Jet Propulsion Laboratory
California Institute of Technology

volume

1

MISSION OVERVIEW, SCIENCE OBJECTIVES AND RESULTS

CASSINI FINAL MISSION REPORT 2019

DEDICATION

Volume One of the Cassini Mission Report is dedicated to the thousands of engineers, scientists, technicians, administrators, storytellers, and artists that took the vision of a few and transformed that vision into the Cassini-Huygens Mission to Saturn and Titan, a 20-year voyage of exploration and discovery and a gift for all of humanity.

The research was carried out at the Jet Propulsion Laboratory, California Institute of Technology, under a contract with the National Aeronautics and Space Administration.

CONTENTS

NOTE: *For Sections 3.1 and 3.2 list of figures and tables, please refer to the individual discipline and instrument reports.*

Figures

Tables

MISSION OVERVIEW, SCIENCE OBJECTIVES, AND RESULTS

1 INTRODUCTION

On September 15, 2017, at about 10:45 a.m. Saturn local time, the Cassini-Huygens mission ended with a high-velocity entry of the Cassini orbiter into Saturn's upper atmosphere. The spacecraft's speed guaranteed destruction, effectively precluding any inadvertent encounter with Saturn's moons, particularly Enceladus and Titan. Intentionally guided to its fiery demise by the flight team at NASA's Jet Propulsion Laboratory, this final mission event represented a triumphant end to one of humanity's greatest missions of deep space exploration.

The Cassini-Huygens spacecraft were launched on October 15, 1997. After a 6.5-year interplanetary cruise with gravity assists from Venus (2), Earth, and Jupiter, the spacecraft entered into orbit around Saturn on June 30, 2004. The ESA-supplied Huygens probe was released from Cassini on December 24, 2004, and made its historic landing on the moon Titan on January 14, 2005. The Cassini orbiter then went on for another 12¾ years exploring the Saturn system.

As a fitting end to 13 incredible years of exploring the Saturn system, the mission concluded with the Grand Finale, a gambit so daring that it could not have been considered during any other phase of the mission. These 22 orbits darted through the gap between the rings and planet itself revealing more unseen wonders and a collection of brand-new puzzles.

Christened a "discovery machine" by its scientists, the Cassini-Huygens mission will be considered one of the most productive chapters in humankind's exploration of the planets. From the moment Cassini-Huygens began science operations until its final moments as it was overcome by the Saturn's encroaching atmosphere, the mission was returning invaluable information on the Saturn system. Cassini-Huygens time and time again shocked and amazed both the science community and the general public.

Using data from the mission, scientists have written nearly 4,000 science publications across five interrelated disciplines: Titan, Icy Satellites, Rings, Magnetosphere and Plasma Science, and Saturn. The Cassini Mission has produced such a wealth of data that the science community will be analyzing the results for decades. While this report attempts to tell the Cassini-Huygens story,

we are aware that no single report can completely cover the history, challenges, successes, results, and lessons learned from the mission. We encourage the reader to seek out the many publications on the mission that we have captured in the references.

The Cassini Mission Report's seven volumes contain an overview of the mission and a science summary and assessment, a performance assessment of the different systems that formed parts of the project, and the major lessons from the mission team during the development and operations phases.

Content for each volume of the Mission Report:

- Volume 1 describes the Cassini Mission and the major systems that formed part of the project, provides an assessment of success in achieving its scientific objectives, summarizes the accomplishments and successes of the project's public and educational outreach program, lists archive locations of project records, and provides a bibliography of scientific and engineering papers, articles, and publications in the appendices.
- Volumes 2 and 3 contain the performance assessment of the spacecraft and the instrument payload, respectively. Spacecraft performance is discussed at the system level, as well as for each of the engineering subsystems. Volume 3 contains the performance assessment for each of the scientific instruments that formed Cassini's payload. These two volumes describe in detail the challenges and successes that the spacecraft, instruments, and flight team went through during the operations phases. Volumes 2 and 3 also provide an overview of the main spacecraft and instrument anomalies and idiosyncrasies that took place during operations.
- Volume 4 contains a performance assessment of the navigation portion of the mission. It includes an overview of the navigation objectives, a detailed description for each navigation model used during operations, the navigation strategies used to predict and reconstruct the spacecraft's trajectory, as well as the methodology for determining the ephemerides (i.e., the positions at a given time) of Saturn and its moons.
- Volume 5 contains a performance assessment for the ground-based Mission Operations System (MOS) used to operate the flight system from the beginning of the cruise phase through end of mission. For each of the major operations processes, this volume also includes a system-level description and a performance assessment.
- Volume 6 contains the lessons that the project and the flight team learned during mission operations, as well as an explanation of the event (or events) that led to each lesson learned. Some of the lessons learned also contain the event's impact on the project or the overall mission.
- Volume 7 contains the end-of-mission Planetary Protection Report. This volume details the Cassini Project's final disposal of launched hardware and the project's compliance with the planetary protection requirements established by NASA policy directive (NPD) 8020.7G and as directed by the NASA Planetary Protection Officer.

2 MISSION DESCRIPTION

> The Cassini-Huygens mission was designed to reveal Saturn's mysteries … using the largest and most sophisticated interplanetary spacecraft that … (NASA) had ever launched.

Perhaps no other place in the solar system is so rich an environment for exploration and scientific discovery as the expansive Saturn system. The planet, its rings, and its several dozen moons have lured and mystified scientists from all over the world. While the solar system's other giant planets—Jupiter, Uranus, and Neptune—have rings, Saturn's are unique in their breadth and brightness. They are the main feature by which Saturn is known. Scientists treat Saturn and its ring system as a physical model for the Sun and the disc of gas and dust from which the planets formed because when humans search for planetary systems elsewhere in the galaxy, their success depends partly upon how well we understand the early stages of planet formation. The Cassini-Huygens mission was designed to reveal Saturn's mysteries by exploring the entire Saturn system in greater detail than ever before, using the largest and most sophisticated interplanetary spacecraft that the National Aeronautics and Space Administration (NASA) had ever launched.

2.1 Program Summary

When Cassini-Huygens left Earth on October 15, 1997, to begin a journey covering 3.5 billion km, it was the most highly instrumented and scientifically capable planetary spacecraft ever flown. The Cassini orbiter carried 12 instruments, and the Huygens probe carried six, for a total of 18 instruments. The mission represented the best technical efforts of thousands of engineers and over 260 scientists from the United States and 18 European countries.

The Cassini-Huygens mission was an enterprise that, from initial vision to mission completion, spanned 30 years. The formal beginning was in 1982, when the European Science Foundation's Space Science Committee and the Space Science Board of the U.S. National Academy of Sciences formed a joint working group. The group's charter was to study how the United States and Europe might cooperate in the field of planetary science. Their precept was that the mission would benefit the scientific, technological, and industrial sectors of their countries. As a result of the studies, European scientists proposed a Saturn orbiter and Titan probe mission to the European Space Agency (ESA), suggesting collaboration with NASA.

The Cassini-Huygens mission became an international venture involving NASA, ESA, the Italian Space Agency (Agenzia Spaziale Italiana (ASI)), and several separate European academic and industrial partners. The large Cassini spacecraft, consisting of an orbiter and the attached ESA Titan probe, carried scientific sensors to support 27 different investigations.

2.1.1 Historical Astronomical Observations Important to Cassini-Huygens

The mission was named in honor of the French-Italian astronomer Jean Dominique Cassini, with the Titan probe named in honor of the Dutch scientist Christiaan Huygens. Those two scientists so enriched human understanding of the Saturn system that the Program was inspired to select their names for the mission.

The Italian astronomer Galileo Galilei was the first to observe Saturn through a telescope in 1609–10. The earliest known record of any telescope is dated to only a year or so before Galileo began studying the night sky. Viewed through Galileo's crude instrument, which he constructed himself, Saturn was a puzzling sight. Unable to make out the rings, Galileo thought he saw two sizable companions close to the planet. Having recently discovered the major moons of Jupiter, he supposed that Saturn could have large moons, too. "... [to] my very great amazement, Saturn was seen to me to be not a single star, but three together, which almost touch each other," Galileo wrote at the time.

Galileo was even more astonished when, two years later, he again looked at Saturn through his telescope only to find that Saturn's companion bodies had apparently disappeared. "I do not know what to say in a case so surprising, so unlooked for and so novel," he wrote in 1612. The rings were simply "invisible" because he was now viewing them edge-on. Two years later, they again reappeared, larger than ever. Galileo concluded that what he saw were some sort of "arms" that grew and disappeared for unknown reasons. He died not knowing that he had been the first person to observe Saturn's (or any planet's) rings.

Nearly half a century later, optics had improved, allowing Dutch scientist Christiaan Huygens to solve the puzzle that had baffled Galileo. Huygens pronounced in 1659 that the companions or arms decorating Saturn were not appendages, but rather the planet "is surrounded by a thin, flat ring, which nowhere touches the body." Some in the science community were opposed to his theory, but the notion of Saturn's rings was later confirmed by the observations of British physicist Robert Hooke and Italian-French astronomer Jean Dominique Cassini.

While observing Saturn, Huygens also discovered Saturn's largest moon Titan. A few years later and using new telescopes, Cassini added several other key Saturn discoveries, including Saturn's four other major moons—Iapetus, Rhea, Tethys, and Dione. In 1675, Cassini discovered that Saturn's rings are split largely into two parts by a narrow gap—known since as the "Cassini Division." In the 19th century, J. E. Keeler, pursuing theoretical studies developed by James Clerk Maxwell, showed that the ring system was not a uniform sheet but is instead made up of small particles orbiting Saturn. Each of those realizations was game-changing. Yet it was only when humans began sending spacecraft to observe the Saturn system up close that the planet, rings, and moons began to truly reveal themselves.

The first detection of Saturn's magnetic field came with the flyby of Saturn by NASA's Pioneer 11 spacecraft in 1979. Then, in 1980 and 1981, the NASA Voyager 1 and Voyager 2

spacecraft flew through Saturn's system to reveal several additional small moons, storms and subtle latitudinal banding in the planet's atmosphere, and a breathtaking collection of thousands of ringlets. The Voyagers found ring particles ranging in size from nearly invisible dust to icebergs the size of a house. The spacing and width of the ringlets were discovered to be orchestrated at least in part by gravitational tugs from a retinue of orbiting moons and moonlets, some near ring edges but most far beyond the outermost main rings. Voyager instruments confirmed what ground-based instruments had suggested—that the rings contain water ice, which may cover rocky particles.

The Hubble Space Telescope then joined the effort, making Saturn a frequent target and producing stunning views of long-lived hurricane-like storms in the planet's atmosphere. The world's major telescopes, including Hubble, have been trained on Saturn to observe phenomenon known to astronomers as a Saturn ring plane crossing. The rings were seen edge-on from Earth's perspective on May 22 and August 10, 1995, and on February 11, 1996. Ring plane crossings provide astronomers with unique views of Saturn's system.

These observations showed that the ring plane was not absolutely flat. Instead, the tilt of the F-ring distorts the appearance of the rings, causing one side to appear brighter than the other during ring plane crossings. Astronomers used observations from the space telescope to search for new moons and turned up several suspects, most of which are now believed to be bright "knots" in the F-ring. Of particular interest were ring arcs, natural "satellites" in the F-ring that appeared cloud-like and spread over a small area, instead of sharp pinpoints. The origin of these clumps of material in the F-ring is not well understood.

Viewing Saturn's ring system edge on also made the faint, outermost E-ring easier to detect due to the greater amount of material in the line of sight. That effect also allowed scientists to get better information about the overall thickness of Saturn's rings. Mission designers used the new information gathered about the location and density of material in the rings to plan the most advantageous and safest course for Cassini's flight through the gap between Saturn's F- and G-rings during Saturn arrival in 2004.

The Hubble Space Telescope not only helped designers plan the spacecraft's trajectory for the Cassini-Huygens mission, but also guided and supported the mission's observations of Saturn, its rings, moons, and magnetosphere. Hubble observations of Saturn's atmosphere were made after storms were discovered by ground-based observers. First in 1990 and again in 1994, apparent upwellings of ammonia clouds appeared and then were spread around the planet by prevailing winds.

Scientists also compared Voyager and Hubble observations of Saturn's moon, Titan. They found that color differences in Titan's hemispheres seen during the Voyager flybys in 1980 and 1981 had reversed themselves by the time Hubble observed the moon.

Some Hubble observations have studied chemical processes in Titan's atmosphere. Images made in the infrared have looked through Titan's clouds (which are opaque in visible wavelengths of light), allowing some mapping of Titan's surface. Hubble has also contributed new information about processes in Saturn's magnetosphere through ultraviolet measurements of Saturn's auroras.

As with any proper science endeavor, Cassini-Huygens used knowledge acquired by its predecessors to refine not only the questions to be asked, but also the best places and times to ask those questions.

2.1.2 HISTORY OF THE EVOLUTION AND DEVELOPMENT OF THE CASSINI MISSION

In 1983, the U.S. Solar System Exploration Committee recommended that NASA include a Titan probe and radar mapper in its core program and also consider a Saturn orbiter. NASA/ESA completed a joint assessment of a Saturn orbiter/Titan probe mission in 1984–85. Then in 1986, ESA's Science Program Committee approved Cassini for initial Phase A study, with conditional start in 1987.

In 1987–88, NASA carried out further work to design and develop the standardized Mariner Mark II spacecraft and a set of outer planets missions to be accomplished with the new line of spacecraft. The program was an early effort to reduce the costs of planetary exploration by producing multiple spacecraft for different missions with the same basic spacecraft components off the same assembly line. Cassini and the Comet Rendezvous/Asteroid Flyby (CRAF) were the first two missions chosen for further study. At the same time in Europe, a Titan probe Phase A study was carried out by ESA in collaboration with a European industrial consortium led by Marconi Space Systems. The Titan probe was named Huygens by ESA as its first medium-sized mission of its Horizon 2000 space science program.

In 1989, the U.S. Congress approved funding for Cassini and the comet-asteroid mission. NASA and ESA simultaneously released announcements of opportunity for scientists to propose scientific investigations for the missions. In 1992, a funding cap was placed on the Mariner Mark II program, effectively ending the new spacecraft line and, at the same time, canceling the CRAF mission. To cut the cost of the mission and simplify the spacecraft and its operation, designers restructured the Cassini spacecraft.

Mission planners performed extensive tradeoff studies considering cost, mass, reliability, durability, suitability, and availability of hardware, which resulted in Cassini's eventual design. They eliminated moving parts from the spacecraft wherever the functions could be performed satisfactorily without them. As a result, early designs that included moving science instrument platforms or turntables were discarded in favor of instruments fixed to the spacecraft body, whose pointing requires rotation of the entire spacecraft. Also, tape recorders were replaced with solid-state recorders, mechanical gyroscopes were replaced with hemispherical resonator gyroscopes, an articulated probe relay antenna was discarded in favor of using Cassini's high-gain antenna to capture the radio signal of the Huygens probe, and a deployable high-gain antenna of the type used for the Galileo mission was considered and abandoned.

Project engineers, both those who designed and built the hardware and those who operated the spacecraft, relied heavily on extensive experience to provide a spacecraft design more

The Cassini-Huygens design also came with a side effect: new spacecraft technology that benefited future missions.

sophisticated and reliable than any other spacecraft ever built for exploration of the planets. That careful design allowed the Cassini spacecraft to return more scientific data about its targets than had been possible in any previous planetary mission.

The Cassini-Huygens design also came with a side effect: new spacecraft technology that benefited future missions.

2.1.3 NEW TECHNOLOGY

A wealth of new technology was developed and qualified for spaceflight by or for the Cassini program. Much of the new technology has already been adopted by other space science programs, in some cases at a reduced cost directly attributable to Cassini, which enabled the development of new classes of low-cost, high-efficiency spacecraft, such as the Discovery and New Millennium spacecraft.

The Cassini orbiter also advanced and extended the technology base of the United States and its partners with several innovations in engineering and information systems. Though they may not seem so today because the pace of technology is so fast, each of the innovations described below was revolutionary at the time of Cassini's launch in 1997.

Cassini pioneered the use of solid-state data recorders with no moving parts. This is now standard hardware on all spacecraft.

Similarly, the main onboard computer that directs operations of the orbiter used an innovative design that employed new types of electronic chips, such as the very high-speed integrated circuit (VHSIC) chips developed under a U.S. government-industry research and development initiative. The Cassini generic VHSIC spaceborne computer (GVSC) 1750A was the first civilian spacecraft to use this technology. Cassini's computer system also used new application-specific integrated circuit (ASIC) parts; each component replaced one hundred or more traditional chips. The ASIC chips allowed the development of a data system for Cassini 10 times more efficient than earlier spacecraft designs, and with less than one-third the mass and volume. Two spacecraft under NASA's Discovery program—Mars Pathfinder and the Near-Earth Asteroid Rendezvous mission—used these chips directly off the Cassini production line.

Also, on the Cassini orbiter, the power system benefited from an innovative solid-state power switch developed for the mission. The switch had a significantly improved component lifetime and eliminated rapid fluctuations called transients that usually occurred with conventional power switches. The Cassini program also developed a low-mass, low-power, radiation-hardened X-band radio transponder (a combined receiver and transmitter). Both the Mars Pathfinder and the Near-Earth Asteroid Rendezvous missions used radio transponders built on the Cassini mission's production line.

The inertial reference units (IRUs) used on Cassini represented the first space version of a revolutionary new gyro called the hemispherical resonator gyroscope. At the time, gyros that were commonly used in spacecraft, aircraft, and ships were large, very delicate mechanical devices whose many moving parts made them susceptible to failure. The new hemispherical resonator gyroscope was more reliable and less vulnerable to failure because it used no moving parts. The new gyroscope relied instead on waves traveling through a hemispherical quartz shell similar to how a note is produced when running a wet finger around the rim of a wine glass, but using electricity instead of one's finger. The Near-Earth Asteroid Rendezvous spacecraft used a slightly modified Cassini gyro.

2.1.4 THE CASSINI-HUYGENS PROGRAM

The Cassini-Huygens program was a cooperative international effort involving NASA, ESA, and ASI, as well as numerous American and European academic and industrial contributors—a partnership that represented an undertaking whose scope and cost would not likely be borne by any single nation, but was made possible through shared investment and participation.

Figure 2.1-1. Flags of the Participating Nations in Cassini-Huygens Development.

Over the course of nearly 30 years, the structure and names of the internal and external structure of the Cassini-Huygens program changed several times but the basic structure remained the same. In the United States, the mission was managed by NASA's Jet Propulsion Laboratory (JPL), a division of the California Institute of Technology (Caltech). Leadership at NASA was provided by the Cassini program executive and program scientist.

The European Space Technology and Research Center (ESTEC) managed the development of the Huygens Titan probe. Many European countries supplied the probe equipment, which were then assembled by ESTEC's prime contractor, Aerospatiale (now Alcatel) in Cannes, France. The U.S. supplied Huygens' batteries and two of its scientific instruments.

ASI supplied Cassini's high-gain and low-gain antenna. ASI also contributed components to the radio frequency instrument subsystem, the Cassini radar, and the visible and infrared mapping spectrometer.

The U.S. Department of Energy provided Cassini's radioisotope thermoelectric generators.

The U.S. Air Force provided the Titan IV/Centaur launch vehicle that was built by Lockheed-Martin. Launch operations were managed by the 45th Space Wing, Cape Canaveral, FL.

2.2 Mission Objectives

Cassini's instrument payload represented a carefully chosen suite of interrelating instruments to address major scientific questions about the Saturn system. The data they returned were, and will continue to be, analyzed by a team of nearly 260 scientists from the United States and Europe.

Following is the set of major science objectives that the Cassini-Huygens mission was charged with accomplishing.

2.2.1 Saturn

The major science objectives for Saturn (Figure 2.2-2) included:

- Determine the temperature field, cloud properties, and composition of Saturn's atmosphere.
- Measure the planet's global wind field, including waves and eddies; make long-term observations of cloud features to see how they grow, evolve, and dissipate.
- Determine the internal structure and rotation of Saturn's deep atmosphere.
- Study daily variations and the relationship between the ionosphere and the planet's magnetic field.

- Determine the composition, heat flux, and radiation environment present during Saturn's formation and evolution.
- Investigate the sources and nature of Saturn's lightning.

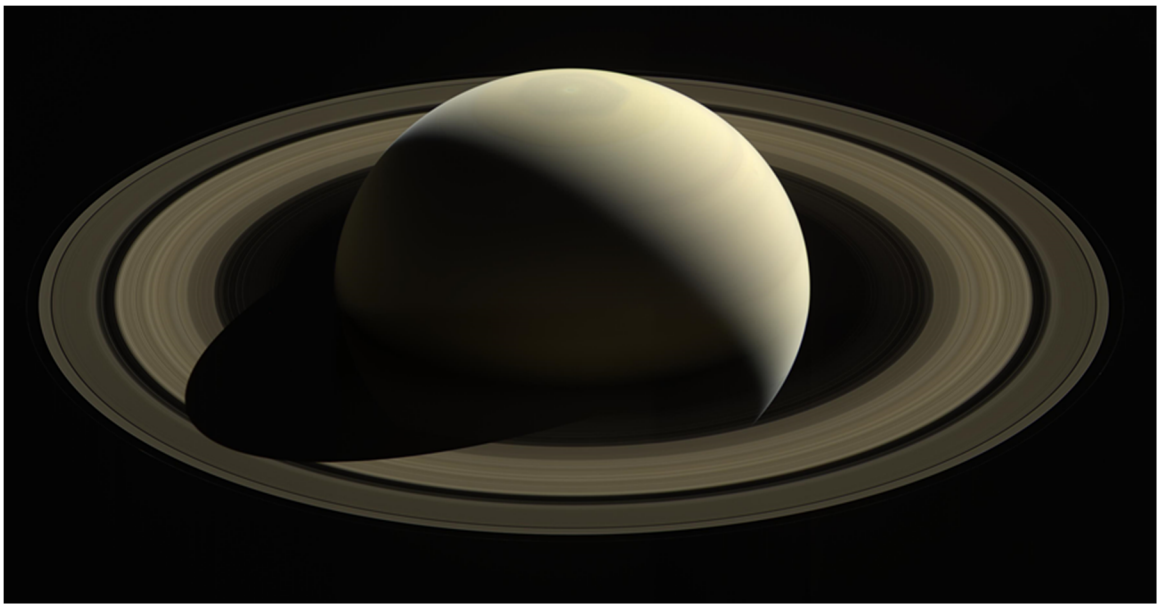

Figure 2.2-2. Saturn.

2.2.2 THE RINGS

The major science objectives for the rings (Figure 2.2-3) included:

- Study configuration of the rings and dynamic processes responsible for ring structure.
- Map the composition and size distribution of ring material.
- Investigate the interrelation of Saturn's rings and moons, including moons embedded in the rings.
- Determine the distribution of dust and meteoroid distribution in the vicinity of the rings.
- Study the interactions between the rings and Saturn's magnetosphere, ionosphere, and atmosphere.

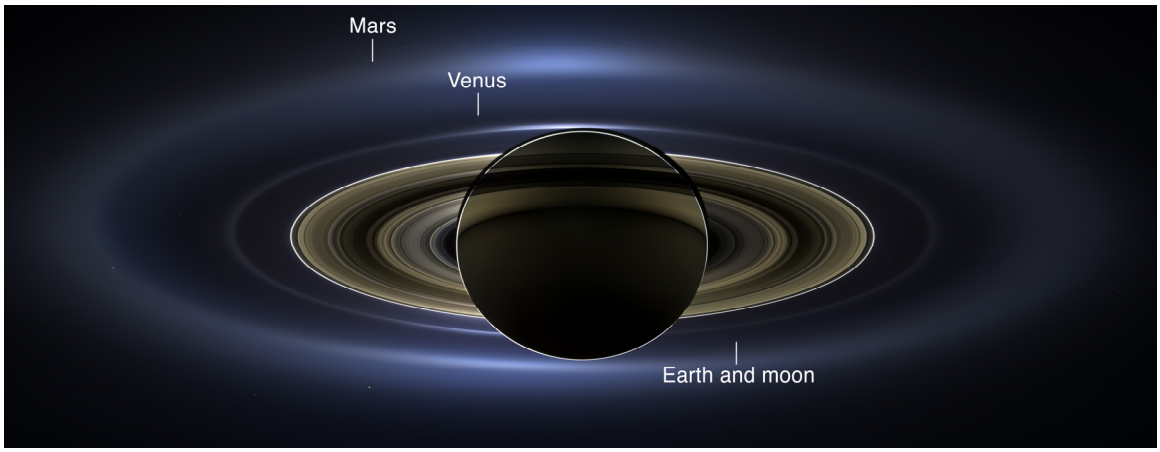

Figure 2.2-3. The Rings.

2.2.3 TITAN

The major science objectives for Titan (Figure 2.2-4) included:

- Determine the relative amounts of different components of the atmosphere; determine the mostly likely scenarios for the formation and evolution of Titan and its atmosphere.
- Observe vertical and horizontal distributions of trace gases; search for complex organic molecules; investigate energy sources for atmospheric chemistry; determine the effects of sunlight on chemicals in the stratosphere; study formation and composition of aerosols (particles suspended in the atmosphere).
- Measure winds and global temperatures; investigate cloud physics, general circulation, and seasonal effects in Titan's atmosphere; search for lightning.
- Determine the physical state, topography, and composition of Titan's surface; characterize its internal structure.
- Investigate Titan's upper atmosphere, its ionization and its role as a source of neutral and ionized material for Saturn's magnetosphere.

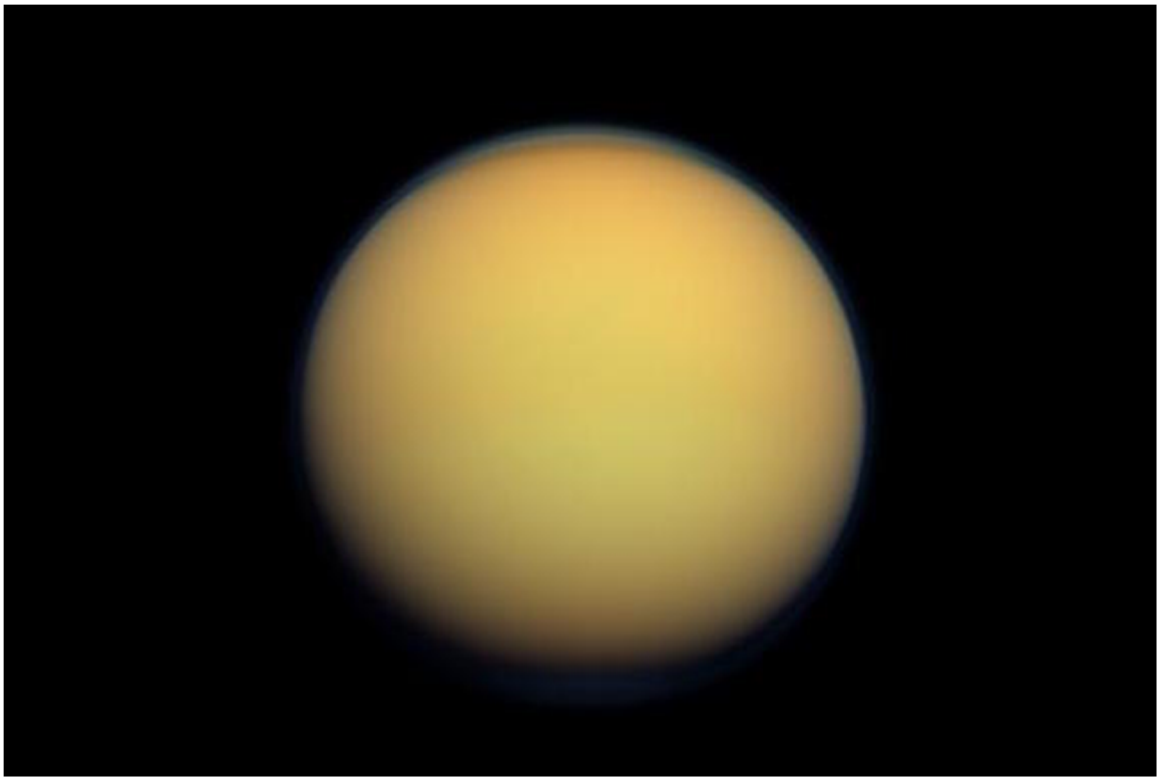

Figure 2.2-4. Titan, Saturn's largest moon.

2.2.4 MAGNETOSPHERE

The major science objectives for the magnetosphere (Figure 2.2-5) included:

- Determine the configuration of Saturn's magnetic field, which is nearly symmetrical with Saturn's rotational axis. Also study its relation to the modulation of Saturn kilometric radiation—a radio emission from Saturn that is believed to be linked to the way electrons in the solar wind interact with the magnetic field at Saturn's poles.
- Determine the current systems, composition, sources, and concentrations of electrons and protons in the magnetosphere.
- Characterize the structure of the magnetosphere and its interactions with the solar wind, Saturn's moons, and rings.
- Study how Titan interacts with the solar wind and with the ionized gases within Saturn's magnetosphere.

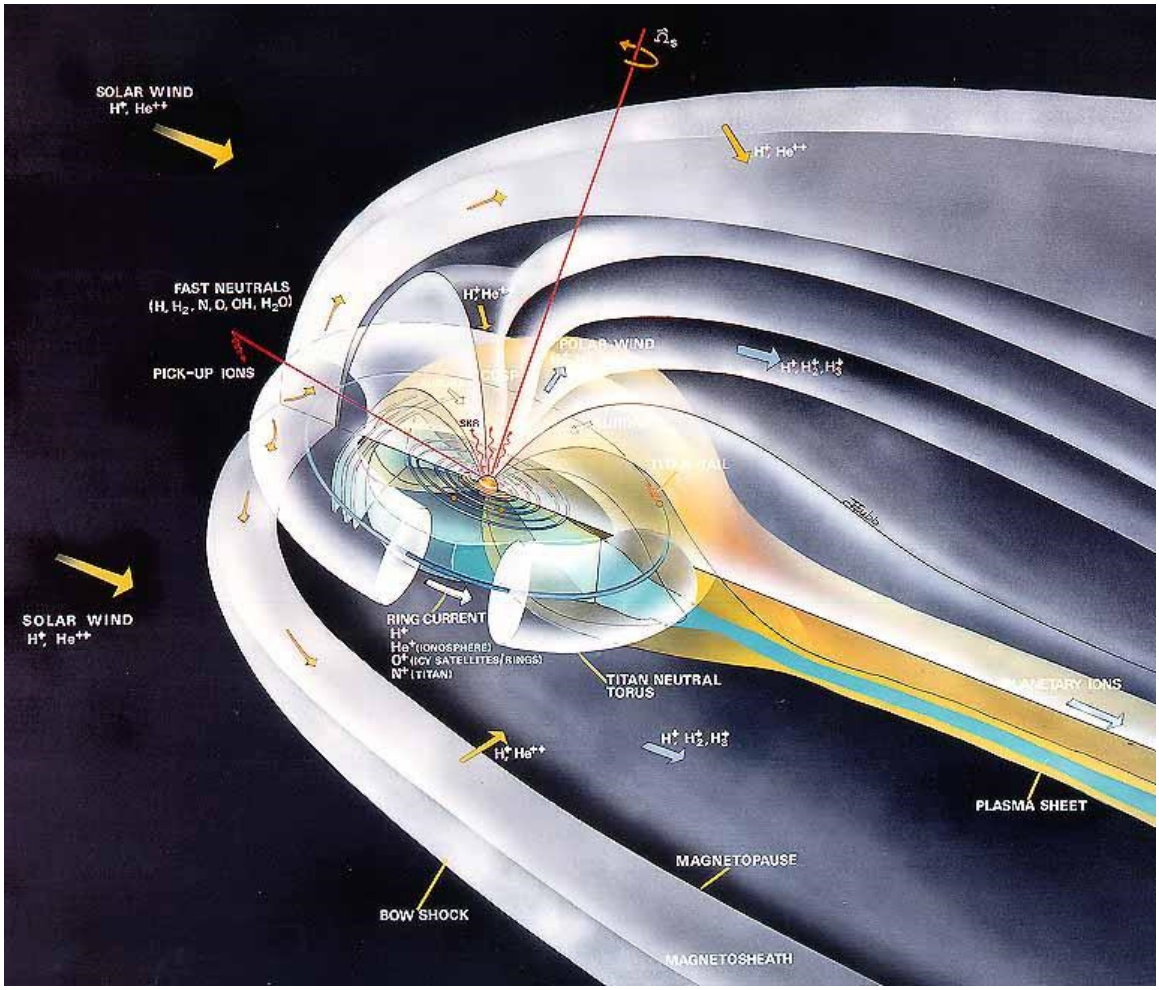

Figure 2.2-5. Magnetosphere.

2.2.5 Icy Moons

The major science objectives for icy moons (Figure 2.2-6) included:

- Determine general characteristics and geological histories of Saturn's moons.
- Define the different physical processes that have created the surfaces, crusts, or sub-surfaces of the moons.
- Investigate compositions and distributions of surface materials, particularly dark, organic-rich materials, and condensed ices with low melting points.
- Determine the bulk compositions and internal structures of the moons.
- Investigate interactions of the moons with Saturn's magnetosphere and ring system and possible gas injections into the magnetosphere.

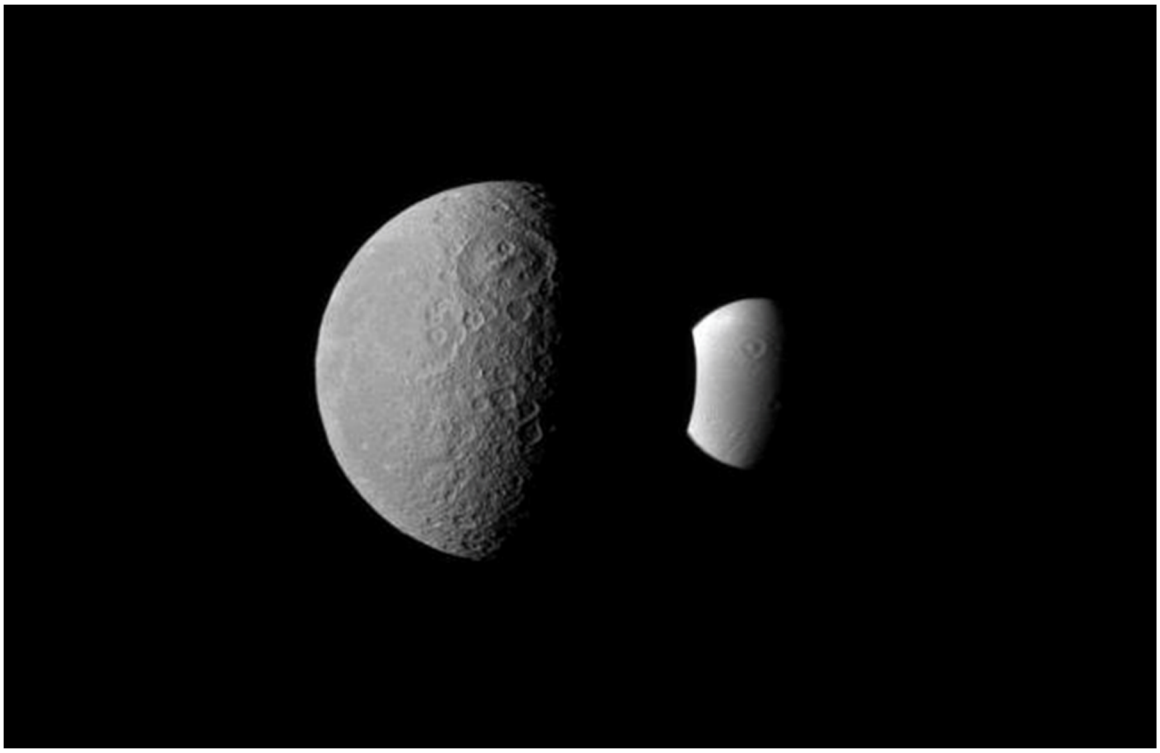

Figure 2.2-6. Saturn's icy moons Rhea (left) and Dione.

In addition to the science objectives at Saturn, the Cassini spacecraft also conducted a gravitational wave search through the ASI-provided high-gain antenna during its interplanetary cruise.

2.3 Mission Overview

The Cassini spacecraft traveled to Saturn for nearly seven years via four planetary gravity assists—two flybys of Venus, and one flyby each of Earth and Jupiter—and in June 2008 completed an outstanding 4-year prime tour of the Saturnian system (Figure 2.3-1). Cassini then embarked on two mission extensions: the Cassini Equinox Mission (completed in 2010) and the Cassini Solstice Mission (completed in 2017). Cassini-Huygens was the fourth spacecraft to visit the Saturnian system but was the first spacecraft to orbit Saturn. In all, Cassini completed 294 Saturn orbits during 13 years.

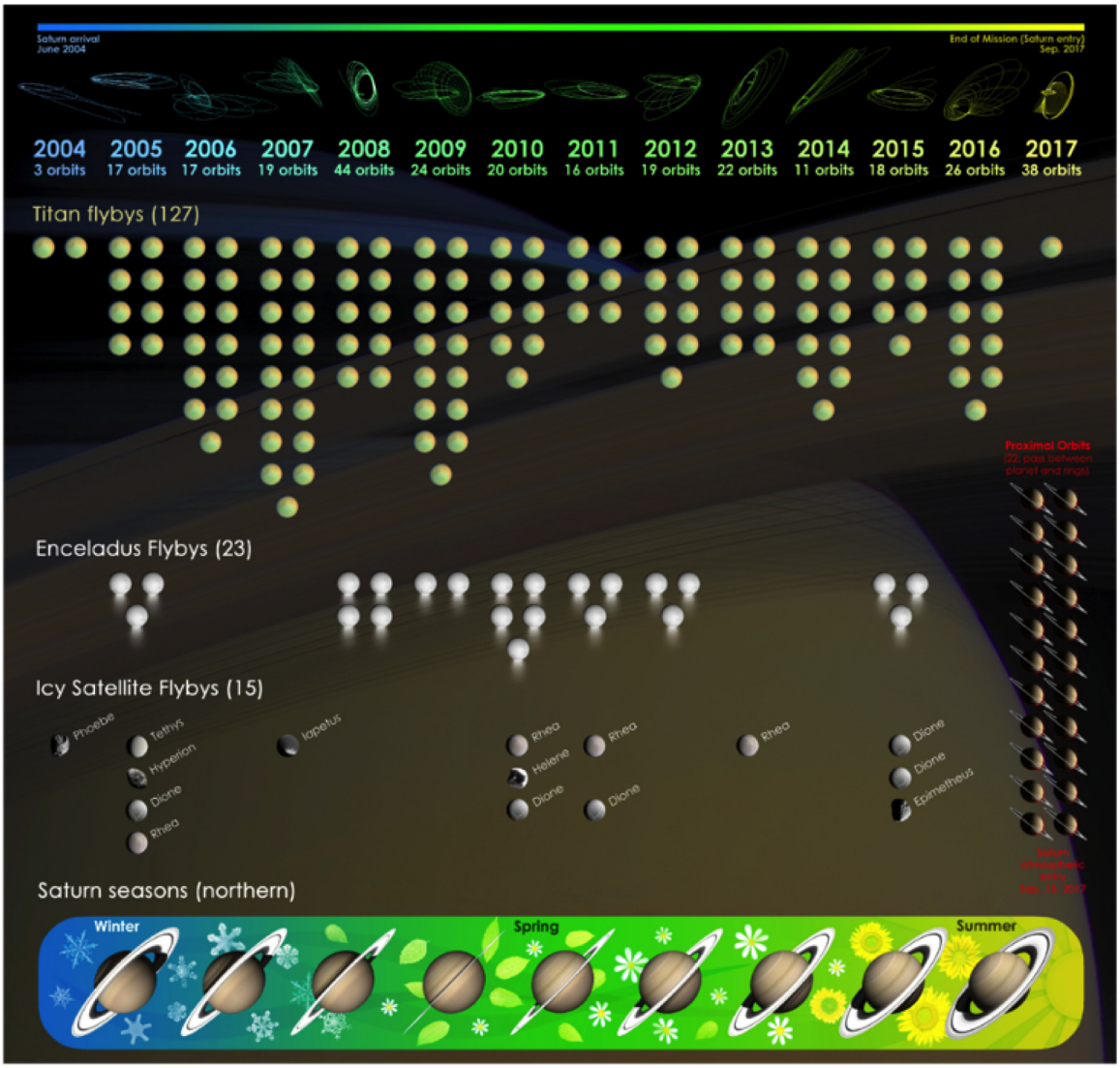

Figure 2.3-1. Cassini Mission overview.

2.3.1 LAUNCH

Cassini's journey to Saturn began on October 15, 1997, with launch on a Titan IVB/Centaur rocket from Florida's Cape Canaveral Air Force Station. The upper-stage booster accelerated the spacecraft out of Earth orbit towards Venus for the first of four planetary gravity assists designed to boost Cassini toward Saturn. In a gravity assist, the spacecraft flies close to enough to a planet to use the gravity of the two bodies—the planet and the spacecraft—to transfer some of the planet's orbital momentum to the spacecraft. As a result, the spacecraft accelerates and the planet decelerates. But because of the enormous difference in mass between the planet and the relatively miniscule spacecraft, the spacecraft accelerates by thousands of kilometers per hour while the planet decelerates by immeasurably little. That is what produces the "slingshot" effect to boost the speed of the spacecraft.

2.3.2 VENUS, EARTH, AND JUPITER FLYBYS

Cassini's mass was so large that it was not possible to use any available launch vehicle to send it on a direct path to Saturn. If Cassini had traveled directly toward Saturn, the Sun's gravity would have slowed the spacecraft and curved its trajectory back toward the inner solar system, and it would have never reached Saturn. To gain enough momentum to overcome the Sun's gravity after launch, the mission used four gravity assists to hurl the spacecraft to Saturn. Cassini travelled an interplanetary trajectory that took it by Venus twice, then past Earth and Jupiter (Figure 2.3-2).

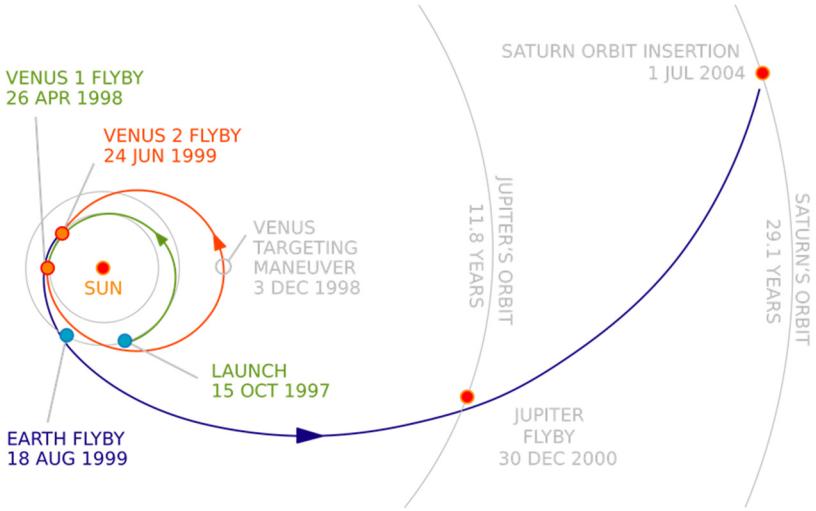

Figure 2.3-2. Venus, Earth, and Jupiter flybys.

2.3.3 PRIME MISSION OVERVIEW

In 1990, NASA announced the selection of seven Principal Investigator (PI) instruments and four facility instruments for the orbiter, and seven interdisciplinary science investigations. The Ion and Neutral Mass Spectrometer instrument was selected in 1992. The assembly, test, and launch operations began in November 1995. NASA received launch approval on October 3, 1997.

Cassini had a 30-day nominal launch period, extending from October 6, 1997 to November 4, 1997, which provided an arrival date at Saturn of July 1, 2004. The launch vehicle was a Titan IV with solid rocket motor upgrades and a Centaur upper stage. After controllers postponed a first attempt on October 13, Cassini successfully lifted off from the Cape Canaveral Air Force Station complex 40 on October 15, 1997 at 08:55 Coordinated Universal Time (UTC).

During the nearly seven years en route to Saturn, ground controllers checked out, calibrated, and maintained the science instruments. They also characterized the instruments and performed limited science observations.

The interplanetary trajectory design was a Venus–Venus–Earth–Jupiter gravity assist. The inner cruise phase spanned the time period from November 14, 1997 through November 7, 1999.

This phase included two Venus flybys (April 26, 1998 and June 24, 1999) and one Earth flyby (August 18, 1999). The outer cruise phase extended from November 8, 1999 to July 7, 2002, and included a flyby of Jupiter on December 30, 2000.

The science cruise phase began on July 8, 2002, and continued through May 15, 2004. As Cassini approached Saturn, it executed the first targeted flyby of the tour, of Phoebe, on June 11, 2004.

Cassini-Huygens entered Saturn orbit (called Saturn Orbit Insertion, or SOI) on July 1, 2004. In January 2005, after the Huygens probe descent to the surface of Titan, Cassini went on to complete its 4-year tour of Saturn, its rings, satellites, and magnetosphere via 75 orbits about Saturn, which included 45 close Titan flybys, four Enceladus flybys, and nine close flybys of other icy satellites along with dozens of Saturn, rings, and Titan radio and solar occultations. Due to the highly successful execution of the 4-year prime tour, NASA approved funding for a mission extension called the Equinox Mission, so named because the spacecraft would observe Saturn's equinox—the period when the planet's equator and the rings face the Sun edge-on.

2.3.4 EQUINOX MISSION OVERVIEW

The Equinox Mission was an aggressive 2-year 3-month extended mission that began on July 1, 2008, and continued to explore the Saturnian system's rings, magnetosphere, and icy satellites, especially Enceladus. The extension also allowed scientists to make observations during Saturn's northern vernal equinox. The Equinox Mission trajectory consisted of 64 more orbits of Saturn, 28 more Titan flybys, and 11 more close icy moon flybys, seven of which were Enceladus flybys.

2.3.5 SOLSTICE MISSION OVERVIEW

At the conclusion of the Equinox Mission, the Cassini team initiated a 7-year mission extension named the Solstice Mission, stretching the tour to September 15, 2017. The overarching goal of the Solstice Mission was to observe the complex and dynamic Saturn system over a wider range of geometries and conditions, including Saturn's May 2017 northern summer solstice. By end of mission, Cassini observed most of the northern winter season and all of the northern spring season (Figure 2.3-3).

On November 30, 2016, Cassini began the penultimate phase of the mission, the ring-grazing orbits. This 20-week phase consisted of 20 high-inclination orbits with apoapses near Titan's orbit and periapses just outside the main ring system, shown in Figure 2.3-4. The final, targeted Titan flyby on April 22, 2017, set Cassini on the Grand Finale—a series of 22 orbits with periapses that passed between Saturn and its rings; a region no spacecraft had explored before.

On September 11, 2017, Titan gave Cassini a "goodbye kiss," a distant non-targeted flyby that put Cassini on its impact trajectory with Saturn. End-of-mission occurred at 11:56 UTC on

September 15, 2017, when Cassini plunged into Saturn's atmosphere and Earth lost the spacecraft's signal forever.

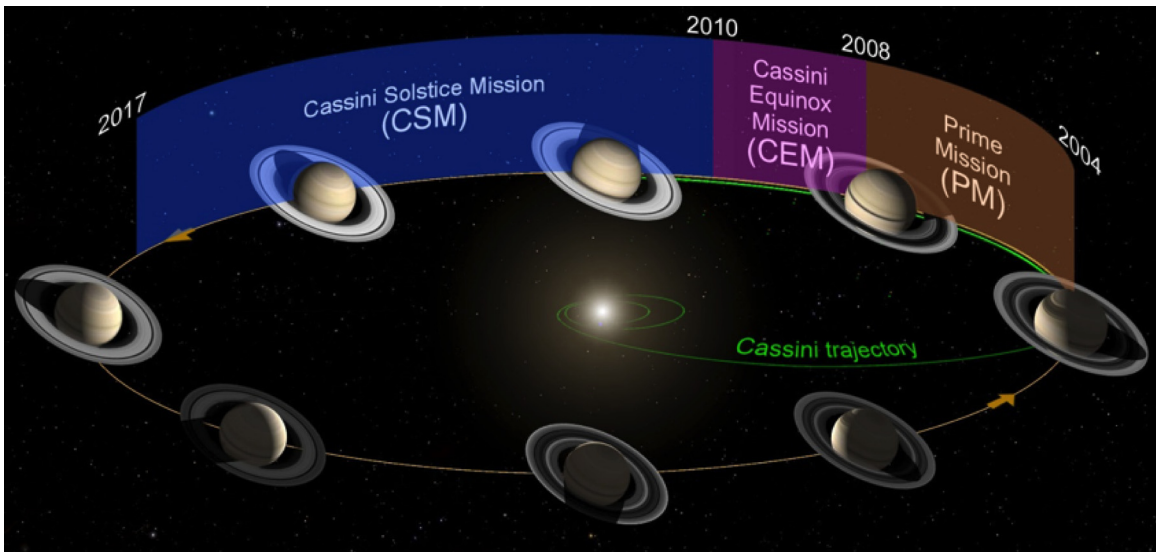

Figure 2.3-3. Cassini Mission Saturn seasonal coverage.

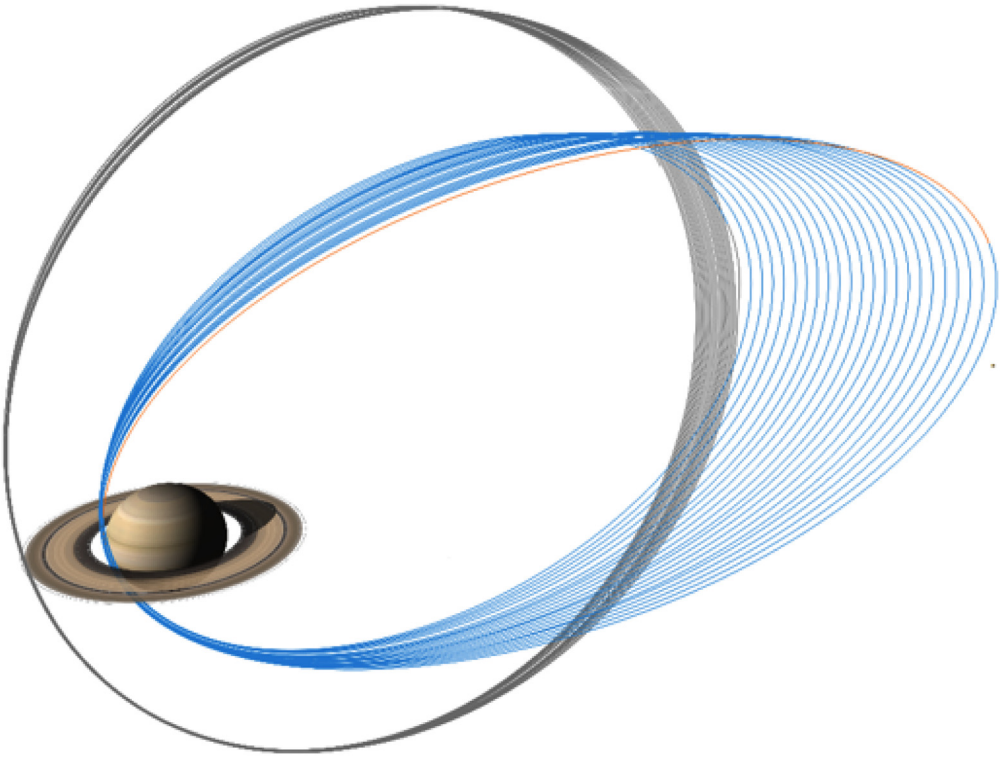

Figure 2.3-4. Ring-grazing orbits (gray), grand finale (blue), and final plunge (orange).

2.4 Flight System Description

2.4.1 SPACECRAFT OVERVIEW

The Cassini orbiter is the largest and most sophisticated outer planet spacecraft built to date (Figure 2.4-1). At launch, the orbiter with the Huygens probe weighed 5,574 kilograms. Over half of that mass was the liquid propellants needed to perform the main engine maneuvers. Right before the end of mission, the spacecraft weighed 2,780 kilograms, having used up the bulk of its propellants and having ejected the 320-kilogram Huygens probe.

The Cassini design had to accommodate a wide range of solar output, from the equivalent of 2.2 Suns at Venus distances to the 0.01 Sun available at Saturn. It was electromagnetically “quiet” to enable sensitive science investigations. The spacecraft’s telecommunications system was designed to function at near-Earth distances and at 1.6 billion kilometers from Earth, in Saturn orbit.

Cassini was a three-axis stabilized spacecraft using reaction wheels and small thrusters for control (Figure 2.4-2). Unlike Galileo, the mission to Jupiter, Cassini had no articulating platform that would allow the imaging instruments to target objects of interest while the spacecraft remained at a fixed attitude. Instead, the entire Cassini spacecraft had to be turned as one for instrument pointing, resulting in more complex design and sequencing of science opportunities. Much of the instrument pointing required the high-gain antenna to point away from Earth, so Earth communications were carefully balanced with data collection in order to maximize science return.

Figure 2.4-1. The Cassini-Huygens orbiter during thermal-vacuum testing.

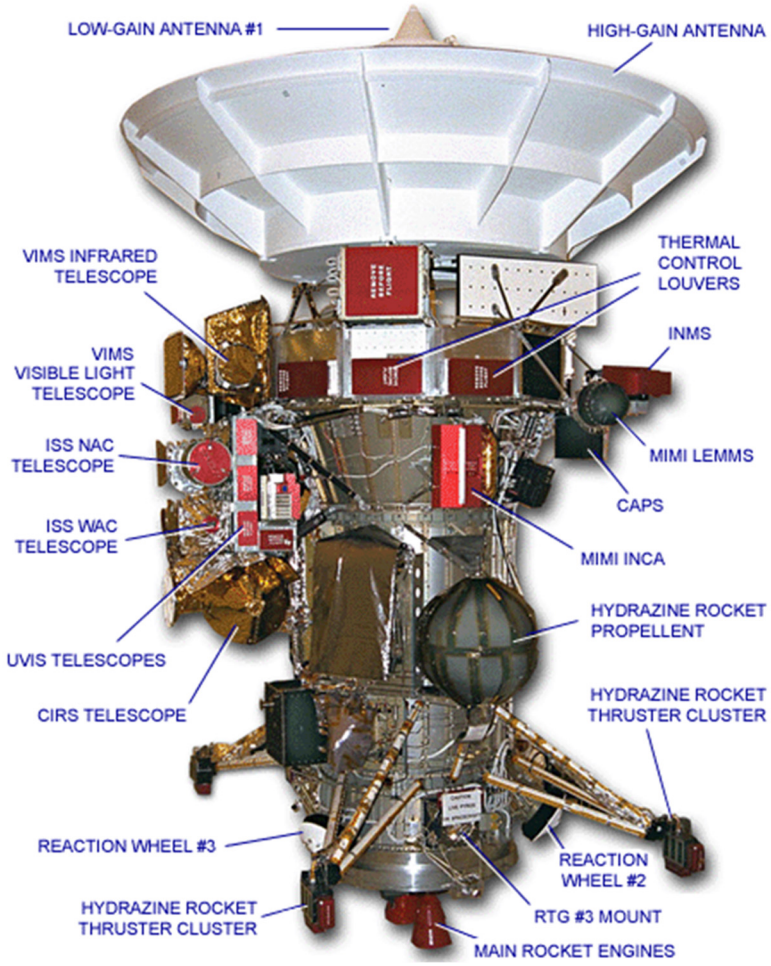

Figure 2.4-2. The Cassini-Huygens orbiter and some of its components.

2.4.2 SPACECRAFT ENGINEERING SUBSYSTEMS OVERVIEW

The Cassini spacecraft was composed of eight engineering subsystems that controlled spacecraft features and functions:

1. Spacecraft structure subsystem
2. Power subsystem
3. Command and data subsystem
4. Attitude and articulation control subsystem
5. Propulsion subsystem
6. Telecommunications subsystem

7. Thermal control subsystem

8. Fault protection

All of the main engineering subsystems had redundant units to serve as a backup in case the main unit failed. This was typical design at JPL when a single spacecraft is planned for a major mission like Cassini.

2.4.2.1 Spacecraft Structure Subsystem

Cassini used the classic JPL multisided ring bus derived from the early Mariner-Mark II spacecraft design. The Cassini bus had 12 sides, or bays, that held most of the engineering subsystems and some of the instrument electronics.

The spacecraft contained five main stacked modules. At top was the 4-meter parabolic high-gain antenna, built by the Italian Space Agency. The high-gain antenna sat atop the 12-bay electronics module, which in turn, was attached to the upper equipment module. These three components were then stacked on top of the domed propulsion module, built by Lockheed Martin Astronautics Company. And at the bottom of the stack was the lower equipment module, holding the small thruster cluster pods and completing the spacecraft's structure.

At 6.8 meters tall, the spacecraft was roughly the size of a school bus. With the magnetometer boom fully extended, the spacecraft was over 15 meters wide. The bulk of the spacecraft was made of aluminum, with some titanium and beryllium pieces for structural integrity. The high-gain antenna and the legs of the lower equipment module were a graphite epoxy structure.

2.4.2.2 Power Subsystem

Three radioisotope thermoelectric generators (RTGs) supplied power for the spacecraft. Their combined power at launch was about 875 watts. Planners predicted that the RTGs' total power output by the end of prime mission in July 2008 would be 692 watts, but because the mission was extended to September 2018 (another 10 years and two months), the actual power measured at the end of the Grand Finale was even lower, at 602 watts. The rate of power decay was quite predictable, allowing for routine power operational modes to be used in sequencing.

The RTG power was supplied to 192 solid-state power switches (SSPS), which acted as circuit breakers. Each individual engineering or science load was allocated one or more SSPS depending on the load required and the criticality of the unit. For example, the Huygens probe used five SSPSs to carry its 260 watts, and the main engineering computers had two redundant SSPSs, each capable of supplying the entire 10 watts.

2.4.2.3 Command and Data Subsystem (CDS)

Cassini had redundant IBM 1750A computers, called engineering flight computers (EFCs) that provided command, data handling, telemetry and timekeeping services. Each EFC had a 7.4 megahertz quartz crystal clock for timekeeping services. The EFC flight code was written in Ada, and the load image had some 45,000 lines of code for each EFC. The flight code was stored in radiation-hardened static random-access memory (SRAM).

As the telecommunication subsystem received commands, they were processed and routed over a MIL-STD-1553B bus to the appropriate instrument or engineering subsystem. There were two 1553B buses (for reliability and redundancy), but only one was active at a time. Each instrument or engineering subsystem had a bus interface unit (BIU) to receive commands from the computer and to send telemetry packets when requested. The 1553B bus was a mostly serial master bus, commanding and collecting data from only one instrument or engineering subsystem at a time, with the exception being broadcast messages, which were transmitted to all BIUs at the same time.

2.4.2.3.1 Solid-State Recorders

Two solid-state recorders (SSRs) handled data storage for the spacecraft, and each had approximately 2.2 gigabits of storage capacity. The SSRs had two functions, the primary one being to store the science and engineering telemetry until the data were downlinked to Earth. The second function was to store copies of the flight software for the attitude and articulation control subsystem (AACS), CDS, and the instruments. Each SSR was able to hold two different flight software loads for each instrument and the engineering computers. That allowed an instrument or the CDS or AACS to uplink and check out a new flight software load while still maintaining an older copy to fall back on if needed.

2.4.2.4 Attitude and Articulation Control Subsystem

The basic system architecture for the AACS flight computer was the same as the CDS. AACS also had a redundant MIL-STD-1553B bus and redundant IBM 1750A computers, called AACS flight computers (AFCs). The AFC received commands from and sent telemetry to the CDS EFC through a special BIU on the CDS buses. It used its own internal AACS 1553B bus to communicate with the sun sensors, stellar reference units (SRUs), IRUs, accelerometer, and the propulsion drive electronics. The AFCs had their own flight software and fault protection routines to always maintain proper attitude knowledge and control. The code was also in Ada, but larger than the EFC, with some 55,000 lines of code.

2.4.2.4.1 Attitude Determination

The prime sensor for attitude knowledge was the SRU, which had a catalog of 3,700 stars that identified up to five of the brightest stars in the field of view at any given time. The SRU was located 90° away from the optical remote sensing platform, on the +X spacecraft orientation. The SRU information was then fed every 5 seconds to the IRU, which propagated the inertial attitude between star updates. Should the SRU star updates be suspended, either by the ground or by some fault on

the spacecraft, the IRU was able to propagate the inertial attitude for many hours before needing a star update from the SRU. The backup, "failsafe" unit was the sun sensor. The two sun sensors were located in cutout holes in the high-gain antenna. The sun sensor was used for initial Sun acquisition and in certain fault protection situations. Should attitude knowledge be lost for any reason, the spacecraft would try to find the Sun and center on it, then it would try to reestablish attitude knowledge.

2.4.2.4.2 Attitude Control

There were two modes of operation for attitude control. One was using the reaction control subsystem (RCS), which used small 1-Newton thrusters to control attitude. The attitude on each axis was allowed to drift within a small range called the "deadband." If the spacecraft's attitude drifted to the edge of that deadband, thrusters would fire to push the spacecraft's attitude back toward its ideal attitude. A typical deadband range was ±2 milliradians. Thrusters provided fairly coarse control of the spacecraft—it was effective for downlink and for large directional instrument control, but not the best for producing good images. For finer control, the spacecraft used three reaction wheel assemblies (RWAs). Each RWA was aligned to be roughly 120° apart and was not co-aligned with the spacecraft X-, Y-, and Z-axes, but rather between any two axes. The RWAs were capable of maintaining a spacecraft attitude to within 40 micro-radians at any given time. In other words, about 50 times finer precision than the thruster system. Now and then, because the RWAs adjusted the spacecraft's attitude by spinning at a higher or lower rate, one or another of the RWAs would become "saturated," or spin excessively fast. To restore the RWAs to a healthier and more useful spin rate, the thrusters held the spacecraft's attitude while the RWAs spun down in a process called "desaturation."

Thrusters provided fairly coarse control of the spacecraft—it was effective for downlink and for large directional instrument control, but not the best for producing good images.

2.4.2.4.3 Propulsive Maneuvers / Trajectory Correction Maneuvers

The AACS used the 445 Newton main engines for all maneuvers with a change in velocity over 0.5-meters per second. The bipropellant system is described below in the propulsion section. Cassini's largest maneuver was the SOI maneuver. With a velocity change of 626 meters per second, the burn used about 27 percent of the total 3,132 kilograms of bipropellant loaded at launch. The main engine gimbals controlled only pitch and yaw direction during actual burns, while the RCS thrusters controlled roll. For very small maneuvers, only the RCS thrusters were used instead of the main engine.

2.4.2.5 Propulsion Subsystem

The propulsion subsystem had two independent systems, the bipropellant and the monopropellant subsystems. The bipropellant system was used strictly for large maneuvers, as described above.

2.4.2.5.1 Bipropellant Subsystem

The bipropellant subsystem consisted of the bipropellant tanks and plumbing to the 445-Newton rocket engine assemblies, also known as the main engines. The bipropellant design used monomethyl hydrazine (MMH) as fuel and nitrogen tetroxide (NTO) as the oxidizer. The separate propellant tanks were pressurized by a common helium system. The plumbing was designed after the Mars Observer loss, and used an extensive pyrotechnic valve ladder configuration to isolate the NTO from the MMH side. The high-pressure helium could also be isolated from both fuel and oxidizer tanks using additional pyro-activated valves. The pyro ladder was used multiple times in flight to pressurize and isolate the NTO tank.

2.4.2.5.2 Monopropellant Subsystem

The monopropellant system was a hydrazine 1-Newton thruster design. Cassini had four thruster clusters on the lower equipment module, each containing two Z–axis facing and two X-axis facing thrusters, for a total of 16 thrusters. Only one thruster in each axis on each cluster was used at a time, the other two were redundant. The thrusters fired in pairs, with the Z-facing thruster used for pitch and yaw control, and the Y-facing thrusters for roll control.

2.4.2.6 Telecommunications Subsystem

The Cassini spacecraft communicated with Earth via an X-band downlink and X-band uplink to and from NASA's Deep Space Network (DSN). The DSN has three main complexes—one near Madrid, Spain, one near Canberra, Australia, and one near Barstow, California. As Earth rotates, at least one of the complexes was able "see" Cassini at any given time. The DSN uses either 34-meter or 70-meter antennas for communication with interplanetary spacecraft, and on a typical day Cassini was allocated a 9-hour DSN pass on one of those antennas. In other words, the spacecraft was transmitting to Earth, and Earth was transmitting to Cassini, for about 9 hours at a time on any given day.

2.4.2.6.1 Antennas

Cassini had three communication antennas. The 4-meter high-gain antenna was used for high-rate telemetry and commanding. Low-gain antenna-1 was located on top of the high-gain antenna and was used for emergency links. A second low-gain antenna, low-gain antenna-2, was located below the Huygens probe and was used extensively for inner cruise communication, when the high-gain antenna was being used as a sunshade and so could not point at Earth without the spacecraft being exposed to dangerously intense sunlight.

2.4.2.6.2 Uplink/Downlink

Commands were routed from JPL to the DSN and uplinked to Cassini via the X-band carrier. The uplink power from the DSN was usually 18 kilowatts. The command uplink rate was from 7.8125 bits per second (bps) over the low-gain antenna to 500 bps over the high-gain antenna. A 20-watt X-band amplifier powered the downlink carrier. The downlink telemetry rate was 5 bps over the low-gain

antenna. Over the high-gain antenna, the bit rate was variable, from 1896 bps up to 165 kilobits per second (kbps). The highest telemetry rates were available only by using the DSN's 70-meter stations.

2.4.2.6.3 Navigation

The downlink carrier was normally made coherent with the uplink carrier to get a two-way Doppler signal. To be coherent, the receiver must lock on the uplink signal, then downlink an exact 880/749 multiple of the uplink carrier. The two-way Doppler signal was used for accurate navigation. The DSN was able to also add ranging or other "tones" on the uplink to obtain radio-metric tracking data for navigation.

2.4.2.7 Thermal Control Subsystem

The thermal control subsystem was distributed all around the spacecraft, using both active and passive components. The spacecraft was covered with thermal multi-layer insulation blankets. The blankets were either gold, from a gold-colored Kapton layer, or black from a black Kapton layer.

Each instrument had its own replacement heater that was normally used when the instrument was turned off. Some of the more isolated instruments had supplemental heaters all designed to keep the electronics within certain temperature limits. The electronics in the 12-bay structure, the upper equipment module, and the propellant control assembly also had supplemental heaters as needed.

The larger heat generators, such as CDS, the Ku-band radar, Radio Frequency Instrument S-band, Ka-band, and X-band amplifiers, all had thermostat-controlled louvers on the outside to actively cool the electronics.

2.4.2.8 Onboard Fault Protection

Because of the billion-plus kilometers between Saturn and Earth, a radio signal from Cassini sometimes took more than an hour to reach Earth. If the spacecraft reported that something had gone wrong (a short-circuit, unusually extreme temperatures in the spacecraft, etc.), it would take an additional hour-plus for commands from the ground to travel the distance back to Cassini. Due to that time-lag, along with the complex nature of spacecraft events, the onboard computers had special sequences that functioned as system fault-protection routines.

Each subsystem had some hardware fault-protection built in, but the system-level fault protection was in the flight software loaded into the CDS EFCs. There were a number of system-level routines that were able to execute a response to any of several monitors if needed. The core system fault protection routine was known as spacecraft safing. Safing refers, literally, to keeping the spacecraft safe for a period of time until the ground is able to intervene. The main purpose of these routines was to establish a safe power-level, attitude reference and attitude control, and a robust telecommunication link to Earth.

2.4.3 HUYGENS PROBE OVERVIEW

The Huygens probe system included the probe itself, which entered the Titan atmosphere, and support equipment that remained attached to the orbiter after the release of the probe. The probe weighed 320 kilograms and consisted of three main elements (see Figure 2.4-3):

1. A **spin-eject device, which was part of the support equipment**, used springs to propel the probe away from the orbiter with a relative velocity of about 0.3 to 0.4 meter per second and simultaneously caused the probe to spin about its axis at 7 revolutions per minute.

2. A **front shield**, 2.7 meters in diameter, protected the probe from the enormous heat generated during entry into Titan's atmosphere. The shield was covered with a special thermal-protection material called AQ60—a low-density mat of silica fibers.

3. An **aft cover** used thermal-protection materials to ensure a slow and stable descent. Its main parachute slowed the probe and allowed the decelerator to fall away when it was released. To limit the duration of the descent to a maximum of 2.5 hours, the main parachute was jettisoned at approximately 900 seconds after atmospheric entry, and was replaced by an approximately 3-meter diameter drogue chute for the remainder of the descent.

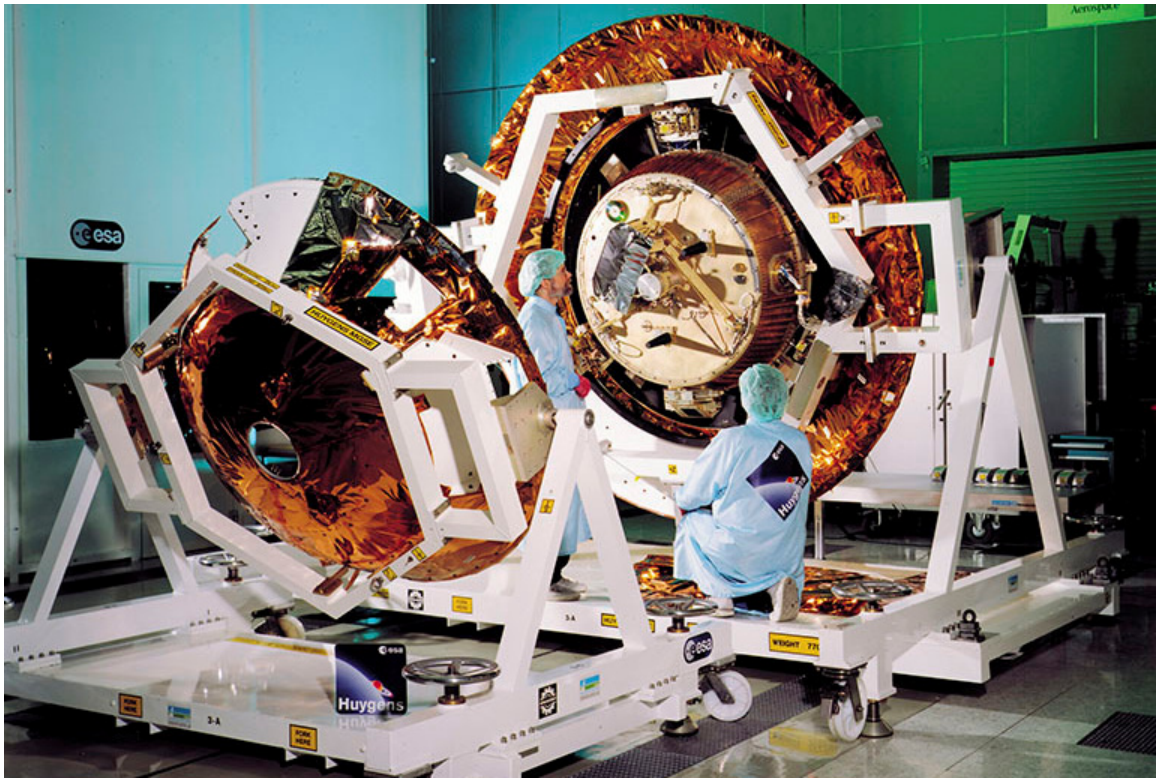

Figure 2.4-3. The Huygens probe during assembly. Image courtesy of the European Space Agency.

The probe's interior consisted of two aluminum honeycomb platforms and an aluminum shell. It was linked by fiberglass struts and pyrotechnically operated release mechanisms to the front shield and aft cover. The central equipment platform carried the boxes containing the electrical subsystems and science experiments. The upper platform carried the stowed parachute and the transmitter used to radio data to the Cassini spacecraft via the microwave S-band.

At different phases of the mission, the Huygens probe was subject to extreme changes of heat and cold requiring a variety of passive controls to maintain the required temperature conditions. When Cassini left the inner solar system, the temperature environment of the probe was greatly reduced. After separation from the Cassini spacecraft, the Huygens probe was at its coldest. To ensure that the equipment stayed operational, 35 radioisotope heater units were placed in the system. Each heater unit contained radioactive plutonium dioxide and produced about 1 watt of heat.

During entry into Titan's atmosphere, the front shield reached temperatures above 1,500° Celsius. Layers of insulation in the probe ensured that the equipment inside stayed below 50° Celsius. Once the chutes were deployed, the probe instruments were exposed to the cold Titan atmosphere at a temperature of approximately −200° Celsius. The probe's internal temperature was kept within operating limits by a thick foam insulation filling the probe and by power dissipation in the experiments and subsystems.

When still attached to the Cassini spacecraft, the probe obtained power from the spacecraft via an umbilical cable. After separation, five lithium-sulfur dioxide batteries provided electrical power, each with 23 cells. A small part of the battery power was used by the Huygens probe's timer for the 21-day coast to Titan.

The Huygens probe's command and data management subsystem controlled the timing and execution of a number of critical events, including the following:

1. Kept time during the coast phase and switched on the probe just before atmospheric entry.

2. Controlled the deployment of various components during descent.

3. Distributed commands to other subsystems and to the experiments.

4. Distributed to the experiments a timeline of conditions that instruments were able to use to schedule operations.

5. Collected scientific and engineering data and forwarded the data to the spacecraft during the cruise to Saturn and during the Huygens mission.

The probe data-relay subsystem provided the one-way communications link between the Huygens probe and the Cassini spacecraft, and included equipment installed in the probe and in the spacecraft. Elements that were part of the probe's support equipment on the Cassini spacecraft included radio-frequency electronics (including an ultra-stable oscillator, USO) and a low-noise

amplifier. For backup, the Huygens probe carried two S-band transmitters, both of which transmitted data during probe descent; each had its own antenna.

2.4.3.1 Huygens Probe Instruments

The Huygens descent probe contained a total of six science instruments, which are shown in Figure 2.4-4 and briefly described below:

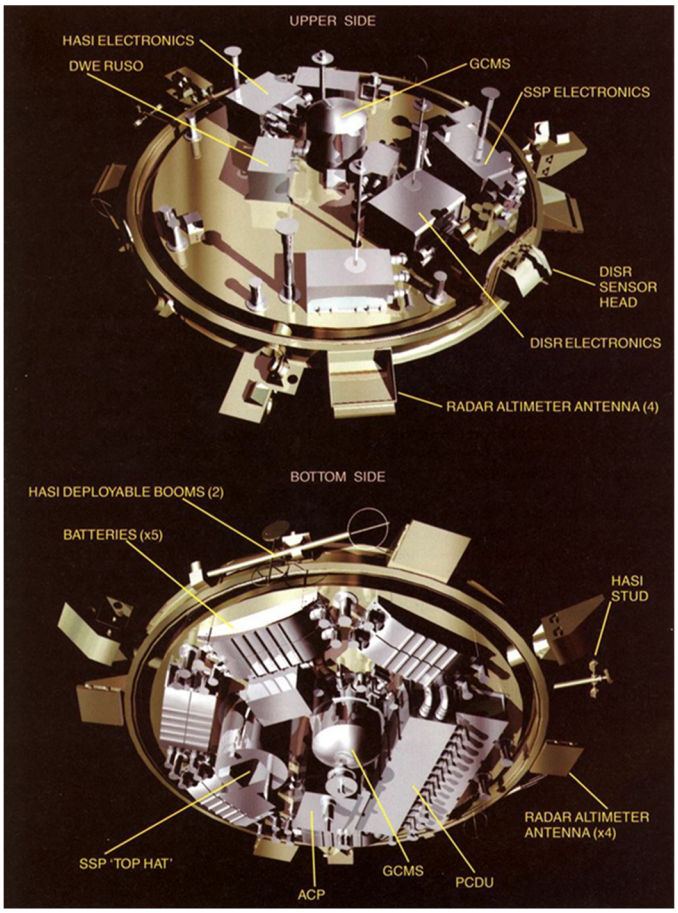

Figure 2.4-4. Huygens probe instruments.

1. **Descent Imager/Spectral Radiometer (DISR).** The imager/spectrometer used 13 fields of view, operating at wavelengths of 350 to 1,700 nanometers, to obtain a variety of imaging and spectral observations: Infrared and visible imagers were used to observe Titan's surface during the latter stages of the descent. By taking advantage of the Huygens probe's rotation, the imagers were able to build a mosaic of pictures around the landing site. A side-looking visible imager was able to view the horizon and the underside of the cloud deck. The spectral radiometer measured concentrations of argon and methane in the atmosphere. It also determined that the

local surface was solid and studied its topography. Solar aureole sensors measured the light intensity around the Sun resulting from scattering by particles suspended in the atmosphere, permitting calculations of their size, number and density. The PI for DISR was Dr. Martin G Tomasko of the University of Arizona, Tucson.

2. **Huygens Atmospheric Structure Instrument (HASI).** This instrument investigated the physical properties of Titan's atmosphere, including temperature, pressure, and atmospheric density as a function of altitude, wind gusts, and liquid surface wave motion. Comprising a variety of sensors, the instrument also measured the ion and electron conductivity of the atmosphere and searched for electromagnetic wave activity. On Titan's surface, the instrument was able to measure the conductivity of surface materials. The instrument also processed the signal from the Huygens probe's radar altimeter to obtain information on surface topography, roughness and electrical properties. The PI for HASI was Dr. Marcello Fulchignoni of the Paris Observatory, Meudon, France.

3. **Aerosol Collector and Pyrolyzer (ACP).** The collector and pyrolyzer instrument trapped particles suspended in Titan's atmosphere using a deployable sampling device. Samples were heated to vaporize the ice particles and decompose the complex organic materials into their component chemicals. The products were then passed to the gas chromatograph/mass spectrometer for analysis. The instrument obtained samples at two altitude ranges. The first sample was taken at altitudes down to about 30 km above the surface. The second sample would be obtained at an altitude of about 20 km. The PI for ACP was Dr. Guy M. Israel of the Service d'Aeronomie du Centre National de la Recherche Scientifique, Verrieres-le-Buisson, France.

4. **Gas Chromatograph Mass Spectrometer (GCMS).** This spectrometer provided a quantitative analysis of Titan's atmosphere. Atmospheric samples were transferred into the instrument by dynamic pressure as the Huygens probe descended through the atmosphere. The mass spectrometer constructed a spectrum of the molecular masses of the gas sampled by the instrument. Just before landing, the instrument's inlet port was heated to vaporize material on contact with the surface. After landing, the instrument was able to determine Titan's surface composition. The mass spectrometer served as the detector for the gas chromatograph, for atmospheric samples, and for samples provided by the aerosol collector and pyrolyzer. The PI for GCMS was Dr. Hasso B. Neimann of NASA's Goddard Space Flight Center, Greenbelt, Maryland.

5. **Doppler Wind Experiment (DWE).** The wind instrument used two ultra-stable oscillators—one on the Huygens probe and one on the Cassini spacecraft—to give the Huygens' radio relay link a stable carrier frequency. Spacecraft measurements of changes in probe frequency caused by Doppler shift provided information on the probe's motion. From this, scientists were able to derive a height profile of wind and its turbulence. The PI for the DWE was Dr. Michael K. Bird of the University of Bonn, Germany.

6. **Surface Science Package (SSP).** This instrument contained a number of sensors to determine the physical properties and composition of Titan's surface. An acoustic sounder measured the rate of descent, surface roughness, and the speed of sound in any fluid. During descent, measurements of the speed of sound provided information on atmospheric composition and temperature. An accelerometer recorded the deceleration profile at impact, indicating the hardness of the surface. Tilt sensors (liquid-filled tubes with electrodes) measured any pendulum motion of the Huygens probe during descent, indicated the Huygens probe orientation after landing, and measured any wave motion. Other sensors measured the surface's density, temperature, refractive index, thermal conductivity, heat capacity, and electrical properties. A group of platinum resistance wires, through which a heating current was passed, measured temperature and thermal conductivity of the surface and lower atmosphere and the heat capacity of the surface material. A transducer, pointed downward and operating at 15 KHz, conducted an acoustic sounding of the liquid's depth. The instrument provided a crude topographic mapping of the surface as the probe descended the last few meters through the atmosphere. The PI for SSP was Dr. John C. Zarnecki of the University of Kent, England.

2.4.4 INSTRUMENTS PAYLOAD OVERVIEW

The Cassini spacecraft carried a total of 12 science instruments, four of which were on the remote sensing experiments pallet, and three of which were on the fields and particles experiments pallet. The other five instruments were fixed at independent locations on the spacecraft. The science instruments are listed and their measurement objectives described in this section. For eight of these instruments, a PI and co-investigators were responsible for their corresponding instrument, as well as for their scientific investigation. The other four instruments were designated as "facility instruments"; these instruments were built at JPL and were used by a Cassini science team. Facility instrument science teams had team leaders rather than PIs.

Following are the PI-led instruments:

1. Cassini Plasma Spectrometer (CAPS)
2. Composite Infrared Spectrometer (CIRS)
3. Cosmic Dust Analyzer (CDA)
4. Ion and Neutral Mass Spectrometer (INMS)
5. Magnetometer (MAG)
6. Magnetospheric Imaging Instrument (MIMI)
7. Radio and Plasma Wave Science (RPWS)
8. Ultraviolet Imaging Spectrograph (UVIS)

Following are the facility instruments:

1. Imaging Science Subsystem (ISS)
2. RADAR
3. Radio Science Subsystem (RSS)*
4. Visible and Infrared Mapping Spectrometer (VIMS)

Note: The INMS was developed as a facility instrument by NASA's Goddard Space Flight Center but was operated as a PI instrument (see Section 2.5.8.2).

2.4.4.1 Optical Remote Sensing Instruments

Cassini was equipped with a set of in situ instruments for studying the environment in the immediate vicinity of the spacecraft (e.g., magnetometers, plasma instruments, cosmic dust analyzer), as well as a set of instruments that studied targets from afar (visible and infrared cameras, spectrometers, etc.) called optical remote sensing instruments (ORS). The ORS instruments were mounted on the remote sensing pallet (RSP) rigidly attached to the upper equipment module (UEM), shown in Figure 2.4-5. These instruments measured properties of targets at a distance and included: CIRS, ISS, UVIS, and VIMS.

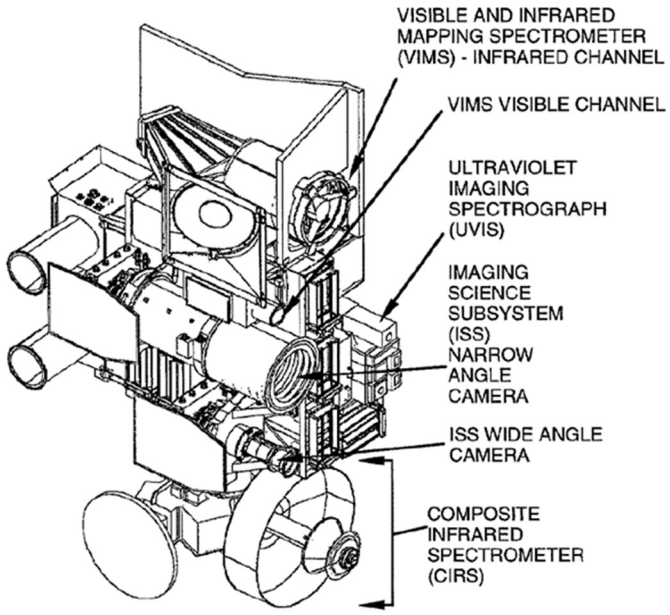

Figure 2.4-5. Remote sensing pallet.

* The RSS was not an instrument, but rather a scientific experiment, which used the capabilities of the radio frequency (RF) subsystem (or telecommunications (telecom) subsystem) onboard the spacecraft to accomplish its science objectives.

Mounted on the RSP, these instruments studied Saturn and its rings and moons in the electromagnetic spectrum:

Composite Infrared Spectrometer (CIRS). The infrared spectrometer functioned as a remote-sensing thermometer. It captured infrared emissions from atmospheres, rings, and surfaces. The instrument then split the light into its component wavelengths (or colors) and then measured the strength of the light at each of those wavelengths primarily to measure the temperature of objects. It also determined the chemical composition of the targets because molecules leave different "fingerprints"—they preferentially absorb and emit infrared radiation at different specific wavelengths in the spectrum. In other words, their presence shows up as different lines in the spectrum.

By analyzing an object's light with a spectrometer, the science community can determine its temperature and some of the materials it is made of. When pointed at Saturn's atmosphere, for example, a spectrometer would reveal a series of bright lines indicating that the spectrometer observed methane gas.

CIRS instrument characteristics:

- Mass (current best estimate) = 39.24 kg
- Peak operating power (current best estimate) = 32.89 W
- Average operating power (current best estimate) = 26.37 W
- Peak data rate (current best estimate) = 6.000 kilobits/sec
- Dimensions (approximate) = 50 cm diameter telescope; 89 × 76 × 52 cm

The PI for CIRS was Dr. Michael Flasar of NASA's Goddard Space Flight Center, Greenbelt, Maryland.

Imaging Science Subsystem (ISS). Cassini's visible-light cameras provided unparalleled images of Saturn, the rings, Titan and the icy moons for various scientific purposes. It would be challenging to overstate how spectacular the images produced by this instrument were. Its images remain iconic (some more than a decade after they were taken) both among the public and among the people who worked on the mission. Yet it was, in both intent and use, a science instrument.

The ISS was one of the facility instruments built at JPL, and one of the six instruments destined to perform scientific investigations of the Saturnian system from a range of remote observing distances. It was also used for optical navigation in order to improve the navigation team's knowledge of the spacecraft's trajectory. The optical navigation method used the known positions of Saturn's moons along with a map of the stars to determine the spacecraft's position based on the images taken of Saturn's moons with stars in the background.

The ISS instrument was composed of two cameras, a wide-angle camera (WAC) and a narrow-angle camera (NAC). Each had its own electronics, detectors, optics, filters wheels, and shutters.

Both were sensitive to visible wavelengths of light and to some infrared and ultraviolet wavelengths. The ISS included spectral filters and imaging capabilities that aided in the attainment of spectacular images of Saturn, its rings, and its numerous icy and rocky moons. In the process, the instrument satisfied several scientific objectives. It studied the contents of Saturn's and Titan's atmospheres, the surfaces of Saturn's moons, and the characteristics and composition of Saturn's rings.

The NAC was a reflecting telescope with a focal length of 2,000 millimeters and a field of view of 0.35°. The WAC was a refractor with a focal length of 200 millimeters and a field of view of 3.5°. Each camera was equipped with a large number of spectral filters which, when used together, spanned the electromagnetic spectrum from 2,000 Angstroms to 1.1 microns. Each of the cameras contained a detector that consisted of a 1,024-square array of pixels each 12 microns. In other words, each of Cassini's cameras was a one mega-pixel camera. The combined spacecraft and instrument data system allowed many options for data collection, including data compression, a method that allowed instrument data reduction to be stored onboard the spacecraft and played back to Earth and expanded to the original set of data collected by the instrument.

Each camera was equipped with a large number of spectral filters which, when used together, spanned the electromagnetic spectrum from 2,000 Angstroms to 1.1 microns.

The WAC captured comprehensive and detailed images of Saturn and its rings from more than 1.5 million kilometers away, and the NAC provided high-resolution images of specific targets, such as craters or fractures on the surfaces of Saturn's moons.

ISS instrument characteristics:

- Wide-angle camera (20 cm f/3.5 refractor; 380–1,100 nm; 18 filters; 3.5° × 3.5°)
- Narrow-angle camera (2 m f/10.5 reflector; 200–1,100 nm; 24 filters; 0.35° × 0.35°)
- Mass (current best estimate) = 57.83 kg
- Peak operating power (current best estimate) = 55.90 W
- Peak data rate (current best estimate) = 365.568 kilobits/sec
- Dimensions (approximate) = 95 × 40 × 33 cm (NAC); 55 × 35 × 33 cm (WAC)

The team leader for ISS was Dr. Carolyn C. Porco of Space Science Institute (SSI) Denver, Colorado.

Ultraviolet Imaging Spectrograph (UVIS). The spectrograph was a set of detectors designed to measure ultraviolet light reflected by or emitted from atmospheres, rings, and surfaces to determine their compositions, distributions, aerosol content, and temperatures. The instrument also measured fluctuations of sunlight and starlight as the Sun and other stars move behind the

rings of Saturn and the atmospheres of Saturn and Titan, and determined the atmospheric concentrations of hydrogen and deuterium.

The instrument included a two-channel, far-ultraviolet and extreme-ultraviolet imaging spectrograph that studied light over wavelengths from 55.8 to 190 nanometers. It also had a hydrogen and deuterium absorption cell and a high-speed photometer. An imaging spectrograph recorded spectral intensity information in one or more wavelengths of light and then outputted digital data that could be displayed in visual form, such as a false-color image. False-color images are not what the eye would see, but are often more useful because enhanced contrast brings out scientifically meaningful details. The hydrogen-deuterium absorption cell measured the quantity of deuterium, a heavier form (isotope) of hydrogen. Hydrogen-deuterium ratio varies widely throughout the solar system and is an important piece of data in understanding planetary evolution. The high-speed photometer determined the radial structure of Saturn's rings by watching starlight that passed through the rings. The PI for UVIS was Dr. Larry L. Esposito of the University of Colorado, Boulder.

Visible and Infrared Mapping Spectrometer (VIMS). The infrared spectrometer mapped the surface spatial distribution of the mineral and chemical features of a number of targets, including Saturn's rings, surfaces of the moons, and the atmospheres of Saturn and Titan. The instrument included a pair of imaging grating spectrometers that were designed to measure reflected and emitted radiation from atmospheres, rings, and surfaces to determine their compositions, temperatures, and structures. A spectrometer is an optical instrument that splits the light received from objects into its component wavelengths; each chemical has a unique spectral signature and thus can be identified. The instrument obtained information over 352 contiguous wavelengths from 0.35 to 5.1 micrometers; it measured intensities of individual wavelengths and used the data to infer the composition and other properties of the object that emitted the light. The mapping function of the instrument provided images in which every pixel contained high-resolution spectra of the corresponding spot on the target body. The team leader for VIMS was Dr. Robert H. Brown of the University of Arizona, Tucson.

2.4.4.2 Fields, Particles, and Waves In Situ Instruments

The fields, particles, and waves (FPW) instruments were mounted in several locations on the spacecraft. The MAG sensors were located on the extensible magnetometer (MAG) boom, attached to the top of the upper equipment module. A small pallet, also mounted on the upper equipment module, carried INMS, MIMI Lower Equipment Module (LEMMS) and Change-Energy-Mass Spectrometer (CHEMS), and CAPS. MIMI Ion and Neutral Camera (INCA), CDA, and the RPWS antennas and Magnetic Search Coils (MSC) were attached elsewhere on the Upper Equipment Module. (Note: MIMI INCA imaged the charged particle population of Saturn's magnetosphere, but despite being a remote sensing instrument rather than an in situ instrument, we included it in this section because it was part of the MIMI instrument and moving it elsewhere might have created confusion.) Figure 2.4-6 depicts the remote sensing pallet and fields and particles pallet.

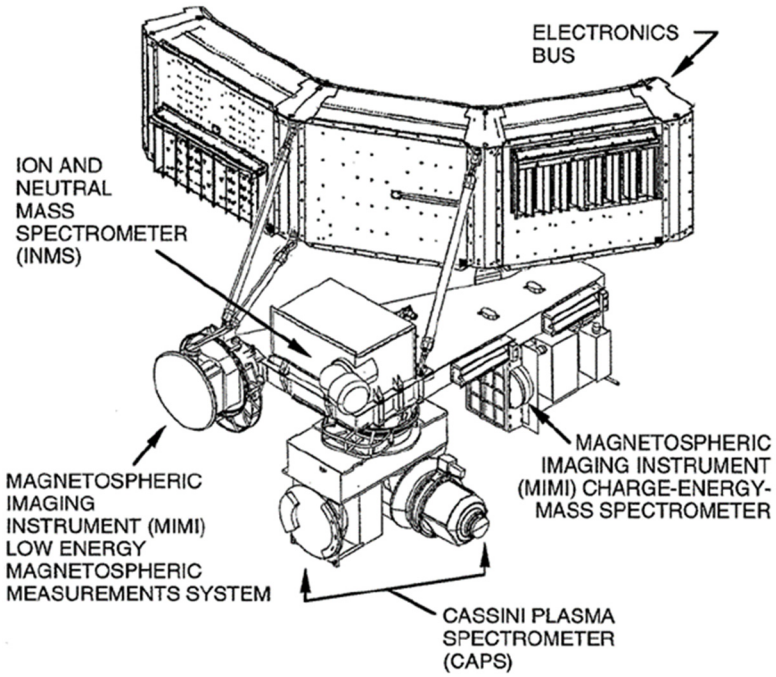

Figure 2.4-6. Remote sensing pallet and fields and particles pallet.

Following is an overview description for each of the FPW instruments.

Cassini Plasma Spectrometer (CAPS). The plasma spectrometer measured the composition, density, flow velocity, and temperature of ions and electrons in Saturn's magnetosphere. CAPS consisted of three sensors: an electron spectrometer, an ion beam spectrometer, and an ion mass spectrometer. A motor-driven actuator rotated the sensor package to provide 208° scanning in the azimuth of the Cassini orbiter. The electron spectrometer performed measurements of the energy of incoming electrons; its energy range was 0.7 to 30,000 electron volts. The ion beam spectrometer determined the energy-to-charge ratio of an ion; its energy range was 1 electron volt to 50 kilo-electron volts. The ion mass spectrometer's energy range was 1 electron volt to 50 kilo-electron volts. The PI for CAPS was Dr. David T. Young of the Southwest Research Institute (SwRI), San Antonio, Texas.

Cosmic Dust Analyzer (CDA). The dust analyzer provided direct observations of small ice or dust particles in the Saturn system to investigate their physical, chemical, and dynamic properties, and to study their interactions with the rings, icy moons, and magnetosphere of Saturn. The instrument measured the amount, velocity, charge, mass, and composition of tiny dust and ice particles. It had two types of sensors—high-rate detectors and a dust analyzer. The two high-rate detectors, intended primarily for measurements in Saturn's rings, counted up to 10,000 impacts per second. The dust analyzer determined the electric charge carried by dust particles, the flight direction and impact speed, mass and chemical composition, at rates up to 1 particle per second, and for speeds of up to about 100 km per second. An articulation mechanism allowed the entire instrument to be rotated or repositioned relative to the body of the Cassini orbiter to investigate

dust particles traveling from specific directions. The PI for CDA was Dr. Ralf Srama of the Max Planck Institute fur Kernphysik, Heidelberg, Germany.

Ion and Neutral Mass Spectrometer (INMS). This spectrometer determined the composition and structure of positive ions and neutral particles in the upper atmosphere of Titan and the magnetosphere of Saturn, and measured the positive ion and neutral environments of Saturn's icy moons and rings. The instrument determined the chemical, elemental, and isotopic composition of the gaseous and volatile components of the neutral particles and the low energy ions in Titan's atmosphere and ionosphere, Saturn's magnetosphere and the ring environment. The PI for INMS was Dr. J. Hunter Waite of SwRI, San Antonio, Texas.

Magnetometer (MAG). Cassini's magnetometer consisted of direct-sensing instruments that detected and measured the strength of magnetic fields in the vicinity of the spacecraft. MAG determined the magnetic fields of the planet and moons and studied dynamic interactions between different magnetic fields in the planetary environment. The instrument included both a flux gate magnetometer and a vector/scalar helium magnetometer. They were used to measure the magnitude and direction of magnetic fields. Since magnetometers are sensitive to electric currents and ferrous metal components, they were placed on an extended boom, as far from the spacecraft as possible. On Cassini, the flux gate magnetometer was located midway out on the 11-meter magnetometer boom, and the vector/scalar helium magnetometer was located at the end of the boom. The boom itself, composed of thin, nonmetallic rods, was folded during launch and deployed about two years after launch. The magnetometer electronics were located in a bay in the Cassini orbiter's spacecraft body. The PIs for MAG were Dr. David J. Southwood and Dr. Michel Dougherty of the Imperial College of Science and Technology, London, England.

Magnetospheric Imaging Instrument (MIMI). This instrument was designed to measure the composition, charge state, and energy distribution of energetic ions and electrons; detect fast neutral particles; and conduct remote imaging of Saturn's magnetosphere. MIMI was the first instrument ever designed to produce an image of a planetary magnetosphere. This information was used to study the overall configuration and dynamics of the magnetosphere and its interactions with the solar wind, Saturn's atmosphere, Titan, rings and the icy moons. The instrument provided images of the ionized gases, called plasma, surrounding Saturn and determined the charge and composition of ions. Like the Cassini plasma spectrometer, this instrument had three sensors that performed various measurements: the low-energy magnetospheric measurement system, the charge-energy-mass spectrometer, and the ion and neutral camera. The low-energy magnetospheric measurement system measured low- and high-energy proton, ion, and electron angular distributions (the number of particles coming from each direction). The charge-energy-mass spectrometer used an electrostatic analyzer, a time-of-flight mass spectrometer, and microchannel plate detectors to measure the charge and composition of ions. The third sensor, the ion and neutral camera, performed two different types of measurements. It obtained three-dimensional distributions, velocities and the rough composition of magnetospheric and interplanetary ions. PIs for MIMI were Dr. Stamatios M. Krimigis and Dr. Mitchel Donald of Johns Hopkins University, Baltimore, Maryland.

Radio and Plasma Wave Science (RPWS). This instrument measured electrical and magnetic fields in the plasma of the interplanetary medium and Saturn's magnetosphere, as well as electron density and temperature. Plasma is essentially a soup of free electrons and positively charged ions, the latter being atoms that have lost one or more electrons. Plasma makes up most of the universe and is created by the heating of gases by stars and other bodies in space. Plasma is distributed by the solar wind; it is also "contained" by magnetic fields (that is, the magnetospheres) of bodies such as Saturn and Titan. The major components of the instrument were an electric field sensor, a magnetic search coil assembly and a Langmuir probe. The electric field sensor was made up of three deployable antenna elements mounted on the upper equipment module of the Cassini spacecraft. Each element was a collapsible beryllium-copper tube that was rolled up during launch and subsequently unrolled to its approximately 10-meter length by a motor drive. The magnetic search coils were mounted on a small platform attached to a support for Cassini's high-gain antenna. The Langmuir probe, which measured electron density and temperature, was a metallic sphere about 50 millimeters in diameter. The probe was attached to the same platform by an approximately 1-meter deployable boom. PIs were Dr. Donald A. Gurnett and Dr. William Kurth of the University of Iowa, Iowa City.

Plasma makes up most of the universe and is created by the heating of gases by stars and other bodies in space.

2.4.4.3 Microwave Sensing Instruments

Cassini carried two microwave sensing instruments: The Titan Radar Mapper (RADAR) and the RSS.

The RADAR instrument investigated the surface of Saturn's largest moon, Titan, whose surface is covered by a thick, cloudy atmosphere that hides the moon's surface in normal optical views, but can be penetrated by radar. The instrument was based on the same imaging radar technology used in missions such as the Magellan mission to Venus and the Earth-orbiting Spaceborne Imaging Radar.

The instrument was composed of the following subsystems: the radio frequency electronics subsystem (RFES), the digital subsystem (DSS), the energy storage subsystem (ESS), and the Antenna Subsystem. The DSS and ESS were located in one of the equipment bays below the high-gain antenna. RFES was in a penthouse-like attachment over the bay. The principal component of the antenna subsystem was the five-beam Ku-band high-gain antenna feed. RADAR shared the high-gain antenna with the RSS for both its active (synthetic aperture radar imaging and altimetry) and passive (radiometry) operations.

The radar was able to take four types of observations: imaging, altimetry, backscatter and radiometry. In imaging mode, the instrument bounced pulses of microwave energy off the surface of Titan from different incidence angles and recorded the time it took the pulses to return to the

spacecraft. These measurements, converted to distances by dividing by the speed of light, allowed construction of visual images of the target surface with a resolution ranging from about 0.3 to 1.7 km.

RADAR altimetry used a similar approach, bouncing microwave pulses off the target body's surface and measuring the time it took the "echo" to return to the spacecraft. In this case, however, the goal was not to create visual images but rather to obtain numerical data on the precise altitude of surface features. The altimeter resolution was about 24 to 27 km horizontally, and 90 to 150 meters vertically.

In backscatter mode, the radar bounced pulses off Titan's surface and measured the intensity of the energy returning. This returning energy, or backscatter, was always less than the original pulse, because surface features reflected the pulse in countless directions, with only a fraction of the original pulse returning to Cassini where the high-gain antenna collected the signal. Scientists drew conclusions about the composition and roughness of the surface from the backscatter measurements.

In radiometry mode, the radar operated as a passive instrument, simply recording the heat energy emanating from the surface of Titan (everything that's not at zero Kelvin emits some radio signal). This information was used to determine the amount of heat absorption by gases and aerosols (such as methane) in Titan's atmosphere, a factor that affected the accuracy of the other measurements taken by the instrument.

The radar was used in different ways at different altitudes. At altitudes between about 22,500 to 9,000 km, the radar switched between scattering measurements and radiometry to obtain low-resolution global maps of Titan's surface roughness, backscatter intensity, and thermal emissions. At altitudes between about 9,000 to 4,000 km, the instrument switched between altimetry and radiometry, collecting surface altitude and thermal emission measurements. Below about 4,000 km, the radar switched between imaging and radiometry. The radar team leader was Dr. Charles Elachi of NASA's Jet Propulsion Laboratory, Pasadena, California.

The RSS "instrument" (experiment) used the spacecraft's radio (telecom) subsystem and the ground antennas of NASA's DSN to study the composition, pressures and temperatures of the atmospheres and ionospheres of Saturn and Titan. RSS also studied the radial structure of and particle size distribution in Saturn's rings, as well as the masses of objects in the Saturn system and the mass of Saturn's ring system as a whole. Radio science also helped search for gravitational waves coming from beyond the solar system. Some of these experiments measured Doppler shifts (frequency shifts) and other changes to radio signals when the spacecraft passed behind planets, moons, atmospheres, or physical features such as planetary rings. From those measurements, scientists derived information about the structures and compositions of the occulting bodies, atmospheres, and rings.

The RSS was composed of elements located in the DSN (part of the ground system) and onboard the spacecraft. The flight RSS instrument consisted of the radio frequency instrument subsystem (RFIS) and elements of the RFS. The main assemblies of the RFIS were the Ka-band

exciter, the Ka-band traveling wave tube amplifier, the Ka-band translator, and the S-band transmitter. In addition, the high-gain antenna was used as part of the RSS instrument to receive the X- and Ka-band signals and to transmit at X-, Ka-, and S-bands. The RSS team leaders were Dr. Arvydas J. Kliore of NASA's Jet Propulsion Laboratory, Pasadena, California, and Dr. Richard French of Wellesley College, Massachusetts.

2.5 Mission Operations System Description (Functional Level)

Two-way communication with the Cassini spacecraft was established through the large dish antennas of the DSN. The spacecraft transmitted and received in the microwave X-band using its parabolic high-gain antenna, which was also used for radio and radar experiments and for receiving signals from the Huygens probe.

Because Cassini's science instruments were fixed to the spacecraft, and the entire spacecraft had to be turned to point them, Cassini was frequently reoriented by using either the reaction wheels or the spacecraft's set of small onboard thrusters. Consequently, most science observations were made without a real-time communications link to Earth. Data were stored on Cassini's two SSRs, each with a capacity of two gigabits.

Each of Cassini's science instruments was run by an instrument microprocessor capable of controlling the instrument and formatting/packetizing science and housekeeping data. Ground engineers controlled the orbiter with a combination of centralized commands to control system-level resources, and some commands issued by the individual science instruments' microprocessors. Packets of data were collected from each instrument on a schedule that varied. Typically, data packets were stored on Cassini's onboard SSRs for later transmission, though once in a while they were transmitted to Earth right away via a real-time transmission. The science instruments had different pointing requirements, which often conflicted with each other and with the need to point the spacecraft toward Earth to transmit data to the ground system. Periods during which the antenna pointed toward Earth were carefully built into the design of the sequence controlling the onboard activities.

Control of the spacecraft was done, for the most part, from autonomous sequences stored onboard the spacecraft. To conduct activities and maintain the health and safety of Cassini, spacecraft sequencing used a combination of centralized commands (for control of the system-level resources) and instrument commands issued by the CDS and the instrument microprocessors. Each instrument's microprocessor formatted that instrument's data (including editing or compression), and the CDS then collected the data on the spacecraft bus on a schedule determined by the active telemetry mode. Packets from the engineering subsystems and instruments were assembled into frames and stored on the SSR or inserted directly into the real-time downlink telemetry stream. Data were normally received by the DSN with one tracking pass by one antenna per day, with occasional extra coverage for special radio science experiments.

Engineering teams and science instrument teams monitored spacecraft telemetry and instruments to ensure a safe and healthy spacecraft. The navigation team processed the tracking data to determine and predict the spacecraft's trajectory.

The spacecraft provided system-level services for each of the 12 science investigations, including instrument command delivery, telemetry collection and transmission, spacecraft pointing and attitude stability, power, and thermal control. The spacecraft was flown with sufficient margins to allow the instruments to operate fairly independently from each other, and with a minimum of real-time ground intervention, but still allowed for collaborative, synergistic collection of data.

Following is a brief description of the teams that formed part of the Mission Operations System, also known as the Ground System.

2.5.1 MANAGEMENT

Project management was responsible for the execution of the Cassini Mission within the resource constraints (cost and schedule). Project management provided technical and programmatic leadership for all aspects of the project, except for science analysis and publications, which were the responsibility of the Cassini project science team. Cassini project management in coordination with the science planning and sequencing team (SPST) manager provided management of the day-to-day operation of the mission (including all flight and ground activities) as well as the planning for future operations.

Cassini project management directed and monitored progress of all MOS activities: mission planning, science planning and analysis, spacecraft planning and analysis, navigation, sequence development, real-time mission operations, data transport and delivery, science data processing, and data archiving. The Cassini Project Manager was the interface between the Cassini flight team and upper JPL management.

2.5.2 PROJECT SCIENCE

The project science team (the Project Scientist and the project science group) was responsible to the Cassini project management and NASA for ensuring that the science objectives of the Cassini mission were being fully met. The project science team was the representative of the Science Team in the day-to-day science activities and decision-making process.

2.5.3 MISSION PLANNING

Prior to launch, the mission planning team was responsible for documenting the Mission Plan. The Mission Plan was the principal reference for high-level descriptions of the Cassini Mission. It documented the interplanetary cruise and Saturn tour trajectories; high-level spacecraft and activity designs; operational strategies and options; and guidelines and constraints for mission operations. The Cassini Mission Plan served to guide the development of detailed event timelines from before

launch through end of mission and it evolved throughout the mission as a living document. The Mission Plan provided the following information:

- An overview of the Cassini Mission, including the spacecraft trajectory during cruise and tour, and a summary of the main events during the flight. It described the science objectives of the mission.
- Descriptions of the spacecraft, probe, instrument, and launch vehicle systems.
- Explanations of the primary operational strategies for the mission.
- Descriptions of the different mission phases.
- Documented mission-level guidelines and constraints, operational modes, and timelines for critical periods.

During operations the mission planning team was responsible for assessing adherence to the mission plan and maintaining and updating the plan. This included responding to unforeseen mission events (e.g., anomalies, idiosyncrasies, and new science requirements), determining the effects of those events on the mission objectives and requirements, and, when required, performing re-planning to accomplish the original objectives or to optimize them.

Specific mission planning activities during operations included:

- Analyzing implications of the actual flight trajectory to achieving the mission goals and objectives.
- Monitoring and evaluating ongoing mission events against mission goals and objectives.
- Monitoring, tracking, and assessing flight system (spacecraft and instruments payload) consumable resources usage against estimates for usage through the end of the mission. Consumable resources included propellant, hydrazine, power, data volume, etc.
- Developing contingency plans necessary to recover from a flight system anomaly or an unforeseen event.
- Developing new mission plans needed in response to new mission objectives.

2.5.4 SCIENCE PLANNING AND SEQUENCING

The SPST was part of the Science and Uplink (SAUL) Office. The SAUL Office was composed of the SPST, the instrument operations team, the Mission Sequencing System (MSS), and science system engineering.

During flight operations, the SPST was responsible for identifying science opportunities by evaluating spacecraft trajectory information, target-body ephemerides, and keep-out periods of time during which spacecraft engineering activities (e.g., spacecraft engineering subsystems

calibrations and orbit trim maneuvers (OTMs)) needed to take place. The science opportunities represented periods of time in the mission where science observations could be performed to achieve the mission's science objectives. The SPST coordinated these observation opportunities with the science teams and the Spacecraft Operations Office to ensure that they were in agreement with performing such observations during the selected times. After several iterations between the SPST, the science teams, and the Spacecraft Operations Office (SCO), an agreement was reached and an integrated science plan was put together by the SPST. Once the integrated science plan was approved by all involved teams, each science/instrument team and the SCO generated their corresponding subsequence files containing the corresponding set of commands for instruments and spacecraft subsystems activities. The SPST accessed these subsequence files and integrated them into a single background sequence. Once generated, the commands were expanded, constraint checked, and compiled by the SPST.

Specific science planning and sequencing activities during operations included:

- Generation of a fully integrated sequence of science events needed to meet the science objectives of the mission.
- Identification of science opportunities based on atmospheric, geological, magnetospheric, ring, and satellite objectives. Opportunities were ranked according to their importance relative to the mission's science objectives.
- Combination of science and instrument engineering inputs into a single, integrated science activity plan.
- Modification of the science activity plan to improve or optimize science return through the use of allocated ground resources (e.g., observation redesign, late updates, "tweaks," etc.) and spacecraft resources (e.g., observation duration, time between activities, etc.).
- Coordination of design observations needed to implement the science activity plan based on spacecraft capabilities and within mission guidelines and flight rules.
- Evaluation of the implementation of the science observation based on initial inputs.
- Ensured that no other activity degraded or inhibited the acquisition of the data.
- Generation and translation of commands (sequence and real-time) needed to implement the activity plan.

2.5.5 MISSION SEQUENCING SUBSYSTEM

The mission sequencing subsystem was part of the SAUL Office.

The MSS team was responsible for defining, creating, maintaining, and delivering the software applications used by the SPST. The MSS team created the requirements and the design for the software applications and then implemented and tested them after the requirements and design had been approved by SPST and the project.

The suite of applications included sequencing and planning software tools that supported the SPST during the execution of the uplink process. Many of the applications were used on previous flight projects and were modified to meet the Cassini requirements. Some of those applications can be traced back more than 25 years. Many of these applications were part of the Advanced Multi-Mission Operations System (AMMOS). These applications were used with minimum modifications because they provided generic capabilities applicable to all missions. Sequence Translator (SEQTRAN) only required the input of Cassini commands to work. This software translated those commands into binary for uplink to the spacecraft. Other applications required some level of Cassini mission-specific adaptation. The required adaptations were designed, implemented and tested by the MSS team. Sequence Generator (SEQ_GEN) was an application that required mission specific adaptation to add Cassini commands and activities. This software checked flight and mission rules. In addition, there were software tools designed and created specifically for Cassini. One of those tools was the Pointing Design Tool (PDT). This software application allowed the teams to create pointing designs that were used to perform science observations. Other software applications were utilities that improved the uplink process. Among the main applications that the MSS was responsible for were: the PDT, SEQ_GEN, and the SEQTRAN, just to mention a few.

2.5.6 SPACECRAFT OPERATIONS

The primary responsibility of SCO was to maintain the health and safety of the Cassini spacecraft, and provide for the return of mission and science data. The spacecraft subsystem engineers prepared telemetry predictions and then analyzed real-time and non-real-time data, identified and resolved anomalies, implemented spacecraft maneuvers, maintained attitude control and flight software, and developed, analyzed, and tested the engineering commands for background sequence uploads and real-time commanding, as required. Spacecraft engineers also utilized the Integrated Test Laboratory (ITL), the hardware testbed, to analyze data, prepare predicts, and simulate commands and sequences. The SCO was also responsible for generating and maintaining various documents (e.g., command and telemetry dictionaries, operations procedures, flight rules and constraints, idiosyncrasies, and plans) and reports (consumables, trends, and subsystem performance) that were necessary to conduct the Cassini Mission.

The primary responsibility of SCO was to maintain the health and safety of the Cassini spacecraft, and provide for the return of mission and science data.

The SCO was responsible for generating all spacecraft subsystem engineering command inputs and for reviewing all system-level commands for uplink to the spacecraft.

Commands were generated (real-time and sequenced) to perform spacecraft subsystem calibrations and to maintain spacecraft health. Spacecraft engineers also reviewed sequenced and real-time command uploads for engineering correctness and completeness. Maneuver designs, using Navigation inputs, were developed by the SCO subsystems and systems engineers, and the appropriate spacecraft commands were determined to carry out the maneuvers.

Spacecraft subsystem engineering data (real-time and non-real-time) were analyzed, and the health, safety, and performance of the spacecraft were determined by the spacecraft subsystem and system engineers. To carry out this responsibility, spacecraft performance models were developed. These models were software programs and/or hardware models that generated predictions of spacecraft performance and analyzed spacecraft data. The spacecraft system engineers analyzed all spacecraft system data (real-time and non-real-time) to assess spacecraft performance. Investigations were conducted of any spacecraft anomalies, and resolutions were developed to correct them.

Spacecraft attitude/pointing determination and planning was the responsibility of the AACS engineer, who prepared attitude predictions, and analyzed/compared pointing data to the predictions, and provided inputs to science, mission planning, and sequencing/commanding, as required. The SCO developed a suite of analysis tools, which included tools that support calibration, contingency planning, downlink analysis, flight software maintenance, maneuvers, modeling, and the uplink process.

The SCO developed and maintained the ITL, a flight system simulator (testbed, simulator, test lab, etc.) that was used to perform testing (validation) of command sequences prior to transmission to the spacecraft. Spacecraft ITL engineers maintained the flight system simulator and operated it for the mission.

Maintenance of the onboard flight software was required in order to assure proper operation of the spacecraft. The CDS and the AACS engineers were responsible for this activity. This activity involved managing spacecraft flight software maintenance, the generation of flight software memory loads, and the control of all changes to flight programs, including databases.

2.5.7 NAVIGATION

The navigation team was responsible for determining the position and predicted flight path of the spacecraft and correcting that flight path to achieve mission objectives. The navigation process involved a sequence of actions:

1. The acquisition of radiometric tracking and/or optical measurements.

2. The determination of the statistically best estimate of the trajectory based on the tracking and/or optical measurements.

3. The computation of trajectory correction maneuvers (TCMs) to achieve the desired targeting objectives.

In addition, the navigation team performed ongoing planning and analysis activities to ensure that the navigation performance was consistent with the mission and science objectives.

Specific navigation team activities during operations included:

- **Orbit Determination:** The navigation team determined the trajectory and location of the Cassini spacecraft by performing precise measurements of line-of-sight coherent Doppler and range acquired at S- or X-band frequency by using the DSN equipment.
- **Maneuver Design and Analysis:** Many propulsive maneuvers were required to navigate the Cassini spacecraft during the cruise phase (TCMs) and to modify the orbit during the tour phase (orbit trajectory maneuvers). The navigation team designed and verified propulsive maneuvers to modify the spacecraft trajectory and to correct navigation errors in order to achieve the Cassini mission targeting objectives, taking into account the mission and spacecraft constraints. The team monitored and evaluated the maneuver performance in real-time. As part of this process, the team also assessed propellant margin through the end of the mission.
- **Trajectory Analysis:** The navigation team generated the spacecraft trajectory that satisfied mission requirements, based on orbit determination estimates and planned maneuvers. The team updated the trajectory design as needed in response to mission events and science objectives.
- **Optical Navigation:** By using the ISS, the navigation team incorporated optical target-relative navigation measurements into the orbit determination process. The team used these measurements in conjunction with tracking data to support approach navigation and/or orbit maintenance.
- **Navigation Operations Software Maintenance:** The navigation team, in conjunction with the multi-mission navigation team, maintained the navigation software and databases in accordance with flight project requirements. The team responded to software failure reports and change requests.

2.5.8 FACILITY AND PI INSTRUMENTS OPERATIONS

The responsibility for operating the Cassini instruments depended on whether the instrument was a facility instrument or a PI instrument. The facility- and PI-developed instruments are listed in Section 2.4.4. Basically, facility instruments were operated at JPL while PI-developed instruments were operated from the PI's home organization.

Operations responsibilities for the Cassini instrument payload are listed in Table 2.5-1. Figure 2.5-1 depicts the geographical locations for all of the teams responsible for instrument operations. More details of the instrument operations roles and responsibilities are described in Sections 2.5.8.1 and 2.5.8.2.

Table 2.5-1. Distributed operations responsibilities for instruments.

Instrument/Experiment	Responsible Team/	Instrument/Experiment
Optical Remote Sensing Instruments		
Composite Infrared Spectrometer (CIRS)	CIRS Ops Team/ Goddard Space Flight Center (GSFC)	Greenbelt, MD, USA
Imaging Science Subsystem (ISS)	Instrument Ops (IO) Team/ Jet Propulsion Laboratory and Space Science Institute	Pasadena, CA, USA Denver, Colorado, USA
Ultraviolet Imaging Spectrograph (UVIS)	UVIS Ops Team/University of Colorado Boulder	Denver, Colorado, USA
Visible and Infrared Mapping Spectrometer (VIMS)	Instrument Ops (IO) Team/ Jet Propulsion Laboratory and University of Arizona	Pasadena, CA, USA Tucson, AZ, USA
Fields Particles and Waves Instruments		
Cassini Plasma Spectrometer (CAPS)	CAPS Ops Team / Southwest Research Institute (SwRI)	San Antonio, TX, USA
Cassini Dust Analyzer (CDA)	CDA Ops Team/Max Planck Institute	Heidelberg and Stuttgart, Germany
Ion and Neutral Mass Spectrometer (INMS)	INMS Ops Team / Southwest Research Institute (SwRI)	San Antonio, TX, USA
Magnetometer (MAG)	MAG Ops Team/Imperial College	London, England
Magnetosphere Imaging Instrument (MIMI)	MIMI Ops Team / Johns Hopkins University, Applied Physics Laboratory (APL)	Laurel, MD, USA
Radio and Plasma Wave Science Instrument (RPWS)	RPWS Ops Team/ University of Iowa	Iowa City, IO, USA
Microwave Remote Sensing		
Titan Radar Mapper (RADAR)	Instrument Ops (IO) Team/ Jet Propulsion Laboratory	Pasadena, CA, USA
Radio Science Subsystem (RSS)	Instrument Ops (IO) Team/ Jet Propulsion Laboratory	Pasadena, CA, USA

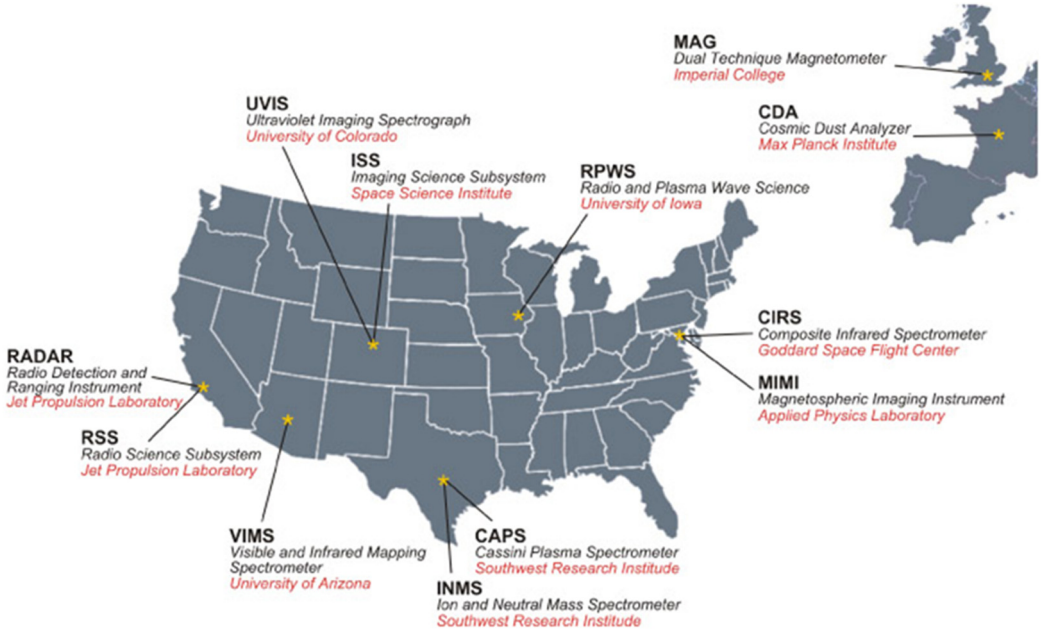

Figure 2.5-1. Geographical location for operations instrument teams.

2.5.8.1 Facility Instrument Operations by the Instrument Operations Team

The operations responsibilities for the three facility instruments (ISS, RADAR, and VIMS) and the RSS investigation were performed by the instrument operations (IO) team at JPL. These operations responsibilities were similar for all instrument, including the PI instrument (see Section 2.5.8.2). These common operations responsibilities are summarized below.

2.5.8.1.1 Facility Instrument (ISS, RADAR, and VIMS) Operations by the IO Team

- Analyzed and assessed the health and safety of the instrument
- Analyzed, predicted, and assessed the performance of the instrument
- Analyzed and predicted instrument resource usage
- Maintained instrument telemetry alarms
- Assessed and resolved instrument anomalies
- Maintained team operations procedures and contingency plans

2.5.8.1.2 Instrument/Science Activity Planning and Command Generation Support by the IO Team

- Participated in the planning of the instrument activities through the SPST
- Generated, verified (constrained check), and validated instrument commands and sequences
  - Generated, verified (constrained check), and validated instrument expanded blocks (IEBs) and instrument non-interactive (or instrument internal) commands
- Generated, verified (constrained check), and validated instrument flight software uploads
- Validated the final instrument command and sequence products via manual review, if required

2.5.8.1.3 Science Data Processing by the IO Team

- Processed instrument raw science data (the processing and generation of facility instrument high-level products were the responsibility of the facility instrument science teams at their home institution)

2.5.8.1.4 Science Data Products Delivery

The delivery of the facility instruments' high-level science data products to the Planetary Data System (PDS) was the responsibility of the facility instruments science teams directed by a corresponding Team Leader. The Team Leaders prepared the high-level science data products at

their home institutions and delivered these products directly to the PDS for permanent archive, except for the RSS. The RSS high-level science data products were generated by the RSS PI science team at its home institution; however, the IO team at JPL prepared and delivered the RSS science data volumes to the PDS for permanent archive.

All of the above roles and responsibilities for the operation of the facility instruments are described in greater detail in Volume 5, under the Uplink Operations Processes and Downlink Operations Processes sections.

2.5.8.2 Principal Investigator Instrument Operations Teams

The PI instrument operations teams were staffed by their corresponding instrument institution and were remotely located at their corresponding institutions. Figure 2.5-1 shows the geographic locations of the instrument institutions. Each PI instrument operations team was responsible for the overall health and safety of their particular instrument. A summary of the common functions performed by the PI instrument operations team during operations is as follows:

2.5.8.2.1 PI Instrument Operations

- Analyzed and assessed the health and safety of the instrument
- Analyzed, predicted, and assessed the performance of the instrument
- Analyzed and predicted instrument resource usage
- Maintained instrument telemetry alarms
- Assessed and resolved instrument anomalies
- Maintained team operations procedures and contingency plans

2.5.8.2.2 Instrument/Science Activity Planning and Command Generation

- Participated in the planning of the instrument activities through the SPST
- Generated, verified (constrained check), and validated instrument commands and sequences
  - Generated, verified (constrained check), and validated IEBs and instrument non-interactive (or instrument internal) commands
- Generated, verified (constrained check), and validated instrument flight software uploads
- Validated the final sequence products via manual review if required

2.5.8.2.3 Science Data Processing

- Processed instrument/science data
- Generated higher-level science data products
- Generated PDS volumes and corresponding labels for all science data products

2.5.8.2.4 Science Data Products Delivery

- Delivered science data products to the PDS for permanent archive

2.5.9 REAL-TIME OPERATIONS TEAM

The real-time operations (RTO) team worked in two functional areas: flight operations and data management. In flight operations, also called mission control, the on-duty Ace† interacted with the DSN, with the multi-mission data services operations team (DSOT), and with other ground-system functions during tracking passes. This constituted the real-time interface between Flight System and Ground System.

The second RTO area was data management. This involved operation of the Telemetry Delivery System (TDS) repositories and cognizance of their content, and creating and maintaining fully documented stores of TLM, MON, and QQC data. (DSN radiometric TRK data acquired under RTO's control was managed and stored separately by the navigation team; RS data was acquired by RSS with RTO's assistance, and stored separately.)

2.5.9.1 RTO Flight Operations Functional Area

Under the flight operations function, the RTO Ops Lead nominally worked dayshifts to provide interface between Aces and the rest of the flight team. Aces worked any time of any day to staff DSN passes (and later, ESA Deep Space Antenna passes), ensuring that there was always a Cassini representative on console when the spacecraft was scheduled to be tracked. Through cross-training, every Ace was also capable of performing the team interface tasks, and the Operations Lead was certified for console work. The Operations Lead developed Ace certification requirements and checklists, and conducted training and certification.

RTO served at the endpoint of the Cassini uplink system, and at the starting point of the Cassini downlink system. At the start of each DSN track, the Ace would verbally brief the station on the latest operational requirements for upcoming activities, and then would monitor both the DSN and the spacecraft while the track progressed, validating the predicted space-link

† "Ace" is the voice-net call sign for the engineer serving as Mission Controller, also called the Flight Controller. The word is not an acronym, but it originated as a reference to a single expert point of contact on the flight project for all real-time interactions, such as for commanding, for decisions about DSN and other ground system configuration activities, problem reporting, and general communications among the project's various science and engineering teams.

performance. On average a track occurred about once a day, and the duration of each track was in the neighborhood of 9 hours plus pre-cal setup time.

Uplink: The Ace radiated CMD data to the spacecraft via the DSN, as authorized per the Command Request Forms, and confirmed spacecraft receipt of the CMD data via TLM. This CMD function came at the end of the long-term processes, largely external to RTO, of sequence development, plus the shorter-term work on subsequences. The Ace also routinely transmitted commands in real-time to reset the spacecraft's fault-protection command-loss timer, and sent other real-time commands as needed. RTO and the SIP lead engineer together exercised great caution to minimize the risks inherent to commanding. RTO coordinated with DSN in real-time to ensure proper reconfiguration when necessary to respond to commanded state changes on the spacecraft, such as for TCMs, OTMs, and other commanded events that caused pointing or telecom configuration changes. RTO also ensured proper radiometric uplink and downlink in service of navigation and radio science requirements.

Downlink and Anomaly Response: RTO managed timely deployment of ancillary files, produced by other teams, which were needed for ground system operation. These included TLM-packet decommutation maps, light-time files, channel parameter table (CPT) files, channel conversion language (CCL) files, spacecraft clock time–spacecraft event time (SCLK-SCET) coefficient files, and Automated Alarm Notification pager files. An important task for the Ace was to keep the TLM red-alarm limit CPT files up-to-date, editing them per user requests, testing and then distributing them throughout the flight team's workstations in coordination with SCO and the science teams.

Naturally, the Ace was often the first flight team member to recognize anomalies in the ground system and the flight system.

Naturally, the Ace was often the first flight team member to recognize anomalies in the ground system and the flight system. The Ace's task was to discriminate between ground or flight system origin, and to take appropriate action under the Anomaly Response Operations Plan (a document which RTO led efforts to keep accurate, usable, and pertinent).

Anomalous conditions may have become evident in many places including the uplink transmitter power, the downlink carrier signal strength, the telemetry-capture performance, TLM and MON channel values, and TLM alarm limit violations. Cassini telemetered thousands of engineering measurements that were limit-checked in the Ground System via the data monitor and display (DMD), and carrying out Cassini's strict policy of maintaining current and meaningful red-alarm limit settings (via CPT edits) ensured the ability to identify and respond to valid flight system anomalies in a timely manner. The Ace documented each anomaly, and resolved it or initiated its resolution within the flight team, and ensured that data continued being loaded to TDSs as soon as possible for access by users. Other parts of the flight team were involved when anomaly resolution required commanding, or for wider procedure or policy changes.

2.5.9.2 RTO Data Management Functional Area

Under the data management function, in coordination with DSOT and the Cassini DGS team, the RTO DMT loaded data to the TDSs, maintained online and off-site data backups and archives, researched and produced reports and explanations of gaps in the data, and interfaced with science teams and DSOT to locate data that various instrument and engineering teams may have had trouble finding. RTO DMT also loaded data to the TDS from archives and backups as required to service some requests, and managed in cases of TDS anomalies, some of which would require extensive rebuilding of the TDS catalogs.

2.5.10 DOWNLINK GROUND SYSTEM TEAM

The Downlink Ground Data System (DGDS) team was responsible for the development and maintenance of the Cassini downlink and data tools. Following is a list of their specific responsibilities:

- Interfaced with the Multi-Mission Ground Data System and Services (MGSS) mission control, data management and accountability, and spacecraft analysis subsystem (MDAS) to develop requirements, resolve problems, and determine integration schedule of core tools
- Interfaced with telemetry, tracking and command (TT&C) subsystem to develop requirements, resolve problems, and determine integration schedule of core tools
- Interfaced with Cassini offices and teams to develop requirements, establish priorities, and determine delivery schedule to the project
- Established and maintained team staffing to meet project commitments
- Oversaw and approved documentation in conjunction with software cognizant engineers
- Provided the tools, training, and resources required for accomplishing development tasks
- Coordinated Cassini use of and compatibility with DSOT
- Maintained ground system compatibility with the telemetry dictionary used for operations
- Maintained Cassini adaptation of multi-mission downlink tools and environment
  - cascat environment
  - Cassini Distributed Object Manager (DOM)
  - DMD customizations
  - CMD customizations
  - ITL telemetry support
  - Administered the Cassini DOM

- Maintained the Cassini downlink, RTO, web tools
  - Rampage
  - Acelog
  - PSG Automation Tool (PAT)
- Managed and performed systems administration of the flight operations, ITL, webnet, Science Operations and Planning Computer (SOPC), and Science Operations (SCIOP) workstations, servers, and networks. Responsible for the oversight of workstation, servers, and network operations, repairs. Responsible for initiation of changes to architectures and design as required, and coordinating implementation with Cassini teams and Office of the Chief Information Officer (OCIO). Maintained spare equipment and logistics support. Managed all maintenance and service contracts, software licenses, and spares.
- Maintained interfaces with external information and technology (IT) entities (MGSS and OCIO).
- Maintained Cassini project compliance with applicable IT security requirements. This included maintaining the Information Technology Security Database (ITSDB) and responding to SPLs (security problem logs). Developed and maintained IT security plans and perimeter access requests (PARs) for the appropriate Cassini systems.

2.5.11 System Engineering and Configuration Management

System engineering (MOS engineering and GDS engineering) ensured that the end-to-end mission operations system was working properly. This included, but it was not limited to, operations documentation, processes, procedures, interfaces, and GDS (ground software and hardware). System engineering was in charge for the following specific responsibilities:

- Ensured that Level-3 (system level, L3) processes were working properly
- Updated L3 processes as needed to factor in lessons learned and experience from the flight team
- Ensured that Level-4 (team level, L4) operations procedures were being followed
- Ensured that L4 teams were maintaining operations procedures and contingency plans properly
- Updated/maintained Flight Operations Plan (FOP), as needed
- Updated/maintained Operational Interface Agreements (OIAs), as needed
- Supported the planning, generation, and execution of verification and validation (V&V) exercises

- Identified and proposed modifications to the GDS (tools and capabilities) needed to successfully support the operations processes and procedures
- Monitored all aspects of the GDS
- Led investigation and resolution of GDS anomalies (incident/surprise/anomaly, ISA)
- Maintained and managed ground software, hardware, and networks consistent with the GDS Software Management Plan
- Coordinated development, testing, integration, and release of GDS upgrades
- Led and managed GDS deliveries
- Assessed GDS change requests
- Ensured proper system and database administration
- Identified improvements to GDS processes and tools
- Ensured that the Software Interface Specifications (SISs) were correct and coordinated any required changes or updates
- Led the update of the VIMS and CIRS thermal models for FRPO

Configuration management (CM) consisted of JPL personnel with MGSS partnership. The CM Engineer was responsible for ensuring that configuration management tasks were properly performed in accordance with the NASA and JPL policies. The CM Engineer had the following specific responsibilities:

- Track, route, close, archive, and report status of change requests
- Run Change Control Board
- Control GDS software baseline
- Audit software installed on project workstations

2.5.12 MISSION OPERATIONS ASSURANCE

Mission operations assurance (MOA) was the responsibility of the Mission Operations Assurance Manager (MOAM). The MOAM was responsible for ensuring that MOA tasks were properly performed in accordance with NASA and JPL policies. The MOAM was responsible for the following specific tasks:

- Anomaly (ISA) management, including criticality rating and team assignment
- Concurrence on ISA closures
- Facilitating anomaly review meetings
- Reviewing operations processes

- Management of project's risk items
- Ensure the existence of adequate and appropriate operations assurance processes that contributed to the success of the project
- Support project staff in recommending/developing solutions to operational problems based on project needs and requirements
- Provide mission assurance interfaces with flight team and remote instrument teams for matters related to mission assurance

2.5.13 DSN Mission Interface

The DSN Mission Interface Manager (MIM) provided the interface between the Cassini mission system and the DSN organization. Also, the DSN MIM was responsible for maintaining and updating the DSN operational interfaces between the Cassini Project and the DSN organization.

2.6 Mission Phases

The Cassini Mission is divided into five major phases, each phase containing several sub-phases. Following are the phases and corresponding sub-phases.

2.6.1 Launch Phase

The Launch Phase spanned the time period between launch (L) and L + 30 days. During this time interval, the spacecraft went through a relatively rapid series of transitions which took it from the launch pad on Earth (see Figures 2.6-1 and 2.6-2) to a Venus-targeted trajectory, then eventually took it to Saturn. Because of the launch environment and the operation of the spacecraft for the first time, the events in the launch phase are geared primarily towards characterizing the spacecraft's behavior in the space environment, performing essential engineering checkouts and calibrations, and preparing the spacecraft for its first main engine maneuver, which occurred at L + 25 days.

The first 30 days of the mission were divided into two sub-phases: the launch sequence sub-phase and the sub-phase containing the first TCM, called the TCM-1 sub-phase. The launch sequence sub-phase was autonomous, lasting two days, and covered the interaction between the spacecraft and launch vehicle through separation, the powering-on of select heaters, and the acquisition of the spacecraft's signal by the DSN. The TCM-1 sub-phase began at L + 2 days and addressed the events that led up to and surrounded the first TCM and included spacecraft system health checks and a limited number of maintenance activities.

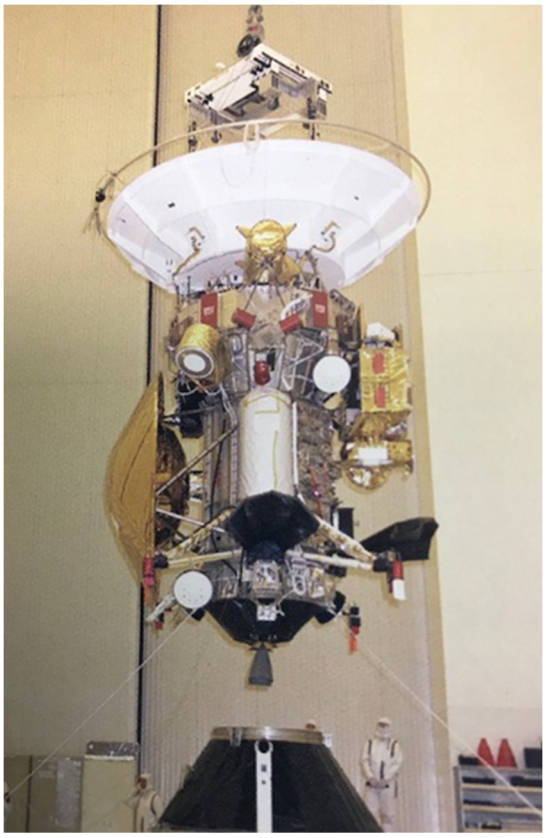

Figure 2.6-1. The Cassini-Huygens installed on the launch adapter.

Figure 2.6-2. Cassini's launch via a Titan IVB vehicle.

2.6.1.1 Launch Sequence Sub-phase

Cassini had a 30-day nominal launch window, extending between October 6 and November 4, 1997, that provided for an arrival date at Saturn of July 1, 2004. If the spacecraft had launched after November 4, Cassini would have missed its ideal arrival date at Saturn. The spacecraft could still have launched into its primary trajectory as late as November 13, but in that case, its arrival date at Saturn would have been pushed back as late as June 25, 2005—practically a year later than planned.

After a first attempt was postponed on October 13, Cassini successfully lifted off from the Cape Canaveral Air Station complex 40 on October 15, 1997 at 08:55 UTC. The solid rocket motors burned from liftoff to separation at 2 minutes, 23 seconds at an altitude of 68,000 meters. Stage 1 ignition began at 2 minutes, 11 seconds at an altitude of 59,000 meters, and Stage 2 ignition (and Stage 1 separation) occurred at 5 minutes, 23 seconds after liftoff at 167,000 meters. During the first 3 minutes and 27 seconds of flight, the payload fairing shrouded the spacecraft protecting it from direct solar illumination.

The Centaur upper stage separated from the launch vehicle at 9 minutes, 13 seconds at 200,000 meters. The first Centaur burn began at 9 minutes, 13 seconds and lasted approximately 2 minutes. This burn placed the Cassini spacecraft into an elliptical, 170-kilometer by 445-kilometer parking orbit with an inclination of about 30°. Cassini's orbit around Earth was designed to provide an orbital lifetime of about 20 days in case the Centaur failed to have a successful second burn and injection. After 17 minutes in parking orbit, the Centaur fired again and launched Cassini toward Venus en route to Saturn. The injection launch energy, or C3, was 16.6 km^2 per $second^2$.

Cassini initiated and completed its first critical on-board subsequence (called TEMP) during parking orbit coast, and actually started the onboard launch sequence in addition to turning on spacecraft heaters.

Cassini's second critical subsequence (called PREP), 30 seconds after the second Centaur burn, prepared the spacecraft for separation from the Centaur. PREP opened the prime thruster branch latch valve, turned on the pyro switching units, and turned on the spacecraft's X-band exciter and amplifiers for the low-gain antenna for acquisition by the DSN's Canberra station.

The third critical subsequence (called SEP) was initiated following the worst-case completion time of PREP (6 minutes after the second Centaur burn). At this point, the spacecraft was separated from the Centaur.

Immediately after separation, the spacecraft's AACS took control and pointed the high-gain antenna toward the Sun to achieve a thermally safe attitude. X-band uplink and downlink was established, the RPWS Langmuir probe was deployed via pyro, instrument replacement heaters and main engine oxidizer valve heaters were turned on, and the SRU, ISS, and VIMS decontaminations were started.

The Centaur, after separation from the spacecraft, executed a collision and contamination avoidance maneuver (C/CAM) that prevented it from impacting either Venus or the spacecraft. This burn occurred approximately 20 minutes after separation to allow the spacecraft and the Centaur to drift apart such that the plume from the Centaur RCS firing would not impact the spacecraft. Approximately 8 minutes after C/CAM, the Centaur executed a blowdown maneuver to expel unused propellant and to further reduce the probability of impact with the spacecraft or Venus. About an hour after separation, the Centaur depleted its hydrazine from the RCS. The Centaur mission ended approximately 87 minutes after separation.

Figure 2.6-3 illustrates the main events executed during the launch sequence.

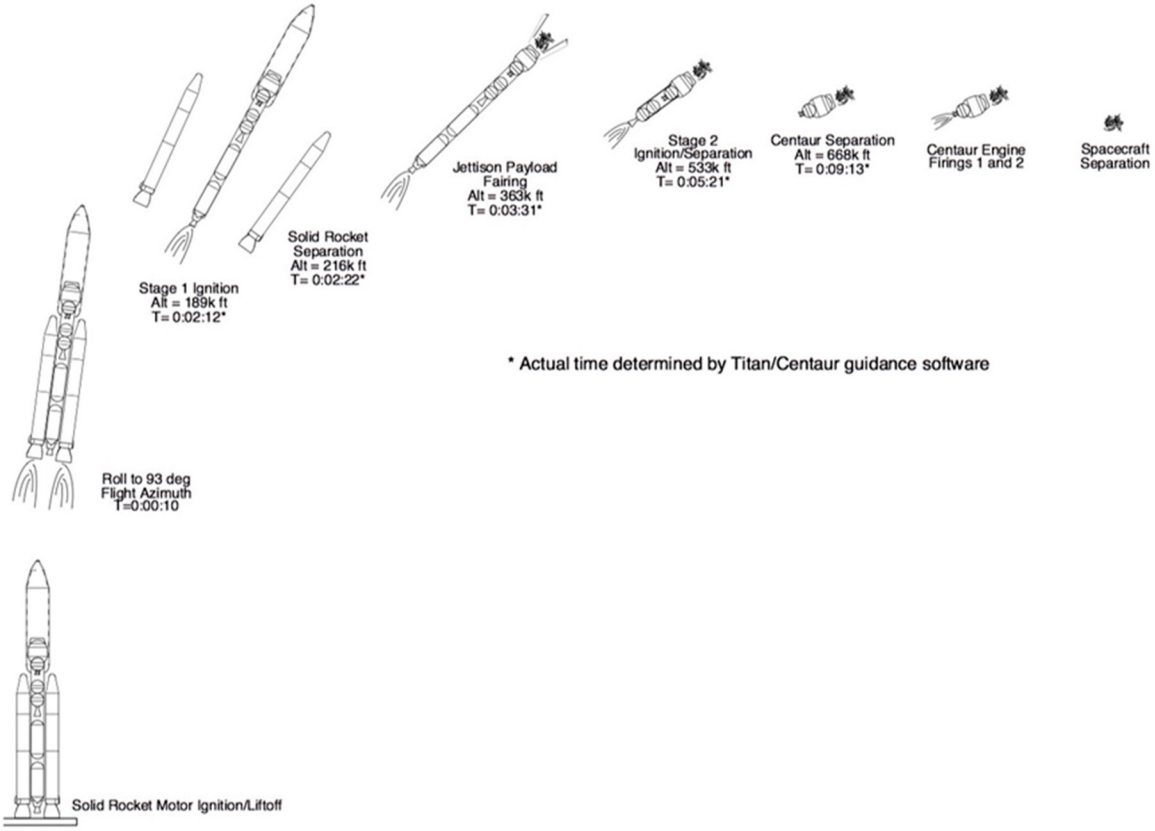

Figure 2.6-3. The Cassini-Huygens launch events.

2.6.1.2 TCM-1 Sub-phase

The TCM-1 sub-phase began on day 291 (October 18) of the mission and was comprised of four 1-week sequences. During the beginning of the TCM-1 sub-phase, the spacecraft was in a relatively inactive state. Ground controllers used telemetry downlinked from the spacecraft to make an initial characterization of the spacecraft and to assess whether its various subsystems survived the launch environment. Controllers also began deployment, decontamination, tank heating, and AACS checkout activities.

During most of the TCM-1 sub-phase, the spacecraft remained Sun-pointed (i.e., with its high-gain antenna aimed at the Sun). The only event requiring the spacecraft to go off Sun-point was the TCM itself, when Cassini's main engine had to be pointed in a specific orientation that prevented Sun-point (CK).

PMS Activities: Before the first trajectory correction maneuver only, the fuel and oxidizer tanks were heated in order to avoid an irreversible overpressure in the propellant lines. If the tanks fully pressurized before the spacecraft passed through the peak temperature regime, when entering the maximum thermal environment, the tank pressure could climb without a way to bring it back down, possibly causing an overpressure.

Each tank had one heater and one redundant backup heater. The oxidizer tank heater was turned on at approximately L + 8 hours. Since the fuel tank requires less heating time, the fuel tank heater was turned on a few days later. The tank heating was interrupted for probe checkout and periodic instrument maintenance due to power constraints. Both heaters were turned off approximately 2 days before TCM-1.

After opening the main engine cover, the spacecraft vented, primed, and pressurized the bipropellant lines (REA-A only) between one and two days before TCM-1. Venting removes the gas between the latch valves and the engines, creating a vacuum in the propellant lines. Priming fills these lines with propellant. The tanks then pressurized at a temperature higher than the peak temperature expected en route to Venus. Each step takes only seconds to complete, but a real-time "Go" command was needed from controllers on Earth (CK) before moving on to the next step, to ensure that the previous step was successful. After pressurizing, the valves were left open until approximately 2 days after TCM-1.

AACS Activities: There was a window to update AACS parameters in real-time at L + 2 days. An IRU characterization, engine gimbal assembly (EGA) exercise, and accelerometer calibration were scheduled during the TCM-1 sub-phase in order to ensure functionality before TCM-1.

TCM-1 and Thermal Characterization: TCM-1 was an Earth injection clean-up maneuver at L + 25 days. The spacecraft executed TCM-1 with its main engine for a ΔV magnitude of 2.8 meters per second. The burn sequence included holding the spacecraft off-Sun after burn completion to allow the spacecraft heating to be characterized in a relatively benign environment. The main engine cover was opened 48 hours before the start of the burn, and closed during the TCM-1 minisequence several hours after burn completion. Because of the high data-rate capability at the beginning of the trajectory, it took less than one DSN pass to downlink the data from TCM-1 using the playback (PB) and real-time engineering (RTE) 948 data mode.

Regulator Leak Problem: As the initial pressurization was being performed just prior to TCM-1, the primary regulator showed an unexpectedly high leak rate of 1,700 standard cubic centimeters per minute (sccm). The specified rate for leakage from this regulator was supposed to be 0.6 sccm or less. In response, ground controllers closed high-pressure latch valve (LV) 10. The incident was addressed in ISA Z44505.

While regulator leakage is a well-known phenomenon, the magnitude of this leak was surprising, especially given the leakage characteristics demonstrated by pressure regulator (PR) 1 during ground testing. Analysis demonstrated that particulate contamination could very easily explain the observed regulator leakage, since the requisite particle size that causes a 1,700 sccm leak is two orders of magnitude smaller than the filter capacity between pyro valve (PV) 1 and PR-1. That is, a particle that just fits and passes through the filter upstream of PR-1 could cause a leak a hundred times larger than the leak observed at initial pressurization. Regardless, analysts recommended that the Cassini Mission continue to use PR-1 unless the leakage had reached 20,000 sccm.

… , a particle that just fits and passes through the filter upstream of PR-1 could cause a leak a hundred times larger than the leak observed at initial pressurization.

Solid-State Recorder: There were SSR pointer resets scheduled for L + 18 and L + 25 days. The primary SSR was switched from SSR-A to SSR-B at L + 18 days, just before the scheduled pointer reset. At L + 29 days, the redundant SSR was turned off.

ISS and VIMS Decontaminations: The spacecraft powered on decontamination heaters for these instruments in order to "boil off" any contaminants deposited on their optics or radiators as a result of the launch environment. VIMS and ISS Level-1 decontaminations began during the launch sequence sub-phase. ISS decontamination was increased to Level-2 at the beginning of C1 (L + 3 days). The VIMS high-power decontamination lasted 150 days. ISS decontamination was reduced to Level-1 and the VIMS infrared (IR) optics heaters were paused for periodic instrument maintenance, probe checkout, and TCM-1. The VIMS visible optics heater were also paused for the periodic instrument maintenance. Level-2 ISS decontamination concluded after the end of the TCM-1 sub-phase, when the decontamination had reached a cumulative 30 days.

The spacecraft executed several instrument cover deployments, antenna deployments, and latch releases during the first 30 days after launch. These included MIMI launch latch release, CAPS launch latch release, CIRS launch latch release, CDA cover jettison, MIMI cover releases, and UVIS membrane puncture. There was also a periodic instrument maintenance scheduled for L + 12 days. However, the Ka-band traveling wave tube amplifier's helix current maintenance could not occur before L + 4 months and was excluded from this first maintenance activity.

The Huygens probe team also requested an early checkout shortly after launch to take advantage of the high downlink data rates. The first probe checkout was scheduled for L + 8 days. This was the earliest time allowable considering post-launch cool-down inside the probe, while also allowing room for subsequent contingency actions that may have been necessary while the downlink rate was still up at 24.885 kilobits per second (until approximately L + 12 days). The checkout provided post-launch verification for all subsystems and experiments, and was of particular importance for the GCMS by pumping out any contaminants introduced during launch.

2.6.2 CRUISE OPERATIONS PHASE

2.6.2.1 Inner Cruise Phase

The inner cruise phase consisted of three sub-phases: Venus-1, instrument checkout, and Venus-2–Earth. Activities accomplished in each sub-phase are described in following subsections.

The inner cruise phase spanned the time period from November 14, 1997 through November 7, 1999. During most of this phase, the spacecraft remained Sun-pointed because it was so close to the Sun, and therefore telecommunications used the low data-rate low-gain antennas. The downlink capability of the low-gain antennas at large spacecraft–Earth ranges was very limited.

Figure 2.6-4 shows the timeline of events for the inner cruise phase. Between L + 30 days and L + 150 days the downlink data rate varied between 20 and 948 bits per second. During this 4-month period, the spacecraft performed routine maintenance activities and engineering calibrations, which enabled the Mission and Science Operations Office to progressively improve their understanding of the spacecraft's health and capabilities.

Routine maintenance was limited to engineering subsystems and instrument maintenance. On some days during inner cruise, the downlink data-rate capability dropped below 40 bps for a

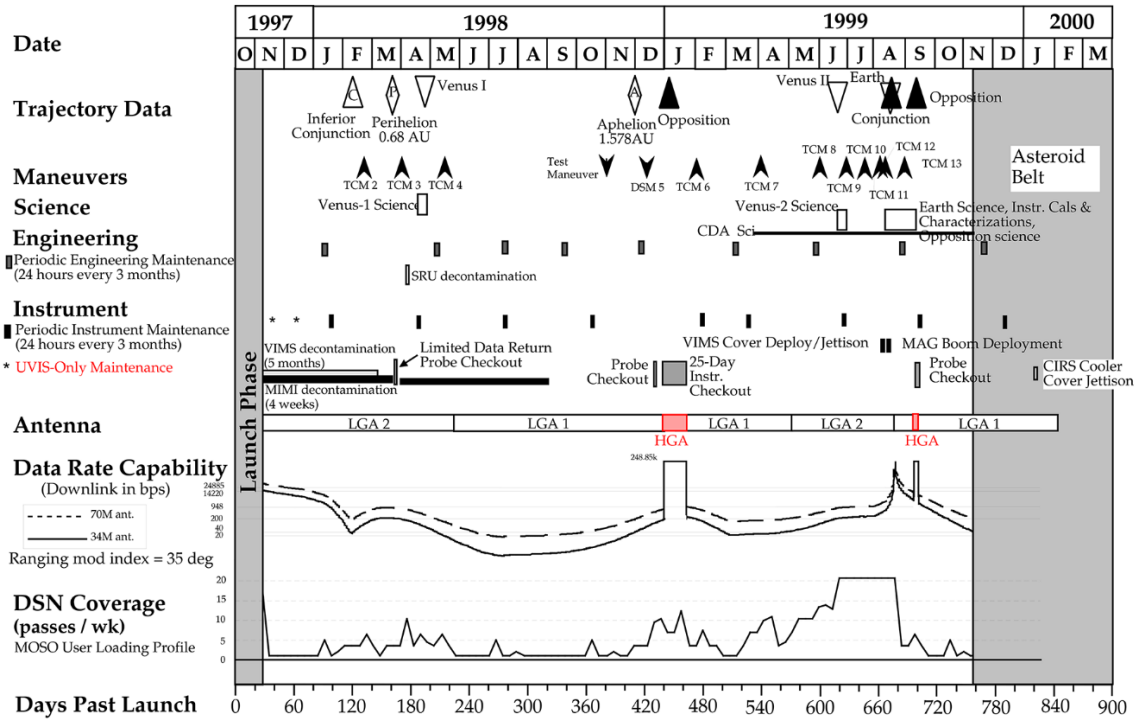

Figure 2.6-4. Cassini Inner Cruise Phase.

short period of time, even with ranging turned off. So during those periods, controllers on the ground avoided spacecraft activities generating large amounts of data.

Beginning on December 28, 1998, the spacecraft approached opposition and pointed its high-gain antenna towards Earth for 25 days and kept the probe equipment temperature within the required range. This provided a high data-rate window in which checkout activities were accomplished. Off-Sun pointing greater than 2.5° was permitted for this 25-day period.

The DSN coverage shown in Figure 2.6-4 reflects the DSN tracking during the inner cruise phase. A detailed description of the project's request to the DSN can be found in the Program Service Level Agreement (PSLA). The number of passes requested per week satisfied navigation radiometric data requirements and provided telemetry visibility during periods of spacecraft activities requiring ground intervention, such as maneuvers or planetary flybys. During the inner cruise phase, Cassini utilized 34-meter DSN coverage. (The 70-meter DSN stations were not available to uplink X-band until the year 2000. X-band uplink is required for 2-way navigation tracking data.)

The transitions from LGA-1 to LGA-2 are based on which antenna has the highest gain for a particular geometry. These transitions occurred at Sun–Spacecraft–Earth (SPE) angles of approximately 44°; when this angle was less than 44°, LGA-1 had the higher gain, and when the angle was at least 44°, LGA-2 provided the higher downlink capability.

During most of the inner cruise phase, the spacecraft remained Sun-pointed and downlinked telemetry via the low-gain antennas. The engineering activities onboard the spacecraft were geared towards maintenance and calibration of the various engineering subsystems, as well as providing support for the trajectory course maneuvers and the deep space maneuver executed during the phase.

Probe checkouts (PCOs) were required about every six months to exercise the probe's internal systems to maintain their health. PCOs are usually accomplished with a 70-meter antenna for downlink to use their high-rate probe checkout telemetry mode, or when circumstances permit, the high-gain antenna.

PCO-1 was done on October 23, 1997, when the spacecraft was still relatively close to Earth and was able to support the high-data-rate downlink on a 34-meter antenna. PCO-2 had no conveniently close high-data-rate period to allow for real-time downlink. ESA agreed to a compromise required downlink of about 40 percent of the data from this checkout. Fortunately, before the Venus-1 flyby, some 70-meter coverage was available, permitting the orbiter to transmit data using PB&RTE-948 data mode for periods at high elevation. PCO-2 was carried on March 27, 1998.

The mission used the January 1999 opposition period for the high downlink of PCO-3. Cassini was able to be Earth-pointed near opposition, so it could use the spacecraft's high-gain antenna. PCO-3 was carried out on December 22, 1998. However, since the spacecraft was Earth-pointed, and the probe was receiving some sunlight, the checkout occurred six days prior to the start of Earth-point to allow time for probe equipment to cool down after the checkout. Therefore, PCO-3

did not return the checkout data in real-time. High data rates during the ICO period allowed rapid playback of the probe data, so the full data set was returned during the first day of the ICO period.

The mission executed PCO-4 just after the Earth flyby, nine months after PCO-3, when the high-gain antenna was available for a limited period near opposition. This checkout occurred on September 15, 1999. Extensive activities before and during the flyby related to the MAG boom deployment and calibration (see the Earth flyby description later in this section) made PCO-4 impractical to be done until the flyby was completed.

2.6.2.2 Venus-1 Flyby Sub-phase

The Venus-1 sub-phase started lasted from November 14, 1997 through September 13, 1998, and encompassed sequences C5 through C9. During this period, the Cassini spacecraft performed two TCMs (one other TCM was cancelled), one planetary swing-by, and three switches between LGA-2 and LGA-1. Most of the period was dedicated to engineering and instrument maintenance activities.

Cassini's encountered Venus for the first time on April 26, 1998 (see Figure 2.6-5). The spacecraft approached Venus from a sunward direction, and made closest approach just after entering Venus's shadow for a period of about 15 minutes. At closest approach, the spacecraft was 284 km from Venus, with a velocity relative to the planet of about 11.8 km per second. The spacecraft was occulted from the Earth for about 2 hours during the flyby. The Earth occultation zone started about 15 minutes after the spacecraft left the Sun occultation zone. The navigation team managed trajectory accuracy for the Venus flyby by using two trajectory correction maneuvers, 60 and 20 days before closest approach, along with a cleanup maneuver 20 days after the flyby.

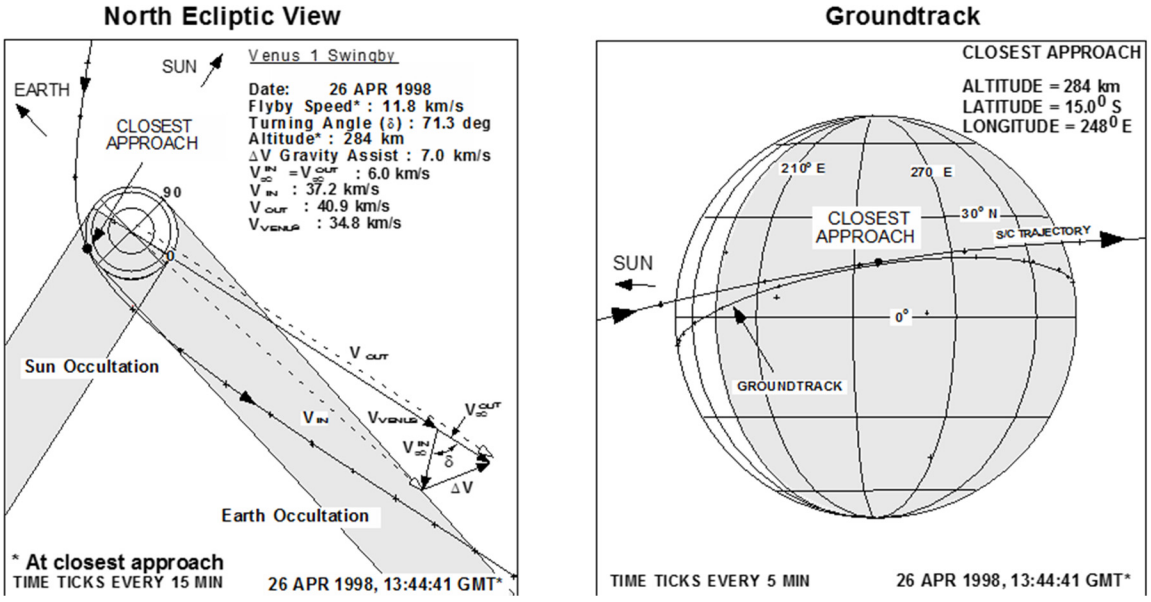

Figure 2.6-5. Venus-1 flyby.

DSN requirements for the Venus-1 flyby consisted of one pass per day on approach, beginning 90 days before the Venus-1 flyby, followed by continuous coverage during the five days around the flyby. Continuous coverage was defined as no gaps greater than 8 hours (Earth Swing-by (ESB) requirement 418-1D(k)in Project Policies document). Coverage was reduced to one pass per day for the five days following the flyby.

Instrument Checkout Sub-phase

The instrument checkout sub-phase lasted from September 14, 1998 through March 14, 1999. The sub-phase consisted of sequences C10–C13 and is characterized by the January 9, 1999 opposition. Because opposition nearly aligned the Earth and Sun (from Cassini's point of view), the spacecraft used the high-gain antenna as both a sunshade and as its downlink antenna, which provided a high data rate for checkout activities. The spacecraft began Earth-point on December 28, 1998, as the spacecraft approached opposition. Cassini kept its high-gain antenna towards Earth for a period of 25 days and kept the probe equipment temperature within the required range. Off-Sun pointing greater than 2.5° was permitted.

All instrument teams scheduled checkout activities for their instruments within that 25-day period centered on opposition. It was the first opportunity since launch to exercise most of the instruments and check their status beyond routine instrument maintenance. One of the tests repeated the "quiet test" performed during assembly test and launch operations, which allowed instruments to monitor other instruments as they turned on and off. This provided valuable insight into how to integrate science observations during the Saturn tour.

During the instrument checkout activities, the spacecraft autonomously went into a safe state due to a slow z-axis turn to keep the Sun in the X-axis direction during opposition, which caused star position errors. These errors caused AACS fault protection to call spacecraft safing. Most of the instrument checkout activities were able to be rescheduled after a 10-day safing period. Those not completed were rescheduled for the ICO-2 sub-phase.

2.6.2.3 Venus-2–Earth Sub-phase

The Venus-2–Earth sub-phase started on March 15, 1999, 45 days prior to the second Venus flyby, and continued through November 7, 1999, or Earth + 82 days. The sub-phase encompassed sequences C13–C16. The period included seven scheduled TCMs, two planetary swing-bys, and 25 science activities in addition to normal engineering activities. Figure 2.6-6 shows the Venus-2–Earth timeline.

At the beginning of the Venus-2–Earth sub-phase, the spacecraft was Sun-pointed and communicating through LGA-2. On approach to the Venus-2 flyby, the mission was allocated one DSN pass per day. The spacecraft executed TCMs 37 days before the flyby (TCM-7) and 14 days before the flyby (TCM-8). In support of the flyby, the DSN coverage increased to three passes per day.

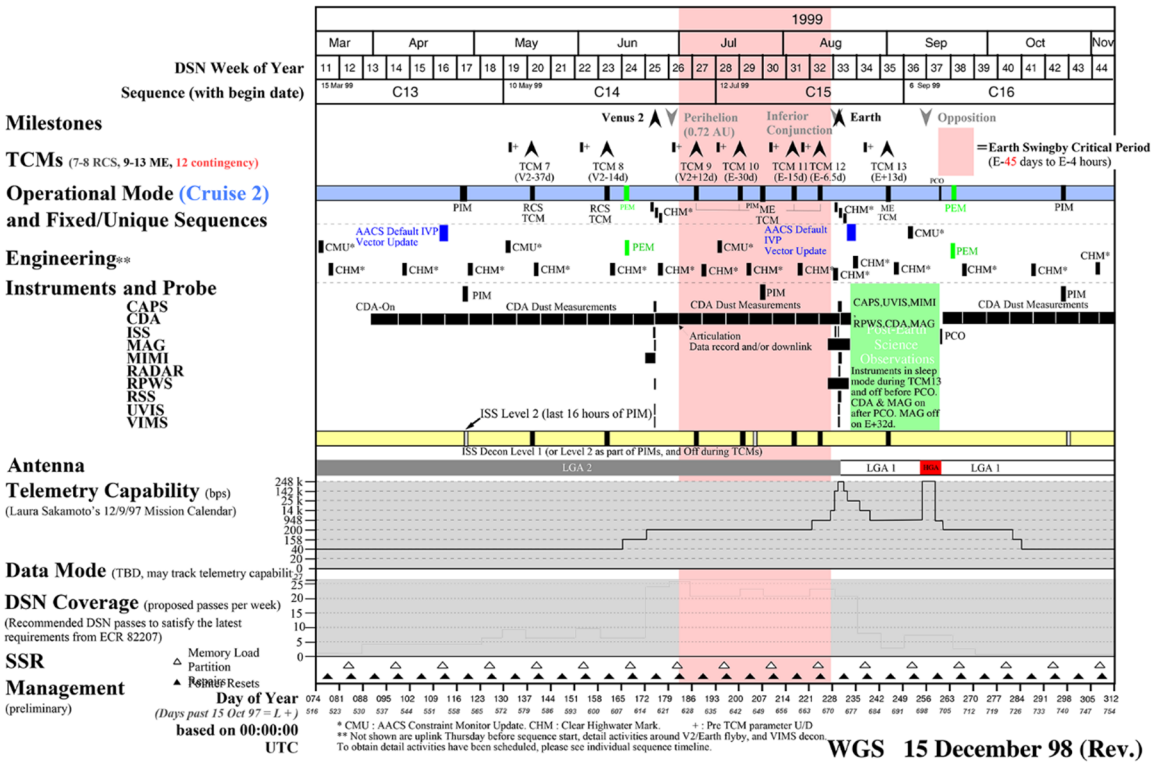

Figure 2.6-6. Cassini Venus-2–Earth Sub-phase Timeline: C13 through C16 sequences.

After perihelion, and 12 days after the Venus flyby, the spacecraft executed the first Earth-targeting maneuver (TCM-9), and then three more pre-Earth maneuvers to ensure a successful Earth flyby. Cassini also performed a post-Earth cleanup maneuver 13 days after the Earth flyby. The DSN coverage-demands then decreased until the spacecraft was switched to the high-gain antenna in February 2000.

Opposition occurred 26 days after the Earth flyby, again presenting an opportunity to use the high-gain antenna for both a sunshade and communication with Earth. For four days the spacecraft was pointed to Earth and stayed within 2.5° of the Sun. Five instruments planned observations as Cassini passed through Earth's magnetotail.

During this sub-phase, about two-dozen activities involving maintenance, calibration, checkout, and science observations were carried out, using all of the Cassini instruments except INMS and CIRS. These activities are summarized in Table 2.6-1.

The first flyby of this sub-phase was the second flyby of Venus (see Figure 2.6-7). This flyby was an energy-increasing (with respect to the Sun) gravity-assist that changed the trajectory to meet Earth about 55 days later. The encounter, along with the Earth flyby, provided the spacecraft with the heliocentric energy to reach Jupiter in late 2000. A timeline for Venus-2 science activities is shown in Figure 2.6-9.

Closest approach occurred by the time the spacecraft left the Earth occultation zone. This occultation lasted approximately 15 minutes. At closest approach, the spacecraft was 603 km from Venus, with a Venus-relative velocity of 13.6 km per second. The spacecraft performed targeting maneuvers at 140, 37, and 14 days before closest approach, and a cleanup maneuver 12 days after the flyby. For the Venus-2 flyby, the spacecraft required one pass with the DSN every two days beginning 90 days before the flyby, plus one pass per day from 50 days before the flyby until three days before the flyby. Then the DSN provided continuous coverage from two days preceding the Venus flyby until two days following the flyby.

Table 2.6-1. Earth spacecraft activities.

Activity	Instr.	Description	Observation Timing (duration usu. less than instrument-on time)
Near Venus-2			
CAPS Observations	CAPS	Characterize interaction of Venus with Solar Wind	2 hrs near C/A
ISS Venus-2 Observations	ISS	Flat-field calib. for ISS WAC and NAC	10 minutes near C/A
Venus-2 MAG Field	MAG	Measure magnetic field	4 hrs centered on C/A
MIMI Venus-2	MIMI	Science obs.; UV sensitivity calib.	4 hrs centered on C/A
RPWS Venus-2 Science	RPWS	Measure plasma waves and search for lightning	At least 2 hrs, beginning 1 hr + 15 min. before C/A
UVIS Venus-2 Activity	UVIS	Measure Venus airglow; determine thermosphere time variation	30 min. near Venus 2
VIMS Observations	VIMS	Map tropospheric motion and night side of Venus	23 min., starting 20 min. prior to boresight viewing the Venus terminator
Venus 2 – ESB			
CDA Activity	CDA	Continuous interplanetary dust measurements	Continuously after Venus 2 to ESB
Near ESB			
CAPS Calibration	CAPS	Calibrate spectra and take data	> = 13 hrs between 3–10 Earth radii
MAG Boom Deployment	MAG	Deploy MAG boom	After Sun range > 0.97 AU (about 5 days before ESB) and before ESB
MAG Calibration	MAG	Calibrate MAG's alignment	From MAG activation for boom deployment until 14.22 kps downlink no longer possible
MIMI Earth Swing-by	MIMI	Calibrate sensors and take data	10 hrs centered on C/A
Radar Operation	RADAR	Transmit and receive pulses for closed-loop test of radar	~30 min of data acquisition, centered around Earth occultation of Sun, following C/A, maximized for ranges < = 40,000 km
RPWS Validation and Testing	RPWS	Validate capability to determine propagation characteristics of plasma waves; test direction-finding capability	> = 13 days + 2 hrs, beginning 2 hrs before C/A
Earth Flyby Trajectory Determination	RSS	Search for anomalous trajectory perturbation by determining pre- and post-flyby trajectory	DSN tracking as continuously as possible from encounter − 10 hrs to encounter + 10 hrs
VIMS Covers Jettison and Deployment	VIMS	Jettison of VIMS IR channel radiator cover; deployment of VIMS IR channel optics cover	After final TCM prior to ESB, prior to MAG boom deploy, and at > 2 days prior to last outbound Earth orbit crossing

Table 2.6-1. Earth spacecraft activities.

Activity	Instr.	Description	Observation Timing (duration usu. less than instrument-on time)
Near ESB; using Moon			
ISS Lunar Calibration	ISS	Image the Moon for several calibrations; study regional compositional differences on Moon	40 min near C/A to Moon, dictated by pointing restrictions
UVIS Characterization	UVIS	Characterize scattered light w/ EUV and FUV; characterize HDAC sensitivity	30 min, beginning when Moon enters the UVIS slit
VIMS Calibration	VIMS	Calibrations and science data using the Moon	1.5 hrs beginning ~2 hrs before C/A, and 2.0 hrs beginning ~1 hrs after C/A
After ESB			
CAPS Earth Observation	CAPS	Observe geomagnetic tail and interstellar particles	~5-day high-gain antenna-to-Earth period centered on opposition
CDA Dust Measurements	CDA	Continuous science dust measurements	29 days, from ESB to high-gain antenna-to-Earth period*
MAG Earth-Extended-Tail Operations	MAG	Measurements of the magnetic field in Earth's magnetotail	29 days, from ESB to high-gain antenna-to-Earth period*
MIMI Earth Magnetotail	MIMI	Calibrate LEMMS, CHEMS, and INCA; magnetotail measurements	29 days, from ESB to high-gain antenna-to-Earth period*
RPWS Magnetotail Observations	RPWS	Look for signatures of the distant geomagnetic tail	29 days, from ESB to high-gain antenna-to-Earth period*
UVIS Observations	UVIS	UV measurements of the geocoronal H tail; measurements of Lyman β, α, and He 584	29 days, from ESB to high-gain antenna-to-Earth period*

* in sleep mode for TCM-13

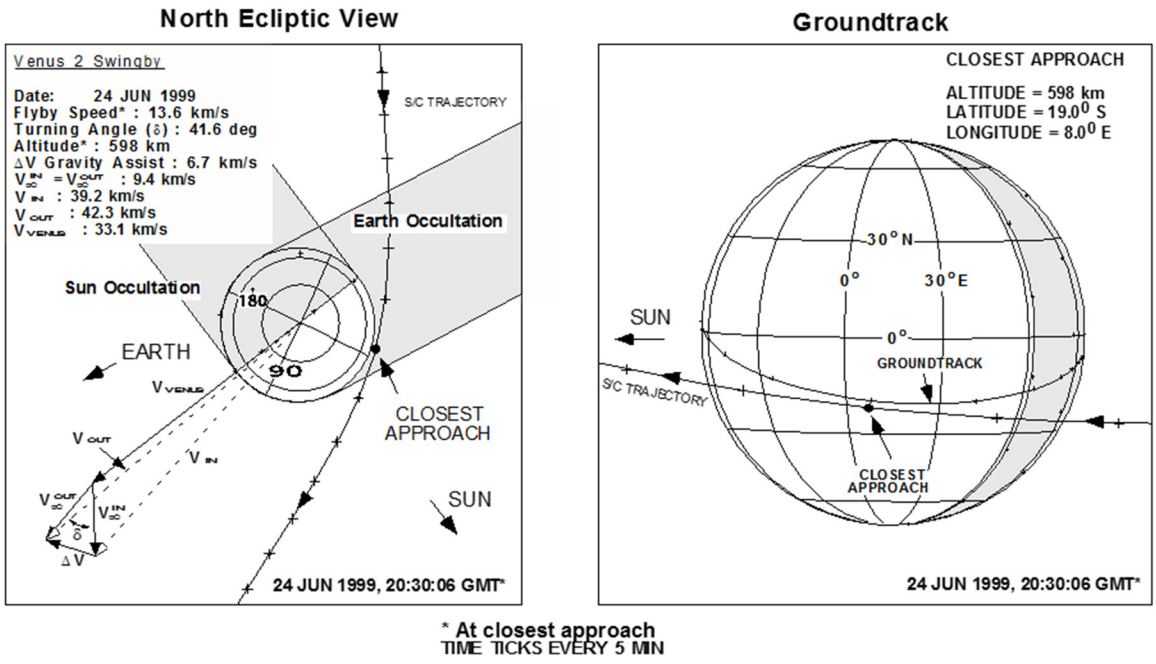

Figure 2.6-7. Venus 2 flyby.

Cassini performed its Earth flyby on August 18, 1999, 55 days after the Venus-2 flyby (see Figure 2.6-8). The spacecraft approached the Earth approximately from the direction of the Sun, and closest approach occurred immediately after the spacecraft entered the Sun occultation zone. The occultation lasted approximately 30 minutes. Cassini's altitude at closest approach to Earth was 1,175 km, with an Earth-relative velocity of 19.0 km per second.

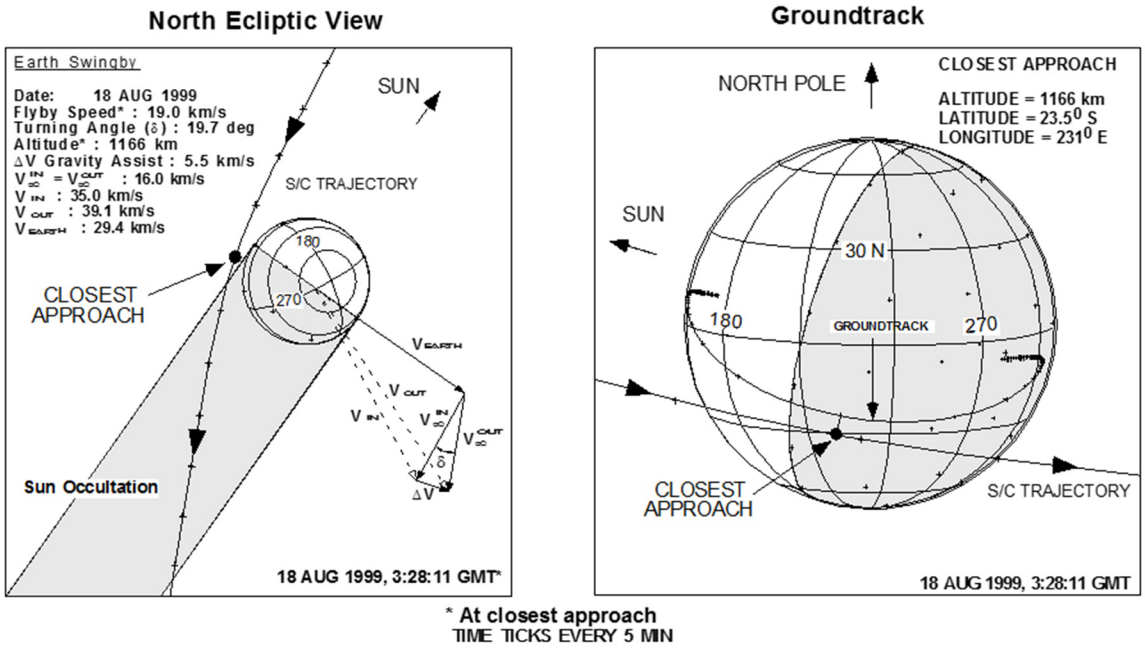

Figure 2.6-8. Earth flyby.

Preceding the Earth flyby, the spacecraft performed four TCMs at 43, 30, 15, and 6.5 days before closest approach. Cassini also had a cleanup maneuver 13 days after the Earth flyby. The DSN provided continuous coverage from the Venus 2 flyby through the Earth flyby. One week after the Earth flyby, that coverage dropped to one pass every two days. A timeline for Earth science activities between Venus and Earth is shown in Figure 2.6-9. The post-Earth science activities through opposition are shown in Figure 2.6-10.

2.6.2.3.1 Earth Swing-by Considerations

The Cassini Project was required to assure that an inadvertent reentry of the spacecraft at Earth be next to impossible (mean probability less than one in a million). As a result, constraints were placed on all project elements, including the mission.

The mission constraints fell mostly in the Venus-2–Earth leg. First, the trajectory design over the launch period was constrained to Earth swing-by altitudes no lower than about 800 km.

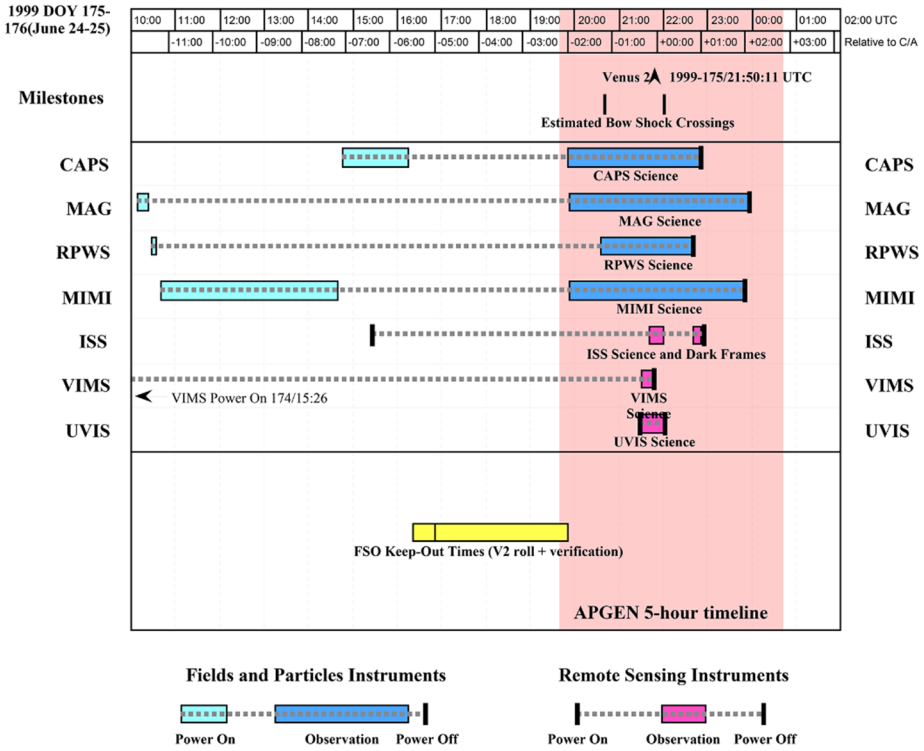

Figure 2.6-9. Cassini Venus-2 Science Timeline (C14 Sequence), Time Frame = 16 hours.

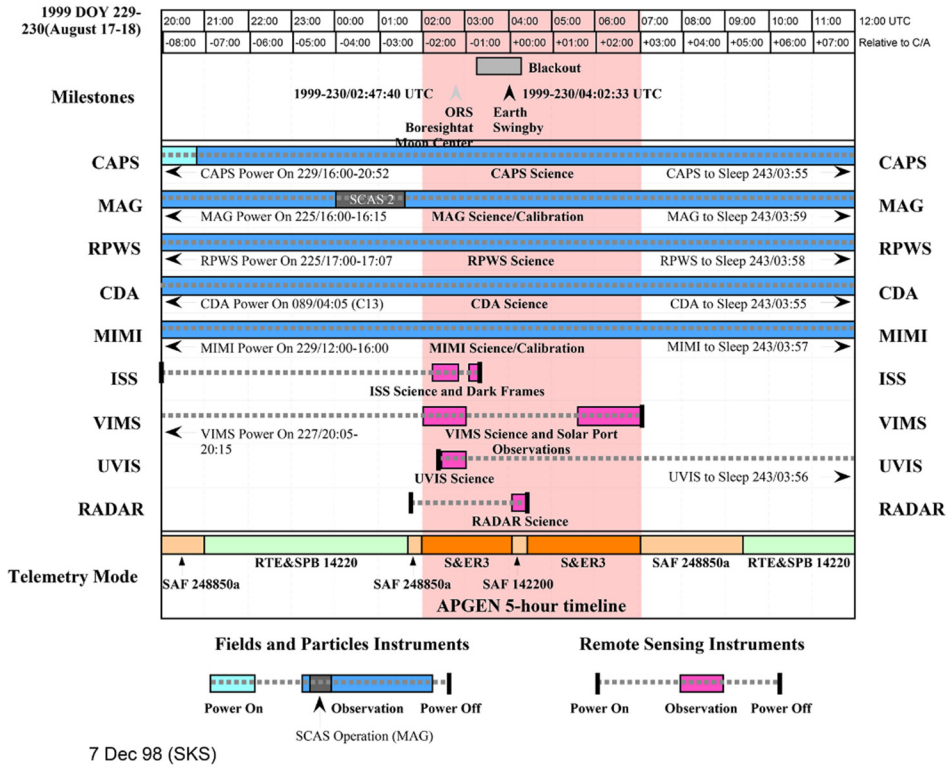

Figure 2.6-10. Cassini Earth Swing-by Science Timeline (C15 Sequence), Time Frame = 16 hours.

Second, the bipropellant system needed to be in blowdown mode for the leg, with no pyro events or any other propulsion activities not needed for TCMs or maintenance of a Sun-pointed attitude between maneuvers.

Third, the orientation of the spacecraft was constrained during the leg to roll the Huygens probe to the ecliptic in the leading direction of the heliocentric trajectory (the high-gain antenna remained Sun-pointed). That attitude was intended to shield some parts of the spacecraft from micrometeoroids, and was compatible with maintaining communications with the spacecraft through LGA-2, which points in the same roll direction as the probe.

Fourth, the spacecraft was required to be tracked continuously to rapidly detect any deviation from the desired course so that corrective actions could be taken if needed.

Fifth, for the final maneuver before the Earth swing-by, ground controllers had to uplink Cassini's magnitude and direction information (parameters) about 24 hours before the maneuver. And then Cassini had to zero out that information from the sequence immediately after the maneuver to protect against inadvertently repeating the maneuver.

The trajectory of this leg was biased away from the Earth aim point until the last 6.5 days. The most important effect of the biasing was to keep the ΔV magnitude required to impact the Earth greater than 1.6 meters per second over the entire leg, which nullified the effect of several small ΔV failure modes. The biasing strategy is detailed in the Earth Swing-by Plan and the Navigation Plan, and was crucial to meeting the Earth swing-by requirement.

The Venus-2–Earth portion of cruise contained not only demanding navigation coverage, but some of the worst conditions for telemetry as well. Continuous DSN coverage was required throughout the Venus-2–Earth leg. From the beginning of the sub-phase through Earth closest approach, the spacecraft used LGA-2. After the Earth flyby, the SPE angle dropped to low values again and the spacecraft used LGA-1 until the thermal constraints allowed the high-gain antenna to be used in February 2000. During the low-gain antenna coverage, ground controllers maintained an uplink/commanding bit-rate of at least 31.25 bps.

The spacecraft downlinked telemetry from each trajectory correction maneuver and flyby. Telemetry coverage for the Earth magnetotail passage, leading up to opposition, required several additional passes since the 14.22 kilobits per second capability was no longer available.

2.6.2.3.2 Mag Boom Deployment and Earth Flyby Calibrations

In the 24-hour period surrounding Earth flyby, the spacecraft passed in and out of the Earth's magnetosphere. This time was the most crucial for magnetometer alignment calibration to ensure that measurements at Saturn are accurate. Without the measurement of Earth's well-defined magnetic field, the measurement threshold of the instrument would be degraded enough to prevent the achievement of at least one major science goal (the measurement of Saturn's magnetic field orientation, or tilt, to an accuracy of 0.1°).

The Cassini Project also accepted activities for CAPS, MIMI, RPWS, Radio Science, and VIMS during the approach to Earth as well as ISS, UVIS, and VIMS observations using the Earth's moon. RADAR observed the Earth just after Earth closest approach.

Figure 2.6-11 shows the MAG boom deployment activities. Thermal restrictions limited the boom deployment to sometime after the last outbound passage of 0.97 AU (which was five days prior to Earth). The MAG boom deployment was scheduled for 44 hours prior to Earth. This timing avoided the scheduled pre-Earth maneuver periods and gave the navigation team enough time to determine whether or not an Earth avoidance contingency maneuver (TCM-12A) was necessary. If the contingency maneuver would have been necessary, the MAG boom deployment and science calibrations would have been dropped from the sequence.

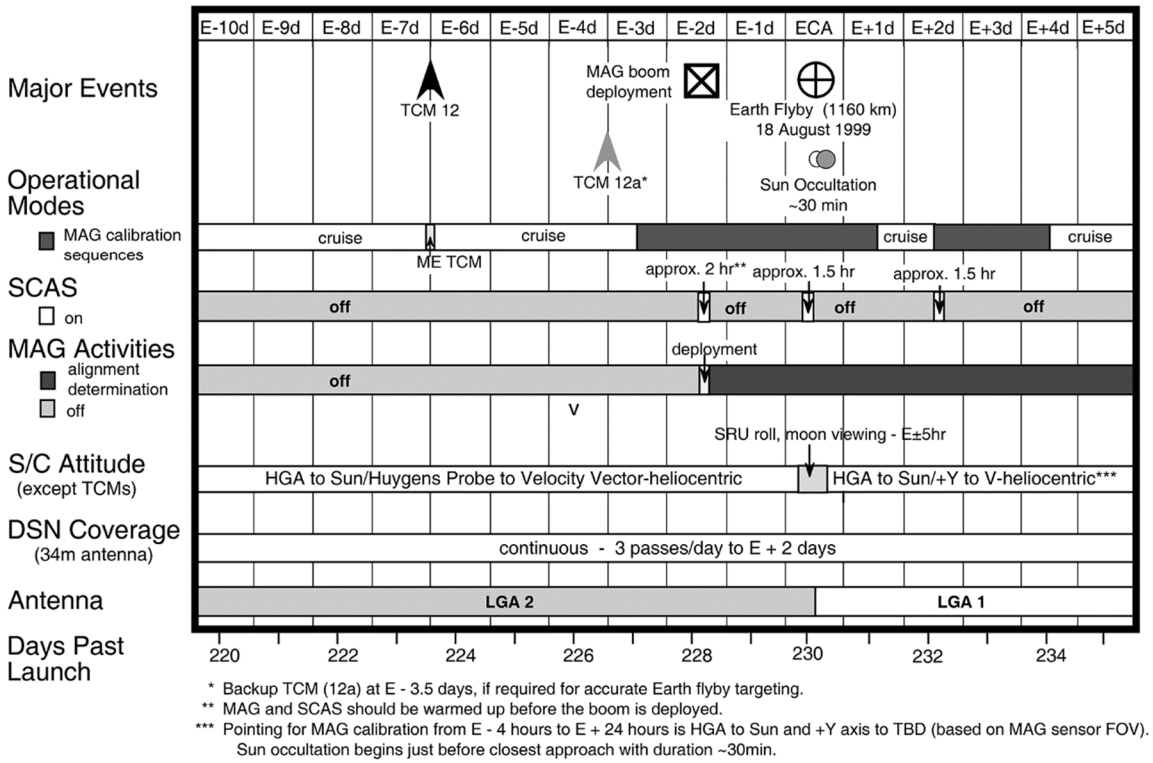

Figure 2.6-11. MAG Boom Deployment and Alignment Determination Activities.

The MAG calibration sequence was planned for a cumulative period of six days, broken up into two blocks. The MAG team used science calibration subsystem (SCAS) for about five hours during near-Earth MAG operation: two hours while the MAG boom was being deployed, about one and one-half hours before entering the Earth's magnetosphere, and one and one-half hours after exiting the Earth's magnetosphere. The purpose of SCAS is to create a known magnetic field for the magnetometer to measure. The high-gain antenna was constantly Sun-pointed throughout this time period, and Earth's magnetic field lay within the magnetometer's 45° field of view, which is along the spacecraft's X-axis.

2.6.2.3.3 Post-Earth Activities

After Earth closest approach, there were several other activities planned. The radar observation performed an end-to-end test of the radar system using Earth as a target. Several instruments finished up their Earth calibrations and science measurements and then remained on, except during TCM-13 (13 days after the Earth flyby) when they were in sleep mode. The instruments came on again after the trajectory correction maneuver and stayed on until just prior to the probe checkout 27 days after the Earth flyby, when they were turned off. The spacecraft turned the high-gain antenna toward Earth 24 days after the flyby, which allowed high data return on the high-gain antenna. The PCO-4 occurred just prior to the end of the high-gain antenna period. After four days on high-gain antenna, the spacecraft was turned back to Sun point, switched to LGA-1, and turned MAG and CDA on. MAG was turned off four days later. CDA remained on throughout the rest of the sequence.

2.6.2.4 Outer Cruise Phase

The outer cruise phase consists of sub-phases for high-gain antenna transition, ICO-2, Jupiter, and quiet cruise. This subsection provides an overview of the activities and plans in the outer cruise phase, which extends from November 8, 1999 (when the spacecraft reached a Sun range of 2.7 AU) to July 7, 2002 (about 2 years prior to SOI). At 2.7 AU, the high-gain antenna began continuous Earth-pointing, with the restriction that the Huygens probe was used as a Sun shield for the rest of the spacecraft, without violating probe thermal restrictions. A timeline for the outer cruise phase and the science cruise phase is shown in Figure 2.6-12.

The outer cruise navigation activities shown on the timeline include the seven trajectory correction maneuvers between the Earth flyby until just after the Jupiter flyby.

A second instrument checkout activity (ICO-2) was added for the summer of 2000, which required additional DSN passes to support science activities and reaction wheel unloading. The one planetary encounter in this phase was the flyby of Jupiter in December 2000. Extensive Jupiter science was accomplished which required additional DSN support. Science at Jupiter was an opportunity to test Saturn observation techniques. Data rates during this phase were much less tightly constrained than during most of the previous mission phases, because of the final transition to exclusive use of the high-gain antenna, which was made on February 1, 2000. This fact made it much easier to perform cruise science and instrument checkout activities.

The outer cruise navigation activities shown on the timeline include the seven trajectory correction maneuvers between the Earth flyby until just after the Jupiter flyby. DSN tracking coverage is also shown, and is driven in large measure by the navigation requirements for radiometric data to determine the spacecraft trajectory and plan the trajectory correction maneuvers. Five of these maneuvers (TCM-14 to TCM-18) occur in the outer cruise phase. The

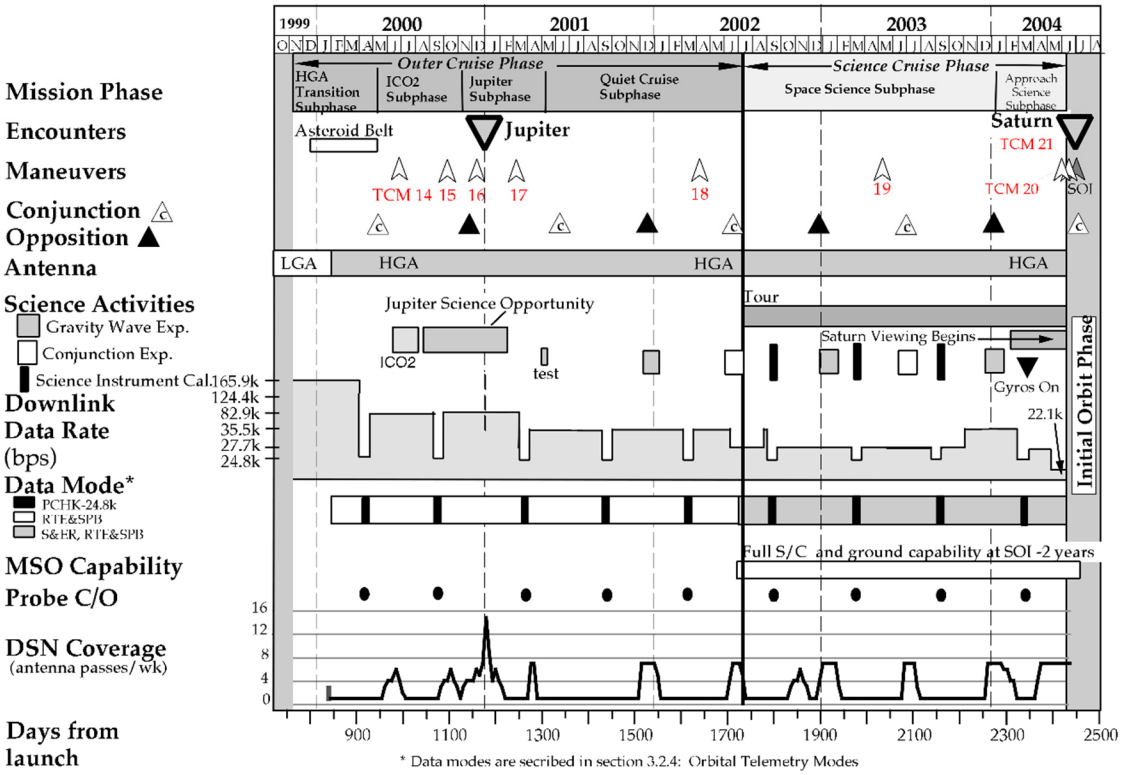

Figure 2.6-12. Cassini Outer Cruise/Science Cruise Phases.

DSN tracking for navigation data was typically one pass per week, with increased tracking around the maneuvers (TCM-21 to TCM-14) and the Jupiter flyby science observation period (October 1, 2000–April 29, 2001).

The engineering maintenance activities continued from the inner cruise phase including EGA exercise, RWA exercise, backup assisted load format injection loader (BAIL) maintenance, SRU calibration, and PMS flushing maneuver.

There were five scheduled probe checkouts in outer cruise. PCO-5 was performed February 2, 2000, one day after the spacecraft switched to the high-gain antenna. This PCO was the first time a probe checkout was performed with the Sun outside the high-gain antenna's main beam. This provided unique circumstances to investigate DWE performance in a noise-free environment.

PCO 6 was performed July 28, 2000. This was moved earlier in time to allow science to use templates during the September timeframe.

PCO 7 was performed on March 22, at the end of the majority of Jupiter observations.

PCO 8 was scheduled in September 2001, in C28.

PCO 9 occurred approximately 6 months after PCO-8.

2.6.2.5 Spacecraft High-Gain Antenna Checkout Sub-phase

The sub-phase followed the Venus-2–Earth sub-phase and preceded the ICO-2 sub-phase, and incorporated sequences C17 to C19. During this sub-phase, the ISS and VIMS instruments' decontamination heaters were on, CDA executed dust calibrations, and MAPS performed some observations after pointing the high-gain antenna to Earth.

During the initial part of the sub-phase (C17 and part of C18), the spacecraft communicated with Earth via LGA-1, but the spacecraft was the farthest it had ever been from Earth and would soon transition to the high-gain antenna for regular use. As a result, data rates before the transition were relatively low and spacecraft activities were kept to a minimum. Sequence C17 included standard maintenance activities and one PEM. Sequence C17 also included the Y2K turnover, which did not cause any problems. To be safe, however, all uplinks and critical activities were avoided for three days around the century change date. Activities during the LGA-1 portion of C18 included a PIM, ORS observations (by ISS, VIMS, and UVIS) of the asteroid Masursky near closest approach (at 1,634,000 km), and ISS dark frame calibration images directly following the ORS observations.

The high-gain antenna was turned toward Earth for regular use on February 1, 2000, during C18. With the greater telemetry capabilities of the high-gain antenna, the spacecraft performed several activities during the rest of C18: playback of the Masursky data and ISS dark frames, a probe checkout, a probe S-band relay test, a telemetry-ranging interference test, MAG calibrations, and a PEM. The spacecraft also began MAPS observations (by CAPS, CDA, MAG, MIMI, and RPWS) within a few days after transitioning to the high-gain antenna.

The first six weeks of C19 were used for a checkout of new flight software. The AACS version A7 software was uploaded near the beginning of this period, and the first two weeks were devoted to AACS tests. The next four weeks were originally scheduled for CDS tests of version 7.0. However, these tests were delayed to late July and August of 2000 to allow time for additional regression testing. During the AACS checkout period, MAPS activity ceased, although ISS and VIMS decontamination heaters remained on. Several activities took place during the last three weeks of C19: the MAPS observations resumed and continued throughout the sequence, three RSS activities (high-gain antenna pattern calibration, high-gain antenna boresight calibration, and USO characterization), the CIRS cooler cover release, and a PIMAll activities were successful.

A few days before the end of sequence C19, the command loss timer setting was increased slightly, to account for the 10-day period at the beginning of sequence C20 during which the geometry of superior conjunction made commanding problematic.

2.6.2.6 Instrument Checkout-2 Sub-phase

The second instrument checkout sub-phase was scheduled from May 6, 2000 to November 5, 2000, after the spacecraft had begun using the high-gain antenna and the spacecraft office

completed their engineering checkout activities. During ICO-2, the flight team performed instrument checkouts that required reaction wheel capability and any instrument checkouts that were not successfully completed during ICO-1. In addition, pre-Jupiter science was requested during this sub-phase. The CDS flight software V7 uplink and checkout, which was delayed from March, was rescheduled to late July through early September 2000, causing many of the ICO-2 activities to be rescheduled into a shorter and denser period. Some activities were postponed until after the Jupiter observations were completed in 2001.

The ICO-2 sub-phase began with a superior conjunction, which precluded early science or engineering activities. MAPS instruments remained on to prevent cycling the instruments but data return was not assumed during conjunction. Two trajectory correction maneuvers were scheduled for Jupiter targeting, in June and September. The latter of the two was moved out of October to allow for Jupiter science to begin using a repeatable template.

Engineering activities included the continuous use of reaction wheels and, beginning October 1, 2000, Cassini's dual SSRs. There were no scheduled instrument PIMs done during ICO-2 since all instruments had other activities that accomplished this function. Other engineering activities included two RWA friction tests, two PEMs, and an SRU calibration.

Science activities began with the MAPS instruments, continuing from sequence C19. New flight software was loaded for eight instruments in late May, and a CDA FSW update was done in September. New quiet tests while operating on reaction wheels, for most instruments were done in July, although the RSS quiet tests were done in September and radar-related tests were done in late June. A probe checkout occurred in late July.

Spacecraft turns were done for radar observations of the Sun and Jupiter in June and again in September. The star Alpha Piscis Austrinus (Fomalhaut) was also observed in September by VIMS with ISS and UVIS doing ride-along science. No other science turns were scheduled until October. On October 1, Jupiter science began using a repeating five-day template with 11 turns per five-day period, including two downlinks. The turns in the five-day template involved four orientations:

- ORS boresights to Jupiter, Z-axis parallel to ecliptic
- High-gain antenna to Sun, rolling about Z-axis
- Probe to Sun, rotating about X-axis
- High-gain antenna to Earth, probe offset from Sun for CDA, not rotating, downlink orientation

Additional instrument activities for calibration, checkout, and science were also scheduled.

2.6.2.7 Jupiter Sub-phase

The Jupiter flyby occurred on December 30, 2000, at an altitude of about 9.7 million kilometers with a velocity relative to Jupiter of about 0.4 km per second. This gravity assist rotated the trajectory 12° and increased the heliocentric velocity by 2 km per second. The Jupiter relative speed at closest approach was about 11.6 km per second. At this distance, Jupiter filled the NAC field of view. The spacecraft performed extensive Jupiter science, which required additional support from the DSN: templates using up to two passes every five days, and a maximum of one pass every 30 hours in the 10 days on either side of closest approach. The mission studied Jupiter with Cassini's science instruments to test how to build and execute viable Saturn sequences. The Jupiter sub-phase was from November 6, 2000 to April 29, 2001, and incorporated sequences C23 to C25. However, Jupiter remote sensing observations actually begin on October 1, 2000, in sequence C22.

Figure 2.6-13 illustrates the flyby geometry for Cassini and for the previous Voyager missions. Although Cassini was not assumed to pass through Jupiter's magnetopause, it actually recorded six crossings as well as 44 bowshock crossings during the Jupiter sub-phase.

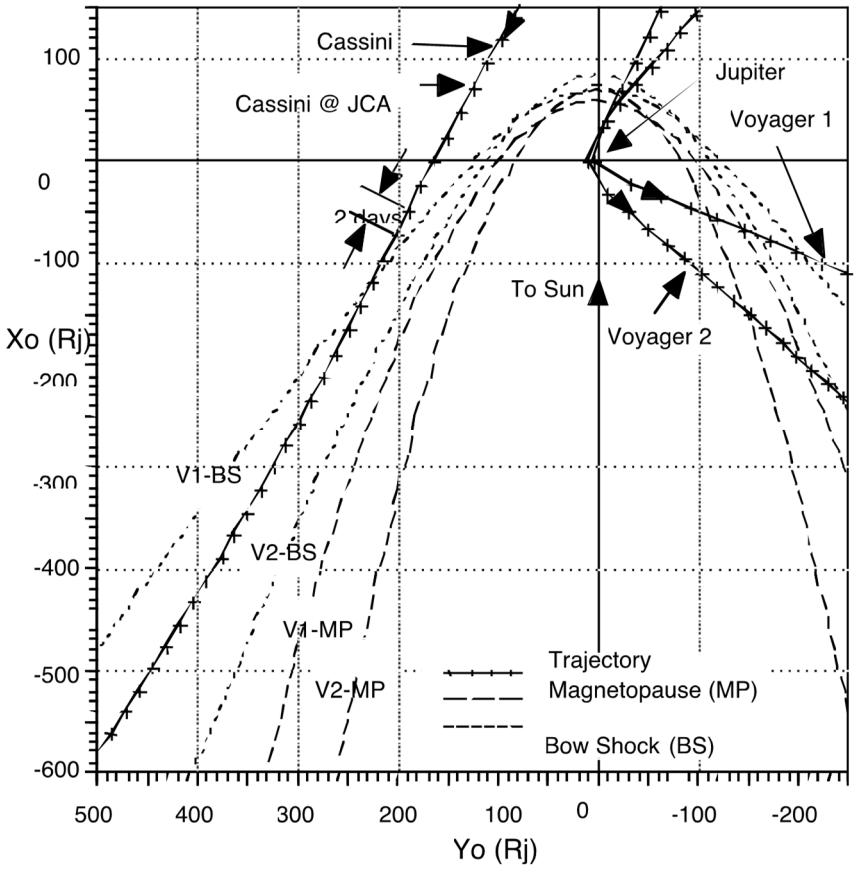

Figure 2.6-13. Cassini-Jupiter magnetotail passages.

The spacecraft performed TCM-17 in sequence C24 and was executed on February 28, 2001, to correct for Jupiter perturbation errors. During Jupiter science operations, the RPWS instrument was calibrated in small blocks, each lasting 10 hours (five blocks before the Jupiter flyby and four after the flyby).

During passage through Jupiter's magnetotail, the spacecraft's reaction wheels and dual solid-state recorders were in continuous use. The Cassini team scheduled no instrument PIMs during the Jupiter sub-phase since all instruments had other activities that accomplished that function. Other engineering activities included: two PEMs, star ID extended bodies test, and RWA unloads. The team performed a Huygens probe checkout on March 22, 2001, following a 5-day probe relay test in early February (in place of a 5-day science template). The spacecraft executed a radar radiometer calibration 89 days after the Jupiter flyby. Beginning 48 days before Jupiter flyby, the spacecraft Ka-band was turned on for the rest of Jupiter sub-phase to perform the Ka-band upgrade task with DSS-25. Most of the RSS activities scheduled between mid-March and the end of April 2001 were in preparation for the gravitational wave experiment (GWE) test #1 performed at the beginning of May 2001. The preparation work for the GWE test included USO characterization, repeat of ICO test E, 3-link test, high-gain antenna boresight calibration, Operational Interface Test (OIT) and its follow-up test, and high-gain antenna pattern calibration. The spacecraft also performed a successful in-flight test for the RTE and science playback (SPB) 35.5 telemetry mode in sequence C25 in preparation for using the new mode extensively in sequence C26.

Jupiter science observations were scheduled between Jupiter flyby − 90 days and Jupiter flyby + 82 days. This period of Jupiter science observations was divided into A, B, C, D, E, F, and G Jupiter science phases. Each of these science phases contained specific Jupiter science objectives and observations. Phase A occurred during the ICO-2 sub-phase.

The Jupiter sub-phase science activities began with science phase B; the first 10 days (Jupiter flyby − 55 days to Jupiter flyby − 45 days) contained two more instances of the late ICO-2 (Phase A) five-day science template. Sequence C23 incorporated phases B, C, D, and E, and covered from Jupiter flyby − 55 days to Jupiter flyby + 15 days. The major science activities during these science phases, except for the science observations continued from the late ICO-2 five-day template, included 2 × 2 mosaics of Jupiter, ring movies, atmospheric and Europa opposition surge observations, north–south maps of Jupiter, Io eclipse observations, dust stream detection, coordinated Hubble Space Telescope and Cassini observations, and the observations of Callisto opposition surge and Himalia closest approach. When the spacecraft neared closest approach, resolution improved and the phase angle changed significantly, satellite and ring observations became more important. During this time frame the spacecraft performed more atmospheric, ring, and satellite observations, such as: the ORS boresights slewed slowly from north to south then stepped in a 1 × 3 mosaic from south to north; 3 × 2 mosaic was executed with full filter set and a 3 × 3 mosaic designed to obtain the best Jupiter picture; Io thermal studies and Io torus monitoring; and satellite eclipse observations. The coordinated Galileo and Cassini observations for Io dust stream and Io eclipses were performed during this closest approach time frame. The solar wind monitoring, which began in Jupiter science phase A, continued in C23. From Jupiter flyby to the

end of C23, the most important science objectives include the coordinated Hubble and Cassini observations of Jupiter's aurora and solar wind, phase angle coverage of Jupiter's atmosphere and ring, coordinated Galileo ring and satellite observations, and the radar observation of Jupiter's synchrotron emission.

The spacecraft experienced a problem with the RWAs on December 16, 2000. Increased friction on one of the wheels caused the spacecraft to autonomously switch to the RCS for attitude control. With the switch to RCS, the spacecraft used more hydrazine. Two of the four joint CAPS-Hubble observations, a Jupiter north–south map, the Himalia "flyby," and a UVIS torus observation were all executed on RCS before the sequence was terminated on December 19, 2000. MAPS data continued to be recorded at a reduced rate. All other planned science activities were cancelled until December 29, when they were resumed.

The reaction wheels began being used again for attitude control on December 22, with constraints imposed to avoid low RPM regions. This was accomplished by biasing the wheels. Continued testing by AACS personnel suggested the anomaly was a transient event so the sequence was restarted on December 29. Subsequent tests and studies eventually led to a project directive to use the RCS system as primary control beginning with sequence C27.

Observations lost due to the anomaly include four Jupiter north–south maps, two CAPS solar wind measurements, numerous Galilean satellite observations at various longitude and phase angles, Europa eclipse, numerous ring and Io torus measurements, and Jupiter feature tracks.

During this time frame, magnetospheric science was one of the most important science objectives since Cassini was in and out of Jupiter's magnetosheath while Galileo was in the solar wind.

The science phases F and G were executed from Jupiter flyby + 15 days to Jupiter flyby + 82 days. Phase F lasted the entire C24 sequence, and Phase G filled the first 2 weeks of the C25 sequence. During this time frame, magnetospheric science was one of the most important science objectives since Cassini was in and out of Jupiter's magnetosheath while Galileo was in the solar wind. This enabled the same type of science as inbound when Cassini was in the solar wind while Galileo was in the magnetosphere. Major science observations for science Phases F and G included coordinated Cassini/Hubble for joint observations of Jupiter's aurora, the outbound crescent movie, a search for lightning, and continuous monitoring of Io's torus emissions and dust streams.

A slightly modified version of the tour ORS operational mode was used for all of the Jupiter science phases (A–G). RADAR activities were performed in SAF-142a and SAF-248 telemetry modes, and all non-radar observation periods were performed in the S&ER-3 telemetry mode.

2.6.2.8 Quiet Cruise Sub-phase

The quiet cruise sub-phase is a 14-month period that started at the end of the Jupiter sub-phase and ended two years before SOI. During this sub-phase, routine maintenance, engineering, and navigation functions were carried out. One GWE was planned for December 2001 and one conjunction experiment for June 2002. The GWE preparation included two 1-week test periods starting in early May 2001 and August 2001.

Many activities that were deferred from ICO-2 and were not accomplished during Jupiter activities were scheduled for quiet cruise. In addition, newly proposed activities for both science and engineering activities were considered for quiet cruise activities. The mission integrated science and engineering activities during the science planning virtual team activity, which began in January 2001. Templates were again used to efficiently plan science and engineering activities for quiet cruise. One change from the Jupiter sub-phase was that data was recorded on only one SSR.

A new telemetry mode of 35.5 kbps was implemented just prior to the start of quiet cruise sub-phase to allow more efficient use of the downlink capability, which was diminishing due to geometry. The Program Manager authorized increasing the requested DSN passes to a minimum of two passes per week to accommodate the increased science activity. Additional passes were also requested for GWEs, GWE tests, conjunction experiment, and TCM-18. Other increases in DSN passes were expected for radio science activities, AACS activities, CDS new FSW, and probe tests. All new requests were documented in the PSLA.

All cruise activities beginning in May 2000 assumed RWA for attitude control. Since the anomalous behavior in December 2000, tests and studies led to a Program decision to use RCS as the primary attitude control system. RWA was allowed for certain activities that required increased stability or pointing accuracy, e.g., GWE and RSS tests. This restriction was in force beginning with sequence C27. Other requests for turns on thrusters required approval by the Program Manager.

2.6.2.8.1 Gravitational Wave Experiments

The project requirements called for support of GWEs while en route to Saturn near at least three oppositions, for periods of at least 40 days each, and with Ka-band tracking coverage from Goldstone of one pass per day. Additional tracking was requested using X-band links with DSN stations at Madrid and Canberra. These experiments were scheduled for the three oppositions after the Jupiter flyby in December 2001, December 2002, and January 2004. However, the 2004 GWE was rescheduled to begin October 20, 2003, to relieve some of the DSN resource contention in January 2004 due to Mars missions and other projects.

During GWEs, the spacecraft was configured into an operational mode with X-band and Ka-band uplinks, and X-band and Ka-band downlinks. The X-band downlink was required for engineering telemetry, including high-gain antenna inertial pointing. Attitude control was on reaction wheels for these 40-day periods. The spacecraft was rolled 180° about the Earth line when needed in order to unload the reaction wheels momentum without having to use thrusters. Since the RTG

thermal torque and the magnetometer-boom solar torque are body fixed, the reaction wheel momentum change due to the X- and Y-axis torque reverses direction under the effect of the 180° roll. The Z-axis momentum continued to accumulate, but the rate was acceptably low. Keeping the turn rate below 180° per four hours assured that the Doppler stability was not compromised. The turns were expected to be performed a few times during each GWE.

Within a month before each GWE, GWE test, and conjunction experiment, there was a high-gain antenna electrical boresight peak calibration. This calibration lasted two hours and included X- and Ka-bands for the GWEs and S-, X-, and Ka-bands for the conjunction experiments. These calibrations required telemetry modulation be turned off. Note that GWEs and conjunction experiments extended into the science cruise phase.

2.6.2.8.2 Conjunction Experiments

The project requirements call for support of conjunction experiments whose purpose is to perform tests of general relativity and to study the solar corona. These experiments were conducted while en route to Saturn, near at least two solar conjunctions, for periods of at least 30 days each, and with Ka-band tracking coverage from Goldstone of one pass per day. Additional tracking was requested at S-band for the study of the solar corona. These experiments were scheduled during the two conjunctions preceding SOI, from June 6, 2002 to July 6, 2002, and from June 16, 2003 to July 16, 2003. The spacecraft was configured in the RSS2/RWA operational mode. For complete calibration of the plasma noise during the general relativity test, X-band and Ka-band uplinks and X-band and Ka-band downlinks were used. The solar corona study required X-band uplink and simultaneous X-band and S-band downlink (for SEP > 2°) and X-band uplink and simultaneous X-band and Ka-band downlink (for SEP ≤ 2°). The team acquired Doppler and range (at X-band) data throughout the conjunction experiment, and the spacecraft-maintained attitude control using reaction wheels during these 30-day periods.

2.6.2.9 Science Cruise Phase

Cruise science and instrument calibrations continued during the science cruise phase, which began on July 8, 2002 and continued through May 15, 2004. Sub-phase activities included instrument calibrations, late cruise science, and preparation for Phoebe flyby science and Saturn approach science. Two sub-phases comprised this phase: space science and approach science. In spring of 2003, new flight software allowed engineering data to be sent to a separate partition on the SSR so that not all engineering data needed to be downlinked on every pass. The impact of this was to increase the SSR data volume available for science data. Mission and science operations software for science pointing, timeline analysis, opportunity analysis (geometric observation models), resource allocation, science data records, etc., were all to be completed by January 2004 to support the approach science sub-phase. The Cassini Mission maintained a complete list of mission and science operations and science deliverables throughout the mission.

2.6.2.9.1 Space Science Sub-phase

The space science sub-phase began on July 8, 2002 and ran through January 10, 2004. TCM-18 and TCM-19 occurred during the space science sub-phase. Activities during this period were requested in the post-Jupiter final scoping package and the space science scoping package. These activities included:

- Two GWEs scheduled during the space science sub-phase for December 2002 and October 2003.
- The second conjunction experiment occurred during the space science sub-phase and was scheduled for June 2003 to July 2003.
- An SOI readiness test to simulate the activities associated with SOI. This took place about one year prior to SOI (June 30, 2004).
- A probe relay operational readiness test in November 2003. This included orienting the orbiter to point the high-gain antenna to a simulation of the probe touchdown point on the rotating surface of Titan.

2.6.2.9.2 Approach Science Sub-phase

The approach science sub-phase covered the period from January 12 through May 15, 2004. At that point in the trajectory, the spacecraft had long since left the Jovian system and was approaching Saturn at a rate of 5 km per second. Most of the activities during that 4-month period were Saturn science observations and preparation for the Phoebe flyby, SOI, and tour operations.

The reaction wheels were turned on for continuous use about six months prior to SOI to provide a more stable viewing platform. Around the same time, the imaging instruments began atmospheric imaging, and making long-term atmospheric movies. CIRS began long integrations of Saturn's disk.

About four months prior to SOI, Saturn filled one third of the NAC field of view and one half of the CIRS far-infrared (FIR) field of view. The Saturn approach was made toward the morning terminator at a phase angle of about 75°, and VIMS gathered data on the temperature difference across Saturn's terminator. UVIS scans of the Saturn system began about three months prior to SOI. Fields, particles, and waves instruments also collected solar wind information and recorded Saturn emissions as the spacecraft neared the planet. Science data gathered during this period was stored on the SSR and transmitted back to Earth. Tracking coverage at the start of the sub-phase was increased to three passes per week even though the first two months were heavily contested with other projects for DSN resources. Daily tracking coverage began 90 days prior to SOI.

2.6.3 ORBITAL OPERATIONS PHASE

2.6.3.1 Saturn Approach and Phoebe

The first event of the tour (though it occurs before SOI) was a targeted encounter with Phoebe 20 days prior to the SOI burn. Among planetary satellites, Saturn's outermost satellite is unusual. Phoebe has a rotation period of about 9.4 hours, an orbital period of 550 days, and a diameter of about 220 km. Its inclined, retrograde, chaotic orbit is strong evidence that the moon is a captured object. Evidence from albedo measurements suggested Phoebe would have craters on its surface. Determining whether or not Phoebe is asteroidal in character was an important scientific goal. Determining the density of Phoebe was important in meeting this goal. As this was the only possible encounter with Phoebe, the data acquisition opportunity was unique. The science operating modes used for this flyby were 1) the ORS mode to allow ISS, CIRS, UVIS, and VIMS observations as well as a more accurate determination of the Phoebe rotation period and 2) the RSS2/RWA mode to allow mass determination. The flyby of Phoebe occurred on June 11, 2004, 19 days before SOI. The Phoebe closest approach was at 2,000 km altitude at 19:32 UTC, at a phase angle of 155°.

The imaging characteristics are shown in Figure 2.6-14. Beginning about 10 hours from Phoebe, the NAC FOV was rapidly filled. At closest approach, the resolution of Phoebe was about

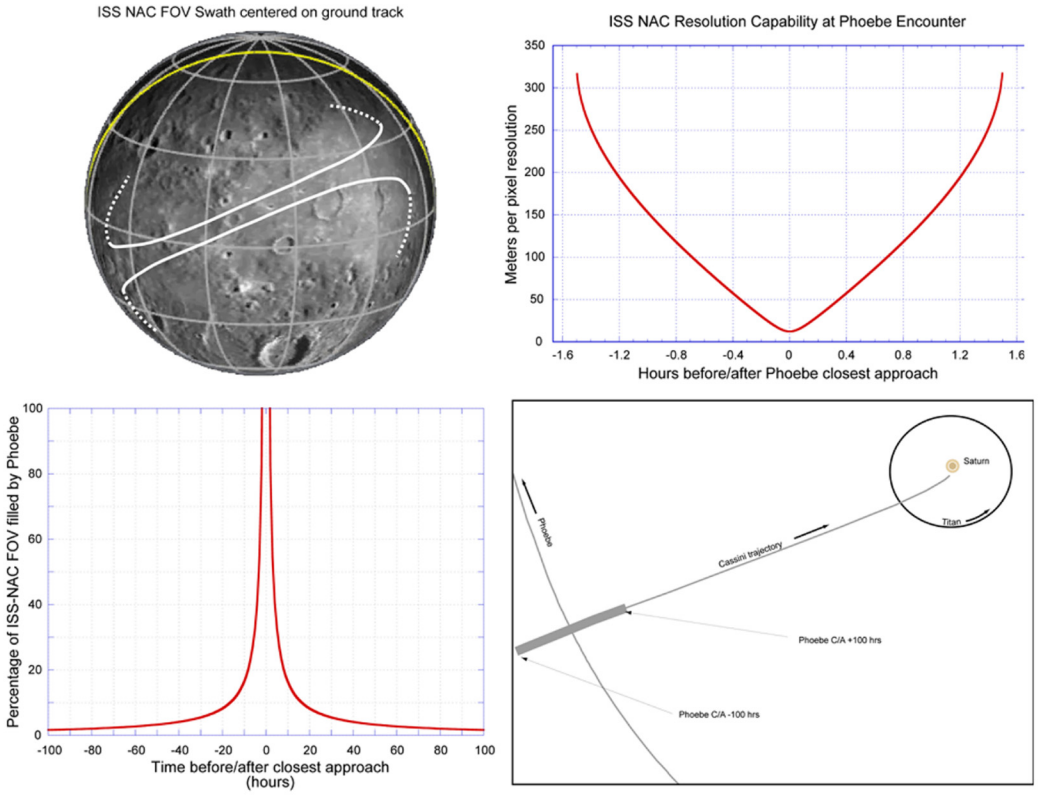

Figure 2.6-14. Characteristics of Phoebe flyby.

12 meters per pixel, a resolution 1,500 times better than Voyager and excellent for morphologic mapping and for studying the geologic character of Phoebe, including surface mapping. A complete map of Phoebe was desired with the range less than 160,000 km.

During the approach to Saturn, the spacecraft performed three approach trajectory correction maneuvers. TCM-20 is the final Phoebe targeting maneuver and was done with pressurized tanks by firing pyro valve 25 and opening latch valve 10. After TCM-20 was complete, LV-10 was closed until 70 seconds before the SOI burn begins. TCM-21 ensured that the B-plane delivery error at the orbit insertion point was less than 130 km (one sigma). The maneuver needed to be done at least 14 days before SOI because the fault protection recovery period (based on Magellan and Voyager experience) can be as long as two weeks if the fault is difficult to diagnose and/or new software uplinks are required. There was another trajectory course maneuver opportunity at S − 10 days, which was available if needed. Two SSRs were used for recording science data beginning June 1, 2004.

2.6.3.2 Saturn Orbit Insertion

As Cassini approached Saturn, it executed the first targeted flyby of the tour of Phoebe on June 11, 2004, 19 days before SOI. The arrival date and trajectory were specifically selected to accommodate this flyby and was the only opportunity during the mission (prime and extended) to study Phoebe at close range. The altitude at closest approach was 2,000 km, offering resolution up to about 10 meters per pixel, many times better than Voyager. The flyby was highly successful.

Saturn Orbit Insertion occurred on June 30, 2004 (Pacific Time, July 1 UTC), where the spacecraft made its closest approach to Saturn's surface during the Prime Mission at an altitude of only 0.3 Saturn radii (18,000 km). Due to this unique opportunity, the 97-minute 626 m/s SOI burn required to place Cassini in orbit around Saturn executed earlier than its optimal point centered on periapsis, and instead ended at periapsis, allowing unique science observations of Saturn's magnetosphere and the main rings immediately after closest approach, and before the descending ring-plane crossing. Due to concerns about ring particle impacts, a protective attitude of HGA to dust ram was assumed for both the ascending (before the SOI burn) and descending ring-plane crossings, and the main engine cover was closed after the burn. Furthermore, an eight-day quiet period was observed prior to SOI, where turns, instrument articulations, and power state changes directly unrelated to orbit insertion were not permitted. SOI science and engineering data were played back twice to ensure ground receipt and make room for post-SOI observations during a distant Titan encounter (named "T0"). Figure 2.6-15 below depicts the major events performed during the approach to Saturn.

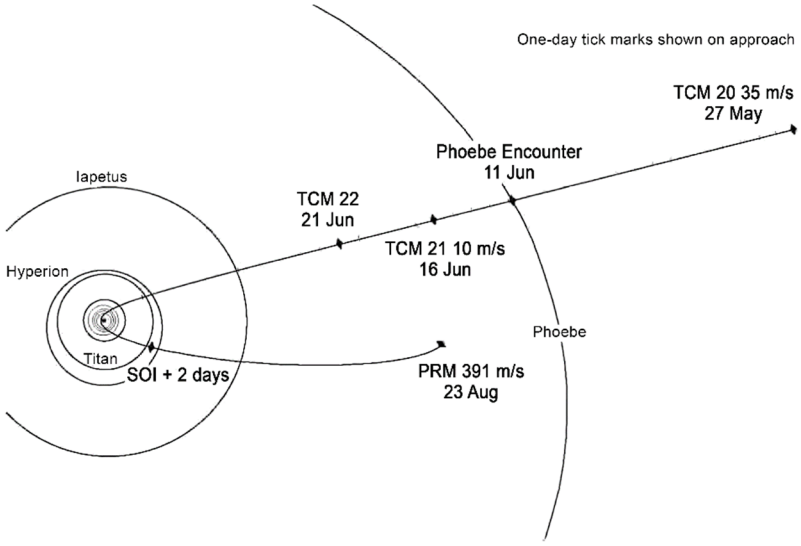

Figure 2.6-15. Cassini-Huygens Saturn Approach and Insertion.

2.6.3.2.1 SOI Overview

Figure 2.6-16 shows the SOI events timeline. After the Phoebe flyby and clean-up trajectory course maneuvers, there was a quiet period that began eight days before the SOI burn. DSN coverage during approach was one pass per day, with continuous coverage on trajectory course maneuver days. Continuous coverage began two days prior to SOI and continued through one day following SOI. The mission considered extending the continuous coverage on both sides of the burn.

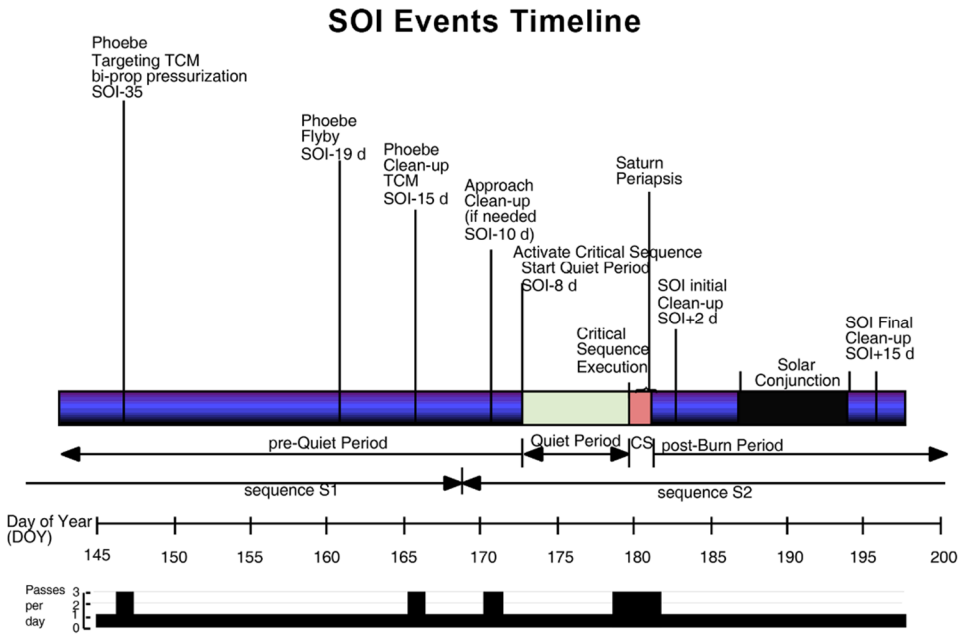

Figure 2.6-16. SOI Events Timeline.

Before the critical sequence began, the spacecraft turned off reaction wheel control and went to thruster attitude control. This allowed turns for safing, SOI burn orientation, and science viewing to be done faster than if on wheels. During the quiet period and burn itself, only FPP instruments were on. Other instruments were either in sleep or off to provide power margins for the critical burn event. Spacecraft vibrations during the main engine firing were likely to degrade remote sensing in any case.

2.6.3.2.2 Initial Orbit

After SOI, the spacecraft performed a pair of cleanup maneuvers to correct for errors in the SOI burn. The first manuever was immediately before the superior conjunction, two days after SOI, and the second was after conjunction, 16 days after SOI. The initial cleanup was based on only one day of tracking after the SOI burn was complete. The trajectory course maneuver could not be delayed much further due to solar noise, which degraded Doppler tracking around the conjunction period (July 5–12, 2004).

Beginning with the periapsis raise maneuver 53 days after SOI, the spacecraft executed a sequence of nine maneuvers to target the Huygens probe and orbiter trajectories for the proper entry and flyby conditions to ensure that Huygens could successfully make its science observations and relay those data to the Cassini orbiter via radio.

Three new Titan encounters, Ta, Tb, and Tc, were designed with a distant flyby during probe delivery on Tc. These three initial Titan encounters replace the first two Titan encounters of the T18-5 tour. If the Huygens probe couldn't be delivered at the Tc flyby, a contingency trajectory existed that allowed a second chance to deliver the probe. This contingency retargeted Tc to a lower altitude and introduced a new distant flyby, Td, for probe delivery. However, this contingency would cause Cassini to fall off of the tour and unable to return to the T18-5 tour until the 13TI (T6) flyby.

The periapsis trajectory course maneuver required 392 m/s and the orbiter deflection maneuver (ODM) required 26 m/s. In addition to the trajectory course maneuvers, the initial orbit also contained three probe checkouts. The data from the last pre-separation checkout, along with orbiter status, determined whether or not to target to the Titan impact point at the Titan-1 flyby. DSN coverage after SOI was generally one pass per day. Additional coverage was required for unique events including maneuvers. Continuous coverage was required on maneuver days. Additional details on the probe mission are given in Section 2.6.4.

The tour consisted of 75 orbits of Saturn with various orientations, orbital periods ranging from 7 to 118 days, and Saturn-centered periapsis radii ranging from about 2.7 to 15.6 R_S (Saturn radii). Orbital inclination with respect to Saturn's equator ranged from 0–75.6°, providing opportunities for ring imaging, magnetospheric coverage, and radio (Earth), solar, and stellar occultations of Saturn, Titan, and the ring system. A total of 45 targeted Titan flybys occurred during the tour. Of these, 41 had flyby altitudes less than 2,800 km and two had flyby altitudes greater than 10,000 km. Titan flybys were used to control the spacecraft's orbit about Saturn as well as for Titan science

acquisition. The tour also contained 13 close flybys of icy satellites and 30 additional distant flybys of icy satellites within 100,000 km.

After SOI, Saturn tour science gathering began in earnest. However, much of the focus was on preparations for successful release and descent of the Huygens probe to the surface of Titan.

2.6.4 HUYGENS PROBE MISSION

The final checkout of the Huygens probe was made 31 days before its separation from the orbiter, and this supports a go/no-go decision to proceed with the probe mission at the Titan-C encounter. Twenty-eight days before separation and 48 days before entry, a depassivation activity was scheduled for the probe batteries to ensure that they were fully functional for entry and descent. The probe targeting maneuver was then executed on December 18, 2004, two days before separation, placing the Huygens spacecraft on an impacting trajectory with Titan. Final commands to the probe were sent three days later to complete preparations for release, and this included setting the probe coast timer.

The spin-stabilized probe was targeted for a southern latitude landing site on the day side of Titan.

Separation of the Huygens probe then occurred on December 24, 2004, which was 20 days before entry to Titan on January 14, 2005. The probe spin/eject device (SED) separated the probe with a relative speed of 0.3–0.4 m/s and spun it up to a rate of >5 rpm. At separation, the probe axis was pointed to achieve a zero-angle-of-attack entry and such that the velocity increment by the SED springs provided the final targeting to the entry aim-point. The last two maneuvers of the orbiter before probe entry provided its final targeting to the required aim-point to achieve the radio relay link geometry and to obtain the required gravity assist from Titan for subsequent encounters in the orbital tour. The first of these maneuvers was the ODM, which was executed four days after separation, or E-17 days. This maneuver of about 26 m/s targeted the orbiter for the planned flyby of Titan at an altitude of 60,000 km and delayed the orbiter's closest approach to occur just over two hours after probe entry. The relative position of the orbiter with respect to Titan during probe entry and descent provided a view toward the probe for approximately four and a half hours after entry. The orbiter high-gain antenna was pointed toward the predicted probe landing site to capture the probe telemetry during descent (maximum duration 150 minutes) and for approximately two hours after probe touchdown.

The spin-stabilized probe was targeted for a southern latitude landing site on the day side of Titan. To minimize trajectory dispersion and thus enhance data relay link performance, and to avoid probe skip-out, the probe entry angle into the atmosphere was relatively steep at 64°. The term "entry" generally refers to the arrival of the probe at the interface altitude of 1,270 km, which defines the interface point for probe targeting requirements. The probe did not experience significant atmospheric drag until a much lower altitude. The B-plane angle of the probe aim point was −190°. This resulted in a landing site at about 10.7° (±7°) N and 160° (±13°) E. The large east–west uncertainty in the landing site was driven by uncertainties in the Titan-relative ephemeris and in the

magnitude and direction of zonal winds on Titan. No Earth or Sun occultations by Titan (as seen from either the probe or orbiter) occurred during the probe-relay flyby.

2.6.4.1 Probe Separation

Successful separation of the Huygens probe from the Cassini orbiter was defined as a separation that did not jeopardize the functional or structural integrity of the probe or orbiter and gave the probe the required post-separation trajectory and attitude within allowable uncertainties. To accomplish this, the pre-separation state vector (position and velocity) and attitude had to be such that, after the dynamics of separation were applied, the probe was left with the proper velocity to reach the aim point, and the proper attitude for atmospheric entry. The pre-separation attitude was achieved by rotating the combined spacecraft under AACS control to an attitude, which left the probe at the desired post-separation attitude.

The Cassini attitude determination system provided an estimate of the spacecraft attitude and turning rates with respect to the J2000 coordinate system. The high accuracy celestial-inertial mode was used for attitude determination in the period prior to the separation event. In this mode, the SRU and an on-board star catalog determined the spacecraft attitude in the J2000 reference frame. Attitude estimates were propagated by the IRU between SRU measurement updates.

The RCS was used to control the combined spacecraft attitude immediately prior to the separation event. RCS control algorithms maintained the spacecraft attitude and rate about all three spacecraft axes within a limit cycle whose angular size was commandable. The control was achieved using four Z-facing thrusters and another four Y-facing thrusters. It was assumed that, following the turn to the probe separation orientation, sufficient time was allowed for the spacecraft to attain a quiescent state with rates below 0.01° per sec on all axes. However, the firing of the RCS thrusters were inhibited 10 seconds prior to probe separation, and re-enabled 60 seconds following probe separation.

After the probe was positioned to its separation orientation, the AACS continually monitored the spacecraft attitude. If the AACS determined that the probe pointing direction had varied beyond a settable threshold, the orbiter/probe separation event would have been aborted.

All of the activity between the time of the separation command and the time at which the orbiter and probe were no longer in physical contact took place in approximately 0.15 seconds.

Once the separation command was initiated, a sequence of dynamic events occurred that resulted in separation of the probe. These events included the firing of pyro bolts, engagement of the separation push-off springs, ramps and rollers, and the separation of the electrical connectors, as well as motion of the orbiter under the separation-induced loads. All of the activity between the

time of the separation command and the time at which the orbiter and probe were no longer in physical contact took place in approximately 0.15 seconds.

The results obtained for the probe separation analysis are shown in Table 2.6-2 for the expected propellant loading case. The probe axial velocity (spacecraft −X-axis direction) of 0.3367 m/s was within the requirement of 0.3 to 0.4 m/s. The probe lateral velocity, the vector sum of the y and z components, was 0.0039 m/s, well within the ICD requirement of <0.032 m/s. The probe axial spin rate was 7.29 rpm, satisfying the requirement of >5 rpm. The maximum orbiter angular rate (the maximum of x, y, or z) is 0.974° per second (0.1624 rpm), satisfying the requirement of <7° per second.

Table 2.6-2. Probe/orbiter post-separation velocity state.

	Δvx (m/s)	Δvy (m/s)	Δvz (m/s)	wx (rpm)	wy (rpm)	wz (rpm)
Probe	−0.3367	0.0014	0.0036	7.2900	−0.0049	−0.0700
Orbiter	0.0471	−0.0011	−0.0006	−0.1624	0.1045	0.018

The dynamics of the probe and the orbiter during the five minutes between the time of separation and the time the two bodies were ~15 meters apart has been studied. The analysis results indicate that the overall minimum clearance obtained was found to occur between the Langmuir probe and the Huygens probe. The minimum clearance of 0.153 m occurred for the low propellant mass scenario. This value of minimum clearance is considered to be satisfactory. To assure that no unmodeled spacecraft motion occurred until the probe cleared the vicinity of the orbiter, the AACS inhibited the firing of the RCS thrusters until 60 seconds following the probe separation event.

The AACS switched from the celestial-inertial mode to the coast mode 10 seconds before probe separation. In the coast mode, the RCS thrusters were inhibited from firing and the spacecraft attitude and rates were continuously sensed by the IRU. Sixty seconds after the separation event, the AACS switched to the detumble mode. In this mode, the RCS thrusters were re-enabled and the spacecraft rates were reduced to low, commandable threshold values. When the orbiter rates were within the prescribed threshold limits, the AACS was switched to the celestial-inertial mode and a turn was commenced to return the orbiter to the attitude that it had just prior to the probe release event.

Post-separation imaging of the probe was considered to improve the knowledge of its ephemeris and entry conditions at Titan. The development team conducted a preliminary feasibility study but important issues remained on the ability to point the WAC and NAC accurately enough given uncertainties in the probe and orbiter velocities after separation. If the pointing was sufficiently accurate, images could be obtained shortly after separation with the WAC and up to six days after separation with the NAC. While studies indicate that all probe mission requirements could be met without post-separation imaging, this option could have enhanced the probe relay pointing margins and provided diagnosis of certain probe separation anomalies.

2.6.4.2 Probe Relay

The probe flew directly into Titan's atmosphere, where it relayed data to the orbiter for about 2.5 hours during its descent to the surface. The probe continued to broadcast data from the surface until the spacecraft passed over the horizon, about 4.5 hours after the probe began broadcasting, which included 2 hours of data while the probe was on the surface. This was the first (and so far only) landing to take place in the outer solar system. Refer to the Titan-C (Huygens) mission description for more information about the Huygens probe mission. Figure 2.6-17 provides a summary of the Huygens probe descent events.

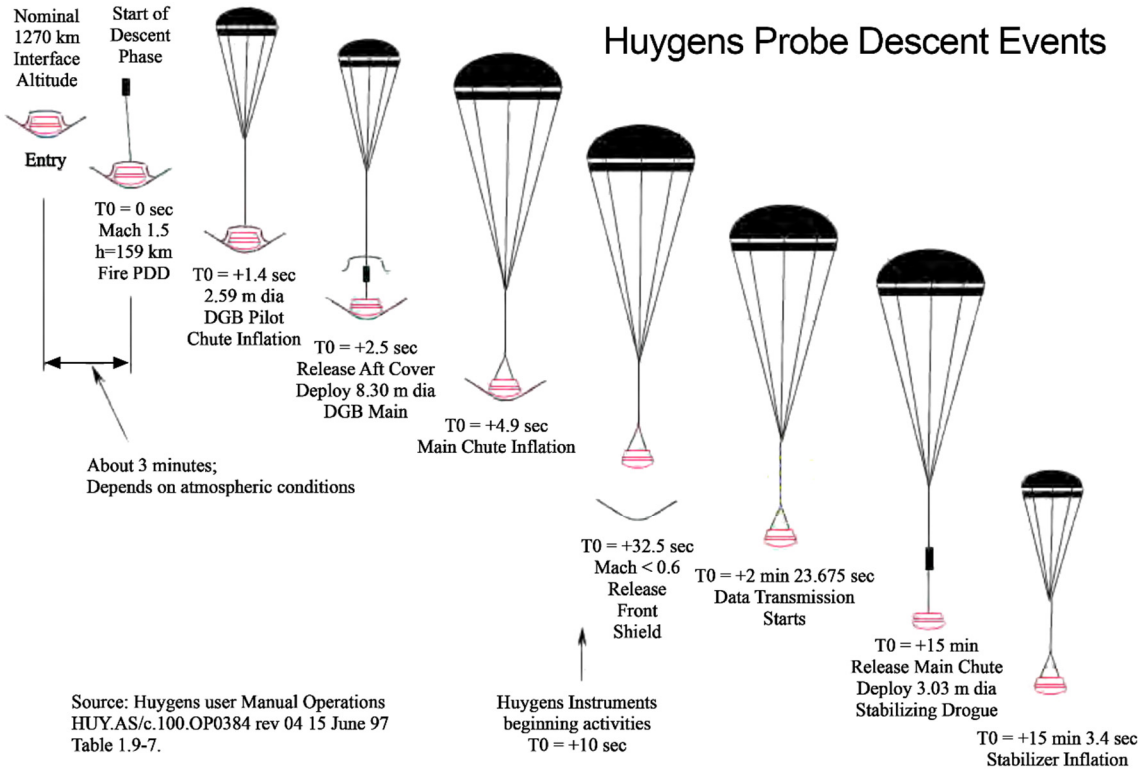

Figure 2.6-17. Huygens probe descent timeline.

The probe entry event occurred over the Goldstone tracking complex at about 0858 UTC (spacecraft event time, with a 67.7-minute one-way light time). Because the orbiter was looking at Titan through most of the Goldstone tracking pass, DSN support on this day was primarily through the 70-meter antennas at the Canberra and Madrid tracking complexes. On approach to Titan, the last downlink before probe relay was to the Madrid station (DSS 63). Following the playback of all data remaining on the solid state recorders, the orbiter was turned nearly 180° to point the high-gain antenna at the predicted probe impact point. The probe support avionics (PSA) were configured to receive data from the probe. Some orbiter instruments were put in a low power state to allow power for the PSA. The data from the probe were transmitted at S-band in two separate data streams, and both were recorded on each SSR.

SSR partitions 4, 5, and 6 were resized as part of the probe-relay critical sequence. Following completion of the predicted descent, the orbiter continued to listen to the probe for 30 minutes, in case the probe transmissions continued after landing. The orbiter was required to stay pointed at the predicted probe landing site for three hours, based on an earlier prediction of the longest descent time being 150 minutes, plus at least 60 minutes after landing. (Current ESA analysis gives an expected descent time of 141 ± 15 minutes, with the principal uncertainties being the Titan atmospheric density, Titan topography, and uncertainties in the probe parachute area and drag coefficients, including wind-induced oscillations.)

To prevent any interference with reception of the probe data, no transmissions from the orbiter were allowed during probe relay (FR80A4) at any frequency. Transmissions from the orbiter high-gain antenna at X-band were turned off by the probe mission sequence shortly after the orbiter turned away from the Earth to point the high-gain antenna at the predicted probe landing site. Additional protection was included in the probe mission sequence and in the configuration of the orbiter fault protection algorithms to ensure no violation of this flight rule; this protection included periodic or cyclic commands to ensure that transmissions were kept off at S, X, Ka, and Ku frequencies.

When the probe data collection was complete, that data were write-protected on each SSR. The spacecraft then turned to view Titan with the optical remote sensing instruments, until about one hour after closest approach. A specific science profile was not defined, but the best combination of remote sensing with fields, particles, and waves, and INMS observations were defined for the first close Titan flyby (Titan-1) within orbiter operating constraints. Instrument data could not overwrite the probe data on the SSRs.

Soon after closest approach, the orbiter turned the high-gain antenna towards Earth and began transmitting the recorded probe data. The complete, four-fold redundant set of probe data was transmitted twice, and its receipt verified, before the write protection on that portion of the SSR was lifted by ground command, marking probe mission completion. The first playback after Titan closest approach was to the Canberra 70-meter antenna and included all of the probe data. The second playback including all of the probe data and the orbiter instrument observations was returned over the subsequent Madrid 70-meter tracking pass, which was at higher tracking elevations.

2.6.5 SATURN ORBITAL OPERATIONS

2.6.5.1 Prime Mission

After the probe data receipt was verified, the orbiter continued on the 75-orbit tour of the Saturnian system, which included 45 close Titan flybys for gravity assist and science acquisition. The Titan flybys and Saturn orbits were designed to maximize science coverage while meeting resource and operations limitations. Figure 2.6-18 shows a view from above Saturn's north pole of all tour orbits in a rotating coordinate system in which the Sun direction is fixed. The broad range of orbit orientations allowed detailed survey of the magnetosphere and atmosphere of Saturn. Figure 2.6-19 shows a side view, from a direction perpendicular to the plane formed by the Saturn–Sun

line and Saturn's North Pole, in which the inclination of the orbits is apparent. The characteristics of the orbits are summarized in Table 2.6-3.

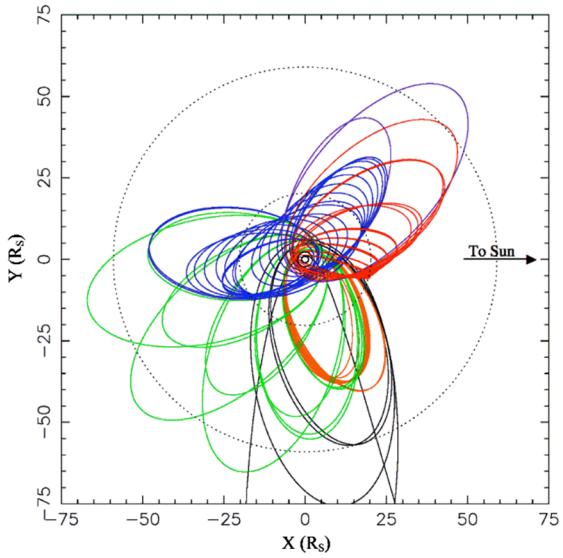

Figure 2.6-18 Tour Petal Plot – North Pole View.

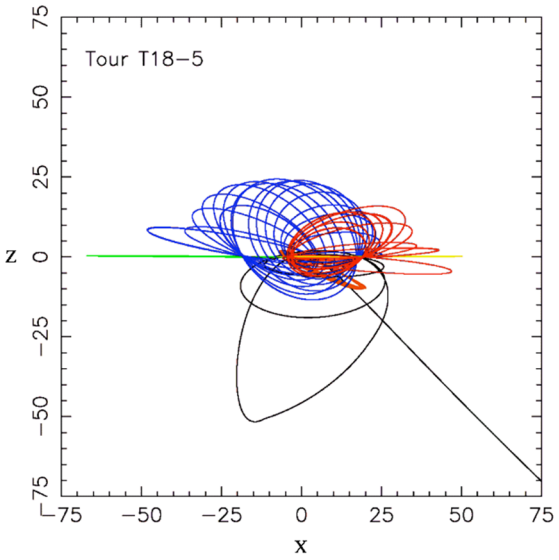

Figure 2.6-19. Tour Petal Plot – Side View.

Table 2.6-3 Characteristics of the orbits.

Cassini Tour Encounters				All times are in SCET. For events with nonzero duration, epoch given is start.			
Seq	Rev	Name	Event	Epoch (SCET)	Date	DOW	Comment
S1	0	0PH (t)	Phoebe	2004 - 163T19 : 33	Jun11	Fri	was P1; inbound 1997 km flyby, v=6.4 km/s, Phase=25 deg
S5	a	aTI (t)	Titan	2004 - 300T15 : 30	Oct26	Tue	T N / A; inbound 1, 200 km flyby, v=6.1 km/s, phase=91 deg
S6	b	bTI (t)	Titan	2004 - 348T11 : 36	Dec13	Mon	T N / A; inbound 2, 336 km flyby, v=6.0 km/s, phase=98 deg
S7	c	cTI (t)	Titan	2005 - 014T11 : 04	Jan14	Fri	T N / A; inbound 60, 000 km flyby, v=5.4 km/s, phase=93 deg
S8	3	3TI (t)	Titan	2005 - 046T06 : 54	Feb15	Tue	T3; inbound 950 km flyby, v=6.0 km/s, phase=102 deg
S9	4	4EN (t)	Enceladus	2005 - 068T09 : 06	Mar09	Wed	was E1; inbound 499 km flyby, v=6.6 km/s, phase=43 deg
S9	5	5TI (t)	Titan	2005 - 090T19 : 55	Mar31	Thu	T4; outbound 2, 523 km flyby, v=5.9 km/s, phase=65 deg
S10	6	6TI (t)	Titan	2005 - 106T19 : 05	Apr16	Sat	T5; outbound 950 km flyby, v=6.1 km/s, phase=127 deg
S12	11	11EN (t)	Enceladus	2005 - 195T19 : 57	Jul14	Thu	was E2; inbound 1000 km flyby, v=8.1 km/s, phase=43 deg
S13	13	13TI (t)	Titan	2005 - 234T08 : 40	Aug22	Mon	T6; outbound 4, 015 km flyby, v=5.8 km/s, phase=42 deg

Table 2.6-3 Characteristics of the orbits.

Cassini Tour Encounters				All times are in SCET. For events with nonzero duration, epoch given is start.			
Seq	Rev	Name	Event	Epoch (SCET)	Date	DOW	Comment
S14	14	14TI (t)	Titan	2005 - 250T07 : 50	Sep07	Wed	T7; outbound 950 km flyby, v=6.1 km/s, phase=84 deg
S14	15	15HY (t)	Hyperion	2005 - 269T01 : 41	Sep26	Mon	was H1; outbound 990 km flyby, v=5.6 km/s, phase=45 deg
S15	16	16DI (t)	Dione	2005 - 284T17 : 58	Oct11	Tue	was D1; inbound 500 km flyby, v=9.0 km/s, phase=66 deg
S15	17	17TI (t)	Titan	2005 - 301T03 : 58	Oct28	Fri	T8; inbound 1, 446 km flyby, v=5.9 km/s, phase=105 deg
S16	18	18RH (t)	Rhea	2005 - 330T22 : 35	Nov26	Sat	was R1; inbound 500 km flyby, v=7.3 km/s, phase=87 deg
S17	19	19TI (t)	Titan	2005 - 360T18 : 54	Dec26	Mon	T9; outbound 10, 429 km flyby, v=5.6 km/s, phase=67 deg
S17	20	20TI (t)	Titan	2006 - 015T11 : 36	Jan15	Sun	T10; inbound 2, 042 km flyby, v=5.8 km/s, phase=121 deg
S18	21	21TI (t)	Titan	2006 - 058T08 : 20	Feb27	Mon	T11; outbound 1, 812 km flyby, v=5.9 km/s, phase=93 deg
S19	22	22TI (t)	Titan	2006 - 077T23 : 58	Mar18	Sat	T12; inbound 1, 947 km flyby, v=5.8 km/s, phase=148 deg
S20	23	23TI (t)	Titan	2006 - 120T20 : 53	Apr30	Sun	T13; outbound 1, 853 km flyby, v=5.8 km/s, phase=121 deg
S20	24	24TI (t)	Titan	2006 - 140T12 : 13	May20	Sat	T14; inbound 1, 879 km flyby, v=5.8 km/s, phase=163 deg
S21	25	25TI (t)	Titan	2006 - 183T09 : 12	Jul02	Sun	T15; outbound 1, 911 km flyby, v=5.8 km/s, phase=148 deg
S22	26	26TI (t)	Titan	2006 - 203T00 : 25	Jul22	Sat	T16; inbound 950 km flyby, v=6.0 km/s, phase=105 deg
S23	28	28TI (t)	Titan	2006 - 250T20 : 12	Sep07	Thu	T17; inbound 950 km flyby, v=6.0 km/s, phase=45 deg
S24	29	29TI (t)	Titan	2006 - 266T18 : 52	Sep23	Sat	T18; inbound 950 km flyby, v=6.0 km/s, phase=90 deg
S24	30	30TI (t)	Titan	2006 - 282T17 : 23	Oct09	Mon	T19; inbound 950 km flyby, v=6.0 km/s, phase=81 deg
S25	31	31TI (t)	Titan	2006 - 298T15 : 51	Oct25	Wed	T20; inbound 950 km flyby, v=6.0 km/s, phase=25 deg
S26	35	35TI (t)	Titan	2006 - 346T11 : 35	Dec12	Tue	T21; inbound 950 km flyby, v=6.0 km/s, phase=124 deg
S26	36	36TI (t)	Titan	2006 - 362T10 : 00	Dec28	Thu	T22; inbound 1, 500 km flyby, v=5.9 km/s, phase=62 deg
S27	37	37TI (t)	Titan	2007 - 013T08 : 34	Jan13	Sat	T23; inbound 950 km flyby, v=6.0 km/s, phase=53 deg
S27	38	38TI (t)	Titan	2007 - 029T07 : 12	Jan29	Mon	T24; inbound 2, 776 km flyby, v=5.8 km/s, phase=73 deg
S28	39	39TI (t)	Titan	2007 - 053T03 : 10	Feb22	Thu	T25; outbound 953 km flyby, v=6.3 km/s, phase=161 deg

Table 2.6-3 Characteristics of the orbits.

Cassini Tour Encounters				All times are in SCET. For events with nonzero duration, epoch given is start.			
Seq	Rev	Name	Event	Epoch (SCET)	Date	DOW	Comment
S28	40	40TI (t)	Titan	2007 - 069T01 : 47	Mar10	Sat	T26; outbound 956 km flyby, v=6.3 km/s, phase=149 deg
S28	41	41TI (t)	Titan	2007 - 085T00 : 21	Mar26	Mon	T27; outbound 953 km flyby, v=6.3 km/s, phase=144 deg
S29	42	42TI (t)	Titan	2007 - 100T22 : 57	Apr10	Tue	T28; outbound 951 km flyby, v=6.3 km/s, phase=137 deg
S29	43	43TI (t)	Titan	2007 - 116T21 : 32	Apr26	Thu	T29; outbound 951 km flyby, v=6.3 km/s, phase=130 deg
S30	44	44TI (t)	Titan	2007 - 132T20 : 08	May12	Sat	T30; outbound 950 km flyby, v=6.3 km/s, phase=121 deg
S30	45	45TI (t)	Titan	2007 - 148T18 : 51	May28	Mon	T31; outbound 2, 425 km flyby, v=6.1 km/s, phase=114 deg
S31	46	46TI (t)	Titan	2007 - 164T17 : 46	Jun13	Wed	T32; outbound 950 km flyby, v=6.3 km/s, phase=107 deg
S31	47	47TI (t)	Titan	2007 - 180T17 : 05	Jun29	Fri	T33; outbound 1, 942 km flyby, v=6.2 km/s, phase=96 deg
S32	48	48TI (t)	Titan	2007 - 200T00 : 39	Jul19	Thu	T34; inbound 1, 302 km flyby, v=6.2 km/s, phase=34 deg
S33	49	49TI (t)	Titan	2007 - 243T06 : 34	Aug31	Fri	T35; outbound 3, 227 km flyby, v=6.1 km/s, phase=87 deg
S33	49	49IA (t)	Iapetus	2007 - 253T12 : 33	Sep10	Mon	was I 1; outbound 1000 km flyby, v=2.4 km/s, phase=65 deg
S34	50	50TI (t)	Titan	2007 - 275T04 : 48	Oct02	Tue	T36; outbound 950 km flyby, v=6.3 km/s, phase=67 deg
S35	52	52TI (t)	Titan	2007 - 323T00 : 52	Nov19	Mon	T37; outbound 950 km flyby, v=6.3 km/s, phase=51 deg
S35	53	53TI (t)	Titan	2007 - 339T00 : 06	Dec05	Wed	T38; outbound 1, 300 km flyby, v=6.3 km/s, phase=70 deg
S36	54	54TI (t)	Titan	2007 - 354T22 : 56	Dec20	Thu	T39; outbound 953 km flyby, v=6.3 km/s, phase=61 deg
S36	55	55TI (t)	Titan	2008 - 005T21 : 26	Jan05	Sat	T40; outbound 949 km flyby, v=6.3 km/s, phase=37 deg
S38	59	59TI (t)	Titan	2008 - 053T17 : 39	Feb22	Fri	T41; outbound 959 km flyby, v=6.4 km/s, phase=30 deg
S38	61	61EN (t)	Enceladus	2008 - 072T19 : 05	Mar12	Wed	was E3; inbound 995 km flyby, v=14.6 km/s, phase=56 deg
S39	62	62TI (t)	Titan	2008 - 085T14 : 35	Mar25	Tue	T42; outbound 950 km flyby, v=6.4 km/s, phase=21 deg
S40	67	67TI (t)	Titan	2008 - 133T10 : 09	May12	Mon	T43; outbound 950 km flyby, v=6.4 km/s, phase=35 deg
S40	69	69TI (t)	Titan	2008 - 149T08 : 33	May28	Wed	T44; outbound 1, 316 km flyby, v=6.3 km/s, phase=23 deg
EM	78	78TI (t)	Titan	2008 - 213T02 : 20	Jul31	Thu	T45; outbound 3, 980 km flyby, v=6.1 km/s, phase=7 deg

Thirteen close flybys and dozens of more distant flybys of selected icy satellites were also completed to determine icy satellite surface compositions and geologic histories. Cassini's orbital inclination varied widely to investigate the field, particle, and wave environment at high latitudes, including the hypothesized source of the unique Saturn kilometric radiation. High inclinations also permitted high-latitude Saturn radio occultations, viewing of Saturn's polar regions, traversal through unknown regions of the magnetosphere, and more vertical viewing of Saturn's rings.

On a typical day in the tour, science data was collected continuously for 15 hours by the spacecraft reorienting itself at a variety of targets. One instrument at a time controlled the pointing of the spacecraft, and other instruments would "ride along" and collect data at the same time.

The remaining 9 hours were spent on Earth-point, downlinking (or playing back) the data. During downlink, since the Z-axis of the spacecraft must be fixed to Earth, the spacecraft could only rotate about the high-gain antenna to collect fields, particles, and waves data. This sweeping during playback allowed three-dimensional and temporal measurements of the fields and particles environment.

The Prime Mission ended on June 30, 2008, for a total mission duration of 10.7 years. The spacecraft and all instruments remained healthy at the end of the tour. The tour was very successful and made many new scientific discoveries about the Saturn system. Several of the mission's achievements are highlighted in the following paragraphs.

- During the 45 targeted flybys of Titan, many important observations were made about Saturn's largest moon. The atmosphere of Titan is composed of 98% nitrogen with the remainder mostly methane. Other observations have revealed sand dunes, ethane and methane lakes in both the northern and southern polar regions, and large ethane clouds. Scientists also theorized that an underground ocean may exist on Titan separating the crust from the core.
- Enceladus is the most geologically active moon in the Saturnian system. Flybys of this moon have revealed varying surface features such as craters in the northern hemisphere and recent resurfacing activity and "tiger stripes" in the southern hemisphere, near the south pole. The "tiger stripes" are the source of jets that spew water vapor away from the surface of Enceladus. The ejected particles are the primary source of Saturn's E-ring.
- When Cassini launched in 1997, Saturn only had 18 known moons. As of 2019, there are 82 known moons in orbit around the planet, of which 53 have received official names. The new moons discovered by Cassini include Methone, Pallene, Polydeuces, Anthe, and Daphnis. Moonlets have also been discovered in the rings, which may have arisen from the shattering of a larger moon.
- Iapetus is one of Saturn's most interesting moons. Observations have revealed that one-half of the moon (the leading hemisphere) is very dark, while the light side is almost five times brighter. Scientists theorize that the dark side of the moon is coated in particles that it has swept up during its orbit. Flybys have also revealed a

13 km ridge around the 1,500 km diameter equator of the moon with mountains larger than the Olympus Mons on Mars.

2.6.5.2 Extended Missions

2.6.5.2.1 Equinox Mission

At the conclusion of the Prime Mission tour phase on June 30, 2008, Cassini initiated a 2-year 3-month extended mission named the Equinox Mission (EM). This extended mission began on July 1, 2008, and was funded through September 30, 2010. The EM continued to explore the Saturn system's rings, magnetosphere, and icy satellites, especially Enceladus. The extension also allowed scientists to make observations during Saturn's northern vernal equinox. The Equinox Mission trajectory consisted of 64 more orbits of Saturn, 28 more Titan flybys, and 11 more close icy moon flybys, seven of which were Enceladus flybys.

2.6.5.2.2 Solstice Mission

At the conclusion of the Equinox Mission, the Cassini team initiated a 7-year mission extension named the Solstice Mission, stretching the tour to September 15, 2017. The overarching goal of the Solstice Mission was to observe the complex and dynamic Saturn system over a wider range of geometries and conditions, including Saturn's May 2017 northern summer solstice. By end of mission, Cassini observed most of the northern winter season and all of the northern spring season.

On November 30, 2016, Cassini began the penultimate phase of the mission, the ring-grazing orbits. This 20-week phase consisted of 20 high-inclination orbits with apoapses near Titan's orbit and periapses just outside the main ring system. The final targeted Titan flyby on April 22, 2017, set Cassini on the Grand Finale—a series of 22 orbits with periapses that passed between Saturn and its rings; a region no spacecraft had explored before.

On September 11, 2017, Titan gave Cassini a "goodbye kiss," a distant non-targeted flyby that put Cassini on its impact trajectory with Saturn. End-of-mission occurred at 11:56 UTC on September 15, 2017, when Cassini plunged into Saturn's atmosphere and Earth lost the spacecraft's signal forever.

section

3

Science Mission Results

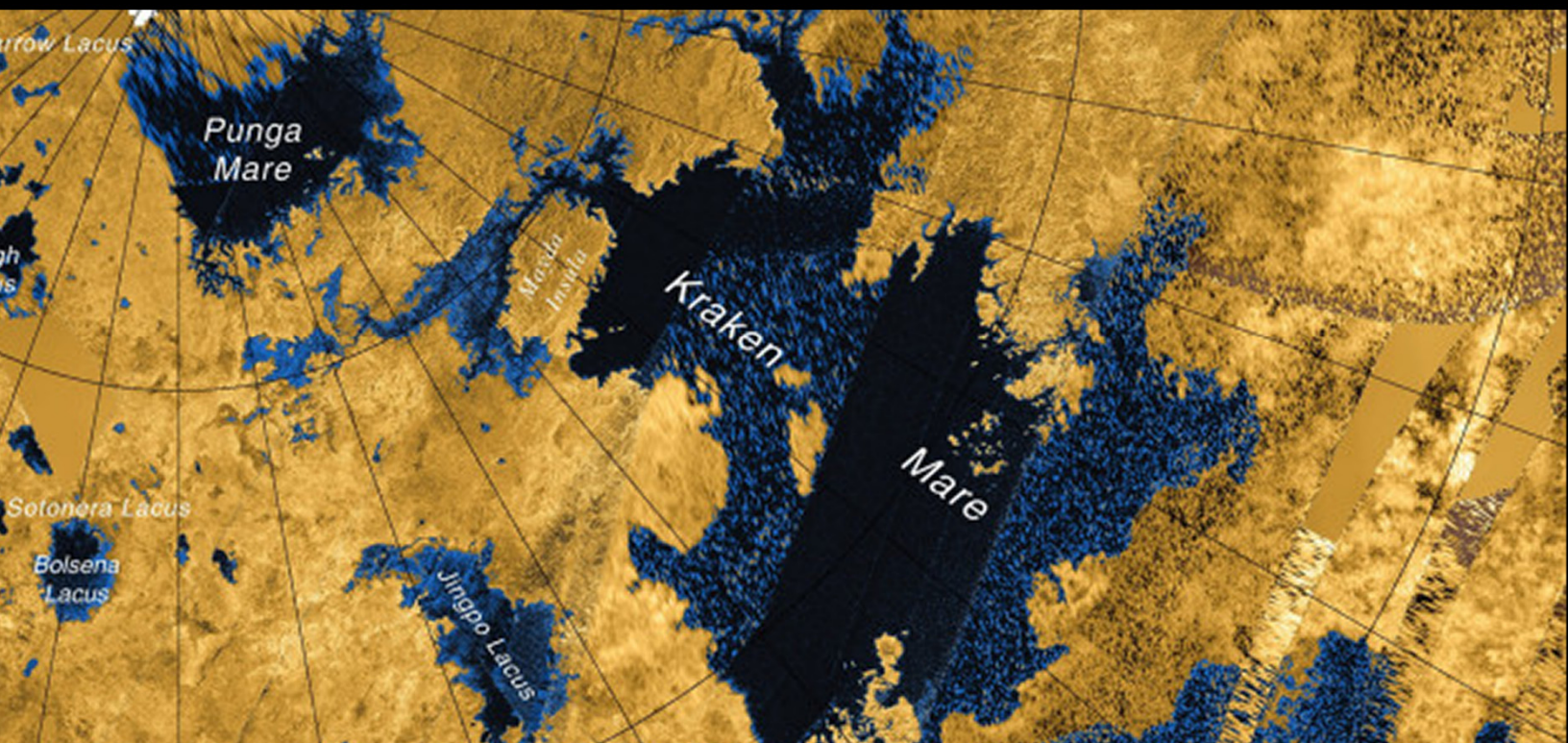

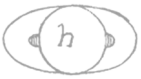

3 SCIENCE MISSION RESULTS

For ease of researchability, Volume 1 Section 3 Science Mission Results is separated into three main categories: 3.0 Mission Science Highlights and Science Objectives Assessment; 3.1 Discipline Science Results; and 3.2 Instrument Science Results. All categories are also available as stand-alone documents.

The 3.1 Discipline Science Results category is separated further into six disciplines:

- Huygens
- Icy Satellites
- MAPS
- Rings
- Saturn
- Titan

The 3.2 Instrument Science Results category is separated into three sub-categories followed by the respective instrument: (totaling 12 instruments)

- Optical Remote Sensing Instruments
  - Composite Infrared Spectrometer (CIRS)
  - Imaging Science Subsystem (ISS)
  - Ultraviolet Imaging Spectrograph (UVIS)
  - Visual and Infrared Mapping Spectrometer (VIMS)
- Fields, Particles, and Waves Sensing Instruments
  - Cassini Plasma Spectrometer (CAPS)
  - Cosmic Dust Analyzer (CDA)
  - Ion and Neutral Mass Spectrometer (INMS)
  - Magnetometer (MAG)
  - Magnetospheric Imaging Instrument (MIMI)
  - Radio and Plasma Wave Science (RPWS)
- Microwave Remote Sensing Instruments
  - Titan Radar Mapper (RADAR)
  - Radio Science Subsystem (RSS)

3.0 Mission Science Highlights and Science Objectives Assessment

NASA/JPL-CALTECH/ASI/USGS

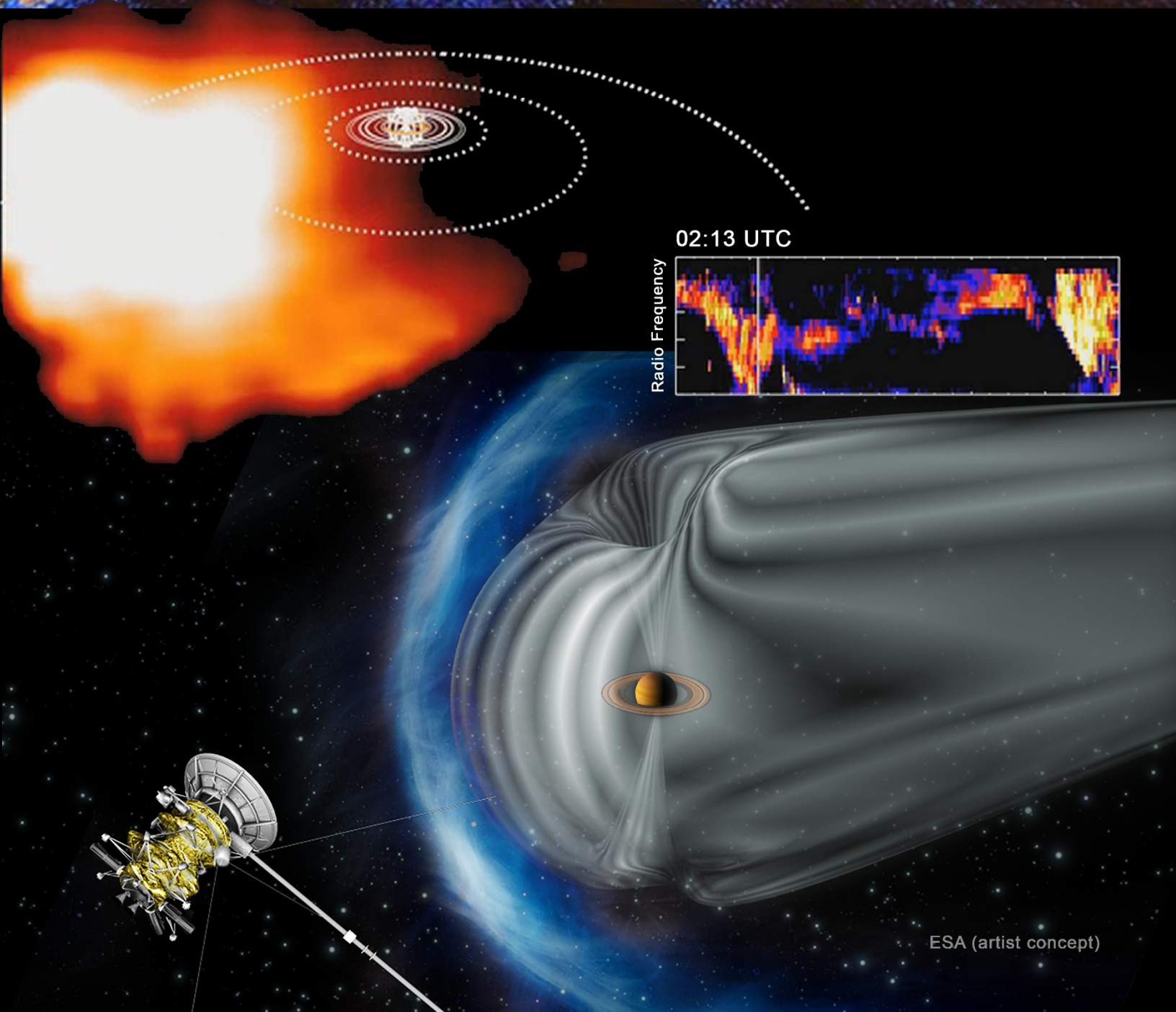

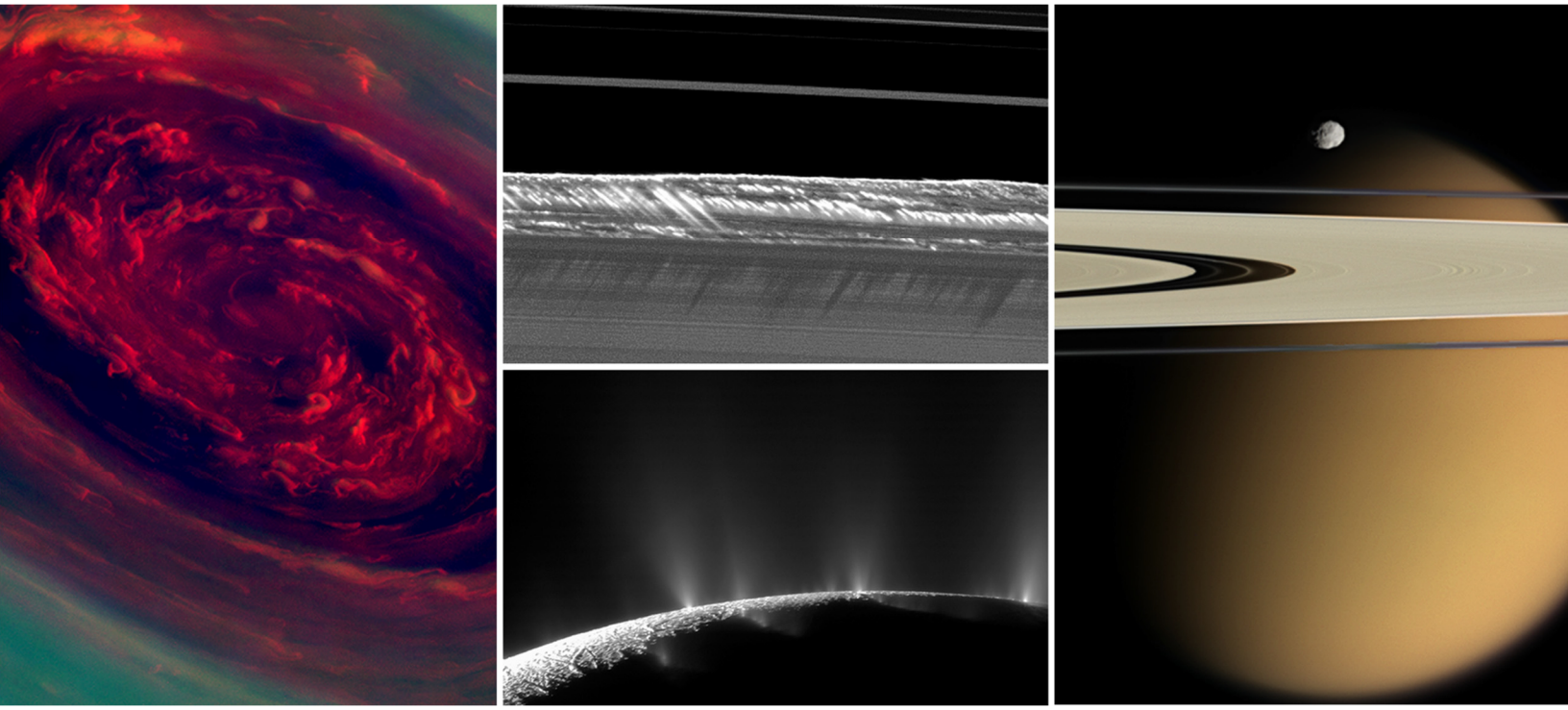

Mission Science Highlights and Science Objectives Assessment

Cassini-Huygens, humanity's most distant planetary orbiter and probe to date, provided the first in-depth, close up study of Saturn, its magnificent rings and unique moons, including Titan and Enceladus, and its giant magnetosphere. Discoveries from the Cassini-Huygens mission revolutionized our understanding of the Saturn system and fundamentally altered many of our concepts of where life might be found in our solar system and beyond. Cassini-Huygens arrived at Saturn in 2004, dropped the parachuted probe named Huygens to study the atmosphere and surface of Saturn's planet-sized moon Titan, and orbited Saturn for the next 13 years making remarkable discoveries. When it was running low on fuel, the Cassini orbiter was programmed to vaporize in Saturn's atmosphere in 2017 to protect the ocean worlds, Enceladus and Titan, where it discovered potential habitats for life.

CONTENTS

Figures

Tables

EXECUTIVE SUMMARY

The scientific findings and discoveries of the Cassini-Huygens mission revolutionized our understanding of the Saturn system. This international mission consisted of the Cassini Saturn orbiter and the Huygens Titan probe. With 19 participating countries, the project was an archetype for effective international collaboration.

> The primary goal of Cassini-Huygens is to conduct an in-depth exploration of the Saturn system [NASA 1989].

Overall, the Cassini-Huygens mission was a tremendous success, meeting or exceeding essentially all of its science goals listed in the 1989 Cassini and Huygens Announcements of Opportunity (AOs) and in the Cassini Traceability Matrices first defined in 2007 near the end of the Prime Mission (PM). A complete assessment of these objectives is given in a set of color-coded tables in the Project Science Assessment section.

Due to the very broad scope of the Cassini-Huygens mission, this short overview just scratches the surface of the breadth and depth of Cassini-Huygens' scientific findings. The details of the scientific findings of the mission, including discipline and team science assessments, can be found in the following reports in Section 3. They provide in-depth information on the many investigations that constitute the Cassini-Huygens mission. A concise overview of the scientific findings of Cassini's 13-year mission can be found in Spilker [2019].

A vast amount of unique scientific data was returned over Cassini's 13-year mission and a large volume of that data has yet to be thoroughly analyzed and interpreted. Planetary scientists continue to analyze these data, and will do so for decades to come. All of the Cassini data and supporting information are stored in the Planetary Data System (PDS), available for analysis by future generations of planetary scientists.

The following sections present a brief history of the mission, ties to the previous Decadal Survey, and a short mission overview. The chapter includes the mission science objectives and a project assessment of those objectives, as well as the mission's top science highlights and major open questions. The Cassini-Huygens mission successfully answered a large number of scientific questions and posed many new ones, setting the stage for future missions to Saturn and the outer planets.

Origin of the Cassini Mission

Three trailblazing spacecraft, Pioneer 11 in 1979, Voyager 1 in 1980, and Voyager 2 in 1981, flew past Saturn and provided short, fleeting glimpses of this unique system, including the giant moon, Titan. Beginning in 2004, NASA's Cassini spacecraft became the first robotic craft to orbit Saturn and perform detailed seasonal and temporal studies. In 2005, the European Space Agency's (ESA) Huygens probe, carried by the Cassini orbiter, was the first human-made object to land on an outer planet moon, Titan.

The Cassini orbiter was named after the Italian/French astronomer Giovanni Domenico Cassini, who discovered several Saturnian satellites and ring features, including the Cassini division, between 1671–1685. The Titan probe was named after the Dutch astronomer Christiaan Huygens who discovered Titan in 1655.

Cassini-Huygens was an international flagship mission, a cooperative undertaking by NASA, ESA, and the Italian space agency (Agenzia Spaziale Italiana (ASI)). Initial conversations about this mission began not long after the Voyager flybys in the early 1980s. The Voyager instruments were unable to penetrate Titan's thick photochemical haze and many new questions were raised by these flybys. Discussions and planning for a return mission to Saturn, including an in-depth study of the system and a probe into Titan's atmosphere, spanned many years. Some of the discussion that follows can also be found in the Space Science Reviews chapter by Matson et al. [2002].

Formal discussions began in June 1982 when a Joint Working Group was formed by the Space Science Committee of the European Science Foundation and the Space Science Board of the National Academy of Science in the United States. The charter of this Joint Working Group was to study possible modes of cooperation between the United States and Europe in the field of planetary science. Seven years later, after much discussion and many meetings between these international partners, the Cassini and Huygens AOs were released in 1989.

The scientific objectives for the mission and the implementation approach were developed further by the work of the Joint NASA/ESA Assessment Study that was carried out in mid-1984 through 1985, and in 1988. These study groups defined the scientific objectives for the Cassini-Huygens mission and published them in the group's final reports [ESA 1985, 1988]. These objectives then became formally established when they were incorporated into both the NASA and ESA Announcements of Opportunity [ESA 1989; NASA 1989, 1991]. Early summaries of the mission can be found in Lebreton [1991], a book edited by Spilker [1997], and in Matson et al. [2002].

Instrument Teams and Interdisciplinary Investigations

Prior to issuing the Announcements of Opportunity, NASA, ESA, and ASI carried out informal discussions regarding organization and management of the Cassini-Huygens mission. These agreements were formalized in a Memoranda of Understanding (MOUs) between NASA and ESA, signed in 1990, and between NASA and ASI, signed in 1993. The scientific organization of the mission evolved from these memoranda.

The selections of scientific instruments and facility teams were coordinated between NASA and ESA. Investigations for the Huygens probe were announced by ESA in September 1990, and NASA announced Saturn orbiter selections in November 1990. Both agencies also selected interdisciplinary investigations. The ESA Huygens selection was comprised of six Principal Investigator (PI) instruments and three interdisciplinary science (IDS) investigations. The initial NASA Cassini selection was comprised of seven PI-led instruments, four facility instruments, and seven IDS investigations. Facility instruments were scientific instruments already selected and defined by NASA

to be part of the Cassini payload (e.g., the imaging cameras). Scientists proposed to be Team Members (TMs) or Team Leaders (TLs) for these predefined instruments. PI-led instruments included a full instrument proposal, along with a proposed list of Co-Investigators (Co-Is). IDSs proposed scientific investigations relevant to the mission. With the death of NASA-selected IDS James Pollock in 1994, the number of NASA-selected IDS investigations was reduced to six. Absent from the proposed Cassini instruments was one capable of measuring the properties of Titan's upper atmosphere. Such an instrument was regarded as critical to the mission, so in May 1991 NASA issued a second AO, for the Ion and Neutral Mass Spectrometer (INMS) TL and TMs. The results of that selection were announced in February 1992. For facility instruments, NASA selected a TL and TMs, while for PI-led instruments, NASA selected the PI along with his/her proposed team of Co-Is.

Cassini and Huygens accommodated 27 major scientific investigations that were supported by 18 specially designed instruments, 12 on the Cassini orbiter and 6 on the Huygens probe. Lists of the instrument and IDS investigations for Cassini and Huygens can be found in Tables 3-1 and 3-2.

The flight operations of the Cassini mission were carried out at the Jet Propulsion Laboratory (JPL) in Pasadena, California. The data were collected at NASA's Deep Space Network (DSN) stations, with support at times from ESA stations, and sent to the instrument teams. The operations of the Cassini instruments were distributed to their home institutions. Cassini's distributed operations represented a paradigm shift from previous flagship missions, such as Voyager and Galileo, where operations were conducted primarily at JPL. The instrument teams analyzed their respective instrumental data and prepared instrumental operation sequences at their home institution and transmitted them to JPL for uplink. The flight operations of the Huygens probe were carried out from ESA's European Space Operations Center (ESOC) in Darmstadt, Germany, where the Huygens Operations Center (HPOC) was also established.

Table 3-1. Cassini orbiter investigations. If two scientists are listed, the first individual was the PI or TL at the time of AO selection in 1990. The second name is the individual who was leading the instrument team at the end of the mission, with a transition at some point during the mission.

Investigation/Acronym	Scientist/Affiliation	Brief Objectives
Cassini Plasma Spectrometer (CAPS)	D. Young (PI), Southwest Research Institute J.H. Waite (PI), Southwest Research Institute	In situ study of plasma within and near Saturn's magnetic field
Cosmic Dust Analyzer (CDA)	E. Grün (PI), Max Planck Institut für Kernphysik R. Srama (PI), Universität Stuttgart	In situ study of ice and dust grains in the Saturn system
Composite Infrared Spectrometer (CIRS)	V. Kunde (PI), NASA Goddard Space Flight Center F.M. Flasar (PI), Goddard Space Flight Center	Temperature and composition of surfaces, atmospheres, and rings within the Saturn system
IDS – Magnetosphere and Plasma	M. Blanc (IDS), Research Institute of Astrophysics and Planetology, Toulouse	Interdisciplinary study of plasma circulation and magnetosphere-ionosphere coupling
IDS – Rings and Dust	J. Cuzzi (IDS), NASA Ames Research Center	Interdisciplinary study of rings and dust within the Saturn system
IDS – Magnetosphere and Plasma	T. Gombosi (IDS), University of Michigan	Interdisciplinary study of the plasma environment in Saturn's magnetosphere
IDS – Atmospheres	T. Owen (IDS), University of Hawaii	Interdisciplinary study of the atmospheres of Titan and Saturn
IDS – Satellites	L. Soderblom (IDS), U.S. Geological Survey	Interdisciplinary study of the satellites of Saturn

Table 3-1. Cassini orbiter investigations. If two scientists are listed, the first individual was the PI or TL at the time of AO selection in 1990. The second name is the individual who was leading the instrument team at the end of the mission, with a transition at some point during the mission.

Investigation/Acronym	Scientist/Affiliation	Brief Objectives
IDS – Aeronomy and Solar Wind Interaction	D. Strobel (IDS), Johns Hopkins University	Interdisciplinary study of aeronomy in the Titan and Saturn atmospheres
IDS – Origins	J. Pollock (IDS), NASA Ames Research Center (deceased 1994)	Interdisciplinary study of the origin and evolution of the Saturn system
Ion and Neutral Mass Spectrometer (INMS)	J.H. Waite (TL), Southwest Research Institute	In-situ compositions of neutral and charged particles within the Saturn magnetosphere
Imaging Science Subsystem (ISS)	C. Porco (TL), Space Science Institute	Multispectral imaging of Saturn, Titan, rings, and the icy satellites to observe their properties
Dual Technique Magnetometer (MAG)	D. Southwood (PI), Imperial College M. Dougherty (PI), Imperial College	Study of Saturn's magnetic field and interactions with the solar wind
Magnetospheric Imaging Instrument (MIMI)	S. Krimigis (PI), Applied Physics Laboratory D. Mitchell (PI), Applied Physics Laboratory	Global magnetospheric imaging and in-situ measurements of Saturn's magnetosphere and solar wind interactions
Titan Radar Mapper (RADAR)	C. Elachi (TL), NASA Jet Propulsion Laboratory	Radar imaging, altimetry, and passive radiometry of Titan's surface
Radio and Plasma Wave Science (RPWS)	D. Gurnett (PI), University of Iowa W. Kurth (PI), University of Iowa	Measure the electric and magnetic fields and electron density and temperature in the interplanetary medium and within the Saturn magnetosphere
Radio Science Subsystem (RSS)	A. Kliore (TL), NASA Jet Propulsion Laboratory D. French (TL), Wellesley College	Study of atmospheric and ring structure, gravity fields, and gravitational waves
Ultraviolet Imaging Spectrograph (UVIS)	L. Esposito (PI), University of Colorado	Spectra and low-resolution imaging of atmospheres and rings for structure, chemistry, and composition
Visible and Infrared Mapping Spectrometer (VIMS)	R. Brown (TL), NASA Jet Propulsion Laboratory	Spectral mapping to study composition and structure of surfaces, atmospheres, and rings

Table 3-2. Huygens probe investigations. The table below lists the Huygens instrument and IDS investigations as selected in response to the Huygens 1989 AO. (Table after Matson et al. [2002])

Investigation/Acronym	Scientist/Affiliation	Brief Objectives
Aerosol Collector Pyrolyser (ACP)	G. Israel (PI), CNRS, Service d'Aéronomie	In situ study of clouds and aerosols in the Titan atmosphere
Descent Imager and Spectral Radiometer (DISR)	M. Tomasko (PI), University of Arizona	Temperatures and images of Titan's atmospheric aerosols and surface
Doppler Wind Experiment (DWE)	M. Bird (PI), Universität Bonn	Study of winds from their effect on the *Probe* during the Titan descent
Gas Chromatograph and Mass Spectrometer (GCMS)	H. Niemann (PI), NASA Goddard Space Flight Center	In situ measurement of chemical composition of gases and aerosols in Titan's atmosphere
Huygens Atmospheric Structure Instrument (HASI)	M. Fulchignoni (PI), Observatoire de Paris-Meudon	In situ study of Titan atmospheric physical and electrical properties
IDS – Titan Aeronomy	D. Gautier (IDS), Observatoire de Paris-Meudon	Interdisciplinary study of the aeronomy of Titan's atmosphere
IDS – Titan Atmosphere-Surface Interactions	J. Lunine (IDS), Cornell University	Interdisciplinary study of Titan atmosphere-surface interactions
IDS – Titan Organic Chemistry	F. Raulin (IDS), Université Paris, Val de Marne	Interdisciplinary study of Titan's chemistry and exobiology
Surface Science Package (SSP)	J. Zarnecki (PI), University of Kent	Measurement of the physical properties of Titan's surface

Defining Scientific Objectives

Further development of the AO scientific objectives for Cassini-Huygens was carried out by the Project Science Group (PSG) and the Huygens Science Working Team (HSWT). These groups, chartered by the AOs, were the Program's scientific advisory bodies. Chaired and managed by the Cassini Project Scientist and Huygens Project Scientist, they included interdisciplinary scientists, and participants from all instrument teams. They provided more detail than that specified in the AO requirements, developed Science Traceability Matrices post 2007 for the Equinox and Solstice Missions, and kept the requirements up to date with respect to any new discoveries. In the PSG, this work was done by a set of committees called Discipline Working Groups (DWGs) specializing in each discipline's science requirements and co-chaired by Interdisciplinary Scientists (IDSs) as was envisioned in the AO.

The Cassini team was an archetype for effective international collaboration, with nineteen participating countries.

The Cassini team of over 350 scientists was organized into five DWGs: Titan, Icy Satellites, Rings, Magnetospheres and Plasma Science (MAPS), and Saturn overseen by the Cassini Project Scientist. These groups were comprised of representatives from the 12 instrument teams and were typically headed by one or more Interdisciplinary Scientists. The Cassini team was an archetype for effective international collaboration, with 19 participating countries. Over the course of the mission, the Cassini family continued to grow by adding a Cassini Participating Scientist Program in addition to the many team associates, postdoctoral fellows, and graduate students. The first class of 12 Participating Scientists was selected in 2011, and included four international scientists. A total of 41 Participating Scientists were selected over five years. A vast amount of unique scientific data was returned over its 13-year mission and a large volume of that data has yet to be thoroughly analyzed and interpreted. Planetary scientists continue to analyze these data, and will do so for decades to come.

The PSG and the HSWT had the responsibility to translate the science requirements into strategies for observing and measuring. The workload was shared by the five DWGs, special working groups such as the Titan Atmospheric Working Group (TAMWG) and Saturn Atmospheric Working Group (SAMWG), and instrument scientific investigation teams under the direction of the PIs and TLs. These strategies were then translated into specific instrumental observations and measurements by the scientists and the engineering and operations staffs of the individual instruments. All of these steps were closely coordinated with the spacecraft operations staffs at JPL and ESOC (for Huygens instruments). Minute-by-minute observation planning was conducted by PSG-sanctioned Operations Science Teams (OSTs; for Titan and Icy Satellite) and project-sanctioned Target Working Teams (TWTs; for Saturn, Rings, and MAPS), which were comprised of instrument team science and engineering representatives along with project-appointed Investigation Scientists (ISs), science planning and spacecraft engineers, and spacecraft operators.

Cassini Rules of the Road

Before Cassini arrived at Saturn in 2004, the Project Science Group crafted a set of Cassini/Huygens Rules of the Road that were created based on the MAPS Rules of the Road (see Appendix A for more details). The Cassini Rules of the Road offered guidelines for multi-investigation studies using data that were not yet in the PDS. Each Cassini instrument team also crafted its own set of Instrument Rules of the Road to govern their investigations. The Cassini Rules of the Road were the overarching set of Rules of the Road for the mission. The goal of these Rules of the Road was to foster collaboration between the instrument teams.

The Cassini/Huygens Rules of the Road were:

- "Rules of the Road" offers guidelines for multi-investigation studies only and it applies equally and fairly to all Cassini/Huygens teams.
- Cassini/Huygens teams are headed by a PSG member (PI, TL, or IDS). Team members are: TL, official Co-Is, NASA/ESA selected Facility Team Members, and their direct associates. Each associate is "authenticated" by the team lead.
- Each Cassini/Huygens Team has overall responsibility for its investigation, including the initial analysis, interpretation, and publication of their data. Results from single investigations should be published first as much as possible.
- All Cassini/Huygens teams are expected to make available their processed data for Cassini/Huygens team use for multi-investigation studies within a reasonable time (up to 6 months).
- The combined data sets are made available to all interested Cassini/Huygens scientists to identify possible scientifically interesting events.
- The combined data sets may not be published or released without the specific authorization of all contributing Cassini/Huygens teams.
- When data from a Cassini/Huygens team are used in a multi-investigation study:
  - The team lead must be immediately informed of their use.
  - The team must be invited at an early time to participate in the study.
  - The team must be invited to participate in any resulting publication or presentation. First authorship should be fairly divided between the participating teams.
  - Disputes should be resolved at the lowest possible level.
- The Cassini/Huygens science team needs to create a positive atmosphere that strongly discourages misconduct and maximizes science return from the mission.
- It is the responsibility of all Cassini/Huygens teams to make sure that all team members and associates are aware of the Rules of the Road and that they abide by them.

- These principles were unanimously accepted by the Cassini PSG Executive Session on October 24, 2002.

Cassini Project Reviews

As the Cassini mission progressed, NASA held a series of reviews during the mission to assess the completed science objectives and to evaluate proposals for extending the mission. In each successive phase of the mission (see Mission Phases section), new science objectives were defined based on Cassini's new findings and discoveries. For example, after the discovery of the Enceladus plume, Enceladus became a science focus for the remainder of the mission, with the addition of 20 more close Enceladus flybys including seven that flew directly through the plume. Other aspects of the mission, such as observing seasonal and temporal changes, were included as well. NASA reviews of Cassini were held in 2007 (proposal for Equinox Mission), 2011 (briefing to Ed Weiler and NASA HQ team), 2012 (Cassini Senior Review 2012), and 2014 (Senior Review 2014), which also included the final year of the mission.

After each review, Cassini received funding to continue its mission. For the 2012 and 2014 Senior Reviews, the Cassini mission proposals were ranked as "Excellent" and at the top of the list of all planetary missions under review.

System Science

The list of scientific objectives for both the Cassini and Huygens missions was quite extensive. Specific objectives were defined for each type of body in the system—Saturn itself, the rings, Titan, icy satellites, and the magnetosphere. Cassini-Huygens was designed to determine the present state of these bodies, the processes operating on or in them, and the interactions occurring among them. A detailed list of these objectives is given in the Cassini Science Objectives section.

This ability to execute system science was a key aspect of this flagship-class international mission and set this superbly instrumented spacecraft apart. The very complex interactions that occur in systems such as those found at Saturn (e.g., Enceladus jets or Titan's atmosphere and seas) could only be addressed by a diverse, broad array of instruments. The advantage of a flagship-class mission like Cassini-Huygens was its ability to perform an extensive set of exploratory studies, and follow up on those findings. In a number of cases, the Cassini orbiter instruments were used in ways not envisioned when the spacecraft first launched; for instance, flying through Enceladus' plume, and flying through the gap between the innermost ring and the top of Saturn's atmosphere for 22 orbits at the end of the mission.

Mission Summary

Cassini's 13 years of scientific study spanned almost half a Saturn year, covering late northern winter, spring, and northern summer. The mission ended just a few months after northern summer

solstice. Cassini was launched in 1997 and arrived at Saturn in 2004. Cassini's four-year Prime Mission began our exploration of the Saturn system, raising puzzling new questions that were addressed in the extended missions. The two-year Equinox Mission continued observations surrounding the equinox crossing in August 2009 when Saturn's rings were edge-on to the Sun. In 2010, the Cassini Solstice Mission began the final seven years of exploration. It contained equatorial orbits with many targeted icy satellite flybys; inclined orbits with optimal views of Saturn's rings and poles; and finally, highly inclined Ring-Grazing and Grand Finale orbits, diving between the innermost D-ring and upper region of Saturn's atmosphere for the first time by any spacecraft prior to the mission's end on September 15, 2017.

Some of Cassini's most surprising scientific discoveries came from encounters with Saturn's intriguing moons. Enceladus harbors a salty, liquid water ocean beneath its icy crust that is the source for icy jets spewing from its south pole. On giant Titan, methane rain carves river channels and fills lakes and seas with liquid hydrocarbons, mixed with complex prebiotic chemicals that form in its atmosphere and rain to the surface. Titan, too, has an internal liquid water ocean. Cassini's discovery of two ocean worlds at Saturn profoundly changed our ideas of where life might exist in our own solar system and beyond.

Some of Cassini's other amazing findings include a myriad of three-dimensional structures in the dynamic rings driven by interactions with Saturn's moons and interior; a giant Saturn storm that circled the entire planet for most of 2011, while a long-lived hexagonal jet stream discovered by Voyager in 1981 continues to encircle the north polar region. Cassini solved the mystery of Iapetus' dual bright-dark surface, and the true rotation rate of Saturn's interior. The final year of the mission, moving the spacecraft closer to Saturn than ever before, provided an astonishing array of discoveries about the interior of Saturn, its rings, and the gap between the rings and the planet. A summary of some of Cassini's key highlights can be found in the section on Cassini's Top Science Highlights and in Spilker [2019], while more detailed summaries and discussion can be found in the discipline and team reports.

At the conclusion of the Cassini mission, many open questions remained. Some of the top open questions are summarized in the Major Open Questions Resulting from Cassini section. Additional open questions can be found in each discipline and team report. These questions will help guide future missions to Saturn and the outer planets.

Ties to Planetary Science Decadal Survey Key Questions, Goals, and Objectives

The Cassini mission enabled significant advances in planetary science and its findings will guide future missions to the outer planets.

Since July 2004, Cassini returned a wealth of data from the Saturn system, yielding amazing discoveries, breathtaking images, expanded awareness of where and how life might exist beyond Earth, and several thousand publications across five interrelated science disciplines: Titan, Icy Satellites, Rings, Magnetosphere and Plasma Science, and Saturn. Over the course of the

mission, Cassini implemented Objective 1.5 of the *NASA Strategic Plan 2014*, and addressed the three *Vision and Voyages* (2013–2022 Planetary Science Decadal Survey) cross-cutting themes, including eight of its top ten Priority Questions (Table 3-3). Cassini also tackled all 25 of its Giant Planets and Satellites goals (Table 3-4). The Cassini mission enabled significant advances in planetary science and its findings will guide future missions to the outer planets.

The 13-year Cassini mission at Saturn took full advantage of the spacecraft's diverse set of high-performance instruments to provide unique science throughout the mission. Some of the outstanding opportunities included: 1) observed seasonal processes on Saturn, Titan, icy satellites, the rings, and in the magnetosphere from northern winter to northern summer; 2) studied the time variability of many phenomena, including plume activity on Enceladus and changes in the ring system; 3) made and pursued discoveries in this exceptionally complex and dynamic environment over a variety of inclination and solar illumination angles that are not available from Earth; and 4) determined the gravitational and magnetic fields of Saturn's interior, measured the main-ring mass, and sampled the composition of Saturn's ring particles and upper atmosphere. Cassini was a mission of extraordinary depth and breadth that produced rich data sets.

The Cassini mission provided new data for all 25 objectives listed in the Planetary Science Decadal Survey's Giant Planets and Satellites chapters (Table 3-4). The check marks in Table 3-4 indicate which Decadal Questions were answered by each of the five disciplines. Huygens probe science is included as part of the Titan column.

Table 3-3. Cassini addressed eight of top ten 2013–2022 Planetary Science Decadal Key Questions.

Cross-Cutting Themes	Priority Questions	Addressed by Cassini?
Origins *Building New Worlds*	1. What were the initial stages, conditions and processes of solar system formation and the nature of the interstellar matter that was incorporated?	✓
	2. How did the giant planets and their satellite systems accrete, and is there evidence that they migrated to new orbital positions?	✓
	3. What governed the accretion, supply of water, chemistry, and internal differentiation of the inner planets and the evolution of their atmospheres, and what roles did bombardment by large projectiles play?	✓
Habitability *Planetary Habitats*	4. What were the primordial sources of organic matter, and where does organic synthesis continue today?	✓
	5. Did Mars or Venus host ancient aqueous environments conducive to early life, and is there evidence that life emerged?	
	6. Beyond Earth, are there modern habitats elsewhere in the solar system with necessary conditions, organic matter, water, energy, and nutrients to sustain life, and do organisms live there now?	✓
Evolution *Workings of Solar Systems*	7. How do the giant planets serve as laboratories to understand Earth, the solar system and extrasolar planetary systems?	✓
	8. What solar system bodies endanger and what mechanisms shield Earth's biosphere?	
	9. Can understanding the roles of physics, chemistry, geology, and dynamics in driving planetary atmospheres lead to a better understanding of climate change on Earth?	✓
	10. How have the myriad chemical and physical processes that shaped the solar system operated, interacted, and evolved over time?	✓

Table 3-4. Cassini's Science Objectives thoroughly addressed all 25 of the Planetary Science Decadal Survey Goals and Objectives for Giant Planets and Satellites.

Vision & Voyages Planetary Science Decadal Survey 2013–022			Cassini Science Disciplines				
Chapters	Science Goals	Objectives	Titan (includes Huygens)	Icy Satellites	Rings	MAPS	Saturn
The Giant Planets: Local Laboratories and Ground Truth for Planets Beyond	Giant planets as ground truth for exoplanets	Understand heat flow and radiation balance in giant planets					✓
		Investigate the chemistry of giant-planet atmospheres				✓	✓
		Probe interiors of giant planets, including with planetary precession			✓	✓	✓
		Explore planetary extrema in the solar system's giant planets			✓	✓	✓
		Analyze the properties and processes in planetary magnetospheres				✓	✓
		Use ring systems as laboratories for planetary formation processes			✓	✓	✓
	Giant planets' role in promoting a habitable planetary system	Search for chemical evidence of planetary migration					✓
		Explore the giant planets' role in creating our habitable Earth through large impacts					✓
		Determine the role of surface modification through smaller impacts	✓	✓	✓		✓
	Giant planets as laboratories for properties and processes on Earth	Investigate atmospheric dynamical processes in the giant-planet laboratory				✓	✓
		Assess tidal evolution within giant-planet systems	✓	✓	✓		✓
		Elucidate seasonal change on giant planets				✓	✓
		Evaluate solar wind and magnetic-field interactions with planets				✓	✓
Satellites: Active Worlds and Extreme Environments	How did the satellites of the outer solar system form and evolve?	What were the conditions during satellite formation?	✓	✓	✓		
		What determines the abundance and composition of satellite volatiles?	✓	✓	✓		
		How are satellite thermal and orbital evolution and internal structure related?	✓	✓	✓		
		What is the diversity of geologic activity and how has it changed over time?	✓	✓			
	What processes control the present-day behavior of these bodies?	How do active endogenic processes shape the satellites' surfaces and influence their interiors?	✓	✓			
		What processes control the chemistry and dynamics of satellite atmospheres?	✓	✓		✓	
		How do exogenic processes modify these bodies?	✓	✓	✓	✓	
		How do satellites influence their own magnetospheres and those of their parent planets?	✓	✓		✓	
	What are the processes that result in habitable environments?	Where are subsurface bodies of liquid water located, and what are their characteristics and histories?	✓	✓			
		What are the sources, sinks, and evolution of organic material?	✓	✓		✓	
		What energy sources are available to sustain life?	✓	✓		✓	
		Is there evidence for life on the satellites?	✓	✓			

Cassini also responded to 41 of 75 of the Giant Planets and Satellites chapters “Important Questions for the next decade,” and also inspired 29 of them. Some of the Cassini-inspired questions, many of which Cassini answered over the course of the mission, included:

- Does Titan have an internal liquid water ocean?
- Is there active cryovolcanism on Titan?
- How do Titan’s clouds originate and evolve?
- What is the spatial distribution of Enceladus’ heat output, and how has it varied with time?
- Does Enceladus have an internal ocean or some other means of providing large tidal dissipation?
- What mechanisms drive and sustain Enceladus’ plumes and tiger stripe tectonics?
- What is the source of the organic material in the plume of Enceladus?
- Do other Saturnian icy satellites such as Dione and Rhea contribute measurable amounts of neutrals or plasma to Saturn’s magnetosphere?

Other Planetary Science Decadal Important Questions included:

- What mechanism has prolonged Saturn’s thermal evolution?
- How is energy dissipated within giant planets?
- Does helium rain play a role in reducing the He/H in Saturn’s molecular envelope?
- What are the natures of periodic outbursts such as the global upheavals on Jupiter and the infrequent great white spots on Saturn?
- How and why does the atmospheric temperature and cloud composition vary with depth and location on the planet?
- What is the source of energy for the hot coronas/upper atmospheres of all four giant planets?
- What processes control Titan’s weather?
- What can our understanding of the giant planet magnetospheres tell us about the conditions to be expected at extra-solar giant planets?
- How do magnetospheres interact with the solar wind?
- What can the significant differences among ring systems teach us about the differing origins, histories, or current states of these giant planet systems?
- What drives orbital evolution of embedded moonlets; how do they interact with their disks?
- What drives mass accretion in a ring system?

Overall, the Cassini mission was a tremendous success. It addressed objectives across a broad array of scientific disciplines, and followed up on many unexpected discoveries. Cassini's many findings and discoveries will provide a pathfinder for outer planet science in the next Planetary Science Decadal Survey.

MISSION OVERVIEW

Mission Phases

Cassini was designed to address a broad array of objectives across five science disciplines: Titan, Icy Satellites, Rings, Magnetospheres and Plasma Science, and Saturn.

The spacecraft flew with 12 science instruments (Table 3-5): four optical remote sensing (ORS) instruments, two microwave remote sensing instruments, and six MAPS instruments. The Class-A spacecraft subsystems launched with full redundancy, and retain full functionality.

Table 3-5. Three suites of instruments enable interdisciplinary science investigations.

Optical Remote-Sensing Instruments (ORS)	
CIRS	Composite Infrared Spectrometer
ISS	Imaging Science Subsystem
UVIS	Ultraviolet Imaging Spectrograph
VIMS	Visible and Infrared Mapping Spectrometer
Microwave Remote-Sensing Instruments	
RADAR	Titan Radar Mapper
RSS	Radio Science Subsystem
Magnetosphere and Plasma Science Instruments (MAPS)	
CAPS	Cassini Plasma Spectrometer
CDA	Cosmic Dust Analyzer
INMS	Ion and Neutral Mass Spectrometer
MAG	Dual Technique Magnetometer
MIMI	Magnetospheric Imaging Instrument
RPWS	Radio and Plasma Wave Science

Cassini-Huygens left the Earth on October 17, 1997, using a Titan IV/Centaur launch vehicle with Solid Rocket Motor Upgrade (SRMU) strap-ons and a Centaur upper stage. During the 6.7-year journey to Saturn, the spacecraft had gravity assistance from Venus on April 26, 1998, and June 24, 1999, from Earth on August 18, 1999, and from Jupiter on December 30, 2000. Cruise activities were planned to checkout, calibrate, and maintain the instruments as well as characterize the instruments and perform limited science observations (limited by flight software available on the spacecraft as well as cost, scheduling, and workforce constraints).

The Venus-1 flyby occurred on April 26, 1998, just six months after launch. The spacecraft approached Venus from a sunward direction and closest approach occurred just after entering the Sun's shadow for a period of about 15 minutes. At closest approach, the altitude was 284 km, with a velocity relative to Venus of 11.8 km/s.

A repetition of the ATLO "Quiet Test" was conducted to allow instruments to monitor other instruments as they turned on and off, thus providing valuable insight into how to integrate science observations during the Saturn tour.

The Instrument Checkout (ICO-1) sub-phase was September 14, 1998, through March 14, 1999. This sub-phase was characterized by the opposition that occurred on January 9, 1999, and which allowed use of the high-gain antenna (HGA) for downlink since the Earth and Sun were nearly aligned as seen from Cassini. All instruments scheduled checkout activities within a 25-day period centered on opposition. This was the first opportunity since launch to exercise most of the instruments and check status other than routine instrument maintenance. A repetition of the ATLO "Quiet Test" was conducted to allow instruments to monitor other instruments as they turned on and off, thus providing valuable insight into how to integrate science observations during the Saturn tour.

The second Venus (Venus-2) flyby occurred on June 24, 1999. Closest approach occurred at 2030 Universal Time (UT) at an altitude of 603 km with a Venus-relative velocity of 13.6 km/s. Approach to Venus was from the dusk side of the planet. Between Venus-2 and the upcoming Earth flyby, about two dozen activities involving maintenance, calibration, checkout, and science observations were carried out, using all of the Cassini instruments except INMS and CIRS, which were subject to thermal constraints.

The Earth flyby occurred 55 days after the Venus 2 flyby on August, 18, 1999. The spacecraft approached the Earth approximately from the direction of the Sun. Closest approach occurred right after the spacecraft entered the Sun occultation zone. The occultation lasted approximately 30 minutes. The altitude at closest approach was 1175 km, with an Earth-relative velocity of 19.0 km/s.

The MAG boom deployment executed 44 hours prior to Earth closest approach. Within the 24-hour period surrounding Earth flyby, the spacecraft passed in and out of the Earth's magnetosphere. Observations during this time were crucial for magnetometer alignment calibration to ensure that measurements at Saturn would be accurate to meet the major science goal of measuring Saturn's magnetic field orientation to an accuracy of 0.1°.

In addition, activities for CAPS, CDA, MIMI, RPWS, RSS, and VIMS were allowed during the approach to Earth, as well as observations of the Earth's moon for ISS, UVIS, and VIMS. After Earth closest approach, RADAR observations were performed as an end-to-end test of the RADAR system using Earth as a target. A few months later, on January 23, 2000, observations by ISS, VIMS, and UVIS of the distant (1,634,000 km) asteroid 2685 Masursky were conducted. No papers or abstracts were written on this observation.

A second Instrument Checkout (ICO-2) was conducted during July and August 2000 when the high-gain antenna was routinely in use and in preparation for the upcoming Jupiter flyby. The Jupiter flyby occurred on December 30, 2000, at a distance of 9.7 million km. On October 1, 2000, Jupiter approach science began using a repeating 5-day template. Science conducted by all instruments at Jupiter provided an opportunity to test Saturn observation techniques, ground and flight software, and building and execution of sequences.

After Jupiter, a Gravitational Wave Experiment (GWE) was executed December 2001 and a Conjunction Experiment in June 2002. The GWE preparation included two 1-week test periods starting in early May 2001 and August 2001. Additional GWEs were performed in December 2002 and October 2003.

Limited calibration and science data collection occurred during the Venus and Earth flybys. The scientific results of this mission phase are described in a collection of 11 scientific articles that appeared together in a special issue, “First Results from Cassini: Venus and Earth Swing-Bys” in the *Journal of Geophysical Research: Space Physics* in December 2001. As the spacecraft approached Jupiter, the number of science activities increased. Jupiter observations served as preparation for the four-year tour of the Saturnian system. Many of the science results are summarized in the Discipline and Instrument Reports that follow in this volume (see Volume 1 Sections 3.1 and 3.2).

Orbit insertion at Saturn occurred on July 1, 2004, thus starting 13 years of Cassini observations. The Saturn year is almost 30 Earth-years long and Saturn has an obliquity of almost 27°. Cassini arrived after the start of northern winter for its Prime Mission (Table 3-6 and Figure 3-1). The Prime Mission, completed in mid-2008, had only begun the exploration of the Saturn system, raising puzzling new questions that focused the science objectives of the upcoming extended missions.

Table 3-6. Summary of Cassini mission phases in the Saturn system.

	Mission Phase	Acronym	Dates (Seasons)
	Prime Mission	PM	July 2004—July 2008
Extended Missions	Cassini Equinox Mission	CEM	July 2008—Oct 2010 (equinox)
	Cassini Solstice Mission	CSM	Oct 2010—Nov 2016 (early northern spring)
	Ring Grazing (F-ring orbits) *Grand Finale (proximal orbits)*	RG *GF*	Nov 2016—April 2017 (late northern spring) April 2017—Sept 2017 (northern summer)

The fully-funded Cassini Equinox Mission (CEM) continued observations throughout a two-year period surrounding the equinox crossing in August 2009. In 2010, the streamlined (reduced budget) Cassini Solstice Mission (CSM) began seven years of exploration in three phases: CSM-1 was characterized by equatorial orbits including many icy-satellite targeted flybys; CSM-2 was characterized by inclined orbits that gave us optimal views of the rings and poles of Saturn; and the Northern Summer Mission (NSM) designed to witnesses the arrival of northern summer continuing the seasonal study of the Saturn system.

The last nine months of the mission was designed to put Cassini onto a collision course with Saturn. For the first five months, the trajectory included a series of 20 inclined orbits with periapses

near the unusually dynamic F-ring and apoapses near Titan's orbit. The last close flyby of Titan put Cassini into orbits with periapse between the innermost D-ring and the upper portions of Saturn's atmosphere for Cassini's last four months. A "goodbye kiss" from Titan, placed Cassini onto its last half orbit and brought the mission to an end collecting data on Saturn's upper atmosphere for as long as the spacecraft could hold steady.

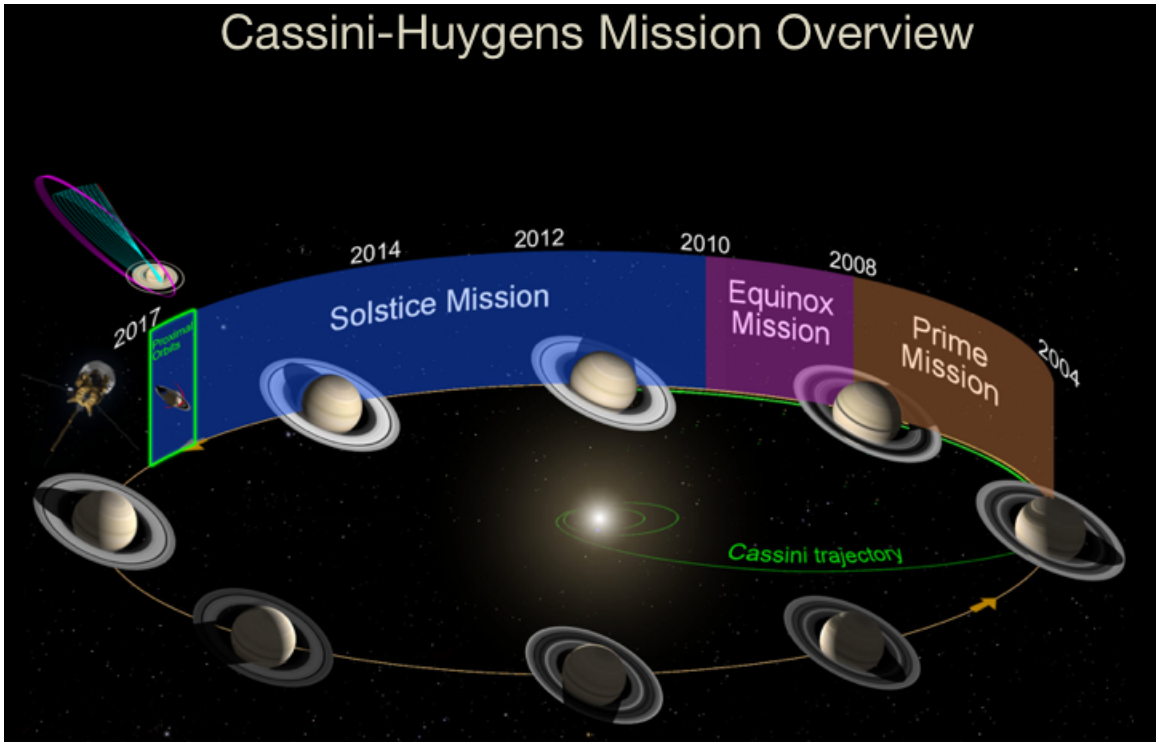

Figure 3-1. Seasonal coverage and associated phases of the Cassini-Huygens mission to Saturn. The Ring Grazing and Grand Finale phases of the mission are shown in the green box.

A Scientifically-Rich Mission

On the surface, Cassini's complete set of orbits, or tour, might look like a giant ball of yarn. When examined more closely, these orbits allowed Cassini to visit multiple targets at key times during the course of half a Saturn year. Multiple flybys of Titan provided gravity assists that shaped the size and orientation of each orbit in Cassini's orbital tour. This unique combination of orbital geometry allowed Cassini to study the complex seasonal changes that occurred throughout the Saturn system as the Sun set in the south and rose to more northerly latitudes in the Saturnian sky. Figure 3-2 illustrates the richness of this tour flown by the spacecraft.

The Prime Mission started roughly two years after northern winter began. It was comprised of 75 orbits, 45 Titan flybys, four (4) Enceladus flyby, and six (6) icy satellite flybys, including Phoebe. Just one year into the exploration, Cassini and Huygens discovered that Titan was an Earth-like world with lakes and rivers and active weather. Cassini also discovered that Enceladus was a

satellite with active plumes for the spacecraft to sample. Already, it was clear that scientists wanted to further study both worlds.

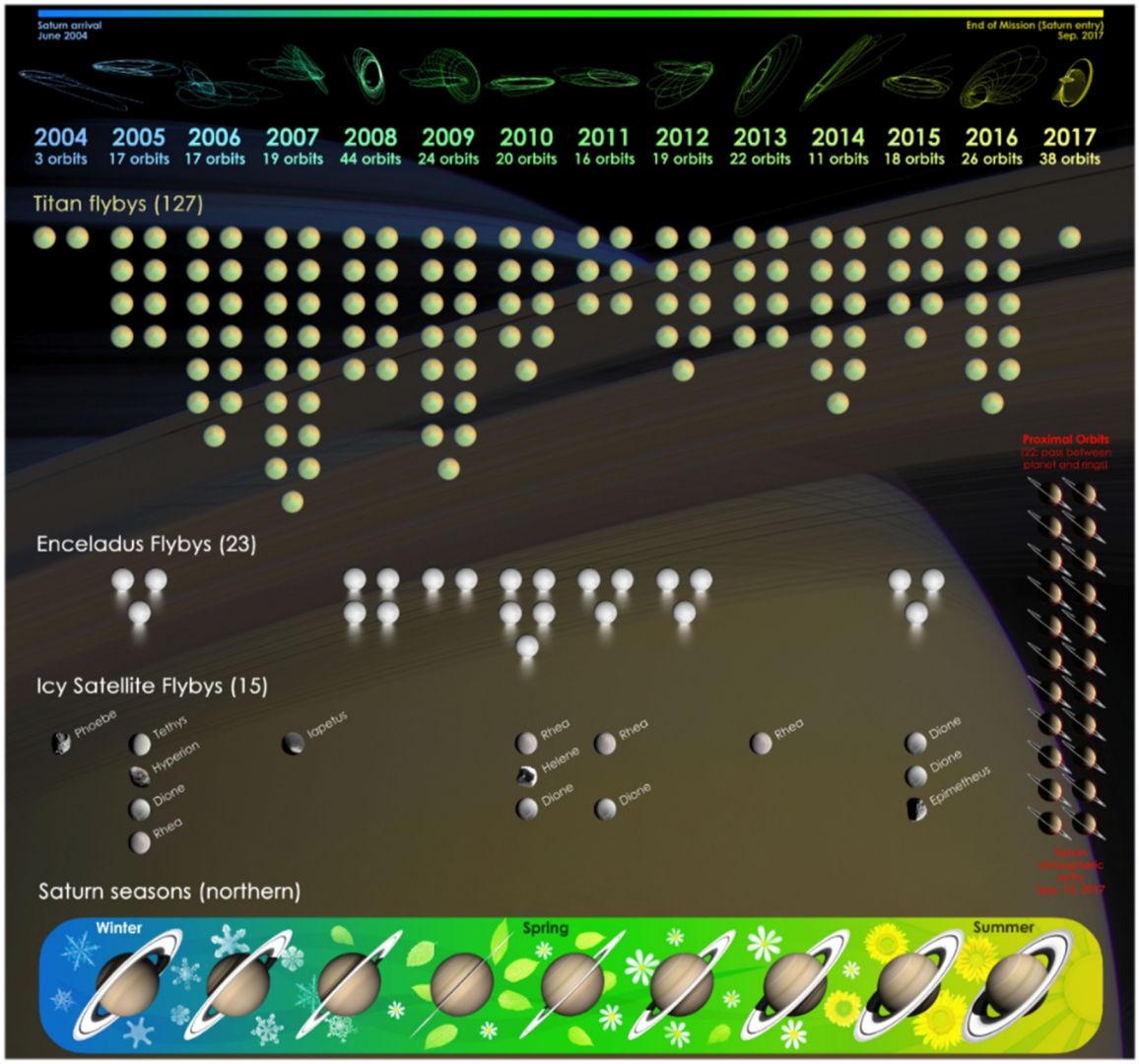

Figure 3-2. A scientifically-rich mission. From top to bottom: year and orbit, number of Titan flybys, number of Enceladus flybys, number of icy satellite flybys, and Saturn seasons. Cassini's 22 Grand Finale orbits are shown at the far right.

Cassini's mission was extended by another two years to encompass the years surrounding Saturn's equinox in August 2009 marking the transition from northern winter to northern spring. Orbits were designed to take advantage of the unique viewing of the rings at the time of equinox and to explore the magnetotail. These 60 orbits contained seven (7) additional Enceladus flybys, 26 Titan flybys, and four (4) icy satellite flybys.

With the knowledge and efficiencies gained from six years of flying a healthy spacecraft, mission designers proposed a plan to effectively make use of the remaining fuel onboard to observe the

Saturn system for the entire spring and into solstice (May 2017). Open scientific questions certainly argued for it and paved the way for profound discoveries to be made and provided the opportunity to observe unexpected events (e.g., Saturn's 2010–2011 Great Storm). A total of 160 orbits were executed containing twelve (12) Enceladus, 56 Titan, and twelve (12) icy satellite flybys. The last nine months, the 42 Ring Grazing and Grand Finale orbits, would be the capstone of a remarkable mission.

Cassini's Last Phase: Capstone of a Remarkable Mission

Ring Grazing Orbits: In late 2016, Cassini's trajectory transitioned to a series of 20 Ring Grazing orbits with periapses located within 10,000 km of Saturn's F-ring (Figure 3-3). These orbits provided the high-resolution views of Saturn's F-ring and outer A-ring, in addition to prime viewing conditions for fine-scale ring structures such as propellers (Figure 3-4). They also included the closest flybys of tiny ring moons, including Pan, Daphnis, and Atlas (Figure 3-4). Plasma and dust composition measurements were also conducted in this region.

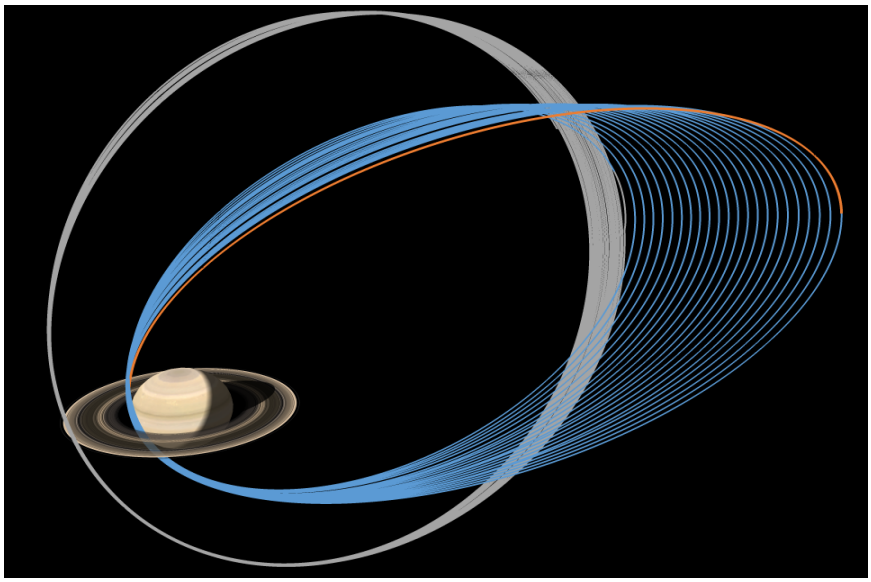

Figure 3-3. Cassini's 20 Ring Grazing (gray) and Grand Finale (blue) orbits. The last half-orbit (orange) took Cassini into Saturn's atmosphere for vaporization.

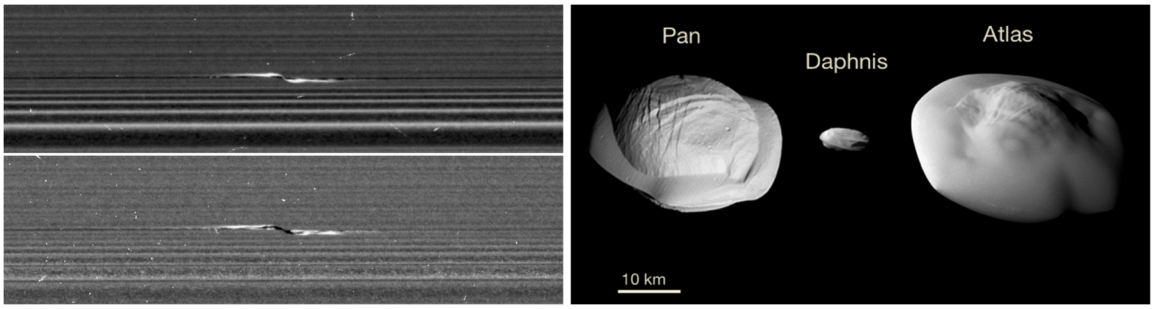

Figure 3-4. Left: Ring propeller Santos-Dumont on lit and unlit sides of the rings. Right: Comparison of highest resolution images of the ring moons, Pan, Daphnis, and Atlas.

Grand Finale Orbits: A final close flyby of Titan in late April 2017 propelled Cassini across Saturn's main rings and into its Grand Finale orbits. Comprised of 22 orbits, the spacecraft repeatedly dove between Saturn's innermost rings and upper atmosphere (Figure 3-4, blue orbits) attempting to answer fundamental questions unattainable earlier in the mission. The Grand Finale was like a brand-new mission, exploring a region of the Saturn system that was unexplored by Cassini and any previous outer planet spacecraft.

Saturn's gravitational field was measured to unprecedented accuracy, providing information from which constraints on the interior structure of the planet, winds in the deep atmosphere, and mass distribution in the rings could be derived (Figure 3-5). Probing the magnetic field provided data for insight into the physics of the magnetic dynamo, on the structure of the internal magnetic field, and on the location of the metallic hydrogen transition region.

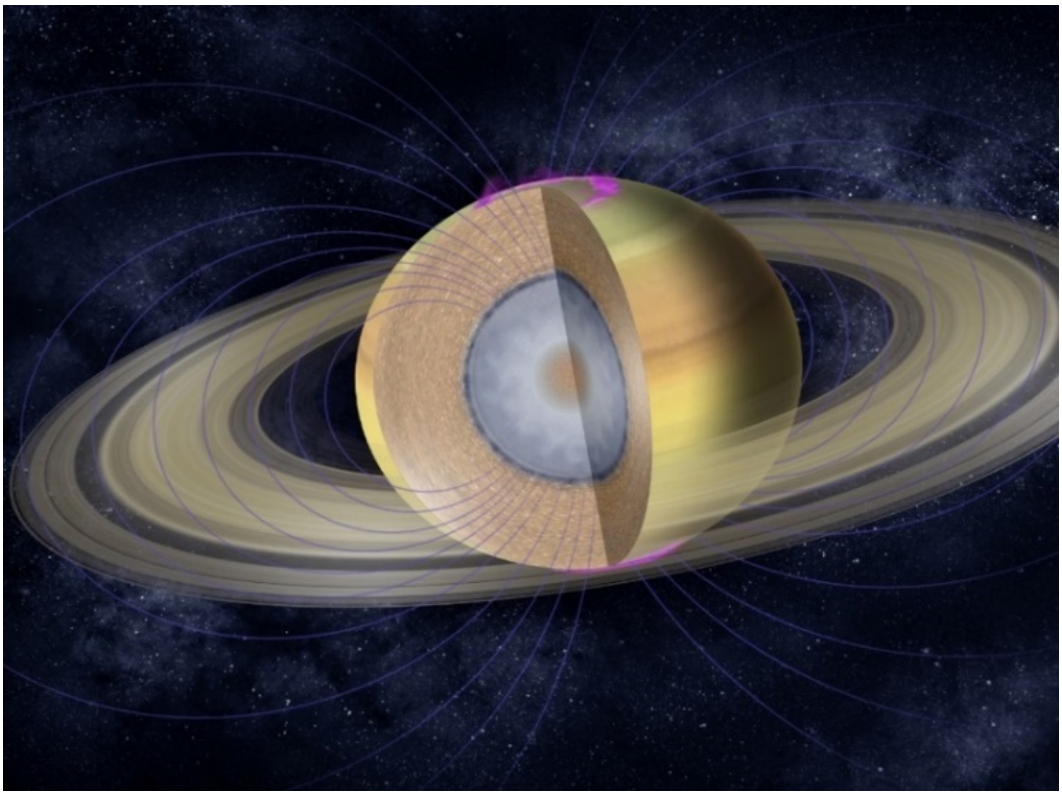

Figure 3-5. Grand Finale science goals focused on studying ring mass and composition, interior structure, magnetic dynamo, aurora, and atmospheric composition.

The Grand Finale orbits provided the highest resolution observations ever of both Saturn's C- and D-rings and Saturn's atmospheric weather layer (Figure 3-6). Direct in situ sampling of the ring particle composition and the innermost radiation belts was also achieved. The INMS sampled the exosphere and upper atmosphere for molecules entering and escaping from the atmosphere and water-based molecules originating from the rings. The CDA directly sampled the composition of ring particles from different regions of the main rings for the first time.

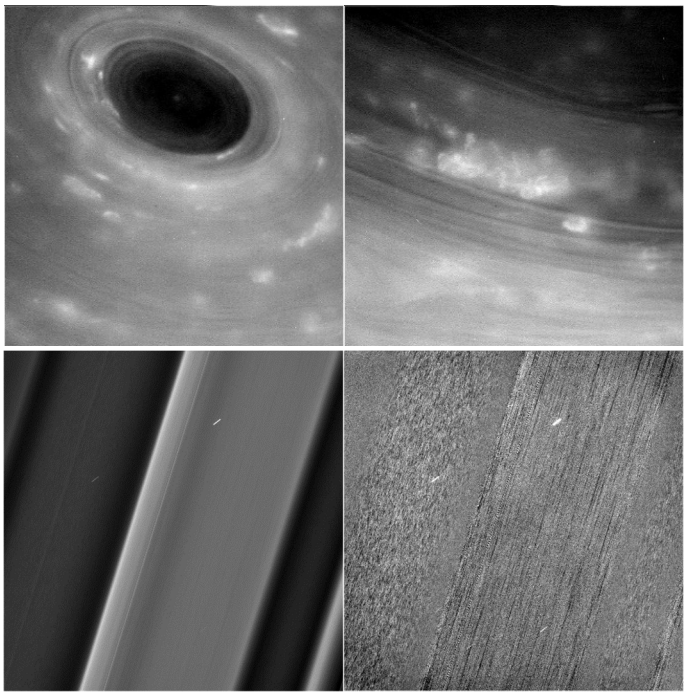

Figure 3-6. Saturn's north polar vortex (upper left) and convective clouds over the hexagon jet stream (upper right). Image of C-ring "Plateau" features (lower left) and same image after processing (lower right) to reveal differing ring particle "textures" in neighboring regions.

Cassini's Final Half-orbit: The last half-orbit turned the spacecraft into the first Saturn atmosphere probe with all of fields and particle instruments gathering data as long as the spacecraft remained stable. Approximately one additional scale height of atmosphere was probed prior to loss of the radio signal from the spacecraft.

The Cassini mission was a remarkable endeavor, revealing the Saturn system in unprecedented detail. Numerous Cassini discoveries reshaped our thinking about this astoundingly complex system.

CASSINI-HUYGENS SCIENCE OBJECTIVES

The Cassini-Huygens science objectives were first defined in the NASA and ESA AOs [ESA 1989; NASA 1989, 1991]. An expanded set of science objectives were later defined in a set of Traceability Matrices that were developed in 2007 as a part of Cassini's first mission extension. As the mission progressed, the Traceability Matrices were updated and refined through three mission extensions, including Senior Reviews in 2012 and 2014 [JPL 2012, 2014], based on Cassini's latest findings. Science objectives from both the AO and Traceability Matrices are briefly listed in the next section, and are explored in more detail in the discipline and instrument team reports in Section 3.2. The Traceability Matrix objectives listed in the following section are those defined for the Cassini Solstice Mission (CSM), and in Cassini's 2014 Senior Review. For the Traceability Matrix objectives, the second letter is either a "C" for seasonal or temporal "Change," or an "N" for "New" science.

Cassini-Huygens Announcements of Opportunity and Traceability Matrices Science Objectives

Huygens Probe AO objectives (see Huygens Discipline Report)

- Titan Atmospheric Formation and Evolution (H_AO1) – Determine abundances of atmospheric constituents (including any noble gases); establish isotope ratios for abundant elements; constrain scenarios of formation and evolution of Titan and its atmosphere.
- Titan Atmospheric Composition and Distribution (H_AO2) – Observe vertical and horizontal distributions of trace gases; search for more complex organic molecules; investigate energy sources for atmospheric chemistry; model the photochemistry of the stratosphere; study formation and composition of aerosols.
- Titan Meteorology (H_AO3) – Measure winds and global temperatures; investigate cloud physics, general circulation and seasonal effects in Titan's atmosphere; search for lightning discharges.
- Titan Surface Characteristics and Internal Structure (H_AO4) – Determine the physical state, topography, and the composition of the surface; infer the internal structure of the satellite.
- Titan Upper Atmosphere (H_AO5) – Investigate the upper atmosphere, its ionization, and its role as a source of neutral and ionized material for the magnetosphere of Saturn.

Icy Satellites AO objectives (see Icy Satellites Discipline Report)

- Icy Satellite Geology and History (I_AO1) – Determine the general characteristics and geological histories of the satellites.
- Icy Satellite Surface and Crustal Modifications (I_AO2) – Define the mechanisms of crustal and surface modifications, both external and internal.
- Icy Satellite Surface Composition (I_AO3) – Investigate the compositions and distributions of surface materials, particularly dark, organic rich materials and low melting point condensed volatiles.
- Icy Satellite Interior Properties (I_AO4) – Constrain models of the satellites' bulk compositions and internal structures.
- Icy Satellite Magnetosphere and Ring Interactions (I_AO5) – Investigate interactions with the magnetosphere and ring systems and possible gas injections into the magnetosphere.

Icy Satellites CSM Traceability Matrix objectives (see Icy Satellites Discipline Report)

- Enceladus Seasonal Changes (IC1a) – Identify long-term secular and seasonal changes at Enceladus, through observations of the south polar region, jets, and plumes.
- Enceladus Ocean (IN1a) – Determine the presence of an ocean at Enceladus as inferred from induced magnetic field and plume composition, search for possible anomalies in the internal structure of Enceladus as associated with plume sources, and constrain the mechanisms driving the endogenic activity by in situ observations and remote sensing.
- Mid-sized Satellites (IN1b) – Complete the comparative study of Saturn's mid-sized satellites, their geological and cratering histories, and interactions with the Saturn system, with remote sensing of Mimas at the highest resolution possible in order to understand the mechanisms behind its unique thermal properties discovered by Cassini.
- Dione (IN1c) – Determine whether Dione exhibits evidence for low-level activity, now or in recent geological time.
- Rhea (IN2a) – Determine whether there is ring material orbiting Rhea, and if so, what its spatial and particle size distribution is.
- Tethys (IN2b) – Determine whether Tethys contributes to the E-ring and the magnetospheric ion and neutral population.
- Satellite Interiors (IN2c) – Determine the extent of differentiation and internal inhomogeneity within the icy satellites, especially Rhea and Dione.
- Small Moons (IN2d) – Observe selected small satellites to quantify the movement of Enceladus material through the system, the history of satellite collisions/breakup, interaction with ring material as indicated by surface properties/composition, and cratering rates deep in the Saturnian system.
- Hyperion (IN2e) – Understand the unusual appearance of Hyperion with remote sensing observations of the highest resolution possible.
- Iapetus (IN2f) – Use remote sensing of Iapetus to test models for the albedo heterogeneity of the satellite. Quantify the effect of the newly-discovered Phoebe ring on the properties of Iapetus' surface.

Titan AO objectives (see Titan Discipline Report)

- Titan Atmospheric Formation and Evolution (T_AO1) – Determine abundances of atmospheric constituents (including any noble gases), establish isotope ratios for abundant elements, constrain scenarios of formation and evolution of Titan and its atmosphere.

- Titan Atmospheric Composition and Distribution (T_AO2) – Observe vertical and horizontal distributions of trace gases, search for more complex organic molecules, investigate energy sources for atmospheric chemistry, model the photochemistry of the stratosphere, study formation and composition of aerosols.
- Titan Meteorology (T_AO3) – Measure winds and global temperatures; investigate cloud physics, general circulation, and seasonal effects in Titan's atmosphere; search for lightning discharges.
- Titan Surface Characteristics and Internal Structure (T_AO4) – Determine the physical state, topography, and composition of the surface; infer the internal structure of the satellite.
- Titan Upper Atmosphere (T_AO5) – Investigate the upper atmosphere, its ionization, and its role as a source of neutral and ionized material for the magnetosphere of Saturn.

Titan CSM Traceability Matrix objectives (see Titan Discipline Report)

- Titan's Great Seas (TC1a) – Determine seasonal changes in the methane-hydrocarbon hydrological cycle: of lakes, clouds, aerosols, and their seasonal transport.
- Titan's Global Seasons (TC1b) – Determine seasonal changes in the high-latitude atmosphere, specifically the temperature structure and formation and breakup of the winter polar vortex.
- Titan-Magnetosphere Interaction (TC2a) – Observe Titan's plasma interaction as it goes from south to north of Saturn's solar-wind-warped magnetodisk from one solstice to the next.
- Titan's Surface (TN1a) – Determine the types, composition, distribution, and ages, of surface units and materials, most notably lakes (i.e., filled vs. dry and depth; liquid vs. solid and composition; polar vs. other latitudes and lake basin origin).
- Titan's Interior Ocean (TN1b) – Determine internal and crustal structure: Liquid mantle, crustal mass distribution, rotational state of the surface with time, intrinsic and/or internal induced magnetic field.
- Titan Atmospheric Composition (TN1c) – Measure aerosol and heavy molecule layers and properties.
- Titan Atmospheric Structure (TN2a) – Resolve current inconsistencies in atmospheric density measurements (critical to a future Flagship mission).
- Titan's Icy Shell (TN2b) – Determine icy shell topography and viscosity.
- Titan Meteorology (TN2c) – Determine the surface temperature distribution, cloud distribution, and tropospheric winds.

Saturn AO objectives (see Saturn Discipline Report)

- Saturn Temperature, Clouds, Composition (S_AO1) – Determine temperature field, cloud properties, and composition of the atmosphere of Saturn.
- Saturn Winds and Weather (S_AO2) – Measure the global wind field, including wave and eddy components; observe synoptic cloud features and processes.
- Saturn Interior Structure and Rotation (S_AO3) – Infer the internal structure and rotation of the deep atmosphere.
- Saturn Ionosphere-Magnetosphere Interaction (S_AO4) – Study the diurnal variations and magnetic control of the ionosphere of Saturn.
- Saturn Formation and Evolution (S_AO5) – Provide observational constraints (gas composition, isotope ratios, heat flux, ...) on scenarios for the formation and the evolution of Saturn.
- Saturn Lightning Sources and Morphology (S_AO6) – Investigate the sources and the morphology of Saturn lightning (Saturn electrostatic discharges (SEDs), lightning whistlers).

Saturn CSM Traceability Matrix objectives (see Saturn Discipline Report)

- Seasonal Variations (SC1a) – Observe seasonal variations in temperature, clouds, and composition in three spatial dimensions.
- Saturn's Winds (SC1b) – Observe seasonal changes in the winds at all accessible altitudes coupled with simultaneous observations of clouds, temperatures, composition, and lightning.
- Aurorae, Chemistry, and Upper Atmosphere (SC2a) – Observe the magnetosphere, ionosphere, and aurora as they change on all time scales—minutes to years—and are affected by seasonal and solar cycle forcing.
- Saturn's Rotation Rate (SN1a) – Determine Saturn's rotation rate and internal structure despite the planet's unexpected high degree of axisymmetry.
- 2010–2011 Great Storm (SN1b) – Observe the aftermath of the 2010–2011 storm. Study the life cycles of Saturn's newly discovered atmospheric waves, south polar hurricane, and rediscovered north polar hexagon.
- Saturn Trace Gases (SN1c) – Measure the spatial and temporal variability of trace gases and isotopes.
- Saturn Storms and Lightning (SN2a) – Monitor the planet for new storms and respond with new observations when the new storms occur.

Rings AO objectives (see Rings Discipline Report)

- Ring Structure and Dynamics (R_AO1) – Study configuration of the rings and dynamical processes (gravitational, viscous, erosional, and electromagnetic) responsible for ring structure.
- Ring Particle Composition and Size (R_AO2) – Map composition and size distribution of ring material.
- Ring-Satellite Interaction (R_AO3) – Investigate interrelation of rings and satellites, including embedded satellites.
- Dust and Meteoroid Distribution (R_AO4) – Determine dust and meteoroid distribution both in the vicinity of the rings and in interplanetary space.
- Ring Magnetosphere-Ionosphere Interactions (R_AO5) – Study interactions between the rings and Saturn's magnetosphere, ionosphere, and atmosphere.

Rings CSM Traceability Matrix objectives (see Rings Discipline Report)

- Changing Rings (RC1a) – Determine the seasonal variation of key ring properties and the microscale properties of ring structure, by observing at the seasonally maximum opening angle of the rings near solstice.
- Ring Temporal Variability (RC1b) – Determine the temporal variability of ring structure on all timescales up to decadal for regions including Encke gap, D-ring, F-ring, and ring edges by substantially increasing the cadence and time baseline of observations.
- F-Ring (RC2a) – Focus on F-ring structure, and distribution of associated moonlets or clumps, as sparse observations show clumps, arcs, and possibly transient objects appearing and disappearing.
- Ring Age and Origin (RN1a) – Constrain the origin and age of the rings by direct determination of the ring mass, and of the composition of ring ejecta trapped on field lines.
- Ring Composition (RN1b) – Determine the composition of the close-in "ringmoons" as targets of opportunity.
- Ring Structure (RN1c) – Determine structural and compositional variations at high resolution across selected ring features of greatest interest, using remote and in situ observations.
- Ring Microstructure (RN2a) – Conduct in-depth studies of ring microstructure such as self-gravity wakes, which permeate the rings.
- New Ring Structures (RN2b) – Perform focused studies of the evolution of newly discovered "propeller" objects.

MAPS AO objectives (see MAPS Discipline Report)

- Saturn Magnetic Field Configuration and SKR (M_AO1) – Determine the configuration of the nearly axially symmetric magnetic field and its relation to the modulation of Saturn kilometric radiation (SKR).
- Magnetosphere Charged Particles (M_AO2) – Determine current systems, composition, sources, and sinks of magnetosphere charged particles.
- Magnetosphere Wave-Particle Interactions (M_AO3) – Investigate wave-particle interactions and dynamics of the dayside magnetosphere and the magnetotail of Saturn and their interactions with the solar wind, the satellites, and the rings.
- Magnetosphere and Solar Interactions with Titan (M_AO4) – Study the effect of Titan's interaction with the solar wind and magnetospheric plasma.
- Plasma Interactions with Titan's Atmosphere and Ionosphere (M_AO5) – Investigate interactions of Titan's atmosphere and exosphere with the surrounding plasma.

MAPS CSM Traceability Matrix objectives (see MAPS Discipline Report)

- Enceladus Plume Variability (MC1a) – Determine the temporal variability of Enceladus' plumes.
- Seasonal and Solar Cycle Variations (MC1b) – Observe Saturn's magnetosphere over a solar cycle, from one solar minimum to the next.
- Titan's Ionosphere (MC2a) – Observe seasonal variation of Titan's ionosphere, from one solstice to the next.
- Magnetotail (MN1a) – Determine the dynamics of Saturn's magnetotail.
- Saturn's Ionosphere and Radiation Belts (MN1b) – Conduct in situ studies of Saturn's ionosphere and inner radiation belt.
- Magntosphere Periodicities (MN1c) – Investigate magnetospheric periodicities, their coupling to the ionosphere, and how the SKR periods are imposed from close to the planet (3–5 Rs) out to the deep tail.
- Ionosphere and Ring Coupling (MN2a) – Determine the coupling between Saturn's rings and ionosphere.

Cruise Science AO objectives

- Cruise Interstellar Ion Composition (C_AO1) – Extend the sensitivity of composition measurements of interstellar ions by approximately three orders of magnitude.
- Cruise Solar Wind Investigations (C_AO2) – Investigate the behavior of the solar wind during solar minimum, for comparison with earlier Galileo and Ulysses measurements.

- Cruise Gravitational Wave Searches (C_AO3) – Extend spacecraft searches for gravitational waves.
- Cruise Interplanetary Dust Studies (C_AO4) – Extend studies of interplanetary dust to the orbit of Saturn.
- Cruise Planetary and Stellar Internal Oscillations (C_AO5) – Attempt to detect internal oscillations of Saturn, Jupiter, and some stars.

Jupiter Flyby AO objectives

- Jupiter and Satellite Studies (J_AO1) – Extend the time for studies of atmospheric dynamics and variable satellite phenomena, specifically Io volcanism, beyond the period accessible to the Galileo nominal mission.
- Jupiter Global Atmospheric Structure and Composition (J_AO2) – Infer global atmospheric thermal structure and composition with instrumentation not carried by the Galileo orbiter, complementing the local in situ measurements of the Galileo probe.
- Jupiter Magnetospheric Studies (J_AO3) – Explore the dusk side of the magnetosphere and intermediate regions of the magnetotail unvisited by previous spacecraft.
- Jupiter Io Torus (J_AO4) – Obtain the first high-resolution images of the Io torus.

Venus Flyby AO objectives

- N/A – There were no specific Venus science objectives called out in the Announcement of Opportunity. It was, however, an opportunity to calibrate and gauge the performance of instruments and test spacecraft functionality.

Asteroid Flyby AO objectives

- Asteroid Flyby Investigation (A_AO1) – Investigate an asteroid not seen by previous missions, possibly a new class of asteroid, thereby adding important new information to the study of asteroids.
  - On January 23, 2000, observations by ISS, VIMS, and UVIS of the distant (1,634,000 km) asteroid 2685 Masursky were conducted. No papers or abstracts were written on the observation.
- Asteroid Global Characteristics (A_AO2) – Characterize global properties, determine composition and morphology of the surface, investigate properties of the regolith.
  - On January 23, 2000, observations by ISS, VIMS, and UVIS of the distant (1,634,000 km) asteroid 2685 Masursky were conducted. No papers or abstracts were written on the observation.

PROJECT SCIENCE ASSESSMENT

Overall, the Cassini-Huygens mission was a tremendous success, accomplishing or exceeding almost all of the science objectives defined in the Cassini and Huygens AOs and in the Cassini Solstice Mission Traceability Matrices. Tables 3-7, 3-8, and 3-9 contain color-coded assessments of the science objectives for the Cassini-Huygens mission. If a science objective was accomplished or exceeded, its box is colored green. The rare exceptions, which are colored yellow or lime green, are instances where an objective was only partially accomplished. A full explanation of why it was not met is included in each yellow or lime green box.

Overall, the Cassini-Huygens mission was a tremendous success, accomplishing or exceeding almost all of the science objectives defined in the Cassini and Huygens AOs and in the Cassini Solstice Mission Traceability Matrices.

The project science assessments shown in Tables 3-7, 3-8, and 3-9 are a compilation of each discipline assessment and Huygens probe assessment. Table 3-7 includes the science assessments for the Icy Satellites, Titan, and Enceladus disciplines. Table 3-8 includes the science assessments for Saturn, Rings, and MAPS disciplines, while Table 3-9 includes the science assessments for Cruise and Jupiter science.

Future analysis of Cassini data may result in some unmet objectives being fully met. For example, at the writing of this report, Saturn's internal rotation rate could not be determined from the magnetometer data taken during Cassini's Grand Finale orbits at the end of the mission. The offset between Saturn's rotation axis and magnetic field axis appears to be too small to provide an estimate of Saturn's internal rotation rate. However, a paper by Mankovich et al. [2019] uses Saturn-driven waves detected in the main rings (kronoseismology) to determine an internal rotation rate for Saturn. Future analysis of Cassini data may provide additional information on Saturn's internal rotation rate. For more details on the specifics of the science assessments for each science objective, please see the discipline and team reports in Section 3, which also include their own color-coded science assessment tables.

Table 3-7. Project Science Assessment (1 of 3 tables): Icy Satellites, Titan disciplines and Huygens.

Table Legend: Green: Fully Accomplished Yellow: Partially Accomplished

Cassini & Huygens Science Objectives		
Icy Satellites	**Titan**	**Huygens**
Prime Mission AO Objectives		
Icy Satellite Geology and History (I_AO1) - Determine the general characteristics and geological histories of the satellites.	**Titan Atmospheric Formation and Evolution (T_AO1)** - Determine abundances of atmospheric constituents (including any noble gases), establish isotope ratios for abundant elements, constrain scenarios of formation and evolution of Titan and its atmosphere.	**Titan Atmospheric Formation and Evolution (H_AO1)** - Determine abundances of atmospheric constituents (including any noble gases); establish isotope ratios for abundant elements; constrain scenarios of formation and evolution of Titan and its atmosphere.

Table 3-7. Project Science Assessment (1 of 3 tables): Icy Satellites, Titan disciplines and Huygens.

Table Legend: Green: Fully Accomplished Yellow: Partially Accomplished

Cassini & Huygens Science Objectives		
Icy Satellites	**Titan**	**Huygens**
Icy Satellite Surface and Crustal Modifications (I_AO2) - Define the mechanisms of crustal and surface modifications, both external and internal.	**Titan Atmospheric Composition and Distribution (T_AO2)** - Observe vertical and horizontal distributions of trace gases, search for more complex organic molecules, investigate energy sources for atmospheric chemistry, model the photochemistry of the stratosphere, study formation and composition of aerosols.	**Titan Atmospheric Composition and Distribution (H_AO2)** - Observe vertical and horizontal distributions of trace gases; search for more complex organic molecules; investigate energy sources for atmospheric chemistry; model the photochemistry of the stratosphere; study formation and composition of aerosols. *Note: This box is not green because the very low concentrations of aerosols collected by ACP limited the results to simple species, rather than complex hydrocarbon hazes.*
Icy Satellite Surface Composition (I_AO3) - Investigate the compositions and distributions of surface materials, particularly dark, organic rich materials and low melting point condensed volatiles.	**Titan Meteorology (T_AO3)** - Measure winds and global temperatures; investigate cloud physics, general circulation, and seasonal effects in Titan's atmosphere; search for lightning discharges.	**Titan Meteorology (H_AO3)** - Measure winds and global temperatures; investigate cloud physics, general circulation and seasonal effects in Titan's atmosphere; search for lightning discharges.
Icy Satellite Interior Properties (I_AO4) - Constrain models of the satellites' bulk compositions and internal structures.	**Titan Surface Characteristics and Internal Structure (T_AO4)** - Determine the physical state, topography, and composition of the surface; infer the internal structure of the satellite. *Note: This box is not green because "Some work was done, but more work remains for future missions."*	**Titan Surface Characteristics and Internal Structure (H_AO4)** - Determine the physical state, topography and the composition of the surface; infer the internal structure of the satellite.
Icy Satellite Magnetosphere and Ring Interactions (I_AO5) - Investigate interactions with the magnetosphere and ring systems and possible gas injections into the magnetosphere.	**Titan Upper Atmosphere (T_AO5)** - Investigate the upper atmosphere, its ionization, and its role as a source of neutral and ionized material for the magnetosphere of Saturn.	**Titan Upper Atmosphere (H_AO5)** - Investigate the upper atmosphere, its ionization, and its role as a source of neutral and ionized material for the magnetosphere of Saturn.
Science Traceability Matrix		
Enceladus Seasonal Changes (IC1a) - Identify long-term secular and seasonal changes at Enceladus, through observations of the south polar region, jets, and plumes.	**Titan's Great Seas (TC1a)** - Determine seasonal changes in the methane-hydrocarbon hydrological cycle: of lakes, clouds, aerosols, and their seasonal transport.	
Enceladus Ocean (IN1a) - Determine the presence of an ocean at Enceladus as inferred from induced magnetic field and plume composition, search for possible anomalies in the internal structure of Enceladus as associated with plume sources, and constrain the mechanisms driving the endogenic activity by in situ observations and remote sensing.	**Titan's Global Seasons (TC1b)** - Determine seasonal changes in the high-latitude atmosphere, specifically the temperature structure and formation and breakup of the winter polar vortex.	

Table 3-7. Project Science Assessment (1 of 3 tables): Icy Satellites, Titan disciplines and Huygens.

Table Legend: Green: Fully Accomplished Yellow: Partially Accomplished

Cassini & Huygens Science Objectives		
Icy Satellites	**Titan**	**Huygens**
Mid-sized Satellites (IN1b) - Complete the comparative study of Saturn's mid-sized satellites, their geological and cratering histories, and interactions with the Saturn system, with remote sensing of Mimas at the highest resolution possible in order to understand the mechanisms behind its unique thermal properties discovered by Cassini.	**Titan-Magnetosphere Interaction (TC2a)** - Observe Titan's plasma interaction as it goes from south to north of Saturn's solar-wind-warped magnetodisk from one solstice to the next.	
Dione (IN1c) - Determine whether Dione exhibits evidence for low-level activity, now or in recent geological time. *Note: This box is not green because extensive data were gathered, but the current results are still ambiguous. No current activity was detected.*	**Titan's Surface (TN1a)** - Determine the types, composition, distribution, and ages, of surface units and materials, most notably lakes (i.e., filled vs. dry & depth; liquid vs. solid & composition; polar vs. other latitudes & lake basin origin).	
Rhea (IN2a) - Determine whether there is ring material orbiting Rhea, and if so, what its spatial and particle size distribution is.	**Titan's Interior Ocean (TN1b)** - Determine internal and crustal structure: Liquid mantle, crustal mass distribution, rotational state of the surface with time, intrinsic and/or internal induced magnetic field. *Note: This box is not green because 1) Cassini only studied a few crustal structures locally and crustal viscosity was not determined by data taken, and 2) induced magnetic fields were difficult to determine due to ionospheric currents.*	
Tethys (IN2b) - Determine whether Tethys contributes to the E-ring and the magnetospheric ion and neutral population. *Note: From a CDA/icy dust perspective, this box is not green because during the Solstice Mission there were no close Tethys flybys to measure potential ejecta [Kempf, Beckmann, and Schmidt 2010]. For MAPS as a whole, enough data were obtained to determine that Tethys does not contribute to the E-ring and magnetospheric ion and neutral population [Burch et al. 2007; Khurana, Russell, and Dougherty 2008], yielding an overall yellow box.*	**Titan Atmospheric Composition (TN1c)** - Measure aerosol and heavy molecule layers and properties.	
Satellite Interiors (IN2c) - Determine the extent of differentiation and internal inhomogeneity within the icy satellites, especially Rhea and Dione.	**Titan Atmospheric Structure (TN2a)** - Resolve current inconsistencies in atmospheric density measurements (critical to a future Flagship mission).	

Table 3-7. Project Science Assessment (1 of 3 tables): Icy Satellites, Titan disciplines and Huygens.

Table Legend: Green: Fully Accomplished Yellow: Partially Accomplished

Cassini & Huygens Science Objectives		
Icy Satellites	**Titan**	**Huygens**
Small Moons (IN2d) - Observe selected small satellites to quantify the movement of Enceladus material through the system, the history of satellite collisions/breakup, interaction with ring material as indicated by surface properties/composition, and cratering rates deep in the Saturnian system.	**Titan's Icy Shell (TN2b)** - Determine icy shell topography and viscosity. *Note: This box is not green because crustal viscosity could not be determined to date from data taken.*	
Hyperion (IN2e) - Understand the unusual appearance of Hyperion with remote sensing observations of the highest resolution possible.	**Titan Meteorology (TN2c)** - Determine the surface temperature distribution, cloud distribution, and tropospheric winds.	
Iapetus (IN2f) - Use remote sensing of Iapetus to test models for the albedo heterogeneity of the satellite. Quantify the effect of the newly-discovered Phoebe ring on the properties of Iapetus' surface.		

Table 3-8. Project Science Assessment (2 of 3 tables): Saturn, Rings and MAPS disciplines.

Table Legend: Green: Fully Accomplished Yellow: Partially Accomplished

Cassini Science Objectives		
Saturn	**Rings**	**MAPS**
Prime Mission AO Objectives		
Saturn Temperature, Clouds, Composition (S_AO1) - Determine temperature field, cloud properties, and composition of the atmosphere of Saturn.	**Ring Structure and Dynamics (R_AO1)** - Study configuration of the rings and dynamical processes (gravitational, viscous, erosional, and electromagnetic) responsible for ring structure.	**Saturn Magnetic Field Configuration and SKR (M_AO1)** - Determine the configuration of the nearly axially symmetric magnetic field and its relation to the modulation of SKR.
Saturn Winds and Weather (S_AO2) - Measure the global wind field, including wave and eddy components; observe synoptic cloud features and processes.	**Ring Particle Composition and Size (R_AO2)** - Map composition and size distribution of ring material.	**Magnetosphere Charged Particles (M_AO2)** - Determine current systems, composition, sources, and sinks of magnetosphere charged particles.
Saturn Interior Structure and Rotation (S_AO3) - Infer the internal structure and rotation of the deep atmosphere. *Note: This box is not green because at the time of this report, Saturn's internal rotation rate could not be determined from the Grand Finale magnetic field data. Mankovich et al. [2019] may have finally determined the rotation rate from patterns related to kronoseismology in Saturn's rings, at which point this box would become green.*	**Ring-Satellite Interaction (R_AO3)** - Investigate interrelation of rings and satellites, including embedded satellites.	**Magnetosphere Wave-Particle Interactions (M_AO3)** - Investigate wave-particle interactions and dynamics of the dayside magnetosphere and the magnetotail of Saturn and their interactions with the solar wind, the satellites, and the rings.
Saturn Ionosphere-Magnetosphere Interaction (S_AO4) - Study the diurnal variations and magnetic control of the ionosphere of Saturn.	**Dust and Meteoroid Distribution (R_AO4)** - Determine dust and meteoroid distribution both in the vicinity of the rings and in interplanetary space.	**Magnetosphere and Solar Interactions with Titan (M_AO4)** - Study the effect of Titan's interaction with the solar wind and magnetospheric plasma.

Table 3-8. Project Science Assessment (2 of 3 tables): Saturn, Rings and MAPS disciplines.

Table Legend: Green: Fully Accomplished Yellow: Partially Accomplished

Cassini Science Objectives		
Saturn	**Rings**	**MAPS**
Saturn Formation and Evolution (S_AO5) - Provide observational constraints (gas composition, isotope ratios, heat flux, ...) on scenarios for the formation and the evolution of Saturn.	**Ring Magnetosphere-Ionosphere Interactions (R_AO5)** - Study interactions between the rings and Saturn's magnetosphere, ionosphere, and atmosphere.	**Plasma Interactions with Titan's Atmosphere and Ionosphere (M_AO5)** - Investigate interactions of Titan's atmosphere and exosphere with the surrounding plasma.
Saturn Lightning Sources and Morphology (S_AO6) - Investigate the sources and the morphology of Saturn lightning (Saturn electrostatic discharges (SEDs), lightning whistlers).		
Science Traceability Matrix		
Seasonal Variations (SC1a) - Observe seasonal variations in temperature, clouds, and composition in three spatial dimensions.	**Changing Rings (RC1a)** - Determine the seasonal variation of key ring properties and the microscale properties of ring structure, by observing at the seasonally maximum opening angle of the rings near solstice.	**Enceladus Plume Variability (MC1a)** - Determine the temporal variability of Enceladus' plumes.
Saturn's Winds (SC1b) - Observe seasonal changes in the winds at all accessible altitudes coupled with simultaneous observations of clouds, temperatures, composition, and lightning.	**Ring Temporal Variability (RC1b)** - Determine the temporal variability of ring structure on all timescales up to decadal for regions including Encke gap, D-ring, F-ring, and ring edges by substantially increasing the cadence and time baseline of observations.	**Seasonal and Solar Cycle Variations (MC1b)** - Observe Saturn's magnetosphere over a solar cycle, from one solar minimum to the next.
Aurorae, Chemistry, and Upper Atmosphere (SC2a) - Observe the magnetosphere, ionosphere, and aurora as they change on all time scales—minutes to years—and are affected by seasonal and solar cycle forcing.	**F-ring (RC2a)** - Focus on F-ring structure, and distribution of associated moonlets or clumps, as sparse observations show clumps, arcs, and possibly transient objects appearing and disappearing.	**Titan's Ionosphere (MC2a)** - Observe seasonal variation of Titan's ionosphere, from one solstice to the next.
Saturn's Rotation Rate (SN1a) - Determine Saturn's rotation rate and internal structure despite the planet's unexpected high degree of axisymmetry.	**Ring Age and Origin (RN1a)** - Constrain the origin and age of the rings by direct determination of the ring mass, and of the composition of ring ejecta trapped on field lines.	**Magnetotail (MN1a)** - Determine the dynamics of Saturn's magnetotail.
2010—2011 Great Storm (SN1b) - Observe the aftermath of the 2010—2011 storm. Study the life cycles of Saturn's newly discovered atmospheric waves, south polar hurricane, and rediscovered north polar hexagon.	**Ring Composition (RN1b)** - Determine the composition of the close-in "ringmoons" as targets of opportunity.	**Saturn's Ionosphere and Radiation Belts (MN1b)** - Conduct in situ studies of Saturn's ionosphere and inner radiation belt.

Table 3-8. Project Science Assessment (2 of 3 tables): Saturn, Rings and MAPS disciplines.

Table Legend: Green: Fully Accomplished Yellow: Partially Accomplished

Cassini Science Objectives		
Saturn	**Rings**	**MAPS**
Saturn Trace Gases (SN1c) - Measure the spatial and temporal variability of trace gases and isotopes.	**Ring Structure (RN1c)** - Determine structural and compositional variations at high resolution across selected ring features of greatest interest, using remote and in situ observations.	**Magntosphere Periodicities (MN1c)** - Investigate magnetospheric periodicities, their coupling to the ionosphere, and how the SKR periods are imposed from close to the planet (3–5 R_S) out to the deep tail. *Note: This box is not green because at the time of this report, Saturn's internal rotation rate could not be determined from the Grand Finale magnetic field data. Mankovich et al. [2019] may have finally determined the rotation rate from patterns related to kronoseismology in Saturn's rings, at which point this box would become green.*
Saturn Storms and Lightning (SN2a) - Monitor the planet for new storms and respond with new observations when the new storms occur.	**Ring Microstructure (RN2a)** - Conduct in-depth studies of ring microstructure such as self-gravity wakes, which permeate the rings.	Ionosphere and Ring Coupling (MN2a) - Determine the coupling between Saturn's rings and ionosphere.
	Ring Microstructure (RN2a) - Conduct in-depth studies of ring microstructure such as self-gravity wakes, which permeate the rings.	

Table 3-9. Project Science Assessment (3 of 3 tables): Cruise Science and Jupiter.

Table Legend: Green: Fully Accomplished Yellow: Partially Accomplished

Cassini Science Cruise & Jupiter Flyby Objectives	
Cruise Science	**Jupiter**
Cruise Interstellar Ion Composition (C_AO1) - Extend the sensitivity of composition measurements of interstellar ions by approximately three orders of magnitude.	**Jupiter and Satellite Studies (J_AO1)** - Extend the time for studies of atmospheric dynamics and variable satellite phenomena, specifically Io volcanism, beyond the period accessible to the Galileo nominal mission.
Cruise Solar Wind Investigations (C_AO2) - Investigate the behavior of the solar wind during solar minimum, for comparison with earlier Galileo and Ulysses measurements.	**Jupiter Global Atmospheric Structure and Composition (J_AO2)** - Infer global atmospheric thermal structure and composition with instrumentation not carried by the Galileo Orbiter, complementing the local in situ measurements of the Galileo Probe.
Cruise Gravitational Wave Searches (C_AO3) - Extend spacecraft searches for gravitational waves.	**Jupiter Magnetospheric Studies (J_AO3)** - Explore the dusk side of the magnetosphere and intermediate regions of the magnetotail unvisited by previous spacecraft.
Cruise Interplanetary Dust Studies (C_AO4) - Extend studies of interplanetary dust to the orbit of Saturn.	**Jupiter Io Torus (J_AO4)** - Obtain the first high-resolution images of the Io torus.
Cruise Planetary and Stellar Internal Oscillations (C_AO5) - Attempt to detect internal oscillations of Saturn, Jupiter, and some stars.	

As can be seen in Tables 3-7, 3-8, and 3-9, the Cassini-Huygens mission was extremely successful in accomplishing its scientific objectives.

- - - - - - - - - - - - - -

CASSINI'S TOP SCIENCE HIGHLIGHTS

Many of Cassini's findings revolutionized our understanding of the Saturn system. Some of Cassini's most surprising scientific discoveries came from encounters with Saturn's intriguing moons. Enceladus harbors a salty, liquid water ocean beneath its icy crust that is the source for icy jets and huge plume spewing from fractures at its south pole. On giant Titan, methane rain carves river channels and fills lakes and seas with hydrocarbons, mixed with complex prebiotic chemicals that form in its atmosphere and rain to the surface. From Huygens probe data it was determined that Titan, too, has an internal liquid water ocean. Some of Cassini's other amazing findings include a myriad of three-dimensional structures in the dynamic rings driven by interactions with Saturn's moons and interior; a giant Saturn storm that circled the entire planet for most of 2011, while a long-lived hexagonal jet stream discovered by Voyager in 1981 continues to encircle the north polar region. Cassini solved the mystery of Iapetus' dual bright-dark surface, and the true rotation rate of Saturn's interior. During the final year of the mission, moving closer to Saturn than ever before, provided an astonishing array of discoveries about the interior of Saturn, its rings and tiny ringmoons, and the gap between the rings and the planet. This section highlights some of Cassini's top scientific discoveries. Additional details about each of them can be found in the discipline and instrument team reports in Section 3 and in Spilker [2019].

Enceladus: Discovery of an Ocean World

The discovery of Enceladus' massive plume spewing into space was such a surprise that mission designers completely reshaped the mission to get a more detailed look, adding 20 more close Enceladus flybys, for a total of 23 during the mission. The discovery became even more important when Cassini found evidence of water vapor and water ice in the plume. Life as we know it relies on water, so the search for life suddenly extended to this small, bright moon. The discovery of a subsurface ocean makes Enceladus one of the most exciting science destinations in our solar system.

Prior to Cassini's arrival, Enceladus, a small moon only about 500 km across, was puzzling because of its very bright surface. As the brightest moon in our solar system, it reflects almost 90% of the sunlight it receives. During Cassini's early flybys, images of the moon (Figure 3-7) revealed a system of extensive cracks and large regions completely devoid of craters. The south polar region contains large tectonic features, is devoid of craters, and is the youngest surface on Enceladus. It includes a system of four nearly parallel fractures, nicknamed "tiger stripes," that are centered near the pole [Helfenstein 2010]. Each "tiger stripe" is about 130 km long and 2–4 km wide. They are separated from each other by approximately 35 km.

Activity on Enceladus was first detected by Cassini's magnetometer as a deflection of Saturn's magnetic field [Dougherty et al. 2006]. During a close targeted flyby in 2005, Cassini's thermal infrared spectrometer discovered a hot spot centered near the South Pole [Spencer et al. 2006]. The four tiger stripe fractures were the warmest regions—more than 100 degrees Celsius warmer than the surrounding areas [Howett et al. 2011]—and were the source of an immense ice plume

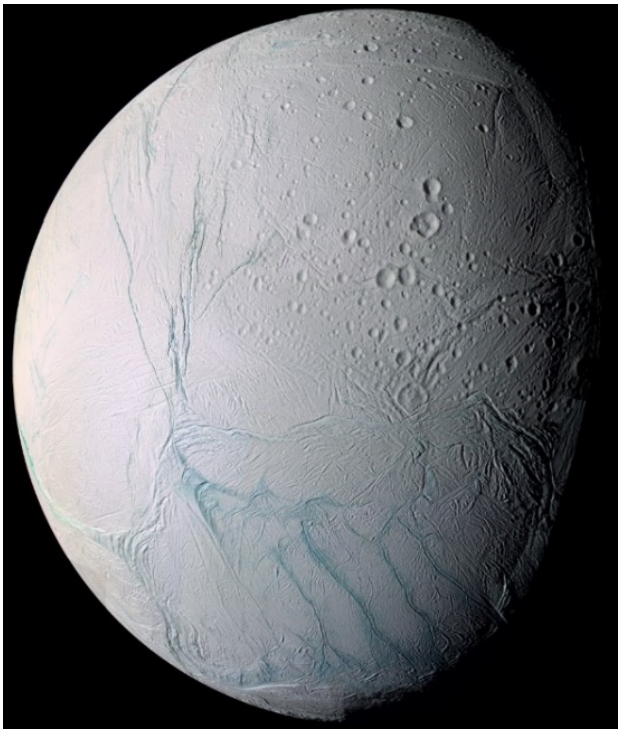

Figure 3-7. Enceladus' bright surface, with very few craters, indicates a young surface. Four bluish "tiger stripe" fractures at the South Pole are the source of the icy jets and plume.

imaged by Cassini's camera [Porco et al. 2006]. The giant cryovolcanic plume of water vapor and ice grains is fed by both discrete jets [Porco, DiNino, and Nimmo 2014] and curtains of material [Spitale et al. 2015] originating inside each tiger stripe (Figure 3-8). The localized jets in the tiger stripes are the warmest regions on the moon [Spencer and Nimmo 2013; Goguen et al. 2013]. The unexpected discovery of Enceladus' extensive water vapor and ice particle plume was such a surprise that future mission phases were reshaped to capitalize on this discovery. Cassini ultimately flew through the Enceladus plume seven times, directly sampling its gas and icy particles.

The lack of impact craters in the tiger stripe region demonstrates that it is a geologically fresh surface that is constantly renewing itself. A fair fraction of the plume material eventually re-impacts Enceladus but some of the smallest grains are the source of the tenuous, distended E-ring [Spencer et al. 2006; Kempf, Beckmann, and Schmidt 2010; Mitchell, Porco, and Weiss 2015], which is densest at the orbit of Enceladus and spreads throughout the system. The E-ring interacts with the inner moons, coating one side with bright, fresh material. Cassini discovered that the source of the plume is a global liquid water ocean beneath Enceladus' crust [Iess et al. 2014; Thomas et al. 2016]. The ocean is about 10 km deep beneath an ice shell that is about 26–31 km thick, and perhaps considerably thinner, as thin as 5 km, in the south polar region.

In addition to water vapor [Hansen et al. 2006], Cassini's INMS discovered that the plume gasses contain carbon dioxide and simple hydrocarbons such as methane, propane, and acetylene [Waite et al. 2009; Waite et al. 2017]. During Cassini's closest dive through the plume in 2015,

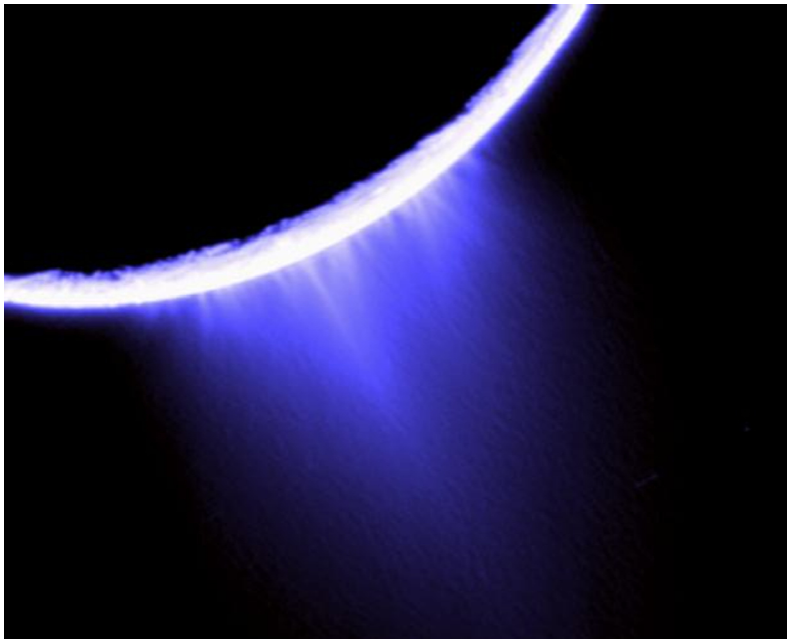

Figure 3-8. Icy jets shoot from Enceladus' South Pole. Jets form a ghostly plume of particles, some fall back to the moon and others create the E-ring. This false-color image was taken by NASA's Cassini spacecraft.

INMS discovered molecular hydrogen (H_2) [Waite et al. 2017]. Cassini's CDA found icy particles as well as salt-rich ice grains containing sodium and potassium that are probably frozen droplets from the underground salty ocean [Postberg et al. 2009; Postberg et al. 2011; Glein, Baross, and Waite 2015]. CDA also discovered tiny grains of silica, less than 10 nanometers in size, originating from Enceladus' ocean [Hsu et al. 2015]. These tiny silica grains most likely condensed from hot water spewing from hydrothermal vents on Enceladus' seafloor. The excess hydrogen discovered by INMS could also be coming from the hydrothermal vents. CDA and INMS also detected evidence for large organic fragments, indicative of complex organic molecules that are created in chemical processes, perhaps including those related to life [Postberg et al. 2018]. The source of energy for the hydrothermal activity on Enceladus is tidal interactions among Enceladus, Dione, and Saturn [Tobie, Cadek, and Sotin 2008]. With liquid water, an energy source, and organic molecules, the subsurface ocean of Enceladus could harbor the ingredients for primitive life. The Cassini orbiter did not carry the instruments needed to detect life so that goal remains for a future mission. Enceladus and the other icy moons of Saturn are discussed in detail in the book edited by Schenk et al. [2018]. For more details about Enceladus science, see the Icy Satellite report and the team reports.

Titan: Earth-like World with Rain, Rivers, Lakes and Seas, Global Ocean, and Prebiotic Chemistry

Titan is the largest moon in the Saturn system, slightly larger than the planet Mercury, and the only moon in our solar system with a dense atmosphere. Titan is also the only body other than Earth that

displays clear evidence for surface liquids: liquid hydrocarbons. Titan's atmosphere is mostly nitrogen with some methane and a haze layer of organics that give Titan its orange appearance. Key Titan results can be found in the books, *Titan: Interior, surface, atmosphere, and space environment* [Müller-Wodarg et al. 2014] and *Titan from Cassini-Huygens* [Brown, Lebreton, and Waite 2009].

Titan has many geologic processes similar to that of Earth. These processes generate methane rains, which build river channels and form lakes and seas containing liquid methane and ethane. Titan's atmosphere is teaming with a variety of molecules—the most chemically complex in the solar system. Beginning with sunlight and methane, ever more complex molecules form until they become large enough to form the smog that covers the giant moon. Nearer the surface, methane, ethane, and other organics condense and fall to the surface where likely other prebiotic chemistry can take place.

Cassini revealed an array of complex hydrocarbons in Titan's atmosphere, created as methane gas is broken apart by sunlight in the upper atmosphere, generating active chemistry [Waite et al. 2007] and a link to haze formation [Lavvas et al. 2013]. The mechanism by which methane is replenished remains a mystery. Over the course of the mission, methane rainfall darkened parts of Titan's surface [Turtle et al. 2009; Turtle et al. 2011], and methane clouds formed and dissipated [Rodriguez et al. 2009]. As the seasons changed, the evolution and breakup of Titan's northern winter polar vortex and the early formation of Titan's southern winter polar vortex were observed [Vinatier et al. 2015; Achterberg et al. 2011]. The polar vortices appear to be tilted by a few degrees relative to the rotational pole of Titan, and the entire stratosphere is also tilted by several degrees [Achterberg et al. 2008].

The surface of Titan was examined from orbit using radar and imaging at both visible and infrared wavelengths, which showed that Titan has many geologic processes reminiscent of those on Earth. Radar wavelengths can pierce the haze, allowing us to see Titan's surface. These processes generate methane clouds and rain, build river channels, form lakes and seas (Figure 3-9) containing liquid methane and ethane, form complex atmospheric hydrocarbons, and generate dunes of hydrocarbon particles. Cassini's studies revealed Titan to be remarkably like a prebiotic Earth. On Titan, methane plays the role of water on Earth and water ice is a key ingredient of the rocky soil. Titan's methane cycle is analogous to Earth's hydrologic cycle, but at temperatures about 200 K lower.

Titan's surface consists of broad regions of light and dark terrain. Some of the dark, equatorial regions generally consist of long, linear dunes [Radebaugh et al. 2008]. Titan's lakes and seas are confined primarily to the polar regions. In the south polar region, one lake, Ontario Lacus, was seen by Cassini while the north polar region small lakes, and large seas about the size of the Great Lakes, abound [Stofan et al. 2007]. A specular reflection observed by VIMS definitively verified that the dark lake regions contain liquid [Stephan et al. 2010]. For more details about Titan, see the Titan report and team reports in Sections 3.1 and 3.2.

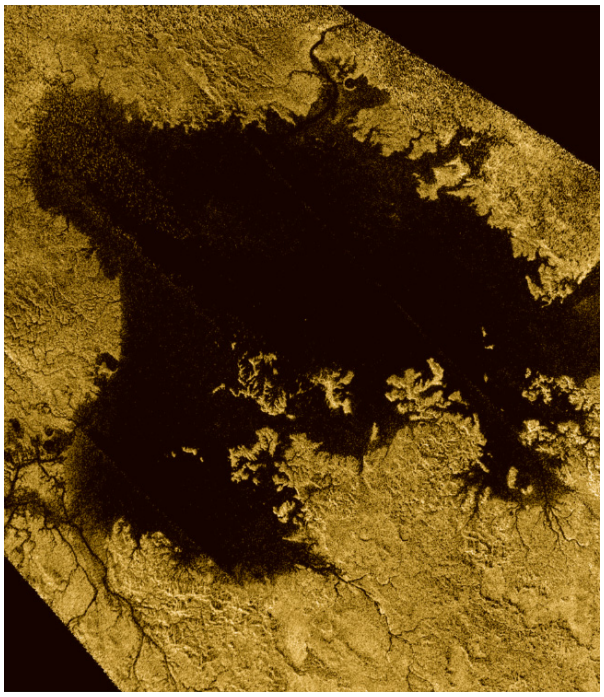

Figure 3-9. Radar view of Titan sea Ligeia Mare with river channels flowing into it. Ligeia Mare is 50% larger than Earth's Lake Superior and ~500 feet deep, also similar to the Great Lakes.

Huygens Probe: First Landing on an Outer Solar System Moon (Titan)

The Huygens probe became the first human-made object to land on Titan. Huygens was built and operated by ESA and was carried as a passenger on the Cassini spacecraft. Huygens separated from Cassini in December 2004 and landed on Titan three weeks later, on January 14, 2005.

Huygens's historic 2005 landing on Titan was the most distant in our solar system to date. The probe's descent revealed Titan to be remarkably like Earth before life evolved, with methane rain, erosion and drainage channels, and dry lake beds. An array of complex hydrocarbons was found in Titan's atmosphere, created by the break-up of methane high in the atmosphere.

Huygen's 2 hour 27 min parachuted descent provided the first in situ atmospheric profile of temperature, pressure, density, wind, and composition, as well as detailed images of the surface. The surface pressure was 1.47 times that on Earth [Fulchignoni et al. 2005]; super-rotating prograde, zonal winds peaked at 430 km hour^{-1}, much greater than Titan's equatorial rotation velocity [Bird et al. 2005]; and atmospheric composition included the noble gases argon, krypton, and xenon [Niemann et al. 2005], whereas nitrogen and methane were confirmed as the primary constituents [Niemann et al. 2010]. After landing, the GCMS measured an increase in abundance of methane gas as the relatively warm GCMS inlet heated Titan's surface [Niemann et al. 2005].

The Cassini spacecraft flew overhead and collected the Huygens data, including about 72 minutes on Titan's surface, before Huygen's link to Cassini was lost as Cassini set over the

horizon. Huygens landed in a dry lakebed filled with rounded pebbles (Figure 3-10), near the Xanadu region, an equatorial area about the size of Australia. Images taken at about 10 km altitude captured dendritic erosional patterns on a hillside with very steep slopes. The rounded, smoothed pebbles at the landing site are evidence of fluid flow [Tomasko et al. 2005].

An overview of Huygens science can be found in Lebreton et al. [2009] and in the Huygens report.

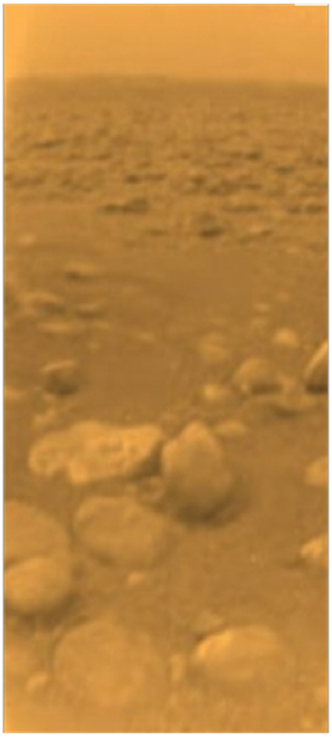

Figure 3-10. Huygens image from the surface of Titan. This colored view was processed to add reflection spectral data, and gives a better indication of the actual color of the surface.

Iapetus: Mystery of the Dual, Bright-dark Surface of the Moon Solved

The origin of Iapetus's two-face, bright-dark surface has been a mystery for more than 300 years (Figure 3-11). The Cassini spacecraft solved the puzzle. Dark, reddish dust in Iapetus' orbital path is swept up and lands on the leading face of the moon. The dark areas absorb energy and become warmer, while uncontaminated areas remain cooler. The moon's long rotation period contributes to this yin-yang effect.

One hemisphere of Iapetus is as dark as charcoal while the other half is nearly as bright as snow. The reason for this light-dark dichotomy was not known prior to Cassini's arrival at Saturn. An Earth-orbiting infrared telescope discovered a very tenuous ring at the orbit of Phoebe [Verbiscer, Skrutskie, and Hamilton 2009], probably dust thrown off the moon by tiny meteor impacts. This dust is swept up by Iapetus as it orbits Saturn. The darkest side of the moon is

centered exactly in the direction of motion of the satellite. A handful of small impact craters on the dark side punch through to bright material below, suggesting that the dark material is not very deep.

Cassini discovered a 20 km high ridge that circles most of the equator [Porco et al. 2005]. The ridge breaks up into mountains in some of the lowest albedo regions. The ridge must have been formed early in the history of Iapetus because it is heavily cratered and eroded. The surface of Iapetus is mainly water ice with small amounts of carbon dioxide, carbon, and complex organic molecules present.

Figure 3-11. The dark surface of Iapetus and the dark, heavily cratered region called Cassini Regio are visible, along with the giant ridge that circles Iapetus's equator.

Moons Mimas and Phoebe

The Saturn system contains 62 known moons, many of them small, captured objects that are distant from Saturn and irregular in shape. Much closer to Saturn are 24 regular moons that probably formed from the same sub-nebula as Saturn. Some of these moons have strong interactions with the ring system, opening gaps and sculpting the rings. More information about Enceladus and the icy satellites can be found in Schenk et al. [2018].

Mimas is the innermost and smallest of the intermediate-sized moons with a diameter of 394 km. During a close flyby in February 2010 the infrared spectrometer discovered that the leading side of Mimas—the hemisphere that faces forward in the moon's orbit about Saturn—is about 15 degrees K colder than the other side [Howett et al. 2011]. This thermal anomaly, in the shape of "Pac-Man," is a result of a contrast in thermal inertia between the leading and trailing sides of Mimas. The leading face is altered by bombardment of highly energetic electrons. This bombardment increases the contact between regolith grains, decreases their porosity and increases thermal inertia [Schenk et al. 2011]. Models of Saturn's E-ring suggest that the side of

Mimas that faces away from the direction of motion should be preferentially coated by particles from the E-ring. Mimas' exceptionally high reflectivity (it is the second most reflective moon in the solar system) supports this hypothesis. Water ice is the primary compound detected on its surface. Its heavily cratered appearance argues against current activity on the moon.

Two weeks before Saturn Orbit Insertion (SOI), Cassini-Huygens flew close to Phoebe, the largest outer irregular moon of Saturn. Phoebe moves in an inclined, retrograde orbit that is 13 million kilometers from Saturn. It is covered with impact craters that were probably created by collisions with smaller outer moons. Some of the craters contain icy patches and layered structures; others have unusual conical shapes. Phoebe reflects only a few percent of the sunlight that falls on it, about the same as that reflected by the dark regions of Earth's moon. In addition to water ice, its surface is composed of carbon and carbon dioxide [Clark et al. 2005]. The presence of carbon and the fact that its density is higher than that of the other medium-sized moons of Saturn suggest that Phoebe was formed near the edge of the solar system and migrated inward to be captured by Saturn [Johnson and Lunine 2005]. Phoebe may have originated in the Kuiper Belt, the reservoir of ice/rock bodies that dwell beyond the orbit of Neptune and that may provide clues to the architecture of the early solar system and its subsequent evolution.

Discovery of seven small moons

Cassini discovered seven small moons in the inner Saturn system [Thomas et al. 2016]. Pallene and Aegaeon are associated with diffuse, dusty rings, and Anthe and Methone are associated with ring arcs. A tiny moon, Daphnis, orbits in the Keeler gap and may help to keep it clear. An even smaller moon causes propeller-like structures in a ring of Saturn (S/2009 S). A new moon, Aegaeon, was discovered inside Saturn's G-ring [Hedman et al. 2010]. Another Cassini discovery is the moon Polydeuces, which moves in a gravitationally stable zone in Dione's orbit known as the Lagrangian point.

Prior to Cassini, Saturn already had a unique family of small satellites, including the co-orbitals Janus and Epimetheus, which switch orbits every four years and appear to have been one body until their violent separation. Other previously known moons include the F-ring shepherds, Prometheus and Pandora, as well as Atlas, orbiting just outside the A-ring edge, and Pan, which clears the Encke gap.

Saturn's Rings: Revealed as Active and Dynamic—A Laboratory for How Planets Form

Cassini's 13 years in orbit made it possible to watch changes in Saturn's dynamic ring system. The spacecraft discovered propeller-like formations, witnessed the possible birth of a new moon and observed what may be one of the most active, chaotic rings in our solar system, Saturn's F-ring.

Saturn's rings are both beautiful and complex, and the processes observed there provide a laboratory for how planets might form. Some of the highest resolution data on the rings were obtained

at SOI in 2004. Tiny propellers and straw-like clumping in the strongest density wave peaks were first detected in the images from the SOI unlit ring scan. For more detailed summaries, see ring chapters in the books, *Saturn from Cassini-Huygens* [Dougherty, Esposito, and Krimigis 2009], and *Planetary Ring Systems: Properties, Structure, and Evolution* [Tiscareno and Murray 2018].

Some places in Saturn's rings were changing on very short timescales of weeks or months. Dozens of objects, 0.1–1 km in size, orbiting in the A-ring, changed their locations as they interacted with neighboring material. These unseen objects opened up tiny propeller-shaped gaps that were captured in the Cassini cameras and in stellar occultations of the rings [Tiscareno et al. 2010] (Figure 3-12). Cassini observed channels opening and closing in the F-ring, in response to close approaches by the tiny moon Prometheus [Murray et al. 2005]. Clumps and dusty jets appeared and disappeared in the F-ring core, excited by embedded moonlets and disturbed by objects with orbits eccentric enough to dive through the ring [Murray et al. 2008; Beurle et al. 2010]. Several new ringlets appeared during Cassini's 13 years in orbit [Hedman et al. 2009]. They were composed mostly of fine dust grains; one in the outer Cassini division was barely visible when Cassini arrived but was among the dustiest features in the rings by the end of the mission.

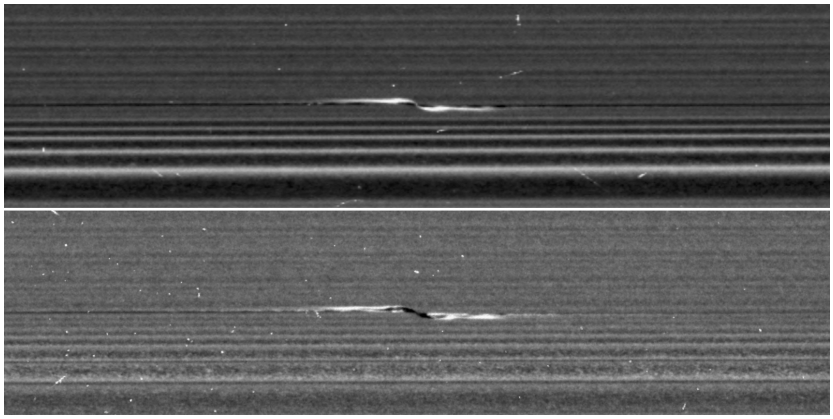

Figure 3-12. Propeller structures are caused by embedded moonlets at their centers, and have much in common with baby planets embedded in protoplanetary disks. View of propeller Santos Dumont on the sunlit side of the rings (top panel) and unlit side of the rings (bottom panel).

The ring particles in Saturn's main A- and B-rings are nearly pure water ice but show a strong ultraviolet absorption that varies in strength from place to place. A reddish color of varying intensity in the rings is deeper where the ice signature is strongest. The rings probably darken with time as they are polluted by meteoroid bombardment. The less massive C-ring and Cassini division look more polluted (redder) than the more massive A-ring and B-ring [Cuzzi et al. 2010].

Hundreds of stellar and radio occultations of the rings were obtained throughout the mission at a large variety of ring geometries, including some of the best-ever radio occultations during the Grand Finale as the radio signal was beamed through the rings while Cassini flew close to Saturn. Detailed horizontal and vertical structure in the rings was revealed at multiple wavelengths. They provided a detailed map of Saturn's rings, including three-dimensional measurements of tendril-like, ephemeral structures in the rings called self-gravity wakes [Colwell, Esposito, and Sremcevic 2006]. These

transient gravitational instabilities form but are torn apart by Saturn's tides. Similar behavior in a protoplanetary disk might play a role in formation of planets in our own solar system and beyond. A different kind of microstructure, which behaves like self-gravity but is due more to viscous forces in the rings than self-gravity, can also be seen throughout the densest parts of the rings [Colwell et al. 2007].

Modeling of the damping behavior of dozens of spiral density and bending waves constrained the mass of most of Saturn's main rings [Tiscareno et al. 2007]. However, occultations were not able to directly probe the densest parts of the B-ring so its mass remained uncertain until gravity measurements in the Grand Finale orbits found that the total mass of the rings was less than all previous estimates, hinting at a young age for the rings [Iess et al. 2019].

Vertical Structures in the Rings Imaged for the First Time

Once about every 15 years, the Sun shines on the edge of the ring plane and northern and southern sides of the rings receive little sunlight. Cassini measured the long shadows from this rare event to determine the heights of structures within the rings.

Many new discoveries were made during equinox in August 2009, the time when the Sun was edge-on to the rings. Once every half Saturn year, the ring plane aligns with the center of the Sun, and for a brief time, the northern and southern sides of the rings receive essentially no sunlight. Vertically extended objects cast long shadows on the rings that provided a measurement of the height of these ring structures. During this unique time, Cassini observed long shadows up to 2.5 km long (Figure 3-13) created by objects larger than the 5-meter vertical thickness of the rings. They included shadows from towering km-sized objects near the outer edge of the B-ring, and the vertical extent of edge waves in the Keeler gap created by the tiny moon Daphnis [Tiscareno and Murray 2018]. The rings also cooled to their lowest temperatures, heated for a few days only by Saturn shine [Spilker, Ferrari, and Morishima 2013].

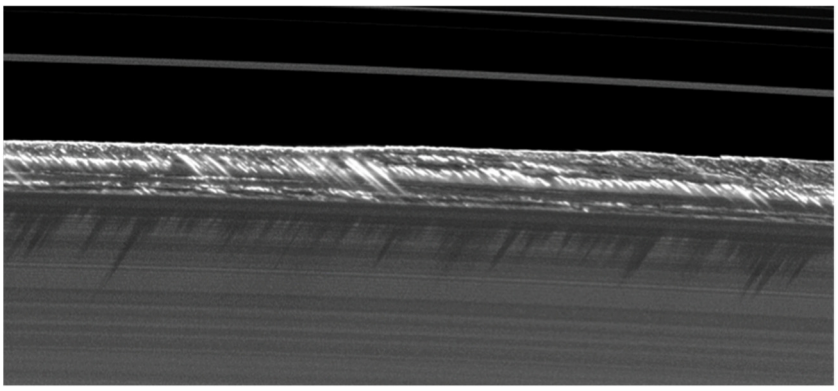

Figure 3-13. Vertical structures at the edge of Saturn's B-ring. Among the tallest structures seen in Saturn's main rings, large objects rise abruptly from the edge of the B ring to cast long shadows on the ring. This image was taken by NASA's Cassini spacecraft two weeks before the planet's August 2009 equinox. (Credit: NASA/JPL/Space Science Institute)

Saturn's Great Northern Storm of 2010–2011

Late in 2010, a giant storm quickly erupted in Saturn's relatively bland atmosphere (Figure 3-14). This type of storm typically occurs only once every 30 years, but this one arrived 10 years early, providing a unique observing opportunity for Cassini [Baines et al. 2018]. Within months, this storm completely encircled the planet with a swirling band of clouds and vortices [Sayanagi et al. 2013]. The largest temperature increases ever recorded for any planet were measured in the stratosphere and molecules never seen before in Saturn's upper atmosphere were detected. The storm began to fade away shortly after the vortex in its "head" collided with one in its "tail," about nine months after it began [Fletcher et al. 2011].

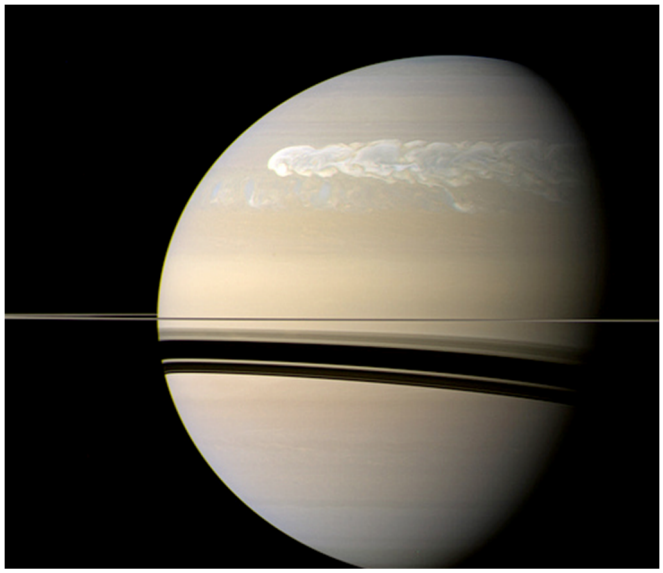

Figure 3-14. Saturn's relatively tranquil atmosphere erupted with a storm of gigantic proportions in late 2010.

Saturn's North Polar Hexagon and Discovery of Giant Hurricanes at Both of Saturn's Poles

Saturn's polar regions surprised scientists with the presence of a long-lived hexagonal-shaped jet stream in the north and two hurricane-like storms at both poles. Their driving forces remain a mystery.

Saturn's alternating eastward and westward jet streams define the cloud bands that circle the planet on lines of constant latitude to within about one degree of each pole. One of the jet streams, near 75 degrees north latitude, forms a hexagonal pattern that is two Earth diameters across [Baines et al. 2009]. Voyager first discovered the hexagon, and it is still present at the same location after 35 years. Small clouds move eastward around the corners of the pattern. This hexagonal-shaped jet stream (Figure 3-15) is remarkable for its stability and longevity. Its source remains a mystery. Using Cassini CIRS thermal data of Saturn's North Pole, a new hexagonal structure,

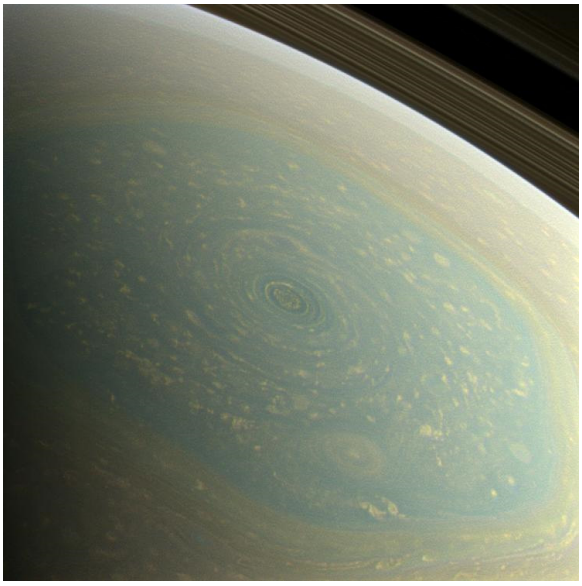

Figure 3-15. The greenish hexagon, about two Earth diameters across, is clearly seen at Saturn's North Pole. (Credit: NASA/JPL/Space Science Institute).

precisely matching the well-known hexagon, was recently discovered towering hundreds of kilometers above the cloud tops [Fletcher et al. 2018]. The presence of a newly detected hexagon in Saturn's northern summer stratosphere, which is connected to the familiar hexagon in some way, suggests that there is a great deal more to be learned about the dynamics at play in Saturn's atmosphere.

Cassini discovered hurricane-like storms at both of Saturn's pole. The hurricanes are about 50 times larger than a typical Earth hurricane and are centered exactly at the poles [Fletcher et al. 2008; Sayanagi et al. 2017]. In the south, Cassini discovered the clear eye of a hurricane-like vortex, with eyewall clouds towering 70 kilometers above the clouds in the center. There is a warm vortex at Saturn's North Pole as well. Each vortex shows well-developed eye walls [Dyudina et al. 2008].

Length of Saturn's day

Saturn emits radio waves known as SKR that were first observed by Voyager in the early 1980s and were interpreted as an indicator of Saturn's internal rotation period. Cassini results showed that the SKR signals were not coming from the interior of Saturn as originally assumed. The SKR period changed from year to year, an impossibility if the SKR is tied to the interior. When Cassini first arrived at Saturn and measured the SKR period, data from the radio and plasma wave instrument also showed that the radio waves' frequencies were different in the northern and southern hemispheres [Gurnett et al. 2009]. In addition, planetary period oscillations observed in magnetic field data reveal a similar story: the period of these oscillations (although close to the expected planetary period of about 10.7 hours) changed over time, particularly with season, and were different in the northern and southern hemispheres [Provan, Cowley, and Nichols 2009]. Clearly the observations of SKR and its associated magnetic field are not coming from the interior.

The origin of the multiple periodicities is not well understood but they are not related to Saturn's internal rotation rate. The magnetometer team searched for an offset between Saturn's rotation axis and magnetic field axis, to use the magnetic field variations from this offset to determine the length of Saturn's day. However, the offset was too small to determine Saturn's internal rotation rate [Dougherty et al. 2018].

Clues to the length of Saturn's day actually came from small waves detected in the rings. Saturn's ring system acts like a sensitive seismograph, providing a measure of Saturn's internal oscillations that allow a determination of its interior rotation rate. These vibrations, determined by Saturn's non-uniform internal structure, are probably driven by convection inside the planet, which cause oscillations in Saturn's gravity field that manifest themselves as waves in the rings. Modeling the propagation behavior of this collection of waves provides an interior rotation rate for Saturn of 10 hours 35.3 minutes ±2 minutes [Mankovich et al. 2019].

Unexplored Territory: Probing the Gap between the Rings and Saturn

After 13 years in orbit, the Cassini-Huygens mission to Saturn ended with a truly unique set of science data. Cassini sent back its final bits of distinctive science data on September 15, 2017, as it plunged into Saturn's atmosphere, vaporizing to satisfy planetary protection requirements. Cassini's final phase covered roughly 10 months and ended after the first ever exploration of the region between the planet and its rings.

In late 2016, Cassini transitioned to a series of 20 Ring Grazing orbits with the closest approach (periapsis) just outside Saturn's F-ring, providing close flybys of tiny ring moons, and high-resolution views of Saturn's A- and F-rings. A final Titan flyby in late April 2017 propelled Cassini's periapsis across Saturn's main rings to initiate the Grand Finale orbits. Comprised of 22 orbits, Cassini repeatedly dove between Saturn's innermost rings and upper atmosphere to answer fundamental questions unaddressed earlier in the mission. The last orbit turned the spacecraft into the first Saturn atmospheric entry probe. Additional details about the science in these final orbits can be found in the discipline and team reports in Sections 3.1 and 3.2.

Close to Saturn: rings and ringmoons

The Ring Grazing and Grand Finale orbits provided some of the highest-resolution remote sensing observations of the mission for studies of the five tiny ringmoons and Saturn's main rings. These orbits also provided a rare opportunity to fly through and directly sample the SKR region.

In the Ring Grazing orbits, Cassini performed the closest ever flybys of five of Saturn's tiny ringmoons, Pan, Daphnis, Atlas, Pandora, and Epimetheus. The surface characteristics of these moons are regulated by both accretion of a reddish material from Saturn's main rings and of icy grains originating in the Enceladus plume [Buratti et al. 2019]. The color and brightness of the moons inside or closest to the main rings (Pan, Daphnis, and Atlas) strongly resemble that of the rings. Figure 3-16 shows a central core surrounded by an equatorial ridge of ring particles for each

of these three moons [Buratti et al. 2019]. For more details about these tiny ringmoons, see the Icy Satellites report in Section 3.1.

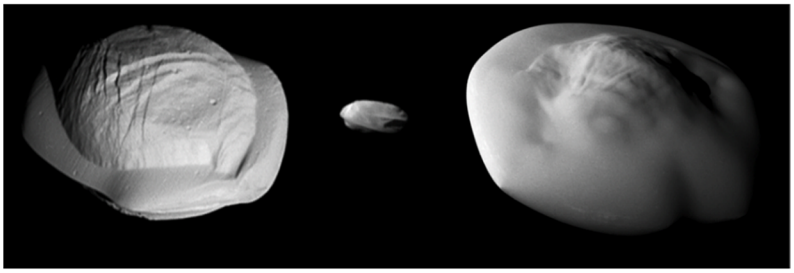

Figure 3-16. Cassini images of Pan (left), Daphnis (center) and Atlas (right) as observed in 2017 during the closest flybys ever of these moons.

The Cassini spacecraft passed very close to Saturn's main rings during its final year, and obtained very high-spatial-resolution images, spectral scans, and temperature scans [Tiscareno et al. 2019]. Embedded masses sculpt the main rings and new structures were discovered in the images, including new ring textures such as streaky C-ring plateaus and unexpected bands of particle clumping throughout the rings (Figure 3-17). Water ice band depths vary across the rings, and weaker ice bands were identified outside the Keeler gap in the A-ring. Many structures throughout the main rings and F-ring were studied in more detail—see Tiscareno and Murray [2018]. For more details about these ring observations, see the Ring report and team reports in Sections 3.1 and 3.2.

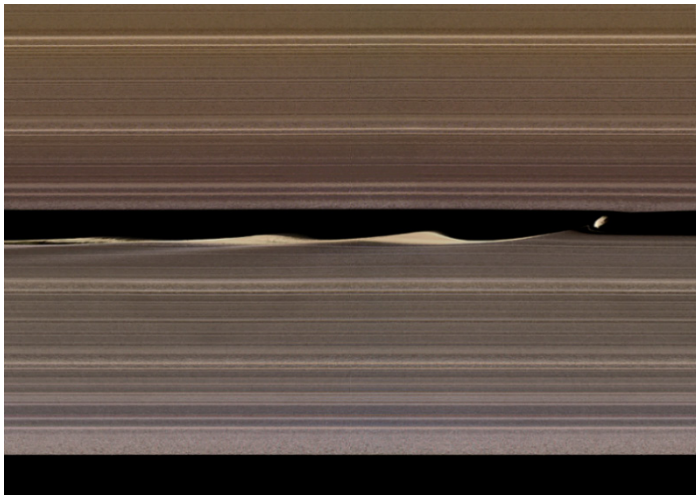

Figure 3-17. Tiny Daphnis opens the Keeler gap and generates waves along one gap edge. The speckled texture is created by ring particles clumping together. This clumping is seen throughout the rings.

The orbits during the final year provided an excellent opportunity to directly and repeatedly sample the top of the SKR emission region to determine its source [Lamy et al. 2018]. SKR is a sensitive diagnostic of Saturn's magnetospheric dynamics and auroral processes. In situ measurements are required to understand how these planetary radio emissions are generated. These emissions were found to be strongly time-variable from orbit to orbit, with a dependence on

local time around Saturn. Only three SKR source regions were identified, all on the dawn side of Saturn, and controlled by the electron densities in the vicinity [Lamy et al. 2018]. These regions were embedded in upward currents associated with Saturn's auroral oval.

Diving through the gap

During the Grand Finale orbits, numerous instruments performed in situ measurements while traversing the gap between the inner D-ring and the planet. MIMI, designed to measure energetic particles, measured an unexpected response to very small dust grains, about the size of large organic molecules [Mitchell et al. 2018]. Ring dust in the submicron range was detected by CDA, and ring composition was directly measured for the first time [Hsu et al. 2018]. The composition of the volatiles in the gap was revealed by INMS, indicating an array of gases and organic compounds [Waite et al. 2018]. The MIMI instrument also identified an inner radiation belt in this gap region [Roussos et al. 2018].

MIMI detected tiny nanograin ring particles, within ±2° of the equator, entering Saturn's equatorial atmosphere directly from the inner D-ring, possibly from the bright D68 ringlet [Mitchell et al. 2018]. Collisions with hydrogen atoms provide enough drag to decelerate the particles, until they plunge into Saturn's atmosphere. This continuous rain of particles produces a lower limit of ~5 kg s^{-1} into the atmosphere. Particles at higher latitudes are charged and transported along the magnetic field lines as "ring rain" [Hsu et al. 2018; Mitchell et al. 2018].

CDA directly measured the mass and composition of particles originating in Saturn's main rings to characterize the material falling into Saturn's atmosphere. CDA primarily detected tiny nanograins with the highest peak flux near Saturn's equator and two secondary peaks at mid-latitudes, one on each side of the rings [Hsu et al. 2018], consistent with previously detected "ring rain" [O'Donoghue et al. 2013]. Two separate nanograin compositions were identified, water ice grains and silicate grains [Hsu et al. 2018]. Silicate grains comprised about one-third of the identified nanograins, much greater than the estimated bulk silicate composition of typically only a few percent [Cuzzi et al. 2010].

The INMS instrument directly observed the interaction between the rings and Saturn's atmosphere, measuring the in situ atmospheric and ionospheric composition of Saturn's equatorial atmosphere for the first time. Ring volatiles from the D-ring were detected, including water, methane, ammonia, carbon monoxide and/or molecular nitrogen, and carbon dioxide enter Saturn's atmosphere along the ring plane. INMS also measured an influx of organic-rich nanoparticles from the rings that further modifies the composition and structure of the equatorial atmosphere (Figure 3-18). The estimated mass influx rate was 5,000 to 40,000 kg s^{-1}, considerably higher than the MIMI estimates [Mitchell et al. 2018; Waite et al. 2018].

During the final orbits, an inner radiation belt was detected by MIMI in the gap between the D-ring and top of Saturn's atmosphere [Roussos et al. 2018]. Saturn's main rings inhibit the inward passage of trapped charged particles that form radiation belts. Hence, the radiation belts outside the main rings cannot interact with the inner radiation belt, providing an opportunity to study the

inner belt and its interactions with the D-ring. One possible source for the inner radiation belt is the Cosmic Ray Albedo Neutron Decay (CRAND). Ringlets in the D-ring, including D68 and D73, control the structure and outer boundary, respectively, of this radiation belt [Roussos et al. 2018].

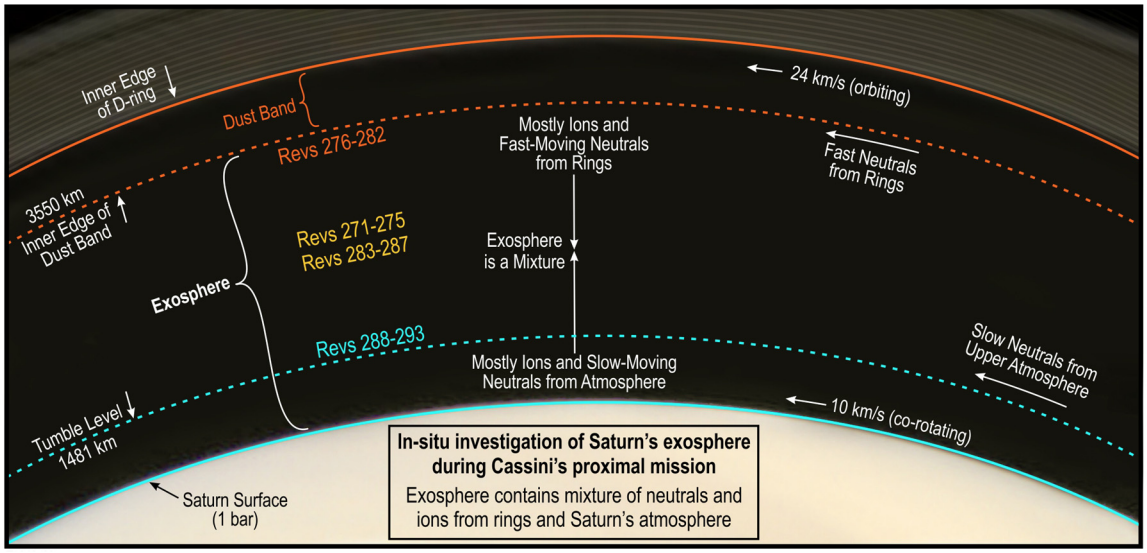

Figure 3-18. Geometry of Cassini's Grand Finale orbits. Left panel: A schematic drawing showing the altitude coverage of the orbits (revs) during the Grand Finale phase of the Cassini mission from a polar perspective. The region is bounded above by the D-ring and below by the 1 bar pressure level of Saturn's atmosphere. From Waite et al. [2018].

Window inside Saturn: Internal Structure from Gravity and Magnetic Fields

Cassini's Grand Finale orbits enabled the highest resolution gravity and magnetic field measurements of Saturn for the entire mission. The behavior of Saturn's internal gravity and magnetic fields provides a window into the interior of the planet.

Six of the Grand Finale orbits were designed for gravity measurements. During these orbits unique gravity signatures were recorded to determine the mass distribution in Saturn's interior and the mass of Saturn's main rings [Iess et al. 2019]. The measured values of Saturn's gravitational harmonics require deep differential rotation to a depth of about ~9,000 km inside the planet (down to about 0.7 Saturn radii). This depth may correspond to the levels of magnetic dissipation. Saturn's rocky core is about 15–18 Earth masses. The ring mass is 0.41 Mimas masses, pointing to a relatively young ring age, perhaps only 10^7–10^8 years old [Iess et al. 2019].

All 22 orbits provided the highest resolution magnetic field measurements of Saturn's internal and external fields since Cassini's passage above

> Cassini's final year was like a brand-new mission as it explored a region of the Saturn system unexplored by any previous outer planet spacecraft.

the rings during SOI. One of the Grand Finale surprises was the exceptionally small observed tilt (less than 0.0095°) between Saturn's spin-axis and its magnetic axis [Dougherty et al. 2018]. Saturn's magnetic field is considerably more axisymmetric than any other planetary magnetic field in our solar system, making it challenging to explain with current theories. MAG data provide interesting insights into Saturn's conducting magnetic region. For instance, zonal flows imply differential rotation, which is consistent with Cassini's gravity measurements [Iess et al. 2019], while the higher order magnetic moments hint that secondary dynamo action may be at work in the semi-conducting region of Saturn [Dougherty et al. 2018].

The magnetometer team also discovered a strong, low latitude field-aligned current (FAC) system, situated between the inner edge of the D-ring and the top of Saturn's atmosphere [Dougherty et al. 2018]. This current is comparable in strength to the currents observed in the auroral zone and as such, may be part of a global current system.

Cassini's final year was like a brand-new mission as it explored a region of the Saturn system unexplored by any previous outer planet spacecraft. These new data required new theories and new ideas. Cassini's final Earth-bound transmission occurred on September 15, 2017, as it plunged into the planet, sending its last bits about the directly sampled atmosphere to Earth, then vaporizing in Saturn's atmosphere. This protective measure ensured that any hardy, Earthly microbes that might have survived onboard Cassini did not inadvertently contaminate either Enceladus or Titan.

Only a few of the many Cassini scientific highlights were discussed here. In the coming years many more Cassini discoveries remain to be found in this incredibly rich data set.

A list of some of Cassini's key discoveries and findings is given in Table 3-10 to illustrate the breadth and depth of this incredible mission. Cassini's rich set of science instruments led to many new discoveries across all five science disciplines. Many more discoveries and findings are discussed in the discipline and team reports in Sections 3.1 and 3.2.

Table 3-10. Cassini discoveries: A partial list of Cassini's key findings and discoveries.

Huygens landing on Titan. Huygens probe lands on the surface of Titan and makes critical atmospheric and surface measurements.
Geologic activity at Enceladus. Active plume discovered at south pole; Enceladus' plume creates Saturn's E-ring and alters other moons' surfaces; spectacular south polar terrain tectonics; enormous measurable endogenic heat.
Lakes and seas on Titan. Discovery of Titan's polar lakes/seas; specular reflection of sunlight confirms liquid in Kraken Mare.
Saturn giant storm. Saturn daytime lightning seen for the first time. Unprecedented, long-lasting 80K stratospheric temperature increase and new molecules observed in aftermath. Thunderstorms uplift carbon, water ice, and ammonia ice from depth.
Saturn kilometric radiation. North-south periods are different and change unpredictably.
Vertical structure in Saturn's rings. The 10 m thick rings, edge-on, show huge vertical structures created by gravitational interaction with moons; rippled rings show evidence for large impacts over the centuries.
Enceladus' variable plume emission. Gravitational tides cause fissures to periodically open and close depending on orbital distance from Saturn.
Subsurface ocean on Titan. Gravity and radar measurements indicate the presence of a subsurface ocean and soft interior.
Two new populations of objects in the rings. Propellers and self-gravity wakes reveal dynamic structure of the rings.

Table 3-10. Cassini discoveries: A partial list of Cassini's key findings and discoveries.

Depth of a Titan sea. Radar sees secondary echo while sounding Ligea Mare, detecting sea bottom. Depth of other seas and small lakes detected also.
Enceladus global ocean. Global ocean discovered beneath Enceladus' icy crust from radio science measurements and detection of excess libration.
Ring impact clouds. The rings make good detectors of meteorite impacts, based on generated debris clouds.
Massive hurricanes at Saturn's north and south pole. Hurricanes discovered at north and south poles.
Phoebe flyby. First encounter with an object in the Saturn system that likely originated in the Kuiper Belt.
Formation of a polar vortex over Titan's south pole. Seasonal changes caught in the act on Titan.
Enceladus plume composition. Jets are shown to contain salty particles, organic molecules, and ammonia ice.
Enceladus hydrothermal vents. Evidence for hydrothermal vents, including detection of nanosilica grains and excess hydrogen in the plume.
Most of Titan's seas and lakes are at its north pole. Discovery of lakes in Titan's polar regions, but with vast majority at the north pole.
Saturn polar hexagon rediscovered. Discovered by Voyager, Cassini found this jet stream long lived.
Thermal anomalies at Mimas and Tethys. Electron bombardment of parts of their surfaces brings about modification of surface thermal properties.
Weather on Titan. Methane rains (part of Titan's methane "hydrological" cycle) cause visible changes on Titan's surface.
Saturn's magnetosphere plentiful with water. H_2O products dominate the magnetospheric chemical species; expected nitrogen not found.
Iapetus' albedo dichotomy and equatorial ridge. Phoebe dust darkens Iapetus surface. Thermal migration of volatiles causes color dichotomy. Equatorial ridge observed, perhaps a relic of ancient ring of impactors.
Menagerie of Moon Surfaces. Satellites exhibit a striking diversity of surface properties, e.g., Hyperion, Iapetus, and tiny ringmoons.
Saturn rotation mystery. Variable SKR rates and apparent lack of magnetic axis tilt leaves internal rotation rate a mystery.
Rings capture Saturn's internal dynamics. Unique spiral waves in rings provide windows into Saturn's atmospheric oscillations and interior. May provide a rotation rate for the interior of Saturn.
Organic 'building blocks' discovered in Titan's atmosphere. The presence of heavy negative ions in Titan's ionosphere appeared to act as organic building blocks in recombination with large positive ions to create more complex molecules as precursors of aerosol and haze particles.
Supernovae shockwaves. Unusually strong solar wind interacted with magnetosphere to accelerate particles to relativistic speeds, a model for stellar-explosion shockwaves.
Nanograins in gap between innermost ring and top of Saturn's atmosphere. Predominant particle population in the gap is tiny nanograins. Complex organic compounds embedded in water nanograins rain down from Saturn's rings into its upper atmosphere. Composition includes water and silicates, and also methane, ammonia, carbon monoxide, nitrogen and carbon dioxide. Some inner-ring particles and gases fall directly into Saturn's atmosphere.
Ring rain. Some ring particles take on electric charges and spiral along magnetic field lines, falling into Saturn at higher latitudes as "ring rain."
New inner radiation belt. New radiation belt discovered very close to the planet and is made up of very energetic particles.
Tilt of magnetic field axis. Saturn's magnetic field axis is almost completely aligned with its spin axis and is very close to zero.
Electric current connects to top of Saturn's atmosphere. A previously unknown electric current system that connects rings to top of Saturn's atmosphere.
Asymmetric ring structure. Ring particle clumping appear to be ubiquitous across the main rings, including within C-ring plateaus.
Mass of rings points to young ring age. The measured mass of the rings, less than 0.5 Mimas masses, points to a ring age much younger than the age of the solar system.
Saturn differential rotation. Gravity measurements indicate differential rotation inside Saturn and wind depths of about 9.000 km.

Major Open Questions Resulting from Cassini

While making amazing discoveries within the Saturn system and changing the paradigm of where to search for life in the solar system, the Cassini mission left a number of open questions for future study. Some of the answers are buried in the wealth of data that will be analyzed by current and future generations of scientists. Some await future exploration of the Saturn system. Below is a summary of some of these questions, organized by science discipline. For more details and other open questions, please see the Sections 3.1 and 3.2 discipline and team reports, all of which have submitted open questions relevant to their own discipline or team.

Icy Satellites

- What are some of the minor constituents of the Saturnian moons, and are they endogenic or exogenic? If exogenic, is the accretional process still ongoing?
- What is the total heat production on Enceladus and how and why does it vary? What does this imply about the cause of activity on the moon? What is the source of the organic material in the plume of Enceladus?
- Is there residual activity on Dione and Tethys, and if so, what does this imply about their recent history? Are the red streaks on Tethys evidence for such activity?
- What caused the ridge on Iapetus? Is it evidence for a past ring? Did other moons have rings in the past?
- Why does the origin of the moons of Jupiter and Saturn seem to diverge, with the Jovian moons being formed relative to their position from Jupiter, and the Saturnian moons being formed by stochastic events?
- To what extent do magnetospheric particles alter the optical properties of the moons? Does contamination by ring particles, including those from the E-ring dominate this process?

Titan

- What are the abundances of the heavy noble gases in Titan’s atmosphere and surface?
- How do you go from the very heavy ions and molecular species to haze particles?
- What are the origin, evolution, and ultimate fate of Titan’s atmosphere?
- How did the lakes and sea basins form?
- What is the nature and extent of the exchange between the surface/atmosphere and deep subsurface and ocean?
- Is there active cryovolcanism on Titan?

Saturn

- What is Saturn's global water abundance and what is its role in bringing heat to the surface? What is the role of moist convection in maintaining the large-scale motions?
- What is Saturn's rotation period, and what is the spread of periods if differential rotation persists into the interior? Has kronoseismology, as exhibited by the Saturn-driven waves in the main rings, finally yielded an answer to this question?
- How will additional insights from the combination of ring seismometry, gravity sounding, and magnetic field sounding improve the understanding of Saturn's internal equation of state, mass distribution, composition, and temperature distribution?
- What is Saturn's noble gas abundances including helium, as done for Jupiter by the Galileo probe? Does helium rain play a role in reducing the He/H in Saturn's molecular envelope?
- Using the power of ring seismometry and gravity sounding, improve the understanding of Saturn's internal equation of state, mass distribution, composition, and temperature distribution.
- What sustains Saturn's north polar hurricane and hexagonal jet stream?

Rings

- What is the radial profile of ring mass?
- What is causing the myriad of unexplained ring structures? For instance, what is creating and sustaining the entire ensemble of so-called "plateaus" in the outer C-ring?
- What is creating the unusually "red" color of the A and B rings, which are more than 95% water ice? Is it due to organic material, based on a combination of remote and in-situ measurements? How does the composition vary from place to place and on a range of scales?
- What is the age of the rings? Current data indicate that the rings seem to be much younger than the age of the solar system.
- How much about Saturn's internal structure and dynamics can be inferred from ring features?

MAPS

- What is the cause of the rotational modulation in axisymmetric magnetosphere configuration?

- How are mass and magnetic flux transported in the middle and outer magnetosphere?
- Need for more plasma measurements in auroral acceleration and source region of related SKR. Will the previously observed hemispheric dichotomy in the Saturn kilometric radiation period reappear?
- Need for better time resolution and coverage to understand the Enceladus' plume-magnetosphere interaction.
- What is the composition of the negative ions at Titan and >100 amu positive ions?
- What is the source of energy for the hot coronas/upper atmospheres of all four giant planets?

The Cassini mission has successfully answered many scientific questions and posed many new ones. A robust combination of future missions to the Saturn system, along with continued research and analysis, may yield answers to some of the questions listed above questions and generate new ones. The next Planetary Science Decadal Survey will pose its own questions based on Cassini results. One thing is clear: the questions left unanswered by Cassini and Huygens cry out for return missions to the Saturn system.

ACKNOWLEDGEMENTS

The Cassini Program is indebted to the hundreds of engineers, scientists, managers, and support staff on the Cassini and Huygens teams who designed, developed, managed, and operated the Cassini-Huygens mission. Their heart-felt dedication made this mission possible.

The Cassini-Huygens mission is a joint undertaking by the National Aeronautics and Space Administration (NASA) and the European Space Agency (ESA). Agenzia Spaziale Italiana (ASI) is also a major partner via a bilateral agreement with NASA. Cassini is managed by the Jet Propulsion Laboratory, California Institute of Technology, under a contract from NASA.

ACRONYMS

Note: For a complete list of Acronyms, refer to Cassini Acronyms – Attachment A.

ACP	Aerosol Collector Pyrolyser
AO	Announcements of Opportunity
ASI	Agenzia Spaziale Italiana
CAPS	Cassini Plasma Spectrometer
CDA	Cosmic Dust Analyzer
CEM	Cassini Equinox Mission
CIRS	Composite Infrared Spectrometer
Co-I	Co-Investigator
CRAND	Cosmic Ray Albedo Neutron Decay
CSM	Cassini Solstice Mission
DISR	Descent Imager and Spectral Radiometer
DSN	Deep Space Network
DWE	Doppler Wind Experiment
DWG	Discipline Working Group
ESA	European Space Agency
ESOC	European Operations Center
FAC	Field-Aligned Current
GCMS	Gas Chromatograph and Mass Spectrometer
GF	Grand Finale
GWE	Gravitational Wave Experiment
HASI	Huygens Atmospheric Structure Instrument
HGA	High-Gain Antenna
HPOC	Huygens Operations Center
HSWT	Huygens Science Working Team
ICO	Instrument Checkout
IDS	Interdisciplinary Scientist
IDS	Interdisciplinary Scientist
INMS	Ion and Neutral Mass Spectrometer
IS	Investigation Scientist
ISS	Imaging Science Subsystem
JPL	Jet Propulsion Laboratory
MAG	Magnetometer
MIMI	Magnetospheric Imaging Instrument
NSM	Northern Summer Mission
ORS	Optical Remote Sensing
OST	Operations Science Team
PI	Principal Investigator

PM	Prime Mission
PSG	Project Science Group
PVO	Pioneer Venus Orbiter
RADAR	Titan Radar Mapper
RG	Ring Grazing (F-ring orbits)
RotR	Rules of the Road
RPWS	Radio and Plasma Wave Science
RSS	Radio Science Subsystem
SAMWG	Saturn Atmospheric Working Group
SED	Saturn Electrostatic Discharge
SKR	Saturn Kilometric Radiation
SOI	Saturn Orbit Insertion
SSP	Surface Science Package
TAMWG	Titan Atmospheric Working Group
TL	Team Leader
TM	Team Member
TWT	Target Working Team
UT	Universal Time
UVIS	Ultraviolet Imaging Spectrograph
VIMS	Visible and Infrared Mapping Spectrometer

REFERENCES

Disclaimer: The partial list of references below correspond with in-text references indicated in this report. For all other Cassini references, refer to Attachment B – References & Bibliographies; Attachment C – Cassini Science Bibliographies; the sections entitled References contributed by individual Cassini instrument and discipline teams located in Volume 1 Sections 3.1 and 3.2 Science Results; and other resources outside of the Cassini Final Mission Report.

Achterberg, R. K., P. J. Gierasch, B. J. Conrath, F. M. Flasar, C. A. Nixon, (2011), Temporal variations of Titan's middle-atmospheric temperatures from 2004 to 2009 observed by Cassini/CIRS, Icarus, 211(1):686–698, doi: 10.1016/j.icarus.2010.08.009.

Achterberg, R. K., B. J. Conrath, P. J. Gierasch, F. M. Flasar, C. A. Nixon, (2008), Observation of a tilt of Titan's middle-atmospheric superrotation, Icarus, 197(2):549–555, doi: 10.1016/j.icarus.2008.05.014.

Baines, K., F. Flasar, N. Krupp, T. Stallard, (2018), Saturn in the 21st Century, Cambridge Planetary Science, Cambridge University Press, Cambridge, MA.

Baines, K. H., T. W. Momary, L. N. Fletcher, A. P. Showman, M. Roos-Serote, R. H. Brown, B. J. Buratti, R. N. Clark, P. D. Nicholson, (2009), Saturn's north polar cyclone and hexagon at depth revealed by Cassini/VIMS, Planetary and Space Science, 57(14–15):1671–1681, doi: 10.1016/j.pss.2009.06.026.

Beurle, K., C. D. Murray, G. A. Williams, M. W. Evans, N. J. Cooper, C. B. Agnor, (2010), Direct evidence for gravitational instability and moonlet formation in Saturn's rings, Astrophysical Journal Letters, 718(2):L176, doi: 10.1088/2041-8205/718/2/l176.

Bird, M. K., M. Allison, S. W. Asmar, D. H. Atkinson, I. M. Avruch, R. Dutta-Roy, Y. Dzierma, P. Edenhofer, W. M. Folkner, L. I. Gurvits, D. V. Johnston, D. Plettemeier, S. V. Pogrebenko, R. A. Preston, G. L. Tyler, (2005), The vertical profile of winds on Titan, Nature, 438(7069):800–802, doi: 10.1038/nature04060.

Brown, R. H., J. -P. Lebreton, J. H. Waite, Jr., (2009), Titan from Cassini-Huygens, Springer, Dordrecht.

Buratti, B. J., P. C. Thomas, E. Roussos, C. Howett, M. Seiß, A. R. Hendrix, P. Helfenstein, R. H. Brown, R. N. Clark, T. Denk, (2019), Close Cassini flybys of Saturn's ring moons Pan, Daphnis, Atlas, Pandora, and Epimetheus, Science, 364(6445):eaat2349.

Burch, J. L., J. Goldstein, W. S. Lewis, D. T. Young, A. J. Coates, M. K. Dougherty, N. Andre, (2007), Tethys and Dione as sources of outward-flowing plasma in Saturn's magnetosphere, Nature, 447(7146):833–835, doi: 10.1038/nature05906.

Clark, R. N., R. H. Brown, R. Jaumann, D. P. Cruikshank, R. M. Nelson, B. J. Buratti, T. B. McCord, J. Lunine, K. H. Baines, G. Bellucci, J. P. Bibring, F. Capaccioni, P. Cerroni, A. Coradini, V. Formisano, Y. Langevin, D. L. Matson, V. Mennella, P. D. Nicholson, B. Sicardy, C. Sotin, T. M. Hoefen, J. M. Curchin, G. Hansen, K. Hibbits, K. D. Matz, (2005),

Compositional maps of Saturn's moon Phoebe from imaging spectroscopy, Nature, 435(7038):66–69, doi: 10.1038/nature03558.

Colwell, J. E., L. W. Esposito, M. Sremcevic, G. R. Stewart, W. E. McClintock, (2007), Self-gravity wakes and radial structure of Saturn's B ring, Icarus, 190(1):127–144.

Colwell, J. E., L. W. Esposito, M. Sremcevic, (2006), Self-gravity wakes in Saturn's A ring measured by stellar occultations from Cassini, Geophysical Research Letters, 33(7), doi: 10.1029/2005gl025163.

National Research Council, (2011), Vision and Voyages for Planetary Science in the Decade 2013–2022, The National Academies Press, Washington, DC.

Cuzzi, J. N., J. A. Burns, S. Charnoz, R. N. Clark, J. E. Colwell, L. Dones, L. W. Esposito, G. Filacchione, R. G. French, M. M. Hedman, S. Kempf, E. A. Marouf, C. D. Murray, P. D. Nicholson, C. C. Porco, J. Schmidt, M. R. Showalter, L. J. Spilker, J. N. Spitale, R. Srama, M. Sremcevic, M. S. Tiscareno, J. Weiss, (2010), An evolving view of Saturn's dynamic rings, Science, 327(5972):1470–1475, doi: 10.1126/science.1179118.

Dougherty, M. K., H. Cao, K. K. Khurana, G. J. Hunt, G. Provan, S. Kellock, M. E. Burton, T. A. Burk, E. J. Bunce, S. W. H. Cowley, M. G. Kivelson, C. T. Russell, D. J. Southwood, (2018), Saturn's magnetic field revealed by the Cassini Grand Finale, Science, 362(6410), doi: 10.1126/science.aat5434.

Dougherty, M., L. Esposito, S. Krimigis, (2009), Saturn from Cassini-Huygens, Springer Science & Business Media.

Dougherty, M. K., K. K. Khurana, F. M. Neubauer, C. T. Russell, J. Saur, J. S. Leisner, M. E. Burton, (2006), Identification of a dynamic atmosphere at Enceladus with the Cassini magnetometer, Science, 311(5766):1406–1409, doi: 10.1126/science.1120985.

Dyudina, U. A., A. P. Ingersoll, S. P. Ewald, A. R. Vasavada, R. A. West, A. D. Del Genio, J. M. Barbara, C. C. Porco, R. K. Achterberg, F. M. Flasar, A. A. Simon-Miller, L. N. Fletcher, (2008), Dynamics of Saturn's south polar vortex, Science, 319:1801–1801.

ESA, (1989), Announcement of Opportunity, Cassini Mission: Huygens.

ESA, (1988), Cassini Saturn Orbiter and Titan Probe, in Report on the Phase A Study.

ESA, (1985), Cassini Saturn Orbiter and Titan Probe, in ESA/NASA Assessment Study.

Fletcher, L. N., P. G. J. Irwin, G. S. Orton, N. A. Teanby, R. K. Achterberg, G. L. Bjoraker, P. Read, A. A. Simon-Miller, C. Howett, R. de Kok, N. Bowles, S. B. Calcutt, B. Hesman, F. M. Flasar, (2008), Thermal structure and dynamics of Saturn's northern springtime disturbance, Science, 319:79–81.

Fletcher, L. N., G. S. Orton, J. A. Sinclair, S. Guerlet, P. L. Read, A. Antunano, R. K. Achterberg, F. M. Flasar, P. G. J. Irwin, G. L. Bjoraker, J. Hurley, B. E. Hesman, M. Segura, N. Gorius, A. Mamoutkine, S. B. Calcutt, (2018), A hexagon in Saturn's northern stratosphere surrounding the emerging summertime polar vortex, Nature Communications, 9(3564), doi: 10.1038/s41467-018-06017-3.

Fletcher, L. N., B. E. Hesman, P. G. J. Irwin, K. H. Baines, T. W. Momary, A. Sanchez-Lavega, F. M. Flasar, P. L. Read, G. S. Orton, A. Simon-Miller, R. Hueso, G. L. Bjoraker,

A. Mamoutkine, T. del Rio-Gaztelurrutia, J. M. Gomez, B. Buratti, R. N. Clark, P. D. Nicholson, C. Sotin, (2011), Thermal structure and dynamics of Saturn's northern springtime disturbance, Science, 332(6036):1413–1417. doi: 10.1126/science.1204774.

Fulchignoni, M., F. Ferri, F. Angrilli, A. J. Ball, A. Bar-Nun, M. A. Barucci, C. Bettanini, G. Bianchini, W. Borucki, G. Colombatti, M. Coradini, A. Coustenis, S. Debei, P. Falkner, G. Fanti, E. Flamini, V. Gaborit, R. Grard, M. Hamelin, A. M. Harri, B. Hathi, I. Jernej, M. R. Leese, A. Lehto, P. F. Lion Stoppato, J. J. Lopez-Moreno, T. Makinen, J. A. M. McDonnell, C. P. McKay, G. Molina-Cuberos, F. M. Neubauer, V. Pirronello, R. Rodrigo, B. Saggin, K. Schwingenschuh, A. Seiff, F. Simoes, H. Svedhem, T. Tokano, M. C. Towner, R. Trautner, P. Withers, J. C. Zarnecki, (2005), In situ measurements of the physical characteristics of Titan's environment, Nature, 438(7069):785–791, doi: 10.1038/nature04314.

Glein, C. R., J. A. Baross, J. H. Waite, (2015), The pH of Enceladus' ocean, Geochimica Et Cosmochimica Acta, 162:202–219, doi: 10.1016/j.gca.2015.04.017.

Goguen, J. D., B. J. Buratti, R. H. Brown, R. N. Clark, P. D. Nicholson, M. M. Hedman, R. R. Howell, C. Sotin, D. P. Cruikshank, K. H. Baines, K. J. Lawrence, J. R. Spencer, D. G. Blackburn, (2013), The temperature and width of an active fissure on Enceladus measured with Cassini VIMS during the 14 April 2012 South Pole flyover, Icarus, 226(1):1128–1137, doi: 10.1016/j.icarus.2013.07.012.

Gurnett, D. A., A. Lecacheux, W. S. Kurth, A. M. Persoon, J. B. Groene, L. Lamy, P. Zarka, J. F. Carbary, (2009), Discovery of a north-south asymmetry in Saturn's radio rotation period, Geophysical Research Letters, 36:L16102, doi: 10.1029/2009gl039621.

Hansen, C. J., L. Esposito, J. Colwell, A. Hendrix, D. Matson, C. Parkinson, W. Pryor, D. Shemansky, I. Stewart, J. Tew, Y. Yung, (2006), Enceladus' water vapour plumes, Planetary Science: Challenges and Discoveries.

Hedman, M. M., N. J. Cooper, C. D. Murray, K. Beurle, M. W. Evans, M. S. Tiscareno, J. A. Burns, (2010), Aegaeon (Saturn LIII), a G-ring object, Icarus, 207(1):433–447, doi: 10.1016/j.icarus.2009.10.024.

Hedman, M. M., C. D. Murray, N. J. Cooper, M. S. Tiscareno, K. Beurle, M. W. Evans, J. A. Burns, (2009), Three tenuous rings/arcs for three tiny moons, Icarus, 199(2):378–386, doi: 10.1016/j.icarus.2008.11.001.

Helfenstein, P., (2010), Tectonic overturn on Enceladus, Nature Geoscience, 3:75–76.

Howett, C. J. A., J. R. Spencer, J. Pearl, M. Segura, (2011), High heat flow from Enceladus' south polar region measured using 10–600 cm− 1 Cassini/CIRS data, Journal of Geophysical Research: Planets, 116(E3).

Hsu, H. W., J. Schmidt, S. Kempf, F. Postberg, G. Moragas-Klostermeyer, M. Seiß, H. Hoffmann, M. Burton, S. Ye, W. S. Kurth, M. Horányi, N. Khawaja, F. Spahn, D. Schirdewahn, J. O'Donoghue, L. Moore, J. Cuzzi, G. H. Jones, R. Srama, (2018), In situ collection of dust grains falling from Saturn's rings into its atmosphere, Science, 362(6410), doi: 10.1126/science.aat3185.

Hsu, H. W., F. Postberg, Y. Sekine, T. Shibuya, S. Kempf, M. Horanyi, A. Juhasz, N. Altobelli, K. Suzuki, Y. Masaki, T. Kuwatani, S. Tachibana, S. Sirono, G. Moragas-Klostermeyer, R. Srama, (2015), Ongoing hydrothermal activities within Enceladus, Nature, 519(7542):207–210+supplemental material, doi: 10.1038/nature14262.

Iess, L., B. Militzer, Y. Kaspi, P. Nicholson, D. Durante, P. Racioppa, A. Anabtawi, E. Galanti, W. Hubbard, M. J. Mariani, (2019), Measurement and implications of Saturn's gravity field and ring mass, Science, 364(6445):eaat2965.

Iess, L., D. J. Stevenson, M. Parisi, D. Hemingway, R. A. Jacobson, J. I. Lunine, F. Nimmo, J. W. Armstrong, S. W. Asmar, M. Ducci, P. Tortora, (2014), The gravity field and interior structure of Enceladus, Science, 344(6179):78–80. doi: 10.1126/science.1250551.

Johnson, T. V., J. I. Lunine, (2005), Saturn's moon Phoebe as a captured body from the outer Solar System, Nature, 435(7038):69–71, doi: 10.1038/nature03384.

JPL, (2014), Cassini 2014 Senior Review, Jet Propulsion Laboratory.

JPL, (2012), Cassini 2012 Senior Review, Jet Propulsion Laboratory.

Kempf, S., U. Beckmann, J. Schmidt, (2010), How the Enceladus dust plume feeds Saturn's E ring, Icarus, 206(2):446–457, doi: 10.1016/j.icarus.2009.09.016.

Khurana, K. K., C. T. Russell, M. K. Dougherty, (2008), Magnetic portraits of Tethys and Rhea, Icarus, 193(2):465–474.

Lamy, L., P. Zarka, B. Cecconi, R. Prange, W. S. Kurth, G. Hospodarsky, A. Persoon, M. Morooka, J. -W. Wahlund, G. J. Hunt, (2018), The low-frequency source of Saturn's Kilometric radiation, Science, 362(6410):eaat2027, doi: 10.1126/science.aat2027.

Lavvas, P., R. V. Yelle, T. Koskinen, A. Bazin, V. Vuitton, E. Vigren, M. Galand, A. Wellbrock, A. J. Coates, J. -E. Wahlund, F. J. Crary, D. Snowden, (2013), Aerosol growth in Titan's ionosphere, Proceedings of the National Academy of Sciences of the United States of America, 110(8):2729–2734, doi: 10.1073/pnas.1217059110.

Lebreton, J. -P., A. Coustenis, J. Lunine, F. Raulin, T. Owen, D. Strobel, (2009), Results from the Huygens probe on Titan, Astronomy and Astrophysics Review, 17(2):149–179, doi: 10.1007/s00159-009-0021-5.

Lebreton, J. -P., (1991), Cassini: A Mission to Saturn and Titan, ESA SP-315, in 24th ESLAB Symposium, Formation of Stars and Planets, and the Evolution of the Solar System, Sept. 17–19, 1990, Friedrichshafen.

Mankovich, C., M. S Marley, J. J. Fortney, N. Movshovitz, (2019), Cassini ring seismology as a probe of Saturn's interior, I. Rigid rotation, The Astrophysical Journal, 871(1):1.

Matson, D. L., L. J. Spilker, J. P. Lebreton, (2002), The Cassini/Huygens mission to the Saturnian system, Space Science Reviews, 104(1):1–58.

Mitchell, D. G., M. E. Perry, D. C. Hamilton, J. H. Westlake, P. Kollmann, H. T. Smith, J. F. Carbary, J. H. Waite, R. Perryman, H. -W. Hsu, J. -E. Wahlund, M. W. Morooka, L. Z. Hadid, A. M. Persoon, W. S. Kurth, (2018), Dust grains fall from Saturn's D-ring into its equatorial upper atmosphere, Science, 362(6410), doi: 10.1126/science.aat2236.

Mitchell, C. J., C. C. Porco, J. W. Weiss, (2015), Tracking the geysers of Enceladus into Saturn's E ring, Astronomical Journal, 149(5):156–172, doi: 10.1088/0004-6256/149/5/156.

Müller-Wodarg, I., C. A. Griffity, E. Lellouch, T. E. Cravens, (2014), Titan: interior, surface, atmosphere, and space environment, Cambridge Planetary Science, Cambridge University Press, New York.

Murray, C. D., K. Beurle, N. J. Cooper, M. W. Evans, G. A. Williams, S. Charnoz, (2008), The determination of the structure of Saturn's F ring by nearby moonlets, Nature, 453(7196):739–744.

Murray, C. D., C. Chavez, K. Beurle, N. Cooper, M. W. Evans, J. A. Burns, C. C. Porco, (2005), How prometheus creates structure in Saturn's F ring, Nature, 437(7063):1326–1329, doi: 10.1038/nature04212.

NASA, (2014), NASA Strategic Plan, 2014.

NASA, (1991), Announcement of Opportunity, Facility Instrument Science Team for the Ion and Neutral Mass Spectrometer on the Cassini Saturn Orbiter.

NASA, (1989), Announcement of Opportunity, Cassini Mission: Saturn Orbiter.

Niemann, H. B., S. K. Atreya, J. E. Demick, D. Gautier, J. A. Haberman, D. N. Harpold, W. T. Kasprzak, J. I. Lunine, T. C. Owen, F. Raulin, (2010), Composition of Titan's lower atmosphere and simple surface volatiles as measured by the Cassini-Huygens probe gas chromatograph mass spectrometer experiment, Journal of Geophysical Research: Planets, 115:E12006, doi: 10.1029/2010je003659.

Niemann, H. B., S. K. Atreya, S. J. Bauer, G. R. Carignan, J. E. Demick, R. L. Frost, D. Gautier, J. A. Haberman, D. N. Harpold, D. M. Hunten, G. Israel, J. I. Lunine, W. T. Kasprzak, T. C. Owen, M. Paulkovich, F. Raulin, E. Raaen, S. H. Way, (2005), The abundances of constituents of Titan's atmosphere from the GCMS instrument on the Huygens probe, Nature, 438(7069):779–784, doi: 10.1038/nature04122.

O'Donoghue, J., T. S. Stallard, H. Melin, G. H. Jones, S. W. H. Cowley, S. Miller, K. H. Baines, J. S. D. Blake, (2013), The domination of Saturn's low-latitude ionosphere by ring 'rain,' Nature, 496(7444):193–195, doi: 10.1038/nature12049.

Porco, C., D. DiNino, F. Nimmo, (2014), How the geysers, tidal stresses, and thermal emission across the south polar terrain of Enceladus are related, Astronomical Journal, 148(3):45–69. doi: 10.1088/0004-6256/148/3/45.

Porco, C. C., P. Helfenstein, P. C. Thomas, A. P. Ingersoll, J. Wisdom, R. West, G. Neukum, T. Denk, R. Wagner, T. Roatsch, S. Kieffer, E. Turtle, A. McEwen, T. V. Johnson, J. Rathbun, J. Veverka, D. Wilson, J. Perry, J. Spitale, A. Brahic, J. A. Burns, A. D. DelGenio, L. Dones, C. D. Murray, S. Squyres, (2006), Cassini observes the active south pole of Enceladus, Science, 311(5766):1393–1401, doi: 10.1126/science.1123013.

Porco, C. C., E. Baker, J. Barbara, K. Beurle, A. Brahic, J. A. Burns, S. Charnoz, N. Cooper, D. D. Dawson, A. D. Del Genio, T. Denk, L. Dones, U. Dyudina, M. W. Evans, B. Giese, K. Grazier, P. Helfenstein, A. P. Ingersoll, R. A. Jacobson, T. V. Johnson, A. McEwen, C. D. Murray, G. Neukum, W. M. Owen, J. Perry, T. Roatsch, J. Spitale, S. Squyres, P. C. Thomas, M. Tiscareno, E. Turtle, A. R. Vasavada, J. Veverka, R. Wagner, R. West, (2005),

Cassini Imaging Science: initial results on Phoebe and Iapetus, Science, 307(5713):1237–1242, doi: 10.1126/science.1107981.

Postberg, F., N. Khawaja, B. Abel, G. Choblet, C. Glein, M. Gudipati, B. L. Henderson, H. W. Hsu, K. Kempf, F. Klenner, G. Moragas-Klostermeyer, B. Magee, L. Nölle, M. Perry, R. Reviol, J. Schmidt, R. Srama, F. Stolz, G. Tobie, M. Trieloff, J. H. Waite, (2018), Macromolecular organic compounds from the depths of Enceladus, Nature, 558(7711):564–568.

Postberg, F., J. Schmidt, J. Hillier, S. Kempf, R. Srama, (2011), A salt-water reservoir as the source of a compositionally stratified plume on Enceladus, Nature, 474(7353):620–622.

Postberg, F., S. Kempf, J. Schmidt, N. Brilliantov, A. Beinsen, B. Abel, U. Buck, R. Srama, (2009), Sodium salts in E-ring ice grains from an ocean below the surface of Enceladus, Nature, 459:1098–1101, doi: 10.1038/nature08046.

Provan, G., S. W. H. Cowley, J. D. Nichols, (2009), Phase relation of oscillations near the planetary period of Saturn's auroral oval and the equatorial magnetospheric magnetic field, Journal of Geophysical Research: Space Physics, 114:A04205, doi: 10.1029/2008ja013988.

Radebaugh, J., R. D. Lorenz, J. I. Lunine, S. D. Wall, G. Boubin, E. Reffet, R. L. Kirk, R. M. Lopes, E. R. Stofan, L. Soderblom, M. Allison, M. Janssen, P. Paillou, P. Callahan, C. Spencer, Cassini RADAR Team, (2008), Dunes on Titan observed by Cassini Radar, Icarus, 194(2):690–703, doi: 10.1016/j.icarus.2007.10.015.

Rodriguez, S., S. Le Mouelic, P. Rannou, G. Tobie, K. H. Baines, J. W. Barnes, C. A. Griffith, M. Hirtzig, K. M. Pitman, C. Sotin, R. H. Brown, B. J. Buratti, R. N. Clark, P. D. Nicholson, (2009), Global circulation as the main source of cloud activity on Titan, Nature, 459(7247):678–682, doi: 10.1038/nature08014.

Roussos, E., P. Kollmann, N. Krupp, A. Kotova, L. Regoli, C. Paranicas, D. G. Mitchell, S. M. Krimigis, D. Hamilton, P. Brandt, J. Carbary, S. Christon, K. Dialynas, I. Dandouras, M. E. Hill, W. H. Ip, G. H. Jones, S. Livi, B. H. Mauk, B. Palmaerts, E. C. Roelof, A. Rymer, N. Sergis, H. T. Smith, (2018), A radiation belt of energetic protons located between Saturn and its rings, Science, 362(6410), doi: 10.1126/science.aat1962.

Sayanagi, K. M., J. J. Blalock, U. A. Dyudina, S. P. Ewald, A. P. Ingersoll, (2017), Cassini ISS observation of Saturn's north polar vortex and comparison to the south polar vortex, Icarus, 285:68–82, doi: 10.1016/j.icarus.2016.12.011.

Sayanagi, K. M., U. A. Dyudina, S. P. Ewald, G. Fischer, A. P. Ingersoll, W. S. Kurth, G. D. Muro, C. C. Porco, R. A. West, (2013), Dynamics of Saturn's great storm of 2010-2011 from Cassini ISS and RPWS, Icarus, 223(1):460–478, doi: 10.1016/j.icarus.2012.12.013.

Schenk, P. M., R. N. Clark, C. J. A. Howett, A. J. Verbiscer, J. H. Waite, (2018), Enceladus and the icy moons of Saturn, in Space Science Series, University of Arizona Press, Tucson.

Schenk, P., D. P. Hamilton, R. E. Johnson, W. B. McKinnon, C. Paranicas, J. Schmidt, M. R. Showalter, (2011), Saturn system dynamics as recorded in global color patterns on its midsize icy satellites, Icarus, 211:740–757.

Spencer, J. R., F. Nimmo, (2013), Enceladus: An active ice world in the Saturn System, Annual Review of Earth and Planetary Sciences, 41:693–717, doi: 10.1146/annurev-earth-050212-124025.

Spencer, J. R., J. C. Pearl, M. Segura, F. M. Flasar, A. Mamoutkine, P. Romani, B. J. Buratti, A. R. Hendrix, L. J. Spilker, R. M. C. Lopes, (2006), Cassini encounters Enceladus: background and the discovery of a south polar hot spot, Science, 311(5766):1401–1405, doi: 10.1126/science.1121661.

Spilker, L., (2019), Cassini-Huygens' exploration of the Saturn system: 13 years of discovery, Science, 364:1046–1051.

Spilker, L., C. Ferrari, R. Morishima, (2013), Saturn's ring temperatures at equinox, Icarus, 226(1):316–322, doi: 10.1016/j.icarus.2013.06.002.

Spilker, L. J., (1997), Passage to a ringed world: The Cassini-Huygens mission to Saturn and Titan, NASA Special Publication, Subfile Database Book Monograph, National Aeronautics and Space Administration (NASA), Washington, DC:.

Spitale, J. N., T. A. Hurford, A. R. Rhoden, E. E. Berkson, S. S. Platts, (2015), Curtain eruptions from Enceladus' south-polar terrain, Nature, 521(7550):57–60, doi: 10.1038/nature14368.

Stephan, K., R. Jaumann, R. H. Brown, J. M. Soderblom, L. A. Soderblom, J. W. Barnes, C. Sotin, C. A. Griffith, R. L. Kirk, K. H. Baines, B. J. Buratti, R. N. Clark, D. M. Lytle, R. M. Nelson, P. D. Nicholson, (2010), Specular reflection on Titan: Liquids in Kraken Mare, Geophysical Research Letters, 37(07):L07104, doi: 10.1029/2009gl042312.

Stofan, E. R., C. Elachi, J. I. Lunine, R. D. Lorenz, B. Stiles, K. L. Mitchel, S. Ostro, L. Soderblom, C. Wood, H. Zebker, S. Wall, M. Janssen, R. Kirk, R. Lopes, F. Paganelli, J. Radebaugh, L. Wye, Y. Anderson, M. Allison, R. Boehmer, P. Callahan, P. Encrenaz, E. Flamini, G. Francescetti, Y. G. Gim, G. Hamilton, S. Hensley, W. T. K. Johnson, K. Kelleher, D. Muhleman, P. Paillou, G. Picardi, F. Posa, L. Roth, R. Seu, S. Shaffer, S. Vetrella, R. West, (2007), The lakes of Titan, Nature, 445(7123):61–64, doi: 10.1038/nature05438.

Thomas, P. C., R. Tajeddine, M. S. Tiscareno, J. A. Burns, J. Joseph, T. J. Loredo, P. Helfenstein, C. Porco, (2016), Enceladus's measured physical libration requires a global subsurface ocean, Icarus, 264:37–47, doi: 10.1016/j.icarus.2015.08.037.

Tiscareno, M. S., P. D. Nicholson, J. N. Cuzzi, L. J. Spilker, C. D. Murray, M. M. Hedman, J. E. Colwell, J. A. Burns, S. M. Brooks, R. N. Clark, N. J. Cooper, E. Deau, C. Ferrari, G. Filacchione, R. G. Jerousek, S. Le Mouélic, R. Morishima, S. Pilorz, S. Rodriguez, M. R. Showalter, S. V. Badman, E. J. Baker, B. J. Buratti, K. H. Baines, C. Sotin, (2019), Close-range remote sensing of Saturn's rings during Cassini's ring-grazing orbits and Grand Finale, Science, 364(6445):eaau1017, doi: 10.1126/science.aau1017.

Tiscareno, M. S., C. D. Murray, (2018), Planetary ring systems: Properties, structure, and evolution, Vol. 19, Cambridge University Press.

Tiscareno, M. S., J. A. Burns, M. Sremcevik, K. Beurle, M. M. Hedman, N. J. Cooper, A. J. Milano, M. W. Evans, C. C. Porco, J. N. Spitale, J. W. Weiss, (2010), Physical characteristics and non-Keplerian orbital motion of propeller moons embedded in Saturn's rings, The Astrophysical Journal Letters, 718(2):L92–L96, doi: 10.1088/2041-8205/718/2/l92.

Tiscareno, M. S., J. A. Burns, P. D. Nicholson, M. A. Hedman, C. C. Porco, (2007), Cassini imaging of Saturn's rings, II. A wavelet technique for analysis of density waves and other radial structure in the rings, Icarus, 189(1):14–34.

Tobie, G., O. Cadek, C. Sotin, (2008), Solid tidal friction above a liquid water reservoir as the origin of the south pole hotspot on Enceladus, Icarus, 196(2):642–652.

Tomasko, M. G., B. Archinal, T. Becker, B. Bézard, M. Bushroe, M. Combes, D. Cook, A. Coustenis, C. de Bergh, L. E. Dafoe, L. Doose, S. Douté, A. Eibl, S. Engel, F. Gliem, B. Grieger, K. Holso, E. Howington-Kraus, E. Karkoschka, H. U. Keller, R. Kirk, R. Kramm, M. Küppers, P. Lanagan, E. Lellouch, M. Lemmon, J. Lunine, E. McFarlane, J. Moores, G. M. Prout, B. Rizk, M. Rosiek, P. Rueffer, S. E. Schröder, B. Schmitt, C. See, P. Smith, L. Soderblom, N. Thomas, R. West, (2005), Rain, winds and haze during the Huygens probe's descent to Titan's surface, Nature, 438:765, doi: 10.1038/nature04126.

Turtle, E. P., J. E. Perry, A. G. Hayes, R. D. Lorenz, J. W. Barnes, A. S. McEwen, R. A. West, A. D. Del Genio, J. M. Barbara, J. I. Lunine, E. L. Schaller, T. L. Ray, R. M. C. Lopes, E. R. Stofan, (2011), Rapid and extensive surface changes near Titan's equator: Evidence of April showers, Science, 331(6023):1414–1417, doi: 10.1126/science.1201063.

Turtle, E. P., J. E. Perry, A. S. McEwen, A. D. DelGenio, J. Barbara, R. A. West, D. D. Dawson, C. C. Porco, (2009), Cassini imaging of Titan's high-latitude lakes, clouds, and south-polar surface changes, Geophysical Research Letters, 36:L02204, doi: 10.1029/2008gl036186.

Verbiscer, A. J, M. F. Skrutskie, D. P. Hamilton, (2009), Saturn's largest ring, Nature, 461(7267):1098–1100.

Vinatier, S., B. Bezard, S. Lebonnois, N. A. Teanby, R. K. Achterberg, N. Gorius, A. Mamoutkine, E. Guandique, A. Jolly, D. E. Jennings, F. M. Flasar, (2015), Seasonal variations in Titan's middle atmosphere during the northern spring derived from Cassini/CIRS observations, Icarus, 250:95–115, doi: 10.1016/j.icarus.2014.11.019.

Waite, J. H., R. S. Perryman, M. E. Perry, K. E. Miller, J. Bell, T. E. Cravens, C. R. Glein, J. Grimes, M. Hedman, J. Cuzzi, T. Brockwell, B. Teolis, L. Moore, D. G. Mitchell, A. Persoon, W. S. Kurth, J.-E. Wahlund, M. Morooka, L. Z. Hadid, S. Chocron, J. Walker, A. Nagy, R. Yelle, S. Ledvina, R. Johnson, W. Tseng, O. J. Tucker, and W. -H. Ip, (2018), Chemical interactions between Saturn's atmosphere and its rings, Science, 362(6410):eaat2382, doi: 10.1126/science.aat2382.

Waite, J. H., C. R. Glein, R. S. Perryman, B. D. Teolis, B. A. Magee, G. Miller, J. Grimes, M. E. Perry, K. E. Miller, A. Bouquet, J. I. Lunine, T. Brockwell, S. J. Bolton, (2017), Cassini finds molecular hydrogen in the Enceladus plume: Evidence for hydrothermal processes, Science, 356(6334):155–159, doi: 10.1126/science.aai8703.

Waite, J. H., W. S. Lewis, B. A. Magee, J. I. Lunine, W. B. McKinnon, C. R. Glein, O. Mousis, D. T. Young, T. Brockwell, J. Westlake, M. J. Nguyen, B. D. Teolis, B. Niemann, R. L. McNutt, M. Perry, W. H. Ip, (2009), Liquid water on Enceladus from observations of ammonia and Ar-40 in the plume, Nature, 460(7254):487–490, doi: 10.1038/nature08153.

Waite, J. H., Jr., D. T. Young, T. E. Cravens, A. J. Coates, F. J. Crary, B. Magee, J. Westlake, (2007), The process of tholin formation in Titan's upper atmosphere, Science, 316(5826):870–5, doi: 10.1126/science.1139727.

Jet Propulsion Laboratory
California Institute of Technology

MAPS Rules of the Road

volume 1 Mission Overview,
Science Objectives and Results

CASSINI FINAL MISSION REPORT 2019

Appendix A

What Are the MAPS Rules of the Road

The original AO for Cassini in 1989 included the following list of goals for the study of the magnetosphere of Saturn.

- Determine the configuration of the nearly axially symmetric magnetic field and its relation to the modulation of the Saturn kilometric radiation.
- Determine current systems, composition, sources and sinks of magnetospheric charged particles.
- Investigate wave-particle interactions and dynamics of the dayside magnetosphere and the magnetotail of Saturn and their interaction with the solar wind, satellites and the rings.
- Study the effect of Titan's interaction with the solar wind and the magnetospheric plasma.
- Investigate the interaction of Titan's atmosphere and exosphere with the surrounding plasma.

These goals are very general and broad reaching and it is clear that they could not be achieved by any single instrument and certainly not without the sharing of data between instrument teams. MAPS, led by its two IDSs, started early to make plans to address this.

One of the important actions by the MAPS IDS team was to propose and manage the creation of the "MAPS Rules of the Road" (hereafter RotR). The overarching goal of the RotR document was to create an environment where collaboration between teams was the norm. Such an environment would require the MAPS PIs and their teams to feel comfortable sharing their data with other teams and to have the assurance that their data would be handled fairly. The MAPS RotR contains an itemized description of what data can and should be shared between the MAPS instrument teams, how that data is allowed to be used, and who is responsible for overseeing the proper use of shared data. Although the MAPS RotR are by no means perfect, they provided a foundation on which the scientific success of the Cassini MAPS team could be built.

Development of the MAPS Rules of the Road

Motivation: MAPS science naturally requires collaboration

The scientific questions studied by the MAPS working group are based heavily on fundamental plasma physics including neutral and charged particles, particle sources and losses, particle

energization and transport, the influence of electric and magnetic fields and coupling with Saturn and its moons. The processes are fundamentally governed by Maxwell's equations, which couple particle related quantities (current, charge) with electric and magnetic fields. Furthermore, Saturn's moons (Titan in particular) are places where chemical processes are highly important. The dependence of MAPS science on fundamental principles naturally results in the need for data from multiple instruments because of:

- Interactions of neutral particles, ions and electrons
- Lower energy particles make up the bulk of the plasma density while higher energy particles contribute significantly to the plasma pressure
- Saturn's magnetic field, coupled with fast planetary rotation, drives particle motion and plasma transport
- Identification of neutral and ion species leads to understanding of sources as well as the fundamental chemical processes involved

Because of the inter-instrumental nature of the MAPS Cassini science questions, it was clear that the MAPS instrument teams could not achieve all of their own, individual science goals or the mission science goals without data sharing. Fortunately, because of the fundamental, physics-based need for data sharing in magnetosphere physics, the magnetospheric and plasma science community has a historical track record of sharing data. Although this community has a long history of sharing mission data, it was recognized that formalizing a data sharing plan would further foster the collaborative environment in the MAPS community and would likely greatly enhance the return from the Cassini Mission. I concluded that a data sharing plan needed to be a topic that was addressed and worked out early in the mission.

Venus Express as a Model

The MAPS RotR were modeled after the Pioneer Venus Orbiter (PVO) rules of the road. Unfortunately, it was not possible to find the original PVO RotR documents to include here and it was also not possible to determine who wrote the original RotR for the PVO. I was a member of the PVO science team and was familiar with the PVO RotR. I concluded that the Cassini MAPS teams could benefit from a formal data sharing agreement that outlined specific regulations for how data would be shared amongst the instruments team. I presented the PVO RotR document to the MAPS PIs around 1995 and to the entire Cassini PSG meeting soon after launch.

The Design and Implementation Process

IDS Gombosi presented the idea that MAPS needed a data sharing plan and suggested to the PIs that the PVO RotR was a document that provided a good place to start a discussion. The

presentation of the PVO RotR document by IDS Gombosi to the MAPS PIs was generally received positively and a discussion of what the MAPS RotR should look like began. It is important to note that the MAPS RotR is a data sharing plan that was mutually developed and agreed on by each of the MAPS instrument PIs. The document was not created from above and forced on the PIs. It was created together with the PIs through discussion and negotiation. This process allowed each PI to be satisfied that their individual needs would be addressed and created an atmosphere of buy in by all instrument teams.

The MAPS RotR document retained all the initial points of the PVO RotR document. However, the MAPS PIs suggested a few modifications, one of which was very significant. In point 1, the MAPS IDS's added the phrase "It is the responsibility of MAPS PIs to ensure that the Rules-of-the-Road are observed by their team." Although the quantity of added text was minimal, the intent of the text became very important during the mission. The PIs felt that it was important to directly indicate who was responsible for ensuring that the RotR where followed. Asking each PI to be responsible for their own team's use of data from other instruments had several important consequences. First, for a PI to fulfill this responsibility it required them to know what research was being conducted by their teams. The PIs did not micromanage the research, but by being aware of what their team members were doing they could enforce the RotR and foster more collaborations. Second, by assigning responsibility for oversight it was relatively straight forward to handle the occasional violation of the RotR.

It is important to note that final text for the document was accepted in the year 2000, four years before the arrival of Cassini at Saturn and before the flyby of Jupiter. The agreement was in place well before any of the truly important scientific data was beginning to be collected. In fact, having the RotR in place during the cruise phase allowed teams to begin to understand how to operate within the rules and to start sharing data with trust and confidence early on. By the time Cassini arrived at Saturn, teams shared data reasonably well because they already had experience.

Beyond indicating that the responsibility for oversight of the use of shared data belonged to the PIs, the MAPS RotR contained several key stipulations. Perhaps equally important to the data sharing oversight, the document makes it very clear that instrument teams are expected to share their data (item 4). Although such data sharing is typical in the magnetosphere and plasma community, the formalized, agreed upon statement put MAPS on a stable foundation for collaborations during the mission. The RotR also outlines several limitations to what data would be shared and how that data could be used. First, the document makes clear that instrument PIs and their Co-Is are responsible for the initial analysis, interpretation, and publication of these data. This statement was very important because it clarified that PIs and instrument teams would have first right to publish unique data or discoveries made by their instrument before having to share data with the MAPS team. The RotR also makes it clear that data is shared for the purpose of conducting correlative and collaborative studies and should not be used for studies that could be done by the instrument team alone. Finally, when data shared by another instrument is being used for a correlative study, the RotR indicate that the instrument PI and the team should be informed of how the data will be used. In addition, the RotR indicates that researchers using other instruments data

should invite members of the appropriate instrument team, through the PI, to participate in the study and that this invitation should be made very early in the research process.

Because data was expected to be shared broadly between the MAPS instrument teams it was important that the RotR indicate with whom data could be shared. MAPS data was to be shared within the MAPS instruments teams, under the direction of the instrument PIs. The data and summary plots created on MAPSview were not to be shared beyond the MAPS team members without approval of the PIs of the relevant instrument.

Finally, two important stipulations of the MAPS RotR related to roles of the IDSs within the MAPS group: proper role of an IDS and summary plots and a key parameter database. Both of these items are addressed in more detail in the MAPS Data Sharing document. Here we note that as the RotR document was being created the MAPS IDSs expressed their strong belief that their job was not to complete with the instrument teams but rather to facilitate individual teams, facilitate collaboration between teams, and to bring skills or models to the table that none of the instrument teams had access to. The MAPS RotR formalized this role. In the context of facilitating collaboration, the MAPS IDSs felt it was important create a key parameter database and summary plots including all MAPS instrument data. These resources where to be used for quickly finding correlations or to quickly evaluate observed events. The RotR document indicates that this key parameter data and the quick look plots are to be treated the same as full quality instrument data products.

Rules of the Road during the Mission

Successes

The most important success of the MAPS RotR is the incredible science return that has come from the MAPS working group. A quick review of papers produced by MAPS investigators shows that a majority of papers have co-authors from more than one instrument. Although it is not possible to determine the quantitative impact the RotR had on the number of collaborative papers published by MAPS, our feeling is that the RotR greatly enhanced the ease of sharing data and teams willingness to share and therefore greatly increased the number of papers produced by MAPS.

During the mission, there was only one serious breach of the MAPS RotR. Given the considerable amount of data shared and the breadth and quality of the collaborations this is clearly a success.

Finally, as mentioned above, the process for creating the MAPS RotR was not top down. It was suggested by the MAPS IDS but it was not forced on the PIs. The process of modifying the PVO RotR to meet the needs of the Cassini mission and of implementing the RotR was in the hands of the PIs. This process assured that each PI could be satisfied that the needs of their individual team would be addressed and that the MAPS RotR would be consistent with individual team's internal policies.

The active support of the PIs for the development and implementation resulted in an atmosphere where sharing of data was the norm and where teams trusted that their data and their interests would be protected.

Challenges

Because the MAPS RotR were agreed upon by each of the MAPS PIs early in the mission, there were no problems with teams complaining about sharing data or teams restricting access to data that was important for collaborative studies. However, with a group as large as the Cassini MAPS team, and with the generally open sharing of data from all the MAPS instruments, it was likely that at some point data would be treated out of accordance with the RotR.

Although the RotR worked remarkably well in helping MAPS teams to share data openly and conduct many collaborative studies, there were a few occasions when the RotR were not followed. In almost every case, the breach was inadvertent, not malicious and did not result from a blatant lack of ethics. Nevertheless, some of the breaches where quite problematic and caused justified concern for the PIs involved. Very minor breaches where typically handled between the PIs whose teams were involved. However, in one or two cases, the RotR had to be reiterated at a MAPS working group meeting at a PSG and the MAPS IDSs were called on to reaffirm the data sharing agreement. At the same time, PIs were reminded to talk with their teams about the issue and to take a firmer role in overseeing how data from other instruments was being used. In each case, the value of the RotR was amplified because it provided a foundation for the discussion and resolution. The RotR could be consulted to clearly delineate how the offending action violated the RotR and what the appropriate course of action should have been.

Cassini Mission Rules of the Road

The MAPS RotR document was clearly a success in fostering data sharing between the MAP teams. This success led the Cassini Mission Project Scientist to consult with the MAPS IDS in implementing a RotR document for the broader mission. The creation of that document was discussed during the 1998–2002 period and the final Cassini RotR was accepted by the Executive PSG in 2002.

Lessons Learned

As outlined above, the most important aspect of the RotR was that it clarified the rights of teams with respect to using their own data, their responsibility to share their data and proper use of other team’s data. In addition, it clearly laid out who was responsible for assuring the team members followed the RotR. These key parts of the RotR greatly reduced the data “ownership” conflicts that often prevent the open sharing of data between instrument teams.

Moving from “the data is ours” point of view to the open sharing of data requires a culture change. Although the MAPS community has a track record of sharing data (for the reasons outlined above), the RotR document gave PIs and their teams confidence that their data would be protected and used correctly. This allowed teams to begin to share data and then to observe the mutual benefit that comes from sharing. This is perhaps one of the most important keys to a culture change. Teams have to see that sharing is mutually beneficial to feel truly comfortable openly sharing their data. The MAPS RotR document, or something like it, can have the effect of opening the door enough for teams to gain confidence and move toward the culture change needed for open sharing of data.

Finally, we note that the collaborative, data sharing culture is easier to achieve for in-situ instruments, as opposed to remote sensing instruments, due to the nature of the science addressed. As outlined above, data from multiple in-situ instruments is typically required in order to fully understand a phenomenon or an event. On the other hand, the nature of the science done by remote sensing teams is such that a single instrument can often make major advanced without the need for data from other teams. The nature of images also makes them more prone to someone outside a team being able to make discovery where for in-situ instrument this is much more unlikely. For this reason, it is clear that achieving a collaborative data sharing culture is easier for in-situ (MAPS) instrument teams than it is for remote sensing teams.

Cassini/Huygens Mission MAPS Discipline Working Group Rules of the Road (September 2000)

The MAPS DWG of the Cassini Huygens Mission agrees to the following set of procedures and rules to assure an orderly and efficient analysis and interpretation of the mission's scientific results.

1. Instrument Principal Investigators (PI), Science Team Leaders (TL) and Interdisciplinary Scientists (IDS) will be designated MAPS PIs. It is the responsibility of MAPS PIs to ensure that the Rules-of-the-Road are observed by their team. MAPS instrument PIs and TLs will be referred to as instrument PIs. The MAPS team is composed of all MAPS PIs, their Co-Is, team members and associates (such as students, postdocs, etc.). Each team member must be sponsored by a MAPS PI.

Gombosi: MAPS Rules-of-the Road 6

1. Each instrument PI is responsible for the analysis of data from his/her instrument. The instrument PIs and their Co-Is are responsible for the initial analysis, interpretation, and publication of these data.

2. IDSs are expected, under normal circumstances, to carry out investigations that involve more than one instrument. This may occur either as a result of their proposing such investigation, or their being invited to participate in investigations by other MAPS PIs. When investigations are proposed in an area in which an IDS is known to have an interest, the normal procedure will be to invite him/her to participate.

3. All instrument PIs are expected to contribute their processed data for MAPS team use. However, these data are to be used for correlative studies only.

4. When data from an instrument are used in a correlative study, the instrument PI responsible for the data must be informed of their use, and invited at an early time (preferably before the investigation begins) to participate (directly or through designated associates) in the study. The collaborators from the data providing instrument should be invited, through the PI, to be co-authors of any resulting publication or presentation (including abstract of a presentation).

5. The combined summary plots are made available to MAPS to identify possible scientifically interesting events. These plots are not intended for publication purposes, and may not be published without the specific authorization of the appropriate instrument PI. However, summary plots can be used in oral presentations to demonstrate potential new science. In such cases appropriate credit must be given to the instrument PI.

6. Each MAPS member entrusted with the summary plots are required to see that they are not distributed beyond the MAPS community without the specific permission of the instrument PIs who contributed data to the summary plot.

7. Any instrument PI can release data from his/her instrument to anyone, but no data can be released or published without the permission of the appropriate instrument PI.

3.1
Discipline Science Results

- Huygens
- Icy Satellites
- MAPS
- Rings
- Saturn
- Titan

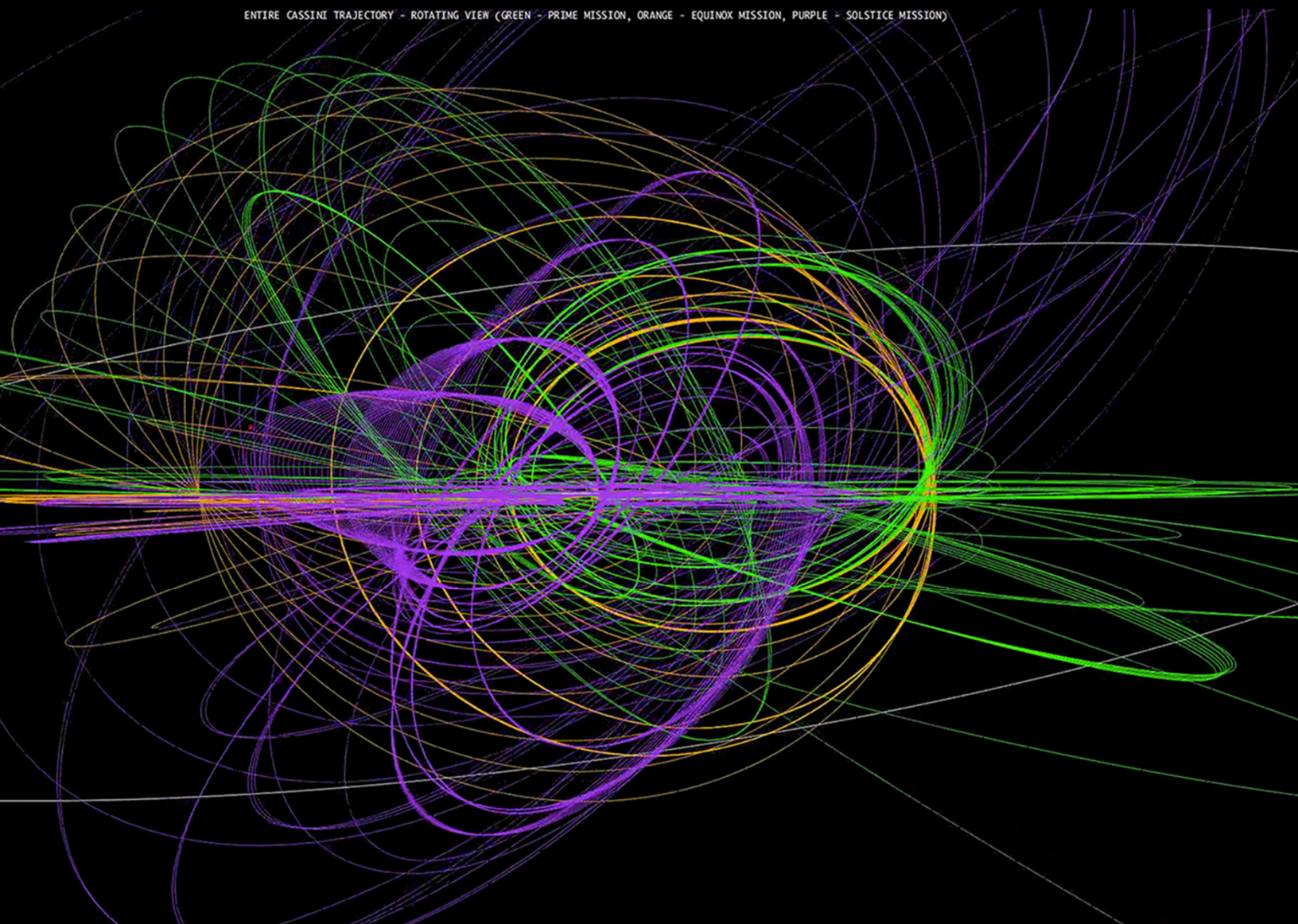

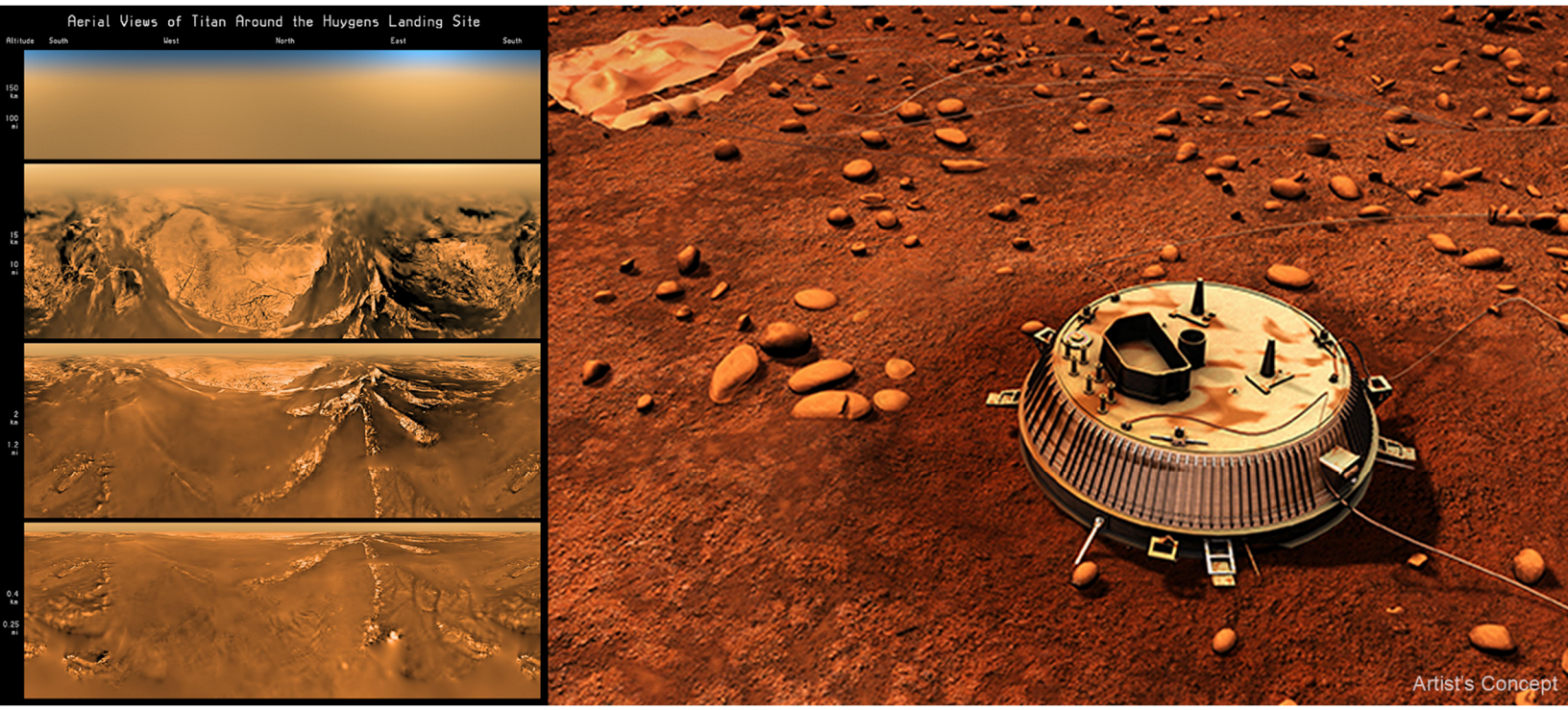

HUYGENS PROBE

The European Space Agency (ESA) Huygens Probe was an entry probe designed to study the atmosphere and the surface of Saturn's largest moon, Titan. Huygens was delivered to Titan by the Cassini Orbiter in January 2005 after a seven-year interplanetary cruise. The Huygens scientific objectives were to carry out detailed in situ measurements of the physical properties, the chemical composition and the dynamics of the atmosphere and to provide a local characterization of the surface near the landing site. Titan's Earth-like surface was revealed in images taken during the probe's descent to the surface.

Huygens was a highly sophisticated robotic laboratory equipped with six scientific instruments including: 1) Aerosol Collector Pyrolyser (ACP), 2) Descent Imager and Spectral Radiometer (DISR), 3) Doppler Wind Experiment (DWE), 4) Gas Chromatograph and Mass Spectrometer (GCMS), 5) Huygens Atmospheric Structure Instrument (HASI), and 6) Surface Science Package (SSP). Additionally, an engineering system, the Radar Altimeter, provided some scientific information about the structure along the ground track. The Doppler signature of the transmitted Huygens radio signal was directly detected by the two largest radio telescopes that were included in a network of 17 telescopes that were part of the very long baseline interferometry (VLBI) project put together a couple years before Huygens' release. These instruments allowed the Huygens probe to investigate Titan's atmospheric composition and dynamics, formation and evolution, to study Titan's meteorology, to investigate Titan's organic haze and to examine Titan's surface characteristics and to infer information about Titan's internal structure. The Huygens science team successfully addressed all the Huygens mission science objectives.

CONTENTS

Figures

Tables

EXECUTIVE SUMMARY

The Cassini-Huygens mission comprising the NASA Saturn Orbiter and the ESA Huygens Probe, arrived at Saturn in late June 2004. Following the separation of the Huygens probe from the Cassini Orbiter on December 25, 2004, Huygens arrived at Titan on January 14, 2005. Following entry protected by its heatshield, Huygens descended under two sequentially deployed parachutes to Titan's surface where it landed safely. It continued to fully operate on Titan's surface for several hours, until its batteries were depleted. Huygens findings and discoveries include new and improved understanding of Titan's atmospheric structure and chemical composition, distribution and composition of atmospheric aerosols, morphology and composition of the surface at the Huygens landing site, the altitude profile of zonal and near-surface winds along the Huygens descent trajectory, and atmospheric electrical properties. The data set collected by Huygens provided significant contribution to the understanding of the origin and evolution of Titan [Lebreton et al. 2009]. Furthermore, Huygens data set also served as the ground truth for several orbiter atmosphere and surface observations, proving the complementarity of in situ and remote sensing observations of a newly explored world.

In situ (accelerometry) measurements were made from about 1400 km altitude under the heatshield configuration. They revealed a very wavy atmospheric temperature/density profile attributed to atmospheric gravity waves. Direct in situ measurements of various atmospheric parameters started after parachute deployment (and heatshield release) at an altitude of about 150 km. During the latter stages of the descent, below about 50–60 km altitude above the surface, clear images of the surface were obtained by DISR, revealing a remarkably Earth-like world, showing strong evidence for erosion due to past epochs of flowing liquids, possibly methane. The Huygens descent trajectory carried the probe across a boundary between a bright, icy, rugged terrain and into a darker flat area where Huygens landed. Measured profiles of pressure and temperature below 150 km by HASI were found to be close to those expected based on Voyager observations. At the landing site, the surface temperature and pressure measured by Huygens were 93.7 K and 1,470 mbar, respectively. Reflectance spectra taken during descent show that the surface is primarily composed of dirty water-ice, and images of the landing site from the surface show a scattering of water-ice cobbles up to several centimeters in diameter. The SSP penetrometer found the surface to be unconsolidated, with the consistency of damp sand.

During the latter stages of the descent, below about 50–60 km altitude above the surface, clear images of the surface were obtained by DISR, revealing a remarkably Earth-like world, showing strong evidence for erosion due to past epochs of flowing liquids, possibly methane.

Atmospheric winds measured by Doppler tracking of the Huygens probe were found to blow predominantly in the direction of Titan's rotation (prograde: west–east) with speeds of about

125 m/s (~450 km/hr) detected above an altitude of 120 km. Although the winds diminished with decreasing altitude as expected from both Voyager and ground-based observations, a somewhat unexpected weakening of the winds was found between 100 km and 60 km. In the planetary boundary layer near the surface, the direction of the winds changed to include a significant north-south component.

Haze was detected from the top of the atmosphere to the surface with no evidence of the haze-free atmosphere predicted below 60 km. At an altitude of about 60 km, an ionosphere-like layer likely produced by galactic cosmic rays predicted by models was characterized, but at an altitude slightly lower than predicted by models [Whitten et al. 2007] was characterized, but at an altitude slightly lower than predicted by models.

The GCMS and ACP measurements of Titan's atmospheric composition and aerosols confirmed the presence of a complex organic chemistry in both the gas and the solid phase, and vertical abundance profiles were obtained for the more abundant species. Although primordial argon ^{36}Ar and radiogenic argon ^{40}Ar were detected, there was no detection of either xenon or krypton. Isotopic ratios of carbon, nitrogen, and deuterium to hydrogen (D/H) were measured, helping to further constrain formation scenarios for Titan's atmosphere [Niemann et al. 2010].

Composition measurements made by GCMS from the surface material vaporized after landing included detection of ^{40}Ar. The time profile of the composition of surface vapors indicated the Huygens probe landed on a surface damp with methane which subsequently evaporated as the cold regolith was heated by the GCMS inlet and the DISR lamp. Compounds such as C_6H_6, C_2N_2, and CO_2 were detected in the gas from the surface material.

Huygens Science Assessment

The Huygens science objectives were defined in the ESA's Announcement of Opportunity (AO), 1989.

Table HUYGENS-1. Huygens Science Assessment.

Fully/Mostly Accomplished: **Partially Accomplished:**

H1 Titan Atmosphere Formation and Evolution: Determine Abundance of atmospheric constituents (including noble gases); establish isotope ratios for abundant elements; constrain scenarios of formation and evolution of Titan and its atmosphere.

Huygens Objectives		Status	Instrument	Notes
H1.1	Determine the abundances of atmospheric constituents and noble gases		GCMS	CH_4 mole fraction 5.65 ±0.18% and CH_4 relative humidity near surface ~50%.
H1.2	Establish isotope ratios for abundant elements		GCMS	Measured isotopes of H (D/H), C, N, Ar
H1.3	Constrain scenarios of formation and evolution of Titan and its atmosphere		GCMS	Detected extremely low quantities of ^{36}Ar which rules out primary origin of N_2 and argues N_2 as secondary like on Earth; Measured isotopic ratios of C, N, and D/H helps constrain atmospheric formation &evolution scenarios; Radiogenic ^{40}Ar measured to constrain Titan outgassing history.

H2 Titan Atmosphere Composition and Distribution: Observe vertical and horizontal distributions of trace gases; search for more complex organic molecules; investigate energy sources for atmospheric chemistry; model the photochemistry of the stratosphere; study formation and composition of aerosols.

Huygens Objectives		Status	Instrument	Notes
H2.1	Observe vertical distribution (profile) of trace gases		GCMS, DISR	DISR: low altitudes; GCMS: Vertical distribution of CH_4 and H mole fractions
H2.2	Search for more complex organic molecules		GCMS	Found evidence of heavy organic molecules
H2.3	Investigate energy sources for atmospheric chemistry		DISR, HASI	DISR measured light absorption vs altitude; HASI detected cosmic ray ionization
H2.4	Model the photochemistry of the stratosphere		GCMS, ACP	Data used in multiple photochemical models
H2.5	Study formation and composition of aerosols		GCMS, ACP	Low mass of ACP sample transferred to GCMS limited the results to simple species, rather than complex hydrocarbon hazes

H3 Titan Meteorology: Measure winds and global temperatures; investigate cloud physics, general circulation and seasonal effects in Titan's atmosphere; search for lightning discharges.

Huygens Objectives		Status	Instrument	Notes
H3.1	Measure winds and global temperatures		DWE, HASI, DISR	DISR: Wind drift near surface via feature tracking; PBL detected at ~7 km; Measurements provided ground truth for global Cassini remote sensing measurements.
H3.2	Investigate cloud physics, general circulation and seasonal effects in Titan's atmosphere		DWE, DISR	Huygens measurements provided ground truth for Cassini global remote sensing studies for seasonal effects.
H3.3	Search for lightning discharges		DISR, HASI	Schumann Resonance seen by HASI PWA, but not linked to lightning activity. No optical or RF signature of lightning found.

H4 Titan Surface Characteristics and Internal Structure: Determine the physical state, topography and the composition of the surface; infer the internal structure of the satellite.

Huygens Objectives		Status	Instrument	Notes
H4.1	Determine the physical state, topography and the composition of the surface		SSP, HASI, DISR, GCMS	DISR: Imaging of surface topography show drainage basins, dry riverbeds, dunes; IR reflectance spectroscopy. GCMS: Trace organic species found in surface measurements. HASI: Surface permittivity SSP: Acoustic Sounding; Surface penetrometry and accelerometry. Radar altimeter: surface topography and reflectivity.
H4.2	Infer the internal structure of the satellite;		HASI	HASI PWA: Measurement of Schumann resonance within ionosphere / subsurface ocean waveguide.

H5 Titan Upper Atmosphere: Investigate the upper atmosphere, its ionization, and its role as a source of neutral and ionized material for the magnetosphere of Saturn.

Huygens Objectives		Status	Instrument	Notes
H5.1	Investigate upper atmosphere, its ionization, and its role as a source of neutral and ionized material for the magnetosphere of Saturn		DISR, HASI	DISR: Hydrocarbon haze number density in upper atmosphere. HASI PWA: Measurement of Schumann resonance within ionosphere / subsurface ocean waveguide.

HUYGENS MISSION OVERVIEW

The Huygens probe was the ESA contribution to the NASA/ESA/ASI Cassini-Huygens mission. The Cassini-Huygens spacecraft arrived in the Saturnian system on June 30, 2004, following a seven-year cruise, and performed a perfect Saturn Orbit Insertion maneuver to initiate a long series of orbits around Saturn that included frequent regular flybys of Titan. For the first three Titan flybys, Cassini was still carrying the Huygens probe. Following the third Titan encounter on December 13, 2004, the Cassini orbiter main engine was fired on December 17 to bring the orbiter and Huygens probe, still attached, onto a collision trajectory with Titan. Small onboard jets were fired on December 23, 2004, to fine-tune the flight path of Cassini-Huygens to align the spacecraft on a trajectory that would target Huygens to the desired entry location, and on December 25, 2004, at 02:00 UTC the Spin/Eject Device separated Huygens from Cassini with a relative speed of approximately 0.35 m/s and a spin rate of 7.5 revolutions per minute. The Huygens probe was targeted for a low southern-latitude site on the dayside of Titan. Constrained by the heat shield design performance and radio visibility conditions between the probe and the orbiter during the descent, the probe entry flight path angle into the atmosphere was set to −65° (25° from the local vertical) with a tolerance of three degrees. The relative position of Cassini, Huygens, and Titan enabled a theoretical maximum telecommunications link between Huygens and Cassini of 4 hours 30 minutes. Huygens and Cassini were effectively in radio contact from the start of the radio transmission after parachute deployment until after about 72 minutes after landing. Two Earth radio telescopes, first Green Bank in West Virginia, and then Parkes in Australia, detected directly the Huygens radio signal (carrier).

The relative position of Cassini, Huygens, and Titan enabled a theoretical maximum telecommunications link between Huygens and Cassini of 4 hours 30 minutes.

Prior to arrival at the atmospheric entry interface point on January 14, 2005, at 11:04 UTC [Lebreton et al. 2005], the Huygens coast timer woke up Huygens. Four and a half hours later, the Huygens probe encountered the Titan atmosphere at an altitude of about 1500 km above the surface, causing the 300 kg probe to aerobrake from its approaching velocity of around 21,600 km/h (6 km/s) to less than 1,400 km/h at 150 km altitude. During entry, Huygens experienced aerodynamic forces up to 12 g (measurements saturated at 10 b by design) and an estimated entry temperature of 12,000° C (21,600° F) in the shock that formed in front of the probe, leading to an expected heat shield temperature of 1,800° C. After the entry, speed had decreased to about Mach 1.4 (290 km/h at about 160 km altitude). The pilot chute was deployed and the backshell of the heat shield was pulled away by the pilot chute and deployed, within less than 2 seconds the 8.3-meter (diameter) main parachute. The heat shield was released 30 seconds later. Following 15 minutes of descent, the main parachute was discarded and replaced at about 110 km altitude by a smaller 3-meter (diameter) parachute to ensure that the probe would reach the surface at least 30 minutes before the orbiter would pass below the horizon as seen from the

landing site. The descent from atmospheric entry to landing took 2 hours 27 minutes 50 seconds. The radio contact between Huygens and Cassini was operational until the orbiter passed below the horizon 72 minutes after landing.

The light level on the surface of Titan was roughly 1,000 times less than experienced on Earth by day, but 500 times brighter than the light of the full moon.

At an altitude of 60 km, the surface-sensing radar was turned on to provide altitude information to the onboard computers, which then broadcast the altitude to the instruments to allow the instruments to adapt their measurement sequence to the measured, rather than to the predicted altitude. Accurate altitude information was in fact provided only below 20 km. DISR, HASI and SSP adapted their measurement sequence to the measured altitude information provided by the onboard computer. This tuning allowed the Huygens surface lamp to be activated at 700 m altitude and the SSP instrument to activate its high-time resolution impact detection measurement mode while approaching the surface. The light level on the surface of Titan was roughly 1,000 times less than experienced on Earth by day, but 500 times brighter than the light of the full moon. Although the natural lighting by the Sun was sufficient to illuminate the landing site, the surface lamp enabled high signal-to-noise multispectral measurements of surface reflectivity.

Due largely to the thick atmosphere and the excellent performance of the parachutes, the surface impact speed was slightly less than 5 m/s (about 18 km/h). Once on the surface, Huygens' five batteries lasted much longer than expected, allowing the probe to continue functioning several hours after landing, providing time for the orbiter to collect surface data for 1 hour 12 minutes before disappearing below the horizon. The Earth-based radio telescope received the Huygens signal for more than 3 hours after landing, until 16:00 GMT, corresponding to the end of the window assigned to that observation.

More than 350 images and numerous spectra were returned by the DISR camera during descent, while four other probe instruments, the HASI, ACP, GCMS, and the SSP sampled Titan's atmosphere to help determine its composition and structure, and to characterize the aerosols. To retrieve the altitude profile of zonal winds, the DWE was designed to provide Doppler tracking of the probe throughout descent. Once on the surface, the SSP, HASI, GCMS, and DISR continued to acquire data (ACP turned off as planned below 10 km). The Huygens probe was also tracked by a VLBI network of 17 radio telescopes, as part of an experimental project put in place about one year before Huygens landing. Two of the VLBI radio telescopes, the Green Bank Telescope and Parkes were equipped with highly sensitive radio receivers provided by the JPL radio science team. They collected the most accurate Doppler information during the descent, as this information could not be retrieved from the channel of the Huygens radio link equipped with ultra-Stable Oscillators as the receiver onboard Cassini was not activated properly due to a programming error. Limited Doppler information was however retrieved from the

second channel of the Huygens-to-Cassini radio link which itself was equipped with less stable crystal oscillators.

The Huygens science data was relayed to the Cassini orbiter at a rate of 8 kilobits per second and stored in solid-state memory on the orbiter. Although the data were transmitted on two nearly redundant channels, A and B, a programming error in the channel A receiver resulted in no data collected through that channel. In the end, because of the redundancy philosophy applied to the Huygens design, almost all of the measurements were recovered. In particular, the exceedingly weak signal from Huygens was captured by two of the Earth-based radio telescopes, Green Bank and then Parkes, both equipped with highly sensitive radio receivers provided by the JPL radio science team, in effect providing a channel C to Doppler-track the probe throughout descent and enabling the DWE to retrieve the Titan zonal wind profile. In the end, radio telescopes on Earth received 5 hours 42 minutes of Huygens data, including 3 hours 14 minutes from the surface. The probe survived the landing and continued transmitting from the surface for a much longer time than expected because Huygens touched down on a relatively soft solid surface. Once the Cassini orbiter flew beyond the horizon as seen from Huygens, the probe continued transmitting for several hours. The Huygens signal was still detected when Parkes stopped tracking it at 16:00 UTC. Flight performance of the probe allowed an estimate that the batteries became depleted about 20–25 minutes later. [Huygens Flight Performance Report, Huygens data set archive, Lorenz 2017].

TOP TEN HUYGENS FINDINGS

The top 10 Huygens discoveries at Titan are listed below and can be found at ESA website http://sci.esa.int/cassini-huygens/55221-huygens-titan-science-highlights/, [ESA 2017].

On 14 January 2005, at 13:34 CET (12:34 UTC), ESA's Huygens probe entered the history books by descending to the surface of Titan, Saturn's largest moon. This was humanity's first successful attempt to land a probe on another world in the outer solar system.

Huygens hitched a ride to the Saturn system during an epic, seven-year voyage attached to NASA's Cassini spacecraft. The final chapter of the interplanetary trek was a 21-day solo cruise toward the haze-shrouded moon. Plunging into Titan's atmosphere, the probe survived the hazardous 2-hour 27 minute descent to touch down safely on Titan's frozen surface.

Huygens continued to transmit back to Earth for another 72 minutes before contact was lost with Cassini as it dipped below the horizon. The stream of data provided a unique treasure trove of in situ measurements from the planet-sized satellite which scientists are still mining today. In the following articles we present 10 important results from the pioneering mission.

1. Profiling the Atmosphere of Titan

The HASI made the first in situ measurements of Titan's atmosphere. HASI determined the atmospheric temperature, pressure, and density from an altitude of 1400 km down to the surface.

Long before ESA's Huygens probe arrived at Titan, scientists knew that the moon's dense atmosphere was mainly composed of nitrogen, with some methane, but the atmosphere's structure—its temperature and pressure at different altitudes —was poorly understood.

By monitoring the probe's rate of deceleration as it plunged into the atmosphere, the HASI instrument directly determined the density of the upper atmosphere. The temperature was derived from models of how it should change with density and altitude. In the lower atmosphere (below 160 km) and on the surface of Titan, HASI directly measured the pressure and temperature, as well as electrical properties such as permittivity and the distribution of ions.

HASI data showed that the upper atmosphere (the thermosphere) was generally warmer and more dense than expected. Titan's atmosphere was also found to be highly stratified.

Above 500 km, the average temperature was about −100° C but strong variations of 10-20° C were detected due to inversion layers and other phenomena, such as, gravity waves and tides. The mesosphere was virtually absent, in contrast with theoretical predictions.

Below 500 km, the temperature increased quite rapidly, reaching a maximum of -87° C at the top of the stratosphere, at an altitude of 250 km. The temperature then decreased steadily throughout the stratosphere, reaching a minimum of −203° C at an altitude of 44 km. This marked the boundary between the stratosphere and the troposphere.

The temperature increased again as the probe neared the surface, rising to a chilly −180° C at the landing site. The surface pressure was 1.47 times that on Earth.

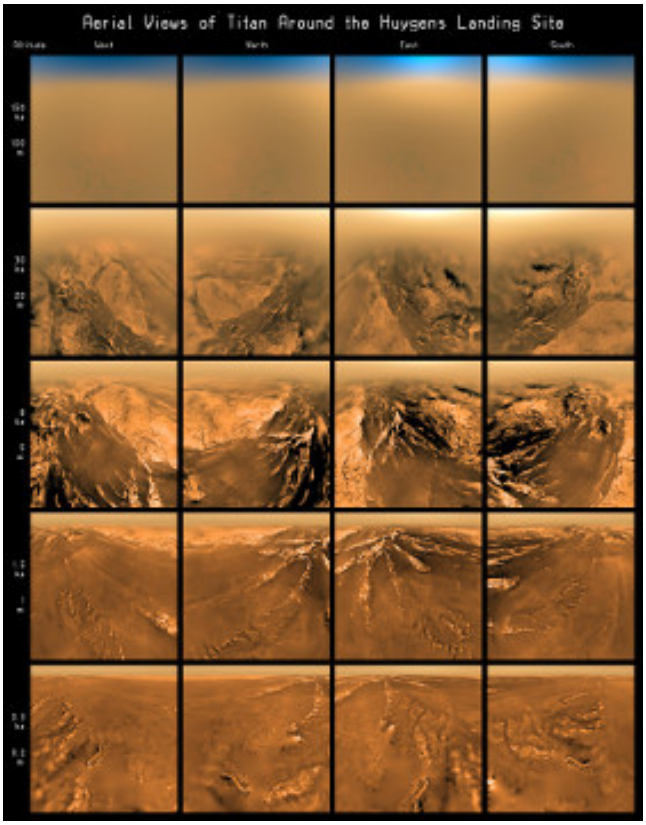

Figure HUYGENS-1. Huygens' view of Titan from five altitudes. Credit: ESA/NASA/JPL/University of Arizona.

2. Titan's Super-rotating Winds

Although spacecraft observations had indicated that strong zonal (east-west) winds may exist in Titan's atmosphere, the first direct measurements were made by the Doppler Wind Experiment on ESA's Huygens probe.

By measuring the Doppler shift of the radio signal from Huygens and studying panoramic mosaics from the onboard imager to work out the descent trajectory, it was possible to create a high resolution vertical profile of Titan's winds, with an estimated accuracy of better than 1 m/s.

Huygens found that the zonal winds were prograde (the same direction as the Moon's rotation) during most of the atmospheric descent. The probe generally drifted east, driven by remarkably strong westerly winds which peaked at roughly 120 m/s (430 km/h) at an altitude of about 120 km.

Down to a height of 60 km, large variations in the Doppler measurements were observed—evidence that Huygens endured a rough ride as the result of significant vertical wind shear. Wind speeds then decreased toward the surface, dropping from 30 m/s (108 km/h) at an altitude of 55 km to 10 m/s (36 km/h) at a height of 30 km, eventually slowing to 4 m/s (14 km/h) at 20 km. The winds dropped to zero and then reversed direction at around 7 km.

The large prograde wind speeds measured between 45 km and 70 km altitude and above 85 km were much faster than Titan's equatorial rotation speed. It was the first in situ confirmation of the predicted super-rotation of the moon's atmosphere, even though the speed observed was slightly lower than expected.

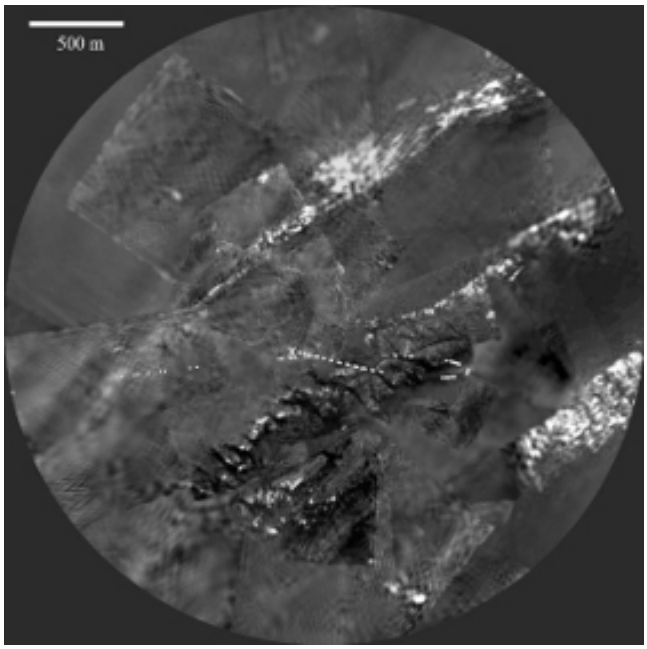

Figure HUYGENS-2. The ground track of Huygens is marked on this aerial view of Titan. Credit: ESA/NASA/JPL/University of Arizona.

A layer with surprisingly slow wind, where the sideways velocity decreased to near zero, was detected at altitudes between 60 km and 100 km.

During the last 15 minutes of the descent, Huygens headed west-northwest at a speed of approximately 1 m/s. The wind speed on the surface was between 0.3 m/s and 1 m/s.

Over the duration of the descent, the probe drifted eastward a distance of 165.8 km with respect to the surface of Titan.

3. Methane Mystery

ESA's Huygens probe made the first direct measurements of the composition of Titan's lower atmosphere. Data returned by the GCMS on Huygens included altitude profiles of the gaseous constituents, isotopic ratios and trace gases (including organic compounds).

Two of the key questions about Titan are the origin of the nitrogen and methane in its atmosphere, and the mechanisms by which methane levels are maintained. Since sunlight destroys methane irreversibly on Titan, its lifetime in the atmosphere is only tens of millions of years. Somehow the methane must be continually or periodically replenished.

The primary constituents of Titan's atmosphere were confirmed to be nitrogen and methane. In the stratosphere, levels of methane were found to be fairly low and the gas was uniformly mixed. Then, at an altitude of 40 km, in the upper troposphere, the relative amount of methane began to increase gradually until approximately 7 km, when it reached 100% relative humidity (saturation level).

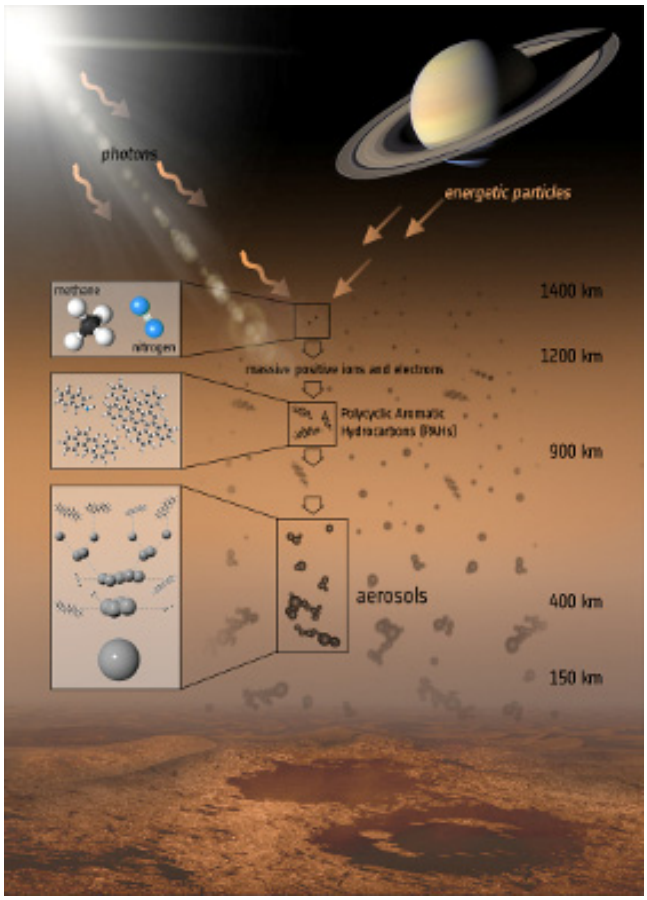

Figure HUYGENS-3. Chemistry in Titan's atmosphere. Credit: ESA/ATG medialab.

For the last part of the descent, methane amounts remained relatively constant until the probe touched down on the surface. A sudden, 40% increase in the methane signal after landing, while the nitrogen count rate remained constant, suggested the presence of liquid methane on the surface. This may have been due to the spacecraft heating the surface material. This increased value for methane remained nearly constant for about one hour, with a hint of a very slight decrease in the level toward the end of this period.

Measurements of the carbon isotopes in the methane provide no support for suggestions that it is generated by active micro-organisms on Titan. The methane was probably accreted by Titan during the moon's formation, and large quantities of liquid methane are now trapped in ices beneath the surface, possibly reaching the surface through some form of cryovolcanism. (Surface features

associated with possible cryovolcanism have been observed by Cassini. See Science highlights from Huygens: #5. Radioactive decay and cryovolcanism [ESA 2019a].) This activity would replace the methane that is lost as a result of photochemistry in the atmosphere.

The spectra taken on the surface also showed signatures characteristic of more complex hydrocarbons, such as ethane, cyanogen and benzene.

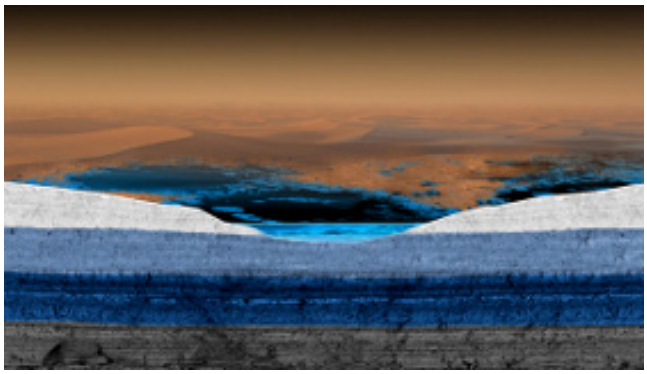

Figure HUYGENS-4. Titan's subsurface reservoirs contain hydrocarbons, including methane. Credit: ESA/ATG medialab.

4. The Origin of Titan's Nitrogen Atmosphere

Titan and Earth are the only worlds in our solar system that have thick nitrogen atmospheres. Although data from the Voyager Mission had implied that nitrogen (N_2) was the main atmospheric gas, the GCMS on ESA's Huygens probe made the first direct identification of bulk atmospheric nitrogen and its abundance. Other GCMS atmospheric measurements provided clues about where this atmosphere came from.

During its descent to the surface, the GCMS measured isotopic ratios and trace species in the atmosphere. One of the objectives for the GCMS was to search for heavy, noble gases such as argon-36 (^{36}Ar), argon-38 (^{38}Ar), krypton (Kr), and xenon (Xe). These primordial gases have been detected and measured in meteorites, in the atmospheres of Earth, Mars, Venus (to some extent), and Jupiter. Differing patterns of relative abundances and isotopic ratios of the gases provide insights into the origin and evolution of these objects. As a result, their measurements in the atmosphere of Titan were eagerly anticipated.

Scientists had theorised that these noble gases were present throughout the solar nebula, and should therefore have been incorporated into both Saturn and Titan during the early stages of planet formation. In the context of the origin of nitrogen, ^{36}Ar is of particular importance, and the GCMS found that the ratio of ^{36}Ar to nitrogen was about one million times less than is found in the Sun.

Direct condensation of gases in the young Titan would have resulted in the capture of ^{36}Ar, as well as nitrogen, in solar proportions. However, the depleted ratio detected by the GCMS on Huygens implies that the nitrogen was captured as ammonia (NH_3) or in other nitrogen-bearing compounds.

The rarity of noble gases on Earth has long been viewed as strong support for the atmosphere having been formed by the impacts of gas-rich planetesimals, and the near absence of noble gases from Titan provides more support for this hypothesis.

5. Radioactive Decay and Cryovolcanism

One of the trace gases detected by the GCMS on ESA's Huygens probe was radiogenic argon-40 (^{40}Ar). This isotope offers a window to the interior of the giant moon.

Radiogenic argon was detected by the GCMS below 18 km. This detection was important because ^{40}Ar originates solely from the decay of potassium-40 (^{40}K), a radioactive isotope of potassium found in rocks. The only possible source of this ^{40}Ar is rocks which exist deep in Titan's interior, below the satellite's mantle of hydrocarbon and water ice.

Since the radioactive half-life of ^{40}K is about 1.3 billion years, much shorter than the lifetime of Titan, the small amount of ^{40}Ar in the atmosphere provides an important indicator of how much outgassing has occurred from the deep interior.

If the rocky component of Titan's interior has the same composition as that of Earth and has outgassed to the same extent, ^{40}Ar should be about ten times more abundant than measured by Huygens, comprising approximately 0.05% of the atmosphere. If the interior was warm enough in the past for a liquid water or water-ammonia mantle to have reached all the way down to the moon's rocky core, potassium could have seeped into the liquid. The radiogenic ^{40}Ar could then have outgassed to the surface.

Certainly, the presence of the ^{40}Ar at the levels seen by Huygens is a strong indication of geological activity on Titan, and consistent with periodic replenishment of atmospheric methane (see Science highlights from Huygens: #3. Methane Mystery [ESA 2019b].) The apparent evidence for cryovolcanism observed by the Cassini orbiter—involving water or a mixture of water and ammonia—provides one possible process for release of both gases from the interior.

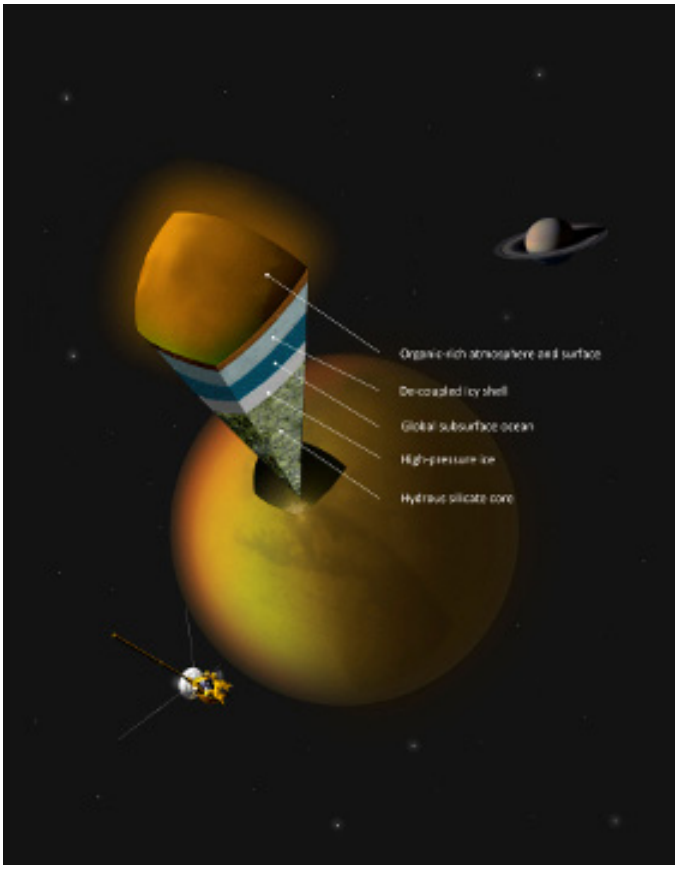

Figure HUYGENS-5. Concept sketch of the interior of Titan. Credit: Angelo Tavani.

6. Hazy Titan

One of the most noticeable features of Titan is the orange blanket of haze that hides its surface. However, no one knew whether the haze extended to the surface until ESA's Huygens probe landed on the icy moon.

The measurements of the DISR on the Huygens probe provided in situ information on the optical properties, size and density of the haze particles. The observations showed that there was a significant amount of haze at all altitudes throughout the descent, extending all the way down to the surface. With decreasing altitude, the haze particles became brighter, and the particle sizes increased, due to collisions which resulted in a 'snowball' effect, as well as condensation of methane, ethane and hydrogen cyanide gases onto small aerosol nuclei at lower levels.

Huygens detected three distinct haze regions (region I above 80 km, region II between 80 and 30 km, and region III between 30 km and the surface), based on the density and optical properties of the atmosphere.

Before the Huygens mission, it was generally believed that the tiny haze particles slowly sink through the stratosphere, eventually acting as condensation nuclei for lower-level clouds. Some scientists theorized that the haze might clear below an altitude of 50 km to 70 km due to condensation of gases such as methane. However, the probe's DISR showed that Huygens began to emerge from the haze only in the troposphere, 30 km above the surface.

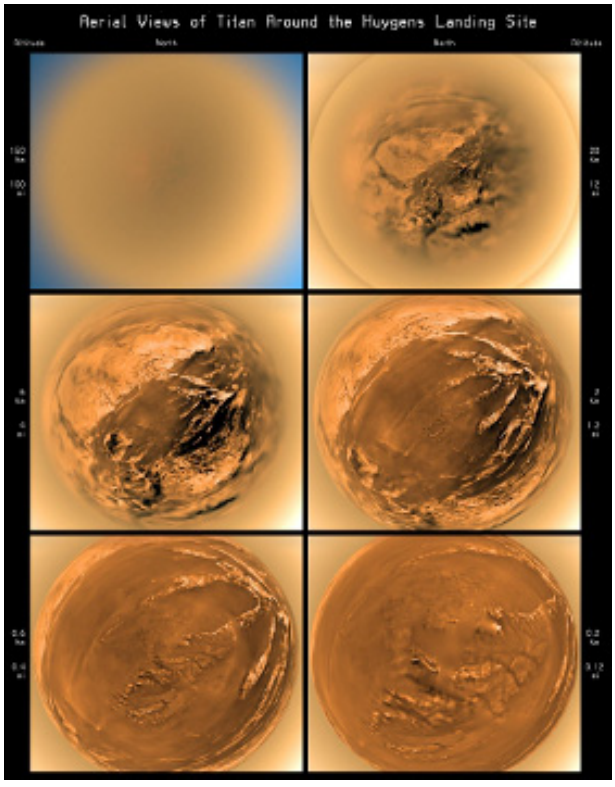

Figure HUYGENS-6. Six stereographic images of Titan's surface taken during Huygens's descent to Titan's surface, showing the haze clearing. Credit: ESA/NASA/JPL/University of Arizona.

Another thin layer of methane haze was detected at an altitude of 21 km, where the local temperature was −197° C and the pressure was 450 mbar. This feature may be an indication of methane condensation. Indeed, the data suggest the presence of layered methane clouds in Titan's troposphere, at altitudes between 8 km and 30 km.

When combined with ground-based measurements, the data suggest an upper methane ice cloud (or haze) between approximately 20 km and 30 km and a liquid methane-nitrogen cloud layer between 8 km and 16 km, perhaps with a gap in between.

7. Titan's Tiny Aerosols

Tiny particles (aerosols) in Titan's atmosphere have long been suspected to play an important role in determining its thermal structure and atmospheric processes. However, until the Huygens mission, no direct measurements had been made of the chemical composition of these particles.

One set of measurements was made by the GCMS and the ACP experiment. The collected aerosol particles were heated in the ACP oven in order to vaporize all volatile components, and the composition of the gases released by each sample was then analyzed by the GCMS.

Two atmospheric samples were obtained during the descent of Huygens. One was taken at 130-35 km (the middle stratosphere) and the other at 25-20 km (the middle troposphere). Ammonia (NH_3) and hydrogen cyanide (HCN) were identified as the main gases released in the oven, confirming that carbon and nitrogen are major constituents of the aerosols.

No substantial difference was found between the two samples, suggesting that the aerosols' composition was the same at both altitudes. This supports the idea that they have a common source in the upper atmosphere, where ultraviolet sunlight photochemically alters gases such as methane.

Meanwhile, the DISR characterized the optical properties of the photochemical aerosols from 150 km altitude to the surface. They were found to match the properties of 'tholins', materials created in laboratories by sending electrical discharges into mixtures of nitrogen and methane.

The aerosols' optical properties can be reproduced by the condensation of hydrogen cyanide close to 80 km, ethane condensation close to the tropopause (44 km), and methane condensation from the tropopause down to 8 km.

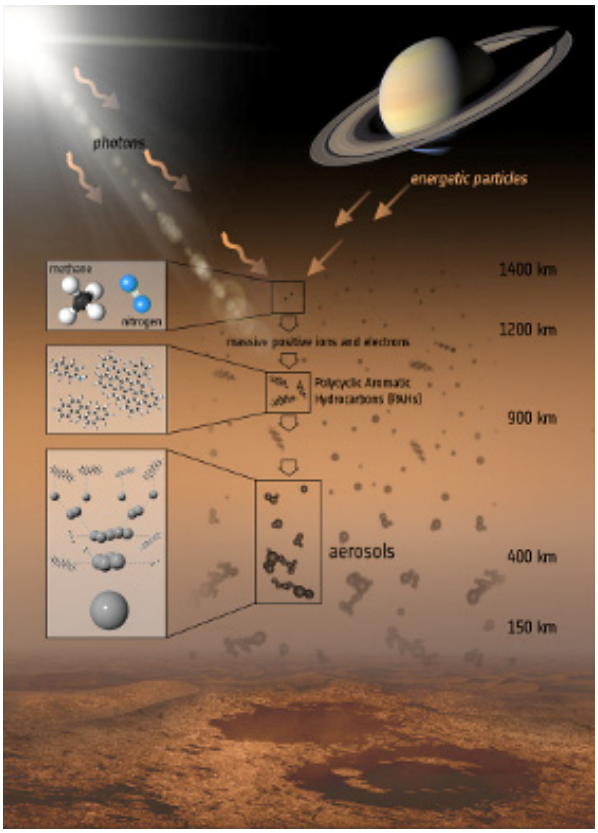

Figure HUYGENS-7. How aerosols form in Titan's haze. Credit: ESA / ATG medialab.

8. Dry River Beds and Lakes

Hidden beneath an all-embracing blanket of haze, Titan's surface remained a mystery until the DISR on ESA's Huygens probe sent back a series of unique, spectacular images.

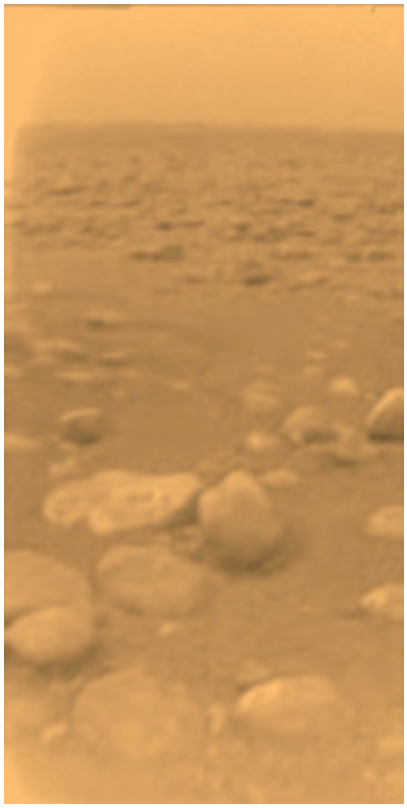

Figure HUYGENS-8. Titan's surface viewed by DISR. Credit: ESA/NASA/JPL/ University of Arizona.

The DISR took several hundred visible-light images with its three cameras during its 2 hour 27 minute descent, including several sets of stereo image pairs which enabled scientists to construct digital terrain models. See Huygens's descent to Titan's surface [ESA 2015] for further details and enhanced video.

The cameras revealed a plateau with a large number of dark channels cut into it, forming drainage networks which bore many similarities to those on Earth. The narrow channels converged into broad rivers, which drained into a broad, dark, lowland region. The ravines cut by the rivers were approximately 100 m deep and their valley slopes were very steep, which suggested rapid erosion due to sudden, violent flows.

No evidence of surface liquid was found at the time of the landing. However, it seems likely that, from time to time, the entire dark region is inundated by floods of liquid methane and ethane. If the darker region is a dry lakebed, it is too large to have been caused by the creeks and channels visible in the images. It may have been created by other larger river systems or some large-scale catastrophic event, which predates deposition by the rivers seen in the images.

Brighter regions north of the landing site displayed two different drainage patterns: 1) bright highlands with rough topography and deeply incised branching (dendritic) drainage networks with dark-floored valleys that indicated erosion by methane rainfall; and 2) short, stubby channels that followed linear fault patterns, forming canyon-like features suggestive of spring sapping by liquid methane.

The topographic data showed that the bright highland terrains are extremely rugged, often with slopes of up to 30 degrees. These drain into relatively flat, dark lowland terrains. The dark material that covers the plains may have been carried along by the flows and could be made up of photochemical deposits rained down from above.

The landing site itself resembled a dried-up riverbed. Rounded cobbles, 10 cm to 15 cm in diameter and probably made of hydrocarbons and water ice, rested on a darker granular surface.

9. Schumann-like Resonances: Hints of a Subsurface Ocean

One of the most surprising discoveries of ESA's Huygens Mission was the detection of an unusual source of electrical excitation in Titan's atmosphere.

Scientists had wondered whether lightning might be generated in Titan's atmosphere, so Huygens was equipped with the permittivity, wave and altimetry (PWA) experiment to detect tell-tale radio signals.

On Earth, thousands of lightning flashes take place every second, and each bolt generates a radio 'crackle'. This means our atmosphere is continuously generating extremely low frequency (ELF) radio signals, known as Schumann resonances. These global electro-magnetic resonances, excited by lightning discharges, occur in the 'cavity' formed between Earth's surface and the ionosphere—a region of electrically charged particles in Earth's upper atmosphere.

Such a resonance is known only on Earth for being released by storm lightning and it had long been considered that its existence on other planets would make it possible to reveal the presence of both storm activity and a conductive ground.

Although no lightning or thunderstorms were detected in Titan's atmosphere, the PWA did detect an unusual ELF signal at a frequency of around 36 Hertz. Huygens also discovered a lower ionospheric layer between 140 km and 40 km, with electrical conductivity peaking near 60 km.

In order to explain the unique pattern of signals, scientists have proposed that Titan's atmosphere behaves like a giant electrical circuit. The electrical currents are generated in the ionosphere when it interacts with Saturn's magnetosphere. This results in a dynamo effect as plasma trapped in the magnetosphere co-rotates with the planet every 10 hours or so.

The lower boundary of Titan's 'cavity', which reflects the radio signals, is thought to be a conductive ocean of water and ammonia which is buried at a depth of 55–80 km below a non-conducting, icy crust.

Huygens' discovery of this unique Schumann resonance is seen as key supporting evidence for the existence of such a subsurface ocean, hidden far beneath the moon's frozen surface.

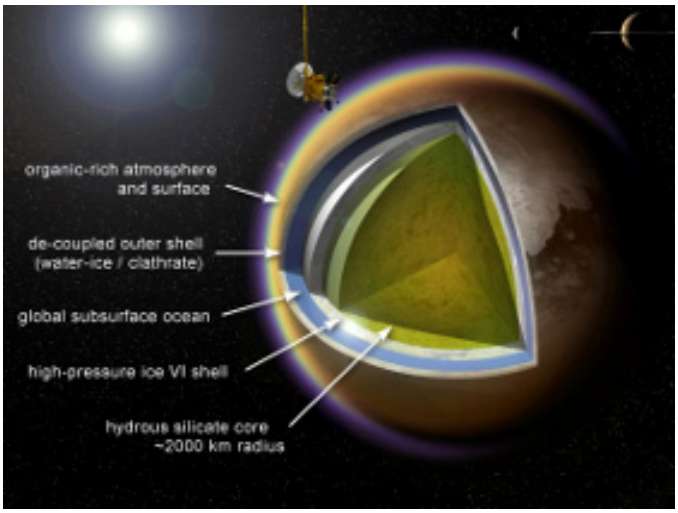

Figure HUYGENS-9. This artist's impression of a possible model for Titan's interior includes a global subsurface ocean. Credit: A. D. Fortes/UCL/STFC.

10. Elusive Dunes

To their surprise, scientists found that locating the Huygens landing site on images taken by the Cassini orbiter was much more difficult than expected.

Although the side-looking imager (SLI), part of the DISR on board ESA's Huygens probe, was able to image surface features located up to 450 km from the Huygens landing site, the images it sent back were hard to match with the synthetic aperture radar (SAR) images obtained by the Cassini orbiter. See Huygens's descent to Titan's surface [ESA 2015] for further details and enhanced video.

The area around the Huygens landing site turned out to be a huge plain of dirty water ice over which lay blankets of organic (carbon-bearing) deposits. These mantles of aerosol were invisible to radar waves, so Cassini SAR images only revealed the underlying water ice. As a result, the boundary between the bright highlands and dark plains that Huygens drifted over simply did not show up in the radar images.

The location of the landing site was only tied down after some time by the detection of two dark, longitudinal "sand" dunes, about 30 km north of the landing site. The elusive landforms were visible in both the SAR and Huygens images. Although dark, longitudinal dunes form vast "sand seas" throughout Titan's optically dark equatorial regions, Huygens descended over a region of bright and dark units that was free of the pervasive dune fields found elsewhere.

The dunes on Titan are probably composed of sand-sized hydrocarbon and/or nitrile grains mixed with lesser amounts of water ice. The particles rained down from above onto the surface and were subsequently eroded and moved by surface and aeolian processes, such as liquid methane runoff and wind erosion.

In order for the sand to migrate across the surface under the influence of Titan's weak surface winds, a process called saltation, scientists have concluded that the dune material must be between 100 microns and 300 microns in diameter.

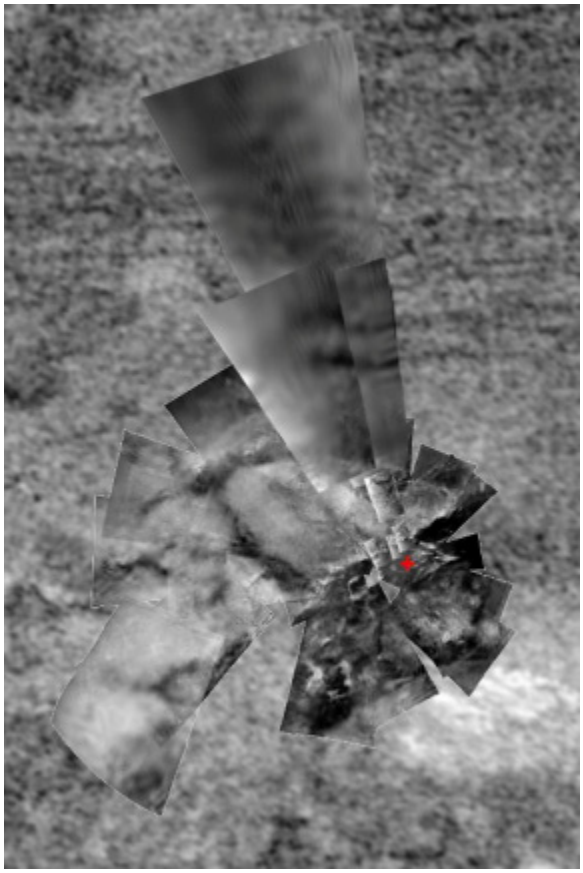

Figure HUYGENS-10. Huygens's landing site. Credit: ESA/NASA/JPL-Caltech/ University of Arizona/USGS.

ACRONYMS

Note: For a complete list of Acronyms, refer to Cassini Acronyms – Attachment A.

ACP	Aerosol Collector Pyrolyser
AO	Announcement of Opportunity
ASI	Italian Space Agency
AU	astronomical unit
CCD	charge coupled device
CIRS	Composite Infrared Spectrometer
CO	carbon monoxide
CSWG	Campaign Science Working Group
D/H	Deuterium to Hydrogen
DISR	Descent Imager and Spectral Radiometer
DWE	Doppler Wind Experiment
ELF	Extremely Low Frequency
ESA	European Space Agency
EUV	extreme ultraviolet
GC	gas chromatographic
GCM	general circulation models
GCMS	Gas Chromatograph and Mass Spectrometer
HASI	Huygens Atmospheric Structure Instrument
HCN	hydrogen cyanide
HST	Hubble Space Telescope
INMS	Ion and Neutral Mass Spectrometer
IRIS	infrared spectrometers
ISS	Imaging Science Subsystem
JPL	Jet Propulsion Laboratory
NH_3	Ammonia
PWA	Permittivity Wave and Altimetry
SAR	Synthetic Aperture Radar
SLI	side-looking imager
SSP	Surface Science Package
TSSM	Titan Saturn System Mission
UTC	Coordinated Universal Time
UV	ultraviolet
VIMS	Visual and Infrared Imaging Spectrometer
VLBI	Very Long Baseline Interferometry

REFERENCES

Disclaimer: *An extensive selection of Huygens references is provided here. For all other Cassini references, refer to the section entitled Other References and Papers, Attachment B – References & Bibliographies; Attachment C – Cassini Science Bibliographies; the sections entitled References contributed by individual Cassini instrument and discipline teams located in Volume 1 Sections 3.1 and 3.2 Science Results; and other resources outside of the Cassini Final Mission Report.*

Aboudan, A., G. Colombatti, F. Ferri, F. Angrilli, (2008), Huygens probe entry trajectory and attitude estimated simultaneously with Titan atmospheric structure by Kalman filtering, Planetary and Space Science, 56, 5, 573–585, doi: 10.1016/j.pss.2007.10.006.

Barnes, J. W., L. Lemke, R. Foch, C. P. McKay, R. A. Beyer, J. Radebaugh, D. H. Atkinson, R. D. Lorenz, S. Le Mouelic, S. Rodriguez, J. Gundlach, F. Giannini, S. Bain, F. M. Flasar, T. Hurford, C. M. Anderson, J. Merrison, M. Adamkovics, S. A. Kattenhorn, J. Mitchell, D. M. Burr, A. Colaprete, E. Schaller, A. J. Friedson, K. S. Edgett, A. Coradini, A. Adriani, K. M. Sayanagi, M. J. Malaska, D. Morabito, K. Reh, (2012), AVIATR-Aerial Vehicle for In-situ and Airborne Titan Reconnaissance A Titan airplane mission concept, Experimental Astronomy 33, 1, 55–127, doi: 10.1007/s10686-011-9275-9.

Beghin, C., O. Randriamboarison, M. Hamelin, E. Karkoschka, C. Sotin, R. C. Whitten, J.-J. Berthelier, R. Grard, F. Simoes, (2012), Analytic theory of Titan's Schumann resonance: Constraints on ionospheric conductivity and buried water ocean, Icarus, 218, 2, 1028–1042, doi: 10.1016/j.icarus.2012.02.005.

Beghin, C., F. Simoes, V. Krasnoselskikh, K. Schwingenschuh, J. J. Berthelier, B. P. Besser, C. Bettanini, R. Grard, M. Hamelin, J. J. Lopez-Moreno, G. J. Molina-Cuberos, T. Tokano, (2007), A Schumann-like resonance on Titan driven by Saturn's magnetosphere possibly revealed by the Huygens Probe, Icarus, 191, 1, 251–266.

Biemann, K., (2006), Astrochemistry: Complex organic matter in Titan's aerosols?, Nature, 444, 7118, 6, doi: 10.1038/nature05417.

Bird, M. K., M. Allison, S. W. Asmar, D. H. Atkinson, I. M. Avruch, R. Dutta-Roy, Y. Dzierma, P. Edenhofer, W. M. Folkner, L. I. Gurvits, D. V. Johnston, D. Plettemeier, S. V. Pogrebenko, R. A. Preston, G. L. Tyler, (2005), The vertical profile of winds on Titan, Nature, 438, 7069, 800–802, doi: 10.1038/nature04060.

Bird, M. K., R. Dutta-Roy, M. Heyl, M. Allison, S. W. Asmar, W. M. Folkner, R. A. Preston, D. H. Atkison, P. Edenhofer, D. Plettemeier, R. Wohlmuth, L. Iess, G. L. Tyler, (2002), The Huygens Doppler wind experiment - Titan winds derived from probe radio frequency measurements, Space Science Reviews, 104, 1, 613–640, doi: 10.1023/A:1023683004351.

Bird, M. K., R. Dutta-Roy, S. W. Asmar, T. A. Rebold, (1997), Detection of Titan's ionosphere from Voyager 1 radio occultation observations, Icarus, 130, 2, 426–436, doi: 10.1006/icar.1997.5831.

Borucki, W. J. and R. C. Whitten, (2008), Influence of high abundances of aerosols on the electrical conductivity of the Titan atmosphere, Planetary and Space Science, 56, 1, 19–26, doi: 10.1016/j.pss.2007.03.013.

Borucki, W. J., Z. Levin, R. C. Whitten, R. G. Keesee, L. A. Capone, A. L. Summers, O. B. Toon, J. Dubach, (1987), Predictions of the electrical conductivity and charging of the aerosols in Titan's atmosphere, Icarus, 72, 3, 604–622.

Brassé, C., A. Buch, P. Coll, F. Raulin, (2017), Low-temperature alkaline pH hydrolysis of oxygen-free Titan tholins: Carbonates' impact, Astrobiology, 17, 1, 8–26, doi: 10.1089/ast.2016.1524.

Cable, M. L., S. M. Hörst, R. Hodyss, P. M. Beauchamp, M. A. Smith, P. A. Willis, (2012) Titan tholins: Simulating Titan organic chemistry in the Cassini-Huygens era, Chemical Reviews, 112, 3, 1882–1909, doi: 10.1021/cr200221x.

Civeit, T., T. Appourchaux, J-P. Lebreton, D. Luz, Courtin R., C. Neiner, O. Witasse, D. Gautier, (2005), On measuring planetary winds using high-resolution spectroscopy in visible wavelengths, Astronomy & Astrophysics, 431, 1157–1166.

Coll, P., D. Coscia, M-C. Gazeau, F. Raulin, (1998), Review and latest results of laboratory investigation of Titan’s aerosols, Origins of Life and Evolution of Biospheres, 28,195–213.

Coustenis, A., S. K. Atreya, T. Balint, R. H. Brown, et al., (2009), TandEM: Titan and Enceladus mission, Experimental Astronomy, 23, 893–946.

Cui, J., R. V. Yelle, K. Volk, (2008), Distribution and escape of molecular hydrogen in Titan's thermosphere and exosphere, Journal of Geophysical Research: Planets, 113, E10, 16, doi: 10.1029/2007je003032.

Elliott, J. O., K. Reh, T. Spilker, (2007), Titan exploration using a radioisotopically-heated montgolfiere balloon, Space Technology and Applications International Forum-STAIF 2007: 11th Conference on Thermophysics Applications in Microgravity; 24th Symposium on Space Nuclear Power and Propulsion; 5th Conference on Human/Robotic Technology and the National Vision for Space Exploration; 5th Symposium on Space Colonization, 4th Symposium on New Frontiers and Future Concepts, (eds.) M. S. El-Genk, Albuquerque, NM, 11–15 February 2007, AIP Conference Proceedings, vol. 880, no. 1, pp. 372–379, doi: 10.1063/1.2437476.

European Space Agency (ESA), (2019a), Science highlights from Huygens: #5. Radioactive decay and cryovolcanism, https://sci.esa.int/web/cassini-huygens/-/55226-science-highlights-from-huygens-5-radioactive-decay-and-cryovolcanism.

European Space Agency (ESA), (2019b), Science highlights from Huygens: #3. Methane mystery, https://sci.esa.int/web/cassini-huygens/-/55224-science-highlights-from-huygens-3-methane-mystery.

European Space Agency (ESA), (2017), Huygens: the top 10 discoveries at Titan, http://sci.esa.int/cassini-huygens/55221-huygens-titan-science-highlights/.

European Space Agency (ESA), (2015), Huygens’ descent to Titan’s surface, Credit: ESA/NASA/JPL/University of Arizona, https://sci.esa.int/web/cassini-huygens/-/39218-huygens-descent-to-titan-surface.

Flasar, F. M., (1998), The dynamic meteorology of Titan, Planetary and Space Science, 46, 9, 1125–1147, doi: 10.1016/S0032-0633(97)00223-7.

Folkner, W. M., S. W. Asmar, J. S. Border, G. W. Franklin, S. G. Finley, J. Gorelik, D. V. Johnston, V. V. Kerzhanovich, S. T. Lowe, R. A. Preston, M. K. Bird, R. Dutta-Roy, M. Allison, D. H. Atkinson, P. Edenhofer, D. Plettemeier, G. L. Tyler, (2006), Winds on Titan from ground-based tracking of the Huygens probe, Journal of Geophysical Research: Planets, 111, 9, doi: 10.1029/2005JE002649.

Fulchignoni, M., F. Ferri, F. Angrilli, A. J. Ball, A. Bar-Nun, M. A. Barucci, C. Bettanini, G. Bianchini, W. Borucki, G. Colombatti, (2005), In situ measurements of the physical characteristics of Titan's environment, Nature, 438, 7069, 785.

Fulchignoni, M., F. Ferri, F. Angrilli, A. Bar-Nun, M. A. Barucci, G. Bianchini, W. Borucki, M. Coradini, A. Coustenis, P. Falkner, E. Flamini, R. Grard, M. Hamelin, A. M. Harri, G. W. Leppelmeier, J. J. Lopez-Moreno, J. A. M. McDonnell, C. P. McKay, F. H. Neubauer, A. Pedersen, G. Picardi, V. Pirronello, R. Rodrigo, K. Schwingenschuh, A. Seiff, H. Svedhem, V. Vanzani, J. Zarnecki, (2002), The characterization of Titan's atmospheric physical properties by the Huygens Atmospheric Structure Instrument (HASI), Space Science Reviews, 104, 1, 395–431, doi: 10.1023/A:1023688607077.

Grard, R., M. Hamelin, J. J. Lopez-Moreno, K. Schwingenschuh, I. Jernej, G. J. Molina-Cuberos, F. Simões, R. Trautner, P. Falkner, F. Ferri, M. Fulchignoni, R. Rodrigo, Svedhem H., C. Béghin, J-J. Bertherlier, V. J. G. Brown, M. Chabassiere, J. M. Jeronimo, L. M. Lara, T. Tokano, (2006), Electric properties and related physical characteristics of the atmosphere of Titan, Planetary and Space Science, 54, 1124–1136.

Grard, R., H. Svedhem, V. Brown, P. Falkner, and M. Hamelin, (1995), An experimental investigation of atmospheric electricity and lightning activity to be performed during the descent of the Huygens probe onto Titan, Journal of Atmospheric and Terrestrial Physics, 57, 5, 575–585, doi: 10.1016/0021-9169(94)00082-y.

Griffith, C. A., P. Penteado, P. Rannou, R. Brown, V. Boudon, K. H. Baines, R. Clark, P. Drossart, B. Buratti, P. Nicholson, C. P. McKay, A. Coustenis, A. Negrao, R. Jaumann, (2006), Evidence for a polar ethane cloud on Titan, Science, 313, 5793, 1620–1622, doi: 10.1126/science.1128245.

Hamelin, M., C. Beghin, R. Grard, J. J. Lopez-Moreno, K. Schwingenschuh, F. Simoes, R. Trautner, J. J. Berthelier, V. J. G. Brown, M. Chabassiere, P. Falkner, F. Ferri, M. Fulchignoni, I. Jernej, J. M. Jeronimo, G. J. Molina-Cuberos, R. Rodrigo, T. Tokano, (2007), Electron conductivity and density profiles derived from the mutual impedance probe measurements performed during the descent of Huygens through the atmosphere of Titan, Planetary and Space Science, 55, 13, 1964–1977, doi: 10.1016/j.pss.2007.04.008.

Hirtzig, M., A. Coustenis, E. Gendron, P. Drossart, A. Negrão, M. Combes, O. Lai, P. Rannou, S. Lebonnois, D. Luz, (2006), Monitoring atmospheric phenomena on Titan, Astronomy & Astrophysics, 456, 2, 761–774.

Hourdin, F., O. Talagrand, R. Sadourny, R. Courtin, D. Gautier, C. P, Mckay, (1995), Numerical simulation of the general circulation of the atmosphere of Titan, Icarus, 117, 2, 358–374.

Imanaka, H., B. N. Khare, J. E. Elsila, E. L. O. Bakes, C. P. McKay, D. P. Cruikshank, S. Sugita, T. Matsui, and R. N. Zare, (2004), Laboratory experiments of Titan tholin formed in cold plasma at various pressures: implications for nitrogen-containing polycyclic aromatic compounds in Titan haze, Icarus, 168, 2, 344–366.

Israël, G., C. Szopa, F. Raulin, M. Cabane, H. B. Niemann, S. K. Atreya, S. J. Bauer, J. F. Brun, E. Chassefière, P. Coll, E. Condé, D. Coscia, A. Hauchecorne, P. Millian, M. J. Nguyen, T. Owen, W. Riedler, R. E. Samuelson, J. M. Siguier, M. Steller, R. Sternberg, C. Vidal-Madjar, (2006), Complex organic matter in Titan's aerosols?, (Reply), Nature, 444, E6, doi: 10.1038/nature05418.

Israël, G., C. Szopa, F. Raulin, M. Cabane, H. B. Niemann, S. K. Atreya, S. J. Bauer, J. F. Brun, E. Chassefiere, P. Coll, E. Conde, D. Coscia, A. Hauchecorne, P. Millian, M. J. Nguyen, T. Owen, W. Riedler, R. E. Samuelson, J. M. Siguier, M. Steller, R. Sternberg, C. Vidal-Madjar, (2005), Complex organic matter in Titan's atmospheric aerosols from in situ pyrolysis and analysis, Nature, 438, 7069, 796–799, doi: 10.1038/nature04349.

Israël, G., M. Cabane, J. F. Brun, H. Niemann, S. Way, W. Riedler, M. Steller, F. Raulin, D. Coscia, (2002), Huygens probe aerosol collector pyrolyser experiment, Space Science Reviews, 104, 1, 433–68, doi: 10.1023/A:1023640723915.

Karkoschka, E., (2016), Titan's meridional wind profile and Huygens' orientation and swing inferred from the geometry of DISR imaging, Icarus, 270, 326–338, doi: 10.1016/j.icarus.2015.06.012.

Karkoschka, E., S. E. Schroder, M. G. Tomasko, H. U. Keller, (2012), The reflectivity spectrum and opposition effect of Titan's surface observed by Huygens' DISR spectrometers, Planetary and Space Science, 60, 1, 342–355, doi: 10.1016/j.pss.2011.10.014.

Karkoschka, E. and M. G. Tomasko, (2009), Rain and dewdrops on titan based on in situ imaging, Icarus, 199, 2, 442–448, doi: 10.1016/j.icarus.2008.09.020.

Karkoschka, E., M. G. Tomasko, L. R. Doose, C. See, E. A. McFarlane, S. E. Schroder, B. Rizk, (2007), DISR imaging and the geometry of the descent of the Huygens probe within Titan's atmosphere, Planetary and Space Science, 55, 13, 1896–1935, doi: 10.1016/j.pss.2007.04.019.

Khare, B. N., C. Sagan, H. Ogino, B. Nagy, C. Er, K. H. Schram, E. T. Arakawa, (1986), Amino acids derived from Titan tholins, Icarus, 68, 1, 176–184.

Kostiuk, T., K. E. Fast, T. A. Livengood, T. Hewagama, J. J. Goldstein, F. Espenak, D. Buhl, (2001), Direct measurement of winds on Titan, Geophysical Research Letters, 28, 12, 2361–2364, doi: 10.1029/2000GL012617.

Leary, J., C. Jones, R. Lorenz, R. D. Strain, J. H. Waite, (2007), Titan explorer NASA flagship mission study, Johns Hopkins University Applied Physics Laboratory, Laurel, MD.

Lebreton, J.-P., A. Coustenis, J. Lunine, F. Raulin, T. Owen, D. Strobel, (2009), Results from the Huygens probe on Titan, Astronomy & Astrophysics Review, 17, 2, 149–179, doi: 10.1007/s00159-009-0021-5.

Lebreton, J.-P., O. Witasse, C. Sollazzo, T. Blancquaert, P. Couzin, A.-M. Schipper, J. B. Jones, D. L. Matson, L. I. Gurvits, D. H. Atkinson, B. Kazeminejad, M. Perez-Ayucar, (2005), An

overview of the descent and landing of the Huygens probe on Titan, Nature, 438, 7069, 758–764. doi: 10.1038/nature04347.

Lellouch, E., A. Coustenis, D. Gautier, F. Raulin, N. Dubouloz, C. Frere, (1989), Titan's atmosphere and hypothesized ocean: A reanalysis of the Voyager 1 radio-occultation and IRIS 7.7-μm data, Icarus, 79, 2, 328–349.

Lorenz, R. D., E. P. Turtle, J. W. Barnes, M. G. Trainer, D. S. Adams, K. E. Hibbard, C. Z. Sheldon, K. Zacny, P. N. Peplowski, D. J. Lawrence, M. A. Ravine, T. G. McGee, K. S. Sotzen, S. M. MacKenzie, J. W. Langelaan, S. Schmitz, L. S. Wolfarth, P. Bedini, (2018), Dragonfly : A rotorcraft lander concept for scientific exploration at Titan, Johns Hopkins Applied Physics Laboratory Technical Digest, 34, 3, 374–387.

Lorenz, R., (2018), Personal communication.

Lorenz, R. D., E. P. Turtle, J. W. Barnes, M. G. Trainer, D. S. Adams, K. E. Hibbard, C. Z. Sheldon, et al., (2017), Dragonfly: a Rotorcraft Lander Concept for scientific exploration at Titan, Johns Hopkins Applied Physics Laboratory Technical Digest.

Lorenz, R. D., (2017), Wind shear and turbulence on Titan: Huygens analysis, Icarus, 295,119–124, doi: 10.1016/j.icarus.2017.06.010.

Lorenz, R. D., H. Svedhem, R. Trautner, W. Kofman, A. Herique, D. Plettemeier, J. P. Lebreton, O. Witasse, P. Falkner, N. Floury, F. Ferri, (2016), Observations of the surface of Titan by the radar altimeters on the Huygens probe, Icarus, 270, 248–259, doi: 10.1016/j.icarus.2015.11.007.

Lorenz, R. D. and J. L. Mann, (2015), Seakeeping on Ligeia Mare: Dynamic response of a floating capsule to waves on the hydrocarbon seas of Saturn's moon titan, Johns Hopkins Applied Physics Laboratory Technical Digest, 33, 2, 82–94.

Lorenz, R. D., M. R. Leese, B. Hathi, J. C. Zarnecki, A. Hagermann, P. Rosenberg, M. C. Towner, J. Garry, H. Svedhem, (2014a), Silence on Shangri-La: Attenuation of Huygens acoustic signals suggests surface volatiles, Planetary and Space Science, 90, 72–80, doi: 10.1016/j.pss.2013.11.003.

Lorenz, R. D., L. A. Young, F. Ferri, (2014b), Gravity waves in Titan's lower stratosphere from Huygens probe in situ temperature measurements, Icarus, 227, 49–55, doi: 10.1016/j.icarus.2013.08.025.

Lorenz, R. D., (2009), Titan Mission Studies - a Historical Review, Journal of the British Interplanetary Society, 62, 5, 162–174.

Lorenz, R. D., B. W. Stiles, R. L. Kirk, M. D. Allison, P. P. del Marmo, L. Iess, J. I. Lunine, S. J. Ostro, S. Hensley, (2008), Titan's rotation reveals an internal ocean and changing zonal winds, Science, 319, 5870, 1649–1651.

Lorenz, R. D., (2008), A review of balloon concepts for Titan, Journal of the British Interplanetary Society, 61, 1, 2.

Lorenz, R. D., H. B. Niemann, D. N. Harpold, S. H. Way, J. C. Zarnecki, (2006), Titan's damp ground: constraints on Titan surface thermal properties from the temperature evolution of the Huygens GCMS inlet, Meteoritics & Planetary Science, 41, 11, 1705–1714.

Lorenz, R. D., (2000), Post-Cassini exploration of Titan: Science rationale and mission concepts, Journal of the British Interplanetary Society, 53, 7–8, 218–234.

Lunine, J. I., C. Elachi, S. D. Wall, M. A. Janssen, M. D. Allison, Y. Anderson, R. Boehmer, et al., (2008), Titan's diverse landscapes as evidenced by Cassini RADAR's third and fourth looks at Titan, Icarus, 195, 1, 415–433.

McKay, C. P., A. Coustenis, R. E. Samuelson, M. T. Lemmon, R. D. Lorenz, M. Cabane, P. Rannou, P. Drossart, (2001), Physical properties of the organic aerosols and clouds on Titan, Planetary and Space Science, 49, 1, 79–99.

Molina-Cuberos, G. J., J. J. López-Moreno, R. Rodrigo, L. M. Lara, (1999a), Chemistry of the galactic cosmic ray induced ionosphere of Titan, Journal of Geophysical Research: Planets, 104, E9, 21997–22024.

Molina-Cuberos, G. J., J. J. López-Moreno, R. Rodrigo, L. M. Lara, and K. O'Brien, (1999b), Ionization by cosmic rays of the atmosphere of Titan, Planetary and Space Science, 47, 10–11, 1347–1354.

Nguyen, M.-J., F. Raulin, P. Coll, S. Derenne, C. Szopa, G. Cernogora, G. Israël, and J. M. Bernard, (2007), Carbon isotopic enrichment in Titan's tholins? Implications for Titan's aerosols, Planetary and Space Science, 55, 13, 2010–2014, doi: 10.1016/j.pss.2007.04.010.

Nguyen, M.-J., (2007), New contraints on the physical and chemical nature of Titan's aerosols (data analysis from the Cassini-Huygens mission and experimental simulations in laboratory), Ph.D. Thesis, Université Paris-Est-Créteil-Val-de-Marne, 12 December 2017.

Niemann, H. B., S. K. Atreya, J. E. Demick, D. Gautier, J. A. Haberman, D. N. Harpold, W. T. Kasprzak, J. I. Lunine, T. C. Owen, F. Raulin, (2010), Composition of Titan's lower atmosphere and simple surface volatiles as measured by the Cassini-Huygens probe gas chromatograph mass spectrometer experiment, Journal of Geophysical Research: Planets, 115, E12006, doi: 10.1029/2010je003659.

Niemann, H. B., S. K. Atreya, S. J. Bauer, G. R. Carignan, J. E. Demick, R. L. Frost, D. Gautier, J. A. Haberman, D. N. Harpold, D. M. Hunten, G. Israël, J. I. Lunine, W. T. Kasprzak, T. C. Owen, M. Paulkovich, F. Raulin, E. Raaen, S. H. Way, (2005), The abundances of constituents of Titan's atmosphere from the GCMS instrument on the Huygens probe, Nature, 438, 7069, 779–784, doi: 10.1038/nature04122.

Niemann, H. B., S. K. Atreya, S. J. Bauer, K. Biemann, B. Block, G. R. Carignan, T. M. Donahue, R. L. Frost, D. Gautier, J. A. Haberman, D. Harpold, D. M. Hunten, G. Israël, J. I. Lunine, K. Mauersberger, T. C. Owen, F. Raulin, J. E. Richards, S. H. Way, (2002), The gas chromatograph mass spectrometer for the Huygens probe, Space Science Reviews, 104, 1, 553–591, doi: 10.1023/A:1023680305259.

Porco, C. C., E. Baker, J. Barbara, K. Beurle, A. Brahic, J. A. Burns, S. Charnoz, N. Cooper, D. D. Dawson, A. D. Del Genio, T. Denk, L. Dones, U. Dyudina, M. W. Evans, et al., (2005), Imaging of Titan from the Cassini spacecraft, Nature, 434, 7030, 159–68. doi: 10.1038/nature03436.

Raulin, F., C. Brassé, O. Poch, P. Coll, (2012), Prebiotic-like chemistry on Titan, Chemical Society Reviews, 41, no. 16, 5380–5393.

Raulin, F., M. C. Gazeau, J. P. Lebreton, (2007a), A new image of Titan. Titan as seen from Huygens, Planetary and Space Science, 55, 13, 1843–1844, doi: 10.1016/j.pss.2007.04.003.

Raulin, F., M. J. Nguyen, P. Coll, (2007b), Titan: an astrobiological laboratory in the solar system, In Instruments, Methods, and Missions for Astrobiology X, International Society for Optics and Photonics, Optical Engineering + Applications 2007, San Diego, CA, vol. 6694, pp. 66940L, doi: 10.1117/12.732883.

Sagan, C. and B. N. Khare, (1979), Tholins: Organic chemistry of interstellar grains and gas, Nature, 277, 102–107.

Schroder, S. E. and H. U. Keller, (2009), The unusual phase curve of Titan's surface observed by Huygens' Descent Imager/Spectral Radiometer, Planetary and Space Science, 57, 14–15, 1963–1974, doi: 10.1016/j.pss.2009.03.012.

Sicardy, B., F. Colas, T. Widemann, A. Fienga, S. Lacour, J. Lecacheux, E. Lellouch, S. Pau, S. Renner, F. Roques, (2004), The two stellar occultations of November 14, 2003: revealing Titan's stratosphere at sub-km resolution, Bulletin of the American Astronomical Society, vol. 36, p. 1119.

Simoes, F., R. Grard, M. Hamelin, J. J. Lopez-Moreno, K. Schwingenschuh, C. Beghin, J. J. Berthelier, B. Besser, V. J. G. Brown, M. Chabassiere, P. Falkner, F. Ferri, M. Fulchignoni, R. Hofe, I. Jernej, J. M. Jeronimo, G. J. Molina-Cuberos, R. Rodrigo, H. Svedhem, T. Tokano, R. Trautner, (2007), A new numerical model for the simulation of ELF wave propagation and the computation of eigenmodes in the atmosphere of Titan: Did Huygens observe any Schumann resonance?, Planetary and Space Science, 55, 13, 1978–1989, doi: 10.1016/j.pss.2007.04.016.

Soderblom, L. A., M. G. Tomasko, B. A. Archinal, T. L. Becker, M. W. Bushroe, D. A. Cook, L. R. Doose, D. M. Galuszka, T. M. Hare, E. Howington-Kraus, E. Karkoschka, R. L. Kirk, J. I. Lunine, E. A. McFarlane, B. L. Redding, B. Rizk, M. R. Rosiek, C. See, P. H. Smith, (2007), Topography and geomorphology of the Huygens landing site on Titan, Planetary and Space Science, 55, 13, 2015–2024, doi: 10.1016/j.pss.2007.04.015.

Stofan, E., R. Lorenz, J. Lunine, E. B. Bierhaus, B. Clark, P. R. Mahaffy, M. Ravine, (2013), TiME-the titan mare explorer, 2013 IEEE Aerospace Conference, AERO 2013, 2–9 March 2013, Big Sky, MT.

Strobel, D. F., (2008), Titan's hydrodynamically escaping atmosphere, Icarus, 193, 2, 588–594.

Strobel, D. F. and B. Sicardy, (1997), Gravity wave and wind shear models, In Huygens: Science, Payload and Mission, Noordwijk, The Netherlands: ESTEC.

Tobie, G., J. I. Lunine, C. Sotin, (2006), Episodic outgassing as the origin of atmospheric methane on Titan, Nature, 440, 7080, 61–64, doi: 10.1038/nature04497.

Tokano, T., (2007), Near-surface winds at the Huygens site on Titan: Interpretation by means of a general circulation model, Planetary and Space Science, 55, 13, 1990–2009, doi: 10.1016/j.pss.2007.04.011.

Tokano, T. and F. M. Neubauer, (2002), Tidal winds on Titan caused by Saturn, Icarus, 158, 2, 499–515, doi: 10.1006/icar.2002.6883.

Tomasko, M. G., L. Doose, S. Engel, L. E. Dafoe, R. West, M. Lemmon, E. Karkoschka, C. See, (2008), A model of Titan's aerosols based on measurements made inside the atmosphere, Planetary and Space Science, 56, 5, 669–707, doi: 10.1016/j.pss.2007.11.019.

Tomasko, M. G., B. Archinal, T. Becker, B. Bézard, M. Bushroe, M. Combes, D. Cook, A. Coustenis, C. de Bergh, L. E. Dafoe, L. Doose, S. Douté, A. Eibl, S. Engel, F. Gliem, B. Grieger, K. Holso, E. Howington-Kraus, E. Karkoschka, H. U. Keller, R. Kirk, et al., (2005), Rain, winds and haze during the Huygens probe's descent to Titan's surface, Nature, 438, 765, doi: 10.1038/nature04126.

Tomasko, M. G., D. Buchhauser, M. Bushroe, L. E. Dafoe, L. R. Doose, A. Eibl, C. Fellows, E. M. Farlane, G. M. Prout, M. J. Pringle, B. Rizk, C. See, P. H. Smith, K. Tsetsenekos, (2002), The Descent Imager/Spectral Radiometer (DISR) experiment on the Huygens entry probe of Titan, Space Science Reviews, 104, 1, 469–551, doi: 10.1023/a:1023632422098.

Vervack Jr., R. J., B. R. Sandel, D. F. Stobel, (2004), New perspectives on Titan's upper atmosphere from a reanalysis of the Voyager 1 UVS solar occultations, Icarus, 170, 1, 91–112, doi: 10.1016/j.icarus.2004.03.005.

Vinatier, S., B. Bezard, C. A. Nixon, (2007), The Titan $^{14}N/^{15}N$ and $^{12}C/^{13}C$ isotopic ratios in HCN from Cassini/CIRS, Icarus, 191, 2, 712–721, doi: 10.1016/j.icarus.2007.06.001.

Walterscheid, R. L. and G. Schubert, (2006), A tidal explanation for the Titan haze layers, Icarus, 183, 2, 471–478.

Whitten, R. C., W. J. Borucki, and S. Tripathi, (2007), Predictions of the electrical conductivity and charging of the aerosols in Titan's nighttime atmosphere, Journal of Geophysical Research: Planets, 112, no. E4.

Yelle, R. V., J. Cui, I. C. F. Mueller-Wodarg, (2008), Methane escape from Titan's atmosphere, Journal of Geophysical Research: Planets, 113, E10, E10003, doi: 10.1029/2007je003031.

Yelle, R. V., D. F. Strobel, E. Lellouch, D. Gautier, (1997), Engineering models for Titan's atmosphere, Huygens: Science, Payload and Mission, pp. 243–256.

Zarnecki, J. C., M. R. Leese, B. Hathi, A. J. Ball, A.Hagermann, M. C. Towner, R. D. Lorenz, et al., (2005), A soft solid surface on Titan as revealed by the Huygens surface science package, Nature, 438, no. 7069, 792, doi: 10.1038/nature04211.

Zarnecki, J. C., (2005), First results from the Huygens surface science package, 36th Annual Lunar and Planetary Science Conference, 14–18 March 2005, in League City, TX, abstract 1295.

Zarnecki, J. C., M. R. Leese, J. R. C. Garry, N. Ghafoor, B. Hathi, (2002), Huygens' surface science package, Space Science Reviews, 104, 1, 593–611, doi: 10.1023/A:1023628321189.

Additional Key Huygens References and Papers (not listed above)

Huygens Space Science Reviews, 2002

Lebreton, J. P. and D. L. Matson, (2002), The Huygens Probe: Science, Payload And Mission Overview, Space Science Review, 104, 59–100.

Lunine, J. I. and L. A. Soderblom, (2002), Cassini-Huygens Investigations of Satellite Surfaces and Interiors, Space Science Review, 118, 191–208.

Owen, T. and D. Gautier, (2002), Touring the Saturnian System: The Atmospheres of Titan and Saturn, Space Science Review, 104, 347–376.

Raulin, F. and T. Owen, (2002), Organic Chemistry and Exobiology on Titan, Space Science Review, 104, 377–394.

Nature, 2005

Owen, T., (2005), Huygens rediscovers Titan, Nature, vol. 438, p. 756.

Planetary and Space Sciences, 2007

Dzierma, Y., M. K. Bird, R. Dutta-Roy, Miguel Pérez-Ayúcar, D. Plettemeier, P. Edenhofer, (2007), Huygens probe descent dynamics inferred from Channel B signal level measurements, Planetary and Space Science, 55, 1886–1895.

Lorenz, R. D., (2007), Titan atmosphere profiles from Huygens engineering (temperature and acceleration) sensors, Planetary and Space Science, 55, 1949–1958.

Lorenz, R. D., J. C. Zarnecki, M. C. Towner, M. R. Leese, A. J. Ball, B. Hathi, A. Hagermann, N. A. L. Ghafoor, (2007), Descent motions of the Huygens probe as measured by the Surface Science Package (SSP): Turbulent evidence for a cloud layer, Planetary and Space Science, 55, 1936–1948.

Withers, P., (2007), A technique to determine the mean molecular mass of a planetary atmosphere using pressure and temperature measurements made by an entry probe: Demonstration using Huygens data, Planetary and Space Science, 55, 1959–1963.

Journal of Geophysical Research, 2006

Perez-Ayucar, M., R. D. Lorenz, N. Floury, R. Prieto-Cerdeira, J-P. Lebreton, (2006), Bistatic observations of Titan's surface with the Huygens probe radio signal, Journal of Geophysical Research, vol. 111, E07001, doi:10.1029/2005JE002613.

Additional Lebreton Astronomy-Astrophysics 2009 References (not listed above)

Atreya, S. K., T. M. Donahue, W. R. Kuhn, (1978), Evolution of a nitrogen atmosphere on Titan, Science, 201, 611–613.

Bar-Nun, A., I. Kleinfeld, E. Kochavi, (1988), Trapping of gas mixtures by amorphous water ice, Physical Review B, 38, 7749–7754.

Bézard, B., C. Nixon, I. Kleiner, D. Jennings, (2007), Detection of 13CH3 D on Titan, Icarus, 191, 397–400.

Bockelée-Morvan, D., D. Gautier, D. C. Lis, K. Young, J. Keene, T. Phillips, T. Owen, J. Crovisier, P. F. Goldsmith, E. A. Bergin, D. Despois, (1998), Deuterated water in comet C/1996 B2 (Hyakutake) and its implications for the origin of comets, Icarus, 133, 147–162.

Cochran, A. L., E. Jehin, J. Manfroid, D. Hutsemékers, C. Arpigny, J.-M. Zucconi, R. Schulz, (2006), Nitrogen isotope ratios in comets, In Precision spectroscopy of astrophysics, (eds.) N. C. Santos, L. Pasquini, A. C. M. Correia, M. Romaniello, Springer, Berlin, Heidelberg, European Southern Observatory (ESO) Astrophysics Symposia, pp. 263–265, doi: 10.1007/978-3-540-75485-5_58.

Cochran, A., (2002), A search for N_2^+ in spectra of comet C/2002 C1 (Ikeya–Zhang), The Astrophysical Journal Letters, 576, L165–L168.

Courtin, R., C. K. Kim, S. J. Kim, D. Gautier, (2007), The tropospheric abundance of H_2 on Titan from the Cassini CIRS Investigation, Bulletin of the American Astronomical Society, vol. 39, p. 529.

Coustenis, A., J. I. Lunine, J.-P. Lebreton, D. Matson, K. Reh, P. Beauchamp, Edr Ch, TSSM team, (2008), TSSM: the in situ exploration, Europlanet Planetary Science Congress, Münster, Germany, 22–26 Sept 2008.

Coustenis, A., R. Achterberg, B. Conrath, D. Jennings, A. Marten, et al., (2007), The composition of Titan's stratosphere from Cassini/CIRS mid-infrared spectra, Icarus, 189, 35–62.

Crovisier, J., (1998), Physics and chemistry of comets: recent results from comets Hyakutake and Hale–Bopp. Answers to old questions and new enigmas, In Chemistry and physics of molecules and grains in space, Faraday Discussions, vol. 109, Royal Society of Chemistry, London pp. 437–452.

Fulchignoni M., F. Ferri, F. Angrilli, et al., (2005), Titan's physical characteristics measured by the Huygens Atmospheric Structure Instrument (HASI), Nature, 438, 785–791, doi: 10.1038/nature04314.

Gautier, D., F. Hersant, (2005), Formation and composition of planetesimals, Space Science Review, 116, 25–52, doi: 10. 1007/s11214-005-1946-2.

Gautier, D., F. Hersant, O. Mousis, J. I. Lunine, (2001), Enrichments in volatiles in Jupiter: a newinterpretation of the Galileo measurements, The Astrophysical Journal Letters, 550, L227–L230.

Gautier, D., F. Hersant, O. Mousis, J. I. Lunine, (2001), Erratum: Enrichments in volatiles in Jupiter: a new interpretation of the Galileo measurements, The Astrophysical Journal, 559, L183–L183.

Geiss, J., (1988), Composition in Halley's Comet: clues to origin and history of cometary matter, Reviews of Modern Physics, 1, 1–27.

Grevesse, N., M. Asplund, J. Sauval, (2005), The new solar chemical composition, In Element stratification in stars: 40 years of atomic diffusion, (eds.) G. Alecian, O. Richard, S. Vauclair, European Astronomical Society (EAS) Publications Series, 17, pp. 21–30.

Hersant, F., D. Gautier, G. Tobie, J. I. Lunine, (2008), An interpretation of the carbon abundance in Saturn measured by Cassini, Planetary and Space Science, 56, 1103–1111.

Hourdin, F., O. Talagrand, R. Sadourny, R. Courtin, D. Gautier, C. P. Mckay, (1995), Numerical simulation of the general circulation of the atmosphere of Titan, Icarus, 117, 358–374.

Israël, G., C. Szopa, F. Raulin, M. Cabane, H. B. Niemann, S. K. Atreya, S. J. Bauer, (2005), Evidence for the presence of complex organic matter in Titan's aerosols by in situ analysis, Nature 438, 796–799.

Israël, G., M. Cabane, J. F. Brun, H. Niemann, et al., (2002), The Cassini–Huygens ACP experiment and exobiological implications, Space Science Review, 104, 435–466.

Lunine, J. I., Y. L. Yung, R. D. Lorenz, (1999), On the volatile inventory of Titan from isotopic abundances in nitrogen and methane, Planetary and Space Science, 47, 1291–1301.

Marty, B., T. Guillot, A. Coustenis, et al., (2008), KRONOS: exploring the depths of Saturn with probes and remote sensing through an international mission, Experimental Astronomy, 23, 947–976, doi:10.1007/s10686-008-9084-9.

Meibom, A., A. N. Krot, F. Robert, S. Mostefaoui, S. S. Russell, M .I. Petaev, M. Gounelle, (2007), Nitrogen and carbon isotopic composition of the Sun inferred from a high-temperature solar nebular condensate, The Astrophysical Journal, 656, L33–L36.

Meier, R. and T. C. Owen, (1999), Cometary deuterium, Space Science Review, 90, 33–43, doi: 10.1023/A:1005269208310

Meier, R., T. C. Owen, D. C. Jewitt, H. E. Matthews, M. Senay, N. Biver, D. Bockelée-Morvan, J. Crovisier, D. Gautier, (1998), Deuterium in comet C/1995 O1 (Hale-Bopp): detection of DCN, Science, 279, 1707– 1710.

Niemann, H. B. et al., (2008), Personal communication.

Owen, T., (2005), Preliminary results from Huygens GCMS, Physics-Uspekhi (Advances in Physical Sciences), 635, 6–38.

Owen, T., P. R. Mahaffy, H. B. Niemann, S. Atreya, M. Wong, (2001), Protosolar nitrogen, The Astrophysical Journal, 553, L77–L79.

Owen, T. and A. Bar-Nun, (2000), Volatile contributions from icy planetesimals, In Origin of the Earth and Moon (eds.) R. M. Canup, K. Righter, University of Arizona Press, pp. 459–475.

Owen, T. and A. Bar-Nun, (1995), Comets, impacts and atmospheres, Icarus, 116, 215–226.

Pollack, J. and P. Bodenheimer, (1989), Theories of the origin and evolution of the giant planets, In Origin and evolution of planetary and satellite atmospheres, (eds.) S. K. Atreya, J. B. Pollack, M. S. Matthews, University of Arizona Press, pp. 564–602.

Strobel, D. F., (1982), Chemistry and evolution of Titan's atmosphere, Planetary and Space Science, 30, 839–848.

Tobie, G., O. Èadek, C. Sotin, (2008), Solid tidal friction above a liquid water reservoir as the origin of the south pole hotspot on Enceladus, Icarus, 196, 642–652.

Tobie, G., O. Grasset, J. I. Lunine, A. Mocquet, C. Sotin, (2005), Titan's internal structure inferred from a coupled thermal–orbital model, Icarus, 175, 496–502.

Van Dishoeck, E. F., G. A. Blake, B. T. Draine, J. I. Lunine, (1993), The chemical evolution of protostellar and protoplanetary matter, In Protostars and planets III, (eds.) L. H. Levy, J. I. Lunine, University of Arizona Press, pp. 163–241.

Waite, H., D. T. Young, T. E. Cravens, A. J. Coates, F. J. Crary, B. Magee, J. Westlake, (2007), The process of tholin formation in Titan's upper atmosphere, Science, 316, 870–875.

Waite Jr., H., H. Niemann, R. V. Yelle, W. T. Kasprzak, et al., (2005), Ion neutral mass spectrometer results from the first flyby of Titan, Science, 308, 982–986.

Yung, Y., M. Allen, J. P. Pinto, (1984), Photochemistry of the atmosphere of Titan - comparison between model and observations, The Astrophysical Journal Supplement Series, 55, 465–506.

Other References

Barnes, J. W., R. H. Brown, L. Soderblom, B. J. Buratti, C. Sotin, et al., (2006), Global-Scale Surface Spectral Variations on Titan Seen from Cassini/VIMS, Icarus, 186, 1, 242–258.

Elachi, C., S. Wall, M. Allison, Y. Anderson, R. Boehmer, et al., (2005), Cassini Radar Views of the Surface of Titan, Science, 308, 970–974.

Harland, D. M., (2003), Mission to Saturn, Praxis-Springer.

Lebreton, J.-P., O. Witasse, C. Sollazzo, T. Bancquaert, P. Couzin, et al., (2005), Huygens descent and landing on Titan: Mission overview and science highlights, Nature, 438, 758–764, (Key scientific results from the experiments onboard Huygens are given in six papers in the subsequent pages of this journal.)

Lorenz, R. D., (2017), Pre-publication draft in Johns Hopkins Applied Physics Laboratory Technical Digest.

Lorenz, R. D. and I. Mitton, (2010), Titan unveiled: Saturn's mysterious moon explored, Princeton University Press.

Lorenz, R. D., (2009), A Review of Titan Mission Studies, Journal of the British Interplanetary Society, 62, 162–174.

Lorenz, R. D., S. Wall, J. Radebaugh, G. Boubin, E. Reffet, et al., (2006), The sand seas of Titan: Cassini RADAR observations of longitudinal dunes, Science, 312, 724–727.

Lorenz, R. D. and J. Mitton, (2002), Lifting Titan's veil, Cambridge University Press.

Sotin, C., R. Jaumann, B. J. Buratti, R. H. Brown, R. N. Clark, et al., (2005), Release of volatiles from a possible cryovolcano from near-infrared imaging of Titan, Nature, 435, 786–789.

Stofan, E. F., C. Elachi, J. I. Lunine, R. D. Lorenz, B. Stiles, et al., (2007), The lakes of Titan, Nature, 445, 61–64.

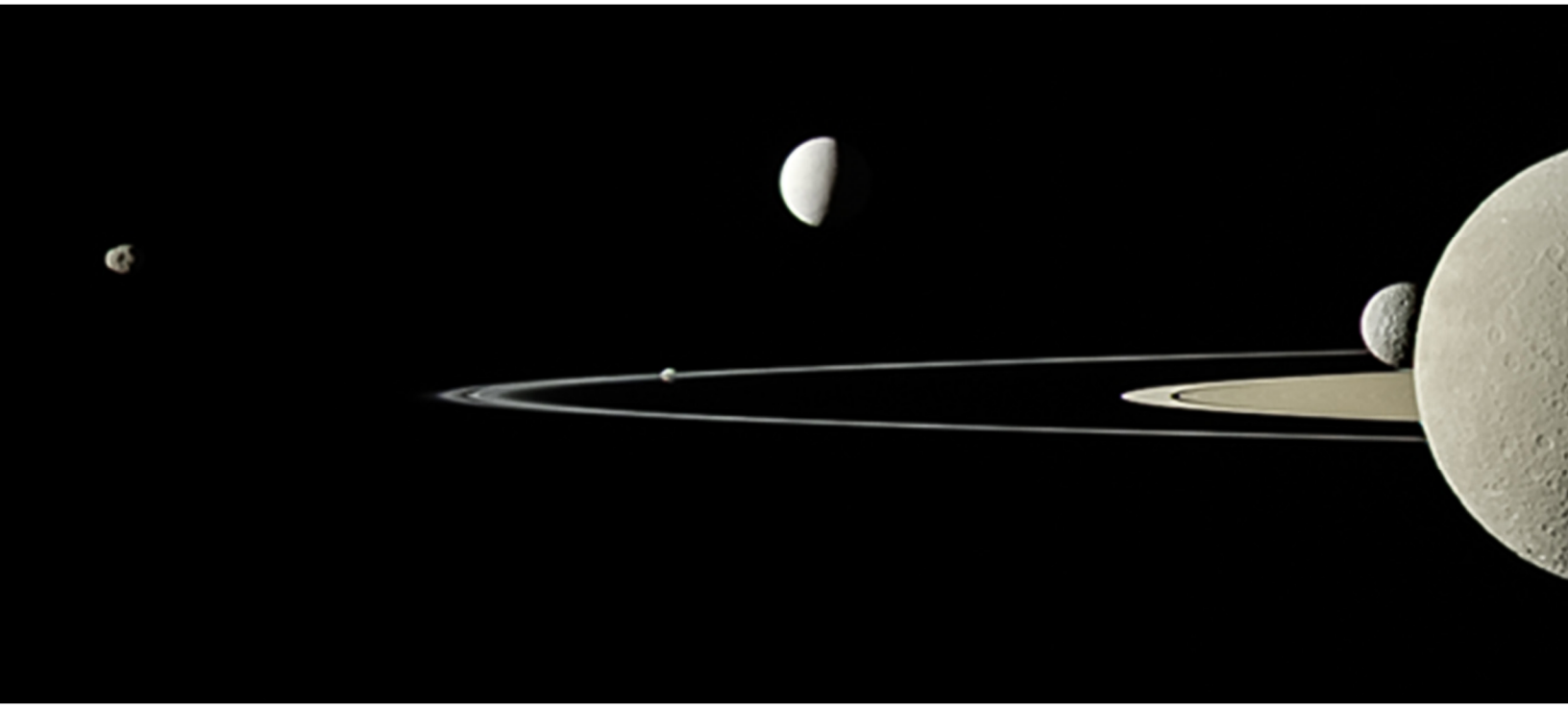

ICY SATELLITES

The Voyager and Pioneer flybys of the 1970s and 1980s provided incomplete views of Saturn's moons. However, during its many years in Saturn orbit, Cassini discovered previously unknown moons, solved mysteries about known ones, studied their interactions with the rings and revealed how sharply different the moons are from one another. Saturn's moons range in size from about a third of a kilometer in size to larger than the planet Mercury, and they vary in color, texture and composition, and internal structure. Cassini data has also hinted at a possibly young age for several of the innermost icy moons.

For decades, scientists did not know why Enceladus was the brightest world in the solar system, or how it related to Saturn's E-ring. Cassini found that both the fresh coating on its surface, and icy material in the E-ring originate from vents connected to a global subsurface saltwater ocean that might host hydrothermal vents and complex organics.

The **Icy Satellites** Working Group (ISWG) working with the Satellites Orbiter Science Team (SOST) coordinated and implemented the icy satellite observation planning and detailed scheduling for the many icy satellite flybys throughout the mission, including 23 close Enceladus flybys, to ensure that Cassini icy satellite objectives were met. The ISWG Discipline Working Group (DWG) has achieved their Cassini mission objectives and has provided the first extended, comprehensive view of the moons of Saturn.

CONTENTS

Figures

Tables

Executive Summary

The Cassini-Huygens mission offered the first extended, comprehensive view of the moons of Saturn. There are existing and upcoming review books and papers that summarize the results from the Cassini mission; as is the case with so many previous missions, major questions remain even after more than a dozen years of exploration [Buratti et al. 2017]. The questions appropriate to the icy satellite discipline that were proposed at the onset of the mission were far-reaching science goals that provided the driving force behind the mission are listed in the section entitled Key Objectives for Icy Satellites DWG, and summarized in Spilker [1997]. As the section entitled Icy Satellites Science Assessment shows, most mission objectives were fully met with only two (not including two objectives associated with asteroid science) partially met. The asteroid flyby investigations were lacking because the spacecraft trajectory did not bring Cassini sufficiently close to an object in the Main Belt.

> … far-reaching science goals provided the driving force behind the mission …

Key Objectives for Icy Satellites DWG

Icy Satellites AO Objectives

- **Icy Satellite Geology and History (I_AO1)** – Determine the general characteristics and geological histories of the satellites.
- **Icy Satellite Surface and Crustal Modifications (I_AO2)** – Define the mechanisms of crustal and surface modifications, both external and internal.
- **Icy Satellite Surface Composition (I_AO3)** – Investigate the compositions and distributions of surface materials, particularly dark, organic rich materials and low melting point condensed volatiles.
- **Icy Satellite Interior Properties (I_AO4)** – Constrain models of the satellites' bulk compositions and internal structures.
- **Icy Satellite Magnetosphere and Ring Interactions (I_AO5)** – Investigate interactions with the magnetosphere and ring systems and possible gas injections into the magnetosphere.

Icy Satellites CSM Traceability Matrix Objectives

- **Enceladus Seasonal Changes (IC1a)** – Identify long-term secular and seasonal changes at Enceladus through observations of the south polar region, jets, and plumes, and through analysis of heat production.

- **Enceladus Ocean (IN1a)** – Determine the presence of an ocean at Enceladus as inferred from induced magnetic field and plume composition, search for possible anomalies in the internal structure of Enceladus as associated with plume sources, and constrain the mechanisms driving the endogenic activity by in situ observations and remote sensing.
- **Mid-sized Satellites (IN1b)** – Complete the comparative study of Saturn's mid-sized satellites, their geological and cratering histories, and interactions with the Saturn system, with remote sensing of Mimas at the highest resolution possible in order to understand the mechanisms behind its unique thermal properties discovered by Cassini. Understand if other moons exhibit similar thermal properties.
- **Dione (IN1c)** – Determine whether Dione exhibits evidence for low-level activity, now or in recent geological time.
- **Rhea (IN2a)** – Determine whether there is ring material orbiting Rhea, and if so, what its spatial and particle size distribution is. Understand the origin of blue pearls discovered on its surface.
- **Tethys (IN2b)** – Determine whether Tethys contributes to the E-ring and the magnetospheric ion and neutral population. Understand the nature of mysterious red streaks discovered on its surface.
- **Satellite Interiors (IN2c)** – Determine the extent of differentiation and internal inhomogeneity within the icy satellites, especially Rhea and Dione. Determine whether Dione has a subsurface ocean.
- **Small Moons (IN2d)** – Observe selected small satellites to quantify the movement of Enceladus material through the system, the history of satellite collisions/breakup, interaction with ring material as indicated by surface properties/composition, and cratering rates deep in the Saturnian system. Understand the composition of these moons and how it relates to kindred bodies in the Saturnian system and beyond.
- **Hyperion (IN2e)** – Understand the unusual appearance of Hyperion with remote sensing observations of the highest resolution possible.
- **Iapetus (IN2f)** – Use remote sensing of Iapetus to test models for the albedo heterogeneity of the satellite. Quantify the effect of the newly-discovered Phoebe ring on the properties of Iapetus' surface.

Jupiter Flyby AO Objectives

- **Jupiter and Satellite Studies (J_AO1)** – Extend the time for studies of atmospheric dynamics and variable satellite phenomena, specifically Io volcanism, beyond the period accessible to the Galileo nominal mission.

Asteroid Flyby AO Objectives

- **Asteroid Flyby Investigation (A_AO1)** – Investigate an asteroid not seen by previous missions, possibly a new class of asteroid, thereby adding important new information to the study of asteroid
- **Asteroid Global Characteristics (A_AO2)** – Characterize global properties, determine composition and morphology of the surface, investigate properties of the regolith.

Icy Satellites Science Assessment

All these objectives have been answered to a large degree (see Table IcySats-1), and specific results can be expressed by this top twenty list of discoveries:

- Discovery of Enceladus jets, their coincidence with small-scale hot spots, the plume they form, and its impact on the Saturnian system.
- Evidence of hydrothermal chemistry and discovery of a strong thermal anomaly on Enceladus.
- Detection of global oceans beneath Enceladus's, and possibly Dione's and Mimas's icy crusts.
- Plume structure connection to both individual jets and curtains along tiger stripes.
- Plume strength modulation by tidal forces and stochastic on/off timing of individual jets.
- The plume of Enceladus as the source of the E-ring of Saturn.
- Detection of plume composition: water (vapor and micron-sized grains), salt, organics, nanograin dust, hydrogen, and ammonia.
- Discovery of supersonic motion in the jets.
- Evidence for subdued ongoing or recently extinguished activity on Dione.
- Red streaks on Tethys signifying potential outgassing along fractures.
- Accretion disks on the ring moons showing they continue to add particles from the main ring system to their bodies.
- Low densities of the small moons.
- Discovery of a globe-girdling equatorial ridge on Iapetus, perhaps akin to those seen on the ring moons.
- Thermal segregation and Phoebe ring particle infall as the cause of the bright/dark dichotomy on Iapetus, first discovered by the astronomer Cassini in 1677.
- Likely formation of Phoebe in the Kuiper Belt.

- The discovery that the high reflectance and albedo/color patterns of the Saturnian inner moons is primarily due to exchange of material between rings and moons specific to the Saturnian system. This includes the accumulation of E-ring particles and subsequent alteration by high-energy elections to produce Pac-Man.
- Discovery of organics and carbon dioxide (and possibly ammonia) on the outer moons. Evidence for iron oxides and space-weathered silicates on the surfaces of Phoebe and Iapetus.
- Wispy streaks on Dione and Rhea are actually fracture systems.
- Evidence for past rings around moons, such as blue pearls on Rhea, and possibly the ridge of Iapetus.
- Evidence that outer irregular moons are low density and slow rotators based on light curve surveys.

It was known before the Cassini mission that the main constituent of the surfaces of the moons is crystalline water ice. CO_2 is present on the surface of most of the moons [Buratti et al. 2005; Brown et al. 2006; Clark et al. 2012, 2008, 2005; Cruikshank et al. 2010], but there are still spectral identifications that are uncertain. Clark et al. [2012] showed that a weak feature at 2.42 μm is due to trapped molecular hydrogen and is observed in dark material on multiple icy satellites, but this feature needs confirmation by an independent instrument. A weak absorption at 2.97 μm corresponds to ammonia [Clark et al. 2012, 2008] and is seen on multiple icy satellites, but the absorption overlaps an order-sorting filter gap in the VIMS instrument where instrument errors are larger. Observations of ammonia need confirmation either by a better calibration of the VIMS data, or by other instruments.

An up-to-date table of the physical and dynamical properties of all the Saturnian moons is given at https://ssd.jpl.nasa.gov/?sat_elem and at https://ssd.jpl.nasa.gov/?phys_data.

The results of the mission can be summarized by Table IcySats-1. The colors refer to the data gathered and the expected results to be obtained by ongoing analyses. Green means the objective was fully met; yellow means it was partially met by the best estimate; and red means it was not met. Note that this assessment is based on whether sufficient data was collected, not on the status of the ongoing analysis and modeling of the data. The first five goals were set out in the mission Announcement of Opportunity, while subsequent goals in the table followed up in Cassini's extended mission on major discoveries. Text below primarily addresses the achievement of the extended mission goals.

Table IcySats-1. Assessment of Mission Goals.

Fully/Mostly Accomplished: **Partially Accomplished:** **Not Accomplished:**

Icy Satellite Science Objectives	AO and TM Science Objectives	Icy Satellite Science Assessment	Comments
Icy Satellite Geology and History: (I_AO1) – Determine the general characteristics and geological histories of the satellites.	I_AO1		

Table IcySats-1. Assessment of Mission Goals.

Fully/Mostly Accomplished: **Partially Accomplished:** **Not Accomplished:**

Icy Satellite Science Objectives	AO and TM Science Objectives	Icy Satellite Science Assessment	Comments
Icy Satellite Surface and Crustal Modifications (I_AO2) – Define the mechanisms of crustal and surface modifications, both external and internal.	I_AO2		
Icy Satellite Surface Composition (I_AO3) – Investigate the compositions and distributions of surface materials, particularly dark, organic rich materials and low melting point condensed volatiles.	I_AO3		
Icy Satellite Interior Properties (I_AO4) – Constrain models of the satellites' bulk compositions and internal structures.	I_AO4		
Icy Satellite Magnetosphere and Ring Interactions (I_AO5) – Investigate interactions with the magnetosphere and ring systems and possible gas injections into the magnetosphere.	I_AO5		
Enceladus Seasonal Changes (IC1a) – Identify long-term secular and seasonal changes at Enceladus through observations of the south polar region, jets, and plumes.	IC1a		
Enceladus Ocean (IN1a) – Determine the presence of an ocean at Enceladus as inferred from induced magnetic field and plume composition, search for possible anomalies in the internal structure of Enceladus as associated with plume sources, and constrain the mechanisms driving the endogenic activity by in situ observations and remote sensing.	IN1a		
Mid-sized Satellites (IN1b) – Complete the comparative study of Saturn's mid-sized satellites, their geological and cratering histories, and interactions with the Saturn system, with remote sensing of Mimas at the highest resolution possible in order to understand the mechanisms behind its unique thermal properties discovered by Cassini.	IN1b		
Dione (IN1c) – Determine whether Dione exhibits evidence for low-level activity, now or in recent geological time.	IN1c		Extensive data were gathered, but the results are still ambiguous. No current activity was detected.
Rhea (IN2a) – Determine whether there is ring material orbiting Rhea, and if so, what its spatial and particle size distribution is.	IN2a		

Table IcySats-1. Assessment of Mission Goals.

Fully/Mostly Accomplished: **Partially Accomplished:** **Not Accomplished:**

Icy Satellite Science Objectives	AO and TM Science Objectives	Icy Satellite Science Assessment	Comments
Tethys (IN2b) – Determine whether Tethys contributes to the E-ring and the magnetospheric ion and neutral population.	IN2b		From a CDA/icy dust perspective, it is red because during the solstice mission there were no close Tethys flybys to measure potential ejecta [Kempf et al. 2010]. For MAPS as a whole, enough data was obtained to determine that Tethys does not contribute to the E-ring and magnetospheric ion and neutral population [Burch et al. 2007; Khurana et al. 2008].
Satellite Interiors (IN2c) – Determine the extent of differentiation and internal inhomogeneity within the icy satellites, especially Rhea and Dione.	IN2c		
Small Moons (IN2d) – Observe selected small satellites to quantify the movement of Enceladus material through the system, the history of satellite collisions/breakup, interaction with ring material as indicated by surface properties/composition, and cratering rates deep in the Saturnian system.	IN2d		
Hyperion (IN2e) – Understand the unusual appearance of Hyperion with remote sensing observations of the highest resolution possible.	IN2e		
Iapetus (IN2f) – Use remote sensing of Iapetus to test models for the albedo heterogeneity of the satellite. Quantify the effect of the newly-discovered Phoebe ring on the properties of Iapetus' surface.	IN2f		
Jupiter and Satellite Studies (J_AO1) – Extend the time for studies of atmospheric dynamics and variable satellite phenomena, specifically Io volcanism, beyond the period accessible to the Galileo nominal mission.	J_AO1		
Asteroid Flyby Investigation (A_AO1) – Investigate an asteroid not seen by previous missions, possibly a new class of asteroid, thereby adding important new information to the study of asteroid	A_AO1		This objective was present for the case where Cassini would have flown close to an asteroid. No asteroid was found to be nearby.
Asteroid Global Characteristics (A_AO2) – Characterize global properties, determine composition and morphology of the surface, investigate properties of the regolith.	A_AO2		This objective was present for the case where Cassini would have flown close to an asteroid. No asteroid was found to be nearby.

ICY SATELLITES DWG SYSTEM RESULTS

Enceladus Seasonal Changes (IC1a)

Enceladus eruptions are mostly water vapor, with a variable amounts of micron-sized ice grains [Porco et al. 2017, 2006; Hedman et al. 2018]. There are ~100 discrete jets and faint sheets of icy particles fountaining from the four tiger stripe fissures across Enceladus' south polar region [Porco et al. 2014; Spitale et al. 2015; Teolis et al. 2017].

The brightness, and hence mass, of the plume created by the particle jets varies diurnally, most likely due to the cycling of tidal extensional/compressional stresses across the south polar terrain [Hedman et al. 2013; Nimmo et al. 2014]. A phase lag of ~45 deg (or ~4.5 hours), compared to the ice-shell response predicted by simple tidal models for an elastic ice shell, is present though its origin is not clear [Nimmo et al. 2014]. Notable is the observation that the plume never goes to zero strength, as seen in particles [Nimmo et al. 2014] as well as vapor [Hansen et al. 2017]. Individual geysers were observed to be time variable, turning on and/or off on timescales that were not comparable to the diurnal cycling of stresses [Porco et al. 2014; Teolis et al. 2017]. This was taken as an indication that condensation of ice in the vents leads to the stochastic clogging of the vents and consequently the shutoff of geysers, but averaged across the SPT, the plume is continuous in time if variable in strength. The estimated timescale for the clogging process is months to a couple of years [Porco et al. 2014, 2006].

Behounkova et al. [2015], in a 3-D numerical model of the viscoelastic tidal response of the ice shell, showed the diurnal brightness variation is best described by the cycling of the normal stresses across the fractures averaged over the SPT. They proposed that the delay in eruption activity may be a natural consequence of the viscosity structure in the south polar region and the size of the putative subsurface ocean, but there are alternate suggestions [Kite and Rubin 2016].

One hot spot was identified on Enceladus with radar observations [Le Gall et al. 2017]. VIMS data were able to place constraints on the size and temperature of one opening, just 9 m wide [Goguen et al. 2013]. VIMS observations of hot spots [Goguen et al. 2013] were used in conjunction with Imaging Science Subsystem (ISS) observations to show that individual jets are spatially coincident with the small-scale (~10 s meters) hot spots [Porco et al. 2014], a result that indicates the heat emerging from the fractures is largely that due to the latent heat of condensation of vapor in the near-surface portion of the vents, and not due to shear heating, and is consistent with a deep source of the eruptive materials.

An analysis of ISS observations of the plume from 2005–2015 suggested there may be seasonal changes in the plumes' brightness.

An analysis of ISS observations of the plume from 2005–2015 suggested there may be seasonal changes in the plumes' brightness [Ingersoll and Ewald 2017] (Figure ICYSATS-1). However, a later analysis of the full suite of Cassini ISS plume observations through the end of the

mission (August 2017) has shown that the long-timescale variations in the plume's brightness are most likely due to two periods (4-year and 11-year) both associated with the Dione-Enceladus 2:1 orbital resonance that also cause the cycling of tidal stresses across the moon's surface [Porco et al. 2018].

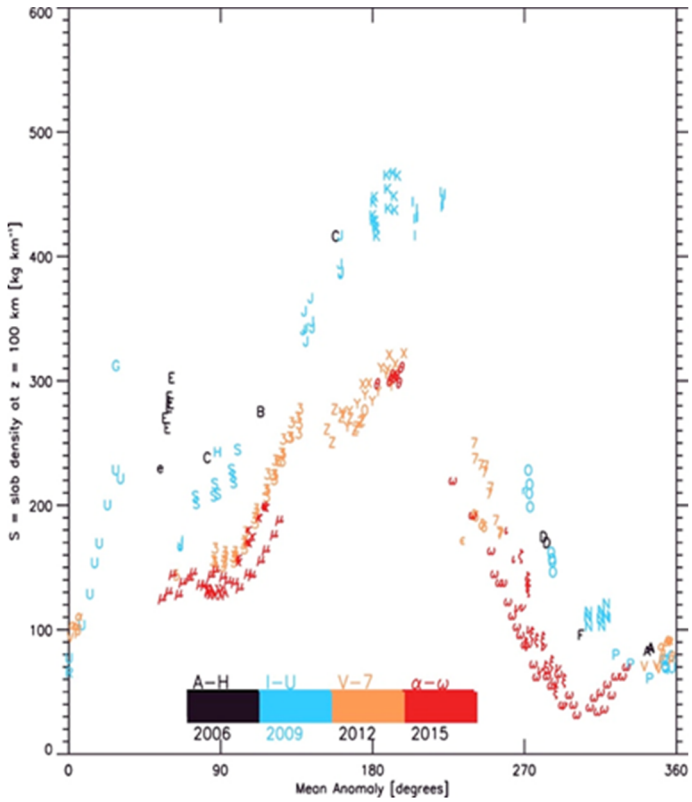

Figure ICYSATS-1. A figure of plume brightness from 2006 through 2015 showing year-to-year changes in the amplitude of the diurnal variations with mean anomaly, including a substantial decrease toward the end of the mission. Figure from Ingersoll and Ewald [2017].

Composite Infrared Spectrometer (CIRS) also carried out a significant investigation on the variability of heat in the tiger stripe region throughout the mission on various time scales, with special focus on this problem at the end of the mission [Howett et al. 2017]. CIRS observations of Enceladus' active south polar region during Cassini's F-ring and Proximal Orbits (FRPO) were designed to investigate whether Enceladus' surface temperatures also vary with time. Preliminary results indicate that Enceladus' surface temperatures vary with mean anomaly, but lag in time behind the plume brightness change. The total heat flux varied by about a factor of two with mean anomaly. A detailed measurement of the heat flux between revs 61 and 91 showed no significant change. Work is continuing in this area, as different analysis techniques give substantially different results for the heat flux (details are in the CIRS Science Results).

A series of Ultraviolet Imaging Spectrograph (UVIS) stellar and solar occulations were spectacularly successful for studying the composition and structure of Enceladus' plume [Hansen et al. 2011, 2008, 2006]. Unlike ISS and CIRS, UVIS detected no significant variations in the

amount of water vapor as seen over the course of the mission, although the strongest jets, which lift the most icy grains, are more variable [Hansen et al. 2017].

Enceladus Ocean (IN1a)

Though the presence of liquid water within the conduits leading to the south polar surface, and then later the proposal that there was liquid water under the ice shell, were suggested early in the mission [Porco et al. 2006; Collins and Goodman 2007; Postberg et al. 2009], the first detection of this long-suspected body of liquid water beneath the moon's crust came from radio science data that showed Enceladus' gravity field combined with topography was consistent with a regional sea beneath Enceladus' south pole, though a global ocean could not be ruled out [Iess et al. 2014]. Subsequent, careful analysis of the rotational motion of Enceladus revealed a libration indicating the ice shell is decoupled from the core and the subsurface liquid ocean is global, as shown in Figure ICYSATS-2 [Thomas et al. 2015]. Figure ICYSATS-2 is a Cassini nugget summarizing our knowledge of the Enceladan Ocean.

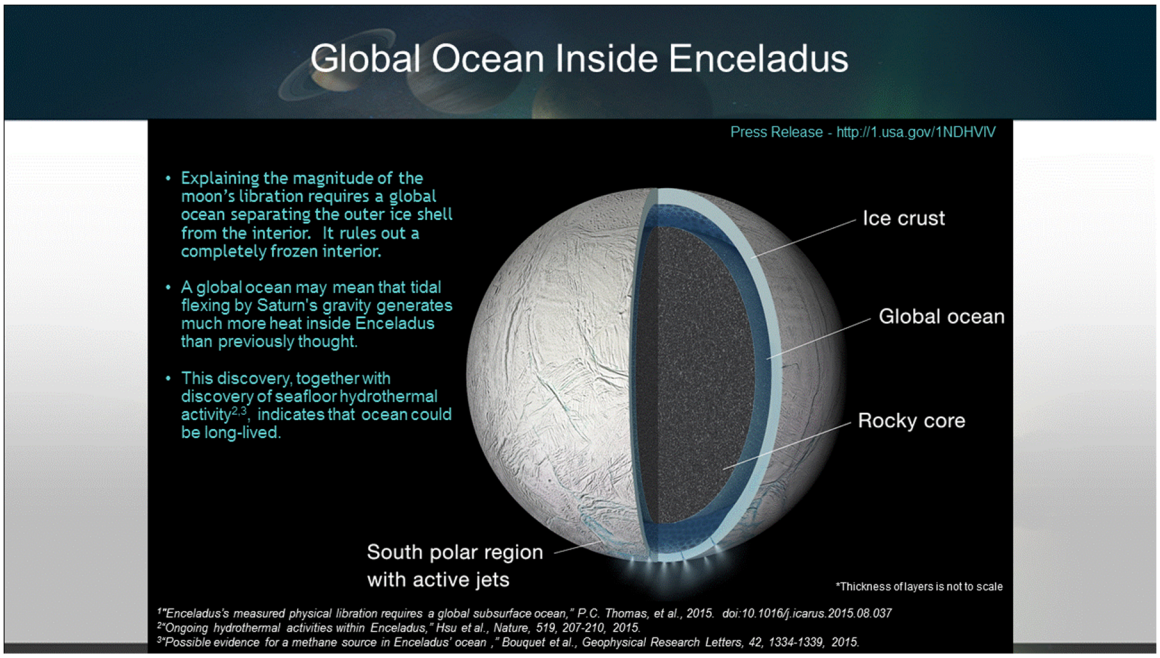

Figure ICYSATS-2. A NASA Nugget summarizing our knowledge of the ocean of Enceladus at the end of the mission.

Cassini's dust analyzer (CDA) determined the particle size and compositional profile for the water ice particles expelled from the tiger stripe fissures [Postberg et al. 2011]. Grain sizes are stratified: the smallest pure-ice particles (< 0.4 micron) condense from gas in the plume, reach escape velocity and go into orbit around Saturn, forming the E-ring. These tiny particles are likely lofted by the supersonic gas jets detected by UVIS [Hansen et al. 2011]. Larger salt-rich particles come from liquid water and may originate as a frozen aerosol spray, which is then carried by the

escaping gas to the surface. These larger grains separate from the gas, fall back to the surface and modify Enceladus' color [Schenk 2014; Postberg et al. 2017].

Observational constraints are necessary to develop models of the nature of the plumbing from the subsurface body of water to the nozzles carrying gas and particles to the surface [Teolis et al. 2017]. Several concepts for the nature of the plumbing that connects the subsurface liquid reservoir to the escaping gas and particles have been proposed. An early idea was a Perrier ocean powered by escaping CO_2: as seawater nears the surface pressure decreases, the dissolved gases come out of solution and bubbles form [Matson et al. 2012]. Another hypothesis is that the gas is accelerated as it goes through nozzle-like channels from the ocean to the surface [Schmidt et al. 2009; Yeoh 2017]. Yet another idea is that water coming up from the ocean separates the solid edges of the fissures and that tidal stresses partially open and close the fissures, keeping the water from freezing [Kite and Rubin 2016].

CDA detected silica nano-particles, confirming that the liquid layer is in contact with the rocky core.

CDA detected silica nano-particles, confirming that the liquid layer is in contact with the rocky core [Hsu et al. 2015]. Very hot water (194° F) is required for these particles to form, suggesting that Enceladus has hydrothermal vents on its seafloor. Furthermore, the abundance of methane gas in the plume can only happen if there are hydrothermal vents preventing the methane from being captured in the icy walls confining the ocean [Bouquet et al. 2015].

What is the pH of Enceladus' ocean? Values reported range from 8 [Hsu et al. 2015] to 12 [Glein et al. 2015], however the most likely range is 9–11 [Waite et al. 2017].

Another important result is provided by the Ion and Neutral Mass Spectrometer (INMS) detection of H_2. The process that likely provides the H_2, serpentinization of rock, could provide the chemical energy required for life [Waite et al. 2017]. Cassini's investigations have shown that Enceladus' ocean is a habitable environment.

Mid-sized Satellites (IN1b)

The mid-sized bodies of Saturn proved to be a collection of unique bodies, ranging from Phoebe, a heavily cratered, relatively dense moon that is probably a captured Kuiper Belt object (KBO) [Johnson and Lunine 2005a] to less dense moons that may have some type of ongoing activity. The optical properties of the surfaces of these moons are largely determined by interactions with rings and high-energy particles. Accurate values for fundamental whole-body physical properties of the moons were obtained. These include mean radii, densities, and shapes—for example, Thomas [2010]; Thomas et al. [2018]; Castillo-Rogez et al. [2018]—and also photometric quantities such as geometric albedo, the phase integral, or Hapke photometric model parameters [Pitman et al. 2013; Verbiscer et al. 2018].

The sizes and shapes of the six mid-sized icy satellites were measured from ISS data. Mimas, Enceladus, Tethys, Dione, and Rhea are well described by triaxial ellipsoids; Iapetus is best represented by an oblate spheroid [Thomas et al. 2007]. Impact craters dominate the surfaces and provide the primary means of estimating terrain ages as well as many other properties of the surfaces [Dones et al. 2009; Kirchoff and Schenk 2010; Schenk et al. 2018; Kirchoff et al. 2018].

None of the unusual crater landforms (such as multi-ring basins or shallow distorted craters on the Galilean moons) seen on icy worlds that have confirmed internal oceans are seen on the mid-sized moons. However, this finding does not preclude possible oceans [Schenk et al. 2018]. Global mapping has revealed geologically complex worlds. All (except perhaps Iapetus) have been tectonically deformed to different degrees. Almost all tectonic landforms are interpreted as extensional structures [Schenk et al. 2018].

All of the icy Saturnian moons are absorbing in the ~0.2–0.5 μm region, making them dark at FUV wavelengths.

The trailing sides of Tethys and Dione, and to a lesser degree of Rhea, are darker than the respective leading sides. This is due to E-ring material infalling preferentially on the leading sides and has originally been discovered in Voyager data [Buratti et al. 1990]. The colors of the trailing sides are also redder than the leading sides of these moons.

All of the icy Saturnian moons are absorbing in the ~0.2–0.5 μm region, making them dark at far ultraviolet (FUV) wavelengths. For instance, Filacchione et al. [2016, 2012] used Cassini VIMS data to show that the spectral slope (0.35–0.55 μm) increases (becomes redder) with distance from Enceladus. While the ultraviolet (UV) absorber causes reddening, sub-micron grains induce increased scattering, causing a bluing effect, so there are competing signatures of these two components throughout the Saturn system.

Deuterium has been found on Phoebe, Iapetus, Hyperion, Rhea, Dione, Enceladus, and the Rings, and carbon 13 has been detected on Phoebe and Iapetus [Clark et al. 2019, 2017a, 2017b, 2016a, 2016b], and the deuterium to hydrogen (D/H) ratio derived. Phoebe is an outlier with D/H more than eight times higher than terrestrial, which the other satellites and rings are close to terrestrial ocean water values, an unexpected result not predicted by current models of solar system formation.

Infrared (IR) spectroscopy is sensitive to grain size of materials, and the multiple absorption in ice allows grain size mapping to be done with VIMS data. On Enceladus, the sizes of ice particles are generally well correlated with geologic features and surface ages, indicating a stratigraphic correlation between tectonic features and cryovolcanic activities [Jaumann et al. 2008]. Grains much smaller than the wavelength of light cause enhanced blue scattering, including a Rayleigh scattering effect. This bluing effect is observed in the Saturn system and quantified by Clark et al. [2012, 2008].

Scipioni et al. [2017] produced image cube maps of Enceladus, and mapped ice grain sizes and identified plume deposits across the surface. The map of the band-depth ratio 1.50/2.02 μm overall shows good agreement with the predicted plumes' deposits on the trailing side, where the amount of sub-micron particles decreases with increasing accumulation of ejecta material. However, this correlation is much weaker, or even absent, on the leading side of Enceladus, where the abundance of sub-micron particles is the highest across the entire surface.

Stephan et al. [2012] showed that the distribution of spectral endmembers as well as global band depth variations of Dione's water ice absorptions measurements imply that the bombardment with charged particles from Saturn's magnetosphere is one of at least two major global processes affecting Dione's surface. Ice deposits dominating its leading hemisphere appear rather associated with rays of the fresh impact crater Creusa on the northern leading hemisphere. These rays cross almost the whole hemisphere masking here any effects of possibly existent but less dominant processes as evident in the transition from the bright to dark regions on the Saturn-facing hemisphere (~0° W). CO_2 is evident in the dark material pointing to a possible formation due to the interaction of the surface material with the impacting particles from Saturn's magnetosphere. Local spectral differences are consistent with impacting particles from the trailing side as described by Clark et al. [2008] with a pronounced ice signature on crater walls facing the leading side direction and shielded from impacting particles and dark material concentrated on interior crater walls facing the trailing hemisphere.

Spectra of ice also varies with temperature, so the surface temperatures of cold icy surfaces can be sensed without needing to measure longer wavelength thermal emission. Filacchione et al. [2016] analyzed the ice spectral to produce daytime temperature maps of the satellite surfaces. Just one more indication of the diversity of science that an imaging spectrometer can provide.

Cassini radar tracks on Saturn's icy satellites through the end of the Prime Mission increased the number of radar albedo estimates to 73.

Cassini radar tracks on Saturn's icy satellites through the end of the Prime Mission increased the number of radar albedo estimates to 73 [Ostro et al. 2010]. The measurements sample diverse subradar locations (and for Dione, Rhea, and Iapetus, almost always use beamwidths less than half the target angular diameters), thereby constraining the satellites' global radar albedo distributions. The echoes result predominantly from volume scattering, and their strength is thus strongly sensitive to ice purity and regolith maturity. The combination of the Cassini data set and Arecibo 13-cm observations of Enceladus, Tethys, Dione, Rhea [Black et al. 2007], and Iapetus [Black et al. 2004] discloses an unexpectedly complex pattern of 13 cm to 2 cm wavelength dependence. The 13-cm albedos are generally smaller than 2-cm albedos and lack the correlation seen between 2 cm and optical geometric albedos. Enceladus and Iapetus are the most interesting cases. The E-ring has a prominent effect on the 13-cm radar lightcurve. The uppermost trailing-side regolith is too fresh for meteoroid bombardment to have developed larger-scale heterogeneities that would be necessary to elevate the 13-cm radar albedo, whereas all of Enceladus is clean and mature enough for the 2-cm albedo to be uniformly high. For, Iapetus, the

2-cm albedo is strongly correlated with optical albedo: low for the optically dark, leading-side material and high for the optically bright, trailing-side material. However, Iapetus' 13-cm albedo values show no significant albedo dichotomy and are several times lower than 2-cm values, being indistinguishable from the weighted mean of 13-cm albedos for main-belt asteroids, 0.15 ±0.10.

A series of UVIS stellar and solar occulations were designed at a wide range of latitudes and longitudes to search for thin atmospheres and plumes indicating possible activity.

The leading side's optically dark contaminant must be present to depths of at least one to several decimeters. A more detailed review of Cassini Radar observations of the icy moons of Saturn is detailed in the RADAR Instrument Science Results.

A series of UVIS stellar and solar occulations were designed at a wide range of latitudes and longitudes to search for thin atmospheres and plumes indicating possible activity. (The Planetary Data System (PDS) includes a list of these occultations.) This technique was spectacularly successful for Enceladus [Hansen et al. 2006]. Searches at Tethys, Iapetus, Rhea, and Dione showed no detectable atmosphere [Hansen et al. 2018].

Under the leadership of the inimitable Amanda Hendrix, UVIS set a gallant lead in obtaining full longitudinal and phase angle coverage of the icy satellites during the long mission, with CIRS, VIMS, and ISS benefitting from ride-a-long observations. The strong UV water absorption band is diagnostic of water ice, a major component of all the icy surfaces. This allows significant constraints on the surface composition and the processes that control the evolution of their surfaces [Hendrix and Hansen 2010, 2008; Hendrix et al. 2018, 2017, 2012; Royer and Hendrix 2014].

Substantial effort was expended on understanding the thermal properties of the medium-sized moons. Observations returned by CIRS and ISS showed a thermal and color anomaly at low latitudes on Mimas and Tethys' leading hemisphere, dubbed Pac-Man, because its shape mimics that of the 1980s' video icon (Figure ICYSATS-3). Pac-Man display warmer nighttime and cooler daytime temperatures than its surroundings and appears darker in IR/UV color ratio maps [Howett et al. 2012, 2011; Schenk et al. 2011]. The color and thermal anomalies are believed to be the result of surface alteration by high-energy electrons, which preferentially bombard this region, altering its surface and increasing its thermal inertia. These high-energy electrons, in Saturn's magnetosphere, drift in a retrograde direction relative to corotation. Recent modeling efforts, supported by the Low Energy Magnetospheric Measurement System (LEMMS) on Cassini's Magnetospheric Imaging Instrument (MIMI), have shown that these electrons preferentially bombard low latitudes on Mimas, Tethys, and Dione's leading hemisphere [Paranicas et al. 2014, 2012; Howett et al. 2011; Schenk et al. 2011]. The thermal anomaly is closely correlated spatially with an IR/UV (0.930/0.338 lm) color ratio anomaly previously observed in global maps of Mimas using Cassini ISS data.

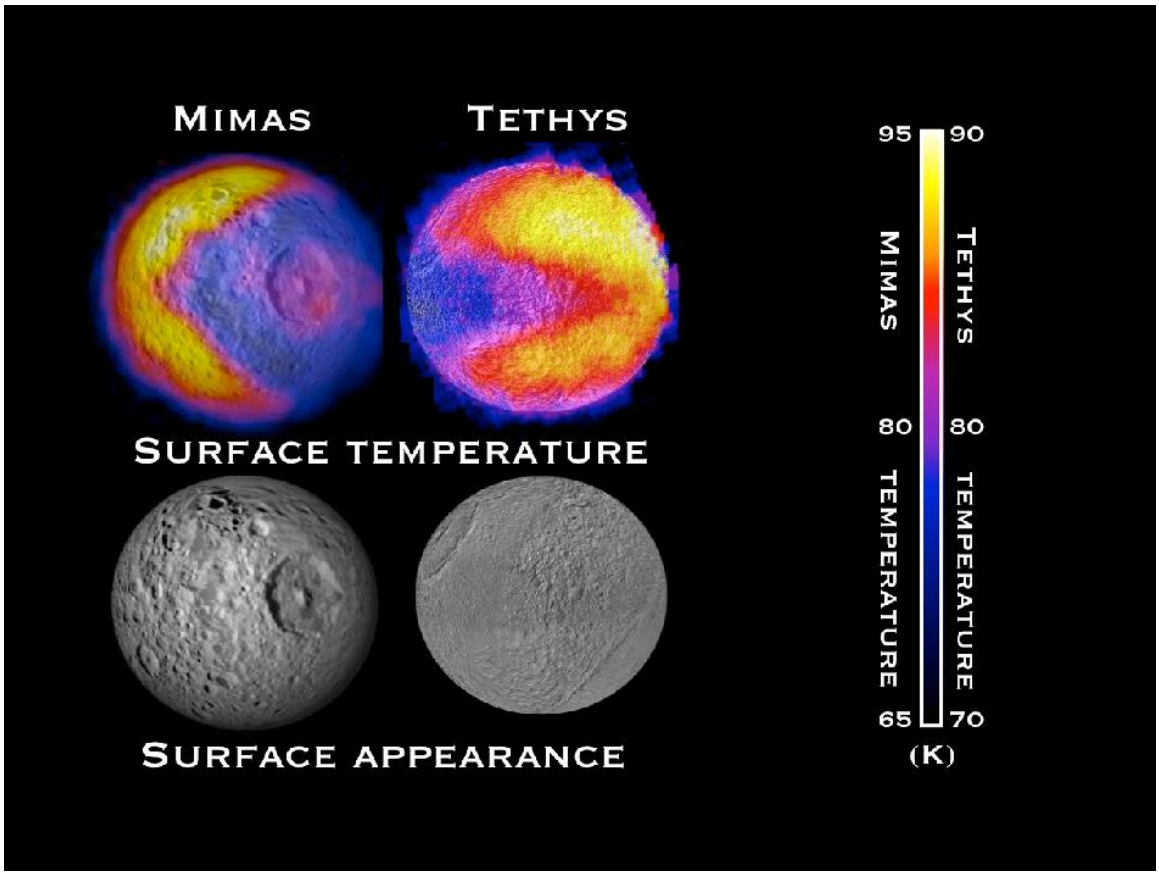

Figure ICYSATS-3. Pac-Man on Mimas and Tethys.

CIRS also measured the bolometric Bond albedo, the thermal inertia, and skindepths of the moons, which are summarized in Table ICYSATS-2 [Howett et al. 2010]. The thermal inertia of all of Saturn's icy satellites is shown to be less than half that of the Galilean satellites, implying less consolidated and more porous surfaces, perhaps partially due to the limited mobility of water ice on the Saturnian satellites due to their low temperatures compared with the Galilean satellites, or to a surface coating of E-ring particles. The latitudinal variation in the thermal inertia of Enceladus implies the surface becomes more consolidated towards the southern pole, whereas the higher albedo in the southern hemisphere implies a cleaner surface, perhaps due to plume fallout. Further work investigating the hemispheric bolometric Bond albedo asymmetries of Dione would be valuable, as although the globally averaged values derived here provide a good fit to the CIRS data, observations of viable wavelength have observed notable differences between the leading and trailing hemispheres [Buratti and Veverka 1984].

In September 2011 (during Cassini's orbit 153), CIRS obtained a daytime medium-spatial resolution observation (the average resolution was 84 km/pixel) of Tethys' leading hemisphere [Howett et al. 2012]. The results clearly show that a thermally anomalous Pac-Man region exists on Tethys' leading hemisphere at low latitudes in both the daytime and nighttime temperatures. The region appears to be ~10 K cooler during the day and ~10 K warmer at night than its

surroundings, quite unlike the pattern expected if surface properties were spatially uniform. The largest thermal contrast occurs at the northern anomaly boundary, particularly towards the east. The thermally anomalous region is lens-shaped with apexes at 0° W and 180° W, and is widest in the center of the leading hemisphere (90° W) reaching latitude ±20°. This anomalous region spatially coincides with a dark (low) albedo region at low latitudes on Tethys' leading hemisphere was first observed in Voyager data [Buratti and Veverka 1984; Buratti et al. 1990; Stooke 2002, 1989]. Photometry applied to Cassini ISS images showed the band to be 2–3% brighter in the narrow angle camera (NAC) CL1-UV3 filter (338 nm) and 8% darker in the NAC CL1-IR3 (930 nm) filter [Elder et al. 2007].

A Pac-Man thermal anomaly was also detected on Mimas [Howett et al. 2011]. It is closely correlated spatially with an IR/UV (0.930/0.338 lm) color ratio anomaly previously observed in global maps of Mimas using Cassini ISS data. The boundaries of the thermal and color anomalies appear to be nearly identical, although the apex of the thermal anomaly appears sharper.

The maximum electron energy flux bombarding Tethys is nearly six times lower than that on Mimas and is constrained to a smaller latitudinal extent, consistent with the relative amplitude and shape of the thermal anomaly on the two bodies [Paranicas et al. 2012; Schenk et al. 2011]. The discovery of Tethys' thermal anomaly, which has a boundary corresponding to an 18 GeV cm 2 s 1 electron flux (compared to 56 GeV cm 2 s 1 on Mimas), greatly strengthens the case that energetic electrons are able to significantly alter an icy satellite surface, and also proves that the threshold electron energy flux able to do so is lower than previously thought. A lower energy flux threshold increases the probability that such alteration occurs on other satellite surfaces. Why high-energy electron bombardment would decrease the IR/UV surface color ratio and why the thermal anomalous region appears darker in visible light images of Tethys, but not on Mimas, remains a mystery.

Table IcySats-2. Thermal properties of the moons.

Target	Bolometric	Thermal Inertia (MKS)	Skindepth (cm)	References
Jovian satellites				
Io	0.52	70	0.39[c]	Rathbun et al. [2003]
Europa	0.55	70 14 ±5	0.55[c] 0.01[d]	Spencer et al. [1999] Hansen [1973]
Ganymede	0.32 ±0.04	70 ±20 12 ±3 14 ±3	0.78[c] 0.01[d] 0.01[d]	Spencer [1987] Hansen [1973] Morrison and Cruikshank [1973]
Callisto	0.2 ±0.4	50 ±10 10 ±1	0.86[c] 0.01[d]	Spencer [1987] Morrison and Cruikshank [1973]
Saturnian satellites				
Mimas	$0.49^{+0.05}_{-0.14}$	19^{+57}_{-9}	0.54	
Enceladus	0.81 ±0.04	15^{+24}_{-9}	0.51	
Tethys	0.67 ±0.11	9^{+10}_{-4}	0.36	
Dione	0.63 ±0.15	11^{+18}_{-6}	0.53	

Table ICYSATS-2. Thermal properties of the moons.

Target	Bolometric	Thermal Inertia (MKS)	Skindepth (cm)	References
Rhea trailing	$0.57^{+0.20}_{-0.26}$	8^{+12}_{-5}	0.50	
Rhea leading	$0.63^{+0.11}_{-0.12}$	9^{+9}_{-5}	0.56	
Iapetus trailing	$0.31^{+0.15}_{-0.17}$	20^{+13}_{-8}	5.22	
Iapetus leading	0.10[a]	$14^{+7^{a}}_{-8}$	3.66	
Phoebe	0.1	20/25[b]		

Dione (IN1c)

The Cassini spacecraft executed five targeted flybys of Dione, passing as close as 500 km to its surface. Three of the flybys were devoted to gravity analysis, designed to understand the interior state of the moon and whether it harbors a subsurface ocean. Such an ocean was inferred from two separate studies: Beuthe et al. [2016] and Hemingway et al. [2016]. Further evidence for a subsurface ocean on Dione, at least at some point, was provided by a geophysical analysis of the formation of Janiculum Dorsae, a raised feature on Dione's surface. The heat flux required to form this feature is 25–60 mW/m^2, much greater than that expected solely from radioactive decay, but which can be generated by tidal heating in a liquid ocean [Hammond et al. 2013]. The evidence for an ocean provides the backdrop to the many lines of evidence for residual geologic activity on Dione.

Another intriguing result was the detection on December 15, 2004, of a transient aura-like ring around Dione at 2.65 μm that suggested the existence of an atmosphere [Clark et al. 2008]. Magnetometer data obtained on October 11, 2005, show a weak field perturbation in the upstream region, indicating a tenuous atmosphere [Simon et al. 2011]. The signature was not seen on April 7, 2010. Observing with CAPS, Tokar et al. [2012] discovered a thin atmosphere (~0.01–0.09 particles/cm^3) of O_2^+ during the close (500 km) flyby on April 7, 2010. A search for forward scattered radiation at solar phase angles > 150°, indicating a plume, was negative [Buratti et al. 2011]. Perhaps the most compelling evidence is the existence of possible cryovolcanic features on Dione. Figure ICYSATS-4 shows an image that includes linear groves and scarps that may be nascent or fossilized activity. Near the center of the image there is an anomalous crater pair that may be a possible volcanic vent. Furthermore, the surrounding area is smooth and relatively crater-free, as if covered by a volcanic deposit. A nearby rampart crater and evidence for amorphous ice suggesting rapid freezing [Newman et al. 2009] also imply some perhaps localized liquid water, although we have previously noted that inferring the existence of amorphous ice is difficult because of the dearth of laboratory data.

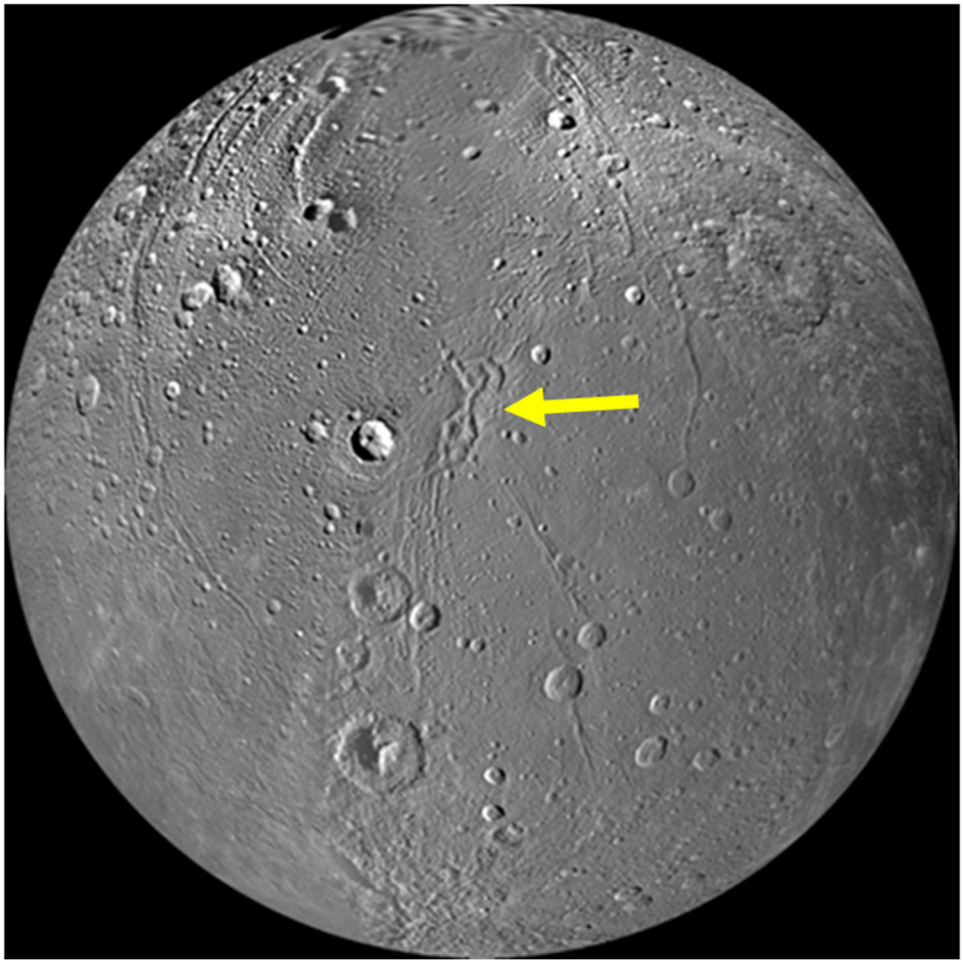

Figure IcySats-4. Possible cryovolcanic features on Dione.

High phase angle observations of Dione and Tethys were sought during the last year of the mission. Analysis of these data failed to detect any evidence for a plume or atmosphere on either body [Hansen et al. 2018; Buratti et al. 2018a]. No thermal signatures were detected either [Schenk et al. 2018]. The atmosphere appears to be transient, as it was seen only one time. Perhaps there is some type of low-level residual activity on Dione that is sporadic in nature. In any case, possible activity on Dione is one of the truly cold cases of the Cassini mission that will be reopened by future missions.

Rhea (IN2a)

The largest of the bright ray craters found in the Saturn system, Inktomi (Ø = 49 km), is a flat-floored crater on Rhea with a ray system radiating several hundred kilometers from the crater rim. It was imaged by ISS in August 2007 in three colors at resolutions up to 32 m/pxl and in stereo. The images are the best for a pristine crater in the Saturnian system and reveal a rugged landscape. Most of the ejecta and floor is essentially free of small craters [Wagner et al. 2011; Schenk et al.

2018]. Many of the tectonic lineaments are normal faults and graben, see for example, Wagner et al. [2010, 2007]. Most of this is concentrated in the trailing hemisphere as two major rift zones (Galunlati and Yasmi Chasmata) that trend roughly northeast–southwest and that are up to 3 km deep. These rifts are morphologically similar to those on Dione.

The blue pearls (bluish spots discovered with ISS in Figure ICYSATS-5) are a series of near-IR dark irregular patches located at the crests of the highest ridges or massifs located along the equator of Rhea. Their origin is speculated to be related to infalling or collapse of a former orbiting debris ring [Schenk et al. 2011]. A dedicated search with ISS showed that present Rhea has no ring system [Tiscareno et al. 2010]. The blue pearls are not associated with any tectonic feature along its length or in near proximity. Instead, they appear to be associated with steep slopes (e.g., crater rims). The lack of any constructional artifacts associated with these color patterns on Rhea implies that they are due to regolith disruption [Schenk et al. 2011].

Wispy streaks seen by Voyager on Dione and Rhea are fracture networks [Schenk et al. 2018].

Tethys (IN2b)

Rugged topography of overlapping craters is typical for wide parts of Tethys [Schenk et al. 2018]. The large 425-km wide impact basin Odysseus is one of the largest well-preserved basins in the Saturnian system. Flat-floor deposits (as commonly found in large craters on the Moon and Mercury) are lacking, suggesting that impact melt ponding did not occur in large quantities. This lack of large melt sheets is characteristic of all craters in the Saturn system [Schenk et al. 2018]. Ithaca Chasma is the dominant tectonic feature. It is a giant rift zone already identified by Voyager, 1,800 km in length and subtending at least 270° of arc, between 70 km and 110 km in width, and 2–5 km deep. It predates the Odysseus basin and thus should not have been formed by this impact feature [Giese et al. 2007].

Red streaks were only found on Tethys and are very enigmatic (Figure ICYSATS-5). They show an enhanced color signature in the near-IR which is a very unusual color for features on Saturn's icy satellites. No associated surface deformation is visible even at image resolutions of 60 m/pxl [Schenk et al. 2015]. The infrared shows distinct compositional changes between the red streaks and the surrounding regions [Buratti et al. 2017].

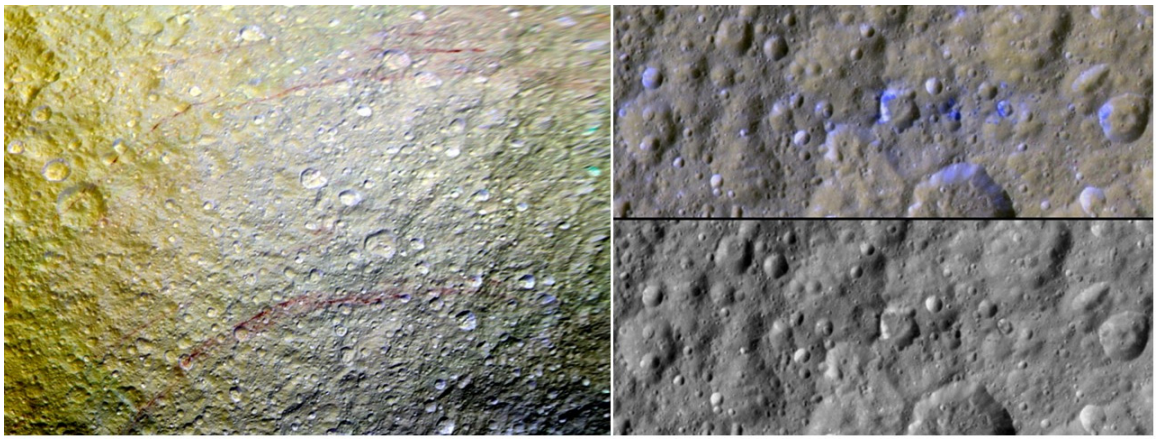

Figure ICYSATS-5. Red streaks on Tethys (left) and blue pearls on Rhea (right).

Tethys' equatorial albedo band, first seen in Voyager images, was analyzed in several ISS NAC wavelengths. The band is symmetric 15° on either side of the equator and extends from 0° to 160° W; that is, almost centered on the leading edge of Tethys. There is no evidence that the band is topographically-based; margins are gradational and there is no visible difference in underlying geology [Elder et al. 2007]. ISS NAC polarization images found no evidence for surface textural variations on size-scales comparable to individual geological features (like crater walls and floors on these size scales, the surface texture of Tethys appears to be uniform). However, a banded pattern on the surface was found and that likely originates in the subtle albedo variations tied to Tethys' equatorial band [Elder et al. 2007] and thermally anomalous terrain [Helfenstein et al. 2005].

Satellite Interiors (IN2c)

Multiple close targeted flybys of the icy moons afforded by an orbital mission as opposed to the single flybys of the Voyager spacecraft provided key data for interior studies. Furthermore, several flybys of Enceladus, Dione, and Rhea were devoted primarily to gravity studies, in which articulations of the spacecraft by reaction wheels or thrusters were avoided. Cassini gravity and imaging experiments teamed up to produce both clear discoveries of internal oceans and interesting mysteries. It appears that multiple Saturnian satellites are well out of hydrostatic equilibrium, reflecting a lack of substantial heat sources and perhaps suggestive of a collisionally dominated history after initial accretion. Rhea is one of these objects, and the gravity data are consistent with a completely undifferentiated body [Tortora et al. 2016]. The lack of evidence for substantial silicates in the surface materials has led to models in which some small amount of differentiation has occurred; however, this is an unstable situation that is difficult to sustain and instead one might look to mechanisms for coating the surface with icy material that obscures a silicate signature.

Cassini data on Mimas and Dione has been interpreted as indicating oceans deep beneath the surfaces of both. For the former, imaging measurements of the moon's unexpectedly large libration imply either a decoupled outer shell (hence, an ocean) or a strongly nonhydrostatic interior

with, for example, an elongated core [Tajeddine et al. 2014]. In the case of Dione, gravity data have been interpreted in terms of a deep ocean via two separate analyses as presented in Beuthe et al. [2016] and Hemingway et al. [2016], but the latter also implies a strongly non-hydrostatic interior. Reconciling these surprising results with models of satellite origin and thermal evolution will be challenging.

The ocean of Enceladus is well-established [Iess et al. 2014; McKinnon 2015; Thomas et al. 2016], but its power source and longevity remain hot topics. Likewise does the question of life, which if present, will (from the point of view of an interiors modeling purist) affect the interpretation of the mass spectrometric data in terms of core-ocean hydrothermal and chemical evolutionary processes.

Iapetus, if in hydrostatic equilibrium, has a shape inconsistent with its present-day spin. This has been interpreted as indicative of a thermal history in which the deep interior was kept hot and dissipative for tidal braking while a thick cold lithosphere retains the shape. If the heat source responsible was short-lived radioactive isotopes, a formation time (since condensation of the first meteorite components) for Iapetus can be derived [Castillo-Rogez et al. 2009]. However, subsequent work revealed that the answer may be very sensitive to ice rheology [Castillo-Rogez et al. 2011], and explanations for the presence of the equatorial ridge in terms of collision with another object [Levison et al. 2011] would severely modify the rotational evolution story.

In contrast with the Jovian system, the intermediate satellite system of Saturn contains objects whose origins and histories, expressed by their interior and surface states, seemed to have been dominated by stochastic events rather than by position relative to their parent planet. Why this is so remains one of the most enduring cold cases left behind by Cassini.

Small Moons (IN2d)

Table IcySats-3 summarizes our current knowledge of the inner small moons of Saturn.

Table IcySats-3. Sizes and mean densities of small Saturnian satellites. Table from Buratti et al. [2018b] and Thomas et al. [2007].

Object	a, km	b, km	c, km	Rm, km	density, kgm^{-3}	gravity, cms^{-2}
Pan	17.3 ±0.2	14.1 ±0.2	10.5 ±0.7	13.7 ±0.3	400 ±32	0.2–1.7
Daphnis	4.9 ±0.3	4.2 ±0.8	2.8 ±0.6	3.9 ±0.5	274 ±142	0.0–0.4
Atlas	20.4 ±0.1	17.7 ±0.2	9.3 ±0.3	14.9 ±0.2	412 ±19	0.0–1.7
Prometheus	68.5 ±0.5	40.5 ±1.4	28.1 ±0.4	42.8 ±0.7	460 ±21	0.8–5.8
Pandora	51.5 ±0.3	39.5 ±0.3	31.5 ±0.2	40.0 ±0.3	509 ±12	2.0–5.9
Epimetheus	64.8 ±0.4	58.1 ±0.8	53.5 ±0.4	58.6 ±0.5	625 ±16	6.6–10.9
Janus	101.8 ±0.9	93.0 ±0.3	74.5 ±0.3	89.0 ±0.5	642 ±10	10.9–16.9
Aegaeon	0.7 ±0.0	0.3 ±0.1	0.2 ±0.0	0.3 ±0.0	539 ±140	0.001–0.005
Methone	1.9 ±0.0	1.3 ±0.0	1.2 ±0.0	1.4 ±0.0	307 ±30	0.1–0.1

Table IcySats-3. Sizes and mean densities of small Saturnian satellites. Table from Buratti et al. [2018b] and Thomas et al. [2007].

Object	a, km	b, km	c, km	Rm, km	density, kgm^{-3}	gravity, cms^{-2}
Pallene	2.9 ±0.4	2.1 ±0.3	1.8 ±0.3	2.2 ±0.3	251 ±75	0.1–0.2
Telesto	16.6 ±0.3	11.7 ±0.3	9.6 ±0.2	12.3 ±0.3		
Calypso	14.7±0.3	9.3 ±0.9	6.4 ±0.3	9.5 ±0.4		
Polydeuces	1.5 ±0.3	1.3 ±0.4	1.0 ±0.2	1.3 ±0.3		
Helene	22.6 ±0.2	19.6 ±0.3	13.3 ±0.2	18.1 ±0.2		
Hyperion	164.1 ±1.7	130.1 ±4.0	107.1 ±4.3	135.9 ±3.1	535 ±37	17.3–20.8

The low densities of the small inner moons of Saturn, which were refined by the close flybys at the end of the mission, is consistent with accretion from ring material. The new data on the moons embedded in the A-ring show that the color of these moons becomes more similar to the rings the closer they are to Saturn. This result suggests there is an ongoing accretion of a reddish chromophore that may be a mixture of organics, silicates, and iron, onto the surfaces of the rings [Buratti et al. 2017]. The difference in color between the moons and their adjacent ring can be explained by the accretion of bright, icy E-ring particles. In essence, each moon's surface is subjected to a balance between these two ongoing processes, with their distance from Saturn and Enceladus determining the final result (Figure IcySats-6). The detection of abundant ice grains by CDA in the region of these moons supports this view. The bluer core of Atlas is also explained by the accretion of E-ring particles, which have a wider range of inclinations than main ring particles. The finding by MIMI of a dearth of high-energy ions also lessens the competing alteration processes from bombardment by magnetospheric particles. The strong crystalline water ice band at 1.65 μm also suggests the lack of importance of these processes. This low energy environment also renders comparisons with the identity of the red chromophore on the trailing hemispheres of main moons of Saturn, especially Dione and Rhea, problematical, as they dwell in a region where alterations by ions is significant and would tend to darken and redden the surfaces. Finally, contamination of Saturn's rings by bright icy particles diminishes the argument that the observed brightness of the rings bespeaks a recent formation [Zhang et al. 2017].

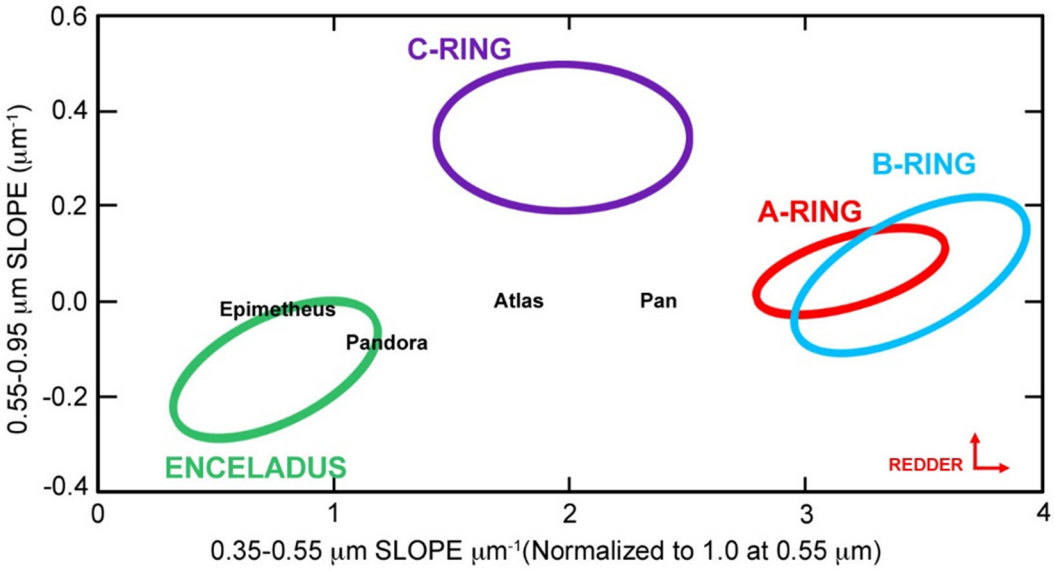

Figure ICYSATS-6. Colors of the ring moons compared to the rings. Figure based on Filacchione et al. [2013, 2012] and Buratti et al. [2018b].

The moons record complex geologic histories including groove formation caused by tidal stresses, accretion of ring particles, and possible accretion of debris from impacts on larger moons. The CDA finding of porous surfaces for the ring moons further supports substantial accretion. Although the topography and surface slopes strongly suggest the equatorial ridges of Pan and Atlas are accreted from rings and are not formed by normal surface transport, the variety of forms of ridges on these objects, and the minimal ridges on Daphnis, show that much remains to be understood about their formation and relation to the main rings. The high-resolution images strongly suggest exposures, especially on Epimetheus, Janus, and Pandora, of a solid substrate distinct from the mobile regolith that generally conceals bedrock on small solar system objects. These exposures may eventually help reveal systematic trends of body history and structures for the whole of the Saturn satellite system. The moons Aegaeon, Methone, and Pallene have shapes of equilibrium ellipsoids indicative of weak or mobile surfaces that cannot support shear stresses [Thomas et al. 2013]. These forms are unique for such small objects, usually fractured or clumpy, and as yet are unexplained. An example of ISS, CIRS, and VIMS data on Atlas is shown in Figure ICYSATS-7.

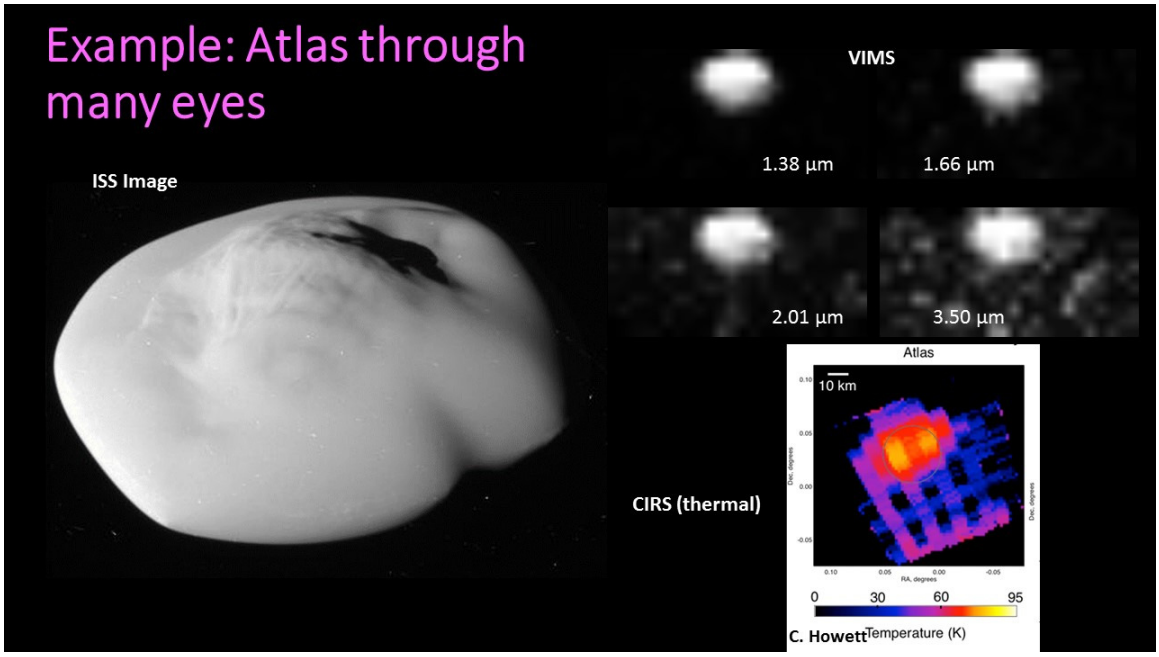

Figure ICYSATS-7. ISS, VIMS, and CIRS observations of Atlas obtained during the F-ring orbits.

Hyperion (IN2e)

The chaotically rotating satellite, Hyperion, has unique sponge-like topography that may reflect sublimation of species more volatile than water ice [Thomas et al. 2007]. The chaotic rotation of Hyperion was analyzed using data from three flybys. The Lyapunov timescale was found to be approximately 100 days [Harbison et al. 2011]. As Iapetus is, Hyperion may be coated with material from the Phoebe ring, but because the moon is in chaotic rotation it is not found preferentially on one hemisphere. Rather, it tends to be located in the bottoms of craters or pits, similar to sun cups on the Earth, in which dark material is concentrated in warmer areas through a process of thermal segregation. This material is rich in organics, including possibly aromatics. The CO_2 on the surface is probably combined in some way with water ice. Dalton et al. [2012] identify aromatic and aliphatic hydrocarbons in the low-albedo material, and possibly H_2. As for Iapetus and the other moons, nanophase iron is thought to act as a coloring agent [Clark et al. 2012].

Iapetus (IN2f)

The global and regional topography of Iapetus is much less smooth than for the other mid-sized icy moons [Thomas et al. 2007; Lee et al. 2010]. A total of 10 basins larger than 300 km have been identified on Iapetus (despite the lack of resolved imaging in some locations), but only four on Rhea. Dione, Tethys, and Mimas are similarly depleted [Schenk et al. 2018]. ISS data show numerous impact craters down to the resolution limit [Denk et al. 2010].

Iapetus' global albedo dichotomy, first described by the spacecraft's eponym Jean-Dominique Cassini in 1677 and unexplained since then, has been solved through Cassini CIRS and ISS data [Spencer and Denk 2010]. Dust from Phoebe or possibly from other retrograde-orbiting irregular moons has likely been painting the surface of Iapetus, forming the newly-detected global color dichotomy of Iapetus [Denk et al. 2010], which triggered the evolution of low-latitude and mid-latitude parts of the leading side into the stark bright and dark patterns we see today as the global albedo dichotomy [Spencer and Denk 2010], accentuated with the thermal migration of water ice [Denk et al. 2010]. A major property of the global color dichotomy is that dark material on the leading side is redder than dark material on the trailing side, and that bright material on the leading side (mainly at high latitudes) is also redder than bright material on the trailing side [Denk et al. 2010]. Cassini ISS data showed that the stark dark-bright contrast is also a local phenomenon. The surface is either bright or dark, but almost never gray, even in the transition zone between the dark Cassini Regio and the bright Roncevaux Terra and Saragossa Terra [Denk et al. 2008].

Observations of small, bright-ray craters within the dark terrain indicate that the dark material corresponds to a blanket of a few meters or less in thickness…

Observations of small, bright-ray craters within the dark terrain indicate that the dark material corresponds to a blanket of a few meters or less in thickness [Denk et al. 2010], a finding also supported by Titan Radar Mapper (RADAR) data [Ostro et al. 2006] and consistent with the thermal migration model of Spencer and Denk [2010].

A huge and enigmatic ridge located exactly at the equator was discovered in ISS images [Porco et al. 2005; Denk et al. 2005a; Denk et al. 2005b]. In places, this ridge is up to 20 km high and 70 km across, and it spans almost 75% of the moon's circumference [Porco et al. 2005; Denk et al. 2008; Giese et al. 2008; Singer and McKinnon 2011]. While the ridge is mainly continuous on the leading side (Toledo Montes), it separates into the isolated mountains of the Carcassone Montes which were already discovered in Voyager data (and thus sometimes dubbed Voyager mountains) [Denk et al. 2000]. In general, it shows a wide range of cross-sections and heights at different longitudes [Denk et al. 2008; Singer et al. 2012]. Singer and McKinnon [2011] did not find potential hints for tectonic or volcanic origin. Defying any obvious explanation, numerous endogenic and exogenic formation mechanisms were proposed, for example, see short review of them by Damptz et al. [2018]. None of them can be favored over the others at this point.

CO_2 was found on Iapetus during an untargeted flyby just prior to the Huygens probe separation [Buratti et al. 2005], and spectra with km-scale resolution were obtained during a targeted flyby on September 10, 2007. Clark et al. [2012] identified additional key components of the surface of Iapetus in addition to CO_2 and H_2O, including bound water, H_2, OH-bearing minerals, trace organics, and possibly ammonia. The CO_2 on Iapetus was enriched in the low-albedo areas, reaching a maximum at the apex of motion where the albedo is lowest. The Clark et al. [2012] posits the presence of nanophase metallic iron particles and an iron oxide, probably hematite to contribute to the observed Rayleigh scattering peak in the visible part of the spectrum. Figure ICYSATS-8 is a summary of the features in the spectrum of Iapetus.

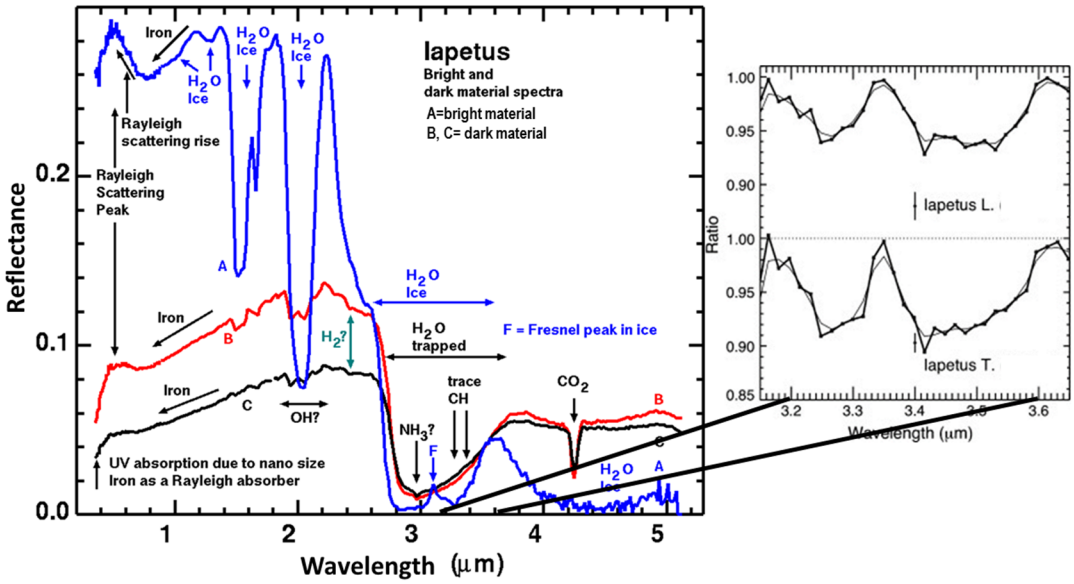

Figure ICYSATS-8. The spectrum of Iapetus showing explanations for the spectral lines of the bright material and two examples of dark material on Iapetus. *B = dark material:* The identification of aromatic hydrocarbons in the spectrum. This graph gives the residuals that result from a best-fit Hapke compositional model to the leading and trailing sides. Absorption bands at 3.28 μm are characteristic of aromatic hydrocarbons, while those between 3.35 and 3.6 μm are characteristic of aliphatic hydrocarbons. *A = bright material:* is based on Clark et al. [2012] and *B = dark material:* is based on Cruikshank et al. [2014].

An analysis of the 2.7 to 4.0 μm spectral region by Cruikshank et al. [2010, 2014] identified the presence of both aromatic and aliphatic hydrocarbons in the dark material on Iapetus. The aromatic band near the CH stretching modes of aromatic hydrocarbons at ~3.28 μm is especially strong, and is likely due to aromatic hydrocarbons. Because surfaces rich in aromatic hydrocarbons are readily carbonized via UV radiation, these substances are not stable on the surface of Iapetus, and thus the process of accretion of Phoebe ring particles must be ongoing.

The dark material on Iapetus is abundant enough to perform compositional modeling. The 3-micron-bound water band was found to match hydrated iron oxides [Clark et al. 2012] and subsequent recalibration of VIMS [Clark et al. 2018] show that spectra of the dark materials also shows a 1.9-micron water absorption that matches hydrated iron oxides. The linear slope, blue peak, and absorption shorter than 0.5 microns, argue for space-weathered silicates (thus nano-metallic iron) as the explanation of the UV-visible spectrum. The lack of any hint of absorptions from tholins in the IR is enough abundance to explain the UV-visible spectrum, and argues for the space-weathered silicates and iron oxide explanation [Clark et al. 2012].

Clark et al. [2012] also explained that the differences in color between the Iapetus dark material and Phoebe is simply due to abundance differences of space-weathered silicates, hydrated iron oxides, and ice. According to this model, the flatter, grayer spectrum of Phoebe compared to Iapetus dark material is due to lower abundance of the iron oxides and space-weathered silicates.

Other Icy Satellites Science not in CSM

Phoebe was the first targeted flyby on June 11, 2004. Its global shape is close to an oblate spheroid, with a = b to within the uncertainties of the data [Thomas 2010; Castillo-Rogez et al. 2012]. Its mean radius is 106.4 ±0.4 km and its mean density is 1.64. This high density along with its compositional differences with the mid-sized regular satellites of Saturn, support the evidence that it is a captured body [Johnson and Lunine 2005b]. Numerous impact craters are visible on the surface; they range in diameter from the lower limit imposed by the ISS image resolution up to ≈100 km [Porco et al. 2005]. Phoebe's topography, relative to an equipotential surface, is within the range of other small objects and is much higher than that for clearly relaxed objects [Thomas 2010]. Digital Terrain Model (DTM) and orthoimage of the surface were produced from ISS data [Giese et al. 2006]. The J2000 spin-axis was found at Dec = 78.0° ±0.1°; RA = 356.6° ±0.3°, substantially different from the former Voyager solution [Giese et al. 2006]. Finally, Phoebe dust ring, discovered from Earth, has also been observed with the ISS Wide Angle Camera [Tamayo et al. 2014].

Mimas was the least studied of the main moons, with no targeted flyby.

Mimas was the least studied of the main moons, with no targeted flyby. The best images obtained at this flyby have a spatial resolution of ~93 m/pxl. There is morphologic evidence for a highly degraded impact basin of ~153 km diameter, northeast of crater Herschel [Schmedemann and Neukum 2011].

All irregular moons except Phoebe were discovered between year 2000 and 2007. Since this was after the launch of Cassini-Huygens, they were not part of the original science goals. Therefore, a dedicated observation campaign with ISS was initiated for the Solstice mission. ISS observed 25 of Saturn's 38 known irregular moons, and precise rotational periods could be derived for most of them. The light curves are indicative for objects with quite different shapes. The rotational periods vary between 5.45 h and 76.13 h. Many asteroids of similar size rotate faster; this indicates that Saturn's irregular moons have rather low densities. Some objects show very distinct 3 maxima/3 minima light curves with an equal spacing of the extrema. Convex-shape models of these moons resemble triangular prisms, but they might actually be contact-binary objects. Other light curves show patterns that might even hint to binary moons. It is likely that non-random correlations were found between the ranges to Saturn, the orbit directions, orbit tilts, object sizes, and the rotation periods. The physical cause, especially for size and spin relations to orbital elements, is unknown at this point. For further reading, we refer to Denk et al. [2018] or Denk and Mottola [2013, 2014].

Open Questions for Icy Satellite Science

The top open questions for icy moon science, as compiled by the Cassini ISWG meeting in March 2018 and compiled in a peer-reviewed paper by Buratti et al. [2017], are:

1. What are some of the minor constituents of the Saturnian moons, and are they endogenic or exogenic? If exogenic, is the accretional process still ongoing?

2. Can the D/H ratio be measured on these moons? If so, how does it compare with that of other regions of the Solar System, and what does that imply about the transport of volatiles on a large scale? Clark et al. [2019] derives the D/H in the ice on the satellites and rings and the 12C/13C on the carbon dioxide. The D/H is similar to terrestrial values for the satellites and rings except for Phoebe, where deuterium and C13 are high.

3. Is ammonia hydrate on the surfaces of any of the moons?

4. What is the identity of the red chromophore on these bodies' surfaces? Is it nano-iron or organic material, and what are the transport processes to move this material around the Solar System? Is it the same chromophore that exists in the main ring system?

5. What is the total heat production on Enceladus; how and why does it vary? What does this imply about the cause of activity on the moon? Why is only the South Pole active and not the North Pole (what is Enceladus' tectonic history)? What is the nature of the plumbing that connects the ocean to the surface? Is there any evidence for seasonal variations in output? Is there life in Enceladus' ocean?

6. Is there residual activity on Dione and Tethys, and if so, what does this imply about their recent history? Are the red streaks on Tethys evidence for such activity?

7. What caused the ridge on Iapetus? Is it evidence for a past ring? Did other moons have rings in the past?

8. Why does the origin of the moons of Jupiter and Saturn seem to diverge, with the Jovian moons being formed relative to their position from Jupiter, and the Saturnian moons being formed by stochastic events?

9. Why are some of the moons not in hydrostatic equilibrium? Rhea and Dione, incompletely, for example.

10. To what extent do magnetospheric particles alter the optical properties of the moons? Does contamination by ring particles, including those from the E-ring, dominate this process?

11. What are the blue pearls on Rhea?

Earth (Moon)

From Clark [2009]:

> "Data from the Visual and Infrared Mapping Spectrometer (VIMS) on Cassini during its flyby of the Moon in 1999 show a broad absorption at 3 micrometers due to adsorbed water and near 2.8 micrometers attributed to hydroxyl in the sunlit surface on the Moon. The amounts of water indicated in the spectra depend on the type of mixing and the grain sizes in the rocks and soils but could be 10 to 1000 parts per million and locally higher. Water in the Polar Regions may be water that has migrated to the colder environments there. Trace hydroxyl is observed in the anorthositic highlands at lower latitudes."

Jupiter (Galilean Satellites)

In December 2000, Cassini flew by Jupiter for a gravity assist to Saturn. The geometry of the flyby was set by the trajectory requirements for Saturn so most of the moons were quite distant, however, several significant new results were obtained. Brown et al. [2003] documents VIMS results from the Jupiter flyby: VIMS documented a surprisingly high opposition surge on Europa, and the first visual-near-IR spectra of Himalia. UVIS observed Europa's O_2 atmosphere. ISS studied Io's volcanic activity.

Io

Io was observed during four eclipses. ISS imaged the glow of Io's ambient atmosphere from the K, Na, O, S_2, and SO_2 coming from its volcanoes. Differences in the altitude of the emissions indicate stratification of the Io atmosphere [Geissler et al. 2004].

Europa

VIMS data provided the first near-IR phase curve of Europa [Simonelli and Buratti 2004]. Europa exhibits a remarkable surge in brightness (~0.2 mag/deg) under 1°, comparable to the lunar opposition surge measured by Clementine [Buratti et al. 1996]. Furthermore, data at small phase angles show a clear trend with albedo, such that wavelengths corresponding to higher albedos have smaller surges, consistent with shadow illumination. The VIMS results suggest that neither CBE nor shadow hiding provide a complete description of Europa's opposition surge below 1° [Brown et al. 2003].

UVIS observed emissions from Europa's O_2 atmosphere and mapped its spatial extent. Atomic oxygen extends further from Europa than O_2, however, it does not form a torus [Hansen et al. 2005]. Analysis of other emissions from other neutrals and ions near Europa constrains the level of eruptive activity and suggests that it can only be intermittent—no plumes comparable to Enceladus were active at the time of the Cassini flyby [Shemansky et al. 2014].

Galilean moons

VIMS spectra of the Galilean satellites confirmed the spectral features in the Galileo Near-Infrared Mapping Spectrometer Subsystem (NIMS) data. Brown et al. [2003] also noted similar spectral structure as in NIMS data attributed to a CN bond near 4.5 microns. This structure was also seen in VIMS data of the Saturnian satellites, see for example, Clark et al. [2005, 2008], but was later found to be due to a calibration error [Clark et al. 2012].

Himalia

The disk of Himalia was resolved in ISS images, and show that it is not spherical [Porco et al. 2003]. If principal axes were visible, the diameters are 150 ±10 km × 120 ±5 km. VIMS data shows that Himalia has a slightly reddish spectrum, an apparent absorption near 3 μm, and a geometric albedo of 0.06 ±0.01 at 2.2 μm (assuming an average 85-km radius). If the 3-μm feature in Himalia's spectrum is eventually confirmed, it would be suggestive of the presence of water in some form, either free, bound, or incorporated in layer-lattice silicates [Brown et al. 2003].

ACRONYMS

Note: For a complete list of Acronyms, refer to Cassini Acronyms – Attachment A.

AO	Announcement of Opportunity
CAPS	Cassini Plasma Spectrometer
CDA	Cosmic Dust Analyzer
CIRS	Composite Infrared Spectrometer
CSM	Cassini Solstice Mission
D/H	Deuterium to Hydrogen
DTM	Digital Terrain Model
DWG	Discipline Working Group
FRPO	F-ring and Proximal Orbits
FUV	far ultraviolet
INMS	Ion and Neutral Mass Spectrometer
IR	infrared
ISS	Imaging Science Subsystem
ISWG	Icy Satellites Working Group
KBO	Kuiper Belt object
LEMMS	Low Energy Magenotospheric Measurement System
MAPS	Magnetospheres and Plasma Science
MIMI	Magnetospheric Imaging Instrument
NAC	narrow angle camera
NIMS	Near Infrared Mapping Spectrometer Subsystem
PDS	Planetary Data System
RADAR	Titan Radar Mapper
SOST	Satellites Orbiter Science Team
TM	Traceability Matrix
UV	ultraviolet
UVIS	Ultraviolet Imaging Spectrograph
VIMS	Visual and Infrared Imaging Spectrometer

REFERENCES

Disclaimer: The partial list of references below correspond with in-text references indicated in this report. For all other Cassini references, refer to Attachment B – References & Bibliographies; Attachment C – Cassini Science Bibliographies; the sections entitled References contributed by individual Cassini instrument and discipline teams located in Volume 1 Sections 3.1 and 3.2 Science Results; and other resources outside of the Cassini Final Mission Report.

Behounkova, M., G. Tobie, O. Cadek, G. Choblet, C. Porco, F. Nimmo, (2015), Timing of water plume eruptions on Enceladus explained by interior viscosity structure, Nature Geoscience 8, 8, 601–604, doi: 10.1038/ngeo2475.

Beuthe, M., A. Rivoldini, A. Trinh, (2016), Enceladus's and Dione's floating ice shells supported by minimum stress isostasy, Geophysical Research Letters 43, 19.

Black, G. J., D. B. Campbell, L. M. Carter, (2007), Arecibo radar observations of Rhea, Dione, Tethys, and Enceladus, Icarus 191, 2, 702–11, doi: 10.1016/j.icarus.2007.06.009.

Black, G. J., D. B. Campbell, L. M. Carter, S. J. Ostro, (2004), Radar detection of Iapetus. Science 304, 5670, 553–553.

Bouquet, A., O. Mousis, J. H. Waite, S. Picaud, (2015), Possible evidence for a methane source in Enceladus' ocean, Geophysical Research Letters 42, 5, 1334–1339, doi: 10.1002/2014GL063013.

Brown, R. H., R. N. Clark, B. J. Buratti, D. P. Cruikshank, J. W. Barnes, R. M. E. Mastrapa, J. Bauer, S. Newman, T. Momary, K. H. Baines, G. Bellucci, F. Capaccioni, P. Cerroni, M. Combes, A. Coradini, P. Drossart, V. Formisano, R. Jaumann, Y. Langevin, D. L. Matson, T. B. McCord, R. M. Nelson, P. D. Nicholson, B. Sicardy, C. Sotin, (2006), Composition and physical properties of Enceladus' surface, Science 311, 5766, 1425–1428. doi: 10.1126/science.1121031.

Brown, R. H., K. H. Baines, G. Bellucci, J. P. Bibring, B. J. Buratti, F. Capaccioni, P. Cerroni, R. N. Clark, A. Coradini, D. P. Cruikshank, P. Drossart, V. Formisano, R. Jaumann, Y. Langevin, D. L. Matson, T. B. McCord, V. Mennella, R. M. Nelson, P. D. Nicholson, B. Sicardy, C. Sotin, S. Amici, M. A., Chamberlain, G. Filacchione, G. Hansen, K. Hibbitts, M. Showalter, (2003), Observations with the Visual and Infrared Mapping spectrometer (VIMS) during Cassini's flyby of Jupiter, Icarus, 164, 2, 461–470. doi: 10.1016/s0019-1035(03)00134-9.

Buratti, B. J. et al., (2018a), First Results from Cassini's Five Fabulous Flybys of Saturn's Ring Moons, Science, revision submitted May 25, 2018.

Buratti, B. J., P. C. Thomas, E. Roussos, C. Howett, M. Seiss, A. R. Hendrix, P. Helfenstein, R. H. Brown, R. N. Clark, T. Denk, G. Filacchione, H. Hoffmann, G. H. Jones, H. Khawaja, P. Kollman, N. Krupp, J. Lunine, T. S. Momary, C. Paranicas, F. Postberg, M. Sachse, F. Spahn, J. Spencer, R. Srama, T. Albin, K. H. Baines, M. Ciarniello, T. Economou, S. Hsu, S. Kempf, S. M. Krimigis, D. Mitchell, G. Moragas-Klostermeyer, P. D. Nicholson, C. C. Porco,

H. Rosenberg, J. Simolka, L. A. Soderblom, (2018b), First Results from Cassini's Flybys of Saturn's Ring Moons at the End of Mission, Science, submitted.

Buratti, B. J., R. N. Clark, F. Crary, C. J., Hansen, A. R. Hendrix, C. J. A. Howett, J. Lunine, C. Paranicas, (2017), Cold cases: What we don't know about Saturn's Moons, Planetary and Space Science, 155, 41–49.

Buratti, B. J., S. P. Faulk, J. A. Mosher, K. H. Baines, R. H. Brown, R. N. Clark, P. D. Nicholson, (2011), Search for and limits on plume activity on Mimas, Tethys, and Dione with the Cassini Visual Infrared Mapping Spectrometer (VIMS), Icarus 214, 2, 534–540. doi: 10.1016/j.icarus.2011.04.030.

Buratti, B. J., D. P. Cruikshank, R. H. Brown, R. N. Clark, J. M. Bauer, R. Jaumann, T. B. McCord, D. P. Simonelli, C. A. Hibbitts, G. B. Hansen, T. C. Owen, K. H. Baines, G. Bellucci, J. P. Bibring, F. Capaccioni, P. Cerroni, A. Coradini, P. Drossart, V. Formisano, Y. Langevin, D. L. Matson, V. Mennella, R. M. Nelson, P. D. Nicholson, B. Sicardy, C. Sotin, T. L. Roush, K. Soderlund, A. Muradyan, (2005), Cassini Visual and Infrared Mapping Spectrometer observations of Iapetus: detection of CO2, Astrophysical Journal Letters, 622, 2, 149–52.

Buratti, B. J., J. K. Hillier, M. Wang, (1996), The lunar opposition surge: Observations by Clementine, Icarus, 124, 2, 490–499.

Buratti, B. J., J. A. Mosher, T. V. Johnson, (1990), Albedo and color maps of the saturnian satellites, Icarus, 87, 2, 339–357.

Buratti, B. and J. Veverka, (1984), Voyager photometry of Rhea, Dione, Tethys, Enceladus and Mimas, Icarus, 58, 2, 254–264.

Burch, J. L., J. Goldstein, W. S. Lewis, D. T. Young, A. J. Coates, M. K. Dougherty, N. Andre, (2007), Tethys and Dione as sources of outward-flowing plasma in Saturn's magnetosphere, Nature 447, 7146, 833–835. doi: 10.1038/nature05906.

Castillo-Rogez, J. C., D. Hemingway, W. B. McKinnon, G. Schubert, G. Tobie, (2018), Origin and Evolution of Saturn's Midsize Moons, Part 3: Saturn's Icy Moons, In Enceladus and the icy moons of Saturn, (eds.) P. M. Schenk, R. N. Clark, C. J. A. Howett, A. J. Verbiscer, J. H. Waite, The University of Arizona Press, Tucson, AZ.

Castillo-Rogez, J. C., T. V. Johnson, P. C. Thomas, M. Choukroun, D. L. Matson, J. I. Lunine, (2012), Geophysical evolution of Saturn's satellite Phoebe, a large planetesimal in the outer Solar System, Icarus, 219, 1, 86–109, doi: 10.1016/j.icarus.2012.02.002.

Castillo-Rogez, J. C., M. Efroimsky, V. Lainey, (2011), The tidal history of Iapetus: Spin dynamics in the light of a refined dissipation model, Journal of Geophysical Research: Planets, 116, E9.

Castillo-Rogez, J., T. V. Johnson, M. H. Lee, N. J. Turner, D. L. Matson, J. Lunine, (2009), Al-26 decay: Heat production and a revised age for Iapetus, Icarus, 204, 2, 658–662, doi: 10.1016/j.icarus.2009.07.025.

Clark, R. N., R. H. Brown, D. P. Cruickshank, D. P. Swayze, (2019), Isotopic ratios of Saturn's Rings and Satellites: Implications for the Origin of Water and Phoebe, Icarus, 321, 791–802.

Clark, R. N, R. H. Brown, D. M. Lytle, M. Hedman, (2018), The VIMS wavelength and radiometric calibration 19, Final Report.

Clark, R. N., R. H. Brown, G. A. Swayze, D. P. Cruikshank, (2017a), Detecting isotopic signatures and measuring isotopic ratios on solid icy surfaces: Implications for origin and evolution, American Geophysical Union (AGU) Fall Meeting, abstract P52B-06.

Clark, R. N., R. H. Brown, G. A. Swayze, D. P. Cruikshank, (2017b), Detection of deuterium in icy surfaces and the D/H ratio of icy objects, American Astronomical Society (AAS), Division for Planetary Sciences Meeting, meeting 49, id 210.01.

Clark, R. N., R. H. Brown, D. P. Cruikshank, (2016a), CO2 and 12C: 13C isotopic ratios on Phoebe and Iapetus, American Geophysical Union (AGU) Fall Meeting, abstract P42A-07.

Clark, R. N., R. H. Brown, D. M. Lytle, D. P. Cruikshank, (2016b), Composition of Phoebe and Iapetus: bound water and possible deuterated water, American Astronomical Society (AAS), Division for Planetary Sciences Meeting, meeting 48, id 519.06.

Clark, R. N., D. P. Cruikshank, R. Jaumann, R. H. Brown, K. Stephan, C. M. D. Ore, K. E. Livo, N. Pearson, J. M. Curchin, T. M. Hoefen, B. J. Buratti, G. Filacchione, K. H. Baines, P. D. Nicholson, (2012), The surface composition of Iapetus: Mapping results from Cassini VIMS, Icarus, 218, 2, 831–860. doi: 10.1016/j.icarus.2012.01.008.

Clark, R. N., (2009), Detection of adsorbed water and hydroxyl on the Moon, Science, 326, 5952, 562–564, doi: 10.1126/science.1178105.

Clark, R. N., J. M. Curchin, R. Jaumann, D. P. Cruikshank, R. H. Brown, T. M. Hoefen, K. Stephan, J. M. Moore, B. J. Buratti, K. H. Baines, P. D. Nicholson, R. M. Nelson, (2008), Compositional mapping of Saturn's satellite Dione with Cassini VIMS and implications of dark material in the Saturn system, Icarus, 193, 2, 372–386.

Clark, R. N., R. H. Brown, R. Jaumann, D. P. Cruikshank, R. M. Nelson, B. J. Buratti, T. B. McCord, J. Lunine, K. H. Baines, G. Bellucci, J. P. Bibring, F. Capaccioni, P. Cerroni, A. Coradini, V. Formisano, Y. Langevin, D. L. Matson, V. Mennella, P. D. Nicholson, B. Sicardy, C. Sotin, T. M. Hoefen, J. M. Curchin, G. Hansen, K. Hibbits, K. D. Matz, (2005), Compositional maps of Saturn's moon Phoebe from imaging spectroscopy, Nature, 435 7038, 66–69, doi: 10.1038/nature03558.

Collins, G. C. and J. C. Goodman, (2007), Enceladus' south polar sea, Icarus, 189, 1, 72–82.

Cruikshank, D. P., C. M. D. Ore, R. N. Clark, Y. J. Pendleton, (2014), Aromatic and aliphatic organic materials on Iapetus: Analysis of Cassini VIMS data, Icarus, 233, 306–315, doi: 10.1016/j.icarus.2014.02.011.

Cruikshank, D. P., A. W. Meyer, R. H. Brown, R. N. Clark, R. Jaumann, K. Stephan, C. A. Hibbitts, S. A. Sandford, R. M. E. Mastrapa, G. Filacchione, C. M. D. Ore, P. D. Nicholson, B. J. Buratti, T. B. McCord, R. M. Nelson, J. B. Dalton, K. H. Baines, D. L. Matsoni, (2010), Carbon dioxide on the satellites of Saturn: Results from the Cassini VIMS investigation and revisions to the VIMS wavelength scale, Icarus, 206, 2, 561–572. doi: 10.1016/j.icarus.2009.07.012.

Dalton III, J. B., D. P. Cruikshank, R. N. Clark, (2012), Compositional analysis of Hyperion with the Cassini Visual and Infrared Mapping Spectrometer, Icarus, 220, 2, 752–776. doi: 10.1016/j.icarus.2012.05.003.

Damptz, A. L., A. J. Dombard, M. R. Kirchoff, (2018), Testing models for the formation of the equatorial ridge on Iapetus via crater counting, Icarus, 302, 134–144. doi: 10.1016/j.icarus.2017.10.049.

Denk, T., S. Mottola, F. Tosi, W. B. Bottke, D. P. Hamilton, (2018), The Irregular Satellites of Saturn, Part 3: Saturn's Icy Moons, In Enceladus and the Icy Moons of Saturn, (eds.) P. M. Schenk, R. N. Clark, C. J. A. Howett, A. J. Verbiscer, J. H. Waite, The University of Arizona Press, Tucson, AZ.

Denk, T. and S. Mottola, (2014), Periods, poles, and shapes of irregular satellites of Saturn from lightcurves, American Astronomical Society (AAS), Division for Planetary Sciences Meeting abstracts 46, id 304.09.

Denk, T. and S. Mottola, (2013), Irregular Saturnian moon lightcurves from Cassini-ISS Observations: Update, 45th American Astronomical Society (AAS), Division for Planetary Sciences Meeting, 6–11 October 2013, Denver, CO, vol. 45, no. 9, p. 170, id 406.08.

Denk, T., G. Neukum, T. Roatsch, C. C. Porco, J. A. Burns, G. G. Galuba, N. Schmedemann, P. Helfenstein, P. C. Thomas, R. J. Wagner, R. A. West, (2010), Iapetus: Unique surface properties and a global color dichotomy from Cassini Imaging, Science, 327, 5964, 435–439, doi: 10.1126/science.1177088.

Denk, T., G. Neukum, N. Schmedemann, T. Roatsch, R. J. Wagner, B. Giese, J. E. Perry, P. Helfenstein, E. P. Turtle, C. C. Porco, (2008), Iapetus imaging during the targeted flyby of the Cassini Spacecraft, 39th Lunar and Planetary Science Conference, League City, TX, 10–14 March 2008.

Denk, T., G. Neukum, T. Roatsch, A. S. McEwen, E. P. Turtle, P. C. Thomas, P. Helfenstein, R. J. Wagner, C. C. Porco, J. E. Perry, (2005a), First imaging results from the Iapetus b/c flyby of the Cassini Spacecraft, NASA Technical Reports Server, Lunar and Planetary Science XXXVI, Part 4, LPI-Contrib-1234-Pt-4.

Denk, T., G. Neukum, P. Helfenstein, P. C. Thomas, E. P. Tulle, A. S. McEwen, T. Roatsch, J. Veverka, T. V. Johnson, J. E. Perry, W. M. Owen, R. J. Wagner, C. C. Porco, (2005b), The first six months of Iapetus observations by the Cassini ISS camera, 36th Lunar and Planetary Science Conference, Houston, TX, 14–18 March 2005.

Denk, T., K. D. Matz, T. Roatsch, U. Wolf, R. J. Wagner, G. Neukum, R. Jaumann, (2000), Iapetus (1): Size, topography, surface structures, craters, 31st Lunar and Planetary Science Conference, Houston, TX, March 13–17, 2000.

Dones, H. C. L., E. B. Bierhaus, K. J. Zahnle, (2009), The population of impactors on the inner Saturnian satellites, American Astronomical Society (AAS), Division for Planetary Sciences Meeting, vol. 41, abstract 41.

Elder, C., P. Helfenstein, P. Thomas, J. Veverka, J. A. Burns, T. Denk, C. Porco, (2007), Tethys' mysterious equatorial band, Bulletin of the American Astronomical Society, vol. 39, p. 429.

Filacchione, G., E. D'Aversa, F. Capaccioni, R. N. Clark, D. P. Cruikshank, M. Ciarniello, P. Cerroni, G. Bellucci, R. H. Brown, B. J. Buratti, P. D. Nicholson, R. Jaumann, T. B. McCord, C. Sotin, K. Stephan, C. M. D. Ore, (2016), Saturn's icy satellites investigated by Cassini-VIMS. IV. Daytime temperature maps, Icarus, 271, 292–313. doi: 10.1016/j.icarus.2016.02.019.

Filacchione, G., F. Capaccioni, R. N. Clark, P. D. Nicholson, D. P. Cruikshank, J. N. Cuzzi, J. I. Lunine, R. H. Brown, P. Cerroni, F. Tosi, M. Ciarniello, B. J. Buratti, M. M. Hedman, E. Flamini, (2013), The radial distribution of water ice and chromophores across Saturn's system, The Astrophysical Journal, 766, 2, 76, doi: 10.1088/0004-637X/766/2/76.

Filacchione, G., F. Capaccioni, M. Ciarniello, R. N. Clark, J. N. Cuzzi, P. D. Nicholson, D. P. Cruikshank, M. M. Hedman, B. J. Buratti, J. I. Lunine, L. A. Soderblom, F. Tosi, P. Cerroni, R. H. Brown, T. B. McCord, R. Jaumann, K. Stephan, K. H. Baines, E. Flamini, (2012), Saturn's icy satellites and rings investigated by Cassini-VIMS: III - Radial compositional variability, Icarus, 220, 2, 1064–1096, doi: 10.1016/j.icarus.2012.06.040.

Geissler, P., A. McEwen, C. Porco, D. Strobel, J. Saur, J. Ajello, R. West, (2004), Cassini observations of Io's visible aurorae, Icarus, 172, 1, 127–40, doi: 10.1016/j.icarus.2004.01.008.

Giese, B., T. Denk, G. Neukum, T. Roatsch, P. Helfenstein, P. C. Thomas, E. P. Turtle, A. McEwen, C. C. Porco, (2008), The topography of Iapetus' leading side, Icarus, vol. 193, Issue 2, pp. 359–371.

Giese, B., R. Wagner, G. Neukum, P. Helfenstein, P. C. Thomas, (2007), Tethys: Lithospheric thickness and heat flux from flexurally supported topography at Ithaca Chasma, Geophysical Research Letters, 34, 21, L21203.

Giese, B., G. Neukum, T. Roatsch, T. Denk, C. C. Porco, (2006), Topographic modeling of Phoebe using Cassini images, Planetary and Space Science, 54, 12, 1156–66, doi: 10.1016/j.pss.2006.05.027.

Glein, C. R., J. A. Baross, J. H. Waite, (2015), The pH of Enceladus' ocean, Geochimica Et Cosmochimica Acta, 162, 202–219, doi: 10.1016/j.gca.2015.04.017.

Goguen, J. D., B. J. Buratti, R. H. Brown, R. N. Clark, P. D. Nicholson, M. M. Hedman, R. R. Howell, C. Sotin, D. P. Cruikshank, K. H. Baines, K. J. Lawrence, J. R. Spencer, D. G. Blackburn, (2013), The temperature and width of an active fissure on Enceladus measured with Cassini VIMS during the 14 April 2012 South Pole flyover, Icarus, 226, 1, 1128–1137, doi: 10.1016/j.icarus.2013.07.012.

Hammond, N. P., C. B. Phillips, F. Nimmo, S. A. Kattenhorn, (2013), Flexure on Dione: Investigating subsurface structure and thermal history, Icarus, 223, 1, 418–422, doi: 10.1016/j.icarus.2012.12.021.

Hansen, C. J., A. R. Hendrix, L. W. Esposito, (2018), Observations of stellar occultations to look for plumes from Dione and Tethys, 49th Lunar and Planetary Science Conference, 19–23 March 2018, The Woodlands, TX, vol. 49, no. 2083, id 2446.

Hansen, C. J., L. W. Esposito, A. R. Hendrix, (2017), UV detection and characterization of plume activity, American Geophysical Union (AGU) Fall Meeting, abstract P23F-05.

Hansen, C. J., L. W. Esposito, B. B. Buffington, J. Colwell, A. R. Hendrix, B. K. Meinke, D. E. Shemansky, I. Stewart, R. A. West, (2011), The structure of Enceladus' plume from Cassini occultation observations, American Geophysical Union (AGU) Fall Meeting, San Francisco, CA, 5–9 December 2011.

Hansen, C. J., L. W. Esposito, A. I. F. Stewart, B. Meinke, B. Wallis, J. E. Colwell, A. R. Hendrix, K. Larsen, W. Pryor, F. Tian, (2008), Water vapour jets inside the plume of gas leaving Enceladus, Nature, 456, 7221, 477–479, doi: 10.1038/nature07542.

Hansen, C. J., L. Esposito, J. Colwell, A. Hendrix, D. Matson, C. Parkinson, W. Pryor, D. Shemansky, I. Stewart, J. Tew, Y. Yung, (2006), Enceladus' water vapour plumes, Science 311, no. 5766, pp. 1422–1425, doi: 10.1126/science.1121254.

Hansen, C. J., D. E. Shemansky, A. R. Hendrix, (2005), Cassini UVIS observations of Europa's oxygen atmosphere and torus, Icarus, 176, 2, 305–315. doi: 10.1016/j.icarus.2005.02.007.

Hansen, O. L., (1973), Ten-micron eclipse observations of Io, Europa, and Ganymede, Icarus, 18, 2, 237–246.

Harbison, R. A., P. C. Thomas, P. C. Nicholson, (2011), Rotational modeling of Hyperion, Celestial Mechanics and Dynamical Astronomy, 110, 1, 1–16. doi: 10.1007/s10569-011-9337-3.

Hedman, M. M., D. Dhingra, P. D. Nicholson, C. J. Hansen, G. Portyankina, S. Ye, Y. Dong, (2018), Spatial variations in the dust-to-gas ratio of Enceladus' plume, Icarus, 305, 123-138. doi: 10.1016/j.icarus.2018.01.006.

Hedman, M. M., C. M. Gosmeyer, P. D. Nicholson, C. Sotin, R. H. Brown, R. N. Clark, K. H. Baines, B. J. Buratti, M. R. Showalter, (2013), An observed correlation between plume activity and tidal stresses on Enceladus, Nature, 500, 7461, 182–184. doi: 10.1038/nature12371.

Helfenstein, P., P. Thomas, J. Veverka, T. Denk, G. Neukum, R. A. West, B. Knowles, C. Porco, (2005), A Cassini ISS search for regolith-texture variations on Tethys, 36th Lunar and Planetary Science Conference, Houston, TX, 14–18 March 2005.

Hemingway, D. J., M. Zannoni, P. Tortora, F. Nimmo, S. W. Asmar, (2016), Dione's internal structure inferred from Cassini gravity and topography, 47th Lunar and Planetary Science Conference, The Woodlands, TX, March 21–25, 2016, vol. 47, p. 1314.

Hendrix, A. R., G. Filacchione, C. Paranicas, P. Schenk, F. Scipioni, (2018), Icy Saturnian satellites: Disk-integrated UV-IR characteristics and links to exogenic processes, Icarus, 300, 103–114, doi: 10.1016/j.icarus.2017.08.037.

Hendrix, A. R, K. S. Noll, J. R. Spencer, (2017), Icy Saturnian satellites: Using UV-Vis data to study surface composition and surface processing, American Astronomical Society (AAS), Division for Planetary Sciences Meeting, abstract 49.

Hendrix, A. R., T. A. Cassidy, B. J. Buratti, C. Paranicas, C. J. Hansen, B. Teolis, E. Roussos, E. T. Bradley, P. Kollmann, R. E. Johnson, (2012), Mimas' far-UV albedo: Spatial variations, Icarus, 220, 2, 922–931, doi: 10.1016/j.icarus.2012.06.012.

Hendrix, A. R. and C. J. Hansen, (2010), The surface composition of Enceladus: clues from the ultraviolet, International Astronomical Union, vol. 5, Issue S263 (Icy Bodies of the Solary System) pp. 126-130, doi: 10.1017/S1743921310001626.

Hendrix, A. R. and C. J. Hansen, (2008), Ultraviolet observations of Phoebe from the Cassini UVIS, Icarus, 193, 2, 323–333.

Howett, C., J. R. Spencer, A. Verbiscer, (2017), Characterizing the heat flow from between Enceladus' tiger stripes, American Geophysical Union (AGU) Fall Meeting, abstract P43B-2881.

Howett, C. J. A., J. R. Spencer, T. Hurford, A. Verbiscer, M. Segura, (2012), Pac-Man returns: An electron-generated thermal anomaly on Tethys, Icarus, 221, 2, 1084–1088, doi: 10.1016/j.icarus.2012.10.013.

Howett, C. J., J. R. Spencer, P. Schenk, R. E. Johnson, C. Paranicas, T. A. Hurford, A. J. Verbiscer, M. Segura, (2011), A high-amplitude thermal inertia anomalies of probable magnetospheric origin in the Saturnian system, American Geophysical Union (AGU) Fall Meeting, San Francisco, CA, 5–9 Dec. 2011.

Howett, C. J. A, J. R. Spencer, J. Pearl, M. Segura, (2010), Thermal inertia and bolometric bond albedo values for Mimas, Enceladus, Tethys, Dione, Rhea and Iapetus as derived from Cassini/CIRS measurements, Icarus, 206, 2, 573–593.

Hsu, H. W., F. Postberg, Y. Sekine, T. Shibuya, S. Kempf, M. Horanyi, A. Juhasz, N. Altobelli, K. Suzuki, Y. Masaki, T. Kuwatani, S. Tachibana, S. Sirono, G. Moragas-Klostermeyer, R. Srama, (2015), Ongoing hydrothermal activities within Enceladus, Nature, 519, 7542, 207–210, plus supplemental material, doi: 10.1038/nature14262.

Iess, L., D. J. Stevenson, M. Parisi, D. Hemingway, R. A. Jacobson, J. I. Lunine, F. Nimmo, J. W. Armstrong, S. W. Asmar, M. Ducci, P. Tortora, (2014), The gravity field and interior structure of Enceladus, Science, 344, 6179, 78–80, doi: 10.1126/science.1250551.

Ingersoll, A. P. and S. P. Ewald, (2017), Decadal timescale variability of the Enceladus plumes inferred from Cassini images, Icarus, 282, 260–275, doi: 10.1016/j.icarus.2016.09.018.

Jaumann, R., K. Stephan, G. B. Hansen, R. N. Clark, B. J. Buratti, R. H. Brown, K. H. Baines, S. F. Newman, G. Bellucci, G. Filacchione, A. Coradini, D. P. Cruikshank, C. A. Griffith, C. A. Hibbitts, T. B. McCord, R. M. Nelson, P. D. Nicholson, C. Sotin, R. Wagner, (2008), Distribution of icy particles across Enceladus' surface as derived from Cassini-VIMS measurements, Icarus, 193, 2, 407–419.

Johnson, T.V. and J. I. Lunine, (2005a), Densities of the Saturnian satellites and the C/O chemistry of the solar Nebula, Bulletin of the American Astronomical Society, vol. 37, p. 704.

Johnson, T. V. and J. I. Lunine, (2005b), Saturn's moon Phoebe as a captured body from the outer solar system, Nature, 435, 7038, 69–71. doi: 10.1038/nature03384.

JPL/CalTech, Solar System Dynamics Website, Physical Data & Dynamical Constants, https://ssd.jpl.nasa.gov/?phys_data.

JPL/CalTech, Solar System Dynamics Website, Planetary Satellite Mean Orbital Parameters, https://ssd.jpl.nasa.gov/?sat_elem.

Kempf, S., J. Schmidt, R. Srama, F. Postberg, F. Spahn, M. Horanyi, (2010), Enceladus dust production – new insights from Cassini, American Geophysical Union (AGU) Fall Meeting 2010, San Francisco, CA, abstract P33A-1562.

Khurana, K. K., C. T. Russell, M. K. Dougherty, (2008), Magnetic portraits of Tethys and Rhea, Icarus, 193, 2, 465–474.

Kirchoff, M. R., E. B. Bierhaus, L. Dones, S. J. Robbins, K. N. Singer, R. J. Wagner, K. J. Zahnle, (2018), Cratering Histories in the Saturnian System, Part 3: Saturn's Icy Moons, In Enceladus and the Icy Moons of Saturn, (eds.) P. M. Schenk, R. N. Clark, C. J. A. Howett, A. J. Verbiscer, J. H. Waite, The University of Arizona Press, Tucson, AZ, pp. 267–284.

Kirchoff, M. R. and P. Schenk, (2010), Impact cratering records of the mid-sized, icy saturnian satellites, Icarus, 206, 2, 485–497, doi: 10.1016/j.icarus.2009.12.007.

Kite, E. S. and A. M. Rubin, (2016), Sustained eruptions on Enceladus explained by turbulent dissipation in tiger stripes, Proceedings National Academy of Sciences, 113, 15, 3972–3975, doi: 10.1073/pnas.1520507113.

Le Gall, A. A., R. West, M. A. Jansses, C. Leyrat, L. Bonnefoy, E. Lellouch, (2017), Cassini radar and radiometry observations of Saturn's airless icy satellites, American Geophysical Union (AGU) Fall Meeting, New Orleans, LA, 11–15 December 2017, abstract P23G-02. 2017.

Lee, J. S., B. J. Buratti, M. Hicks, J. Mosher, (2010), The roughness of the dark side of Iapetus from the 2004 to 2005 flyby, Icarus, 206, 2, 623–630, doi: 10.1016/j.icarus.2009.11.008.

Levison, H. F., K. J. Walsh, A. C. Barr, L. Dones, (2011), Ridge formation and de-spinning of Iapetus via an impact-generated satellite, Icarus, 214, 2, 773–778, doi: 10.1016/j.icarus.2011.05.031.

Matson, D. L., J. C. Castillo-Rogez, A. G. Davies, T. V. Johnson, (2012), Enceladus: A hypothesis for bringing both heat and chemicals to the surface, Icarus, 221, 1, 53–62, doi: 10.1016/j.icarus.2012.05.031.

McKinnon, W. B., (2015), Effect of Enceladus's rapid synchronous spin on interpretation of Cassini gravity, Geophysical Research Letters, 42, 7, 2137–2143, doi: 10.1002/2015GL063384.

Morrison, D. and D. P. Cruikshank, (1973), Thermal properties of the Galilean satellites, Icarus, 18, 2, 224–236.

Newman, S. F., B. J. Buratti, R. H. Brown, R. Jaumann, J. Bauer, T. Momary, (2009), Water ice crystallinity and grain sizes on Dione, Icarus, 203, 2, 553–559, doi: 10.1016/j.icarus.2009.04.034.

Nimmo, F., C. Porco, C. Mitchell, (2014), Tidally modulated eruptions on Enceladus: Cassini ISS observations and models, The Astronomical Journal, 148, 3, 46, doi: 10.1088/0004-6256/148/3/46.

Ostro, S. J., R. D. West, L. C. Wye, H. A. Zebker, M. A. Janssen, B. Stiles, K. Kelleher, Y. Z. Anderson, R. A. Boehmer, P. Callahan, Y. Gim, G. A. Hamilton, W. T. K. Johnson, C. Veeramachaneni, R. D. Lorenz, Radar Team Cassini, (2010), New Cassini RADAR results for Saturn's icy satellites, Icarus, 206, 2, 498–506, doi: 10.1016/j.icarus.2009.07.041.

Ostro, S. J., R. D. West, M. A. Janssen, R. D. Lorenz, H. A. Zebker, G. J. Black, J. I. Lunine, L. C. Wye, R. M. Lopes, S. D. Wall, C. Elachi, L. Roth, S. Hensley, K. Kelleher, G. A. Hamilton, Y. Gim, Y. Z. Anderson, R. A. Boehmer, W. T. K. Johnson, (2006), Cassini RADAR observations of Enceladus, Tethys, Dione, Rhea, Iapetus, Hyperion, and Phoebe, Icarus, 183, 2, 479–90, doi: 10.1016/j.icarus.2006.02.019.

Paranicas, C., E. Roussos, R. B. Decker, R. E. Johnson, A. R. Hendrix, P. Schenk, T. A. Cassidy, J. B. Dalton III, C. J. A. Howett, P. Kollmann, W. Patterson, K. P. Hand, T. A. Nordheim, N. Krupp, D. G. Mitchell, (2014), The lens feature on the inner saturnian satellites, Icarus, 234, 155–161, doi: 10.1016/j.icarus.2014.02.026.

Paranicas, C., E. Roussos, N. Krupp, P. Kollmann, A. R. Hendrix, T. Cassidy, R. E. Johnson, P. Schenk, G. Jones, J. Carbary, D. G. Mitchell, K. Dialynas, (2012), Energetic charged particle weathering of Saturn's inner satellites, Planetary and Space Science, 61, 1, 60–65, doi: 10.1016/j.pss.2011.02.012.

Pitman, K. M., L. Kolokolova, A. J. Verbiscer, (2013), Coherent backscattering effect in Icy Satellites: Model, Cassini VIMS, and Ground-Based Near-Infrared Spectra, American Astronomical Society (AAS), Division for Planetary Sciences Meeting, abstract 45.

Porco, C., C. Mitchell, F. Nimmo, M. Tiscareno, (2018), Enceladus' plume temporal variability from analysis of Cassini ISS images, 49th Lunar and Planetary Science Conference, 19–23 March 2018, The Woodlands, TX, LPI Contribution No. 2083, id 2003.

Porco, C. C., L. Dones, C. Mitchell, (2017), Could it be snowing microbes on Enceladus? Assessing conditions in its plume and implications for future missions, Astrobiology, 17, 9, 876–901.

Porco, C., D. DiNino, F. Nimmo, (2014), How the geysers, tidal stresses, and thermal emission across the south polar terrain of Enceladus are related, The Astronomical Journal, 148, 3, 45–69, doi: 10.1088/0004-6256/148/3/45.

Porco, C. C., P. Helfenstein, P. C. Thomas, A. P. Ingersoll, J. Wisdom, R. West, G. Neukum, T. Denk, R. Wagner, T. Roatsch, S. Kieffer, E. Turtle, A. McEwen, T. V. Johnson, J. Rathbun, J. Veverka, D. Wilson, J. Perry, J. Spitale, A. Brahic, J. A. Burns, A. D. DelGenio, L. Dones, C. D. Murray, S. Squyres, (2006), Cassini observes the active south pole of Enceladus, Science, 311, 5766, 1393–1401, doi: 10.1126/science.1123013.

Porco, C. C., E. Baker, J. Barbara, K. Beurle, A. Brahic, J. A. Burns, S. Charnoz, N. Cooper, D. D. Dawson, A. D. Del Genio, T. Denk, L. Dones, U. Dyudina, M. W. Evans, B. Giese, K. Grazier, P. Helfenstein, A. P. Ingersoll, R. A. Jacobson, T. V. Johnson, A. McEwen, C. D. Murray, G. Neukum, W. M. Owen, J. Perry, T. Roatsch, J. Spitale, S. Squyres, P. C. Thomas, M. Tiscareno, E. Turtle, A. R. Vasavada, J. Veverka, R. Wagner, R. West, (2005), Cassini Imaging Science: Initial results on Phoebe and Iapetus, Science, 307, 5713, 1237–1242, doi: 10.1126/science.1107981.

Porco, C. C., R. A. West, A. McEwen, A. D. Del Genio, A. P. Ingersoll, P. Thomas, S. Squyres, L. Dones, C. D. Murray, T. V. Johnson, J. A. Burns, A. Brahic, G. Neukum, J. Veverka, J. M. Barbara, T. Denk, M. Evans, J. J. Ferrier, P. Geissler, P. Helfenstein, T. Roatsch, H. Throop, M. Tiscareno, A. R. Vasavada, (2003), Cassini imaging of Jupiter's atmosphere,

satellites, and rings, Science, vol. 299, Issue 5612, pp. 1541–1547, doi: 10.1126/science.1079462.

Postberg, F., N. Khawaja, S. Kempf, J. H. Waite, C. Glein, H. W. Hsu, R. Srama, (2017), Complex organic macromolecular compounds in ice grains from Enceladus, , 48th Lunar and Planetary Science Conference, Houston, TX, abstract 1401.

Postberg, F., J. Schmidt, J. Hillier, S. Kempf, R. Srama, (2011), A salt-water reservoir as the source of a compositionally stratified plume on Enceladus, Nature, 474, 7353, 620–622, doi: 10.1038/nature10175.

Postberg, F., S. Kempf, J. Schmidt, N. Brilliantov, A. Beinsen, B. Abel, U. Buck, R. Srama, (2009), Sodium salts in E-ring ice grains from an ocean below the surface of Enceladus, Nature, 459, 7250, 1098–1101, doi: 10.1038/nature08046.

Rathbun, J. A., J. R. Spencer, L. K. Tamppari, T. Z. Martin, L. Barnard, L. D. Travis, (2003), Galileo PPR at Io: High-resolution scans taken in conjunction with SSA and NIMS data, 34th Annual Lunar and Planetary Science Conference, March 17–21, 2003, League City, TX, abstract 385.

Royer, E. M. and A. R. Hendrix, (2014), First far-ultraviolet disk-integrated phase curve analysis of Mimas, Tethys and Dione from the Cassini-UVIS data sets, Icarus, 242, 158–171, doi: 10.1016/j.icarus.2014.07.026.

Schenk, P. M., R. N. Clark, C. J. A. Howett, A. J. Verbiscer, J. H. Waite, (2018), Enceladus and the Icy Moons of Saturn, Space Science, The University of Arizona Press in collaboration with Lunar and Planetary Institute.

Schenk, P. M., B. Buratti, P. Byrne, W. B. McKinnon, F. Nimmo, F. Scipioni, (2015), Blood stains on Tethys: evidence of recent activity, EOS p P21B-02.

Schenk, P., (2014), The colors of Enceladus: From plumes and particles to active fractures, 45th Lunar and Planetary Science Conference, The Woodlands, TX, 17–21 March 2014, LPI Contribution No. 1777, p. 2618.

Schenk, P., D. P. Hamilton, R. E. Johnson, W. B. McKinnon, C. Paranicas, J. Schmidt, M. R. Showalter, (2011), Plasma, plumes and rings: Saturn system dynamics as recorded in global color patterns on its midsize icy satellites, Icarus, 211, 1, 740–757, doi: 10.1016/j.icarus.2010.08.016.

Schmedemann, N. and G. Neukum, (2011), Impact crater size-frequency distribution (SFD) and surface ages on Mimas, 42nd Lunar and Planetary Science Conference, The Woodlands, TX, LPI Contribution No. 1608, p. 2772.

Schmidt, J., F. Postberg, N. V. Brilliantov, S. Kempf, A. Beinsen, B. Abel, U. Buck, R. Srama, (2009), On the Formation of sodium bearing E-ring ice grains on Enceladus, American Astronomical Society (AAS), Division for Planetary Sciences Meeting, abstract 41.

Scipioni, F., P. Schenk, F. Tosi, E. D'Aversa, R. Clark, J. P. Combe, C. M. D. Ore, (2017), Deciphering sub-micron ice particles on Enceladus surface, Icarus, 290, 183–200, doi: 10.1016/j.icarus.2017.02.012.

Shemansky, D. E., Y. L. Yung, X. Liu, J. Yoshii, C. J. Hansen, A. R. Hendrix, L. W. Esposito, (2014), A new understanding of the Europa atmosphere and limits on geophysical activity, The Astrophysical Journal, 797, 2, 84.

Simon, S., J. Saur, F. M. Neubauer, A. Wennmacher, M. K. Dougherty, (2011), Magnetic signatures of a tenuous atmosphere at Dione, Geophysical Research Letters, 38, 15, L15102, doi: 10.1029/2011GL048454.

Simonelli, D. P. and B. J. Buratti, (2004), Europa's opposition surge in the near-infrared: interpreting disk-integrated observations by Cassini VIMS, Icarus, 172, 1, 149–62, doi: 10.1016/j.icarus.2004.06.004.

Singer, K. N., W. B. McKinnon, P. M. Schenk, J. M. Moore, (2012), Massive ice avalanches on Iapetus mobilized by friction reduction during flash heating, Nature Geoscience, 5, 8, 574–578, doi: 10.1038/NGEO1526.

Singer, K. N. and W. B. McKinnon, (2011), Tectonics on Iapetus: Despinning, respinning, or something completely different? Icarus, 216, 1, 198–211, doi: 10.1016/j.icarus.2011.08.023.

Spencer, J. R. and T. Denk, (2010), Formation of Iapetus' extreme albedo dichotomy by exogenically triggered thermal ice migration, Science, 327, 5964, 432–435, doi: 10.1126/science.1177132.

Spencer, J. R., L. K. Tamppari, T. Z. Martin, L. D. Travis, (1999), Temperatures on Europa from Galileo photopolarimeter-radiometer: nighttime thermal anomalies, Science, 284, 5419, 1514–1516.

Spencer, J. R., (1987), The surfaces of Europa, Ganymede, and Callisto: an Investigation using Voyager IRIS thermal infrared spectra (Jupiter), The University of Arizona, Dissertation.

Spilker, L. J., (1997), Passage to a Ringed World: The Cassini-Huygens Mission to Saturn and Titan, National Aeronautics and Space Administration Technical Report, NASA-SP-533, NAS 1.21:533.

Spitale, J. N., T. A. Hurford, A. R. Rhoden, E. E. Berkson, S. S. Platts, (2015), Curtain eruptions from Enceladus' south-polar terrain, Nature, 521, 7550, 57–60, doi: 10.1038/nature14368.

Stephan, K., R. Jaumann, R. Wagner, R. N. Clark, D. P. Cruikshank, B. Giese, C. A. Hibbitts, T. Roatsch, K.-D. Matz, R. H. Brown, G. Filacchione, F. Cappacioni, F. Scholten, B. J. Buratti, G. B. Hansen, P. D. Nicholson, K. H. Baines, R. M. Nelson, D. L. Matson, (2012), The Saturnian satellite Rhea as seen by Cassini VIMS, Planetary and Space Science, 61, 1, 142–160, doi: 10.1016/j.pss.2011.07.019.

Stooke, P. J., (2002), Tethys and Dione: New geological interpretations, 33rd Annual Lunar and Planetary Science Conference, March 11–15, 2002, Houston, TX, abstract 1553.

Stooke, P. J., (1989), Tethys: Volcanic and structural geology, Lunar and Planetary Science Conference, vol. 20, p. 1071.

Tajeddine, R., N. Rambaux, V. Lainey, S. Charnoz, A. Richard, A. Rivoldini, B. Noyelles, (2014), Constraints on Mimas' interior from Cassini ISS libration measurements, Science, 346, 6207, 322–324, doi: 10.1126/science.1255299.

Tamayo, D., M. M. Hedman, J. A. Burns, (2014), First observations of the Phoebe ring in optical light, Icarus, 233, 1–8, doi: 10.1016/j.icarus.2014.01.021.

Teolis, B. D., M. E. Perry, C. J. Hansen, J. H. Waite, C. C. Porco, J. R. Spencer, C. J. A. Howett, (2017), Enceladus plume structure and time variability: Comparison of Cassini observations, Astrobiology, vol. 17, no. 9, 926–940, doi: 10.1089/ast.2017.1647.

Thomas, P. C., M. S. Tiscareno, P. Helfenstein, (2018), The Inner Small Satellites of Saturn and Hyperion, Part 3: Saturn's Icy Moons, In Enceladus and the Icy Moons of Saturn, (eds.) P. M. Schenk, R. N. Clark, C. J. A. Howett, A. J. Verbiscer, J. H. Waite, The University of Arizona Press, Tucson, AZ.

Thomas, P. C., R. Tajeddine, M. S. Tiscareno, J. A. Burns, J. Joseph, T. J. Loredo, P. Helfenstein, C. Porco, (2016), Enceladus's measured physical libration requires a global subsurface ocean, Icarus, 264, 37–47.

Thomas, P., R. Tajeddine, M. S. Tiscareno, J. A. Burns, J. Joseph, T. J. Loredo, P. Helfenstein, C. Porco, (2015), Enceladus's subsurface sea is part of a global ocean as shown by measured physical libration, American Geophysical Union (AGU) Fall Meeting, abstract P11D-05.

Thomas, P. C., J. A. Burns, M. Hedman, P. Helfenstein, S. Morrison, M. S. Tiscareno, J. Veverka, (2013), The inner small satellites of Saturn: A variety of worlds, Icarus, 226, 1, 999–1019, doi: 10.1016/j.icarus.2013.07.022.

Thomas, P. C., (2010), Sizes, shapes, and derived properties of the saturnian satellites after the Cassini nominal mission, Icarus, 208, 1, 395–401, doi: 10.1016/j.icarus.2010.01.025.

Thomas, P. C., J. A. Burns, R. Helfenstein, S. Squyres, J. Veverka, C. Porco, E. P. Turtle, A. McEwen, T. Denk, B. Giese, T. Roatsch, T. V. Johnson, R. A. Jacobson, (2007), Shapes of the saturnian icy satellites and their significance, Icarus, 190, 2, 573–584, doi: 10.1016/j.icarus.2007.03.012.

Tiscareno, M. S., J. A. Burns, J. N. Cuzzi, M. M. Hedman, (2010), Cassini imaging search rules out rings around Rhea, Geophysical Research Letters, 37, 14, L14205, doi: 10.1029/2010GL043663.

Tokar, R. L., R. E. Johnson, M. F. Thomsen, E. C. Sittler, A. J. Coates, R. J. Wilson, F. J. Crary, D. T. Young, G. H. Jones, (2012), Detection of exospheric O2+ at Saturn's moon Dione, Geophysical Research Letters, 39, 3, L03105, doi: 10.1029/2011GL050452.

Tortora, P., M. Zannoni, D. Hemingway, F. Nimmo, R. A. Jacobson, L. Iess, M. Parisi, (2016), Rhea gravity field and interior modeling from Cassini data analysis, Icarus, 264, 264–273, doi: 10.1016/j.icarus.2015.09.022.

Verbiscer, A. J., Helfenstein, P., Buratti, B. J., and Royer, E., (2018), Surface Properties of Saturn's Icy Moons from Optical Remote Sensing, Part 3: Saturn's Icy Moons, In Enceladus and the Icy Moons of Saturn, (eds.) Schenk, P. M., Clark, R. N., Howett, C. J. A., Verbiscer, A. J., and Waite, J. H., The University of Arizona Press, Tucson, AZ.

Wagner, R. J., G. Neukum, U. Wolf, N. Schmedemann, T. Denk, K. Stephan, T. Roatsch, C. C. Porco, (2011), Bright ray craters on Rhea and Dione, 42nd Lunar and Planetary Science Conference, March 7–11, 2011, Houston, TX, LPI Contribution no. 1608, p.2249.

Wagner, R. J., G. Neukum, B. Giese, T. Roatsch, T. Denk, U. Wolf, C. C. Porco, (2010), The geology of Rhea; a first look at the ISS camera data from orbit 121 (Nov. 21, 2009) in Cassini's extended mission, 41st Lunar and Planetary Science Conference XLI, March 1–5, 2010, The Woodlands, TX, LPI Contribution no. 1533, p.1672.

Wagner, R. J., G. Neukum, B. Giese, T. Roatsch, T. Denk, (2007), Geology and Geomorphology of Rhea: a First Look at the High-Resolution Cassini ISS Images from the Targeted Flyby on Aug. 30, 2007, American Geophysical Union (AGU) Fall Meeting, abstract P12B-06.

Waite, J. H., C. R. Glein, R. S. Perryman, B. D. Teolis, B. A. Magee, G. Miller, J. Grimes, M. E. Perry, K. E. Miller, A. Bouquet, J. I. Lunine, T. Brockwell, S. J. Bolton, (2017), Cassini finds molecular hydrogen in the Enceladus plume: Evidence for hydrothermal processes, Science, 356, 6334, 155–159, doi: 10.1126/science.aai8703.

Yeoh, S. K., Z. Li, D. B. Goldstein, P. L. Varghese, D. A. Levin, L. M. Trafton, (2017), Constraining the Enceladus plume using numerical simulation and Cassini data, Icarus, 281, 357–378, doi: 10.1016/j.icarus.2016.08.028.

Zhang, Z., A. G. Hayes, M. A. Janssen, P. D. Nicholson, J. N. Cuzzi, I. de Pater, D. E. Dunn, (2017), Exposure age of Saturn's A and B rings, and the Cassini Division as suggested by their non-icy material content, Icarus, 294, 14–42, doi: 10.1016/j.icarus.2017.04.008.

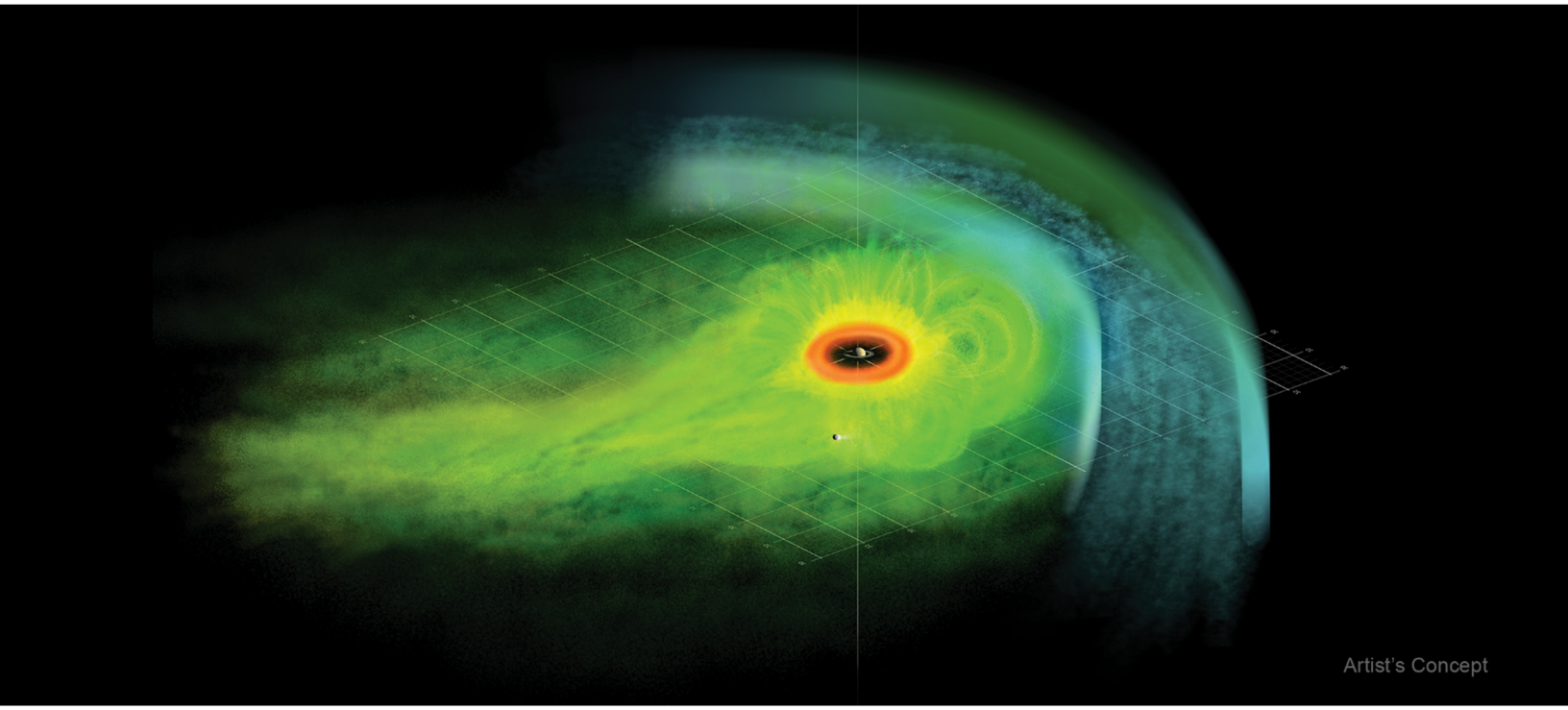

MAPS

Prior to Cassini's arrival, scientists had little information about Saturn's magnetosphere, the giant, invisible magnetic bubble surrounding the planet. Cassini studied Saturn's magnetosphere as never before by mapping the magnetic field, studying the flow of excited plasma within, and observing the influence of the solar wind and how it affects Saturn's auroras. Fields and particles data have provided powerful insights about how Saturn's magnetic field provide linkages between charged particle sources and the rings, moons, and atmospheres, in addition to the inner workings of Saturn's interior.

The **Magnetospheres and Plasma Science (MAPS)** Discipline Working Group (DWG) facilitated and coordinated the data sharing and collective science among the six MAPS instrument teams to ensure that all Cassini's MAPS mission objectives were successfully met. The MAPS DWG has achieved and exceeded in every way the Cassini mission goals and objectives, and has provided a legacy for the outer planets community that will reach far into the future.

CONTENTS

Figures

Tables

EXECUTIVE SUMMARY

…it is clear that the MAPS DWG achieved and exceeded in every way the AO and extended mission goals, and provided a legacy … that will reach far into the future.

The purpose of the Magnetospheres and Plasma Science (MAPS) Discipline Working Group (DWG) was to facilitate and coordinate the data sharing and collective science among the MAPS instruments teams to ensure that all Cassini Announcement of Opportunity (AO) and extended mission objectives were achieved. Without reservation it is clear that the MAPS DWG achieved and exceeded in every way the AO and extended mission goals, and provided a legacy for the outer planets community that will reach far into the future.

Perhaps the most important single contribution to the MAPS science coming from the Interdisciplinary scientist of the MAPS DWG was the creation of the MAPS Rules-of-the-Road. This document outlined a very clear policy that MAPS instruments would share data, that PIs would take responsibility for their teams, and that collaborative work would be the norm for MAPS not the exception. A separate closeout document describes in detail the creation and execution of the Rules-of-the-Road. While the MAPS DWG was not without its conflicts, the legacy of this document was a DWG that shared data that fostered collaborations between instrument teams and created new investigations without significant conflict.

In addition to the MAPS Rules-of-the-Road, another operating principle of the MAPS DWG and the DWG Interdisciplinary Scientists (IDSs) was that the instrument teams should take the lead, and thereby receive the glory, on nearly all investigations. With this guiding principle, the DWG was able to have the most relevant team lead, most investigations, and then have other teams contribute.

KEY SCIENCE RESULTS

Top Science Findings for MAPS

Discovery of the Enceladus plumes and their interaction with Saturn's magnetosphere

One of the most important and surprising discoveries of the entire Cassini mission was the discovery of an atmospheric plume at Enceladus by the magnetometer team [Dougherty et al. 2006] on February 17, 2005. The discovery was confirmed and strengthened by subsequent measurements on later flybys and other instruments. This dynamic atmospheric plume was later shown by the Imaging team to be due to geyser activity on the southern hemisphere of Enceladus. Subsequent modeling based on analytical theory clearly showed that the magnetometer results

required the presence of negatively charged dust particles [Simon et al. 2011]. As a unique feature at Enceladus, dust–plasma interactions play an important role to explain the observations.

The discovery of a large and neutral plasma source at Enceladus led to the potential that the moon's interaction with Saturn would result in currents along the magnetic flux tube that could cause an auroral footprint in Saturn's ionosphere. Although initial Hubble Space Telescope (HST) observations did not detect such an auroral footprint [Wannawichian et al. 2008], a follow-on study discovered an Enceladus-associated aurora in a few percent of the scans of the moon's footprint [Pryor et al. 2011]. The footprint varies in emission magnitude more than can plausibly be explained by changes in magnetospheric parameters, and as such is probably indicative of variable plume activity.

Identifying the highly axisymmetric internal magnetic field of Saturn

Early in the mission the Magnetometer (MAG) team determined that the tilt of Saturn's dipole must be smaller than 0.06 degrees from the spin-axis of Saturn which was further constrained by the Grand Finale measurements to <0.01 degrees [Dougherty et al. 2018]. The time variation of Saturn's intrinsic magnetic field must be an order of magnitude slower than that of Earth's [Cao et al. 2011]. These results are very challenging for dynamo theory, as Cowling's theorem excludes the possibility of a purely axisymmetric magnetic field being maintained by dynamo action. The Cassini Grand Finale gravity measurements indicate that the ~100 m/s zonal flows observed at the cloud deck of Saturn extend almost 10,000 kilometers into the planetary interior. Given that the electrical conductivity at such depth are high enough for significant magnetohydrodynamic (MHD) effects, zonal flow magnetic field interaction in the semi-conducting region of Saturn is now a central issue in understanding the interior dynamics. The amplitude of the wind-induced magnetic perturbations would depend on the amplitude of the deep differential rotation as well as the amplitude of the small-scale deep convective flow. Thus, measuring/constraining wind-induced magnetic perturbations along the Cassini Grand Finale orbits would place important constraints on the properties (profile and amplitude) of deep differential rotation and convective flow in the semi-conducting region of Saturn. This work is still ongoing and we expect additional discoveries.

Discovery of periodicities while the intrinsic rotation rate remains elusive

Many properties of Saturn's magnetosphere exhibit periodicities at approximately the planetary rotation rate, a significant puzzle given the near-alignment of the magnetic and rotational axes. Saturn's kilometric radiation (SKR) is the most intense radio emission component, produced in the auroral regions. The first SKR periodicity measured by Cassini witnessed a value differing by 1% to the SKR period identified from Voyager/Planetary Radio Astronomy (PRA) observations 25 years earlier [Gurnett et al. 2005]. Such a large variation implies that the SKR period does not probe the internal rotation rate. The major discovery was the identification of two SKR periods [Kurth et al. 2008] corresponding to the two Kronian hemispheres, differing by ~1%. Both of those periods were found to vary with time in anti-correlation over yearly timescales and crossed closely after equinox, a trend which was interpreted as a seasonal driving of solar illumination [Gurnett et al. 2011a,

2010a, 2009; Lamy 2011]. These dual periods were also observed in numerous magnetospheric observables including magnetic oscillations, energetic neutral atom (ENA) emissions, and aurorae [Mitchell et al. 2009b; Carbary et al. 2011a, 2010a; Nichols et al. 2010; Andrews et al. 2011, 2010; Provan et al. 2011; Badman et al. 2012a, 2012b]. It is now accepted that these dual rotational modulations all originate from two rotating hemispheric systems of field-aligned currents, whose origin may be atmospheric vortices [Jia et al. 2012].

Discovery of new radiation belts

The Magnetospheric Imaging Instrument (MIMI)/Low Energy Magnetospheric Measurement System (LEMMS) instrument discovered a previously unknown radiation belt collocated with the D-ring and extending up to the dense atmosphere of Saturn. This belt was discovered earlier in the Cassini mission [Kollmann et al. 2015], but its properties were unknown. It was found that the belt is dominated by protons up the GeV range, which is the first time that such high energies were directly observed at any of the giant planets. Their pitch angle distribution is very steep, likely due to a strong interaction with Saturn's atmosphere. The suggested source is Cosmic Ray Albedo Neutron Decay (CRAND). There is no evidence for the presence of energetic electrons or ions heavier than protons [Roussos et al. 2018a; Kollmann et al. 2018].

Identifying the main plasma sources in Saturn's magnetosphere

The dominant ion species seen throughout the magnetosphere are well explained by ionization of material from the water plumes of Enceladus that are estimated to produce ~60–100 kg/s [Fleshman et al. 2013]. Enceladus is also the probable source of most of the N^+ observed in Saturn's inner magnetosphere [Smith et al. 2010]. The finding of very little N^+ in the outer magnetosphere [Smith et al. 2005] indicated that Titan's contribution to the heavy-ion plasma is limited, whereas the fact that H_2^+ becomes comparable to H^+ and W^+ in the outer magnetosphere [Thomsen et al. 2010] indicates that Titan is an important source of lighter ions in that region producing ~0.8 kg/s [Coates et al. 2012]. Observation of probable plasma outflows from Saturn's ionosphere led to an estimate of some 10 s of kg/s lofted from the ionosphere [Felici et al. 2016]. It is, however, not yet clear how often such outflow occurs. During Saturn Orbit Insertion (SOI) a layer of O_2^+ and O^+ was discovered over the A-ring and B-ring [Young et al. 2005]. The ring atmosphere and ionosphere are likely produced by ultraviolet (UV) photo sputtering of the icy rings and subsequent photoionization of O^+. Significant O^+ was also detected outside the main rings, near the F-ring [Tokar et al. 2005], and analysis of the O^+ and W^+ profiles showed seasonal dependence consistent with a ring source that depends on the solar illumination angle [Elrod et al. 2014, 2012]. In contrast, Gurnett et al. [2005] show evidence of deep density depletions over the ring during SOI. These results indicate that the rings are an important source of heavy ions inside the orbit of Mimas.

Global configuration and dynamics of the magnetosphere

Cassini discovered that most of the magnetospheric plasma is produced by Enceladus deep inside the magnetosphere. Combined with very strong centrifugal forces this source controls most of Saturn's magnetospheric dynamics. Cassini has also discovered evidence that, unlike at the Earth, the solar wind plays a relatively small role in magnetospheric dynamics, primarily associated with large dynamic pressure enhancements. Saturn's giant magnetic field is the principal cause of the transport of material between the many bodies in this still evolving system, dumping oxygen into the atmospheres of Titan and Saturn. Cassini detected radially outward plasma flows of ~800 km/s during observation of a plasmoid (magnetically detached plasma bubble) on March 4, 2006.

Understanding the transport of plasma through the magnetosphere and the mechanisms for its eventual loss of plasma has been one of the major points of focus of the MAPS investigation. Plasma transport occurs through convection, plasma interchange, reconnective processes, and plasmoid formation. At the time of Cassini's arrival to Saturn the relative importance of these different processes was poorly understood. Now with 13 years of magnetospheric data we have a much better understanding of these different processes. MAPS studies have addressed the relative importance of Vasyliunas-cycle and Dungey-cycle reconnection, and the formation process and frequency of plasmoids and how they are related to dipolarizations. There have been a whole host of studies on the frequency, distribution, source region, life time, size, and plasma properties of the different interchange events that Cassini has observed.

First in situ measurements of Saturn's topside ionosphere

During the Cassini Grand Finale, Cassini MAPS instruments made an unprecedented series of measurements of Saturn's upper atmosphere, sampling from ~3500–1370 km altitude above the 1 bar pressure level. Prior to these orbits, it was anticipated that Saturn's upper atmosphere consisted primarily of H, H_2, with trace amounts of H_2O and He. The in situ measurements of Saturn's ionosphere allowed the first determination of ion mixing ratios and number densities as well as their temporal variabilities. The measurements of helium provided constraints on possible deep-atmosphere mixing ratios of helium and whether or not Saturn has a solar-like composition or something else. In the equatorial region of Saturn's ionosphere where the ring-ionosphere interaction is important, combined with Radio and Plasma Wave Science (RPWS) and MIMI measurements, Ion and Neutral Mass Spectrometer (INMS) in situ data paint a clear picture of Saturn's equatorial ionosphere being dominated by heavy molecular ions that result from ring-derived material. Near the end of the mission, during the proximal orbits, INMS measured densities of H^+, H_2^+, H_3^+, and He^+ in Saturn's ionosphere.

> All of these unanticipated results have effectively turned our understanding of the high-altitude thermosphere-ionosphere chemistry on its head.

In addition to the primary and expected species, the INMS measurements revealed an atmosphere with an

unexpectedly rich composition, containing significant amounts of organics spanning the entire mass range sampled by INMS and specifically the presence of several species of high mass neutrals, for example, CH_4, CO, CO_2. All of these unanticipated results have effectively turned our understanding of the high-altitude thermosphere-ionosphere chemistry on its head.

Detection of lightning in Saturn's atmosphere and the evolution of a once-per-Saturn-year Great White Spot storm

The first indication of lightning in Saturn's atmosphere was obtained in November 1980 by the radio instrument onboard Voyager 1. Strong impulsive signals in the frequency range of a few MHz were detected and termed SEDs for Saturn Electrostatic Discharges [Warwick et al. 1981]. The Cassini mission has greatly enhanced our knowledge about Saturn lightning, and combined radio and imaging observations, have clearly established the atmospheric origin of the SEDs.

RPWS provided the most complete census of lightning activity from near continuous observations of Saturn electrostatic discharges (SED) and established the frequency of convective storms on Saturn, their duration, and lightning flash rates, see for example, Fischer et al. [2011a, 2011b]. Saturn lightning flashes were first detected optically on the nightside of Saturn around equinox. The Cassini cameras spotted flash-illuminated cloud tops with a diameter of about 200 km, suggesting that the lightning comes from 125–250 km below [Dyudina et al. 2010], and most likely from the water-cloud layer. At Earth the charging of water cloud particles in thunderstorms is most effective in a temperature range of −10° C to −25° C. At Saturn this temperature range is located at a level of 8–10 bars, about 200 km below the cloud tops, i.e., consistent with the altitude range found by Dyudina et al. [2010]. Another indication that the Saturn lightning source is in the water cloud layer comes from Cassini Visual and Infrared Imaging Spectrometer (VIMS) near-infrared spectra of the Great White Spot. They revealed spectroscopic evidence for ammonia and water ices [Sromovsky et al. 2013] brought up to higher altitudes by strong vertical convection. So, it is thought that the same particle charging mechanisms are at work on Saturn and Earth. As most of the sunlight is absorbed above 2 bars, Saturn's weather and thunderstorms at deep pressure levels should be powered by the planet's internal energy [Desch et al. 2006]. It drives the vertical convection which brings up the water cloud to the visible atmospheric level where it is observed as a bright eruption by Cassini Imaging Science Subsystem (ISS) and VIMS. Dyudina et al. [2010] also measured the optical flash energy to be about 10^9 J, which suggests that Saturn lightning is superbolt-like with total energies of about 10^{12} J [Fischer et al. 2011c].

Detailed studies of Saturn's auroras

For the first time, Cassini's presence inside the magnetosphere facilitated the coordinated optical observations of the aurora and in situ measurements of the plasma properties, the magnetic structure, and the field-aligned currents. While there have been various studies of the aurora as reviewed in Grodent [2015], the best way to summarize Cassini work is to highlight one of these coordinated studies. One coordinated auroral observing campaign occurred April 21–22,

2013, involving instruments onboard Cassini and the Hubble Space Telescope. During this campaign both Saturn's northern and southern aurora were observed while Cassini traversed Saturn's high-latitude auroral field lines [Badman et al. 2016]. Signatures of upward field-aligned currents were detected that corresponded to the bright ultraviolet auroral arc seen in the auroral images and various auroral features observed included a bulge that appeared along the pre-dawn auroral oval and an intensification of the auroral field-aligned currents. These observations are interpreted as the response to tail reconnection events instigated by solar wind compression, initially involving Vasyliunas-type reconnection of closed mass-loaded magnetotail field lines, and then proceeding onto open lobe field lines, causing the contraction of the polar cap region on the post-midnight sector. At the same time Kurth et al. [2016] reports on the RPWS monitoring of the Saturn kilometric radiation. This study found that there is a good correlation between the 10 h averages of SKR power flux and the estimated power input to the aurora on the basis of the UV brightness, justifying the SKR as a simple proxy for auroral activity through the campaign. The SKR emissions also give evidence for a recurrent pattern of solar wind interaction with Saturn's magnetosphere, suggesting a two-sector structure and associated corotating interaction regions that influence the level of auroral activity on Saturn. But there are other SKR intensifications that may be due to internal processes. This coordinated campaign is a perfect example of the many coordinated studies that have been performed by the Cassini MAPS teams in working to understand the aurora at Saturn.

Discovery of ring-ionosphere-magnetosphere interaction

Cassini MAPS instruments discovered and characterized a unique ring–ionosphere–magnetosphere interaction. INMS first observed O_2^+, O^+, and H^+ ions over the A-ring in its ion mode during SOI [Waite et al. 2005]. Further Cassini observations revealed that the ring–ionosphere–magnetosphere interaction is driven by photolytic processes, not impact processes [Farrell et al. 2017]. Specifically, the Sun-facing side of the main rings are a source of photo-dissociated neutrals that get ionized to form a relatively low energy exo-ionosphere. This exo-ionosphere cannot directly access the shadowed/unlit side of the rings: the ring particles represent obstacles to their transport. Thus, the plasma density on the unlit side is modulated by ring density, being lowest where the ring obstruction is the highest in the central B-ring. Local maxima are expected where the local ring particle density is low, such as across the Cassini Division. There is little evidence of impact-generated plasma like that which was predicted during the Voyager era. Cassini observation suggested that there is a current system driven by the rings–magnetosphere interaction. While the plasma on field lines over the rings would be corotating, the particles and associated photo-dissociated gas of the rings would be moving in Keplerian motion, creating drag on the plasma. This drag creates an associated change in plasma speed. Beyond the synchronous point, the plasma is slowed by the Keplerian-moving particles and gas, creating a radially outward directed electric field in order to maintain the new sub-corotation speed. This new electric field drives an outward current that then acts to form a magnetohydrodynamic JxB force to balance the plasma-ring drag force. Inward of the synchronous point, the corotating plasma is accelerated by the ring drag force, creating an inward radial electric field and current that forms a JxB force to offset the acceleration. At the edges of the rings, these cross-ring currents become a field-aligned parallel

current that closes down to the ionosphere along connecting magnetic field lines at the outer edge of the A-ring near L = 2.25 and inner edge of the D-ring near L ~1.11. The rings thus behave as an electrical generator in the plasma, driving currents from the ring surfaces along magnetic field lines down to the ionosphere.

Discovery of heavy positive and negative ions in Titan's ionosphere

This is one of the major surprises of the Cassini mission—the high level of chemical complexity observed in Titan's ionosphere. The first in situ ion composition measurements of Titan's ionosphere were made by the INMS in its ion mode and showed a complex composition [Cravens et al. 2006]. From the earliest close encounters Cassini Plasma Spectrometer (CAPS) detected heavy negatively charged ions with mass/charge up to 13,800 amu/q. In addition, heavy positive ions up to ~350 amu/q [Crary et al. 2009] and as high as 1000 amu/q [Coates et al. 2010] were also detected. An unexpected level of chemical complexity was seen in the neutrals as well [Waite et al. 2007]. The existence of negative ions was completely unexpected at the altitudes sampled by Cassini.

Dust–plasma interactions

The discovery of the dense neutral water vapor jets at Enceladus resulted in a continuous, detailed examination of all aspects of the Enceladus plume and the extended effects on the magnetosphere. A major result of this examination is the detection of singly charged nanometer-size water-ice grains [Coates et al. 2009; Jones et al. 2009; Hill et al. 2012; Meier et al. 2014; Dong et al. 2015; Meier et al. 2015]. Such nanograins had been inferred to exist in various cold, tenuous geophysical and astrophysical environments, but the close Enceladus plume encounters by Cassini offered the first (and still the only) opportunity to measure and characterize the nanograins in situ.

This analysis confirms that the nanograins are largely uncharged when they emerge from the surface vents and become increasingly (mostly negatively) charged as they approach Cassini a few tenths of Enceladus radii away. The most plausible charging mechanism is electron attachment from the dense plume plasma. The non-neutrality of the nanograins observed by CAPS, n(−) >> n(+), plausibly cancels the opposite non-neutrality of the plume plasma observed by RPWS Langmuir Probe (LP). Most of the electrons missing from the plume plasma reside on the nanograins.

Discovery of nanodust between the planet and the D-ring

An exciting result of the proximal orbits during the final months of the Cassini mission was the discovery of nanograins between the planet/ionosphere and the D-ring. Understanding the implications of these particles is still a work in progress, and the first in situ measurements by RPWS of the cold ionosphere properties have just been reported [Wahlund et al. 2018]. Several other manuscripts have been submitted by MAPS instrument teams, and they all show a very strong interaction between the D-ring and the ionosphere of Saturn, causing the ionosphere to

become extremely variable with more than two orders of magnitude and trigger a dust-ionosphere layer near the equator.

Discovery of the shape of the heliosphere

Beyond the Saturn system, one of the most important contributions of Cassini to our understanding of the solar heliosphere came from the MIMI/Ion and Neutral Camera (INCA), first ever images of the global heliosphere in > 5.2 keV ENA measurements [Krimigis et al. 2009]. These images identified two striking, previously unexpected, heliospheric signatures: a) the Belt, a broad band of emission in the sky, identified as a high intensity, relatively wide ENA region that wraps around the celestial sphere in ecliptic coordinates, passing through the nose, the anti-nose (tail), and the north and south heliosphere poles; and b) the basins, identified as two extended heliosphere lobes where the ENA minima occur. In addition, INCA measurements could be used to image the shape of our heliosphere with a surprising result that it is now thought to be a sphere rather a structure with a nose and a tail, like a magnetosphere [Dialynas et al. 2018].

MIMI's images came at a time when Voyager 1 and Voyager 2 crossed the termination shock, where the supersonic solar wind presumably terminates at the shock front, at respective distances of ~94 and ~84 AU in 2004 and 2007 at +35° and −26° ecliptic latitudes [Decker et al. 2008, 2005], pinpointing both the size of the local heliosphere and the scale of the heliospheric asymmetry. After this crossing, V1 additionally unexpectedly passed through the heliopause [Krimigis et al. 2013] at a distance of ~122 AU. Due to the powerful synergy between in situ ions from V1 Low Energy Charged Particle (LECP) instrument and ENAs from INCA (in overlapping energy bands), MIMI has made key discoveries, beginning in about 2009, that altered our past notions on the formation and interactions of the heliosphere, and led to a number of surprises concerning the physics that governs this enormous system and also provided insights on the plasma processes at ~100 AU that were substantially at variance with previous theories and models.

Assessment of Overall DWG Science

The Cassini MAPS DWG was successful in carrying out a robust and complete science investigation over the seven-year cruise and more than thirteen years in orbit at Saturn (the nominal mission plus extensions). The Cassini mission addressed each of the nominal and extended mission science objectives. As is typical in scientific investigation, the process of answering questions typically creates new unanticipated questions. This was certainly the case for the Cassini mission and MAPS science, in particular. Cassini was able to make advances in these unanticipated areas due to the capabilities of the Cassini spacecraft and the ability to plan robust and exciting extended mission designs. Although there are certainly questions that are left for future mission to answer (see section entitled Open Questions for Saturn System Science), all of the MAPS science objectives were addressed and advances were made. In the section entitled MAPS DWG Science Assessment, Table MAPS-1 indicates that all MAPS key science objectives were completed except for the determination of Saturn's internal rotation rate. Although tremendous advances have been made to address this determination, as outlined in the Key Open Questions,

the relationship of the SKR to the true rotation period of Saturn is still under investigation. For this reason, this science objective is marked as partially completed.

Key Open Questions

- Internal rotation rate of Saturn.
- Rotational modulation in axisymmetric configuration.
- How are mass and magnetic flux transported in the middle and outer magnetosphere?
- Solar wind control of the Saturnian magnetosphere.
- Why do neutral particles dominate the Saturnian magnetosphere in contrast to Jupiter?
- Very limited plasma measurements in auroral acceleration and source region of related SKR.
- Understanding the Enceladus plume-magnetosphere interaction. Crossing too fast for better time resolution. Limited plasma measurements.
- Composition of the negative ions at Titan and > 100 amu positive ions.

KEY OBJECTIVES FOR MAPS DWG

The scientific goals of the MAPS DWG were, simply stated, to seek to understand as much about Saturn's magnetosphere, ionosphere, moon interaction, and plasma physics as possible. The key science objectives are listed below.

Characterize the vector fields as a function of position and time.

- **MC1b:** Observe Saturn's magnetosphere over a solar cycle, from one solar minimum to the next.
  - Investigate what controls the interplay between the Dungey and Vasyliunas cycles.
  - Study the solar cycle dependence of the magnetospheric dynamics.
  - Investigate magnetospheric structure: variations in force balance.
  - Investigate non-static and other variant radiation belt features.
- **MN1a:** Determine the dynamics of Saturn's magnetotail.
  - Study thoroughly the plasma sheet in Saturn's magnetotail.

- Investigate the relation between solar wind compression events and magnetotail dynamics.
- Investigate the plasma sheet thickness and scale height as functions of radial distance and local time.
- Statistically characterize magnetotail variations, especially those associated with plasmoids, and correlate them with changes in the inner magnetosphere.
- Critically evaluate the Dungey and Vasyliunas cycles in light of the new observations, especially those of flow speeds.

Characterize Saturn's interaction with the magnetosphere.

- **MN1b:** Conduct in situ studies of Saturn's ionosphere and inner radiation belt.
  - Investigate the effects on aurora of solar wind and seasons.
  - Are there UV satellite footprints on Saturn? (like at Jupiter)
  - Is there a seasonal variation in auroral activity?
  - Investigate solar wind–ionosphere–magnetosphere coupling through the auroral regions.
  - Investigate whether there are UV satellite footprints on Saturn and whether there are Region 1 currents connecting the ionosphere and the magnetopause.
  - Investigate the composition of Saturn's ionosphere.
  - Study whether there is a significant polar outflow from Saturn's high latitude ionosphere and whether the outflow exhibits seasonal or solar cycle variation.
  - Determine whether there is a radiation belt between the D-ring inner edge and the atmosphere.
- **MN2a:** Determine the coupling between Saturn's rings and ionosphere.
  - Study how field-aligned currents are coupled to the rings and satellites.
  - Explore the dust dynamics in the proximity region.
  - Investigate the mid-plane of Saturn's D-ring.
  - Determine the grain composition in the proximity region.
  - Investigate the possible interaction of lightning with the inner magnetosphere and the rings.
  - Investigate coupling between E-ring and the Enceladus neutral and plasma tori.

Characterize the absolute energy spectra, composition, and angular distribution of energetic charged particles and plasma, including plasma wave phenomena, as a function of position and time.

- **M_AO2:** Determine current systems, composition, sources, and sinks of magnetosphere-charged particles.
- **M_AO3:** Investigate wave-particle interactions and dynamics of the dayside magnetosphere and the magnetotail of Saturn and their interactions with the solar wind, the satellites, and the rings.

Determine the rotational, seasonal, solar cycle, and secular variations of SKR and its relation to magnetic field oscillations.

- **M_AO1:** Determine the configuration of the nearly axially symmetric magnetic field and its relation to the modulation of SKR.
- **MN1c:** Investigate magnetospheric periodicities, their coupling to the ionosphere, and how the SKR periods are imposed from close to the planet (3–5 R_S) out to the deep tail.
  - Determine what controls the SKR periods and whether there is a solar cycle and/or seasonal variation.
  - Investigate the coupling mechanism between the SKR periods and the internal rotation rate.
  - Study whether the ionosphere and/or thermosphere is differentially rotating.
  - Determine which hemispherical SKR period dominates other periodicities in the magnetosphere and whether this varies with time.

Investigate satellite–magnetosphere interactions.

- **M_AO5:** Investigate interactions of Titan's atmosphere and exosphere with the surrounding plasma.
- **M_AO4:** Study the effect of Titan's interaction with the solar wind and magnetospheric plasma.
- **MC1a:** Determine the temporal variability of Enceladus' plumes.
  - Investigate temporal variations in Enceladus gas production and plume composition, on the scale of seasons and solar cycle.
  - Study plume neutral gas composition.
  - Investigate the physics of the dusty plasma environment.
  - Determine how the magnetosphere reacts to changes in (plume?) gas production rates by studying Enceladus' auroral footprint.
  - Study variability in dust-to-gas mass ratio.

- **MC2a:** Observe seasonal variation of Titan's ionosphere from one solstice to the next.
  - Study how intensity variations of energetic ions and electrons affect the energy deposition in the atmosphere, and the degree of ionization at different depths.
  - Investigate how the energy input from energetic particles varies when Titan resides in the plasma sheet or magnetosheath.

Cruise science and Jupiter objectives.

- **J_AO3:** Explore the dusk side of Jupiter's magnetosphere and intermediate regions of the magnetotail unvisited by previous spacecraft.
- **J_AO4:** Obtain the first high-resolution images of the Io torus.
- **C_AO1:** Extend the sensitivity of composition measurements of interstellar ions by approximately three orders of magnitude.
- **C_AO2:** Investigate the behavior of the solar wind during solar minimum, for comparison with earlier Galileo and Ulysses measurements.
- **C_AO4:** Extend studies of interplanetary dust to the orbit of Saturn.
- **S_AO4:** Study the diurnal variations and magnetic control of the ionosphere of Saturn.

MAPS DWG Science Assessment

Table MAPS-1. MAPS Science Assessment. AO and TM Objectives are paired with MAPS science objectives.

Fully/Mostly Accomplished: **Partially Accomplished:** **Not Accomplished:**

MAPS Science Objectives	AO and TM Science Objectives	MAPS Science Assessment	Comments
Characterize the vector fields			
Seasonal and solar cycle variations	MC1b		
Magnetotail configuration and dynamics	MN1a		
High-order magnetic moments of Saturn	M_AO1, MN1c		
Saturn's interaction with the magnetosphere			
Magnetospheric convection	MN1b		
Aurora and satellite footprints	MN1b		
Plasma loss into the magnetotail	MC1a, MN1a		
Ionospheric convection	MN1b, S_AO4		
Composition of ionosphere/thermosphere	MN1b, MN2a		
Particle distributions			
Plasma sources and sinks	M_AO2		

Table MAPS-1. MAPS Science Assessment. AO and TM Objectives are paired with MAPS science objectives.

Fully/Mostly Accomplished: **Partially Accomplished:** **Not Accomplished:**

MAPS Science Objectives	AO and TM Science Objectives	MAPS Science Assessment	Comments
Plasma kinetics	M_AO3		
Radiation belts	M_AO3, MC1b, MN1b		
Wave-particle interactions	M_AO3		
Periodicities			
Saturn's magnetic field and its relation to the modulation of SKR	M_AO1, MN1c		
Solar cycle/seasonal variation of SKR periods	MN1c		
SKR periods and Saturn's internal rotation rate	MN1c		Rotation rate is still not known
Differential rotation of the ionosphere and/or thermosphere	MN1c		
Satellite/ring magnetosphere interactions			
Titan's interaction with the surrounding plasma	M_AO4, M_AO5, MC2a		
Interaction of the Enceladus plume with the magnetosphere	M_AO2, M_AO3, MC1a, MN2a		
Ring-magnetosphere interaction	M_AO3, MN2a		
Cruise science & other science			
Jupiter's magnetotail, Io Torus	J_AO3, J_AO4		In spite of no-cruise science decision by Project Management
Interstellar particles	C_AO1		
Solar wind from Earth to Saturn	C_AO2		
Interplanetary dust studies of Saturn	C_AO4		

MAPS DWG Magnetosphere Science Results

Titan Science

Instruments on the Cassini Orbiter carried out extensive measurements of the upper atmosphere and ionosphere of Titan as well as its interaction with Saturn's magnetosphere. Over the course of the Cassini mission, the spacecraft performed 127 flybys of Titan. The flybys, varying in trajectory and closest approach altitude, served as gravity assists to change Cassini's trajectory, but also to bring our understanding of the moon's environment to an unprecedented level.

Titan's upper atmosphere and its interaction with the surrounding plasma

- **M_AO5:** Investigate interactions of Titan's atmosphere and exosphere with the surrounding plasma.

- **M_AO4:** Study the effect of Titan's interaction with the solar wind and magnetospheric plasma.
- **MC2a:** Observe seasonal variation of Titan's ionosphere from one solstice to the next.

TITAN'S NEUTRAL ATMOSPHERE

The first neutral measurements made by MAPS instruments were made during the TA pass. These measurements were made in order to characterize the initial ionospheric density and thereby assess safe altitudes for future flybys.

Observations of neutral densities (mainly N_2) have allowed us to make inferences into the thermal structure of Titan's upper atmosphere [cf. Müeller-Wodarg et al. 2008, 2006a; Cui et al. 2009, 2008; Magee et al. 2009; Westlake et al. 2011; Snowden et al. 2013]. The average thermospheric temperature derived from Ion and Neutral Mass Spectrometer (INMS) data is approximately 150 K, which is in good agreement with pre-Cassini estimates [Müeller-Wodarg 2003, 2000; Müeller-Wodarg and Yelle 2002]. However, the temperature of Titan's thermosphere exhibits a high degree of variability that was not predicted prior to Cassini, see for example, Müeller-Wodarg [2003, 2000; Müeller-Wodarg and Yelle 2002]. Pre-Cassini models calculated day–night variations on the order of 10–15 K. Cassini has observed temperature variations much larger than this over the course of a single Titan day, even when observing the same region of atmosphere at a similar local time. The variations in temperature are not correlated with solar input, indicating there are additional heating/cooling mechanisms with magnitudes that are similar to solar insulation. The short-timescales associated with the large variations in temperature has led some to postulate that the magnetosphere may provide sporadic and localized inputs [Westlake et al. 2011] or internal gravity waves may be depositing significant energy into the upper atmosphere [Müeller-Wodarg et al. 2006b; Snowden et al. 2013]. Atmospheric escape may also significantly alter the temperature of the upper thermosphere [Tucker et al. 2013] as can spatial and temporal variation of minor species that are strong sources of radiative cooling such as hydrogen cyanide (HCN) and CH_4.

Prior to the arrival of Cassini at Saturn, modeling of the production of energetic neutral atoms (ENAs) began as a preparation for the first observations.

The INCA instrument had the capability of remotely measuring the exosphere of Titan, an ambient neutral population too tenuous to be measured by in situ mass spectrometers. Prior to the arrival of Cassini at Saturn, modeling of the production of energetic neutral atoms (ENAs) began as a preparation for the first observations. Amsif et al. [1997] developed a model that included the inner and outer exosphere, as well as the five major species contained in Titan's atmosphere, namely, H, H_2, N, N_2, and CH_4. The ENA production was modeled using a proton spectrum from the Voyager flyby. Taking into account the production from both the inner and outer exosphere (estimated using a Chamberlain model), they predicted that Cassini would be able to image the

exosphere out to at least five Titan radii. Dandouras and Amsif [1999] analyzed the production of synthetic ENA images while taking into account the same exospheric model from Amsif et al. [1997], but included the geometry of the interaction region and the expected ENA trajectories. They concluded that the INCA instrument would be able to provide information regarding the ion fluxes and spectra, as well as the magnetic field environment in the vicinity of Titan, based on a shadowing effect produced by the presence of the moon itself.

Combining data from the INCA and the INMS instruments, Dandouras et al. [2008] calculated profiles of the main exospheric species that revealed the non-thermal nature of their distributions. They also found that the ENA emissions from the interaction region get absorbed below an altitude of about 1000 km, where energetic ions deposit their energy. In terms of the extension of the atmosphere, they were able to measure it up to an altitude of 40,000 km.

Using data from SOI to 2007, Brandt et al. [2012] studied the exospheric composition of Titan. For this, 36-minute accumulation time hydrogen data from the INCA detector when observing Titan without the magnetosphere behind it were analyzed. Combining these observations with a model for the production of ENAs, they found that the molecular hydrogen exosphere of Titan extends to a distance of about 50,000 km (almost 20 Titan radii) confirming the lower limit of 5 Titan radii obtained by Amsif et al. [1997]. Taking into account the profiles obtained and the fact that ENAs have direct access to Titan's atmosphere, they estimated a precipitating energy flux from ENAs of 5×10^6 keV/(cm^2 s), a number comparable to previous estimates of precipitating energetic ions [Sittler et al. 2009a] and solar extreme ultraviolet (EUV) [Tobiska 2004].

TITAN'S IONOSPHERE

Voyager measurements, both in situ of the magnetotail and radio occultation of the main ionosphere, showed the existence of an ionosphere at Titan [Neubauer et al. 1984; Bird et al. 1997]. Subsequent theoretical modeling suggested that the ionospheric composition could be quite complex, largely due to the presence of hydrocarbons associated with dissociation and ionization of methane [Nagy and Cravens 1998; Keller et al. 1998, 1992; Fox and Yelle 1997]. But the series of Cassini measurements by the MAPS instruments quantified the ionospheric densities and the extent of the ionosphere.

The main structure of Titan's ionosphere emerged after a few flybys [Ågren et al. 2009, 2007; Robertson et al. 2009] and it became clear that solar EUV radiation dominated the ionization of Titan's upper atmosphere, and varied with the long-term EUV output from the Sun [Edberg et al. 2013a; Madanian et al. 2016; Shebanits et al. 2017] (Figure MAPS-1). Energetic particle precipitation from the magnetosphere is important on the nightside of Titan, but only occasionally makes a significant difference on the dayside [Edberg et al. 2013b]. A most surprising find was the importance of the ionosphere for the production of complex organic chemistry and aerosol particles (dust) below about 1100-km altitude, see for example, Coates et al. [2011, 2007]; Wahlund et al. [2009]; Vuitton et al. [2009]; Ågren et al. [2012]; Lavvas et al. [2013]; Shebanits et al. [2016; 2013], where the Langmuir probe provided a measure of the detailed amounts of organic ions and charged

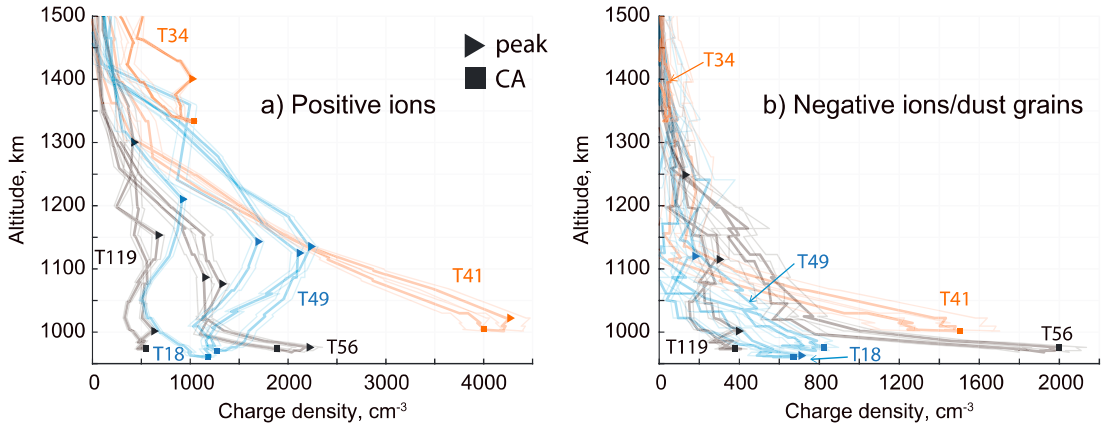

Figure MAPS-1. Examples from six flybys of Titan of altitude profiles of the positive ion and negative ion/aerosol number densities as derived from the RPWS Langmuir probe measurements [Shebanits et al. 2017]. Note the dominance of charged aerosol particles below 1100 km. Dayside flybys are colored in orange, terminator in blue, and nightside in black; the triangles mark the peaks and the squares mark the closest-approach (CA) maxima.

aerosol particles. The mechanism starts with EUV producing an N_2^+ ion that then reacts primarily with methane, with subsequently more complex C-H-N chemistry and aerosol formation [Lavvas et al. 2013].

The major ion species produced in the ionosphere is N_2^+, since N_2 is the major neutral species. However, chemical considerations told us that the main ion species at mass 28 is not N_2^+ but $HCNH^+$, so another ion species, CH_3^+, was used to almost directly deduce ion production rates [Richard et al. 2015a, 2015b; Vigren et al. 2015; Sagnières et al. 2015]. The rapid chemical reaction of N_2^+ with CH_4 produces CH_3^+ (mass 15). The ionization rate of CH_4 can be deduced by the measured CH_4^+ ions at mass 16 [Richard et al. 2015a, 2015b].

Sources of ionization deep on the nightside were also studied by Cassini. Globally, solar radiation accounts for 90% of total ionization, but precipitation of energetic electrons and ions leading to ionization is obviously locally important on the nightside [Ågren et al. 2007; Cravens et al. 2009a, 2008a, 2008b; Vigren et al. 2015; Snowden and Yelle 2014a, 2014b; Edberg et al. 2013a, 2013b; Robertson et al. 2009; Galand et al. 2014]. As on Venus and Mars, the two possible sources of the nightside ionosphere are local/direct ionization from precipitation (i.e., a diffuse aurora) and transport of plasma from the dayside. Evidence for the precipitation source is provided by INMS measurements of primary or almost primary ion species (CH_3^+, CH_4^+, CH_5^+, …), which have short chemical lifetimes and could only be produced locally and also by MIMI data which provided in situ data to understand the upstream conditions at Titan's orbit as well as the energy deposition by energetic ions in the atmosphere. Cassini data from the T5 and T18 flybys has been used to study the energy deposition by energetic ions as well as the energetic protons [Cravens et al. 2008a, 2008b; Cui et al. 2009; Smith et al. 2009].

Modeling combined with Cassini data determined that the precipitation ionization source depends on magnetic topology and on the location of Titan in Saturn's magnetosphere. Incident

magnetospheric electron fluxes and the associated nightside ionosphere were more robust when Titan was located in the plasma sheet region as opposed to the magnetic lobes of Saturn's magnetosphere [Richard et al. 2015a; Rymer et al. 2009a] and that ionization rates can vary by up to 80% from one location to another due to finite gyro radius effects [Regoli et al. 2016].

The chemistry of Titan's upper atmosphere and ionosphere is complex due to the presence of a large number of organic species extending up to high mass numbers. The neutral and ion chemistry is linked together [Waite et al. 2007]. The INMS has played a key role in improving our understanding of this chemistry. Photodissociation and photoionization of N_2 and CH_4 form ion and neutral species that are very reactive and that initiate a series of reactions that produce increasing larger species, up to aerosol-sized particles [Waite et al. 2007]. Primary N_2^+ ions react with CH_4 to produce CH_3^+, which again reacts with CH_4 to produce $C_2H_5^+$. $C_2H_5^+$ reacts with HCN to produce the very abundant species $HCNH^+$. Reactions of $C_2H_5^+$ and $HCNH^+$ with C_2H_2, C_2H_4, and C_4H_2 drive a chain of reactions leading to families of $C_nH_m^+$ species, including protonated benzene ($C_6H_7^+$), and up to masses exceeding 99 Da [Anicich and McEwan 1997; Cravens et al. 2006; Vuitton et al. 2009, 2007, 2006; Westlake et al. 2014; Cui et al. 2009; Mandt et al. 2012]. See Figure MAPS-2.

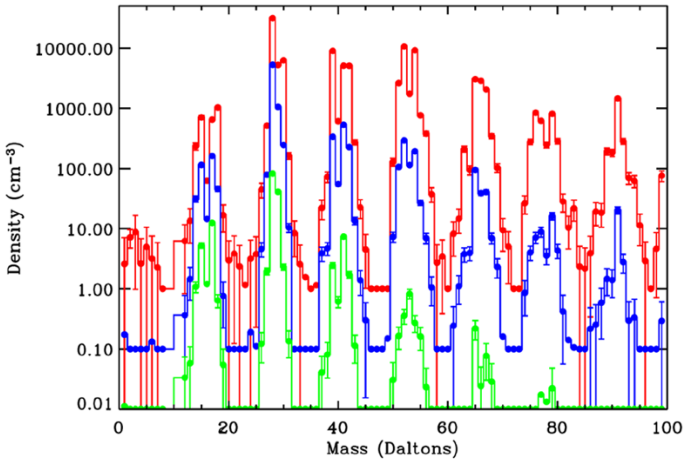

Figure MAPS-2. Shown are the first INMS measurements of ion densities versus Mass number at three different altitudes for the T5 nightside ionosphere [Cravens et al. 2006]. *Red*: 1027–1200 km. *Blue*: 1200–1400 km. *Green*: 1400–1600 km. Chemical complexity increases with decreasing altitude.

Titan's ionosphere consists of positive and negative ions, some of which have masses of up to and possibly beyond thousands of Da [Waite et al. 2007; Coates et al. 2007; Crary et al. 2009]. The study of Vuitton et al. [2007] identified over 100 ions in the INMS spectrum including several N-bearing species such as protonated ammonia (NH_4^+), $CH_2NH_2^+$, and CH_3CNH^+. Titan's atmosphere is a reducing atmosphere (little or no oxygen species are present) and as such the ionization will flow from species whose parent neutral molecules have low proton affinities (PAs) to those whose parent neutral molecules have greater PAs.

Measurements made by CAPS and INMS between altitudes of 950 to 1400 km were responsible for one of the major surprises of the Cassini mission, the high level of chemical

complexity observed in Titan's ionosphere. From the earliest close encounters electron spectrometer (ELS) detected heavy negatively charged ions with mass/charge up to 13,800 amu/q. In addition, heavy positive ions up to ~350 amu/q [Crary et al. 2009] and as high as 1000 amu/q [Coates et al. 2010] were detected by Ion Beam Spectrometer (IBS) (Figure MAPS-3). An unexpected level of chemical complexity was seen in the neutrals as well [Waite et al. 2007]. Before Cassini, models of Titan's chemistry had shown some complexity in the interaction of the neutral atmosphere with positive ions [Wilson and Atreya 2004]. The observations from Cassini necessitated more sophisticated modelling of the positive ion composition [Cravens et al. 2009b]. The negative ion observations by ELS were completely unexpected at the altitudes sampled by Cassini, opening up a whole new field for modeling and understanding the complex chemistry of Titan's atmosphere.

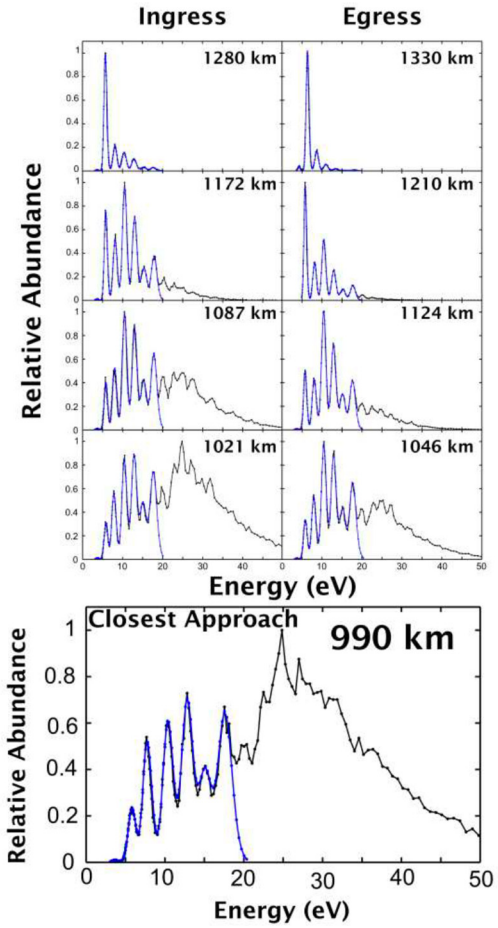

Figure MAPS-3. Shown are nine ion mass spectra obtained by the CAPS-IBS instrument at various altitudes during the T26 flyby. The blue lines show the INMS data converted using the CAPS-IBS instrument response model.

Westlake et al. [2014] analyzed the T57 flyby in detail between the CAPS and INMS observations to determine the characteristics of the processes responsible for the production and

loss of the large hydrocarbons observed at Titan. The work suggested that an ion-molecule reaction pathway could be responsible for the production of the heavy ions, namely reactions that utilize abundant building blocks such as C_2H_2 and C_2H_4, which have been shown to be energetically favorable and that have already been identified as ion growth patterns for the lighter ions detected by the INMS.

An additional discovery made by the Cassini MAPS instruments is the presence of large negative ions in Titan's ionosphere. After initial discovery by CAPS, further studies have been made of the spatial distribution and density of these ions on parameters including altitude and solar zenith angle [Wellbrock et al. 2013; Desai et al. 2017]. Wellbrock et al. [2013] have shown that the highest densities of negative ions are found at lower altitudes. Moreover, the average altitudes where peak ion densities occur decrease with increasing ion mass. In addition, the maximum altitudes at which ions from a specific mass group are observed (the reference altitude) decrease with increasing mass group. The highest mass negative ions were observed during the T16 encounter. A recent analysis of this data shows that polar winter is where the heaviest negative ions are seen [Wellbrock et al. 2019]. This helps to constrain the chemical processes at work to produce these large ions. The relativity low-mass negative ions were identified as CN^-, C_3N^-, and C_5N^- in the first chemical models used to describe the negative ions seen at these altitudes [Vuitton et al. 2009].

While some progress has been made on formation of higher mass ions, this topic is still under study. The geometric configuration of heavy ions is relatively unconstrained, and chains, rings or even fullerenes may be possible. Sittler et al. [2009a, 2009b] have suggested that the latter may trap and transport oxygen to the surface although there are as yet no observations that confirm this hypothesis. Agglomeration of large molecules caused by charging [Michael et al. 2011] or chemical processes [Lavvas et al. 2013] have been suggested as potential mechanisms to produce the large negative ions. However recent work by Desai et al. [2017] shows that chains of negative ions at intermediate masses may provide another pathway for heavy ion formation. Heavy negative and positive ions may also link up to form embryo aerosols of both negative and positive charge [Coates et al. 2007; Crary et al. 2009].

Desai et al. [2017] used observations of negative ions by CAPS/ELS to show mass peaks where unsaturated carbon-chain negative ions such as CN^-/C_2H^-, C_3N^-/C_4H^-, C_5N^-/C_6H^-, etc., might exist. Higher mass ions ~117 ± 3 amu/q and 154 ± 8 amu/q could be longer negative carbon chains with 10 or 12 or more carbon atoms in saturated aromatic versions. Thus, negative ions exist at masses where INMS cannot measure positive ions, which makes the two instruments not only complementary in their measurements but make them highly dependent on each other if we are going to have deeper insight into the composition of Titan's ionosphere. A second example of INMS/CAPS interdependence are IBS observations of heavy positive ions above 1000 amu/q [Crary et al. 2009] which complements INMS measurements that are limited to $m/q \leq 100$ amu/q.

TITAN'S MAGNETOSPHERIC INTERACTION

All the Cassini MAPS instruments have provided data, that with associated modeling, has increased our understanding of Titan's plasma interaction with Saturn's magnetosphere and, rarely, with the solar wind plasma. Titan's interaction with the magnetosphere of Saturn results in the formation of an induced magnetosphere around Titan. The virtual absence of an intrinsic field at Titan makes this interaction mainly atmospheric as fields and charged particles from Saturn or the Sun impinge on the moon's chemically complex atmosphere, exosphere and ionosphere. Atmospheric interactions are common elsewhere in the solar system with Mars and Venus as their most typical examples. In these cases, as well as in Titan's, charged particles from its atmosphere (originating from photoionization, charge exchange and electron impact) become electromagnetically coupled to those carried by the plasma winds that flow past it [Bertucci et al. 2011].

The Cassini/RPWS sensors have mapped the interaction region—for example, Modolo et al. [2007a, 2007b]—proved the existence of cold ionospheric flows from Titan—for example, Edberg et al. [2011, 2010]—as well as more energetic ion pick-up [Modolo et al. 2007b] (Figure MAPS-4), and studied how these processes change when Titan enters the magnetosheath [Bertucci et al. 2008; Garnier et al. 2009]. Titan's ionosphere also acts as a conductive medium where electric currents generated in the induced magnetosphere close [Rosenqvist et al. 2009; Ågren et al. 2011]. The escape rate through the cold plasma was determined to be a few kg/s (10^{25} ions/s), which is considered small compared to the exosphere escape rates.

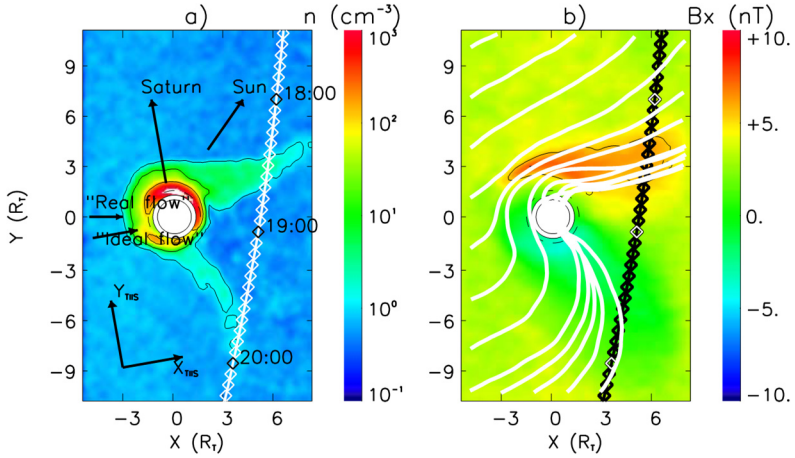

Figure MAPS-4. The induced magnetosphere of Titan as measured and modelled during the T9 flyby through the tail [Modolo et al. 2007b].

Many of the individual encounters with Titan have been studied. In joint studies of the TA flyby a comparison between MAG and RPWS-data was done by Wahlund et al. [2005] and a comparison between Cassini and Voyager data using both plasma spectrometer (PLS) and magnetic field data by Hartle et al. [2006a, 2006b]. Magnetic field and PLS electron data from flybys TA, TB, and T3 [Neubauer et al. 2006] showed a draping boundary as the outer boundary of strong magnetic field draping. In addition, the shape of the tail was found to be similar to a delta wing in aerodynamics.

It was shown that the long travel time of frozen-in magnetic field lines into the lower ionosphere of Titan led to the observation of old or fossil field lines compared with their times of arrival in front of Titan. This concept was later called memory effect by Bertucci et al. [2008] in a paper discussing Titan encounter T32 which occurred for the first time in the Saturnian magnetosheath but also contained old Saturnian magnetospheric field as a memory effect, see also Ma et al. [2009]. A special study of the magnetotails has investigated the tails by wake flybys with closest approach (CA) distances > 2.5 R_T in the whole set of flybys TA-T84 [Simon et al. 2014]. The resulting eight flybys confirmed the delta wing structure found in Neubauer et al. [2006] leading to a thickness of the wing of ±3 R_T.

The interaction between Titan and the corotating Saturnian plasma forms an induced magnetosphere with an elongated Alfven-wing-style magnetotail. During the first mid-tail flyby T9, Cassini plasma and magnetic field instruments detected in one tail lobe a magnetic flux tube connected with ionosphere and filled with cold ionospheric plasma. This magnetic structure indicates that Titan's ionosphere appears to be escaping along field lines down the tail, leading to particle loss from the atmosphere [Wei et al. 2007].

The first opportunity to study the induced tail at medium distances occurred at T9 [Bertucci et al. 2007]. This data analysis led to a number of modelling papers which helped to disentangle the detailed plasma and magnetic field characteristics [Kallio et al. 2007; Wei et al. 2007; Ma et al. 2007] of the complex magnetotail. All the early papers also led to the conclusion that an internal magnetic field of Titan was at most very small. Using the magnetic field observations on flyby orbits very close to Titan, Wei et al. [2010] found an upper limit on the moment of 0.78 nT × R_{Ti}^3 improving the Voyager 1 upper limit by a factor of five.

One most remarkable features revealed by Cassini MAG instrument was that Titan's induced magnetosphere is formed by layers of different polarity of the external magnetic field that allow to reconstruct the history of the moon's magnetic environment. Indeed, in the same way as older sediments lay beneath more recent deposits in geology, the magnetic fields fossilized in the deep layers of Titan's induced magnetosphere provide information about the orientation of the field Titan was exposed up to three hours before the encounter with Cassini [Bertucci et al. 2008]. This magnetic memory of Titan is significantly longer than at Venus and Mars and is a result of the capacity of Titan plasma to remove momentum form the external plasma. A further study of the ionosphere of Titan with its embedded magnetic field on the nightside ionosphere was published by Cravens et al. [2009a]. During the interaction between Titan's ionosphere and its ambient plasma, Cassini observations find that the lower ionosphere of Titan is often magnetized, with large scale magnetic fields and some structures resemble magnetic flux ropes. These flux ropes are either starting to form or maturely formed, with their axial orientations in agreement with the formation mechanism [Wei et al. 2010].

This magnetic memory of Titan is significantly longer than at Venus and Mars and is a result of the capacity of Titan plasma to remove momentum form the external plasma.

Titan's orbit is typically located inside Saturn's magnetosphere, but could occasionally move outside it into the magnetosheath or even into the solar wind. T96 was the first encounter presumably occurring in the supersonic solar wind and the observed structures at Titan's unique example of interaction with the supersonic solar wind were similar to structures found at Mars and Venus (an induced magnetospheric boundary and a collisional bow shock) [Bertucci et al. 2015]. Omidi et al. [2017] made simulations which showed that a deformed bow shock could form that would encompass both Titan and Saturn's magnetosphere.

To understand the internal magnetic moments of Titan, we use the radial component of Cassini magnetometer observations near Titan surface (from 950 km to 1100 km) is used to calculate the permanent dipole moment. The upper limit to Titan's permanent dipole moment is 1.25 nT × R_{Ti}^3, using the observations during the southern summer season of Saturn (April 2005 to March 2009). This weak internal field indicates the interior of Titan may not contain a liquid core sufficiently electrically conductive for a magnetic dynamo to be generated inside Titan or even for the simple amplification of the external magnetic field [Wei et al. 2010]. For the signs of the calculated internal field components, the g11 and h11 component, corresponding with the Titan-to-Saturn direction and the corotation direction, respectively, are in agreement with the signs of the averaged ambient field around Titan during the observation period. This indicates that these estimated internal moments may be due to the penetration of the ambient field into the interior of Titan, generating induced fields. After Saturn's equinox, August 2009, the ambient of field of Titan changes sign in the Titan-to-Saturn direction and the corotation direction, as Titan moved from below Saturn's current sheet to above it. Thus, we compare the calculated internal moments using the observations before and after Saturn's equinox, and find that the g11 and h11 moment change sign in agreement with the sign of Titan's ambient field.

The Cassini/CAPS instrument measured pick-up ions in the form of beams of CH_4^+ and N_2^+ that can be explained theoretically as the result of kinetic interactions between Titan and the magnetosphere [Hartle and Killen 2006; Hartle and Sittler 2007; Hartle et al. 2011]. It is no surprise that beam composition is consistent with the composition Titan's exosphere and atmosphere which is dominated by N_2 (98.4%) and CH_4 (1.4%) [cf. Waite et al. 2005].

Sittler et al. [2010] observed nearly field aligned outflows from the topside ionosphere during the T9 flyby and estimated the loss of methane ions due to pick-up from the exosphere at ~5 × 10^{22} mol/s [Sittler et al. 2009a]. The outflows serve ultimately as a sink from Titan's atmosphere of roughly ~5 × 10^{24} mol/s. Later, Coates et al. [2012] observed similar amounts of ionospheric outflows during the T9, T63, and T75 flybys. The theoretical cause of these outflows was originally discussed in Hartle et al. [2008]. It is produced by a field-aligned polarization electric field E_{pol} ~−$1/n_e e \nabla_{||} P_e$ so that above the ionospheric density peak the outward acceleration is > 10 times the force of gravity for m/q ~28 amu/q ions. (Note: the ionospheric electron temperature T_e ~1000° K is much greater than the ionospheric ion temperature T_{ION} < 180° K, which gives rise to charge separation and hence the dipolar electric field.) Sittler et al. [2010] found that the resulting ion outflow speeds were ~7 km/s with T_{ION} ~50,000° K. Therefore both significant accelerations and heating must have occurred at altitudes above 5000 km. Later, using electron observations, Coates et al. [2015] measured the total potential

drop of this electric field to be ~0.2 μV/m to heights ~15,000 km, which is sufficient to accelerate methane ions to the observed speeds ~5–6 km/s. Future 3-D hybrid simulations similar to that done by Lipatov et al. [2014, 2012, 2011] will be required to understand the heating, for example, due to wave-particle interactions, of ions to the observed high temperatures. In addition to the outflows, Sittler et al. [2010] also found evidence of Alfven waves during the T9 flyby with transverse velocity and magnetic field fluctuations that were anti-correlated with time and thus consistent with field-aligned propagation of these waves.

One other surprising observation that affects Titan atmospheric chemistry was CAPS' discovery of kilovolt oxygen ions with inflows ranging up to ~1023 O^+/s [Hartle et al. 2006a, 2006b] arriving from the magnetosphere at the exobase of Titan's atmosphere. Its likely origins are Enceladus and the rings, see Johnson et al. [2005]; Cassidy and Johnson [2010]. Oxygen combined with the complex chemical makeup of the ionosphere is most likely the source of CO in the atmosphere [Hörst et al. 2008; Krasnopolsky 2012]. The influx of O^+ into the atmosphere, where it undoubtedly affects Titan's already complex chemistry, is one more unusual and interesting aspect of Saturn's magnetosphere in which it acts as a conduit for the chemistry of one moon (Enceladus plumes) to affect the chemistry of another.

The peak ionospheric density at Titan was found to be dependent on solar cycle variations by Edberg et al. [2013a]. RPWS measurements of the electron density in the ionospheric peak region made during 2012 (T83–T88) showed significant increases compared to previous averages. These measurements suggest that a solar cycle variation caused by the rise of EUV fluxes during solar maximum. The study uses a power law to estimate the peak electron density at the subsolar point of Titan during solar maximum conditions and find it to be about 6500 cm^{-3}, i.e., 85–160% more than had been previously measured during the entire Cassini mission.

TITAN'S ATMOSPHERIC LOSS

Both CAPS and the INMS have provided crucial data for estimating processes that contribute to atmospheric loss. The review article by Johnson et al. [2009] highlights mechanisms and estimates of loss. They are primarily H_2 thermal (or Jeans) escape, CH_4 destruction/precipitation, N_2/CH_4 sputtering, ion pick-up causing ionospheric outflows, CH_4 hydrodynamic outflow [Yelle et al. 2008], and CH_4 plus H_2 hydrodynamic outflow [Strobel 2008].

Waite et al. [2005] presented the first observations of H_2, CH_4 and N_2 altitude profiles extending above the exobase to ~1400 km. There is a break in the altitude profiles above the exobase that is consistent with atmospheric escape. Cui et al. [2008] and Bell et al. [2009] estimated H_2 escape to be ~10^{10} amu/q/cm^2/s locally, and ~1.6×10^{28} amu/q/s globally (integrated over the entire surface area of the atmosphere). Sittler et al. [2010] reported that during the T9 and T18 flybys H^+ and H_2^+ ions were present in the flow of plasma moving towards Titan. The ions also happened to be moving perpendicular to the local magnetic field, leading Sittler et al. [2010] to conclude that they were seeing pick-up ions from Titan's hydrogen corona which can extend to ~20 Titan radii (i.e., out to the Hill sphere).

The primary chemical losses occur when methane is dissociated and ionized by photochemical reactions initiated by solar UV and particle impact. Further reactions with neutrals and ions then make heavier hydrocarbons and nitriles, which can eventually grow into aerosols that precipitate to Titan's surface. Sittler et al. [2009a], using an analogy to molecular clouds and planetary nebulas, suggested that negative chains of carbon atoms form and eventually fold into fullerenes, implying that the same might be going on at Titan. They then estimated precipitation to the surface to be ~2.7 × 10^{-14} kg/m^2/s at 950 km altitude and a global rate of ~4 × 10^{27} amu/q/s. This mass loss rate appears to dominate all other present day atmospheric loss mechanisms [e.g., Johnson et al. 2009] and, because it is large, in order to maintain a steady state methane concentration would require upward diffusion of methane, presumably from a source of methane from Titan's surface.

Sittler et al. [2009a] estimated the loss rate due to pick-up ions to be between ~5 × 10^{22} ions/s and ~10^{24} amu/q/s, which is much smaller than the lower bound given by Johnson et al. [2009] of ~10^{26} amu/q/s possibly due to the inclusion of scavenging down Titan's ion tail, see for example, Sillanpää et al. [2006]; Hartle et al. [2006b]. Escape caused by ionospheric outflows are ~5 × 10^{24} mol/s or ~10^{26} amu/q/s [Sittler et al. 2010; Coates et al. 2012] which may be included in the Johnson et al. [2009] estimate. The escape fluxes caused by sputtering, hot atomic recoils and charge transfer by ENAs also cause heating of the thermosphere and corona [De LaHaye et al. 2007a, 2007b]. Adding all these terms Johnson et al. [2009] find a total escape rate of ~0.32 to ~3.8 × 10^{28} amu/q/s.

Recent work highlights the need to reanalyze INMS data using detailed models of sputtering and energy deposition in the upper atmosphere in order to understand the energy distribution of neutral molecules in the exosphere region. Snowden and Yelle [2014a, 2014b] used Fourier's Law to extract energy deposition rates in the upper atmosphere from INMS data. They determined that precipitation of magnetospheric ions observed by CAPS is too small to explain the observed temperature variations and escape rates. They suggest that gravity waves produced in the lower atmosphere could produce the variability, but a source for the waves has not been identified.

Tucker et al. [2016] showed that using the Louisville Theorem approach, with a non-thermal energy distribution at the exobase, can lead to incorrect estimations of the upper atmospheric thermal structure and, consequently, escape rates due to collisions in the transitional region. Furthermore, such corona fits obtain different exobase energy distributions for N_2 and CH_4 density distributions, which is suggestive of different heating mechanisms occurring between species. Therefore, ion/pick-up fluxes and spectra extracted from CAPS data and model development of gas-kinetic models are needed for detailed simulations of the ion-neutral interaction. Such models can consider the ion - neutral interaction at the microscopic level, and include the production of hot recoil molecules.

The final topic is hydrodynamic loss proposed by Yelle et al. [2008] and Strobel [2008]. By using CH_4 and N_2 ingress altitude profiles with methane diffusing through atmospheric N_2, and then using the ^{40}Ar density profiles, they were able to separate the molecular and eddy diffusivities, which then required an upward methane flux ~4–5 × 10^{10} amu/q/cm^2/s and globally

~4.5 × 10^{28} amu/q/s. This estimate is close to the chemical destruction/precipitation of methane to heavier molecules and aerosols. The model by Strobel [2008] called slow wind argues that solar UV penetrates below the ionosphere where it is deposited. This excess heat is then conducted upward to higher altitudes to drive the hydrodynamic slow wind. But, in order to meet the upward flux required by Yelle et al. [2008] this heat must be transported above the exobase where there are no collisions to conduct the heat, which is its major weakness. Direct Simulation Monte Carlo (DSMC) simulations by Tucker and Johnson [2009] did not show any enhancement of the methane escape rate significantly greater than the Jeans escape rate ~3 × 10^{22} amu/q/s. Therefore, it is highly unlikely that Titan is currently undergoing hydrodynamic escape of CH_4. Tucker et al. [2013] showed that H_2 escape cools the background gas resulting in non-isothermal density profiles without requiring a significant escape rate. Volkov et al. [2011a, 2011b] examined the hydrodynamic escape problem in detail using DSMC simulations. They found that above a Jeans parameter of 6 at the exobase the thermal escape rate is enhanced towards the analytical Jeans rate only by a factor of 1.4–1.7. This is in contrast to Strobel [2008] which predicts a CH_4 escape rate orders of magnitude larger than the Jeans rates, due to an overestimation of heat conduction in the transitional region.

Icy Satellite Science

Interaction of the Enceladus plume with the magnetosphere

- **M_AO2:** Determine current systems, composition, sources, and sinks of magnetosphere charged particles.
- **M_AO3:** Investigate wave-particle interactions and dynamics of the dayside magnetosphere and the magnetotail of Saturn and their interactions with the solar wind, the satellites, and the rings.
- **MC1a:** Determine the temporal variability of Enceladus' plumes.
  - Investigate temporal variations in Enceladus gas production and plume composition, on the scale of seasons and solar cycle.
  - Study plume neutral gas composition.
  - Investigate the physics of the dusty plasma environment.
  - Determine how the magnetosphere reacts to changes in (plume?) gas production rates by studying Enceladus' auroral footprint.
  - Study variability in dust-to-gas mass ratio.
- **MN2a:** Determine the coupling between Saturn's rings and ionosphere.
  - Study how field aligned currents are coupled to the rings and satellites.
  - Explore the dust dynamics in the proximity region.
  - Investigate the mid-plane of Saturn's D-ring.

- Determine the grain composition in the proximity region.
- Investigate the possible interaction of lightning with the inner magnetosphere and the rings.
- Investigate Coupling Between E-ring and the Enceladus neutral and plasma tori.

The initial Cassini MAPS teams began planning for Enceladus encounters as if Enceladus was just another small icy satellite albeit of some additional interest due to the fact that it was embedded in the E-ring. All this changed with discovery of an atmospheric plume at Enceladus by the magnetometer team [Dougherty et al. 2006] on February 17, 2005. With later confirmation by subsequent measurements by many Cassini instruments on later flybys Enceladus quickly became one of the most important objects in the Saturnian system. The main question to answer, "Does Enceladus have liquid water beneath the surface?", because the answer could be the major determining factor if life could exist there.

With the discovery of a thin neutral atmosphere by the magnetic signature of an electrodynamic interaction, all the other Cassini MAPS teams began to reexamine their previous data and to also plan new observing strategies for future encounters.

In 2005, and far from Enceladus, CAPS/Ion Mass Spectrometer (IMS) measured pick-up water group ions (O^+, OH^+, H_2O^+ and H_3O^+ or, collectively, W^+) throughout Saturn's inner magnetosphere [Young et al. 2005; Sittler et al. 2006a, 2006b, 2005; Tokar et al. 2008]. The source of these ions is charge exchange collisions that scatter water group neutrals, replacing a fraction of the co-rotating core distribution with a new and slower-moving ion population without changing the total ion content. The newly-created ions are moving near the local Keplerian speed, which is slower than the co-rotation speed, and hence are picked-up by Saturn's magnetic field. IMS detected these water-group ions within their source region, the Enceladus torus, thus providing the first measurements of W^+ ions throughout their toroidal source region and far from Enceladus. High ion count rates in IMS were observed at the ion pick-up energies, with largest signals near the Enceladus and Dione orbits.

Although encounters with Enceladus later in the mission would be at much closer distances, CAPS was still able to detect indications of a strong interaction between Enceladus and magnetospheric plasma … .

Striking observations were also obtained with IMS during the close encounters of Cassini with Enceladus. On the same encounter where MAG made its discovery, the spacecraft flew within 175 km of Enceladus, and passed through its surrounding cloud of neutrals and plasma. Although encounters with Enceladus later in the mission would be at much closer distances, CAPS was still able to detect indications of a strong interaction between Enceladus and magnetospheric plasma [Tokar et al. 2006]. Originally detected by the Hubble space telescope, Enceladus was known to sit in a cloud of neutral OH forming a torus around Saturn. The cloud detected by CAPS extends from about 3 to 8 R_S with maximum concentration of ~10^3 cm^{-3} inferred to exist near the orbit of

Enceladus (3.95 R_S). The OH cloud is produced by dissociation of H_2O, and although the peak concentration suggested that the largest source of water molecules was in the region near the orbit of Enceladus, the nature of this source was unknown. IMS measurements during the 2005 encounter established a strong perturbation of the plasma flow caused by Enceladus, and perhaps most importantly, the presence of W^+ ions. This population had been detected earlier during SOI [Young et al. 2005].

Later in the mission, during closer encounters with Enceladus, CAPS obtained in situ measurements of W^+ ions freshly produced in the dense Enceladus plume. The dominant species there are light ions (H^+, H_2^+), W^+ ions, and single water cluster ions, ($H_2O \times H_2O^+$). All were observed close to, and nearly due south, of Enceladus. The ions have kinetic energies in the IMS frame roughly equal to ions that are at rest with respect to Enceladus and rammed into the CAPS sensors at the spacecraft speed. This is the signature of freshly produced ions in the plume due, e.g., to charge exchange interactions of incoming magnetospheric ions with neutral plume gas. Figure MAPS-5 shows an example of these ions detected by IMS during the E3 encounter only 52 km from Enceladus. The high count rates close to the ion ram energies in CAPS (denoted by vertical arrows) are clearly visible. Further details of these data are discussed in Tokar et al. [2009].

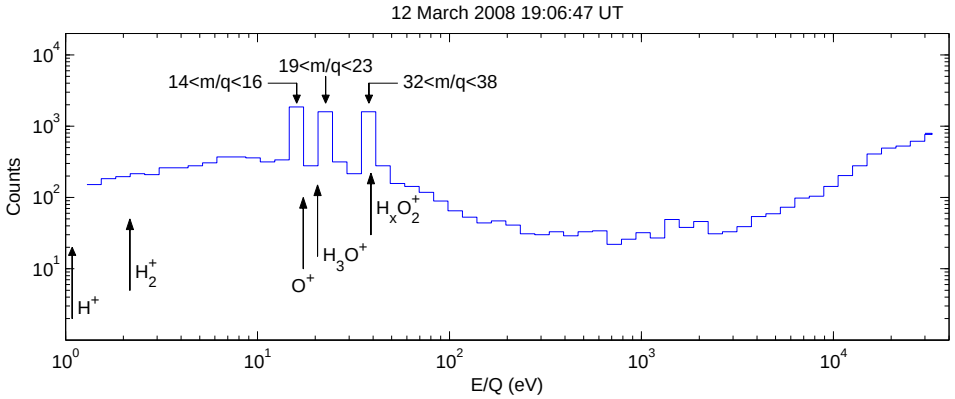

Figure MAPS-5. Individual ion counting rates versus energy per charge measured by IMS anode 5 within the plume during the March 12, 2008 (E3) flyby of Enceladus. Figure from Tokar et al. [2009].

The E7 encounter on November 2, 2009 provided additional observations of the plume stagnation region as Cassini passed directly through the Enceladus plume. The IMS detector sensitive to rammed ions observed stagnation and fresh ions at the ion ram energies. The strong interaction region within the plume is clearly visible in the CAPS IMS data as are the water group ions near 10 eV that are at rest in the Enceladus frame.

The E7 encounter also exhibited the close correspondence between IMS observations of ion slowing and the observed entry into the dense water vapor plume measured by INMS. The data suggest that magnetospheric plasma enters the dense plume leading to charge exchange with plume water vapor followed by subsequent pick-up into the corotating flow. The signature of this process is very sharp on the Saturn-ward side of the plume as the new ions are picked-up and gyrate away from Saturn. The transition out of the plume opposite Saturn for E7 is more extended

due to a number of factors—for example, ion drift velocity and variable ion gyro radii for the various masses created. Note that the IMS observed ion flow speed from the count distributions in the ram direction imply speeds as low as a few km/s in the Enceladus frame.

RPWS results from the E8 flyby reported observations of whistler mode auroral hiss emissions produced by magnetic field-aligned electron beams [Gurnett et al. 2011b]. A ray path analysis of the funnel emission shows the hiss source region within a few moon radii of the Enceladus surface. Figure MAPS-6 is adapted from Gurnett et al. [2011b] Figure 2, and shows the auroral hiss funnel from the E8 flyby in the top panel and the nearly field-aligned electron beams from the CAPS ELS instrument in the second panel. The magnetometer observations of the field-aligned currents which accelerate the electron beams are shown in the bottom panel. The ramp-like signature of the southward current is associated with a shear-mode Alfven wave excited by the moon-plasma interaction. Parallel electric fields, often associated with the Alfven wave, are believed to be accelerated by these waves along magnetic field lines that map to the Enceladus footprint in Saturn's aurora [Gurnett and Pryor 2012]. Sulaiman et al. [2018] showed evidence of currents

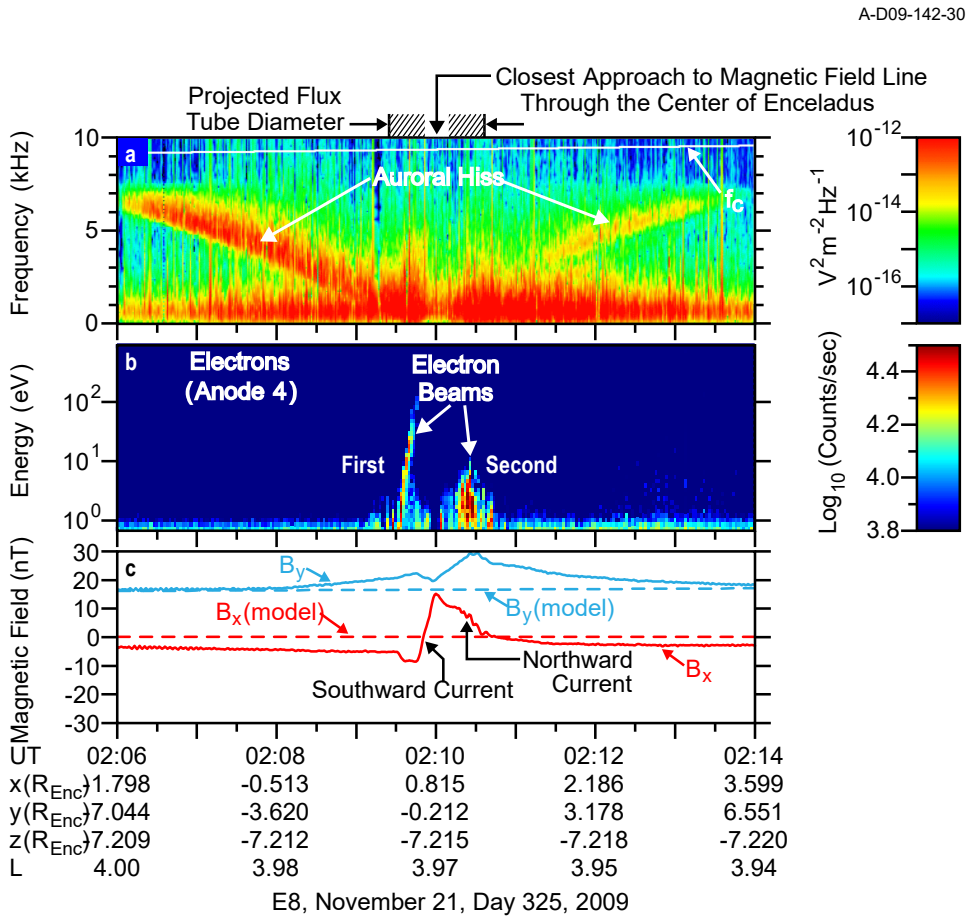

Figure MAPS-6. The auroral hiss funnel from the E8 flyby in the top panel and the nearly field-aligned electron beams from the CAPS ELS instrument in the second panel. Figure from Gurnett et al. [2011a].

between Enceladus and Saturn in the form of very low frequency (VLF) saucers generated by electron beams from Saturn's ionosphere on the Enceladus flux tube.

In addition to the dense neutral water vapor measured by INMS and the resulting cold plasma measured by CAPS and RPWS-LP, the south-polar plume of Enceladus was also found by CAPS and INMS to carry singly charged nanometer-size water-ice grains [Coates et al. 2009; Farrell et al. 2009; Jones et al. 2009; Hill et al. 2012; Morooka et al. 2011; Meier et al. 2015, 2014; Dong et al. 2015]. Such nanograins had been inferred to exist in various cold, tenuous geophysical and astrophysical environments, but the close Enceladus plume encounters by Cassini offered the first (and still the only) opportunity to measure and characterize the nanograins in situ. Before the CAPS shutdown in June 2012 there were three close Enceladus encounters that provided the CAPS ram pointing required to measure these high mass-per-charge particles—E3 on March 12, 2008, E5 on October 9, 2008, and E7 on November 2, 2009. The detailed analysis was reported by Hill et al. [2012]. RPWS data was used by Farrell et al. [2009] to present high-time resolution spectral evidence from the E3 flyby of small water-ice grain impacts on the electric antennas in the vicinity of Enceladus and a sudden, large drop in the electron density in the same region, a density depletion that they attribute to the absorption of electrons by sub-millimeter-sized icy particles. Morooka et al. [2011] presented Langmuir Probe observations to provide evidence for the presence of dusty plasma in the Enceladus plume region. The data show large increases in the ion and electron densities just south of the equatorial plane in the plume region for four Enceladus flybys in 2008, but there is a two order of magnitude difference in these plasma densities with $n_e/n_i < 0.01$. This plasma signature is attributed to electron absorption by dust grains in the plume, which subsequently become negatively charged. Data shows the strong drop in the ne/ni density ratio in this same region where the presence of dust grains had been previously determined [Farrell et al. 2009]. The density profiles of these micron size dust grains was measured by the CDA and RPWS instruments [Ye et al. 2014a]. Additionally, RPWS measurements show almost Keplerian ion speeds measured by the Langmuir Probe which are well below the plasma corotation speed, reaching a minimum below Keplerian speeds in the plume region. The interaction between the cold plasma and the negatively charged small dust grains is believed to cause this slowing of the plasma that moves with Enceladus, explaining the lack of a plasma wake behind the moon.

The presence of dust grains inferred by the ion-electron density difference led to a number of research results. Ye et al. [2014b] discovered that, after a dust grain impacted the RPWS electric antennas, a dust ringing effect was observed by the RPWS wideband receiver, characterized as periodic plasma oscillations. The frequency of these oscillations was shown to be consistent with the local electron plasma frequency, providing a measurement of the electron density. Densities derived from this method in the Enceladus plume region were found to be consistent with electron densities derived by the Langmuir Probe for four consecutive Enceladus flybys in 2008. Shafiq et al. [2011] presented Langmuir Probe observations of the E3 flyby to derive estimates of the dusty plasma parameters and found that the dust density would vary depending on the grain size. The submicron-sized dust grains dominate in the plume region with densities of 10^2 cm^{-3}. The micrometer-sized and larger sized grains are estimated to have densities of only 6.3×10^{-5} cm^{-3}.

Analysis by the CAPS team confirms that the nanograins are largely uncharged when they emerge from the surface vents, and become increasingly (mostly negatively) charged as they approach Cassini a few tenths of Enceladus radii away. The charged nanograin density versus distance from the surface source is shown in Figure MAPS-7, from Hill et al. [2012]. The dashed line shows the r^{-2} dependence that would be expected if the grains were already charged when they emerged from the source. The most plausible charging mechanism is electron attachment from the dense plume plasma. The non-neutrality of the nanograins observed by CAPS, n(−) >> n(+), plausibly cancels the opposite non-neutrality of the plume plasma observed by RPWS-LP. Most of the electrons missing from the plume plasma reside on the nanograins.

This dynamic atmospheric plume was shown by the Imaging team to be due to geyser activity on the southern hemisphere of Enceladus. The electrodynamic interaction involves southern and northern Alfvén wings such that the atmospheric influence not only shows up in the southern, but also the northern wing, hemispheric coupling [Saur et al. 2007]. Using these concepts and magnetic field observations of flybys E0, E1, E2, and neutral density measurements at E2 the time variability of the plumes was investigated [Saur et al. 2008]. Subsequent modelling based on analytical theory clearly showed that the magnetometer results required the presence of negatively charged dust particles [Simon et al. 2011]. The paper also proves the presence of the hemispheric coupling currents required by Saur et al. [2007]. The interaction was later modelled numerically in detail using a hybrid (fluid electron) kinetic code including charged dust particles [Kriegel et al. 2011]. As a unique feature at Enceladus dust–plasma interactions play an important role to explain the observations.

Further modeling has been applied to a spherical obstacle in a plasma flow to show the effect of the moon and local pick-up separately [Jia et al. 2010a]. With this model, we have refined the plume geometry with E2 data [Jia et al. 2010b] and constrained the outgassing rate of the Enceladus plume with data from the nine early flybys [Jia et al. 2010c, 2010d].

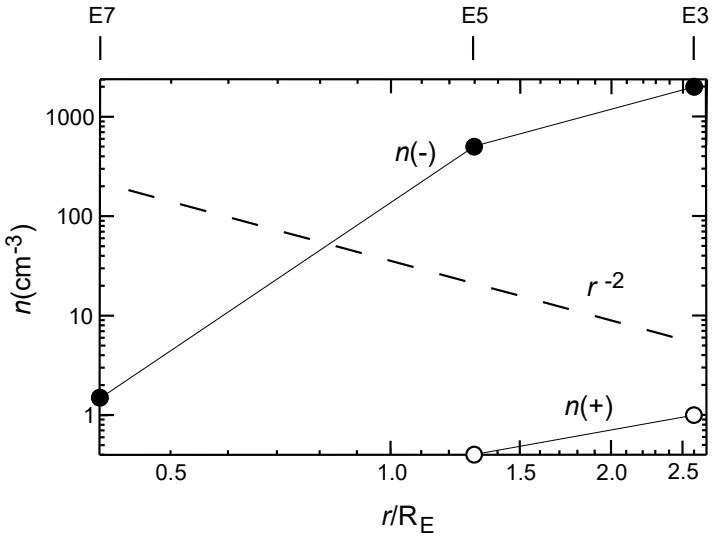

Figure MAPS-7. Total charged nanograin number density within the CAPS E/q range versus distance from the south-pole source vent.

Plume brightness is found to be varying by a factor of a few around the apocenter of Enceladus orbit, using visual images. In contrast, when we plot our deduced outgassing rate against time, we have found 50% variation in gas production rate during the first nine passes E0–E8. The magnetometer could not confirm this postulation with local interaction data. Then, the field perturbation perpendicular to both the direction of magnetospheric flow, and to the magnetic field has been studied with our multi-fluid code, to illustrate the effect of charged dust in creating such a field perturbation [Jia et al. 2011].

Beyond the plasma interaction physics that has been explored by the Cassini/MAPS team, extensive measurements by the INMS team has contributed to characterization of the neutral species in the plume, the plume distribution and to questions about the internal ocean.

The first close flyby of Enceladus with a ram pointing orientation for INMS occurred during the E2 encounter on the July 14, 2005 when Cassini passed with 168.2 km of the flank of Enceladus. The presence of water vapor emanating from the south polar cap was noted over 4000 km before the encounter. A day later on July 15, 2005, the first INMS measurements of the plume's composition were made in the plume's outer edge, and revealed that the plume consists predominantly of water vapor, with small amounts of carbon dioxide, methane, a species of mass 28 (carbon dioxide and molecular nitrogen were suggested), and trace quantities of acetylene and propane.

The next major milestone for INMS occurred during the E5 flyby that occurred at a much higher relative velocity of ~18 km/s, approached from the Northern hemisphere and fly out along the south polar axis. This produced the highest signal to noise mass spectra of Enceladus of the entire mission due to the long outbound duration in the plume. The integrated mass spectra, reproduced from Waite et al. [2009] Figure 1, shows a much more complex spectrum extending out to the limits of the INMS mass range (99 u) (Figure MAPS-8).

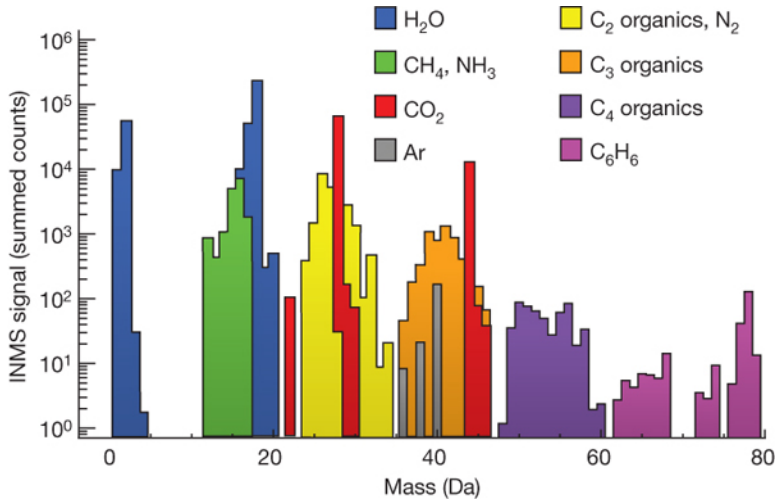

Figure MAPS-8. A complex spectrum extending out to the limits of the INMS mass range (99 u). Figure from Waite et al. [2009] Figure 1.

A mass deconvolution of the E5 integrated mass spectra indicates a host of complex organic compounds, as well as, the compounds previously cited on flyby E2: water, carbon dioxide, methane, mass 28, ammonia, acetylene, and propane. Of particular note was that water seems to be converted into molecular hydrogen and some other compounds abundance altered due to the high flyby speed. This conversion was interpreted and later verified [Walker et al. 2015] as due to raw titanium vapor from ice grain impacts reacting with water to form TiO and TiO_2 and leaving behind the H_2. The serendipitous side effect of this reaction allowed the INMS team to determine the D/H ratio in water from Enceladus, which was found to be similar to comet Halley ($2.9\ (+1.5/-0.7) \times 10^{-4}$) suggesting that Enceladus had never come into chemical equilibrium with the protoplanetary nebula of Saturn otherwise the ratio would have been much closer to the protoplanetary value of 2×10^{-5}.

The INMS data obtained during the E14, E17, and E18 flybys, all at relative flyby speeds of 7–8 km/s and all along or in parallel tracks near the Baghdad tiger stripe, provide a consistent and repeatable depiction of the mass spectra at relative speeds low enough that fragmentation effects are minimized. The spectra above 50 u (not shown) were near the noise level and further reinforce the point that the relative speeds above 8 km/s can lead to significant fragmentation of heavy organics buried in ice grains that complicate the interpretation of the mass spectra from E3 (~14 km/s) and E5 (~18 km/s). One can mass deconvolve the combined spectra from the slower flybys (E14, E17, and E18) (see Figure MAPS-9). The detailed analysis of this data set is the subject of a paper in preparation by Magee et al. [2018].

During six encounters between 2008 and 2013, the Cassini INMS made in situ measurements deep within the Enceladus plumes. Throughout each encounter, those measurements showed density variations that reflected the nature of the source, particularly of the high-velocity jets. Since

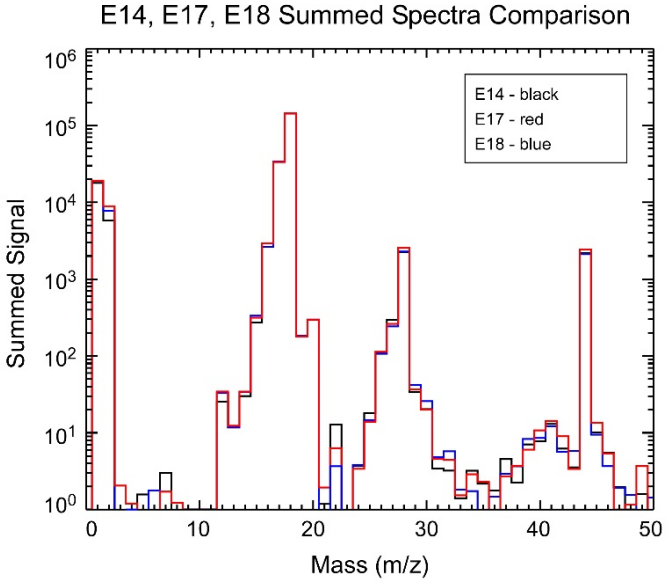

Figure MAPS-9. Overlaid mass spectra for flybys E14, E17, and E18. Note the consistency of the spectra.

the dominant constituent of the vapor, H_2O, interacted with the walls of the INMS inlet, changes in the external vapor density are tracked by using more-volatile species that responded promptly to those changes. To understand the plumes requires examination of each of the three components of Enceladus ejecta, fast and dense jets, slower diffuse gas, and ice grains.

The vapor plumes show variability that was first reported by Hedman et al. [2013]. A comparison of data from the last three encounters, E14, E17, and E18, are consistent with the VIMS observation of variability in jet production and a slower, more diffuse gas flux from the four sulci or tiger stripes. Teolis et al. [2017] used data from all INMS and Ultraviolet Imaging Spectrograph (UVIS) encounters to constrain a time-dependent and high-resolution model of the plumes.

During the final low-altitude flybys of Enceladus, the most abundant, non-sticky species in the plume, CO_2 at 44 u, was sampled at a higher rate, to enable higher-resolution measurements of local density variations along Cassini's trajectory, achieving resolution of 0.25 s temporal and 1.9 km spatial. As shown in Figure MAPS-10, CO_2 data from E17 clearly resolved density variations, indicative of gas jets, along Cassini's trajectory. Hurley et al. [2015] suggested on the basis of Monte Carlo models that the plume source may be continuously distributed, albeit variable, along the tiger stripes. These models included one lower-velocity component for the tiger stripes and a second, higher-velocity component for the jets. The complete plume three-dimensional structure is difficult to uniquely constrain solely on the basis of the few INMS flybys as multiple combinations of jet pointing directions and intensities can fit the data, and temporal variability further increases the potential solutions.

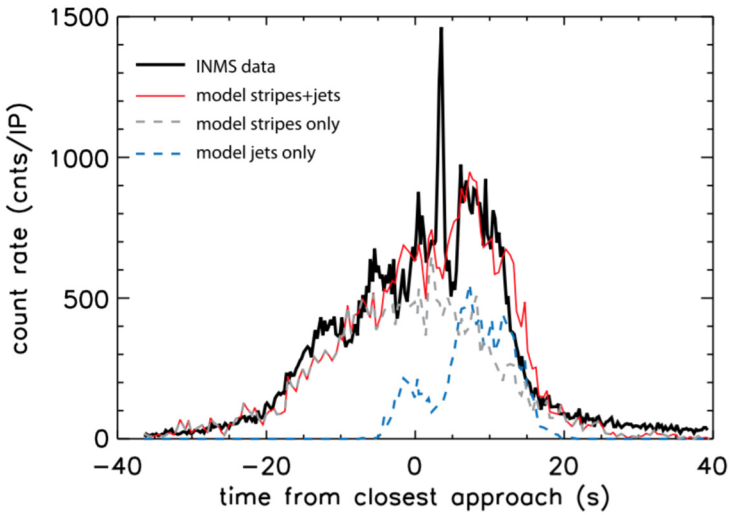

Figure MAPS-10. INMS measurements of mass 44 u species during the E17 flyby are shown in black. Model [Hurley et al. 2015] predictions using constant emission along the tiger stripes at 500 m/s and 270 K (gray dashed line) are selected to match the rise and fall on the outskirts of the plume. The jet model using Mach 4 (1500 m/s and 270 K) are included (blue dashed line) to reproduce the overall enhancement near closest approach. The sum of the two models, shown in red, reproduces the overall structure of the plume, but misses some of the fine structure.

During Cassini's close (99, 74, 74 km) E14, E17, and E18 flybys through the Enceladus gas/dust plume on October 1, 2011, March 27, 2012, and April 14, 2012, the INMS measured in situ the detailed spatial structure of the neutral gas along the trajectories. These encounters were the first to fly close enough to the plume sources with the required pointing and sufficient data acquisition rate, to enable resolution of individual gas jets within the broad plume by INMS. During these flybys two INMS objectives were to: 1) constrain the locations, magnitudes and gas velocity from the plume surface sources; and 2) extrapolate the three-dimensional structure of the plume, including the diffuse plume and individual major jets. Since these flybys, the INMS team have carried out detailed plume modeling, combining the along-track densities measured at different times/dates by INMS, with and occultation, surface temperature, and imaging data from UVIS, Composite Infrared Spectrometer (CIRS) and ISS. The goals were to constrain the physics of the jet sources, that is, the nozzle dimension and gas thermodynamic properties including temperature, density, flow and expansion rate, and provide necessary inputs for future modeling of the plume interaction with the Saturn system, that is, the E-ring and magnetospheric sources and mass loading.

The results of our studies are now published in the papers by Perry et al. [2015] and Teolis et al. [2017]. Teolis et al. [2017] describes a detailed comparison of several plume source scenarios. The findings indicate that a time variable source, consisting of: 1) a source continuously (but non-uniformly) distributed along the tiger stripes; and 2) sharp gas jets as inferred from ISS data [Porco et al. 2014], provide the best fit to the INMS and UVIS data.

In the curtain and jet cases, the model suggests that a gas source with a Mach number distribution, containing a slow (with thermal velocity, Mach 0) isotropic emission, and a super-sonic (high velocity) component, was required to fit the broad distribution, and the fine structure, respectively, observed in the UVIS/INMS data. The fits use a 4-point Mach number distribution ranging from zero (gas at rest) to 16 (the fast component), as necessary to best fit the shapes of the features in the INMS and UVIS data. The curtain model considered three cases: 1) a uniform emission along the tiger stripes; 2) emission correlated to the tiger stripe temperature from CIRS data (Figure MAPS-11); and 3) emission optimized to fit the INMS and UVIS data. For jets, the model considered two cases: 1) jets with equal intensities; and 2) jet intensity optimized to fit the data. The optimized models typically give multiple solutions, corresponding to reductions/enhancements in different combinations of jets, or different vapor source distributions along the tiger stripes. Figures MAPS-26–MAPS-30 show the averages over these solution 'families' to compare and contrast the quality of the fits in the cases of continuous distributed emission and of discrete gas jets. It is clear on the basis of the plots, that neither the thermal plume cases, nor the cases of uniform curtains or jets, provide very good fits to the data. Both optimized curtains and jets yield rough agreement with the data but, as shown in the plots, some features of the data are better matched by the jets. The models could not fit all of the INMS and UVIS data simultaneously with a unique model solution. Therefore, given the curtain and [Porco et al. 2014], jets as a modeling constraint, an assumption of time variability of plume source distribution and/or individual jets between the Cassini flybys, is required to fit the data. The changes over time of the individual jets appears to be chaotic, exhibiting no obvious correlation to the Enceladus mean anomaly, as seen (for the plume as a whole) in VIMS data [Hedman et al. 2013].

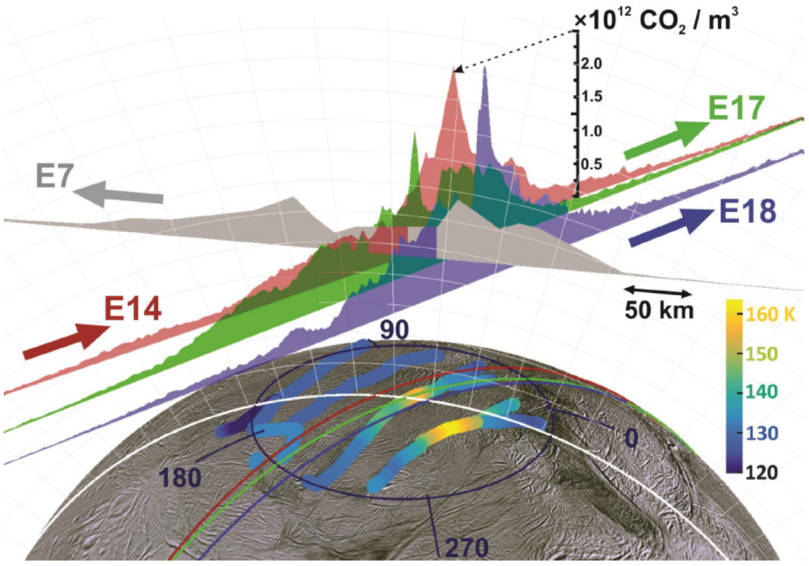

Figure MAPS-11. To scale 3-D representation of the E14, E17, E18 and also (lower resolution) E7 INMS data, with vertical areas representing (in linear scale) the density, and the flat base of the areas corresponding to the Cassini trajectories. Lines across the surface are the ground tracks. The Tiger stripes are colored according to the temperature estimated by CIRS. Figure from Teolis et al. [2017].

Table MAPS-2 shows the major species composition of Enceladus' plume gas and the volume mixing ratios reproduced from Waite et al. [2017] Table 1.

Table MAPS-2. The major species composition of Enceladus' plume gas. Volume mixing ratios are derived from Cassini INMS measurements [Waite et al. 2017].

Constituent	Mixing Ratio (%)
H_2O	96 to 99
CO_2	0.3 to 0.8
CH_4	0.1 to 0.3
NH_3	0.4 to 1.3
H_2	0.4 to 1.4

Ring Science

Ring-magnetosphere-ionosphere interaction

- **MN2a:** Determine the coupling between Saturn's rings and ionosphere.
  - Study how field aligned currents are coupled to the rings and satellites.
  - Explore the dust dynamics in the proximity region.
  - Investigate the mid-plane of Saturn's D-ring.
  - Determine the grain composition in the proximity region.

  - Investigate the possible interaction of lightning with the inner magnetosphere and the rings.
  - Investigate Coupling Between E-ring and the Enceladus neutral and plasma tori.
- **M_AO2:** Determine current systems, composition, sources, and sinks of magnetosphere charged particles.
- **M_AO3:** Investigate wave-particle interactions and dynamics of the dayside magnetosphere and the magnetotail of Saturn and their interactions with the solar wind, the satellites, and the rings.

The Cassini mission brought about a profound new view the interaction of the amazing Saturnian main ring system with the magnetospheric space environment. During the Voyager era, it was presumed that meteors continually bombarded the rings. The spokes were thought to represent a stunning visual manifestation of these intense impacts. The associated impact-ionized vapor plume then delivered ring water and oxygen ions along connecting magnetic field lines to the ionosphere. These water ions were thought to chemically disrupt the ionosphere hydrogen cycle and deplete the ionosphere locally of electrons. It was also thought that these ring-generated ions possibly modify the color of the cloud tops. In this view, the rings were considered a source of quasi-energetic plasma delivering heavy ions to the exobase above the cloud-tops. Figure MAPS-12 shows the predicted impact-generated plasma flux from the rings, with peak densities over the dense portion of the central B-ring [Wilson and Waite 1989]. Voyager, unfortunately, did not actually fly over the rings and thus confirmation of this impact-driven ring plasma source could only be inferred.

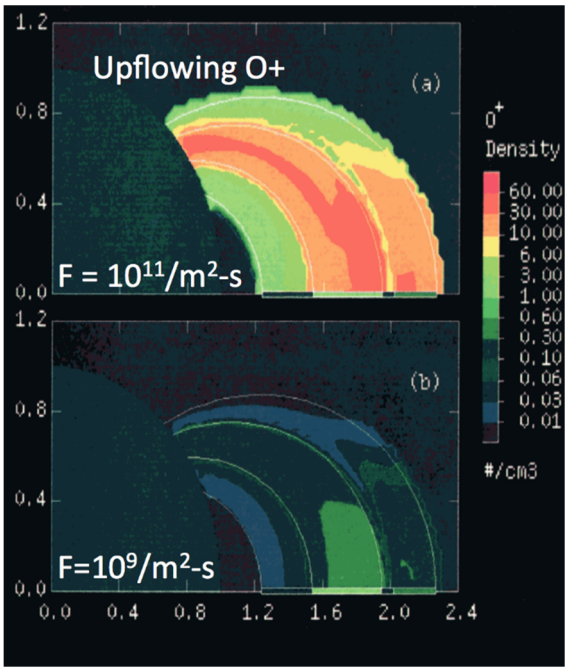

Figure MAPS-12. Wilson and Waite Impact-Driven Ring Plasma Model [Wilson and Waite 1989].

Cassini's orbit provided several important periods during which measurements were made of the rings and their interaction with the magnetosphere and ionosphere. First measurements of this important system began with Cassini's very first passage through the magnetosphere during SOI. During this period, Cassini crossed the ring plane in a gap between the F-ring and G-ring and also flew directly across magnetic field lines that connect back down to the main rings. The RPWS instrument thus obtained unique direct measurements of the plasma environment across the main A-ring, B-ring, and C-ring [Gurnett et al. 2005; Wang et al. 2006]. Near the very end of the mission, Cassini again was able to make measurements while crossing these flux tubes, this time by many instruments. After SOI, during the first few years of the mission, Cassini made a number of inclined and equatorial crossings of the E-ring, particularly near the orbit of Enceladus. Later, Cassini shifted to high inclination orbits and crossed the E-ring multiple times in 2016, providing opportunities to compare the vertical dust density profiles to those measured before equinox [Kurth et al. 2006; Ye et al. 2016a].

During Cassini's SOI on July 1, 2004, the spacecraft passed over the B-ring, A-ring, F-ring, and the Cassini division before descending (inside the G-ring) through the ring plane. The trajectory provided the first in situ plasma measurements over Saturn's main rings, complementing data obtained by the Voyager 2 plasma science instrument outside the main rings. During SOI, data form the MAPS instruments presented a new view of the plasma environment over the main rings. Data from RPWS [Gurnett et al. 2005] shows the plasma density as derived from the narrow-banded upper hybrid waves, electron plasma oscillations, and high frequency edge of the auroral hiss (see Figure MAPS-13). From the same RPWS measurements, Wang et al. [2006] were able

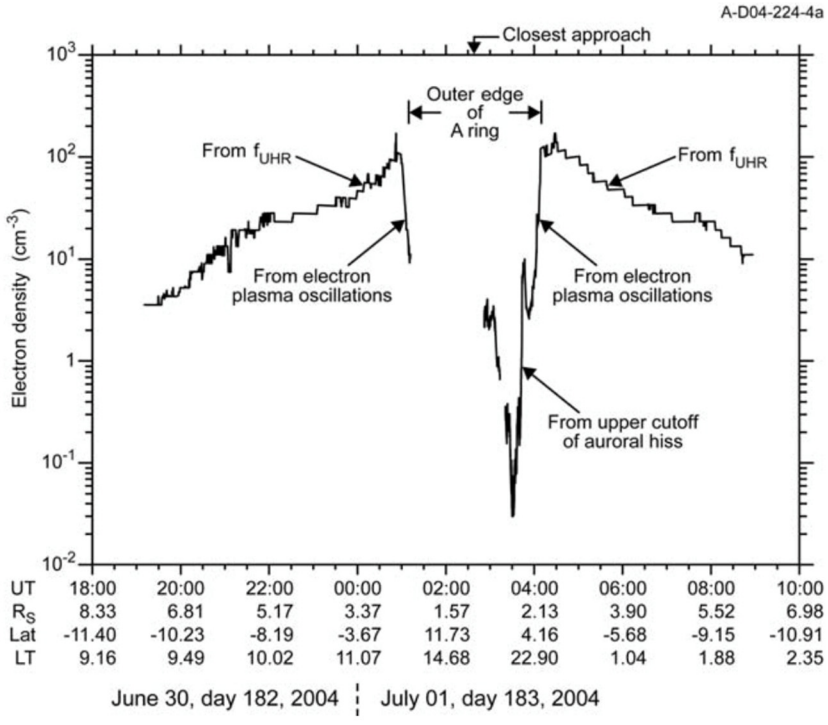

Figure MAPS-13. The electron density over the main rings as derived by the plasma waves detected by RPWS. See Gurnett et al. [2005] for more details.

to provide information on the micron sized dust at the inbound and outbound ring plane crossings before and after SOI.

This RPWS electron density profile was unexpected and almost diametrically opposite to what would have been predicted from an impact-driven ring plasma system, where the maximum in plasma density is expected in the central B-ring. There are two stunning features to this profile. First, immediately adjacent to the dense A-ring, there is an electron density maximum at over 100 electrons/cm^3 , with the high density region (>10/cm^3) extending out to beyond L = 5. It would later be found [Persoon et al. 2015, 2009] that this high density region is a plasma torus created by ionization and pick-up of new ions born in the Enceladus plume and a seasonal contribution from photo-ionized neutrals originating from the rings themselves. Second, the region over the main rings is devoid of plasma, with an electron density drop of near 10000 from the outer edge of the A-ring to values of 0.04 electrons/cm^3 at 1.76 R_S over the central portion of the B-ring [Xin et al. 2006; Farrell et al. 2017]. This void region has been identified as a ring plasma cavity (RPC) with its lowest density near the synchronous location. The profile of electron density over the main rings varied inversely with ring optical depth, with the lowest plasma densities observed over the central dense B-ring and a local maxima sense when passing over field lines connected to the Cassini Division. (In Figure MAPS-13, this Cassini Division plasma maxima is seen near 03:45 spacecraft event time (SCET) with the local peak near 10/cm^3.)

During the same period (SOI) CAPS IMS observed an enhanced ion flux (compared to background outside the rings) outside of the main rings and in the vicinity of the F-ring and G-ring as Cassini crossed the ring plane during orbit insertion on July 1, 2004. Near the edge of the main rings the IMS ion flux as a function of energy per charge provided strong evidence for the presence of O_2^+. Analysis led to the conclusion that the enhanced ion flux between the F-ring and G-ring consisted of the water group ions O^+, OH^+, and H_2O^+ (the other water group ion H_3O^+ could not be identified) coming from Enceladus with an admixture of O_2^+, predominantly from the extended ring O_2 atmosphere. The O_2^+ component appeared to be dominant at SOI and was later found to vary with season [Elrod et al. 2014, 2012] due to the changing orientation of the ring plane relative to the solar UV flux (Figure MAPS-14).

Near the edge of the main rings the IMS ion flux as a function of energy per charge provided strong evidence for the presence of O_2^+.

RPWS observations confirm the model of Tseng et al. [2013a] that the ring-ionosphere-magnetosphere interaction is driven by photolytic processes, not impact processes [Farrell et al. 2017]. Specifically, the Sun-facing side of the main rings are a source of photo-dissociated neutrals that then get ionized to form a relatively low energy exo-ionosphere. This exo-ionosphere cannot directly access the shadowed/unlit side of the rings: the ring particles represent obstacles to their transport. Thus, the plasma density on the unlit side is modulated by ring density, being lowest where the ring obstruction is the highest, (in the central B-ring). Local maxima are expected where the local ring particle density is low, like across the Cassini Division. There is little evidence of impact-generated plasma like that predicted during the Voyager era.

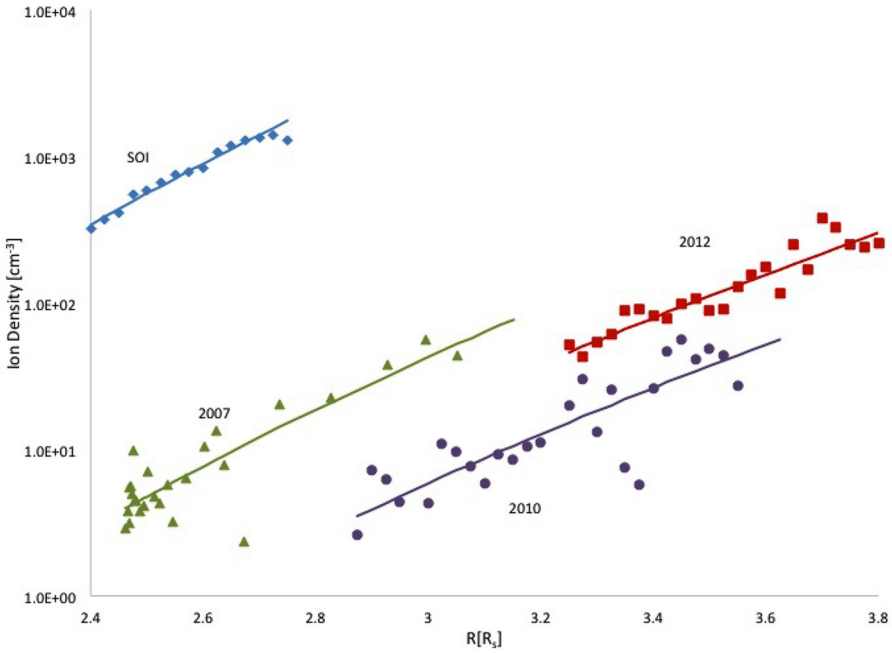

Figure MAPS-14. Ion densities extracted from CAPS IMS data at SOI in 2004, and inferred for subsequent years by modelling. The modeling indicates the seasonal dependence of ring plasma. This region contains ions formed from neutrals scattered out of the ring atmosphere as well as ions formed from neutrals in the Enceladus torus. SOI was dominated by O_2^+ and the later years by water group ions. Figure from Elrod et al. [2014].

The seasonal dependence observed and modeled using CAPS data confirmed that the O_2^+ ionization source was indeed solar UV acting on oxygen in the ring atmosphere as predicted by Tseng et al. [2010]. Seasonally varying oxygen was subsequently observed at much larger radii by the MIMI instrument, confirming that oxygen originating in the rings can be scattered throughout the inner magnetosphere and, consequently, also into Saturn's atmosphere. This likely accounts for oxygen observed in Saturn's thermosphere. Subsequent modeling [Tseng et al. 2013a] shows that model calculations based on the CAPS data were in reasonable agreement with that data.

Laboratory data showed that radiation decomposition of ice would lead to the production of roughly twice as much H_2 as O_2, thereby maintaining the near stoichiometry of irradiated ice grains —for example, Brown et al. [1982]. Indeed CAPS measurements have shown that the Saturnian magnetosphere is permeated with H_2^+ and H^+ from a variety of sources (Titan, the Enceladus torus, and Saturn's atmosphere), including the ring atmosphere [Tseng et al. 2013b, 2011]. Since H_2 is much lighter than O_2 it has a proportionately larger neutral scale height, and can also be easily scattered throughout the magnetosphere by the heavier molecules. Ionization of the H_2 component of the extended ring atmosphere, and the pick-up of H_2^+ formed by this process, was shown by Tseng et al. [2011] to be an important component of magnetospheric H_2^+ detected by CAPS [Thomsen et al. 2010].

Surprisingly, the IMS ion densities observed between the outer edge of the main rings and Mimas and populated by ionization of neutrals from the ring atmosphere and the Enceladus torus,

exhibited an unexpected radial dependence [Elrod et al. 2014, 2012]. Not only did the plasma detected by CAPS in this region exhibit a seasonal dependence, with the O_2^+ component dominated by the water products from the Enceladus torus at Equinox, but the observed radial dependence suggested that an ion loss process other that electron-ion recombination, charge exchange or diffusion was acting [Elrod et al. 2014; Tseng et al. 2013a]. Since the CAPS ion densities and the RPWS electron densities differed, particularly at SOI, the observed radial dependence of the CAPS ion data was subsequently determined to be due quenching of the ions on nano-grains. These grains, a fraction of which were negatively charged, were presumed to be emitted from the edge of the main rings and present in the tenuous F-ring and G-ring, acted as ion sinks [Johnson et al. 2017]. That this process was occurring in this region of the magnetosphere was subsequently confirmed by the RPWS instrument during the F-ring orbits when, unfortunately, the CAPS instrument was turned off.

IMS observed ion fluxes over the main rings consistent with the presence of atomic and molecular oxygen ions [Young et al. 2005]. CAPS IMS observations over the main rings detected both O^+ and O_2^+ at densities of a few per cm^3 using the IMS time-of-flight (TOF) sensor (Figure MAPS-15) [Tokar et al. 2005; Elrod et al. 2012]. Further analysis by Elrod et al. [2012] shows much higher densities of O^+ when CAPS was over the outer edge of the B-ring and again when CAPS was over the inner edge of the A-ring.

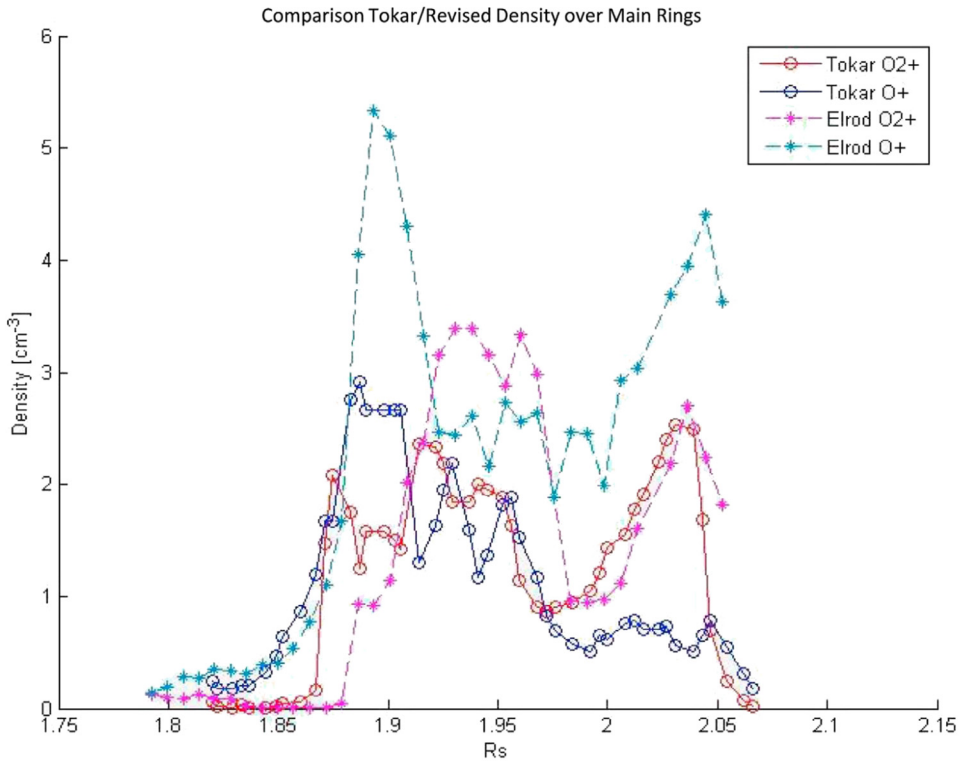

Figure MAPS-15. Densities of O^+ and O_2^+ obtained from IMS data over the main rings as a function of radial distance from Saturn in R_S. Data from Tokar et al. [2005] and re-analyzed by Elrod et al. [2012].

The IMS data suggested the presence of a ring atmosphere that was predominantly O_2 rather than H_2O and much more robust than predicted. Since the energetic ion density in this region is highly depleted due to absorption by ring particles, for example, Cooper et al. [2017], the CAPS team proposed that the atmosphere was produced by UV-induced decomposition of ice on the ring particles [Johnson et al. 2006]. Such a neutral atmosphere would have a scale height confining it close to the ring plane. Because ions were detected well above the ring plane, this also led to the prediction that ion-neutral scattering would produce both a ring ionosphere with a much larger scale height, and a neutral oxygen cloud that permeated Saturn's magnetosphere [Johnson et al. 2006; Luhman et al. 2006; Bouhram et al. 2006]. Following ionization, pick-up and scattering of the neutrals from this atmosphere was shown to populate the magnetosphere with oxygen atoms and molecules which are eventually ionized far from the main rings [Johnson et al. 2006]. Molecular oxygen ions in were eventually discovered in the inner magnetosphere as well [Martens et al. 2008]. This has been subsequently confirmed by additional data and modeling.

Interestingly, the INMS instrument also observed only water-group ions in the F-ring. Unlike the neutrals, the ion densities were not symmetrical with respect to the equatorial plane, varying in both total density and the relative fractions within the water group. The predominance of O^+ versus the other water-group ions indicates that there may be a source of O^+ other than as a byproduct of water. One possibility is that CH_4^+ contributes a fraction of the 16 u ions. The lack of O_2^+, which INMS observed during Cassini's insertion into orbit about Saturn, is likely due to the INMS energy limit: at the F-ring speeds, O_2^+ exceeds the INMS limit for ions. The lack of H_2^+ is surprising and not yet explained. As with neutrals, noise prevents INMS measurement of H^+ at 1 u.

In addition to the ion and electron plasma population detected in the vicinity of the ring, the INMS instruments was able to detect the neutral parent molecules. INMS found two neutrals with remarkable consistency during the F-ring passes: H_2 and a species at 28 u (Figure MAPS-16). The scale height, or the half-width-half-max of the INMS counts, for both of these species was approximately 3,000 km, or 0.05 Saturn radii (R_S). This parameter and the total counts were nearly identical in each pass.

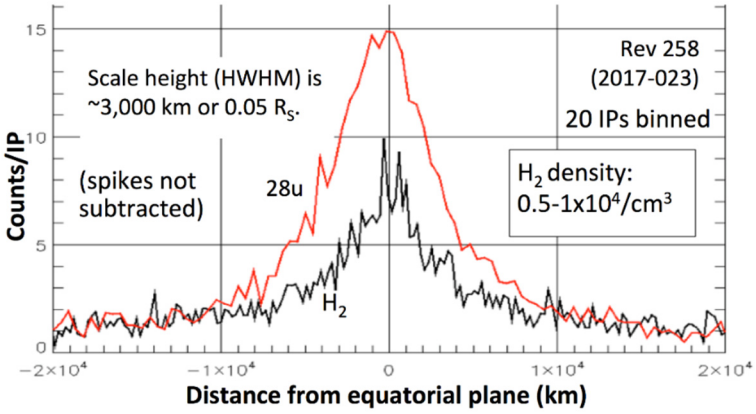

Figure MAPS-16. The major neutrals measured by INMS in the F-ring. Twenty measurements (integration periods or IPs) were binned for this plot.

Although H_2 was expected in this area of the rings, models and Earth-based observations predicted a larger scale height for H_2 from Saturn's atmosphere, and the narrow distribution of the observed H_2 suggests that it is more liked to originate in the rings. The lack of variability indicates a stable ring atmosphere. Atomic hydrogen is not measured by INMS due to instrumental noise at 1 u.

CH_4 (16 u) and CO_2 (44 u) are the only other measured species. They both have a count rate that is approximately 20% of the H_2 rate. CH_4 is confirmed by the presence of 15 u counts at the correct electron impact dissociative ionization ratio, the amount produced from CH_4 in the INMS ionization chamber. CO_2 is not a common dissociation product and may be a native species. It exists on the surface of several icy moons. Count rates for both CH_4 and CO_2 are depressed due to dissociation and they may be more abundant than indicated by the measurements. There are small amounts of 26 u and 27 u, which are expected products from ionization of C_2H_4, one possibility for the 28 u measurements. However, the count rates for these two cracking products are lower than expected if the entire 28 u signal was produced by C_2H_4. This deficiency implies that another species such as CO may contribute to the 28 u signal.

Several expected neutrals are missing, most notably H_2O and O_2. Since water is temporarily adsorbed onto the walls of the INMS inlet, H_2O counts are suppressed and delayed. Combined with the radiation background, which increases after passing through the equatorial plane, INMS would not detect low densities of H_2O, particularly after some loss due to high-velocity dissociation. Models show that O_2 could be abundant, but that densities decrease a factor of 1,000 approaching the location of Cassini's trajectory; moreover, much of the O_2 would be lost due to dissociation.

The observation suggested that there is a current system driven by the rings-magnetosphere interaction, with the electron beams and currents near the synchronous point … possibly being part of the current closure system.

In addition to the surprising neutral and plasma composition and the existence of a unique ring ionosphere, Cassini instruments were also able to the study the current systems that connects the rings, the ring ionosphere, Saturn's magnetosphere, and Saturn's own ionosphere. Xin et al. [2006] reported a strong auroral hiss signal detected at the deepest depletion of the electrons within the RPC near 1.76 R_S. The whistler-mode auroral hiss emission is a classic signature of the presence of energetic field aligned electron beams, in this case flowing outward from the rings along field lines connecting to the ionosphere. They reported that the RPC environment had a stunning similarity to plasma cavities found in polar auroral regions, usually associated with field aligned currents that drive the aurora. The observation suggested that there is a current system driven by the rings-magnetosphere interaction, with the electron beams and currents near the synchronous point at 1.76 R_S possibly being part of the current closure system.

Figure MAPS-17 illustrates the concept of this new ring current system presented in Xin et al. [2006]. While the plasma on field lines over the rings would be corotating, the particles and associated photo-dissociated gas of the rings would be moving in Keplerian motion, creating drag

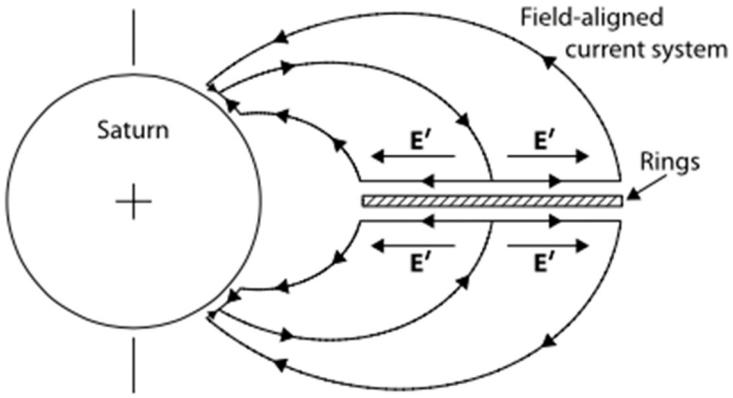

Figure MAPS-17. The proposed large-scale current system that would be induced in Saturn's magnetosphere by the interaction of the rings (including any associated gas) with the corotating magnetospheric plasma. Figure from Xin et al. [2006].

on the plasma. This drag creates an associated change in plasma speed, ΔV. Beyond the synchronous point, the plasma is slowed by the Keplerian-moving particles and gas, creating an outward radially-directed E-field in order to maintain the new sub-corotation speed E′ = ΔV × B. This new E-field drives an outward current, J, which acts to then form a magnetohydrodynamic J × B force to balance the plasma-ring drag force. Inward of the synchronous point, the corotating plasma is accelerated by the ring drag force, creating an inward radial E-field and current that forms a J × B force to offset the acceleration. At the edges of the rings, these cross-ring currents become field-aligned parallel current that close down to the ionosphere along connecting magnetic field lines at the outer edge of the A-ring near L = 2.25 and inner edge of the D-ring near L ~1.11. The rings thus behave as an electrical generator in the plasma, driving currents from the ring surfaces along magnetic field lines down to the ionosphere.

While detailed analysis of the proximal orbits is still ongoing, Wahlund et al. [2018] reported on a very strong Saturnian ionosphere D-ring electrical connection, which would represent the current closure of the Xin et al. [2006] model at the inner radial edge of the main rings. Using the RPWS Langmuir Probe, they found that Cassini passed through a cold, dense electron region during proximal perigee, which has been interpreted to be entry into the Saturnian ionosphere.

At higher altitude proximal perigee passes, like orbit 277, Cassini passed through the inner edge of the D-ring (also immersed in the outer edge of the ionosphere). In these cases, the electron density had a distinct bite-out or decrease near the equator which is believed to be due to the presence of D-ring particulates that have absorbed the local ionospheric plasma. The RPWS instrument also detected micron-sized dust grain impacts revealing the presence of these D-ring particulates. The complex dusty plasma interactions remain a subject of considerable study even after the end of the mission [Ye et al. 2018].

An additional surprise during the proximal orbits was that the MIMI/INCA and Charge-Energy-Mass Spectrometer (CHEMS) instruments, that were designed to measure energetic particles, were detecting signatures of D-ring dust falling into Saturn's equatorial atmosphere. These particles

are of 1–3 nm size, much smaller than what is detected by the CDA instrument designed to measure dust. The dust is reaching the atmosphere within 4 h and provides a continuous influx of about 5 kg/s from the rings into the atmosphere [Hsu et al. 2018; Mitchell et al. 2018].

The ionosphere of Saturn and its connection to the ring ionosphere system is still a work in progress. First in situ measurements by RPWS of the cold ionosphere properties have just been reported [Wahlund et al. 2018]. Several other manuscripts have been submitted, and they all show a very strong interaction between the D-ring and the ionosphere of Saturn, causing the ionosphere to become extremely variable with more than two orders of magnitude and trigger a dust-ionosphere layer near the equator.

Magnetosphere Science

Seasonal and solar cycle variations

- **MC1b:** Observe Saturn's magnetosphere over a solar cycle, from one solar minimum to the next.
  - Investigate what controls the interplay between the Dungey and Vasyliunas cycles?
  - Study the solar cycle dependence of the magnetospheric dynamics.
  - Investigate magnetospheric structure: variations in force balance.
  - Investigate non-static and other variant radiation belt features.

Cassini spent 13 years in Saturn's magnetosphere. This allowed the MAPS instruments aboard the spacecraft to make measurements of Saturn's magnetosphere and of the important moons such as Enceladus and Titan over more than a solar cycle and over nearly half of a Saturnian year. This allowed MAPS scientists to study the effects of both the solar cycle and the Kronian season on the magnetosphere. Many of the results of the seasonal and solar cycle variation are detailed in the section of this summary where their underlying processes are addressed. For example, see sections entitled:

- Titan's upper atmosphere and its interaction with the surrounding plasma
- Magnetotail configuration and dynamics
- Magnetospheric structure and convection
- Plasma loss into the magnetotail; Radiation belts
- Time varying modulation of SKR and associated planetary period oscillation (PPO) signals

In this section we will highlight just a few of the results related to solar cycle and seasonal effects produced by the MAPS instruments teams.

One of the most important discoveries of the Cassini mission was the identification the ring ionosphere, the ring sources of plasma and the activity of Enceladus. Many of these interesting new phenomena exhibited seasonal dependence due to the inclination of the rings relative to the activating solar UV. Amount these effects was the discovery of a seasonally-dependent source of plasma between the A-ring and Enceladus. Additionally, a seasonal dependence was observed and modeled using CAPS data that confirmed that the O_2^+ ionization source was indeed solar UV acting on oxygen in the ring atmosphere as predicted by Tseng et al. [2010]. Seasonally varying oxygen was subsequently observed at much larger radii by the MIMI instrument, confirming that oxygen originating in the rings can be scattered throughout the inner magnetosphere and, consequently, also into Saturn's atmosphere. Surprisingly, the IMS ion densities observed between the outer edge of the main rings and Mimas, and populated by ionization of neutrals from the ring atmosphere and the Enceladus torus, exhibited an unexpected radial dependence [Elrod et al. 2014, 2012]. Not only did the plasma detected by CAPS in this region exhibit a seasonal dependence, with the O_2^+ component dominated by the water products from the Enceladus torus at Equinox, but the observed radial dependence suggested that an ion loss process other that electron-ion recombination, charge exchange or diffusion was acting [Elrod et al. 2014; Tseng et al. 2013a].

As outlined in the section entitled Time varying modulation of SKR and associated PPO signals, many aspects of Saturn's magnetosphere are modulated at the assumed rotation period as approximated by the SKR signal. Extensive studies of the SKR period as well as associated auroral activity have shown a mark dependence on the Saturnian season. The SKR spectrum was studied statistically with RPWS observations from a wide variety of Cassini's positions. Southern SKR was predominant during Saturn's southern summer up to 2010–mid 2011 (slightly after the equinox of 2009), while the northern SKR was predominant after, consistent with a seasonal control of field-aligned currents driving auroral emissions by solar illumination of Saturn's ionosphere.

The major discovery brought by RPWS was then the identification of 2 SKR periods [Kurth et al. 2008] corresponding to the 2 Kronian hemispheres, differing by ~1%. These periods were found to both vary with time in anti-correlation over yearly timescales and crossed closely after equinox, a trend which was interpreted as a seasonal driving of solar illumination [Gurnett et al. 2011a, 2010b, 2009; Lamy 2011]. These dual periods were later noticed in narrowband (NB) emissions and auroral hiss as well [Gurnett et al. 2010b; Ye et al. 2017, 2010] and more generally observed in numerous magnetospheric observables including magnetic oscillations, ENA emissions, aurorae [Mitchell et al. 2009b; Carbary et al. 2011a, 2010a; Nichols et al. 2010; Andrews et al. 2011, 2010a; Provan et al. 2011; Badman et al. 2012a, 2012b]. It is now accepted that these dual rotational modulations all originate from two rotating hemispheric systems of field-aligned currents, whose origin may be atmospheric vortices [Jia et al. 2012].

Clearly related to the variation in aurora and the SKR signal, the PPO current were found to have similar seasonal dependence. MAG data comparing high-latitude data sets from 2006/2007 and 2008 in Saturn's late southern summer to a third interval of high-latitude data was obtained in 2012/2013 during northern spring [Bradley et al. 2018]. The PPO currents were found to be of similar form but somewhat weaker than in 2008, while the sub-corotation currents exhibited strong

opposite seasonal asymmetries in the north and south polar regions, indicative of weak polar ionospheric conductivity in the winter polar cap. Investigation of the current signatures observed on the F-ring and proximal orbits spanning northern summer solstice at the end of the Cassini mission are currently ongoing [Hunt et al. 2018a].

Thus far we have outlined several seasonal variations at Saturn. Most of these have been related to either the ring plane inclination or to current system. The CAPS instrument measurements of the in situ plasma do not show such a strong variation. In fact, on the time scale of months to years, most of Saturn's magnetospheric plasma does not exhibit strong variability, less than a factor of three [Wilson et al. 2017], in spite of the fact that the Enceladus plume source does appear to vary on the scale of several months [Smith et al. 2010]. In the very inner magnetosphere, just outside the main rings, heavy ion densities (O_2^+ and W^+) show a seasonal dependence, as could be expected for a ring source that depends on the solar illumination angle [Elrod et al. 2014, 2012]. Utilizing many measurements by the RPWS instrument in the inner magnetosphere, Persoon et al. [2013, 2009] were able to develop an empirical plasma density model for the Saturnian system.

Beyond the seasonal dependence, there was an expectation that the solar cycle would have effects on Saturn's magnetosphere. The strength of this dependence would depend on the overall capability of the solar wind to feed energy into and drive the magnetosphere. Sections entitled Magnetotail configuration and dynamics, Magnetospheric structure and convection, Plasma loss into the magnetotail, and Time varying modulation of SKR and associated PPO signals address how efficient the solar wind is at influencing the global magnetosphere and therefore many results related to solar cycle can be found in studies highlighted in those sections.

Above in the previous paragraphs, we outline the dependence of the SKR on seasonal effects. The SKR also exhibit solar cycle effects. [Kimura et al. 2013] investigated the very long-term (six years of measurements) variations of northern and southern SKR spectra, separated by polarization. This study confirms the prominent role of solar wind pressure over one solar cycle, and additionally identified a seasonal dependence of the SKR activity, with a maximum in summer.

Saturn is often placed in between Earth (solar wind driven) and Jupiter (internally driven) in terms of its magnetospheric dynamics, but this is an overly-simplistic picture. Much work has been done to characterize the structure of the solar wind upstream of the planet. Jackman et al. [2004] analyzed several solar rotations worth of upstream interplanetary magnetic field (IMF) data while Cassini was approaching Saturn, and Jackman et al. [2005a] followed up with an analysis of the solar wind excursion on Cassini's long first capture orbit. Overall it was found that during the declining phase of the solar cycle, the IMF is structured into a very clear pattern of two compressions per solar rotation separated by rarefactions. This structuring is very useful because it helps to predict

Saturn is often placed in between Earth (solar wind driven) and Jupiter (internally driven) in terms of its magnetospheric dynamics, but this is an overly-simplistic picture.

the phasing of intermittent driving of the magnetosphere by the solar wind. Jackman et al. [2004] developed an empirical formula to calculate how much open flux is generated through dayside reconnection, dependent on the IMF direction, the solar wind velocity, and assuming a certain length of a predicted reconnection x-line at the dayside magnetopause. This formula has since been widely used by many other authors, in particular to compare to auroral images which seem to indicate addition and removal of flux, for example, Badman et al. [2012a, 2005]. The solar wind conditions at Saturn (and Jupiter) spanning all stages of the solar cycle were summarized in Jackman and Arridge [2011a]. Reconnection voltages were predicted to be slightly lower at solar minimum than solar maximum, while increased photoionization of the Enceladus torus at solar maximum can lead to a more plasma dominated system at this stage of the solar cycle.

In addition to the MAG results, MIMI also discovered that energetic particles with oscillations at the solar wind period (~26 d) likely display solar cycle variations. This solar wind periodicity was discerned during solar minimum (i.e., 2008–2010) when the solar wind structure was not disrupted by solar activity. The solar wind periodicity was first recognized in the energetic electrons [Carbary et al. 2009a], but was perhaps even stronger in the energetic ions [Carbary et al. 2013]. Because solar activity varied with the ~22-year solar cycle, the appearance of this 26-day periodicity itself should vary with the solar cycle.

The solar cycle is also evident in MIMI/LEMMS measurements of Saturn's radiation belts. The very energetic protons (E > 1 MeV) that form Saturn's ionic radiation belts were found to be modulated with the solar cycle, which provided clues that they might derive from CRAND from Saturn's atmosphere [Roussos et al. 2011]. As at Earth, the cosmic rays causing CRAND at Saturn are themselves modulated by the solar cycle, and LEMMS detected this for the first time using observations over many years. The ring current boundary, deduced from LEMMS observations, also appears to fluctuate in response to solar energetic particle (SEP) events, which are themselves conditioned according to the solar cycle [Roussos et al. 2014].

The section entitled Radiation belts outlines the MAPS contribution to our understanding of the radiation environment at Saturn. The MIMI measurements achieved a comprehensive description of the radiation belts of Saturn during approximately 200 orbits which crossed into the radiation belts, allowing us to understand and quantify their average structure, but also to monitor time variations, despite the single point measurements. Studies by Christon et al. [2014a, 2014b, 2013] provide the most detailed characterization of trace energetic ions and their charge states at an outer planet, showing how their origin may be connected to the planet's rings, the activity of Enceladus and seasonal or solar cycle effects.

Finally, a recent study by Roussos et al. [2018c] uses a novel technique to overcome the lack of an upstream solar wind monitor at Saturn. Cassini MIMI/LEMMS observations of SEP and Galactic Cosmic Ray (GCR) transients, that are both linked to energetic processes in the heliosphere such as Interplanetary Coronal Mass Ejections (ICMEs) and Corotating Interaction Regions (CIRs), are used to trace enhanced solar wind conditions at Saturn's distance. A survey of the MIMI/LEMMS dataset between 2004 and 2016 resulted in the identification of 46 SEP events. Most events last more than two weeks and have their lowest occurrence rate around the extended

solar minimum between 2008 and 2010, suggesting that they are associated to ICMEs rather than CIRs, which are the main source of activity during the declining phase and the minimum of the solar cycle. Also, 17 time periods (> 50 days each) are identified where GCRs show a clear solar periodicity (~13 or 26 days). The 13-day period that derives from two CIRs per solar rotation dominates over the 26-day period in only one of the 17 cases catalogued. This interval belongs to the second half of 2008 when expansions of Saturn's electron radiation belts were previously reported to show a similar periodicity. That observation not only links the variability of Saturn's electron belts to solar wind processes, but also indicates that the source of the observed periodicity in GCRs may be local. In this case, GCR measurements can be used to provide the phase of CIRs at Saturn. The survey results also suggest that magnetospheric convection induced by solar wind disturbances associated with SEPs is a necessary driver for the formation of transient radiation belts that were observed throughout Saturn's magnetosphere on several occasions during 2005 and on day 105 of 2012. Also, an enhanced solar wind perturbation period that is connected to an SEP of day 332/2013 was the definite source of a strong magnetospheric compression (enhanced SKR and low frequency extension (LFE) were also detected at this time) which led to open flux loading in the magnetotail. This event lists can a guide to better constrain or identify the arrival times of interplanetary shocks or solar wind compressions for single case studies or statistical investigations on how Saturn and its moons (particularly Titan) respond to extreme solar wind conditions or on the transport of SEPs and GCRs in the heliosphere.

Magnetotail configuration and dynamics

- **MN1a:** Determine the dynamics of Saturn's magnetotail.
  - Study thoroughly the plasma sheet in Saturn's magnetotail.
  - Investigate the relation between solar wind compression events and magnetotail dynamics.
  - Investigate the plasma sheet thickness and scale height as functions of radial distance and local time.
  - Statistically characterize magnetotail variations, especially those associated with plasmoids, and correlate them with changes in the inner magnetosphere.
  - Critically evaluate the Dungey and Vasyliunas cycles in light of the new observations, especially those of flow speeds.

Measurements made by Cassini in the magnetotail, have allowed MAPS team members to study the dynamic nature of this region of the magnetosphere. Studies include characterizing reconnection, the observation and characterization of plasmoid-like structures, observation of dipolarization events, describing the warping of Saturn's current sheet and studying the response of the magnetosphere to the solar wind.

Since the outer magnetosphere is very dynamic, it is very challenging to describe its average properties. Still, the continuous in situ measurements by CHEMS and LEMMS and the remote

monitoring by INCA have provided unique insights into that region. A detailed study of the outer magnetosphere's average structure is given by Krimigis et al. [2007]; Sergis et al. [2009], which highlight the distinct day-night asymmetry in the vertical extent of the ring current (or plasma sheet). INCA images have been used to determine the most active sites for dipolarization (or large-scale injection events) in the outer magnetosphere being in the post-midnight sector of the magnetosphere [Mitchell et al. 2009b, 2005; Carbary et al. 2008a]. They have revealed the wavy structure of the magnetodisk [Carbary et al. 2016, 2015, 2008b; Carbary 2013] and links to auroral emissions. Energetic electrons have been used to identify an unexpected source of high energy electrons, seen as quasi-periodic pulsations with a period of about 65 minutes. These events are seen globally, they can accelerate electrons to the MeV range instantly and have been linked to reconnection, auroral transients, and similar periodic observations in magnetic field and plasma wave data [Roussos et al. 2016b; Palmaerts et al. 2016a, 2016b; Carbary et al. 2016]. The magnetospheric topology (e.g., open versus closed field lines or the cusp) has been discussed in the context of MIMI observations—for example, Gurnett et al. [2010b]; Arridge et al. [2016a], while MIMI data have been central in the study and interpretation of reconnection/dipolarization events, in combination with other datasets—for example, Badman et al. [2016, 2013]; Jackman et al. [2015, 2008]; Masters et al. [2010]. CHEMS observations also revealed outer magnetosphere asymmetries in the fractional abundance of solar wind-originating ions penetrating into the magnetosphere of Saturn [Allen et al. 2018]. These asymmetries indicate that solar wind He^{++} particles may be entering the magnetosphere due to a combination of Dungey-type reconnection as well as Kelvin-Helmholtz (K-H) instabilities [Allen et al. 2018].

Cassini MAG measurements (often in concert with plasma measurements) have been used to characterize the tail in terms of distinguishing the lobe and plasma sheet regions and exploring how they change with distance from the planet. The current sheet is found to be warped out of the equatorial plane [Arridge et al. 2008a], with a characteristic hinging distance of ~25 R_S. This warping made a significant impact in Saturn's southern hemisphere summer in 2006 when Cassini executed its deepest tail orbits, first in the equatorial plane (below the hinged current sheet) and later at higher latitudes (close to the hinged current sheet). The current sheet has also been found to flap, or oscillate vertically with a period close to the ~10 hours linked to the mysterious planetary periodicities. Jackman and Arridge [2011b] performed a statistical study of Saturn's lobes and plasma sheet during 2006, developing numerical definitions for these regions, and deriving the falloff of the field strength in the lobes with radial distance. They found that the near magnetotail of Saturn is similar to that of Jupiter and Earth (when scaled to a common distance). Unlike at Earth, we do not have spacecraft coverage of the asymptotic tail region, but rather have likely only covered the part of the tail where the magnetopause boundary is still flaring outward and where the lobe field strength is falling off before reaching a steady asymptotic level. We do not know the exact length of Saturn's tail, but can consider arguments first made by Dungey [1965] for the Earth where length was estimated by time for open field lines to be dragged over the poles before ultimately sinking in toward the center of the tail before reconnection (giving ~1000 R_E). Milan et al. [2005] examined the case at Saturn where the polar cap refresh time (i.e., the time for magnetic flux to be cycled through dayside to nightside reconnection) is expected to be many days—for example, Jackman et al. [2004], compared to a much shorter (~10–11 hours) planetary rotation period. This may be expected to twist the lobes of the tail

and Milan argued each turn of a twisted lobe could be ~900 R_S long. They theorized that Saturn is a last-in-first-out system in which recently opened field lines are the first to be closed by reconnection in the tail, due to this twist. This implies that Saturn's tail lobes contain a core of old open field lines that can be stretched to incredible lengths (>15000 R_S).

Saturn's magnetosphere is observed to undergo dramatic, explosive energy release events. The first indication of such behavior was on the outbound pass of SOI where Bunce et al. [2005] reported an episode of solar wind compression-induced tail reconnection, with dipolarizing field and injection of hot plasma. The products of reconnection tailward of the x-line (plasmoids and travelling compression regions, TCRs), were first observed with the Cassini magnetometer by Jackman et al. [2007]. They are identified primarily by a bipolar deflection in the north-south component of the field, with northward turnings implying reconnection products tailward of the x-line and southward turnings implying dipolarizations planetward of the x-line. Multi-instrument views of reconnection events reveal changes in the flow pattern from azimuthal to tailward and local heating of the plasma, for example, Jackman et al. [2008]. It is sometimes observed that northward turnings are not purely bipolar but instead have an extended interval where the field remains northward. This has been interpreted as the Kronian equivalent of the post-plasmoid plasma sheet [Jackman et al. 2011], which represents an interval where previously open flux is being closed by reconnection.

Over the years, catalogues of reconnection events were built up from by-eye surveys and basic automation involving simple background thresholding of the magnetic field and searching for significant deflections above or below these thresholds. Surveys covering the deepest tail orbits of 2006 revealed a significant imbalance between the rate of mass loss inferred from plasmoid release and the rate of mass loading from the moon Enceladus, which has been termed the mass budget problem [Jackman et al. 2014]. More sophisticated automated event searches have returned surveys of > 2000 events from tail orbits during 2006, 2009, and 2010, and Smith et al. [2016] revealed that the rate of observed reconnection events peaked post-midnight, with a highly variable radial location of the reconnection x-line, with an average ranging from 20–30 R_S from the planet. To date only one study has identified the x-line region itself [Arridge et al. 2016b], while more recently Smith et al. [2018a] presented a series of very short duration reconnection-related inward and outward flows in quick succession on the dusk flank. Their interpretation was that over a 7-hour interval investigated, reconnection sites had formed both tailward and planetward of the spacecraft, showing that reconnection can operate on small spatial/temporal scales. A second case study showed an event during which the reconnection site was inferred to retreat tailward, resulting in progressively hotter, dipolarizing material reaching Cassini.

The properties of dipolarizations planetward of the x-line give us another view of the impact of reconnection on the magnetosphere. Jackman et al. [2013] published a case study which showed rapid acceleration of newly-reconnected field lines back toward the planet. The transition from a radially stretched to dipolar field configuration can cause a current which usually flows across the tail to divert into the ionosphere, potentially leading to bright, distinct spots of auroral emission. Jackman et al. [2015] further showed that dipolarization of the field can be accompanied by ion flows at speeds of up to 1500 km/s toward the planet following tail reconnection, representing a significant departure

from the slower, sub-corotational flow typically seen in the tail. A reconnection event that starts at a small x-line can have a big impact on the magnetosphere as a whole.

Dipolarizations themselves have also been shown to have a dramatic effect on the local plasma: Smith et al. [2018b] investigated dipolarizations as identified from southward deflections of the magnetic field and found they were clustered preferentially post-midnight. The analysis of the accompanying CAPS data showed that the dipolarizing material was systematically hotter and less dense than the ambient plasma sheet. This density depletion and heating was found to be much more variable post-midnight, suggesting a more variable reconnection site.

By analyzing Cassini's MAG and CAPS data, Yao et al. [2017a] revealed that there are two fundamentally different drivers of dipolarization (i.e., magnetic reconnection and electrical current re-distribution) at Saturn, similarly to what is found in the terrestrial magnetotail.

Beyond reconnection and dipolarizations, several studies have been done of larger scale reconfigurations of the magnetotail. Some of this work is reported in a series of papers by Jackman and coauthors. Jackman et al. [2009a] revealed evidence of plasmoid-like magnetic structures and other phenomena indicative of the Saturnian equivalent of terrestrial substorms. In general, there was a good correlation between the timing of reconnection events and enhancements in the auroral SKR emission. Eight of nine reconnection events studied occur at SKR phases where the SKR power would be expected to be rising with time. Thus, while the recurrence rate of substorm-like events at Saturn is likely much longer than the planetary rotation timescale, the events are favored to occur at a particular phase of the rotation. Three examples were found in which the SKR spectrum extended to lower frequencies than usual. These low frequency extension SKR events were labeled LFEs and were interpreted as an expansion of the auroral particle acceleration region to higher altitudes (lower radio frequency) along magnetic field lines as a direct consequence of an increase in the magnetosphere-ionosphere current density driven by substorm-like events. Saturnian substorms are likely a much more prevalent phenomenon than this small number of observations suggests, but the statistics in this study were hampered by viewing geometries, primary the small amount of time that Cassini spent in the deep magnetotail near the nominal current sheet location. Many examples of LFEs are observed by Cassini from a wide set of vantage points, but the spacecraft is only in the right position to observe the corresponding magnetic signature (if any) a fraction of the time.

In general, there was a good correlation between the timing of reconnection events and enhancements in the auroral SKR emission.

Jackman et al. [2010] also explored the dynamic response of Saturn's magnetotail to an episode of solar wind compression that took place while Cassini was sampling Saturn's nightside equatorial magnetosphere in 2006. Following an initial increase in solar wind dynamic pressure, the magnetosphere was compressed and became more streamlined, with an elevated lobe field strength as external pressure compressed the tail. Then, assuming a favorable IMF direction (for

at least part of the interval, as seems entirely plausible), dayside reconnection may have been ongoing, leading to an increase in the amount of open flux inside the magnetosphere, flaring of the magnetotail, and continued elevated lobe field strength. Because of the longer time scales involved at Saturn for loading of the tail with open flux, it can take several days for the tail to be inflated to a point where reconnection is likely to occur, and this study suggested that the time scale observed in this case was of order ~6–7 days. No strong evidence for magnetotail reconnection events during this loading phase were detected, however, toward the end of this period a sharp decrease in lobe field strength and what appears to be significant current sheet deflection toward the equator from its previously hinged position was observed. Several days later the current sheet was displaced southward from its previously hinged position, and magnetic signatures consistent with the passage of a plasmoid were observed. These field signatures are closely correlated with intense radio emission, evidenced by low-frequency extensions (LFEs) of radio emission, corresponding to radio sources detected at higher altitudes. All of the above features are believed to be a common consequence of the impact of a solar wind compression on Saturn's magnetosphere.

Additional evidence for significant dynamical effects attributable to solar wind variability has been reported by the CAPS team. CAPS observations from SOI outbound, in the pre-dawn tail, showed sudden energization of plasma associated with a field dipolarization, which was interpreted as evidence of a solar wind compression-related tail collapse via magnetic reconnection. Under conditions of high solar wind dynamic pressure, the magnetotail appears to enter a state of sustained lobe reconnection, resulting in a more Dungey-like configuration [Thomsen et al. 2015a]. In the inner magnetosphere, there is no apparent relation between the depth of electron penetration and solar wind properties [Thomsen et al. 2016], although the energization of ions in a large-scale standing wave might be caused by a solar wind pressure impulse [Thomsen et al. 2017a].

Jackman et al. [2015] presented a rare observation of strong planetward flow following a reconnection episode in Saturn's tail from August of 2006, when the Cassini spacecraft was sampling the region near 32 R_S and 22 h local time (LT). Cassini observed a strong northward-to-southward turning of the magnetic field, which is interpreted as the signature of dipolarization of the field as seen by the spacecraft planetward of the reconnection X-line. This event was accompanied by very rapid (up to ~1500 km s^{-1}) thermal plasma flow toward the planet. At energies above 28 keV, energetic hydrogen and oxygen ion flow bursts were observed to stream planetward from a reconnection site downtail of the spacecraft. Meanwhile, a strong field-aligned beam of energetic hydrogen was also observed to stream tailward, likely from an ionospheric source. SKR radio emissions enhancements similar to ones previously associated with plasmoid formation and release were detected slightly more than an hour after the observation of the dipolarization. The reconnection episode as inferred from the planetward directional flow duration lasts on the order of ~1.5 h, a significant fraction of a planetary rotation. The continuing presence of energetic O^+ ions throughout the event demonstrates that this must be a case of long-lasting Vasyliunas-type reconnection occurring beyond 32 R_S in the premidnight region, perhaps indicating quasi-steady reconnection of the type. Because of the persistent presence of O^+, we find little evidence for lobe involvement in the reconnection.

Kimura et al. [2013] investigated the very long-term (six years of measurements) variations of northern and southern SKR spectra, separated by polarization. This study confirms the prominent role of solar wind pressure over one solar cycle, and additionally identified a seasonal dependence of the SKR activity, with a maximum in summer.

Felici et al. [2016] presented a case study of data from Saturn's magnetotail, when Cassini was located at ~22 hour Local Time at 36 R_S from Saturn that suggests for the first time that a low-energy ionospheric outflow event has been detected at planets other than Earth. During several entries into the magnetotail lobe, tailward flowing cold electrons and a cold ion beam were observed directly adjacent to the plasma sheet and extending deeper into the lobe. The electrons and ions appear to be dispersed, dropping to lower energies with time. The composition of both the plasma sheet and lobe ions show very low fluxes (sometimes zero within measurement error) of water group ions. The magnetic field has a swept-forward configuration which is atypical for this region, and the total magnetic field strength is larger than expected at this distance from the planet. Ultraviolet auroral observations show a dawn brightening, SKR is enhanced and extends down to lower frequencies, and upstream heliospheric models suggest that the magnetosphere is being compressed by a region of high solar wind ram pressure. This event is interpreted as the observation of ionospheric outflow in Saturn's magnetotail, with the active atmospheric regions most likely the main auroral oval.

The majority of the previously discussed studies involved periods where Saturn's magnetosphere encountered a high density solar wind. The study by Kinrade et al. [2017] discusses observations during a period that Saturn's magnetosphere was in a rarified solar wind region. During this period on June 14, 2014 (day 165), the Hubble Space Telescope observed an unusual auroral morphology, where for 2 h, the Saturn's far ultraviolet (FUV) aurora faded almost entirely, with the exception of a distinct emission spot at high latitude. The spot remained fixed in local time between 10 and 15 LT and moved poleward to a minimum colatitude of ~4°. Interestingly, the spot constituted the entirety of the northern auroral emission, with no emissions present at any other local time, including Saturn's characteristic dawn arc, the complete absence of which is rarely observed. Solar wind parameters from propagation models, together with a Cassini magnetopause bow shock crossing, indicate that Saturn's magnetosphere in an expanded magnetosphere configuration during the interval, suggesting it was likely embedded in a rarefaction region. The spot was possibly sustained by reconnection either poleward of the cusp or at low latitudes under a strong component of interplanetary magnetic field transverse to the solar wind flow. The subsequent poleward motion could then arise from either reconfiguration of successive open field lines across the polar cap or convection of newly opened field lines. The spot's fixed LT position may be attributed to the negative IMF BY conditions incident at the time, combined with increased subcorotation of open flux toward higher latitudes. The emission intensity was also possibly enhanced by a sector of upward PPO current rotating through the region. These observations show conclusively that the mechanisms producing noon auroral spots and the main oval auroras (i.e., the dawn arc) are distinct, since in this case the cusp spot occurred without the arc. These observations also suggest that reconnection can occur in an expanded magnetosphere, in agreement with the cusp observations of Arridge et al. [2016a], who found evidence of reconnection under a range of upstream solar wind conditions.

Magnetospheric structure and convection

- **MN1b:** Conduct in situ studies of Saturn's ionosphere and inner radiation belt.
  - Investigate the effects on aurora of solar wind and seasons.
  - Are there UV satellite footprints on Saturn? (like at Jupiter)
  - Is there a seasonal variation in auroral activity?
  - Investigate solar wind - ionosphere - magnetosphere coupling through the auroral regions.
  - Investigate whether there are UV satellite footprints on Saturn and whether there are Region 1 currents connecting the ionosphere and the magnetopause.
  - Investigate the composition of Saturn's ionosphere.
  - Study whether there is a significant polar outflow from Saturn's high latitude ionosphere and whether the outflow exhibits seasonal or solar cycle variation.
  - Determine whether there is a radiation belt between the D-ring inner edge and the atmosphere.

Understanding the structure of the magnetosphere and the convection systems within the magnetosphere are clearly two of the most important goals of the MAPS investigation. Each MAPS instrument team and the IDS teams have contributed extensively to the study of this aspect of Saturn and have published extensive literature. In this summary document it is only possible to summarize a small fraction of the work done by the MAPS instruments. We refer the interested read to the individual MAPS instrument team reports and the published literature for a more complete coverage of the extensive contribution of Cassini to understanding Saturn's magnetospheric structure.

The Cassini spacecraft crossed the bow shock of Saturn for the first time at 09:45 UT on June 27, 2004, at a radial distance of 49.2 R_S from Saturn. After the initial crossing, the large apoapsis orbits by the Cassini spacecraft around Saturn over many years enabled hundreds of bow shock crossings. This allowed for thorough analyses of the three-dimensional shape, a capability to predict the location of the boundary and to investigating the microphysics of high Mach number shocks. Studying the global shape, location, and dynamics of the bow shock offers important insights into the physics governing its formation and the magnetosphere's response to solar wind dynamics.

Studying the global shape, location, and dynamics of the bow shock offers important insights into the physics governing its formation and the magnetosphere's response to solar wind dynamics.

A number of authors have used the Cassini data to develop models of the average shape of Saturn's bow shock as well as the response of this surface to changes in the dynamic pressure of the upstream solar wind. Masters et al. [2008] and Went et al. [2011] developed an exhaustive semi-empirical model of Saturn's dayside bow shock. The average three-dimensional shape of the boundary was constructed and equations relating the response of the subsolar point to variations in solar wind dynamic pressure derived. Achilleos et al. [2006] presented magnetic field signatures of some of the earliest crossings in the mission. Their results showed clearly defined overshoot and foot signatures that are typical of quasi-perpendicular shocks. This is by virtue of the Parker spiral structure of the IMF at 10 AU, where the magnetic fields met the bow shock with very large azimuthal components.

In addition, a number of studies have investigated the properties of the bow shocks themselves at Saturn [Masters et al. 2017, 2013a, 2013b; Sulaiman et al. 2015; Sundberg et al. 2017], and the particles and regions associated with the bow shock, including hot flow anomalies [Masters et al. 2009], superthermal electrons [Masters et al. 2016], and upstream whistler mode waves [Sulaiman et al. 2017] occurred during a period of high solar wind pressure that caused Saturn's bow shock to be pushed inside Titan's orbit, exposing the moon and its ionosphere to the solar wind. Omidi et al. [2017] using electromagnetic hybrid (kinetic ions and fluid electrons) simulations and Cassini observations, showed a formation of a single deformed bow shock for the Titan-Saturn system. Sulaiman et al. [2016] characterized Saturn's bow shock using the largest sample of crossings to date. They showed Saturn's dayside bow shock was in the quasi-perpendicular configuration for a large majority of the time. The bow shock was found to exhibit characteristics akin to both terrestrial and astrophysical regimes. Clarke et al. [2010a] investigated 35 Cassini orbits on which the spacecraft crossed Saturn's magnetopause and bow shock during 2004–2007, and concluded that the bow shock and magnetopause oscillate approximately in phase, within a phase uncertainty of about ±25°. The typical amplitude is 1–2 R_S and the period is significantly organized by the phase of the interior magnetic field oscillations, with a period near that of planetary rotation. Saturn's (dayside) bow shocks are predominantly quasi-perpendicular by virtue of the Parker spiral at 10 AU.

The Cassini spacecraft has shown that Saturn's bow shock can occasionally reach a high-Mach number typical of astrophysical shocks. In this regime Cassini has provided the first in situ evidence for suprathermal electron acceleration under quasi-parallel upstream magnetic conditions [Masters et al. 2016]. Masters et al. [2013b, 2011a] explore several different aspects of Saturn's shock structure. They investigated the Mach number dependence of electron heating across a bow shock. Their work presented a positive correlation between the electron temperature increase across the shock and kinetic energy of an incident proton, where electron heating accounts for ~3%–~7% [Masters et al. 2011a]. In addition, they compared observations of overshoots between Mercury's and Saturn's bow shocks, both of which represent drastically different Mach numbers in parameter space. They showed, on average, the overshoots at Saturn's bow shock were much higher than those observed at Mercury's. This supported the larger role of particle dynamics at higher Mach numbers [Masters et al. 2013b]. In addition, Sulaiman et al. [2015] showed evidence for cyclic reformation controlled by specular ion reflection occurring at the predicted time scale of

~0.3 τ c, where τ c is the ion gyroperiod. In addition, they experimentally revealed the relationship between reformation and alfvenic Mach number (Figure MAPS-18).

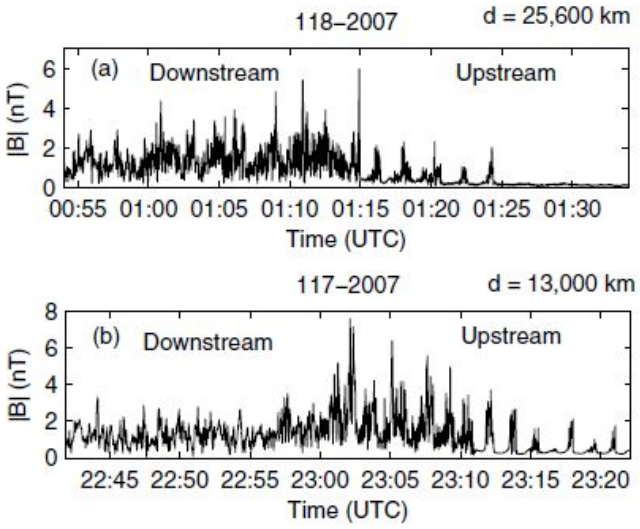

Figure MAPS-18. The panels are two examples of magnetic field plots showing quasi-perpendicular bow shock crossings with re-formation cycles occurring upstream of the shock. Figure adapted from Sulaiman et al. [2015] Figure 2.

Collisionless shock waves are also known to be efficient particle accelerators. It is widely believed that a large proportion of cosmic rays originate from energetic charged particles accelerated at collisionless shocks associated with supernova explosions in our galaxy. Masters et al. [2013a] confirmed, for the first time, electron acceleration up to relativistic energies at an unusually strong Saturn bow shock under a quasi-perpendicular configuration. This contradicted previous knowledge purporting a magnetic dependence on this phenomenon. Further works by Masters et al. [2016] and Masters et al. [2017] provided the full picture of suprathermal electrons at Saturn's bow shock. They showed results that are consistent with the theory in which the "injection" of thermal electrons into an acceleration process is possible for all magnetic field configurations at high Mach numbers.

Long-term sampling of Saturn's magnetosheath by Cassini afforded the most complete coverage of this intermediary region between the unshocked solar wind and Saturn's magnetosphere. A relatively high Alfvén Mach number solar wind and a polar-flattened magnetosphere make Saturn's magnetosheath both physically and geometrically distinct from the Earth's. Fast rotating gas giants, such as Saturn, are bulged along the equator and flattened along the poles owing to their embedded plasma disks and for this reason, Sulaiman et al. [2014] showed that the magnetic structure of Saturn's magnetosheath significantly deviated from axisymmetry. Their results showed large northward/southward components in the magnetic field despite the prevailing Parker spiral configuration being largely in the equatorial plane.

Using CAPS and other MAPS data, Sergis et al. [2013] investigated the properties of the magnetosheath. At energies of a few keV the magnetosheath is comprised of shocked solar wind plasma, while at energies above a few keV there is a strong presence of water group ions forming localized structures that are being convected downstream in the plasma flow. Under average magnetic field conditions in the magnetosheath, the kinetic properties of these hot water group ions can enable escape upstream from the bow shock. To help future scientists access the CAPS data to study the magnetosheath, Thomsen et al. [2017a] provides a comprehensive survey of intervals in which the observed magnetosheath flow was encompassed within the plasma analyzer field of view, and for which the computed numerical moments are accurate. The data extend over eight years from 2004 day 299 to 2012 day 151. The magnetosheath population is characterized by ion energies between ~100 eV and ~2 keV and electrons up to about 100 eV. The solar wind is best identified in the electrons, which have energies generally below 10 eV.

Saturn's magnetopause marks the boundary between the impinging solar wind and the region of space dominated by Saturn's intrinsic magnetic field. The magnetopause presents an obstacle to the solar wind. Cassini MAPS instruments have made extensive measurements of crossing of the magnetopause and have allowed us to examine the ways in which energy can be transferred in to and out of near-Saturn space. Understanding this is crucial for revealing the dynamics of the coupled planetary system of magnetosphere, moons, rings, and atmosphere.

A good understanding of the geometry of the magnetopause, and how its position changes with the pressure of the solar wind, is important for characterizing the distant dayside magnetosphere and in developing a three-dimensional global model of the magnetospheric magnetic field. Arridge et al. [2006] used early measurements of the magnetopause from Cassini/MAG, combined with measurements from Voyager 1/2 and Pioneer 11, to develop a new model of Saturn's magnetopause. This new model revealed that Saturn's magnetosphere was more compressible than previously thought: more compressible than Earth's magnetosphere, but less than Jupiter. This was confirmed and enhanced in further studies using larger datasets from Cassini/MAG [Kanani et al. 2010; Pilkington et al. 2015]. In a study by Achilleos et al. [2008], the MAG team analyzed some of the early orbits and the points along those orbits where the spacecraft crossed the magnetopause. By analyzing the distribution of the magnetopause crossings, it was concluded that the size of the magnetosphere was certainly being controlled by the dynamic pressure of the solar wind upstream of the planet, but that there was also evidence for an additional influence, probably due to a process internal to the magnetosphere. The system preferentially spent most of the time in one of two states, characterized by subsolar magnetopause distances near ~22 and ~27 Saturn radii.

A study some years later [Pilkington et al. 2015] built upon this work by constructing an up-to-date empirical model of Saturn's magnetopause. The work found that one could not satisfactorily fit these crossings in their entirety by assuming a system whose size responded only to solar wind pressure. By separating the crossings into subsets based on additional plasma data from the MIMI instrument, the study demonstrated that Saturn's magnetosphere plausibly made transitions between states which were plasma-light and plasma-loaded.

Magnetic reconnection is a fundamental process that can operate at a current sheet. It results in the release of energy stored in the local magnetic field, leading to acceleration of charged particles and allowing the direct transfer of mass and energy across an otherwise closed boundary. While evidence for the known operation of reconnection at Saturn's magnetopause has been sparse, MAG observations have formed the basis of important assessments that have broad implications. The first such assessment demonstrated that conditions at the magnetopause boundary of Saturn's magnetosphere are dramatically unlike those at Earth's magnetopause. As a result, reconnection at Saturn's magnetopause should be more restricted to regions where magnetic field lines adjacent to the boundary are locally anti-parallel to each other [Masters et al. 2012a]. This Cassini result began a shift in how we think about the solar wind-magnetosphere interaction at Saturn, with implications for other magnetized planets.

MAG data has also shown that when reconnection operates at Saturn's magnetopause it likely does so at a speed that is far slower than that associated with reconnection in environments closer to the Sun, for example, the solar corona, the solar wind, Earth's magnetopause, Earth's magnetotail [Masters et al. 2014]. The reason for this is the way that solar wind properties change as the plasma moves away from the Sun. The Alfvén speed, which dictates the speed of reconnection, drops with heliocentric distance, producing a relatively slow reconnection process at Saturn's magnetopause and consistent with the lack of evidence for rapid boundary later response discussed above. This result directly contributed to further work that showed that driving of Saturn's magnetosphere by global magnetopause reconnection is rarely strong enough to compete with the internal driving of the system that results from the combination of fast planetary rotation and plasma production due to the plumes of Enceladus [Masters 2015].

Magnetic reconnection at Earth has been proposed to occur only at the magnetopause and in the nightside magnetotail. At Saturn and Jupiter, internal sources are additional drivers for magnetospheric dynamics, and it is usually believed that internal sources could drive magnetic reconnection in the nightside inner magnetosphere. However, Guo et al. [2018] report in situ evidence of active magnetic reconnection process in the dayside of Saturn's magnetodisc at ~2 R_S away from Saturn's magnetopause. This study would directly support drizzle magnetic reconnection picture proposed by Delamere et al. [2015], and is also consistent with the rotating reconnection site picture proposed by Yao et al. [2017b].

The other important mechanism by which solar wind energy can enter a planetary magnetosphere is via a viscous-like interaction. This is underpinned by another fundamental process: Growth of the K-H instability. Where there are large plasma flow shears across a magnetopause this instability can lead to the evolution of small boundary perturbations in to gentle waves and eventually in to large, rolled-up vortices. The first evidence for magnetopause surface waves from Cassini came in the form of normal to the boundary determined from magnetic field observations that exhibited an oscillation in a preferred direction from one magnetopause crossing to the next [Masters et al. 2009]. The direction of wave propagation (direction of boundary normal oscillation) was controlled by the local direction of the magnetic field inside the boundary, consistent with K-H-driven waves. After this first observation, extensive continued studies of the K-H waves at magnetopause crossings has shown that such waves are ubiquitous [Masters et al. 2012b].

In addition to understanding reconnection and the K-H interaction at lower latitudes, it is important to understand how the magnetic cusps play a role in energy and particle transfer between the solar wind and the magnetosphere. At Earth, the solar wind is the primary energy source which can drive dynamical processes, and it is also a primary source of plasma. Before Cassini's arrival it was not clear what role the solar wind played in driving the magnetosphere, and so understanding the coupling between the solar wind and the magnetosphere, characterizing the phenomena of the distant dayside/flank planetary environment, was an important goal. This included studying viscous and magnetic reconnection processes at the magnetopause. Flux transfer events are a signature of dayside magnetic reconnection at Earth, Mercury and Jupiter, and consist of a rope of magnetic flux and plasma peeling away from the magnetopause. Jasinksi et al. [2016] presented an example of a flux transfer event at Saturn (the only one) and showed that this single event made a fairly small contribution (< 10%) to the magnetic flux transport budget, although it was not clear how typical this event was, and if they are more prevalent at locations on the magnetopause not sampled by Cassini.

… it is important to understand how the magnetic cusps play a role in energy and particle transfer between the solar wind and the magnetosphere.

At higher latitudes, a region known as the cusp maps to a very wide region of the magnetopause and so is ideal for remote monitoring of the magnetopause for reconnection signatures, revealing coupling between the solar wind and the magnetosphere. Cassini's inclined orbits during 2007/2008 and 2013/2014 were ideal to study this coupling process in plasma (CAPS) and the magnetic field (MAG). Some of the early inclined orbits in early 2007 showed evidence of solar wind plasma gaining entry into the magnetosphere [Arridge et al. 2016a]. This work showed evidence for movement of the cusp region in phase with magnetospheric (so-called planetary-period) oscillations, indicating the presence of current systems in the magnetosphere. It was also found that magnetopause reconnection was possible under both compressed and expanded magnetospheric conditions [Jasinski et al. 2016; Arridge et al. 2016a] and that the reconnection process could proceed in an unsteady fashion and at various locations on the magnetopause [Jasinski et al. 2016, 2014; Arridge et al. 2016a]. During SOI, the CAPS instrument showed that at latitudes above the extended plasma sheet/ring current there is a region that is largely devoid of plasma, known as the magnetospheric lobe [Young et al. 2005]. The lobe is commonly seen in the magnetotail, for example, Thomsen et al. [2015a], as the plasma sheet rocks and flaps up and down. Lobe field lines are thought to be connected by magnetopause reconnection into the solar wind and have thus lost their magnetospheric contents. At low altitudes, the lobe maps into the polar cap. The polar cap boundary is identified based on a sharp drop in ELS electron fluxes and corresponding signatures in other data sets (Figure MAPS-19), for example, Jinks et al. [2014]. A survey of polar cap boundary crossings showed that the main upward field-aligned currents associated with the aurorae reside equatorward of the open-closed boundary [Jinks et al. 2014].

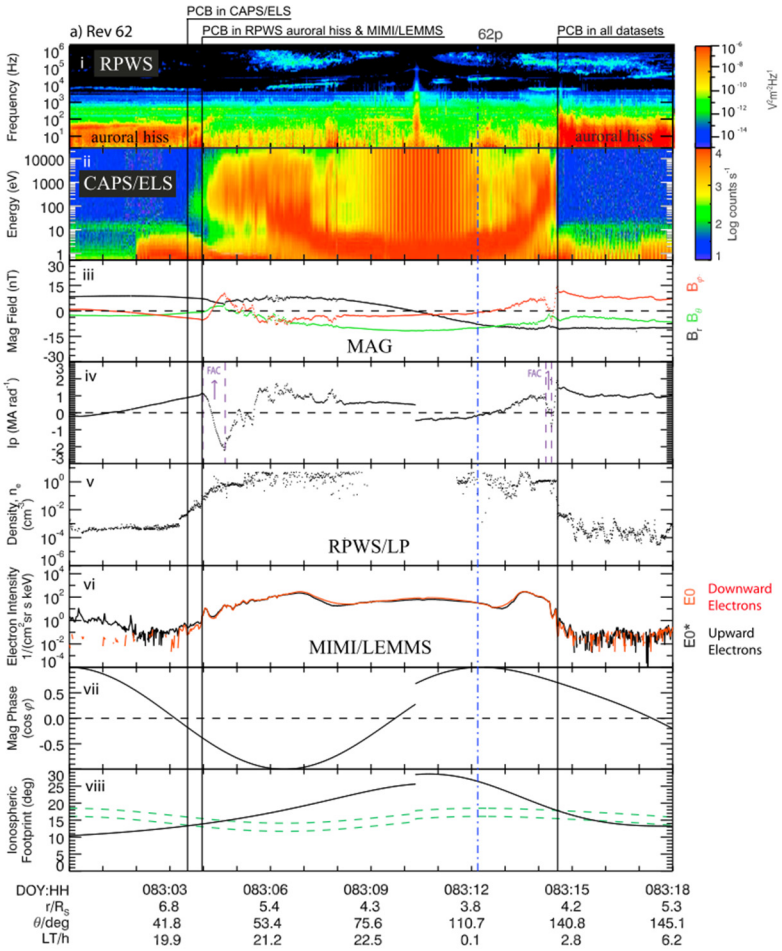

Figure MAPS-19. Polar cap boundary as seen in several different Cassini data sets. The sharp change in the ELS electron spectrum is the most definitive signature. The polar cap is largely devoid of electrons (counts below ~20 eV are due to spacecraft photoelectrons). Figure from Jinks et al. [2014].

Near noon, open magnetic field lines (which will ultimately become the lobe/polar cap) are filled with incoming magnetosheath plasma, which penetrates down to low altitudes. CAPS observations of this region, known as the cusp, demonstrate that the process of reconnection occurs at Saturn's magnetopause, with indications that the reconnection is pulsed [Jasinski et al. 2014]. The first reported cusp observation was associated with the arrival of a solar wind shock front, which compressed the magnetosphere and probably provided more favorable conditions for magnetopause reconnection [Jasinski et al. 2014]. Evidence for both bursty and more continuous reconnection is observed at different cusp events, and the locations of the reconnection site vary along the subsolar magnetopause. Magnetic reconnection and plasma injection into the cusp can occur for a variety of upstream conditions [Jasinski et al. 2017, 2016; Arridge et al. 2016a].

Saturn's magnetosphere is an example of a rapidly rotating system dominated over much of its extent by a large magnetodisk of rotating plasma, this material falling further behind corotation with the planet as we go to larger distances from the planet. Because the system is so large,

centrifugal force becomes very effective at keeping the cold plasma confined as this near-equatorial disk. In order to develop a first-principles model of Saturn's magnetodisk region, Achilleos et al. [2010a] adapted a model of field and plasma developed for the Jovian system by Caudal [1986], using plasma data available at that time to constrain the model's boundary conditions. This model was successfully used to explain the observed response of the planet's magnetospheric field to changes in system size. We were also able to compare the model contributions to the total magnetodisk current associated with the various forces on the plasma (centrifugal force and pressure gradient force) for both the Kronian and Jovian magnetodisk systems. A follow-up study by Achilleos et al. [2010b] explored particularly the influence of global changes in the energetic particle population on Saturn's magnetodisk structure. This model was also used in a study by Sorba et al. [2017], who developed theoretical compressibility curves showing how the magnetodisk size responds to changes in solar wind pressure and internal plasma content (energetic particles). These theoretical results were in good agreement with the observational analysis of Pilkington et al. [2015] and we were also able to use the model to explain why one would expect the compressibility of the system to vary with system size. We have also had some success in using this magnetodisc model, combined with the current sheet elevation model of Arridge et al. [2011a], in order to model global, near-planetary-period oscillations in the magnetic field and plasma properties [Achilleos et al. 2014].

It has been shown that periodic variations of the plasma density peak at different rotation phases depending on radial distance in the magnetosphere. We showed that this variation arises as a consequence of the interaction between simple rotation and the expansion and contraction of the magnetosphere associated with propagating compressional disturbances [Ramer et al. 2017]. Propagating compressional disturbances also cause the magnetopause to move in and out non-sinusoidally and somewhat asymmetrically [Kivelson and Jia 2014]. The simulation also explains the dawn-dusk asymmetry of field configuration and plasma flows in Saturn's magnetosphere [Jia and Kivelson 2016].

The rotation period of Saturn's magnetosphere was found to vary with time, and changing periodicities were identified in magnetic fields, radio emissions, and charged particles [Andrews et al. 2012, 2011, 2008; Provan et al. 2014, 2013, 2011, 2009]. The plasma motion of the magnetodisk is very much affected by the oscillating magnetic field of Saturn, which is different in the two hemispheres. These planetary period oscillations strongly influence the magnetic and plasma properties of the outer magnetosphere [Andrews et al. 2010a; Provan et al. 2012] as well as the density of thermal ions [Nemeth et al. 2011; Szego et al. 2011]. The thermal plasma sheet properties are different for the different ion species. The proton sheet is smoothly modulated by the flapping of the magnetodisk while heavy ions form a narrow sheet surrounding the magnetic equator. The periodicity of the observed heavy-ion rich events was found to be close to the SKR period of the southern hemisphere.

Szego et al. [2012] observed that the ion density moments derived by Thomsen et al. [2010] from Cassini CAPS measurements exhibit peaks around zero-crossings of the magnetic field. The proton peaks are broader while the heavy ion peaks are sharper. They found that the positions of these peaks can be explained by the simple structural model of Arridge et al. [2011a]. Szego et al.

[2013] modified this simple structural model to include the dual periodicity of the magnetic field, and found an even better agreement for the positions of the ion peaks.

Using numerical ion moments, Nemeth et al. [2015] investigated the azimuthal flow velocities measured by CAPS along with their periodicities. They observed a significant positive correlation between the azimuthal plasma speed and the plasma density, both anti-correlating with the magnitude of the radial component of the magnetic field. They found that the dense plasma near the magnetic equator rotates around the planet at high speed, but the dilute plasma of higher latitudes is rotating significantly slower.

Nemeth et al. [2016] analyzed the quasi-periodic variation of several plasma parameters. The variation of the magnetic field was used to recover the position of the magnetodisk, and the position information was further used to model the variation of the density and azimuthal velocity moments of the thermal ions. This simple technique provides very good fits for all three parameters simultaneously.

Saturn's disk-like magnetosphere produces a unique and interesting current system. The magnetodisk current flows in the equatorial magnetosphere eastward around the planet extending the field lines radially outward, carried by the differential drift of ions and electrons in the plasma trapped on Saturn's magnetic field lines, which grades into the cross-tail plasma sheet current separating the lobes of the magnetic tail on the nightside. Although the existence of the ring current was first established from magnetic data acquired during the Pioneer-11 and Voyager flybys, little was known of the variability of the current, and its physical nature remained a matter of controversy, whether due to centrifugal action of the plasma mass or to the effect of plasma pressure. Data from the initial sequence of near-equatorial Cassini orbits was first used to determine the strength and radial extent of the current, showing that this varies strongly with the size of the magnetosphere dependent on the dynamic pressure of the impinging solar wind [Bunce et al. 2007]. While the inner edge of the current lies nearly unvaryingly at an equatorial radial distance of ~7 R_S, the radius of the outer edge varies between ~15 R_S when the magnetosphere is strongly compressed to ~22 R_S when it is significantly expanded, these distances typically lying a only few R_S inside the dayside magnetopause. Correspondingly, the total eastward current varies from ~9 to ~15 MA, with a magnetic dipole moment that varies between ~0.2 and ~0.6 that of the internal field of the planet. A consequence is that while the dayside and comparably-near nightside field is quasi-dipolar in form when the system is compressed, the field lines extend into an equatorial magnetodisk when it is expanded [Bunce et al. 2008]. Later, when data from the first highly inclined Cassini orbits became available, the first direct measurements of the north-south thickness of the current sheet were also made, with values being typically ~3 R_S on the dayside, while varying between ~1 and ~5 R_S on the nightside [Kellett et al. 2009].

Cassini/MAG data revealed the magnetodisc [Arridge et al. 2008b; Bunce et al. 2008] was particularly sensitive to the solar wind pressure, essentially disappearing on the dayside when the magnetosphere was compressed by the solar wind and explaining why it was not detected by Pioneer 11 or Voyagers 1/2 [Arridge et al. 2008b].

The current sheet was also found to be warped out of the equatorial plane, as expected by analogy with Earth and Jupiter, but it was also found to be deformed at noon. Effectively the current sheet had the geometry of a shallow bowl, or upturned umbrella [Arridge et al. 2008a]. Subsequently, a detailed study of data from Earth's magnetosphere has revealed a similar effect at Earth [Tsyganenko and Andreeva 2014], inspired by Cassini/MAG measurements at Saturn. Superimposed upon this global warping was a flapping motion that occurred in phased with other periodicities in Saturn's magnetosphere [Arridge et al. 2011a, 2008c] and which had a lag or delay that propagated into the outer magnetosphere. However, latitudinal effects were also shown to play an important role, connected with differing periods in the northern and southern hemispheres [Provan et al. 2012].

Small ripples were also found superimposed on this bowl-shape [Arridge et al. 2007] that are largely propagating away from Saturn, indicating a source closer to the planet, possibly produced by plasma transport in the inner/middle magnetosphere [Martin and Arridge 2017].

The presence of the current sheet, and its deformation into a bowl-shape, has important consequences for Titan's magnetic and plasma environment, and so the structure of its induced magnetosphere [Backes et al. 2005; Arridge et al. 2011b; Simon et al. 2013], as not only is the magnetic field (oriented in a different location to that found by Voyager 1), but also the bowl-shaped current sheet means that the Titan is not continuously immersed in Saturn's magnetospheric plasma.

Detailed collaborative work of the MAPS teams also examined the physical nature of the current [Kellett et al. 2011, 2010; Sergis et al. 2018]. It was shown that inside ~10–12 R_S the current is carried principally by the relatively unvarying population of warm (~100 eV) water plasma picked-up from the Enceladus torus, comprising principally of inertia and pressure anisotropy currents. Beyond these distances it is carried mainly by the more variable hot tenuous plasma. While, by analogy with Earth, the term ring current particles is often taken to be synonymous with hot injected plasma, this usage has thus proven to be inappropriate at Saturn, since the outwardly-transported warm water plasma is at least as significant in carrying the current.

The middle magnetosphere is the region where the so-called ring current of Saturn resides. This current likely has important components below the energy range of MIMI. But it has been found to contain energetic ions and electron below 1 MeV, with relatively high fluxes. It is populated by large scale injections in the nightside magnetosphere of Saturn, which populate the ring current with a series of rotating, energetic ion and electron bundles, called sometimes blobs due to their appearance as such in remote sensing images by MIMI/INCA. The energy density of the energetic ion population is high enough to increase the plasma beta (the ratio of total particle pressure divided by magnetic pressure) above one, therefore causing a significant stretching of the magnetic field lines. Depending on the abundance of oxygen in the energetic ion distributions, the dynamics of the current

Depending on the abundance of oxygen in the energetic ion distributions, the dynamics of the current sheet may be dominated by the presence of energetic particles.

sheet may be dominated by the presence of energetic particles. All these results are summarized in a series of studies by Sergis et al. [2017, 2013, 2011, 2010, 2009, 2007]; Krimigis et al. [2007]; Dialynas et al. [2013, 2009]; Carbary et al. [2014, 2012, 2010b, 2008b]; Kollmann et al. [2011]. All these measurements provided a most comprehensive, average description of Saturn's ring current, which can inform numerous empirical and physical models of Saturn's magnetosphere, for example, Achilleos et al. [2010a]. The time variations in the ring current have been linked to changes in the radiation belts [Roussos et al. 2018b, 2014; Kollmann et al. 2017], injections [Mitchell et al. 2016, 2015, 2009a], revealing the coupling of the system with different regions of the magnetosphere and the interplanetary space and the aurora, for example, Mitchell et al. [2009b]. The average properties of the ring current, as monitored by ENAs, have been inverted in order to probe the characteristics of Saturn's neutral gas cloud [Dialynas et al. 2013]. Meanwhile, the average distribution of the middle magnetosphere energetic particles has been studies using observations from CHEMS [Allen et al. 2018].

Many of the studies focusing of the inner magnetosphere extended into the region of the ring current, meaning that energy spectra, angular and L-shell distributions, composition, as well as asymmetries are equally well quantified for $9 < L < 15$.

In the inner and middle magnetospheres, significant work has been done to characterize not only the current systems, but also the plasma properties. In these regions the primary spatial dependence of magnetospheric properties is in the radial direction. From the first SOI pass through the magnetosphere [Young et al. 2005], several distinct magnetospheric regions could be identified: an outer region (inside the magnetopause) with extremely low density, later understood as magnetospheric lobe; then a significantly denser region with variable density and dominantly H^+, later understood as the higher-latitude manifestation of the plasma sheet/ring current; and finally, a much denser inner plasmasphere with W^+. Subsequent analyses of the SOI data [Sittler et al. 2008, 2006a, 2006b, 2005] provided quantitative estimates of the H^+, W^+, and electron plasma parameters in the inner magnetosphere and demonstrated that the plasma flow velocity is near corotation throughout the region (corotation is the azimuthal flow that results from essentially rigid rotation with the planet; it is enforced by currents flowing along the magnetic field lines between the upper atmosphere and the magnetospheric plasma). The proton and water-group temperatures were consistent with local ionization and pick-up into the corotating flow. The electrons in the inner magnetosphere consist of two populations: a cool component whose temperature tracks the proton temperature and a hotter population that increases in energy with decreasing radial distance [Young et al. 2005; Sittler et al. 2006a, 2006b; Schippers et al. 2008]. Later work [Rymer et al. 2007; Rymer 2010] showed that the cold electron component was consistent with a local pick-up source and subsequent heating via Coulomb collisions with the protons. The hot component was consistent with adiabatic transport inwards from a source in the plasma sheet/ring current region.

Calculation of the ion plasma moments (density, temperature, flow velocity) from CAPS data is complicated by incomplete and variable viewing. Nonetheless, application of a numerical computational scheme to the full data set through March 2009 enabled a survey of the properties of H^+, W^+, and H_2^+ (the third most common ion species in the magnetosphere, as revealed by CAPS time-of-flight measurements) throughout the magnetosphere [Thomsen et al. 2010]. The survey

confirmed that densities decrease and temperatures increase with radial distance inside ~20 R_S, and the W^+ density declines more rapidly than light ions. The flow velocity remains primarily in the corotational direction essentially all the way to the magnetopause, but the speed is lower than full corotation. Combined with the higher-energy measurements of MIMI, the CAPS data enabled a comprehensive survey of the total plasma pressure throughout the magnetosphere and thus an understanding of the currents that distort the dipole field within the plasma sheet and ring current region [Sergis et al. 2017, 2010]. A more recent survey of plasma moments calculated with a forward modeling approach that includes anisotropic temperatures explores both the radial and local time variations of the plasma (Figure MAPS-20), [Wilson et al. 2017].

Due to strong centrifugal forces on corotating plasma, Saturn's magnetosphere is flattened into a disk shape, especially on the night side and during times of relatively low solar wind dynamic pressure, for example, Arridge et al. [2008b, 2007]. CAPS data allow determination of the latitudinal scale heights of H^+, W^+, and H_2^+ and show that the heavy ions are more strongly confined to the equatorial plane, for example, Thomsen et al. [2010]. In the magnetotail, the magnetodisk structure is particularly prominent, with the current flowing in a relatively thin region of dense plasma separating the lobes of oppositely-directed magnetic field. The magnetodisk consists of a structured plasma sheet: a low-latitude heavy ion layer displaying narrow substructures, and a higher-latitude, smooth, broad ion layer composed dominantly of light ions (Figure MAPS-20), [Szego et al. 2011]. The density and azimuthal flow speed decline with increasing latitude [Nemeth et al. 2015] as a direct consequence of the sub-corotation of the plasma in the outer magnetosphere, for example, McAndrews et al. [2009]; Thomsen et al. [2014a, 2013]; Wilson et al. [2017]. Highest speeds occur on field lines at lowest latitudes mapping to the rapidly rotating inner regions of the plasma sheet, and the speed falls as one moves to higher latitudes, where the field lines are connected to strongly sub-corotating plasma at large radial distances.

An extremely important aspect of understanding the magnetosphere of Saturn is understanding the convection patterns and transport of plasma through and out of the magnetosphere. Saturn's magnetosphere is dominated throughout the equatorial magnetosphere by (partial) corotation with the planet. This was widely expected before the Cassini encounter, and although the expectation was not universally held, the basic result was no big surprise.

It is now clear that the dominant source of plasma for Saturn's entire equatorial magnetosphere is the inner icy satellites, in particular, the south-polar geyser plumes of Enceladus orbiting Saturn at L = 3.95, where L is the planet-centered distance normalized to Saturn's equatorial radius, $R_S \approx 60{,}300$ km [Young et al. 2005]. If tiny Enceladus is to dominate the source of Saturn's magnetospheric plasma, and hence its magnetospheric dynamics, there must be a mechanism for transporting this plasma radially from its inner-magnetospheric source to a sink in the outer magnetosphere and ultimately to the downstream solar wind. This transport mechanism is now known to be the centrifugal interchange instability.

In Saturn's magnetosphere, the centrifugal acceleration $\Omega 2/r$ is outward, and exceeds Saturn's inward gravitational acceleration beyond L ~ 2. Outward moving flux tubes release centrifugal potential energy from the system at a rate $\Omega 2/r$ per unit mass, and inward moving flux

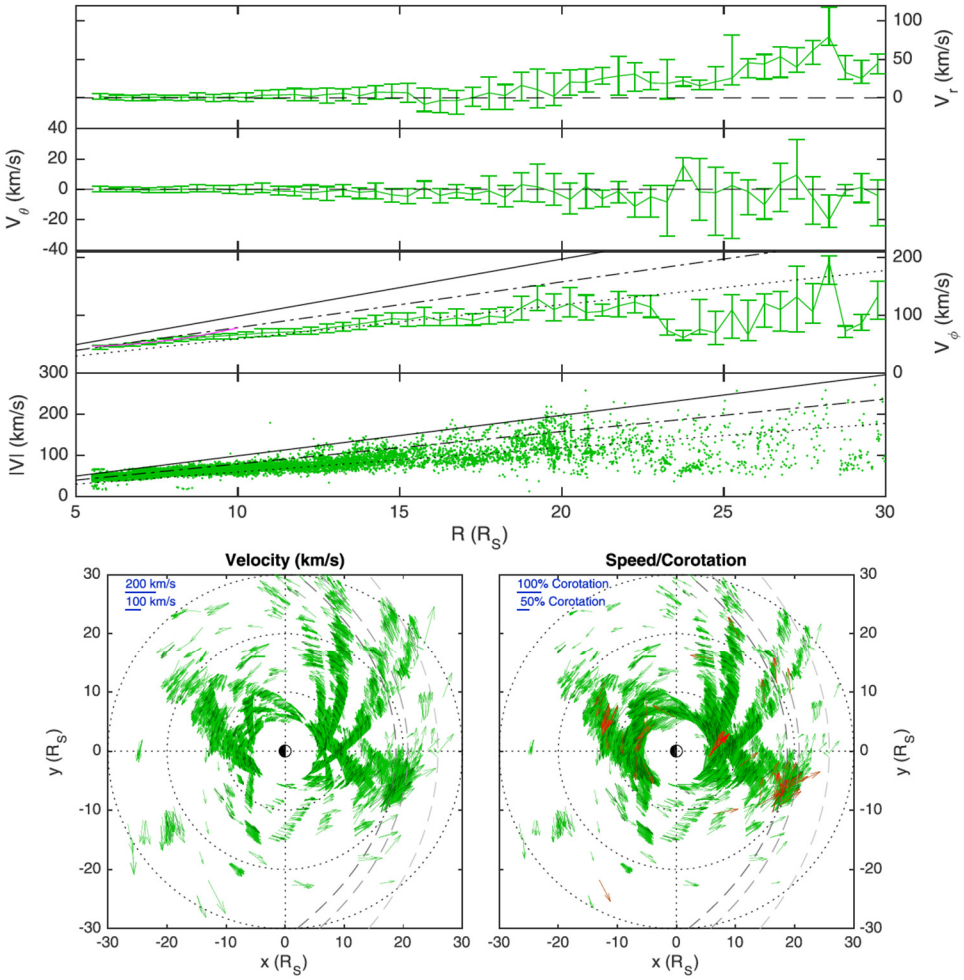

Figure MAPS-20. A recent survey of plasma moments calculated with a forward modeling approach that includes anisotropic temperatures explores both the radial and local time variations of the plasma. *Top three panels*: Radial profiles of plasma velocity components, in 0.5-Rs bins. *Fourth panel from the top*: All measured flow speeds. *Bottom left panel*: Equatorial plane projections of flow vectors with length proportional to flow speed. *Bottom right panel*: Same as the panel to the left, but with length proportional to the fraction of corotation. All data points are shown in green, while dark green shows every thirtieth data point. Figure from Wilson et al. [2017].

tubes add centrifugal potential energy to the system at the same rate per unit mass. Because of the inward density gradient of the combined plasma distribution (per unit magnetic flux), the combined flux-tube interchange process releases potential energy from the system and is therefore gravitationally unstable. The reverse would be true if the background density gradient (per unit magnetic flux) were reversed. In this sense the interchange motion is centrifugally driven. (Flux-tube interchange motions, by definition, involve no net radial transport of magnetic flux.)

It is also important to note that the azimuthal gradient and curvature drifts of the hot tenuous plasma result in plasma being injected inward by the interchange process, relative to a corotating frame of reference. This drift is prograde (eastward) for positive ions and retrograde (westward) for

negative ions and electrons. Its speed at a given distance is proportional to particle thermal energy. The injection process thus gives rise to an energy-longitude dispersion signature of the injected plasma, which has been called the smoking gun of interchange convection. This signature was repeatedly observed by CAPS on every Cassini pass through the inner magnetosphere, (L between ~5 and ~12), where the magnetic configuration is well described by an aligned dipole model [Burch et al. 2005; Hill et al. 2005; Young et al. 2005; Chen and Hill 2008; Chen et al. 2010; Rymer et al. 2009b, 2008]. An early example of this injection-dispersion signature, appropriate to this off-equatorial orbit, is shown in Figure MAPS-21 from Hill et al. [2005].

One unexpected feature of these CAPS observations was that Saturn's inflow channels (containing hot tenuous plasma) were always narrower in longitude than the neighboring outflow channels (containing cooler denser plasma), by a factor ~10 [Chen and Hill 2008; Chen et al. 2010]. All previous theoretical models of interchange convection had inflow and outflow channels of equal width, because of assumptions made for analytical convenience. Recent numerical simulations using the more flexible Rice Convection Model (RCM), driven by CAPS observational inputs [Liu et al. 2010; Liu and Hill 2012; Hill 2017, 2016; Hill et al. 2018], have clarified the reason for this apparent discrepancy between observation and theory. At Saturn (unlike at Jupiter) the source region for newly injected plasma, both from new ionization and from charge-exchange reactions with ambient neutral molecules, is broadly distributed throughout the radial range in which the resultant interchange radial transport occurs (L between ~5 and ~12).

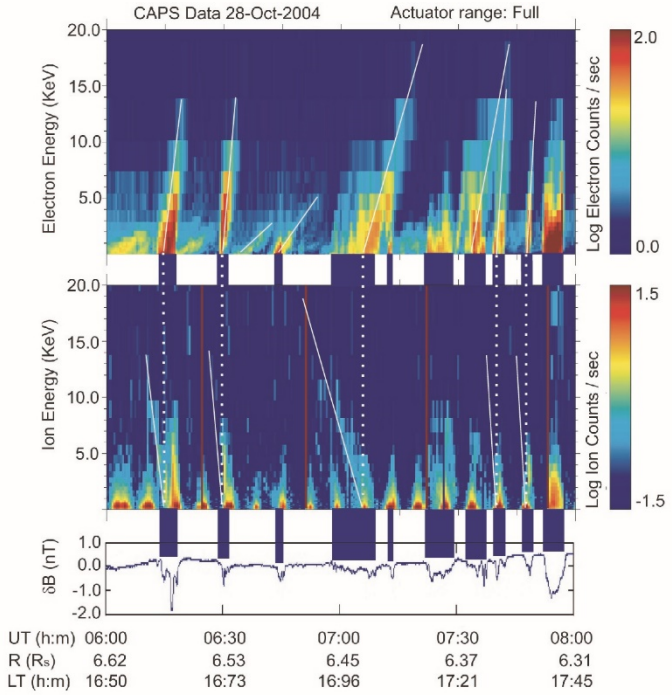

Figure MAPS-21. Early example of injection-dispersion signature, appropriate to off equatorial orbit. Linear energy-time spectrograms for electrons (*Top panel*) and positive ions (*Middle panel*) from the CAPS detectors during the second Cassini orbit of Saturn. *Bottom panel* shows simultaneous magnetic-field magnitude perturbations.

Injections at Saturn have been coarsely characterized as small and large scale. The latter would likely be accompanied by reconfigurations of the planetary magnetic field. Small-scale injections are probably confined to a small range of planetary longitudes and physically can be flux tube bundles, flow channels, or more elaborate structures. This group of injections also perturbs the magnetic field locally, for example, Andre et al. [2007, 2005], but probably at the level of a few percent of the planetary field. Andre et al. [2007] and Rymer et al. [2009b] present multi-instrument displays of interchange events in the magnetosphere of Saturn. This group of injections have been characterized as particle distributions with phase space densities that are very different from the surrounding medium in which they are observed [Mauk et al. 1998; Paranicas et al. 2016]. Mitchell et al. [2015] summarized the observational differences between small- and large-scale injections at Saturn. They found that small scale injections tended to be found inward of about 12–15 R_S, although they also found large-scale injections that could be inward of that distance. It is probably the case that small-scale injections (which are found very frequently in the data) extend in energy up to the tens of keV or so. Rymer et al. [2007] used phase space density profiles derived from CAPS data to approximate a starting radial distance of interchange injections that are observed by Cassini. Paranicas et al. [2016] approximated the inward flow speed of injections and found values comparable to the theoretical computations of Hill [2016] for $5 < L < 10$. It is believed that the radial speed of injections decreases as they approach Saturn.

Large-scale injections at Saturn have received much less attention in the literature than small scale ones. Thomsen et al. [2013] has provided a good summary of the situation. Large scale injections have been characterized by the MIMI data set. Mitchell et al. [2009b] linked some of these injections to UV data from HST and Cassini. Paranicas et al. [2010, 2007] looked at the radial range of injection remnants. Because these extend into the hundreds of keV, it is likely Paranicas was studying large-scale injections. The effects of tail collapse, plasmoid production, and related processes have been documented with the help of magnetometer data, for example, Jackman et al. [2015, 2011].

Because of their ubiquity, injections at Saturn have been used to characterize other features of the magnetosphere. Mauk et al. [2005] and Müeller et al. [2010] created azimuthal plasma flow speeds as a function of Saturn distance using MIMI injection data. Plasma flow speeds were later found using the plasma data, for example, Thomsen et al. [2010].

There are useful and well-established relationships between the local rate of plasma mass or momentum loading (through new ionization, charge exchange, or outward mass transport), on one hand, and the radial variation of the rotational lag behind rigid corotation with the planet, on the other hand. Rates of ionization, charge exchange, and net outward mass transport are difficult if not impossible to measure directly. But the corotation lag is straightforward to measure directly if one has access to reliable in situ plasma measurements. Tokar et al. [2006] reported surprisingly strong and asymmetric plasma flow perturbations during the distant and highly inclined July 2005 Cassini encounter with Enceladus. This study also concluded that plasma mass is added to Saturn's magnetosphere at a rate > ~100 kg/s in the near vicinity of Enceladus, a conclusion that was controversial at the time but was subsequently verified by many independent analyses, for example, Chen et al. [2010]. Pontius and Hill [2009] applied a similar analysis, not to the localized plasma

loading in the immediate vicinity of Enceladus, but to the much broader region 3 < ~L < ~10 where significant corotation lag was reported by Wilson et al. [2009, 2008] from their analysis of CAPS data. The study showed that the corotation lag as a fraction of the local rigid corotation speed. The data-model comparison of Pontius and Hill [2009] concludes that the plasma loading rate in this much larger volume is also > ~100 kg/s, comparable to that in the near vicinity of Enceladus.

Plasma loss into the magnetotail

- **MC1a:** Determine the temporal variability of Enceladus' plumes.
  - Investigate temporal variations in Enceladus gas production and plume composition, on the scale of seasons and solar cycle.
  - Study plume neutral gas composition.
  - Investigate the physics of the dusty plasma environment
  - Determine how the magnetosphere reacts to changes in (plume?) gas production rates by studying Enceladus' auroral footprint.
  - Study variability in dust-to-gas mass ratio.
- **MN1a:** Determine the dynamics of Saturn's magnetotail.
  - Study thoroughly the plasma sheet in Saturn's magnetotail.
  - Investigate the relation between solar wind compression events and magnetotail dynamics.
  - Investigate the plasma sheet thickness and scale height as functions of radial distance and local time.
  - Statistically characterize magnetotail variations, especially those associated with plasmoids, and correlate them with changes in the inner magnetosphere.
  - Critically evaluate the Dungey and Vasyliunas cycles in light of the new observations, especially those of flow speeds.

Enceladus, the rings, and Titan are all sources of plasma in Saturn's magnetosphere. The roughly 100 kg/s of mass being added must eventually find its way out of the inner and middle magnetosphere and into the magnetotail where it can be lost. Large-scale reconnection events that may produce plasmoids provides one potential escape route for the cool W^+ plasma that has accumulated from the interior source region. There remains some controversy as to whether this escape route is adequate to balance the interior source rate, estimated to be roughly 100 kg/s or more as noted above. It is plausible, but not yet demonstrated, that an unseen spectrum of smaller but more frequent plasmoids could contribute importantly to the escape rate.

Magnetic reconnection in the magnetotail current sheet can produce plasmoids, magnetic flux ropes (or closed magnetic loops) that are disconnected from the planet at one (or both) ends. These structures have been routinely observed in the magnetotails of Earth and Jupiter. Their detection

at Saturn by Cassini was limited by orbital geometry because the 2006 deep magnetotail passes by Cassini occurred near Saturn's northern winter solstice, when the warped magnetotail current sheet was presumably displaced well northward of Cassini's orbital plane (see Figure MAPS-22). Despite this problem, three plasmoid-like magnetic signatures were identified in the Cassini magnetometer data [Jackman et al. 2007]. Two of these events actually crossed the current sheet, where ion fluxes were sufficient to permit composition and velocity-moment information to be extracted from CAPS data. These two events were analyzed in detail by Hill et al. [2008]. The most dramatic event occurred on March 4, 2006, at a planet-centered distance of 44 R_S and at 0300 LT. Results are shown in Figure MAPS-23 and Figure MAPS-24.

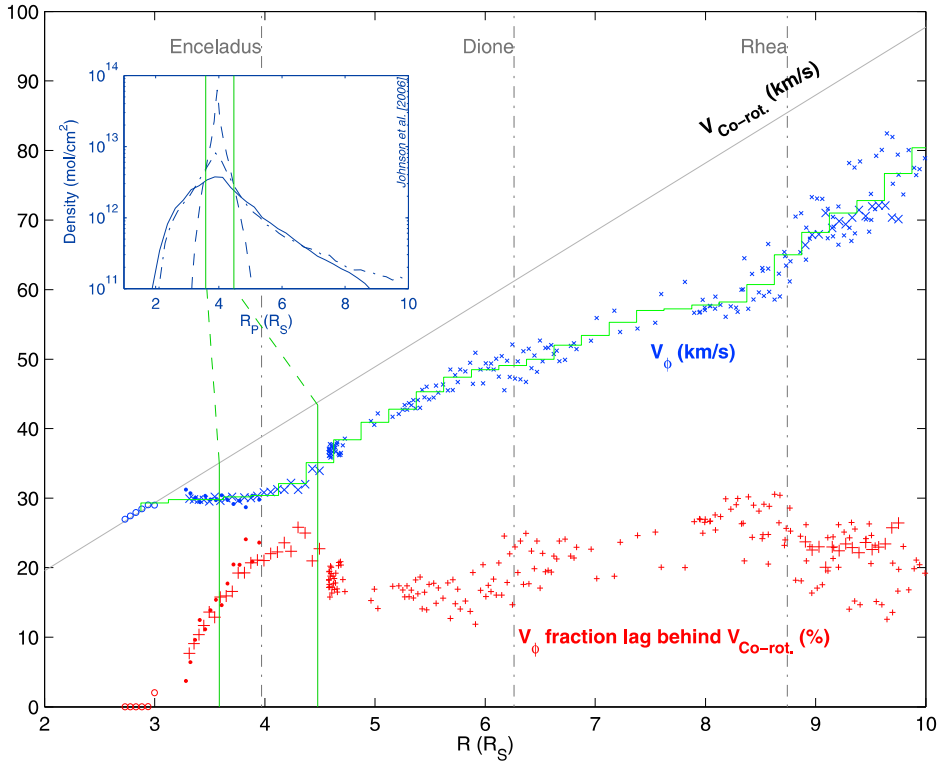

Figure MAPS-22. CAPS plasma flow measurements. Data for L > 5.5 are from forward modeling of thermalized ion velocity moments [Wilson et al. 2008]. Data for L < 5.5 are obtained from analysis of freshly picked-up charge-exchange products under the assumption of gyrotropy. Red symbols at the bottom show azimuthal speeds as a fraction of the local corotation speed. Figure from Wilson et al. [2009] Figure 4.

Early in this event, before the sharp B_θ reversal near 2300 UT, water-group ions (W^+) dominated the plasma composition, indicating a pinching off of a formerly closed flux tube containing plasma from the interior source, as in Vasyliunas-cycle reconnection. At about 23:10 UT the W^+ peak went off-scale above the energy-per-charge range of the CAPS IMS (50 V), so W^+ velocity moments became unavailable though their flux remained high. The velocity moments (based on H^+ after 23:10) indicate sub-corotational azimuthal flow throughout the event and a dramatic tailward acceleration (with Vr increasing up to ~800 km/s) late in the event. Rigid corotation at this distance would be 430 km/s in the V_Φ direction.

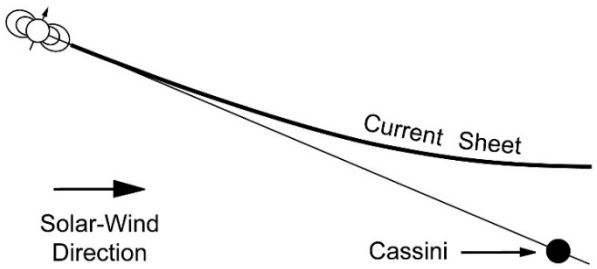

Figure MAPS-23. Orbital geometry during the deep-tail passes of Cassini. Figure from Hill et al. [2008] Figure 1.

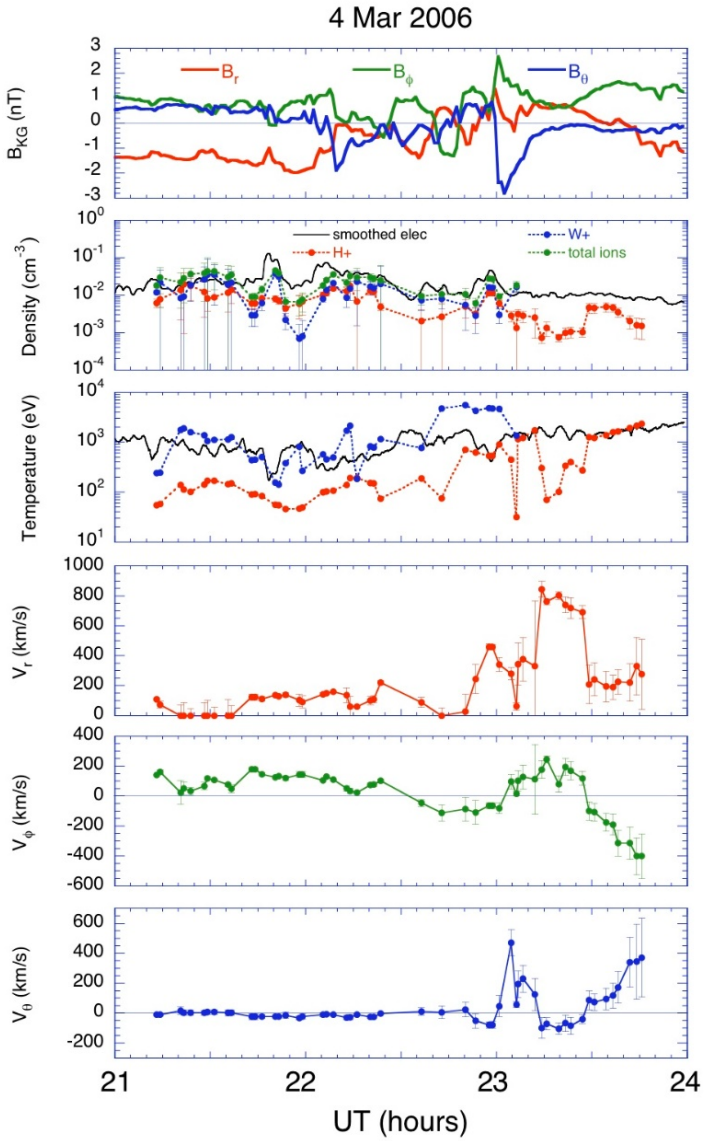

Figure MAPS-24. Magnetic field components and particle velocity moments for the plasmoid encountered by Cassini at 44 R_S near 0300 LT. Figure from Hill et al. [2008] Figure 3.

A particularly interesting feature of this event is that Cassini was in a position to see not only the plasmoid properties observed in situ by CAPS and MAG, but also the plasmoids earlier initiation closer to Saturn as observed by MIMI in ENA bursts. The viewing geometry is shown in Figure MAPS-25. The ENAs were hydrogen and oxygen atoms having speeds consistent with covering the distance from source to Cassini (~26.5 R_S) in the allotted time (~25 min). The plasmoid structure itself could also have covered the same distance in the same time interval [Hill et al. 2008].

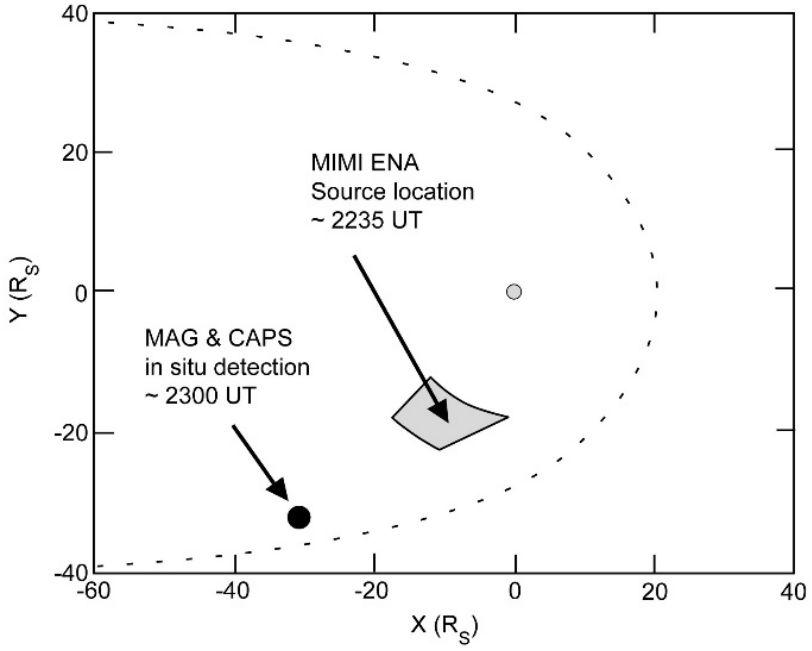

Figure MAPS-25. During the in situ CAPS and MAG plasmoid observations on March 4, 2006, Cassini was within the large dot indicated, and the ENA bursts observed from the same location ~25 min earlier were deduced to have a source within the quasi-rectangular shaded box. The dashed contour is a cartoon depiction of the typical shape and location of Saturn's magnetopause.

Magnetotail reconnection also provides a fresh source of hot, tenuous plasma to the region planetward of the reconnection site, where it produces a dipolarization signature in the magnetic field. It can also provide seed particles both for the inflow channels of the interchange cells in the inner magnetosphere, as described earlier, and for the intermittent ENA bursts observed by MIMI from the middle and outer magnetosphere, and the associated SKR bursts observed by RPWS from the footprints of the same field lines.

Theoretically, there is a clear distinction between Vasyliunas-cycle reconnection involving the pinching off of formerly closed flux tubes, containing cool dense plasma from the inner-magnetosphere source, and the more Earth-like Dungey-cycle reconnection involving the closure of formerly open flux tubes of the magnetotail lobes, containing hotter and more tenuous plasma of magnetosheath origin. The large plasmoid described above is readily explained by the Vasyliunas cycle alone. But two detailed multi-instrument event studies [Thomsen et al. 2015a, 2015b] have also found evidence of both Vasyliunas and Dungey cycles occurring either

simultaneously or sequentially. In addition, Cowley et al. [2015] estimate that based on the duration of observed plasmoid field perturbations the mass loss due to plasmoids is at least an order of magnitude smaller than necessary. Given the typically several-hour interval between plasmoid releases it has been suggested that the overall plasma structure released by such events may be at least an order of magnitude longer than the few tens of R_S lengths inferred from the magnetic data direct.

Thomsen et al. [2015b] examined a high-latitude dawnside Cassini pass from the low-density lobe region into the higher-density closed field-line region. They inferred a stripping of plasma from the outer region of closed magnetic flux tubes as those tubes cross the night side magnetosphere from dusk to dawn, attributable to Vasyliunas-cycle reconnection, together with an interval (or region) of Dungey-cycle reconnection at the high-latitude boundary between open and closed field lines.

On the other hand, Thomsen et al. [2015a] examined a deep-tail near-equatorial Cassini pass near 37 R_S near midnight LT. They found a prolonged period (~5 hours) of planet-ward plasma-sheet flow attributable to an even more prolonged period of magnetotail compression due to the passage of a recurrent solar-wind structure containing enhanced dynamic pressure. They conclude that Dungey-cycle reconnection takes precedence over Vasyliunas-cycle reconnection when the solar-wind pressure is high.

In addition, numerous reconnection-related events during the main Cassini tail exploration interval in 2006, namely planetward-travelling dipolarizations and tailward-travelling plasmoid structures, which were found to be related in timing to both the pulsing of the SKR emissions and the magnetic PPO phase [Jackman et al. 2016, 2009a]. Specifically, the events were found to be preferentially initiated during intervals when the PPO perturbations stretch the field lines radially outward from the planet and thin the plasma sheet leading to instability (see entitled Time varying modulation of SKR and associated PPO signals), especially when the two PPO systems act in this manner in concert, i.e., when they are near antiphase. Ongoing work is presently investigating dipolarization events and auroral storms during the sequence of proximal orbits observed just prior to end of mission.

Plasma composition, distribution, sources, and sinks

- **M_AO2:** Determine current systems, composition, sources, and sinks of magnetosphere charged particles.

Understanding the plasma composition, distribution, sources and sink in Saturn's magnetosphere begins with understanding the neutral gas sources. Prior to the arrival of Cassini in the Saturn system, Voyager measurements seemed to indicate that Titan was the main sources of the neutral gas in the system and therefore the main sources of plasma. However, with the discovery of the activity of Enceladus and better mass resolved measurements of the neutral and the plasma composition it became clear that Enceladus, the other icy satellites and the rings are the major source of distributed mass in the Saturn system.

Our understanding of the neutral gas distribution comes from measurements made by the INMS instrument. In 2008, the INMS investigation made in situ measurements of neutral species near Saturn's equatorial plane within 0.5 R_S of the orbit of Enceladus. After removing the large background and modeling to interpret instrumental effects, the data provide constraints on the neutral distribution and composition. These data show an azimuthal asymmetry in the neutral densities and provide measurements used to compare to simulations of neutral H_2O emitted from Enceladus (Figure MAPS-26). Far from Enceladus, the neutral water densities, at a few times 10^3 molecules/cm^3, are near the detection limit of INMS. Near Enceladus, but outside of the plumes and north of the equatorial plane, the INMS detects particles within 5,000 km of Enceladus, with the density increasing to approximately 10^5 molecules/cm^3 at the equatorial plane.

INMS observes inner-magnetosphere neutrals with a mass of 28 u that have unexpectedly high densities, no apparent source, and no clear molecular identification. With densities as high as 30% of the neutral-water density, the candidate molecules, N_2 and CO, should be abundant in the Enceladus emissions, but multiple observational approaches show that neither molecule comprises more than 3% of the H_2O density.

Although RPWS cannot distinguish the species of ions in the magnetosphere, measurements of the electron density in the inner magnetosphere show that adjacent to the dense A-ring there is an electron density maximum at over 100 electrons/cm^3, with the high density region (> 10/cm^3)

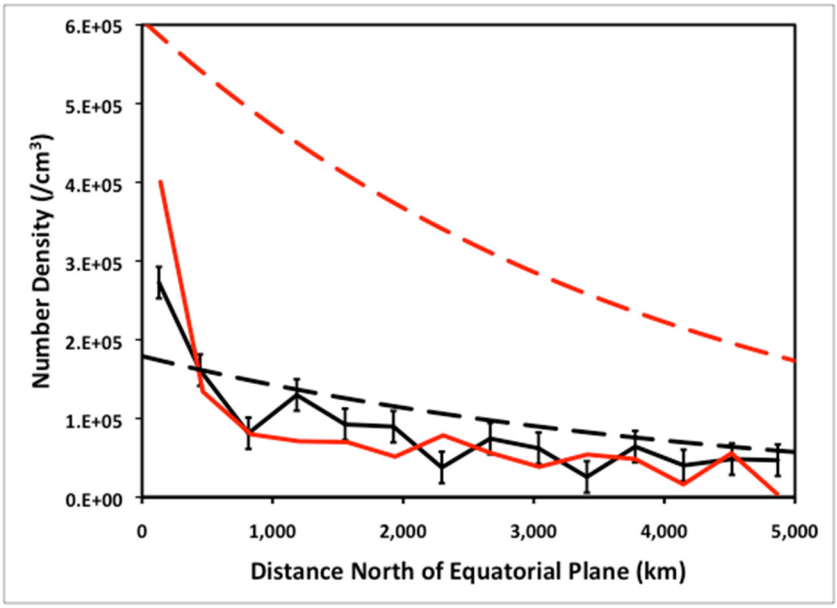

Figure MAPS-26. Neutral cloud density north of Enceladus, before close approach and outside of proximal influence of the south-pole plumes. The solid lines are the INMS data. The dashed lines are simulations using the charge-exchange model of the neutral cloud [Smith 2010]. The E5 simulation is based on the source rate derived from modeling the E5 plumes, and the E3 simulation is based on the source rate derived from modeling the E3 plumes. The E3 and E5 INMS densities are similar to each other and to the E3 simulation. E5 error bars (not shown to reduce clutter) are the same size as E3 error bars.

extending out to beyond L = 5. Persoon et al. [2015, 2009] found that this high density region is a plasma torus created by ionization and pick-up of new ions born in the Enceladus plume and a seasonal contribution from photo-ionized neutrals originating from the rings themselves. Thus, at equinox, the maximum in plasma density in this torus shifts radially outward to 4 R_S, but at solstice, the sun-facing rings become a neutral and plasma source shifting the torus plasma maximum closer to the A-ring—see Persoon et al. [2015] Figures 6 and 7. The peak density in the torus is about 10% of the Io torus at Jupiter and represents a dominant controlling element in the inner magnetosphere of Saturn [Gurnett et al. 2007]. These RPWS measurements in the inner magnetosphere have allowed Persoon et al. [2013, 2009] to develop an empirical plasma density model for the Saturnian system.

In addition to the direct measurements of the neutral distribution by the INMS instrument, one of the best pointers to the source of plasma in the magnetosphere is the composition. CAPS finds that the dominant magnetospheric ions are W^+, H^+, and H_2^+ [Young et al. 2005; Thomsen et al. 2010] were well explained by the later discovery of the prodigious output of water from the south-polar plumes of Enceladus. It was noted by Young et al. [2005] that the presence of H_3O^+ within the W^+ ion group indicated ion-molecule reactions occurring in a water-rich atmosphere, attributed to the E-ring and inner icy satellites, which ultimately was determined to be Enceladus. A careful separation of the individual components of the water-group species and determination of the radial distance dependence of their relative proportions [Wilson et al. 2015] provided vital constraints on models of the physics and chemistry of Enceladus-originating material.

INMS has extracted the water-group ion fractions from open source ion (OSI) measurements in Saturn's inner magnetosphere. These fractions are sensitive probes of the source, transport, and loss mechanisms that govern Saturn's magnetosphere. INMS samples only a small portion of velocity space at a time, which enables investigation of the distributions within velocity space but also limits sensitivity and complicates the separation of various factors that affect the relative ion fractions. Densities and count rates can be low, sometimes requiring the sum of 10,000 IPs for a two-sigma result. Figure MAPS-27 shows that ion fractions depend on distance from the orbit of Enceladus. Models show that the water-group fractions depend most strongly on the local fraction of neutrals. In contrast to CAPS results, INMS data show H_3O^+ fractions less than 0.1 except for measurements taken directly in the plumes. These fractions are now being used to calibration ion and neutral models of Saturn's magnetosphere.

Another example of source determination through composition is N^+ [Smith et al. 2008, 2007, 2005] (see Figure MAPS-28). Originally expected from Titan, the radial dependence of the N^+ phase space density and the energy of this population suggested instead an inner magnetosphere source, probably Enceladus, with both molecular nitrogen and ammonia emitted there. Surprisingly little N^+ has been found in the outer magnetosphere, indicating that nitrogen ions coming from Titan do not accumulate to significant densities.

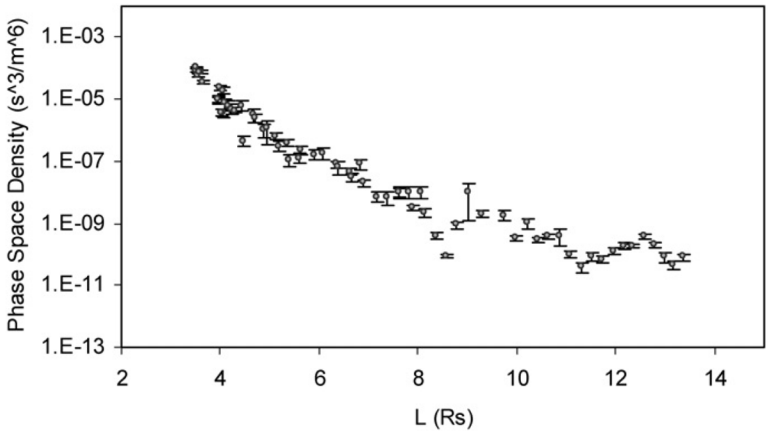

Figure MAPS-27. Nitrogen ion phase space density averaged over energy and angle, as a function of distance from Saturn. Clear decline with distance indicates a source in the inner region, inconsistent with a Titan source in the outer magnetosphere (L ~20). Figure from Smith et al. [2007].

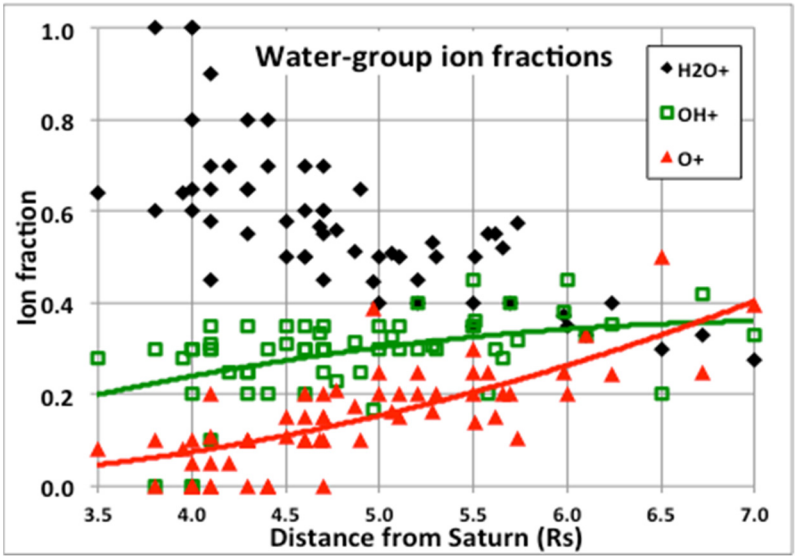

Figure MAPS-28. The fraction of water-group ions plotted as a function of distance from Saturn. INMS finds that the highest fraction of H_3O^+ is near 4 R_S, as expected, as that is the orbit of Enceladus, the source of the neutral water that becomes the plasma.

As indicated above, the dominant ion species seen throughout the magnetosphere are well explained by ionization of material from the water plumes of Enceladus. Cassini MAPS instruments observations of the plumes themselves are detailed in the section entitled Interaction of the Enceladus plume with the magnetosphere. In addition, MAPS instruments and CAPS in particular showed Enceladus to be the probable source of most of the N^+ observed in Saturn's inner magnetosphere, and CAPS measurements further helped reveal the existence of temporal variability in the plume source [Smith et al. 2010].

Before the arrival of Cassini in the Saturn system, Titan was regarded as the major source of neutrals and hence ions to the Saturn magnetosphere. The primary tracers of Titan's contributions to magnetospheric plasma have been N^+ and H_2^+. The finding of very little N^+ in the outer magnetosphere [Smith et al. 2005] indicated that Titan's contribution to the heavy-ion plasma is limited, whereas the fact that H_2^+ becomes comparable to H^+ and W^+ in the outer magnetosphere [Thomsen et al. 2010] indicates that Titan is an important source of lighter ions in that region. From observations during passage through Titan's wake region, the total mass loss rate from Titan is estimated to be a few × 10^{25} amu/q/sec (~0.8 kg/s) [Coates et al. 2012], compared to estimates of ~60–100 kg/s from Enceladus [Fleshman et al. 2013].

CAPS was turned off before the F-Ring and proximal orbits, so the only direct exploration of ring-associated plasma occurred during SOI, where a layer of O^+ and O_2^+ was discovered over the A-ring and B-ring [Young et al. 2005]. Subsequent analysis of the SOI data [Tokar et al. 2005] produced densities and temperatures of these two species (Figure MAPS-29). The ring atmosphere and ionosphere are likely produced by UV photo sputtering of the icy rings and subsequent photoionization of O_2^+. Significant O_2^+ was also detected outside the main rings, near the F-ring [Tokar et al. 2005], and analysis of the O_2^+ and W^+ profiles showed the seasonal dependence mentioned above, consistent with a ring source that depends on the solar illumination angle [Elrod et al. 2014, 2012]. The result indicates that the rings are an important source of O_2^+ and O^+ ions inside the orbit of Mimas.

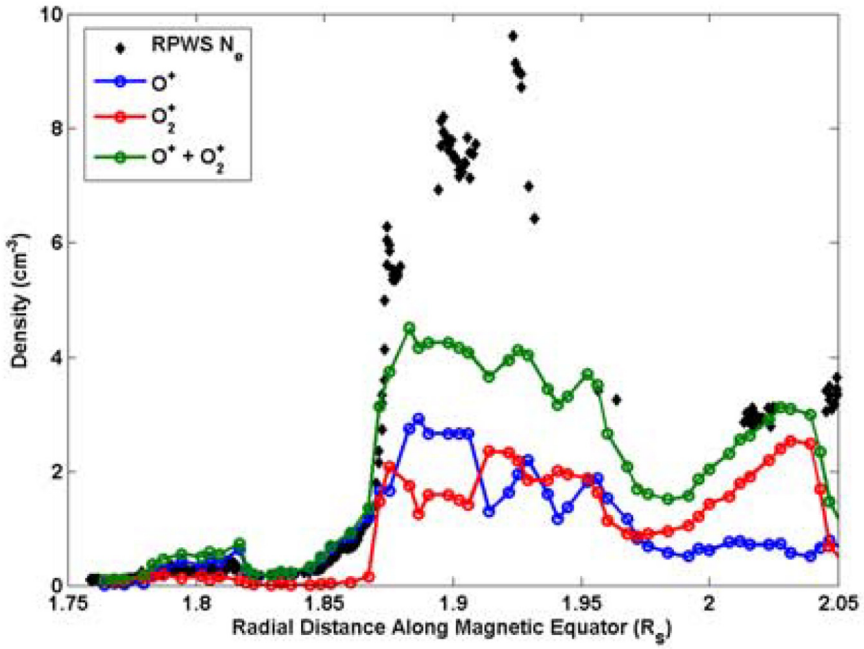

Figure MAPS-29. Radial dependence of O^+ and O_2^+ densities from CAPS observations over the main rings during SOI. Figure from Tokar et al. [2005].

CAPS has also detected O_2^+ in the vicinity of Dione [Tokar et al. 2012], and the observed radial dependence of the ratio O_2^+/W^+ suggested that there is a neutral O_2 source in the vicinity of Rhea [Martens et al. 2008]. Although the evidence for oxygen from Rhea is somewhat skimpy, CAPS has clearly detected non-gyrotropic outflowing CO_2^+ there, as well as another negatively-charged species, previously thought to be O^- but now found to be closer to mass 23 [Desai et al. 2018]. The latter is perhaps a carbon-based ion deriving from implanted exogenic compounds. Examination of the plasma conditions on flybys of Rhea [Wilson et al. 2010] revealed that the plasma flowing near it had no radial component on the Saturn-side of the moon, but had a radially outward component on the anti-Saturn-side. This is potentially due to an electric field enhancement near the moon, as observed in hybrid simulations.

Observation of probable plasma outflows from the ionosphere at the outer edge of the night side plasma sheet and extending into the lobes led to an estimate of some 10 s of kg/s lofted from the ionosphere (Figure MAPS-30) [Felici et al. 2016]. The observations occurred during a probable solar wind dynamic pressure enhancement, which may be important for producing significant outflow. It is not yet clear how often such outflow occurs, nor whether the outflow is actually captured into the closed region of the magnetosphere, rather than just escaping into the solar wind. Additionally, the field-aligned angular distributions of the suprathermal electrons within the plasma sheet/ring current region may indicate an ionospheric origin [Schippers et al. 2008], but no supporting evidence from the ion data has been reported.

With regard to dayside entry of solar wind plasma via reconnection or the K-H instability, there is considerable evidence that both processes take place. Magnetopause encounters frequently exhibit a low-latitude boundary layer (LLBL), in which magnetosheath plasma can be found just inside the magnetopause. From a survey of 354 crossings of the LLBL [Masters et al. 2011b, 2011c], the estimated thickness of the LLBL is only of the order of 1 Saturn radius, with no clear dawn-dusk asymmetry. Thus, while solar wind plasma can and does enter the magnetosphere on the dayside, it does not get very far in. This is supported by the fact that the ratio of m/q = 2 to H^+ ions in the outer magnetosphere is almost always significantly greater than the values of 1 to 10% typically seen within the solar wind [Thomsen et al. 2010], indicating that the plasma in the outer magnetosphere is dominantly of inner magnetospheric and/or Titan origin, with very little contribution from solar wind plasma there.

On the night side, plasma with solar wind-like composition has been observed at 37 R_S near local midnight [Thomsen et al. 2015a]. In that event, it appeared that prolonged high solar wind dynamic pressure may have caused erosion of the tail plasma sheet through ongoing Vasyliunas-type reconnection that then involved open lobe field lines and created a more Earth-like, Dungey-style outer plasma sheet dominantly of solar wind origin. Other evidence for Dungey-style reconnection following a Vasyliunas-style reconnection event is the post-plasmoid plasma sheet, for example, Jackman et al. [2011]. One other event that showed the possibility of a Dungey region, in which field lines were probably closed but the densities were quite low and there was very little O^+, was seen in a rapid high-latitude pass near dawn with clear evidence of Vasyliunas-type reconnection at latitudes just equatorward of the Dungey region [Thomsen et al. 2015b].

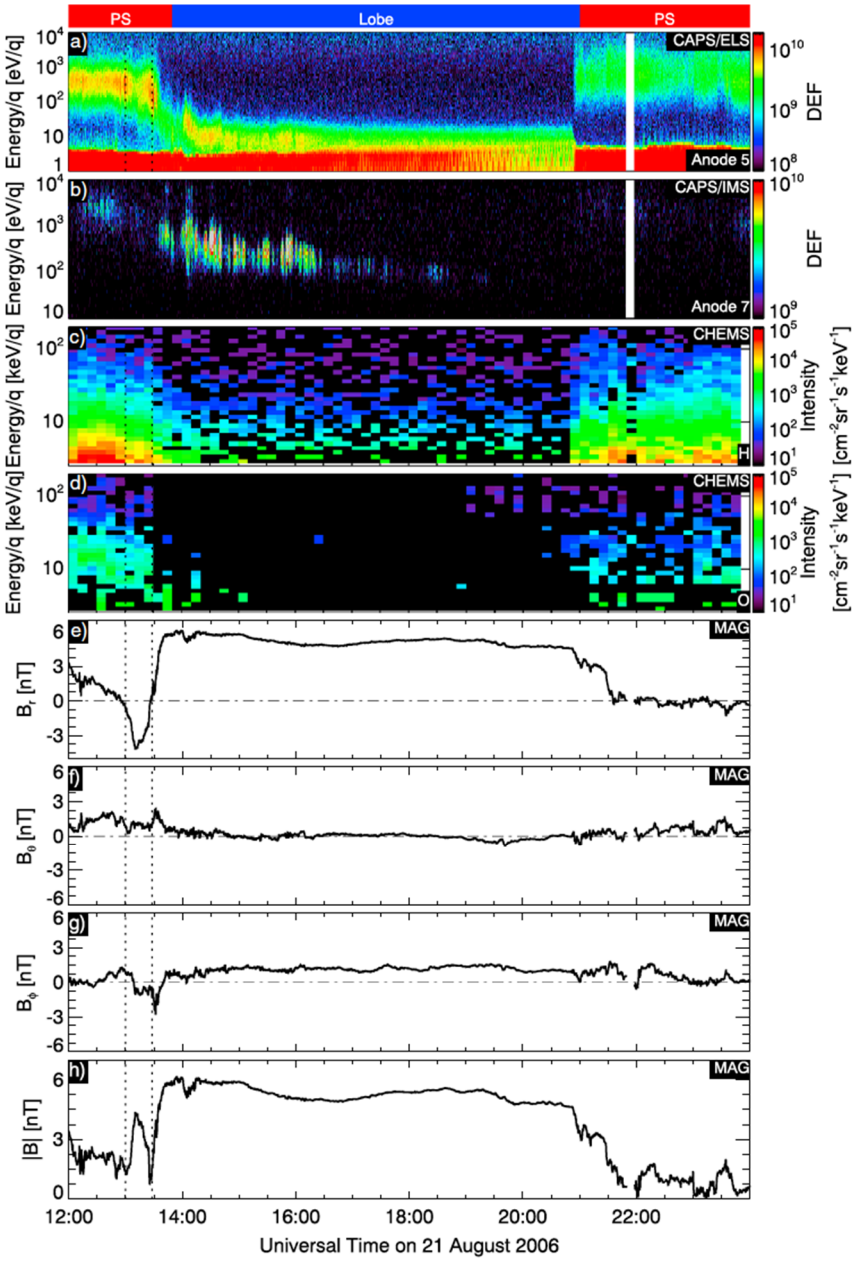

Figure MAPS-30. CAPS observations of an outflowing H^+ population from Saturn's ionosphere, seen in the lobe near the plasma sheet boundary at 36 RJ down tail. Figure from Felici et al. [2016].

CAPS measurements consistently show that plasma flow in the inner magnetosphere is dominantly in the corotation direction, with a magnitude near full corotation at low radial distances but tending toward a fraction (~60%) of full corotation by 10 R_S, see Sittler et al. [2005]; Wilson et al. [2017, 2009, 2008]; Thomsen et al. [2010]; Livi et al. [2014]. Radial velocities are much smaller and difficult to measure [Wilson et al. 2008].

There is widespread agreement that the primary mechanism for radial transport within the inner magnetosphere, which is needed to remove the continuously-produced plasma from Enceladus, is the process of centrifugally-driven flux-tube interchange. This process is described in detail in the section entitled Magnetospheric Structure and Convection, but CAPS data have been instrumental in the discovery [Young et al. 2005; Hill et al. 2005; Burch et al. 2005] and diagnosis [Andre et al. 2007; Chen and Hill 2008; Menietti et al. 2008; Rymer et al. 2009b; Chen et al. 2010; DeJong et al. 2010; Thomsen et al. 2014b; Paranicas et al. 2016] of the hot-plasma injection events that are the inward-moving half of the flux-tube interchange. There has been only one reported observation of the outward-moving cold plasma fingers that should form the other half of the process [Thomsen et al. 2015b]. Estimates of the inflow speeds within the injection channels range from a few km/s to ~260 km/s [Burch et al. 2005; Rymer et al. 2009b; Chen et al. 2010; Paranicas et al. 2016]. Composition suggests that the plasma inside the injection channels comes from the outer magnetosphere [Thomsen et al. 2014b].

One unanticipated discovery of the Cassini mission is the existence of an inner magnetospheric convection pattern superimposed on the dominant corotation pattern [Andriopoulou et al. 2014, 2012; Thomsen et al. 2012; Wilson et al. 2013]. The pattern consists of a general dusk-to-dawn drift, such that particles drift inward while they corotate from noon to midnight and outward as they return from midnight to noon (Figure MAPS-31). The result is an inward displacement at midnight compared to noon. A number of hypotheses regarding this convection have been advanced, but it remains an unsolved puzzle.

Beyond 10 R_S, CAPS measurements show consistently that the plasma flow overwhelmingly remains in the corotational direction at essentially all local times, indicating continued influence of connection to the corotating ionosphere, but the speed of the flow is well below full corotation, for example, McAndrews et al. [2009]; Thomsen et al. [2014a, 2013, 2010]; Wilson et al. [2017]. Beyond about 15–20 R_S, there is little evidence for inflowing plasma on the night side, where, particularly near the flanks, flows tend to have more of an outward component. From the lack of inward flow in the pre-dawn sector, it appears that dense plasma is not often able to make the turn and return sunward to the dayside magnetosphere at distances beyond ~15 R_S.

One of the principal ways in which plasma produced in the inner magnetosphere can be shed to the solar wind is through the process of magnetic reconnection in the tail. This is covered in greater detail in the section entitled Plasma loss into the magnetotail and Magnetotail configuration and dynamics flux tubes loaded with inner magnetospheric plasma are transported via interchange to the outer magnetosphere. Strong centrifugal forces distend them radially, especially near the equatorial plane. On the dayside, the pressure of the solar wind helps confine the distended flux tubes, but when they rotate into the night side, that confinement goes away, and centrifugal force can overwhelm the magnetic tension. The result is that the flux tubes pinch off (or reconnect), shedding a plasmoid that is no longer connected to the planet and which carries away the load of plasma the flux tube bore before reconnection occurred. This is the so-called Vasyliunas cycle. CAPS data have been instrumental in identifying the resulting down tail flows of the disconnected plasmoids [Hill et al. 2008; McAndrews et al. 2009; Jackman et al. 2015, 2014; Arridge et al. 2015;

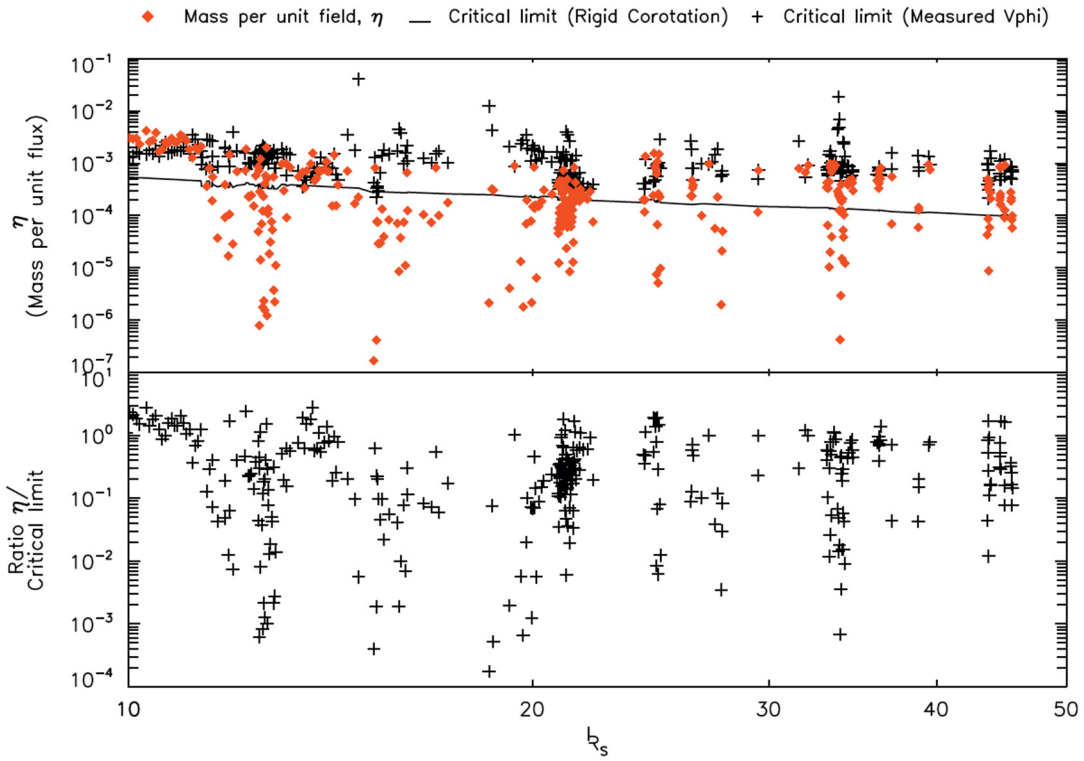

Figure MAPS-31. Comparison of nightside flux-tube content (red diamonds), estimated from CAPS/IMS data, with the theoretical critical limit above which the flux tube will pinch off and release a plasmoid downtail (black +). The observed flux-tube content is roughly bounded by the critical limit, suggesting that nightside reconnection and plasmoid formation keep the tail near marginal stability. Figure from McAndrews et al. [2009].

Smith et al. 2018a, 2018b, 2016]. There is ongoing debate as to whether plasmoids can carry away enough plasma to balance the new production in the inner magnetosphere.

Magnetic reconnection and nonlinear K-H waves at the magnetopause could both potentially allow magnetospheric mass loss. Evidence for the operation of both processes has been seen, for example, McAndrews et al. [2008]; Masters et al. [2012b, 2010, 2009]; Wilson et al. [2012]; Delamere et al. [2013]; Fuselier et al. [2014]; Jasinski et al. [2016]. However, to date the contribution of neither process to the overall mass balance problem has been quantitatively assessed. While energetic W^+ ions are commonly seen in the dayside magnetosheath, there is no evidence for thermal W^+ there [Sergis et al. 2013] or in the upstream region [Thomsen et al. 2007].

As mentioned in the section entitled Magnetotail configuration and dynamics, plasma flows along the night-side flanks of the magnetosphere tend to have an outward component, suggesting the likelihood that plasma is lost as a planetary wind down the flanks. An estimate of total mass loss from the tail (excluding plasmoids) [Thomsen et al. 2014a] is within the range of previous estimates of the total mass-loading rate from ionization of water gas from Enceladus.

Plasma kinetics and wave-particle interactions

- **M_AO3:** Investigate wave-particle interactions and dynamics of the dayside magnetosphere and the magnetotail of Saturn and their interactions with the solar wind, the satellites, and the rings.

Similar to the section entitled Seasonal and solar cycle variations, many of the kinetic and wave-particle interaction results of the MAPS instruments is outlined in other sections of this document. Specifically, effects related to the magnetospheric interaction with Titan are outlined in the section entitled Titan's upper atmosphere and its interaction with the surrounding plasma, results related to the magnetosphere can be found in the sections entitled Magnetotail configuration and dynamics, Magnetospheric structure and convection, and Plasma loss into the magnetotail, and many results can be additionally found in the section entitled Time varying modulation of SKR and associated PPO signals. In this section, we reiterate just a few of those results.

Several MAPS instruments found that Titan's interaction with the magnetosphere of Saturn features important plasma kinetic physics. The CAPS instruments, for example, discovered pick-up ions in the form of beams of CH_4^+ and N_2^+ that can be explained theoretically as the result of kinetic interactions between Titan and the magnetosphere [Hartle and Killen 2006; Hartle and Sittler 2007; Hartle et al. 2011]. It is no surprise that beam composition is consistent with the composition Titan's exosphere and atmosphere which is dominated by N_2 (98.4%) and CH_4 (1.4%) [cf. Waite et al. 2005].

Sittler et al. [2010] observed nearly field aligned outflows from the topside ionosphere during the T9 flyby and estimated the loss of methane ions due to pick-up from the exosphere at ~5×10^{22} mol/s [Sittler et al. 2009a]. The outflows serve ultimately as a sink from Titan's atmosphere of roughly ~5×10^{24} mol/s. Later, Coates et al. [2012] observed similar amounts of ionospheric outflows during the T9, T63, and T75 flybys. The theoretical cause of these outflows was originally discussed in Hartle et al. [2008]. It is produced by a field-aligned polarization electric field Epol ~$-1/n_e e \nabla_{||} P_e$ so that above the ionospheric density peak the outward acceleration is > 10 times the force of gravity for m/q ~28 amu/q ions. Sittler et al. [2010] found that the resulting ion outflow speeds were ~7 km/s with T_{ION} ~50,000° K. Therefore, both significant accelerations and heating must have occurred at altitudes above 5000 km. Later, using electron observations, Coates et al. [2015] measured the total potential drop of this electric field to be ~0.2 μV/m to heights ~15,000 km, which is sufficient to accelerate methane ions to the observed speeds ~5–6 km/s. Future 3-D hybrid simulations similar to that done by Lipatov et al. [2014, 2012, 2011] will be required to understand the heating, for example, due to wave-particle interactions, of ions to the observed high temperatures. In addition to the outflows, Sittler et al. [2010] also found evidence of Alfven waves during the T9 flyby with transverse velocity and magnetic field fluctuations that were anti-correlated with time and thus consistent with field-aligned propagation of these waves.

The T9 flyby was further studied by magnetometer team, which considered the ionosphere of Titan with its embedded magnetic field a study of Titan's nightside ionosphere was published by Cravens et al. [2009a]. T96, the first encounter presumably occurring in the supersonic solar wind, was also modelled using a hybrid kinetic code [Feyerabend et al. 2016]. An important kinetic process

in the interaction between a streaming magnetized plasma and Titan's atmosphere is the pick-up process, which has been observed to lead to the generation of often strong ion cyclotron waves in the cases of atmospheric interactions (Venus, Mars, Galilean satellites of Jupiter, Saturnian satellites, comets). In the case of Titan only two flybys T63 and T98 were associated with ion cyclotron waves are of relatively high amplitude, as a study of the MAG team shows [Russell et al. 2016].

The T9 flyby was modeled by Ma et al. [2007]. The wake region of Titan is an important component of Titan's interaction with its surrounding plasma. The Cassini spacecraft passed through the distant downstream region of Titan on December 26, 2005 (T9 flyby). In this study, we compared the observational data with numerical results using a 7-species Hall MHD Titan model. There is a good agreement between the observed and modeled parameters, given the uncertainties in plasma measurements and the approximations inherent in the Hall MHD model. Our simulation results also show that Hall MHD model results fit the observations better than the non-Hall MHD model for the flyby, consistent with the importance of kinetic effects in the Titan interaction. Based on the model results, we also identified the controlling physical processes in different plasma regions based on ion gyradius.

Beyond Titan, kinetic effects also play a role at other satellite interactions. The current system, detected by MAG in Rhea's plasma wake, results from the combination of: i) ion kinetic effects in a hot plasma; and ii) relative motion between the plasma and an inert plasma absorbing body like Rhea. As the wake is refilled with plasma in the downstream co-rotation flow [Roussos et al. 2008a], the plasma pressure gradient directed back toward Rhea results in diamagnetic current closure across the wake and perpendicular to the co-rotation flow. The pressure gradient exerts a force directed towards Rhea and mimics a real exosphere by generating a field-aligned Alfvénic current system, which extracts momentum from the co-rotating plasma outside the wake and transfers it to the wake. The Alfvén wings from the wake [Khurana et al. 2017] produce flow-directed magnetic field perturbations north and south of Rhea's equatorial plane, detected by MAG at the locations of R2 and R3 and also during two distant (102 R_H and 54 R_H away from Rhea on June 3, 2010, and October 17, 2010) [Khurana et al. 2012] downstream flybys.

Finally, we highlight the acceleration of particles that can occur at the bow shock of Saturn. In the presence of an obstacle, shock waves in a neutral gas efficiently dissipate the supersonic flow to subsonic through the action of collisions. In space plasmas however, shocks cannot rely on collisions to adequately dissipate the flow since the collisional mean free path is many orders of magnitude larger than the shock's width. Here, electromagnetic forces play a role to compensate for the additional dissipation required. Their roles are well understood for modest Mach numbers (e.g., 2–10), however this becomes more problematic at larger Mach numbers since additional kinetic processes, namely ion reflection and reformation, come into play to complete the dissipation process. Fortunately, such high Mach number phenomena were explored using the Cassini magnetometer dataset. Sulaiman et al. [2015] showed evidence for the timescales of ions reflection at a shock undergoing reformation to be 0.3 times the upstream gyro period. This was in excellent agreement with what had been theorized.

Radiation belts

- **M_AO3:** Investigate wave-particle interactions and dynamics of the dayside magnetosphere and the magnetotail of Saturn and their interactions with the solar wind, the satellites, and the rings.
- **MC1b:** Observe Saturn's magnetosphere over a solar cycle, from one solar minimum to the next.
  - Investigate what controls the interplay between the Dungey and Vasyliunas cycles?
  - Study the solar cycle dependence of the magnetospheric dynamics.
  - Investigate magnetospheric structure: variations in force balance.
  - Investigate non-static and other variant radiation belt features.
- **MN1b:** Conduct in situ studies of Saturn's ionosphere and inner radiation belt.
  - Investigate the effects on aurora of solar wind and seasons.
  - Are there UV satellite footprints on Saturn? (like at Jupiter)
  - Is there a seasonal variation in auroral activity?
  - Investigate solar wind–ionosphere–magnetosphere coupling through the auroral regions.
  - Investigate whether there are UV satellite footprints on Saturn and whether there are Region 1 currents connecting the ionosphere and the magnetopause.
  - Investigate the composition of Saturn's ionosphere.
  - Study whether there is a significant polar outflow from Saturn's high latitude ionosphere and whether the outflow exhibits seasonal or solar cycle variation.
  - Determine whether there is a radiation belt between the D-ring inner edge and the atmosphere.

Cassini MAPS instruments, especially the MIMI instrument, have made measurements of Saturn's magnetosphere that provide the most comprehensive description of the radiation belts of a planet besides Earth. More than 200 orbits crossed into the radiation belts, allowing us to understand and quantify their average structure, but also to monitor time variations, despite the single point measurements. The most detailed description of the radiation belts is given by Kollmann et al. [2011] where the L-shell, local time, and pitch angle (latitudinal) structure of the belts is given for electrons and protons of different energies. Heavier ions and their charge states are studied by DiFabio et al. [2011]; Dialynas et al. [2009]; Carbary et al. [2010c]; Christon et al. [2014a, 2014b, 2013]. The latter three studies provide the most detailed characterization of trace energetic ions and their charge states at an outer planet, showing how their origin may be connected to the planet's rings, the activity of Enceladus and seasonal or solar cycle effects.

Allen et al. [2018] conducted a mission long overview of internal to external sources of energetic plasma at Saturn. They found that solar wind-originating He^{++} ions are able to penetrate into the inner magnetosphere, although the fractional abundance in the inner magnetosphere is only about 0.001%.

Detailed investigations of the proton radiation belts in the MeV range have been published by Roussos et al. [2018a, 2016a, 2011]; Kollmann et al. [2017, 2015, 2013]; Armstrong et al. [2009]; Paranicas et al. [2010, 2008]; Buratti et al. [2018]. All studies establish how the protons belts are segmented by the icy moons of Saturn (Pandora, Prometheus, Janus, Epimetheus, Mimas, Enceladus, and Tethys) and the planet's main rings. They highlight interaction features with minor rings or ring arcs, such as those from Methone, Pallene, the G-ring, and the ringlets of the D-ring, most of which were unknown prior to Cassini. All studies established that the proton radiation belts inward of Tethys are disconnected from the short-term and large-scale changes that occur in the rest of the magnetosphere, and develop only over long time-scales due to the combined influence from variable particle transport effects and the solar cycle, with the former being much more important. The origin of those belts is attributed to CRAND, rather than to extreme solar wind transients, a possibility that was considered before Cassini. Transient extensions of these belts, outside Tethys, have been linked with certainty to the occurrence of Interplanetary Coronal Mass Ejections (CMEs) in the vicinity of Saturn [Roussos et al. 2008b, 2018c], one of the first direct demonstrations of space weather at an outer planet with in situ data.

The electron radiation belts in the MeV range have been studied in a series of papers by Roussos et al. [2018b, 2016a, 2014, 2006]; Paranicas et al. [2014, 2012, 2010]; Mauk et al. [2010]; Buratti [2019]. They are much more variable and longitudinally asymmetric than the corresponding proton belts, but on average they tend to increase monotonically in intensity inward towards the main rings at which point electrons get instantly absorbed. They evolve in time scales of weeks (as opposed to years for the protons) and are controlled by numerous factors, including the solar wind and internal magnetospheric dynamics. Interaction features of MeV electrons with material (e.g., scattering and energy loss in collisions with material) and moons have help to constrain radial transport rates in the magnetosphere and discover previously unknown ring arcs. The source population of the MeV electron belts is now believed to reside in the ring current (middle magnetosphere).

Between energies of tens of keV and few hundred keV, both electrons and ions are on average diminished significantly inward of the orbit of Tethys, due to interactions of these particles with the neutral cloud of Enceladus, the dust of the E-ring, or due to absorption by the moons [Paranicas et al. 2007; Kollmann et al. 2011; Carbary et al. 2009b; Kurth et al. 2006; Ye et al. 2016a]. The region between 5 and 9 R_S has been found to be dominated by transient population of interchange injection events, which have been analyzed in single case studies and statistically [Paranicas et al. 2010, 2008, 2007; Müeller et al. 2010; Mauk et al. 2005; Rymer et al. 2009b, 2008, 2007]. The results have been used to constrain the plasma corotation speed in the inner magnetosphere, the inward radial transport velocities of plasma, and assess the importance of interchange for energetic particle transport and acceleration with respect to other processes like diffusion. The inner magnetosphere is also dominated by energetic electron microsignatures (gaps

in the electron fluxes caused by electron absorption by Saturn's moons), which have been used to define the convective flows in the inner magnetosphere (a noon-to-midnight electric field) and radial diffusion rates [Paranicas et al. 2005; Roussos et al. 2018b, 2013, 2008a, 2007; Andriopoulou et al. 2014, 2012; Thomsen et al. 2012]. Statistically significant results on the angular distributions and energy spectra of electrons have been described for the first time in Carbary et al. [2011a, 2011b] and Clark et al. [2014].

In April 2017, the proximal orbits began, also called the mission Grand Finale. This enabled a comprehensive study of the proton radiation belt trapped approximately between the F-ring and A-ring. MIMI also found a previously unknown partial, transient electron belt within the F-ring, partial because it is only observed outbound at local noon, transient because it is very variable. These results are compiled in Buratti et al. [2019].

The LEMMS instrument discovered a previously unknown radiation belt collocated with the D-ring and extending up to the dense atmosphere of Saturn. This belt was predicted earlier [Kollmann et al. 2015], but its properties were unknown. It was found that the belt is dominated by protons up to the GeV range, which is the first time that such high energies were directly observed at any of the giant planets. Their pitch angle distribution is very steep, likely due to a strong interaction with Saturn's atmosphere. The suggested source is CRAND. There is no evidence for the presence of energetic electrons or ions heavier than protons. These results are compiled in Roussos et al. [2018c].

During SOI, Cassini remotely detected protons at tens of keV from low (atmospheric) altitudes [Krimigis et al. 2005]. The proximal orbits revealed that this was a huge coincidence since similar observations were only found once during the proximal orbits [Roussos and Kollmann et al. 2018], suggesting this this ion population is transient. Since the ions derive from ENAs produced in the magnetosphere, their intensity likely depends on the conditions in the magnetosphere. Because these ions were not observed in situ, they must be located at altitudes below 3800 km.

Saturn Science

High-order magnetic moments of Saturn

- **M_AO1:** Determine the configuration of the nearly axially symmetric magnetic field and its relation to the modulation of SKR.
- **MN1c:** Investigate magnetospheric periodicities, their coupling to the ionosphere, and how the SKR periods are imposed from close to the planet (3–5 R_S) out to the deep tail.
  - Determine what controls the SKR periods and whether there is a solar cycle and/or seasonal variation.
  - Investigate the coupling mechanism between the SKR periods and the internal rotation rate.

- Study whether the ionosphere and/or thermosphere is differentially rotating.
- Determine which hemispherical SKR period dominates other periodicities in the magnetosphere and whether this varies with time.

Numerous planetary magnetic field models have been developed over the time of the Cassini orbital mission at Saturn beginning with SOI [Dougherty et al. 2005]. Burton [2009] derived a model of Saturn's internal planetary magnetic field based on data obtained from the first three years of the mission, from July 1, 2004–July 1, 2007. Due to the uncertainty in the rotation rate, the model was constrained to be axisymmetric. In that analysis, one-minute averages of the vector magnetic field data obtained by the fluxgate magnetometer from all orbits within 10 R_S (1 R_S = 60,268 km). Data from 45 orbits were used in that study. The contribution of the eastward flowing ring current is known to be significantly close to the planet. Its contribution was modeled using the analytical expression derived by Giampieri and Dougherty [2004] based on the simple axisymmetric equatorial current sheet centered on the planet's equator, first described by Connerney et al. [1981]. The ring current magnetic field was modeled separately for the inbound and outbound legs of each orbit because the current sheet structure and characteristics are known to vary with local time [Arridge et al. 2008b] and temporal variations in the solar wind and magnetosphere are likely to occur over time scales corresponding to that of a periapsis pass (several days). The ring current field was modeled and removed from the data and standard generalized inversion techniques were used to model the magnetic field presumed to originate in Saturn's interior.

The contribution of the eastward flowing ring current is known to be significantly close to the planet.

The internal field model derived in that study was found to be quite consistent with previous models. An axisymmetric octupolar (degree 3) model was found to fit the data adequately based on an examination of the root-mean-square misfit or residual for each orbit. The spherical harmonic coefficients derived were g10 = 21,162, g20 = 1,514, g30 = 2,283. (Units are nano-Teslas (nT) and are based on a planetary radius of 60,268 km.) Saturn's magnetic was found to be offset northward by 0.036 Saturn radii, consistent with earlier Pioneer-11 and Voyager models. Reanalysis and comparison with data obtained by Pioneer-11 and Voyager-1 and Voyager-2 showed little evidence for secular variation in the field in the almost thirty years since those data were obtained.

A subsequent study [Burton et al. 2010] used data from the entire Cassini prime mission (through July 2008) and a methodology that differed in significant ways from the earlier modeling approach [Burton et al. 2009]. Only data obtained at radial distances closer than the L-shell of Enceladus (dipole L-value of 3.8) were used to derive the model. Measurements obtained by all Cassini fields and particles instruments had demonstrated that the structure and dynamics of Saturn's inner magnetosphere are governed by plasma created at Enceladus [Kivelson 2006]. The observed field at radial distances outside the orbit of Enceladus is modified by processes in the inner magnetosphere and does not necessarily reflect the magnetic field generated in Saturn's interior.

The approach to modeling the external ring current field also differed from the earlier modeling approach. As time went on our understanding of Saturn's magnetodisc had evolved and a simple symmetric ring current centered on the equator was no longer thought to an accurately representation. Instead the current sheet was found to be displaced from Saturn's rotational equator and to assume the shape of a bowl or basin, referred to as a magnetodisc [Arridge et al. 2008a]. Instead of modeling the external field as an oversimplified axisymmetric ring current as in Burton [2009], the internal plus external field was modeled using the standard spherical harmonic formulation and a single set of spherical harmonic coefficients was obtained that describes the internal and external field in a least squares sense. Accordingly, the axisymmetric model coefficients differ somewhat from the previous model.

In Burton [2010] an attempt was made to determine the planetary rotation rate by deriving a number of non-axisymmetric magnetic field models for a plausible range of planetary rotation periods and assessing the power in the non-axisymmetric components of the field and the root-mean-square misfit between the model and the data. The methodology is as follows. A presumed planetary rotation period was varied in 1 second increments from 10 hours 28 minutes to 10 hours 40 minutes and a pseudo-longitude calculated for each measured data point. A degree 3, non-axisymmetric magnetic field model was derived and the power in the non-axial magnetic field and the misfit were calculated. The underlying premise is that the planetary rotation period could be determined based on a peak in the non-axial power and minimum in the misfit. Although no such peak was identified unambiguously, the analysis did provide an upper limit on the extent of the dipole tilt. Based on the distribution of the non-axial spherical harmonic model coefficients for the range of rotation rates, a mean value for the dipole tilt was determined to be 0.03 degrees. The upper limit of all tilt angles was found to be 0.1 degrees.

The magnetometer team have developed the state-of-the-art internal magnetic field model for Saturn using Cassini magnetometer measurements prior to the Grand Finale, which placed the most stringent constraint to date on the tilt and secular variation of Saturn's intrinsic magnetic field [Cao et al. 2011]. The tilt of Saturn's dipole must be smaller than 0.06 degrees from the spin-axis of Saturn, and the time variation of Saturn's intrinsic magnetic field must be an order of magnitude slower than that of the Earth's [Cao et al. 2011]. These results are very challenging for dynamo theory, as Cowling's theorem excludes the possibility of a purely axisymmetric magnetic field being maintained by dynamo action.

The magnetometer team have also derived degree 4 and degree 5 internal magnetic moments for Saturn, albeit with relatively large uncertainties, from re-analyzing the Cassini SOI magnetometer measurements [Cao et al. 2012]. Based on these observational findings, we worked out the implications on helium rain inside Saturn [Cao et al. 2012, 2011]. These also provided the framework for our current analysis of the magnetometer measurements from the Cassini Grand Finale.

The latest Cassini Grand Finale gravity measurements indicate that the ~100 m/s zonal flows observed at the cloud deck of Saturn extend almost ten thousand kilometers into the planetary interior. Given that the electrical conductivity at such depth are high enough for significant MHD

effects, zonal flow magnetic field interaction in the semi-conducting region of Saturn is now a central issue in understanding the interior dynamics. On the theoretical side, we have developed a mean-field model for zonal flow magnetic field interaction in the semi-conducting region of Saturn [Cao and Stevenson 2017]. In this work, we proposed that the interaction between zonal flow and magnetic field in the semi-conduction region of Saturn would generate small-scale axisymmetric magnetic field that are spatially correlated with zonal flows [Cao and Stevenson 2017]. The amplitude of the wind-induced magnetic perturbations would depend on the amplitude of the deep differential rotation as well as the amplitude of the small-scale deep convective flow. Thus, measuring/constraining wind-induced magnetic perturbations along the Cassini Grand Finale orbits would place important constraints on the properties (profile and amplitude) of deep differential rotation and convective flow in the semi-conducting region of Saturn.

With magnetic field measurements at unprecedented proximity to Saturn by Cassini Grand Finale [Dougherty et al. 2018], we are working on deriving: i) non-axisymmetric internal magnetic moments of Saturn from Cassini Grand Finale magnetometer measurements, which can tell us about the deep interior rotation rate of Saturn and/or helium rainout and stable stratification inside Saturn; ii) small-scale axisymmetric magnetic features (e.g., high-degree axisymmetric internal magnetic moments) which can be used to constrain deep differential rotation inside Saturn; and iii) time variations in the internal magnetic fields, which would reveal characteristic time scale in Saturn's internal magnetic field and deep interior dynamics. These expected results would constitute the observational facts about the internal magnetic fields of Saturn for many years to come, which would further serve as tests for theories about giant planet interiors and have profound implications about giant planets outside the solar system.

Time varying modulation of SKR and associated PPO signals

- **M_AO1:** Determine the configuration of the nearly axially symmetric magnetic field and its relation to the modulation of SKR.
- **MN1c:** Investigate magnetospheric periodicities, their coupling to the ionosphere, and how the SKR periods are imposed from close to the planet (3–5 R_S) out to the deep tail.
  - Determine what controls the SKR periods and whether there is a solar cycle and/or seasonal variation.
  - Investigate the coupling mechanism between the SKR periods and the internal rotation rate.
  - Study whether the ionosphere and/or thermosphere is differentially rotating.
  - Determine which hemispherical SKR period dominates other periodicities in the magnetosphere and whether this varies with time.

Saturn's radio emissions started to be observed by Cassini/RPWS over the 10–1000 kHz range from distances of a few astronomical units. From late 2002 to early 2003, they were embedded in Jovian radio emissions and solar radio bursts. Their signal-to-noise ratio increasing with decreasing distance to Saturn, they became the dominant emission for the mid-2003 to mid-2004 preceding Saturn's orbit insertion. The most important and the most intense radio component is the SKR produced in the auroral regions. Several reviews of SKR properties have accompanied the Cassini mission [Kurth et al. 2009; Badman et al. 2015], the most recent one summarizing our current knowledge before Cassini Grand Finale [Lamy 2017].

The most important and the most intense radio component is the SKR produced in the auroral regions.

There are two important features of the SKR signal that we highlight here: 1) the SKR spectrum appears to be most intense when observed from the dawn-side at mid-latitude [Lamy et al. 2008; Kimura et al. 2013]. Southern SKR was predominant up to 2010-mid 2011 (slightly after the equinox of 2009), while the northern SKR was predominant after, consistent with a seasonal control of field-aligned currents driving auroral emissions by solar illumination of Saturn's ionosphere; and 2) the important feature of the SKR is that at the timescales of 11 hours (Saturn's rotation period), the emission is strongly rotationally modulated [Kurth et al. 2016, 2005; Clarke et al. 2005; Crary et al. 2005; Jackman et al. 2010, 2009a, 2005; Badman et al. 2016, 2008; Nichols et al. 2009; Lamy et al. 2013; Reed et al. 2018].

The remaining comments in this section concentrate on the modulation of the SKR.

Until the cruise phase of Cassini, the modulation of the SKR signal was taken to mark the rotation rate of the core of Saturn. Similar radio signals at Jupiter are clearly indicative of the rotation of the magnetic core of planet and therefore a similar interpretation was made for Saturn. Such magnetic rotation should theoretically be stable for planets as large as Jupiter and Saturn on a timescale not measurable by Cassini. However, the first SKR periodicity measured by RPWS witnessed a value differing by 1% to the SKR period identified from Voyager/PRA observations 25 years earlier [Gurnett et al. 2005]. Such a large variation implies that the SKR period does not probe the internal rotation rate. The measured SKR period was then found to display weak variations associated with those of solar wind speed [Cecconi and Zarka 2005; Zarka et al. 2007].

The major discovery brought by RPWS was the identification of two SKR periods [Kurth et al. 2008] corresponding to the two Kronian hemispheres, differing by ~1%. These periods were found to both vary with time in anti-correlation over yearly timescales and crossed closely after equinox, a trend which was interpreted as a seasonal driving of solar illumination [Gurnett et al. 2011a, 2010b, 2009; Lamy 2011], for example see Figure MAPS-32. These dual periods were later noticed in NB emissions and auroral hiss as well [Gurnett et al. 2010b; Ye et al. 2017, 2010] and more generally observed in numerous magnetospheric observables including magnetic oscillations, ENA emissions, aurorae [Mitchell et al. 2009b; Carbary et al. 2011a, 2010a; Nichols et al. 2010; Andrews et al. 2011, 2010a; Provan et al. 2011; Badman et al. 2012a, 2012b]. It is now accepted that these

dual rotational modulations all originate from two rotating hemispheric systems of field-aligned currents, whose origin may be atmospheric vortices [Jia et al. 2012].

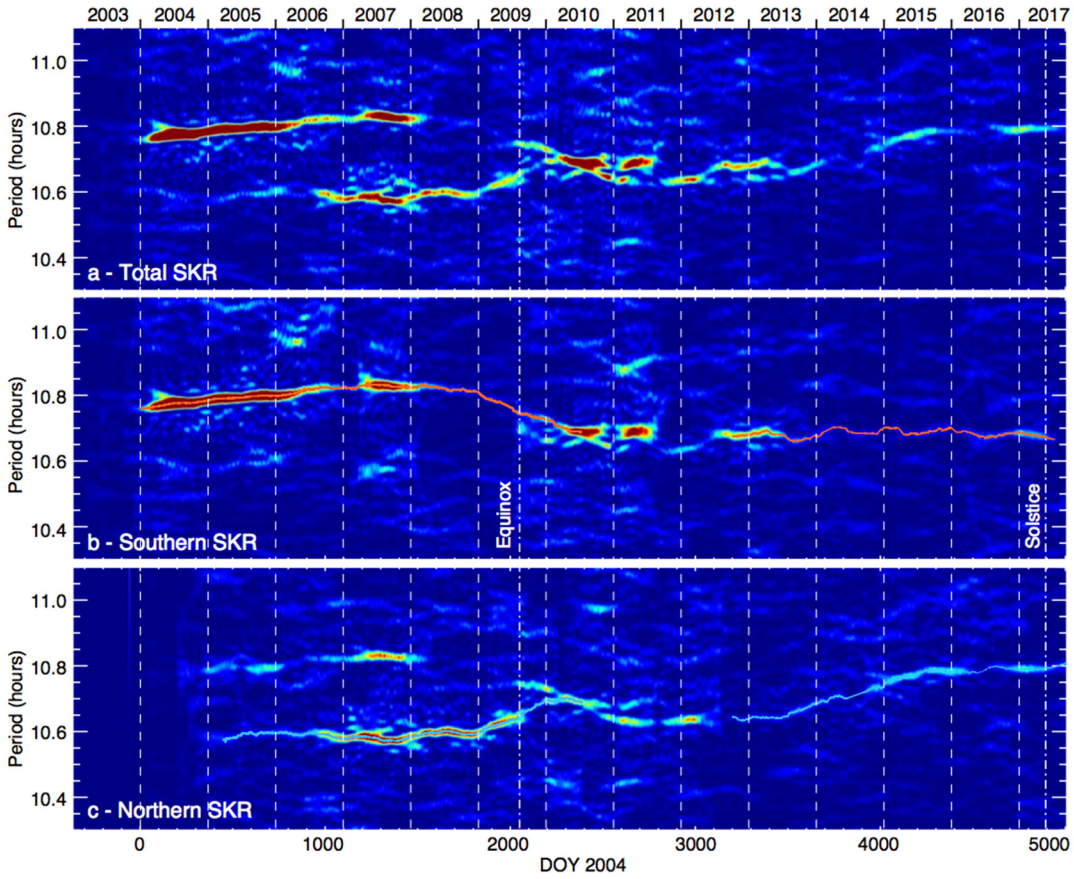

Figure MAPS-32. Lomb-Scargle periodograms of *Panel a*: total, *Panel b*: southern and *Panel c*: northern SKR flux density integrated over 100–500 kHz as a function of period and time from 2003-001 to 2017-258, extending of Lamy [2011] Figure 1. Southern and northern SKR were originally identified as LH and RH (X-mode) emission, excluding scarce intervals displaying ambiguous polarization measurements. The latter intervals were noticed to be more frequent at close distances and high latitudes which prevailed in the past two years. To improve the signal-to-noise ratio of *Panel b* and *Panel c*, southern and northern SKR were therefore identified as the total SKR signal observed beyond 10° latitude after days 2016-001 and 2016-180, respectively. Solid red and blue lines plot the southern and northern SKR periods derived by [Lamy 2011] from day 2004-001 to 2010-193, [Provan et al. 2016] from day 2012-278 to 2015-365 and tracked here from day 2016-001 to 2017-258. The latter will serve to build southern and northern SKR phases covering most of the Cassini mission.

This dual periodicity is not always detected, however, which may be a consequence of the observer location and/or its actual disappearance [Carbary 2016, 2014]. Single and dual periodicities were also observed in ENA fluxes detected by INCA [Carbary et al. 2014, 2008a; Carbary and Mitchell 2017]. INCA's global view of these periodicities revealed a local time dependence, namely, that one period might be detected at one local time but absent at another [Carbary et al. 2014]. Finally, the energetic electrons apparently have the same period (~10.8 h)

during the summer season when either the north or the South Pole tilts with respect to the direction to the Sun [Carbary et al. 2017]. This discovery, made possible by Cassini's solstice-to-solstice extension, has strong implications for the solar driving of these planetary periodicities. A complete review of Saturn's magnetospheric periodicities, as of 2013, appeared in Reviews of Geophysics [Carbary and Mitchell 2013], and should be consulted for the overall context within which particle periodicities can be placed.

The post-equinox period displayed a confused situation with poorly determined radio and magnetospheric periods. Over 2010–2012, they remained close to each other at locked phases, suggesting retro-interaction between both currents systems [Garnier et al. 2014], while sudden jumps of periods were tentatively attributed to Saturn's great white spot activity [Fischer et al. 2014] or to variable solar wind conditions [Provan et al. 2015]. Both periods eventually merged between mid-2013 and mid-2014 before crossing and diverging from each other after mid-2014 up to September 2017 [Provan et al. 2016; Ye et al. 2017, 2016b; Lamy 2017].

With the discovery that the SKR periodicity was not constant, the search for understanding began by all the MAPS instruments. Cassini observations have demonstrated the near ubiquity of oscillations near the planetary rotation period in essentially all magnetospheric plasma, field, and wave data despite the close axisymmetry of the internal planetary magnetic field. Due to the ubiquitous presence of these oscillations over most of the magnetosphere they were given the terminology PPO. Studying the PPO, with the goal to understand by the SKR period variation and the influence of PPO's on the magnetosphere has been a significant part of the Cassini mission.

Initial work on the magnetic PPOs established their basic properties, first confirming the rotational nature of the oscillations via the Doppler effect of the azimuthal spacecraft motion [Cowley et al. 2006], and second showing that while the perturbation fields in the equatorial region are quasi-uniform in nature [Andrews et al. 2010a], rotating in the equatorial plane as indicated by the earlier flyby studies, the fields at high latitudes are instead quasi-dipolar in form [Provan et al. 2009], associated with a rotating transverse dipole. The dipole moment is not internally generated by the planet, however, but by an external current system coupling the ionosphere and magnetosphere (see the section entitled Magnetospheric structure and convection). The PPOs are thus associated with a second large-scale current system, and, due to their ubiquitous nature, have proved to be a major aspect of the Cassini Magnetic Field Investigation throughout the mission. In addition, their imprint is seen more widely in the entire Cassini magnetosphere data set. It was shown that the radial distance of the dayside magnetopause and bow shock are also significantly modulated by this phenomenon [Clarke et al. 2010a, 2010b, 2006].

In the plasma data, the periodicities are clearest in the plasma sheet region. The density varies by more than an order of magnitude, depending on the SLS3 longitude [Arridge et al. 2008c]. This variability is likely due to periodic up-and-down motion of the plasma sheet. The temporal and spatial variations in plasma and field parameters are well organized by the flapping of the plasma disk about a periodically varying position [Arridge et al. 2008a; Szego et al. 2013, 2012, 2011; Nemeth et al. 2016]. Asymmetries in Cassini's periodic plasma sheet crossings [Thomsen et al. 2017b] are consistent with predictions of plasma sheet rocking and thickness variation made both

by the global MHD models that incorporate the effects of hypothesized atmospheric vortices [Jia and Kivelson 2012] and by the closely-related dual rotating current systems inferred from magnetic field observations, for example, Cowley et al. [2017] and references therein.

In the inner to middle magnetosphere, evidence was found for a plasma cam, in which the plasma density varies roughly sinusoidally with SLS3 [Burch et al. 2009; Goldstein et al. 2016] (see Figure MAPS-33). Theoretical arguments suggest that an asymmetric ring-current pressure coupled to Saturn's ionosphere can initiate a rotating two-cell interchange potential that is long-lived and stable [Goldstein et al. 2014]. Outflow from the dense sector was suggested as the driver of recurrent tail reconnection and plasmoid production (see sections entitled Plasma Loss Into The Magnetotail, and Magnetotail Configuration and Dynamics) inferred from periodic magnetic field variations in the tail [Burch et al. 2009], but subsequent authors argued that the field variations were more consistent with simple wave-like motion or periodic rocking of the plasma sheet rather than plasmoid formation [Jackman et al. 2009b]. In the more recent forward-modeling dataset of

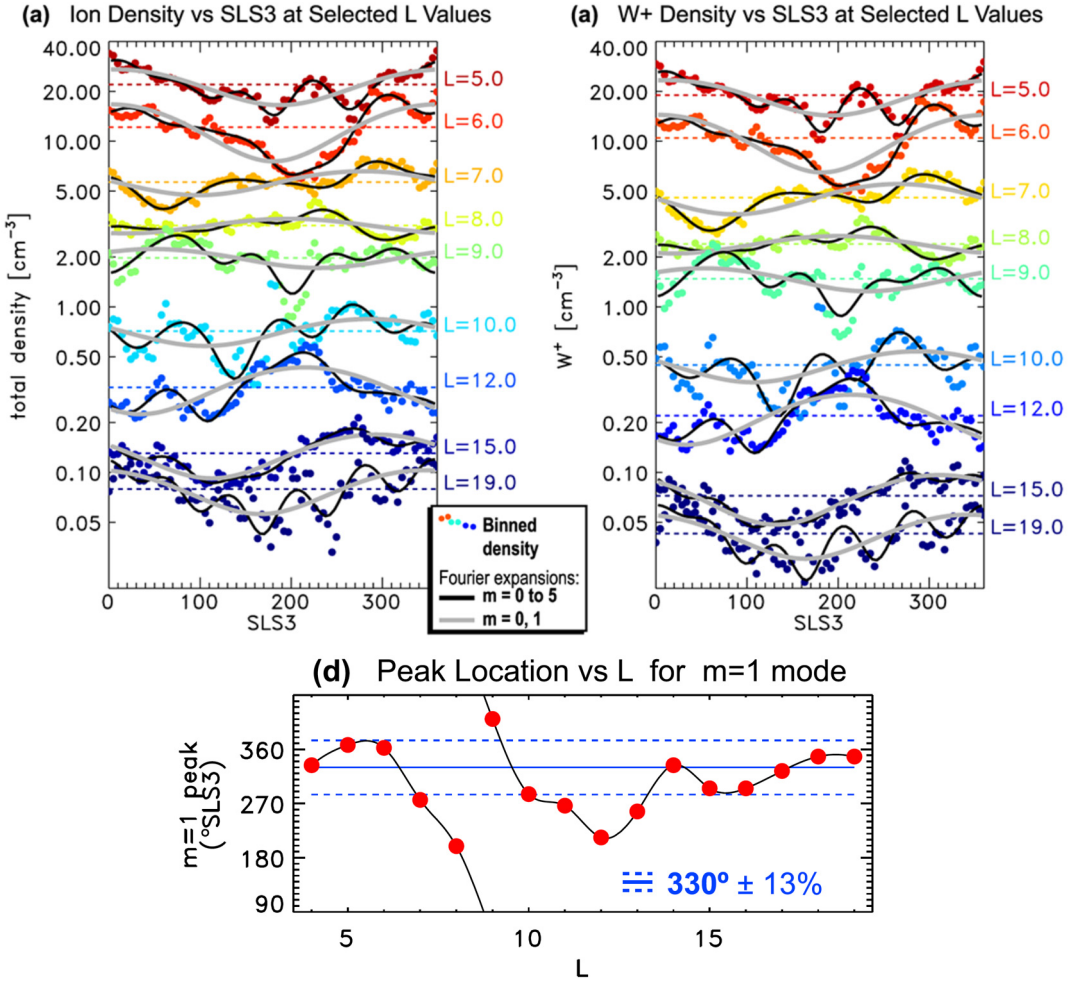

Figure MAPS-33. Evidence for the existence of a plasma cam, in which the density is generally highest in a particular SLS3 longitude sector. Figure from Goldstein et al. [2016].

ion densities [Wilson et al. 2017], the cam is not seen, so there remain questions about its existence and its consequences.

With the further realization, initially from SKR data, that two such oscillations are generally present with slightly different periods, one associated with the northern polar region and the other with the southern, it was shown that the phase jitter in the equatorial magnetic oscillations previously observed is due to the vector superposition of the two systems [Provan et al. 2011], while the polar oscillations were found to be pure northern and southern on the central polar field lines in the two hemispheres [Andrews et al. 2012]. Cassini data from the deeper tail passes in 2006 correspondingly showed that while the two tail lobes are modulated at their separate polar periods, mixed signals are again present within the plasma sheet that are associated with both north-south oscillations of the current layer together with significant modulations in its thickness [Provan et al. 2012; Szego et al. 2013; Nemeth et al. 2016, 2015]. A model of these PPO-related variations has been derived which provides a simple explanation of the sawtooth plasma sheet field variations observed during equinoctial conditions of near-equal northern and southern PPO amplitudes [Cowley et al. 2017; Thomsen et al. 2017a]. The model has further been successfully applied to the more northern-dominated conditions prevailing during northern spring [Cowley and Provan 2017].

With the additional realization that the two PPO periods slowly change with Saturn's seasons by ~ ±1% about ~ 10.7 h (i.e., ~ ±6 min), a long-term program of precise (~ ±10 s) measurement of the magnetic oscillation rotation period and phase has been carried out over the whole Cassini mission [Andrews et al. 2012, 2010b, 2008; Provan et al. 2018, 2016, 2014, 2013]. The results have subsequently been employed by many Cassini and HST teams as a framework to organize their data. The two PPO periods were found to be well-separated in late southern summer conditions at the beginning of the Cassini mission, ~10.6 h for the northern system and ~10.8 h for the dominant southern system, but then slowly converged with near-equal amplitudes to a near-common value ~10.7 h over a ~2 (Earth)-year interval centered near vernal equinox (August 2009) [Andrews et al. 2012]. There followed a ~3-year interval in early northern spring when the relative amplitudes changed abruptly at ~100–200-day intervals between southern and northern dominance and near-equal amplitudes [Provan et al. 2013], the southern period ~10.69 h remaining slightly longer than the northern ~10.65 h, before the periods of the two systems coalesced at ~10.70 h in antiphase during the first half of 2014 [Provan et al. 2016]. In mid-2014 the period of the then-dominant northern system began to increase towards ~10.8 h, similar to the southern system in southern summer, while the southern period remained near-fixed at ~10.7 h, thus leading to the first enduring reversal in PPO periods, northern longer than southern, during the Cassini era. The periods remained close to these values across northern summer solstice in May 2017 to the end of mission [Provan et al. 2018]. Possible physical origins of the post-equinox interval of abrupt changes have been discussed in terms of both atmospheric effects [Cowley and Provan 2013] and solar wind influences during the rising phase of the solar cycle [Provan et al. 2015], though clear causality remains to be demonstrated. An additional important theme of these studies has been the comparison of the magnetic field phases and periods with the related data derived independently by others from analysis of SKR modulations. Although some areas of contention

have been debated [Yates et al. 2015a, 2015b; Cowley and Provan 2016, 2015], the overall picture is one of good agreement [Andrews et al. 2012, 2011, 2010b, 2008; Provan et al. 2016, 2014].

The final proximal orbits have provided access to previously unexplored field lines crossing and inside Saturn's ring system. The behavior of the PPO oscillations on these field lines is presently under intense investigation.

Theoretical work [Southwood and Kivelson 2007] describes how a system of rotating field-aligned currents (cam currents) located on a magnetic shell in the range L = 12–15 would account for the periodicity observed in the magnetic field perturbations near the equator. Later it was shown that the interaction of the rotating cam currents would interact with the global magnetic structure of the magnetosphere to produce periodic variations of current intensity and account for the modulation of the power of SKR [Southwood and Kivelson 2009].

A series of papers elucidated how appropriately placed vertical flows in a rotating ionosphere drive field-aligned currents consistent with the cam current previously proposed. These rotating currents were shown to provide a quantitatively consistent description of all of the periodic dynamics reported in the system [Jia et al. 2012; Jia and Kivelson 2016; Kivelson and Jia 2014]. Theoretical work continues to best understand the origin of the two rotations rates [Southwood 2015, 2014, 2011; Southwood and Cowley 2014; Southwood and Chané 2016].

One important aspect of the PPO signal is to consider how reconnection fits into the bigger picture of global magnetospheric dynamics. Jackman et al. [2016] reported that, like so many other phenomena, tail reconnection at Saturn is organized by northern and southern magnetic phase. Events are specifically linked to current sheet thinning and outward displacement of field and plasma. Little evidence was found for visibility effects associated with the north-south motion of the plasma sheet.

One important aspect of the PPO signal is to consider how reconnection fits into the bigger picture of global magnetospheric dynamics.

Initial studies detected numerous reconnection-related events during the main Cassini tail exploration interval in 2006, namely planetward-travelling dipolarizations and tailward-travelling plasmoid structures, which were found to be related in timing to both the pulsing of the SKR emissions and the magnetic PPO phase [Jackman et al. 2016, 2009a]. Specifically, the events were found to be preferentially initiated during intervals when the PPO perturbations stretch the field lines radially outward from the planet and thin the plasma sheet leading to instability, especially when the two PPO systems act in this manner in concert, i.e., when they are near antiphase. Ongoing work is presently investigating dipolarization events and auroral storms during the sequence of proximal orbits observed just prior to end of mission.

The question of whether reconnection is linked to internal or external drivers is an important one, and one approach to exploring this is to examine the radio data which accompany the

magnetometer observations. Jackman et al. [2005b] explored concurrent IMF and SKR data from Cassini during SOI. They showed that the SKR intensified and extended to lower frequencies coincident with the arrival of a solar wind compression, while many other authors have also explored this strong link between the radio power (and frequency) and the nature of the solar wind.

Jackman et al. [2009a] explored the SKR in more detail, focusing on several case studies where reconnection had been observed in Saturn's magnetotail. In general, they found a good correlation between the timing of reconnection events and enhancements in the SKR emissions. A physical mechanism was put forward whereby reconnection increases the precipitation of energetic particles into the auroral zones, leads to the formation of a potential drop, and thus stimulates the motion of the SKR source region to higher altitudes along the field line (and hence lower frequencies of radio emission). These LFEs of the SKR were seen as strong proxies for dynamic solar wind compression and/or tail reconnection events.

Reed et al. [2018] attempted to automate the search for these LFEs in the SKR data and correlated 282 LFEs found during 2006 with a larger catalogue of reconnection events. LFEs were grouped into two categories, with short events of duration < 20 hours separated by a median waiting time of ~10 hours, and strongly correlated with the northern and southern SKR phases. Sixty percent of short LFEs have a reconnection event within the preceding six hours. The second category, long events, had duration > 20 hours, often lasting multiple planetary rotations and associated with increases in solar wind dynamic pressure.

Aurora and satellite footprints

- **MN1b:** Conduct in situ studies of Saturn's ionosphere and inner radiation belt.
  - Investigate the effects on aurora of solar wind and seasons.
  - Are there UV satellite footprints on Saturn? (like at Jupiter)
  - Is there a seasonal variation in auroral activity?
  - Investigate solar wind–ionosphere–magnetosphere coupling through the auroral regions.
  - Investigate whether there are UV satellite footprints on Saturn and whether there are Region 1 currents connecting the ionosphere and the magnetopause.
  - Investigate the composition of Saturn's ionosphere.
  - Study whether there is a significant polar outflow from Saturn's high latitude ionosphere and whether the outflow exhibits seasonal or solar cycle variation.
  - Determine whether there is a radiation belt between the D-ring inner edge and the atmosphere.

Cassini instruments have provided the first ever in situ measurements of the currents and particle populations that result in the Aurora and satellite footprints at Saturn. In addition to in situ measurements made by MAPS instruments, remote sensing images have been made by a range or Cassini instruments. This amazing set of Cassini data, together with a significant data from Earth-based observing platforms has resulted in a much more complete picture of the Kronian auroral processes. Fine structures of the aurora and nightside emissions have been revealed for the first time thanks to the observations acquired by the UVIS spectrograph on board Cassini. Spatial and dynamical characteristics of the complex pattern of auroral emissions at Saturn have been thoroughly described during the Cassini mission.

Previously observed with HST [Gérard et al. 2004; Grodent et al. 2005], the principal auroral component, so-called main emission, appeared through UVIS eyes as multiple substructures of various sizes. The dawn side of the main emission usually consists in a continuous narrow arc, rotating with the planet at approximately 70% of rigid corotation [Grodent et al. 2005]. This arc can get particularly bright during several hours while the emission rotates from midnight to noon, for example, Mitchell et al. [2009b]; Meredith et al. [2014]; Radioti et al. [2016]. Thanks to the combination between Cassini in situ measurements and auroral data, such a brightening has been associated with important magnetotail reconnection activity either induced by solar wind compression and closing magnetic flux [Cowley et al. 2005] or internally driven by stretching of the field lines in the nightside magnetosphere [Mitchell et al. 2009b; Radioti et al. 2016]. In both cases, the auroral intensification is produced by intense field-aligned currents on flux tubes moving from tail reconnection site to the dayside. Occasionally, these flux tubes could experience a blockage in the equatorial plane around noon local time, leading to the stagnation of the main emission dawn arc close to noon, as reported by Radioti et al. [2017a]. Furthermore, Yao et al. [2017c] surveyed Cassini-UVIS dataset, and revealed that transient auroral intensification near the noon local time is a systematic phenomenon, and proposed two potential mechanisms in driving such auroral phenomenon by analyzing simultaneous measurements from Cassini's magnetic field, plasma and auroral instruments.

In addition to the dawn arc, the main emission can exhibit isolated features of a few hundred kilometers wide which could be observed during the low-altitude orbits of Cassini. These individual spots have been tentatively interpreted as signatures of K-H vortices at the magnetopause [Grodent et al. 2011]. Alternatively, Meredith et al. [2013] argued that these spots might be produced by field-aligned currents of second harmonic ultra-low frequency (ULF) FLR waves propagating in Saturn's equatorial outer magnetosphere.

Furthermore, the main emission sometimes exhibits a localized brightening on the dayside which gradually gives birth to an extended arc-like structure rotating to the nightside with one extremity attached to the main emission while the other is moving towards the pole [Radioti et al. 2011; Badman et al. 2013]. These so-called bifurcations, together with an increase of the region threaded by open field lines (i.e., the polar cap), suggest that they are the signatures of dayside reconnection at the magnetopause, whereas the existence of magnetopause reconnection at Saturn was still subject of debate. Consecutive bifurcations and quasi-periodic brightening of an

individual bifurcation even suggest that such a dayside reconnection process can be pulsed [Radioti et al. 2013b, 2011; Mitchell et al. 2016].

Fixed in local time around noon, an auroral spot poleward of the main emission has been attributed to the auroral footprint of the cusp [Gérard et al. 2005, 2004; Palmaerts et al. 2016a; Kinrade et al. 2017] for which theoretical considerations connect it to high-latitude lobe reconnection [Bunce et al. 2005]. Thanks to extended UVIS observation time of Saturn's aurora, it has been shown that this polar cusp aurora can exhibit brightening with a periodicity of around one hour, indicative of a pulsed reconnection process [Palmaerts et al. 2016a]. In addition, Radioti et al. [2014] discovered a rare nightside auroral arc extending from the nightside main emission towards dayside, across the polar cap region. This polar arc is likely a tongue of closed flux tubes in the open field line region which appears during a period of enhanced tail reconnection combined with an absence of dayside reconnection.

Using the low-altitude UVIS observations during the Grand Finale phase of the Cassini mission, Radioti et al. [2017b] identified some auroral arcs which are azimuthally spread from high to low altitudes in the nightside sector. These arcs could be produced by plasma flows propagating from the outer tail magnetosphere toward the planet, akin to the terrestrial auroral streamers. Such plasma flows result from ballooning instability in the plasma sheet which has been shown to occur in Saturn's magnetosphere [Yao et al. 2017d].

Equatorward to the main auroral emission, two types of auroral structures can be encountered. The presence of a quasi-permanent partial ring of faint emissions mainly on the nightside sector has been established by Grodent et al. [2010]. These outer emissions are thought to be generated by an upward current layer carried by warm electrons detected by Cassini [Schippers et al. 2012]. Additionally, isolated transient auroral patches are occasionally observed along the equatorward edge of the dayside main emission. The combination of HST, in situ and remote Cassini observations, and simulations provided evidence that these spots behave as UV auroral signatures of energetic particle injections [Radioti et al. 2013a, 2009]. Furthermore, large-scale injections with strong corotation velocity gradients can give rise to spiral-shaped auroral features propagating from predawn to noon, as revealed by Radioti et al. [2015].

The combination of HST, in situ and remote Cassini observations, and simulations provided evidence that these spots behave as UV auroral signatures of energetic particle injections … .

During a coordinated auroral observing campaign on April 21–22, 2013, instruments onboard Cassini and the Hubble Space Telescope observed Saturn's northern and southern aurora while Cassini traversed Saturn's high latitude auroral field lines [Badman et al. 2016]. Signatures of upward and downward field-aligned currents were detected in the nightside magnetosphere, with the location of the upward current corresponded to the bright ultraviolet auroral arc seen in the auroral images, and the downward current region located poleward of the upward current in an

aurorally dark region. In the area poleward of the auroral oval, magnetic field and plasma fluctuations were identified with periods of ~20 and ~60 min. During April 11, the northern and southern auroral ovals were observed to rock in latitude in phase with the respective northern and southern planetary period oscillations. A solar wind compression impacted Saturn's magnetosphere at the start of April 22, 2013, identified by the intensification and extension to lower frequencies of the SKR. At this time a bulge appeared along the pre-dawn auroral oval, which appeared to have moved sunward when this region was next observed. The midnight sector aurora remained a narrow arc at this time. Subsequently, the post-midnight aurora broadened in latitude and contracted towards the pole. The motion in this sector was in the opposite direction to that expected from the planetary period oscillation. There was also an intensification of the auroral field-aligned currents. These observations are interpreted as the response to tail reconnection events instigated by solar wind compression, initially involving Vasyliunas-type reconnection of closed mass-loaded magnetotail field lines, and then proceeding onto open lobe field lines, causing the contraction of the polar cap region on the post-midnight sector.

During the same auroral campaign, Kurth et al. [2016] reports on the SKR measurements obtained during a Saturn auroral campaign carried out in the spring of 2013 which used multiple Earth-based observations, remote-sensing observations from Cassini, and in situ-observations from Cassini. Saturn kilometric radiation was remotely monitored nearly continuously providing a measure of the auroral activity and a means of understanding the temporal relationships between the sometimes widely spaced remote sensing observations of the auroral activity. While beaming characteristics of the radio emissions are known to prevent single spacecraft observations of this emission from being a perfect auroral activity indicator, a good correlation between the radio emission intensity and the level of UV auroral activity was observed, when both measurements are available, similar to what the previous studies had shown. Given the known influence of solar wind dynamics on both SKR intensity and auroral activity as discussed above, the SKR integrated power is also a proxy for solar wind activity. This study found that there is a good correlation between the 10 h averages of SKR power flux and the power estimated input to the aurora on the basis of the UV brightness, justifying the SKR as a simple proxy for auroral activity through the campaign. The SKR emissions also give evidence for a recurrent pattern of solar wind interaction with Saturn's magnetosphere, suggesting a two-sector structure and associated corotating interaction regions influencing the level of auroral activity on Saturn. But there are other SKR intensifications that may be due to internal processes.

Bunce et al. [2014] presented an unusual case in January 2009, where UVIS observes the entire northern UV auroral oval during a 2 h interval while Cassini traverses the magnetic flux tubes connecting to the auroral regions near 21 LT, sampling the related magnetic field, particle, and radio and plasma wave signatures. The motion of the auroral oval evident from the UVIS images was found to be consistent with the appropriate phase of the magnetosphere oscillations in the northern hemisphere, whereas previous interpretations have assumed a static current system. Concurrent observations of the auroral hiss (typically generated in regions of downward directed field-aligned current) support this revised interpretation of an oscillating current system.

Field-aligned current systems are at the heart of all aurora observed in the solar system. Large-scale field-aligned current systems which couple the magnetosphere to the planet's upper atmosphere, ultimately produce the auroral displays seen in, for example, UV images. As in other magnetized environments, field-aligned currents in Saturn's magnetosphere play a fundamental role in the transfer of momentum along field lines between the ionosphere, the magnetosphere, and (potentially) the solar wind. At their ends such currents close cross-field in association with j × B forces on the corresponding plasmas. Field-aligned currents further relate to the generation of bright discrete auroral forms at ionospheric heights, if current densities directed away from the planet exceed that which can be carried by the ambient precipitating magnetospheric electrons, at which point the latter are accelerated downward into the ionosphere by field-aligned voltages where they deposit their charge and energy. Initial theoretical expectations for Saturn related to meridional magnetosphere-ionosphere currents associated with the transfer of angular momentum from the planet's ionosphere to the net radially-outward transported equatorial plasma principally of Enceladus origin, i.e., the sub-corotation currents [Cowley et al. 2004], together with dawn–dusk asymmetries associated with the solar wind interaction [Jackman and Cowley 2006].

Observationally, field-aligned currents are detected and quantified via variations in the azimuthal magnetic field on high-latitude and relatively low-altitude passes across the planet's polar regions. The first such data were acquired by Cassini in 2006/2007, with simultaneous HST UV imagery on one pass confirming that Saturn's auroral oval indeed maps into a region of upward current requiring downward acceleration of the observed magnetospheric electrons [Bunce et al. 2008; Cowley et al. 2008]. An overall survey of these data showed that while their basic properties are consistent with theoretical expectations for subcorotation currents, with ~6 MA flowing down into the central polar ionosphere and the same return current flowing upward at lower latitudes in the auroral region, the currents are also modulated by the PPOs [Talboys et al. 2009a]. A much larger data set was then acquired in 2008 which allowed statistical studies to be undertaken [Talboys et al. 2011, 2009b]. It further allowed detailed exploration of the PPO dependence by comparing currents observed under conditions of differing PPO phase [Hunt et al. 2018b, 2015, 2014].

The principal PPO currents in a given hemisphere are found to be directed upward and downward on opposite sides of the planet's polar ionosphere and rotate around the pole at the PPO period of the corresponding hemisphere. They are also approximately co-located with the upward current region of the sub-corotation system, and of comparable strength, such that where the PPO current flows down, the total field-aligned current is reduced near to zero, while where it flows up the current is doubled, thus suggesting a dynamical connection. It is also found that the auroral region oscillates in latitude with amplitude ~1° in concert with these rotating modulations [Nichols et al. 2008; Provan et al. 2009; Hunt et al. 2014; Bunce et al. 2014]. A complementary multi-instrument study also established the typical locations of the boundary of open field lines in the two hemispheres at ~13° co-latitude in the north and ~16° in the south [Jinks et al. 2014], showing that the main PPO field-aligned currents flow just equatorward of this boundary on closed field lines. Correspondingly, inter-hemispheric coupling along closed magnetospheric field lines also occurs between the two PPO systems [Hunt et al. 2015; Provan et al. 2018]. Overall, the form of the PPO currents is consistent with driving by rotating twin-vortex flows in the two polar thermosphere/ionosphere [Hunt et al. 2014; Southwood and Cowley 2014].

Comparison between the 2008 data, obtained in the midnight sector, with the dawn-dayside data from 2006/2007 showed little difference, confounding expectations of observing long-term current asymmetries associated with the solar wind interaction [Hunt et al. 2016]. Highly unusual current distributions are observed in a small subset of passes, however, some of which have been associated with Saturn auroral storm solar wind compression events [Bunce et al. 2010]. Significant solar wind-related currents thus do flow in Saturn's magnetosphere at least intermittently. Indirect evidence of less dramatic solar wind effects have been obtained from HST studies of the dayside auroras (though not directly in field data), using Cassini as an upstream monitor of the IMF. Morphological auroral differences are found depending on the sense of the north-south component of the IMF, suggestive of dayside reconnection and related driving of flows and currents when the IMF points north [Meredith et al. 2014]. More generally, collaboration with colleagues at Moscow State University has resulted in the development of Saturn magnetospheric field models validated with Cassini data which incorporate ring/tail and magnetopause currents, and are also parameterized by the strength and direction of the IMF [Alexeev et al. 2006; Belenkaya et al. 2016, 2014, 2011, 2010, 2007, 2006]. These models have been used during intervals when Cassini was located in the solar wind measuring the impinging IMF to map auroral features observed by the HST along field lines into their magnetospheric source regions, namely the middle and outer ring current region typically at dawn, and to the vicinity of the open-closed field boundary for high-latitude emissions near noon.

While the 2006/2007 and 2008 high-latitude data sets both correspond to Saturn's late southern summer, a third interval of high-latitude data was obtained in 2012/2013 during northern spring [Bradley et al. 2018]. The PPO currents were found to be of similar form but somewhat weaker than in 2008, while the sub-corotation currents exhibited strong opposite seasonal asymmetries in the north and south Polar Regions, indicative of weak polar ionospheric conductivity in the winter polar cap. Investigation of the current signatures observed on the F-ring and proximal orbits spanning northern summer solstice at the end of the Cassini mission are currently ongoing [Hunt et al. 2018a].

Although Voyager radio data had previously demonstrated that SKR emissions are strongly positively correlated with solar wind dynamic pressure, the nature of the related magnetospheric dynamics remained unknown. This was partially revealed in early 2004 during Cassini approach to Saturn when an intensive HST campaign imaging Saturn's UV auroras was undertaken, with Cassini acting as upstream solar wind/IMF monitor. As expected during the declining phase of the solar cycle, the recurrent solar wind structure consisted of two corotating interaction regions (CIRs) per ~25-day solar rotation, exhibiting two few-day compression events of enhanced dynamic pressure, one major and one minor [Jackman et al. 2004]. The HST caught the impingement of the major compression region on Saturn's magnetosphere towards the end of the campaign, and observed a major increase in UV and SKR emissions with bright auroral forms extending throughout the dawn sector up to the planetary pole itself [Clarke et al. 2005; Bunce et al. 2006]. It was suggested that such auroral storms are caused by major bursts of compression-induced reconnection in Saturn's nightside tail, that inject hot plasma towards Saturn, which subsequently flows around the planet via dawn under the action of magnetosphere-ionosphere coupling [Cowley et al. 2005]. Estimates of the reconnection rate yielded associated voltages of at least several

hundred kV [Badman et al. 2005]. Monitoring of the interplanetary field prior to SOI showed that the same compression region would likely impinge on the system during the SOI fly-through of the magnetosphere [Jackman et al. 2005a, 2005b], and indeed did, with a corresponding magnetic dipolarization event, plasma energization, and enhanced SKR emissions being observed in the nightside magnetosphere on the outbound pass [Bunce et al. 2005]. Analysis of a larger number of compression events observed by Cassini acting as upstream IMF monitor during the approach phase, as well as outbound after SOI in late 2004, also showed characteristic enhancements in SKR, but with the regular pulsing at the PPO period generally being undisturbed in phase [Badman et al. 2008].

The passage of a moon through the magnetospheric plasmas of Jupiter, Saturn or the other giant planets is well known to create the potential for an auroral display at the footprint of the magnetic flux tube connecting the satellite and the planet's ionosphere. However, prior to Cassini all evidence of this process and of satellite footprints has been obtained at Jupiter. With the arrival of Cassini, the capability to perform coordinate in situ measurements yielded several new studies with the goal of observing the any such footprint if they existed. An initial study using a series of UV images of Saturn's aurora taken by the HST January 2004 and between February 2005 and January 2007 could not detect the faint auroral emission that would have been a signature of the Enceladus footprint [Wannawichian et al. 2008]. However, a follow-on study was able to report the detection of magnetic-field-aligned ion and electron beams (offset several moon radii downstream from Enceladus) with sufficient power to stimulate detectable aurora, and the subsequent discovery of Enceladus-associated aurora in a few per cent of the scans of the moon's footprint. The footprint varies in emission magnitude more than can plausibly be explained by changes in magnetospheric parameters, and as such is probably indicative of variable plume activity [Pryor et al. 2011].

Finally, using the spectra acquired by UVIS from 56 to 191 nm, it was possible to retrieve the characteristics of the energetic particles generating Saturn's aurora [Gustin et al. 2017, 2010, 2009]. Gustin et al. [2017] examined about 2000 FUV UVIS spectra to derive the mean energy of precipitating electrons for the different components of the aurora, using two different methods. The first one uses the absorption of the auroral emissions by hydrocarbons while the second one is based on the brightness ratio between the Lyman-α line and the total H_2 UV emission. Both methods give similar results with an average energy of the primary electrons ranging between 1 and 17 keV depending on the aurora component.

Composition of ionosphere and thermosphere

- **MN1b:** Conduct in situ studies of Saturn's ionosphere and inner radiation belt.
  - Investigate the effects on aurora of solar wind and seasons.
  - Are there UV satellite footprints on Saturn? (like at Jupiter)
  - Is there a seasonal variation in auroral activity?
  - Investigate solar wind–ionosphere–magnetosphere coupling through the auroral regions.

  - Investigate whether there are UV satellite footprints on Saturn and whether there are Region 1 currents connecting the ionosphere and the magnetopause.
  - Investigate the composition of Saturn's ionosphere.
  - Study whether there is a significant polar outflow from Saturn's high latitude ionosphere and whether the outflow exhibits seasonal or solar cycle variation.
  - Determine whether there is a radiation belt between the D-ring inner edge and the atmosphere.
- **MN2a:** Determine the coupling between Saturn's rings and ionosphere.
  - Study how field aligned currents are coupled to the rings and satellites.
  - Explore the dust dynamics in the proximity region.
  - Investigate the mid-plane of Saturn's D-ring.
  - Determine the grain composition in the proximity region.
  - Investigate the possible interaction of lightning with the inner magnetosphere and the rings.
  - Investigate Coupling Between E-ring and the Enceladus neutral and plasma tori.

Cassini was able to make unprecedented measurements of Saturn's topside atmosphere, neutral thermosphere and ionosphere. Some of these measurements were made possible by the Grand Finale orbits which dipped to the top of the atmosphere and allowed the first ever in situ measurements of Saturn's atmosphere and ionosphere.

Saturn Upper Atmosphere Major Findings (Neutral Thermosphere):

- INMS made first in situ measurements of Saturn's atmosphere, discovering the unexpected presence of several species of high mass neutrals, e.g., CH_4, CO, CO_2.
- The INMS made the first in situ characterization of the thermal structure in the upper atmosphere of Saturn, indirectly through its measurements of the H_2 densities.
- Helium has been measured for the first time in Saturn's upper atmosphere, providing constraints on possible deep-atmosphere mixing ratios of Helium and whether or not Saturn has a solar-like composition or something else.

During the Cassini Grand Finale, the INMS made an unprecedented series of measurements of Saturn's upper atmosphere during the proximal orbit phase, sampling from ~3500–1370 km altitude above the 1-bar pressure level. Prior to these orbits, it was anticipated that Saturn's upper atmosphere consisted primarily of H, H_2, with trace amounts of H_2O, and He. However, the INMS measurements revealed an atmosphere with an unexpectedly rich composition, containing significant amounts of organics spanning the entire mass range sampled by INMS, as seen in Figure MAPS-34. These results were completely unanticipated and they have effectively turned our understanding of the high-altitude thermosphere-ionosphere chemistry on its head.

In particular, INMS has identified methane, CH_4, as a significant component of the upper atmosphere of Saturn above 1370 km. As seen in Figure MAPS-35, INMS has found significant amounts of methane that reach up to ~10% of the composition near 3500-km altitude above the

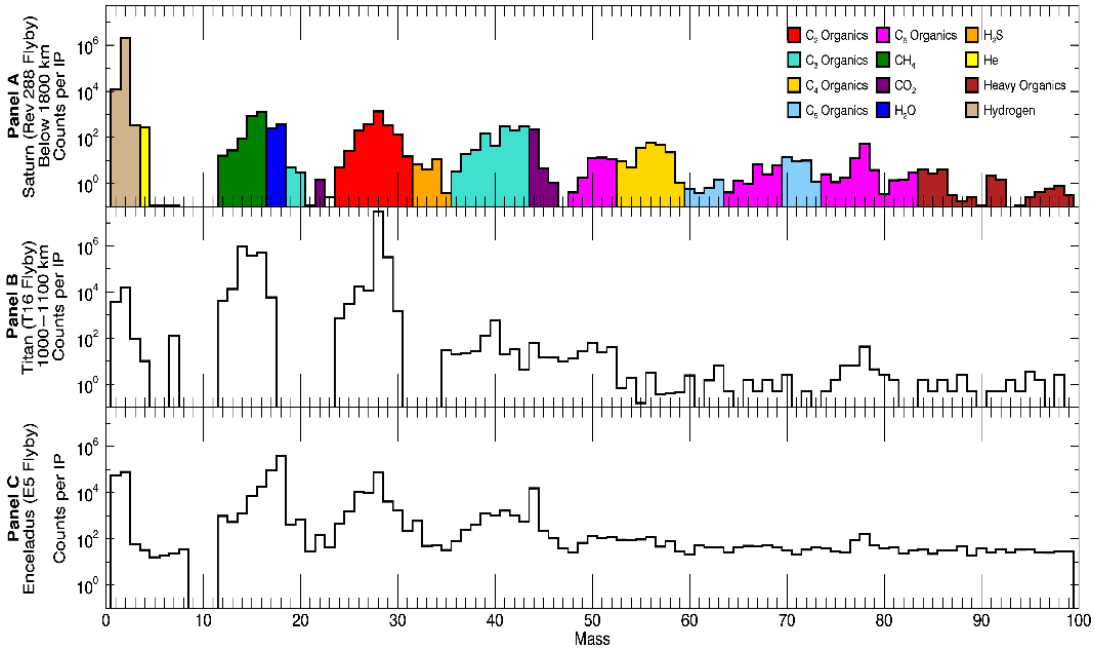

Figure MAPS-34. INMS Mass spectra from the Grand Finale orbits at Saturn (*Panel A*), compared with those of Titan (*Panel B*), and Enceladus (*Panel C*). Horizontal axis is in units of mass per charge.

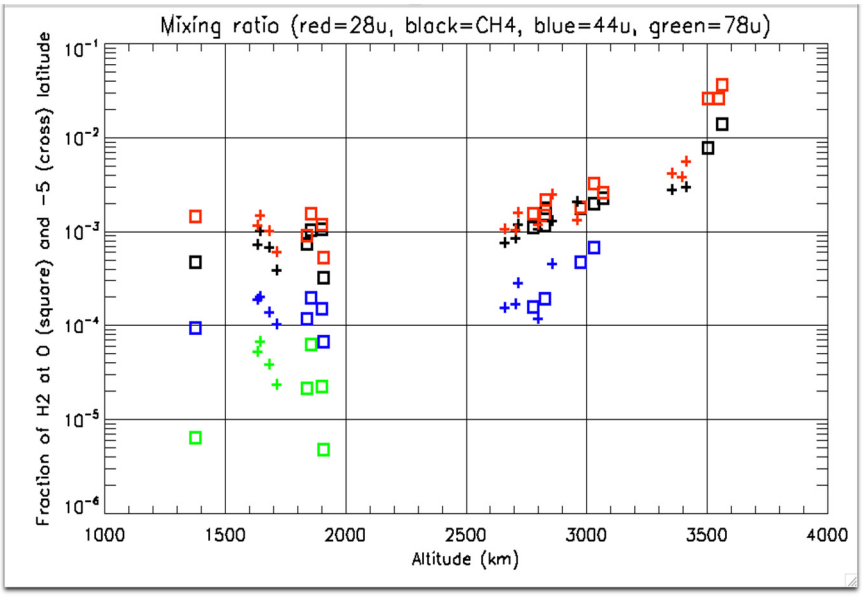

Figure MAPS-35. Volume mixing ratios (vertical axis) of the heavy species identified by INMS in the Saturnian upper atmosphere as a function of altitude above the 1 bar pressure level (horizontal axis).

1-bar pressure level. Additional heavy species (masses 28 u, 44 u, and 78 u) have also been identified. All of these species can potentially play major photochemical roles in the atmosphere of Saturn [cf. Moses and Bass 2000; Kim et al. 2014].

Using a combination of National Institute of Standards and Technology (NIST) data and calibration data collected using the refurbished engineering unit, preliminary fits to spectra at altitudes between 1700 and 1800 km for three representative orbits were made to identify contributing species. In general, the spectrum below ~70 u can be fit by a combination of species that is dominated by hydrocarbons. Ammonia (NH_3) is detected at 17 u. Other N-bearing species are neither excluded nor required by the spectra. The same is true for O-bearing organics. Inclusion of S species, especially H_2S, improves the fit of the spectrum. However, of the non-H_2, non-He material, less than 1 mol.% is contributed by S-bearing species. We estimate that between 30 and 50 mol.% of the non-H_2, non-He material measured by INMS is comprised of organics other than methane, which may constitute an additional 20 to 35 mol.%. C_4 species, including butane (C_4H_{10}) at 58 u, are particularly abundant compared to other hydrocarbons. Above 70 u, the spectra are consistent with contributions from heavier aromatic species, including species such as naphthalene ($C_{10}H_8$, 128 amu) with primary peaks that are beyond the range of INMS.

Other Cassini instruments, including the CHEMS from the MIMI, reported detections of heavy (8,000 to 40,000 amu) particles during the Grand Finale orbits [Mitchell et al. 2018, submitted]. To understand the relationship of these particles to INMS data, we compared the total amount of material detected by INMS to the particle sizes observed by MIMI. The results suggest that INMS may have mainly sampled smaller particles that were dominated by volatile and organic material with very little contribution from refractory mineral phases. The altitude-density profiles of these particles indicate very low densities, likely on the order of 0.1 g/cm^3 or less. These densities may be consistent with the densities of interplanetary dust particles from small bodies [Rietmeijer 1993]. Some masses, including 15 u (mainly from CH_4), 28 u (possibly N_2 or CO), and 17 u (mainly NH_3), have altitude-density profiles that are consistent with molecular radii. Other masses, including 58 u (possibly butane, C_4H_{10}) and 78 u (possibly benzene, C_6H_6), have profiles that suggest larger radii, on the order of nanometers or tens of nanometers.

In addition to the heavy species in the upper atmosphere of Saturn, INMS has also made the first in situ measurements of H_2, He, and H-D in the atmosphere of Saturn. Molecular hydrogen (H_2) is the dominant species in the thermosphere, and its density scale height reveals the expected background temperature of Saturn's upper atmosphere. Thus, measurements of H_2 reveal information about the thermal state of Saturn's upper atmosphere. Prior to the INMS measurements, only remote sensing observations were possible [cf. Koskinen et al. 2015; Vervack and Moses 2015], which provide temperatures through inversion techniques. The measurements in SIA3, however, provide the first-ever direct sampling of the Saturn atmosphere, allowing us to infer thermal structure from these measurements using models of the atmosphere, such as Müeller-Wodarg et al. [2012, 2006b].

Finally, there has been considerable uncertainty about the amount of Helium in the Saturnian atmosphere [Ben-Jaffel and Abbes 2015]. Helium abundances are key to determining the most

likely formation scenarios for Saturn's atmosphere. Currently, it has been suggested that Saturn would be depleted in Helium relative to Jupiter (~13.5% volume mixing ratio) or the protosolar value (~15.6%), due to Helium raining out in the lower atmosphere. The measurements provided by INMS, combined with diffusive modeling, can lead to constraints on the Helium content in the lower atmosphere, providing a missing component in our understanding of planetary evolution.

Saturn Upper Atmosphere Major Findings (Charged Ionosphere):

- INMS made repeated in situ measurements of Saturn's ionosphere, allowing the first determination of ion mixing ratios and number densities as well as their temporal variabilities.
- INMS measurements of the minor ion, H_2^+, represent a strong constraint on local ion production rates, providing a check on outer planet projections of solar irradiances.
- Combined with RWPS and MIMI measurements, INMS in situ data paint a clear picture of Saturn's equatorial ionosphere being dominated by heavy molecular ions that result from ring-derived material.

Prior to the Cassini Grand Finale, observations of Saturn's ionosphere were limited to altitude profiles of electron density (the presumed sum of the ion densities) at dawn or dusk, periods of rapid change in an ionosphere. Trace emissions from an expected major ion, H_3^+, were also detected, but column-integrated densities could only be derived at auroral latitudes. Therefore, ion densities throughout the majority of Saturn's ionosphere were based solely on model comparisons with radio occultation measurements, for example, Moses and Bass [2000]; Moore et al. [2010, 2006]. In situ measurements by INMS provided key constraints on the expected major ion species, H^+ and H_3^+, finally providing closure on a decades-long debate regarding the dominant chemical losses of H^+, for example, Connerney and Waite [1984].

In addition, INMS was able to measure the expected minor ion species H_2^+ and He^+. The chemistry of these ions is relatively straightforward, and the extremely short chemical lifetime of H_2^+ makes it an ideal marker for the in situ ion production rate. Therefore, H_2^+ densities from INMS measurements can be used to gauge the accuracy of commonly used projections of solar irradiances at Saturn. These projections rely on Earth-based data, and the assumption of a relatively stable solar irradiance over a period of days. Comparisons between measured H_2^+ with modeled H_2^+ based on projected solar irradiances find a ~50% discrepancy, implying that future outer planet modeling will require better estimates of the solar irradiance.

Finally, Cassini's high speed near periapse during the Grand Finale (~32 km s^{-1}), meant that INMS could only sample ions with mass up to 7 u. The sums of the light ions measured by INMS were found to be an excellent match with the electron density from RPWS at high altitudes (> ~2200 km), implying that Saturn's high-altitude ionosphere was charge-neutral and dominated by H^+ with minor contributions from H_3^+, as expected (Figures MAPS-36 and MAPS-37). However, at low altitudes the total ion densities from INMS differed significantly from the electron density.

This massive discrepancy could be interpreted as a signature of an ionosphere dominated by heavy (> 7 u) ions, which would be entirely consistent with the expected ion chemistry to follow from the ring-derived influx of complex neutrals measured by INMS.

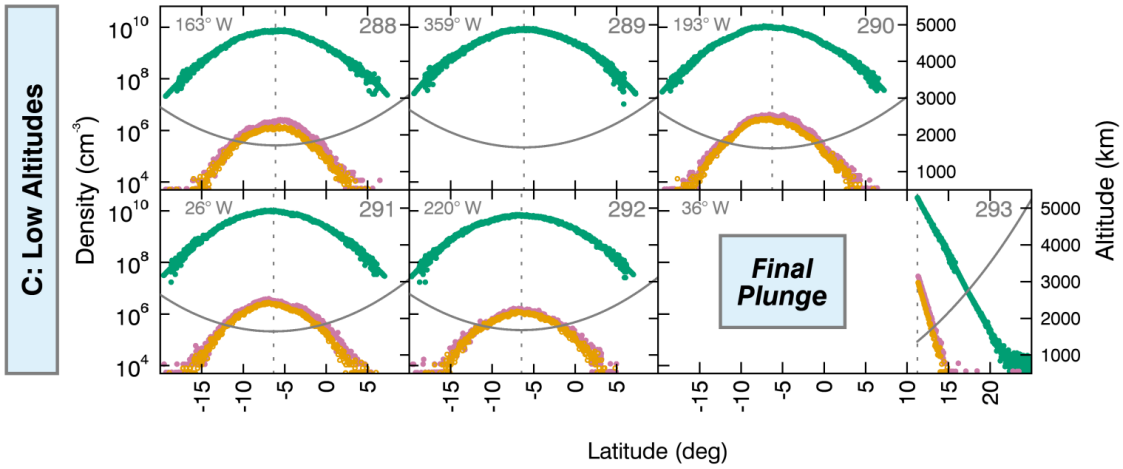

Figure MAPS-36. INMS measurements of H_2 (green), He (red), and Mass 3u (orange) as a function of altitude (right-hand axis) and latitude (horizontal axis).

Open Questions for Saturn System Science

Internal rotation rate and internal magnetic field of Saturn

- What is the rotation period of Saturn? How do the multiple, variable magnetospheric periods observed in radio, magnetic fields, energetic particles, plasma, aurora, and other phenomena tied to the internally-generated magnetic field at Saturn?
- How are the observed periodicities related to the actual rotation of Saturn, and does it matter? Most investigators agree that the observed periods of Saturn, which are generally magnetospheric in nature, do reflect the true rotation of the planet, and that such periods are probably slower than the real rotation period, which may be intimated from the planet's oblateness, see Helled et al. [2015] and references therein. If Saturn is a differential rotator, such as the Sun, then, indeed, the period may be ephemeral and not meaningful, for example, Dessler [1985].
- What are the implications of the extremely axisymmetric planetary magnetic field for the internal structure of Saturn? What is the dynamo process generating this planetary field?

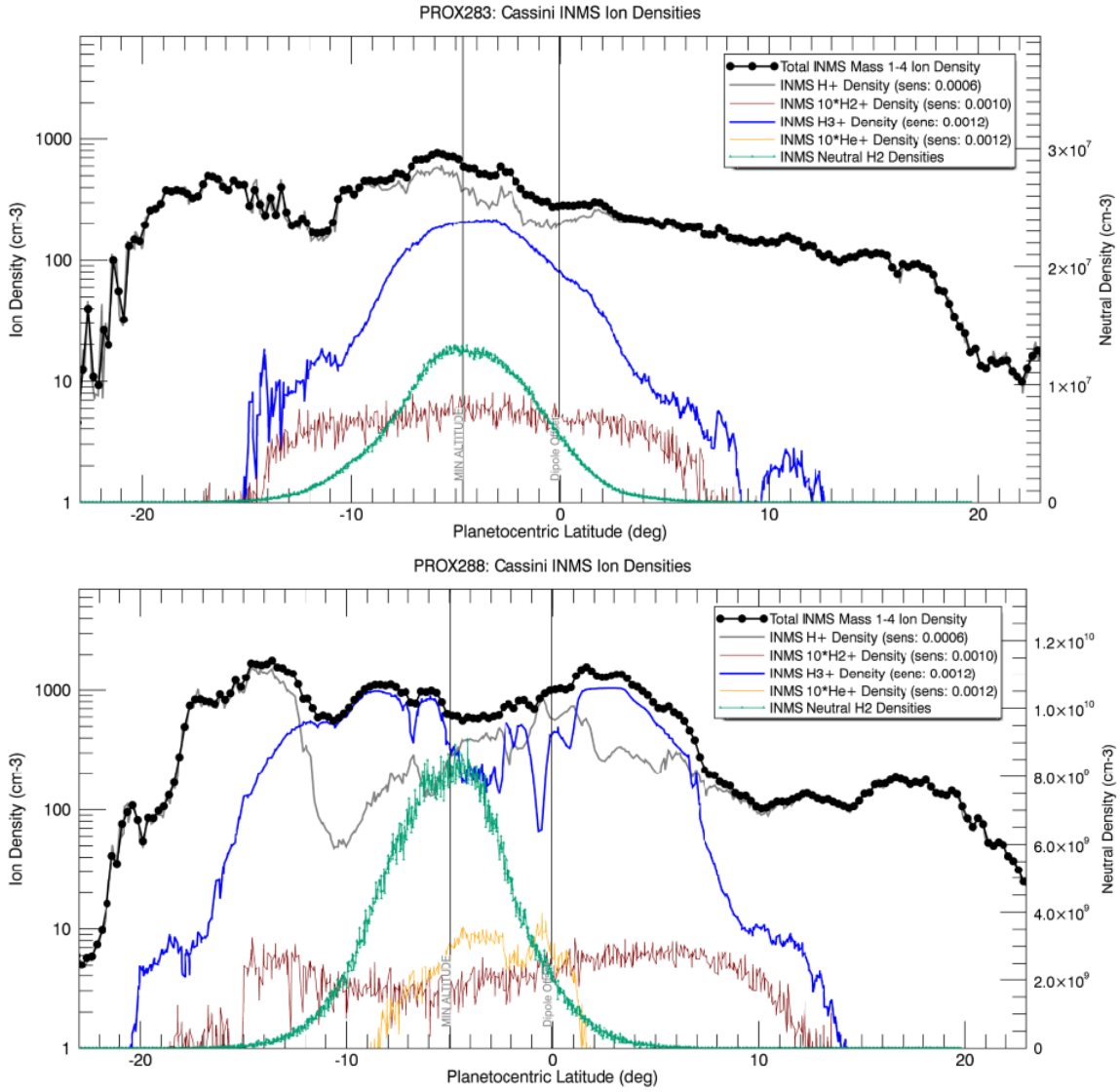

Figure MAPS-37. INMS measurements of H_2 (green), H^+ (gray), H_2^+ (red, multiplied by 10), H_3^+ (blue), He^+ (gold, multiplied by 10), and total light ion density (1–4 u, black) as a function of planetocentric latitude (horizontal axis). Ion measurements were taken for four proximal orbits, 283, 287, 288, and 292, though only one representative high altitude (283, *Top panel*) and low altitude (288, *Bottom panel*) orbit is presented here.

Rotational modulation in axisymmetric configuration

- Given the extraordinarily axisymmetric magnetic field, why are there such prominent rotational PPO modulations in Saturn's magnetosphere?
- What is the underlying cause of Saturn's periodicities? The current thinking is that the periodicities are related to disturbances, possibly vortices, in the upper polar atmosphere or lower ionosphere. The periodicities are not thought to arise in the

magnetosphere, although the magnetosphere probably provides a linkage, via field-aligned currents, between periods in the north and the south.

- How are the PPOs driven in the atmosphere, thermosphere and ionosphere of Saturn?

How are mass and magnetic flux transported in the middle and outer magnetosphere?

- Where and how does the magnetosphere unload its cold, dense plasma?
- How is plasma transported outward, and magnetic flux returned, in the region between 12 and 20 to 25 R_S?
- What is the connection between large-scale and small-scale injections at Saturn? How much material do injections transport relative to radial diffusion? What drives radial diffusion?
- What is the relationship between large-scale, tail-reconnection-driven injections and small-scale interchange injections?
- What determines the scale size and inflow speed of interchange injections? What determines the apparently variable rate and depth of such injections?
- Are the growth of the K-H instability and magnetic reconnection coupled?
- Where in the Saturnian system does Vasyliunas-type reconnection take place, and where does Dungey-type reconnection take place? Is there a region in Saturn's magnetosphere where one or the other dominates?

Solar wind control of the Saturnian magnetosphere

- What is the dominant mode of solar wind interaction with the magnetosphere, the viscous interaction or the large-scale reconnection interaction?
- How does the solar wind drive magnetospheric dynamics at Saturn? Is solar wind dynamic pressure the primary influence?

Neutral particle dominated Saturnian magnetosphere related to difference if compared to Jupiter?

- How does the abundant neutral population in Saturn's magnetosphere make it different from fully or mostly ionized magnetospheres?

Very limited plasma measurements in auroral acceleration and source region of related SKR

- What is the predominant form of the electron distribution function at the source of SKR?

Understanding the Enceladus plume-magnetosphere interaction

- What are the various populations of charged dust and molecules that balance charges in dusty media such as in the plumes of Enceladus and in Saturn's topside equatorial ionosphere?
- In the Enceladus plumes, the 28 u species measured during CSN operations is a fragment of a larger molecule. The identity of the larger molecule and of the 28 u fragment would help constrain the chemistry in the subsurface oceans of Enceladus. Similarly, the highly abundant 28 u neutral measured in Saturn's inner magnetosphere could be CO, N_2, or a fragment of a heavier molecule, and none of these is consistent with CAPS observations or with the Enceladus plume composition.
- How are heavy negative ions formed in the plume at Enceladus, and what is their contribution to nano-grain formation?

Composition of the negative ions at Titan and > 100 amu positive ions

- What are the detailed process that create the large ions and the negatively charge ions in Titan's upper atmosphere and ionosphere?

MAPS DWG Non-Saturn Science Results

Cruise-specific Science

Solar wind from Earth to Saturn

- **C_AO1:** Extend the sensitivity of composition measurements of interstellar ions by approximately three orders of magnitude.

The Cassini spacecraft obtained gravity-assists at Earth (August 1999) and Jupiter (December 2000–January 2001) arriving at Saturn July 2004. This extensive time spent in the solar wind allowed Cassini to make measurements that could be used, together with Galileo and Ulysses measurements, to better understand the evolution of the solar wind outward in the solar system.

During the cruise to Saturn the MIMI suite was able to make unique measurements of heliospheric suprathermal particles in the 2–60 keV/nuc range. There has never been an

investigation with species separation of this important class of particles, which ties the solar wind plasma to the energetic particles, beyond Jupiter. Hill et al. [2009] made CHEMS measurements that revealed that the radial intensity profiles of He^{+} and He^{++} are very different from both analytical and numerical theory, with the observations showing an increasing intensity with distance from the Sun, while the theory predicts the intensity should fall. This observation remains unexplained.

During same time period, the CAPS investigation made the first in situ observation of interstellar pick-up ions beyond the orbit of Jupiter. This was the first direct detection of mass-resolved interstellar pick-up ions, and confirmed the existence of helium focusing at these distances. Focusing of helium atoms at these distances is caused by the solar gravitational field (Figure MAPS-38). CAPS also made the first direct, in situ, measurements of a large shadow in the interstellar hydrogen population downstream from the Sun caused by motion through the interstellar medium [McComas et al. 2004]. The shape of the measured distribution function of the observed He+ as a function of energy was characteristic of a pick-up distribution with a flat top and cut off at about four times of the solar wind energy.

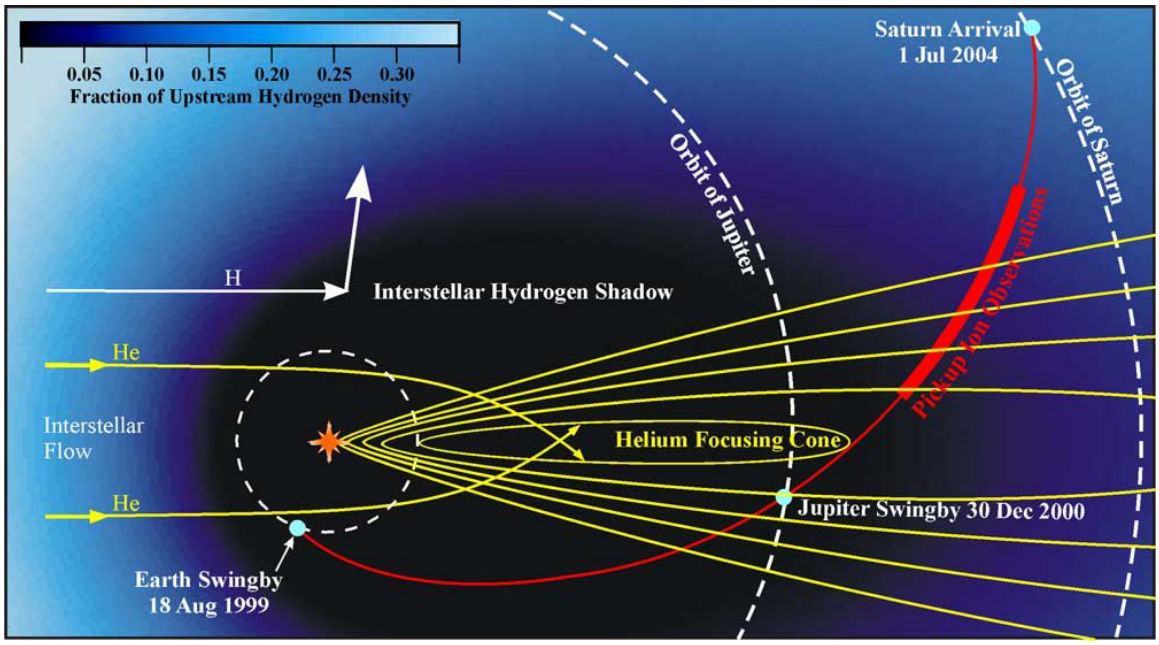

Figure MAPS-38. Schematic diagram of Cassini's trajectory between Earth swing-by and arrival at Saturn. Pick-up ion measurements were made between 6.4 and 8.2 AU (heavy line) as Cassini emerged from the down-stream direction. Simulation results show: i) the gravitational focusing of interstellar He in contours of 5/3, 2, 7/3, 8/3, and 3 times the upstream He density; and ii) the color-coded H density as a fraction of the interstellar value. The dark region downstream from the Sun is the interstellar hydrogen shadow. Figure from McComas et al. [2004].

CHEMS measurements of pick-up ions were used to determine solar wind speeds, which enabled a study [Hill and Hamilton 2010] of the spectral index of suprathermal particles. The slopes of the spectra were reported and widely put into and used to create context by the community, but Hill and Hamilton [2010] showed that the expected velocity v dependence was approximately v^{-5}

as reported by Fisk and Gloeckler [2008]. The solar wind speeds themselves are of inherent value for investigating the heliosphere and, near Saturn, as an input to magnetospheric studies. In 2014, data from 2001 to 2004, inclusive, at a 12-hour cadence, were published on the Cassini project's MAPSview website: [http://mapskp.cesr.fr/index.php].

The energetic particle population was further studied by Lario et al. [2004] using LEMMS observations. They found that intensity enhancements up to ~1 MeV were due to the passage of interplanetary shocks while at the highest energy (> 25 MeV), the prompt component of solar energetic particle events was responsible. For all but the largest SEP events the presence of magnetic field structures between the Sun and the spacecraft significantly modulates the intensity enhancements.

In addition to the measurements Cassini MAPS instruments made of solar system plasmas and neutrals, the RPWS instrument was able to make measurements of nanograin dust. During the flyby of Jupiter, Meyer-Vernet et al. [2009] reported wave measurements that corresponded to observations of nanograin dust streams moving at the solar wind speed made by the Cassini dust sensor. The result is the first wave detection simultaneous with a conventional detection by a dust analyzer attributed to nanoparticles. Following this detection, RPWS data from the cruise phase (between 1–5 AU) was analyzed in more detail. Schippers et al. [2015, 2014] analyze the low frequency bursty noise identified in the Cassini radio and plasma wave data during the spacecraft cruise phase and find the magnitude, spectral shape, and waveform of this broadband noise are consistent with the signatures of the nanoparticles that traveled at solar wind speed and impinged on the spacecraft surface. Nanoparticles were observed whenever the radio instrument was turned on and able to detect them at different heliocentric distances between Earth and Jupiter, suggesting their ubiquitous presence in the heliosphere. Analysis of the radial dependence of the nanodust flux with heliospheric distance and found that it is consistent with the dynamics of nanodust originating from the inner heliosphere and picked-up by the solar wind. The contribution of the nanodust produced in the asteroid belt appears to be negligible compared to the trapping region in the inner heliosphere. In contrast, further out, nanodust is mainly produced by the volcanism of active moons such as Io and Enceladus.

Due to a fortuitous alignment of the Earth and Jupiter during the Cassini Jupiter flyby Hanlon et al. [2004] were able to study the evolution of an interplanetary mass ejection during solar maximum. The pre-Jupiter data set reveals clear and numerous transient perturbations to the Parker Spiral solar wind structure typical of solar maximum. The limited plasma data is available at Cassini due to instrument pointing restrictions and this renders the identification of the nature of such structures ambiguous. However, the alignment of Jupiter and Earth during this encounter allowed the tracing of these structures back to those observed by the Wind spacecraft near the Earth. Of the phenomena that are satisfactorily able to

Due to a fortuitous alignment of the Earth and Jupiter during the Cassini Jupiter flyby Hanlon et al. [2004] were able to study the evolution of an interplanetary mass ejection during solar maximum.

trace back to their manifestation at 1 AU, two are identified as being due to interplanetary coronal mass ejections. One event at Cassini is shown to be a merged interaction region, which is formed from the compression of a magnetic cloud by two anomalously fast solar wind streams. The flux-rope structure associated with this magnetic cloud is not as apparent at Cassini and has most likely been compressed and deformed.

Other Non-Saturn System Science

Interstellar neutrals and the Heliotail

- **C_AO1:** Extend the sensitivity of composition measurements of interstellar ions by approximately three orders of magnitude.
- **J_AO4:** Obtain the first high-resolution images of the Io torus.

The Sun's atmosphere is not static but expands in the form of a magnetized fluid called the solar wind [Parker 1958], reaching to distances of potentially hundreds of Astronomical Units (1 AU = 1.5 × 10^8 km), shaping our local bubble, called the heliosphere, through its interaction with the Local Interstellar Medium (LISM). Voyager 1 and Voyager 2 (hereafter, V1 and V2) crossed the termination shock, where the supersonic solar wind presumably terminates at the shock front, at respective distances of ~94 and ~84 AU in 2004 and 2007 at +35° and −26° ecliptic latitudes [Decker et al. 2008, 2005], pinpointing both the—previously unanticipated—size of the local heliosphere and the scale of the heliospheric asymmetry.

After the discovery of the reservoir of ions and electrons that constitute the heliosheath (a region past the termination shock), V1 passed through an unexpected depletion region, where a decrease in ions of solar origin (by a factor of ~10^3) and a simultaneous increase of high energy cosmic rays (~9.3%) occurred, that forms part of the interface between the solar plasma and the galaxy, namely the heliopause [Krimigis et al. 2013], at a distance of ~122 AU. Since August 2012, V1 has continued its journey to the galaxy, measuring the distant and unexplored LISM (V1 is currently located at a distance of ~19 AU past the heliopause), while V2 is still surveying the heliosheath (expected to cross the heliopause in the next few years). Due to the powerful synergy between in situ ions from V1/LECP (Low Energy Charged Particle) instrument and ENAs from INCA (in overlapping energy bands), MIMI, beginning in about 2009, has made key discoveries that altered our past notions on the formation and interactions of the heliosphere, leading to a number of surprises concerning the physics that governs this enormous system, and providing insights on the plasma processes at ~100 AU that were substantially at variance with previous theories and models.

In 2009, an important paper by the MIMI team [Krimigis et al. 2009] showed, for the first time, images of the global heliosphere using > 5.2 keV ENA measurements obtained with INCA over the 2003–2009 time period, and identified two striking, previously unexpected, heliospheric signatures: i) the Belt, a broad band of emission in the sky, identified as a high intensity, relatively wide ENA region that wraps around the celestial sphere in ecliptic coordinates, passing through the nose the anti-nose (tail) and the north and south heliosphere poles; and (ii) the basins,

identified as two extended heliosphere lobes where the ENA minima occur. Interestingly, the ENA measurements are moderately well organized in galactic coordinates, with the Belt presenting a prominent tilt of ~30° with respect to the galactic equator, whereas the Basins were found to roughly coincide with the galactic north and south poles, although their boundaries were also tilted ~30° to the galactic equator. The same science issue hosted yet another significant publication (with contribution from the then-MIMI PI, Stamatios M. Krimigis), from the Interstellar Boundary Explorer team [McComas et al. 2009], showing, for the first time, images of the heliosphere in < 6 keV ENAs. A narrow bright ENA stripe known as the ribbon forms an incomplete circle around the heliospheric nose, most prominent at ~1.1 keV, surrounded by a broad ENA emission that became known as Globally Distributed Flux (GDF).

In a later publication, Dialynas et al. [2013] found that the deviation of the ENA emissions from the equator is effectively minimized in a rotated frame (interpreted interstellar magnetic field frame (ISMF)) where its north pole points toward 190° ecliptic longitude and 15° ecliptic latitude. The ENA spectra showed a power-law form in energy, presenting higher spectral slopes in the belt region and lower outside ($3.4 < \gamma < 4.4$), which are almost indistinguishable between the tail and the nose regions, i.e., no noticeable asymmetry was observed. Notably, the morphology of the belt (peak, width, and structure) is nearly energy independent of energy from 5.2 keV to 30 keV. The authors speculated that Interstellar Boundary Explorer (IBEX)-GDF evolves with increasing ENA energy to form the belt at high GDF energies, explaining that the GDF and the ribbon are distinct features that originate from different source plasma populations (heliosheath and outside the heliopause, respectively). This was recently confirmed by the IBEX team [McComas et al. 2017].

Taking into account the local partial pressure over the $\sim 5 < E < 4000$ keV energy range from V1, V2 and INCA (~ 0.1 pPa), an assumed thickness of the heliosheath (~50 AU) and the simulated pick-up ions (PUI) distribution [Giacalone and Decker 2010] that was used to estimate the $E < 6$ keV contribution (~0.12 pPa), Krimigis et al. [2010] concluded that there is a need for a substantially stronger magnetic field upstream of the heliopause than assumed before, in order to balance the non-thermal PUI pressure against the stagnation pressure of the interstellar plasma and the local ISMF at the heliospheric nose. The interstellar magnetic field was estimated to be ~0.5 nT and have an upper bound of ~0.64 nT. This calculation was confirmed a few years later after V1 crossed the heliopause and measured a strong interstellar magnetic field of ~0.5 nT [Burlaga et al. 2013] that exhibited a jump right outside the heliopause of ~0.6 nT. V1 is currently located at ~19 AU past the heliopause and still measures a magnetic field of ~0.5 nT, Burlaga and Ness [2016], and a relatively dense plasma of > 0.09/cm^3 that reached densities of ~0.12/cm^3 [Gurnett et al. 2015, 2013].

A different study, Dialynas et al. [2015] analyzed separately INCA images of the heliosphere and found that the very low (basin) and high (tail) ENA emissions in the heliosheath are separated with a relatively smooth boundary (called transition region), with a spatial width of ~30° in ecliptic longitude, which no theory had predicted to date. The ENA intensity gradient in this transition region was found to be almost invariant as a function of both ecliptic latitude and energy, with an average value of ~2.4% per degree and translates to a corresponding partial pressure gradient that occurs in the transition region, enabling a discussion on the Parker field towards the tail. Bearing in mind

that the plasma-β inside the heliosheath showed large fluctuations about an average of ~5–10, i.e., much larger than unity [Decker et al. 2015], this pressure gradient is possibly not consistent with a tail magnetic field configuration that is similar to the measured magnetic fields by the Voyagers in the nose hemisphere. Notably, the pick-up ion populations in the keV range play a dominant role in maintaining the pressure balance in the heliosheath.

In the pre-INCA imaging era, the size of the heliosphere had been estimated using several different models, where the heliosheath varied between 70 and 160 AU. By combining Voyager in situ ion measurements and remotely sensed INCA ENAs in overlapping energy bands, Krimigis et al. [2010, 2009], calculated that the heliosheath thickness should be ~54 (+30, −15) AU. A more detailed analysis performed by the MIMI team, included also the possible contributions from the Compton-Getting effect due to the radial velocity of the heliosheath plasma and concluded that the heliosheath appears to be twice as thick along the V2 line-of-sight (LOS) as it is along the LOS to V1: L_{V1} = 31(+31, −18) AU and L_{V2} = 71(+30, −15) AU [Roelof et al. 2012]. A breakthrough on this came in 2011, when the MIMI and Voyager teams published a brief report [Krimigis et al. 2011] showing that the radial component of the bulk plasma velocity had been decreasing almost linearly for three years, from 70 km/s to 0 km/s, and then it stabilized around this value for ~8 months. This study concluded that the ENA and ion spectra could be brought into agreement at V2 with a heliosheath thickness of L_{V2} ~54(+30, −15) AU, whereas the same normalization procedure applied to Voyager 1 results in L_{V1} ~27(+26, −11) AU. Surprisingly, the V1 crossing from the heliopause occurred ~1 month later than anticipated by Krimigis et al. [2011], in August 2012 [Krimigis et al. 2013], showing that the heliosheath thickness towards the nose (at V1 direction) is ~29 AU, i.e., much smaller and more compressed than expected in past models.

Admittedly, one of the milestones in the heliosphere research concerns the shape of this enormous system, because it strongly relates to the interpretation of several phenomena that were either theorized in the literature and/or resulted from measurements performed by modern detectors. For more than five decades, the shape and interactions of the heliosphere with the local interstellar medium have been discussed in the context of either a magnetosphere-like heliotail or a more symmetric bubble shape, posited in 1961 [Parker 1961]. Although past models broadly assumed the magnetosphere-like concept, the accurate heliospheric configuration remained largely undetermined due to lack of measurements.

Building upon previous analyses made by Krimigis et al. [2009] and Dialynas et al. [2013], and employing both Voyager in situ and INCA remote measurements, a recent MIMI publication, Dialynas et al. [2017a] used > 5.2 keV ENA measurements, obtained with MIMI/INCA over the 2003–2014 time period and provided a new paradigm on the heliosphere interaction with the LISM: the belt corresponds to a reservoir of particles that exist within the heliosheath, constantly replenished by new particles from the solar wind, while the ENAs that INCA detects are most likely associated with a region of enhanced particle pressure that is formed inside the heliopause and contributes to balancing the pressure of the ISMF (see Figures MAPS-39). The authors showed that the heliosheath ions are the source of > 5.2 keV ENA and that the heliosphere responds

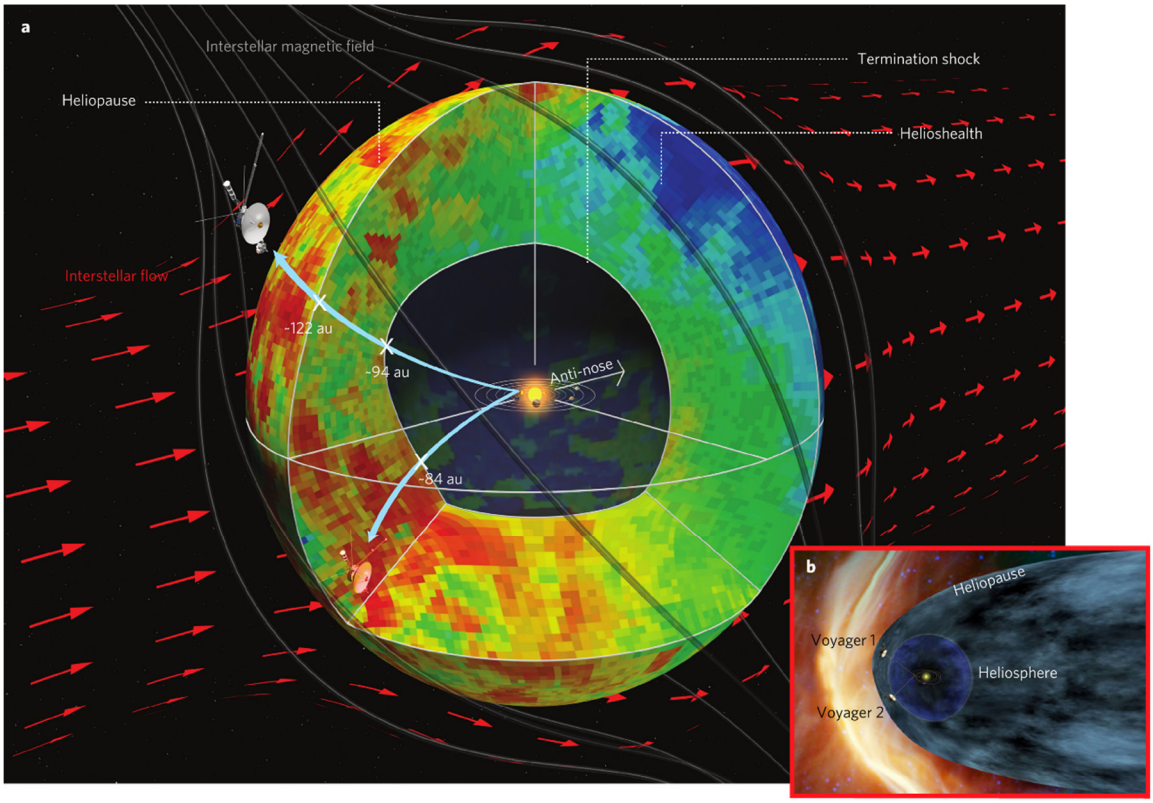

Figure MAPS-39. Adapted from Dialynas et al. [2017a] showing a conceptual model of the global heliosphere: (a) The gross shape and basic properties of the global heliosphere in three dimensions, summarizing our current understanding, based on both remote ENA and in situ ion measurements from Cassini/INCA and LECP/V1&V2, respectively. It shows a belt of varying ENA intensities surrounding the termination shock and extending to the outer boundary of the Heliosphere, called the heliopause, as identified by V1; it is anticipated that the heliopause south of the ecliptic will be crossed by V2 within the next few years. The red arrows represent the interstellar plasma flow deflected around the heliosphere bubble. The termination shock and heliopause are marked at the distances (in AU) observed by the Voyagers from 2004 through 2012 in their traversal of the heliosheath. The cutout illustrates the possible distribution of hot ion plasma in the heliosheath discerned by line-of-sight ENA images (E > 5.2 keV); relative scale ranging from 1 *(blue)* to 12 *(red)*. As the ENA emissions detected by INCA are LOS integrated, the 3rd dimension in this composite, conceptual representation of the global heliosheath (presenting the possible ENA distribution confined between the termination shock and the heliopause) is based on the knowledge of the variation of ion intensities measured at the Voyagers towards the nose hemisphere. These ion intensities are representative of the average ENA intensities along any LOS inside the heliosheath. Note that this concept of the heliosphere does not imply a closed system that cannot change its shape towards the tail to release the solar wind energy input. Inside the termination shock the ion intensities are lower by at least ×100. The orbits of the outer planets are drawn to scale around the Sun. Concept *(a)* is compared with *(b)*, a magnetosphere-like configuration (http://voyager.jpl.nasa.gov/mission/) widely adopted as one of two possibilities put forward by Parker [1961]. The termination shock is ~10 AU further out in the V1 direction, but the HS is possibly ~30–50% thicker towards the V2 direction (as detailed in the text), inconsistent with a compressed heliosheath in the southern hemisphere. That will be determined when V2 crosses the HP, expected in the next few years.

promptly, within ~2–3 years, to outward propagating solar wind changes (controlled by solar sunspot numbers and solar wind energy input) in both the upstream (nose) and downstream (tail) directions. These observations, taken together with the V1 measurement of a ~0.5 nT interstellar magnetic field, plasma density of > 0.09/cm^3 and the enhanced ratio between particle pressure and magnetic pressure in the heliosheath, strongly suggest a diamagnetic bubble-like heliosphere with few substantial tail-like features. A follow-up MIMI publication [Dialynas et al. 2017b] discussed the details of these results, and by calculating the recovery times of ENAs in the heliosphere, they found that the rough width of the heliosheath can be ~80–120 AU (or more) towards the tail, due to the ~2–3 year delay after solar minimum.

Dialynas et al. [2017a] also included two important implications concerning the heliosphere interaction with the LISM: 1) A perfectly symmetric and stable heliosphere in time would not be possible and/or physically correct, i.e., as the heliosphere cannot be a closed system, the heliosphere bubble can (and must) inflate with time in either the anti-nose direction (tail models) or along the direction of the interstellar magnetic field (Note: the polar jets [Opher et al. 2015; Drake et al. 2015], provide one of the possible mechanisms through which the solar wind input is evacuated from the system); and 2) due to the strong interstellar magnetic field, the Mach number of the local interstellar medium can be significantly decreased and the flow can become submagnetosonic, leading to the inability of forming a bow shock, as previously explained by Fahr et al. [1986] and simulated from Kivelson and Jia [2013] using the mini magnetosphere of Ganymede as a rough analogy to the heliosphere.

Jupiter

Jupiter's magnetotail

- **J_AO3:** Explore the dusk side of Jupiter's magnetosphere and intermediate regions of the magnetotail unvisited by previous spacecraft

Cassini flew by Jupiter on December 30, 2000, on its way to Saturn. Arriving from the pre-noon sector, closest approach occurred in the afternoon sector at 138 Jovian radii (~107 km) from the planet and was followed by an exploration of the dusk flank of the Jovian magnetosphere. During the Cassini flyby, the Galileo probe was still active (Figure MAPS-40).

In spite of the large distance of the flyby, several Cassini-MAPS instruments recorded high-quality data for about six months around closest approach. These observations benefited from the simultaneous presence of Galileo in orbit around Jupiter, enabling two-point measurements, and were complemented by remote observations by HST, Chandra, and ground-based radio. This resulted in a very rich data set that was the basis of many publications and will be further exploited in the coming years.

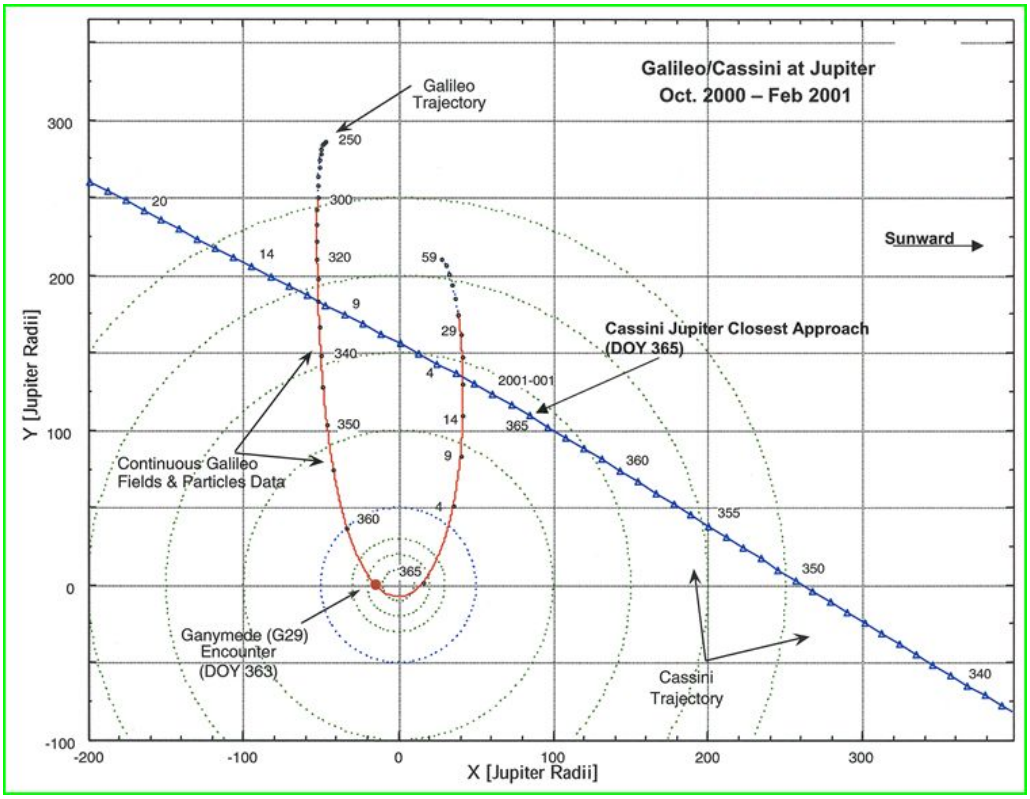

Figure MAPS-40. The orbits of Galileo and Cassini at Jupiter.

The dual Cassini/MAPS and Galileo measurements provided a chance to study the dynamic effects of the solar wind perturbations on the global configuration of the Jovian magnetosphere. These measurements showed clearly that magnetospheric particles leak directly into the interplanetary medium from the closed magnetosphere and are the source for the upstream particle events [Krupp 2002].

During its passage along Jupiter's dusk flank, Cassini made at least five bow shock crossings, one at ~1929 LT and four more between 2100 and 2130 LT on DOY 21. During the flyby, shock activity was high and variable, making a moving target for Cassini instruments. Cassini found that the shock is enormous, extending at least 700 R_J down the flank.

All three CAPS sensors were used to identify shock conditions and the times at which Cassini crossed into and out of it. See Szego et al. [2003] for a full description of shock studies based on all Cassini observations. By combining RPWS identification of Langmuir waves and IBS energy spectra, the upstream density could be measured at 0.5 to 1 cm^{-3} while at the same time ELS provided a measure of electron temperature at 2.6 eV. The data allowed the team to solve the Rankine-Hugoniot relations for transitions between the upstream and downstream conditions, deriving plasma density ratios of 2.74, and a downstream ion bulk energy of ~360 eV. The calculated downstream electron bulk temperature prediction was ~44 eV whereas ELS data gave ~11 eV and IMS ~24 eV, in fairly good agreement with the total energy jump predicted by theory.

IBS energy-time spectrograms were used to identify shock crossings far down the flank of the magnetosphere (Figure MAPS-41 is one example). Four examples that were observed using IBS data took place at 576, 618, 744, and 770 R_J were studied in detail by Szego et al. [2003].

Using CAPS, MAG, and RPWS, Cassini was able to investigate features of the downstream Jovian shock and magnetosheath out to ~700 R_R; a region not previously visited by any other spacecraft. As might be expected, the shock transition layer was broad and turbulent at that distance, but the transits were always easily observed using IBS data.

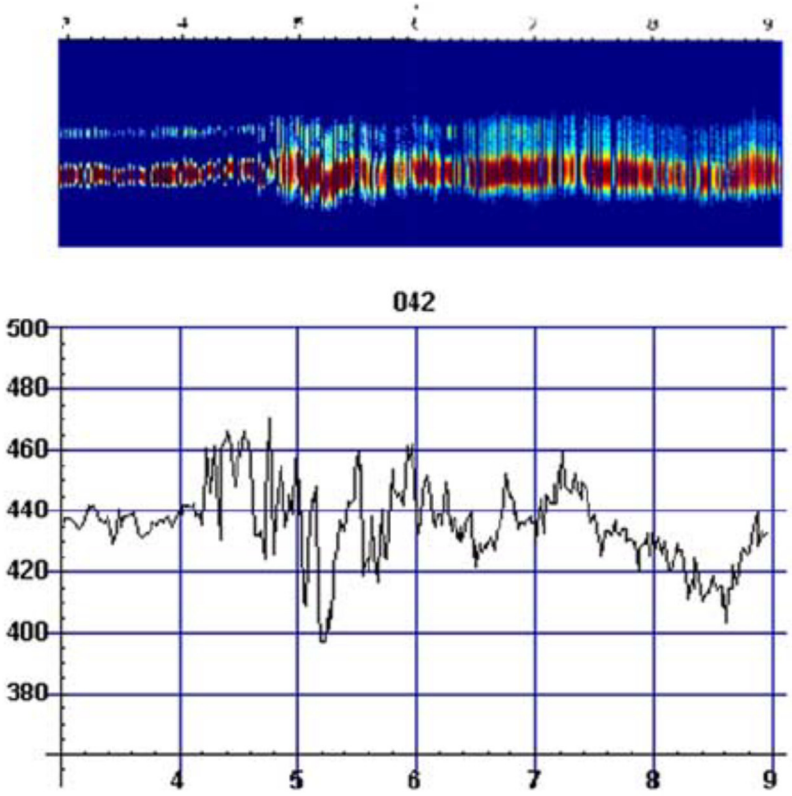

Figure MAPS-41. IBS data taken on DOY 042, 2000, 0300 to 0900 UT along the flanks of the Jovian magnetosphere. The velocity jump across the shock shows up as a jump in the velocity measured by IBS beginning at approximately 0420 UT. The most apparent feature is at ~4:40 UT when Cassini is inside the sheath and density and temperature both increase.

An important result of the coordinated measurements of Cassini and Galileo was good evidence of a change in magnetospheric shape in response to local solar wind magnetic field changes in the north-south component. There is increased flaring when the field is northward, opposite as to what happens at Earth. As the Jovian dipole is oppositely oriented, this is consistent with reconnection being important to magnetospheric configuration at Jupiter despite the high planetary rotation [Kivelson and Southwood 2005, 2003].

Not only did the passage of Cassini allow two-point measurements, but the MIMI/LEMMS and RPWS instruments on Cassini were very similar to instruments flown on Galileo. This allowed direct comparison of energetic particle and wave phenomena both inside and outside the magnetosphere of Jupiter. The comparison of energetic particle measurements made by both spacecraft is summarized in Krupp et al. [2004, 2002]. Figure MAPS-42 shows the differential fluxes and the pitch angle distributions of ions and electrons measured with LEMMS onboard Galileo and Cassini in the vicinity of the Jovian magnetopause.

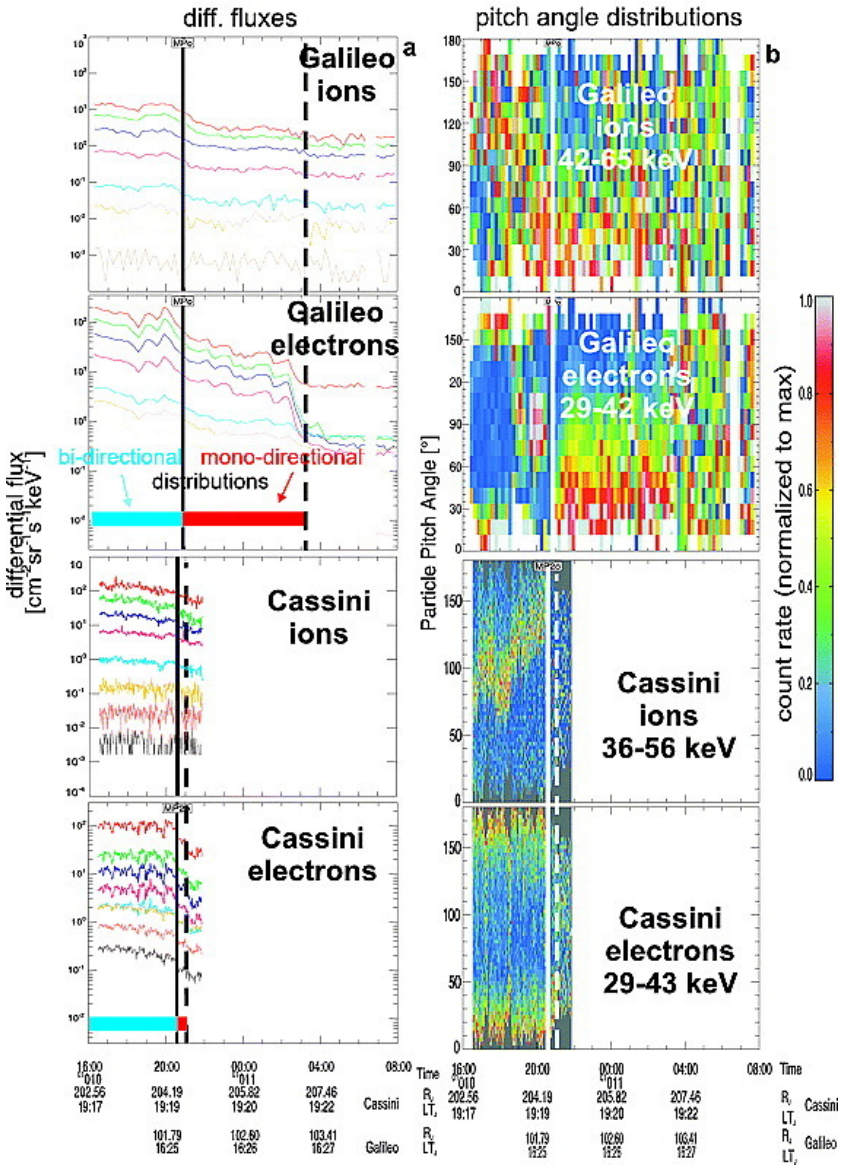

Figure MAPS-42. Differential fluxes and pitch angle distributions of ions and electrons measured with the LEMMS sensors onboard Galileo and Cassini in the vicinity of the magnetopause of Jupiter. Figure from Krupp et al. [2002].

Significant results from the coordinated measurements of the energetic particles include:

- Passage of closed to open planetary field lines with distributions from bi-directional to mono-directional, with respect to the magnetic field near the magnetopause.
- Periodic variations of electron fluxes on both spacecraft with 40 min periods near Cassini and about 60 min at Galileo's location.
- Leakage of magnetospheric particles into the interplanetary space.
- Sporadic electron beams outside the magnetosphere (Cassini at 300–900 R_J and Galileo at 130 R_J).

In addition, during the Jupiter flyby, INCA observed large fluxes of ENAs, primarily H and O, from the planet [Mitchell et al. 2004]. INCA discovered an ENA torus associated with and located just outside the orbit of Europa [Mauk et al. 2003]. The neutral densities in this torus were comparable to those found in the Io-associated cloud, and suggested that Europa is a strong source of neutrals. Figure MAPS-43 shows the discovery ENA image of the Europa torus.

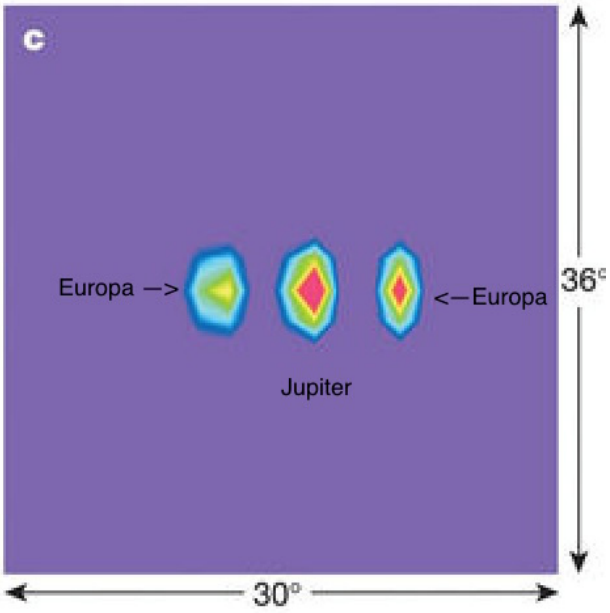

Figure MAPS-43. ENA image of the Europa torus, seen from the side, during the Cassini flyby of Jupiter in early 2001. The Europa torus appears on either side of Jupiter. The image was deconvolved for point sources and corrected for background. The intensity scale is linear.

Jupiter's radio emissions

The distant observations that Cassin made along the dusk flank of Jupiter's magnetosphere were well adapted to the study of the complex zoo of Jupiter's magnetospheric radio emissions, nicely covered by the Kronos receiver of RPWS, an example of which is given in Figure MAPS-44. An early overview is given in [Lecacheux 2001]. The intensity spectrum of all Jovian radio components was

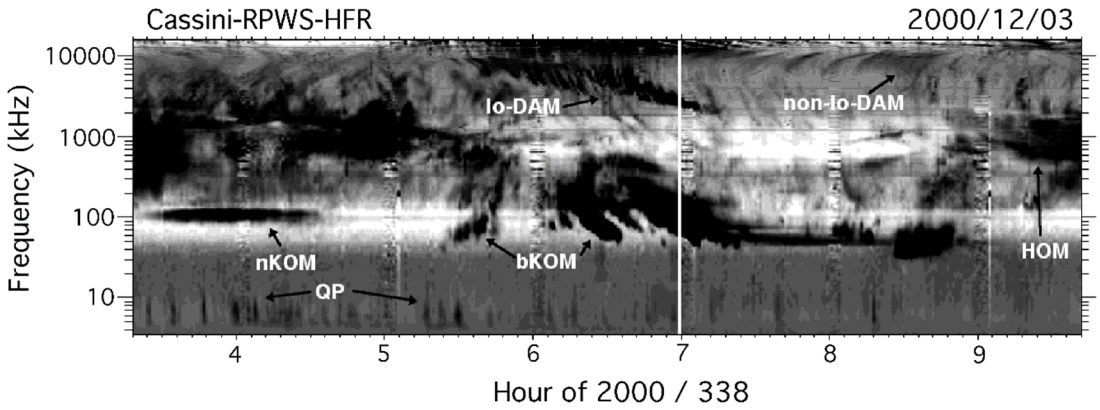

Figure MAPS-44. Jovian low-frequency radio emissions detected on December 3, 2000, by the RPWS experiment onboard Cassini approaching Jupiter. Frequency range is 3.5 kHz to 16.1 MHz. The Io-induced decameter emission (Io-DAM) appears here down to about 2 MHz, while weaker Io-independent (non-Io-DAM) arcs merge with the hectometer component (HOM) detected down to ~400 kHz. The auroral broadband kilometer component (bKOM) is detected down to ~40 kHz. The narrowband emission (nKOM) about 100 kHz is generated at or near the plasma frequency f_{pe} in Io's torus. The quasi-periodic (QP) bursts, spaced by 5 to > 15 min, are detected in the ~5 to 20 kHz range. Distance to Jupiter was 383 R_J (2.7×10^7 km) at the time of this observation.

accurately measured [Zarka et al. 2004] through calibration on the galactic background and Nançay observations, demonstrating in particular the absence of peak at 10 MHz in the decameter spectrum. The beaming of the decametric (DAM) and hectometric (HOM) components (a widely opened hollow cone of a few degrees thickness) were measured via two-point Cassini-Wind measurements [Kaiser et al. 2000] as well as frequency-longitude statistics and modelling [Imai et al. 2011a, 2011b, 2008]. The HOM low-frequency cutoff measured by Ulysses and Cassini provided constraints of its source location, in the outer regions of the Io plasma torus [Zarka et al. 2001].

The 6-month series of continuous homogeneous measurements provided unique measurements of time variations of the radio emission. Burst of auroral (non-Io) DAM emission were found to reoccur at a period slightly longer than the system III rotation period [Panchenko et al. 2013, 2010; Panchenko and Rucker 2011]. Gurnett et al. [2002] found from Cassini and Galileo observations that Jupiter's auroral radio and UV emissions were triggered by interplanetary shocks inducing magnetospheric compressions, in disagreement with theoretical predictions [Southwood and Kivelson 2001]. Hess et al. [2014] reconciled these views by a finer analysis of dawn and dusk radio emissions seen by Cassini, Galileo and Nançay, only dusk emissions being driven by both compressions and dilatations of the magnetosphere. They also used radio observations to deduce the subcorotation velocity of the magnetospheric plasma. Clarke et al. [2009] compared the effect of solar wind compressions on radio and UV aurora at Jupiter and Saturn, and found a weaker effect at Jupiter. Radio (non-Io-DAM, HOM and bKOM) and UV comparisons are used quite systematically in the study of Jupiter's aurora [Clarke et al. 2005, 2004; Pryor et al. 2005]. Comparison of Galileo/Jupiter and Cassini/Saturn observations also revealed similar energetic events where auroral radio intensifications are related to centrifugal plasma ejections, from the Io torus at Jupiter and from the equatorial plasma sheet at Saturn [Louarn et al. 2007].

Cassini, Galileo and Voyager radio observations were used to try to demonstrate the influence of satellites other than Io on DAM emissions. Marginal results were obtained statistically [Hospodarsky et al. 2001a], whereas clear evidence was obtained for Europa and Ganymede by comparison of observations with modelled dynamic spectra [Louis et al. 2017].

Fast recording modes of RPWS (spectral and waveform) allowed us to characterize the fine structure of Jovian radio emissions in the kilometer (bKOM) to decameter range [Kurth et al. 2001a; Lecacheux et al. 2001], including zebra-like patterns in the bKOM emission. Those were tentatively interpreted by bubble-like plasma inhomogeneities [Farrell et al. 2004] or the double plasma resonance mechanism involving ion cyclotron waves [Zlotnik et al. 2016]. Similar patterns have been observed at decameter wavelengths [Panchenko et al. 2018a, 2018b].

At the very low-frequency end of the radio spectrum (below a few 10 s of kHz), Cassini together with Ulysses and Galileo characterized the Jovian quasi-periodic bursts [Kaiser et al. 2004, 2001]. Stereoscopic observations demonstrated their strobe-like behavior and wide beaming [Hospodarsky et al. 2004], and direction-finding techniques localized their sources at high latitude regions of the magnetopause, implying complex propagation [Hospodarsky et al. 2004; Kimura et al. 2012]. Quasi-periodic (QP) bursts were tentatively related to the so-called Jovian anomalous continuum radiation [Ye et al. 2012]. Propagation of radio waves near the edges of the Io plasma torus were shown to generate the HOM attenuation lane, an intensity gap oscillating between ~1 and ~3 MHz, described by Boudjada et al. [2011] and modeled by Menietti et al. [2003] and Imai et al. [2015]. Occultations of Jovian radio emissions were used to probe the Io plasma torus [Boudjada et al. 2014].

Analysis of local low-frequency plasma waves recorded by RPWS was used to study the Jovian dust flank magnetopause and bow shock [Kurth et al. 2002; Szego et al. 2003], magnetosheath [Bebesi et al. 2011, 2010] and pre-shock [Szego et al. 2006]. The magnetopause was found to be in the process of being compressed by a solar wind pressure increase at the time of the Cassini flyby [Kurth et al. 2002]. Langmuir waves were detected upstream of the bow shock, and their level compared with that at other planets: the ratio of the energy density of the waves electric field to the plasma was found to increase with distance from the Sun [Hospodarsky et al. 2006].

Observations of Jupiter radio emissions were used to calibrate the Direction-Finding (actually Gonio-Polarimetric) capability of RPWS/Kronos [Vogl et al. 2004, 2001], which proved extremely successful at Saturn. Early use of this directional capability permitted to check the origin of lightning-like signals observed in Cassini's inbound leg to Saturn, which proved to be Jovian radio bursts [Fischer et al. 2006].

Overall, the radio observations made by the Cassini RPWS experiment were very successful at Jupiter. The obtained results were reported in several review papers about comparisons of radio waves [Zarka 2004, 2000; Zarka and Kurth 2005; de Pater and Kurth 2007; Rucker et al. 2014] and plasma waves [Hospodarsky et al. 2012] at the magnetized planets, as well as in reviews about auroras [Badman et al. 2015], magnetospheric processes [Blanc et al. 2002; Seki et al. 2015], or dust detection [Meyer-Vernet et al. 2017]. They greatly helped to prepare the magnetospheric measurements of the Juno mission in Jovian polar orbit [Bagenal et al. 2017].

Venus

Cassini made two very close gravity-assist flybys of Venus in route to Saturn. The first of the two flybys occurred on April 26, 1998, and the second occurred 14 months later on June 24. 1999. During the Venus flybys, the RPWS instrument conducted a search for high-frequency (0.125 to 16 MHz) radio impulses from Venus lightning. Despite the excellent sensitivity of the high-frequency RPWS receiver (down to the cosmic background), no impulses were detected [Gurnett et al. 2001]. During a subsequent close gravity-assist flyby of Earth on August 18, 1999, radio signals from lightning were observed essentially continuously at all radial distances inside of about 14 Earth radii, with maximum occurrence rates up to about 30 pulses per minute. These radio measurements made at Earth by Cassini are characteristic of terrestrial lightning and are commonly observed. The clear detection at Earth and the non-detection at Venus indicate that if lightning exists in the atmosphere of Venus, it is either extremely rare or is much weaker and at much lower frequencies than terrestrial lightning.

Earth

Cassini executed a flyby of Earth only 54 days after the second Venus encounter on August 18, 1999 in order to gain sufficient energy to continue its planned trajectory to Saturn. Although the principle purpose for the flyby was related to orbital mechanics, the flyby also offered an important opportunity for the Cassini MAPS instruments to operate in a well characterized magnetosphere. Operating the instruments in the Earth's magnetosphere allowed the MAPS teams to test planned operation modes and capabilities and to further characterize instrument performance in a planetary magnetosphere nearly five years prior to arrival at Saturn. Although the principle purpose of operating the MAPS instrument during the swift flyby of Earth was for calibration and other operational purposes, measurements made during flyby of Earth provided interesting scientific results [Burton et al. 2001; Kurth et al. 2001b; Lagg et al. 2001; Rymer et al. 2001; Southwood et al. 2001].

Figure MAPS-45, from Burton et al. [2001], shows the trajectory of the Cassini spacecraft during its encounter with Earth. The trajectory brings Cassini into the magnetosphere just past noon local time and carries it down the magnetotail in the post-midnight sector. Closest approach to Earth was just under 1200 km and was at a high rate of speed (~9 Earth radii per hour). The quick passage of the spacecraft through the magnetosphere provided a snapshot of the Earth's magnetosphere on a uniquely short timescale. In addition, Cassini's unique trajectory allowed near-continuous observations covering a range of distances down the magnetotail for the first time. Previous mission to the magnetotail (IMP 6, ISEE 1, ISEE 3, and Geotail), effectively made observations in the lobe at a single downtail distance due to their bound orbits. As Cassini flew by Earth, MAPS instruments were able to identify each of the typical magnetospheric boundaries and regions including the bow shock, magnetosheath, magnetopause, radiation belts, plasmasphere, plasma sheet, lobes, and crossings of the tail magnetopause [Burton et al. 2001; Kurth et al. 2001b; Lagg et al. 2001; Rymer et al. 2001; Southwood et al. 2001].

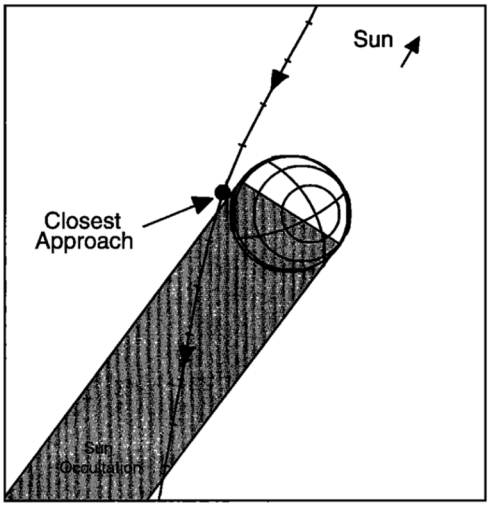

Figure MAPS-45. Trajectory of the Cassini spacecraft during it flyby of Earth on August 18, 1999. Reproduced from Burton et al. [2001] Figure 4.

During the Earth flyby the CAPS ELS sensor collected almost 9-hours of data in the Earth's magnetosphere and almost 10-hours of solar wind data upstream of the Earth. As noted above, CAPS, along with other MAPS instruments, sampled many plasma regions of the magnetosphere including electrons in the solar wind, bow shock, magnetosheath, magnetopause, radiation belts, plasmasphere, plasma sheet, lobes, and during crossings of the tail magnetopause. CAPS measurements were consistent with previous observations with a few exceptions and allowed the CAPS sensor to prepare for future operations at Saturn [Rymer et al. 2001]. In addition to anticipated results, CAPS found evidence of a low-energy field-aligned beam in the plasma sheet [Abel et al. 2001]. Bidirectional electrons were measured in the northern magnetotail lobe and were consistent with previous studies. However, measurements showed that was believed to be the first observations of a returning electron population in the magnetosheath. Bidirectional electrons were observed up to 0.02 keV, while at higher energies only unidirectional electrons were observed. The low energy of the returning electrons arises as a result of the electron populations' passage through the magnetopause twice and losses due to precipitation [Abel et al. 2001]. CAPS also found evidence of asymmetry on the dayside and nightside plasmapause position.

During the Earth flyby, the magnetometer performed important test and was able to make fairly original observations. One of the most important results of the Earth flyby for the magnetometer team was the testing of the helium magnetometer operating in the scalar mode and measuring the magnetic field magnitude with extremely high accuracy. Similar scalar mode measurements would be very important at Saturn for determining Saturn's intrinsic field, the near-Earth flyby provided a unique opportunity to test the magnetometer before arrival at Saturn [Smith et al. 2001]. In addition, the magnetometer observed what appeared to be interchange motions on the nightside outbound pass. Inbound, high resolution measurements of the whistler waves in the electron foreshock were reported [Southwood et al. 2001; Tsurutani et al. 2001].

Another important result of the Earth flyby was the large, international campaign of data gathering that was carried out on behalf of the magnetometer team by the Radio and Space Plasma Physics Group of the University of Leicester, United Kingdom [Khan et al. 2001]. Data obtained from various sources, together with the Cassini data, showed that during Cassini's outbound passage through the geomagnetic tail the magnetosphere underwent two complete classic substorm cycles and the data obtained by the fields and particles instruments on board Cassini confirmed that the flyby took place when the Earth's magnetosphere was generally in a disturbed state [Khan et al. 2001]. During the tail passage, RPWS observed a marked increase in the integrated auroral kilometric radiation power while at the same time CAPS and MIMI also saw evidence of these two substorm events in their data [Kurth et al. 2001b; Lagg et al. 2001; Rymer et al. 2001].

Finally, the RPWS instrument was able to make several different investigations to study Earth's magnetosphere and to test its capabilities in different modes. Figure MAPS-46 shows an overview of the RPWS observations during the Earth flyby. As one would expect, the RPWS observed broadband electrostatic waves at the bow shock, electron cyclotron harmonics and whistler mode chorus in the outer radiation belts and emissions between the plasma frequency and upper hybrid frequency in the ionosphere. Evidence for electron phase space holes was found in the near-Earth plasma sheet. At higher frequencies auroral kilometric radiation was observed on

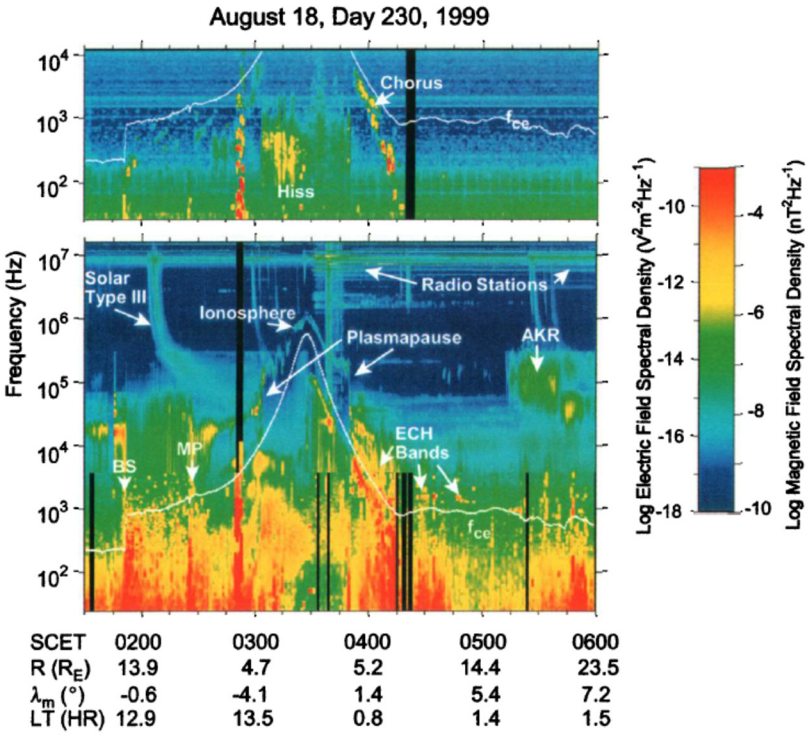

Figure MAPS-46. An overview of RPWS observations of the Earth flyby with magnetic fields shown in the top panel and electric fields below. The white trace is the electron cyclotron frequency f_{ce} derived from |B|. BS refers to the bow shock, MP refers to the magnetopause, ECH refers to electron cyclotron harmonics, and AKR refers to auroral kilometric radiation.

the night side indicating a series of auroral substorms and fixed frequency narrowband lines from man-made terrestrial radio stations were observed. Even Jovian hectometric radiation was observed from a position far downstream from Earth.

The RPWS instruments used a number of techniques to determine the plasma density from different wave excitations. The electron plasma frequency and upper hybrid resonance frequency are characteristic frequencies of the plasma dependent on the electron density. RPWS also includes a Langmuir probe that can determine the electron density and temperature. Finally, a relaxation sounder was used to stimulate the plasma frequency.

Another feature of the RPWS instrument that was tested during the Earth flyby was the capability of determining the wave normal angle of whistler mode waves using 5-channel waveform (WFR) measurements of three magnetic and two electric sensors. Hospodarsky et al. [2001b] used the WFR measurements to examine the propagation characteristics of a lightning whistler, chorus, and electromagnetic emissions in the magnetosheath, presumably lion roars.

Hospodarsky et al. [2001b] determined that the whistler analyzed was also detected at Palmer Station in Antarctica. The chorus waves were observed near the magnetic equator and appeared to reverse their direction of propagation at the equator, consistently propagating away from the equator where it is assumed the chorus source is located. The lion roars were found to consistently propagate nearly along the magnetic field but varied from burst to burst with some propagating near parallel and others near antiparallel to the field, suggesting multiple sources.

Cassini detected intense, fixed frequency emissions at close range to Earth in the frequency range above about 1 MHz that are attributed to man-made radio transmissions. Fischer and Rucker [2006] studied the occurrence of these in detail and demonstrated that most of the emissions could be identified with shortwave radio bands. A few brief detections of scientific transmitters include the High-frequency Active Auroral Research Program (HAARP) and the Russian SURA station, see also Tokarev et al. [2006]. Fischer and Rucker [2006] point out an interesting quiet period when Cassini was near closest approach over the Pacific Ocean where a combination of the rarity of transmitters in this location and ionospheric propagation characteristics effectively shielded Cassini from the radio transmission for a period of about 20 minutes.

ACRONYMS

Note: For a complete list of Acronyms, refer to Cassini Acronyms – Attachment A.

amu	atomic mass unit
AO	Announcement of Opportunity
AU	astronomical unit
bKOM	broadband kilometer
CA	closest approach
CAPS	Cassini Plasma Spectrometer
CHEMS	Charge-Energy-Mass Spectrometer
CRAND	Cosmic Ray Albedo Neutron Decay
DAM	decametric
DOY	day of year
DSMC	Direct Simulation Monte Carlo
DWG	Discipline Working Group
ELS	electron spectrometer
ENA	energetic neutral atom
EUV	extreme ultraviolet
FUV	far ultraviolet
GCR	Galactic Cosmic Ray
GDF	Globally Distributed Flux
HAARP	High-frequency Active Auroral Research Program
HCN	hydrogen cyanide
HOM	hectometric
HST	Hubble Space Telescope
IBEX	Interstellar Boundary Explorer
IBS	Ion Beam Spectrometer
IDS	Interdisciplinary Scientist
IMF	interplanetary magnetic field
IMS	Ion Mass Spectrometer
INCA	Ion and Neutral Camera
INMS	Ion and Neutral Mass Spectrometer
ISMF	interstellar magnetic field frame
ISS	Imaging Science Subsystem
K-H	Kelvin-Helmholtz
LECP	Low Energy Charged Particle
LEMMS	Low Energy Magnetospheric Measurement System
LFE	low frequency extension
LISM	Local Interstellar Medium
LLBL	low-latitude boundary layer

LOS	line-of-sight
LP	Langmuir Probe
LT	local time
MAG	Magnetometer
MAPS	Magnetospheres and Plasma Science
MHD	magnetohydrodynamic
MIMI	Magnetospheric Imaging Instrument
NB	narrowband
NIST	National Institute of Standards and Technology
OSI	open source ion
PLS	plasma spectrometer
PPO	planetary period oscillation
PRA	Planetary Radio Astronomy
PUI	pick-up ions
QP	quasi-periodic
RCM	Rice Convection Model
RPC	ring plasma cavity
RPWS	Radio and Plasma Wave Science
RS	Saturn radii
SCET	spacecraft event time
SED	Saturn electrostatic discharges
SEP	solar energetic particle
SKR	Saturn's kilometric radiation
SOI	Saturn Orbit Insertion
TOF	time-of-flight
ULF	ultra-low frequency
UT	universal time
UV	ultraviolet
UVIS	Ultraviolet Imaging Spectrograph
VIMS	Visual and Infrared Imaging Spectrometer
VLF	very low frequency
WFR	waveform

REFERENCES

Disclaimer: The partial list of references below correspond with in-text references indicated in this report. For all other Cassini references, refer to Attachment B – References & Bibliographies; Attachment C – Cassini Science Bibliographies; the sections entitled References contributed by individual Cassini instrument and discipline teams located in Volume 1 Sections 3.1 and 3.2 Science Results; and other resources outside of the Cassini Final Mission Report.

Abel, G., A. Coates, A. Rymer, D. Linder, M. Thomsen, D. Young, M. Dougherty, (2001), Cassini plasma spectrometer observations of bidirectional lobe electrons during the Earth flyby, August 18, 1999, Journal of Geophysical Research: Space Physics, 106, no. A12, pp. 30199-30208.

Achilleos, N., C. S. Arridge, C. Bertucci, P. Guio, N. Romanelli, N. Sergis, (2014), A combined model of pressure variations in Titan's plasma environment, Geophysical Research Letters 41 (24), 8730-8735, doi: 10.1002/2014GL061747.

Achilleos, N., P. Guio, C. S. Arridge, (2010a), A model of force balance in Saturn's magnetodisc, Monthly Notices of the Royal Astronomical Society, 401(4):2349–2371, doi: 10.1111/j.1365-2966.2009.15865.x.

Achilleos, N., P. Guio, C. S. Arridge, N. Sergis, R. J. Wilson, M. F. Thomsen, A. J. Coates, (2010b), Influence of hot plasma pressure on the global structure of Saturn's magnetodisk, Geophysical Research Letters, 37, L20201, doi: 10.1029/2010GL045159.

Achilleos, N., C. S. Arridge, C. Bertucci, C. M. Jackman, M. K. Dougherty, K. K. Khurana, C. T. Russell, (2008) Large-scale dynamics of Saturn's magnetopause: Observations by Cassini, Journal of Geophysical Research-Space Physics, 113 (A11), A11209, doi: 10.1029/2008ja013265.

Achilleos, N., C. Bertucci, C. T. Russell, G. B. Hospodarsky, A. M. Rymer, C. S. Arridge, M. E. Burton, M. K. Dougherty, S. Hendricks, E. J. Smith, B. T. Tsurutani, (2006), Orientation, location, and velocity of Saturn's bow shock: Initial results from the Cassini spacecraft, Journal of Geophysical Research, 111(A03201), doi: 10.1029/2005JA011297.

Ågren, K., N. J. T. Edberg, J. -E. Wahlund, (2012), Detection of negative ions in the deep ionosphere of Titan during the Cassini T70 flyby, Geophysical Research Letters, 39, L10201, doi: 10.1029/2012GL051714.

Ågren, K., D. J. Andrews, S. C. Buchert, A. J. Coates, S. W. H. Cowley, M. K. Dougherty, N. J. T. Edberg, P. Garnier, G. R. Lewis, R. Modolo, H. Opgenoorth, G. Provan, L. Rosenqvist, D. L. Talboys, J. E. Wahlund, A. Wellbrock, (2011), Detection of currents and associated electric fields in Titan's ionosphere from Cassini data, Journal of Geophysical Research-Space Physics 116, A04313, doi: 10.1029/2010ja016100.

Ågren, K., J. E. Wahlund, P. Garnier, R. Modolo, J. Cui, M. Galand, I. Müeller-Wodarg, (2009), On the ionospheric structure of Titan, Planetary and Space Science 57 (14-15), 1821-1827, doi: 10.1016/j.pss.2009.04.012.

Ågren, K., J. E. Wahlund, R. Modolo, D. Lummerzheim, M. Galand, I. Müeller-Wodarg, P. Canu, W. S. Kurth, T. E. Cravens, R. V. Yelle, J. H. Waite, A. J. Coates, G. R. Lewis, D. T. Young, C. Bertucci, M. K. Dougherty, (2007), On magnetospheric electron impact ionisation and dynamics in Titan's ram-side and polar ionosphere - a Cassini case study, Annales Geophysicae 25 (11), 2359-2369.

Alexeev, I. I., V. V. Kalegaev, E. S. Belenkaya, S. Y. Bobrovnikov, E. J. Bunce, S. W. H. Cowley, J. D. Nichols, (2006), A global magnetic model of Saturn's magnetosphere and a comparison with Cassini SOI data, Geophysical Research Letters 33 (8), L08101. doi: 10.1029/2006GL025896.

Allen, R. C., D. G. Mitchell, C. P. Paranicas, D. C. Hamilton, G. Clark, A. M. Rymer, S. K. Vines, E. C. Roelof, S. M. Krimigis, J. Vandegriff, (2018), Internal versus external sources of plasma at Saturn: Overview from magnetospheric imaging investigation/charge-energy-mass spectrometer data, Journal of Geophysical Research: Space Physics, submitted, doi: 10.1029/2018JA025262.

Amsif, A., J. Dandouras, E. C. Roelof, (1997), Modeling the production and the imaging of energetic neutral atoms from Titan's exosphere, Journal of Geophysical Research: Space Physics 102 (A10), 22169-22181, doi: 10.1029/97JA01597.

Andre, N., A. M. Persoon, J. Goldstein, J. L. Burch, P. Louarn, G. R. Lewis, A. M. Rymer, A. J. Coates, W. S. Kurth, E. C. Sittler, Jr., M. F. Thomsen, F. J. Crary, M. K. Dougherty, D. A. Gurnett, D. T. Young, (2007), Magnetic signatures of plasma-depleted flux tubes in the Saturnian inner magnetosphere, Geophysical Research Letters 34 (14), 14108, doi: 10.1029/2007GL030374.

Andre, N., M. K. Dougherty, C. T. Russell, J. S. Leisner, K. K. Khurana, (2005), Dynamics of the Saturnian inner magnetosphere: First inferences from the Cassini magnetometers about small-scale plasma transport in the magnetosphere, Geophysical Research Letters 32 (14), 14-06, doi: 10.1029/2005GL022643.

Andrews, D. J., S. W. H. Cowley, M. K. Dougherty, L. Lamy, G. Provan, D. J. Southwood, (2012), Planetary period oscillations in Saturn's magnetosphere: Evolution of magnetic oscillation properties from southern summer to post-equinox, Journal of Geophysical Research: Space Physics 117, A04224, doi: 10.1029/2011JA017444.

Andrews, D. J., B. Cecconi, S. W. H. Cowley, M. K. Dougherty, L. Lamy, G. Provan, P. Zarka, (2011), Planetary period oscillations in Saturn's magnetosphere: Evidence in magnetic field phase data for rotational modulation of Saturn kilometric radiation emissions, Journal of Geophysical Research: Space Physics 116, A09206, doi: 10.1029/2011ja016636.

Andrews, D. J., A. J. Coates, S. W. H. Cowley, M. K. Dougherty, L. Lamy, G. Provan, P. Zarka, (2010a), Magnetospheric period oscillations at Saturn: Comparison of equatorial and high-latitude magnetic field periods with north and south Saturn kilometric radiation periods, Journal of Geophysical Research: Space Physics, 115: 21 pp., doi: 10.1029/2010JA015666.

Andrews, D. J., S. W. H. Cowley, M. K. Dougherty, G. Provan, (2010b), Magnetic field oscillations near the planetary period in Saturn's equatorial magnetosphere: Variation of amplitude and

phase with radial distance and local time, Journal of Geophysical Research: Space Physics, 115: 28 pp., doi: 10.1029/2009JA014729.

Andrews, D. J., E. J. Bunce, S. W. H. Cowley, M. K. Dougherty, G. Provan, D. J. Southwood, (2008), Planetary period oscillations in Saturn's magnetosphere: Phase relation of equatorial magnetic field oscillations and Saturn kilometric radiation modulation, Journal of Geophysical Research: Space Physics 113 (A9), A09205, doi: 10.1029/2007ja012937.

Andriopoulou, M., E. Roussos, N. Krupp, C. Paranicas, M. Thomsen, S. Krimigis, M. K. Dougherty, K. H. Glassmeier, (2014), Spatial and temporal dependence of the convective electric field in Saturn's inner magnetosphere, Icarus 229, 57-70, doi: 10.1016/j.icarus.2013.10.028.

Andriopoulou, M., E. Roussos, N. Krupp, C. Paranicas, M. Thomsen, S. Krimigis, M. K. Dougherty, K. H. Glassmeier, (2012), A noon-to-midnight electric field and nightside dynamics in Saturn's inner magnetosphere, using microsignature observations, Icarus 220 (2), 503-513, doi: 10.1016/j.icarus.2012.05.010.

Anicich, V. G. and M. J. McEwan, (1997), Ion-molecule chemistry in Titan's ionosphere, Planetary and Space Science, 45 (8), 897-921.

Armstrong, T. P., S. Taherion, J. Manweiler, S. Krimigis, C. Paranicas, D. Mitchell, N. Krupp, (2009), Energetic ions trapped in Saturn's inner magnetosphere, Planetary and Space Science 57 (14-15),1723-1731, doi: 10.1016/j.pss.2009.03.008.

Arridge, C. S., J. M. Jasinski, N. Achilleos, Y. V. Bogdanova, E. J. Bunce, S. W. H. Cowley, A. N. Fazakerley, K. K. Khurana, L. Lamy, J. S. Leisner, E. Roussos, C. T. Russell, P. Zarka, A. J. Coates, M. K. Dougherty, G. H. Jones, S. M. Krimigis, N. Krupp, (2016a), Cassini observations of Saturn's southern polar cusp, Journal of Geophysical Research: Space Physics 121 (4), 3006-3030, doi: 10.1002/2015ja021957.

Arridge, C. S., J. P. Eastwood, C. M. Jackman, G. K. Poh, J. A. Slavin, M. F. Thomsen, N. Andre, X. Jia, A. Kidder, L. Lamy, A. Radioti, D. B. Reisenfeld, N. Sergis, M. Volwerk, A. P. Walsh, P. Zarka, A. J. Coates, M. K. Dougherty, (2016b), Cassini in situ observations of long-duration magnetic reconnection in Saturn's magnetotail, Nature Physics 12 (3), 268-271, doi: 10.1038/nphys3565.

Arridge, C. S., M. Kane, N. Sergis, K. K. Khurana, C. M. Jackman, (2015), Sources of local time asymmetries in magnetodiscs, Space Science Reviews 187 (1-4), 301-333, doi: 10.1007/s11214-015-0145-z.

Arridge, C. S., N. Andre, K. K. Khurana, C. T. Russell, S. W. H. Cowley, G. Provan, D. T. Young, (2011a), Periodic motion of Saturn's nightside plasma sheet, Journal of Geophysical Research: Space Physics, 116:22 pp., doi: 10.1029/2011JA016827.

Arridge, C. S., N. Achilleos, P. Guio, (2011b), Electric field variability and classifications of Titan's magnetoplasma environment, AnGeo Communicates, 29:1253–1258, doi: 10.5194/angeo-29-1253-2011.

Arridge, C. S., K. K. Khurana, C. T. Russell, D. J. Southwood, N. Achilleos, M. K. Dougherty, H. K. Leinweber, (2008a), Warping of Saturn's magnetospheric and magnetotail current

sheets, Journal of Geophysical Research: Space Physics, 113(A8), doi: 10.1029/2007JA012963.

Arridge, C. S., C. T. Russell, K. K. Khurana, N. Achilleos, S. W. H. Cowley, M. K. Dougherty, E. J. Bunce, (2008b), Saturn's magnetodisc current sheet, Journal of Geophysical Research: Space Physics, 113(A4):9 pp., doi: 10.1029/2007JA012540.

Arridge, C. S., N. Andre, N. Achilleos, K. K. Khurana, C. L. Bertucci, L. K. Gilbert, M. K. Dougherty, (2008c), Thermal electron periodicities at 20R_S in Saturn's magnetosphere, Geophysical Research Letters, 35(15):5 pp., doi: 10.1029/2008GL034132.

Arridge, C. S., C. T. Russell, K. K. Khurana, N. Achilleos, N. Andre, A. M. Rymer, M. K. Dougherty, A. J. Coates, (2007), Mass of Saturn's magnetodisc: Cassini observations, Geophysical Research Letters 34 (9), L09108.

Arridge, C. S., N. Achilleos, M. K. Dougherty, K. K., Khurana, C. T. Russell, (2006), Modeling the size and shape of Saturn's magnetopause with variable dynamic pressure, Journal of Geophysical Research: Space Physics, 111(A11):13 pp., doi: 10.1029/2005JA011574.

Backes, H., F. M. Neubauer, M. K. Dougherty, N. Achilleos, N. Andre, C. S. Arridge, C. Bertucci, G. H. Jones, K. K. Khurana, C. T. Russell, A. Wennmacher, (2005), Titan's magnetic field signature during the first Cassini encounter, Science 308 (5724), 992-995, doi: 10.1126/science.1109763.

Badman, S. V., G. Provan, E. J. Bunce, D. G. Mitchell, H. Melin, S. W. H. Cowley, A. Radioti, W. S. Kurth, W. R. Pryor, J. D. Nichols, S. L. Jinks, T. S. Stallard, R. H. Brown, K. H. Baines, M. K. Dougherty, (2016), Saturn's auroral morphology and field-aligned currents during a solar wind compression, Icarus 263, 83-93, doi: 10.1016/j.icarus.2014.11.014.

Badman, S.V., G. Branduardi-Raymont, M. Galand, S. L. Hess, N. Krupp, L. Lamy, H. Melin, C. Tao, (2015), Auroral processes at the giant planets: Energy deposition, emission mechanisms, morphology and spectra, Space Science Reviews, 187(1–4):99–179.

Badman, S. V., A. Masters, H. Hasegawa, M. Fujimoto, A. Radioti, D. Grodent, N. Sergis, M. K. Dougherty, A. J. Coates, (2013), Bursty magnetic reconnection at Saturn's magnetopause, Geophysical Research Letters 40 (6), 1027-1031, doi: 10.1002/grl.50199.

Badman, S. V., N. Achilleos, C. S. Arridge, K. H. Baines, R. H. Brown, E. J. Bunce, A. J. Coates, S. W. H. Cowley, M. K. Dougherty, M. Fujimoto, G. Hospodarsky, S. Kasahara, T. Kimura, H. Melin, D. G. Mitchell, T. Stallard, C. Tao, (2012a), Cassini observations of ion and electron beams at Saturn and their relationship to infrared auroral arcs, Journal of Geophysical Research: Space Physics 117, A01211, doi: 10.1029/2011JA017222.

Badman, S. V., D. J. Andrews, S. W. H. Cowley, L. Lamy, G. Provan, C. Tao, S. Kasahara, T. Kimura, M. Fujimoto, H. Melin, T. Stallard, R. H. Brown, K. H. Baines, (2012b), Rotational modulation and local time dependence of Saturn's infrared H_3^+ auroral intensity, Journal of Geophysical Research: Space Physics 117, doi: 10.1029/2012ja017990.

Badman, S. V., S. W. H. Cowley, B. Cecconi, L. Lamy, and P. Zarka, (2008), Relationship between solar wind corotating interaction regions and the phasing and intensity of Saturn kilometric radiation bursts, Annales Geophysicae, 26:3641–3651.

Badman, S. V., E. J. Bunce, J. T. Clarke, S. W. H. Cowley, J-C. Gérard, D. Grodent, S. E. Milan, (2005), Open flux estimates in Saturn's magnetosphere during the January 2004 Cassini-HST campaign, and implications for reconnection rates, Journal of Geophysical Research, 110(A11216), doi: 10.1029/2005JA011240.

Bagenal, F., A. Adriani, F. Allegrini, S. J. Bolton, B. Bonfond, E. J. Bunce, J. E. P. Connerney, S. W. H. Cowley, R. W. Ebert, G. R. Gladstone, C. J. Hansen, W. S. Kurth, S. M. Levin, B. H. Mauk, D. J. McComas, C. P. Paranicas, D. Santos-Costas, R. M. Thorne, P. Valek, J. H. Waite, P. Zarka, (2017), Magnetospheric science objectives of the Juno Mission, Space Science Reviews, 213, 219–287, doi: 10.1007/s11214-014-0036-8.

Bebesi, Z., K. Szego, A. Balogh, N. Krupp, G. Erdos, A. M. Rymer, G. R. Lewis, W. S. Kurth, D. T. Young, and M. K. Dougherty, (2011), Response to Comment on Slow-mode shock candidate in the Jovian magnetosheath, Planetary and Space Science 59 (5-6), 445-446, doi: 10.1016/j.pss.2010.10.007.

Bebesi, Z., K. Szego, A. Balogh, N. Krupp, G. Erdos, A. M. Rymer, G. R. Lewis, W. S. Kurth, D. T. Young, M. K. Dougherty, (2010), Slow-mode shock candidate in the Jovian magnetosheath, Planetary and Space Science 58 (5), 807-813. doi: 10.1016/j.pss.2009.12.008.

Belenkaya, E. S., V. V. Kalegaev, S. W. H. Cowley, G. Provan, M. S. Blokhina, O. G. Barinov, A. A. Kirillov, M. S. Grigoryan, (2016), Optimization of Saturn paraboloid magnetospheric field model parameters using Cassini equatorial magnetic field data, Annales Geophysicae 34 (7), 641-656, doi: 10.5194/angeo-34-641-2016.

Belenkaya, E. S., S. W. H. Cowley, C. J. Meredith, J. D. Nichols, V. V. Kalegaev, I. I. Alexeev, O. G. Barinov, W. O. Barinova, M. S. Blokhina, (2014), Magnetospheric magnetic field modelling for the 2011 and 2012 HST Saturn aurora campaigns – implications for auroral source regions, Annales Geophysicae, 32:689–704, doi: 10.5914/angeo-32-689-2014.

Belenkaya, E. S., S. W. H. Cowley, J. D. Nichols, M. S. Blokhina, V. V. Kalegaev, (2011), Magnetospheric mapping of the dayside UV auroral oval at Saturn using simultaneous HST images, Cassini IMF data, and a global magnetic field model, Annales Geophysicae 29 (7), 1233-1246, doi: 10.5194/angeo-29-1233-2011.

Belenkaya, E. S., I. I. Alexeev, M. S. Blokhina, E. J. Bunce, S. W. H. Cowley, J. D. Nichols, V. V. Kalegaev, V. G. Petrov, G. Provan, (2010), IMF dependence of Saturn's auroras: Modelling study of HST and Cassini data from 12-15 February 2008, Annales Geophysicae 28 (8), 1559-1570, doi: 10.5194/angeo-28-1559-2010.

Belenkaya, E. S., I. I. Alexeev, M. S. Blokhina, S. W. H. Cowley, S. V. Badman, V. V. Kalegaev, M. S. Grigoryan, (2007), IMF dependence of the open-closed field line boundary in Saturn's ionosphere, and its relation to the UV auroral oval observed by the Hubble Space Telescope, Annales Geophysicae 25 (5), 1215-1226.

Belenkaya, E. S., S. W. H. Cowley, I. I. Alexeev, (2006), Saturn's aurora in the January 2004 events, Annales Geophysicae 24 (6), 1649-1663.

Bell, J. M., H. Waite, J. Westlake, B. Magee, (2009), Simulating the 3-D structure of Titan's upper atmosphere, American Geophysical Union (AGU) Spring Meeting, abstract.

Ben-Jaffel, L. and I. Abbes, (2015), Helium abundance in giant planets and the local interstellar medium, In Journal of Physics: Conference Series, vol. 577, no. 1, p. 012003, Institute Of Physics Publishing, Bristol, United Kingdom.

Bertucci, C., D. C. Hamilton, W. S. Kurth, G. Hospodarsky, D. Mitchell, N. Sergis, N. J. T. Edberg, M. K. Dougherty, (2015), Titan's interaction with the supersonic solar wind, Geophysical Research Letters 42 (2), 193-200.

Bertucci, C., F. Duru, N. Edberg, M. Fraenz, C. Martinecz, K. Szego, O. Vaisberg, (2011), The induced magnetospheres of Mars, Venus, and Titan, Space Science Reviews 162 (1-4), 113-171, doi: 10.1007/s11214-011-9845-1.

Bertucci, C., N. Achilleos, M. K. Dougherty, R. Modolo, A. J. Coates, K. Szego, A. Masters, Y. Ma, F. M. Neubauer, P. Garnier, J. E. Wahlund, D. T. Young, (2008), The magnetic memory of Titan's ionized atmosphere, Science 321 (5895), 1475-1478. doi: 10.1126/science.1159780.

Bertucci, C., F. M. Neubauer, K. Szego, J. -E. Wahlund, A. J. Coates, M. K. Dougherty, D. T. Young, W. S. Kurth, (2007), Structure of Titan's mid-range magnetic tail: Cassini magnetometer observations during the T9 flyby, Geophysical Research Letters, 34(24):4 pp., doi: 10.1029/2007GL030865.

Bird, M. K., R. Dutta-Roy, S. W. Asmar, T. A. Rebold, (1997), Detection of Titan's ionosphere from Voyager 1 radio occultation observations, Icarus 130 (2), 426-436. doi: 10.1006/icar.1997.5831.

Blanc, M., S. Bolton, J. Bradley, M. Burton, T. E. Cravens, I. Dandouras, M. K. Dougherty, M. C. Festou, J. Feynman, R. E. Johnson, T. G. Gombosi, W. S. Kurth, P. C. Liewer, B. H. Mauk, S. Maurice, D. Mitchell, F. M. Neubauer, J. D. Richardson, D. E. Shemansky, E. C. Sittler, B. T. Tsurutani, P. H. Zarka, L. W. Esposito, E. Grun, D. A. Gurnett, A. J. Kliore, S. M. Krimigis, D. Southwood, J. H. Waite, D. T. Young, (2002), Magnetospheric and plasma science with Cassini-Huygens, Space Science Reviews 104 (1), 253-346. doi: 10.1023/A:1023605110711.

Boudjada, M. Y., P. H. M. Galopeau, S. Sawas, H. Lammer, (2014), Remote sensing of the Io torus plasma ribbon using natural radio occultation of the Jovian radio emission, Annales Geophysicae, 32, 1119–1128, doi: 10.5194/angeo-32-1119-2014.Boudjada, M. Y., P. H. M. Galopeau, H. O. Rucker, A. Lecacheux, N. Mebarki, W. Macher, and W. Voller, (2011), Morphological aspects of the attenuation bands associated with Jovian hectometric radiation, Journal of Geophysical Research-Space Physics 116, A11208, doi: 10.1029/2010JA016354.

Bouhram, M., R. E. Johnson, J.-J. Berthelier, J.-M. Illiano, R. L. Tokar, D. T. Young, F. J. Crary, (2006), A test-particle model of the atmosphere/ionosphere system of Saturn's main rings, Geophysical Research Letters, 33, L05106, doi: 10.1029/2005GL025011.

Bradley, T. J., S. W. H. Cowley, G. Provan, G. J. Hunt, E. J. Bunce, S. J. Wharton, I. I. Alexeev, E. S. Belenkaya, V. V. Kalegaev, M. K. Dougherty, (2018), Field-aligned currents in Saturn's nightside magnetosphere: Subcorotation and planetary period oscillation components

during northern spring, Journal of Geophysical Research: Space Physics, 123(5):3602–3636, doi: 10.1029/2017JA024885.

Brandt, P. C., K. Dialynas, I. Dandouras, D. G. Mitchell, P. Garnier, S. M. Krimigis, (2012), The distribution of Titan's high-altitude (out to 50,000 km) exosphere from energetic neutral atom (ENA) measurements by Cassini/INCA, Planetary and Space Science 60 (1), 107-114. doi: 10.1016/j.pss.2011.04.014.

Brown, W. L., W. M. Augustyniak, E. Simmons, K. J. Marcantonio, L. J. Lanzerotti, R. E. Johnson, J. W. Boring, C. T. Reimann, G. Foti, V. Pirronello, (1982), Erosion and molecule formation in condensed gas films by electronic energy loss of fast ions, Nuclear Instruments and Methods in Physics Research 198 (1), 1-8. doi: 10.1016/0167-5087(82)90043-6.

Bunce, E. J., D. C. Grodent, S. L. Jinks, D. J. Andrews, S. V. Badman, A. J. Coates, S. W. H. Cowley, M. K. Dougherty, W. S. Kurth, D. G. Mitchell, G. Provan, (2014), Cassini nightside observations of the oscillatory motion of Saturn's northern auroral oval, Journal of Geophysical Research-Space Physics 119 (5), 3528-3543. doi: 10.1002/2013ja019527.

Bunce, E. J., S. W. H. Cowley, D. L. Talboys, M. K. Dougherty, L. Lamy, W. S. Kurth, P. Schippers, B. Cecconi, P. Zarka, C. S. Arridge, A. J. Coates, (2010), Extraordinary field-aligned current signatures in Saturn's high-latitude magnetosphere: Analysis of Cassini data during Revolution 89, Journal of Geophysical Research-Space Physics 115, A10238. doi: 10.1029/2010ja015612.

Bunce, E. J., C. S. Arridge, S. W. H. Cowley, M. K. Dougherty, (2008), Magnetic field structure of Saturn's dayside magnetosphere and its mapping to the ionosphere: Results from ring current modeling, Journal of Geophysical Research-Space Physics 113 (A2), A02207.

Bunce, E. J., S. W. H. Cowley, I. I. Alexeev, C. S. Arridge, M. K. Dougherty, J. D. Nichols, C. T. Russell, (2007), Cassini observations of the variation of Saturn's ring current parameters with system size, Journal of Geophysical Research-Space Physics 112 (A10).

Bunce, E. J., S. W. H. Cowley, C. M. Jackman, J. T. Clarke, F. J. Crary, M. K. Dougherty, (2006), Cassini observations of the Interplanetary Medium Upstream of Saturn and their relation to the Hubble Space Telescope aurora data, Advances in Space Research, mercury, mars and saturn, 38(4):806–814, doi: 10.1016/j.asr.2005.08.005.

Bunce, E. J., S. W. H. Cowley, S. E. Milan, (2005), Interplanetary magnetic field control of Saturn's polar cusp aurora, Annales Geophysicae 23, 1405, doi: 10.5194/angeo-23-1405.

Buratti, B. J., P. C. Thomas, E. Roussos, C. Howett, M. Seiß, A. R. Hendrix, P. Helfenstein, R. H. Brown, R. N. Clark, T. Denk, (2019), Close Cassini flybys of Saturn's ring moons Pan, Daphnis, Atlas, Pandora, and Epimetheus, Science, 364(6445):eaat2349.

Burch, J. L., A. D. Dejong, J. Goldstein, D. T. Young, (2009), Periodicity in Saturn's magnetosphere: Plasma cam, Geophysical Research Letters, doi: 10.1029/2009GL039043.

Burch, J. L., J. Goldstein, T. W. Hill, D. T. Young, F. J. Crary, A. J. Coates, N. Andre, W. S. Kurth, E. C. Sittler Jr., (2005), Properties of local plasma injections in Saturn's magnetosphere, Geophysical Research Letters 32 (14), 14-02. doi: 10.1029/2005GL022611.

Burlaga, L. F. and N. F. Ness, (2016), Observations of the interstellar magnetic field in the outer heliosheath: Voyager 1, The Astrophysical Journal 829 (2), 134.

Burlaga, L. F., N. F. Ness, E. C. Stone, (2013), Magnetic field observations as Voyager 1 entered the heliosheath depletion region, Science 341 (6142), 147-150.

Burton, M. E., M. K. Dougherty, C. T. Russell, (2010), Saturn's internal planetary magnetic field, Geophysical Research Letters 37, L24105, doi: 10.1029/2010gl045148.

Burton, M. E., M. K. Dougherty, C. T. Russell, (2009), Model of Saturn's internal planetary magnetic field based on Cassini observations, Planetary and Space Science 57 (14-15), 1706-1713, doi: 10.1016/j.pss.2009.04.008.

Burton, M. E., B. Buratti, D. L. Matson, J. -P. Lebreton, (2001), The Cassini/Huygens Venus and Earth flybys: An overview of operations and results, Journal of Geophysical Research, 106(A12):30099–30107, doi: 10.1029/2001JA900088.

Cao, H. and D. J. Stevenson, (2017), Gravity and zonal flows of giant planets: From the Euler equation to the thermal wind equation, Journal of Geophysical Research-Planets 122 (4), 686-700, doi: 10.1002/2017je005272.

Cao, H., C. T. Russell, J. Wicht, U. R. Christensen, M. K. Dougherty, (2012), Saturn's high degree magnetic moments: Evidence for a unique planetary dynamo, Icarus, 221(1):388–394, doi: 10.1016/j.Icarus.2012.08.007.

Cao, H., C. T. Russell, U. R. Christensen, M. K. Dougherty, M. E. Burton, (2011), Saturn's very axisymmetric magnetic field: No detectable secular variation or tilt, Earth and Planetary Science Letters 304 (1-2), 22-28. doi: 10.1016/j.epsl.2011.02.035.

Carbary, J. F., D. G. Mitchell, P. Kollmann, N. Krupp, E. Roussos, (2017), Energetic electron periodicities during the Cassini Grand Finale, Journal of Geophysical Research-Space Physics 122 (12), 12229-12235, doi: 10.1002/2017ja024836.

Carbary, J. F. and D. G. Mitchell, (2017), Midnight flash model of ENA periodicities at Saturn, Journal of Geophysical Research: Space Physics, doi: 10.1002/2017JA024296.

Carbary, J. F., D. G. Mitchell, P. Kollmann, N. Krupp, E. Roussos, (2017), Energetic electron periodicities during the Cassini grand finale, Journal of Geophysical Research: Space Physics, 122, doi: 10.1002/2017JA024836.

Carbary, J. F., W. S. Kurth, D. G. Mitchell, (2016), Short periodicities in low-frequency plasma waves at Saturn, Journal of Geophysical Research: Space Physics, 121:6562–6572.

Carbary, J. F., N. Sergis, D. G. Mitchell, N. Krupp, (2015), Saturn's hinge parameter from Cassini magnetotail passes in 2013–2014, Journal of Geophysical Research: Space Physics, 120:4438.

Carbary, J. F., M. Kane, B. H. Mauk, S. M. Krimigis, (2014a), Using the kappa function to investigate hot plasmas in the magnetospheres of the giant planets, Journal of Geophysical Research, 119, doi: 10.1002/2014JA020324.

Carbary, J. F., D. G. Mitchell, P. C. Brandt, (2014b), Local time dependences of oxygen ENA periodicities at Saturn, Journal of Geophysical Research, 119, 2014JA020214.

Carbary, J. F., (2013), Wavy magnetodisk in Saturn's outer magnetosphere, Geophysical Research Letters, 40:5024.

Carbary, J. F., E. C. Roelof, D. G. Mitchell, D. C. Hamilton, (2013), Solar periodicity in energetic ions at Saturn, Journal of Geophysical Research, 118, doi: 10.1002/jgra.50282.

Carbary, J. F., N. Achilleos, C. S. Arridge, (2012), Statistical ring current of Saturn, Journal of Geophysical Research, 117(A06223).

Carbary, J. F., D. G. Mitchell, S. M. Krimigis, N. Krupp, (2011a), Post-equinox periodicities in Saturn's energetic electrons, Geophysical Research Letters, 28(L24104), 2011GL050259.

Carbary, J. F., C. Paranicas, D. G. Mitchell, S. M. Krimigis, N. Krupp, (2011b), Energetic electron spectra in Saturn's plasma sheet, Journal of Geophysical Research, 116(A07210).

Carbary, J. F., D. G. Mitchell, S. M. Krimigis, D. A. Gurnett, W. S. Kurth, (2010a), Phase relations between energetic neutral atom intensities and kilometric radio emissions at Saturn, Journal of Geophysical Research, 115(A01203).

Carbary, J. F., N. Achilleos, C. S. Arridge, K. K. Khurana, M. K. Dougherty, (2010b), Global configuration of Saturn's magnetic field derived from observations, Geophysical Research Letters, 37(L21806), doi: 10.1029/2010GL044622.

Carbary, J. F., D. C. Hamilton, S. P. Christon, D. G. Mitchell, S. M. Krimigis, (2010c), Longitude dependencies of energetic H+ and O+ at Saturn, Journal of Geophysical Research, 115(A07226), doi: 10.1029/2009JA015133.

Carbary, J. F., E. C. Roelof, D. G. Mitchell, S. M. Krimigis, N. Krupp, (2009a), Solar wind periodicity in energetic electrons at Saturn, Geophysical Research Letters, 36(L22104), doi: 10.1029/2009GL041086.

Carbary, J. F., D. G. Mitchell, N. Krupp, S. M. Krimigis, (2009b), L shell distribution of energetic electrons at Saturn, Journal of Geophysical Research, 114(A09210), doi: 10.1029/2009JA014341.

Carbary, J. F., D. G. Mitchell, P. Brandt, E. C. Reolof, S. M. Krimigis, (2008a), Track analysis of energetic neutral atom blobs at Saturn, Journal of Geophysical Research, 113(A01209), doi: 10.1029/2007JA012708.

Carbary, J. F., D. G. Mitchell, C. Paranicas, E. C. Roelof, S. M. Krimigis, (2008b), Direct observation of warping in the plasma sheet of Saturn, Geophysical Research Letters, 35(L24201), doi: 10.1029/2008GL035970.

Cassidy, T. A. and R. E. Johnson, (2010), Collisional spreading of Enceladus' neutral cloud, Icarus 209 (2), 696-703, doi: 10.1016/j.icarus.2010.04.010.

Caudal, G., (1986), A self-consistent model of Jupiter's magnetodisc including the effects of centrifugal force and pressure, Journal of Geophysical Research: Space Physics 91, no. A4, 4201-4221.

Cecconi, B. and P. Zarka, (2005), Model of a variable radio period for Saturn, Journal of Geophysical Research, 110, A12203, doi: 10.1029/2005JA011085.

Chen, Y., T. W. Hill, A. M. Rymer, R. J. Wilson, (2010), Rate of radial transport of plasma in Saturn's inner magnetosphere, Journal of Geophysical Research, 115(A10211), doi: 10.1029/2010JA015412.

Chen, Y. and T. W. Hill, (2008), Statistical analysis of injection dispersion events in Saturn's inner magnetosphere, Journal of Geophysical Research-Space Physics 113 (A7), A07215.

Christon, S. P., D. C. Hamilton, D. G. Mitchell, R. B. DiFabio, S. M. Krimigis (2014a), Suprathermal magnetospheric minor ions heavier than water at Saturn: Discovery of 28M+ seasonal variations, J. Geophys. Res., 119, 2014JA020010.

Christon, S.P., D. C. Hamilton, D. G. Mitchell, J. M. C. Plane, R. D. DiFabio, S. M. Krimigis, S. R. Nylund, A. Lui, (2014b), December. Discovery of suprathermal Fe+ in the magnetospheres of Earth and Saturn, American Geophysical Union (AGU) Fall Meeting, abstract.

Christon, S. P., D. C. Hamilton, R. D. DiFabio, D. G. Mitchell, S. M. Krimigis, D. S. Jontof-Hutter, (2013), Saturn suprathermal O-2(+) and mass-28(+) molecular ions: Long-term seasonal and solar variation, Journal of Geophysical Research-Space Physics 118 (6), 3446-3462. doi: 10.1002/jgra.50383.

Clark, G., C. Paranicas, D. Santos-Costa, S. Livi, N. Krupp, D. G. Mitchell, E. Roussos, W. L. Tseng, (2014), Evolution of electron pitch angle distributions across Saturn's middle magnetospheric region from MIMI/LEMMS, Planetary and Space Science, 104:18–28, doi: 10.1016/pss.2014.07.004.

Clarke, J. T., J. Nichols, J. C. Gerard, D. Grodent, K. C. Hansen, W. Kurth, G. R. Gladstone, J. Duval, S. Wannawichian, E. Bunce, S. W. H. Cowley, F. Crary, M. Dougherty, L. Lamy, D. Mitchell, W. Pryor, K. Retherford, T. Stallard, B. Zieger, (2009), Response of Jupiter's and Saturn's auroral activity to the solar wind, Journal of Geophysical Research Space Physics 114 (A5), A05210, doi: 10.1029/2008ja013694.

Clarke, J. T., J. C. Gerard, D. Grodent, S. Wannawichian, J. Gustin, J. Connerney, F. Crary, M. Dougherty, W. Kurth, S. W. H. Cowley, E. J. Bunce, T. Hill, J. Kim, (2005), Morphological differences between Saturn's ultraviolet aurorae and those of Earth and Jupiter, Nature 433 (7027), 717-719, doi: 10.1038/nature03331.

Clarke, J. T., D. Grodent, S. W. H. Cowley, E. J. Bunce, P. Zarka, J. E. P. Connerney, T. Satoh, (2004), Jupiter's aurora, In Jupiter: the Planet, Satellites, and Magnetosphere, (eds.) F. Bagenal, W. McKinnon, T. Dowling, Cambridge University Press, Cambridge.

Clarke, K. E., D. J. Andrews, A. J. Coates, S. W. H. Cowley, A. Masters, (2010a), Magnetospheric period oscillations of Saturn's bow shock, Journal of Geophysical Research-Space Physics 115, A05202, doi: 10.1029/2009ja015164.

Clarke, K. E., D. J. Andrews, C. S. Arridge, A. J. Coates, S. W. H. Cowley, (2010b), Magnetopause oscillations near the planetary period at Saturn: Occurrence, phase, and amplitude, Journal of Geophysical Research, 115(A08209), doi: 10.1029/2009JA014745.

Clarke, K. E., N. Andre, D. J. Andrews, A. J. Coates, S. W. H. Cowley, M. K. Dougherty, D. M. Wright, (2006), Cassini observations of planetary-period oscillations of Saturn's magnetopause, Geophysical Research Letters, 33(23), doi: 10.1029/2006GL027821.

Coates, A. J., A. Wellbrock, J. H. Waite, G. H. Jones, (2015), A new upper limit to the field-aligned potential near Titan, Geophysical Research Letters 42 (12), 4676–4684, doi: 10.1002/2015GL064474.

Coates, A. J., A. Wellbrock, G. R. Lewis, C. S. Arridge, F. J. Crary, D. T. Young, M. F. Thomsen, D. B. Reisenfeld, E. C. Sittler Jr., R. E. Johnson, K. Szego, Z. Bebesi, G. H. Jones, (2012), Cassini in Titan's tail: CAPS observations of plasma escape, Journal of Geophysical Research, 117(A5), doi:10.1029/2012JA017595.

Coates, A. J., J. -E. Wahlund, K. Ågren, N. J. T. Edberg, J. Cui, A. Wellbrock, K. Szego, (2011), Recent results from Titan's ionosphere, Space Science Review, 162:85–211, doi: 10.1007/s11214-011-9826-4.

Coates, A. J., A. Wellbrock, G. R. Lewis, G. H.Jones, D. T. Young, F. J. Crary, J. H. Waite, R. E. Johnson, T. W. Hill, E. C. Sittler Jr., (2010), Negative ions at Titan and Enceladus: recent results, Faraday Discussion, 147(1):293–305, doi: 10.1039/C004700G.

Coates, A. J., A. Wellbrock, G. R. Lewis, G. H. Jones, D. T. Young, F. J. Crary, J. H. Waite Jr., (2009), Heavy negative ions in Titan's ionosphere: altitude and latitude dependence, Planetary and Space Science, 57(14–15):1866–1871, doi: 10.1016/j.pss.2009.05.009.

Coates, A.J ., F. J. Crary, G. R. Lewis, D. T. Young, J. H. Waite Jr., E. C. Sittler Jr., (2007), Discovery of heavy negative ions in Titan's ionosphere, Geophysical Research Letters, 34, L22103, doi: 10.1029/2007GL030978.

Connerney, J. E. P. and J. H. Waite, (1984), New model of Saturn's ionosphere with an influx of water from the rings, Nature 312 (5990), 136.

Connerney, J. E. P., (1981), The magnetic field of Jupiter: A generalized inverse approach, Journal of Geophysical Research: Space Physics, 86(A9):7679–7693, doi: 10.1029/JA086iA09p07679.

Cooper, N. J., C. D. Murray, S. Renner, (2017), F-ring objects, Cassini End of Mission, Project Science Group (PSG), September 16, 2017, Pasadena, California.

Cowley, S. W. H. and G. Provan, (2017), Planetary period modulations of Saturn's magnetotail current sheet during northern spring: Observations and modeling, Journal of Geophysical Research, 122:6049–6077, doi: 10.1002/2017JA023993.

Cowley, S. W. H., G. Provan, G. J. Hunt, C. M. Jackman, (2017), Planetary period modulations of Saturn's magnetotail current sheet: A simple illustrative mathematical model, Journal of Geophysical Research, 122:258–279, doi: 10.1002/2016JA023367.

Cowley, S. W. H. and G. Provan, (2016), Planetary period oscillations in Saturn's magnetosphere: Further comments on the relationship between post-equinox properties deduced from magnetic field and Saturn kilometric radiation measurements, Icarus, 272:258–276, doi: 10.1016/j.Icarus.2016.02.051.

Cowley, S. W. H. and G. Provan, (2015), Planetary period oscillations in Saturn's magnetosphere: Comments on the relation between post-equinox periods determined from magnetic field and SKR emission data, Annales Geophysicae, 33:901–912.

Cowley, S. W. H., J. D. Nichols, C. M. Jackman, (2015), Down-tail mass loss by plasmoids in Jupiter's and Saturn's magnetospheres, Journal of Geophysical Research-Space Physics 120 (8), 6347-6356, doi: 10.1002/2015ja021500.

Cowley, S. W. H. and G. Provan, (2013), Saturn's magnetospheric planetary period oscillations, neutral atmosphere circulation, and thunderstorm activity: Implications, or otherwise, for physical links, Journal of Geophysical Research, 118:7246–7261, doi: 10.1002/2013JA019200.

Cowley, S. W. H., C. S. Arridge, E. J. Bunce, J. T. Clarke, A. J. Coates, M. K. Dougherty, J. C. Gerard, D. Grodent, J. D. Nichols, D. L. Talboys, (2008), Auroral current systems in Saturn's magnetosphere: Comparison of theoretical models with Cassini and HST observations, Annales Geophysicae 26 (9), 2613-2630.

Cowley, S. W. H., D. M. Wright, E. J. Bunce, A. C. Carter, M. K. Dougherty, G. Giampieri, T. R. Robinson, (2006), Cassini observations of planetary-period magnetic field oscillations in Saturn's magnetosphere: Doppler shifts and phase motion, Geophysical Research Letters, 33(7):4 pp., doi: 10.1029/2005GL025522.

Cowley, S. W. H., S. V. Badman, E. J. Bunce, J. T. Clarke, J. C. Gérard, D. Grodent, C. M. Jackman, S. E. Milan, T. K. Yeoman, (2005), Reconnection in a rotation-dominated magnetosphere and its relation to Saturn's auroral dynamics, Journal of Geophysical Research, 110(A02201), doi: 10.1029/2004JA010796.

Cowley, S. W. H., E. J. Bunce, J. M. O'Rourke, (2004), A simple quantitative model of plasma flows and currents in Saturn's polar ionosphere, Journal of Geophysical Research Space Physics 109 (A5).

Crary, F. J., B. A. Magee, K. Mandt, J. H. Waite Jr., J. Westlake, D. T. Young, (2009), Heavy ions, temperatures and winds in Titan's ionosphere: Combined Cassini CAPS and INMS observations, Planetary and Space Science 57 (14-15), 1847-1856. doi: 10.1016/j.pss.2009.09.006.

Crary, F. J., J. T. Clarke, M. K. Dougherty, P. G. Hanton, K. C. Hansen, J. T. Steinberg, B. L. Barraclough, A. J. Coates, J. C. Gerard, D. Grodent, W. S. Kurth, D. G. Mitchell, A. M. Rymer, D. T. Young, (2005), Solar wind dynamic pressure and electric field as the main factors controlling Saturn's aurorae, Nature Volume 433 (no. 7027), 720-722. doi: 10.1038/nature03333.

Cravens, T. E., I. P. Robertson, J. H. Waite, R. V. Yelle, V. Vuitton, A. J. Coates, J.-E. Wahlund, K. Ågren, M. S. Richard, V. de La Haye, A. Wellbrock, F. M. Neubauer, (2009a), Model-data comparisons for Titan's nightside ionosphere, Icarus, 199:174–188, doi: 10.1016/j.icarus.2008.09.005.

Cravens, T. E., R. V. Yelle, J.-E. Wahlund, D. E. Shemansky, A. F. Nagy, (2009b), Composition and structure of the ionosphere and thermosphere, in Titan from Cassini-Huygens, (eds.) R. H. Brown, J.-P. Lebreton, J. H. Waite, Springer, Dordrecht, doi: 10.1007/978-1-420-9215-2_11, pp. 259-295.

Cravens, T. E., I. P. Robertson, S. A. Ledvina, D. Mitchell, S. M. Krimigis, J. H. Waite Jr., et al., (2008a), Energetic ion precipitation at Titan, Geophysical Research Letters, 35(3), doi: 10.1029/2007GL032451.

Cravens, T. E., I. P. Robertson, J. H. Waite Jr., R. V. Yelle, V. Vuitton, A. J. Coates, J. -E. Wahlund, K. Ågren, M. S. Richard, V. De La Haye, A. Wellbrock, F. N. Neubauer, (2008b),

Model-data comparisons for Titan's nightside ionosphere, Icarus, doi: 10.1016/j.icarus.2008.09.005.

Cravens, T. E., I. P. Robertson, J. H. Waite, W. T. Kasprzak, R. V. Yelle, V. Vuitton, J. Clark, J. G. Luhmann, S. A. Ledvina, R. L. McNutt, W. Ip, I. Müeller-Wodarg, J. Wahlund, A. J. Coates, (2006), Solar radiation and magnetospheric electron sources of the ionosphere of Titan: Model comparisons with Cassini data, American Geophysical Union (AGU) Fall Meeting, San Francisco, California, 11-15 Dec. 2006.

Cui, J., R. V. Yelle, V. Vuitton, J. H. Waite, W. T. Kasprzak, D. A. Gell, H. B. Niemann, I. C. F. Müller-Wodarg, N. Borggren, G. G. Fletcher, E. L. Patrick, E. Raaen, B. A. Magee, (2009), Analysis of Titan's neutral upper atmosphere from Cassini ion neutral mass spectrometer measurements, Icarus, 200:581–615, doi: 10.1016/j.icarus.2008.12.005.

Cui, J., R. V. Yelle, K. Volk, (2008), Distribution and escape of molecular hydrogen in Titan's thermosphere and exosphere, Journal of Geophysical Research, 113, E10004, doi: 10.1029/2007JE003032.

Dandouras, I., P. Garnier, D. G. Mitchell, E. C. Roelof, P. C. Brandt, N. Krupp, S. M. Krimigis, (2008), Titan's exosphere and its interaction with Saturn's magnetosphere, Philosophical Transactions of the Royal Society A: Mathematical, Physical and Engineering Sciences, 367(1889):743-752.

Dandouras, J. and A. Amsif, (1999), Production and imaging of energetic neutral atoms from Titan's exosphere: A 3-D model, Planetary and Space Science 47 (10), 1355-1369, doi: 10.1016/S0032-0633(99)00057-4.

De La Haye, V., J. H. Waite, E. Cravens, A. F. Nagy, R. E. Johnson, S. Lebonnois, I. P. Robertson, (2007a), Titan's corona: The contribution of exothermic chemistry, Icarus 191 (1), 236-250, doi: 10.1016/j.icarus.2007.04.031.

De La Haye, V., J. H. Waite, R. E. Johnson, R. V. Yelle, T. E. Cravens, J. G. Luhmann, W. T. Kasprzak, D. A. Gell, B. Magee, F. Leblanc, M. Michael, S. Jurac, I. P. Robertson, (2007b), Cassini ion and neutral mass spectrometer data in Titan's upper atmosphere and exosphere: Observation of a suprathermal corona, Journal of Geophysical Research-Space Physics 112 (A7), A07309, doi: 10.1029/2006JA012222.

de Pater, I, and W. S. Kurth, (2007), The solar system at radio wavelengths, In Encyclopedia of the Solar System, (eds.), L.-A. Adams McFadden, P. R. Weissman, T. V. Johnson, 695-718, San Diego, California, Academic Press/Elsevier.

Decker, R. B., S. M. Krimigis, E. C. Roelof, M. E. Hill, (2015), Recent particle measurements from Voyagers 1 and 2, Journal of Physics: Conference Series, vol. 577, doi: 10.1088/1742-6596/577/1/012006.

Decker, R. B., S. M. Krimigis, E. C. Roelof, M. E. Hill, T. P. Armstrong, G. Gloeckler, D. C. Hamilton, L. J. Lanzerotti, (2008), Mediation of the solar wind termination shock by non-thermal ions, Nature, 454, 67-70.

Decker, R. B., S. M. Krimigis, E. C. Roelof, M. E. Hill, T. P. Armstrong, G. Gloeckler, D. C. Hamilton, L. J. Lanzerotti, (2005), Voyager 1 in the foreshock, termination shock, and heliosheath, Science 309 (5743), 2020-2024.

DeJong, A. D., J. L. Burch, J. Goldstein, A. J. Coates, D. T. Young, (2010), Low-energy electrons in Saturn's inner magnetosphere and their role in interchange injections, Journal of Geophysical Research-Space Physics 115, A10229, doi: 10.1029/2010ja015510.

Delamere, P. A., A. Otto, X. Ma, F. Bagenal, R. J. Wilson, (2015), Magnetic flux circulation in the rotationally driven giant magnetospheres, Journal of Geophysical Research: Space Physics 120, no. 6, 4229-4245, doi: 10.1002/2015JA021036

Delamere, P. A., R. J. Wilson, S. Eriksson, F. Bagenal, (2013), Magnetic signatures of Kelvin-Helmholtz vortices on Saturn's magnetopause: Global survey, Journal of Geophysical Research: Space Physics, 118, 393–404, doi: 10.1029/2012JA018197.

Desai, R. T., S. A. Taylor, L. H. Regoli, A. J. Coates, T. A. Nordheim, M. A. Cordiner, B. D. Teolis, M. F. Thomsen, R. E. Johnson, G. H. Jones, M. M. Cowee, J. H. Waite, (2018), Cassini CAPS identification of pickup ion compositions at Rhea, Geophysical Research Letters 45 (4), 1704-1712, doi: 10.1002/2017GL076588.

Desai, R. T., A. J. Coates, A. Wellbrock, V. Vuitton, F. J. Crary, D. Gonzalez-Caniulef, O. Shebanits, G. H. Jones, G. R. Lewis, J. H. Waite, M. Cordiner, S. A. Taylor, D. O. Kataria, J. E. Wahlund, N. J. T. Edberg, E. C. Sittler, (2017), Carbon chain anions and the growth of complex organic molecules in Titan's ionosphere, Astrophysical Journal Letters 844 (2), doi: 10.3847/2041-8213/aa7851.

Desch, M. D., G. Fischer, M. L. Kaiser, W. M. Farrell, W. S. Kurth, D. A. Gurnet, P. Zarka, A. Lecacheax, C. C. Porco, A. P. Ingersoll, U. Dyudina, (2006), Cassini RPWS and imaging observations of Saturn lightning, Planetary Radio Emissions VI: 6th International Workshop on Planetary and Solar Radio Emissions, 2005, Graz, Austria.

Dessler, A. J., (1985), Differential rotation of the magnetic fields of gaseous planets, Geophysical Research Letters 12 (5), 299-302.

Dialynas, K., E. Roussos, L. Regoli, C. P. Paranicas, S. M. Krimigis, M. Kane, D. G. Mitchell, D. C. Hamilton, N. Krupp, J. F. Carbary, (2018), Energetic ion moments and polytropic index in Saturn's magnetosphere using Cassini/MIMI measurements: A simple model based on *K*-Distribution functions, Journal of Geophysical Research: Space Physics 123, no. 10, 8066-8086.

Dialynas, K., S. M. Krimigis, D. G. Mitchell, R. B. Decker, E. C. Roelof, (2017a), The bubble-like shape of the heliosphere observed by Voyager and Cassini, Nature Astronomy, 1, 115.

Dialynas, K., S. M. Krimigis, D. G. Mitchell, R. B. Decker, E. C. Roelof, (2017b), Response times of Cassini/INCA > 5.2 keV ENAs and Voyager ions in the heliosheath over the solar cycle, Journal of Physics: Conference Series, 900(1).

Dialynas, K., S. M. Krimigis, D. G. Mitchell, E. C. Roelof, (2015), Energetic neutral atom (ENA) intensity gradients in the heliotail during year 2003, using Cassini/INCA measurements, Journal of Physics: Conference Series 577 (1), 12007-12016, doi: 10.1088/1742-6596/577/1/012007.

Dialynas, K., S. M. Krimigis, D. G. Mitchell, E. C. Roelof, R. B. Decker, (2013), A three-coordinate system (Ecliptic, Galactic, ISMF) spectral analysis of heliospheric ENA emissions using

Cassini/INCA measurements, Astrophysical Journal 778 (1), 40, doi: 10.1088/0004-637X/778/1/40.

Dialynas, K., S. M. Krimigis, D. G. Mitchell, D. C. Hamilton, N. Krupp, P. C. Brandt, (2009), Energetic ion spectral characteristics in the Saturnian magnetosphere using Cassini/MIMI measurements, Journal of Geophysical Research-Space Physics 114, A01212, doi: 10.1029/2008ja013761.

DiFabio, R. D., D. C. Hamilton, S. M. Krimigis, D. G. Mitchell, (2011), Long term time variations of the suprathermal ions in Saturn's magnetosphere, Geophysical Research Letters 38 (18), L18103, doi: 10.1029/2011GL048841.

Dong, Y., T. W. Hill, S. Y. Ye, (2015), Characteristics of ice grains in the Enceladus plume from Cassini observations, Journal of Geophysical Research-Space Physics 120 (2), 915-937, doi: 10.1002/2014ja020288.

Dougherty, M. K., H. Cao, K. K. Khurana, G. J. Hunt, G. Provan, S. Kellock, M. E. Burton, T. A. Burk, E. J. Bunce, S. W. H. Cowley, M. G. Kivelson, C. T. Russell, D. J. Southwood, (2018), Saturn's magnetic field revealed by the Cassini Grand Finale, Science 362 (6410), doi: 10.1126/science.aat5434.

Dougherty, M. K., K. K. Khurana, F. M. Neubauer, C. T. Russell, J. Saur, J. S. Leisner, M. E. Burton, (2006), Identification of a dynamic atmosphere at Enceladus with the Cassini magnetometer, Science 311 (5766), 1406-1409. doi: 10.1126/science.1120985.

Dougherty, M. K., N. Achilleos, N. Andre, C. S. Arridge, A. Balogh, C. Bertucci, B. T. Tsurutani, (2005), Cassini magnetometer observations during Saturn orbit insertion, Science, 307(5713):1266–1270, doi: 10.1126/science.1106098.

Drake, J. F., M. Swisdak, M. Opher, (2015), A model of the heliosphere with jets, The Astrophysical Journal Letters 808 (2), L44.

Dungey, J. W., (1965), The length of the magnetospheric tail, Journal of Geophysical Research 70 (7), 1753-1753, doi: 10.1029/JZ070i007p01753.

Dyudina, U. A., A. P. Ingersoll, S. P. Ewald, C. C. Porco, G. Fischer, W. S. Kurth, R. A. West, (2010), Detection of visible lightning on Saturn, Geophysical Research Letters 37, L09205. doi: 10.1029/2010gl043188.

Edberg, N. J. T., D. J. Andrews, O. Shebanits, K. Ågren, J.-E. Wahlund, H. J. Opgenoorth, T. E. Cravens, Z. Girazian, (2013a), Solar cycle modulation of Titan's ionosphere, Journal of Geophysical Research, 118, 5255–5264, doi: 10.1002/jgra.50463.

Edberg, N. J. T., D. J. Andrews, O. Shebanits, K. Ögren, J.-E. Wahlund, H. J. Opgenoorth, E. Roussos, P. Garnier, T. E. Cravens, S. V. Badman, R. Modolo, C. Bertucci, M. K. Dougherty, (2013b), Extreme densities in Titan's ionosphere during the T85 magnetosheath encounter, Geophysical Research Letters, 40, 2879–2883, doi: 10.1002/grl.50579.

Edberg, N. J. T., K. Ågren, J. E. Wahlund, M. W. Morooka, D. J. Andrews, S. W. H. Cowley, A. Wellbrock, A. J. Coates, C. Bertucci, M. K. Dougherty, (2011), Structured ionospheric outflow during the Cassini T55-T59 Titan flybys, Planetary and Space Science 59 (8), 788-797, doi: 10.1016/j.pss.2011.03.007.

Edberg, N. J. T., J. E. Wahlund, K. Ågren, M. W. Morooka, R. Modolo, C. Bertucci, M. K. Dougherty, (2010), Electron density and temperature measurements in the cold plasma environment of Titan: Implications for atmospheric escape, Geophysical Research Letters 37 (20), L20105, doi: 10.1029/2010GL044544.

Elrod, M. K., W. L. Tseng, A. K. Woodson, R. E. Johnson, (2014), Seasonal and radial trends in Saturn's thermal plasma between the main rings and Enceladus, Icarus 242:130-137, doi: 10.1016/j.icarus.2014.07.020.

Elrod, M. K., W. L. Tseng, R. J. Wilson, R. E. Johnson, (2012), Seasonal variations in Saturn's plasma between the main rings and Enceladus, Journal of Geophysical Research-Space Physics 117, A03207, doi: 10.1029/2011JA017332.

Fahr, H. J., (1986), Is the heliospheric interface submagnetosonic? Consequences for the LISM presence in the heliosphere, Advances in Space Research 6 (2), 13-25.

Farrell, W. M., W. S. Kurth, D. A. Gurnett, A. M. Persoon, R. J. MacDowall, (2017), Saturn's rings and associated ring plasma cavity: Evidence for slow ring erosion, Icarus, 292, 48–52, doi: 10.1016/j.icarus.2017.03.022.

Farrell, W. M., W. S. Kurth, D. A. Gurnett, R. E. Johnson, M. L. Kaiser, J. E. Wahlund, J. H. Waite Jr., (2009), Electron density dropout near Enceladus in the context of water-vapor and water-ice, Geophysical Research Letters 36, L10203, doi: 10.1029/2008gl037108.

Farrell, W. M., M. L. Kaiser, W. S. Kurth, M. D. Desch, D. A. Gurnett, G. B. Hospodarsky, and R. J. MacDowall, (2004), Remote sensing of possible plasma density bubbles in the inner Jovian dayside magnetosphere, Journal of Geophysical Research-Space Physics 109 (A9), 14, doi: 10.1029/2003JA010130.

Felici, M., C. S. Arridge, A. J. Coates, S. V. Badman, M. K. Dougherty, C. M. Jackman, W. S. Kurth, H. Melin, D. G. Mitchell, D. B. Reisenfeld, N. Sergis, (2016), Cassini observations of ionospheric plasma in Saturn's magnetotail lobes, Journal of Geophysical Research-Space Physics 121 (1), 338-357, doi: 10.1002/2015ja021648.

Feyerabend, M., S. Simon, F. M. Neubauer, U. Motschmann, C. Bertucci, N. J. T. Edberg, G. B. Hospodarsky, W. S. Kurth, (2016), Hybrid simulation of Titan's interaction with the supersonic solar wind during Cassini's T96 flyby, Geophysical Research Letters 43 (1), 35-42.

Fischer, G., S.-Y. Ye, J. B. Groene, A. P. Ingersoll, K. Sayanagi, J. D. Menietti, W. S. Kurth, D. A. Gurnett, (2014), A possible influence of the Great White Spot on Saturn kilometric radiation periodicity, Annales Geophysicae, 32, 1463–1476, doi: 10.5194/angeo-32-1463-2014.

Fischer, G., W. S. Kurth, D. A. Gurnett, P. Zarka, U. A. Dyudina, A. P. Ingersoll, S. P. Ewald, C. C. Porco, A. Wesley, C. Go, M. Delcroix, (2011a), A giant thunderstorm on Saturn, Nature, 475, 75–77, doi: 10.1038/nature10205.

Fischer, G., U. A. Dyudina, W. S. Kurth, D. A. Gurnett, P. Zarka, T. Barry, M. Delcroix, C. Go, D. Peach, R. Vandebergh, A. Wesley, (2011b), Overview of Saturn lightning observations, in Planetary Radio Emissions VII, (eds.) H. O. Rucker, W. S. Kurth, P. Louarn, G. Fischer, Austrian Academy of Sciences, Vienna, Austria, pp. 135–144.

Fischer, G., D. A. Gurnett, Y. Yair, (2011c), Extraterrestrial lightning and its past and future investigation, lightning; properties, formation and types, (eds.) M. D. Wood, NOVA Science Publishers, Inc., New York.

Fischer, G., W. Macher, D. A. Gurnett, M. D. Desch, A. Lecacheux, P. Zarka, W. S. Kurth, M. L. Kaiser, (2006), The discrimination between Jovian radio emissions and Saturn electrostatic discharges, Geophysical Research Letters, 33, L21201, doi: 10.1029/2006GL026766.

Fischer, G. and H. O. Rucker, (2006), Man-made radio emissions recorded by Cassini/RPWS during Earth flyby, Planetary Radio Emissions VI, Proceedings from the 6th International Workshop on Planetary and Solar Radio Emissions, April 20-22, 2005, Graz, Austria.

Fisk, L. A. and G. Gloeckler, (2008), Acceleration of suprathermal tails in the solar wind, The Astrophysical Journal 686 (2), 1466.

Fleshman, B. L., P. A. Delamere, F. Bagenal, T. Cassidy, (2013), A 1-D model of physical chemistry in Saturn's inner magnetosphere, Journal of Geophysical Research-Planets 118 (8), 1567-1581, doi: 10.1002/jgre.20106.

Fox, J. L. and R. V. Yelle, (1997), Hydrocarbon ions in the ionosphere of Titan, Geophysical Research Letters 24 (17), 2179-2182.

Fuselier, S. A., R. Frahm, W. S. Lewis, A. Masters, J. Mukherjee, S. M. Petrinec, I. J. Sillanpää, (2014), The location of magnetic reconnection at Saturn's magnetopause: A comparison with Earth, Journal of Geophysical Research-Space Physics 119 (4), 2563-2578, doi: 10.1002/2013ja019684.

Galand, M., A. J. Coates, T. E. Cravens, J. -E. Wahlund, (2014), Titan's ionosphere, in Titan: Interior, Surface, Atmosphere, and Space Environment, Chapter 11, (eds.) I. Müller-Wodarg, C. A. Griffith, E. Lellouch, T. E. Cravens, Cambridge University Press, pp. 376–419.

Garnier, P., M. K. G. Holmberg, J. E. Wahlund, G. R. Lewis, P. Schippers, A. Coates, D. A. Gurnett, J. H. Waite, I. Dandouras, (2014), Deriving the characteristics of warm electrons (100-500 eV) in the magnetosphere of Saturn with the Cassini Langmuir probe, Planetary and Space Science 104 (Part B), 173-184. doi: 10.1016/j.pss.2014.09.008.

Garnier, P., J. E. Wahlund, L. Rosenqvist, R. Modolo, K. Ågren, N. Sergis, P. Canu, M. Andre, D. A. Gurnett, W. S. Kurth, S. M. Krimigis, A. Coates, M. Dougherty, J. H. Waite, (2009), Titan's ionosphere in the magnetosheath: Cassini RPWS results during the T32 flyby, Annales Geophysicae 27 (11), 4257-4272, doi: 10.5194/angeo-27-4257-2009.

Gérard, J.-C., E. J. Bunce, D. Grodent, S. W. H. Cowley, J. T. Clarke, S. V. Badman, (2005), Signature of Saturn's auroral cusp: Simultaneous Hubble Space Telescope FUV observations and upstream solar wind monitoring, Journal of Geophysical Research Space Physics 110, A11201, doi: 10.1029/2005JA011094.

Gérard, J.-C., D. Grodent, J. Gustin, A. Saglam, J. T. Clarke, J. T. Trauger, (2004), Characteristics of Saturn's FUV aurora observed with the Space Telescope Imaging Spectrograph, Journal of Geophysical Research Space Physics 109, A09207, doi: 10.1029/2004JA010513.

Giacalone, J. and R. Decker, (2010), The origin of low-energy anomalous cosmic rays at the solar-wind termination shock, The Astrophysical Journal 710 (1), 91.

Giampieri, G. and M. K. Dougherty, (2004), Modelling of the ring current in Saturn's magnetosphere, Annales Geophysicae, 22(2):653–659, doi: 10.5194/angeo-22-653-2004.

Goldstein, J., J. H. Waite, J. L. Burch, R. Livi, (2016), Evidence of m=1 density mode (plasma cam) in Saturn's rotating magnetosphere, Journal of Geophysical Research-Space Physics 121 (3), 2335-2348, doi: 10.1002/2015ja022131.

Goldstein, J., T. W. Hill, J. H. Waite, J. L. Burch, (2014), Analytical model of rotating two-cell convection at Saturn, Journal of Geophysical Research-Space Physics 119 (3), 1980-1993. doi: 10.1002/2013ja019615.

Grodent, D., (2015), A brief review of ultraviolet auroral emissions on giant planets, Space Science Reviews 187, (1-4), 23-50, doi: 10.1007/s11214-014-0052-8.

Grodent, D., J. Gustin, J. C. Gerard, A. Radioti, B. Bonfond, W. R. Pryor, (2011), Small-scale structures in Saturn's ultraviolet aurora, Journal of Geophysical Research Space Physics 116, A09225, doi: 10.1029/2011JA016818.

Grodent, D., A. Radioti, B. Bonfond, J.-C. Gérard, (2010), On the origin of Saturn's outer auroral emission, Journal of Geophysical Research Space Physics 115, A08219, doi: 10.1029/2009JA014901.

Grodent, D., J.-C. Gérard, S. W. H. Cowley, E. J. Bunce, J. T. Clarke, (2005), Variable morphology of Saturn's southern ultraviolet aurora, Journal of Geophysical Research Space Physics 110, 16, A07215, doi: 10.1029/2004JA010983.

Guo, R. L., Z. H. Yao, Y. Wei, L. C. Ray, I. J. Rae, C. S. Arridge, A. J. Coates, P. A. Delamere, N. Sergis, P. Kollmann, (2018), Rotationally driven magnetic reconnection in Saturn's dayside, Nature Astronomy 2, no. 8, 640, doi: 10.1038/s41550-018-0461-9.

Gurnett, D. A., W. S. Kurth, E. C. Stone, A. C. Cummings, S. M. Krimigis, R. B. Decker, N. F. Ness, L. F. Burlaga, (2015), Precursors to interstellar shocks of solar origin, The Astrophysical Journal 809 (2), 121.

Gurnett, D. A., W. S. Kurth, L. F. Burlaga, N. F. Ness, (2013), In situ observations of interstellar plasma with Voyager 1, Science 341, 1489-1492.

Gurnett, D. A. and W. R. Pryor, (2012), Auroral processes associated with Saturn's moon Enceladus, In Auroral Phenomenology and Magnetospheric Processes: Earth and Other Planets, (eds.), A. Keiling, E. Donovan, F. Bagenal, T. Karlsson, Geographical Monograph Series, vol. 197, pp. 305-313, Washington, DC, American Geophysical Union, doi:10.1029/2011GM001174.

Gurnett, D. A., J. B. Groene, T. F. Averkamp, W. S. Kurth, S.-Y. Ye, G. Fischer, (2011a), A SLS4 longitude system based on a tracking filter analysis of the rotational modulation of Saturn kilometric radiation, in Planetary Radio Emissions VII, (eds.) H. O. Rucker, W. S. Kurth, P. Louarn, G. Fischer, Austrian Academy of Sciences, Vienna, Austria, pp. 51–63.

Gurnett, D. A., T. F. Averkamp, P. Schippers, A. M. Persoon, G. B. Hospodarsky, J. S. Leisner, W. S. Kurth, G. H. Jones, A. J. Coates, F. J. Crary, M. K. Dougherty, (2011b), Auroral hiss,

electron beams and standing Alfven wave currents near Saturn's moon Enceladus, Geophysical Research Letters, 38, L06102, doi: 10.1029/2011GL046854.

Gurnett, D. A., J. B. Groene, A. M. Persoon, J. D. Menietti, S.-Y. Ye, W. S. Kurth, R. J. MacDowall, A. Lecacheux, (2010a), The reversal of the rotational modulation rates of the north and south components of Saturn kilometric radiation near equinox, Geophysical Research Letters, 37, L24101, doi: 10.1029/2010GL045796.

Gurnett, D. A., A. M. Persoon, A. J. Kopf, W. S. Kurth, M. W. Morooka, J.-E. Wahlund, K. K. Khurana, M. K. Dougherty, D. G. Mitchell, S. M. Krimigis, N. Krupp, (2010b), A plasmapause-like density boundary at high latitudes in Saturn's magnetosphere, Geophysical Research Letters, 37, L16806, doi: 10.1029/2010GL044466.

Gurnett, D. A., A. Lecacheux, W. S. Kurth, A. M. Persoon, J. B. Groene, L. Lamy, P. Zarka, J. F. Carbary, (2009), Discovery of a north-south asymmetry in Saturn's radio rotation period, Geophysical Research Letters, 36, L16102, doi: 10.1029/2009GL039621.

Gurnett, D. A., A. M. Persoon, W. S. Kurth, J. B. Groene, T. F. Averkamp, M. K. Dougherty, D. J. Southwood, (2007), The variable rotation period of the inner region of Saturn's plasma disk, Science, 316(5823):442–445, doi: 10.1126/science.1138562.

Gurnett, D. A., W. S. Kurth, G. B. Hospodarsky, A. M. Persoon, T. F. Averkamp, B. Cecconi, A. Lecacheux, P. Zarka, P. Canu, N. Cornilleau-Wehrlin, P. Galopeau, A. Roux, C. Harvey, P. Louarn, R. Bostrom, G. Gustafsson, J. -E. Wahlund, M. D. Desch, W. M. Farrell, M. L. Kaiser, K. Goetz, P. J. Kellogg, G. Fischer, H.-P. Ladreiter, H. Rucker, H. Alleyne, A. Pedersen, (2005), Radio and plasma wave observations at Saturn from Cassini's approach and first orbit, Science, 307, 1255–1259, doi: 10.1126/science.1105356.

Gurnett, D. A., W. S. Kurth, G. B. Hospodarsky, A. M. Persoon, P. Zarka, A. Lecacheux, S. J. Bolton, M. D. Desch, W. M. Farrell, M. L. Kalser, H. P. Ladreiter, H. O. Rucker, P. Galopeau, P. Louarn, D. T. Young, W. R. Pryor, M. K. Dougherty, (2002), Control of Jupiter’s radio emission and aurorae by the solar wind, Nature 415 (6875), 985-987, doi: 10.1038/415985a.

Gurnett, D. A., P. Zarka, R. Manning, W. S. Kurth, G. B. Hospodarsky, T. F. Averkamp, M. L. Kaiser, W. M. Farrell, (2001), Non-detection at Venus of high-frequency radio signals characteristic of terrestrial lightning, Nature 409 (6818), 313-315. doi: 10.1038/35053009.

Gustin, J., D. Grodent, A. Radioti, W. Pryor, L. Lamy, J. Ajello, (2017), Statistical study of Saturn’s auroral electron properties with Cassini/UVIS FUV spectral images, Icarus 284, 264-283 doi: 10.1016/j.icarus.2016.11.017.

Gustin, J., I. Stewart, J.-C. Gérard, L. Esposito, (2010), Characteristics of Saturn’s FUV airglow from limb-viewing spectra obtained with Cassini-UVIS, Icarus 210 (1), 270-283. doi: 10.1016/j.icarus.2010.06.031.

Gustin, J., J.-C. Gérard, W. Pryor, P. D. Feldman, D. Grodent, G. Holsclaw, (2009), Characteristics of Saturn’s polar atmosphere and auroral electrons derived from HST/STIS, FUSE and Cassini/UVIS spectra, Icarus 200 (1), 176-187, doi: 10.1016/j.icarus.2008.11.013.

Hanlon, P. G., M. K. Dougherty, R. J. Forsyth, M. J. Owens, K. C. Hansen, G. Toth, D. T. Young, (2004), On the evolution of the solar wind between 1 and 5 AU at the time of the Cassini Jupiter flyby: Multispacecraft observations of interplanetary coronal mass ejections including the formation of a merged interaction region, Journal of Geophysical Research: Space Physics, 109(A9):10 pp., doi: 10.1029/2003JA010112.

Hartle, R. E., M. Sarantos, E. C. Sittler Jr., (2011), Pickup ion distributions from three-dimensional neutral exospheres, Journal of Geophysical Research-Space Physics 116, A10101. doi: 10.1029/2011JA016859.

Hartle, R. E., E. C. Sittler Jr., A. Lipatov, (2008), Ion Escape from the Ionosphere of Titan, European Geosciences Union Annual Meeting, Vienna Austria, 14–18 April 2008.

Hartle, R. E. and E. C. Sittler Jr., (2007), Pickup ion phase space distributions: effects of atmospheric spatial gradients, Journal of Geophysical Research-Part A-Space Physics 112:A07104, doi: 10.1029/2006JA012157.

Hartle, R. E., E. C. Sittler Jr., F. M. Neubauer, R. E. Johnson, H. T. Smith, F. Crary, D. J. McComas, D. T. Young, A. J. Coates, D. Simpson, S. Bolton, D. Reisenfeld, K. Szego, J. J. Berthelier, A. Rymer, J. Vilppola, J. T. Steinberg, N. Andre, (2006a), Preliminary interpretation of Titan plasma interaction as observed by the Cassini plasma spectrometer: Comparisons with Voyager 1, Geophysical Research Letters, 33, L08201, doi: 10.1029/2005GL024817.

Hartle, R. E., E. C. Sittler Jr., F. M. Neubauer, R. E. Johnson, H. T. Smith, F. Crary, D. J. McComas, D. T. Young, A. J. Coates, D. Simpson, S. Bolton, D. Reisenfeld, K. Szego, J. J. Berthelier, A. Rymer, J. Vilppola, J. T. Steinberg, N. Andre, (2006b), Initial interpretation of Titan plasma interaction as observed by the Cassini plasma spectrometer: Comparisons with Voyager 1, Planetary and Space Science, 54, 1211.

Hartle, R. E. and R. Killen, (2006), Measuring pickup ions to characterize the surfaces and exospheres of planetary bodies: Applications to the Moon, Geophysical Research Letters 33 (5), doi: 10.1029/2005GL024520.

Hartle, R., E. C. Sittler Jr., F. M. Neubauer, R. E. Johnson, H. T. Smith, F. Crary, D. J. McComas, D. T. Young, A. J. Coates, D. Simpson, S. Boltan, D. Reisenfeld, K. Szego, J. J. Berthelier, A. Rymer, J. Vilppola, J. T. Steinberg, N. Andre, (2006), Preliminary interpretation of Titan plasma interaction as observed by the Cassini plasma spectrometer: Comparisons with Voyager 1, Geophysical Research Letters, vol. 33(8), L08201, doi: 10.1029/2005GL024817.

Hedman, M. M., C. M. Gosmeyer, P. D. Nicholson, C. Sotin, Robert H. Brown, R. N. Clark, K. H. Baines, B. J. Buratti, M. R. Showalter, (2013), An observed correlation between plume activity and tidal stresses on Enceladus, Nature, 500, 182–184, doi: 10.1038/nature12371.

Helled, R., E. Galanti, Y. Kaspi, (2015), Saturn's fast spin determined from its gravitational field and oblateness, Nature 520 (7546):202-204, doi: 10.1038/nature14278.

Hess, S. L. G., E. Echer, P. Zarka, L. Lamy, P. A. Delamere, (2014), Multi-instrument study of the Jovian radio emissions triggered by solar wind shocks and inferred magnetospheric subcorotation rates, Planetary and Space Science 99, 136-148, doi: 10.1016/j.pss.2014.05.015.

- - - - - - - - - - - - - -

Hill, M. E. and D. C. Hamilton, (2010), Interim report on the power law index of interplanetary suprathermal ion spectra, In AIP Conference Proceedings, vol. 1302, no. 1, pp. 58-63, American Institute of Physics, doi: 10.1063/1.3529991.

Hill, M. E., N. A. Schwadron, D. C. Hamilton, R. D. DiFabio, R. K. Squier, (2009), Interplanetary suprathermal He+ and He++ observations during quiet periods from 1 to 9 AU and implications for particle acceleration, Astrophysical Journal Letters 699 (1), L26-L30, doi: 10.1088/0004-637x/699/1/l26.

Hill, T. W., A. Jaggi, S. Sazykin, R. A. Wolf, (2018), Plasma circulation time scale of Saturn's magnetosphere.

Hill, T. W., (2017), Magnetosphere-Ionosphere coupling at Jupiter and Saturn, in Magnetosphere-Ionosphere Coupling in the Solar System, Part VI: Chapter 24, (eds.) C. R. Chappell, R. W. Schunk, P. M. Banks, J. L. Burch, R. M. Thorne, pp. 307–318, doi: 10.1002/9781119066880.ch24.

Hill, T. W., (2016), Penetration of external plasma into a rotation-driven magnetosphere, Journal of Geophysical Research: Space Physics, 121, doi: 10.1002/ 2016JA023430.

Hill, T. W., M. F. Thomsen, R. L. Tokar, A. J. Coates, G. R. Lewis, D. T. Young, F. J. Crary, et al., (2012), Charged nanograins in the Enceladus plume, Journal of Geophysical Research: Space Physics, 117(A5).

Hill, T. W., M. F. Thomsen, M. G. Henderson, R. L. Tokar, A. J. Coates, H. J. McAndrews, G. R. Lewis, D. G. Mitchell, C. M. Jackman, C. T. Russell, M. K. Dougherty, F. J. Crary, D. T. Young, (2008), Plasmoids in Saturn's magnetotail, Journal of Geophysical Research, 113, A01214, doi: 10.1029/2007JA012626.

Hill, T. W., A. M. Rymer, J. L. Burch, F. J. Crary, D. T. Young, M. F. Thomsen, D. Delapp, N. Andre, A. J. Coates, G. R. Lewis, (2005), Evidence for rotationally driven plasma transport in Saturn's magnetosphere, Geophysical Research Letters 32 (14), 14-10, doi: 10.1029/2005GL022620.

Hörst, S. M., V. Vuitton, R. V. Yelle, (2008), Origin of oxygen species in Titan's atmosphere, Journal of Geophysical Research-Planets 113 (E10), E10006. doi: 10.1029/2008je003135.

Hospodarsky, G. B., J. S. Leisner, K. Sigsbee, J. D. Menietti, W. S. Kurth, D. A. Gurnett, C. A. Kletzing, O. Santolik, (2012), Plasma wave observations at Earth, Jupiter, and Saturn in dynamics of Earth's radiation belts and inner magnetosphere, vol. 199, American Geophysical Union, Washington, DC.

Hospodarsky, G. B., J. E. Nelson, W. S. Kurth, D. A. Gurnett, P. Zarka, P. Canu, M. K. Dougherty, A. J. Coates, D. T. Young, A. M. Rymer, (2006), Solar wind electron densities upstream of Saturn determined from Langmuir Wave observations by the Cassini RPWS instrument, American Geophysical Union (AGU) Fall Meeting, San Francisco, California, 11-15 Dec. 2006.

Hospodarsky, G. B., W. S. Kurth, B. Cecconi, D. A. Gumett, M. L. Kaiser, M. D. Desch, P. Zarka, (2004), Simultaneous observations of Jovian quasi-periodic radio emissions by the Galileo and Cassini spacecraft, Journal of Geophysical Research-Space Physics 109 (A9), A09S07, doi: 10.1029/2003JA010263.

Hospodarsky, G. B., I. W. Christopher, J. D. Menietti, W. S. Kurth, D. A. Gurnett, T. F. Averkamp, J. B. Groene, P. Zarka, (2001a), Control of Jovian radio emissions by the Galilean moons as observed by Cassini and Galileo, in Planetary Radio Emissions V, (eds.) H. O. Rucker, M. L. Kaiser, Y. Leblanc, Austrian Academy of Sciences Press, Vienna, Austria, pp. 155–164.

Hospodarsky, G. B., T. F. Averkamp, W. S. Kurth, D. A. Gurnett, M. Dougherty, U. Inan, T. Wood, (2001b), Wave normal and poynting vector calculations using the Cassini Radio and Plasma Wave instrument, Journal of Geophysical Research, 106, 30253–30269, doi: 10.1029/10.1029/2001JA900114.

Hsu, H. W., J. Schmidt, S. Kempf, F. Postberg, G. Moragas-Klostermeyer, M. Seiss, H. Hoffmann, M. Burton, S. Y. Ye, W. S. Kurth, M. Horanyi, N. Khawaja, F. Spahn, D. Schirdewahn, J. O'Donoghue, L. Moore, J. Cuzzi, G. H. Jones, R. Srama, (2018), Cosmic dust analyser onboard Cassini collects material from Saturn's main rings, Science 362, 49.

Hunt, G. J., G. Provan, E. J. Bunce, S. W. H. Cowley, M. K. Dougherty, D. J. Southwood, (2018a), Field-aligned currents in Saturn's magnetosphere: Observations from the F-ring orbits, Journal of Geophysical Research, 123(5):3806–3821, doi: 10.1029/2017JA025067.

Hunt, G. J., S. W. H. Cowley, J. D. Nichols, (2018b), Ionospheric currents due to ionosphere-magnetosphere coupling at Jupiter and Saturn, in Electric Currents in Geospace and Beyond, (eds.) A. Keiling, O. Marghitu, M. Wheatland, John Wiley & Sons, Inc., p. 459.

Hunt, G. J., S. W. H. Cowley, G. Provan, E. J. Bunce, I. I. Alexeev, E. S. Belenkaya, V. V. Kalegaev, M. K. Dougherty, A. J. Coates, (2016), Field-aligned currents in Saturn's magnetosphere: Local time dependence of southern summer currents in the dawn sector between midnight and noon, Journal of Geophysical Research: Space Physics 121, no. 8, 7785-7804, doi: 10.1002/2016ja022712.

Hunt, G. J., S. W. H. Cowley, G. Provan, E. J. Bunce, I. I. Alexeev, E. S. Belenkaya, V. V. Kalegaev, M. K. Dougherty, A. J. Coates, (2015), Field-aligned currents in Saturn's northern nightside magnetosphere: Evidence for interhemispheric current flow associated with planetary period oscillations, Journal of Geophysical Research-Space Physics 120 (9), 7552-7584, doi: 10.1002/2015ja021454.

Hunt, G. J., S. W. H. Cowley, G. Provan, E. J. Bunce, I. I. Alexeev, E. S. Belenkaya, V. V. Kalegaev, M. K. Dougherty, A. J. Coates, (2014), Field-aligned currents in Saturn's southern nightside magnetosphere: Subcorotation and planetary period oscillation components, Journal of Geophysical Research-Space Physics 119 (12), 9847-9899, doi: 10.1002/2014ja020506.

Hurley, D. M., M. E. Perry, J. H. Waite, (2015), Modeling insights into the locations of density enhancements from the Enceladus water vapor jets, Journal of Geophysical Research: Planets 120 (11), 1763-1773.

Imai, M., A. Lecacheux, M. Moncuquet, F. Bagenal, C. A. Higgins, K. Imai, J. R. Thieman, (2015), Modeling Jovian hectometric attenuation lanes during the Cassini flyby of Jupiter, Journal of Geophysical Research-Space Physics 120 (3), 1888-1907, doi: 10.1002/2014ja020815.

Imai, M., A. Lecacheux, K. Imai, C. A. Higgins, J. R. Thieman, (2011a), Jupiter's decametric and hectomectric radio emissions observed by Voyager PRA and Cassini RPWS, in Planetary Radio Emissions VII, (eds.) H. O. Rucker, W. S. Kurth, P. Louarn, G. Fischer, Austrian Academy of Sciences, Vienna, Austria, pp. 167–176.

Imai, M., K. Imai, C. A. Higgins, J. R. Thieman, (2011b), Comparison between Cassini and Voyager observations of Jupiter's decametric and hectometric radio emissions, Journal of Geophysical Research, 116, A12233, doi: 10.1029/2011JA016456.

Imai, M., K. Imai, C. A. Higgins, J. R. Thieman, (2008), Angular beaming model of Jupiter's decametric radio emissions based on Cassini RPWS data analysis, Geophysical Research Letters 35 (17), L17103, doi: 10.1029/2008gl034987.

Jackman, C. M., G. Provan, S. W. H. Cowley, (2016), Reconnection events in Saturn's magnetotail: Dependence of plasmoid occurrence on planetary period oscillation phase, Journal of Geophysical Research-Space Physics 121 (4), 2922-2934. doi: 10.1002/2015ja021985.

Jackman, C. M., M. F. Thomsen, D. G. Mitchell, N. Sergis, C. S. Arridge, M. Felici, S. V. Badman, C. Paranicas, X. Jia, G. B. Hospodarksy, (2015), Field dipolarization in Saturn's magnetotail with planetward ion flows and energetic particle flow bursts: Evidence of quasi-steady reconnection, Journal of Geophysical Research Space Physics 120 (5), 3603-3617.

Jackman, C. M., J. A. Slavin, M. G. Kivelson, D. J. Southwood, N. Achilleos, M. F. Thomsen, G. A. DiBraccio, J. P. Eastwood, M. P. Freeman, M. K. Dougherty, M. F. Vogt, (2014), Saturn's dynamic magnetotail: A comprehensive magnetic field and plasma survey of plasmoids and traveling compression regions and their role in global magnetospheric dynamics, Journal of Geophysical Research-Space Physics 119 (7), 5465-5494, doi: 10.1002/2013ja019388.

Jackman, C. M., N. Achilleos, S. W. H. Cowley, E. J. Bunce, A. Radioti, D. Grodent, S. V. Badman, M. K. Dougherty, W. Pryor, (2013), Auroral counterpart of magnetic field dipolarizations in Saturn's tail, Planetary and Space Science 82-83, 34-42, doi: 10.1016/j.pss.2013.03.010.

Jackman, C. M., J. A. Slavin, S. W. H. Cowley, (2011), Cassini observations of plasmoid structure and dynamics: Implications for the role of magnetic reconnection in magnetospheric circulation at Saturn, Journal of Geophysical Research, 116, A10212, doi: 10.1029/2011JA016682.

Jackman, C. M. and C. S. Arridge, (2011a), Solar cycle effects on the dynamics of Jupiter's and Saturn's magnetospheres, Solar Physics, 274:481–502, doi 10.1007/s11207-011-9748-z.

Jackman, C. M. and C. S. Arridge, (2011b), Statistical properties of the magnetic field in the Kronian magnetotail lobes and current sheet, Journal of Geophysical Research, 116(A05224), doi: 10.1029/2010JA015973.

Jackman, C. M., C. S. Arridge, J. A. Slavin, S. E. Milan, L. Lamy, M. K. Dougherty, A. J. Coates, (2010), In situ observations of the effect of a solar wind compression on Saturn's magnetotail, Journal of Geophysical Research-Space Physics 115:A10240. doi: 10.1029/2010ja015312.

Jackman, C. M., L. Lamy, M. P. Freeman, P. Zarka, B. Cecconi, W. S. Kurth, M. K. Dougherty, (2009a), On the character and distribution of lower-frequency radio emissions at Saturn and their relationship to substorm-like events, Journal of Geophysical Research: Space Physics, 114:13 pp., doi: 10.1029/2008JA013997.

Jackman, C. M., C. S. Arridge, H. J. McAndrews, M. G. Henderson, R. J. Wilson, (2009b), Northward field excursions in Saturn's magnetotail and their relationship to magnetospheric periodicities, Geophysical Research Letters, 36(L16101), doi: 10.1029/2009GL039149.

Jackman, C. M., C. S. Arridge, N. Krupp, E. J. Bunce, D. G. Mitchell, H. J. McAndrews, M. K. Dougherty, C. T. Russell, N. Achilleos, G. H. Jones, A. J. Coates, (2008), A multi-instrument view of tail reconnection at Saturn, Journal of Geophysical Research-Space Physics 113 (A11), A11213, doi: 10.1029/2008ja013592.

Jackman, C. M., C. T. Russell, D. J. Southwood, C. S. Arridge, N. Achilleos, M. K. Dougherty, (2007), Strong rapid dipolarizations in Saturn's magnetotail: In situ evidence of reconnection, Geophysical Research Letters 34 (11), L11203.

Jackman, C. M. and S. W. H. Cowley, (2006), A model of the plasma flow and current in Saturn's polar ionosphere under conditions of strong Dungey cycle driving, Annales Geophysicae 24(3), pp. 1029-1055, European Geosciences Union.

Jackman, C. M., N. Achilleos, E. J. Bunce, S. W. H. Cowley, S. E. Milan, (2005a), Structure of the interplanetary magnetic field during the interval spanning the first Cassini fly-through of Saturn's magnetosphere and its implications for Saturn's magnetospheric dynamics, Advances in Space Research, 36:2120–2126, doi: 10.1016/j.asr.2004.12.023.

Jackman, C. M., N. Achilleos, E. J. Bunce, B. Cecconi, J. T. Clarke, S. W. H. Cowley, W. S. Kurth, P. Zarka, (2005b), Interplanetary conditions and magnetospheric dynamics during the Cassini orbit insertion fly-through of Saturn's magnetosphere, Journal of Geophysical Research, 110(A10212), doi: 10.1029/2005JA011054.

Jackman, C. M., N. Achilleos, E. J. Bunce, S. W. H. Cowley, M. K. Dougherty, G. H. Jones, S. E. Milan, E. J. Smith, (2004), Interplanetary magnetic field at ~9 AU during the declining phase of the solar cycle and its implications for Saturn's magnetospheric dynamics, Journal of Geophysical Research-Space Physics 109 (A11), 19. doi: 10.1029/2004JA010614.

Jasinski, J. M., C. S. Arridge, A. J. Coates, G. H. Jones, N. Sergis, M. F. Thomsen, N. Krupp, (2017), Diamagnetic depression observations at Saturn's magnetospheric cusp by the Cassini spacecraft, Journal of Geophysical Research Space Physics 122 (6), 6283-6303, doi: 10.1002/2016ja023738.

Jasinski, J. M., C. S. Arridge, A. J. Coates, G. H. Jones, N. Sergis, M. F. Thomsen, D. B. Reisenfeld, N. Krupp, J. H. Waite, (2016), Cassini plasma observations of Saturn's magnetospheric cusp, Journal of Geophysical Research Space Physics 121 (12), 12047-12067, doi: 10.1002/2016ja023310.

Jasinski, J. M., C. S. Arridge, L. Lamy, J. S. Leisner, M. F. Thomsen, D. G. Mitchell, A. J. Coates, A. Radioti, G. H. Jones, E. Roussos, N. Krupp, D. Grodent, M. K. Dougherty, J. H. Waite, (2014), Cusp observation at Saturn's high latitude magnetosphere by the Cassini spacecraft, Geophysical Research Letters, 41, 1382–1388, doi: 10.1002/2014GL059319.

Jia, X. Z. and M. G. Kivelson, (2016), Dawn-dusk asymmetries in rotating magnetospheres: Lessons from modeling Saturn, Journal of Geophysical Research Space Physics 121 (2), 1413-1424, doi: 10.1002/2015ja021950.

Jia, X. and M. G. Kivelson, (2012), Driving Saturn's magnetospheric periodicities from the upper atmosphere/ionosphere: Magnetotail response to dual sources, Journal of Geophysical Research-Space Physics 117, A11219, doi: 10.1029/2012JA018183.

Jia, X., M. G. Kivelson, T. I. Gombosi, (2012), Driving Saturn's magnetospheric periodicities from the upper atmosphere/ionosphere, Journal of Geophysical Research, 117(A04215), doi: 10.1029/2011JA017367.

Jia, Y. D., C. T. Russell, K. K. Khurana, H. Y. Wei, Y. J. Ma, J. S. Leisner, A. M. Persoon, M. K. Dougherty, (2011), Cassini magnetometer observations over the Enceladus poles, Geophysical Research Letters 38 (19), L19109, doi: 10.1029/2011GL049013.

Jia, Y. -D., C. T. Russell, K. K. Khurana, J. S. Leisner, T. I. Gombosi, (2010a), The interaction of Saturn's magnetosphere and its moons 1: Interaction between co-rotating plasma and standard obstacles, Journal of Geophysical Research, 115(A04214), doi: 10.1029/2009JA014630.

Jia, Y. -D., C. T. Russell, K. K. Khurana, Y. J. Ma, D. Najib, T. I. Gombosi, (2010b), The interaction of Saturn's magnetosphere and its moons 2: Shape of the Enceladus plume, Journal of Geophysical Research, 115(A04215), doi: 10.1029/2009JA014873.

Jia, Y. -D., C. T. Russell, K. K. Khurana, J. S. Leisner, Y. J. Ma, M. K. Dougherty, (2010c), Time-varying magnetospheric environment near Enceladus as seen by the Cassini magnetometer, Geophysical Research Letters, 37:5 pp., doi: 10.1029/2010GL042948.

Jia, Y. -D., C. T. Russell, Y. J. Ma, K. K. Khurana, W. Kurth, T. I. Gombosi, (2010d), The interaction of Saturn's magnetosphere and its moons 3: Time Variation of the Enceladus Plume, Journal of Geophysical Research, 115(12):A12243, doi: 10.1029/2010JA015534.

Jinks, S. L., E. J. Bunce, S. W. H. Cowley, G. Provan, T. K. Yeoman, C. S. Arridge, M. K. Dougherty, D. A. Gurnett, N. Krupp, W. S. Kurth, D. G. Mitchell, M. Morooka, J. E. Wahlund, (2014), Cassini multi-instrument assessment of Saturn's polar cap boundary, Journal of Geophysical Research-Space Physics 119 (10), 8161-8177, doi: 10.1002/2014ja020367.

Johnson, R. E., W. L. Tseng, M. K. Elrod, A. M. Persoon, (2017), Nanograin density outside Saturn's A ring, Astrophysical Journal Letters 834 (1), doi: 10.3847/2041-8213/834/1/l6.

Johnson, R. E., O. J. Tucker, M. Michael, E. C. Sittler, H. T. Smith, D. T. Young, J. H. Waite, (2009), Mass loss processes in Titan's upper atmosphere, in Titan from Cassini-Huygens, R. H. Brown, J.-P. Lebreton, and J. H. White (eds.), pp. 373-391, Springer, Dordrecht.

Johnson, R. E., J. G.Luhmann, R. L. Tokar, M. Bouhram, J. J. Berthelier, E. C. Sittler, J. F. Cooper, T. W. Hill, H. T. Smith, M. Michael, M. Liu, F. J. Crary, D. T. Young, (2006), Production, ionization and redistribution of O2 Saturn's ring atmosphere, Icarus180, 393–402.

Johnson, R. E., M. Liu, E. C. Sittler Jr., (2005), Plasma-induced clearing and redistribution of material embedded in planetary magnetospheres, Geophysical Research Letters, 32, L24201, doi: 10.1029/2005GL024275.

Jones, G. H., C. S. Arridge, A. J. Coates, G. R. Lewis, S. Kanani, A. Wellbrock, D. T. Young, F. J. Crary, R. L. Tokar, R. J. Wilson, T. W. Hill, R. E. Johnson, D. G. Mitchell, J. Schmidt, S. Kempf, U. Beckmann, C. T. Russell, Y. D. Jia, M. K. Dougherty, J. H. Waite Jr., B. A. Magee, (2009), Fine jet structure of electrically charged grains in Enceladus' plume, Geophysical Research Letters 36, L16204, doi: 10.1029/2009gl038284.

Kaiser, M. L., W. M. Farrell, W. S. Kurth, G. B. Hospodarsky, D. A. Gurnett, (2004), New observations from Cassini and Ulysses of Jovian VLF radio emissions, Journal of Geophysical Research, 109, A09S08, doi: 10.1029/2003JA010233.

Kaiser, M. L., W. M. Farrell, M. D. Desch, G. B. Hospodarsky, W. S. Kurth, D. A. Gurnett, (2001), Ulysses and Cassini at Jupiter: Comparison of the quasi-periodic radio bursts, In Planetary Radio Emissions V, (eds.) H. O. Rucker, M. L. Kaiser, Y. Leblanc, Austrian Academy of Sciences Press, Vienna, Austria, pp. 41–48.

Kaiser, M. L., P. Zarka, W. S. Kurth, G. B. Hospodarsky, D. A. Gurnett, (2000), Cassini and wind stereoscopic observations of Jovian nonthermal radio emissions – Measurement of beam widths, Journal of Geophysical Research-Space Physics 105 (A7), 16, 053-16, 062.

Kallio, E., I. Sillanpää, R. Jarvinen, P. Janhunen, M. Dougherty, C. Bertucci, F. Neubauer, (2007), Morphology of the magnetic field near Titan: Hybrid model study of the Cassini T9 flyby, Geophysical Research Letters 34 (24), L24S09.

Kanani, S. J., C. S. Arridge, G. H. Jones, A. N. Fazakerley, H. J. McAndrews, N. Sergis, S. M. Krimigis, M. K. Dougherty, A. J. Coates, D. T. Young, K. C. Hansen, N. Krupp, (2010), A new form of Saturn's magnetopause using a dynamic pressure balance model, based on in situ, multi-instrument Cassini measurements, Journal of Geophysical Research-Space Physics 115, A06207, doi: 10.1029/2009ja014262.

Keller, C. N., V. G. Anicich, T. E. Cravens, (1998), Model of Titan's ionosphere with detailed hydrocarbon ion chemistry, Planetary and Space Science 46 (9), 1157-1174, doi: 10.1016/S0032-0633(98)00053-1.

Keller, C. N., T. E. Cravens, L. Gan, (1992), A model of the ionosphere of Titan, Journal of Geophysical Research Space Physics 97 (A8), 12117-12135.

Kellett, S., C. S. Arridge, E. J. Bunce, A. J. Coates, S. W. H. Cowley, M. K. Dougherty, A. M. Persoon, N. Sergis, R. J. Wilson, (2011), Saturn's ring current: Local time dependence and temporal variability, Journal of Geophysical Research Space Physics 116, A05220, doi: 10.1029/2010ja016216.

Kellett, S., C. S. Arridge, E. J. Bunce, A. J. Coates, S. W. H. Cowley, M. K. Dougherty, A. M. Persoon, N. Sergis, R. J. Wilson, (2010), Nature of the ring current in Saturn's dayside magnetosphere, Journal of Geophysical Research Space Physics 115, A08201. doi: 10.1029/2009ja015146.

Kellett, S., E. J. Bunce, A. J. Coates, S. W. H. Cowley, (2009), Thickness of Saturn's ring current determined from north-south Cassini passes through the current layer, Journal of Geophysical Research Space Physics 114, A04209, doi: 10.1029/2008ja013942.

Khan, H., S. W. H. Cowley, E. Kolesnikova, M. Lester, M. J. Brittnacher, T. J. Hughes, W. J. Hughes, W. S. Kurth, D. J. McComas, L. Newitt, C. J. Owen, G. D. Reeves, H. J. Singer, C. W. Smith, D. J. Southwood, J. F. Watermann, (2001), Observations of two complete substorm cycles during the Cassini Earth swing-by: Cassini magnetometer data in a global context, Journal of Geophysical Research Space Physics 106 (A12), 30141-75, doi: 10.1029/2001JA900049.

Khurana, K. K., S. Fatemi, J. Lindkvist, E. Roussos, N. Krupp, M. Holmstrom, C. T. Russell, M. K. Dougherty, (2017), The role of plasma slowdown in the generation of Rhea's Alfven wings, Journal of Geophysical Research Space Physics 122 (2), 1778-1788, doi: 10.1002/2016ja023595.

Khurana, K. K., N. Krupp, M. G. Kivelson, E. Roussos, C. T. Russell, M. K. Dougherty, (2012), Cassini's flyby through Rhea's distant Alfven wing, European Planetary Science Congress 2012.

Kim, Y. H., J. L. Fox, J. H. Black, J. I. Moses, (2014), Hydrocarbon ions in the lower ionosphere of Saturn, Journal of Geophysical Research Space Physics 119 (1), 384-395, doi: 10.1002/2013JA019022.

Kimura, T., L. Lamy, C. Tao, S. V. Badman, S. Kasahara, B. Cecconi, P. Zarka, A. Morioka, Y. Miyoshi, D. Maruno, Y. Kasaba, M. Fujimoto, (2013), Long-term modulations of Saturn's auroral radio emissions by the solar wind and seasonal variations controlled by the solar ultraviolet flux, Journal of Geophysical Research Space Physics 118 (11), 7019-7035, doi: 10.1002/2013JA018833.

Kimura, T., B. Cecconi, P. Zarka, Y. Kasaba, F. Tsuchiya, H. Misawa, A. Morioka, (2012), Polarization and direction of arrival of Jovian quasiperiodic bursts observed by Cassini, Journal of Geophysical Research Space Physics 117, A11209, doi: 10.1029/2012JA017506.

Kinrade, J., S. V. Badman, E. J. Bunce, C. Tao, G. Provan, S. W. H. Cowley, A. Grocott, R. L. Gray, D. Grodent, T. Kimura, J. D. Nichols, C. S. Arridge, A. Radioti, J. T. Clarke, F. J. Crary, W. R. Pryor, H. Melin, K. H. Baines, M. K. Dougherty, (2017), An isolated, bright cusp aurora at Saturn, Journal of Geophysical Research Space Physics 122 (6), 6121-6138, doi: 10.1002/2016ja023792.

Kivelson, M. G. and X. Z. Jia, (2014), Control of periodic variations in Saturn's magnetosphere by compressional waves, Journal of Geophysical Research Space Physics 119 (10), 8030-8045, doi: 10.1002/2014ja020258.

Kivelson, M. G. and X. Jia, (2013), An MHD model of Ganymede's mini-magnetosphere suggests that the heliosphere forms in a sub-Alfvénic flow, Journal of Geophysical Research Space Physics 118 (11), 6839-6846.

Kivelson, M. G., (2006), Does Enceladus govern magnetospheric dynamics at Saturn?, Science 311 (5766), 1391-2, doi: 10.1126/science.1124494.

Kivelson, M. G. and D. J. Southwood, (2005), Dynamical consequences of two modes of centrifugal instability in Jupiter's outer magnetosphere, Journal of Geophysical Research Space Physics 110 (A12).

Kivelson, M. G. and D. J. Southwood, (2003), First evidence of IMF control of Jovian magnetospheric boundary locations: Cassini and Galileo magnetic field measurements compared, Planetary and Space Science 51 (13), 891-8, doi: 10.1016/S0032-0633(03)00075-8.

Kollmann, P., E. Roussos, C. Paranicas, E. E. Woodfield, B. H. Mauk, G. Clark, D. C. Smith, J. Vandegriff, (2018), Electron acceleration to MeV energies at Jupiter and Saturn, Journal of Geophysical Physics 123 (11), 9110-9129.

Kollmann, P., E. Roussos, A. Kotova, C. Paranicas, N. Krupp, (2017), The evolution of Saturn's radiation belts modulated by changes in radial diffusion, Nature Astronomy 1 (12), 872-877, doi: 10.1038/s41550-017-0287-x.

Kollmann, P., E. Roussos, A. Kotova, J. F. Cooper, D. G. Mitchell, N. Krupp, C. Paranicas, (2015), MeV proton flux predictions near Saturn's D ring, Journal of Geophysical Research Space Physics 120 (10), 8586-8602, doi: 10.1002/2015ja021621.

Kollmann, P., E. Roussos, C. Paranicas, N. Krupp, D. K. Haggerty, (2013), Processes forming and sustaining Saturn's proton radiation belts, Icarus 222 (1), 323-341, doi: 10.1016/j.icarus.2012.10.033.

Kollmann, P., E. Roussos, C. Paranicas, N. Krupp, C. M. Jackman, E. Kirsch, K. H. Glassmeier, (2011), Energetic particle phase space densities at Saturn: Cassini observations and interpretations, Journal of Geophysical Research Space Physics 116, A05222, doi: 10.1029/2010ja016221.

Koskinen, T. T., B. R. Sandel, R. V. Yelle, D. F. Strobel, I. C. F. Müeller-Wodarg, J. T. Erwin, (2015), Saturn's variable thermosphere from Cassini/UVIS occultations, Icarus 260, 174-189, doi: 10.1016/j.icarus.2015.07.008.

Krasnopolsky, V. A., (2012), Titan's photochemical model: Further update, oxygen species, and comparison with Triton and Pluto, Planetary and Space Science 73 (1), 318-326, doi: 10.1016/j.pss.2012.08.013.

Kriegel, H., S. Simon, U. Motschmann, J. Saur, F. M. Neubauer, A. M. Persoon, M. K. Dougherty, D. A. Gurnett, (2011), Influence of negatively charged plume grains on the structure of Enceladus' Alfven wings: Hybrid simulations versus Cassini Magnetometer data, Journal of Geophysical Research Space Physics 116, A10223, doi: 10.1029/2011JA016842.

Krimigis, S. M., R. B. Decker, E. C. Roelof, M. E. Hill, T. P. Armstrong, G. Gloeckler, D. C. Hamilton, L. J. Lanzerotti, (2013), Search for the exit: Voyager 1 at heliosphere's border with the galaxy, Science 341 (6142), 144-147.

Krimigis, S. M., E. C. Roelof, R. B. Decker, M. E. Hill, (2011), Zero outward flow velocity for plasma in a heliosheath transition layer, Nature, 474, 359–361.

Krimigis, S. M., D. G. Mitchell, E. C. Roelof, R. B. Decker, (2010), ENA (E>5 keV) images from Cassini and Voyager "ground truth": Suprathermal pressure in the heliosheath, In AIP

Conference Proceedings, vol. 1302, no. 1, pp. 79-85, American Institute of Physics, doi: 10.1063/1.3529994.

Krimigis, S. M., D. G. Mitchell, E. C. Roelof, K. C. Hsieh, D. J. McComas, (2009), Imaging the interaction of the heliosphere with the interstellar medium from Saturn with Cassini, Science 326 (5955), 971-973, doi: 10.1126/science.1181079.

Krimigis, S. M., N. Sergis, D. G. Mitchell, N. Krupp, (2007), A dynamic, rotating ring current around Saturn, Nature, 450, 1050-1053.

Krimigis, S. M., Krimigis, S. M., D. G. Mitchell, D. C. Hamilton, N. Krupp, S. Livi, E. C. Roelof, J. Dandouras, et al., (2005), Dynamics of Saturn's magnetosphere from MIMI during Cassini's orbital insertion, Science, 307, 1270-1273.

Krupp, N., J. Woch, A. Lagg, S. Livi, D. G. Mitchell, S. M. Krimigis, M. K. Dougherty, P. G. Hanlon, T. P. Armstrong, S. A. Espinosa, (2004), Energetic particle observations in the vicinity of Jupiter: Cassini MIMI/LEMMS results, Journal of Geophysical Research Space Physics 109 (A9), 10, doi: 10.1029/2003JA0101.

Krupp, N., J. Woch, A. Lagg, S. A. Espinosa, S. Livi, S. M. Krimigis, D. G. Mitchell, D. J. Williams, A. F. Cheng, B. H. Mauk, R. W. McEntire, T. P. Armstrong, D. C. Hamilton, G. Gloeckler, J. Dandouras, L. J. Lanzerotti, (2002), Leakage of energetic particles from Jupiter's dusk magnetosphere: dual spacecraft observations, Geophysical Research Letters 29 (15), 26-1, doi: 10.1029/2001GL014290.

Krupp, N., J. Woch, A. Lagg, S. A. Espinosa, S. Livi, S. M. Krimigis, D. G. Mi, et al., (2002), Leakage of energetic particles from Jupiter's dusk magnetosphere: Dual spacecraft observations, Geophysical Research Letters, 29, doi: 10.1029/2001GL014290.

Kurth, W. S., G. B. Hospodarsky, D. A. Gurnett, L. Lamy, M. K. Dougherty, J. Nichols, E. J. Bunce, W. Pryor, K. Baines, T. Stallard, H. Melin, F. J. Crary, (2016), Saturn kilometric radiation intensities during the Saturn auroral campaign of 2013, Icarus 263, 2-9, doi: 10.1016/j.icarus.2015.01.003.

Kurth, W. S., E. J. Bunce, J. T. Clarke, F. J. Crary, D. C. Grodent, A. P. Ingersoll, U. A. Dyudina, L. Lamy, D. G. Mitchell, A. M. Persoon, W. R. Pryor, J. Saur, T. Stallard, (2009), Auroral Processes, In Saturn from Cassini-Huygens, (eds.), M. K. Dougherty, L. W. Esposito S. M. Krimigis, 333-374, Dordrecht, New York, Springer.

Kurth, W. S., T. F. Averkamp, D. A. Gurnett, J. B. Groene, A. Lecacheux, (2008), An update to a Saturnian longitude system based on kilometric radio emissions, Journal of Geophysical Research Space Physics 113 (A5), A05222.

Kurth, W. S., T. F. Averkamp, D. A. Gurnett, Z. Wang, (2006), Cassini RPWS observations of dust in Saturn's E ring, Planetary and Space Science, 54, 988–998, doi: 10.1016/j.pss.2006.05011.

Kurth, W. S., G. B. Hospodarsky, D. A. Gurnett, B. Cecconi, P. Louarn, A. Lecacheux, P. Zarka, H. O. Rucker, M. Boudjada, M. L. Kaiser, (2005), High spectral and temporal resolution observations of Saturn kilometric radiation, Geophysical Research Letters, 32, L20S07, doi: 10.1029/2005GL022648.

Kurth, W. S., D. A. Gurnett, G. B. Hospodarsky, W. M. Farrell, A. Roux, M. K. Dougherty, S. P. Joy, M. G. Kivelson, R. J. Walker, F. J. Crary, C. J. Alexander, (2002), The dusk flank of Jupiter's magnetosphere, Nature 415 (6875), 991-994.

Kurth, W. S., G. B. Hospodarsky, D. A. Gurnett, A. Lecacheux, P. Zarka, M. D. Desch, M. L. Kaiser, W. M. Farrell, (2001a), High-resolution observations of low-frequency Jovian radio emissions by Cassini, In Planetary Radio Emissions V, (eds.) H. O. Rucker, M. L. Kaiser, Y. Leblanc, Austrian Academy of Sciences Press, Vienna, Austria, pp. 15–28.

Kurth, W. S., G. B. Hospodarsky, D. A. Gurnett, M. L. Kaiser, J.-E. Wahlund, A. Roux, P. Canu, P. Zarka, Y. Tokarev, (2001b), An overview of observations by the Cassini radio and plasma wave investigation at Earth, Journal of Geophysical Research, 106, 30,239-30,252, doi: 10.1029/2001JA900033.

Lagg, A., N. Krupp, S. Livi, J. Woch, S. Krimigis, M. Dougherty, (2001), Energetic particle measurements during the Earth swing-by of the Cassini spacecraft in August 1999, Journal of Geophysical Research Space Physics 106 (A12), 30, 209-30, 222.

Lamy, L., (2017), The Saturnian kilometric radiation before the Cassini grand finale, arXiv preprint arXiv:1709.07693.

Lamy, L., R. Prange, W. Pryor, J. Gustin, S. V. Badman, H. Melin, T. Stallard, D. G. Mitchell, P. C. Brandt, (2013), Multispectral simultaneous diagnosis of Saturn's aurorae throughout a planetary rotation, Journal of Geophysical Research Space Physics 118 (8), 4817-4843, doi: 10.1002/jgra.50404.

Lamy, L., (2011), Variability of southern and northern periodicities of Saturn Kilometric Radiation, arXiv preprint arXiv:1102.3099.

Lamy, L., P. Zarka, B. Cecconi, R. Prangé, W. S. Kurth, D. A. Gurnett, (2008), Saturn kilometric radiation: Average and statistical properties, Journal of Geophysical Research: Space Physics, 113, no. A7.

Lario, D., S. Livi, E. C. Roelof, R. B. Decker, S. M. Krimigis, M. K. Dougherty, (2004), Heliospheric energetic particle observations by the Cassini spacecraft: Correlation with 1 AU observations, Journal of Geophysical Research: Space Physics, 109, no. A9.

Lavvas, P., R. V. Yelle, T. Koskinen, A. Bazin, V. Vuitton, E. Vigren, M. Galand, A. Wellbrock, A. J. Coates, J.-E. Wahlund, F. J. Crary, D. Snowden, (2013), Aerosol growth in Titan's ionosphere, Proceedings of the National Academy of Sciences of the United States of America 110 (8), 2729-2734, doi: 10.1073/pnas.1217059110.

Lecacheux, A., W. S. Kurth, R. Manning, (2001), Sub-second time scales in jovian radio emissions as measured by Cassini/RPWS: Comparison with ground-based observations, https://austriaca.at/pre5/lecacheux2.pdf.

Lecacheux, A., (2001), Radio observations during the Cassini flyby of Jupiter, http://austriaca.at/pre5/lecacheux1.pdf.

Lipatov, A. S., E. C. Sittler Jr., R. E. Hartle, J. F. Cooper, and D. G. Simpson, (2014), Titan's plasma environment: 3D hybrid kinetic modeling of the TA flyby and comparison with CAPS-ELS and RPWS LP observations, Planetary and Space Science 93-94, 119-128, doi: 10.1016/j.pss.2014.02.012.

Lipatov, A. S., E. C. Sittler Jr., R. E. Hartle, J. F. Cooper, D. G. Simpson, (2012), Saturn's magnetosphere interaction with Titan for T9 encounter: 3D hybrid modeling and comparison with CAPS observations, Planetary and Space Science 61 (1), 66-78, doi: 10.1016/j.pss.2011.08.017.

Lipatov, A. S., E. C. Sittler Jr., R. E. Hartle, J. F. Cooper, D. G. Simpson, (2011), Background and pickup ion velocity distribution dynamics in Titan's plasma environment: 3D hybrid simulation and comparison with CAPS T9 observations, Advances in Space Research 48 (6), 1114-1125, doi: 10.1016/j.asr.2011.05.026.

Liu, X. and T. W. Hill, (2012), Effects of finite plasma pressure on centrifugally driven convection in Saturn's inner magnetosphere, Journal of Geophysical Research Space Physics 117, A07216, doi: 10.1029/2012JA017827.

Liu, X., T. W. Hill, R. A. Wolf, S. Sazykin, R. W. Spiro, H. Wu, (2010), Numerical simulation of plasma transport in Saturn's inner magnetosphere using the Rice Convection Model, Journal of Geophysical Research Space Physics 115, A12254, doi: 10.1029/2010ja015859.

Livi, R., J. Goldstein, J. L. Burch, F. Crary, A. M. Rymer, D. G. Mitchell, A. M. Persoon, (2014), Multi-instrument analysis of plasma parameters in Saturn's equatorial, inner magnetosphere using corrections for corrections for spacecraft potential and penetrating background radiation, Journal of Geophysical Research: Space Physics, 119, no. 5, 3683—3707.

Louarn, P., W. S. Kurth, D. A. Gurnett, G. B. Hospodarsky, A. M. Persoon, B. Cecconi, A. Lecacheux, P. Zarka, P. Canu, A. Roux, H. O. Rucker, W. M. Farrell, M. L. Kaiser, N. Andre, C. Harvey, M. Blanc, (2007), Observation of similar radio signatures at Saturn and Jupiter: Implications for the magnetospheric dynamics, Geophysical Research Letters 34 (20), L20113.

Louis, C. K., L. Lamy, P. Zarka, B. Cecconi, S. L. G. Hess, (2017), Detection of Jupiter decametric emissions controlled by Europa and Ganymede with Voyager/PRA and Cassini/RPWS, Journal of Geophysical Research: Space Physics, 122, no. 9, 9228–9247.

Luhmann, J. G., R. E. Johnson, R. L. Tokar, S. A. Ledvina, T. E. Cravens, (2006), A model of the ionosphere of Saturn's rings and its implications, Icarus 181 (2), 465-74. doi: 10.1016/j.icarus.2005.11.022.

Ma, Y.-J., C. T. Russell, A. F. Nagy, G. Toth, C. Bertucci, M. K. Dougherty, F. M. Neubauer, A. Wellbrock, A. J. Coates, P. Garnier, J. E. Wahlund, T. E. Cravens, F. J. Crary, (2009), Time-dependent global MHD simulations of Cassini T32 flyby: From magnetosphere to magnetosheath, Journal of Geophysical Research-Space Physics 114, A03204, doi: 10.1029/2008ja013676.

Ma, Y.-J., A. F. Nagy, G. Toth, T. E. Cravens, C. T. Russell, T. I. Gombosi, J.-E. Wahlund, et al., (2007), 3D global multi-species Hall-MHD simulation of the Cassini T9 flyby, Geophysical Research Letters, 34, no. 24.

Madanian, H., T. E. Cravens, M. S. Richard, J. H. Waite, N. J. T. Edberg, J. H. Westlake, J. E. Wahlund, (2016), Solar cycle variations in ion composition in the dayside ionosphere of Titan, Journal of Geophysical Research Space Physics 121 (8), 8013-8037, doi: 10.1002/2015ja022274.

Magee, B. A., et al., (2018), in preparation.

Magee, B. A., J. H. Waite, K. E. Mandt, J. Westlake, J. Bell, D. A. Gell, (2009), INMS-derived composition of Titan's upper atmosphere: Analysis methods and model comparison, Planetary and Space Science 57 (14-15), 1895-1916, doi: 10.1016/j.pss.2009.06.016.

Mandt, K. E., D. A. Gell, M. Perry, J. H.r Waite, F. A. Crary, D. Young, B. A. Magee, et al., (2012), Ion densities and composition of Titan's upper atmosphere derived from the Cassini Ion Neutral Mass Spectrometer: Analysis methods and comparison of measured ion densities to photochemical model simulations, Journal of Geophysical Research: Planets 117, no. E10.

MAPSview, (2019), MAPS Key Parameter Database, Regents of the University of Michigan & IRAP Toulouse, France, http://mapskp.cesr.fr/index.php.

Martens, H. R., D. B. Reisenfeld, J. D. Williams, R. E. Johnson, H. T. Smith, (2008), Observations of molecular oxygen ions in Saturn's inner magnetosphere, Geophysical Research Letters 35 (20), 20103, doi: 10.1029/2008GL035433.

Martin, C. J. and C. S. Arridge, (2017), Cassini observations of aperiodic waves on Saturn's magnetodisc, Journal of Geophysical Research: Space Physics, 122, no. 8, 8063–8077.

Masters, A., A. H. Sulaiman, L. Stawarz, B. Reville, N. Sergis, M. Fujimoto, D. Burgess, A. J. Coates, M. K. Dougherty, (2017), An in situ comparison of electron acceleration at collisionless shocks under differing upstream magnetic field orientations, Astrophysical Journal 843 (2), doi: 10.3847/1538-4357/aa76ea.

Masters, A., A. H. Sulaiman, N. Sergis, L. Stawarz, M. Fujimoto, A. J. Coates, M. K. Dougherty, (2016), Suprathermal electrons at Saturn's bow shock, Astrophysical Journal 826 (1), doi: 10.3847/0004-637x/826/1/48.

Masters, A., (2015), The dayside reconnection voltage applied to Saturn's magnetosphere, Geophysical Research Letters 42 (8), 2577-2585, doi: 10.1002/2015GL063361.

Masters, A., M. Fujimoto, H. Hasegawa, C. T. Russell, A. J. Coates, M. K. Dougherty, (2014), Can magnetopause reconnection drive Saturn's magnetosphere?, Geophysical Research Letters 41 (6), 1862-1868, doi: 10.1002/2014GL059288.

Masters, A., J. A. Slavin, G. A. DiBraccio, T. Sundberg, R. M. Winslow, C. L. Johnson, B. J. Anderson, H. Korth, (2013a), A comparison of magnetic overshoots at the bow shocks of Mercury and Saturn, Journal of Geophysical Research: Space Physics, 118, no. 7, 4381–4390.

Masters, A., L. Stawarz, M. Fujimoto, S. J. Schwartz, N. Sergis, M. F. Thomsen, A. Retino, et al., (2013b), Electron acceleration to relativistic energies at a strong quasi-parallel shock wave, Nature Physics, 9, no. 3, 164.

Masters, A., J. P. Eastwood, M. Swisdak, M. F. Thomsen, C. T. Russell, N. Sergis, F. J. Crary, M. K. Dougherty, A. J. Coates, S. M. Krimigis, (2012a), The importance of plasma β conditions for magnetic reconnection at Saturn's magnetopause, Geophysical Research Letters, 39, no. 8.

Masters, A., N. Achilleos, J. C. Cutler, A. J. Coates, M. K. Dougherty, G. H. Jones, (2012b), Surface waves on Saturn's magnetopause, Planetary and Space Science, 65, no. 1, 109-121.

Masters, A., S. J. Schwartz, E. M. Henley, M. F. Thomsen, B. Zieger, A. J. Coates, N. Achilleos, J. Mitchell, K. C. Hansen, M. K. Dougherty, (2011a), Electron heating at Saturn's bow shock, Journal of Geophysical Research Space Physics 116, A10107, doi: 10.1029/2011JA016941.

Masters, A., D. G. Mitchell, A. J. Coates, M. K. Dougherty, (2011b), Saturn's low-latitude boundary layer: 1. Properties and variability, Journal of Geophysical Research: Space Physics, 116, no. A6.

Masters, A., A. P. Walsh, A. N. Fazakerley, A. J. Coates, M. K. Dougherty, (2011c), Saturn's low-latitude boundary layer: 2. Electron structure, Journal of Geophysical Research: Space Physics, 116, no. A6.

Masters, A., N. Achilleos, M. G. Kivelson, N. Sergis, M. K. Dougherty, M. F. Thomsen, C. S. Arridge, S. M. Krimigis, H. J. McAndrews, S. J. Kanani, N. Krupp, A. J. Coates, (2010), Cassini observations of a Kelvin-Helmholtz vortex in Saturn's outer magnetosphere, Journal of Geophysical Research Space Physics 115, A07225, doi: 10.1029/2010ja015351.

Masters, A., H. J. McAndrews, J. T. Steinberg, M. F. Thomsen, C. S. Arridge, M. K. Dougherty, L. Billingham, S. J. Schwartz, N. Sergis, G. B. Hospodarsky, A. J. Coates, (2009), Hot flow anomalies at Saturn's bow shock, Journal of Geophysical Research Space Physics 114, A08217, doi: 10.1029/2009ja014112.

Masters, A., N. Achilleos, M. K. Dougherty, J. A. Slavin, G. B. Hospodarsky, C. S. Arridge, A. J. Coates, (2008), An empirical model of Saturn's bow shock: Cassini observations of shock location and shape, Journal of Geophysical Research: Space Physics, 113, no. A10.

Mauk, B. H. and N. J. Fox, (2010), Electron radiation belts of the solar system, Journal of Geophysical Research Space Physics 115 (A12), doi: 10.1029/2010JA015660.

Mauk, B. H., J. Saur, D. G. Mitchell, E. C. Roelof, P. C. Brandt, T. P. Armstrong, D. C. Hamilton, S. M. Krimigis, N. Krupp, S. A. Livi, J. W. Manweiler, C. P. Paranicas, (2005), Energetic particle injections in Saturn's magnetosphere, Geophysical Research Letters 32 (14), 14-05, doi: 10.1029/2005GL022485.

Mauk, B. H., D. G. Mitchell, S. M. Krimigis, E. C. Roelof, C. P. Paranicas, (2003), Energetic neutral atoms from a trans-Europa gas torus at Jupiter, Nature 421, no. 6926, 920.

Mauk, B. H., S. M. Krimigis, D. G. Mitchell, E. C. Roelof, E. P. Keath, J. Dandouras, (1998), Imaging Saturns dust rings using energetic neutral atoms, Planetary and Space Science, 46, no. 9–10, 1349–1362.

McAndrews, H. J., M. F. Thomsen, C. S. Arridge, C. M. Jackman, R. J. Wilson, M. G. Henderson, R. L. Tokar, K. K. Khurana, E. C. Sittler, A. J. Coates, M. K. Dougherty, (2009), Plasma in Saturn's nightside magnetosphere and the implications for global circulation, Planetary and Space Science 57 (14-15), 1714-1722, doi: 10.1016/j.pss.2009.03.003.

McAndrews, H. J., C. J. Owen, M. F. Thomsen, B. Lavraud, A. J. Coates, M. K. Dougherty, D. T. Young, (2008), Evidence for reconnection at Saturn's magnetopause, Journal of Geophysical Research Space Physics 113 (A4), A04210.

McComas, D. J., E. J. Zirnstein, M. Bzowski, M. A. Dayeh, H. O. Funsten, S. A. Fuselier, P. H. Janzen, M. A. Kubiak, H. Kucharek, E. Möbius, (2017), Seven years of imaging the global heliosphere with IBEX, The Astrophysical Journal Supplement Series 229 (2), 41.

McComas, D. J., F. Allegrini, P. Bochsler, M. Bzowski, E. R. Christian, G. B. Crew, R. DeMajistre, H. Fahr, H. Fichtner, P. C. Frisch, (2009), Global observations of the interstellar interaction from the Interstellar Boundary Explorer (IBEX), Science.

McComas, D. J., N. A. Schwadron, F. J. Crary, H. A. Elliott, D. T. Young, J. T. Gosling, M. F. Thomsen, E. Sittler, J. J. Berthelier, K. Szego, A. J. Coates, (2004), The interstellar hydrogen shadow: observations of interstellar pickup ions beyond Jupiter, Journal of Geophysical Research Space Physics 109 (A2), 6. doi: 10.1029/2003JA010217.

Meier, P., U. Motschmann, J. Schmidt, F. Spahn, T. W. Hill, Y. Dong, G. H. Jones, H. Kriegel, (2015), Modeling the total dust production of Enceladus from stochastic charge equilibrium and simulations, Planetary and Space Science, 119, 208–221.

Meier, P., H. Kriegel, U. Motschmann, J. Schmidt, F. Spahn, T. W. Hill, Y. Dong, G. H. Jones, (2014), A model of the spatial and size distribution of Enceladus' dust plume, Planetary and Space Science 104 (Part B), 216-233, doi: 10.1016/j.pss.2014.09.016.

Menietti, J. D., O. Santolik, A. M. Rymer, G. B. Hospodarsky, D. A. Gurnett, A. J. Coates, (2008), Analysis of plasma waves observed in the inner Saturn magnetosphere, Annales Geophysicae 26 (9), 2631-2644.

Menietti, J. D., D. A. Gurnett, G. B. Hospodarsky, C. A. Higgions, W. S. Kurth, P. Zarka, (2003), Modeling radio emission attenuation lanes observed by the Galileo and Cassini spacecraft, Planetary and Space Science 51 (9), 533-40, doi: 10.1016/S0032-0633(03)00078-3.

Meredith, C. J., S. W. H. Cowley, J. D. Nichols, (2014), Survey of Saturn auroral storms observed by the Hubble Space Telescope: Implications for storm time scales, Journal of Geophysical Research Space Physics 119 (12), 9624-9642, doi: 10.1002/2014JA020601.

Meredith, C. J., S. W. H. Cowley, K. C. Hansen, J. D. Nichols, T. K. Yeoman, (2013), Simultaneous conjugate observations of small-scale structures in Saturn's dayside ultraviolet auroras: Implications for physical origins, Journal of Geophysical Research Space Physics 118 (5), 2244-2266, doi: 10.1002/jgra.50270.

Meyer-Vernet, N., M. Moncuquet, K. Issautier, P. Schippers, (2017), Frequency range of dust detection in space with radio and plasma wave receivers: Theory and application to interplanetary nanodust impacts on Cassini, Journal of Geophysical Research Space Physics 122 (1), 8-22, doi: 10.1002/2016ja023081.

Meyer-Vernet, N., A. Lecacheux, M. L. Kaiser, D. A. Gurnett, (2009), Detecting nanoparticles at radio frequencies: Jovian dust stream impacts on Cassini/RPWS, Geophysical Research Letters 36, L03103, doi: 10.1029/2008gl036752.

Michael, M., S. N. Tripathi, P. Arya, A. Coates, A. Wellbrock, D. T. Young, (2011), High-altitude charged aerosols in the atmosphere of Titan, Planetary and Space Science 59 (9), 880-885. doi: 10.1016/j.pss.2011.03.010.

Milan, S. E., E. J. Bunce, S. W. H. Cowley, C. M. Jackman, (2005), Implications of rapid planetary rotation for the Dungey magnetotail of Saturn, Journal of Geophysical Research Space Physics 110 (A3), 10, doi: 10.1029/2004JA010716.

Mitchell, D. G., et al., (2018), submitted.

Mitchell, D. G., M. E. Perry, D. C. Hamilton, J. H. Westlake, P. Kollmann, H. T. Smith, J. F. Carbary, Jr. J. H. Waite, R. Perryman, H.-W. Hsu, J.-E. Wahlund, M. W. Morooka, L. Z. Hadid, A. M. Persoon, W. S. Kurth, (2018), Dust grains fall from Saturn's D-ring into its equatorial upper atmosphere, Science 362, no. 6410, eaat2236.

Mitchell, D. G., J. F. Carbary, E. J. Bunce, Aikaterini Radioti, S. V. Badman, W. R. Pryor, G. B. Hospodarsky, W. S. Kurth, (2016), Recurrent pulsations in Saturn's high latitude magnetosphere, Icarus, 263, 94-100.

Mitchell, D. G., P. C. Brandt, J. F. Carbary, W. S. Kurth, S. M. Krimigis, C. Paranicas, N. Krupp, D. C. Hamilton, B. H. Mauk, G. B. Hospodarsky, M. K. Dougherty, W. R. Pryor, (2015), Injection, interchange, and reconnection: Energetic particle observations in Saturn's magnetosphere, In Magnetotails in the Solar System, (eds.), A. Keiling, C. M. Jackman P. A. Delamere, 327-343, Hoboken, New Jersey, John Wiley & Sons, Inc.

Mitchell, D. G., W. S. Kurth, G. B. Hospodarsky, N. Krupp, J. Saur, B. H. Mauk, J. F. Carbary, S. M. Krimigis, M. K. Dougherty, D. C. Hamilton, (2009a), Ion conics and electron beams associated with auroral processes on Saturn, Journal of Geophysical Research: Space Physics, 114, no. A2.

Mitchell, D. G., S. M. Krimigis, C. Paranicas, P. C. Brandt, J. F. Carbary, E. C. Roelof, W. S. Kurth, et al., (2009b), Recurrent energization of plasma in the midnight-to-dawn quadrant of Saturn's magnetosphere, and its relationship to auroral UV and radio emissions, Planetary and Space Science, 57, no. 14–15, 1732–1742.

Mitchell, D. G., P. C. Brandt, E. C. Roelof, J. Dandouras, S. M. Krimigis, B. H. Mauk, C. P. Paranicas, et al., (2005), Energetic ion acceleration in Saturn's magnetotail: Substorms at Saturn?, Geophysical Research Letters, 32, no. 20.

Mitchell, D. G., C. P. Paranicas, B. H. Mauk, E. C. Roelof, S. M. Krimigis, (2004), Energetic neutral atoms from Jupiter measured with the Cassini magnetospheric imaging instrument: Time dependence and composition, Journal of Geophysical Research: Space Physics, 109, no. A9.

Modolo, R., M. Chanteur, J. E. Wahlund, P. Canu, W. S. Kurth, D. Gurnett, A. P. Matthews, C. Bertucci, (2007a), Plasma environment in the wake of Titan from hybrid simulation: A case study, Geophysical Research Letters 34 (24), L24S07.

Modolo, R., J. E. Wahlund, R. Bostrom, P. Canu, W. S. Kurth, D. Gurnett, G. R. Lewis, A. J. Coates, (2007b), Far plasma wake of Titan from the RPWS observations: A case study, Geophysical Research Letters 34 (24), L24S04.

Moore, L., I. Müeller-Wodarg, M. Galand, A. Kliore, M. Mendillo, (2010), Latitudinal variations in Saturn's ionosphere: Cassini measurements and model comparisons, Journal of Geophysical Research: Space Physics, 115, no. A11.

Moore, L., A. F. Nagy, A. J. Kliore, I. Müller-Wodarg, J. D. Richardson, M. Mendillo, (2006), Cassini radio occultations of Saturn's ionosphere: Model comparisons using a constant water flux, Geophysical Research Letters, 33, no. 22.

Morooka, M. W., J. E. Wahlund, A. I. Eriksson, W. M. Farrell, D. A. Gurnett, W. S. Kurth, A. M. Persoon, M. Shafiq, M. Andre, M. K. G. Holmberg, (2011), Dusty plasma in the vicinity of Enceladus, Journal of Geophysical Research Space Physics 116, A12221, doi: 10.1029/2011JA017038.

Moses, J. I. and S. F. Bass, (2000), The effects of external material on the chemistry and structure of Saturn's ionosphere, Journal of Geophysical Research Planets 105 (E3), 7013-7052, doi: 10.1029/1999JE001172.

Müeller, A. L., J. Saur, N. Krupp, E. Roussos, B. H. Mauk, A. M. Rymer, D. G. Mitchell, S. M. Krimigis, (2010), Azimuthal plasma flow in the Kronian magnetosphere, Journal of Geophysical Research Space Physics 115, A08203, doi: 10.1029/2009ja015122.

Müeller-Wodarg, I. C. F., L. Moore, M. Galand, S. Miller, M. Mendillo, (2012), Magnetosphere-atmosphere coupling at Saturn: 1-Response of thermosphere and ionosphere to steady state polar forcing, Icarus 221(2), 481-494, doi: 10.1016/j.icarus.2012.08.034.

Müeller-Wodarg, I. C. F., R. V. Yelle, J. Cui, J. H. Waite, (2008), Horizontal structures and dynamics of Titan's thermosphere, Journal of Geophysical Research: Planets, 113, no. E10.

Müeller-Wodarg, I. C. F., R. V. Yelle, N. Borggren, J. H. Waite, (2006a), Waves and horizontal structures in Titan's thermosphere, Journal of Geophysical Research Space Physics 111 (A12), A12315.

Müeller-Wodarg, I. C. F., M. Mendillo, R. V. Yelle, A. D. Aylward, (2006b), A global circulation model of Saturn's thermosphere, Icarus, 180, no. 1, 147–160.

Müeller-Wodarg, I. C. F., R. V. Yelle, M. J. Mendillo, A. D. Aylward, (2003), On the global distribution of neutral gases in Titan's upper atmosphere and its effect on the thermal structure, Journal of Geophysical Research: Space Physics, 108, no. A12.

Müeller-Wodarg, I. C. F. and R. V. Yelle, (2002), The effect of dynamics on the composition of Titan's upper atmosphere, Geophysical Research Letters, 29, no. 23, 54-1–54-4.

Müeller-Wodarg, I. C. F., R. V. Yelle, M. Mendillo, L. A. Young, A. D. Aylward, (2002), The thermosphere of Titan simulated by a global three-dimensional time-dependent model, Journal of Geophysical Research: Space Physics, 105, no. A9, 20833–20856.

Nagy, A. and T. Cravens, (1998), Titan's ionosphere: A review, Planetary and Space Science 46, no. 9-10, 1149-1155, doi: 10.1016/S0032-0633(98)00049-X.

Nemeth, Z., K. Szego, L. Foldy, S. W. H. Cowley, G. Provan, M. Thomsen, (2016), Periodic motion of the magnetodisk as a cause of quasi-periodic variations in the Kronian magnetosphere, Planetary and Space Science 130, 54-59.

Nemeth, Z., K. Szego, L. Foldy, M. G. Kivelson, X. Jia, K. M. Ramer, S. W. H. Cowley, G. Provan, M. Thomsen, (2015), The latitudinal structure of the nightside outer magnetosphere of Saturn as revealed by velocity moments of thermal ions, Annales Geophysicae 33 (9), 1195-1202, doi: 10.5194/angeo-33-1195-2015.

Nemeth, Z., K. Szego, Z. Bebesi, G. Erdos, L. Foldy, A. Rymer, E. C. Sittler, A. J. Coates, A. Wellbrock, (2011), Ion distributions of different Kronian plasma regions, Journal of Geophysical Research Space Physics 116, A09212, doi: 10.1029/2011JA016585.

Neubauer, F. M., H. Backes, M. K. Dougherty, A. Wennmacher, C. T. Russell, A. Coates, D. Young, et al, (2006), Titan's near magnetotail from magnetic field and electron plasma observations and modeling: Cassini flybys TA, TB, and T3, Journal of Geophysical Research: Space Physics, 111, no. A10.Neubauer, F. M., D. A. Gurnett, J. D. Scudder, and R. E. Hartle, (1984), Titan’s magnetospheric interaction, Saturn 1, 760-787.

Nichols, J. D., B. Cecconi, J. T. Clarke, S. W. H. Cowley, J. C. Gerard, A. Grocott, D. Grodent, L. Lamy, P. Zarka, (2010), Variation of Saturn’s UV aurora with SKR phase, Geophysical Research Letters 37, L15102, doi: 10.1029/2010gl044057.

Nichols, J. D., S. V. Badman, E. J. Bunce, J. T. Clarke, S. W. H. Cowley, F. J. Crary, M. K. Dougherty, J. C. Gerard, D. Grodent, K. C. Hansen, W. S. Kurth, D. G. Mitchell, W. R. Pryor, T. S. Stallard, D. L. Talboys, S. Wannawichian, (2009), Saturn’s equinoctial auroras, Geophysical Research Letters 36, doi: 10.1029/2009gl041491.

Nichols, J. D., J. T. Clarke, S. W. H. Cowley, J. Duval, A. J. Farmer, J.-C. Gérard, D. Grodent, S. Wannawichian, (2008), Oscillation of Saturn's southern auroral oval, Journal of Geophysical Research: Space Physics, 113, no. A11.

Omidi, N., A. H. Sulaiman, W. Kurth, H. Madanian, T. Cravens, N. Sergis, M. K. Dougherty, N. J. T. Edberg, (2017), A single deformed bow shock for Titan-Saturn system, Journal of Geophysical Research Space Physics 122 (11), 11058-11075, doi: 10.1002/2017ja024672.

Opher, M., J. F. Drake, B. Zieger, T. I. Gombosi, (2015), Magnetized jets driven by the Sun: The structure of the heliosphere revisited, The Astrophysical Journal Letters 800 (2), L28, doi: 10.1088/2041-8205/800/2/L28.

Palmaerts, B., A. Radioti, E. Roussos, D. Grodent, J.-C. Gérard, N. Krupp, D. G. Mitchell., (2016a), Pulsations of the polar cusp aurora at Saturn, Journal of Geophysical Research: Space Physics, 121, no. 12, 11–952.

Palmaerts, B., E. Roussos, N. Krupp, W. S. Kurth, D. G. Mitchell, J. N. Yates, (2016b), Statistical analysis and multi-instrument overview of the quasi-periodic 1-hour pulsations in Saturn’s outer magnetosphere, Icarus, 271, 1–18.

Panchenko, M., S. Rošker, H. O. Rucker, A. Brazhenko, P. Zarka, G. Litvinenko, V. E. Shaposhnikov, A. A. Konovalenko, V. Melnik, A. V. Franzuzenko, (2018a), Zebra pattern in decametric radio emission of Jupiter, Astronomy & Astrophysics 610, A69.

Panchenko, M., S. Rosker, H. O. Rucker, A. Brazhenko, A. A. Konovalenko, G. Litvinenko, P. Zarka, V. Melnik, V. E. Shaposhnikov, A. V. Frantsuzenko, (2018b), Zebra-like fine spectral structures in Jovian decametric radio emission, 103–116.

Panchenko, M., H. O. Rucker, W. M. Farrell, (2013), Periodic bursts of Jovian non-Io decametric radio emission, Planetary and Space Science 77 (SI), 3-11. doi: 10.1016/j.pss.2012.08.015.

Panchenko, M. and H. O. Rucker, (2011), New type of periodic bursts of non-Io Jovian decametric radio emission, Planetary, Solar and Heliospheric Radio Emissions, Planetary Radio Emissions VII, Proceedings of the 7th International Workshop held at Graz, Austria, September 15-17, 2010, (eds.), H. O. Rucker, W. S. Kurth, P. Louarn, G. Fischer. Austrian Academy of Sciences Press, Vienna, p. 157-166.

Panchenko, M., H. O. Rucker, M. L. Kaiser, O. C. St Cyr, J. L. Bougeret, K. Goetz, S. D. Bale, (2010), New periodicity in Jovian decametric radio emission, Geophysical Research Letters 37, L05106, doi: 10.1029/2010gl042488.

Paranicas, C., M. F. Thomsen, N. Achilleos, M. Andriopoulou, S. V. Badman, G. Hospodarsky, C. M. Jackman, X. Jia, T. Kennelly, K. Khurana, P. Kollmann, N. Krupp, P. Louarn, E. Roussos, N. Sergis, (2016), Effects of radial motion on interchange injections at Saturn, Icarus 264, 342-351, doi: 10.1016/j.icarus.2015.10.002.

Paranicas, C., E. Roussos, R. B. Decker, R. E. Johnson, A. R. Hendrix, P. Schenk, T. A. Cassidy, J. B. Dalton, III, C. J. A. Howett, P. Kollmann, W. Patterson, K. P. Hand, T. A. Nordheim, N. Krupp, D. G. Mitchell, (2014), The lens feature on the inner saturnian satellites, Icarus 234, 155-161, doi: 10.1016/j.icarus.2014.02.026.

Paranicas, C., E. Roussos, N. Krupp, P. Kollmann, A. R. Hendrix, T. Cassidy, R. E. Johnson, P. Schenk, G. Jones, J. Carbary, D. G. Mitchell, K. Dialynas, (2012), Energetic charged particle weathering of Saturn's inner satellites, Planetary and Space Science 61 (1), 60-65, doi: 10.1016/j.pss.2011.02.012.

Paranicas, C., D. G. Mitchell, E. Roussos, P. Kollmann, N. Krupp, A. L. Müeller, S. M. Krimigis, F. S. Turner, P. C. Brandt, A. M. Rymer, R. E. Johnson, (2010), Transport of energetic electrons into Saturn's inner magnetosphere, Journal of Geophysical Research Space Physics 115, A09214, doi: 10.1029/2010ja015853.

Paranicas, C., D. G. Mitchell, S. M. Krimigis, D. C. Hamilton, E. Roussos, N. Krupp, G. H. Jones, R. E. Johnson, J. F. Cooper, T. P. Armstrong, (2008), Sources and losses of energetic protons in Saturn's magnetosphere, Icarus 197 (2), 519-525, doi: 10.1016/j.icarus.2008.05.011.

Paranicas, C., D. G. Mitchell, E. C. Roelof, B. H. Mauk, S. M. Krimigis, P. C. Brandt, M. Kusterer, F. S. Turner, J. Vandegriff, N. Krupp, (2007), Energetic electrons injected into Saturn's neutral gas cloud, Geophysical Research Letters 34 (2), L02109.

Paranicas, C., D. G. Mitchell, S. Livi, S. M. Krimigis, E. Roussos, N. Krupp, J. Woch, A. Lagg, J. Saur, F. S. Turner, (2005), Evidence of Enceladus and Tethys microsignatures, Geophysical Research Letters, 32, no. 20.

Parker, E. N., (1961), The stellar-wind regions, The Astrophysical Journal 134, 20-27.

Parker, E. N., (1958), Dynamics of the interplanetary gas and magnetic fields, The Astrophysical Journal, 128, 664.

Perry, M. E., B. D. Teolis, D. M. Hurley, B. A. Magee, J. H. Waite, T. G. Brockwell, R. S. Perryman, R. L. McNutt, (2015), Cassini INMS measurements of Enceladus plume density, Icarus 257, 139-162, doi: 10.1016/j.icarus.2015.04.037.

Persoon, A. M., D. A. Gurnett, W. S. Kurth, J. B. Groene, J. B. Faden, (2015), Evidence for a seasonally dependent ring plasma in the region between Saturn's A ring and Enceladus' orbit, Journal of Geophysical Research Space Physics 120 (8), 6276-6285, doi: 10.1002/2015ja021180.

Persoon, A. M., D. A. Gurnett, J. S. Leisner, W. S. Kurth, J. B. Groene, J. B. Faden, (2013), The plasma density distribution in the inner region of Saturn's magnetosphere, Journal of Geophysical Research Space Physics 118 (6), 2970-2974, doi: 10.1002/jgra.50182.

Persoon, A. M., D. A. Gurnett, O. Santolik, W. S. Kurth, J. B. Faden, J. B. Groene, G. R. Lewis, A. J. Coates, R. J. Wilson, R. L. Tokar, J. E. Wahlund, M. Moncuquet, (2009), A diffusive equilibrium model for the plasma density in Saturn's magnetosphere, Journal of Geophysical Research Space Physics 114, A04211, doi: 10.1029/2008ja013912.

Pilkington, N. M., N. Achilleos, C. S. Arridge, P. Guio, A. Masters, L. C. Ray, N. Sergis, M. F. Thomsen, A. J. Coates, M. K. Dougherty, (2015), Internally driven large-scale changes in the size of Saturn's magnetosphere, Journal of Geophysical Research Space Physics 120 (9), 7289-7306, doi: 10.1002/2015ja021290.

Pontius Jr., D. H. and T. W. Hill, (2009), Plasma mass loading from the extended neutral gas torus of Enceladus as inferred from the observed plasma corotation lag, Geophysical Research Letters 36, L23103, doi: 10.1029/2009gl041030.

Porco, C., D. DiNino, F. Nimmo, (2014), How the geysers, tidal stresses, and thermal emission across the south polar terrain of Enceladus are related, Astronomical Journal 148 (3), 45-69, doi: 10.1088/0004-6256/148/3/45.

Provan, G., S. W. H. Cowley, T. J. Bradley, E. J. Bunce, G. J. Hunt, M. K. Dougherty, (2018), Planetary period oscillations in Saturn's magnetosphere: Cassini magnetic field observations over the northern summer solstice interval, Journal of Geophysical Research: Space Physics, 123, no. 5, 3859–3899.

Provan, G., S. W. H. Cowley, L. Lamy, E. J. Bunce, G. J. Hunt, P. Zarka, M. K. Dougherty, (2016), Planetary period oscillations in Saturn's magnetosphere: Coalescence and reversal of northern and southern periods in late northern spring, Journal of Geophysical Research: Space Physics, 121, no. 10, 9829–9862.

Provan, G., C. Tao, S. W. H. Cowley, M. K. Dougherty, A. J. Coates, (2015), Planetary period oscillations in Saturn's magnetosphere: Examining the relationship between abrupt changes in behavior and solar wind-induced magnetospheric compressions and expansions, Journal of Geophysical Research: Space Physics, 120, no. 11, 9524–9544.

Provan, G., L. Lamy, S. W. H. Cowley, M. K. Dougherty, (2014), Planetary period oscillations in Saturn's magnetosphere: Comparison of magnetic oscillations and SKR modulations in the postequinox interval, Journal of Geophysical Research Space Physics 119 (9), 7380–7401, doi: 10.1002/2014ja020011.

Provan, G., S. W. H. Cowley, J. Sandhu, D. J. Andrews, M. K. Dougherty, (2013), Planetary period magnetic field oscillations in Saturn's magnetosphere: Postequinox abrupt nonmonotonic transitions to northern system dominance, Journal of Geophysical Research Space Physics 118 (6), 3243-3264, doi: 10.1002/jgra.50186.

Provan, G., D. J. Andrews, C. S. Arridge, A. J. Coates, S. W. H Cowley, G. Cox, M. K. Dougherty, C. M. Jackman, (2012), Dual periodicities in planetary-period magnetic field oscillations in Saturn's tail, Journal of Geophysical Research Space Physics 117 (A01), A01209, doi: 10.1029/2011JA017104.

Provan, G., D. J. Andrews, B. Cecconi, S. W. H. Cowley, M. K. Dougherty, L. Lamy, P. M. Zarka, (2011), Magnetospheric period magnetic field oscillations at Saturn: Equatorial phase "jitter" produced by superposition of southern and northern period oscillations, Journal of Geophysical Research Space Physics 116, A04225, doi: 10.1029/2010ja016213.

Provan, G., D. J. Andrews, C. S. Arridge, A. J. Coates, S. W. H. Cowley, S. E. Milan, M. K. Dougherty, D. M. Wright, (2009), Polarization and phase of planetary-period magnetic field oscillations on high-latitude field lines in Saturn's magnetosphere, Journal of Geophysical Research: Space Physics, 114, no. A2.

Pryor, W. R., A. M. Rymer, D. G. Mitchell, T. W. Hill, D. T. Young, J. Saur, G. H. Jones, S. Jacobsen, S. W. H. Cowley, B. H. Mauk, A. J. Coates, J. Gustin, D. Grodent, J.-C. Gerard, L. Lamy, J. D. Nichols, S. M. Krimigis, L. W. Esposito, M. K. Dougherty, A. J. Jouchoux, A. I. F. Stewart, W. E. McClintock, G. M. Holsclaw, J. M. Ajello, J. E. Colwell, A. R. Hendrix, F. J. Crary, J. T. Clarke, X. Zhou, (2011), The auroral footprint of Enceladus on Saturn, Nature 472 (7343), 331-333, doi: 10.1038/nature09928.

Pryor, W. R., A. I. F. Stewart, L. W. Esposito, W. E. McClintock, J. E. Colwell, A. J. Jouchoux, A. J. Steffl, D. E. Shemansky, J. M. Ajello, R. A. West, C. J. Hansen, B. T. Tsurutani, W. S. Kurth, G. B. Hospodarsky, D. A. Gurnett, K. C. Hansen, J. H. Waite, Jr., F. J. Crary, D. T. Young, N. Krupp, J. T. Clarke, D. Grodent, M. K. Dougherty, (2005), Cassini UVIS observations of Jupiter's auroral variability, Icarus 178 (2), 312-26, doi: 10.1016/j.icarus.2005.05.021.

Radioti, A., D. Grodent, J.-C. Gérard, D. J. Southwood, E. Chané, B. Bonfond, W. Pryor, (2017a), Stagnation of Saturn's auroral emission at noon, Journal of Geophysical Research: Space Physics, 122, no. 6, 6078–6087.

Radioti, A., D. Grodent, Z. H. Yao, J.-C. Gérard, S. V. Badman, W. Pryor, B. Bonfond, (2017b), Dawn auroral breakup at Saturn initiated by auroral arcs: UVIS/Cassini beginning of Grand Finale Phase, Journal of Geophysical Research: Space Physics, 122, 12, doi: 10.1002/2017JA024653.

Radioti, A., D. Grodent, X. Jia, J. C. Gerard, B. Bonfond, W. Pryor, J. Gustin, D. G. Mitchell, C. M. Jackman, (2016), A multi-scale magnetotail reconnection event at Saturn and associated flows: Cassini/UVIS observations, Icarus 263, 75-82, doi: 10.1016/j.icarus.2014.12.016.

Radioti, A., D. Grodent, J. C. Gerard, E. Roussos, D. Mitchell, B. Bonfond, W. Pryor, (2015), Auroral spirals at Saturn, Journal of Geophysical Research Space Physics 120 (10), 8633-8643, doi: 10.1002/2015ja021442.

Radioti, A., D. Grodent, J.-C. Gérard, S. E. Milan, R. C. Fear, C. M. Jackman, B. Bonfond, W. Pryor, (2014), Saturn's elusive nightside polar arc, Geophysical Research Letters 41, 6321, doi: 10.1002/2014GL061081.

Radioti, A., E. Roussos, D. Grodent, J.-C. Gérard, N. Krupp, D. G. Mitchell, J. Gustin, B. Bonfond, W. Pryor, (2013a), Signatures of magnetospheric injections in Saturn's aurora, Journal of Geophysical Research Space Physics 118, 1922, doi: 10.1002/jgra.50161.

Radioti, A., D. Grodent, J.-C. Gérard, B. Bonfond, J. Gustin, W. Pryor, J. M. Jasinski, C. S. Arridge, (2013b), Auroral signatures of multiple magnetopause reconnection at Saturn, Geophysical Research Letters 40, 4498, doi: 10.1002/grl.50889.

Radioti, A., D. Grodent, J. C. Gerard, S. E. Milan, B. Bonfond, J. Gustin, W. Pryor, (2011), Bifurcations of the main auroral ring at Saturn: ionospheric signatures of consecutive reconnection events at the magnetopause, Journal of Geophysical Research Space Physics 116, A11209, doi: 10.1029/2011JA016661.

Radioti, A., D. Grodent, J. C. Gerard, E. Roussos, C. Paranicas, B. Bonfond, D. G. Mitchell, N. Krupp, S. Krimigis, J. T. Clarke, (2009), Transient auroral features at Saturn: Signatures of energetic particle injections in the magnetosphere, Journal of Geophysical Research Space Physics 114, A03210, doi: 10.1029/2008ja013632.

Ramer, K. M., M. G. Kivelson, N. Sergis, K. K. Khurana, X. Jia, (2017), Spinning, breathing, and flapping: Periodicities in Saturn's middle magnetosphere, Journal of Geophysical Research: Space Physics 122 (1), 393-416.

Reed, J. J., C. M. Jackman, L. Lamy, W. S. Kurth, D. K. Whiter, (2018), Low-frequency extensions of the Saturn kilometric radiation as a proxy for magnetospheric dynamics, Journal of Geophysical Research Space Physics 123 (1), 443-463, doi: 10.1002/2017ja024499.

Regoli, L. H., A. J. Coates, M. F. Thomsen, G. H. Jones, E. Roussos, J. H. Waite, N. Krupp, G. Cox, (2016), Survey of pickup ion signatures in the vicinity of Titan using CAPS/IMS, Journal of Geophysical Research Space Physics 121 (9), 8317-8328, doi: 10.1002/2016ja022617.

Richard, M. S., T. E. Cravens, C. Wylie, D. Webb, Q. Chediak, K. Mandt, J. H. Waite, A. Rymer, C. Bertucci, A. Wellbrock, A. Windsor, A. J. Coates, (2015a), An empirical approach to modeling ion production rates in Titan's ionosphere II: Ion production rates on the nightside, Journal of Geophysical Research Space Physics 120 (2), 1281-1298, doi: 10.1002/2014ja020343.

Richard, M. S., T. E. Cravens, C. Wylie, D. Webb, Q. Chediak, R. Perryman, K. Mandt, J. Westlake, J. H. Waite, I. Robertson, B. A. Magee, N. J. T. Edberg, (2015b), An empirical approach to modeling ion production rates in Titan's ionosphere I: Ion production rates on the dayside and globally, Journal of Geophysical Research Space Physics 120 (2), 1264-1280, doi: 10.1002/2013ja019706.

Rietmeijer, F. J. M., (1993), Size distributions in two porous chondritic micrometeorites, Earth and Planetary Science Letters 117 (3-4), 609-617.

Robertson, I. P., T. E. Cravens, J. H. Waite Jr., R. V. Yelle, V. Vuitton, A. J. Coates, J. E. Wahlund, K. Ågren, K. Mandt, B. Magee, M. S. Richard, E. Fattig, (2009), Structure of Titan's ionosphere: Model comparisons with Cassini data, Planetary and Space Science 57 (14-15), 1834-1846, doi: 10.1016/j.pss.2009.07.011.

Roelof, E. C., S. M. Krimigis, D. G. Mitchell, R. B. Decker, K. Dialynas, (2012), Cassini ENA images of the heliosheath and Voyager "ground truth": Thickness of the heliosheath, In AIP Conference Proceedings, vol. 1436, no. 1, pp. 239-244, American Institute of Physics, doi: 10.1063/1.4723614.

Rosenqvist, L., J. E. Wahlund, K. Ågren, R. Modolo, H. J. Opgenoorth, D. Strobel, I. Müeller-Wodarg, P. Garnier, C. Bertucci, (2009), Titan ionospheric conductivities from Cassini measurements, Planetary and Space Science 57 (14-15), 1828-1833, doi: 10.1016/j.pss.2009.01.007.

Roussos, E., P. Kollmann, N. Krupp, A. Kotova, L. Regoli, C. Paranicas, D. G. Mitchell, et al., (2018a), A radiation belt of energetic protons located between Saturn and its rings, Science, 362, no. 6410, eaat1962.

Roussos, E., P. Kollmann, N. Krupp, C. Paranicas, K. Dialynas, N. Sergis, D. G. Mitchell, D. C. Hamilton, S. M. Krimigis, (2018b), Drift-resonant, relativistic electron acceleration at the outer planets: Insights from the response of Saturn's radiation belts to magnetospheric storms, Icarus, 305, 160–173.

Roussos, E., C. M. Jackman, M. F. Thomsen, W. S. Kurth, S. V. Badman, C. Paranicas, P. Kollmann, et al., (2018c), Solar Energetic Particles (SEP) and Galactic Cosmic Rays (GCR) as tracers of solar wind conditions near Saturn: Event lists and applications, Icarus, 300, 47–71.

Roussos, E., N. Krupp, P. Kollmann, C. Paranicas, D. G. Mitchell, S. M. Krimigis, M. Andriopoulou, (2016a), Evidence for dust-driven, radial plasma transport in Saturn's inner radiation belts, Icarus, 274, 272–283.

Roussos, E., N. Krupp, D. G. Mitchell, C. Paranicas, S. M. Krimigis, M. Andriopoulou, B. Palmaerts, et al., (2016b), Quasi-periodic injections of relativistic electrons in Saturn's outer magnetosphere, Icarus, 263, 101–116.

Roussos, E., N. Krupp, C. Paranicas, J. F. Carbary, P. Kollmann, S. M. Krimigis, D. G. Mitchell, (2014), The variable extension of Saturn's electron radiation belts, Planetary and Space Science 104, 3-17, doi: 10.1016/j.pss.2014.03.021.

Roussos, E., M. Andriopoulou, N. Krupp, A. Kotova, C. Paranicas, S. M. Krimigis, D. G. Mitchell, (2013), Numerical simulation of energetic electron microsignature drifts at Saturn: Methods and applications, Icarus 226 (2), 1595-1611, doi: 10.1016/j.icarus.2013.08.023.

Roussos, E., N. Krupp, C. P. Paranicas, P. Kollmann, D. G. Mitchell, S. M. Krimigis, T. P. Armstrong, D. R. Went, M. K. Dougherty, G. H. Jones, (2011), Long- and short-term variability of Saturn's ionic radiation belts, Journal of Geophysical Research Space Physics 116, A02217, doi: 10.1029/2010ja015954.

Roussos, E., J. Wuller, S. Simon, (2008a), Plasma and fields in the wake of Rhea: 3-D hybrid simulation and comparison with Cassini data, In Annales geophysicae: atmospheres, hydrospheres and space sciences, vol. 26, no. 3, p. 619.

Roussos, E., N. Krupp, T. P. Armstrong, C. Paranicas, D. G. Mitchell, S. M. Krimigis, G. H. Jones, K. Dialynas, N. Sergis, D. C. Hamilton, Discovery of a transient radiation belt at Saturn, Geophysical Research Letters, 35, no. 22.

Roussos, E., G. H. Jones, N. Krupp, C. Paranicas, D. G. Mitchell, A. Lagg, J. Woch, U. Motschmann, S. M. Krimigis, M. K. Dougherty, (2007), Electron microdiffusion in the Saturnian radiation belts: Cassini MIMI/LEMMS observations of energetic electron absorption by the icy moons, Journal of Geophysical Research Space Physics 112 (A6), doi: 10.1029/2006ja012027.

Roussos, E., N. Krupp, G. H. Jones, C. Paranicas, D. G. Mitchell, S. M. Krimigis, U. Motschmann, M. K. Dougherty, A. Lagg, J. Woch, (2006), Icy Moon Absorption Signatures: Probes of Saturnian Magnetospheric Dynamics and Moon Activity, American Geophysical Union (AGU) Fall Meeting, abstract.

Rucker, H. O., M. Panchenko, C. Weber, (2014), Planetary radio astronomy: Earth, giant planets, and beyond, Advances in Radio Science 12, 211-220, doi: 10.5194/ars-12-211-2014.

Russell, C. T., H. Y. Wei, M. M. Cowee, F. M. Neubauer, M. K. Dougherty, (2016), Ion cyclotron waves at Titan, Journal of Geophysical Research Space Physics 121 (3), 2095-2103, doi: 10.1002/2015ja022293.

Rymer, A. M., (2010), Electron-ion thermal equilibration at Saturn: Electron signatures of ion pick-up?, In AIP Conference Proceedings, American Institute of Physics, vol. 1302, no. 1, pp. 250-255, doi: 10.1063/1.3529979.

Rymer, A. M., H. T. Smith, A. Wellbrock, A. J. Coates, D. T. Young, (2009a), Discrete classification and electron energy spectra of Titan's varied magnetospheric environment, Geophysical Research Letters, 36, no. 15.

Rymer, A. M., B. H. Mauk, T. W. Hill, N. Andre, D. G. Mitchell, C. Paranicas, D. T. Young, H. T. Smith, A. M. Persoon, J. D. Menietti, G. B. Hospodarsky, A. J. Coates, M. K. Dougherty, (2009b), Cassini evidence for rapid interchange transport at Saturn, Planetary and Space Science 57 (14-15), 1779-1784, doi: 10.1016/j.pss.2009.04.010.

Rymer, A. M., B. H. Mauk, T. W. Hill, C. Paranicas, D. G. Mitchell, A. J. Coates, D. T. Young, (2008), Electron circulation in Saturn’s magnetosphere, Journal of Geophysical Research Space Physics 113 (A1).

Rymer, A. M., B. H. Mauk, T. W. Hill, C. Paranicas, N. Andre, E. C. Sittler, D. G. Mitchell, H. T. Smith, R. E. Johnson, A. J. Coates, D. T. Young, S. J. Bolton, M. F. Thomsen, M. K. Dougherty, (2007), Electron sources in Saturn’s magnetosphere, Journal of Geophysical Research Space Physics 112 (A2), A02201.

Rymer, A., A. Coates, K. Svenes, G. Abel, D. Linder, B. Narheim, M. Thomsen, T. Young, (2001), Cassini plasma spectrometer electron spectrometer measurements during the Earth swing-by on August 18, 1999, Journal of Geophysical Research Space Physics 106 (A12), 30, 177-30, 198.

Sagnieres, L. B. M., M. Galand, J. Cui, P. P. Lavvas, E. Vigren, V. Vuitton, R. V. Yelle, A. Wellbrock, A. J. Coates, (2015), Influence of local ionization on ionospheric densities in Titan's upper atmosphere, Journal of Geophysical Research Space Physics 120 (7), 5899-5921, doi: 10.1002/2014ja020890.

Saur, J, N. Schilling, F. M. Neubauer, D. F. Strobel, S. Simon, M. K. Dougherty, C. T. Russell, R. T. Pappalardo, (2008), Evidence for temporal variability of Enceladus' gas jets: Modeling of Cassini observations, Geophysical Research Letters, 35, no. 20.

Saur, J., F. M. Neubauer, N. Schilling, (2007), Hemisphere coupling in Enceladus' asymmetric plasma interaction, Journal of Geophysical Research Space Physics 112 (A11), A11209.

Schippers, P., N. Meyer-Vernet, A. Lecacheux, S. Belheouane, M. Moncuquet, W. S. Kurth, I. Mann, D. G. Mitchell, N. Andre, (2015), Nanodust detection between 1 and 5AU using Cassini wave measurements, Astrophysical Journal 806 (1), 77, doi: 10.1088/0004-637x/806/1/77.

Schippers, P., N. Meyer-Vernet, A. Lecacheux, W. S. Kurth, D. G. Mitchell, N. Andre, (2014), Nanodust detection near 1AU from spectral analysis of Cassini/radio and plasma wave science data, Geophysical Research Letters 41 (15), 5382-5388, doi: 10.1002/2014GL060566.

Schippers, P., N. André, D. A. Gurnett, G. R. Lewis, A. M. Persoon, A. J. Coates, (2012), Identification of electron field-aligned current systems in Saturn's magnetosphere, Journal of Geophysical Research Space Physics 117 (A5).

Schippers, P., M. Blanc, N. Andre, I. Dandouras, G. R. Lewis, L. K. Gilbert, A. M. Persoon, N. Krupp, D. A. Gurnett, A. J. Coates, S. M. Krimigis, D. T. Young, M. K. Dougherty, (2008), Multi-instrument analysis of electron populations in Saturn's magnetosphere, Journal of Geophysical Research Space Physics 113 (A7), A07208, doi: 10.1029/2008ja013098.

Seki, K., A. Nagy, C. M. Jackman, F. Crary, D. Fontaine, P. Zarka, P. Wurz, et al., (2015), A review of general physical and chemical processes related to plasma sources and losses for Solar System magnetospheres, Space Science Reviews, 192, no. 1–4, 27–89.

Sergis, N., E. J. Bunce, J. F. Carbary, S. W. H. Cowley, X. Jia, D. C. Hamilton, S. M. Krimigis, D. G. Mitchell, M. K. Dougherty, (2018), The ring current of Saturn, In Electric Currents in Geospace and Beyond, (eds.) A. Keiling, O. Marghitu, and M. Wheatland, vol. 235, pp. 139-154, Hoboken, New Jersey, American Geophysical Union and John Wiley & Sons.

Sergis, N., C. M. Jackman, M. F. Thomsen, S. M. Krimigis, D. G. Mitchell, D. C. Hamilton, M. K. Dougherty, N. Krupp, R. J. Wilson, (2017), Radial and local time structure of the Saturnian ring current, revealed by Cassini, Journal of Geophysical Research Space Physics 122 (2), 1803-1815, doi: 10.1002/2016ja023742.

Sergis, N., C. M. Jackman, A. Masters, S. M. Krimigis, M. F. Thomsen, D. C. Hamilton, D. G. Mitchell, M. K. Dougherty, A. J. Coates, (2013), Particle and magnetic field properties of the Saturnian magnetosheath: Presence and upstream escape of hot magnetospheric plasma, Journal of Geophysical Research Space Physics 118 (4), 1620-1634, doi: 10.1002/jgra.50164.

Sergis, N., C. S. Arridge, S. M. Krimigis, D. G. Mitchell, A. M. Rymer, D. C. Hamilton, N. Krupp, M. K. Dougherty, A. J. Coates, (2011), Dynamics and seasonal variations in Saturn's magnetospheric plasma sheet, as measured by Cassini, Journal of Geophysical Research Space Physics 116, A04203, doi: 10.1029/2010ja016180.

Sergis, N., S. M. Krimigis, E. C. Roelof, C. S. Arridge, A. M. Rymer, D. G. Mitchell, D. C. Hamilton, N. Krupp, M. F. Thomsen, M. K. Dougherty, A. J. Coates, D. T. Young, (2010), Particle pressure, inertial force, and ring current density profiles in the magnetosphere of Saturn, based on Cassini measurements, Geophysical Research Letters 37, L02102, doi: 10.1029/2009gl041920.

Sergis, N., S. M. Krimigis, D. G. Mitchell, D. C. Hamilton, N. Krupp, B. H. Mauk, E. C. Roelof, M. K. Dougherty, (2009), Energetic particle pressure in Saturn's magnetosphere measured with the magnetospheric imaging instrument on Cassini, Journal of Geophysical Research Space Physics 114, A02214, doi: 10.1029/2008ja013774.

Sergis, N., S. M. Krimigis, D. G. Mitchell, D. C. Hamilton, N. Krupp, B. M. Mauk, E. C. Roelof, M. Dougherty, (2007), Ring current at Saturn: Energetic particle pressure in Saturn's equatorial magnetosphere measured with Cassini/MIMI, Geophysical Research Letters 34 (9), L09102.

Shafiq, Muhammad, J. E. Wahlund, M. W. Morooka, W. S. Kurth, W. M. Farrell, (2011), Characteristics of the dust-plasma interaction near Enceladus' South Pole, Planetary and Space Science 59 (1), 17-25, doi: h10.1016/j.pss.2010.10.006.

Shebanits, O., E. Vigren, J. E. Wahlund, M. Holmberg, M. Morooka, N. Edberg, K. Mandt, J. Waite, (2017), Titan's ionosphere: A survey of solar EUV influences, Journal of Geophysical Research Space Physics 122, no. 7, 7491-7503, doi: 10.1002/2017JA023987.

Shebanits, O., J. E. Wahlund, N. J. T. Edberg, F. J. Crary, A. Wellbrock, D. J. Andrews, E. Vigren, R. T. Desai, A. J. Coates, K. E. Mandt, J. H. Waite, (2016), Ion and aerosol precursor densities in Titan's ionosphere: A multi-instrument case study, Journal of Geophysical Research Space Physics 121 (10), 10075-10090, doi: 10.1002/2016ja022980.

Shebanits, O., J. E. Wahlund, K. Mandt, K. Ågren, N. J. T. Edberg, J. H. Waite Jr., (2013), Negative ion densities in the ionosphere of Titan-Cassini RPWS/LP results, Planetary and Space Science 84, 153-162, doi: 10.1016/j.pss.2013.05.021.

Sillanpää, I., E. Kallio, P. Janhunen, W. Schmidt, K. Mursula, J. Vilppola, P. Tanskanen, (2006), Hybrid simulation study of ion escape at Titan for different orbital positions, Advances in Space Research 38 (4), 799-805.

Simon, S., F. M. Neubauer, A. Wennmacher, M. K. Dougherty, (2014), Variability of Titan's induced magnetotail: Cassini magnetometer observations, Journal of Geophysical Research Space Physics 119 (3), 2024-2037, doi: 10.1002/2013ja019608.

Simon, S., S. C. van Treeck, A. Wennmacher, J. Saur, F. M. Neubauer, C. L. Bertucci, M. K. Dougherty, (2013), Structure of Titan's induced magnetosphere under varying background magnetic field conditions: Survey of Cassini magnetometer data from flybys TA–T85, Journal of Geophysical Research: Space Physics, 118, no. 4, 1679–1699.

Simon, S., J. Saur, H. Kriegel, F. M. Neubauer, U. Motschmann, M. K. Dougherty, (2011), Influence of negatively charged plume grains and hemisphere coupling currents on the

structure of Enceladus' Alfvén wings: Analytical modeling of Cassini magnetometer observations, Journal of Geophysical Research: Space Physics, 116, no. A4.

Sittler Jr., E. C., R. E. Hartle, R. E. Johnson, J. F. Cooper, A. S. Lipatov, C. Bertucci, A. J. Coates, et al., (2010), Saturn's magnetospheric interaction with Titan as defined by Cassini encounters T9 and T18: New results, Planetary and Space Science, 58, no. 3, 327–350.

Sittler, E. C., R. E. Hartle, C. Bertucci, A. Coates, T. Cravens, I. Dandouras, D. Shemansky, (2009a), Energy deposition processes in Titan's upper atmosphere and its induced magnetosphere, In Titan from Cassini-Huygens, (eds.) R. H. Brown, J.-P. Lebreton, J. H. Waite, Jr., 393-453, Dordrecht, New York, Springer.

Sittler Jr., E. C., A. Ali, J. F. Cooper, R. E. Hartle, R. E. Johnson, A. J. Coates, D. T. Young, (2009b), Heavy ion formation in Titan's ionosphere: Magnetospheric introduction of free oxygen and a source of Titan's aerosols?, Planetary and Space Science, 57, no. 13, 1547–1557.

Sittler Jr., E. C., N. Andre, M. Blanc, M. Burger, R. E. Johnson, A. Coates, A. Rymer, et al, (2008), Ion and neutral sources and sinks within Saturn's inner magnetosphere: Cassini results, Planetary and Space Science, 56, no. 1, 3–18.

Sittler, E. C., M. Blanc, J. D. Richardson, A. Rymer, N. Andre, M. Thomsen, J. F. Cooper, et al., (2006a), Cassini Observations of Saturn's Dawn-Magnetotail Region and their Relation to Models of Saturn's Aurora: Preliminary results, American Geophysical Union (AGU) Fall Meeting, abstract.

Sittler Jr., E. C., R. E. Johnson, H. T. Smith, J. D. Richardson, S. Jurac, M. Moore, J. F. Cooper, et al., (2006b), Energetic nitrogen ions within the inner magnetosphere of Saturn, Journal of Geophysical Research: Space Physics, 111, no. A9.

Sittler Jr., E. C., M. Thomsen, D. Chornay, M. D. Shappirio, D. Simpson, R. E. Johnson, H. T. Smith, A. J. Coates, A. M. Rymer, F. Crary, D. J. McComas, D. T. Young, D. Reisenfeld, M. Dougherty, N. Andre, (2005), Preliminary results on Saturn's inner plasmasphere as observed by Cassini: Comparison with Voyager, Geophysical Research Letters 32 (14), 5, doi: 10.1029/2005GL022653.

Smith, A. W., C. M. Jackman, M. F. Thomsen, L. Lamy, N. Sergis, (2018a), Multi-instrument investigation of the location of Saturn's magnetotail X-line, Journal of Geophysical Research: Space Physics, 123, no. 7, 5494–5505.

Smith, A. W., C. M. Jackman, M. F. Thomsen, N. Sergis, D. G. Mitchell, E. Roussos, (2018b), Dipolarization fronts with associated energized electrons in Saturn's magnetotail, Journal of Geophysical Research: Space Physics, 123, no. 4, 2714–2735.

Smith, A. W., C. M. Jackman, M. F. Thomsen, (2016), Magnetic reconnection in Saturn's magnetotail: A comprehensive magnetic field survey, Journal of Geophysical Research Space Physics 121 (4), 2984-3005, doi: 10.1002/2015ja022005.

Smith, E. J., M. K. Dougherty, C. T. Russell, D. J. Southwood, (2001), Scalar helium magnetometer observations at Cassini Earth swing-by, Journal of Geophysical Research Space Physics 106 (A12), 30129-39, doi: 10.1029/2001JA900115.

Smith, H. T., R. E. Johnson, M. E. Perry, D. G. Mitchell, R. L. McNutt, D. T. Young, (2010), Enceladus plume variability and the neutral gas densities in Saturn's magnetosphere, Journal of Geophysical Research Space Physics 115, A10252, doi: 10.1029/2009ja015184.

Smith, H. T., (2010), Neutral Clouds and Their Influence on Pick-up Ions in Saturn's Magnetosphere, In AIP Conference Proceedings, vol. 1302, no. 1, pp. 256–262.

Smith, H. T., D. G. Mitchell, R. E. Johnson, C. P. Paranicas, (2009), Investigation of energetic proton penetration in Titan's atmosphere using the Cassini INCA instrument, Planetary and Space Science 57, no. 13, 1538–1546.

Smith, H. T., M. Shappirio, R. E. Johnson, D. Reisenfeld, E. C. Sittler, F. J. Crary, D. J. McComas, D. T. Young, (2008), Enceladus: A potential source of ammonia products and molecular nitrogen for Saturn's magnetosphere, Journal of Geophysical Research: Space Physics 113, no. A11.

Smith, H. T., R. E. Johnson, E. C. Sittler, M. Shappirio, D. Reisenfeld, O. J. Tucker, M. Burger, F. J. Crary, D. J. McComas, D. T. Young, (2007), Enceladus: The likely dominant nitrogen source in Saturn's magnetosphere, Icarus 188, no. 2, 356–366.

Smith, H. T., M. Shappirio, E. C. Sittler, D. Reisenfeld, R. E. Johnson, R. A. Baragiola, F. J. Crary, D. J. McComas, D. T. Young, (2005), Discovery of nitrogen in Saturn's inner magnetosphere, Geophysical Research Letters 32 (14), 14-03, doi: 10.1029/2005GL022654.

Snowden, D. and R. V. Yelle, (2014a), The global precipitation of magnetospheric electrons into Titan's upper atmosphere, Icarus 243, 1-15. doi: 10.1016/j.icarus.2014.08.027.

Snowden, D. and R. V. Yelle, (2014b), The thermal structure of Titan's upper atmosphere, II: Energetics, Icarus 228, 64-77, doi: 10.1016/j.icarus.2013.08.027.

Snowden, D., R. V. Yelle, J. Cui, J.-E. Wahlund, N. J. T. Edberg, K. Ågren, (2013), The thermal structure of Titan's upper atmosphere, I: Temperature profiles from Cassini INMS observations, Icarus, 226, no. 1, 552–582.

Sorba, A. M., N. A. Achilleos, P. Guio, C. S. Arridge, N. M. Pilkington, A. Masters, N. Sergis, A. J. Coates, M. K. Dougherty, (2017), Modeling the compressibility of Saturn's magnetosphere in response to internal and external influences, Journal of Geophysical Research Space Physics 122 (2),1572-1589, doi: 10.1002/2016ja023544.

Southwood, D. J. and E. Chané, (2016), High-latitude circulation in giant planet magnetospheres, Journal of Geophysical Research: Space Physics, 121, no. 6, 5394–5403.

Southwood, D. J., (2015), Formation of magnetotails: Fast and slow rotators compared, In Magnetotails in the Solar System, (eds.) A. Keiling, C. M. Jackman, P. A. Delamere, pp. 199-215, Hoboken, New Jersey, John Wiley & Sons, Inc., doi: 10.1002/9781118842324.ch12.

Southwood, D. J. and S. W. H. Cowley, (2014), The origin of Saturn's magnetic periodicities: Northern and southern current systems, Journal of Geophysical Research Space Physics 119 (3), 1563-1571, doi: 10.1002/2013ja019632.

Southwood, D. J., (2014), Saturn's mysterious magnetism, Astronomy & Geophysics, vol. 55, Issue 1, pp. 1.13–1.18, doi: 10.1093/astrogeo/atu034.

Southwood, D., (2011), Direct evidence of differences in magnetic rotation rate between Saturn's northern and southern polar regions, Journal of Geophysical Research Space Physics 116, A01201, doi: 10.1029/2010ja016070.

Southwood, D. J. and M. G. Kivelson, (2009), The source of Saturn's periodic radio emission, Journal of Geophysical Research Space Physics 114, A09201, doi: 10.1029/2008ja013800.

Southwood, D. J. and M. G. Kivelson, (2007), Saturnian magnetospheric dynamics: Elucidation of a camshaft model, Journal of Geophysical Research Space Physics 112 (A12), A12222.

Southwood, D. J., M. K. Dougherty, A. Balogh, S. W. H. Cowley, E. J. Smith, B. T. Tsurutani, C. T. Russell, et al., (2001), Magnetometer measurements from the Cassini Earth swing-by, Journal of Geophysical Research: Space Physics, 106, no. A12, 30109–30128.

Southwood, D. J. and M. G. Kivelson, (2001), A new perspective concerning the influence of the solar wind on the Jovian magnetosphere, Journal of Geophysical Research Space Physics 106 (A4), 6123-6130.

Sromovsky, L. A., K. H. Baines, P. M. Fry, (2013), Saturn's Great Storm of 2010-2011: Evidence for ammonia and water ices from analysis of VIMS spectra, Icarus 226 (1), 402-418, doi: 10.1016/j.icarus.2013.05.043.

Strobel, D. F., (2008), Titan's hydrodynamically escaping atmosphere, Icarus 193 (2), 588-594.

Sulaiman, A. H., W. S. Kurth, G. B. Hospodarsky, T. F. Averkamp, A. M. Persoon, J. D. Menietti, S.-Y. Ye, et al., (2018), Auroral hiss emissions during Cassini's Grand Finale: Diverse electrodynamic interactions between Saturn and its rings, Geophysical Research Letters, 45, no. 14, 6782–6789.

Sulaiman, A. H., D. A. Gurnett, J. S. Halekas, J. N. Yates, W. S. Kurth, M. K. Dougherty, (2017), Whistler mode waves upstream of Saturn, Journal of Geophysical Research: Space Physics, 122, no. 1, 227–234.

Sulaiman, A. H., A. Masters, M. K. Dougherty, (2016), Characterization of Saturn's bow shock: Magnetic field observations of quasi-perpendicular shocks, Journal of Geophysical Research-Space Physics 121 (5), 4425-4434, doi: 10.1002/2016ja022449.

Sulaiman, A. H., A. Masters, M. K. Dougherty, D. Burgess, M. Fujimoto, G. B. Hospodarsky, (2015),Quasiperpendicular high Mach number shocks, Physical Review Letters 115 (12), 125001, doi: 10.1103/PhysRevLett.115.125001.

Sulaiman, A. H., A. Masters, M. K. Dougherty, X. Jia, (2014), The magnetic structure of Saturn's magnetosheath, Journal of Geophysical Research Space Physics 119 (7), 5651-5661, doi: 10.1002/2014ja020019.

Sundberg, T., D. Burgess, M. Scholer, A. Masters, A. Haidar, (2017), The dynamics of very high Alfvén Mach number shocks in space plasmas, The Astrophysical Journal Letters 836, no. 1, L4, doi: 10.3847/2041-8213/836/1/L4.

Szego, K., Z. Nemeth, L. Foldy, S. W. H. Cowley, G. Provan, (2013), Dual periodicities in the flapping of Saturn's magnetodisk, Journal of Geophysical Research Space Physics 118 (6), 2883-2887, doi: 10.1002/jgra.50316.

Szego, K., Z. Nemeth, G. Erdos, L. Foldy, Z. Bebesi, M. Thomsen, D. Delapp, (2012), Location of the magnetodisk in the nightside outer magnetosphere of Saturn near equinox based on ion densities, Journal of Geophysical Research Space Physics 117, A09225, doi: 10.1029/2012JA017817.

Szego, K., Z. Nemeth, G. Erdos, L. Foldy, M. Thomsen, D. Delapp, (2011), The plasma environment of Titan: The magnetodisk of Saturn near the encounters as derived from ion densities measured by the Cassini/CAPS plasma spectrometer, Journal of Geophysical Research Space Physics 116, A10219, doi: 10.1029/2011JA016629.

Szego, K., C. Bertucci, A. J. Coates, Z. Bebesi, G. Erdos, L. Foldy, D. T. Young, F. Crary, E. C. Sittler, R. Hartle, M. Thomsen, (2006), On the flowside plasma environment of Titan, American Geophysical Union (AGU) Fall Meeting, San Francisco, CA, 11-15 Dec. 2006.

Szego, K., D. T. Young, B. Barraclough, J. J. Berthelier, A. J. Coates, D. J. McComas, F. J. Crary, M. K. Dougherty, G. Erdos, D. A. Gurnett, W. S. Kurth, M. F. Thomsen, (2003), Cassini plasma spectrometer measurements of Jovian bow shock structure, Journal of Geophysical Research Space Physics 108 (A7), 11-1. doi: 10.1029/2002JA009517.

Talboys, D. L., E. J. Bunce, S. W. H. Cowley, C. S. Arridge, A. J. Coates, M. K. Dougherty, (2011), Statistical characteristics of field-aligned currents in Saturn's nightside magnetosphere, Journal of Geophysical Research Space Physics 116, A04213, doi: 10.1029/2010ja016102.

Talboys, D. L., C. S. Arridge, E. J. Bunce, A. J. Coates, S. W. H. Cowley, M. K. Dougherty, (2009a), Characterization of auroral current systems in Saturn's magnetosphere: High-latitude Cassini observations, Journal of Geophysical Research: Space Physics, 114, no. A6.

Talboys, D. L., C. S. Arridge, E. J. Bunce, A. J. Coates, S. W. H. Cowley, M. K. Dougherty, K. K. Khurana, (2009b), Signatures of field-aligned currents in Saturn's nightside magnetosphere, Geophysical Research Letters, 36, no. 19.

Teolis, B. D., M. E. Perry, C. J. Hansen, J. H. Waite, C. C. Porco, J. R. Spencer, C. J. A. Howett, (2017), Enceladus plume structure and time variability: comparison of Cassini observations, Astrobiology, 17, no. 9, 926–940.

Thomsen, M. F., S. V. Badman, C. M. Jackman, X. Jia, M. G. Kivelson, W. S. Kurth, (2017a), Energy-banded ions in Saturn's magnetosphere, Journal of Geophysical Research Space Physics 122 (5), 5181-5202, doi: 10.1002/2017ja024147.

Thomsen, M. F., C. M. Jackman, S. W. H. Cowley, X. Jia, M. G. Kivelson, G. Provan, (2017b), Evidence for periodic variations in the thickness of Saturn's nightside plasma sheet, Journal of Geophysical Research: Space Physics, 122, no. 1, 280–292.

Thomsen, M. F., A. J. Coates, E. Roussos, R. J. Wilson, K. C. Hansen, G. R. Lewis, (2016), Suprathermal electron penetration into the inner magnetosphere of Saturn, Journal of Geophysical Research: Space Physics, 121, no. 6, 5436–5448.

- - - - - - - - - - - - - -

Thomsen, M. F., C. M. Jackman, D. G. Mitchell, G. Hospodarsky, W. S. Kurth, K. C. Hansen, (2015a), Sustained lobe reconnection in Saturn's magnetotail, Journal of Geophysical Research: Space Physics, 120, no. 12, 10257–10274.

Thomsen, M. F., D. G. Mitchell, X. Jia, C. M. Jackman, G. Hospodarsky, A. J. Coates, (2015b), Plasmapause formation at Saturn, Journal of Geophysical Research: Space Physics, 120, no. 4, 2571–2583.

Thomsen, M. F., C. M. Jackman, R. L. Tokar, R. J. Wilson, (2014a), Plasma flows in Saturn's nightside magnetosphere, Journal of Geophysical Research Space Physics 119 (6), 4521-4535, doi: 10.1002/2014ja019912.

Thomsen, M. F., D.B. Reisenfeld, R. J. Wilson, M. Andriopoulou, F. J. Crary, G. B. Hospodarsky, C. M. Jackman, et al, (2014b), Ion composition in interchange injection events in Saturn's magnetosphere, Journal of Geophysical Research: Space Physics, 119, no. 12, 9761–9772.

Thomsen, M. F., (2013), Saturn's magnetospheric dynamics, Geophysical Research Letters 40 (20), 5337-5344, doi: 10.1002/2013GL057967.

Thomsen, M. F., E. Roussos, M. Andriopoulou, P. Kollmann, C. S. Arridge, C. P. Paranicas, D. A. Gurnett, R. L. Powell, R. L. Tokar, D. T. Young, (2012), Saturn's inner magnetospheric convection pattern: Further evidence, Journal of Geophysical Research Space Physics 117, A09208, doi: 10.1029/2011JA017482.

Thomsen, M. F., D. B. Reisenfeld, D. M. Delapp, R. L. Tokar, D. T. Young, F. J. Crary, E. C. Sittler, M. A. McGraw, J. D. Williams, (2010), Survey of ion plasma parameters in Saturn's magnetosphere, Journal of Geophysical Research Space Physics 115, A10220, doi: 10.1029/2010ja015267.

Thomsen, M. F., J. P. DiLorenzo, D. J. McComas, D. T. Young, F. J. Crary, D. Delapp, D. B. Reisenfeld, N. Andre, (2007), Assessment of the magnetospheric contribution to the suprathermal ions in Saturn's foreshock region, Journal of Geophysical Research: Space Physics 112, no. A5.

Tobiska, W. K., (2004), SOLAR2000 irradiances for climate change research, aeronomy and space system engineering, Advances in Space Research 34 (8), 1736-1746.

Tokar, R. L., R. E. Johnson, M. F. Thomsen, E. C. Sittler, A. J. Coates, R. J. Wilson, F. J. Crary, D. T. Young, G. H. Jones, (2012), Detection of exospheric O2+ at Saturn's moon Dione, Geophysical Research Letters 39 (3), L03105, doi: 10.1029/2011GL050452.

Tokar, R. L., R. E. Johnson, M. F. Thomsen, R. J. Wilson, D. T. Young, F. J. Crary, A. J. Coates, G. H. Jones, C. S. Paty, (2009), Cassini detection of Enceladus' cold water-group plume ionosphere, Geophysical Research Letters 36 (13), doi: 10.1029/2009GL038923.

Tokar, R. L., R. J. Wilson, R. E. Johnson, M. G. Henderson, M. F. Thomsen, M. M. Cowee, E. C. Sittler, D. T. Young, F. J. Crary, H. J. McAndrews, H. T. Smith, (2008), Cassini detection of water-group pick-up ions in the Enceladus torus, Geophysical Research Letters 35 (14), L14202.

Tokar, R. L., R. E. Johnson, T. W. Hill, D. H. Pontius, W. S. Kurth, F. J. Crary, D. T. Young, M. F. Thomsen, D. B. Reisenfeld, A. J. Coates, G. R. Lewis, E. C. Sittler, D. A. Gurnett,

(2006), The interaction of the atmosphere of Enceladus with Saturn's plasma, Science 311 (5766), 1409-12, doi: 10.1126/science.1121061.

Tokar, R. L., R. E. Johnson, M. F. Thomsen, D. M. Delapp, R. A. Baragiola, M. F. Francis, D. B. Reisenfeld, B. A. Fish, D. T. Young, F. J. Crary, A. J. Coates, D. A. Gurnett, W. S. Kurth, (2005), Cassini observations of the thermal plasma in the vicinity of Saturn's main rings and the F and G rings, Geophysical Research Letters 32 (14), L14S04.

Tokarev, Y., J.-L. Bougeret, B. Cecconi, A. Lecacheux, M. L. Kaiser, W. S. Kurth, (2006), Sura-waves experiments: calibration of the Cassini/RPWS/HFR instrumentation, Verlag der Österreichischen Akademie der Wissenschaften, https://austriaca.at/0xc1aa5576_0x0015cbe6.pdf.

Tseng, W.-L., R. E. Johnson, M. K. Elrod, (2013a), Modeling the seasonal variability of the plasma environment in Saturn's magnetosphere between main rings and Mimas, Planetary and Space Science 77, 126-135, doi: 10.1016/j.pss.2012.05.001.

Tseng, W.-L., R. E. Johnson, W.-H. Ip, (2013b), The atomic hydrogen cloud in the saturnian system, Planetary and Space Science, 85, 164–174.

Tseng, W.-L., R. E. Johnson, M. F. Thomsen, T. A. Cassidy, M. K. Elrod, (2011), Neutral H_2 and H_2^+ ions in the Saturnian magnetosphere, (2011), Journal of Geophysical Research: Space Physics, 116, no. A3.

Tseng, W. L., W. H. Ip, R. E. Johnson, T. A. Cassidy, M. K. Elrod, (2010), The structure and time variability of the ring atmosphere and ionosphere, Icarus 206 (2), 382-389, doi: 10.1016/j.icarus.2009.05.019.

Tsurutani, B. T., E. J. Smith, M. E. Burton, J. K. Arballo, C. Galvan, Xiao-Yan Zhou, D. J. Southwood, M. K. Dougherty, K. H. Glassmeier, F. M. Neubauer, J. K. Chao, (2001), Oblique "1-Hz" whistler mode waves in an electron foreshock: The Cassini near-Earth encounter, Journal of Geophysical Research Space Physics 106 (A12), 30223-30238, doi: 10.1029/2001JA900108.

Tsyganenko, N. A. and V. A. Andreeva, (2014), On the "bowl-shaped" deformation of planetary equatorial current sheets, Geophysical Research Letters 41, no. 4, 1079-1084, doi: 10.1002/2014GL059295.

Tucker, O. J., W. Waalkes, V. M. Tenishev, R. E. Johnson, A. Bieler, M. R. Combi, A. F. Nagy, (2016), Examining the exobase approximation: DSMC models of Titan's upper atmosphere, Icarus 272:290-300, doi: 10.1016/j.icarus.2016.02.044.

Tucker, O. J., R. E. Johnson, J. I. Deighan, A. N. Volkov, (2013), Diffusion and thermal escape of H-2 from Titan's atmosphere: Monte Carlo simulations, Icarus 222 (1), 149-158, doi: 10.1016/j.icarus.2012.10.016.

Tucker, O. J. and R. E. Johnson, (2009), Thermally driven atmospheric escape: Monte Carlo simulations for Titan's atmosphere, Planetary and Space Science, 57, no. 14-15, 1889–1894.

Vervack, R. J. and J. I. Moses, (2015), Saturn's upper atmosphere during the Voyager era: Reanalysis and modeling of the UVS occultations, Icarus 258, 135-163, doi: 10.1016/j.icarus.2015.06.007.

Vigren, E., M. Galand, R. V. Yelle, A. Wellbrock, A. J. Coates, D. Snowden, J. Cui, P. Lavvas, N. J. T. Edberg, O. Shebanits, J. E. Wahlund, V. Vuitton, K. Mandt, (2015), Ionization balance in Titan's nightside ionosphere, Icarus 248, 539-546, doi: 10.1016/j.icarus.2014.11.012.

Vogl, D. F., B. Cecconi, W. Macher, P. Zarka, H. P. Ladreiter, P. Fedou, A. Lecacheux, T. Averkamp, G. Fischer, H. O. Rucker, D. A. Gurnett, W. S. Kurth, G. B. Hospodarsky, (2004), In-flight calibration of the Cassini-Radio and Plasma Wave Science (RPWS) antenna system for direction-finding and polarization measurements, Journal of Geophysical Research Space Physics 109 (A9), 15, doi: 10.1029/2003JA010261.

Vogl, D. F., H. P. Ladreiter, P. Zarka, H. O. Rucker, W. Macher, W. S. Kurth, D. A. Gurnett, G. Fischer, (2001), First results on the calibration of the Cassini RPWS antenna system: Verlag der Österreichischen Akademie der Wissenschaften.

Volkov, A. N., O. J. Tucker, J. T. Erwin, R. E. Johnson, (2011a), Kinetic simulations of thermal escape from a single component atmosphere, Physics of Fluids, 23, no. 6, 066601.

Volkov, A. N., R. E. Johnson, O. J. Tucker, J. T. Erwin, (2011b), Thermally driven atmospheric escape: Transition from hydrodynamic to Jeans escape, The Astrophysical Journal Letters, 729, no. 2, L24.

Vuitton, V., P. Lavvas, R. V. Yelle, M. Galand, A. Wellbrock, G. R. Lewis, A. J. Coates, J.-E. Wahlund, (2009), Negative ion chemistry in Titan's upper atmosphere, Planetary and Space Science 57, no. 13, 1558–1572.

Vuitton, V., R. V. Yelle, M. J. McEwan, (2007), Ion chemistry and N-containing molecules in Titan's upper atmosphere, Icarus 191, no. 2, 722–742.

Vuitton, V., R. V. Yelle, V. G. Anicich, (2006), The nitrogen chemistry of Titan's upper atmosphere revealed, The Astrophysical Journal Letters, 647, no. 2, L175.

Wahlund, J. E., M. W. Morooka, L. Z. Hadid, A. M. Persoon, W. M. Farrell, D. A. Gurnett, G. Hospodarsky, W. S. Kurth, S. Y. Ye, D. J. Andrews, N. J. T. Edberg, A. I. Eriksson, E. Vigren, (2018), In situ measurements of Saturn's ionosphere show that it is dynamic and interacts with the rings, Science 359 (6371), 66-68, doi: 10.1126/science.aao4134.

Wahlund, J.-E., M. Galand, I. Müeller-Wodarg, J. Cui, R. V. Yelle, F. J. Crary, K. Mandt, et al., (2009), On the amount of heavy molecular ions in Titan's ionosphere, Planetary and Space Science, 57, no. 14–15, 1857–1865.

Wahlund, J.-E., R. Boström, G. A. G. D. Gustafsson, D. A. Gurnett, W. S. Kurth, A. Pedersen, T. F. Averkamp, et al., (2005), Cassini measurements of cold plasma in the ionosphere of Titan, Science, 308, no. 5724, 986–989.

Waite, J. H., C. R. Glein, R. S. Perryman, B. D. Teolis, B. A. Magee, G. Miller, J. Grimes, M. E. Perry, K. E. Miller, A. Bouquet, J. I. Lunine, T. Brockwell, S. J. Bolton, (2017), Cassini finds molecular hydrogen in the Enceladus plume: Evidence for hydrothermal processes, Science 356 (6334), 155-159, doi: 10.1126/science.aai8703.

Waite, J. H., W. S. Lewis, B. A. Magee, J. I. Lunine, W. B. McKinnon, C. R. Glein, O. Mousis, D. T. Young, T. Brockwell, J. Westlake, M. J. Nguyen, B. D. Teolis, B. Niemann,

R. L. McNutt, M. Perry, W. H. Ip, (2009), Liquid water on Enceladus from observations of ammonia and ^{40}Ar in the plume, Nature 460 (7254), 487-490, doi: 10.1038/nature08153.

Waite, J. H., D. T. Young, T. E. Cravens, A. J. Coates, F. J. Crary, B. Magee, J. Westlake, (2007), The process of tholin formation in Titan's upper atmosphere, Science, 316, no. 5826, 870–875.

Waite, J. H., T. E. Cravens, W. H. Ip, W. T. Kasprzak, J. G. Luhmann, R. L. McNutt, H. B. Niemann, R. V. Yelle, I. Müeller-Wodarg, S. A. Ledvina, S. Scherer, (2005), Oxygen ions observed near Saturn's A ring, Science 307 (5713), 1260-1262, doi: 10.1126/science.1105734.

Walker, J. D., S. Chocron, J. H. Waite, T. Brockwell, (2015), The vaporization threshold: Hypervelocity impacts of ice grains into a titanium Cassini spacecraft instrument chamber, Procedia Engineering, 103, 628–635.

Wang, Z., D. A. Gurnett, T. F. Averkamp, A. M. Persoon, W. S. Kurth, (2006), Characteristics of dust particles detected near Saturn's ring plane with the Cassini Radio and Plasma Wave instrument, Planetary and Space Science, 54, no. 9–10, 957–966.

Wannawichian, S., J. T. Clarke, D. H. Pontius, (2008), Interaction evidence between Enceladus' atmosphere and Saturn's magnetosphere, Journal of Geophysical Research Space Physics 113, A07217, doi: 10.1029/2007JA012899.

Warwick, J. W., J. B. Pearce, D. R. Evans, T. D. Carr, J. J. Schauble, J. K. Alexander, M. L. Kaiser, M. D. Desch, M. Pedersen, A. Lecacheux, (1981), Planetary radio astronomy observations from Voyager 1 near Saturn, Science 212 (4491), 239-243.

Wei, H. Y., C. T. Russell, M. K. Dougherty, F. M. Neubauer, Y. J. Ma, (2010), Upper limits on Titan's magnetic moment and implications for its interior, Journal of Geophysical Research: Planets, 115, no. E10.

Wei, H. Y., C. T. Russell, J.-E. Wahlund, M. K. Dougherty, C. Bertucci, R. Modolo, Y. J. Ma, F. M. Neubauer, (2007), Cold ionospheric plasma in Titan's magnetotail, Geophysical Research Letters, 34, no. 24.

Wellbrock, A., A. J. Coates, G. H. Jones, V. Vuitton, P. Lavvas, R. T. Desai, J. H. Waite, (2019), Heavy negative ion growth in Titan's polar winter, Monthly Notices of the Royal Astronomical Society 490, no. 2, 2254–2261.

Wellbrock, A., A. J. Coates, G. H. Jones, G. R. Lewis, J. H. Waite, (2013), Cassini CAPS-ELS observations of negative ions in Titan's ionosphere: Trends of density with altitude, Geophysical Research Letters 40 (17), 4481-4485, doi: 10.1002/grl.50751.

Went, D. R., G. B. Hospodarsky, A. Masters, K. C. Hansen, M. K. Dougherty, (2011), A new semiempirical model of Saturn's bow shock based on propagated solar wind parameters, Journal of Geophysical Research: Space Physics, 116, no. A7.

Westlake, J. H., J. H. Waite, N. Carrasco, M. Richard, T. Cravens, (2014), The role of ion-molecule reactions in the growth of heavy ions in Titan's ionosphere,Journal of Geophysical Research: Space Physics, 119, no. 7, 5951–5963.

Westlake, J. H., J. M. Bell, J. H. Waite Jr., R. E. Johnson, J. G. Luhmann, K. E. Mandt, B. A. Magee, A. M. Rymer, (2011), Titan's thermospheric response to various plasma environments, Journal of Geophysical Research: Space Physics, 116, no. A3.

Wilson, A., (2004), Planetary probe atmospheric entry and descent trajectory analysis and science, Proceedings of the International Workshop Planetary Probe Atmospheric Entry and Descent Trajectory Analysis and Science, 6-9 October 2003, Lisbon, Portugal, (ed.), A. Wilson, ESA SP-544, Noordwijk, Netherlands: ESA Publications Division, pp. VI + 364.

Wilson, E. H. and S. K. Atreya, (2004), Current state of modeling the photochemistry of Titan’s mutually dependent atmosphere and ionosphere, Journal of Geophysical Research-Planets 109 (E6), E06002, doi: 10.1029/2003JE002181.

Wilson, G. R. and J. H. Waite Jr., (1989), Kinetic modeling of the Saturn ring-ionosphere plasma environment, Journal of Geophysical Research: Space Physics, 94, no. A12, 17287–17298.

Wilson, R. J., F. Bagenal, A. M. Persoon, (2017), Survey of thermal plasma ions in Saturn’s magnetosphere utilizing a forward model, Journal of Geophysical Research Space Physics 122 (7), 7256-7278, doi: 10.1002/2017ja024117.

Wilson, R. J., F. Bagenal, T. Cassidy, B. L. Fleshman, F. Crary, (2015), The relative proportions of water group ions in Saturn's inner magnetosphere: A preliminary study, Journal of Geophysical Research: Space Physics, 120, no. 8, 6624–6632.

Wilson, R. J., F. Bagenal, P. A. Delamere, M. Desroche, B. L. Fleshman, V. Dols, (2013), Evidence from radial velocity measurements of a global electric field in Saturn’s inner magnetosphere, Journal of Geophysical Research Space Physics 118 (5), 2122-2132, doi: 10.1002/jgra.50251.

Wilson, R. J., P. A. Delamere, F. Bagenal, Adam Masters, (2012), Kelvin-Helmholtz instability at Saturn's magnetopause: Cassini ion data analysis, Journal of Geophysical Research: Space Physics, 117, no. A3.

Wilson, R. J., R. L. Tokar, W. S. Kurth, A. M. Persoon, (2010), Properties of the thermal ion plasma near Rhea as measured by the Cassini plasma spectrometer, Journal of Geophysical Research Space Physics 115, A05201, doi: 10.1029/2009ja014679.

Wilson, R. J., R. L. Tokar, M. G. Henderson, (2009), Thermal ion flow in Saturn’s inner magnetosphere measured by the Cassini plasma spectrometer: A signature of the Enceladus torus?, Geophysical Research Letters 36, L23104, doi: 10.1029/2009gl040225.

Wilson, R. J., R. L. Tokar, M. G. Henderson, T. W. Hill, M. F. Thomsen, D. H. Pontius Jr., (2008), Cassini plasma spectrometer thermal ion measurements in Saturn’s inner magnetosphere, Journal of Geophysical Research Space Physics 113 (A12), A12218, doi: 10.1029/2008ja013486.

Xin, L., D. A. Gurnett, O. Santolik, W. S. Kurth, G. B. Hospodarsky, (2006), Whistler-mode auroral hiss emissions observed near Saturn’s B ring, Journal of Geophysical Research Space Physics 111 (A6), A06214.

Yao, Z. H., D. Grodent, L. C. Ray, I. J. Rae, A. J. Coates, Z. Y. Pu, A. T. Lui et al., (2017a), Two fundamentally different drivers of dipolarizations at Saturn, Journal of Geophysical Research: Space Physics, 122, no. 4, 4348–4356.

Yao, Z. H., A. J. Coates, L. C. Ray, I. J. Rae, D. Grodent, G. H. Jones, M. K. Dougherty, C. J. Owen, R. L. Guo, W. R. Dunn, A. Radioti, Z. Y. Pu, G. R. Lewis, J. H. Waite, J.-C. Gérard, (2017b), Corotating magnetic reconnection site in Saturn's magnetosphere, The Astrophysical Journal 846, L25, doi: 10.3847/2041-8213/aa88af.

Yao, Z. H., A. Radioti, I. J. Rae, J. Liu, D. Grodent, L. C. Ray, S. V. Badman, A. J. Coates, J.-C. Gérard, J. H. Waite, J. N. Yates, Q. Q. Shi, Y. Wei, B. Bonfond, M. K. Dougherty, E. Roussos, N. Sergis, B. Palmaerts, (2017c), Mechanisms of Saturn's near-noon transient aurora: In situ evidence from Cassini measurements, Geophysical Research Letters 44, 11, doi: 10.1002/2017GL075108.

Yao, Z., Z. Y. Pu, I. J. Rae, A. Radioti, M. V. Kubyshkina, (2017d), Auroral streamer and its role in driving wave-like pre-onset aurora, Geoscience Letters 4, no. 1, 8.

Yates, J. N., D. J. Southwood, M. K. Dougherty, (2015a), Magnetic phase structure of Saturn's 10.7 h oscillations, Journal of Geophysical Research: Space Physics, 120, no. 4, 2631–2648.

Yates, J. N., D. J. Southwood, M. K. Dougherty, (2015b), Reply to the comment by Cowley et al. on Magnetic phase structure of Saturn's 10.7 h oscillations.

Ye, S.-Y., W. S. Kurth, G. B. Hospodarsky, A. M. Persoon, A. H. Sulaiman, D. A. Gurnett, M. Morooka et al., (2018), Dust Observations by the Radio and Plasma Wave Science Instrument During Cassini's Grand Finale, Geophysical Research Letters, 45, no. 19, 10–101.

Ye, S.-Y., G. Fischer, W. S. Kurth, J. D. Menietti, D. A. Gurnett, (2017), Rotational modulation of Saturn kilometric radiation, narrrowband emission and auroral hiss, 191-204, doi: 10.1553/PRE8s191.

Ye, S.-Y., D. A. Gurnett, W. S. Kurth, (2016a), In-situ measurements of Saturn's dusty rings based on dust impact signals detected by Cassini RPWS, Icarus, 279, 51–61.

Ye, S.-Y., G. Fischer, W. S. Kurth, J. D. Menietti, D. A. Gurnett, (2016b), Rotational modulation of Saturn's radio emissions after equinox, Journal of Geophysical Research: Space Physics, 121, no. 12, 11714–11728.

Ye, S.-Y., D. A. Gurnett, W. S. Kurth, T. F. Averkamp, S. Kempf, H.-W. Hsu, R. Srama, E. Grün, (2014a), Properties of dust particles near Saturn inferred from voltage pulses induced by dust impacts on Cassini spacecraft, Journal of Geophysical Research: Space Physics, 119, no. 8, 6294–6312.

Ye, S.-Y., D. A. Gurnett, W. S. Kurth, T. F. Averkamp, M. Morooka, S. Sakai, J.-E. Wahlund, (2014b), Electron density inside Enceladus plume inferred from plasma oscillations excited by dust impacts, Journal of Geophysical Research: Space Physics, 119, no. 5, 3373–3380.

Ye, S., H. Hsu, T. F. Averkamp, W. S. Kurth, D. A. Gurnett, S. Kempf, (2012), Cassini/RPWS Dust Measurements During Enceladus Flybys, American Geophysical Union (AGU) Fall Meeting, abstract.

Ye, S.-Y., D. A. Gurnett, J. B. Groene, Z. Wang, W. S. Kurth, (2010), Dual periodicities in the rotational modulation of Saturn narrowband emissions, Journal of Geophysical Research: Space Physics, 115, no. A12.

Yelle, R. V., J. Cui, I. C. F. Müeller-Wodarg, (2008), Methane escape from Titan's atmosphere, Journal of Geophysical Research Planets 113 (E10), E10003, doi: 10.1029/2007je003031.

Young, D. T., J. J. Berthelier, M. Blanc, J. L. Burch, S. Bolton, A. J. Coates, F. J. Crary, R. Goldstein, M. Grande, et al., (2005), Composition and dynamics of plasma in Saturn's magnetosphere, Science 307 (5713), 1262-1266, doi: 10.1126/science.1106151.

Zarka, P., L. Lamy, B. Cecconi, R. Prange, H. O. Rucker, (2007), Modulation of Saturn's radio clock by solar wind speed, Nature 450 (7167), 265-267, doi: 10.1038/nature06237.

Zarka, P. and W. S. Kurth, (2005), Radio wave emission from the outer planets before Cassini, Space Science Reviews 116 (1), 371-397, doi: 10.1007/s11214-005-1962-2.

Zarka, P., B. Cecconi, W. S. Kurth, (2004), Jupiter's low-frequency radio spectrum from Cassini/Radio and Plasma Wave Science (RPWS) absolute flux density measurements, Journal of Geophysical Research: Space Physics, 109, no. A9.

Zarka, P., (2004), Radio and plasma waves at the outer planets, Advances in Space Research, 33, no. 11, 2045–2060.

Zarka, P., J. Queinnec, F. J. Crary, (2001), Low-frequency limit of Jovian radio emissions and implications on source locations and Io plasma wake, Planetary and Space Science, 49, no. 10–11, 1137–1149.

Zarka, P., (2000), Radio emissions from the planets and their moons, Geophysical Monograph American Geophysical Union 119, 167-178.

Zlotnik, E. Y., V. E. Shaposhnikov, V. V. Zaitsev, (2016), Interpretation of the zebra pattern in the Jovian kilometric radiation, Journal of Geophysical Research, Space Physics 121 (6), 5307-5318.

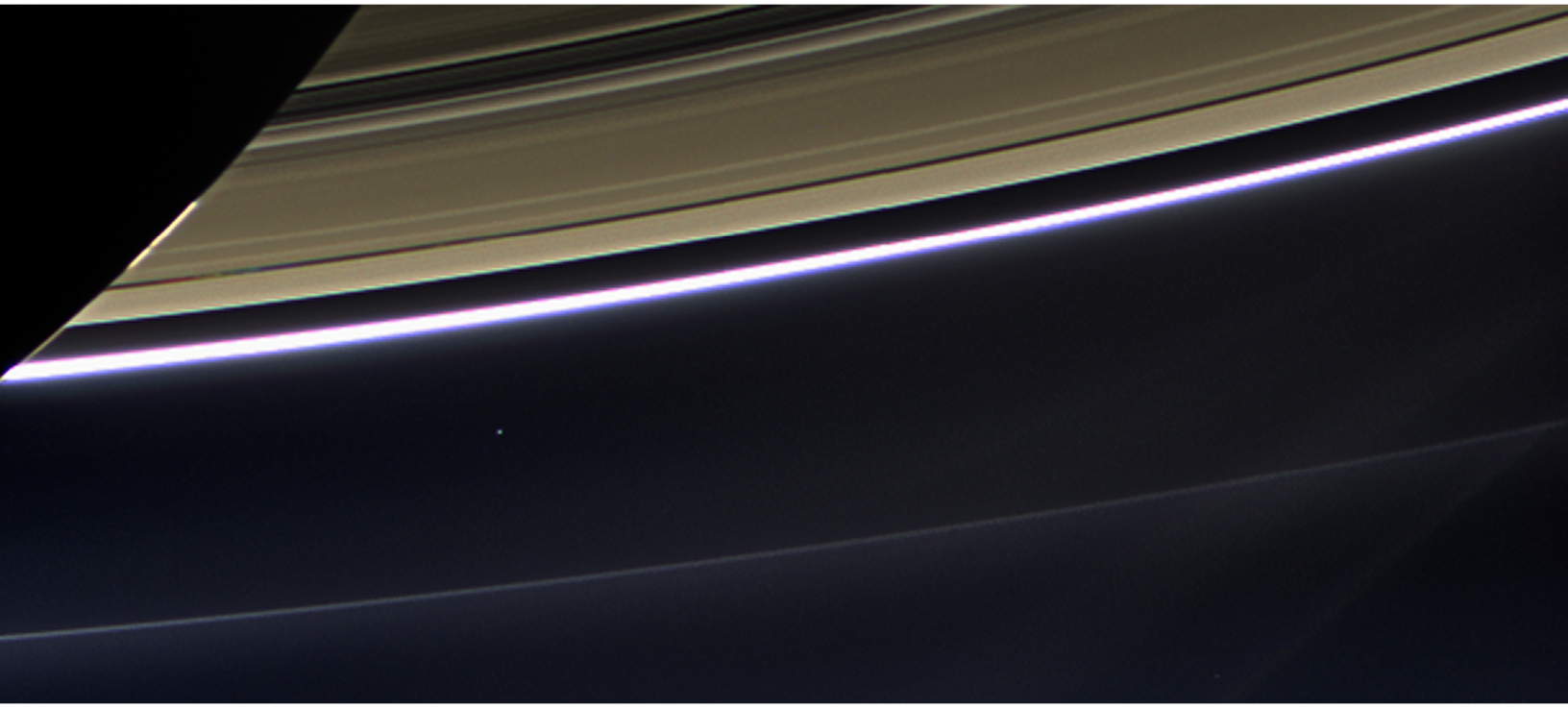

RINGS

Scientists had never before studied the particle size, temperature, composition and dynamics of Saturn's rings from Saturn orbit. Cassini discovered new rings, captured extraordinary ring-moon interactions, observed the lowest ring-temperature ever recorded at Saturn, discovered that the moon Enceladus is the source for Saturn's E-ring, and viewed the rings at equinox when sunlight strikes the rings edge-on, revealing never-before-seen ring features and details. Cassini data have swayed the lively debate over the age of the rings in favor of young rings.

The Ring Working Group (RWG) actively coordinated and enabled Cassini ring observations throughout the mission. Cassini has rewritten the textbooks regarding our understanding of Saturn's Rings, a full generation after Voyager first revealed their complex structure. Not only were all key science objectives successfully accomplished over the course of the Cassini mission, but a number of new science objectives were formulated and addressed along the way, either in response to unexpected results or capitalizing on observational opportunities. The Grand Finale orbits opened up new science opportunities not originally envisioned. There is no question that the science return of Cassini vastly exceeded the expectations as described in the original announcement of opportunity.

CONTENTS

Figures

Tables

EXECUTIVE SUMMARY

… the rings are changing before our eyes dynamically and they are much younger than the solar system compositionally.

Cassini has rewritten the textbooks regarding our understanding of Saturn's Rings, a full generation after Voyager first revealed their complex structure. In fact, Cassini studies of Saturn's rings have already been thoroughly reviewed in two sets of review chapters and articles. In the first major review volume, Saturn after Cassini-Huygens, very thorough reviews are given by Colwell et al. [2009]; Charnoz et al. [2009]; Cuzzi et al. [2009]; Horanyi et al. [2009]; and Schmidt et al. [2009], which remain largely valid as of this writing even if they predate many important results. A short, nonspecialist review is given by Cuzzi et al. [2010]. More recent complete reviews can be found in the Cambridge Planetary Rings book, including Cassini's results prior to the Ring-Grazing and Grand Finale orbits [Charnoz et al. 2018; Cuzzi et al. 2018a; Estrada et al. 2018; Hedman et al. 2018a; Murray and French 2018; Nicholson et al. 2018; Spahn et al. 2018; Spilker et al. 2018]. Finally, Section 3.2 Instrument Science Results updates the story to the very end of the mission, including results from Cassini's last moments and chapters with exhaustive bibliographies. We attempt to cover the highlights of ring science from beginning to end of the mission as organized by our own goals and objectives, and in a readable way we provide a thread of continuity connecting Cassini's vast accomplishments to the big picture of ring origin and evolution. In summary, the rings are changing before our eyes dynamically and they are much younger than the solar system compositionally. Following is a list of our top 20 highlights.

Waves and Collective Dynamics

Spiral density and bending waves were discovered by Voyager. They are driven at orbital resonances with various satellites, blanket the A-ring, and are sprinkled throughout the B-ring and C-ring. Improved analysis tools have allowed even the weakest of these features to be studied in detail, and they provide powerful constraints on the underlying, local surface mass density on several-km spatial scales. About a dozen spiral density and bending waves in the C-ring have been shown to be caused by gravitational and pressure modes inside the planet, and most recently, even constrain the interior structure of Saturn and its rotation rate.

Ring microstructure on sub-km scales is seen everywhere by stellar and radio occultations, and varies on short timescales. Ubiquitous transient gravitational instabilities called self-gravity wakes arise and are torn apart by differential rotation. These wakes vary in configuration across the rings, and their properties imply a ring vertical thickness of tens of meters or less. An unrelated axisymmetric kind of microstructure, due more to viscous forces than self-gravity, can also be seen at various places in the denser parts of the rings. Images taken from close orbits, with sub-km resolution, show that fine-scale structure is widespread in optically thick regions (some of it granular and some axisymmetric or streaky). Dense clumps called straw, each the size of a convoy of aircraft

carriers, are seen in between the dense crests of strong spiral density waves, are probably compacted as particles pass through the crests, and are subsequently broken apart by collisions.

Embedded Moonlets

Analysis of Cassini images have now shown that skirted, embedded 10 km size moonlets are responsible for opening both the Encke and Keeler gaps in the A-ring (see the Icy Satellites chapter). In general, the small ringmoons lying within and near to the rings have very low densities and are likely rubble piles with dense cores. However, moonlets have not been found in similar gaps in the Cassini Division or C-ring with the ~1 km sizes previously thought necessary to clear them.

Flocks of smaller propeller objects of 100–200 m size, detectable only in their disturbance of nearby ring material, occupy three radial bands in the A-ring. A dozen or so of the largest of these objects, 0.1–1 km in size, wander in semi-major axis, perhaps because of gravitational scattering by the clumpy ring material they interact with. Discrete km-size objects have also been inferred from disturbances at the outer edges of the A-ring and B-ring and in the Huygens ringlet of the Cassini Division. One such object has been imaged in the B-ring. Some of these objects seem to disaggregate and perhaps reaggregate in place, on timescales of months or years, suggesting ongoing recycling of material driven by satellite forcing, self-gravity, and collisions.

Rings in 3-D

Cassini discovered dramatic vertical distortions of the rings, in addition to the well-known spiral bending waves, near Equinox when the sun's illumination was at a grazing angle. The edges of the Keeler gap are noticeably warped, consistent with the small inclination of its central ringmoon Daphnis, but those of the Encke gap are not. The outer edge of the B-ring showed alpen-like, spiky peaks and shadows. The outer edge of the A-ring showed a very clumpy structure, lacking distinct peaks, but with shadows suggesting vertical relief.

Ring Particle Properties

Voyager showed that the main ring particle size distributions tend towards powerlaws ranging between cm-m radii. Cassini has shown that the slope and the minimum and maximum sizes of these powerlaws vary across the rings. Enhanced collisions in spiral density waves create blizzards of small particles, which seem to affect the brightness and color of the surrounding region. As shown by comparison of occultations at ultraviolet (UV), near-infrared (IR), mid-IR, and radio wavelengths, and by the ring spectra and color, this effect is especially significant in the outermost A-ring, the region most strongly stirred by spiral density waves.

A combination of 10–400 μm thermal emission and scattering, and 2.2 cm radiometry, suggests that ring particles probably have a low density mantle (i.e., are porous aggregates), but

might also have more dense cores. The rings' thermal emission suggests a regolith of nearly pure water ice grains of 10–100 μm size. Cassini 2.2 cm radiometry detects a fraction of a percent of non-icy material through the A-ring and B-ring, greatly improving on pre-Cassini microwave observations which could constrain the total non-icy material only to less than a few percent relative abundance. However, when combined with spiral density wave surface densities/opacities, 2.2 cm radiometry has also revealed what looks like a buried silicate-rich rubble belt in the mid C-ring; possibly the remains of the core of the ring parent.

Visual and Infrared Imaging Spectrometer (VIMS) spectra show that A-ring and B-ring composition is nearly pure water ice without any other identifiable ices such as CO, CO_2, NH_3, or CH_4, but there is a strong UV absorption making the rings unusually reddish, that varies in strength from place to place. The red color of the rings is strongest where the water ice absorption bands are deepest, suggesting that the red material resides within the icy regolith grains, and increases radially inwards at a steady rate. A third, more neutral non-icy material has a completely different radial distribution. The very low mass fraction of non-icy material (except perhaps in the C-ring rubble belt) provides our strongest constraint on the age and origin of the Rings, as discussed below. The rings' red color in the UV-visible region may be explained by fragments of carbon-bearing tholins (perhaps similar to material blanketing the surface of comet C-G as observed by Rosetta), or (some argue) by tiny iron-rich particles, embedded in the dominant water ice. Recent Cassini in situ results and remote sensing analyses, and Hubble Space Telescope (HST)-Space Telescope Imaging Spectrograph (STIS) observations, favor the organics.

New in situ data from Cosmic Dust Analyzer (CDA) and Ion and Neutral Mass Spectrometer (INMS) on the Ring-Grazing (RG) and Grand Finale (GF) orbits have greatly enriched the ring composition story. Abundant, Fe-poor silicates and organic molecules are associated with the innermost D-ring and perhaps C-ring. Evidence for organics is also found outside the rings by INMS. Reconciliation of these in situ results with remote sensing is only beginning.

Ring Variability with Time

The outer edges of the dense A-ring and B-ring vary in complex ways with both longitude and time, indicating the interference of multiple free or normal modes; possibly the result of large-scale non-axisymmetric viscous overstabilities, with the expected satellite-driven forced modes. The outer 100 km of the B-ring shows complex, fine-scale brightness variations possibly caused by these deformations. Gravitational effects of the modes might even play a role in sculpting the narrower gaps in the Cassini Division; so far found to be free of small moonlets.

Channels open and close in Saturn's F-ring strands, in response to close approaches by Prometheus, and these effects vary as the orbits of Prometheus and the F-ring mutually precess, leading to stronger and weaker gravitational interactions. Kinks and mini-jets come and go in the F-ring core, excited by small unseen objects at low relative velocities, and more dramatic jets of material lasting months are triggered by objects eccentric enough to crash through the ring at high relative velocities. These violent collisions continue because the entire F-ring region is dynamically

chaotic, mostly because of Prometheus, and for this reason the long-term stability of the F-ring core has been problematic. The F-ring has a narrow true core of large particles, as characterized best by Radio Science Subsystem (RSS), confined into discontinuous arcs and stabilized by a corotational resonance due only to Prometheus. The fine dust seen in images and stellar occultations is a tiny fraction of the F-ring total mass. Clump activity has varied dramatically between Voyager and Cassini.

Vertical ripples or warps covering the inner part of the rings, which have changed even over the duration of the mission, suggest that Saturn's D-ring and inner C-ring were tipped relative to its equator several times over the last millennium, and as recently as a few decades ago. Impacts by rubble streams produced by disrupted objects are the most likely cause. Several impacts by individual m-size projectiles have actually been seen and catalogued.

Diffuse Rings Dominated by Tiny Dust Grains are Affected by Sunlight and Magnetic Fields

The source of the E-ring particles has been confirmed as the south polar jets of Enceladus (see the Icy Satellites chapter). Several new arcs and ringlets are associated with erosion of small embedded moons. The E-ring and other diffuse rings and ringlets (such as those in the Encke gap) are affected by sunlight and electromagnetic forces as well as by gravity, and thus show seasonal variations in their structure. Some diffuse rings, notably the D-ring and the faint material between the A-ring and F-ring, are modulated by azimuthal variations in Saturn's magnetic field.

The duration and behavior of the spokes Voyager discovered in the B-ring have been further constrained, though their ultimate cause or trigger remains unknown. Cassini found that they seasonally appear and disappear, probably due to variable photo-charging of the main ring layer, and their temporal periodicities match best that of the northern hemisphere Saturn Kilometric Radiation (SKR) during the 2008–2009 timeframe, though contributions from the southern SKR source could not be ruled out. Any association with the Saturn Electrostatic Discharges (SEDs) was ruled out.

Ring Mass

Voyager-era estimates of the ring mass were roughly 0.7–0.8 Mimas masses. It was since suggested that the breakdown of the ring layer into opaque clumps (the self-gravity wakes), separated by nearly empty gaps, could allow a lot of mass to be hidden in the clumps. Modeling of dozens of spiral density and bending waves over Cassini’s first decade had constrained the mass of the A-ring, C-ring, and inner B-ring, so any hidden mass had to reside in the densest parts of the B-ring. In the Grand Finale orbits, the Cassini RSS team tracked the spacecraft to constrain the ring mass by its perturbation on Cassini's orbit, and concluded that the ring mass is not very different from, and likely lower than, our Voyager-era expectations.

Origin and Age of the Rings

The strongest constraint on ring age is provided by the gradual darkening and restructuring of the rings with time by infalling meteoroids. Inferring the actual ring age requires knowledge of the current mass fraction in non-icy pollutant, as well as both the incoming meteoroid mass flux and the total mass of the rings. The Cassini CDA experiment has determined, cumulatively over the entire mission, the infalling meteoroid mass flux and dynamical population. The mass flux far from the planet is not too different from pre-Cassini estimates. However, the dynamical population is like that of Kuiper Belt objects, so has a lower encounter velocity and is more strongly focused by Saturn's gravity than thought previously. This means that the flux of meteoritic material actually hitting the rings is probably even larger than previously thought. Combining the ring mass with the CDA-determined meteoroid mass flux, and estimates of non-icy pollution currently in the rings, leads to a ring exposure age of 100–200 million years, perhaps even a little younger than Voyager-era young-ring scenarios.

Combining the ring mass with the CDA-determined meteoroid mass flux, and estimates of non-icy pollution currently in the rings, leads to a ring exposure age of 100–200 million years … .

The associated puzzles of “Why is Saturn the only giant planet with rings?” and “Is the ring system young?” have been, if not yet explained, at least illuminated by an emerging hypothesis involving a closely-coupled tidal evolution of the mid-sized icy moons leading to a Saturn-specific dynamical instability of the inner satellite system, with possible disruptions and reaccretion, on the order of 100 million years ago. Constraints from satellite surface geology will need to be folded in to evaluate the plausibility of the scenario.

Overall Assessment of Ring and Dust Science

All key science objectives listed in the Announcement of Opportunity (AO) and Solstice Traceability Matrix (TM) were successfully accomplished over the course of the Cassini mission. In addition, a number of new science objectives were formulated and addressed along the way either in response to unexpected results or capitalizing on observational opportunities (some not originally envisioned, and some in greater numbers than envisioned). When the mission was approved, the AO Objectives reflected a 4-year baseline tour with only 59 orbits, allowing at most 16 Radio occultations, and of course did not incorporate the RG or GF observing geometries.

By the end of the mission, even the four-year baseline tour had been optimized to include 74 (generally shorter) orbits, wasting less time far from the planet, and had also been extended by nine years, tripling the total time baseline for observations relative to the AO. The final tour lasted 13 years, sampling three different seasons and reaching northern summer solstice (the maximum opening angle of the rings as seen from Earth and the Sun) which allowed the radio occultations to better penetrate the optically thickest parts of the B-ring. The mission included 282 orbits capturing

many new combinations of illumination and viewing angles important for imaging—VIMS and Ultraviolet Imaging Spectrograph (UVIS) spectral reflectance mapping, and Composite Infrared Spectrometer (CIRS) thermal mapping. Datasets returned included 135 ring radio occultations (each at 3 wavelengths), 170,000 ring images (many at < 1 km/pxl), over 200 UV stellar occultations, 170 near-IR stellar occultations, 30 solar occultations, and even a few occultations at thermal, mid-IR wavelengths.

The stellar occultations made use of dozens of stars with different elevation angle relative to the rings; low-optical depth rings are best studied by low-elevation stars, and high optical depth rings by high-elevation stars. In addition, several complete 2.2 cm microwave emission maps or radial scan combinations were obtained in different geometries and resolutions, and three active radar backscattering scans were obtained in the RG and GF orbits when the spacecraft was close enough to overcome the fourth-power dependence of radar sensitivity on distance. Moreover, the RG and GF orbits provided in situ ring particle composition sampling opportunities for CDA, INMS, and Magnetospheric Imaging Instrument (MIMI) that were not part of the AO plan, and enabled direct determination of the ring mass from spacecraft tracking of the RSS signal. VIMS stellar occultations were not even envisioned in the AO, but were added after selection of the instruments. This new stellar occultation capability provided a very useful wavelength difference compared to UVIS, and an entirely different angular distribution of sources on the sky. Using the Radar as a passive pencil-beam microwave ring brightness mapper, or to obtain active radar backscattering radial profiles from the rings were also not part of the original plan.

The overall science data volume return of Cassini was more than 100 times that of Voyager in the instruments they both carried (not to mention the roughly 200 times longer time baseline at interesting resolution) and the numerous unique new remote and in situ observations provided by Cassini. There is no question that the science return of Cassini vastly exceeded the expectations as described in the AO.

Summary of Key Open Questions

Overall, Cassini has answered many of the questions raised by Voyager, raised new ones, and leaves us with a largely untapped reservoir of data with which to answer. These questions and others are discussed in more detail in the section entitled Unsolved Problems Suitable for Ongoing Research and Future Missions.

The overall ring mass is known now, but with low precision and no radial resolution. Is the B-ring mass uniformly distributed according to optical depth, or is it even more strongly concentrated in the still nearly opaque central regions? Does the C-ring contain a rocky rubble belt? Future missions with tracking capability and multiple close passes will be needed, and should be planned to also provide a better understanding of why Saturn's own interior is so different from Jupiter's.

Most ring structure is still a puzzle. The irregular structure blanketing the entire B-ring, with lengthscales narrowly concentrated near 80 km in the inner B-ring, but covering a wider range of scales from the resolution limit to several hundred km in the mid-and outer B-ring, remains a mystery. In the inner-mid B-ring there are very sharp optical-depth jumps (but not to empty space) that are barely explored and remain unexplained.

The entire ensemble of so-called plateaus in the outer C-ring, symmetrically placed around the Maxwell gap in the C-ring, which is known to be caused by structure in Saturn's interior, and incorporating other empty gaps is not understood. The plateaus also contain a unique kind of streaky microstructure not seen elsewhere, which was only seen in a limited way during the final orbits.

There are several significant features (A-ring inner edge, C-ring plateaus), which have sharp well-defined boundaries, that are defined only by changes in the particle size distribution across which the surface mass density does not change. This structural control of particle size distribution, or vice versa, is not understood.

The mere presence of the Cassini Division is an unsolved problem, although it is plausible that a strong density wave driven by the 2:1 resonance with Mimas had a role in creating it when the rings were more massive and material filled the region. The apparent lack of moonlets capable of clearing the 13 gaps in the Cassini Division and C-ring, especially the 5–6 that have no embedded ringlets[1], is a puzzle. A clue may be found in the apparently non-random spacings of the edges of the Cassini Division bands and gaps, perhaps somehow manifesting gravitational influence of the B-ring outer edge.

The unusually red color of the A-ring and B-ring, which are surely more than 95% water ice and probably more than 99%, seems to be due to organic material based on a combination of remote and in situ measurements. However, composition varies from place to place and on a range of scales. Models capable of interpreting color and spectral data quantitatively in terms of underlying composition are inadequate and need improvement. The hint of a rubble belt of non-icy material buried in the mid-C-ring is intriguing, but remote observations are ambiguous and the analysis of in situ observations is only getting underway. Whether or not organics explain the similarity, but relatively weak, UV absorption seen in most icy moons is not yet known—the dark side of Iapetus has been fit by carbon, nano-iron, and metal oxides. Why is the G-ring parent body, so close to the icy main rings, so dark?

Are the A-ring (and B-ring) propeller objects the shards left over from the ring parent? Why do the dozen or so giant propellers found only outside of the Encke gap wander in semi-major axis, and what (if any) patterns are present in the evolution? Are there cyclic, self-limiting processes of growth and disruption of sub-km sized objects in the outer A-ring (and B-ring)? The F-ring core is stabilized by Prometheus, but what causes its uniformly precessing eccentricity? Do relatively large

[1] Cassini Division gaps with ringlets: Huygens, Herschel, Laplace; and without ringlets: Russell, Jeffreys, Kuiper, Bessel, Barnard. C-ring gaps with ringlets: G1, Colombo, Maxwell, Bond; and without ringlets: Dawes.

objects form in regions compressed by Prometheus and go on to crash through the core, creating clumps and strands?

The rings seem to be much younger than the solar system based on nominal results to date, and there is one encouraging hypothesis (a 200-million year ago system-wide instability) providing the proper context. However, questions remain including consistency (or lack of it) of the observed icy moon cratering distributions with reaccretion of most of the inner icy moons on that same timescale.

Key Objectives of the Rings Working Group

The original ring objectives from the AO, and those added for the extended Cassini Solstice Mission, are given in Table RINGS-1. We assess Cassini as fully successful, at least in all regards. It is emphasized that in almost all cases there has been far more data obtained, reduced, and archived than the teams have had time to analyze and interpret.

Rings AO Objectives

- **Ring Structure and Dynamics (R_AO1)** – Study configuration of the rings and dynamical processes (gravitational, viscous, erosional, and electromagnetic) responsible for ring structure.
- **Ring Particle Composition and Size (R_AO2)** – Map composition and size distribution of ring material.
- **Ring-Satellite Interaction (R_AO3)** – Investigate interrelation of rings and satellites, including embedded satellites.
- **Dust and Meteoroid Distribution (R_AO4)** – Determine dust and meteoroid distribution both in the vicinity of the rings and in interplanetary space.
- **Ring Magnetosphere-Ionosphere Interactions (R_AO5)** – Study interactions between the rings and Saturn's magnetosphere, ionosphere, and atmosphere.

Rings CSM Traceability Matrix Objectives

- **Changing Rings (RC1a)** – Determine the seasonal variation of key ring properties and the microscale properties of ring structure, by observing at the seasonally maximum opening angle of the rings near Solstice.
- **Ring Temporal Variability (RC1b)** – Determine the temporal variability of ring structure on all timescales up to decadal for regions including Encke gap, D-ring, F-ring, and ring edges by substantially increasing the cadence and time baseline of observations.

- **F-ring (RC2a)** – Focus on F-ring structure, and distribution of associated moonlets or clumps, as sparse observations show clumps, arcs, and possibly transient objects appearing and disappearing.
- **Ring Age and Origin (RN1a)** – Constrain the origin and age of the rings by direct determination of the ring mass, and of the composition of ring ejecta trapped on field lines.
- **Ringmoons – Composition (RN1b)** – Determine the composition of the close-in ringmoons as targets of opportunity.
- **Ring Structure – High Resolution and Composition (RN1c)** – Determine structural and compositional variations at high resolution across selected ring features of greatest interest, using remote and in situ observations.
- **Ring Microstructure (RN2a)** – Conduct in-depth studies of ring microstructure such as self-gravity wakes, which permeate the rings.
- **New Ring Structures (RN2b)** – Perform focused studies of the evolution of newly discovered propeller objects.

Table RINGS-1. RWG Science Assessment.

Fully/Mostly Accomplished: **Partially Accomplished:** **Not Accomplished:**

RWG Science Objectives	AO and TM Science Objectives	RWG Science Assessment	Comments (if yellow, partially fulfilled)
Ring Structure and Dynamics	R_AO1		
Ring Particle Composition and Size	R_AO2		
Ring-Satellite Interactions	R_AO3		
Dust and Meteoroid Distribution	R_AO4		
Ring-Magnetosphere-Ionosphere Interactions	R_AO5		
Changing Rings	RC1a		
Ring Temporal Variability	RC1b		
F-ring	RC2a		
Ring Age and Origin	RN1a		
Ring Composition - ringmoons	RN1b		
Ring Structure - high resolution and composition	RN1c		
Ring Microstructure	RN2a		
New Ring Structures	RN2b		

These objectives are discussed below in more detail.

RWG SCIENCE RESULTS

Prime Mission (AO) Original Objectives (Highest, Top-level Results)

Ring structure and dynamics (R_AO1)

Studies configuration of the rings and dynamical processes (gravitational, viscous, erosional, and electromagnetic) responsible for ring structure.

This objective, perhaps the broadest and deepest, was satisfied beyond our initial expectations. Stellar and radio occultations are the most powerful tool for exploring structure at high resolution. During initial planning sessions, the UVIS team was considering dozens of stellar occultations as an optimistic goal, and ended up with over 200, including the novel turnaround occultations in which the line of sight to the star moves parallel to the particle orbits, at very low velocity, allowing azimuthal structure to be determined with high resolution at perhaps a dozen radii and structure on the scale of a ring thickness to be addressed statistically. Moreover, VIMS developed a stellar occultation capability of their own that was not part of the original plan, and went on to produce almost 200 occultations of their own in geometries that were independent of and complementary to those available to UVIS, because they observed a different set of stars. All these stellar occultations reside on the Rings Planetary Data System (PDS) node in 1 and 10 km resolution format. In addition, RSS conducted 135 occultations at three radio wavelengths (0.94, 3.6, and 13 cm), which all reside on the Rings PDS node in 1 and 10 km resolution format, and for which further processing (by diffraction correction) can generally provide 100 m or even better radial resolution. More analysis of these data will provide additional surprises and constraints. Review chapters by Colwell et al. [2009] and Cuzzi et al. [2018] cover the major advances regarding observed ring structure, Schmidt et al. [2009] review advances in the theory of dense ring structure, and Horanyi et al. [2009] review advances in the theory of electromagnetic influences (most significant on tiny dust grains).

CONFIGURATION OF THE RINGS

The Grand Structure of the rings (Figure RINGS-1) was elucidated for the first time by Voyager, reviewed by Orton et al. [2009] and Colwell et al. [2009]. In this section we will discuss the so-called main rings (A-ring, B-ring, and C-ring) and the Cassini Division, all of which have optical depth > ~0.1 (Figure RINGS-1). The A-ring is the best understood by Voyager-era theory; blanketed by spiral density and bending waves from nearby moons, with embedded moonlets that carve empty gaps by the process of gravitational shepherding, and a ubiquitous non-axisymmetric microstructure having scales comparable to the ring thickness due to local gravitational instabilities. All of these structural properties have been closely observed by Cassini, in greater numbers, with greater radial coverage, in more geometries, in finer detail, and at better sensitivity than ever before. The B-ring and C-ring contain a few of these well-understood features too, but are overwhelmingly dominated by structure on all scales that is simply not understood at present (see

section entitled Electromagnetic and Radiative Processes). The so-called diffuse rings (D-ring, E-ring, and G-ring) and dusty rings associated with various moonlets, have optical depths much less than unity and are a separate class of structure discussed in sections entitled Dust and Meteoroid Distribution, and Ring Magnetosphere-Ionosphere Interactions. The narrow, kinky F-ring lying just outside the A-ring has captured a niche of its own and is discussed mostly in the section entitled F-ring.

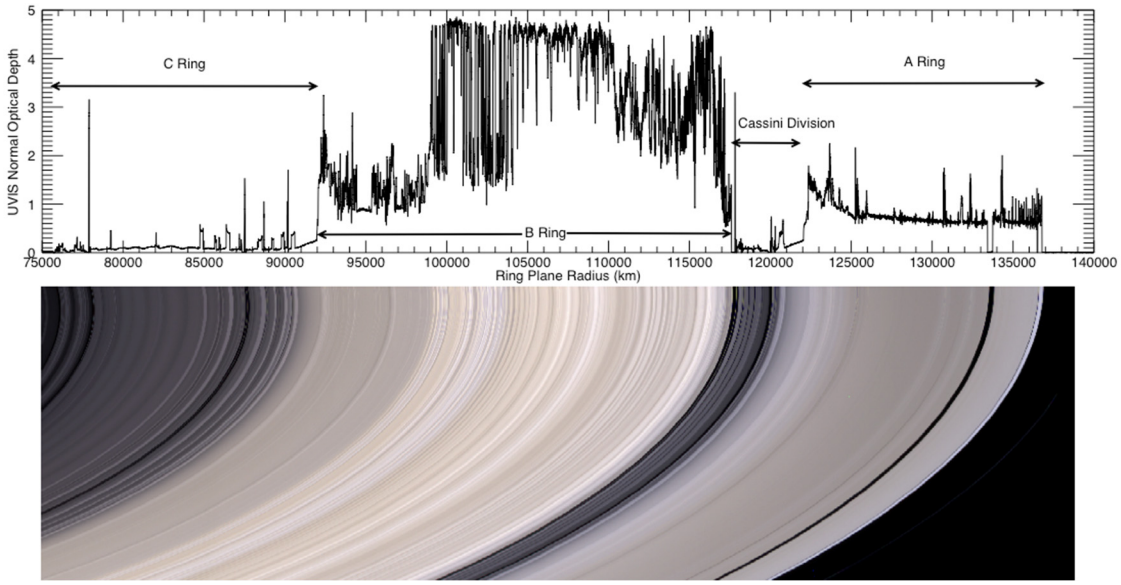

Figure RINGS-1: Main rings of Saturn. The image is registered along its top edge with a radial profile of the ring optical depth from a Cassini UVIS stellar occultation. The optical depth (usually denoted τ) is the vertical integral through the ring layer of the particle number density times its cross-sectional area, times extinction efficiency (for the plot above, the efficiency is unity). The B-ring (especially its central part) has the highest optical depth, but the highest values shown are just noise limits. Unlabeled regions mentioned in the following text include the series of plateaus in the outer C-ring, centered on the Maxwell gap near 87500 km, which contains an elliptical ringlet. The Encke gap is visible in the outer A-ring, around 133600 km. The narrow, stranded F-ring is just off the figure at right. Figure from Colwell et al. [2009].

The local ring thickness was a perennial topic of discussion before Voyager and measurements of kilometers were reported (now known to be better explained by vertical corrugations and/or the inclined F-ring). The single Voyager stellar and Radio occultations showed that ring edges were so sharp that the local thickness (at least at edges) could be no more than tens of meters. Cassini's hundreds of stellar and radio occultations have extended this knowledge to nearly all locations except the opaque central B-ring [Colwell et al. 2006, 2009; Hedman et al. 2007b]; see also Tiscareno et al. [2007]. This small vertical thickness means that the rings are not the many particle thick classical layer envisioned even in the Voyager era, and have a moderate volume density of 0.01–0.1 [Salo and French 2010] or even larger. There are implications of high volume density for ring viscosity (see section entitled Viscous Processes). Another indication of volume density (and thus local dynamics) comes from mutual shadowing. Visual brightness observations have long shown a sharp opposition peak that was traditionally interpreted in terms

of shadowing in a many-particle-thick layer; however, dynamical constraints and the increased recognition of the importance of coherent backscattering in grainy particle regoliths (see Cuzzi et al. [2009] for a review) complicate this interpretation [Salo and French 2010]. CIRS observations show a much broader phase effect in particle temperatures; however, that is plausibly shadowing-related (unlikely to be contaminated by coherent backscattering) and consistent with non-classical rings [Altobelli et al. 2007, 2009; Reffet et al. 2015; Morishima et al. 2017; Deau et al. 2019]. These thermal studies lead to midplane particle volume densities as large as 0.3–0.4 in the B-ring. Finally, analysis of 2.2 cm radiometry is best fit by modeling closely packed cm-m size particles in the near-field scattering regime [Zhang et al. 2017b, 2019].

There has been a start taken on modeling of imaging observations of the rings over a wide range of geometries, with an emphasis on unraveling opposition effects of different kinds using classical radiative transfer models [Deau et al. 2013, 2018; Deau 2015]. However, interpreting UV, visual, and near-IR observations using realistic models of closely packed particles with rough shadowed surfaces, which might provide more insight into radial variations of local particle volume density and thus local dynamics, remains in its infancy (see Porco et al. [2008] for the only example).

Gravitational processes (self-gravity wakes, spiral waves, and shepherding torques)

Probably the longest-known and most widespread gravitational process leads to the self-gravity wakes, caused by local, transient, incipient gravitational instabilities which are stretched into trailing clumps of scale comparable to the ring thickness (indeed defining the ring thickness) by Keplerian shear, keeping the ring in a constant state of frustrated satellite formation [Orton et al. 2009; Schmidt et al. 2009; Colwell et al. 2009]. Imaging observations have characterized the effect in the A-ring, using the azimuthal brightness asymmetry known for decades, but finding the particle collisional elasticity to be smaller than thought; indicating either a rough surface or a porous regolith [Porco et al. 2008]. The effect has also been observed and modeled in the thermal IR [Leyrat et al. 2008; Ferrari et al. 2009; Morishima et al. 2014]—see also section entitled Extended Mission (CSM) Objectives, Section 3.2 Instrument Science Results chapter entitled CIRS, and Spilker et al. [2018]. A CAT-scan technique of characterizing the horizontal and vertical scales of these structures as well as their angle relative to the orbit direction was developed based on stellar occultations from a variety of slant directions. These models of the dense gravitational wakes as optically thick granola bars or elliptical cylinders [Colwell et al. 2006, 2007; Hedman et al. 2007a; Nicholson and Hedman 2010] (see also Colwell et al. [2009] for a review) provide valuable mean values of the orientation, width, height, and separation of dense clumps for use in models of ring brightness. The pitch angle of the wakes, relative to the orbit direction, decreases radially inwards as differential rotation becomes stronger.

Perhaps the most obvious, beautiful, and useful gravitational ring structures are spiral density and bending waves at isolated satellite resonances. These striking features share the physics of the arms of spiral galaxies, but are tightly wrapped like watchsprings [Shu 1984; Schmidt et al.

2009]. They propagate away from their driving resonance with a decreasing wavelength—density waves move outwards and bending waves inwards. The wavelength itself is diagnostic of the underlying surface mass density on scales smaller than a wavelength. Thus, spiral density wave measurements provide our best idea of the radial profile of mass density, in regions where they are found. This property is extremely important, because the almost ubiquitous clumping due to self-gravity wakes breaks the rings into a set of opaque regions separated by nearly empty gaps, for which the optical depth (see Figure RINGS-1) is of questionable basic value.

For this reason, Robbins et al. [2010] suggested that inferences of ring surface mass density from a combination of observed optical depth and particle size distribution might greatly underestimate the ring mass. This reasoning led to a debate as to whether the ring mass could be much larger than Voyager-era estimates, because most of the B-ring (which contains most of the mass) is unsampled by diagnostic density and bending waves, with implications for ring age (see section entitled Ring Age and Origin). The debate tilted in favor of low mass when Hedman and Nicholson [2016] succeeded in obtaining some B-ring density wave measurements despite the noisy background, and has now been definitively resolved in that direction by the RSS total mass measurements based on gravitational tracking (see section entitled Determination of Ring Mass). The RSS gravity measurements have little or no radial resolution, but used A-ring and C-ring masses as determined from these waves [Colwell et al. 2009; Tiscareno et al. 2013] and assumed the remainder of the measured mass to be that of the B-ring. They do suggest, though, that the surface mass densities obtained from spiral density waves are insensitive to the suggested clumping difficulty.

One important surprise from measuring surface mass density is that several important structural features, long seen in images and occultations, actually manifest as distinct structures not because they have higher local mass density as was usually assumed, but because their local particle size distribution changes in a dramatic way making them more opaque than their surroundings without much change in their underlying surface mass density. This happens because the surface-to-mass ratio of a particle, or of a distribution of particles, increases as particle size decreases. The effect is seen at the inner edge of the A-ring and all of the C-ring plateaus—sharp optical depth jumps are seen where there is at most a gradual change in surface mass density [Tiscareno et al. 2007, 2013a; Tiscareno and Harris 2018]. Baillié et al. [2011] and Hedman and Nicholson [2014] show surface mass densities for the plateaus and background C-ring, and Colwell et al. [2018] show drops in effective particle size in the plateaus, consistent with a small change in surface mass density despite a large increase in optical depth. This important phenomenon of locally abrupt changes in the particle size distribution is not currently understood, but is clearly of central importance to understanding the formation of these structures.

Another important clue from density and bending waves is obtained from sparse sampling of the C-ring, showing that the surface mass density radial profile differs from the optical depth profile in a fashion most easily explained if the local particles (whose sizes are well known from RSS occultations) are several times more dense in the central C-ring than elsewhere in it; possibly hinting at buried rocks in unusually high abundance and perhaps to a hidden rocky rubble belt [Zhang et al. 2017a], see also section entitled Ring Particle Composition and Size. Sampling of the

B-ring is even sparser, but generally points to surface mass densities somewhat lower than previously thought [Hedman and Nicholson 2016; Tiscareno and Harris 2018].

An interdisciplinary bonus was the confirmation of the prediction by Marley et al. [1987, 1989]; Marley [1990]; and Marley and Porco [1993] that density fluctuations in Saturn's interior produced by planetary scale acoustic oscillations (modes) can drive spiral density and bending waves similar to those driven by an external satellite. A number of unidentified waves had been noted by Rosen et al. [1991] in Voyager RSS occultation data. Marley and Porco [1993] suggested several specific associations between predicted resonance locations and these Rosen waves. They also suggested that the strongest predicted (two-lobed, or m = 2) planetary interior resonance might be associated with the unexplained Maxwell gap, where there was an unexplained eccentric (m = 1) ringlet.

Cassini, along with subsequent improvements in the Saturn interior model, have confirmed the Marley and Porco [1993] predictions, putting the study of ring seismology on firm ground and finding in the process other features likely due to variations in internal structure not accounted for in the simple 1993 interior model. The great advantage of Cassini data is multiplicity and accuracy of occultation measurements, allowing both the number of spiral arms and the pattern speed of the waves to be determined unambiguously, and thus finer associations to be made with theoretical predictions [Hedman and Nicholson 2013, 2014; Marley 2014; French et al. 2019; Mankovich et al. 2019; Hedman et al. 2019]. Initially, some Rosen waves, and newly discovered ones [Baillié et al. 2011] were found to have the same value of m, something not predicted by Marley and Porco [1993]. However, Fuller et al. [2016] showed that allowing a compositionally-stratified layer deep inside Saturn could explain these multiplicities because such a gradual density transition would allow different types of modes to mix inside the planet. Next, a two-armed spiral density wave was discovered within the (m = 1) Maxwell gap ringlet [French et al. 2016b] validating the association of the gap with the strongest (m = 2) mode as predicted by Marley and Porco [1993]. Finally, Mankovich et al. [2019] have recently shown that slightly changing the interior rotation period of Saturn allows the detailed predictions of Marley and Porco [1993] to be very well matched across 16 sets of waves over a wide range of relative strengths, with the strongest perturbation opening the Maxwell gap. In fact, this excellent agreement provides the best constraint yet on the deep interior rotation period of Saturn—a fundamental property that has been elusive because of the almost complete lack of magnetic field azimuthal asymmetry [Dougherty et al. 2018] (see also Section 3.1 Discipline Science Results chapter entitled MAPS). In addition, a new class of density waves has been found in the B-ring and A-ring; waves that are driven by density structures of unknown origin, fixed to the body of Saturn [El Moutamid et al. 2016a, 2016b]. Surprisingly, some of these wave features are actually seen to drift radially inwards in the rings, indicating temporal changes in Saturn's interior structure on a decade timescale [Hedman et al. 2017, 2018b; Hedman and Nicholson 2014]. Therefore, ring properties and physics have led to three new important insights into the deep interior of Saturn. See section entitled Ring-Satellite Interaction for more

… a new class of density waves has been found in the B-ring and A-ring—waves that are driven by density structures of unknown origin, fixed to the body of Saturn .

discussion of interactions between satellites and moonlets with the rings, which are mostly gravitational.

VISCOUS PROCESSES

Because of their innumerable particles in a constant state of gentle collisions, the rings act like a gas or fluid and obey the equations of fluid dynamics with local pressure and viscosity. They spread radially due to viscosity, an important aspect of their evolution that combines with other angular momentum and mass transport processes like shepherding, wave torques, and ballistic transport of meteoroid ejecta. The theory of spiral density waves is mature enough that the rate at which their amplitude damps as they propagate can be used to constrain the local ring viscosity [Schmidt et al. 2009, 2016; Colwell et al. 2009].

A second kind of so-called ring microstructure, called a viscous overstability, occurs on scales of the ring vertical thickness and is partly driven by viscosity [Schmidt et al. 2009]. In this effect, a stable (non-growing) radial oscillation can develop that comprises axisymmetric, alternating ringlets of high and low density that pulsate on the orbital timescale. These structures are aligned with the orbital direction and were first distinguished by subtle Doppler effects in off-axis scattering during Cassini RSS occultations [Thomson et al. 2007], but have also been detected using statistical analysis of stellar occultations [Colwell et al. 2009; Hedman et al. 2014a]. They are widespread across the rings and generally found with the expected lengthscales (comparable to a ring thickness) in regions where the optical depth is moderate to high. Self-gravity plays only a small role in these structures.

Viscous overstabilities can take on non-axisymmetric forms as well. For example, in a densely packed ring, collective behaviors akin to those seen in granular flow can occur and viscous stress can actually decrease the damping between adjacent orbital motions effectively by locking particles and their orbits together. Where there is also the opportunity for double reflection of spiral density waves, as within a narrow isolated ring bounded by sharp edges, or a so-called resonant cavity, they can become amplified [Borderies et al. 1985; Hedman and Nicholson 2019] generating low-order (m = 1, 2, 3, etc.) modes. The m = 1 and m = 2 structure of the narrow sharp-edged rings of Saturn and Uranus may be explained in this way. For instance, the Maxwell ringlet exhibits an m = 2 spiral density wave forced by an m = 2 acoustic mode within Saturn (see section entitled Gravitational Process), but attains an m = 1 overall structure. However, Cassini discovered large-scale, unforced, or free modes with m = 1, 2 and 3 in the outer portion of the B-ring, in addition to the resonant m = 2 mode forced by Mimas at the B-ring's edge [Spitale and Porco 2010], see also section entitled Ring Temporal Variability). The large-amplitude m = 1 mode, in particular, would damp quickly without both the overstabilizing viscous effects described above and the amplification accompanying multiple reflections within the resonant cavity formed by the B-ring outer edge and the mode's own resonant radius some 250 km inwards. The discovery of these unforced modes is the first indication of substantial wave amplification on large scales, in broad rings. These modes may have applications to other celestial disks, such as protoplanetary nebulae [Laughlin et al. 1997] and spiral galaxies.

Viscosity and pressure due to ring particle collisions determines the ability of ring particles to move from one face of the rings (lit face) to the other (unlit) face, and models have been applied to CIRS thermal observations to address this constraint [Flandes et al. 2010; Pilorz et al. 2015; Morishima et al. 2016]. Another manifestation of particle collisions would be to pack surface regoliths to varying degrees, depending on local dynamics. CIRS tried to measure radial variations in particle thermal inertia (higher for more packed particle surfaces), but the complexities of the models, the complications due to small and/or rapidly rotating particles, and the incompleteness of the observing phase space has so far precluded more than a basic determination that the ring particles look like other frosty outer solar system objects. Section 3.2 Instrument Science Results chapter entitled CIRS describes how models of ring thermal observations can address these and other issues in more detail.

Erosional processes

Pollution of the mostly icy ring material by meteoroid bombardment, erosion of ring particles into impact ejecta, and restructuring of the rings by Ballistic Transport of the ejecta, were first suggested and discussed in the pre-Cassini era—see Durisen et al. [1989, 1992]; Cuzzi and Estrada [1998]; and see also the section entitled Ring Origin and Age for more discussion. The process is a little subtle and counterintuitive—see more recent work in Charnoz et al. [2009] and Estrada et al. [2015]. Extrinsic meteoroids hit the rings at tens of km/s, not only depositing their substantial amount of non-icy material, but ejecting chips of the target ring particle at 1–100 m/s. These chips go off on orbits that re-impact the rings where they become part of a new ring particle. Exchanges of losses and gains of mass and angular momentum can result in significant radial restructuring of the ring surface mass density over a time short compared to the age of the Solar System, given what we now understand about the meteoroid flux—see section entitled Dust and Meteoroid Distribution.

Signatures of this process can be found both in ring structure and ring composition. To date, intriguing possible correspondences to observed structure have been seen (amongst them the abrupt inner edges of the A-ring and B-ring and the odd linear ramps inward of them, and the 80 km scale irregular structure in the inner B-ring and inner A-ring) and a good match is provided to the smooth compositional profile that accompanies the abrupt B-ring–C-ring boundary. These independent structural and compositional properties suggest a young ring age of a few hundred million years, extending the simpler pollution argument relying on deposition of non-icy material alone, see section entitled Ring Particle Composition and Size, but the models have many parameters and face new challenges from new discoveries of several kinds (see section entitled Non-Saturn-System Science Results).

Electromagnetic and radiative processes

Particles in the space environment tend to attain a maximum charge that is only large enough to affect the dynamics of tiny (at most 10 micron size) grains. An entire branch of ring dynamics has to do with resonances involving forcing of tiny charged grains by the periodically fluctuating

planetary magnetic field; so-called Lorentz Resonances [Burns et al. 1985; Schaffer and Burns 1987], see also Horanyi et al. [2009] and Hedman et al. [2018a] for reviews of these and other electrodynamical effects. The most obvious places where these processes will be important is in the diffuse rings, such as the D-ring, E-ring, and G-ring, which are known to be most easily delineated by their tiny particles [Hedman et al. 2009a, 2018a; Chancia et al. 2019]. The E-ring shows the most clear influences, including its preference for a near-monodispersion of particle size at around one micron radius, a radial profile with a local minimum in vertical thickness at the location of Enceladus, and 3-D variations that correlate with the orientation relative to the Sun [Hedman et al. 2012; Ye et al. 2016]. It is now known that the E-ring is the frosty breath of Enceladus, and analyses of ISS images have clarified how it is fed in some detail [Mitchell et al. 2015].

A second ring phenomenon widely thought to be connected to electromagnetic forces is the flickering of shadowy spokes across the A-ring and B-ring, discovered by Voyager, see reviews by Orton et al. [2009] and Horanyi et al. [2009]. Various periodicities in the Voyager spoke occurrence rates, rotation rates at spoke boundaries, and the angular and spectral scattering properties of spoke regions have implicated electromagnetic effects acting on tiny grains; with sizes most recently shown by D'Aversa et al. [2010]. The tiny grains are probably released sporadically from ring particle surfaces somehow, perhaps by m-size particle impacts, energy beamed from the planet, or magnetic field/plasma instabilities near the ring, reviewed by Horanyi et al. [2009]. Earth-based observations also contributed to this understanding [McGhee et al. 2005]. Surprisingly to most of the Cassini team, spokes were invisible on approach and for the first year or more of the mission, and initially seen only weakly in late 2005 [Mitchell et al. 2006]. This observation supported an idea first suggested by Nitter et al. [1998] that seasonal changes in photocharging by the Sun were responsible. In this theory, dust is constantly being lofted out of the ring plane by impacts, but when the solar elevation is high, electrons are photosputtered out of the dense main ring layer causing the main rings to be positively charged while embedded in a vertically extended negatively charged electron plasma. Grains ejected from the rings become negatively charged in this plasma and are swept immediately back into the rings by the strong vertical electric field. The process is like an electrostatic dust precipitator in an industrial smokestack. The theory predicted that at a certain low elevation angle, the electrostatic precipitation would cease and spokes would reappear (Voyager 1 and 2 flybys were both at a time of low solar elevation) and indeed their disappearance again a year or so after equinox proved this to be the case. During the brief time spokes were abundant (roughly 2009–2011), detailed studies of their morphology [Mitchell et al. 2013] showed that the spokes had extended active growth times, both radially and azimuthally, and that their activity level was most likely associated with one of the SKR periods, but maximizes at a different longitude in that system than found by Voyager.

Finally, certain dusty ringlets in various otherwise empty gaps in the rings suggest evidence for electromagnetic or even solar radiative control on their predominantly micron-sized grains. The very obvious dusty, eccentric so-called "charming" ringlet in the outermost Cassini Division gap, that was not very noticeable during either Voyager encounter, always points its apoapse towards the Sun due to radiation pressure [Hedman et al. 2010a]. Several dusty, clumpy ringlets in the Encke gap have similar properties [Hedman et al. 2013b]. In general, one would expect that these tiny grains are constantly resupplied by generally unseen strands or clumps of macroscopic

particles with comparably low optical depths, but such a belt of more massive particles would not be influenced by electromagnetic or radiative forces.

Ring particle composition and size (R_AO2)

Maps composition and size distribution of ring material.

As described in more detail in the section entitled Ring Origin and Age, understanding the non-icy mass fraction in the rings is critical, as it provides perhaps the strongest constraint on the age and origin of the rings.

COMPOSITION (REMOTE SENSING)

The goal was to determine the composition of the ring material with the best possible radial resolution across the main rings. Spectral observations at UV, visual, and near-IR (NIR) wavelengths are generally insensitive to ring particle size because the ring particles were known to be much larger than these wavelengths from groundbased and Voyager observations. Known ring structure is on scales of 100–300 km, so observations needed to be planned to enable VIMS, UVIS and CIRS; all having much lower resolution than ISS, to resolve these scales. Longer observation times allowing deeper integrations were possible at greater distances, and high SNR spectra of broad segments of the A-ring, B-ring, and C-ring were also obtained. As time went on, we learned more about the observations and about the rings. For instance, Saturnshine was found to contribute organic-looking spectral features in certain geometries (ring longitudes between 120–240° solar hour angles as observed from high phase angles, for instance). The VIMS and UVIS calibration pipelines evolved and improved as the mission went on, and data analyzed and published early in the mission might still profit from reanalysis. ISS, while having much higher resolution and typically obtaining 3–5 km/pxl in extended color sequences, has very limited spectral resolution. In-depth ISS sequences were planned, but only one lit face observation in all 15 filters was obtained in Prime Mission, which was corrupted, so extensive and redundant follow-up was planned for the extended or Cassini Solstice Mission (CSM), over a range of illumination and viewing geometries (see section entitled High-resolution Ring Structure and Composition). Regional and local radial variations in color and spectra were seen by UVIS, ISS, and VIMS, greatly expanding geometrical and wavelength coverage to a depth of data that has yet to be plumbed. However, going from observed reflectivity (or I/F, the ratio of observed intensity to that of a colocated Lambert surface) to quantitative constraints on ring particle composition is a somewhat imperfect modeling step, involving the poorly understood way closely spaced particles with rough, grainy regoliths scatter light (see section entitled Non-Saturn System Science Results).

Allowing for most of these complexities, VIMS spectral data has been especially powerful in connecting the abundance and regolith grain size of water ice with the relative abundance of other materials. Early in the mission, Nicholson et al. [2008] found, and subsequently Hedman et al. [2013a] showed in more detail, that the redness of the main rings correlated very well with the water ice band depth suggesting that the UV absorber was spatially colocated with water ice, most likely

as tiny submicron or smaller size inclusions within the water ice regolith grains (new in situ observations may have even detected these tiny few-nm-size inclusions directly, see section entitled Composition of Rings From Ring Ejecta). Detailed studies of radial variation of color and spectra are reviewed by Cuzzi et al. [2009, 2018b, and references therein]. Regarding the actual nature of the UV absorber, a lively debate has continued for a decade as to whether the rings' redness can be better explained by good old-fashioned rust or other metal oxides, as on Mars, or by large organic molecules like Polycyclic Aromatic Hydrocarbons (PAHs) that give fruits and vegetables their orange-red color, see Cuzzi et al. [2009] for a discussion.

Broadly speaking, the optically thinner C-ring and Cassini division are more polluted by some spectrally neutral non-icy material than the A-ring or B-ring, making them darker at visual wavelengths and decreasing the strengths of the near-IR water ice bands; this is the natural outcome if the darkening material is deposited from extrinsic meteoroid bombardment [Cuzzi and Estrada 1998; Elliott and Esposito 2011], see also Cuzzi et al. 2009 for a review. More recent results from CIRS thermal models give the ring particle bolometric albedo; another measurement of their non-icy pollutants. It is interesting that, like inferences from visual wavelength reflectivities, the bolometric albedos are not only lower in the C-ring and Cassini division, but also vary smoothly across the sharp A-ring and B-ring boundaries [Morishima et al. 2010], as generally predicted by ballistic transport models.

Cassini's late-orbit in situ observations find plenty of organic material and some silicates, but no discernible free metal or metal oxides … .

Cassini's late-orbit in situ observations find plenty of organic material and some silicates, but no discernible free metal or metal oxides—see section entitled Composition of Rings from Ring Ejecta for details. Moreover, the most recent Cassini and non-Cassini studies using both classical and Monte-Carlo ring radiative transfer models agree that the spectra are more consistent with reddish organics than with other suggested materials [Ciarniello et al. 2019; Cuzzi et al. 2018b]. However, even the best current regolith scattering models simplify the physics and involve several parameters. Because different flavors of Hapke-like regolith scattering models lead to systematic, model-based uncertainties in absolute abundances at the factor-or-several level, or even worse, quantitative inferences about abundances must be treated with caution. For instance, Hedman et al. [2013a] interpreted fine-scale radial color variations in terms of regolith grain size, but this may have been because of the limitations of their (classical) model, whereas other secondary optical-depth-related effects may likely be the cause. On the other hand, Cassini's UV spectrometer UVIS observed the strong 170 nm water ice absorption edge and how it varies across the rings [Bradley et al. 2010, 2013]. These analyses provide a sensitive measurement of the regolith grain size, which can remove ambiguities in regolith models at comparable wavelengths and lead to absolute abundances of non-icy material—see section entitled Ring Particle Composition and Size for more discussion of grain size effects. Therefore, while the compositional debate has clarified regarding overall composition, there is a need for considerably more work regarding radial variation and inference of quantitative abundances of non-icy material, see section entitled Non-Saturn-System Science Results.

Other new contributors to the ring composition were the CIRS far-IR capability[2] and the Cassini 2.2 cm Titan Radar Mapper (RADAR), used in radiometer mode[3]. These observations have considerable historical motivation, as microwave observations were the first to constrain the ring composition as nearly pure water ice particles of cm-m size, see Esposito et al. [1984] for a review. The basic observation is that the brightness temperature of the rings drops from the physical temperature in the thermal IR, to a small fraction of it in the microwave (thus requiring a low particle emissivity). CIRS was able to get ring spectra covering the transition spectral range between thermal IR and several hundred micron wavelength, resolving inconsistent Voyager-era observations [Spilker et al. 2005, 2018]. CIRS and 2.2 cm radiometry was used to create sensitive high-resolution maps of the very low microwave brightness temperature [Zhang et al. 2017a, 2017b]. Microwave radiometry is unique because the long wavelengths penetrate to depths of several meters in cold water ice that has a very low microwave absorption coefficient, thus microwaves sample the bulk composition of the ring particles in a way that micron and submicron wavelengths cannot. The Cassini 2.2 cm radiometry had sufficiently high resolution to separate the A-ring, B-ring, and C-ring into dozens of radial bins and greatly improved on groundbased interferometry by setting upper limits of a fraction of a percent on non-icy material in the A-ring and B-ring.

Analysis of the 2.2 cm radar radiometry observations also found that the C-ring (with up to 6% non-icy material uniformly mixed) is much dirtier than the A-ring and B-ring [Zhang et al. 2017a, 2017b]. The assumption of uniform mixing may seriously underestimate the C-ring non-icy material abundance. Constraints on surface mass density from a handful of spiral density and bending waves strongly suggest that the particles in the same belt of the central C-ring, where unusually high abundances of silicates are found, have an internal density several times higher than water ice; far heavier than explained by a mere 6% in uniformly mixed silicate dust. The situation suggests buried solid chunks of non-icy material (silicate or carbonaceous) in large volume fraction. This rubble belt is what we might expect the remains of a disrupted core of a differentiated object to look like. However, modeling the microwave emission/scattering problem in the main rings is very difficult since the particle sizes and separations are not much larger than the wavelength and are in the near field of each other. Therefore, approximations are needed even in the very best current models, leading to some degree of compositional uncertainty. Moreover, these analyses are insensitive to the nature of the non-icy material.

Recent comparisons of spectral properties of the main rings with those of the ringmoons and classical icy moons are provided by Filacchione et al. [2012, 2013, 2014], and other recent reviews are by Cuzzi et al. [2009, 2018a]. For complementary discussion of the ring composition based on in situ observations (not part of the AO objectives), which are especially relevant to the D-ring, see section entitled Ring Age and Origin. The so-called diffuse rings (D-ring, E-ring, F-ring, and G-ring)

[2] It had been hoped that the longest wavelength channel of CIRS – advertised as 0.5mm wavelength, but more realistically 1 mm, could be used as a radiometer in this way. However, complicated calibration problems with the Michelson interferometry technique precluded this even after considerable effort by the team.

[3] Little was proposed or expected along the lines of ring science from RADAR in the AO or early discussions, as the team was exclusively focused on Titan. However, as the mission went on and the antenna beam was carefully calibrated, the very low ring brightness temperature was mapped even in the presence of the 10-times-brighter, huge globe of Saturn looming in the complex sidelobes.

and smaller rubble belts are discussed in the section entitled Dust and Meteoroid Distribution, both regarding structure and composition.

SIZE DISTRIBUTION

Even before Voyager, it was known from groundbased microwave observations that by far most of the main ring particles were in the cm-few meters size range [Orton et al. 2009], and for this reason microwave wavelengths were expected to be the most powerful at specifying their details. To this end, Cassini's observation planning incorporated 135 radio occultations of the main and F-rings, at three wavelengths: 0.94, 3.6, and 13 cm. These occultations provide the direct-path optical depth at all three wavelengths, clearly showing local and regional differences in the abundance of the smaller particles (a few cm in radius). In addition, the off-axis scattering (so-called bistatic scattering) of the radio beam can be used to constrain variations in the particles at the large-size end of a (usually) powerlaw size distribution, as well as the slope of the powerlaw, for example, Zebker et al. [1985]; Cuzzi et al. [2009]. The RSS occultation profiling observations have been reduced, corrected for diffraction, and provided to the Rings Node of the PDS, some examples are shown in Cuzzi et al. [2009] Figures 16.1a–16.2. Distinctions as subtle as changes in the slope of the powerlaw size distribution and the minimum and maximum particle size between typically a few mm and a few meters can be discerned. In addition, stellar occultations contribute information on the relative abundance of smaller particles.

Some generalities can be extracted even at this preliminary stage of the investigation. The fraction of small particles increases outwards through the A-ring based on the RSS data, consistent with more vigorous collisions associated with the increasing radial density of resonances and spiral density waves [Cuzzi et al. 2009; Becker et al. 2016; Jerousek et al. 2016].

In the RSS data, C-ring "plateau" structures show local drops in the differential optical depth, characteristic of locally fewer (short-)wavelength-size particles, and a similar effect is seen crossing from the outer C-ring to the inner B-ring, and from the outer Cassini Division to the inner A-ring; with the optically thicker rings having relatively fewer wavelength-size particles lying near the small end of the size distribution [Cuzzi et al. 2009].

Stellar occultation variance data[4] from UVIS provides an independent and complementary particle size determination to the RSS data. Analysis of this type reveals that all of the C-ring plateaus and narrower embedded ringlets have a smaller mean particle size compared to the background C-ring. The background C-ring has an undulating optical depth over scales of hundreds of km, and effective particle size correlates positively with this structure, this may suggest size-dependent dynamical transport within the ring. The innermost 700 km of the B-ring, and regions around the strong resonances in the A-ring, exhibit different effective particle sizes based on occultation variance (even though self-gravity wakes in these regions dominate the signal). There is a marked decrease in effective particle size coinciding with the Mimas 5:3 bending wave in the

[4] Showalter and Nicholson [1990] introduced this technique to relate the excess variance in the occultation signal (about a radially variable, locally defined mean) to the size of the largest local particles.

outer A-ring. This and other observations suggest a vertically extended haze of small particles across the wave; oddly, the effect is not seen in the nearby density waves where collisions might be expected to be even more vigorous. The variance in the Cassini Division ramp reveals the particle size distribution there to be more similar to the A-ring than to the Cassini Division, with a discrete increase in effective particle size at the inner edge of the ramp. On the other hand, the comparable C-ring–B-ring boundary transition is more gradual in variance and implied particle size [Colwell et al. 2018].

Because the optical depth does change abruptly by a factor of several, there must be a corresponding abrupt change in the opacity at these locations, requiring a change in the particle size distribution.

More information on particle sizes can be gained by comparing the local surface mass density from wavelengths of spiral density and bending waves, see Colwell et al. [2009]; Schmidt et al. [2009], with the local optical depth. For identical particles, the opacity (ratio of optical depth to surface mass density) is inversely proportional to particle size. Based on a number of observations of spiral density waves, there seem to be only very smooth, or no, dramatic changes in surface mass density across the plateaus or across the inner A-ring boundary [Tiscareno et al. 2013a; Colwell et al. 2009], see also the section entitled Gravitational processes. Because the optical depth does change abruptly by a factor of several, there must be a corresponding abrupt change in the opacity at these locations requiring a change in the particle size distribution. The sense of this is that the particles are on average smaller in the plateaus, and in the inner A-ring and B-ring, than in adjacent material, consistent with the variance data noted above. However, RSS occultations show that these same regions have fewer cm-size particles, requiring either that there must also be fewer large particles or that the largest particles are smaller, in the plateaus and similar regions. All together this suggests narrower size distributions for the plateaus, and inner A-ring and B-ring, than for their surroundings; relatively fewer particles at both size extremes. There is currently no explanation for this strong structural control on particle size, with very abrupt boundaries.

An important kind of size distribution is the size distribution of regolith grains on the surfaces of ring particles. While not what a dynamicist would call a ring particle, these grains along with their underlying material composition determine the spectral signature at any wavelength. Regolith grain sizes are usually best determined in and around strong absorption bands. UVIS, for instance, sees the strong water ice edge at 170 nm, and from the details of its position determines a regolith grain size of about 5 microns [Bradley et al. 2010, 2013]. However, at longer wavelengths (the near-IR water bands) larger grain sizes in the tens of microns are generally derived [Cuzzi et al. 2009; Clark et al. 2012; Filacchione et al. 2012, 2013]. This is consistent with the idea that shorter wavelengths sense and are scattered by smaller scale structures. Indeed, even before Cassini, models by Poulet and Cuzzi [2002] and Poulet et al. [2003] of Earth-based spectra of the rings covering the 0.3–4.5 um spectral range required very broad regolith size distributions; from 10 microns to several millimeters. Analyses of the long-wavelength roll off from much longer wavelength CIRS data [Spilker et al. 2005], and a 30 micron ice absorption feature [Morishima et al. 2012] suggest (not

surprisingly) a broad size distribution from tens of microns to centimeters radius with the larger ones perhaps starting to merge from regolith particles to freely-floating particles. Much more work is needed with improved regolith radiative transfer models and broader spectral ranges.

The so-called diffuse rings (D-ring, E-ring, F-ring and G-ring) have their own distinct size distribution; generally dominated by micron-sized particles that diffract, rather than backscatter, light at UV, visual, and NIR wavelengths (see section entitled Dust and Meteoroid Distribution).

Ring-satellite interaction (R_AO3)

Investigate interrelation of rings and satellites, including embedded satellites.

The first actual sighting of a small moon embedded in a clear gap was Pan, in the A-ring Encke gap … .

The first actual sighting of a small moon embedded in a clear gap was Pan, in the A-ring Encke gap [Showalter 1991], see also Colwell et al. [2009]; Orton et al. [2009]. Cassini quickly found a second example: Daphnis, in the Keeler gap, has an inclined orbit and the wavy edges it imparts to the gap flap vertically [Weiss et al. 2009]. The known dimensions and masses of these objects [Porco et al. 2005, 2007], combined with the estimated ring viscosity, provides our best validation of the shepherding torque theory [Goldreich and Tremaine 1980, 1982; Schmidt et al. 2009]. Cassini then embarked on an extensive systematic mapping of the other multiple empty gaps in the Cassini Division and C-ring over the duration of the mission, coming up empty handed, and (even though not every longitude of every gap was mapped) concluding that these gaps do not seem to be cleared by moonlets [Spitale 2017], at least based on the shepherding torque theory as currently understood [Schmidt et al. 2009]. Clues about other gap-clearing processes may be found in some of the details of the edge locations of the Cassini Division gaps [Nicholson and Hedman 2010; Spitale and Porco 2010; French et al. 2016a]. However, there are no corresponding clues regarding the few C-ring gaps lacking moonlets, which may instead be explained in the context of whatever mystery process generates the C-ring plateau ensemble, with which the unexplained gaps are associated. It is ironic that the Voyager imaging team redirected resources late in the planning phase to test a (then-new) hypothesis for gap-clearing by searching for gap-embedded moonlets, but resource and time constraints forced a choice of targeting only one gap, and as it turns out, the Cassini Division where they looked was not the right place [Smith et al. 1982].

Ring edges can also be maintained by single, isolated resonances, as at the outer edges of the B-ring (Mimas 2:1 resonance) [Spitale and Porco 2010, and references therein] and the A-ring outer edge (Janus 7:6 resonance) [Porco et al. 1984]. Recently El Moutamid et al. [2016c] and Tajeddine et al. [2017a] showed in detail how Janus actually is able to create an abrupt edge for the outer A-ring and restrain its spreading, even as it swaps orbits back and forth with Epimetheus, in somewhat of a team effort with all the other ringmoons and resonances acting on different parts of the A-ring, so the classical shepherding theory seems to be in good shape. The kinky, stranded

F-ring has a more complicated, often chaotic, relationship with its nearby moons, though (see section entitled F-ring).

A special kind of embedded moonlet is one that is too small (smaller than 1 km radius) to actually open a gap; these were predicted by Spahn et al. [1994], but most Cassini scientists were surprised to actually see some, initially in the Saturn Orbit Insertion (SOI) images [Tiscareno et al. 2006]. These have been dubbed “propellers” by virtue of the disturbances they create, which are too weak to prevent viscosity from backfilling the disturbance before the next encounter of the moonlet with the same material. It seems there are on the order of a million of these objects in the A-ring, and they are confined mostly to three distinct bands in the A-ring [Sremčević et al. 2007; Tiscareno et al. 2008]. There have been reports of propellers in the B-ring as well [Sremčević et al. 2012, 2013, 2014a, 2014b]. It is not currently understood whether these objects are shards of a ring parent, or are somehow spontaneously forming and perhaps dispersing in place [Esposito et al. 2012]. The three A-ring propeller bands are anti-correlated with the halos of large spiral density waves, and correlated with the strength of self-gravity wakes, which might favor the local formation idea or might simply indicate changes in the photometric balance or local viscosity that causes propellers to be visible. A subset of much larger objects, dubbed Giant Propellers, was discovered, which could be tracked and found to be evolving in semi-major axis [Tiscareno et al. 2010]. This discovery motivated significant dedicated observing during the extended mission (see section entitled New Ring Structure). Meanwhile, the theory of these disturbances has been actively discussed and continues to advance [Schmidt et al. 2009; Crida et al. 2010; Pan and Chiang 2010, 2012; Rein and Papaloizou 2010; Pan et al. 2012; Bromley and Kenyon 2013; Tiscareno 2013; Seiler et al. 2017; Seiß et al. 2018].

A possible physical extension of these objects to smaller sizes has been seen in the optically thicker bands of the C-ring (including the plateaus) and Cassini Division (including its outer ramp); so-called ghosts or partial clearings appear in UVIS occultations with very small lengthscales [Baillié et al. 2013]. These are thought to be caused by relatively large ring particles (maybe meters to tens of meters in size) smaller than the A-ring and B-ring propellers (objects so small would not clear gaps in the generally higher optical depth, and more strongly stirred, A-ring and B-ring). These objects would need to be more than three times larger than the largest ring particle in a powerlaw size distribution in order to create the ghost clearings.

Fleeting glimpses of what appear to be embedded Keplerian objects have also been obtained near the edges of several rings and ringlets. At the outer edge of the A-ring, the so-called “Peggy” object was seen briefly [Murray et al. 2014], seemingly getting ready to break free of the main rings. This exciting moment might, it was thought, allow the object to be spun away from the rings due to ring torques such as modeled by Charnoz et al. [2010]; an effect by which the age of the rings might be constrained (see section entitled Ring Origin and Age). However, Peggy actually was reabsorbed back into the rings and apparently broke into several pieces, proving that leaving home can be difficult. Moderately large Keplerian objects, but still too small to be seen directly, were also seen near the edges of the A-ring Keeler gap [Tajeddine et al. 2017b], in the Huygens ringlet of the Cassini Division [Spitale and Hahn 2016], and near the outer edge of the B-ring itself [Spitale and Porco 2010—see also Cuzzi et al. [2018a]. It has been suggested that many or even all of these

objects are transient, forming by compaction due to satellite perturbations, and then being disrupted as they increasingly stir the regions around them [Esposito et al. 2012].

Finally, it cannot be forgotten that all the wonderful dynamical relationships we are starting to understand between the rings and various moons depend on a good understanding of the orbital dynamics of the moons themselves, and the so-called ringmoons in particular, that interact strongly with the rings [Spitale et al. 2006; Jacobson et al. 2008; Tajeddine et al. 2013]. Additional results can be found in the ISS Instrument Science Results. Of special importance is the paradigm-breaking observational result of Lainey et al. [2017] that the midsize icy moons of Saturn, from Mimas through at least Rhea, are tidally evolving outwards much faster than had been previously assumed based on traditional tidal "Q" theory. This was extremely surprising, because Saturn's interior had been thought to be quite non-dissipative, like Jupiter, with a high "Q" value (see section entitled Saturn System Science Results). A more recent tidal theory suggests that "Q" is highly frequency dependent, and that moons get trapped on a comb of low-Q frequencies that slowly decrease as Saturn's interior structure evolves, driving the entire set of moderate-sized icy moons outward at a more or less distance-independent rate instead of the strongly distance-dependent rate of traditional tidal theory—see for example, Fuller et al. [2016]. This new perspective has profound implications for the origin and (now increasingly believed to be) geologically youthful age of the rings (see section entitled Ring Origin and Age).

Dust and meteoroid distribution (R_AO4)

Determines dust and meteoroid distribution both in the vicinity of the rings and in interplanetary space.

THE DIFFUSE RINGS

The so-called diffuse rings (D-ring, E-ring, F-ring and G-ring) are best studied by tracing their micron-size particles. Such small particles scatter UV, visual, and near-IR light into small solid angles in the forward direction so they may be more easily detected than in the lower brightness of their larger particles, which is spread over more angles near backscattering and also may be subject to the low brightness of individual particles. In all these cases where only fine dust belts are observed, it is generally accepted that a larger-particle skeleton (or some small parent moonlet) must be present to resupply the micron-sized material, which is rather quickly lost [Burns et al. 1984; Hedman et al. 2018a]. Based partly on observations of charged particle depletions [Van Allen 1982]—see also Section 3.1 Discipline Science Results chapter entitled MAPS for Cassini-based examples; the G-ring has long been known to contain an underlying rubble belt or arc of macroscopic particles—see reviews by Orton et al. [2009] and Hedman et al. [2018a]. Cassini discovered that the ultimate source of this rubble belt is a 0.5 km size, highly non-spherical object called Aegaeon, which has a very dark primitive-body type surface [Hedman et al. 2011a]. Moreover, Aegaeon is trapped in a 7:6 resonance with Mimas [Hedman et al. 2007c, 2010].

Several other dusty arcs of material were discovered, supplied by the small moonlets Anthe, Pallene, and Methone—of these, Methone and Anthe are trapped in Mimas resonances [Hedman et al. 2009b]. A composite dusty ring phase function and size distribution was obtained from wide phase angle coverage of the D-ring and G-ring, for application to so-called Debris Disks around young stars [Hedman and Stark 2015]; a certain similarity in the two ring phase functions may point to some family and/or process similarity in the particles; such as an aggregate, fractal structure. The D-ring shows several kinds of time variability, and is discussed more in the section entitled Ring Temporal Variability. Also, the giant, diffuse Phoebe ring, discovered in 1999 by the Spitzer Space Telescope [Verbiscer et al. 2009], was further constrained in extent, dynamics, and particle size using shadow-edge imaging observations [Tamayo et al. 2014, 2016].

A disadvantage of necessary reliance on forward scattering for the diffuse rings, is that it is essentially diffraction, and only weakly dependent on composition, so the composition of these rings is not quite as well known. Even when there is some signal in backscattered intensity or reflectivity, it remains problematic to derive even albedos for the large F-ring and G-ring particles (whose scattering would be compositionally diagnostic) because their optical depths are variable and/or small, and so uncertain. The F-ring is known to be dominated by crystalline water ice [Vahidinia et al. 2011; Hedman et al. 2011b], but may be significantly polluted by drifting G-ring material [Clark et al. 2012]—see also Cuzzi et al. [2018a], Figure 3.22, and the section entitled F-ring for more discussion. By comparison, the composition of the E-ring is known very well from CDA in situ sampling (mostly water ice, with embedded organics and salt, all characteristic of the underground Enceladus Ocean from which it comes), and its structure is discussed in the section entitled Changing Rings. In situ sampling of nanoparticles in the D-ring is discussed in sections entitled Ring Magnetosphere and Determination of Ring Mass.

THE EXTRINSIC (INTERPLANETARY) MASS FLUX - A PRIMARY GOAL OF CASSINI

The CDA instrument [Srama et al. 2005] estimated detecting 100 extrinsic particles of micron-size and larger. However, early in the mission it started to look difficult or impossible to measure it directly (it is a very dusty system in reality), so an indirect approach was explored to look for dust ejecta haloes around Rhea and Tethys, by analogy to Galileo results at Jupiter [Sremčević et al. 2005]. This led to only upper limits and an initial conclusion that the extrinsic meteoroid flux was lower than previously assumed. However, the basic direct approach simply counting up the detections and velocities of small particles with identifiably extrinsic orbits was ultimately successful partly due to the much longer time baseline of the CSM (13 years) relative to the baseline mission. The lack of indirect detection (satellite dust haloes) was reconciled after the fact by uncertainties in the ejecta yield model. For example, the ongoing snowfall caused by Enceladus' geysers might have influenced/changed the mechanical surface properties of Rhea and Tethys compared to the Jovian icy moons. Future analyses of thermal inertias might provide useful constraints on satellite surface properties, in this regard.

The CDA meteoroid mass flux measurement works as follows [Kempf et al. 2019], see Section 3.2 Instruments Science Results chapter entitled CDA. For each particle detected entering

the instrument there is an instrumental ambiguity that allows two equally valid predetection velocity vectors. A lower limit to the incident mass flux comes from only the 25 particles for which both velocity vectors trace back to extrinsic projectiles, from beyond Saturn. An upper limit of a sort also includes the 75 or so particles for which only one of the velocity vectors requires an extrinsic origin. Because the size distribution of the detected particles is not well known, the largest particles might carry most of the mass, and their rarity suggests that the nominal detection values could be a lower limit. For instance, a solitary 250 μm particle was not included in the mass flux calculations (including it would increase the mass flux by a factor of five) and another year of mission time might have captured more large particles. Future, more detailed (perhaps Bayesian) analyses might refine the uncertainties more, but at present it seems that the nominal CDA minimum flux is conservative. The values for the minimum flux at infinity (before gravitational focusing by Saturn) are within a factor of order unity of pre-Cassini assumptions [Cuzzi and Estrada 1998]. However, the CDA discovery that the pre-Saturn orbits were dynamically Kuiper Belt object (KBO)-like (low eccentricity and inclination) rather than comet-like (and thus have lower encounter velocities), leads to an order of magnitude increase in Saturn's gravitational focusing factor and thus in the flux at the rings. The implications of this new result for models of ring structural and compositional evolution, which have multiple parameters [Estrada et al. 2015] are not yet well understood, but they are unlikely to allow a ring age older than previous estimates of some hundreds of millions of years.

Perhaps a simple, large field-of-view (FOV), NIR photometer experiment to monitor impacts might be considered for a future mission.

Along the lines of mass flux into the rings, we should mention flux at larger sizes as perhaps providing additional constraints on ring evolution; as yet, no effort has gone into merging these datasets and results. An observation by RPWS only reported at meetings [Gurnett et al. 2004] may suggest impacts by dozens of particles during the 30 minutes Cassini was skimming across the face of the rings at SOI. Significant theoretical development is needed to translate these observations into responsible projectile sizes (sand-grains?), but if this can be done, the rates would surely be of interest. Impact ejecta trails from a handful of meter-sized particle impacts were imaged by ISS [Tiscareno et al. 2013; Schmidt and Tiscareno 2013]. UVIS mounted an early attempt to detect actual impact flashes themselves, but subsequent thought and modeling concluded that the flash could only be seen in the near-IR [Chambers et al. 2008] so the UVIS searches were discontinued. Perhaps a simple, large field-of-view (FOV), NIR photometer experiment to monitor impacts might be considered for a future mission. Finally, as discussed in the section entitled Ring Temporal Variability, there is evidence for multiple impacts on the rings by 1–10 km size objects over decades and centuries.

Ring magnetosphere-ionosphere interactions (R_AO5)

Studies interactions between the rings and Saturn's magnetosphere, ionosphere, and atmosphere.

It has long been known that the rings have an atmosphere of their own due to photosputtering and meteoroid bombardment, and interact with both the magnetosphere and the planet, even reducing the ionospheric electron density [Shimizu 1982; Connerney and Waite 1984]. During SOI, Cassini obtained the first-ever in situ measurement of the ring atmosphere, and it was a big surprise. It had been expected to be dominated by water products (WP) (molecules and ions of H_2O and its fragments), but instead Cassini Plasma Spectrometer (CAPS) found it was dominated by neutral and ionized O and O_2 [Tseng et al. 2010]. The observations and theory are reviewed in Cuzzi et al. [2009]; essentially, WP recombine on ring particle surfaces, but O and O_2 do not, building up in the ring atmosphere without freezing out or adsorbing onto ring particle surfaces, and ultimately filtering out to the magnetosphere and into the planet [Tseng et al. 2010]. Since that review, the effect has been modeled in more detail, and the observed seasonal variation of magnetospheric oxygen ions transported from the rings (see Section 3.1 Disciplines Science Results chapter entitled MAPS) suggests that photosputtering of ring ices dominates over material from Enceladus in producing the ring atmosphere [Tseng et al. 2010, 2013; Elrod et al. 2014]. This discovery of the ring atmosphere alone would satisfy the AO objective, but indeed during the RG and GF orbits, Cassini discovered far more about the particulate component of the ring atmosphere and its flux into the planet; the so-called ring rain long speculated upon, for example, Connerney and Waite [1984]. We discuss this in detail in the section entitled Ring Age and Origin.

The D-ring is now known to be embedded in a high-energy-particle radiation belt that is separated from Saturn's main radiation belts [Kollmann et al. 2019; Roussos et al. 2019]. This may help explain its possible shortage of water ice (see section entitled Composition of Rings from Ring Ejecta). The diffuse E-ring and G-ring interact in more intimate ways with the magnetosphere; their tiny grains get charged and undergo electromagnetic forces (see section entitled Electromagnetic and Radiative Processes).

Extended Mission (CSM) Objectives

The objectives below were developed in 2010, to prioritize upcoming planning by focusing on specific problems, either unresolved AO goals or unexpected new phenomena, and to take advantage of the unique geometries of the CSM.

Changing rings (RC1a)

Determines the seasonal variation of key ring properties and the microscale properties of ring structure, by observing at the seasonally maximum opening angle of the rings near Solstice.

The emphasis here is on observing at the seasonally maximum opening angle of the rings near Solstice. The dominant operative intention was to take advantage of the maximum ring opening angle as seen from Earth and the Sun to: a) allow CIRS to determine the energetics of thermal heating and cooling of the rings as they opened to their maximum opening angle to the sun; and b) allow RSS occultations to penetrate the most opaque parts of the rings (the central B-ring), which they had not yet been able to do even during the maximum opening angle allowed

during Prime Mission (21°). The difference relative to true maximum opening angle of 23.7° can be critical for RSS, as it appears in the exponential of the optical depth term. The objective was very well satisfied, in that 36 more radio occultations were obtained, with various combinations of resolution and sensitivity, at opening angles larger than available during prime mission and more suitable for probing the dense B-ring. The data have been reduced and deposited in the Rings PDS node at 1 and 10 km spatial resolution. CIRS also obtained data over a wide range of opening angles; one important conclusion has to do with the seasonal cooling of the rings through equinox; their minimum temperature is considerably larger than instantaneous thermal equilibrium with Saturn's reflected and emitted energy, constraining the internal density of the particles (at least in the A-ring where the model was applied) to be closer to solid ice in the central A-ring than in its inner or outer regions [Morishima et al. 2016]. Perhaps this can be correlated with the radial variation of self-gravity wakes and/or the radial distribution of propeller objects.

When this goal was written, it was still not known as to whether the spokes would vanish again, and if so, exactly when and under what geometrical conditions. Indeed that situation is now well understood in terms of photocharging of the main rings (see section entitled Electromagnetic and Radiative Processes).

The diffuse E-ring, composed largely of micron-sized grains jetted out of Enceladus, deforms and changes shape with the seasons in response to the elevation angle of the sun, as solar radiation pressure influences the orbits of these tiny grains [Hedman et al. 2012].

The waxing and waning of the magnetospheric oxygen ion content is dominantly seasonal; implicating photosputtering of ice in the main rings rather than impacts by grains from Enceladus, one previous candidate [Tseng et al. 2013].

Ring temporal variability (RC1b)

Determines the temporal variability of ring structure on all timescales up to decadal for regions including Encke gap, D-ring, F-ring, and ring edges by substantially increasing the cadence and time baseline of observations.

The rings are changing before our eyes. The F-ring may be the most extreme example of time variability, and merited its own strategic objective (see section entitled F-ring). Here we discuss other aspects of ring temporal variability.

The sharp edges of the A-ring and B-ring flop around loosely, revealing the fluid nature of the rings. The A-ring outer edge seven-lobed structure derives from a 7:6 resonance with (mostly) Janus, and it reorganizes itself, diminishing in amplitude, when Janus swaps to its outer orbit and the resonance moves off of the A-ring edge [Spitale and Porco 2009; El Moutamid et al. 2016c]. The B-ring outer edge is more complicated, showing the predicted two-lobed forcing of the Mimas 2:1 resonance, but in addition, showing interference with m = 1, 2, and 3 patterns that are probably free modes driven by ring pressure and viscosity. Sometimes the pattern almost vanishes because

of this interference [French et al. 2010; Hedman et al. 2010b; Esposito et al. 2012; Nicholson et al. 2014; Spitale and Porco 2010]—see section entitled Viscous Processes.

Saturn's innermost ring (D-ring) is only visible with effort and in favorable geometry. However, after the F-ring fireworks, it has provided some of the most interesting evidence for time variations (usually observed by virtue of its fine dust component, in forward scattering geometries, as discussed in the section entitled The Diffuse Rings). Hedman et al. [2007b] first noticed that its structure of irregularly spaced bands or belts had changed dramatically since Voyager. They also pointed out a pattern that they interpreted as a vertical spiral ripple, and suggested that the ripple was the result of an ongoing wrapping up by differential node regression of a tilted mean ring plane. From the wavelength of the wrap, which shortens with time, they dated the event to the early 1980s. Hedman et al. [2011c] found the ripple to extend through the C-ring, and suggested that the tilt was imposed by an impacting stream of rubble, perhaps from a disrupted, 1–10 km size, Shoemaker-Levy-9 type object, with an extended node crossing the D-ring and C-ring. Hedman et al. [2015] determined, from further analysis, that the event may have had two parts, separated by months. Hedman and Showalter [2016] subsequently found pattern evidence for two other disturbances that occurred in 1979 (in Voyager data) and 2011. Marouf et al. [2011] discovered a similar pattern in the C-ring, from higher-resolution radio occultation data, that they interpreted as two events, separated by 50 years that occurred in the late 1300s. It is fascinating that the rings still bear silent witness to these long-lasting scars of cometary impacts. A related example of time variability is ongoing impacts onto the ring by discrete particles large enough to create detectable disturbances; the little cousins of these ripple-forming comet-size objects. Impacts by meter-size particles have been observed directly; once a leading candidate for triggering spokes (see section entitled Electromagnetic and Radiative Processes), the connection between the observed meter-size impact rates and spoke formation rates has not been pursued in depth. These impact effects were discussed in the section entitled The Extrinsic (Interplanetary) Mass Flux.

The D-ring and C-ring show two other, still unexplained, kinds of time variation. Hedman et al. [2014b] found that one of the most prominent bright ringlets in the D-ring, also seen by Voyager, is moving inwards at more than 2 km/year, and apparently moved outwards to its current position between Voyager and Cassini. The ringlet also has strong azimuthal clumpiness that seems stable, but cannot be associated with any plausible resonance with either some known moon, or some known planetary interior modes or rotating structures; all in all it is a puzzling dynamical feature. Also, there are time-variable aspects to several C-ring spiral density waves that appear to be driven by density fluctuations fixed to Saturn's internal structure and rotating with its winds; so-called tesseral resonances (see section entitled Gravitational Processes). Hedman et al. 2017, 2018b; Hedman and Nicholson 2014] have found that some of these wavetrains seem to be drifting inwards at about 1 km/year, as if the density fluctuations causing them were moving in latitude or depth inside the planet. The D-ring also revealed a new set of bright clumps near the end of the mission, possibly related to time variation in the INMS GF observations (see section on Composition of Rings from Ring Ejecta).

F-ring (RC2a)

Focuses on F-ring structure, and distribution of associated moonlets or clumps, as sparse observations show clumps, arcs, and possibly transient objects appearing and disappearing.

Because of the strong time variations seen during prime mission, the F-ring became a central focus for Cassini imaging observations during CSM. The F-ring lies about 3000 km outside the A-ring edge, and is unique in the family of planetary rings. Faintly glimpsed by Pioneer 11, its kinky, multi-stranded structure was revealed in Voyager images to be dominated by small dust grains, and Voyager radio and stellar occultations showed it to have a very narrow core of larger objects. Earth-based observations between Voyager and Cassini showed it to be highly variable, with large clumps coming and going, having orbital periods that differed slightly from that of its central strand [McGhee et al. 2001]. As it was straddled by the 100 km diameter ringmoons Prometheus and Pandora, classical shepherding theory was quickly proposed to explain its survival. However, almost immediately, problems arose with that interpretation, growing over the years when it was realized that not only were the so-called shepherds on chaotic orbits themselves, but objects orbiting between them were excited to even more chaotic orbits [Cuzzi et al. 2014]. In fact, Cassini very quickly observed some of these objects (2004S6, etc.) [Porco et al. 2005] on orbits that crossed the F-ring, but could not be tracked for more than a few months before they vanished [Cooper et al. 2017]. Meanwhile, large jets of material were seen splashed out from the central core due to collisions by these careening objects [Charnoz et al. 2005; Murray et al. 2008; Becker et al. 2018], and evidence was found for smaller, unseen objects embedded within the F-ring strands themselves. Dynamical models showed how the perturbations of Prometheus alone could explain the alternating streamer-channel appearance of the F-ring [Murray et al. 2005; Beurle et al. 2010].

Several new classes of embedded objects were inferred and modeled, based on often faint and initially obscure patterns seen to come and go. Mini-jets (small spikes poking out of the central strand) were catalogued and understood as caused by large embedded objects (meters or tens of meters in size perhaps) colliding at low (few m/sec) speeds within the dense central ring strand [Charnoz 2009; Murray et al. 2008; Esposito et al. 2008; Beurle et al. 2010; Albers et al. 2012; Meinke et al. 2012; Attree et al. 2012, 2014]. Fans or localized regular brightness fluctuations were shown to be due to small embedded objects on slightly eccentric orbits relative to the F-ring [Murray et al. 2008]. Some of these fans were localized to parts of the ring where Prometheus compressed ring material, perhaps actually forming new small moonlets [Beurle et al. 2010].

RSS occultations only detected the F-ring's very narrow (< 1 km) true core of cm-and-larger-size particles about 1/3 of the time, showing it had to be azimuthally broken and discontinuous. Using these observations, a new theory was developed in which the stability of the true core, in the presence of strong orbital chaos driven locally by Prometheus, seems to be due to longitudinal confinement into separated clumps or arcs by a corotational resonance in which the stable clumps never encounter Prometheus at its apoapse where strong chaos-inducing perturbations can result [Cuzzi et al. 2018c], see also Albers et al. [2012]; Cooper et al. [2013]. The reason why only this one of many nearby corotational resonances is occupied remains unclear. This arrangement of incomplete arcs of macroscopic particles must occasionally make small

adjustments, given the occasional chaotic changes in Prometheus' orbit to which the clumps must readjust. Hedman et al. [2011b] observed variations in crystalline ice band depth due to variations in the relative abundance of macroscopic bodies and dust, which have yet to be correlated with the RSS clumping. Large objects forming in fans, and usually outside the very narrowly defined stable true core orbit [Cuzzi et al. 2014, 2018c], can become strongly perturbed by Prometheus and evolve into 2004S6-like objects, ultimately recolliding with the F-ring at high speeds. Indeed, while 2004S6 was tracked in 2006–2008 as it collided with the F-ring several times and then lost, similar objects have since appeared. Different frequencies and intensities of such big eruptions as seen by Cassini and by Voyager observations underline the sporadic nature of these variations [French et al. 2012, 2014].

Ring age and origin (RN1a)

Constrains the origin and age of the rings by: a) direct determination of the ring mass; and b) of the composition of ring ejecta trapped on field lines.

Over the years the ring composition has emerged as perhaps the best gauge of ring age and clue to ring origin. While ring composition is powerfully addressed using traditional remote sensing techniques (see section entitled Ring Particle Composition and Size), this objective focused on in situ measurements that were only achievable during Cassini's RG and GF orbits.

Determination of ring mass

It was not known, when Cassini was initially planned, that we would be able to obtain a direct measurement of the ring mass; this only became possible in the CSM GF orbits when the spacecraft was able to fly between the rings and the planet 22 times. The original AO mission plan was to constrain the ring mass by measuring the ring optical depth and particle size distributions together, and sample all available spiral density waves, using stellar and radio occultations. However, because of the possible ambiguities associated with hidden mass in the B-ring that arose during the prime mission (see section entitled Gravitational Processes), six complete close passes were allocated in the GF orbits, during which the spacecraft remained quiet while RSS transmitted a carrier signal to Earth, to allow the small gravitational effects of the rings to be separated from those of Saturn; a mini-Juno mission. The details of the technique, and difficulties encountered, are described by Iess et al. [2019] and in this volume. Unexpected and probably azimuthally variable internal properties of the planet (very unlike those of Jupiter) contaminate the gravitational signature of the rings, increasing the measurement uncertainty to perhaps 50% of the signal. It is puzzling that, if the RSS variance is interpreted as internal mass irregularities, the amplitude of these seems considerably larger than would be

It was not known, …, that we would be able to obtain a direct measurement of the ring mass; this only became possible …, when the spacecraft was able to fly between the rings and the planet 22 times.

inferred from the dozen or so spiral density and bending waves currently seen in the rings that have been identified as being driven by mass fluctuations inside the planet (see section entitled Gravitational Processes). Nevertheless, it can be concluded with confidence that the ring mass is probably less than the Voyager-era estimate to within the uncertainty, see Section 3.2 Instruments Science Results chapter entitled RSS, and Iess et al. [2019]. A total ring mass even as large as 0.8 Mimas masses is regarded as unlikely, and the nominal value is 0.4 Mimas masses. While RSS has been as yet unable to obtain a radial profile of surface mass density, there is a clue from CIRS thermal models that the central B-ring region called B3 (105000–110000 km) is actually a quite sharply bounded annulus containing 2–3 times the surface mass density of the rest of the B-ring [Reffet et al. 2015].

Composition of Rings from Ring Ejecta

The AO mission provided for no direct, in situ measurement of main ring particle composition; it was planned to rely on remote observations by VIMS and CIRS, and eventually RADAR 2.2 cm radiometry, sensing the non-icy component of ring material (see section entitled Ring Particle Composition and Size). Unfortunately, no unambiguous compositional signatures of any materials besides water ice were seen by VIMS, UVIS, or ISS; and other instruments such as CIRS and RADAR could only constrain the amount of non-icy material in a nonspecific way. Fortunately, in the GF orbits, when Cassini crossed the ring plane inside of the D-ring (and indeed skimmed through the planet's tenuous upper atmosphere) synergistic, dedicated in situ observations by CDA, INMS, MIMI, and RPWS hit pay dirt.

CDA detected grains at a variety of vertical distances above the rings, with varying silicate/ice fraction [Hsu et al. 2018]. The Fe/Si ratio suggested low-Fe silicates. The order-unity silicate/ice ratio in material detected by CDA (primarily at high latitudes) is far higher than seen in the main rings or even the more polluted C-ring, and suggests that detected grains have been stripped of most of their ice before detection, perhaps by photosputtering [Hsu et al. 2018], but this remains an active area of research. No evidence was found for free iron or FexOy compounds (candidates for reddening the rings)—see section entitled Composition (Remote Sensing) and Cuzzi et al. [2009] for a review and discussion—even though their presence had been suggested in true interstellar grains detected by CDA [Altobelli et al. 2016]. CDA observations of organics are expected to be limited to large grains, which were rare because the dust abundance at the radii of ring plane crossings was much lower than had been (conservatively) estimated from spacecraft hazard studies, and most of the detected grains were too tiny to get good mass spectra in the presence of known carbon contamination of CDA. For the larger grains, CDA can say that the concentration of organics is low in any single detected grain, compared to the amount of ice or silicate. Nevertheless, the data are still being analyzed and new results along these lines are anticipated—see, for instance, Hsu et al. [2018], and Section 3.2 Instruments Science Results chapter entitled CDA.

MIMI detected an equatorial layer of 4–5 nm radius grains with vertical thickness of a few thousand km [Mitchell D. et al. 2018] blending into the very rare upper atmosphere of Saturn. These

tiny grains plausibly derive from the even flatter D-ring and drift inwards under gas drag while spreading vertically. They are too small to pick up much charge, so orbit at nearly Keplerian speeds, obtaining their few-thousand km vertical thickness by scattering collisions with differentially rotating exospheric H atoms. MIMI could not determine the composition of these grains directly, but estimates their mass flux into the atmosphere at 5 kg/s [Mitchell et al. 2018] (and Section 3.2 Instrument Science Results chapter entitled MIMI).

Meanwhile, as Cassini skimmed through the very rarified upper atmosphere on the GF orbits closest to Saturn, INMS detected strong signals due to a very wide range of masses, up to their limit at 100 amu [Waite et al. 2018; Perry et al. 2018]. The abundance of these molecules actually decreased downwards into Saturn, so they are entering from above, not diffusing up from depth. The overall pattern observed is roughly dominated by multiples of carbon atoms, up to C6, but given the likelihood that large molecules fragment into smaller ones within the INMS chamber prior to actually being sampled, detailed inferences require a complex deconvolution process [Waite et al. 2018; Miller et al. 2019]. INMS is unable to detect nonvolatile material like iron or silicates, and is even subject to underestimation of H_2O. The good agreement between the INMS latitudinal signal strength and the thickness of the MIMI 4–5 nm particle layer suggests that the INMS compositions refer to impact fragments of the MIMI particles. Also seen in the INMS spectra are N and O; however, the complexity of the deconvolution leaves some ambiguity about whether the O, N (and even some of the C) were carried as part of the organics or in smaller molecules like NH_3 or CH_4 [Waite et al. 2018; Perry et al. 2018; Miller et al. 2019]. For comparison, Cassini VIMS observations see no CH_4 or CO_2 [Cuzzi et al. 2009] and STIS spectra see no NH_3 [Cuzzi et al. 2018b]. INMS estimated a total flux of these materials into Saturn's upper atmosphere, over a latitudinal band of 5–10° wide, that is about 1000 times larger than the MIMI estimate [Perry et al. 2018], and propose that it must be carried dominantly by particles of 1–2 nm radius, too small for MIMI to detect, but following roughly the same vertical distribution. This flux is so high that INMS suggests it is probably due to a flareup in the D-ring, perhaps due to recent activity in the D68 ringlet [Hedman et al. 2014b; Hedman and Showalter 2016; Hedman 2019].

Ring origin and age

The age of the rings has been debated since the Voyager era, when two general lines of argument arose suggesting they may be much younger than the solar system. These are described in more detail in several recent review chapters [Cuzzi et al. 2009, 2018a; Charnoz et al. 2009]. First, angular momentum transfer by spiral density waves between the rings and the inner moons should quickly collapse the A-ring and spin the close ringmoons outwards, a tidal effect like our own Earth-moon tidal interaction [Goldreich and Tremaine 1982], see also Poulet and Sicardy [2001] or Charnoz et al. [2009] for loopholes. Second, pollution of the dominantly icy A-ring and B-ring, more than 90% ice, as known since pre-Voyager [Esposito et al. 1984; Orton et al. 2009], by dominantly non-icy meteoroid infall should darken them in much less than the age of the solar system [Doyle et al. 1989; Cuzzi and Estrada 1998; Elliott and Esposito 2011]. It had been argued, however, that the ring mass could be much larger than generally accepted during the Voyager era, because gravitational clumping and lack of sampling by spiral density waves of the most massive B-ring

might allow most of the mass to escape detection (see section entitled Gravitational Processes). Also, the meteoroid mass flux was very poorly known, and if it had been overestimated by an order of magnitude or so, the rings could remain unpolluted for the age of the solar system.

The combination of ring mass determined by RSS [Iess et al. 2019], and the extrinsic meteoroid mass flux measured by CDA [Kempf et al. 2019] (see section entitled The Extrinsic (Interplanetary) Mass Flux) at last allows us to constrain the ring age to be less than 250 million years or so (observational and model-based uncertainties remain), i.e., no older than the dinosau [O'Donoghue et al. 2019]. If we must reluctantly relinquish our otherwise physically plausible primordial ring origin scenarios, at least there is one plausible recent origin scenario, related to a dynamical instability incurred 100 million years ago by a stably evolving Saturn inner moon system [Cuk et al. 2016]. There are many current issues associated with connecting such an instability (near Rhea's orbit) and actual formation of a massive ring inside the Roche zone. However, it offers both an independently derived, recent age and also an indication why Saturn is the only giant planet to sport such a young, massive, icy ring. Constraints from cratering of icy moon surfaces and internal evolution will play an important role in testing the idea. There are also several Titan-related puzzles pointing to short timescales [Nixon et al. 2018]. A possibly important constraint is that the D/H ratio in the rings is similar to the regular icy moons and terrestrial values, while that of Phoebe is more comet-like [Clark et al. 2019]. The current implications that the rings are colored by organics, that there may be a silicate-rich rubble belt buried within the C-ring (see section entitled Composition (Remote Sensing)), and even the dark, enigmatic G-ring parent Aegaeon [Hedman et al. 2011a] provide important constraints as well.

Ring composition (RN1b) - ringmoons

Determines the composition of the close-in ringmoons as targets of opportunity. This is discussed in detail in Section 3.1 Discipline Science Results chapter entitled Icy Satellites.

Ring structure (RN1c) – high resolution and composition

Determines structural and compositional variations at high resolution across selected ring features of greatest interest, using remote and in situ observations.

A substantial number of new, dedicated observations were prioritized, integrated, and implemented to make use of the unique, up-close-and-personal geometry of Cassini's RG and GF orbits to address radial structure, meaning on scales larger than the vertical thickness. Also, a large number of ISS 8–15 filter color scans with 3–5 km radial resolution were integrated and successfully implemented well before the RG and GF orbits, to address compositional variations, over a large range of illumination and viewing angles, as well as different solar hour angles to assess the role of Saturnshine and the wavelength variation of ring particle phase functions.

Much higher spatial resolution is needed to assess fine scale structural variations. Recall that the unique SOI observations (400 m resolution) were sparsely sampled, were of the unlit face, and were taken at a large relative velocity requiring short exposures and producing noisy images. On

the other hand, the RG and GF orbits provided similar 100–300 m resolution on the lit face as well as of the unlit face, and at low phase angles, with the opportunity to use smear removal tracking. Moreover, one new kind of observation was enabled during the RG and GF orbits; active radar backscattering. Radar observations (from the ground) opened the modern era of Saturn's Rings research 40 years ago, but their sensitivity decreases as distance to the fourth power, so they only became feasible for Cassini in these very close-in geometries. The Radar team did carry out three active radar backscattering radial profiles with the potential to reach several km radial resolution, but reduction of this sort of data has not been previously done by the team and is still in progress (see Section 3.2 Instruments Science Results chapter entitled RADAR). Indeed, as of this writing, a number of observations taken on the RG and GF orbits remain in the early stages of analysis. However, an overview of high resolution observations by ISS, VIMS, UVIS, and CIRS may be found in Tiscareno et al. [2019].

Ring microstructure (RN2a)

Conducts in-depth studies of ring microstructure such as self-gravity wakes, which permeate the rings.

Microstructure has the connotation of structure comparable in scale to the ring vertical thickness (see section entitled Gravitational Processes). During the CSM, a number of exceptionally high radial resolution scans were implemented of the lit and unlit faces, using smear removal tracking (the so-called SUPERHRES scans) and targeted observations of, for instance, the Keeler gap in the vicinity of Daphnis, the C-ring plateaus, and other specific regions of interest. Spatial clumping, of several different types and on scales still larger than the expected self-gravity wakes, is widely seen in images with these sub-km resolutions [Tiscareno et al. 2019a]. A number of specially designed Turnaround stellar occultations were prioritized and included; these are chord occultations in which the path of the star becomes tangent to the orbital direction at some radius. The implication is that radial stellar velocity vanishes and ultra-high radial resolution can be obtained, along with very good tangential resolution. Finally, the technique of variance analysis 4 has been widely applied and a variety of interesting differences seen from place to place. This sort of analysis is only getting underway [Colwell et al. 2018].

New ring structures (RN2b)

Performs focused studies of the evolution of newly discovered propeller objects. Extend to studies of streaky plateau structure.

A dedicated campaign to image selected giant propellers (> 1 km size) as often as possible was conducted over the last five years of the mission. This campaign yielded several hundred images that successfully targeted propellers, with rich sampling in time. Ongoing analysis of these images—for example, see section entitled Ring-Satellite Interaction) finds excursions from Keplerian orbit of diverse kinds, including both gradual trends and sharp changes of direction. In the RG orbits, three giant propellers were specifically targeted for close-flyby imaging, which

successfully revealed their detailed structure. Also in the RG orbits, high-resolution images of the Propeller Belts yielded the first full view of a size distribution in which the largest propellers are 4× to 5× larger than the smallest [Tiscareno et al. 2019a]. In the GF orbits, images of the plateaus spectacularly confirmed previous suspicions of streaky texture, and further revealed sharp-edged belts of textures (some streaky, some clumpy) at other locations in the main rings [Tiscareno et al. 2019b]. Most of these data encompass both the lit and unlit faces of the rings, and are still under reduction and analysis.

Saturn System Science Results

The possibility of young rings now has broadened to the possibility of a young inner icy moon (and ring) system. The evection resonance theory of Cuk et al. [2016] not only independently arrives at a similar timescale as ring ages, but also points to Saturn as the most likely planet to incur such a fate. More studies of the icy moon surfaces (especially cratering statistics) are needed to constrain the validity of this hypothesis, and the composition of the moons and rings needs to be taken into account together.

Along these lines, results obtained through the study of rings have led us to a new understanding of the deep interior of Saturn. The discipline, now known as Kronoseismology, is in its infancy, and has led to the suggestion of a diffuse core boundary and rapidly changing internal structure at Saturn, see section entitled Gravitational Processes. Recent results have even shown that the elusive deep interior rotation period of the planet can be determined very precisely by matching internal structure predictions with spiral waves seen in the C-ring [Mankovich et al. 2019].

CDA also detected 46 grains coming from the Interstellar Flux stream (its velocity apex or ram direction is known from the velocity of the solar system through the local diffuse Interstellar medium) and constrained their composition [Altobelli et al. 2016]. This profoundly important in situ determination of the composition of interstellar medium (ISM) grains complements and informs often ambiguous remote sensing determinations, see section entitled Ring Age and Origin. The grains populating the diffuse ISM; those detected here and the most easily studied by remote sensing, include Mg-rich silicates and, perhaps, iron metal or oxides, but are depleted in sulfur. By comparison, the silicates detected by CDA during the GF orbits were also Mg-rich, but showed no evidence of companion Fe metal or oxides. The ISM grains were quite homogeneous, probably by repeated processing in the ISM by shocks and radiation. As these grains become embedded in the dark, dense, presolar parent cloud; they accumulate more volatile organics and ices (apparently some sulfur-bearing ices) before flowing into the forming solar system. However, their very refractory mix of silicates and metal would not be expected to change at the low temperatures of these clouds.

Non-Saturn-System Science Results

Cassini ISS took nearly 1200 images of the Jovian ring system during its 6-month encounter with Jupiter … .

Cassini ISS took nearly 1200 images of the Jovian ring system during its 6-month encounter with Jupiter [Porco et al. 2003]. These observations constitute the most complete data set on the ring taken by a single instrument, both in phase angle (0.5°–120° at seven angles) and wavelength (0.45–0.93 μm through eight filters). The optical depth and radial profile of the main ring are consistent with previous observations. No broad asymmetries within the ring were seen, but possible hints of 1000 km-scale azimuthal clumps were detected. Throop et al. [2004] combined the Cassini ISS and VIMS observations with those from Voyager, HST, Keck, Galileo, and groundbased telescopes, and fit the entire dataset using a photometric model including microscopic silicate dust grains and larger, long-lived parent bodies. Main ring optical depths for the large bodies, and the dust, of about 1–5 × 10^{-6}, respectively, were obtained, and the grains appear to be nonspherical. The larger bodies must be very red between 0.4–2.5 μm wavelengths, and may have absorption features near 0.8 and 2.2 μm.

Unsolved Problems Suitable for Ongoing Research and Future Missions

Figure RINGS-2 shows a montage of views displaying Saturn's main rings structure.

Why is the interior of Saturn different from that of Jupiter (as seen by the RSS gravity passes) and, why are the mass irregularities inferred so different and so much larger than what are inferred from Kronoseismology spiral density and bending waves in the rings? Are these differences tied to the faster tidal evolution rates seen for the Saturnian moons than for the Jovian moons (the so-called larger Q for Jupiter than for Saturn)? What are the embedded mass concentrations responsible for the tesseral spiral density waves that rotate at harmonics of Saturn's spin rate, and moreover change with time?

The ring mass and in particular its radial distribution were not as well constrained as hoped, because of unexpected internal structure within Saturn. Only a total ring mass could be determined, and the B-ring component inferred by backing out the already very well-known A-ring and C-ring masses (from spiral density waves). This remaining uncertainty provides an opportunity for a future mission to use repeated close gravitational flybys to separate out and fully understand the apparently unusual and intriguing internal structure of the planet, from the radial mass distribution within the rings, hopefully at a few hundred km radial resolution even, and to determine which parts of the opaque B-ring actually hold how much of the mass. Better radial mass resolution would be useful in the C-ring also, because the possibility that the middle C-ring hides a fossil silicate rubble belt has implications for ring origin; it is currently constrained by a small handful of surface mass densities. There is some evidence that the visual wavelength

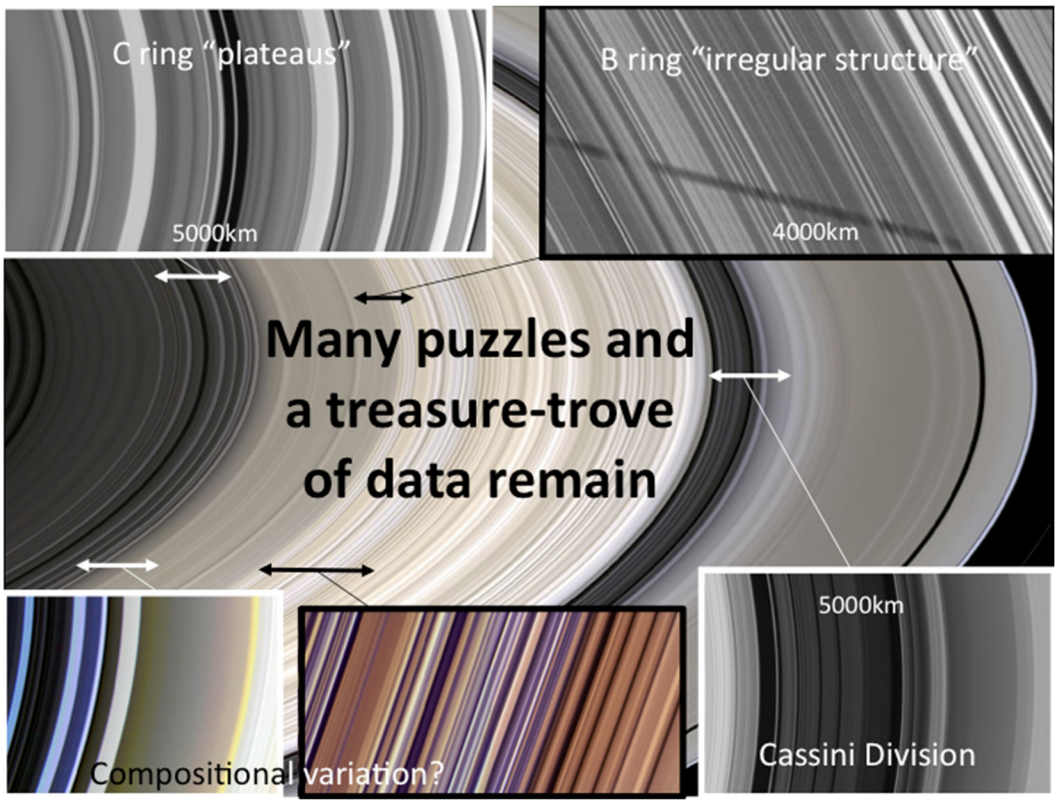

Figure RINGS-2: A montage of still-puzzling structure. A mosaic view of Saturn's main rings is shown in the central panel. Certain selected regions are indicated by double-header arrows, and by close-up images shown as insets.

spectra of the central C-ring differ from the otherwise similar Cassini Division; might this be another clue regarding a buried silicate belt?

The smooth, undulating 80 km scale irregular structure in the inner B-ring may be related to ballistic transport, but the array of finer-to-coarser scale structure in the middle and outer B-ring seems to be something different. Could it be some form of viscous overstability, operating at longer wavelengths than models show, and possibly coupling to the even larger scale azimuthal B-ring edge variations? In the region between 100,000–104,500 km, radio and stellar occultations both see successions of very sharp transitions between large and very large optical depth, for which no explanations exist. At the time of this writing, RSS occultations of the very densest B-ring regions, taken at the largest ring opening angles where they would be most likely to be even partially transparent, have not been analyzed or released, but are eagerly anticipated.

The outer C-ring hosts a series of 5–8 plateau features in optical depth, nearly symmetrically arrayed about the Maxwell gap which is now known to be caused by a 2:1 resonance with the strongest planetary internal vibration mode [Marley and Porco 1993; French et al. 2016b; Fuller 2014]; the reason why a dense, elliptical m = 1 ringlet dominates the gap, apparently caused by an m = 2 resonance, is not understood. A similar situation occurs at a Titan resonance in the C-ring, but that is an m = 1 resonance. The plateaus do not have any special association with resonances

from known or predicted planetary internal modes [Marley 2014]. They are odd in that their appearance as features is due primarily to locally abrupt changes in particle size distribution rather than surface mass density, see section entitled Size Distribution, and the following paragraphs. Moreover, ultra-high resolution Cassini images reveal a novel and unique streaky structure in the plateaus that is not understood [Tiscareno et al. 2019a].

Why is there a Cassini Division and why are there no embedded moonlets clearing its several empty gaps? It has been suggested that weak perturbations from the fluctuating B-ring edge might play a role [Hedman et al. 2010b]. Presumably the Cassini Division was originally cleared by a powerful Mimas 2:1 spiral density wave, at a time when the rings were continuous through the region [Baillié et al 2019] , but how did that early, vigorous evolution lead to today's quiet, banded structure? And, how are the moonlet-free C-ring gaps formed?

In the A-ring, a million propeller objects populate three distinct radial belts. Are these objects transient clumps that emerge from the background material with low, but finite probability and then disperse again? Giant propellers (found only outside the Encke gap) seem especially hard to create by spontaneous, or triggered formation. Gravitational encounters with smaller masses seem to explain their wandering behavior, but the mass clumps needed are larger than the largest ring particles and even typical self-gravity wakes. There are a few propeller objects in the B-ring, but their locations and abundances have not been well characterized. What else could be hiding in the densest parts of the B-ring? What causes the ghost gaps in the C-ring and outer Cassini Division?

In the F-ring, telltale signatures of embedded, relatively large objects are seen preferentially in strands where they are maximally compressed by Prometheus. If the semi-major axes of these newly created objects lie outside the stable true core (see section entitled F-ring), they will develop chaotic orbital perturbations, diffusing away from their formation location as their eccentricity increases, and ultimately recolliding sporadically with the F-ring core. Cycles of such activity may be expected (and there is some evidence from comparing Voyager and Cassini), but no systematic assessment has been obtained. Meanwhile, even the most recent hypothesis for the stability of the F-ring true core cannot explain the stable precession of dozens of separated arcs as a single, well defined ellipse. Could the (mostly unconstrained) mass of the F-ring be playing a role?

The systematic increase of the redness of the rings inwards across the B-ring remains a puzzle. In situ observations (albeit in the D-ring) seem to favor large organic molecules, polycyclic aromatic hydrocarbons (PAHs) or fragments of tholins, possibly containing N and maybe even O, as the UV absorber responsible for the ring redness. These red organics seem to be intrinsic to the dominant icy material. Whether or not organics also explain the weaker UV absorption seen in most of the icy moons will be an important clue regarding ring origin scenarios; such as recent ones that connect their origin to a moderately recent collisional erosion/destruction of pre-existing, mature, differentiated icy moons. Can organic material remain associated with liquid water when a moon differentiates, and remain with it when it freezes?

Unexplained microstructure is seen in many places across the rings, at optical depths large and small, in late, high-resolution images which have resolution even better than those taken at SOI, … .

Color and brightness variations within the rings on tens to hundreds of km scale have been interpreted as small-scale, optical-depth dependent regolith grain size variations, but models capable of treating the difficult ring radiative transfer problem have yet to be deployed in compositional analyses. That is, secondary optical-depth dependent effects (like collisional packing or smoothing of particle surfaces) may change the particle phase functions, or volume density effects may change the layer scattering function. Much more analysis needs to be done with more sophisticated, nonclassical radiative transfer models, fitting observations over wide ranges of illumination and viewing geometry, as well as assessing wider ranges of wavelength simultaneously, to understand the situation before compositional implications can be derived with confidence. Shadowing on the surely very ragged ring particle surfaces needs to be studied [Cuzzi et al. 2017]. Also on the subject of radiative transfer models, Cassini's three high-radial-resolution active radar backscattering scans require new models for their interpretation that can adequately treat coherent backscattering.

Unexplained jumps in particle size distribution are seen at a number of places in the rings where sharp edges appear in optical depth, but across these edges there are only small (or no) contrasts in surface mass density. Basically, this means the features are caused by abrupt changes in particle size distribution. The inner edge of the A-ring, where it transitions to the Cassini Division, is one such place. The series of C-ring plateaus, nearly symmetrically surrounding the Maxwell gap (which is known to be associated with a 2:1 resonance with a mode inside Saturn) are like that as well. What causes this effect? Why do the slopes and minimum or maximum sizes in generally powerlaw size distributions of ring particles vary from place to place? Are most particles porous throughout or do they conceal dense, solid cores?

Unexplained microstructure is seen in many places across the rings, at optical depths large and small, in late, high-resolution images which have resolution even better than those taken at SOI, as well as combinations of lit and unlit face geometries, lower smear, and higher signal to noise ratio [Tiscareno et al. 2019a]. The texture can change rather quickly with radius and is not always related to optical depth changes.

The process actually responsible for the initial formation of spokes; whether it be bursts of ionizing radiation from planetary superstorms, magnetic field instabilities, or impacts, remains unclear.

The Ballistic transport process usually believed to explain the sharp inner edges of the A-ring and B-ring, and hypothesized to explain the C-ring plateaus, has been modeled assuming the boundaries of these features manifested jumps in surface mass density without particle size changes, and we now know the underlying surface mass density is only slowly varying while the particle size changes abruptly. How do these new realizations affect the models? Could the ejection

velocity change from place to place, depending on the nature of the local particle regoliths? How will the results change under new assumptions about meteoroid impact flux and dynamical population? The theory of ring pollution and restructuring by meteoroid bombardment and ballistic transport needs to be tested more carefully against other structures and compositional profiles, and revised to capture more realistic impact outcomes and newly constrained incoming meteoroid fluxes. Matching radial scans of ring color and spectral reflectance with models of compositional evolution must incorporate new understanding about ring surface mass density, particle size, and viscosity. Inclusion of regolith thermal inertias would provide another handle on how particle surfaces respond to meteoroid bombardment.

More sophisticated models of impact chemistry and radiation chemistry are needed; both in micrometeoroid impacts on ring particles, possibly resulting in some C-O chemistry, and by nm-size grain impacts into the INMS entry chamber. INMS sees a variety of molecules (CH_4, CO_2, and NH_3 in particular) that are not evident in VIMS or HST-STIS spectra of the rings. Are some of these created in hypervelocity impacts, transforming absorbing carbon compounds into volatiles or transparent ices? If so (or if not) this would have implications for ring pollution and inferred ring age. How does the water ice throughout the rings remain crystalline given constant radiation and meteoroid bombardment? VIMS spectral and occultation observations strongly support crystalline ice.

Explanation for the geologically recent formation of the rings: We now have a new set of constraints, and even an appealing theoretical hypothesis to explore; however, we are still lacking a complete understanding as to how the rings formed in their current location, within Saturn's Roche limit, from a differentiated icy object with a trace, intimately mixed organic component, 250 million years ago, even given disruptive collisions near the current orbit of Rhea. Observations and interpretation of icy moon surfaces can contribute meaningful constraints.

CONCLUSION

This short review can in no way capture the depth and complexity of the analysis that has gone into every one of the incomplete list of ~200 publications cited here, each of them several years work for multiple scientists. Each of these papers has contributed one critical and unique stone to the edifice of knowledge we now possess about the rings of Saturn; stones all formed from bits returned by Cassini's spectacular 13-year mission. Nor can it adequately convey the even larger and deeper, still unanalyzed and uninterpreted amount of data so thoughtfully conceived, passionately argued for, painstakingly planned, obtained, carefully calibrated, and stored in the Planetary Data System that awaits the attention of future generations of ring scientists. However, we hope it can provide an idea of the scope of where we stand today, and hints at future directions of research. Even this summary would be different if it were written a year from now. The Cassini Rings Discipline Working Group has nothing but admiration and deep appreciation for the dedication of the hundreds of engineers and dozens of managers at Jet Propulsion Laboratory (JPL) who made this mission possible, some of whom may be lucky enough to return to Saturn on a future mission and help answer these outstanding questions.

ACRONYMS

Note: For a complete list of Acronyms, refer to Cassini Acronyms – Attachment A.

AO	Announcement of Opportunity
CAPS	Cassini Plasma Spectrometer
CDA	Cosmic Dust Analyzer
CIRS	Composite Infrared Spectrometer
CSM	Cassini Solstice Mission
FOV	field-of-view
GF	Grand Finale
HST	Hubble Space Telescope
INMS	Ion and Neutral Mass Spectrometer
IR	infrared
ISM	interstellar medium
JPL	Jet Propulsion Laboratory
KBO	Kuiper Belt object
MAPS	Magnetospheres and Plasma Science
MIMI	Magnetospheric Imaging Instrument
NIR	near-IR
PAH	polycyclic aromatic hydrocarbon
PDS	Planetary Data System
RADAR	Titan Radar Mapper
RG	Ring-Grazing
RSS	Radio Science Subsystem
RWG	Ring Working Group
SED	Saturn Electrostatic Discharge
SKR	Saturn Kilometric Radiation
SOI	Saturn Orbit Insertion
STIS	Space Telescope Imaging Spectrograph
TM	Traceability Matrix
UV	ultraviolet
UVIS	Ultraviolet Imaging Spectrograph
VIMS	Visual and Infrared Imaging Spectrometer
WP	water products

REFERENCES

Disclaimer: The partial list of references below correspond with in-text references indicated in this report. For all other Cassini references, refer to Attachment B – References & Bibliographies; Attachment C – Cassini Science Bibliographies; the sections entitled References contributed by individual Cassini instrument and discipline teams located in Volume 1 Sections 3.1 and 3.2 Science Results; and other resources outside of the Cassini Final Mission Report.

Albers, N., M. Sremčević, J. E. Colwell, L. W. Esposito, (2012), Saturn's F-ring as seen by Cassini UVIS: Kinematics and statistics, Icarus, 217, 367−388.

Altobelli, N., F. Postberg, K. Fiege, M. Trieloff, H. Kimura, V. J. Sterken, H.-W. Hsu, J. Hillier, N. Khawaja, G. Moragas-Klostermeyer, J. Blum, M. Burton, R. Srama, S. Kempf, E. Gruen, (2016), Flux and composition of interstellar dust at Saturn from Cassini's Cosmic Dust Analyzer, Science, 352, 312−318.

Altobelli, N., L. Spilker, S. Pilorz, C. Leyrat, S. Eddgington, B. Wallis, A. Flandes, (2009), Thermal phase curves observed in Saturn's main rings by Cassini-CIRS: Detection of an opposition effect?, Geophysical Research Letters 36, L10105, doi: 10.1029/2009gl038163.

Altobelli, N., L. Spilker, S. Pilorz, S. Brooks, S. Edgington, B. Wallis, M. Flasar, (2007), C-ring fine structures revealed in the thermal infrared, Icarus, 191, 2, 691−701, doi: 10.1016/j.icarus.2007.06.014.

Attree, N. O., C. D. Murray, G. A. Williams, N. J. Cooper, (2014), A survey of low-velocity collisional features in Saturn's F-ring, Icarus, 227, 56−66.

Attree, N. O., C. D. Murray, N. J. Cooper, G. A. Williams, (2012), Detection of low-velocity collisions in Saturn's F-ring, The Astrophysical Journal Letters, vol. 755, no. 2, doi: 10.1088/2041-8205/755/2/L27.

Baillié, K., B. Noyelles, V. Lainey, S. Charnoz, G. Tobie, (2019), Formation of the Cassini Division-I, Shaping the rings by Mimas inward migration, Monthly Notices of the Royal Astronomical Society, 486, 2933−2946, doi: 10.1093/mnras/stz548.

Baillié, K., J. E. Colwell, L. W. Esposito, M. C. Lewis, (2013), Meter-sized moonlet population in Saturn's C-ring and Cassini Division, The Astronomical Journal, vol. 145, no. 6, doi: 10.1088/0004-6256/145/6/171.

Baillié, K., J. E. Colwell, J. J. Lissauer, L. W. Esposito, M. Sremčević, (2011), Waves in Cassini UVIS stellar occultations, 2, The C-ring, Icarus, 216, 292−308.

Becker, T. M., J. E. Colwell, L. W. Esposito, N. O. Attree, C. D. Murray, (2018), Cassini UVIS solar occultations by Saturn's F-ring and the detection of collision-produced micron-sized dust, Icarus, 306, 171−199.

Becker, T. M., J. E. Colwell, L. W. Esposito, A. D. Bratcher, (2016), Characterizing the particle size distribution of Saturn's A-ring with Cassini UVIS occultation data, Icarus, 279, 20−35.

Beurle, K., C. D. Murray, G. A. Williams, M. W. Evans, N. J. Cooper, C. B. Agnor, (2010), Direct Evidence for gravitational instability and moonlet formation in Saturn's rings, The Astrophysical Journal, 718, L176-L180.

Borderies, N., P. Goldreich, S. Tremaine, (1985), A granular flow model for dense planetary rings, Icarus, 63, 406−420.

Bradley, E. T., J. E. Colwell, L. W. Esposito, (2013), Scattering properties of Saturn's rings in the far ultraviolet from Cassini UVIS spectra, Icarus, 225, 726−739.

Bradley, E. T., J. E. Colwell, L. W. Esposito, J. N. Cuzzi, H. Tollerud, L. Chambers, (2010), Far ultraviolet spectral properties of Saturn's rings from Cassini UVIS, Icarus 206, 458−466.

Bromley, B. C. and Kenyon, S. J., (2013), Migration of small moons in Saturn's rings, The Astrophysical Journal, vol. 764, no. 2.

Burns, J. A., L. E. Schaffer, R. J. Greenberg, M. R. Showalter, (1985), Lorentz resonances and the structure of the Jovian ring, Nature, 316, 115−119.

Burns, J. A., M. R. Showalter, G. E. Morfill, (1984), The ethereal rings of Jupiter and Saturn, In Planetary rings, (eds.) R. Greenberg, A. Braphic, (A85-34401 15-88), University of Arizona Press, Tucson, AZ, 200−272.

Chambers, L. S., J. N. Cuzzi, E. Asphaug, J. Colwell, S. Sugita, (2008), Hydrodynamical and radiative transfer modeling of meteoroid impacts into Saturn's rings, Icarus, 194, 623−635.

Chancia, R. O., M. M. Hedman, S. W. H. Cowley, G. Provan, S. -Y. Ye, (2019), Seasonal structures in Saturn's dusty Roche Division correspond to periodicities of the planet's magnetosphere, Icarus, vol. 330, pp. 230−255, doi: 10.1016/j.icarus.2019.04.012.

Charnoz, S., R. M. Canup, A. Crida, L. Dones, (2018), The Origin of Planetary Ring Systems, Chapter 18, In Planetary Rings, (eds.) M. Tiscareno, C. Murray, Cambridge University Press pp. 515−536, doi: 10.1017/9781316286791.018.

Charnoz, S., J. Salmon, A. Crida, (2010), The recent formation of Saturn's moonlets from viscous spreading of the main rings, Nature, 465, 752−754.

Charnoz, S., L. Dones, L. W. Esposito, P. R. Estrada, M. M. Hedman, (2009), Origin and Evolution of Saturn's Ring System, Chapter 17, In Saturn from Cassini-Huygens, (eds.) M. K. Dougherty, L. W. Esposito, S. M. Krimigis, Springer, Dordrecht, pp. 537–575, doi: 10.1007/978-1-4020-9217-6_17.

Charnoz, S., (2009), Physical collisions of moonlets and clumps with the Saturn's F-ring core, Icarus, 201, 191−197.

Charnoz, S., C. C. Porco, E. Déau, A. Brahic, J. N. Spitale, G. Bacques, K. Baillié, (2005), Cassini Discovers a Kinematic Spiral Ring Around Saturn, Science, 310, 1300−1304.

Ciarniello, M., G. Filacchione, E. D'Aversa, F. Capaccioni, P. D. Nicholson, J. N. Cuzzi, R. N. Clark, M. M. Hedman, C. M. Dalle Ore, P. Cerroni, C. Plainaki, L. J. Spilker, (2019), Cassini-VIMS observations of Saturn's main rings II: A spectrophotometric study by means of Monte Carlo ray-tracing and Hapke's theory, Icarus, 317, pp. 242−265, doi: 10.1016/j.icarus.2018.07.010.

Clark, R. N., R. H. Brown, D. P. Cruikshank, G. A. Swayze, (2019), Isotopic ratios of Saturn's rings and satellites: Implications for the origin of water and Phoebe, Icarus, 791−802, doi: 10.1016/j.icarus.2018.11.029.

Clark, R. N., D. P. Cruikshank, R. Jaumann, R. H. Brown, K. Stephan, C. M. Dalle Ore, K. E. Livo, N. Pearson, J. M. Curchin, T. M. Hoefen, B. J. Buratti, G. Filacchione, K. H. Baines, P. D. Nicholson, (2012), The surface composition of Iapetus: Mapping results from Cassini VIMS, Icarus, 218, 831−860.

Colwell, J. E., L. W. Esposito, J. H. Cooney, (2018), Particle sizes in Saturn's rings from UVIS stellar occultations 1, Variations with ring region, Icarus, 300, 150−166.

Colwell, J. E., P. D. Nicholson, M. S. Tiscareno, C. D. Murray, R. G. French, E. A. Marouf, (2009), The Structure of Saturn's Rings, Chapter 13, In Saturn from Cassini-Huygens, (eds.) M. K. Dougherty, L. W. Esposito, S. M. Krimigis, Springer, Dordrecht, pp. 375−412, doi: 10.1007/978-1-4020-9217-6_13.

Colwell, J. E., L. W. Esposito, M. Sremčević, G. R. Stewart, W. E. McClintock, (2007), Self-gravity wakes and radial structure of Saturn's B-ring, Icarus, 190, 127−144.

Colwell, J. E., L. W. Esposito, M. Sremčević, (2006), Self-gravity wakes in Saturn’s A-ring measured by stellar occultations from Cassini, Geophysical Research Letters, 33, L07201.

Connerney, J. E. P. and J. H. Waite, (1984), New model of Saturn's ionosphere with an influx of water from the rings, Nature, 312, 136−138.

Cooper, N. J., C. D. Murray, S. Renner, (2017), F-ring Objects, Presented at Cassini End of Mission Project Science Group (PSG), Pasadena, CA, September 16, 2017.

Cooper, N. J., C. D. Murray, G. A. Williams, (2013), Local variability in the orbit of Saturn's F-ring, The Astronomical Journal, vol. 145, no. 6, doi: 10.1088/0004-6256/145/6/161.

Crida, A., J. C. B. Papaloizou, H. Rein, S. Charnoz, J. Salmon, (2010), Migration of a moonlet in A-ring of solid particles: Theory and application to Saturn's propellers, The Astrophysical Journal, 140, 944−953.

Ćuk, M., L. Dones, D. Nesvorný, (2016), Dynamical evidence for a late formation of Saturn’s Moons, The Astrophysical Journal, 820, 2, 97.

Cuzzi, J. N., G. Filacchione, E. A. Marouf, et al., (2018a), The Rings of Saturn, Chapter 3, In Planetary Ring Systems, (eds.) M. Tiscareno and C. Murray, Cambridge University Press, pp. 51−92, doi: 10.1017/9781316286791.003.

Cuzzi, J. N., R.G. French, A. R. Hendrix, D. M. Olson, T. Roush, S. Vahidinia, (2018b), HST-STIS spectra and the redness of Saturn's rings, Icarus, 309, 363−388.

Cuzzi, J. N., E. A. Marouf, R. G. French, R. A. Jacobson, C. D. Murray, N. J. Cooper, (2018c), Saturn’s F-ring is shepherded by Prometheus, Science Advances, in review.

Cuzzi, J. N., L. B. Chambers, A. R. Hendrix, (2017), Rough surfaces: Is the dark stuff just shadow? Icarus, 289, 281−294.

Cuzzi, J. N., A. D. Whizin, R. C. Hogan, A. R. Dobrovolskis, L. Dones, M. R. Showalter, J. E. Colwell, J. D. Scargle, (2014) ,Saturn’s F-ring core: Calm in the midst of chaos, Icarus, 232, 157−175.

Cuzzi, J. N., J. A. Burns, S. Charnoz, R. N. Clark, J. E. Colwell, L. Dones, L. W. Esposito, G. Filacchione, R. G. French, M. M. Hedman, S. Kempf, E. A. Marouf, C. D. Murray, P. D. Nicholson, C. C. Porco, J. Schmidt, M. R. Showalter, L. J. Spilker, J. N. Spitale, R. Srama, M. Sremčević, M. S. Tiscareno, J. Weiss, (2010), An evolving view of Saturn's dynamic rings, Science, 327, 1470−1475.

Cuzzi, J., R. Clark, G. Filacchione, R. French, R. Johnson, E. Marouf, L. Spilker, (2009), Ring Particle Composition and Size Distribution, Chapter 15, In Saturn from Cassini-Huygens, (eds.) M. K. Dougherty, L. W. Esposito, S. M. Krimigis, Springer, Dordrecht, pp. 459−509, doi: 10.1007/978-1-4020-9217-6.

Cuzzi, J. N. and P. R. Estrada, (1998), Compositional evolution of Saturn's rings due to meteoroid bombardment, Icarus, 132, 1−35.

D'Aversa, E., G. Bellucci, P. D. Nicholson, M. M. Hedman, R. H. Brown, M. R. Showalter, F. Altieri, F. G. Carrozzo, G. Filacchione, F. Tosi, (2010), The spectrum of a Saturn ring spoke from Cassini/VIMS, Geophysical Research Letters, 37, 1.

Déau, E., L. Dones, L. Spilker, A. Flandes, K. Baillié, S. Pilorz, M. Showalter, M. El Moutamid, J. E. Colwell, (2019), Cassini CIRS and ISS opposition effects of Saturn's rings: 1, C-ring narrow or broad surge? Monthly Notices of the Royal Astronomical Society, vol. 489, Issue 2, pp. 2775–2791, doi: 10.1093/mnras/sty2587.

Déau, E., L. Dones, M. I. Mishchenko, R. A. West, P. Helfenstein, M. M. Hedman, C.C. Porco, (2018), The opposition effect in Saturn's main rings as seen by Cassini ISS: 4, Correlations of the surge morphology with surface albedos and VIMS spectral properties, Icarus, 305, 324−349.

Déau, E., (2015), The opposition effect in Saturn's main rings as seen by Cassini ISS: 2, Constraints on the ring particles and their regolith with analytical radiative transfer models, Icarus, 253, 311−345.

Déau, E., L. Dones, S. Charnoz, R. A. West, A. Brahic, J. Decriem, C. C. Porco, (2013), The opposition effect in Saturn's main rings as seen by Cassini ISS: 1, Morphology of phase functions and dependence on the local optical depth, Icarus, 226, 591−603.

Dougherty, M. K., H. Cao, K. K. Khurana, G. J. Hunt, G. Provan, S. Kellock, M. E. Burton, et al., (2018), Saturn's magnetic field revealed by the Cassini Grand Finale, Science, 362, 6410, doi: 10.1126/science.aat5434.

Doyle, L. R., L. Dones, J. N. Cuzzi, (1989), Radiative transfer modeling of Saturn's outer B-ring, Icarus, vol. 80, pp. 104−135, doi: 10.1016/0019-1035(89)90163−-2.

Durisen, R. H., P. W. Bode, J. N. Cuzzi, S. E. Cederbloom, B. W. Murphy, (1992), Ballistic transport in planetary ring systems due to particle erosion mechanisms II: Theoretical models for Saturn's A- and B-ring inner edges, Icarus, 100, 364−393.

Durisen, R. H., N. L. Cramer, B. W. Murphy, J. N. Cuzzi, T. L. Mullikin, S. E. Cederbloom, (1989), Ballistic transport in planetary ring systems due to particle erosion mechanisms I: Theory, numerical methods, and illustrative examples, Icarus, 80, 136−166.

El Moutamid, M., P. D. Nicholson, M. M. Hedman, P. J. Gierasch, J. A. Burns, R. G. French, (2016a), Tesseral resonances in the rings of Saturn, American Astronomical Society (AAS),

Division on Dynamical Astronomy (DDA), meeting 47, id. 400.05, Vanderbilt University, Nashville, TN, May 22−26, 2016.

El Moutamid, M., M. M. Hedman, P. D. Nicholson, P.J. Gierasch, J. A. Burns, (2016b), Evidence of differential rotation inside Saturn from waves of its rings, American Astronomical Society (AAS), Division for Planetary Sciences (DPS), meeting 48, id. 114.0, Pasadena, CA, October 16−21, 2016.

El Moutamid, M., P. D. Nicholson, R. G. French, M. S. Tiscareno, C. D. Murray, M. W. Evans, C. M. French, M. M. Hedman, J. A. Burns, (2016c), How Janus' orbital swap affects the edge of Saturn's A-ring?, Icarus, 279, 125−140.

Elliott, J. P. and L. W. Esposito, (2011), Regolith depth growth on an icy body orbiting Saturn and evolution of bidirectional reflectance due to surface composition changes, Icarus, 2012, 268−274.

Elrod, M. K., W.-L. Tseng, A. K. Woodson, R. E. Johnson, (2014), Seasonal and radial trends in Saturn's thermal plasma between the main rings and Enceladus, Icarus, 242, 130−137.

Esposito, L. W., N. Albers, B. K. Meinke, M. Sremčević, P. Madhusudhanan, J. E. Colwell, R. G. Jerousek, (2012), A predator-prey model for moon-triggered clumping in Saturn's rings, Icarus, 217, 103−114.

Esposito, L. W., B. K. Meinke, J. E. Colwell, P. D. Nicholson, M. M. Hedman, (2008), Moonlets and clumps in Saturn's F-ring, Icarus, 194, 278−289.

Esposito, L. W., J. N. Cuzzi, J. B. Holberg, E. A. Marouf, G. L. Tyler, C. C. Porco, (1984), Saturn's rings-structure, dynamics, and particle properties, Saturn, 463−545.

Estrada, P. R., R. H. Durisen, H. N. Latter, (2018), Meteoroid bombardment and ballistic transport in planetary rings, Chapter 9, In Planetary Rings, (eds.) M. Tiscareno, C. Murray, Cambridge University Press, pp. 198−224, doi: 10.1017/9781316286791.009.

Estrada, P. R., R. H. Durisen, J. N. Cuzzi, D. A. Morgan, (2015), Combined structural and compositional evolution of planetary rings due to micrometeoroid impacts and ballistic transport, Icarus, 252, 415−439.

Ferrari, C., S. Brooks, S. Edgington, et al., (2009), Structure of self- gravity wakes in Saturn's A-ring as measured by Cassini CIRS, Icarus, 199, 145–153.

Filacchione, G., M. Ciarniello, F. Capaccioni, R. N. Clark, P. D. Nicholson, M. M. Hedman, J. N. Cuzzi, D. P. Cruikshank, C. M. Dalle Ore, R. H. Brown, P. Cerroni, N. Altobelli, L. J. Spilker, (2014), Cassini-VIMS observations of Saturn's main rings I: Spectral properties and temperature radial profiles variability with phase angle and elevation, Icarus, 241, 45−65.

Filacchione, G., F. Capaccioni, R. N. Clark, P. D. Nicholson, D. P. Cruikshank, J. N. Cuzzi, J. I. Lunine, R. H. Brown, P. Cerroni, F. Tosi, M. Ciarniello, B. J. Buratti, M. M. Hedman, E. Flamini, (2013), The radial distribution of water ice and chromophores across Saturn's System, The Astrophysical Journal, vol. 766, no. 2, doi: 10.1088/0004-637X/766/2/76.

Filacchione, G., F. Capaccioni, M. Ciarniello, R. N. Clark, J. N. Cuzzi, P. D. Nicholson, D. P. Cruikshank, M. M. Hedman, B. J. Buratti, J. I. Lunine, L. A. Soderblom, F. Tosi, P. Cerroni, R. H. Brown, T. B. McCord, R. Jaumann, K. Stephan, K. H. Baines, E. Flamini, (2012),

Saturn's icy satellites and rings investigated by Cassini-VIMS III: Radial compositional variability, Icarus, 220, 1064−1096.

Flandes, A., L. Spilker, R. Morishima, S. Pilorz, C. Leyrat, N. Altobelli, S. Brooks, S. G. Edgington, (2010), Brightness of Saturn's rings with decreasing solar elevation, Planetary and Space Science, 58, 1758–1765.

French, R. G., C. A. McGhee-French, P. D. Nicholson, M. M. Hedman, (2019), Kronoseismology III: Waves in Saturn's inner C-ring, Icarus, 319, pp. 599−626, doi: 10.1016/j.icarus.

French, R. G., P. D. Nicholson, C. A. McGhee-French, K. Lonergan, T. Sepersky, M. M. Hedman, E. A. Marouf, J. E. Colwell, (2016a), Noncircular features in Saturn's rings III: The Cassini Division, Icarus, 274, 131−162.

French, R. G., P. D. Nicholson, M. M. Hedman, J. M. Hahn, C. A. McGhee-French, J. E. Colwell, E. A. Marouf, N. J. Rappaport, (2016b), Deciphering the embedded wave in Saturn's Maxwell ringlet, Icarus, 279, 62−77.

French, R. S., S. K. Hicks, M. R. Showalter, A. K. Antonsen, D. R. Packard, (2014), Analysis of clumps in Saturn's F-ring from Voyager and Cassini, Icarus, 241, 200−220.

French, R. S., M. R. Showalter, R. Sfair, C. A. Argüelles, M. Pajuelo, P. Becerra, M. M. Hedman, P. D. Nicholson, (2012), The brightening of Saturn's F-ring, Icarus, 219, 181−193.

French, R. G., E. A. Marouf, N. J. Rappaport, C. A. McGhee, (2010), Occultation Observations of Saturn's B-ring and Cassini Division, The Astronomical Journal, 139, 1649−1667.

Fuller, J., J. Luan, E. Quataert, (2016), Resonance locking as the source of rapid tidal migration in the Jupiter and Saturn moon systems, Monthly Notices of the Royal Astronomical Society, 458, 3867−3879.

Fuller, J., (2014), Saturn ring seismology: Evidence for stable stratification in the deep interior of Saturn, Icarus, 242, 283−296.

Goldreich, P. and S. Tremaine, (1982), The dynamics of planetary rings, Annual Review of Astronomy and Astrophysics, 20, 249−283.

Goldreich, P. and S. Tremaine, (1980), Disk-satellite interactions, The Astrophysical Journal, 241, 425−441.

Gurnett, D. A., W. S. Kurth, G. B. Hospodarsky, A. M. Persoon, L. Xin, W. Farrell, A. Lecacheux, J.-E. Wahlund, (2004), Cassini Observations of Radio and Plasma Wave Phenomena Associated with the Saturn's Rings, Bulletin of the American Astronomical Society, vol. 36, p. 1067.

Harbison, R. A., P. D. Nicholson, M. M. Hedman, (2013), The smallest particles in Saturn's A- and C-ings, Icarus, 226, 1225−1240.

Hedman, M. M., P. D. Nicholson, R. G. French, (2019), Kronoseismology IV: Six Previously Unidentified waves in Saturn's middle C-ring, The Astronomical Journal, vol. 157, no. 1, doi: 10.3847/1538-3881/aaf0a6.

Hedman, M. M. and P. D. Nicholson, (2019), Axisymmetric density waves in Saturn's rings, Monthly Notices of the Royal Astronomical Society, 485, 13−29, doi: 10.1093/mnras/stz301.

Hedman, M. M., (2019), Bright clumps in the D68 ringlet near the end of the Cassini Mission, Icarus, 323, 62−75, doi: 10.1016/j.icarus.2019.01.007.

Hedman, M. M., F. Postberg, D. P. Hamilton, S. Renner, H.-W. Hsu, (2018a), Dusty Rings, Chapter 12, In Planetary Rings, (eds.) M. Tiscareno, C. Murray, Cambridge University Press, pp. 308−337, doi: 10.1017/9781316286791.012.

Hedman, M. M., P. D. Nicholson, M. El Moutamid, (2018b), Evidence for changes in Saturn's interior from structures in its rings, 49th Lunar and Planetary Science Conference, Houston, TX, March 19−23, 2018, LPI Contribution no. 2083, id. 1288.

Hedman, M. M., M. El Moutamid, P. D. Nicholson, (2017), Drifting waves in Saturn's C-ring, evidence for changes in Saturn's interior, American Astronomical Society (AAS), Division on Dynamical Astronomy (DDA) meeting 48, id. 401.03.

Hedman, M. M. and P. D. Nicholson, (2016), The B-ring's surface mass density from hidden density waves: Less than meets the eye?, Icarus, 279, 109−124.

Hedman, M. M. and M. R. Showalter, (2016), A new pattern in Saturn's D-ring created in late 2011, Icarus, 279, 155−165.

Hedman, M. M., J. A. Burns, M. R. Showalter, (2015), Corrugations and eccentric spirals in Saturn's D-ring: New insights into what happened at Saturn in 1983, Icarus, 248, 137−161.

Hedman, M, M. and C, C. Stark, (2015), Saturn's G- and D-rings provide nearly complete measured scattering phase functions of nearby debris disks, The Astrophysical Journal, vol. 811, no. 1, doi: 10.1088/0004-637X/811/1/67.

Hedman, M. M., P. D. Nicholson, H. Salo, (2014a), Exploring overstabilities in Saturn's A-ring using two stellar occultations, The Astronomical Journal, 148, 15, doi: 10.1088/0004-6256/148/1/15.

Hedman, M. M., J. A. Burt, J. A. Burns, M. R. Showalter, (2014b), Non-circular features in Saturn’s D-ring: D68, Icarus, 233, 147−162.

Hedman, M. M. and P. D. Nicholson, (2014), More Kronoseismology with Saturn's rings, Monthly Notices of the Royal Astronomical Society, 444, 1369−1388.

Hedman, M. M., P. D. Nicholson, J. N. Cuzzi, R. N. Clark, G. Filacchione, F. Capaccioni, M. Ciarniello, (2013a), Connections between spectra and structure in Saturn’s main rings based on Cassini VIMS data, Icarus, 223, 105−130.

Hedman, M. M., J. A. Burns, D. P. Hamilton, M. R. Showalter, (2013b), Of horseshoes and heliotropes: Dynamics of dust in the Encke Gap, Icarus, 223, 252−276.

Hedman, M. M. and P. D. Nicholson, (2013), Kronoseismology: Using density waves in Saturn's C-ring to probe the planet's interior, The Astronomical Journal, vol. 146, no. 1, doi: 10.1088/0004-6256/146/1/12.

Hedman, M. M., J. A. Burns, D. P. Hamilton, M. R. Showalter, (2012), The three-dimensional structure of Saturn's E-ring, Icarus, 217, 322−338.

Hedman, M. M., J. A. Burns, P. C. Thomas, M. S. Tiscareno, M. W. Evans, (2011a), Physical properties of the small moon Aegaeon (Saturn LIII), European Planetary Science Congress-

Division for Planetary Sciences (EPSC-DPS) Joint Meeting, 02–07 October 2011, Nantes, France.

Hedman, M. M., P. D. Nicholson, M. R. Showalter, R. H. Brown, B. J. Buratti, R. N. Clark, K. Baines, C. Sotin, (2011b), The Christiansen Effect in Saturn's narrow dusty rings and the spectral identification of clumps in the F-ring, Icarus, 215, 695−711.

Hedman, M. M., J. A. Burns, M. W. Evans, M. S. Tiscareno, C. C. Porco, (2011c), Saturn's curiously corrugated C-ring , Science, 332, 708.

Hedman, M. M., J. A. Burt, J. A. Burns, M. S. Tiscareno, (2010a), The shape and dynamics of a heliotropic dusty ringlet in the Cassini Division, Icarus, 210, 284−297.

Hedman, M. M., P. D. Nicholson, K. H. Baines, B. J. Buratti, C. Sotin, R. N. Clark, R. H. Brown, R. G. French, E. A. Marouf, (2010b), The architecture of the Cassini Division, The Astronomical Journal, 139, 228−251.

Hedman, M. M., N. J. Cooper, C. D. Murray, K. Beurle, M. W. Evans, M. S. Tiscareno, J. A. Burns, (2010c), Aegaeon (Saturn LIII), a G-ring object, Icarus, 207, 433−447.

Hedman, M. M., J. A. Burns, M. S. Tiscareno, C. C. Porco, (2009a), Organizing some very tenuous things: Resonant structures in Saturn's faint rings, Icarus, 202, 260−279.

Hedman, M. M., C. D. Murray, N. J. Cooper, M. S. Tiscareno, K. Beurle, M. W. Evans, J. A. Burns, (2009b), Three tenuous rings/arcs for three tiny moons, Icarus, 199, 378−386.

Hedman, M. M., P. D. Nicholson, H. Salo, B. D. Wallis, B. J. Buratti, K. H. Baines, R. H. Brown, R. N. Clark, (2007a), Self-gravity wake structures in Saturn's A-ring revealed by Cassini VIMS, The Astronomical Journal, 133, 2624–2629.

Hedman, M. M., J. A. Burns, M. R. Showalter, C. C. Porco, P. D. Nicholson, A. S. Bosh, M. S. Tiscareno, et al., (2007b), Saturn's dynamic D-ring, Icarus, 188, 1, 89–107, doi: 10.1016/j.icarus.2006.11.017.

Hedman, M. M., J. A. Burns, M. S. Tiscareno, C. C. Porco, G. H. Jones, E. Roussos, N. Krupp, C. Paranicas, S. Kempf, (2007), The source of Saturn's G ring, Science, 317, no. 5838, 653–656.

Horanyi, M., J. A. Burns, M. M. Hedman, G. H. Jones, S. Kempf, (2009), Diffuse Rings, Chapter 16, In Saturn from Cassini-Huygens, (eds.) M. K. Dougherty, L. W. Esposito, S. M. Krimigis, Springer, Dordrecht, pp. 511–536, doi: 10.1007/978-1-4020-9217-6_16.

Hsu, H.-W., J. Schmidt, S. Kempf, F. Postberg, G. Moragas-Klostermeyer, M. Seiß, H. Hoffmann, et al., (2018), In situ collection of dust grains falling from Saturn's rings into its atmosphere, Science, 362, 6410, doi: 10.1126/science.aat3185.

Iess, L., B. Militzer, Y. Kaspi, P. Nicholson, D. Durante, P. Racioppa, A. Anabtawi, E. Galanti, W. Hubbard, M. J. Mariani, P. Tortora, S. Wahl, M. Zannoni, (2019), Measurement and implications of Saturn's gravity field and ring mass, Science, 364, Issue 6445, eaat2965, doi: 10.1126/science.aat2965.

Jacobson, R. A., J. Spitale, C. C. Porco, K. Beurle, N. J. Cooper, M. W. Evans, C. D. Murray, (2008), Revised orbits of Saturn's small inner satellites, The Astronomical Journal, 135, 261−263.

Jerousek, R. G., J. E. Colwell, L. W. Esposito, P. D. Nicholson, M. M. Hedman, (2016), Small particles and self-gravity wakes in Saturn's rings from UVIS and VIMS stellar occultations, Icarus, 279, 36−50.

Johnson, R. E., W.-L. Tseng, M. K. Elrod, A. M. Persoon, (2017), Nanograin density outside Saturn’s A-ring, The Astrophysical Journal, vol. 834, no. 1, doi: 10.3847/2041-8213/834/1/L6.

Kempf, S., N. Altobelli, J. N. Cuzzi, P. R. Estrada, R. Srama, (2019), Exogenous dust delivery into the Saturnian system constrains ring age to 10**8 years, in preparation.

Kollmann, P., E. Roussos, A. Kotova, L. Regoli, D. G. Mitchell, J. Carbary, G. Clark, N. Krupp, C. Paranicas, (2019), Saturn's innermost radiation belt throughout and inward of the D-ring, Geophysical Research Letters, 45, 10912−10920, doi: 10.1029/2018GL077954.

Lainey, V., R. A. Jacobson, R. Tajeddine, N. J. Cooper, C. Murray, V. Robert, G. Tobie, T. Guillot, S. Mathis, F. Remus, J. Desmars, J.-E. Arlot, J.-P. De Cuyper, V. Dehant, D. Pascu, W. Thuillot, C. Le Poncin-Lafitte, J.-P. Zahn, (2017), New constraints on Saturn's interior from Cassini astrometric data, Icarus, 281, 286−296.

Laughlin, G., V. Korchagin, F. C. Adams, (1997), Spiral mode saturation in self-gravitating disks, The Astrophysical Journal, 477, 410-423.

Leyrat, C., L. J. Spilker, N. Altobelli, S. Pilorz, C. Ferrari, (2008), Infrared observations of Saturn’s rings by Cassini CIRS: Phase angle and local time dependence, Planetary and Space Science, 56, 117–133.

Mankovich, C., M. S. Marley, J. J. Fortney, N. Movshovitz, (2019), Cassini ring seismology as a probe of Saturn’s interior I: Rigid rotation, The Astrophysical Journal, vol. 871, no. 1, doi: 10.3847/1538-4357/aaf798.

Marley, M. S., (2014), Saturn ring seismology: Looking beyond first order resonances, Icarus, 234, 194−199.

Marley, M. S. and C. C. Porco, (1993), Planetary acoustic mode seismology - Saturn's rings, Icarus, 106, 508.

Marley, M, S., (1990), Nonradial oscillations of Saturn: Implications for ring system structure, Ph.D. Thesis, University of Arizona, Tucson.

Marley, M. S., W. B. Hubbard, C. C. Porco, (1989), C-ring features and f-mode oscillations of Saturn, Bulletin of the American Astronomical Society (BAAS) 21, pp. 928.

Marley, M. S., W. B. Hubbard, C. C. Porco, (1987), Saturnian nonradial p-mode oscillations and C-ring structure, Bulletin of the American Astronomical Society (BAAS) 19, pp 889.

Marouf, E. A., R. G. French, N. J. Rappaport, K. Wong, C. McGhee, A. Anabtawi, (2011), Six centuries old spiral of vertical corrugations in Saturn's C-ring, American Geophysical Union (AGU), Fall Meeting, December 3−7, 2011, San Francisco, CA, abstract P12B-01.

McGhee, C. A., R. G. French, L. Dones, J. N. Cuzzi, H. J. Salo, R. Danos, (2005), HST observations of spokes in Saturn's B-ring, Icarus, 173, 508−521.

McGhee, C. A., P. D. Nicholson, R. G. French, K. J. Hall, (2001), HST observations of Saturnian satellites during the 1995 ring plane crossings, Icarus, 152, 282−315.

Meinke, B. K., L. W. Esposito, N. Albers, M. Sremčević, (2012), Classification of F-ring features observed in Cassini UVIS occultations, Icarus, 218, 545−554.

Miller, K. et al., (2019), in preparation.

Mitchell, C. J., C. C. Porco, J. W. Weiss, (2015), Tracking the Geysers of Enceladus into Saturn's E-ring, The Astronomical Journal, vol. 149, no. 5, doi: 10.1088/0004-6256/149/5/156.

Mitchell, C. J., C. C. Porco, H. L. Dones, J. N. Spitale, (2013), The behavior of spokes in Saturn's B-ring, Icarus, 225, 446−474.

Mitchell, C. J., M. Horányi, O. Havnes, C. C. Porco, (2006), Saturn's spokes: Lost and found, Science, 311, 1587−1589.

Mitchell, D. G., M. E. Perry, D. C. Hamilton, J. H. Westlake, P. Kollmann, H. T. Smith, J. F. Carbary, et al., (2018), Dust grains fall from Saturn's D-ring into its equatorial upper atmosphere, Science, 362, 6410, doi: 10.1126/science.aat2236.

Morishima, R., N. Turner, L. Spilker, (2017), Surface roughness of Saturn's rings and ring particles inferred from thermal phase curves, Icarus, 295, 74–88.

Morishima, R., L. Spilker, S. Brooks, E. Deau, S. Pilorz, (2016), Incomplete cooling down of Saturn's A-ring at solar equinox: Implication for seasonal thermal inertia and internal structure of ring particles, Icarus, 279, 2–19.

Morishima, R., L. Spilker, N. Truner, (2014), Azimuthal temperature modulations of Saturn's A-ring caused by self-gravity wakes, Icarus, 228, 247–259.

Morishima, R., S. G., Edgington, L. Spilker, (2012), Regolith grain sizes of Saturn's rings inferred from Cassini-CIRS far-infrared spectra, Icarus, 221, 888–899.

Morishima, R., L. Spilker, H. Salo, et al., (2010), A multilayer model for thermal infrared emission of Saturns rings II: Albedo, spins, and vertical mixing of ring particles inferred from Cassini CIRS, Icarus, 210, 330–345.

Murray, C. D. and R. C. French, (2018), The F-ring, Chapter 13, In Planetary Rings, (eds.) M. Tiscareno, C. Murray, Cambridge University Press, pp. 338−362, doi: 10.1017/9781316286791.013.

Murray, C. D., N. J. Cooper, G. A. Williams, N. O. Attree, J. S. Boyer, (2014), The discovery and dynamical evolution of an object at the outer edge of Saturn's A-ring, Icarus, 236, 165−168.

Murray, C. D., K. Beurle, N. J. Cooper, M. W. Evans, G. A. Williams, S. Charnoz, (2008), The determination of the structure of Saturn's F-ring by nearby moonlets, Nature, 453, 7196, 739−744.

Murray, C. D., C. Chavez, K. Beurle, N. Cooper, M. W. Evans, J. A. Burns, C. C. Porco, (2005), How Prometheus creates structure in Saturn's F-ring, Nature, 437, 1326−1329.

Nicholson, P. D., R. G. French, J. N. Spitale, (2018), Narrow rings, gaps and sharp edges, Chapter 11, In Planetary Rings, (eds.) M. Tiscareno and C. Murray, Cambridge University Press, pp. 276−307, doi: 10.1017/9781316286791.011.

Nicholson, P. D., R. G. French, M. M. Hedman, et al., (2014), Noncircular features in Saturn's rings I: The edge of the B-ring, Icarus, 227, 152−175.

Nicholson, P. D. and M. M. Hedman, (2010), Self-gravity wake parameters in Saturn's A- and B-rings, Icarus, 206, 410−423.

Nicholson, P. D., M. M. Hedman, R. N. Clark, M. R. Showalter, D. P. Cruikshank, J. N. Cuzzi, G. Filacchione, F. Capaccioni, P. Cerroni, G. B. Hansen, B. Sicardy, P. Drossart, R. H. Brown, B. J. Buratti, K. H. Baines, A. Coradini, (2008), A close look at Saturn's rings with Cassini VIMS, Icarus, 193, 182−212.

Nitter, T., O. Havnes, F. Melandsø, (1998), Levitation and dynamics of charged dust in the photoelectron sheath above surfaces in space, Journal of Geophysical Research, 103, 6605−6620.

Nixon, C. A., R. D. Lorenz, R. K. Achterberg, A. Buch, P. Coll, R. N. Clark, R. Courtin, A. Hayes, L. Iess, R. E. Johnson, R. M. C. Lopes, M. Mastrogiuseppe, K. Mandt, D. G. Mitchell, F. Raulin, A. M. Rymer, H. T. Smith, A. Solomonidou, C. Sotin, D. Strobel, et al., (2018), Titan's cold case files - Outstanding questions after Cassini-Huygens, Planetary and Space Science, 155, 50−72, doi: 10.1016/j.pss.2018.02.009.

O'Donoghue, J., L. Moore, J. Connerney, H. Melin, T. S. Stallard, S. Miller, K. H. Baines, (2019), Observations of the chemical and thermal response of 'ring rain' on Saturn's ionosphere Icarus, 322, 251−260, doi: 10.1016/j.icarus.2018.10.027.

Orton, G. S., K. H. Baines, D. Cruikshank, J. N. Cuzzi, S. M. Krimigis, S. Miller, E. Lellouch, (2009), Review of knowledge prior to the Cassini-Huygens Mission and concurrent research, Chapter 2, In Saturn from Cassini-Huygens, (eds.) M. K. Dougherty, L. W. Esposito, S. M. Krimigis, Springer, Dordrecht, pp. 9−54, doi: 10.1007/978-1-4020-9217-6_2.

Pan, M., H. Rein, E. Chiang, S. N. Evans, (2012), Stochastic flights of propellers, Monthly Notices of the Royal Astronomical Society, vol. 427, Issue 4, pp. 2788−2796, doi: 10.1111/j.1365-2966.2012.22023.x.

Pan, M. and E. Chiang, (2012), Care and feeding of frogs, The Astronomical Journal, vol. 143, no. 1, doi: 10.1088/0004-6256/143/1/9.

Pan, M. and E. Chiang, (2010), The propeller and the frog, The Astrophysical Journal, vol. 722, no. 2, doi: 10.1088/2041-8205/722/2/L178.

Perry, M. E., J. H. Waite Jr., D. G. Mitchell, K. E. Miller, T. E. Cravens, R. S. Perryman, L. Moore, et al., (2018), Material flux from the rings of Saturn into its atmosphere, Geophysical Research Letters, vol. 45, Issue 19, pp. 10,093−10,100, doi: 10.1029/2018GL078575.

Pilorz, S., N. Altobelli, J. Colwell, M. Showalter, (2015), Thermal transport in Saturn’s B-ring inferred from Cassini CIRS, Icarus, 254, 157–177.

Porco, C. C., J. W. Weiss, D. C. Richardson, L. Dones, T. Quinn, H. Throop, (2008), Simulations of the dynamical and light-scattering behavior of Saturn's rings and the derivation of ring particle and disk properties, The Astronomical Journal, vol. 136, no. 5, pp. 2172–2200, doi: 10.1088/0004-6256/136/5/2172.

Porco, C. C., P. C. Thomas, J. W. Weiss, D. C. Richardson, (2007) Saturn’s small inner satellites: Clues to their origins, Science, 318, 1602.

Porco, C. C., E. Baker, J. Barbara, K. Beurle, A. Brahic, J. A. Burns, S. Charnoz, N. Cooper, D. D. Dawson, A. D. Del Genio, T. Denk, L. Dones, U. Dyudina, M. W. Evans, B. Giese, K. Grazier, P. Helfenstein, A. P. Ingersoll, R. A. Jacobson, T. V. Johnson, A. McEwen, C. D. Murray, G. Neukum, W. M. Owen, J. Perry, T. Roatsch, J. Spitale, S. Squyres, P. Thomas, M. Tiscareno, E. Turtle, A. R. Vasavada, J. Veverka, R. Wagner, R. West, (2005), Cassini imaging science: Initial results on Saturn's rings and small satellites, Science, 307, 5713, 1226−1236.

Porco, C. C., R. A. West, A. McEwen, A. D. Del Genio, A. P. Ingersoll, P. Thomas, S. Squyres, L. Dones, C. D. Murray, T. V. Johnson, J.A. Burns, A. Brahic, G. Neukum, J. Veverka, J. M. Barbara, T. Denk, M. Evans, J. J. Ferrier, P. Geissler, P. Helfenstein, T. Roatsch, H. Throop, M. Tiscareno, A. R. Vasavada, (2003), Cassini imaging of Jupiter's atmosphere, satellites, and rings, Science, 299, no. 5612, 1541−1547.

Porco, C., G. E. Danielson, P. Goldreich, J. B. Holberg, A. L. Lane, (1984), Saturn's nonaxisymmetric ring edges at 1.95 R_s and 2.27 R_s, Icarus, 60, 17−28.

Poulet, F., D. P. Cruikshank, J. N. Cuzzi, T. L. Roush, R. G. French, (2003), Compositions of Saturn's rings A, B, and C from high resolution near-infrared spectroscopic observations, Astronomy & Astrophysics, 412, 305−316.

Poulet, F. and J. N. Cuzzi, (2002), The Composition of Saturn's Rings, Icarus, 160, 350−358.

Poulet, F. and B. Sicardy, (2001), Dynamical evolution of the Prometheus-Pandora system, Monthly Notices of the Royal Astronomical Society, vol. 322, pp 343−355.

Reffet, E., M. Verdier, C. Ferrari, (2015) Thickness of Saturn’s B-ring as derived from seasonal temperature variations measured by Cassini CIRS, Icarus, 254, 276–286.

Rein, H. and J. C. B. Papaloizou, (2010), Stochastic orbital migration of small bodies in Saturn's rings, Astronomy & Astrophysics, 524, A22, doi: 10.1051/0004-6361/201015177.

Robbins, S. J., G. R. Stewart, M. C. Lewis, J. E. Colwell, M. Sremcević, (2010), Estimating the masses of Saturn’s A- and B-rings from high-optical depth N-body simulations and stellar occultations, Icarus, 206, 431–445.

Rosen, P. A., G. L. Tyler, E. A. Marouf, J. J. Lissauer, (1991), Resonance structures in Saturn's rings probed by radio occultation II: Results and interpretation, Icarus, 93, 1, 25−44.

Roussos, E., P. Kollmann, N. Krupp, A. Kotova, L. Regoli, C. Paranicas, D. G. Mitchell, S. M. Krimigis, D. Hamilton, P. Brandt, J. Carbary, S. Christon, K. Dialynas, I. Dandouras, M. E. Hill, W. H. Ip, G. H. Jones, S. Livi, B. H. Mauk, B. Palmaerts, et al., (2019), A radiation belt of energetic protons located between Saturn and its rings, Science, vol. 362, Issue 6410, eaat1962, doi: 10.1126/science.aat1962.

Salo, H. and R. G. French, (2010), The opposition and tilt effects of Saturn’s rings from HST observations, Icarus, 210, 785−816.

Schaffer, L. and J. A. Burns, (1987), The dynamics of weakly charged dust - Motion through Jupiter's gravitational and magnetic fields, Journal of Geophysical Research, 92, 2264−2280.

Schmidt, J., J. E. Colwell, M. Lehmann, E. A. Marouf, H. Salo, F. Spahn, M. S. Tiscareno, (2016), On the linear damping relation for density waves in Saturn's rings, The Astrophysical Journal, vol. 824, no. 1, doi: 10.3847/0004-637X/824/1/33.

Schmidt, J. and M. S. Tiscareno, (2013), Ejecta clouds from meteoroid impacts on Saturn's rings: Constraints on the orbital elements and size of the projectiles, American Geophysical Union (AGU), Fall Meeting, abstract P23D-1820.

Schmidt, J., K. Ohtsuki, N. Rappaport, H. Salo, F. Spahn, (2009), Dynamics of Saturn's dense rings, In Saturn from Cassini-Huygens, Chapter 14, (eds.) M. K. Dougherty, L. W. Esposito, S. M. Krimigis, Springer, Dordrecht, pp. 413−458, doi: 10.1007/978-1-4020-9217-6_14.

Seiler, M., M. Sremčević, M. Seiß, H. Hoffmann, F. Spahn, (2017), A librational model for the propeller Blériot in the Saturnian ring system, The Astrophysical Journal, vol. 840, no. 2, doi: 10.3847/2041-8213/aa6d73.

Seiß, M., N. Albers, M. Sremčević, J. Schmidt, H. Salo, M. Seiler, H. Hoffmann, F. Spahn, (2018), Hydrodynamic simulations of moonlet-induced propellers in Saturn's rings: Application to Blériot, The Astronomical Journal, vol 157, no. 1, doi: 10.3847/1538-3881/aaed44.

Shimizu, M., (1982), Strong interaction between the ring system and the ionosphere of Saturn, Moon and the Planets, 22, pp. 521−522.

Showalter, M. R., (1991), Visual detection of 1981S13, Saturn's eighteenth satellite, and its role in the Encke gap, Nature, 351, 709−713.

Showalter, M. R. and P. D. Nicholson, (1990), Saturn's rings through a microscope - Particle size constraints from the Voyager PPS scan, Icarus, 87, 285−306.

Shu, F. H., (1984), Waves in planetary rings, Chapter 9, In Planetary Rings, (A85-34401 15-88), (eds.) R. Greenberg, A. Brahic, University of Arizona Press, pp. 513−561.

Smith, B. A., L. Soderblom, R. M. Batson, P. M. Bridges, J. L. Inge, H. Masursky, E. Shoemaker, R. F. Beebe, J. Boyce, G. Briggs, A. Bunker, S. A. Collins, C. Hansen, T. V. Johnson, J. L. Mitchell, R. J. Terrile, A. F. Cook, J. N. Cuzzi, J. B. Pollack, G. E. Danielson, A. P. Ingersoll, M. E. Davies, G. E. Hunt, D. Morrison, T. Owen, C. Sagan, J. Veverka, R. Strom, V. E. Suomi, (1982), A new look at the Saturn system - The Voyager 2 images, Science, 215, 504−537.

Spahn, F., H. Hoffmann, H. Rein, M. Seiß, M. Sremčević, M. Tiscareno, (2018), Moonlets in dense planetary rings, Chapter 8, In Planetary Ring Systems, (eds.) M. Tiscareno, C. Murray, Cambridge University Press, pp. 157−197, doi: 10.1017/9781316286791.008.

Spahn, F., H. Scholl, J.-M. Hertzsch, (1994), Structures in planetary rings caused by embedded moonlets, Icarus, 111, 514−535.

Spilker, L. J., C. Ferrari, N. Altobelli, S. Pilorz, R. Morishima, (2018), Thermal properties of rings and ring particles, Chapter 15, In Planetary Ring Systems, (eds.) M. Tiscareno, C. Murray, Cambridge University Press, pp. 399−433, doi: 10.1017/9781316286791.015.

Spilker, L. J., S. H. Pilorz, S. G. Edgington, et al., (2005), Cassini CIRS observations of a roll-off in Saturn ring spectra at submillimeter wavelengths, Earth Moon Planets, 96, 149–163.

Spitale, J. N., (2017), Saturn's misbegotten moonlets, American Astronomical Society (AAS), Division on Dynamical Astronomy (DDA), meeting 48, id. 400.04.

Spitale, J. N. and J. M. Hahn, (2016), The shape of Saturn's Huygens ringlet viewed by Cassini ISS, Icarus, 279, 141−154.

Spitale, J. N. and C. C. Porco, (2010), Detection of free unstable modes and massive bodies in Saturn's outer B-ring, The Astronomical Journal, vol. 140, no. 6, pp. 1747−1757, doi: 10.1088/0004-6256/140/6/1747.

Spitale, J. N. and C. C. Porco, (2009), Time variability in the outer edge of Saturn's A-ring revealed by Cassini imaging, The Astronomical Journal, vol. 138, no. 5, pp. 1520−1528, doi: 10.1088/0004-6256/138/5/1520.

Spitale, J. N., R. A. Jacobson, C. C. Porco, W. M. Owen Jr., (2006), The orbits of Saturn's small satellites derived from combined historic and cassini imaging observations, The Astronomical Journal, vol. 132, no. 2, pp. 692−710.

Srama, R., M. Burton, S. Helfert, S. Kempf, G. Moragas-Klostermeyer, A. Mocker, F. Postberg, M. Roy, E. Grün, (2005), Cassini Saturn dust measurements, Workshop on Dust in Planetary Systems, Kaua‘i, HI, Sep. 26–30, 2005, LPI Contribution No. 1280, p. 133, https://www.lpi.usra.edu/lpi/contribution_docs/LPI-001280.pdf.

Sremčević, M., G. R. Stewart, N. Albers, L. W. Esposito, (2014a), Propellers in Saturn's rings, European Planetary Science Congress (EPSC), Abstract, vol. 9, id. EPSC2014-633.

Sremčević, M., G. R. Stewart, N. Albers, L. W. Esposito, (2014b), Propellers in Saturn A- and B-rings, American Astronomical Society (AAS), Division for Planetary Sciences (/DPS) 46th Annual Meeting, November 9−14, 2014, Tucson, AZ, meeting 46, id. 417.01.

Sremčević, M., G. R. Stewart, N. Albers, L. W. Esposito, (2013), Propellers in Saturn's rings American Geophysical Union (AGU), Fall Meeting, December 9−13, 2013, San Francisco, CA, abstract P21E-07.

Sremčević, M., G. R. Stewart, N. Albers, L. W. Esposito, (2012), Discovery of B-ring propellers In Cassini UVIS and ISS, American Astronomical Society (AAS), Division for Planetary Sciences (DPS), October 14−19, 2012, Reno, NV, meeting 44, id. 513.06.

Sremčević, M., J. Schmidt, H. Salo, M. Seisz, F. Spahn, N. Albers, (2007), A belt of moonlets in Saturn's A-ring, Nature, 449, 1019−1021.

Sremčević, M., A. V. Krivov, H. Krüger, F. Spahn, (2005), Impact-generated dust clouds around planetary satellites: Model versus Galileo data, Planetary and Space Science, 53, 625−641.

Tajeddine, R., P. D. Nicholson, P.-Y. Longaretti, M. El Moutamid, J. A. Burns, (2017a), What Confines the Rings of Saturn?, The Astrophysical Journal Supplement Seried, vol. 232, no. 2, doi: 10.3847/1538-4365/aa8c09.

Tajeddine, R., P. D. Nicholson, M. S. Tiscareno, M. M. Hedman, J. A. Burns, M. El Moutamid, (2017b), Dynamical phenomena at the inner edge of the Keeler gap, Icarus, 289, 80−93.

Tajeddine, R., V. Lainey, N. J. Cooper, C. D. Murray, (2013), Cassini ISS astrometry of the Saturnian satellites: Tethys, Dione, Rhea, Iapetus, and Phoebe 2004−2012, Astronomy & Astrophysics, 575, A73, doi: 10.1051/0004-6361/201425605.

- - - - - - - - - - - - - -

Tamayo, D., S. R. Markham, M. M. Hedman, J. A. Burns, D. P. Hamilton, (2016), Radial profiles of the Phoebe ring: A vast debris disk around Saturn, Icarus, 275, 117−131.

Tamayo, D., M. M. Hedman, J. A. Burns, (2014), First observations of the Phoebe ring in optical light, Icarus, 233, pp. 1−8.

Thomson, F. S., E. A. Marouf, G. L. Tyler, R. G. French, N. J. Rappoport, (2007), Periodic microstructure in Saturn's rings A and B, Geophysical Research Letters, vol. 34, Issue 24, doi: 10.1029/2007GL032526|.

Throop, H. B., C. C. Porco, R. A. West, J. A. Burns, M. R. Showalter, P. D. Nicholson, (2004), The Jovian rings: New results derived from Cassini, Galileo, Voyager, and Earth-based observations, Icarus, 172, 59−77.

Tiscareno, M. S., P. D. Nicholson, J. N. Cuzzi, L. J. Spilker, C. D. Murray, M. M. Hedman, J. E. Colwell, J. A. Burns, S. M. Brooks, R. N. Clark, N. J. Cooper, E. Deau, C. Ferrari, G. Filacchione, R. G. Jerousek, S. Le Mouélic, R. Morishima, S. Pilorz, S. Rodriguez, M. R. Showalter, (2019a), Close-range remote sensing of Saturn's rings during Cassini's ring-grazing orbits and Grand Finale, Science, vol. 364, Issue 6445, eaau1017, doi: 10.1126/science.aau1017.

Tiscareno, M. S., P. D. Nicholson, J. N. Cuzzi, L. J. Spilker, C. D. Murray, M. M. Hedman, J. E. Colwell, et al., (2019b), Close-range remote sensing of Saturn’s rings during Cassini’s ring-grazing orbits and Grand Finale, Science, vol. 364, no. 6445, eaau1017, doi: 10.1126/science.aau1017.

Tiscareno, M. S. and B. E. Harris, (2018), Mapping spiral waves and other radial features in Saturn's rings, Icarus, 312, 157−171, doi: 10.1016/j.icarus.2018.04.023.

Tiscareno, M. S., M. M. Hedman, J. A. Burns, J. W. Weiss, C. C. Porco, (2013a), Probing the inner boundaries of Saturn's A-ring with the Iapetus -1:0 nodal bending wave, Icarus, 224, 201−208.

Tiscareno, M. S., C. J. Mitchell, C. D. Murray, D. Di Nino, M. M. Hedman, J. Schmidt, J. A. Burns, J. N. Cuzzi, C. C. Porco, K. Beurle, M. W. Evans, (2013b), Observations of ejecta clouds produced by impacts onto Saturn’s rings, Science, 340, Issue 6131, 460−464.

Tiscareno, M. S., (2013), A modified “Type I migration” model for propeller moons in Saturn's rings, Planetary and Space Science, 77, 36−142.

Tiscareno, M. S., J. A. Burns, M. Sremčević, K. Beurle, M. M. Hedman, N. J. Cooper, A. J. Milano, M. W. Evans, C. C. Porco, J. N. Spitale, J. W. Weiss, (2010), Physical characteristics and non-keplerian orbital motion of "propeller" moons embedded in Saturn's rings, The Astrophysical Journal, vol. 718, no. 2, doi: 10.1088/2041-8205/718/2/L92.

Tiscareno, M. S., J. A. Burns, M. M. Hedman, C. C. Porco, (2008), The population of propellers in Saturn's A-ring, The Astronomical Journal, vol. 135, no. 3, pp. 1083−1091, doi: 10.1088/0004-6256/135/3/1083.

Tiscareno, M. S., J. A. Burns, P. D. Nicholson, M. M. Hedman, C. C. Porco, (2007), Cassini imaging of Saturn's rings II: A wavelet technique for analysis of density waves and other radial structure in the rings, Icarus, 189, 14−34.

Tiscareno, M. S., J. A. Burns, M. M. Hedman, C. C. Porco, J. W. Weiss, L. Dones, D. C. Richardson, C. D. Murray, (2006), 100-metre-diameter moonlets in Saturn's A-ring from observations of ‘propeller’ structures, Nature, 440, Issue 7084, 648−650.

Tseng, W.-L., R. E. Johnson, M. K. Elrod, (2013), Modeling the seasonal variability of the plasma environment in Saturn's magnetosphere between main rings and Mimas, Planetary and Space Science, 77, 126−135.

Tseng, W.-L., W.-H. Ip, R. E. Johnson, T. A. Cassidy, M. K. Elrod, (2010), The structure and time variability of the ring atmosphere and ionosphere, Icarus, 206, 382−389.

Vahidinia, S., J. N. Cuzzi, M. Hedman, B. Draine, R. N. Clark, T. Roush, G. Filacchione, P. D. Nicholson, R. H. Brown, B. Buratti, C. Sotin, (2011), Saturn's F-ring grains: Aggregates made of crystalline water ice, Icarus, 215, Issue 2, pp. 682−694.

Van Allen, J. A., (1982), Findings on rings and inner satellites of Saturn of Pioneer 11, Icarus, 51, 509−527.

Verbiscer, A. J., M. F. Skrutskie, D. P. Hamilton, (2009), Saturn's largest ring, Nature, 461, 1098−1100.

Waite Jr., J. H., R. Perryman, M. Perry, K. Miller, J. Bell, T. E. Cravens, C. R. Glein, J. Grimes, M. Hedman, J. Cuzzi, T. Brockwell, B. Teolis, L. Moore, D. Mitchell, A. Persoon, W. S. Kurth, J.-E. Wahlund, M. Morooka, L. Hadid, S. Chocron, J. Walker, A. Nagy, R. Yelle, S. Ledvina, R. Johnson, W. Tseng, O. J. Tucker, W.-H. Ip, (2018), Chemical interactions between Saturn’s atmosphere and its rings, Science, vol. 362, Issue 6410, eaat2382, doi: 10.1126/science.aat2382.

Weiss, J. W., C. C. Porco, M. S. Tiscareno, (2009), Ring edge waves and the masses of nearby satellites, The Astronomical Journal, vol. 138, no. 1, pp. 272−286, doi: 10.1088/0004-6256/138/1/272.

Ye, S. Y., D. A. Gurnett, W. S. Kurth, (2016), In-situ measurements of Saturn's dusty rings based on dust impact signals detected by Cassini RPWS, Icarus, 279, 51−61.

Zebker, H. A., E. A. Marouf, G. L. Tyler, (1985), Saturn's rings - Particle size distributions for thin layer model, Icarus, 64, 531−548.

Zhang, Z., A. G. Hayes, I. de Pater, D. E. Dunn, M. A. Janssen, P. D. Nicholson, J. N. Cuzzi, B. J. Butler, R. J. Sault, S. Chatterjee, (2019), VLA multi-wavelength microwave observations of Saturn's C- and B-rings, Icarus, 317, 518−548, doi: 10.1016/j.icarus.2018.08.014.

Zhang, Z., A. G. Hayes, M. A. Janssen, P. D. Nicholson, J. N. Cuzzi, I. de Pater, D. E. Dunn, P. R. Estrada, M. M. Hedman, (2017a), Cassini microwave observations provide clues to the origin of Saturn's C-ring, Icarus, 281, 297−321.

Zhang, Z., A. G. Hayes, M. A. Janssen, P. D. Nicholson, J. N. Cuzzi, I. de Pater, D. E. Dunn, (2017b), Exposure age of Saturn's A- and B-rings, and the Cassini Division as suggested by their non-icy material content, Icarus, 294, 14−42.

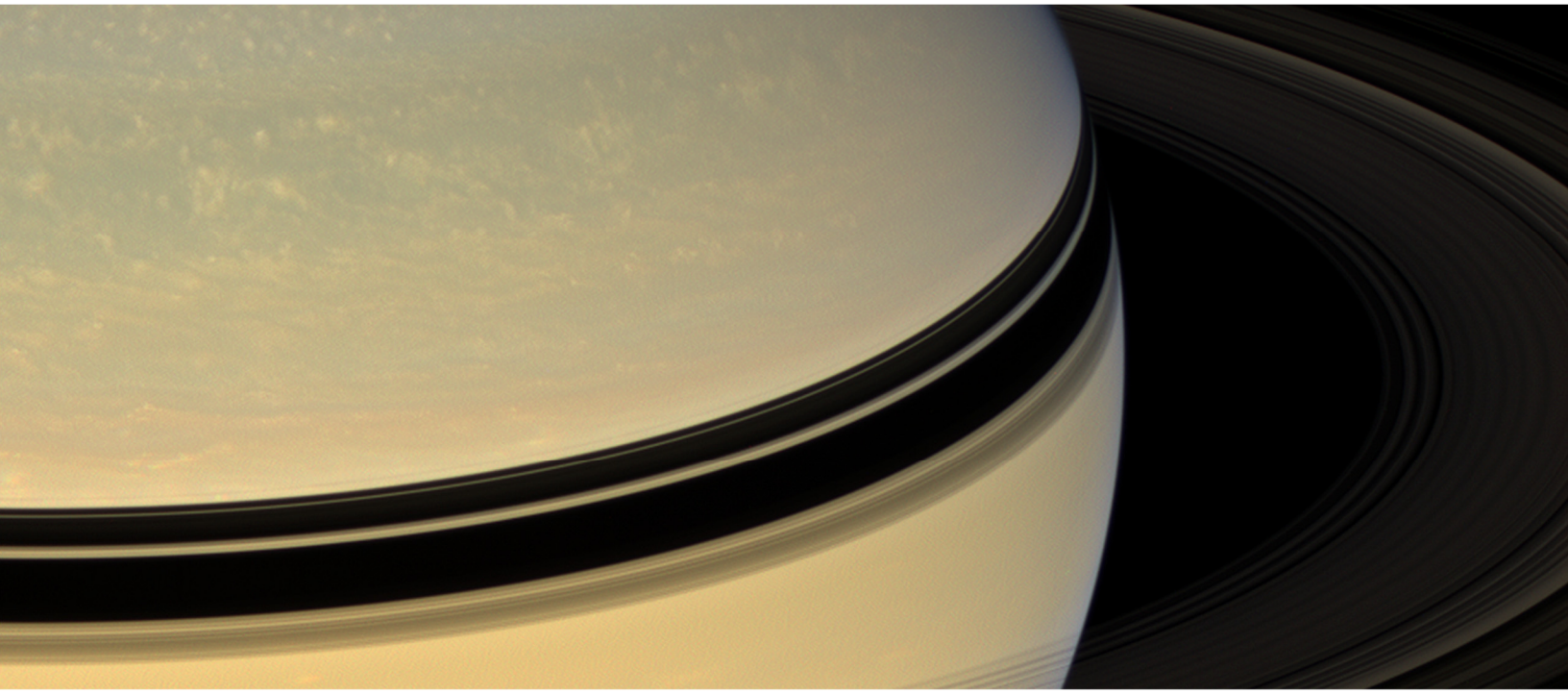

SATURN

Before Cassini, scientists viewed Saturn's unique features only from Earth and from a few spacecraft flybys. During more than a decade orbiting the gas giant, Cassini studied the composition and temperature of Saturn's upper atmosphere as the seasons changed there. Cassini also provided up-close observations of Saturn's exotic storms and jet streams, and heard Saturn's lightning, which cannot be detected from Earth. The Grand Finale orbits provided valuable data for understanding Saturn's interior structure and magnetic dynamo, in addition to providing insight into material falling into the atmosphere from parts of the rings.

Cassini's Saturn science objectives were overseen by the Saturn Working Group (SWG). This group consisted of the scientists on the mission interested in studying the planet itself and phenomena which influenced it. The Saturn Atmospheric Modeling Working Group (SAMWG) was formed to specifically characterize Saturn's uppermost atmosphere (thermosphere) and its variation with time, define the shape of Saturn's 100 mbar and 1 bar pressure levels, and determine when the Saturn safely eclipsed Cassini from the Sun. Its membership consisted of experts in studying Saturn's upper atmosphere and members of the engineering team.

CONTENTS

Figures

Tables

EXECUTIVE SUMMARY

The Executive Summary is organized into the 10 major discoveries that Cassini made about the planets during its 13 years at Saturn and its months-long flyby of Jupiter.

The planets themselves were an important scientific objective of the Cassini mission, and they are the focus of this Saturn Discipline Working Group (DWG) science results. The Executive Summary is organized into the 10 major discoveries that Cassini made about the planets during its 13 years at Saturn and its months-long flyby of Jupiter. Measurements for the future, after Cassini, are given at the end. The main parts are organized by objectives listed in the Cassini Announcement of Opportunity (AO) and the Traceability Matrix (TM) of the Cassini Solstice Mission (CSM). The bold items in parenthesis that appear with the 10 major discoveries in the Executive Summary refer to the sub-sections in the Saturn DWG Science Results and Saturn DWG Non-Saturn Science Results sections. Figures are found in these sub-sections.

1. **Great Storm on Saturn – (Storms (SN1b, SN2a))**

    a. **Storm Evolution.** Saturn's weather is generally quieter and blander than Jupiter's and Earth's, but every few decades a latitude band erupts with turbulent clouds, high winds, and lightning. Typically the disturbed region spreads eastward or westward around the planet and fades after a few months of violent activity. Five such eruptions, sometimes called great white spots, were observed from Earth during the period 1876–1990. Cassini was fortunate to be in orbit, routinely taking images and searching for radio signals from Saturn lightning, when the great storm of 2010–2011 began. The storm appeared on December 5, 2010 as a small dot in an Imaging Science Subsystem (ISS) image and a sudden start of lightning activity recorded by the Radio and Plasma Wave Science (RPWS) instrument. Within a few days, amateur astronomers were tracking its progress from Earth, and within a month a new set of observing commands had been uploaded onto the Cassini spacecraft to bring its powerful instruments to bear on the new target. Figure SATURN-7 shows an ISS image of the storm on February 25, 2011, after the storm's head, trailing westward, had wrapped around the planet and caught the tail. The giant storm of 2010–2011 is extensively reviewed by Sanchez-Lavega et al. [2018].

    b. **Lightning.** For months or years at a time, Saturn does not emit the broad-band radio signals called atmospherics (sferics) that are produced by lightning. In contrast, the great storm of 2010–2011 was emitting constantly, often faster than the RPWS counting rate of ten per second. The ISS is only ON when the shutter is open, for about 0.1 second depending on the filter, but sometimes it detects lightning. Figure SATURN-8 shows a color image, a superposition of three ISS

images in different filters taken in rapid succession. The blue filter happened to capture a lightning flash, which shows up as a blue dot near the right edge of the image. Further to the right, a second color image taken 30 minutes later at the same location failed to capture a lightning flash. The size of the observed flash is comparable to the depth from the tops of the clouds down to the light source, which is probably in the water cloud. This data could give an estimate of the amount of water on Saturn, and the analysis is ongoing.

c. **Ammonia Precipitation.** The great storm affected all levels in the atmosphere. Figure SATURN-9 [Janssen et al. 2013] shows images from 2009, 2010, and 2011 taken by the Cassini Titan Radar Mapper (RADAR) with its transmitter turned OFF. Operated this way, the instrument sees thermal radiation coming up through dry spots, which are gaps in the otherwise uniform distribution of ammonia vapor. The gaps show up as bright areas, and on March 20, 2011 the great storm, at 30–40° planetocentric latitude, shows up as a low-ammonia band [Sromovsky et al. 2016]. This tells us something about the updrafts and downdrafts, since the vapor falls out when the air is rising. The first models of this process have been published [Li and Ingersoll 2015], and the research is ongoing.

d. **Upward-Propagating Waves.** The great storm sent waves propagating up into the stratosphere, where they break and deposit their energy. The heating is strong enough to cause chemical changes of the stratospheric gases, which are still somewhat of a mystery. Figure SATURN-10 [Fletcher et al. 2011] shows an Earth-based image, left, and two infrared images taken by Cassini Composite Infrared Spectrometer (CIRS) on January 19, 2011. The center image records temperature in the upper troposphere, at the 200–500 mbar level, and the right image shows temperatures at the 1–10 mbar level. The stratospheric beacon stands out in the right image.

e. **Temperatures, Molecular Hydrogen, and Heat Budget.** Figure SATURN-11 [Achterberg et al. 2014], from Cassini CIRS, shows evidence of air being dredged up from below. The top two panels show tropospheric temperature before and after the storm, and the band from 30–40° planetographic has warmed by several degrees. The bottom two panels show the two chemical states (nuclear spins parallel and nuclear spins anti-parallel) of molecular hydrogen H_2 before and after the great storm. The 30–40° band shows a low para fraction, which indicates that the air has risen from below cloud base. Figure SATURN-4 [Li et al. 2015] shows the thermal emission of the planet, in units of W m^{-2}, also from Cassini CIRS. Comparing the years before and after 2011, it is clear that the storm increased the thermal emission by 5–10% in the 30–40° latitude band, and that the anomaly persisted for several years. These details are important for understanding why Saturn erupts and are a necessary test of atmospheric models.

2. Saturn's Rotation and Interior – (Saturn's Rotation Rate (SN1a))

a. **Rotation.** The giant planets reveal their rotation in several ways—from cloud motions in the atmosphere, from the wobble of the internally-driven magnetic field, from radio waves, from the equatorial bulge, and for Saturn at least, from internal oscillations revealed in slight eccentricities in the orbits of ring particles. Cloud motions have two problems. Different latitudes give different periods ranging from about 10 h 12 m to about 10 h 40 m, and the atmosphere can slide relative to deeper levels. Saturn's internally-driven magnetic field is aligned within 0.06° of the rotation axis [Cao et al. 2011], so it does not wobble. As a random event, such alignment is highly improbable, given that the other giant planets are misaligned by tens of degrees and the probability goes as the area on the surface of the sphere rather than the angle from the pole. Voyager detected radio waves with a period of 10 h 39 m 22 s, but the radio periods turned out to vary over the years in ways that strongly suggested they originated in the upper atmosphere and magnetosphere.

b. **Gravity.** The other methods, involving gravity, are being developed and tested. Rotation causes the planet to bulge at the equator, but to interpret the shape it is necessary to know the equation of state to high accuracy. The shape of the atmosphere just gives the rotation of the atmosphere. The axisymmetric components of the gravity field indicate that the zonal winds extend 9000 km down into the fluid interior [Iess et al. 2019; Galanti et al. 2019]. The depth is greater than that for Jupiter, and that is consistent with the greater depth on Saturn at which magnetic drag reduces the winds to zero. The method involves tracking the orbit of the spacecraft using the Doppler shift of the craft's radio signal, which is observed to high precision.

c. **Ring seismology.** The orbits of Saturn's ring particles are exquisitely sensitive to non-axisymmetric (tesseral) harmonics of the gravity field. These could be due to normal mode oscillations in Saturn's interior or masses floating in the interior and rotating with it. Figure SATURN-15 [Hedman and Nicholson 2014] shows observed periods that are close to the atmospheric periods and are therefore likely be the signature of floating masses. The observed periods are just as diverse as those derived from cloud motions, which may indicate floating masses moving at different speeds. The frequencies of the normal modes depend on the planet's rotation. The implied rotation period turns out to be intermediate between the shortest and longest atmospheric periods defined from cloud motions at different latitudes [Mankovich et al. 2019]. Although the possibility of using the rings as a seismometer was predicted before Cassini, there was no guarantee that the irregularities inside the planet would be large enough.

3. **Energy for the Zonal Jet Streams – (Atmospheric dynamical processes (S_AO2))**

    a. **Mean Zonal Winds.** The eastward-flowing and westward-flowing jet streams are an iconic feature of giant planet atmospheres. They are remarkably fast and remarkably steady in time by terrestrial standards. Figure SATURN-18 [Porco et al. 2003] shows the zonal jet streams for Jupiter. The black curve is from Cassini ISS data in late 2000, and the red curve is from Voyager data in mid-1979. The jets are remarkably steady over this interval of 21 years. Figure SATURN-5 [Garcia-Melendo et al. 2011b] shows Saturn data from Cassini ISS. The black curve represents data from the 350 to 700 mbar levels, and the red curve represents data from 100 to 200 mbar. The differences are small except for a latitude band within ±15° of the equator. This could be part of a 15-year periodicity that resembles the quasi-biennial oscillation in the stratosphere of Earth. We have more to say about that oscillation in the section entitled Saturn DWG Non-Saturn Science Results.

    b. **Eddy Input.** Figure SATURN-13 [Del Genio and Barbara 2012] and Figure SATURN-19 [Salyk et al. 2006] show how eddies are pumping energy and momentum into the jets for Saturn and Jupiter, respectively. Both studies use Cassini ISS data. An eddy in this context is a departure of wind from the zonal mean. The eddy eastward wind u′ is the residual after the mean zonal wind has been subtracted off, and similarly for the eddy northward wind v′. The zonal means of u′ and v′ are zero by definition, but the mean of their product, $\overline{u'v'}$, may be non-zero. Multiplied by the density, this quantity is the northward flux of eastward momentum. If this quantity has the same sign as $\partial\bar{u}/\partial y$, which is the increase of the mean eastward wind with latitude, then the eddies are putting energy into the jets and not the reverse. Figures SATURN-13 and SATURN-19 show that this is the case. The data are less noisy for Jupiter because Jupiter has more small-scale features with which to measure winds from a series of images. This type of eddy mean-flow interaction is an important topic in fluid dynamics and atmospheric science, and the giant planets provide the best examples.

4. **Elemental Abundances and Chemical Tracers – (Composition and chemistry (SN1c); Saturn Formation and Evolution (S_AO5))**

    a. **Helium.** For the Sun, the abundances of major elements relative to hydrogen are known to better than ±10%. Jupiter and Saturn come close to solar composition, but the actual ratios range from less than 1 to at least 10. Each element tells its own story of how and when it was incorporated into the giant planet when it was forming and how the atmospheric ratio has evolved since then. Helium, being the second most abundant element after hydrogen, has special relevance. Direct detection by mass spectrometry when the spacecraft is dipping into the

exosphere on its final proximal orbits is possible, but the determination of the planet's He/H ratio involves extrapolating down to the well-mixed troposphere and is difficult. Remote sensing is difficult because helium has no spectral signature at visible or infrared wavelengths, so one has to use its effect on the molecular mass. Traditionally this is done by finding temperature as a function of pressure from infrared radiometry and then finding density as a function of altitude by preforming an occultation. Hydrostatic equilibrium then gives density as a function of pressure. With T, P, and density, one can solve for the molecular mass. Another approach uses the difference between He and H_2 in their effects on the infrared spectrum of hydrogen itself. The most recent estimate [Koskinen and Guerlet 2018] uses Cassini UVIS for the occultations and CIRS for temperature versus pressure. They get a helium mass fraction Y of 0.16−0.22, which is about 70% of the protosolar mass fraction of 0.27, implying that a certain amount of settling has occurred in Saturn's interior.

b. **Carbon.** The C/H ratio is perhaps the most accurately known ratio of all elements beyond helium. This is because its molecular form, methane, does not condense at Saturn temperatures and is not readily destroyed in chemical reactions. Cassini CIRS probes the far-infrared rotational lines of the molecule and has determined a volume mixing ratio of $(4.7 \pm 0.2) \times 10^{-3}$, corresponding to a C/H enrichment relative to solar of 10.4. This is more than a factor of 2 greater than that for Jupiter and points to a fundamental difference between the gas giants' origin and evolution. The O/H ratio is largely unknown because its molecular form, water, condenses out at the 15–20 bar level, which is well below the levels reachable by remote sensing. CO and H_2O, which are observed in trace amounts in the upper atmosphere, are probably supplied by comets. Without direct observation, the best one can do is to assume that the enrichment factor relative to solar of O/H is the same as that of C/H.

c. **Phosphorus, Arsenic, and Nitrogen.** Although phosphine, PH_3, is also enriched relative to solar by a factor of ~10, its abundance is highly variable and is often used as tracer of vertical motion. The standard view is that PH_3 is brought up from below on updrafts and is destroyed by sunlight in the upper troposphere and stratosphere. Arsine (AsH_3) is supposed to work the same way, and so is ammonia, although it is removed from the upper troposphere by precipitation rather than destruction by sunlight. However, Figure SATURN-2, from Cassini Visual and Infrared Mapping Spectrometer (VIMS) [Fletcher et al. 2011], does not tell a consistent story according to this picture. NH_3 shows a high mole fraction at the equator, consistent with upwelling there and downwelling on either side at 10–12° latitude, but PH_3 and AsH_3 show low abundances at the equator. Low para fraction, discussed in connection with Figure SATURN-11, also implies upwelling at the equator—an observation dating back to Voyager. On the other hand, the Cassini CIRS data [Fletcher et al. 2009a] show a maximum of PH_3 at the equator, which seems to contradict the Cassini VIMS data (Figure SATURN-

2). All the data are good, and the resolution may be that there are two circulations, one on top of the other, with rising motion at high altitude and sinking motion deeper down. This is compatible with all the data, since VIMS is sensitive to deeper levels, 1.3 to 4 bars, where the equatorial downwelling might occur, and CIRS is sensitive above the 1.3 bar level, where the equatorial upwelling might occur. These complications are one of the surprises of the Cassini mission, and tell us important things about how atmospheres work. Upwelling and downwelling are what drive atmospheric circulations and give energy to the winds.

5. **Hexagon and Polar Vortex – (Storms (SN1b, SN2a); Atmospheric dynamical processes (S_AO2))**

a. **Discovery.** Saturn has five or six eastward jets in each hemisphere, but only the one at 75° meanders in latitude, forming a six-lobed pattern. Small clouds within the jet move eastward along the hexagonal pattern at 100 m s^{-1}, but the pattern stays stationary in a reference frame close to Saturn's radio emissions. There is no consensus on why only this jet meanders, although there are numerical models and laboratory experiments that can simulate the phenomenon, given the right boundary and initial conditions. The hexagon was discovered in images taken by the two Voyager spacecraft as they flew past Saturn in 1980 and 1981. It was re-discovered in infrared VIMS images in 2006. ISS images had to wait until the start of spring in the northern hemisphere when the North Pole was in full sunlight. Figure SATURN-12 shows a false color image taken on November 27, 2012. The MT3 and MT2 images, which are dark where the light is passing through methane gas, are projected as blue and green, respectively. The CB2 image, which is not sensitive to methane absorption, is projected as red. The color balance is chosen to make the planet's atmosphere look realistic. The rings look bright blue because there is no methane gas between the rings and the spacecraft.

The hexagon was discovered in images taken by the two Voyager spacecraft as they flew past Saturn in 1980 and 1981.

b. **Polar Cyclone.** The red spot in the center of Figure SATURN-12 extends from the pole to a latitude of 88–89°. It looks red in the false-color image because the clouds are deep and methane gas absorbs the sunlight before it can reflect off the clouds and reach the spacecraft. There is a similar zone in the south, and there the clouds just outside the zone appear to cast shadows, either because they are 50–70 km higher than the clouds inside [Dyudina et al. 2009] or because there is a step-wise poleward decrease in optical depth of the overlying haze [Sromovsky et al. 2019]. The outer ring of clouds circulates counterclockwise around the pole at a speed of 100 m s^{-1}. In these respects the structure is like a

tropical cyclone on Earth—a hurricane—but it is not in the tropics and it is not drawing energy from an ocean underneath. It is known that cyclonic vortices drift poleward, but how they originate and why there is only one on Saturn is still being investigated.

6. **Equatorial Oscillation – (Saturn's Winds (SC1b))**

   a. **Quasi-biennial oscillation.** On Earth, waves generated by storms in the troposphere propagate into the stratosphere and break, depositing energy and momentum there. A symmetry-breaking instability develops in which the eastward waves break preferentially at altitudes where the mean zonal wind is eastward, and similarly for the westward waves and the westward wind. The result is that the mean zonal wind forms an oscillation with altitude that propagates downward with time. The amplitude of the waves sets the period, and on Earth it averages out to 22 months and is known as the quasi-biennial oscillation (QBO). The period of the oscillation on Jupiter is ~4 years, and on Saturn it is ~15 years. Figure SATURN-6 [Fouchet et al. 2008], from Cassini CIRS, documents the oscillation in greater detail, as reflected both in the temperature field, upper panel, and its associated zonal velocity, lower panel. The wave generation mechanism is still uncertain, but presumably the longer period as one moves out in the solar system is due to the lower energy flux available to drive the waves.

7. **Upper Atmosphere – (Seasonal Variations (SC1a); Upper atmosphere (SC2a); Aurora (SC2a); (SN1c))**

   a. **Stratosphere.** Upwelling and downwelling in the stratosphere are detected by chemical tracers as in the troposphere. For both Saturn and Jupiter, the best tracers are probably ethane and acetylene, C_2H_6 and C_2H_2, respectively. Both gases are formed from photodissociation of methane at mbar levels and are destroyed in the troposphere where they revert back to methane. Thus an enhancement at the 200 mbar level is indicative of downwelling.
   Figure SATURN-20 [Nixon et al. 2007] shows the picture for Jupiter, as derived from Cassini CIRS data. C_2H_2 has a shorter lifetime once it is formed than C_2H_6 does, so it decays on the downdrafts faster than C_2H_6. Thus the lower panel of Figure SATURN-20 shows downdrafts at the pole and updrafts at the equator. The upper panel shows that the time constant of this circulation is longer than the lifetime of the C_2H_2 molecule, because it has decayed before reaching the 200 mbar level.

   b. **Thermosphere.** An ongoing mystery is why the thermosphere is so warm outside the polar auroral zones. The problem is illustrated in Figure SATURN-16 [Koskinen et al. 2015], which compares Cassini Ultraviolet Imaging Spectrograph (UVIS) observations with Voyager observations and with a 3-D general

circulation model. The model result is represented by the smooth dot-dashed line, and it is significantly low (colder) equatorward of ±60° in both hemispheres. The problem is that the air from the polar regions, heated by auroral currents, cools before it reaches the lower latitudes. One proposal is that drag forces due to atmospheric gravity waves, which are often overlooked in the models, could speed up the pole-to-equator circulation [Müeller-Wodarg et al. 2019]. The Cassini data confirm that the observations are good and not restricted to the Voyager era.

8. **Seasonal Change, Energy Budget and Temperatures – (Temperature and clouds (S_AO1); Saturn Formation and Evolution (S_AO5))**

   a. **Radiation.** Seasonal change begins with the changing distribution of sunlight falling on the two hemispheres. The rings amplify this effect by putting the winter hemisphere in shadow, but the effect on temperatures is moderated by the large heat capacity of Saturn's deep atmosphere and the small radiative fluxes far out in the solar system. Figure SATURN-4 [Li et al. 2015], which we have already discussed in connection with the great storm, also shows the reduction of emitted long-wave radiation in the south and increase in the north as the latter changed from early winter in 2004 to late spring in 2013.These changes in the emitted radiation reflect changes in temperature at the emitting levels, but they also could reflect changes in gaseous and cloud opacity.

   b. **Temperature Change.** The emitted radiation of Figure SATURN-2 includes the radiation at all wavelengths. Radiation at specific wavelengths allows one to probe to different levels and deduce temperature as a function of latitude and altitude. Figure SATURN-3 [Fletcher et al. 2010] shows this for years 2005 and 2008, also using CIRS data. The south is warmer than the north in both years, although most of the hemispheric contrast and most of the difference between 2005 and 2008 is confined to high altitudes. There the sunlight is strongest and the atmospheric density is low, so the seasonal effect on temperature is greatest.

   c. **Chemical Change.** The other seasonal effect is on the chemistry of the atmosphere. Figure SATURN-1 was taken by the ISS in 2004 as Cassini was approaching Saturn. It was summer in the south, and the sunlight was driving a rich hydrocarbon chemistry, resulting in an orange haze of small particles. The north was mostly shielded from sunlight, and the skies were blue, as shown by the sliver of atmosphere visible above the ring. Toward the end of the mission, the colors reversed. The rate of the shift reveals much about the photochemical processes that produce the haze.

9. **Lightning – (Saturn Lightning Sources and Morphology (S_AO6, SN2a))**

    a. **Quiet Times.** We have already mentioned that the Cassini RPWS recorded lightning strikes from the 2010–2011 great storm at rates exceeding 10 s^{-1}. But normally Saturn is a quiet place, with no lightning storms at all, which contrasts starkly with Earth's average of 2000 storms per day. Figure SATURN-14 [Dyudina et al. 2007] shows the Saturn electrostatic discharge counts, SED's, which are roughly equivalent to lightning strikes, over a 2-year period starting in 2004. The SED's are detected by the RPWS instrument, which is ON continuously. The lower panel shows ISS coverage of latitudes −34° to −36°, where all the storms were occurring, and it is clear that no storms were present when the RPWS was detecting nothing.

10. **Jupiter Colors and Movies – (Jupiter atmospheric dynamics (J_AO1))**

    a. **Chromophores.** The agent that colors the particles in Jupiter's clouds has been a mystery for decades. The principal cloud-forming gases are NH_3, H_2S, and H_2O, but they form particles that are white. Disequilibrium species involving phosphorus, sulfur, and/or hydrocarbons have been suggested, and it is difficult to choose one candidate over another. A new, Cassini-era candidate, a red (blue-absorbing) chromophore made from ammonia reacting with acetylene has been proposed [Carlson et al. 2016; Baines et al. 2019]. It seems to account for almost all of the color variation on the planet [Sromovsky et al. 2017]. Figure SATURN-17 shows the highest-resolution, full-disk color mosaic of Jupiter ever taken.

    b. **Movies.** With its powerful imaging system, Cassini took images continuously during its 70-day approach to Jupiter at the end of year 2000. A 70-day movie shows the clouds in motion at all longitudes and latitudes up to within ~10 degrees of the poles. The movie can be seen at these site(s): https://photojournal.jpl.nasa.gov/catalog/PIA03452; https://photojournal.jpl.nasa.gov/catalog/PIA03453; https://photojournal.jpl.nasa.gov/catalog/PIA03454. It is a modern sequel to the successful Voyager approach movie and an important research tool for measuring winds and the evolution of cloud features.

11. **For the Future, the Next Generation**

    a. **Water.** Measure the global water abundance and determine its role in bringing heat to the surface. Determine the role of moist convection in maintaining the large-scale motions. A Saturn probe to the base of the water cloud is a challenging but possible objective. Juno-type microwave remote sensing, in addition, is potentially valuable.

b. **Ammonia.** Determine the global ammonia abundance, and map its distribution with depth over the planet. Currently available data are good down to only about 3 bars, which do not necessarily represent the deep well mixed abundance of ammonia. A Saturn probe to 10 bars could make this measurement, and microwave remote sensing is potentially valuable.

c. **Noble Gases.** Determine Saturn's noble gas abundances including helium, and their isotopic ratios, as done for Jupiter by the Galileo probe. A Saturn probe could measure noble gases to exquisite precision.

d. **Interior Motions.** Determine Saturn's rotation period if such a number exists, or determine the spread of periods if differential motions persist into the interior. Document the time dependence of motions in Saturn's interior.

e. **Weather Layer.** Determine the vertical profiles of temperature, winds, clouds, condensable gases, longwave and shortwave radiation, and turbulence levels. A cloud-resolving model like those used in tropical meteorology, but tailored to the giant planets, is both timely and valuable. Again, a Saturn probe is needed.

f. **Interior.** Using the power of ring seismometry and gravity sounding, improve the understanding of Saturn's internal equation of state, mass distribution, composition, and temperature distribution. Develop a fully coupled interior/weather-layer model as done for Earth's oceans and atmosphere.

SATURN DWG SUMMARY

Cassini's Saturn science objectives were overseen by the Saturn DWG. This group consisted of the scientists on the mission interested in studying the planet itself and phenomena which influenced it. Leadership consisted of Interdisciplinary Scientists (IDS). The Saturn DWG would meet roughly three times a year at the Project Science Group (PSG) meetings and occasionally via telecon to discuss the executed and upcoming planned Saturn science, in addition to any high-priority science issues that the Project Scientist would request. This group would participate in tour selection (Prime, Equinox, and Solstice, and Grand Finale), define campaigns for focused Saturn science and define activities that eventually become the highest-priority observations—Pre Integration Event (PIE) and Cassini Apoapses for Kronian Exploration (CAKE)—to be negotiated with other Cassini DWGs.

The day-to-day work of the Saturn DWG was carried out by the Saturn Target Working Team (TWT). The Saturn TWT consisted of a subset of Saturn scientists who were interested in negotiating on a weekly basis with other scientists to layout a timeline of observations to be conducted in Saturn-centric windows of time (segments) within the constraints of the

Cassini's Saturn science objectives were overseen by the Saturn DWG.

spacecraft and of the mission. Its leadership consisted of an appointed Saturn scientist, a supporting Investigation Scientist, and one or more Science Planning Engineers. This group would implement both individual stand-alone team observations and campaign templates involving multiple of Cassini's instruments. Most issues were nicely negotiated and resolved during the weekly (and ultimately monthly) telecons. Where there were major science conflicts to be resolved amongst the scientists, the Saturn DWG would offer recommendations for their resolution.

The SAMWG was formed by the Project Scientist to specifically answer the following three questions: 1) characterize Saturn's uppermost atmosphere (thermosphere) and its variation with time; 2) define the shape of Saturn's 100 mbar and 1 bar pressure levels; and 3) determine when the Saturn safely eclipsed Cassini from the Sun. Its membership consisted of experts in studying Saturn's upper atmosphere and members of the engineering team. The SAMWG reported to the Saturn DWG on a periodic basis.

SATURN KEY OBJECTIVES

Cassini's Saturn and Jupiter science objectives originate from those spelled out in the AO and CSM TMs. They are briefly called out here.

- **Saturn Temperature, Clouds, Composition (S_AO1)**
  - **Temperature and clouds (S_AO1)** – Determine temperature field, cloud properties, and composition of the atmosphere of Saturn.
  - **Composition and chemistry (SN1c)** – Measure the spatial and temporal variability of trace gases and isotopes.
- **Saturn Winds and Weather (S_AO2)**
  - **Seasonal Variations (SC1a)** – Observe seasonal variations in temperature, clouds, and composition in three spatial dimensions.
  - **Saturn's Winds (SC1b)** – Observe seasonal changes in the winds at all accessible altitudes coupled with simultaneous observations of clouds, temperatures, composition, and lightning.
  - **Storms (SN1b, SN2a)** – Observe the aftermath of the 2010–2011 storm. Study the life cycles of Saturn's newly discovered atmospheric waves, south polar hurricane, and rediscovered north polar hexagon. Monitor the planet for new storms and respond with observations when they occur.
  - **Atmospheric dynamical processes (S_AO2)** – Measure the global wind field, including wave and eddy components; observe synoptic cloud features and processes.

  - **Saturn Lightning Sources and Morphology (S_AO6, SN2a)** – Investigate the sources and the morphology of Saturn lightning—Saturn Electrostatic Discharges (SED)—lightning whistlers.
- **Saturn Interior Structure and Rotation (S_AO3)**
  - **Saturn's Rotation Rate (SN1a)** – Determine Saturn's rotation rate and internal structure despite the planet's unexpected high degree of axisymmetry.
  - **Saturn Formation and Evolution (S_AO5)** – Provide observational constraints (gas composition, isotope ratios, heat flux, …) on scenarios for the formation and the evolution of Saturn.
- **Aurora, Chemistry, and Upper Atmosphere (SC2a)** – Observe the upper atmosphere and the aurora as it changes on all time scales—minutes to years—and is affected by seasonal and solar cycle forcing.
- **Jupiter atmospheric dynamics (J_AO1)** – Extend the time for studies of atmospheric dynamics beyond the period accessible to the Galileo nominal mission.
- **Jupiter Global Atmospheric Structure and Composition (J_AO2)** – Infer global atmospheric thermal structure and composition with instrumentation not carried by the Galileo Orbiter, complementing the local in situ measurements of the Galileo Probe.
- **Venus atmosphere observations** – No specific objectives were called out.
- **Cruise Planetary and Stellar Internal Oscillations (C_AO5)** – Attempt to detect internal oscillations of Saturn, Jupiter, and some stars.
- **Saturn Ionosphere-Magnetospheric Interaction (S_AO4)** – Study the diurnal variations and magnetic control of the ionosphere of Saturn.

Saturn Science Assessment

Table SATURN-1 is an assessment of data collected to satisfy an objective. It is not as assessment of the status of data analysis/publications.

Table SATURN-1. Science Assessment.

Fully/Mostly Accomplished: **Partially Accomplished:** **Not Accomplished:**

Saturn DWG Science Objectives	AO and TM Science Objectives	Saturn DWG Assessment	Comments (if yellow, partially fulfilled)
Saturn Temperature, Clouds, Composition	S_AO1		
– Temperature and clouds	S_AO1		
– Composition and chemistry	SN1c		
Saturn Winds and Weather	S_AO2		
– Seasonal variations	SC1a		

Table SATURN-1. Science Assessment.

Fully/Mostly Accomplished: **Partially Accomplished:** **Not Accomplished:**

Saturn DWG Science Objectives	AO and TM Science Objectives	Saturn DWG Assessment	Comments (if yellow, partially fulfilled)
– Saturn's winds	SC1b		
– Storms	SN1b, SN2a		
– Atmospheric dynamical processes	S_AO2		
– Saturn lightning	S_AO6, SN2a		
Saturn Interior Structure and Rotation	S_AO3		
– Saturn's rotation rate	S_AO3, SN1a		
– Saturn formation and evolution	S_AO3, S_AO5		
Aurorae, Chemistry, and Upper Atmosphere	SC2a		
– Upper atmosphere	SC2a		
– Aurora	SC2a		
Jupiter Atmospheric Dynamics	J_AO1		
– Dynamics observations	J_AO1		
– Dynamics modeling and theory	J_AO1		
Jupiter Global Atmospheric Structure and Composition	J_AO2		
– Thermal and cloud structure	J_AO2		
– Composition and chemistry	J_AO2		
Venus Atmosphere Observations	N/A		
Cruise Planetary and Stellar Internal Oscillations	C_AO5		NOTE: Planetary and stellar cruise observations were not conducted.
Saturn Ionosphere-Magnetosphere Interaction	S_AO4		NOTE: This is primarily a MAPS WG objective. See their objectives MN1b, MN1c, MN2a, and MC1a. The green assessment reflects the status of both WG's data analysis.

SATURN DWG SCIENCE RESULTS

Saturn Temperature, Clouds, Composition (S_AO1)

- **Temperature and clouds (S_AO1)** – Determine temperature field, cloud properties, and composition of the atmosphere of Saturn.

The temperature field, cloud properties, and composition are an interacting system that controls the energy budget of the planet and the clouds and haze that we see in the planet's atmosphere (Figure SATURN-1). Clouds are a tracer of the motion. They form on updrafts, which are part of the energy cycle that controls the zonal winds. Also, clouds interact with the temperature field through condensation and evaporation. Cassini, with its comprehensive array

of instruments and unique perspective from different positions in the orbit, has contributed critical data on all of these objectives. In addition, Cassini has spawned exploration of Saturn from Earth-based telescopes.

Timed with the start of Cassini's exploration of the Saturn system, Beebe [2005] presented the case for comparative study of the outer planets. Papers on the Cassini instruments and their ability to measure clouds and haze include: Baines et al. [2005] on VIMS; Porco et al. [2005] on ISS; Flasar et al. [2005] and Jennings et al. [2017] on CIRS; and Janssen et al. [2013] on the Cassini RADAR radiometer. Schinder et al. [2015] give the techniques for probing the electron density and temperature structure with radio occultations.

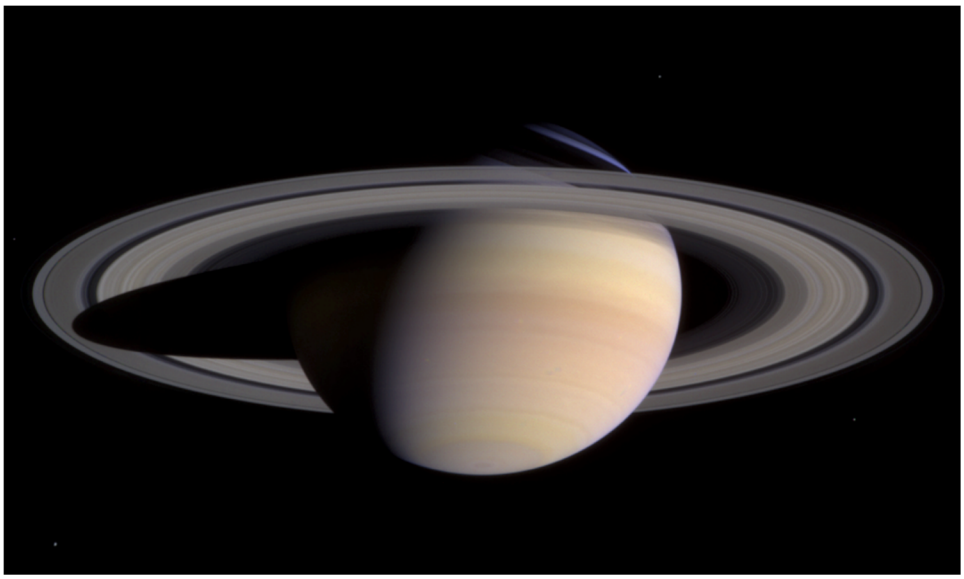

Figure SATURN-1. Image taken by the ISS in 2004 as Cassini was approaching Saturn. It was summer in the south, and the sunlight was driving a rich hydrocarbon chemistry, resulting in an orange haze of small particles. The north was mostly shielded from sunlight, and the skies were blue, as shown by the sliver of atmosphere visible above the ring (PIA05389).

Banfield et al. [1998] described the use near-infrared (IR) spectroscopy from the 5-m Hale telescope at Palomar, California, to measure the altitudes and scattering properties of clouds and haze. Similarly, Sanchez-Lavega et al. [2004] described Hubble Space Telescope observations of cloud morphology in Saturn's atmosphere. Temma et al. [2005] used Earth-based telescopic observations to probe the vertical structure of Saturn's cloud layers. Using Hubble Space Telescope (HST) data, Perez-Hoyos et al. [2006] documented short-term variability (weeks to months) associated with cloud reflectivity of the belts and zones. West et al. [2009] gives a comprehensive survey of clouds and haze in Saturn's atmosphere as inferred from Cassini VIMS and ISS, as well as HST and other Earth-based telescopes. Ingersoll et al. [2018] present images taken during the last few months of the mission at resolutions down to 0.5 km per pixel. The interesting features include filamentary clouds coherent over 20,000 km and puffy clouds resembling terrestrial cumulus.

Fletcher et al. [2007b] used Cassini CIRS data to probe the vertical and horizontal temperature structure and its relation to the belt and zone cloud structure. Roman et al. [2013] used ISS data to probe the layered cloud structure from the haze layers at 40 mbar to tropospheric clouds at 2.5 bar. Laraia et al. [2013] used Cassini RADAR radiometer data to probe the vertical distribution of NH_3 to depths below its nominal cloud base. Barstow et al. [2016] used Cassini VIMS to document a photochemical origin for the stratospheric haze and either NH_3 or NH_4SH for the deeper tropospheric cloud. Using Cassini ISS data, Dyudina et al. [2016] and Perez-Hoyos et al. [2016] quantified the way the atmosphere scatters light, including the phase function and the spherical and Bond albedos.

Del Genio et al. [2009] give a comprehensive review of Saturn's atmospheric structure and dynamics. The early data come from the Voyager flybys and Earth-based telescopes and then from the remote-sensing instruments on Cassini. The review covers the deep atmosphere, the troposphere, the stratosphere, and dynamical features such as the jets, waves, discrete features. Del Genio and Barbara [2016] provide a classification scheme based on cloud morphology for revealing the underlying dynamics.

- **Composition and chemistry (SN1c)** – Measure the spatial and temporal variability of trace gases and isotopes

The gaseous composition of a giant planet atmosphere varies due to several processes: condensation and precipitation that remove the particles from the gas, updrafts and downdrafts that alter the chemical equilibrium of the various reacting species, and photochemical reactions that lead to dissociation and/or ionization (Figure SATURN-2). The reacting species include CH_4, NH_3, PH_3, and their chemical byproducts like C_2H_2 and C_2H_6. In addition, the upper atmosphere may receive molecules and solid particles from the rings and satellites.

Fouchet et al. [2009] give a comprehensive review of Saturn composition and chemistry. Fletcher et al. [2011a] review the elements that appear in simple compounds that are detectable in VIMS spectra, including PH_3, NH_3, AsH_3, GeH_3, CO, CH_3D, and $^{13}CH_4$. Howett et al. [2007] and [Guerlet et al. 2009] focus on C_2H_2, C_2H_6, and C_3H_8, which are produced in the stratosphere by photodissociation of methane. They use Cassini CIRS data to infer a stratospheric circulation from south to north during the southern summer. Guerlet et al. [2010] added C_3H_8 and CH_3C_2H to the list of tracers and again found evidence of upwelling in the south and downwelling in the north. Fletcher et al. [2007a] also used CIRS data, focusing on phosphine, PH_3. It is in chemical equilibrium below the cloud tops and is destroyed by photolysis in the stratosphere. The altitudes of sources and sinks are opposite to that of C_2H_2 and C_2H_6, but the inferred circulation is similar.

Cassini CIRS data stimulated photochemical modeling in order to quantify the inferred circulations [Dobrijevic et al. 2011; Hue et al. 2015]. The data also stimulated laboratory measurements [Auwera et al. 2007; Devi et al. 2014] to refine the infrared absorptions of these gases. Gases like CH_4, C_2H_2, and C_2H_6 absorb and emit in the infrared, and their spatial and temporal variations create temperature variations, which in turn affect the circulation. These

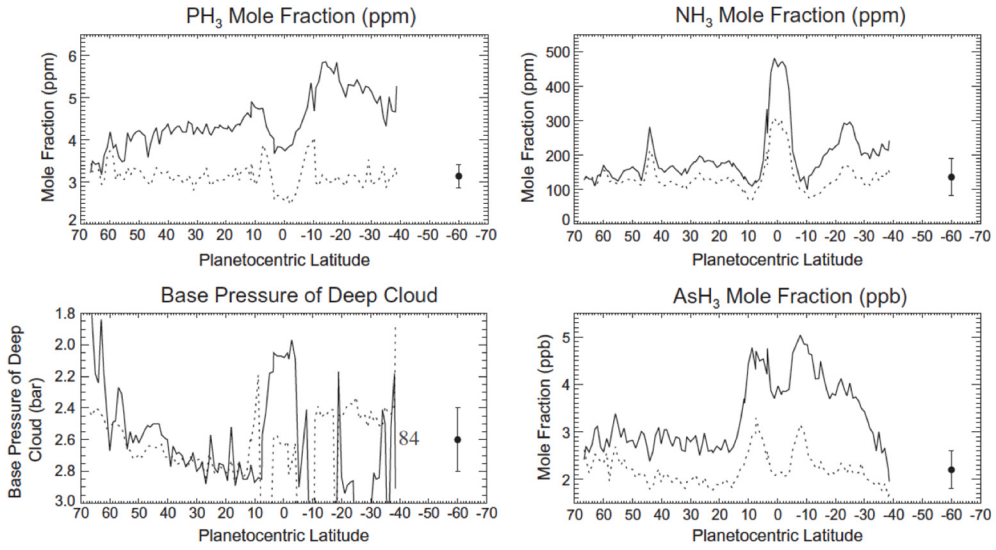

Figure SATURN-2. Tropospheric chemical abundances from Cassini VIMS. The profiles do not tell a consistent story according to this picture. NH_3 shows a high mole fraction at the equator, consistent with upwelling there and downwelling on either side at 10–12° latitude, but PH_3 and AsH_3 show low abundances at the equator, consistent with downwelling. The data may be indicating a double Hadley cell, with rising motion at the higher altitudes at the equator and sinking motion deeper down [Fletcher et al. 2011a].

interactions are studied with 2-D photochemical models, which have been another desirable outgrowth of Cassini observations [Hue et al. 2016].

Intensified Earth-based observations are a further desirable result of Cassini's mission to Saturn. Some of the observations immediately preceded the outpouring of Cassini data [Kim and Geballe 2005; Tejfel 2005], both to extend the range of temporal variability and to compare inferences based on different data sets. For instance, microwaves are sensitive to ammonia vapor at deeper levels than those probed by infrared radiation. The Cassini RADAR used in passive mode collects thermal radiation at 2.2 cm wavelength. With laboratory measurements of the ammonia opacity [Hanley et al. 2009], the Cassini 2.2 cm data were used to infer depletion of ammonia below the expected base of the ammonia cloud [Janssen et al. 2013; Laraia et al. 2013]. This depletion is observed on Jupiter as well and has not been fully explained. The NH_3 abundance is controlled mostly by condensation and evaporation, which is more tied to the cloud structure, so it reveals different aspects of the circulation [Hurley et al. 2012b] than that of the hydrocarbons.

In giant planet atmospheres, the principal oxygen-bearing molecules are H_2O and CO, with the latter in equilibrium at higher temperatures and pressures than the former. However, water is frozen out at high altitudes, so the presence of CO_2 at the 1 mbar level suggests a source outside the planet. Cassini CIRS observations were used to show that the source is probably interstellar dust grains [Abbas et al. 2013].

Saturn Winds and Weather (S_AO2)

- **Seasonal Variations (SC1a)** – Observe seasonal variations in temperature, clouds, and composition in three spatial dimensions.

Two opposing effects control the amplitude of seasonal variations on Saturn (Figure SATURN-3). The obliquity is 26.73°, which is larger than that of Earth, and is tending to produce large seasonal variations in incident sunlight. These variations are augmented by the rings, which block sunlight from reaching large parts of the winter hemisphere. On the other hand, Saturn's troposphere is massive, with clouds of water down to the 20-bar level, assuming the enrichment of water relative

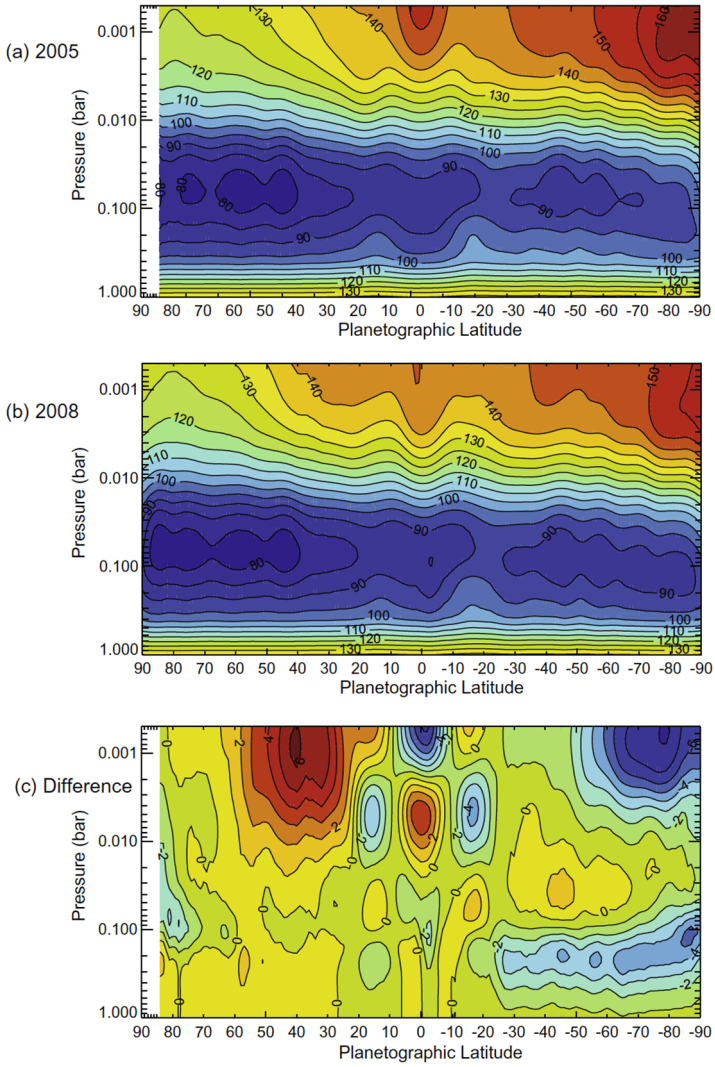

Figure SATURN-3. Temperature as a function of latitude and altitude from Cassini CIRS. In 2005 the season was early winter in the north, and in 2008 the season was mid-winter. The south is warmer than the north in both years, although most of the hemispheric contrast and most of the difference between 2005 and 2008 is confined to high altitudes [Fletcher et al. 2010].

to solar composition is the same as that of methane, whose abundance can be measured spectroscopically. Further, the high specific heat of hydrogen gives the troposphere a huge thermal inertia, so the atmosphere tends to average over the seasonal cycle rather than respond to it. Seasonal averaging is reduced in the stratosphere, because it has less thermal inertia than the troposphere. Seasonal change is reflected in the emitted power as a function of latitude [Li et al. 2015], as the northern hemisphere season changed from winter to late spring over the period 2004-2013 (Figure SATURN-4).

Using Cassini CIRS data Fletcher et al. [2010] showed that the stratosphere has a greater range of temperatures than the troposphere, which is consistent with the greater thermal inertia of the latter. They point out that a photochemical haze develops in the spring/summer hemisphere (Figure SATURN-1). Fletcher et al. [2015] observed polar cooling and depletion of acetylene in the southern hemisphere during fall and winter. Tropospheric temperature variations are small [Fletcher et al. 2016] and show a substantial seasonal lag time, as expected. These seasonal changes are superposed on a general upwelling in the tropics and downwelling at the poles, as revealed by the two states (ortho and para) of the H_2 molecule [Fletcher et al. 2016, 2017]. Sinclair et al. [2013] and Sylvestre et al. [2015] compare CIRS observations of temperature, C_2H_2, C_2H_6, and C_3H_8 with a static photochemical model and find substantial effects of circulation and transport in addition to variations due to chemistry. Seasonal change of thermal structure, composition and aerosol is extensively reviewed by Fletcher et al. [2018].

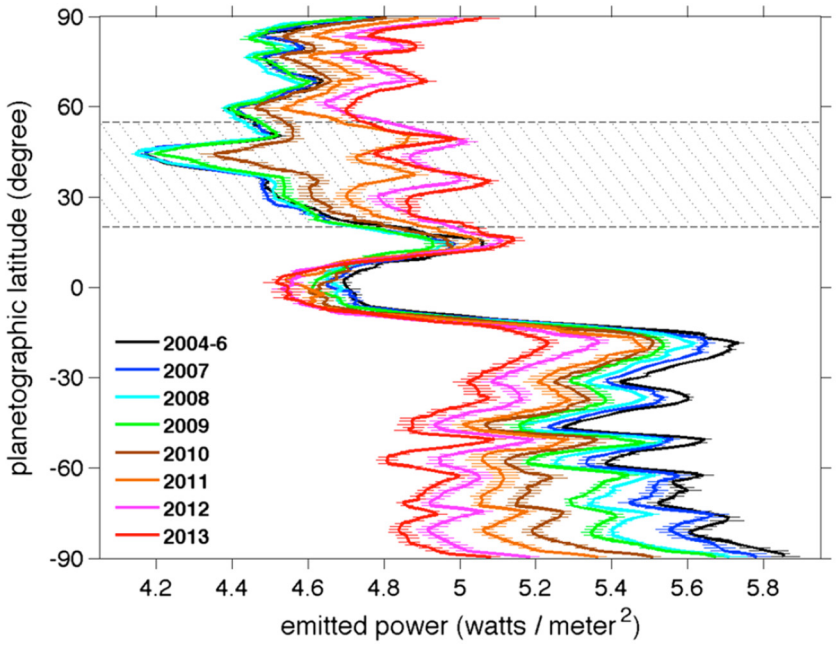

Figure SATURN-4. Thermal emission of the planet in units of W m^{-2} from Cassini CIRS. In the south the season was early summer in 2004 and mid fall in 2013. The decrease in thermal emission in the south was due to cooling of the atmosphere. Comparing the years before and after 2011, it is clear that the great storm increased the thermal emission by 5–10% in the 30–40° latitude band, and that the anomaly persisted for several years [Li et al. 2015].

- **Saturn's Winds (SC1b)** – Observe seasonal changes in the winds at all accessible altitudes coupled with simultaneous observations of clouds, temperatures, composition, and lightning.

Tracking small clouds in sequences of images is the principal way of measuring the winds (Figure SATURN-5). Both ISS and VIMS can measure the winds directly. CIRS can measure the gradient of the wind with respect to altitude by measuring the horizontal gradient of temperature and applying the thermal wind equation. Except at the equator, the mean zonal winds—the

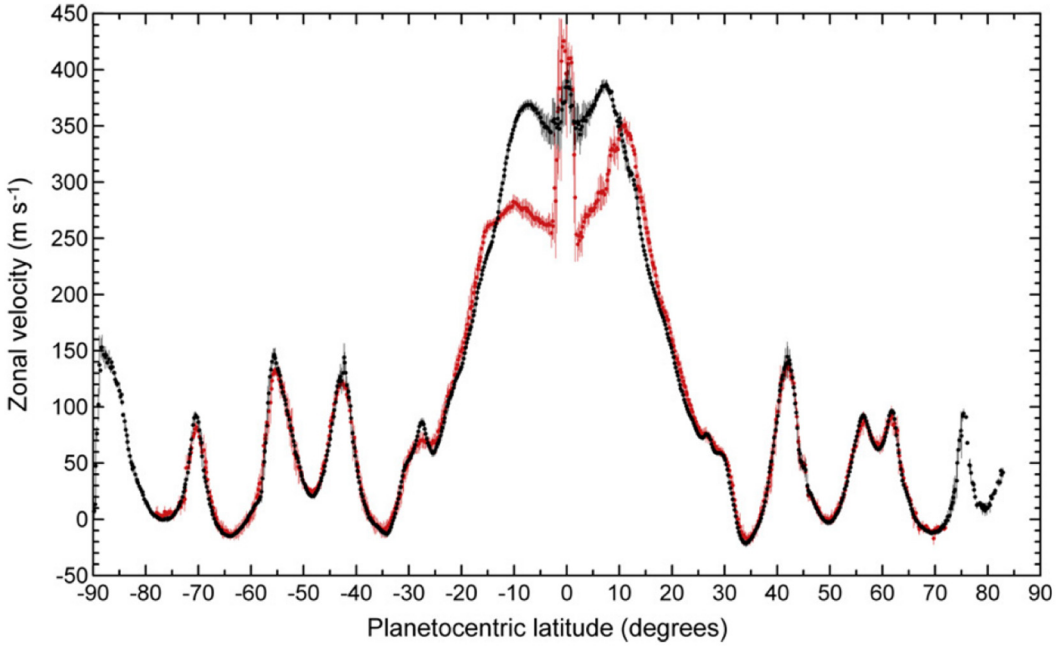

Figure SATURN-5. Atmospheric zonal velocity for Saturn from Cassini ISS. The black curve is data from the 350 to 700 mbar levels, and the red curve is data from 100 to 200 mbar. The differences are small except for a latitude band ±15° from the equator [Garcia-Melendo et al. 2011b].

eastward winds averaged with respect to longitude—are remarkably steady. This conclusion follows, in part, by comparing the mean zonal winds during Voyager times with those measured by Cassini 25–30 years later [Antunano et al. 2015; Choi et al. 2009; Li et al. 2011, 2013; Vasavada et al. 2006]. Images taken at wavelengths where methane is a strong absorber tend to sample higher altitudes than those where methane is transparent. Vertical shears show up in the eastward jets [Garcia-Melendo et al. 2009, 2011], which is consistent with the horizontal temperature gradient and the thermal wind equation.

At the equator, the speed of the zonal wind in the upper troposphere and stratosphere oscillates with a 15-year period [Fouchet et al. 2008] (Figure SATURN-6). Similar oscillations occur in the stratospheres of Earth and Jupiter. On Earth the period is about 22 months, and the oscillation is called QBO. On Jupiter, the period is about four years. On Earth, the mechanism is feedback between the wind profile and the altitude where waves propagating up from the troposphere deposit their zonal momentum. The period is inversely related to the intensity of the waves. A similar

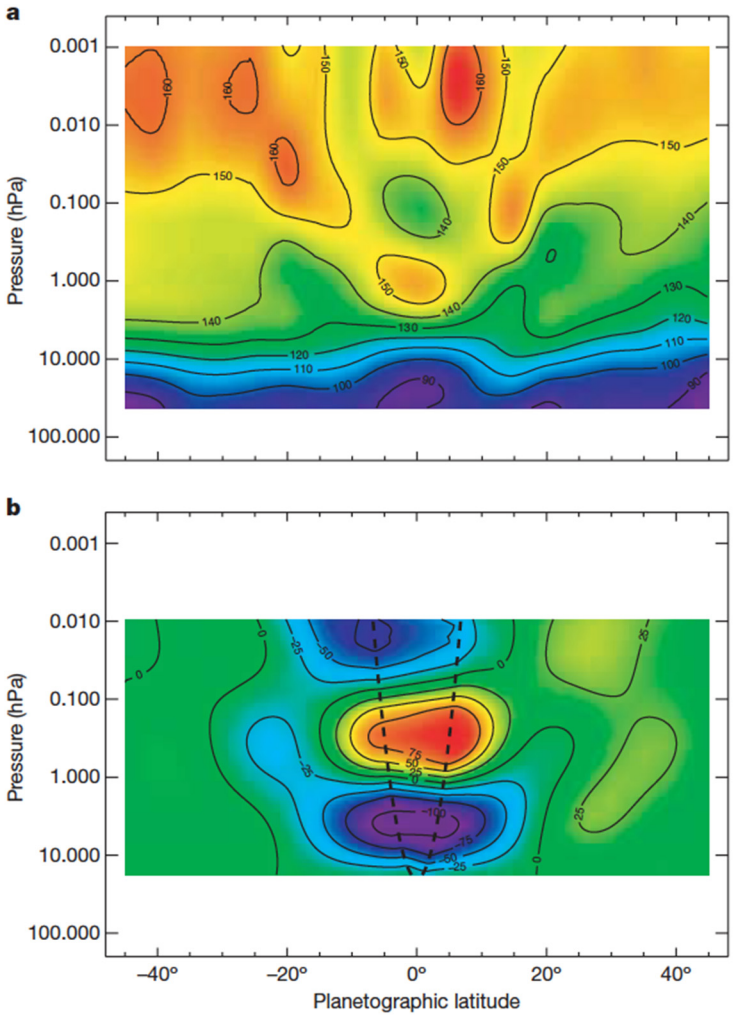

Figure SATURN-6. Oscillation of temperature (upper panel) and mean zonal wind (lower panel) at the equator from Cassini CIRS. The pattern moves down with time and has a ~15-year period. A similar pattern on Earth has a ~22 month period and is known as the QBO. The period of the oscillation on Jupiter is ~4 years. The longer period as one moves out in the solar system is probably due to the lower energy available to drive the oscillation [Fouchet et al. 2008].

mechanism is likely to operate on Jupiter and Saturn. Since vertical shear in the zonal wind is related to horizontal gradients of temperature through the thermal wind equation, the oscillation reveals itself in the temperatures on either side of the equator.

In preparation for the Cassini encounter, Voyager and Hubble Space Telescope observations were used to document the variability of the zonal wind in the equatorial stratosphere [Perez-Hoyos and Sanchez-Lavega 2006; Sanchez-Lavega et al. 2000]. Sanchez-Lavega et al. [2007] and Garcia-Melendo et al. [2010] used Cassini ISS images in the methane bands to further document the vertical wind shear and its temporal variability. Li et al. [2008] used Cassini CIRS data, where the oscillation is revealed in stratospheric temperatures, and Li et al. [2011] showed that the temperatures and cloud-tracked winds are consistent with the QBO oscillation mechanism.

Schinder et al. [2011] used radio occultations by the Cassini spacecraft to measure temperature and showed that the zonal wind profile propagates downward as on Earth, consistent with the wave forcing mechanism of the QBO. Downward propagation also shows up in the thermal infrared maps based on CIRS data [Fouchet et al. 2008; Guerlet et al. 2011]. Sanchez-Lavega et al. [2016] used ISS data to track individual features in the upper haze and clouds and further demonstrated the intense vertical shears and temporal variability.

- **Storms (SN1b, SN2a)** – Observe the aftermath of the 2010–2011 storm. Study the life cycles of Saturn's newly discovered atmospheric waves, south polar hurricane, and rediscovered north polar hexagon. Monitor the planet for new storms and respond with observations when they occur.

Saturn is prone to large-scale eruptions (Figure SATURN-7). They start with a small cloud that grows rapidly during its first week and expands zonally, until after two or three months the

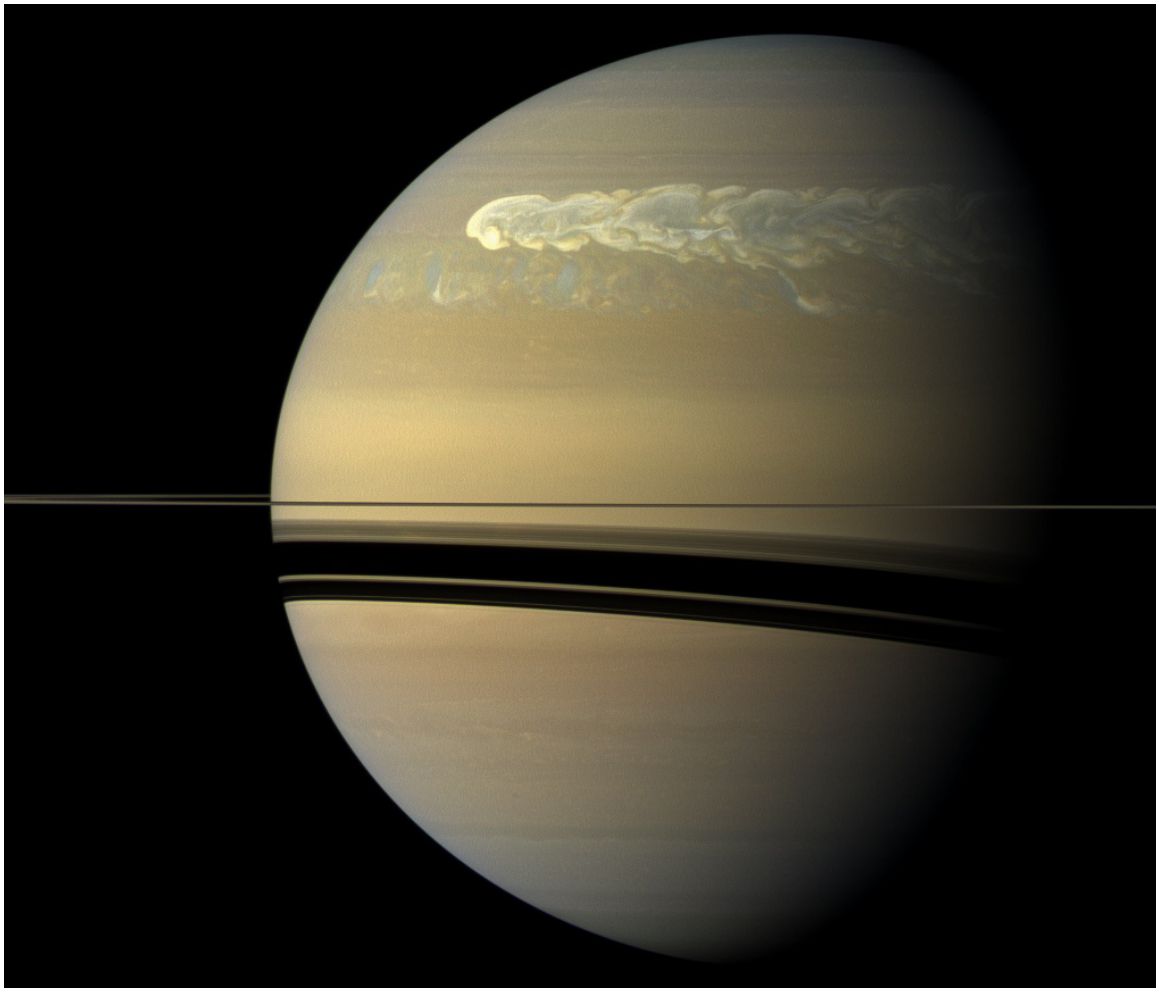

Figure SATURN-7. Saturn imaged by Cassini ISS on February 25, 2011. The great storm of 2010–2011 is clearly visible in a band centered at 30–40° latitude. Since its appearance on December 5, 2010, the head of the storm had drifted west and overtaken the tail.

disturbance has fully encircled the planet within its latitude band. The paper by Sanchez-Lavega [1994] is the definitive pre-Cassini review of these phenomena. He calls them Great White Spots, and he lists five of them before the Cassini era: 1876, 1903, 1933, 1960, and 1990. This gives an average periodicity of 28.5 Earth years, which is close to Saturn's year of 29.46 Earth years. The corresponding latitude bands of these storms are 8 ±3°, 36 ±2°, 2 ±3°, 58 ±1°, and 12 ±1°, all in the northern hemisphere. Whether the disturbances are in a unique class or just the largest in a continuous distribution of sizes is uncertain. And whether the disturbances are locked in phase to Saturn's year is also uncertain, because within each latitude band the period is much longer than a Saturn year. And the great storm of 2010–2011 came 10 years too early to satisfy the annual cycle hypothesis.

Saturn's great storm of 2010–2011 was a singular event in Cassini's 13 year tour of the Saturn system [Sanchez-Lavega et al. 2018]. It began as a small (~1000 km) spot captured in a routine ISS image on December 5, 2010. Cassini RPWS had been detecting lighting discharges (Figure SATURN-8) from the storm for a few hours when the image was taken [Fischer et al. 2011]. The lightning continued for the ~7 month lifetime of the storm as the westward-moving head left behind a tail that eventually wrapped around the planet. In its mature phase, the storm filled a latitude band 10,000 km wide that was centered at a planetocentric latitude of 35°. Earth-based telescopes were following the storm within days of its appearance [Sanchez-Lavega et al. 2011], and systematic Cassini imaging began in January 2011.

Visible-light images of clouds in the troposphere [Sanchez-Lavega et al. 2012; Sayanagi et al. 2013] showed that the head spawned large (10,000 km diameter) anticyclones that drifted off to the east and became part of the tail. The storm seems to have originated from a feature called the string of pearls, a train of cyclones at the latitude of the great storm [Sayanagi et al. 2014]. Garcia-Melendo et al. [2013] are able to reproduce many of the observed morphological features of the storm with a prescribed heat source moving at a prescribed velocity. Li and Ingersoll [2015] present a theory that reproduces the observed drying (low mixing rate of ammonia) of the storm's latitude band (Figure SATURN-9) [Janssen et al. 2013; Laraia et al. 2013] as well as the multi-decadal

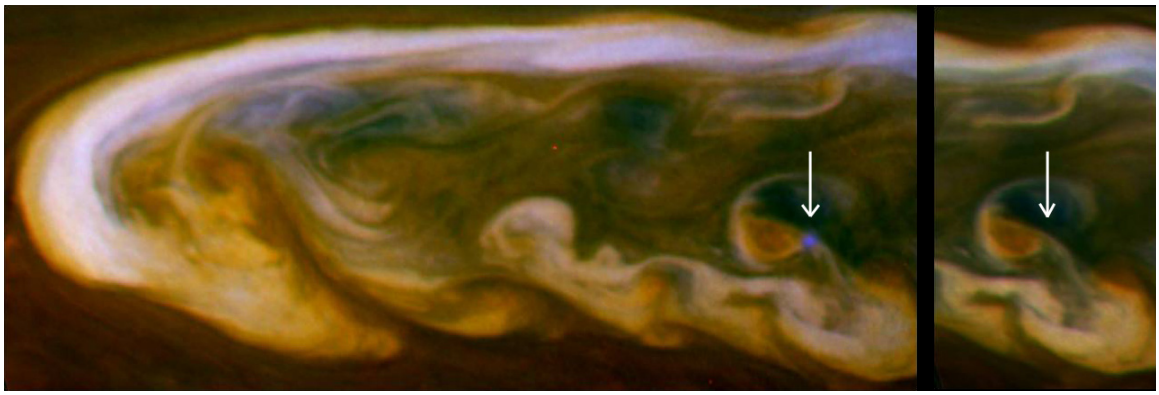

Figure SATURN-8. Lightning flash in Saturn's great storm of 2010–2011. The color composite consists of three images taken in rapid succession at three different wavelengths. A lightning flash occurred while the blue-filtered image was taken, making a blue spot in the composite image, left. The same region was imaged 30 minutes later and did not see a lightning flash, right (PIA14921).

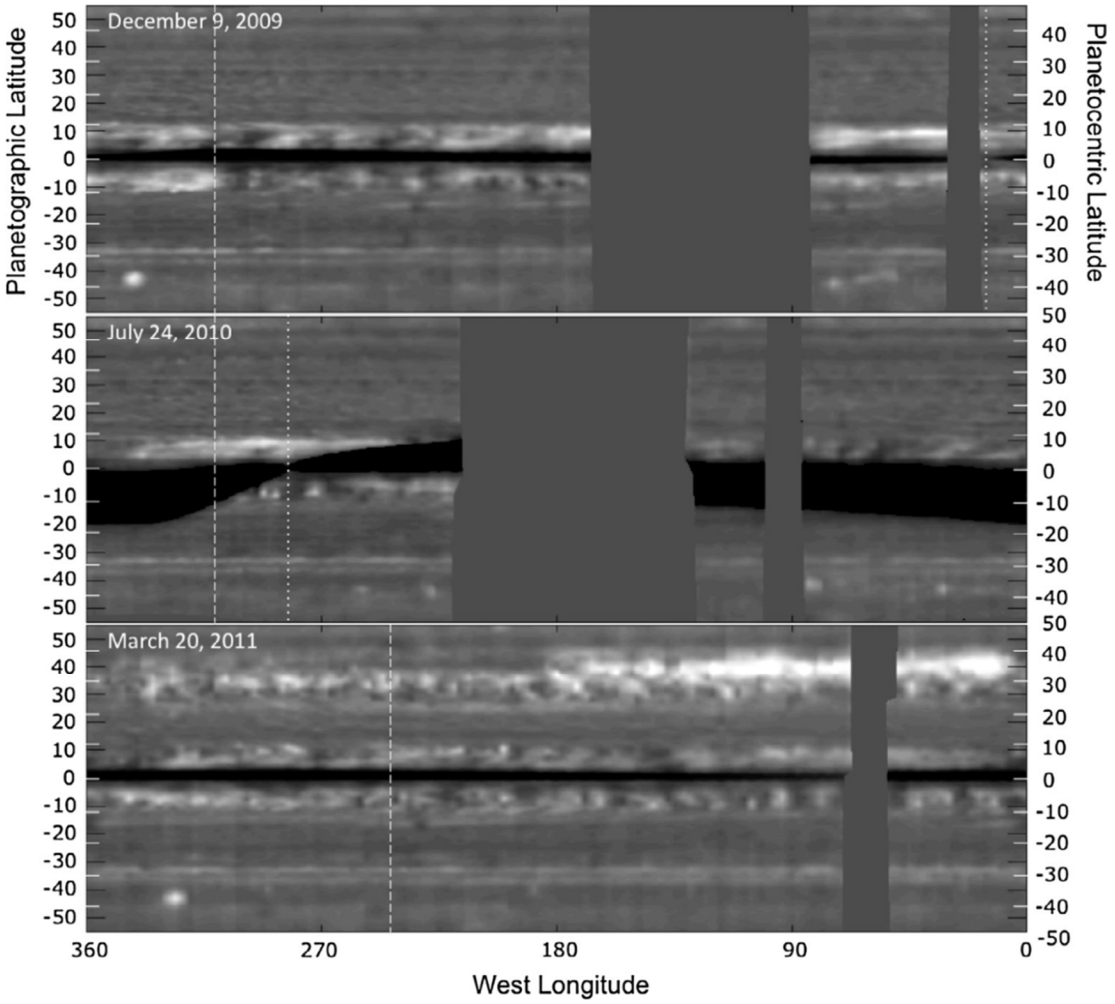

Figure SATURN-9. Cylindrical projection of Jupiter thermal emission at 2.2 cm wavelength, obtained by the Cassini RADAR in passive (non-transmitting) mode. The dark band at the equator is due to the rings, which are colder than the planet itself. The top two panels show the planet before the great storm. The lower panel shows warm emission at the location of the storm. Ammonia is the principal absorber at 2.2 cm wavelength, so the warm emission is due to ammonia depletion allowing radiation from deeper levels to reach the detector [Janssen et al. 2013].

interval between great storms. The latter is tied to mass loading, i.e., the stabilizing effect of water and ammonia condensation in a low molecular weight (H_2 and He) atmosphere. Above a critical abundance of the condensates, the atmosphere becomes stable after a convective event, and the time needed to destabilize the atmosphere is decades. Based on the C/H ratios for Jupiter and Saturn, assuming the same enrichment factors relative to solar for O/H, Saturn is above the critical value and Jupiter is below it, which could explain why only Saturn has these great storms.

Thermal infrared spectroscopy by Cassini CIRS revealed effects of the storm that penetrated into the stratosphere to the 1 mbar level [Fletcher et al. 2011b]. Subsidence of air in the stably-stratified stratosphere produced beacons as much as 16 K warmer than their surroundings

(Figure SATURN-10). By May 5, 2011, the beacons had reached temperatures of 226 K, about 80 K warmer than the surrounding stratosphere [Fletcher et al. 2012; Fouchet et al. 2016]. The storm produced a 100-fold increase of ethylene in the stratosphere near the beacon [Hesman et al. 2012]. Photochemical models cannot explain this increase, so some dynamical mechanism must be at work [Cavalie et al. 2015; Moses et al. 2015]. Temperatures in the troposphere at the latitude of the storm increased by 3 K, and the para fraction of H_2 decreased by about 0.4, indicating warm air upwelling from below (Figure SATURN-11) [Achterberg et al. 2014].

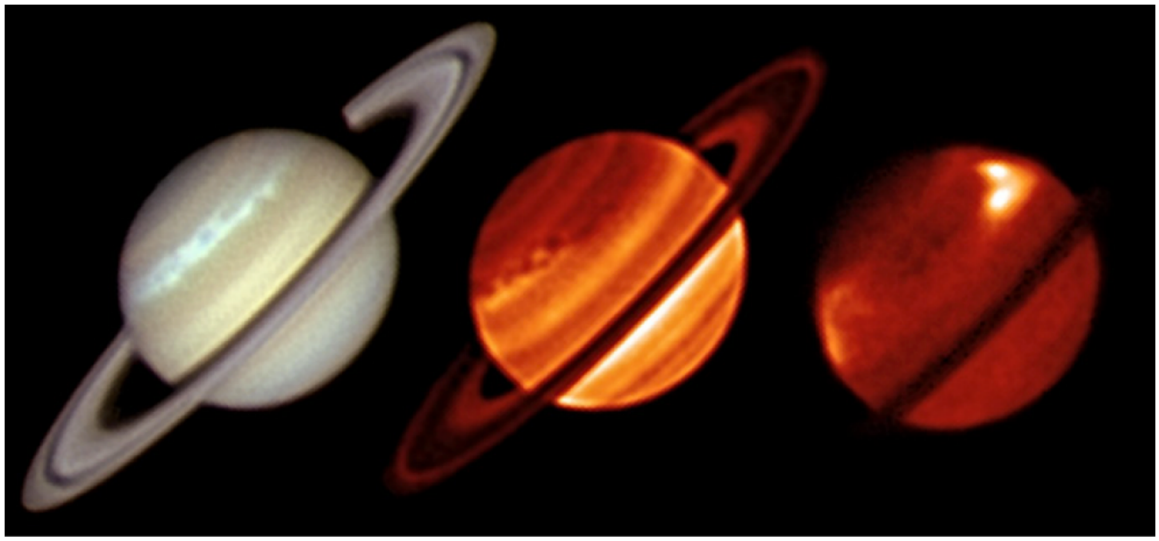

Figure SATURN-10. Earth-based image, left, and two infrared images taken by Cassini CIRS on January 19, 2011. The center image records temperature in the upper troposphere, at the 200–500 mbar level, and the right image shows temperatures at the 1–10 mbar level. The stratospheric beacon stands out in the right image [Fletcher et al. 2011b].

The 2010–2011 storm seems to have affected clouds and haze, both at the latitude of the storm and farther away. Sromovsky et al. [2013] used VIMS spectra to study the composition of the cloud particles lofted by the storm, and found evidence of ammonia ice, water ice, and ammonium hydrosulfide. This is the first spectroscopic evidence of water ice in Saturn's atmosphere and indicates upwelling from 200 km below the tops of the ammonia clouds. Further study of the aftermath of the storm reveals clearing of the ammonia cloud with some residual particles of other species [Sromovsky et al. 2016]. According to an analysis of VIMS data, a residual haze layer persisted in the upper troposphere and lower stratosphere as well [Oliva et al. 2016]. The great storm seems to have caused a 10 K warming of the middle atmosphere (0.5-5 mbar) at the equator, providing evidence of teleconnections between latitudes [Fletcher et al. 2017].

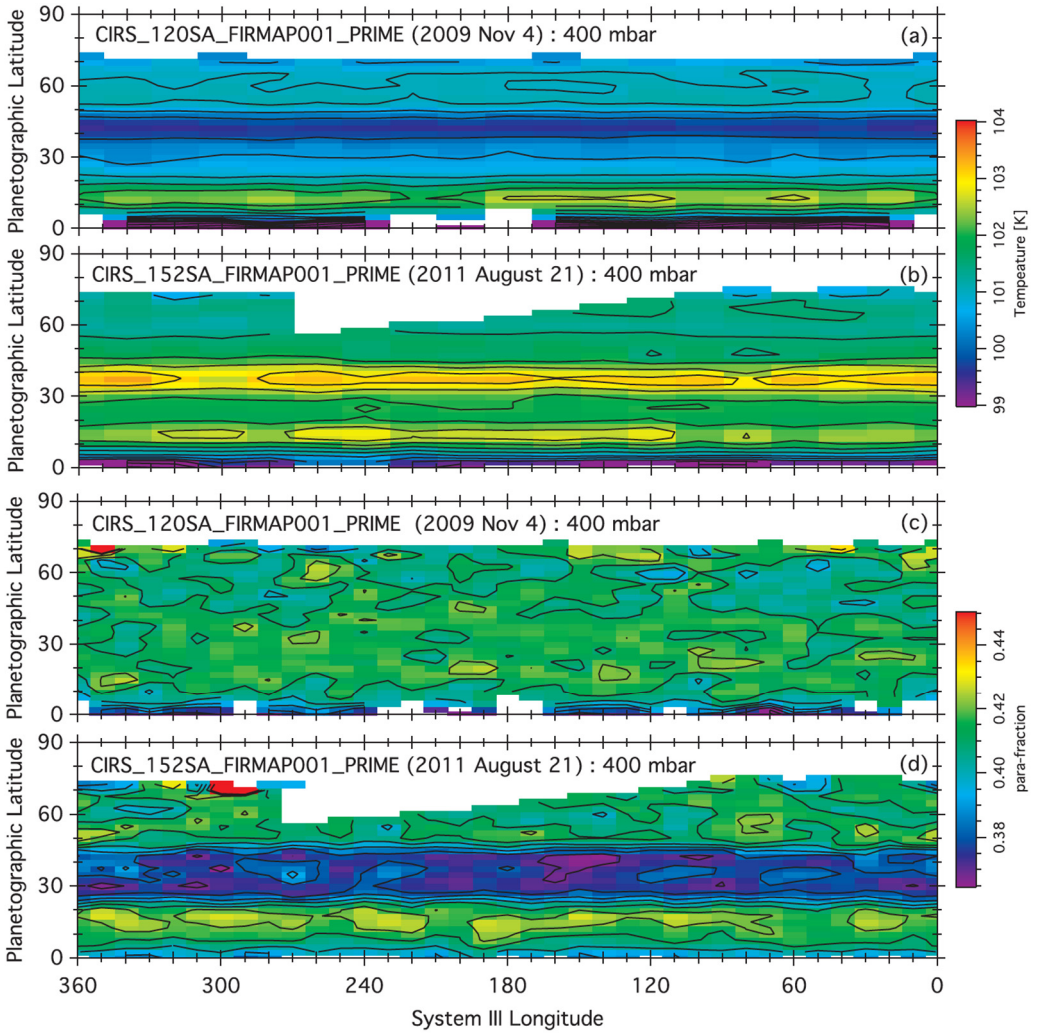

Figure SATURN-11. Cassini CIRS cylindrical projections showing evidence of air being dredged up from below. The top two panels show tropospheric temperature before and after the storm and the band from 30–40° planetographic has warmed by several degrees. The bottom two panels show the two chemical states (nuclear spins parallel and nuclear spins anti-parallel) of molecular hydrogen H_2 before and after the great storm. The 30–40° band shows a low para fraction, which indicates that the air has risen from below cloud base [Achterberg et al. 2014].

Saturn's hexagon is a six-lobed meandering pattern in an eastward jet centered at 75° north latitude (Figure SATURN-12). The excursions in latitude are approximately ±1°, which gives the structure its polygonal shape. Larger excursions would give it a more sinusoidal, wave-like shape. The hexagon was discovered in Voyager images taken in 1980 and was discovered again by Cassini VIMS, before the spring equinox when the North Pole was still in darkness [Baines et al. 2009b]. Its effects extend into the stratosphere to altitudes of 0.5 mbar [Adriani et al. 2015]. Based on ISS and VIMS imaging, the clouds on either side of the jet move slowly or not at all relative to the nominal rotation rate for Saturn, which was defined following the Voyager encounter [Desch and Kaiser 1981]. Relative to these clouds and to the hexagon pattern, the jet's speed is

~125 m s^{-1}. Thus the hexagon is like a road fixed in the Voyager reference frame, and the clouds in the jet move along it. Based on the hexagon's long-term stability, Sanchez-Lavega et al. [2014] argue that it is a deep-seated feature that could reveal the true rotation of the planet.

Each pole of Saturn is occupied by a single isolated cyclonic vortex with peak winds of ~150 m s^{-1} [Dyudina et al. 2008, 2009; Sanchez-Lavega et al. 2006]. The latitude of the peak winds

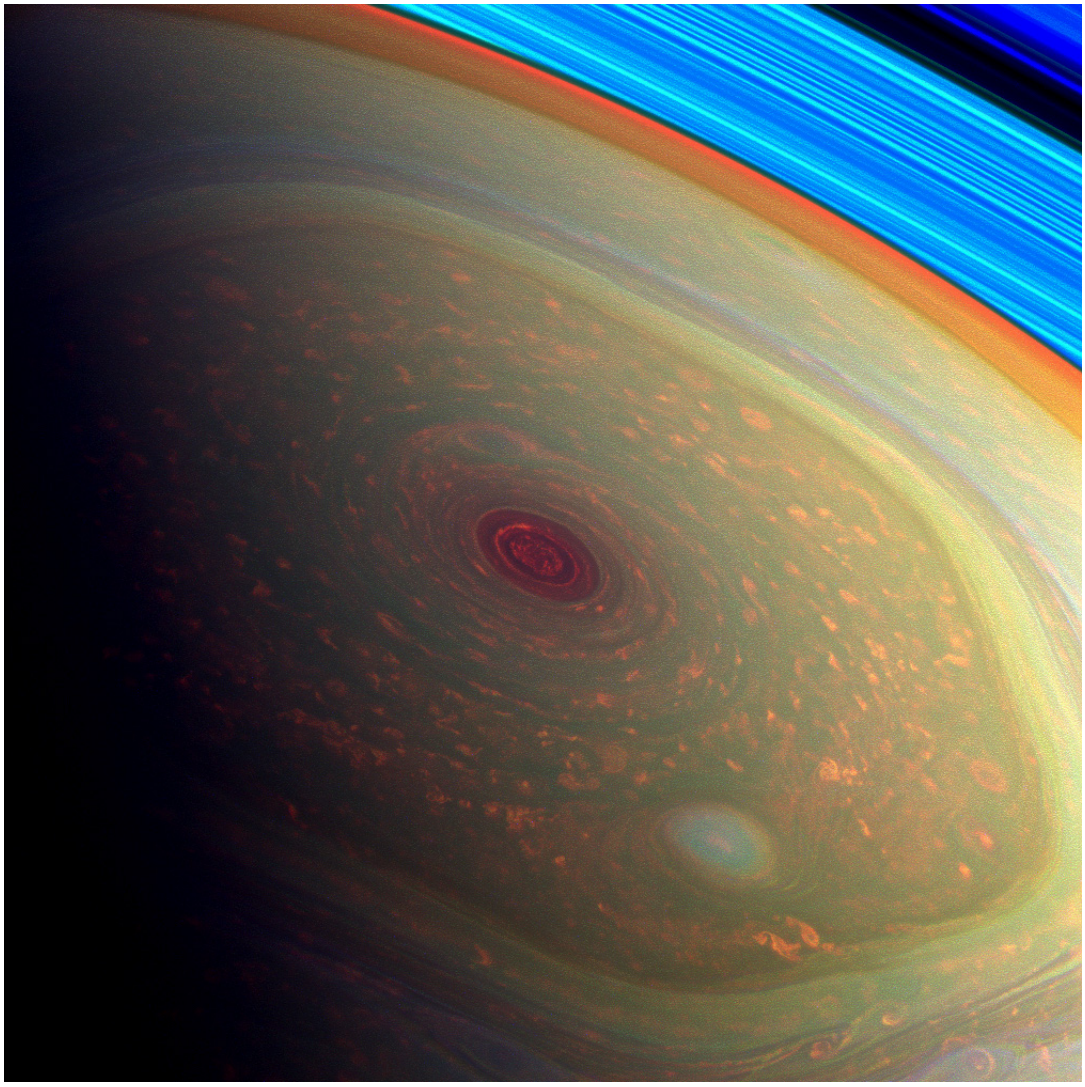

Figure SATURN-12. Saturn's north polar hexagon and polar cyclone. This false color image was taken on November 27, 2012 by the Cassini ISS. The MT3 and MT2 images, which are sensitive to absorption by methane gas in the atmosphere, are projected as blue and green, respectively. The CB2 image, which is not sensitive to methane absorption, is projected as red. The color balance is chosen to make the planet's atmosphere look realistic. The rings look bright blue because there is no methane gas between the rings and the spacecraft. The red spot in the center extends from the pole to a latitude of 88–89°. It looks red in the false-color image because the clouds are deep and methane gas absorbs the sunlight before it can reflect off the clouds and reach the spacecraft. The spot is a cyclone with winds of ~100 m s^{-1}.

is ~88°, which means that the average relative vorticity within 2° of the poles is equal to 0.4 times the local planetary vorticity. Based on Cassini ISS, VIMS, and CIRS data, Dyudina et al. [2008] and Dyudina et al. [2009] interpreted the vortex as a hurricane-like eye with eyewall clouds at 88° extending 20–70 km above the clouds at the pole. Sromovsky and Fry [2019] argued that an abrupt change of optical thickness could mimic the apparent eyewalls. The region has a 4–7 K warm core extending from the upper troposphere into the stratosphere [Achterberg et al. 2018]. The warm core and stable stratification implies downwelling, which is consistent with low phosphine abundance in the core [Fletcher et al. 2008]. Outside the eyewall are numerous anticyclonic vortices suggesting a convective origin [Dyudina et al. 2009]. Sayanagi et al. [2017] compared the north and south polar cyclones and attributed the differences to seasonal effects. Polar phenomena are extensively reviewed by Sayanagi et al. [2018].

- **Atmospheric dynamical processes (S_AO2)a**

Giant planet atmospheres are a superb laboratory for studying the dynamics of rotating fluids. Cloud tracking provides estimates of the winds, and the lack of continents and oceans provides a simpler setting than on Earth. The Cassini mission advanced this field, not only by providing 13 years of observations of Saturn but also by providing a 3-month flyby of Jupiter with an upgraded suite of instruments compared with those on the Voyager flybys. The Jupiter observations are discussed in the section entitled Saturn DWG non-Saturn science results. Here we focus on observations and models of the jets and vortices in Saturn's atmosphere. Saturn's atmospheric dynamics is extensively reviewed by Showman et al. [2018].

The zonal wind profile is a fundamental observation. ISS provided the first data at the start of the Cassini mission [Garcia-Melendo et al. 2011b; Porco et al. 2005; Vasavada et al. 2006] and a valuable comparison with Voyager 25 years earlier. The second fundamental observation is the eddy momentum flux (Figure SATURN-13). Eddies are the time- and longitude-dependent motions that carry heat and momentum across latitude circles. Using ISS data, Del Genio et al. [2007] and Del Genio and Barbara [2012] found a clear positive correlation between eddy momentum fluxes and meridional shear of the zonal wind, implying that eddies supply eastward momentum to the eastward jets and westward momentum to the westward jets. Similar correlations are found on Jupiter and Earth, although the energy supply for Earth's eddies could be different from that for Saturn and Jupiter.

> The eddies north and south of the equator supply positive angular momentum to the equator, so the meridional circulation replaces it with air from higher latitudes on both sides, implying convergence.

Since the eddies supply positive angular momentum to the eastward jets, the meridional circulation must replace it with low angular momentum air, which is found at higher latitudes. Conversely, the westward jets must have flow from lower latitudes. The result is that the meridional circulation diverges in the latitude bands that have westward jets on their poleward sides and eastward jets on their equatorward sides. These are the cyclonic shear zones—called belts on Jupiter.

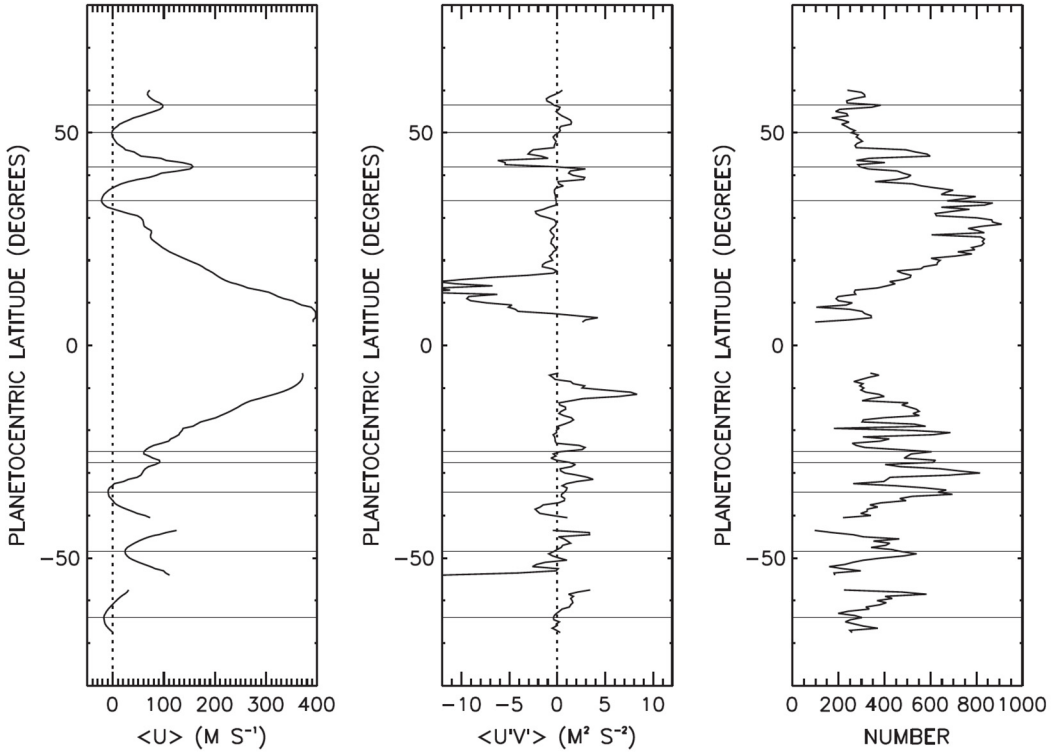

Figure SATURN-13. Eddy momentum transport for Saturn from Cassini ISS. The eastward and northward eddy winds u′ and v′ are the departures from the zonal means. Their product $\overline{u'v'}$ averaged over longitude and multiplied by density is the northward eddy flux of eastward momentum. The fact that this quantity has the same sign as $\partial\bar{u}/\partial y$, which is the increase of the mean eastward wind with latitude, says that the eddies are putting energy into the jets and not the reverse [Del Genio and Barbara 2012].

Anticyclonic shear zones—called zones on Jupiter—are the reverse, so they have convergence. The eddies north and south of the equator supply positive angular momentum to the equator, so the meridional circulation replaces it with air from higher latitudes on both sides, implying convergence. Horizontal convergence implies vertical divergence—either upwelling into the stratosphere or downwelling into the deep troposphere, or both. Using CIRS data Fletcher et al. [2009a] observed phosphine (PH_3), which is destroyed by photochemistry in the upper troposphere, to infer upwelling at the equator above the 0.5 bar level. However using VIMS data, which is sensitive to deeper levels, Fletcher et al. [2011a] inferred downwelling at the equator below the 1.3 bar level. Zuchowski et al. [2009] showed how this pair of stacked, oppositely-directed Hadley cells could arise from a balance between the effects of radiative heating and eddy momentum flux convergence. There is evidence of stacked Hadley cells on Jupiter as well [Gierasch et al. 2000; Ingersoll et al. 2000, 2017; Showman and de Pater 2005], but the subject of upwelling and downwelling is still open.

Zonal jet stability is the third important observation. Stability depends on the potential vorticity [Antunano et al. 2019], which depends on vertical structure, both of temperature and wind, but a simple but relevant criterion is that the flow is stable if the curvature of the zonal wind profile with respect to latitude does not exceed β, which is twice the planet's angular velocity times the cosine

of latitude divided by the planetary radius. Interestingly, this stability criterion is violated on Saturn near the peaks of the westward jets, especially at high latitudes, indicating that the zonal jets could be unstable [Antunano et al. 2015; Read et al. 2009a]. That does not mean the flow is unstable, however, as there are other stability criteria that involve vertical structure [Dowling 1995]. Liao et al. [2007] argue that a statistical equilibrium occurs as the zonal flow saturates. In their global vortex analysis, Trammell et al. [2014] find a correlation between the number of vortices and the westward jet peaks, implying at least some degree of instability at those latitudes.

Waves and vortices are another important feature of giant planet atmospheres. Saturn currently has nothing like the Great Red Spot, which has endured for over 100 years, but it has similar structures. Generally, anticyclones last longer than cyclones, but del Rio-Gaztelurrutia et al. [2010, 2018] document a cyclone that lasted for four years. Convective storms can generate waves that transport westward momentum away from their source regions, helping to accelerate eastward jets at the latitudes of the convection [Gunnarson et al. 2018; Liu and Schneider 2015; Sayanagi and Showman 2007]. This acceleration must be balanced somewhere, and [Schneider and Liu 2009] argue that the balance occurs through magneto-hydrodynamic drag at 0.3 to 1.4 Mbar where the atmosphere becomes electrically conducting [Liu et al. 2014; Liu and Schneider 2015].

Saturn's north polar hexagon at 75° latitude has inspired several modeling studies, both in the laboratory [Aguiar et al. 2010] and on the computer [Morales-Juberias et al. 2011, 2015]. Saturn's ribbon at 47° latitude is a less dramatic relative of the hexagon [Sayanagi et al. 2010] since both seem to represent a steady meandering pattern on an eastward jet stream. The models do not explain why the conditions necessary for a long-lived meandering jet stream exist only at certain latitudes on Saturn or why there are no such jet streams on Jupiter. O'Neill et al. [2015, 2016] propose a model of Saturn's polar cyclones in which convection at mid latitudes produces a vortex that is cyclonic at the bottom and anticyclonic at the top. The two halves separate, and the cyclonic vortex drifts to the pole and merges with other cyclonic vortices to make a single polar vortex. Brueshaber et al. [2019] one-layer shallow-water simulations also show that poleward drifting cyclonic vortices merge to form polar vortices, and also revealed a mechanism that separates the polar dynamical regimes of Jupiter, Saturn, and Uranus/Neptune. On the other hand, Antunano et al. [2018] report no meridional migration in the region north of the hexagon, and suggest that mergers do not contribute to the maintenance of the polar vortex. Sanz-Requena et al. [2018, 2019] describe the haze and cloud structure in the north pole and hexagon region.

Saturn's great storm has also inspired modeling studies. One model uses an imposed heat pulse and studies its interaction with the ambient zonal flow [Garcia-Melendo and Sanchez-Lavega 2017]. Another model studies how precipitation of water, which has a high molecular mass relative to hydrogen, from the troposphere, can inhibit convection for decades due to the long radiative time constant of Saturn's atmosphere [Li and Ingersoll 2015]. A third model uses a long-term numerical integration of moist convection in a giant planet atmosphere [Sugiyama et al. 2014]. The simulations are conducted using a two-dimensional cloud-resolving model that explicitly represents the convective motions and microphysics of NH_3, NH_4SH, and H_2O. It produces intermittent cumulonimbus activity. The time scale is ~60 days, although it is proportional to the water abundance and is therefore likely to be greater for Saturn than for Jupiter.

Numerical models of Saturn's jets and vortices fall into two categories. One is the conventional general circulation model (GCM), which uses hydrostatic balance in the vertical and is valid for large horizontal scales and small vertical scales [Friedson and Moses 2012; Garcia-Melendo et al. 2007; Trammell et al. 2016]. The other is the fluid sphere model in which the vertical and horizontal scales are comparable and the flow takes place in thick spherical shells [Aurnou et al. 2008; Heimpel and Aurnou 2007; Liu et al. 2014]. Computational limitations make it difficult to develop a single model that includes both small and large vertical scales, although the effort is being made [Heimpel et al. 2016]. More often, the practitioners divide in separate camps and work with different tools.

- **Saturn Lightning Sources and Morphology (S_AO6, SN2a)** – Investigate the sources and the morphology of Saturn lightning SED, lightning whistlers.

The Cassini RPWS detects the radio waves from lightning at frequencies starting at 1.3 MHz and ranging up to 40 MHz [Fischer et al. 2006a; Fischer et al. 2006b; Fischer et al. 2007; Fischer et al. 2008]. A single flash is called a SED, and it lasts for less than the 35.2 ms integration time of the RPWS instrument (Figure SATURN-14). Fundamentally, the duration of an SED is unknown [Farrell et al. 2007]. An SED is not a whistler; it is a freely-propagating radio wave that follows a straight-line path from the source. Although the RPWS is listening virtually all the time, sometimes it detects nothing for months. SED activity is often from a single storm, with SEDs every few seconds for a 5-hour ON period followed by a 5-hour OFF period, when the storm is hidden behind Saturn. Often the storm itself is visible, both in ISS images [Dyudina et al. 2007] and in the images gathered by amateur astronomers at Earth. Criteria used to identify the storm are that it appeared within a day or two after the onset of SED activity and it was always on the side of the planet facing the spacecraft when the RPWS was detecting signals. Thus the number of lightning storms at any one time is likely to be either 0 or 1. In contrast, Earth has ~2000 lightning storms over the globe at all times, and Jupiter has dozens of storms at all times [Little et al. 1999].

Cassini ISS eventually detected the lightning flashes [Dyudina et al. 2010], even on the day side despite the bright background of clouds in sunlight. The secret is to take many short exposures, since a short exposure reduces the background but not the lightning; it does reduce the probability of capturing a flash, so one needs to take many exposures. The diameter of the illuminated spot is about 200 km, indicating that the lightning is 125–250 km below cloud tops. This depth is above the liquid H_2O–NH_3 cloud and may be either in the NH_4SH cloud or the H_2O ice cloud.

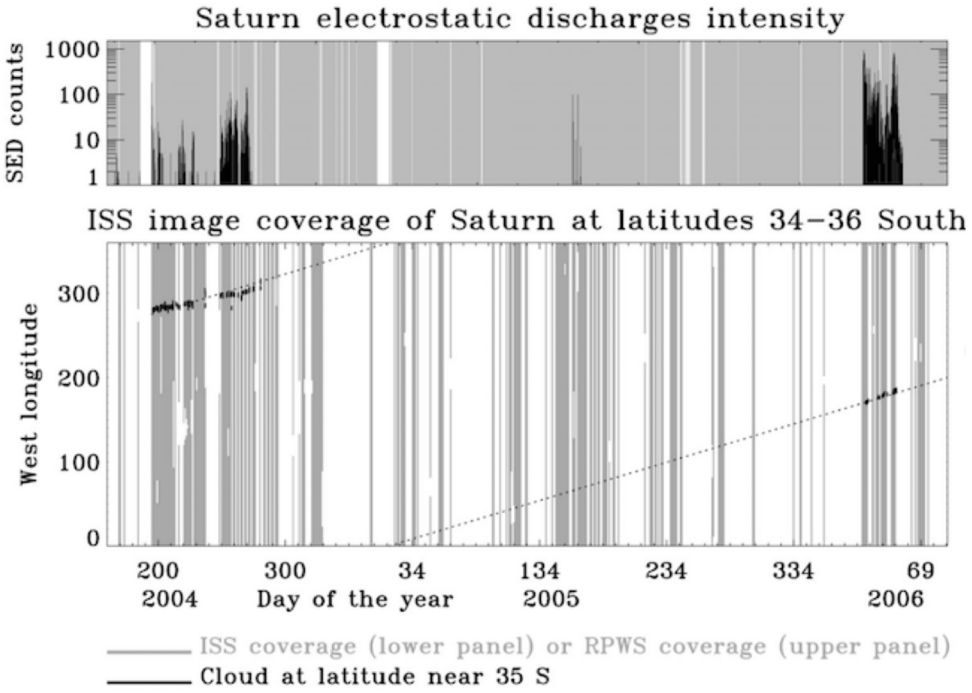

Figure SATURN-14. Saturn electrostatic discharge counts, SEDs, which are roughly equivalent to lightning strikes, over a 2-year period starting in 2004. The SEDs are detected by the RPWS instrument, which is ON continuously. The lower panel shows ISS coverage of latitudes −34° to −36°, where all the storms were occurring, and it is clear that storms were seen only when the RPWS was detecting SED's [Dyudina et al. 2007].

The great northern storm of 2010–2011 was a copious lightning emitter [Dyudina et al. 2013; Fischer et al. 2011]. The RPWS recorded flashes every 0.2 s. The optical energy per flash was about equal to that of the radio energy [Dyudina et al. 2013], although there is considerable uncertainty in both. The optical energy in single flashes ranged up to 8×10^9 J. The flash rate and total power were hundreds of times greater than those of the smaller southern storms that had been appearing intermittently since the start of Cassini observations. Fischer et al. [2014] proposed that the northern storm could account for a change in the Saturn kilometric radiation (SKR) frequency through its effect on thermospheric winds.

The Saturn lighting results stimulated two reviews of planetary lightning [Yair et al. 2008; Yair 2012]. Lightning is an agent of chemical change. Based on VIMS observations, Baines et al. [2009a] proposed that the dark and spectrally featureless clouds associated with giant planet thunderstorms represent small particles of elemental carbon. The particles are postulated to arise from atmospheric methane exposed to high temperatures during the lightning discharge, but Sromovsky et al. [2018] argue that the dark features are more likely regions of reduced optical depth. Dubrovin et al. [2014] studied the effect of lightning on the lower ionosphere of Saturn finding that H_3^+ ions are rapidly produced from the parent H_2^+ ion. On the other hand [Hurley et al. 2012a] searched for but found no correlation between acetylene and thunderstorm activity on Saturn. The Saturn results also

stimulated lightning searches throughout the solar system and on exoplanets from Earth-based radio telescopes and from spacecraft [Hodosan et al. 2016; Zarka et al. 2008].

Saturn Interior Structure and Rotation (S_AO3)

- **Saturn Formation and Evolution (S_AO5)** – Provide observational constraints (gas composition, isotope ratios, heat flux, …) on scenarios for the formation and the evolution of Saturn

The internal heat coming out of the planet is a fundamental quantity relevant to formation and evolution. Because giant planets in our solar system are massive and their surfaces are cold, they cool off slowly. Their interiors are still warm, and they are still releasing some of their heat of formation. To measure the internal power one takes the difference between the emitted infrared power and the absorbed solar power, which is the difference between the incident and reflected sunlight. Using Voyager data, Hanel et al. [1983] estimated the effective emission temperature as 95.0 ±0.4 K, corresponding to an average emitted heat flux of 4.62 ±0.8 W m^{-2}, and the ratio of emitted power to absorbed power as 1.78 ±0.09. Thus the internal power divided by the absorbed solar power is 0.78. Using data from Cassini CIRS, Li et al. [2010] estimated the emitted heat flux as 4.952 ±0.035 W m^{-2} during 2004–2009, although it decreased by 2% during that time and was 16% higher in the southern hemisphere than in the northern hemisphere. These were likely seasonal changes associated with the approach of vernal equinox in 2009. Li et al. [2015] measured the emitted power vs. latitude from 2004 to 2013 and documented the 2010 great storm's effect, which was to increase the global emitted power by 2% and the power at the latitude of the storm by 9% (Figure SATURN-4). These changes were in addition to a seasonal warming of the north and cooling of the south from 2004 to 2013.

The settling releases gravitational potential energy, which affects the cooling history and planetary evolution.

The helium to hydrogen ratio in the atmosphere reflects the value in the solar nebula when the planets were forming as well as the degree to which helium has settled toward the core. Settling is thought to happen because helium becomes immiscible in metallic hydrogen, which is the dominant constituent at megabar pressures. The settling releases gravitational potential energy, which affects the cooling history and planetary evolution. In principle, helium is detected by remote sensing through its effect on the molecular weight of the gas. One uses occultation data to get density vs. altitude, and from the hydrostatic equation one gets density vs. pressure. Then one uses infrared data to get temperature vs. pressure, and with the equation of state one can solve for the molecular weight. The method was used for Jupiter and Saturn using Voyager data [Conrath et al. 1984], but the Galileo probe gave a different result for Jupiter and forced a reanalysis for Saturn [Conrath and Gautier 2000]. Cassini has collected excellent data using CIRS for the temperature and occultations by several instruments—radio science, VIMS, and UVIS, but getting a consistent estimate of the helium abundance is difficult. The occultation result depends on the ray path, and that depends on unknown winds and temperatures above the

occultation point. The most recent estimate [Koskinen and Guerlet 2018] uses Cassini UVIS for the occultations and CIRS for temperature versus pressure. They get a helium mass fraction Y of 0.16−0.22, which is about 70% of the protosolar mass fraction of 0.27, implying that a certain amount of settling has occurred in Saturn's interior.

Before Cassini reached Saturn, the C/H abundance ratio was known to be higher on Saturn than on Jupiter, which was known to be higher than that on the Sun [Atreya et al. 1999, 2003; Owen and Encrenaz 2003]. The C/H ratio is perhaps the most accurately known ratio of all the heavy elements because its molecular form, methane, doesn't condense at Saturn temperatures and isn't readily destroyed in chemical reactions. Cassini CIRS probes the far-infrared rotational lines of the molecule and has determined a volume mixing ratio of $(4.7 \pm 0.2) \times 10^{-3}$, corresponding to a C/H enrichment relative to solar of 10.4 [Fletcher et al. 2009b]. This is more than a factor of 2 greater than that for Jupiter but consistent with conventional models of the formation and evolution of the giant planets, which predict increasing ratios to H of the heavy element abundances relative to the Sun from Jupiter to Neptune [Atreya et al. 2019].

Saturn's greater enrichment is also qualitatively consistent with the masses and radii of the two giant planets. These, coupled with the gravitational moments, rotation rate, and an equation of state, give information about the core mass and amount of heavy elements in the molecular envelope [Guillot 1999; Nettelmann et al. 2013]. Chemical models preceding the arrival of Galileo and Cassini listed many gases that were potentially observable in the atmospheres of Jupiter and Saturn [Fegley and Lodders 1994].

The high C/H ratio is taken as evidence of heavy element enrichment in general and has implications for possible differential sedimentation in the planet's interior over its lifetime [Mousis et al. 2006]. Measurements of NH_3, PH_3, C_2H_2, C_2H_6, and CH_4 all are consistent with these gases trapped as clathrate hydrate in the feeding zone of Saturn as the planets were forming [Hersant et al. 2008]. Clathrate hydrates require water, and our lack of knowledge of the oxygen abundance allows for a number of interior models with a range of values for the C/O ratio [Lunine 2011]. Cassini CIRS measurements suggest that Saturn's D/H ratio is less than that for Jupiter, which mostly reminds us that our understanding planetary formation and evolution is incomplete [Pierel et al. 2017].

Although ammonia is the main carrier of nitrogen on Jupiter and Saturn, the isotopic ratio $^{15}N/^{14}N$ can reveal insights into the molecular carrier (N_2 versus NH_3) in the protoplanetary nebula. The Saturnian and Jovian isotopic ratios appear indistinguishable [Fletcher et al. 2014; Fouchet et al. 2004a]. That result favors accretion of primordial N_2 on both planets, either in the gas phase from the solar nebula or as ices formed at very low temperature [Fletcher et al. 2014].

- **Saturn's Rotation Rate (SN1a)** – Determine Saturn's rotation rate and internal structure despite the planet's unexpected high degree of axisymmetry.

The periodic variation of the dynamo field has been used to estimate the interior rotation rates of Jupiter, Uranus, and Neptune. However, Saturn's magnetic field axis is so closely aligned with its rotation axis that is has no periodic variation. Taking the misalignment of the other three giant

planets, 10° for Jupiter, 60° for Uranus, and 47° for Neptune, the 0.1° upper bound for Saturn is highly improbable (1 chance in 10^4 or 10^5), given that the probability of the magnetic axis aligning with the rotation axis goes as the square of the angle between them [Dougherty 2017]. The close alignment means that there is no detectable wobble in the field as the planet rotates and therefore no periodic signal with which to estimate the rotation period of the planet's interior. The SKR radio emissions are tied to currents in the magnetosphere and ionosphere, and the period is variable from year to year [Fischer et al. 2014], which rules out a direct tie to the interior of Saturn.

There have been various attempts to use the atmospheric periods to estimate the interior rotation rate. They use the data in different ways, but they all derive a period that is near the midpoint of the atmospheric periods. Smith et al. [1982] use cloud tracking and choose a reference frame that minimizes the variance of the cloud-tracked zonal wind with respect to latitude, with 10 h 31 m 30 ±30 s as the result. Anderson and Schubert [2007] chose the reference frame that minimizes the measured shape of the 100 mbar surface from an equipotential, with 10 h 32 m 35 ±13 s as the result. Read et al. [2009b] use the reference frame in which the atmosphere is marginally stable with respect to Arnol'd's second stability criterion, with 10 h 34 m 13 ±20 s as the result. Their method uses ISS and CIRS wind and temperature data to estimate potential vorticity in the range 2–270 mbar. The problem with these approaches is that they ignore the thermal wind equation, which allows vertical shear in the zonal winds. Thus the speed at depth might not match the average speed at the tops of the clouds where the winds and temperatures are measured. Read et al. [2009b] argue that the stability criterion depends on the speed of the longest Rossby waves, which are deeply rooted, but still the problem remains. For instance, the midpoint of the wind distribution at Earth's upper troposphere would give a period between 22 hours and 23 hours for the rotation of the planet, because the average wind at the top of the troposphere is to the east.

Saturn is a fluid planet, and if it were in equilibrium only the zonal harmonics with even *n* would be present.

The gravity field [Jacobson et al. 2006] also has information about the rotation rate of the interior [Hubbard 2009]. As with all planets, Saturn's gravitational potential can be expanded into spherical harmonics, the leading term of which is the spherically symmetric potential −GM/R, followed by the zonal harmonics and the tesseral harmonics. The zonal harmonics are axially symmetric, and each term is proportional to a Legendre polynomial of degree n and a dimensionless amplitude factor J_n. The tesseral harmonics are the longitudinally-varying part of the gravitational potential. Saturn is a fluid planet, and if it were in equilibrium only the zonal harmonics with even n would be present. The J_n reflect the response of the planet to its own rotation, so one could use them to infer the interior rotation rate if the interior structure were known. Conversely, one could infer the interior structure, e.g., core mass, metallic hydrogen, degree of helium separation, heavy elements in the molecular envelope, etc., if the rotation rate were known [Helled and Guillot 2013; Helled et al. 2015; Hubbard 2009]. Further information about the interior could come from the tidal Love number—the magnitude of the planet's response to tidal forces [Lainey et al. 2017]. The observations are astrometric data on the orbits of Saturn's moons spanning more than a century and include a large set of Cassini data. The study indicates significant tidal

dissipation inside the planet. In all cases, an independent measure of the rotation rate is important for probing the internal structure.

The tesseral harmonics have an effect on the rings, which are a sensitive seismometer for detecting the non-zonal gravity field [Hedman and Nicholson 2013, 2014]. The harmonics are of two types. One type has pattern speeds ranging from 807 to 834 degrees per day, for which the corresponding periods are 10 h 42 m to 10 h 22 m, respectively (Figure SATURN-15). These nearly bracket the periods derived from tracking the clouds at various latitudes in Saturn's atmosphere, and could be due to non-zonal structures rotating with the planet. The large range of periods prevents improving on cloud tracking estimates alone. The other types of tesseral harmonics have pattern speeds near five hours and are thought to be due to normal mode oscillations inside the planet. The precise frequencies of these normal modes depend both on the interior structure and the interior rotation rate, but as with the zonal harmonics, it is difficult to separate the two effects. This is an ongoing effort.

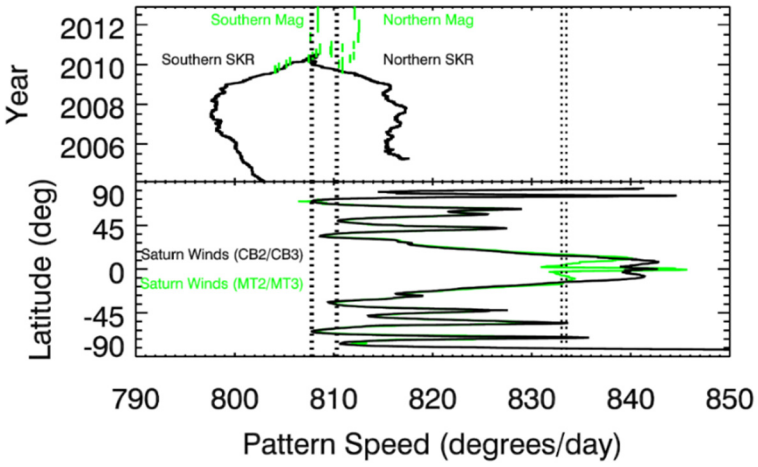

Figure SATURN-15. Ring seismology. The vertical dotted lines are the speeds of non-axisymmetric patterns in Saturn's rings. Only the patterns that match the planet's rotation are shown. They could be due to floating masses in the interior of Saturn. For comparison, periods of exterior magnetic fields, radio emissions, and clouds in the atmosphere are shown. Other patterns with speeds twice as fast are likely due to normal mode oscillations of the planet [Hedman and Nicholson 2014].

The precise frequencies of the normal modes depend both on the interior structure and the interior rotation rate. Parameters of the interior structure include the mass of the core, the helium mass fraction and the heavy-element mass fraction in the metallic and molecular envelopes, and the pressure at the metallic-molecular transition [Mankovich et al. 2019]. For a given rotation rate, the interior parameters are adjusted to give the observed values of J_2 and J_4. The rotation rate is varied to give the best fit to the observed frequencies of the ~20 normal modes whose resonant effect on the ring orbits makes them detectable. The planet's rotation affects the frequencies through the Coriolis and centrifugal forces and the ellipticity of level surfaces. The distribution of rotation periods resulting from a broad sample of interior models can be summarized as $10^h\ 33^m\ 38s^{+1m52s}_{-1m19s}$ [Mankovich et al. 2019]. The residuals of the fit do not exhibit any strong evidence of differential rotation inside the planet, but differential rotation cannot be ruled out. The rotation period

is consistent with predictions by Militzer et al. [2019] who combined interior models, which were constrained by Cassini's gravity measurements, with observations of the planet's oblateness by the Voyager spacecraft. Based on this analysis, a rotation period of 10:33:34 ±55 s is predicted for the planet's deep interior.

The even zonal harmonics, especially n = 6 and above, can be used to detect differential rotation inside the planet [Galanti and Kaspi 2017; Kaspi 2013]. This method is being used both with Cassini at Saturn and with Juno at Jupiter. The odd harmonics have been used only at Jupiter. The software to analyze these data was developed to be used on both planets [Galanti and Kaspi 2016; Galanti et al. 2017; Kaspi et al. 2016]. Cassini produced its best gravity data during six dives between the planet and the innermost ring during the final five months of the mission [Iess et al. 2019]. On these dives the spacecraft skimmed 2600–3900 km above the cloud tops while the radio link to Earth was monitored to determine the gravitational field of the planet and the mass of the rings. The gravity measurements yielded unexpectedly large values of the even zonal harmonics J_6, J_8 and J_{10}. These values do not match any interior model that assumes uniform rotation and makes reasonable assumptions about the equation of state and helium rain [Iess et al. 2019]. Galanti et al. [2019] confirmed that an acceptable solution can only be found for J_2 and J_4.

One can fit all the even harmonics J_2-J_{10} with a model where unknown winds extend through the planet on cylinders. The best fit is where the atmosphere at the equator rotates 4% faster than the deep interior, but the models also require a region that rotates more slowly than the deep interior, which is surprising because it is not seen in the cloud tracking data. One can also fit the harmonics by assuming the observed cloud-top winds extend to a finite depth. The best fit is with a finite depth of 9000 km. Qualitatively the two results are the same, since the cloud-top winds are fastest at the equator. The depth of the winds for Saturn is 2–3 times deeper than that for Jupiter, but the difference is explained by the more rapid increase of electrical conductivity with depth on Jupiter and the shallower point where magnetic drag suppresses differential rotation [Guillot et al. 2018].

Once the gravity signal of the deep winds is adequately incorporated into models for Saturn's interior, reasonable structures are obtained: The conditions of helium rain are compatible with predictions from ab initio computer simulations. Cores of heavy elements with 15–18 Earth masses are compatible with the core-accretion hypothesis, which requires a ~8 Earth mass core to trigger run-away gas accretion. The enrichment of heavy elements in the planet's molecular envelope of 1–3 times solar is lower than expected but still reasonable. This contrasts with the persistent conundrum for Jupiter, for which the inferred heavy abundances are near or subsolar.

A puzzling feature of this analysis is that the same model of the gravitational field cannot fit all of the six passes in a combined, multi-arc orbital solution [Iess et al. 2019]. The residuals represent unmodeled accelerations acting on Cassini over time scales of 20–60 min and could be due to time-varying tesseral harmonics. Convection in Saturn's interior is one possible source. Normal modes varying in amplitude and frequency is another. The data were eventually fit by assuming random accelerations of 10 minute duration acting within ±1 hour from pericenter [Iess

et al. 2019]. The hope is that these high-frequency accelerations do not significantly affect the determination of the even harmonics J_2-J_{10}.

Aurora, Chemistry, and Upper Atmosphere (SC2a)

Observe the upper atmosphere and the aurora as it changes on all time scales—minutes to years—and is affected by seasonal and solar cycle forcing.

- **Upper atmosphere (SC2a)**

The stratosphere entered in the discussion in the sections entitled Composition and chemistry, Seasonal variations, and Saturn's winds. To reduce the overlap between those sections and this one, we focus here on theoretical models and on the parts of the atmosphere above the stratosphere. The entire subject, upper atmosphere and ionosphere, is reviewed in the book chapter by Nagy [2009]. Species like C_2H_2 and C_2H_6 have chemical lifetimes in the stratosphere that are comparable to a season on Saturn, so they can be used as tracers of the meridional circulation and its annual reversal from north to south. At the equator the zonal winds in the stratosphere exhibit a 15-year oscillation that is accompanied by an oscillation of the temperature distribution symmetric about the equator to maintain thermal wind balance.

The simplest chemical model is a diurnally averaged 1D photochemical model with eddy diffusion chosen to represent dynamical processes. Moses et al. [2000a] developed a model that couples hydrocarbon and oxygen photochemistry, molecular and eddy diffusion, radiative transfer, and condensation to better constrain the chemical species and to identify the important physical processes that control the abundances. Moses et al. [2000b] consider the role of oxygen by comparing their model results with the observed abundances of H_2O and CO_2. They find that an external source of oxygen is necessary, and they estimate its magnitude. They mention micrometeoroid ablation and ring particle diffusion as likely sources.

In particular, electrostatic charging could lead to ejection of nanograins out of the ring plane and into the atmosphere by the electromagnetic force [Ip et al. 2016]. Further evidence of ring rain is seen in enhanced H_3^+ emissions at latitudes tied to magnetic field lines that cross the equatorial plane at the locations of the inner edges of the A-ring and B-ring and at the orbit of Enceladus [O'Donoghue et al. 2013, 2017].

Hesman et al. [2009] compare the output of the static photochemical model with observations of C_2H_2 and C_2H_6, and they find evidence of a meridional circulation. Guerlet et al. [2014] compare the temperatures computed from a radiative equilibrium model with temperatures observed by Cassini CIRS, and they find evidence that other processes, presumably related to dynamics, control Saturn's stratospheric thermal structure. Teanby et al. [2006] place new upper limits on halides in Saturn's stratosphere, but they advise that the abundances in the troposphere could be much larger. Sinclair et al. [2014] compare temperatures and gaseous abundances from Cassini with those from Voyager exactly one Saturn year later. They find that most of the change is due to the opposite phase of the 15-year oscillation and that other types of interannual variability are small.

Above the stratosphere, diffusive separation takes over and each gas's density falls off with altitude at its own individual scale height, which depends on its molecular weight. The altitude of the transition is called the homopause. Below the homopause, one finds gaseous hydrocarbons ranging in molecular weight at least up to benzene [Koskinen et al. 2016; Vervack and Moses 2015]. These hydrocarbons are the source of stratospheric haze particles at non-auroral latitudes [Moses et al. 2000a; Kim et al. 2012]. Above the homopause the major constituent is H_2, which continues into the exosphere where the molecules don't collide with each other except at the exobase [Koskinen et al. 2013]. The relatively high (380 K to 590 K) exospheric temperature at low to mid latitudes is a long-standing mystery [Shemansky and Liu 2012; Stallard et al. 2012b]. Despite the changing seasons, the high temperatures have persisted from the period of the Voyager flybys through the Cassini era [Koskinen et al. 2015]. High temperatures do occur in the auroral zones, but dynamical models strongly suggest that the upper atmosphere is geostrophically balanced and cannot convey the high-temperature air to lower latitudes (Figure SATURN-16). One possibility is that atmospheric gravity waves, which are often overlooked in models, could supply enough torque to overcome the Coriolis force and allow enough meridional overturning to warm the equatorial thermosphere [Müeller-Wodarg et al. 2019].

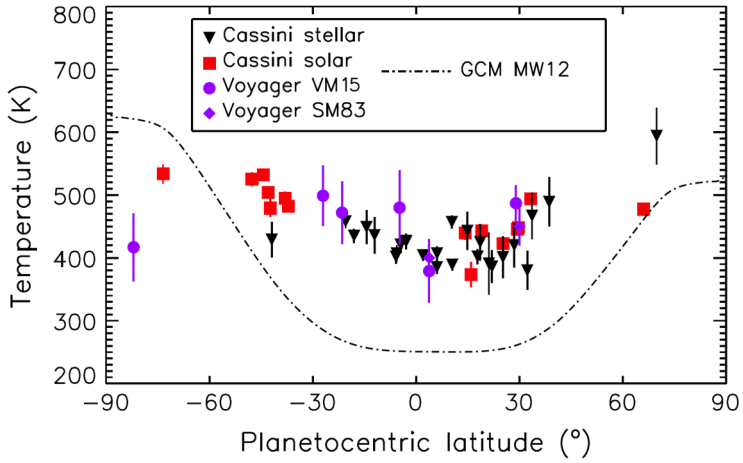

Figure SATURN-16. Comparison of Cassini UVIS observations with Voyager observations and with a 3-D general circulation model. The model result is represented by the smooth dot-dashed line, and it is significantly low (colder) equatorward of ±60° in both hemispheres. The problem is that the air from the polar regions, heated by auroral currents, cools before it reaches the lower latitudes. What keeps it warm is an ongoing mystery [Koskinen et al. 2015].

The first in situ measurements of the equatorial thermosphere occurred during the final month of the Cassini mission, when the spacecraft skimmed through the upper atmosphere on four periapses and also during the final plunge. The Ion Neutral Mass Spectrometer (INMS) measured the profiles of temperature and composition [Yelle et al. 2018]. The best fit to the exospheric temperature is in the range 340 to 370 K, with a value during the final plunge of 354 K. The helium profiles are consistent with diffusive equilibrium, but the methane profiles are not. Even well above the homopause, the CH_4/H_2 ratio is nearly constant with height. This points to an external source, the most likely being Saturn's rings [Yelle et al. 2018].

- **Aurora (SC2a)**

The aurora is caused by precipitating electrons striking the upper atmosphere. The source of the electrons is in the magnetosphere, and the subject is covered mainly in the section entitled Magnetospheres and Plasma Science (MAPS) Discipline Science Results. Some of the questions involve the energy and source of the electrons, how deep they penetrate into the atmosphere, and what effects they have on the temperatures, chemistry, and electromagnetic emissions associated with the aurora.

The aurora is observed in the ultraviolet [Gerard et al. 2013; Gustin et al. 2009, 2010, 2017], visible [Dyudina et al. 2016], infrared [Melin et al. 2011, 2016; O'Donoghue et al. 2014; Stallard et al. 2012a], and radio wavelengths [Lamy et al. 2009, 2013; Ye et al. 2016]. The currents associated with the electrons can be observed when the spacecraft flies through an auroral flux tube [Bunce et al. 2014]. And although the magnetosphere of Saturn is much less energetic than that of Jupiter, the footprint of the Enceladus flux tube has detectable emissions [Pryor et al. 2011], though not so bright as those of the Jovian moons: The geysers of Enceladus are weaker than the volcanoes of Io, and the magnetic field of Saturn is weaker than the magnetic field of Jupiter.

For a short, broad-brush summary of the magnetosphere, ionosphere, and atmosphere, we recommend Gombosi and Ingersoll [2010].

- **Ionosphere (S_AO4)** – Study the diurnal variations and magnetic control of the ionosphere of Saturn.

This science objective is captured in detail in the Magnetospheres and Plasma Science (MAPS) Discipline Science Results under the following AO and TM science objectives: **MN1b:** Conduct in situ studies of Saturn's ionosphere and inner radiation belt; **MN1c:** Investigate magnetospheric periodicities, their coupling to the ionosphere, and how the SKR periods are imposed from close to the planet (3–5 R_S) out to the deep tail; **MN2a:** Determine the coupling between Saturn's rings and ionosphere; and **MC1a:** Determine the temporal variability of Enceladus' plume (relevant to the Enceladus auroral footprint).

Further Science Objectives for Saturn Science

- **Water.** Measure the global water abundance and determine its role in bringing heat to the surface. Determine the role of moist convection in maintaining the large-scale motions. A Saturn probe to the base of the water cloud is a challenging but possible objective.
- **Rotation.** Determine Saturn's rotation period if such a number exists, or determine the spread of periods if differential rotation persists into the interior.
- **Noble gases.** Determine Saturn's noble gas abundances including helium, as done for Jupiter by the Galileo probe. A Saturn probe could measure noble gases to exquisite precision.

- **Weather layer.** Determine the vertical profiles of temperature, winds, clouds, condensable gases, longwave and shortwave radiation, and turbulence levels. A cloud-resolving model like those used in tropical meteorology, but tailored to the giant planets, is both timely and valuable. Again, a Saturn probe is needed.
- **Interior.** Using the power of ring seismometry and gravity sounding, improve the understanding of Saturn's internal equation of state, mass distribution, composition, and temperature distribution. Develop a fully coupled interior/weather-layer model as done for Earth's oceans and atmosphere.

SATURN DWG NON-SATURN SCIENCE RESULTS

- **Jupiter atmospheric dynamics (J_AO1)** – Extend the time for studies of atmospheric dynamics beyond the period accessible to the Galileo nominal mission.

Jupiter has a photogenic atmosphere; its colorful clouds provide ideal tracers of the winds (Figure SATURN-17). The light and dark bands—the zones and belts—and their associated jet streams have been observed from Earth for more than 100 years. The Great Red Spot (GRS) and its smaller cousins have been observed for just as long. Thus Jupiter is an atmospheric dynamics laboratory, where dynamical phenomena like waves, jets, eddies, and vortices can be studied without the complications of continents, oceans, and large seasonal swings. As it approached and flew past Jupiter in late 2000, Cassini provided three months of valuable data about the atmosphere. A 70-day movie shows the clouds in motion at all longitudes and latitudes up to within ~10 degrees of the poles. That movie in cylindrical and polar projections is PIA03452, PIA03453, and PIA03454, and is available at https://photojournal.jpl.nasa.gov/.

The GRS is at least 150 years old, although it could be much older. The three white ovals to the south of the GRS formed in the late 1930s and merged into one oval named BA in the late 1990s. All of these features are anticyclones with circumferential winds greater than 100 m s^{-1}. They drift slowly in longitude but stay fixed in latitude. Combined with Hubble Space Telescope and Galileo data, Cassini data were used to show that the GRS shrank by 15% from 1996 to 2006, both in terms of its visible appearance and its ring of circumferential winds [Asay-Davis et al. 2009; Shetty and Marcus 2010].

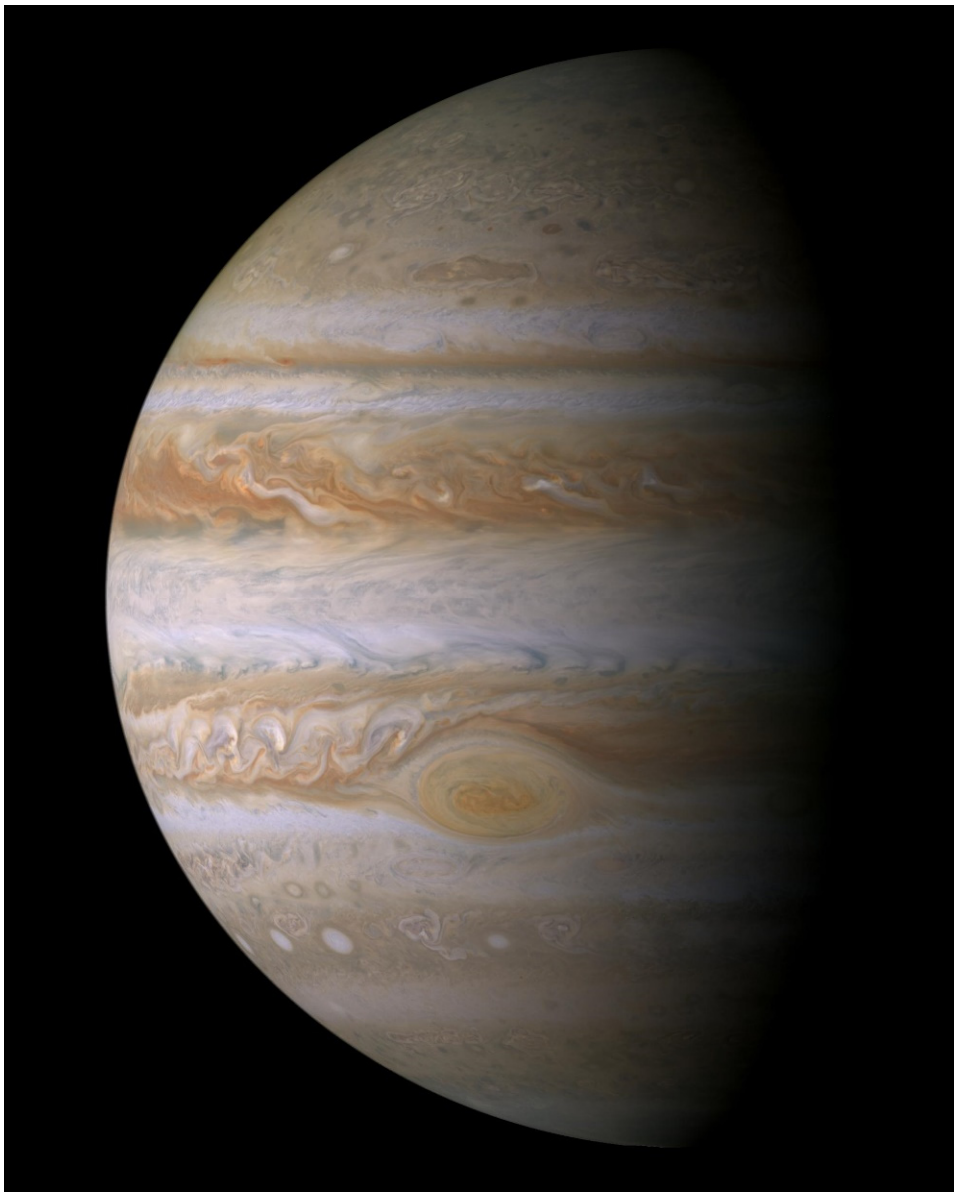

Figure SATURN-17. The highest-resolution, full-disk color mosaic of Jupiter ever taken. Jupiter more than filled the field of view of the ISS, so the mosaic was assembled from over 30 individual images, allowing for the planet's rotation as the images were taken.

The white ovals occupied a single latitude band with anticyclonic vorticity. They avoided each other for 60 years because they were separated by cyclonic regions encroaching into the band from the equatorward side [Youssef and Marcus 2003]. When the cyclonic regions got pushed out, the ovals merged. Peak velocities around oval BA remained steady while the color changed from white to red several years later. Using different techniques to measure winds and different definitions of the oval's edge, different groups have documented small changes in the properties of

BA over similar time periods [Hueso et al. 2009; Choi et al. 2010; Sussman et al. 2010]. The combination of Cassini ISS data and Hubble methane band data was used to understand the changes in vertical cloud structure as BA changed from white to red [Wong et al. 2011]. Using ISS data from the Cassini flyby [Li et al. 2004; Choi et al. 2013] and amateur telescopic data [Rogers et al. 2006], several authors have documented the life cycles—formation, shape, lifetime, mergers—of the more numerous smaller spots on Jupiter.

Jupiter's zonal jets are remarkably steady in comparison with Earth's jet streams, which change on time scales of one or two weeks (Figure SATURN-18). Cassini ISS documented only one latitude outside the equator, near 21° planetocentric, where the jet speed had changed by a modest amount from Voyager in 1979 to Cassini in 2000 [Porco et al. 2003; Asay-Davis et al. 2011]. Most of the observed variability is at the equator [Garcia-Melendo et al. 2011a] and is part of a regular ~4-year oscillation similar to the QBO on Earth [Simon-Miller et al. 2007; Simon-Miller and

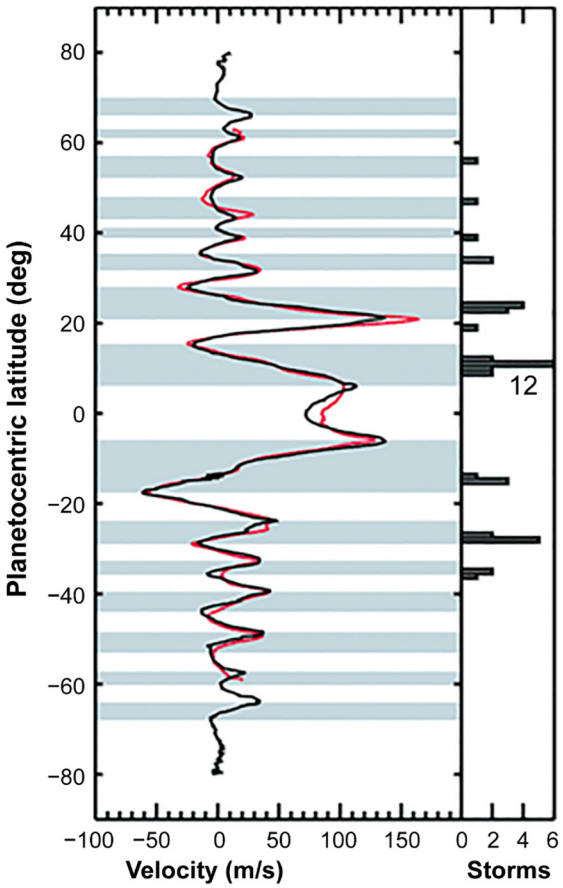

Figure SATURN-18. Atmospheric zonal velocity for Jupiter. The black curve is from Cassini ISS data in late 2000, and the red curve is from Voyager data in mid1979. The jets are remarkably steady over this 21-year interval [Porco et al. 2003].

Gierasch 2010]. Meridional transport is inferred indirectly from Cassini CIRS data that give the latitudinal distribution of C_2H_2 and C_2H_6, which have known chemical lifetimes and thereby track

the age of air masses in the stratosphere [Liang et al. 2005; Zhang et al. 2013b]. Vertical wind shear of the zonal winds is studied by tracking features at different wavelengths that probe different altitudes [Li et al. 2006c].

Waves in a planetary atmosphere provide information about the medium in which they propagate and also about the sources that excite them. Mesoscale waves—wavelengths ~100 km—are visible from space if the crests and troughs are marked by clouds. The thunder following a lightning strike and the sonic boom following a meteor impact are examples of intense sound waves. Cassini could not detect sound waves, but it did detect thunderstorms and lightning [Dyudina et al. 2004; Porco et al. 2003; Baines et al. 2007]. Voyager, Galileo, and New Horizons detected mesoscale wave trains with crests and troughs aligned north-south and wavelengths of ~300 km. Cassini apparently did not detect mesoscale waves [Arregi et al. 2009]. They may have been absent at the time of the Cassini flyby or perhaps the waves were unobservable due to lack of cloud tracers. One theory says the mesoscale waves are propagating gravity waves [Flasar and Gierasch 1986], and another theory says they are shear instabilities [Bosak and Ingersoll 2002]. The measured phase velocities seem inconsistent with both models [Simon et al. 2015] given reasonable assumptions about the vertical wind shears, so the nature of the mesoscale waves is uncertain.

Cassini also detected large scale periodic patterns with wavelengths ranging up to 20,000 km. Circumpolar waves have wavelengths and phase speeds that suggest they are Rossby waves [Barrado-Izagirre et al. 2008, 2009]. Simultaneous observations by ISS, UVIS, and CIRS allow one to probe the vertical structure and opacity sources of the waves [Li et al. 2006b]. Radio observations allow one to study how the passage of a wave affects the distribution of ammonia [Cosentino et al. 2017]. Cassini observations have been used to support various theories of wave-like features in the South Equatorial Belt—that they are either inertia-gravity waves or Rossby waves [Simon-Miller et al. 2012] or a pattern associated with baroclinic instability at that latitude [Rogers et al. 2016].

Wave mean-flow interactions and cascades of energy from one scale to another are fundamental processes in the dynamics of planetary atmospheres. One theory says that the zonal mean flow forms into a potential vorticity (PV) staircase. PV is a conserved dynamical tracer and the staircase consists of latitude bands with constant PV and sharp boundaries in between. However, quantitative analysis of the Cassini 70-day movie shows that the PV gradient reverses sign and is not zero as the staircase model predicts [Li et al. 2004; Read et al. 2006; Shetty and Marcus 2010]. The 70-day movie was also used to show that the eddy momentum transport is into the jets from neighboring latitudes, meaning that the eddies are supplying energy to the jets and not the reverse (Figure SATURN-19) [Salyk et al. 2006]. The eddies could be getting their energy from convection [Li et al. 2006a] or the latitudinal gradient of radiative heating, or both [Schneider and Liu 2009]. Fourier spectra of the 70-day movie data generally reveal an inverse energy cascade, where kinetic energy flows from intermediate scales to large scales [Choi and Showman 2011; Galperin et al. 2014; Hadjighasem and Haller 2016], but there is evidence of a forward cascade from intermediate scales down to small scales, which has been interpreted as energy input at the intermediate scales, perhaps associated with the radius of

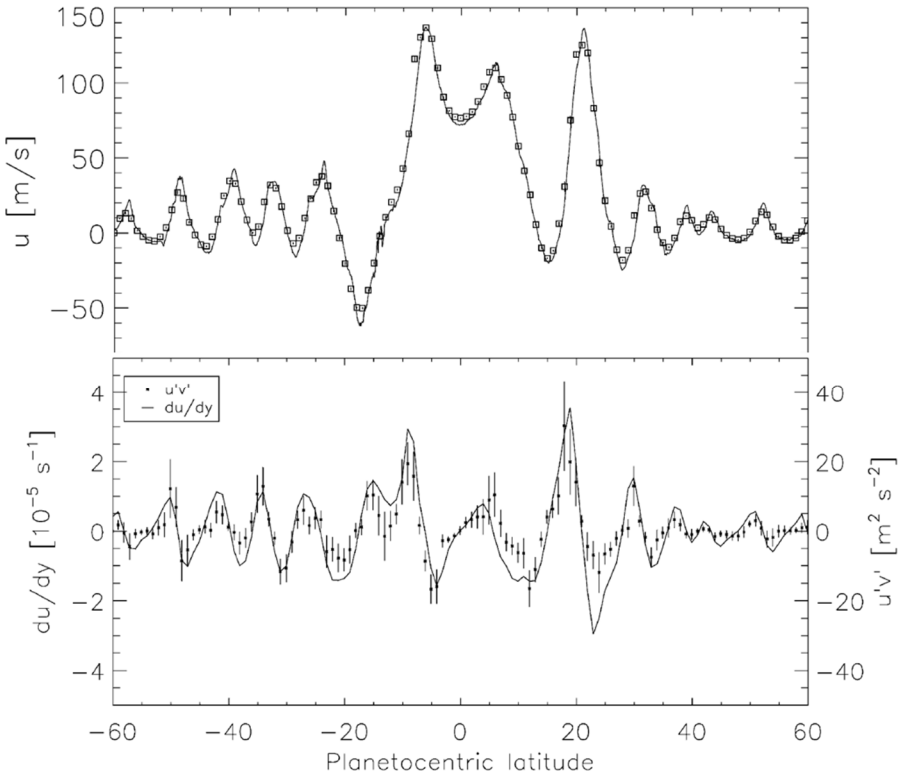

Figure SATURN-19. Eddy momentum transport for Jupiter from Cassini ISS. The eastward and northward eddy winds u′ and v′ are the departures from the zonal means. Their product $\overline{u'v'}$ averaged over longitude and multiplied by density is the northward eddy flux of eastward momentum. The fact that this quantity has the same sign as $\partial\overline{u}/\partial y$, which is the increase of the mean eastward wind with latitude, says that the eddies are putting energy into the jets and not the reverse [Salyk et al. 2006].

deformation through baroclinic instability [Young and Read 2017]. Others have compared visible features in the 70-day movie with fine-scale features in their 3-dimensional numerical models to test the models' treatment of unknown processes and parameters [Heimpel et al. 2005, 2016; Morales-Juberias and Dowling 2013].

- **Jupiter Global Atmospheric Structure and Composition (J_AO2)** – Infer global atmospheric thermal structure and composition with instrumentation not carried by the Galileo Orbiter, complementing the local in situ measurements of the Galileo Probe.

Reactive gases can serve as tracers that reveal regions of upwelling, downwelling, and meridional motion (Figure SATURN-20). During the Jupiter flyby, Cassini CIRS measured the latitude distributions of C_2H_2 and C_2H_6, which are produced in the upper stratosphere by photodissociation of methane. The rate of production is greatest at the equator where the solar ultraviolet (UV) is greatest. C_2H_2 has a chemical lifetime that is short compared to the meridional overturning, so it decreases toward the poles in response to the reduced solar UV. C_2H_6 has a longer chemical lifetime, so following a fluid parcel it increases with time the longer the parcel

spends in the stratosphere. The abundance of C_2H_6 increases toward the poles [Nixon et al. 2007, 2010], suggesting a meridional circulation in the stratosphere with upwelling at the equator and downwelling at the poles. The circulation revealed from the distributions of C_2H_2 and C_2H_6 aids in understanding the origin and chemical lifetimes of HCN and CO_2, which were also measured by CIRS [Lellouch et al. 2006].

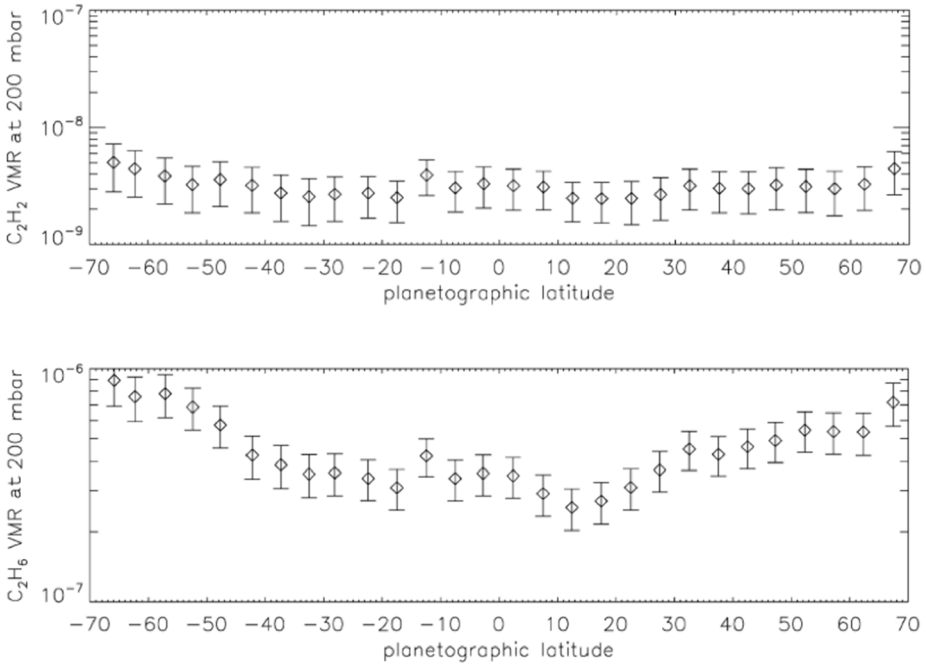

Figure SATURN-20. Chemical tracers in Jupiter's atmosphere at 200 mbar from Cassini CIRS. Both acetylene and ethane are formed at higher altitudes than these observations. C_2H_2 has a shorter lifetime once it is formed than C_2H_6 does, so it decays on the downdrafts faster than C_2H_6. The lower panel indicates downdrafts at the pole and updrafts at the equator. The upper panel shows that the time constant of this circulation is longer than the lifetime of the C_2H_2 molecule, because it has decayed before reaching the 200 mbar level [Nixon et al. 2007].

Since the stratosphere is stably stratified, to maintain steady state the updrafts must be heated and the downdrafts must be cooled. The decrease of sunlight toward the poles is consistent with updrafts at the equator and downdrafts at the poles. CIRS measurements of stratospheric temperatures and abundances of radiatively active gases are used to model the radiative forcing [Zhang et al. 2013a, 2013b], which includes the effects of stratospheric aerosols [Zhang et al. 2013c, 2015].

Cassini CIRS also measured the latitude distributions of phosphine [Irwin et al. 2004; Fletcher et al. 2009a] and ammonia [Achterberg et al. 2006]. The measurements refer to the upper troposphere, at the 100–500 mbar level, and they tell a consistent story. Both gases are removed from the atmosphere at upper levels, phosphine by photodissociation and ammonia by condensation, and both have maximum abundance at the equator and reduced abundance in the cyclonic belts on either side of the equator. This indicates rapid uplift or strong vertical mixing in

the equatorial zone and descent in the neighboring belts. Probing still deeper into the troposphere, Cassini VIMS detected a 3 μm absorption that could be a mixture of NH_4SH and NH_3 [Brown et al. 2003; Sromovsky and Fry 2010] and provided new insights into the composition of fresh ammonia clouds [Sromovsky and Fry 2018].

Gaseous abundances can provide clues to planet formation. CIRS measured the nitrogen isotopic ratio in ammonia [Abbas et al. 2004; Fouchet et al. 2004a]. The ratio is similar to that on the Sun but different from that on Earth, suggesting that the Earth was somehow isolated from the main reservoir of nitrogen during solar system formation. The hydrogen halides, on the other hand, are depleted relative to solar composition and support the halogens' condensation in ammonium salts [Fouchet et al. 2004b].

The Cassini flyby provided insights into aurora-related phenomena on Jupiter as well. UVIS observations of the He 584 Å line were used to infer enhanced eddy mixing in the polar regions, which may account for the enhancement of heavy hydrocarbons there [Parkinson et al. 2006]. Alternately, the enhancement of C_2H_2 and C_2H_6 in the polar regions could be explained by a combination of auroral-driven chemistry and advection by the meridional circulation [Sinclair et al. 2017]. CIRS observations have also been used to study the sources of heating in the polar stratosphere from 1–10 mbar [Sinclair et al. 2018]. The result is that heating by auroral soot particles dominates at 1 mbar altitude, and that heating by charged particles dominates at 10 mbar. Cassini VIMS observations have been used to produce the first maps of H_3^+ emission, temperature, and column density on Jupiter's nightside [Stallard et al. 2015]. The enhanced emission in the polar regions is produced by enhanced H_3^+ density rather than higher temperatures, which further points to the importance of auroral chemistry in that region.

Because of its high spatial and spectral resolution and full angular coverage during the flyby, Cassini obtained useful information about the clouds of Jupiter. Cloud color is a long-standing uncertainty: What chemical gives the Red Spot its redness? How many coloring agents are there? Comparison of laboratory experiments and visible spectra from Cassini VIMS suggests that the red chromophore is the product of photolyzed ammonia reacting with acetylene [Carlson et al. 2016; Baines et al. 2019]. The chromophore occurs in an optically thin layer above the main cloud deck, and may require upward displacement of the air mass to form. A principal component analysis of Cassini ISS data indicates that the red chromophore explains most of the variance across the planet, but a second coloring agent is required to explain the brownish color of the cyclones in Jupiter's North Equatorial Belt [Ordonez-Etxeberria et al. 2016].

The vertical structure of the cloud layers is another long-standing unknown. Cassini CIRS thermal spectra were used to probe into the clouds at a wavelength of 7.18 μm, where the ammonia gas is relatively transparent [Matcheva et al. 2005]. The result is that cloud base is at 0.9–1.1 bar, which is deeper than the nominal ammonia cloud base and might imply another, deeper cloud, possibly NH_4SH. Cassini VIMS covers 4.5–5.1 μm, another wavelength range where the gas is relatively transparent. Holes in the cloud allow thermal radiation to space, so the holes appear as hot spots. The cloud is found to be spectrally flat and at a pressure of 1.2 bar or deeper [Giles et al. 2015]. Pure NH_3 cloud and pure NH_4SH cloud do not match the spectra, and some kind of

coating is implied. Despite the possibility of coatings, CIRS has detected the spectral signature of NH_3 ice particles in the upper tropospheric clouds [Wong et al. 2004].

The planet's global energy budget is a key to its evolution and internal processes, including the separation of helium from hydrogen in the metallic interior. To determine the energy budget accurately, one would have to measure the thermal emission and scattered sunlight at all seasons, latitudes, longitudes, wavelengths, emission angles, incident angles, and phase angles. In practice, one samples these quantities and uses models to fill the gaps. Cassini CIRS, VIMS, and ISS all contribute to this estimate [Simon-Miller et al. 2006; Li et al. 2012; Sato et al. 2013; Mayorga et al. 2016]. North-south asymmetries and changes from Voyager to Cassini are present at the level of a few percent, but whether these are random fluctuations or systematic trends is uncertain.

Venus Atmosphere Observations

The Venus flybys yielded useful data at a variety of wavelengths. The VIMS instrument detected thermal emission from the hot surface at wavelengths of 0.85 and 0.90 μm, and thereby provided a new technique for exploring the surface mineralogy [Baines et al. 2000]. In an attempt to image the surface, the RADAR instrument was operated at 2.2 cm in both scatterometric and radiometric modes during the encounters, but only the thermal emission from the thick absorbing atmosphere was detected [Lorenz et al. 2001]. The UVIS instrument studied the airglow of Venus, focusing on N_2, C, O, and CO as clues to the excitation mechanisms and abundances [Hubert et al. 2010, 2012; Gerard et al. 2011]. Lightning on Venus is a long-standing controversial subject. The RPWS instrument on Cassini searched for lightning signals in the frequency range 0.125 to 16 MHz and found none, even though they easily detected lightning at rates of 70 s^{-1} during the Earth flyby several months later [Gurnett et al. 2001].

ACRONYMS

Note: For a complete list of Acronyms, refer to Cassini Acronyms – Attachment A.

AO	Announcement of Opportunity
CAKE	Cassini Apoapses for Kronian Exploration
CIRS	Composite Infrared Spectrometer
CSM	Cassini Solstice Mission
DWG	Discipline Working Group
GCM	General Circulation Model
GRS	Great Red Spot
HST	Hubble Space Telescope
IDS	Interdisciplinary Scientists
IR	Infrared
ISS	Imaging Science Subsystem
MAG	Magnetometer
MAPS	Magnetospheres and Plasma Science
PIE	Pre Integration Event
PSG	Project Science Group
PV	Potential Vorticity
QBO	Quasi-Biennial Oscillation
RADAR	Titan Radar Mapper
RPWS	Radio and Plasma Wave Science
SAMWG	Saturn Atmospheric Modeling Working Group
SED	Saturn Electrostatic Discharges
SKR	Saturn Kilometric Radiation
SWG	Saturn Working Group
TM	Traceability Matrix
TWT	Target Working Team
UV	Ultraviolet
UVIS	Ultraviolet Imaging Spectrograph
VIMS	Visual and Infrared Mapping Spectrometer
WG	Working Group

REFERENCES

Disclaimer: The partial list of references below correspond with in-text references indicated in this report. For all other Cassini references, refer to Attachment B – References & Bibliographies; Attachment C – Cassini Science Bibliographies; the sections entitled References contributed by individual Cassini instrument and discipline teams located in Volume 1 Sections 3.1 and 3.2 Science Results; and other resources outside of the Cassini Final Mission Report.

Abbas, M. M., A. LeClair, E. Woodard, M. Young, M. Stanbro, F. M. Flasar, et al., (2013), Distribution of CO2 in Saturn's atmosphere from Cassini/CIRS infrared observations, The Astrophysical Journal, 776, 2, 73, doi: 10.1088/0004-637x/776/2/73.

Abbas, M. M., A. LeClair, T. Owen, B. J. Conrath, F. M. Flasar, V. G. Kunde, et al., (2004), The nitrogen isotopic ratio in Jupiter's atmosphere from observations by the Composite Infrared Spectrometer on the Cassini spacecraft, The Astrophysical Journal, 602, 1063–1074, doi: 10.1086/381084.

Achterberg, R. K., Flasar, F. M., Bjoraker, G. L., Hesman, B. E., Gorius, N. J. P., Mamoutkine, A. A., et al., (2018), Thermal emission from Saturn's polar cyclones, Geophysical Research Letters, 45, 11, 5312–5319, doi: 10.1029/2018GL078157.

Achterberg, R. K., P. J. Gierasch, B. J. Conrath, L. N. Fletcher, B. E. Hesman, G. L. Bjoraker, F. M. Flasar, (2014), Changes to Saturn's zonal-mean tropospheric thermal structure after the 2010-2011 northern hemisphere storm, The Astrophysical Journal, 786, 2, 92, doi: 10.1088/0004-637x/786/2/92.

Achterberg, R. K., B. J. Conrath, P. J. Gierasch, (2006), Cassini CIRS retrievals of ammonia in Jupiter's upper troposphere, Icarus, 182, 169–180, doi: 10.1016/j.icarus.2005.12.020.

Adriani, A., M. L. Moriconi, E. D'Aversa, F. Oliva, G. Filacchione, (2015), Faint luminescent ring over Saturn's polar hexagon, The Astrophysical Journal, 808, L16, doi: 10.1088/2041-8205/808/1/l16.

Aguiar, A. C. B., P. L. Read, R. D. Wordsworth, T. Salter, Y. H. Yamazaki, (2010), A laboratory model of Saturn's north polar hexagon, Icarus, 206, 2, 755-763, doi: 10.1016/j.icarus.2009.10.022.

Anderson, J. D., and G. Schubert, (2007), Saturn's gravitational field, internal rotation, and interior structure. Science, 317, 1384–1387, doi: 10.1126/science.1144835.

Antunano, A., T. del Río-Gaztelurrutia, A. Sánchez-Lavega, P. L. Read, L. N. Fletcher, (2019), Potential vorticity of Saturn's polar regions, J. Geophys. Res., 124, 186-201, doi: 10.1029/2018JE005764.

Antunano, A., T. del Rio-Gaztelurrutia, A. Sanchez-Lavega, J. Rodriguez-Aseguinolaza, (2018), Cloud morphology and dynamics in Saturn's northern polar region, Icarus, 299, 117–132, doi: 10.1016/j.icarus.2017.07.017.

Antunano, A., T. del Rio-Gaztelurrutia, A. Sanchez-Lavega, R. Hueso, (2015), Dynamics of Saturn's polar regions, Journal of Geophysical Research-Planets, 120, 2, 155–176, doi: 10.1002/2014je004709.

Arregi, J., J. F. Rojas, R. Hueso, A. Sanchez-Lavega, (2009), Gravity waves in Jupiter's equatorial clouds observed by the Galileo orbiter, Icarus, 202, 358–360, doi: 10.1016/j.icarus.2009.03.028.

Asay-Davis, X. S., P. S. Marcus, M. H. Wong, I. de Pater, (2011), Changes in Jupiter's zonal velocity between 1979 and 2008, Icarus, 211, 1215–1232, doi: 10.1016/j.icarus.2010.11.018.

Asay-Davis, X. S., P. S. Marcus, M. H. Wong, I. de Pater, (2009), Jupiter's shrinking Great Red Spot and steady Oval BA: Velocity measurements with the "Advection Corrected Correlation Image Velocimetry" automated cloud-tracking method, Icarus, 203, 164–188, doi: 10.1016/j.icarus.2009.05.001.

Atreya, S. K., A. Crida, T. Guillot, J. I. Lunine, N. Madhusudhan, M. Mousis, (2019), The origin and evolution of Saturn, with exoplanet perspective, in Saturn in the 21st Century, (eds.) K. Baines, M. Flasar, N. Krupp, T. Stallard), Cambridge University Press, pp. 5–43.

Atreya, S. K., P. R. Mahaffy, H. B. Niemann, M. H. Wong, T. C. Owen, (2003), Composition and origin of the atmosphere of Jupiter - an update, and implications for the extrasolar giant planets, Planetary and Space Science 51, 2, 105–112, doi: 10.1016/s0032-0633(02)00144-7.

Atreya, S. K., M. H. Wong, T. C. Owen, P. R. Mahaffy, H. B. Niemann, I. de Pater, P. Drossart, T. Encrenaz, (1999), A comparison of the atmospheres of Jupiter and Saturn: deep atmospheric composition, cloud structure, vertical mixing, and origin, Planetary and Space Science, 47,10–11, 1243–1262, doi: 10.1016/s0032-0633(99)00047-1.

Aurnou, J., M. Heimpel, L. Allen, E. King, J. Wicht, (2008), Convective heat transfer and the pattern of thermal emission on the gas giants, Geophysical Journal International, 173, 3, 793–801, doi: 10.1111/j.1365-246X.2008.03764.x.

Auwera, J. V., N. Moazzen-Ahmadi, J. M. Flaud, (2007), Toward an accurate database for the 12 μm region of the ethane spectrum, Astrophysical Journal, 662, 1, 750–757.

Baines, K. H., L. A. Sromovsky, R. W. Carlson, T. W. Momary, T. W., P. M. Fry, (2019), The visual spectrum of Jupiter's Great Red Spot accurately modeled with aerosols produced by photolyzed ammonia reacting with acetylene, Icarus 330, 217–229.

Baines, K. H., M. L. Delitsky, T. W. Momary, R. H. Brown, B. J. Buratti, R. N. Clark, P. D. Nicholson, (2009a), Storm clouds on Saturn: Lightning-induced chemistry and associated materials consistent with Cassini/VIMS spectra, Planetary and Space Science, 57, 14–15, 1650–1658, doi: 10.1016/j.pss.2009.06.025.

Baines, K. H., T. W. Momary, L. N. Fletcher, A. P. Showman, M. Roos-Serote, R. H. Brown, B. J. Buratti, R. N. Clark, P. D. Nicholson, (2009b), Saturn's north polar cyclone and hexagon at depth revealed by Cassini/VIMS, Planetary and Space Science, 57, 14–15, 1671–1681, doi: 10.1016/j.pss.2009.06.026.

Baines, K. H., A. A. Simon-Miller, G. S. Orton, H. A. Weaver, A. Lunsford, T. W. Momary, et al., (2007), Polar lightning and decadal-scale cloud variability on Jupiter, Science, 318, 226–229, doi: 10.1126/science.1147912.

Baines, K. H., P. Drossart, T. W. Momary, V. Formisano, C. Griffith, G. Bellucci, J. P. Bibring, et al., (2005), The atmospheres of Saturn and Titan in the near-infrared: First results of Cassini/VIMS, Earth Moon and Planets, 96, 3–4, 119–147, doi: 10.1007/s11038-005-9058-2.

Baines, K. H., G. Bellucci, J. P. Bibring, R. H. Brown, B. J. Buratti, E. Bussoletti, et al., (2000), Detection of sub-micron radiation from the surface of Venus by Cassini/VIMS, Icarus, 148, 307–311, doi: 10.1006/icar.2000.6519.

Banfield, D., B. J. Conrath, P. J. Gierasch, P. D. Nicholson, K. Matthews, (1998), Near-IR spectrophotometry of Jovian aerosols - Meridional and vertical distributions, Icarus, 134, 1, 11–23, doi: 10.1006/icar.1998.5942.

Barrado-Izagirre, N., S. Perez-Hoyos, A. Sanchez-Lavega, (2009), Brightness power spectral distribution and waves in Jupiter's upper cloud and hazes, Icarus, 202, 181–196, doi: 10.1016/j.icarus.2009.02.015.

Barrado-Izagirre, N., A. Sanchez-Lavega, S. Perez-Hoyos, R. Hueso, (2008), Jupiter's polar clouds and waves from Cassini and HST images: 1993-2006. Icarus, 194, 173–185, doi: 10.1016/j.icarus.2007.08.025.

Barstow, J. K., P. G. J. Irwin, L. N. Fletcher, R. S. Giles, C. Merlet, (2016), Probing Saturn's tropospheric cloud with Cassini/VIMS, Icarus, 271, 400–417, doi: 10.1016/j.icarus.2016.01.013.

Beebe, R. F., (2005), Comparative study of the dynamics of the outer planets, Space Science Reviews, 116, 1–2, 137–154, doi: 10.1007/s11214-005-1952-4.

Bosak, T., and A. P. Ingersoll, (2002), Shear instabilities as a probe of Jupiter's atmosphere, Icarus, 158, 2, 401–409, doi: 10.1006/icar.2002.6886.

Brown, R. H., K. H. Baines, G. Bellucci, J. P. Bibring, B. J. Buratti, F. Capaccioni, et al., (2003), Observations with the Visual and Infrared Mapping Spectrometer (VIMS) during Cassini's flyby of Jupiter, Icarus, 164, 461–470, doi: 10.1016/s0019-1035(03)00134-9.

Brueshaber, S. R., K. M. Sayanagi, T. E. Dowling, (2019), Dynamical regimes of giant planet polar vortices, Icarus 323, 46–61.

Bunce, E. J., D. C. Grodent, S. L. Jinks, David J. Andrews, S. V. Badman, Andrew J. Coates, S. W. H. Cowley, et al., (2014), Cassini nightside observations of the oscillatory motion of Saturn's northern auroral oval, Journal of Geophysical Research-Space Physics, 119, 5, 3528–3543, doi: 10.1002/2013ja019527.

Cao, Hao, C. T. Russell, U. R. Christensen, M. K. Dougherty, M. E. Burtonm (2011), Saturn's very axisymmetric magnetic field: No detectable secular variation or tilt, Earth and Planetary Science Letters 304, no. 1–2, 22–28.

Carlson, R. W., K. H. Baines, M. S. Anderson, G. Filacchione, A. A. Simon, (2016), Chromophores from photolyzed ammonia reacting with acetylene: Application to Jupiter's Great Red Spot, Icarus, 274, 106–115, doi: 10.1016/j.icarus.2016.03.008.

Cavalie, T., M. Dobrijevic, L. N. Fletcher, J. C. Loison, K. M. Hickson, V. Hue, P. Hartogh, (2015), Photochemical response to the variation of temperature in the 2011–2012 stratospheric vortex of Saturn, Astronomy & Astrophysics, 580, doi: 10.1051/0004-6361/201425444.

Choi, D. S., A. P. Showman, A. R. Vasavada, A. A. Simon-Miller, (2013), Meteorology of Jupiter's equatorial hot spots and plumes from Cassini, Icarus, 223, 832–843, doi: 10.1016/j.icarus.2013.02.001.

Choi, D. S., and A. P. Showman, (2011), Power spectral analysis of Jupiter's clouds and kinetic energy from Cassini, Icarus, 216, 597–609, doi: 10.1016/j.icarus.2011.10.001.

Choi, D. S., A. P. Showman, A. R. Vasavada, (2010), The evolving flow of Jupiter's White Ovals and adjacent cyclones, Icarus, 207, 359–372, doi: 10.1016/j.icarus.2009.10.013.

Choi, D. S., A. P. Showman, R. H. Brown, (2009), Cloud features and zonal wind measurements of Saturn's atmosphere as observed by Cassini/VIMS, Journal of Geophysical Research-Planets, 114, doi: 10.1029/2008je003254.

Conrath, B. J., and D. Gautier, (2000), Saturn helium abundance: A reanalysis of Voyager measurements, Icarus, 144, 1, 124–134, doi: 10.1006/icar.1999.6265.

Conrath, B. J., D. Gautier, R. A. Hanel, J. S. Hornstein, (1984), The helium abundance of Saturn from Voyager measurements, Astrophysical Journal, 282, 2, 807-815, doi: 10.1086/162267.

Cosentino, R. G., B. Butler, B. Sault, R. Morales-Juberias, A. Simon, I. de Pater, (2017), Atmospheric waves and dynamics beneath Jupiter's clouds from radio wavelength observations, Icarus, 292, 168–181, doi: 10.1016/j.icarus.2017.01.006.

Del Genio, A. D., and J. M. Barbara, (2016), An objective classification of Saturn cloud features from Cassini ISS images, Icarus, 271, 222–236, doi: 10.1016/j.icarus.2016.02.011.

Del Genio, A. D., and J. M. Barbara, (2012), Constraints on Saturn's tropospheric general circulation from Cassini ISS images, Icarus, 219, 2, 689–700, doi: 10.1016/j.icarus.2012.03.035.

Del Genio, A. D., R. K. Achterberg, K. H. Baines, F. M. Flasar, P. L. Read, A. Sanchez-Lavega, A. P. Showman, (2009), Saturn atmospheric structure and dynamics, In Saturn from Cassini-Huygens, (eds.) M. K. Doughterty, L. W. Esposito, S. M. Krimigis, pp. 113–159, Springer, Dordrecht, Netherlands.

Del Genio, A. D., J. M. Barbara, J. Ferrier, A. P. Ingersoll, R. A. West, A. R. Vasavada, J. Spitale, C. C. Porco, (2007), Saturn eddy momentum fluxes and convection: First estimates from Cassini images, Icarus, 189, 2, 479–492, doi: 10.1016/j.icarus.2007.02.013.

del Rio-Gaztelurrutia, T., A. Sanchez-Lavega, A. Antunano, J. Legarreta, E. Garcia-Melendo, K. M. Sayanagi, et al., (2018), A planetary-scale disturbance in a long living three vortex coupled system in Saturn's atmosphere, Icarus, 302, 499–513, doi: 10.1016/j.icarus.2017.11.029.

del Rio-Gaztelurrutia, T., J. Legarreta, R. Hueso, S. Perez-Hoyos, A. Sanchez-Lavega, (2010), A long-lived cyclone in Saturn's atmosphere: Observations and models, Icarus, 209, 2, 665–681, doi: 10.1016/j.icarus.2010.04.002.

Desch, M. D., and M. L. Kaiser, (1981), Voyager measurement of the rotation period of Saturn's magnetic field, Geophysical Research Letters, 8, 3, 253–256, doi: 10.1029/GL008i003p00253.

Devi, V. M., I. Kleiner, R. L. Sams, L. R. Brown, D. C. Benner, L. N. Fletcher, (2014), Line positions and intensities of the phosphine (PH3) pentad near 4.5 μm, Journal of Molecular Spectroscopy, 298, 11–23, doi: 10.1016/j.jms.2014.01.0130022-2852.

Dobrijevic, M., T. Cavalie, F. Billebaud, (2011), A methodology to construct a reduced chemical scheme for 2D-3D photochemical models: Application to Saturn, Icarus, 214, 1, 275–285, doi: 10.1016/j.icarus.2011.04.027.

Dougherty, M., and Cassini Magnetometer Team, (2017), Cassini's magnetometer at Saturn, Astronomy & Geophysics, 58, 4, 36–42, doi: 10.1093/astrogeo/atx140.

Dowling, T. E., (1995), Dynamics of Jovian atmospheres, Annual Review of Fluid Mechanics, 27, 293–334, doi: 10.1146/annurev.fl.27.010195.001453.

Dubrovin, D., A. Luque, F. J. Gordillo-Vazquez, Y. Yair, F. C. Parra-Rojas, U. Ebert, C. Price, (2014), Impact of lightning on the lower ionosphere of Saturn and possible generation of halos and sprites, Icarus, 241, 313–328, doi: 10.1016/j.icarus.2014.06.025.

Dyudina, U. A., X. Zhang, L. Li, P. Kopparla, A. P. Ingersoll, L. Dones, A. Verbiscer, Y. L. Yung, (2016), Reflected light curves, spherical and Bond albedos of Jupiter- and Saturn-like exoplanets, The Astrophysical Journal, 822, 2, 76, doi: 10.3847/0004-637x/822/2/76.

Dyudina, U. A., A. P. Ingersoll, S. P. Ewald, C. C. Porco, G. Fischer, Y. Yair, (2013), Saturn's visible lightning, its radio emissions, and the structure of the 2009-2011 lightning storms, Icarus, 226, 1, 1020–1037, doi: 10.1016/j.icarus.2013.07.013.

Dyudina, U. A., A. P. Ingersoll, S. P. Ewald, C. C. Porco, G. Fischer, W. S. Kurth, R. A. West, (2010), Detection of visible lightning on Saturn, Geophysical Research Letters, 37, doi: 10.1029/2010gl043188.

Dyudina, U. A., A. P. Ingersoll, S. P. Ewald, A. R. Vasavada, R. A. West, K. H. Baines, T. W. Momary, et al., (2009), Saturn's south polar vortex compared to other large vortices in the Solar System, Icarus, 202, 1, 240–248, doi: 10.1016/j.icarus.2009.02.014.

Dyudina, U. A., A. P. Ingersoll, S. P. Ewald, A. R. Vasavada, R. A. West, A. D. Del Genio, J. M. Barbara, et al., (2008), Dynamics of Saturn's south polar vortex, Science, 319, 5871, 1801–1801, doi: 10.1126/science.1153633.

Dyudina, U. A., A. P. Ingersoll, S. P. Ewald, C. C. Porco, G. Fischer, W. Kurth, M. Desch, A. Del Genio, J. Barbara, J. Ferrier, (2007), Lightning storms on Saturn observed by Cassini ISS and RPWS during 2004-2006, Icarus, 190(2), 545-555, doi: 10.1016/j.icarus.2007.03.035.

Dyudina, U. A., A. D. Del Genio, A. P. Ingersoll, C. C. Porco, R. A. West, A. R. Vasavada, J. M. Barbara, (2004), Lightning on Jupiter observed in the H-alpha line by the Cassini imaging science subsystem, Icarus, 172, 24–36, doi: 10.1016/j.icarus.2004.07.014.

Farrell, W. M., M. L. Kaiser, G. Fischer, P. Zarka, W. S. Kurth, D. A. Gurnett, (2007), Are Saturn electrostatic discharges really superbolts? A temporal dilemma, Geophysical Research Letters, 34, 6, doi: 10.1029/2006gl028841.

Fegley, B., and K. Lodders, (1994), Chemical Models of the deep atmospheres of Jupiter and Saturn, Icarus, 110, 1, 117–154, doi: 10.1006/icar.1994.1111.

Fischer, G., S. Y. Ye, J. B. Groene, A. P. Ingersoll, K. M. Sayanagi, J. D. Menietti, W. S. Kurth, D. A. Gurnett, (2014), A possible influence of the Great White Spot on Saturn kilometric radiation periodicity, Annales Geophysicae, 32, 12, 1463–1476, doi: 10.5194/angeo-32-1463-2014.

Fischer, G., W. S. Kurth, D. A. Gurnett, P. Zarka, U. A. Dyudina, A. P. Ingersoll, S. P. Ewald, et al., (2011), A giant thunderstorm on Saturn, Nature, 475, 7354, 75–77, doi: 10.1038/nature10205.

Fischer, G., D. A. Gurnett, W. S. Kurth, F. Akalin, P. Zarka, U. A. Dyudina, W. M. Farrell, M. L. Kaiser, (2008), Atmospheric electricity at Saturn, Space Science Reviews, 137, 1–4, 271–285, doi: 10.1007/s11214-008-9370-z.

Fischer, G., W. S. Kurth, U. A. Dyudina, M. L. Kalser, P. Zarka, A. Lecacheux, A. P. Ingersoll, D. A. Gurnett, (2007), Analysis of a giant lightning storm on Saturn, Icarus, 190, 2, 528–544, doi: 10.1016/j.icarus.2007.04.002.

Fischer, G., M. D. Desch, P. Zarka, M. L. Kaiser, D. A. Gurnett, W. S. Kurth, W. Macher, et al., (2006a), Saturn lightning recorded by Cassini/RPWS in 2004, Icarus, 183, 1, 135–152, doi: 10.1016/j.icarus.2006.02.010.

Fischer, G., W. Macher, D. A. Gurnett, M. D. Desch, A. Lecacheux, P. Zarka, W. S. Kurth, M. L. Kaiser, (2006b), Discrimination between Jovian radio emissions and Saturn electrostatic discharges, Geophysical Research Letters, 33, 21, doi: 10.1029/2006gl026766.

Flasar, F. M., (2005), Temperatures, winds, and composition in the Saturnian system, Science, 307, 5713, 1247–1251. doi: 10.1126/science.1105806.

Flasar, F., and P. Gierasch, (1986), Mesoscale waves as a probe of Jupiter's deep atmosphere, Journal of the Atmospheric Sciences, 43, 22, 2683–2707, doi: 10.1175/1520-0469(1986)043<2683:MWAAPO>2.0.CO;2.

Fletcher, L. N., T. K. Greathouse, S. Guerlet, J. I. Moses, R. A. West, (2018), Saturn’s seasonally changing atmosphere: thermal structure, composition and aerosols. In Saturn in the 21st Century, (eds.) K. H. Baines, F. M. Flasar, N. Krupp, T. Stallard, Cambridge University Press, pp. 251–294, doi: 10.1017/9781316227220.010.

Fletcher, L. N., S. Guerlet, G. S. Orton, R. G. Cosentino, T. Fouchet, P. G. J. Irwin, L. M. Li, F. M. Flasar, N. Gorius, R. Morales-Juberias, (2017), Disruption of Saturn's quasi-periodic equatorial oscillation by the great northern storm, Nature Astronomy, 1, 11, 765–770, doi: 10.1038/s41550-017-0271-5.

Fletcher, L. N., P. G. J. Irwin, R. K. Achterberg, G. S. Orton, F. M. Flasar, (2016), Seasonal variability of Saturn's tropospheric temperatures, winds and para-H2 from Cassini far-IR spectroscopy, Icarus, 264, 137–159, doi: 10.1016/j.icarus.2015.09.009.

Fletcher, L. N., P. G. J. Irwin, J. A. Sinclair, G. S. Orton, R. S. Giles, J. Hurley, N. Gorius, R. K. Achterberg, B. E. Hesman, G. L. Bjoraker, (2015), Seasonal evolution of Saturn's polar temperatures and composition, Icarus, 250, 131–153, doi: 10.1016/j.icarus.2014.11.022.

Fletcher, L. N., T. K. Greathouse, G. S. Orton, P. G. J. Irwin, O. Mousis, J. A. Sinclair, R. S. Giles, (2014), The origin of nitrogen on Jupiter and Saturn from the 15N/14N ratio, Icarus, 238, 170–190, doi: 10.1016/j.icarus.2014.05.007.

Fletcher, L. N., B. E. Hesman, R. K. Achterberg, P. G. J. Irwin, G. Bjoraker, N. Gorius, J. Hurley, et al., (2012), The origin and evolution of Saturn's 2011-2012 stratospheric vortex, Icarus, 221, 2, 560–586, doi: 10.1016/j.icarus.2012.08.024.

Fletcher, L. N., B. E. Hesman, P. G. J. Irwin, K. H. Baines, T. W. Momary, A. Sanchez-Lavega, F. M. Flasar, P. L. Read, G. S. Orton, A. Simon-Miller, R. Hueso, G. L. Bjoraker, A. Mamoutkine, T. del Rio-Gaztelurrutia, J. M. Gomez, B. Buratti, R. N. Clark, P. D. Nicholson, C. Sotin, (2011), Thermal structure and dynamics of Saturn’s northern springtime disturbance, Science 332, no. 6036, 1413–1417, doi: 10.1126/science.1204774.

Fletcher, L. N., K. H. Baines, T. W. Momary, A. P. Showman, P. G. J. Irwin, G. S. Orton, M. Roos-Serote, C. Merlet, (2011a), Saturn's tropospheric composition and clouds from Cassini/VIMS 4.6-5.1 μm nightside spectroscopy, Icarus, 214, 2, 510-533, doi: 10.1016/j.icarus.2011.06.006.

Fletcher, L. N., B. E. Hesman, P. G. J. Irwin, K. H. Baines, T. W. Momary, A. Sanchez-Lavega, F. M. Flasar, et al., (2011b), Thermal structure and dynamics of Saturn's northern springtime disturbance, Science, 332, 6036, 1413–1417, doi: 10.1126/science.1204774.

Fletcher, L. N., R. K. Achterberg, T. K. Greathouse, G. S. Orton, B. J. Conrath, A. A. Simon-Miller, N. Teanby, S. Guerlet, P. G. J. Irwin, F. M. Flasar, (2010), Seasonal change on Saturn from Cassini/CIRS observations, 2004–2009, Icarus, 208, 1, 337-352, doi: 10.1016/j.icarus.2010.01.022.

Fletcher, L. N., G. S. Orton, N. A. Teanby, P. G. J. Irwin, (2009a), Phosphine on Jupiter and Saturn from Cassini/CIRS, Icarus, 202, 543–564, doi: 10.1016/j.icarus.2009.03.023.

Fletcher, L. N., G. S. Orton, N. A. Teanby, P. G. J. Irwin, G. L. Bjoraker, (2009b), Methane and its isotopologues on Saturn from Cassini/CIRS observations, Icarus, 199, 2, 351–367, doi: 10.1016/j.icarus.2008.09.019.

Fletcher, L. N., P. G. J. Irwin, G. S. Orton, N. A. Teanby, R. K. Achterberg, G. L. Bjoraker, P. L. Read, A. A. Simon-Miller, C. Howett, R. de Kok, N. Bowles, S. B. Calcutt, B. Hesman, F. M. Flasar, (2008), Temperature and composition of Saturn’s polar hot spots and hexagon, Science, 319, 5859, 79–81.

Fletcher, L. N., P. G. J. Irwin, N. A. Teanby, G. S. Orton, P. D. Parrish, S. B. Calcutt, N. Bowles, R. de Kok, C. Howett, F. W. Taylor, (2007a), The meridional phosphine distribution in Saturn's upper troposphere from Cassini/CIRS observations, Icarus, 188, 1, 72–88, doi: 10.1016/j.icarus.2006.10.029.

Fletcher, L. N., P. G. J. Irwin, N. A. Teanby, G. S. Orton, P. D. Parrish, R. de Kok, C. Howett, S. B. Calcutt, N. Bowles, F. W. Taylor, (2007b), Characterizing Saturn's vertical temperature structure from Cassini/CIRS, Icarus, 189, 2, 457–478, doi: 10.1016/j.icarus.2007.02.006.

Fouchet, T., T. K. Greathouse, A. Spiga, L. N. Fletcher, S. Guerlet, J. Leconte, G. S. Orton, (2016), Stratospheric aftermath of the 2010 Storm on Saturn as observed by the TEXES instrument. I. Temperature structure, Icarus, 277, 196–214, doi: 10.1016/j.icarus.2016.04.030.

Fouchet, T., J. I. Moses, B. J. Conrath, (2009), Saturn: Composition and chemistry, In Saturn from Cassini-Huygens, (eds.) M. K. Doughterty, L. W. Esposito, S. M. Krimigis, pp. 83–112, Springer, Dordrecht, Netherlands.

Fouchet, T., S. Guerlet, D. F. Strobel, A. A. Simon-Miller, B. Bézard, F. M. Flasar, (2008), An equatorial oscillation in Saturn’s middle atmosphere, Nature, 453, 7192, 200–202, doi: 10.1038/nature06912.

Fouchet, T., P. G. J. Irwin, P. Parrish, S. B. Calcutt, F. W. Taylor, C. A. Nixon, T. Owen, (2004a), Search for spatial variation in the jovian 15N/14N ratio from Cassini/CIRS observations, Icarus, 172, 1, 50–58, doi: 10.1016/j.icarus.2003.11.011.

Fouchet, T., G. Orton, P. G. J. Irwin, S. B. Calcutt, C. A. Nixon, (2004b), Upper limits on hydrogen halides in Jupiter from Cassini/CIRS observations, Icarus, 170, 237–241, doi: 10.1016/j.icarus.2004.03.013.

Friedson, A. J., and J. I. Moses, (2012), General circulation and transport in Saturn's upper troposphere and stratosphere, Icarus, 218, 2, 861–875, doi: 10.1016/j.icarus.2012.02.004.

Galanti, E., Y. Kaspi, Y. Miguel, T. Guillot, D. Durante, P. Racioppa, L. Iess, (2019), Saturn’s deep atmospheric flows revealed by the Cassini grand finale gravity measurements, Geophysical Research Letters, 46, 2, 616–624, doi: 10.1029/2018GL078087.

Galanti, E., and Y. Kaspi, (2017), Prediction for the flow-induced gravity field of Saturn: Implications for Cassini's Grand Finale, Astrophysical Journal Letters, 843, 2, doi: 10.3847/2041-8213/aa7aec.

Galanti, E., Y. Kaspi, E. Tziperman, (2017), A full, self-consistent treatment of thermal wind balance on oblate fluid planets, Journal of Fluid Mechanics, 810, 175–195, doi: 10.1017/jfm.2016.687.

Galanti, E., and Y. Kaspi, (2016), An adjoint-based method for the inversion of the Juno and Cassini gravity measurements into wind fields, The Astrophysical Journal, 820, 2, 91, doi: 10.3847/0004-637x/820/2/91.

Galperin, B., R. M. B. Young, S. Sukoriansky, N. Dikovskaya, P. L. Read, A. J. Lancaster, D. Armstrong, (2014), Cassini observations reveal a regime of zonostrophic macroturbulence on Jupiter, Icarus, 229, 295–320, doi: 10.1016/j.icarus.2013.08.030.

Garcia-Melendo, E., and A. Sanchez-Lavega, (2017), Shallow water simulations of Saturn's giant storms at different latitudes, Icarus, 286, 241–260, doi: 10.1016/j.icarus.2016.10.006.

Garcia-Melendo, E., R. Hueso, A. Sanchez-Lavega, J. Legarreta, T. del Rio-Gaztelurrutia, S. Perez-Hoyos, J. F. Sanz-Requena, (2013), Atmospheric dynamics of Saturn's 2010 giant storm, Nature Geoscience, 6, 7, 525–529, doi: 10.1038/ngeo1860.

Garcia-Melendo, E., Arregi, J., Rojas, J. F., Hueso, R., Barrado-Izagirre, N., Gomez-Forrellad, J. M., et al., (2011a), Dynamics of Jupiter's equatorial region at cloud top level from Cassini and HST images, Icarus, 211, 1242–1257, doi: 10.1016/j.icarus.2010.11.020.

Garcia-Melendo, E., S. Perez-Hoyos, A. Sanchez-Lavega, R. Hueso, (2011b), Saturn's zonal wind profile in 2004-2009 from Cassini ISS images and its long-term variability, Icarus, 215, 1, 62–74, doi: 10.1016/j.icarus.2011.07.005.

Garcia-Melendo, E., A. Sanchez-Lavega, J. Legarreta, S. Perez-Hoyos, R. Hueso, (2010), A strong high altitude narrow jet detected at Saturn's equator, Geophysical Research Letters, 37, doi: 10.1029/2010gl045434.

Garcia-Melendo, E., A. Sanchez-Lavega, J. F. Rojas, S. Perez-Hoyos, R. Hueso, (2009), Vertical shears in Saturn's eastward jets at cloud level, Icarus, 201, 2, 818–820, doi: 10.1016/j.icarus.2009.02.022.

Garcia-Melendo, E., A. Sanchez-Lavega, R. Hueso, (2007), Numerical models of Saturn's long-lived anticyclones, Icarus, 191, 2, 665–677, doi: 10.1016/j.icarus.2007.05.020.

Gerard, J. C., J. Gustin, W. R. Pryor, D. Grodent, B. Bonfond, A. Radioti, G. R. Gladstone, J. T. Clarke, J. D. Nichols, (2013), Remote sensing of the energy of auroral electrons in Saturn's atmosphere: Hubble and Cassini spectral observations, Icarus, 223, 1, 211–221, doi: 10.1016/j.icarus.2012.11.033.

Gerard, J. C., B. Hubert, J. Gustin, V. I. Shematovich, D. Bisikalo, G. R. Gladstone, L. W. Esposito, (2011), EUV spectroscopy of the Venus dayglow with UVIS on Cassini, Icarus, 211, 70–80. doi: 10.1016/j.icarus.2010.09.020.

Gierasch, P. J., A. P. Ingersoll, D. Banfield, S. P. Ewald, P. Helfenstein, A. Simon-Miller, A. Vasavada, H. H. Breneman, D. A. Senske, Galileo Imaging Team, (2000), Observation of moist convection in Jupiter's atmosphere, Nature, 403, 6770, 628–630, doi: 10.1038/35001017.

Giles, R. S., L. N. Fletcher, P. G. J. Irwin, (2015), Cloud structure and composition of Jupiter's troposphere from 5 μm Cassini VIMS spectroscopy, Icarus, 257, 457–470, doi: 10.1016/j.icarus.2015.05.030.

Gombosi, T. I., and A. P. Ingersoll, (2010), Saturn: atmosphere, ionosphere, and magnetosphere, Science, 327, 5972, 1476–1479, doi: 10.1126/science.1179119.

Guerlet, S., A. Spiga, M. Sylvestre, M. Indurain, T. Fouchet, J. Leconte, E. Millour, et al., (2014), Global climate modeling of Saturn's atmosphere. Part I: Evaluation of the radiative transfer model, Icarus, 238, 110-124, doi: 10.1016/j.icarus.2014.05.010.

Guerlet, S., T. Fouchet, B. Bezard, F. M. Flasar, A. A. Simon-Miller, (2011), Evolution of the equatorial oscillation in Saturn's stratosphere between 2005 and 2010 from Cassini/CIRS limb data analysis, Geophysical Research Letters, 38, doi: 10.1029/2011gl047192.

Guerlet, S., T. Fouchet, B. Bezard, J. I. Moses, L. N. Fletcher, A. A. Simon-Miller, F. M. Flasar, (2010), Meridional distribution of CH_3C_2H and C_4H_2 in Saturn's stratosphere from CIRS/Cassini limb and nadir observations, Icarus, 209, 2, 682-695, doi: 10.1016/j.icarus.2010.03.033.

Guerlet, S., T. Fouchet, B. Bezard, A. A. Simon-Miller, F. M. Flasar, (2009), Vertical and meridional distribution of ethane, acetylene and propane in Saturn's stratosphere from CIRS/Cassini limb observations, Icarus, 203, 214–232, doi: 10.1016/j.icarus.2009.04.002.

Guillot, T., Y. Miguel, B. Militzer, W. B. Hubbard, Y. Kaspi, E. Galanti, et al., (2018), A suppression of differential rotation in Jupiter's deep interior, Nature, 555(7695), 227, doi: 10.1038/nature25775.

Guillot, T., (1999), A comparison of the interiors of Jupiter and Saturn, Planetary and Space Science, 47, 10–11, 1183-1200, doi: 10.1016/s0032-0633(99)00043-4.

Gunnarson, J. L., K. M. Sayanagi, J. J. Blalock, L. N. Fletcher, A. P. Ingersoll, U. A. Dyudina, et al., (2018), Saturn's new ribbons: Cassini observations of planetary waves in Saturn's 42N atmospheric jet, Geophysical Research Letters, 45, 15, 7399–7408, doi: 10.1029/2018GL078156.

Gurnett, D. A., P. Zarka, R. Manning, W. S. Kurth, G. B. Hospodarsky, T. F. Averkamp, et al., (2001), Non-detection at Venus of high-frequency radio signals characteristic of terrestrial lightning, Nature, 409, 313–315, doi: 10.1038/35053009.

Gustin, J., D. Grodent, A. Radioti, W. Pryor, L. Lamy, J. Ajello, (2017), Statistical study of Saturn's auroral electron properties with Cassini/UVIS FUV spectral images, Icarus, 284, 264–283, doi: 10.1016/j.icarus.2016.11.017.

Gustin, J., I. Stewart, J. C. Gerard, L. Esposito, (2010), Characteristics of Saturn's FUV airglow from limb-viewing spectra obtained with Cassini-UVIS, Icarus, 210, 1, 270–283, doi: 10.1016/j.icarus.2010.06.031.

Gustin, J., J. C. Gerard, W. Pryor, P. D. Feldman, D. Grodent, G. Holsclaw, (2009), Characteristics of Saturn's polar atmosphere and auroral electrons derived from HST/STIS, FUSE and Cassini/UVIS spectra, Icarus, 200, 1, 176–187, doi: 10.1016/j.icarus.2008.11.013.

Hadjighasem, A., and G. Haller, (2016), Geodesic transport barriers in Jupiter's atmosphere: A video-based analysis, Siam Review, 58, 69–89, doi: 10.1137/140983665.

Hanel, R. A., B. J. Conrath, V. G. Kunde, J. C. Pearl, J. A. Pirraglia, (1983), Albedo, internal heat flux, and energy balance of Saturn, Icarus, 53, 2, 262–285, doi: 10.1016/0019-1035(83)90147-1.

Hanley, T. R., P. G. Steffes, B. M. Karpowicz, (2009), A new model of the hydrogen and helium-broadened microwave opacity of ammonia based on extensive laboratory measurements, Icarus, 202, 1, 316–335, doi: 10.1016/j.icarus.2009.02.002.

Hedman, M. M., and P. D. Nicholson, (2014), More kronoseismology with Saturn's rings, Monthly Notices of the Royal Astronomical Society, 444, 2, 1369–1388, doi: 10.1093/mnras/stu1503.

Hedman, M. M., and P. D. Nicholson, (2013), Kronoseismology: Using density waves in Saturn's C ring to probe the planet's interior, Astronomical Journal, 146, 1, doi: 10.1088/0004-6256/146/1/12.

Heimpel, M., T. Gastine, J. Wicht, (2016), Simulation of deep-seated zonal jets and shallow vortices in gas giant atmospheres, Nature Geoscience, 9, 19, doi: 10.1038/ngeo2601.

Heimpel, M., and J. Aurnou, (2007), Turbulent convection in rapidly rotating spherical shells: A model for equatorial and high latitude jets on Jupiter and Saturn, Icarus, 187, 2, 540–557, doi: 10.1016/j.icarus.2006.10.023.

Heimpel, M., J. Aurnou, J. Wicht, (2005), Simulation of equatorial and high-latitude jets on Jupiter in a deep convection model, Nature, 438, 193–196, doi: 10.1038/nature04208.

Helled, R., E. Galanti, Y. Kaspi, (2015), Saturn's fast spin determined from its gravitational field and oblateness, Nature, 520, 7546, 202-U140, doi: 10.1038/nature14278.

Helled, R., and T. Guillot, (2013), Interior models of Saturn: Including the uncertainties in shape and rotation, The Astrophysical Journal, 767, 2, 113, doi: 10.1088/0004-637x/767/2/113.

Hersant, F., D. Gautier, G. Tobie, J. I. Lunine, (2008), Interpretation of the carbon abundance in Saturn measured by Cassini, Planetary and Space Science, 56, 8, 1103–1111, doi: 10.1016/j.pss.2008.02.007.

Hesman, B. E., G. L. Bjoraker, P. V. Sada, R. K. Achterberg, D. E. Jennings, P. N. Romani, A. W. Lunsford, et al., (2012), Elusive ethylene detected in Saturn's northern storm region, The Astrophysical Journal, 760, 1, 24, doi: 10.1088/0004-637x/760/1/24.

Hesman, B. E., D. E. Jennings, P. V. Sada, G. L. Bjoraker, R. K. Achterberg, A. A. Simon-Miller, C. M. Anderson, et al., (2009), Saturn's latitudinal C_2H_2 and C_2H_6 abundance profiles from Cassini/CIRS and ground-based observations, Icarus, 202, 1, 249–259, doi: 10.1016/j.icarus.2009.02.013.

Hodosan, G., C. Helling, R. Asensio-Torres, I. Vorgul, P. B. Rimmer, (2016), Lightning climatology of exoplanets and brown dwarfs guided by Solar system data, Monthly Notices of the Royal Astronomical Society, 461, 4, 3927–3947, doi: 10.1093/mnras/stw1571.

Howett, C. J. A., P. G. J. Irwin, N. A. Teanby, A. Simon-Miller, S. B. Calcutt, L. N. Fletcher, R. de Kok, (2007), Meridional variations in stratospheric acetylene and ethane in the southern hemisphere of the saturnian atmosphere as determined from Cassini/CIRS measurements, Icarus, 190, 2, 556–572, doi: 10.1016/j.icarus.2007.03.009.

Hubbard, W. B., M. K. Dougherty, D. Gautier, R. Jacobson, (2009), The interior of Saturn, In Saturn from Cassini-Huygens,(eds.) M. K. Doughterty, L. W. Esposito, S. M. Krimigis, pp. 75–81, Springer, Dordrecht, Netherlands.

Hubert, B., J. C. Gerard, J. Gustin, D. V. Bisikalo, V. I. Shematovich, G. R. Gladstone, (2012), Cassini-UVIS observation of dayglow FUV emissions of carbon in the thermosphere of Venus, Icarus, 220, 635–646, doi: 10.1016/j.icarus.2012.06.002.

Hubert, B., J. C. Gerard, J. Gustin, V. I. Shematovich, D. V. Bisikalo, A. I. Stewart, G. R. Gladstone, (2010), UVIS observations of the FUV OI and CO 4P Venus dayglow during the Cassini flyby, Icarus, 207, 549–557, doi: 10.1016/j.icarus.2009.12.029.

Hue, V., T. K. Greathouse, T. Cavalie, M. Dobrijevic, F. Hersant, (2016), 2D photochemical modeling of Saturn's stratosphere. Part II: Feedback between composition and temperature, Icarus, 267, 334–343, doi: 10.1016/j.icarus.2015.12.007.

Hue, V., T. Cavalie, M. Dobrijevic, F. Hersant, T. K. Greathouse, (2015), 2D photochemical modeling of Saturn's stratosphere. Part I: Seasonal variation of atmospheric composition without meridional transport, Icarus, 257, 163–184, doi: 10.1016/j.icarus.2015.04.001.

Hueso, R., J. Legarreta, E. Garcia-Melendo, A. Sanchez-Lavega, S. Perez-Hoyos, (2009), The Jovian anticyclone BA II. Circulation and interaction with the zonal jets, Icarus, 203, 499–515, doi: 10.1016/j.icarus.2009.05.004.

Hurley, J., P. G. J. Irwin, L. N. Fletcher, J. I. Moses, B. Hesman, J. Sinclair, C. Merlet, (2012a), Observations of upper tropospheric acetylene on Saturn: No apparent correlation with 2000 km-sized thunderstorms, Planetary and Space Science, 65, 21–37. doi: 10.1016/j.pss.2011.12.026.

Hurley, J., L. N. Fletcher, P. G. J. Irwin, S. B. Calcutt, J. A. Sinclair, C. Merlet, (2012b), Latitudinal variation of upper tropospheric NH3 on Saturn derived from Cassini/CIRS far-infrared measurements, Planetary and Space Science, 73, 1, 347–363, doi: 10.1016/j.pss.2012.08.003.

Iess, L., B. Militzer, Y. Kaspi, P. Nicholson, D. Durante, P. Pacioppa, A. Anabtawi, E. Galanti, W. Hubbard, M. J. Mariani, P. Tortora, S. Wahl, M. Zannoni, (2019), Measurement and implications of Saturn's gravity field and ring mass, Science, doi: 10.1125/science.aat2965.

Ingersoll, A. P., S. P. Ewald, K. M. Sayanagi, J. J. Blalock, (2018), Saturn’s atmosphere at 1-10 kilometer resolution, Geophysical Research Letters, 45, 15, 7851–7856, doi: 10.1029/2018GL079255.

Ingersoll, A. P., V. Adumitroaie, M. D. Allison, S. Atreya, A. A. Bellotti, S. J. Bolton, et al., (2017), Implications of the ammonia distribution on Jupiter from 1 to 100 bars as measured by the Juno microwave radiometer, Geophysical Research Letters, 44, 15, 7676–7685, doi: 10.1002/2017GL074277.

Ingersoll, A. P., P. J. Gierasch, D. Banfield, A. R. Vasavada, Galileo Imaging Team, (2000), Moist convection as an energy source for the large-scale motions in Jupiter’s atmosphere, Nature, 403, 6770, 630–632, doi: 10.1038/35001021.

Ip, W. H., C. M. Liu, K. C. Pan, (2016), Transport and electrodynamical coupling of nano-grains ejected from the Saturnian rings and their possible ionospheric signatures, Icarus, 276, 163–169, doi: 10.1016/j.icarus.2016.04.004.

Irwin, P. G. J., P. Parrish, T. Fouchet, S. B. Calcutt, F. W. Taylor, A. A. Simon-Miller, C. A. Nixon, (2004), Retrievals of Jovian tropospheric phosphine from Cassini/CIRS, Icarus, 172, 37–49, doi: 10.1016/j.icarus.2003.09.027.

Jacobson, R. A., P. G. Antreasian, J. J. Bordi, K. E. Criddle, R. Ionasescu, J. B. Jones, R. A. Mackenzie, et al., (2006), The gravity field of the Saturnian system from satellite observations and spacecraft tracking data, Astronomical Journal, 132, 6, 2520–2526, doi: 10.1086/508812.

Janssen, M. A., A. P. Ingersoll, M. D. Allison, S. Gulkis, A. L. Laraia, K. H. Baines, S. G. Edgington, Y. Z. Anderson, K. Kelleher, F. A. Oyafuso, (2013), Saturn's thermal emission at 2.2-cm wavelength as imaged by the Cassini RADAR radiometer, Icarus, 226, 1, 522–535, doi: 10.1016/j.icarus.2013.06.008.

Jennings, D. E., F. M. Flasar, V. G. Kunde, C. A. Nixon, M. E. Segura, P. N. Romani, N. Gorius, et al., (2017), Composite infrared spectrometer (CIRS) on Cassini, Applied Optics, 56, 18, 5274-5294, doi: 10.1364/ao.56.005274.

Kaspi, Y., J. E. Davighi, E. Galanti, W. B. Hubbard, (2016), The gravitational signature of internal flows in giant planets: Comparing the thermal wind approach with barotropic potential-surface methods, Icarus, 276, 170–181, doi: 10.1016/j.icarus.2016.04.001.

Kaspi, Y., (2013), Inferring the depth of the zonal jets on Jupiter and Saturn from odd gravity harmonics, Geophysical Research Letters, 40, 4, 676–680, doi: 10.1029/2012gl053873.

Kim, S. J., C. K. Sim, D. W. Lee, R. Courtin, J. I. Moses, Y. C. Minh, (2012), The three-micron spectral feature of the Saturnian haze: Implications for the haze composition and formation process, Planetary and Space Science, 65, 122–129, doi: 10.1016/j.pss.2012.02.013.

Kim, S. J., and T. R. Geballe, (2005), The 2.9-4.2 micron spectrum of Saturn: Clouds and CH4, PH3, and NH3, Icarus, 179, 2, 449–458, doi: 10.1016/j.icarus.2005.06.015.

Koskinen, T. T., and S. Guerlet, (2018), Atmospheric structure and helium abundance on Saturn from Cassini/UVIS and CIRS observations, Icarus, 307, 161–171, doi: 10.1016/j.icarus.2018.02.020.

Koskinen, T. T., J. I. Moses, R. A. West, S. Guerlet, A. Jouchoux, (2016), The detection of benzene in Saturn's upper atmosphere, Geophysical Research Letters, 43, 15, 7895–7901, doi: 10.1002/2016gl070000.

Koskinen, T. T., B. R. Sandel, R. V. Yelle, D. F. Strobel, I. C. F. Müeller-Wodarg, J. T. Erwin, (2015), Saturn's variable thermosphere from Cassini/UVIS occultations, Icarus, 260, 174-189, doi: 10.1016/j.icarus.2015.07.008.

Koskinen, T. T., B. R. Sandel, R. V. Yelle, F. J. Capalbo, G. M. Holsclaw, W. E. McClintock, S. Edgington, (2013), The density and temperature structure near the exobase of Saturn from Cassini UVIS solar occultations, Icarus, 226, 2, 1318-1330, doi: 10.1016/j.icarus.2013.07.037.

Lainey, V., R. A. Jacobson, R. Tajeddine, N. J. Cooper, C. Murray, V. Robert, et al., (2017), New constraints on Saturn’s interior from Cassini astrometric data, Icarus, 281, 286–296, doi: 10.1016/j.icarus.2016.07.014.

Lamy, L., R. Prange, W. Pryor, J. Gustin, S. V. Badman, H. Melin, T. Stallard, D. G. Mitchell, P. C. Brandt, (2013), Multispectral simultaneous diagnosis of Saturn's aurorae throughout a planetary rotation, Journal of Geophysical Research-Space Physics, 118, 8, 4817–4843, doi: 10.1002/jgra.50404.

Lamy, L., B. Cecconi, R. Prange, P. Zarka, J. D. Nichols, J. T. Clarke, (2009), An auroral oval at the footprint of Saturn's kilometric radio sources, colocated with the UV aurorae, Journal of Geophysical Research-Space Physics, 114, doi: 10.1029/2009ja014401.

Laraia, A. L., A. P. Ingersoll, M. A. Janssen, S. Gulkis, F. Oyafuso, M. Allison, (2013), Analysis of Saturn's thermal emission at 2.2-cm wavelength: Spatial distribution of ammonia vapor, Icarus, 226, 1, 641–654, doi: 10.1016/j.icarus.2013.06.017.

Lellouch, E., B. Bezard, D. F. Strobel, G. L. Bjoraker, F. M. Flasar, P. N. Romani, (2006), On the HCN and CO2 abundance and distribution in Jupiter's stratosphere. Icarus, 184, 478–497, doi: 10.1016/j.icarus.2006.05.018.

Li, C., and A. P. Ingersoll, (2015), Moist convection in hydrogen atmospheres and the frequency of Saturn's giant storms, Nature Geoscience, 8, 5, 398–403, doi: 10.1038/ngeo2405.

Li, L. M., X. Jiang, H. J. Trammell, Y. F. Pan, J. Hernandez, B. J. Conrath, et al., (2015), Saturn's giant storm and global radiant energy, Geophysical Research Letters, 42, 2144–2148, doi: 10.1002/2015gl063763.

Li, L. M., R. K. Achterberg, B. J. Conrath, P. J. Gierasch, M. A. Smith, A. A. Simon-Miller, C. A. Nixon, et al., (2013), Strong temporal variation over one saturnian year: From Voyager to Cassini, Scientific Reports, 3, doi: 10.1038/srep02410.

Li, L. M., K. H. Baines, M. A. Smith, R. A. West, S. Perez-Hoyos, H. J. Trammell, et al., (2012), Emitted power of Jupiter based on Cassini CIRS and VIMS observations, Journal of Geophysical Research-Planets, 117, doi: 10.1029/2012je004191.

Li, L. M., X. Jiang, A. P. Ingersoll, A. D. Del Genio, C. C. Porco, R. A. West, A. R. Vasavada, et al., (2011), Equatorial winds on Saturn and the stratospheric oscillation, Nature Geoscience, 4, 11, 750–752, doi: 10.1038/ngeo1292.

Li, L. M., B.J. Conrath, P. J. Gierasch, R. K. Achterberg, C. A. Nixon, A. A. Simon-Miller, F. M. Flasar, et al., (2010), Saturn's emitted power, Journal of Geophysical Research-Planets, 115, doi: 10.1029/2010je003631.

Li, L. M., P. J. Gierasch, R. K. Achterberg, B. J. Conrath, F. M. Flasar, A. R. Vasavada, A. P. Ingersoll, D. Banfield, A. A. Simon-Miller, L. N. Fletcher, (2008), Strong jet and a new thermal wave in Saturn's equatorial stratosphere, Geophysical Research Letters, 35, 23, doi: 10.1029/2008gl035515.

Li, L. M., A. P. Ingersoll, X. L. Huang, (2006a), Interaction of moist convection with zonal jets on Jupiter and Saturn, Icarus, 180, 113–123. doi: 10.1016/j.icarus.2005.08.016.

Li, L. M., A. P. Ingersoll, A. R. Vasavada, A. A. Simon-Miller, R. K. Achterberg, S. P. Ewald, et al., (2006b), Waves in Jupiter's atmosphere observed by the Cassini ISS and CIRS instruments, Icarus, 185, 416–429, doi: 10.1016/j.icarus.2006.08.005.

Li, L. M., A. P. Ingersoll, A. R. Vasavada, A. A. Simon-Miller, A. D. Del Genio, S. P. Ewald, et al., (2006c), Vertical wind shear on Jupiter from Cassini images, Journal of Geophysical Research-Planets, 111, doi: 10.1029/2005je002556.

Li, L. M., A. P. Ingersoll, A. R. Vasavada, C. C. Porco, A. D. Del Genio, S. P. Ewald, (2004), Life cycles of spots on Jupiter from Cassini images, Icarus, 172, 9–23, doi: 10.1016/j.icarus.2003.10.015.

Liang, M. C., R. L. Shia, A. Y. T. Lee, M. Allen, A. J. Friedson, Y. L. Yung, (2005), Meridional transport in the stratosphere of Jupiter, Astrophysical Journal, 635, L177–L180, doi: 10.1086/499624.

Liao, X. H., T. H. Feng, K. K. Zhang, (2007), On the saturation and temporal variation of mean zonal flows: An implication for equatorial jets on giant planets, Astrophysical Journal, 666, 1, L41-L44, doi: 10.1086/521526.

Little, B., C. D. Anger, A. P. Ingersoll, A. R. Vasavada, D. A. Senske, H. H. Breneman, W. J. Borucki, S. S. I. T. Galileo, (1999), Galileo images of lightning on Jupiter, Icarus, 142, 2, 306-323, doi: 10.1006/icar.1999.6195.

Liu, J. J., and T. Schneider (2015), Scaling of off-equatorial jets in giant planet atmospheres, Journal of the Atmospheric Sciences, 72, 1, 389–408, doi: 10.1175/jas-d-13-0391.1.

Liu, J. J., T. Schneider, L. N. Fletcher, (2014), Constraining the depth of Saturn's zonal winds by measuring thermal and gravitational signals, Icarus, 239, 260–272, doi: 10.1016/j.icarus.2014.05.036.

Lorenz, R. D., C. Elachi, R. D. West, W. T. K. Johnson, M. A. Janssen, M. Moghaddam, et al., (2001), Cassini Radio Detection and Ranging (RADAR): Earth and Venus observations. Journal of Geophysical Research-Space Physics, 106, 30271–30279, doi: 10.1029/2001ja900035.

Lunine, J., (2011), Chemistry of the Solar System revealed in the interiors of the giant planets, Proceedings of the International Astronomical Union, The Molecular Universe, 7(S280), 249–260, doi: 10.1017/S1743921311025026.

Mankovich, C., M. S. Marley, J. J. Fortney, N. Movshovitz, (2019), Cassini ring seismology as a probe of Saturn’s interior. I. Rigid Rotation. Astrophysical Journal, 871, 1, 1, doi: 10.3847/1538-4357/aaf798.

Matcheva, K. I., B. J. Conrath, P. J. Gierasch, F. M. Flasar, (2005), The cloud structure of the Jovian atmosphere as seen by the Cassini/CIRS experiment. Icarus, 179, 432–448. doi: 10.1016/j.icarus.2005.06.020.

Mayorga, L. C., J. Jackiewicz, K. Rages, R. A. West, B. Knowles, N. Lewis, M. S. Marley, (2016), Jupiter’s phase variations from Cassini: A testbed for future direct-imaging missions, The Astronomical Journal, 152, 209, doi: 10.3847/0004-6256/152/6/209.

Melin, H., S. V. Badman, T. S. Stallard, Stanley William Herbert Cowley, U. Dyudina, J. D. Nichols, G. Provan, et al., (2016), Simultaneous multi-scale and multi-instrument observations of Saturn's aurorae during the 2013 observing campaign, Icarus, 263, 56–74, doi: 10.1016/j.icarus.2015.08.021.

Melin, H., T. Stallard, S. Miller, J. Gustin, M. Galand, S. V. Badman, W. R. Pryor, J. O'Donoghue, R. H. Brown, K. H. Baines, (2011), Simultaneous Cassini VIMS and UVIS observations of Saturn's southern aurora: Comparing emissions from H, H-2 and H-3(+) at a high spatial resolution, Geophysical Research Letters, 38, doi: 10.1029/2011gl048457.

Militzer, B., S. Wahl, W. B. Hubbard, (2019), Models of Saturn's interior constructed with an accelerated concentric Maclaurin spheroid method, Astrophysical Journal 879, 78.

Morales-Juberias, R., K. M. Sayanagi, A. A. Simon, L. N. Fletcher, R. G. Cosentino, (2015), Meandering shallow atmospheric jet as a model of saturn's north-polar hexagon, Astrophysical Journal Letters, 806, 1, doi: 10.1088/2041-8205/806/1/l18.

Morales-Juberias, R., and T. E. Dowling, (2013), Jupiter's Great Red Spot: Fine-scale matches of model vorticity patterns to prevailing cloud patterns, Icarus, 225, 216–227, doi: 10.1016/j.icarus.2013.03.026.

Morales-Juberias, R., K. M. Sayanagi, T. E. Dowling, A. P. Ingersoll, (2011), Emergence of polar-jet polygons from jet instabilities in a Saturn model, Icarus, 211, 2, 1284–1293, doi: 10.1016/j.icarus.2010.11.006.

Moses, J. I., E. S. Armstrong, L. N. Fletcher, A. J. Friedson, P. G. J. Irwin, J. A. Sinclair, B. E. Hesman, (2015), Evolution of stratospheric chemistry in the Saturn storm beacon region, Icarus, 261, 149–168, doi: 10.1016/j.icarus.2015.08.012.

Moses, J. I., B. Bezard, E. Lellouch, G. R. Gladstone, H. Feuchtgruber, M. Allen, (2000a), Photochemistry of Saturn's atmosphere - I. Hydrocarbon chemistry and comparisons with ISO observations, Icarus, 143, 244–298, doi: 10.1006/icar.1999.6270.

Moses, J. I., E. Lellouch, B. Bezard, G. R. Gladstone, H. Feuchtgruber, M. Allen, (2000b), Photochemistry of Saturn's atmosphere II. Effects of an influx of external oxygen, Icarus, 145, 1, 166–202, doi: 10.1006/icar.1999.6320.

Mousis, O., Y. Alibert, W. Benz, (2006), Saturn's internal structure and carbon enrichment, Astronomy & Astrophysics, 449, 1, 411–415, doi: 10.1051/0004-6361:20054224.

Müeller-Wodarg, I. C. F., T. T. Koskinen, L. Moore, J. Serigano, R. V. Yelle, S. Horst, et al., (2019), Atmospheric Waves and Their Possible Effect on the Thermal Structure of Saturn's Thermosphere, Geophysical Research Letters, 46, 5, 2372–2380, doi: 10.1029/2018GL081124.

Nagy, A. F., A. J. Kliore, M. Mendillo, S. Miller, L. Moore, J. I. Moses, I. Müeller-Wodarg, D. Shemansky, (2009), Upper atmosphere and ionosphere of Saturn, In Saturn from Cassini-Huygens, (eds.) M. K. Doughterty, L. W. Esposito, S. M. Krimigis, pp. 181–201, Springer, Dordrecht, Netherlands.

NASA/JPL/Southwest Research Institute, PhotoJournal, (2001), Jupiter Polar Winds Movie, PIA03452, https://photojournal.jpl.nasa.gov/catalog/PIA03452

NASA/JPL/Southwest Research Institute, PhotoJournal, (2001), Jupiter Polar Winds Movie Blownup, PIA03453, https://photojournal.jpl.nasa.gov/catalog/PIA03453

NASA/JPL/Southwest Research Institute, PhotoJournal, (2001), 70 Days of Jupiter Winds, PIA03454, https://photojournal.jpl.nasa.gov/catalog/PIA03454

Nettelmann, N., R. Pustow, R. Redmer, (2013), Saturn layered structure and homogeneous evolution models with different EOSs, Icarus, 225, 1, 548–557, doi: 10.1016/j.icarus.2013.04.018.

Nixon, C. A., R. K. Achterberg, P. N. Romani, M. Allen, X. Zhang, N. A. Teanby, et al., (2010), Abundances of Jupiter's trace hydrocarbons from Voyager and Cassini. Planetary and Space Science, 58, 1667–1680, doi: 10.1016/j.pss.010.05.008.

Nixon, C. A., R. K. Achterberg, B. J. Conrath, P. G. J. Irwin, N. A. Teanby, T. Fouchet, et al., (2007), Meridional variations of C_2H_2 and C_2H_6 in Jupiter's atmosphere from Cassini CIRS infrared spectra, Icarus, 188, 47–71, doi: 10.1016/j.icarus.2006.11.016.

O'Donoghue, J., L. Moore, J. E. P. Connerney, H. Melin, T. S. Stallard, S. Miller, K. H. Baines, (2017), Redetection of the Ionospheric H-3(+) Signature of Saturn's ring rain, Geophysical Research Letters, 44, 11762–11769, doi.org/10.1002/2017gl075932.

O'Donoghue, J., T. S. Stallard, H. Melin, S. W. H. Cowley, S. V. Badman, L. Moore, S. Miller, C. Tao, K. H. Baines, J. S. D. Blake, (2014), Conjugate observations of Saturn's northern and southern H3+ aurorae, Icarus, 229, 214–220, doi: 10.1016/j.icarus.2013.11.009.

O'Donoghue, J., T. S. Stallard, H. Melin, G. H. Jones, S. W. H. Cowley, S. Miller, et al., (2013), The domination of Saturn's low-latitude ionosphere by ring rain, Nature, 496, 7444, 193–195, doi: 10.1038/nature12049.

O'Neill, M. E., K. A. Emanuel, G. R. Flierl, (2016), Weak jets and strong cyclones: shallow water modeling of giant planet polar caps, Journal of the Atmospheric Sciences, 73, 1841–1855, doi: 10.1175/JAS-D-15-0314.1.

O'Neill, M. E., K. A. Emanuel, G. R. Flierl, (2015), Polar vortex formation in giant-planet atmospheres dues to moist convection, Nature Geoscience, 8, 7, 523-U118, doi: 10.1038/ngeo2459.

Oliva, F., A. Adriani, M. L. Moriconi, G. L. Liberti, E. D'Aversa, G. Filacchione, (2016), Clouds and hazes vertical structure of a Saturn's giant vortex from Cassini/VIMS-V data analysis, Icarus, 278, 215–237, doi: 10.1016/j.icarus.2016.06.021.

Ordonez-Etxeberria, I., R. Hueso, A. Sanchez-Lavega, S. Perez-Hoyos, (2016), Spatial distribution of Jovian clouds, hazes and colors from Cassini ISS multi-spectral images, Icarus, 267, 34–50, doi: 10.1016/j.icarus.2015.12.008.

Owen, T., and T. Encrenaz, (2003), Element abundances and isotope ratios in the Giant Planets and Titan, Space Science Reviews, 106, 1–4, 121–138, doi: 10.1023/a:1024633603624.

Parkinson, C. D., A. I. F. Stewart, A. S. Wong, Y. L. Yung, J. M. Ajello, (2006), Enhanced transport in the polar mesosphere of Jupiter: Evidence from Cassini UVIS helium 584 angstrom airglow, Journal of Geophysical Research-Planets, 111, doi: 10.1029/2005je002539.

Perez-Hoyos, S., J. F. Sanz-Requena, A. Sanchez-Lavega, P. G. J. Irwin, A. Smith, (2016), Saturn's tropospheric particles phase function and spatial distribution from Cassini ISS 2010-11 observations, Icarus, 277, 1–18, doi: 10.1016/j.icarus.2016.04.022.

Perez-Hoyos, S., and A. Sanchez-Lavega, (2006), On the vertical wind shear of Saturn's Equatorial Jet at cloud level, Icarus, 180, 1, 161–175, doi: 10.1016/j.icarus.2005.07.011.

Perez-Hoyos, S., A. Sanchez-Lavega, R. G. French, (2006), Short-term changes in the belt/zone structure of Saturn's Southern Hemisphere (1996-2004), Astronomy & Astrophysics, 460, 2, 641–645, doi: 10.1051/0004-6361:20065972.

Pierel, J. D. R., C. A. Nixon, E. Lellouch, L. N. Fletcher, G. L. Bjoraker, R. K. Achterberg, B. Bezard, B. E. Hesman, P. G. J. Irwin, F. M. Flasar, (2017), D/H Ratios on Saturn and Jupiter from Cassini CIRS, Astronomical Journal, 154, 5, doi: 10.3847/1538-3881/aa899d.

Porco, C. C., E. Baker, J. Barbara, K. Beurle, A. Brahic, J. A. Burns, S. Charnoz, et al., (2005), Cassini Imaging Science: Initial results on Saturn's atmosphere, Science, 307, 5713, 1243–1247, doi: 10.1126/science.1107691.

Porco, C. C., R. A. West, A. McEwen, A. D. Del Genio, A. P. Ingersoll, P. Thomas, et al., (2003), Cassini imaging of Jupiter's atmosphere, satellites, and rings, Science, 299, 1541–1547, doi: 10.1126/science.1079462.

Pryor, W. R., A. M. Rymer, D. G. Mitchell, T. W. Hill, D. T. Young, J. Saur, G. H. Jones, et al., (2011), The auroral footprint of Enceladus on Saturn, Nature, 472(7343), 331–333, doi: 10.1038/nature09928.

Read, P. L., B. J. Conrath, L. N. Fletcher, P. J. Gierasch, A. A. Simon-Miller, L. C. Zuchowski, (2009a), Mapping potential vorticity dynamics on Saturn: Zonal mean circulation from Cassini and Voyager data, Planetary and Space Science, 57, 1682–1698, doi: 10.1016/j.pss.2009.03.004.

Read, P. L., T. E. Dowling, G. Schubert, (2009b), Saturn's rotation period from its atmospheric planetary-wave configuration, Nature, 460, 7255, 608–610, doi: 10.1038/nature08194.

Read, P. L., P. J. Gierasch, B. J. Conrath, A. Simon-Miller, T. Fouchet, Y. H. Yamazaki, (2006), Mapping potential-vorticity dynamics on Jupiter. I: Zonal-mean circulation from Cassini and Voyager 1 data, Quarterly Journal of the Royal Meteorological Society, 132, 1577–1603, doi: 10.1256/qj.05.34.

Rogers, J. H., L. N. Fletcher, G. Adamoli, M. Jacquesson, M. Vedovato, G. S. Orton, (2016), A dispersive wave pattern on Jupiter's fastest retrograde jet at 20°S, Icarus, 277, 354–369, doi: 10.1016/j.icarus.2016.05.028.

Rogers, J. H., H. J. Mettig, A. Cidadao, P. C. Sherrod, D. Peach, (2006), Merging circulations on Jupiter: Observed differences between cyclonic and anticyclonic mergers, Icarus, 185, 244–257, doi: 10.1016/j.icarus.2006.05.022.

Roman, M. T., D. Banfield, P. J. Gierasch, (2013), Saturn's cloud structure inferred from Cassini ISS, Icarus, 225, 1, 93–110, doi: 10.1016/j.icarus.2013.03.015.

Salyk, C., A. P. Ingersoll, J. Lorre, A. Vasavada, A. D. Del Genio, (2006), Interaction between eddies and mean flow in Jupiter's atmosphere: Analysis of Cassini imaging data, Icarus, 185, 430–442, doi: 10.1016/j.icarus.2006.08.007.

Sánchez-Lavega, A., G. Fischer, L. Fletcher, E. García-Melendo, B. Hesman, S. Pérez-Hoyos, L. Sromovsky, (2018), The Great Saturn Storm of 2010–2011, In Saturn in the 21st Century, (eds.) K. Baines, F. Flasar, N. Krupp, T. Stallard, Cambridge Planetary Science, Cambridge University Press, pp. 377–416, doi: 10.1017/9781316227220.013.

Sanchez-Lavega, A., E. García-Melendo, S. Perez-Hoyos, R. Hueso, M. H. Wong, A. Simon, J. F. Sanz-Requena, et al., (2016), An enduring rapidly moving storm as a guide to Saturn's Equatorial jet's complex structure, Nature Communications, 7, doi: 10.1038/ncomms13262.

Sanchez-Lavega, A., T. del Río-Gaztelurrutia, R. Hueso, S. Pérez-Hoyos, E. García-Melendo, A. Antuñano, I. Mendikoa, et al., (2014), The long- term steady motion of Saturn's hexagon and the stability of its enclosed jet stream under seasonal changes, Geophysical Research Letters, 41, 5, 1425–1431, doi: 10.1002/2013gl059078.

Sanchez-Lavega, A., T. del Río-Gaztelurrutia, M. Delcroix, J. J. Legarreta, J. M. Gómez-Forrellad, R. Hueso, E. García-Melendo, et al., (2012), Ground-based observations of the long-term evolution and death of Saturn's 2010 Great White Spot, Icarus, 220, 2, 561–576, doi: 10.1016/j.icarus.2012.05.033.

Sanchez-Lavega, A., T. del Río-Gaztelurrutia, R. Hueso, J. M. Gómez-Forrellad, J. F. Sanz-Requena, J. Legarreta, E. García-Melendo, et al., (2011), Deep winds beneath Saturn's upper clouds from a seasonal long-lived planetary-scale storm, Nature, 475, 7354, 71–74, doi: 10.1038/nature10203.

Sanchez-Lavega, A., R. Hueso, S. Perez-Hoyos, (2007), The three-dimensional structure of Saturn's equatorial jet at cloud level, Icarus, 187, 2, 510–519, doi: 10.1016/j.icarus.2006.10.022.

Sanchez-Lavega, A., R. Hueso, S. Perez-Hoyos, J. F. Rojas, (2006), A strong vortex in Saturn's South Pole, Icarus, 184, 2, 524–531, doi: 10.1016/j.icarus.2006.05.020.

Sanchez-Lavega, A., R. Hueso, S. Perez-Hoyos, J. F. Rojas, R. G. French, (2004), Saturn's cloud morphology and zonal winds before the Cassini encounter, Icarus, 170, 2, 519–523, doi: 10.1016/j.icarus.2004.05.002.

Sanchez-Lavega, A., J. F. Rojas, P. V. Sada, P. V. Sada, (2000), Saturn's zonal winds at cloud level, Icarus, 147, 2, 405–420, doi: 10.1006/icar.2000.6449.

Sanchez-Lavega, A., (1994), Saturn's Great White Spots, Chaos: An Interdisciplinary Journal of Nonlinear Science, 4, 2, 341–353, doi: 10.1063/1.166012.

Sanz-Requena J. F., S. Pérez-Hoyos, A. Sánchez-Lavega, T. del Rio-Gaztelurrutia, P. G. J. Irwin, (2019), Hazes and clouds in a singular triple vortex in Saturn's atmosphere from HST/WFC3 multispectral imaging, Icarus, 333, 22–36, doi: 10.1016/j.icarus.2019.05.037.

Sanz-Requena J. F. , S. Pérez-Hoyos, A. Sánchez-Lavega, A. Antuñano, P. G. J. Irwin, (2018), Haze and cloud structure of Saturn’s north pole and hexagon wave from Cassini/ISS imaging, Icarus, 305, 284–300, doi.org/10.1016/j.icarus.2017.12.043.

Sato, T. M., T. Satoh, Y. Kasaba, (2013), Retrieval of Jovian cloud structure from the Cassini ISS limb-darkening data I. Continuum scattering phase functions for cloud and haze in the South Tropical Zone, Icarus, 222, 100–121, doi: 10.1016/j.icarus.2012.09.035.

Sayanagi, K. M., K. H. Baines, U. Dyudina, L. N. Fletcher, A. Sánchez-Lavega, R. A. West, (2018), Saturn’s polar atmosphere, In Saturn in the 21st Century, (eds.) K. H. Baines, F. M. Flasar, N. Krupp, T. Stallard, Cambridge University Press, pp. 337–376, doi: 10.1017/9781316227220.012.

Sayanagi, K. M., J. J. Blalock, U. A. Dyudina, S. P. Ewald, A. P. Ingersoll, (2017), Cassini ISS observation of Saturn's north polar vortex and comparison to the south polar vortex, Icarus, 285, 68–82, doi: 10.1016/j.icarus.2016.12.011.

Sayanagi, K. M., U. A. Dyudina, S. P. Ewald, G. D. Muro, A. P. Ingersoll, (2014), Cassini ISS observation of Saturn's String of Pearls, Icarus, 229, 170–180, doi: 10.1016/j.icarus.2013.10.032.

Sayanagi, K. M., U. A. Dyudina, S. P. Ewald, G. Fischer, A. P. Ingersoll, W. S. Kurth, G. D. Muro, C. C. Porco, R. A. West, (2013), Dynamics of Saturn's great storm of 2010–2011 from Cassini ISS and RPWS, Icarus, 223, 1, 460–478, doi: 10.1016/j.icarus.2012.12.013.

Sayanagi, K. M., R. Morales-Juberias, A. P. Ingersoll, (2010), Saturn's northern hemisphere ribbon: Simulations and comparison with the meandering Gulf Stream, Journal of the Atmospheric Sciences, 67, 2658–2678, doi: 10.1175/2010jas3315.1.

Sayanagi, K. M., and A. P. Showman, (2007), Effects of a large convective storm on Saturn's equatorial jet, Icarus, 187, 2, 520–539, doi: 10.1016/j.icarus.2006.10.020.

Schinder, P. J., F. M. Flasar, E. A. Marouf, R. G. French, A. Anabtawi, E. Barbinis, A. J. Kliore, (2015), A numerical technique for two-way radio occultations by oblate axisymmetric atmospheres with zonal winds, Radio Science, 50, 7, 712–727, doi: 10.1002/2015rs005690.

Schinder, P. J., F. M. Flasar, E. A. Marouf, R. G. French, C. A. McGhee, A. J. Kliore, N. J. Rappaport, E. Barbinis, D. Fleischman, and A. Anabtawi, (2011), Saturn's equatorial oscillation: Evidence of descending thermal structure from Cassini radio occultations, Geophysical Research Letters, 38, doi: 10.1029/2011gl047191.

Schneider, T., and J. Liu, (2009), Formation of jets and equatorial superrotation on Jupiter, Journal of the Atmospheric Sciences, 66, 3, 579–601, doi.org/10.1175/2008JAS2798.1.

Shemansky, D. E., and X. Liu, (2012), Saturn upper atmospheric structure from Cassini EUV and FUV occultations, Canadian Journal of Physics, 90, 8, 817–831, doi: 10.1139/p2012-036.

Shetty, S., and P. S. Marcus, (2010), Changes in Jupiter's Great Red Spot (1979-2006) and Oval BA (2000-2006), Icarus, 210, 182–201, doi: 10.1016/j.icarus.2010.06.026.

Showman, A. P., A. P. Ingersoll, R. Achterberg, Y. Kaspi, (2018), The global atmospheric circulation of Saturn, In Saturn in the 21st Century, (eds.) K. H. Baines, F. M. Flasar, N. Krupp, T. Stallard, Cambridge University Press, pp. 295–336, doi: 10.1017/9781316227220.011.

Showman, A. P., and I. de Pater, (2005), Dynamical implications of Jupiter's tropospheric ammonia abundance, Icarus, 174, 1, 192–204, doi.org/10.1016/j.icarus.2004.10.004.

Simon, A. A., L. Li, D. C. Reuter, (2015), Small-scale waves on Jupiter: A reanalysis of New Horizons, Voyager, and Galileo data, Geophysical Research Letters, 42, 8, 2612–2618, doi: 10.1002/2015GL063433.

Simon-Miller, A. A., J. H. Rogers, P. J. Gierasch, D. Choi, M. D. Allison, G. Adamoli, H. J. Mettig, (2012), Longitudinal variation and waves in Jupiter's south equatorial wind jet, Icarus, 218, 817–830, doi: 10.1016/j.icarus.2012.01.022.

Simon-Miller, A. A., and P. J. Gierasch, (2010), On the long-term variability of Jupiter's winds and brightness as observed from Hubble, Icarus, 210, 258–269. doi: 10.1016/j.icarus.2010.06.020.

Simon-Miller, A. A., B. W. Poston, G. S. Orton, B. Fisher, (2007), Wind variations in Jupiter's equatorial atmosphere: A QQO counterpart?, Icarus, 186, 192–203. doi: 10.1016/j.icarus.2006.08.009.

Simon-Miller, A. A., B. J. Conrath, P. J. Gierasch, G. S. Orton, R. K. Achterberg, F. M. Flasar, B. M. Fisher, (2006), Jupiter's atmospheric temperatures: From Voyager IRIS to Cassini CIRS, Icarus, 180, 98–112. doi: 10.1016/j.icarus.2005.07.019.

Sinclair, J. A., G. S. Orton, T. K. Greathouse, L. N. Fletcher, J. I. Moses, V. Hue, P. G. J. Irwin, (2018), Jupiter's auroral-related stratospheric heating and chemistry II: Analysis of IRTF-TEXES spectra measured in December 2014, Icarus, 300, 305–326, doi: 10.1016/j.icarus.2017.09.016.

Sinclair, J. A., G. S. Orton, T. K. Greathouse, L. N. Fletcher, J. I. Moses, V. Hue, P. G. J. Irwin, (2017), Jupiter's auroral-related stratospheric heating and chemistry I: Analysis of Voyager-IRIS and Cassini-CIRS spectra, Icarus, 292, 182–207, doi: 10.1016/j.icarus.2016.12.033.

Sinclair, J. A., P. G. J. Irwin, L. N. Fletcher, T. Greathouse, S. Guerlet, J. Hurley, C. Merlet, (2014), From Voyager-IRIS to Cassini-CIRS: Interannual variability in Saturn's stratosphere?, Icarus, 233, 281–292, doi: 10.1016/j.icarus.2014.02.009.

Sinclair, J. A., P. G. J. Irwin, L. N. Fletcher, J. I. Moses, T. K. Greathouse, A. J. Friedson, B. Hesman, J. Hurley, C. Merlet, (2013), Seasonal variations of temperature, acetylene and ethane in Saturn's atmosphere from 2005 to 2010, as observed by Cassini-CIRS, Icarus, 225, 1, 257–271, doi: 10.1016/j.icarus.2013.03.011.

Smith, B. A., L. Soderblom, R. M. Batson, P. M. Bridges, J. L. Inge, H. Masursky, E. Shoemaker, R. F. Beebe, J. Boyce, G. Briggs, A. Bunker, S. A. Collins, C. Hansen, T. V. Johnson, J. L. Mitchell, R. J. Terrile, A. F. Cook, J. N. Cuzzi, J. B. Pollack, G. E. Danielson, A. P. Ingersoll, M. E. Davies, G. E. Hunt, D. Morrison, T. Owen, C. Sagan, J. Veverka, R. Strom, V. E. Suomi, (1982), A new look at the Saturn system: The Voyager 2 Images, Science, 215, 4532, 504–537, doi.org/10.1126/science.215.4532.504.

Sromovsky, L. A., K. H. Baines, P. M. Fry, (2019), Saturn's south polar cloud composition and structure inferred from 2006 Cassini/VIMS spectra and ISS images, Icarus in press, doi: 10.1016/j.icarus.2019.113398.

Sromovsky, L. A. and P. M. Fry, (2019), Interpretation of shadows and antishadows on Saturn and the evidence against south polar eyewalls, Icarus in press, doi: 10.1016/j.icarus.2019.113399.

Sromovsky, L. A., K. H. Baines, P. M. Fry, (2018), Models of bright storm clouds and related dark ovals in Saturn's Storm Alley as constrained by 2008 Cassini/VIMS spectra, Icarus 302, 360.

Sromovsky, L. A., and P. M. Fry, (2018), Composition and structure of fresh ammonia clouds on Jupiter based on quantitative analysis of Galileo/NIMS and New Horizons/LEISA spectra, Icarus 307, 347.

Sromovsky, L. A., K. H. Baines, P. M. Fry, R. W. Carlson, (2017), A possibly universal red chromophore for modeling color variations on Jupiter, Icarus, 291, 232–244, doi: 10.1016/j.icarus.2016.12.014.

Sromovsky, L. A., K. H. Baines, P. M. Fry, T. W. Momary, (2016), Cloud clearing in the wake of Saturn's Great Storm of 2010-2011 and suggested new constraints on Saturn's He/H2 ratio, Icarus, 276, 141–162, doi: 10.1016/j.icarus.2016.04.031.

Sromovsky, L. A., K. H. Baines, P. M. Fry, (2013), Saturn's Great Storm of 2010-2011: Evidence for ammonia and water ices from analysis of VIMS spectra, Icarus, 226, 1, 402–418, doi: 10.1016/j.icarus.2013.05.043.

Sromovsky, L. A., and P. M. Fry, (2010), The source of widespread 3 μm absorption in Jupiter's clouds: Constraints from 2000 Cassini VIMS observations, Icarus, 210, 230–257, doi: 10.1016/j.icarus.2010.06.039.

Stallard, T. S., H. Melin, S. Miller, S. V. Badman, K. H. Baines, R. H. Brown, et al., (2015), Cassini VIMS observations of H3+ emission on the nightside of Jupiter, Journal of Geophysical Research-Space Physics, 120, 6948–6973, doi: 10.1002/2015ja021097.

Stallard, T. S., H. Melin, S. Miller, S. V. Badman, R. H. Brown, K. H. Baines, (2012a), Peak emission altitude of Saturn's H3+ aurora, Geophysical Research Letters, 39, doi: 10.1029/2012gl052806.

Stallard, T. S., H. Melin, S. Miller, J. O'Donoghue, S. W. Cowley, S. V. Badman, A. Adriani, R. H. Brown, K. H. Baines, (2012b), Temperature changes and energy inputs in giant planet atmospheres: what we are learning from H3+, Philos Trans A Math Phys Eng Sci, 370, 1978, 5213–5224, doi: 10.1098/rsta.2012.0028.

Sugiyama, K., K. Nakajima, M. Odaka, K. Kuramoto, Y. Y. Hayashi, (2014), Numerical simulations of Jupiter's moist convection layer: Structure and dynamics in statistically steady states, Icarus, 229, 71–91, doi: 10.1016/j.icarus.2013.10.016.

Sussman, M. G., N. J. Chanover, A. A. Simon-Miller, A. R. Vasavada, R. F. Beebe, (2010), Analysis of Jupiter's Oval BA: A streamlined approach, Icarus, 210, 202–210, doi: 10.1016/j.icarus.2010.06.044.

Sylvestre, M., S. Guerlet, T. Fouchet, A. Spiga, F. M. Flasar, B. Hesman, G. L. Bjoraker, (2015), Seasonal changes in Saturn's stratosphere inferred from Cassini/CIRS limb observations, Icarus, 258, 224–238, doi: 10.1016/j.icarus.2015.05.025.

Teanby, N. A., L. N. Fletcher, P. G. J. Irwin, T. Fouchet, G. S. Orton, (2006), New upper limits for hydrogen halides on Saturn derived from Cassini-CIRS data, Icarus, 185, 2, 466–475, doi: 10.1016/j.icarus.2006.07.011.

Tejfel, V. G., (2005), Latitudinal variations of the molecular absorption on Saturn and seasonal changes of the atmospheric state at S- and N-hemispheres, Terrestrial Atmospheric and Oceanic Sciences, 16, 1, 231–240, doi: 10.3319/tao.2005.16.1.231(aa).

Temma, T., N. J. Chanover, A. A. Simon-Miller, D. A. Glenar, J. J. Hillman, D. M. Kuehn, (2005), Vertical structure modeling of Saturn's equatorial region using high spectral resolution imaging, Icarus, 175, 2, 464–489, doi: 10.1016/j.icarus.2004.11.006.

Trammell, H. J., L. Li, X. Jiang, Y. Pan, M. A. Smith, E. A. Bering III, S. M. Hörst, et al., (2016), Vortices in Saturn's Northern Hemisphere (2008–2015) observed by Cassini ISS, Journal of Geophysical Research-Planets, 121, 9, 1814–1826, doi: 10.1002/2016je005122.

Trammell, H. J., L. M. Li, X. Jiang, M. Smith, S. Horst, A. Vasavada, (2014), The global vortex analysis of Jupiter and Saturn based on Cassini Imaging Science Subsystem, Icarus, 242, 122–129, doi: 10.1016/j.icarus.2014.07.019.

Vasavada, A. R., S. M. Horst, M. R. Kennedy, A. P. Ingersoll, C. C. Porco, A. D. Del Genio, R. A. West, (2006), Cassini imaging of Saturn: Southern hemisphere winds and vortices, Journal of Geophysical Research-Planets, 111, E5, doi: 10.1029/2005je002563.

Vervack, R. J., and J. I. Moses, (2015), Saturn's upper atmosphere during the Voyager era: Reanalysis and modeling of the UVS occultations, Icarus, 258, 135–163, doi: 10.1016/j.icarus.2015.06.007.

West, R. A., K.H. Baines, E. Karkoschka, A. Sanchez-Lavega, (2009), Clouds and aerosols in Saturn's atmosphere, In Saturn from Cassini-Huygens, (eds.) M. K. Doughterty, L.W. Esposito, S.M. Krimigis, pp. 161–179, Springer, Dordrecht, Netherlands.

Wong, M. H., I. de Pater, X. Asay-Davis, P. S. Marcus, C. Y. Go, (2011), Vertical structure of Jupiter’s Oval BA before and after it reddened: What changed?, Icarus, 215, 211–225, doi: 10.1016/j.icarus.2011.06.032.

Wong, M. H., G. L. Bjoraker, M. D. Smith, F. M. Flasar, C. A. Nixon, (2004), Identification of the 10-μm ammonia ice feature on Jupiter, Planetary and Space Science, 52, 385–395, doi: 10.1016/j.pss.2003.06.005.

Yair, Y., (2012), New results on planetary lightning, Advances in Space Research, 50, 3, 293–310, doi: 10.1016/j.asr.2012.04.013.

Yair, Y., G. Fischer, F. Simoes, N. Renno, P. Zarka, (2008), Updated review of planetary atmospheric electricity, Space Science Reviews, 137, 1–4, 29–49, doi: 10.1007/s11214-008-9349-9.

Ye, S. Y., G. Fischer, W. S. Kurth, J. D. Menietti, D. A. Gurnett, (2016), Rotational modulation of Saturn's radio emissions after equinox, Journal of Geophysical Research-Space Physics, 121, 12, 11714–11728, doi: 10.1002/2016ja023281.

Yelle, R. V., J. Serigano, T. T. Koskinen, S. M. Horst, M. E. Perry, R. S. Perryman, J. H, Waite, (2018), Thermal Structure and Composition of Saturn’s Upper Atmosphere From Cassini/Ion Neutral Mass Spectrometer Measurements, Geophysical Research Letters, 45, 20, 10951–10958, doi: 10.1029/2018GL078454.

Young, R. M. B., and P. L. Read, (2017), Forward and inverse kinetic energy cascades in Jupiter’s turbulent weather layer, Nature Physics, 13, 1135, doi: 10.1038/nphys4227.

Youssef, A., and P. S. Marcus, (2003), The dynamics of Jovian white ovals from formation to merger, Icarus, 162, 1, 74–93, doi: 10.1016/S0019-1035(02)00060-X.

Zarka, P., W. Farrell, G. Fischer, A. Konovalenko, (2008), Ground-based and space-based radio observations of planetary lightning, Space Science Reviews, 137, 1–4, 257–269, doi: 10.1007/s11214-008-9366-8.

Zhang, X., R. A. West, P. G. J. Irwin, C. A. Nixon, Y. L. Yung, (2015), Aerosol influence on energy balance of the middle atmosphere of Jupiter, Nature Communications, 6, doi: 10.1038/ncomms10231.

Zhang, X., C. A. Nixon, R. L. Shia, R. A. West, P. G. J. Irwin, R. V. Yelle, et al., (2013a), Radiative forcing of the stratosphere of Jupiter, Part I: Atmospheric cooling rates from

Voyager to Cassini, Planetary and Space Science, 88, 3–25, doi: 10.1016/j.pss.2013.07.005.

Zhang, X., R.-L. Shia, Y. L. Yung, (2013b), Jovian stratosphere as a chemical transport system: Benchmark analytical solutions, The Astrophysical Journal, 767, 172, doi: 10.1088/0004-637x/767/2/172.

Zhang, X., R. A. West, D. Banfield, Y. L. Yung, (2013c), Stratospheric aerosols on Jupiter from Cassini observations, Icarus, 226, 159–171, doi: 10.1016/j.icarus.2013.05.020.

Zuchowski, L. C., Y. H. Yamazaki, P. L. Read, (2009), Modeling Jupiter's cloud bands and decks 1, Jet scale meridional circulations, Icarus, 200, 548–562, doi: 10.1016/j.icarus.2008.11.024.

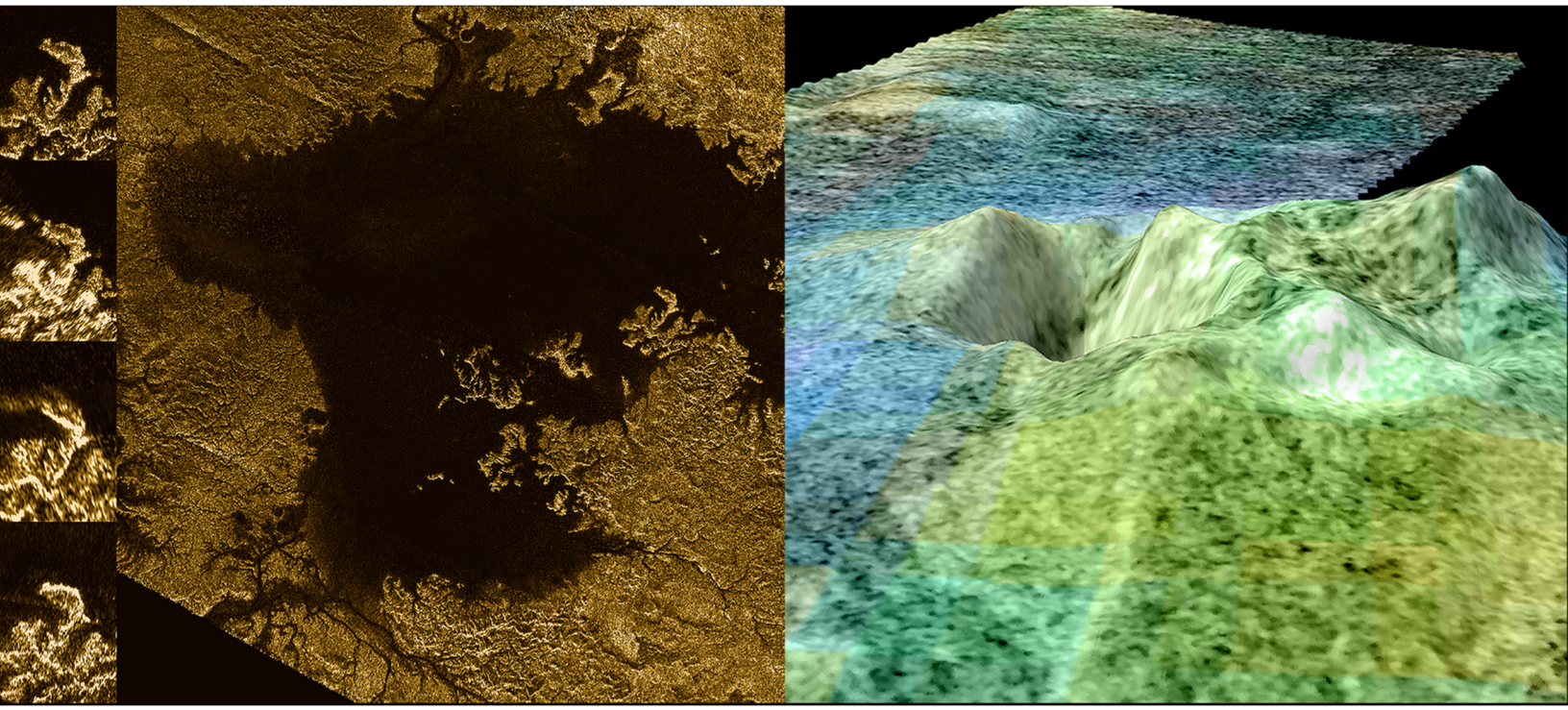

TITAN

Until the Cassini-Huygens mission, very little was known about Saturn's largest moon Titan, except that it was a Mercury-sized world whose surface was veiled beneath a thick, nitrogen-rich atmosphere. But Cassini mapped Titan's surface, studied its atmospheric reactions, discovered liquid seas there and even sent the Huygens probe to the moon's surface, completely rewriting our understanding of this remarkable world, including the detection of a large internal ocean deep below the surface. By the conclusion of the mission, Cassini-Huygens had revealed a complex Titan surface with a striking resemblance to the total geomorphology of the Earth, including dunes, rivers, gullies, lakes, seas, volcanic constructs, and mountains.

The Titan Discipline Working Group and Science Teams accomplished all surface and atmospheric science objectives in the traceability matrices for the mission. The Titan Observation Science Team (TOST) coordinated every Titan observation and planned all 127 close Titan flybys to ensure that Cassini Titan objectives were met. The Titan Atmospheric Modeling Working Group (TAMWG), comprised of experts in Titan's upper atmosphere and members of the engineering team, was formed to characterize Titan's uppermost atmosphere and its variation with seasons to give advice to the project on how close the spacecraft could approach Titan.

CONTENTS

Figures

Tables

Executive Summary

By the conclusion of the mission Cassini-Huygens had revealed a complex Titan surface with a striking resemblance to the total geomorphology of the Earth. Dunes, rivers, gullies, lakes, seas, volcanic constructs, mountains, are all present. Titan's methane cycle, analogous to the Earth's hydrologic cycle, drives processes including sedimentary transport that lead to the most geologically diverse surface after that of the Earth. Most spectacular was the discovery of several polar seas and hundreds of lakes, covering multiple hundreds of thousands of square kilometers. Some of the coastlines appear very Earth-like, with bays, cliffs, coves and river estuaries, while other boundaries are puzzling and may reflect a tectonic origin of the sea basins. Changes in two of the seas have been seen, suggesting dynamic processes driven by seasonal or other influences. Bathymetry and compositional measurements by Cassini lead to a liquid hydrocarbon inventory of about 70,000 square kilometers, mostly methane.

> The entire duration of the Cassini Mission exceeded 13 years, permitting observations over close to half of a seasonal cycle (almost half of Saturnian year) on Titan and revealed that seasonal variations are not symmetrical.

Cassini and the close-up images provided by Huygens establish fluvial erosion and rainfall as important processes tying together Titan's surface and atmosphere. A variety of cloud and weather patterns, including those generating rain, occur in the lower atmosphere. Comparison of cloud patterns with general circulation models supports the presence of a substantial amount of liquid methane in Titan's crust. From a variety of Cassini data, a surface age between ~0.5–1 billion years is derived. Although Cassini has not detected emission of methane from the crust, various indirect lines of evidence from Cassini point to episodic release of methane from the deep crust, with ethane soaked up by the ice in the form of clathrate hydrate or other trapping mechanisms.

Cassini measured Titan's gravity field and dynamic tidal response, indicating (together with Huygens electric field data) the presence of a deep subsurface water ocean, one denser than liquid water and thus possibly salty. A relatively low density, possibly hydrated, core was detected. The measurement of isotopic argon in the atmosphere supports significant outgassing over Titan's history, while the low abundance of primordial argon along with other isotopic measurements support ammonia as the original parent molecule of Titan's atmospheric nitrogen.

At the end of the Cassini-Huygens Nominal Mission, we had a good first order knowledge of the density and thermal structure of the atmosphere except for the ~ 500–950 km region, variously called the ignorosphere, agnostosphere, etc. Although Huygens Atmospheric Structure Instrument (HASI) inferred the thermal structure at equatorial latitudes through this region, it did not yield a pronounced mesopause as was widely expected from theory. Composite Infrared Spectrometer (CIRS) data provided detailed altitudinal and latitudinal composition and temperature

measurements of the stratosphere. The latter allowed the derivation of stratospheric zonal winds at substantial super-rotation speeds.

The Cassini Equinox and Solstice Missions enabled the study of seasonal variations of composition, temperatures and inferred zonal winds to understand the transition from summer in the southern hemisphere to equinoctial conditions to summer in the northern hemisphere, especially as the northern polar region emerges out of the polar winter night and its strong circumpolar vortex was breaking up. The entire duration of the Cassini Mission exceeded 13 years, permitting observations over close to half of a seasonal cycle (almost half of Saturnian year) on Titan and revealed that seasonal variations are not symmetrical. The eccentricity of Saturn's orbit and the obliquity of its rotational pole is sufficient to produce the observed asymmetry in Titan's seasonal response. But its entire stratosphere is tilted by several degrees from the rotational pole. Seasonal variations in composition, density, and thermal structure of Titan's upper atmosphere were characterized in particular by Ion and Neutral Mass Spectrometer (INMS) with complementary data from Ultraviolet Imaging Spectrograph (UVIS) measurements.

Cassini data determined that the thermosphere is a chemical factory that initiates the formation of complex positive and negative ions in the high thermosphere as a consequence of magnetospheric-ionospheric-atmospheric interaction involving solar extreme ultraviolet (EUV) and ultraviolet (UV) radiation, energetic ions and electrons. This factory produces very heavy positive and negative ions and large molecules, which condense out and are detectable in solar and stellar UV occultations at ~1000 km and initiate the haze formation process. As these particles fall through the 500–950 km region and grow, they become detectable by remote sensing: UVIS at ~1000 km, Imaging Science Subsystem (ISS) at ~500 km and eventually become ubiquitous throughout the stratosphere. These haze particles are strong absorbers of solar UV and visible radiation, play a fundamental role in heating Titan's stratosphere and mesosphere and provide a surface for heterogeneous reactions. The differential heating with latitude drives wind systems in Titan's middle atmosphere, much as ozone does in the Earth's middle atmosphere.

In summary the Titan Discipline Working Group and Science Teams accomplished all surface and atmospheric science objectives in the traceability matrices for the mission.

TOP 10–20 LIST OF SCIENTIFIC DISCOVERIES/ACCOMPLISHMENTS

- Cassini measured the shape of Titan's gravity field, including the tidal response. Cassini-Huygens discovered a global ocean of liquid water below a thick crust, and a relatively low density (hence hydrated?) core were discovered. Gravity and rotational data hint at the ocean being over dense and hence salty.
- Cassini-Huygens measured argon ($^{36,\,40}$Ar) in the atmosphere. Primordial argon was very low, indicating ammonia as the origin of the nitrogen atmosphere. Radiogenic argon indicated communication of the interior with the surface.

- Cassini-Huygens revealed a complex Titan surface with a striking resemblance to the total geomorphology of Earth. Dunes, rivers, gullies, lakes, seas, volcanic constructs, mountains, are all present. Titan's methane cycle, analogous to the Earth's hydrologic cycle, drives processes including sedimentary transport that lead to the most geologically diverse surface after that of Earth.
- Cassini discovered that Titan has several polar seas and hundreds of lakes, covering hundreds of thousands of square kilometers. Cassini determined the composition and bathymetry of the seas and a few lakes. The marine coastlines are very Earth-like, with bays, coves, cliffs and river estuaries, and dynamic changes occur in the seas. The total observable liquid hydrocarbon inventory was constrained (70,000 cubic km).
- Cassini-Huygens determined a range of crustal ages on Titan's surface; the average age is hundreds of millions to a billion years.
- Cassini-Huygens observed dynamic meteorology in cloud behavior and rainstorms, changes in the lakes and seas, and evaporation of liquids from the surface.
- Cassini-Huygens discovered a variety of weather patterns, including rainstorms, in Titan's lower atmosphere and documented seasonal changes therein.
- Cassini further explored the evolution and composition of the winter circumpolar vortex that switches hemispheres seasonally. Titan has strong parallels to Earth with strong winter polar vortices.
- Cassini discovered the entire stratosphere is tilted by several degrees from the rotational pole.
- Cassini discovered ice condensate clouds in the stratosphere.
- Cassini discovered complex, heavy molecules and ions (both positive and surprisingly, negative) in the upper atmosphere, pointing to active chemistry and a link to the initiation of haze formation. The richness and complexity (going up to hundreds, maybe thousands of species) of the heavy molecules.
- Cassini-Huygens discovered Enceladus as one possible source for oxygen compounds in Titan's atmosphere.
- Cassini discovered Titan's thermosphere to be highly variable, contradicting model predictions.
- Cassini firmly established no intrinsic magnetic field.
- Cassini-Huygens came up with the surprising result that lightning is absent despite observed methane moist convection.

Table TITAN-1 shows the assessment of data collected to satisfy an objective. It is not as assessment of the status of data analysis/publications.

Table TITAN-1. Science Assessment. This table is an assessment of data collected to satisfy an objective. It is not as assessment of the status of data analysis/publications.

Fully/Mostly Accomplished: **Partially Accomplished:** **Not Accomplished:**

Titan Discipline Science Objectives	AO and TM Science Objectives	Titan DWG Assessment	Comments (if yellow, partially fulfilled)
Titan's Great Seas	(TC1a)		
Titan's Global Seasons	(TC1b)		
Titan-Magnetosphere Interaction	(TC2a), (T_AO5)		
Titan's Surface	(TN1a), (T_AO4)		Some work was done, but more work remains for future missions.
Titan's Interior Ocean	(TN1b)		A few crustal structures locally; induced magnetic field difficult due to ionospheric currents.
Titan Atmospheric Composition	(TN1c), (T_AO1, 2)		
Titan Atmospheric Structure	(TN2a), (T_AO5)		
Titan's Icy Shell	(TN2b)		Crustal viscosity not determined from data taken.
Titan Meteorology	(TN2c), (T_AO3)		
Other Titan Science not in CSM Traceability Matrix			
Open Questions for Titan Science			

KEY SCIENCE OBJECTIVES FOR TITAN

- **Titan Atmospheric Formation and Evolution (T_AO1)** – Determine abundances of atmospheric constituents (including any noble gases), establish isotope ratios for abundant elements, constrain scenarios of formation and evolution of Titan and its atmosphere.
- **Titan Atmospheric Composition and Distribution (T_AO2)** – Observe vertical and horizontal distributions of trace gases, search for more complex organic molecules, investigate energy sources for atmospheric chemistry, model the photochemistry of the stratosphere, study formation and composition of aerosols.
- **Titan Meteorology (T_AO3)** – Measure winds and global temperatures; investigate cloud physics, general circulation, and seasonal effects in Titan's atmosphere; search for lightning discharges.
- **Titan Surface Characteristics and Internal Structure (T_AO4)** – Determine the physical state, topography, and composition of the surface; infer the internal structure of the satellite.
- **Titan Upper Atmosphere (T_AO5)** – Investigate the upper atmosphere, its ionization, and its role as a source of neutral and ionized material for the magnetosphere of Saturn.

Titan CSM Traceability Matrix Objectives

- **Titan's Great Seas (TC1a)** – Determine seasonal changes in the methane-hydrocarbon hydrological cycle: of lakes, clouds, aerosols, and their seasonal transport.
- **Titan's Global Seasons (TC1b)** – Determine seasonal changes in the high-latitude atmosphere, specifically the temperature structure and formation and breakup of the winter polar vortex.
- **Titan-Magnetosphere Interaction (TC2a)** – Observe Titan's plasma interaction as it goes from south to north of Saturn's solar-wind-warped magnetodisk from one solstice to the next.
- T**itan's Surface (TN1a)** – Determine the types, composition, distribution, and ages, of surface units and materials, most notably lakes (i.e., filled versus dry and depth; liquid versus solid and composition; polar versus other latitudes and lake basin origin).
- **Titan's Interior Ocean (TN1b)** – Determine internal and crustal structure: Liquid mantle, crustal mass distribution, rotational state of the surface with time, intrinsic and/or internal induced magnetic field.
- **Titan Atmospheric Composition (TN1c)** – Measure aerosol and heavy molecule layers and properties.
- **Titan Atmospheric Structure (TN2a)** – Resolve current inconsistencies in atmospheric density measurements (critical to a future Flagship mission).
- **Titan's Icy Shell (TN2b)** – Determine icy shell topography and viscosity.
- **Titan Meteorology (TN2c)** – Determine the surface temperature distribution, cloud distribution, and tropospheric winds.

Titan DWG System Results

Titan

Titan's great seas (TC1a) T_AO2) [Hayes, Lorenz, Lunine]

Titan's lakes and seas encompass 1% of the total surface area and are restricted to latitudes poleward of ~55° [Hayes 2016]. The majority (97% by area) of surface liquids reside in the north polar region, with 80% of all liquid-filled surface area contained in three large seas; Kraken Mare (5.0×10^5 km^2), Ligeia Mare (1.3×10^5 km^2), and Punga Mare (6.1×10^4 km^2). The only large liquid body in the south polar region is Ontario Lacus (1.6×10^4 km^2), although several large empty basins that encompass an area similar to the northern Maria (7.6×10^5 km^2) have been identified and interpreted as paleoseas [Birch et al. 2018; Hayes et al. 2010, 2011]. While a few small lakes have

been observed to disappear or brighten in both the north and south over the thirteen years of Cassini observations, no large-scale changes have been reported in the shorelines of the northern seas [Hayes et al. 2011]. Although confirmed and stable liquid deposits are currently restricted to polar terrain, the equatorial features Hotei and Tui Regiones have been interpreted as possible low-latitude paleoseas [Moore and Howard 2011]. Both regions are surrounded by fluvial networks that appear to converge on a field of radar-bright, lobate, depressions that are morphologically similar to high-latitude lakes [Moore and Howard 2011]. Dark flow-like features identified adjacent to the radar-bright depressions have been interpreted as cryovolcanic deposits [Barnes et al. 2006; Wall et al. 2009], suggesting that both paleo-lakes and cryovolcanic flows may be present at Tui Regio and Hotei Regio [Lopes et al. 2013]. The existence of modern equatorial lakes has been proposed based on the longevity of low albedo localities observed by Cassini Visual and Infrared Imaging Spectrometer (VIMS) [Griffith et al. 2012; Vixie et al. 2015], although none of these features have been confirmed by higher-resolution Synthetic Aperture Radar (SAR) or altimetry datasets.

For the majority of the Cassini mission, the surfaces of the Titan's lakes and seas were observed to be incredibly flat, …, suggesting little to no wind or currents capable of ruffling liquid surfaces … .

For the majority of the Cassini mission, the surfaces of the Titan's lakes and seas were observed to be incredibly flat, with maximum average surface deviations of order millimeters, suggesting little to no wind or currents capable of ruffling liquid surfaces [Grima et al. 2017; Stephan et al. 2010; Wye et al. 2009; Zebker et al. 2014]. As northern spring approached, evidence for surface waves and other transient features began to emerge [Barnes et al. 2014; Hofgartner et al. 2014]. This increase in activity has been attributed to the increase in solar insolation and surface winds expected with the changing seasons [Hayes et al. 2013; Lorenz and Hayes 2012]. Prior to northern springtime, surface winds were presumably below the threshold for wind-wave generation in hydrocarbon liquids (~0.4 m/s) [Hayes et al. 2013].

During an observation designed to look for surface waves on Ligeia Mare, the Cassini Titan Radar Mapper (RADAR) acquired altimetry echoes that displayed two distinct returns, one from the surface of Ligeia Mare and one from its seabed [Mastrogiuseppe et al. 2014]. The difference in received timing between these returns was a measure of Ligeia Mare's depth (160 m), while their relative intensity provided a measurement of the microwave loss-tangent (i.e., absorbance) of the liquid ($\tan \Delta = \varepsilon''/\varepsilon' = 4.4 \pm 0.8 \times 10^{-5}$, where ε is the complex dielectric constant). Following the identification of Ligeia Mare's seabed, several of the final radar passes of Titan were modified to repeat the experiment over Punga Mare, Kraken Mare, and several small lakes [Mastrogiuseppe et al. 2016, 2017]. As a result, bathymetry measurements over all three of Titan's maria and several small lakes are now available. When combined with SAR observations that also penetrate the shallower seas and assuming a maximum depth of ~300 m for Kraken Mare [Lorenz et al. 2014; 2008b], for which a reflection from the bottom was not observed, the volume of Titan's lakes and seas is estimated at 70,000 km^3 [Hayes 2016]. This represents only ~1/7 the volume of atmospheric methane suggesting that, unlike on Earth, Titan's seas have little influence on the global climate.

This also means that the lakes and seas are not plausible as a long-term resupply reservoir of atmospheric methane.

Laboratory experiments [Mitchell et al. 2015] demonstrated that the microwave loss-tangents measured by Cassini require methane-dominated liquids. If higher-order hydrocarbons (e.g., propane) are considered in addition to ethane, then the loss-tangents measured over Ligeia, Punga, and Kraken Mare require near pure methane-nitrogen mixtures. If a methane-nitrogen-ethane ternary mixture is considered, Ligeia's loss tangent is consistent with 71% methane and 12% ethane by volume [Mastrogiuseppe et al. 2016]. These abundances are generally consistent with predicted equilibrium compositions [Glein and Shock 2013; Tan et al 2015], although higher-order components (e.g., propane) were not taken into account. The loss-tangent of Punga Mare and Kraken are similar (to within error) to Ligeia Mare, while Ontario Lacus was observed to be more absorbent, consistent with a greater ethane content or an increased abundance of more involatile hydrocarbons (e.g., propane). Regardless, the primary constituent of Ontario must still be methane in order to match the derived loss tangent [Mastrogiuseppe et al. 2017]. Earlier in the Cassini mission, VIMS infrared spectra were used to identify the presence of ethane in Ontario [Brown et al. 2008]. The fact that Titan's seas are methane-dominated further exacerbates the long-standing mystery of Titan's missing ethane [Lunine et al. 1983].

Titan's global seasons (TC1b) [Teanby et al. 2017]

Determine seasonal changes in the high-latitude atmosphere, specifically the temperature structure and formation and breakup of the winter polar vortex.

To understand the structure of Titan's atmosphere one must keep in mind certain basic facts from solar system dynamics. First, the axial tilt of Saturn and Titan is 26.73°; and second, Saturn's orbital eccentricity is 0.05415, which yield variations in the distance from the Sun from 9.04 to 10.07 AU and in the total solar flux of ~20 %. Titan's atmospheric seasonal evolution is driven by three mechanisms: the seasonal change in solar declination, the orbital eccentricity of Saturn with Titan receding from the Sun since 2002, and the solar cycle variation of the Sun with activity increasing from its minimum in late 2009 to peak solar activity for cycle 24 in April 2014. Perihelion last occurred in February 25, 2003. Summer solstice in Titan's southern hemisphere was March 17, 2002; summer solstice in the northern hemisphere was on May 24, 2017 after spring equinox on August 11, 2009.

The variation in solar distance and thus solar flux will be most important in the troposphere, stratosphere, and mesosphere, whereas the much larger solar cycle variations in UV and EUV solar radiation will overwhelm the smaller eccentricity effects in situ in the thermosphere. But the contraction and expansion of the underlying stratosphere/mesosphere with increasing and decreasing solar distance must be considered in determining thermospheric seasonal changes. The Voyager spacecraft flybys were at high solar activity, whereas orbit insertion of the Cassini spacecraft in July 2004 was during the descending phase from peak activity, which occurred in April 2000, to deep solar minimum conditions in the August–November 2009 timeframe.

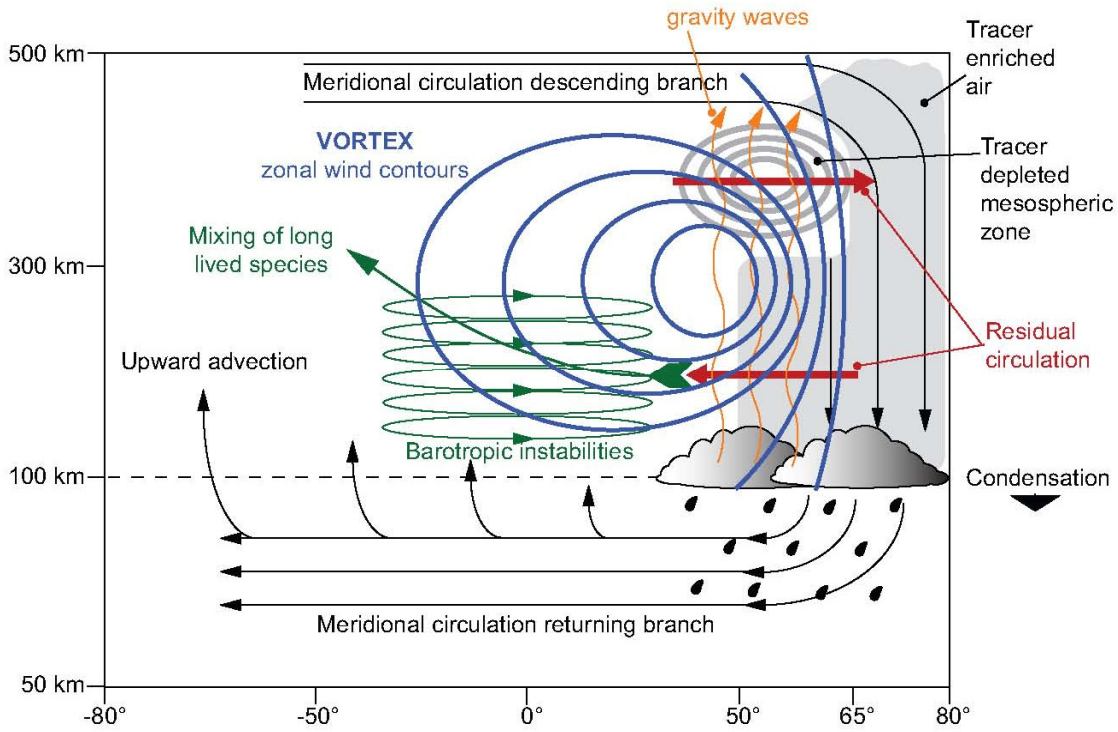

Figure TITAN-1. Schematic of dynamical processes thought to be important in Titan's winter north polar region. A single cell meridional circulation, a polar vortex of strong zonal winds, wave induced mixing by inferred equatorial barotropic and gravity waves. Figure from Teanby et al. [2008].

Accordingly, the nominal Cassini-Huygens Mission was mostly at low solar activity. Peak solar activity for cycle 24 occurred in April 2014.

When the Cassini spacecraft arrived at Titan, there was a well-developed winter polar vortex in the northern hemisphere inferred from the stratospheric temperatures with peak zonal wind velocities on the order of 200 m/s [Achterberg et al. 2008a]. From July 1, 2004 to September 15, 2017, the spacecraft made a total of 127 Titan flybys, spanning nearly half of Titan's 29.5-year orbit around the Sun that allowed observations of the detailed evolution and breakup of Titan's northern winter polar vortex and the formation and early evolution of Titan's southern winter polar vortex (Figure TITAN-1). The former was characterized by the decrease in the upper stratospheric temperatures, weakening of the zonal winds, and the reduction in the enhancement of photochemically produced compounds [Vinatier et al. 2010, 2015; Achterberg et al. 2011].

> "Associated with the polar vortex was a meridional circulation dominated by a single pole-to-pole cell that ascended at southern and equatorial latitudes and subsided over the northern winter pole. Strong vortex winds formed a mixing barrier and effectively isolated the polar air mass, permitting a distinct temperature and composition within the vortex. Pre-equinox observations of the north polar region show the mid-winter vortex is characterized by: trace gas enrichment due to subsidence from upper-

atmosphere photochemical source regions, a cold lower stratosphere due to long-wave radiative cooling and a lack of insolation; and a hot stratopause/mesosphere due to subsidence and adiabatic heating with a peak temperature of ~200 K. Pre-equinox observations detail the nominal configuration of the mid-winter polar vortex, which is broadly consistent with results from numerical models" [Teanby et al. 2017].

"Following Titan's 2009 northern spring equinox, peak solar heating moved to the northern hemisphere, initiating south-polar subsidence and winter south-polar vortex formation with reversal almost immediately of the vertical circulation at the south pole [Vinatier et al. 2015]. Throughout 2010–2011, strengthening subsidence produced a mesospheric hot-spot (~180 K at 300–400 km altitude) and caused extreme enrichment of high-altitude photochemically produced trace gases. The reversal was accompanied by a two-cell transitional global circulation, with upwelling around the equator and subsidence at both poles, which persisted for two years before a fully reversed single circulation cell was established [Vinatier et al. 2015]. The timing of these circulation changes is consistent with numerical models, which subsequently predicted a gradual evolution of the south polar vortex towards a state similar to that observed in the north prior to equinox." [Teanby et al. 2017].

"However, contrary to expectations, in 2012 spectral features of HCN ice were identified at 300 km altitude over the southern winter pole with VIMS [de Kok et al. 2014]".

In addition, CIRS detected C_6H_6 ice in the south polar cloud [Vinatier et al. 2018] and an undetermined 220 cm^{-1} spectral signature suddenly appeared as well in July 2012 but not February 2012 CIRS data set taken there [Jennings et al. 2012].

"This cloud was also observed in high spatial resolution images from ISS. The presence of HCN ice was surprising as it requires temperatures of ~125 K to form at 300 km altitude—over 50 K colder than temperatures observed in mid-2011 at similar altitudes and latitudes. Therefore, development of Titan's winter south polar vortex is more complex than expected. There is not a simple monotonic increase of mesospheric temperatures following equinox to eventually mirror the ~200 K temperatures observed in northern winter at the start of the mission—instead rapid and unexpected cooling occurred accompanied by extreme trace gas enrichment within the polar vortex that dramatically increased mesospheric long-wave radiative cooling efficiency, causing unusually cold temperatures 2–6 years post-equinox. The long timeframe to reach a stable vortex configuration results from the high infrared opacity of Titan's trace gases and the relatively long atmospheric radiative time constant. Whereas winter polar hotspots have been observed on other planets, detection of post-equinox cooling is so far unique to Titan." [Teanby et al. 2017].

Titan-magnetosphere interaction (TC2a) [Strobel et al. 2009; Strobel and Cui 2014; Simon et al. 2010]

Observe Titan's plasma interaction as it goes from south to north of Saturn's solar-wind-warped magnetodisk from one solstice to the next.

Titan's ambient plasma conditions heavily depend on the properties of Saturn's magnetodisk, which in turn is controlled by the solar wind pressure, Saturn seasons, and inner magnetospheric effects (periodicities and mass loading by rings + Enceladus). Thermal electron [Rymer et al. 2009], ion [Németh et al. 2011], energetic particle [Garnier et al. 2010], and field [Simon et al. 2010] flyby classifications are described extensively in Arridge et al. [2011]. Thermal ion composition in Saturn's magnetodisk is also strongly dependent on magnetic latitude, with heavy (water group) ion density maximizing near Br = 0. [Szego et al. 2011].

The classification of Titan's magnetospheric environment by energetic electrons relies on the four broad types identified by Rymer et al. [2009]: plasma sheet, lobe-like, magnetosheath, and bimodal, which result from variable solar wind pressure, day/night asymmetry, and the vertical flapping of the plasma sheet with respect to the equatorial plane. The plasma sheet region contains relatively high electron densities (~0.05 cm^{-3}) and temperatures (~110 eV), whereas the lobe-like region has high temperatures (~110 eV), but much lower densities (~0.003 cm^{-3}). Their respective energy fluxes into Titan's atmosphere are ~1.6 × 10^{9} eV cm^{-2} s^{-1} (2.6 × 10^{-3} erg cm^{-2} s^{-1}) and ~1.2 × 10^{8} eV cm^{-2} s^{-1} (1.9 × 10^{-4} erg cm^{-2} s^{-1}). Higher thermospheric temperatures have been associated with the plasma sheet environment, which is consistent with the factor of 10 enhancements in electron density. The magnetosheath is encountered, of course only when Titan is outside of Saturn's magnetosphere and characterized by high electron densities (~0.4 cm^{-3}) but cold temperatures (~30 eV) with an energy flux of ~2.5 × 10^{9} eV cm^{-2} s^{-1} (4.0 × 10^{-3} erg cm^{-2} s^{-1}). The bimodal regions have two distinct electron populations: the more energetic population being plasma sheet or lobe-like (electron densities (~0.004 cm^{-3}) and temperatures (~350 eV)) and the less energetic population suggestive of local pick-up (electron densities (~0.1 cm−^{3}) and temperatures (~10 eV)) [Rymer et al. 2009]. For bimodal regions the energy flux is approximately 1 × 10^{9} eV cm^{-2} s^{-1} (1.6 × 10^{-3} erg cm^{-2} s^{-1}).

Titan's location with respect to Saturn's magnetodisk is also dependent on the phase of a rotating perturbation within Saturn's inner magnetosphere [Southwood and Kivelson 2007]. In particular, Titan's proximity to Saturn's magnetodisk current sheet depends [Arridge et al. 2008; Bertucci et al. 2009] on the so-called Saturn Longitude System [Kurth et al. 2008] which organizes fields and particle periodicities inside Saturn's magnetosphere. Vertical and radial excursions of the upstream plasma flow are expected to be influenced by this effect [Sillanpaa et al. 2011; Achilleos et al. 2014].

The solar wind dynamic pressure also influences Titan's interaction by distorting Saturn's magnetodisk into a bowl shape during off-equinox periods [Achilleos et al. 2014]; and in coincidence with the arrival of ICMEs and CIRs [Roussos et al. 2018], by controlling the location of Saturn's magnetopause and bow shock [Kanani et al. 2010].

During solar wind excursions [Bertucci et al. 2008, 2015] the orientation and strength bundles of draped magnetic field lines inside Titan's magnetosphere suggest field lines take between 20 min to 3 h to travel across the interaction region in agreement with predictions [Neubauer et al. 2006]. The geometry of the magnetotail/magnetosphere agrees with upstream conditions for most orbits [Simon et al. 2010].

While a search for an intrinsic Titan magnetic field has yielded negative results, the magnetometer data show that the moon's magnetic environment is strongly affected by its proximity to Saturn's warped and highly dynamic magnetodisk [Simon et al. 2010]. In the nightside sector of Saturn's magnetosphere, the magnetic field near Titan is controlled by intense vertical flapping motions of the magnetodisk current sheet, alternately exposing the moon to radially stretched lobe-type fields and to more dipolar, but highly distorted current sheet fields [Simon et al. 2010]. The upper limit to the intrinsic magnetic moment is 0.78 nT R_T^3 according to Wei et al. [2010].

Titan's thermosphere and exosphere are also very dynamic and temporally variable.

Titan's thermosphere and exosphere are also very dynamic and temporally variable. Qualitatively, Cassini in situ measurements point to an important role for Saturn's magnetospheric interaction as a key driver of this observed variability. Quantitatively based on Cassini data, the measured and derived magnetospheric power inputs to the upper atmosphere are smaller than solar EUV and UV power input on a globally averaged, orbital averaged basis. Only on very rare occasions does magnetospheric power input equal solar input. This leads to the conclusion that solar radiation mostly heats the upper atmosphere, whereas magnetospheric particle precipitation plays a more important role in the ionization of the atmosphere below the main ionosphere ($z < 900$ km). This is consistent with the absence of N_2 ultraviolet signatures of magnetospheric power input to Titan's upper atmosphere in nightside EUV spectra [Ajello et al. 2007; West et al. 2012] and UV dayglow observations [Stevens et al. 2011] with UVIS.

On a related issue, we note that the evidences for a link between magnetospheric inputs and Titan's ionosphere are scarce. The fact that an ionospheric response to magnetospheric inputs is harder to observe than a thermospheric response is associated with the different timescales involved. Characteristic ion-chemical time constants in Titan's ionosphere are ~ (10–1000) sec, shorter than or comparable to the time interval that the Cassini spacecraft typically spent below Titan's exobase. This means any ionospheric response to Saturn's magnetosphere can only be captured as it occurs luckily during a Titan encounter.

Analysis of Cassini data has not yielded any proven correlation between the temperature of Titan's thermosphere and ionospheric signatures attributed to enhanced particle precipitation, which suggests that the correlation is not indicative of a physical connection. In summary based on all of Cassini observational data analyzed to date in conjunction with theoretical studies, an upper limit of 10% on the ratio of magnetospheric power input to solar EUV and far ultraviolet (FUV) power input into Titan's upper atmosphere can be placed on an orbital, globally averaged basis.

Table TITAN-2. Titan energy source magnitudes.

Energy Source	Reference	r at peak (km)	Energy Flux (erg/cm^2/s)	Global Input (GW)
Solar Lyman-alpha	LASP- solar min	3400	0.017	2.4
Solar Lyman-alpha	LASP- solar med	3400	0.022	3.2
Solar Lyman-alpha	LASP- solar max	3400	0.027	4
Solar EUV	SEE- solar min	3700	0.008	1.5
Solar EUV	SEE- solar med	3700	0.018	3.1
Solar EUV	SEE- solar max	3700	0.022	4
Mag e- PS	Rymer [2009]	4000	0.0026	0.5
Mag e- Lobe	Rymer [2009]	4000	0.0002	0.04
Mag e- MS	Rymer [2009]	4000	0.004	0.8
Mag e- Bimodal	Rymer [2009]	4000	0.0016	0.3
Mag i+ PS				
Mag i+ Lobe				
Mag i+ MS				
Mag i+ Bimodal				
ENAs	Brandt [2001]	3400	0.008	1.1
O+ ions	Shah [2009]	3500	0.01	1.4

The entries in Table TITAN-2 correct the UV entries in Sittler et al. [2009], Table 16.1 shown in Table TITAN-3.

Table TITAN-3. Titan upper atmosphere and its induced magnetosphere. Table from Sittler et al. [2009], Table 16.1.1.

Energy Source	Energy Flux (erg/cm2/s)	Global Input (Watts)[d]	Comments
Plasma protons	1.6e-4	3.4e7	Magnetized
Plasma electrons	1.6e-4	3.4e7	Magnetize
Plasma heavy ions	1.5e-3	3.2e8	Unmagnetized
Energetic ions	5.0e-4 to 1.0e-2	1.05e8 to 2.0e9	$27 < E_p < 255$ keV[a]
Energetic electrons	2.0e-4	4.0e7	$28 < E_e < 533$ keV[a,b]
UV airglow	1.6e-3	3.5e8	Altitude ~1,300 km[c]
UV ionization	1.6e-4	3.4e7	Altitude ~1,300 km[c]
Ohmic heating			Not yet known
GCR	1.6e-4 to 2.7e-3	3.2e7 to 5.4e8	Integrated flux
Dust	1.8e-3	1.8e8	Interplanetary dust

[a] Model by Ledvina et al. [2005] show some magnetic channeling of 50 keV protons. If heavy ions (0^+) Unmagnetized. Expect energetic electrons to be more magnetized than protons.

[b] Energetic electron energy flux derived from Krupp et al. [2005].

[c] For T0 at 90° phase angle UV absorption peaked at 1,325 km, while for TB at 0° phase angle absorption peaked at 1,095 km altitude.

[d] Exobase at r ~4,000 km and 4π area 2×10^{18} cm^2.

Titan's surface (TN1a) (T_AO4)

The Cassini-Huygens mission has revealed the surface of Titan in unprecedented detail, enabling us to discern the different geomorphologic units on the surface, constrain the relative times of emplacement and place constraints on composition. Titan has an icy crust, but water ice signatures are not easily detected due to atmospheric scattering and absorption that hamper the observations, as well as the presence of complex organic molecules on the surface. The extended, dense, and hazy N_2−CH_4 dominated atmosphere shields the surface from direct optical observations, except at certain wavelengths where the methane absorption is weak. These atmospheric windows are exploited by the Cassini VIMS to obtain compositional information and by VIMS and the ISS to map surface features. In addition, Cassini RADAR altimetry and SARTopo [Stiles et al. 2009] have documented elevations ranging over ~2300 m [Corlies et al. 2017; Lorenz et al. 2013] and put constraints on Titan's global topography. Compared to the Moon's or the Earth's surfaces, off-nadir radar response from most of Titan's surface is quite strong at Ku-band, indicating that more complex processes than simple surface scattering, such as a significant volume scattering component, have to be considered [Wye et al. 2007; Janssen et al. 2016]. Indeed, signals from Cassini RADAR Ku-band instrument, given the low Titan surface temperatures and the low loss tangent of material analogs relevant to Titan's surface, should produce radar waves that can penetrate the surface down to a depth ranging from a few decameters, for an organic and compacted near-surface, Paillou et al. [2008], to several meters, for a pure water ice near-surface, Paillou et al. [2008], and have thus multiple opportunities to be scattered. The above referenced observations of Titan's surface are themselves consistent with sub-surface and volume scattering processes, in addition to pure surface scattering. Scatterometer and radiometer measurements alike are even, in some locations, best fit using models where volume scattering is enhanced by coherent backscatter processes [Zebker et al. 2008; Janssen et al. 2011].

Janssen et al. [2016] further advance that a regionally enhanced degree of volume scattering is indicative of a higher abundance of water-ice in the near-surface, water-ice being more transparent to microwaves than organics and thus allowing for more opportunities for scattering. Based on this idea, about 10% of Titan's near-surface is water ice-rich while the composition of the remaining terrains is dominated by more absorbing organic materials, by-products of the intense atmospheric photochemistry (Figure TITAN-2). The regions with a high degree of volume scattering include mountainous terrains, craters as well as fan-like features, possibly corresponding to flowing material resulting from cryovolcanism, the radar signature of which could be explained by a strong volume scattering effect in a thick water-ammonia ice layer using a two-layers scattering model [Paillou et al. 2006] as shown in Figure TITAN-3. Radar-bright sinuous channels in the southwest of Xanadu, showing very large radar cross-sections, are also consistent with the presence of icy low-loss rounded scatterers, acting as efficient natural retro-reflectors [Le Gall et al. 2010].

Weaker radar reflectors such as Titan's dunes are most likely organic in nature, as also supported by VIMS [Soderblom et al. 2009]. However, we note that they exhibit high-amplitude scattering as compared to Earth analogs, which is consistent with a volume scattering component added to the surface component due to the radar wave penetration in aeolian sediments, implying that the dune material is either inhomogeneous or presents a high porosity [Paillou et al. 2014].

Mega-yardang structures were observed on Titan, and they also present a much brighter radar signature than their terrestrial analogs, indicating that additional scattering processes, such as volume scattering, should occur [Paillou et al. 2016].

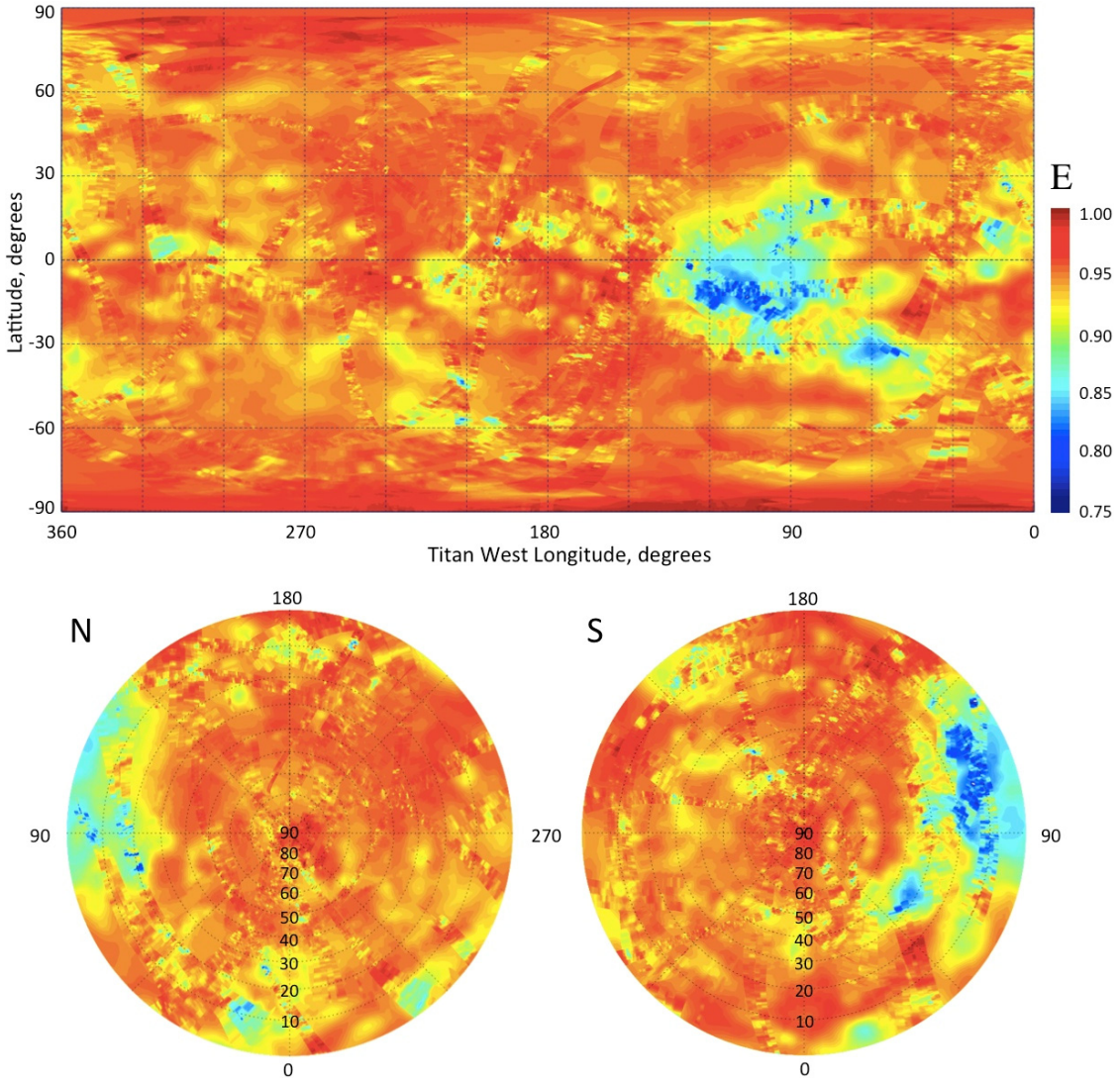

Figure TITAN-2. Global mosaic of emissivity of Titan at the 2 cm wavelength of the Cassini RADAR. This is the final result of the brightness temperature mapping of Titan incorporating all radiometric data obtained from Titan passes Ta through T98, a nearly ten-year span. The brightness temperature was measured as a function of position, polarization and time over a wide range of geometries and ranges and calibrated to about 1% absolute accuracy using Huygens probe and CIRS temperature measurements as described in Janssen et al. [2016]. The polarization data were used to construct a global mosaic of effective dielectric constant, enabling the conversion of all measured brightness temperatures to their equivalent values at normal incidence. The data were then folded into a massive least squares solution for the seasonally varying brightness temperature distribution of Titan over the time scale of the observations. Comparison with surface temperature measurements obtained in the infrared (IR) using Kirchhoff's law then enabled the construction of the emissivity map shown.

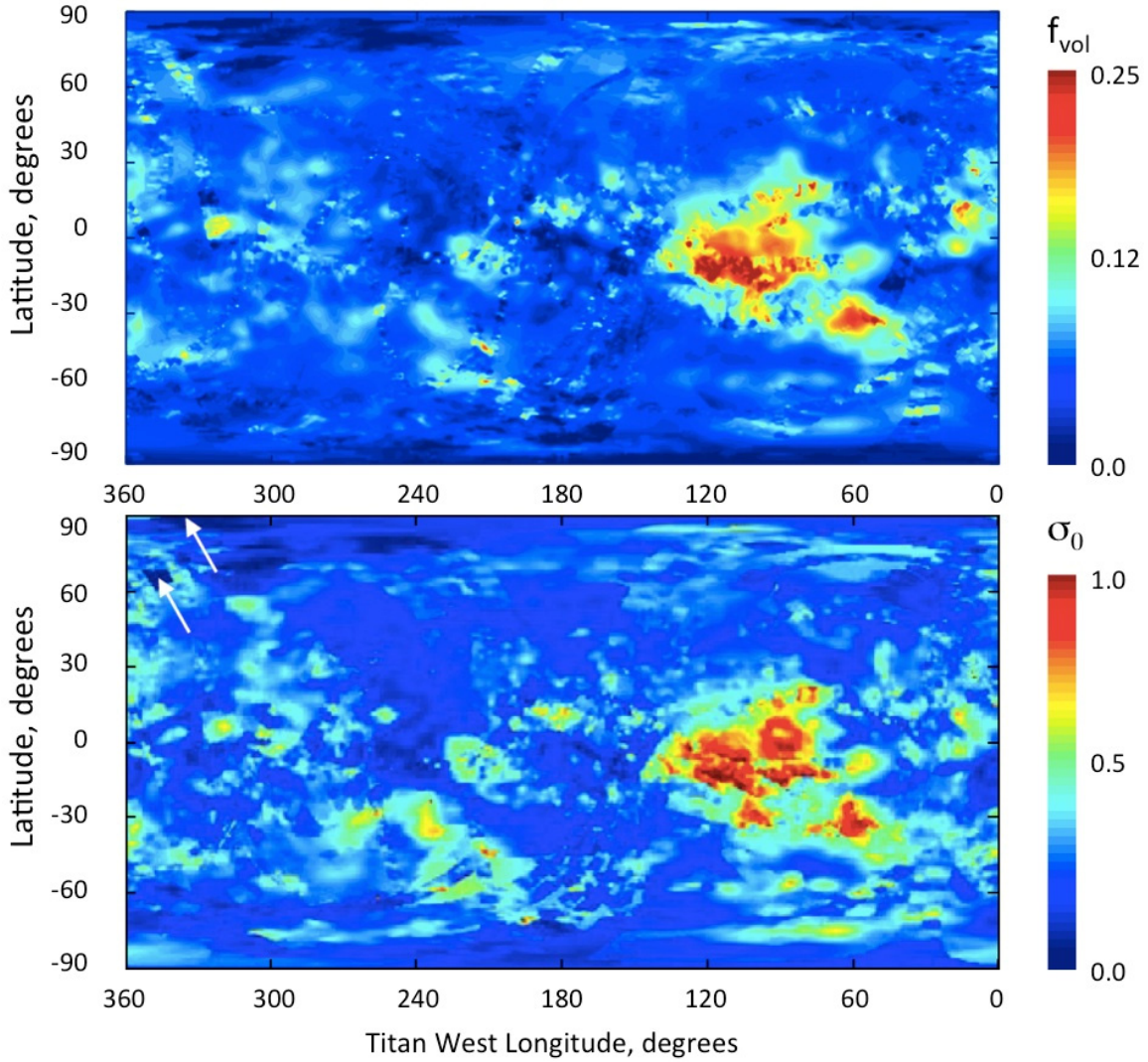

Figure TITAN-3. Predicted and observed maps of scattering from Titan's surface. The upper panel is a map of the volume scattering parameter f_{vol} for a simple surface model composed of a smooth dielectric interface separating free space from an inhomogeneous and isotropically scattering subsurface. f_{vol} is the probability that a photon entering the surface (as determined by the effective dielectric constant) scatters and escapes from the subsurface before it is absorbed. The map of f_{vol} reconciles the maps of effective dielectric constant and emissivity and predicts the overall magnitude of the scattering. The lower panel is a global mosaic of Titan's normalized radar cross-section from all real aperture data through T71 [Wye 2011], showing the actually observed scattering. The white arrows in the upper left-hand corner indicate two small regions that were not mapped.

Lastly and of particular interest is the case of Titan's methane-dominated seas and lakes, where radar waves can penetrate down to several thousands of wavelengths (at least 150 m), and be subsequently backscattered by the lakebeds [Mastrogiuseppe et al. 2014, 2019], consistent with recent laboratory investigation of the electrical properties of liquid hydrocarbons [Mitchell et al. 2015].

Surface observations analyzed in view of deriving the surface albedo and determining the composition are rendered difficult on Titan due to the atmospheric interference with the main opacity due to methane and which allows direct access to the surface only at a few specific frequencies in the near-infrared where the methane absorption is weak—for example, Niemann et al. [2010]. Nonetheless, re-analysis of the entire ISS dataset acquired in the 938 nm methane window has yielded a complete global map of Titan's surface at resolutions better than a few kilometers with albedos calibrated to Huygens Descent Imager/Spectral Radiometer (DISR) ranging from 0.25 in the dunes to 0.9 at Hotei Arcus [Karkoschka et al. 2017]. A combination of RADAR and spectral imaging data—VIMS—is required in order to distinguish and categorize the geomorphological features into units with distinct chemical compositions that remain to be identified. Several investigators have applied radiative transfer codes in addition to data set comparisons—for example, Hirtzig et al. [2013]; Solomonidou et al. [2014]; Lopes et al. [2016]. These studies allow definition of both the surface and the atmospheric contributions in VIMS spectral imaging data in the near-IR after performing the appropriate pixel selection of areas of interest with the help of SAR data.

The radiative transfer code application to the VIMS Titan data yields extracted weighted surface albedos in the seven methane windows tested against a variety of Titan candidate ice and organic constituents to provide constraints on the possible material present at various geomorphological units, as reported in Solomonidou et al. [2018]. An updated material library is being used based on Bernard et al. [2006]; Brassé et al. [2015]; Grenoble Astrophysics and Planetology Solid Spectroscopy and Thermodynamics (GhoSST) database [https://ghosst.osug.fr]. The library includes several materials at different grain sizes, such as ices of acetylene (C_2H_2), ethylene (C_2H_4), ethane (C_2H_6), propane (C_3H_8), cyanoacetylene (HC_3N), water (H_2O), ammonia (NH_3), methane (CH_4) and carbon dioxide (CO_2), in addition to spectra of laboratory tholins [Bernard et al. 2006; Brassé et al. 2015], and spectra of dark materials such as asphalite, kerite, different types of anthraxolite and amorphous carbon, which have been proposed as capable of lowering the total surface albedo of Titan's surface [Lellouch 2006; GhoSST]. Considering the different grain sizes, the library consists of 148 different constituent possibilities that can also be mixed. By using this constituent library spectral simulations are made and via an iterative process the best fit to the observations is obtained, bearing in mind that there is no unique solution for all of the mixtures. With these and other caveats described in Solomonidou et al. [2018], these authors have derived constraints on the possible major constituent for each geological unit and reported a latitudinal dependence of Titan's surface composition, with water ice being the major constituent at latitudes poleward of 30° N and 30° S, while Titan's equatorial region appears to be dominated partly by a tholin-like or by a very dark unknown material. The surface albedo differences and similarities among the various geomorphological units constrain the implications for the geological processes that govern Titan's surface and interior (for example, aeolian, cryovolcanic, tectonic).

Data from SAR and other RADAR modes, aided by data from VIMS and ISS, have provided sufficient information on Titan's surface to distinguish different types of geologic units [Lopes et al. 2010, 2016; Malaska et al. 2016] and establish the major geomorphologic unit classes on Titan and their relative ages using contacts between units. The classes of units are mountainous/ hummocky terrains, plains, dunes, labyrinthic terrains, craters and lakes. The oldest units are the

mountainous/hummocky and the labyrinthic terrains; it is not possible with currently available data to differentiate the relative ages of these two oldest types of terrain. The mountainous/hummocky terrains consist of mountain chains and isolated radar-bright terrains. The labyrinthic terrains consist of highly incised dissected plateaus with medium radar backscatter. The plains are younger than both mountainous/hummocky and labyrinthic unit classes. Dunes and lakes of liquid hydrocarbons are the youngest unit classes on Titan. Additionally, we have identified individual features such as crater rims, channels, and candidate cryovolcanic features. Crater rims and candidate cryovolcanic features are locations more likely to expose materials from the icy crust, while the hummocky/mountainous materials are thought to be exposed remnants of the icy crust.

Characterization and comparison of the properties of the unit classes and the individual features with data from radar radiometry, ISS, and VIMS provides information on their composition and possible provenance. The hummocky/mountainous terrains and impact crater rim features have relatively low emissivity (and greater radar scattering) in radiometric data, consistent with more water ice near the surface. We can also use these correlations to infer global distribution on regions not covered by SAR. This is particularly important as SAR data will not provide complete coverage of Titan by the end of the Cassini mission.

Matching the different surface units with specified mixtures of materials sheds light on the interconnection between the interior, the surface, and the atmosphere.

Matching the different surface units with specified mixtures of materials sheds light on the interconnection between the interior, the surface, and the atmosphere. In Solomonidou et al. [2018] three groups of compositional mixtures are reported, which include the major geomorphological units mentioned in the previous section, among three candidates (water ice, tholin, and a dark component). The units with spectral response similar to water ice are the labyrinth terrains and a number of plains such as the streak-like, the scalloped, and the undifferentiated plains that are concentrated at the higher parts of the midlatitudes. The crater ejecta and the alluvial fans are part of a different compositional group in which a tholin-like material is dominant. Furthermore, the units covered with an unknown dark constituent are the hummocky/mountainous terrains, the variable plains, the dunes, and the undifferentiated plains that are close to the equator and possibly contaminated by dune material [Lopes et al. 2016; Solomonidou et al. 2018].

Plains are the most widespread type of terrain on Titan [Lopes et al. 2016]. Although there are several different types of plains, by far the most extensive are the Undifferentiated Plains, first mapped by Lopes et al. [2010]. These are vast expanses of radar-dark terrains that appear fairly uniform in SAR images, with no major topographic units, and are for this reason often referred to as blandlands. Lopes et al. [2016] mapped the distribution of the Undifferentiated Plains using SAR swaths up to flyby T92 (July 2013) and found that these terrains are located mainly at mid-latitudes. Their gradational boundaries and paucity of recognizable features in SAR data make geologic interpretation challenging, so Lopes et al. [2016] used all the RADAR datasets available, plus VIMS and ISS, to examine and evaluate different formation mechanisms including: (i) cryovolcanic origin, consisting of overlapping flows of low relief; or (ii) sedimentary origins, resulting from

fluvial/lacustrine or aeolian deposition, or accumulation of photolysis products created in the atmosphere. Their analysis showed that the Undifferentiated Plains unit is consistent with a composition predominantly containing organic rather than icy materials and formed by depositional and/or sedimentary processes. They concluded that aeolian processes played a major part in the formation of the Undifferentiated Plains, although other processes (fluvial, deposition of photolysis products) are likely to have contributed, possibly in differing proportions depending on location. However, the distribution of Undifferentiated Plains, both at local and global scales, is consistent with aeolian deposition being the major process contributing to their formation. Spectral differences between the Plains and Dunes seen in VIMS data imply that the materials, at least on the top layers of the surface, are not exactly the same. Spectral differences in terms of surface albedo values between locations of Undifferentiated Plains [Lopes et al. 2016; Solomonidou et al. 2018] show that Plains at lower latitudes (closer to the dune seas) are more spectrally similar to dune materials, implying that they are related and supporting the idea that dunes materials are transported by wind to mid-latitudes. The Undifferentiated Plains appear to be composed of insoluble organic materials which may have been cemented by an organic substance and/or wetted by methane, causing them to become spectrally different from dune materials, at least at a surficial level. If the Undifferentiated Plains materials are the result of aeolian deposition, but contain liquids due to methane rain or fluids transported by channels, this would explain why they show relatively high emissivity (lower global dielectric constant, less efficient volume scattering) as well as why they are free of dunes (reduced sediment mobility). It would also be consistent with the high level of degradation of craters found at mid-latitudes—efficient erosion by fluvial/pluvial/subsurface flow activity, [Neish et al. 2016]. Le Gall et al. [2011] suggested that the latitudinal changes in dune-to-interdune ratio and possible variations in the thickness of the interdunal sand cover are likely related to changes in sediment availability at higher latitudes. These changes may be due to a decrease in sediment supply with distance from sediment source areas, an increased soil moisture content at higher latitudes (reflecting Titan's climate integrated over several seasonal cycles), or an enhanced wind transport capacity.

DUNES

Tens of thousands of sand dunes are found across the surface of Titan at the equatorial regions [Lorenz et al. 2006b]. These appear as long, narrow, and SAR-dark features against a SAR-brighter substrate or interdune (Figure TITAN-4), because dune sands are smooth at the 2.17 cm Cassini SAR wavelength. The dunes are generally 1–2 km wide, spaced by 1–4 km and can be over 100 km long [Lorenz et al. 2006b; Radebaugh et al. 2008]. Limited measurements of heights from radarclinometry suggest they are 80–130 m tall [Neish et al. 2010]. They are grouped together in large dune fields, or sand seas, equatorward of ±30 degrees latitude. Rodriguez et al. [2014] found that dunes cover 13 ±2% of the 58.1% of Titan's surface observed with SAR and HiSAR, and closer to ≈17% (≈14.10^6 km^2, 1.5 × the entire Sahara Desert on Earth), using VIMS.

Titan's dunes interact with topographic obstacles, seen as SAR-bright and generally isolated mountains, in a way that indicates general W-E transport of sand; they pile up on the west side of obstacles, divert in their azimuth around the obstacles, and are sparser on the east side

Figure TITAN-4. Dunes on Titan as seen by the Cassini SAR (wavelength 2.17 cm, with spatial resolution of 350 m) in the Belet Sand Sea, from the T61 (August 2009) swath on the equatorial leading hemisphere, at 11° S, 255° W. Dune surfaces are generally smooth and absorbing to SAR and thus appear as SAR-dark lines against a rougher and/or fractured, SAR-bright substrate. Open arrows indicate the direction of SAR illumination and incidence angle. Figure from Radebaugh et al. [2013].

[Lunine et al. 2008a; Radebaugh et al. 2010]. Their size, general morphology and relationship with underlying terrain and obstacles, and their style of collection are nearly identical to large, linear dunes in Earth's sand seas of the Sahara, Arabia and Namibia [Lorenz et al. 2006b; Radebaugh et al. 2008; Le Gall et al. 2011, 2012]. Such dunes on Earth typically form under bimodal winds [Fryberger and Dean 1979; Tsoar 1983] or a dominant, slightly off-axis wind and a secondary wind causing sand flux down the dune long axis [Courrech du Pont et al. 2014; Lucas et al. 2014].

A fundamental challenge raised by the SAR observations of the dunes is the eastward direction of growth and sand transport [Lorenz et al. 2006b; Lorenz and Radebaugh 2009; Radebaugh et al. 2010]. This contrasts with expectations that low-latitude near-surface winds should generally blow to the west. The solution appears to be that the dunes reflect strong but infrequent eastward winds, either associated with vertical mixing in the atmosphere at equinox leading to strong westerly gusts [Tokano 2010] or methane rainstorms having a similar effect [Charnay et al. 2015]. Additionally, convergence of the meridional transport predicted in models—for example, Lucas et al. [2014] can further explain why Titan's dunes are confined within ±30° latitudes, where sediment fluxes converge—see also Malaska et al. [2016].

Titan's dune sands are not only dark to SAR but they are some of the darkest materials seen by ISS [Porco et al. 2005; Karkoschka et al. 2017] and have a low albedo and red slope as seen by VIMS, thus comprising the VIMS dark brown spectral unit, and highest-resolution VIMS images distinguish individual dunes as dark [Soderblom et al. 2007; Barnes et al. 2008; Clark et al. 2010; Rodriguez et al. 2014]. Volume scattering within the dunes is very low, consistent with smooth,

homogeneous surfaces in general, and lacking large voids or clasts [Janssen et al. 2009, 2016; Le Gall et al. 2011], although modeling by Paillou et al. [2014] suggests possible surface ripples and some volume scattering. The observations indicate the dunes cannot be composed of water ice, but rather must be made of organics, ultimately derived from photolytic processing of methane in the upper atmosphere and precipitation to the surface [Lorenz et al. 2006b, 2008a; Soderblom et al. 2007]. Sand sources could include river channels, as on Earth [Radebaugh 2013]; low-latitude evaporite deposits, which can show similar VIMS properties [Barnes et al. 2011]; or the midlatitude blandlands, though it is more likely that sands are being transported there from the equatorial regions [Lopes et al. 2016; Malaska et al. 2016]. The extent of the dunes indicates that sands have been generated and transported in great volumes across Titan and that processes have acted on the surface long enough to produce extensive and morphologically consistent landforms [Radebaugh 2013], with some evidence of change over time [Ewing et al. 2015].

In addition to dunes, other aeolian features and landforms on Titan's surface include wind streaks and yardangs, or wind-carved ridges. The wind streaks are visible in ISS images as bright features that extend in the downwind direction from obstacles, for example, Porco et al. [2005]; Lorenz et al. [2006b]; Malaska et al. [2016]. SAR-bright, rough, elevated domes are crosscut by a series of parallel, long lineations ~1 km wide, spaced by a few km, and tens of kilometers long [Paillou et al. 2016]. They are similar in appearance and SAR brightness, radiometry and scatterometry to yardangs [Paillou et al. 2016]. These appear to have formed in easily eroded materials, similar to yardangs on Earth and Mars and further indicate the action of wind at moderate to high latitudes now or in the past. Craters: Before Cassini arrived at Saturn, the cratering history on Titan was unknown from direct observations. Estimates of the cratering rate were made by extrapolating the crater distributions observed on other Saturnian satellites, or by predicting impact rates by comet populations. Such estimates suggested that at least several hundred craters larger than 20 km in diameter should be present on Titan [Zahnle et al. 2003]; projectiles that create craters smaller than 20 km in diameter are expected to be disrupted by Titan's thick atmosphere [O'Brien et al. 2005; Korycansky and Zahnle 2005]. However, Cassini observed an extreme paucity of craters compared to these predictions. Only 23 certain or nearly certain craters and ~10 probable craters have been documented on Titan in this size range, with a handful of smaller crater candidates [Wood et al. 2010; Neish and Lorenz 2012; Buratti et al. 2012; Neish et al. 2016]. This population suggests that Titan has a crater retention time of several hundred million years [Wood et al. 2010; Neish and Lorenz 2012], with the oldest regions located near the equator and the youngest regions located near the poles [Neish et al. 2016].

The craters that are observed on Titan all show evidence for extensive modification by exogenic processes (Figure TITAN-5.). River valleys are observed to cut through the ejecta blankets and floors of several impact craters [Wood et al. 2010; Soderblom et al. 2010; Neish et al. 2015]. Many of Titan's impact craters are located in its equatorial sand seas, and also show evidence for extensive infilling by sand [Wood et al. 2010; Neish et al. 2013]. In addition to the morphologic evidence for erosion and burial, Titan's craters are consistently shallower than similarly sized fresh craters on Ganymede (often by many hundreds of meters), suggestive of infill [Neish et al. 2013]. Given the distribution of depths, aeolian infilling appears to be the dominant modification process on Titan [Neish et al. 2013], but fluvial erosion seems to play an important

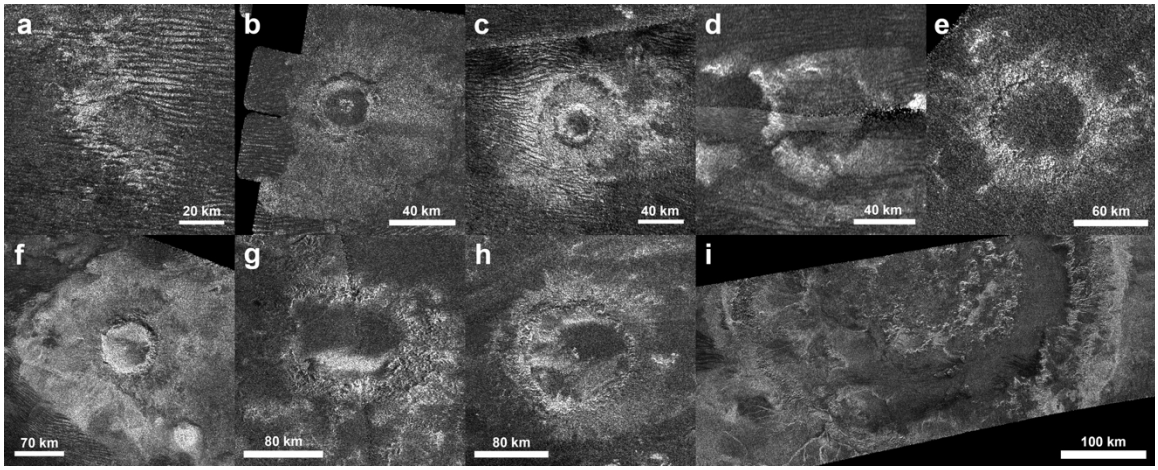

Figure TITAN-5. Nine probable impact craters observed on Titan by Cassini RADAR, from smallest (a) to largest (i). Impact craters on Titan show modification by exogenic processes such as fluvial erosion and infilling by sand. Figure from Neish et al. [2013].

secondary role [Neish et al. 2016]. Modification by viscous relaxation is expected to be minimal given the cold surface temperatures on Titan, although insulation by sand can enable some relaxation in Titan's larger craters [Schurmeier and Dombard 2018].

In addition to being highly modified, Titan's impact craters are not uniformly distributed across the moon. There is an almost complete absence of impact craters near Titan's poles, with the majority of the craters found in the topographically high, equatorial sand seas [Neish and Lorenz 2014]. There have been several hypotheses advanced to explain this observation. Neish and Lorenz [2014] proposed the lack of craters near Titan's poles may be indicative of marine impacts into a former ocean in this region. Moore et al. [2014] suggested that extreme climate change occurred in Titan's recent past, causing global methane rainfall that produced sediment that settled in Titan's topographically low poles, burying any craters there. Finally, Neish et al. [2016] suggested that an increased rate of fluvial erosion near the poles could degrade Titan's craters to the point where they would be unrecognizable from orbit. In any case, it appears that Titan is an extremely dynamic world, and studying its impact craters can reveal much about the processes that have shaped it.

Cryovolcanism: The possibility of finding cryovolcanic features on Titan had been discussed prior to Cassini, for example, Lorenz [1993b, 1996a]. The case for cryovolcanism was strengthened by results from the Gas Chromatograph Mass Spectrometer (GCMS) instrument on board the Huygens probe, which detected the radiogenic isotope of Argon-40 in Titan's atmosphere [Niemann et al. 2005] in concentrations suggesting that the atmosphere was in communication with a reservoir of the parent atom. Prior to the first Titan flyby using RADAR, VIMS imaged a bright feature (later named Tortola Facula) that Sotin et al. [2005] proposed to be cryovolcanic in origin, although SAR images obtained later in the mission showed Tortola Facula to be a local topographic high similar to others elsewhere on Titan [Lopes et al. 2013] and not a candidate for a cryovolcanic feature. Sotin et al. [2005] further suggested that the upwelling of large cryovolcanic plumes might be releasing sufficient methane into the atmosphere to account for the current atmospheric composition.

Cassini RADAR and VIMS revealed several features that have been interpreted as cryovolcanic in origin [Lopes et al. 2007, 2013; Soderblom et al. 2009; Wall et al. 2009; Solomonidou et al. 2016]. However, the interpretation has been the subject of some debate—for example, Moore and Pappalardo [2011]—and has not been entirely resolved by Cassini data [Nixon et al. 2018], primarily due to limitations in spectral resolution and coverage. The interpretations of RADAR—SAR, stereogrammetry [Kirk et. al. 2010], SARTopo [Stiles et al. 2009], and radiometry—and VIMS surface albedos and compositional constraints are based on morphology, albedo differences between the cryovolcanic areas, their surrounding terrains and several other geomorphological features, and temporal variations detected by VIMS [Solomonidou et al. 2014, 2016, 2018]. However, the Cassini mission did not reveal any hot spots, i.e., thermal enhancements that would have provided conclusive proof. The detection of thermal activity at Titan's surface using radiometry data (which is sensitive to variations of ~1K) or VIMS, would require Cassini's instruments to be observing the right locations at the right times and on multiple occasions, an unlikely scenario given the relatively small number of candidate-cryovolcanic features [Lopes et al. 2010].

The strongest evidence for cryovolcanic features on Titan was put forward by Lopes et al. [2013] who combined SAR imaging (including stereogrammetry) and VIMS data for a region that includes two mountains, Doom Mons (40.4° W, 14.7° S) and Erebor Mons (36.2° W, 5.0° S), as well as a depression, Sotra Patera (40.0° W, 14.5° S), and a region consisting of flow-like features, Mohini Fluctus (centered at 38.5° W, 11.8° S). Doom and Erebor Montes are high mountains (Doom being ~70 km in diameter and 1.45 ±0.2 km high), and Sotra Patera is the deepest depression found on Titan (1.7 ±0.2 km deep). It is non-circular, and interpreted as a collapse feature adjacent to Doom Mons. Mohini Fluctus appears to emerge from Doom Mons. Other non-circular, depressions are located between the two Montes, and flow-like features also surround Erebor Mons.

A criticism by Moore and Pappalardo [2011] of initial interpretations by RADAR of cryovolcanic candidates reported by Lopes et al. [2007] is that flow-like features could have been produced by fluvial activity, as channels are seen in areas such as Hotei Regio and Ganesa Macula (which topography later showed was not a shield or dome as initially interpreted). However, the Doom Mons-Sotra Patera-Erebor Mons region is totally devoid of fluvial channels, making a fluvial origin for Mohini Fluctus and other flows unlikely. Moreover, a vast dune field is located between Doom and Erebor Montes, indicating a dry region. The depressions seen in the region, including Sotra Patera, are not circular and are therefore unlikely to have had an impact origin [Lopes et al. 2013]. Additionally, analysis of VIMS data using a radiative transfer code [Solomonidou et al. 2014] showed that the surface albedo of the candidate cryovolcanic features is different from that of plains or dunes, indicating differences in composition [Solomonidou et al. 2014]. Following this, and using a radiative transfer code on a large selection of VIMS data, Solomonidou et al. [2016] revealed temporal changes for the Sotra Patera and Mohini Fluctus area, potentially brightening by up to a factor of two in terms of pure surface albedo and brightness during one year (2005–2006), while surrounding areas and the undifferentiated plains and dunes did not present any significant change for the same period of time. The surface albedo variations, together with the presence of volcanic morphological features, suggest possible relation to the deep interior via cryovolcanic processes. Additional support for the cryovolcanic origin of these features comes from interior structure models

of Titan and corresponding calculations of the spatial pattern of maximum tidal stresses [Sohl et al. 2014], which indicate that the Sotra Patera-Doom Mons-Erebor Mons area is a likely region for cryovolcanic activity.

Titan's interior (TN1b) (T_AO4)

Static and time-varying gravity field measurements [Iess et al. 2010, 2012], rotational dynamics measurements [Stiles et al. 2008, 2010; Meriggiola et al. 2016] and shape models [Zebker et al. 2009; Mitri et al. 2014; Corlies et al. 2017] are used to infer the interior structure of Titan. Magnetic field measurements have shown that an intrinsic magnetic field is not present on Titan [Wei et al. 2010]. The determination of the rotational dynamics from Cassini RADAR SAR images is key to constrain the interior structure of Titan. As described above, Cassini RADAR SAR coverage of Titan is dependent on orbit dynamics and competition for observation time. As a result, SAR swaths appear randomly distributed with coincidental overlaps (with only a few exceptions). Where overlap occurs, and assuming that the same surface features appear in both images, it has been possible to determine how the surface of Titan has moved between observations and thus estimate Titan's pole location and spin rate [Stiles et al. 2008, 2010], analogous to previous work using Magellan SAR imagery to estimate the spin model of Venus [Davies et al. 1992]. First, a set of recognizable landmarks were selected that are observed in two different SAR images obtained at different times. A pixel is chosen in each SAR image that corresponds as closely as possible to the same point on the landmark, using several techniques to minimize landmark mismatches. These pixels are then located in a Titan-centered inertial, non-rotating (J2000) frame. Finally, spin state parameters are estimated by minimizing the misregistration error, i.e., the apparent movement in Titan body-fixed coordinates of the landmarks between observation times. Thus, estimates of Titan's spin state parameters and their error bars are obtained. Using similar methodology, Meriggiola et al. [2016] also provided a rotational model of Titan estimating the spin pole location, the spin rate, the precession and the nutation. Further, these authors have shown that the pole location is compatible with the Cassini state 1.

Stiles et al. [2008] and Meriggiola et al. [2016] have provided an estimate of Titan's obliquity (0.31°). The obliquity together with the quadrupole moment of the gravity field (J_2 and C_{22}) measurements [Iess et al. 2010, 2012] can be used to infer the moment of inertia of Titan and, consequently, the radial mass distribution of Titan [Bills and Nimmo 2011]. Bills and Nimmo [2011] and Meriggiola et al. [2016] have shown that the estimated obliquity is compatible with a deep interior decoupled from the outer ice shell by a global subsurface ocean. The presence of a subsurface ocean inferred from the rotational dynamics of Titan is consistent with the large tidal response of Titan (tidal Love number $k_2 = 0.589 \pm 0.150$) [Iess et al. 2012], see also Mitri et al. [2014]. In agreement with this scenario, the Permittivity, Wave and Altimetry (PWA) instrument on board Huygens' probe has measured a Schumann-like resonance, suggesting also the presence of a subsurface ocean [Bèghin et al. 2012]. In summary, the gravity, topography and rotational dynamics measurements in combination with thermal-evolution models indicate that Titan presents internal differentiation, with an outer ice shell, a subsurface ocean, a high-pressure layer at the base of the ocean, and a deep rocky interior [Hemingway et al. 2013; Mitri et al. 2014; Tobie et al. 2014].

Bills and Nimmo [2011] next used these results, combined with low-degree gravity field derived from Cassini spacecraft Doppler tracking data [Iess et al. 2010], to suggest that Titan's outer shell is mechanically decoupled from the deeper interior, plausibly an outer ice layer which is mechanically decoupled from the deeper interior by an ocean. Taking this conclusion together with other evidence, there is emerging consensus that Titan possesses an internal ocean. Implications for the crustal and internal composition and origin of Titan are discussed by Tobie et al. [2014].

Cassini radar observations in both its altimeter and SARTopo modes reveal its global shape and yield insights to its interior structure. The roughly 60 satellite-derived elevation surface traces (Figure TITAN-6) show that Titan's polar radius is less and equatorial radii greater than predicted by its gravity field.

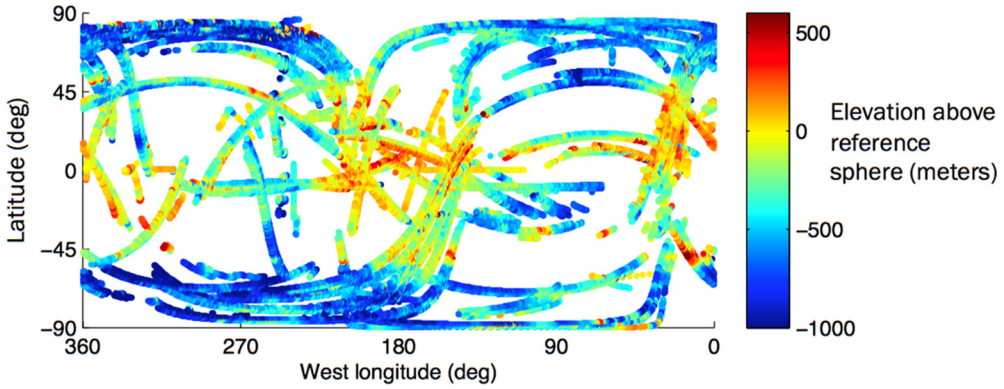

Figure TITAN-6. Cassini measurements of Titan surface height above a reference sphere of 2575 km. Clear triaxial ellipsoid shape implies a body not in hydrostatic equilibrium, suggesting that depth to a subsurface ocean is less at the poles than at the equator.

The ratio (a−c) / (b−c), which is exactly 4 for a spin-locked satellite in hydrostatic equilibrium, for Titan's figure is thus observed to be only 2.65. The corresponding third-degree gravity hydrostatic ratio is 3.83. While the gravity field is consistent with a hydrostatically relaxed body, the figure does not. If both of these data constraints pertain, Titan's interior do not conform to a set of spherically symmetric shells, as these data imply that the average satellite density at the equator is less than that at the poles. If Titan has a vast interior ocean of liquid water, then some ice layers (less dense than liquid water) are thinner at the poles than the equator. A simple model satisfying both sets of data and assuming isostatic compensation (Figure TITAN-7) could be the result of uneven heat dissipation in Titan's interior, such as may result from tidal interaction with Saturn or its other moons.

Another simple model realizing these is greater precipitation of hydrocarbon snow or loosely packed particulates at the equator than at the poles, perhaps with a net equatorward transport from the poles. We note that this is consistent with the observation of 100 m tall dune structures near Titan's equator, so that poorly consolidated material may indeed collect there. Several hundred m of deposition at the equator would match the mean equatorial radii of both models, but precipitation would have to preferentially occur in the directions toward and away from Saturn, which seems unlikely.

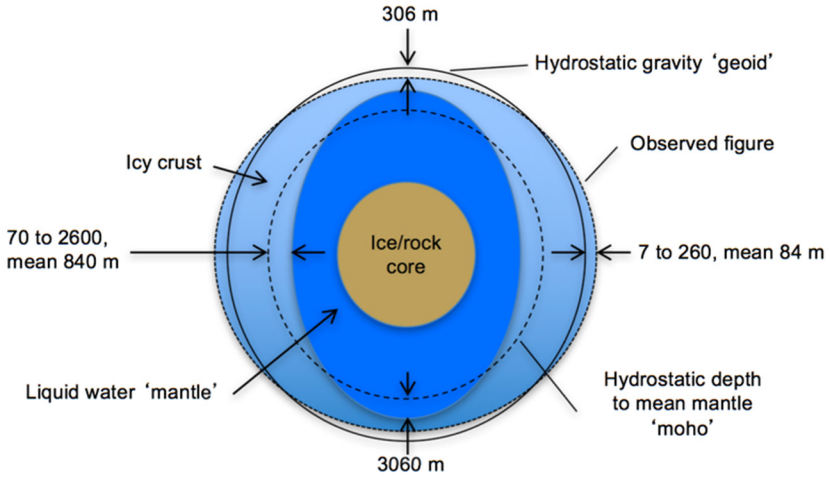

Figure TITAN-7. A model consistent with Cassini gravity and figure measurements, assuming isostatic compensation. The thinner ice shell at the poles could result from uneven heat dissipation within Titan from tidal interactions, and the higher "geoid" at the poles is one explanation for the preponderance of lakes at the most northern and southern latitudes.

Further comparison of the gravity and shape observations constrain the depth of any outer ice shell enclosing a global subsurface ocean. While the exact value varies depending on how the spherical expansion is constrained, our observed gravity to topography ratio is 0.070 for the third order terms and 0.042 for fourth order. These imply ice shell thicknesses of 327 and 187 km, respectively, twice or more of the 100 km expected from thermal models [Sohl at al. 2003; Nimmo and Bills 2010]. Our solution yields a tidal Love number h_{2t} of about 0.5, and a basal heat flow of 2.5 mW/m^2. This would suggest that heat from Titan's core is lower than often assumed, hence the amount of radiogenic material in the core is likely less as well.

These data also constrain the depth of Titan's mantle and density of its core, placing added restrictions on its composition and evolution. Supposing that Titan has an undifferentiated ice/rock core beneath the ocean, and that its moment of inertia is most likely in the range 0.33–0.34 [Iess et al. 2010], a 200 km crust estimate from above, and Titan's well-known mean density of 1.88 g cm^{-3} implies an ocean depth and core density ranging from 308 km and 2.74 g cm^{-3} (MOI = 0.33) to 226 km and 2.55 g cm^{-3} (MOI = 0.34).

Titan atmospheric composition (TN1c) (T_AO2)

Observe vertical and horizontal distributions of trace gases, search for more complex organic molecules. Determine abundances of atmospheric constituents (including any noble gases), derive isotope ratios for abundant elements. Measure aerosol and heavy molecule layers and properties. Investigate energy sources for atmospheric chemistry, model the photochemistry of the stratosphere, study formation and composition of aerosols.

The chemistry of Titan's atmosphere is driven by CH_4 photolysis in the thermosphere and catalytic reactions in the stratosphere, and by N_2 dissociation due to both UV photons and energetic

electrons. Ethane is the most abundant gas product and HCN is the dominant nitrile. The mixing ratios of all photochemical species, except C_2H_4, increase with altitude at equatorial and southern latitudes, indicative of transport from a high-altitude source to a condensation sink in the lower stratosphere. Poleward of 45°, most product compounds are enriched as a consequence of subsidence in the winter polar vortex, particularly for nitriles and more complex hydrocarbons than C_2H_6 and C_2H_2. Most products have lower increases with altitude at high latitudes than at low latitudes. The vertical and horizontal distribution of trace gases with season have been well-reported and documented in publications by Coustenis et al. [2007]; Vinatier et al. [2010, 2015]. The gases include hydrocarbons ($^{12}CH_4$, $^{13}CH_4$, CH_3D, C_2H_2, C_2HD, C_2H_4, C_2H_6, C_3H_4, C_3H_8, C_4H_2, C_6H_6), nitriles (HCN, HC_3N), H_2O, CO, and CO_2, as well as the detection of long sought after propene (C_3H_6) by Nixon et al. [2013] to remove a three-decade gap in the hydrocarbon sequence. Vuitton et al. [2019] give a detailed review of our current understanding of Titan's atmospheric chemistry at the end of the Cassini Mission.

Measurements of C, H, N isotopes provide constraints on photochemical fractionation mechanisms. While the Huygens GCMS measured ^{36}Ar, ^{40}Ar, and possibly ^{22}Ne, only upper limits were placed on Kr and Xe. As a consequence, the origin of CH_4 in the solar versus Saturnian nebula or conversion of CO_2 to CH_4 in Titan's interior remains unconstrained. Also, CIRS tracer gas distributions have been used to diagnose models of stratospheric dynamics [Crespin et al. 2008]. The carbon isotope ratio $^{12}C/^{13}C$ was determined in CH_3D [Bézard et al. 2007]; in HCN [Vinatier et al. 2007]; in HC_3N [Jennings et al. 2008]; in CO_2 [Nixon et al. 2008]; in CH_4, C_2H_2, C_2H_6 [Nixon et al. 2008, 2012]; in C_4H_2 [Jolly et al. 2010]. The hydrogen isotope ratio D/H was derived from CH_4 by Bézard et al. [2007] and C_2H_2 by Coustenis et al. [2008], whereas Nixon et al. [2008] obtained the oxygen isotope ratio $^{16}O/^{18}O$ from CO_2.

The thermosphere is a chemical factory that initiates the formation of complex positive and negative ions in the high thermosphere as a consequence of magnetospheric-ionospheric-atmospheric interaction involving solar EUV and UV radiation, energetic ions and electrons. This factory produces very heavy positive and negative ions and large molecules [Shebanits et al. 2016], for example, benzene, naphthalene, nitriles, which apparently condense out and are detectable in solar and stellar UV occultations at ~1000 km [Liang et al. 2007; Kammer 2015], and initiate the haze formation process [Lavvas et al. 2013]. As these particles fall through the agnostosphere/ ignorosphere/mesosphere and grow, they become detectable by remote sensing: UVIS at ~900 down to ~300 km, ISS at ~500 km and below and eventual become ubiquitous throughout the stratosphere. These haze particles are strong absorbers of solar UV and visible radiation and play a fundamental role in heating Titan's stratosphere [Bézard et al. 2018] and probably the mesosphere [Lavvas et al. 2009]. The differential heating with latitude drives wind systems in Titan's middle atmosphere, much as ozone does in the Earth's middle atmosphere.

The Huygens Probe measurements, and the Cassini orbiter measurements over a significant fraction of the Titan season, in particular, were responsible for major advances. The Descent Imager/Spectral Radiometer (DISR) measured intensity and polarization from the near-UV to 1.6 microns in the near-IR. Haze density profiles along the descent path from the ground to 160 km altitude were derived from these measurements, along with tight constraints on the size of the

monomers that make up aggregate particles, as well as the mean size of the aggregates [Tomasko et al. 2008, 2009; Doose et al. 2016].

All of the Cassini orbiter optical instruments contributed new measurements and insights regarding the Titan haze. Solar and stellar occultations by the UVIS and VIMS instruments provided detailed vertical profiles over near-surface to high altitude (>700 km) [Koskinen et al. 2011]. Limb measurements by the CIRS instrument revealed vertical profiles of haze opacity in the thermal-IR and identified two polar haze layers, probably condensate layers, with spectral signatures near 50 microns. The components of aerosol composition have been inferred from CIRS observed spectral signatures of functional group vibrational modes and compared with laboratory produced Titan tholins [Vinatier et al. 2012] The ISS and VIMS instruments detected a high-altitude winter polar HCN cloud that formed shortly after equinox. The ISS instrument measured Titan's detached haze and followed its altitude changes over a significant part of the seasonal cycle [West et al. 2018].

Titan atmospheric structure (TN2a) (T_AO5)

Resolve current inconsistencies in atmospheric density measurements (critical to a future Flagship mission). Investigate the upper atmosphere, its ionization, and its role as a source of neutral and ionized material for the magnetosphere of Saturn (**Titan Upper Atmosphere (T_AO5)**).

Remarkably in the middle stratosphere, the warmest temperatures occur at the equator and the largest meridional temperature gradients are found in the winter hemisphere.

Titan's atmosphere is predominantly N_2 with CH_4 the next most abundant molecule. It has a mole fraction of 0.05 just above the surface decreasing to 0.014 in the stratosphere. Above the homopause (~800–850 km), it increases to 0.12 at the exobase. The third abundant molecule is H_2 with a tropospheric mole fraction of 0.001 increasing to 0.004 at ~1000 km and ~0.02 at the exobase (~1500–1600 km). There is a large suite of hydrocarbons, nitriles, other nitrogen and also oxygen bearing compounds. Titan possesses a mostly stable troposphere with a well-defined tropopause (T ~70 K at ~44 km) and a lower stratosphere with a high static stability, which is extremely cold over the winter polar region and warm over the summer pole (Figure TITAN-8 and Figure TITAN-9). Remarkably in the middle stratosphere, the warmest temperatures occur at the equator and the largest meridional temperature gradients are found in the winter hemisphere. The stratopause from the summer pole to about 45° winter hemisphere remains at a relatively constant pressure of 0.1 mbar/300 km and then it rises rapidly upward to ~0.01 mbar/400 km at the winter north pole, where it is the warmest region in the entire atmosphere. One possible interpretation of the HASI temperature profile is that Titan's atmosphere is essentially isothermal ~170 K from 500–1100 km, with large amplitude thermal waves (10 K) superimposed. The existence and location of a well-defined mesopause is an open question.

The Huygens HASI instrument provided along its trajectory essentially continuous profiles of mass density, pressure, and temperature from an altitude of 1350 km down to the surface. While

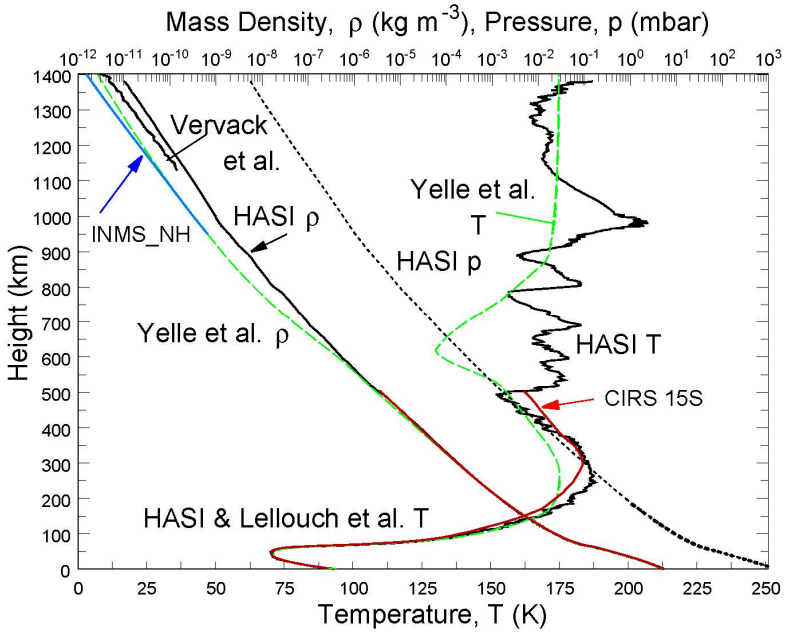

Figure TITAN-8. Titan possesses a mostly stable troposphere with a well-defined tropopause and a lower stratosphere with a high static stability. Black Lines: Comparison of Cassini-Huygens HASI density, pressure, and temperature profiles [Fulchignoni et al. 2005]. Red Lines: CIRS density and temperature profiles at 15 S [Vinatier et al. 2007]. Blue Lines: Average INMS Northern Hemisphere density profile mission with preflight calibration [Müller-Wodarg et al. 2008], needs to be increased by a factor of 2.2 [Teolis et al. 2015]. Green Lines: With the Voyager [Lellouch et al. 1989; Vervack et al. 2004] results, and the Yelle et al. [1997] engineering model, all as functions of altitude above surface.

only at one time and location, it provided an important reference atmosphere to compare with measurements by other instruments of latitudinal and seasonal variations over the 13 years of active observations. But Lellouch et al. [2014] found that the CH_4 mole fraction near 15 mbar (~85 km) varied from ~1.0 % at low latitudes, in disagreement with the Huygens GCMS measurement of 1.48 %, and near ±50–55°, but ~1.5 % at ±30–35° and polar latitudes. The retrieved thermal profile from CIRS is about 3–5 K colder than HASI in the 2–20 mbar region with CH_4 = 1.48 % (cf. Figure TITAN-8). But with CH_4 = 1.0 %, the CIRS derived temperature below 147 km altitude (2.7 mbar), agrees with the HASI direct measurements by its temperature sensor and would resolve the CIRS/HASI differences in the temperatures below 147 km at the Huygens landing site.

The chemistry of Titan's atmosphere is driven by CH_4 photolysis in the thermosphere and catalytic reactions in the stratosphere, and by N_2 dissociation due to both UV photons and energetic electrons. Ethane is the most abundant gas product and HCN is the dominant nitrile. The mixing ratios of all photochemical species, except C_2H_4, increase with altitude at equatorial and southern latitudes, indicative of transport from a high-altitude source to a condensation sink in the lower stratosphere. In northern hemisphere winter northward of 45° N, most photochemically produced compounds are enriched as a consequence of subsidence in the polar vortex, particularly for nitriles

and more complex hydrocarbons than C_2H_6 and C_2H_2, and have lower increases with altitude at high latitudes than at low latitudes.

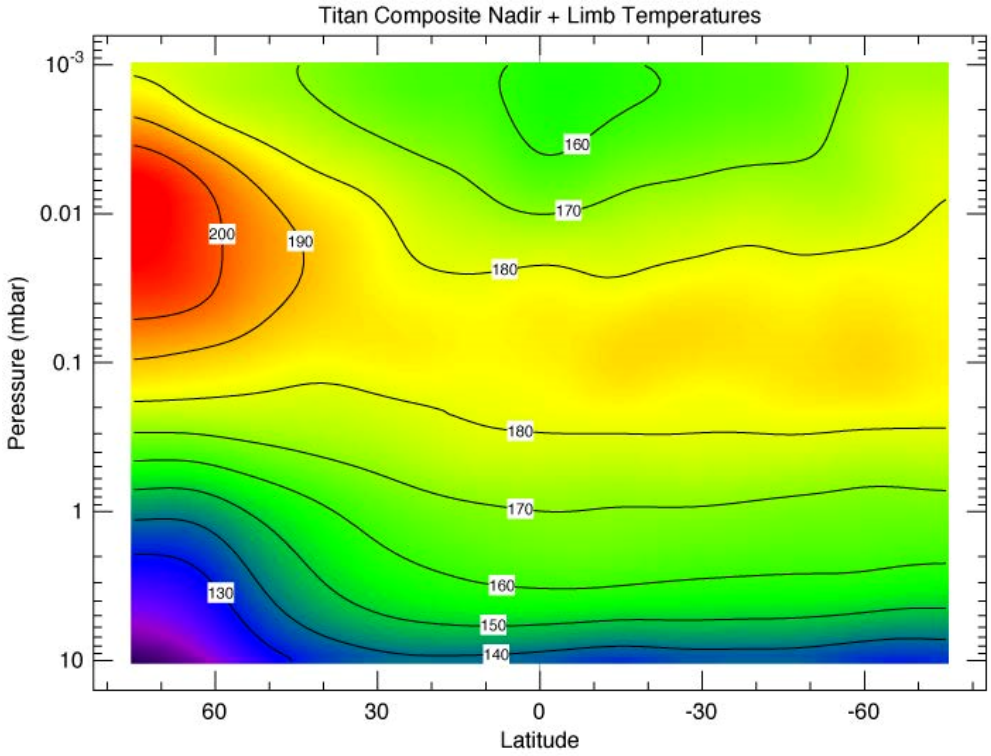

Figure TITAN-9. CIRS zonal mean temperatures (K) from limb and nadir spectra recorded between July 2004 and September 2006. Retrieved temperatures were averaged over 5° latitudinal intervals and smoothed three times with 10° boxcar function, Note that the north pole is on the left. [After Achterberg et al. 2008].

The thermosphere is a chemical factory that initiates the formation of complex positive and negative ions in the high thermosphere because of magnetospheric-ionospheric-atmospheric interaction involving solar EUV and UV radiation, energetic ions and electrons (Figure TITAN-11). This factory produces very heavy positive and negative ions and large molecules—for example, benzene, naphthalene, nitriles—which apparently condense out and are detectable in solar and stellar UV occultations at ~1000 km [Liang et al. 2007] and initiate the haze formation process [Lavvas et al. 2013]. As these particles fall through the mesosphere and grow, they become detectable by remote sensing: UVIS at ~1000 km, ISS at ~500 km and eventually become ubiquitous throughout the stratosphere. These haze particles are strong absorbers of solar UV and visible radiation and play a fundamental role in heating Titan's stratosphere and perhaps the mesosphere [Lavvas et al. 2009]. The differential heating with latitude drives wind systems in Titan's middle atmosphere, much as ozone does in the Earth's middle atmosphere.

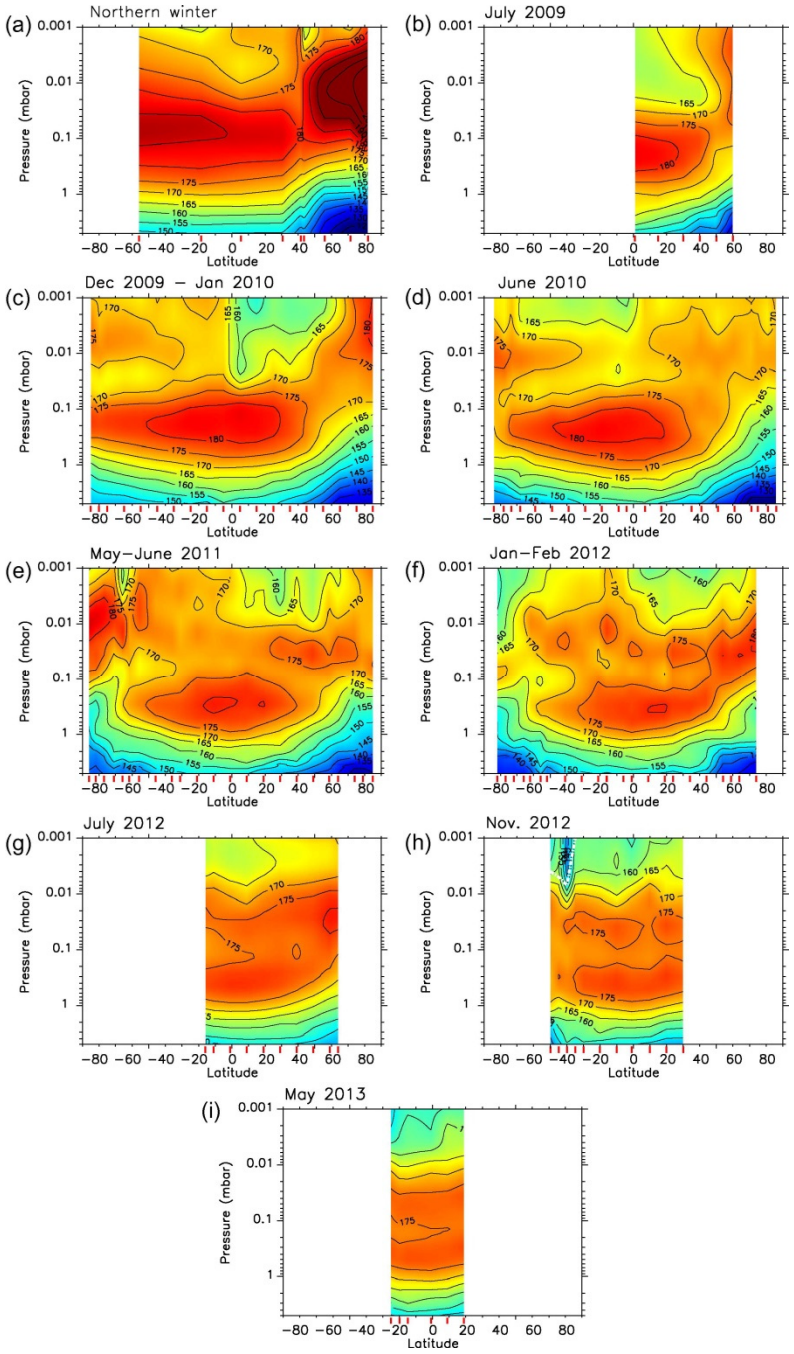

Figure TITAN-10. Pressure/latitudes maps of temperature as a function of season from northern winter through late spring. Note that the north pole is on the right. Red marks on the horizontal scale give the latitudes where limb spectra were analyzed. White areas indicate regions where CIRS did not acquire limb spectra. White dashed lines show the levels above which the constraints on the thermal profiles are poor (typically because of a too low signal-to-noise ratio) [Vinatier et al. 2015].

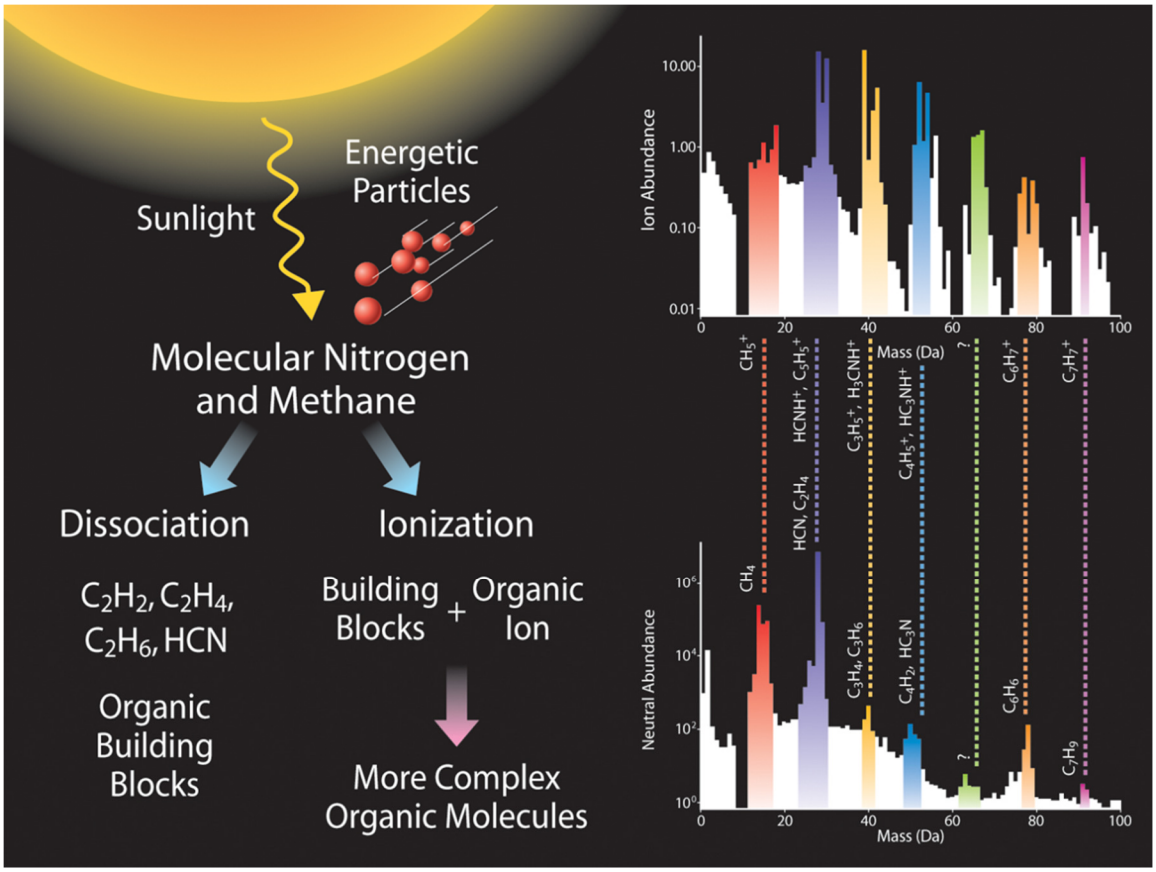

Figure TITAN-11. A cartoon of complex ion/neutral chemistry in Titan's upper atmosphere (950-1000 km) as observed by the Cassini INMS on flyby T16. The upper insert is an ion mass spectrum from 1–100 Daltons and the lower insert a neutral mass spectrum from 1 to 100 Daltons. Note benzene at 78 Daltons. Organic ions can be either negatively (~20 to ~8000 Da) or positively (up to ~350 Da) charged. The end result is the pervasive haze that envelopes Titan and whose particles (called Titan tholins) are eventually deposited on the surface [After Waite et al. 2007].

Escape of atoms and molecules from Titan is a source for mass loading of Saturn's magnetosphere. Strobel and Cui [2014] reviewed the strong evidence for significant escape of hydrogen as atoms (~1 × 10^{27} s^{-1}) and molecules (~1 × 10^{28} s^{-1}) for a total of ~2 × 10^{28} amu s^{-1}, and by far a major source of mass for the magnetosphere. Their escape is controlled by the maximum rate that they diffuse through Titan's atmosphere and confirmation of the principle behind Hunten's limiting flux [Hunten, 1973]. While they escape Titan, they are still gravitationally bound to Saturn and thus subject to ionization. If ionized, they have less impact on the magnetosphere by virtue of Titan's location at the outer boundary of the magnetosphere in comparison to Enceladus with a comparable mass source rate, but in the inner magnetosphere.

In contrast the controversy concerning the escape rate of CH_4 is linked to the analysis of measured CH_4 density profiles and the inference of the magnitude and radial direction of CH_4 diffusion fluxes. Initial INMS results yielded upward flow of ~2 × 10^{27} CH_4 s^{-1}. This suggested escaping CH_4, if there were no compensating downward flow elsewhere in the atmosphere. But not

every INMS flyby data set yielded high CH_4 escape rates. In Cui et al. [2012], Table 5 and Strobel and Cui [2014], Table 10.1, occasionally, the CH_4 flux is downward and/or indistinguishable from diffusion equilibrium, although about half of the orbits yielded preferentially strong upward flow of CH_4. Titan's upper atmosphere has shown considerably variability in the CH_4 density profiles and temperature structure inferred from N_2 density profiles from orbit to orbit—for example, Snowden et al. [2013]. Attempts to identify the drivers for this structure variability and inferred CH_4 escape/loss rates yielded larger escape on the nightside over the dayside, whereas magnetospheric lobe-like conditions (factor of 10 reduction in energetic electron flux) yielded diffusive equilibrium, no net CH_4 fluxes [Cui et al. 2012, Table 6], albeit in the latter case, it is the statistics of few flybys. Given this observed variability, one can question whether 1-D models are appropriate to derive only a single number: the globally averaged, Titan orbit averaged CH_4 escape rate. Whereas one can present arguments that solar heating of Titan's thermosphere is sufficient to support large CH_4 escape rates, to date no models have been capable of accelerating a sufficient number of CH_4 molecules in the collisional atmosphere to speeds that exceed the escape velocity at the exobase [Tucker and Johnson 2009].

Cassini INMS measurements based on roughly 100 Titan flybys during the Cassini mission yielded neutral and ion densities systematically lower, by factors approximately 2 to 3, than alternate methods to derive and infer densities, specifically, torque on the spacecraft measured by the Attitude and Articulation Control System (AACS) and the spacecraft atmospheric drag derived by the Navigation system [Teolis et al. 2015]. By correcting for an under-estimation of gas leakage out of the instrument into space by the original calibration model, and adjusting for the gain change, Teolis et al. [2015] developed a new calibration model that raises INMS densities upward by a constant detector sensitivity correction factor of 1.55 ±21%. With this new model the density ratio of AACS to INMS is now 1.47, but outside of the INMS error bars, and the density ratio of navigation (NAV) to INMS is now 1.16 and within the error bars. Although the three methods of determining atmospheric densities are much closer, one would want to know whether AACS or NAV is the more accurate method to derive densities.

The UVIS stellar and solar occultations are self-calibrating. In the case of the solar occultations one can retrieve density profiles in the altitude range 1120–1400 km for N_2 and 850-1300 km for CH_4, whereas UVIS stellar occultations are limited by interstellar hydrogen absorption to wavelengths above 91.1 nm. The CH_4 dissociation cross-sections vary smoothly with wavelength and allow measurements of CH_4 optical depths and densities, while complex N_2 electronic band systems between 80–100 nm are not accessible to analysis with any confidence. T118 was the only flyby in the mission where UVIS and INMS observe Titan's atmosphere simultaneously at the same latitude. UVIS sampled remotely by observing a solar occultation; INMS sampled the upper atmospheric density in situ with the hypersonic Cassini Spacecraft flying through the atmosphere at Mach 20–25.

The TAMWG report will discuss attempts to resolve current inconsistencies in atmospheric density measurements (critical to a future Flagship mission).

Titan's icy shell (TN2b) (T_AO2)

Work in this area is discussed in the section entitled *Titan's interior (TN1b) (T_AO4)*.

Titan meteorology (TN2c) (T_AO3)

Determine the surface temperature distribution, cloud distribution, and tropospheric winds. Measure winds and global temperatures; investigate cloud physics, general circulation, and seasonal effects in Titan's atmosphere; search for lightning discharges.

Titan surface temperature maps from CIRS measurements over the period of 2004–2016 [Jennings et al. 2016] can be visualized at https://www.nasa.gov/image-feature/jpl/pia20020/titan-temperature-lag-maps-animation.

Winds were directly measured by the Doppler Wind Experiment (DWE) and inferred from DISR measurements during the descent of the Huygens Probe. From CIRS global mapping of stratospheric temperatures, zonal winds can be inferred via the gradient wind relationship from 10 mbar (~140 km) up to 0.001 mbar (~500 km) as a function of altitude and latitude with season. From the zonal winds one derives information on the location and structure of the polar vortex as a function of season. In conjunction with trace gas enrichment due to subsidence from upper-atmosphere photochemical source regions, the associated meridional circulation structure can be deduced as characteristically a single cell circulation with broad summer hemispheric upwelling and winter polar-confined subsidence or a two-cell transitional global circulation, with upwelling around the equator and subsidence at both poles, characteristic of equinoctial circulation reversal [Vinatier et al. 2015; Teanby et al. 2017]. Also, CIRS tracer gas distributions have been used to diagnose 2-D GCM models of stratospheric dynamics, for example, Crespin et al. [2008].

Cassini discovered not only that the polar vortices appear to be tilted by a few degrees relative to the spin axis of Titan but also that the entire stratosphere is tilted by a several degrees from the rotational pole [Achterberg et al. 2008b].

The radio occultation measurements by Radio Science Subsystem (RSS) have yielded density, pressure, and temperature radial profiles from the surface to ~ 300 km at discrete locations that yield information on the latitudinal structure of the atmosphere and can be coupled with the CIRS remote sensing data [Schinder et al. 2012]. The latitudinal temperature gradients in these radio occultation measurements imply that the velocity minimum in the zonal wind profile detected by the DWE between 70–80 km is a global phenomenon.

Guided by RSS and HASI measurements, Charnay and Lebonnois [2012] used a GCM to simulate the dynamics that governs the thermal structure of Titan's planetary boundary layer, the lowermost atmosphere. From observations of dune spacing (~3 km) and the knowledge that the spacing is limited by the height of the planetary boundary layer [Andreotti et al. 2009], the boundary layer is ~3 km thick. The simulations yielded a convective boundary layer during the day, rising to an altitude of 800 m and a seasonal boundary of 2 km depth produced by the reversal of the Hadley

cell at the equinox, with a dramatic impact on atmospheric circulation. Boundary layer clouds are a better interpretation of the previous discovery claim of fog at Titan's south pole. They concluded that Titan's troposphere possesses two boundary layers that control wind patterns, dune spacing and cloud formation at low altitudes.

Although liquids have flowed on the surface at Titan's equator in the past, currently liquids are only found on the surface at polar latitudes. The vast expanses of dunes that dominate Titan's equatorial regions require a predominantly arid climate.

VIMS near-infrared images of Titan's clouds were acquired between July 2004 and September 2017 [Rodriguez et al. 2009, 2011; Turtle et al. 2018], following the evolution of clouds over 13 years including the equinox and northern summer solstice, greatly helping to further constrain global circulation models (GCMs). After four years of regular outbursts observed by Cassini between 2004 and 2008, southern polar cloud activity started declining. The extensive cloud system over the north pole, stable between 2004 and 2008, progressively fractionated and vanished as Titan entered into northern spring. At southern mid-latitudes, clouds were observed even after equinox, in a latitude band between 30 S and 60 S. Fewer clouds were observed closer to the equator, although they were slightly more frequent as equinox approached. As northern summer approached, cloud activity picked up at mid- and high northern latitudes as well.

ISS observations from April 2004 through September 2017 showed that clouds were generally more prevalent in the summer hemisphere, but revealed some surprises in locations and timing: with clouds remaining common at southern mid-latitudes longer than expected; north-polar clouds initially appearing much sooner than model predictions; and large north-polar summer convective systems not appearing before the mission ended, standing in marked contrast with south-polar activity observed over several years leading up to the southern summer solstice. Twice during the Cassini mission, ISS observations revealed changes in surface brightness consistent with methane rainfall darkening the surface [Turtle et al. 2009, 2011], first at Arrakis Planitia near the south pole in 2004–2005, Titan's southern summer, and secondly along the southern boundary of the Belet dune field in 2010, following the equinox. Comparison of ISS and VIMS cloud observations to GCMs suggests that a polar-wetlands scenario, with subsurface reservoirs at both poles and relatively dry lower latitudes, better matches cloud locations and timing as well as the sporadic nature of the activity documented [Lora and Mitchell 2015; Mitchell and Lora 2016; Faulk et al. 2017; Turtle et al. 2018]. For a comprehensive discussion on weather, clouds, and storms on Titan from Cassini observations, see also Griffith et al. [2014].

Searches have been conducted for lightning by HASI, RPWS, and ISS with negative results. The full seasonality of the methane hydrological cycle has not been observed, in particular the pole to pole transport of methane, which may operate on the timescale of Milankovitch cycles [Aharonson et al. 2009].

Other Titan science not in CSM TM: Titan as a system – its origin and mysteries

Titan Atmospheric Formation and Evolution (T_AO1) – Constrain scenarios of formation and evolution of Titan and its atmosphere.

Titan is the only moon in the solar system with an atmosphere so massive that it dominates the total volatile inventory in the surface-atmosphere system as well as providing strong radiative forcing and an active meteorology [Lorenz et al. 2005]. It also obscures the surface from view in both the optical and infrared, which is why the Cassini RADAR has been such a crucial tool. However, by the irreversible deposition of heavy hydrocarbons, nitriles, and other photochemical products from methane and nitrogen, the atmosphere also obscures the underlying surface geology to some extent. Were the current inventory of methane to condense onto the surface, it would form a layer 5 meters thick [Mitchell and Lora 2016], but a variety of evidence suggests that many times that number is present in various solid and liquid deposits of organics on and within the crust [Hayes et al. 2018].

Therefore, Titan's geologic history is poorly constrained and in particular there is a significant uncertainty as to what fraction of body's 4.5 billion year of existence is recorded in the surface. Observations relevant to its history include:

1. The low observed numbers of impact craters [Porco et al. 2005] yield an age of hundreds of millions of years, not billions [Lorenz et al. 2007; Wood et al. 2010; Neish and Lorenz 2012].

2. The rate of photodissociation of methane in Titan's atmosphere implies that the current gaseous inventory will be depleted in some tens of millions of years [Yung et al. 1984].

3. Titan's interior has at least partially differentiated, resulting in a rock-metal core, a high-pressure ice mantle of uncertain thickness, a liquid water ocean [less et al. 2010] perhaps with salts and ammonia [Mitri et al. 2014], and an ice crust 50 to 100 km thick. The core is either significantly hydrated [Castillo-Rogez and Lunine 2010], or there is a mixed rock-ice layer somewhere in the interior, see for example, Tobie et al. [2014].

4. A range of chemical and physical data from the atmosphere to the interior suggest that a significant event, or change in the way Titan evolves, occurred sometime between a few hundred million and a billion years ago [Hörst 2017].

The relatively youthful age of the surface, which may be the result of geologic activity or substantial burial in organic matter, or both, means that there is little if any geologic evidence of the first 3/4 of Titan's history. Two unanswered questions are what was the process(es) that eroded or covered older impact craters and other landforms? and, Did the obscuration of features older than a few hundred million years occur continuously over time, or in some singular event?

There is no evidence of the answer to the second question, but a theoretical model of the evolution of Titan's interior by Tobie et al. [2006] provides an intriguing scenario that implies Titan had a significant change in the working of its interior, crust, and atmosphere about 500 million years ago [Wood 2018]. In the Tobie et al. [2006] model, Titan has a thin and rigid clathrate crust (with methane as the dominant guest species) up until 500 million to one billion years ago. During that earlier epoch, several major heating events resulted in the release of large (compared to the present atmospheric inventory) amounts of methane from the clathrate hydrate into the surface-atmosphere system. Within the last 500–1000 million years the interior has cooled sufficiently to allow an ice I crust to form underneath the buoyant clathrate hydrate crust, with diapirism in the thickening ice I crust providing one or several episodes of further release of methane into the surface-atmosphere system.

… a theoretical model of the evolution of Titan's interior by Tobie et al. [2006] provides an intriguing scenario that implies Titan had a significant change in the working of its interior, crust, and atmosphere about 500 million years ago … .

Wood [2018] called the onset of the ice I subcrust the "Great Crustal Thickening Event" and noted that the mode of geologic processes would change dramatically as Titan transitioned from a body with a thin rigid conductive crust over the ocean to one with a thicker and rheologically heterogenous crust.

This is but one model for Titan's interior [Tobie et al. 2014]. What remains unresolved, however, is whether the methane hydrological cycle that we see today shaping so many aspects of Titan's surface is ancient or recent, episodic [Lunine et al. 1998] or continuous. While the idea is commonly held that the source of the methane to resupply the atmosphere is in crustal clathrate hydrate, such a crust going back to pre-Voyager days [Lewis 1971], how the resupply works is unclear. Simple forcing out of the methane from the clathrate by the photochemically produced ethane eventually fails because of the stoichiometry (two methane molecules making one ethane), although this replacement could eventually weigh down the crust and cause an overturn because clathrate with predominantly ethane is heavier than ice I [Choukroun and Sotin 2012]. This could cause interesting geologic consequences in the present era when the clathrate is nominally underlain by warm ice I.

Birch et al. [2017] have pointed to geologic evidence (notably the presence of evaporite deposits seen in Cassini/VIMS data), for example, Mackenzie et al. 2014, suggesting that the present epoch of lakes and seas of methane, ethane, and nitrogen might have been preceded by one with a widespread ocean of methane and other hydrocarbons. However, it is not possible to constrain the longevity of such an ocean, and the implications in terms of tidal dissipation of the orbital eccentricity during ocean shrinkage [Sagan and Dermott 1982; Sears 1995] have yet to be evaluated for the known Titan topography. Finally, it is possible that Titan has run out of atmospheric and surface methane multiple times in its history, leading to dramatic atmospheric

changes [Lorenz et al. 1997] and possibly epochs in the which the surface is worked by liquid nitrogen seas and rivers [Charnay et al. 2014].

If Titan's geologic and atmospheric nature have changed in a secular way over its history, it would join the other terrestrial planets—Venus, Earth, and Mars, in this regard. In each case, interior and surface-atmosphere changes over time have led to present-day characteristics that are likely to have been dramatically different from those in the past.

Open questions for Titan science

Some questions are taken directly from Hörst [2017], see also Nixon et al. [2018].

1. What are the abundances of the heavy noble gases in Titan's atmosphere and surface?
2. What is the ice phase that dominates the crust?
3. How intimately coupled are the various atmospheric layers?
4. How do you go from the very heavy ions and molecular species to haze particles?
5. What is the role of heterogeneous reactions in determining the partitioning of gas phase molecules and the composition of haze particles?
6. The controversy concerning the escape rate of CH_4 is linked to the analysis of INMS and UVIS measured CH_4 density profiles and the inference of the magnitude and radial direction of CH_4 diffusion fluxes.
7. What are the very heavy ions in the ionosphere, how do they form, and what are the implications for complexity of prebiotic chemistry?
8. How do the organic compounds produced in the atmosphere evolve on the surface?
9. What are the dynamics of Titan's surface-atmosphere interactions? Fluvial erosion?
10. How variable is the climate over 104 years and longer?
11. How old is Titan's current atmosphere and what happened on Titan 300–500 million years ago?
12. Is Titan's atmospheric methane episodic, and what are the implications on habitability?
13. What are the origin of Titan's methane and the fate of the photochemically produced ethane?

14. What is controlling Titan's H_2 profile and potential spatial variations?
15. What is the organic and inorganic composition of the surface?
16. What is the circulation in the lakes and seas and how is it affected by the atmosphere?
17. What is the composition of the dune particles and how are they produced?
18. How did the lakes and sea basins form?
19. Does cryovolcanism occur on Titan?
20. What is the salinity and composition of the deep ocean and is it in contact with rock beneath?
21. Is there life in the deep ocean, and some exotic life in hydrocarbon solvents?
22. What are the characteristics of the methane meteorology (of often clouds form, how typical is the half Titan year that we observed, etc.)?
23. What is the nature of the asymmetry in seasonal effects?
24. What is the nature and extent of the exchange between the surface/atmosphere and deep subsurface and ocean?
25. What is the depth and thickness of the subsurface ocean?
26. To what extent is the surface fluvially dissected?
27. What is the role of heterogeneous reactions in determining the partitioning of gas phase molecules and the composition of haze particles?
28. What are the sources of the stratospheric tilt?
29. What is the origin of Xanadu as a distinct geologic province?
30. What are the origin, evolution, and ultimate fate of Titan's atmosphere?
31. What is the impact of the influx of water and water vapor from Enceladus to Titan's upper atmosphere?

ACRONYMS

Note: For a complete list of Acronyms, refer to Cassini Acronyms – Attachment A.

AACS	Attitude and Articulation Control System
AO	Announcement of Opportunity
AU	astronomical unit
CIRS	Composite Infrared Spectrometer
CSM	Cassini Solstice Mission
DISR	Descent Imager/Spectral Radiometer
DWE	Doppler Wind Experiment
DWG	Discipline Working Group
EUV	extreme ultraviolet
FUV	far ultraviolet
GCMS	Gas Chromatograph Mass Spectrometer
HASI	Huygens Atmospheric Structure Instrument
INMS	Ion and Neutral Mass Spectrometer
IR	infrared
ISS	Imaging Science Subsystem
PWA	Permittivity, Wave and Altimetry
RADAR	Titan Radar Mapper
RSS	Radio Science Subsystem
SAR	Synthetic Aperture Radar
TAMWG	Titan Atmospheric Modeling Working Group
TM	Traceability Matrix
TOST	Titan Observation Science Team
UV	ultraviolet
UVIS	Ultraviolet Imaging Spectrograph
VIMS	Visual and Infrared Imaging Spectrometer

REFERENCES

Disclaimer: The partial list of references below correspond with in-text references indicated in this report. For all other Cassini references, refer to Attachment B – References & Bibliographies; Attachment C – Cassini Science Bibliographies; the sections entitled References contributed by individual Cassini instrument and discipline teams located in Volume 1 Sections 3.1 and 3.2 Science Results; and other resources outside of the Cassini Final Mission Report.

Achilleos, N., C. S. Arridge, C. Bertucci,P. Guio, N. Romanelli, N. Sergis, (2014), A combined model of pressure variations in Titan's plasma environment, Geophysical Research Letters, 41, 8730–8735, doi: 10.1002/2014GL061747.

Achterberg, R. K., P. J. Gierasch, B. J. Conrath, F. M. Flasar, C. A. Nixon, (2011), Temporal variations of Titan's middle-atmospheric temperatures from 2004 to 2009 observed by Cassini/CIRS, Icarus 211, 686–698.

Achterberg, R. K., B. J. Conrath, P. J. Gierasch, F. M. Flasar, C. A. Nixon, (2008a), Titan's middle-atmospheric temperatures and dynamics observed by the Cassini Composite Infrared Spectrometer, Icarus, 194, 263–277, doi: 10.1016/j.icarus.2007.09.

Achterberg, R. K., B. J. Conrath, P. J. Gierasch, F. M. Flasar, C. A. Nixon, (2008b), Observation of a tilt of Titan's middle-atmospheric superrotation, Icarus, 197, 549–555, doi: 10.1016/j.icarus.2008.05.014.

Ádámkovics, M., J. L. Mitchell, A. G. Hayes, P. M. Rojo, P. Collies, et al., (2016), Meridional variation in tropospheric methane on Titan observed with AO spectroscopy at Keck and VLT, Icarus, 270, 376–888.

Ádámkovics, M., J. W. Barnes, M. Hartung, I. de Pater, (2010), Observations of a stationary mid-latitude cloud system on Titan, Icarus, 208, 868–877.

Aharonson, O., A. G. Hayes, J. I. Lunine, R. D. Lorenz, M. D. Allison, C. Elachi, (2009), An asymmetric distribution of lakes on Titan as a possible consequence of orbital forcing, Nature Geoscience, 2, 851–854.

Ajello, J. M., M. H. Stevens, I. Stewart, K. Larsen, L. Esposito, J. Colwell, W. McClintock, G. Holsclaw, J. Gustin, W. Pryor, (2007), Titan airglow spectra from Cassini Ultraviolet Imaging Spectrograph (UVIS): EUV analysis, Geophysical Research Letters, 34, L24204, doi: 10.1029/2007GL031555.

Allen, M. R. and W. J. Ingram, (2002), Constraints on future changes in climate and the hydrologic cycle, Nature, 419, 224.

Andreotti, B., A. Fourriere, F. Ould-Kaddour, B. Murray, and P. Claudin, (2009), Giant Aeolian dune size determined by the average depth of the atmospheric boundary layer, Nature, 457, 1120–1123, doi: 10.1038/nature07787.

Arridge, C. S., N. André, C. L. Bertucci, P. Garnier, C. M. Jackman, Z. Németh, A. M. Rymer, N. Sergis, K. Szego, A.J . Coates, F. J. Crary, (2011), Upstream of Saturn and Titan, Space Science Reviews, 162, 1–4, 25–83, doi: 10.1007/s11214-011-9849-x.

Arridge, C. S., N. André, N. Achilleos, K. K. Khurana, C. L. Bertucci, L. K. Gilbert, G. R. Lewis, A. J. Coates, M. K. Dougherty, (2008), Thermal electron periodicities at 20R_S in Saturn's magnetosphere, Geophysical Research Letters, 35, L15107, doi: 10.1029/2008GL034132.

Artemieva, N. and J. Lunine, (2003), Cratering on Titan: impact melt, ejecta, and the fate of surface organics, Icarus, 164, 471–480.

Atreya, S. K., E. Y. Adams, H. B. Niemann, J. E. Demick-Montelara, T. C. Owen, et al., (2006), Titan's methane cycle, Planetary and Space Science, 54, 1177–1187.

Awal, M. and J. I. Lunine, (1994) Moist convective clouds in Titan atmosphere, Geophysical Research Letters, 21, 2491–2494.

Barnes, J., C. Sotin, J. Soderblom, R. Brown, A. Hayes, et al., (2014), Cassini/VIMS observes rough surfaces on Titan’s Punga Mare in specular reflection, Planetary Science, 3, 1–17, doi: 10.1186/s13535-014-0003-4.

Barnes, J. W., J. Bow, J. Schwartz, R. H. Brown, J. M. Soderblom, A. G. Hayes, G. Vixie, S. Le Mouelic, S. Rodriguez, C. Sotin, R. Jaumann, K. Stephan, L. A. Soderblom, R. N. Clark, B. J. Buratti, K. H. Baines, P. D. Nicholson, (2011), Organic sedimentary deposits in Titan’s dry lakebeds: Probable evaporate, Icarus, 216, 136–140.

Barnes, J. W., R. H. Brown, J. M. Soderblom, L. A. Soderblom, R. Jaumann, et al., (2009), Shoreline features of Titan's Ontario Lacus from Cassini/VIMS observations, Icarus, 201, 217–225.

Barnes, J. W., R. H. Brown, L. Soderblom, C. Sotin, S. Le Mouelic, S. Rodriguez, R. Jaumann, R. A. Beyer, R. Clark, P. Nicholson, (2008), Spectroscopy, morphometry, and photoclinometry of Titan’s dunefields from Cassini/VIMS, Icarus, 195, 400–414.

Barnes, J. W., R. H. Brown, J. Radebaugh, B. J. Buratti, C. Sotin, et al., (2006), Cassini observations of flow-like features in western Tui Regio, Titan, Geophysical Research Letters vol. 33, Issue 16, doi: 10.1029/2006GL026843.

Barth, E. L., S. C R. Rafkin, (2007), TRAMS: A new dynamic cloud model for Titan's methane clouds, Geophysical Research Letters 34.

Béghin, C., O. Randriamboarison, M. Hamelin, E. Karkoschka, C. Sotin, R.C. Whitten, J.-J. Berthelier, R. Grard, F. Simoes, (2012), Analytic theory of Titan’s Schumann resonance: Constraints on ionospheric conductivity and buried water ocean, Icarus, 218, 1028–1042.

Béghin, C., C. Sotin, M. Hamelin, (2010), Titan's native ocean revealed beneath some 45 km of ice by a Schumann-like resonance, Comptes Rendus Geoscience 342, 425–433.

Bernard, J.-M., E. Quirico, O. Brissaud, G. Montagnac, B. Reynard, B.P. McMillan, P. Coll, M.-J. Nguyen, F. Raulin, B. Schmitt, (2006), Reflectance spectra and chemical structure of Titan's tholins: Application to the analysis of Cassini Huygens observations, Icarus, 185, 301–307.

Bertucci, C., D. C. Hamilton, W. S. Kurth, G. Hospodarsky, D. Mitchell, N. Sergis, N. J. T. Edberg, M. K. Dougherty, (2015), Titan's interaction with the supersonic solar wind, Geophysical Research Letters, 42, 193–200, doi: 10.1002/2014GL062106.

Bertucci, C., B. Sinclair, N. Achilleos, P. Hunt, M. K. Dougherty, C. S. Arridge, (2009), The variability of Titan's magnetic environment, Planetary and Space Science, 57, no. 14–15, 1813–1820.

Bertucci, C., N. Achilleos, M. K. Dougherty, R. Modolo, A. J. Coates, K. Szego, A. Masters, et al., (2008), The magnetic memory of Titan's ionized atmosphere, Science, 321, 5895, 1475–1478, doi: 10.1126/science.1159780.

Bézard, B., S. Vinatier, R. K. Achterberg, (2018), Seasonal radiative modeling of Titan's stratospheric temperatures at low latitudes, Icarus, 302, 437–450, doi 10.1016/j.icarus.2017.11.034.

Bézard, B., C. A. Nixon, I. Kleiner, D. E. Jennings, (2007), Detection of $^{13}CH_3D$ on Titan, Icarus, 191, 1, 397–400, doi: 10.1016/j.icarus.2007.06.004.

Bills, B. G. and F. Nimmo, (2011), Rotational dynamics and internal structure of Titan, Icarus, vol. 214, Issue 1, pp. 351–355.

Birch, S. P. D., A. G. Hayes, P. Corlies, E. R. Stofan, J. D. Hofgartner, R. M. C. Lopes, R. D. Lorenz, J. I. Lunine, S. M. MacKenzie, M. J. Malaska, C. A. Wood, Cassini RADAR Team, (2018), Morphologic evidence that Titan’s southern hemisphere basins are paleoseas, Icarus, 310, 140–148.

Birch, S. P. D., A. G. Hayes, W. E. Dietrich, A. D. Howard, C. S. Bristow, et al., (2017), Geomorphologic mapping of titan's polar terrains: Constraining surface processes and landscape evolution, Icarus, 282, 214–236.

Birch, S. P. D., A. G. Hayes, A. D. Howard, J. Moore, J. Radebaugh, (2016), Alluvial fan morphology, distribution, and formation on Titan, Icarus, 270, 238–247.

Black, B. A., J. T. Perron, D. Hemingway, E. Bailey, F. Nimmo, H. Zebker, (2017), Global drainage patterns and the origins of topographic relief on Earth, Mars, and Titan, Science, 356, 727–731.

Black, B. A., J. T. Perron, D. M. Burr, S. A. Drummond, (2012), Estimating erosional exhumation on Titan from drainage network morphology, Journal of Geophysical Research: Planets, vol. 117, Issue E8, doi: 10.1029/2012JE004085.

Brandt, P. C., K. Dialynas, I. Dandouras, D. G. Mitchell, P. Garnier, S. M. Krimigis, (2012), The distribution of Titan’s high-altitude (out to 50,000 km) exosphere from energetic neutral atom (ENA) measurements by Cassini/INCA, Planetary and Space Science, 60, 107–114, doi: 10.1016/j.pss.2011.04.014.

Brassé, C., O. Munoz, P. Coll, F. Raulin, (2015), Optical constants of Titan aerosols and their tholins analogs: Experimental results and modeling/observational data, Planetary and Space Science, vol. 109–110, pp. 159–174.

Brown, M. E., J. E. Roberts, E. L. Schaller, (2010), Clouds on Titan during the Cassini prime mission: A complete analysis of the VIMS data, Icarus, 205, 571–580.

Brown, R. H., L. A. Soderblom, J. M. Soderblom, R. N. Clark, R. Jaumann, et al., (2008), The identification of liquid ethane in Titan's Ontario Lacus, Nature, 454, 607–610.

Brown, R. H., C. A. Griffith, J. I. Lunine, J. W. Barnes, (2006), Polar caps on Titan?, In European Planetary Science Congress, p. 602.

Brown, M. E., A. H. Bouchez, C. A. Griffith, (2002), Direct detection of variable tropospheric clouds near Titan's south pole, Nature, 420, no. 6917, p. 795.

Buratti, B. J., C. Sotin, K. Lawrence, R. H. Brown, S. Le Mouélic, J. M. Soderblom, et al., (2012), A newly discovered impact crater in Titan's Senkyo Cassini VIMS observations and comparison with other impact features, Planetary and Space Science, 60, 18–25.

Burr, D. M., N. T. Bridges, J. R. Marshall, J. K. Smith, B. R. White, J. P. Emery, (2015), Higher-than-predicted saltation threshold wind speeds on Titan, Nature, 517, 7532, p. 60.

Burr, D. M., S. A. Drummond, R. Cartwright, B. A. Black, J. T. Perron, (2013a), Morphology of fluvial networks on Titan: Evidence for structural control, Icarus, 226, 742–759.

Burr, D. M., J. T. Perron, M. P. Lamb, R. P. Irwin, G. C. Collins, et al., (2013b), Fluvial features on Titan: Insights from morphology and modeling, Geological Society of America Bulletin, 125, 299–321.

Burr, D. M., R. E. Jacobsen, D. L. Roth, C. B. Phillips, K. L. Mitchell, D. Viola, (2009), Fluvial network analysis on Titan: Evidence for subsurface structures and west-to-east wind flow, southwestern Xanadu, Geophysical Research Letters, 36.

Burr, D. M., J. P. Emery, R. D. Lorenz, G. C. Collins, P. A. Carling, (2006), Sediment transport by liquid surficial flow: Application to Titan, Icarus, 181, 235–242.

Castillo-Rogez, J. C. and J. I. Lunine, (2010), Evolution of Titan's rocky core constrained by Cassini observations, Geophysical Research Letters, 37, L20205, doi: 10.1029/2010GL044398.

Charnay, B., E. Barth, S. Rafkin, C. Narteau, S. Lebonnois, S. Rodriguez, S. C. Du Pont, A. Lucas, (2015), Methane storms as a driver of Titan’s dune orientation, Nature Geoscience, 8, 5, p. 362.

Charnay, B., F. Forget, G. Tobie, C. Sotin, R. Wordsworth, (2014), Titan’s past and future: 3D modeling of a pure nitrogen atmosphere and geological implications, Icarus, 241, 269–279.

Charnay, B. and S. Lebonnois, (2012), Two boundary layers in Titan's lower troposphere inferred from a climate model, Nature Geoscience, 5, 106–109, doi: 10.1038/ngeo1374.

Choukroun, M. and C. Sotin, (2012), Is Titan's shape caused by its meteorology and carbon cycle?, Geophysical Research Letters, 39.

Choukroun, M., O. Grasset, G. Tobie, C. Sotin, (2010), Stability of methane clathrate hydrates under pressure: Influence on outgassing processes of methane on Titan, Icarus, 205, 581–593.

Clark, R. N., J. M. Curchin, J. W. Barnes, R. Jaumann, L. Soderblom, D. P. Cruikshank, R. H. Brown, S. Rodriguez, J. Lunine, K. Stephan, T. M. Hoefen, (2010) Detection and mapping of hydrocarbon deposits on Titan, Journal of Geophysical Research: Planets, 115, E10, doi: 10.1029/2009JE003369.

Corlies, P., A. G. Hayes, S. P. D. Birch, R. Lorenz, B. W. Stiles, R. Kirk, V. Poggiali, H. Zebker, L. Iess, (2017), Titan's topography and shape at the end of the Cassini mission, Geophysical Research Letters, 44, 23.

Courrech du Pont, S., C. Narteau, X. Gao, (2014), Two modes for dune orientation, Geology, doi: 10.1130/G35657.1.

Coustenis, A., D. E. Jennings, C. A. Nixon, (2010), Titan trace gaseous composition from CIRS at the end of the Cassini-Huygens prime mission, Icarus, 207, 461v476, doi: 10.1016/j.icarus.2009.11.027.

Coustenis, A., D. E. Jennings, A. Jolly, Y. Bénilan, C. A. Nixon, S. Vinatier, D. Gautier, et al., (2008), Detection of C_2HD and the D/H ratio on Titan, Icarus, 197, 2, 539–548, doi: 10.1016/j.icarus.2008.06.003.

Coustenis, A. (2007), The atmospheric structure of Titan from Voyager to Cassini, American Geophysical Union (AGU) Spring Meeting Abstracts.

Crespin, A., S. Lebonnois, S. Vinatier, (2008), Diagnostics of Titan's stratospheric dynamics using Cassini/CIRS data and the 2-dimensional IPSL circulation model, Icarus, 197, 556–571, doi: 10.1016/j.icarus.2008.05.010.

Cui, J., R. V. Yelle, D. F. Strobel, I. C. F. Müller-Wodarg, D. S. Snowden, T. T. Koskinen, M. Galand, (2012), The CH_4 structure in Titan’s upper atmosphere revisited, Journal of Geophysical Research, E11, doi: 10.1029/2012JE004222.

Davies, M. E., T. R. Colvin, P. G. Rogers, P. W. Chodas, W. L. Sjogren, E. L. Akim, V. A. Stepaniants, Z. P. Vlasova, A. I. Zakharov, (1992), The rotation period, direction of the north pole, and geodetic control network of Venus, Journal of Geophysical Research: Planets, vol. 97, Issue E8, pp. 13141–13151, doi: 10.1029/92JE01166.

de Kok, R. J., N. A. Teanby, L. Maltagliati, et al., (2014), HCN ice in Titan’s high-altitude southern polar cloud, Nature, 514, 65, doi: 10.1038/nature13789.

Doose, L. R., E. Karkoschka, M. G. Tomasko, et al., (2016), Vertical structure and optical properties of Titan's aerosols from radiance measurements made inside and outside the atmosphere, Icarus, 270, 355–375.

Durham, W. B., S. H. Kirby, L. A. Stern, W. Zhang, (2003), The strength and rheology of methane clathrate hydrate, Journal of Geophysical Research: Solid Earth, vol. 108, Issue B4, doi: 10.1029/2002JB001872.

Elachi, C., S. Wall, M. Allison, Y. Anderson, R. Boehmer, et al., (2005), Cassini radar views the surface of Titan, Science, 308, 970–974.

Elachi, C., M. D. Allison, L. Borgarelli, P. Encrenaz, E. Im, M. A. Janssen, W. T. K. Johnson, R. L. Kirk, R. D. Lorenz, J. I. Lunine, D. O. Muhleman, S. J. Ostro, G. Picardi, F. Posa, C. G. Rapley, L. E. Roth, R. Seu, L. A. Soderblom, S. Vetrella, S. D. Wall, C. A. Wood, H. A. Zebker, (2005), RADAR: The Cassini Titan Radar Mapper, Space Science Review, 117, 71–110.

Ewing, R. C., A. G. Hayes, A. Lucas, (2015), Sand dune patterns on Titan controlled by long-term climate cycles, Nature Geoscience, 8, 1, pp.15–19.

Faulk, S. P., J. L. Mitchell, S. Moon, J. M. Lora, (2017), Regional patterns of extreme precipitation on Titan consistent with observed alluvial fan distribution, Nature Geoscience, 10, 827.

Flasar, F. M., (1983), Oceans on Titan?, Science, 221, 55–57.

Fryberger, S. G. and G. Dean, (1979), Dune forms and wind regime, In A study of global sand seas, U.S. Government Printing Office Washington, vol. 1052, pp. 137–169.

Fulchignoni, M., F. Angrilli, G. Borouki W. Bianchini, (2005), Physical characterization of Titan Atmosphere by the Huygens Atmospheric Structure Instrument (HASI), Thirty-Sixth Lunar and Planetary Science Conference, 14–18 March 2005, Houston, TX.

Garnier, P., I. Dandouras, D. Toublanc, E. C. Roelof, P. C. Brandt, D. G. Mitchell, S. M. Krimigis, N. Krupp, D. C. Hamilton, J.-E. Wahlund, (2010), Statistical analysis of the energetic ion and ENA data for the Titan environment, Planetary and Space Science, vol. 58, Issues 14–15, pp. 1811–1822, doi: 10.1016/j.pss.2010.08.009.

Grenoble Astrophysics and Planetology Solid Spectroscopy and Thermodynamics (GhoSST) v0.6, (2014), database service, https://ghosst.osug.fr.

Gibbard, S. G., B. Macintosh, D. Gavel, C. E. Max, I. de Pater, et al., (2004), Speckle imaging of Titan at 2 microns: surface albedo, haze optical depth, and tropospheric clouds 1996–1998, Icarus, 169, 429–439.

Glein, C. R. and E. L. Shock, (2013), A geochemical model of non-ideal solutions in the methane-ethane-propane-nitrogen-acetylene system on Titan, Geochimica Et Cosmochimica Acta, 115, 217–240.

Graves, S. D. B., C. P. McKay, C. A. Griffith, F. Ferri, M. Fulchignoni, (2008), Rain and hail can reach the surface of Titan, Planetary and Space Science, 56, 346–357.

Greeley, R. and J. D. Iversen, (1985), Wind as a geological process: on Earth, Mars, Venus and Titan, Cambridge Planetary Science Series, 4, Cambridge University Press.

Griffith, C., S. Rafkin, P. Rannou, and C. McKay, (2014), Storms, clouds, and weather, Chapter 6, In Titan: Interior, surface, atmosphere, and space environment, (eds.) I. Müller-Wodarg, C. Griffith, E. Lellouch, T. Cravens, Cambridge University Press, pp. 190–223, doi: 10.1017/CBO9780511667398.009.

Griffith, C. A., J. M. Lora, J. Turner, P. F. Penteado, R. H. Brown, et al., (2012), Possible tropical lakes on Titan from observations of dark terrain, Nature, 486, 237–239.

Griffith, C. A., P. Penteado, S. Rodriguez, S. Le Mouélic, K. H. Baines, et al., (2009), Characterization of clouds in Titan's tropical atmosphere, The Astrophysical Journal Letters, 702, L105-L9.

Griffith, C. A., P. Penteado, P. Rannou, R. Brown, V. Boudon, et al., (2006), Evidence for a polar ethane cloud on Titan, Science, 313, 1620.

Griffith, C. A., P. Penteado, K. Baines, P. Drossart, J. Barnes, et al., (2005), The evolution of Titan's mid-latitude clouds, Science, 310, 474–477.

Griffith, C. A., T. Owen, G. A. Miller, T. Geballe, (1998), Transient clouds in Titan's lower atmosphere, Nature, 395, 575–578.

Grima, C., M. Mastrogiuseppe, A. G. Hayes, S. D. Wall, R. D. Lorenz, et al., (2017), Surface roughness of Titan's hydrocarbon seas, Earth and Planetary Science Letters, 474, 20–24.

Harper, J. M., G. D. McDonald, J. Dufek, M. J. Malaska, D. M. Burr, A. G. Hayes, J. McAdams, J. J. Wray, (2017), Electrification of sand on Titan and its influence on sediment transport, Nature Geoscience, 10, 4, p.260.

Hayes, A. G., R. D. Lorenz, J. I. Lunine, (2018) A post-Cassini view of Titan's methane-based hydrologic cycle, Nature Geoscience, 11, no. 5, 306.

Hayes, A. G., S. P. D. Birch, W. E. Dietrich, A. D. Howard, R. Kirk, et al., (2017), Topographic constraints on the evolution and connectivity of Titan's lacustrine basins, Geophysical Research Letters, vol. 44, Issue 23, pp. 11745–11753, doi: 10.1002/2017GL075468.

Hayes, A. G., (2016), The lakes and seas of Titan, Annual Review of Earth and Planetary Sciences, vol. 44, pp. 57–83, doi: 10.1146/annurev-earth-060115-012247.

Hayes, A. G., R. D. Lorenz, M. A. Donelan, M. Manga, J. I. Lunine, et al., (2013), Wind driven capillary-gravity waves on Titan's lakes: Hard to detect or non-existent?, Icarus, 225, 403–412.

Hayes, A. G., O. Aharonson, J. I. Lunine, R. L. Kirk, H. A. Zebker, et al., (2011), Transient surface liquid in Titan's polar regions from Cassini, Icarus, 211, 655–671.

Hayes, A. G., A. S. Wolf, O. Aharonson, H. Zebker, R. Lorenz, et al., (2010), Bathymetry and absorptivity of Titan's Ontario Lacus, Journal of Geophysical Research: Planets, 115.

Hayes, A., O. Aharonson, P. Callahan, C. Elachi, Y. Gim, et al., (2008), Hydrocarbon lakes on Titan: Distribution and interaction with a porous regolith, Geophysical Research Letters, 35.

Hemingway, D., F. Nimmo, H. Zebker, L. Iess, (2013), A rigid and weathered ice shell on Titan, Nature, 500, 550–552.

Hersant, F., D. Gautier, G. Tobie, J. I. Lunine, (2008), Interpretation of the carbon abundance in Saturn measured by Cassini, Planetary and Space Science, 56, 1103–1111.

Hirtzig, M., B. Bézard, E. Lellouch, A. Coustenis, C. de Bergh, P. Drossart, A. Campargue, V. Boudon, V. Tyuterev, P. Rannou, T. Cours, S. Kassi, A. Nikitin, D. Mondelain, S. Rodriguez,, S. Le Mouélic, (2013), Titan's surface and atmosphere from Cassini/VIMS data with updated methane opacity, Icarus, 226, 470–486.

Hirtzig, M., A. Coustenis, E. Gendron, P. Drossart, A. Negrao, et al., (2006), Monitoring atmospheric phenomena on Titan, Astronomy & Astrophysics, 456, 761–774.

Hofgartner, J. D., A. G. Hayes, J. I. Lunine, H. Zebker, B. W. Stiles, et al., (2014), Transient features in a Titan sea, Nature Geoscience, 7, 493–496.

Hörst, S., (2017), Titan's atmosphere and climate, Journal of Geophysical Research: Planets, 122, 432–482, doi: 10.1002/2016JE005240.

Horvath, D. G., J. C. Andrews-Hanna, C. E. Newman, K. L. Mitchell, B. W. Stiles, (2016), The influence of subsurface flow on lake formation and north polar lake distribution on Titan, Icarus, 277, 103–124.

Hueso, R., A. Sanchez-Lavega, (2006), Methane storms on Saturn's moon Titan, Nature, 442, 428–431.

Hunten, D. M., (1973), The escape of H_2 from Titan, Journal of the Atmospheric Sciences, 30, 726–732, doi: 10.1175/1520- 0469.

Iess, L., R. A. Jacobson, M. Ducci, D. J. Stevenson, J. I. Lunine, et al., (2012), The tides of Titan, Science, 337, 457–459, doi: 10.1126/science.1219631.

Iess, L., N. J. Rappaport, R. A. Jacobson, P. Racioppa, D. J. Stevenson, P. Tortora, J. W. Armstrong, S. W. Asmar, (2010), Gravity field, shape, and moment of inertia of Titan, Science, 327, 1367, doi: 10.1126/science.1182583.

Janssen, M. A., A. Le Gall, R. M. Lopes, R. D. Lorenz, M. J. Malaska, A. G. Hayes, C. D. Neish, A. Solomonidou, K. L. Mitchell, J. Radebaugh, S. J. Keihm, (2016) Titan's surface at 2.18-cm wavelength imaged by the Cassini RADAR radiometer: Results and interpretations through the first ten years of observation, Icarus, 270, pp. 443–459.

Janssen, M. A., A. Le Gall, L. C. Wye, (2011), Anomalous radar backscatter from Titan's surface?, Icarus, 212, 1, 321–328.

Janssen, M. A., R. D. Lorenz, R. West, F. Paganelli, R. M. Lopes, R. L. Kirk, C. Elachi, S. D. Wall, W. T. K. Johnson, Y. Anderson, R. A. Boehmer, P. Callahan, Y. Gim, G. A. Hamilton, K. D. Kelleher, L. Roth, B. Stiles, A. Le Gall, Cassini Radar Team, (2009), Titan's surface at 2.2-cm wavelength imaged by the Cassini RADAR Radiometer: Calibration and first results, Icarus, 200, 222–239, doi: 10.1016/j.icarus.2008.10.017.

Jaumann, R., R. H. Brown, K. Stephan, J. W. Barnes, L. A. Soderblom, et al., (2008), Fluvial erosion and post-erosional processes on Titan, Icarus, 197, 526–538.

Jennings, D. E., V. Cottini, C. A. Nixon, R. K. Achterberg, F. M. Flasar, V. G. Kunde, P. N. Romani, R. E. Samuelson, A. Mamoutkine, N. J. P. Gorius, A. Coustenis, (2016), Surface temperatures on Titan during northern winter and spring, The Astrophysical Journal Letters, vol. 816, no. 1, doi: 10.3847/2041-8205/816/1/L17.

Jennings, D. E., C. M. Anderson, R. E. Samuelson, F. M. Flasar, C. A. Nixon, G. L. Bjoraker, P. N. Romani, et al., (2012), First observation in the south of Titan's far-infrared 220 cm^{-1} Cloud, The Astrophysical Journal Letters, 761, 1, doi: 10.1088/2041-8205/761/1/l15.

Jennings, D. E., F. M. Flasar, V. G. Kunde, R. E. Samuelson, J. C. Pearl, C. A. Nixon, R. C. Carlson, et al., (2009) Titan's surface brightness temperatures, The Astrophysical Journal, 691, 2, L103–L105.

Jennings, D. E., C. A. Nixon, A. Jolly, B. Bézard, A. Coustenis, S. Vinatier, P. G. J. Irwin, et al., (2008), Isotopic ratios in Titan's atmosphere from Cassini CIRS limb sounding: HC_3N in the north, The Astrophysical Journal Letters, 681, 2, L109–L111, doi: 10.1086/590534.

Jolly, A., A. Fayt, Y. Benilan, D. Jacquemart, C. A. Nixon, D. E. Jennings, (2010), The v_8 Bending mode of diacetylene: from laboratory spectroscopy to the detection of ^{13}C isotopologues in Titan's atmosphere, The Astrophysical Journal, 714, 1, 852–859, doi: 10.1088/0004-637X/714/1/852.

Kammer, J. A., (2015), Analyses of planetary atmospheres across the spectrum: From Titan to exoplanets Dissertation (Ph.D.), California Institute of Technology, doi: 10.7907/Z9GX48HD, http://resolver.caltech.edu/CaltechTHESIS:08312014-134619300.

Kanani, S. J., C. S. Arridge, G. H. Jones, A. N. Fazakerley, H. J. McAndrews, N. Sergis, S. M. Krimigis, et al., (2010), A new form of Saturn's magnetopause using a dynamic pressure balance model, based on in situ, multi-instrument Cassini measurements, Journal of Geophysical Research, 115, A06207, doi: 10.1029/2009JA014262.

Karkoschka, E., A. McEwen, J. Perry, (2017), Creating the best global mosaic of Titan's surface albedo using Cassini images, American Astronomical Society (AAS), Division for Planetary Sciences (DPS), meeting 49, id 301.06.

Kasting, J. F., (1988), Runaway and moist greenhouse atmospheres and the evolution of Earth and Venus, Icarus, 74, 472–494.

Kirk, R. L., E. Howington-Kraus, A. G. Hayes, R. M. C. Lopes, R. D. Lorenz, J. I. Lunine, K. L. Mitchell, E. R. Stofan, S. D. Wall, (2010), La Sotra y los otros: Topographic evidence for (and against) cryovolcanism on Titan, American Geophysical Union (AGU) Fall Meeting, December 13–17, 2010, San Francisco, CA, abstract P22A-03.

Klinger, J., (1981), Some consequences of a phase transition of water ice on the heat balance of comet nuclei, Icarus, 47, no. 3, 320–324.

Korycansky, D. G. and K. J. Zahnle, (2005), Modeling crater populations on Venus and Titan, Planetary and Space Science, 53, 695–710.

Koskinen, T. T., R. V. Yelle, D. S. Snowden, P. Lavvas, B. R. Sandel, F. J. Capalbo, Y. Benilan, and R. A. West, (2011), The mesosphere and thermosphere of Titan revealed by Cassini/UVIS stellar occultations, Icarus, 216, 507–534.

Krupp, N., A. Lagg, J. Woch, S. M. Krimigis, S. Livi, D. G. Mitchell, E. C. Roelof, C. Paranicas, B. H. Mauk, D. C. Hamilton, T. P. Armstrong, M. K. Dougherty, (2005), The Saturnian plasma sheet as revealed by energetic particle measurements, Geophysical Research Letters, 32, L20S03, doi: 10.1029/2005GL022829.

Kuiper, G. P., (1944), Titan: A satellite with an atmosphere, The Astrophysical Journal, 100, 378–383, doi: 10.1086/144679.

Kurth, W. S., T. F. Averkamp, D. A. Gurnett, J. B. Groene, A. Lecacheux, (2008), An update to a Saturnian longitude system based on kilometric radio emissions, Journal of Geophysical Research, 113, A05222, doi: 10.1029/2007JA012861.

Langhans, M. H., R. Jaumann, K. Stephan, R. H. Brown, B. J. Buratti, et al., (2012), Titan's fluvial valleys: Morphology, distribution, and spectral properties, Planetary and Space Science, 60, 34–51.

Lavvas, P., R. V. Yelle, T. Koskinen, et al., (2013), Aerosol growth in Titan's ionosphere, Proceedings of the National Academy of Sciences, 110, 8, 2729–2734, doi: 10.1073/pnas.1217059110.

Lavvas, P. P., R. V. Yelle, V. Vuitton, (2009), The detached haze layer in Titan's mesosphere, Icarus, 201, 626–633, doi: 10.1016/j.icarus.2009.01.004.

Lavvas, P. P., A. Coustenis, I. M. Vardavas, (2008), Coupling photochemistry with haze formation in Titan's atmosphere, Part I: Model description, Planetary and Space Science, 56, 27–66.

Le Gall, A., M. J. Malaska, R. D. Lorenz, M. A. Janssen, T. Tokano, A. G. Hayes, M. Mastrogiuseppe, J. I. Lunine, G. Veyssière, P.,Encrenaz, O. Karatekin, (2016), Composition, seasonal change and bathymetry of Ligeia Mare, Titan, derived from its microwave thermal emission, Journal of Geophysical Research: Planets, 121, 233–251.

Le Gall, A., A. G. Hayes, R. Ewing, M. A. Janssen, J. Radebaugh, C. Savage, P. Encrenaz, Cassini Radar Team, (2012), Latitudinal and altitudinal controls on Titan's dune field morphometry, Icarus, 217, 231–242.

Le Gall, A., M. A. Janssen, L. C. Wye, A. G. Hayes, J. Radebaugh, C. Savage, H. Zebker, R. D. Lorenz, J. I. Lunine, R. L. Kirk, R. M. C. Lopes, S. Wall, P. Callahan, E. R. Stofan, T. Farr, Cassini Radar Team, (2011), Cassini SAR, radiometry, scatterometry and altimetry observations of Titan's dune fields, Icarus, 213, 608–624.

Le Gall, A., M. A. Janssen, P. Paillou, R. D. Lorenz, S. D. Wall, (2010), Radar-bright channels on Titan, Icarus, vol. 207, pp. 948–958.

Ledvina, S. A., T. E. Cravens, K. Kecskemety, (2005), Ion distributions in Saturn's magnetosphere near Titan, Journal of Geophysical Research: Space Physics, 110, A06211.

Lellouch, E., B. Bézard, F. M. Flasar, S. Vinatier, R. Achterberg, et al., (2014), The distribution of methane in Titan's stratosphere from Cassini/CIRS observations, Icarus 231, 323–337.

Lellouch, E., (2006), Titan's zoo of clouds, Science, vol. 311, Issue 5758, pp. 186–187, doi: 10.1126/science.1122628.

Lellouch, E., A. Coustenis, D. Gautier, F. Raulin, N. Dubouloz, C. Frere, (1989), Titans atmosphere and hypothesized ocean - a reanalysis of the Voyager-1 radio-occultation and IRIS 7.7-μm data, Icarus, 79, 328–349.

Leovy, C. B. and J. B. Pollack, (1973), First look at atmospheric dynamics and temperature variations on Titan, Icarus, 19, 195–201.

Lewis, J. S., (1971), Satellites of outer planets - their physical and chemical nature, Icarus, 15, 174–185.

Liang, M-C., Y. L. Yung, D. E. Shemansky, (2007), Photolytically generated aerosols in the mesosphere and thermosphere of Titan, The Astronomical Journal, 661, L199–L202.

Lindal, G. F., G. E. Wood, H. B. Hotz, D. N. Sweetnam, V. R. Eshleman, G. L. Tyler, (1983), The atmosphere of Titan - an analysis of the Voyager-1 radio occultation measurements, Icarus, 53, 348–363.

Lopes, R. M. C., M. J. Malaska, A. Solomonidou, A. LeGall, M. A. Janssen, C. Neish, E. P. Turtle, S. P. D. Birch, A. G. Hayes, J. Radebaugh, A. Coustenis, A. Schoenfeld, B. W. Stiles, R. L. Kirk, K. L. Mitchell, E. R. Stofan, K. J. Lawrence, Cassini RADAR Team, (2016), Nature, distribution, and origin of Titan's undifferentiated plains, Icarus, 270, 162–182.

Lopes, R. M. C., R. L. Kirk, K. L. Mitchell, A. LeGall, J. W. Barnes, A. Hayes, J. Kargel, L. Wye, J. Radebaugh, E. R. Stofan, M. Janssen, C. Neish, S. Wall, C. A. Wood, J. I. Lunine, M. Malaska, (2013), Cryovolcanism on Titan: New results from Cassini RADAR and VIMS. Journal of Geophysical Research: Planets, 118, no. 3, 416–435.

Lopes, R. M. C., E. R. Stofan, R. Peckyno, J. Radebaugh, K. L. Mitchell, G. Mitri, C. A. Wood, R. L. Kirk, S. D. Wall, J. I. Lunine, A. Hayes , R. Lorenz, T. Farr, L. Wye, J. Craig, R. J. Ollerenshaw, M. Janssen, A. LeGall, F. Paganelli, R. West, B. Stiles, P. Callahan, Y. Anderson, P. Valora, L. Soderblom, Cassini RADAR Team, (2010), Distribution and interplay of geologic processes on Titan from Cassini RADAR data, Icarus, 205, 540–588, doi: 10.1016/j.icarus.2009.08.010.

Lopes, R. M. C., K. L. Mitchell, E. R. Stofan, J. I. Lunine, R. Lorenz, F. Paganelli, R. L. Kirk, C. A. Wood, S. D. Wall, L. E. Robshaw, A. D. Fortes, C. D. Neish, J. Radebaugh, E. Reffet, S. J. Ostro, C. Elachi, M. D. Allison, Y. Anderson, R. Boehmer, G. Boubin, P. Callahan, P. Encrenaz, E. Flamini, G. Francescetti, Y. Gim, G. Hamilton, S. Hensley, M. A. Janssen, W. T. K. Johnson, K. Kelleher, D. O. Muhleman, G. Ori, R. Orosei, G. Picardi, F. Posa, L. E. Roth, R. Seu, S. Shaffer, L. A. Soderblom, B. Stiles, S. Vetrella, R. D. West, L. Wye, H. A. Zebker, (2007), Cryovolcanic features on Titan’s surface as revealed by the Cassini Titan RADAR Mapper, Icarus, 186, 395–412.

Lora, J. M. and M. Ádámkovics, (2017), The near-surface methane humidity on Titan, Icarus, 286, 270–279.

Lora, J. M., J. I. Lunine, J. L. Russell, (2015), GCM simulations of Titan's middle and lower atmosphere and comparison to observations, Icarus, 250, 516–528.

Lora, J. M. and J. L. Mitchell, (2015), Titan's asymmetric lake distribution mediated by methane transport due to atmospheric eddies, Geophysical Research Letters, 42, 6213–6220.

Lora, J. M., J. I. Lunine, J. L. Russell, A. G. Hayes, (2014), Simulations of Titan's paleoclimate, Icarus, 243, pp. 264–273.

Lorenz, R. D., R. L. Kirk, A. G. Hayes, Y. Z. Anderson, J. I. Lunine, et al., (2014), A radar map of Titan Seas: Tidal dissipation and ocean mixing through the throat of Kraken, Icarus 237, 9–15, doi: 10.1016/j.icarus.2014.04.005.

Lorenz, R. D. and Zimbelman, J. R., (2014), Dune worlds: How windblown sand shapes planetary landscapes, Springer, Science & Business Media.

Lorenz, R. D., (2014), Physics of saltation and sand transport on Titan: A brief review. Icarus, 230, pp.162–167.

Lorenz, R. D., B. W. Stiles, O. Aharonson, A. Lucas, A. G. Hayes, R. L. Kirk, H. A. Zebker, et al., (2013), A global topographic map of Titan, Icarus, 225, 367–377, doi: 10.1016/j.icarus.2013.04.002.

Lorenz, R. D. and A. G. Hayes, (2012), The growth of wind-waves in Titan’s hydrocarbon seas, Icarus, 219, 468–475.

Lorenz, R. D., (2012), Titan is to Earth's hydrological cycle what Venus is to its greenhouse effect, Comparative Climatology of Terrestrial Planets, Boulder, CO, June 25–28, 2012, LPI Contribution No. 1675, id 8053.

Lorenz, R. D., P. Claudin, B. Andreotti, J. Radebaugh, T. Tokano, (2010), A 3 km atmospheric boundary layer on Titan indicated by dune spacing and Huygens data, Icarus, 205, 2, pp. 719–721.

Lorenz, R. D. and J. Radebaugh, (2009), Global pattern of Titan's dunes: radar survey from the Cassini prime mission, Geophysical Research Letters, 36, 3.

Lorenz, R. D., R. M. Lopes, F. Paganelli, J. I. Lunine, R. L. Kirk, K. L. Mitchell, L. A. Soderblom, E. R. Stofan, G. Ori, M. Myers, H. Miyamoto, J. Radebaugh, B. Stiles, S. D. Wall, C. A. Wood, Cassini RADAR Team, (2008a), Fluvial channels on Titan: Initial Cassini RADAR observations, Planetary and Space Science, 56, 1132–1144.

Lorenz, R. D., K. L. Mitchell, R. L. Kirk, A. G. Hayes, H. A. Zebker, P. Paillou, J. Radebaugh, J. I. Lunine, M. A. Janssen, S. D. Wall, R. M. Lopes, B. Stiles, S. Ostro, G. Mitri, E. R. Stofan, Cassini RADAR Team, (2008b), Titan's Inventory of Organic Surface Materials, Geophysical Research Letters, 35, L02206, doi: 10.1029/2007GL032118.

Lorenz, R. D., C. A. Wood, J. I. Lunine, S. D. Wall, R. M. Lopes, K. L. Mitchell, F. Paganelli, Y. Z. Anderson, L. Wye, C. Tsai, H. Zebker, E. R. Stofan, (2007), Titan's young surface: Initial impact crater survey by Cassini RADAR and model comparison, Geophysical Research Letters, 34, L07204.

Lorenz, R. D., H. B. Niemann, D. N. Harpold, S. H. Way, J. C. Zarnecki, (2006a), Titan's damp ground: Constraints on Titan surface thermal properties from the temperature evolution of the Huygens GCMS inlet, Meteoritics & Planetary Science, 41, 1705–1714.

Lorenz, R. D., S. Wall, J. Radebaugh, G. Boubin, E. Reffet, M. Janssen, E. Stofan, R. Lopes, R. Kirk, C. Elachi, J. Lunine, F. Paganelli, L. Soderblom, C. Wood, L. Wye, H. Zebker, Y. Anderson, S. Ostro, M. Allison, R. Boehmer, P. Callahan, P. Encrenaz, G. G. Ori, G. Francescetti, Y. Gim, G. Hamilton, S. Hensley, W. Johnson, K. Kelleher, K. Mitchell, D. Muhleman, G. Picardi, F. Posa, L. Roth, R. Seu, S. Shaffer, B. Stiles, S. Vetrella, E. Flamini R. West, (2006b), The sand seas of Titan: Cassini RADAR observations of longitudinal dunes, Science, 312, 724–727.

Lorenz, R. D., C. A. Griffith, J. I. Lunine, C. P. McKay, N. O. Rennò, (2005), Convective plumes and the scarcity of Titan's clouds, Geophysical Research Letters, 32, 1.

Lorenz, R. D., G. Biolluz, P. Encrenaz, M. A. Janssen, R. D. West, D.O. Muhleman, (2003), Cassini RADAR: prospects for Titan surface investigations using the microwave radiometer, Planetary and Space Science, 51, 4–5, pp. 353–364.

Lorenz, R. D., (2000), Planetary science - The weather on Titan, Science, 290, 467–468.

Lorenz, R. D., C. P. McKay, J. I. Lunine, (1997), Photochemically driven collapse of Titan's atmosphere, Science, 275, 642–644.

Lorenz, R. D., (1996a), Pillow lava on Titan: expectations and constraints on cryovolcanic processes, Planetary and Space Science, 44, no. 9, 1021–1028.

Lorenz, R. D. and J. I. Lunine, (1996b), Erosion on Titan: Past and present, Icarus, 122, 79–91.

Lorenz, R. D., J. I. Lunine, J. A. Grier, M. A. Fisher, (1995), Prediction of aeolian features on planets: Application to Titan paleoclimatology, Journal of Geophysical Research: Planets, 100, E12, pp. 26377–26386.

Lorenz, R. D., (1993a), The life, death and afterlife of a raindrop on Titan, Planetary and Space Science, 41, 647–655.

Lorenz, R. D., (1993b), The surface of Titan in the context of ESA's Huygens probe, European Space Agency Journal, vol. 17, pp. 275–292.

Loveday, J. S., R. J. Nelmes, M. Guthrie, S. A. Belmonte, D. R. Allan, et al., (2001), Stable methane hydrate above 2-GPa and the source of Titan's atmospheric methane, Nature, 410, 661–663.

Lucas, A., S. Rodriguez, C. Narteau, B. Charnay, S. C. Pont, T. Tokano, A. Garcia, M. Thiriet, A. G. Hayes, R. D. Lorenz, O. Aharonson, (2014), Growth mechanisms and dune orientation on Titan, Geophysical Research Letters, 41, 17, pp. 6093–6100, doi: 10.1002/2014GL060971.

Lunine, J. I. and S. M. Hörst, (2011), Organic chemistry on the surface of Titan, Rendiconti Lincei-Scienze Fisiche E Naturali, 22, 183–189.

Lunine, J. I., C. Elachi, S. D. Wall, M. A. Janssen, M. D. Allison, Y. Anderson, et al., (2008a), Titan's diverse landscapes as evidenced by Cassini RADAR's third and fourth looks, Icarus, 195, 415–433.

Lunine, J. I. and S. K. Atreya, (2008b), The methane cycle on Titan, Nature Geoscience, 1, 159–164.

Lunine, J. I., R. D. Lorenz, W. K. Hartmann, (1998), Some speculations on Titan's past, present and future, Planetary and Space Science, 46, 1099–1107.

Lunine, J. I. and D. J. Stevenson, (1987), Clathrate and ammonia hydrates at high-pressure - application to the origin of methane on Titan, Icarus, 70, 61–77.

Lunine, J. I., D. J. Stevenson, Y. L. Yung, (1983), Ethane ocean on Titan, Science, 222, 1229–1230.

MacKenzie, S. M., J. W. Barnes, C. Sotin, J. M. Soderblom, S. Le Mouélic, S. Rodriguez, K. H. Baines, B. J. Buratti, R. N. Clark, P. D. Nicholson, T. B. McCord, (2014), Evidence of Titan's climate history from evaporite distribution, Icarus, 243, pp. 191–207.

Malaska, M. J., R. M. Lopes, A. G. Hayes, J. Radebaugh, R. D. Lorenz, E. P. Turtle, (2016), Material transport map of Titan: The fate of dunes, Icarus, 270, pp. 183–196, doi: 10.1016/j.icarus.2015.09.029.

Mastrogiuseppe, M., V. Poggiali, A. G. Hayes, J. I. Lunine, R. Seu, G. Mitri, R. D. Lorenz, (2019), Depp and methane-rich lakes on Titan, Nature Astronomy, 3, 535–542.

Mastrogiuseppe, M., A. G. Hayes, V. Poggiali, J. I. Lunine, R. D. Lorenz, et al., (2017), Bathymetry and composition of Titan's Ontario Lacus derived from Monte Carlo-based waveform inversion of Cassini RADAR altimetry data, Icarus, 300, 203–209.

Mastrogiuseppe, M., A. Hayes, V. Poggiali, R. Seu, J. I. Lunine, J. D. Hofgartner, (2016), Radar sounding using the Cassini altimeter: Waveform modeling and Monte Carlo approach for data inversion of observations of Titan's seas, IEEE Transactions on Geoscience and Remote Sensing, vol. 54, Issue 10, pp. 5646–5656, doi: 10.1109/TGRS.2016.2563426.

Mastrogiuseppe, M., V. Poggiali, A. Hayes, R. Lorenz, J. Lunine, G. Picardi, R. Seu, E. Flamini, G. Mitri, C. Notarnicola, P. Paillou, H. Zebker, (2014), The bathymetry of a Titan sea, Geophysical Research Letters, vol. 41, no. 5, pp. 1432–1437.

McDonald, G. D., A. G. Hayes, R. C. Ewing, J. M. Lora, C. E. Newman, T. Tokano, A. Lucas, A. Soto, G. Chen, (2016) Variations in Titan's dune orientations as a result of orbital forcing, Icarus, 270, pp.197–210.

McKay, C. P., J. B. Pollack, R. Courtin, (1989), The Thermal Structure of Titans Atmosphere, Icarus, 80, 23-53.

Meriggiola, R., L. Iess, B. W. Stiles, J. I. Lunine, G. Mitri, (2016), The rotational dynamics of Titan from Cassini RADAR images, Icarus, 275, 183–192.

Mitchell, J. L. and J. M. Lora, (2016), The climate of Titan, Annual Review of Earth and Planetary Sciences, vol. 44, 353–380, doi: 10.1146/annurev-earth-060115-012428.

Mitchell, K. L., M. B. Barmatz, C. S. Jamieson, R. D. Lorenz, J. I. Lunine, (2015), Laboratory measurements of cryogenic liquid alkane microwave absorptivity and implications for the composition of Ligeia Mare, Titan, Geophysical Research Letters, 42, 1340–1345.

Mitchell, J. L., M. Adamkovics, R. Caballero, E. P. Turtle, (2011), Locally enhanced precipitation organized by planetary-scale waves on Titan, Nature Geoscience, 4, 589–592.

Mitchell, J. L., (2008), The drying of Titan's dunes: Titan's methane hydrology and its impact on atmospheric circulation, Journal of Geophysical Research: Planets, 113, E8.

Mitri, G., R. Meriggiola, A. Hayes, L. Axel, G. Tobie, et al., (2014), Shape, topography, gravity anomalies and tidal deformation of Titan, Icarus, 236, 169–177.

Moore, J. M., A. D. Howard, A. M. Morgan, (2014), The landscape of Titan as witness to its climate evolution, Journal of Geophysical Research: Planets, 119, 2060–2077, doi: 10.1002/2014JE004608.

Moore, J. M. and Howard A. D., (2011), Are the basins of Titan's Hotei Regio and Tui Regio sites of former low latitude seas?, Geophysical Research Letters, vol. 38, L04201.

Moore, J. M. and R. T. Pappalardo, (2011), Titan: An Exogenic World?, Icarus, 212, 790–806.

Mousis, O., M. Choukroun, J. I. Lunine, C. Sotin, (2014), Equilibrium composition between liquid and clathrate reservoirs on Titan, Icarus, 239, 39–45.

Müller-Wodarg, I. C. F., R. V. Yelle, J. Cui, J. H. Waite, (2008), Horizontal structures and dynamics of Titan's thermosphere, Journal of Geophysical Research: Planets, vol. 113, Issue E10, doi: 10.1029/2007JE003033.

NASA/JPL-Caltech/GSFC, (2016), Titan Temperature Lag Maps & Animation, https://www.nasa.gov/image-feature/jpl/pia20020/titan-temperature-lag-maps-animation.

Neish, C. D., J. L. Molaro, J. M. Lora, A. D. Howard, R. L. Kirk, P. Schenk, et al., (2016), Fluvial erosion as a mechanism for crater modification on Titan, Icarus, 270, 114–129.

Neish, C. D., J. W. Barnes, C. Sotin, S. MacKenzie, J. M. Soderblom, S. Le Mouélic, et al., (2015), Spectral properties of Titan's impact craters imply chemical weathering of its surface, Geophysical Research Letters, 42, 3746–3754.

Neish, C. D. and R. D. Lorenz, (2014), Elevation distribution of Titan's craters suggests extensive wetlands, Icarus, 228, 27–34.

Neish, C. D., R. L. Kirk, R. D. Lorenz, V. J. Bray, P. Schenk, B. W. Stiles, et al., (2013), Crater topography on Titan: Implications for landscape evolution, Icarus, 223, 82–90.

- - - - - - - - - - - - - -

Neish, C. D. and R. D. Lorenz, (2012), Titan's global crater population: A new assessment, Planetary and Space Science, 60, 1, pp. 26–33.

Neish, C. D., R. D. Lorenz, R. L. Kirk, L. C. Wye, (2010), Radarclinometry of the sand seas of Africa's Namibia and Saturn's moon Titan, Icarus, 208, 385–394.

Németh, Z., K. Szego, Z. Bebesi, G. Erdős, L. Foldy, A. Rymer, E. C. Sittler, A. J. Coates, A. Wellbrock, (2011), Ion distributions of different Kronian plasma regions, Journal of Geophysical Research: Space Physics, vol. 116, Issue A9, doi: 10.1029/2011JA016585.

Neubauer, F. M., H. Backes, M. K. Dougherty, A. Wennmacher, C. T. Russell, A. Coates, D. Young, N. Achilleos, N. Andre, C. S. Arridge, C. Bertucci, G. H. Jones, K. K. Khurana, T. Knetter, A. Law, G. R. Lewis, J. Saur, (2006), Titan's near magnetotail from magnetic field and electron plasma observations and modeling: Cassini flybys TA, TB and T3, Journal of Geophysical Research: Space Physics, vol. 111, Issue A10, doi: 10.1029/2006JA011676.

Niemann, H. B., S. K. Atreya, J. Demick, D. Gautier, J. Haverman, D. Harpold, W. Kasprzak, J. Lunine, T. Owen, F. Raulin, (2010), Composition of Titan's lower atmosphere and simple surface volatiles as measured by the Cassini-Huygens probe gas chromatograph mass spectrometer experiment, Journal of Geophysical Research, vol. 115, Issue E12, doi: 10.1029/2010JE003659.

Niemann, H. B., S. K. Atreya, S. J. Bauer, G. R. Carignan, J. E. Demick, et al., (2005), The abundances of constituents of Titan's atmosphere from the GCMS instrument on the Huygens probe, Nature, 438, 779–784, doi: 10.1038/nature04122.

Niemann, H. B., S. K. Atreya, S. J. Bauer, G. R. Carignan, J. E. Demick, R. L. Frost, D. Gautier, J. A. Haberman, D. N. Harpold, D. M. Hunten, G. Israel, J. I. Lunine, W. T. Kasprzak, T. C. Owen, M. Paulkovich, F. Raulin, E. Raaen, S. H. Way, (2005), Huygens probe gas chromatograph mass spectrometer: The atmosphere and surface of Titan, Nature, 438, 779–784.

Nimmo, F. and B. G. Bills, (2010), Shell thickness variations and the long-wavelength topography of Titan, Icarus, 208, 896–904.

Nixon, C., R. Clark, R. Courtin, A. Hayes, R. Lopes, R. Yelle, C. Sotin, A. Rymer, R. Johnson, R. Lorenz, M. Mastroguiseppe, H. Smith, D. Strobel, R. Achterberg, A. Buch, K. Mandt, D. Mitchell, F. Raulin, E. Turtle, L. Iess, V. Vuitton, A. Solomonidou, R. West, P. Coll, (2018), Titan's cold case files – Outstanding questions after Cassini-Huygens, Planetary and Space Science, 155, pp. 50–72, doi: 10.1016/j.pss.2018.02.009.

Nixon, C. A., D. E. Jennings, B. Bézard, S. Vinatier, N. A. Teanby, K. Sung, T. M. Ansty, et al., (2013), Detection of propene in Titan's stratosphere, The Astrophysical Journal Letters, vol. 776, no. 1, doi: 10.1088/2041-8205/776/1/L14.

Nixon, C. A., B. Temelso, S. Vinatier, N. A. Teanby, B. Bézard, et al., (2012), Isotopic ratios in Titan's methan: Measurements and modeling, The Astrophysical Journal, 749, 2, doi: 10.1088/0004-637X/749/2/159.

Nixon, C. A., R. K. Achterberg, S. Vinatier, B. Bézard, A. Coustenis, P. G. J. Irwin, N. A. Teanby, et al., (2008), The $^{12}C/^{13}C$ isotopic ratio in Titan hydrocarbons from Cassini/CIRS infrared spectra, Icarus, 195, 2, 778–791, doi: 10.1016/j.icarus.2008.01.012.

Nixon, C., D. Jennings, B. Bézard, et al., (2008), Isotopic ratios in Titan's atmosphere from Cassini CIRS limb sounding: CO_2 at low and midlatitudes, The Astrophysical Journal Letters, 681, 2, L101-L103, doi: 10.1086/590553.

O'Brien, D. P., R. D. Lorenz, J. I. Lunine, (2005), Numerical calculations of the longevity of impact oases on Titan, Icarus, 173, 1, 243–253, doi: 10.1016/j.icarus.2004.08.001.

Osegovic, J. P., M. D. Max, (2005), Compound clathrate hydrate on Titan's surface, Journal of Geophysical Research: Planets, vol. 110, Issue E8, doi: 10.1029/2005JE002435.

Paillou, P., B. Seignovert, J. Radebaugh, S. Wall, (2016), Radar scattering of linear dunes and mega-yardangs: Application to Titan, Icarus, vol. 270, pp. 211–221.

Paillou, P., D. Bernard, J. Radebaugh, R. Lorenz, A. Le Gall, T. Farr, (2014), Modeling the SAR backscatter of linear dunes on Earth and Titan, Icarus, vol. 230, pp. 208–214.

Paillou, P., K. L. Mitchell, S. D. Wall, G. Ruffié, C.A. Wood, R. D. Lorenz, E. R. Stofan, J. I. Lunine, R. M. Lopes, P. Encrenaz, (2008), Microwave dielectric constant of liquid hydrocarbons: Application to the depth estimation of Titan's lakes, Geophysical Research Letters, vol. 35, Issue 5, doi: 10.1029/2007GL032515.

Paillou, P., M. Crapeau, C. Elachi, S. Wall, P. Encrenaz, (2006), Models of SAR backscattering for bright flows and dark spots on Titan, Journal of Geophysical Research, vol. 111, E11011, doi: 10.1029/2006JE002724.

Perron, J. T., M. P. Lamb, C .D. Koven, I. Y. Fung, E. Yager, M. Adamkovics, (2006), Valley formation and methane precipitation rates on Titan, Journal of Geophysical Research: Planets, 111, E11001.

Pierrehumbert, R. T., (2002), The hydrologic cycle in deep-time climate problems, Nature, 419, 191–198.

Poggiali, V., M. Mastrogiuseppe, A. G. Hayes, R. Seu, S. P. D. Birch, R. Lorenz, C. Grima, J. D. Hofgartner, (2016), Liquid-filled canyons on Titan, Geophysical Research Letters, 43, 7887–7894.

Porco, C. C., E. Baker, J. Barbara, K. Beurle, A. Brahic, J. A. Burns, S. Charnoz, N. Cooper, D. D. Dawson, A. D. DelGenio, T. Denk, L. Dones, U. Dyudina, M. W. Evans, S. Fussner, B. Giese, K. Grazier, P. Helfenstein, A. P. Ingersoll, R. A. Jacobson, T. V. Johnson, A. McEwen, C. D. Murray, G. Neukum, W. M. Owen, J. Perry, T. Roatsch, J. Spitale, S. Squyres, P. Thomas, M. Tiscareno, E. P. Turtle, A. R. Vasavada, J. Veverka, R. Wagner, R. West, (2005), Imaging of Titan from the Cassini spacecraft, Nature, 434, 159–168, doi: 10.1038/nature03436.

Radebaugh, J., D. Ventra, R. D. Lorenz, T. Farr, R. Kirk, et al., (2016), Alluvial and fluvial fans on Saturn's moon Titan reveal processes, materials and regional geology, Geological Society, London, Special Publications, 440, no. 1, 281–305.

Radebaugh, J., (2013), Dunes on Saturn’s moon Titan as revealed by the Cassini Mission, Aeolian Research, 11, 23–41.

Radebaugh, J., R. Lorenz, T. Farr, P. Paillou, C. Savage, C. Spencer, (2010), Linear dunes on Titan and Earth: Initial remote sensing comparisons, Geomorphology, 121, 122–132, doi: 10.1016/j.geomorph.2009.02.022.

Radebaugh, J., R. D. Lorenz, J. I. Lunine, S. D. Wall, G. Boubin, E. Reffet, R. L. Kirk, R. M. Lopes, E. R. Stofan, L. Soderblom, M. Allison, Cassini Radar Team, (2008), Dunes on Titan observed by Cassini RADAR, Icarus, 194, 2, pp.690–703, doi: 10.1016/j.icarus.2007.10.015.

Rannou, P., F. Montmessin, F. Hourdin, S. Lebonnois, (2006), The latitudinal distribution of clouds on Titan, Science, 311, 5758, pp.201–205.

Rodriguez, S., A. Garcia, A. Lucas, T. Appéré, A. Le Gall, E. Reffet, L. Le Corre, S. Le Mouélic, T. Cornet, S. Courrech du Pont, C. Narteau, O. Bourgeois, J. Radebaugh, K. Arnold, J. W. Barnes, K. Stephan, R. Jaumann, C. Sotin, R. H. Brown, R. D. Lorenz, E. P. Turtle, (2014), Global mapping and characterization of Titan’s dune fields with Cassini: correlation between RADAR and VIMS observations, Icarus, 230, 168–179.

Rodriguez, S., S. Le Mouélic, P. Rannou, C. Sotin, R. H. Brown, et al., (2011), Titan's cloud seasonal activity from winter to spring with Cassini/VIMS, Icarus, 216, 89–110, doi: 10.1016/j.icarus.2011.07.031.

Rodriguez, S., S. Le Mouélic, P. Rannou, J.-P. Combe, L. Le Corre, G. Tobie, J. W. Barnes, et al., (2009), Fast forward modeling of Titan's infrared spectra to invert VIMS/Cassini hyperspectral images, IEEE First Workshop on Hyperspectral Image and Signal Processing: Evolution in Remote Sensing, pp. 1-4.

Roe, H. G., I. de Pater, B. A. Macintosh, C. P. McKay, (2002), Titan's clouds from Gemini and Keck adaptive optics imaging, The Astrophysical Journal, 581, 1399–1406.

Roussos, E., P. Kollmann, N. Krupp, C. Paranicas, K. Dialynas, N. Sergis, D. G. Mitchell, D. C. Hamilton, S. M. Krimigis, (2018), Drift-resonant, relativistic electron acceleration at the outer planets: Insights from the response of Saturn’s radiation belts to magnetospheric storms, Icarus, 305, 160–173, doi: 10.1016/j.icarus.2018.01.016.

Rubin, D. M. and P. A. Hesp, (2009), Multiple origins of linear dunes on Earth and Titan, Nature Geoscience, 2, 9, p. 653.

Rymer, A. M., H. T. Smith, A. Wellbrock, A. J. Coates, D. T. Young, (2009), Discrete classification and electron energy spectra of Titan’s varied magnetospheric environment, Geophysical Research Letters, 36, 15109, doi: 10.1029/2009GL039427.

Sagan, C. and S. F. Dermott, (1982) The tide in the seas of Titan, Nature, 300, 731–733.

Savage, C. J., J. Radebaugh, E. H. Christiansen, R. D. Lorenz, (2014), Implications of dune pattern analysis for Titan’s surface history, Icarus, 230, pp. 180–190.

Schaller, E. L., H. G. Roe, T. Schneider, M. E. Brown, (2009), Storms in the tropics of Titan, Nature, 460, 873–875.

Schaller, E. L., M. E. Brown, H. G. Roe, A. H. Bouchez, C. A. Trujillo, (2006), Dissipation of Titan's south polar clouds, Icarus, 184, 517–523.

Schinder, P. J., F. M. Flasar, E. A. Marouf, et al., (2012), The structure of Titan's atmosphere from Cassini radio occultations: Occultations from the Prime and Equinox missions, Icarus, 221, 1020–1031, doi: 10.1016/j.icarus.2012.10.021.

Schneider, T., S. D. B. Graves, E. L. Schaller, M. E. Brown, (2012), Polar methane accumulation and rainstorms on Titan from simulations of the methane cycle, Nature, 481, 58–61.

Schurmeier, L. R. and A. J. Dombard, (2018), Crater relaxation on Titan aided by low thermal conductivity sand infill, Icarus, 305, 314–323.

Sears, W. D., (1995), Tidal dissipation in oceans on Titan, Icarus, 113, 1, 39–56, doi: 10.1006/icar.1995.1004.

Shah, M. B., C. J. Latimer, E. C. Montenegro, O. J. Tucker, R. E. Johnson, H. T. Smith, (2009), The implantation and interactions of O^+ in Titan's atmosphere: Laboratory measurements of collision-induced dissociation of N_2 and modeling of positive ion formation, The Astrophysical Journal, 703, 1947–1954, doi: 10.1088/0004-637X/703/2/1947.

Shebanits, O., J.-E. Wahlund, N. J. T. Edberg, et al., (2016), Ion and aerosol precursor densities in Titan's ionosphere: A multi-instrument case study, Journal of Geophysical Research: Space Physics, 121, 10075–10090, doi: 10.1002/2016JA022980.

Sillanpää, I., D. T. Young, F. Crary, M. Thomsen, D. Reisenfeld, J.-E. Wahlund, C. Bertucci, E. Kallio, R. Jarvinen, P. Janhunen, (2011), Cassini plasma spectrometer and hybrid model study on Titan's interaction: Effect of oxygen ions, Journal of Geophysical Research, 116, A7, doi: 10.1029/2011JA016443.

Simon, S., A. Wennmacher, F. M. Neubauer, et al., (2010), Titan's highly dynamic magnetic environment: A systematic survey of Cassini magnetometer observations from flybys TA-T62, Planetary and Space Science, 58, 1230–1251, doi: 10.1016/j.pss.2010.04.021.

Singh, S., T. B. McCord, J. P. Combe, S. Rodriguez, T. Cornet, et al., (2016), Acetylene on Titan's surface, The Astrophysical Journal, vol. 828, no. 1, doi: 10.3847/0004-637X/828/1/55.

Sittler, E. C., R. E. Hartle, C. Bertucci, A. Coates, T. Cravens, I. Dandouras, D. Shemansky, (2009), Energy deposition processes in Titan's upper atmosphere and its induced magnetosphere, Chapter 16, In Titan from Cassini-Huygens, (eds.) R. H. Brown, J. P. Lebreton, J. H. Waite, Springer, Dordrecht, pp. 393–453, doi: 10.1007/978-1-4020-9215-2_16.

Snowden, D., R. V. Yelle, J. Cui, J.-E. Wahlund, K. Ågren, N. J. T. Edberg, (2013), The thermal structure of Titan's upper atmosphere, I: Temperature profiles from Cassini INMS observations, Icarus, 226, 522–582, doi: 10.1016/j.icarus.2013.06.006.

Soderblom, J. M., R. H. Brown, L. A. Soderblom, J. W. Barnes, R. Jaumann, S. Le Mouélic, et al., (2010), Geology of the Selk crater region on Titan from Cassini VIMS observations, Icarus, 208, 905–912.

Soderblom, L. A., R. H. Brown, J. M. Soderblom, J. W. Barnes, R. L. Kirk, C. Sotin, R. Jaumann, D. J. MacKinnon, D. W. Mackowski, K. H. Baines, B. J. Buratti, R. N. Clark, P. D. Nicholson, (2009), The geology of Hotei Regio, Titan: Correlation of Cassini VIMS and RADAR, Icarus, 204, 610–618, doi: 10.1016/j.icarus.2009.07.033.

- - - - - - - - - - - - - -

Soderblom, L. A., M. G. Tomasko, B. A. Archinal, T. L. Becker, M. W. Bushroe, et al., (2007) Topography and geomorphology of the Huygens landing site on Titan, Planetary and Space Science, 55, 2015–2024.

Soderblom, L., J. Anderson, K. Baines, J. Barnes, J. Barrett, R. Brown, B. Buratti, R. Clark, D. Cruikshank, C. Elachi, M. Janssen, R. Jaumann, R. Kirk, E. Karkoschka, S. Lemouelic, R. Lopes, R. Lorenz, J. Lunine, T. McCord, P. Nicholson, J. Radebaugh, B. Rizk, C. Sotin, E. Stofan, T. Sucharski, M. Tomasko, S. Wall, (2007), Correlations between Cassini VIMS spectra and RADAR SAR images: Implications for Titan's surface composition and the character of the Huygens Probe landing site, Planetary and Space Science, 55, 2025–2036.

Sohl, F., A. Solomonidou, F.W. Wagner, A. Coustenis, H. Hussmann, D. Schulze-Makuch, (2014), Tidal stresses on Titan and implications for its geology and habitability, Journal of Geophysical Research, 119, 1013–1036.

Sohl, F., H. Hussmann, B. Schwentker, T. Spohn, R. D. Lorenz, (2003), Interior structure models and tidal Love numbers of Titan, Journal of Geophysical Research, 108, E12, 5130, doi: 10.1029/2003JE002044.

Solomonidou, A., A. Coustenis, R. M. C. Lopes, M. Malaska, S. Rodriguez, P. Drossart, C. Elachi, B. Schmitt, S. Philippe, M. Janssen, M. Hirtzig, S. Wall, C. Sotin, K. Lawrence, N. Altobelli, E. Bratsolis, J. Radebaugh, K. Stephan, R. H. Brown, S. Le Mouélic, A. Le Gall, E. V. Villanueva, J. F. Brossier, A. A. Bloom, O. Witasse, C. Matsoukas, A. Schoenfeld, (2018), The spectral nature of Titan's major geomorphological units: Constraints on surface composition, Journal of Geophysical Research: Planets, 123, no. 2, 489–507.

Solomonidou, A., A. Coustenis, M. Hirtzig, S. Rodriguez, K. Stephan, R. M. C. Lopes, P. Drossart, C. Sotin, S. Le Mouélic, K. Lawrence, E. Bratsolis, R. Jaumann, R. H. Brown, (2016), Temporal variations of Titan's surface with Cassini/VIMS, Icarus, 270, 85–99.

Solomonidou, A., M. Hirtzig, A. Coustenis, E. Bratsolis, S. Le Mouélic, S. Rodriguez, K. Stephan, et al., (2014), Surface albedo spectral properties of geologically interesting areas on Titan, Journal of Geophysical Research, 119, 1729–1747.

Sotin, C. R. Jaunmann, B. J. Buratti, R. H. Brown, R. N. Clark, L. A. Soderblom, K. H. Baines, G. Bellucci, J.-P. Bribing, F. Capaccioni, P. Cerroni, A. Coradini, D. P. Cruikshank, P. Drossart, V. Formisano, Y. Langevin, D. L. Matson, T. B. McCord, R. M. Nelson, P. D. Nicholson, B. Sicardy, S. LeMouelic, S. Rodriguez, K. Stephan, C. K. Scholz, (2005), Release of Volatiles from a possible cryovolcano from near-infrared imaging of Titan, Nature, 435, 786–789.

Southwood, D. J. and M. G. Kivelson, (2007), Saturnian magnetospheric dynamics: Elucidation of a camshaft model, Journal of Geophysical Research, vol. 112, Issue A12, doi: 10.1029/2007JA012254.

Stephan, K., R. Jaumann, R. H. Brown, J. M. Soderblom, L. A. Soderblom, et al., (2010), Specular reflection on Titan: Liquids in Kraken Mare, Geophysical Research Letters, 37.

Stevens, M. H., J. Gustin, J. M. Ajello, J. S. Evans, R. R. Meier, A. J. Kochenash, A. W. Stephan, A. I. F. Stewart, L. W. Esposito, W. E. McClintock, G. Holsclaw, E. T. Bradley, B. R. Lewis,

A. N. Heays, (2011), The production of Titan's ultraviolet nitrogen airglow, Journal of Geophysical Research: Space Physics, 116, A15, 5304, doi: 10.1029/2010JA016284.

Stiles, B. W., R. L. Kirk, R. D. Lorenz, S. Hensley, E. Lee, S. J. Ostro, M. D. Allison, P. S. Callahan, Y. Gim, L. Iess, P. Perci del Marmo, G. Hamilton, W. T. K. Johnson, R. D. West, Cassini RADAR Team, (2010), Erratum: Determining titan's spin state from Cassini radar images, (2008, AJ, 135, 1669), Published 2009 December 10 © 2010, The American Astronomical Society, The Astronomical Journal, vol. 139, no. 1, doi: 10.1088/0004-6256/139/1/311.

Stiles, B. W., S. Hensley, Y. Gim, D. M. Bates, R. L. Kirk, A. Hayes, J. Radebaugh, R. Lorenz, K. L. Mitchell, P. S. Callahan, H. Zebker, W. T. K. Johnson, S. D. Wall, J. I. Lunine, C. A. Wood, M. Janssen, F. Pelletier, R. D. West, C. Veeramachenenia, Cassini RADAR Team, (2009), Determining Titan surface topography from Cassini SAR data, Icarus, 202, 584–598.

Stiles, B. W., R. L. Kirk, R. D. Lorenz, S. Hensley, E. Lee, S. J. Ostro, M. D. Allison, et al., (2008), Determining Titan's spin state from Cassini RADAR images, The Astronomical Journal, 135, no. 5, 1669.

Stofan, E. R., C. Elachi, J. I. Lunine, R. D. Lorenz, B. Stiles, et al., (2007), The lakes of Titan, Nature, 445, 61–64.

Strobel, D. F. and J. Cui, (2014), Titan's upper atmosphere/exosphere, escape processes and rates, Chapter 10, In Titan: Interior, Surface, Atmosphere and Space Environment, (eds.) I. Müeller-Wodarg, C. Griffith, E. Lellouch, T. Cravens, Cambridge University Press, pp. 355–375, doi: 10.1017/CBO9780511667398.013.

Strobel, D. F., S. K. Atreya, B. Bézard, F. Ferri, F. M. Flasar, M. Fulchignoni, E. Lellouch, I. Müller-Wodarg, (2009), Atmospheric structure and composition, Chapter 10, In Titan from Cassini-Huygens, (eds.) R. H. Brown, J. P. Lebreton, J. H. Waite, Springer, Dordrecht, pp. 235–257, doi: 10.1007/978-1-4020-9215-2_10.

Szego, K., Z. Nemeth, G. Erdos, L. Foldy, M. Thomsen, D. Delapp, (2011), The plasma environment of Titan: The magnetodisk of Saturn near the encounters as derived from ion densities measured by the Cassini/CAPS plasma spectrometer, Journal of Geophysical Research, vol. 116, Issue A10, doi: 10.1029/2011JA016629.

Tan, S. P., J. S. Kargel, D. E. Jennings, M. Mastrogiuseppe, H. Adidharma, G. M. Marion, (2015), Titan's liquids: Exotic behavior and its implications on global fluid circulation, Icarus, 250, 64–75.

Teanby, N. A. B. Bézard, S. Vinatier, (2017), The formation and evolution of Titan's winter polar vortex, Nature Communications, 8, 1586, doi: 10.1038/s41467-017-01839-z.

Teanby, N.A., R. de Kok, P. G. J. Irwin, S. Osprey, S. Vinatier, P. J. Gierasch, P. L. Read, et al., (2008), Titan's winter polar vortex structure revealed by chemical tracers, Journal of Geophysical Research, 113, E12003, doi: 10.1029/2008JE003218.

Teolis, B. D., H. B. Niemann, J. H. Waite Jr., et al., (2015), A revised sensitivity model for Cassini INMS: Results at Titan, Space Science Review, 190, 47–84, doi: 10.1007/s11214-014-0133-8.

Tobie, G., J. Lunine, J. Monteux, O. Mousis, and F. Nimmo, (2014), The origin and evolution of Titan, In Titan: Interior, Surface, Atmosphere, and Space Environment, (eds.) I. Müller-Wodarg, C. Griffith, E. Lellouch, T. Cravens, Cambridge University Press, pp. 29–62), doi: 10.1017/CBO9780511667398.004.

Tobie, G., M. Choukroun, O. Grasset, S. Le Mouelic, J. I. Lunine, et al., (2009), Evolution of Titan and implications for its hydrocarbon cycle, Philosophical Transactions of the Royal Society A: Mathematical, Physical and Engineering Sciences, 367, 617–631, doi: 10.1098/rsta.2008.0246.

Tobie, G., J. I. Lunine, C. Sotin, (2006), Episodic outgassing as the origin of atmospheric methane on Titan, Nature, 440, 61–64.

Tokano, T., (2010), Relevance of fast westerlies at equinox for the eastward elongation of Titan's dunes, Aeolian Research, vol. 2, Issues 2–3, pp.113–127, doi: 10.1016/j.aeolia.2010.04.003.

Tokano, T., (2008), Dune-forming winds on Titan and the influence of topography, Icarus, vol. 194, Issue 1, pp. 243–262, doi: 10.1016/j.icarus.2007.10.007.

Tokano, T., (2005), Meteorological assessment of the surface temperatures on Titan: Constraints on the surface type, Icarus, 173, 222–242.

Tomasko, M. G. and R. A. West, (2009), Aerosols in Titan's atmosphere, Chapter 12, In Titan from Cassini-Huygens, (eds.) R. H. Brown, J. P. Lebreton, J. H. Waite, Springer, Dordrecht, doi: 10.1007/978-1-4020-9215-2_12.

Tomasko, M. G., L. R. Doose, L. E. Dafoe, C. See, (2009), Limits on the size of aerosols from measurements of linear polarization in Titan's atmosphere, Icarus, 204, 271–283.

Tomasko, M. G., L. Doose, S. Engel, L. E. Dafoe, R. West, M. Lemmon, E. Karkoschka, C. See, (2008), A model of Titan's aerosols based on measurements made inside the atmosphere, Planetary and Space Science, 56, 669–707.

Tomasko, M., B. Archinal, T. Becker, B. Bézard, M. Bushroe, M. Combes, D. Cook, A. Coustenis, C. de Bergh, L. Dafoe, L. Doose, S. Douté, A. Eibl, S. Engel, F. Gliem, B. Grieger, K. Holso, E. Howington-Kraus, E. Karkoschka, H. Keller, R. Kirk, R. Kramm, M. Küppers, P. Lanagan, E. Lellouch, M. Lemmon, J. Lunine, E. McFarlane, J. Moores, M. Prout, B. Rizk, M. Rosiek, P. Rueffer, S. Schröder, B. Schmitt, C. See, P. Smith, L. Soderblom, N. Thomas, R. West, (2005), Rain, winds, and haze during the Huygens probe descent to Titan's surface, Nature, 438, 765–778.

Toon, O. B., C. P. McKay, R. Courtin, T. P. Ackerman, (1988), Methane Rain on Titan, Icarus, 75, 255–284.

Tsoar, H., (1983), Dynamic processes acting on a longitudinal (seif) dune, Sedimentology, vol. 30, Issue 4, pp. 567–578, doi: 10.1111/j.1365-3091.1983.tb00694.x.

Tucker, O. J. and R. E. Johnson, (2009), Thermally driven atmospheric escape: Monte Carlo simulations for Titan's atmosphere, Planetary and Space Science, vol. 57, Issues 14–15, pp. 1889–1894, doi: 10.1016/j.pss.2009.06.003.

Turtle, E. P., J. E. Perry, J. M. Barbara, A. D. DelGenio, S. Rodriguez, S. Le Mouélic, C. Sotin, et al., (2018), Titan's meteorology over the Cassini Mission: Evidence for extensive subsurface methane reservoirs, Geophysical Research Letters, vol. 45, Issue 11, pp. 5320–5328, doi: 10.1029/2018GL078170.

Turtle, E. P., J. E. Perry, A. G. Hayes, R. D. Lorenz, J. W. Barnes, et al., (2011), Rapid and extensive surface changes near Titan's equator: Evidence of April showers, Science, 331, 1414–1417, doi: 10.1126/science.1201063.

Turtle, E. P., J. E. Perry, A. S. McEwen, A. D. DelGenio, J. Barbara, et al., (2009) Cassini imaging of Titan's high-latitude lakes, clouds, and south-polar surface changes, Geophysical Research Letters, 36, no. 2.

Vervack Jr., R. J., B. R. Sandel, D. F. Strobel, (2004), New perspectives on Titan's upper atmosphere from a reanalysis of the Voyager 1 UVS solar occultations, Icarus, 170, 91–112.

Vinatier, S., B. Schmitt, B. Bézard, et al., (2018), Study of Titan's fall southern stratospheric polar cloud composition with Cassini/CIRS: Detection of benzene ice, Icarus, vol. 310, pp. 89-104, doi: 10.1016/j.icarus.2017.12.040.

Vinatier, S., B. Bézard, S. Lebonnois, et al., (2015), Seasonal variations in Titan's middle atmosphere during the northern spring derived from Cassini/CIRS observations, Icarus, vol. 250, pp. 95–115, doi: 10.1016/j.icarus.2014.11.019.

Vinatier, S., P. Rannou, C. A. Anderson, et al., (2012), Optical constants of Titan's stratospheric aerosols in the 70–1500 cm^{-1} spectral range constrained by Cassini/CIRS observations, Icarus, vol. 219, Issue 1, pp. 5–12, doi: 10.1016/j.icarus.2012.02.009.

Vinatier, S., B. Bézard, C. A. Nixon, A. Mamoutkine, R. C. Carlson, et al., (2010), Analysis of Cassini/CIRS limb spectra of Titan acquired during the nominal mission: I. Hydrocarbons, nitriles and CO_2 vertical mixing ratio profiles, Icarus, vol. 205, Issue 2, pp. 559–570, doi: 10.1016/j.icarus.2009.08.013.

Vinatier, S., B. Bézard, C. A. Nixon, (2007), The Titan $^{14}N/^{15}N$ and $^{12}C/^{13}C$ isotopic ratios in HCN from Cassini/CIRS, Icarus, vol. 191, Issue 2, pp. 712–721, doi: 10.1016/j.icarus.2007.06.001.

Vixie, G., J. W. Barnes, B. Jackson, S. Rodriguez, S. Le Mouélic, et al., (2015), Possible temperate lakes on Titan, Icarus, vol. 257, pp. 313–323, doi: 10.1016/j.icarus.2015.05.009.

Vuitton, V., R. V. Yelle, S. J. Klippenstein, S. M. Hörst, P. Lavvas, (2019), Simulating the density of organic species in the atmosphere of Titan with a coupled ion-neutral photochemical model, Icarus, 324, 120–197, doi: 10.1016/j.icarus.2018.06.013.

Waite Jr., J. H., D. T. Young, T. E. Cravens, A. J. Coates, F. J. Crary, B. Magee, J. Westlake, (2007), The process of tholin formation in Titan's upper atmosphere, Science, 316, 870, doi: 10.1126/science.1139727.

Wall, S., A. Hayes, C. Bristow, R. Lorenz, E. Stofan, et al., (2010), Active shoreline of Ontario Lacus, Titan: A morphological study of the lake and its surroundings, Geophysical Research Letters, vol. 37, Issue 5, doi: 10.1029/2009GL041821.

Wall, S. D., R. M. Lopes, E. R. Stofan, C. A. Wood, J. L. Radebaugh, et al., (2009), Cassini RADAR images at Hotei Arcus and western Xanadu, Titan: Evidence for geologically recent cryovolcanic activity, Geophysical Research Letters, vol. 36, Issue 4, doi: 10.1029/2008GL036415.

Ward, W. R. and D. P. Hamilton, (2004), Tilting Saturn: I. Analytic model. Astronomical Journal vol. 128, no. 5, pp. 2501–2509.

Wei, H. Y., C. T. Russell, M. K. Dougherty, F. M. Neubauer, Y. J. Ma, (2010), Upper limits on Titan's magnetic moment and implications for its interior, J. Geophys. Res., 115, E10007, doi: 10.1029/2009JE003538.

Wei, H. Y., Russell, C. T., Dougherty, M. K., Neubauer, F. M., Ma, Y. J., (2010), Upper limits on Titan's magnetic moment and implications for its interior, Journal of Geophysical Research, vol. 115, Issue E10, doi: 10.1029/2009JE003538.

West, R., B. Seignovert, P. Rannou, P. Dumont, E. P. Turtle, J. Perry, M. Roy, A. Ovanessian, (2018), The seasonal cycle of Titan's detached haze, Nature Astronomy, 2, 495–500.

West, R. A., P. Lavvas, C. Anderson, H. Imanaka, (2014), Titan's Haze, Chapter 8, In Titan: Surface, Atmosphere and Magnetosphere, (eds.) I. Müller-Wodarg, C. Griffith, E. Lellouch, T. Cravens, Cambridge University Press, pp. 285–321.

West, R. A., J. M. Ajello, M. H. Stevens, D. F. Strobel, G. R. Gladstone, J. S. Evans, E. T. Bradley, (2012), Titan Airglow During Eclipse, Geophys. Res. Lett., 39, L18204, doi: 10.1029/2012GL053230.

Wilson, E. H. and S. K. Atreya, (2009), Titan's carbon budget and the case of the missing ethane, The Journal of Physical Chemistry A, 113, 42, 11221–11226, doi: 10.1021/jp905535a.

Wood, C. A., (2018), Titan's great crustal thickening event and recent geologic history, Lunar and Planetary Science Conference, vol. 49, 1343.

Wood, C. A., R. Lorenz, R. Kirk, R. Lopes, K. Mitchell, E. Stofan, (2010), Impact craters on Titan, Icarus, 206, 334–344.

Wye, L. C., (2011), Radar scattering from Titan and Saturn's icy satellites using the Cassini spacecraft, Ph.D. Thesis, Stanford University.

Wye, L. C., H. A. Zebker, R. D. Lorenz, (2009), Smoothness of Titan's Ontario Lacus: Constraints from Cassini RADAR specular reflection data, Geophysical Research Letters, vol. 36, Issue 16, doi: 10.1029/2009GL039588.

Wye, L. C., H. A. Zebker, S. J. Ostro, R. D. West, Y. Gim, R. D. Lorenz, Cassini RADAR Team, (2007), Electrical properties of Titan's surface from Cassini RADAR scatterometer measurements, Icarus, vol. 188, Issue 2, pp. 367–385, doi: 10.1016/j.icarus.2006.12.008.

Yelle, R. V., J. Cui, I. C. F. Müller-Wodarg, (2008), Methane escape from Titan's atmosphere, Journal of Geophysical Research: Planets, vol. 113, Issue E10, doi: 10.1029/2007JE003031.

Yelle, R. V., D. F. Strobel, E. Lellouch, D. Gautier, (1997), Engineering models for Titan's atmosphere, Huygens: Science, Payload and Mission, vol. 1177, pp. 243–256.

Yu, X., S. M. Hörst, C. He, N. T. Bridges, D. M. Burr, J. A. Sebree, J. K. Smith, (2017), The effect of adsorbed liquid and material density on saltation threshold: Insight from laboratory and wind tunnel experiments, Icarus, 297, pp.97–109.

Yung, Y. L., M. Allen, J. P. Pinto, (1984) Photochemistry of the atmosphere of Titan - Comparison between model and observations, The Astrophysical Journal Supplement Series, 55, 465–506, doi: 10.1086/190963.

Zahnle, K., P. Schenk, H. Levison, L. Dones, (2003), Cratering rates in the outer Solar System, Icarus, 163, 263–289.

Zebker, H., A. Hayes, M. Janssen, A. Le Gall, R. Lorenz, L. Wye, (2014), Surface of Ligeia Mare, Titan, from Cassini altimeter and radiometer analysis, Geophysical Research Letters ,41, 308–313.

Zebker, H. A., B. Stiles, S. Hensley, R. Lorenz, R. L. Kirk, J. I. Lunine, (2009), Size and shape of Saturn’s moon Titan, Science, 324, 921–923.

Zebker, H., L. Wye, M. Janssen, Cassini Radar Team, (2008),Titan's surface from reconciled Cassini microwave reflectivity and emissivity observations, Icarus, vol. 194, Issue 2, pp. 704–710.

3.2
Instrument Science Results

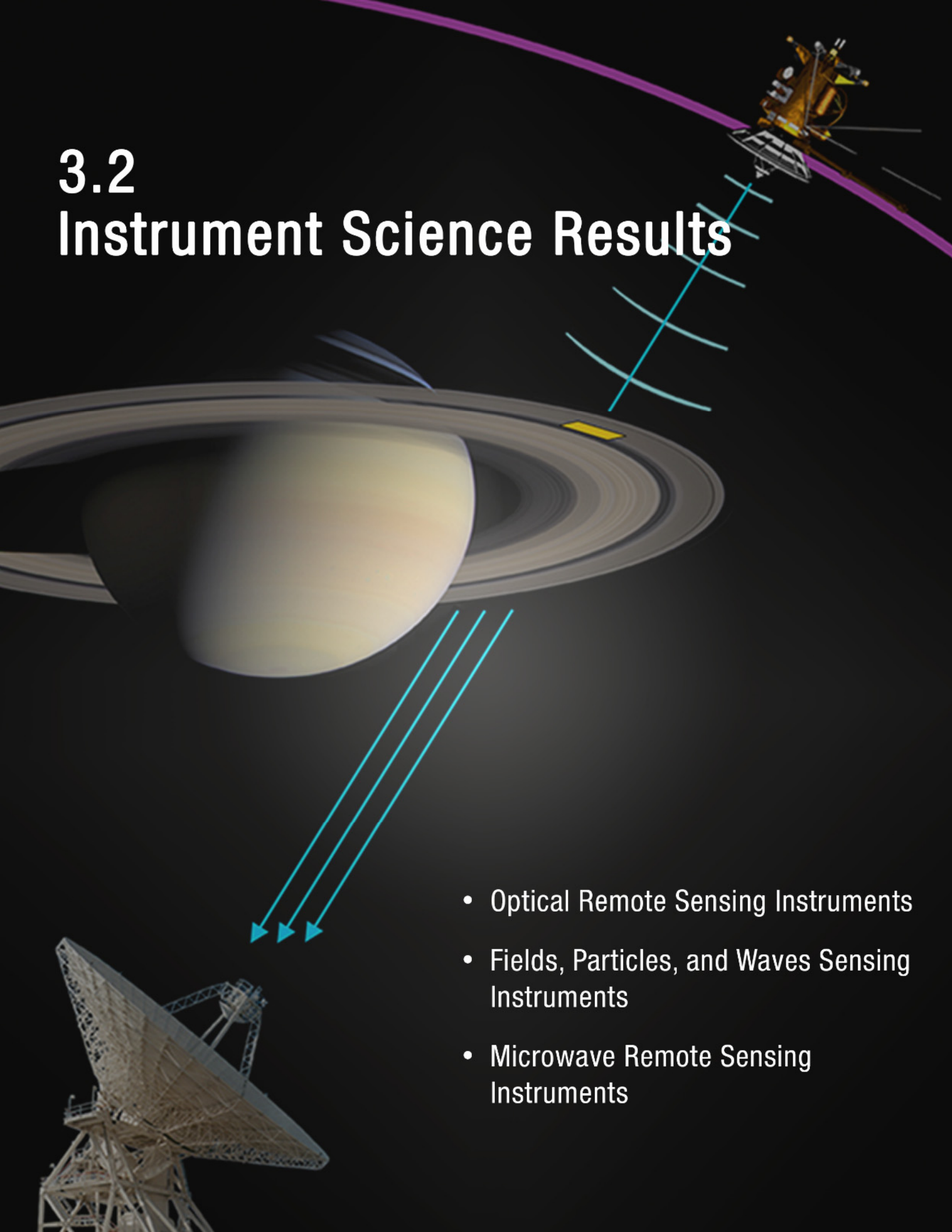

- Optical Remote Sensing Instruments
- Fields, Particles, and Waves Sensing Instruments
- Microwave Remote Sensing Instruments

Optical Remote Sensing Instruments

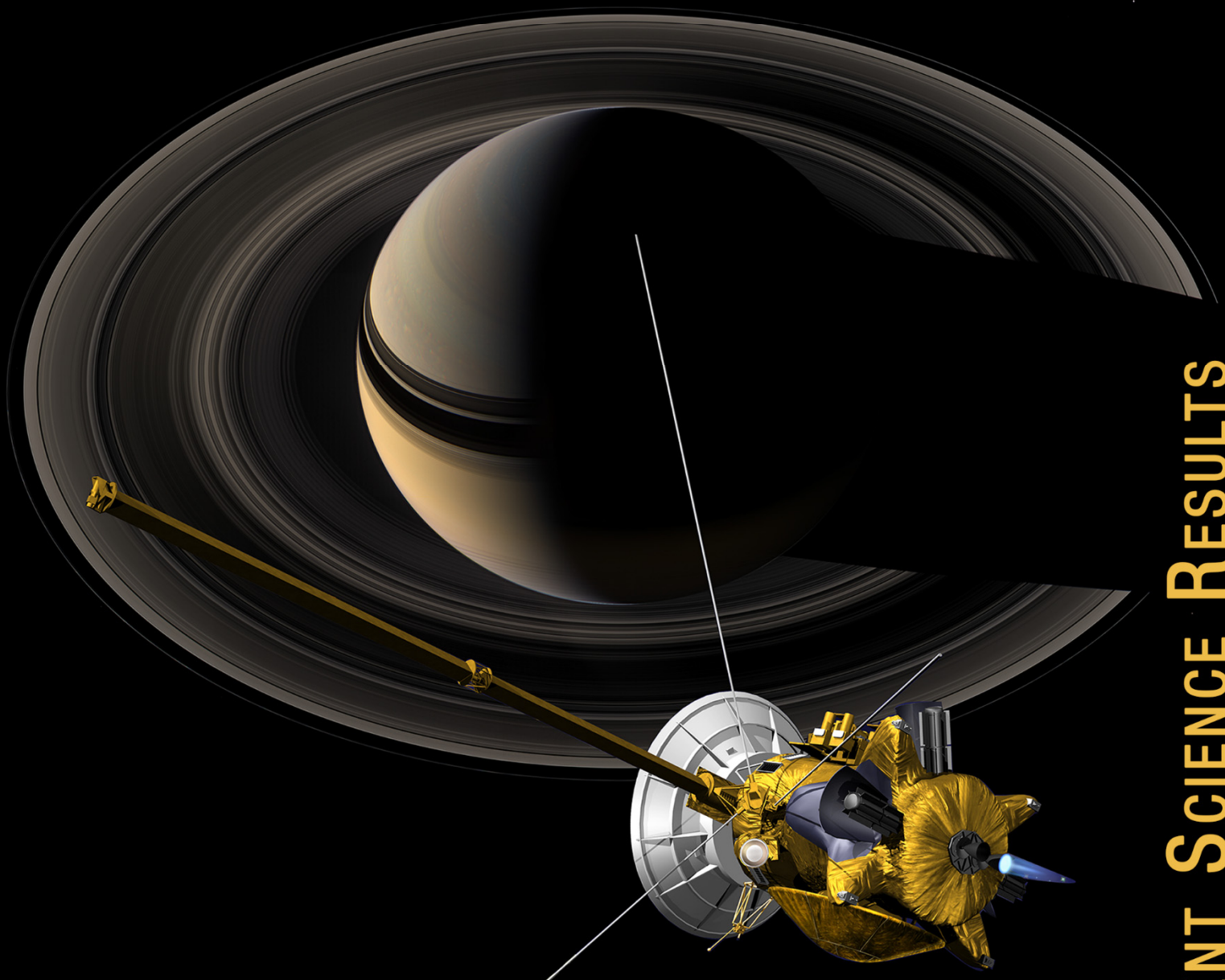

– Composite Infrared Spectrometer (CIRS)

– Imaging Science Subsystem (ISS)

– Ultraviolet Imaging Spectrograph (UVIS)

– Visual and Infrared Mapping Spectrometer (VIMS)

INSTRUMENT SCIENCE RESULTS

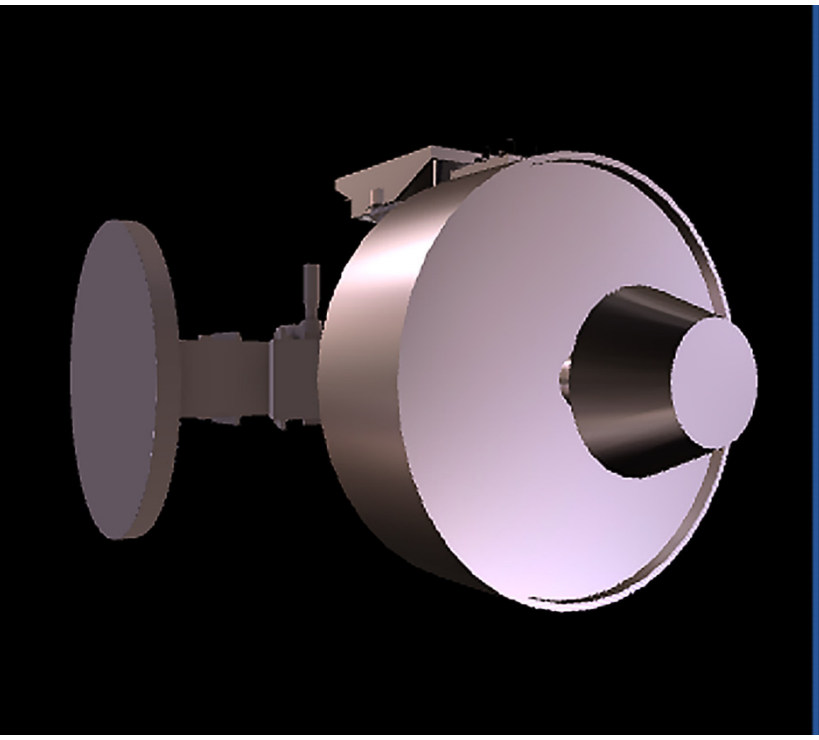

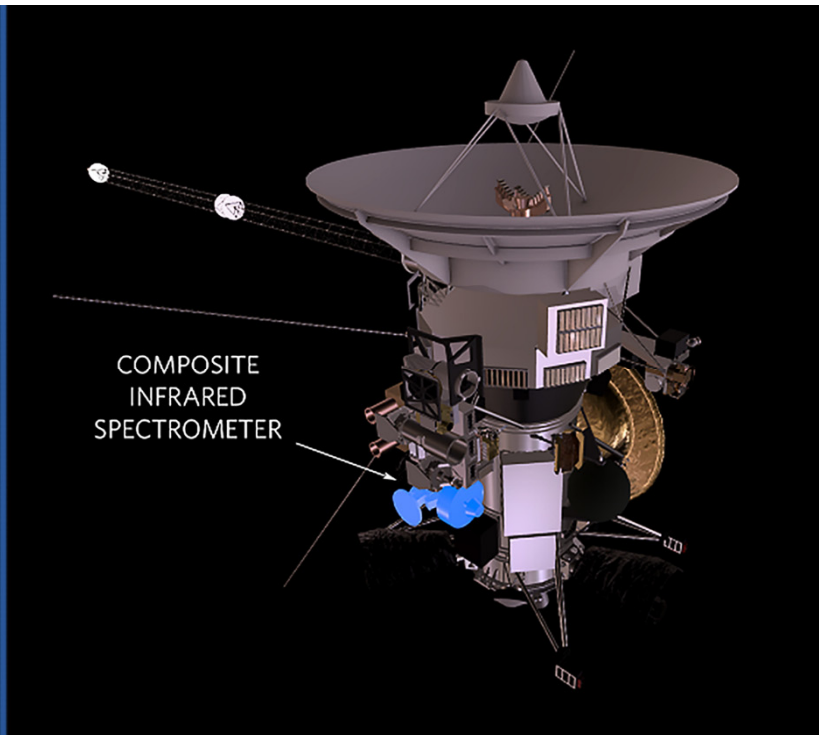

Composite Infrared Spectrometer

The Composite Infrared Spectrometer (CIRS) was an infrared Fourier Transform Spectrometer that measured infrared radiation from 7-1,000 μm that was emitted by Saturn, its rings and its moons. The **science objectives** of CIRS were to measure infrared emissions from atmospheres, rings and surfaces in the Saturn system to determine their composition, temperatures and thermal properties; to map the atmospheres of Saturn and Titan in three dimensions to determine temperature and pressure profiles with altitude, gas composition, and the distribution of aerosols and clouds. Molecular composition is determined in the infrared by the emitted or absorbed energy at specific wavelengths. The infrared spectrum identifies the gases or solids present and their relative amounts.

CIRS consisted of two interferometers that operated in the far-infrared and mid-infrared. They shared a common telescope and scan mechanism. CIRS included three sets of infrared detectors (Focal planes 1, 3, and 4) and a passive radiative cooler plate.

CONTENTS

Figures

Tables

EXECUTIVE SUMMARY

Key Science Results

Saturn

- Characterization of the great northern storm in the troposphere and stratosphere, which erupted unexpectedly in northern spring. For the first time, a detailed picture was obtained of the major disturbance in the stratosphere (warm, anticyclonic vortices, enhancement of trace hydrocarbons) that persisted for nearly three years.
- Determination for the first time of the vertical structure of Saturn's equatorial oscillation; measurement of the descending pattern of temperatures and zonal winds with time and its disruption by the great northern storm.
- Improvement in the abundance determination of methane, and as a result, of carbon.
- Characterization of the temperature and zonal wind structure of polar vortices at high spatial resolution.
- Determination of the vertical and latitude distribution and seasonal variation of stratospheric hydrocarbons.

Rings

- Slowly rotating ring particles discovered in Saturn’s main rings. These slowly rotating particles provided the first direct evidence for anisotropic thermal emission of rings versus a broad range of phase and emission angles at geometries not visible from Earth.
- First complete far-infrared (IR) roll-off measured in main ring temperature. Cassini CIRS obtained the first continuous submillimeter spectrum of Saturn’s main rings over a broad range of wavenumbers, from 25 microns to 0.5 millimeters. Until these observations, the location and shape of the spectral roll-off was not well determined. The roll-off in emissivity occurs around 200 microns and contains key information on material properties of the particles.
- A-ring particles with dense cores inferred from incomplete cooling down at solar equinox. At the solar equinox in August 2009, the CIRS onboard Cassini showed the lowest Saturn's ring temperatures ever observed. The observed equinox temperatures of Saturn's A-ring are much higher than model predictions as long as only the flux from Saturn is taken into account. This means that A-ring particles did not completely cool down at the equinox. The detailed seasonal model showed that A-ring particles have dense cores beneath the fluffy regolith mantles.

- Vertical thermal gradient detected in B-ring. A vertical thermal gradient was detected in the B-ring, which yields constraints on the diffusivity of this porous medium, and by extension on its thickness (which is unique for the thick B-ring).
- First cooling profile of main rings from near solstice through equinox CIRS observed the main rings of Saturn cool down from the orbit insertion of the spacecraft in 2004 until Saturn's equinox in 2009, and through northern summer solstice in 2017. The solar elevation varied from 26 degrees to 0 degrees with respect to the rings. The data showed that the A-ring, B-ring, and C-ring temperatures varied as much as 29–38, 22–34 and 18–23 K, respectively. Interestingly the unlit sides of the rings showed important temperature variations as well.
- First far-IR radial profile in optical depth CIRS obtained the first radial profile in optical depth in far-IR, filling in gap between near-IR and radio observations. CIRS observed a ring occultation of the far-IR source, Eta Carinae, to derive the ring optical depth.

Titan

- Discovery of a tilted stratospheric rotation [Achterberg et al. 2008].
- Observation of seasonal change in the 220 cm^{-1} absorber [Jennings et al. 2012a, 2012b, 2015].
- Observation of a late onset to the reversal of the seasonal gas distribution [Teanby et al. 2012b].
- Measurement of the vertical profile of water [Cottini et al. 2012a].
- Detection of the important $^{13}CH_3D$ [Bézard et al. 2007] and C_2HD isotopes [Coustenis et al. 2008].
- Detection of propene in the stratosphere [Nixon et al. 2013a].
- Characterization of hydrogen cyanide (HCN) ice above the south pole [de Kok et al. 2014].
- Hypothesis of grain surface chemistry to explain far-infrared absorption [Anderson et al.2016].
- Measurement of aerosol spectral opacity [Vinatier et al. 2012].
- Discovery of benzene ice [Vinatier et al. 2018].

Icy satellites

- Endogenic thermal emission from the Enceladus tiger stripes at temperatures up to 190 K, with large spatial variations on scales from 10 s of kilometers to 10 s of meters.

- Endogenic heat flow from Enceladus' south pole is larger than can be explained by simple steady-state tidal heating.
- Large spatial variations in thermal inertia on Mimas, Tethys, and Dione due to electron bombardment.
- High daytime temperature of Iapetus dark terrain, implying that thermal segregation is a major contributor to the extreme albedo dichotomy on Iapetus.
- Determining low thermal inertia throughout the Saturnian system.
- Ruling out significant activity on Dione and Tethys.
- Detecting surface temperatures of Ring Satellites.

Jupiter

- First characterization of the detailed vertical structure of Jupiter's equatorial oscillation and the discovery of an intense jet in the stratosphere centered at 4 mbar.
- Detection of the puzzling distribution of HCN and CO_2 in Jupiter's stratosphere, originally thought to be products of the SL9 impact in 1994.
- Mapping of the northern infrared auroral hot spot, and the determination of the lower limit to its penetration (4 mbar) and the composition of acetylene and ethane within the spot.
- First detection of diacetylene and the methyl radical in the northern and southern auroral hotspots.
- Discovery of anticorrelated abundance trends with latitude for acetylene and ethane.

CIRS Summary

The CIRS is an infrared Fourier Transform Spectrometer (FTS) on the Cassini orbiter that measures thermal radiation over more than two decades in wavenumber (ν) from 10 to 1400 cm^{-1} (1 mm to 7 μm). CIRS is described in detail in Kunde et al. [1996]; Flasar et al. [2004]; and Jennings et al. [2017]. Further information on CIRS and its operation throughout the mission is given in the Cassini Final Mission Report Volume 3 Instrument Performance Assessment, and the Cassini Final Mission Report Volume 5 Mission Operations System Performance Assessment.

The CIRS instrument consists of two interferometers, sharing a common telescope and scan mechanism. They operate in the far-infrared (10–600 cm^{-1}) and mid-infrared (600–1400 cm^{-1}) with a commandable, apodized spectral resolution as high as 0.5 cm^{-1}. The far-IR interferometer is a polarization interferometer, with a single focal plane consisting of two thermopile detectors with a 3.9 microradians (mrad) circular field of view (FOV), labeled FP1. The mid-IR interferometer is a

conventional Michelson interferometer with two linear focal plane arrays (FP3, FP4), each containing 10 HgCdTe detectors, with 0.273 mrad FOV per pixel. The center of the FP3 and FP4 arrays is aligned with the boresights of the other optical remote sensing instruments—Imaging Science Subsystem (ISS), wide-angle camera (WAC) and narrow-angle camera (NAC), Visual and Infrared Mapping Spectrometer (VIMS), and Ultraviolet Imaging Spectrograph (UVIS). The FP1 boresight is offset by 4 mrad [Flasar et al. 2004a; Jennings et al. 2017].

CIRS instrument operation allows data to be acquired at spectral resolutions between 0.5 cm^{-1} and 15 cm^{-1} by varying the scan length of the moving mirror. The low-resolution data have the highest signal to noise ratio (SNR) and the shortest scan length. The calibration for FP1 utilizes deep space spectra while FP3 and FP4 have, in addition, a shuttered target source at 170 K.

KEY OBJECTIVES FOR CIRS

Key Science Objectives for Saturn

1. **Formation, evolution, and internal structure:** Helium, carbon, nitrogen, and sulfur abundances in Saturn's atmosphere.

2. **Atmospheric gas composition:** Disequilibrium tropospheric compounds (PH_3, CO…), ortho-para H_2 conversion, disequilibrium stratospheric compounds (hydrocarbons), external sources—oxygen compounds.

3. **Clouds and aerosols.**

4. **Atmospheric structure and circulation:** Temperatures, zonal winds, meridional circulations, waves, eddies, compact vortices.

5. **Temporal behavior:** Seasonal, internal dynamical (northern Saturn storm, equatorial oscillation, neither fully anticipated).

Key Science Objectives for the Rings

CIRS has provided major advances over previous spacecraft infrared observations of Saturn's rings in three respects: 1) extension of the spectral range to submillimeter wavelengths; 2) higher spatial resolution on the rings as result of closer proximity during the Cassini tour, as well as of a linear detector array with much finer spatial resolution in the mid-infrared; and 3) temporal extent of the mission, which provided greatly improved sampling in illumination and viewing geometries. With its enhanced capabilities, CIRS addressed many of the rings science objectives of the Cassini mission, particularly those pertaining to radial thermal structure, ring optical depth in the mid-IR, ring particle thermal properties and rotation states, ring-scale

CIRS has provided major advances over previous spacecraft infrared observations of Saturn's rings.

properties including vertical structure, and thermal roll-off in the submillimeter. The key CIRS ring science objectives are listed below and each one is discussed in the section entitled Science Results.

1. **Ring Thermal Structure:** Determine Saturn's ring thermal structure and how the ring temperatures vary with ring optical depth, solar elevation, phase angle, azimuth angle and distance to the planet. What is the source of the temperature variations? Determine the azimuthal asymmetries in the rings, apart from the diurnal cooling/heating cycle. What is their origin?

2. **Ring optical depth at mid-IR wavelengths:** Determine the variation of ring optical depths at mid-IR wavelengths and compare to ultraviolet (UV) and near-IR optical depths.

3. **Particle-scale Properties:** Determine key particle properties such as Bond albedo, thermal inertia and particle spin. On what factors do they depend? Determine the distribution of particle spins of the ring particles. What does this distribution tell us about local dynamics? Compare the diurnal and seasonal thermal inertia and any differences between them.

4. **Ring-scale Properties:** Determine the volume filling factors for the rings. Search for an opposition surge in the thermal infrared. Is it driven by mutual shadowing alone? Determine vertical temperature gradient between lit and unlit sides of the rings. What does this tell us about the ring vertical structure and dynamics? Determine the ring thermal inertia and compare it to the particle thermal inertia. Does it change with seasons?

5. **Regolith Properties deduced from CIRS Emissivity Roll-off:** Determine the wavelength of the roll-off in ring emissivity. What do we learn from this roll-off about particle structure and composition?

Key Science Objectives for Titan

1. **Formation and evolution:** Volatiles—methane.

2. **Atmospheric composition:** Organics (hydrocarbons and nitriles), oxygen compounds, new species.

3. **Aerosols and condensates.**

4. **Atmospheric structure and circulation:** Temperatures, zonal winds, meridional transports, eddies and waves.

5. **Seasonal behavior:** Evolution of polar vortices—gas composition, condensates, temperatures and winds.

Key Science Objectives for the Icy Satellites

1. **Enceladus' Activity:** Determine Enceladus' heat flow, to help constrain its activity mechanism. Determine whether Enceladus' activity varies with seasonal change.

2. **Activity on other Satellites:** Search for activity on Dione and Tethys, and search for a ring and debris disk around Rhea.

3. **Comparative study of Saturn's icy satellites:** Compare the surface properties of Saturn's mid-sized icy satellites. Determine the uniqueness of Mimas' thermally anomalous region. Observe Saturn's small satellites as opportunities arise (including but not limited to Epimethus, Janus, Methone and Promethus).

4. **Better understand unusual surfaces:** Constrain Hyperion's unusual surface's thermophysical properties, constrain Iapetus' albedo dichotomy.

CIRS Science Assessment

Saturn

Table CIRS-1 contains an assessment of CIRS Saturn science based on the objectives in the original Announcement of Opportunity (AO) and the Cassini Traceability Matrix (TM) developed for the Equinox and Solstice missions. Each CIRS Saturn science objective is paired with an AO and TM science objective. The key AO and TM objectives addressed by CIRS are:

- **Saturn Temperature, Clouds, Composition (S_AO1):** Determine temperature field, cloud properties, and composition of the atmosphere of Saturn.
- **Saturn Winds and Weather (S_AO2):** Measure the global wind field, including wave and eddy components; observe synoptic cloud features and processes.
- **Saturn Interior Structure and Rotation (S_AO3):** Infer the internal structure and rotation of the deep atmosphere.
- **Saturn Formation and Evolution (S_AO5):** Provide observational constraints (gas composition, isotope ratios, heat flux...) on scenarios for the formation and the evolution of Saturn.
- **Seasonal Variations (SC1a):** Observe seasonal variations in temperature, clouds, and composition in three spatial dimensions.
- **Saturn's Winds (SC1b):** Observe seasonal changes in the winds at all accessible altitudes coupled with simultaneous observations of clouds, temperatures, composition, and lightning.

- **Saturn's Rotation Rate (SN1a):** Determine Saturn's rotation rate and internal structure despite the planet's unexpected high degree of axisymmetry.
- **2010–2011 Great Storm (SN1b):** Observe the aftermath of the 2010–2011 storm. Study the life cycles of Saturn's newly discovered atmospheric waves, south polar hurricane, and rediscovered north polar hexagon.
- **Saturn Trace Gases (SN1c):** Measure the spatial and temporal variability of trace gases and isotopes.

Table CIRS-1. CIRS Saturn Science Assessment: AO and TM Objectives are paired with CIRS Science objectives.

Fully/Mostly Accomplished: Partially Accomplished: Not Accomplished:

CIRS Saturn Science Objectives	AO and TM Science Objectives	CIRS Saturn Science Assessment	Comments if yellow (partially fulfilled)
Formation, evolution, internal structure			
Helium	S_AO1, S_AO5		Analysis in progress.
Carbon	S_AO1, S_AO5		
Nitrogen	S_AO1, S_AO5		
Carbon monoxide	S_AO1, S_AO5		
Internal rotation	S_AO3, SN1a		
Atmospheric gas composition			
Disequilibrium tropospheric compounds: PH_3, CO, halides	S_AO1,SN1c		
Ortho-para H_2	S_AO1,SC1b,SN1c		
Stratospheric hydrocarbons	S_AO1,SN1c		
External sources—oxygen compounds	S_AO1		Analysis in progress.
Atmospheric structure and circulation			
Temperatures & zonal winds	S_AO1, S_AO2, SC1b		
Meridional circulations	S_AO1,SC1b,SN1c		
Waves & eddies	S_AO2,SN1c		Larger scale waves done: N. hexagon, equatorial waves.
Compact vortices	S_AO2		Polar vortices.
Temporal behavior			
Seasonal	SC1a		
Northern storm	SN1b		Persisted to 2013 in stratosphere.
Equatorial oscillation	SC1a,SN1b		

Rings

Table CIRS-2 contains an assessment of CIRS ring science based on the objectives in the original AO and the Cassini TM developed for the Equinox and Solstice missions. Each CIRS ring science objective is paired with an AO and TM science objective. The key AO and TM objectives addressed by CIRS are:

- **Ring Structure and Dynamics (R_AO1):** Study configuration of the rings and dynamical processes (gravitational, viscous, erosional, and electromagnetic) responsible for ring structure.

Table CIRS-2. CIRS Ring Science Assessment: AO and TM Objectives are paired with CIRS Science objectives.

Fully/Mostly Accomplished: **Partially Accomplished:** **Not Accomplished:**

CIRS Ring Science Objectives	AO and TM Science Objectives	CIRS Ring Science Assessment	Comments if yellow (partially fulfilled)
Ring Thermal Structure			
Radius and Ring Optical Depth	R_AO1, RC1a		
Solar elevation	R_AO1, RC1a		
Phase angle	R_AO1, RC1a		
Ring Equinox temperatures	R_AO1, RC1a		
Azimuthal dependence	R_AO1, RC1a		
Ring Optical Depth at mid-IR Wavelengths	R_AO1, RC1a		
Particle-scale Properties			
Bolometric Bond Albedo	R_AO1, RC1a		
Particle Spin	R_AO1, RC1a		
Diurnal Thermal Inertia	R_AO1, RC1a		
Seasonal Thermal Inertia and Particle Size	R_AO1, RC1a		
Average Thermal Emissivity	R_AO1, RC1a		
Ring-scale Properties			
Volume Filling Factors of A-ring and B-ring	R_AO1, RC1a		
Opposition Surge	R_AO1, RC1a		
Energy budget and heat transfer in B-ring	R_AO1, RC1a		
Thermal Properties, Thickness and Surface Mass Density of B-ring	R_AO1, RC1a		
Self-gravity wakes in the A-ring	R_AO1, RC1a		
Regolith Properties Deduced from CIRS Emissivity Roll-off			
Thermal Emissivity Roll-off at Submillimeter wavelengths	R_AO1, RC1a		
F-ring Clumps	RC2a		

- **Changing Rings (RC1a):** Determine the production mechanisms of spokes, and the microscale properties of ring structure, by observing at the seasonally maximum opening angle of the rings near Solstice.
- **Ring Temporal Variability (RC1b):** Understand the time-variability of ring phenomena on decadal timescales (Encke gap, D-ring, ring edges, etc.) by substantially increasing the time baseline of observations.

Titan

Table CIRS-3 contains an assessment of CIRS Titan science based on the objectives in the original AO and the Cassini TM developed for the Equinox and Solstice missions. Each CIRS Titan science objective is paired with an AO and TM science objective. The key AO and TM objectives addressed by CIRS are:

Titan AO objectives

- **Titan Atmospheric Formation and Evolution (T_AO1):** Determine abundances of atmospheric constituents (including any noble gases), establish isotope ratios for abundant elements, constrain scenarios of formation and evolution of Titan and its atmosphere.
- **Titan Atmospheric Composition and Distribution (T_AO2):** Observe vertical and horizontal distributions of trace gases, search for more complex organic molecules, investigate energy sources for atmospheric chemistry, model the photochemistry of the stratosphere, study formation and composition of aerosols.
- **Titan Meteorology (T_AO3):** Measure winds and global temperatures; investigate cloud physics, general circulation, and seasonal effects in Titan's atmosphere; search for lightning discharges.
- **Titan Surface Characteristics and Internal Structure (T_AO4):** Determine the physical state, topography, and composition of the surface; infer the internal structure of the satellite.

Titan Cassini Solstice Mission (CSM) traceability matrix objectives

- **Titan’s Great Seas (TC1a):** Determine seasonal changes in the methane-hydrocarbon hydrological cycle: of lakes, clouds, aerosols, and their seasonal transport.
- **Titan’s Global Seasons (TC1b):** Determine seasonal changes in the high-latitude atmosphere, specifically the temperature structure and formation and breakup of the winter polar vortex.

- **Titan's Surface (TN1a):** Determine the types, composition, distribution, and ages, of surface units and materials, most notably lakes (i.e., filled versus dry and depth; liquid versus solid and composition; polar versus other latitudes and lake basin origin).
- **Titan Atmospheric Composition (TN1c):** Measure aerosol and heavy molecule layers and properties.
- **Titan Atmospheric Structure (TN2a):** Resolve current inconsistencies in atmospheric density measurements (critical to a future Flagship mission).
- **Titan Meteorology (TN2c):** Determine the surface temperature distribution, cloud distribution, and tropospheric winds.

Table CIRS-3. CIRS Titan Science Assessment: AO and TM Objectives are paired with CIRS Science objectives.

Fully/Mostly Accomplished: **Partially Accomplished:** **Not Accomplished:**

CIRS Titan Science Objectives	AO and TM Science Objectives	CIRS Titan Science Assessment	Comments if yellow (partially fulfilled)
Surface Temperature	T_AO4, TN2c		
Latitudinal variation	T_AO4, TN2c		
Temporal changes	T_AO4, TN2c		
Variation with topography and terrain	T_AO4, TN1a		Insufficient data and S/N, footprint too large.
Atmospheric Thermal and Dynamical State	T_AO3, TC1b		
Global temperature mapping	T_AO3, TC1b		
Winds and jets	T_AO3, TC1b		
Rotation axis	T_AO3, TC1b		
Global Energy Balance	T_AO3, TC1b		
Seasonal changes	T_AO3, TC1b		
Gas Composition and Chemistry	T_AO2, TN1c		
Global gas distribution near equinox	T_AO2, TN1c		
Seasonal changes	T_AO2, TN1c		
Search for new gas species	T_AO2, TC1a		
Isotopic ratios	T_AO1, N/A		Still under study to reduce errors, improve agreement between measurements.
Hazes and Condensates	T_AO2/3, TN1c		Hazes and condensates mapped, but ongoing work to elucidate composition.
Haze characteristics	T_AO2, TN1c		
Condensates: location and identification	T_AO3, TN1c		

The majority of the science goals for Titan laid down at the start of the mission (Key Objectives for CIRS) have been achieved successfully, and much progress has also been made on the revised goals from the Cassini Solstice Mission. Table CIRS-3 shows a final assessment for the surface temperatures, only the issue of correlation with topography remains uncertain, and is unlikely to be gleaned from the CIRS dataset given the large FP1 detector footprint. All atmospheric temperature science goals have been achieved, although a discrepancy between CIRS and Huygens stratopause levels may require further investigation, as described later. Gas abundance measurements have also been largely met, although isotopic ratios, which require the highest accuracy, have proved susceptible to systematic errors. More analysis is needed of the dataset in this area to resolve remaining differences between published values. Finally, much new information has been returned about hazes and condensates, although work is still ongoing to determine composition, for example with regard to the notorious 220 cm^{-1} emission feature.

Icy Satellites

The key TM questions of Icy Satellite science that CIRS has helped address are:

Level 1

- **Changes on Enceladus (IC1a):** Determine whether Enceladus exhibits any seasonal changes. Other temporal changes (e.g., mean anomaly) are also considered.
- **Enceladus' interior (IN1a):** Determine the surface temperature in active regions and constrain Enceladus' heat flow, to better constrain models of its activity.
- **Compare Saturn's mid-sized satellites (IN1b):** Compare the surface characteristics of Saturn's mid-sized satellites, including the thermally anomalous Pac-Man regions.
- **Activity on Dione (IN1c):** Determine whether Dione is currently active, or has been so on recent geological timescales.

Level 2

- **Rhea's Ring (IN2a):** Determine if there is a ring (or debris disk) around Rhea, and if so, characterize the spatial and particle size distribution.
- **Tethys and the E-ring (IN2b):** Determine whether Tethys is geologically active, and thus could be contributing to the E-ring.
- **Characterize the surfaces of Saturn's small satellites (IN2d):** Derive the surface thermophysical properties of Saturn's small satellites, including (but not limited to) Epimethys, Janus, Methone, and Promethus.

Table CIRS-4. CIRS Ice Satellite Science Assessment: AO and TM Objectives are paired with CIRS Science objectives.

Fully/Mostly Accomplished: **Partially Accomplished:** **Not Accomplished:**

CIRS Icy Satellite Science Objectives	AO and TM Science Objectives	CIRS Ring Science Assessment	Comments only if yellow or red
Enceladus			
Enceladus' Surface Temperatures	IC1a, IN1a		
Constrain Enceladus' heat flow	IC1a, IN1a		
Activity On Other Satellites			
Dione	IN1c		
Tethys	IN2b		No evidence for activity was found when looking at temperature maps of Tethys using CIRS data for in Howett et al. [2012].
Ring around Rhea	IN2a		No thermal inertia signature connected with ring infall were observed on Rhea in Howett et al. [2014], but any signature (including the 'blue dots') are likely to be too small to be resolved in this work.
Comparative Study of Saturn's Icy Satellites			
Search for thermally anomalous regions on Tethys	IN1b		
Search for thermally anomalous regions on Dione	IN1b		
Search for thermally anomalous regions on Rhea	IN1b		
Characterizing the properties of small satellites	IN2d		Work is in progress.
Unusual Surfaces			
Constrain Hyperion's thermophysical surface properties	IN2d		CIRS work included in paper by Howard et al. [2012].
Constrain Iapetus' albedo	IN1b		

CIRS Saturn System Science Results

Saturn

Formation, evolution, and internal structure

Helium, carbon, nitrogen, halides

In principle, the helium abundance can be retrieved from thermal infrared spectra, but placing tight bounds on helium has proved elusive. Three approaches have received the most attention so far.

1. Using far-infrared spectra alone. Here the helium abundance is derived from its effect on the collisionally induced absorption S(0) and S(1) lines of H_2 at 320 cm^{-1} and 600 cm^{-1}, respectively, and the translational continuum at 50–200 cm^{-1}. The difficulty arises in that the para-fraction of H_2 (f_p) deviates from its equilibrium value, and it must be retrieved along temperature and helium mole fraction [Achterberg et al. 2014b]. These variables are not independent, and as a result the problem becomes poorly constrained. One can only place a rough upper limit to [He]/[H_2] of 0.15. The smallest deviations from equilibrium f_p occur when the ratio is ~0.05.

2. Using far-infrared spectra with temperatures retrieved from radio-occultation soundings. With helium uniformly distributed the retrieved refractivity profiles translate into profiles of temperature divided by the molecular mass and of pressure times the refractivity per molecule divided by the molecular mass. In this case one greatly increases the precision of the helium abundance determination. One proceeds as before, except now the temperature-pressure profile is constrained, and determines f_p and the helium abundance. One iterates until the synthetic spectrum, computed for a particular T(P), f_p, and [He]/[H_2], matches the observed spectrum. With this technique Achterberg et al. [2016] obtained ratios [He]/[H_2] ~0.065–0.085. However, there is some evidence that systematic errors are present, particularly at mid and high latitudes, where the shape of the best-fit synthetic spectrum can exhibit large deviations from the observed one. The source of this discrepancy is under study.

3. Koskinen and Guerlet [2018] have combined Cassini stellar occultation soundings with the UVIS with CIRS mid-infrared limb spectra. The UVIS soundings provide vertical profiles the H_2 density versus radius down to the base of the thermosphere near 0.03 μbar. The CIRS observations retrieve temperature versus pressure up to the 1–3 μbar level. Hence, there is a gap of 30 or more in barometric pressure over the region that presumably contains the homopause. The pressure scale height decreases with molecular mass, and the trick here is to find a solution that matches the CIRS T-P condition at the bottom of the gap with the correct density-altitude condition from the UVIS sounding in the thermosphere. Koskinen and Guerlet [2018] argue that an isothermal profile across the gap provides the most viable solution, which yields an estimate of [He]/[H_2] = 0.124.

Saturn is enriched in carbon, relative to the Sun. Flasar et al. [2005b] reported the mole fraction of CH_4 as 4.5 ±0.9 × 10^{-3}. This was later refined by Fletcher et al. [2009b], who averaged over a larger number of CIRS observations, as 4.7 ±0.2 × 10^{-3}, about 10 times the solar value of C/H—see also the review by Fouchet et al. [2009].

Teanby et al. [2006] analyzed CIRS far-infrared spectra (10–600 cm^{-1}) to improve upper limits on hydrogen halides. Their derived 3 σ upper limits indicated that HF, HCl, and HBr were sub-solar at 500 mbar, similar to what was found for Jupiter (see the section entitled Halides). Because the

line strengths of HI are so weak and its solar abundance so small, they were not able to constrain its abundance to sub-solar values.

ISOTOPES

Fletcher et al. [2009] derived isotopic ratios in methane by modeling the emissions of $^{12}CH_4$, $^{13}CH_4$ and $^{12}CH_3D$. The derived D/H ratio in methane of (1.6 ±0.2) × 10^{-5} appears to be smaller than on Jupiter, in contrast with expectations that D-enriched ices would form a progressively larger proportional of the giant planets, moving outward from Jupiter to Neptune. The reason for this is still unclear. In contrast, the carbon isotopic ratio $^{12}C/^{13}C$ = 91.8 (+8.4/−7.8, is consistent with both the terrestrial ratio and Jovian ratio, suggesting that carbon was accreted from a shared reservoir for all of the planets.

D/H from HD/H_2. Pierel et al. [2017] made a careful modeling of the far-IR HD rotational lines on CIRS FP1. The modeling effort uncovered substantial uncertainties in current knowledge of the HD line parameters, especially the line widths at low temperatures, which contributed to substantial error bars dominated by systematic uncertainties rather than spectral noise. The bulk D/H was found to be (2.95 ±0.55) × 10^{-5} on Jupiter and somewhat lower (2.10 ±0.13) × 10^{-5} on Saturn, indicating potential interior differences. The results were compared to previous estimates from ISO and Herschel data, as well as to inferences about bulk D/H extrapolated from methane measurements. Overall, Saturn shows a trend toward slightly lower D/H than Jupiter, in contrast to expectations of a higher value, due to a larger ice/gas ratio at formation. However, the errors and spread in values is large and the difference remains statistically marginal. Further work is needed, first on better laboratory estimates of the HD and H_2 quadrapole line strengths and widths at low temperatures, followed by re-retrievals of the spectral data.

INTERNAL ROTATION

Saturn's internal rotation rate remains a subject of interest and controversy.

Saturn's internal rotation rate remains a subject of interest and controversy. Read et al. [2009] proposed a novel way to estimate the internal rotation period based on the potential vorticity, observed at the cloud tops. The authors assumed that the zonal flow was marginally stable with respect to the nonlinear stability as prescribed in Arnol'd's 2nd stability theorem. The theorem is couched in terms of the zonal phase velocity of the longest, fastest, and mostly deeply rooted Rossby waves, which presumably are closest to the internal rotation. Using the tracked cloud-top winds from Cassini imaging and temperatures retrieved from CIRS spectra, the authors computed the potential vorticity and used the stability criterion to infer an internal rotation period of 10 h 34 min 13 ±20 s for the interior.

Atmospheric gas composition

DISEQUILIBRIUM TROPOSPHERIC COMPOUNDS

Phosphine (PH_3) is a disequilibrium compound in the upper troposphere. It is generally believed to be a product of rapid vertical mixing from deep atmospheric levels. PH_3 is transported upwards in a time much shorter than the chemical depletion time in the upper troposphere, so the observed abundances represent the quenched equilibrium conditions deeper down. Hence, meridional variations in the observed abundance are diagnostic of the vertical motion. CIRS observations indicate an enhancement of PH_3 in the equatorial region [Fletcher et al. 2007a, 2009a, 2018], which is consistent with rapid vertical upwelling and the cold temperatures observed there. At 23° N (planetographic), PH_3 is depleted, suggesting subsidence, perhaps indicative of a Hadley-type cell. Lower values of PH_3 have also been inferred in the upper troposphere in the cores of the polar vortices, where there is subsidence [Fletcher et al. 2008, 2010] found a hemispheric asymmetry in the phosphine distribution over 2004–2009, with the southern hemisphere (in summer) on average having higher abundances.

Hurley et al. [2012b] investigated whether thermal disassociation associated with lightning and shock waves generated by thunder in Saturn's water clouds could generate an enhancement of tropospheric acetylene (C_2H_2) that would be transported upward to the tropopause region, and thereby serve as a chemical fingerprint of thunderstorm activity. Analyzing CIRS mid-infrared spectra, they found no systematic enhancement around regions in which there are known occurrences of normally sized (2000 km) thunderstorms, beyond what would be expected from photolysis under ambient conditions.

ORTHO-PARA H_2

CIRS far-infrared spectra can probe the para-fraction of H_2 (f_p) in the upper troposphere (100–400 mbar). Because the equilibration time between the ortho and para states are thought to be long compared to seasonal time scales, the distribution of f_p should provide an indication of vertical motion from deeper levels of the atmosphere. In the equilibrated state, f_p increases with decreasing temperature. CIRS observations show that f_p remains depressed near the equator, relative to the average over latitude in the upper troposphere, indicating upwelling, throughout the Cassini tour [Fletcher et al. 2007a, 2010, 2016, 2018]. The meridional structure at mid and high latitudes is more difficult to interpret. An exception is the depression of f_p at 20°–50° N, resulting from upward transport after the outbreak of the Saturn storm (see the section entitled Temporal behavior).

DISEQUILIBRIUM STRATOSPHERIC COMPOUNDS (HYDROCARBONS)

The review chapter by Fletcher et al. [2018] provides a good summary of CIRS observations of stratospheric hydrocarbons. Observations in nadir-viewing [Howett et al. 2007; Hesman et al. 2009; Sinclair et al. 2013; Fletcher et al. 2015] and limb-viewing [Guerlet et al. 2009; Sylvestre et al. 2015]

geometries have provided information on meridional and vertical structure of C_2H_2 and C_2H_6. Quantitative differences exist among the spatial distributions and temporal behaviors identified by different authors, but some general common trends can be identified: (i) C_2H_2 decreases from equator to pole while C_2H_6 is largely uniform with latitude; (ii) There are regional enhancements of both species at the highest latitudes within polar vortices, possibly associated with auroral chemistry and entrainment; (iii) There are general spring hemisphere enhancements and autumn hemisphere depletions in the millibar region, suggestive of stratospheric transport from the southern to the northern hemisphere that may be related to the local meridional cells associated with the equatorial oscillation (see section the entitled Equatorial Oscillation).

CIRS limb observations [Guerlet et al. 2009, 2010, 2015; Sylvestre et al. 2015] have also provided information on the spatial distributions of C_3H_8, CH_3C_2H, C_4H_2, and C_6H_6. Like those of C_2H_2 and C_2H_6, these bear little resemblance to photochemical model predictions in the absence of dynamical transport.

External sources—oxygen compounds

Prior analysis of the rotational lines of H_2O and CO has been based on disk average measurements. While CIRS observations spatially resolve Saturn, the rotational lines are weak at its spectral resolution, the relatively cold temperatures require large spectral averages for analysis. Little on this has been published as yet. Using spectral averages of nadir and limb observations, Abbas et al. [2013] analyzed the Q-branch of the ν_2 band of CO_2 in the 667 cm^{-1} region, and they did not find any discernable meridional trends, obtaining a mixing ratio ~5 × 10^{10} near ~1 mbar.

Clouds and aerosols

CIRS thermal-infrared spectra have placed fewer constraints on clouds and aerosols on Saturn that on Jupiter (see the section entitled Jupiter - Clouds and Aerosols). In part this can be attributed to the lower temperatures and signal-to-noise ratios of spectral features. Constraints from observations near-infrared, visible, and ultraviolet wavelengths have been more definitive. And unlike Titan, limb sounding in the far-infrared was not feasible at Saturn, because of the greater distance between the spacecraft and atmosphere.

There have, however been more indirect indications of the haze distribution from retrieved CIRS temperatures. One of the interesting features of Saturn's vertical temperature profile is the knee, which is an undulation that occurs over the range ~150–300 mbar and effectively broadens the tropopause region. This was originally seen in temperatures retrieved from Voyager IRIS spectra, obtained in early northern spring, mainly in the southern hemisphere. Retrieving temperatures from Cassini CIRS spectra obtained in early northern winter, Fletcher et al. [2007b] detected the temperature knee and mapped its variation with latitude. They found it to be larger in the summer hemisphere than in the winter, smaller and higher at the equator, deeper and larger in the equatorial belts, and small at the poles. They proposed solar heating of tropospheric haze as a possible mechanism for the temperature knee, with larger aerosols in the summer hemisphere.

Atmospheric structure and circulation

GLOBAL STRUCTURE

Flasar et al. [2005a] reported the first observations of Saturn by CIRS. From nadir-viewing observations, they found little variation with altitude of the zonal winds in the upper troposphere and stratosphere, except near the equator, where they found a general decay with altitude between 500 mbar and 2 mbar. Later limb and more detailed nadir observations would reveal the oscillatory undulation of the zonal winds in the stratosphere associated with the equatorial oscillation (see the section entitled Equatorial Oscillation). The earlier CIRS observation also found that the south pole was warmer than the equator in the stratosphere near 1 mbar by 15 K—about 3 times that expected just from the radiative response to solar heating in southern summer—suggesting that descending motion and adiabatic compression and heating played an important role over the south pole. Fletcher et al. [2007b] found that the south pole in the same season was 25–30 K warmer than the north pole at 1 mbar. They also quantified the knee in the vertical temperature profiles, a flattening of the temperature lapse rates between 150 and 300 mbar in the tropopause region, which was first seen in temperatures retrieved from Voyager IRIS spectra obtained in 1980–1981. This was most noticeable in the southern hemisphere, becoming more compact in the equatorial region. They suggested that this could result from solar heating of heterogeneously distributed aerosol hazes.

Li et al. [2010] undertook a careful study of Saturn's thermal emission during 2004–2009. They found an effective temperature of 96.7 K, but found that the emission from the southern hemisphere (in summer) was 17% higher than in the north. They also found evidence of seasonal and variations in the total power ~2% and some interannual variability.

POLAR STRUCTURE

During northern winter, both poles exhibited compact spots in the upper troposphere, associated with cyclonic vortices, with subsidence and adiabatic heating [Fletcher et al. 2008]. At the southern (summer) pole, the warm structure persisted into the stratosphere near 1 mbar, where the warm region was slightly broader in extent. In the north, the warm pole was less compact and intense in the stratosphere. Evidence for polar subsidence was further supported by the depletion in PH_{3}¬, a disequilibrium compound thought to be transported upward from the deeper atmosphere. CIRS observations also detected the cold anticyclonic zone (warm cyclonic belt) poleward (equatorward) of the jet at 77° N, associated with the polar hexagon. (The hexagonal shape actually represents the orthographic projection of a wavenumber 6 sinusoidal variation of the amplitude in latitude with longitude.) As Saturn's seasons moved from northern winter to northern summer, the hexagon retained its structure in the thermal infrared and the north polar stratosphere developed a well-defined warm region that is broader than in the troposphere [Fletcher et al. 2015; Sayanagi et al. 2018]. On the other hand, the warm stratosphere over the south pole has weakened considerably. More recently, the recent Grand Finale orbits have provided observations of the poles with the highest spatial resolution of the mission. Tropopause temperatures over the north pole, now in

summer, increase sharply between 89° and 90° N [Achterberg et al. 2018]. The average subsidence velocity in this region, assuming a balance between adiabatic heating and radiative damping, are modest, ~0.05 mm/s. However, the circulation appears to be deeply rooted, still depressing the isentropes over the pole at the deepest levels probed by CIRS, ~600 mbar.

Temporal behavior

SATURN STORM

One of the key advantages of having a long-term orbiting spacecraft about a planet is the ability to map the fourth dimension—time—in addition to the three spatial dimensions. Geophysical systems are inherently nonlinear, and their temporal behavior is often not easily predictable. This is particularly true of meteorology. Our terrestrial experience has taught us that continued observation is critical to understanding an atmosphere's dynamical behavior.

One of the key advantages of having a long-term orbiting spacecraft about a planet is the ability to map the fourth dimension—time . . .

An intriguing phenomenon is the outbreak of the great Saturn storms. These originate as the appearance of a white compact spot that quickly spreads and encircles the planet with clouds within a latitude band. The storms recur in the northern hemisphere roughly every 30 years (approximately Saturn's orbital period) generally in northern summer, when Saturn is near periapsis—see, for example, the review by Sánchez-Lavega et al. [2016]. However, storms prior to the last one, which erupted in December 2010, were observed by Earth observatories, and this may have introduced some bias in the detections because of obscuration by the rings. The last storm, which was observed by Cassini, was unexpected in that it erupted early, just after the northern spring equinox. For the first time, an observatory was in hand to observe the storm evolution, not only up close, but with a full array of instruments spanning much of the electromagnetic spectrum as well as obtaining in situ data.

CIRS observations were critical in characterizing the effect of the storm on atmospheric structure. Current thinking attributes the storm outbreak as driven by a moist convective instability associated with Saturn's water clouds. Retrievals from CIRS spectra, obtained over the course of 18 months after the outbreak, indicated that tropospheric temperatures in the latitude band encircled by the clouds were elevated and the para ratio of H_2 was lower, relative to the ambient atmosphere at adjacent latitudes [Achterberg et al. 2014a]. This is broadly consistent with the notion of a rapid convectively unstable updraft that transports a higher fraction of ortho H_2, in equilibrium with the higher temperatures at depth. If, as on Earth, the convective updrafts are confined to narrow towers, surrounded by compensating downdrafts, which occupy most of the horizontal surface area in the perturbed latitude band, the adiabatic compression and warming would produce the higher temperatures observed, rather than lateral mixing of latent released in the updrafts. The mean zonal winds and temperatures are coupled via the thermal wind equation.

The warmer tropospheric temperatures at the storm latitude band means that winds become more westward with altitude equatorward of the band and eastward with altitude poleward, hence increasing the mean zonal anticyclonic vorticity with altitude. This is roughly consistent with the behavior inferred from cloud tracking studies using various filters [Sayanagi et al. 2013].

Li et al. [2015] examined the effect of the storm on Saturn's radiant power. The storm increased the total power near 45° by 9%, causing the globally emitted power to increase by 2%.

For the first time, the effects of the storm on the stratosphere was observed. CIRS observations indicated that initially two warm spots were observed near 2 mbar at the same latitude as the storm [Fletcher et al. 2012]. It was quickly realized that these could not have resulted directly from updrafts, because, with the sharp increase in static stability above the tropopause, any updraft would quickly become negatively buoyant. Instead, the effect of any updrafts hitting the tropopause region would be analogous to tossing a stone into a pond, generating waves that would propagate upward. The waves would likely be nonlinear, with the warm spots resulting from local subsidence and adiabatic heating. There were no accompanying colder regions at other longitudes, perhaps because of the presumed nonlinearity. It should be appreciated that Cassini observations, because they had been pre-programmed several months in advance, were not optimally configured to track the storm. Therefore, ground-based observations were brought to bear to fill in the gaps. VLA observations tracked the evolution of the two warm spots initially detected [Fletcher et al. 2012]. Because zonal pressure gradients were relatively weak in the troposphere, application of hydrostatic balance implied that the warm regions were high pressure centers, hence anticyclonic vortices with clockwise flow, with wind velocities ~200 m/s. Both anticyclonic vortices moved slowly westward at different speeds with respect to the background zonal flow. Eventually, in May 2011, they merged, with the vortex increasing in strength. At that time, the vortex temperature at 2 mbar was 80 K warmer than the ambient atmosphere at this isobaric level, unheard of in the normally quiescent Saturn stratosphere. CIRS observations indicated that not only were temperatures elevated, but there was a 100-fold enhancement of ethylene (C_2H_4) [Hesman et al. 2012]. The cause of this enhancement is not understood, but it may result from the release of condensed C_2H_4 bound onto aerosols that was released by the higher temperatures in the merged vortex.

The tropospheric disturbances associated with the storm dissipated over eight months. In contrast the stratospheric disturbance lasted nearly three years after the storm began [Fletcher et al. 2017]. The persistence of the stratospheric disturbance shows evidence of interfering with the descending phase of the equatorial oscillation (see next sectional paragraph below).

EQUATORIAL OSCILLATION

One of the remarkable phenomena on Jupiter and Saturn is the occurrence of equatorial oscillations in the planets' stratospheres. Equatorial oscillations on Earth—the quasi-biennial oscillation (QBO), with an irregular period ranging from 22–34 months, and the semi-annual oscillation (SAO) with a well-defined periodicity—have been extensively studied. The zonally symmetric structure in the equatorial middle atmosphere (stratosphere and mesosphere) is

characterized by an alternating series of warmer and colder layers with height. Because of Earth's rapid rotation, temperatures and zonal winds are in thermal wind balance, and the warm and cold regions are associated with decreasing and increasing zonal wind shear, respectively. The alternating shears are large enough that the zonal winds alternate between eastward and westward with altitude. Associated with the temperature and wind structure are a series of stacked meridional circulation cells. At equatorial levels where there is subsidence (ascent), adiabatic warming (cooling) produces warmer (colder) temperatures. These meridional cells close at higher latitudes in each hemisphere, and thus affect the structure of temperatures and winds at higher altitude. Indeed, there is evidence that the strength of the winter polar vortices on Earth, is correlated with the phase of the QBO. The terrestrial equatorial oscillations are thought to be mechanically driven, from the absorption of upwardly propagating atmospheric waves with both eastward and westward zonal phase velocities.

Ground-based observations [Orton et al. 2008] have indicated an oscillatory behavior in Saturn's equatorial stratosphere for decades, but they did not spatially resolve the vertical structure. Cassini CIRS observations resolved this structure for the first time. Fouchet et al. [2008] found the analogous warm and cold anomalies at the equator from limb-viewing spectra. The warm and cold anomalies were spaced apart by approximately two pressure scale heights. The zonal winds implied by the thermal wind equation did not reverse, as on Earth, but remained eastward. However, the peak-to-peak variation between the largest and smallest eastward winds was roughly 200 m/s, compared to the characteristic value between 400 and 500 m/s for the cloud-top winds. Some evidence for the extratropical extent of the implied meridional circulations associated with the equatorial oscillation was seen in the enhancement of C_2H_6 near 20° N. Since ethane increases with altitude, this suggested that subsidence was transporting it downward. The CIRS limb observations were limited and did not provide direct evidence that the observed undulatory structure in the temperatures and winds was indicative of the zonal mean structure, like on Earth. The evidence for that came from Cassini radio occultations [Schinder et al. 2011a]. Occultations at several different longitudes over the course of a few months indicated larger-scale undulations in the retrieved temperature profiles that agreed with those found with CIRS and which did not differ markedly with longitude. In addition, there was much smaller-scale structure that did vary from profile to profile, that could be indicative of atmospheric wave structure, perhaps of internal gravity waves.

Cassini not only provided close-up viewing of Saturn, but also an opportunity to observe the temporal behavior of the oscillation. Guerlet et al. [2011] compared CIRS limb observations 4–5 years apart of the equatorial regions. They observed that the pattern reported by Fouchet et al. [2008] had descended. The descent rate of warm and cold layers was consistent with the ~15-year period—approximately half of Saturn's year—that had been inferred from the ground-based observations by Orton et al. [2011]. Cassini radio occultations [Schinder et al. 2011a] also indicated a roughly comparable descent rate. During the descent the pattern is not rigid, and the vertical structure undergoes some modulation. The Earth's QBO and SAO also exhibit descending patterns that modulate. This behavior is linked to the deposition of zonal momentum of the absorbed vertically propagating waves that drive the oscillation—see, for example, Baldwin

et al. [2001]. More recent limb observations of Saturn, from 2015 [Guerlet et al. 2018] have shown the descent continues.

Li et al. [2011a] have combined cloud-tracking of Cassini imaging data and application of the thermal wind equation to CIRS temperature retrievals from nadir-viewing observations to assess the temporal variation of the zonal winds near the equator. Although they cannot access the higher altitudes associated with limb-sounding observations, they can probe the tropopause region better. They find variations in the zonal winds consistent with the previously cited work, but with the amplitude reduced near the tropopause.

The question arises whether the Saturn equatorial oscillation is really semi-annual, like the SAO on Earth. Comparison of temperatures retrieved from Voyager measurements in 1980–1981 with Cassini observations one Saturnian year later in 2009–2010 by Sinclair et al. [2014] and Li et al. [2013] at 2.1 mbar and 50–100 mbar, respectively, indicated that the later temperatures were noticeably warmer than expected if the oscillation were strictly periodic [see also the review by Fletcher et al. 2018]. More recently, Fletcher et al. [2017] found that the descent of the equatorial oscillation was significantly affected by the great northern storm, described earlier, at the beginning of 2011, when the equatorial region at pressures less than 5 mbar cooled by 10–12 K. This disruption persisted until at least 2014, after which the normal phasing of descending warm and cold equatorial anomalies appears to have resumed. Recent observations of Earth's QBO have revealed a disruption in the phase of the descending pattern in 2016. The origin of this disruption is not known, although zonal momentum transport from the northern hemisphere by mid-latitude planetary waves has been suggested. There have been a few analyses of Saturn's temperatures to characterize wave structure, from the Voyager Infrared Interferometer Spectrometer—IRIS—measurements [Achterberg and Flasar 1996] and from Cassini CIRS [Li et al. 2008; Guerlet et al. 2018], and these have suggested the presence of planetary waves with low to intermediate zonal wavenumbers. More effort is warranted.

Rings

This section contains an introduction which outlines the nature of ring thermal emission, a brief overview of Saturn's rings and their key characteristics, and a brief discussion of CIRS ring data analysis. Following the introduction is a discussion of CIRS ring models, the key CIRS ring results, the modeling of those results organized by the CIRS science objectives and the science assessments, and conclusions and future work. Thermal measurements of Saturn's rings by ground-based or spacecraft-based observations are summarized in book chapters by Cuzzi et al. [1984]; Cuzzi et al. [2009]; and Spilker et al. [2018]. The CIRS ring material in the following sections is taken primarily from Flasar et al. [2004] and Spilker et al. [2018], and a multitude of CIRS ring papers.

Introduction

The thermal response of a ring is determined by the way particles absorb, transfer heat in their interior and re-radiate it through the ring. The radiation source functions depend upon the ring structure. Energy sources include direct, reflected and scattered solar light, mutual heating by neighboring ring particles, and thermal and visible radiation from Saturn. Because of mutual shading and heating between particles, the thermal emission is determined not only by the physical properties of the particles, but also by the structural and dynamical properties of the ring disk itself. Friction in mutual dissipative collisions between particles, due to their possibly irregular surfaces, transforms orbital kinetic energy into spin. The particle surface temperature and its thermal emission are expected to vary on the surface along the rotation axis and azimuthally. Ring particles, as they collide into each other, are tumbling around the ring mid-plane with a vertical excursion governed by the local ring dynamics. The thermal history of a particle along its orbit is then an indicator of vertical dynamics. The particle is conditioned by the time it spends in sunlight and in the planetary shadow. At the exit of the shadow, its thermal inertia scales its ability to warm up as a function of time. Any difference in the heating curves between the lit and unlit sides should reveal the time each particle spends on each side.

Friction in mutual dissipative collisions between particles, due to their possibly irregular surfaces, transforms orbital kinetic energy into spin.

The thermal emission of planetary rings is thus expected to be a complex function of ring particle properties, ring disk structure, and observed geometry. Individual particle properties include size, regolith characteristics, Bond albedo, thermal emissivity and inertia, spin rate, and spin axis orientation. Ring structural and dynamical properties include optical depth, particle size distribution, vertical thickness and excursion, filling factor, and thermal inertia, too [Spilker et al. 2003a; Ferrari and Leyrat 2006; Morishima et al. 2009; Ferrari and Reffet 2013]. The emission observed from Saturn's rings also depends on the illumination and viewing conditions and to the position of the targeted ring segment relative to those two. Phase angle, solar elevation angle, observer elevation angle, local hour angle, and radial location in the rings are thus parameters of variable impact on that thermal emission.

SATURN RINGS OVERVIEW

The major ring features, from closest to farthest from Saturn, are the D-ring, C-ring, B-ring, Cassini Division, A-ring, narrow F-ring, faint G-ring and extended, and faint E-ring. The main rings (D through A) range from ~67,900 km to 136,800 km from the center of Saturn, and lie in a thin disk that is typically less than 10 meters thick [Tiscareno et al. 2007]. The C-ring and Cassini Division optical depths are lowest; 0.05–0.35 and 0–0.1, respectively. The B-ring optical depth is highest, 0.4 to >5, while the A-ring optical depth is intermediate, 0.4 to 1. Some gravitational wakes—temporary clumping of particles—have been detected in these to rings. Such a diversity in

the opacity of the rings versus distance is expected to play a role in the temperatures measured by CIRS and allowed us to address additional key questions such as: how does clumping affect the thermal radiation from the rings, and what does this tell us about the nature of these aggregates? Are the rings organized in a multi-particle-layer or mono-particle-layer, and how does the clumping affect this structure? How does the thermal inertia of the rings vary with the disk structure (thickness, filling factor, particle vertical excursion, etc.) or with particle properties such as albedo, surface roughness, porosity, or spin?

CIRS was indeed able to observe all but the faint and optically thin D-ring, G-ring, and E-ring, with optical depths ranging from ~10^{-5} to 10^{-6}. CIRS results from Saturn's F-ring, with the best data taken during the ring-grazing orbits near the end of the mission, are still under study.

CIRS RING DATA ANALYSIS

The ring spectra (Figure CIRS-1) delivered by the FP1 focal plane have been predominantly used for obtaining information about the ring temperatures because they contain the peak of the Planck function for typical ring temperatures (50–100 K). This allows a determination of the characteristic temperature within the FOV. Nearly every uncontaminated FP1 spectrum taken during the mission is well fit by a Planck function such that [Spilker et al. 2006; Pilorz et al. 2015]

$$I(\nu) = \beta B(\nu, T)$$

where $I(\nu)$ is the spectral intensity in W cm^{-2}sr^{-1}cm, $B(\nu, T)$ is the Planck function dependent on the wavenumber ν, T the effective temperature in the FOV. The β-factor is scalar, and stands for the product of the geometric filling factor β_{geo}, the infrared emissivity ε_{IR}, and the factor β_{therm} that arises due to a distribution of temperatures within the FOV [Altobelli et al. 2007]:

$$\beta = \beta_{geo}\varepsilon_{IR}\beta_{therm}$$

The expected deviations from the single-temperature fit resulting from the presence of multiple temperatures within the FOV are relatively small [Spilker et al. 2005].

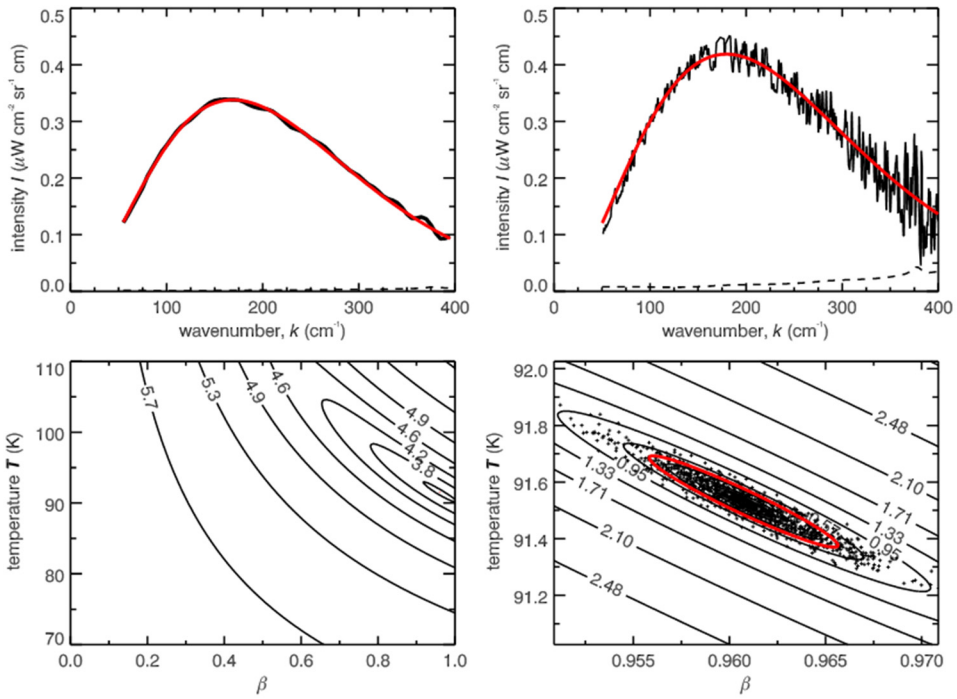

Figure CIRS-1. *Top panels*: show examples of low and high spectral resolution spectra used in the fitting process. We show two spectra selected from the B-ring at 105,000 km from Saturn. *Top left panel*: is from the lit, high-phase low-resolution (15.5 cm^{-1}) scan. *Top right panel*: is from the lit, low-phase high-resolution (1 cm^{-1}) scan. Noise spikes have been removed from these spectra. Each spectrum is plotted with the best fit to the single-temperature Planck function. The NESR at these wave numbers are shown as dashed lines. *Bottom panels*: show an example of the chi-square fitting procedure for the high-resolution spectrum. *Bottom left panel*: contours of the chi-square are shown over a large range of possible values. These contours are typical, and there are no local minima other than around the best fit (shown as a red dot). *Bottom right panel*: is an expanded plot of the contours in the vicinity of the best fit. Here, the theoretical 1 σ contour that we use in our error analysis is highlighted in red; the crosses represent the temperature and beta values derived from 1000 perturbations to the best fit spectrum, using uncorrelated, randomly generated noise with a standard deviation equal to the NESR at any wavenumber. In this realization 672 of the 1000 points lie within the theoretical contour, in close agreement with the expected 68%. Figure from Spilker et al. [2006], Figure 2.

Ring thermal structure

The main result obtained on the way the thermal emission, first as a function of the distance from the planet and of optical depth, then as a function of the solar elevation about the ring plane or as a function of the spacecraft position relatively to the Sun and finally with local hour angle, are presented below.

TEMPERATURE VARIATION WITH DISTANCE AND RING OPTICAL DEPTH

The effective temperature of Saturn's rings, as defined above, varies with radial distance from the planet. Radial temperature variations (Figure CIRS-2) are observed across both the lit and unlit

rings at both low and high phase angles [Spilker et al. 2006]. On the lit side of the rings, at low phase angle, the dominant trend across the ring system is a rough anti-correlation between optical depth and temperature. The optically thin C-ring and Cassini Division are considerably warmer than the optically thick A-ring and B-ring. However, within the A-ring and B-ring, the correlation between optical depth and temperature is distinctly positive and stronger at low phase angles (phase angle dependence will be discussed in more detail below). At high enough optical depth, the sunlight does not penetrate so deeply into the ring. The C-ring and Cassini Division also have lower albedos than the A-ring and B-ring. The lower albedos, lower optical depth and reduced mutual shadowing in these rings all contribute to their higher temperatures.

The temperatures of the A-ring and B-ring are correlated with their optical depths when viewed from the lit side of the rings and are anti-correlated when viewed from the unlit side. On the unlit side of the B-ring the lowest temperatures correlate with the largest optical depths and are also the same at both low and high phase angles, indicating that very little sunlight penetrates to the unlit side of the densest ring region. This also suggests that vertical mixing of ring particles is not very efficient in the optically thickest part of the rings. In the densest part of the unlit B-ring the phase variation nearly vanishes, indicating that direct sunlight does not play a significant role in heating these particles.

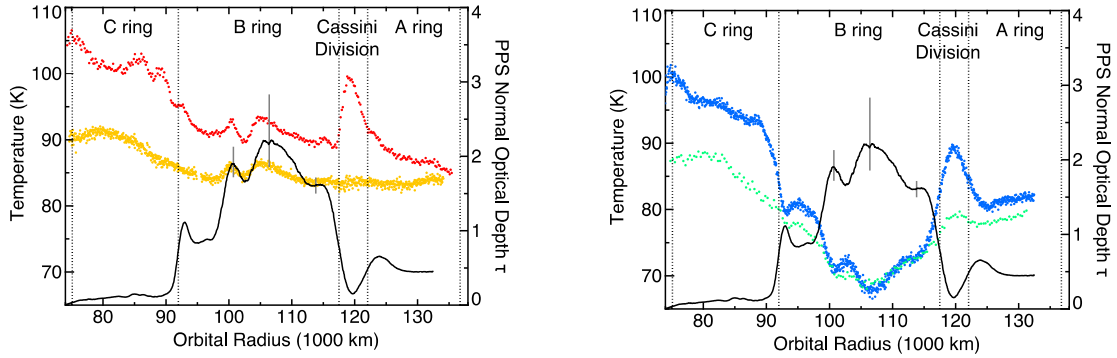

Figure CIRS-2. Radial temperature variations. *Left*: Radial temperature variation across the lit rings at both low and high phase angle. The ring temperatures at low phase (red symbols) and high phase (gold symbols) are shown as a function of ring radius, with boundaries between rings indicated by dashed lines. Both scans were taken at afternoon local times. The Voyager PPS optical depth profile is superposed, smoothed to the CIRS FP1 resolution. Vertical gray bars indicate the calibration uncertainty (1σ) in the PPS-derived B ring optical depths. Elsewhere the uncertainties are narrower than the width of the plotted line. *Right*: Same as the left, but for the ring temperatures at low phase (blue symbols) and high phase (green symbols). Figures from Spilker et al. [2006].

TEMPERATURE VARIATION WITH SOLAR ELEVATION AND THE EQUINOX CASE

One of the strongest effects observed in the ring thermal data is the decrease of temperature with decreasing solar elevation [Flandes et al. 2010]. The solar insolation is therefore, to first order, the main driver of the ring temperature. This effect is observed in all ring regions. Regions with low optical depth, the C-ring and Cassini Division, appear to have more limited amplitudes in

temperature variations. In contrast, larger differences are found between solar solstice and equinox in the B-ring and A-ring. The measurements of ring temperature with solar elevation (Figure CIRS-3) now cover a full seasonal cycle. The analytical model from Froidevaux [1981] assuming a monolayer with only slow rotators was fit to each ring data set using the visible bond albedo as the only model parameter—see Flandes et al. [2010] for model details—and can reproduce the observed temperature changes.

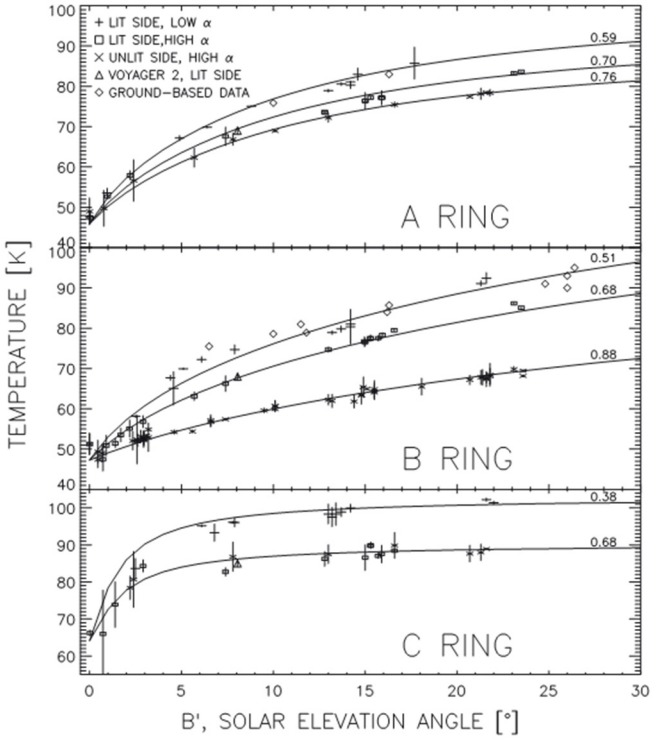

Figure CIRS-3. Saturn's ring temperatures as a function of solar elevation angle for the A-ring, B-ring, and C-ring. Observational data from Cassini CIRS (plus mark, cross and square), ground-based (diamond) and Voyager 2 (triangle) are shown. Data are presented at low (α ~ 30 deg) and high (α > 120 deg) phase angles for lit and unlit sides of the rings. The error bars represent the observed standard deviation. The analytical model from Froidevaux [1981] was used to fit the CIRS data assuming a mono-particle-layer of a ring and only slowly rotating particles. Figure from Flandes et al. [2010].

The solar equinox occurred on August 11, 2009. During the equinox period (August 11–13), CIRS obtained 15 radial scans [Spilker et al. 2013]. These observations took place when the solar elevation was between 0° and 0.036° above the ring-plane, mostly after the equinox. The very low solar elevation angle guarantees that the direct solar illumination is negligible. The absolute spacecraft elevation angle was about 20° for all the scans. Assuming that the heat source at the equinox is simply the infrared flux from Saturn, the simplest zeroth-order model gives the expected particle temperatures (Figure CIRS-4) [Spilker et al. [2013]. Saturn infrared emission is definitely structuring the radial variations of ring temperatures at equinox. The anti-correlation between the

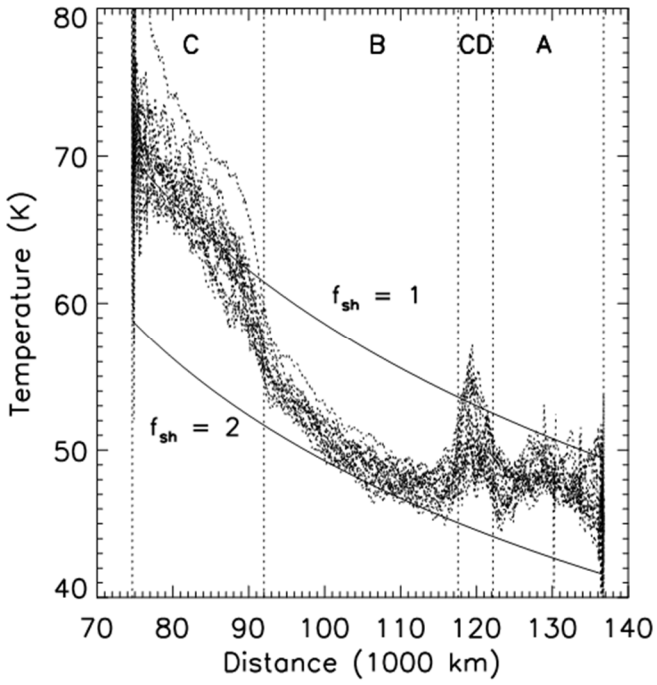

Figure CIRS-4. Ring temperature versus saturnocentric distance at the solar equinox (dotted curves). The temperature and the optical depth are anticorrelated and the temperature decreases with distance, as expected for the case of central heating. The temperature profiles from a simple model are also shown for optically thin (f_{sh} = 1) and thick (f_{sh} = 2) rings. See Spilker et al. [2013] for details.

ring temperature and the optical depth strongly supports the idea that nearby particles partially block Saturn's radiation depending on their optical depth.

The local observed temperature variations from scan to scan are caused by a change in observer geometry if the particles are not isotropic emitters. We found that the leading hemisphere of the particle is warmer than the trailing hemisphere at least for the C-ring and probably for the A-ring and B-ring too, although the temperature differences are as small as the error bars. This asymmetry indicates that some fraction of particles has spin rates lower than the synchronous rotation rate, provided that their thermal inertia is not zero. Spins slower than synchronous are indeed expected for the largest particles in N-body simulations [Salo 1987; Ohtsuki and Toyama 2005; Morishima and Salo 2006].

A multi-particle-layer model of Morishima et al. [2009] can reproduce the observed equinox temperatures for the C-ring and B-ring. C-ring temperatures were being well reproduced by the mono-particle-layer model of Ferrari and Leyrat [2006] while the multi-particle-layer model significantly underestimated the A-ring temperatures. This, in fact, indicates that the A-ring was not completely cooled down at the equinox and that it is possible to give constraints on the size and seasonal thermal inertia of A-ring particles. For further detail see the section entitled Seasonal Thermal Inertia and Particle Size, and the paper by Morishima et al. [2016].

TEMPERATURE VARIATION WITH PHASE ANGLE

The analysis of the temperature variations with phase angle across the main rings (Figure CIRS-5) reveals a variable dependence on optical depth and solar elevation [Altobelli et al. 2007, 2009; Morishima et al. 2017]. A surge in temperature is observed at low phase angles, if the solar elevation is low enough and the (normal) optical depth of the ring region observed (high enough) typically above ~0.3.

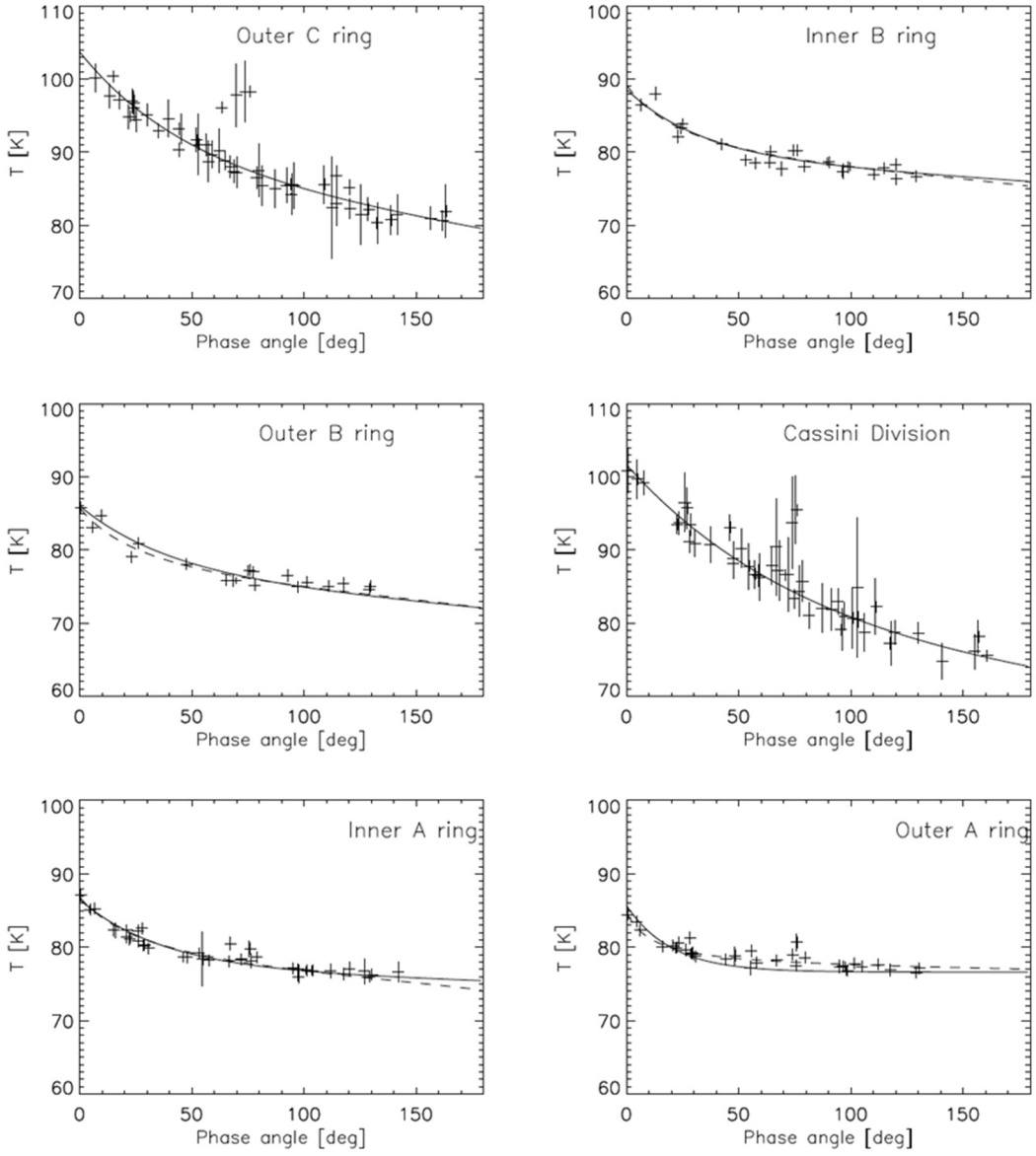

Figure CIRS-5. Temperature versus phase angle obtained at different ring locations. In all ring regions, an exponential-linear fit is applied (plain curve). In the A-ring and B-ring only, a fit based on the shadowing function of Hapke [1993] is also plotted (dashed curve).

The shape of thermal phase curves does not vary with solar elevation in the optically thin portions of the C-ring and Cassini Division. However, the shape does vary in the optically thicker regions of the B-ring, with an opposition surge at low solar elevation [Altobelli et al. 2007]. A similar behavior is observed in the C-ring plateaus [Altobelli et al. 2009] which are optically thicker than the surrounding background. The temperature surge is more pronounced for the plateaus than the C-ring background at low phase angle while similar phase curves are seen for both the plateaus and background at large phase angle.

The morphology of the phase curve, in particular the thermal surge in optically thicker regions for combinations of low phase angles and low solar elevation, can be explained by mutual shadowing between particles. Lower solar elevations obviously favor mutual shadowing by increasing the length of shadows projected on the ring-plane. (For futher detail see the section entitled Modeling of Opposition Surge for Packed Particulate Medium.)

AZIMUTHAL DEPENDENCE

CIRS executed azimuthal scans (Figure CIRS-6) of the lit and unlit rings at constant radial distance from the planet to measure ring temperature variations with local hour angle [Leyrat et al. 2008a]. Some scans investigated eclipse cooling, from which the thermal inertia of the rings and possibly of wake structures within dense rings were inferred.

Temperature scans of A-ring, B-ring, and C-ring versus local hour angle all exhibit a large drop in temperature from the entry into the shadow to a few hours after the shadow exit. This eclipse event is the major source of azimuthal temperature variations. The thermal gradient between entry

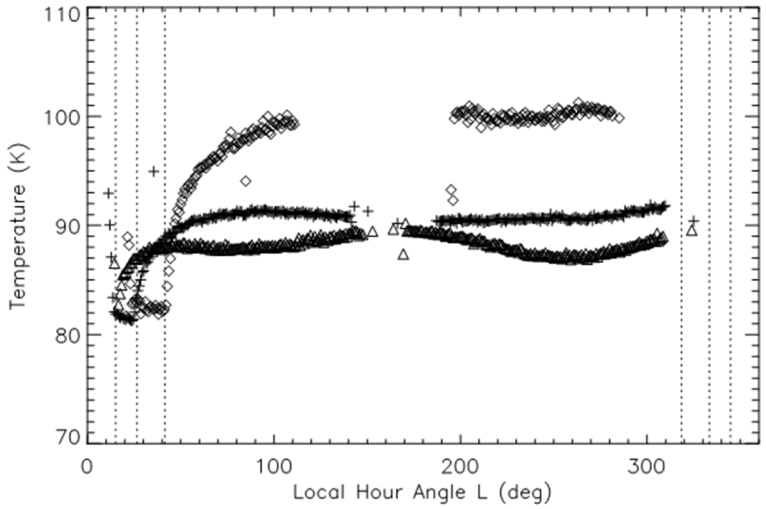

Figure CIRS-6. Typical azimuthal scans of ring temperatures versus local hour angle: C-ring (diamond), B-ring (cross), and A-ring (triangle). The vertical dotted lines mark the shadow boundaries for each ring. At this epoch, the Sun is relatively high above the ring plane (*B'*=-21.4 deg) and the shadow sector is significantly smaller for the A-ring. The phase angle ranges between 14 deg and 25 deg.

and exit from the shadow increases with solar elevation and decreases with phase angle [Leyrat et al. 2008a]. The shadow crossing is not detectable on the unlit side of the thick B-ring [Leyrat et al. 2008a; Reffet et al. 2015], which is consistent with the expectation that no direct sunlight reaches this side.

The temperature of the A-ring exhibits a quadrupole azimuthal modulation of 2–3 K on top of the eclipse drop, which is about 5–6 K [Leyrat et al. 2008a]. This modulation appears to vary with viewing and lighting geometry [Morishima et al. 2014]. Ferrari et al. [2009] showed that the model fit for the A-ring azimuthal variations of the scaling factor β at different solar elevations were improved using the regularly spaced, infinitely long, opaque elliptical cylinders, first introduced by Hedman et al. [2007] (Figure CIRS-7).

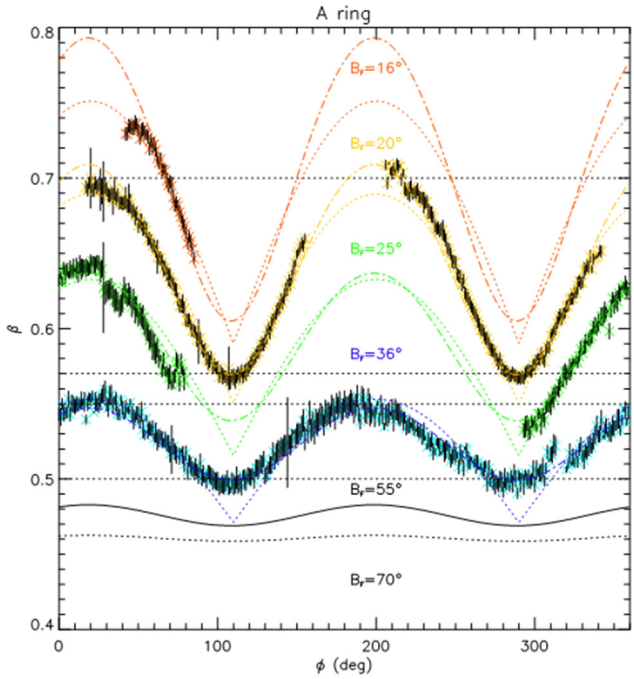

Figure CIRS-7. Averaged azimuthal profiles of the A-ring filling factor as a function of S/C azimuthal angle in the rotating frame ϕ at various spacecraft elevation *B* (shown as B_F in the figure). Best fit for elliptical cylinders wake model (dash-dot) or rectangular bars wake model (dot) are superimposed with the same color. Expected profiles at elevation *B* = 55 deg and *B* = 70 deg are also plotted. Figure from Ferrari et al. [2009].

Ring optical depth at mid-IR wavelengths

Differences between radial profile of optical depths at different wavelengths provide information on changes in the size distribution versus distance. Such profile was definitely missing at infrared wavelengths. Several CIRS ring occultations of the bright stars Eta Carinae and CW Leo were observed using the CIRS FP3 10-pixel array, with the objective of obtaining such mid-infrared (MIR) optical depths of Saturn's main rings (Figure CIRS-8). Since the rings also emit thermal photons at these wavelengths, the FP3 array was aligned along the occultation track. The stars and their

extended dust clouds were observed across two pixels, and the remaining pixels were used for background subtraction of the rings. CIRS optical depths were compared to UVIS optical depths from a high-resolution UVIS occultation of the star β Persei. It was expected that the cross-sections in the UV and MIR would behave similarly, but a linear fit of the observed MIR power to the UVIS-derived line of sight filling factor for a UV occultation indicates that the observed MIR filling factor is approximately 4% smaller than that predicted from the ultraviolet occultation of Saturn's rings [Pilorz et al. 2018a]. The optical depths agree well in the C-ring and A-ring, but in the B-ring the CIRS derived optical depth is smaller. This could result from the simplistic calibration, or be due to details related to the saturation of the CIRS signal in that region due to strong B-ring emission in the MIR. Additional CIRS Eta Carinae occultations obtained late in the mission are still to be processed.

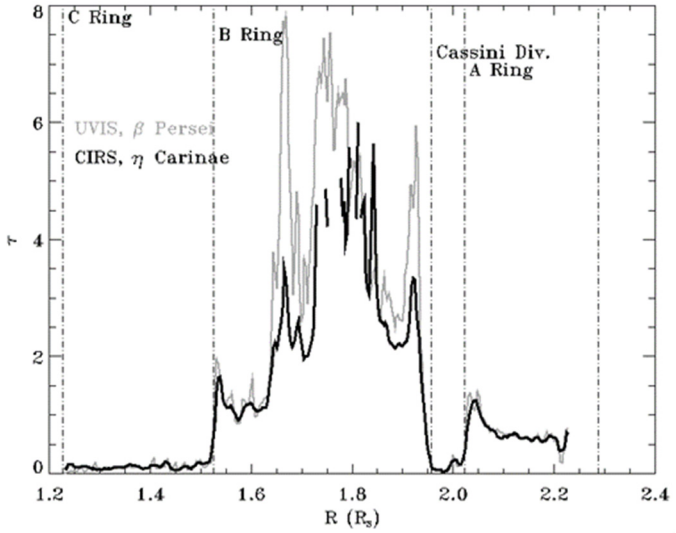

Figure CIRS-8. MIR optical thickness. This is an estimate obtained from the Eta Carini occultation, which may change pending ongoing work to correct for the response of the FP3 detectors, the location of the star within the FOV, the thermal signal from the rings, and the maximum signal received. Figure from Pilorz et al. [2018a].

Ring thermal models

Saturn's rings offer a wide diversity of optical depths and dynamical contexts. Particle properties are expected to be more easily probed in optically thin rings or in rings with very low volume filling factor *D*. As the volume filling factor increases or as tidal effects diminish, particles may interact dynamically to form wakes, gravitational instabilities of any form, like typically suggested for Saturn's A-ring and B-ring. The thermal behavior of the ring depends on the structure of group ensembles or on the dynamics of colliding particles, which is still not well known. If *D* is low, particle-based models are generally used. In case of high volume filling factor, the ring can be treated either as infinitesimally long elliptical or rectangular cylinders or as a slab or static packed bed with limited excursion of ring particles. These latter slab-based models do not usually consider individual particles but can eventually treat heat transfer both at the particle scale and

the scale of the ring itself. They may be suitable for the thick A-ring and B-ring and for the wake structures seen in these rings.

Various models have recently been developed to tentatively reproduce the observed thermal behaviors of Saturn's rings. They rely on different a priori hypotheses and produce various observables to be fitted to data. At this stage, none of these models is able to reproduce all observed thermal behaviors at once. We describe here models for the ring geometric filling factor and temperatures that have been developed in the past decade. These thermal models are classified into particle-based models and slab-based models.

Heat transfer

The particle-based models solve the heat diffusion equation at the scale of the particle and its facets, whereas the slab models solve it at the scale of the ring. Both ring and particle can be considered as porous media. In order to follow the change of the temperature T with time in such media, the thermal diffusion equation needs to be solved with appropriate boundary conditions, i.e., energy balance, assuming effective thermal properties of a mixture of voids and matter.

The temporal variation of the incoming flux at the chosen scale occurs due to the particle spin, to azimuthal motion around the planet, or to vertical motion of particles in optically thick rings. While some models explicitly take into account these variations by solving the thermal diffusion equation, the heat conduction term is often ignored in simple models. On a long timescale, seasonal variation occurs due to the obliquity of Saturn. It is reasonable to ignore the heat conduction term for the seasonal effect as the thermal relaxation time is much shorter than the Saturn's orbital period. An exception is at equinox, at which the rings may not completely cool down to the equilibrium temperatures that are determined in the absence of direct solar illumination.

The total radiation flux consists of the sum of the direct solar radiation, the thermal radiation from Saturn, the sunlight reflected by Saturn, the thermal radiation from nearby particles, and the radiation of visible light multiply scattered by neighboring particles. Methods to calculate these fluxes vary among models but the direct solar radiation term dominates other terms except near solar equinox.

Particle-based models

The two extreme examples of the particle-based models are the mono-particle-layer model [Froidevaux et al. 1981; Ferrari and Leyrat 2006] and the multi-particle-layer model [Kawata 1983; Morishima et al. 2009]. The particle-based thermal models that have been recently developed [Ferrari and Leyrat 2006; Morishima et al. 2009] calculate temperature distribution over the surfaces of individual particles. The ring temperature is derived by integrating the emitted spectrum averaged over the particle surfaces. Therefore, these models are applicable to any observational geometries while the early models are practically applicable only to ground-based observations. Particles may oscillate around the ring mid-plane and exhibit spin. Their properties are characterized by various

parameters such as bolometric Bond albedo, distribution of spins, thermal inertia, infrared emissivity, or surface roughness.

Monolayer Model: Ferrari and Leyrat [2006] proposed a standard spin model that calculates the temperature of a monolayer ring of spinning particles with finite thermal inertia. It calculates exactly the surface temperature pattern as a function of spin rate, obliquity and thermal inertia. The surface temperature map of a particle is calculated over time along its specified orbit, taking into account the periodic crossing of the planetary shadow and the changing directions of the heating sources in the particle rotating frame.

For each particle facet the heat diffusion equation is solved in 1D-spherical coordinates over several times the larger one of the skin depth associated with the particle spin or that with the rotation around Saturn. The energy balance is applied at the scale of a facet of a particle. It takes into account mutual shadowing between particles, visible light scattered and infrared heating by nearby particles or by the planet. The effective temperature of the unresolved particle is calculated from its integrated thermal spectrum as seen from the spacecraft position. Model parameters are the probability density functions for spin rates and orientations, the particle Bond albedo, emissivity, and thermal inertia.

Ferrari and Leyrat [2006] showed that the spin rate, orientation and thermal inertia significantly modulate the ring temperature along local hour angle L and that the longitude of the peak temperature mainly depends on the spacecraft local hour angle, as it alternatively observes the morning, noon, afternoon, or night-time face of particles. The distribution in spin rates or obliquities, prograde or retrograde, the thermal inertia affects this modulation to a lesser extent.

Multilayer Model: In the multi-particle-layer model of Morishima et al. [2009], the vertical thickness of a ring is assumed to be much larger than the particle size or equivalently the ring's volume filling factor $D = 0$. The model numerically solves the classical radiative transfer equation [Chandrasekhar 1960; Modest 2003] using the multi-stream method. The model adopts the plane-parallel approximation so rings are horizontally homogeneous.

The model takes into account heat transport due to particle motion in the vertical and azimuth directions by following temporal thermal evolution of thousands of ring particles. The model employs two different types of vertical motion of particles: sinusoidal motion without collision and cycloidal motion that mimics bouncing at the mid-plane. The model assumes, instead of an actual continuous size distribution, a bimodal size distribution consisting of fast and slow rotators. Fast rotators are small rapidly spinning particles having spherically symmetric thermal structure whereas slow rotators are large non-spinning Lambertian particles. The areal fraction of fast rotators and the ratio of the scale height of fast rotators to that of slow rotators are the input parameters. The ring effective temperature is derived by summing up the thermal emission of all ring particles toward the observer, taking into account the attenuation factor due to other particles on the line of sight.

MODELING OF OPPOSITION SURGE FOR PACKED PARTICULATE MEDIUM

Models for packed particulate medium [Lumme and Bowell 1981a; Hapke 1993], which were originally derived to explain reflectance measurements of atmosphereless bodies, was used by Altobelli et al. [2007, 2009]. These models envision Saturn's rings as a packed particulate medium. In this approach, the drop-off in temperature with increasing phase angle is related to a net reduction of the particles' illuminated cross-section as a result of mutual shadowing. In addition, particles must be big enough and far enough apart with respect to the wavelength so that diffraction effects are negligible, which is certainly the case for Saturn's rings at visible and thermal infrared wavelengths. For a given optical depth, the relevant physical parameter for particles to cast shadow is their volume filling factor *D*.

SLAB-BASED RING STRUCTURE MODELS

Current slab-based ring thermal models follow diverse objectives. They aim at predicting ring lit side temperatures with no attempt to implement the physical processes at the origin of the thermal emission [Altobelli et al. 2014], at reproducing the thermal opposition surge with a varying degree of surface roughness [Morishima et al. 2017], or at estimating the thickness of rings from thermal gradients between lit and unlit sides [Ferrari et al. 2005; Ferrari and Reffet 2013; Pilorz et al. 2015]. The slab-based models that reproduce the diurnal or seasonal temperature variations of lit and unlit sides help us understand how heat transfers from one side to the other and why the thermal inertias observed are so low.

Empirical modeling of lit side ring temperatures: Altobelli et al. [2014] attempted to fit the entire CIRS data set using a slab-based model with correction factors due to variations of observation geometries defined empirically. They focused on only the lit side, non-shadowed by the planet. This analytical model has proven to be a good predictor of temperature variations for most of the viewing geometries. The model has been tested over the whole ring radial extent, using radial slices 1500–4000 km wide. The radial resolution is constrained by requiring at least one hundred individual measurements with an error below 2 K within each ring slice. The resulting full parameter values are provided in Altobelli et al. [2014].

Particle scale properties

The models cited below have been compared to CIRS ring temperatures to provide constraints on ring and particle properties. They share some basic common parameters like albedo, spin or thermal inertia, which can be defined at both the scales of the particle and the ring. Some models include unique parameters.

BOLOMETRIC BOND ALBEDO

The bolometric albedo A_V (Figure CIRS-9) is the albedo averaged over ultraviolet to near-infrared wavelengths, weighted by the solar intensity. It controls the overall temperature level at any

observational geometry: the temperature increases with decreasing A_V. From Morishima et al. [2010] the albedo A_V derived from CIRS data is lowest, ~0.1, at the innermost C-ring and increases with increasing saturnocentric distance up to 0.6 at the mid B-ring. Through the mid B-ring to the outer B-ring, A_V is nearly constant. The Cassini division shows $A_V \sim 0.4$. The A-ring has a nearly constant A_V of ~0.5. The values of A_V derived from this thermal model can be compared with those from photometric observations and models. Although overall agreements are good, the thermal data generally give lower values of A_V than those from the photometric data, particularly for the C-ring. One possible explanation for the deviation is that the infrared emissivity ε_{IR} is less than unity while the thermal model assumes $\varepsilon_{IR} = 1$. Other studies (see the section entitled Scalar Thermal Emissivity for particle and ring emissivity) derive values for ε_{IR} of ~0.9 across all rings.

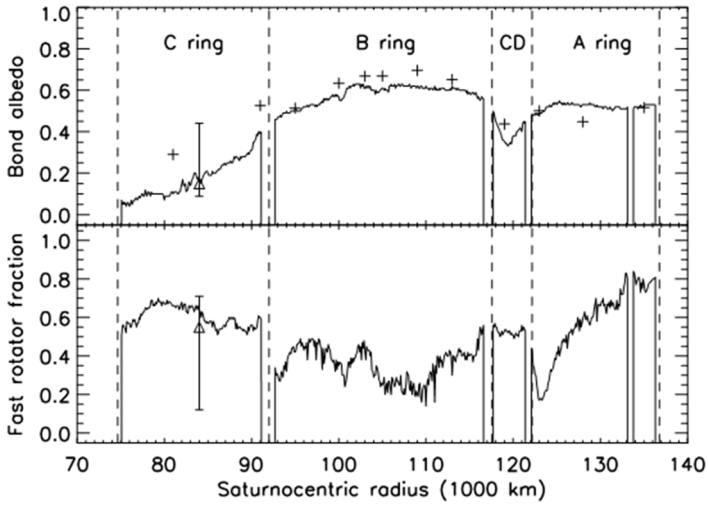

Figure CIRS-9. Bolometric Bond albedo A_V and areal fraction of fast rotators f_{fast} estimated from CIRS radial scans and the multi-particle-layer model. [Morishima et al. 2009, 2010]. The triangles are A_V and f_{fast} estimated from Voyager IRIS data and the mono-particle-layer model [Leyrat et al. 2008a]. *Top panel*: plus marks are the values of A_V calculated using visible and near-infrared albedos [Poulet et al. 2003; Porco et al. 2005].

SPIN RATE

The phase dependence and first-order azimuthal variations of ring temperatures can be interpreted as being caused by spherical spinning particles, as demonstrated by particle-based models. Slowly spinning particles emit predominantly toward the heat source, while fast spinning particles emit more isotropically.

The multi-particle-layer model of Morishima et al. [2009] employs a bimodal spin distribution consisting of slow rotators and isotropic emitters fast rotators with fraction f_{fast} which is roughly half for the all rings although some regional variations, such as smaller particles and more fast rotators in the outer A-ring, are seen. Roughly speaking, fast rotators are defined so that their spin periods are shorter than the thermal relaxation time [Morishima et al. 2011]. The spin periods of the largest particles are about the orbital period while the orbital periods of smaller particles are proportional

to particle sizes [Salo 1987; Ohtsuki 2006a, 2006b; Morishima and Salo 2006]. Therefore, f_{fast} increases with increasing particle-size distribution width and with increasing thermal inertia. Morishima et al. [2011] found good agreements between the size distribution width suggested from f_{fast} and thermal inertia and those estimated from stellar occultations [French and Nicholson 2000]. The analysis with Ferrari and Leyrat [2006] model of the temperatures of the C-ring at equinox epoch implied that both population are indeed present [Spilker et al. 2013].

DIURNAL THERMAL INERTIA

The thermal inertia Γ is a measure of the thermal responsiveness of a material to variations in the incoming flux. When Γ is small enough the particle temperature quickly reaches the equilibrium value determined by the instantaneous flux. Morishima et al. [2011] applied their multi-particle-layer model to CIRS azimuthal scans (Figure CIRS-10) that include data in Saturn's shadow and estimated the diurnal thermal inertia (diurnal here represents a variation due to rotation around Saturn).

The values of Γ are estimated from individual CIRS azimuthal scans at different solar phase angles. The values are about 10–20 $Jm^{-2}\ K^{-1}\ s^{-1/2}$ for all the rings. The Cassini division shows the lowest values. These are comparable to or slightly higher than those estimated with the mono-layer spin model both for pre-Cassini studies [Leyrat et al. 2008b] or Cassini observations of the C-ring at 10 $Jm^{-2}\ K^{-1}\ s^{-1/2}$ [Ferrari 2006; Spilker et al. 2013].

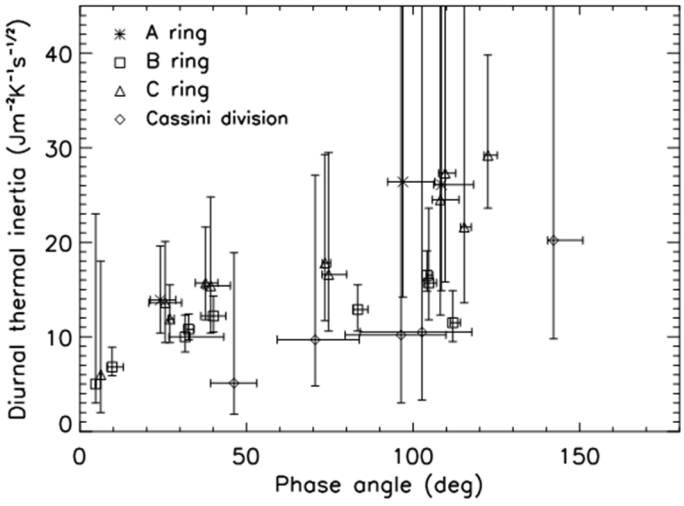

Figure CIRS-10. Diurnal thermal inertia estimated from CIRS azimuthal scans. The multi-particle-layer model [Morishima et al. 2009, 2011] is used. Thermal inertias of the B-ring and C-ring at the lowest phase angles (~5 deg) are those estimated by Ferrari et al. [2005] who applied their mono-particle-layer model to the ground-based data.

However, it was found that Γ increases with solar phase angle for all the rings. Morishima et al. [2011] interpreted this trend as caused by the size-dependent thermal inertia; large slow rotators have lower thermal inertia values than those for small fast rotators because the thermal emission

of slow rotators is relatively stronger than that of fast rotators at low phase and vice versa. Their additional parameter fits, which assume that slow and fast rotators have different thermal inertia values, showed the thermal inertia of fast rotators are 30–80 $Jm^{-2}\ K^{-1}\ s^{-1/2}$ and that of slow rotators are 5–9 $Jm^{-2}\ K^{-1}\ s^{-1/2}$. A probable reason for the large thermal inertia of fast rotators is that they cannot hold very fluffy regolith layers because of their fast spins while the slow rotators can accumulate a thicker, porous regolith layer leading to smaller thermal inertias.

SEASONAL THERMAL INERTIA AND PARTICLE SIZE

Morishima et al. [2016] applied both the multi-particle-layer model [Morishima et al. 2009] and the wake model [Morishima et al. 2014] to the equinox data of the A-ring. They found that the observed equinox temperatures are much higher than model predictions as long as only the flux from Saturn is taken into account. In addition, the post-equinox temperatures are lower than the pre-equinox temperatures at the same absolute solar elevation angle. These facts indicate that the A-ring was not completely cooled down at the equinox and that it is possible to give constraints on the size and seasonal thermal inertia of ring particles.

A simple seasonal model based on the monolayer model (Figure CIRS-11) was used to estimate the seasonal thermal inertia and the particle size for the A-ring [Morishima et al. 2016]. If the internal density and the thermal inertia of a ring particle are assumed to be uniform with depth, the seasonal thermal inertia is found to be 30–50 $Jm^{-2}\ K^{-1}\ s^{-1/2}$ in the middle A-ring, whereas it is ~10 $Jm^{-2}\ K^{-1}\ s^{-1/2}$ or as low as the diurnal thermal inertia in the inner and outermost regions of the A-ring. The particle size is estimated to be 1–2 m. Another internal structure model, in which a particle has a high-density core surrounded by a fluffy regolith mantle with Γ of 10 $Jm^{-2}\ K^{-1}\ s^{-1/2}$ shows that

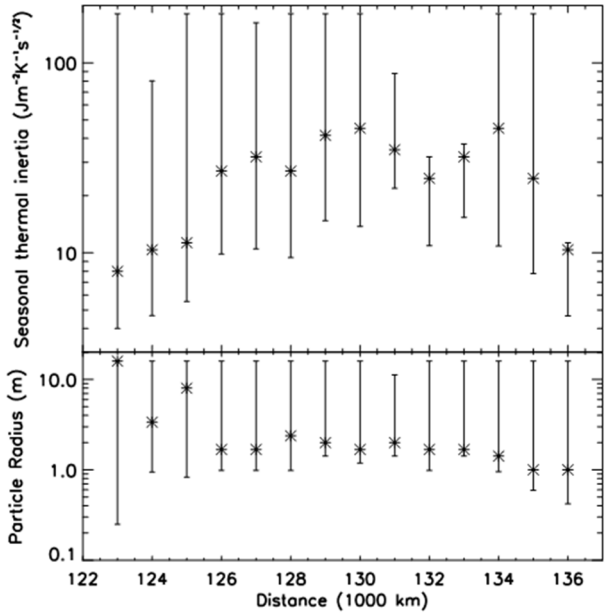

Figure CIRS-11. Seasonal thermal inertia and size of particles for the A-ring [Morishima et al. 2016].

the core radius relative to the particle radius is about 0.9 for the middle A-ring and is much less for the inner and outer regions of the A-ring [Morishima et al. 2016]. This means that the radial variation of the internal density of ring particles exists across the A-ring. Some mechanisms may be confining dense particles in the middle A-ring against viscous diffusion. Alternatively, the middle A-ring might have recently formed ($<10^8$ yr) by destruction of an icy satellite, so that dense particles have not yet diffused over the A-ring and regolith mantles of particles have not grown thick.

Scalar Thermal Emissivity

Since the thermal infrared emission of the particle is proportional to the scalar emissivity ε_{IR}, the temperature increases with decreasing ε_{IR}. A degeneracy between A_V and ε_{IR} is expected, as the particle temperature is proportional to $((1 - A_V)/\varepsilon IR)^{1/4}$ with a single heat source emitting visible light (e.g., the Sun).

It is possible to constrain ε_{IR}, if the ring temperature and the geometric filling factor are known [Altobelli et al. 2008]. For optically thin rings, the geometric filling factor is well represented by the formulation of the multi-particle-layer model. Using the formulation, Altobelli et al. [2008] derived $\varepsilon_{IR} = 0.9$ for the C-ring. For the thickest part of the B-ring, the geometric filling factor is almost unity, and $\varepsilon_{IR} = 0.9$ is derived, too [Spilker et al. 2005; Altobelli et al. 2008]. Morishima et al. [2016] applied the wake model of Morishima et al. [2014] to the A-ring equinox data and estimated the lower limit of ε_{IR} to be ~0.9. The most recent work by Pilorz et al. [2018b] supports the previous results (Figure CIRS-12).

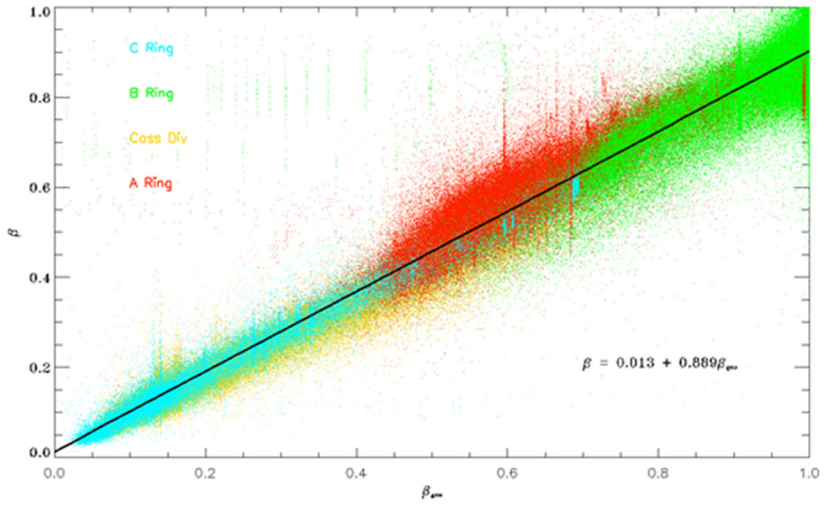

Figure CIRS-12. Scaling factor β versus convolved geometric filling factor β_{geo}. Figure from Pilorz et al. [2018b].

Ring-scale properties

When compared with the orbital and seasonal temperature variations of the lit and unlit sides, slab-based thermal models have provided new insights into the structure of dense rings, their volume filling factor, thickness, mass and thermal properties. The observed correlation of the vertical thermal gradient between both sides with optical depth proved useful in this regard.

VOLUME FILLING FACTORS OF A-RING AND B-RING

Both the thermal opposition effect model [Altobelli et al. 2009] and the multi-scale slab model favor a relatively high volume filling factor for the dense central B-ring. For a mono-disperse population of spherical particles, the half-width-half-maximum (HWHM) of the thermal opposition peak $h \approx -(3/8)\ \ln(1-D)$ yields $0.3 < D < 0.4$ in the B-ring. In the outer A-ring, $D < 0.2$. The C-ring background and Cassini division thermal phase curves could hardly be reproduced by this model, suggesting that, as expected, the thermal emission is not modulated by mutual shadowing in these thin rings. The C-ring plateaus, on the other hand, show strong opposition surge and Altobelli et al. [2007] yielded $D = 0.001–0.01$.

Reffet et al. [2015] also demonstrated that, in the frame of a multi-scale slab approach, the correlation between the lit-unlit face temperature difference and the optical depth seen in the B-ring [Spilker et al. 2006] could not be explained by an increasing compaction D but rather by an increasing slab thickness. The fit of this model to orbital and seasonal temperatures all along the Prime Mission in the central B-ring (across the B2 and B3 thickest regions of the B-ring yielded a volume filling factor $D = 0.34 \pm 0.01$, remarkably consistent with the value derived from the opposition surge [Altobelli et al. 2009] and with expectations from numerical simulations of ring dynamics [Salo and Karjalainen 2003; Salo and French 2010].

ENERGY BUDGET AND HEAT TRANSFER IN B-RING

The optically thick B-ring is a good region for a slab-based modeling approach because the ring particles are expected to be close together, as confirmed by its measured filling factor. The slab approach allows the heat transfer to be quantified through such a dense ring structure and provides an effective thermal inertia or thermal conductivity through a vertical slab from the lit to the unlit side of the B-ring. The heat transfer can be by conduction through the solid phase of particles, by radiation through voids or by the vertical particle motion.

Ignoring vertical particle motion in the thick B-ring, Ferrari and Reffet [2013] proposed a model for the B-ring slab, including both heat transport by radiation and conduction and being able to disentangle ring and particle thermal inertias thanks to a multi-scale approach (Figure CIRS-13). This model was successfully fitted to more than 600 temperature measurements of both lit and unlit sides of the B-ring and spread all along the Cassini Prime mission (2004–2009) [Reffet et al. 2015]. Only mid-phase angle data were used to avoid the low-phase angle thermal hotspot, which the model cannot account for, assuming particles are isothermal. Self-gravity wakes have been

observed in the B-ring and the reduced width of the inter-wake gap allows them to be considered as a continuous slab. This is not the case for these structures observed in the A-ring.

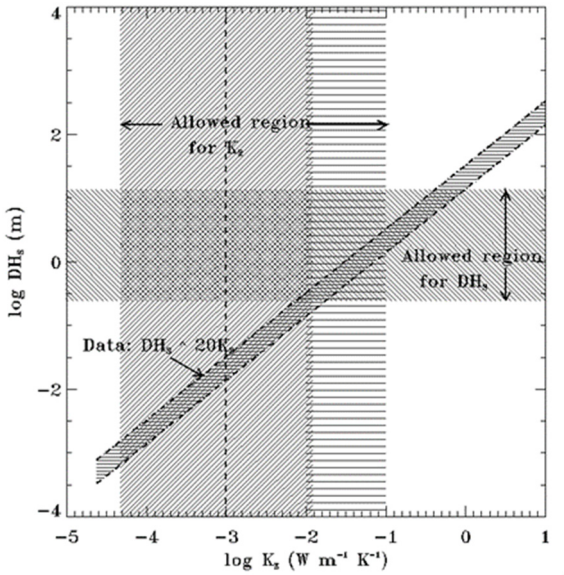

Figure CIRS-13. Diagram of the allowed values of effective ring thickness, DH_S, and effective heat conductivity, K_E, for the B-ring. These values are consistent with the ratio K_E/DH_S constrained in Pilorz et al. [2015]. The diagonal hashed region indicates combinations of values of DH_S and K_E such that ratio K_E/DH_S agrees with observations of the seasonal variation of heat throughput. The horizontal and vertical hashed regions indicate ranges of values for DH_S and K_E, respectively that are currently accepted as reasonable for ring thickness and the conductivity of icy moon regoliths or ring models.

THERMAL PROPERTIES, THICKNESS, AND SURFACE MASS DENSITY OF B-RING

Fitting of the model of Ferrari and Reffet [2013] to the central B-ring at the distance of 105,000 km from Saturn, where most data on the transient thermal regime about the planetary shadow were focused, Reffet et al. [2015] found a slab Bond albedo of A_V = 0.402 ±0.005 for an emissivity nearly unity, in total agreement with the energy balance studied by Pilorz et al. [2015].

Assuming no heat transport by the vertical motion of particles, but solely by conduction through the particles and radiation through voids, the particles have to be relatively conductive to ensure vertical heat transport through the slab. The effective slab conductivity estimated by Reffet et al. [2015] is on the order of 0.06–0.08 W m^{-1} K^{-1} at 80 K. Despite very different approaches but fitted on similar data sets, Reffet et al. [2015] and Pilorz et al. [2015] yield similar slab effective conductivity. The seasonal thermal inertia for the B-ring was found to be 30–35 Jm^{-2} K^{-1} s$^{-1/2}$, comparable to the seasonal thermal inertia of particles measured in the A-ring by Morishima et al. [2016].

The empirical model of Altobelli et al. [2014], using the entire CIRS data set to that date, and including radial scans near the shadow boundaries, yields a thermal relaxation time of 15–25

minutes, almost radially constant for the A-ring and B-ring. Since the thermal relaxation time is expected to be linearly proportional to the slab thermal inertia [Morishima et al. 2011], the radial variation of the slab thermal inertia is likely to be small for these rings.

Assuming that the vertical thermal gradient in the B-ring mainly fluctuates with the slab thickness and that ring and particle properties across the whole ring are similar to the one derived at 105 000 km distance, Reffet et al. [2015] have derived two radial profiles of the B-ring thickness $H_S(R)$ at two different epochs, where B_0 = −15.7° and B_0 = −4.5°. They happen to be highly consistent and exhibit variations in between 1 m and 3 m in the highest optical depth regions of the B-ring (Figure CIRS-14). If this thickness is assumed to be the same as the thickness of self-gravity wakes in the B-ring, it can be combined with their aspect ratios to derive a surface mass density across the thickest regions (B_2 to B_4) of the B-ring. It is found that the surface mass density is about 400 kg m^{-2} in the B_2 region, about 500 kg m^{-2} in the B_4 region and larger than 1000 kg m^{-2} in the B_3 region as self-gravity wakes are observed with difficulty in this dense region.

The resulting minimum mass of the B-ring derived by this method is $M_B = 8.7 \pm 1.7 \times 10^{18}$ kg [Reffet et al. 2015]. The minimum total mass of Saturn's rings, given the estimates of the C-ring, CD-ring, A-ring, and B_1-ring, for a total mass of 5.3×10^{18} kg [Baillié et al. 2011; Colwell et al. 2009; Tiscareno et al. 2007; Esposito et al. 1984], would then be $M_R = 1.4 \pm 0.2 \times 10^{19}$ kg. It is consistent with larger estimates provided by Esposito et al. [1983] and Robbins et al. [2010]. The minimum mass of the B-ring estimated by this method compares rather well to the residual mass of a viscous ring which has evolved over the age of the solar system, i.e., $M_R = 1.5 \times 10^{19}$ kg, whatever the initial (larger) mass is [Salmon et al. 2010].

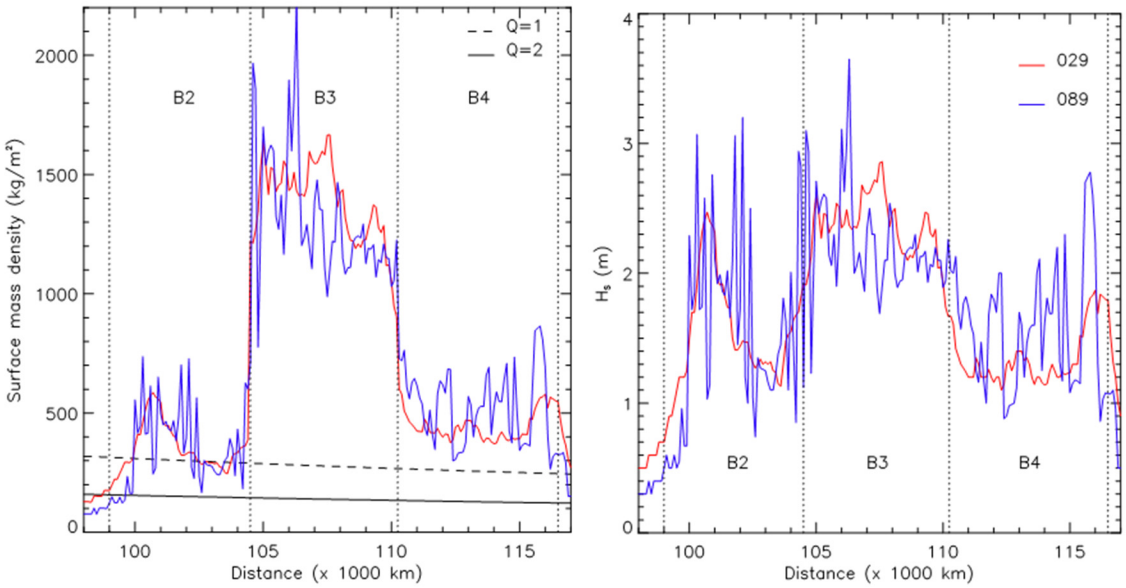

Figure CIRS-14. *Left*: Vertical thickness of the B-ring slab as a function of distance to Saturn. Both profiles have been estimated from vertical gradient measured at B_0 = -15.7 deg (rev. 29) and B_0 = −4.5 deg (rev. 89). *Right*: Radial variations of surface mass density of the B-ring as derived from ring thickness H_S. See Reffet et al. [2015] for details.

SELF-GRAVITY WAKES IN THE A-RING

The quadrupole azimuthal asymmetry first discovered in the A-ring in visible light from the ground [Lumme and Irvine 1976; French et al. 2007] has been since observed with the Cassini remote sensing instruments [Colwell et al. 2006; Hedman et al. 2007; Thomson et al. 2007]. It is caused by the presence of self-gravity wakes forming in this ring close to the Roche limit. As trains of gravitationally bounded particles, separated by gaps of low optical depth [Salo 1995; Robbins et al. 2010], self-gravity wakes are expected to modulate both the filling factor of the instrument field of view and the ring observed temperature along azimuth. These structures were satisfactorily modeled as rectangular bars or elliptical cylinders mainly after the analysis of occultation data [Colwell et al. 2006; Hedman et al. 2007].

Ferrari et al. [2009] showed that the fit with azimuthal variation of the beta factor at different solar elevations was improved using the regularly spaced, infinitely long, opaque elliptical cylinders using the geometric filling factor from Hedman et al. [2007]. In the wake model of Morishima et al. [2014], the temperature distribution over the wake surface is calculated instead of considering the temperatures of individual particles. Wakes are approximately represented by opaque elliptical cylinders as adopted in Hedman et al. [2007] and Ferrari et al. [2009]. The model ignores inter-wake particles for simplicity. The surface of an elliptical cylinder is divided into multiple facets and interactions between facets (inter-wake mutual heating and multiple scattering of photometric light) are calculated using a radiosity method. The ring effective temperature is calculated by summing up the thermal emission from facets that can be seen from the observer.

SURFACE ROUGHNESS OF THE B-RING

Morishima et al. [2017] reanalyzed the seasonal variation of thermal phase curves for the B-ring, first found by Altobelli et al. [2009]. Morishima et al. [2017] approximated the B-ring as a slab covered by craters and the surface roughness of the B-ring was found to be moderate. The modeled phase curves of optically thick rings are shallow if the phase angle change is primarily due to change of observer azimuthal angle. On the other hand, the phase curves are steep if the phase angle change is due to change of observer elevation angle, as inter-particle shadows become visible at higher observer elevation. In addition, the area of shadowed facets increases with decreasing solar elevation angle. These combined effects explain the large seasonal change of the phase curve steepness observed for the B-ring.

Regolith properties deduced from CIRS emissivity roll-off

Ring particles are often assumed to be covered by tiny regolith grains. In rings with low volume filling factor *D*, ring properties can be relatively easily related to the particle and grain properties. Under this assumption, rings are clouds of particles and their thermal emission is a function of the individual particle properties. The ring emissivity can be retrieved from observations and compared to a model which links it to the average emissivity of individual particles and then regolith grains. Rings then are multi-scale worlds made of cm-to-m-sized particles themselves covered by μm-to-

cm-sized grains. Morishima et al. [2012] after the work of Spilker et al. [2005] in the earlier stages of the Cassini mission propose a model to interpret the ring emissivity in terms of regolith grain size and chemical composition.

THERMAL EMISSIVITY ROLL-OFF AT SUBMILLIMETER WAVELENGTHS

The infrared spectrometer provides the thermal radiance *I* (ν) of the ring as a function of wavenumber, ν. If the emissivity ε(ν) is assumed constant over a footprint, using a single temperature approximation, Spilker et al. [2005] derived the ring emissivity as:

$$\varepsilon(\nu) = I(\nu) / \left(\beta_{geo} B(\nu, T_0)\right)$$

where they obtained β_{geo} using Voyager Power & Pyrotechnics Subsystem (PPS) occultation data and the multilayer approximation. The spectral roll off occurs for $\nu < 50$ cm^{-1} for all rings.

While Spilker et al. [2005] analyzed a limited number of CIRS spectra measured in the very early stage of the Cassini mission from relatively large distances, Morishima et al. [2012] analyzed a much larger number of spectra more comprehensively. In their emissivity model, two warm and cold portions, with temperatures T_w and T_c, are considered where f_w is the fraction of the warm portion. A superposition of spectra with two different temperature portions produces a downward convex function of the emissivity when applied to a Planck fit with a single temperature. On the other hand, the emissivity spectrum of water ice has a downward convex function in far-infrared wavelengths. Because these two effects cancel each other out to some degree, degeneracy is generated between the retrieved emissivity spectrum and the temperature distribution. To avoid this issue, Morishima et al. [2012] applied simultaneous fits of the emissivity model parameters (grain sizes) and of hot and cold temperature distributions. They also derived β_{geo} using Cassini UVIS data, taking into account the spacecraft elevation dependence on the photometric optical depth.

The emissivity of Saturn's rings at far-infrared wavelength (Figure CIRS-15) is high basically because of absorption caused by intermolecular vibrations of water ice. A dip seen at 230 cm^{-1} corresponds to the maximum of the imaginary part of the refractive index of the water ice (transverse-optical mode). As found by Spilker et al. [2005], the emissivity decreases with decreasing wavenumber for $\nu < 50$ cm^{-1} because water ice becomes increasingly transparent at longer wavelengths (thus opening a view into the deeper ring particle). The exact wavelength of the roll-off is a strong function of the size of an individual particle, with larger particles having flatter emissivity as the geometric optics limit is approached. No one particle or grain size fits any spectrum and the emissivity is reflective of the collective distribution of ring particle and their regolith grain sizes.

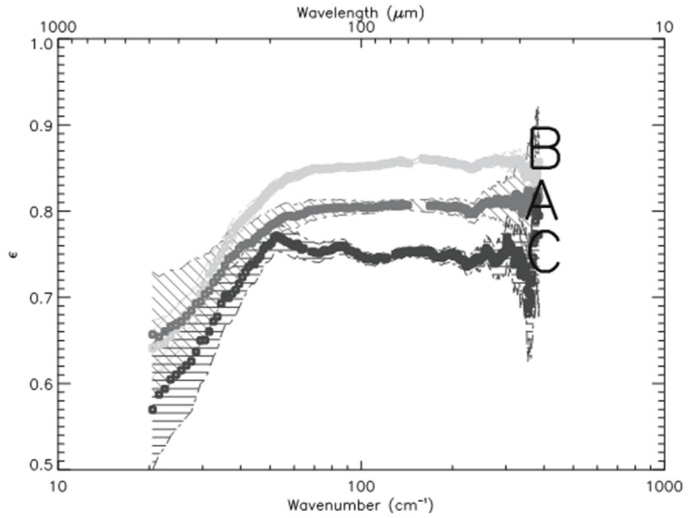

Figure CIRS-15. Emissivity spectra for the A-ring, B-ring, and C-ring. Figure from Spilker et al. [2005].

REGOLITH GRAIN SIZES INFERRED BY EMISSIVITY MODELING

A ring emissivity model was proposed by Morishima et al. [2012] to interpret the ring emissivity in terms of regolith grain size and chemical composition. The single scattering albedos of regolith grains are calculated using the Mie theory [Mie 1908; Bohren and Hoffman 1983], diffraction is removed with the delta-Eddington approximation [Joseph et al. 1976], and the hemispherical emissivities for macroscopic particles are calculated using Hapke's isotropic scattering model [Hapke 1993]. The composition of regolith grains is assumed to be pure water ice *Ih*. The intra-grain porosity of 0.7 is introduced to reproduce the shallow 230 cm^{-1} feature seen in the ring spectra in Morishima et al. [2012]. The maximum ring particle size that CIRS is sensitive to is estimated to be 1–100 cm in most of the rings, although the C-ring shows very different values of maximum grain size, and is dependent on the temperature of the ring. The median size is typically between 100 and 1000 μm. The reason for the temperature dependence of the estimated size distributions, particularly seen in the C-ring, is not clearly understood. Morishima et al. [2012] suggested that it is caused by the effect of eclipse cooling; only small grains are heated to very high temperatures.

The retrieved grain sizes are larger than those estimated from UVIS [Bradley et al. 2010, 2013] and VIMS [Nicholson et al. 2008; Cuzzi et al. 2009; Filacchione et al. 2012; Hedman et al. 2013] reflectances. An interpretation of this discrepancy is that large regolith grains are covered by small grains. At short wavelengths, the incoming light is primarily reflected by these small grains while at longer wavelengths the light can penetrate deeper into the regolith layers.

Exploring possible contaminants using CIRS spectra remains for future work, although the range of wavelengths covered by CIRS is not very suitable for this purpose due to strong water absorptions. Preliminary work [Edgington et al. 2008, unpublished] looked for the presence of silicates, carbon monoxide, and several other simple ices to no avail. This work also sought to determine the relative amounts of amorphous versus crystalline water ice. During Cassini's Solstice

Mission, a great many additional observations at high spectral and higher spatial resolution were acquired. Given this additional data, along with improved calibration of the CIRS data set, a proper statistical analysis and spatial trend analysis is warranteed to look for spatial variations in particle sizes and the presence of contaminant ring material. Another potential area of investigation would couple analysis of the longest wavelengths of the roll-off region with Titan Radar Mapper (RADAR) observations of the rings which probe the deeper particle cores.

Possible polarization effects have been studied. A few CIRS observations where designed to make use of the polarization nature of the FP1 interferometer (accomplished by rotating the spacecraft to three distinct orientations separated by 60°) to look for polarization effects in the far-IR. Theoretically possible with non-spherical thermal emitters, the data were inconclusive as observed patterns could be explained by other physical effects such as thermal opposition surges. These individual observations do not take into account the advantage that the entire CIRS FP1 data set picks off a particular polarization direction. The possibility that there is a polarization signal hidden in the global data set remains to be seen.

Conclusions and future work

Considering the Cassini CIRS data set in its entirety showed us that the ring can be characterized as a thermal system whose properties result from multi-scale phenomena, including the physical properties of individual particles as well as large-scale interactions, resulting in shadowing and thermal transport across the ring. Future analysis will aim at combining the global approach yielding empirical models of the ring thermal behavior, with the forward modeling of individual particles, such as to reject solutions possibly acceptable at one scale but not at the other. The key CIRS ring results are discussed in the next several paragraphs.

The global modeling of all measurements obtained over the illuminated rings yields radial profiles of the ring emissivity and albedo with the highest spatial resolution ever achieved in the thermal infrared. The anisotropy of the temperature distribution with viewing geometry, and in particular the effect of mutual shadowing between particles in regions with higher optical depth, is directly inferred from the global empirical modeling. Thermal surges at low phase angle, most likely resulting from shadow hiding, have been observed in all ring regions, except those with the lowest optical depth like the C-ring background. A contribution to shadow hiding from the particle's regolith cannot be excluded, in particular if regolith properties are driven by the frequency of particle collision, correlated with the ring optical depth. Combining the empirical model of the ring, constrained by all measurements, with dynamical simulations and with realistic temperature distributions on irregular, regolith covered icy surfaces, is the next logical step to disentangle the large-scale properties of the rings from those of its individual constituents.

There is a correlation between the bolometric Bond albedo and the ring optical depth. This is also found by photometric observations and is probably produced by meteoritic bombardment. The areal fractions of fast and slow rotators are similar to each other, although the fast rotator's fraction is larger for thin rings. This produces large range of size distributions for thin rings. A large fraction

of fast rotators is seen in the outer A-ring, suggesting enhanced impact velocities in this region, possibly due to satellite perturbations or strong self-gravitational wakes.

The diurnal thermal inertia is estimated to be about 10 J m^{-2} K^{-1} $s^{-1/2}$ for all the main rings from eclipse cooling data, although the Cassini division shows the lowest values. The low diurnal thermal inertia may indicate a very fluffy surface regolith layer. The thermal skin depth associated with eclipse cooling is on the order of 1 mm. The seasonal temperature variations can provide constraints on thermal inertia of deep interiors of particles, if they do not completely cool down at equinox to their equilibrium temperatures that are determined by the flux from Saturn only. The equinox temperature of the middle A-ring is found to not completely cool down. The seasonal thermal inertia of the middle A-ring particles is estimated to be 30–50 J m^{-2} K^{-1} $s^{-1/2}$, while it is as low as the diurnal thermal inertia for the outer and inner parts of the A-ring. The ring particles in the middle A-ring are likely to have a dense core under a thin fluffy regolith mantle. This indicates that unknown mechanisms confine dense particles in the middle A-ring or that the A-ring has been recently formed (~100 million years) by destruction of a pre-existing icy satellite. The seasonal thermal inertia of the thick B-ring is also found to be of the order of 30–50 J m^{-2} K^{-1} $s^{-1/2}$, assuming no heat transport by the vertical motion of particles. The seasonal inertia of particles in this multi-scale approach is found to be much larger, about 160–200 J m^{-2} K^{-1} $s^{-1/2}$, and the difference is due to the ring porosity that limits heat transfer through the solid phase. At this stage more effort is needed to understand why the thermal inertia of particles is so low, how heat transfer actually happens at their scale, and how deep the thermal waves are actually penetrating and sounding the particles on short and long timescales. Seasonal thermal effects should be able to probe particle interiors. But current thermal models, which attempt to explore them, are still facing an abnormally high porosity which yields a very low bulk density.

The ring particles in the middle A-ring are likely to have a dense core under a thin fluffy regolith mantle.

The particle properties are mostly derived using the multi-particle-layer model of Morishima et al. [2009], which ignores any effects of particle clumping (i.e., finite volume filling factor of a ring). Although this model can reproduce temperatures observed at various observational geometries, it does not accurately model the data in some cases. These failures are most likely all related to effects of particle clumping. Models that handle the effects of particle clumping are also discussed. In models of geometric filling factor and temperature of the A-ring, wakes are represented by elliptical or rectangular cylinders. These models can reproduce azimuthal modulations of geometric filling factor or temperature. The ratio of the vertical thickness to the horizontal width of wakes estimated from CIRS data at the middle A-ring is found to be slightly larger than those from stellar occultations.

Thermal opposition surges are seen in the dense A-ring and B-ring, and C-ring plateaus, but not in C-ring backgrounds. The volume filling factors estimated from the phase curves near the opposition are 0.2 and 0.4 for the A-ring and B-ring and 0.001–0.01 for the C-ring plateaus. The

temperature difference between the lit and unlit faces of the B-ring suggests very efficient heat transport is taking place from the lit face to the unlit face. The multilayer model can reproduce the lit–unlit face temperature difference if ring particles have vertical motion. In the densest part of the B-ring, particles likely bounce near the mid-plane. The lit–unlit face temperature can also be reproduced by a slab-type model in which vertical heat transport is taking place primarily by radiation and conduction, provided ring particles are isothermal. This model also yields a volume filling factor for the B-ring consistent with that estimated from opposition effects, i.e., on the order of 0.3.

The models that take into account the effects of particle clumping are only applicable to rather specific data sets. Universal models that are applicable to various geometries are required. A possible new model is one that directly uses the outputs of *N*-body simulations. Ray-tracing models that are applicable to photometric observations of packed particulate mediums have been developed by several authors [Salo and Karjalainen 2003; Porco et al. 2008; Ciarniello et al. 2015]. Modeling of thermal infrared emission using packed particulate mediums is much more complicated because various heat sources need to be included such as mutual heating. In addition, since the problem is time-dependent (particle spins and particle motion), radiative transfer needs to be solved at every time-step. Full modeling is very challenging and some approximations may be necessary for the first step.

Analysis of CIRS data using currently existing models also have not been fully conducted. For example, we do not clearly know the radial variation of the diurnal thermal inertia. The spatial resolution of the data that we have used were also limited. A part of the issue may be resolved by using FP3 data in addition to FP1 data. FP3 data have so far been used only for the opposition surge of the outer C-ring. During the final phase of the Cassini mission, the spacecraft's orbit carried it high above the planet's north pole and then sent it plunging between the planet and the innermost edge of its rings. In this orbital geometry, the Cassini spacecraft flew closer to some of Saturn's rings than ever before, and this encounter provided unprecedentedly high spatial resolution data. The CIRS instrument resolved some fine structures such as the F-ring, Cassini division, and C-ring plateau region, even with FP1. Future work will also include multi-analysis of data from multiple instruments, combining other temperature indicators provided by the VIMS for the top surface layer, and microwave radiometry for the interior of the particles.

CIRS emissivity spectra give constraints on sizes of regolith grains. The deduced sizes range from 1 μm to 10 cm and are on average larger than those estimated from data at short wavelengths. This may suggest that large grains are covered by small grains or that regolith structure is fractal. Modeling of such structures remains for future work, as does the effect of possible contaminants on CIRS spectra.

Other studies that are related to thermal emission but have not been covered by the present review are orbital migration of ring particles due to thermal effects that include the Yarkovsky effect, the Yarkovsky–Schach effect, and the Pointing–Robertson effect [Rubincam 2006; Vokrouhlický et al. 2007]. Vokrouhlický et al. [2007] found that the total torques on ring particles due to these effects are negative for all rings with a plausible range of thermal parameters that

are consistent with those reviewed in Spilker et al. [2018]. CIRS data of Saturn's rings will be analyzed for decades to come.

Titan

This section contains an introduction which outlines the broad nature of Titan's atmosphere and crust and the nature of thermal emissions from the gases, particulates and surface. Following the introduction is a discussion describing the typical means of modeling Titan spectra to retrieve information, the CIRS Titan science results and their implications organized by the CIRS science objective, the science assessments, and the conclusions and future work. See also book chapters and reviews that include CIRS results [Bézard 2009; Bézard et al. 2013; Flasar et al. 2009, 2014; Lebonnois et al. 2014; Lorenz et al. 2009; Strobel et al. 2009].

Introduction

Titan is the second-largest moon in the solar system (diameter 5150 km), the largest moon of Saturn, and the only moon with a significant atmosphere. The atmosphere is now known to have a bulk composition of ~94.5–98.5% nitrogen (N_2) and 5.5–1.5% methane (CH_4) [Niemann et al. 2010]. With a surface pressure of ~1.5 bar and temperature of ~90 K, and a similar molecular weight to Earth's air, the surface atmospheric density is almost 5× denser than Earth's according to the ideal gas equation. However due to the lower gravity, the scale height (*RT/Mg*) is much greater than Earth (~45 km versus 11 km) leading to a greatly extended atmosphere (~1500 km to the exobase [Yelle et al. 2008]). Titan is tidally locked to Saturn, orbiting with a 15.95-day period, and a substantial eccentricity of 3%. Titan's obliquity relative to Saturn is near-zero, leading to identical solar insolation cycle and seasons.

Titan is the second-largest moon in the solar system (diameter 5150 km), the largest moon of Saturn, and the only moon with a significant atmosphere.

ATMOSPHERIC STRUCTURE

Titan has a mild greenhouse (21 K) and anti-greenhouse effect (9 K) [McKay et al. 1991] leading to a surface temperature of 94 K, considerably warmer than the predicted effective temperature (82 K) for an airless body at 9.5 AU. The greenhouse effect arises from the long-wavelength opacity at ~25–200 μm from collisions primarily of N_2 and CH_4 molecules. The anti-greenhouse effect is due to the high-altitude hazes and condensates that absorb and reflect sunlight in the visible and UV, while being almost transparent in the thermal infrared. Due to these effects, Titan has a similar atmospheric structure to the Earth although caused by different gases. Convection in the lower atmosphere leads to decreasing temperatures up to the tropopause (~45 km, 70 K) with temperatures increasing again in the stratosphere, due to solar heating from methane and aerosols,

up to a well-defined stratopause at ~300 km. Above this altitude the temperature falls through the mesosphere (300–550 km) due to enhanced gas and aerosol cooling, and rises through the thermosphere (550–850 km) due to non-local thermodynamic equilibrium (non-LTE) processes. Above this homopause altitude gases begin to separate and have different scale heights, and ionization has a major effect up to the exobase (1500 km) where gases may escape to space due to Jeans escape [Hunten 1973], sputtering [De La Haye et al. 2007] and possibly slow hydrodynamic escape [Strobel 2008; Yelle et al. 2008].

Titan's global circulation in the stratosphere is dominated by single or dual cell meridional circulations. Following the solstices, warm air in the summer hemisphere rises (to 400–500 km) and circulates to the winter pole, where it cools and descends. Adiabatic compression leads to a hot, elevated stratopause, and a much cooler stratosphere beneath. Near to the equinoxes, a two-cell circulation is briefly in existence, with rising warm air at the equator forming two high-altitude circulation branches towards either pole.

ATMOSPHERIC CHEMISTRY

The dual action of solar UV (primarily Lyman α) and charged particle bombardment (primarily electrons) from Saturn's magnetosphere photolyzes the major atmospheric gases—N_2 and CH_4—leading to radicals of N, C, CH, CH_2, and CH_3 and associated ions. These react and recombine forming larger molecules—primarily hydrocarbons (C_xH_y) and nitriles ($C_xH_y(CN)_z$). The primary photolysis product of methane is ethane (40%, [Wilson and Atreya 2009]):

$$2\,CH_4 + 2\,h\nu \rightarrow C_2H_6 + H_2,$$

leading to escape and permanent loss of hydrogen. Other major photolysis products are acetylene (C_2H_2) and HCN. Small amounts of oxygen reaching Titan mostly from Enceladus lead to trace amounts of CO_2 and H_2O, and a larger amount of CO (50 ppm), which is very long-lived and accumulates over time.

These chemicals diffuse or are transported downwards, creating a vertical concentration gradient that is normally positive upwards. In the cold lower stratosphere, most gases reach saturation and condense onto haze particles (next section), using these as condensation nuclei, and falling out of the atmosphere towards the surface (some re-evaporation may occur). The tropopause thus acts as a cold trap for both methane in the upward sense, and other gases in the downward sense. The few non-condensing gases are: N_2, H_2, CO, and C_2H_4, plus light noble gases (Ne, Ar).

Due to the Hadley circulation (previous section) the minor gases are entrained, and become decaying tracers of atmospheric motions with lifetimes varying from hours to decades or longer. Many minor gas species are highly enriched in the stratosphere over the winter pole, as first detected by Voyager.

PARTICULATES

Two types of particulates are common in Titan's atmosphere: 1) aerosols, defined for our purposes as photochemically-produced microscopic organic particles and assumed to be agglomerations of macromolecules bonded by Van Der Waals forces as seen in terrestrial smog, smoke and laboratory simulations (tholins); and 2) condensates (liquid and solids) formed by condensation of trace gases (methane, ethane, etc.) into small droplets (liquid) or grains (ice) similar to terrestrial tropospheric and stratospheric clouds. Condensates can be, and likely are, mixtures of several molecular types with similar freezing/boiling points. Further grain-surface photochemistry may change the composition (see the section entitled Surface).

SURFACE

Titan's surface was only coarsely imaged as late as 1996 [Smith et al. 1996] using the Hubble Space Telescope (HST), and subsequently with ground-based telescopes employing adaptive optics. Detailed imaging awaited the Huygens probe, which descended to Titan's surface in 2005 [Tomasko et al. 2005]. The Cassini orbiter followed up with mapping at visible (ISS), near-IR (VIMS) and RADAR wavelengths; the latter providing the most detailed morphological picture. RADAR was the key to discovering Titan's dune fields [Lorenz et al. 2006], polar lakes and seas [Stofan et al. 2007], and surface cratering [Neish and Lorenz 2011]. Overall, Titan's topography remains low in relief [Lorenz et al. 2013], with the tallest surface prominences reaching only 1.4 km [Lopes et al. 2013]. Proposed geologic activity remains controversial [Nixon et al. 2018]. Key goals for CIRS included measurement of an expected equator-to-pole thermal gradient and diurnal variation due to insolation effects, and any possible local differences over the seas, dunes and impacted terrain (Xanadu) due to differences in altitude and thermal inertia, related to porosity and composition.

Spectral modeling and inversion

Once CIRS spectra have been calibrated, and usually averaged together (co-added) to increase the signal-to-noise (S/N) ratio, they are modeled using a radiative transfer program to retrieve atmospheric quantities such as temperature, gas abundances, and particle column densities. The CIRS team used multiple radiative programs—for example, ARTT Coustenis et al. [2007], NEMESIS Irwin et al. [2008]—and other modeling codes developed at the University of Maryland, Paris Observatory, NASA Goddard Space Flight Center (GSFC), and elsewhere, to retrieve atmospheric and surface information.

The process of modeling a spectrum usually follows these principal steps:

1. Define a reference atmospheric profile of vertical temperature, gas abundances, and particle sizes and number densities.

2. Run a forward model for the reference atmosphere and compare to the CIRS spectrum.

3. Adjust model parameters (reference atmosphere) iteratively and rerun forward model, until a fit to the spectrum is obtained, usually defined as reaching the noise threshold, or some other pre-determined measure of convergence.

In many cases, atmospheric gas abundances are obtained in a two-step process: (i) model the emission of a well-mixed gas of known (or assumed) abundance (often methane) to retrieve atmospheric temperatures; and (ii) fix the temperature profile and model other parts of the spectrum to obtain gas abundances. However, this paradigm is often modified by assuming or ingesting temperatures from other sources such as the Huygens probe, or radio occultation measurements. In other cases, gas or particle abundances and temperatures are obtained simultaneously.

Steps of the model process are described in the following section.

REFERENCE ATMOSPHERE

The first step is to construct an initial model atmosphere that includes temperature profiles and vertical profiles of gases and aerosols. An excellent starting point is the vertical profile data recorded by the Huygens probe, which provided in situ measurements at the landing site coordinates (10.3° S, 192.3° W) of Titan's temperature profile, gas abundances, and an aerosol altitude profile below 150 km [Fulchignoni et al. 2005; Niemann et al. 2010; Tomasko et al. 2005]. Further reference temperatures profiles are available from Cassini CIRS [Achterberg et al. 2008a, 2011] and radio occultations [Schinder et al. 2011a, 2012]. The temperature profiles are combined with trial gas abundances based on previous measurements or photochemical model predictions to create an a priori (initial-guess) profile for Titan's atmosphere.

FORWARD MODEL

The outgoing spectral radiance along a single atmospheric path is obtained by evaluating the Schwarzchild integral for emission:

$$I_{\tilde{\nu}} = \int_0^{z_\infty} \frac{\partial \tau_{\tilde{\nu}}(z_\infty, z)}{\partial z} B_{\tilde{\nu}}\big(T(z)\big) dz, \qquad \text{(Eq. 1)}$$

where $I_{\tilde{\nu}}$ is the outgoing radiance, $\tau_{\tilde{\nu}}$ is the transmittance from height z to the top of the (sensible) atmosphere at height z_∞, $B_{\tilde{\nu}}(T)$ is the Planck function (local thermodynamic equilibrium, or LTE, as assumed), and the subscript $\tilde{\nu}$ indicates wavenumber. Including the surface with an emissivity ε_s, and dropping the wavenumber subscripts for convenience, the outgoing intensity is:

$$I = \int_0^{z_\infty} \frac{\partial \tau(z_\infty, z)}{\partial z} B\big(T(z)\big) dz + \varepsilon_s B(T_s)\tau_s + (1-\varepsilon_s)\tau_s \int_{z_\infty}^{0} \frac{\partial \tau(0,z)}{\partial z} B\big(T(z)\big) dz, \qquad \text{(Eq. 2)}$$

where τ_s is the transmittance evaluated from the surface to the top of the atmosphere. Note that the third term accounts for the down-welling radiation which is reflected from the surface and suffers extinction on return; this term vanishes when the surface emissivity is unity. The transmittance is defined as: $\tau_{\tilde{\nu}} = \exp(-\chi_{\tilde{\nu}})$ where $\chi_{\tilde{\nu}}$ is the spectral opacity due to all sources in the atmosphere

integrated over the path. The radiative transfer program evaluates the discretized form, replacing the integral by a summation over *N* atmospheric layers, e.g., for unit surface emissivity:

$$I_\infty = B_s\tau_{N_L} + \sum_{l=1}^{N_L}\left[B_l exp\left(-\sum_{i=1}^{l}\Delta\chi_i\right)\right]. \quad \text{(Eq. 3)}$$

The opacity increment at each layer $\Delta\chi_i$ is typically the sum of three sources: $\Delta\chi_i = \Delta\chi_{L,i} + \Delta\chi_{C,i} + \Delta\chi_{P,i}$, which are the opacities due to spectral lines, collision-induced absorption (CIA) and particles, respectively. These are:

$$\Delta\chi_{L,i}(\tilde{\nu}) = \sum_{j=1}^{N_g}\left[k_j(\tilde{\nu})q_{ij}\right]\rho_i\,\Delta z_i \quad \text{(LINES)} \quad \text{(Eq. 4)}$$

$$\Delta\chi_{C,i}(\tilde{\nu}) = \sum_{j=1}^{N_g}\sum_{k=1}^{N_g}\alpha_{jk}\,(\tilde{\nu})q_{ij}q_{ik}\left(\frac{p_i}{p_0}\right)^2\left(\frac{T_0}{T_i}\right)^2\Delta z_i \quad \text{(CIA)} \quad \text{(Eq. 5)}$$

$$\Delta\chi_{P,i}(\tilde{\nu}) = \sum_{j=1}^{N_P}\sigma_j\,(\tilde{\nu})n_{ji}\Delta z_i \quad \text{(PARTICLES)} \quad \text{(Eq. 6)}$$

where *kj* is the absorption co-efficient (per unit mass) due to spectral lines for the j^{th} of N_q gases in the atmosphere, q_{ij} is the volume mixing ratio of each gas at each level, ρ_i is the total atmospheric mass density of the layer, Δz_i is the thickness of the layer, α_{jk} is the spectral CIA coefficient for the (*j,k*) gas pair normalized to nominal pressure p_0 and temperature T_0, p_i and T_i are the pressure and temperature of the layer respectively, σ_j is the extinction cross-section of the j^{th} particle type and n_{ji} is the number density of each particle type in the layer. The exact method of computing the spectral line absorption coefficient *k* varies: it may be a line-by-line model, or more usually a band model of correlated-k technique, which preserves accuracy but at much shorter computational time.

SPECTRAL LINE DATA

Infrared spectral line data are taken from the standard line atlases: GEISA [Jacquinet-Husson et al. 2016] and/or HITRAN [Rothman and Gordon 2013], supplemented by additional line lists provided by colleagues for some gases and bands that have been measured recently, but not yet included in the standard atlases. The CIA coefficients of are those of Borysow and colleagues as detailed in [Teanby et al. 2006b]. Extinction cross-sections for stratospheric aerosols are often based on laboratory tholin coefficients measured by Khare et al. [1984a, 1984b], but more recent laboratory work and CIRS-derived coefficients are now available [Khare et al. [1984a, 1984b]. A list of principal detected infrared bands is given in Table CIRS-5. See also Figure CIRS-16.

Table CIRS-5. Principal gases in Titan's stratosphere, and infrared spectral bands seen by Cassini CIRS.

	Gas Name	Chemical Formula	Emission Bands Detected in Mid-/Far-IR (center or range in cm^{-1})	VMR (equator at 5 mbar)
Major Species	Nitrogen	N_2	~100 (collision-induced opacity)	9.85×10^{-1}
	Methane	CH_4	60–140 (pure rotations); 1304 (n4)	1.40×10^{-2}
	Argon	*Ar*	*none*	
	Hydrogen	H_2	355 and 585 (dimers)	1.00×10^{-3}
Hydrocarbons	Acetylene	C_2H_2	729 (n5)	3.00×10^{-6}
	Ethylene	C_2H_4	949 (n7)	1.50×10^{-7}
	Ethane	C_2H_6	822 (n9), 1379 (n6), 1468 (n8)	1.00×10^{-5}
	Propyne	C_3H_4	328 (n10), 633 (n9)	7.00×10^{-9}
	Propene	C_3H_6	913 (n19)	$2{:}00 \times 10^{-9}$
	Propane	C_3H_8	748 (n21), 870 (n8), 922 (n16), 1054 (n15), 1158 (n7), 1376 (n13), 1472 (n19)	5.00×10^{-7}
	Diacetylene	C_4H_2	220 (n9), 628 (n6)	1.40×10^{-9}
	Benzene	C_6H_6	674 (n4)	5.00×10^{-10}
Nitriles	Hydrogen Cyanide	HCN	40–100 (pure rotations), 712 (n2)	1.00×10^{-7}
	Cyanoacetylene	HC_3N	499 (n6), 663 (n5)	4.00×10^{-10}
	Cyanogen	C_2N_2	233 (n5)	(north only)
Oxygen Species	Carbon Monoxide	CO	50–100 (pure rotations)	4.50×10^{-5}
	Carbon Dioxide	CO_2	667 (n2)	1.40×10^{-8}
	Water	H_2O	80–300	1.00×10^{-10}

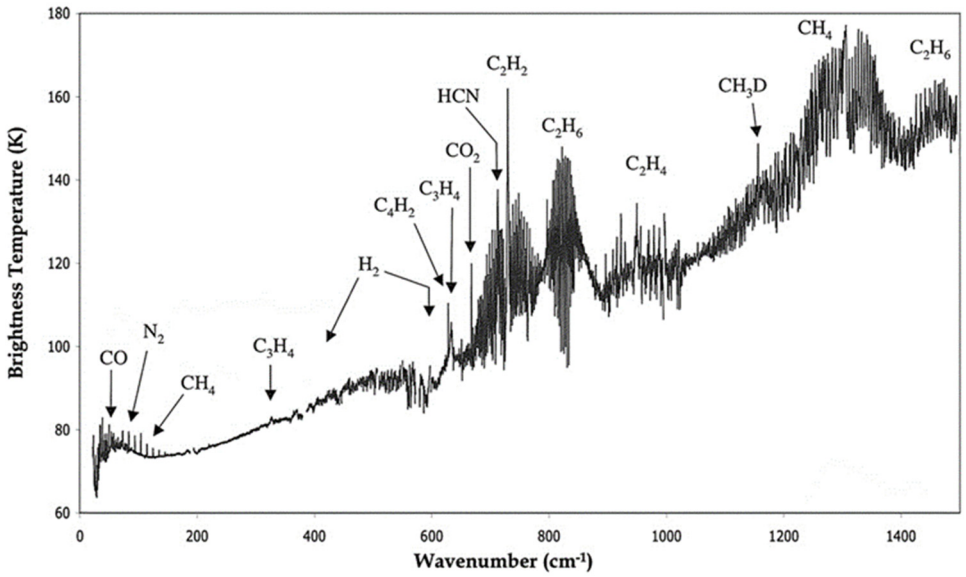

Figure CIRS-16. A complete composite unapodized CIRS spectrum in brightness temperature taken during TB at medium resolution (1.7 cm^{-1}) at mid-latitudes. Figure from Coustenis et al. [2007].

RETRIEVAL/INVERSION

Coupled to the forward model, many radiative transfer models also include a retrieval (or inversion) methodology—for example, Rodgers [2000], which attempts to find the set of model parameters $\underline{x}$ which best fits the spectral data, $\underline{y}$. The measurement process may be written as: $F(\underline{x}) = \underline{y} + \varepsilon$, where F is the physics and ε is the measurement error. The inverse problem is therefore to find a self-consistent atmospheric state $\underline{\hat{x}}$ such that $F(\underline{\hat{x}}) = \underline{y} \pm \varepsilon$. The retrieval proceeds by defining a goodness of fit metric similar to a chi-squared test, and sometimes called the cost function, that is minimized to achieve a best fit atmospheric state $\underline{\hat{x}}$; e.g., the cost function ϕ used by NEMESIS:

$$\phi = \left(\underline{y} - F(\underline{\hat{x}})\right)^T \underline{S}_{\varepsilon}^{-1} \left(\underline{y} - F(\underline{\hat{x}})\right) + (\underline{\hat{x}} - \underline{\hat{a}})^T \underline{S}_a^{-1} (\underline{\hat{x}} - \underline{\hat{a}}), \quad \text{(Eq. 7)}$$

is comprised of two terms, the first being the traditional χ^2 difference between the model and data spectra, while the second is a constraint term that is proportional to the square of the deviation between the solution vector and the a priori (best-guess) vector $\underline{\hat{a}}$, required to obtain a solution to the ill-posed problem. The retrieval procedure iterates to solve the non-linear problem, until the cost function or other fitness measure ceases to decrease appreciably (converges). This combination of forward model and retrieval scheme is a powerful tool to retrieve values and error estimates for the temperature, gas abundance profiles, and haze opacities from CIRS spectral data.

Titan's surface

Titan's surface temperature can be directly sensed in the far-infrared through a window of low opacity near 530 cm^{-1} (19 μm), as discovered by Voyager 1 [Flasar et al. 1981; Hanel et al. 1981; Samuelson et al. 1981]. This wavelength is sensed by CIRS FP1, which being a single pixel of relatively large angular diameter, places some limits on resolution and mapping capability. Nevertheless, CIRS was able to significantly expand on the science of Voyager, giving global context for the Huygens measurements, and comparison for RADAR temperature measurements at longer wavelengths [Janssen et al. 2009].

LATITUDINAL VARIATION

The first surface temperature results from CIRS were published by Jennings et al. [2009], who averaged data from 43 flybys of the prime mission (2004–2008). They found T = 93.7 ±0.6 K at the Huygens landing site, in good agreement with the in situ measurements, and also the maximum recorded at any latitude. The temperature decreased to 90.5 ±0.8 K at 87° N and 91.7 ±0.7 K at 88° S, in broad agreement with the season (late northern winter).

TEMPORAL CHANGES

Jennings et al. [2011] followed up on the earlier work, showing the first time-resolved measurements covering two time periods: 2006–2008 (L_S = 335°) and 2008–2010 (L_S = 0°), the latter coinciding with northern spring equinox (NSE) in 2009. By the time of NSE, the temperature distribution had become symmetric, with polar temperatures in both hemispheres leveling off at ~91 K, and an equatorial maximum of 93.4 K. A slight phase lag relative to solar insolation of ΔL_S ~9° was recorded, consistent with the observations of Voyager 1, and general circulation modeling (GCM).

Cottini et al. [2012b] followed up with a comprehensive analysis of data from 2004–2010, this time dividing the data temporally into three two-year periods. Agreement with HASI was again noted at the Huygens landing site, and changes of several degrees near the poles were in good agreement with Jennings et al. [2011]. Cottini et al. [2012b] were also able to detect diurnal variations in surface temperature, based on data from −20° to +20° latitude. A slow warming of ~1 K was observed from daybreak to late afternoon, followed by a plateau, and then a more rapid cooling from midnight to dawn. By comparing to models from Tokano [2005], the authors found consistency with a thermal inertia of 300–600 J m^{-2} $s^{-1/2}$ K^{-1} and albedo 0.3, in agreement with a surface crust of porous icy material.

A surface temperature update was published by Jennings et al. [2016], who divided the period 2004 to 2014 into five two-year periods (Figure CIRS-17). During this time the north polar temperature rose by about 1 K from 90.7 ±0.5 to 91.5 ±0.2 K, while that at the south pole dropped by a larger amount from 91.7 ±0.3 to 89.7 ±0.5 K. The low latitude temperature maximum stayed constant at 93.65 ±0.15 K, while moving northwards from 19° S to 16° N. In general, temperature changes were in agreement with GCM models, excepting in the north polar regions from 2014 onwards, where the rise was about 1 K less than expected. This anomaly was tentatively attributed to surface cooling through increased precipitation and methane evaporation. Recently Jennings et al. [2019] extended the analysis to the end of mission in September 2017.

VARIATION WITH TOPOGRAPHY AND TERRAIN

A search for localized temperature differences has been made by members of the CIRS team including V. Cottini and D. E. Jennings, including over the northern lakes/seas, and over low-latitude albedo features such as Xanadu with no conclusive evidence to date—unlike the thermal anomalies seen by RADAR [Janssen et al. 2009]. This has been attributed to the much lower S/N and larger spatial resolution footprint of CIRS that may not be sufficient to see small temperature contrasts over small features, including lakes and seas.

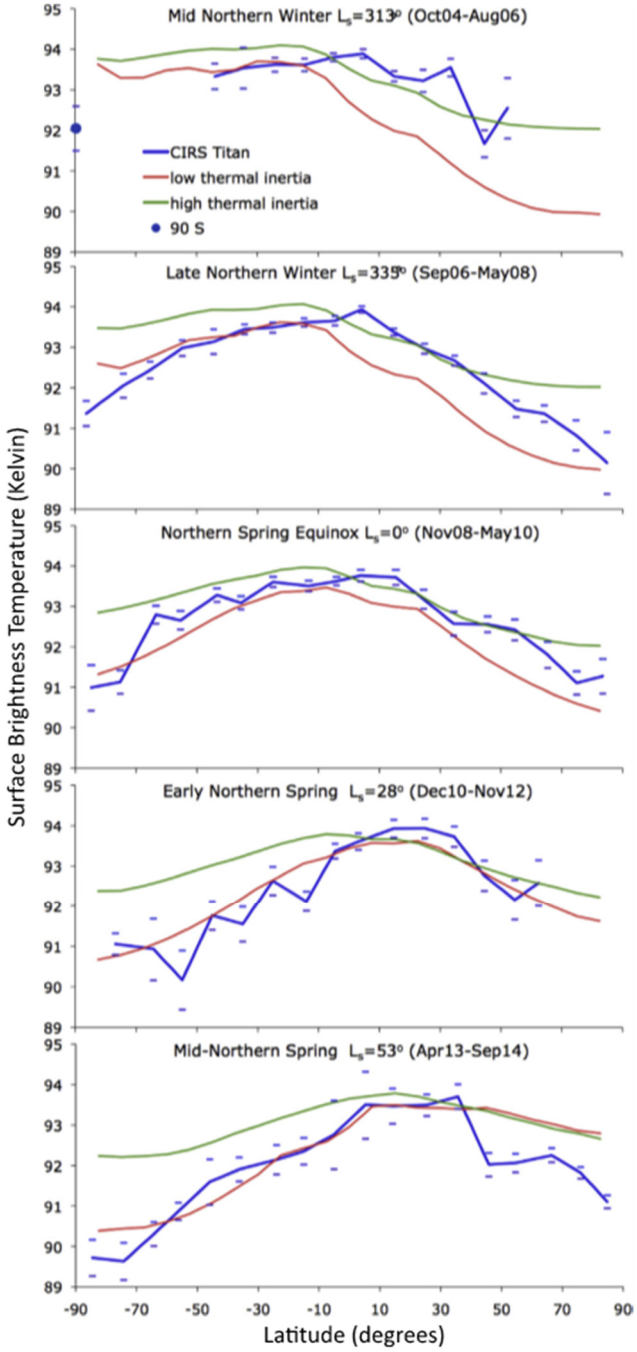

Figure CIRS-17. Measured surface brightness temperatures (blue) on Titan compared with GCM predictions, for five approximately two-year periods during the Cassini mission. The error bars are two standard deviations, calculated from the average that produced each data point. Variation in the size of the error bars is due primarily to differences in the number of spectra averaged. The two GCM curves [Tokano 2005] correspond to low thermal inertia (red) and high thermal inertia (green). Two of the periods, L_S = 313° and 28°, did not have sufficient data to completely map the high latitudes. The single data point at 90° S for L_S = 313°, added here to extend the coverage to the south pole, was from June 6, 2005. Figure from Jennings et al. [2016].

Atmospheric dynamical state

CIRS has mapped Titan's atmospheric temperatures primarily through two spectral regions: the ν_4 band of methane centered on 1305 cm^{-1} (visible on FP4) that sense the stratosphere, and the far-infrared (100–400 cm^{-1}) that gives temperatures in the troposphere. By assuming abundances of CH_4 and H_2, typically from Huygens Gas Chromatograph Mass Spectrometer (GCMS), the temperatures may be retrieved. Temperature (and gas abundance) retrievals use either one of two observing geometries: nadir viewing, where the sightline intercepts the surface, although not necessarily normal (90° to surface); and limb, where the line of sight passes above the surface (tangential). Limb viewing is often preferable for two reasons: (i) the emission is usually strongly localized at the tangent point altitude, allowing for more precise altitude sensing; and (ii) the longer path length compared to nadir viewing increases S/N, allowing retrievals to proceed to higher altitudes.

Limb viewing on Titan encounters a problem not usually significant on the Earth: the larger scale height of the atmosphere causes the depth of the sensible atmosphere to be greatly extended relative to the solid body diameter. This means that the weighting function extends significantly to either side of the tangent point, and therefore latitudinal/longitudinal variations in composition and temperature are important. This causes problems for 1-D radiative transfer models (such as NEMESIS), which cannot capture the 2-D nature of the problem (Figure CIRS-18), although at least one full 2-D temperature retrieval model has now been developed [Achterberg et al. 2008a].

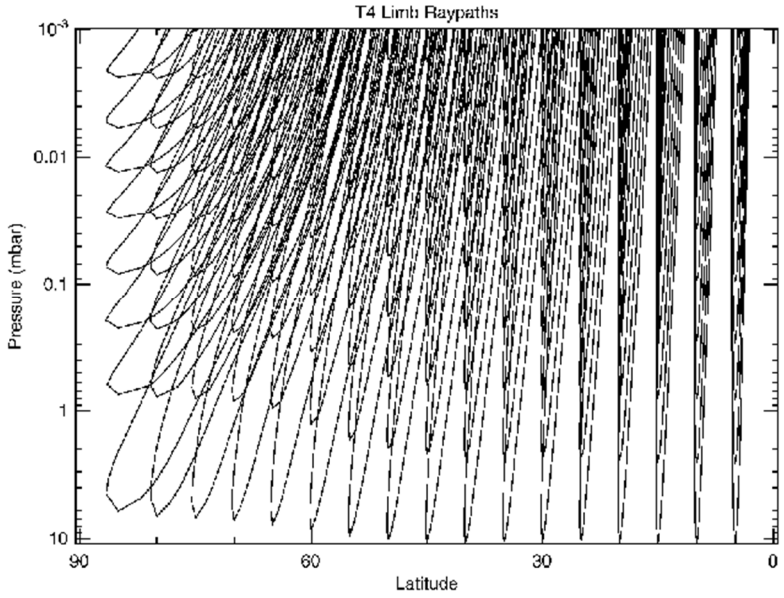

Figure CIRS-18. Ray paths for limb measurements acquired on the T4 Titan flyby, illustrating the nature of the 2-D retrieval problem. Tangent views towards high latitudes traverse a significant range of latitudes. The equatorward branch of each trajectory extends from the spacecraft to the tangent point of the ray, while the poleward branch is the extension of the ray path beyond the tangent point. Figure from Achterberg et al. [2008a].

GLOBAL TEMPERATURE MAPPING

The first maps of Titan's global temperatures were published by Flasar et al. [2005a], showing the first Titan results from Cassini CIRS. The stratopause was distinct at ~310 km (186 K) at low latitudes, and showed a cooling of 4–5 K towards the south pole. The northern hemisphere above 60° N was not measured. Shortly thereafter, Huygens HASI results [Fulchignoni et al. 2005] were to show disagreement with the CIRS low latitude stratopause altitude, a discrepancy that has long persisted, although may recently have been resolved [Lellouch et al. 2014].

The first and so-far only model to successfully retrieve the 2-D atmospheric structure on Titan was devised by Achterberg et al. [2008a]. The authors showed the significant errors that can occur in 1-D models, by comparing to a fully 2-D model (Figure CIRS-19). Temperatures were retrieved from 90° S to 60° N and 5 to 0.2 mbar from nadir mapping data, and from 75° S and 85° N and 1 to 0.005 mbar from limb data. The higher-altitude limb data allowed the stratopause to be fully captured, and showed that it was 20 K warmer in the northern polar atmosphere than at low latitudes (<40° N) and higher by about 100 km (0.01 mbar N polar, versus 0.1 mbar low latitudes) (Figure CIRS-20). This is in agreement with GCM models [Lebonnois et al. 2009, 2012] that predict subsidence in the stratosphere over the winter pole and consequent adiabatic warming.

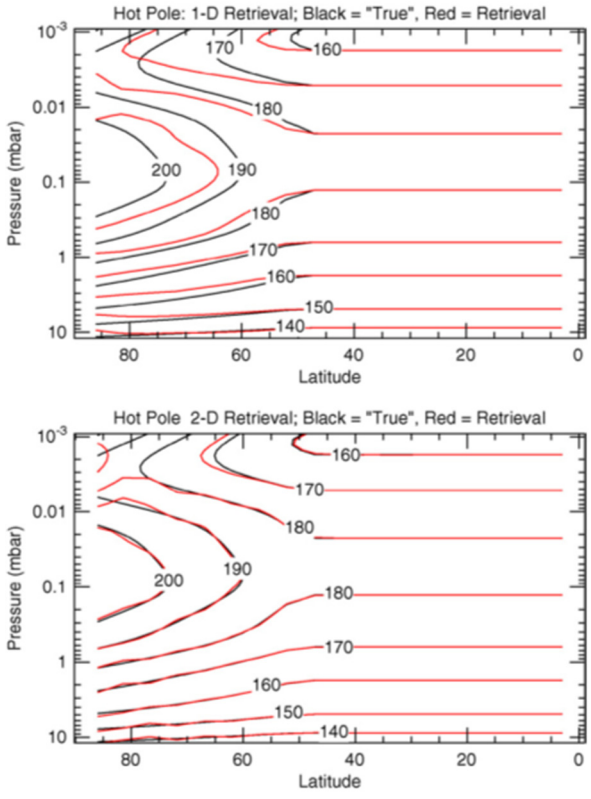

Figure CIRS-19. One- and two-dimensional retrieval results on synthetic data with a warm pole. The one-dimensional retrieval does not recover the polar warm spot well. Figure from Achterberg [2008a].

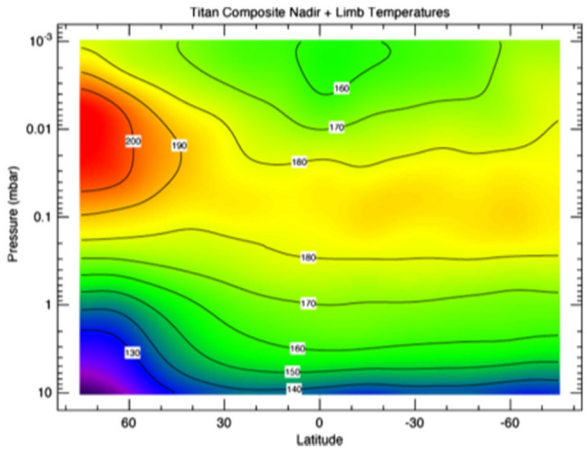

Figure CIRS-20. Zonal mean temperatures from all limb and nadir maps. Retrieved temperatures were averaged in 5° latitude bins, then smoothed with a 10° boxcar function applied three times. Contours are labeled in K. Figure from Achterberg et al. [2008a].

Winds and Jets

The first CIRS derivation of the stratospheric wind was shown in Flasar et al. [2005a], with zonal winds reaching 160 m/s in mid-northern latitudes above 200 km (1 mbar). Achterberg et al. [2008a] also applied the thermal wind equation to derive zonal winds, finding a jet of 190 ms^{-1} at 30–60° N, and peaking near 1 mbar (Figure CIRS-21).

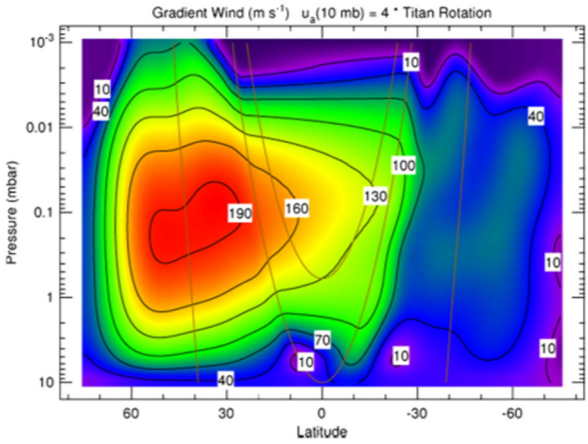

Figure CIRS-21. Zonal winds calculated from the temperatures in Figure CIRS-19 from the gradient wind equation, assuming solid-body rotation at the 10 mbar level at four times Titan's rotation rate. Wind speed contours (black lines) are labeled in ms^{-1}. The gray lines indicate cylindrical surfaces parallel to the rotation axis along which the gradient wind equation is integrated. Equatorward and above the gray line tangent to the equator at 10 mbar, the winds are unconstrained by the gradient wind equation, and have been linearly interpolated on constant pressure surfaces. Figure from Achterberg et al. [2008a].

ATMOSPHERIC ROTATION AXIS

A curious and hitherto unknown phenomenon was observed at the end of the prime mission by Achterberg et al. [2008b]—that isotherm contours plotted in a polar frame are not concentric about the solid body pole, but offset by ~3.5° (Figure CIRS-22). This axial offset was observed most clearly in the north due to the steeper temperature contours, but was also observed in the opposite sense in the south. The atmospheric tilt was later confirmed in other datasets, including an analysis of Titan's brightness banding in ISS images [de Kok et al. 2010b; Roman et al. 2009] and in composition contours of HCN gas from CIRS [Teanby et al. 2010a].

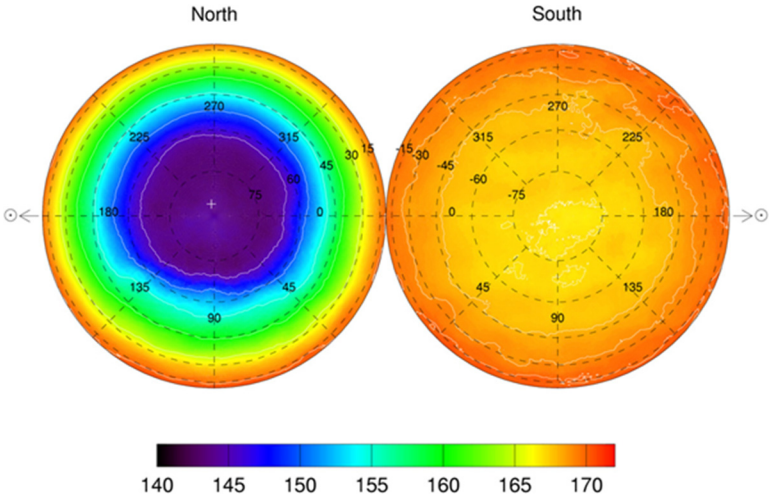

Figure CIRS-22. Polar projection maps of retrieved temperatures at the 1 mbar level. The northern hemisphere is shown on the *left* and the southern hemisphere on the *right*. The color-coded temperature scale in kelvins is shown at the bottom. The superposed grid represents latitude and west longitude in a Sun-fixed frame with the longitude of the subsolar point at 180° W, such that the Sun direction is towards the left and right edges of the figure. Temperature contours are plotted at intervals of 5 K in the northern hemisphere, and 1 K in the southern hemisphere. The fitted axis of symmetry is indicated by a white cross (+). Figure from Achterberg et al. [2008b].

In 2008, it was unclear whether this axis was fixed in a solar frame, or a sidereal (inertial) frame, and Achterberg et al. [2008b] suggested that the observed pole tilt might represent a compromise between two competing effects. The first is the need to maintain Titan's global super-rotation, which requires the upward transport of angular momentum. For an axisymmetric circulation the most favorable configuration for achieving this with upwelling at the equator. The second is the transport of heat by a Hadley circulation, which is most efficient when the upwelling is centered about the subsolar latitude. If this hypothesis were correct, the axial tile should remain fixed in the solar frame. However, more recent, unpublished work by the same authors, which includes observations from the remainder of the Cassini mission, indicates that the axial tilt, remains fixed in the inertial frame. The origin of the tilt still lacks an explanation.

GLOBAL ENERGY BALANCE

Li et al. [2011b] considered whether Titan is in overall thermal equilibrium: as it should be if there is no significant internal energy source. One the strengths of CIRS is the very broad spectral coverage, which includes almost the entire Planck function of cold outer solar system bodies. By carefully integrating across the entire spectrum and accounting for emission angle, Li and colleagues found a global power emission of (2.84 ±0.01) × 10^{14} watts. This compares very closely to the global absorbed solar energy of (2.89 ±0.12) × 10^{14}, which has a significantly larger associated error due to the bond albedo, and places any possible thermal imbalance at ≤ 6%.

In a follow-up paper, Li [2015] searched for temporal variability of the emitted power. In the northern hemisphere, the radiant energy dropped from 2007–2009, then increased 2009–2013, whereas in the southern hemisphere, the power continuously dropped by eventually 5% from 2.40 to 2.28 W/m^2 (Figure CIRS-23). This drop was attributed to seasonal variation. Taken together, the overall global power drop was 2.5%: much less than the decrease (13%) in the solar constant at Titan in the same period, showing the significant thermal inertia of Titan's atmosphere.

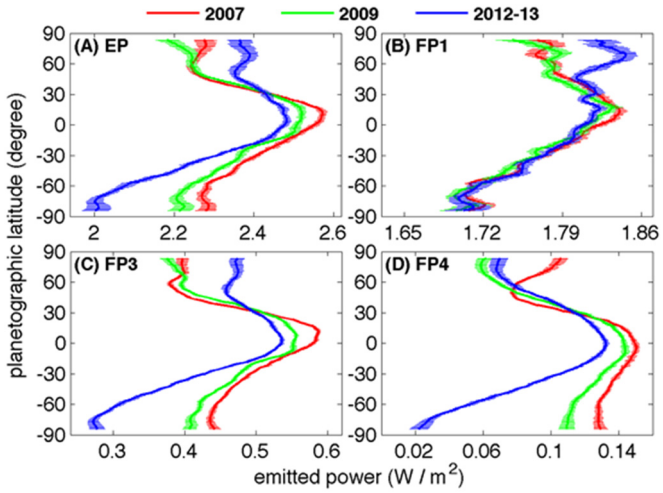

Figure CIRS-23. Meridional distribution of Titan's emitted power. Panel (A): total emitted power. *Panels (B), (C), and (D):* are thermal radiance recorded by the focal planes FP1, FP3, and FP4, respectively. The thick line is the profile of the emitted power and horizontal lines represent the uncertainties. The estimated uncertainty is combined by the uncertainty related to the filling observational gaps and the uncertainty related to the CIRS data calibration. Figure from Li [2015].

A more detailed picture of the global energy balance was presented by Bézard et al. [2018], who developed a seasonal radiative-dynamical model. Constrained by gas and haze data from CIRS and Huygens Descent Imager/Spectral Radiometer (DISR), the model was capable of investigating the net heating and cooling rates at varying latitudes as a function of time. A significant revision downward of the radiative relaxation time in the stratosphere was proposed, and the change in the solar flux due to Saturn's orbital eccentricity was found to be enough to explain a 4 K drop in equatorial temperature at 1 mbar noted between 2009 and 2016. At mid-latitudes on the other hand, the model predicted changes in temperature much larger than observed, which put new constraints on the vertical mixing.

SEASONAL CHANGE

Achterberg et al. [2011] followed up on the original work of [Achterberg et al. 2008a], showing time variation in the stratospheric temperatures from 2004–2009 (L_S 293° to 4°, from late northern winter to just after equinox). Significant cooling (20 K) of the northern stratopause had occurred, consistent with a weakening of the descending branch of the stratospheric circulation cell. Smaller changes were noted elsewhere in the atmosphere.

Teanby et al. [2012a] reported rapid changes in the south polar temperature field shortly after equinox (Figure CIRS-24). They measured elevated mesospheric temperatures in early 2010, which were indicative of south polar subsidence. This is opposite to the south polar upwelling inferred at the start of the mission and was the first observation of Titan's circulation reversing. The reversal was extremely rapid and was evident in both temperature and composition 2-D cross-sections.

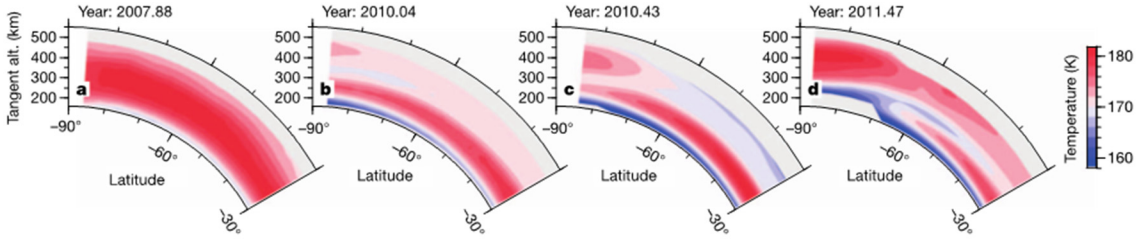

Figure CIRS-24. South polar seasonal temperature changes. Cross-sections were derived from low-spectral-resolution limb-mapping sequences and cover pre-equinox (a) and post-equinox (b–d) periods. Substantial stratospheric (300 km) cooling occurs after the equinox, consistent with reduced total solar flux during this time, as Titan moves towards southern winter. After the equinox (after mid-2009), there is evidence for high-altitude (450 km) polar warming relative to more equatorial latitudes. This is initially present as a small (2 K) temperature anomaly almost immediately proceeding the equinox (b), which increases to 6 K (c) and then to 8 K (d) in subsequent sequences. This implies that the mesospheric circulation has reversed and is now subsiding at the south pole. The strongest polar warming occurs in the most recent observation, indicating the fastest subsidence speeds. The gray regions indicate latitudes and altitudes where observations exist but have insufficient signal-to-noise ratios for an accurate temperature determination. Contour spacing is 2 K, which is the maximum uncertainty for this altitude range. These changes are confirmed by additional single-latitude observations at both high and low spectral resolution. Figure from Teanby et al. [2012a].

Teanby et al. [2017] reported another new discovery about Titan's winter polar vortex, this time in the south, during the early winter time period that Cassini had not been able to observe in the north (happening in 2002 just prior to arrival of the spacecraft). Previously, a hot elevated stratopause had been seen in the late winter vortex in the north, and also in the early winter vortex in the south. Abruptly however, in 2012 three years post-equinox, the mesosphere in southern winter vortex cooled dramatically, and did not recover its previous temperature until 2015. This phenomenon, not seen elsewhere in the solar system, was interpreted as being due to the huge enrichment occurring in trace gases, which were efficiently cooling the mesosphere. This observation provided a unique glimpse at the interplay between thermodynamic and radiative effects on controlling atmospheric temperature (Figure CIRS-25).

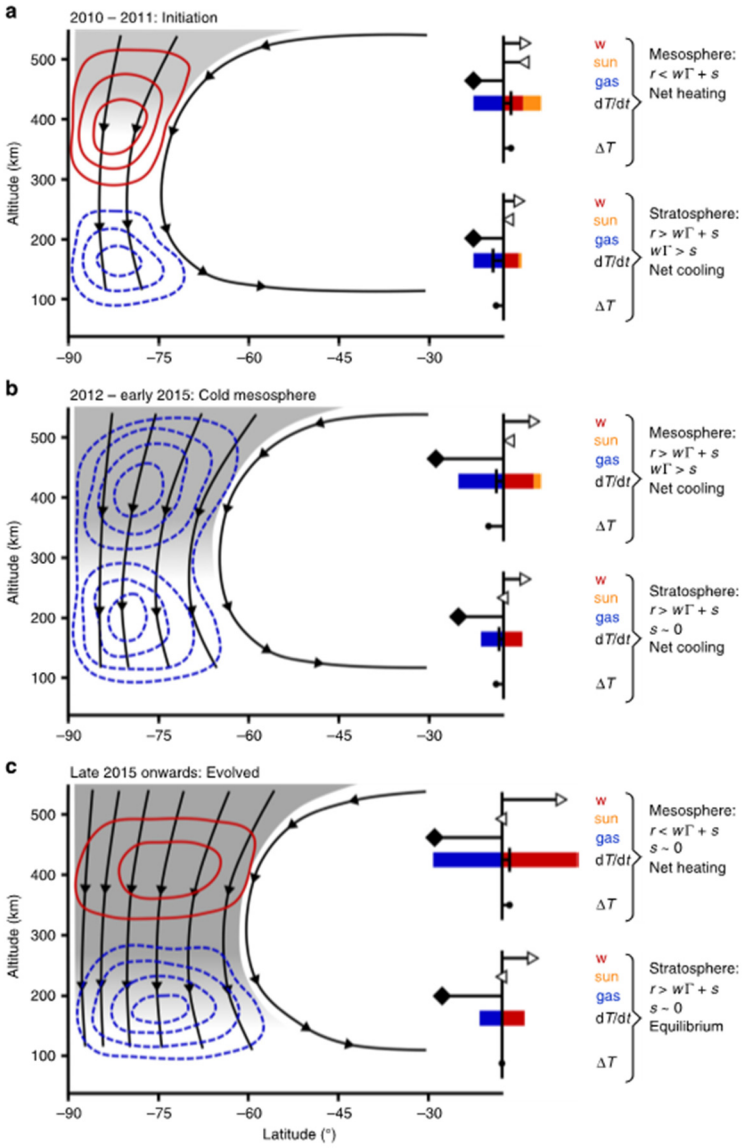

Figure CIRS-25. Schematic of the three stages of Titan's vortex evolution. Shaded areas represent trace gas abundance, which increases with time due to the subsiding flow (black streamlines). Red contours indicate hot anomalies and blue-dashed contours represent cold anomalies. Inset bar plots in each panel represent mesospheric and stratospheric heating and cooling processes; right-pointing triangles indicate subsidence speed w, which drives adiabatic heating rate wΓ (red bar); left-pointing triangles indicate solar heating rate s (orange bar); and diamonds indicate trace gas relative abundance, which drives long-wave radiative cooling rate r (blue bar). The overall net heating rate ∂T/∂t = −r + wΓ + s (vertical line) produces either a hot or cold temperature anomaly ΔT (filled circle). Estimated long-wave cooling rates range from 0.75 to 3.3 K per day in the mesosphere (~0.01 mbar, 400 km) and 0.04–0.17 K per day in the stratosphere (~1 mbar, 175 km). The three stages are: *Panel a*: vortex initiation, with a hot mesosphere driven by modest subsidence-induced adiabatic heating combined with weak cooling from trace gases; *Panel b*: cold mesosphere, caused by enhanced net cooling from increased trace gas opacity; and *Panel c*: evolved vortex, with a hot mesosphere driven by strong subsidence-induced adiabatic heating that exceeds enhanced cooling from trace gas enrichment. Figure from Teanby et al. [2017].

Gas composition and chemistry

The gas composition of Titan's atmosphere is highly informative in many respects: it yields information on the chemistry, it acts as a tracer of dynamical motions, and informs about the possible composition of aerosols and condensates. As previously mentioned, measurement of the gas abundances through thermal infrared emissions is contingent on first knowing the temperature profile, either through external (non-CIRS) measurements or models, or through CIRS modeling based on a prior well known/well mixed gas such as CH_4, CO, or H_2. However, in some instances these well-known gas abundances are instead the object of study, necessitating a joint retrieval which complicates the analysis.

GLOBAL GAS DISTRIBUTION

The first latitudinal trends in Titan's gases from CIRS data were published in Flasar et al. [2005a], showing similar qualitative trends in the lower stratosphere to those seen in Voyager flyby data 24 years earlier, i.e., short-lived trace gases (HCN, HC_3N, C_4H_2) showed sharp increases towards the north pole by 1–2 orders of magnitude, while longer-lived gases (such as CO_2 and C_3H_4) showed smaller increases or none at all. C_2H_4 showed an unexpected decrease from 0 to 60° N, which remains unexplained. Shortly thereafter, a focused follow-up study of the latitudinal variation of nitriles by Teanby et al. [2006] using medium resolution nadir spectra confirmed the trends reported in the 2005 paper.

The year 2007 was a watershed year for CIRS Titan results, with publications by Coustenis, Teanby, Vinatier and de Kok describing gas composition measurements.

Coustenis et al. [2007] modeled observations encompassing the first half of the Cassini prime mission (2004–2006), and including medium (2.5 cm^{-1}) and high (0.5 cm-) spectral resolution observations. All previous gases seen by Voyager IRIS and the Infrared Space Observatory (ISO) were detected, including a robust confirmation of benzene, tentatively detected by ISO [Coustenis et al. 2003]. Latitudinal variations of all species were mapped (Figure CIRS-26), showing the greatest polar increases for HCN, HC_3N, C_4H_2, C_3H_4, and C_6H_6. The D/H ratio was measured from CH_3D, and found to be $(1.17 \pm 0.25) \times 10^{-4}$.

The first results from analysis of CIRS limb observations, yielding vertical-latitudinal profiles of HCN, HC_3N, and C_2H_2, were shown in the paper of Teanby et al. [2007], and was also the first to include CIRS data covering 60–90°N. It clearly revealed for the first time the 2-D structure of the atmospheric trace gas concentrations, and dramatically showed the difference in distributions between the three decaying tracers of differing lifetimes (Figure CIRS-27). The longest-lived species, C_2H_2 showed only marginal polar enhancement, while the shortest-lived species, HC_3N showed the steepest vertical gradient at low latitudes, and the most intense enhancement over the northern (winter) pole where the descending branch of stratospheric global circulation was occurring. The intermediate lifetime species, HCN, showed the most interesting and unexpectedly distribution, with a tongue of enriched air reaching from the lower N polar stratosphere back

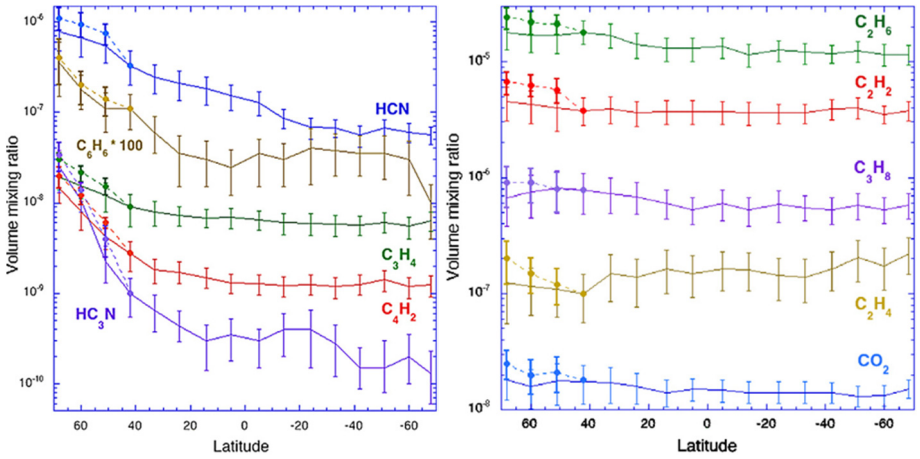

Figure CIRS-26. Meridional variations in the composition of trace gases in Titan's stratosphere and associated error bars. The latitudes indicated take into account the latitude smearing effect. The abundances shown are the averages of the results from fitting tours TB–T10. In dotted lines are shown the results at high northern latitudes when using the limb-based profiles instead of the nadir-based ones, highlighting the uncertainty on the higher northern inferences. Figure from Coustenis et al. [2007].

equatorwards. This was interpreted as the returning branch of the stratospheric circulation, seen clearly for the first time outside of GCM models.

Vinatier et al. [2007a] retrieved temperatures and vertical profiles for a wider array of gases at two latitudes on Titan—15° S and 80° N—from early flybys in 2004–2005. The temperature profiles confirmed the existence of a well-defined stratopause on Titan that was elevated (380 km versus 310 km) and hotter (207 K versus 183 K) in the north, in agreement with model expectations. The gas distributions largely confirmed the predicted picture from photochemical and dynamical models, however, there were unexpected details. Two of the heavier gases (C_3H_4 and C_4H_2) showed a minimum at 300 km in the north, perhaps related to haze formation. C_2H_4 showed a decreasing profile with altitude in the south: the opposite trend to other species, and possibly indicative of a secondary formation peak at low altitudes.

Oxygen-containing molecules were the focus of work by de Kok et al. [2007a], who retrieved a global mean abundance of CO equal to 47 ±8 ppm, and an upper limit for H_2O of 0.9 ppb, from CIRS FP1 far-IR spectra. CO_2 was found to have a typical abundance of 15 ppb in the lower stratosphere (100–200 km) with little latitude variation, in agreement with its expected long photochemical lifetime.

Teanby et al. [2008a] made a more detailed study of the northern polar vortex, this time using limb observation data to find the vertical gas distributions. A primary focus was to infer dynamical information from the distribution of trace gas species. A clear mixing barrier was detected at the edge of the northern vortex, preventing the enriched air from mixing laterally into the mesosphere at lower latitudes. However, at the base of the vortex, a tongue of tracer-enriched was spotted extending to lower latitudes, suggesting cross-vortex mixing and a residual polar circulation:

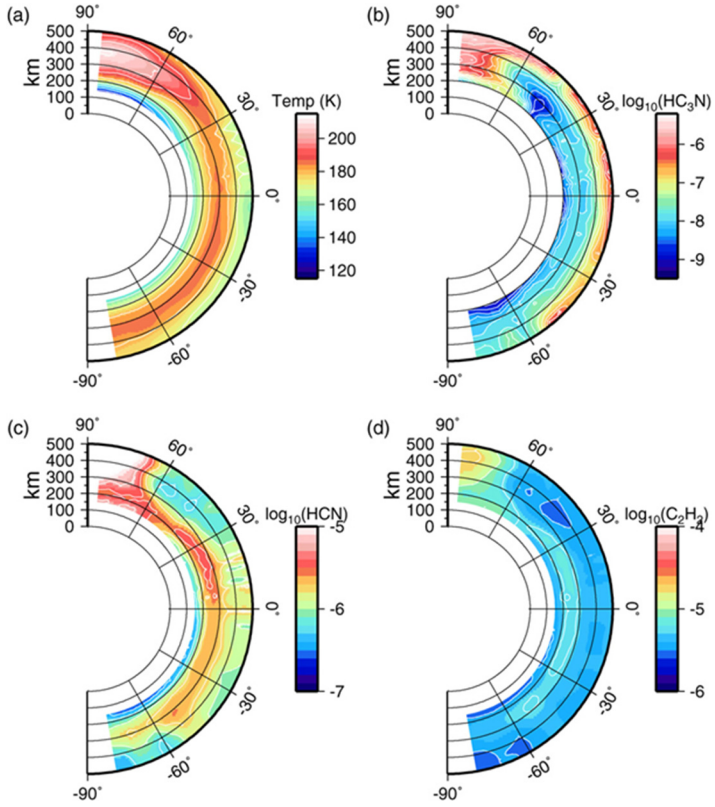

Figure CIRS-27. Cross-sections through Titan's atmosphere obtained using the three low resolution mapping sequences displaying temperature, HC_3N, HCN, and C_2H_2 abundance. Temperature is increased over the northern winter pole in the upper stratosphere and mesosphere and the stratopause is elevated with respect to the equator. The stratopause in the south also appears to be slightly higher than at the equator. The lower stratosphere in the north is much colder than at the equator. HC_3N shows a massive enrichment over the north pole, which appears to be confined to latitudes above 60° N. There is a suggestion of a tongue of enriched air extending from the north to the south at 200 km and 60° N. Note that HC_3N retrievals are not reliable southward of 50° N as the signal from HC_3N is too small. HCN is also enriched in the north, but the most striking feature is the layer of HCN enriched air at 200–250 km extending from the north pole to lower latitudes, which is suggestive of entrainment of enriched air in a meridional circulation cell. C_2H_2 appears to be well mixed throughout the atmosphere and does not vary significantly with latitude. There appears to be some slight enrichment over the north pole, which may be an artifact due to the correlation between HCN and C_2H_2 retrievals. Figure from Teanby et al. [2007].

features not reproduced in contemporary GCM models. Evidence was also seen for possible polymerization of C_2H_2 to C_4H_2.

A 2-D circulation model (CM) appeared soon thereafter, due to the work of Crespin et al. [2008] at the Institute Pierre-Simon Laplace, and with extensive collaboration from CIRS investigators. This model attempted to replicate the temperature fields measured by Achterberg, and vertical gas distributions retrieved by Vinatier and Teanby, especially. This represented an important step forward in modeling the new Cassini data, and provided an explanation for some of the observed phenomena. For example, the low-altitude increase in C_2H_2 was explained as the

presence of a long-lived, non-condensing gas species in the returning branch of the global circulation cell. However, some difficulties were encountered, such as the inability of the model to replicate a well-defined stratopause, and to reproduce the amplitude of the residual (previous season) winter polar enhancement in the south. These model deficiencies were important in pointing the way to further future work.

Hydrocarbon and nitrile composition from CIRS far-infrared spectra were first reported by Teanby et al. [2009c], who aggregated data from the first four years of the Cassini mission, encompassing the entirety of the prime mission (2004–2008). Three gases previously seen in this spectral region (200–400 cm^{-1}) by Voyager IRIS were detected: C_3H_4, C_4H_2, and C_2N_2, the last of which (cyanogen) is not seen in the mid-infrared spectrum of CIRS (600–1400 cm^{-1}). The abundance of C_3H_4 was about 2× greater than inferred from mid-infrared data, suggesting that coefficients for one or other of the bands were incorrect. For the first time, C_2N_2 was detected at low latitudes, where its abundance ($5.5 \pm 1.4 \times 10^{-11}$) is amongst the lowest of any gas detections by CIRS. Like other nitriles (HCN, HC_3N), cyanogen showed a greater polar enhancement than hydrocarbons with similar lifetimes, suggesting that chemical processes were missing from contemporary models.

In a study by Coustenis et al. [2010], the 2007 survey was expanded to include nadir data from all flybys of the Cassini prime mission (2004–2008), and including latitudes 90° S to 90° N, and also using revised spectroscopic parameters for C_2H_2, C_2H_6, and HCN to improve accuracy of results. By and large, the results were in agreement with GCM predictions [Crespin et al. 2008], but discrepancies were noted, such as lack of observational support for a secondary circulation cell.

Vinatier et al. [2010b] provided a comprehensive look at vertical profiles of a nearly-complete suite of Titan gases in the CIRS spectrum (C_2H_2, C_2H_4, C_2H_6, C_3H_8, CH_3C_2H, C_4H_2, C_6H_6, HCN, HC_3N, and CO_2) including first-ever maps of the 2-D distribution of C_2H_4, C_2H_6, C_3H_8, C_6H_6 and CO_2 at nine latitudes from 56° S to 80° N (Figure CIRS-28). This confirmed earlier results [Vinatier et al., 2007a], such as the decreasing abundance of C_2H_4 with altitude, in contrast to other gas species. Other previously unknown details of the gas distribution emerged, including depleted regions of C_2H_2, HCN, and C_4H_2 at 400 km (0.01 mbar) and 55° N. In contrast an enhanced region of CO_2 was seen at 30–40° N between 2–0.7 mbar. Finally, nearly all molecules showed a local minimum in abundance at (300 km, 80° N) in contrast with GCM models that predicted vertically constant profiles inside the vortex.

Far-infrared spectral lines of HCN were modeled by Teanby et al. [2010b] to confirm the earlier polar enhancement derived from mid-infrared spectral emissions [Teanby et al. 2007]. The data also supported the conclusion of Teanby et al. [2009c] that nitriles were missing a chemical sink in current photochemical schemes, since the emission versus lifetime distribution did not match that of hydrocarbons. In addition, the abundance of CO was re-derived and found to be: 55 ±6 ppm at 20 mbar, in good agreement with de Kok et al. [2007a].

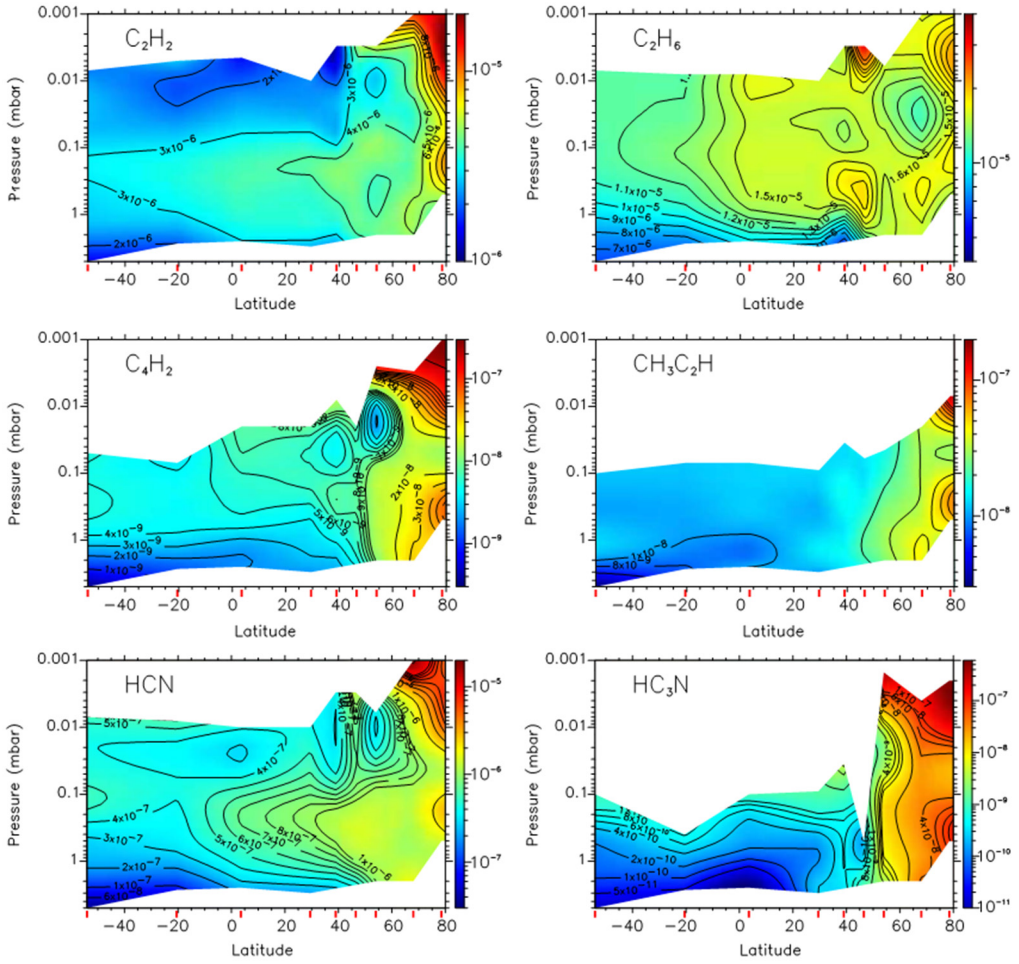

Figure CIRS-28. Latitude/pressure map of mixing ratios of C_2H_2, C_2H_6, C_4H_2, CH_3C_2H, HCN, and HC_3N. The regions of insufficient information content appear in white. Latitudes of the observed spectra are displayed as red vertical bars on the latitude axis. Figure from Vinatier et al. [2010b].

The global abundance of H_2 was the objective of a study by Courtin et al. [2012], who modeled the H_2–N_2 dimer S_0 (0) feature around 355 cm^{-1} seen on CIRS FP1 using data from 2006–2007. The mean abundance found was (9.6 ±2.4) × 10^{-4}, in good agreement with the Huygens GCMS value of (1.01 ±0.16) × 10^{-3} [Niemann et al. 2010]. This value is however some 4× lower than the ionospheric value: (4.05 ±0.03) × 10^{-3} at ~1200 km [Waite et al. 2005], which causes significant difficulty for modeling to explain. Interestingly, the CIRS measurements of the hydrogen abundance showed some evidence of increase towards the poles (Figure CIRS-29), by 30–70%, which would only make sense if it was due to downward transport in the presence of a vertically increasing hydrogen profile, as implied by the joint CIRS-GCMS-INMS results. Whether or not such a large hydrogen gradient is consistent with photochemical timescales from modeling remains an open question.

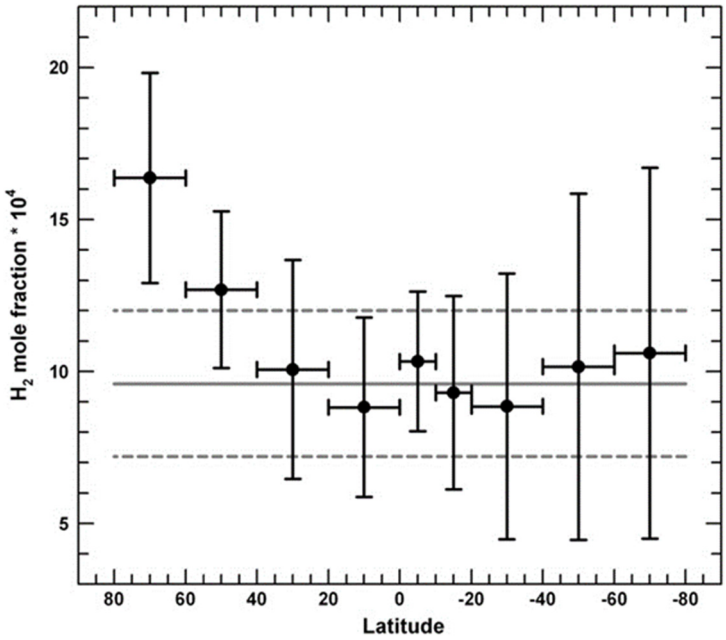

Figure CIRS-29. Values of the H_2 mole fraction (in unit of 10^4) derived from the CIRS average spectra in the nine latitude bands. The horizontal lines represent the global average value we derived, $(9.6 \pm 2.4) \times 10^{-4}$. Figure from Courtin et al. [2012].

Cottini et al. [2012a] made the first measurement of water latitude distribution from Cassini CIRS far-IR data, following the upper limit published by de Kok et al. [2007a] and a southern hemisphere average by Teanby et al. [2009b]. Globally, nadir measurements yielded an abundance of 0.14 ±0.05 ppb for an altitude of 97 km for a well-mixed vertical profile, somewhat lower than previously inferred from ISO (0.4 ppb). Two vertical profile points were also retrieved (Figure CIRS-30), showing a steep gradient that was in agreement with some photochemical models. No latitude variation was noted in the data.

In 2014, an interesting result emerged from the work of Lellouch et al. [2014] to constrain the abundance of methane, normally assumed to be constant with latitude in CIRS analysis, and fixed to the Huygens probe GCMS values [Niemann et al. 2010]. Lellouch and colleagues sought instead to retrieve the atmospheric temperature and the abundance of CH_4, via simultaneous modeling of mid-infrared rovibrational lines and far-infrared pure rotational lines. The result was unexpected, showing a variation in the abundance of methane from 1.0 to 1.5% at 85 km (15 mbar) in the lower stratosphere, a large fluctuation that was difficult to explain. Intriguingly, the low value (1.0%) near the equator allowed a temperature profile that agreed for the first time with Huygens HASI measurements, at the cost of losing agreement with GCMS. An explanation was offered for the mid-latitude increases in methane abundance as being due to tropospheric convection events percolating and persisting into the stratosphere.

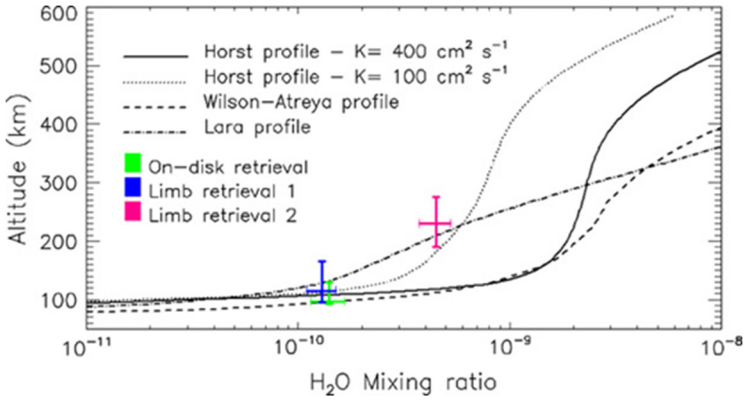

Figure CIRS-30. Water vapor mole fraction retrieved from CIRS on-disk and two limb observations assuming a water profile constant with altitude over the condensation level. Water profiles from three photochemistry models are also shown for comparison. The Hörst et al. [2008] water vapor profile was derived assuming two different eddy diffusion coefficients—100 cm^2 s^1 and 400 cm^2 s^1 (the second being the one recommended in their model; dotted curve plus solid curve). Also the profiles in Wilson and Atreya [2004] (dashed curve) and in Lara et al. [1996] (dot-dash curve). Figure from Cottini et al. [2012a].

Titan's water abundance was further constrained by the work of Bauduin et al. [2018], who analyzed a unique set of distant (~10^6 km) observations of Titan by CIRS, taken so that the entire moon was contained inside the FP1 pixel. This was done for intercomparison purposes with earlier studies using ISO and Herschel data, where Titan was similarly unresolved from the Earth-orbiting telescopes. Bauduin and colleagues found that the original discrepancy of a factor ~5 between Herschel (0.023 ppb at 12.1 mbar) and CIRS (0.14 ppb at 10.7 mbar) was sustained in the reanalysis, opening the possibility of seasonal change in the water abundance.

Lombardo et al. [2019] used a new line list for propene, first detected by Nixon et al. [2013a] to make the first spectral retrievals for this gas species. The results indicate that propene has a significantly different latitudinal profile from the other C_3H_x species: propyne and propane. Instead of being concentrated over the winter pole, the greatest abundance was found at the equator. Differences from photochemical model predictions were also found.

SEASONAL CHANGES

The paper of Teanby et al. [2008b] marked the start of papers focused on a new dimension of the dataset: seasonal changes in the gas distributions, from (L_S = 293°–328°). Teanby and colleagues used nadir spectra at medium (2.5 cm^{-1}) and high spectral resolution (0.5 cm^{-1}) to elucidate spatial and temporal changes in the abundances of C_2H_2, C_3H_4, C_4H_2, HCN, and HC_3N. A major new result was the gas distribution for the north polar region, showing that abundances continued to increase right up to 90° N (Figure CIRS-31). No secondary circulation cell was seen at the south pole, in contrast to GCM models predictions. A decline in southern gases was noted, as the residual southern winter enhancement faded.

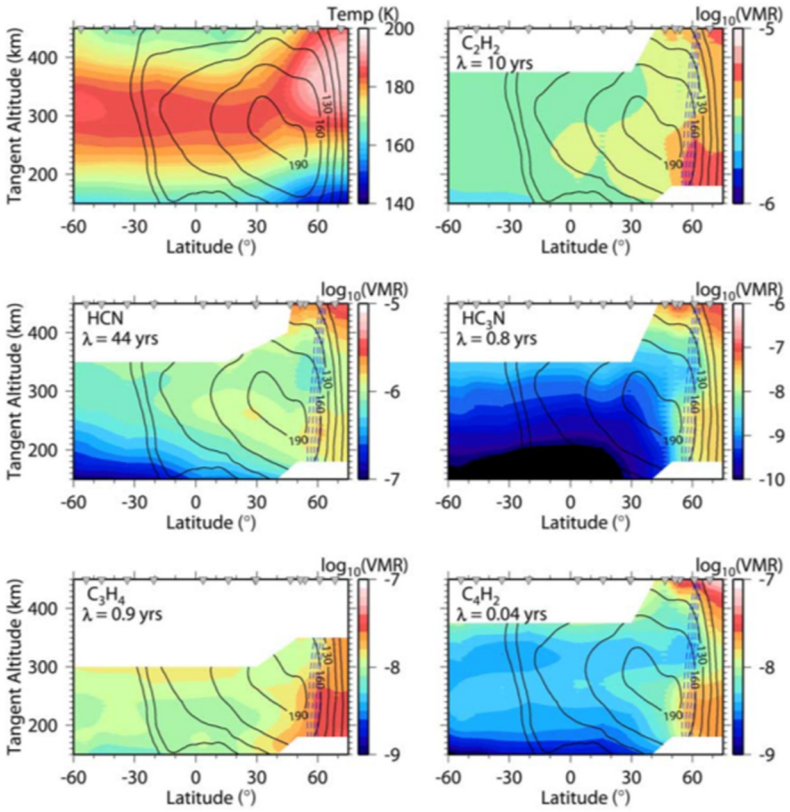

Figure CIRS-31. Cross-sections of temperature and composition through Titan's atmosphere. Composition is given as a volume mixing ratio, and the positions of the observed profiles are denoted by inverted triangles at the top of each plot. Contours indicate the vortex zonal wind speeds (in m s^{-1}) derived by Achterberg et al. [2008a], and blue dashed lines show the region with the steepest horizontal potential vorticity gradient, which indicates a dynamical mixing barrier (see Figure CIRS-5 and the section entitled Jupiter). Altitudes with low signal to noise or where the atmosphere becomes opaque are not plotted. VMR is the volume mixing ratio, and lambda is the photochemical lifetime at 300 km. Figure from Teanby et al. [2008b].

Teanby et al. [2009b] elaborated on the previous work, and showed that nitriles have different enhancements over the winter pole compared to hydrocarbons of similar photochemical lifetimes, which suggests some missing reactions in chemical models. A further update to seasonal and temporal trends in gas abundances was published by Teanby et al. [2010c], enlarging the dataset to include the six-year period from 2004–2010. Post-equinox (August 2009), increases in gases at both poles was seen, the first tentative evidence that Titan was transitioning to a two-cell circulation.

Seasonal changes in temperature and composition were also reported by Bampasidis et al. [2012], who modeled CIRS high resolution (0.5 cm^{-1}) nadir spectra from 50° S to 50° N, and spanning a time range from 2006–2012. At northern latitudes, the temperature profile evolved during the time period from a strong positive gradient to a more isothermal profile, with a cooling mesosphere and warming stratosphere. A maximum in the polar trace gas enrichment was found at the time of northern spring equinox (August 2009), followed by a sharp decrease as the polar descending circulation weakened and gases began to dissipate.

The first clear evidence for reversal of the stratospheric circulation was reported by Teanby et al. [2012a], who reported a build-up in trace gases over the south pole, some two years after equinox. A primary result was that the transition was very rapid, taking less than six months. The gas enrichments were used to estimate subsidence velocities within the vortex. Furthermore, gas and temperature distributions showed that upper atmosphere circulation must extend too much higher altitudes than previously thought: 600 km or more. This placed an imperative for revision of GCM models that did not at the time reach to such altitudes. In addition, the data suggested that the detached haze layer at ~500 km could not be solely generated by the circulation.

Coustenis et al. [2013] tackled the important question of intercomparison of findings from Cassini CIRS and Voyager IRIS, spanning a full Titan year, albeit with incomplete coverage. Temperature profiles and gas abundances in the lower stratosphere were measured and compared between 1980 and 2010, one Titan year apart. The results indicated little inter-annual variability, although the detailed distributions of the shortest-lived molecules C_3H_4 and C_4H_2 did exhibit differences.

Most recently, Vinatier et al. [2015] provided an update on the vertical profiles for the majority of Titan gas species seen in the CIRS data (Figure CIRS-32), using data from 2006–2013, focusing on seasonal changes. This provided a clear picture of the changes occurring in seasonal circulation, most especially around equinox, when the two-cell system persisted for just six months (January 2010–June 2010). By 2011, the single-cell winter circulation pattern had become established, reversing the direction of the circulation seen at the start of the mission. A sudden unexpected temperature drop was seen soon afterwards above the south pole, hypothesized to be due to enrichment in trace gases acting as coolants. In late 2012, a detached haze layer was seen in the CIRS data at 320–330 km, corresponding to the altitude of the detached haze layer seen by Cassini's cameras in the UV.

Seasonal change in Titan's temperatures and gases at high latitudes was studied by Coustenis et al. [2016], focusing especially on the comparison of ±50° and ±70° from 2010–2014, following Coustenis et al. [2010] (Figure CIRS-33). For the longest-lived hydrocarbons there was minimal change at all latitudes prior to 2013, with a small trend for increase in the south thereafter. At 70° S there was a strong enhancement in heavier hydrocarbons from late 2011 (equinox), including the appearance of HC_3N and C_6H_6 that were undetectable at this latitude at earlier times. A possible link between the gases and haze formation was postulated.

Sylvestre et al. [2018] followed up on the work of Teanby et al. [2009c], this time searching for seasonal changes in Titan's gases via the far-infrared spectrum. The heavy molecules C_3H_4, C_4H_2, and C_2N_2 were measured, showing a dramatic increase in abundance over the south pole in a short period from 2012–2013, while north polar abundances remained nearly unchanged. However, at northern mid-latitudes the shorter-lived species C_4H_2 and C_2N_2 did exhibit a decrease, while C_3H_4 did not. These results provide further constraint on photochemical and dynamical models.

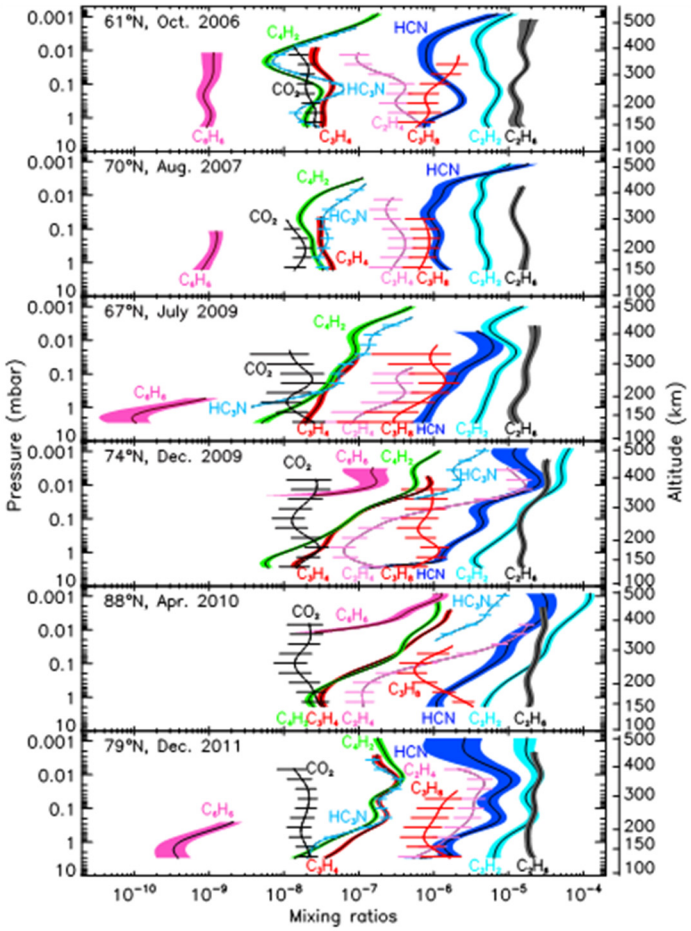

Figure CIRS-32. Seasonal variations of the mixing ratio profiles of C_2H_2 (cyan), C_2H_4 (pink with horizontal bars), C_2H_6 (gray), C_3H_8 (red with horizontal bars), C_3H_4 (red envelope), C_4H_2 (green), C_6H_6 (pink envelope), HCN (dark blue), HC_3N (blue with horizontal bars), and CO_2 (black with horizontal bars) at the north pole, derived from 0.5 cm^{-1} resolution limb spectra. Envelops and horizontal bars give the 1 r error bars. Figure from Vinatier et al. [2015].

A follow-up to the trends in seasonal changes of trace gases reported by Coustenis and colleagues in 2010 and 2016 was made by Coustenis et al. [2018], who focused on the polar regions 60°–90° north and 60°–90° south from CIRS nadir data. Notably different behavior was found for the onset of southern winter gas enhancement, which began in 2012, versus the decline in northern winter enhancement, beginning in 2015. The asymmetry in heating was dramatically evidenced in lower stratospheric temperatures: from 2013–2016 the north, entering spring, showed a mild temperature increase of 10 K, while the south, tending towards winter showed a more dramatic decrease of 25 K in the same period.

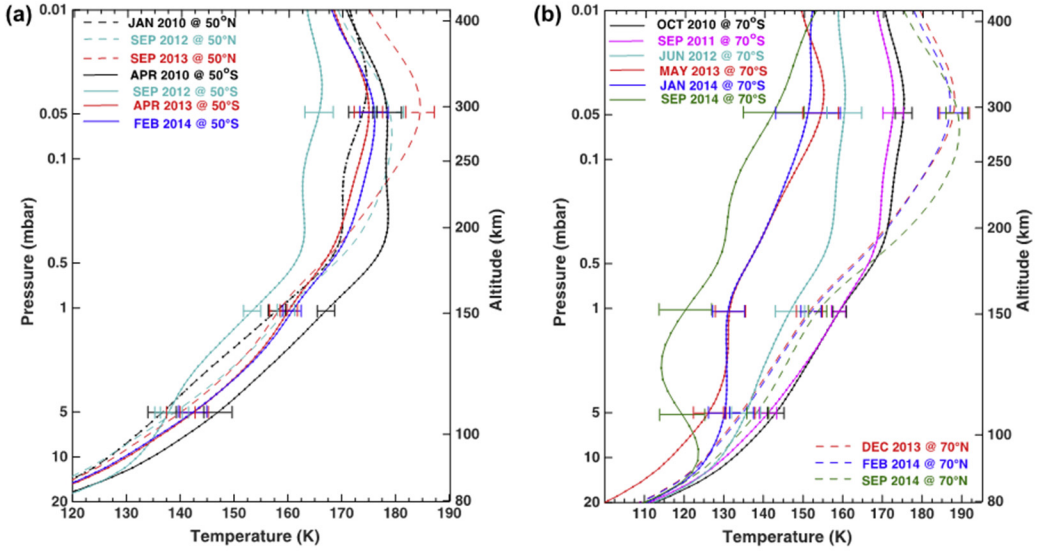

Figure CIRS-33. Seasonal change in Titan's temperatures and gases at high latitudes. (a): temperature variations at 50° S (solid lines) and 50° N (dashed lines) in Titan's stratosphere from January 2010 until February 2014; (b): temperature profiles of Titan at 70° S (solid lines) and 70° N (dashed lines) with dates ranging from October 2010 to September 2014 (in different colors).The pressure/altitude ranges probed by these profiles vary with latitude, but are generally in the 0.1–20 mbar region. The 3-r error bars on the temperature are plotted at 0.05, 1, and 5 mbar (see text for details). As can be seen, the stratospheric temperatures in the 0.1–1 mbar pressure range dropped by about 40 K near the southern pole within the past four years. At the same time, the temperatures in the north had not indicated similar dramatic changes, but rather an increase in temperature is found since February 2014, as the north moves into summer. The dashed lines, thus, show that within about seven months since December 2013, the NORTH POLE had warmed up by about 6 K. Figure from Coustenis et al. [2016].

SEARCH FOR NEW GAS SPECIES

Nixon et al. [2009a] made a detailed survey of the CIRS mid-infrared spectrum of Titan, searching for previously unseen gas species, and focusing especially on the region from 850–1050 cm^{-1} where there are few strong emissions. While a null result was obtained, numerous weak bands of propane (C_3H_8) were seen clearly for the first time that were not present in existing line lists used by the team, prompting a renewed round of laboratory work to provide line parameters.

In a follow-up paper, Nixon et al. [2010b] computed upper limits for several of gases expected to be found on Titan, from dedicated search observations (FP3/4 pair mode) at latitudes 25° S and 75° N. By comparing the results to photochemical model predictions they concluded that NH_3 and CH_3OH are likely present at levels far below the CIRS detection threshold, while CH_3CN, CH_2CCH_2 and H_2CO are closer to detection limits. In a later paper, Nixon et al. [2013b] added upper limits for biologically important sulfur and phosphorus-bearing compounds: H_2S and PH_3.

The first, and to this date only, new gas species detection on Titan from Cassini CIRS data was announced by Nixon et al. [2013a], following the availability of new propane line parameters from

several sources. This enabled the isolation of a propene (C_3H_6) emission at 912 cm^{-1} from stronger over-lying propane and ethylene bands (Figure CIRS-34), with an abundance of 2–4 ppb depending on altitude. This detection marked the completion of the triad of C_3H_x hydrocarbons, although the search for isotopologues such as allene (CH_2CCH_2) and cyclopropane (c-C_3H_6) continues.

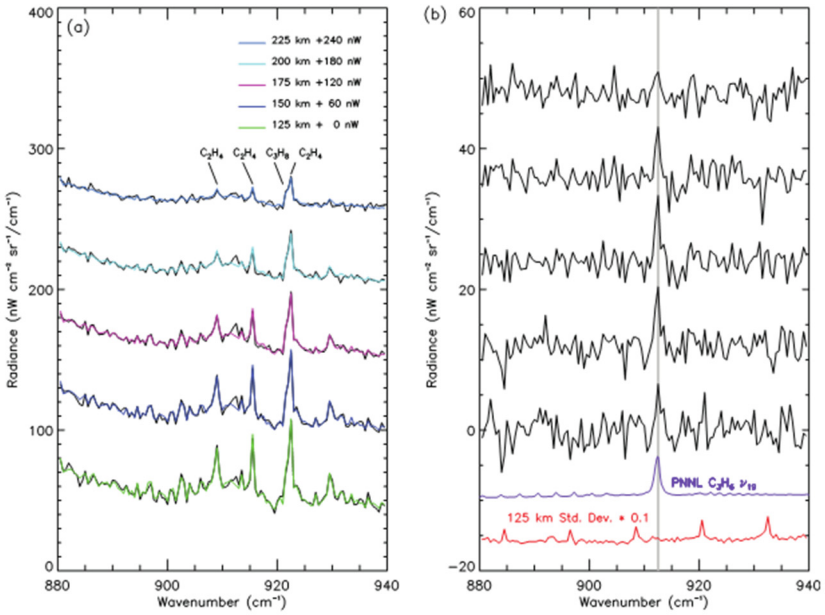

Figure CIRS-34. New gas species detection on Titan from Cassini CIRS data. (a) Co-added data spectrum (black) from weighted average of lowest (125 km), middle (175 km), and topmost (225 km) vertical bins. Also shown are the model spectra with propane (red) and without propane (blue) from the JPL pseudo-line list. (b) Residuals from subtracting data–model: blue line is model without propane and red line is with propane. The purple line shows the smoothed laboratory absorbance spectrum of propene recorded at PNNL, scaled by 1 × 10^4 and offset by −10. The detection significance is ~5 σ. Figure from Nixon et al. [2013a].

A detailed study was made by Jolly et al. [2015] to search for dicyanoacetylene (C_4N_2) in the far-infrared spectrum of CIRS, based on both theoretical expectations for its presence, and also the tentative identification of the ice at 478 cm^{-1} from Voyager IRIS data. Previous searches for the v8 band gas emissions at 472 cm^{-1} had been unsuccessful, causing a dilemma: how could there be ice clouds without vapor? New laboratory work indicated that the ν_9 band at 107 cm^{-1} was in fact stronger than ν_8, and a better candidate for detection given the better S/N in this part of the spectrum. However, only an upper limit on non-detection of 5–7 × 10^{-10} at the 1 σ level was found, leaving the question open about the origin of C_4N_2 ice.

ISOTOPIC RATIOS

Bézard et al. [2007] made a distinguished first detection of the first known double isotopologue on Titan: $^{13}CH_3D$ (Figure CIRS-35). By modeling the emission to measure the gas abundance they were able to estimate isotopic ratios of: $^{12}C/^{13}C$ = 82 (+27/−18) and D/H = (1.32 +0.15/−0.11) × 10^{-4}.

The carbon ratio was in good agreement with the terrestrial ratio (89), however the D/H appeared slightly lower than terrestrial (1.56×10^{-4}), though still substantially higher than in the giant planets, in accordance with expectations.

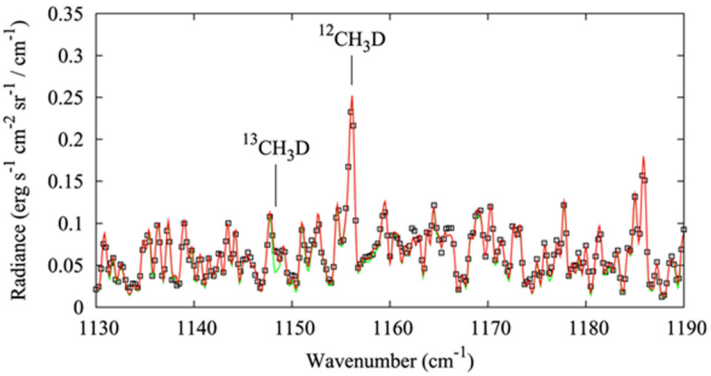

Figure CIRS-35. Comparison between a CIRS spectral selection centered at 15° S (symbols) and synthetic spectra calculated with (red line) and without (green line) $^{13}CH_3D$ line opacity, assuming a $^{12}C/^{13}C$ ratio of 89. Spectral resolution is 0.52 cm^{-1} (apodized). Both calculations use the same haze model, a CH_4 mole fraction of 1.4% and a CH_3D mole fraction corresponding to D/H = 1.34°ø 10^{-4}. Figure from Bézard et al. [2007].

Isotopic ratios in HCN were presented by Vinatier et al. [2007b] from CIRS limb spectra near 700 cm^{-1} on two early flybys. Abundances of HCN, $H^{13}CN$ and $HC^{15}N$ were individually measured, yielding isotopic ratios: $^{13}C/^{12}C = 75 \pm 12$, consistent with the current GCMS measurement at the time (82 ±1); and $^{14}N/^{15}N = 56 \pm 8$, lower than the value measured by GCMS in N_2 (183 ±5), but consistent with previous determinations in HCN from ground-based submillimeter investigations, and confirming that nitrogen-15 is preferentially depleted from the atmospheric reservoir in N_2 and incorporated into HCN.

The year 2008 proved to be a bumper year for new isotopic measurements, with four papers based on CIRS data. Coustenis et al. [2008] made the first detection of C_2HD, enabling for the first time the measurement of D/H in this chemical species. The modal value of $(2.09 \pm 0.45) \times 10^{-4}$ was significantly lower than the D/H in methane found by Bézard et al. [2007]: 1.56×10^{-4}, indicating possible fractionation from the parent (CH_4) to daughter molecule via photolysis or chemical selection.

Jennings et al. [2008] provided the first detection of carbon isotopes of HC_3N, most especially the strong detection of $H^{13}CCCN$ at 658.7 cm^{-1}, well separated from the main gas at 663.3 cm^{-1}. The derived isotopic ratio $^{12}C/^{13}C = 79 \pm 17$ was in good agreement with the terrestrial inorganic standard (89), and confirmed the growing body of evidence that carbon does not incur photochemical fractionation in Titan's atmosphere.

In a companion paper, Nixon et al. [2008b] showed the first detection of CO_2 isotopes on Titan, including both $^{13}CO_2$ and $CO^{18}O$. The carbon ratio ($^{12}C/^{13}C$) was 84 ±17, again in agreement with terrestrial levels, while the oxygen ratio ($^{16}O/^{18}O$) showed some evidence for enrichment: 346 ±110, versus the terrestrial 506. This value was later revised upwards to 380 ±142 by Nixon et

al. [2009b] using a more sophisticated and accurate model for the detector responses, moving the oxygen ratio closer to consistency with terrestrial values.

First remote-sensing measurements of the $^{12}C/^{13}C$ ratio in prominent hydrocarbons: methane, ethane, and acetylene were made by Nixon et al. [2008a], using CIRS high-resolution limb spectra. The results were: 76.6 ±2.7, 84.8 ±3.2, and 89.8 ±7.3 for CH_4, C_2H_2, and C_2H_6, respectively. While the acetylene and ethane values were close to terrestrial, the methane value was markedly lower: a perplexing result, lower even than the GCMS value (at the time) of 82.3 ±1 [Niemann et al. 2005]. Possible explanations were offered in terms of line strength errors or else some strong fractionation effect, however, unknown systematic errors may have contributed.

Following small irregularities in the modeling of the strong ν_8 band of diacetylene (C_4H_2), Jolly et al. [2010] were able to identify the carbon-13 isotopologue: $H^{13}CCCCH$ at 622.3 cm^{-1} (Figure CIRS-36). By modeling emission and comparing to the main isotopologue, a ratio $^{12}C/^{13}C$ = 88 ±7 was derived. This is in good agreement with the ratio in C_2H_2 [Nixon et al. 2008] and also the terrestrial and giant planet values, confirming an emerging picture that carbon undergoes very little isotopic fractionation across the solar system, in comparison to hydrogen and nitrogen.

Nixon et al. [2012] attempted a more accurate measurement of $^{12}CH_4/^{13}CH_4$ to resolve the uncertainty, this time including the other known methane isotopologues: $^{12}CH_3D$ and $^{13}CH_3D$. The

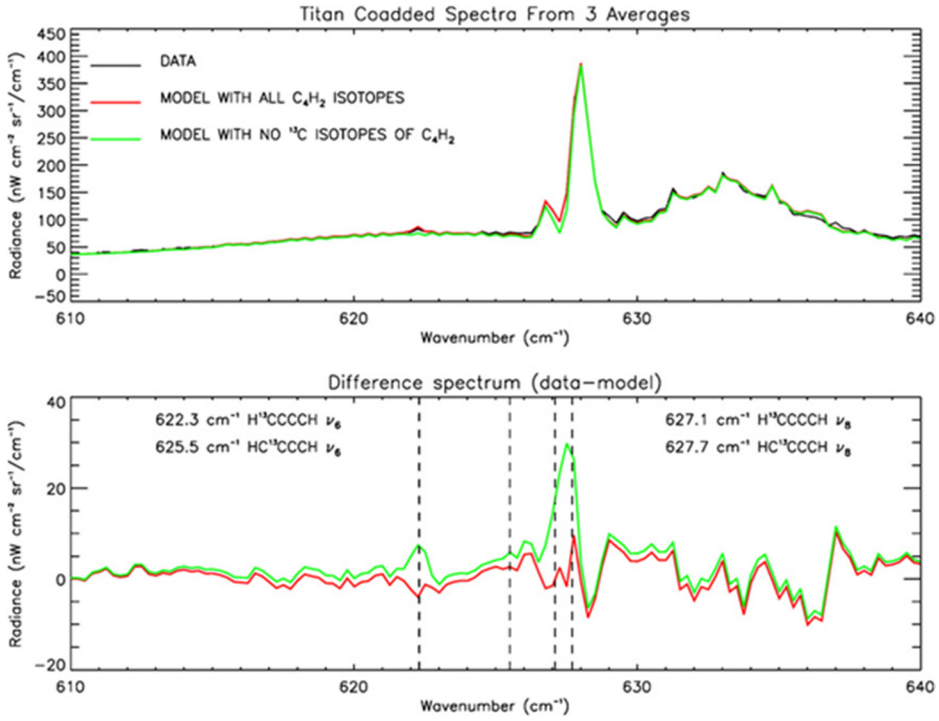

Figure CIRS-36. Modeling emission and comparing to the main isotopologue. *Top*: mean observed spectrum of Titan, compared to model spectra with and without the contribution of ^{13}C isotopologues of C_4H_2. *Bottom*: residual emission obtained after subtracting the observed spectrum and both model spectra. Figure from Jolly et al. [2010].

$^{12}C/^{13}C$ from these new measurements: 86.5 ±8.2 was now in much closer agreement with Huygens GCMS, also revised upwards to 91.1 ±1.4, and both in agreement with terrestrial (89), removing any need for significant fractionation. D/H was also measured to be (1.59 ±0.33) × 10^{-4}, in good agreement with the Huygens GCMS value in H_2: (1.35 ±0.30) × 10^{-4}. By considering the limited divergence of these ratios from primordial values, the authors were able to place an upper bound on the age of Titan's atmosphere of 1600 million years.

Hazes and condensates

In this section, we discuss the rich information derived from CIRS data regarding hazes and condensates in Titan's atmosphere. Although the definitions are sometimes blurred, we will here use the term haze in a narrow sense to mean photochemically-derived, refractory organic particles that are heterogenous in size, composition, and structure at the microscopic level. We use "condensate" to refer to clouds of droplets of ice particles of relatively pure substances that have reached their condensation/freezing point. We note that haze particles are thought to act as nuclei for condensation, and would, therefore, be present in the cores of condensate cloud droplets, although at that point, undetectable. In addition, condensates may undergo photochemical reactions and change their composition, as described the following sections.

HAZE

The first paper tackling the derivation of haze properties from CIRS data was the work of de Kok et al. [2007b], who studied far-infrared (10–600 cm^{-1}) spectral limb data. The authors were able to measure the fractional scale height of the main, ubiquitous haze, in addition to identifying three specific spectral components that could be modeled with Gaussian signatures at 140, 190, and 220 cm^{-1}. These spectral features were localized in both latitude and altitude on Titan, and were in fact condensates of unknown composition, with B and C being seen preferentially in the northern (winter) hemisphere. Haze B appeared to be the re-detection of a strong feature seen by Voyager IRIS, whose composition remains uncertain (Figure CIRS-37).

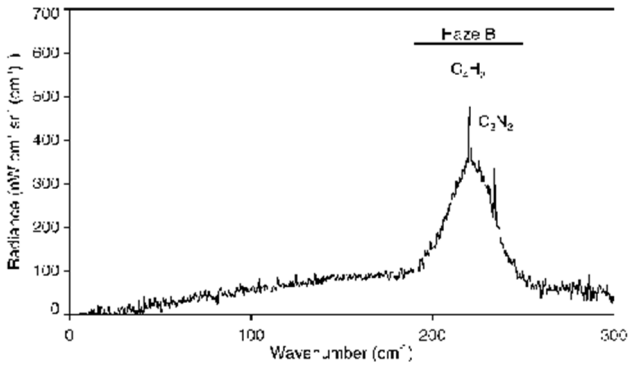

Figure CIRS-37. The average of 13 limb spectra at 85°N at 0.5 cm^{-1} resolution. The FOV centre is at 135 km and the FOV size is 135 km. This spectrum clearly shows a broad feature (Haze B) with gas emissions super-imposed on it. Figure from de Kok et al. [2007b].

A possible anti-correlation between gas and haze vertical abundances was proposed by Teanby et al. [2009a], based on joint analysis of CIRS and ISS data from 150–450 km. Periodic density enhancements were noted, with a length scale of ~50 km, and especially visible over the north pole and vortex boundary. A dynamical origin for the layering was proposed, based on cross-vortex (latitudinal) motions.

Vinatier et al. [2010a] provided the first survey of haze features in the mid-infrared regime of CIRS (600–1400 cm^{-1}), using nine limb integrations from 55° S to 80° N during the prime mission (Figure CIRS-38). Vertical profiles of haze opacity in 17 spectral bins were found, showing near-identical vertical trends, and indicating the haze composition is relatively unvarying with altitude. Distinct spectral features were found at 630 cm^{-1}, 745 cm^{-1}, and 1390 cm^{-1}. A global trend for increasing mass mixing ratio with altitude was taken as strong evidence that the haze is created at high altitudes, above the level of CIRS detection.

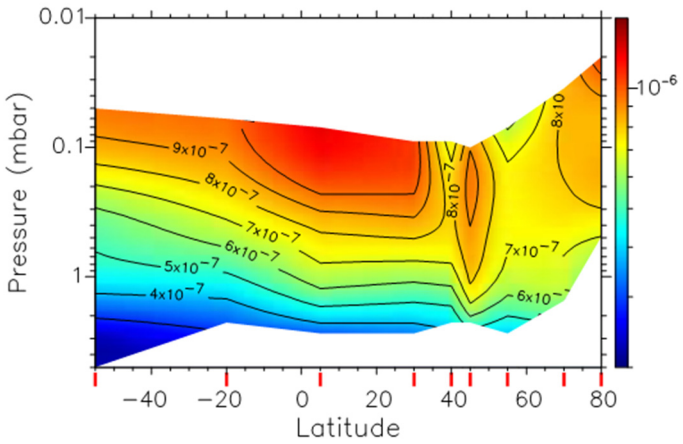

Figure CIRS-38. Latitudinal/pressure map of the haze mass mixing ratio. Latitudes of the observed spectra are displayed as red vertical bars on the latitude axis. Figure from Vinatier et al. [2010a].

A multi-instrument study of the haze banding on Titan was presented by de Kok et al. [2010b], using data from Cassini's ISS and VIMS instruments as well as CIRS. The imagery showed a prominent tropical haze band, and its orientation confirmed the tilt of the atmospheric rotation axis suggested by Achterberg et al. [2008b]. Haze profile retrievals from CIRS data at 640–670 cm^{-1} also reinforced the result.

A comprehensive follow-study by Vinatier et al. [2012] derived the optical properties of Titan's haze from the far-IR to mid-IR (70–1500 cm^{-1}), by modeling the haze particles as aggregates of ~3000 spherical monomers (0.05 micron radius) with fractal dimension n = 2. Real and imaginary refractive indices were derived across the entire range, and several distinct spectral features were found corresponding to vibrations of methyl and methylene. The same features were found across a wide array of altitudes and latitudes, indicating that Titan's haze is relatively uniform in composition.

The notorious, unidentified haze feature at 220 cm^{-1} in the CIRS far-IR was the subject of a study by Jennings et al. [2012b], who observed its seasonal change over the northern (polar) winter pole. From 2004–2012, the intensity of the feature decreased by a factor four, and the authors speculated that this could be due to either: (i) increased photolytic destruction of source chemicals, (ii) decreased condensation due to warmer temperatures, or (iii) a weakening of the subsiding branch of the seasonal circulation. In a follow-up paper [Jennings et al. 2012a] the authors reported the rapid appearance of the 220 cm^{-1} haze in the south (Figure CIRS-39), in July 2012, following non-detection in February the same year. In a 2015 paper on the same feature, it was definitively attributed to a cloud instead of a haze, as described in the following paragraph.

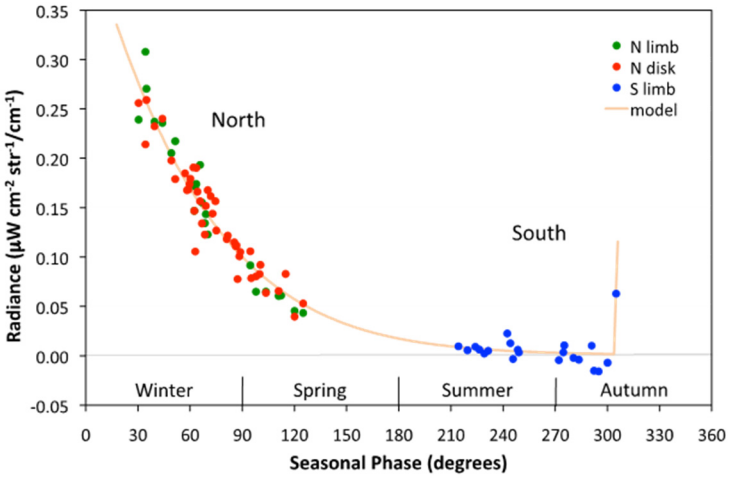

Figure CIRS-39. North and south polar radiances of the 220 cm^{-1} feature plotted on the same seasonal scale. Data from Titan's north represents winter–spring behavior and the data from the south represents summer–autumn behavior. The northern values were adapted from Jennings et al. [2012b], with the addition of a data point in the north from July 24, 2012. The southern values are from Figure CIRS-2 in this report. The seasonal phase scale begins at winter solstice and each 30° increment equals one Titan month. The model is described in the text. Figure from Jennings et al. [2012b].

CONDENSATES

Samuelson et al. [2007] provided the first update on condensates (ices) from CIRS data, comparing the spectral features seen in the far-infrared by CIRS to those seen previously by Voyager. Two definite ice/condensate features were identified in north polar (winter) spectra: the large emission feature at 220 cm^{-1}, previously seen by Voyager IRIS, and also called Haze B by de Kok the same year; and a weaker signature at 160 cm^{-1}. This latter feature was attributed to HCN ice particles of r < = 5 μm at altitudes less than 160 km, while the former was compared to pure crystalline water ice, and also ice of propionitrile (C_2H_5CN), and both candidates found to be produce insufficient spectral fits.

de Kok et al. [2008] further considered gases that might be condensing at Titan's winter (north) pole, especially the open question of C_4N_2 ice first raised by Khanna et al. [1987], and the

origin of Haze B. As with Samuelson et al. [1997], the authors found an upper limit for C_4N_2 gas based on the absence of the gas feature at 471 cm^{-1}, and therefore found the case for the ice identification to be uncertain. Likewise, an upper limit for propionitrile (C_2H_5CN) gas was found to be too low to support the large emission at 220 cm^{-1}, and an alternative explanation in terms of a mixed condensate including an HCN component was postulated instead.

A search for evidence of a tropospheric methane cloud was conducted by de Kok et al. [2010a], using CIRS far-infrared nadir and limb spectra. The authors concluded that the CIRS data were consistent with a cloud at 30 km, however this explanation was in conflict with findings from Cassini VIMS and Huygens DISR. A strong conclusion however was that the collision-induced opacity coefficients for N_2-CH_4 should be in increased by 50%, pending laboratory reevaluation.

The first confirmation for an HC_3N ice cloud on Titan was found by Anderson et al. [2010] at 62° N and 70° N, based on analysis of far-infrared spectral data (Figure CIRS-40). HC_3N ice (506 cm^{-1}) was clearly separated from HC_3N gas (499 cm^{-1}) for the first time, confirming earlier hints of its existence from Voyager IRIS [Samuelson 1985]. Cloud top altitudes were determined for HC_3N ice as 165 km (70° N) and 150 km (62° N), while upper limits for cloud abundances were measured at latitudes of 85° N, 55° N, 30° N, 10° N, and 15° S.

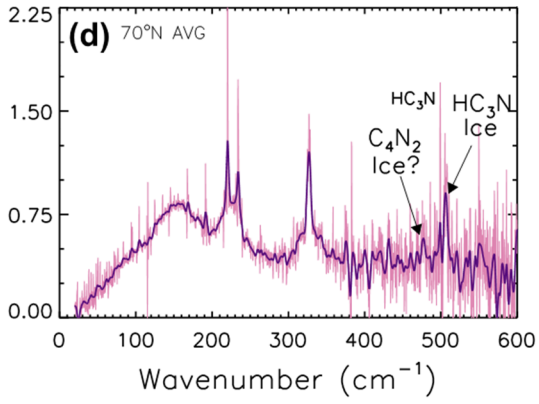

Figure CIRS-40. Weighted vertical average of both sit-and-stares at 70° N. Light pink curves are the data at the original spectral resolution (Dm) of 0.5 cm^1 and the dark purple curves represent the data smoothed by a Gaussian kernel to Dm = 3.0 cm^1. Condensed HC_3N and possibly C_4N_2 emission features are indicated by the arrows. Figure from Anderson et al. [2010].

Anderson and Samuelson [2011] derived the vertical and spectral properties of hazes and condensates at four latitudes (62° N, 15° N, 15° S, 58° S) using CIRS data at both high (0.5 cm^{-1}) and low (15 cm^{-1}) spectral resolution. While haze abundance was comparable, ices were found to be 3× more abundant at 62 °N compared to 15° S. A nitrile (HCN, HC_3N) ice cloud was inferred from a spectral signature at 160 cm^{-1}, 90 km and a second ice cloud was tentatively inferred at 80 cm^{-1}, 60 km. Aerosols were found to be uniformly mixed from the surface to the top of the stratosphere, with a broad emission feature at 140 cm^{-1} possibly due to PAHs.

In de Kok et al. [2014] looked for evidence in the CIRS data to explain the curious high-altitude (300 km) cloud seen by Cassini ISS above Titan's south polar in May 2012. The CIRS data showed

a strong cooling at this altitude (Figure CIRS-41), in contrast with previously observed warming during winter stratospheric subsidence. In addition, the saturation vapor pressure profile of HCN was found to reach 100% at this temperature minimum, providing a strong explanation for the ISS images in terms of an HCN ice cloud.

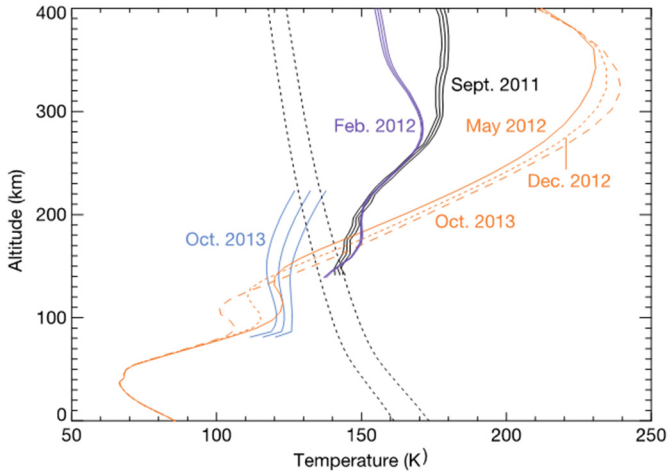

Figure CIRS-41. South-polar temperatures from models and retrievals. Retrieved temperatures and their 1 s errors at 86 u S in September 2011 (black solid line) and February 2012 (purple) from CIRS limb measurements and at 87u S in October 2013 from CIRS nadir measurements (blue). We plot only regions where the observations provide reliable temperature information. Orange lines are circulation model output for May 2012 (solid), December 2012 (dotted), and October 2013 (dashed). Black dotted lines indicate saturation temperatures for HCN volume mixing ratios of 10^{26} (*left*) and 10^{25} (*right*), which cover the measured concentrations of HCN in the south polar vortex. A cloud at 300 km would require temperatures of 125 K there [de Kok et al. 2014].

Anderson et al. [2014] proposed the existence of subsidence-induced methane clouds (SIMCs) over Titan's north pole, based on an analysis of far-infrared rotational lines of methane. By ingesting a radio science (RS) temperature profile and then deriving the vertical profile of methane, the authors showed that methane could exceed its saturation vapor pressure between 20–48 km, and that subsidence in the winter polar vortex could therefore induce condensation. A near-infrared counterpart and possible identification of this cloud was found in Cassini VIMS data.

Jennings et al. [2015] further studied the 220 cm^{-1} feature seen in the far-infrared spectrum of CIRS, and previously referred to as a haze in papers by de Kok et al. [2007b] and Jennings et al. [2012a, 2012b]. The 2015 paper showed the evolution of the condensate cloud at both poles, which was seen to be different. The northern cloud was decreasing in intensity since the start of the mission, with a half-life of 3.8 years. The southern cloud was doubling in intensity every year from 2012, confined to a ring centered on 80° S. In contrast, south polar trace gases had a bi-modal structure with a peak abundance at 90° S, minimum at 80° S, and ring of increased emission at 70° S. The authors concluded that the condensate and gases exhibited an anti-correlation, possibly due to condensation.

Chemical changes on grains of Titan's polar ice clouds were the subject of a 2016 paper by Anderson et al. [2016]. The authors proposed that the previously observed ice signature of C_4N_2 at 478 cm^{-1} (Figure CIRS-42) could arise naturally without condensation from the vapor phase, due to the action of sunlight acting on existing HCN-HC_3N mixed condensates. This process has a counterpart in terrestrial polar stratospheric clouds, where solid state photochemistry leads to condensed nitric acid trihydrate (NAT) particles and loss of ozone.

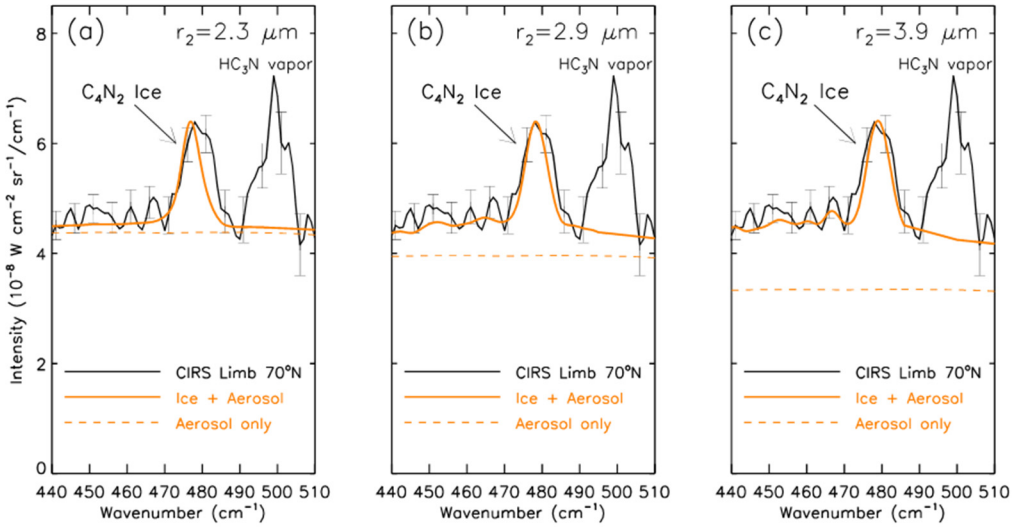

Figure CIRS-42. Radiative transfer fits (solid orange curves) to the continuum of CIRS limb-tangent spectral averages at 70° N (solid black curve). The spectral range is limited to 440–510 cm^{-1}, and the C_4N_2 ice feature at 478 cm^{-1} is included in the fits. A simplified two-stream plane-parallel model, patterned after the one by Hanel et al. [2003], is used to include effects due to anisotropic multiple scattering. Single-scattering parameters are calculated for various C_4N_2-HCN abundance ratios and mean particle radii: (a) pure C_4N_2 ice, r_2 = 2.3 μm; (b) 50:50 C_4N_2-HCN ice mixture, r_2 = 2.9 μm; and (c) 20:80 C_4N_2-HCN ice mixture, r_2 = 3.9 μm. Orange dashed curves show aerosol contributions. The 1σ error bars are spaced every 5 cm^{-1}. Figure from Anderson et al. [2016].

The south polar winter stratosphere again featured in the research of Vinatier et al. [2018], who investigated condensate signatures in the mid-infrared spectral region of CIRS. A weak feature isolated for the first time at 682 cm^{-1} was attributed to benzene ice, and a feature at 695 cm^{-1} was tentatively attributed to C_2H_3CN ice. Mass mixing ratios of both ices were determined, and it was shown that the cloud top for benzene was 300 km at the pole, decreasing to lower latitudes. An upper size limit of 1.5 micron was determined for the benzene ice particles.

Anderson et al. [2018] described their laboratory work dedicated to unraveling the spectral signatures of Titan ices, by deposition and spectroscopy of thin ice films. Pure condensates and co-condensates of HCN, HC_3N, and C_4N_2 were investigated, and the application to modeling and interpretation of CIRS spectra discussed.

Conclusions and further work

The Cassini CIRS instrument in general, and CIRS Titan science in particular, have been hugely successful relative to mission goals, as described in the section entitled CIRS Science Assessment. The original mission was projected to last for four years: in the end Cassini and CIRS returned data for 13 years, allowing an undreamt level of insight into Titan's atmospheric workings, and interactions with the surface. GCM and photochemical models that were largely speculative at the outset of the mission now have large, detailed and time-resolved datasets to use as constraints, providing fodder for study many years into the future.

In the absence of an active mission in the Saturn system, the focus will now turn to observations with ground and space-based observatories such as JWST [Nixon et al. 2016], ALMA, SOFIA, and large optical telescopes. However, given the difficulties of observing through Earth's atmosphere, significant sections of the infrared spectrum remain out reach (for all but JWST). It will be vital to continue monitoring seasonal changes in Titan's atmosphere to extend the time-base of Cassini observations, and prepare the way for the next generation of missions to visit this complex and fascinating world.

Icy Satellites

The key TM questions of Icy Satellite science that CIRS has helped address are:

Level 1

Changes on Enceladus (IC1a)

IC1a: Determine whether Enceladus exhibits any seasonal changes. Other temporal changes (e.g., mean anomaly) are also considered.

Enceladus' plume mass varies as a function time and of orbital position [Ingersoll and Ewald 2017], as shown in Figure CIRS-43. CIRS observations of Enceladus' active south polar region during Cassini's F-ring and proximal orbits (FRPO) were designed to investigate whether Enceladus' surface temperatures also vary with time. Preliminary results indicate that Enceladus' surface temperatures do vary with mean anomaly, but lag in time behind the plume change.

To determine whether the thermal emission of Enceladus varies with mean anomaly a series of observations were planned in the FRPO. A summary of the observations is given in Table CIRS-6.

Howett et al. [2017] presented analysis of this CIRS data at AGU 2017. They used focal plane 3 (FP3) observations since they offer the best compromise between spatial and spectral coverage of Enceladus' active region. The CIRS observations taken of Enceladus clearly show the active region. Figure CIRS-44 shows the original plane of sky data. The figure clearly shows the higher surface emissions from the active south polar terrain.

Table CIRS-6. Summary of the CIRS FP3 observations of Enceladus' south polar terrain. Those in bold have the best SNR, and therefore have been focused upon.

Orbit (Rev)	Date	# FP3 Observations	Mean Anomaly Range
250	**11/27/16**	**5**	**244 to 265**
251	12/4/16	9	8 to 46
254	**12/26/16**	**13**	**247 to 300**
255	1/2/17	5	1 to 18
259	**1/30/17 to 1/31/2017**	**19**	**303 to 24**
263	**2/28/2017 to 3/01/2017**	**21**	**272 to 50**
267	3/29/17	11	215 to 278
286	**8/1/17**	**17**	**280 to 252**

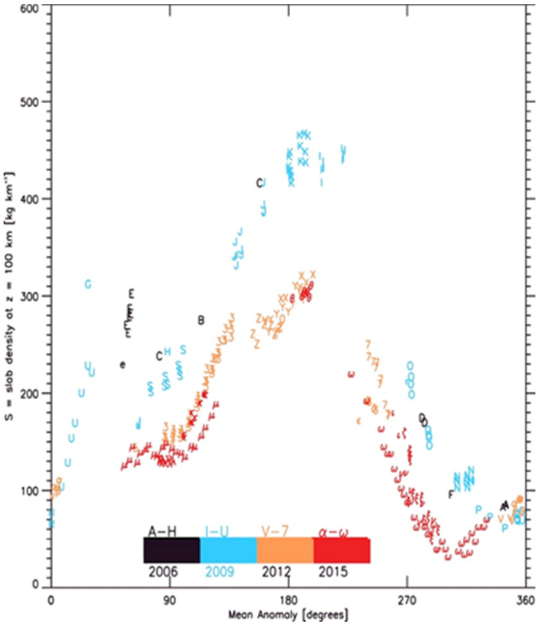

Figure CIRS-43. Enceladus' plume mass vis. Orbital position (mean anomaly). Figure from Ingersoll and Ewald [2017].

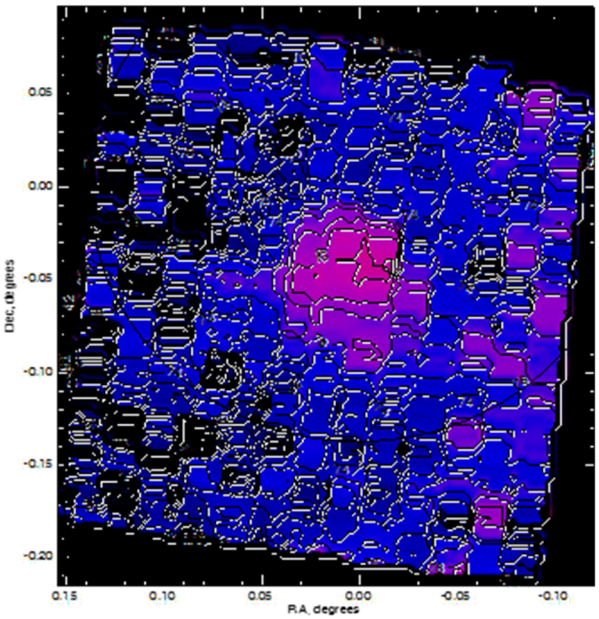

Figure CIRS-44. Typical FP3 scan shown in the plane of sky. Enceladus' active south polar terrain is clearly visible as the warmer purple region.

To properly account for the poles these data were binned into triangles, which are tessellated across the sphere. The area of each triangle is almost constant. The triangles are much smaller than the size of a single FP3 field of view, but since CIRS scans FP3 slowly across the disk subpixel resolution is achieved. Example of the resulting binned total integrated flux between 610 and 800 cm^{-1} are shown in Figure CIRS-45, at the start or end of each observation sequence.

The integrated radiances of all the high SNR observations were totaled for all bins inside of 70° S. The results are shown in Figure CIRS-46. As the figure shows only mean anomalies between ~270 and 10° are covered by these observations, but they appear to show the flux from Enceladus' surface decreasing by about a factor of two during that time.

This is smaller than the 3–5× decrease observed in the plume mass, and occurs at slightly higher mean anomalies. However, the difference is notable and tentatively implies that the temperature of Enceladus' surface in its active region does vary with its orbital location, but the change lags the plume emission change. More work is required to firm up this preliminary result, and analyze the lower signal-to-noise observations to fill in the mean anomaly coverage.

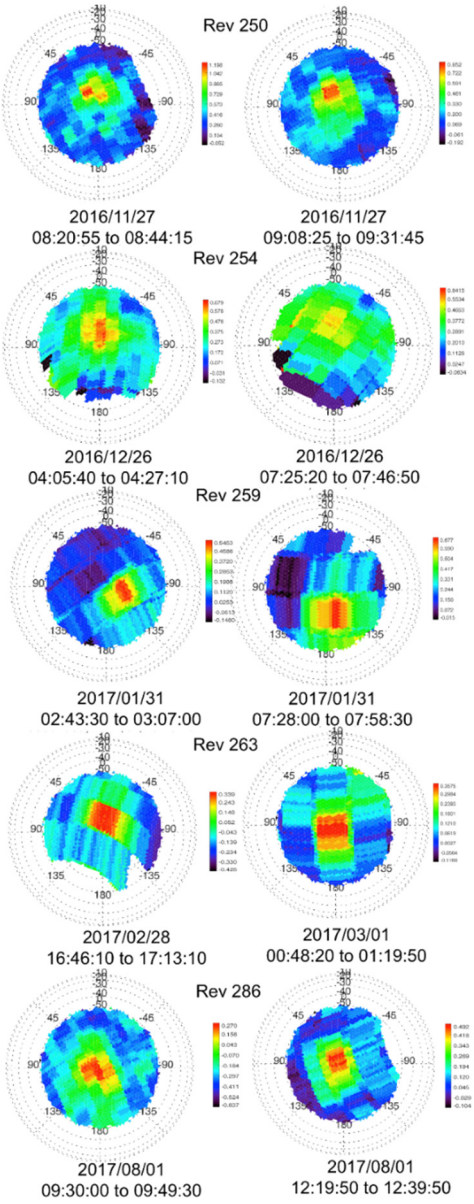

Figure CIRS-45. Binned integrated radiances (610 to 800 cm^{-1}) at the start and end of every rev considered.

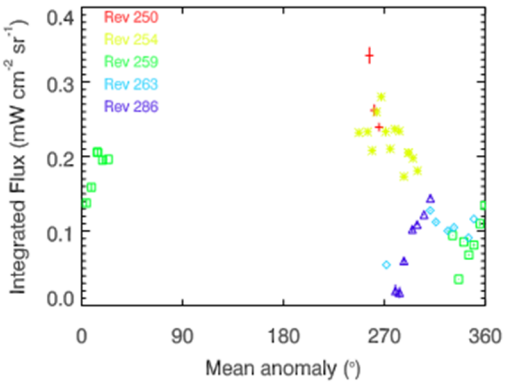

Figure CIRS-46. Total integrated flux (from 610 to 800 cm^{-1}) observed inside of 70° S for all high S/N observations.

CONCLUSIONS

Preliminary analysis indicated that Enceladus' surface emission could be varying with its orbital position, but perhaps lags behind changes in the plume emission. More work is required to firm-up this result, and increase the mean anomaly coverage.

Enceladus' interior (IN1a)

IN1a: Determine the surface temperature in active regions and constrain Enceladus' heat flow, to better constrain models of its activity.

INTRODUCTION

Much work has been done on this subject. An overview of the major results is provided chronologically.

SPENCER ET AL. [2006]

Initial analysis of mid-infrared data (600 to 1100 cm^{-1}) taken by CIRS FP3 onboard Cassini indicated that the endogenic power of Enceladus' south polar region was 5.8 ±1.9 GW [Spencer et al. 2006], much higher than the expected radiogenically produced power of 0.3 GW [Porco et al. 2006; Schubert et al. 2007]. Dissipation of tidally produced energy, most likely from the Dione and Enceladus 2:1 resonance, has been suggested as a possible production mechanism of the observed endogenic power [Spencer et al. 2006; Porco et al. 2006; Yoder 1979; Ross and Schubert 1989].

The Spencer et al. [2006] calculation of Enceladus' endogenic power found that blackbody emission at 133 ±12K over an area of 345 (−160, +320) km^2 matched the total >600 cm^{-1} CIRS FP3 spectrum of the south polar region. However, at this temperature only 10% of the blackbody spectral energy falls within the FP3 wave number range, while the remaining 90% of it falls within the 10 to 600 cm^{-1} wave number range of CIRS' FP1. The percentage of the spectral energy in the FP3 wave number range decreases further with decreasing temperature, rendering FP3 insensitive to low temperature emission, and it was noted by Spencer et al. [2006] that additional power might be radiated at lower temperatures.

HOWETT ET AL. [2011A]

Since the Spencer et al. [2006] analysis used FP3 data it was unable to quantify low-temperature endogenic emission. So another attempt was made to determine Enceladus' heat flow, this time using FP1 data [Howett et al. 2011a]. Long integrations (known as stares) were targeted at Enceladus' south polar region on March 12, 2008 (orbit or revolution, rev 61), and October 31, 2008 (rev 91). The signal to noise of each data set is increased by averaging the stares together. These stares are the only FP1 observations that will be made over the entire Cassini mission which both cover the entire south polar terrain and are sensitive to the wave number region where the bulk of

the endogenic power is radiated. Figure CIRS-47 shows the stare locations: each of the 73 integrations in rev 61 and the 48 integrations in rev 91 has comparable geometry.

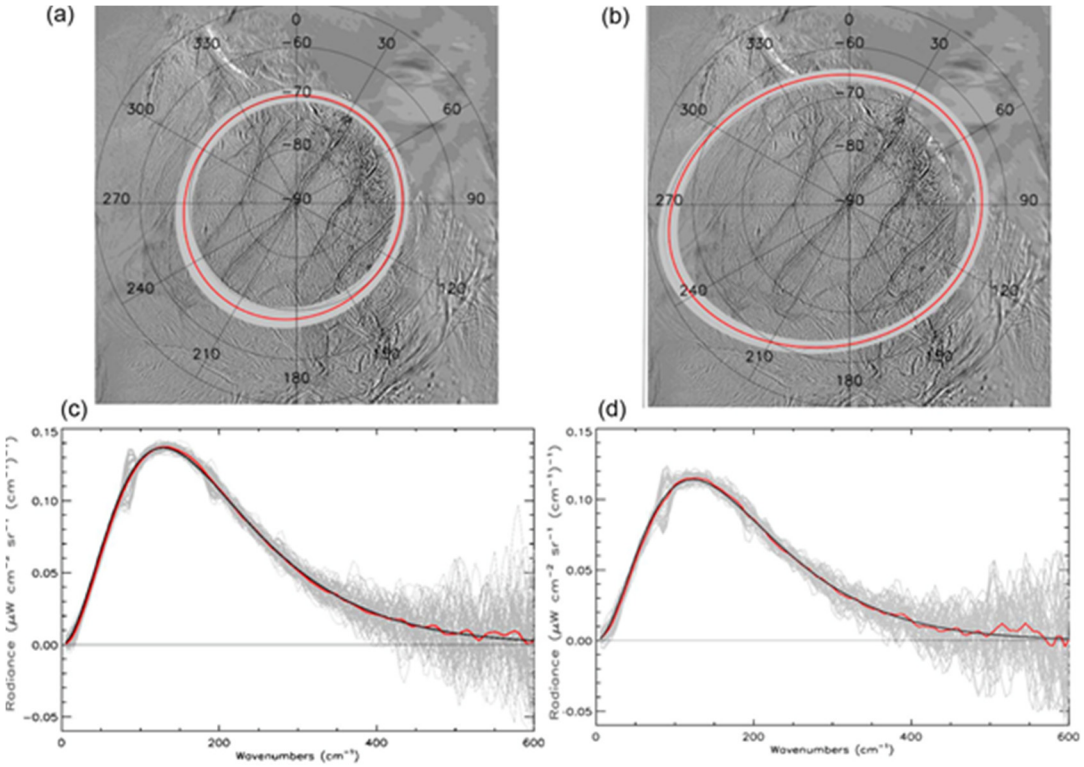

Figure CIRS-47. The range of locations of the FP1 field of view during the stare observations of rev 61 *Panel (a)*, and rev 91 *Panel (b)* over Enceladus' south pole (shown in gray). The field of view at the observation mid-time is also shown (red). The four prominent fractures within the rev 61 field of view are the active tiger stripes. The base map used is the 2006 ISS mosaic PIA 08342. In *Panel (c)* and *Panel (d)*, the spectra of each stare observation (gray), the mean spectrum (red), and the best fit two-temperature to this mean value (black) for revs 61 (*panel c*) and 91 *Panel (d)*.

FP1 is sensitive to the passive emission from the solar-heated surface, which has temperatures in the 35–80 K range [Spencer et al. 2006]. Thus, to obtain the endogenic component of the spectra this passive emission must first be removed. Passive emission is modeled for each epoch and observational geometry using a seasonal and diurnal 1-D numerical thermal model [Spencer et al. 1989]. The model determines surface temperatures by calculating conductive heat flow into and out of the subsurface through every diurnal cycle of an entire Saturnian year, accounting for insolation variations resulting from the 29° tilt of Enceladus' rotation axis relative to the sun, and the concurrent changes in heliocentric distance (9.03–10.05 AU) resulting from Saturn's orbital eccentricity. The model assumes that albedo does not vary with incidence angle, and does not initially account for the effects of heating by radiation from Saturn, or solar eclipses by Saturn, though these are discussed in the section entitled Characterize the Surfaces of Saturn's Small Satellites (IN2d) below. The thermal inertia values it uses are based on previous observations but require assumptions about the thermophysical properties at depth.

For each observation the temperatures predicted by this model are used to calculate the passive background across the FP1 field of view, assuming blackbody emission. These temperatures are weighted by the spatial sensitivity pattern of the FP1 detector, which is approximated as a 2-D Gaussian with a FWHM of 2.42 mrads [Flasar et al. 2004a]. The results from this model were validated by demonstrating the good agreement between the modeled spectrum produced, and CIRS data taken within Enceladus' south polar terrain but away from the tiger stripes themselves. For each observation, this passive thermal background is subtracted from the CIRS spectra leaving a residual, the spectrum of the endogenic emission. The residual is then weighted to correct for the assumed spatial distribution of the endogenic emissions. Three possible scenarios are considered: (i) that emission from the tiger stripes is uniform along their length, (ii) that the emission from the stripes varies in the same way as previously observed by higher spatial resolution higher wave number observations by the CIRS FP3 detector and, (iii) to set a lower limit on the endogenic power, a scenario which all emission arises from the most sensitive central 10% of the field of view is also considered. The effects these scenarios have on the endogenic emission determination are discussed further in the section entitled Tethys and the E-ring (IN2b) below. In the case of the stare observation the corrected residuals for each rev are averaged to increase the signal to noise. The final corrected residual is then fitted by a blackbody temperature curve with a filling factor, which allows the residual to be fitted by emission from only a fraction of the field of view if required. The endogenic power of that residual is then derived using the Stefan-Boltzmann law, the fitted temperature, filling factor and area of the projected FP1 field of view.

Since the response of the FP1 detector is non-uniform we also had to consider the spatial distribution of the endogenic emission. To estimate the dependence of the derived endogenic emission on its spatial distribution we evaluated three different scenarios: (i) that the tiger stripes are the sole source of the power and have uniform emission along their lengths, (ii) that the tiger stripes are the sole source of the power but that the emission intensity varies along each stripe, and (iii) finally that the emission is independent of the tiger stripes location but arises instead from an area within the most sensitive central 10% of the FP1 field of view. The last scenario is unrealistic, but is designed to determine a lower limit to the endogenic emission. The FP1 detector is most sensitive to emission from its central region and thus concentration of the emission in this region would minimize the true power required to produce the observed signal. Under the second scenario the variation in brightness along the length of the tiger stripes is assumed to be the same as that determined from high spatial resolution 600–1100 cm^{-1} FP3 observations made on rev 61 (Figure CIRS-48) from 1922:00 to 1944:00 UT. These observations had a spatial resolution of 4.1-9.6 km, sufficient to resolve the tiger stripes and the spatial distribution of emission along their lengths (Figure CIRS-48). Almost the entire tiger stripe region was covered, with the exception of the Saturn-facing end of Alexandria Sulcus, for which we have included approximate brightness values based on other CIRS observations [Spencer et al. 2006]. For the uniform case, we assigned equal brightness to all spatial bins with nonzero normalized brightness.

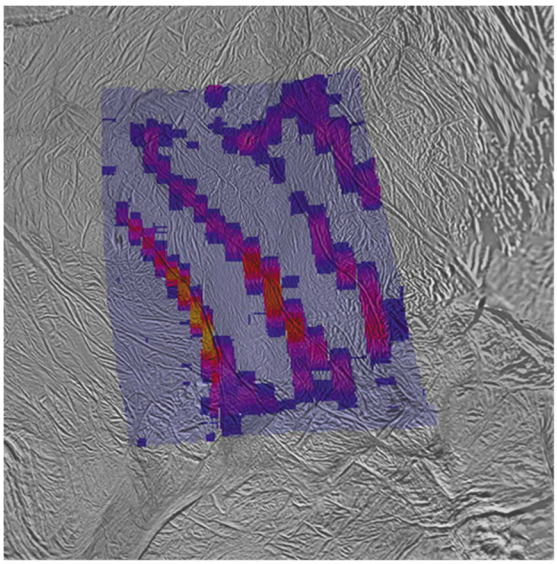

Figure CIRS-48. CIRS FP3 map of the spatial distribution of radiated 600–1100 cm^{-1} brightness along the four tiger stripes, as observed on March 12, 2008 (rev 61). Relative brightness is shown by colors ranging from blue (faintest) to yellow (brightest). The pale blue area shows regions that were mapped, but showed negligible radiated power. The data used in this scan was taken between 1922:00 and 1944:00UT on March 12, 2008.

Finally, the emission from a surface also depends on its albedo and thermal inertia. These properties are not known for Enceladus' active south polar terrain, although they are known for regions close to it [Howett et al. 2010]. By modeling FP1 observations close to, but not over the active part of Enceladus south polar terrain, it was possible to narrow down the range of albedo to ~0.80. Since constraining thermal inertia was not possible three scenarios are considered: (i) a constant thermal inertia of 27 MKS at all depths, (ii) two scenarios both of which have a thermal inertia of 27 MKS from the surface to a depth of 1 cm, but have higher thermal inertias of 100 MKS, and (iii) 1000 MKS below 1 cm. A near- surface thermal inertia of 27 MKS was derived for the latitude bin 60° S to 50° S [Howett et al. 2010], this is the closest location to the south polar terrain (SPT) for which thermal inertia has been determined. The lower deep layer thermal inertia value of 100 MKS was selected using results from 2005 Cassini CIRS observations of Enceladus' winter north pole that showed the north polar thermal inertia to be less than 100 MKS to a depth of ~1 m [Spencer et al. 2006]. The higher deep layer thermal inertia value of 1000 MKS was selected to be close to that of solid water ice [Paige et al. 1994]. The results are shown in Figure CIRS-49, and a summary of the endogenic emission predicted using these different scenarios is given in Table CIRS-7.

The maximum and minimum endogenic emission values given in boldface in Table CIRS-7, excluding the extreme and unlikely scenario where all emission is concentrated at the center of the FP1 field of view, are used as our estimate of the uncertainty range of the total endogenic emission. Thus, it is estimated that Enceladus' south polar endogenic emission of 14.8 ±1.9 GW for rev 61 and 16.9 ±2.4 GW for rev 91, which agree within error and give a combined value of 15.8 ±3.1 GW.

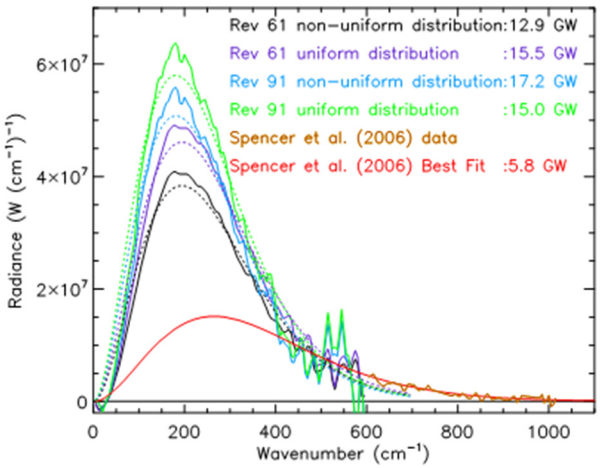

Figure CIRS-49. The mean endogenic emission of the FP1 stare observations taken during revs 61 and 91, assuming both uniform and nonuniform emission along the tiger stripes (see the section entitled Tethys and the E-ring (IN2b)). The best fitting blackbody temperature fits are given by the dotted lines, which are correspondingly colored. Temperatures of 99.1 K and 92.4 K provide the best fit to rev 61 and 91 for both of the assumed spatial distributions. However, the total surface area of the emission decreases from 2657 km^2 to 2211 km^2 for rev 61 and from 4121 km^2 to 3609 km^2 for rev 91 as the assumed spatial distribution varies from uniform to nonuniform. The 2005 FP3 endogenic emission spectrum used by Spencer et al. [2006] to determine the previous lower estimate of endogenic power is also shown, along with the extrapolation of a blackbody fit to that spectrum over the wave number range of the FP1 detector.

Table CIRS-7. Summary of the predicted endogenic emission from Enceladus under a variety of reasonable assumptions about the thermophysical properties of Enceladus' surface. See text for a full description.

Assumed Subsurface Conditions for Thermal Model	Rev 61 Endogenic Power Uniform Spatial Distribution (GW)	Rev 61 Endogenic Power FP3-like Spatial Distribution (GW)	Rev 61 Endogenic Power Central Spatial Distribution (GW)	Rev 91 Endogenic Power Uniform Spatial Distribution (GW)	Rev 91 Endogenic Power FP3-like Spatial Distribution (GW)	Rev 91 Endogenic Power Central Spatial Distribution (GW)
Scenario 1	16.6	13.8	8.2	**19.3**	16.9	11.9
Scenario 2	15.5	**12.9**	7.6	17.2	15.0	10.6
Scenario 3	**16.6**	13.8	8.1	16.6	**14.5**	10.2

SPENCER ET AL. [2012]

The previous heat flow estimates were based on observations that did not resolve the tiger stripes from their surroundings, so passive emission from the surroundings had to be modeled and subtracted to determine endogenic heat. In this work, Spencer et al. [2012] used higher spatial resolution observations to spatially separate the tiger stripe emission, which must be endogenic, from background emission, which is expected to be partly or entirely passive.

They model the surfaces radiating the endogenic emission as continuous ribbons of material of temperature T (l) and width W (l) which vary smoothly with distance l along the tiger stripes and associated warm fractures. T and W are adjusted to match the spatial and wavelength dependence

of the emission seen in specific CIRS observations, using a forward model. The most extensive FP3 map of the tiger stripes, obtained on orbit 61 in March 2008 (Figure CIRS-48 and Figure CIRS-50), can be matched with a single relatively high temperature endogenic component, denoted by subscript H , with TH (I) varying spatially between 120 and 165 K, and WH (I) varying between 60 and 330 meters. The best spatially resolved constraint on lower-wavenumber emission, an FP1 scan across the tiger stripes Damascus, Baghdad, and Cairo from orbit 136 in August 2010 (Figure CIRS-50) shows that an additional lower temperature component is also needed (Figure CIRS-51). However the limited spatial coverage of this and other FP1 scans does not allow unique constraints on the spatial distribution of the low temperature component. To estimate the contribution of this component (denoted by subscript L), we constrain TL and WL from the wavelength-dependent FP1signature where the rev 136 scan crosses the tiger stripes (Figure CIRS-51), and extrapolate to the rest of the system by assuming that both TL and WL /WH are independent of location. We then re-fit all parameters using these assumptions.

The resulting total heat flow is 2.7 GW and 1.5 GW from the high and low temperature components respectively, for a total of 4.2 GW. Enceladus' power output also includes the latent heat of the escaping plume (~0.5 GW [Ingersoll and Pankine 2010]), giving a total output of ~4.7 GW. There may be additional endogenic heat from the regions between the tiger stripes, included in previous estimates but excluded here, which may account for some of the discrepancy with earlier estimates. It is also possible that previous models under-estimated the passive contribution to the integrated south polar emission (e.g., due to spatial variability of thermophysical properties), and thus, over-estimated of the endogenic component.

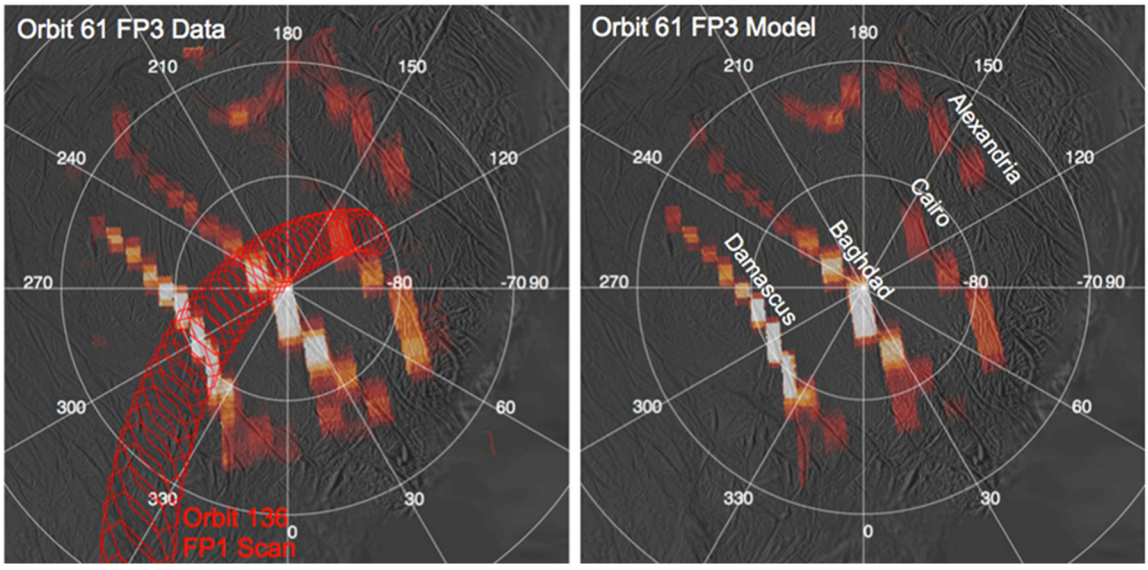

Figure CIRS-50. Constraining the tiger stripe emission distribution model using the orbit 61 CIRS FP3 scan of the tiger stripe system. *Left*: shows observed 600–850 cm^{-1} radiance. *Right*: shows the simulated observation derived from the best-fit model. *Left*: also shows (red) the location of the orbit 136 FP1 scan used to constrain the longer wavelength emission from the tiger stripes (Figure CIRS-51).

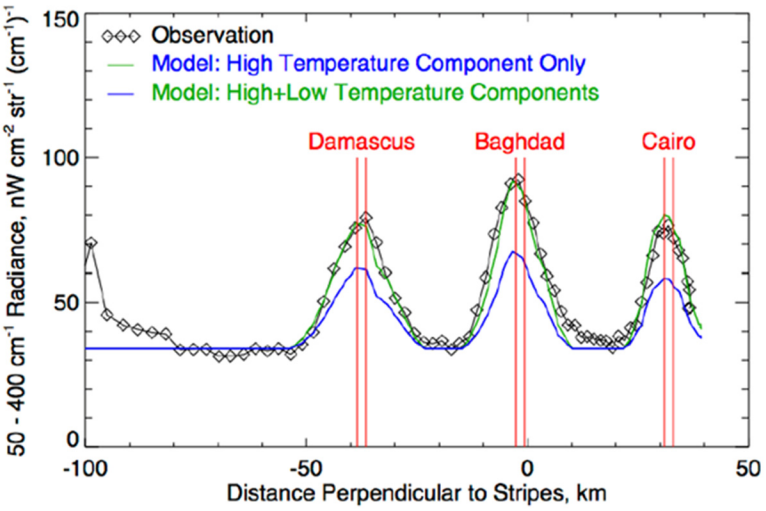

Figure CIRS-51. Profile of low-wavenumber FP1 radiation across three of the tiger stripes (Figure CIRS-50) from orbit 136, compared to predictions from our best-fit model of tiger stripe temperatures, with and without the inclusion of a low-temperature component. The model also includes a constant background radiance, assumed here to be passive re-radiated sunlight. This FP1 scan reveals that the high-temperature component fitted to the FP3 observations (Figure CIRS-50) does not account for all the radiated power at low wavenumbers, and an additional low temperature component is need to match the data.

The inconsistency of heat flows derived from different techniques highlights the difficulty of these measurements, indicating that all heat flow estimates should be treated with caution. However, all estimates are much larger than the expected maximum steady-state tidal heating of 1.1 GW [Meyer and Wisdom 2007].

CURRENT WORK

To minimize the effect of passive emission observations of Enceladus were made with FP1 late in the Cassini mission, when Enceladus' active south pole was in winter. During such time, the effect of low-temperature passive emission is minimized (Figure CIRS-52). Observations taken during rev 250 by FP1 offer one of the best opportunities for determining Enceladus' heat flow. In this rev, a scan of Enceladus entire south polar terrain was made by FP1. Preliminary analysis has been performed using two methods and provides similar results.

The first method was to look at individual spectra taken over Enceladus' active region, remove the (small) expected passive emission, and assume the remaining emission is endogenic (Figure CIRS-52). The resulting endogenic emission is ~9 GW.

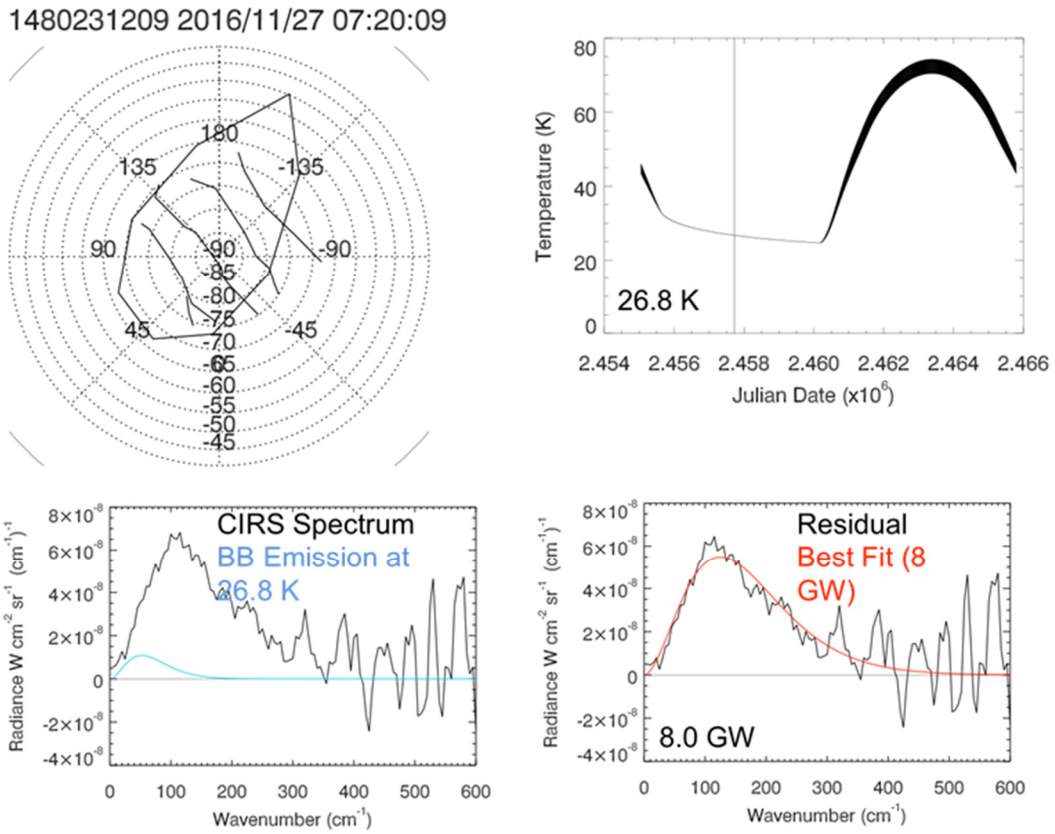

Figure CIRS-52. Individual spectra taken over Enceladus' active region. *Top left*: location of the observation analyzed, spacecraft event time (SCET) relative to Earth time, it was taken. The position of the tiger stripes is indicated. *Top right*: Seasonal model for a surface with an albedo of 0.80 and a constant thermal inertia with depth of 27 MKS. The temperature this model predicts for Enceladus' passive emission at the time the observation was taken is 26.8 K. *Bottom left*: calibrated CIRS FP1 spectrum taken, compared to the predicted passive emission. *Bottom right*: residual CIRS spectrum and the best fit.

The second technique is to use observations close to the tiger stripe but away from the activity as a proxy for the expected passive emission (see Figure CIRS-53). These results imply that the total south polar power (in one FP1 FOV) is ~6–8 GW. However, further work is required to determine to what extent power spills into multiple field of views.

Conclusions

Determining the heat flow of Enceladus' active region is a particularly difficult thing to do, since in order to determine the low-temperature heat flow Enceladus passive emission must be removed (particularly early on in Cassini's mission when the south pole was not in winter). This modeling effort is hampered by a somewhat chicken-and-egg problem: in order to model the passive emission the thermophysical properties of Enceladus' surface are needed to be accurately known, but it is difficult to determine these properties because of the activity.

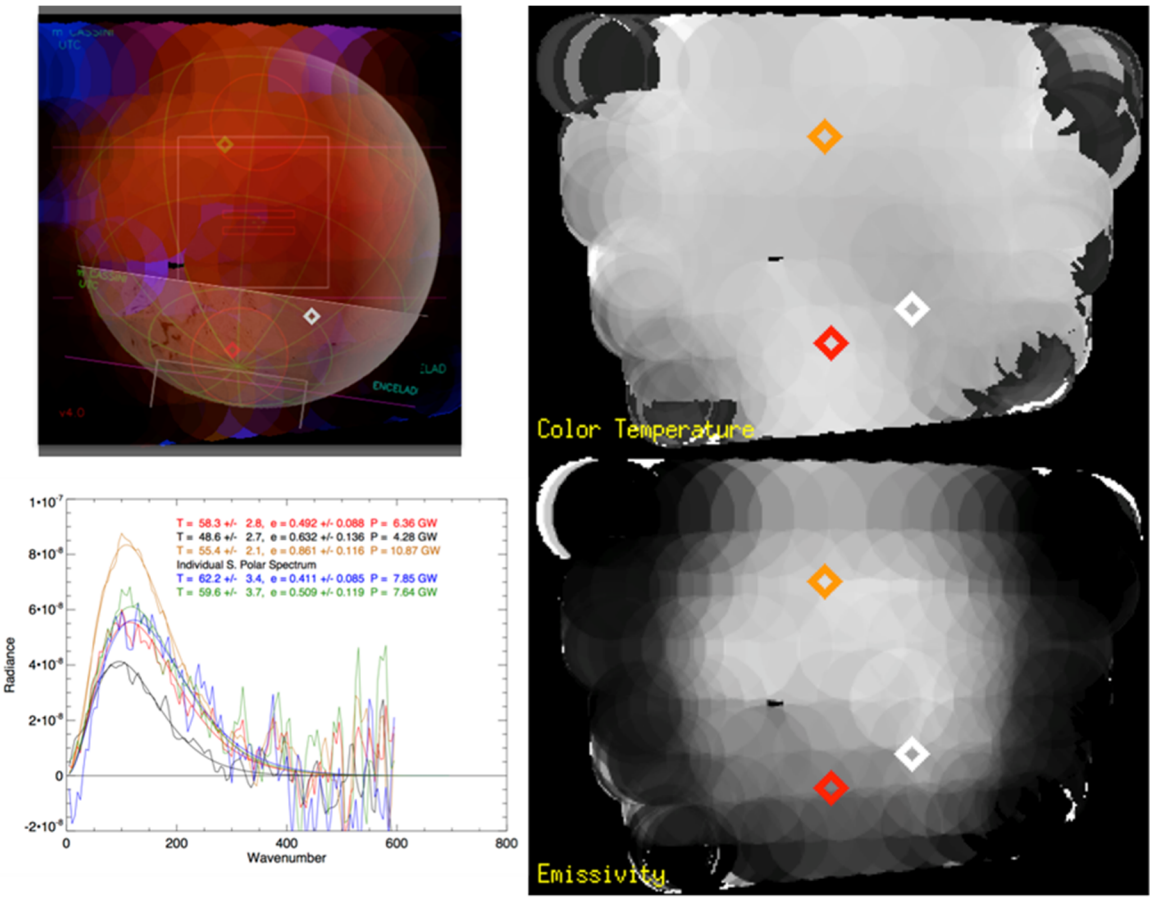

Figure CIRS-53. Observations close to the tiger stripe but away from the activity as a proxy for the expected passive emission. *Top Left*: Temperature map of Enceladus, with geometry overlaid. The position of three reference points are indicated: one away from the tiger stripes (orange), another close but not in the active south polar terrain (white) and another in the heart of the active region (red). *Bottom Left*: calibrated CIRS FP1 spectra and their best fits at the reference points. *Top/Bottom Right*: The radiance map plotted as a function of color temperature and emissivity variations. The plots show the temperature highest over the south polar terrain, which also displays the lowest emissivity.

Early attempts set a limit based on the high-temperature endogenic emission: 5.8 ±1.9 GW [Spencer et al. 2006]. Later attempts characterized both the high- and low-temperature emission: 15.8 ±3.1 GW [Howett et al. 2011a]. Continued modeling of the high- and low-temperature emission from only the stripes themselves pointed to a lower value of ~4.7 GW [Spencer et al. 2018]. New and ongoing work trying to characterize Enceladus' heat flow while the southern polar region is in winter (i.e., has a reduced passive emission) provides an estimate between 6 and 8 GW, but more work is required to fully characterize this emission.

So, more work is required! And even then, there will always be some ambiguity over this number—particularly if it is varying, as preliminary results from Howett et al. [2017] suggest. However, what is certain is that Enceladus' activity is continuing and impressive.

Compare Saturn's mid-sized satellites (IN1b)

IN1b: Compare the surface characteristics of Saturn's mid-sized satellites, including the thermally anomalous Pac-Man regions.

INTRODUCTION

Observations returned by CIRS and ISS showed a thermal and color anomaly at low latitudes on Mimas and Tethys' leading hemisphere (see Figure CIRS-54). This anomaly, dubbed Pac-Man (because its shape mimics that of the 1980s' video icon), displays warmer nighttime and cooler daytime temperatures than its surroundings and appears darker in IR/UV color ratio maps [Howett et al. 2011b, 2012; Schenk et al. 2011]. The color and thermal anomalies are believed to be the result of surface alteration by high-energy electrons, which preferentially bombard this region, altering its surface and increasing its thermal inertia. These high-energy electrons, in Saturn's magnetosphere, drift in a retrograde direction relative to corotation. Recent modeling efforts, supported by the Low Energy Magnetospheric Measurement System (LEMMS) on Cassini's Magnetospheric Imaging Instrument (MIMI), have shown that these electrons preferentially bombard low latitudes on Mimas, Tethys, and Dione's leading hemisphere [Paranicas et al. 2012, 2014; Howett et al. 2011b; Schenk et al. 2011].

COMPARISON OF THE SURFACE PROPERTIES OF THE SATELLITES, HOWETT ET AL. [2010]

We measure surface temperatures by determining the temperature that best match the observed thermal radiation, on the assumption of blackbody radiation. Nighttime temperatures provide the strongest constraints on thermal inertia, and of the icy satellites only Phoebe (due to its low ABB and rapid rotation) has nighttime temperatures warm enough to be detectable by FP3 Flasar et al. [2005a]. The higher wavenumbers detected by FP4 are insensitive to all of the Saturnian icy satellite's passive daytime and nighttime temperatures. This investigation therefore solely uses FP1 data, which is sensitive to both daytime and nighttime radiation from Saturn's icy moons. The

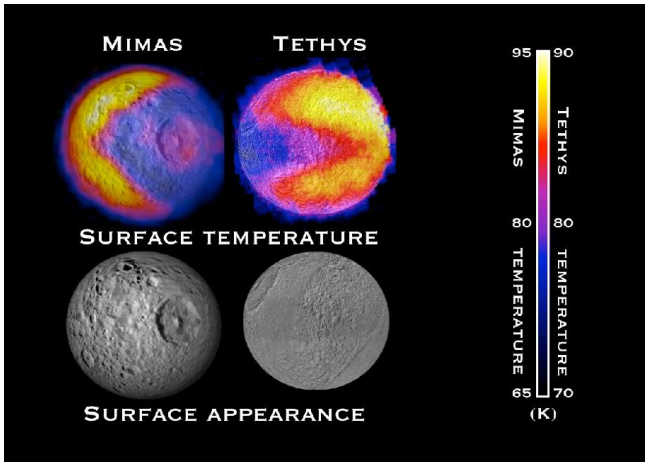

Figure CIRS-54. Summary of the two Pac-Man.

consistency of temperatures derived from FP1 and FP3 observations were spot-checked using selected daytime observations of Rhea and Dione that included near-simultaneous measurements with both detectors. Derived temperature were consistent to within 2–3 K.

The best fitting values for each of Saturn's icy moons is summarized in Table CIRS-8. For Enceladus, the local time coverage of each 10° latitude bin was good enough to constrain the thermal inertia and albedo as a function of latitude between latitude 60° S and 70° N.

Table CIRS-8. Summary of the CIRS derived thermal inertia and albedo for icy satellites in the Saturn system. Table data from Howett et al. [2010].

Target	Bolometric albedo	Thermal inertia (MKS)	Skin Depth (cm)	References
Jovian Satellites				
Io	0.52	70	0.39[c]	Rathbun et al. [2004]
Europa	0.55	70 14 ± 5	0.55[c] 0.01[d]	Spencer et al. [1999] Hansen [1973]
Ganymede	0.32 ± 0.04	70 ± 20 12 ± 3 14 ± 3	0.78[c] 0.01[d] 0.01[d]	Spencer [1987] Hansen [1973] Morrison and Cruikshank [1973]
Callisto	0.2 ± 0.4	50 ± 10 10 ± 1	0.86[c] 0.01[d]	Spencer [1987] Morrison and Cruikshank [1973]
Saturnian Satellites				
Mimas	$0.49^{+0.05}_{-0.14}$	19^{+57}_{-9}	0.54	
Enceladus	0.81 ±0.04	15^{+24}_{-9}	0.51	
Tethys	0.67 ±0.11	9^{+10}_{-4}	0.36	
Dione	0.63 ±0.15	11^{+18}_{-6}	0.53	
Rhea trailing	$0.57^{+0.20}_{-0.26}$	8^{+12}_{-5}	0.50	
Rhea leading	$0.63^{+0.11}_{-0.12}$	9^{+9}_{-5}	0.56	
Iapetus trailing	$0.31^{+0.15}_{-0.17}$	20^{+13}_{-8}	5.22	
Iapetus leading	0.10[a]	$14^{+7^{a}}_{-8}$	3.66	
Phoebe	0.1	20/25[b]		

Latitude bin	Bolometric Bond albedo	Thermal inertia (MKS)
60° N to 70° N	0.76 ±0.06	16^{+17}_{-13}
40° N to 50° N	$0.74^{+0.06}_{-0.04}$	9^{+5}_{-4}
30° N to 40° N	0.77 ±0.05	10^{+10}_{-6}
20° N to 30° N	$0.78^{+0.05}_{-0.04}$	12^{+15}_{-7}
10° N to 20° N	0.75 ±0.03	17^{+10}_{-7}
0° to 10° N	$0.79^{+0.04}_{-0.05}$	25^{+25}_{-14}
10° S to 0°	$0.78^{+0.03}_{-0.02}$	25^{+22}_{-12}
20° S to 10° S	$0.81^{+0.03}_{-0.05}$	18^{+21}_{-9}
30° S to 20° S	$0.81^{+0.05}_{-0.06}$	20^{+19}_{-12}
40° S to 30° S	$0.82^{+0.02}_{-0.03}$	26^{+12}_{-13}
50° S to 40° S	$0.79^{+0.02}_{-0.01}$	40^{+10}_{-18}
60° S to 50° S	$0.80^{+0.03}_{-0.04}$	27^{+13}_{-20}

Accurate determination of the endogenic south polar heat flow from Enceladus [Spencer et al. 2006] requires subtraction of the passive component from the total thermal emission, making knowledge of the thermophysical properties of Enceladus, and their latitudinal variation, particularly important. The CIRS observations previously used to determine the global surface properties between 60° S and 70° N were separated into 10° latitude bins and the same analysis techniques as previously described were applied to each bin. The number of high resolution spectra available between 50° N and 60° N and north of 70° were not high enough to allow the albedo and thermal inertia to be adequately constrained.

However, the bolometric Bond albedos and thermal inertias of Mimas, Enceladus, Tethys, Dione, the leading and trailing hemisphere of Rhea, and the trailing hemisphere of Iapetus have been determined. The diurnal curves derived using these values provide good fits to the calculated black body temperatures fits to the CIRS spectra. The bolometric Bond albedo of the leading side of Iapetus is too low to accurately determine a value; however, an upper limit is found and the local time coverage is adequate to determine its thermal inertia. The thermal inertia of all of Saturn's icy satellites is shown to be less than half that of the Galilean satellites, implying less consolidated and more porous surfaces, perhaps partially due to the limited mobility of water ice on the Saturnian satellites due to their low temperatures compared with the Galilean satellites, or to a surface coating of E-ring particles. The latitudinal variation in the thermal inertia of Enceladus implies the surface becomes more consolidated towards the southern pole, whereas the higher albedo in the southern hemisphere implies a cleaner surface, perhaps due to plume fallout. Further work investigating the hemispheric bolometric Bond albedo asymmetries of Dione would be valuable, as although the globally averaged values derived here provide a good fit to the CIRS data, observations of viable wavelength have observed notable differences between the leading and trailing hemispheres [Buratti and Veverka 1984].

MIMAS, HOWETT ET AL. [2011B]

CIRS day- and nighttime observations of Mimas taken in rev 126 and 139 are shown in Figure CIRS-55. Both the orbit 126 and 139 maps show a V-shaped boundary, sharp at CIRS resolution, separating warmer and cooler temperatures. The apex of the V is at 0° N and 180° W, and the boundary extends in a northeasterly and southeasterly direction, during orbit 144 indicates the eastern edge of the thermal anomaly is near 0_ longitude. The region east of the boundary, on Mimas' leading hemisphere, is colder than its surroundings in the orbit 126 daytime observations, but is warmer than its surroundings in the orbit 139 nighttime and early morning data. This region thus displays much smaller-amplitude diurnal temperature variations than regions to the west, north, and south, which show thermal behavior more typical of other Mimas longitudes and most of the surfaces of Mimas' neighboring satellites, Tethys, Dione, and Rhea [Howett et al. 2010]. Thus, we refer to the region east of the boundary, on the anti-Saturn hemisphere, as the thermally-anomalous region.

Overlaid on Figure CIRS-55 are new estimates of the energy flux of MeV electrons bombarding Mimas, updating those given in Schenk et al. [2011]. Because energetic electrons in Saturn's magnetosphere drift in a retrograde direction relative to corotation they preferentially

bombard Mimas' leading hemisphere. Notable improvements in the new model include the use of additional data from the LEMMS on Cassini's MIMI (several-year averages were used) and the introduction of data from the channel E7 on LEMMS. The E7 channel is the highest energy electron channel on LEMMS and adding these data modifies the spectral slope at high energies, which turns out to be very important for the behavior of the contours particularly away from the equator. Further details on the mission averaged electron data are given in Paranicas et al. [2012, 2014].

The thermal anomaly is closely correlated spatially with an IR/UV (0.930/0.338 lm) color ratio anomaly previously observed in global maps of Mimas using Cassini ISS data. An updated version of the global IR/UV map of Mimas, originally given in Schenk et al. [2011], is shown in Figure CIRS-55. Though there are some inconsistencies in the latitudes and longitudes of features on the two maps, the location of the thermal and color anomalies can be compared by reference to craters near the anomaly boundaries appearing on both maps (red circles, Figure CIRS-55).

Figure CIRS-55 boundaries of the thermal and color anomalies appear to be nearly identical, although the apex of the thermal anomaly appears sharper. In the absence of endogenic emission, surface temperatures are controlled by surface bolometric Bond albedo and thermal inertia. A surface's thermal inertia describes how well it is able to store and release thermal energy. To investigate the cause of the anomalous temperatures seen by CIRS we determine albedo and thermal inertia for two representative regions, one outside and another inside the anomaly (shown by the boxes in Figure CIRS-55). The surface temperature for each of the two regions in orbits 126 and 139 was determined by fitting a single blackbody curve to the mean CIRS FP3 spectra of all the observations taken of that region. Following the example of Spencer et al. [2006], the spectral noise was estimated using the difference between a blackbody emission spectra. These two steps are repeated numerous times and the temperature error estimate is given by the standard deviation of the temperatures whose best able to fit the created spectra.

The ranges of bolometric Bond albedos capable of fitting the data outside and inside of the anomaly overlap: 0.49–0.70 and 0.56–0.62 respectively. This is consistent with the lack of a noticeable albedo boundary in visible-wavelength images. These albedos are comparable in value with those observed on Tethys, Dione and Rhea. As expected, it is the thermal inertias that vary significantly: <16 J m^2 K^{-1} $s^{-1/2}$ outside the anomaly (these units henceforth referred to as MKS) and 66 ±23 MKS within it. The low thermal inertias outside of the anomaly are similar to those observed on Tethys, Dione and Rhea [Howett et al. 2010], whilst those inside the anomaly are greater than but more comparable with values observed on the icy Galilean satellites. The higher thermal inertias inside the anomalous region indicate that the surface there is less porous and/or has a higher thermal conductivity.

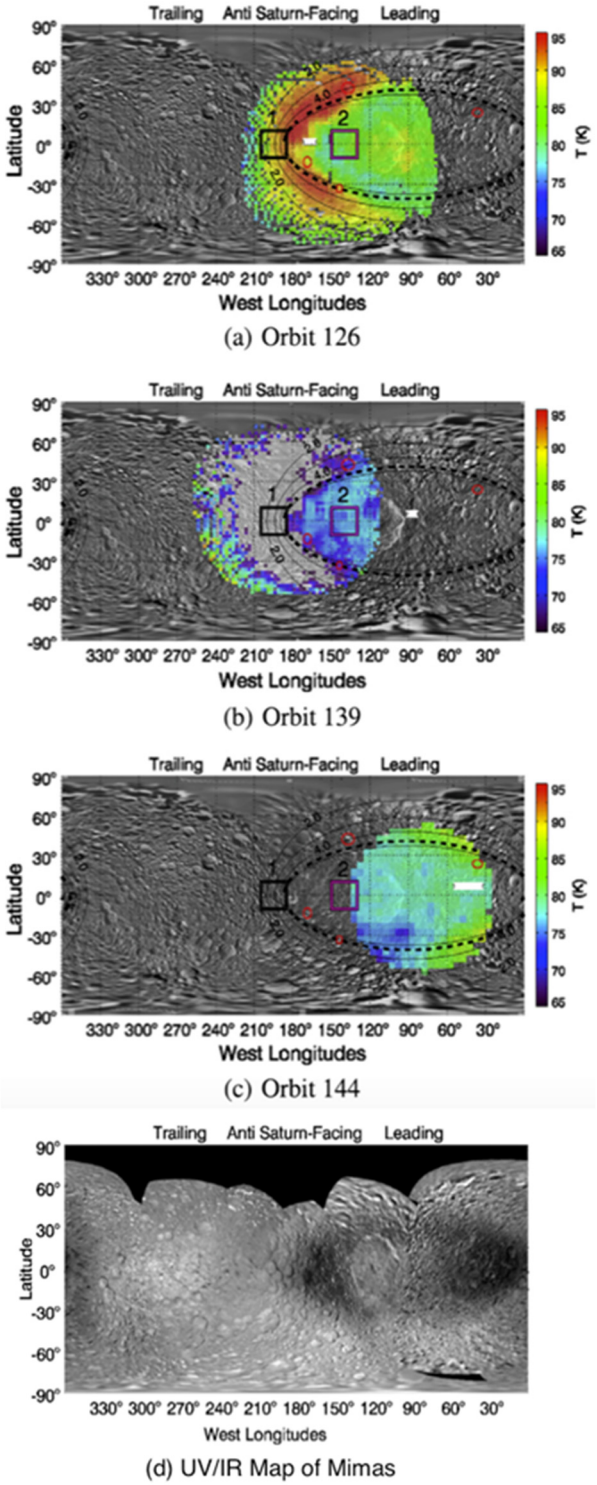

Figure CIRS-55. CIRS day- and nighttime observations of Mimas. *Panel (a)*: Orbit 126 daytime surface temperatures. *Panel (b)*: Orbit 139 nighttime surface temperatures of Mimas. *Panel (c)*: Orbit 144 daytime surface temperatures. *Panel (d)*: IR/UV (0.930/0.338 lm) color ratio map of Mimas' surface determine from Cassini ISS data.

The close spatial correlation of the thermal and IR/UV color ratio anomalies suggests a common origin. It has been proposed that high-energy (MeV) electron bombardment of Mimas' surface is responsible for the observed IR/UV color ratio variation [Schenk et al. 2011]. Plasma corotates with the planet and thus flows around Saturn in a prograde sense, overtaking Mimas in its orbit and impacting its trailing hemisphere. However, electrons with energies above about 1 MeV flow retrograde with respect to Mimas. Their north–south motion is much faster than their longitudinal motion and these electrons therefore bombard the moon close to its leading equator. The impact patterns are represented by lens-shaped contours of energy deposition very similar in shape to the color and thermal boundary (Figure CIRS-55). The color boundary at Mimas corresponds to an electron energy deposition rate contour of about 5.6×10^4 MeV cm^2 s^{-1} [Schenk et al. 2011]. The contour corresponding to the boundary of the thermal anomaly is harder to determine due to its poorer spatial correlation, however it appears to be similar to that of the color anomaly.

TETHYS, HOWETT ET AL. [2012]

In September 2011 (during Cassini's orbit 153) CIRS obtained a daytime medium-spatial resolution observation (the average resolution was 84 km/pixel) of Tethys' leading hemisphere. FP3 was used for these observations since it provides the best compromise between sensitivity to thermal radiation and spatial resolution for daytime observations of icy satellites. These observations were at a significantly better spatial resolution than the previous best thermal map of this hemisphere, a nighttime map obtained in June 2007 (Cassini's orbit 47; 150 km/pixel) using FP1. The lower spatial resolution FP1 is the only CIRS detector sensitive to the cool nighttime surface emission of Saturn's icy satellites; therefore, spatial resolution differences in the night-day-time coverage with CIRS are common. Combination of the orbit 47 and orbit 153 observations provides sufficient local time coverage to constrain surface albedo and thermal inertia.

The results, given in Figure CIRS-56, clearly show a thermally anomalous region exists on Tethys' leading hemisphere at low latitudes in both the daytime and nighttime temperatures. The region appears to be ~10 K cooler during the day and ~10 K warmer at night than its surroundings, quite unlike the pattern expected if surface properties were spatially uniform (also shown in Figure CIRS-56), with largest thermal contrast occurring at the northern anomaly boundary, particularly towards the east. The thermally anomalous region is lens-shaped with apexes at 0° W and 180° W, and is widest in the center of the leading hemisphere (90° W) reaching latitude ±20°. This anomalous region spatially coincides with a dark (low) albedo region at low latitudes on Tethys' leading hemisphere was first observed in Voyager data [Stooke 1989, 2002]. Photometry applied to Cassini ISS images showed the band to be 2–3% brighter in the NAC CL1-UV3 filter (338 nm) and 8% darker in the NAC CL1-IR3 (930 nm) filter [Elder et al. 2007].

The best-fit bolometric Bond albedo for all three of these regions is remarkably constant: 0.67 ±0.02, whilst the best-fit thermal inertia increases from 5 ±1 MKS outside the anomaly, to 11 ±1 MKS at the western boundary and 25 ±3 MKS inside the anomaly. The values outside the thermal anomaly are comparable to those seen on other Saturnian satellites [Howett et al. 2010]. The derived albedo is also consistent with previous estimates.

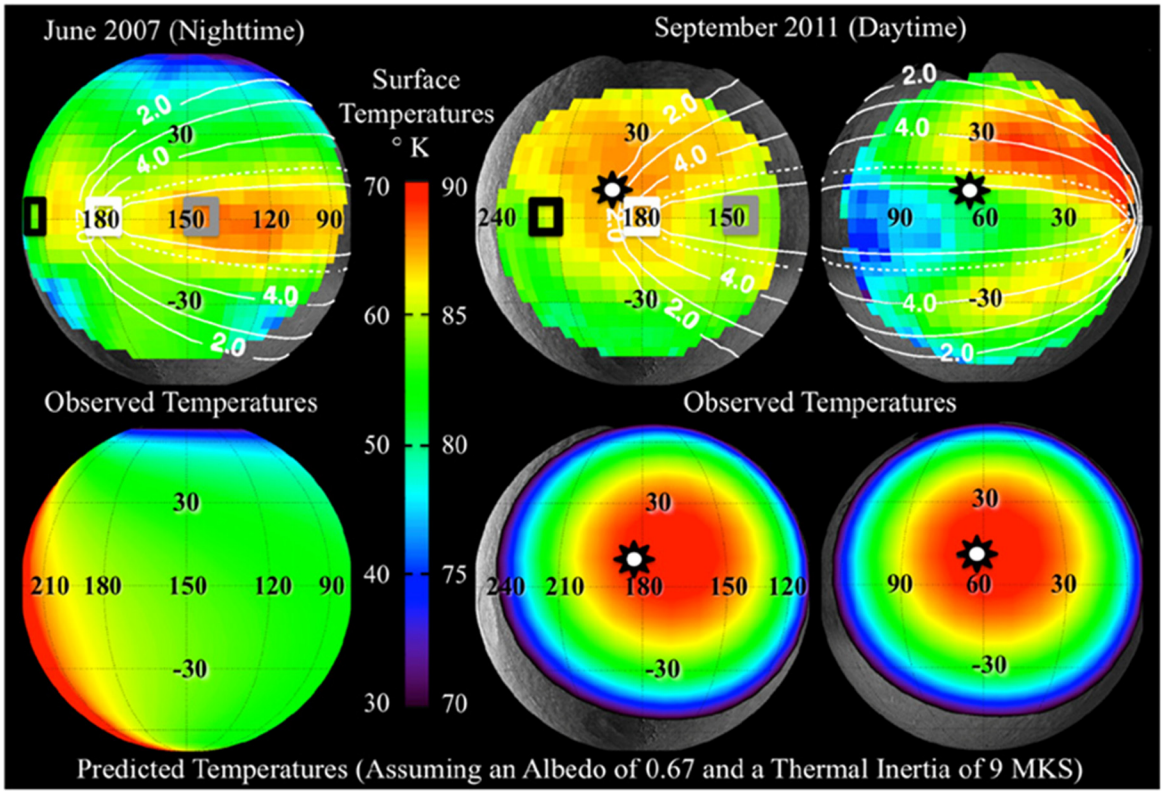

Figure CIRS-56. Tethys' thermal anomaly can be seen by comparing the observed and predicted surface temperatures of Tethys at night (June 2007) and during the day (September 2011). Contours overlaid on the observed temperatures show the predicted electron energy flux onto Tethys' surface, in units of log10(MeV cm^{-2} s^{-1}), with the white dashed line contour representing the best fit electron energy flux contour to the observed surface color alteration (18 GeV cm^{-2} s^{-1}) [Schenk et al. 2011]. The black stars-shapes with the white centers indicate the location of the subsolar point.

The maximum electron energy flux bombarding Tethys is nearly six times lower than that on Mimas and is constrained to a smaller latitudinal extent, consistent with the relative amplitude and shape of the thermal anomaly on the two bodies [Paranicas et al. 2012; Schenk et al. 2011]. The discovery of Tethys' thermal anomaly, which as Figure CIRS-56 shows has a boundary corresponding to an 18 GeV cm^{-2} s^{-1} electron flux (compared to 56 GeV cm^{-2} s^{-1} on Mimas), greatly strengthens the case that energetic electrons are able to significantly alter an icy satellite surface, and also proves that the threshold electron energy flux able to do so is lower than previously thought. A lower energy flux threshold increases the probability that such alteration occurs on other satellite surfaces. Why high-energy electron bombardment would decrease the IR/UV surface color ratio and why the thermal anomalous region appears darker in visible light images of Tethys, but not on Mimas, remains a mystery.

DIONE, HOWETT ET AL. [2014]

Maps of variations in albedo and thermal inertia were derived for Dione, using eight separate CIRS observations taken from 2005 until 2012, which provided both day and nighttime coverage. Figure CIRS-57 shows the thermally-derived bolometric Bond albedo variation across Dione. The map shows that the bolometric Bond albedo of Dione's trailing hemisphere (0.39 ±0.13) is much darker than its leading hemisphere (0.49 ±0.11). The disk-integrated value (0.44 ±0.13) is consistent (to within error) of previously determined values: 0.52 ±0.08 Pitman et al. [2010] and 0.63 ±0.15 Howett et al. [2010]. The trailing/leading hemisphere albedo trend has been previously observed on Dione from visible-wavelength observations (e.g., in the geometric albedo map by Blackburn et al. [2012]) and, as noted in the introduction, is thought to be due to the preferential bombardment of Dione's leading hemisphere by E-ring particles [Hamilton and Burns 1994], which plausibly cause surface brightening [Verbiscer et al. 2007].

Dione displays a different trend in its thermal inertia, which is highest at low latitudes on its leading hemisphere. Between 30° S and 30° N, 180° W and 360° W, the mean thermal inertia is 8 MKS, while between the same latitudes and 30°–150° W, the mean thermal inertia is 11 MKS.

As noted above, Mimas and Tethys display similar anomalies [Howett et al. 2011b, 2012]. However, on Dione the magnitude of the thermal inertia increase is too subtle for its effect to be easily observed in maps of the surface temperature (unlike on Mimas and Tethys). Nonetheless, the inference of high thermal inertia in these regions becomes clear when diurnal temperature curves are compared with Dione's observed surface temperatures; the lower thermal inertia value (8 MKS) is unable to fit Dione's leading hemisphere's higher nighttime temperatures. Diurnal temperatures probe thermophysical properties over a range given by the thermal skin depth, which for these thermal inertias is 0.4–0.6 cm (assumptions as in Howett et al. [2010]). The location of Dione's higher thermal inertia region is spatially correlated with the region preferentially bombarded by high energy electrons. This is the same trend that is observed on Mimas and Tethys. On Mimas E-ring grain particles bombard opposite hemispheres, while on Tethys (and Dione) they both bombard the leading hemisphere. The similarity between Mimas' and Tethys' thermal anomalies (their location on the leading hemisphere and strong spatial correlation to the region preferentially bombarded by high-energy electrons) provides a compelling argument for them having the same formation mechanism, which on Mimas cannot be E-ring grain bombardment. Thus, it is concluded that surface alteration by high-energy electrons is the dominant process on Tethys, and by extension, the same is likely on Dione.

The magnitude of the thermal inertia difference between the background and inside the thermal anomaly is greatest on Mimas and then decreases from Tethys to Dione. However, on Dione the thermal anomalous region does not appear to be spatially correlated with a decrease in the IR/UV albedo ratio as it is on Mimas and Tethys, which suggests either that the surface alteration on Dione is below the threshold for UV darkening to occur or that the color change is too subtle to be detected. No such anomaly is observed on Enceladus, presumably due to its high resurfacing rates.

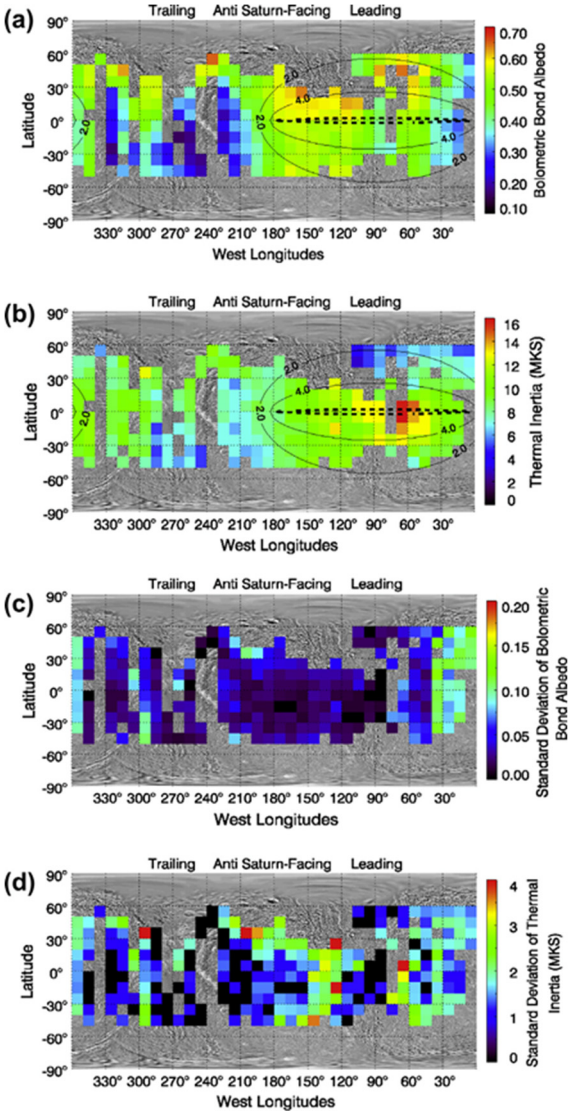

Figure CIRS-57. Maps of derived thermophysical properties for Dione. *Panel (a)*: Bolometric Bond albedo map of Dione. Overlaid are contours of energetic electron power deposited into the surface per unit area (log10 MeV cm^2 s_1). *Panel (b)*: Thermal inertia map of Dione. Overlaid are contours of high-energy electron flux, see the description in *Panel (a)* for details. *Panel (c)*: The standard deviation of the bolometric Bond albedo values given in *Panel (a)*. *Panel (d)*: The standard deviation of the thermal inertia values given in *Panel (b)*.

RHEA, HOWETT ET AL. [2014]

Maps of variations in albedo and thermal inertia were derived for Rhea, using eight separate CIRS observations taken from 2005 until 2012, which provided both day and nighttime coverage. The bolometric Bond albedo and thermal inertia maps of Rhea are given in Figure CIRS-58. Two trends are obvious in the maps: the trailing hemisphere of Rhea is somewhat darker and there is a region of high thermal inertia centered on 110° W, 20° S. Rhea's hemispherical albedo pattern has been previously observed directly at visible wavelengths—for example, Verbiscer and Veverka [1989] and via thermal observations [Howett et al. 2010]. The bolometric Bond albedo maps give a disk-integrated value of 0.58 ±0.12, and leading and trailing hemisphere value of 0.59 ±0.11 and 0.56 ±0.13, respectively. Within error these results agree with the literature values: 0.48 ±0.09 disk-integrated Pitman et al. [2010]; 0:63 (+0.11, −0.12) leading hemisphere Howett et al. [2010]; 0:57 (+0:20, −0:26) trailing hemisphere Howett et al. [2010].

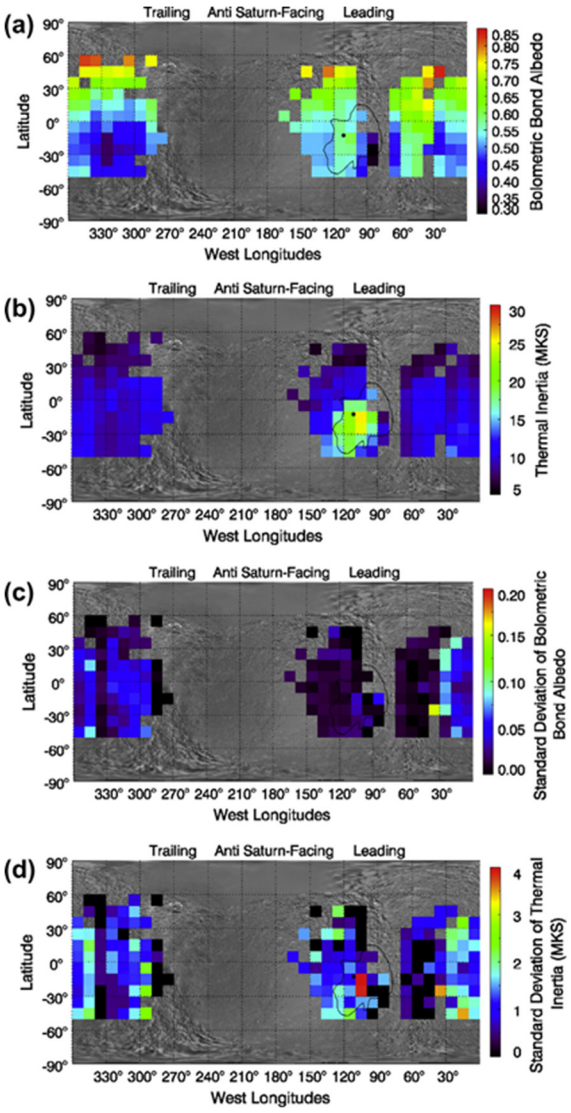

Figure CIRS-58. Maps of derived thermophysical properties for Rhea. The black solid contour shows the approximate edge of the Inktomi ejecta blanket, while the dark circle at 14.1° S and 112.1° W shows the location of the Inktomi crater. *Panel (a)*: Bolometric Bond albedo map of Rhea. *Panel (b)*: Thermal inertia map of Rhea. *Panel (c)*: The standard deviation of the albedo values given in *Panel (a)*. *Panel (d)*: The standard deviation of the thermal inertia values given in *Panel (b)*.

The high thermal inertia region in the southern hemisphere of Rhea's leading hemisphere is a new discovery. The anomalous region does not bear the characteristics of the high thermal inertia regions observed on Mimas, Tethys, and Dione (described in Howett et al. [2011b, 2012, 2014] for Mimas, Tethys and Dione respectively), and Rhea does not display a darkening on this hemisphere in the IR/UV associated with Mimas and Tethys' thermally anomalous region. Rather the thermally anomalous region on Rhea appears to be spatially correlated with the ejecta blanket of Rhea's bright ray crater, Inktomi. Here the thermal inertia increase is more dramatic than on Dione: the background value (the mean value from 30° to 60° W and 10° to 30° S) is 10 MKS, whilst the value on the Inktomi crater ejecta blanket (the mean value between 100° and 120° W, and 10° and 30° S) is 19 MKS. Craters floors with a high thermal inertia compared to the background value have been observed on Mars—for example, Edwards et al. [2013], and the Moon [Bauch et al. 2011], but this is the first time such change in thermal inertia has been observed over a crater on an icy saturnian satellite. This range of thermal inertias corresponds to a thermal skin depth of 0.7–1.3 cm.

Activity on Dione (IN1c), Howett et al. [2018]

IN1c: Determine whether Dione is currently active, or has been so on recent geological timescales.

There are hints that maybe activity does occur on Dione: Dione has smooth plains (indicative of recent resurfacing). Plasma was detected flowing from Dione, which could have been caused by recent geological activity [Burch et al. 2007], although this can also be explained without activity.

FP1 Cassini CIRS data to make nighttime temperature maps of Dione's surface, and model temperature maps were produced by modeling Dione's seasonal temperature change (using previously published thermal inertia and albedo values from Howett et al. [2014]): thermal inertia: 5, 11, and 29 MKS, and albedo values: 0.48, 0.63, and 0.78. Then observed versus modeled temperatures were compared, and temperatures outside of the expected range were looked for. The results are shown in Figure CIRS-59, which shows that for this preliminary example no temperatures are observed outside of those predicted by a passive emission model. When this is repeated for all nighttime CIRS FP1 and FP3 observations of Dione no evidence for activity was found. Therefore, we conclude that there is no evidence in CIRS observations of Dione for activity, and upper-limits of undetected activity have been placed. These results were published in Howett et al. [2018].

The maximum temperature of a 50, 100 and 200 km^2 hot spot is then derived using the highest resolution observation at a given location. The results are shown in Figure CIRS-60.

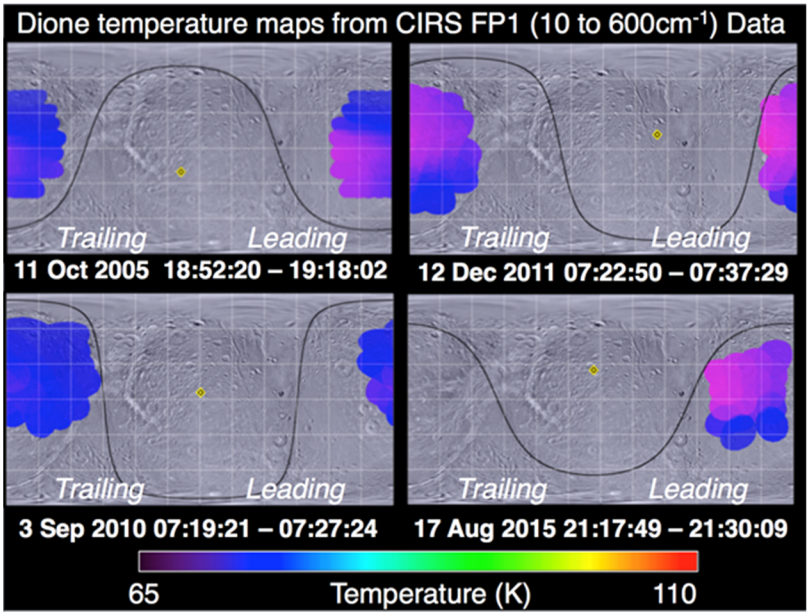

Figure CIRS-59. Comparison of surface temperatures derived from Cassini CIRS FP1 observations to those predicted by a passive emission model.

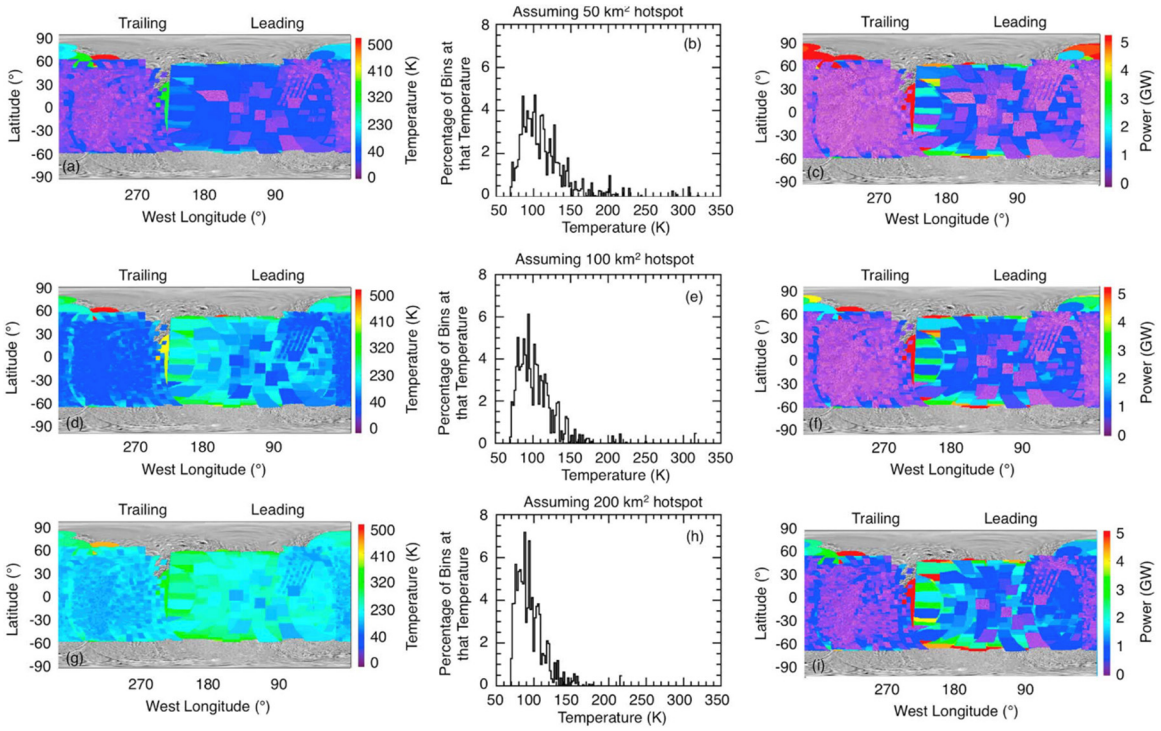

Figure CIRS-60. Details of the upper limits for a 50, 100, and 200 km2 hot spot that could exist on Dione and not be detected in this work. *Panels (a), (d), (g)*: The maximum temperature of a hot spot that could exist on Dione and have remained undetected in this work. *Panels (b), (e), (h)*: The maximum power of a hot spot that could exist on Dione and have remained undetected in this work. *Panels (c), (f), (i)*: Histograms of the maximum temperature a hot spot could have and remain undetected in this study.

Level 2

Rhea's ring (IN2a)

IN2a: Determine if there is a ring (or debris disk) around Rhea, and if so, characterize the spatial and particle size distribution.

ALTERATION OF RHEA'S SURFACE BY INFALL FROM AN ANCIENT RING

Schenk et al. [2011] found blue patches along Rhea's equator, which they believe are evidence for infall from a ring around Rhea. This is because the patches are not associated with any obvious, endogenic tectonic process, as no linear or other tectonic fabric is apparent. Furthermore, a thin ring (or halo) around Rhea was tentatively discovered by Jones et al. [2008] (although this has not been upheld by further observations) [Pitman et al. 2008; Tiscareno et al. 2010].

These patches are small (<1 km), and often well-below the spatial resolution of CIRS thus making them hard to detect. The best estimate of how the surface properties of Rhea vary was

given by Howett et al. [2014], and is shown in Figure CIRS-58. As the figure shows, no obvious change in albedo or thermal inertia is observed along Rhea's equator. We conclude CIRS is unable to contribute to whether infall from an ancient ring around Rhea has altered its surface.

Tethys and the E-ring (IN2b)

IN2b: Determine whether Tethys is geologically active, and thus could be contributing to the E-ring.

Nighttime observations of Tethys have been investigated—see Howett et al. [2012] and this section—and show no evidence for high temperatures expected from activity. Further work is required to set explicit limits on such activity.

Characterize the surfaces of Saturn's small satellites (IN2d)

IN2d: Derive the surface thermophysical properties of Saturn's small satellites, including (but not limited to) Epimethys, Janus, Methone, and Promethus.

CIRS made positive detections of two moons: Epimetheus and Atlas. These results have been submitted as part of a multi-instrument paper [Buratti et al. 2018].

Detections of both Epimetheus and Atlas were made using dedicated CIRS scans bracketed by ISS observations. Epimetheus was detected on January 30, 2017, during a scan that occurred between 19:54:20 to 20:05:50 UTC, at a distance that decreased from 80,179 to 67,237 km. During this time, the sub-spacecraft position changed from 345.0° W / 73.5° N to 346.5° W / 73.7° N, the local time at the sub-spacecraft point increased from 271° to 276° and the phase increased slightly from 68.0° to 68.5°.

Atlas was detected a few months later on April 12, 2017, during a scan that ran from 13:16:39 to 13:24:40 UTC, at a distance that decreased from 33,572 km to 24,580 km. During that time, the phase at the sub-spacecraft point decreased from 51.2° to 47.2°, the sub-spacecraft position changed from 141.9° W / 60.1° N to 149.8° W / 52.1° N, and the local time at the sub-spacecraft point decreased from 226° to 221°.

In both detections, CIRS used its focal plane 3 (FP3, which covers 570–1125 cm^{-1}) to scan the target and background sky. The results are given in Figure CIRS-61, which shows the temperature that has a blackbody emission curve best able to fit the observed radiance over all wavelengths. Both Epimetheus and Atlas are clearly visible above the background dark sky. The mean surface temperature observed on Epimetheus is 90.1 ±2.7 K, and 82.4 ±4.7 K on Atlas.

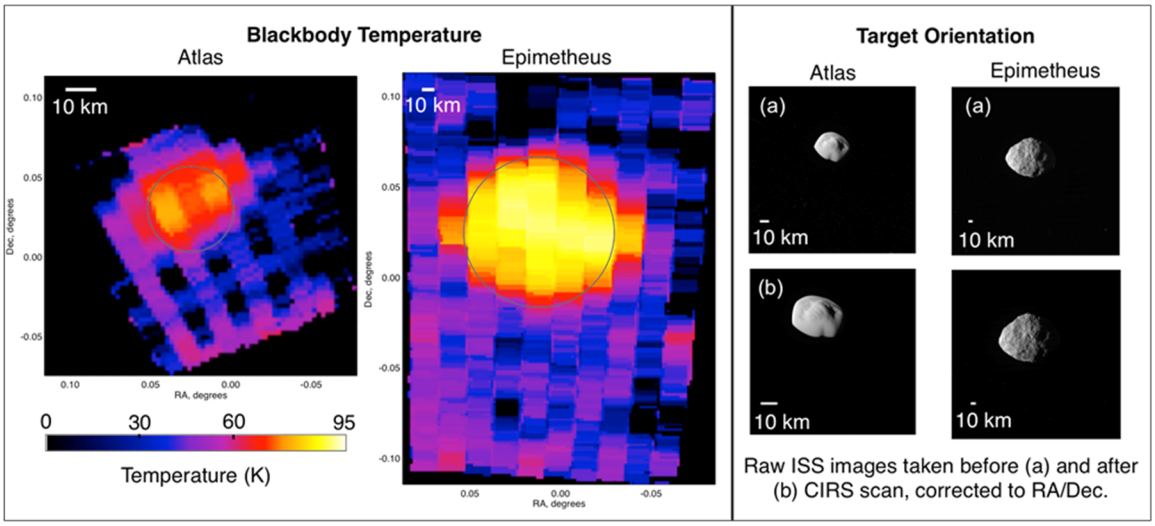

Figure CIRS-61. CIRS and ISS observations of Atlas and Epimetheus. *Left*: The blackbody temperature of the two targets, as determined by fitting a blackbody curve to the full CIRS radiance spectrum at each location. The results are shown in Right Ascension/Declination (RA/Dec) space, which has been corrected so the center of the target lies at 0°/0°. *Right*: Raw ISS observations of both targets taken before and after the CIRS scan, the images have been rotated so they are also in RA/Dec coordinates. However, the scale of the CIRS data and the ISS images is notably different, as indicated by the 10 km scale bar given in every image. Images of Atlas *Panel (a)*: ISS image N00279648 taken using CL1 and CL2 filters on April 12, 2017, at 1:15 UT; *Panel (b)*: ISS image N00279649 taken using CL1 and CL2 filters on April 12, 2017, 1:27 UT. Images of Epimetheus *Panel (a)*: ISS image N00275708 taken using CL1 and CL2 filters on January 30, 2017, 7:53 UT; *Panel (b)*: ISS mage N00275709 taken using CL1 and UV3 filters on January 30, 2017, 8:07 UT.

Open Questions

Saturn

- Exactly how does tropospheric eruption of the great storms perturb the stratosphere so strongly? Presumably by waves generated near the tropopause, but what is the nature of these nonlinear waves?
- What are the waves driving the equatorial oscillation, compared to those identified as drivers for Earth's equatorial oscillations?
- What are the systematic errors affecting the different estimates of the helium abundance from remote sensing techniques (thermal infrared spectra, thermal infrared and radio occultations, thermal infrared and ultraviolet stellar occultations)?
- How important is interannual variability?
- Geophysical systems are complex, nonlinear, and their behavior can be difficult to understand or predict. Cassini, given its proximity and duration, provided us a unique 4-dimensional slice of Saturn. When can we go back?

Rings

Some key open questions on rings are listed below. Other CIRS-specific questions are discussed in the Conclusions and Future Work.

- Why is the ring thermal inertia so low?
- What is the internal structure of ring particles?
- How does the thermal inertia vary with radial distance from Saturn?
- What will even higher spatial resolution data tell us about radial and azimuthal thermal variations in Saturn's rings?
- At higher spatial resolution, which ring regions exhibit a thermal surge and which do not?
- Are there spectral signatures of compounds other than water ice in infrared spectra?
- What are the thermal properties of the faint rings (D-ring, E-ring, G-ring, Phoebe ring) and ringlets (A-ring/Encke gap, F-ring)?
- Do the thermal properties of rings with clumps (A-ring/Encke gap, F-ring, G-ring, E-ring) vary with time?

Titan

- What is the nature of the 220 cm^{-1} absorber?
- How high in altitude does the stratospheric/mesospheric circulation extend?
- Does Titan have a well-defined mesopause?
- Are the nitriles CH_3CN, C_2H_3CN and C_2H_5CN, already seen at sub-mm wavelengths, detectable in the infrared with sufficiently high resolution?
- What functional groups are causing the aerosol absorption features in the mid-IR?
- What is mechanism driving the tilted stratospheric pole?
- How is stratospheric super-rotation generated and maintained?
- What is the link between gas chemistry and aerosol production, and are the abundances anti-correlated?
- Are there condensate clouds of homogenous composition, or are all clouds co-condensates?
- Can we make inferences about Titan's methane history from isotopic ratios?
- Why is the $^{15}N/^{14}N$ much higher in HCN than in N_2?

- Do the abundances of H_2 and CH_4 vary with latitude?
- Are there oxygen bearing molecules beyond CO, CO_2 and H_2O?

Icy satellites

Mimas

- Is there evidence on Mimas' trailing hemisphere for surface alteration due to (low) energy electron bombardment?

Enceladus

- Does the thermal emission of Enceladus' tiger stripes increase over the jet positions predicted by Helfenstein and Porco [2015]?
- Does the thermal emission of Enceladus' tiger stripes show any temporal variability, both in the short-term (with mean anomaly) and long-term (decadal)?
- Are there any more small-scale hot spots?
- Is there any evidence for a thermal anomaly in the location of the radar ones—for example, Le Gall [2017]; Ries et al. [2015]?
- Is there any evidence for a change in thermophysical properties in plume fallout regions?

Tethys

- How does the thermophysical properties vary across Tethys' trailing hemisphere?

Dione

- What is the lower limit of activity on Dione?
- Does the Creusa on Dione show a lower thermal inertia than its surroundings (like Inktomi on Rhea)?
- How do the thermophysical properties of Dione's surface change across its wispy terrain?

Rhea

- What are the thermophysical properties of Rhea's anti-Saturn hemisphere?

Iapetus

- How does the thermal inertia of Iapetus' dark and light terrain vary?

Other Questions

- Can we say anything useful about the surface properties of Saturn's other icy moons?
- What can we learn by combining data sets?
- Is there other evidence of emissivity signatures in the CIRS data?

CIRS Non-Saturn Science Results

Jupiter

Formation and evolution

D/H

See the section entitled Saturn isotopes.

N^{15}/N^{14}

Fouchet et al. [2004a] used large averages of mid-infrared CIRS spectra at the highest apodized resolution (0.5 cm^{-1}) to isolate the weak $^{15}NH_3$ lines from the forest of strong $^{14}NH_3$ lines. The averages were segregated into latitude bins. They found no measurable variation with latitude. The mean global value ($(2.22 \pm 0.52) \times 10^{-3}$) agreed with previous measurements obtained from the Infrared Space Observatory and from the Galileo Probe Mass Spectrometer. They interpreted these values as representative of the proto-solar value. The terrestrial value is a factor nearly 1.7 larger, which they interpreted as originating in a reservoir isolated from the main reservoir of the proto-solar nebula. Abbas et al. [2004] independently analyzed comparable data sets and obtained essentially the identical result for the global average.

Atmospheric gas composition

Disequilibrium Tropospheric Compounds

Phosphine. As noted earlier for Saturn, PH_3 is generally believed to be a product of rapid vertical mixing from deep atmospheric levels, and the observed abundances in the upper troposphere

represent the quenched equilibrium conditions deeper down. Irwin et al. [2004] analyzed CIRS mid-IR spectra over the ranges 600 and 700 cm^{-1} and 1000–1200 cm^{-1} to retrieve jointly the temperature profile, the deep phosphine abundance (~1 bar), the deep ammonia abundance and fractional scale height, and the total cloud (or haze) opacity. They found PH_3 to be greatest within the equatorial zone, indicating upward transport, and smaller within the north and south equatorial belts. The mid latitudes seem to be asymmetric, with PH_3 larger near 40° N at the corresponding latitude in the south. The cause of this is not understood. PH_3 was also enhanced over the Great Red Spot, consistent with upwelling there. Using a more extended spectral range and consideration of tropospheric clouds and aerosols, Fletcher et al. [2009] verified the equatorial enhancement and hemispheric asymmetry. They found Jupiter's mid-IR spectrum is best reproduced by a dual-cloud model, with a compact 10 μm NH_3 ice layer existing at the predicted condensation altitude, and a deeper source of gray opacity (possibly due to NH_4SH clouds). They also found that Jupiter's infrared aerosol opacity is elevated at the equator and within other zones.

Halides. Fouchet et al. [2004b] analyzed CIRS far-infrared spectra to place upper limits on the abundances of HF, HCl, HBr, and HI. The upper limits on the first two were sufficiently small to lie well below solar abundances and support the notion of the halogens' condensation in ammonium salts predicted by thermochemical models for the upper Jovian troposphere.

DISEQUILIBRIUM STRATOSPHERIC COMPOUNDS

Ethane and Acetylene. The thermal infrared spectrometers (IRIS) on the Voyager spacecraft provided meridional profiles of C_2H_6 and C_2H_2, but with limited sensitivity and spatial resolution. Even at a swing-by distance ~138 RJ CIRS vastly improved the latter, and had much better sensitivity. Kunde et al. [2004] found that the latitude profile of C_2H_6 was relatively flat, whereas that of C_2H_2 followed the insolation pattern. The former pattern could be explained if the meridional transport is much faster than the loss of C_2H_6 by vertical mixing (~100 years). That of C_2H_2 suggested that its distribution is mostly governed by local photochemistry with a lifetime of ~1 year. Kunde et al. [2004] concluded that the different distributions would be expected if the dynamical timescale for horizontal transport was between the lifetimes of these two gases, ~10 years.

Kunde et al. [2004] used the emission intensities of C_2H_6 and C_2H_2, relative to the adjacent continuum, as surrogates for the abundances. They corrected for airmass variations using a model of limb brightening. Nixon et al. [2007] noted that the assumption that relative abundance variations with latitude will not, in general, proportionally follow the relative variations of the line intensities, because it ignores the saturation that can occur in the stronger emission lines. As a result, the actual abundance variations are somewhat greater than the intensity analysis would suggest. Nixon et al. [2007] retrieved C_2H_6 and C_2H_2 from the CIRS mid-infrared spectra using a rigorous inversion scheme. They found that the observed spectral emission from C_2H_6 and C_2H_2 was the combination of stratospheric emission, with a peak contribution at ~5 mbar, and tropospheric absorption at 100-400 mbar. For acetylene, they found: (i) the stratospheric volume mixing ratio (VMR) at 5 mbar decreases sharply from a peak around 20° N towards both poles, by a factor ~4; (ii) the northern hemisphere stratosphere is apparently enriched compared to the southern hemisphere at the time

of observation; (iii) in the upper troposphere at 200 mbar the abundance is near constant at ~3 × 10^{-9}. For ethane, the VMR in the equatorial stratosphere at 5 mbar is around 4 × 10^{-6}, in line with previous findings; and increases by factors of ~1.75 to 70° N and ~2.0 to 70° S. The tropospheric VMR at 200 mbar shows similar increases. Nixon et al. [2010a] redid their retrievals using improved modeling of the instrument spectral resolution, and a more recent and improved line list for C_2H_6. They found little change in the meridional distribution of C_2H_2, but found observable changes in the C_2H_6, mainly attributable to the newer line list used. They then analyzed Voyager IRIS spectra from the Jupiter flyby in 1979 (northern fall equinox) and compared the resulting distributions with those from CIRS in 2000 (northern summer solstice). They found the 2-D distribution of ethane was quite similar for the two epochs, although the Cassini distribution was more symmetric than that of Voyager, where C_2H_6 was somewhat depleted in the north relative to the south. Also, the Cassini abundances were mostly higher overall, perhaps because the solar distance was smaller. Acetylene exhibited a much more dramatic change, having a uniform meridional profile at equinox, but strong depletions towards both poles at solstice. The solstice distribution seemed to match the annual-mean picture that would be predicted by a 1-D photochemical model.

HCN and CO_2. The Cassini swing-by also facilitated the mapping of HCN and CO_2 [Kunde et al. 2004]. Both species were thought to be products of the impact of the comet SL9 in 1994, near 45° S. However, observed distributions in latitude were markedly different. HCN exhibited a broad distribution with a maximum near 45° S, a steep fall-off poleward, and a smooth decrease northward to 60° N. The CO_2 profile, however, was much narrower, and its maximum lay southward of 60° S, decreasing abruptly northward of 50° S. Kunde et al. [2004] suggested that the sharp decrease in HCN could result from the inhabitation of horizontal wave-induced diffusion by the south polar vortex. The difference in the meridional distribution of CO_2, compared to that of HCN, particularly at southern latitudes, indicated that it might have other sources in addition to the SL9 impact, and the authors suggested that the precipitation of energetic oxygen ions in the southern auroral regions might be important. Another possibility is that HCN and CO_2 are located at different altitudes. The abundances of both species are so low that their emission features are optically thin; that only restricts their altitude range to be in the stratosphere. Lellouch et al. [2006] revisited the issue, considering various scenarios for transport by eddies and mean meridional circulations. They suggested that the meridional distributions were consistent with HCN and CO_2 residing at different altitudes, with the latter being at the 5-mbar level or lower, and HCN ~3 scale heights higher. However, this possibility is not exclusive, and the enigma remains.

Auroral compounds: C_4H_2 and CH_3. Two new stratospheric species were discovered on Jupiter by CIRS during the 2000-2001 flyby: methyl (CH_3) and diacetylene (C_4H_2) [Kunde et al. 2004]. Diacetylene had previously been detected on Titan, but the detection of the methyl radical marked a first for the solar system. These were detected at 606 cm^{-1} (methyl) and 628 cm^{-1} (diacetylene) on FP3 in both northern and southern hotspots using unapodized data at a resolution of 0.26 cm^{-1}. Simulations were able to replicate the spectral detections, but due to uncertainties in the non-LTE temperatures of the emissions, abundances were not determined.

Clouds and aerosols

Ammonia ice. Thermochemical models suggest that Jupiter's visible cloud deck is composed of ammonia but spectroscopic proof has been difficult to obtain. Ammonia ice can be identified by two infrared absorption features: the ν_3 absorption band (N–H stretch) at 2.96 μm (3376 cm^{-1}) and the ν_2 absorption band (N–H bend) at 9.46 μm (1057 cm_{-1}). The NH_3 ice features cannot be detected from the ground because of telluric CO_2 and H_2O absorption at 3 μm, and terrestrial ozone absorption at 10 μm. Attempts to use mid-infrared spectra from the Voyager IRIS to detect the ν_2 NH_3 ice feature were unsuccessful. Wong et al. [2004] did identify the feature in CIRS spectra, by taking the difference in brightness temperatures, T1040–T1060. They found the highest concentrations of ice at the equator and near 23° N. At the latter location, their spectral fit required at least two types of cloud particles. The NH_3 ice feature at 1060 cm^{-1} required ~1 μm particles in an extended cloud with a scale height equal to the total gas scale height, while the spectrum from 1125 to 1200 cm^{-1} can be matched by a more compact gray cloud with a scale height 20% of the gas scale height and an optical depth of 5.

A good candidate for the deeper cloud layer is NH_4SH, since it could easily form clouds at pressures lower than the predicted condensation pressure level.

Matcheva et al. [2005] used a narrow spectral window centered at 1392 cm^{-1} to map cloud opacities. At this wavenumber atmospheric absorption from ammonia gas is very weak and uncertainties in the ammonia abundance do not impact the cloud retrieval results. In the absence of clouds, the atmospheric transmission is limited by absorption of H_2 and CH_4, and the optical depth is unity near 1200 mbar. The authors found a large variation in latitude, more or less correlated with the zone-belt structure. Their results imply two distinct cloud layers: (i) an optically thick cloud layer of ammonia ice with a base pressure at about 900 mbar or larger; and (ii) a thinner cloud layer with a cloud base at about 1100 mbar that is seen through the gaps of the ammonia ice cloud layer. A good candidate for the deeper cloud layer is NH_4SH, since it could easily form clouds at pressures lower than the predicted condensation pressure level.

Gaseous NH_3. Achterberg et al. [2006] mapped the zonal-mean NH_3 gas abundance between 400 and 500 mbar as a function of latitude. They found the Equatorial Zone is rich in ammonia, with a relative humidity near unity. The North and South Equatorial Belts are depleted relative to the Equatorial Zone by an order of magnitude. The Great Red Spot shows a local maximum in the ammonia abundance. They found NH_3 abundance to be highly correlated with temperature perturbations at the same altitude. Under the assumption that anomalies in ammonia and temperature are both perturbed from equilibrium by vertical motion, they concluded that the adjustment time constant for ammonia equilibration is about one third of the radiative time constant.

Atmospheric structure and circulation

GLOBAL AND ZONAL MEAN STRUCTURE

The 138 RJ swing-by of Jupiter in December 2000–January 2001 provided the best opportunity to map the temperatures of its stratosphere and upper troposphere since the Voyager flybys in 1979. Despite the large distance, the smaller detectors in the mid-infrared focal planes enabled CIRS to achieve a spatial resolution (2.4° latitude near the equator), exceeding the global-mapping resolution obtained by IRIS on Voyager. Application of the thermal wind equation to the retrieved zonal-mean temperatures provided a meridional cross-section of the mean zonal winds [Flasar et al. 2004b]. As expected from the Voyager IRIS observations, the winds decayed with altitude above the visible clouds. However, near the equator, they began to increase with altitude above the ~20 mbar level, reaching a maximum of ~140 m/s near 4 mbar. This stratospheric jet is comparable to the winds lower in the troposphere, obtained from cloud-feature tracking. The undulating structure in altitude is reminiscent of an equatorial oscillation similar to that on Earth. Orton et al. [1991]—see also Simon-Miller et al. [2006]—had observed a temporal oscillation in equatorial brightness temperatures that was not strictly periodic, but cyclic over 4–5 years. Leovy et al. [1991] pointed out that this was reminiscent of the terrestrial quasi-biennial oscillation in the stratosphere. This is mechanically forced by the absorption of atmospheric waves, and they suggested that a similar mechanism operates on Jupiter. A similar phenomenon exists on Saturn (see the section entitled Equatorial Oscillation).

Potential vorticity (PV) has been extensively used in studies of geophysical fluid flows, because under many conditions it is approximately conserved and can serve as a tracer of motion. Moreover, it figures in several stability criteria. Read et al. [2006] used velocity measurements, obtained from tracking cloud features in Voyager and Cassini images, and thermal measurements obtained from Voyager IRIS and Cassini CIRS observations, to derive the PV associated with Jupiter's zonal-mean atmospheric flow. The profiles show some evidence for a step-like pattern suggestive of local PV homogenization, separated by strong PV gradients in association with eastward jets, though on differing scales in the northern and southern hemispheres. The northward gradient of PV is found to change sign in several places in each hemisphere, and the relationship between PV and the mean zonal flow indicate that the northern hemisphere may be closer to marginal stability with respect to Arnol'd's second stability theorem (see the section entitled Internal Rotation) than the southern hemisphere.

The zonal-mean meridional motion can be inferred from the meridional distribution of hydrocarbons discussed earlier.

Li et al. [2012] analyzed the global thermal emission from Jupiter and its meridional distribution from CIRS and VIMS observations. They found Jupiter's mean effective temperature to be 125.6° K. The hemispheric distribution of emitted power was asymmetric, with the emitted power in the north 3.0% larger than in the south. The distribution in the Voyager epoch was more symmetric. Moreover, the Cassini total power was 4% higher than that from Voyager. The authors

suggest that this difference is attributable to the warming of atmospheric layers around 200 mbar, but the cause of this is not understood.

Waves

Flasar et al. [2004b] examined the zonal structure in the 2000–2001 Jupiter swing-by data to search for planetary-scale waves in the troposphere and stratosphere. They observed structure near the equator, which conceivably could be related to the forcing of the equatorial oscillation, but they also observed a variety of thermal features well away from the equator. In the troposphere long trains of regularly spaced features were observed, and they appeared to be quasi-stationary relative to Jupiter's internal rotation. These types of waves had been observed earlier in Voyager and ground-based observations. The stratospheric thermal perturbations also exhibit regularly spaced zonal features, but they were less confined in latitude. Moreover, there was a tendency for many of the features to drift westward relative to the ambient zonal flow, consistent with Rossby waves, although an unambiguous identification could not be made. At many latitudes, the connection between the tropospheric and stratospheric disturbances was not conclusive, either in wavenumber or in zonal phase velocity.

In a later study, Li et al. [2006] compared wave structure in both the CIRS and Cassini imaging data sets. They identified a quasi-stationary wave in the north equatorial belt as a Rossby wave in both data sets that had a slow westward drift.

Aurora

Flasar et al. [2004b] detected an intense warm region at 1 mbar at high northern latitudes, centered near 65° N, 180° W. This had been extensively observed in infrared ground-based observations; however, the morphology of the spot differs from that of the Jovian aurorae described at ultraviolet, visible, and near infrared wavelengths. Because the spectra were of necessity obtained in the nadir-viewing mode (138 RJ), Flasar et al. [2004b] could not place limits on how much higher in altitude the hot spot extended. They were, however, able to place a lower limit on the altitude, because the hot spot was not visible at the 4 mbar level. From the thermal wind equation, strong anticyclonic winds would be expected to bound the hot spot, with vertical shears ~30 m/s per scale height. Kunde et al. [2004], observed enhanced emission from several hydrocarbons within the northern auroral hot spot, for example, from the Q branch of C_2H_2 at 729 cm^{-1}. They also detected enhanced emission from C_2H_2, albeit weaker, at 75°–85° S (higher latitudes were not well observed) over longitudes spanning 0° to 70° W. They estimated the excess thermal emission from the northern spot to be ~1013 W, about an order of magnitude larger than that expected from far-ultraviolet spectra from precipitating particles. They suggested that Joule heating could be a viable alternative source.

Sinclair et al. [2017] analyzed Jupiter's auroral hot spots, using spectra from IRIS on Voyager 1 and CIRS on Cassini. They attempted to separate the effects of temperature from concentration in the observed enhanced emission from C_2H_2 and C_2H_6 within the spot at mid-

infrared wavelengths. To do this, they retrieved vertical profiles of temperature for the upper troposphere and tropopause region from the 600–625 cm^{-1} and 640–665 cm^{-1} portions of the spectrum (both collision induced absorption regions associated with the S(1) line of H_2 but with the emission features of C_3H_4, C_4H_2 and C_6H_6 omitted) and stratospheric temperatures from 1230-1380 cm^{-1} (CH_4 emission) regions. This leaves a range from ~50 mbar to ~5 mbar where the information content of nadir-viewing spectra is minimal, and temperature profiles must be interpolated. However, as noted above, most of the lateral contrast associated with the aurora occurs above the 4 mbar level. The vertical profiles of C_2H_2 and C_2H_6 were retrieved from their respective emission features at 710–750 cm^{-1} and 770–890 cm^{-1}. The authors conclude that the vertical temperature profiles retrieved from CIRS spectra covering the auroral-related spots indicate the presence of two discrete vertical regions of heating, at the 1 mbar level and at pressures of 10 µbar and lower. They argued that the temperatures at 10 µbar and lower pressures were likely indicative of joule heating, ion drag, and/or electron precipitation, ion-drag and energy released from exothermic ion-chemistry. On the other hand, they concluded that the heating at the 1 mbar level is the result of either a layer of aurorally-produced haze particles, which are heated by incident sunlight and/or adiabatic heating by subsidence within the auroral hot-spot region. Retrievals of indicated that C_2H_2 is enriched but C_2H_6 is depleted in auroral regions relative to quiescent regions. They suggested that the contrast between C_2H_2 and C_2H_6 can be explained by a coupling of auroral-driven chemistry and horizontal advection. Ion-neutral and electron recombination chemistry in the auroral region enriches all C_2 hydrocarbons but in particular, the unsaturated C_2H_2 and C_2H_4 hydrocarbons. Once advected outside of the auroral region, the unsaturated C_2 hydrocarbons are converted into C_2H_6 by neutral photochemistry thereby enriching C_2H_6 in quiescent regions, which gives the impression it is depleted inside the auroral region.

Open Questions

- What is the descending pattern of Jupiter's equatorial oscillation? Is it similar to Saturn's? What are the waves driving the oscillation, compared to those identified as drivers for Earth's?
- What is the nature of the physical process causing the apparent discrepancy of stratospheric HCN and CO_2? Is ion chemistry involving exogenic H_2O important, or are the meridional circulations in the high stratosphere multi-layered?
- Why does Jupiter not exhibit the intense storms disrupting broad latitude bands that are observed on Saturn?

ACRONYMS

Note: For a complete list of Acronyms, refer to Cassini Acronyms – Attachment A.

AO	Announcement of Opportunity
CIA	collision-induced absorption
CIRS	Composite Infrared Spectrometer
CM	circulation model
DISR	Descent Imager/Spectral Radiometer
FOV	field of view
FRPO	F-ring and proximal orbits
FTS	Fourier Transform Spectrometer
GCM	general circulation modeling
GCMS	Gas Chromatograph Mass Spectrometer
GSFC	Goddard Space Flight Center
HCN	hydrogen cyanide
HST	Hubble Space Telescope
HWHM	half-width-half-maximum
IR	infrared
IRIS	infrared spectrometers
ISO	Infrared Space Observatory
ISS	Imaging Science Subsystem
LEMMS	Low Energy Magnetospheric Measurement System
LTE	local thermodynamic equilibrium
MIMI	Magnetospheric Imaging Instrument
MIR	mid-infrared
mrad	microradians
NAC	narrow-angle camera
NAT	nitric acid trihydrate
NSE	northern spring equinox
PPS	Power & Pyrotechnics Subsystem
PV	potential vorticity
QBO	quasi-biennial oscillation
RA/Dec	Right Ascension/Declination
RADAR	Titan Radar Mapper
RS	radio science
SAO	semi-annual oscillation
SCET	spacecraft event time
SNR	signal to noise ratio
SPT	South polar terrain
TM	Traceability Matrix

UV	ultraviolet
UVIS	Ultraviolet Imaging Spectrograph
UVIS	Ultraviolet Imaging Spectrometer
VIMS	Visual and Infrared Mapping Spectrometer
VMR	volume mixing ratio
VMR	volume mixing ratio
WAC	wide-angle camera

REFERENCES

Disclaimer: The partial list of references below correspond with in-text references indicated in this report. For all other Cassini references, refer to Attachment B – References & Bibliographies; Attachment C – Cassini Science Bibliographies; the sections entitled References contributed by individual Cassini instrument and discipline teams located in Volume 1 Sections 3.1 and 3.2 Science Results; and other resources outside of the Cassini Final Mission Report.

Abbas, M. M., A. LeClair, E. Woodard, M. Young, M. Stanbro, F. M. Flasar, V. G. Kunde, et al., (2013), Distribution of CO_2 in Saturn's atmosphere from Cassini/CIRS infrared observations, The Astrophysical Journal, 776, 2, doi: 10.1088/0004-637X/776/2/73.

Abbas, M. M., A. LeClair, T. Owen, B. J. Conrath, F. M. Flasar, V. G. Kunde, et al., (2004), The nitrogen isotopic ratio in Jupiter's atmosphere from observations by the Composite Infrared Spectrometer on the Cassini spacecraft, The Astrophysical Journal, 602, 2, 1063–1074, doi: 10.1086/381084.

Achterberg, R. K., F. M. Flasar, G. L. Bjoraker, B. E. Hesman, N. J. Gorius, A. A. Mamoutkine, L. N. Fletcher, M. E. Segura, S. G. Edgington, S. M. Brooks, (2018), Thermal emission from Saturn's polar cyclones, Geophysical Research Letters, vol. 45, Issue 11, pp. 5312–5319, Geophysical Research Letters, doi: 10.1029/2018gl078157.

Achterberg, R. K., P. J. Schinder, et al., (2016), CIRS team meeting notes.

Achterberg, R. K., P. J. Gierasch, B. J. Conrath, L. N. Fletcher, B. E. Hesman, G. L. Bjoraker, F. M. Flasar, (2014a), Changes to Saturn's zonal-mean tropospheric thermal structure after the 2010–2011 northern hemishere storm, The Astrophysical Journal, 786, 2, doi: 10.1088/0004-637X/786/2/92.

Achterberg, R. K., et al., (2014b), CIRS team meeting notes.

Achterberg, R. K., P. J. Gierasch, B. J. Conrath, F. M. Flasar, C. A. Nixon, (2011), Temporal variations of Titan's middle-atmospheric temperatures from 2004 to 2009 observed by Cassini/CIRS, Icarus, 211, 1, 686–698, doi: 10.1016/j.icarus.2010.08.009.

Achterberg, R. K., B. J. Conrath, P. J. Gierasch, E. M. Flasar, C. A. Nixon, (2008a), Titan's middle-atmospheric temperatures and dynamics observed by the Cassini Composite Infrared Spectrometer, Icarus, 194, 1, 263–277, doi: 10.1016/j.icarus.2007.09.029.

Achterberg, R. K., B. J. Conrath, P. J. Gierasch, F. M. Flasar, C. A. Nixon, (2008b), Observation of a tilt of Titan's middle-atmospheric superrotation, Icarus, 197, 2, 549–555, doi: 10.1016/j.icarus.2008.05.014.

Achterberg, R. K., B. J. Conrath, P. J. Gierasch, (2006), Cassini CIRS retrievals of ammonia in Jupiter's upper troposphere, Icarus, 182, 1, 169–180, doi: 10.1016/j.icarus.2005.12.020.

Achterberg, R. K. and F. M. Flasar, (1996), Planetary-scale thermal waves in Saturn's upper troposphere, Icarus, 119, 2, 350–369, doi: 10.1006/icar.1996.0024.

Altobelli, N., D. Lopez-Paz, S. Pilorz, L. J. Spilker, R. Morishima, S. Brooks, C. Leyrat, E. Deau, S. Edgington, A. Flandes, (2014), Two numerical models designed to reproduce Saturn ring temperatures as measured by Cassini-CIRS, Icarus, 238, 205–220.

Altobelli, N., L. Spilker, S. Pilorz, et al. (2009). Thermal phase curves observed in Saturn's main rings by Cassini-CIRS: Detection of an opposition effect? Geophysical Research Letters, vol. 36, Issue 10, doi: 10.1029/2009GL038163.

Altobelli, N., L. Spilker, C. Leyrat, S. Pilorz, (2008), Thermal observations of Saturn's main rings by Cassini CIRS: Phase, emission and solar elevation dependence, Planetary and Space Science, 56, 134–146.

Altobelli, N., L. Spilker, S. Pilorz, et al., (2007), C-ring fine structures revealed in the thermal infrared, Icarus, 191, 691–701.

Anderson, C. M., R. E. Samuelson, D. Nna-Mvondo, (2018), Organic Ices in Titan's Stratosphere, Space Science Reviews, 214, no. 8, 125.

Anderson, C. M., R. E. Samuelson, Y. L. Yung, J. L. McLain (2016), Solid-state photochemistry as a formation mechanism for Titan's stratospheric C4N2 ice clouds, Geophysical Research Letters, 43, 7, 3088–3094, doi: 10.1002/2016gl067795.

Anderson, C. M., R. E. Samuelson, R. K. Achterberg, J. W. Barnes, F. M. Flasar, (2014), Subsidence-induced methane clouds in Titan's winter polar stratosphere and upper troposphere, Icarus, 243, 129–138, doi: 10.1016/j.icarus.2014.09.007.

Anderson, C. M. and R. E. Samuelson (2011), Titan's aerosol and stratospheric ice opacities between 18 and 500 μm: Vertical and spectral characteristics from Cassini CIRS, Icarus, 212, 2, 762–778, doi: 10.1016/j.icarus.2011.01.024.

Anderson, C. M., R. E. Samuelson, G. L. Bjoraker, R. K. Achterberg, (2010), Particle size and abundance of HC_3N ice in Titan's lower stratosphere at high northern latitudes, Icarus, 207, 2, 914–922, doi: 10.1016/j.icarus.2009.12.024.

Baillié, K., J. E. Colwell, J. J. Lissauer, L. W. Esposito, M. Sremčević, (2011), Waves in Cassini UVIS stellar occultations: 2. The C ring, Icarus, 216, no. 1, 292–308.

Baldwin, M. P., L. J. Gray, T. J. Dunkerton, K. Hamilton, P. H. Haynes, W. J. Randel, J. R. Holton, et al., (2001), The quasi-biennial oscillation, Reviews of Geophysics, vol. 39, Issue 2, pp. 179–229, doi: 10.1029/1999rg000073.

Bampasidis, G., A. Coustenis, R. K. Achterberg, S. Vinatier, P. Lavvas, C. A. Nixon, D. E. Jennings, et al., (2012), Thermal and chemical structure variations in Titan's stratosphere during the Cassini Mission, The Astrophysical Journal, 760, 2, doi: 10.1088/0004-637x/760/2/144.

Bauch, K. E., H. Hiesinger, M. S. Robinson, F. Scholten, (2011), Thermophysical properties of selected lunar study regions determined from LROC and diviner data, 42nd Lunar and Planetary Science Conference, 2278pdf.

Bauduin, S., P. G. J. Irwin, E. Lellouch, V. Cottini, R. Moreno, C. A. Nixon, N. A. Teanby, T. Ansty, F. M. Flasar, (2018), Retrieval of H_2O abundance in Titan's stratosphere: A (re) analysis of CIRS/Cassini and PACS/Herschel observations, Icarus, 311, 288–305.

Bézard, B., S. Vinatier, R. K. Achterberg, (2018), Seasonal radiative modeling of Titan's stratospheric temperatures at low latitudes, Icarus, 302, 437–450.

Bézard, B., R. V. Yelle, C. A. Nixon (2013), The composition of Titan's atmosphere, Titan: Interior, Surface, Atmosphere, and Space Environment, 14, 158–189.

Bézard, B., (2009), Composition and chemistry of Titan's stratosphere, Philosophical Transactions of the Royal Society a-Mathematical Physical and Engineering Sciences, 367, 1889, 683–695, doi: 10.1098/rsta.2008.0186.

Bézard, B., C. A. Nixon, I. Kleiner, D. E. Jennings (2007), Detection of $^{13}CH_3D$ on Titan, Icarus, 191, 1, 397–400, doi: 10.1016/j.icarus.2007.06.004.

Blackburn, D. G., B. J. Buratti, E. G. Rivera-Valentin, (2012), Exploring the impact of thermal segregation on Dione through a bolometric bond albedo map, 43rd Lunar Planetary Science Conference, 1536pdf.

Bohren, C. F. and D. R. Huffman, (1983), Absorption and scattering of light by small particles, Wiley-Interscience, NY.

Bradley, E. T., J. E. Colwell, L. W. Esposito, (2013). Scattering properties of Saturn's rings in far ultraviolet from Cassini UVIS spectra, Icarus, 225, 726–739.

Bradley, E. T., J. E. Colwell, L. W. Esposito, et al., (2010), Far ultraviolet spectral properties of Saturn's rings from Cassini UVIS, Icarus, 206, 458–466.

Buratti, B. J., T. Momary, R. N. Clark, et al., (2018), First results from five fabulous flybys of Saturn's ring moons, Science, submitted February 6, 2018.

Buratti, B. and J. Veverka, (1984), Voyager photometry of Rhea, Dione, Tethys, Enceladus and Mimas, Icarus, 258, 254–264.

Burch, J. L., J. Goldstein, W. S. Lewis, D. T. Young, A. J. Coates, M. K. Dougherty, N. André (2007) Tethys and Dione as sources of outward-flowing plasma in Saturn's magnetosphere, Nature, 447, 833–835, doi: 10.1038/nature05906.

Ciarniello, M., F. Capaccioni, G. Filacchione, A. Raponi, F. Tosi, M. C. De Sanctis, M. T. Capria, et al., (2015), Photometric properties of comet 67P/Churyumov-Gerasimenko from VIRTIS-M onboard Rosetta, Astronomy & Astrophysics, 583, A31, doi: 10.1051/0004-6361/201526307.

Chandrasekhar, S., (1960), Radiative Transfer, Dover Publications, https://books.google.com/books?id=CK3HDRwCT5YC.

Charnoz, S., J. Salmon, A. Crida, (2010), The recent formation of Saturn's moonlets from viscous spreading of the main rings, Nature, 465, 752–754.

Colwell, J. E., J. H. Cooney, L. W. Esposito, M. Sremčević, (2009), Density waves in Cassini UVIS stellar occulations: 1, The Cassini division, Icarus, 200, 574–580.

Colwell, J. E., L. W. Esposito, M. Sremčević, G. R. Stewart, W. E. McClintock, (2007), Self-gravity wakes and radial structure of Saturn's B-ring, Icarus, 190, 127–144.

Colwell, J. E., L. W. Esposito, M. Sremčević, (2006), Self-gravity wakes in Saturn's A-ring measured by stellar occultations from Cassini, Geophysical Research Letters, vol. 33, Issue 7, doi: 10.1029/2005GL025163.

Cottini, V., C. A. Nixon, D. E. Jennings, C. M. Anderson, N. Gorius, G. L. Bjoraker, A. Coustenis, et al., (2012a), Water vapor in Titan's stratosphere from Cassini CIRS far-infrared spectra, Icarus, 220, 2, 855–862, doi: 10.1016/j.icarus.2012.06.014.

Cottini, V., C. A. Nixon, D. E. Jennings, R. de Kok, N. A. Teanby, P. G. J. Irwin, F. M. Flasar, (2012b), Spatial and temporal variations in Titan's surface temperatures from Cassini CIRS observations, Planetary and Space Science, 60, 1, 62–71, doi: 10.1016/j.pss.2011.03.015.

Courtin, R., C. K. Sim, S. J. Kim, D. Gautier, (2012), The abundance of H_2 in Titan's troposphere from the Cassini CIRS investigation, Planetary and Space Science, 69, 1, 89–99, doi: 10.1016/j.pss.2012.03.012.

Coustenis, A., D. E. Jennings, R. K. Achterberg, G. Bampasidis, C. A. Nixon, P. Lavvas, V. Cottini, F. M. Flasar, (2018), Seasonal evolution of Titan's stratosphere near the poles, The Astrophysical Journal Letters, 854, no. 2, L30, doi: 10.3847/2041-8213/aaadbd.

Coustenis, A., D. E. Jennings, R. K. Achterberg, G. Bampasidis, P. Lavvas, C. A. Nixon, N. A. Teanby, C. M. Anderson, V. Cottini, F. M. Flasar, (2016), Titan's temporal evolution in stratospheric trace gases near the poles, Icarus, 270, 409–420, doi: 10.1016/j.icarus.2015.08.027.

Coustenis, A., G. Bampasidis, R. K. Achterberg, P. Lavvas, D. E. Jennings, C. A. Nixon, N. A. Teanby, S. Vinatier, F. M. Flasar, R. C. Carlson, G. Orton, (2013), Evolution of the stratospheric temperature and chemical composition over one Titanian year, The Astrophysical Journal, 779, 2, doi: 10.1088/0004-637x/779/2/177.

Coustenis, A., D. E. Jennings, C. A. Nixon, R. K. Achterberg, P. Lavvas, S. Vinatier, N. A. Teanby, et al. (2010), Titan trace gaseous composition from CIRS at the end of the Cassini-Huygens prime mission, Icarus, 207, 1, 461–476, doi: 10.1016/j.icarus.2009.11.027.

Coustenis, A., D. E. Jennings, A. Jolly, Y. Bénilan, C. A. Nixon, S. Vinatier, D. Gautier et al., (2008), Detection of C_2HD and the D/H ratio on Titan, Icarus, 197, 2, 539–548, doi: 10.1016/j.icarus.2008.06.003.

Coustenis, A., R. K. Achterberg, B. J. Conrath, D. E. Jennings, A. Marten, D. Gautier, C. A. Nixon, et al. (2007), The composition of Titan's stratosphere from Cassini/CIRS mid-infrared spectra, Icarus, 189, 1, 35–62, doi: 10.1016/j.icarus.2006.12.022.

Coustenis, A., A. Salama, B. Schulz, S. Ott, E. Lellouch, T. Encrenaz, D. Gautier, H. Feuchtgruber, (2003), Titan's atmosphere from ISO mid-infrared spectroscopy, Icarus, 161, no. 2, 383–403.

Crespin, A., S. Lebonnois, S. Vinatier, B. Bézard, A. Coustenis, N. A. Teanby, R. K. Achterberg, P. Rannou, F. Hourdin, (2008), Diagnostics of Titan's stratospheric dynamics using Cassini/CIRS data and the 2-dimensional IPSL circulation model, Icarus, 197, 2, 556–571, doi: 10.1016/j.icarus.2008.05.010.

Cuzzi, J. N., R. Clark, G. Filacchione, R. French, R. Johnson, E. Marouf, L. Spilker, (2009), Ring particle composition and size distribution, Chapter 15, In Saturn from Cassini-Huygens, (eds.) M. K. Dougherty, L. W. Esposito, S. M. Krimingis, Springer, Dordrecht, pp. 459–509, doi: 10.1007/978-1-4020-9217-6_15.

Cuzzi, J. N. and P. R. Estrada, (1998), Compositional evolution of Saturn's rings due to meteoroid bombardment, Icarus, 132, 1–35.

Cuzzi, J. N., J. J. Lissauer, L. W. Esposito, J. B. Holberg, E. A Marouf, G. L. Tyler, A. Boischot, (1984), Saturn's rings - Properties and processes, In International Astronomical Union (IAU) Colloquia 75: Anneaux des Planetes (Planetary Rings), University of Arizona Press. Tucson, AZ, pp. 73–199.

de Kok, R. J., N. A. Teanby, L. Maltagliati, P. G. J. Irwin, S. Vinatier, (2014), HCN ice in Titan's high-altitude southern polar cloud, Nature, 514, 7520, 65–67, doi: 10.1038/nature13789.

de Kok, R., P. G. J. Irwin, N. A. Teanby, (2010a), Far-infrared opacity sources in Titan's troposphere reconsidered, Icarus, 209, 2, 854–857, doi: 10.1016/j.icarus.2010.06.035.

de Kok, R., P. G. J. Irwin, N. A. Teanby, S. Vinatier, F. Tosi, A. Negrao, S. Osprey, A. Adriani, M. L. Moriconi, A. Coradini (2010b), A tropical haze band in Titan's stratosphere, Icarus, 207, 1, 485–490, doi: 10.1016/j.icarus.2009.10.021.

de Kok, R., P. G. J. Irwin, N. A. Teanby (2008), Condensation in Titan's stratosphere during polar winter, Icarus, 197, 2, 572–578, doi: 10.1016/j.icarus.2008.05.024.

de Kok, R., P. G. J. Irwin, N. A. Teanby, E. Lellouch, B. Bézard, S. Vinatier, C. A. Nixon, et al., (2007a), Oxygen compounds in Titan's stratosphere as observed by Cassini CIRS, Icarus, 186, 2, 354–363, doi: 10.1016/j.icarus.2006.09.016.

de Kok, R., P. G. J. Irwin, N. A. Teanby, C. A. Nixon, D. E. Jennings, L. Fletcher, C. Howett, et al., (2007b), Characteristics of Titan's stratospheric aerosols and condensate clouds from Cassini CIRS far-infrared spectra, Icarus, 191, 1, 223–235, doi: 10.1016/j.icarus.2007.04.003.

De La Haye, V., J. H. Waite Jr, R. E. Johnson, R. V. Yelle, T. E. Cravens, J. G. Luhmann, et al., (2007), Cassini Ion and Neutral Mass Spectrometer data in Titan's upper atmosphere and exosphere: Observation of a suprathermal corona, Journal of Geophysical Research: Space Physics, 112, A7, doi: 10.1029/2006ja012222.

Del Genio, A. D., R. K. Achterberg, K. H. Baines, F. M. Flasar, P. L. Read, A. Sánchez-Lavega, A. P. Showman, (2009), Saturn Atmospheric Structure and Dynamics, Chapter 6, In Saturn

from Cassini-Huygens, (eds.) M. K. Dougherty, L. W. Esposito, S. M. Krimigis, Springer, Dordrecht, pp. 113–159, doi: 10.1007/978-1-4020-9217-6_6.

Dyudina, U. A., A. P. Ingersoll, S. P. Ewald, A. R. Vasavada, R. A. West, K. H. Baines, T. W. Momary, et al., (2009), Saturn's south polar vortex compared to other large vortices in the Solar System, Icarus, 202, 1, 240–248, doi: 10.1016/j.icarus.2009.02.014.

Dyudina, U. A., A. P. Ingersoll, S. P. Ewald, A. R. Vasavada, R. A. West, A. D. Del Genio, J. M. Barbara, et al., (2008), Dynamics of Saturn's south polar vortex, Science, 319, 5871, 1801–1801, doi: 10.1126/science.1153633.

Edgington, S. G., et al., (2008), unpublished.

Edwards, C. S., J. L. Bandfield, P. R. Christensen, A. D. Rogers, (2013), The formation of infilled craters by impact induced decompression melting of the martian mantle, 44th Lunar Planetary Science Conference, 2153pdf.

Elder, C., P. Helfenstein, P. Thomas, J. Veverka, J. A. Burns, T. Denk, C. Porco, (2007), Tethys'mysterious equatorial band, Bulletin American Astronomical Society, 39, 429.

Esposito, L. W., J. N. Cuzzi, J. B. Holberg, et al., (1984), Saturn's rings - Structure, dynamics, and particle properties, Saturn, pp. 463–545.

Ferrari, C. and E. Reffet, (2013), The dark side of Saturn's B-ring: Seasons as clues to its structure, Icarus, 223, 28–39.

Ferrari, C., S. Brooks, S. Edgington, et al., (2009), Structure of self-gravity wakes in Saturn's A-ring as measured by Cassini CIRS, Icarus, 199, 145–153.

Ferrari, C. and C. Leyrat, (2006), Thermal emission of spherical spinning ring particles, Astronomy & Astrophysics, 447, 745–760.

Ferrari, C. (2006), Cassini-CIRS observations of Saturn's rings, Asia Oceania Geosciences Society 3rd Annual Meeting.

Ferrari, C., P. Galdemard, P. O. Lagage, E. Pantin, C. Quorin, (2005), Imaging Saturn's rings with CAMIRAS: thermal inertia of B and C rings, Astronomy & Astrophysics, 441, 379–389.

Ferrari, C., P. Galdemard, P. O. Lagage, E. Pantin, (1999), Thermal inertia of Saturn's ring particles. Bulletin of the American Astronomical Society, 31, 1588–1588.

Filacchione, G., F. Capaccioni, M. Ciarniello, R. N. Clark, J. N. Cuzzi, P. D. Nicholson, D. P. Cruikshank, et al., (2012), Saturn's icy satellites and rings investigated by Cassini-VIMS: III – Radial compositional variability, Icarus, 220, 1064–1096.

Flandes, A., L. Spilker, R. Morishima, S. Pilorz, C. Leyrat, N. Altobelli, S. Brooks, S. G. Edgington, et al., (2010), Brightness of Saturn's rings with decreasing solar elevation, Planetary and Space Science, 58, 1758–1765.

Flasar, F. M., R. K. Achterberg, P. J. Schinder, (2014), Thermal structure of Titan's troposphere and middle atmosphere, Chapter 3, In Titan: Interior, Surface, Atmosphere, and Space

Environment, (eds.) I. Müller-Wodarg, C. A. Griffith, E. Lellouch, T. E. Cravens, Cambridge University Press, New York, NY, pp. 102–121.

Flasar, F. M. and R. K. Achterberg, (2009), The structure and dynamics of Titan's middle atmosphere, Philosophical Transactions of the Royal Society a-Mathematical Physical and Engineering Sciences, 367, 1889, 649–664, doi: 10.1098/rsta.2008.0242.

Flasar, F. M., K. H. Baines, M. K. Bird, T. Tokano, R. A. West, (2009), Atmospheric Dynamics and Meteorology, Chapter 13, In Titan from Cassini-Huygens, (eds.) R. H. Brown, J.-P. Lebreton, J. H. Waite, Springer, Dordrecht, pp. 323–352, doi: 10.1007/978-1-4020-9215-2_13.

Flasar, F. M., R. K. Achterberg, B. J. Conrath, P. J. Gierasch, V. G. Kunde, C. A. Nixon, G. L. Bjoraker, et al., (2005a), Titan's atmospheric temperatures, winds, and composition, Science, 308, 5724, 975–978, doi: 10.1126/science.1111150.

Flasar, F. M., R. K. Achterberg, B. J. Conrath, J. C. Pearl, G. L. Bjoraker, D. E. Jennings, P. N. Romani, et al., (2005b), Temperatures, winds, and composition in the Saturnian system, Science, 307, 5713, 1247–1251, doi: 10.1126/science.1105806.

Flasar, F. M., V. G. Kunde, M. M. Abbas, R. K. Achterberg, P. Ade, A. Barucci, B. Bézard, et al., (2004a), Exploring the Saturn system in the thermal infrared: The composite infrared spectrometer, Space Science Reviews, 115, 169–297, doi: 10.1007/s11214-004-1454-9.

Flasar, F. M., V. G. Kunde, R. K. Achterberg, B. J. Conrath, A. A. Simon-Miller, C. A. Nixon, P. J. Gierasch, et al. (2004b), An intense stratospheric jet on Jupiter, Nature, 427(6970), 132–135, doi: 10.1038/nature02142.

Flasar, F. M., R. E. Samuelson, B. J. Conrath, (1981), Titans atmosphere - temperature and dynamics, Nature, 292, 5825, 693–698, doi: 10.1038/292693a0.

Fletcher, L. N., T. K. Greathouse, S. Guerlet, J. I. Moses, R. A. West, (2018), Saturn’s Seasonally Changing Atmosphere - Thermal Structure, Composition, and Aerosols, Chapter 10, In Saturn in the 21st Century, (ed.) K. H. Baines, F. M. Flasar, N. Krupp, T. Stallard, Cambridge University Press, pp. 251–294, doi: 10.1017/9781316227220.010.

Fletcher, L. N., S. Guerlet, G. S. Orton, R. G. Cosentino, T. Fouchet, P. G. J. Irwin, L. Li, F. M. Flasar, N. Gorius, R. Morales-Juberias, (2017), Disruption of Saturn's quasi-periodic equatorial oscillation by the great northern storm, Nature Astronomy, 1, 11, 765–770, doi: 10.1038/s41550-017-0271-5.

Fletcher, L. N., P. G. J. Irwin, R. K. Achterberg, G. S. Orton, F. M. Flasar, (2016), Seasonal variability of Saturn's tropospheric temperatures, winds and para-H_2 from Cassini far-IR spectroscopy, Icarus, 264, 137–159, doi: 10.1016/j.icarus.2015.09.009.

Fletcher, L. N., P. G. J. Irwin, J. A. Sinclair, G. S. Orton, R. S. Giles, J. Hurley, N. Gorius, R. K. Achterberg, B. E. Hesman, G. L. Bjoraker, (2015), Seasonal evolution of Saturn's polar temperatures and composition, Icarus, 250, 131–153, doi: 10.1016/j.icarus.2014.11.022.

Fletcher, L. N., T. K. Greathouse, G. S. Orton, P. G. J. Irwin, O. Mousis, J. A. Sinclair, R. S. Giles (2014), The origin of nitrogen on Jupiter and Saturn from the N15/N14 ratio, Icarus, 238, 170–190, doi: 10.1016/j.icarus.2014.05.007.

Fletcher, L. N., B. E. Hesman, R. K. Achterberg, P. G. J. Irwin, G. Bjoraker, N. Gorius, J. Hurley, et al., (2012), The origin and evolution of Saturn's 2011–2012 stratospheric vortex, Icarus, 221, 2, 560–586, doi: 10.1016/j.icarus.2012.08.024.

Fletcher, L. N., B. E. Hesman, P. G. J. Irwin, K. H. Baines, T. W. Momary, A. Sanchez-Lavega, F. M. Flasar, et al. (2011), Thermal structure and dynamics of Saturn's northern springtime disturbance, Science, 332, 6036, 1413–1417, doi: 10.1126/science.1204774.

Fletcher, L. N., R. K. Achterberg, T. K. Greathouse, G. S. Orton, B. J. Conrath, A. A. Simon-Miller, N. Teanby, S. Guerlet, P. G. J. Irwin, F. M. Flasar, (2010), Seasonal change on Saturn from Cassini/CIRS observations, 2004–2009, Icarus, 208, 1, 337–352, doi: 10.1016/j.icarus.2010.01.022.

Fletcher, L. N., G. S. Orton, N. A. Teanby, P. G. J. Irwin, (2009a), Phosphine on Jupiter and Saturn from Cassini/CIRS, Icarus, 202, 2, 543–564, doi: 10.1016/j.icarus.2009.03.023.

Fletcher, L. N., G. S. Orton, N. A. Teanby, P. G. J. Irwin, G. L. Bjoraker, (2009b), Methane and its isotopologues on Saturn from Cassini/CIRS observations, Icarus, 199, 2, 351–367, doi: 10.1016/j.icarus.2008.09.019.

Fletcher, L. N., G. J. Irwin, G. S. Orton, N. A. Teanby, R. K. Achterberg, G. L. Bjoraker, P. L. Read, et al., (2008), Temperature and composition of Saturn's polar hot spots and hexagon, Science, 319, 5859, 79–81, doi: 10.1126/science.1149514.

Fletcher, L. N., P. G. J. Irwin, N. A. Teanby, G. S. Orton, P. D. Parrish, S. B. Calcutt, N. Bowles, R. de Kok, C. Howett, F. W. Taylor, (2007a), The meridional phosphine distribution in Saturn's upper troposphere from Cassini/CIRS observations, Icarus, 188, 1, 72–88, doi: 10.1016/j.icarus.2006.10.029.

Fletcher, L. N., P. G. J. Irwin, N. A. Teanby, G. S. Orton, P. D. Parrish, R. de Kok, C. Howett, S. B. Calcutt, N. Bowles, F. W. Taylor, (2007b), Characterising Saturn's vertical temperature structure from Cassini/CIRS, Icarus, 189, 2, 457–478, doi: 10.1016/j.icarus.2007.02.006.

Fouchet, T., J. I. Moses, B. J. Conrath, (2009), Saturn: Composition and Chemistry, Chapter 5, In Saturn from Cassini-Huygens, (eds.) M. K. Dougherty, L. W. Esposito, S. M. Krimigis, pp. 83–112, Springer, Netherlands, doi: 10.1007/978-1-4020-9217-6_5.

Fouchet, T., S. Guerlet, D. F. Strobel, A. A. Simon-Miller, B. Bézard, F. M. Flasar, (2008), An equatorial oscillation in Saturn's middle atmosphere, Nature, 453, 7192, 200–202, doi: 10.1038/nature06912.

Fouchet, T., P. G. J. Irwin, P. Parrish, S. B. Calcutt, F. W. Taylor, C. A. Nixon, T. Owen, (2004a), Search for spatial variation in the jovian $^{15}N/^{14}N$ ratio from Cassini/CIRS observations, Icarus, 172, 1, 50–58, doi: 10.1016/j.icarus.2003.11.011.

Fouchet, T., G. Orton, P. G. J. Irwin, S. B. Calcutt, C. A. Nixon, (2004b), Upper limits on hydrogen halides in Jupiter from Cassini/CIRS observations, Icarus, 170, 1, 237–241, doi: 10.1016/j.icarus.2004.03.013.

French, R. G., H. Salo, C. A. McGhee, L. Dones, (2007), HST observations of azimuthal asymmetry in Saturn's rings, Icarus, 189, no. 2, 493–522.

French, R. G. and P. D. Nicholson, (2000), Saturn's rings II: Particle sizes inferred from stellar occultation data, Icarus, 145, no. 2, 502–523.

Froidevaux, L., K. Matthews, G. Neugebauer, (1981), Thermal response of Saturn's ring particles during and after eclipse, Icarus, 46, no. 1, 18–26, doi: 10.1016/0019-1035(81)90071-3.

Froidevaux, L., (1981), Saturn's rings: Infrared brightness variation with solar elevation, Icarus, 46, no. 1, 4–17, doi: 10.1016/0019-1035(81)90070-1.

Fulchignoni, M., F. Ferri, F. Angrilli, A.J. Ball, A. Bar-Nun, M.A. Barucci, C. Bettanini, G. Bianchini, W. Borucki, G. Colombatti, M. Coradini, et al., (2005), In situ measurements of the physical characteristics of Titan's environment, Nature, 438, 7069, 785–791, doi: 10.1038/nature04314.

Guerlet, S., T. Fouchet, A. Spiga, F. M. Flasar, L. N. Fletcher, B. E. Hesman, N. Gorius, (2018), Equatorial Oscillation and Planetary Wave Activity in Saturn's Stratosphere Through the Cassini Epoch, Journal of Geophysical Research-Planets, 123, 1, 246–261, doi: 10.1002/2017je005419.

Guerlet, S., T. Fouchet, S. Vinatier, A. A. Simon, E. Dartois, A. Spiga, (2015), Stratospheric benzene and hydrocarbon aerosols detected in Saturn's auroral regions, Astronomy & Astrophysics, 580, doi: 10.1051/0004-6361/201424745.

Guerlet, S., T. Fouchet, B. Bézard, F. M. Flasar, A. A. Simon-Miller, (2011), Evolution of the equatorial oscillation in Saturn's stratosphere between 2005 and 2010 from Cassini/CIRS limb data analysis, Geophysical Research Letters, 38, doi: 10.1029/2011GL047192.

Guerlet, S., T. Fouchet, B. Bézard, J. I. Moses, L. N. Fletcher, A. A. Simon-Miller, F. M. Flasar, (2010), Meridional distribution of CH_3C_2H and C_4H_2 in Saturn's stratosphere from CIRS/Cassini limb and nadir observations, Icarus, 209, 2, 682–695, doi: 10.1016/j.icarus.2010.03.033.

Guerlet, S., T. Fouchet, B. Bézard, A. A. Simon-Miller, F. M. Flasar, (2009), Vertical and meridional distribution of ethane, acetylene and propane in Saturn's stratosphere from CIRS/Cassini limb observations, Icarus, 203, 1, 214–232, doi: 10.1016/j.icarus.2009.04.002.

Hamilton, D.P. and J.A. Burns, (1994), Origin of Saturn’s E-ring: Self-sustained, naturally, Nature 264, 550–553, doi: 10.1126/science.264.5158.550.

Hanel, R. A., B. J. Conrath, D. E. Jennings, R. E. Samuelson, (2003), Exploration of the solar system by infrared remote sensing, Cambridge University Press.

Hanel, R., B. Conrath, F. M. Flasar, V. Kunde, W. Maguire, J. Pearl, J. Pirraglia, et al., (1981), Infrared observations of the Saturnian system from Voyager-1, Science, 212, 4491, 192–200, doi: 10.1126/science.212.4491.192.

Hansen, O., (1973), Ten-micron eclipse observations of Io, Europa, and Ganymede, Icarus, 18, 237–246, doi: 10.1016/0019-1035(73)90208-X.

Hapke, B., (1993), Theory of reflectance and emittance spectroscopy, Cambridge University Press, New York.

Hapke, B., (2012), Theory of Reflectance and Emittance Spectroscopy, Cambridge University Press, New York.

Hedman, M. M., P. D. Nicholson, J. N. Cuzzi, et al., (2013) Connections between spectra and structure in Saturn's main rings based on Cassini VIMS data, Icarus, 223, 105–130.

Hedman, M. M., J. A. Burt, J. A. Burns, M. S. Tiscareno, (2010) The shape and dynamics of a heliotropic dusty ringlet in the Cassini division, Icarus, 210, 284–297.

Hedman, M. M., P. D. Nicholson, H. Salo, B. D. Wallis, B. J. Buratti, K. H. Baines, R. H. Brown, R. N. Clark, (2007), Self-gravity wake structures in Saturn's A-ring revealed by Cassini VIMS, The Astronomical Journal, 133, 2624–2629.

Helfenstein, P. and C. C. Porco, (2015), Enceladus' geysers: relation to Geological Features, The Astronomical Journal, 150, no. 3, 96, doi: 10.1088/0004-6256/150/3/96.

Hesman, B. E., G. L. Bjoraker, P. V. Sada, R. K. Achterberg, D. E. Jennings, P. N. Romani, A. W. Lunsford, et al., (2012), Elusive ethylene detected in Saturn's northern storm region, The Astrophysical Journal, 760, 1, doi: 10.1088/0004-637x/760/1/24.

Hesman, B. E., D. E. Jennings, P. V. Sada, G. L. Bjoraker, R. K. Achterberg, A. A. Simon-Miller, C. M. Anderson, et al. (2009), Saturn's latitudinal C_2H_2 and C_2H_6 abundance profiles from Cassini/CIRS and ground-based observations, Icarus, 202, 1, 249–259, doi: 10.1016/j.icarus.2009.02.013.

Hörst, S. M., V. Vuitton, R. V. Yelle, (2008), Origin of oxygen species in Titan's atmosphere, Journal of Geophysical Research: Planets, 113, no. E10, doi: 10.1029/2008JE003135.

Howett, C. J. A., J. R. Spencer, T. Hurford, A. Verbiscer, M. Segura, (2018), Limits on Dione's activity using Cassini/CIRS data, Geophysical Research Letters, vol. 45, Issue 12, pp. 5876–5898, doi: 10.1029/2018GL078161.

Howett, C. J. A., J. R. Spencer, A. Verbiscer, (2017), Characterizing the heat flow from between Enceladus' Tiger Stripes, American Geophysical Union (AGU) Fall Meeting, abstract 272459.

Howett, C. J. A., J. R. Spencer, T. Hurford, A. Verbiscer, M. Segura, (2014), Thermophysical property variations across Dione and Rhea, Icarus, 241, 239–247, doi: 10.1016/j.icarus.2014.05.047.

Howett, C. J. A., J. R. Spencer, T. Hurford, A. Verbiscer, M. Segura, (2012), PacMan returns: An electron-generated thermal anomaly on Tethys, Icarus, 221, 1084–1088, doi: 10.1016/j.icarus.2012.10.013.

Howett C., J .R. Spencer, J. Pearl, M. Segura, (2011a), High heat flow from Enceladus' south polar region measured using 10–600 cm^{-1} Cassini/CIRS data, Journal of Geophysical Research, 116, E03003, doi: 10.1029/2010JE003718.

Howett, C. J. A., J. R. Spencer, P. Schenk, R. E. Johnson, C. Paranicas, T. A Hurford, A. Verbiscer, M. Segura, (2011b), A high-amplitude thermal inertia anomaly of probable magnetospheric origin on Saturn's moon Mimas, Icarus, 216, 221–226, doi: 10.1016/j.icarus.2011.09.007.

Howett, C. J. A., J. R. Spencer, J. Pearl, M. Segura, (2010), Thermal inertia and bolometric Bond albedo values for Mimas, Enceladus, Tethys, Dione, Rhea and Iapetus as derived from Cassini/CIRS measurements, Icarus, 206, 573–593, doi: 10.1016/j.icarus.2009.07.016.

Howett, C. J. A., P. G. J. Irwin, N. A. Teanby, A. Simon-Miller, S. B. Calcutt, L. N. Fletcher, R. de Kok (2007), Meridional variations in stratospheric acetylene and ethane in the southern hemisphere of the saturnian atmosphere as determined from Cassini/CIRS measurements, Icarus, 190, 2, 556–572, doi: 10.1016/j.icarus.2007.03.009.

Hunten, D. M. (1973), Escape of light gases from planetary atmospheres, Journal of the Atmospheric Sciences, 30, 8, 1481–1494, doi: 1 10.1175/1520-0469(1973)030<1481:TEOLGF>2.0.CO;2.

Hurley, J., L. N. Fletcher, P. G. J. Irwin, S. B. Calcutt, J. A. Sinclair, C. Merlet (2012a), Latitudinal variation of upper tropospheric NH_3 on Saturn derived from Cassini/CIRS far-infrared measurements, Planetary and Space Science, 73, 1, 347–363, doi: 10.1016/j.pss.2012.08.003.

Hurley, J., P. G. J. Irwin, L. N. Fletcher, J. I. Moses, B. Hesman, J. Sinclair, C. Merlet, (2012b), Observations of upper tropospheric acetylene on Saturn: No apparent correlation with 2000 km-sized thunderstorms, Planetary and Space Science, 65, 1, 21–37, doi: 10.1016/j.pss.2011.12.026.

Ingersoll, A. and S. P Ewald, (2017), Decadal timescale variability of the Enceladus plumes inferred from Cassini images, Icarus, 282, 260–272, doi: 10.1016/j.icarus.2016.09.018.

Ingersoll, A. and A. Pankine, (2010), Subsurface heat transfer on Enceladus: conditions under which melting occurs, Icarus, 20, 594–607, doi: 10.1016/j.icarus.2009.09.015.

Irwin, P., N. Teanby, R. de Kok, et al., (2008), The Nemesis planetary atmosphere radiative transfer and retrieval tool, Journal of Quantitative Spectroscopy & Radiative Transfer, 109, 6, 1136–1150, doi: 10.1016/j.jqsrt.2007.11.006.

Irwin, P. G. J., P. Parrish, T. Fouchet, S. B. Calcutt, F. W. Taylor, A. A. Simon-Miller, C. A. Nixon, (2004), Retrievals of jovian tropospheric phosphine from Cassini/CIRS, Icarus, 172, 1, 37–49, doi: 10.1016/j.icarus.2003.09.027.

Jacquinet-Husson, N., R. Armante, N. A. Scott, A. Chédin, L. Crépeau, C. Boutammine, A. Bouhdaoui, et al., (2016), The 2015 edition of the GEISA spectroscopic database, Journal of Molecular Spectroscopy, 327, 31–72, doi: 10.1016/j.jms.2016.06.007.

- - - - - - - - - - - - - -

Janssen, M. A., R. D. Lorenz, R. West, F. Paganelli, R. M. Lopes, Randolph L. Kirk, C. Elachi, et al., (2009), Titan's surface at 2.2-cm wavelength imaged by the Cassini RADAR radiometer: Calibration and first results, Icarus, 200, 1, 222–239, doi: 10.1016/j.icarus.2008.10.017.

Jennings, D. E., T. Tokano, V. Cottini, C. A. Nixon, R. K. Achterberg, F. M. Flasar, V. G. Kunde, et al., (2019), Titan surface temperatures during the Cassini Mission, The Astrophysical Journal Letters, 877, 1, L8, doi: 10.3847/2041-8213/ab1f91.

Jennings, D. E., F. M. Flasar, V. G. Kunde, C. A. Nixon, M. E. Segura, P. N. Romani, N. Gorius, et al., (2017), Composite infrared spectrometer (CIRS) on Cassini, Applied Optics, 56, no. 18, 5274–5294, doi: 10.1364/AO.56.005274.

Jennings, D. E., V. Cottini, C. A. Nixon, R. K. Achterberg, F. M. Flasar, V. G. Kunde, P. N. Romani, et al., (2016), Surface temperatures on Titan during northern winter and spring, The Astrophysical Journal Letters, 816, 1, doi: 10.3847/2041-8205/816/1/l17.

Jennings, D. E., R. K. Achterberg, V. Cottini, C. M. Anderson, F. M. Flasar, C. A. Nixon, G. L. Bjoraker, et al., (2015), Evolution of the far-infrared cloud at Titan's south pole, The Astrophysical Journal Letters, 804, 2, doi: 10.1088/2041-8205/804/2/l34.

Jennings, D. E., C. M. Anderson, R. E. Samuelson, F. M. Flasar, C. A. Nixon, G. L. Bjoraker, P. N. Romani, et al., (2012a), First observation in the south of Titan's far-infrared 220 cm^{-1} cloud, The Astrophysical Journal Letters, 761, 1, doi: 10.1088/2041-8205/761/1/l15.

Jennings, D. E., C. M. Anderson, R. E. Samuelson, F. M. Flasar, C. A. Nixon, V. G. Kunde, R. K. Achterberg, et al., (2012b), Seasonal disappearance of far-infrared haze in Titan's stratosphere, The Astrophysical Journal Letters, 754, 1, doi: 10.1088/2041-8205/754/1/l3.

Jennings, D. E., V. Cottini, C. A. Nixon, F. M. Flasar, V. G. Kunde, R. E. Samuelson, P. N. Romani, et al. (2011), Seasonal changes in Titan's surface temperatures, The Astrophysical Journal Letters, 737, 1, doi: 10.1088/2041-8205/737/1/L15.

Jennings, D. E., F. M. Flasar, V. G. Kunde, R. E. Samuelson, J. C. Pearl, C. A. Nixon, R. C. Carlson, et al., (2009), Titan's surface brightness temperatures, The Astrophysical Journal Letters, 691, 2, L103–L105, doi: 10.1088/0004-637X/691/2/L103.

Jennings, D. E., C. A. Nixon, A. Jolly, B. Bézard, A. Coustenis, S. Vinatier, P. G. J. Irwin, et al. (2008), Isotopic ratios in Titan's atmosphere from Cassini CIRS limb sounding: HC_3N in the north, The Astrophysical Journal Letters, 681, 2, L109–L111, doi: 10.1086/590534.

Jolly, A., V. Cottini, A. Fayt, L. Manceron, F. Kwabia-Tchana, Y. Benilan, J. C. Guillemin, C. Nixon, P. Irwin, (2015), Gas phase dicyanoacetylene (C_4N_2) on Titan: New experimental and theoretical spectroscopy results applied to Cassini CIRS data, Icarus, 248, 340–346, doi: 10.1016/j.icarus.2014.10.049.

Jolly, A., A. Fayt, Y. Benilan, D. Jacquemart, C. A. Nixon, D. E. Jennings, (2010), The v^8 bending mode of diacetylene: from laboratory spectroscopy to the detection of ^{13}C isotopologues in Titan's atmosphere, The Astrophysical Journal, 714, 1, 852–859, doi: 10.1088/0004-637X/714/1/852.

Jones, G. H., E. Roussos, N. Krupp, U. Beckmann, A. J. Coates, F. Crary, I. Dandouras, et al., (2008), The dust halo of Saturn's largest icy moon, Rhea, Science, 319, no. 5868, 1380–1384.

Joseph, J. H., W. J. Wiscombe, J. A. Weinman, (1976), The delta-Eddington approximation for radiative flux transfer, Journal of the Atmospheric Sciences, 33, pp. 2452–2459.

Kawata, Y., (1983), Infrared brightness temperature of Saturn's rings based on the inhomogeneous multilayer assumption, Icarus 56, no. 3, 453–464.

Khanna, R. K., M. A. Perera-Jarmer, M. J. Ospina, (1987), Vibrational infrared and Raman spectra of dicyanoacetylene, Spectrochimica Acta Part A: Molecular Spectroscopy, 43, no. 3, 421–425.

Khare, B. N., C. Sagan, E. T. Arakawa, F. Suits, T. A. Callcott, M. W. Williams, (1984), Optical constants of organic tholins produced in a simulated Titanian atmosphere: From soft X-ray to microwave frequencies, Icarus, 60, no. 1, 127–137.

Khare, B. N., C. Sagan, W. R. Thompson, E. T. Arakawa, F. Suits, T. A. Callcott, M. W. Williams, et al., (1984), The organic aerosols of Titan, Advances in Space Research, 4, no. 12, 59–68.

Koskinen, T. T. and S. Guerlet, (2018), Atmospheric structure and helium abundance on Saturn from Cassini/UVIS and CIRS observations, Icarus, 307, 161–171, doi: 10.1016/j.icarus.2018.02.020.

Kunde, V. G., F. M. Flasar, D. E. Jennings, B. Bézard, D. F. Strobel, B. J. Conrath, C. A. Nixon, et al., (2004), Jupiter's atmospheric composition from the Cassini thermal infrared spectroscopy experiment, Science, 305, 5690, 1582–1586, doi: 10.1126/science.1100240.

Kunde, V. G., P. A. R. Ade, R. D. Barney, D. Bergman, J.-F. Bonnal, R. Borelli, D. Boyd, et al., (1996), Cassini infrared Fourier spectroscopic investigation, In Cassini-Huygens: A Mission to the Saturnian Systems, International Symposium on Optical Science, Engineering, and Instrumentation, Denver, CO, vol. 2803, pp. 162–177, doi: 10.1117/12.253416.

Lara, L. M., E. Lellouch, J. J. López-Moreno, R. Rodrigo, (1996), Vertical distribution of Titan's atmospheric neutral constituents, Journal of Geophysical Research: Planets, 101, no. E10, 23261–23283.

Le Gall, A., C. Leyrat, M. A. Janssen, G. Choblet, G. Tobie, O. Bourgeois, A. Lucas, et al., (2017), Thermally anomalous features in the subsurface of Enceladus’s south polar terrain, Nature, Astronomy, 1, no. 4, article 0063, doi: 10.1038/s41550-017-0063.

Lebonnois, S., F. M. Flasar, T. Tokano, C. E. Newman, (2014), The general circulation of Titan's lower and middle atmosphere, Chapter 4, In Titan: Interior, Surface, Atmosphere, and Space Environment, (eds.) I. Müller-Wodarg, C. A. Griffith, E. Lellouch, T. E. Cravens, Cambridge University Press, pp. 122–157.

Lebonnois, S., J. Burgalat, P. Rannou, B. Charnay, (2012), Titan global climate model: A new 3-dimensional version of the IPSL Titan GCM, Icarus, 218, 1, 707–722, doi: 10.1016/j.icarus.2011.11.032.

Lebonnois, S., P. Rannou, F. Hourdin (2009), The coupling of winds, aerosols and chemistry in Titan's atmosphere, Philosophical Transactions of the Royal Society a-Mathematical Physical and Engineering Sciences, 367, 1889, 665–682, doi: 10.1098/rsta.2008.0243.

Lellouch, E., B. Bézard, F. M. Flasar, S. Vinatier, R. Achterberg, C. A. Nixon, G. L. Bjoraker, N. Gorius, (2014), The distribution of methane in Titan's stratosphere from Cassini/CIRS observations, Icarus, 231, 323–337, doi: 10.1016/j.icarus.2013.12.016.

Lellouch, E., B. Bézard, D. F. Strobel, G. L. Bjoraker, F. M. Flasar, P. N. Romani, (2006), On the HCN and CO_2 abundance and distribution in Jupiter's stratosphere, Icarus, 184, 2, 478–497, doi: 10.1016/j.icarus.2006.05.018.

Leovy, C. B., A. J. Friedson, G. S. Orton, (1991), The quasiquadrennial oscillation of Jupiter's equatorial stratosphere, Nature, 354, 6352, 380–382, doi: 10.1038/354380a0.

Leyrat, C., L. J. Spilker, N. Altobelli, S. Pilorz, C. Ferrari, (2008a). Infrared observations of Saturn's rings by Cassini CIRS: Phase angle and local time dependence, Planetary and Space Science, 56, 117–133.

Leyrat, C., C. Ferrari, S. Charnoz, et al., (2008b), Spinning particles in Saturn's C-ring from mid-infrared observations: Pre-Cassini mission results, Icarus, 196, 625–641.

Li, L., X. Jiang, H. J. Trammell, Y. Pan, J. Hernandez, B. J. Conrath, P. J. Gierasch, et al., (2015), Saturn's giant storm and global radiant energy, Geophysical Research Letters, 42, 7, 2144–2148, doi: 10.1002/2015GL063763.

Li, L., (2015), Dimming Titan revealed by the Cassini observations, Scientific Reports 5, article 8239, doi: 10.1038/srep08239.

Li, L., R. K. Achterberg, B. J. Conrath, P. J. Gierasch, M. A. Smith, A. A. Simon-Miller, C. A. Nixon, et al. (2013), Strong temporal variation over one Saturnian year: from Voyager to Cassini, Scientific Reports, 3, doi: 10.1038/srep02410.

Li, L. M., K. H. Baines, M. A. Smith, R. A. West, S. Pérez-Hoyos, H. J. Trammell, A. A. Simon-Miller, et al. (2012), Emitted power of Jupiter based on Cassini CIRS and VIMS observations, Journal of Geophysical Research: Planets, 117, doi: 10.1029/2012je004191.

Li, L. M., X. Jiang, A. P. Ingersoll, A. D. Del Genio, C. C. Porco, R. A. West, A. R. Vasavada, et al., (2011a), Equatorial winds on Saturn and the stratospheric oscillation, Nature Geoscience, 4, 11, 750–752, doi: 10.1038/ngeo1292.

Li, L. M., C. A. Nixon, R. K. Achterberg, M. A. Smith, N. J. P. Gorius, X. Jiang, B. J. Conrath, et al. (2011b), The global energy balance of Titan, Geophysical Research Letters, 38, doi: L2320110.1029/2011gl050053.

Li, L., B. J. Conrath, P. J. Gierasch, R. K. Achterberg, C. A. Nixon, A. A. Simon-Miller, F. M. Flasar, et al., (2010), Saturn's emitted power, Journal of Geophysical Research: Planets, 115, doi: 10.1029/2010JE003631.

Li, L., P. J. Gierasch, R. K. Achterberg, B. J. Conrath, F. M. Flasar, A. R. Vasavada, A. P. Ingersoll, D. Banfield, A. A. Simon-Miller, L. N. Fletcher, (2008), Strong jet and a new

thermal wave in Saturn's equatorial stratosphere, Geophysical Research Letters, 35, 23, doi: 10.1029/2008GL035515.

Li, L. M., A. P. Ingersoll, A. R. Vasavada, A. A. Simon-Miller, R. K. Achterberg, S. P. Ewald, U. A. Dyudina, C. C. Porco, R. A. West, F. M. Flasar, (2006), Waves in Jupiter's atmosphere observed by the Cassini ISS and CIRS instruments, Icarus, 185, 2, 416–429, doi: 10.1016/j.icarus.2006.08.005.

Lombardo, N. A., C. A. Nixon, R. K. Achterberg, A. Jolly, K. Sung, P. G. J. Irwin, F. M. Flasar, (2019), Spatial and seasonal variations in C_3H_x hydrocarbon abundance in Titan's stratosphere from Cassini CIRS observations, Icarus, 317, 454–469.

Lopes, R. M. C., R. L. Kirk, K. L. Mitchell, A. LeGall, J. W. Barnes, A. Hayes, J. Kargel, et al., (2013), Cryovolcanism on Titan: New results from Cassini RADAR and VIMS, Journal of Geophysical Research: Planets, 118, 3, 416–435, doi: 10.1002/jgre.20062.

Lorenz, R. D., B. W. Stiles, O. Aharonson, A. Lucas, A. G. Hayes, R. L. Kirk, H. A. Zebker, et al., (2013), A global topographic map of Titan, Icarus, 225, 1, 367–377, doi: 10.1016/j.icarus.2013.04.002.

Lorenz, R. D., M. E. Brown, F. M. Flasar, (2009), Seasonal change on Titan, Chapter 14, In Titan from Cassini-Huygens, (eds.) R. H. Brown, J.-P. Lebreton, J. H. Waite, Springer Netherlands, pp. 353–372, doi: 10.1007/978-1-4020-9215-2_14.

Lorenz, R. D., S. Wall, J. Radebaugh, G. Boubin, E. Reffet, M. Janssen, E. Stofan, et al., (2006), The sand seas of Titan: Cassini RADAR observations of longitudinal dunes, Science, 312, 5774, 724–727, doi: 10.1126/science.1123257.

Lumme, K. and E. Bowell, (1981a) Radiative transfer in the surfaces of atmosphereless bodies. I. Theory, The Astronomical Journal, 86, 1694–1704.

Lumme, K. and E. Bowell, (1981b). Radiative transfer in the surfaces of atmosphereless bodies. II. Interpretation of phase curves, The Astronomical Journal, 86, 1705–1721.

Lumme, K. and W. M. Irvine, (1976), Photometry of Saturn's rings, The Astronomical Journal, 81, 863–893.

Matcheva, K. I., B. J. Conrath, P. J. Gierasch, F. M. Flasar, (2005), The cloud structure of the jovian atmosphere as seen by the Cassini/CIRS experiment, Icarus, 179, 2, 432–448, doi: 10.1016/j.icarus.2005.06.020.

McKay, C. P., J. B. Pollack, R. Courtin, (1991), The greenhouse and antigreenhouse effects on Titan, Science, 253, 5024, 1118–1121, doi: 10.1126/science.11538492.

Meyer, J. and J. Wisdom (2007), Tidal heating in Enceladus, Icarus 188, 535–539, doi: 10.1016/j.icarus.2007.03.001.

Mie, G. (1908), Beiträge zur Optik trüber Medien, speziell kolloidaler Metallösungen, Annalen der physic, 330, no. 3, 377–445, doi: 10.1002/andp.19083300302.

Modest, M. F., (2003), Radiative heat transfer, Academic Press, An imprint of Elsevier Science, San Diego, CA.

Morishima, R., N. Turner, L. Spilker, (2017), Surface roughness of Saturn's rings and ring particles inferred from thermal phase curves, Icarus, 295, 74–88.

Morishima, R., L. Spilker, S. Brooks, E. Deau, S. Pilorz, (2016). Incomplete cooling down of Saturn's A-ring at solar equinox: Implication for seasonal thermal inertia and internal structure of ring particles, Icarus, 279, 2–19.

Morishima, R., L. Spilker, N. Truner, (2014), Azimuthal temperature modulations of Saturn's A-ring caused by self-gravity wakes, Icarus, 228, 247–259.

Morishima, R., S. G. Edgington, L. Spilker, (2012). Regolith grain sizes of Saturn's rings inferred from Cassini-CIRS far-infrared spectra, Icarus, 221, 888–899.

Morishima, R., L. Spilker, K. Ohtsuki, (2011), A multilayer model for thermal infrared emission of Saturns rings III: Thermal inertia inferred from Cassini CIRS, Icarus, 215, 107–127.

Morishima, R., L. Spilker, H. Salo, et al., (2010). A multilayer model for thermal infrared emission of Saturns rings II: Albedo, spins, and vertical mixing of ring particles inferred from Cassini CIRS, Icarus, 210, 330–345.

Morishima, R., H. Salo, K. Ohtsuki, (2009), A multilayer model for thermal infrared emission of Saturns rings: Basic formulation and implications for Earth-based observations, Icarus, 201, 634–654.

Morishima, R. and H. Salo, (2006), Simulations of dense planetary rings: IV. Spinning self-gravitating particles with size distribution, Icarus, 181, 272–291.

Morishima, R. and H. Salo, (2004), Spin rates of small moonlets embedded in planetary rings. I. Three-body calculations, Icarus, 167, 330–346.

Morrison, D. and D. Cruikshank, (1973), Thermal properties of the Galilean satellites, Icarus, 18, 224–236, doi: 10.1016/0019-1035(73)90207-8.

Neish, C. D. and R. D. Lorenz, (2011), Titan's global crater population: A new assessment, Planetary and Space Science, 60, 1, 26–33, doi: 10.1016/j.pss.2011.02.016.

Nicholson, P. D. and M. M. Hedman, (2010). Self-gravity wake parameters in Saturn's A and B rings, Icarus, 206, 410–423.

Nicholson, P. D., M. M. Hedman, R. N. Clark, M. R. Showalter, D. P. Cruikshank, J. N. Cuzzi, G. Filacchione, et al., (2008), A close look at Saturn's rings with Cassini VIMS, Icaurs, 193, 182–212.

Niemann, H. B., S. K. Atreya, J. E. Demick, D. Gautier, J. A. Haberman, D. N. Harpold, W. T. Kasprzak, J. I. Lunine, T. C. Owen, F. Raulin, (2010), Composition of Titan's lower atmosphere and simple surface volatiles as measured by the Cassini-Huygens probe gas chromatograph mass spectrometer experiment, Journal of Geophysical Research: Planets, 115, doi: 10.1029/2010je003659.

Niemann, H. B., S. K. Atreya, S. J. Bauer, G. R. Carignan, J. E. Demick, R. L. Frost, D. Gautier, et al., (2005), The abundances of constituents of Titan's atmosphere from the GCMS instrument on the Huygens probe, Nature, 438, 7069, 779–784, doi: 10.1038/nature04122.

Nixon, C. A., R. D. Lorenz, R. K. Achterberg, A. Buch, P. Coll, R. N. Clark, R. Courtin, et al., (2018), Titan's cold case files-Outstanding questions after Cassini-Huygens, Planetary and Space Science, 155, 50–72, doi: 10.1016/j.pss.2018.02.009.

Nixon, C. A., R. K. Achterberg, M. Adamkovics, B. Bézard, G. L. Bjoraker, T. Cornet, A. G. Hayes, et al., (2016), Titan Science with the James Webb Space Telescope, Publications of the Astronomical Society of the Pacific, 128, 959, doi: 10.1088/1538-3873/128/959/018007.

Nixon, C. A., D. E. Jennings, B. Bézard, S. Vinatier, N. A. Teanby, K. Sung, T. M. Ansty, et al., (2013a), Detection of propene in Titan's stratosphere, Astrophysical Journal Letters, 776, 1, doi: 10.1088/2041-8205/776/1/l14.

Nixon, C. A., N. A. Teanby, P. G. J. Irwin, S. M. Horst, (2013b), Upper limits for PH_3 and H_2S in Titan's atmosphere from Cassini CIRS, Icarus, 224, 1, 253–256, doi: 10.1016/j.icarus.2013.02.024.

Nixon, C. A., B. Temelso, S. Vinatier, N. A. Teanby, B. Bézard, R. K. Achterberg, K. E. Mandt, et al., (2012), Isotopic ratios in Titan's methane: measurements and modeling, The Astrophysical Journal, 749, 2, doi: 10.1088/0004-637X/749/2/159.

Nixon, C. A., R. K. Achterberg, P. N. Romani, M. Allen, X. Zhang, N. A. Teanby, P. G. J. Irwin, F. M. Flasar, (2010a), Abundances of Jupiter's trace hydrocarbons from Voyager and Cassini, Planetary and Space Science, 58, 13, 1667–1680, doi: 10.1016/j.pss.010.05.008.

Nixon, C. A., R. K. Achterberg, N. A. Teanby, P. G. J. Irwin, J.-M. Flaud, I. Kleiner, A. Dehayem-Kamadjeu, et al. (2010b), Upper limits for undetected trace species in the stratosphere of Titan, Faraday Discussions, 147, 65–81, doi: 10.1039/c003771k.

Nixon, C. A., D. E. Jennings, J. M. Flaud, B. Bézard, N. A. Teanby, P. G. J. Irwin, T. M. Ansty, A. Coustenis, S. Vinatier, F. M. Flasar, (2009a), Titan's prolific propane: The Cassini CIRS perspective, Planetary and Space Science, 57, 13, 1573–1585, doi: 10.1016/j.pss.2009.06.021.

Nixon, C. A., N. A. Teanby, S. B. Calcutt, S. Aslam, D. E. Jennings, V. G. Kunde, F. M. Flasar, et al, (2009b), Infrared limb sounding of Titan with the Cassini Composite InfraRed Spectrometer: effects of the mid-IR detector spatial responses, Applied Optics, 48, no. 10, 1912–1925.

Nixon, C. A., et al. (2008a), The 12C/13C isotopic ratio in Titan hydrocarbons from Cassini/CIRS infrared spectra, Icarus, 195, 2, 778–791, doi: 10.1016/j.icarus.2008.01.012.

Nixon, C., D. Jennings, B. Bézard, et al., (2008b), Isotopic ratios in Titan's atmosphere from Cassini CIRS limb sounding: CO2 at low and midlatitudes, The Astrophysical Journal Letters, 681, 2, L101–L103, doi: 10.1086/590553.

Nixon, C. A., R. K. Achterberg, B. J. Conrath, P. G. J. Irwin, N. A. Teanby, T. Fouchet, P. D. Parrish, et al., (2007), Meridional variations of C_2H_2 and C_2H_6 in Jupiter's atmosphere from Cassini CIRS infrared spectra, Icarus, 188, 1, 47–71, doi: 10.1016/j.icarus.2006.11.016.

Ohtsuki, K., (2006a), Rotation rate and velocity dispersion of planetary ring particles with size distribution: I. Formulation and analytic calculation, Icarus, 183, no. 2, 373–383.

Ohtsuki, K., (2006b), Rotation rate and velocity dispersion of planetary ring particles with size distribution II. Numerical simulation for gravitating particles, Icarus, 183, no. 2, 384–395.

Ohtsuki, K. and D. Toyama, (2005), Local N-body simulations for the rotation rates of particles in planetary rings, The Astronomical Journal, 130, no. 3, 1302.

Orton, G. S., L. N. Fletcher, C. M. Lisse, P. W. Chodas, A. Cheng, P. A. Yanamandra-Fisher, K. H. Baines, et al., (2011), The atmospheric influence, size and possible asteroidal nature of the July 2009 Jupiter impactor, Icarus, 211, no. 1, 587–602.

Orton, G. S., P. A. Yanamandra-Fisher, B. M. Fisher, A. J. Friedson, P. D. Parrish, J. F. Nelson, A. S. Bauermeister, et al., (2008), Semi-annual oscillations in Saturn's low-latitude stratospheric temperatures, Nature, 453, 7192, 196–199, doi: 10.1038/nature06897.

Orton, G. S., A. James Friedson, K. H. Baines, T. Z. Martin, R. A. West, J. Caldwell, H. B. Hammel, et al., (1991), Thermal maps of Jupiter: Spatial organization and time dependence of stratospheric temperatures, 1980 to 1990, Science, 252, 5005, 537–542, doi: 10.1126/science.252.5005.537.

Paige, D., J. Bachman, K. Keegan, (1994), Thermal and albedo mapping of the polar regions of Mars using Viking thermal mapper observations: 1. North polar region, Journal of Geophysical Research, vol. 99, Issue E12, pp. 25959–25991, doi: 10.1029/93JE03428.

Paranicas, C., E. Roussos, R. Decker, R. Johnson, A. Hendrix, P. Schenk, T. Cassidy, B. Dalton, C. J. Howett, P. Kollmann, W. Patterson, K. Hand, T. Nordheim, N. Krupp, D. Mitchell, (2014), The lens feature on the inner saturnian satellites, Icarus, 234, 155–161, doi: 10.1016/j.icarus.2014.02.026.

Paranicas, C., E. Roussos, N. Krupp, P. Kollmann, A. R. Hendrix, T. Cassidy, R. E. Johnson, P. Schenk G. Jones, J. Carbary, D. G. Mitchell, K. Dialynas, (2012), Energetic charged particle weathering of Saturn’s inner satellites, Planetary Space Science, 61, 60–65, doi: 10.1016/j.pss.2011.02.012.

Pierel, J. D. R., C. A. Nixon, E. Lellouch, L. N. Fletcher, G. L. Bjoraker, R. K. Achterberg, B. Bézard, B. E. Hesman, P. G. J. Irwin, F. M. Flasar, (2017), D/H Ratios on Saturn and Jupiter from Cassini CIRS, the Astronomical Journal, 154, 5, doi: 10.3847/1538-3881/aa899d.

Pilorz, S., M. Showalter, S. Edgington, (2018a), Occultations of the star Eta Carinae observed with Cassini CIRS, Icarus, in preparation.

Pilorz, S., et al., (2018b). Thermal emissivity, Icarus, in preparation.

Pilorz, S., N. Altobelli, J. Colwell, M. Showalter, (2015), Thermal transport in Saturn’s B-ring inferred from Cassini CIRS, Icarus, 254, 157–177.

Pitman, K. M., B. J. Buratti, J. A. Mosher, (2010), Disk-integrated bolometric Bond albedos and rotational light curves of saturnian satellites from Cassini Visual and Infrared Mapping Spectrometer, Icarus ,206, 537–560, doi: 10.1016/j.icarus.2009.12.001.

Pitman, K. M., B. J. Buratti, J. A. Mosher, J. M. Bauer, T. W. Momary, Robert H. Brown, P. D. Nicholson, M. M. Hedman, (2008), First high solar phase angle observations of Rhea using Cassini VIMS: Upper limits on water vapor and geologic activity, The Astrophysical Journal Letters, 680, no. 1, L65.

Porco, C. C., J. W. Weiss, D. C. Richardson, L. Dones, T. Quinn, H. Throop, (2008), Simulations of the dynamical and light-scattering behavior of Saturn's rings and the derivation of ring particle and disk properties, The Astronomical Journal, 136, no. 5, 2172.

Porco, C. C., P. Helfenstein, P. C. Thomas, A. P. Ingersoll, J. Wisdom, R. West, G. Neukum, et al., (2006), Cassini observes the active south pole of Enceladus, Science, 311, 1393–1401, doi: 10.1126/science.1123013.

Porco, C. C., E. Baker, J. Barbara, K. Beurle, A. Brahic, J. A. Burns, S. Charnoz, et al, (2005), Cassini imaging science: Initial results on Saturn's rings and small satellites, Science, 307, no. 5713, 1226–1236.

Poulet, F., D. P. Cruikshank, J. N. Cuzzi, T. L. Roush, R. G. French, (2003), Compositions of Saturn's rings A, B, and C from high resolution near-infrared spectroscopic observations, Astronomy & Astrophysics, 412, no. 1, 305–316.

Rathbun, J., J. Spencer, L. Tamppari, T. Martin, L. Bernard, L.Travis, (2004), Mapping of Io's thermal radiation by the Galileo Photopolarimeter–Radiometer (PPR) Instrument, Icarus, 169, 127–139, doi: 10.1016/j.icarus.2003.12.021.

Read, P. L., T. E. Dowling, G. Schubert, (2009), Saturn's rotation period from its atmospheric planetary-wave configuration, Nature, 460, 7255, 608–610, doi: 10.1038/nature08194.

Read, P. L., P. J. Gierasch, B. J. Conrath, A. Simon-Miller, T. Fouchet, Y. H. Yamazaki, (2006), Mapping potential-vorticity dynamics on Jupiter. I: Zonal-mean circulation from Cassini and Voyager 1 data, Quarterly Journal of the Royal Meteorological Society, 132, 618, 1577–1603, doi: 10.1256/qj.05.34.

Reffet, E., M. Verdier, C. Ferrari, (2015). Thickness of Saturn's B-ring as derived from seasonal temperature variations measured by Cassini CIRS, Icarus, 254, 276–286.

Ries, P. A. and M. Janssen, (2015), A large-scale anomaly in Enceladus' microwave emission, Icarus, 257, 88–102.

Robbins, S. J., G. R. Stewart, M. C. Lewis, J. E. Colwell, M. Sremčević, (2010), Estimating the masses of Saturn's A and B rings from high-optical depth N-body simulations and stellar occultations, Icarus, 206, no. 2, 431–445.

Rodgers, C. D., (2000), Inverse Methods for Atmospheric Sounding-Theory and Practice, Series on Atmospheric Oceanic and Planetary Physics, World Scientific Publishing Co. Pte. Ltd., Singapore, vol. 2.

- - - - - - - - - - - - - -

Roman, M. T., R. A. West, D. J. Banfield, P. J. Gierasch, R. K. Achterberg, C. A. Nixon, P. C. Thomas (2009), Determining a tilt in Titan's north-south albedo asymmetry from Cassini images, Icarus, 203, 1, 242–249, doi: 10.1016/j.icarus.2009.04.021.

Ross, M. and G. Schubert, (1989), Viscoelastic models of tidal heating in Enceladus, Icarus, 78, 90–101, doi: 10.1016/0019-1035(89)90071-7.

Rothman, L. S. and I. E. Gordon, (2013), The HITRAN molecular database, In Eighth International Conference on Atomic and Molecular Data and Their Applications (ICAMDATA), (eds.) J. D. Gillaspy, W. L. Wiese, Y. A. Podpaly, 30 September–4 October 2012, Gaithersburg, MD, vol. 1545, pp. 223–231, doi: 10.1063/1.4815858.

Rubincam, D. P., (2006), Saturn's rings, the Yarkovsky effects, and the Ring of Fire, Icarus 184, no. 2, 532–542.

Salmon, J., S. Charnoz, A. Crida, A. Brahic, (2010), Long-term and large-scale viscous evolution of dense planetary rings, Icarus, 209, no. 2, 771–785.

Salo, H. and R. G. French, (2010). The opposition and tilt effects of Saturn’s rings from HST observations, Icarus, 210, 785–816.

Salo, H. and R. Karjalainen, (2003), Photometric modeling of Saturn’s rings. I. Monte Carlo method and the effect of nonzero volume filling factor, Icarus, 164, 428–460.

Salo, H., (1995), Simulations of dense planetary rings. III. Self-gravitating identical particles, Icarus, 117, 287–312.

Salo, H., (1987), Numerical simulations of collisions between rotating particles, Icarus, 70, 37–51.

Samuelson, R. E., M. D. Smith, R. K. Achterberg, J. C. Pearl, (2007), Cassini CIRS update on stratospheric ices at Titan's winter pole, Icarus, 18, 1, 63–71, doi: 10.1016/j.icarus.2007.02.005.

Samuelson, R. E., L. A. Mayo, M. A. Knuckles, R. J. Khanna, (1997), C_4N_2 ice in Titan's north polar stratosphere, Planetary and Space Science, 45, 8, 941–948, doi: 10.1016/s0032-0633(97)00088-3.

Samuelson, R. E., (1985), Clouds and aerosols of Titan's atmosphere, In ESA Special Publication, vol. 241.

Samuelson, R. E., R. A. Hanel, V. G. Kunde, W. C. Maguire, (1981), Mean molecular-weight and hydrogen abundance of titans atmosphere, Nature, 292, 5825, 688-693, doi: 10.1038/292688a0.

Sánchez-Lavega, A., G. Fischer, L. N. Fletcher, E. García-Melendo, B. Hesman, S. Pérez-Hoyos, K. M. Sayanagi, L. A. Sromovsky, (2016), The great Saturn storm of 2010–2011, Chapter 13, In Saturn in the 21st Century, (eds.) K. H. Baines, F. M. Flasar, N. Krupp, T. Stallard, Cambridge University Press, pp. 377–416, doi: 10.1017/9781316227220.013.

Sayanagi, K. M., K. H. Baines, U. A. Dyudina, L. N. Fletcher, A. Sánchez-Lavega, R. A. West, (2018), Saturn’s Polar Atmosphere, Chapter 12, In Saturn in the 21st Century, (eds.)

K. H. Baines, F. M. Flasar, N. Krupp, T. Stallard, Cambridge University Press, pp. 337–376, doi: 10.1017/9781316227220.013.

Sayanagi, K. M., U. A. Dyudina, S. P. Ewald, G. Fischer, A. P. Ingersoll, W. S. Kurth, G. D. Muro, C. C. Porco, R. A. West, (2013), Dynamics of Saturn's great storm of 2010–2011 from Cassini ISS and RPWS, Icarus 223, no. 1, 460–478.

Schenk, P., D. P. Hamilton, R. E. Johnson, W. B. McKinnon, C. Paranicas, J. Schmidt, M. R. Showalter, (2011), Plasma, plumes and rings: Saturn system dynamics as recorded in global color patters on its midsize icy satellites, Icarus, 211, 740–757, doi: 10.1016/j.icarus.2010.08.016.

Schinder, P. J., F. M. Flasar, E. A. Marouf, R. G. French, C. A. McGhee, A. J. Kliore, N. J. Rappaport, E. Barbinis, D. Fleischman, A. Anabtawi, (2012), The structure of Titan's atmosphere from Cassini radio occultations: Occultations from the Prime and Equinox missions, Icarus, 221, 2, 1020–1031, doi: 10.1016/j.icarus.2012.10.021.

Schinder, P. J., F. M. Flasar, E. A. Marouf, R. G. French, C. A. McGhee, A. J. Kliore, N. J. Rappaport, E. Barbinis, D. Fleischman, A. Anabtawi (2011a), Saturn's equatorial oscillation: Evidence of descending thermal structure from Cassini radio occultations, Geophysical Research Letters, 38, doi: 10.1029/2011GL047191.

Schinder, P. J., F. M. Flasar, E. A. Marouf, R. G. French, C. A. McGhee, A. J. Kliore, N. J. Rappaport, E. Barbinis, D. Fleischman, A. Anabtawi, (2011b), The structure of Titan's atmosphere from Cassini radio occultations, Icarus, 215, 2, 460–474, doi: 10.1016/j.icarus.2011.07.030.

Schubert, G., J. D. Anderson, B. J. Travis, J. Palguta, (2007), Enceladus: Present internal structure and differentiation by early and long-term radiogenic heating, Icarus, 188, no. 2, 345–355.

Simon-Miller, A. A., B. J. Conrath, P. J. Gierasch, G. S. Orton, R. K. Achterberg, F. M. Flasar, B. M. Fisher (2006), Jupiter's atmospheric temperatures: from Voyager IRIS to Cassini CIRS, Icarus, 180, 1, 98–112, doi: 10.1016/j.icarus.2005.07.019.

Simon-Miller, A. A., P. J. Gierasch, R. F. Beebe, B. Conrath, F. M. Flasar, R. K. Achterberg, Cassini CIRS Team, (2002), New observational results concerning Jupiter's Great Red Spot, Icarus, 158, 1, 249–266, doi: 10.1006/icar.2002.6867.

Sinclair, J. A., G. S. Orton, T. K. Greathouse, L. N. Fletcher, J. I. Moses, V. Hue, P. G. J. Irwin, (2017), Jupiter's auroral-related stratospheric heating and chemistry I: Analysis of Voyager-IRIS and Cassini-CIRS spectra, Icarus, 292, 182–207, doi: 10.1016/j.icarus.2016.12.033.

Sinclair, J. A., P. G. J. Irwin, L. N. Fletcher, T. Greathouse, S. Guerlet, J. Hurley, C. Merlet, (2014), From Voyager-IRIS to Cassini-CIRS: Interannual variability in Saturn's stratosphere?, Icarus, 233, 281–292, doi: 10.1016/j.icarus.2014.02.009.

Sinclair, J. A., P. G. J. Irwin, L. N. Fletcher, J. I. Moses, T. K. Greathouse, A. J. Friedson, B. Hesman, J. Hurley, C. Merlet, (2013), Seasonal variations of temperature, acetylene and

- - - - - - - - - - - - - -

ethane in Saturn's atmosphere from 2005 to 2010, as observed by Cassini-CIRS, Icarus, 225, 1, 257–271, doi: 10.1016/j.icarus.2013.03.011.

Smith, P. H., M. T. Lemmon, R. D. Lorenz, L. A. Sromovsky, J. J. Caldwell, M. D. Allison, (1996), Titan's surface, revealed by HST imaging, Icarus, 119, 2, 336–349, doi: 10.1006/icar.1996.0023.

Spencer, J. R., F. Nimmo, Andrew P. Ingersoll, T. A. Hurford, E. S. Kite, A. R. Rhoden, J. Schmidt, C. J. A. Howett, (2018), Plume origins and plumbing: from ocean to surface, Enceladus and the Icy Moons of Saturn, 163.

Spencer, J. and F. Nimmo, (2013), Enceladus: An active ice world in the Saturn system, Annual Review Earth Planetary Science, 41, 693–717, doi: 10.1146/annurev-earth-050212-124025.

Spencer, J. R., J. C. Pearl, M. Segura, F. M. Flasar, A. Mamoutkine, P. Romani, B. Buratti, A. Hendrix, L. J. Spilker, R. M. C. Lopes, (2006), Cassini encounters Enceladus: Background and the discovery of a south polar hot spot, Science, 311, 1401–1405, doi: 10.1126/science.1121661.

Spencer, J., L. Tamppari, T. Martin, L. Travis, (1999), Temperatures on Europa from Galileo PPR: Nighttime thermal anomalies, Science, 284, 1514–1516.

Spencer, J. R., L. A. Lebofsky, M. V. Sykes, (1989), Systematic biases in radiometric diameter determinations, Icarus, 78, 337–354, doi: 10.1016/0019-1035(89)90182-6.

Spencer, J., (1987), The surfaces of Europa, Ganymede, and Callisto: An investigation using Voyager IRIS thermal infrared spectra, PhD thesis, University of Arizona.

Spilker, L. J., C. Ferrari, A. Altobelli, S. Pilorz, R. Morishima, (2018), Thermal properties of rings and ring particles, Chapter 15, In Planetary Ring Systems. Properties, Structure, and Evolution, (eds.) M. Tiscareno, A. Murray, University of Arizona Press, Tucson, AZ, pp. 399–433, doi: 10.1017/9781316286791.015.

Spilker, L. J., C. Ferrari, R. Morishima, (2013), Saturn’s ring temperatures at equinox, Icarus, 226, 316–322.

Spilker, L. J., S. H. Pilorz, B. D. Wallis, J. C. Pearl, J. N. Cuzzi, S. M. Brooks, N. Altobelli, et al., (2006), Cassini thermal observations of Saturn’s main rings: Implications for particle rotation and vertical mixing, Planetary and Space Science, 54, 1167–1176.

Spilker, L. J., S. H. Pilorz, S. G. Edgington, et al., (2005), Cassini CIRS observations of a roll-off in Saturn ring spectra at submillimeter wavelengths, Earth Moon Planets, 96, 149–163.

Spilker, L. J., C. Ferrari, J. N. Cuzzi, et al., (2003a), Saturn’s rings in the thermal infrared, Planetary and Space Science, 51, 929–935.

Spilker, L. J., S. Pilorz, C. Ferrari, J. Pearl, B. Wallis, (2003b), Thermal and energy balance measurements of Saturn’s C-ring, Bulletin of the American Astronomical Society, 35, 929.

Stofan, E., C. Elachi, J. Lunine, et al., (2007), The lakes of Titan, Nature, 445, 61–64, doi: 10.1038/nature05438.

Stooke, P.J., (2002), Tethys and Dione: New geological interpretations, Lunar Planetary Science Conference, vol. 33, 1553, https://www.lpi.usra.edu/meetings/lpsc2002/pdf/1553.pdf.

Stooke, P.J., (1989), Tethys: Volcanic and structural geology, Lunar Planetary Science Conference, March 13–17, Houston, TX, vol. 20, no. 1543.

Strobel, D. F., S. K. Atreya, B. Bézard, F. Ferri, F. M. Flasar, M. Fulchignoni, E. Lellouch, I. Müller-Wodarg (2009), Atmospheric Structure and Composition, Chapter 10, In Titan from Cassini-Huygens, (eds.) R. H. Brown, J.-P. Lebreton, J. H. Waite, Springer Netherlands, pp. 235–257, doi: 10.1007/978-1-4020-9215-2_10.

Strobel, D. F., (2008), Titan's hydrodynamically escaping atmosphere, Icarus, 193, 2, 588–594, doi: 10.1016/j.icarus.2007.08.014.

Sylvestre, M., N. A. Teanby, S. Vinatier, S. Lebonnois, P. G. J. Irwin, (2018), Seasonal evolution of C_2N_2, C_3H_4, and C_4H_2 abundances in Titan's lower stratosphere, Astronomy & Astrophysics, 609, doi: 10.1051/0004-6361/201630255.

Sylvestre, M., S. Guerlet, T. Fouchet, A. Spiga, F. M. Flasar, B. Hesman, G. L. Bjoraker, (2015), Seasonal changes in Saturn's stratosphere inferred from Cassini/CIRS limb observations, Icarus, 258, 224–238, doi: 10.1016/j.icarus.2015.05.025.

Teanby, N. A., B. Bézard, S. Vinatier, M. Sylvestre, C. A. Nixon, P. G. J. Irwin, R. J. de Kok, S. B. Calcutt, F. M. Flasar, (2017), The formation and evolution of Titan's winter polar vortex, Nature Communications, 8, doi: 10.1038/s41467-017-01839-z.

Teanby, N. A., P. G. J. Irwin, C. A. Nixon, R. de Kok, S. Vinatier, A. Coustenis, E. Sefton-Nash, S. B. Calcutt, F. M. Flasar, (2012), Active upper-atmosphere chemistry and dynamics polar circulation reversal on Titan, Nature, 491, 7426, 732–735, doi: 10.1038/nature11611.

Teanby, N. A., P. G. J. Irwin, C. A. Nixon, and R. de Kok, (2012b), Seasonal change at Titan’s poles, 43rd Lunar and Planetary Science Conference, Woodlands, TX, March 19-23, 2012, 1500.pdf

Teanby, N. A., P. G. J. Irwin, R. de Kok, (2010a), Compositional evidence for Titan's stratospheric tilt, Planetary and Space Science, 58, 5, 792–800, doi: 10.1016/j.pss.2009.12.005.

Teanby, N. A., P. G. J. Irwin, R. de Kok, C. A. Nixon, (2010b), Mapping Titan's HCN in the far infra-red: implications for photochemistry, Faraday Discussions, 147, 51–64, doi: 10.1039/c001690j.

Teanby, N. A., P. G. J. Irwin, R. de Kok, C. A. Nixon, (2010c), Seasonal changes in Titan's polar trace gas abundance observed by Cassini, The Astrophysical Journal Letters, 724, 1, L84–L89, doi: 10.1088/2041-8205/724/1/l84.

Teanby, N. A., R. de Kok, P. G. J. Irwin, (2009a), Small-scale composition and haze layering in Titan's polar vortex, Icarus, 204, 2, 645–657, doi: 10.1016/j.icarus.2009.07.027.

Teanby, N. A., P. G. J. Irwin, R. de Kok, A. Jolly, B. Bézard, C. A. Nixon, S. B. Calcutt, (2009b), Titan's stratospheric C_2N_2, C_3H_4, and C_4H_2 abundances Cassini/CIRS far-infrared spectra, Icarus, 202, 2, 620–631, doi: 10.1016/j.icarus.2009.03.022.

Teanby, N., P. Irwin, R. de Kok, et al., (2009c), Dynamical implications of seasonal and spatial variations in Titan's stratospheric composition, Philosophical Transactions of The Royal Society A-Mathematical Physical and Engineering Sciences, 367, 1889, 697–711, doi: 10.1098/rsta.2008.0164.

Teanby, N. A., R. de Kok, P. G. J. Irwin, S. Osprey, S. Vinatier, P. J. Gierasch, P. L. Read, et al., (2008a), Titan's winter polar vortex structure revealed by chemical tracers, Journal of Geophysical Research-Planets, 113, E12, doi: 10.1029/2008je003218.

Teanby, N. A., P. G. J. Irwin, R. De Kok, C. A. Nixon, A. Coustenis, E. Royer, S. B. Calcutt, et al., (2008b), Global and temporal variations in hydrocarbons and nitriles in Titan's stratosphere for northern winter observed by Cassini/CIRS, Icarus, 193, 2, 595–611, doi: 10.1016/j.icarus.2007.08.017.

Teanby, N. A., P. G. J. Irwin, R. De Kok, S. Vinatier, B. Bézard, C. A. Nixon, F. M. Flasar, et al., (2007), Vertical profiles of HCN, HC_3N, and C_2H_2 in Titan's atmosphere derived Cassini/CIRS data, Icarus, 186, 2, 364–384, doi: 10.1016/j.icarus.2006.09.024.

Teanby, N. A., L. N. Fletcher, P. G. J. Irwin, T. Fouchet, G. S. Orton, (2006a), New upper limits for hydrogen halides on Saturn derived Cassini-CIRS data, Icarus, 185, 2, 466–475, doi: 10.1016/j.icarus.2006.07.011.

Teanby, N., P. G. J. Irwin, R. De Kok, C. A. Nixon, A. Coustenis, B. Bézard, S. B. Calcutt, et al., (2006b), Latitudinal variations of HCN, HC3N, and C2N2 in Titan's stratosphere derived Cassini CIRS data, Icarus, 181, 1, 243–255, doi: 10.1016/j.icarus.2005.11.008.

Thomson, F. S., E. A. Marouf, G. L. Tyler, R. G. French, N. J. Rappoport, (2007), Periodic microstructure in Saturn's rings A and B, Geophysical Research Letters, 34, no. 24.

Tiscareno, M. S., J. A. Burns, J. N. Cuzzi, M. M. Hedman, (2010), Cassini imaging search rules out rings around Rhea, Geophysical Research Letters, vol. 37, Issue 14, L14205, doi: 10.1029/2010GL043663.

Tiscareno, M. S., J. A. Burns, P. D. Nicholson, M. M. Hedman, C. C. Porco, (2007), Cassini imaging of Saturn’s rings: II. A wavelet technique for analysis of density waves and other radial structure in the rings, Icarus, 189, 14–34.

Tokano, T., (2005), Meteorological assessment of the surface temperatures on Titan: constraints on the surface type, Icarus, 173, 1, 222–242, doi: 10.1016/j.icarus.2004.08.019.

Tomasko, M. G., B. Archinal, T. Becker, B. Bézard, M. Bushroe, M. Combes, D. Cook, et al., (2005), Rain, winds and haze during the Huygens probe's descent to Titan's surface, Nature, 438, 7069, 765–778, doi: 10.1038/nature04126.

Verbiscer, A., R. French, M. Showalter, P. Helfenstein, (2007), Enceladus: Cosmic graffiti artist caught in the act, Science, 315, 815, doi: 10.1126/ science.1134681.

Verbiscer, A. and J. Veverka, (1989), Albedo dichotomy of Rhea: Hapke analysis of Voyager photometry, Icarus, 82, 336–353, doi: 10.1016/0019-1035(89)90042-0.

Vinatier, S., B. Schmitt, B. Bézard, P. Rannou, C. Dauphin, R. De Kok, D. E. Jennings, F. M. Flasar, (2018), Study of Titan's fall southern stratospheric polar cloud composition with Cassini/CIRS: detection of benzene ice, Icarus, 310, 89–104.

Vinatier, S., B. Bézard, S. Lebonnois, N. A. Teanby, R. K. Achterberg, N. Gorius, A. Mamoutkine, et al., (2015), Seasonal variations in Titan's middle atmosphere during the northern spring derived Cassini/CIRS observations, Icarus, 250, 95–115, doi: 10.1016/j.icarus.2014.11.019.

Vinatier, S., P. Rannou, C. M. Anderson, B. Bézard, R. de Kok, R. E. Samuelson, (2012), Optical constants of Titan's stratospheric aerosols in the 70–1500 cm^{-1} spectral range constrained by Cassini/CIRS observations, Icarus, 21, 1, 5–12, doi: 10.1016/j.icarus.2012.02.009.

Vinatier, S., B. Bézard, R. de Kok, C. M. Anderson, R. E. Samuelson, C. A. Nixon, A. Mamoutkine, et al., (2010a), Analysis of Cassini/CIRS limb spectra of Titan acquired during the nominal mission II: Aerosol extinction profiles in the 600–1420 cm^{-1} spectral range, Icarus, 210, 2, 852–866, doi: 10.1016/j.icarus.2010.06.024.

Vinatier, S., B. Bézard, C. A. Nixon, A. Mamoutkine, R. C. Carlson, D. E. Jennings, E. A. Guandique, et al., (2010b), Analysis of Cassini/CIRS limb spectra of Titan acquired during the nominal mission: I. Hydrocarbons, nitriles and CO_2 vertical mixing ratio profiles, Icarus, 205, 2, 559–570, doi: 10.1016/j.icarus.2009.08.013.

Vinatier, S., B. Bézard, T. Fouchet, N. A. Teanby, R. de Kok, P. G. J. Irwin, B. J. Conrath, et al., (2007a), Vertical abundance profiles of hydrocarbons in Titan's atmosphere at 15° S and 80° N retrieved Cassini/CIRS spectra, Icarus, 188, 1, 120–138, doi: 10.1016/j.icarus.2006.10.031.

Vinatier, S., B. Bézard, C. A. Nixon, (2007b), The Titan $^{14}N/^{15}N$ and $^{12}C/^{13}C$ isotopic ratios in HCN Cassini/CIRS, Icarus, 191, 2, 712–721, doi: 10.1016/j.icarus.2007.06.001.

Vokrouhlický, D., D. Nesvorný, L. Dones, W. F. Bottke, Thermal forces on planetary ring particles: Application to the main system of Saturn, Astronomy & Astrophysics, 471, no. 2, 717–730.

Waite, J. H., H. Niemann, R. V. Yelle, W. T. Kasprzak, T. E. Cravens, J. G. Luhmann, R. L. McNutt, et al., (2005), Ion Neutral Mass Spectrometer results the first flyby of Titan, Science, 308, 5724, 982–986, doi: 10.1126/science.1110652.

Wilson, E. H. and S. K. Atreya, (2009), Titan's carbon budget and the case of the missing ethane, Journal of Physical Chemistry A, 113, 42, 11221–11226, doi: 10.1021/jp905535a.

Wilson, E. H. and S. K. Atreya, (2004), Current state of modeling the photochemistry of Titan's mutually dependent atmosphere and ionosphere, Journal of Geophysical Research: Planets 109, no. E6, doi: 10.1029/2003JE002181.

Wong, M. H., G. L. Bjoraker, M. D. Smith, F. M. Flasar, C. A. Nixon, (2004), Identification of the 10-μm ammonia ice feature on Jupiter, Planetary and Space Science, 52, 5–6, 385–395, doi: 10.1016/j.pss.2003.06.005.

Yelle, R. V., J. Cui, I. C. F. Müller-Wodarg, (2008), Methane escape Titan's atmosphere, Journal of Geophysical Research: Planets, 113, E10, doi: 10.1029/2007je003031.

Yoder, C. F., (1979), How tidal heating in Io drives the Galilean orbital resonance locks, Nature 279, 76.

Zhang, X., C. A. Nixon, R. L. Shia, R. A. West, P. G. J. Irwin, R. V. Yelle, M. A. Allen, Y. L. Yung, (2013), Radiative forcing of the stratosphere of Jupiter, Part I: Atmospheric cooling rates Voyager to Cassini, Planetary and Space Science, 88, 3–25, doi: 10.1016/j.pss.2013.07.005.

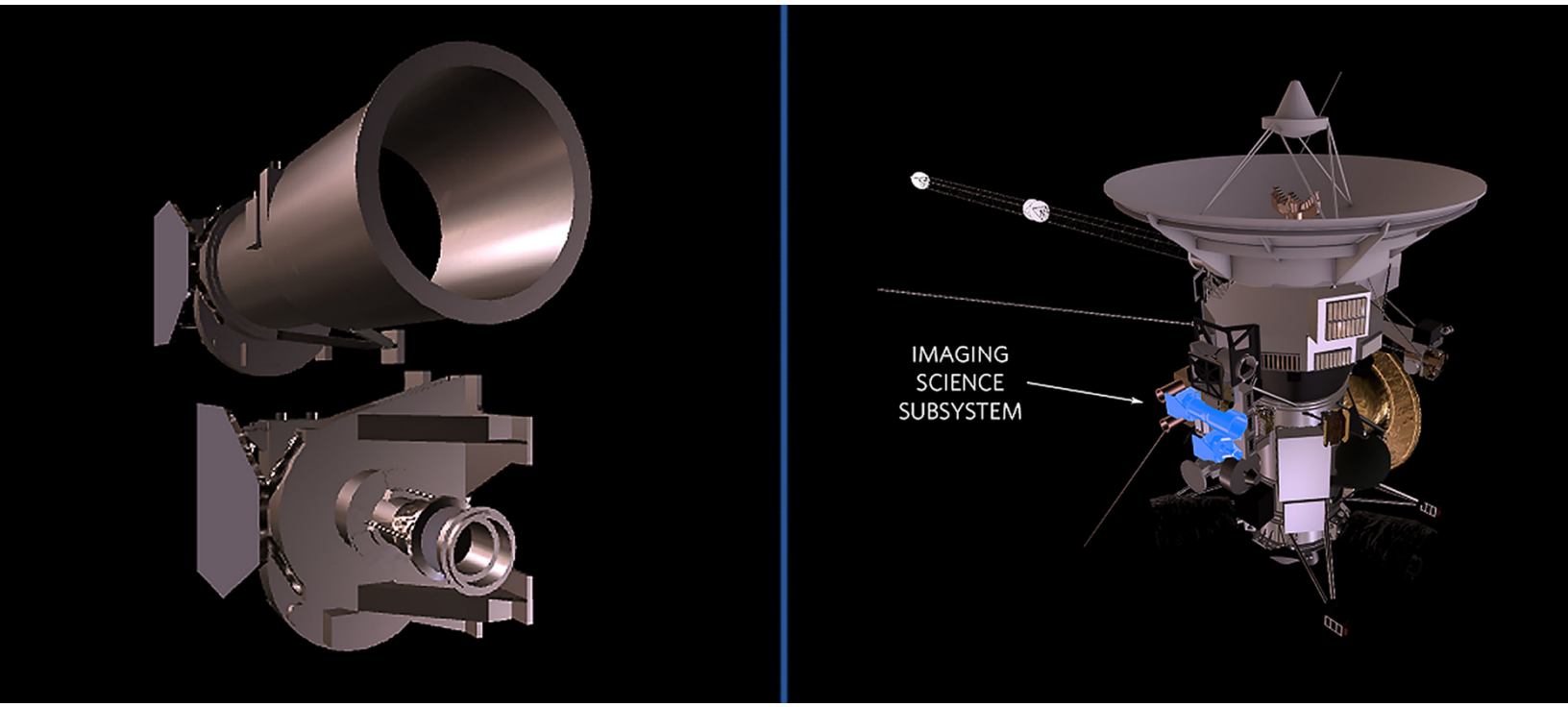

Imaging Science Subsystem

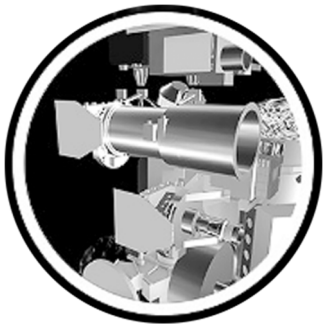

The Imaging Science Subsystem (ISS) consisted of both a wide-angle and a narrow-angle digital camera specifically designed for exploring the Saturn system. The **science objectives** included capturing lightning, investigating three-dimensional cloud structure and meteorology of Saturn's and Titan's atmospheres, imaging the surfaces of icy satellites, determining the composition and structure of Saturn's enormous ring system, and peering through the hazy Titan atmosphere to study its surface. The two cameras were able to capture beautiful images of the Saturn system as well, which inspired the public. In addition to acquiring scientific images, the cameras were also used for optical navigation to refine the knowledge of the spacecraft's trajectory and the position of the satellites.

Each camera included optics, two filter wheels, a shutter and detector head, plus their electronics. The cameras were sensitive to visible wavelengths of light and to some infrared and ultraviolet wavelengths. The filters for each camera were mounted on wheels to select the wavelengths to be sampled in each image. They were also capable of filtering for linear polarization.

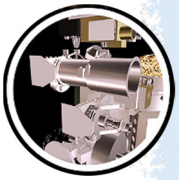

CONTENTS

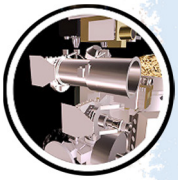

Figures

Tables

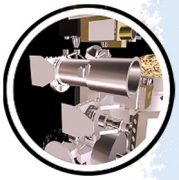

EXECUTIVE SUMMARY

The Cassini Imaging Science Subsystem (ISS) was the highest resolution imaging device on the Cassini mission and was specifically designed to image the bodies in the Saturn system. In its photometric sensitivity, linearity, dynamic range, spectral range—from near-ultraviolet (UV) to near-infrared (IR)—filter complement, resolving power, and variety of data collection and compression modes, it represented a significant advance over its predecessor carried on the Voyager spacecraft to Saturn in 1980 and 1981. The ISS was also the instrument used for optical navigation of the spacecraft.

The Cassini Imaging Science Subsystem (ISS) was the highest resolution imaging device on the Cassini mission and was specifically designed to image the bodies in the Saturn system.

The range of scientific objectives addressed by the ISS, as set forth early on by the Imaging Science team, included surveys of new phenomena and new moons/moonlets, as well as deeper characterization of known phenomena and features, throughout the Saturnian system out to the orbit of Iapetus, though seminal scientific results were obtained in a late-mission study of Saturn's irregular satellites, lying well beyond Iapetus. Among the specific goals of the ISS team were: determining the life-cycle of eddies and storms, and measuring wind speeds and photometric properties, in the Saturn atmosphere; revealing the geomorphology of the surface of Titan, searching for liquid hydrocarbons on the moon's surface, and characterizing the meteorology of the moon's atmosphere and its interactions with the surface; revealing at very high-resolution the architecture and dynamics of Saturn's rings; and mapping the surfaces of Saturn's ring-region and main icy satellites at high-resolution, including a search for plumes spouting from the surface of Enceladus.

This document summarizes the results of the imaging investigations conducted at Jupiter during Cassini's flyby of that planet on the eve of the year 2001, and at Saturn between the years 2004 and 2017. A perfectly engineered Jupiter flyby and several extensions that added nine years to the prime four-year Cassini mission at Saturn, the outstanding technical skill of the mission designers and the exquisite accuracy and richness of the 13-year Saturn orbital tour they produced, the commitment of the spacecraft flight team, the excellent performance of both the ISS and the spacecraft, and the perseverance, intelligence and sheer love of exploration of the imaging science team and the operations staff that supported it, together ensured the unqualified success of the ISS investigations at Saturn and Jupiter.

ISS INSTRUMENT SUMMARY

The ISS As-Built description is documented in Porco et al. [2004]. What follows in this section are excerpts from that paper.

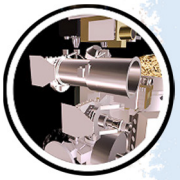

The Cassini ISS consists of two fixed focal length telescopes called cameras. The narrow-angle camera is 95 cm long and 40 cm × 33 cm wide (Figure ISS-1); the wide-angle camera is 55 cm long and 35 × 33 cm wide (Figure ISS-2). Both camera systems together have a mass of 57.83 kg. They sit on the remote sensing palette, fixed to the body of the Cassini orbiter, between the Visual and Infrared Mapping Spectrometer (VIMS) and the Composite Infrared Spectrometer (CIRS), and above the Ultraviolet Imaging Spectrometer (UVIS). The apertures and radiators of both telescopes are parallel to each other.

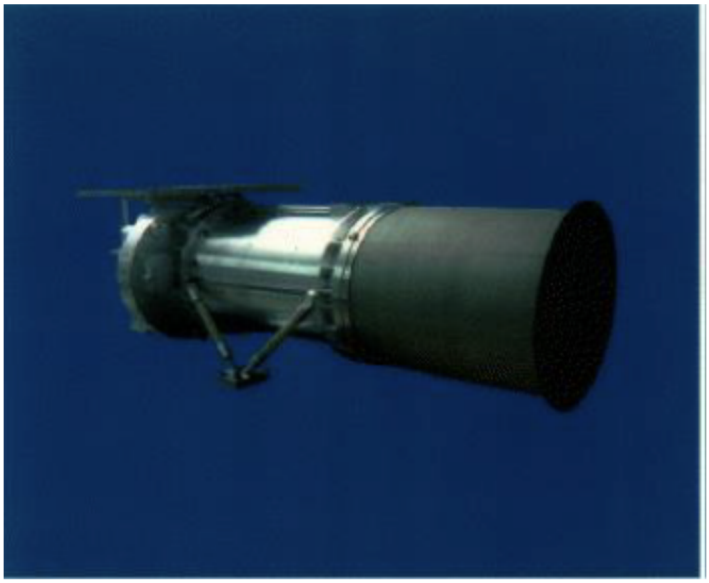

Figure ISS-1. Cassini ISS narrow-angle camera.

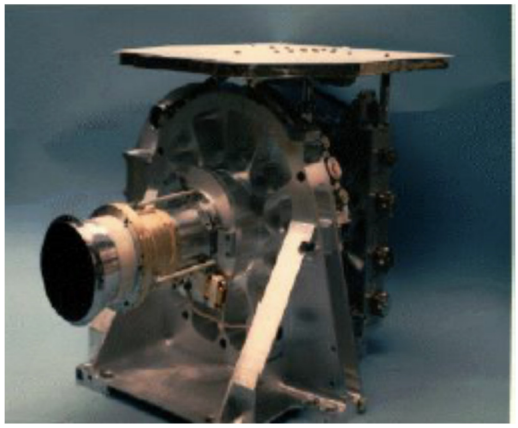

Figure ISS-2. Cassini ISS wide angle camera.

Each camera has its own set of optics, mechanical mountings, charge coupled device (CCD), shutter, filter wheel assembly, temperature sensors, heaters, various control electronics, engineering flight computer, and bus interface unit (BIU) to the central spacecraft command & data system (CDS). The electronics that control each camera consist of two parts: sensor head subassembly and the main electronics subassembly. The sensor head electronics supports the

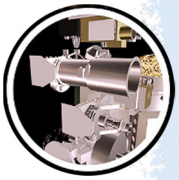

operation of the CCD detector and the preprocessing of the pixel data. The main electronics provide the power and perform all other ISS control functions, including generating and maintaining internal timing which is synchronized to the CDS timing of 8 Hz, control of heaters, and the two hardware data compressors. The Cassini engineering flight computer (EFC) is a radiation-hardened version of IBM's standard, general purpose MIL-STD-1750A 16-bit computer and is the ISS processor that controls the timing, internal sequencing, mechanism control, engineering and status data acquisition, and data packetization.

The narrow angle camera (NAC) is an f/10.5 reflecting telescope with an image scale of ~6 µrad/pixel, a 0.35° × 0.35° field of view (FOV), and a spectral range from 200 nm–1100 nm. Its filter wheel subassembly carries 24 spectral filters: 12 filters on each of two wheels. The optical train of the wide-angle camera (WAC), a Voyager flight spare, is an f/3.5 refractor with a ~60 µrad/pixel image scale and a 3.5° × 3.5° FOV. The refractor objective lens transmission limits the lower end of the spectral range on the WAC which is 380 nm–1100 nm. The WAC filter subassembly carries 9 filters in each of two filter wheels, for a total of 18 filters. In both cameras, images are acquired through two filters, one on each wheel, allowing in-line combinations of filters for greater flexibility, i.e., polarizers in line with other spectral filters, new band-passes created by the overlap of two spectral filters, etc.

KEY OBJECTIVES FOR ISS INSTRUMENT

The Cassini ISS instrument is designed to perform multispectral imaging of Saturn, Titan, rings, and icy satellites to observe their properties. Specific science objectives are as follows:

Cassini Early Mission (2004–2010)

Saturn and Titan atmospheres

1. Motions and dynamics.
    a. Basic flow regime (Titan).
    b. Poleward flux of momentum (u′v′).
    c. Poleward flux of heat (with CIRS).
    d. Life cycles and small-scale dynamics of eddies.
    e. Radiative heating for dynamical studies.
2. Clouds and aerosols.
    a. Cloud and haze stratigraphy (strongly couples with wind studies).

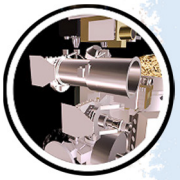

b. Particle optical properties.

c. Particle physical properties.

d. Auroral processes and particle formation.

e. Haze microphysical models.

3. Lightning (related to water clouds on Saturn, unknown for Titan).

4. Auroras (H and H_2 emissions on Saturn, N and N_2 emissions on Titan).

Titan surface

a. Map the surface of Titan in haze-penetrating spectral regions.

b. Search for bodies of liquid hydrocarbons (morphology, glints, etc.).

c. Determine surface/atmospheric interactions.

Rings

a. Ring architecture/evolution—azimuthal, radial, temporal variations across tour.

b. New satellites—orbits, masses/densities, effects on rings; complete inventory of Saturn's ring-region moons.

c. Search and characterize material potentially hazardous to Cassini—diffuse rings, arcs, Hill's sphere material, etc.

d. Orbit refinement of known satellites; temporal variations; resonant effects.

e. Particle/disk properties—vertical disk structure; particle physical properties and size distribution; variations across disk.

f. Spokes—formation timescales/process; periodic variations.

g. Diffuse rings (E-ring, G-ring)—structure, characterize particle properties.

Icy satellite objectives

a. Determine the general characteristics and geological histories of the satellites.

b. Define the mechanisms of crustal and surface modifications, both external and internal.

c. Investigate the compositions and distributions of surface materials, particularly dark, organic rich materials and low melting point condensed volatiles.

d. Constrain models of the satellites' bulk compositions and internal structures.

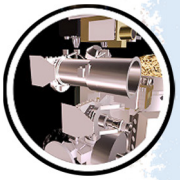

e. Investigate interactions with the magnetosphere and ring systems and possible gas and particle injections into the magnetosphere.

f. Search for plumes erupting from the surface of Enceladus.

Cassini Solstice Mission (2010–2017)

The ISS objectives for Cassini's late mission, or Solstice Mission, have been captured, by discipline, in a series of matrices outlined in the section entitled Science Objectives and Traceability Matrices.

ISS Science Assessment

The ISS Science Assessment describes if and how well ISS observations met the objectives listed in the sections entitled Key Objectives for ISS Instrument and Science Objectives and Traceability Matrices. Evaluation of the objectives are highlighted below. The Cassini Solstice Mission evaluation is given in the section entitled Science Objectives and Traceability Matrices.

Saturn and Titan Atmospheres

1. Motions and dynamics.

   a. Basic flow regime (Saturn and Titan). This goal was met on Saturn and Titan (see Porco et al. [2005a, 2005b] and subsequent ISS papers on Saturn's dynamics). ISS images confirm the discovery by the CIRS team that Titan's zonal flow has a pole location that is offset by a few degrees from Titan's solid body rotation pole [Roman et al. 2009; West et al. 2016].

   b. Poleward flux of momentum ($u'v'$). This goal was met for Saturn [Del Genio et al. 2007].

   c. Poleward flux of heat (with CIRS). This goal has not yet been met for Titan or Saturn. The appropriate ISS data were obtained but the analysis is not complete. However, there have been new global circulation models for Titan constrained by Cassini data [Lora et al. 2015].

   d. Life cycles and small-scale dynamics of eddies. This goal was partially met for Saturn (see Porco et al. [2005a]; Antuñano et al. [2018] and parts of other ISS papers on Saturn's clouds and dynamics).

   e. Radiative heating for dynamical studies. This goal was met [Li et al. 2011, 2013, 2015; Li et al. 2018].

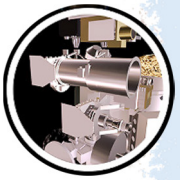

2. Clouds and aerosols.

    a. Cloud and haze stratigraphy (strongly couples with wind studies). This goal was partially met [West et al. 2009, 2016].

    b. Particle optical properties. This goal was met for a restricted latitude band on Saturn [Pérez-Hoyos et al. 2016]. Appropriate data were obtained for other latitudes but the analysis is not complete.

    c. Particle physical properties. This goal has not yet been met. The appropriate data were obtained but the analysis is not complete.

    d. Auroral processes and particle formation. The goal was met for Saturn [Dyudina et al. 2010, 2015].

    e. Haze microphysical models. This goal has not yet been met. The appropriate data were obtained but the analysis is not complete.

3. Lightning (related to water clouds on Saturn, did not know what to expect for Titan). Lighting on Saturn was detected and studied. It was found correlated with Saturn Electrostatic Discharges (see Porco et al. [2005a] and subsequent ISS papers). No lightning was detected for Titan.

4. Auroras (H and H_2 emissions on Saturn, N and N_2 emissions on Titan). Auroras on Saturn were studied [Dyudina et al. 2010, 2015]. Airglow on Titan was discovered [West et al. 2012; Lavvas et al. 2014].

Titan Surface

a. Map the surface of Titan in haze-penetrating spectral regions. The goal was met, providing a global albedo map of Titan [McEwen et al. 2005a, 2005b; Turtle et al. 2009, 2011a, 2011b, 2011c, 2013, 2018a; Perry et al. 2005, 2007; Stephan et al. 2009]. Reprocessing using the complete ISS dataset for much improved signal/noise is underway [Karkoschka et al. 2017a, 2017b].

b. Search for bodies of liquid hydrocarbons (morphology, glints, etc.). The goal was met, with the ISS discovery of the largest lakes and seas in both the south and northern polar regions, from morphology [http://ciclops.org/view.php?id=1161; http://ciclops.org/view.php?id=1194; http://ciclops.org/view.php?id=2607; http://ciclops.org/view.php?id=2631] and temporal changes [Turtle et al. 2009; Turtle et al. 2011b, 2011c, 2018a] and by searching for glints [Fussner et al. 2005], although no glints were found at ISS wavelengths.

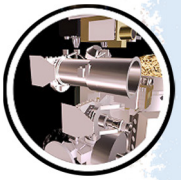

c. Determine surface/atmospheric interactions. The goal was met [Porco et al. 2005b], especially via co-analysis of ISS with other datasets [Turtle et al. 2009, 2011a, 2011b, 2011c, 2018a, 2018b; Barnes et al. 2013; Birch et al. 2017].

Rings

a. Ring architecture/evolution—azimuthal, radial, temporal variations across tour. This goal was met, with substantial discoveries about the azimuthal, radial, and temporal characteristics of the rings [Porco et al. 2005c]. See reviews by Cuzzi et al. [2018]; Murray and French [2018]; Nicholson et al. [2018].

b. New satellites: orbits, masses/densities, effects on rings; complete inventory of Saturn's inner moons. This goal was met. See Porco et al. [2005c] and subsequent papers reporting discovery of Daphnis, Aegaeon, Methone, Pallene, Anthe, Polydeuces; and a survey that verified the non-existence of shepherd moons in most of the gaps within the main rings [Spitale 2017].

c. Search and characterize material potentially hazardous to Cassini—diffuse rings, arcs, Hill's sphere material, etc. This goal was met, with substantial discoveries about current resonant characteristics and long-term evolution of satellite orbits [Porco et al. 2005c; Jacobson et al. 2006a, 2006b, 2008; Lainey et al. 2017], as well as an unexpected sudden change in the orbit of Daphnis [Jacobson 2014].

d. Orbit refinement of known satellites; temporal variations; resonant effects. This goal was met, with substantial discoveries about current resonant characteristics and long-term evolution of satellite orbits [Porco et al. 2005c; Jacobson et al. 2006a, 2006b, 2008; Lainey et al. 2017], as well as an unexpected sudden change in the orbit of Daphnis [Jacobson 2014].

e. Particle/disk properties—vertical disk structure; particle physical properties and size distribution; variations across disk. This goal was met, with substantial discoveries about particle and disk properties [Porco et al. 2005c]. See reviews by Cuzzi et al. [2018]; Estrada et al. [2018]; Murray and French [2018]; Spahn et al. [2018]; Spilker et al. [2018].

f. Spokes—formation timescales/process; periodic variations. This goal was met, with detailed studies of the workings of spokes [Mitchell et al. 2006, 2013].

g. Diffuse rings (E-ring, G-ring): structure, characterize particle properties. This goal was met, with substantial discoveries about the structure and particle properties of diffuse rings [Porco et al. 2005c]. See review by Hedman et al. [2018].

Icy Satellites

a. Determine the general characteristics and geological histories of the satellites. These goals were met [Porco et al. 2005d; Porco et al. 2006]. See comprehensive reviews

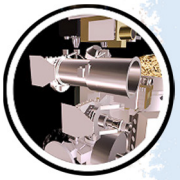

and references therein: Patterson et al. [2018]; Schenk et al. [2018]; Verbiscer et al. [2018]; Postberg et al. [2018]; Kirchoff et al. [2018]; Goldstein et al. [2018]; Thomas et al. [2018]; Spencer et al. [2009]; Matson et al. [2009]; Jaumann et al. [2009a]; Roatsch et al. [2009a]; Dones et al. [2009].

b. Define the mechanisms of crustal and surface modifications, both external and internal. This goal was partially met [Porco et al. 2005d; Porco et al. 2006; Patterson et al. 2018; Schenk et al. 2018; Thomas et al. 2018; Kirchoff et al. 2018; Postberg et al. 2018; Wagner et al. 2006, 2007, 2009, 2010; Matson et al. 2009; Dones et al. 2009].

c. Investigate the compositions and distributions of surface materials, particularly dark, organic rich materials and low melting point condensed volatiles. This goal was partially met [Porco et al. 2005d]. See comprehensive reviews and references therein: Verbiscer et al. [2018]; Schenk et al. [2018]; Thomas et al. [2018].

d. Constrain models of the satellites' bulk compositions and internal structures. This goal was met [Porco et al. 2006; Thomas et al. 2007a, 2016, 2018; Thomas 2010; Castillo-Rogez et al. 2018].

e. Investigate interactions with the magnetosphere and ring systems and possible gas and particle injections into the magnetosphere. This goal was partially met [Thomas et al. 2018; Verbiscer et al. 2014; Annex et al. 2013; Verbiscer et al. 2018; Schenk et al. 2017; Spencer and Denk 2010].

f. Search for plumes emerging from the surface of Enceladus. This goal was met [Porco et al. 2006; Porco et al. 2014].

ISS Saturn System Science Results

Titan

Imaging of Titan's surface, with global mapping at 4 km or better resolution, shows the distribution and wide variety of surface features, including first sighting of a hydrocarbon lake in the south polar region (Ontario Lacus) [http://ciclops.org/view.php?id=1161; http://ciclops.org/view.php?id=1194], the first sighting of Titan’s largest sea in the north polar region (Kraken Mare) [http://ciclops.org/view.php?id=2607; http://ciclops.org/view.php?id=2631], both confirmed as liquid-filled later by other Cassini instruments and Titan's largest impact crater (Menrva). Analysis of the entire equatorial dataset acquired over the duration of the mission indicates surface albedos range from 0.25 in the dunes to 0.9 at Hotei Arcus [Porco et al. 2005b; Perry et al. 2005, 2007; McEwen et al. 2005a, 2005b; Turtle et al. 2009; Stephan et al. 2009; Karkoschka et al. 2017a, 2017b].

Strategies have been developed for effective imaging of Titan's atmosphere and surface as well as image processing techniques to achieve as high signal-to-noise ratio from the surface as

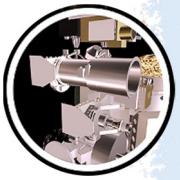

possible. [Porco et al. 2005b; Perry et al. 2005, 2007; Fussner et al. 2005; McEwen et al. 2005a, 2005b; Turtle et al. 2009, supplementary material; Karkoschka et al. 2017a, 2017b].

Features ISS has identified and mapped on the surface include:

- Equatorial dune fields and Xanadu, impact craters, polar lakes and seas, and undifferentiated mid-latitude plains [Porco et al. 2005b; McEwen et al. 2005a, 2005b; Turtle et al. 2009; Lopes et al. 2016].
- Possible shoreline changes at Titan lakes [Turtle et al. 2009, 2011c].
- Identification of a bright surface deposit at Titan's North Pole [Turtle et al. 2013].
- Joint analyses of surface processes and features, including Hotei Arcus; Tui Regio; surface modification associated with seasonal rainfall; and polar lakes, seas, and implications for Titan hydrology [Barnes et al. 2005, 2006; Turtle et al. 2009, 2011b, 2011c; Hayes et al. 2011; Jaumann et al. 2009b].

Surface darkening was observed from Titan rainstorms at Arrakis Planitia in 2004-2005 [Turtle et al. 2009] and at ~30° south latitude, including Concordia Regio, Adiri, in 2010–2011 [Turtle et al. 2011b, 2011c] as well as subsequent isolated brightening [Turtle et al. 2011b; Barnes et al. 2013].

Titan's main haze is almost featureless but shows hemispheric contrast that changes with season. This was known from Voyager images. Work with Cassini images [Roman et al. 2009] showed that the pole of rotational symmetry determined by the shape of the contrast boundary is displaced from Titan's solid body rotational pole by a few degrees, and corroborates the finding of pole displacement by Achterberg et al. [2008]. This finding opens up a new mystery about Titan's atmospheric dynamics.

The behavior of the detached haze provides new information to test and improve Titan dynamical models of the mesosphere and upper stratosphere.

Titan's detached haze, first seen in Voyager images, was again seen in Cassini images, but at altitudes that depend on season [Porco et al. 2005b; West et al. 2011, 2018]. West et al. [2011] showed that the detached haze underwent rapid descent centered around the northern spring equinox in 2009. It reached the same altitude as seen in Voyager images (near 350 km) one Titan year after the Voyager images were obtained. From about mid-2012 to early 2016 the detached haze was not seen in ISS images. It emerged in early 2016 but was weak, and showed irregular variations in latitude and time. The behavior of the detached haze provides new information to test and improve Titan dynamical models of the mesosphere and upper stratosphere.

In 2012, a distinct cloud was observed at an altitude of 300 km near Titan's south pole [West et al. 2016]. Spectral measurements by the VIMS instrument indicate an HCN ice composition [de Kok et al. 2014]. ISS measured altitude, morphology, texture, and motions of the cloud and showed that the atmospheric rotation at 300 km altitude is around a pole that is offset from Titan's solid

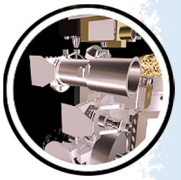

body rotational pole. Texture suggests that the cloud is undergoing open-cell convection, an unusual configuration for high-altitude clouds initiated by downwelling.

ISS documented the distribution, morphology, speeds, and seasonal behavior of Titan's tropospheric clouds starting on approach in April 2004 (late southern summer on Titan) through September 2017 (after the northern summer solstice in May 2017), as well as implications for atmospheric general circulation models and Titan's methane cycle including sub-surface reservoirs. During Titan's late southern summer, extensive convective cloud systems were common over Titan's south pole, and in the case of a large cloud in October 2004 led to substantial precipitation. Starting in 2007 as the Sun rose in Titan's north, clouds began to appear at northern latitudes >55° N and were relatively common until the equinox when northern cloud activity dropped off precipitously. The expectation from atmospheric models had been that cloud activity would increase at high northern latitudes as northern summer approached. However, only small isolated cells were seen near Titan's north pole, leaving the mystery of when/if north polar cloud systems form during northern summer. [Porco et al. 2005b; Turtle et al. 2009, 2011a, 2018a, 2018b; Mitchell et al. 2011].

In addition to polar clouds, Titan exhibited a preference for mid-latitude clouds, at ~40° S early in the mission during late southern summer, and gradually drifting poleward to ~60° S by equinox and beyond [Porco et al. 2005b; Turtle et al. 2009, 2011a]. After equinox, similar mid-latitude clouds were expected in the northern hemisphere but were not observed with any regularity until early 2016 (first at ~50° N and drifting poleward to 60° N). These cloud bands imply a seasonal Hadley circulation with rising motion at these latitudes, a feature that can only be predicted by models that include methane moist convection. However, the timing of the transition from the southern summer to the northern summer configuration is observed to be several Earth years later than predicted by the models [Turtle et al. 2018b]. Similar clouds appeared with lower frequency near ~15° S earlier in the mission and ~30° N late in the mission.

Spectral dependence of detection of some north-polar cloud features was observed starting in 2016, with VIMS detecting features at 2.1 μm that are not seen by ISS at 938 nm [Turtle et al. 2016, 2018a, 2018b] or by VIMS at wavelengths both shorter and longer than 2.1 μm.

Atmospheric airglow observations were made while Titan was in Saturn's shadow. [West et al. 2012; Lavvas et al. 2014].

Enceladus

Early ISS observations of Enceladus and its plume yielded many new discoveries, all refined in subsequent papers. Only the major highlights from these papers are presented next.

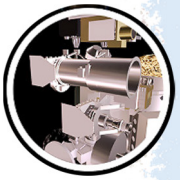

Plume

- A plume of fine, icy particles was discovered erupting from the south polar region of Enceladus in images taken in January and February 2005 [Porco et al. 2006]. In November 2005 the plume was resolved into discrete jets, or geysers, that eject the particles that eventually supply Saturn's E-ring, carried aloft by water vapor in the jets.
- The first argument is presented that the jetting activity at the South Pole is the result of venting from subsurface reservoirs of liquid water [Porco et al. 2006].
- Cassini's revised estimates of the bulk density of Enceladus and the inferred rock mass fraction suggest that radiogenic heating is not the dominant source of heat within the moon, compared with estimates of tidal heating via the Dione:Enceladus 2:1 resonance [Porco et al. 2006].
- In a multi-year high-resolution imaging survey of the south polar terrain (SPT), ~100 discrete geysers were found erupting from the four main fractures crossing the SPT [Porco et al. 2014]. A later claim—that the majority of the jet detections were not real and rather the result of observational bias [Spitale et al. 2015]—was refuted [Porco et al. 2015].
- Anomalously hot regions observed by CIRS at low resolution were found to be coincident with the SPT fractures [Porco et al. 2006; Spitale and Porco 2007]. At very high-resolution, very small scale (~10 m) hot spots reported by VIMS were found coincident with the surface locations of individual discrete geysers [Porco et al. 2014]. This correlation, along with the small size estimates of the hot spots derived from the observations of other instruments, strongly suggests that the source of the surface warmth is not shear heating but latent heat from the condensation of vapor onto the near-surface walls of the vents [Porco et al. 2014], allowing for a deep source of the venting materials.
- The plume that is formed from the geysers varies diurnally due to the varying extensional tidal stresses across the surface, with a phase lag of ~45° (or ~4.5 hours) compared to simple tidal models that assume an elastic ice shell [Nimmo et al. 2014]. The origin of the phase lag is not yet clear. Notable is the observation that the plume never goes to zero strength. Behounkova et al. [2015] showed the variation is best described by the cyclical variation in the normal stresses across the fractures, averaged over the SPT, and simulated the viscoelastic tidal response of Enceladus with a full 3-D numerical model. The delay in eruption activity may be a natural consequence of the viscosity structure in the south-polar region and the size of the putative subsurface ocean.
- Individual geysers were observed to be time variable, turning on and/or off on timescales that were not comparable to the diurnal cycling of stresses [Porco et al. 2014]. This was taken as an indication that condensation of ice in the vents leads to the stochastic clogging of the vents and consequently the shutoff of geysers, but

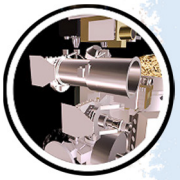

averaged across the SPT, the plume is continuous in time while variable in strength. The estimated timescale for the clogging process is months to a couple of years [Porco et al. 2006].

- Models of vapor arising by sublimation from the walls of the cracks and then condensing to make ice particles [Ingersoll and Pankine 2010] yield ice mass fractions no greater than 1.3%, confirming an earlier argument [Porco et al. 2006] that ice/vapor ratios of order unity favor a liquid source rather than sublimating ice.
- Observations by ISS of plume brightness at scattering angles ranging from 2.25° to 5.30°, which are only possible when the spacecraft is in Saturn's shadow, yield estimates of the particle size distribution in the plumes [Ingersoll and Ewald 2011]. The best-fitting distributions have a median mass-weighted radius r0 = 3.6 μm and differential power laws of r1 and r-3 for r << r0 and r >> r0, respectively. If the particles were solid ice spheres, the ice/vapor ratio is in the range 0.35–0.70, which would favor a liquid source.
- The ISS observations at scattering angles of 2.25–5.30° yield estimates of 51 ±18 kg s^{-1} for the mass leaving the vents and 9% for the fraction that escapes into the E-ring [Ingersoll and Ewald 2011]. The implied lifetime of particles in the E-ring is then ~8 years, but this assumes the particles are solid ice spheres. The estimate would be longer if the particles were fluffy aggregates rather than solid ice.
- Modeling the particles as irregular aggregates of spherical monomers yields ice/vapor ratios of 0.07 ±0.01 for the plume [Gao et al. 2016]. Therefore, a vapor-based origin for the plume particles cannot be ruled out if plume brightness is the only criterion.
- Comparison of ISS measurements of plume particle number density with those taken by other Cassini instruments has significantly reduced initial differences among them (factors of 10–20) by accounting for the temporal variability of the plume and the differing times and geometries of the different observations [Porco et al. 2017]. These results remove the need to assume low-density particle aggregates [Gao et al. 2016] to bring about agreement among all Cassini measurements. The preferred exponent in a differential size distribution was q = 3 at an altitude of 50 km.
- During the early years of the Cassini mission, 2006–2010, the computed diurnally averaged ice mass production rate that reproduces ISS observations of plume mass at 50 km altitude was 29 ±7 kg/s [Porco et al. 2017]. This new value is likely a lower limit as it does not account for heavier ice particles that don’t make it up to 50 km altitude. Because of the time-varying behavior of the plume, comparison of quantities of interest must be made at the same time and geometries, or nearly so. Utilizing a diurnally averaged estimate from other Cassini instruments of vapor production rate for the same time period, a solid to vapor ratio > 0.06 was computed. At 50 km altitude, the plume’s peak optical depth during the same time period was ~10^{-3}; by 2015, it was ~10^{-4}.

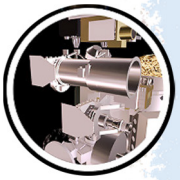

- Analysis of ISS observations from 2005–2015 reveals a decrease of plume brightness by roughly a factor of two [Ingersoll and Ewald 2017]; suggested explanations included a long-period tide (the decreasing phase of an 11-year cycle in orbital eccentricity), clogging of vents over time, or seasonal thermal effects. (The observations are from 47 individual days, usually with many observations per day, and document in great detail the four-fold to five-fold variation with orbital phase.)
- Thousands of ISS observations of the plume extending over the entire Cassini mission, through late 2017 [Porco et al. 2018], showed, after a multi-year decline in plume brightness, a resurgence to a brightness level exceeding that earlier in the mission. The analysis of this result confirmed previous suggestions [Nimmo et al. 2016] that the plume is varying on three time periods associated with the Dione/Enceladus 2:1 orbital resonance (diurnal, ~4 years and ~11 years) and that secular clogging and seasonal effects can be dismissed. The brightness of the secondary peak at MA ≈55°, near mission's end, declined substantially from its early-mission and mid-mission levels.
- A model of flow of vapor in vertical cracks yields estimates of crack width in the range 0.05–0.075 m [Nakajima and Ingersoll 2016]. A wider crack would yield an unacceptably high ratio of escaping vapor compared to that condensing on the walls as inferred from the observed radiated power.
- A model of the liquid-filled cracks introduces the concept of controlled boiling, in which backpressure limits the rate of evaporation [Ingersoll and Nakajima 2016]. The backpressure arises from frictional stress of the walls on the upward-flowing vapor, and leads to a steady state in which the evaporation rate is proportional to the width of the crack divided by its depth.
- The average geothermal flux into the sea beneath Enceladus' SPT was estimated to be comparable to that of the average Atlantic, of order 0.1 W/m^2 [Porco et al. 2017]. Based on this value, microbes could be present on Enceladus and concentrations at its seafloor hydrothermal vents could be comparable to those on Earth, ~10^5 cells/mL. Bubble-scrubbing, a process well-known to marine microbiologists, could enhance microbial concentrations over native ocean values by up to factors of 1000's in the Enceladus' plume. Estimates of microbial concentrations that might be collected in future missions of various designs were given.

Body and surface

- Fracturing and tectonic modification of Enceladus' surface is much more pervasive than predicted from Voyager imaging—tectonic resurfacing has likely played a major role in shaping youthful appearance of Enceladus. Intensely modified expanses are regionally divided by diverse styles of tectonic features among which are deep rifts, horst-and-graben terrains, folded ridges, braided or vermicular

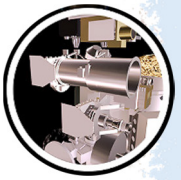

networks of grooves, and curvilinear ridges and fractures [Helfenstein et al. 2005a; Rathbun et al. 2005; Porco et al. 2006].

- An ubiquitous spidery network of sub-parallel, curvilinear, high-angle cracks appear to dissect topographic structures into vertical slabs. Numerous impact craters have been modified by cracks, the orientations of which appear to have a radial component, indicating that the extensional stress field that caused the fractures was influenced by stresses due to the craters themselves [Helfenstein et al. 2005a; Rathbun et al. 2005].
- A network of kilometer-scale ridges (now called Dorsa) and linear arrays of rounded domes are present on the trailing hemisphere of Enceladus and they appear to have extruded through preexisting surface fractures. Some wrinkled, flow-like features with lobate margins are found near the ridge and dome features. New details of viscously-relaxed craters, first seen by Voyager, include central dome features with structurally breached summits [Helfenstein et al. 2005a].
- A geologically active province at the south pole of Saturn's moon Enceladus is circumscribed by south-facing scarps and a chain of folded ridges and troughs at ~55° S latitude. The terrain southward of this boundary is distinguished by its albedo and color contrasts, elevated temperatures, extreme geologic youth, and narrow tectonic rifts that exhibit coarse-grained ice and coincide with the hottest temperatures measured in the region [Porco et al. 2006].
- The placement, morphology, and orientations of the SPT boundary is consistent with its interpretation as a convergent tectonic boundary arising from global deformation due to axial shortening along Enceladus' spin axis. Youthful systems of N-S tending fractures extending from Y-shaped discontinuities (i.e., a Y-shaped tectonic pattern of scarps and confined arcuate ridges that interrupt the SPT boundary) are also consistent with this deformation mechanism [Porco et al. 2006; Helfenstein et al. 2006; Helfenstein 2014].
- Flexural uplift along the ~3.5 Ga aged Harran Sulci rift zone in the tectonically resurfaced trailing hemisphere of Enceladus indicates that, at the time of formation, the mechanical lithospheric thickness was 2.5 km with heat fluxes comparable to average values measured in the active south polar region [Giese et al. 2008b].
- Tiger stripe fractures fall into a family of gradational morphological types. Smooth Flank formations coincide with volcanically active sections. The highest-resolution images (<10 m/pixel) show ice blocks up to tens of meters in size that are widely but non-uniformly distributed over a variety of terrain units. The upraised flanks and valley walls are mantled in places by smooth fluffy-looking deposits, most likely accumulations of coarse-grained plume fallout. Peculiar narrow lenticular ridges (now called shark fins), perhaps emplaced by extrusion or as icy pyroclastic deposits, rise from tens to hundreds of meters along the medial fissures of some tiger stripes. The Smooth Flank formations grade into Platy Flank formations near the ends of the tiger stripes. Platy Flank formations are notably less covered by

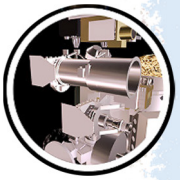

smooth materials giving a somewhat armored surface that reveals small surface cracks. Relict tiger stripe materials exist at the segmented, distal ends of tiger stripes and in at least one large system of parallel ridges and medial troughs eastward of Damascus Sulcus that are superficially similar in appearance and scale to the tiger stripes, but with smooth, strongly muted topography [Helfenstein et al. 2008; Spencer et al. 2009].

- The active Tiger Stripe rifts are separated by a system rounded, platy-textured, elongate hills and a conspicuous system of quasi-parallel ropy ridges and grooves that have spacings and dimensions comparable to the tiger stripe flanks themselves (now called funiscular terrain) [Porco et al. 2006; Helfenstein et al. 2008; Spencer et al. 2009].
- Enceladus' shape deviates slightly from a nominal equilibrium ellipsoid and has a south polar basin with a depth of ~0.4 km [Porco et al. 2006; Thomas et al. 2007a; Thomas 2010; Nimmo et al. 2011].
- The leading hemisphere of Enceladus has distinct geological provinces that exhibit diverse tectonic styles and different cratering histories. The highly tectonized terrains are bounded by a prominent broad annulus of grooved and striated terrains that ranges from about 60 km to over 140 km in width. It surrounds a complex arrangement of tectonic structures, including a conspicuous province near 30° N, 90° W of curvilinear massifs and roughly orthogonal-trending ridged-troughs that define a crudely radial and concentric pattern relative to a point near 25° N, 125° W. This angular sector, about 65° in width, may be the partial remains of an ancient impact basin with a diameter of about 180 km. It could also be the surface expression of an ancient, large diapir. Peculiar quasi-radial ridged-troughs superficially resemble extinct, topographically degraded examples of tiger stripes seen elsewhere on Enceladus. While these features may have a different fracture origin from tiger stripes, their comparable morphology suggests that long ago they may have expressed a similar style of fissure volcanism. Among our other significant findings is a region near 10° S, 60° W of rounded, rope-like sub-parallel ridges similar to ropy (funiscular) plains materials previously found only in the SPT region near active tiger stripes [Helfenstein 2010].
- The topography of a ~1 km high, 250 km wide bulge on the leading side of Enceladus has undergone strong resurfacing and has distinct boundaries to surrounding lower lying cratered terrains; it is consistent with the presence of convection-related warm ice at depth in isostatic equilibrium with surrounding non-convecting cooler ice. [Giese et al. 2010b].
- Tectonic deformation is a major source of blocky-ice features in the SPT. Impact cratering as well as mass wasting, perhaps triggered by seismic events, cannot account for a majority of ice-block features within the inner SPT [Martens et al. 2015; Giese et al. 2010a].

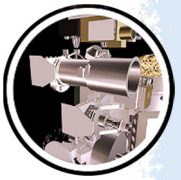

- Geologically young cycloidal fracture segments are found over a variety of different locations on the surface of Enceladus, including the SPT. These features likely have initiated as tension cracks with their form being controlled by diurnal variation of tides, as suggested for Europa. Such a mechanism requires that the ice be mechanically weak and, to allow for sufficient tidal amplitude, there must be a fluid layer below the icy surface. Thus, rather than being confined to just southern latitudes, our observations hint at the presence of fluid layers beneath other areas on Enceladus, potentially at a global sub-surface ocean in recent times [Giese et al. 2011a].
- Geysers emplaced along the three most active tiger stripe fractures (Damascus Sulcus, Baghdad Sulcus, and Cairo Sulcus) occur in local groupings with relatively uniform nearest-neighbor separation distances (~5 km). Their placement may be controlled by uniformly spaced *en echelon* Riedel-type shear cracks originating from left-lateral strike-slip fault motion inferred to occur along tiger stripes. The spacing would imply a lithosphere thickness of ~5 km in the vicinity of the tiger stripes [Helfenstein and Porco 2015].
- The orientations of tilted geyser jets are not randomly distributed; rather their azimuths correlate with the directions either of tiger stripes, cross-cutting fractures, or else fine-scale local tectonic fabrics. Periodic changes of plume activity may be significantly affected by crosscutting fractures that open and close at different times than the tiger stripes that they intersect [Helfenstein and Porco 2015].
- Geyser jets and their associated local hot-spots have the capacity to alter the morphology of surrounding icy geological features, possibly through ablation and sublimation-aided erosion, but also through condensation (which is the source of the heat) and the creation of vent plugs. Plausible morphological examples of ablation and sublimation-erosion include formations of pinnacles along the ridge crests surrounding active areas on and near tiger stripes fractures, possible scour marks or dust trails surrounding active vents, and the excavation of circular pit-like enlargements of active fracture troughs [Helfenstein and Porco 2015].
- Enceladus has a global subsurface ocean which was detected by multi-year imaging observations of forced librations in Enceladus' rotation [Thomas et al. 2016].

Geyser jets and their associated local hot-spots have the capacity to alter the morphology of surrounding icy geological features, possibly through ablation and sublimation-aided erosion, but also through condensation … and the creation of vent plugs.

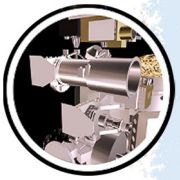

- An exceptionally high-standing (1750 m), 100 km long sawtooth-shaped ridge in the Samarkand Sulci fault band likely initiated by rift flank-uplift caused by extension followed by sinistral shear and compression 3.7 ±0.7 Ga ago, emplacing small-scale fragments sticking out of the surface and creating a (previously enigmatic) pattern of black spots on the sun-facing side of the ridge [Helfenstein et al. 2005a]. The estimated effective elastic lithospheric thickness is ~0.36 km at the time of formation compared to a present-day lower limit of 1.5 km obtained from lithospheric loading modelling [Giese et al. 2017; Wagner et al. 2017; Roatsch et al. 2016].
- A global chain of topographic depressions on Enceladus indicate that this synchronously locked moon has likely undergone True Polar Wander by ~55° about the tidal axis, from an early orientation in which the present terrain near (77° W, 40° N) would have been located at the paleo north pole [Tajeddine et al. 2017a].
- The large collection of high-resolution Cassini ISS images of Enceladus has provided a complete global photomosaic Enceladus base map at 100 m/pixel resolution [Roatsch et al. 2008a; Becker et al. 2016].

Main Icy Satellites (except Enceladus)

Mid-sized icy moons overview

- Accurate values for fundamental whole-body physical properties of the moons were obtained. These include mean radii, densities, shapes, etc., for example, Thomas [2010]; Thomas et al. [2018]; Castillo-Rogez et al. [2018], and also photometric quantities like geometric albedo, the phase integral, or Hapke photometric model parameters [Verbiscer et al. 2018].
- The sizes and shapes of the six mid-sized icy satellites were measured from ISS data. Mimas, Enceladus, Tethys, Dione and Rhea are well described by triaxial ellipsoids; Iapetus is best represented by an oblate spheroid [Thomas et al. 2007a].
- Global photomosaic base maps (ISS CL1:CL2 filter) were completed at better than ~400 m/pxl over the surfaces (Mimas to Rhea; ~800 m/pxl for wide parts of Iapetus) [Roatsch et al. 2009a; Roatsch et al. 2006, 2008a, 2008b, 2009b, 2012, 2013; Schenk et al. 2011; Schenk et al. 2018].
- Images of selected or serendipitous targets at very high-resolution (up to ~3 m/pxl) included bright-ray crater Inktomi (Rhea), fracture networks on Tethys, Dione, and Rhea, equatorial spots on Rhea, parts of Iapetus's ridge (Toledo Montes), etc.
- Almost complete stereo imaging was acquired for all mid-sized icy satellites from Mimas to Rhea (and > 50% for Iapetus), and global topographic maps are now essentially complete for each of the five moons [Schenk et al. 2018].

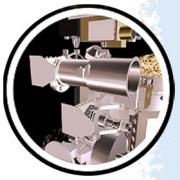

- Impact craters dominate the surfaces and provide the primary means of estimating terrain ages as well as many other properties of the surfaces [Dones et al. 2009; Kirchoff and Schenk 2010; Schenk et al. 2018; Kirchoff et al. 2018].
- However, crater saturation (crater density has reached a point where the formation of new craters erases the same area of older craters, and crater density has reached an equilibrium) is found on probably most, if not all, heavily cratered terrains on the mid-sized icy moons [Dones et al. 2009; Kirchoff et al. 2018].
- A predicted apex-antapex asymmetry in crater density is not observed at all on the Saturnian moons. Non-synchronous rotation is considered unlikely as the cause [Kirchoff et al. 2018].
- Secondary craters have been identified [Schmedemann et al. 2017; Schenk et al. 2018].
- None of the unusual crater landforms (like multi-ring basins or shallow distorted craters on the Galilean moons) seen on icy worlds that have confirmed internal oceans are seen on the mid-sized moons. However, this does not preclude possible oceans [Schenk et al. 2018].
- Global mapping has revealed geologically complex worlds. All (except perhaps Iapetus) have been tectonically deformed to different degrees. Almost all tectonic landforms are interpreted as extensional structures [Schenk et al. 2018].
- The trailing sides of Tethys and Dione and to a lesser degree of Rhea are darker than the respective leading sides. This is due to E-ring material infalling preferentially on the leading sides and has originally been discovered in Voyager data. The colors of the trailing sides are also redder than the leading sides of these moons.
- Potential endogenic processes acting on Saturn's mid-sized moons are cryovolcanism, tectonism, and viscous relaxation, see Kirchoff et al. [2018] and numerous references therein.
- Smooth plains were observed on Tethys and Dione by Voyager, and Cassini mapping confirmed that these are the only moons with such plains [Jaumann et al. 2009b].
- Wispy terrains, discovered on the trailing hemispheres of Dione and Rhea by Voyager, are rather recent and relatively pristine fracture networks. Their morphology and distribution are similar on these two moons [Schenk et al. 2018].
- The orbits and masses of the mid-sized moons have been largely improved.

Mimas

- Mimas was globally mapped at 216 m/pxl [Roatsch et al. 2013].

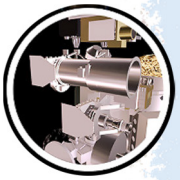

- It is a heavily cratered object with little evidence of endogenic resurfacing [Schmedemann et al. 2015].
- There was no targeted Mimas flyby of Cassini. Closest approach occurred on February 13, 2010 during rev 126, and the best images obtained at this flyby have a spatial resolution of ~93 m/pxl.
- There is morphologic evidence for a highly degraded impact basin of ~153 km diameter northeast of crater Herschel [Schmedemann and Neukum 2011].

Tethys

- Tethys was globally mapped at 292 m/pxl [Roatsch et al. 2009b].
- The highest definition view of Tethys' surface has a spatial resolution of 18 m/pxl and was obtained during the targeted flyby in rev 15 on September 24, 2005.
- Rugged topography of overlapping craters is typical for wide parts of Tethys [Schenk et al. 2018].
- Large 425 km-wide impact basin Odysseus is one of the largest well-preserved basins in the Saturnian system. Flat-floor deposits (as commonly found in large craters on the Moon and Mercury) are lacking, suggesting that impact melt ponding did not occur in large quantities. This lack of large melt sheets is characteristic of all craters in the Saturn system [Schenk et al. 2018].
- Tectonic structures on Tethys are all extensional [Schenk et al. 2018].
- Ithaca Chasma is the dominant tectonic feature. It is a giant rift zone already identified by Voyager, 1,800 km in length and subtending at least 270° of arc, between 70 km and 110 km in width, and 2–5 km deep. It predates the Odysseus basin and thus should not have been formed by this impact feature [Giese et al. 2007].
- Red streaks were only found on Tethys and are very enigmatic. They show an enhanced color signature in the near-IR which is a very unusual color for features on Saturn's icy satellites. No associated surface deformation is visible even at image resolutions of 60 m/pxl [Schenk et al. 2015].

Red streaks were only found on Tethys and are very enigmatic.

- Tethys's equatorial albedo band, first seen in Voyager images, was analyzed in several ISS NAC wavelengths. The band is symmetric 15° on either side of the equator and extends from 0° to 160° W that is, almost centered on the leading edge of Tethys. There is no evidence that the band is topographically-based; margins are gradational and there is no visible difference in underlying geology [Elder et al. 2007].

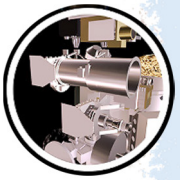

- ISS NAC polarization images found no evidence for surface textural variations on size-scales comparable to individual geological features, like crater walls and floors—on these size scales, the surface texture of Tethys appears to be uniform. However, a banded pattern on the surface was found and that likely originates in the subtle albedo variations tied to Tethys equatorial band [Elder et al. 2007] and thermally anomalous terrain [Helfenstein et al. 2005b].

Dione

- Dione was globally mapped at 153 m/pxl [Roatsch et al. 2013].
- Some Dione images taken from very close range are formally better than 6 m/pxl (rev 129 on April 7, 2010 and rev 220 on August 17, 2015), but these are somewhat smeared because of the large speed of the spacecraft.
- Dione is the geologically most-complex of the mid-sized moons except Enceladus.
- Although the Magnetometer (MAG) instrument detected a small mass loading from Dione toward space, ISS did not detect plumes or jets like those on Enceladus.
- The 345 km-wide Evander basin, discovered in Cassini images (this area was not covered by Voyager) features a prominent central peak ~4 km high, surrounded by a nearly complete peak ring. Unlike Odysseus on Tethys, Evander is strongly relaxed, with the floor nearly elevated up to the ground level. Despite this, relief of up to 4 km is preserved within the basin. Outside the rim, low topographic lobes radiate out from Evander ~1 crater radius from the rim [Schenk et al. 2018].
- Dione's most dramatic tectonic features are a distributed network of linear walled depressions interpreted as normal-fault-bound graben and half graben, for example, Wagner et al. [2006, 2009]. The so-called wispy terrain (associated directly with these extensional tectonic structures) might reflect exposures of clean water ice along normal fault scarps [Stephan et al. 2010; Beddingfield et al. 2016].
- There are only few positive-relief tectonic landforms on Dione. The most obvious is Janiculum Dorsa, a single ridge ~900 km long that trends approximately north-south in the moon’s leading hemisphere. Most other positive-relief landforms are related to impact craters, for example, Wagner et al. [2006].
- At the center of the smooth plains on the leading side of Dione is a pair of oblong craters (named Murranus and Metiscus). They are 45 to 70 km across, but only ~1 km deep. Their irregular shapes and the central mounds do not resemble the circular conical relaxed craters elsewhere on Dione [White et al. 2017]. It is suggested that Murranus and Metiscus might be volcanic craters. If so, these irregular craters were the only evidence for explosive or collapse-forming volcanism on Saturn's icy moons [Schenk et al. 2018].

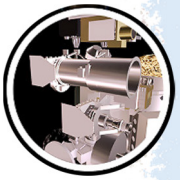

Rhea

- Rhea was globally mapped at 416 m/pxl [Roatsch et al. 2012].
- The best-resolved images of Rhea were acquired from rev 143 (January 11, 2011) and show details as small as ~5 m in size.
- The largest of the bright ray craters found in the Saturn system, the 49 km diameter Inktomi, is a flat-floored crater with a ray system radiating several hundred kilometers from the crater rim. It was imaged by ISS in August 2007 in 3 colors at resolutions up to 32 m/pxl and in stereo. The images are the best for a pristine crater in the Saturnian system and reveal a rugged landscape. Most of the ejecta and floor is essentially free of small craters [Wagner et al. 2011; Schenk et al. 2018].
- Many of the tectonic lineaments are normal faults and graben, for example, Wagner et al. [2007, 2010]. Most of this is concentrated in the trailing hemisphere as two major rift zones (Galunlati and Yasmi Chasmata) that trend roughly northeast–southwest and that are up to 3 km deep. These rifts are morphologically similar to those on Dione.
- The blue pearls (bluish spots; discovered with ISS) are a series of near-IR-dark irregular patches located at the crests of the highest ridges or massifs located along the equator of Rhea. Their origin is speculated to be related to infalling or collapse of a former orbiting debris ring [Schenk et al. 2011]. A dedicated search with ISS showed that present Rhea has no ring system [Tiscareno et al. 2010a].
- The blue pearls are not associated with any tectonic feature along its length or in near proximity. Instead, they appear to be associated with steep slopes (e.g., crater rims). The lack of any constructional artifacts associated with these color patterns on Rhea implies that they are due to regolith disruption [Schenk et al. 2011].

Iapetus

- About 75% of the surface of Iapetus was mapped at better than ~500 m/pxl [Schenk et al. 2018]. The scale of the global map from Roatsch et al. [2009b] is 802 m/pxl.
- Iapetus's unusual shape is best represented by an oblate spheroid; it supports a fossil bulge of ~34 km [Thomas et al. 2007a; Castillo-Rogez et al. 2007].
- A total of 10 basins larger than 300 km have been identified on Iapetus (despite the lack of resolved imaging in some locations), but only four on Rhea. Dione, Tethys, and Mimas are similarly depleted [Schenk et al. 2018].
- These three points show that there must be something fundamentally different between Iapetus and the inner mid-sized moons.
- Global and regional topography is much less smooth than for the other mid-sized icy moons [Thomas et al. 2007a].

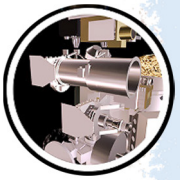

- The close targeted flyby in September 2007 revealed many properties of the anti-Saturn and the trailing hemisphere at high spatial resolution. The best-resolved images have resolutions of 10 m/pxl and show parts of the equatorial ridge within the dark terrain on the anti-Saturn side near 165° W longitude [Denk et al. 2008].
- ISS data show numerous impact craters down to the resolution limit [Denk et al. 2010].
- Iapetus's global albedo dichotomy, first described by the spacecraft's eponym Jean-Dominique Cassini in 1677 and unexplained since then, has been solved through Cassini CIRS and ISS data [Spencer and Denk 2010].
- Dust from Phoebe or possibly from other retrogradely-orbiting irregular moons has likely been painting the surface of Iapetus, forming the newly-detected global color dichotomy of Iapetus [Denk et al. 2010], which triggered the evolution of low-latitude and mid-latitude parts of the leading side into the stark bright and dark patterns we see today as the global albedo dichotomy [Spencer and Denk 2010].
- The global color dichotomy is identified as a fuzzy margin located approximately at the boundary between the leading and the trailing hemisphere; it is consistent with infalling material from Phoebe or the other irregular moons, while the boundary of the global albedo dichotomy is sharp, abrupt, irregular, and somewhat lens-shaped with equatorial parts extending from the leading to the trailing side and completely avoiding the polar areas. The global albedo dichotomy is not consistent with infalling material, but with thermal migration of water ice [Denk et al. 2010].
- A major property of the global color dichotomy is that dark material on the leading side is redder than dark material on the trailing side, and that bright material on the leading side (mainly at high latitudes) is also redder than bright material on the trailing side [Denk et al. 2010].
- Observations of small, bright-ray craters within the dark terrain indicate that the dark material corresponds to a blanket of a few meters or less in thickness [Denk et al. 2010], a finding also supported by Titan Radar Mapper (RADAR) data and consistent with the thermal migration model of Spencer and Denk [2010]. Bright ice, excavated through an impact, presumably sublimates away quickly; fading down to about twice the brightness of the dark surroundings happens within some ~107 years [Denk et al. 2008, 2010].
- While the global albedo dichotomy was known for centuries, Cassini ISS data showed that the stark dark-bright contrast is also a local phenomenon. The surface is either bright or dark, but almost never gray, even in the transition zone between the dark Cassini Regio and the bright Roncevaux Terra and Saragossa Terra [Denk et al. 2008].
- At mid-latitudes on the leading side and also low-latitudes on the trailing side, most of the equator-facing crater walls are covered by dark material, while

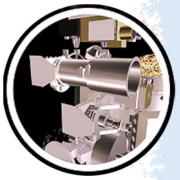

poleward-facing walls are mostly bright. Thermal segregation of water ice is again the explanation [Denk et al. 2008].

- The crater size-frequency distribution of Iapetus could be measured over almost four orders of magnitude (from > 60 m to ~600 km) [Denk et al. 2010].
- Iapetus's equatorial ridge—a huge and enigmatic ridge located exactly at the equator was discovered in ISS images [Porco et al. 2005d; Denk et al. 2005a, 2005b]. In places, this ridge is up to 20 km high and 70 km across, and it spans almost 75% of the moon's circumference [Porco et al. 2005d; Denk et al. 2008; Giese et al. 2008a; Singer and McKinnon 2011].
- While the ridge is mainly continuous on the leading side (Toledo Montes), it separates into the isolated mountains of the Carcassone Montes which were already discovered in Voyager data (and thus sometimes dubbed Voyager mountains) [Denk et al. 2000]. In general, it shows a wide range of cross-sections and heights at different longitudes [Denk et al. 2008; Singer et al. 2012]. Singer and McKinnon [2011] did not find potential hints for tectonic or volcanic origin.
- Defying any obvious explanation, numerous endogenic and exogenic formation mechanisms were proposed—for example, see short review of them by Damptz et al. [2018]. None of them can be favored over the others at this point.
- ISS NAC CL1:GRN-filter polarization images of Iapetus's highly contrasting terrains demonstrate that the degree linear polarization correlates almost linearly with the terrain albedo, thus verifying that Umov's Law broadly holds for all terrains visible in our Iapetus images even though there are stark albedo contrasts across the boundary of Cassini Regio and adjacent high-albedo regions. Thus, at sub-centimeter size scales, Iapetus's regolith most likely has a fairly uniform surface texture [Burleigh et al. 2010].

Satellite Orbits (including OpNav) and Orbital Evolution

Determination of gravitational mass (GM) for Mimas using an analysis of its resonant motion with Tethys and its effect on Methone [Jacobson et al. 2006a].

Pioneering use of systematic ISS astrometric observations (including OpNav images), including the use of mutual events, to improve the orbits of the Saturnian satellites [Spitale et al. 2006; Jacobson et al. 2008; Tajeddine et al. 2013; Cooper et al. 2014; Tajeddine et al. 2015].

The discovery and orbital dynamics of Polydeuces, establishing that it is an L5 co-orbital of Dione [Murray et al. 2005a].

The discovery and orbital dynamics of Anthe, establishing that Anthe is librating in the 11:10 resonance with Mimas: the first known example of a planetary satellite in a coupled inner Lindblad

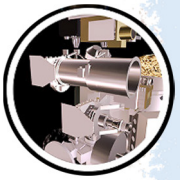

resonance (ILR) / co-rotation-eccentricity resonance (CER), leading to a new determination of the GM of Mimas [Cooper et al. 2008].

Association of Anthe's libration with the structure of its newly-discovered ring arc, in accordance with theory [Hedman et al. 2009b].

The discovery and orbital dynamics of Aegaeon in the G-ring, establishing that Aegaeon is also librating in a coupled first-order ILR/CER, in common with Anthe and Methone [Hedman et al. 2010b].

Improved orbits of the inner satellites and demonstration that the motion of Atlas is chaotic and can be modelled using the CoraLin theory applied to the 54:53 Lindblad and co-rotation resonances with Prometheus [Cooper et al. 2015; Renner et al. 2016].

The first determination of Saturn's tidal parameters incorporating Cassini astrometric data, including the tidal dissipation number Q and the Love number k_2, with confirmation that Q has previously been overestimated by a factor of 10. Important consequences for tidal heating of Enceladus [Lainey et al. 2017].

Small Satellites

Six new moons were discovered in Cassini images …

Six new moons were discovered in Cassini images: Daphnis, Aegaeon, Anthe, Pallene, Methone, and Polydeuces [Murray et al. 2005a; Cooper et al. 2008; Hedman et al. 2009b; Hedman et al. 2010b].

Cassini showed small satellites in the rings had a two-step origin. The innermost ones—Daphnis, Pan, Atlas, even Prometheus and Pandora—are likely not homogenous bodies and must have formed through aggregation of material around a denser core [Porco et al. 2007]. Pan and Atlas later developed equatorial ridges from late-stage accretion from the rings [Charnoz et al. 2007].

The inner small satellites of Saturn have distinctive physical properties and surface morphologies in each of several dynamical niches [Thomas et al. 2013].

Cassini image monitoring of Janus and Epimetheus revealed forced libration for Epimetheus which placed limits on any inhomogeneous mass distribution [Tiscareno et al. 2009].

Cassini showed that small (< 5 km) solid bodies can assume hydrostatic equilibrium ellipsoid shapes [Thomas et al. 2013].

The chaotically rotating satellite Hyperion has unique sponge-like topography that may reflect sublimation of species more volatile than water ice [Thomas et al. 2007b].

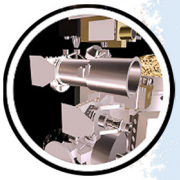

The chaotic rotation of Hyperion was analyzed using data from three flybys. The Lyapunov timescale was found to be approximately 100 days [Harbison et al. 2011].

Cassini images showed some small satellites had surface grooves, and the morphology and patterns of some of these were consistent with tidal effects [Morrison et al. 2009].

Phoebe and the Irregular Satellites

Phoebe

- June 11, 2004—only close flyby of Cassini-Huygens at Phoebe.
- ISS obtained images at better than 2 km pxl^{-1} over slightly more than three Phoebe rotations. The highest resolution ISS images have a pixel scale of 12.3 m.
- A global map was produced and delivered to the United States Geological Survey (USGS). Scale: 1:1,000,000; resolution: 8 pxl deg^{-1} or 233 m pxl^{-1} [Roatsch et al. 2006].
- Phoebe's global shape is close to an oblate spheroid, with a = b to within the uncertainties of the data [Thomas 2010; Castillo-Rogez et al. 2012; Thomas 2010].
- Mean radius: 106.4 ±0.4 km; Ellipsoidal radii (a × b × c):
  109.3 ±0.9 km × 108.4 ±0.4 km × 101.8 ±0.2 km [Thomas et al. 2018].
- Mean density: 1.642 ±0.018 g cm^{-3} [Thomas 2010].
- Even if the porosity of Phoebe were zero, its density would be 1σ above that of the regular icy Saturnian satellites. Therefore, Phoebe appears to be compositionally different from the mid-sized regular satellites of Saturn, ultimately supporting the evidence that it is a captured body [Johnson and Lunine 2005].
- Numerous impact craters are visible on the surface; they range in diameter from the lower limit imposed by the ISS image resolution up to ≈100 km [Porco et al. 2005d].
- Phoebe's topography, relative to an equipotential surface, is within the range of other small objects and is much higher than that for clearly relaxed objects [Thomas 2010].
- Digital terrain model (DTM) and orthoimage of the surface were produced from ISS data [Giese et al. 2006].
- J2000 spin-axis was found at Dec = 78.0° ±0.1°; RA = 356.6° ±0.3°, substantially different from the former Voyager solution [Giese et al. 2006].
- Two ISS observations from remote were designed to obtain light-curves at low and high phase angles [Denk et al. 2018].
- The Phoebe dust ring, discovered from Earth, has also been observed with the ISS WAC [Tamayo et al. 2014].

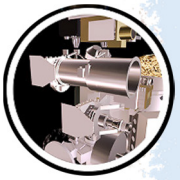

Other irregular satellites

- The irregular-moon observation campaign with ISS was the first use of an interplanetary spacecraft for a systematic photometric survey of a relatively large group of solar-system objects. They were not part of the original science goals of Cassini ISS.
- With 38 known members, the outer or irregular moons constitute the largest group of satellites in the Saturnian system. Except Phoebe, all were discovered between 2000 and 2007 from Earth (Cassini itself did not discover an irregular moon).
- Due to the large distance to the Cassini orbiter and the small sizes of the objects, the irregulars except Phoebe were always smaller than the size of a NAC pixel. The goal of the observations was thus to obtain light curves. The information for this sub-section stems from the summary chapter on irregular moons from Denk et al. [2018].
- All 9 known prograde plus 16 of the known 29 retrograde irregular moons were successfully observed with ISS, mainly with the NAC. Rotational periods could be derived for most of them (from light curve phasing), and also minimum ratios of the equatorial axes (from light curve amplitudes).
- Due to the position of the spacecraft inside the orbits of the moons, a large range of phase angles was available (and used) for the ISS observations.
- Most measured light curves show either four or six extrema (2-maxima/2-minima or 3-maxima/3-minima patterns), indicative that the objects have quite different shapes.
- All but Phoebe's light curves are primarily shape-driven, as expected for such small bodies.
- Average rotational period of 22 objects is 11.4 ±0.1 h (spin rate 2.10 ±0.02 d^{-1}). This is quite slow compared to main-belt asteroids of similar size range (~4 to ~45 km), but maybe not much different from the Jupiter Trojans, Hildas, or objects beyond Saturn's orbit.
- The fastest measured period is 5.45 h (Hati). This is the fastest reliably known rotational period of all moons in the solar system.
- However, the Hati period is much slower than the fastest rotations of asteroids, indicating that the outer moons may have rather low densities, possibly as low as comets.
- The slowest measured period is slightly longer than three days (Tarqeq).
- All light curves of moon Kiviuq show large amplitudes and are relatively symmetric. This makes Kiviuq a potential candidate for a binary or contact-binary object.
- The spin of Tarqeq is only ~0.5% off the 1:5 orbit resonance of Titan.

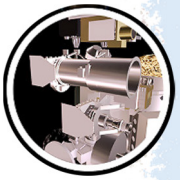

- Siarnaq and Ymir show very distinct 3-maxima/3-minima light curves. Convex-shape models of these moons resemble triangular prisms.
- Siarnaq and Ymir light curves from color filters do not show measurable deviations from the clear-filter light curves, indicating that their surfaces are not colorful at regional scales.
- Siarnaq's pole axis points to low ecliptic latitudes, indicating that this moon experiences strong seasons similar to the regular Uranian moons.
- Contrary to this, the pole axes of Phoebe and Ymir point close to one of the ecliptic poles.
- Most rotational periods of the prograde moons were found to be longer than those of the retrograde moons.
- Most rotational periods of the moons on higher tilted orbits were found to be longer than those on lower tilted orbits.
- Most rotational periods of the moons closer to Saturn were found to be longer than those of the moons farther away.
- Most rotational periods of the larger moons were found to be longer than those of the smaller moons.

Saturn

Cloud top zonal winds in Saturn's equatorial region were documented to be ~100 m s^{-1} weaker than those measured by Voyager, while winds outside the equatorial region were shown to be stable over this same time interval [Porco et al. 2005a; Pérez-Hoyos and Sánchez-Lavega 2006; Sánchez-Lavega et al. 2007; Li et al. 2013]. Stratospheric winds appear to vary over the Cassini mission, perhaps affecting the semi-annual equatorial oscillation [Li et al. 2011; Sánchez-Lavega et al. 2016].

The first direct measurements of vertical wind shear on Saturn showed that the equatorial zonal wind decreases sharply with increasing altitude, suggesting that the observed decrease in cloud top winds since Voyager may be a combination of time variation in the wind itself and time variation in the altitude of the equatorial cloud top [Porco et al. 2005a; Sayanagi and Showman 2007; Garcia-Melendo et al. 2010].

A giant long-lived dragon storm at 35° S appeared in 2004 and was found to be correlated with repeatable Saturn electrostatic discharges (SEDs), implying that the cloud feature is indeed an organized convective disturbance and that the origin of the SEDs is lightning discharges [Porco et al. 2005a; Dyudina et al. 2007; Fischer et al. 2007]. This in turn implies that Saturn's water abundance at depth must not be substantially less than Earth's.

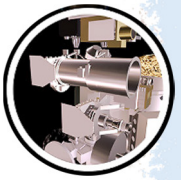

An even larger and longer-lasting giant storm was discovered by ISS at 33° N in 2010. This storm eventually encircled the entire latitude band, was also accompanied by SEDs, and created the largest tropospheric vortex ever seen on Saturn. The storm originated from the string of pearls feature previously discovered by VIMS. The string of pearls was found to be accompanied by a chain of dark cyclonic spots [Fischer et al. 2011, 2014; Sánchez-Lavega et al. 2011; Garcia-Melendo et al. 2013; Sayanagi et al. 2014]. The giant storm has a non-negligible effect on Saturn's global reflected sunlight and emitted thermal radiation [Li et al. 2015].

The first direct detection of lightning flashes on Saturn was made by ISS at the dragon storm latitude in the southern hemisphere [Dyudina et al. 2010]. This was followed by a similar direct lightning detection at the latitude of the giant northern hemisphere storm [Dyudina et al. 2013]. The lightning originates at a depth 125–250 km below the cloud tops, consistent with it being generated by water convective cloud systems.

The quasi-periodic occurrence of giant storms on Saturn on time scales of decades may be explained as the result of suppression of moist convection by the relatively high molecular weight of water in a hydrogen-helium atmosphere [Li and Ingersoll 2015].

Vortices occur preferentially in latitude bands containing westward jets, preferentially on the anticyclonic side of the jet maximum but sometimes on the cyclonic side. Most vortices last for less than a year, but the largest one observed has lasted for at least four years. The southern hemisphere has more vortices than the northern hemisphere [Vasavada et al. 2006; del Rio-Gaztelurrutia et al. 2010; Trammell et al. 2014, 2016].

Horizontal eddy momentum fluxes are directed into eastward jet cores and away from westward jet cores, converting eddy kinetic energy to zonal kinetic energy [Del Genio et al. 2007; Del Genio and Barbara 2012], as on Jupiter. Deep convective clouds exist at all latitudes but preferentially at cyclonic latitudes, as on Jupiter. This behavior is consistent with the idea that the rising branch of the mean meridional circulation occurs at cyclonic shear latitudes and the sinking branch at anticyclonic shear latitudes, implying that the jets are maintained by eddies due to instabilities of the large-scale flow [Del Genio et al. 2009].

Zonal winds weaken with increasing altitude in the cores of eastward jets [Garcia-Melendo et al. 2009, 2011a] and strengthen on either side of the jet core, implying that the jets broaden with increasing altitude [Del Genio and Barbara, 2012]. Eddy momentum fluxes weaken with altitude on the flanks of the jets, consistent with the broadening with altitude and suggesting that the eddy source is near or below cloud level [Del Genio and Barbara 2012].

Inferences about meridional circulation and convective storms from ISS images were found to be consistent with some of the spatial variations in ammonia abundance derived from Cassini RADAR radiometer [Laraia et al. 2013].

Objective analysis of cloud types in ISS continuum and methane band images suggests that dynamically, there are three distinct types of latitude bands on Saturn: 1) deep convectively

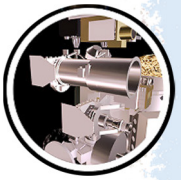

disturbed cyclonic shear regions poleward of the eastward jets; 2) convectively suppressed regions near and surrounding the westward jets; and 3) baroclinically unstable regions near eastward jet cores and in anti-cyclonic regions equatorward of them. These are roughly analogous to Earth's tropics, subtropics, and mid-latitudes [Del Genio and Barbara 2016].

Saturn has distinct vortices at both poles, with cyclonic winds, a warm core and cloud clearing near the pole, and high eyewall clouds surrounding the core. This feature resembles polar vortices found on several other planets [Dyudina et al. 2008, 2009; Sánchez-Lavega et al. 2006; Sayanagi et al. 2017].

The Saturn ribbon feature embedded in the 47° N eastward jet has properties in common with meandering western boundary currents in Earth's oceans such as the Gulf Stream and may be explained by a nonlinearly saturated shear instability [Sayanagi et al. 2010].

The ~78° N polar hexagon first seen by Voyager has persisted through the Cassini era [Sánchez-Lavega et al. 2014; Antuñano et al. 2015, 2018]. Simulations suggest that stable meandering polygonal structures resembling the hexagon can emerge without forcing when dynamical instabilities in a shallow eastward jet nonlinearly equilibrate. The wavenumber of the feature and its phase speed depend on the wind speed both at the cloud level and at the base of the flow [Morales-Juberías et al. 2011, 2015].

Stratospheric haze in Saturn's atmosphere produces photometric and polarimetric signatures that are most apparent in the short (near-UV and blue) wavelengths, in methane absorption bands at 619, 727, and 889 nm, and in polarization at visible and near-IR wavelengths. When Cassini arrived at Saturn in 2004, and earlier during the cruise phase, the northern high latitudes were blue, indicating an atmosphere with little haze content, emerging from a long period of little or no photochemical activity. During the course of the mission the northern high latitudes became exposed to sunlight, leading to photochemical haze formation and a trend toward redder colors [Fletcher et al. 2018]. Hemispheric differences in cloud feature contrast and decreases in contrast in the northern hemisphere over the course of the Cassini mission occur as a result [Del Genio et al. 2009; Del Genio and Barbara 2016].

Most latitudes on Saturn show little polarization, a consequence of reflection from an optically thick layer of large (relative to the observation wavelength), nonspherical ammonia ice or ammonia ice crystals mixed with an unknown component (since the near-infrared spectral feature of ammonia ice is rarely observed for Saturn). Cassini polarization images show enhanced polarization, enhanced forward scattering and darker particles in the region contained within the north polar hexagon [West et al. 2015; Pérez-Hoyos et al. 2016; Sayanagi et al. 2018]. These features indicate that, like Jupiter's poles, auroral input to the high atmosphere leads to the breakup of methane molecules and the subsequent

ISS made the first detection of Saturn's aurora at visible wavelengths in both hemispheres.

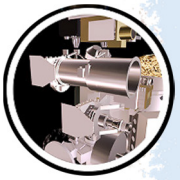

formation of heavier hydrocarbons leading to formation of a UV-dark haze of aggregate particles [Sayanagi et al. 2018].

ISS made the first detection of Saturn's aurora at visible wavelengths in both hemispheres. The color of the aurora varies with altitude and contains a distinct H-alpha line. The auroras form as bright arcs that sometimes spiral around the poles and sometimes form double arcs. The period of the north aurora is close to that of the Saturn Kilometric Radiation [Dyudina et al. 2015].

Rings

Discovery of many new ring phenomena, and more detailed observations of known phenomena, occurred very early in the Cassini mission in ISS observations [Porco 2005], all refined or extended in subsequent papers:

- Moonlets in the F-ring.
- New moons, Methone, Pallene and Polydeuces, among the mid-sized satellites, and estimates of their orbital elements,
- Refined orbits and sizes of ring region satellites Janus, Epimetheus, Prometheus, Pandora, Atlas, and Pan.
- High-resolution images of the edge of the Encke gap revealing in clear detail the edge waves created by Pan.
- Wakes created by Pan seen at large distances from the moon and the inference of low damping, and importance of self-gravity and collective effects, in the rings.
- Many previously undetected spiral waves, Atlas 5:4, 9:8, and 10:9, and Pan 7:6, producing estimates of ring and satellite properties in some cases.
- A wave in the middle of the narrow eccentric Maxwell ringlet.
- A wave in the Huygens ringlet.
- Very fine scale (~0.1 to 1 km) in high optical depth regions in the inner and outer B-ring, attributed to pulsation instabilities (or overstabilities).
- Mottled, ropy, and straw-like structure in the rings at fine scales (few km), indicative of particle clumping.
- New diffuse but relatively narrow tenuous rings between the A-ring edge and the F-ring, and within gaps (Encke, Huygens and Maxwell) in the main rings.
- Spikes and wisps, sharp and broad structures, that extend into the Keeler gap from its outer edge, predicting the presence of an embedded moon (which was discovered later to be Daphnis).
- Spectrophotometric results on the rings.

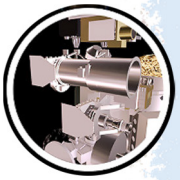

Discovery of characteristic gravitational signature of Prometheus in the F-ring core [Porco 2005].

Discovery of mirroring of F-ring core structure at opposite ansae confirming the effect of eccentricity/periapse perturbations [Porco 2005].

Discovery that the apparent multiple strands of the F-ring are kinematic spirals due to Keplerian shear following collisions [Charnoz et al. 2005].

Detailed understanding of how the gravitational perturbations from Prometheus combined with Keplerian shear produce the characteristic streamer and channel structures visible in the F-ring core [Murray et al. 2005b].

First observation of spokes with Cassini, confirming (with theoretical explanation) that they are a seasonal phenomenon [Mitchell et al. 2006].

Discovery of small moons embedded in the mid A-ring via the propeller-shaped disturbance they create in the ring [Tiscareno et al. 2006a].

First understanding of the complex morphology of spiral density waves due to the co-orbital moons Janus and Epimetheus, tracing their history as recorded in the rings and deriving ring surface mass density values for wave locations [Tiscareno et al. 2006b].

Discovery that the D-ring has undergone substantial changes in the 25 years between Voyager and Cassini [Hedman et al. 2007a].

Discovery of a vertical corrugation in the D-ring with a wavelength that decreases with time, interpreted as a winding spiral due to differential nodal regression after the ring was initially very slightly tilted in the early 1980s [Hedman et al. 2007a].

Discovery of a denser arc within the G-ring, confirming initial indications from Cassini Magnetospheric Imaging Instrument (MIMI). The ISS images are dominated by dust, but the MIMI absorptions must be due to a population of meter-sized objects [Hedman et al. 2007b].

Discovery that the G-ring arc material is trapped in a 7:6 corotation eccentricity resonance with Mimas [Hedman et al. 2007b].

Detailed understanding of spiral density waves and other radial structure from Cassini images taken during Saturn orbit insertion (SOI), deriving surface mass density and ring viscosity values for many locations within the rings with much higher fidelity than pre-Cassini measurements [Tiscareno et al. 2007].

New upper limit on the vertical thickness of the ring, 3–5 meters in the Cassini Division, 10-15 meters in the inner A-ring [Tiscareno et al. 2007].

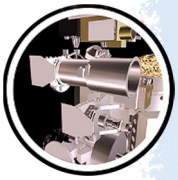

Detailed understanding of propellers in the Propeller Belts of the mid A-ring from analysis of ~150 objects seen in Cassini images [Tiscareno et al. 2008].

Discovery of moonlets embedded in the F-ring core and that the combined gravitational and collisional effects of Prometheus and small satellites produces the F-ring's unusual morphology [Murray et al. 2008].

In studies of the azimuthal asymmetry in Saturn's A-ring, the coefficient of restitution of the particles was found to be ~3.5 times lower than previously assumed, suggesting that particle collisions in the A-ring are more lossy than previously expected, possibly due to particle surface roughness, a regolith, and/or a large degree of porosity [Porco et al. 2008].

Discovery of the time variability of the outer edge of the A-ring due to the 7:6 inner Lindblad resonance with Janus and the effect of the Janus-Epimetheus orbital swap in January 2006 [Spitale and Porco 2009].

Detailed understanding of the relationship between the mass of a moon in a gap and the amplitude of the wavy edges of that gap, with more accurate measurements of the masses of Pan and Daphnis [Weiss et al. 2009].

Measurement of the inclination of Daphnis' orbit, via measurement of shadow lengths of scalloped gap edges and understanding of how those two quantities are related [Weiss et al. 2009].

Discovery of resonance-sculpted patterns within three dusty ring regions (the G-ring, the D-ring, and the Roche Division) with the latter two linked to periodicities within Saturn [Hedman et al. 2009a].

Discovery of three dusty ring structures at the orbits of three small Cassini-discovered moons (Methone, Anthe, and Pallene) confirming, in the case of Pallene, initial indications from Cassini MIMI. The Methone and Anthe ring structures are arcs centered on their moon and are associated with Mimas resonances, while the Pallene ring is circumferential and does not appear to be associated with any strong resonance [Hedman et al. 2009b].

Discovery of the mechanism by which perturbations from Prometheus produce gravitational instabilities in the F-ring core leading to moonlet formation and evolution [Beurle et al. 2010].

Discovery of unforced 1-lobed, 2-lobed, and 3-lobed self-excited patterns in the outer edge of the B-ring, in addition to the previously known 2-lobed pattern forced by Mimas, which implies the importance of viscous overstability in sculpting this region of the rings [Spitale and Porco 2010].

Discovery of localized structures, up to 3.5 km in vertical height, near the outer edge of the B-ring, implying the presence of embedded massive bodies [Spitale and Porco 2010].

Discovery of a single compact object or structure near the outer edge of the B-ring, designated S/2009 S1, casting a shadow implying a size of ~0.3 km [Spitale and Porco 2010].

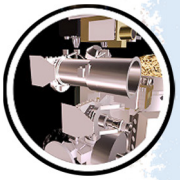

Detailed understanding of the Charming Ringlet, a dusty structure within the Laplace gap of the Cassini Division, as a heliotropic ring whose apoapse always points towards the Sun due to radiation pressure [Hedman et al. 2010a].

Discovery of Aegaeon, a 1 km moon embedded in the G-ring at the heart of the arc in that ring. Determination that Aegaeon is trapped in a strong resonance with Mimas, like Methone and Anthe [Hedman et al. 2010b].

Careful examination of the region around Rhea at both high and low phase angles, with the conclusion that there is no system of rings around that moon, contradicting an earlier report [Tiscareno et al. 2010a].

Discovery of giant propellers and long-term tracking of their orbits [Tiscareno et al. 2010b]. These constitute the first objects in the history of astronomy to have their orbits tracked while they are embedded in a disk, rather than orbiting in free space.

Measurement of shadow lengths for giant propellers during equinox, inferring sizes up to 1-2 km [Tiscareno et al. 2010b].

Discovery of corrugations in the C-ring, like those previously identified in the D-ring, consistent with being caused by an event that occurred in 1983. The identification of such a pattern in the more massive C-ring points to a massive but dispersed cloud of interplanetary debris as the cause [Hedman et al. 2011].

Detailed understanding of the three-dimensional structure of the E-ring, including a radial profile with a local minimum at the location of Enceladus, and variations that correlate with the orientation relative to the Sun [Hedman et al. 2012].

More detailed understanding of the shadow-casting compact object near the B-ring outer edge, S/2009 S1, indicating that it is an unresolved propeller structure and not an isolated embedded moon [Spitale and Tiscareno 2012].

Discovery that, compared to the Voyager epoch, the F-ring core was brighter by a factor two, was three times wider, and had a higher optical depth [French et al. 2012].

The use of geometrical fits of the F-ring core to show the extent of local variability in the orbital elements even though the average values are consistent with those determined from stellar occultations [Cooper et al. 2013]. Discovery of an empirical commensurability between the precession rates of Prometheus and the F-ring.

Discovery and detailed understanding of dusty ringlets in the Encke Gap, one sharing the orbit of Pan and two others on either side, with determination that the radial structure of these ringlets indicates heliotropic behavior as previously described for the Charming Ringlet, while the azimuthal structure constitutes many clumps that are moving with respect to Pan and corotation [Hedman et al. 2013].

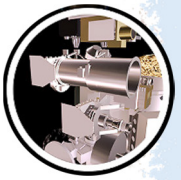

Detailed understanding of the spokes in the B-ring, following their growth and decline as seen in ISS images. Discovery that spokes undergo an active phase during which they grow in size and optical depth, with one edge apparently governed by Lorentz forces and the other edge apparently governed by Keplerian motion. Discovery via light-scattering behavior that spoke particles are irregularly shaped, not spherical. Discovery that spoke activity on both sides of the rings occurs with a period commensurate with the period of northern Saturn kilometric radiation (SKR) emission, though a period commensurate with the southern SKR also seems to be present. Discovery that peak spoke activity is near 200 degrees SLS4, which is divergent from the Voyager value (Mitchell et al. 2013)

Use of the Iapetus—1:0 spiral bending wave to derive a continuous mass density profile for the outer Cassini division and the inner A-ring, in particular finding that the sharp change in optical depth that defines the inner edge of the A-ring does not in fact correspond to any sharp change in surface mass density [Tiscareno et al. 2013a].

Discovery of impact ejecta clouds rising above the rings, and use of those clouds to infer the population of decimeter-to-meter-sized objects in heliocentric orbits near Saturn [Tiscareno et al. 2013b].

Discovery that the exceptionally bright, extended clumps which were common during the Voyager epoch were much rarer in the Cassini era with only two having been seen [French et al. 2014].

Detection and explanation of mini-jets in the F-ring as collisional products due to low velocity impacts with nearby objects [Attree et al. 2012; Attree et al. 2014].

Discovery of an object (Peggy) at the edge of the A-ring. Subsequent tracking of radial discontinuity (probably due to gravitational effect of embedded object) suggests stochastic behavior possibly due to encounters with smaller, nearby objects [Murray et al. 2014].

Discovery of an anti-resonance mechanism which can provide a stabilizing effect to reduce the effect of chaotic evolution of ring particle orbits at the F-ring's location.

Discovery of an anti-resonance mechanism which can provide a stabilizing effect to reduce the effect of chaotic evolution of ring particle orbits at the F-ring's location. The core may be located at a unique location where an anti-resonance and a co-rotation resonance with Prometheus are coincident [Cuzzi et al. 2014].

Detailed understanding of D68, a ringlet in the D-ring, with explication of patterns whose evolution may place important constraints on the ringlet's local dynamical environment and/or the planet's gravitational field [Hedman et al. 2014].

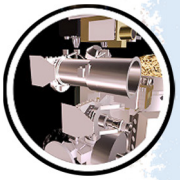

First observation of the Phoebe Ring in visible light, by Cassini images tracing Saturn's shadow as it recedes through that ring, placing new constraints on the properties of Phoebe Ring particles [Tamayo et al. 2014].

Detailed understanding of the tendrils of the E-ring surrounding Enceladus, and the mechanisms by which the E-ring is fed by the Enceladus geysers [Mitchell et al. 2015].

More detailed understanding of corrugations in the D-ring, including a time-variable periodic modulation that likely indicates organized eccentric motions of ring particles, suggesting that the 1983 event that started the spiral had an in-plane component as well as a vertical component, with the vertical component some 2.3 times larger. Mismatch between wavelengths in the D-ring and C-ring may indicate a two-stage initiating event [Hedman et al. 2015].

Detailed understanding of the wide range of viewing geometries available for Cassini ISS photometric measurements of the D-ring and G-ring, and application of the derived functions to understanding similar debris disks around other stars [Hedman and Stark 2015].

Discovery that the Janus-Epimetheus orbital swap in 2010 led to the disappearance of the characteristic 7-lobed pattern as the Janus resonance moved away from the ring edge. Other signatures in the edge pattern could be due to inhomogeneities in Saturn's gravity field [El Moutamid et al. 2016].

Discovery of a new evolving pattern in the D-ring, apparently created by an event that occurred in 2011, possibly debris striking the rings or a disturbance in the planet's electromagnetic environment, with explanation of similar patterns seen by Voyager having possibly resulted from an event that occurred in 1979 [Hedman and Showalter 2015].

Further observations of the Phoebe Ring, yielding a radial profile from 80 to 260 Saturn radii. Evidence of a change in behavior around 110 Saturn radii that may be due to interactions between the dust grains and Iapetus, or to other orbital instabilities. Evidence of material beyond the orbit of Phoebe, which may be due to other moons that contribute material to the ring. Evidence that the Phoebe ring is unusually rich in particles smaller than 20 μm, compared to particles larger than that size, which may be due to a steep size distribution of ejecta or to a subsequent process that preferentially breaks up larger grains [Tamayo et al. 2016].

Detailed understanding of the Huygens ringlet in the C-ring, with each edge modelled separately, finding one 2-lobed pattern forced by a resonance with Mimas as well as a self-excited 2-lobed pattern, and substantial additional structure that is not easily explained [Spitale and Hahn 2016].

Discovery of signs of embedded massive bodies within the Huygens ringlet, especially at two particular co-rotating longitudes [Spitale and Hahn 2016].

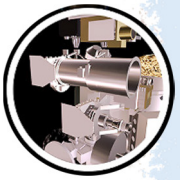

Detailed understanding of the inner edge of the Keeler Gap from ISS images, finding not only strong evidence for a 32-lobed pattern generated by Prometheus, but also 18-lobed and 20-lobed normal modes rising from within the ring. Also, discovery of multiple localized features on eccentric orbits that appear to move at the local Keplerian rate and persist for only a few months. Hypothetical explanations may include differences in how ring particles respond to resonances, and/or unseen embedded objects [Tajeddine et al. 2017b].

Detailed understanding of spiral density waves and their role in holding the ring system in place, using Cassini results for surface mass density and viscosity combined with improved theoretical understanding, demonstration that the A-ring is held in place by many resonances involving at least seven moons [Tajeddine et al. 2017c].

Detailed understanding of spiral density waves and their role in holding the ring system in place, … .

Discovery of a dusty ring that shares the orbit of Prometheus but precesses at a rate characteristic of the F-ring [Hedman and Carter 2017].

Discovery of previously unseen structures in the D-ring and the Roche Division, as well as novel fine-scaled structures in the core of the E-ring, in high-resolution high-phase images obtained during the Ring Grazing Orbits and Grand Finale [Hedman et al. 2017].

Determination that many of the gaps in the C-ring and the Cassini division are not held open by shepherd moons, based on non-detection during intensive Cassini searches for such moons [Spitale 2017].

Discovery of radial variations in the degree of visible clumpiness in the ring, in high-resolution images obtained during the Ring Grazing Orbits and Grand Finale [Tiscareno 2017].

Measurement of the particle-size distribution for small propellers in the Propeller Belts of the mid A-ring, in high-resolution images obtained during the Ring Grazing Orbits and Grand Finale [Tiscareno 2017].

Detailed images of the fine structure of giant propellers, obtained during the Ring Grazing Orbits and Grand Finale [Tiscareno 2017].

Detailed images of impact ejecta clouds in the A-ring and C-ring, with unprecedented color and frequency information, obtained during the Ring Grazing Orbits and Grand Finale [Tiscareno 2017].

Corrected and more complete profile of spiral density in the A-ring [Tiscareno and Harris 2018].

Measurement via spiral density and bending waves of surprisingly low surface density, 25 g/cm^2, in the inner B-ring [Tiscareno and Harris 2018].

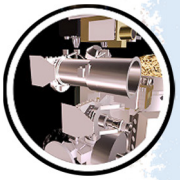

Creation of an atlas of resonant features in Saturn's rings [Tiscareno and Harris, 2018].

Systematic identification of resonant features with moons that drive each wave, and of apparently resonant features with no known driving source [Tiscareno and Harris 2018].

Open Questions for Saturn System Science

Titan (summarized in Nixon et al. [2018])

- What is the timing of the onset of north-polar summer storms?
- Is the weather Cassini observed typical for these seasons on Titan? If so, why does the implied seasonal transition in the mean meridional circulation lag that predicted by models by several Earth years?
- What explains the spectral behavior of some north-polar cloud features visible to VIMS at 2.1 μm but not to ISS at 938 nm or VIMS at other wavelengths (shorter and longer than 2.1 μm)?
- Over what timescale do changes occur in north-polar lakes and seas? And are liquid reservoirs exchanged between the north and south poles, and if so, over what timescale?
- What is the nature of exchange between surface organics and subsurface water? Is there cryovolcanism? Do tectonics facilitate exchange combined with icy mantle convection?
- What are the implications of seasonal behavior of haze for production processes?

Enceladus

- What mechanism(s) produce the phase lag between the maximum normal tidal stresses across the fractures and the maximum plume brightness (and hence mass) over the course of an Enceladus day? Is this phase lag also present in the response of the plume to the 4-year and 11-year periodic variations in tidal stresses across the SPT?
- What processes are occurring in the conduits leading from the ocean to the surface, and how do they change the contents of the plume? How wide are the conduits?
- Does liquid water ever reach the surface?
- How does the magnitude of the flux of curtain-style venting products compare with those of discrete geysers?
- How did the SPT form and how has it evolved with time?

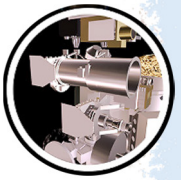

- Was the region of anomalous high thermal flux, presently under the SPT, much more extensive in the past? Did it extend to the equatorial regions on the leading-hemisphere and trailing-hemisphere, where there is widespread evidence for a strongly elevated thermal flux in the past, or where these regions affected by separate hot spots that have diminished over time? Has the activity been constant over time, or does it periodically diminish and return due to tectonic overturn? [Helfenstein 2010].
- To what extent might true polar wander (TPW) have resulted in the formation of tectonic features that are visible today? Are there regions of Enceladus outside the SPT that show evidence of elevated thermal flux due to the lithosphere passing over one or more regional hot spots?
- What does ancient terrain tell us about the early history of Enceladus?
- Are there unique, specific types of local geological structures that discrete geysers deposit or sculp which are diagnostic of their presence, activity, and persistence?
- Can extinct or relict tiger stripe structures be reliably identified outside of the SPT region?
- Are there examples of possibly relict structures other than tiger stripes on Enceladus that have been shaped by some form of ancient venting or cryovolcanism?
- Are the fine, gossamer cracks that slice though terrains throughout the SPT region part of the pervasive system of fine cracks that exist outside of the SPT region? What is their origin and what does it indicate about the mechanical structure of the surface and the nature of stresses that produced them?
- How does the thickness of the icy crust, and its thickness relative to the underlying ocean, vary with location on Enceladus? How has it changed over time?
- What role have tidal interactions played in controlling the evolution of Enceladus' global ocean, lithosphere, tectonism, and water eruptions? [cf. Thomas et al. 2016; Giese et al. 2011b].
- To what extent have plume fallout and accretion of E-ring particles affected the surface physical properties of Enceladus' surface materials [cf. Schenk et al. 2017]? Is there evidence that these interactions have changed over time producing observable records in:
  - Spectral properties and regolith composition?
  - Surface physical properties like regolith porosity and macroscopic texture, particle properties such as grain transparency and particle microstructure?
- Are there observable spectral and/or photometric effects of sintering by thermal hot spots that are diagnostic of the age and persistence of eruptive activity and/or subsurface convection on Enceladus [cf. Helfenstein 2012]?

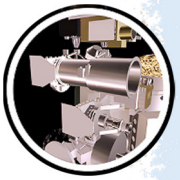

Main icy satellites (except Enceladus)

- What is the absolute timing of all surface-modifying events on the moons?
- How old (or young) is Saturn's satellite system? Based on the hypotheses that orbital instability caused massive collisions within a previous generation of Saturnian mid-sized moons inside the orbit of Titan, it has been speculated that the icy moons (except Iapetus) might be very young relative to the age of the Solar System, maybe just in the order of ~100 Ma [Ćuk et al. 2016]. This possibility is at least not precluded by the geologic record of these mid-sized bodies, but appears to pose major theoretical problems [Schenk et al. 2018]. How likely is it that all moons underwent major formation processes in a short period of time, but look old today? What would be diagnostic signatures of such a scenario? How could kilometer-sized topography of large basins like Evander or Odysseus survive in such a scenario? What is the source of the numerous impact craters?
- Determine the source of the impactors: Is the assumption of heliocentric projectiles (mainly Centaurs/ecliptic comets) as the origin causes of the craters really correct? Or could planetocentric sesquinary impactors (these are secondaries that remained in orbit around Saturn for a while before falling back on a surface) from impacts on the inner moon system and/or from catastrophic break-ups of moons within Titan's orbit [Movshovitz et al. 2015; Ćuk et al. 2016] and/or from the outer irregular moon system (which experienced a violent collisional history, but less likely except for Iapetus and possibly Hyperion because Titan appears to be an effective barrier [Denk et al. 2018] do the job? Alternatively, could there be a completely different impactor population? In case the Ćuk et al. [2016] scenario of a young satellite system is correct, the majority of the craters on the moons inside Titan must come from a planetocentric impactor population.
- How should any early bombardment events be incorporated into the rates? [Kirchoff et al. 2018]. (Only relevant if the moons are old.)
- Crater counts revealed relative paucities of craters with D < ≈10 km on Rhea and Iapetus, and of craters 10–20 km < D < ≈200 km on Mimas, Enceladus, Tethys, and Dione. Cryovolcanism, tectonism, or viscous relaxation are likely not the cause for these differences [Kirchoff et al. 2018]—but what else?
- How have the thermal profiles and physical structure of each satellite evolved over time?
  - How do visible geological and tectonic features record these changes?
- What past or current heating sources ever modified the mid-sized moons of Saturn?
- Why do we see no central pits in craters on these moons, while we do see them on water or ice-bearing bodies like Ceres, Ganymede, Callisto, Europa, Mars, and even examples on Earth?

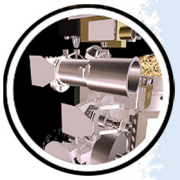

- What is the origin(s) of crater chains on Rhea, Dione, Tethys, and Iapetus? (Are they mostly from secondary cratering, or do split projectiles also form crater chains at Saturn?)
- To what extent have subsurface oceans been present over the geological evolution of each main icy satellite and what role have they played in shaping the present-day surface of each?
  - Is there evidence of tectonism that would require a subsurface water layer?
  - Are there geological features present that are diagnostic of ancient cryovolcanic activity?
  - If such features are present, is there stratigraphic information about their placement in time?
- To what extent have interactions between the outer diffuse rings and the regoliths on the main icy satellites affected the surface physical properties of the regoliths?
  - Spectral properties and regolith composition.
  - Surface physical properties like regolith porosity and macroscopic texture, particle properties such as grain transparency and particle microstructure.
  - Is there any observable evidence that the ring-satellite interactions have changed over time?
- Mimas is similar in size to neighboring, active Enceladus and the closest midsize icy satellite to Saturn, but it is devoid of any but the most rudimentary deformation. Why are these two bodies so different?
- What is the origin of Mimas's trough system?
- Has Mimas an irregularly shaped core or even a sub-surface ocean?
- Did a potential core of Mimas focus seismic energy during the Herschel impact, resulting in the irregular troughs and knobs found antipodal to the crater? (also known as, a scenario somewhat similar to Mercury and the Caloris basin?)
- Why is Tethys so geologically complex despite its very low density (~1 g/cm^3) and the consequently low abundance of radiogenic nuclides?

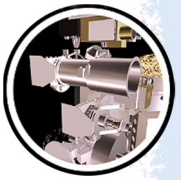

- Are the Odysseus basin and Ithaca Chasma on Tethys genetically linked? Giese et al. [2007] say no, but this has been questioned [Schenk et al. 2018]. What are the relative, what are the absolute ages of these two major features on Tethys?

What is the nature, age, and origin of the enigmatic red streaks on Tethys?

- What is the nature, age, and origin of the enigmatic red streaks on Tethys?
  - Are such spectral features observable on other Saturnian icy satellites? If not, why not?
- Smooth plains emplacement on Tethys and Dione: How did the smooth plains become smooth? The volcanic hypothesis remains, but many challenging questions do so as well: Cassini did not resolve flow fronts on the smooth plains unit—the margins of the smooth terrain grade into heavily cratered highlands over a significant distance, implying that there may be no recognizable discrete contact (boundary) between the two terrains [Kirchoff and Schenk 2010]. Could the smooth plains instead be the result of crater erasure by extremely high heat flow (despite the lack of any cryptic rings representing nearly flattened impact craters)?
- How are thermal anomalies such as those on Tethys and Mimas manifested in terms of surface physical properties of the regolith?
  - Are thermally anomalous features like the Pac-Man terrain observable or more subdued on other main icy satellites of Saturn?
- Does Dione host an ocean [Beuthe et al. 2016]? Difficult to confirm geologically—if the outer shell is on order of 100 km deep as suggested, it may be difficult to fracture.
- Is large basin Evander so much relaxed due to a sub-surface ocean?
- Origin of the wispy terrains (fracture networks) on Dione and Rhea.
- On Rhea, rare high-resolution views (at < 20 m/pixel, e.g., ISS frame N1741547885) reveal occasional isolated fault scarps. Are these far more common than might be guessed from lower resolution global imaging? [Schenk et al. 2018].
- Rhea's blue pearls—on Saturn's mid-sized icy moons, bluish colors are usually associated with young features and fade with time. Thus, we would expect that a color signature like Rhea's equatorial blue spots would also fade with time, implying that it might be a geologically recent phenomenon. Is this really the case? If so, how has a young ring feature formed around Rhea in more recent times? If not, how could the bluish color be preserved?
- Why does Iapetus have so many more large basins and a much more rugged topography than the inner moons? (Was the incoming projectile flux different? Was there a major heating event on the inner moons, erasing the topographic record of early giant impacts? Were the inner moons formed later? Was Iapetus formed elsewhere? ...?)

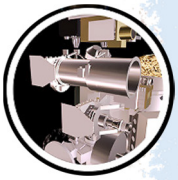

- Iapetus—how did the equatorial ridge form?
- Why is the shape of the cumulative crater size-frequency distribution of Iapetus so close to the size-frequency distribution of the Earth's moon [Denk et al. 2010 Figure 3]?

Satellite orbits and orbital evolution

- Are the orbits of the inner satellites stable in the long-term?
- Did the small inner satellites form from the rings?
- What are the masses of Anthe, Methone, Pallene, Polydeuces and Aegaeon?
- What mechanism determines the secular evolution of the Saturnian satellites, in particular Enceladus?

Small satellites

- Do the mean densities of the satellites restrict possible origin mechanisms?
- Can we assign relative ages to the small satellites and relate those to surface ages of large satellites, or to the age of the main ring system?
- How many types of surface grooves are there, and do any reveal internal structures?
- What are the mechanisms that allow small (few km) objects to assume a hydrostatic shape?

Phoebe and the irregular satellites

- What are the spin rates of the 13 irregular moons not observed by Cassini?
- What are the precise sizes of Saturn's irregular moons?
- How are they looking like? (What are their shapes?)
- What are their exact albedos, how much do they differ between the objects?
- What are their densities? Might they be even lower than ~500 kg/m^3, as indicated by the rotational periods? Are the irregulars indeed rubble piles of cometary nature?
- Are there noticeable albedo variations on the surfaces (other than Phoebe)?
- Is there any irregular moon with color variations on the surface?
- Are there really significant color variations between different objects, as suggested from ground-based observations?
- Is the distribution of pole-axis orientations random, or is there a preferred orientation?

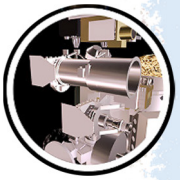

- How are the phase curves looking like, and what will they tell us about the surface properties?
- Do contact-binary irregular moons exist; might they even be common in the Saturn system?
- Do binary moons exist?
- Is there a spin-orbit resonance of Tarqeq with Titan?
- How old are the irregulars that exist today?
- How many progenitor objects were captured by Saturn? When did this happen (when was the first, when the last capture event)? How did Saturn do that? How many of them (or what fraction) were trapped in prograde, in retrograde, in low-tilted, in highly tilted orbits?
- Where in the solar nebula did they originally form? (Inside or outside the Saturn orbit? Were they former asteroids, Hildas, Trojans, Centaurs, Kuiper-Belt objects, comets?)
- Might some of the retrograde moons (especially the Mundilfari and the Suttungr families) be ejecta from large impacts on Phoebe?
- Likely non-random correlations were found between the ranges to Saturn, the orbit directions, the orbit tilts, the object sizes, and the rotation periods. While there are reasonable hypotheses for some of these correlations, a compelling physical cause for size and spin relations to orbital elements is not known.

Saturn

- Does Saturn actually have a much stronger equatorial jet than Jupiter, or are estimates of Saturn's rotation period biased? If Saturn actually has a stronger jet, what makes the two planets different in this regard?
- What is the water abundance at depth on Saturn? If Saturn is wetter than Jupiter, why? Does the water abundance dictate the frequency of major convective storms? Why are giant storms preferentially observed at about the same latitude in both hemispheres?
- Does the sign of the mean meridional circulation at cloud level reverse in the upper troposphere? How does the circulation at cloud level relate to the circulation between cloud level and the water condensation level?
- To what extent do processes deep in Saturn's atmosphere versus processing operating above the water condensation level contribute to the dynamical behavior observed at cloud level? What process provides the energy that drives the eddies at cloud level?
- Why do the north and south poles of Saturn differ in their dynamical behavior?

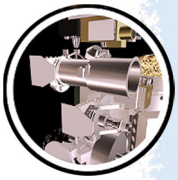

- What explains the lack of coherence between the latitudinal variation of Saturn's visible albedo and the jets at cloud level? Why do cloud features observed at deeper levels by VIMS look different from those observed by ISS at somewhat higher altitude?
- What constituent in Saturn's upper tropospheric haze explains the absence of a near-IR ammonia feature?

Why do cloud features observed at deeper levels by VIMS look different from those observed by ISS at somewhat higher altitude?

Rings

- What causes the C-ring plateaus and sharp optical-depth jumps within the B-ring?
- Are all of the irregular structures in the high optical depth regions of the A-ring and B-ring caused by overstabilities?
- Why are the inner edges of the A-ring and B-ring, and the edges of the C-ring plateaus, sharp only in optical depth, while their mass density profiles are much more gradual?
- What causes the red color of the A-ring and B-ring, and its dramatic increase inwards across the B-ring?
- Why do different ring textures appear in sharp-edged belts that are adjacent to each other? What do these textures tell us about ring particle properties?
- What is the velocity distribution of ring impact ejecta? How does it vary across the radial extent of the rings? How does ballistic transport sculpt the structural and compositional character of the rings?
- What are the kronoseismology waves in the rings telling us about the structure and history of Saturn's interior?
- Are there cyclic, self-limiting processes of growth and disruption of small planetesimal-sized objects, especially in the outer A-ring and F-ring?
- What is the mass of the F-ring?
- Why does the F-ring precess uniformly despite all the local variability? (Collisions? Self-gravity?)
- Is the F-ring in a stable, long-term location or will it eventually dissipate?
- What is the origin and long-term fate of propeller moons? What do they teach us about astrophysical disks?
- Why do propellers have such complex photometry? What do these characteristics tell us about the particles and their properties?

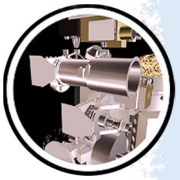

- How was Peggy formed—evolving propeller object or formed from streamline bunching due to 7:6 resonance?)
- What is Peggy's ultimate fate? Will it move inwards, or will it move outwards and escape?
- What forms the spokes?
- How old are the rings?
- How are small dust grains transported, confined and lost throughout the Saturn system?
- What controls the shape and brightness of narrow dusty ringlets within gaps in Saturn's rings?
- What controls the distribution and evolution of bright clumps in the Encke Gap ringlets? Why are such clumps rare in other narrow dusty ringlets?
- What determines the distribution of dust in the D-ring and Roche Division?
- How do the dusty rings respond to seasonal changes in solar radiation forces and magnetospheric asymmetries?
- How much do the dusty rings change over time?

ISS Non-Saturn Science Results

Jupiter Atmosphere and Rings

During a several-month approach to Jupiter, the ISS NAC captured the evolution of a large spot near latitude 65 degrees [Porco et al. 2003]. The lifetime of this UV Great Dark Spot is apparently a few months. A nearly-identical spot was seen in earlier Hubble near-UV images, but only once [West et al. 2004]. Initially the spot resides near System III longitude 180 degrees, coincident with the location Jupiter's deep thermal-IR auroral emission. Over the course of a few months repeated images from Cassini show that the spot morphs and shears, apparently from Jupiter's differential zonal flow field at high latitude. The spot is not visible at wavelengths longer than near-UV, and not seen in methane filters, indicated the absence of particles.

The Cassini ISS took images every ~2 hours as it approached Jupiter starting on October 1, 2000 [Porco et al. 2003]. The phase angle was 20° at the start and passed through 0° in mid-December. In this way, every point on the planet up to ±60° latitude was viewed in sunlight at least once per Jovian day, which is about 10 hours. The images at a given longitude could be played in sequence to make an ~70-day movie with a time step of 10 hours that showed the clouds in motion in Jupiter's atmosphere. This data set was an invaluable aid in measuring the winds, lightning, waves, clouds, turbulence, and discrete features, leading to a greater understanding of the planet's weather.

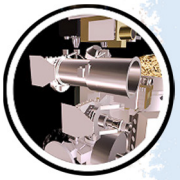

The colored cloud bands that circle Jupiter on lines of constant latitude are an obvious visible feature. The bands are accompanied by zonal winds—the eastward and westward jets that are strongest at the north and south boundaries of the bands. The winds are measured by tracking the positions of clouds in sequences of images, usually with a time step of ~10 hours. The jets are more stable than the cloud colors, and a comparison of jet speeds over the 20-year period from Voyager to Cassini shows almost no change [Porco et al. 2003].

Comparison of data from Cassini, Voyager, and Hubble Space Telescope reveals small changes with a 4–5 year period near the equator [Simon-Miller and Gierasch 2010]. These oscillations are similar to the quasi-biennial oscillation in Earth's atmosphere. The high-speed jet at 24° N varied from 2000 to 2008 [Asay-Davis et al. 2011], but generally the zonal jets are remarkably stable.

Cassini ISS documented changes in the large ovals like the Great Red Spot and the Oval BA. The Red Spot, an anticyclonic vortex that has existed for at least 150 years, was found to be shrinking from 1996–2006 [Asay-Davis et al. 2009; Shetty and Marcus 2010]. The wind speeds in the Oval BA did not change in 2005–2006 when the cloud color became redder [Hueso et al. 2009]. The wind structure around Oval BA is ring-like, and the winds at the periphery strengthened from 1997 to 2007 [Choi et al. 2010; Sussman et al. 2010]. Lifetime is proportional to size. A study of 500 spots over the 70 days of the Cassini movie reveals lifetimes of 3.5 days for convective spots and 16.8 days for all other spots [Li et al. 2004].

Cassini ISS revealed important properties of wave clouds visible in Jupiter's atmosphere. The small-scale (300 km wavelength) gravity waves seen in Voyager and Galileo images were remarkably absent in the Cassini 70-day movie [Arregi et al. 2009]. A chevron-shaped pattern centered on a high-speed (140 m/s) jet at 7.5° S could be an inertia-gravity wave or a Rossby wave [Simon-Miller et al. 2012]. On a larger scale, the equatorial plumes and hot spots seem to form a wave that circles the planet at constant latitude [Li et al. 2006a; Choi et al. 2013]. Hot spots are holes in the clouds, and it is important to understand them if one is to properly interpret the Galileo probe results. Slowly varying westward propagating waves are likely to be Rossby waves, and these were observed in ISS images of the Polar Regions [Barrado-Izagirre et al. 2008].

Around closest approach, Cassini imaged Jupiter over a wide range of phase angles. Cassini ISS observed four clusters of lightning on the night side, where a cluster is a site that produces multiple lightning flashes. Cassini saw lightning flashes that were more than 10 times more powerful than any seen before on Jupiter [Dyudina et al. 2004]. Brightness versus phase angle revealed scattering properties, color, and number of chromophores of the clouds [Ordonez-Etxeberria et al. 2016]. Jupiter provided surface truth for use in interpreting exoplanet phase curves [Dyudina et al. 2016]. The phase angle dependence was useful in inferring vertical structure in Jupiter's clouds [Li et al. 2006b; Garcia-Melendo et al. 2011b; Sato et al. 2013; Dyudina et al. 2016].

> Cassini ISS confirmed a result from Voyager that the eddies, … , are accelerating the zonal jets … .

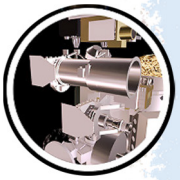

The high-resolution and dense coverage of the Cassini ISS images made possible a number of fundamental statistical studies of turbulence, eddies, and eddy mean flow interaction. Cassini ISS confirmed a result from Voyager that the eddies, which are transient structures ranging in size up to a few thousand km, are accelerating the zonal jets [Salyk et al. 2006]. Other processes, invisible to Cassini, must be decelerating the jets in order to maintain a steady state.

Other fundamental properties of the flow include the scale and power spectrum of the motions [Barrado-Izagirre et al. 2009, 2010; Choi and Showman 2011], for which one often uses brightness variations as a proxy for the wind itself. When the spatial resolution is good enough, as it is with Cassini ISS, one can use the derived velocity field to get the kinetic energy spectrum. The spectral slope implies an inverse cascade of kinetic energy from small scales to the scale of the zonal jets [Galperin et al. 2014; Young and Read 2017]. The velocity field derived from the Cassini movie was used to derive the transport barriers to horizontal mixing [Hadjighasem and Haller 2016].

The basic dynamical features (the zonal wind profile versus latitude, the flow around the large ovals, and their time-dependent behavior) become the target quantities that numerical models try to reproduce. Thus the published zonal wind profiles from Voyager and Cassini were used to compute potential vorticity, which is an important dynamic quantity in modeling studies [Read et al. 2006]. Specific features of the flow within the Red Spot were matched with numerical models to solve for uncertain atmospheric parameters [Morales-Juberias and Dowling 2013]. Finally, the general features of the zonal jets were used to address the basic question of whether the flow is shallow or deep [Heimpel et al. 2005].

Cassini images of the Jovian main ring sampled a broad range of wavelengths and viewing geometries over a period of 37 days during the Jupiter flyby [Porco et al. 2003]. The ring's phase curve was found to be flat from low to medium phase angles.

The color of the Jupiter ring is indicative of the parent bodies' intrinsic color, and not an effect of scattering by small dust grains [Throop et al. 2004]. The main ring is composed of a combination of small grains with a normal optical depth of ~4.7×10^{-6}, and larger bodies of optical depth ~1.3×10^{-6}. The ring's flat phase curve between 1° and 130° confirms the irregular-sized, rather than spherical, particles.

Jupiter/Exoplanet Studies

Disk-integrated reflected light curves derived from Cassini images indicate that for gas giant exoplanets, an assumption that they behave as Lambertian scatterers will underestimate stellar absorption and thus equilibrium temperature of the atmosphere. Saturn-size rings can be confused for a larger planet size, but produce an asymmetry in the phase curve that may help to resolve the ambiguity [Dyudina et al. 2005, 2016].

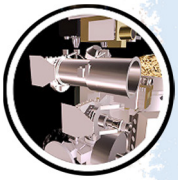

Jupiter Satellites

Discovery of previously unseen ~400 km high plume over the north pole of Io. Joint Galileo imaging showed that the location of the vent was Tvashtar Catena [Porco et al. 2003].

Spatially resolved images of Europa in eclipse show that its visible aurorae are brightest around the limb, indicating an atmospheric rather than surface source [Porco et al. 2003].

First disk resolved imaging of a Jovian outer satellite. The measured size range of Himalia is four to six NAC pixels indicating that it is not spherically shaped. These values correspond to a diameter of 150 ±10 km × 120 ±5 km, if the principal axes (or diameters close to them) were measured. From this size, the surface albedo is calculated as 0.05 ±0.01 [Porco et al. 2003].

The fitted orbital parameters of the inner satellites Amalthea and Thebe confirm the relatively high inclinations of these satellites, equivalent to maximum vertical displacements from the equatorial plane consistent with current estimates of the half-thickness of the Amalthea and Thebe gossamer rings [Cooper et al. 2006]. This supports the conclusion that these satellites are sources of the ring material.

There are no undiscovered satellites between 2.6 R_J and 20 R_J with inclinations < 1.6°, eccentricities < 0.0002 and visual magnitudes (as seen from 40 million km) brighter than 14.5 [Porco et al. 2003].

Observations of auroral emissions in Io's atmosphere throughout the duration of eclipse indicate that the atmosphere must be substantially supported by volcanism [Geissler et al. 2004].

Open Questions for Non-Saturn Science

Jupiter's atmosphere

- Are the zonal winds shallow, or do they extend downward thousands of km along cylinders concentric with the rotation axis? This question applied immediately after Cassini's encounter with Jupiter in 2000. It may have been answered since then by Juno observations of Jupiter and Cassini observations of Saturn.
- What powers the eddies, given that the eddies seem to be powering the zonal jets? The possibilities are: horizontal gradients of temperature due to excess sunlight absorbed at the equator, and unstable vertical gradients due to internal heat from below.
- What limits the speed of Jupiter's zonal jets compared to the higher speeds of the zonal jets of the other giant planets?
- How does the Red Spot maintain itself against turbulent friction? Does it cannibalize smaller spots? Why is the Red Spot shrinking?

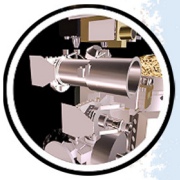

- What caused the three white ovals to merge into the single Oval BA after almost 60 years of separate existence?
- What generates the waves seen in the Jovian clouds? Can one feature act as an obstacle to the flow and generate lee waves? Can an energetic transient event generate waves radiating off to infinity? What role do breaking waves play in redistributing energy and momentum? The question applies to each wave type separately.
- What are the visible clouds made of, and what gives them their color?
- What does lightning tell us about the atmosphere below the cloud tops? Does lightning imply water, or could charge separation occur in the ammonia cloud?
- What do the numerical flow models tell us about the depth of the flow, the source of energy for the flow, and the processes that operate below the tops of the clouds?

Jupiter/exoplanet studies

- What do ISS measurements of disk-integrated polarization of Jupiter and Saturn tell us about what can be learned from exoplanet polarization measurements (cloud and haze particle properties)?
- What do ISS measurements of disk-integrated reflected flux from Jupiter and Saturn tell us about what can be learned from time-series measurements of flux from exoplanet flux (rotation rates, differential rotation)?
- What can ISS measurements of Jupiter and Saturn tell us about the amplitudes of flux and polarization variations for giant planets, providing insight for signal/noise estimates for exoplanet time-series measurements?

Jupiter's satellites

- What are the masses and densities of the small inner satellites Metis, Adrastea and Thebe?
- What are the rotational periods of the irregular satellites? So far, a reliable spin period is only available for Himalia. For the other 60 known irregulars, none has been published to date. An inventory is highly desired.
- Determine to good accuracy the sizes, albedos, colors, pole-axis orientations, object shapes, phase curves of the Jovian irregulars.
- What are the densities, composition and internal structure of the Jovian irregulars?
- Does Jupiter have binary or contact-binary satellites?

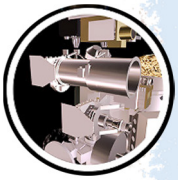

- For the Saturnian irregulars, likely non-random correlations were found between ranges to the planet, orbit tilts, object sizes, and rotation periods. Do the Jovian irregulars show something similar as well?
- Origin—are the irregulars former Jupiter Trojans, or do they come from the inner solar system, or the outer solar system? Was it the same source that also fed Saturn's irregular moon system?
- Origin—how many progenitor objects did Jupiter capture, and when? How massive were they? What is their collisional history?

Science Objectives and Traceability Matrices

Table ISS-1 is the Cassini Solstice Mission Science Objectives. Tables ISS-2 through ISS-6 are the Saturn, Rings, Magnetospheres, Icy Satellites, and Titan Cassini Solstice Mission detailed Traceability Matrices.

Cell codes for Table ISS-1 through Table ISS-6 are as follows:

- First letter = discipline (**S**aturn, **R**ings, **M**agnetospheric and Plasma Science (**M**APS), **I**cy Satellites, **T**itan)
- Second letter = objective type (**C**hange related or **N**ew question)
- Third number = priority level (**1**, **2**)
- Fourth letter = distinction within priority level (**a**, **b**, **c**, etc.)

Color key for Table ISS-1 through Table ISS-6 are as follows:

- Not an ISS objective
- Measurement objectives satisfied
- Measurement objectives partially satisfied
- Measurement objectives not satisfied

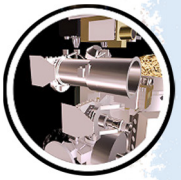

Table ISS-1. Cassini Solstice Mission Science Objectives—Prioritized Summary. Goal: Observe seasonal change in the Saturn system, to understand the underlying process and prepare for future missions.

Saturn	Rings	MAPS	Icy Satellites	Titan
Seasonal-Temporal Change				
Priority 1				
SC1a: Observe seasonal variation in temperature, clouds, and composition in three spatial dimensions.	**RC1a:** Determine the seasonal variation of key ring properties and the microscale properties of ring structure, by observing at the seasonally maximum opening angle of the rings near Solstice.	**MC1a:** Determine the temporal variability of Enceladus' plumes.	**IC1a:** Identify long-term secular and seasonal changes at Enceladus, through observations of the south polar region, jets, and plumes.	**TC1a:** Determine seasonal changes in the methane-hydrocarbon hydrological cycle: of lakes, clouds, aerosols, and their seasonal transport.
SC1b: Observe seasonal changes in the winds at all accessible altitudes coupled with simultaneous observations of clouds, temperatures, composition, and lightning.	**RC1b:** Determine the temporal variability of ring structure on all timescales up to decadal for regions including Encke gap, D-ring, F-ring, and ring edges by substantially increasing the cadence and time baseline of observations.	**MC1b:** Observe Saturn's magnetosphere over a solar cycle, from one solar minimum to the next.		**TC1b:** Determine seasonal changes in the high-latitude atmosphere, specifically the temperature structure and formation and breakup of the winter polar vortex.
Priority 2				
SC2a: Observe the magnetosphere, ionosphere, and aurora as they change on all time scales—minutes to years—and are affected by seasonal and solar cycle forcing.	**RC2a:** Focus on F-ring structure, and distribution of associated moonlets or clumps, as sparse observations show clumps, arcs, and possibly transient objects appearing and disappearing.	**MC2a:** Observe seasonal variation of Titan's ionosphere, from on Solstice to the next.		**TC2a:** Observe Titan's plasma interaction as it goes from south to north of Saturn's solar-wind-warped magnetodisk from one solstice to the next.
New Questions				
Priority 1				
SN1a: Determine Saturn's rotation rate and internal structure despite the planet's unexpected high degree of axisymmetry.	**RN1a:** Constrain the origin and age of the rings by direct determination of the ring mass, and of the composition of ring ejects trapped on field lines.	**MN1a:** Determine the dynamics of Saturn's magnetotail.	**IN1a:** Determine the presence of an ocean at Enceladus as inferred from induces magnetic field and plume composition, search for possible anomalies in the internal structure of Enceladus as associate with plume sources, and constrain the mechanisms driving the endogenic activity by in situ observations and remote sensing.	**TN1a:** Determine the types, composition, distribution, and ages, of surface units and materials, most notably lakes (i.e., filled versus dry and depth; liquid versus solid and composition; polar versus other latitudes and lake basin origin).

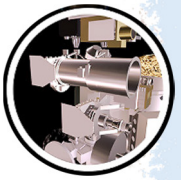

Table ISS-1. Cassini Solstice Mission Science Objectives—Prioritized Summary. Goal: Observe seasonal change in the Saturn system, to understand the underlying process and prepare for future missions.

Saturn	Rings	MAPS	Icy Satellites	Titan
SN1b: Observe the aftermath of the 2010–2011 storm. Study the life cycles of Saturn's newly discovered atmospheric waves, south polar hurricane, and rediscovered north polar hexagon.	**RN1b:** Determine the composition of the close-in ring moons as targets of opportunity.	**MN1b:** Conduct in situ and remote sensing studies of Saturn's ionosphere and inner radiation belt.	**IN1b:** Complete the comparative study of Saturn's mid-sized satellites, their geological and cratering histories, and interactions with the Saturn system, with remote sensing of Mimas at the highest resolution possible in order to understand the mechanisms behind its unique thermal properties discovered by Cassini.	**TN1b:** Determine internal and crustal structure: Liquid mantle, crustal mass distribution, rotational state of the surface with time, intrinsic and/or internal induced magnetic field.
SN1c: Measure the spatial and temporal variability of trace gases and isotopes.	**RN1c:** Determine structural and compositional variations at high-resolution across selected ring features of greatest interest, using remote and in situ observations.	**MN1c:** Investigate magnetospheric periodicities, their coupling to the ionosphere, and how the SKR periods are imposed from close to the planet (3–5 R_S) out to the deep tail.	**IN1c:** Determine whether Dione exhibits evidence for low-level activity, now or in recent geological time.	**TN1c:** Measure aerosol and heavy molecule layers and properties.
		Priority 2		
SN2a: Monitor the planet for new storms and respond with new observations when the new storms occur.	**RN2a:** Conduct in-depth studies of ring microstructure such as self-gravity wakes, which permeate the rings.	**MN2a:** Determine the coupling between Saturn's rings and ionosphere.	**IN2a:** Determine whether there is ring material orbiting Rhea, and if so, what its spatial and particle size distribution is.	**TN2a:** Resolve current inconsistencies in atmospheric density measurements (critical to a future Flagship mission).
	RN2b: Perform focused studies of the evolution of newly discovered propeller objects.		**IN2b:** Determine whether Tethys contributes to the E-ring and the magnetospheric ion and neutral population.	**TN2b:** Determine icy shell topography and viscosity.
			IN2c: Determine the extent of differentiation and internal inhomogeneity within the icy satellites, especially Rhea and Dione.	**TN2c:** Determine the surface temperature distribution, cloud distribution, and tropospheric winds.

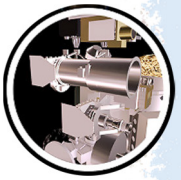

Table ISS-1. Cassini Solstice Mission Science Objectives—Prioritized Summary. Goal: Observe seasonal change in the Saturn system, to understand the underlying process and prepare for future missions.

Saturn	Rings	MAPS	Icy Satellites	Titan
			IN2d: Observe selected small satellites to quantify the movement of Enceladus material through the system, the history of satellite collisions/breakup, interaction with ring material as indicated by surface properties/ composition, and cratering rates deep in the Saturnian system.	

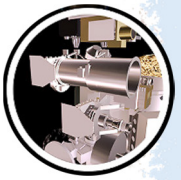

Table ISS-2. Cassini Solstice Mission Saturn Traceability Matrix.

Science Objective	Science Investigation	Measurement	Instrument(s)	Geometric Contraint(s)	Science Investigation Achieved? If No, Explain Further. New/Open Questions.
Seasonal-Temporal Change					
Priority 1					
SC1a - Observe seasonal variations in temperature, clouds, and composition in three spatial dimensions.	1. Investigate seasonal distribution of clouds.	1a. Observations at medium spatial resolution of visible-near-infrared cloud reflectivity, cloud-top altitude, and opacity. Full global daylit and nightside views (10.5 hrs continuous for each dayside and nightside observation) every ~6 months.	1a. VIMS (may be combinable with ISS designs).	1a. Dayside views: phase angle lower than 80 deg; distance between 12 and 20 R_S; Nightside views: phase angle greater than 120 degrees; Distance between 12 and 20 R_S. Polar views every ~6 months during high-inclination revs.	
		1b. Apoapse imaging every ~6 months in ~10 filters. May or may not be combined with part of 1a. Spread out over an orbit to get ~10 uniformly spaced phase angles from 0 to 165 degrees.	1b. ISS/WAC (may or may not be combined with VIMS/UVIS).	1b. Must be done over one almost complete rev to get phase angle coverage. Needs to be done in the range 20-40 R_S.	Phase angle coverage in the F-ring and proximal orbits was sparse due to close proximity to Saturn and fast sweep of phase angle near Periapse.
		1c. Apoapse high-res global map in true color (3 filters) every 2 years for public outreach, 10 hour observation.	1c. ISS/NAC (may or may not be combined with VIMS/UVIS).	1c. At < 90 deg phase angle (dayside). Distance of >30 R_S. From the equatorial plane.	
	2. Characterize seasonal distribution of aerosols.	2c. Observe the sunlight limb from pole to pole every ~6 months.	2c. ISS/NAC	2c. Spacecraft must be in eclipse.	
	4. Determine seasonal changes in the high latitude atmosphere, specifically the north and south polar vortices.	4b. Image both poles every ~6 months at start of Solstice Mission, only the north pole later in Solstice Mission.	4b. ISS (may be combined with other ORS instruments).	4b. Phase angles < 90 degrees. Need duration of ~5 hours for winds. Inclined orbits (i > 20 degrees is sufficient).	

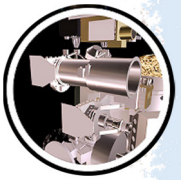

Table ISS-2. Cassini Solstice Mission Saturn Traceability Matrix.

Science Objective	Science Investigation	Measurement	Instrument(s)	Geometric Contraint(s)	Science Investigation Achieved? If No, Explain Further. New/Open Questions.
SC1b - Observe seasonal changes in the winds at all accessible altitudes coupled with simultaneous observations of clouds, temperatures, composition, and lightning.	1. Study the winds at high spatial resolution by observing the planet on successive rotations. Derive thermal winds from temperatures.	1a. Pairs of blocks (each of duration several hours): the second block should begin 11 hours after the first block begins. Cover each latitude every ~6 months.	1a. ISS Observation may be part of the VIMS/UVIS/CIRS template, e.g., 5-6-5 hour template.	1a. At < 100 deg phase angle, equatorial orbits, use 2-9-2 template if time is limited. Need ~8 repetitions to cover all latitudes (fewer than 8 at > 50 R_S).	Study of winds is best done at low phase angle. At high phase angle the contrast is too low. Too little time was available at low phase angle during the F-ring and Proximal orbits.
		1b. 5 µm observations of deep clouds. Pairs of blocks (each of duration several hours): the second block should begin 11 hours after the first block begins. Cover each latitude every ~6 months.	1b. VIMS; observation may be part of the ISS/UVIS template, e.g., 5-6-5 hour template.	1b. Distance between 3 and 15 R_S encompassing both 11 hour observation blocks.	
	3. Study seasonal change in convective storms and lightning.	3a. Night side visible images to see lightning, multiple short exposures to minimize scattered light. Cover each latitude every ~6 months.	3a. ISS; VIMS may ride along.	3a. Phase angle 90 to 130 degrees.	
		3c. Look for sudden appearance of convective storms. Day side imaging at Saturn waypoint. This is a monitoring activity. The idea is to have minimum impact on spacecraft operations.	3c. ISS.	3c. WAC in 1–3 filters whenever pointing at Saturn waypoint, range > 20 R_S, phase angle < 135 deg. Try to repeat every 2 hours, but whenever conflict arises, drop it.	
Priority 2					
SC2a - Observe the magnetosphere, ionosphere, and aurora as they change on all time scales - minutes to years - and are affected by seasonal and solar cycle forcing.	1. Investigate the northern and southern aurora using remote sensing.	1a. High spatial resolution imaging of visible aurora. An 80 hour movie every ~6 months plus ride-alongs.	1a. ISS rides along with UVIS/VIMS/CAPS auroral campaign.	1a. Phase angle > 90 degree (night side).	

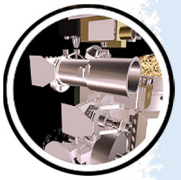

Table ISS-2. Cassini Solstice Mission Saturn Traceability Matrix.

Science Objective	Science Investigation	Measurement	Instrument(s)	Geometric Contraint(s)	Science Investigation Achieved? If No, Explain Further. New/Open Questions.
New Questions					
Priority 1					
SN1b - Observe the aftermath of the 2010-2011 storm. Study the life cycles of Saturn's newly discovered atmospheric waves, south polar hurricane, and rediscovered north polar hexagon.	1. Study Saturn atmospheric features (special features, defined by their latitudes) including the 2010–2011 northern storm region, the north polar vortex and hexagon, the ribbon, donuts, the string of pearls at 30 N, the QXO near the equator, the thunderstorm region at 35 S, and the eye region of the south polar vortex.	1a. High-resolution (few km/pix) visible observations of special latitudes. 11 hour repeat cycle to measure winds. Observe each feature every year.	1a. ISS may be combined with VIMS.	1a. At < 100 deg phase angle.	Study of winds is best done at low phase angle. At high phase angle the contrast is too low. Too little time was available at low phase angle during the F ring and Proximal orbits.
Priority 2					
SN2a - Monitor the planet for new storms and respond with new observations when the new storms occur.	1. Investigate recently active northern storm latitudes and storm alley at 35 S for new lightning storms and other phenomena.	1a. Visible imaging of both hemispheres: 2010–2011 active northern region and southern hemisphere and the "dragon storms" at ~35 S. Take 1–3 images every time the spacecraft is already pointed toward Saturn's center, up to once every 2 hours.	1a. ISS/WAC; VIMS may or may not ride along.	1a. Dayside only (phase angle < 90). ~3.5 Mbits/image.	

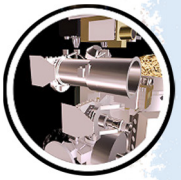

Table ISS-3. Cassini Solstice Mission Rings Traceability Matrix.

Science Objective	Science Investigation	Measurement	Instrument(s)	Geometric Contraint(s)	Science Investigation Achieved? If No, Explain Further. New/Open Questions.
Seasonal-Temporal Change					
Priority 1					
RC1a -Determine the seasonal variation of key ring properties and the microscale properties of ring structure, by observing at the seasonally maximum opening angle of the rings near Solstice.	1. Determine seasonal variability of ring particle temperature.	1c. Measure ring particle albedo at visible-IR wavelengths as a function of radius using radial scans in inclined orbits throughout Solstice Mission.	1c. ISS, VIMS	1c. Take photometric measurements in 3 filters and VIMS plus clear at 5–10 phase angles and 3–5 ring opening angles (lit and unlit face). Distance from Saturn of around 20 R_S is acceptable.	In many or perhaps most cases, there was inadequate data volume to make all the images 12 bits, but this was not a serious problem because the SNR was high. In some cases, allocated time backed us off from 8 filters to maybe 7. But overall, the spirit of them was satisfied. Two of them (RN1b1a and RN1b2c) were more VIMS-emphasis.
	2. Investigate how spoke occurrence varies with season.	2a. Point and Stare observations pointed at a fixed position in the B-ring to look for spokes before they fade in ~2013. Long time baseline needed for accurate measurement of periodicity. 500 h of observation time is required for each of the three types of observations shown in the geometric constraints. (1500 h total.)	2a. ISS	2a. Observations must be performed before the spokes fade out as the ring plane opening angle to the Sun increases beyond 20.5 degrees (~late 2013). Observations must be performed for low phase (less than 50 degrees) lit face, high phase (greater than 100 degrees) lit face and high phase dark face. Spacecraft elevation angle must be greater than 3 degrees.	For the CSM, we were assigned about 1072 hours' worth of observing time, but only about 718 of those hours happened before the spokes faded out. So we roughly got half of the 1500 hours that we were looking for.
	3. Characterize seasonal variation of Saturn's E-ring structure.	3a. Edge-on images of both ansa of the E-ring every 1–2 years to measure changes in sun-driven warp of the rings.	3a. ISS/WAC	3a. Ring opening angle must be less than 0.1 degrees, and range must be greater than 20 R_S, greater than 30 R_S is preferred. There are no strong constraints on the phase angle for these observations. Low (< 30 degrees), high (> 120 degrees) and moderate (~90 degrees) are preferred.	

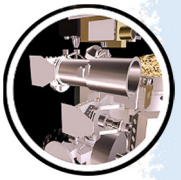

Table ISS-3. Cassini Solstice Mission Rings Traceability Matrix.

Science Objective	Science Investigation	Measurement	Instrument(s)	Geometric Contraint(s)	Science Investigation Achieved? If No, Explain Further. New/Open Questions.
		3b. Imaging of all longitudes in the E-ring at high signal-to-noise in multiple filters every 2 years to measure changes in the spatial distribution of different sized particles.	3b. ISS/WAC	3b. Ideally performed while Cassini is in Saturn's Shadow and more than 10 R_S from the planet. Additional information can be obtained at phase angles between 130 and 145 degrees and ring elevations between 5 and 15 degrees.	We were able to observe all longitudes in 2012 and 2013, and a large fraction of longitudes in 2017 during eclipse periods. We did not have a similar opportunity in the 2014–2016 time frame.
	5. Determine ring microstructure, especially in the optically-thickest regions.	5d. Image rings at 50 meter resolution. One complete lit-face radial profile and one complete unlit-face radial profile are required.	5d. ISS	5d. Range must be less than 0.1 R_S, and spacecraft elevation angle must be greater than 10 degrees. Lit and unlit faces are desired.	Practically no images achieved the stated resolution, much less with full radial coverage. Regions of particular interest were imaged at 400 meter resolution, full coverage at 800 meter resolution.
		5f. Radial profiles of ring brightness of A-ring and B-ring, and Cassini Division over at least 6 longitudes at 3 or more tilt angles to measure amplitude of azimuthal asymmetry at radial resolution better than 5 km. Coverage of the C-ring is desirable, but not required.	5f. ISS	5f. Observations that cover A-rings, Cassini division and B-rings. Sampling is spacecraft relative and should occur over at least 6 longitudes at 3 or more tilt angles (> 20 degrees, 10–20 degrees, and < 20 degrees). Range must be less than 13 R_S, and phase angle must be less than 60 degrees to minimize Saturn-shine.	
	6. Characterize ring properties in geometries that are comparable to Voyager and Earth observations for purposes of cross comparison.	6c. Multi-color radial profiles of lit ring brightness in at least 5 broadband filters in the near-UV, visual wavelengths and near-IR that cover A-rings, Cassini division, B-rings and C-rings at 5 or more solar elevation angles.	6c. ISS	6c. Observations of the lit face of the rings at 5 or more solar elevation angles in the range 5-27 degrees to compare with HST and ground-based observations of the rings. Range must be less than 25 R_S. Phase angles should be as small as possible, preferably < 7 degrees, to allow direct comparison with ground-based data.	

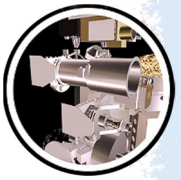

Table ISS-3. Cassini Solstice Mission Rings Traceability Matrix.

Science Objective	Science Investigation	Measurement	Instrument(s)	Geometric Contraint(s)	Science Investigation Achieved? If No, Explain Further. New/Open Questions.
RC1b - Determine the temporal variability of ring structure on all timescales up to decadal for regions including Encke gap, D-ring, F-ring, and ring edges by substantially increasing the cadence and time baseline of observations.	1. Study Encke gap, other gaps and associated ringlets over long-time baseline.	1a. Ansa stare for one full orbital period in each of 5 zones at resolutions of better than 15 km/pixel: i) Inner C/D: Huygens, Russell and Herschel gaps; ii) Outer C/D: Laplace and Jeffreys gaps; iii) Outer C-ring: 1.470, 1.495 R_S gaps; iv) Maxwell gap; v) Columbo gap.	1a. ISS	1a. Phase angle must be less than 60 degrees. Prefer unlit rings, but observation can be performed on lit rings if necessary. Ranges must be between 15 and 40 R_S, and ring opening angles must be greater than 5 degrees.	
		1b. Image multiple longitudes in Laplace Gap, Huygens Gap, Maxwell Gap and D68 at resolutions of better than 15 km/pixel every 1–2 years to measure time evolution of eccentric and heliotropic features.	1b. ISS	1b. For Laplace Gap and D68, no strong constraints on phase angles (although higher phase has higher SNR). For Huygens and Maxwell Gaps, phase angles greater than 130 degrees are preferred. Ranges must be between 15 and 40 R_S and ring opening angles must be greater than 5 degrees.	
	2. Study the D-ring over long-time baseline.	2a. High-Resolution (3-5 km/NAC pixel) imaging of the outer part of the D-ring every year to measure time evolution of corrugation.	2a. ISS	2a. No strong constraints on phase angle. Range must be between 8 and 15 R_S. Both low (0.3–5 degree) and high (5–20 degree) ring opening angles are useful.	
		2b. 12-hour (1 Saturn Rotation) ansa movies of the D-ring between 71,500–74,500 km and the Roche Division between the A-ring and F-ring where a related pattern appears. Desire 2–3 movies of each region within a time span of 6–12 months every 2–3 years to measure structures in the rings tied to SKR.	2b. ISS	2b. Phase must be above 140 degrees. Ring opening angle must be above 5 degrees, and range must be between 15 and 40 R_S.	

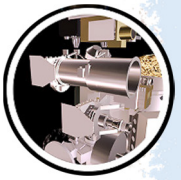

Table ISS-3. Cassini Solstice Mission Rings Traceability Matrix.

Science Objective	Science Investigation	Measurement	Instrument(s)	Geometric Contraint(s)	Science Investigation Achieved? If No, Explain Further. New/Open Questions.
	3. Characterize the G and other narrow faint rings over long time baselines.	3a. Ansa movies of J/E-ring, G-ring, Pallene Ring, Anthe and Methone Rings every 1–2 years. Movies should be longer than 12 hours (1/3 rotation period) and include time when the appropriate moon moves through the ansa.	3a. ISS	3a. No strong constraints on phase angle. Range must be greater than 20 R_S, and ring opening angle must be less than 10 degrees.	For G-ring/ Pallene/Anthe/ Methone the goal was basically achieved, in that we have images around each of these moons with appropriate exposures for the arcs/rings. For the J/E-ring, we made a few attempts to image the relevant region, but it was not clearly visible outside of the HIPHASE/ eclipse periods. We therefore have more limited data on this, but we do have looks in 2013 and 2016/2017.
	4. Determine the temporal evolution of individual propeller.	4a. Scan the outer A-ring (from 133700-136700 km from Saturn Center) at all longitudes at least annually.	4a. ISS	4a. Range must be between 3.5 and 10 R_S. Sub-S/C latitude must be greater than 10 degrees. Observations must be at least 16–18 hours in duration. Observations need not be contiguous, but must be in the same periapse and configured such that all co-rotating longitudes can be sampled.	
		4b. Perform follow-up images of known propellers roughly twice monthly during RTWT segments.	4b. ISS	4b. Range must be less than 15 R_S. (Less than 23 R_S is acceptable for one of the known targets.) Sub-spacecraft latitude must be greater than 10 degrees. Duration of observations require at least 5 minutes (actual dwell time) per target. No connection with 4a is required.	For the J/E-ring, we made a few attempts to image the relevant region, but it was not clearly visible outside of the HIPHASE/ eclipse periods. We therefore have more limited data on this, but we do have looks in 2013 and 2016/2017.

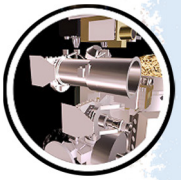

Table ISS-3. Cassini Solstice Mission Rings Traceability Matrix.

Science Objective	Science Investigation	Measurement	Instrument(s)	Geometric Contraint(s)	Science Investigation Achieved? If No, Explain Further. New/Open Questions.
Priority 2					
RC2a - Focus on F-ring structure, and distribution of associated moonlets or clumps, as sparse observations show clumps, arcs, and possibly transient objects appearing and disappearing.	1. Study apse anti-alignment (F-ring/ Prometheus).	1a. Follow Prometheus for one orbital period (15 hours) twice per year, 4–6 times in all, to observe one complete cycle of streamer-channel feature raised in F-ring.	1a. ISS	1a. Range must be between 13 and 22 R_S. Spacecraft elevation angle must be greater than 15 degrees. Execute once early in IN1, the rest later.	
		1b. Ansa stare observations with a duration of 15 hours once per apoapse. Observe complete co-rotating 360 degrees of F-ring as material passes through the NAC field of view.	1b. ISS, VIMS	1b. Range must be less than 30 R_S, and spacecraft elevation angle must be greater than 15 degrees.	We had > 100 FMOVIE observations over the duration of the tour but only ~30 covered the full 360 degrees. Some of the FMOVIEs were intentionally split between ansae to highlight effect of eccentricity. It was impossible to make the "once per apoapse" requirement on every orbit.
	2. Search for and characterize new clumps/strands.	2a. Ansa stare observations with a duration of approximately 15 hours once per apoapse. Observe complete co-rotating 360 degrees of F-ring material as it passes through the NAC field of view.	2a. ISS, VIMS, CIRS	2a. Range must be less than 30 R_S, and spacecraft elevation angle must be greater than 15 degrees.	We had > 100 FMOVIE observations over the duration of the tour but only ~30 covered the full 360 degrees. Some of the FMOVIEs were intentionally split between ansae to highlight effect of eccentricity. It was impossible to make the "once per apoapse" requirement on every orbit.

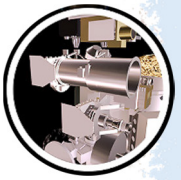

Table ISS-3. Cassini Solstice Mission Rings Traceability Matrix.

Science Objective	Science Investigation	Measurement	Instrument(s)	Geometric Contraint(s)	Science Investigation Achieved? If No, Explain Further. New/Open Questions.
	3. Investigate clumps and moonlets on short timescales.	3a. Obtain high-resolution maps and movies on short time scales for clump and moonlet tracking purposes. Ansa stare observations with a duration of approximately 15 hours should occur once every 2–3 months. Observe F-ring material as it passes through the NAC field of view.	3a. ISS, VIMS	3a. Range must be less than 15 R_S for both instruments, and spacecraft elevation angle must be greater than 15 degrees. If possible, observations should also capture the A-ring edge into ~136000 km without impacting F-ring science in order to partially address RN1c(4a).	We did obtain partial high-resolution coverage but never for the full 360 degrees in this geometry (given the time constraints at peripase this would have been difficult) and never at a frequency of once every 2–3 months. Nevertheless, we did manage to observe and track moonlets.
New Questions					
Priority 1					
RN1b - Determine the composition of the close-in "ringmoons" as targets of opportunity.	1. Obtain spatially resolved spectral and color maps of ringmoons at UV, visual, and NIR wavelengths.	1a. 12-bit images in multiple filters. RED, GRN, BL1, UV3, IR3 and clear at a minimum. Observational opportunities are rare and will be taken as available.	1a. ISS, VIMS, UVIS, CIRS	1a. Phase angle at the satellite must be less than 90 degrees, and ranges must be less than 50,000 km. VIMS requires a minimum object diameter of 1 mrad in order to get at least one filled pixel on the moon. ISS demands are less restrictive. Target will depend on opportunity.	(RN1b1a and RN1b2c) were more VIMS-emphasis
	2. Characterize radial structure of rings at high-resolution.	2b. Two or more multi-filter (at least 8 filters, 12 bit) radial scans across ansa from 68000 km to 141000 km.	2b. ISS, UVIS rider	2b. Observe lit-side. Range must be less than 15 R_S. Elevation angle must be greater than 15 degrees. Phase angle must be less than 60 degrees.	

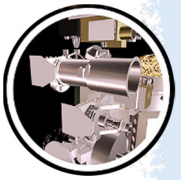

Table ISS-3. Cassini Solstice Mission Rings Traceability Matrix.

Science Objective	Science Investigation	Measurement	Instrument(s)	Geometric Contraint(s)	Science Investigation Achieved? If No, Explain Further. New/Open Questions.
		2c. Radial scans of the entire main ring system during the proximal orbits, supplemented by observations of selected regions such as the outer C-ring and outer B-ring with targeted pointings and/or continuous drift scans. Resolutions better than 30 km/VIMS pixel desired. Require at least two full scans and at least two targeted observations. (RN1b1a and RN1b2c) were more VIMS-emphasis.	2c. VIMS, ISS rider	2c. Range less than 2-3 R_S to observation target and ring opening angles greater than 20 degrees. Lit side preferred. Only proximal orbits will provide these geometries.	
		2d. Radial scans of entire main ring system: 4 lit face and 4 unlit face, at multiple phase angles in at least 4 filters.	2d. ISS	2d. Range must be less than 20 R_S. At least 4 observations of the lit face *and* 4 observations of the unlit face are required, covering a range of phase angles.	
RN1c - Determine structural and compositional variations at high-resolution across selected ring features of greatest interest, using remote and in situ observations.	3. Study gap edges for azimuthal and temporal variations at varying scales and search for potential wakes produced by gap-embedded satellites.	3c. Map the edges of known empty gaps for one full orbital period at least once each.	3c. ISS	3c. Satisfied by requested surveys for undiscovered moonlets and for propellers. Both the lit and unlit sides are acceptable for mapping gap edges.	
		3d. Image Encke and Keeler Gaps at least three times at all available longitudes at 45 degree intervals in less than two hours to disentangle azimuthal and temporal effects.	3d. ISS	3d. Range must be less than 10 R_S, and spacecraft elevation angle must be greater than 15 degrees.	People freaked out about anything that sounded like an "azscan," so this was not done.

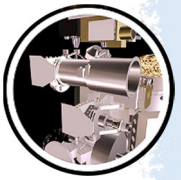

Table ISS-3. Cassini Solstice Mission Rings Traceability Matrix.

Science Objective	Science Investigation	Measurement	Instrument(s)	Geometric Contraint(s)	Science Investigation Achieved? If No, Explain Further. New/Open Questions.
RN2a - Conduct in-depth studies of ring microstructure such as self-gravity wakes, which permeate the rings.	4. Study A-ring and B-ring outer edge modes to improve our understanding of them.	4a. Ansa-stare movies on the ring edges at least twice per year. B-ring requires at least 12 hours per observation, and A-ring requires at least 15 hours per observation. A minimum of 100 images is required for each movie.	4a. ISS	4a. Observe lit side. Elevation angle must be greater than 15 degrees, and phase angle must be less than 60 degrees. A-ring range must be less than 15 R_S. B-ring range must be less than 30 R_S.	
	1. Study self-gravity wakes and over stabilities in depth.	1c. Perform multi-filter lit face radial drift scan from 74,000 km to 141,000 km during the proximal phase of the tour. At least three scans are required.	1c. ISS	1c. Range less than 1 R_S. Lit face required.	
	2. Study "straw" and other packing effects.	2d. Perform multi-filter radial scans from 74,000 km to 141,000 km during the proximal phase of the tour. At least three scans are required.	2d. ISS	2d. Range less than 1 R_S. Lit and unlit face desired, but lit is preferred.	
Priority 2					
RN2b - Perform focused studies of the evolution of newly discovered "propeller" objects.	1. Investigate propeller structure and photometric properties.	1a. Perform focused studies to refine propeller structure and photometric properties at a range of sizes. Scan the "Propeller Belts" in the mid A-ring (from 127000–130000 km from Saturn center) at all longitudes, at least once. Observations must be at least 16–18 hours in duration.	1a. ISS	1a. Range must be between 3.5 and 10 R_S. Sub-spacecraft latitude must be greater than 10 degrees. Observations need not be contiguous, but must be in the same periapse and configured such that all co-rotating longitudes can be sampled.	
		1b. Obtain very-high-resolution images of propellers in the "Propeller Belts" of the mid A-ring. Use multiple color filters while keplerian tracking. Must target at least 3 different radii, at least once each.	1b. ISS	1b. Range must be less than 4 R_S. Sub-spacecraft latitude must be greater than 10 degrees. Observation length (dwell time) of at least 20 minutes per target location required.	Close-range imaging of the Propeller Belts was done, but color imaging proved impractical.

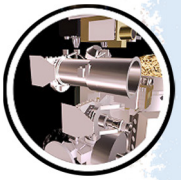

Table ISS-3. Cassini Solstice Mission Rings Traceability Matrix.

Science Objective	Science Investigation	Measurement	Instrument(s)	Geometric Contraint(s)	Science Investigation Achieved? If No, Explain Further. New/Open Questions.
		1c. Obtain very-high-resolution images of known large propellers in the outer A-ring. Use multiple color filters while keplerian tracking. Must target at least 3 known propellers once each.	1c. ISS	1c. Range to the known propeller's position must be less than 4 R_S. Sub-spacecraft latitude must be greater than 10 degrees. Observation length (dwell time) of at least 20 minutes per target required.	Targeted imaging of three propellers was done, but color imaging proved impractical.
		1d. Obtain lit and unlit face images at a range of phase angles and sub-spacecraft latitudes (as shown in the geometric constraints) of known large propellers in the outer A-ring. Use multiple color filters while keplerian tracking. Require at least one observation in each of the eight geometries described.	1d. ISS	1d. Range must be less than 7 R_S. Observe targets for at least 20 minutes when: 1) Sub-spacecraft latitude is between 10 and 20 degrees and phase angle is less than 30 degrees; 2) Sub-spacecraft latitude is between 10 and 20 degrees and phase angle is greater than 130 degrees; 3) Sub-spacecraft latitude is greater than 40 degrees and phase angle is less than 30 degrees; and 4) Sub-spacecraft latitude is greater than 40 degrees and phase angle is greater than 130 degrees. Both lit and unlit faces are desirable.	
		1e. Perform full azimuthal scans of the outer C-ring and Cassini Division, once each.	1e. ISS	1e. Satisfied by the constraints for RC1b(1a).	See RC1b(1a)

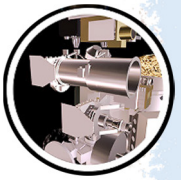

Table ISS-4. Cassini Solstice Mission Magnetospheres Traceability Matrix.

Science Objective	Science Investigation	Measurement	Instrument(s)	Geometric Contraint(s)	Science Investigation Achieved? If No, Explain Further. New/Open Questions.
New Questions					
Priority 1					
MN1b - Conduct in situ and remote sensing studies of Saturn's ionosphere and inner radiation belt.	1. Investigate the effects on aurora of solar wind and seasons.	1a. Sample auroral photon emission, ENA emission, SKR, solar wind conditions.	1a. HST, UVIS, VIMS and/or ISS auroral images; CAPS ions, electrons; MIMI INCA ENA; MAG, RPWS.	1a. In sheath or solar wind, -Y to Saturn aurora.	

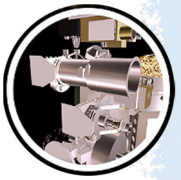

Table ISS-5. Cassini Solstice Mission Icy Satellites Traceability Matrix.

Science Objective	Science Investigation	Measurement	Instrument(s)	Geometric Contraint(s)	Science Investigation Achieved? If No, Explain Further. New/Open Questions.
Seasonal-Temporal Change					
Priority 1					
IC1a - Identify long-term secular and seasonal changes at Enceladus, through observations of the south polar region, jets, and plumes.	1. Understand seasonal changes in Enceladus' south polar region.	1c. Visible imaging of the south polar region illuminated by the sun or Saturn shine with 40 m or better resolution during at least 2 flybys.	1c. ISS	1c. Flybys with views of south pole; 2,000-7,000 km altitude.	As subsolar latitudes moved further north over time, secondary illumination was too poor for imaging surface details except near terminator. However, excellent coverage was obtained early during the CSM. Final high-resolution images of the active SPT region was not obtained in December 2015. However excellent imaging was obtained just outside of the south polar province.
	2. Understand seasonal changes in Enceladus' jets.	2a. High-resolution imaging of jets on temporal scales of at least every 2 months.	2a. ISS	2a. Observations at a range of viewing geometries, including latitudes and longitudes.	As subsolar latitudes moved further north over time, imaging of jets at the surface became problematic due to solar terminator geometry.
	3. Understand seasonal changes in Enceladus' plumes.	3c. Plume imaging, evenly spaced throughout Solstice mission, with observations at a minimum of every two months if possible.	3c. ISS	3c. Very high phase distant views, ideally with spacecraft in Saturn shadow (for plume "tendril" movies).	
		3d. Plume monitoring throughout Solstice mission, with observations at a minimum of every two months if possible.	3d. ISS	3d. Imaging from 60,000 km altitude, 140–165 deg phase, throughout tour.	
	4. Investigate effects on the inner mid-sized and small satellites due to interaction with the E-ring.	4a. Medium and high-resolution imaging and compositional mapping of satellites out to and including Rhea.	4a. ISS, VIMS, UVIS	4a. Medium and high-resolution flybys of leading/trailing hemispheres (1000-100,000 km) at least once per satellite.	

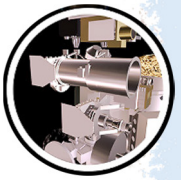

Table ISS-5. Cassini Solstice Mission Icy Satellites Traceability Matrix.

Science Objective	Science Investigation	Measurement	Instrument(s)	Geometric Contraint(s)	Science Investigation Achieved? If No, Explain Further. New/Open Questions.
New Questions					
Priority 1					
IN1a - Determine the presence of an ocean at Enceladus as inferred from induced magnetic field and plume composition, search for possible anomalies in the internal structure of Enceladus as associated with plume sources, and constrain the mechanisms driving the endogenic activity by in situ observations and remote sensing.	3. Determine internal structure and any possible anomalies.	3b. Imaging to determine a more accurate shape model for Enceladus (to determine bulk density and regions of isostatic compensation) on at least 3 compensation) on at least 3.	3b. ISS	3b. Flybys in the 2000-50,000 km range with a range of viewing geometries as available from the mission design.	
	4. Determine mechanisms of activity using in situ observations and remote sensing.	4e. High-resolution (40 m or better in the visible, 0.5 km or better in the IR) imaging, compositional mapping and radiometry of south polar.	4e. ISS, VIMS, RADAR	4e. Flybys with views of south pole; 2,000-7,000 km altitude.	
		4f. Measure dust in plume using visible & IR imaging, every two months if possible.	4f. ISS, VIMS	4f. Long stares (1-2 hours) of plumes.	
IN1b - Complete the comparative study of Saturn's mid-sized satellites, their geological and cratering histories, and interactions with the Saturn system, with remote sensing of Mimas at the highest resolution possible in order to understand the mechanisms behind its unique thermal properties discovered by Cassini.	1. Investigate Mimas' geological and cratering history	1a. Imaging of both leading and trailing hemispheres to complete mapping coverage.	1a. ISS	1a. At least 4 flybys in the 100,000 km range.	

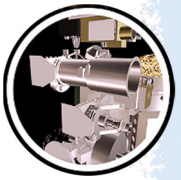

Table ISS-5. Cassini Solstice Mission Icy Satellites Traceability Matrix.

Science Objective	Science Investigation	Measurement	Instrument(s)	Geometric Contraint(s)	Science Investigation Achieved? If No, Explain Further. New/Open Questions.
IN1c - Determine whether Dione exhibits evidence for low-level activity, now or in recent geological time.	1. Investigate Dione's level of current activity.	1f. Seek forward scattered component in solar phase function during flybys by making high phase angle measurements.	1f. VIMS, ISS, UVIS	1f. Observations at large solar phase angles (150-165 degrees; the higher the better).	
		1g. Search for tenuous atmosphere using off-limb.	1g. VIMS, ISS, UVIS	1g. Long integration times off limb.	
	2. Investigate Dione's past geologic activity.	2a. Imaging surface to complete mapping coverage.	2a. ISS	2a. Medium and high-resolution mapping (3000-50,000 km).	
Priority 2					
IN2a - Determine whether there is ring material orbiting Rhea, and if so, what its spatial and particle size distribution is.	1. Investigate Rhea and its environment to search for a ring (or debris disk).	1a. High-resolution imaging of the surface to complete mapping coverage.	1a. ISS	1a. Flybys in 3000-50,000 km altitude range.	
IN2b - Determine whether Tethys contributes to the E ring and the magnetospheric ion and neutral population.	2. Investigate Tethys's level of current activity.	2d. High phase angle measurements to complete phase angle coverage & seek forward-scattered component to the solar phase curve.	2d. VIMS, ISS, UVIS	2d. Observations at large solar phase angles (150-165 degrees, the larger the better).	
	3. Investigate whether Tethys appears to be currently geologically active.	3b. High-resolution imaging of the surface to complete mapping coverage.	3b. ISS	3b. Flybys at 3000-150,000 km.	
	4e. Investigate whether Tethys has a tenuous atmosphere.	4a. Off-limb imaging of Tethys, at least once during Solstice.	4a. VIMS, UVIS, ISS	4a. Long integration time near limb.	
IN2c - Determine the extent of differentiation and internal inhomogeneity within the icy satellites, especially Rhea and Dione.	2. Determine a more detailed shape model for Rhea and Dione.	2a. Medium and high-resolution imaging of Rhea to complete coverage.	2a. ISS	2a. Flybys in the 3000-50,000 km range	
		2b. Medium and high-resolution imaging of Dione to complete coverage.	2b. ISS	2b. Flybys in the 3000-50,000 km range.	

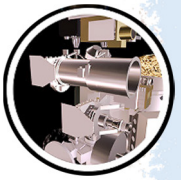

Table ISS-5. Cassini Solstice Mission Icy Satellites Traceability Matrix.

Science Objective	Science Investigation	Measurement	Instrument(s)	Geometric Contraint(s)	Science Investigation Achieved? If No, Explain Further. New/Open Questions.
IN2d - Observe selected small satellites to quantify the movement of Enceladus material through the system, the history of satellite collisions/ breakup, interaction with ring material as indicated by surface properties/compo sition, and cratering rates deep in the Saturnian system	1. Observe Epimetheus, Janus, Methone, Prometheus, and others as opportunities arise.	1a. Visible imaging of surface	1a. ISS	1a. Flybys in the 1000-100,000 km range over solar phase angles 0-120 degrees	Some close flyby images were not obtained due to ephemeris and/or pointing errors especially during very close flybys. This was especially true for close flybys of Helene (2008, 2010), Atlas (2015) and Daphnis (2016).

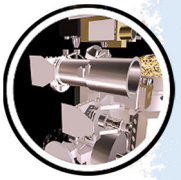

Table ISS-6. Cassini Solstice Mission Titan Traceability Matrix.

Science Objective	Science Investigation	Measurement	Instrument(s)	Geometric Contraint(s)	Science Investigation Achieved? If No, Explain Further. New/Open Questions.
Seasonal-Temporal Change					
Priority 1					
TC1a - Determine seasonal changes in the methane-hydrocarbon hydrological cycle: of lakes, clouds, aerosols, and their seasonal transport.	1. Determine the seasonal distribution of the lakes.	1c. Repeated, as allocated by TOST, medium resolution (≤ 10km/pixel), high-latitude (> 70° N and S; > 50° N for Kraken Mare) observations to look for changes (preferably close (in time) to RADAR observations for comparison and to provide context).	1c. ISS	1c. High latitude (> 70 N and S); > 50° N for Kraken Mare); resolution ≤ 10 km	Limited constraints on the rate of surface changes and extent of seasonal interaction between surface, atmosphere, and subsurface methane reservoirs due to later than predicted onset of summer weather at the north pole. Another question is what is the nature of the bright north-polar surface deposit and how does it relate to the lakes and seas?
	2. Determine the seasonal distribution of clouds.	2b. Repeated, ideally weekly, low-resolution (≤ 50 km/pixel) imaging throughout a seasonal cycle. Desire several opportunities/month throughout the Solstice Mission.	2b. ISS	2b. Phase angle < 120°; any longitude and any latitude—high northern latitudes (> 60°) preferred for development of summer clouds; pixel scale ≤ 50 km (range < 8.4e6 km)	Onset of north-polar cloud activity did not occur before EOM; timing of predicted seasonal weather pattern remains unknown. What causes differences from model predictions and how typical are the weather patterns we observed? What is the nature of the north-polar cloud features VIMS detected at 2.1 μm starting in June 2016 that were not visible at other wavelengths?

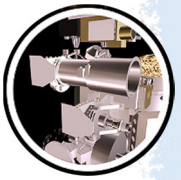

Table ISS-6. Cassini Solstice Mission Titan Traceability Matrix.

Science Objective	Science Investigation	Measurement	Instrument(s)	Geometric Contraint(s)	Science Investigation Achieved? If No, Explain Further. New/Open Questions.
	3. Characterize the seasonal distribution of aerosols.	3c. Repeated limb observations at various latitudes, and resolutions (few to several km) Desire several opportunities/year during distant/non-targeted encounters (or at distant times during targeted encounters) throughout Solstice Mission.	3c. ISS	3c. Variety of phase angles (0–180°) and latitudes (90° S to 90° N) desired	
TC1b - Determine seasonal changes in the high-latitude atmosphere, specifically the temperature structure and formation and breakup of the winter polar vortex.	1. Study wintertime polar vortices.	1b. Repeated polar imaging throughout Solstice Mission at pixel scales of a few to several km. Desire a few opportunities per month throughout the Solstice Mission.	1b. ISS	1b. Latitude > |70°|; resolutions ≤ few to several km	
	2. Understand the tilted pole.	2b. Whole-disk imaging in methane bands, with a frequency of a few opportunities per month throughout the Solstice Mission.	2b. ISS	2b. Phase angles < 90°; latitudes > |60| deg	
New Questions					
Priority 1					
TN1a - Determine the types, composition, distribution, and ages of surface units and materials, most notably lakes (i.e. filled versus dry and depth; liquid versus solid and composition; polar versus other latitudes and lake basin origin).	1. Characterize lakes as liquid or dry and their composition.	1c. ISS context beyond the swaths. ISS/VIMS/RADAR comparisons, i.e. overlapping coverage, for interpretation beyond RADAR swaths/VIMS noodles. (As much ISS coverage overlapping RADAR and VIMS swaths as possible within TOST allocation.)	1c. ISS	1c. Previous RADAR/VIMS observations	Detailed compositions of different geologic surface units and interactions between materials on the surface and in the subsurface remain unknown. What is the bright north-polar surface unit? How does it relate to the lakes and seas? What are the implications of a lack of a comparable surface unit at the south pole?

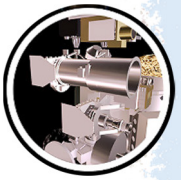

Table ISS-6. Cassini Solstice Mission Titan Traceability Matrix.

Science Objective	Science Investigation	Measurement	Instrument(s)	Geometric Contraint(s)	Science Investigation Achieved? If No, Explain Further. New/Open Questions.
	3. Study surface modifications due to geological activity. Determine the origin of depressions, Xanadu, fluvial features, and crypto-circles	3d. Repeated, as allocated by TOST, medium-high resolution (≤few km) observations throughout the Solstice Mission, especially at high latitudes. Most important to get some observations near equinox and some near northern summer solstice to extend the temporal baseline as long as possible	3d. ISS	3d. Phase < 90 deg; resolutions ≤ few km	Limited constraints on the rate of surface changes and extent of seasonal interaction between surface, atmosphere, and subsurface methane reservoirs due to later than predicted onset of summer weather at the north pole.
TN1c - Measure aerosol and heavy molecule layers and properties.	1. Characterize aerosol properties	1b. Repeated limb observations at various latitudes, and resolutions (few to several km). Desire several opportunities/ year during distant/non-targeted encounters (or at distant times during targeted encounters) throughout Solstice Mission.	1b. ISS	1b. Variety of phase angles (0–180°) and latitudes (90° S to 90° N) desired	
Priority 2					
TN2c - Determine the surface temperature distribution, cloud distribution, and tropospheric winds.	1. Study tropospheric cloud distribution	1a. Repeated (ideally weekly) low-resolution (≤ 50 km/pixel) imaging throughout a seasonal cycle. Desire several opportunities/month throughout the Solstice Mission.	1a. ISS	1a. Phase angle < 120°; any longitude and any latitude—high northern latitudes (> 60°) preferred for development of summer clouds; NAC pixel scale ≤ 50 km (range < 8.4e6 km)	Onset of north-polar cloud activity did not occur before EOM; timing of predicted seasonal weather pattern remains unknown. What causes differences from model predictions and how typical are the weather patterns we observed? What is the nature of the north-polar cloud features VIMS detected at 2.1 μm starting in June 2016 that were not visible at other wavelengths?

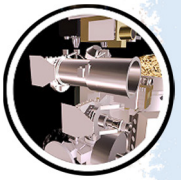

Table ISS-6. Cassini Solstice Mission Titan Traceability Matrix.

Science Objective	Science Investigation	Measurement	Instrument(s)	Geometric Contraint(s)	Science Investigation Achieved? If No, Explain Further. New/Open Questions.
	3. Infer surface and tropospheric winds	3b. Repeated medium-resolution (≤ few to several km/pixel) imaging over several hours; can be distant, e.g. non-targeted encounters (range < 1e6 km)—these are more opportunistic observations than tour/encounter drivers, with as many opportunities as are available throughout the Solstice Mission.	3b. ISS Cloud Tracking	3b. Phase angle < 120°; high northern latitudes (> 60°) preferred for development of summer clouds; resolutions ≤ few to several km (range < 1e6 km)	Onset of north-polar cloud activity did not occur before EOM; timing of predicted seasonal weather pattern remains unknown. What causes differences from model predictions and how typical are the weather patterns we observed? What is the nature of the north-polar cloud features VIMS detected at 2.1 µm starting in June 2016 that were not visible at other wavelengths?

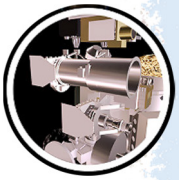

ACRONYMS

Note: For a complete list of Acronyms, refer to Cassini Acronyms – Attachment A.

BIU	Bus Interface Unit
CAPS	Cassini Plasma Spectrometer
CCD	Change Coupled Device
CDS	Command & Data System
CER	Co-rotation-eccentricity Resonance
CIRS	Composite Infrared Spectrometer
CSM	Cassini Solstice Mission
DTM	Digital Terrain Model
EFC	Engineering Flight Computer
FOV	Field of View
GM	Gravitational Mass
ILR	Inner Lindblad Resonance
IR	Infrared
ISS	Imaging Science Subsystem
MAG	Magnetometer
MAPS	Magnetospheric and Plasma Science
MIMI	Magnetospheric Imaging Instrument
NAC	Narrow Angle Camera
RADAR	Titan Radar Mapper
SKR	Saturn Kilometric Radiation
SOI	Saturn orbit insertion
SPT	South Polar Terrain
TPW	True Polar Wander
USGS	United States Geological Survey
UV	Ultraviolet
UVIS	Ultraviolet Imaging Spectrometer
VIMS	Visual and Infrared Mapping Spectrometer
WAC	Wide Angle Camera

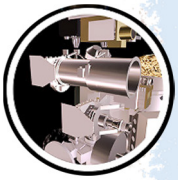

REFERENCES

Disclaimer: The partial list of references below correspond with in-text references indicated in this report. For all other Cassini references, refer to Attachment B – References & Bibliographies; Attachment C – Cassini Science Bibliographies; the sections entitled References contributed by individual Cassini instrument and discipline teams located in Volume 1 Sections 3.1 and 3.2 Science Results; and other resources outside of the Cassini Final Mission Report.

Achterberg, R. K., B. J. Conrath, P. J. Gierasch, F. M. Flasar, C. A. Nixon, (2008), Observation of a tilt of Titan's middle-atmospheric super-rotation, Icarus 197, 549–555.

Annex, A. M., A. J. Verbiscer, P. Helfenstein, C. Howett, P. Schenk, (2013), Photometric properties of thermally anomalous terrains on icy Saturnian satellites, American Astronomical Society DPS meeting #45, 417.02.

Antuñano, A., T. del Rio-Gaztelurrutia, A. Sánchez-Lavega, J. Rodreiguez-Aseguinolaza, (2018), Cloud morphology and dynamics in Saturn's northern polar region, Icarus 299, 117–132.

Antuñano, A., T. del Rio-Gaztelurrutia, A. Sánchez-Lavega, R. Hueso, (2015), Dynamics of Saturn's polar regions, Journal of Geophysical Research, Planets 120, 155–176.

Arregi, J., J. F. Rojas, R. Hueso, A. Sanchez-Lavega, (2009), Gravity waves in Jupiter's equatorial clouds observed by the Galileo orbiter, Icarus, 202, 1, 358–360, doi: 10.1016/j.icarus.2009.03.028.

Asay-Davis, X. S., P. S. Marcus, M. H. Wong, I. de Pater, (2011), Changes in Jupiter's zonal velocity between 1979 and 2008, Icarus, 211(2), 1215–1232, doi: 10.1016/j.icarus.2010.11.018.

Asay-Davis, X. S., P. S. Marcus, M. H. Wong, I. de Pater, (2009), Jupiter's shrinking Great Red Spot and steady Oval BA: Velocity measurements with the 'Advection Corrected Correlation Image Velocimetry' automated cloud-tracking method, Icarus, 203, 1, 164–188, doi: 10.1016/j.icarus.2009.05.001.

Attree, N., C. Murray, G. Williams, N. Cooper, (2014), Survey of low-velocity collisional features in Saturn's F-ring, Icarus 277, 56–66.

Attree, N. O, C. D. Murray, N. J. Cooper, G. A. Williams, (2012), Detection of low-velocity collisions in Saturn's F-ring, The Astrophysical Journal Letters 755, L27–L31.

Barnes, J. W., B. J. Buratti, E. P. Turtle, et al., (2013), Precipitation-induced surface brightenings seen on Titan by Cassini VIMS and ISS, Planetary Science 2, doi: 10.1186/2191-2521-2-1.

Barnes, J. W., R. H. Brown, J. Radebaugh, et al., (2006), Cassini observations of flow-like features in western Tui Regio, Titan, Geophysical Research Letters 33, L16204.

Barnes, J. W., R. H. Brown, E. P. Turtle, et al., (2005), A 5-μm bright spot on Titan: Evidence for surface diversity, Science 310, 92–95.

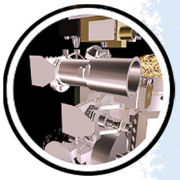

Barrado-Izagirre, N., S. Perez-Hoyos, A. Sanchez-Lavega, (2010), Turbulence in Jupiter's clouds, In Highlights of Spanish Astrophysics V, (eds.) J. M. Diego, L. J. Goicoechea, J. I. GonzalezSerrano, J. Gorgas, pp. 451–451, doi: 10.1007/978-3-642-11250-8_123.

Barrado-Izagirre, N., S. Perez-Hoyos, A. Sanchez-Lavega, (2009), Brightness power spectral distribution and waves in Jupiter's upper cloud and hazes, Icarus, 202, 1, 181–196, doi: 10.1016/j.icarus.2009.02.015.

Barrado-Izagirre, N., A. Sanchez-Lavega, S. Perez-Hoyos, R. Hueso, (2008), Jupiter's polar clouds and waves from Cassini and HST images: 1993–2006, Icarus, 194, 1, 173–185, doi: 10.1016/j.icarus.2007.08.025.

Becker, T. L., M. T. Bland, K. L. Edmundson, L. A. Soderblom, et al., (2016), Completed global control network and basemap of Enceladus, 47th Lunar Planetary Science Conference, p. 2342.

Beddingfield, C. B., D. M. Burr. L. T. Tran, (2016), Polygonal impact craters on Dione: Evidence for tectonic structures outside the wispy terrain, Icarus 274, 163–194.

Behounková, M., G. Tobie, O. Cadek, G. Choblet, C. Porco, F. Nimmo, (2015), Timing of water plume eruptions on Enceladus explained by interior viscosity structure, Nature Geoscience 8, 601–604.

Beurle, K., C. D. Murray, G. A. Williams, M. W. Evans, N. J. Cooper, C. B. Agnor, (2010), Direct evidence for gravitational instability and moonlet formation in Saturn's Rings, Astrophysical Journal Letters 718, L176–L180.

Beuthe, M., A. Rivoldini, A. Trinh, (2016), Enceladus's and Dione's floating ice shells supported by minimum stress isostasy, Geophysical Research Letters 43, no. 19, 10-088.

Birch, S. P. D., A. G. Hayes, W. E. Dietrich, A. D. Howard, et al., (2017), Geomorphologic mapping of Titan's polar terrains: Constraining surface processes and landscape evolution. Icarus, volume 282, p. 214–236.

Burleigh, K. J., P. Helfenstein, B. Carcich, J. Veverka, et al., (2010), Linear polarization and albedo reconnaissance for regolith texture on Saturn's moon Iapetus, 41st Lunar Planetary Science Conference, abstract 1533, p.2607.

Castillo-Rogez, J. C., D. Hemingway, G. Tobie, W. B. McKinnon, G. Schubert, (2018), Origin and evolution of Saturn's midsize moons, In Enceladus and the Icy Moons of Saturn, Part 3: Saturn’s Icy Moons, (eds.) P. M. Schenk, R. N. Clark, C. J. A. Howett, A. J. Verbiscer, J. H. Waite, Space Science Series, The University of Arizona Press, Tucson, AZ, pp. 285–305.

Castillo-Rogez, J. C., T. V. Johnson, P. C. Thomas, M. Choukroun, D. L. Matson, J. I. Lunine, (2012), Geophysical evolution of Saturn's satellite Phoebe, a large planetesimal in the outer Solar System, Icarus 219, 86–109, doi: 10.1016/j.icarus.2012.02.002.

Castillo-Rogez, J. C., D. L. Matson, C. Sotin, T. V. Johnson, J. I. Lunine, P. C. Thomas, (2007), Iapetus’ geophysics: Rotation rate, shape and equatorial ridge, Icarus 190, 179–202.

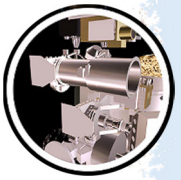

Charnoz S., A. Brahic, P. Thomas, C. Porco, (2007), The equatorial ridges of Pan and Atlas: terminal accretionary ornaments?, Science, vol. 318, issue 5856, pp. 1622–1624, doi: 10.1126/science.1148631.

Charnoz, S., C. C. Porco, E. Deau, A. Brahic, J. N. Spitale, G. Bacques, K. Baillie, (2005), Cassini discovers a kinematic spiral ring around Saturn, Science 310, 1241–1351.

Choi, D. S., A. P. Showman, A. R. Vasavada, A. A. Simon-Miller, (2013), Meteorology of Jupiter's equatorial hot spots and plumes from Cassini, Icarus, 223, 2, 832–843, doi: 10.1016/j.icarus.2013.02.001.

Choi, D. S., and A. P. Showman, (2011), Power spectral analysis of Jupiter's clouds and kinetic energy from Cassini, Icarus, 216, 2, 597–609, doi: 10.1016/j.icarus.2011.10.001.

Choi, D. S., A. P. Showman, A. R. Vasavada, (2010), The evolving flow of Jupiter's white ovals and adjacent cyclones, Icarus, 207, 1, 359–372, doi: 10.1016/j.icarus.2009.10.013.

Cooper, N., S. Renner, C. Murray, M. Evans, (2015), Saturn’s inner satellites: Orbits, masses, and the chaotic motion of Atlas from new Cassini imaging observations, The Astronomical Journal 149, 27.

Cooper, N., C. Murray, V. Lainey, R. Tajeddine, M. Evans, G. Williams, (2014), Cassini ISS mutual event astrometry of the mid-sized Saturnian satellites 2005–2012. Astronomy and Astrophysics 572, A43.

Cooper, N., C. Murray, G. Williams, (2013), Local variability in the orbit of Saturn's F-ring, The Astronomical Journal 145, 161–175.

Cooper, N. J., C. D. Murray, M. W. Evans, K. Beurle, R. A. Jacobson, C. C. Porco, (2008), Astrometry and dynamics of Anthe (S/2007 S 4), a new satellite of Saturn, Icarus, 195, 765–777.

Cooper, N. J., C. D. Murray, C. C. Porco, J. N. Spitale, (2006), Cassini ISS astrometric observations of the inner Jovian satellites, Amalthea and Thebe, Icarus, 181, 223–234.

Ćuk, M., L. Dones, D. Nesvorny, (2016), Dynamical evidence for a late formation of Saturn’s moons, The Astrophysical Journal, 820, 97.

Cuzzi, J. N.,G. Filacchione, E. A. Marouf, M. S. Tiscareno, C. D. Murray, (2018), The Rings of Saturn, Chapter 3, In Planetary Ring Systems: Properties, Structure, and Evolution, (eds.) M. S. Tiscareno, C. D. Murray, Queen Mary University of London, pp. 51–92, doi: 10.1017/9781316286791.003.

Cuzzi, J. N., A. D. Whizin, R. C. Hogan, A. R. Dobrovolskis, L. Dones, M. R. Showalter, J. E. Colwell, J. D. Scargle, (2014), Saturn’s F-ring core: Calm in the midst of chaos?, Icarus 232, 157–175.

Damptz, A. L., A. J. Dombard, M. R. Kirchoff, (2018), Testing models for the formation of the equatorial ridge on Iapetus via crater counting, Icarus 302, 134–144.

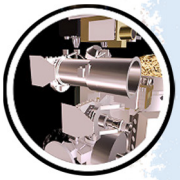

de Kok, R. J., N. A. Teanby, L. Maltagliati, P. G. J. Irwin, and S. Vinatier, (2014), HCN ice in Titan's high-altitude southern polar cloud, Nature, 514, no. 7520, 65, doi: 10.1038/nature13789.

Del Genio, A., and J. Barbara, (2016), An objective classification of Saturn cloud features from Cassini ISS images, Icarus 271, 222–236.

Del Genio, A. D., and J. M. Barbara, (2012), Constraints on Saturn's tropospheric general circulation from Cassini ISS images, Icarus 219, 689–700.

Del Genio, A. D., R. K. Achterberg, K. H. Baines, F. M. Flasar, P. L. Read, Sanchez-Lavega, A., Showman, A. P., (2009), Saturn atmospheric structure and dynamics, Saturn from Cassini-Huygens, (eds.) M. Dougherty, L. Esposito, S. Krimigis, Springer-Verlag, Dordrecht, Netherlands, pp. 113–159.

Del Genio, A. D., J. M. Barbara, J. Ferrier, A. P. Ingersoll, R. A. West, A. R. Vasavada, J. Spitale, C. C. Porco, (2007), Saturn eddy momentum fluxes and convection: First estimates from Cassini images, Icarus 189, 479–492.

del Rio-Gaztelurrutia, T., J. Legarreta, R. Hueso, S. Pérez-Hoyos, A. Sánchez-Lavega, (2010), A long-lived cyclone in Saturn's atmosphere: Observations and models, Icarus 209, 665–681.

Denk, T., S. Mottola, F. Tosi, W. B. Bottke, D. P. Hamilton, (2018), The Irregular satellites of Saturn, In Enceladus and the icy moons of Saturn, (eds.) P. M. Schenk, R. N. Clark, C. J. A. Howett, A. J. Verbiscer, J. H. Waite, Space Science Series, The University of Arizona Press, Tucson, AZ.

Denk, T., G. Neukum, T. Roatsch, C. C. Porco, J. A. Burns, et al., (2010), Iapetus: Unique surface properties and a global color dichotomy from Cassini imaging, Science 327, no. 5964, 435–439, doi: 10.1126/science.1177088.

Denk, T., G. Neukum, N. Schmedemann, T. Roatsch, R. J. Wagner, B. Giese, J. E. Perry, P. Helfenstein, E. P. Turtle, C. C. Porco, (2008), Iapetus Imaging during the targeted flyby of the Cassini spacecraft, 39th Lunar and Planetary Science Conference, abstract 2533.

Denk, T., G. Neukum, P. Helfenstein, P. C. Thomas, E. P. Turtle, A. S. McEwen, T. Roatsch, J. Veverka, T. V. Johnson, J. E. Perry, W. M. Owen, R. J. Wagner, C. C. Porco, Cassini ISS team, (2005a), The first six months of Iapetus observations by the Cassini ISS camera, 36th Lunar and Planetary Science Conference, abstract 2262.

Denk, T., G. Neukum, T. Roatsch, A. S. McEwen, E. P. Turtle, P. C. Thomas, P. Helfenstein, R. J. Wagner, C. C. Porco, J. E. Perry, B. Giese, T. V. Johnson, J. Veverka, Cassini ISS team, (2005b), First imaging results from the Iapetus B/C flyby of the Cassini spacecraft, 36th Lunar and Planetary Science Conference, abstract 2268.

Denk, T., K.-D. Matz, T. Roatsch, U. Wolf, R. J. Wagner, G. Neukum, R. Jaumann, (2000), Iapetus (1): Size, topography, surface structures, craters, 31st Lunar and Planetary Science Conference, abstract 1596.

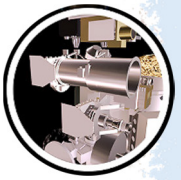

Dones, L., C. R. Chapman, W. B. McKinnon, H. J. Melosh, M. R. Kirchoff, G. Neukum, K. J. Zahnle, (2009), Icy satellites of Saturn: Impact cratering and age determination, Saturn from Cassini-Huygens, (eds.) M. Dougherty, L. Esposito, S. Krimigis, Springer-Verlag, Dordrecht, Netherlands, pp. 613–35.

Dyudina, U., X. Zhang, L. Li, P. Kopparla, A. P. Ingersoll, L. Dones, A. Verbiscer, Y. L. Yung, (2016), Reflected light curves, spherical and bond albedos of Jupiter- and Saturn-like exoplanets, The Astrophysical Journal, 822, 2, 76, doi: 10.3847/0004-637x/822/2/76.

Dyudina, U. A., A. P. Ingersoll, S. P. Ewald, D. Wellington, (2015), Saturn’s aurora observed by the Cassini camera at visible wavelengths, Icarus 263, 32–43.

Dyudina, U. A., A. P. Ingersoll, S. P. Ewald, C. C. Porco, G. Fischer, Y. Yair, (2013), Saturn’s visible lightning, its radio emissions, and the structure of the 2009–2011 lightning storms, Icarus 226, 1020–1037.

Dyudina, U. A., A. P. Ingersoll, S. P. Ewald, C. C. Porco, G. Fischer, W. S. Kurth, R. A. West, (2010), Detection of visible lightning on Saturn, Geophysical Research Letters 37, L09205.

Dyudina, U. A., A. P. Ingersoll, S. P. Ewald, A. R. Vasavada, R. A. West, K. H. Baines, et al., (2009), Saturn's south polar vortex compared to other large vortices in the solar system, Icarus 202, 240–248.

Dyudina, U. A., A. P. Ingersoll, S. P. Ewald, A. R. Vasavada, et al., (2008), Dynamics of Saturn's south polar vortex, Science 319, 1801.

Dyudina, U., A. Ingersoll, S. Ewald, C. Porco, G. Fischer, W. Kurth, et al., (2007), Lightning storms on Saturn observed by Cassini ISS and RPWS during 2004–2006, Icarus 190, 545–555.

Dyudina, U. A., P. D. Sackett, D. D. R. Bayliss, S. Seager, C. C. Porco, H. B. Throop, L. Dones, (2005), Phase light curves for extrasolar Jupiters and Saturns, Astrophysical Journal 618, 973–986.

Dyudina, U. A., A. D. Del Genio, A. P. Ingersoll, C. C. Porco, R. A. West, A. R. Vasavada, J. M. Barbara, (2004), Lightning on Jupiter observed in the H-alpha line by the Cassini imaging science subsystem, Icarus, 172(1), 24–36, doi: 10.1016/j.icarus.2004.07.014.

El Moutamid, M., Nicholson, P., French, R., Tiscareno, M., Murray, C., Evans, M., French, C., Hedman, M., Burns, J., (2016), How Janus' orbital swap affects the edge of Saturn's A-ring?, Icarus 279, 125–140.

Elder, C., P. Helfenstein, P. Thomas, J. Veverka, J. A. Burns, T. Denk, C. Porco, (2007), Tethys’ mysterious equatorial band, Bulletin of the American Astronomical Society 39, p. 429.

Estrada, P. R., R. H. Durisen, and H. N. Latter, (2018), Meteoroid bombardment and ballistic transport in planetary rings, In Planetary Ring Systems: Properties, Structure, and Evolution, (eds.) M. S. Tiscareno, C. D. Murray, Cambridge, United Kingdom, Cambridge University Press, 198–224.

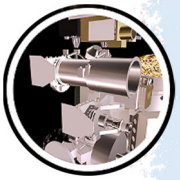

Fischer, G., S. Ye, J. Groene, A. Ingersoll, K. Sayanagi, J. Menietti, W. Kurth, D. Gurnett, (2014), A possible influence of the Great White Spot on Saturn kilometric radiation periodicity, Annales Geophysicae 32, 1463–1476.

Fischer, G., W. S. Kurth, D. A. Gurnett, P. Zarka, U. A. Dyudina, A. P. Ingersoll, S. P. Ewald, C. Porco, A. Wesley, C. Go, M. Delcroix, (2011), A giant thunderstorm on Saturn, Nature 475, 75-77.

Fischer, G., W. Kurth, U. Dyudina, M. Kaiser, P. Zarka, A. Lecacheux, A. Ingersoll, D. Gurnett, (2007), Analysis of a giant lightning storm on Saturn, Icarus 190, 528–544.

Flasar, F. M., K. H. Baines, M. K. Bird, T. Tokano, R. A. West, (2009), Atmospheric dynamics and meteorology, Chapter 13, In Titan from Cassini-Huygens, (eds.) R. Brown, J. P. Lebreton, J. Waite, Springer-Verlag, Dordrecht, Netherlands, pp. 323–353.

Fletcher, L. N., T. K. Greathouse, S. Guerlet, J. I. Moses, and R. A. West, (2018), Saturn's seasonally changing atmosphere: Thermal structure, composition and aerosols, Chapter 10, In Saturn in the 21st Century, (eds.) K. H. Baines, F. M. Flasar, N. Krupp, T. Stallard, Cambridge University Press, pp, 251–294, doi: 10.1017/9781316227220.010.

French, R. S., S. K. Hicks, M. R. Showalter, A. K. Antonsen, D. R. Packard, (2014), Analysis of clumps in Saturn’s F-ring from Voyager and Cassini, Icarus 241, 200–220.

French, R. S., M. R. Showalter, R. Sfair, C. A. Argüelles, M. Pajuelo, P. Becerra, M. Hedman, P. D. Nicholson, (2012), The brightening of Saturn’s F-ring, Icarus 219, 181–193.

Fussner S., A. S. McEwen, J. E. Perry, E. P. Turtle, D. D. Dawson, C. C. Porco, R. A. West, Cassini ISS team,(2005), Dependence of surface contrast on emission angle in Cassini ISS 938-nm images of Titan, Lunar and Planetary Science XXXVI, Part 6.

Galperin, B., R. M. B Young, S. Sukoriansky, N. Dikovskaya, P. L. Read, A. J. Lancaster, D. Armstrong, (2014), Cassini observations reveal a regime of zonostrophic macroturbulence on Jupiter, Icarus, 229, 295–320, doi: 10.1016/j.icarus.2013.08.030.

Gao, P., P. Kopparla, X. Zhang, A. P. Ingersoll, (2016), Aggregate particles in the plumes of Enceladus, Icarus 264, 227–238, doi: 10.1016/j.icarus.2015.09.030.

Garcia-Melendo, E., R. Hueso, A. Sánchez-Lavega, J. Legarreta, T. del Rio-Gaztelurrutia, J. F. Rojas, S. Pérez-Hoyos, J. F. Sanz-Requenna, (2013), Atmospheric dynamics of Saturn’s 2010 giant storm, Nature Geoscience, 6, 525–529.

Garcia-Melendo, E., S. Pérez-Hoyos, A. Sánchez-Lavega, R. Hueso, (2011a), Saturn’s zonal wind profile in 2004–2009 from Cassini ISS images and its long-term variability, Icarus 215, 62–74.

Garcia-Melendo, E., J. Arregi, J. F. Rojas, R. Hueso, N. Barrado-Izagirre, J. M. Gomez-Forrellad, S. Perez-Hoyos, J. F. Sanz-Requena, A. Sanchez-Lavega, (2011b), Dynamics of Jupiter's equatorial region at cloud top level from Cassini and HST images, Icarus, 211, 2, 1242–1257, doi: 10.1016/j.icarus.2010.11.020.

- - - - - - - - - - - - - -

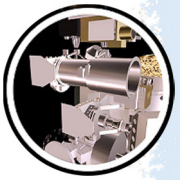

Garcia-Melendo, E., A. Sanchez-Lavega, J. Legarreta, S. Perez-Hoyos, R. Hueso, (2010), A strong high altitude narrow jet detected at Saturn's equator, Geophysical Research Letters, 37, doi: 10.1029/2010gl045434.

Garcia-Melendo, E., A. Sánchez-Lavega, J. F. Rojas, S. Pérez-Hoyos, R. Hueso, (2009), Vertical shears in Saturn's eastward jets at cloud level, Icarus 201, 818–820.

Geissler, P., A. McEwen, C. Porco, D. Strobel, J. Saur, J. Ajello, R. West, (2004), Cassini observations of Io's visible Aurorae, Icarus 172, 127–140.

Giese, B., P. Helfenstein, E. Hauber, H. Hussmann, R. Wagner, (2017), An exceptionally high standing ridge on Enceladus, European Planetary Science Congress 2017, abstract, vol 11, EPSC2017-28-1.

Giese, B., P. Helfenstein, T. A. Hurford, G. Neukum, C. C. Porco, (2011a), Observation of cycloidal features on Enceladus, 42nd Lunar Planetary Science Conference, abstract 1608.

Giese, B., H. Hussmann, T. Roatsch, P. Helfenstein, P. C. Thomas, G. Neukum, (2011b), Enceladus: Evidence for librations forced by Dione, EPSC-DPS Joint Meeting 2011, 976–977.

Giese, B., P. Helfenstein, P. C. Thomas, A. P. Ingersoll, J. Perry, R. Wagner, G. Neukum, C. C. Porco, (2010a), The morphology of an active zone near Enceladus' south pole and implications. In European Geosciences Union General Assembly Conference Abstracts, vol. 12, p. 11085.

Giese, B., and Cassini ISS team, (2010b), The topography of Enceladus, European Planetary Science Congress 2010, abstract, vol. 5, EPSC2010-675.

Giese, B., T. Denk, G. Neukum, T. Roatsch, P. Helfenstein, P. C. Thomas, E. P. Turtle, A. McEwen, C. C. Porco, (2008a), The topography of Iapetus' leading side, Icarus 193, 359–371.

Giese, B., R. Wagner, H. Hussmann, G. Neukum, J. Perry, P. Helfenstein, P. C. Thomas, (2008b), Enceladus: An estimate of heat flux and lithospheric thickness from flexurally supported topography, Geophysical Research Letters 35, Issue 24, CiteID L24204.

Giese, B., R. Wagner, G. Neukum, P. Helfenstein, P. C Thomas, (2007), Tethys: Lithospheric thickness and heat flux from flexurally supported topography at Ithaca Chasma, Geophysical Research Letters 34, L21203.

Giese, B., G. Neukum, T. Roatsch, T. Denk, C. C. Porco, (2006), Topographic modeling of Phoebe using Cassini images, Planetary and Space Science 54, 1156–1166.

Goldstein, D. B., M. Hedman, M. Manga, M. Perry, J. Spitale, B. Teolis, (2018), Enceladus plume dynamics: From surface to space, In Enceladus and the Icy Moons of Saturn, Part 2: Enceladus Plume and the E-ring, (eds.) P. M. Schenk, R. N. Clark, C. J. A. Howett, A. J. Verbiscer, J. H. Waite, Space Science Series, The University of Arizona Press, Tucson, AZ, pp. 175–194.

Hadjighasem, A., and G. Haller, (2016), Geodesic transport barriers in Jupiter's atmosphere: A video-based analysis, Siam Review, 58, 1, 69–89, doi: 10.1137/140983665.

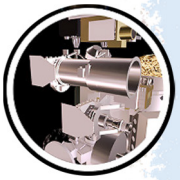

Harbison, R. A., P. C. Thomas, and P. D. Nicholson, (2011), Rotational modeling of Hyperion, Celestial Mechanics and Dynamical Astronomy, vol 110, issue 1, pp. 1–16, doi: 10.1007/s10569-011-9337-3.

Hayes A. G., O. Aharonson, J. I. Lunine, R. L. Kirk, H. A. Zebker, L. C. Wye, R. D. Lorenz, E. P. Turtle, P. Paillou, G. Mitri, S. D. Wall, E. R. Stofan, K. L. Mitchell, C. Elachi, Cassini RADAR team, (2011), Transient surface liquid in Titan's polar regions from Cassini, Icarus 211, 655–671.

Hedman, M. M., F. Postberg, D. P. Hamilton, S. Renner, H.-W. Hsu, (2018), Dusty rings, In Planetary Ring Systems: Properties, Structure, and Evolution, (eds.) M. S. Tiscareno, C. D. Murray, Cambridge, United Kingdom, Cambridge University Press, pp. 308–337.

Hedman, M. M., J. A. Burns, P. D. Nicholson, M. S. Tiscareno, M. W. Evans, E. Baker, (2017), One last look from the dark side: Cassini's final views of Saturn's rings from within the planet's shadow, AAS/DPS Meeting, abstracts 49, 212.01.

Hedman, M. M., and B. J. Carter, (2017), A curious ringlet that shares Prometheus' orbit but precesses like the F-ring, Icarus 281, 322–333.

Hedman, M. M., J. A. Burns, M. R. Showalter, (2015), Corrugations and eccentric spirals in Saturn's D-ring: New insights into what happened at Saturn in 1983, Icarus 248, 137–161.

Hedman, M. M., and C. C. Stark, (2015), Saturn's G- and D-rings provide nearly complete measured scattering phase functions of nearby debris disks, Astrophysical Journal 811, 67.

Hedman, M., and M. Showalter, (2015), A new pattern in Saturn's D-ring created in late 2011, Icarus 279, 155–165.

Hedman, M., J. Burt, J. Burns, M. Showalter, (2014), Non-circular features in Saturn's D-ring: D68, Icarus 223, 147–162.

Hedman, M., J. Burns, D. Hamilton, M. Showalter, (2013), Of horseshoes and heliotropes, dynamics of dust in the Encke Gap, Icarus, vol. 223, issue 1, pp. 252–276, doi: 10.1016/j.icarus.2012.11.036.

Hedman, M. M., J. A. Burns, D. P. Hamilton, M. R. Showalter, (2012), The three-dimensional structure of Saturn's E-ring, Icarus 217, 322–338.

Hedman, M. M., J. A. Burns, M. W. Evans, M. S. Tiscareno, C. C. Porco, (2011), Saturn's curiously corrugated C-ring, Science 332, 708–711.

Hedman, M. M., J. A. Burt, J. A. Burns, M. S. Tiscareno, (2010a), The shape and dynamics of a heliotropic dusty ringlet in the Cassini Division, Icarus 210, 284–297.

Hedman, M. M., N. J. Cooper, C. D. Murray, K. Beurle, M. W. Evans, M. S. Tiscareno, J. A. Burns, (2010b), Aegaeon (Saturn LIII), a G-ring object, Icarus 207, 433–447.

Hedman, M. M., J. A. Burns, M. S. Tiscareno, C. C. Porco, (2009a), Organizing some very tenuous things: Resonant structures in Saturn's faint rings, Icarus 202, 260–279.

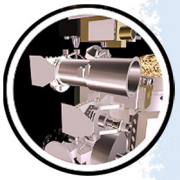

Hedman, M. M., C. D. Murray, N. J. Cooper, M. S. Tiscareno, K. Beurle, M. W. Evans, J.A. Burns, (2009b), Three tenuous rings/arcs for three tiny moons, Icarus 199, 378–386.

Hedman, M. M., J. A. Burns, M. R. Showalter, C. C. Porco, P. D. Nicholson, A. S. Bosh, M. S. Tiscareno, R. H. Brown, B. J. Buratti, K. H. Baines, R. Clark, (2007a), Saturn's dynamic D-ring, Icarus 188, 89–107.

Hedman, M. M., J. A. Burns, M. S. Tiscareno, C. C. Porco, G. H. Jones, E. Roussos, N. Krupp, C. Paranicas, S. Kempf, (2007b), The source of Saturn's G-ring, Science 317, 653–656.

Heimpel, M., J. Aurnou, J. Wicht, (2005), Simulation of equatorial and high-latitude jets on Jupiter in a deep convection model, Nature, 438, 7065, 193–196, doi: 10.1038/nature04208.

Helfenstein, P. and C. C. Porco, (2015), Enceladus' geysers: Relation to geological features, The Astronomical Journal, 150, 96.

Helfenstein, P., (2014), Y-shaped discontinuity, In Encyclopedia of Planetary Landforms, Springer, New York, NY, doi: 10.1007/978-1-4614-9213-9_576-1, pp. 2347–2350.

Helfenstein, P., (2012), Seeing through frost on Enceladus, American Geophysical Union (AGU), Fall Meeting 2012, abstract P32A-09.

Helfenstein, P., (2010), Tectonic overturn on Enceladus, Nature Geoscience, 3, 75–76.

Helfenstein, P., T. Denk, B. Giese, A. Ingersoll, T. V. Johnson, A. S. McEwen, G. Neukum, J. Perry, C. C. Porco, T. Roatsch, P. C. Thomas, E. P. Turtle, A. Verbiscer, J. Veverka, (2008), Enceladus south polar terrain geology: New details from Cassini ISS high resolution imaging, American Geophysical Union (AGU), Fall Meeting 2008, abstract P13D-02.

Helfenstein, P., P. C. Thomas, J. Veverka, J. Rathbun, J. Perry, E. Turtle, T. Denk, G. Neukum, T. Roatsch, R. Wagner, B. Giese, S. Squyres, J. Burns, A. McEwen, C. Porco, T. V. Johnson, Cassini ISS team, (2006), Patterns of fracture and tectonic convergence near the south pole of Enceladus, 35th Lunar Planetary Science Conference, abstract 2182.

Helfenstein, P., P. C. Thomas, J. Veverka, S. Squyres, J. A. Rathbun, T. Denk, G. Neukum, T. Roatsch, R. Wagner, J. Perry, E. Turtle, A. S. McEwen, T. V. Johnson, C. Porco, Cassini ISS team, (2005a), Geological features and terrains on Enceladus as seen by Cassini ISS, Bulletin of the American Astronomical Society 37, p. 701.

Helfenstein, P., P. Thomas, J. Veverka, T. Denk, G. Neukum, R. A. West, B. Knowles, C. C. Porco, Cassini ISS team, (2005b), A Cassini ISS search for regolith-texture variations on Tethys, 36th Lunar Planetary Science Conference, abstract 2399.

Hueso, R., J. Legarreta, E. Garcia-Melendo, A. Sanchez-Lavega, S. Perez-Hoyos, (2009), The jovian anticyclone BA II: Circulation and interaction with the zonal jets, Icarus, 203, 2, 499-515, doi: 10.1016/j.icarus.2009.05.004.

Hurford, T., B. Bills, P. Helfenstein, R. Greenberg, G. Hoppa, D. Hamilton, (2009), Geological implications of a physical libration on Enceladus, Icarus 203, 541–552.

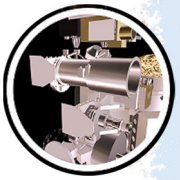

Hurford, T., P. Helfenstein, J. Spitale, (2012), Tidal control of jet eruptions on Enceladus as observed by Cassini ISS between 2005 and 2007, Icarus 220, 896–903.

Ingersoll, A. P., and S. P. Ewald, (2017), Decadal timescale variability of the Enceladus plumes inferred from Cassini images, Icarus 282, 260–275, doi: 10.1016/j.icarus.2016.09.018.

Ingersoll, A. P., and M. Nakajima, (2016), Controlled boiling on Enceladus. 2. Model of the liquid-filled cracks, Icarus 272, 319–326, doi: 10.1016/j.icarus.2015.12.040.

Ingersoll, A. P., and S. P. Ewald, (2011), Total particulate mass in Enceladus plumes and mass of Saturn's E-ring inferred from Cassini ISS images, Icarus 216, 492–506, doi: 10.1016/j.icarus.2011.09.018.

Ingersoll, A. P., and A. A. Pankine, (2010), Subsurface heat transfer on Enceladus: Conditions under which melting occurs, Icarus 206, 594–607, doi: 10.1016/j.icarus.2009.09.015.

Jacobson, R. A., (2014), The small Saturnian satellites—chaos and conundrum, AAS Division on Dynamical Astronomy Meeting Abstracts 45, 304.05, Philadelphia, PA.

Jacobson, R., J. Spitale, C. Porco, K. Beurle, N. Cooper, M. Evans, C. Murray, (2008), Revised orbits of Saturn's small inner satellites, Astronomical Journal 135, 261–263.

Jacobson, R. A., J. Spitale, C. C. Porco, W. M. Owen Jr., (2006a), The GM values of Mimas and Tethys and the libration of Methone, The Astronomical Journal 132, 711–713.

Jacobson, R. A., P. G. Antreasian, J. J. Bordi, K. E. Cridle, R. Ionasescu, J. B. Jones, R. A. Mackenzie, M. C. Meek, D. Parcher, F. J. Pelletier, W. M. Owen, D. C. Roth, I. M. Roundhill, J. R. Stauch, (2006b), The gravity field of the Saturnian system from satellite observations and spacecraft tracking data, The Astronomical Journal 132, 2520–2526.

Jaumann, R., R. N. Clark, F. Nimmo, A. R. Hendrix, B. J. Buratti, T. Denk, J. M. Moore, P. M. Schenk, S. J. Ostro, R. Srama, (2009a), Icy Satellites: Geological evolution and surface processes, In Saturn from Cassini-Huygens, Chapter 20, (eds.) M. Dougherty, L. Esposito, S. Krimigis, Springer, Dordrecht, pp. 637–681, doi: 10.1007/978-1-4020-9217-6_20.

Jaumann R., R. Kirk, R. Lorenz, R. Lopes, E. Stofan, E. P. Turtle, H. U. Keller, C. A. Wood, C. Sotin, L. Soderblom, M. Tomasko, (2009b), Geology and surface processes on Titan, In Titan from Cassini-Huygens, (eds.) R. Brown, J.-P. Lebreton, and H. Waite, Springer, New York, NY, pp. 75–140.

Johnson, T. V., and J. I. Lunine, (2005), Saturn's moon Phoebe as a captured body from the outer solar system, Nature 435, 69–71.

Karkoschka E., A. McEwen, J. Perry, (2017a), Producing the best global mosaic of Titan's surface albedo using Cassini images, LPSC 48 #2518, 48th Lunar and Planetary Science Conference, March 20–24, 2017, The Woodlands, TX.

Karkoschka E., A. McEwen, J. Perry, (2017b), Creating the best global mosaic of Titan's surface albedo using Cassini images, American Astronomical Society, DPS 49, #301.06.

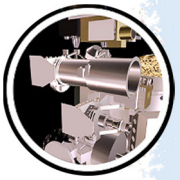

Kirchoff, M. R., E. B. Bierhaus, L. Dones, S. J. Robbins, K. N. Singer, R. J. Wagner, and K. J. Zahnle, (2018), Cratering histories in the Saturnian system, In Enceladus and the Icy Moons of Saturn, (eds.) P. M. Schenk, R. N. Clark, C. J. A. Howett, A. J. Verbiscer, J. H. Waite, Space Science Series, The University of Arizona Press, Tucson, AZ.

Kirchoff, M. R., and P. M. Schenk, (2010), Impact cratering records of the mid-sized, icy Saturnian satellites, Icarus 206, 485–497.

Lainey, V., R. A. Jacobson, R. Tajeddine, N. J. Cooper, C. Murray, V. Robert, G. Tobie, T. Guillot, S. Mathis, F. Remus, J. Desmars, J.-E. Arlot, J.-P. De Cuyper, V. Dehant, D. Pascu, W. Thuillot, C. Le Poncin-Lafitte, J.-P Zahn, (2017), New constraints on Saturn's interior from Cassini astrometric data, Icarus 281, 286–296.

Laraia, A. L., A. P. Ingersoll, M. A. Janssen, S. Gulkis, F. Oyafuso, M. Allison, (2013), Analysis of Saturn’s thermal emission at 2.2-cm wavelength: Spatial distribution of ammonia vapor, Icarus 226, 641–654.

Lavvas P., R. A. West, G. Gronoff, P. Rannou, (2014), Titan’s emission processes during eclipse, Icarus 241, 397–408.

Li, C., and A. P. Ingersoll, (2015), Moist convection in hydrogen atmospheres and the frequency of Saturn’s giant storms, Nature Geoscience 8, 398–403.

Li, J., Q. Xiang, R. Ze, M. Ma, S. Wang, Q. Xie, Y. Xiang (2018), Thermal and electrical analysis of SiGe thermoelectric unicouple filled with thermal insulation materials, Applied Thermal Engineering 134, 266–274.

Li, L., X. Jiang, H. J. Trammell, Y. Pan, J. Hernandez, B. J. Conrath, P. J. Gierasch, et al., (2015), Saturn’s giant storm and global radiant energy, Geophysical Research Letters 42, doi: 10.1002/2015GL063763.

Li, L., R. K. Achterberg, B. J. Conrath, P. J. Gierasch, M. A. Smith, A. A. Simon-Miller, C. A. Nixon, et al., (2013), Strong temporal variation over one Saturnian year: From Voyager to Cassini, Scientific Reports 3, 2410.

Li, L., X. Jiang, A. P. Ingersoll, A. D. Del Genio, C. C. Porco, R. A. West, A. R. Vasavada, et al., (2011), Equatorial winds on Saturn and the stratospheric oscillation, Nature Geoscience 4, 750–752.

Li, L. M., A. P. Ingersoll, A. R. Vasavada, A. A. Simon-Miller, R. K. Achterberg, S. P. Ewald, U. A. Dyudina, C. C. Porco, R. A. West, F. M. Flasar, (2006a), Waves in Jupiter's atmosphere observed by the Cassini ISS and CIRS instruments, Icarus, 185, 2, 416–429, doi: 10.1016/j.icarus.2006.08.005.

Li, L. M., A. P. Ingersoll, A. R. Vasavada, A. A. Simon-Miller, A. D. Del Genio, S. P. Ewald, Porco, C. C., R. A. West, (2006b), Vertical wind shear on Jupiter from Cassini images, Journal of Geophysical Research-Planets, 111(E4), doi: 10.1029/2005je002556.

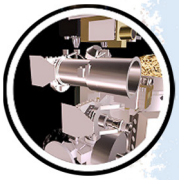

Li, L., Ingersoll, A. P., Vasavada, A. R., Porco, C. C., Del Genio, A. D.,Ewald, S. P., (2004), Life cycles of spots on Jupiter from Cassini images, Icarus, 172, 1, 9–23, doi: 10.1016/j.icarus.2003.10.015.

Lopes R. M. C, M. J. Malaska, A. Solomonidou, A. Le Gall, M. A. Janssen, C. D. Neish, E. P. Turtle et al., (2016), Nature, distribution, and origin of Titan's undifferentiated plains, Icarus 270, pp. 162–182.

Lora, J. M., J. I. Lunine, J. L. Russell, (2015), GCM simulations of Titan's middle and lower atmosphere and comparison to observations, Icarus, volume 250, pp. 516–528.

Martens, H. R., A. P. Ingersoll, S. P. Ewald, P. Helfenstein, B. Giese, (2015), Spatial distribution of ice blocks on Enceladus and implications for their origin and emplacement, Icarus 245, pp. 162–176.

Matson, D. L., J. C. Castillo-Rogez, G. Schubert, C. Sotin, W. B. McKinnon, (2009), The thermal evolution and internal structure of Saturn’s mid-sized Icy satellites, In Saturn from Cassini-Huygens, (eds.) M. K. Dougherty, L. W. Esposito, S. M. Krimigis, Springer, Dordrecht, pp. 577–612 doi: 10.1007/978-1-4020-9217-6_18.

McEwen A. S., E. P. Turtle, J. E. Perry, S. Fussner, C. C. Porco, R. A. West, T. V. Johnson, G. C. Collins, T. del Genio, J. Barbara, Cassini ISS team, (2005a), Cassini Imaging results at Titan, Lunar and Planetary Science XXXVI, Part 13, LPI-Contrib-1234-Pt-13.

McEwen A., E. Turtle, J. Perry, D. Dawson, S. Fussner, G. Collins, C. Porco, T. Johnson, L. Soderblom, (2005b), Mapping and monitoring the surface of Titan, Bulletin of the American Astronomical Society, vol. 37, p. 739.

Mitchell, C., C. Porco, J. Weiss, (2015), Tracking the geysers of Enceladus into Saturn's E-ring, The Astronomical Journal 149, 156.

Mitchell, C., C. Porco, H. Dones, J. Spitale, (2013), The behavior of spokes in Saturn's B-ring, Icarus 225, 446–474.

Mitchell J. L., M. Ádámkovics, R. Caballero, E. P. Turtle, (2011), Locally enhanced precipitation organized by planetary-scale waves on Titan, Nature Geoscience 4, doi: 10.1038/NGEO1219.

Mitchell, C. J., M. Horanyi, O. Havnes, C. C. Porco, (2006), Saturn's spokes: Lost and found, Science 311, 1587–1589.

Morales-Juberías, R., K. M. Sayanagi, A. A. Simon, L. N. Fletcher, R. G. Cosentino, (2015) Meandering shallow atmospheric jet as a model of Saturn’s north-polar hexagon, The Astrophysical Journal 806, L18.

Morales-Juberias, R., and T. E. Dowling, (2013), Jupiter's Great Red Spot: Fine-scale matches of model vorticity patterns to prevailing cloud patterns, Icarus, 225, 1, 216–227, doi: 10.1016/j.icarus.2013.03.026.

Morales-Juberías, R., K. M. Sayanagi, T. E. Dowling, A. P. Ingersoll, (2011), Emergence of polar-jet polygons from jet instabilities in a Saturn model, Icarus 211, 1284–1293.

- - - - - - - - - - - - - -

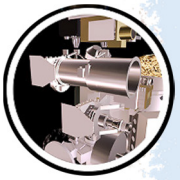

Morrison, S. J., P. C. Thomas, M. S. Tiscareno, J. A. Burns, J. Veverka, (2009), Grooves on small Saturnian satellites and other objects: Characteristics and significance, Icarus 204, 262–270.

Movshovitz N., F. Nimmo, D. G. Korycansky, E. Asphaug, J. M. Owen, (2015), Disruption and reaccretion of midsized moons during an outer solar system Late Heavy Bombardment, Geophysical Research Letters 42, 256–263.

Murray, C. D., and R. S. French, (2018), The F-ring of Saturn, In Planetary Ring Systems: Properties, Structure, and Evolution, (eds.) M. S. Tiscareno, C. D. Murray, Cambridge, United Kingdom, Cambridge University Press, 338–362.

Murray, C. D., N. J. Cooper, G. A. Williams, N. O. Attree, J. S. Boyer, (2014), The discovery and dynamical evolution of an object at the outer edge of Saturn's A-ring, Icarus 236, 165–168.

Murray, C. D., K. Beurle, N. J. Cooper, M. W. Evans, G. A. Williams, S. Charnoz, (2008), The determination of the structure of Saturn's F-ring by nearby moonlets, Nature 453, 739–744.

Murray, C. D., N. Cooper, M. W. Evans, K. Beurle, (2005a), S/2004 S5: A New co-orbital companion for Dione, Icarus 179, 222–234.

Murray, C. D., C. Chavez, K. Beurle, N. Cooper, M. W. Evans, J. A Burns, C. C. Porco, (2005b), How Prometheus creates structure in Saturn's F-ring, Nature 437, 1326–1329.

Nakajima, M., and A. P. Ingersoll, (2016), Controlled boiling on Enceladus. 1. Model of the vapor-driven jets, Icarus 272, 309–318, doi: 10.1016/j.icarus.2016.02.027.

Nicholson, P., R. French, and J. Spitale, (2018), Narrow rings, gaps, and sharp edges. In Planetary Ring Systems: Properties, Structure, and Evolution, (eds.) M. Tiscareno and C. Murray, Cambridge, United Kingdom, Cambridge University Press, pp. 276–307, doi: 10.1017/9781316286791.011.

Nimmo, F., C. Porco, C. Mitchell, T. Van Hoolst, M. Hedman, (2016), The tidally-modulated plume of Enceladus: An update, AGU abstract P33A-2118 presented at 2016 Fall Meeting, AGU, San Francisco, CA, 12–16 Dec.

Nimmo, F., C. Porco, C. Mitchell, (2014), Tidally modulated eruptions on Enceladus: Cassini ISS observations and models, The Astronomical Journal 148, 46.

Nimmo, F., B. C. Bills, and P. C. Thomas, (2011), Geophysical implications of the long-wavelength topography of the Saturnian satellites, Journal of Geophysical Research, 116, E11001, doi: 10.1029/2011JE003835.

NASA/JPL/Space Science Institute, (2007), Released February 27, 2007, Giant Lake on Titan, PIA 08363, 08364, http://ciclops.org/view.php?id=2607.

NASA/JPL/Space Science Institute, (2007), Released March 15, 2007, Exploring the wetlands of Titan, PIA 08365, http://ciclops.org/view.php?id=2631.

NASA/JPL/Space Science Institute, (2005), Land of lakes, Released June 28, 2005 and March 15, 2007, PIA 06240, http://ciclops.org/view.php?id=1161.

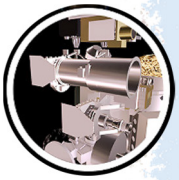

NASA/JPL/Space Science Institute, (2005), NASA'S Cassini reveals lake-like feature on Titan, Released June 28, 2005, http://ciclops.org/view.php?id=1194.

Nixon, C. A., R. D. Lorenz, R. K. Achterberg, A. Buch, P. Coll, R. N. Clark, R. Courtin, et al., (2018), Titan's cold case files-outstanding questions after Cassini-Huygens, Planetary and Space Science 155, 50–72.

O'Neill, C. & F. Nimmo, (2010), The role of episodic overturn in generating the surface geology and heat flow on Enceladus, Nature Geoscience 3, 88–91.

Ordonez-Etxeberria, I., R. Hueso, A. Sanchez-Lavega, S. Perez-Hoyos, (2016), Spatial distribution of Jovian clouds, hazes and colors from Cassini ISS multi-spectral images, Icarus, 267, 34–50, doi: 10.1016/j.icarus.2015.12.008.

Patterson, G. W., S. J. Kattenhorn, P. Helfenstein, G. C. Collins, R. T. Pappalardo, (2018), The geology of Enceladus, In Enceladus and the Icy Moons of Saturn, (eds.) P. M. Schenk, R. N. Clark, C. J. A. Howett, A. J. Verbiscer, J. H. Waite, Space Science Series, The University of Arizona Press, Tucson, AZ.

Pérez-Hoyos, S., J. F. Sanz-Requena, A. Sánchez-Lavega, P. G. J. Irwin, A. Smith, (2016), Saturn's tropospheric particles phase function and spatial distribution from Cassini ISS 2010-11 observations, Icarus 277, 1–18, doi: 10.1016/j.icarus.2016.04.022.

Pérez-Hoyos, S., and A. Sánchez-Lavega, (2006), On the vertical wind shear of Saturn's equatorial jet at cloud level, Icarus 180, 161–175.

Perry, J., E. P. Turtle, A. S. McEwen, D. D. Dawson, C. C. Porco, (2007), Cassini ISS observations of Titan's trailing hemisphere, Bulletin of the American Astronomical Society, 39, #44.04.

Perry J. E., A. S. McEwen, S. Fussner, E. P. Turtle, R. A. West, C. C. Porco, B. Knowles, D. D. Dawson, Cassini ISS team, (2005), Processing ISS images of Titan's surface, Lunar and Planetary Science XXXVI, Part 16, LPI-Contrib-1234-Pt-16.

Porco, C., C. Mitchell, F. Nimmo, M. Tiscareno, (2018), Enceladus' plume temporal variability from analysis of Cassini ISS images, 49th Lunar and Planetary Institute Conference, abstract 2083.

Porco, C., L. Dones, C. Mitchell, (2017), Could it be snowing microbes on Enceladus? Assessing conditions in its plume and implications for future missions, Astrobiology 17, 876–901.

Porco, C., F. Nimmo, and D. DiNino, (2015), Enceladus' 101 Geysers: Phantoms? Hardly, In American Geophysical Union (AGU) Fall Meeting, San Francisco, CA, 14–18 December, abstract P13A-2118.

Porco, C., D. DiNino, F. Nimmo, (2014), How the geysers, tidal stresses, and thermal emissions across the south polar terrain of Enceladus are related, The Astronomical Journal 148, 45.

Porco, C., J. Weiss, D. Richardson, L. Dones, T. Quinn, H. Throop, (2008), Simulations of the dynamical and light-scattering behavior of Saturn's rings and the derivation of ring particle and disk properties, The Astronomical Journal 136, 2172–2200.

- - - - - - - - - - - - - -

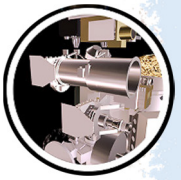

Porco, C., P. Thomas, J. Weiss, D. Richardson, (2007), Saturn's small inner satellites: Clues to their origins, Science 318, 1602–1607.

Porco, C. C., P. Helfenstein, P. C. Thomas, A. P. Ingersoll, J. Wisdom, R. West, G. Neukum, et al., (2006), Cassini observes the active south pole of Enceladus, Science 311, 1393–1401.

Porco, C. C., E. Baker, J. Barbara, K. Beurle, A. Brahic, et al., (2005a), Cassini Imaging Science: Initial results on Saturn's atmosphere, Science 307, 1243–1247.

Porco, C. C., E. Baker, J. Barbara, K. Beurle, A. Brahic, et al., (2005b), Imaging of Titan from the Cassini spacecraft, Nature 434, pp. 159–168.

Porco, C. C., E. Baker, J. Barbara, K. Beurle, A. Brahic, et al., (2005c), Cassini Imaging Science: Initial results on Saturn's rings and small satellites, Science 307, 1226–1236.

Porco, C. C., E. Baker, J. Barbara, K. Beurle, A. Brahic, et al., (2005d), Cassini Imaging Science: Initial results on Phoebe and Iapetus, Science 307, 1237–1242.

Porco, C. C., (2005), Cassini Imaging Science: Saturn's rings and small satellites, Geological Society of America, 2005 annual meeting, Salt Lake City, UT, Oct. 16-19, vol 37, 7, p. 236

Porco, C. C., R. A. West, S. Squyres, A. McEwen, P. Thomas, C. D. Murray, A. Delgenio, et al., (2004), Cassini Imaging Science: Instrument characteristics and anticipated scientific investigations at Saturn, Space Science Reviews 115, 363–497.

Porco, C. C., R. A. West, A. McEwen, A. D. Del Genio, A. P. Ingersoll, P. Thomas, S. Squyres et al., (2003), Cassini imaging of Jupiter's atmosphere, satellites, and rings, Science, 299, 5612, 1541–1547, doi: 10.1126/science.1079462.

Postberg, F., R. N. Clark, C. J. Hansen, A. J. Coates, C. M. D. Ore, F. Scipioni, M. M. Hedman, J. Hunter Waite, (2018), Plume and surface composition of Enceladus, In Enceladus and the Icy Moons of Saturn, (eds.) P. M. Schenk, R. N. Clark, C. J. A. Howett, A. J. Verbiscer, J. H. Waite, Space Science Series, The University of Arizona Press, Tucson, AZ.

Rathbun, J. A., E. P. Turtle, P. Helfenstein, S. W. Squyres, P. Thomas, J. Veverka, T. Denk, G. Neukum, T. Roatsch, R. Wagner, J. Perry, D. Smith, T. V. Johnson, C. C. Porco, (2005), Enceladus' global geology as seen by Cassini ISS, American Geophysical Union (AGU), Fall Meeting 2005, abstract P32A-03.

Read, P. L., P. J. Gierasch, B. J. Conrath, A. Simon-Miller, T. Fouchet, Y. H. Yamazaki, (2006), Mapping potential-vorticity dynamics on Jupiter. I: Zonal-mean circulation from Cassini and Voyager 1 data, Quarterly Journal of the Royal Meteorological Society, 132, 618, 1577–1603, doi: 10.1256/qj.05.34.

Renner, S., N. Cooper, M. El Moutamid, B. Sicardy, A. Vienne, C. Murray, M. Saillenfest, (2016), Origin of the chaotic motion of the Saturnian satellite Atlas, The Astronomical Journal 151, 122–129.

Roatsch, T., R. J. Wagner, N. Schmedemann, P. Helfenstein, K. Stephan, J. Voigt, R. Jaumann, B. Giese, C. Porco, (2016), Stratigraphy in the Samarkand Sulci Region of Enceladus, American Geophysical Union (AGU), Fall Meeting 2016, abstract P33A-2125.

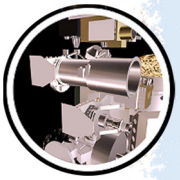

Roatsch T., E. Kersten, A. Hoffmeister, M. Wählisch, K.-D. Matz, C. C. Porco, (2013), Recent improvements of the Saturnian satellites atlases: Mimas, Enceladus, and Dione. Planetary Space Science 77, 118–125.

Roatsch, T., E. Kersten, M. Wählisch, A. Hoffmeister, K.-D. Matz, F. Scholten, R. Wagner, T. Denk, G. Neukum, C. C. Porco, (2012), High resolution atlas of Rhea as derived from Cassini ISS Images, Planetary and Space Sciences 61, 135–141.

Roatsch, T., R. Jaumann, K. Stephan, P.C. Thomas, (2009a), Cartographic mapping of the Icy Satellites using ISS and VIMS data, In Saturn from Cassini-Huygens, (eds.) M. Dougherty, L. Esposito, S. Krimigis, Springer, Dordrecht, pp. 763–781, doi: 10.1007/978-1-4020-9217-6_24.

Roatsch, T., M. Wählisch, A. Hoffmeister, E. Kersten, K.-D. Matz, F. Scholten, R. Wagner, T. Denk, G. Neukum, P. Helfenstein, C. C. Porco, (2009b), High resolution atlases of Mimas, Tethys, and Iapetus derived from Cassini ISS images, Planetary and Space Science 57, pp. 83–92.

Roatsch, T., M. Wählisch, B. Giese, A. Hoffmeister, K.-D. Matz, F. Scholten, R. Wagner, G. Neukum, P. Helfenstein, C. C. Porco, (2008a), High resolution Enceladus atlas derived from Cassini ISS Images, Planetary and Space Sciences 56, 109–116.

Roatsch, T., M. Wählisch, A. Hoffmeister, K.-D. Matz, F. Scholten, E. Kersten, R. Wagner, T. Denk, G. Neukum, C. C. Porco, (2008b), High resolution Dione atlas derived from Cassini ISS Images, Planetary and Space Science 56, 1499–1505.

Roatsch, T., M. Wählisch, F. Scholten, A. Hoffmeister, K.-D. Matz, T. Denk, G. Neukum, P.C. Thomas, P. Helfenstein, C.C. Porco, (2006), Mapping of the icy Saturnian satellites: First results from Cassini ISS, Planetary and Space Science 54, 1137–1145.

Roman, M. T., R. A. West, D. J. Banfield, P. J. Gierasch, R. K. Achterberg, C. A. Nixon, P. C. Thomas, (2009), Determining a tilt in Titan's north-south Albedo asymmetry from Cassini Images, Icarus 203, 242–249.

Salyk, C., A. P. Ingersoll, J. Lorre, A. Vasavada, A. D. Del Genio, (2006), Interaction between eddies and mean flow in Jupiter's atmosphere: Analysis of Cassini imaging data, Icarus, 185, 2, 430–442, doi: 10.1016/j.icarus.2006.08.007.

Sánchez-Lavega, A., E. García-Melendo, S. Perez-Hoyos, R. Hueso, M. H. Wong, A. Simon, J. Francisco Sanz-Requena, et al., (2016), An enduring rapidly moving storm as a guide to Saturn’s equatorial jet’s complex structure, Nature Communications 7, 13262.

Sánchez-Lavega, A., T. del Río-Gaztelurrutia, R. Hueso, S. Pérez-Hoyos, E. García-Melendo, et al., (2014), The long-term steady motion of Saturn’s hexagon and the stability of its enclosed jet stream under seasonal changes, Geophysical Research Letters 41, 1425–1431.

Sánchez-Lavega, A., T. del Río-Gaztelurrutia, R. Hueso, J. M. Gómez-Forrellad, J. F. Sanz-Requena, J. Legarreta, E. García-Melendo, et al., (2011), Deep winds beneath Saturn’s upper clouds from a seasonal long-lived planetary-scale storm, Nature 475, 71–74.

- - - - - - - - - - - - - -

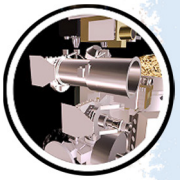

Sánchez-Lavega, A., R. Hueso, S. Pérez-Hoyos, (2007), The three-dimensional structure of Saturn's equatorial jet at cloud level, Icarus 187, 510–519.

Sánchez-Lavega, A., R. Hueso, S. Pérez-Hoyos, J. F. Rojas, (2006), A strong vortex in Saturn's South Pole, Icarus 184, 524–531.

Sato, T. M., T. Satoh, Y. Kasaba, (2013), Retrieval of jovian cloud structure from the Cassini ISS limb-darkening data I. Continuum scattering phase functions for cloud and haze in the south tropical zone, Icarus, 222, 1, 100–121, doi: 10.1016/j.icarus.2012.09.035.

Sayanagi, K. M., K. H. Baines, U. A. Dyudina, L. N. Fletcher, A. Sanchez-Lavega, R. A. West, (2018), Saturn's polar atmosphere, In Saturn in the 21st Century, (eds.) Baines et al., in press.

Sayanagi, K. M., J. J. Blalock, U. A. Dyudina, S. P. Ewald, A. P. Ingersoll, (2017), Cassini ISS observation of Saturn's north polar vortex and comparison to the south polar vortex, Icarus 285, 68–82.

Sayanagi, K., U. Dyudina, S. Ewald, G. Muro, A. Ingersoll, (2014), Cassini ISS observation of Saturn's string of pearls, Icarus 229, 170–180.

Sayanagi, K., U. Dyudina, S. Ewald, G. Fischer, A. Ingersoll, W. Kurth, G. Muro, C. Porco, R. West, (2013), Dynamics of Saturn's great storm of 2010–2011 from Cassini ISS and RPWS, Icarus 223, 460–478.

Sayanagi, K. M., R. Morales-Juberias, and A. P. Ingersoll, (2010), Saturn's northern hemisphere ribbon: Simulations and comparison with the meandering gulf stream, Journal of the Atmospheric Sciences 67, 2658–2678.

Sayanagi, K. M., and A. P. Showman, (2007), Effects of a large convective storm on Saturn's equatorial jet, Icarus 187, 520–539.

Schenk, P., O. White, P. K. Byrne, J. M. Moore, (2018), Saturn's other icy moons: Geologic entities in their own right, In Enceladus and the Icy Moons of Saturn, (eds.) P. M. Schenk, R. N. Clark, C. J. A. Howett, A. J. Verbiscer, J. H. Waite, Space Science Series, The University of Arizona Press, Tucson, AZ, doi: 10.2458/azu_uapress_9780816537075-ch012.

Schenk, P., B. Buratti, P. Helfenstein, S. Kempf, J. Schmidt, (2017), Colors of Enceladus: Plume redeposition and lessons for Europa, 48th Lunar and Planetary Science Conference, LPI Contribution No. 1964, id. 2601.

Schenk, P. M., B. J. Buratti, P. K. Byrne, W. B. McKinnon, F. Nimmo, F. Scipioni, (2015), Blood stains on Tethys: Evidence for recent activity? European Planetary Science Congress 2015, vol. 10, EPSC2015-893.

Schenk, P. M., D. P. Hamilton, R. E. Johnson, W. B. McKinnon, C. Paranicas, J. Schmidt, M. R. Showalter, (2011), Plasma, plumes and rings: Saturn system dynamics as recorded in global color patterns on its midsize icy satellites, Icarus 211, 740–757.

Schmedemann, N., A. Neesemann, F. Schulzeck, K. Krohn, I. van der Gathen, K. A. Otto, R. Jaumann, R. J. Wagner, G. Michael, C. A. Raymond, C. T. Russell, (2017), How the

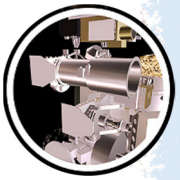

distribution of impact Ejecta may explain surface features on Ceres and Saturnian satellites. European Planetary Science Congress, EPSC2017-119, Riga, 17–22 Sep 2017.

Schmedemann, N., R. J. Wagner, G. Michael, T. Denk, T. Kneissl, (2015), The crater production functions for Mimas. Workshop on Early Solar System Impact Bombardment III, abstract 3021, Houston, TX, 4–5 Feb 2015.

Schmedemann, N., and G. Neukum, (2011), Impact crater size-frequency distribution (SFD) and surface Ages on Mimas. 42nd Lunar and Planetary Science Conference, abstract 2772.

Shetty, S., and P. S. Marcus, (2010), Changes in Jupiter's Great Red Spot (1979–2006) and Oval BA (2000–2006), Icarus, 210, 1, 182–201, doi: 10.1016/j.icarus.2010.06.026.

Simon-Miller, A. A., J. H. Rogers, P. J. Gierasch, D. Choi, M. D. Allison, G. Adamoli, H. J. Mettig, (2012), Longitudinal variation and waves in Jupiter's south equatorial wind jet, Icarus, 218, 2, 817–830, doi: 10.1016/j.icarus.2012.01.022.

Simon-Miller, A. A., and P. J. Gierasch, (2010), On the long-term variability of Jupiter's winds and brightness as observed from Hubble, Icarus, 210, 1, 258–269, doi: 10.1016/j.icarus.2010.06.020.

Singer, K. N., W. B. McKinnon, P. M. Schenk, J. M. Moore, (2012), Massive ice avalanches on Iapetus mobilized by friction reduction during flash heating. Nature Geoscience 5, 574–578.

Singer, K. N., and W. B. McKinnon, (2011), Tectonics on Iapetus: Despinning, respinning, or something completely different? Icarus 216, 198–211.

Spahn, F., H. Hoffmann, H. Rein, M. Seiß, M. Sremcevic, M. S. Tiscareno, (2018), Moonlets in dense planetary rings, In Planetary Ring Systems: Properties, Structure, and Evolution, (eds.) M. S. Tiscareno, C. D. Murray, Cambridge, United Kingdom Cambridge University Press, 157–197.

Spencer, J. R., and T. Denk, (2010), Formation of Iapetus's extreme albedo dichotomy by exogenically-triggered thermal ice migration, Science 327, no. 5964, 432–435, doi: 10.1126/science.1177132).

Spencer, J. R., et al., (2009), Enceladus: An active cryovolcanic satellite, In Saturn from Cassini-Huygens, Springer, Netherlands, 683–724.

Spilker, L. J., A. C. Barr, L. W. Esposito, P. Helfenstein, A. P. Ingersoll, R. Jaumann, C. P. McKay, F. Nimmo, J. H. Waite, (2018), Thermal properties of rings and ring particles, In Planetary Ring Systems: Properties, Structure, and Evolution, (eds.) M. S. Tiscareno, C. D. Murray, Cambridge, United Kingdom, Cambridge University Press, 399–433.

Spitale, J. N., (2017), Saturn’s misbegotten moonlets, AAS/DDA Meeting, abstracts 48, 400.04.

Spitale, J. N., and J. M. Hahn, (2016), The shape of Saturn’s Huygens ringlet viewed by Cassini ISS, Icarus 279, 141–154.

Spitale, J. N., T. A. Hurford, A. R. Rhoden, E. E. Berkson, and S. P. Symeon, (2015), Curtain eruptions from Enceladus’ south-polar terrain, Nature 521, 57.

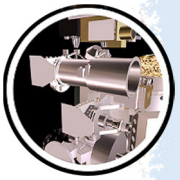

Spitale, J. N., and M. S. Tiscareno, (2012), Cassini images a propeller in Saturn's B-ring, AAS/DPS Meeting, abstracts 44, 414.04.

Spitale, J. N., and C. C. Porco, (2010), Free unstable modes and massive bodies in Saturn's Outer B-ring, The Astronomical Journal 140, 1747–1757.

Spitale, J. N., and C. C. Porco, (2009), Time variability in the outer edge of Saturn's A-ring revealed by Cassini Imaging, The Astronomical Journal 138, 1520–1528.

Spitale, J., and C. Porco, (2007), Association of the jets of Enceladus with the warmest regions on its south polar fractures, Nature 449, 695–697.

Spitale, J. N., R. A. Jacobson, C. C. Porco, W. M. Owen Jr., (2006), The orbits of Saturn's small Satellites derived from combined historic and Cassini imaging observations, The Astronomical Journal 132, 692–710.

Stephan, K., R. Jaumann, R. Wagner, R. N. Clark et al., (2010), Dione's spectral and geological properties, Icarus 206, 631–652.

Stephan K., R. Jaumann, E. Karkoschka, R. L. Kirk, J. W. Barnes, M. G. Tomasko, E. P. Turtle, L. LeCorre, M. Langhans, S. Le Mouélic, R. D. Lorenz, J. Perry, (2009), Mapping products of Titan's surface, In Titan from Cassini-Huygens, (eds.) R. Brown, J.-P. Lebreton, and H. Waite, Springer, New York, NY, pp. 489–510.

Sussman, M. G., N. J. Chanover, A. A. Simon-Miller, A. R. Vasavada, R. F. Beebe, (2010), Analysis of Jupiter's Oval BA: A streamlined approach, Icarus, 210, 1, 202–210, doi: 10.1016/j.icarus.2010.06.044.

Tajeddine, R., K. M. Soderlund, P. C. Thomas, P. Helfenstein, M. M. Hedman, J. A. Burns, P.M. Schenk, (2017a), True polar wander of Enceladus from topographic data, Icarus 295, pp. 46–60.

Tajeddine, R., P. Nicholson, M. Tiscareno, M. Hedman, J. Burns, M. El Moutamid, (2017b), Dynamical phenomena at the inner edge of the Keeler gap, Icarus 289, 80–93.

Tajeddine, R., P. D. Nicholson, P.-Y. Longaretti, M. El Moutamid, J. A. Burns, (2017c), What confines the rings of Saturn?, The Astrophysical Journal Supplement 232, 28.

Tajeddine, R., V. Lainey, N. Cooper, C. Murray, (2015), Cassini ISS astrometry of the Saturnian satellites: Tethys, Dione, Rhea, Iapetus, and Phoebe 2004–2012, Astronomy & Astrophysics 575, A73.

Tajeddine, R., N. J. Cooper, V. Lainey, S. Charnoz, C. D. Murray, (2013), Astrometric reduction of Cassini ISS images of the Saturnian satellites Mimas and Enceladus, Astronomy & Astrophysics 551, A129–A139.

Tamayo, D., S. R., Markham, M. M. Hedman, J. A. Burns, D. P. Hamilton, (2016), Radial profiles of the Phoebe ring: A vast debris disk around Saturn, Icarus 275, 117–131.

Tamayo, D., M. M. Hedman, J. A. Burns, (2014), First observations of the Phoebe ring in optical light, Icarus 233, 1–8.

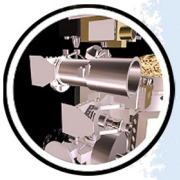

Teolis, B., M. Perry, C. Hansen, H. Waite, C. Porco, J. Spencer, C. Howett, (2017), Enceladus plume structure and time variability: Comparison of Cassini observations, Astrobiology 17, 9, 926–940.

Thomas, P. C., M. S. Tiscareno, P. Helfenstein, (2018), The inner small satellites of Saturn and Hyperion, In Enceladus and the Icy Moons of Saturn, (eds.) P. M. Schenk, R. N. Clark, C. J. A. Howett, A. J. Verbiscer, J. H. Waite, Space Science Series, The University of Arizona Press, Tucson, AZ.

Thomas, P., R. Tajeddine, M. Tiscareno, J. Burns, J. Joseph, T. Loredo, P. Helfenstein, C. Porco, (2016), Enceladus's measured physical libration requires a global subsurface ocean, Icarus 264, 37–47.

Thomas, P., J. Burns, M. Hedman, P. Helfenstein, S. Morrison, M. Tiscareno, J. Veverka, (2013), The inner small satellites of Saturn: A variety of worlds, Icarus 226, 99–1019.

Thomas, P. C., (2010), Sizes, shapes, and derived properties of the Saturnian satellites after the Cassini nominal mission, Icarus 208, 395–401, doi: 10.1016/j.icarus.2010.01.025.

Thomas, P. C., J. A. Burns, P. Helfenstein, S. Squyres, J. Veverka, C. Porco, E. P. Turtle, A. McEwen, T. Denk, B. Giese, T. V. Roatsch, R. A. Jacobson, (2007a), Shapes of the Saturnian icy satellites and their significance, Icarus 190, 573–584.

Thomas, P., J. Armstrong, S. W. Asmar, J. A. Burns, T. Denk, B. Giese, P. Helfenstein, L. Iess, T. V. Johnson, A. McEwen, L. Nicolaisen, C. Porco, N. Rappaport, J. Richardson, L. Somenzi, P. Tottora, E. P. Turtle, J. Veverka, (2007b), Hyperion's sponge-like appearance, Nature 448, 50–53.

Throop, H. B., C. C. Porco, R. A. West, J. A. Burns, M. R. Showalter, P. D. Nicholson, (2004), The Jovian rings: new results derived from Cassini, Galileo, Voyager, and Earth-based observations, Icarus 172, 59–77.

Tiscareno, M., and B. Harris, (2018), Mapping spiral waves and other radial features in Saturn's rings, Icarus, 312, 157–171, doi: 10.1016/j.icarus.2018.04.023.

Tiscareno, M. S., (2017), Imaging of Saturn's main rings during the Cassini Ring-Grazing Orbits and Grand Finale, EPSC Meeting, abstracts, EPSC2017-996.

Tiscareno, M., M. Hedman, J. Burns, J. Weiss, C. Porco, (2013a), Probing the inner boundaries of Saturn's A-ring with the Iapetus -1:0 nodal bending wave, Icarus 224, 221.

Tiscareno, M., C. Mitchell, C. Murray, D. Di Nino, M. Hedman, J. Schmidt, J. Burns, J. Cuzzi, C. Porco, K. Beurle, M. Evans, (2013b), Observations of ejecta clouds produced by impacts onto Saturn's rings, Science 340, 460.

Tiscareno, M. S., J. A. Burns, J. N. Cuzzi, M. W. Hedman, (2010a), Cassini imaging search rules out rings around Rhea, Geophysical Research Letters 37, L14205.

Tiscareno, M. S., J. A. Burns, M. Sremcevic, K. Beurle, M. M. Hedman, N. J. Cooper, A. J. Milano, M. W. Evans, C. C. Porco, J. N. Spitale, J. W. Weiss, (2010b), Physical characteristics

- - - - - - - - - - - - - -

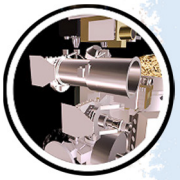

and non-Keplerian orbital motion of propeller, Moons Embedded in Saturn's Rings, Astrophysical Journal Letters 718, L92–L96.

Tiscareno, M., P. C. Thomas, J. A. Burns, (2009), The rotation of Janus and Epimetheus, Icarus 204, 254–261.

Tiscareno, M. S., J. A. Burns, M. M. Hedman, C. C. Porco, (2008), The population of propellers in Saturn's A-ring, The Astronomical Journal 135, 1083–1091.

Tiscareno, M. S., J. A. Burns, P. D. Nicholson, M. M. Hedman, C. C. Porco, (2007), Cassini imaging of Saturn's rings II: A wavelet technique for analysis of density waves and other radial structure in the rings, Icarus 189, 14–34.

Tiscareno, M. S., J. A. Burns, M. M. Hedman, C. C. Porco, J. W. Weiss, L. Dones, D. C. Richardson, C. D. Murray, (2006a), 100-metre-diameter moonlets in Saturn's A-ring from observations of propeller structures., Nature 440, 648–650.

Tiscareno, M. S., P. D. Nicholson, J. A. Burns, M. M. Hedman, C. C. Porco, (2006b), Unraveling temporal variability in Saturn's spiral density waves: Results and predictions, Astrophysical Journal Letters 651, L65–L68.

Tomasko, M. G., R. A. West, (2009), Aerosols in Titan's atmosphere, In Titan from Cassini-Huygens, (eds.) R. Brown, J. P. Lebreton, H. Waite, Springer, Dordrecht, pp. 297–322.

Trammell, H. J., L. Li, X. Jiang, Y. Pan, M. A. Smith, et al., (2016), Vortices in Saturn’s northern hemisphere (2008–2015) observed by Cassini ISS, Journal of Geophysical Research: Planets 121, 1814–1826.

Trammell, H. J., L. Li, X. Jiang, M. Smith, S. Hörst, A. Vasavada, (2014), The global vortex analysis of Jupiter and Saturn based on Cassini Imaging Science Subsystem, Icarus 242, pp. 122–129.

Turtle E. P., J. E. Perry, J. M. Barbara, A. D. Del Genio, C. Sotin, S. Rodriguez, J. M. Lora, S. Faulk, R. A. West, E. Karkoschka, A. S. McEwen, M. Mastrogiuseppe, J. D. Hofgartner, P. Corlies, J. Kelland, A. G. Hayes, J. Pitesky, T.L. Ray, (2018a), Titan insights during the final year of the Cassini Mission, LPSC 49, #1656.

Turtle E. P., J. E. Perry, J. M. Barbara, A. D. Del Genio, S. Rodriguez, S. Le Mouélic, C. Sotin, J. M. Lora, S. Faulk, P. Corlies, J. Kelland, S. M. MacKenzie, R. A. West, A. S. McEwen, J. I. Lunine, J. Pitesky, T. L. Ray, M. Roy, (2018b), Titan's meteorology over the Cassini mission: Evidence for extensive subsurface methane reservoirs, Geophysical Research Letters 45, no. 11, 5320–5328.

Turtle E .P., J. W. Barnes, J. E. Perry, J. M. Barbara, A. G. Hayes, P. Corlies, J. Kelland, R. A. West, A. D. Del Genio, J. M. Soderblom, A. S. McEwen, C. Sotin, (2016), Cassini ISS and VIMS observations of Titan's north polar region during the T120 and T121 flybys: The Curious case of the clouds, Fall Meeting American Geophysical Union (AGU), abstract P33F-05.

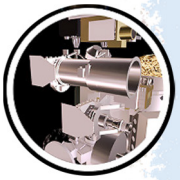

Turtle E. P., J. E. Perry, A. S. McEwen, A. G. Hayes, J. W. Barnes, R. A. West, (2013), ISS observations of Titan's northern lakes and evidence for a north-polar surface unit, Fall Meeting American Geophysical Union (AGU), 9–13 Dec. 2013, abstract P53D-1897.

Turtle E. P., A. D. DelGenio, J. M. Barbara, J. E. Perry, E. L. Schaller, A. S. McEwen, R. A. West, T. L. Ray, (2011a) Seasonal changes in Titan's meteorology, Geophysical Research Letters 38, L03203, doi: 10.1029/2010GL046266.

Turtle E. P., J. E. Perry, A. G. Hayes, R. D. Lorenz, J. W. Barnes, A. S. McEwen, R. A. West, A. D. Del Genio, J. M. Barbara, J. I. Lunine, E. L. Schaller, T. L. Ray, R. M. C. Lopes, E. R. Stofan, (2011b), Rapid and extensive surface changes near Titan's equator: Evidence of April Showers, Science 331, 1414–1417, doi: 10.1126/science.1201063.

Turtle E. P., J. E. Perry, A. G. Hayes, A. S. McEwen, (2011c), Shoreline retreat at Titan's Ontario Lacus and Arrakis Planitia from Cassini Imaging Science Subsystem observations, Icarus 212, 957–959, doi: 10.1016/j.icarus.2011.02.005.

Turtle E. P., J. E. Perry, A. S. McEwen, A. D. DelGenio, J. Barbara, R. A. West, D. D. Dawson, C. C. Porco, (2009), Cassini imaging of Titan's high-latitude lakes, clouds, and south-polar surface changes, Geophysical Research Letters 36, L02204, doi: 10.1029/2008GL036186.

Vasavada, A. R., S. M. Hörst, M. R. Kennedy, A. P. Ingersoll, C. C. Porco, A. D. Del Genio, R. A. West, (2006), Cassini imaging of Saturn: Southern hemisphere winds and vortices, Journal of Geophysical Research-Planets 111, E05004.

Verbiscer, A. J., P. Helfenstein, B. J. Buratti, E. Royer, (2018), Surface properties of Saturn's Icy Moons from optical remote sensing, In Enceladus and the Icy Moons of Saturn, (eds.) P. M. Schenk, R. N. Clark, C. J. A. Howett, A. J. Verbiscer, J. H. Waite, Space Science Series, The University of Arizona Press, Tucson, AZ.

Verbiscer, A. J., P. Helfenstein, C. Howett, A. Annex, P. Schenk, (2014), Spectrophotometric properties of thermally anomalous terrain on Mimas, American Astronomical Society DPS meeting #46, 502.08.

Wagner, R. J., B. Giese, N. Schmedemann, K. Stephan, J. Voigt, P. Helfenstein, E. Kersten, T. Roatsch, R. Jaumann, C. C., (2017), Samarkand Sulci, Enceladus: Topography and geology from the data of the Cassini 2 Porco, 28EN Non-Targeted Flyby in Global Context, 48th Lunar & Planetary Science Conference, LPI Contribution no. 1964, id. 2262.

Wagner, R. J., G. Neukum, U. Wolf, N. Schmedemann, T. Denk, K. Steohan, T. Roatsch, C. C. Porco, (2011), Bright ray craters on Rhea and Dione, 42nd Lunar and Planetary Science Conference, abstract 2249.

Wagner, R. J., G. Neukum, B. Giese, T. Roatsch, T. Denk, U. Wolf, C. C. Porco, (2010), The Geology of Rhea: A first look at the ISS camera data from Orbit 121 (Nov. 21, 2009) in Cassini's Extended Mission, 41st Lunar and Planetary Science Conference, abstract 1672, LPI, The Woodlands (Texas), 1–5 March 2010.

Wagner, R. J., G. Neukum, K. Stephan, T. Roatsch, U. Wolf, and C. C. Porco, (2009), Stratigraphy of tectonic features on Saturn's satellite Dione derived from Cassini ISS camera

- - - - - - - - - - - - - -

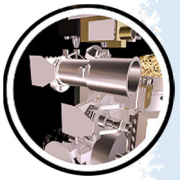

data. 40th Lunar and Planetary Science Conference, abstract 2142, LPI, Houston (Texas), 23-37 March 2009.

Wagner, R., G. Neukum, B. Giese, T. Roatsch, and T. Denk, (2007), Geology and geomorphology of Rhea: A first look at the high-resolution Cassini ISS images from the targeted flyby on Aug. 30, 2007, EOS Transactions American Geophysical Union (AGU), Fall Meeting Supplement, abstract P12B-06.

Wagner, R. J., G. Neukum, B. Giese, T. Roatsch, U. Wolf, T. Denk, Cassini ISS team, (2006), Geology, ages, and topography of Saturn's satellite Dione observed by the Cassini ISS camera, 37th Lunar and Planetary Science Conference, abstract 1805, LPI, Houston (Texas), 13–17 March 2006.

Weiss, J. W., C. C. Porco, M. S. Tiscareno, (2009), Ring edge waves and the masses of nearby satellites, The Astronomical Journal 138, 272–286.

West, R. A., B. Seignovert, P. Rannou, P. Dumont, E. P. Turtle, J. E. Perry, M. Roy, A. Ovanessian, (2018), Titan’s detached haze seasonal cycle, Nature Astronomy vol. 2, pp. 495-500, doi: 10.1038/s41550-018-0434-z.

West, R. A., A. D. Del Genio, J. M. Barbara, D. Toledo, P. Lavvas, P. Rannou, E. P. Turtle, J. Perry, (2016), Cassini Imaging Science subsystem observations of Titan's south polar cloud, Icarus 270, 399–408, doi: 10.1016/ j.icarus.2014.11.038.

West, R. A., P. Yanamandra-Fisher, V. Korokhin, (2015), Gas giant planets, Saturn’s rings, and Titan, In Polarimetry of Stars and Planetary Systems, (eds.) L. Kolokolova, J. Hough, A.-C. Levasseur-Regourd, Cambridge University Press.

West, R., P. Lavvas, C. Anderson, H. Imanaka, (2014), Titan haze, Titan: Surface, atmosphere and magnetosphere 285–321, http://ciclops.org/media/sp/2015/8014_19222_0.pdf.

West, R. A., J. M. Ajello, M. H. Stevens, D. F. Strobel, G. R. Gladstone, J. S. Evans, E. T. Bradley, (2012), Titan airglow during eclipse, Geophysical Research Letters 39, L18204, doi: 10.1029/2012GL053230.

West R. A., J. Balloch, P. Dumont, P. Lavvas, R. Lorenz, P. Rannou, T. Ray, E. P. Turtle, (2011), The evolution of Titan’s detached haze layer near equinox in 2009, Geophysical Research Letters 38, L06204, doi: 10.1029/2011GL046843.

West, R. A., B. Knowles, E. Birath, S. Charnoz, D. Di Nino, M. Hedman, P Helfenstein, A. McEwen, J. Perry, C. Porco, J. Salmon, H. Throop, D. Wilson, (2010), In-flight calibration of the Cassini Imaging Science Subsystem cameras, Planetary and Space Science 58, 1475–1488, doi 10.1016/j.pss.2010.07.006.

West, R. A., K. H. Baines, E. Karkoschka and A. Sánchez-Lavega, (2009), Clouds and aerosols in Saturn's atmosphere, In Saturn from Cassini-Huygens, (eds.) M. K. Dougherty, L. W. Esposito and S. M. Krimigis, Springer, Dordrecht, pp. 161–179.

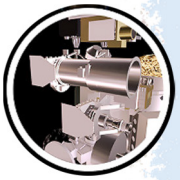

West, R. A., K. H. Baines, A. J. Friedson, D. Baneld, B. Ragent, and F. Taylor, (2004), Jovian clouds and haze, In Jupiter - The Planet, Satellites and Magnetosphere, (eds.) F. Bagenal, T. Dowling, W. McKinnon, Cambridge University Press.

White, O. L., P. M. Schenk, A. W. Bellagamba, A. M. Grimm, A. J. Dombard, V. J. Bray, (2017), Impact crater relaxation on Dione and Tethys and relation to past heat flow, Icarus 288, 37–52.

Young, R. M. B., and P. L. Read, (2017), Forward and inverse kinetic energy cascades in Jupiter's turbulent weather layer, Nature Physics, 13, 11, 1135.

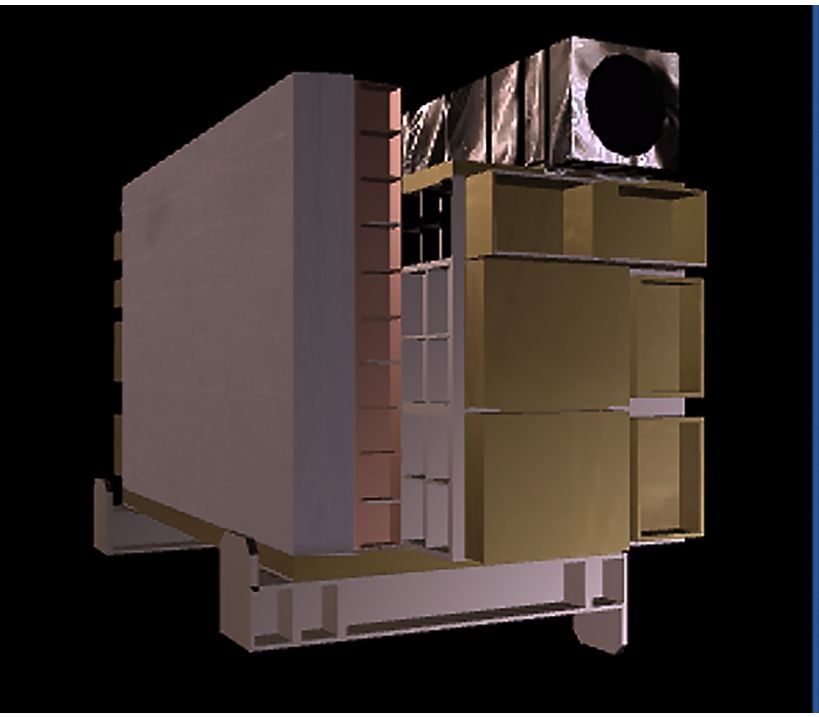

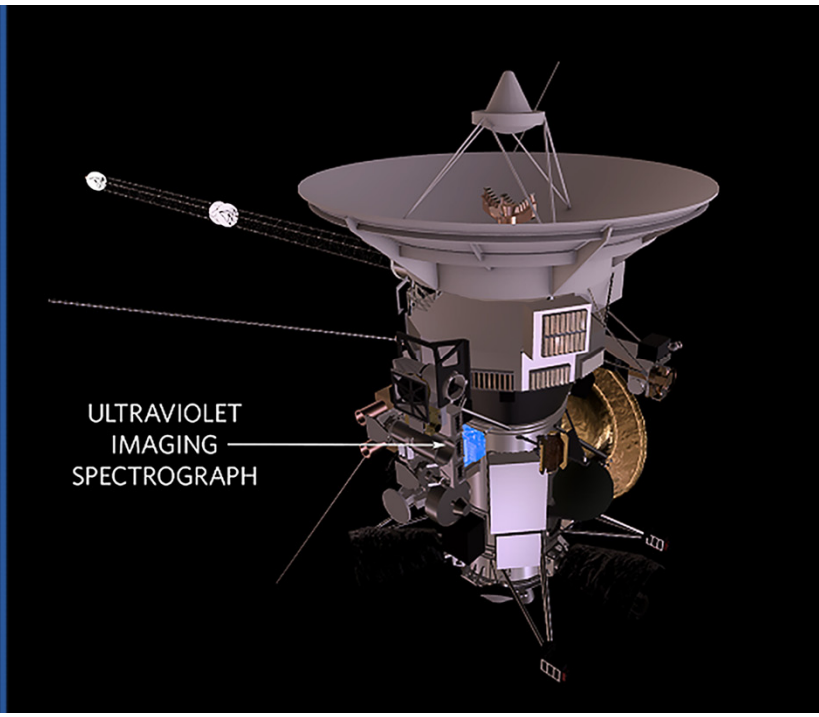

Ultraviolet Imaging Spectrograph

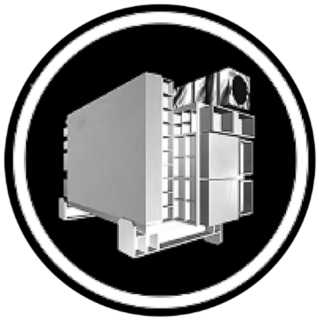

The Ultraviolet Imaging Spectrograph (UVIS) measured ultraviolet light (from 55.8 to 190 nanometers) invisible to the human eye from the Saturn system's atmospheres, rings, and surfaces. The **science objectives** of UVIS were to produce ultraviolet maps of Saturn's rings and many moons, to study the composition of atmospheres of the planet and its moon Titan, and also to look at how light from the Sun and the stars passed through atmospheres and rings in the Saturn system to determine their size characteristics and composition.

UVIS had two spectrographic channels: the extreme ultraviolet channel (EUV) and the far ultraviolet (FUV) channel, and also included a high-speed photometer (HSP) to perform stellar occultations, and a hydrogen-deuterium absorption cell (HDAC). The spectrograph could determine the atomic composition of those gases by splitting the light into its component wavelengths.

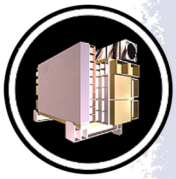

CONTENTS

Tables

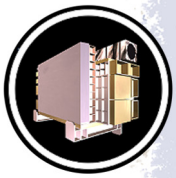

Mission Objectives and Science Objectives and Results

The top ten discoveries from UVIS are listed here:

1. Enceladus icy jets spew 200 kg/sec of water, with no significant variations over the mission. The strongest jets are more variable, though.

2. Titan's airglow is primarily from sunlight and photoelectrons, but the weak night airglow is from magnetospheric particle impacts.

3. An atomic oxygen torus surrounds Saturn, peaking at its source, Enceladus.

4. The Europa atmosphere is dominated by atomic oxygen at low density, inconsistent with water plume activity at the time of the Cassini Jupiter flyby. The Enceladus plumes are significantly different from those found at Europa.

5. UVIS observations of propellers, gaps, ghosts, kittens, self-gravity wakes indicate ongoing aggregation in Saturn's rings; ring statistics, wavelet analysis, haloes, small particles show aggregation/disaggregation on an orbital time scale; we can understand this with an analogy to a predator-prey ecosystem.

6. UVIS and Visual and Infrared Imaging Spectrometer (VIMS) comparisons find small particles in the outer A-ring, and other regions that are strongly perturbed by moon resonances.

7. The ultraviolet (UV) spectrum of Saturn's rings can be matched by pure water ice polluted over the age of the solar system by material having the reflectance of Comet 67P (as measured by Rosetta's Alice). Using Cassini results for the ring mass from Radio Science Subsystem (RSS) and the polluting flux from Cosmic Dust Analyzer (CDA), we constrain the ring age to less than about 200 million years.

8. A solitary wave is excited by the Janus-Epimetheus swap, when Janus moves inward every eight years. This is evidence for non-linear dynamics, and may limit the application of previous conclusions based on a linear theory.

9. UVIS star and solar occultations quantify the profiles of aerosols, nitriles and organics in Titan's atmosphere; and show that Saturn's thermosphere breathes in and out. It was 'in' at the Grand Finale.

10. UVIS sees the auroral footprint of Enceladus and also time varying arcs and spots that indicate magnetospheric variations. Bombarding charged particle radiation may explain the dark color of the polar hexagon.

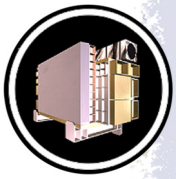

KEY OBJECTIVES

The UVIS science objectives include determination of the composition, structure and processes in the atmospheres of Saturn and Titan, composition of neutrals in the Saturn magnetosphere, morphology and active processes in the Saturn aurora, icy satellite surface and exosphere properties, the deuterium-to-hydrogen ratio in the atmospheres of Saturn and Titan, and the structure, dynamics and history of Saturn's rings.

SCIENCE ASSESSMENT, WITH TABLES

UVIS met or exceeded all science objectives with the exception of those related to D/H, which was due to a failure of the HDAC oxygen cell.

UVIS AO Mission Science Objectives

The UVIS instrument is designed to produce spatial UV maps, map ring radial structure, and to determine hydrogen/deuterium ratios. Specific science objectives for the Cassini mission are as follows.

1. Saturn System Scans
    a. EUV and FUV low resolution spectra of magnetosphere neutral and ion emissions.
    b. System scans at every apoapsis.
2. Satellites
    a. Latitude, longitude, and phase coverage coordinated through Satellite Surfaces Working Group (SSWG).
    b. Distant stellar occultations to determine satellite orbits and Saturn reference frame.
3. Atmosphere
    a. Vertical profiles of H, H_2, hydrocarbons, temp in exo, thermosphere.
    b. Long integrations map of hydrocarbons, airglow.
    c. Map emissions with highest resolution at the limb.
    d. Auroral Map: H and H_2 emissions over several rotations.

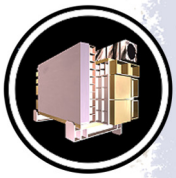

4. Ring Stellar Occultation Objectives

    a. Highest Radial resolution (20 m) structure of rings

    b. Discovery and precise characterization of dynamical features generated by ring-satellite interactions.

        - Density waves and bending waves.
        - Edge waves and ring shepherding.
        - Embedded moonlets and discovery of new moons from dynamical response in rings.

    c. Discovery and precise characterization of azimuthal structure in rings.

        - Eccentric rings.
        - Density waves and edge waves.
        - Small-scale self-gravitational clumping in rings.

    d. Measure temporal variability in ring structure.

    e. Simultaneously measure UV reflectance spectrum of rings.

        - Determine microstructure on particle surfaces.
        - Compositional information on ring particles.

    f. Measure size distribution of large particles through occultation statistics.

    g. Measure dust abundance in diffraction aureole.

    h. Simultaneously search for flashes from 0.1 m–1.0 m meteoroid impacts.

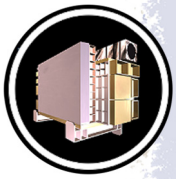

Science Assessment Table

This table is an Assessment of Data collected to satisfy an objective. It is not an assessment of the status of data analysis/publications.

Table UVIS-1. Assessment of data collected to satisfy an objective.

Fully/Mostly Accomplished: **Partially Accomplished:** **Not Accomplished:**

UVIS Science Objectives	AO and TM Science Objectives	Science Assessment	Comments—if yellow (partially fulfilled)
1) Saturn System Scans			
EUV and FUV low resolution spectra of magnetosphere neutral and ion emissions.	S_AO4		
System scans at every apoapsis.	S_AO4, S_AO5, T_AO2, TN1c		Not every apo
2) Satellites			
Latitude, longitude and phase coverage coordinated through SSWG.	I_AO3		
Distant stellar occultations to determine satellite orbits and Saturn reference frame.			Not done
3) Atmosphere			
Vertical profiles of H, H2, hydrocarbons, temp in exo, thermosphere.	S_AO1		
Long integrations map of hydrocarbons, airglow.	S_AO1		
Map emissions with highest resolution at the limb.	S_AO1		
Auroral Map: H and H2 emissions over several rotations.	S_AO1		
4) Ring Stellar Occultation Objectives			
Highest Radial resolution (20 m) structure of rings.	R_AO1, R_AO3, R_AO4, RC1a, RC1b, RC2a, RN1c, RN2a, RN2b		
Discovery and precise characterization of dynamical features generated by ring-satellite interactions.	R_AO1, RC1a, b		
Density waves and bending waves.	R_AO1, RC1a, b		
Edge waves and ring shepherding.	R_AO1, RC1a, b		
Embedded moonlets and discovery of new moons from dynamical response in rings.	R_AO1, RC1a, b		
Discovery and precise characterization of azimuthal structure in rings.	R_AO1, RC1a, b		
Eccentric rings.	R_AO1, RN1c		
Measure temporal variability in ring structure.	R_AO1, RC1b		
Simultaneously measure UV reflectance structure.	R_AO1, R_AO2, RC1a		
Measure size distribution of large particles through occultation statistics.	R_AO1, R_AO2, RC1a		
Measure dust abundance in diffraction aureole.	R_AO2		
Simultaneously search for flashes from 0.1 m—1.0 m meteoroid impacts.	R_AO4		

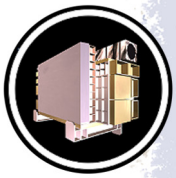

SATURN SYSTEM RESULTS, INCLUDING SYNERGISTIC SCIENCE AND OPEN QUESTIONS

Saturn Atmosphere

Koskinen et al. [2015]; West et al. [2009]; Shemansky et al. [2012] give details of some of the UVIS results, which show the variability of Saturn's thermosphere; clouds and hazes in Saturn's atmosphere; and the structure of Saturn's upper atmosphere. Saturn's thermosphere was cooler at the time of the Grand Finale.

Titan Atmosphere

Solar and stellar occultations provide a probe of the Titan atmosphere [Shemansky et al. 2005]. Hazes [West et al. 2014] are created by photochemical processes [Liang et al. 2007a; Kammer et al. 2016]. The Titan airglow is primarily from sunlight and photo-electrons [Ajello et al. 2007, 2008b, 2012]. The weak nightside airglow is from magnetospheric particle impacts [Royer et al. 2017].

Saturn Magnetosphere

Contrary to pre-Cassini expectations, [Sittler et al. 2009], Saturn's magnetosphere is dominated by neutrals, unlike Jupiter [Shemansky et al. 2009; Melin et al. 2009]. This is the result of water vapor eruptions from Enceladus [Hansen et al. 2006].

Saturn Aurora

UVIS auroral observations have been correlated with those from Hubble Space Telescope (HST) [Gérard et al. 2005, 2013; Grodent et al. 2011, 2015; Gustin et al. 2010, 2012, 2013, 2017] to characterize the interactions with Saturn magnetosphere that give rise to these emissions [Radiotti et al. 2011, 2013a, 2013b, 2014a, 2014b, 2016a, 2016b, 2017a, 2017b].

Titan Airglow and Aurora

Stevens et al. [2011, 2015] and Lavvas et al. [2015] characterize the Titan airglow and compare the Nitrogen emissions to Earth's.

Icy Satellite Surfaces

The long Cassini mission provided full longitudinal and phase angle coverage of the icy satellites. The strong UV water absorption band is diagnostic of water ice, a major component of all the icy surfaces. This allows significant constraints on the surface composition and the processes that

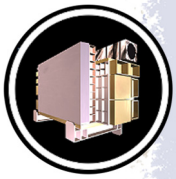

control the evolution of their surfaces [Hendrix et al. 2008a, 2008b, 2010a, 2012, 2017, 2018a, 2018b; Royer et al. 2014].

Icy Satellite Atmospheres

UVIS used stellar occultations and remote sensing to search for thin atmospheres. This was spectacularly successful for Enceladus [Hansen et al. 2006], see section entitled Enceladus Plumes and Jets. Searches at Tethys, Rhea and Dione showed no detectable atmosphere [Hansen et al. 2018].

Enceladus Plumes and Jets

The search for an atmosphere around Enceladus was successful when a stellar occultation probed the region above the south pole [Hansen et al. 2006]. Subsequent stellar and solar occultations mapped the structure and variability of the Enceladus plume and jets [Hansen et al. 2008, 2011, 2017]. Enceladus eruptions are mostly water vapor, with a variable amount of ice grains [Hedman et al. 2018]. No significant variations in the amount of water vapor is seen over the course of the mission, although the strongest jets, which lift the most icy grains, are more variable [Hansen et al. 2017].

Saturn's Rings

UVIS star, sun occultations and remote sensing of UV reflectance provide clues to the structure and composition of Saturn's rings.

UVIS star, sun occultations and remote sensing of UV reflectance provide clues to the structure and composition of Saturn's rings. In turn, these results constrain the dynamics, history and origin of the rings, and parallels to other flattened systems, like proto-planetary disks. UVIS observations of propellers [Sremcevic et al. 2007], gaps, ghosts [Baillié et al. 2013], kittens [Esposito et al. 2008; Meinke et al. 2012], self-gravity wakes [Colwell et al. 2006, 2007] indicate ongoing aggregation in Saturn's rings; ring statistics [Colwell et al. 2017b], wavelet analysis [Esposito et al. 2012], haloes [Madhusudhanan et al. 2018], small particles [Colwell et al. 2009a, 2018b; Becker et al. 2016, 2018; Jerousek et al. 2016] show aggregation/disaggregation on an orbital time scale; we can understand this with an analogy to a predator-prey ecosystem [Esposito et al. 2012].

UVIS and VIMS comparisons find small particles in the outer A-ring, and other regions that are strongly perturbed by moon resonances [Colwell et al. 2018b].

The UV spectrum of Saturn's rings can be matched by pure water ice polluted over the age of the solar system by material having the reflectance of Comet 67P (as measured by Rosetta's

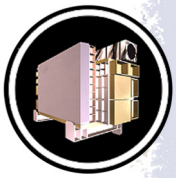

Alice). Using Cassini results for the ring mass from RSS and the polluting flux from CDA, we constrain the ring age to less than about 200 million years [Esposito 2018].

A solitary wave is excited by the Janus-Epimetheus swap, when Janus moves inward every eight years [Rehnberg et al. 2017]. This is evidence for non-linear dynamics, and may limit the application of previous conclusions based on a linear theory.

Key Open Questions

1. What is the mechanism that creates the Enceladus plume, giving rise to its stability over the Cassini mission and the variability of its individual jets? How does it re-supply the E-ring?

2. How do magnetospheric processes mediate Titan's airglow emissions?

3. How do the possible plumes on Europa compare to Enceladus?

4. What is the basic mechanism for creation of aggregates in Saturn's rings and their subsequent dis-aggregation? What does this say about planet formation?

5. What is the origin of Saturn's rings, consistent with Cassini data?

6. How do chemical processes in Titan's haze layers give them seasonal variability?

7. What is the cause of the variability of Saturn's thermosphere?

8. How do magnetospheric phenomena produce the Saturn auroral variations?

Non-Saturn Results, including heliosphere, Venus, Moon, and Jupiter system

Heliosphere

Background

IPHSurvey (Interplanetary Hydrogen Survey) data were taken by the Cassini UVIS instrument with the EUV, FUV, and HDAC instruments throughout the mission, generally when not looking at a planet or moon. The objectives were to:

1. Monitor interstellar hydrogen and helium and their brightness variations in response to changing solar illumination at the H Lyman-alpha 121.6 nm and He 58.4 nm lines, changing solar EUV photoionization, and changing solar wind flows. In the case of H,

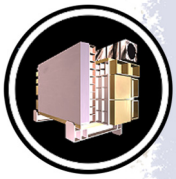

solar wind charge exchange of protons with neutral H is a dominant loss process for slow interstellar H passing through the solar system.

2. Monitor changes in instrumental flat-fields and spectral response because the emissions are spatially extended and always available.

3. Obtain information on H, He, O and other gases that may be present in the Saturn system.

Additional detail on the IPHSurveys can be found in Chapter 11 of the Cassini UVIS Users Guide written by Wayne Pryor.

Operational lessons

There was intense competition for observation time throughout the mission, except during downlink periods when the Cassini spacecraft was pointed to Earth. For this reason, we requested IPHSurveys for most downlink periods, and were usually granted these requests. In some later orbits, additional IPHSurveys were requested in non-downlink periods.

IPHSurveys were usually at low data rates, such as 74 bits per second, or 76 bits per second, but proved adequate for our purposes. The HDAC instrument participated in these IPHSurveys, and has obtained partial maps of the sky at Lyman-alpha.

Careful attention to Lyman-alpha degradation is necessary before analyzing UVIS IPHSurvey FUV data. The standard calibration pipeline degradation corrections may not be adequate and future work to improve corrections is needed.

Science lessons

There is interest in the heliospheric community in future studies of the Cassini IPHSurvey data.

Interplanetary hydrogen has been extensively studied on other missions and is fairly well understood. Pryor et al. [2008] explored how varying solar brightness (27-day variations as seen from Earth) varied going from solar observations at Earth to observations of hydrogen at Cassini and on out to observations of hydrogen at Voyager. As discussed previously by Quemerais et al. [1996], the initial 27-day brightness wave becomes increasingly damped with distance in the outer heliosphere due to multiple scattering effects, constraining the still poorly-known absolute H density values.

There is interest in the heliospheric community in future studies of the Cassini IPHSurvey data. For example, mutual observations—e.g., Hall [1992] obtained by two spacecraft looking towards and away from each other are useful for determining their relative calibrations. Future proposers to data analysis programs should be aware that there is a tremendous amount of data

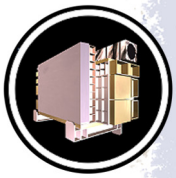

available obtained with varying geometries. H and He brightness data is available throughout the mission. We have recently applied interstellar wind He models developed for Mariner 10 [Ajello 1978] to Lunar Reconnaissance Orbiter (LRO) Lyman-Alpha Mapping Project (LAMP) heliospheric observations [Grava et al. 2018]; these models may be adapted for future Cassini studies. IPHSurvey Observations obtained near Saturn especially merit further study as they may contain magnetospheric H and O, as was found by Melin et al. [2009] in Cassini UVIS system scan observations.

Venus

Cassini observed the Venus airglow during the Cassini Venus flyby [Gérard et al. 2011a, 2011b]

Moon

Cassini observed the lunar reflectance during the Cassini Earth flyby [Hendrix 2005].

Jupiter System

UVIS observed the Io plasma torus for a period of six months surrounding the Cassini Jupiter flyby [Steffl et al. 2004a, 2006] showing radial and temporal variations that extend the Voyager and Galileo measurements.

Europa's oxygen atmosphere and torus were also characterized by these data [Hansen et al. 2004, 2005]. These results place an upper limit on eruptive activity on Europa at the time of the Cassini Jupiter flyby [Shemansky et al. 2014].

Key Open Questions for Non-Saturn Science

1. How do the different eruptive styles of Europa and Enceladus lead to the remarkably different effects in the Jovian and Saturnian magnetospheres?

UVIS Investigations

Planned UVIS Science Investigations with Saturn AO and Solstice Mission Objectives

The UVIS instrument is designed to produce spatial UV maps, map ring radial structure, and determine hydrogen/deuterium ratios. Specific Announcement of Opportunity (AO) science objectives for the Cassini mission are:

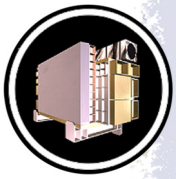

1. Saturn System Scans
    a. EUV and FUV low resolution spectra of magnetosphere neutral and ion emissions.
    b. System scans at every apoapsis.
2. Satellites
    a. Latitude, longitude and phase coverage coordinated through SSWG.
    b. Distant stellar occultations to determine satellite orbits and Saturn reference frame.
3. Atmosphere
    a. Vertical profiles of H, H2, hydrocarbons, temp in exo, thermosphere.
    b. Long integrations map of hydrocarbons, airglow.
    c. Map emissions with highest resolution at the limb.
    d. Auroral Map: H and H2 emissions over several rotations.
4. Ring Stellar Occultation Objectives
    a. Highest Radial resolution (20 m) structure of rings
    b. Discovery and precise characterization of dynamical features generated by ring-satellite interactions.
        - Density waves and bending waves.
        - Edge waves and ring shepherding.
        - Embedded moonlets and discovery of new moons from dynamical response in rings.
    c. Discovery and precise characterization of azimuthal structure in rings.
        - Eccentric rings.
        - Density waves and edge waves.
        - Small-scale self-gravitational clumping in rings.
    d. Measure temporal variability in ring structure.
    e. Simultaneously measure UV reflectance spectrum of rings.

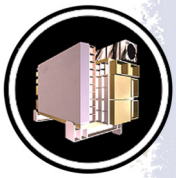

- Determine microstructure on particle surfaces.
- Compositional information on ring particles.

f. Measure size distribution of large particles through occultation statistics.

g. Measure dust abundance in diffraction aureole.

h. Simultaneously search for flashes from 0.1 m–1.0 m meteoroid impacts.

Implementation Challenges and Achievements

a. Distributed operations was a challenge, but gave the science team control.

b. Data limitations forced binning and windowing of the UVIS spectral images.

c. Evil pixels limited photometric accuracy and the spectral/spatial resolution.

d. UVIS calibration involved disparate approaches by different team members: Investigators used the approach most suited to their science.

e. Loss of the near ultraviolet (NUV) channel during mission de-scoping limited science for Saturn and icy satellites.

f. New scientific discoveries motivated new observational strategies to address them: Tracking occultations, shorter occultation integration periods, Enceladus star and solar occultations, Dione, Tethys and Rhea plume searches.

g. The multiplicity of ring occultations allowed investigations and discoveries not expected from our original proposal: Self-gravity wakes, gaps and ghosts, kittens and clumps, solitary waves.

Summary and Suggestions

The broad capability of UVIS allowed us to address our prime objectives and many new science questions that arose during the long mission. We were able to corroborate and/or extend findings from other instruments by riding along whenever possible.

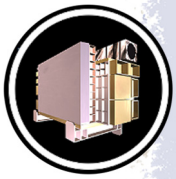

AO OBJECTIVES

Table UVIS-2 shows the prioritized summary of the Cassini Solstice Mission Science Objectives.

Table UVIS-2. Prime Mission AO Science Objectives.

Saturn	Rings	MAPS	Icy Satellites	Titan
		Cassini		
Determine temperature field, cloud properties, and composition of the atmosphere of Saturn.	Study configuration of the rings and dynamical processes (gravitational, viscous, erosional, and electromagnetic) responsible for ring structure.	Determine the configuration of the nearly axially symmetric magnetic field and its relation to the modulation of Saturn Kilometric Radiation (SKR).	Determine the general characteristics and geological histories of the satellites.	Determine abundance of atmospheric constituents (including any noble gases), establish isotope ratios for abundant elements, constrain scenarios of formation and evolution of Titan and its atmosphere.
Measure the global wind field, including wave and eddy components; observe synoptic cloud features and processes.	Map composition and size distribution of ring material.	Determine current systems, composition, sources, and sinks of magnetosphere charged particles.	Define the mechanisms of crustal and surface modifications, both external and internal.	Observe vertical and horizontal distributions of trace gases, search for more complex organic molecules, investigate energy sources for atmospheric chemistry, model the photochemistry of the stratosphere, study formation and composition of aerosols.
Infer the internal structure and rotation of the deep atmosphere.	Investigate interrelation of rings and satellites, including embedded satellites.	Investigate wave-particle interactions and dynamics of the dayside magnetosphere and the magnetotail of Saturn and their interactions with the solar wind, the satellites, and rings.	Investigate the compositions and distributions of surface materials, particularly dark, organic rich materials and low melting point condensed volatiles.	Measure winds and global temperatures; investigate cloud physics, general circulation, and seasonal effects in Titan's atmosphere; search for lightning discharges.
Study the diurnal variations and magnetic control of the ionosphere of Saturn.	Determine dust and meteoroid distribution both in the vicinity of the rings and in interplanetary space.	Study the effect of Titan's interaction with the solar wind and magnetospheric plasma.	Investigate interactions with the magnetosphere and ring systems and possible gas injections into the magnetosphere.	Determine the physical state, topography, and composition of the surface; infer the internal structure of the satellite.
Provide observational constraints (gas composition, isotope ratios, heat flux, …) on scenarios for the formation and evolution of Saturn.	Study interactions between the rings and Saturn's magnetosphere, ionosphere, and atmosphere.	Investigate interactions of Titan's atmosphere and exosphere with the surrounding plasma.		Investigate the upper atmosphere, its ionization, and its role as a source of neutral and ionized material for the magnetosphere of Saturn.
Investigate the sources and the morphology of Saturn lightning (Saturn Electrostatic Discharges (SED), lightning whistlers).				

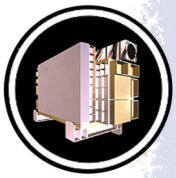

Table UVIS-2. Prime Mission AO Science Objectives.

Saturn	Rings	MAPS	Icy Satellites	Titan
		Huygens		
				Huygens: Determine abundances of atmospheric constituents (including any noble gases); establish isotope ratios for abundant elements; constrain scenarios of formation and evolution of Titan and its atmosphere.
				Huygens: Observe vertical and horizontal distribution of trace gases; search for more complex organic molecules; investigate energy sources for atmospheric chemistry; model the photochemistry of the stratosphere; study formation and composition of aerosols.
				Huygens: Measure winds and global temperatures; investigate cloud physics, general circulation and seasonal effects in Titan's atmosphere; search for lightning discharges.
				Huygens: Determine the physical state, topography and the composition of the surface; infer the internal structure of the satellite.
				Huygens: Investigate the upper atmosphere, its ionization, and its role as a source of neutral and ionized material for the magnetosphere of Saturn.

UVIS Traceability Matrix (TM)

Table UVIS-3 shows the prioritized summary of the Cassini Solstice Mission Science Objectives, and the goals to observe seasonal change in the Saturn system to understand the underlying process and prepare for future missions.

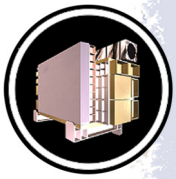

Table UVIS-3. Seasonal-Temporal Change and New Questions. Source: 2014 Senior Review Traceability Matrix (Table) + N2e (Hyperion) and IN2f (Iapetus) from 2010 Senior Review Traceability Matrix.

Saturn	Rings	MAPS	Icy Satellites	Titan
Seasonal-Temporal Change				
Priority 1				
SC1a: Observe seasonal variation in temperature, clouds, and composition in three spatial dimensions.	**RC1a:** Determine the seasonal variation of key ring properties and the microscale properties of ring structure, by observing at the seasonally maximum opening angle of the rings near Solstice.	**MC1a:** Determine the temporal variability of Enceladus' plumes.	**IC1a:** Identify long-term secular and seasonal changes at Enceladus, through observations of the south polar region, jets, and plumes.	**TC1a:** Determine seasonal changes in the methane-hydrocarbon hydrological cycle: of lakes, clouds, aerosols, and their seasonal transport.
SC1b: Observe seasonal changes in the winds at all accessible altitudes coupled with simultaneous observations of clouds, temperatures, composition, and lightning.	**RC1b:** Determine the temporal variability of ring structure on all timescales up to decadal for regions including Encke gap, D-ring, F-ring, and ring edges by substantially increasing the cadence and time baseline of observations.	**MC1b:** Observe Saturn's magnetosphere over a solar cycle, from one solar minimum to the next.		**TC1b:** Determine seasonal changes in the high-latitude atmosphere, specifically the temperature structure and formation and breakup of the winter polar vortex.
Priority 2				
SC2a: Observe the magnetosphere, ionosphere, and aurora as they change on all time scales—minutes to years—and are affected by seasonal and solar cycle forcing.	**RC2a:** Focus on F-ring structure, and distribution of associated moonlets or clumps, as sparse observations show clumps, arcs, and possibly transient objects appearing and disappearing.	**MC2a:** Observe seasonal variation of Titan's ionosphere, from on Solstice to the next.		**TC2a:** Observe Titan's plasma interaction as it goes from south to north of Saturn's solar-wind-warped magnetodisk from one solstice to the next.
New Questions				
Priority 1				
SN1a: Determine Saturn's rotation rate and internal structure despite the planet's unexpected high degree of axisymmetry.	**RN1a:** Constrain the origin and age of the rings by direct determination of the ring mass, and of the composition of ring ejects trapped on field lines.	**MN1a:** Determine the dynamics of Saturn's magnetotail.	**IN1a:** Determine the presence of an ocean at Enceladus as inferred from induces magnetic field and plume composition, search for possible anomalies in the internal structure of Enceladus as associate with plume sources, and constrain the mechanisms driving the endogenic activity by in situ observations and remote sensing.	**TN1a:** Determine the types, composition, distribution, and ages, of surface units and materials, most notably lakes (i.e., filled versus dry and depth; liquid versus solid and composition; polar versus other latitudes and lake basin origin).

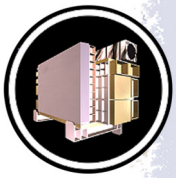

Table UVIS-3. Seasonal-Temporal Change and New Questions. Source: 2014 Senior Review Traceability Matrix (Table) + N2e (Hyperion) and IN2f (Iapetus) from 2010 Senior Review Traceability Matrix.

Saturn	Rings	MAPS	Icy Satellites	Titan
SN1b: Observe the aftermath of the 2010–2011 storm. Study the life cycles of Saturn's newly discovered atmospheric waves, south polar hurricane, and rediscovered north polar hexagon.	**RN1b:** Determine the composition of the close-in ring moons as targets of opportunity.	**MN1b:** Conduct in situ and remote sensing studies of Saturn's ionosphere and inner radiation belt.	**IN1b:** Complete the comparative study of Saturn's mid-sized satellites, their geological and cratering histories, and interactions with the Saturn system, with remote sensing of Mimas at the highest resolution possible in order to understand the mechanisms behind its unique thermal properties discovered by Cassini.	**TN1b:** Determine internal and crustal structure: Liquid mantle, crustal mass distribution, rotational state of the surface with time, intrinsic and/or internal induced magnetic field.
SN1c: Measure the spatial and temporal variability of trace gases and isotopes.	**RN1c:** Determine structural and compositional variations at high resolution across selected ring features of greatest interest, using remote and in situ observations.	**MN1c:** Investigate magnetospheric periodicities, their coupling to the ionosphere, and how the SKR periods are imposed from close to the planet (3–5 R_S) out to the deep tail.	**IN1c:** Determine whether Dione exhibits evidence for low-level activity, now or in recent geological time.	**TN1c:** Measure aerosol and heavy molecule layers and properties.
Priority 2				
SN2a: Monitor the planet for new storms and respond with new observations when the new storms occur.	**RN2a:** Conduct in-depth studies of ring microstructure such as self-gravity wakes, which permeate the rings.	**MN2a:** Determine the coupling between Saturn's rings and ionosphere.	**IN2a:** Determine whether there is ring material orbiting Rhea, and if so, what its spatial and particle size distribution is.	**TN2a:** Resolve current inconsistencies in atmospheric density measurements (critical to a future Flagship mission).
	RN2b: Perform focused studies of the evolution of newly discovered propeller objects.		**IN2b:** Determine whether Tethys contributes to the E-ring and the magnetospheric ion and neutral population.	**TN2b:** Determine icy shell topography and viscosity.
			IN2c: Determine the extent of differentiation and internal inhomogeneity within the icy satellites, especially Rhea and Dione.	**TN2c:** Determine the surface temperature distribution, cloud distribution, and tropospheric winds.

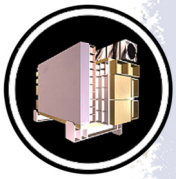

Table UVIS-3. Seasonal-Temporal Change and New Questions. Source: 2014 Senior Review Traceability Matrix (Table) + N2e (Hyperion) and IN2f (Iapetus) from 2010 Senior Review Traceability Matrix.

Saturn	Rings	MAPS	Icy Satellites	Titan
			IN2d: Observe selected small satellites to quantify the movement of Enceladus material through the system, the history of satellite collisions/breakup, interaction with ring material as indicated by surface properties/ composition, and cratering rates deep in the Saturnian system.	
			IN2e: Understand the unusual appearance of Hyperion with remote sensing observations of the highest resolution possible.	
			IN2f: Use remote sensing of Iapetus to test models for the albedo heterogeneity of the satellite. Quantify the effect of the newly-discovered Phoebe ring on the properties of Iapetus' surface.	

Cell Codes:

First Letter = Discipline (**S**aturn, **R**ings, **M**agnetospheric and Plasma Science (MAPS), **I**cy Satellites, **T**itan)

Second Letter = Objective Type (**C**hange related or **N**ew question)

Third number = Priority Level (**1**, **2**)

Fourth Letter = Distinction within Priority Level (**a**, **b**, **c**, etc.)

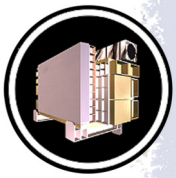

ACRONYMS

Note: For a complete list of Acronyms, refer to Cassini Acronyms – Attachment A.

AO	Announcement of Opportunity
CDA	Cosmic Dust Analyzer
EUV	extreme ultraviolet channel
FUV	far ultraviolet channel
HDAC	hydrogen-deuterium absorption cell
HSP	high-speed photometer
HST	Hubble Space Telescope
LAMP	Lyman-Alpha Mapping Project
LRO	Lunar Reconnaissance Orbiter
MAPS	Magnetospheres and Plasma Science
NUV	near ultraviolet
RSS	Radio Science Subsystem
SED	Saturn Electrostatic Discharges
SKR	Saturn Kilometric Radiation
SSWG	Satellite Surfaces Working Group
TM	Traceability Matrix
UV	ultraviolet
UVIS	Ultraviolet Imaging Spectrograph
VIMS	Visual and Infrared Imaging Spectrometer

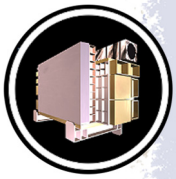

REFERENCES

Disclaimer: *The partial list of references below correspond with in-text references indicated in this report. For all other Cassini references, refer to Attachment B – References & Bibliographies; Attachment C – Cassini Science Bibliographies; the sections entitled References contributed by individual Cassini instrument and discipline teams located in Volume 1 Sections 3.1 and 3.2 Science Results; and other resources outside of the Cassini Final Mission Report.*

Aguilar, A., J. M, Ajello, R. S. Mangina, G. K. James, (2008), The electron excited middle UV to near IR spectrum of H_2: Cross sections and transition probabilities, The Astrophysical Journal Supplement, 177, 388–407, doi: 10.1086/587690.

Ajello, J. M., C. P. Malone, G. M. Holsclaw, A. C. Hoskins, R. W. Eastes, W. E. McClintock, P. V. Johnson, (2017), Electron impact study of the 100 eV emission cross-section and lifetime of the Lyman-Birge-Hopfield band system of N_2: Direct excitation and cascade, Journal of Geophysical Research Physics, 122, doi: 10.1002/2017JA024087.

Ajello, J. M, M. H. West, R. A., Gustin, K. Larsen, A. I. F. Stewart, L. W. Esposito, W. E. McClintock, G. M. Holsclaw, E. T. Bradley, (2012), Cassini UVIS observations of Titan nightglow spectra, Journal of Geophysical Research, vol. 117, A12315, doi: 10.1029/2012JA017888.

Ajello, J. M, R. S. Mangina, D. J. Strickland, D. Dziczek, (2011), Laboratory studies of UV emissions from proton impact on N_2: The Lyman-Birge-Hopfield band system for aurora analysis, Journal of Geophysical Research, vol. 116, A00K03, doi: 10.1029/2010JA016103.

Ajello, J. M., R. S. Mangina, R. R. Meier, (2010), UV molecular spectroscopy from electron impact for applications to planetary atmospheres and astrophysics, Chapter 28, In Charged Particle and Photon Interactions with Matter, Recent Advances, Applications, and Interfaces, (eds.) Y. Hatano, Y. Katsumura, A. Mozumder, CRC Press, pp. 761–804.

Ajello J. M., A. Aguilar, R. S. Mangina, G. K. James, P. Geissler, L. Trafton, (2008a), The middle UV to near IR spectrum of electron excited SO_2, Journal of Geophysical Research: Planets, 113, E03002, doi: 10.1029/2007JE002921.

Ajello, J. M., J. Gustin, A. I. F. Stewart, K. Larsen, L. W. Esposito, W. Pryor, W. McClintock, M. H. Stevens, C. P. Malone, D. Dziczek, (2008b), Titan airglow spectra from the Cassini Ultraviolet Imaging Spectrograph: FUV disk analysis, Geophysical Research Letters, 35, L06102, doi: 10.1029/2007GL032315.

Ajello, J. M., M. H. Stevens, A. I. F. Stewart, K. Larsen, L. W. Esposito, J. E. Colwell, W. E. McClintock, G. Holsclaw, J. Gustin, W. R. Pryor, (2007), Titan airglow spectra from Cassini UVIS: I. EUV analysis, Geophysical Research Letters, 34, L24204, doi: 10.1029/2007GL031555.

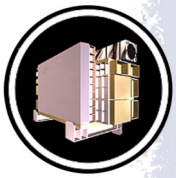

Ajello J. M., W. Pryor, L. W. Esposito, A. I. F. Stewart, W. McClintock, J. Gustin, D. Grodent, J.-C. Gérard, J. T. Clarke, (2005), The Cassini campaign observations of the Jupiter aurora by the Ultraviolet Imaging Spectrograph and the Space Telescope Imaging Spectrograph, Icarus, 178, Issue 2, 327–345, doi: 10.1016/j.icarus.2005.01.023.

Ajello, J. M., (1978), An interpretation of Mariner 10 helium (584 A) and hydrogen (1216 A) interplanetary emission observations, The Astrophysical Journal, 222, 1068.

Ajello, J. M., N. Witt, P. Blum, A. L. Broadfoot, (1977), H (1216A) and He (584A) interplanetary emission observations from Mariner-10, Transactions-American Geophysical Union, 58, 12, 1224–1224.

Albers, N., M. Sremcevic, J. E. Colwell, L. W. Esposito, (2012), Saturn's F-ring as seen by Cassini UVIS: kinematics and statistics, Icarus, vol. 217, pp. 367–388, doi: 10.1016/j.icarus.2011.11.016.

Albers, N., F. Spahn, (2006), The influence of particle adhesion on the stability of agglomerates in Saturn's rings, Icarus, 181, 292–301.

Anderson C. M., R. E. Samuelson, Y. L. Yung, J. L. McLain, (2016), Solid-state chemistry as a formation mechanism for Titan's stratospheric C_4N_2 ice clouds, Geophysical Research Letters, 43, 7, 3088–3094, doi: 10.1002/2016GL067795/abstract.

André, N., M. Blanc, S. Maurice, P. Schippers, E. Pallier, T. I. Gombosi, K. C. Hansen, D. T. Young, F. J. Crary, S. Bolton, E. C. Sittler, H. T. Smith, R. E. Johnson, R. A. Baragiola, A. J. Coates, A. M. Rymer, M. K. Dougherty, N. Achilleos, C. S. Arridge, S. M. Krimigis, D. G. Mitchell, N. Krupp, D. C. Hamilton, I. Dandouras, D. A. Gurnett, W. S. Kurth, P. Louarn, R. Srama, S. Kempf, H. J. Waite, L. W. Esposito, J. T. Clarke, (2008), Identification of Saturn's magnetospheric regions and associated plasma processes: Synopsis of Cassini observations during orbit insertion, Reviews of Geophysics, 46, RG4008, doi: 10.1029/2007RG000238.

Babichenko, S. I., E. V. Deregusov, V. G. Kurt, N. N. Romanova, V. A. Skliankin, A. S. Smirnov, et al., (1977), Measurements in interplanetary space and in the Martian upper atmosphere with a hydrogen absorption-cell-spectrophotometer for L alpha-radiation on-board Mars 4-7 Spaceprobes, Space Science Instrumentation, 3, 271.

Badman S., G. Provan, E. Bunce, D. G. Mitchell, Henrik Melin, S. W. Cowley, A. Radioti, W. Kurth, W. Pryor, J. D. Nichols, S. L. Jinks, T. S. Stallard, R. H. Brown, K. H. Baines, M. K. Dougherty, (2016), Saturn's auroral morphology and field-aligned currents during a solar wind compression, Icarus special issue, 263, 83–93, doi: 10.1016/j.icarus.2014.11.014.

Badman, S. V., A. Masters, H. Hasegawa, M. Fujimoto, A. Radioti, D. Grodent, N. Sergis, M. K. Dougherty, A. J. Coates, (2013), Bursty magnetic reconnection at Saturn's magnetopause, Geophysical Research Letters, 40, doi: 10.1002/grl.50199/abstract.

Badman, S. V., E. J. Bunce, J. T. Clarke, S. W. H. Cowley, J. C. Gérard, D. Grodent, S. E. Milan, (2005), Open flux estimates in Saturn's magnetosphere during the January 2004 Cassini-HST campaign, and implications for reconnection rates, Journal of Geophysical Research: Space Physics, vol. 110, Issue A11, doi: 10.1029/2005JA011240.

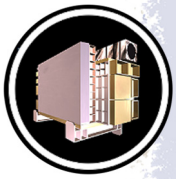

Baillié, K., J. E. Colwell, L. W. Esposito, M. C. Lewis, (2013), Meter-sized moonlet population in Saturn's C ring and Cassini Division, The Astronomical Journal, 145, 171.

Baillié, K., J. E. Colwell, J. J. Lissauer, L. W. Esposito, M. Sremcevic, (2011), Waves in Cassini UVIS stellar occultations 2. Waves in the C ring, Icarus, vol. 216, Issue 1, pp. 292–308, doi: 10.1016/j.icarus.2011.05.019.

Barbara, J. M. and L. W. Esposito, (2002), Moonlet collisions and the effects of tidally modified accretion in Saturn's F ring, Icarus, 160, Issue 1, 161–171, doi: 10.1006/icar.2002.6962.

Barnes, J. W., R. H. Brown, E. P. Turtle, A. S. McEwen, R. D. Lorenz, M. Janssen, E. L. Schaller, M. E. Brown, B. J. Buratti, C. Sotin, C. Griffith, R. Clark, J. Perry, S. Fussner, J. Barbara, R. West, C. Elachi, A. H. Bouchez, H. G. Roe, K. H. Baines, G. Bellucci, J. P. Bibring, F. Capaccioni, P. Cerroni, M. Combes, A. Coradini, D. P. Cruikshank, P. Drossart, V. Formisano, R. Jaumann, Y. Langevin, D. L. Matson, T. B. McCord, P. D. Nicholson, B. Sicardy, (2005), A 5-micron-bright spot on Titan: Evidence for surface diversity, Science, vol. 310, Issue 5745, doi: 10.1126/science.1117075.

Becker, T. M., J. E. Colwell, L. W. Esposito, N. O. Attree, C. D. Murray, (2018), Cassini UVIS solar occultations by Saturn's F ring and the detection of collision-produced micron-sized dust, Icarus, 306, 171–199.

Becker, T. M., J. E. Colwell, L. W. Esposito, A. D. Bratcher, (2016), Characterizing the particle size distribution of Saturn's A-ring with Cassini UVIS, Icarus, 279, 20–35, doi: 10.1016/j.icarus.2015.11.001.

Bertaux, J. L., F. Goutail, E. Dimarellis, G. Kockarts, E. Van Ransbeeck, (1984), First optical detection of atomic deuterium in the upper atmosphere from Spacelab 1, Nature, 309, 771.

Bertaux, J. L., J. Blamont, M. Marcelin, V. G. Kurt, N. N. Romanova, A. S. Smirnov, (1978), Lyman-alpha observations of Venera-9 and 10 I. The non-thermal hydrogen population in the exosphere of Venus, Planetary and Space Science, vol. 26, Issue 9, pp. 817–831.

Blanc, M., S. Bolton, J. Bradley, M. Burton, T. E. Cravens, I. Dandouras, M. K. Dougherty, M. C. Festou, J. Feynman, R. E. Johnson, T. G. Gombosi, W. S. Kurth, P. C. Liewer, B. H. Mauk, S. Maurice, D. Mitchell, F. M. Neubauer, J. D. Richardson, D. E. Shemansky, E. C. Sittler, B. T. Tsurutani, P. Zarka, L. W. Esposito, E. Grun, D. A. Gurnett, A. J. Kliore, S. M. Krimigis, D. Southwood, J. H. Waite, D. T. Young, (2002), Magnetospheric and plasma science with Cassini-Huygens, Space Science Reviews, 104, Issue 1–2, 253–346.

Bolton, S. J., C. J. Hansen, D. L. Matson, L. J. Spilker, J. P. Lebreton, (2004), Cassini-Huygens flyby of the Jovian system, Journal of Geophysical Research: Space Physics, vol. 109, Issue A9.

Bolton, S. J., M. Janssen, R. Thorne, S. Levin, M. Klein, S. Gulkis, T. Bastian, R. Sault, C. Elachi, M. Hofstadter, A. Bunker, G. Dulk, E. Gudim, G. Hamilton, W. T. K. Johnson, Y. Leblanc, O. Liepack, R. McLeod, J. Roller, L. Roth, R. West, (2002), Ultra-relativistic electrons in Jupiter's radiation belts, Nature, vol. 415, Issue 6875.

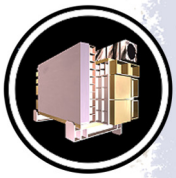

Bradley, E. T., J. E. Colwell, L. W. Esposito, (2013), Scattering properties of Saturn's rings from Cassini UVIS spectra, Icarus, 225, 1, 726–739, doi: 10.1016/j.icarus.2013.04.008.

Bradley, E. T., J. E. Colwell, L. W. Esposito, J. M. Cuzzi, H. Tollerud, L. Chambers, (2010), Far ultraviolet spectral properties of Saturn's rings from Cassini UVIS, Icarus, 206, 458–466.

Brilliantov, N. V., N. Albers, F. Spahn, T. Pöschel, (2013), Erratum: Collision dynamics of granular particles with adhesion [Phys. Rev. E 76, 051302 (2007)], Physical Review E, 87, 039904, doi: 10.1103/PhysRevE.87.039904.

Brilliantov, N., N. Albers, F. Spahn, T. Poeschel, (2007), Collision dynamics of granular particles with adhesion, Physical Review E, 76, 051302-1.

Broadfoot, A. L., B. R. Sandel, D. E. Shemansky, S. K. Atreya, T. M. Donahue, H. W. Moos, J. L. Bertaux, et al., (1977), Ultraviolet spectrometer experiment for the Voyager mission, Space Science Reviews 21, no. 2, 183–205.

Broadfoot, A. L., S. Kumar, M. J. S. Belton, M. B. McElroy, (1974), Ultraviolet observations of Venus from Mariner 10: Preliminary results, Science, 183, no. 4131, 1315–1318.

Brune, W. H., G. H. Mount, P. D. Feldman, (1979), Vacuum ultraviolet spectrophotometry and effective temperatures of hot stars, The Astrophysical Journal, part 1, vol. 227, pp. 884–899.

Canup, R. M., L. W. Esposito, (1997), Evolution of the G ring and the population of macroscopic ring particles, Icarus, 126, Issue 1, 28–41.

Capalbo, F. J., Y. Benilan, N. Fray, M. Schwell, N. Champion, E. Es-sebbar, T. T. Koskinen, I. Lehocki, R. V. Yelle, (2016) New benzene absorption cross sections in the VUV, relevance for Titan's upper atmosphere, Icarus, 265, 95–109, doi: 10.1016/j.icarus.2015.10.006.

Capalbo, F. J., Y. Benilan, R. V. Yelle, T. T. Koskinen, (2015), Titan's upper atmosphere from Cassini/UVIS solar occultations, The Astronomical Journal, 814, 86, doi: 10.1088/0004-637X/814/2/86.

Charnoz, S., L. Dones, L. W. Esposito, P. R. Estrada, M. M. Hedman, (2009), Origin and evolution of Saturn's ring system, Chapter 17, In Saturn From Cassini-Huygens, (eds.) M. Dougherty, L. Esposito, S. Krimigis, Springer Dordrecht, Netherlands, pp. 537–575, doi: 10.1007/978-1-4020-9217-6.

Clarke, J. T., T. L. Graeme, M. Friedman, (2016), Little evidence for enhanced phenotypic evolution in early teleosts relative to their living fossil sister group, Proceedings of the National Academy of Sciences, 113, no. 41, 11531–11536.

Clarke, J. T., J. Nichols, J-C. Gérard, D. Grodent, K. C. Hansen, W. Kurth, G. R. Gladstone, et al., (2009), The response of Jupiter's and Saturn's auroral activity to the solar wind, Journal of Geophysical Research, 114, doi: 10.1029/2008JA013694.

Clarke, J. T., J. C. Gérard, D. Grodent, S. Wannawichian, J. Gustin, J. Connerney, F. Crary, M. Dougherty, W. Kurth, S. W. H. Cowley, E. J. Bunce, T. Hill, J. Kim, (2005), Morphological differences between Saturn's ultraviolet aurorae and those of Earth and Jupiter, Nature, vol. 433, Issue 7027.

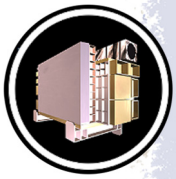

Colwell, J. E., J. Blum, R. Clark, S. Kempf, R. Nelson, (2018a), Laboratory studies of planetary ring systems, Chapter 17, Planetary Ring Systems, (eds.) M. S. Tiscareno, C. D. Murray, Cambridge University Press, pp. 494–516, doi: 10.1017/9781316286791.017.

Colwell, J. E., L. W. Esposito, J. H. Cooney, (2018b), Particle sizes in Saturn's rings from UVIS stellar occultations 1. Variations with ring region, Icarus 300, 150–166, doi: 10.1016/j.icarus.2017.08.036.

Colwell, J. E., (2017a), Cassini's grand finale, Physics World, vol. 30, no. 9, 25–28, doi: 10.1088/2058-7058/30/9/34.

Colwell, J. E., (2017b), The ringed planet: Cassini's voyage of discovery at Saturn, Morgan and Claypool Publishers, doi: 10.1088/978-1-6817-4497-1.

Colwell, J. E., L. W. Esposito, R. G. Jerousek, M. Sremcevic, D. Pettis, E. T. Bradley, (2010), Cassini UVIS stellar occultation observations of Saturn's rings, The Astronomical Journal, vol. 140, Issue 6, pp. 1569–1578.

Colwell, J. E., J. H. Cooney, L. W. Esposito, M. Sremcevic, (2009a), Density waves in Cassini UVIS stellar occultations 1. The Cassini division, Icarus, 200, 574–580.

Colwell, J. E., P. D. Nicholson, M. S. Tiscareno, C. D. Murray, R. G. French, E. A. Marouf, (2009b), The structure of Saturn's rings, Chapter 13, In Saturn From Cassini-Huygens, (eds.) M. Dougherty, L. Esposito, S. Krimigis, Springer Dordrecht, Netherlands, pp. 375–412, doi: 10.1007/978-1-4020-9217-6.

Colwell, J. E., L. W.Esposito, M. Sremcevic, G. R. Stewart, W. E. McClintock, (2007), Self-gravity wakes and radial structure of Saturn's B ring, Icarus, 190, 127–144.

Colwell, J. E., L. W. Esposito, M. Sremcevic, (2006), Self-gravity wakes in Saturn's A-ring measured by stellar occultations from Cassini, Geophysical Research Letters, 33, L07201, doi: 10.1029/2005GL025163.

Cowley, S. W. H., S. V. Badman, E. J. Bunce, J. T. Clarke, J. C. Gérard, D. Grodent, C. M. Jackman, S. E. Milan, T. K. Yeoman, (2005), Reconnection in a rotation-dominated magnetosphere and its relation to Saturn's auroral dynamics, Journal of Geophysical Research: Space Physics, vol. 110, Issue A2.

Crary, F. J., J. T. Clarke, M. K. Dougherty, P. G. Hanlon, K. C. Hansen, J. T. Steinberg, B. L. Barraclough, A. J. Coates, J. C. Gérard, D. Grodent, W. E. Kurth, D. G. Mitchell, A. M. Rymer, D. T. Young, (2005), Solar wind dynamic pressure and electric field as the main factors controlling Saturn's aurorae, Nature, vol. 433, Issue 7027.

Cravens, T. E., R. V. Yelle, J.-E. Wahlund, D. E. Shemansky, (2009), Composition and structure of the ionosphere and thermosphere, Chapter 11, In Titan from Cassini Huygens, (eds.) R. H. Brown, J.-P. Lebreton, H. Waite, Springer Dordrecht, Netherlands, pp. 259–296, doi: 10.1007/978-1-4020-9215-2.

Croteau, P., J. B. Randazzo, O. Kostko, M. Ahmed, M.-C. Liang, Y. L. Yung, K. A. Boering, (2011), Measurements of isotope effects in the photoionization of N_2 and implications for

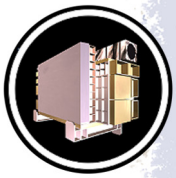

Titan’s atmosphere, The Astrophysical Journal Letters, vol. 728, no. 2, doi: 10.1088/2041-8205/728/2/L32.

Cruikshank, D. P., J. B. Dalton, C. M. Dalle Ore, J. Bauer, K. Stephan, G. Filacchione, A. R. Hendrix, C. J. Hansen, A. Coradini, P. Cerroni, F. Tosi, F. Capaccioni, R. Jaumann, B. J. Buratti, R. N. Clark, R. H. Brown, R. M. Nelson, T. B. McCord, K. H. Baines, P. D. Nicholson, C. Sotin, A. W. Meyer, G. Bellucci, M. Combes, J.-P. Bibring, Y. Langevin, B. Sicardy, D. L. Matson, V. Formisano, P. Drossart V. Mennella, (2007), The surface composition of Hyperion, Nature, vol. 448, 54–56.

Cuzzi, J. N., A. D. Whizin, R. C. Hogan, A. R. Dobrovolskis, L. Dones, M. R. Showalter, J. E. Colwell, J. D. Scargle, (2014), Saturn’s F ring core: Calm in the midst of chaos, Icarus, 232, 157–175, doi: 10.1016/j.icarus.2013.12.027.

Cuzzi, J. N., J. A. Burns, S. Charnoz, R. N. Clark, J. E. Colwell, L. Dones, L. W. Esposito, G. Filacchione, R. G. French, M. M. Hedman, S. Kempf, E. A. Marouf, C. D. Murray, P. D. Nicholson, C. C. Porco, J. Schmidt, M. R. Showalter, L. J. Spilker, J. N. Spitale, R. Srama, M. Sremcevic, M. S. Tiscareno, J. Weiss, (2010), An evolving view of Saturn’s dynamic rings, Science, 327, 1470–1475, doi: 10.1126/science.1179118.

Cuzzi, J., R. Clark, G. Filacchione, R. French, R. Johnson, E. Marouf, L. Spilker, (2009), Ring particle composition and size distribution, Chapter 15, In Saturn from Cassini-Huygens, (eds.) M. Dougherty, L. Esposito, S. Krimigis, Springer Dordrecht, Netherlands, pp. 459–509, doi: 10.1007/978-1-4020-9217-6.

Cuzzi, J. N., J. E. Colwell, L. W. Esposito, C. C. Porco. C. D. Murray, P. D. Nicholson, L. J. Spilker, E. A. Marouf, R. C. French, N. Rappaport, D. Muhleman, (2002), Saturn's rings: Pre-Cassini status and mission goals, Space Science Reviews, 104, Issue 1–2, 209–251.

Delamere, P. A., F. Bagenal, C. Paranicas, A. Masters, A. Radioti, B. Bonfond, L. Ray, X. Jia, J. Nichols, C. Arridge, (2014), Solar wind and internally driven dynamics: Influences on magnetodiscs and auroral responses, Space Science Reviews, Published online, doi: 10.1007/s11214-014-0075-1.

Delamere, P. A., F. Bagenal, A. Steffl, (2005), Radial variations in the Io plasma torus during the Cassini era, Journal of Geophysical Research: Space Physics, vol. 110, Issue A12.

Dougherty, M. K., L. W. Esposito, S. M. Krimigis, (2009a), Overview, In Saturn from Cassini-Huygens, Springer Dordrecht, Netherlands, pp. 1–8, doi: 10.1007/978-1-4020-9217-6.

Dougherty, M. K., L. W. Esposito, S. M. Krimigis, (2009b), Saturn from Cassini-Huygens. Dordrecht, Netherlands.

Dyudina, U. A., A. D. Del Genio, A. P. Ingersoll, C. C. Porco, R. A. West, A. R. Vasavada, J. M. Barbara, (2004), Lightning on Jupiter observed in the H-alpha line by the Cassini imaging science subsystem, Icarus, vol. 172, Issue 1.

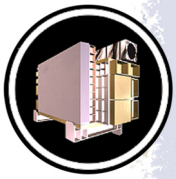

Dzhanoev, A. R., A. Loskutov, J. E. Howard, M. A. F. Sanjuan, (2010), Chaos stabilization in the three body problem, Chapter 14, In Recent Progress in Controlling Chaos, (eds.) M. A. F. Sanjuan, C. Grebogi, World Scientific Review, pp. 395–408.

Dzhanoev, A. R., A. Loskutov, J. E. Howard, M. A. F. Sanjuán, (2009), Stabilized Chaos in The Sitnikov Problem, Part II Celestial Mechanics, In Chaos in Astronomy, (eds.) G. Contopoulos, P. A. Patsis, Research Center for Astronomy Academy of Athens, Athens, Greece, Springer, pp 301–305.

Elliott, J. P. and L. W. Esposito, (2011), Regolith depth growth on an icy body orbiting Saturn and Evolution of bidirectional reflectance due to surface composition changes, Icarus, 212, 268–274.

Esposito, L. W. and M. De Stefano, (2018), Space age studies of planetary rings, Chapter 1, Planetary Ring Systems: Properties, Structure, and Evolution, (eds.), M. S. Tiscareno, C. D. Murray, Cambridge University Press, pp. 3–29.

Esposito, L, W., (2018), Cassini UVIS Top Ten Discoveries, In 42nd COSPAR Scientific Assembly, vol. 42, 14–22 July 2018, Pasadena, CA, abstract id B5.2-4-18.

Esposito, L. W., (2014a), Planetary Rings: A post-equinox view, Cambridge University Press, ISBN-13: 978-1107028821.

Esposito, L. W., (2014b), Saturn's Rings, Discoveries in Modern Science: Exploration, Invention, Technology, (eds.) J. Trefil, vol. 3. Farmington Hills, MI, Macmillan Reference, pp. 987–991, ISBN-13: 978-0028662442.

Esposito, L. W., N. Albers, B. K. Meinke, M. Sremcevic, Pr. Madhusudhanan, J. Colwell, R. G. Jerousek, (2012), A predator-prey model for moon-triggered clumping in Saturn's rings, Icarus, 217, 1, 103–114, doi: 10.1016/j.icarus.2011.09.029.

Esposito, L. W., (2010), Composition, structure, dynamics and evolution of Saturn's rings, Annual Review of Earth & Planetary Sciences, 38, 383–410.

Esposito, L. W. and A. R. Hendrix, (2010), Introduction to special issue, Saturn's rings and icy satellites from Cassini, Icarus, 206, 381, doi: 10.1016/j.icarus.2010.02.001.

Esposito, L. W., B. K. Meinke, J. E. Colwell, P. D. Nicholson, M. M. Hedman, (2008), Moonlets and clumps in Saturn's F ring, Icarus, vol 194, 1, 278–289, doi: 10.1016/j.icarus.2007.10.001.

Esposito, L. W., (2006), Planetary Rings, Cambridge University Press, Cambridge, U. K.

Esposito, L. W., J. E. Colwell, K. Larsen, W. E. McClintock, A. I. F. Stewart, J. Tew Hallett, D. E. Shemansky, J. M. Ajello, C. J. Hansen, A. R. Hendrix, R. A. West, H. U. Keller, A. Korth, W. R. Pryor, R. Reulke, Y. L. Yung, (2005), Ultra-Violet Imaging Spectroscopy shows an active Saturn system, Science, 307, 1251–1255, doi: 10.1126/science.1105606.

Esposito, L. W., C. A. Barth, J. E. Colwell, G. M. Lawrence, W. E. McClintock, A. I. F. Stewart, H. U. Keller, A. Korth, H. Lauche, M. C. Festou, A. L. Lane, C. J. Hansen, J. N. Maki, R. A. West, H. Jahn, R. Reulke, K. Warlich, D. E. Shemansky, Y. L. Yung, (2004), The Cassini Ultraviolet Imaging Spectrograph investigation, Space Science Reviews, 115, 294–361.

- - - - - - - - - - - - - -

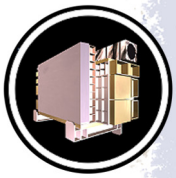

Esposito, L. W., (2003) Cassini imaging at Jupiter, Science, 299, 1529–1530, doi: 10.1126/science.1081517.

Esposito, L. W., J. E. Colwell, W. E. McClintock, (1998), Cassini UVIS observations of Saturn's rings, Planetary and Space Science, 46, 1221–1235.

Flasar, F. M., K. H. Baines, M. K. Bird, T. Tokano, R. A. West, (2009), Atmospheric dynamics and meteorology, Chapter 13, In Titan from Cassini Huygens, (eds.) R. Brown, J.-P. Lebreton, H. Waite, Springer Dordrecht, Netherlands, pp. 323–352, doi: 10.1007/978-1-4020-9215-2.

Fletcher, L. N., T. K. Greathouse, J. I. Moses, S. Guerlet, R. A. West, (2015), Saturn's seasonally changing atmosphere: thermal structure, composition and aerosols, arXiv preprint arXiv:1510.05690.

French, R. G., P. D. Nicholson, C. A. McGhee-French, K. Longergan, T. Sepersky, M. M. Hedman, E. A. Marouf, J. E. Colwell, (2016), Noncircular features in Saturn's rings III: The Cassini Division, Icarus, 274, 131–162, doi: 10.1016/j.icarus.2016.03.017.

French, R. G., P. D. Nicholson, M. M. Hedman, J. M. Hahn, C. A. McGhee-French, J. E. Colwell, E. A. Marouf, N. J. Rappaport, (2016), Deciphering the embedded wave in Saturn's Maxwell ringlet, Icarus, 279, 62–77, doi: 10.1016/j.icarus.2015.08.020.

Geissler, P., A. McEwen, C. Porco, D. Strobel, J. Saur, J. Ajello, R. West, (2004), Cassini observations of Io's visible aurorae, Icarus, vol. 172, Issue 1.

Gérard, J. C., Gustin, J., Pryor, W. R., Grodent, D., Bonfond, B., Radioti, A., Gladstone, R. G., Clarke, J. T., Nichols, J. D., (2013), Remote sensing of the energy of auroral electrons in Saturn's atmosphere: Hubble and Cassini spectral observations, Icarus, vol. 223, Issue 1, 211–221.

Gérard, J.-C., J. Gustin, B, Hubert, G. R. Gladstone, L. W. Esposito, (2011a), Measurements of the Helium 584-Å airglow during the Cassini flyby of Venus, Planetary and Space Science, vol. 59, Issue 13, pp. 1524–1528.

Gérard, J-C., B. Hubert, J. Gustin, V. I. Shematovich, D. Bisikalo, L. Esposito, A.I. Stewart, (2011b), EUV spectroscopy of the Venus dayglow with UVIS on Cassini, Icarus, 211, 1, 70–80.

Gérard, J-C, E. J. Bunce, D. Grodent, S. W. H. Cowley, J. T. Clarke, S. V. Badman, (2005), Signature of Saturn's auroral cusp: Simultaneous Hubble Space Telescope FUV observations and upstream solar wind monitoring, Journal of Geophysical Research: Space Physics, vol. 110, Issue A11.

Glass-Maujean, M., X. Liu, D. E. Shemansky, (2009), Analysis of electron-impact excitation and emission of the $np\sigma^1\Sigma^+_u$ and $np\pi^1\Pi_u$ Rydberg Series of H_2, The Astrophysical Journal Supplement Series, 180, no.1, 38–53.

Grava, C., W. R. Pryor, P. D. Feldman, K. D. Retherford, G. R. Gladstone, T. K. Greathouse, (2018), LRO/LAMP study of the interstellar medium via the HeI 58.4 nm resonance line, Astronomy & Astrophysics, 616, A159.

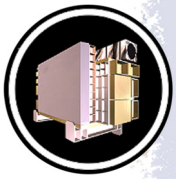

Grodent, D. A., (2015), Brief review of ultraviolet auroral emissions on giant planets, Space Science Review, vol. 187, Issue 1, 23–50, doi: 10.1007/s11214-014-0052-8.

Grodent, D., J. Gustin, J.-C. Gérard, A. Radioti, B. Bonfond, W. Pryor, (2011), Small-scale structures in Saturn's ultraviolet aurora, Journal of Geophysical Research, vol. 116, A09225, doi: 10.1029/2011JA016818.

Guimaraes, A. H. F., N. Albers, F. Spahn, M. Seiss, E. Vieira-Neto, N. V. Brilliantov, (2012), Aggregates in the strength and gravity regime: Particle sizes in Saturn’s rings, Icarus, 220, 2, 660–678, doi: 10.1016/j.icarus.2012.06.005.

Gurnett, D. and W. Pryor, (2012), Auroral processes associated with Saturn's moon Enceladus, In Relationship Between Auroral Phenomenology and Magnetospheric Processes, (eds.), A. Keiling, E. Donovan, F. Bagenal, T. Karlsson, Geophysical Monograph Series, American Geophysical Union (AGU), Washington, DC, pp. 305–313, doi: 10.1029/2011BK001174.

Gurnett, D. A., W. S. Kurth, G. B. Hospodarsky, A. M. Persoon, P. Zarka, A. Lecacheux, S. J. Bolton, M. D. Desch, W. M. Farrell, M. L. Kaiser, H. P. Ladreiter, H. O. Rucker, P. Galopeau, P. Louarn, D. T. Young, W. R. Pryor, M. K. Dougherty, (2002), Control of Jupiter's radio emission and aurorae by the solar wind, Nature, 415, Issue 6875, 985–987.

Gustin, J., D. Grodent, A. Radioti, W. Pryor, L. Lamy, J. Ajello, (2017), Statistical study of Saturn’s auroral electron properties with Cassini/UVIS FUV spectral images, Icarus, 284, 264–283, doi: 10.1016/j.icarus.2016.11.017.

Gustin, J., J. C. Gérard, D. Grodent, G. R. Gladstone, J. T. Clarke, W. R. Pryor, V. Dols, J. M. Ajello, (2013), Effects of methane on giant planet's UV emissions and implications for the auroral characteristics, Journal of Molecular Spectroscopy, 291, 108–117, doi: 10.1016/j.jms.2013.03.010.

Gustin, J., B. Bonfond, D. Grodent, J.-C. Gérard, (2012), Conversion from HST ACS and STIS auroral counts into brightness, precipitated power, and radiated power for H_2 giant planets, Journal of Geophysical Research, 117, A07316, doi: 10.1029/2012JA017607.

Gustin, J., I. Stewart, J.-C. Gérard, L. W. Esposito, (2010), Characteristics of Saturn’s FUV airglow from limb viewing spectra obtained with Cassini-UVIS, Icarus, 210, 270–283.

Gustin, J., J.-C. Grerard, W. Pryor, P. D. Feldman, D. Grodent and G.Holsclaw, (2009), Characteristics of Saturn's polar atmosphere and auroral electrons derived from HST/ STIS, FUSE and Cassini/UVIS spectra, Icarus, 200, Issue 1, 176–187.

Hall, D. T., (1992), Ultraviolet resonance radiation and the structure of the heliosphere, Ph.D. dissertation, University of Michigan.

Hallett, J. T., D. E. Shemansky, X. Liu, (2005a), Fine-structure physical chemistry modeling of Uranus H_2 X quadrupole emission, Geophysical Research Letters, 32, L02204.

Hallett, J. T., D. E. Shemansky, X. Liu., (2005b), A rotational-level hydrogen physical chemistry model for general astrophysical application, The Astrophysical Journal, 624, 448–461.

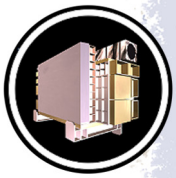

Hansen, C. J., L. W. Esposito, A. R. Hendrix, (2018), Use of ultraviolet observations to find and characterize water vapor plumes at Enceladus and Europa, Geophysical Research Letters, submitted.

Hansen, C. J., L. W. Esposito, K.-M. Aye, J. E. Colwell, A. R. Hendrix, G. Portyankina, D. Shemansky, (2017), Investigation of diurnal variability of water vapor in Enceladus' plume by the Cassini ultraviolet imaging spectrograph, Geophysical Research Letters, 44, 2, 672–677, doi: 10.1002/2016GL071853.

Hansen, C. J., D. E. Shemansky, L. W. Esposito, A. I. F. Stewart, B. R. Lewis, J. E. Colwell, A. R. Hendrix, R. A. West, (2011), The composition and structure of the Enceladus plume, Geophysical Research Letters, 38, L11202, doi: 10.1029/2011GL047415.

Hansen, C. J., H. Waite, S. Bolton, (2009), Titan in the Cassini-Huygens Extended Mission, Chapter 17, In Titan from Cassini Huygens, (eds.) R. H. Brown, J.-P. Lebreton, H. Waite, Springer Dordrecht, Netherlands, pp. 455–478, doi: 10.1007/978-1-4020-9215-2.

Hansen, C. J., L. W. Esposito, A. I. F. Stewart, B. Meinke, B. Wallis, J. Colwell, A. R. Hendrix, K. Larsen, W. Pryor, W. F. Tian, (2008), Water vapor jets in Enceladus, Nature, 456, 477–479.

Hansen, C. J., L. W. Esposito, A. I. F. Stewart, J. Colwell, A. R. Hendrix, W. Pryor, D. E. Shemansky, R. A. West, (2006), Enceladus' water vapor plume, Science, 311, no. 5766, 1422–1425.

Hansen, C. J., D. E. Shemansky, A. R. Hendrix, (2005), Cassini UVIS observations of Europa's oxygen atmosphere and torus, Icarus, 176, Issue 2, 305–315.

Hansen, C. J., S. J. Bolton, D. L Matson, L. J. Spilker, J. P. Lebreton, (2004), The Cassini-Huygens flyby of Jupiter, Icarus, vol. 172, Issue 1.

Heays, A. N., J. M. Ajello, A. Aguilar, B. R. Lewis, S. T. Gibson, (2014), The high resolution extreme-ultraviolet spectrum of N_2 by electron impact, The Astrophysical Journal Supplement Series, vol. 211, Issue 2.

Hedelt, P., Y. Ito, H. U. Keller, R. Reulke, P. Wurz, H. Lammer, H. Rauer, L. Esposito, (2010), Titan's atomic hydrogen corona, Icarus, vol. 210, Issue 1, p. 424–435.

Hedman, M. M., D. Dhingra, P. D. Nicholson, C. J. Hansen, G. Portyankina, S. Ye, Y. Dong, (2018), Spatial variations in the dust-to-gas ratio of Enceladus' plume, Icarus, 305, 123–138.

Hendrix, A. R., B. J. Buratti, D. P. Cruikshank, R. N. Clark, F. Scipioni, C. J. A. Howett, (2018a), Surface composition of Saturn's icy moons, Part 3: Saturn's Icy Moons, In Enceladus and the Icy Moons of Saturn, (eds.) P. M. Schenk, R. N. Clark, C. J. A. Howett, A. J. Verbiscer, J. H. Waite, The University of Arizona Press, Tucson, AZ, pp. 307–322.

Hendrix, A. R., G. Filacchione, C. Paranicas, P. Schenk, F. Scipioni, (2018b), Icy Saturnian Satellites: Disk-integrated UV-IR characteristics and links to exogenic processes, Icarus, 300, 103–114, doi: 10.1016/j.icarus.2017.08.037.

Hendrix, A. R. and Y. L. Yung, (2017), Energy options for future humans on Titan, Journal of Astrobiology & Outreach, vol. 5, Issue 2, doi: 10.4172/2332-2519.1000157.

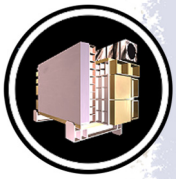

Hendrix, A. R., T. A. Cassidy, B. J. Buratti, C. Paranicas, C. J. Hansen, B. D. Teolis, E. Roussos, P. Kollmann, T. Bradley, R. Johnson, (2012), Mimas' far-UV albedo: Spatial variations, Icarus, 220, 922–931.

Hendrix, A. R., Hansen, C. J., Holsclaw, G. M., (2010a), The ultraviolet reflectance of Enceladus: Implications for surface composition, Icarus, 206, 608–617.

Hendrix, A. R. and C. J. Hansen, (2010b), The surface composition of Enceladus: Clues from the ultraviolet, Proceedings of the International Astronomical Union, vol. 5, no. S263, pp. 126–130, doi: 10.1017/S1743921310001626.

Hendrix, A. R. and C. J. Hansen, (2008a), The albedo dichotomy of Iapetus measured at UV wavelengths, Icarus, 193, 344–351, doi: 10.1016/j.icarus.2007.07.025.

Hendrix, A. R. and C. J. Hansen, (2008b), Ultraviolet observations of Phoebe from Cassini UVIS, Icarus, 193, 323–333, doi: 10.1016/j.icarus.2007.06.030.

Hendrix, A., (2005), The Icy Saturnian Satellites as seen by Cassini UVIS, In American Geophysical Union (AGU) Fall Meeting Abstracts.

Hord, C. W., W. E. McClintock, A. I. F. Stewart, C. A. Barth, L. W. Esposito, G. E. Thomas, B. R. Sandel, et al., (1992), Galileo ultraviolet spectrometer experiment, Space Science Review, 60. 1–4, 503–530.

Howard, J. E. and J. D. Meiss, (2009), Straight-line orbits in Hamiltonian flows, Celestial Mechanics and Dynamical Astronomy, 105, Issue 4, 337–352.

Howard, J. E., (2007), Recent progress on planetary dust grain dynamics, AIP Conference Proceedings, 946, 1, 215–223, doi: 10.1063/1.2806057.

Hubert, B., J.-C. Gérard, J. Gustin, D. V. Bisikalo, V. I. Shematovich, R. G. Gladstone, (2012), Cassini-UVIS observation of dayglow FUV emissions of carbon in the thermosphere of Venus, Icarus, 220, 2, 635–646, doi: 10.1016/j.icarus.2012.06.002.

Hubert, B., J. C. Gérard, J. Gustin, V. I. Shematovich, D. V. Bisikalo, A. I. Stewart, G. R. Gladstone, (2010), Cassini-UVIS observations of the FUV OI and CO Venus dayglow, Icarus, 207, 549–557.

Jackman, C. M., N. Achilleos, S. W. H. Cowley, E. J. Bunce, A. Radioti, D. Grodent, S. V. Badman, M. K. Dougherty, W. Pryor, (2013), Auroral counterpart of magnetic field dipolarizations in Saturn's tail, Planetary and Space Science, vol. 82–83, pp. 34–42.

Jasinski, J. M., C. S. Arridge, L. Lamy, J. S. Leisner, M. F. Thomsen, D. G. Mitchell, A. J. Coates, A. Radioti, G. H. Jones, E. Roussos, N. Krupp, D. Grodent, M. K. Dougherty, J. H. Waite, (2014), Cusp observation at Saturn's high-latitude magnetosphere by the Cassini spacecraft, Geophysical Research Letters, 41, 5, 1382–1388, doi: 10.1002/2014GL059319/abstract.

Jaumann R., R. L. Kirk, R. D. Lorenz, R. M.C. Lopes, E. Stofan, E. P. Turtle, H. U. Keller, C. A. Wood, C. Sotin, L. A. Soderblom, M. G. Tomasko, (2009a), Geology and surface processes on Titan, Chapter 5, In Titan from Cassini Huygens, (eds.) R. H. Brown, J.-P. Lebreton, H. Waite, Springer Dordrecht, Netherlands, pp. 75–140, doi: 10.1007/978-1-4020-9215-2.

- - - - - - - - - - - - - -

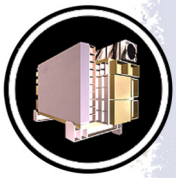

Jaumann, R., R. Clark, Fr. Nimmo , A. Hendrix, B. Buratti, T. Denk, J. Moore, P. Schenk, S. Ostro, R. Srama, (2009b), Icy Satellites: Geological evolution and surface processes, Chapter 20, In Saturn from Cassini-Huygens, (eds.) M. Dougherty, L. Esposito, S. Krimigis, Springer Dordrecht, Netherlands, pp. 637–681, doi: 10.1007/978-1-4020-9217-6.

Jerousek, R. G., J. E. Colwell, P. D. Nicholson, M. M. Hedman, L. W. Esposito, (2016), The smallest particles in Saturn's rings from self-gravity wake observations, Icarus, 279, 36–50.

Jerousek, R. G., J. E. Colwell, L. W. Esposito, (2011), Morphology and Variability of The Titan Ringlet and Huygens Ringlet Edges. Icarus. Volume 216, Issue 1, pp. 280–291.

Jones, G. H., E. Roussos, N. Krupp, U. Beckmann, A. J. Coates, F. Crary, I. Dandouras, V. Kikarev, M. K. Dougerty, P. Garnier, C. J. Hansen, A. R. Hendrix, G. B. Hospodarsky, R. E. Johnson, S. Kempf, K. K. Khurana, S. M. Krimigis, H. Krueger, W. S. Kurth, A. Lagg, H. J. McAndrews, D. G. Mitchell, C. Paranicas, F. Postberg, C. T. Russell, J. Saur, M. Seiss, F. Spahn, R. Srama, D. F. Strobel, R. Tokar, J.-E. Wahlund, R. J. Wilson, J. Woch, D. Young, (2008), The dust halo of Saturn's largest icy moon, Rhea, Science, 319. no. 5868, pp. 1380–1384, doi: 10.1126/science.1151524.

Kammer, J. A., D. E. Shemansky, S. Fan, P. Gao, Y. L. Yung, (2018), Morphology and properties of Titan's atmospheric aerosols, Icarus.

Kammer, J. A., D. E. Shemansky, S. Fan, P. Gao, Y. L. Yung, (2016), Morphology and properties of Titan's atmospheric aerosols, Icarus, submitted January 5, 2016.

Kammer, J. A., D. E. Shemansky, X. Zhang, Y. L. Yung, (2013), Composition of Titan's upper atmosphere from Cassini UVIS EUV stellar occultations, Planetary and Space Science, vol. 88, pp. 86–92, doi: 10.1016/j.pss.2013.08.003.

Kinrade, J., S. V. Badman, E. J. Bunce, C. Tao, G. Provan, S. W. H. Cowley, A. Grocott, et al., (2017), An isolated, bright cusp aurora at Saturn, Journal of Geophysical Research: Space Physics, vol. 122, Issue 6, pp. 6121–6138, doi: 10.1002/2016JA023792.

Koskinen, T. T. and S. Guerlet, (2018), Atmospheric structure and helium abundance on Saturn from Cassini/UVIS and CIRS observations, Icarus, 307, 161–171.

Koskinen, T. T., J. I Moses, R. A. West, S. Guerlet, A. Jouchoux, (2016), The detection of benzene in Saturn's upper atmosphere, Geophysical Research Letters, 43, 7895–7901, doi: 10.1002/2016GL070000/abstract.

Koskinen, T. T., B. R. Sandel, R. V. Yelle, D. F. Strobel, I. C. F. Müller-Wodarg, J. T. Erwin, (2015), Saturn's variable thermosphere from Cassini/UVIS occultations, Icarus, 260, 174–189.

Kurth, W., G. B. Hospodarsky, D. A. Gurnett, L. Lamy, M. K. Dougherty, J. Nichols, E. J. Bunce, W. Pryor, K. Baines, T. Stallard, H. Melin, F. J. Crary, (2016), Saturn kilometric radiation intensities during the Saturn auroral campaign of 2013, Icarus, 263, 2–9.

Kurth, W. S., E. J. Bunce, J. T. Clarke, F. J. Crary, D. C. Grodent, A. P. Ingersoll, U. A. Dyudina, L. Lamy, D. G.Mitchell, A. M. Persoon, W. R. Pryor, J. Saur, T. Stallard, (2009), Auroral

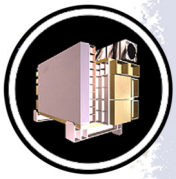

processes, Chapter 12, In Saturn from Cassini-Huygens, (eds.) M. Dougherty, L. Esposito, S. Krimigis, Springer Dordrecht, Netherlands, pp. 333–374, doi: 10.1007/978-1-4020-9217-6.

Kurth, W. S., D. A. Gurnett, J. T. Clarke, P. Zarka, M. D. Desch, M. L. Kaiser, B. Cecconi, A. Lecacheux, W. M. Farrell, P. Galopeau, J. C. Gérard, D. Grodent, R. Prange, M. K. Dougherty, F. J. Crary, (2005), An Earth-like correspondence between Saturn's auroral features and radio emission, Nature, vol. 433, Issue 7027.

Lamy, L., R. Prangé, W. Pryor, Jacques Gustin, S. V. Badman, H. Melin, T. Stallard, D. G. Mitchell, P. C. Brandt, (2013), Multispectral simulations diagnosis of Saturn’s aurorae throughout a planetary rotation, Journal of Geophysical Research: Space Physics, vol. 118, Issue 8, pp. 4817–4843, doi: 10.1002/jgra.50404.

Lavvas, P., R. V. Yelle, A. N. Heays, L. Campbell, M. J. Brunger, M. Galand, V. Vuitton, (2015), N_2 state population in Titan’s atmosphere, Icarus, 260, p.29–59.

Lavvas, P., R. A. West, G. Gronoff, (2014), Titan’s emission processes during eclipse, Icarus, 241, 397–408.

Lewis, M. C. and G. R. Stewart, (2005), Expectations for Cassini observations of ring material with nearby moons, Icarus, vol. 178, Issue 1.

Li, C., X. Zhang, P. Gao, Y. L. Yung, (2015), Vertical distribution of C_3-Hydrocarbons in the stratosphere of Titan, The Astrophysical Journal, 803, L19, doi: 10.1088/2041-8205/803/2/L19.

Li, C., X. Zhang, J. A. Kammer, M.-C. Liang, R-L. Shia, Y.L. Yung, (2014), A non-monotonic eddy diffusivity profile of Titan's atmosphere revealed by Cassini observations, Planetary and Space Science, 104, 8–58, doi: 10.1016/j.pss.2013.10.009.

Liang, M-C, Y. Yung, D. E. Shemansky, (2007a), Photolytically generated aerosols in the mesosphere and thermosphere of Titan, The Astrophysical Journal Letters, 661, L199-L202.

Liang, M-C., A. N. Heays, B. R. Lewis, S. T. Gibson, Y. L. Yung, (2007b), Source of nitrogen isotope anomaly in HCN in the atmosphere of Titan, The Astrophysical Journal Letters, 664, L115-L118.

Liang, M. C., R. L. Shia, A. Y. T. Lee, M. Allen, A. J. Friedson, Y. L. Yung, (2005), Meridional transport in the stratosphere of Jupiter, The Astrophysical Journal, vol. 635, Issue 2.

Liu, X., D. E. Shemansky, J. Yoshii, M. J. Liu, P. V. Johnson, C. P. Malone, (2017a), Energies, transition probabilities, predissociation rates, and lifetimes of the H_2, HD, and D_2 $c^3\prod_{\bar{u}}$ state, Journal of Physics B: Atomic, Molecular and Optical Physics, 50, 035101, doi: 10.1088/1361-6455/50/3/035101.

Liu, X., D. E. Shemansky, J. Yoshii, M. J. Liu, P. V. Johnson, C. P. Malone, M. A. Khakoo, (2017b), $H_2 \times {}^1\Sigma^+_g - c\ {}^3\prod_u$ excitation by electron impact: Energies, spectra, emission yields, cross sections, and H(1s) kinetic energy distributions, The Astrophysical Journal Supplement Series, vol. 232, no. 2, doi: 10.3847/1538-4365/aa89f0.

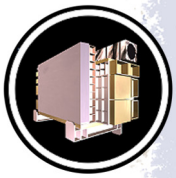

Liu, X., D. E. Shemansky, J. Yoshii, P. V. Johnson, C. P. Malone, J. M. Ajello, (2016), Spectra, emission yields, cross sections, and kinetic energy distributions of hydrogen atoms from H_2 X $^1\Sigma^+_g$ − d $^3\prod_u$ excitation by electron impact, The Astrophysical Journal, 818, 2, 120.

Liu, X., D. E. Shemansky, P. V. Johnson, C. P. Malone, M. A. Khakoo, I. Kanik, (2012a), Electron and photon dissociation cross sections of H_2 singlet-ungerade continua, Journal of Physics B: Atomic, Molecular and Optical Physics 45, no. 1, 015201.

Liu, X., D. E. Shemansky, P. V. Johnson, C. P. Malone, M. A. Khakoo, (2012b), Electron and photon dissociation cross sections of D_2 singlet-ungerade continua, Journal of Physics B: Atomic, Molecular and Optical Physics 45, no. 10, 105203.

Liu, X. and D. E. Shemansky, (2012) Nondissociative electron and photon ionization cross sections of molecular hydrogen and deuterium, Journal of Physics B: Atomic, Molecular and Optical Physics, 45, 095203, doi: 10.1088/0953-4075/45/9/095203.

Liu, X., D. E. Shemansky, P. V. Johnson, C. P. Malone, H. Melin, J. A. Young, I. Kanik, (2010a), The Saturn hot atomic hydrogen plume: Quantum mechanical investigation of H_2 dissociation mechanisms, Chapter 30, In Advances in Geosciences, Volume 19, Planetary Science, (eds.) A. Bhardwaj, World Scientific, pp. 405–426, doi: 10.1142/9789812838162_0030.

Liu, X., P. V. Johnson, C. P. Malone, J. A. Young, I. Kanik, D. E. Shemansky, (2010b), Kinetic energy distribution of H(1s) from the H_2 X $^1\Sigma^+_g$ - a $^3\Sigma^+_g$ excitation and lifetimes and transition probabilities of $a^3\Sigma^+_g(v,J)$, The Astrophysical Journal, 716, 701–711.

Liu, X., A. Heays, D. E. Shemansky, B. R. Lewis, P. D. Feldman, (2009a), Analysis of terrestrial-thermospheric N2 c4′ 1Σ+u (0) ~ b′ 1Σ+u (1)− X1Σ+g dayglow emission observed by the Far Ultraviolet Spectroscopic Explorer, Journal of Geophysical Research, 114, D07304.

Liu, X., P. V. Johnson, C. P. Malone, J. A. Young, D. E. Shemansky, I. Kanik, (2009b), Electron-impact excitation and emission cross sections of the H_2 $B'\,^1\Sigma^+_u$ and D $^1\prod_u$ states and rotational dependence of photodissociation cross sections of the $B'\,^1\Sigma^+_u$ and D $^1\prod_u$ continua, Journal of Physics B: Atomic, Molecular and Optical Physics, 42, 185203.

Liu, X., D. E. Shemansky, C. P. Malone, P. V. Johnson, J. M. Ajello, I. Kanik, A. N. Heays, B. R. Lewis, S. T. Gibson, G. Stark, (2008), Experimental and coupled-channels investigation of the radiative properties of the N_2 $c^1{}_4{}^1\Sigma_u^+ - X^1\Sigma_g^+$ band system, Journal of Geophysical Research, 113, A02304, doi: 10.1029/2007JA012787.

Liu, X., D. E. Shemansky, J. T. Hallett, H. A. Weaver, (2007), Extreme Non-LTE H_2 in comets C/2000 WM1 (LINEAR) and C/2001 A2 (LINEAR), The Astrophysical Journal Supplement Series, 169, 458–471.

Liu, X. and D. E. Shemansky, (2006a), A simple model for N2 line oscillator strengths of the b′ 1Σu+ (1), c4′ 1Σ u+ (0), b 1Πu+ (4), b 1Πu+ (5), and c3 1Πu+ (0)–X 1Σg+ (0) bands, The Astrophysical Journal, 645, 1560–1567.

Liu, X. and D. E. Shemansky, (2006b), Analysis of electron impact ionization properties of methane, Journal of Geophysical Research, 111, A04303, doi: 10.1029/2005JA011454.

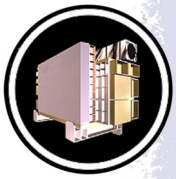

Liu, X., D. E. Shemansky. M. Ciocca, I. Kanik, J. Ajello, (2005), Analysis of the physical properties of the N2 c' 1Σ+u(0)-X 1Σ+g(0) transition, The Astrophysical Journal Letters, vol. 623, Issue 1, pp. 579–584, doi: 10.1086/428641.

Liu, X. and D. E. Shemansky, (2004), Ionization of Molecular Hydrogen, The Astrophysical Journal, 614, 1132–1142.

Lunine, J. I., Y. L. Yung, R. D. Lorenz, (1999), On the volatile inventory of Titan from isotopic abundances in nitrogen and methane, Planetary and Space Science, vol. 47, Issue 10–11.

Madhusudhanan, P., L. W. Esposito, P. J. Torres, (2018), A combined dynamical transport model for producing haloes at resonances in Saturn's rings, Icarus, (submitted 2015), resubmitted 2018.

Mangina, R., S., J. M. Ajello, R. A. West, D Dziczek, (2011), High-resolution electron-impact emission spectra and vibrational emission cross sections from 330–1100 nm for N_2, The Astrophysical Journal Supplement Series, 196, 13.

Mauk, B. H., J. Cuzzi, D. Hamilton, T. Hill, G. Hospodarsky, R. Johnson, C. Paranicas, E. Roussos, C. Russell, D. Shemansky, E. Sittler, R. Thorne, (2009), Fundamental plasma processes in Saturn's magnetosphere, Chapter 11, In Saturn from Cassini-Huygens, (eds.) M. Dougherty, L. Esposito, S. Krimigis, Springer Dordrecht, Netherlands, pp. 281–331, doi: 10.1007/978-1-4020-9217-6.

McClintock, W. E., N. M. Schneider, G. M. Holsclaw, J. T. Clarke, A. C. Hoskins, I. Stewart, F. Montmessin, R. V. Yelle, J. Deighan, (2015), The imaging ultraviolet spectrograph (IUVS) for the MAVEN mission, Space Science Reviews, 195, no. 1–4, 75–124.

McClintock, W. E. and M. R. Lankton, (2007), The Mercury atmospheric and surface composition spectrometer for the MESSENGER mission, Space Science Reviews, 131, no. 1–4, 481–521.

McGrath, M., C. J. Hansen, A. R. Hendrix, (2009), Observations of Europa's tenuous atmosphere, Chapter in Europa, (eds.) R. Pappalardo, W. McKinnon, K. Khurana, University of Arizona Press Space Science Series.

Meinke, B. K., L. W Esposito, N. Albers, M. Sremcevic, C. Murray, (2012), Classification of F ring features observed in Cassini UVIS occultations, Icarus, 218, 1, pp. 545–554, doi: 10.1016/j.icarus.2011.12.020.

Melin, H., S. V. Badman, T. S. Stallard, S. W. H. Cowley, U. Dyudina, J. D. Nichols, G. Provan, J. O'Donoghue, W. R. Pryor, K. H. Baines, S. Miller, J. Gustin, A. Radioti, C. Tao, C.J. Meredith, J. S. D. Blake, R. E. Johnson, (2016), Simultaneous multi-scale and multi-instrument observations of Saturn's aurorae during the 2013 observing campaign, Icarus, 263, 56–74.

Melin, H. and T. S. Stallard, (2016), Jupiter's hydrogen bulge: A Cassini perspective, Icarus, 278, 238–247.

Melin, H., T. Stallard, S. Miller, J. Gustin, M. Galand, S. V. Badman, W. Pryor, J. O'Donoghue, R. H. Brown, K. H. Baines, (2011), Simultaneous Cassini VIMS and UVIS observations of

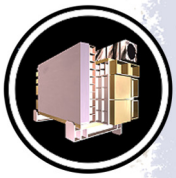

Saturn's southern aurora—comparing emissions from H, H_2, and H_3^+ at a high spatial resolution, Geophysical Research Letters, 38, L15203, doi: 10.1029/2011GL048457.

Melin, H., Shemansky, D. E., Liu, X., (2009), The distribution of atomic hydrogen and oxygen in the magnetosphere of Saturn, Planetary and Space Science, 57, no. 14–15, 1743–1753.

Mitchell, C. J., J. E. Colwell, M. Horanyi, (2005), Tenuous ring formation by the capture of interplanetary dust at Saturn, Journal of Geophysical Research: Space Physics, vol. 110, Issue A9.

Mitchell, D. G., J. F. Carbary, E. J. Bunce, A. Radioti, S. V. Badman, W. R. Pryor, G. B. Hospodarsky, W. S. Kurth, (2016), Recurrent pulsations in Saturn's high latitude magnetosphere, Icarus, 263, 94–100.

Mitchell, D. G., P. C. Brandt, J. F. Carbary, W. S. Kurth, S. M. Krimigis, C. Paranicas, N. Krupp, D. C. Hamilton, B. H. Mauk, G. B. Hospadarsky, M. K. Dougherty, W. R. Pryor, (2015), Injection, Interchange, and Reconnection: Energetic Particle Observations in Saturn's Magnetosphere, Chapter 19, In Magnetotails in the Solar System, (eds.) A. Keiling, C. M. Jackman, P. A. Delamere, John Wiley & Sons, Inc., p.327–343, doi: 10.1002/9781118842324.

Mitchell, D. G., S. M. Krimigisa, C. Paranicas, P. C. Brandt, J. F. Carbary, E. C. Roelof, W. S. Kurth, D. A. Gurnett, J. T. Clarke, J. D. Nichols, J.-C. Gérard, D. C. Grodent, M. K. Dougherty, W. R. Pryor, (2009), Recurrent energization of plasma in the midnight-to-dawn quadrant of Saturn's magnetosphere, and its relationship to auroral UV and radio emissions, Planetary and Space Science, 57, 1732–1742.

Mitchell, D. G., P. C. Brandt E. C. Roelof, J. Dandouras, S. M. Krimigis, B. H. Mauk, C. P. Paranicas, N. Krupp, D. C. Hamilton, W. S. Kurth, P. Zarka, M. K. Dougherty, E. J. Bunce, D. E. Shemansky, (2005), Energetic ion acceleration in Saturn's magnetotail: Substorms at Saturn?, Geophysical Research Letters, vol. 32, Issue 20, L20S01, doi: 10.1029/2005GL022647.

Mitchell, T. R. and G. R. Stewart, (2010), Evolution of the solar nebula and planet growth under the influence of photoevaporation, The Astrophysical Journal, 722, 1115–1130.

Moebius, E., M. Bzowski, H.-J. Fahr, P. Frisch, P. Gangopadhyay, G. Gloeckler, V. Izmodenov, R. Lallement, H.-R. Müller, W. Pryor, J. Raymond, J. Richardson, K. Scherer, J. Slavin, M. Witte., (2005), Consolidation of the Physical Interstellar Medium Parameters and Neutral Gas Filtration – Coordinated Effort at ISSI, Proceedings of Solar Wind 11/SOHO 16, Connecting Sun and Heliosphere Conference, ESA SP-592.

Munoz, G. A., T. T. Koskinen, P. Lavvas, (2018), Upper atmospheres and ionospheres of Planets and Satellites, Chapter 17, In Handbook of Exoplanets, (eds.) H. J. Deeg, J. A. Belmonte, Springer International Publishing AG, Cham, Switzerland, pp. 349–374, doi: 10.1007/978-3-319-55333-7_52.

Nagy, A. F., A. J. Kliore, M. Mendillo, S. Miller, L. Moore, J. I. Moses, I. Muller-Wodarg, D. Shemansky, (2009), Upper atmosphere and ionosphere of Saturn, Chapter 8, In Saturn

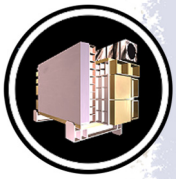

from Cassini-Huygens, (eds.) M. Dougherty, L. Esposito, S. Krimigis, Springer Dordrecht, Netherlands, pp. 181–201, doi: 10.1007/978-1-4020-9217-6.

Nichols, J. D., S. V.Badman, K. H. Baines, R. H. Brown, E. J. Bunce, J. T. Clarke, S. W. H. Cowley, F. J. Crary, M. K. Dougherty, J.-C. Gérard, A. Grocott, D. Grodent, W. S. Kurth, H. Melin, D. G. Mitchell, W. R. Pryor, T. S. Stallard, (2014), Dynamic auroral storms on Saturn as observed by the Hubble Space Telescope, Geophysical Research Letters, vol. 41, Issue 10, pp. 3323–3330, doi: 10.1002/2014GL060186.

Nichols, J. D., S. V. Badman, E. J. Bunce, J. T. Clarke, S. W. H. Cowley, F. J. Crary, M. K. Dougherty, et al., (2009), Saturn's equinoctial auroras, Geophysical Research Letters, 36, L24102, doi: 10.1029/2009GL041491/full.

Nichols, J. D., E. J. Bunce, J. T. Clarke, S. W. H. Cowley, J.-C. Gérard, D. Grodent, W. R. Pryor, (2007), Response of Jupiter's UV auroras to interplanetary conditions as observed by the Hubble Space Telescope during the Cassini fly-by campaign, Journal of Geophysical Research, 112, A02203, doi: 10.1029/2006JA012005.

Nicholson, P. and L. W. Esposito, (2016), Introduction: Special issue on planetary rings, Icarus, vol. 279, doi: 10.1016/j.icarus.2016.08.002.

Nicholson, P. D., R. G. French, M. M. Hedman, E. A. Marouf, J. E. Colwell, (2014a), Noncircular features in Saturn’s rings I: The edge of the B ring, Icarus, 227, 152–175.

Nicholson, P. D., R. G. French, C. A. McGhee-French, K. Lonergan, T. Sepersky, M. M. Hedman, E. A. Marouf, J. E. Colwell, (2014b), Noncircular features in Saturn’s rings II: The C ring, Icarus, 241, 373–396.

Palmaerts, B., A. Radioti, E. Roussos, D. Grodent, J.-C. Gérard, N. Krupp, D. G. Mitchell, (2016) Pulsations of the polar cusp aurora at Saturn, Journal of Geophysical Research, 121, 11952–11963.

Parkinson, C. D., Y. L. Yung, L. W. Esposito, P. Gao, S. W. Bougher, M. Hirtzig, (2014), Photochemical control of the distribution of venusian water, Planetary and Space Science, vols. 113–114, pp. 226–236, doi: 10.1016/j.pss.2015.02.015.

Parkinson, C. D., M-C. Liang, Y. L. Yung, J. L. Kirschivnk, (2008), Habitability of Enceladus: Planetary conditions for life, Origins of Life and Evolution of Biospheres, vol. 38, Issue 4, pp. 355–369, doi: 10.1007/s11084-008-9135-4.

Parkinson, C. D., M-C. Liang, H. Hartman, C. J. Hansen, G. Tinetti, V. Meadows, J. L. Kirschvink, Y. L. Yung, (2007) Enceladus: Cassini observations and implications for the search for life, Astronomy & Astrophysics, 463, no. 1, 353–357, doi: 10.1051/0004-6361:20065773.

Parkinson, C. D., A. I. F. Stewart, A. S. Wong, Y. L. Yung, J. M. Ajello, (2006), Enhanced transport in the polar mesosphere of Jupiter: evidence from Cassini UVIS helium 584 angstrom airglow, Journal of Geophysical Research: Planets, vol. 111, Issue E2, doi: 10.1029/2005JE002539.

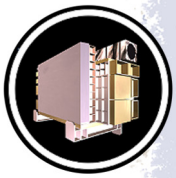

Pilorz, S., N. Altobelli, J. E. Colwell, M. Showalter, (2014) Thermal transport in Saturn's B ring inferred from Cassini CIRS, Icarus, 254, 157–177, doi: 10.1016/j.icarus.2015.01.002.

Pryor W. R., A. M. Rymer, D. G. Mitchell, T. W. Hill, D. T. Young, J. Saur, G. H. Jones, S. Jacobsen, S. W. H. Cowley, B. H. Mauk, A. J. Coates, J. Gustin, D. Grodent, J.-C. Gérard, L. Lamy, J. D. Nichols, S. M. Krimigis, L. W. Esposito, M. K. Dougherty, A., Jouchoux, A.I.F. Stewart, W. E. McClintock, G. M. Holsclaw, J. M. Ajello, J. E. Colwell, A. R. Hendrix, F. J. Crary, J. T. Clarke, X. Zhou, (2011), Discovery of the Enceladus auroral footprint at Saturn, Nature, 472, 331–333, doi: 10.1038/nature09928.

Pryor, W., P. Gangopadhyay, B. Sandel, T. Forrester, E. Quemerais, E. Moebius, L. Esposito, I. Stewart, B. McClintock, A. Jouchoux, J. Colwell, V. Izmodenov, Y. Malama, K. Tobiska, D. Shemansky, J. Ajello, C.Hansen, M. Bzowski, (2008), Radiation transport of heliospheric Lyman-alpha from combined Cassini and Voyager data sets, Astronomy & Astrophysics, 491, 21–28.

Pryor, W. R., A. I. F. Stewart, L. W. Esposito, W. E. McClintock, J. E. Colwell, A. J. Jouchoux, A. J. Steffl, D. E. Shemansky, J. M. Ajello, R. A. West, C. J. Hansen, B. T. Tsurutani, W. S. Kurth, G. B. Hospodarsky, D. A. Gurnett, K. C. Hansen, J. H. Waite, Jr., F. J. Crary, D. T. Young, N. Krupp, J. T. Clarke, D. Grodent, M. K. Dougherty, (2005), Cassini UVIS observations of Jupiter's auroral variability, Icarus, 178, Issue 2, 312–326, doi: 10.1016/j.icarus.2005.05.021.

Quemerais, E., B. R. Sandel, G. de Toma, (1996), 26-day modulation of the sky background Ly alpha brightness: Estimating the interplanetary hydrogen density, The Astrophysical Journal, 463, 349–358.

Radioti, A., D. Grodent, Z. H. Yao, J-C. Gérard, S. V. Badman, W. Pryor, B. Bonfond, (2017a), Dawn auroral breakup at Saturn initiated by auroral arcs: UVIS/Cassini beginning of Grand Finale phase, Journal of Geophysical Research: Space Physics, vol. 122, Issue 12, pp. 12111–12119, doi: 10.1002/2017JA024653.

Radioti, A., D. Grodent, J.-C. Gérard, D. J. Southwood, E. Chané, B. Bonfond, W. Pryor, (2017b), Stagnation of Saturn's auroral emission at noon, Journal of Geophysical Research: Space Physics, 122, 6078–6087, doi: 10.1002/2016JA023820.

Radioti, A., (2017), Saturn's auroral arc, Nature Astronomy, 1, 576, doi: 10.1038/s41550-017-0247-5.

Radioti, A., D. Grodent, J.-C. Grard, E. Roussos, D. Mitchell, B. Bonfond, W. Pryor, (2016a), Auroral spirals at Saturn, Journal of Geophysical Research: Space Physics, 120, 8633–8643, doi: 10.1002/2015JA021442/full.

Radioti, A., D. Grodent, X. Jia, J.-C. Gérard, B. Bonfond, W. Pryor, J. Gustin, D. G. Mitchell, C. M. Jackman, (2016b), A multi-scale magnetotail reconnection event at Saturn and associated flows: Cassini/UVIS observations, Icarus special issue, 263, 75–82.

Radioti, A., D. Grodent, J.-C. Gérard, S. E. Milan, R. C. Fear, C. M. Jackman B. Bonfond, W. Pryor, (2014a), Saturn's elusive nightside polar arc, Geophysical Research Letters, vol. 41, Issue 18, pp. 6321–6328, doi: 10.1002/2014GL061081.

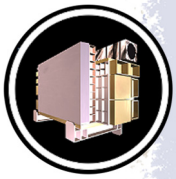

Radioti, A., D. Grodent, J.-C. Gérard, S. E. Milan, R. C. Fear, C. M. Jackman B. Bonfond, W. Pryor, (2014b), Saturn's elusive transpolar arc, European Geoscience Union (EGU) General Assembly Conference Abstracts, vol. 16.

Radioti, A., E. Roussos, D. Grodent, J.-C. Gérard, N. Krupp, D. G. Mitchell, J. Gustin, B. Bonfond, and W. Pryor, (2013a), Signatures of magnetospheric injections in Saturn's aurora, Journal of Geophysical Research, vol. 118, Issue 5, pp. 1922–1933, doi: 10.1002/jgra.50161.

Radioti, A., D. Grodent, J.-C. Gérard, B. Bonfond, W. Pryor, (2013b), Auroral signatures of multiple magnetopause reconnection at Saturn, Geophysical Research Letters, 40, 1–5, doi: 10.1002/grl.50889.

Radioti, A., D. Grodent, J.-C. Gérard, S. E. Milan, B. Bonfond, J. Gustin, W. Pryor, (2011), Bifurcations of the main auroral ring at Saturn: Ionospheric signatures of consecutive reconnection events at the magnetopause, Journal of Geophysical Research, vol 116, A11209, doi: 10.1029/2011JA016661.

Rehnberg, M. E., Z. L. Brown, L. W. Esposito, N. Albers, (2017), Direct detection of gaps in Saturn's A-ring, Icarus, 297, 110–118.

Rehnberg, M., L. W. Esposito, Z. Brown, N. Albers, M. A. Sremcevic, (2016), A Traveling feature in Saturn's rings, Icarus, 279, 100–108.

Robbins, S. J., G. R. Stewart, M. C. Lewis, J. E. Colwell, M. Sremčević, (2010), Estimating the masses of Saturn's A and B rings from high-optical depth N-body simulations and stellar occultations, Icarus, 206, 431–445.

Royer, E. M., J. M. Ajello, G. M. Holsclaw, R. A. West, L. W. Esposito, E. T. Bradley, (2017), Cassini UVIS observations of Titan ultraviolet airglow intensity dependence with solar zenith angle, Geophysical Research Letters, 44, 1, 88–96, doi: 10.1002/2016GL071756/full.

Royer, E. M. and A. R. Hendrix, (2014), First far-ultraviolet disk-integrated phase curve analysis of Mimas, Tethys and Dione from the Cassini-UVIS data sets, Icarus, 242, 158–171.

Sayanagi, K., K. H. Baines, U. Dyudina, L. N. Fletcher, A. Sánchez-Lavega, R. A. West, (2019), Saturn's polar atmoshpere, Chapter 12, In Saturn in the 21st Century, (eds.) K. H. Baines, F. M. Flasar, N. Krupp, T. Stallard, Cambridge University Press, pp. 337–376.

Seiß, M., F. Spahn, M. Sremcevic, H. Salo, (2005), Structures induced by small moonlets in Saturn's rings: Implications for the Cassini Mission, Geophysical Research Letters, vol. 32, Issue 11.

Shemansky, D. E., Y. L. Yung, X. Liu, J. Yoshii, C. J. Hansen, A. R. Hendrix, L. W. Esposito, (2014), A new understanding of the Europa atmosphere and limits on geophysical activity, The Astrophysical Journal, 797, 84, doi: 10.1088/0004-637X/797/2/84.

Shemansky, D. E. and X. Liu, (2012), Saturn upper atmospheric structure from Cassini EUV/FUV occulations, Canadian Journal of Physics, 90, 817–831, doi: 10.1139/p2012-036.

Shemansky, D.E., X. Liu, H. Melin, (2009), The Saturn hydrogen plume, Planetary and Space Science, doi: 10.1016/j.pss.2009.05.002.

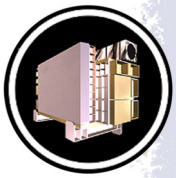

Shemansky, D. E., A. I. F. Stewart, R. A. West, L. W. Esposito, J. T. Hallet, X. Liu, (2005), The Cassini UVIS stellar probe of the Titan atmosphere, Science, 308, 978–982.

Shemansky, D. E. and X. Liu, (2005), Evaluation of electron impact excitation of N2 X 1Σg+ (0) into the N2+ X 2Σg+ (v), A 2Πu (v), and B 2Σu+ (v) states, Journal of Geophysical Research: Space Physics, 110, no. A7.

Sittler, E., C. Bertucci, A. Coates, T. Cravens, I. Dandouras, D. Shemansky, (2009), Energy deposition processes in Titan's upper atmosphere and its induced magnetosphere, Chapter 16, In Titan from Cassini Huygens, (eds.) R. H. Brown, J.-P. Lebreton, H. Waite, Springer Dordrecht, Netherlands, pp. 393—454, doi: 10.1007/978-1-4020-9215-2.

Spahn, F., J. Schmidt, N. Albers, M. Horning, M. Makuch, M. Seiss, S. Kempf, R. Srama, V. V. Dikarev, S. Helfert, G. Moragas-Klostermeyer, A. V. Krivov, M. Sremcevik, A. J. Tuzzolino, T. Economou, E. Grun, (2006a), Cassini dust measurements at Enceladus and implications for the origin of the E ring, Science, vol. 311, Issue 5766.

Spahn, F., N. Albers, M. Horning, S. Kempf, A. V. Krivov, M. Makuch, J. Schmidt, M. Seiss, M. Sremcevic, (2006b), E ring dust sources: Implications from Cassini's dust measurements, Planetary and Space Science, vol. 54, Issue 9.

Spahn, F. and M. Sremcevic, (2000), Density patterns induced by small moonlets in Saturn's rings?, Astronomy & Astrophysics, vol. 358, Issue 1.

Spahn, F., K. U. Thiessenhusen, J. E. Colwell, R. Srama, E. Grun, (1999), Dynamics of dust ejected from Enceladus: Application to the Cassini dust detector, Journal of Geophysical Research: Planets, vol. 104, Issue E10.

Spencer, J. R., A. C. Barr, L. W. Esposito, P. Helfenstein, A. P. Ingersoll, R. Jaumann, C. P. McKay, F. Nimmo, C. C. Porco, J. H. Waite, (2009), Enceladus: An active cryovolcanic satellite, Chapter 21, In Saturn from Cassini-Huygens, (eds.) M. Dougherty, L. Esposito, S. Krimigis, Springer Dordrecht, Netherlands, pp. 683-724, doi: 10.1007/978-1-4020-9217-6.

Spencer, J. R., J. C. Pearl, M. Segura, F. M. Flasar, A. Mamoutkine, P. Romani, B. J. Buratti, A. R. Hendrix, L. J. Spilker, R. M. C. Lopes, (2006) Cassini encounters Enceladus: background and the discovery of a south polar hot spot, Science, vol. 311, Issue 5766.

Sremcevic, M., J. Schmidt, H. Salo, M. Seiß, F. Spahn, N. Albers, (2007), A belt of moonlets in Saturn's A-ring, Nature, 449, pp. 1019–1021, doi: 10.1038/nature06224.

Steffl, A. J., P. A. Delamere, F. Bagenal, (2006), Cassini UVIS observations of the Io plasma torus: III. Observations of temporal and azimuthal variability, Icarus, vol. 180, Issue 1, pp. 124–140, doi: 10.1016/j.icarus.2005.07.013.

Steffl, A. J., A. I. F. Stewart, F. Bagenal, (2004a), Cassini UVIS observations of the Io plasma torus: I. Initial results, Icarus, vol. 172, Issue 1, pp. 78–90, doi: 10.1016/j.icarus.2003.12.027.

Steffl, A. J., F. Bagenal, A. I. F. Stewart, (2004b), Cassini UVIS observations of the Io plasma torus: II. Radial variations, Icarus, vol. 172, Issue 1, pp. 91–103, doi: 10.1016/j.icarus.2004.04.016.

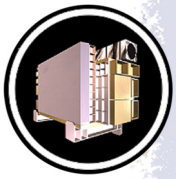

Stevens M. H., J. S. Evans, J. Lumpe, J. H. Westlake, J. M. Ajello, E. T. Bradley, L. W. Esposito, (2015), Molecular nitrogen and methane density retrievals from Cassini UVIS dayglow observations of Titan's upper atmosphere, Icarus, 247, 301–312.

Stevens, M. H., J. Gustin, J. M. Ajello, J. S. Evans, R. R. Meier, A. J. Kochenash, A. W. Stephan, A. I. F. Stewart, L. W. Esposito, W. E. McClintock, G. Holsclaw, E. T. Bradley, B. R. Lewis, (2011), The production of Titan's far ultraviolet nitrogen airglow, Journal of Geophysical Research, 116, A05304, doi: 10.1029/2010JA016284.

Strobel, D. F., T. T. Koskinen, I. C. F. Mueller-Wodarg, (2018), Saturn's variable thermosphere, Chapter 9, In Saturn in the 21st Century, (eds.) K. H. Baines, F. M. Flasar, N. Krupp, T. Stallard, Cambridge University Press, pp. 224–250.

Tian, F., A. I. F. Stewart, O. B. Toon, K. Larsen, L. W. Esposito, (2007), Monte Carlo simulations of the water vapor plume on Enceladus, Icarus, 188, 154–161.

Tomasko, M. G. and R. A. West, (2009), Aerosols in Titan's atmosphere, Chapter 12, In Titan from Cassini-Huygens, (eds.) R. H. Brown, J.-P. Lebreton, H. Waite, Springer Dordrecht, Netherlands, pp. 297–322, doi: 10.1007/978-1-4020-9215-2.

Torres, P. J., P. Madhusudhanan, L. W. Esposito, (2013), Mathematical analysis of a model for moon-triggered clumping in Saturn's rings, Physica D: Nonlinear Phenomena, vol. 259, pp. 55–62, doi: 10.1016/j.physd.2013.06.002.

Verbiscer, A. J., P. Helfenstein, B. J. Buratti, E. Royer, (2018), Surface properties of Saturn's icy moons from optical remote sensing, Part 3 Saturn's Icy Moons, In Enceladus and the icy moons of Saturn, (eds.) P. M. Schenk, R. N. Clark, C. J. A. Howett, A. J. Verbiscer, J. H. Waite, The University of Arizona, pp. 323–341, doi: 10.2458/azu_uapress_9780816537075-ch016.

Warlich, K., H. Jahn, R. Reulke, (1998), Simulation and methods for the data analysis of the hydrogen-deuterium-absorption-cell-experiment on Cassini, Advances in Space Research, vol. 21, Issue 3, pp. 419–423, doi: 10.1016/S0273-1177(97)00922-8.

West, R., P. Lavvas, C. Anderson, H. Imanaka, (2014), Titan Haze, Chapter 8, In Titan: Interior, Surface, Atmosphere and Space Environment, (eds.), I. Mueller-Wodarg, C. Griffith, T. Cravens, E. Lellouch, Cambridge University Press.

West, R. A, J. M. Ajello, M. H. Stevens, D. F. Strobel, G. R. Gladstone, J. S. Evans, E. T. Bradley, (2012), Titan airglow during eclipse, Geophysical Research Letters, 39, L18204, doi: 10.1029/2012GL053230.

West, R. A., K. H. Baines, E. Karkoschka, A. Sanchez-Lavega, (2009), Clouds and aerosols in Saturn's atmosphere, Chapter 7, In Saturn From Cassini-Huygens, (eds.) M. Dougherty, L. Esposito, S. Krimigis, Springer Dordrecht, Netherlands, pp. 161–179, doi: 10.1007/978-1-4020-9217-6.

Willacy, K., M. Allen, Y. L. Yung, (2016), A new photochemical model for Titan astrobiology, The Astrophysical Journal, 829, 2, 79.

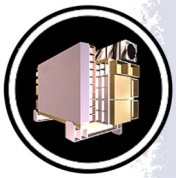

Woods, T. N., P. D. Feldman, G. H. Bruner, (1985), The absolute flux of 6 hot stars in the ultraviolet (912-1600-A), The Astrophysical Journal, 292, 2, 676–686, doi: 10.1086/163199.

Xu, F., A. B. Davis, R. A. West, L. W. Esposito, (2011), Markov chain formalism for polarized light transfer in plane-parallel atmospheres, with numerical comparison to the Monte Carlo method, Optics Express, vol. 19, 2, 946–967.

Yao Z. H., Z. Y. Pu, I. J. Rae, A. Radioti, M. V. Kubyshkina, (2017a), Auroral streamer and its role in driving wave-like pre-onset aurora, Geoscience Letters, 4, 8.

Yao, Z. H., A. Radioti, I. J. Rae, J. Liu, D. Grodent, L. C. Ray, S. V. Badman, et al., (2017b), Mechanisms of Saturn's near-noon transient aurora: In situ evidence from Cassini measurements, Geophysical Research Letters, 44, no. 22.

Yao, Z. H., D. Grodent, L. C. Ray, I. J. Rae, A. J. Coates, Z. Y. Pu, A. T. Lui, et al., (2017c), Two fundamentally different drivers of dipolarizations at Saturn, Journal of Geophysical Research: Space Physics, 122, no. 4, pp. 4348–4356.

Young, J. A., C. P. Malone, P. V. Johnson, J. M. Ajello, X. Liu, I. Kanik, (2010), Lyman–Birge–Hopfield emissions from electron-impact excited N_2, Journal of Physics B: Atomic, Molecular and Optical Physics, vol. 43, no. 13, doi: 10.1088/0953-4075/43/13/135201.

Zastrow, M., J. T. Clarke, A. R. Hendrix. K. S. Noll, (2012), UV spectrum of Enceladus, Icarus, 220, 29–35.

Zhang X., J. M. Ajello, Y. L. Yung, (2011), Atomic carbon in the upper atmosphere of Titan, The Astrophysical Journal Letters, 708, 1, L18-L21.

Zhou L., W. Zheng, R. I. Kaiser, A. Landera, A. M. Mebel, M-C. Liang, Y. Yung, (2010), Cosmic-ray-mediated formation of Benzene on the surface of Saturn’s moon Titan, The Astrophysical Journal, 718, 1243–1251.

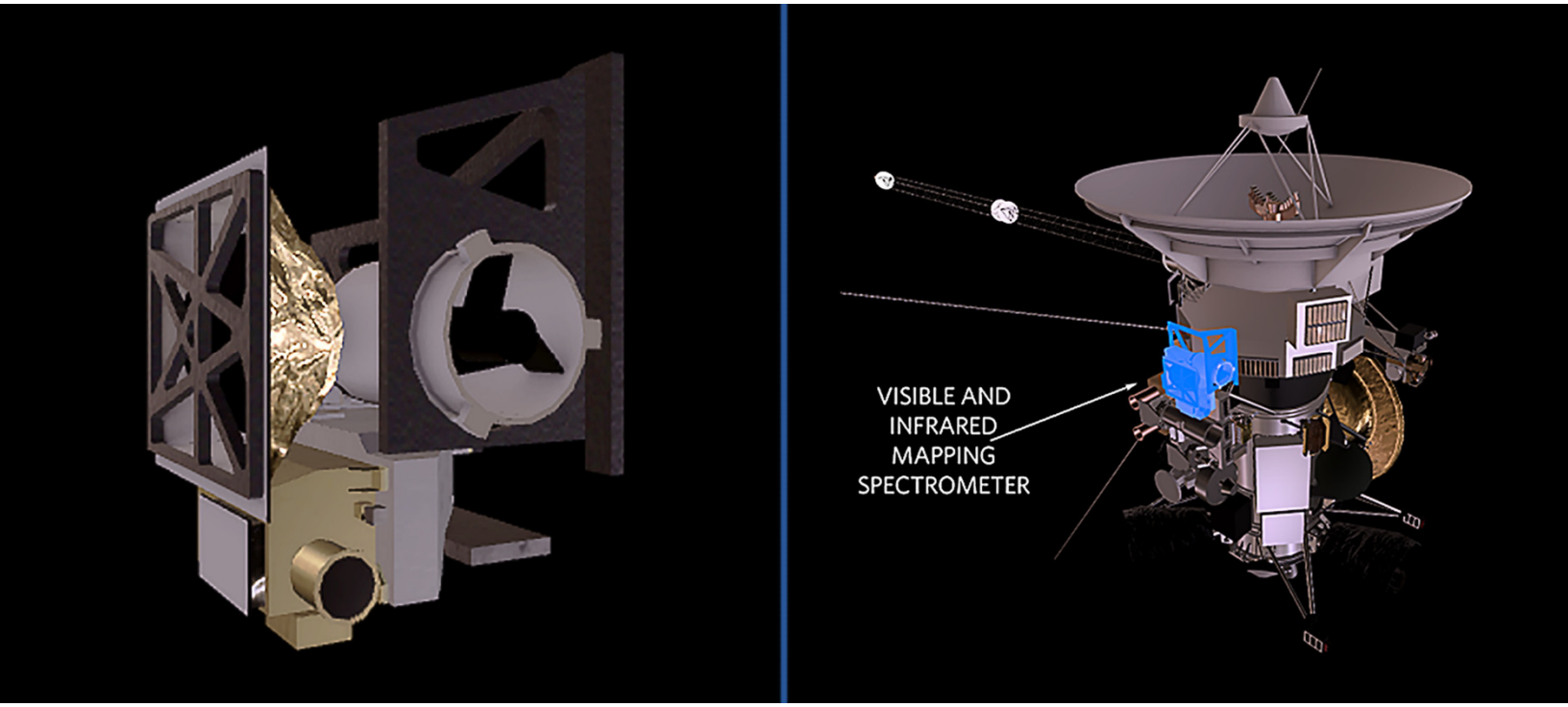

Visible and Infrared Mapping Spectrometer

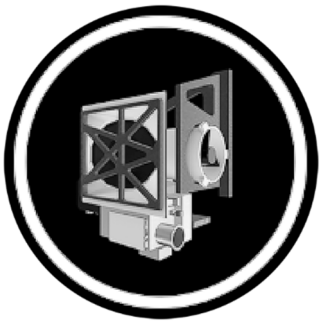

The Visual and Infrared Mapping Spectrometer (VIMS) was a pair of imaging grating spectrometers that were designed to measure reflected and emitted visible and near-infrared light from atmospheres, rings and surfaces over wavelengths from 0.35 to 5.1 microns. The **science objectives** of VIMS were to determine the composition and structure of atmospheres, rings and surfaces in the Saturn system using visual and infrared spectral mapping. Of Cassini's instruments, VIMS was uniquely capable of simultaneously collecting both images and spectra of satellite surfaces, the rings, and the atmospheres of Saturn and Titan without having to scan to make images.

VIMS separated the light into its various wavelengths providing information about the composition of materials from the measured reflected or emitted light. The instrument had the capability to detect 352 different wavelengths of light, many of which are beyond the capability of the human eye to detect. Images could be created from light collected at the various VIMS wavelengths.

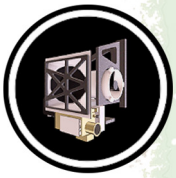

CONTENTS

Figures

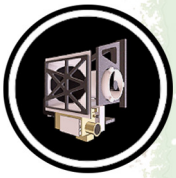

Tables

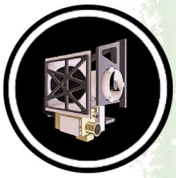

VIMS Science Performance Assessment

R. H. Brown, S. V. Badman, K. H. Baines, B. J. Buratti, R. N. Clark, P. D. Nicholson, C. Sotin and E. Joseph, April 27, 2018.

Instrument Description

The development, performance specifications and detailed design of the Cassini VIMS are well described in the literature and will not be repeated here. For detailed technical descriptions, the reader is referred to the refereed literature [Miller et al. 1996; Reininger et al. 1994; Brown et al. 2004] and Cassini project documents that describe the technical aspects of the VIMS instrument. For a complete discussion of the operational aspects of the Cassini VIMS the reader is directed to the VIMS User's Manual (JPL document D-14200).

> … the Team of people that eventually designed, built and used the VIMS instrument managed to extend the reach of the investigation well beyond what was envisioned by NASA … .

The VIMS instrument is an imaging spectrometer that is a composite of two channels: the VIMS visible (V) channel and the VIMS infrared (IR) channel. In its normal operating mode, the VIMS-V channel covers the wavelength region 0.35–1.05 μm in 96 spectral channels, with a spectral resolution of 0.0073 μm, an angular resolution of 0.5 microradians (mrad) and a 3.6 degree field of view. In its normal operating mode, the VIMS IR channel covers the wavelength region 0.85–5.1 μm in 256 channels at a spectral resolution of 0.0166 μm, an angular resolution of 0.5 mrad and a 3.6 degree field of view. The VIMS-V channel uses push-broom scanning to cover its 64 × 64 pixel field of view, while the IR instrument uses whisk-broom scanning to cover its 64 × 64 pixel field of view. The VIMS instrument is capable of a large range of operating modes, varying scan sizes and shapes, varying exposure times, and varying angular and spectral resolution, while incorporating a wide range of options for onboard processing of data such as spectral summing and spectral editing. For a detailed description of VIMS' various operating modes and parameters, the reader is again referred to the papers cited above. This document will focus on the scientific output of the VIMS investigation, and a few post-selection changes in the instrument and the investigation team that had a major effect on the scope and depth of the VIMS science investigation.

Several changes and developmental branches occurred during the designing and building of the VIMS instrument, and were not in the original specifications of the instrument as described in the Cassini Mission Announcement of Opportunity (AO), or in the original selection of the investigation team. Those changes, nevertheless, had dramatic and transformative effects on the science accomplished by the VIMS investigation. In essence, the Team of people that eventually designed, built and used the VIMS instrument managed to extend the reach of the investigation well beyond what was envisioned by NASA, the review panels that determined the original

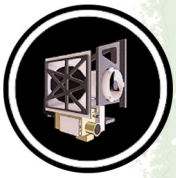

specifications of the instrument, its notional development budget, and the team of scientists originally chosen to use the instrument.

VIMS, as a facility instrument with its associated investigation team, was originally defined by several groups of people, most of whom had relevant expertise, but who would have no direct connection to the VIMS investigation, determination of its ultimate design and its development budget, or its overall scientific objectives. In addition, other individuals would judge the proposals submitted by scientists interested in becoming part of the VIMS science investigation team, and as such would determine to a great extent the depth and scope of the notional VIMS science investigation. Such an approach, though legitimate, necessarily cannot provide the deeply integrated vision and planning inherent in an instrument proposed by a principal investigator and a carefully picked team of associate scientists. Such teams have a more detailed and deeper understanding of the important scientific problems to be addressed, as well as the required specifications and capabilities of the instrumentation needed to achieve the science objectives, than that of a team and an instrument designed by committees. As such, though the committees that provided the initial input did as well as they could be given the constraints lain out by NASA, both the instrument configuration and the composition of the core VIMS science team changed significantly prior to and after Cassini's launch, reflecting the core team's vision of the scope and range of the eventual VIMS science investigation. As such, the VIMS investigation has far exceeded the scope and depth originally envisioned for it. For that, the entire team of scientists and engineers that have contributed to the development and use of VIMS on Cassini deserve a great amount of credit.

Changes to Hardware, Software and Personnel Post Announcement of Opportunity

There were several major changes made to the configuration of the VIMS instrument relative to that which was originally specified in the Cassini AO. The most significant of those changes were: i) incorporation of a separate channel to cover the visible spectral region from 0.35–1.05 microns; ii) incorporation of the ability to operate the VIMS instrument in a mode that resembled that of an occultation photometer; iii) the loss of the calibration plaque originally envisioned for the instrument, which drove the addition of a solar port to calibrate VIMS, along with the evolution of in-flight calibration strategies addressing that loss and the resulting capability to use the solar port to conduct solar-occultation studies of objects in the Saturn system; iv) the loss of Cassini's scan platform necessitating large changes in the operation plans envisioned for the entire package of remote-sensing instruments on Cassini; v) the addition of a second, orthogonal scanning direction for the VIMS secondary mirror, allowing for greater operational flexibility and scientific utility, specifically enabling collaborative studies with other remote sensing instruments having entrance slits; and vi) the use of H_3^+ emission measurements to study magnetospheric processes in the Saturn system. There were also several, minor changes to the flight software developed for the VIMS instrument, allowing for greater operational and scientific flexibility, among which were modes that allowed onboard processing of VIMS data such as data compression, spectral summing and spectral editing.

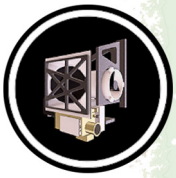

In addition to changes to both the hardware and software of the VIMS instrument relative to its AO configuration, after the original selections the VIMS core science team was embellished to better exploit the hardware and software changes. In particular, Dr. Phillip Nicholson was added to the team by NASA in response to a VIMS team request, specifically in the area of ring science and the use of occultation data to probe the structure and dynamics of Saturn's ring system. Dr. Alberto Adriani, Dr. Giancarlo Bellucci and Dr. Ezio Bussoletti were added to provide more expertise for scientific investigations using the VIMS-V channel. To enhance the expertise in the area of icy satellite surfaces, the VIMS team requested that Dr. Bonnie Buratti be added to the team. There have been other additions and subtractions to the VIMS core science team over the 29 years of its existence, but the aforementioned people were specifically added to expand the scope and depth of the VIMS investigation.

Another fundamental change in the scope of the VIMS investigation accrued from the realization that the lower atmosphere and surface of Titan could be imaged by VIMS. This opened up an entire sub discipline of the VIMS investigation concerning Titan geology, lakes, and methane cloud meteorology. The Titan sub-discipline grew explosively in the years following Cassini Saturn Orbit Insertion (SOI), eventually growing to become the largest of the VIMS sub-disciplines, both in number of investigators as well as production of scientific papers.

Stellar Occultation Mode

Were Cassini able to point its instruments at a specified celestial position (i.e., a star) with accuracy significantly better than 1 VIMS pixel, then occultation observations would be straightforward. In reality, however, the spacecraft's a priori pointing error was designed to be no worse than ~2 mrad, and in practice was approximately 1 mrad. It was thus impossible to predict in which VIMS pixel the stellar image would fall, though the uncertainty was at most 2–4 pixels. Fortunately, however, the spacecraft pointing was extremely stable once a new target was acquired, with typical pointing variations being only a few tens of narrow angle camera (NAC) pixels, or <<1 VIMS pixel. To solve the problem of initial targeting on board, the VIMS instrument was reprogrammed during cruise to first obtain a small image of the star 5–10 min before the predicted start of an occultation. Hardware constraints required this image to contain 64 pixels; in practice it was fixed at 16 × 4 pixels. The instrument's internal data compression software was then used to identify the brightest pixel in the scene (assumed to be the star of interest), and this was used to calculate the 2-D mirror offset necessary to place the star in the single pixel to be observed for the remainder of the occultation period. The star-finding cube was also returned to the ground, should it prove necessary to examine this later, as were the 2-D scanning mirror coordinates selected by the on-board star-finding software.

Although this simple procedure had its limitations, chiefly that it did not cope well with situations where the star fell more or less midway between two pixels, in practice it worked well in over 90% of the occultations we attempted. In only 4 cases out of 190 ring occultations did VIMS fail to acquire the star, or lose it after the initial acquisition, and in a further 11 cases (or 5% of the time) the occultation was recorded but the stellar signal was observed to be less than one-third of

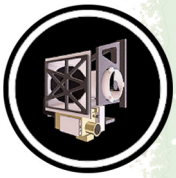

the predicted level, suggesting that the stellar image was not in fact centered within the pixel selected by the onboard algorithm.

Because the addition of both the stellar and solar occultation modes was such a substantial contributor to the overall VIMS science legacy, we detail the observation statistics in Table VIMS-1.

Table VIMS-1. Stellar and solar occultation mode observation statistics.

Type	Number tried	Successful	Failures	Comments
Ring stellar	190	182	8	~20 (10%) have poor SNR due to bad pointing
Saturn stellar	106	92	14	~10 (10%) have poor SNR due to bad pointing
Titan stellar	14	13	1	2 have poor SNR due to bad pointing
Ring solar	31	30	1	
Saturn solar	28	26	2	
Titan solar	16	12	1	3 were confused by bright limb in main port

A quick inspection of the above will reveal that VIMS attempted 310 stellar occultation measurements of Saturn, Saturn's rings and Titan, with only 23 failing to produce useful data. The remaining 287 produced data which was in general very high quality, resulting in 15 important scientific papers, and many new insights into the Saturn system. Those new insights ranged from atmospheric composition measurements for both Saturn and Titan, to studies of the structure and dynamics of Saturn's rings, to discovering features in Saturn's rings that resulted from gravitational perturbations driven by oscillations of Saturn's interior, thus allowing the VIMS team to virtually pioneer the field of space-based, observational Krono-seismology. In addition, VIMS attempted 75 solar occultation measurements of Saturn, Saturn's rings and Titan, all but four of which produced useful data, resulting in new insights into the composition and dynamics of those objects. It is useful to again note that the capabilities to conduct solar and stellar occultation measurements using VIMS were never envisioned by the committees that defined ether VIMS' notional design, or its complement of science team members. These capabilities, and the subsequent large contribution of scientific knowledge that resulted from their employ, were a huge bonus delivered to NASA by the talented people of the VIMS core science and engineering teams.

Impacts on the Scientific Community

As these efforts continue to grow over the next few years, the impact of the VIMS effort will continue to grow as well.

Further evidence of the seminality of the VIMS investigation is in the impact of its people and data on Planetary Science. At the time of writing, VIMS has had over 100 collaborators, postdocs and students associated with the investigation who are or have been participating in the analysis and publication of the data. Over 10 Ph.D. dissertations have made extensive use of the VIMS data, and there are at least four research groups studying Titan using VIMS data that have nucleated at the University of Idaho, M.I.T., Cornell, and The University of Paris around former students and postdocs who went on to become faculty at those institutions. As these efforts

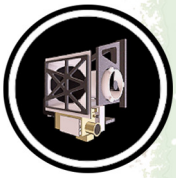

continue to grow over the next few years, the impact of the VIMS effort will continue to grow as well.

In the following we summarize the most significant of the VIMS science results in each of the disciplines where VIMS made contributions; i.e., atmospheres, magnetospheres, icy satellites, rings and Titan. After the science summaries follow detailed descriptions of the important results in the disciplines mentioned above. This document will then conclude with a bibliography of publications that have resulted from both the use of VIMS data and VIMS science results in scientific research driven and inspired by Cassini.

Summary of the Main Scientific Contributions of VIMS

In the following, we summarize in a list the most important scientific accomplishments of the VIMS investigation, organized by discipline.

Atmospheres and magnetospheres

1. Study and characterization of discrete clouds, silhouetted by 5-μm thermal radiation from Saturn's interior, resulting in important new insights into Saturn's atmospheric structure and circulation.

2. Study and characterization of Saturn's north-polar hexagon using 5-μm illumination while Saturn's north pole was in total darkness.

3. Discovery and characterization of Saturn's north polar vortex.

4. First spectral identification of ammonia ice in Saturn's clouds.

5. Discovery of carbon soot as a component of Saturn's dark clouds, likely produced by lightning in Saturn's atmosphere.

6. First detection of water ice in Saturn's clouds, from studies of the great storm of 2011–2012.

7. Determination of the abundance and spatial/temporal distribution of phosphine and arsine in Saturn's atmosphere.

8. Provision of additional constraints on Saturn's important He/H ratio.

9. Detailed mapping of the spatial and temporal character of Saturn's wind fields.

10. Discovery and characterization of Saturn's string of pearls storm system.

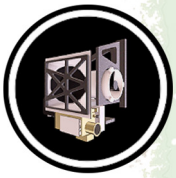

11. Extensive imaging of H_3^+ emission from Saturn's aurorae at the highest resolution ever resulting in new insights into Saturn's magnetospheric processes.

12. Discovery of a temperature asymmetry in Saturn's aurorae with the southern aurora being hotter than that of the north.

13. Elucidation of magnetospheric-ionospheric coupling in Saturn's aurorae.

14. First observations of surface emission features at sub-micron wavelengths on Venus.

15. Proved the existence of spectrally-identifiable ammonia and ammonium hydrosulfide ices in most zones and belts across Jupiter.

16. Provided new insights into the identity of the potential red chromophores responsible for the reddish tint of Jupiter and its Great Red Spot.

17. Discovery of a 3% asymmetry in Jupiter's thermal emission possibly due to hemispherical differences in the structure of Jupiter's interior.

Satellites

1. Discovery of widespread water on Earth's Moon at concentrations of 10 to 1000 parts per million, and locally higher.

2. Discovery of a surprisingly high opposition surge on Europa.

3. Discovery of a 3-μm feature in Himalia's spectrum of Jupiter's satellite Himalia, suggestive of the presence of water, either free, bound, or incorporated in layer-lattice silicates.

4. Provided the first near-IR phase curve of Europa, suggesting that neither coherent backscatter nor shadow hiding provide a complete description of Europa's opposition surge below 1°.

5. First spatially resolved spectra of Phoebe showing iron-bearing minerals, bound water, trapped CO_2, probable phyllosilicates, organics, and NH-bearing compounds, showing Phoebe to be one of the most compositionally diverse objects yet observed in our Solar System.

6. The recognition, through both chemical and isotopic composition measurements by VIMS, that Phoebe is very likely a captured object, probably from well beyond the orbit of Saturn.

7. The recognition that the water ice on the icy satellites is crystalline, rather than amorphous as had been thought.

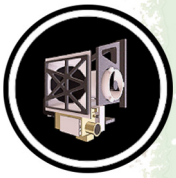

8. The discovery that CO_2 is present on the surface of most of Saturn's icy moons, extensive mapping of the spatial distribution of that CO_2, and elucidation of its physical state, both bound and free.

9. Discovery of spectral absorptions attributed to the presence of aromatic hydrocarbons on Iapetus and Phoebe.

10. Tentative identification of trapped H_2 and ammonia on the surfaces of several of Saturn's icy satellites.

11. Discovery of Deuterium on Phoebe, Iapetus, Hyperion, Rhea, Dione, Enceladus and the Saturn's rings, and measurement of the associated D/H ratios.

12. Detection of ^{13}C on Phoebe and Iapetus.

13. Recognition that VIMS' measurements of high D/H and $^{13}C/^{12}C$ isotopic ratios imply that the materials comprising Phoebe's surface came from a different reservoir than that of the other icy satellites of Saturn, and its rings.

14. Discovery that the plumes of Enceladus vary in intensity with mean anomaly over short-timescales in VIMS data, with subsequent attribution to tidal stresses induced by variations in Enceladus' orbital distance from Saturn.

15. Derived a temperature of 197 ±20 K, and a linear size of 9 meters for one of the plume sources on Enceladus using VIMS observations at 5 μm.

16. Discovered that the particulate component of Enceladus' plumes consist primarily of fine-grained water ice, ejected at velocities of 80 and 160 m/s, with size distributions strongly depleted in particles with radii larger than 3 μm, and that only a small fraction of 3-μm particles can escape from Enceladus.

17. Particle sizes on Enceladus are correlated with geologic features and surface ages, suggesting a stratigraphic relationship between tectonic features and cryovolcanic activity.

18. Constructed daytime temperature maps of the icy satellite surfaces using temperature-dependent spectral changes observed by VIMS in the spectrum of water ice on their surfaces.

19. Discovery of nano-phase iron oxides and metallic iron together explain the varied color and ultraviolet (UV) absorber on Iapetus, Phoebe, and Hyperion. The metallic iron must be embedded in another material like a silicate, thus characteristic of space-weathered meteoric dust. The 3-μm absorber in the Iapetus dark material is only matched by hydrated iron oxides. The 1.9-micron bound water absorption in

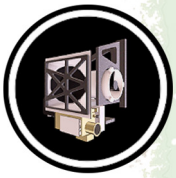

spectra of the dark material is also a constraining absorption characteristic of hydrated iron oxides.

Saturn's rings

1. VIMS spectral observations at SOI revealed that the mysterious red coloring agent in the rings resides within the water ice grains that make up the regolith on the ring particles.

2. Observations of ring occultations of o Ceti (aka Mira) in 2005 confirmed the existence of strong self-gravity wakes in the A-ring, leading to the first reliable estimates for the ring thickness of ~6 meters in this region.

3. Observations of multiple stellar and radio occultations in 2005–2009 leading to the discovery that the amplitude of the radial perturbations at the outer edge of the B-ring (due to the Mimas 2:1 resonance) varies from ~70 km to < 5 km, and that these may also be indirectly responsible for the regular spacing of the multiple gaps within the Cassini Division.

4. The observation of reststrahlen bands of H_2O ice in a stellar occultation by the F-ring permitted discrimination between clumps of macroscopic source bodies and the background of micron-sized dust.

5. A comparative analysis of visible-infrared (VIS-IR) spectral indicators (slopes and band depths) of rings, regular satellites and small moons has allowed VIMS to map the distribution of water ice and red contaminant materials across the Saturn system. However, in the main rings, the abundance of the red coloring agent is lower and there is at present no way to distinguish definitively between the nano-iron model and more traditional carbon-tholin models. Recent modeling results obtained with Hapke theory indicate that both intimate and intra-particle mixing of water ice, amorphous carbon and organic material (Titan tholins) can reproduce the observed ring spectra.

6. VIMS investigations of numerous small-scale wavelike structures in the C-ring have provided strong evidence that several of these are density waves driven by global oscillations within Saturn itself, opening up a new window on the planet's internal structure and rotation rate.

7. A pair of stellar occultations with turnaround radii in the inner A-ring yielded strong evidence for viscous over-stability in the denser parts of Saturn's rings, supporting previous work based on radio occultation data.

8. Together with occultation data from Radio Science Subsystem (RSS) and Ultraviolet Imaging Spectrograph (UVIS), VIMS data from more than 100 stellar occultations has led to the characterization of numerous non-circular features in the C-ring and

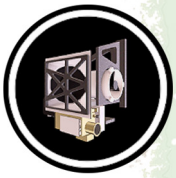

Cassini Division, including the discovery of a large number of normal mode oscillations on the edges of both narrow gaps and their associated ringlets.

9. Ring temperature maps have been built from VIMS spectra by using an indirect method based on the wavelength of the temperature-dependent reflectance peak at 3.6 μm.

10. Application of a new, phase-sensitive wavelet analysis technique to selected VIMS stellar occultation profiles has led to the identification of several satellite-driven density waves in the optically-thick B-ring, resulting in the first estimates of surface mass density in this most opaque part of Saturn's rings. The results are unexpectedly low, and imply a total mass for the rings of ~40 percent that of Mimas.

Titan

1. Observation and characterization of the first specular reflection from an extraterrestrial body of liquid.

2. Detection of liquid ethane in Ontario Lacus.

3. First observation and characterization of waves on Titanian lakes.

4. Discovery and characterization of cryovolcanic deposits near Hotei Regio and Tui Regio on Titan.

5. Discovery and characterization of evaporite deposits on Titan's surface.

6. Global mapping of Titan's surface composition.

7. Discovery of solid benzene on Titan.

8. Discovery of acetylene on Titan.

9. Mapping of the composition and distribution of material near or around Selk crater on Titan.

10. Discovery and characterization of dust storms on Titan.

11. Mapping, characterization and analysis of the global cloud distribution on Titan during the entire 13-year orbital tour.

12. Discovery and characterization of the extreme smoothness of Ontario Lacus during the early part of the Cassini orbital tour.

13. Discovery of CO nighttime emissions on Titan.

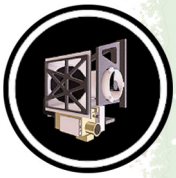

14. Discovery and characterization of precipitation-induced surface brightening seen on Titan.

15. Discovery of fog at the south pole of Titan.

16. Discovery of giant, infrared palimpsest on Titan's Xanadu region.

17. Observation and characterization of the shoreline of Ontario Lacus showing no changes over five years.

18. Discovery of ethane in Titan's rainfall.

19. Characterization of fluvial erosion and post-erosional processes on Titan.

20. Characterization of the evolution of Titan's north polar hood.

21. Evidence for tropical and temperate lakes on Titan.

Details of the Most Significant Scientific Results

Jupiter's Atmosphere, Saturn's Atmosphere and Aurorae

Cloud properties

Upon arrival at Saturn, VIMS used its 5-μm thermal spectral imaging capability to quickly discover that discrete clouds lie below the traditional levels observed in reflected sunlight. Across the planet, localized clouds were observed in silhouette against the planet's indigenous background thermal radiation and found to reside near the 1.5-bar level [Baines et al. 2005, 2009b; Fletcher et al. 2011a], revealing that a different dynamical atmospheric regime resides below the visible cloud tops. Upon observing the north polar region during the first set of inclined orbits in 2006 under full nighttime polar winter conditions, these clouds allowed the north polar hexagon to be clearly imaged for the first time and revealed the existence of a classical polar vortex via the determination of the north polar windfield by VIMS 5 μm cloud-tracking [Baines et al. 2009b].

Ammonia ice was found by VIMS to be a spectrally-identifiable component of thunderstorm-related clouds in southern mid-latitudes, the first spectral identification of ammonia ice in Saturn [Baines et al. 2009a]. Neighboring clouds were found to be exceptionally dark over all visible and near-IR reflective wavelengths, consistent with carbon soot being a significant component of these features, as perhaps produced by lightning observed in the region by Radio and Plasma Wave Spectrometer (RPWS) [Baines et al. 2009a]. More recent modeling by Sromovsky et al. [2018] confirms the excellent spectral fits for both the bright spectrally-identifiable ammonia-ice clouds and the dark neighboring features. This paper also finds excellent fits for the dark clouds via relatively bright cloud models characterized by depressed cloud tops, although depressed cloud tops are

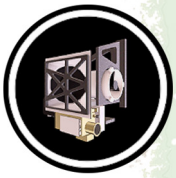

dynamically inconsistent with the anticyclonic nature of these features found by Imaging Science Subsystem (ISS).

Water ice was spectrally identified by VIMS in the cloud tops of the Great Storm of 2010–2011, the first identification of water ice on Saturn [Sromovsky et al. 2013]. The particle size, number density, and structure of the clouds in the nucleus of the Great Storm clouds were also determined from VIMS spectral imagery. The high cloud tops found (near 300 mbar) where the water ice is seen by VIMS implies that water is lofted over 150 km within this storm from its condensation level near the 20 bar level.

Composition

VIMS constrained the gaseous abundances of phosphine and arsine in Saturn's north polar region [Baines et al. 2009b], in the Great Storm of 2010–2011 [Fletcher et al. 2011b], and across the planet in various zonal structures [Fletcher et al. 2011a]. As noted above, VIMS also determined spectroscopically the presence of both ammonia and water ice in a variety of clouds. The He/H_2 ratio (important for understanding Saturn's internal heat) was constrained from VIMS 4– to 5-μm spectroscopy from a unique analysis of the unusually aerosol-free mid-northern-latitude band created in the aftermath of the Great Storm of 2010–2011, leveraging the effect of helium on the pressure/temperature gradient [Sromovsky et al. 2016].

Global and regional wind fields

The zonal wind field was mapped globally over the planet from ~60 degrees north latitude to 30 degrees south latitude by Choi et al. [2009]. In the north polar region, the zonal winds were mapped under winter nighttime conditions from Cassini's highly-inclined orbit in 2006, revealing the presence of a classical polar vortex [Baines et al. 2009b]. As well, a similar vortex structure was mapped by VIMS for the south pole [Dyudina et al. 2009] observed under the daylit conditions of southern summer, confirming the simultaneously-measured ISS cloud-tracked results obtained at significantly higher spatial resolution.

Synoptic cloud features and processes

VIMS followed the enigmatic String of Pearls which it discovered (and named) for five years, until its demise with the eruption of the Great Storm in December 2010 [Del Genio et al. 2009; Baines et al. 2018]. This feature was likely a Vortex Street, perhaps stimulated by undetected upwellings from below that eventually erupted into the Great Storm of 2010–2011.

The aftermath of the Great Storm of 2010–2011 left an unexpectedly clear atmosphere over the ~10 degrees of latitude that had been occupied by the storm. With its 5-μm observing capabilities, VIMS followed the evolution of this region, quantifying its rate of recovery back to its pre-storm state [Sromovsky et al. 2016].

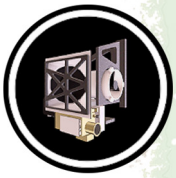

Auroral science

VIMS imaged Saturn's infrared aurora, emitted by the ionized molecule H_3^+, at unprecedented spatial and temporal resolution. New features were identified, including polar infilling for which no ultraviolet counterpart has yet been identified [Stallard et al. 2008]. Limb observations showed that the aurora peaks at ~1100 km altitude, similarly to the UV aurora, but has a narrower profile [Stallard et al. 2012a].

Observations of both hemispheres (not possible from Earth-based telescopes) revealed that the southern auroral oval was brighter than the north, implying a higher temperature [Badman et al. 2011b]. The southern temperature was estimated to be 440 ±50 K [Melin et al. 2011].

Comparison with UV observations showed that the infrared H_3^+ emission has a lifetime of ~500 s, and is morphologically identical to the UV H and H_2 emission only at the main auroral arc [Badman et al. 2011a; Melin et al. 2011, 2016].

Magnetosphere-ionosphere coupling was revealed in arcs conjugate with energetic ions and electrons [Badman et al. 2012a] and modulated by a rotating current system [Badman et al. 2012b; Lamy et al. 2013].

Venus science

During the Venus flyby in June 1999, the visual channel of VIMS was able to obtain the first observations of surface emission features at sub-micron wavelengths surface emission, proving the previously theorized existence of emissions at 0.85 and 0.90 μm [Baines et al. 2000]. This result extended the number of spectral windows useful for surface spectroscopy from 3 to 5 μm, expanding the useful surface-sensitive spectral range from 1.01 to 1.18 μm pre-VIMS/Cassini to 0.85–1.18 μm post-VIMS.

Jupiter science

During the Jupiter flyby of late 2000–early 2001, VIMS 0.35– to 5.1-μm spectral maps of the planet obtained at higher spatial resolution than available heretofore resulted in proving the existence of spectrally-identifiable ammonia and ammonium hydrosulfide ices in most zones and belts across the planet [Sromovsky et al. 2010]. Visual spectral imagery in the 0.35– to 0.6-μm range proved particularly useful for modeling the potential red chromophores responsible for the reddish tint of the planet [Sromovsky et al. 2017]. Spectral fits were particularly fine in the core of the Great Red Spot [Baines et al. 2019], providing significant clues to the centuries-long mystery of why the Great Red Spot is red.

Jupiter's emitted power was evaluated over latitude from a combination of VIMS and Composite Infrared Spectrometer (CIRS) and observations [Li et al. 2012]. The analysis found a north/south hemispherical difference of a 3% in emitted power, with the northern hemisphere being warmer. This is despite the low obliquity of the planet that theoretically prevents

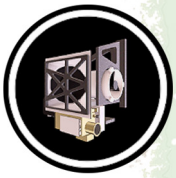

seasonal/hemispherical variations. The cause may then be due to hemispherical differences in the structure of Jupiter's thermally-emitting interior.

VIMS observed the night-side auroral emission with a peak at the equatorward edge of the main emission attributed to enhanced H_3^+ density, but very little emission, and hence particle precipitation, at the equator [Stallard et al. 2015].

Some open questions

1. What is the helium abundance on Saturn? The answer may still rest in the proper interpretation of the joint VIMS/CIRS data sets, but perhaps by better joint observational scenarios by future VIMS occultation and mid-IR thermal mapping instruments on a future mission are needed (or, finally, measured directly by an in situ atmospheric probe).

2. What, exactly, occurs in the initial development of major storms on Saturn? VIMS-like studies of the development of a major storm (particularly the composition of condensates seen in the early stages) would be able to determine more accurately what the energetics are in lofting materials from 100s of km down. Continued studies would then be able better constrain the energetics throughout the lifetime of a storm.

3. More studies are needed of smaller storms in the mid-southern-latitude storm alley, in particular, looking for and characterizing the dark carbon soot observed in storms in this region. VIMS had just one amazing set of images that revealed these, but that then limited us to just one set of lighting and viewing angles. Had we had some views of the these features near the limb or at a different phase angle we could have distinguished better between different scenarios of just how much of what we were seeing was actually due to soot vs unexpected but perhaps large depressions in both cloud tops and cloud thinning.

4. The String of Pearls. How often and why do such features appear? Like the Hexagon, this was a very strange phenomenon unseen on any other planet. The huge storm of 2010–2011, which actually erupted amongst the Pearls, obliterated it. Were these connected? Was the String of Pearls a harbinger of the Great Storm (somewhat like earthquakes can be a harbinger of volcanic eruptions).

5. The polar hexagon. What is its lifetime/variability? The very large shear in the winds rising from a more typical 10–20 m/s to over 125 m/s in just a few degrees of latitude, and then back down again to 10–20 m/s on the other side of the hexagon, is still perplexing. Why does not it diffuse away? Something is organizing it which is still very poorly understood. In addition, the whole north polar region seems to have some seasonal variability in its upper atmosphere aerosol coloring which should be studied by a VIMS or ISS instrument (or both) on a future mission. It is possible that Hubble

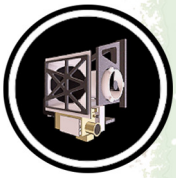

Space Telescope (HST) and some ground-based telescopes will continue to observe this, but as Saturn tilts back to its northern fall season it will be problematic to view.

6. What is Saturn's bulk rotation rate (or perhaps set of rates, if there are actually different rates for various 10,000 km depth-scale regimes, as some folks are starting to suggest)? The new Krono-seismology technique that Matt Hedman and Phil Nicholson have developed from VIMS observations may be a key contributor to answering this with future missions.

Icy Satellites and the Earth's Moon

Earth's moon

Clark [2009] wrote:

> *"Data from the Visual and Infrared Mapping Spectrometer (VIMS) on Cassini during its flyby of the Moon in 1999 show a broad absorption at 3 micrometers due to adsorbed water and near 2.8 μm attributed to hydroxyl in the sunlit surface on the Moon. The amounts of water indicated in the spectra depend on the type of mixing and the grain sizes in the rocks and soils but could be 10 to 1000 parts per million and locally higher. Water in the polar regions may be water that has migrated to the colder environments there. Trace hydroxyl is observed in the anorthositic highlands at lower latitudes."*

The discovery of widespread water on the Moon was evident in the data returned right after the Earth flyby, … .

See Figure VIMS-1 for image.

The discovery of widespread water on the Moon was evident in the data returned right after the Earth flyby, but calibration of the VIMS data was uncertain at that time. It was not until after Cassini orbit insertion at Saturn had the VIMS calibration been refined enough to be certain of the water signature. The VIMS results were later verified by the Moon Mineralogy Mapper on Chandrayan-1, and EPOXI on Deep Impact and the three instruments showed proof that the water signature was real, changing our understanding of the Moon.

Jupiter system

Brown et al. [2003] presented results from the Jupiter flyby. VIMS documented a surprisingly high opposition surge on Europa, the first visual-near-IR spectra of Himalia. Himalia has a slightly reddish spectrum, an apparent absorption near 3 μm, and a geometric albedo of 0.06 to 0.01 at 2.2 μm (assuming an 85 km radius). If the 3-μm feature in Himalia's spectrum is eventually confirmed, it would be suggestive of the presence of water in some form, either free, bound, or incorporated in layer-lattice silicates.

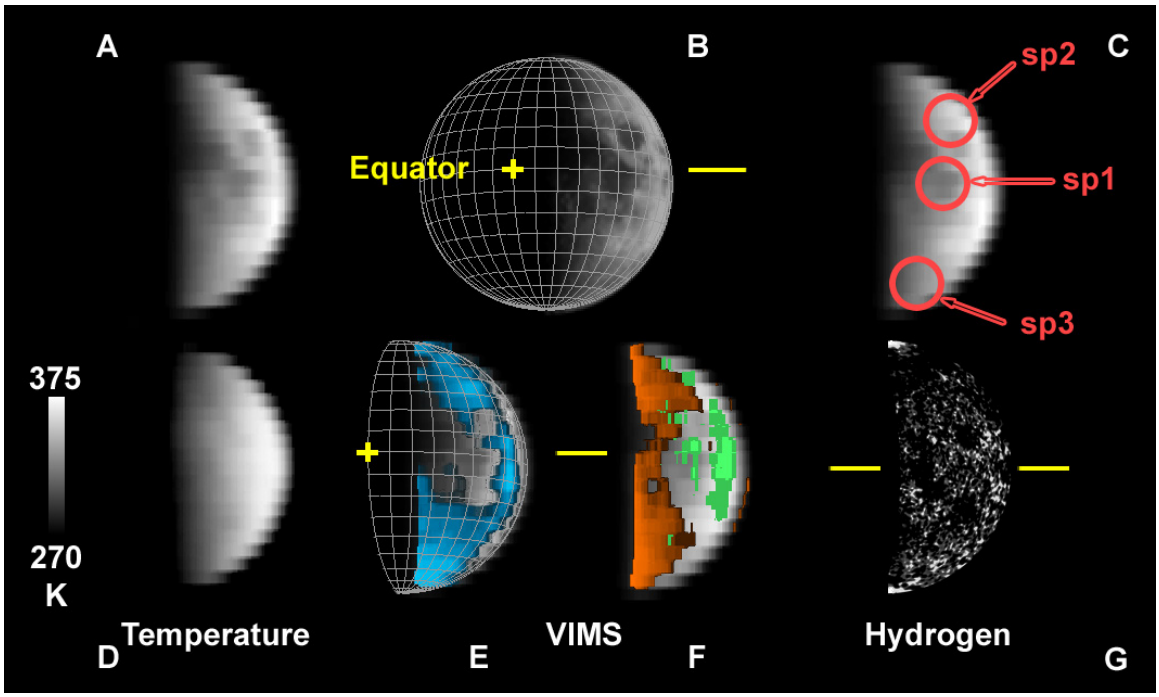

Figure VIMS-1. Cassini VIMS observations of the Moon on August 19, 1999. *A*: VIMS 2.4 µm apparent reflectance. *B*: Cassini Imaging Science Subsystem image obtained during the flyby. The yellow bars indicated the equator position. The yellow cross indicates latitude 0, longitude 0. *C*: Locations of VIMS spectra discussed in Clark [2009]. *D*: VIMS-derived temperatures. Maps of *E*: the 3 micron absorption strength (blue), and *F*: the 2.8 µm OH strength (orange and green). *G*: Hydrogen map from LP [Feldman et al. 2000] masked to give a similar view as the VIMS observation. Figure from Clark [2009].

VIMS spectra of the Galilean satellites confirmed the spectral features in the Near Infrared Mapping Spectrometer Subsystem (NIMS) data. Brown et al. [2003] also noted similar spectral structure as in NIMS data attributed to a CN bond near 4.5 µm. This structure was also seen in VIMS data of the Saturnian satellites—for example, Clark et al. [2005, 2008]—but as later found to be due to a calibration error [Clark et al. 2012]. VIMS data also provided the first near-IR phase curve of Europa. Europa exhibits a remarkable surge in brightness (~0.2 mag/deg) under 1°, comparable to the lunar opposition surge measured by Clementine [Buratti et al. 1996]. Furthermore, data at small phase angles show a clear trend with albedo, such that wavelengths corresponding to higher albedos have smaller surges, consistent with shadow illumination. The VIMS results suggest that neither CBE nor shadow hiding provide a complete description of Europa's opposition surge below 1° [Brown et al. 2003].

Saturn system

The first VIMS observations of the Saturnian satellites were of Phoebe on June 11, 2004, before Saturn orbit insertion [Clark et al. 2005]. VIMS spatially resolved the surface of Phoebe, and data have been registered and projected into simple cylindrical maps: low to medium resolution with near hemispheric coverage, and high resolution of a small area. Clark et al. [2005] mapped ferrous-

iron-bearing minerals, bound water, trapped CO_2, probable phyllosilicates, organics, nitriles and cyanide compounds. Detection of these compounds on Phoebe makes it one of the most compositionally diverse objects yet observed in our Solar System. It is likely that Phoebe's surface contains primitive materials from the outer Solar System, indicating a surface of cometary origin. Improved calibration [Clark et al. 2012] showed that the nitrile detection was due to an error in the calibration to reflectance. The ferrous-iron-bearing minerals was subsequently shown by Clark et al. [2012] to be nano-iron oxides plus nano-metallic iron (e.g., in space-weathered silicates) and scattering effects.

This nitrile identification error originated in the NIMS calibration and propagated into the VIMS calibration from cross instrument calibrations. A calibration target was descoped early in the mission, which led to the error. The diversity of targets and phase angles during the Cassini orbital tour led to continuing improvements in the VIMS calibration [Clark et al. 2016b, 2018]. Figure VIMS-2 shows the quality of spectra obtained using the new calibration.

We now know that the iron signatures in Phoebe's spectrum are due to a combination of nano-phase iron oxides and nano-metallic iron [Clark et al. 2012]. This is the same composition as the dark material on Iapetus (Figure VIMS-2). The 3-μm absorber was also identified as a definitive match by Clark et al. [2012] as a unique signature of hydrated nano-iron oxides (the water may be adsorbed water). The nano-phase metallic iron must be embedded in another matrix, e.g., silicates.

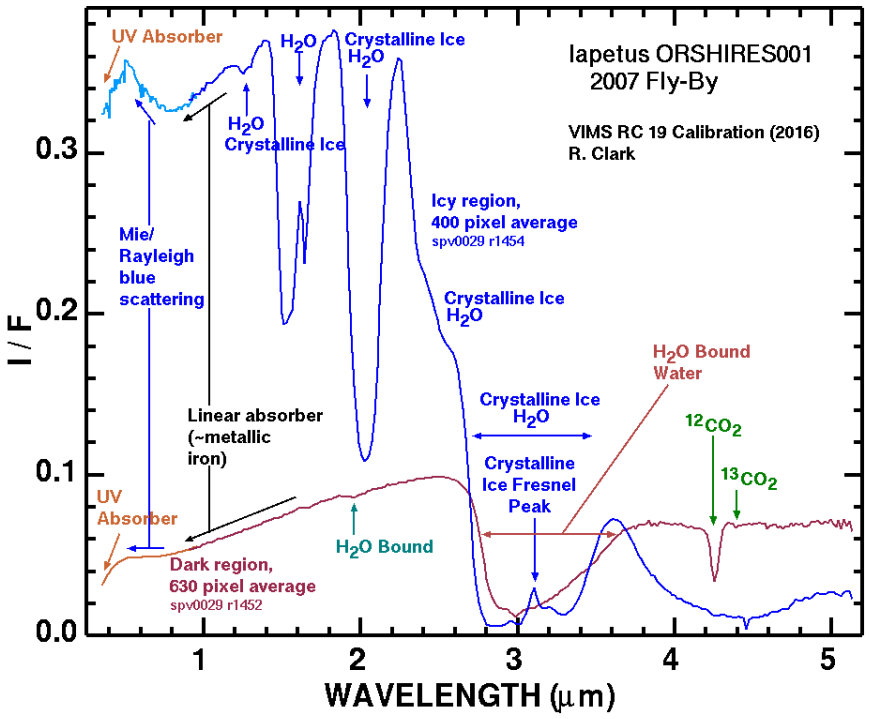

Figure VIMS-2. Illustration of VIMS spectra of two regions on Iapetus with causes of spectral features labeled. After Clark et al. [2012] with the RC 19 calibration [Clark et al. 2016b].

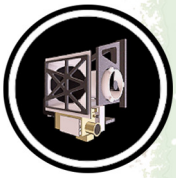

VIMS has shown that the water ice on the icy satellites is crystalline. While initial reports showed indications of amorphous ice, it was subsequently found that sub-micron ice grains modify the reflectance spectrum mimicking some aspects of amorphous ice signatures. Mastrapa et al. [2008] publication of crystalline and amorphous ice optical constants enabled better comparisons to observed spectra, and along with improved radiative transfer models that included diffraction effects of small particles [Clark et al. 2012], the differentiation between amorphous and crystalline ice could be made with more confidence. These results are summarized in Buratti et al. [2018a].

CO_2 is present on the surface of most of the moons [Buratti et al. 2005; Brown et al. 2006; Clark et al. 2005, 2008, 2012; Cruikshank et al. 2010 and references therein], but there are still spectral identifications that are uncertain. Clark et al. [2012] showed that a weak feature at 2.42 μm is due to trapped molecular hydrogen and is observed in dark material on multiple icy satellites, but this feature needs confirmation by an independent instrument. A weak absorption at 2.97 μm corresponds to ammonia [Clark et al. 2008, 2012] and is seen on multiple icy satellites, but the absorption overlaps an order-sorting filter gap in the VIMS instrument where instrument errors are larger. Observations of ammonia need confirmation either by a better calibration of the VIMS data, or by other instruments. Iapetus and Hyperion have many unidentified spectral bands in the 1- to 5-μm region [Cruikshank et al. 2007; Clark et al. 2012; Dalton et al. 2012] that may be the signature of higher order hydrocarbons, some of which have not been measured in the laboratory. Absorptions attributed to aromatic hydrocarbons have been detected in the spectrum of Iapetus and Phoebe [Cruikshank et al. 2008, 2014; Dalle Ore et al. 2012].

All of the icy Saturnian moons are absorbing in the ~0.2 to 0.5 μm region, making them dark at far ultraviolet channel (FUV) wavelengths. For instance, Filacchione et al. [2012, 2016] used Cassini VIMS data to show that the spectral slope (0.35–0.55 μm) increases (becomes redder) with distance from Enceladus. While the UV absorber causes reddening, sub-micron grains induce increased scattering, causing a bluing effect, so there are competing signatures of these two components throughout the Saturn system.

Deuterium has been found on Phoebe, Iapetus, Hyperion, Rhea, Dione, Enceladus and the Rings and carbon 13 has been detected on Phoebe and Iapetus (Figure VIMS-2) [Clark et al. 2018, 2017a, 2017b, 2016, 2012] and the D/H ratio derived. Phoebe is an outlier with D/H more than seven times higher than terrestrial, which the other satellites and rings are close to terrestrial ocean water values, an unexpected result not predicted by current models of Solar System formation.

The plumes of Enceladus were observed by VIMS to vary in intensity with mean anomaly over short-timescales [Hedman et al. 2013a]. Results from the VIMS, which measured the short-wavelength end of the blackbody curve for the south pole of Enceladus, calculated a temperature of 197 ±20 K and a linear size of 9 meters [Goguen et al. 2013]. Further analysis of VIMS data will enable this result to be refined and will place limits on additional emitting regions. The amount and/or size of particles spewing from the fissures varies as a function of the orbital position of Enceladus, implicating tidal forces as the source of energy driving eruptive activity [Hedman et al. 2013a; Nimmo et al. 2014]. Hedman et al. [2009] analyzed VIMS plume spectra as a function of altitude to derive composition and grain sizes. These spectra show that the particulate component

of the plume consists primarily of fine-grained water ice. The spectral data are used to derive profiles of particle densities versus height, which are in turn converted into measurements of the velocity distribution of particles launched from the surface between 80 and 160 m/s (i.e., between one-third and two-thirds of the escape velocity). The size distributions show that the parts of the plume observed by VIMS are strongly depleted in particles with radii larger than 3 μm. Furthermore, the velocity distributions indicate that only a small fraction of 3-μm particles can escape from Enceladus.

One of the most intriguing results of the mission was the discovery of global red streaks on Tethys and blue pearls on Rhea that do not appear to be connected to any underlying geologic structures [Schenk et al. 2011, 2015] VIMS analysis of the streaks on Tethys shows a clear spectral difference [Buratti et al. 2017], but it is not clear whether this difference is caused by composition, such as an enhanced amount of organic material, magnetospheric effects, or simply grain size.

Another intriguing result was the detection on December 15, 2004, of a transient aura-like ring around Dione at 2.65 μm that suggested the existence of an atmosphere [Clark et al. 2008] (Figure VIMS-3). Magnetometer data obtained on October 11, 2005, show a weak field perturbation in the upstream region, indicating a tenuous atmosphere [Simon et al. 2011]. Observing with Cassini Plasma Spectrometer (CAPS), Tokar et al. [2012] discovered a thin atmosphere (~0.01-0.09 particles/cm^3) of O_2^+ during the close (500 km) flyby on April 7, 2010. A search for forward scattered radiation at solar phase angles >150°, indicating a plume, was negative [Buratti et al. 2011]. No clear evidence of ongoing activity on Dione was discovered during the mission, although more thorough inspection of the 2.65-μm band is an ongoing task.

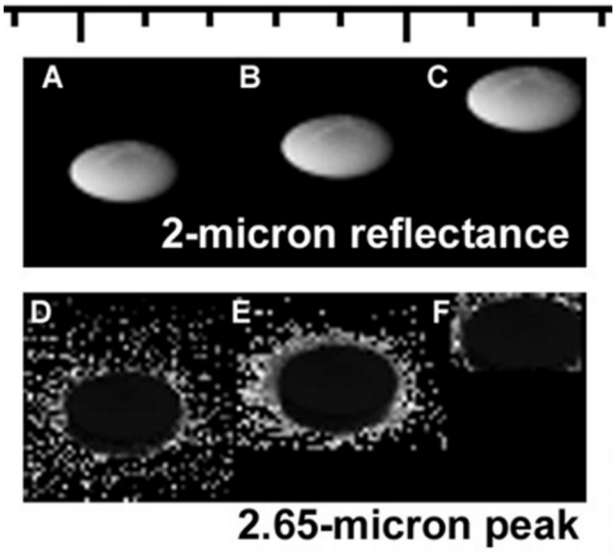

Figure VIMS-3. The 2.65-μm transient atmosphere on Dione [Clark et al. 2008].

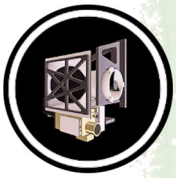

IR spectroscopy is sensitive to grain size of materials, and the multiple absorption in ice allow grain size mapping to be done with VIMS data. On Enceladus, the sizes of ice particles are generally well correlated with geologic features and surface ages, indicating a stratigraphic correlation between tectonic features and cryovolcanic activities [Jaumann et al. 2008b]. Grains much smaller than the wavelength of light cause enhanced blue scattering, including a Rayleigh scattering effect. This bluing effect is observed in the Saturn system and quantified by Clark et al. [2008, 2012].

Scipioni et al. [2017] produced image-cube maps of Enceladus,mapped ice grain sizes and identified plume deposits across the surface. The map showing the band-depths-ratio 1.50/2.02 μm overall shows a good agreement with the predicted plumes' deposits on the trailing side, where the amount of sub-micron particles decreases with increasing accumulation of ejecta material. However, this correlation is much weaker, or even absent, on the leading side of Enceladus, where the abundance of sub-micron particles is the highest across the entire surface.

Stephan et al. [2012] showed that the distribution of spectral endmembers as well as global band-depth variations of Dione's water-ice absorptions measurements imply that the bombardment with charged particles from Saturn's magnetosphere is one of at least two major global processes affecting Dione's surface. Ice deposits dominating its leading hemisphere appear rather associated with rays of the fresh impact crater Creusa on the northern leading hemisphere. These rays cross almost the whole hemisphere masking here any effects of possibly existent, but less dominant, processes as evident in the transition from the bright to dark regions on the Saturn-facing hemisphere (~0° W). CO_2 is evident in the dark material pointing to a possibly formation due to the interaction of the surface material with the impacting particles from Saturn's magnetosphere. Local spectral differences are consistent with impacting particles from the trailing side as described by Clark et al. [2008] with a pronounced ice signature on crater walls facing the leading side direction and shielded from impacting particles and dark material concentrated on interior crater walls facing the trailing hemisphere.

Spectra of ice also vary with temperature, so the surface temperatures of cold icy surfaces can be sensed without needing to measure longer wavelength thermal emission. Filachione et al. [2016] analyzed the ice spectra to produce daytime temperature maps of the satellite surfaces, just one more indication of the diversity of science that an imaging spectrometer can provide.

Observations of the small inner moons of Saturn were also obtained during the mission, including five best ever flybys of the ring moons Pan, Daphnis, Atlas, Pandora, and Epimetheus that were obtained between December 2016 and April 2017 during the Ring-grazing Orbits. An example of an observation is shown in Figure VIMS-4. Views of the moons' morphology, structure, particle environment, and composition were obtained, as well as VIMS maps in its full spectral range, except for Daphnis, which as of now is lacking a visible VIMS spectrum [Buratti et al. 2018b]. The optical properties of the moons are determined by two competing processes: contamination by a red chromophore in Saturn's main ring system, and accretion of bright particles from the E-ring originating from Enceladus.

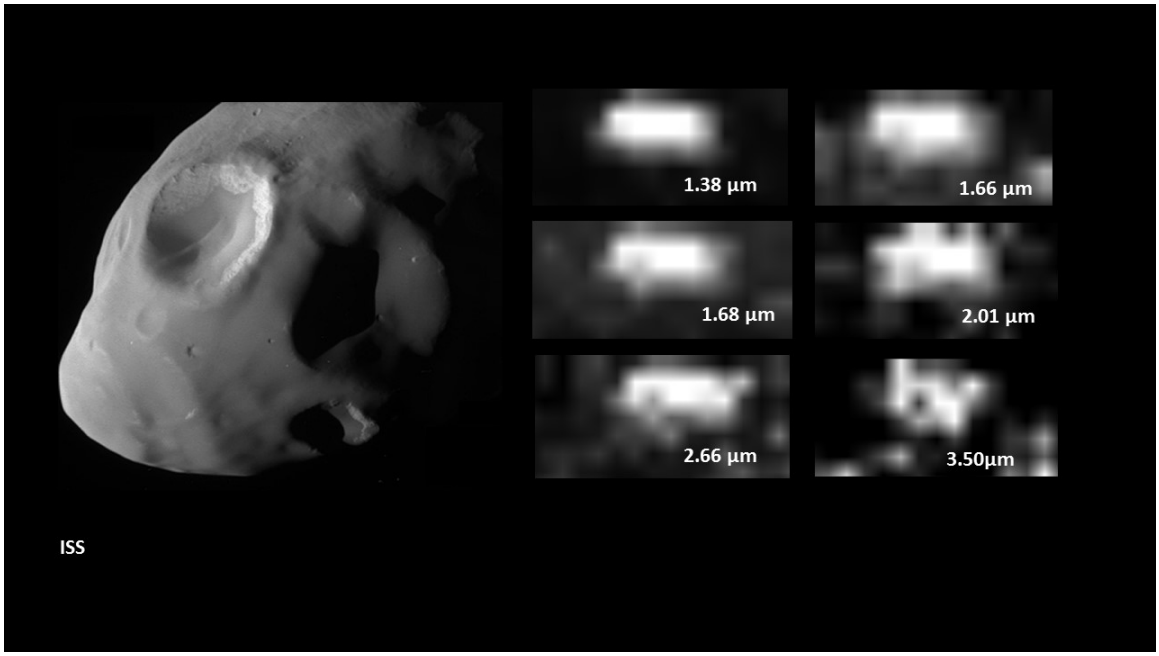

Figure VIMS-4. VIMS images of Pandora (*Right*), obtained on December 12, 2016 during a flyby that approached the shepherd moon to within a distance of 22,000 km. The ISS image is shown (*Left*) for context.

Open questions

Is there a connection between the composition of the plume and the regions on Enceladus where plume deposits exist, for example, Schenk et al. [2011]. How are the plume fallout zones compositionally different from the other zones on Enceladus that are affected by particles from the E-ring? What is the chemical make-up of the trailing side of Tethys, and why is it so reddish [Schenk et al. 2011] compared to regions dominated by the in-fall of E-ring grains?

What is the nature of possible activity on Dione? Is this moon still active, or has it been active in the recent past?

Similar to Dione, Tethys exhibits regions of smooth plains in which large craters have been removed. Cryovolcanic activity on Tethys is problematic: with a density even less than that of water, what is the driver for the activity?

What is the cause of the red streaks on Tethys and the blue dots on Rhea? Are they compositionally different, or can their appearance be explained solely by the effects of grain size?

What is the time scale for plume variability on Enceladus beyond the simple correlation with distance from Saturn, which is due to the magnitude of tidal effects? Is there a correlation with seasons? Can the variability be monitored from the ground?

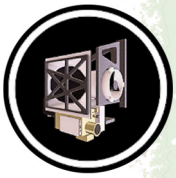

What is the identity of the red chromophore on the inner icy satellite surfaces? Is it nano-iron or organic material (tholins), and what are the transport processes to move this material around the Solar System? We have excellent evidence that Iapetus', Phoebe's and Hyperion's color is dominated by nano-iron and nano-iron oxide, but the red absorber is weaker on the inner satellites, and it cannot be established which possibility is correct for those satellites. Does radiation play a greater role in surface modification of these materials on the inner satellites?

What are some of the minor constituents of the Saturnian moons, and are the endogenic or exogenic? If exogenic, is the accretional process still ongoing?

How does the D/H ratio compare with that of other regions of the solar system, and what does that imply about the transport of volatiles on a large scale?

Is the detection of ammonia hydrate on the surfaces of the moons definitive?

Some of these unanswered questions might be answered with further research with the vast trove of archived data and with continuing ground-based observations, including the James Webb Space Telescope (JWST).

Science Assessment Summary

The VIMS instrument illustrated that the data an imaging spectrometer can deliver led to an amazing diversity in science. For icy satellites alone, from unexpected compositions, to geologic mapping, grain size distribution, temperature mapping, isotopic ratios, to plume dynamics, VIMS and the science team delivered far more than what was envisioned at the start of the mission. No single other instrument has shown such science diversity.

No single other instrument has shown such science diversity.

While the above science assessment documents huge accomplishments in satellite science with imaging spectroscopy data obtained by VIMS, interpretation of such data has been and remains difficult due to limited laboratory data and sophistication of models. For example, one of the main, seemingly simple, science questions yet to be answered is the nature of the coloring agent(s) on the inner icy Saturnian satellites and rings. While we obtained a definitive answer for the satellites beyond Titan, the origin of the coloring on the icy moons inside the orbit of Titan remain uncertain. This is largely due to lack of lab data and sophistication of radiative transfer models. Similarly, it was not until near the end of the prime mission before it was realized that the spectral effects of sub-micron ice particles affected the spectra in such profound ways, because there was no lab work or radiative transfer models for those conditions. Early on we wondered if there were calibration errors in VIMS causing unusual shapes of ice absorptions in VIMS data. If we had more extensive spectral libraries at the start of the mission, so much time would not have been lost going down blind alleys. Similar blind alleys were also traveled trying to identify other spectral features, like the 2.42 micron absorption. Initial thoughts were it was due to a C-N bond,

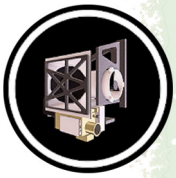

but the stronger absorptions of C-N bearing compounds at longer wavelengths were not seen. It took substantial resources to find the origin as trapped H_2. To date, the organics absorptions observed in VIMS data on several satellites still have not been precisely identified, only general categories like aliphatic versus aromatic can be determined. What major chemistry and implications are we missing with this lack of knowledge? Only additional resources put into lab work and modeling, funded by future NASA research programs will solve these problems. This should also be a lesson for future missions: the science output of the mission will be limited by current knowledge, including laboratory data and models.

Ring science

This part of the VIMS efforts had five principal components that are described below, along with their principal scientific goals, and major scientific results.

Ring macrostructure and dynamical processes

Our goal here was to study the radial structure of the main rings at the sub-km scale, at a variety of ring opening angles, and to examine their large-scale azimuthal variations (eccentricities, normal modes, etc.). Also of interest is the vertical structure of the rings, in those regions where it can be resolved.

Stellar occultations provide radial structure; over 170 were observed over the course of the mission, using ~40 different stars to provide different ring opening angles. A number of different investigations have been carried out using these data, as documented below. Particularly valuable for low-optical-depth regions such as the C-ring have been occultations of bright, low-latitude stars such as alpha Ori, omicron Ceti, and alpha CMa. But probably our most scientifically-productive data set is a sequence of ~17 occultations of the bright, high-latitude star gamma Crucis done on nearly-successive orbits with very similar geometry in 2008 and 2009.

Ring Plane Crossing observations were done on several near-equatorial orbits in order to provide measurements of the rings' photometric thickness as a function of radius and phase angle. Modeling of these data confirms that the ring's edge-on brightness is dominated by the vertically-extended F-ring.

Extended movies were obtained of the F-ring to study its complex azimuthal variations and also obtain high-quality spectra. Most of these observations were efficiently done as riders on ISS movies.

Ring microstructure and particle size distribution

Cassini observations, primarily radio and stellar occultations, have revealed the presence of various types of small-scale structure in the rings, notably self-gravity wakes (due to a completion between Keplerian shear and self-gravity) and radial oscillations caused by a viscous over-stability in dense

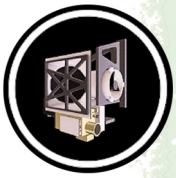

parts of the rings. The ring particle size distribution is critical to numerical models of ring structure and evolution, but can only be approached indirectly by Cassini.

Stellar occultations are again our main tool here, providing 100-m scale resolution or even better in some cases. The most useful observations here are occultations where the track of the star reaches a minimum radius in the rings. In hindsight, more of these events would have been useful. Occultations of low-latitude stars also provide quantitative data on the azimuthal variations in optical depth produced by self-gravity (S-G) wakes.

VIMS solar occultations by the main rings have provided valuable (and unique) information on the distribution of the smallest ring particles, in the mm–cm size range.

Spectral images of the rings obtained at phase angles of 165° or higher have provided very valuable data on the particle size distributions of the diffuse D-ring, F-ring, G-ring and E-ring that are not obtainable in any other way short of in situ sampling. Because the key scattering parameter in this geometry is the ratio $\Theta\lambda/r$, where Θ is the scattering angle, lambda is the wavelength, and r is the mean particle radius. VIMS 1– to 5-μm spectra effectively extend the range of observed scattering angles by a factor of 5.

Compositional variations

A primary goal of VIMS ring observations, not surprisingly, was to establish their composition and map radial variations in the fraction of non-icy material, suspected on the basis of Earth-based spectroscopy. This has turned out to be a very difficult problem, chiefly because of the very tiny amounts of non-icy material, estimated to be a few tenths of a per cent in most places. Although radial variations in the rings' spectral characteristics have been well-established, in the form of ice band depths and continuum slopes, there is still no consensus on the nature of the non-icy material. Recent Hapke modeling of spectra in selected regions indicate that both intimate and intra-particle mixing of water ice, amorphous carbon and organic material (modeled as Titan tholins) can reproduce the observed ring spectra, but nano-phase Fe-bearing materials such as these seen on Iapetus remain a possibility. A large variety of both Prime and Rider observations have been devoted to this problem.

VIMS radial scans generally provide the highest-quality data. This includes several high-resolution (30–60 km/pixel) complete radial scans obtained on the F-ring and Proximal orbits in 2017.

A unique set of radial scans were done at Saturn orbit insertion in 2004 that still provide our highest-resolution spectral data of the unlit side of the rings.

VIMS scans along the edge of Saturn's shadow on the rings are lower in resolution but were designed to minimize interference from Saturn-shine.

Several riders on ISS high-resolution radial scans also provide excellent-quality VIMS spectral data.

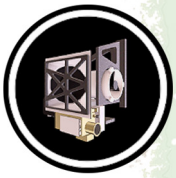

A large number of riders on lower-resolution CIRS radial scans provide useful data at a variety of ring opening and phase angles.

PHOTOMETRY AND LIGHT-SCATTERING PROCESSES

A number of observations were designed to provide lower spatial resolution spectral data on the rings at a wider range of observing geometries than are covered by the above compositional scans. The goal was to provide data with which to model light-scattering processes in the main rings, in particular the degree of multiple scattering between particles and the characteristics of the rings' well-known opposition brightening at low phase angles. The principal sets of observations are:

a. Standardized ring ansa mosaics done at ~20 R_S.

b. Scans and small mosaics at phase angles of 165° or higher.

c. Full system mosaics at distances of 30–40 R_S.

d. Radial scans across the rings immediately before and after the Equinox in August 2009, when the solar illumination was almost edge-on.

e. Riders on ISS photometry observations.

DIFFUSE RING STRUCTURE, PARTICLE SIZE, AND COMPOSITION

VIMS was well-suited to obtain reflected-light observations of Saturn's diffuse rings, including the D-ring, F-ring G-ring and E-ring as well as several smaller-scale structures such as narrow ringlets and clumps within gaps in the main rings and arcs associated with the small satellites such as Aegaeon. This is because of the instrument's very low level of scattered off-axis light (unlike the ISS-wide angle camera (WAC), which is also used for such studies), its spectral range, and its capacity to take long exposures. A mixture of VIMS-prime and ISS-rider observations was employed, with most observations being made at high phase angles where dust-sized particles are brightest. The principle sets of observations are:

a. Radial mosaics of one ansa of the E-ring at various phase angles.

b. Image cubes targeted to one ansa of the G-ring at various phase angles. Most E_ and GPHASE observations were made when the rings were viewed edge-on, on equatorial orbits, in order to increase the line-of-sight optical depth of these very diffuse structures.

c. Movies of the F-ring, intended to cover all (or most) co-moving longitudes of the ring in a single observation. This was done initially as VIMS-prime and later as ISS-riders, on non-equatorial orbits to resolve radial structure.

d. Riders on various ISS faint ring observations.

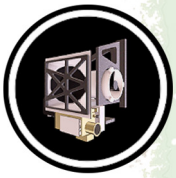

Cornell non-rings observations

In addition to observations of the rings, the Cornell group also took on responsibility for several categories of non-ring observations which used similar techniques or designs as some Rings observations.

> … VIMS proved to be an effective instrument for observing atmospheric occultations by Saturn and Titan.

Saturn and Titan stellar occultations

Using the same technique developed for ring stellar occultations, as discussed in the section entitled Saturn and Titan Stellar Occultations, VIMS proved to be an effective instrument for observing atmospheric occultations by Saturn and Titan. With sampling intervals of 20–40 msec, the altitude resolution is typically 100–400 m. The science obtained from such observations includes vertical profiles of temperature, atmospheric composition (chiefly methane) and aerosol abundance, as functions of latitude, as well as information on the shape of Saturn's geoid. Over the course of the mission ~70 stellar occultations by Saturn were planned, with all but 13 returning useful data. Another 35 were observed as bonuses at the end of ring occultations, but many of these were seen against a sunlit limb and suffer badly from background light from the planet. A total of 14 stellar occultations by Titan were observed, all but one successfully. Some of the latter show noticeable aerosol layers. An important limitation of such observations is atmospheric refraction, which eventually causes the star to leave the VIMS pixel. This limits the maximum depth of Saturn occultations to a pressure level of ~5 mbar.

Saturn and Titan solar occultations

Using the solar port originally designed for spectral calibrations, VIMS has observed 29 solar occultations by Saturn and 16 by Titan. Because the angular diameter of the sun exceeds the VIMS instantaneous field of view (IFOV) of 0.5 mrad, solar occultations were observed in IMAGE mode rather than in the special mode designed for stellar occultations, thus reducing the vertical resolution to10–30 km. All of these observations were done as riders on UVIS occultations. Analysis of several Titan solar occultations has led to vertical profiles of methane and CO, as well as characterization of the aerosol size distribution. All but one of the solar occultations attempted returned data, but in several cases the Titan observation were corrupted because the bright limb of Titan itself appeared in the main VIMS aperture while the sun was in the solarport.

Enceladus plume observations

VIMS made several important observations of the plumes of Enceladus, including both high-phase images that led to the discovery of the plumes' significant variations with orbital phase and a solar occultation from which the volume density of water ice particles could be measured directly.

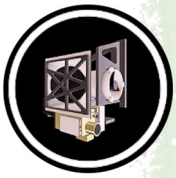

STELLAR CALIBRATIONS

In addition to regular observations of standard stars for instrumental calibration purposes, VIMS also obtained near-IR spectra for ~40 of the brightest stars in the sky, many of which were published in an IR spectral atlas. Many of the stars are late-type variables that exhibit strong absorptions due to CO and water vapor.

SOLAR PORT CALIBRATIONS

Over the course of the mission, a substantial number of calibration observations of the Sun were made with the VIMS solar port. Some of these simply provide routine monitoring of the solar spectrum, as check on instrumental sensitivity drifts while others were used to map the spatial variations in its throughput.

EXOPLANET AND VENUS TRANSITS

In 2010 and 2011 several attempts were made to observe stellar transits of the giant exoplanet, HD189533b. VIMS was used in 2 × 2 IMAGE mode in order to provide simultaneous background measurements and some insurance against pointing variations. Unfortunately the star was much fainter than normal VIMS point source targets and no transit was detected. Analysis of the data, however, demonstrated that VIMS sensitivity scaled with integration time as expected, even down to signal levels of order 0.1 DN. In December 2012 a very similar technique was used to monitor a predicted transit of Venus across the sun using the VIMS solar port. This observation, which involved a reduction in the solar flux of only 0.01% was successfully observed, though the signal-to-noise ratio was too low to detect the absorption signature of Venus' atmosphere in the transit spectra.

PRINCIPAL RESULTS

1. VIMS spectral observations at SOI revealed that the mysterious red coloring agent in the rings resides within the water ice grains that make up the regoliths on the ring particles [Nicholson et al. 2008].

2. Observations of ring occultations of o Ceti (aka Mira) in 2005 confirmed the existence of strong self-gravity wakes in the A-ring, leading to the first reliable estimates for the ring thickness of ~6 meters in this region [Hedman et al. 2007b].

3. Observations of multiple stellar and radio occultations in 2005–2009 led to the discovery that the amplitude of the radial perturbations at the outer edge of the B-ring (due to the Mimas 2:1 resonance) varies from ~70 km to < 5 km, and that these may also be indirectly responsible for the regular spacing of the multiple gaps within the Cassini Division [Hedman et al. 2010].

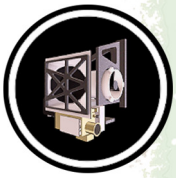

4. The observation of restrahlung bands of H_2O ice in a stellar occultation by the F-ring permitted discrimination between clumps of macroscopic source bodies and the background of micron-sized dust [Hedman et al. 2011].

5. A comparative analysis of VIS-IR spectral indicators (slopes and band depths) of rings, regular satellites and small moons has allowed VIMS to map the distribution of water ice and red contaminant materials across the Saturn system [Filacchione et al. 2012, 2013; Clark et al. 2012]. However, in the main rings, the abundance of the red coloring agent is lower and there is at present no way to distinguish definitively between the nano-iron model and more traditional carbon-tholin models. Recent modeling results obtained with Hapke theory indicate that both intimate and intraparticle mixing of water ice, amorphous carbon and organic material (Titan tholins) can reproduce the observed ring spectra [Ciarniello et al. 2019].

6. VIMS investigations of numerous, small-scale, wavelike structures in the C-ring have provided strong evidence that several of these are density waves driven by global oscillations within Saturn itself, opening up a new window on the planet's internal structure and rotation rate [Hedman and Nicholson 2013; Hedman and Nicholson 2014].

7. A pair of stellar occultations with turnaround radii in the inner A-ring yielded strong evidence for viscous over-stability in the denser parts of Saturn's rings, supporting previous work based on radio occultation data. [Hedman et al. 2014].

8. Together with occultation data from RSS and UVIS, VIMS data from more than 100 stellar occultations has led to the characterization of numerous non-circular features in the C-ring and Cassini Division, including the discovery of a large number of normal mode oscillations on the edges of both narrow gaps and their associated ringlets. [Nicholson et al. 2014a, 2014b; French et al. 2016].

9. Ring temperature maps have been built from VIMS spectra by using an indirect method based on the wavelength of the temperature-dependent reflectance peak at 3.6 μm [Filacchione et al. 2014].

10. Application of a new phase-sensitive wavelet analysis technique to selected VIMS stellar occultation profiles has led to the identification of several satellite-driven density waves in the optically-thick B-ring, resulting in the first estimates of surface mass density in this most opaque part of Saturn's rings. The results are unexpectedly low, and imply a total mass for the rings of ~40 percent that of Mimas [Hedman and Nicholson 2016].

EXAMPLES OF STELLAR OCCULTATION OBSERVATIONS

Figures VIMS-5 through VIMS-10 show examples of stellar occulation observations.

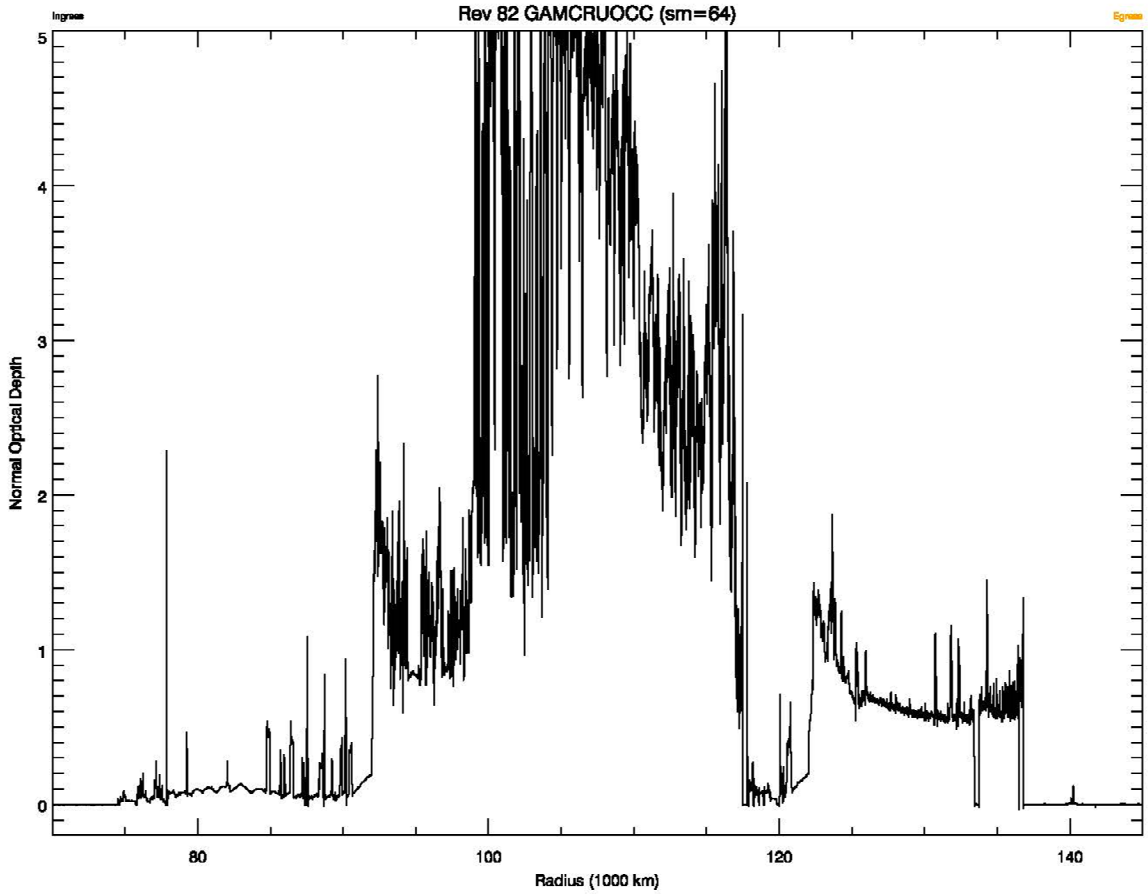

Figure VIMS-5. An optical depth profile of Saturn's rings at a wavelength of 2.92 microns, derived from a VIMS occultation of the star gamma Crucis on rev 82, obtained in August 2008. This is one of the highest-quality VIMS occultation observations, as evidenced by the very flat baselines exterior to the A-ring's edge at 136,770 km and interior to the C-ring at 74,500 km. Note that the optical depth exceeds 5 in some regions of the central B-ring.

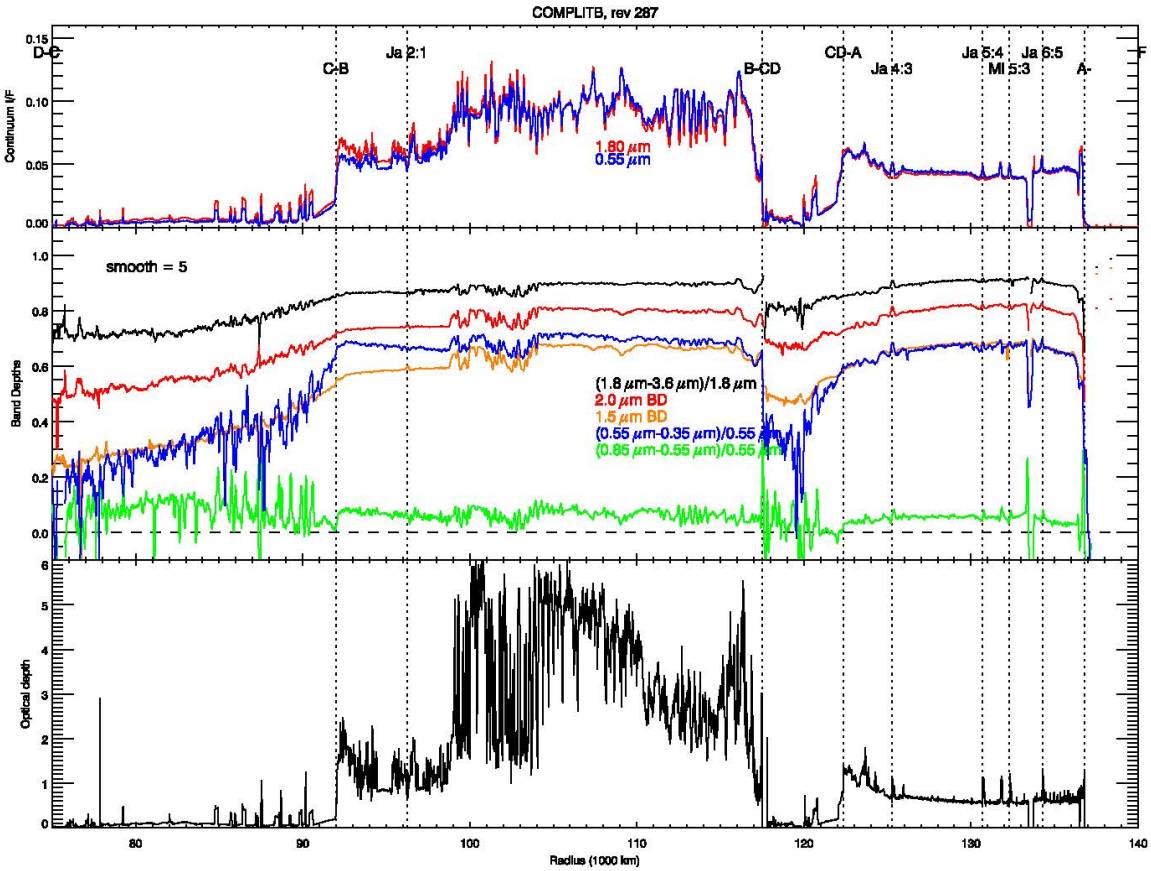

Figure VIMS-6. Radial profiles of IR spectral parameters derived from the final VIMS scan across the sunlit rings on rev 287, rebinned to a uniform sampling resolution of 20 km. *Upper panel*: shows the reflectivity of the rings at continuum wavelengths of 0.55 and 1.8 microns, with the locations of major ring boundaries and the strongest density waves identified by vertical dotted lines. *Middle panel*: shows the fractional depths of the IR water ice bands at 1.55, 2.0 and 3.6 microns, coded by line color, as well as the UV and red slopes measured with the visual channel, all smoothed to a resolution of 100 km. *Lower panel*: shows the optical depth profile of the rings obtained from a VIMS occultation of the star gamma Crucis on rev 82, binned to 10-km resolution, as context for the spectral scans.

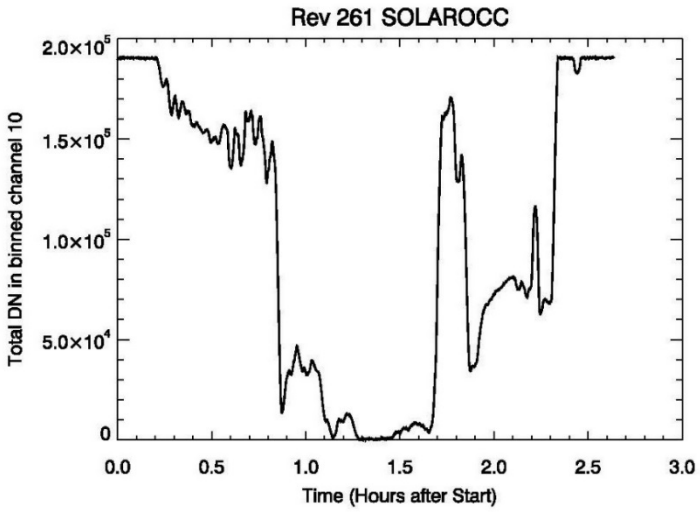

Figure VIMS-7. A transmission profile of the rings at a wavelength of 1.06 microns derived from a VIMS solar occultation on rev 261, obtained in February 2017. Note the lower spatial resolution compared to the stellar occultation in Figure VIMS-5, but the much higher signal-to-noise ratio.

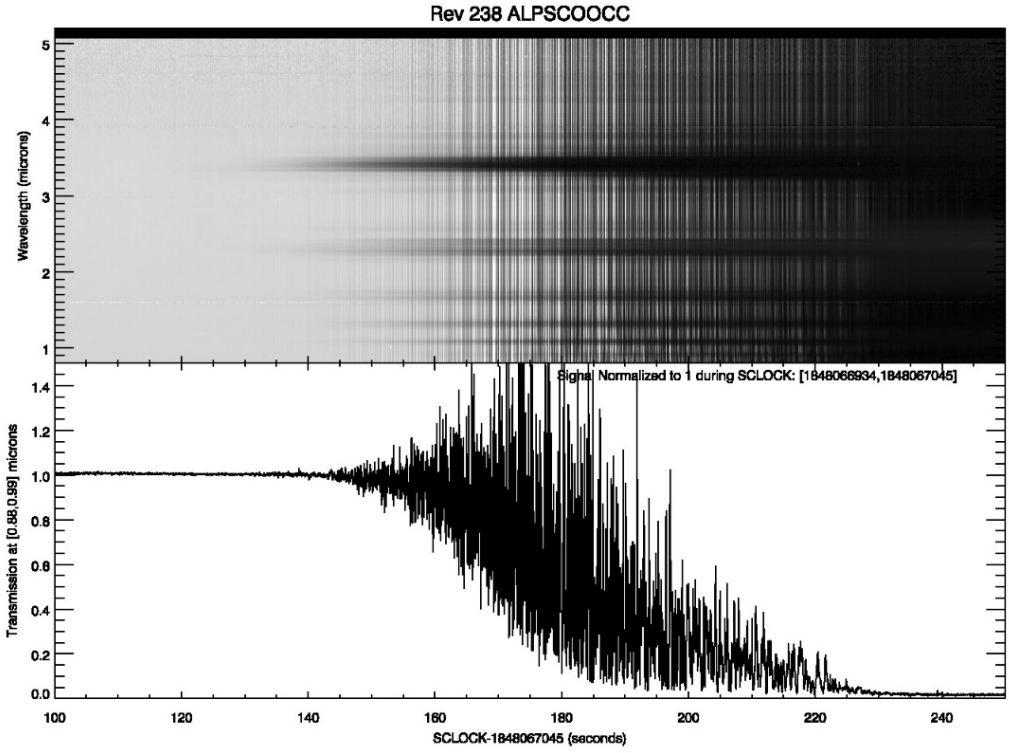

Figure VIMS-8. An ingress stellar occultation by Saturn's atmosphere at 63 deg south latitude on rev 238, obtained in July 2016. Time is shown on the abscissa, in seconds, with wavelength on the ordinate, from 0.85 to 5.1 microns. The greyscale indicates the measured stellar brightness, normalized to unity before the occultation began. In addition to a gradual loss of signal due to differential refraction, punctuated by rapid oscillations due to turbulent scintillation, one sees absorption at several discrete wavelengths (3.4, 2.3, 1.7 microns, etc.) due to stratospheric gasses, chiefly methane.

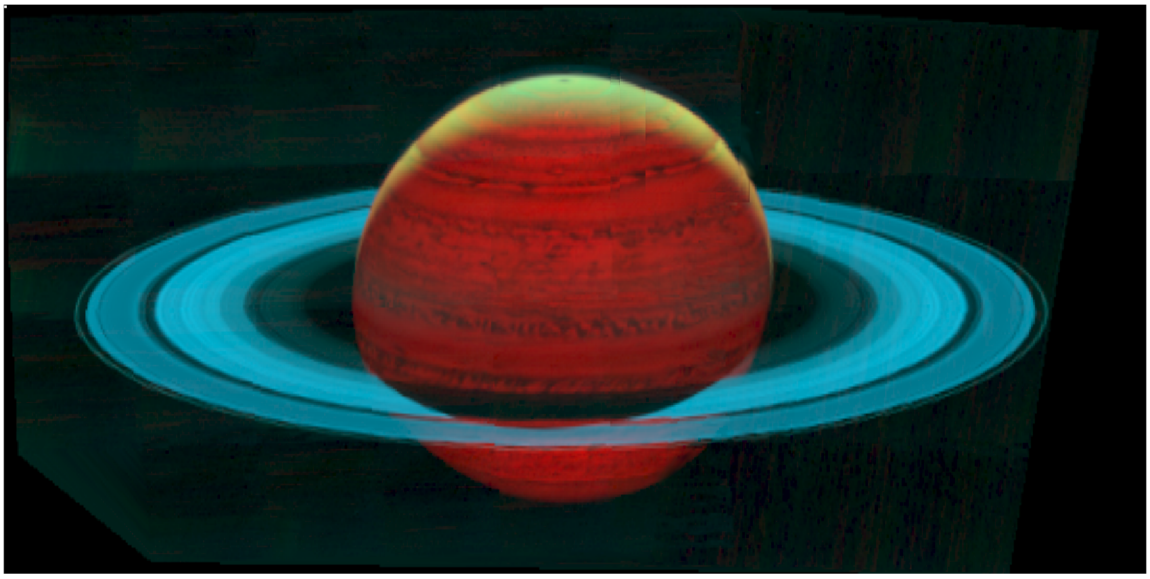

Figure VIMS-9. A mosaic of Saturn and its rings obtained by VIMS on revs 287/289, in August 2017. A total of 35 VIMS cubes were combined to produce this false-color image, with *Red* showing thermal emission from Saturn's deep atmosphere at 5 microns, *Green* showing reflected sunlight from the clouds at 3 microns, and *Blue* showing reflected sunlight from the icy rings at 1.8 microns. The view is at a phase angle of 140 degrees, with only a thin crescent in the north illuminated by sunlight. This close to summer solstice, the planet's shadow on the rings extends only just beyond the Cassini Division. Dark mottling on the planet is due to the variable thickness of clouds in the upper atmosphere. Saturn's oblateness is slightly exaggerated here by changes in the viewing geometry during the total observation period of almost 12 hours.

Open questions

A big unanswered question remains that of the nature of the non-icy component. We know that some of it is meteoritic (or cometary) debris, but the true nature of the UV-absorbing component(s) remains elusive. More sophisticated spectral modeling might eventually solve this problem, as we certainly have acquired plenty of spectra.

Titan

Before Cassini, Titan's surface was unknown territory because aerosols in its dense nitrogen and methane atmosphere hide the surface in the optical wavelengths. It was believed that only radar waves would be able to cross the atmosphere and provide images of the surface, thus it was not expected that the VIMS instrument would be able to image Titan's surface. During Cassini's cruise phase, telescopic observations hinted that Titan's surface may be observable by VIMS at 1.6 and 2.0 μm [Meier et al. 2000], providing impetus for VIMS prime time observations during the first Titan flyby (T00A). Since it had been added to solve the issue of the transmission between the Huygens probe and the Cassini spacecraft, this flyby had not yet been allocated to any instrument. During that first flyby, the VIMS instrument demonstrated its potential to observe Titan's surface in seven atmospheric windows [Sotin et al. 2005]. The 5-μm band in particular was shown to have very little

scattering from atmospheric aerosols, while the 2-μm band proved to be the best compromise between solar flux, atmospheric scattering, and detector sensitivity. That discovery propelled the VIMS instrument into a key mapping role for Titan, and provided information very complementary to radar images. Most of the VIMS images of Titan's surface were acquired during the extended mission because the flybys during the Prime Mission were already allocated.

As history has shown, VIMS made some fundamental observations of Titan's atmosphere with implications for both its composition and dynamics. A solar port, aligned with the UVIS solar port, was set up to allow for solar occultation as riding along with UVIS, and a dozen solar occultation observations of Titan were performed at different latitudes and seasons, providing key information on the aerosol content of the atmosphere. Finally, specular reflections from Titan's seas were observed at 5 μm and have provided key information on the presence and dynamics of Titan's seas. The following three sections provide the main scientific results obtained by the VIMS instrument.

TITAN'S SOLID SURFACE

The VIMS instrument can see Titan's surface through seven atmospheric windows in the near infrared between 0.9 and 5 μm [Sotin et al. 2005; Rodriguez et al. 2006]. Because atmospheric scattering decreases with wavelength, and observations of specular reflection (Figure VIMS-10) show that there is very little scattering at 5 μm, it was determined that optimum imaging occurred at 2 μm. RGB, synthetic color images can be constructed by choosing three out of the seven wavelengths from a VIMS image cube, enhancing the visibility of geological features, which can be

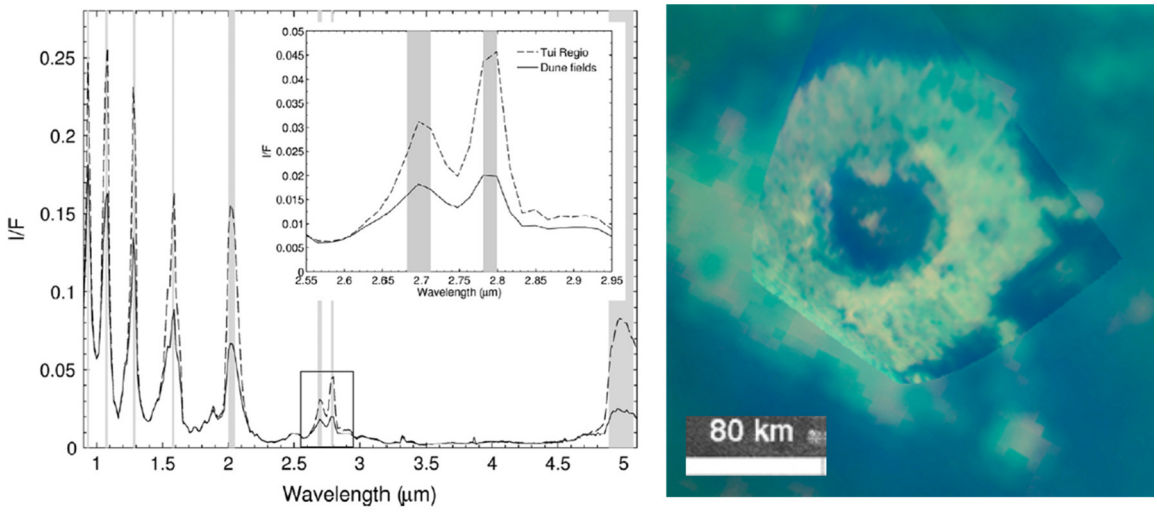

Figure VIMS-10. Titan's surface. *Left*: Typical spectrum of Titan's surface with the dark spectrum taken over dune fields and the bright spectrum taken on the bright feature known as Tui regio. *Right*: Sinlap crater is considered as the least altered impact crater on Titan [Neish et al. 2015]. Resolution ranges from 1 to 4 km. The RGB image was constructed with R=4.8–5.2 μm, G=2.00 μm, B=1.28 μm.

observed with pixel size as small as 500 m in a few spots. The resolution depends on the distance between the Cassini spacecraft and Titan's surface and the global maps are mosaics of images with very different pixel scales and viewing geometry. The VIMS images enable detailed comparisons to be carried out with Titan Radar Mapper (RADAR) images, for example, Soderblom et al. [2007a] demonstrated the very strong correlation of the dark brown VIMS units with the radar dune fields. They suggested that the bright areas surrounded by these dune fields are deposits of bright, fine, precipitating tholin-aerosol-dust, and hypothesized that chemical/mechanical processes may be converting the bright, fine-grained aerosol deposits into the dark, saltating, hydrocarbon and/or nitrile grains. Alternatively the dark dune materials may be derived from a different type of air aerosol photochemical product than Titan's bright materials.

VIMS mapped a few impact craters [Le Mouélic et al. 2008; Buratti et al. 2012; Neish et al. 2015]. These impact craters exhibit various degrees of degradation, with Sinlap being the least degraded. Buratti et al. [2012] studied the crater Paxsi, located in the dune field known as Senkyo. This crater's dark brown interior was attributed to infilling by dune material. The number density of impact craters on Titan is small suggesting a young surface.

At the end of the Cassini mission, it is not clear that Titan's surface displays cryovolcanic features. 5-µm-bright lobate features at Tui regio [Barnes et al. 2006] suggest an endogenic origin, but, other authors have attributed this 5-µm-bright feature to evaporitic material [MacKenzie et al. 2014], which suggests that Tui regio may be located in a depression near Titan's equator. Similarly, Hotei Regio, also located in the Xanadu area to the East of Hotei, exhibits a 5 µm bright feature also interpreted as evaporitic material. The interpretation that the 5-µm-bright feature is evaporitic material comes from the observation of such features at the North poles, next to the large hydrocarbons seas.

The composition of Titan's surface has stimulating much debate since the observation of the surface at seven infrared wavelengths, and one, important unsettled question is the presence or absence of convincing water ice deposits on Titan's surface. Water ice has a clear spectral signature in the 2.7-µm window, characterized by two peaks at 2.7 and 2.8 µm. Its spectrum shows a strong decrease in albedo between 2.7 and 2.8, suggesting that the 2.8-µm peak should be much less pronounced than the 2.7-µm peak. This is not what is observed, suggesting that Titan's surface is covered by organic material which masks the spectral signature of water ice. The composition of Titan's surface has been studied by Clark et al. [2010], using absorption bands in the 5-µm atmospheric window. They discovered a benzene absorption (5.05 µm), alkane absorptions (near 4.97 µm), and a component yet to be identified which has an absorption at 5.01 µm.

TITAN'S SEAS

Titan is the only place in the solar system, other than Earth, that has seas of liquids at its surface. That many very dark areas on Titan are bodies of liquid was confirmed by the solar glint (secular reflection) at 5 µm (Figure VIMS-11), first observed by Stephan et al. [2010d] over Jingpo Lacus.

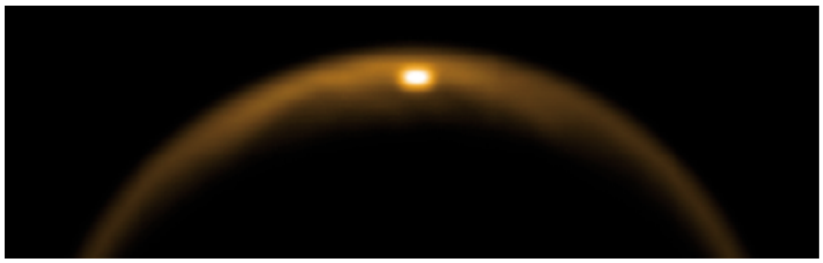

Figure VIMS-11. The 5 μm solar glint during the T58 flyby.

This glint demonstrated that the lake's surface is smooth and free of scatterers, at the observation wavelength of 5 μm. Just before Cassini arrived at Saturn, Lorenz and Lunine [2005] wrote:

> *"The glint may be observable at longer wavelengths by VIMS (although this will not be trivial, since the specular point moves across the surface as the sub-spacecraft point moves, and VIMS is a mapping spectrometer, not a framing camera, so its image is not built instantaneously)".*

Despite these difficulties, several observations of 5-μm specular reflections have been made. Measuring the intensity of specular reflections was employed by Barnes et al. [2011b], to demonstrate that the surfaces of many of Titan's lake and seas are very smooth, with waves which have slopes 2 orders of magnitude lower than those on Earthly lakes and seas.

Titan's lakes and seas are very dark in Titan's atmospheric windows, and their distribution correlates very well with the radar observations [Sotin et al. 2012]. Besides the specular points that provide information on the waves, VIMS observations also provide information on transport processes operating to move liquids between Kraken Mare and Ligeia Mare through a channel known as Trevize fretum [Sotin et al. 2015].

VIMS also determined that ethane is one of the components present in a large lake, Ontario lacus, located in the southern hemisphere [Brown et al. 2008]. The VIMS instrument cannot determine whether methane is present because of its abundance in the atmosphere. However, in the solid surface, liquid ethane/methane was detected by VIMS in some non-polar locations [Clark et al. 2010].

TITAN'S ATMOSPHERE

VIMS provided data important to understanding on Titan's climate by observing the appearance and evolution of clouds [Rodriguez et al. 2009, 2011], as well as determining their composition using solar occultation observations [Bellucci et al. 2009; Maltagliati et al. 2015]. Two types of clouds were detected during the period 2005–2009 during northern winter (Figure VIMS-12). Initially the north pole was covered by a polar hood, while later clouds with a short lifetime were detected at southern mid-latitudes.

The composition of Titan's atmosphere was derived from solar occultation observations by Bellucci et al. [2009], who determined the mixing ration of methane above an altitude of 200 km to

be between 1.4 and 1.7%, while the amount of CO was 33 ±10 ppm. Maltagliati et al. [2015] used solar occultation observations to refine measurement of the mixing ratio of CH_4, finding it be 1.28% ±0.08% and the CO abundance equal to 46 ±1 6 ppm, comparable with the previous measurements. Their work showed the presence of ethane, explaining many of the remaining, and previously unattributed absorption bands.

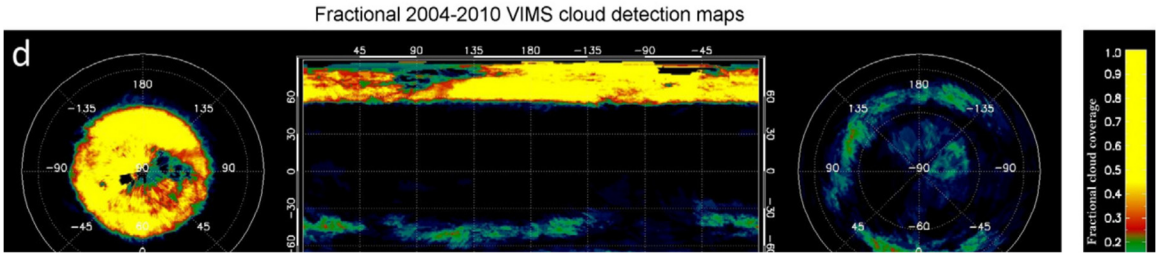

Figure VIMS-12. Fraction of cloud coverage on Titan during the period 2004–2010.

Conclusion

The VIMS instrument exceeded all expectations with regard to its studies of Titan, with major advances in understanding of Titan's surface and atmosphere. It made fundamental discoveries regarding the composition of Titan's surface and atmosphere, the dynamics of Titan's atmosphere, and the morphology of its surface. VIMS paved the way for the development of an infrared camera that may eventually enable us to obtain global maps of Titan's surface at 25-meter resolution (Huygens type resolution), providing important information on unanswered questions about Titan's geology, such as why is the surface so young; why are there geomorphological features that trace outgassing; is there fluvial erosion; what are the ages of any methane outbursts; are there tectonic features; is there aeolian transport of organics?

Open questions

Are there water ice outcrops on the surface?

What is the composition of the river beds?

Where are located the ethane reservoirs?

Are there morphological features related to the release of methane in the atmosphere?

What is the nature of the organic material covering Titan's surface?

What is the nature of the very bright deposits?

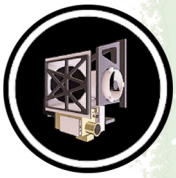

ACRONYMS

Note: For a complete list of Acronyms, refer to Cassini Acronyms – Attachment A.

AO	Announcement of Opportunity
CAPS	Cassini Plasma Spectrometer
CIRS	Composite Infrared Spectrometer
D/H	Deuterium to Hydrogen
FUV	far ultraviolet channel
HST	Hubble Space Telescope
IFOV	instantaneous field of view
IR	infrared
ISS	Imaging Science Subsystem
JWST	James Webb Space Telescope
mrad	microradians
NAC	narrow angle camera
NIMS	Near Infrared Mapping Spectrometer Subsystem
RADAR	Titan Radar Mapper
RPWS	Radio and Plasma Wave Spectrometer
RSS	Radio Science Subsystem
S-G	self-gravity
SNR	signal to noise ratio
SOI	Saturn Orbit Insertion
UV	ultraviolet
UVIS	Ultraviolet Imaging Spectrograph
V	visible
VIMS	Visual and Infrared Mapping Spectrometer
VIS-IR	visible-infrared
WAC	wide angle camera

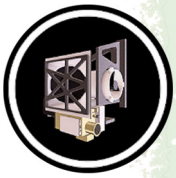

THE VIMS BIBLIOGRAPHY SUMMARY

The Cassini VIMS and its team contributed to 373 peer-reviewed articles, book chapters, and reviewed conference proceedings. The publications span 29 years (and counting) from 1990 to 2018.

This bibliography was compiled from the online databases Scopus, Science Direct, and the SAO/NASA Astrophysics Data System. Generally, the databases were searched for “Cassini VIMS” as a keyword, and the returned entries were evaluated to determine if VIMS data were the main driver of a publication or made significant contributions to its scientific conclusions. Publications were also considered for inclusion at the recommendation of VIMS Science Team members based on the above criteria. These entries were assembled in an EndNote Database (available on request), and further organized and analyzed (also available on request).

The contributions appeared in 54 different publications in at least 5 different countries. Icarus published 198 of the references (53%), and 48 (15%) appeared in Planetary & Space Science. Geophysical Research Letters had 17 articles, all other sources had 10 or less. Twenty journals had only a single paper. Also represented were the proceedings of three conferences, eight books, and four graduate dissertations.

The references were categorized based on their target, discipline of study, and technique. Almost the same number of publications was contributed on the study of Saturn and on the study of Titan, 164 & 167 respectively. Also represented were Venus (2), Earth & its moon (5), Mars (1), Jupiter (23), stars (7), and the hardware and software systems used by the instrument (10).

There are 3,272 author listings in the bibliography, representing over 720 individuals. Three hundred and ninty-six of them appear only once, while P.D. Nicholson is the most prolific with 129 entries (Appearing in 35% of the references, representing 4% of the total author listings). The largest number of authors on a single paper is 34. The median number of authors for a reference is 7, the mode is 3.

Almost 190 different people lead the publications, with M. M. Hedman appearing as first author most often (15 times).

Citation numbers were collected for all but two of the entries. The VIMS h-index as calculated from the 371 references with available data is 47. The highest number of reported citations is 248, and the average is 21.

Further details of analysis are available on request. Please direct any requests, additions, or corrections to ejoseph@lpl.arizona.edu.

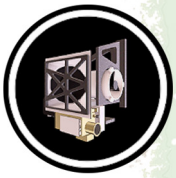

REFERENCES

Disclaimer: The partial list of references below correspond with in-text references indicated in this report. For all other Cassini references, refer to Attachment B – References & Bibliographies; Attachment C – Cassini Science Bibliographies; the sections entitled References contributed by individual Cassini instrument and discipline teams located in Volume 1 Sections 3.1 and 3.2 Science Results; and other resources outside of the Cassini Final Mission Report.

Ádámkovics, M., J. W. Barnes, M. Hartung, I. de Pater, (2010), Observations of a stationary mid-latitude cloud system on Titan, Icarus, 208, 2, 868–877, doi: 10.1016/j.icarus.2010.03.006.

Ádámkovics, M., I. de Pater, M. Hartung, J. W. Barnes, (2009), Evidence for condensed-phase methane enhancement over Xanadu on Titan, Planetary and Space Science, 57, 13, 1586–1595, doi: 10.1016/j.pss.2009.07.001.

Adriani, A., B. M. Dinelli, M. López-Puertas, M. García-Comas, M. L. Moriconi, E. D'Aversa, B. Funke, A. Coradini, (2011), Distribution of HCN in Titan's upper atmosphere from Cassini/VIMS observations at 3μm, Icarus, 214, 2, 584–595, doi: 10.1016/j.icarus.2011.04.016.

Adriani, A., A. Gardini, E. D'Aversa, A. Coradini, M. L. Moriconi, G. L. Liberti, R. Orosei, G. Filacchione, (2005), Titan's ground reflectance retrieval from Cassini-VIMS data taken during the July 2nd, 2004 fly-by at 2 am ut, Earth, Moon and Planets, 96, 3–4, 109–117, doi: 10.1007/s11038-005-9057-3.

Anderson, C. M., R. E. Samuelson, D. Nna-Mvondo, (2018), Organic Ices in Titan's Stratosphere, Space Science Reviews, 214, 8, doi:10.1007/s11214-018-0559-5.

Anderson, C. M., R. E. Samuelson, R. K. Achterberg, J. W. Barnes, F. M. Flasar, (2014), Subsidence-induced methane clouds in Titan's winter polar stratosphere and upper troposphere, Icarus, 243, 129–138, doi: 10.1016/j.icarus.2014.09.007.

Atreya, S. K., E. Y. Adams, H. B. Niemann, J. E. Demick-Montelara, T. C. Owen, M. Fulchignoni, F. Ferri, E. H. Wilson, (2006), Titan's methane cycle, Planetary and Space Science, 54, 12, 1177–1187, doi: 10.1016/j.pss.2006.05.028.

Badman, S. V., G. Provan, E. J. Bunce, D. G. Mitchell, H. Melin, S. W. H. Cowley, A. Radioti, et al., (2016), Saturn's auroral morphology and field-aligned currents during a solar wind compression, Icarus, 263, 83–93, doi: 10.1016/j.icarus.2014.11.014.

Badman, S. V., N. Achilleos, C. S. Arridge, K. H. Baines, R. H. Brown, E. J. Bunce, A. J. Coates, et al., (2012a), Cassini observations of ion and electron beams at Saturn and their relationship to infrared auroral arcs, Journal of Geophysical Research: Space Physics, 117, no. A1.

Badman, S. V., D. J. Andrews, S. W. H. Cowley, L. Lamy, G. Provan, C. Tao, S. Kasahara, et al., (2012b), Rotational modulation and local time dependence of Saturn's infrared H_3^+ auroral intensity, Journal of Geophysical Research: Space Physics, 117, 9, doi: 10.1029/2012JA017990.

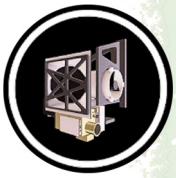

Badman, S. V., N. Achilleos, K. H. Baines, R. H. Brown, E. J. Bunce, M. K. Dougherty, H. Melin, J. D. Nichols, T. Stallard, (2011a), Location of Saturn's northern infrared aurora determined from Cassini VIMS images, Geophysical Research Letters, 38, 3, doi: 10.1029/2010GL046193.

Badman, S. V., C. Tao, A. Grocott, S. Kasahara, H. Melin, R. H. Brown, K. H. Baines, M. Fujimoto, T. Stallard, (2011b), Cassini VIMS observations of latitudinal and hemispheric variations in Saturn's infrared auroral intensity, Icarus, 216, 2, 367–375, doi: 10.1016/j.icarus.2011.09.031.

Baines, K. H., L. A. Sromovsky, R. W. Carlson, T. W. Momary, P. M. Fry, (2019), The visual spectrum of Jupiter's Great Red Spot accurately modeled with aerosols produced by photolyzed ammonia reacting with acetylene, Icarus, 330, 217–229, doi: 10.1016/j.icarus.2019.04.008.

Baines, K. H., L. A. Sromovsky, R. W. Carlson, T. W. Momary, P. M. Fry, (2019) The visual spectrum of Jupiter's Great Red Spot accurately modeled with aerosols produced by photolyzed ammonia reacting with acetylene, Icarus, 330, 217–229.

Baines, K. H., L. A. Sromovsky, P. M. Fry, T. W. Momary, R. H. Brown, B. J. Buratti, R. N. Clark, P. D. Nicholson, C. Sotin, (2018), The eye of Saturn's north polar vortex: Unexpected cloud structures observed at high spatial resolution by Cassini/VIMS, Geophysical Research Letters, 45, 12, 5867–5875, doi:10.1029/2018GL078168.

Baines, K. H., P. A. Yanamandra-Fisher, T. W. Momary, G. S. Orton, G. G. Villar Iii, L. N. Fletcher, H. Campins, A. S. Rivkin, M. Shara, (2013), The temporal evolution of the July 2009 Jupiter impact cloud, Planetary and Space Science, 77, 25–39, doi: 10.1016/j.pss.2012.05.007.

Baines, K. H., M. L. Delitsky, T. W. Momary, R. H. Brown, B. J. Buratti, R. N. Clark, P. D. Nicholson, (2009a), Storm clouds on Saturn: Lightning-induced chemistry and associated materials consistent with Cassini/VIMS spectra, Planetary and Space Science, 57, 1650–1658, doi: 10:1016/j.pss.2009.06.025.

Baines, K. H., T. W. Momary, L. N. Fletcher, A. P. Showman, M. Roos-Serote, R. H. Brown, B. J. Buratti, R. N. Clark, P. D. Nicholson, (2009b), Saturn's north polar cyclone and hexagon at depth revealed by Cassini/VIMS. Planetary and Space Science, 57, 1671–1681, doi: 10.1016/j.pss.2009.06.026.

Baines, K. H., S. Atreya, R. W. Carlson, D. Crisp, P. Drossart, V. Formisano, S. S. Limaye, W. J. Markiewicz, G. Piccioni, (2006a), To the depths of Venus: Exploring the deep atmosphere and surface of our sister world with Venus Express, Planetary and Space Science, 54, 13–14, 1263–1278, doi: 10.1016/j.pss.2006.04.034.

Baines, K. H., P. Drossart, M. A. Lopez-Valverde, S. K. Atreya, C. Sotin, T. W. Momary, R. H. Brown, B. J. Buratti, R. N. Clark, P. D. Nicholson, (2006b), On the discovery of CO nighttime emissions on Titan by Cassini/VIMS: Derived stratospheric abundances and geological

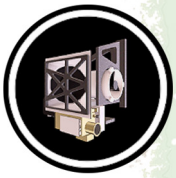

implications, Planetary and Space Science, 54, 15, 1552–1562, doi: 10.1016/j.pss.2006.06.020.

Baines, K. H., P. Drossart, T. W. Momary, V. Formisano, C. Griffith, G. Bellucci, J. P. Bibring, et al., (2006c), The atmospheres of Saturn and Titan in the near-infrared: First results of Cassini/Vims, Earth, Moon and Planets, 96, 3–4, 119–147, doi: 10.1007/s11038-005-9058-2.

Baines, K. H., P. Drossart, T. W. Momary, V. Formisano, C. Griffith, G. Bellucci, J. P. Bibring, et al., (2005), The atmospheres of Saturn and Titan in the near-infrared: First results of Cassini/VIMS, Earth, Moon, and Planets, 96, no. 3–4, 119–147.

Baines, K. H., G. Bellucci, J.-P. Bibring, R. H. Brown, B. J. Buratti, E. Bussoletti, F. Capaccioni, et al., (2000), Detection of Sub-Micron Radiation from the Surface of Venus by Cassini/VIMS, Icarus, 148, 1, 307–311, doi: 10.1006/icar.2000.6519.

Banfield, D., B. J. Conrath, P. J. Gierasch, P. D. Nicholson, K. Matthews, (1998), Near-IR Spectrophotometry of Jovian Aerosols - Meridional and Vertical Distributions, Icarus, 134, 1, 11–23, doi: 10.1006/icar.1998.5942.

Barbosa Aguiar, A. C., P. L. Read, R. D. Wordsworth, T. Salter, Y. Hiro Yamazaki, (2010), A laboratory model of Saturn’s north polar hexagon, Icarus, 206, 2, 755–763, doi: 10.1016/j.icarus.2009.10.022.

Barnes, J. W., S. M. Mackenzie, E. F. Young, L. E. Trouille, S. Rodriguez, T. Cornet, B. K. Jackson, M. Ádámkovics, C. Sotin, J. M. Soderblom, (2018), Spherical radiative transfer in C++ (SRTC++): A parallel Monte Carlo radiative transfer model for Titan, The Astronomical Journal, 155, 6, doi:10.3847/1538-3881/aac2db.

Barnes, J. W., C. Sotin, J. M. Soderblom, R. H. Brown, A. G. Hayes, (2014), Cassini/VIMS observes rough surfaces on Titan's Punga Mare in specular reflection, Planetary Science, 3, 1, doi: 10.1186/s13535-014-0003-4.

Barnes, J. W., B. J. Buratti, E. P. Turtle, J. Bow, P. A. Dalba, J. Perry, R. H. Brown, et al., (2013a), Precipitation-induced surface brightenings seen on Titan by Cassini VIMS and ISS, Planetary Science, 2, 1, doi: 10.1186/2191-2521-2-1.

Barnes, J. W., R. N. Clark, C. Sotin, M. Ádámkovics, T. Appéré, S. Rodriguez, J. M. Soderblom, et al., (2013b), A transmission spectrum of Titan's north polar atmosphere from a specular reflection of the Sun, The Astrophysical Journal, 777, 2, 161, doi: 10.1088/0004-637X/777/2/161.

Barnes, J. W., J. Bow, J. Schwartz, R. H. Brown, J. M. Soderblom, A. G. Hayes, G. Vixie, et al., (2011a), Organic sedimentary deposits in Titan's dry lakebeds: Probable evaporite, Icarus, 216, 1, 136–140, doi: 10.1016/j.icarus.2011.08.022.

Barnes, J. W., J. M. Soderblom, R. H. Brown, L. A. Soderblom, K. Stephan, R. Jaumann, S. Le Mouélic, et al., (2011b), Wave constraints for Titan's Jingpo Lacus and Kraken Mare from VIMS specular reflection lightcurves, Icarus, 211, 1, 722–731, doi: 10.1016/j.icarus.2010.09.022.

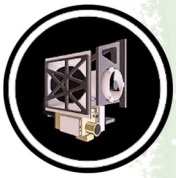

Barnes, J. W., R. H. Brown, J. M. Soderblom, L. A. Soderblom, R. Jaumann, B. Jackson, S. Le Mouélic, et al., (2009a), Shoreline features of Titan's Ontario Lacus from Cassini/VIMS observations, Icarus, 201, 1, 217–225, doi: 10.1016/j.icarus.2008.12.028.

Barnes, J. W., J. M. Soderblom, R. H. Brown, B. J. Buratti, C. Sotin, K. H. Baines, R. N. Clark, et al., (2009b), VIMS spectral mapping observations of Titan during the Cassini prime mission, Planetary and Space Science, 57, 14–15, 1950–1962, doi: 10.1016/j.pss.2009.04.013.

Barnes, J. W., R. H. Brown, L. Soderblom, C. Sotin, S. Le Mouèlic, S. Rodriguez, R. Jaumann, et al., (2008), Spectroscopy, morphometry, and photoclinometry of Titan's dunefields from Cassini/VIMS, Icarus, 195, 1, 400–414, doi: 10.1016/j.icarus.2007.12.006.

Barnes, J. W., R. H. Brown, L. Soderblom, B. J. Buratti, C. Sotin, S. Rodriguez, S. Le Mouèlic, K. H. Baines, R. Clark, P. Nicholson, (2007a), Global-scale surface spectral variations on Titan seen from Cassini/VIMS, Icarus, 186, 1, 242–258, doi: 10.1016/j.icarus.2006.08.021.

Barnes, J. W., J. Radebaugh, R. H. Brown, S. Wall, L. Soderblom, J. Lunine, D. Burr, et al., (2007b), Near-infrared spectral mapping of Titan's mountains and channels, Journal of Geophysical Research E: Planets, 112, 11, doi: 10.1029/2007JE002932.

Barnes, J. W., R. H. Brown, J. Radebaugh, B. J. Buratti, C. Sotin, S. Le Mouelic, S. Rodriguez, et al, (2006), Studies of Titan's 5-Micron-Bright Regions Using Combined VIMS and ISS Observations, American Geophysical Union (AGU) Fall Meeting, abstract.

Barstow, J. K., P. G. J. Irwin, L. N. Fletcher, R. S. Giles, C. Merlet, (2016), Probing Saturn's tropospheric cloud with Cassini/VIMS, Icarus, 271, 400–417, doi: 10.1016/j.icarus.2016.01.013.

Barth, E. L., (2017), Modeling survey of ices in Titan's stratosphere, Planetary and Space Science, 137, 20–31, doi: 10.1016/j.pss.2017.01.003.

Barth, E. L. and S. C. R. Rafkin, (2010), Convective cloud heights as a diagnostic for methane environment on Titan, Icarus, 206, 2, 467–484, doi: 10.1016/j.icarus.2009.01.032.

Bauerecker, S. and E. Dartois, (2009), Ethane aerosol phase evolution in Titan's atmosphere, Icarus, 199, 2, 564–567, doi: 10.1016/j.icarus.2008.09.014.

Bellini, B., G. Bellucci, V. Formisano, (1998), Atmospheric studies with spectro-imaging: Prospects for the VIMS experiment on Cassini, Planetary and Space Science, 46, 9–10, 1305–1314, doi: 10.1016/S0032-0633(98)00004-X.

Bellucci, A. S., B., Drossart, P., Rannou, P., Nicholson, P. D., Hedman, M., Baines, K. H., Burrati, B., (2009), Titan solar occultation observed by Cassini/VIMS: Gas absorption and constraints on aerosol composition, Icarus, 201(1), 198–216, doi: 10.1016/j.icarus.2008.12.024.

Bellucci, A., (2008), Analyse d'occultations solaires et stellaires par Titan observées par l'instrument Cassini/VIMS, Université Paris VI - Pierre et Marie Curie.

Bellucci, G., E. D'Aversa, V. Formisano, D. Cruikshank, R. M. Nelson, R. N. Clark, K. H. Baines, et al., (2004a), Cassini/VIMS observation of an Io post-eclipse brightening event, Icarus, 172, 1, 141–148, doi: 10.1016/j.icarus.2004.05.012.

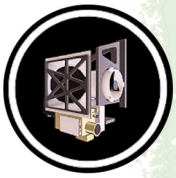

Bellucci, G. F., V., D'Aversa, E., Brown, R. H., Baines, K. H., Bibring, J. P., Buratti, B. J., Capaccioni, F., Cerroni, P., Clark, R. N., Coradini, A., Cruikshank, D. P., Drossart, P., Jaumann, R., Langevin, Y., Matson, D. L., McCord, T. B., Mennella, V., Nelson, R. M., Nicholson, P. D., Sicardy, B., Sotin, C., Chamberlain, M. C., Hansen, G., Hibbits, K., Showalter, M., Filacchione, G., (2004b), Principal components analysis of Jupiter VIMS spectra, Advances in Space Research, 34, 8, 1640–1646, doi: 10.1016/j.asr.2003.05.062.

Bellucci, G., R. H. Brown, V. Formisano, K. H. Baines, J.-P. Bibring, B. J. Buratti, F. Capaccioni, et al., (2002), Cassini/VIMS observations of the moon, Advances in Space Research, 30, 8, 1889–1894, doi: 10.1016/S0273-1177(02)00484-2.

Bellucci, G. and V. Formisano, (1997), Regional mapping of planetary surfaces with imaging spectroscopy, Planetary and Space Science, 45, 11, 1371–1381, doi: 10.1016/S0032-0633(97)00074-3.

Bernard, J. M., E. Quirico, O. Brissaud, G. Montagnac, B. Reynard, P. McMillan, P. Coll, M. J. Nguyen, F. Raulin, B. Schmitt, (2006), Reflectance spectra and chemical structure of Titan's tholins: Application to the analysis of Cassini–Huygens observations, Icarus, 185, 1, 301–307, doi: 10.1016/j.icarus.2006.06.004.

Bézard, B., S. Vinatier, R. K. Achterberg, (2018), Seasonal radiative modeling of Titan's stratospheric temperatures at low latitudes, Icarus, 302, 437–450, doi: 10.1016/j.icarus.2017.11.034.

Birch, S. P. D., A. G. Hayes, P. Corlies, E. R. Stofan, J. D. Hofgartner, R. M. C. Lopes, R. D. Lorenz, et al., (2017), Morphological evidence that Titan’s southern hemisphere basins are paleoseas, Icarus, doi: 10.1016/j.icarus.2017.12.016.

Blackburn, D. G., (2011), An analysis of the stability and transport of carbon dioxide on Mars and Iapetus: Increasing accuracy via experiments and photometry, University of Arkansas.

Blackburn, D. G., B. J. Buratti, R. Ulrich, (2011), A bolometric Bond albedo map of Iapetus: Observations from Cassini VIMS and ISS and Voyager ISS, Icarus, 212, 1, 329–338, doi: 10.1016/j.icarus.2010.12.022.

Blackburn, D. G., B. J. Buratti, R. Ulrich, J. A. Mosher, (2010), Solar phase curves and phase integrals for the leading and trailing hemispheres of Iapetus from the Cassini Visual Infrared Mapping Spectrometer, Icarus, 209, 2, 738–744, doi: 10.1016/j.icarus.2010.04.011.

Bonnefoy, L. E., A. G. Hayes, P. O. Hayne, M. J. Malaska, A. Le Gall, A. Solomonidou, A. Lucas, (2016), Compositional and spatial variations in Titan dune and interdune regions from Cassini VIMS and RADAR, Icarus, 270, 222–237, doi: 10.1016/j.icarus.2015.09.014.

Bourke, M. C., N. Lancaster, L. K. Fenton, E. J. R. Parteli, J. R. Zimbelman, J. Radebaugh, (2010), Extraterrestrial dunes: An introduction to the special issue on planetary dune systems, Geomorphology, 121, 1–2, 1–14, doi: 10.1016/j.geomorph.2010.04.007.

Brassé, C., O. Muñoz, P. Coll, F. Raulin, (2015), Optical constants of Titan aerosols and their tholins analogs: Experimental results and modeling/observational data, Planetary and Space Science, 109–110, 159–174, doi: 10.1016/j.pss.2015.02.012.

Brossier, J. F., S. Rodriguez, T. Cornet, Antoine Lucas, J. Radebaugh, L. Maltagliati, S. Le Mouélic, et al., (2018), Geological evolution of Titan's equatorial regions: Possible nature and origin of the dune material, Journal of Geophysical Research: Planets, 123, 5, 1089–1112, doi: 10.1029/2017JE00539.

Brown, A. J., (2014), Spectral bluing induced by small particles under the Mie and Rayleigh regimes, Icarus, 239, 85–95, doi: 10.1016/j.icarus.2014.05.042.

Brown, M. E., J. E. Roberts, E. L. Schaller, (2010), Clouds on Titan during the Cassini prime mission: A complete analysis of the VIMS data, Icarus, 205, 2, 571–580, doi: 10.1016/j.icarus.2009.08.024.

Brown, M. E., A. L. Smith, C. Chen, M. Ádámkovics, (2009), Discovery of fog at the south pole of Titan, The Astrophysical Journal Letters, 706, no. 1, L110, doi: 10.1088/0004-637X/706/1/L110.

Brown, R. H., J. W. Barnes, H. J. Melosh, (2011), On Titan’s Xanadu region, Icarus, 214, 2, 556–560, doi: 10.1016/j.icarus.2011.03.018.

Brown, R. H., L. A. Soderblom, J. M. Soderblom, R. N. Clark, R. Jaumann, J. W. Barnes, C. Sotin, B. Buratti, K. H. Baines, P. D. Nicholson, (2008), The identification of liquid ethane in Titan's Ontario Lacus, Nature, 454, 7204, 607–610, doi: 10.1038/nature07100.

Brown, R. H. B., K. H., Bellucci, G., Buratti, B. J., Capaccioni, F., Cerroni, P., Clark, R. N., Coradini, A., Cruikshank, D. P., Drossart, P., Formisano, V., Jaumann, R., Langevin, Y., Matson, D. L., McCord, T. B., Mennella, V., Nelson, R. M., Nicholson, P. D., Sicardy, B., Sotin, C., Baugh, N., Griffith, C. A., Hansen, G. B., Hibbitts, C. A., Momary, T. W., Showalter, M. R., (2006), Observations in the Saturn system during approach and orbital insertion, with Cassini's visual and infrared mapping spectrometer (VIMS), Astronomy and Astrophysics, 446, 2, 707–716, doi: 10.1051/0004-6361:20053054.

Brown, R. H., K. H. Baines, G. Bellucci, J.-P. Bibring, B. J. Buratti, F. Capaccioni, P. Cerroni, et al., (2004), The Cassini visual and infrared mapping spectrometer (VIMS) investigation, Space Science Reviews, 115, 1–4, 111–168, doi: 10.1007/s11214-004-1453-x.

Brown, R. H. B., K. H., Bellucci, G., Bibring, J. P., Buratti, B. J., Capaccioni, F., Cerroni, P., Clark, R. N., Coradini, A., Cruikshank, D. P., Drossart, P., Formisano, V., Jaumann, R., Langevin, Y., Matson, D. L., McCord, T. B., Mennella, V., Nelson, R. M., Nicholson, P. D., Sicardy, B., Sotin, C., Amici, S., Chamberlain, M. A., Filacchione, G., Hansen, G., Hibbitts, K., Showalter, M., (2003), Observations with the Visual and Infrared Mapping Spectrometer (VIMS) during Cassini's flyby of Jupiter, Icarus, 164, 2, 461–470, doi: 10.1016/S0019-1035(03)00134-9.

Buratti, B. J., R. N. Clark, F. Crary, C. J. Hansen, A. R. Hendrix, C. J. A.Howett, J. Lunine, C. Paranicas, (2018a), Cold cases: What we don't know about Saturn's Moons, Planetary and Space Science, vol. 155, pp. 41–49, doi.org/10.1016/j.pss.2017.11.017.

Buratti, B. J., C. J. Hansen, A. R. Hendrix, L. W. Esposito, J. A. Mosher, R. H. Brown, R. N. Clark, K. H. Baines, P. D. Nicholson, (2018b), The search for activity on Dione and Tethys with

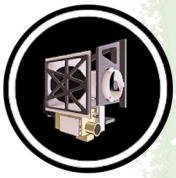

Cassini VIMS and UVIS, Geophysical Research Letters, 45, 12, 5860–5866, doi: 10.1029/2018GL078165.

Buratti, B. J., R. H. Brown, R. N. Clark, D. P. Cruikshank, G. Filacchione, (2017), Spectral analyses of Saturn's moons using Cassini-VIMS, In Remote Sensing, (eds.) J. Bishop, J. Bell, Cambridge, In press.

Buratti, B. J., C. Sotin, K. Lawrence, R. H. Brown, S. Le Mouélic, J. M. Soderblom, J. Barnes, R. N. Clark, K. H. Baines, P. D. Nicholson, (2012), A newly discovered impact crater in Titan's Senkyo: Cassini VIMS observations and comparison with other impact features, Planetary and Space Science, 60, 1, 18–25, doi: 10.1016/j.pss.2011.05.004.

Buratti, B. J., S. P. Faulk, J. Mosher, K. H. Baines, R. H. Brown, R. N. Clark, P. D. Nicholson, (2011), Search for and limits on plume activity on Mimas, Tethys, and Dione with the Cassini Visual Infrared Mapping Spectrometer (VIMS), Icarus, 214, 2, 534–540, doi: 10.1016/j.icarus.2011.04.030.

Buratti, B. J., J. M. Bauer, M. D. Hicks, J. A. Mosher, G. Filacchione, T. Momary, K. H. Baines, R. H. Brown, R. N. Clark, P. D. Nicholson, (2010), Cassini spectra and photometry 0.25-5.1 μm of the small inner satellites of Saturn, Icarus, 206, 2, 524–536, doi: 10.1016/j.icarus.2009.08.015.

Buratti, B. J., K. Soderlund, J. Bauer, J. A. Mosher, M. D. Hicks, D. P. Simonelli, R. Jaumann, et al., (2008), Infrared (0.83-5.1 μm) photometry of Phoebe from the Cassini Visual Infrared Mapping Spectrometer, Icarus, 193, 2, 309–322, doi: 10.1016/j.icarus.2007.09.014.

Buratti, B. J., C. Sotin, R. H. Brown, M. D. Hicks, R. N. Clark, J. A. Mosher, T. B. McCord, et al., (2006), Titan: Preliminary results on surface properties and photometry from VIMS observations of the early flybys, Planetary and Space Science, 54, 15, 1498–1509, doi: 10.1016/j.pss.2006.06.015.

Buratti, B. J., D. P. Cruikshank, R. H. Brown, R. N. Clark, J. M. Bauer, R. Jaumann, T. B. McCord, et al., (2005), Cassini Visual and Infrared Mapping Spectrometer observations of Iapetus: Detection of CO_2, The Astrophysical Journal Letters, 622, 2, L149–L152, doi: 10.1086/429800.

Buratti, B. J., J. K. Hillier, M. Wang, (1996), The lunar opposition surge: Observations by Clementine, Icarus, 124, no. 2, 490–499.

Buratti, B. J., J. A. Mosher, T. V. Johnson, (1990), Albedo and color maps of the Saturnian satellites, Icarus, 87, 2, 339–357, doi: 10.1016/0019-1035(90)90138-Y.

Campargue, A., L. Wang, D. Mondelain, S. Kassi, B. Bézard, E. Lellouch, A. Coustenis, C. De Bergh, M. Hirtzig, P. Drossart, (2012), An empirical line list for methane in the 1.26–1.71 μm region for planetary investigations (T = 80–300 K). Application to Titan, Icarus, 219, 1, 110–128, doi: 10.1016/j.icarus.2012.02.015.

Campbell, J., P. Sidiropoulos, J. P. Muller, (2016), IR spectral mapping of the martian south polar residual cap using CRISM, The International Archives of the Photogrammetry, Remote Sensing and Spatial Information Sciences, XXIII ISPRS Congress, 12–19 July 2016, Prague, Czech Republic, vol. XLI-B7, doi: 10.5194/isprsarchives-XLI-B7-71-2016

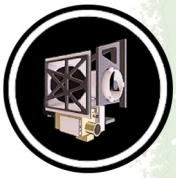

Capaccioni, F., A. Coradini, P. Cerroni, S. Amici, (1998), Imaging spectroscopy of Saturn and its satellites: VIMS-V onboard Cassini, Planetary and Space Science, 46, 9-10, 1263–1276, doi: 10.1016/S0032-0633(98)00037-3.

Carlson, R. E., (2010), Spatial and seasonal variations in Saturn's haze and vertical phosphine distribution at 3 microns from 2005 to 2010, New Mexico State University.

Carlson, R. W., K. H. Baines, M. S. Anderson, G. Filacchione, A. A. Simon, (2016), Chromophores from photolyzed ammonia reacting with acetylene: Application to Jupiter's Great Red Spot, Icarus, 274, 106–115, doi: 10.1016/j.icarus.2016.03.008.

Castillo-Rogez, J. C., D. L. Matson, C. Sotin, T. V. Johnson, J. I. Lunine, P. C. Thomas, (2007), Iapetus' geophysics: Rotation rate, shape, and equatorial ridge, Icarus, 190, 1, 179–202, doi: 10.1016/j.icarus.2007.02.018.

Chaban, G. M., M. Bernstein, D. P. Cruikshank, (2007), Carbon dioxide on planetary bodies: Theoretical and experimental studies of molecular complexes, Icarus, 187, 2, 592–599, doi: 10.1016/j.icarus.2006.10.010.

Chamberlain, M. A. and R. H. Brown, (2004), Near-infrared spectroscopy of Himalia, Icarus, 172, 163–169, doi: 10.1016/j.icarus.2003.12.016.

Chauhan, P., P. Kaur, N. Srivastava, R. K. Sinha, N. Jain, S. V. S. Murty, (2015), Hyperspectral remote sensing of planetary surfaces: An insight into composition of inner planets and small bodies in the solar system, Current Science, 108, 5, 915–924.

Choi, D. S., A. P. Showman, R. H. Brown, (2009), Cloud features and zonal wind measurements of saturn's atmosphere as observed by Cassini/VIMS, Journal of Geophysical Research: Planets, 114, 4, doi: 10.1029/2008JE003254.

Ciarniello, M., G. Filacchione, E. D'Aversa, F. Capaccioni, P. D. Nicholson, J. N. Cuzzi, R. N. Clark, et al., (2019), Cassini-VIMS observations of Saturn's main rings: II. A spectrophotometric study by means of Monte Carlo ray-tracing and Hapke's theory, Icarus, 317, 242–265.

Ciarniello, M., F. Capaccioni, G. Filacchione, R. N. Clark, D. P. Cruikshank, P. Cerroni, A. Coradini, et al., (2011), Hapke modeling of Rhea surface properties through Cassini-VIMS spectra, Icarus, 214, 2, 541–555, doi: 10.1016/j.icarus.2011.05.010.

Clark, R. N., R. H. Brown, D. P. Cruikshank, G. A. Swayze, (2019), Isotopic ratios of Saturn's rings and satellites: Implications for the origin of water and Phoebe, Icarus, 321, 791–802, doi: 10.1016/j.icarus.2018.11.029.

Clark, R. N., R. H. Brown, D. M. Lytle, M. Hedman, (2018), The VIMS Wavelength and Radiometric Calibration 19, Final Report, NASA Planetary Data System.

Clark, R. N., R. H. Brown, G. A. Swayze, D. P. Cruikshank, (2017a), Detecting Isotopic Signatures and Measuring Isotopic Ratios on Solid Icy Surfaces: Implications for Origin and Evolution, American Geophysical Union (AGU) Fall Meeting, abstracts.

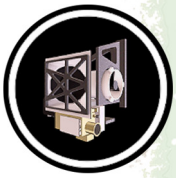

Clark, R. N., R. H. Brown, G. A. Swayze, D. P. Cruikshank, (2017b), Detection of Deuterium in Icy Surfaces and the D/H Ratio of Icy Objects, American Astronomical Society (AAS)/Division for Planetary Sciences Meeting, abstract 49, vol. 49.

Clark, R. N., R. H. Brown, D. P. Cruikshank, (2016a), CO_2 and ^{12}C: ^{13}C Isotopic Ratios on Phoebe and Iapetus, AGU Fall Meeting, abstract.

Clark, R. N., R. H. Brown, D. M. Lytle, (2016b), The VIMS wavelength and radiometric calibration, NASA Planetary Data System, The Planetary Atmospheres Node.

Clark, R. N., G. A. Swayze, R. Carlson, W. Grundy, K. Noll, (2014), Spectroscopy from Space, Reviews in Mineralogy and Geochemistry, pp. 399–446, doi: 10.2138/rmg.2014.78.10.

Clark, R. N., R. Carlson, W. Grundy, K. Noll, (2013), Observed Ices in the Solar System, In The Science of Solar System Ices, (eds.) M. Gudipati, J. Castillo-Rogez, Astrophysics and Space Science Library (ASSL), Springer, NY, vol. 356, Part 1, pp. 3–46, doi: 10.1007/978-1-4614-3076-6_1.

Clark, R. N., D. P. Cruikshank, R. Jaumann, R. H. Brown, K. Stephan, C. M. Dalle Ore, K. E. Livo, N. Pearson, J. M. Curchin, T. M. Hoefen, B. J. Buratti, G. Filacchione, K. H. Baines, P. D. Nicholson, (2012), The surface composition of Iapetus: Mapping results from Cassini VIMS, Icarus, 218, 831–860, doi: 10.1016/j.icarus.2012.01.008.

Clark, R. N., J. M. Curchin, J. W. Barnes, R. Jaumann, L. Soderblom, D. P. Cruikshank, R. H. Brown, S. Rodriguez, J. Lunine, K. Stephan, T. M. Hoefen, (2010), Detection and mapping of hydrocarbon deposits on Titan, Journal of Geophysical Research: Planets, 115, 10, doi: 10.1029/2009JE003369.

Clark, R. N., (2009), Detection of adsorbed water and hydroxyl on the Moon, Science, 326, 562–564, doi: 10.1126/science.1178105.

Clark, R. N., R. H. Brown, R. Jaumann, D. P. Cruikshank, B. Buratti, K. H. Baines, R. M. Nelson, P. D. Nicholson, J. M. Moore, J. Curchin, T. Hoefen, K. Stephan, (2008), Compositional mapping of Saturn's satellite Dione with Cassini VIMS and implications of dark material in the Saturn system, Icarus, 193, p 372–386, doi: 10.1016/j.icarus.2007.08.035.

Clark, R. N., R. H. Brown, R. Jaumann, D. P. Cruikshank, R. M. Nelson, B. J. Buratti, T. B. McCord, J. Lunine, K. H. Baines, G. Bellucci, J.-P. Bibring, F. Capaccioni, P. Cerroni, A. Coradini, V. Formisano, Y. Langevin, D. L. Matson, V. Mennella, P. D. Nicholson, B. Sicardy, C. Sotin, T. M. Hoefen, J. M. Curchin, G. Hansen, K. Hibbits, K.-D. Matz, (2005), Compositional maps of Saturn's moon Phoebe from imaging spectroscopy, Nature, doi: 10.1038/nature03558.

Cohen-Zada, A. L., D. G. Blumberg, S. Maman, (2016), Earth and planetary aeolian streaks: A review, Aeolian Research, 20, 108–125, doi: 10.1016/j.aeolia.2015.12.002.

Colwell, J. E., P. D. Nicholson, M. S. Tiscareno, C. D. Murray, R. G. French, E. A. Marouf, (2009), The structure of Saturn's rings, Chapter 13, In Saturn from Cassini-Huygens, (eds.) M. Dougherty, L. Esposito, S. Krimigis, Springer Dordrecht, pp. 375– 412, doi: 10.1007/978-1-4020-9217-6_13.

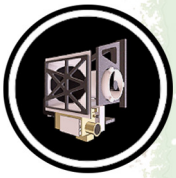

Combe, J. P., T. B. McCord, D. L. Matson, T. V. Johnson, A. G. Davies, F. Scipioni, F. Tosi, (2019), Nature, distribution and origin of CO_2 on Enceladus, Icarus, 317, 491–508, doi: 10.1016/j.icarus.2018.08.007.

Cooper, J. F., P. D. Cooper, E. C. Sittler, S. J. Sturner, A. M. Rymer, (2009), Old faithful model for radiolytic gas-driven cryovolcanism at Enceladus, Planetary and Space Science, 57, 13, 1607–1620, doi: 10.1016/j.pss.2009.08.002.

Coradini, A., F. Capaccioni, P. Cerroni, G. Filacchione, G. Magni, R. Orosei, F. Tosi, D. Turrini, (2009), Saturn satellites as seen by Cassini Mission, Earth, Moon and Planets, 105, no. 2–4, pp. 289–310, doi: 10.1007/s11038-009-9334-7.

Coradini, A., F. Tosi, A. I. Gavrishin, F. Capaccioni, P. Cerroni, G. Filacchione, A. Adriani, et al., (2008), Identification of spectral units on Phoebe, Icarus, 193, 1, 233–251, doi: 10.1016/j.icarus.2007.07.023.

Coradini, A., (2005), Planetary observations and landers, Chapter 8, In Payload and Mission Definition in Space Sciences, (eds.) V. M. Pillet, A. Aparicio, F. Sanchez, Cambridge University Press, pp. 323–394, doi: 10.1017/CBO9780511550591.009.

Coradini, A., G. Filacchione, F. Capaccioni, P. Cerroni, A. Adriani, Robert H. Brown, Y. Langevin, B. Gondet, (2004), Cassini/VIMS-V at Jupiter: Radiometric calibration test and data results, Planetary and Space Science, 52, 7, 661–670, doi: 10.1016/j.pss.2003.11.005.

Cordier, D., T. Cornet, J. W. Barnes, S. M. MacKenzie, T. Le Bahers, D. Nna-Mvondo, P. Rannou, A. G. Ferreira, (2016), Structure of Titan’s evaporites, Icarus, 270, 41–56, doi: 10.1016/j.icarus.2015.12.034.

Cordier, D., J. W. Barnes, A. G. Ferreira, (2013), On the chemical composition of Titan’s dry lakebed evaporites, Icarus, 226, 2, 1431–1437, doi: 10.1016/j.icarus.2013.07.026.

Cordier, D., O. Mousis, J. I. Lunine, S. Lebonnois, P. Rannou, P. Lavvas, L. Q. Lobo, A. G. M. Ferreira, (2012), Titan's lakes chemical composition: Sources of uncertainties and variability, Planetary and Space Science, 61, 1, 99–107, doi: 10.1016/j.pss.2011.05.009.

Cornet, T., O. Bourgeois, S. Le Mouélic, S. Rodriguez, T. Lopez Gonzalez, C. Sotin, G. Tobie, et al, (2012a), Geomorphological significance of Ontario Lacus on Titan: Integrated interpretation of Cassini VIMS, ISS and RADAR data and comparison with the Etosha Pan (Namibia), Icarus, 218, 2, 788–806, doi: 10.1016/j.icarus.2012.01.013.

Cornet, T., O. Bourgeois, S. Le Mouélic, S. Rodriguez, C. Sotin, J. W. Barnes, R. H. Brown et al., (2012b), Edge detection applied to Cassini images reveals no measurable displacement of Ontario Lacus' margin between 2005 and 2010, Journal of Geophysical Research: Planets, 117, 7, doi: 10.1029/2012JE004073.

Cours, T., P. Rannou, A. Coustenis, A. Hamdouni, (2010), A new analysis of the ESO very large telescope (VLT) observations of Titan at 2 μm, Planetary and Space Science, 58, 13, 1708–1714, doi: 10.1016/j.pss.2009.12.009.

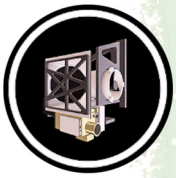

Courtin, R., H. Feuchtgruber, S. J. Kim, E. Lellouch, (2016), The 6–7 μm spectrum of Titan from ISO/SWS observations, Icarus, 270, 389–398, doi: 10.1016/j.icarus.2015.07.021.

Courtin, R., S. J. Kim, A. Bar-Nun, (2015), Three-micron extinction of the Titan haze in the 250–700 km altitude range: Possible evidence of a particle-aging process, Astronomy & Astrophysics, 573, A21, doi: 10.1051/0004-6361/201424977.

Couturier-Tamburelli, I., M. S. Gudipati, A. Lignell, R. Jacovi, N. Piétri, (2014), Spectroscopic studies of non-volatile residue formed by photochemistry of solid C_4N_2: A model of condensed aerosol formation on Titan, Icarus, 234, 81–90, doi: 10.1016/j.icarus.2014.02.016.

Cruikshank, D. P., C. M. Dalle Ore, R. N. Clark, Y. J. Pendleton, (2014), Aromatic and aliphatic organic materials on Iapetus: Analysis of Cassini VIMS data, Icarus, 233, 306–315, doi: 10.1016/j.icarus.2014.02.011.

Cruikshank, D. P., J. P. Emery, K. A. Kornei, G. Bellucci, E. d'Aversa, (2010a), Eclipse reappearances of Io: Time-resolved spectroscopy (1.9–4.2 μm), Icarus, 205, 2, 516–527, doi: 10.1016/j.icarus.2009.05.035.

Cruikshank, D. P., A. W. Meyer, R. H. Brown, R. N. Clark, R. Jaumann, K. Stephan, C. A. Hibbitts, et al, (2010b), Carbon dioxide on the satellites of Saturn: Results from the Cassini VIMS investigation and revisions to the VIMS wavelength scale, Icarus, 206, 561–572, doi: 10.1016/j.icarus.2009.07.012.

Cruikshank, D. P., A. W. Meyer, R. H. Brown, R. N. Clark, R. Jaumann, K. Stephan, C. A. Hibbitts, et al., (2010), Carbon dioxide on the satellites of Saturn: Results from the Cassini VIMS investigation and revisions to the VIMS wavelength scale, Icarus 206, no. 2, 561–572.

Cruikshank, D. P., E. Wegryn, C. M. Dalle Ore, R. H. Brown, K. H. Baines, J.-P. Bibring, B. J. Buratti, R. N. Clark, T .B. McCord, P. D. Nicholson, Y. J. Pendleton, T. C. Owen, G. Filacchione, VIMS Team, (2008), Hydrocarbons on Saturn's Satellites Iapetus and Phoebe, Icarus, Icarus, 193, 334–343, doi: 10.1016/j.icarus.2007.04.036.

Cruikshank, D. P., J. B. Dalton, C. M. Dalle Ore, J. Bauer. K. Stephan, G. Filacchione, A. R. Hendrix, C. J. Hansen, A. Coradini, P. Cerroni, F. Tosi, F. Capaccioni, R. Jaumann, B. J. Buratti, R. N. Clark, R. H. Brown, R. M. Nelson, T. B. McCord, K. H. Baines, P. D. Nicholson, C. Sotin, A. W. Meyer, G. Bellucci, M. Combes, J.-P. Bibring, Y. Langevin, B. Sicardy, D. L. Matson, V. Formisano, P. Drossart, V. Mennella, (2007), Surface composition of Hyperion, Nature, 448, pp. 54–56, doi: 10.1038/nature05948.

Cruikshank, D. P., T. C. Owen, C. M. Dalle Ore, T. R. Geballe, T. L. Roush, C. De Bergh, S. A. Sandford, F. Poulet, G. K. Benedix, J. P. Emery, (2005), A spectroscopic study of the surfaces of Saturn's large satellites: H_2O ice, tholins, and minor constituents, Icarus, 175, 1, 268–283, doi: 10.1016/j.icarus.2004.09.003.

Cuzzi, J., R. Clark, G. Filacchione, R. French, R. Johnson, E. Marouf, L. Spilker, (2009), Ring particle composition and size distribution, Chapter 15, In Saturn from Cassini-Huygens, (eds.) M. Dougherty, L. Esposito, S. Krimigis, Springer Dordrecht, pp. 459–510, doi: 10.1007/978-1-4020-9217-6_15.

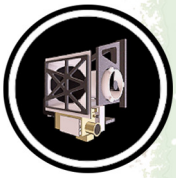

Dalba, P. A., P. S. Muirhead, J. J. Fortney, M. M. Hedman, P. D. Nicholson, M. J. Veyette, (2015), The transit transmission spectrum of a cold gas giant planet, The Astrophysical Journal, 814, 154, doi: 10.1088/0004-637X/814/2/154.

Dalba, P. A., B. J. Buratti, R. H. Brown, J. W. Barnes, K. H. Baines, C. Sotin, R. N. Clark, K. J. Lawrence, P. D. Nicholson, (2012), Cassini VIMS observations show ethane is present in Titan's rainfall, The Astrophysical Journal Letters, 761, 2, doi: 10.1088/2041-8205/761/2/L24.

Dalle Ore, C. M., D. P. Cruikshank, R. M. E. Mastrapa, E. Lewis, O. L. White, (2015), Impact craters: An ice study on Rhea, Icarus, 261, 80–90, doi: 10.1016/j.icarus.2015.08.008.

Dalle Ore, C. M., D. P. Cruikshank, R. N. Clark, (2012), Infrared spectroscopic characterization of the low-albedo materials on Iapetus, Icarus, 221, 2, 735–743, doi: 10.1016/j.icarus.2012.09.010.

Dalton III, J. B., D. P. Cruikshank, R. N. Clark, (2012), Compositional analysis of Hyperion with the Cassini Visual and Infrared Mapping Spectrometer, Icarus, 220, 752–776, doi: 10.1016/j.icarus.2012.05.003.

D'Aversa, E., G. Bellucci, F. Altieri, F. G. Carrozzo, G. Filacchione, F. Tosi, P. D. Nicholson, M. M. Hedman, R. H. Brown, M. R. Showalter, (2011), Spectral characteristics of a spoke on the Saturn Rings, Memorie della Societa Astronomica Italiana Supplementi, 16, 70.

D'Aversa, E., G. Bellucci, P. D. Nicholson, M. M. Hedman, R. H. Brown, M. R. Showalter, F. Altieri, F. G. Carrozzo, G. Filacchione, F. Tosi, (2010), The spectrum of a Saturn ring spoke from Cassini/VIMS, Geophysical Research Letters, 37, 1, doi: 10.1029/2009GL041427.

Davies, A. G., C. Sotin, M. Choukroun, D. L. Matson, T. V. Johnson, (2016), Cryolava flow destabilization of crustal methane clathrate hydrate on Titan, Icarus, 274, 23–32, doi: 10.1016/j.icarus.2016.02.046.

Davies, A. G., L. P. Keszthelyi, A. J. L. Harris, (2010a), The thermal signature of volcanic eruptions on Io and Earth, Journal of Volcanology and Geothermal Research, 194, 4, 75–99, doi: 10.1016/j.jvolgeores.2010.04.009.

Davies, A. G., C. Sotin, D. L. Matson, J. Castillo-Rogez, T. V. Johnson, M. Choukroun, K. H. Baines, (2010b), Atmospheric control of the cooling rate of impact melts and cryolavas on Titan’s surface, Icarus, 208, 2, 887–895, doi: 10.1016/j.icarus.2010.02.025.

De Bergh, C., R. Courtin, B. Bézard, A. Coustenis, E. Lellouch, M. Hirtzig, P. Rannou, et al., (2012), Applications of a new set of methane line parameters to the modeling of Titan's spectrum in the 1.58 μm window, Planetary and Space Science, 61, 1, 85–98, doi: 10.1016/j.pss.2011.05.003.

de Kok, R., P. G. J. Irwin, N. A. Teanby, (2010a), Far-infrared opacity sources in Titan’s troposphere reconsidered, Icarus, 209, 2, 854–857, doi: 10.1016/j.icarus.2010.06.035.

de Kok, R., P. G. J. Irwin, N. A. Teanby, S. Vinatier, F. Tosi, A. Negrão, S. Osprey, A. Adriani, M. L. Moriconi, A. Coradini, (2010b), A tropical haze band in Titan’s stratosphere, Icarus, 207, 1, 485–490, doi: 10.1016/j.icarus.2009.10.021.

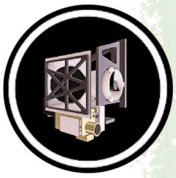

Déau, E., L. Dones, M. I. Mishchenko, R. A. West, P. Helfenstein, M. M. Hedman, C. C. Porco, (2018), The opposition effect in Saturn's main rings as seen by Cassini ISS: 4. Correlations of the surge morphology with surface albedos and VIMS spectral properties, Icarus, 305, 324–349, doi:10.1016/j.icarus.2017.12.025.

Degruyter, W. and M. Manga, (2011), Cryoclastic origin of particles on the surface of Enceladus, Geophysical Research Letters, 38, 16, doi: 10.1029/2011GL048235.

Del Genio, A. D., R. K. Achterberg, K. H. Baines, F. M. Flasar, P. L. Read, A. Sánchez-Lavega, A. P. Showman, (2009), Saturn atmospheric structure and dynamics, Chapter 6, In Saturn from Cassini-Huygens, (eds.) M. K. Dougherty, L. W. Esposito, S. M. Krimigis, Springer Dordrecht, pp. 113–159, doi:10.1007/978-1-4020-9217-6_6.

Dhingra, R. D., J. W. Barnes, R. H. Brown, B. J. Burrati, C. Sotin, P. D. Nicholson, K. H. Baines, et al., (2019), Observational evidence for summer rainfall at Titan's north pole, Geophysical Research Letters, 46, 3, 1205–1212, doi:10.1029/2018GL080943.

Dhingra, R. D., J. W. Barnes, B. J. Yanites, R. L. Kirk, (2018), Large catchment area recharges Titan's Ontario Lacus, Icarus, 299, 331–338, doi:10.1016/j.icarus.2017.08.009

Dhingra, D., M. M. Hedman, R. N. Clark, P. D. Nicholson, (2017), Spatially resolved near infrared observations of Enceladus' tiger stripe eruptions from Cassini VIMS, Icarus, 292, 1–12, doi: 10.1016/j.icarus.2017.03.002.

Dinelli, B. M., M. Lõpez-Puertas, A. Adriani, M. L. Moriconi, B. Funke, M. García-Comas, E. D'Aversa, (2013), An unidentified emission in Titan's upper atmosphere, Geophysical Research Letters, 40, 8, 1489–1493, doi: 10.1002/grl.50332.

Dyudina, U. A., A. P. Ingersoll, S. P. Ewald, D. Wellington, (2016), Saturn's aurora observed by the Cassini camera at visible wavelengths, Icarus, 263, 32–43, doi: 10.1016/j.icarus.2015.05.022.

Dyudina, U. A., A. P. Ingersoll, S. P. Ewald, A.R. Vasavada, R. A. West, K. H. Baines, T. W. Momary, A. D. Del Genio, J. M. Barbara, C. C. Porco, R. K. Achterberg, F. M. Flasar, A. A. Simon-Miller, L. N. Fletcher, (2009), Saturn's south pole vortex compared to other large vortices in the solar system, Icarus, 202, 240–248, doi:10.1016/j.icarus.2009.02.014.

El Moutamid, M., P. D. Nicholson, R. G. French, M. S. Tiscareno, C. D. Murray, M. W. Evans, C. M. French, M. M. Hedman, J. A. Burns, (2016), How Janus' orbital swap affects the edge of Saturn's A-ring?, Icarus, 279, 125–140, doi: 10.1016/j.icarus.2015.10.025.

Esposito, L. W., B. K. Meinke, J. E. Colwell, P. D. Nicholson, M. M. Hedman, (2008), Moonlets and clumps in Saturn's F ring, Icarus, 194, 1, 278–289, doi: 10.1016/j.icarus.2007.10.001.

Fabiano, F., M. López Puertas, A. Adriani, M. L. Moriconi, E. D'Aversa, B. Funke, M. A. López-Valverde, M. Ridolfi, B. M. Dinelli, (2017), CO concentration in the upper stratosphere and mesosphere of Titan from VIMS dayside limb observations at 4.7 μm, Icarus, 293, 119–131, doi: 10.1016/j.icarus.2017.04.014.

Feldman, W. C., D. J. Lawrence, R. C. Elphic, B. L. Barraclough, S. Maurice, I. Genetay, A. B. Binder, (2000), Polar hydrogen deposits on the Moon, Journal of Geophysical Research: Planets, 105, no. E2, 4175–4195.

Filacchione, G., M. Ciarniello, E. D'Aversa, F. Capaccioni, P. Cerroni, B. Buratti, R. N. Clark, K. Stephan, C. Plainaki, (2018a), Photometric modeling and VIS-IR albedo maps of Tethys from Cassini-VIMS, Geophysical Research Letters, 45, 13, 6400–6407, doi: 10.1029/2018GL078602.

Filacchione, G., M. Ciarniello, E. D'Aversa, F. Capaccioni, P. Cerroni, B. J. Buratti, R. N. Clark, K. Stephan, C. Plainaki, (2018b), Photometric modeling and VIS-IR albedo maps of Dione from Cassini-VIMS, Geophysical Research Letters, 45, 5, 2184–2192, doi: 10.1002/2017GL076869.

Filacchione, G., E. D'Aversa, F. Capaccioni, R. N. Clark, D. P. Cruikshank, M. Ciarniello, P. Cerroni, et al., (2016), Saturn's icy satellites investigated by Cassini-VIMS, IV, Daytime temperature maps, Icarus, 271, 292–313, doi: 10.1016/j.icarus.2016.02.019.

Filacchione, G., M. Ciarniello, F. Capaccioni, R. N. Clark, P. D. Nicholson, M. M. Hedman, J. N. Cuzzi, et al., (2014), Cassini-VIMS observations of Saturn's main rings: I, Spectral properties and temperature radial profiles variability with phase angle and elevation, Icarus, 241, 45–65, doi: 10.1016/j.icarus.2014.06.001.

Filacchione, G., F. Capaccioni, R. N. Clark, P. D. Nicholson, D. P. Cruikshank, J. N. Cuzzi, J. I. Lunine, et al., (2013), The radial distribution of water ice and chromophores across Saturn's system, The Astrophysical Journal, 766, 2, doi: 10.1088/0004-637X/766/2/76.

Filacchione, G., F. Capaccioni, M. Ciarniello, R. N. Clark, J. N. Cuzzi, P. D. Nicholson, D. P. Cruikshank, et al., (2012), Saturn's icy satellites and rings investigated by Cassini-VIMS: III - Radial compositional variability, Icarus, 220, 2, 1064–1096, doi: 10.1016/j.icarus.2012.06.040.

Filacchione, G., F. Capaccioni, R. N. Clark, J. N. Cuzzi, D. P. Cruikshank, A. Coradini, P. Cerroni, et al., (2010), Saturn's icy satellites investigated by Cassini-VIMS, II, Results at the end of nominal mission, Icarus, 206, 2, 507–523, doi: 10.1016/j.icarus.2009.11.006.

Filacchione, G., F. Capaccioni, T. B. McCord, A. Coradini, P. Cerroni, G. Bellucci, F. Tosi, et al., (2007), Saturn's icy satellites investigated by Cassini-VIMS – I, Full-disk properties: 350–5100 nm reflectance spectra and phase curves, Icarus, 186, 1, 259–290, doi: 10.1016/j.icarus.2006.08.001.

Fischer, G., U. A. Dyudina, W. S. Kurth, D. A. Gurnett, P. Zarka, T. Barry, M. Delcroix, et al., (2011), Overview of Saturn lightning observations, Planetary Radio Emissions VII, (eds.) H. O. Rucker, W. S. Kurth, P. Louarn, G. Fischer, Austrian Academy of Sciences Press, Vienna, 135–144, arXiv:1111.4919.

Flasar, F. M., K. H. Baines, M. K. Bird, T. Tokano, R. A. West, (2009), Atmospheric dynamics and meteorology, Chapter 13, In Titan from Cassini-Huygens, (eds.) R. H. Brown, J.-P. Lebreton, J. H. Waite, Springer Dordrecht, pp. 323–352, doi: 10.1007/978-1-4020-9215-2_13.

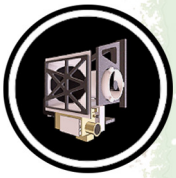

Fletcher, L. N., K. H. Baines, T. W. Momary, A. P. Showman, P. G. J. Irwin, G. S. Orton, M. Roos-Serote, C. Merlet, (2011a), Saturn's tropospheric composition and clouds from Cassini/VIMS 4.6-5.1 μm nightside spectroscopy, Icarus, 214, 2, 510–533, doi: 10.1016/j.icarus.2011.06.006.

Fletcher, L. N., B. E. Hesman, P. G. J. Irwin, K. H. Baines, T. W. Momary, A. Sanchez-Lavega, F. M. Flasar et al, (2011b), Thermal structure and dynamics of Saturn’s northern springtime disturbance, Science, 332, no. 6036, 1413–1417.

Fleury, B., M. S. Gudipati, I. Couturier-Tamburelli, N. Carrasco, (2019), Photoreactivity of condensed acetylene on Titan aerosols analogues, Icarus, 321, 358–366, doi: 10.1016/j.icarus.2018.11.030.

Formisano, V., E. D'Aversa, G. Bellucci, K. H. Baines, J. P. Bibring, Robert H. Brown, B. J. Buratti et al., (2003), Cassini-VIMS at Jupiter: Solar occultation measurements using Io, Icarus, 166, 1, 75–84, doi: 10.1016/S0019-1035(03)00178-7.

Formisano, V., A. Adriani, G. Bellucci, (1992), The VNIR-VIMS experiment for Craf/Cassini, Il Nuovo Cimento C, 15, 6, 1179–1192, doi: 10.1007/BF02506711.

Fortes, A. D., P. M. Grindrod, S. K. Trickett, L. Vočadlo, (2007), Ammonium sulfate on Titan: Possible origin and role in cryovolcanism, Icarus, 188, 1, 139–153, doi: 10.1016/j.icarus.2006.11.002.

French, R. G., C. A. McGhee-French, P. D. Nicholson, M. M. Hedman, (2019), Kronoseismology III: Waves in Saturn's inner C ring, Icarus, 319, 599–626, doi:10.1016/j.icarus.2018.10.013.

French, R. G., C. A. McGhee-French, K. Lonergan, T. Sepersky, R. A. Jacobson, P. D. Nicholson, M. M. Hedman, E. A. Marouf, J. E. Colwell, (2017), Noncircular features in Saturn's rings IV: Absolute radius scale and Saturn's pole direction, Icarus, 290, 14–45, doi: 10.1016/j.icarus.2017.02.007.

French, R. G., P. D. Nicholson, M. M. Hedman, J. M. Hahn, C. A. McGhee-French, J. E. Colwell, E. A. Marouf, N. J. Rappaport, (2016a), Deciphering the embedded wave in Saturn’s Maxwell ringlet, Icarus, 279, 62–77, doi: 10.1016/j.icarus.2015.08.020.

French, R. G., P. D. Nicholson, C. A. McGhee-French, K. Lonergan, T. Sepersky, M. M. Hedman, E. A. Marouf, J. E. Colwell, (2016b), Noncircular features in Saturn's rings III: The Cassini Division, Icarus, 274, 131–162, doi: 10.1016/j.icarus.2016.03.017.

French, R. G., P. D. Nicholson, C. A. McGhee-French, K. Lonergan, T. Sepersky, M. M. Hedman, E. A. Marouf, J. E. Colwell, (2016), Noncircular features in saturn’s rings III: the cassini division, Icarus, 274, 131–162.

French, R. S., M. R. Showalter, R. Sfair, C. A. Argüelles, M. Pajuelo, P. Becerra, M. M. Hedman, P. D. Nicholson, (2012), The brightening of Saturn's F ring, Icarus, 219, 1, 181–193, doi: 10.1016/j.icarus.2012.02.020.

García-Comas, M., M. López-Puertas, B. Funke, B. M. Dinelli, M. Luisa Moriconi, A. Adriani, A. Molina, A. Coradini, (2011), Analysis of Titan CH_4 3.3μm upper atmospheric emission as measured by Cassini/VIMS, Icarus, 214, 2, 571–583, doi: 10.1016/j.icarus.2011.03.020.

Gautier, T., J. A. Sebree, X. Li, V. T. Pinnick, A. Grubisic, M. J. Loeffler, S. A. Getty, M. G. Trainer, W. B. Brinckerhoff, (2017), Influence of trace aromatics on the chemical growth mechanisms of Titan aerosol analogues, Planetary and Space Science, 140, 27–34, doi: 10.1016/j.pss.2017.03.012.

Gautier, T., N. Carrasco, A. Mahjoub, S. Vinatier, A. Giuliani, C. Szopa, C. M. Anderson, J. J. Correia, P. Dumas, G. Cernogora, (2012), Mid- and far-infrared absorption spectroscopy of Titan's aerosols analogues, Icarus, 221, 1, 320–327, doi: 10.1016/j.icarus.2012.07.025.

Giles, R. S., L. N. Fletcher, P. G. J. Irwin, (2015), Cloud structure and composition of Jupiter's troposphere from 5-μm Cassini VIMS spectroscopy, Icarus, 257, 457–470, doi: 10.1016/j.icarus.2015.05.030.

Gilliam, A. E. and A. Lerman, (2016), Formation mechanisms of channels on Titan through dissolution by ammonium sulfate and erosion by liquid ammonia and ethane, Planetary and Space Science, 132, 13–22, doi: 10.1016/j.pss.2016.08.009.

Goguen, J. D., B. J. Buratti, R. H. Brown, R. N. Clark, P. D. Nicholson, M. M. Hedman, R. R. Howell, C. Sotin, D. P. Cruikshank, K. H. Baines, K. J. Lawrence, J. R. Spencer, D. G. Blackburn, (2013), The temperature and width of an active fissure on Enceladus measured with Cassini VIMS during the 14 April 2012, south pole flyover, Icarus, 226 p1128–1137, doi: 10.1016/j.icarus.2013.07.012.

Griffith, C. A., P. F. Penteado, J. D. Turner, C. D. Neish, G. Mitri, N. J. Montiel, A. Schoenfeld, R. M. C. Lopes, (2019), A corridor of exposed ice-rich bedrock across Titan’s tropical region, Nature Astronomy, doi: 10.1038/s41550-019-0756-5.

Griffith, C. A., L. Doose, M. G. Tomasko, P. F. Penteado, C. See, (2012), Radiative transfer analyses of Titan's tropical atmosphere, Icarus, 218, 2, 975–988, doi: 10.1016/j.icarus.2011.11.034.

Hansen, C. J., S. J. Bolton, D. L. Matson, L. J. Spilker, J.-P. Lebreton, (2004), The Cassini–Huygens flyby of Jupiter, Icarus, 172, 1, 1–8, doi: 10.1016/j.icarus.2004.06.018.

Hansen, G. B., E. C. Hollenbeck, K. Stephan, S. K. Apple, E. J. Z. Shin-White, (2012), Water ice abundance and CO_2 band strength on the saturnian satellite Phoebe from Cassini/VIMS observations, Icarus, 220, 2, 331–338, doi: 10.1016/j.icarus.2012.05.004.

Hansen, G. B., (2009), Calculation of single-scattering albedos: Comparison of Mie results with Hapke approximations, Icarus, 203, 2, 672–676, doi: 10.1016/j.icarus.2009.05.025.

Harbison, R. A., P. D. Nicholson, M. M. Hedman, (2013), The smallest particles in Saturn's A and C rings, Icarus, 226, 2, 1225–1240, doi: 10.1016/j.icarus.2013.08.015.

Hayes, A. G., J. M. Soderblom, M. Ádámkovics, (2016), Titan’s surface and atmosphere, Icarus, 270, 1, doi: 10.1016/j.icarus.2016.02.029.

Hayes, A. G., R. D. Lorenz, M. A. Donelan, M. Manga, J. I. Lunine, T. Schneider, M. P. Lamb, et al., (2013), Wind driven capillary-gravity waves on Titan’s lakes: Hard to detect or non-existent?, Icarus, 225, 1, 403–412, doi: 10.1016/j.icarus.2013.04.004.

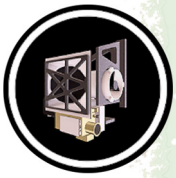

Hayne, P. O., T. B. McCord, C. Sotin, (2014), Titan's surface composition and atmospheric transmission with solar occultation measurements by Cassini VIMS, Icarus, 243, 158–172, doi: 10.1016/j.icarus.2014.08.045.

Hedman, M. M., P. D. Nicholson, R. G. French, (2019), Kronoseismology. IV. Six Previously Unidentified Waves in Saturn's Middle C Ring, The Astronomical Journal, 157, 1, 18, doi: 10.3847/1538-3881/aaf0a6.

Hedman, M. M., D. Dhingra, P. D. Nicholson, C. J. Hansen, G. Portyankina, S. Ye, Y. Dong, (2018a), Spatial variations in the dust-to-gas ratio of Enceladus' plume, Icarus, 305, 123–138, doi: 10.1016/j.icarus.2018.01.006.

Hedman, M. M., F. Postberg, D. P. Hamilton, S. Renner, H. W. Hsu, (2018b), Dusty rings, Chapter 12, In Planetary Ring Systems: Properties, Structure, and Evolution, (eds.) M. S. Tiscareno, C. D. Murraypp, Cambridge University Press, pp. 308–337, doi: 10.1017/9781316286791.012.

Hedman, M. M., (2018), An introduction to planetary ring dynamics, Chapter 2, In Planetary Ring Systems: Properties, Structure, and Evolution, (eds.) M. S. Tiscareno, C. D. Murraypp, Cambridge University Press, pp. 30–47, doi: 10.1017/9781316286791.002.

Hedman, M. M. and P. D. Nicholson, (2016), The B-ring's surface mass density from hidden density waves: Less than meets the eye?, Icarus, 279, 109–124, doi: 10.1016/j.icarus.2016.01.007.

Hedman, M. M. and P. D. Nicholson, (2014), More Kronoseismology with Saturn's rings, Monthly Notices of the Royal Astronomical Society, 444, 1369–1388, doi: 10.1093/mnras/stu1503.

Hedman, M. M., P. D. Nicholson, H. Salo, (2014), Exploring overstabilities in Saturn's A-ring using two stellar occultations, The Astronomical Journal, 148, 15, doi: 10.1088/0004-6256/148/1/15.

Hedman, M. M., C. M. Gosmeyer, P. D. Nicholson, C. Sotin, R. H. Brown, R. N. Clark, K. H. Baines, B. J. Buratti, M. R. Showalter, (2013a), An observed correlation between plume activity and tidal stresses on Enceladus, Nature, 500, 182–184, doi: 10.1038/nature12371.

Hedman, M. M., P. D. Nicholson, J. N. Cuzzi, R. N. Clark, G. Filacchione, F. Capaccioni, M. Ciarniello, (2013b), Connections between spectra and structure in Saturn's main rings based on Cassini VIMS data, Icarus, 223, 1, 105–130, doi: 10.1016/j.icarus.2012.10.014.

Hedman, M. M. and P. D. Nicholson, (2013c), Kronoseismology: Using density waves in Saturn's C ring to Probe the planet's interior, The Astronomical Journal, 146, 12, doi: 10.1088/0004-6256/146/1/12.

Hedman, M. M., P. D. Nicholson, M. R. Showalter, R. H. Brown, B. J. Buratti, R. N. Clark, K. Baines, C. Sotin, (2011), The Christiansen Effect in Saturn's narrow dusty rings and the spectral identification of clumps in the F ring, Icarus, 215, 2, 695–711, erratum in Icarus 218, 735, doi: 10.1016/j.icarus.2011.02.025.

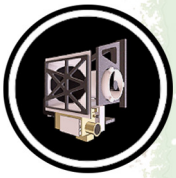

Hedman, M. M., P. D. Nicholson, K. H. Baines, B. J. Buratti, C. Sotin, R. N. Clark, R. H. Brown, R. G. French, E. A. Marouf, (2010), The architecture of the Cassini Division, The Astronomical Journal, 139, 228–251, doi: 10.1088/0004-6256/139/1/228.

Hedman, M. M., P. D. Nicholson, M. R. Showalter, R. H. Brown, B. J. Buratti, R. N. Clark, (2009), Spectral observations of the enceladus plume with Cassini-VIMS, The Astrophysical Journal, 693, 2, 1749–1762, doi: 10.1088/0004-637X/693/2/1749.

Hedman, M. M., J. A. Burns, M. R. Showalter, C. C. Porco, P. D. Nicholson, A. S. Bosh, M. S. Tiscareno, et al., (2007a), Saturn's dynamic D ring, Icarus, 188, 1, 89–107, doi: 10.1016/j.icarus.2006.11.017.

Hedman, M. M., P. D. Nicholson, H. Salo, B. D. Wallis, B. J. Buratti, K. H. Baines, R. H. Brown, R. N. Clark, (2007b), Self-gravity wake structures in Saturn's A-ring revealed by Cassini VIMS, The Astronomical Journal, 133, 6, 2624–2629, doi: 10.1086/516828.

Hendrix, A. R., G. Filacchione, C. Paranicas, P. Schenk, F. Scipioni, (2018), Icy Saturnian satellites: Disk-integrated UV-IR characteristics and links to exogenic processes, Icarus, 300, 103–114, doi: 10.1016/j.icarus.2017.08.037.

Hendrix, A. R., T. A. Cassidy, B. J. Buratti, C. Paranicas, C. J. Hansen, B. Teolis, E. Roussos, E. Todd Bradley, P. Kollmann, R. E. Johnson, (2012), Mimas' far-UV albedo: Spatial variations, Icarus, 220, 2, 922–931, doi: 10.1016/j.icarus.2012.06.012.

Hirtzig, M., B. Bézard, E. Lellouch, A. Coustenis, C. De Bergh, P. Drossart, A. Campargue, et al., (2013a), Corrigendum to– Titan's surface and atmosphere from Cassini/VIMS data with updated methane opacity, Icarus, vol. 226, Issue 1, p. 1182, doi: 10.1016/j.icarus.2013.07.015.

Hirtzig, M., B. Bézard, E. Lellouch, A. Coustenis, C. De Bergh, P. Drossart, A. Campargue, et al., (2013b), Titan's surface and atmosphere from Cassini/VIMS data with updated methane opacity, Icarus, vol. 226, Issue 1, pp. 470–486, doi: 10.1016/j.icarus.2013.05.033.

Hodyss, R., P. V. Johnson, J. V. Stern, J. D. Goguen, I. Kanik, (2009), Photochemistry of methane–water ices, Icarus, 200, 1, 338–342, doi: 10.1016/j.icarus.2008.10.024.

Hofgartner, J. D., A. G. Hayes, J. I. Lunine, H. Zebker, R. D. Lorenz, M. J. Malaska, M. Mastrogiuseppe, C. Notarnicola, J. M. Soderblom, (2016), Titan's "Magic Islands": Transient features in a hydrocarbon sea, Icarus, 271, 338–349, doi:10.1016/j.icarus.2016.02.022.

Imanaka, H., D. P. Cruikshank, B. N. Khare, C. P. McKay, (2012), Optical constants of Titan tholins at mid-infrared wavelengths (2.5–25 μm) and the possible chemical nature of Titan's haze particles, Icarus, 218, 1, 247–261, doi: 10.1016/j.icarus.2011.11.018.

Ingersoll, A. P. and S. P. Ewald, (2017), Decadal timescale variability of the Enceladus plumes inferred from Cassini images, Icarus, 282, 260–275, doi: 10.1016/j.icarus.2016.09.018.

Izawa, M. R. M., E. A. Cloutis, D. M. Applin, M. A. Craig, P. Mann, M. Cuddy, (2014), Laboratory spectroscopic detection of hydration in pristine lunar regolith, Earth and Planetary Science Letters, 390, 157–164, doi: 10.1016/j.epsl.2014.01.007.

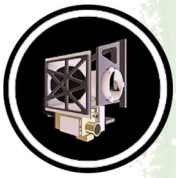

Jaumann, R., R. H. Brown, K. Stephan, J. W. Barnes, L. A. Soderblom, C. Sotin, S. Le Mouélic, et al., (2008a), Fluvial erosion and post-erosional processes on Titan, Icarus, 197, 2, 526–538, doi: 10.1016/j.icarus.2008.06.002.

Jaumann, R., K. Stephan, G. B. Hansen, R. N. Clark, B. J. Buratti, R. H. Brown, K. H. Baines, G. Bellucci, A. Coradini, D. P. Cruikshank, C. A. Griffith, C. A. Hibbitts, T. B. McCord, R. M. Nelson, P. D. Nicholson, C. Sotin, R. Wagner, (2008b), Distribution of icy particles across Enceladus' surface as derived from Cassini-VIMS measurements, Icarus 193, 407–419, doi: 10.1016/j.icarus.2007.09.013.

Jaumann, R., K. Stephan, R. H. Brown, B. J. Buratti, R. N. Clark, T. B. McCord, A. Coradini, (2006), High-resolution Cassini-VIMS mosaics of Titan and the icy Saturnian satellites, Planetary and Space Science, 54, 12, 1146–1155, doi: 10.1016/j.pss.2006.05.034.

Jerousek, R. G., J. E. Colwell, L. W. Esposito, P. D. Nicholson, M. M. Hedman, (2016), Small particles and self-gravity wakes in Saturn's rings from UVIS and VIMS stellar occultations, Icarus, 279, 36–50, doi: 10.1016/j.icarus.2016.04.039.

Juergens, D. W., J. E. Duval, R. F. Lockhart, Y. Langevin, V. Formisano, G. Bellucci, (1991), Visible and infrared mapping spectrometer for exploration of comets, asteroids, and the saturnian system of rings and moons, International Journal of Imaging Systems and Technology, 3, 2, 108–120, doi: 10.1002/ima.1850030207.

Karkoschka, E. and S. E. Schröder, (2016), Eight-color maps of Titan's surface from spectroscopy with Huygens' DISR, Icarus, 270, 260–271, doi: 10.1016/j.icarus.2015.06.010.

Kazeminejad, B., D. H. Atkinson, J. P. Lebreton, (2011), Titan's new pole: Implications for the Huygens entry and descent trajectory and landing coordinates, Advances in Space Research, 47, 9, 1622–1632, doi: 10.1016/j.asr.2011.01.019.

Kim, S. J., C. K. Sim, T. S. Stallard, R. Courtin, (2019), Spectral characteristics and formation of high-altitude haze in the south-polar regions of Saturn, Icarus, 321, 436–444, doi: 10.1016/j.icarus.2018.12.004.

Kim, S. J., D. W. Lee, C. K. Sim, K. I. Seon, R. Courtin, T. R. Geballe, (2018), Retrieval of haze properties and HCN concentrations from the three-micron spectrum of Titan, Journal of Quantitative Spectroscopy and Radiative Transfer, 210, 197–203, doi: 10.1016/j.jqsrt.2018.02.024.

Kim, S. J. and R. Courtin, (2013), Spectral characteristics of the Titanian haze at 1–5 micron from Cassini/VIMS solar occultation data, Astronomy & Astrophysics, 557, doi: 10.1051/0004-6361/201322173.

Kim, S. J., C. K. Sim, D. W. Lee, R. Courtin, J. I. Moses, Y. C. Minh, (2012), The three-micron spectral feature of the Saturnian haze: Implications for the haze composition and formation process, Planetary and Space Science, 65, 1, 122–129, doi: 10.1016/j.pss.2012.02.013.

Kim, S. J., A. Jung, C. K. Sim, R. Courtin, A. Bellucci, B. Sicardy, I. O. Song, Y. C. Minh, (2011), Retrieval and tentative indentification of the 3 μm spectral feature in Titans haze, Planetary and Space Science, 59, 8, 699–704, doi: 10.1016/j.pss.2011.02.002.

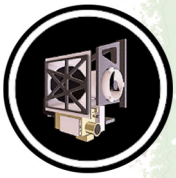

Kim, Y. S., C. Ennis, S. J. Kim, (2013), Simulating the 3.4-micron feature of titan's haze, Bulletin of the Korean Chemical Society, 34, 3, 759–762, doi: 10.5012/bkcs.2013.34.3.759.

Kolokolova, L., L. Liu, B. Buratti, M. I. Mishchenko, (2011), Modeling variations in near-infrared spectra caused by the coherent backscattering effect, Journal of Quantitative Spectroscopy and Radiative Transfer, 112, 13, 2175–2181, doi: 10.1016/j.jqsrt.2011.03.010.

Kolokolova, L., B. Buratti, V. Tishkovets, (2010), Impact of coherent backscattering on the spectra of icy satellites of Saturn and the implications of its effects for remote sensing, The Astrophysical Journal Letters, 711, L71–L74, doi: 10.1088/2041-8205/711/2/L71.

Lamy, L., R. Prangé, W. Pryor, Jacques Gustin, S. V. Badman, H. Melin, T. Stallard, D. G. Mitchell, P. C. Brandt, (2011), Multispectral simultaneous diagnosis of Saturn's aurorae throughout a planetary rotation, Journal of Geophysical Research: Space Physics, 118, no. 8, 4817–4843.

Langhans, M., J. I. Lunine, G. Mitri, (2013), Titan’s Xanadu region: Geomorphology and formation scenario, Icarus, 223, 2, 796–803, doi: 10.1016/j.icarus.2013.01.016.

Langhans, M. H., R. Jaumann, K. Stephan, R. H. Brown, B. J. Buratti, R. N. Clark, K. H. Baines, et al., (2012), Titan's fluvial valleys: Morphology, distribution, and spectral properties, Planetary and Space Science, 60, 1, 34–51, doi: 10.1016/j.pss.2011.01.020.

Langhans, M., (2011), Erosion on saturn's moon Titan - Analyses of the distribution, morphology, and spectral properties of Titan's fluvial valleys, Ph.D. dissertation, doi: 10.17169/refubium-6689.

Larson, E. J. L., O. B. Toon, A. J. Friedson, (2014), Simulating Titan’s aerosols in a three dimensional general circulation model, Icarus, 243, 400–419, doi: 10.1016/j.icarus.2014.09.003.

Launeau, P., C. Sotin, J. Girardeau, (2002), Cartography of the Ronda peridotite (Spain) by hyperspectral remote sensing, Bulletin de la Societe Geologique de France, 173, 6, 491–508, doi: 10.2113/173.6.491.

Le Corre, L., S. Le Mouélic, C. Sotin, J.-P. Combe, S. Rodriguez, J. W. Barnes, R. H. Brown, et al., (2009), Analysis of a cryolava flow-like feature on Titan, Planetary and Space Science, 57, 7, 870–879, doi: 10.1016/j.pss.2009.03.005.

Le Gall, A., M. A. Janssen, L. C. Wye, A. G. Hayes, J. Radebaugh, C. Savage, H. Zebker, et al., (2011), Cassini SAR, radiometry, scatterometry and altimetry observations of Titan's dune fields, Icarus, 213, 2, 608–624, doi: 10.1016/j.icarus.2011.03.026.

Le Mouélic, S., T. Cornet, S. Rodriguez, C. Sotin, B. Seignovert, J. W. Barnes, R. H. Brown, et al., (2019), The Cassini VIMS archive of Titan: From browse products to global infrared color maps, Icarus, 319, 121–132, doi: 10.1016/j.icarus.2018.09.017.

Le Mouélic, S., S. Rodriguez, R. Robidel, B. Rousseau, B. Seignovert, C. Sotin, J. W. Barnes, et al., (2018), Mapping polar atmospheric features on Titan with VIMS: From the dissipation of

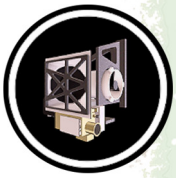

the northern cloud to the onset of a southern polar vortex, Icarus, 311, 371–383, doi: 10.1016/j.icarus.2018.04.028.

Le Mouélic, S., T. Cornet, S. Rodriguez, C. Sotin, J. W. Barnes, K. H. Baines, R. H. Brown, et al., (2012a), Global mapping of Titan′s surface using an empirical processing method for the atmospheric and photometric correction of Cassini/VIMS images, Planetary and Space Science, 73, 1, 178–190, doi: 10.1016/j.pss.2012.09.008.

Le Mouélic, S., P. Rannou, S. Rodriguez, C. Sotin, C. A. Griffith, L. Le Corre, J. W. Barnes, et al., (2012b), Dissipation of Titans north polar cloud at northern spring equinox, Planetary and Space Science, 60, 1, 86–92, doi: 10.1016/j.pss.2011.04.006.

Le Mouélic, S., P. Paillou, M. A. Janssen, J. W. Barnes, S. Rodriguez, C. Sotin, R. H. Brown, et al., (2008), Mapping and interpretation of Sinlap crater on Titan using Cassini VIMS and RADAR data, Journal of Geophysical Research: Planets, 113, 4, doi: 10.1029/2007JE002965.

Lee, J. S., B. J. Buratti, M. Hicks, J. Mosher, (2010), The roughness of the dark side of Iapetus from the 2004 to 2005 flyby, Icarus, 206, 2, 623–630, doi: 10.1016/j.icarus.2009.11.008.

Li, L., K. H. Baines, M. A. Smith, R. A. West, S. Pérez-Hoyos, H. J. Trannell, A. A. Simon-Miller, B. J. Conrath, G. S. Orton, C. A. Nixon, G. Filacchione, P. M. Fry, T. W. Momary, (2012), Emitted power of Jupiter based on Cassini CIRS and VIMS observations, Journal of Geophysical Research: Planets, doi: 10.1029/2012JE004191.

Loeffler, J. and A. Baragiola, (2009), Is the 3.5 μm infrared feature on Enceladus due to hydrogen peroxide?, The Astrophysical Journal, 694, L92–L94, doi: 10.1088/0004-637X/694/1/L92.

Lopes, R. M. C., M. J. Malaska, A. Solomonidou, A. Le Gall, M. A. Janssen, C. D. Neish, E. P. Turtle, et al., (2016), Nature, distribution, and origin of Titan's Undifferentiated Plains, Icarus, 270, 162–182, doi: 10.1016/j.icarus.2015.11.034.

Lopes, R. M. C., R. L. Kirk, K. L. Mitchell, A. LeGall, J. W. Barnes, A. Hayes, J. Kargel, et al., (2013), Cryovolcanism on Titan: New results from Cassini RADAR and VIMS, Journal of Geophysical Research: Planets, 118, 3, 416–435, doi: 10.1002/jgre.20062.

Lopes, R. M. C., B. J. Buratti, A. R. Hendrix, (2008), The Saturn system's icy satellites: New results from Cassini, Icarus, 193, 2, 305–308, doi: 10.1016/j.icarus.2007.11.002.

Lora, J. M., J. I. Lunine, J. L. Russell, (2015), GCM simulations of Titan’s middle and lower atmosphere and comparison to observations, Icarus, 250, 516–528, doi: 10.1016/j.icarus.2014.12.030.

Lorenz, R. D., J. I. Lunine, (2005), Titan's surface before Cassini, Planetary and Space Science, 53, no. 5, 557–576.

MacKenzie, S. M., J. W. Barnes, C. Sotin, J. M. Soderblom, S. Le Mouélic, S. Rodriguez, K. H. Baines, et al., (2014), Evidence of Titan's climate history from evaporite distribution, Icarus, 243, 191–207, doi: 10.1016/j.icarus.2014.08.022.

Mahjoub, A., M. Choukroun, R. Hodyss, C. Sotin, P. Beauchamp, M. Barmatz, (2018), Titan Lakes Simulation System (TiLSS): A cryogenic experimental setup to simulate Titan's liquid

hydrocarbon surfaces, Review of Scientific Instruments, 89, 12, 124502, doi: 10.1063/1.5053126.

Mahjoub, A., M. Schwell, N. Carrasco, Y. Benilan, G. Cernogora, C. Szopa, M. C. Gazeau (2016), Characterization of aromaticity in analogues of titan's atmospheric aerosols with two-step laser desorption ionization mass spectrometry, Planetary and Space Science, 131, 1–13, doi: 10.1016/j.pss.2016.05.003.

Mahjoub, A., N. Carrasco, P. R. Dahoo, T. Gautier, C. Szopa, G. Cernogora, (2012), Influence of methane concentration on the optical indices of Titan's aerosols analogues, Icarus, 221, 2, 670–677, doi: 10.1016/j.icarus.2012.08.015.

Malaska, M. J., R. M. C. Lopes, D. A. Williams, C. D. Neish, A. Solomonidou, J. M. Soderblom, A. M. Schoenfeld, et al., (2016), Geomorphological map of the Afekan Crater region, Titan: Terrain relationships in the equatorial and mid-latitude regions, Icarus, 270, 130–161, doi: 10.1016/j.icarus.2016.02.021.

Malathy Devi, V., I. Kleiner, R. L. Sams, L. R. Brown, D. C. Benner, L. N. Fletcher, (2014), Line positions and intensities of the phosphine (PH_3) Pentad near 4.5 μm, Journal of Molecular Spectroscopy, 298, 11–23, doi: 10.1016/j.jms.2014.01.013.

Maltagliati, L., B. Bézard, S. Vinatier, M. M. Hedman, E. Lellouch, P. D. Nicholson, C. Sotin, R. J. de Kok, B. Sicardy, (2015), Titan's atmosphere as observed by Cassini/VIMS solar occultations: CH_4, CO and evidence for C_2H_6 absorption, Icarus, 248, 1–24, doi: 10.1016/j.icarus.2014.10.004.

Mastrapa, R. M., M. P. Bernstein, S. A. Sandford, T. L. Roush, D. P. Cruikshank, C. M. Dalle Ore, (2008), Optical constants of amorphous and crystalline H_2O-ice in the near infrared from 1.1 to 2.6 μm, Icarus, 197, no. 1, 307–320.

Mastrogiuseppe, M., A. G. Hayes, V. Poggiali, J. I. Lunine, R. D. Lorenz, R. Seu, A. Le Gall, et al., (2018), Bathymetry and composition of Titan's Ontario Lacus derived from Monte Carlo-based waveform inversion of Cassini RADAR altimetry data, Icarus, 300, 203–209, doi: 10.1016/j.icarus.2017.09.009.

Mathé, C., T. Gautier, M. G. Trainer, N. Carrasco, (2018), Detection Opportunity for Aromatic Signature in Titan's Aerosols in the 4.1–5.3 μm Range, The Astrophysical Journal Letters, 861, 2, doi:10.3847/2041-8213/aacf88.

Matson, D. L., A. G. Davies, T. V. Johnson, J. P. Combe, T. B. McCord, J. Radebaugh, S. Singh, (2018), Enceladus' near-surface CO_2 gas pockets and surface frost deposits, Icarus, 302, 18–26, doi: 10.1016/j.icarus.2017.10.025.

McCord, T. B., et al., (2008), Titan's surface: Search for spectral diversity and composition using the Cassini VIMS investigation, Icarus, 194(1), 212–242, doi: 10.1016/j.icarus.2007.08.039.

McCord, T. B., P. Hayne, J.-P. Combe, G. B. Hansen, J. W. Barnes, S. Rodriguez, S. Le Mouélic, et al., (2006), Composition of Titan's surface from Cassini VIMS, Planetary and Space Science, 54, 15, 1524–1539, doi: 10.1016/j.pss.2006.06.007.

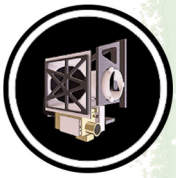

McCord, T. B., A. Coradini, C. A. Hibbitts, F. Capaccioni, G. B. Hansen, G. Filacchione, R. N. Clark, et al., (2004), Cassini VIMS observations of the Galilean satellites including the VIMS calibration procedure, Icarus, 172, 104–126, doi: 10.1016/j.icarus.2004.07.001.

Meier, R., B. A. Smith, T. C. Owen, R. J. Terrile, (2000), The surface of Titan from NICMOS observations with the Hubble Space Telescope, Icarus, 145, no. 2, 462–473.

Melin, H., S. V. Badman, T. S. Stallard, U. Dyudina, J. D. Nichols, G. Provan, J. O'Donoghue, W. R. Pryor, K. H. Baines, S. Miller, J. Gustin, A. Radioti, C. Tao, C. J. Meredith, J. S. D. Blake, (2016), Simultaneous multi-scale and multiinstrument observations of Saturn's aurorae during the 2013 Observing Campaign, Icarus, 263, 56–74, doi: 10.1016/j.icarus.2015.08.021.

Melin, H., T. Stallard, S. Miller, J. Gustin, M. Galand, S. V. Badman, W. R. Pryor, J. O'Donoghue, R. H. Brown, K. H. Baines, (2011), Simultaneous Cassini/VIMS and UVIS observations of Saturn's southern aurora: Comparing emissions from H, H_2 and H_3^+ at a high spatial resolution, Geophysical Research Letters, 38, L15203, doi: 10.1029/2011GL048457.

Miller, E. A., G. Klein, D. W. Juergens, K. Mehaffey, J. M. Oseas, R. A. Garcia, A. Giandomenico, et al., (1996), The visual and infrared mapping spectrometer for Cassini, In Cassini/Huygens: A Mission to the Saturnian Systems, International Symposium on Optical Science, Engineering, and Instrumentation, Denver, CO, vol. 2803, pp. 206–220, doi: 10.1117/12.253421.

Moore, J. M. and R. T. Pappalardo, (2011), Titan: An exogenic world?, Icarus, 212, 2, 790–806, doi: 10.1016/j.icarus.2011.01.019.

Moore, J. M. and A. D. Howard, (2010), Are the basins of Titan's Hotei Regio and Tui Regio sites of former low latitude seas?, Geophysical Research Letters, 37, 22, doi: 10.1029/2010GL045234.

Morales-Juberías, R., K. M. Sayanagi, T. E. Dowling, A. P. Ingersoll, (2011), Emergence of polar-jet polygons from jet instabilities in a Saturn model, Icarus, 211, 2, 1284–1293, doi: 10.1016/j.icarus.2010.11.006.

Moriconi, M. L., A. Adriani, E. D'Aversa, G. L. Liberti, G. Filacchione, F. Oliva, (2016), Unbiased estimations of atmosphere vortices: The Saturn's storm by Cassini VIMS-V as case study, Journal of Signal and Information Processing, 7, no. 02, 75–83, doi: 10.4236/jsip.2016.72009.

Moriconi, M. L., J. I. Lunine, A. Adriani, E. D'Aversa, A. Negrão, G. Filacchione, A. Coradini, (2010), Characterization of Titan's Ontario Lacus region from Cassini/VIMS observations, Icarus, 210, 2, 823–831, doi: 10.1016/j.icarus.2010.07.023.

Neish, C. D., J. W. Barnes, C. Sotin, S. MacKenzie, J. M. Soderblom, S. Le Mouélic, R. L. Kirk, et al., (2015), Spectral properties of Titan's impact craters imply chemical weathering of its surface, Geophysical Research Letters, 42, 10, 3746–3754, doi:10.1002/2015gl063824.

Nelson, R. M., L. W. Kamp, R. M. C. Lopes, D. L. Matson, R. L. Kirk, B. W. Hapke, S. D. Wall., et al., (2009a), Photometric changes on Saturn's Titan: Evidence for active cryovolcanism, Geophysical Research Letters, 36, 4, doi: 10.1029/2008GL036206.

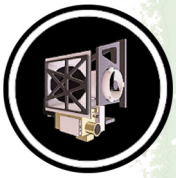

Nelson, R. M., L. W. Kamp, D. L. Matson, P. G. J. Irwin, K. H. Baines, M. D. Boryta, F. E. Leader, et al., (2009b), Saturn's Titan: Surface change, ammonia, and implications for atmospheric and tectonic activity, Icarus, 199, 2, 429–441, doi: 10.1016/j.icarus.2008.08.013.

Nelson, R. M., R. H. Brown, B. W. Hapke, W. D. Smythe, L. Kamp, M. D. Boryta, F. Leader, et al., (2006), Photometric properties of Titan's surface from Cassini VIMS: Relevance to titan's hemispherical albedo dichotomy and surface stability, Planetary and Space Science, 54, 15, 1540–1551, doi: 10.1016/j.pss.2006.06.014.

Nelson, R. M., W. D. Smythe, B. W. Hapke, A. S. Hale, (2002), Low phase angle laboratory studies of the opposition effect: search for wavelength dependence, Planetary and Space Science, 50, 9, 849–856, doi: 10.1016/S0032-0633(02)00059-4.

Nelson, R. M., B. W. Hapke, W. D. Smythe, L. J. Horn, (1998), Phase curves of selected particulate materials: The contribution of coherent backscattering to the opposition surge, Icarus, 131, 1, 223–230, doi: 10.1006/icar.1997.5850.

Newman, S. F., B. J. Buratti, R. H. Brown, R. Jaumann, J. Bauer, T. Momary, (2009), Water ice crystallinity and grain sizes on Dione, Icarus, 203, 2, 553–559, doi: 10.1016/j.icarus.2009.04.034.

Newman, S. F., B. J. Buratti, R. H. Brown, R. Jaumann, J. Bauer, T. Momary, (2008), Photometric and spectral analysis of the distribution of crystalline and amorphous ices on Enceladus as seen by Cassini, Icarus, 193, 2, 397–406, doi: 10.1016/j.icarus.2007.04.019.

Newman, S. F., B. J. Buratti, R. Jaumann, J. M. Bauer, T. W. Momary, (2007), Hydrogen peroxide on Enceladus, The Astrophysical Journal, 670, L143–L146, doi: 10.1086/524403.

Nichols, J. D., S. V. Badman, E. J. Bunce, J. T. Clarke, S. W. H. Cowley, G. J. Hunt, G. Provan, (2016), Saturn’s northern auroras as observed using the Hubble Space Telescope, Icarus, 263, 17–31, doi: 10.1016/j.icarus.2015.09.008.

Nicholson, P. D., R. G. French, J. N. Spitale, (2018), Narrow rings, gaps and sharp edges, Chapter 11, In Planetary Ring Systems: Properties, Structure, and Evolution, (eds.) M. S. Tiscareno, C. D. Murraypp, Cambridge University Press, pp. 276–307, doi: 10.1017/9781316286791.011.

Nicholson, P. D. and M. M. Hedman, (2016), A vertical rift in Saturn's inner C ring, Icarus, 279, 78–99, doi: 10.1016/j.icarus.2016.01.024.

Nicholson, P. D., R. G. French, M. M. Hedman, E. A. Marouf, J. E. Colwell, (2014a), Noncircular features in Saturn’s rings I: The edge of the B ring, Icarus, 227, 152–175, doi: 10.1016/j.icarus.2013.09.002.

Nicholson, P. D., R. G. French, C. A. McGhee-French, M. M. Hedman, E. A. Marouf, J. E. Colwell, K. Lonergan, T. Sepersky, (2014b), Noncircular features in Saturn’s rings II: The C ring, Icarus, 241, 373–396, doi: 10.1016/j.icarus.2014.06.024.

Nicholson, P. D. and M. M. Hedman, (2010), Self-gravity wake parameters in Saturn's A and B rings, Icarus, 206, 2, 410–423, doi: 10.1016/j.icarus.2009.07.028.

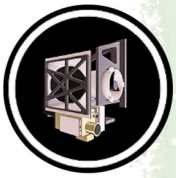

Nicholson, P. D., M. M. Hedman, R. N. Clark, M. R. Showalter, D. P. Cruikshank, J. N. Cuzzi, G. Filacchione et al., (2008), A close look at Saturn's rings with Cassini VIMS, Icarus 193, 182–212, doi: 10.1016/j.icarus.2007.08.036.

Nimmo, F., C. Porco, C. Mitchell, (2014), Tidally modulated eruptions on Enceladus: Cassini ISS observations and models, The Astronomical Journal, 148, no. 3, 46.

Nordheim, T. A., K. P. Hand, C. Paranicas, C. J. A. Howett, A. R. Hendrix, G. H. Jones, A. J. Coates, (2017), The near-surface electron radiation environment of Saturn's moon Mimas, Icarus, 286, 56–68, doi: 10.1016/j.icarus.2017.01.002.

Oancea, A., O. Grasset, E. Le Menn, O. Bollengier, L. Bezacier, S. Le Mouélic, G. Tobie, (2012), Laboratory infrared reflection spectrum of carbon dioxide clathrate hydrates for astrophysical remote sensing applications, Icarus, 221, 2, 900–910, doi: 10.1016/j.icarus.2012.09.020.

Oliva, F., A. Adriani, M. L. Moriconi, G. L. Liberti, E. D'Aversa, G. Filacchione, (2016), Clouds and hazes vertical structure of a Saturn's giant vortex from Cassini/VIMS-V data analysis, Icarus, 278, 215–237, doi: 10.1016/j.icarus.2016.06.021.

Orton, G. S., L. N. Fletcher, C. M. Lisse, P. W. Chodas, A. Cheng, P. A. Yanamandra-Fisher, K. H. Baines, et al., (2011), The atmospheric influence, size and possible asteroidal nature of the July 2009 Jupiter impactor, Icarus, 211, 1, 587–602, doi: 10.1016/j.icarus.2010.10.010.

Palmer, E. E. and R. H. Brown, (2011), Production and detection of carbon dioxide on Iapetus, Icarus, 212, 2, 807–818, doi: 10.1016/j.icarus.2010.12.007.

Palmer, E. E. and R. H. Brown, (2008), The stability and transport of carbon dioxide on Iapetus, Icarus, 195, 1, 434–446, doi: 10.1016/j.icarus.2007.11.020.

Pasek, V. and Lytle, D., (2011), Mission-critical software development for a distributed and diverse user base, paper presented at IEEE Aerospace Conference Proceedings.

Penteado, P. F. and C. A. Griffith, (2010), Ground-based measurements of the methane distribution on Titan, Icarus, 206, 1, 345–351, doi: 10.1016/j.icarus.2009.08.022.

Penteado, P. F., C. A. Griffith, M. G. Tomasko, S. Engel, C. See, L. Doose, K. H. Baines, et al., (2010), Latitudinal variations in Titan's methane and haze from Cassini VIMS observations, Icarus, 206, 1, 352–365, doi: 10.1016/j.icarus.2009.11.003.

Penteado, P. F., (2009), Study of Titan's methane cycle, University of Arizona.

Pinilla-Alonso, N., T. L. Roush, G. A. Marzo, D. P. Cruikshank, C. M. Dalle Ore, (2011), Iapetus surface variability revealed from statistical clustering of a VIMS mosaic: The distribution of CO2, Icarus, 215, 1, 75–82, doi: 10.1016/j.icarus.2011.07.004.

Pirim, C., R. D. Gann, J. L. McLain, T. M. Orlando, (2015), Electron-molecule chemistry and charging processes on organic ices and Titan's icy aerosol surrogates, Icarus, 258, 109–119, doi: 10.1016/j.icarus.2015.06.006.

Pitman, K. M., L. Kolokolova, A. J. Verbiscer, D. W. Mackowski, E. C. S. Joseph, (2017), Coherent backscattering effect in spectra of icy satellites and its modeling using multi-sphere

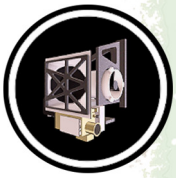

T-matrix (MSTM) code for layers of particles, Planetary and Space Science, 149, 23–31, doi: 10.1016/j.pss.2017.08.005.

Pitman, K. M., B. J. Buratti, J. A. Mosher, (2010), Disk-integrated bolometric Bond albedos and rotational light curves of saturnian satellites from Cassini Visual and Infrared Mapping Spectrometer, Icarus, 206, 2, 537–560, doi: 10.1016/j.icarus.2009.12.001.

Pitman, K. M., B. J. Buratti, J. A. Mosher, J. M. Bauer, T. W. Momary, R. H. Brown, P. D. Nicholson, M. M. Hedman, (2008), First high solar phase angle observations of rhea using Cassini VIMS: Upper limits on water vapor and geologic activity, The Astrophysical Journal, 680, L65–L68, doi: 10.1086/589745.

Porco, C., D. Dinino, F. Nimmo, (2014), How the geysers, tidal stresses, and thermal emission across the south polar terrain of Enceladus are related, The Astronomical Journal, 148, 3, doi: 10.1088/0004-6256/148/3/45.

Radebaugh, J., (2013), Dunes on Saturn’s moon Titan as revealed by the Cassini Mission, Aeolian Research, 11, 23–41, doi: 10.1016/j.aeolia.2013.07.001.

Radebaugh, J., R. D. Lorenz, S. D. Wall, R. L. Kirk, C. A. Wood, J. I. Lunine, E. R. Stofan, et al., (2011), Regional geomorphology and history of Titan’s Xanadu province, Icarus, 211, 1, 672–685, doi: 10.1016/j.icarus.2010.07.022.

Rannou, P., B. Seignovert, S. Le Mouélic, L. Maltagliati, M. Rey, C. Sotin, (2018), Transparency of 2 μm window of Titan's atmosphere, Planetary and Space Science, doi: 10.1016/j.pss.2017.11.015.

Rannou, P., D. Toledo, P. Lavvas, E. D’Aversa, M. L. Moriconi, A. Adriani, S. Le Mouélic, C. Sotin, R. Brown, (2016), Titan’s surface spectra at the Huygens landing site and Shangri-La, Icarus, 270, 291–306, doi: 10.1016/j.icarus.2015.09.016.

Rannou, P., S. Le Mouélic, C. Sotin, R. H. Brown, (2012), Cloud and haze in the winter polar region of titan observed with visual and infrared mapping spectrometer on board Cassini, The Astrophysical Journal, 748, 1, doi: 10.1088/0004-637X/748/1/4.

Rannou, P., T. Cours, S. Le Mouélic, S. Rodriguez, C. Sotin, P. Drossart, R. Brown, (2010), Titan haze distribution and optical properties retrieved from recent observations, Icarus, 208, 2, 850–867, doi: 10.1016/j.icarus.2010.03.016.

Reininger, F. M., M. Dami, R. Paolinetti, S. Pieri, S. Falugiani, (1994), Visible Infrared Mapping Spectrometer--visible channel (VIMS-V), In Instrumentation in Astronomy VIII, Symposium on Astronomical Telescopes and Instrumentation for the 21st Century, Kailua, Kona, HI, vol. 2198, pp. 239–250, doi: 10.1117/12.176753.

Rey, M., A. V. Nikitin, B. Bézard, P. Rannou, A. Coustenis, V. G. Tyuterev, (2018), New accurate theoretical line lists of $^{12}CH_4$ and $^{13}CH_4$ in the 0–13400 cm range: Application to the modeling of methane absorption in Titan’s atmosphere, Icarus, 303, 114–130, doi: 10.1016/j.icarus.2017.12.045.

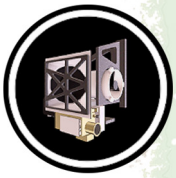

Rivera-Valentin, E. G., D. G. Blackburn, R. Ulrich, (2011), Revisiting the thermal inertia of Iapetus: Clues to the thickness of the dark material, Icarus, 216, 1, 347–358, doi: 10.1016/j.icarus.2011.09.006.

Roatsch, T., R. Jaumann, K. Stephan, P. C. Thomas, (2009), Cartographic mapping of the icy satellites using ISS and VIMS data, in Saturn from Cassini-Huygens, pp. 763–781, doi: 10.1007/978-1-4020-9217-6_24.

Robinson, T. D., L. Maltagliati, M. S. Marley, J. J. Fortney, (2014), Titan solar occultation observations reveal transit spectra of a hazy world, Proceedings of the National Academy of Science, 111, 9042–9047, doi: 10.1073/pnas.1403473111.

Rodriguez, S., S. Le Mouélic, J. W. Barnes, J. F. Kok, S. C. R. Rafkin, R. D. Lorenz, B. Charnay, et al., (2018), Observational evidence for active dust storms on Titan at equinox, Nature Geoscience, 11, 10, 727–732, doi:10.1038/s41561-018-0233-2.

Rodriguez, S., A. Garcia, A. Lucas, T. Appéré, Alice Le Gall, E. Reffet, L. Le Corre, et al., (2014), Global mapping and characterization of Titan's dune fields with Cassini: Correlation between RADAR and VIMS observations, Icarus, 230, 168–179, doi: 10.1016/j.icarus.2013.11.017.

Rodriguez, S., S. Le Mouélic, P. Rannou, C. Sotin, R. H. Brown, J. W. Barnes, C. A. Griffith, et al., (2011), Titan's cloud seasonal activity from winter to spring with Cassini/VIMS, Icarus, 216, 1, 89–110, doi: 10.1016/j.icarus.2011.07.031.

Rodriguez, S., S. Le Mouélic, P. Rannou, G. Tobie, K. H. Baines, J. W. Barnes, C. A. Griffith, et al., (2009), Global circulation as the main source of cloud activity on Titan, Nature, 459, 678, doi: 10.1038/nature08014.

Rodriguez, S., S. Le Mouélic, C. Sotin, H. Clénet, R. N. Clark, B. Buratti, R. H. Brown, T. B. McCord, P. D. Nicholson, K. H. Baines, (2006), Cassini/VIMS hyperspectral observations of the HUYGENS landing site on Titan, Planetary and Space Science, 54, 15, 1510–1523, doi: 10.1016/j.pss.2006.06.016

Sayanagi, K. M., K. H. Baines, U. Dyudina, L. N. Fletcher, A. Sánchez-Lavega, R. A. West, (2018), Saturn’s polar atmosphere, Chapter 12, In Saturn in the 21st Century, (eds.), F. M. Flasar, K. H. Baines, N. Krupp, T. Stallard, Cambridge University Press, pp. 337–376, doi: 10.1017/9781316227220.012.

Sayanagi, K. M., R. Morales-Juberías, A. P. Ingersoll, (2010), Saturn's northern hemisphere ribbon: Simulations and comparison with the meandering Gulf Stream, Journal of the Atmospheric Sciences, 67, 8, 2658–2678, doi: 10.1175/2010JAS3315.1.

Schenk, P. M., B. J. Buratti, P. K. Byrne, W. B. McKinnon, F. Nimmo, F. Scipioni, (2015), Blood stains on Tethys: evidence of recent activity, European Planetary Science Congress (EPSC), vol. 10, abstract EPSC2015-893.

Schenk, P., D. P. Hamilton, R. E. Johnson, W. B. McKinnon, C. Paranicas, J. Schmidt, M. R. Showalter, (2011), Plasma, plumes and rings: Saturn system dynamics as recorded in global color patterns on its midsize icy satellites, Icarus, 211, no. 1, 740–757.

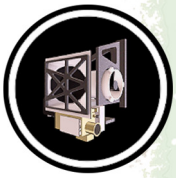

Schurmeier, L. R. and A. J. Dombard, (2018), Crater relaxation on Titan aided by low thermal conductivity sand infill, Icarus, doi: 10.1016/j.icarus.2017.10.034.

Sciamma-O'Brien, E., K. T. Upton, F. Salama, (2017), The Titan Haze Simulation (THS) experiment on COSmIC, Part II, Ex-situ analysis of aerosols produced at low temperature, Icarus, 289, 214–226, doi: 10.1016/j.icarus.2017.02.004.

Sciamma-O'Brien, E., P. R. Dahoo, E. Hadamcik, N. Carrasco, E. Quirico, C. Szopa, G. Cernogora, (2012), Optical constants from 370 nm to 900 nm of Titan tholins produced in a low pressure RF plasma discharge, Icarus, 218, 1, 356–363, doi: 10.1016/j.icarus.2011.12.014.

Scipioni, F., P. Schenk, F. Tosi, E. D'Aversa, R. Clark, J. P. Combe, C. M. D. Ore, (2017), Deciphering sub-micron ice particles on Enceladus surface, Icarus, 290, 183–200, doi: 10.1016/j.icarus.2017.02.012.

Scipioni, F., F. Tosi, K. Stephan, G. Filacchione, M. Ciarniello, F. Capaccioni, P. Cerroni, (2014), Spectroscopic classification of icy satellites of Saturn II: Identification of terrain units on Rhea, Icarus, 234, 1–16, doi: 10.1016/j.icarus.2014.02.010.

Scipioni, F., F. Tosi, K. Stephan, G. Filacchione, M. Ciarniello, F. Capaccioni, P. Cerroni, (2013), Spectroscopic classification of icy satellites of Saturn I: Identification of terrain units on Dione, Icarus, 226, 2, 1331–1349, doi: 10.1016/j.icarus.2013.08.008.

Scipioni, F., A. Coradini, F. Tosi, F. Capaccioni, P. Cerroni, G. Filacchione, C. Federico, (2012), Spectroscopic investigation of Dione' surface using Cassini VIMS images, Memorie della Societa Astronomica Italiana Supplementi, vol. 20, p. 114.

Sim, C. K., S. J. Kim, R. Courtin, M. Sohn, D.-H. Lee, (2013), The two-micron spectral characteristics of the Titanian haze derived from Cassini/VIMS solar occultation spectra, Planetary and Space Science, 88, 93–99, doi: 10.1016/j.pss.2013.10.003.

Simon, S., J. Saur, F. M. Neubauer, A. Wennmacher, M. K. Dougherty, (2011), Magnetic signatures of a tenuous atmosphere at Dione, Geophysical Research Letters 38, no. 15, doi: 10.1029/2011GL048454.

Simonelli, D. P. and B. J. Buratti, (2004), Europa's opposition surge in the near-infrared: Interpreting disk-integrated observations by Cassini VIMS, Icarus, 172, 149–162, doi: 10.1016/j.icarus.2004.06.004.

Sinclair, J. A., P. G. J. Irwin, L. N. Fletcher, J. I. Moses, T. K. Greathouse, A. J. Friedson, B. Hesman, J. Hurley, C. Merlet, (2013), Seasonal variations of temperature, acetylene and ethane in Saturn's atmosphere from 2005 to 2010, as observed by Cassini-CIRS, Icarus, 225, 1, 257–271, doi: 10.1016/j.icarus.2013.03.011.

Singh, G., S. Singh, A. Wagner, V. F. Chevrier, J. P. Combe, M. Gainor, (2017a), Experimental reflectance study of methane and ethane ice at Titan's surface conditions, Astrophysics and Space Science, 362, 10, doi: 10.1007/s10509-017-3166-0.

Singh, S., J. P. Combe, D. Cordier, A. Wagner, V. F. Chevrier, Z. McMahon, (2017b), Experimental determination of acetylene and ethylene solubility in liquid methane and ethane:

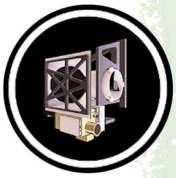

Implications to Titan's surface, Geochimica et Cosmochimica Acta, 208, 86–101, doi: 10.1016/j.gca.2017.03.007.

Singh, S., T. Cornet, V. F. Chevrier, J. P. Combe, T. B. McCord, L. A. Roe, S. Le Mouélic, E. Le Menn, F. C. Wasiak, (2016), Near-infrared spectra of liquid/solid acetylene under Titan relevant conditions and implications for Cassini/VIMS detections, Icarus, 270, 429–434, doi: 10.1016/j.icarus.2015.11.002.

Soderblom, J. M., J. W. Barnes, L. A. Soderblom, R. H. Brown, C. A. Griffith, P. D. Nicholson, K. Stephan, et al., (2012), Modeling specular reflections from hydrocarbon lakes on Titan, Icarus, 220, 2, 744–751, doi: 10.1016/j.icarus.2012.05.030.

Soderblom, J. M., R. H. Brown, L. A. Soderblom, J. W. Barnes, R. Jaumann, S. Le Mouélic, C. Sotin, et al., (2010a), Geology of the Selk crater region on Titan from Cassini VIMS observations, Icarus, 208, 2, 905–912, doi: 10.1016/j.icarus.2010.03.001.

Soderblom, L. A., J. W. Barnes, R. H. Brown, R. N. Clark, M. A. Janssen, T. B. McCord, H. B. Niemann, M. G. Tomasko, (2010b), Composition of titan's surface, in Titan from Cassini-Huygens, pp. 141–175, doi:10.1007/978-1-4020-9215-2_6.

Soderblom, L. A., R. H. Brown, J. M. Soderblom, J. W. Barnes, R. L. Kirk, C. Sotin, R. Jaumann, et al., (2009), The geology of Hotei Regio, Titan: Correlation of Cassini VIMS and RADAR, Icarus, 204, 2, 610–618, doi: 10.1016/j.icarus.2009.07.033.

Soderblom, L. A., R. L. Kirk, J. I. Lunine, J. A. Anderson, K. H. Baines, J. W. Barnes, J. M. Barrett, et al., (2007a), Correlations between Cassini VIMS spectra and RADAR SAR images: Implications for Titan's surface composition and the character of the Huygens Probe Landing Site, Planetary and Space Science, 55, 13, 2025–2036, doi: 10.1016/j.pss.2007.04.014.

Soderblom, L. A., M. G. Tomasko, B. A. Archinal, T. L. Becker, M. W. Bushroe, D. A. Cook, L. R. Doose, et al., (2007b), Topography and geomorphology of the Huygens landing site on Titan, Planetary and Space Science, 55, 13, 2015–2024, doi: 10.1016/j.pss.2007.04.015.

Solomonidou, A., A. Coustenis, M. Hirtzig, S. Rodriguez, K. Stephan, R. M. C. Lopes, P. Drossart, et al., (2016), Temporal variations of Titan's surface with Cassini/VIMS, Icarus, 270, 85–99, doi: 10.1016/j.icarus.2015.05.003.

Solomonidou, A., G. Bampasidis, M. Hirtzig, A. Coustenis, K. Kyriakopoulos, K. St. Seymour, E. Bratsolis, X. Moussas, (2013), Morphotectonic features on Titan and their possible origin, Planetary and Space Science, 77, 104–117, doi: 10.1016/j.pss.2012.05.003.

Sotin, C., J. W. Barnes, K. J. Lawrence, J. M. Soderblom, E. Audi, R. Hamilton Brown, S. Le Mouelic, et al, (2015), Tidal Currents between Titan's Seas Detected by Solar Glints, In American Geophysical Union (AGU) Fall Meeting, abstract.

Sotin, C., K. J. Lawrence, B. Reinhardt, J. W. Barnes, Robert H. Brown, A. G. Hayes, S. Le Mouélic, et al., (2012), Observations of Titan's Northern lakes at 5μm: Implications for the organic cycle and geology, Icarus, 221, 2, 768–786, doi: 10.1016/j.icarus.2012.08.017.

Sotin, C., R. Jaumann, B. J. Buratti, Robert H. Brown, R. N. Clark, L. A. Soderblom, K. H. Baines, et al., (2005), Release of volatiles from a possible cryovolcano from near-infrared imaging of Titan, Nature, 435, 7043, 786–789, doi:10.1038/nature03596.

Sromovsky, L. A., K. H. Baines, P. M. Fry, (2018), Models of bright storm clouds and related dark ovals in Saturn's Storm Alley as constrained by 2008 Cassini/VIMS spectra, Icarus, 302, 360–385, doi: 10.1016/j.icarus.2017.11.027.

Sromovsky, L. A., K. H. Baines, P. M. Fry, R. W. Carlson, (2017), A possibly universal red chromophore for modeling color variations on Jupiter, Icarus, 291, 232–244, doi: 10.1016/j.icarus.2016.12.014.

Sromovsky, L. A., K. H. Baines, P. M. Fry, T. W. Momary, (2016), Cloud clearing in the wake of Saturn’s Great Storm of 2010–2011 and suggested new constraints on Saturn’s He/H_2 ratio, Icarus, 276, 141–162, doi: 10.1016/j.icarus.2016.04.031.

Sromovsky, L. A., K. H. Baines, P. M. Fry, (2013), Saturn's Great Storm of 2010–2011: Evidence for ammonia and water ices from analysis of VIMS spectra, Icarus, 226, 1, 402–418, doi: 10.1016/j.icarus.2013.05.043.

Sromovsky, L. A. and P. M. Fry, (2010), The source of widespread 3-μm absorption in Jupiter's clouds: Constraints from 2000 Cassini VIMS observations, Icarus, 210, 1, 230–257, doi: 10.1016/j.icarus.2010.06.039.

Stallard, T. S., H. Melin, S. Miller, S. V. Badman, K. H. Baines, R. H. Brown, J. S. D. Blake, J. O’Donoghue, R. E. Johnson, B. Bools, N. M. Pilkington, O. T. L. East, M. Fletcher, (2015), Cassini VIMS observations of H_3^+ emission on the nightside of Jupiter, Journal of Geophysical Research, 120, 6948–6973, doi: 10.1002/2015JA021097.

Stallard, T. S., H. Melin, S. Miller, S. V. Badman, R. H. Brown, K. H. Baines, (2012a), Peak emission altitude of Saturn's H_3^+ aurora, Geophysical Research Letters, 39, 15, doi: 10.1029/2012GL052806.

Stallard, T. S., H. Melin, S. Miller, J. O'Donoghue, S. W. Cowley, S. V. Badman, A. Adriani, R. H. Brown, K. H. Baines, (2012b), Temperature changes and energy inputs in giant planet atmospheres: what we are learning from H_3^+, Philosophical Transactions of the Royal Society of London Series A 370, 370, 1978, 5213–5224, doi: 10.1098/rsta.2012.0028.

Stallard et al. 2012

Stallard, T., S. Miller, M. Lystrup, N. Achilleos, E. J. Bunce., C. S. Arridge, M. K. Dougherty, S. W. H. Cowley, S. V. Badman, D. L. Talboys, R. H. Brown, K. H. Baines, B. J. Buratti, R. N. Clark, C. Sotin, P. D. Nicholson, P. Drossart, (2008), Complex structure within Saturn’s infrared aurora, Nature, 456, 214–217, doi:10.1038/nature07440.

Stephan, K., R. Wagner, R. Jaumann, R. N. Clark, D. P. Cruikshank, R. H. Brown, B. Giese, et al., (2016), Cassini's geological and compositional view of Tethys, Icarus, 274, 1–22, doi: 10.1016/j.icarus.2016.03.002.

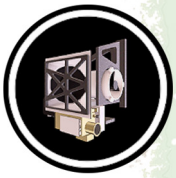

Stephan, K., R. Jaumann, R. Wagner, R. N. Clark, D. P. Cruikshank, B. Giese, C. A. Hibbitts, et al., (2012), The Saturnian satellite Rhea as seen by Cassini VIMS, Planetary and Space Science, 61, 1, 142–160, doi: 10.1016/j.pss.2011.07.019.

Stephan, K., R. Jaumann, R. H. Brown, J. M. Soderblom, L. A. Soderblom, J. W. Barnes, C. Sotin, et al., (2010a), Specular reflection on Titan: Liquids in Kraken Mare, Geophysical Research Letters, 37, L07104, doi: 10.1029/2009GL042312.

Stephan, K., R. Jaumann, E. Karkoschka, R. L. Kirk, J. W. Barnes, M. G. Tomasko, E. P. Turtle, et al., (2010b), Mapping products of titan's surface, Chapter 19, In Titan from Cassini-Huygens, (eds.) R. H. Brown, J. P. Lebreton, J. H. Waite, Springer Dordrecht, pp. 489–510, doi: 10.1007/978-1-4020-9215-2_19.

Stephan, K., R. Jaumann, R. Wagner, R. N. Clark, D. P. Cruikshank, C. A. Hibbitts, T. Roatsch, et al., (2010c), Dione's spectral and geological properties, Icarus, 206, 2, 631–652, doi: 10.1016/j.icarus.2009.07.036.

Stephan, K., R. Jaumann, R. H. Brown, J. M. Soderblom, L. A. Soderblom, J. W. Barnes, C. Sotin, et al., (2010d), Detection of a specular reflection on Titan by Cassini-VIMS, In Lunar and Planetary Science Conference, vol. 41, p. 1692.

Stewart, P. N., P. G. Tuthill, J. D. Monnier, M. J. Ireland, M. M. Hedman, P. D. Nicholson, S. Lacour, (2016a), The weather report from IRC+10216: evolving irregular clouds envelop carbon star, Monthly Notices of the Royal Astronomical Society, 455, 3102–3109, doi: 10.1093/mnras/stv2454.

Stewart, P. N., P. G. Tuthill, P. D. Nicholson, M. M. Hedman, (2016b), High-angular-resolution stellar imaging with occultations from the Cassini spacecraft - III. Mira, Monthly Notices of the Royal Astronomical Society, 457, 1410–1418, doi: 10.1093/mnras/stw045.

Stewart, P. N., P. G. Tuthill, P. D. Nicholson, M. M. Hedman, J. P. Lloyd, (2015a), High angular resolution stellar imaging with occultations from the Cassini spacecraft - II. Kronocyclic tomography, Monthly Notices of the Royal Astronomical Society, 449, 1760–1766, doi: 10.1093/mnras/stv446.

Stewart, P. N., P. G. Tuthill, P. D. Nicholson, G. C. Sloan, M. M. Hedman, (2015b), An Atlas of Bright Star Spectra in the Near-infrared from Cassini-VIMS, The Astrophysical Journal Supplement Series, 221, 2, doi: 10.1088/0067-0049/221/2/30.

Stewart, P. N., P. G. Tuthill, P. D. Nicholson, M. M. Hedman, J. P. Lloyd, (2014), Advances in stellar imaging with occultations from the Cassini spacecraft, Space Telescopes and Instrumentation 2014: Optical, Infrared, and Millimeter Wave, SPIE Astronomical Telescopes + Instrumentation, 2014, Montréal, Quebec, Canada, vol. 9143, p. 91431G, doi: 10.1117/12.2055631.

Stewart, P. N., P. G. Tuthill, M. M. Hedman, P. D. Nicholson, J. P. Lloyd, (2013), High-angular-resolution stellar imaging with occultations from the Cassini spacecraft - I. Observational technique, Monthly Notices of the Royal Astronomical Society, 433, 2286–2293, doi: 10.1093/mnras/stt894.

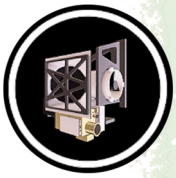

Studwell, A., L. Li, X. Jiang, K. H. Baines, P. M. Fry, T. W. Momary, U. A. Dyudina, (2018), Saturn's global zonal winds explored by Cassini/VIMS 5-μm Images, Geophysical Research Letters, 45, 14, 6823–6831, doi:10.1029/2018GL078139.

Taffin, C., O. Grasset, E. Le Menn, O. Bollengier, M. Giraud, S. Le Mouélic, (2012), Temperature and grain size dependence of near-IR spectral signature of crystalline water ice: From lab experiments to Enceladus' south pole, Planetary and Space Science, 61, 1, 124–134, doi: 10.1016/j.pss.2011.08.015.

Tajeddine, R., P. D. Nicholson, P. Y. Longaretti, M. E. Moutamid, J. A. Burns, (2017a), What Confines the Rings of Saturn?, The Astrophysical Journal Supplement Series, 232, 2, doi: 10.3847/1538-4365/aa8c09.

Tajeddine, R., P. D. Nicholson, M. S. Tiscareno, M. M. Hedman, J. A. Burns, M. E. Moutamid, (2017b), Dynamical phenomena at the inner edge of the Keeler gap, Icarus, 289, 80–93, doi: 10.1016/j.icarus.2017.02.002.

Tao, C., S. V. Badman, T. Uno, M. Fujimoto, (2012), On the feasibility of characterizing Jovian auroral electrons via infrared line-emission analysis, Icarus, 221, 1, 236–247, doi: 10.1016/j.icarus.2012.07.015.

Throop, H. B., C. C. Porco, R. A. West, J. A. Burns, M. R. Showalter, P. D. Nicholson, (2004), The Jovian rings: New results derived from Cassini, Galileo, Voyager, and Earth-based observations, Icarus, 172, 59–77, doi: 10.1016/j.icarus.2003.12.020.

Tiscareno, M. S., M. M. Hedman, J. A. Burns, J. W. Weiss, C. C. Porco, (2013), Probing the inner boundaries of Saturn’s A-ring with the Iapetus −1:0 nodal bending wave, Icarus, 224, 1, 201–208, doi: 10.1016/j.icarus.2013.02.026.

Tobie, G., N. A. Teanby, A. Coustenis, R. Jaumann, F. Raulin, J. Schmidt, N. Carrasco, et al., (2014), Science goals and mission concept for the future exploration of Titan and Enceladus, Planetary and Space Science, 104, 59–77, doi: 10.1016/j.pss.2014.10.002.

Tokar, R. L., R. E. Johnson, M. F. Thomsen, E. C. Sittler, A. J. Coates, R. J. Wilson, F. J. Crary, D. T. Young, G. H. Jones, (2012), Detection of exospheric O_2^+ at Saturn's moon Dione, Geophysical Research Letters, 39, no. 3, doi: 10.1029/2011GL050452.

Tosi, F., R. Orosei, R. Seu, A. Coradini, J. I. Lunine, G. Filacchione, A. I. Gavrishin, et al., (2010a), Correlations between VIMS and RADAR data over the surface of Titan: Implications for Titan's surface properties, Icarus, 208, 1, 366–384, doi: 10.1016/j.icarus.2010.02.003.

Tosi, F., D. Turrini, A. Coradini, G. Filacchione, (2010b), Probing the origin of the dark material on Iapetus, Monthly Notices of the Royal Astronomical Society, 403, 3, 1113–1130, doi: 10.1111/j.1365-2966.2010.16044.x.

Tosi, F., A. Coradini, A. Adriani, F. Capaccioni, P. Cerroni, G. Filacchione, A. I. Gavrishin, R. H. Brown, (2006), G-mode classification of spectroscopic data, Earth, Moon and Planets, 96, 3–4, 165–197, doi: 10.1007/s11038-005-9061-7.

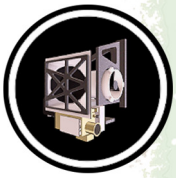

Turtle, E. P., J. E. Perry, J. M. Barbara, A. D. Del Genio, S. Rodriguez, S. Le Mouélic, C. Sotin, et al., (2018), Titan's Meteorology Over the Cassini Mission: Evidence for Extensive Subsurface Methane Reservoirs, Geophysical Research Letters, 45, 1, 5320–5328, doi: 10.1029/2018GL078170.

Vahidinia, S., J. N. Cuzzi, M. Hedman, B. Draine, R. N. Clark, T. Roush, G. Filacchione, et al., (2011), Saturn's F ring grains: Aggregates made of crystalline water ice, Icarus, 215, 2, 682–694, doi: 10.1016/j.icarus.2011.04.011.

Veeder, G. J., A. G. Davies, D. L. Matson, T. V. Johnson, D. A. Williams, J. Radebaugh, (2012), Io: Volcanic thermal sources and global heat flow, Icarus, 219, 2, 701–722, doi: 10.1016/j.icarus.2012.04.004.

Verbiscer, A. J., D. E. Peterson, M. F. Skrutskie, M. Cushing, P. Helfenstein, M. J. Nelson, J. D. Smith, J. C. Wilson, (2006), Near-infrared spectra of the leading and trailing hemispheres of Enceladus, Icarus, 182, 1, 211–223, doi: 10.1016/j.icarus.2005.12.008.

Vilas, F., S. M. Lederer, S. L. Gill, K. S. Jarvis, J. E. Thomas-Osip, (2006), Aqueous alteration affecting the irregular outer planets satellites: Evidence from spectral reflectance, Icarus, 180, 2, 453–463, doi: 10.1016/j.icarus.2005.10.004.

Vincendon, M. and Y. Langevin, (2010), A spherical Monte-Carlo model of aerosols: Validation and first applications to Mars and Titan, Icarus, 207, 2, 923–931, doi: 10.1016/j.icarus.2009.12.018.

Vixie, G., J. W. Barnes, B. Jackson, S. Rodriguez, S. Le Mouélic, C. Sotin, S. MacKenzie, P. Wilson, (2015), Possible temperate lakes on Titan, Icarus, 257, 313–323, doi: 10.1016/j.icarus.2015.05.009.

Vixie, G., J. W. Barnes, J. Bow, S. Le Mouélic, S. Rodriguez, R. H. Brown, P. Cerroni, et al., (2012), Mapping Titan's surface features within the visible spectrum via Cassini VIMS, Planetary and Space Science, 60, 1, 52–61, doi: 10.1016/j.pss.2011.03.021.

Vuitton, V., R. V. Yelle, S. J. Klippenstein, S. M. Hörst, P. Lavvas, (2018), Simulating the density of organic species in the atmosphere of Titan with a coupled ion-neutral photochemical model, Icarus, 324, 120–197, doi: 10.1016/j.icarus.2018.06.013.

Waite, J. H., J. Bell, R. Lorenz, R. Achterberg, F. M. Flasar, (2013), A model of variability in Titan's atmospheric structure, Planetary and Space Science, 86, 45–56, doi: 10.1016/j.pss.2013.05.018.

Walch, M., D. W. Juergens, S. Anthony, P. D. Nicholson, (1993), Stellar occultation experiment with the Cassini VIMS instrument, Infrared Technology XVIII, International Society for Optics and Photonics, San Diego, CA, vol. 1762, pp. 483–494, doi: 10.1117/12.138989.

Waldmann, I. P. and C. A. Griffith, (2019), Mapping Saturn using deep learning, Nature Astronomy, doi: 10.1038/s41550-019-0753-8.

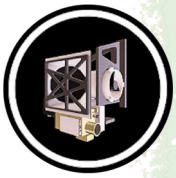

Werynski, A., C. D. Neish, A. L. Gall, M. A. Janssen, R. T. The Cassini, (2019), Compositional variations of Titan's impact craters indicates active surface erosion, Icarus, 321, 508–521, doi: 10.1016/j.icarus.2018.12.007.

West, R. A., K. H. Baines, E. Karkoschka, A. Sánchez-Lavega, (2009), Clouds and aerosols in Saturn’s atmosphere, Chapter 7, In Saturn from Cassini-Huygens, (eds.) M. Dougherty, L. Esposito, S. Krimigis, Springer Dordrecht, pp. 161–179, doi: 10.1007/978-1-4020-9217-6_7.

Fields, Particles, and Waves Sensing Instruments

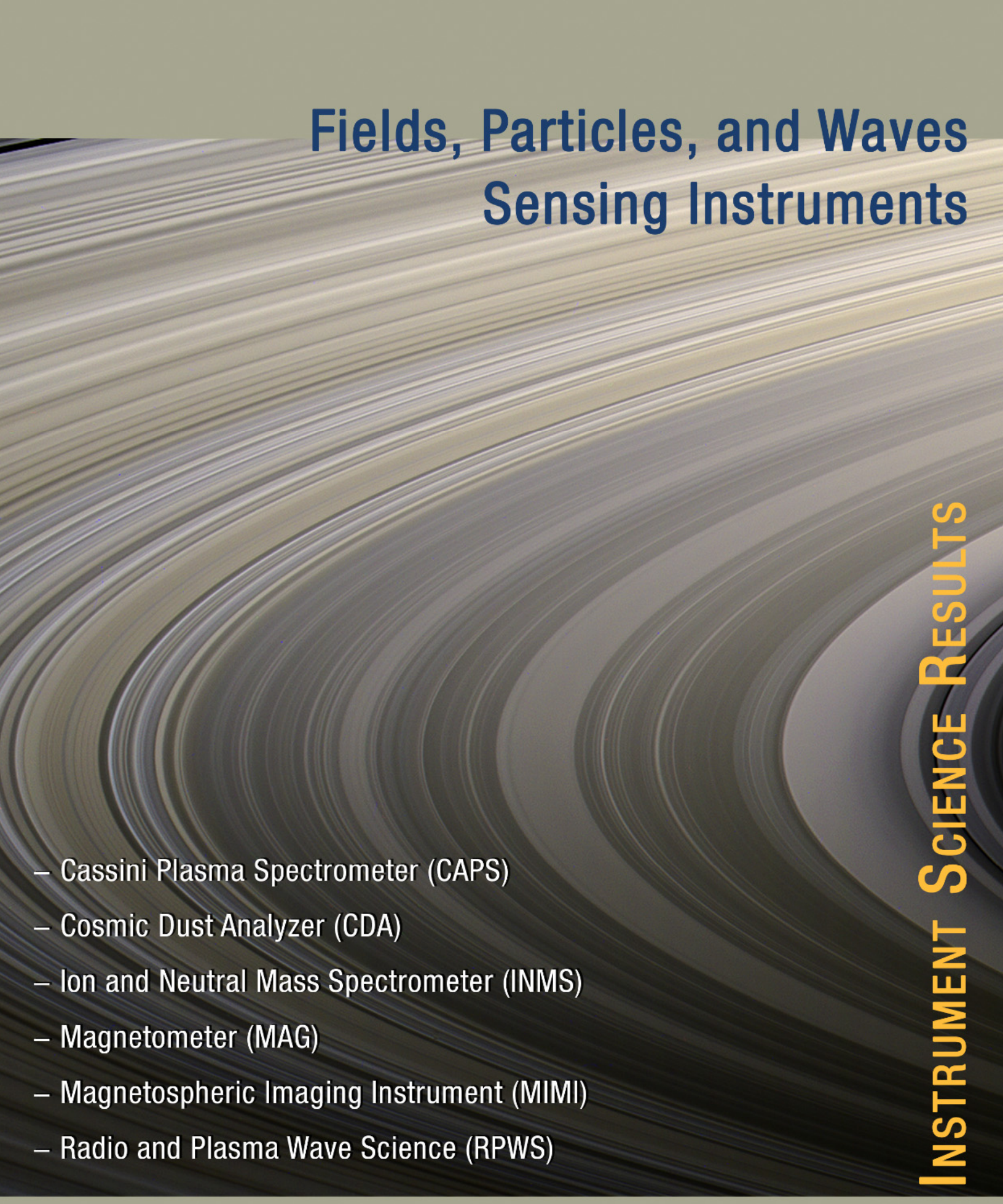

- Cassini Plasma Spectrometer (CAPS)
- Cosmic Dust Analyzer (CDA)
- Ion and Neutral Mass Spectrometer (INMS)
- Magnetometer (MAG)
- Magnetospheric Imaging Instrument (MIMI)
- Radio and Plasma Wave Science (RPWS)

INSTRUMENT SCIENCE RESULTS

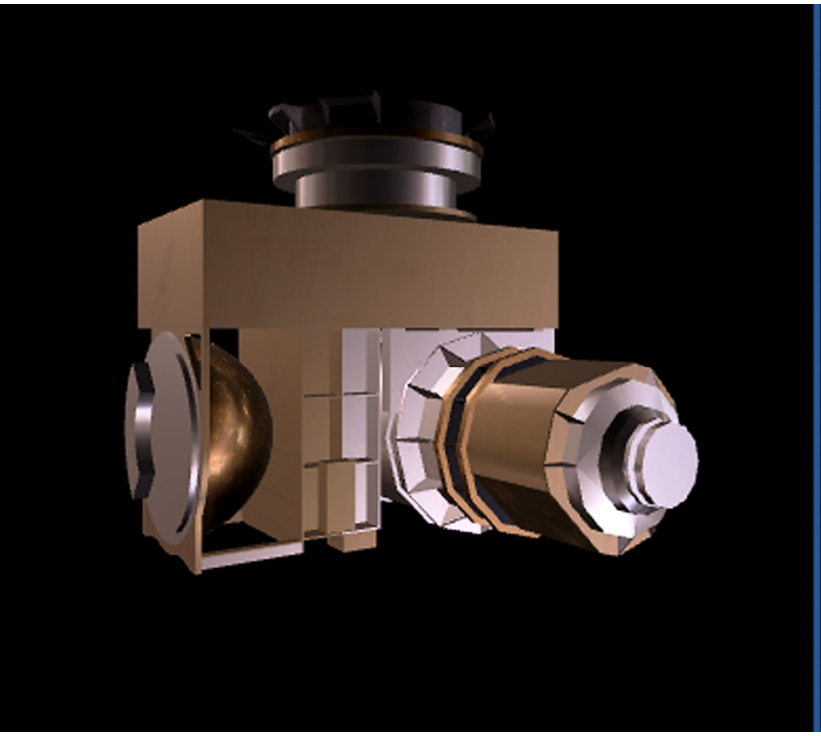

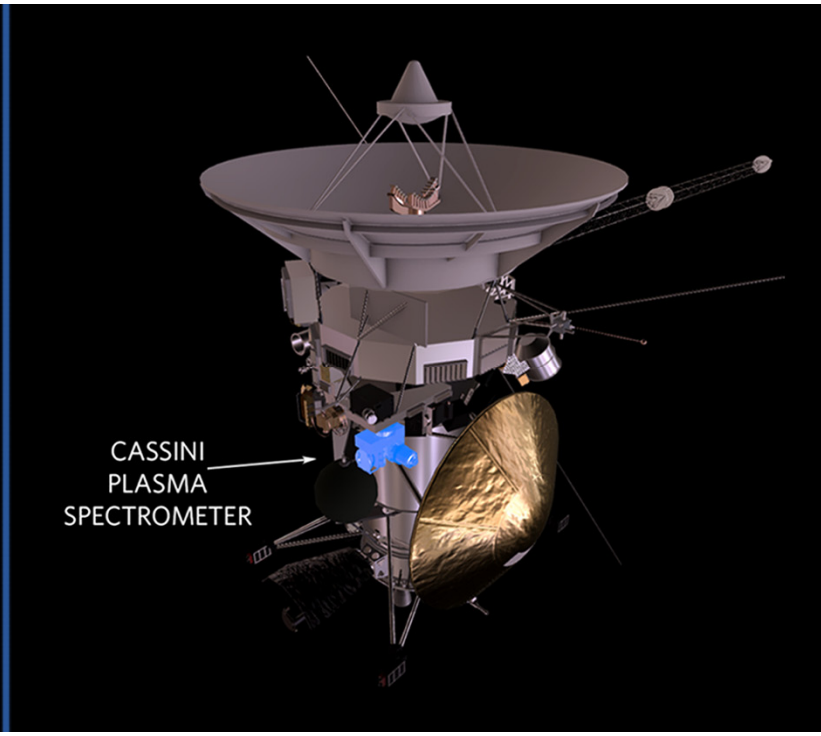

Cassini Plasma Spectrometer

The Cassini Plasma Spectrometer (CAPS) was an in situ instrument that investigated the plasma environment in and near Saturn's magnetosphere. CAPS made measurements of the plasma composition, density, flow velocity, and temperature. The **science objectives** of CAPS were to determine the sources of plasma in the magnetosphere, characterize dynamic magnetospheric processes, and study the interaction of plasma sources, including Enceladus, the rings, and Titan, with the magnetosphere.

CAPS comprised three sensors, a time-of-flight Ion Mass Spectrometer (IMS), an Electron Spectrometer (ELS), and an Ion Beam Spectrometer (IBS) that together measured the composition and velocity distributions of positively and negatively charged ions and electrons from approximately 1 eV to several tens of keV depending on the sensor. CAPS was mounted on an actuator platform that rotated the sensor fields-of-view parallel to the spacecraft Z-axis in order to compensate for 3-axis stabilization of the Cassini spacecraft.

CONTENTS

Figures

Tables

EXECUTIVE SUMMARY

The CAPS instrument was designed to make comprehensive three-dimensional mass-resolved measurements of the full variety of plasma phenomena found in Saturn's magnetosphere. The CAPS science objectives can be broken into four general categories: 1) investigate the structure, composition, and boundaries of the magnetosphere; 2) identify plasma sources and sinks and the physical processes by which they are created and quenched; 3) understand dynamical processes of plasma acceleration, transport, and loss; and 4) study the interactions of plasma sources, including Enceladus, the rings, and Titan, with the magnetosphere.

> … CAPS made significant discoveries and contributions to our understanding of a wide range of phenomena including the unexpected composition and interactions of the ionospheres of Titan, Enceladus, and the rings, as well as the structure and dynamics of the magnetosphere.

By the end of CAPS operations, the investigation met all of the goals and objectives listed above, thereby fulfilling objectives laid out in the Announcement of Opportunity (AO) and Cassini Solstice Mission (CSM). In doing so CAPS made significant discoveries and contributions to our understanding of a wide range of phenomena including the unexpected composition and interactions of the ionospheres of Titan, Enceladus, and the rings, as well as the structure and dynamics of the magnetosphere. Examples of the former include discovery of massive negative and positive ions at Titan and Enceladus, while the latter include radial transport driven by centrifugal interchange instabilities and the massive co-rotating magnetodisk in the middle magnetosphere. CAPS also showed itself to be uniquely capable of measuring the composition and energy distributions of hot plasmas found in the magnetotail and outer magnetosphere. During cruise to Saturn CAPS made the first observations of interstellar pickup ions beyond the orbit of Jupiter as well as the sun's hydrogen shadow.

CAPS operated from checkout through the Cruise phase (1997 through 2004), the primary mission (2004 through June 2008), the extended mission (2008 through 2010) and well into the Solstice Mission (2010 through 2012). Due to an unfortunate and very unusual power anomaly (see National Electrical Safety Code (NESC) RP-12-00803) CAPS did not operate from June 2012 through the end of mission.

During cruise CAPS measured the plasma environments inside the Earth's magnetosphere, and the upstream solar wind, bow shock and magnetosheath conditions at Jupiter. Following the Jupiter swing-by, CAPS made its first major discovery when it captured the first direct, mass-resolved observations of heliospheric pickup ions (H^+, He^+, He^{++}, and O^+) beyond the orbit of Jupiter [McComas et al. 2004]. The neutral interstellar atoms corresponding to these ion species were ionized by solar ultraviolet (UV) and then picked up by the solar wind. The observations were made

between 6.4 and 8.2 astronomical unit (AU) consistent with gravitational focusing of the neutral atoms by the Sun.

During orbital insertion on July 1, 2004, CAPS discovered a completely unexpected atmosphere and ionosphere hovering over the main rings [Young et al. 2005]. The ring plasma is created by photon sputtering of ring ices, creating O_2 molecules that are ionized by solar UV, leading to an admixture of O^+, OH^+, H_2O^+ and O_2^+ ions between the F-ring and G-ring [Tokar et al. 2005].

CAPS contributions to understanding the complexity of the magnetosphere began with the ring plasma, followed by further discoveries of unusual plasma populations and phenomena with each new satellite encounter. During the initial flyby of Titan, the ELS, which was designed to measure electron velocity distributions, showed that in fact the high-altitude (~1000 km) ionosphere is rich in negatively charged ions with masses up to and greater than 13,800 amu/q. At the same time the IBS, designed primarily for solar wind and high Mach number flows, identified heavy positive ions with masses up to 350 amu/q and occasionally above 1000 amu/q [Coates et al. 2007a; Coates et al. 2010a] that were an extension of lower-mass (1 to 100 amu/q) ion spectra measured by Ion and Neutral Mass Spectrometer (INMS) [Coates 2005; Waite et al. 2005, 2007a]. Analysis of these data, combined with chemical modeling, suggests that the heavy ions are precursors of aerosols and tholins seen much lower in the atmosphere (~few hundreds of km). Estimates suggest that this process results in ~0.1 to ~1.0 metric tons per year of tholins added to the atmosphere. These discoveries, together with modeling of the atmosphere and its chemistry, reveal that Titan has what is easily the most complex atmosphere in the solar system.

Titan's ion wake is the most prominent example of Titan-magnetosphere interactions [Hartle et al. 2006b; Wellbrock et al. 2012]. It consists primarily of heavy (m/q ~16 and 28) and light (m/q = 1–2) ions stripped off by the co-rotating flow at a rate estimated to be ~0.3 to 4.0×10^{28} amu/q/s down Titan's wake (or tail as some prefer).

Extensive measurements of the distribution of ion density, temperature and flow velocity made over a period of 4.5 years have revealed the major structures and flow patterns in the magnetosphere [Thomsen et al. 2010]. From Voyager data it was expected that N^+ originating at Titan would be a major plasma component; however, Thomsen et al. [2010] established that water group ions (O^+, OH^+, H_2O^+ and H_3O^+ collectively referred to as W^+) are the dominant species, coming primarily from ion pickup near the orbit of Enceladus. Titan is a relatively weak source with most magnetospheric N^+ originating at Enceladus—yet another surprising feature of the chemical composition of Saturn's magnetosphere [Smith et al. 2008]. CAPS also found that the plumes of Enceladus contain large amounts of negative ions and heavy positive ions with a mass continuum that extends up into the tens of thousands of amu/q reaching into the realm of nano-grains at densities up to 10^3 particles/cm^3 [Hill et al. 2012]. It is thought that as plume gases are ionized they load and deflect the passing co-rotating magnetic flux tubes, leading to the addition of approximately 100 kg/s of fresh Enceladus plasma. This amount of mass loading was confirmed by an analysis of stresses in the distended magnetodisk located in the equatorial plane [Sergis et al. 2010]. Calculation of stress balance in the magnetodisk leads to estimates of a total mass

~10^6 kg for the closed portion of the magnetosphere. Extensive studies of magnetotail dynamics showed that the primary magnetospheric plasma sink is associated with plasmoid generation and subsequent losses down the magnetotail into the solar wind [Hill et al. 2008].

As the number of orbits piled up and their geometric relation to magnetosphere boundaries changed with local time and latitude, the structure of the magnetosphere became apparent. The distribution of plasma is highest near the orbit of Enceladus (3.95 R_S) with an average density ~100 ions/cm^3 and then drops by a factor of ~1000 near ~16 R_S [Thomsen et al. 2010]. Plasma structures in Saturn's magnetosphere do not appear to have strong long-term annual or seasonal variability although on scales of hours to days plasma structures created by interchange instabilities create marked variation in plasma properties [Hill et al. 2005].

From the very first orbits passing through the high-altitude magnetosphere, it was apparent that the magnetosphere is far more dynamic than previously thought. Hundreds of plasma injection events were observed in which hotter plasma from beyond ~10 R_S invaded cold plasma deeper in the magnetosphere. Detailed analysis revealed that the injections were the result of a centrifugal instability set up by forces generated by the co-rotating inner magnetosphere [Hill et al. 2005]. Transport driven by these instabilities is largely responsible for moving the hundreds of kilograms of plasma produced by Enceladus into the outer magnetosphere.

Many plasma observations and analyses featured data collected simultaneously by most if not all of the particles and fields instruments. Prior to the mission it was understood that collaboration by the entire Magnetospheres and Plasma Science (MAPS) suite (CAPS, INMS, MAG, MIMI, and RPWS) was essential to the success of Cassini, and would lead to synergistic science opportunities on many spatial and temporal scales. A glance at the references included with this report, and the complete CAPS publication list of papers in the refereed literature, shows that the goal was indeed achieved.

The CAPS investigation team met or exceeded all of the objectives of both the Primary and Cassini Solstice Missions.

CAPS operated for the first eight years of the Cassini mission before a power anomaly forced the instrument to be turned off in 2012 [NASA Engineering and Safety Center (NESC)-2013]. Understandably this left behind numerous science questions (see the section below on Top Open Questions). Thus there are many significant issues remaining, one in particular is the processes responsible for creating heavy negative and positive ions in the atmosphere of Titan and the plumes of Enceladus. Other important open questions about the magnetosphere include: how is plasma transported outward, and magnetic flux returned inward, in the region between 12 and ~20 to ~25 R_S? and where and how does the magnetosphere unload tons of cold, dense plasma?

As this cursory summary shows, the CAPS investigation met or exceeded all of the objectives of both the Primary and Cassini Solstice Missions. During the Primary Mission CAPS achieved all of its highest-priority goals and major objectives. Moreover, serendipity at Titan and Enceladus

allowed CAPS ELS to make the completely unanticipated discovery of negative ions in both ionospheres. This, and heavy positive ion measurements by IBS, have led to an entirely new understanding of the chemistry of planetary atmospheres with features that were not anticipated in the initial instrument objectives. CAPS measurements of the global composition of the magnetosphere, the surprisingly wide range of plasma sources and sinks, and the primary drivers of plasma transport all mark major contributions to our understanding of magnetospheric physics. Solstice Mission objectives were to enhance our knowledge of the general workings of the magnetosphere and to increase our understanding of long-term temporal variations in plasma sources and sinks from one solstice to the next.

Top Science Highlights

1. Discovered heavy negative ions with masses up to and greater than 13,800 amu/q, and heavy positive ions with masses up to and greater than 1000 amu/q in Titan's upper atmosphere.

2. Discovered that the newly found massive ions are precursors to the formation of atmospheric aerosols and tholins that form the haze components of Titan's upper atmosphere, and that may eventually settle to its surface.

3. Discovered that the plumes of Enceladus contain heavy negatively and positively charged water cluster ions and ice grains with masses extending well above 10,000 amu/q.

4. Discovered that the Enceladus plume emits ~100 kg/s of water-based ions (O^+, OH^+, H_2O^+ and H_3O^+) that become the dominant source of plasma in the magnetosphere.

5. Discovered that Enceladus, not Titan, is the primary source of nitrogen ions in the magnetosphere as was previously thought from Voyager data.

6. Discovered that the main rings of Saturn have an atmosphere consisting of molecular oxygen and water ion products.

7. Discovered that plasma found outside the edge of the A-ring is quenched by nanograins from the rings.

8. Discovered that the ring atmosphere changes with season because of changes in illumination by solar UV.

9. Discovered molecular oxygen exospheres around Dione and Rhea and a dust ring or halo at Rhea.

10. Discovered hydrogen ion outflows leaving Saturn's high latitude atmosphere along magnetic field lines.

11. Discovered hundreds of hot plasma injections in the middle magnetosphere. These result from centrifugal interchange instabilities that drive the radial transport of plasma out of the inner magnetosphere.

12. Discovered a massive heavy-ion co-rotating magnetodisk in the middle magnetosphere weighing ~1000 tons.

13. Discovered an unknown and unexplained plasma convection pattern in the inner magnetosphere that displaces plasma inward near local midnight and outward near noon.

14. Discovered plasmoids carrying water ions down the magnetotail at distances greater than 3 million km at a rate consistent with removal of plasma originating from Enceladus.

15. Discovered that both Dungey-style and Vasyliunas-style reconnection events, which propel plasma down the magnetotail, may occur depending on solar wind conditions.

16. Discovered heliospheric pickup ions (H^+, He^+, He^{++}, and O^+) beyond the orbit of Jupiter. This is the first evidence for interstellar helium atoms and is only the second observation of the Sun's hydrogen shadow.

17. Discovered that Jupiter's bow shock and magnetosheath extend as far as 700 Jupiter radii downstream from the planet.

Top Open Questions

1. What are the chemical and physical mechanisms that create and destroy large negative and positive ions at Titan, and what are their lifetimes?

2. Sunlight clearly plays a key role in determining the maximum negative ion masses found in Titan's atmosphere, but does it control production, loss, or the balance between the two?

3. What is the mechanism causing heavy ions in Titan's atmosphere to form aerosols? And do the aerosols then grow to form tholins? Or are they all the same thing?

4. Are heavy ions (above ~100 amu/q) at Titan picked up by co-rotating plasma, and negative ions picked up in a way that is analogous to positive ions? If so then what is their fate? Are they ejected or destroyed?

5. The loss mechanisms for some species such as N_2 and CH_4 are critical to understanding Titan's atmosphere. Can the daughter ion species be detected in the magnetosphere and the loss rates estimated?

6. What are the chemical and physical mechanisms that create and destroy large negative and positive water ions and neutrals in the Enceladus plume?

7. How are the nano-grain ice-particles in the Enceladus plume formed?

8. How is cold heavy plasma transported outward from the middle magnetosphere (~12 R_S) and magnetic flux returned from the outer magnetosphere (~25 R_S)?

9. Where and how does the magnetosphere unload its cold, dense plasma?

10. How do the sources of magnetospheric plasma (Enceladus plumes, Titan's ionosphere, Saturn, solar wind) match up with the sinks removing plasma (solid surface adsorption, reconnection and plasmoids) to keep the mass budget of the magnetosphere in equilibrium? Does this change with season?

11. What role does the ring atmosphere play in determining the composition of Saturn's upper atmosphere?

12. What causes the inner magnetosphere's dawn-ward convection that drives the noon-midnight asymmetry in plasma temperature, plasma density, energetic particle intensity, etc.?

13. What determines the scale size and inflow speed of interchange injections, and what determines the apparently variable rate and depth of such injections?

14. What is the relationship between large-scale, tail-reconnection-driven plasma injections and small-scale interchange injections?

15. Jupiter's magnetosheath was observed as far as 700 R_J downstream—how far does it extend?

Instrument Summary

The CAPS instrument was a novel design comprising three high-performance sensors that together measured the velocity distributions of electrons and ions from approximately one electron volt (eV) to several tens of kiloelectron volts (keVs) [Young et al. 2004]. The CAPS sensors exceeded their design goals, leading to discoveries of new charged particle populations that reveal the magnetosphere and Saturn's satellites to be a far richer and more complex environment than earlier Voyager data and scientific modeling would have led us to believe. In particular, the discovery at Titan of heavy and ultra-heavy negatively and positively charged ions will lead the way to an understanding of the origin and growth of tholins in Titan's atmosphere. The discovery at Enceladus of a broad range of charged particles including heavy and ultra-heavy negatively and positively charged ions, charged water cluster ions, and charged nano-grains, has helped establish the unique characteristics of the plumes as well as chemical and ionization processes in dusty plasmas.

The photograph in Figure CAPS-1 shows the location and orientation of the three sensors (arrows point to their apertures), and the data processing unit (DPU) which contains command and control electronics, data processors, spacecraft interfaces, and most of the low- and high-voltage power supplies. The entire instrument including the DPU is mounted on an actuator capable of rotating the CAPS sensors through a range of 160º parallel to the spacecraft z-axis at a nominal rate of 1°/s. This compensates in part for the three-axis stabilization of the Cassini spacecraft. Figure CAPS-2 is a cross-section of the optical design of the three sensors in simplified form.

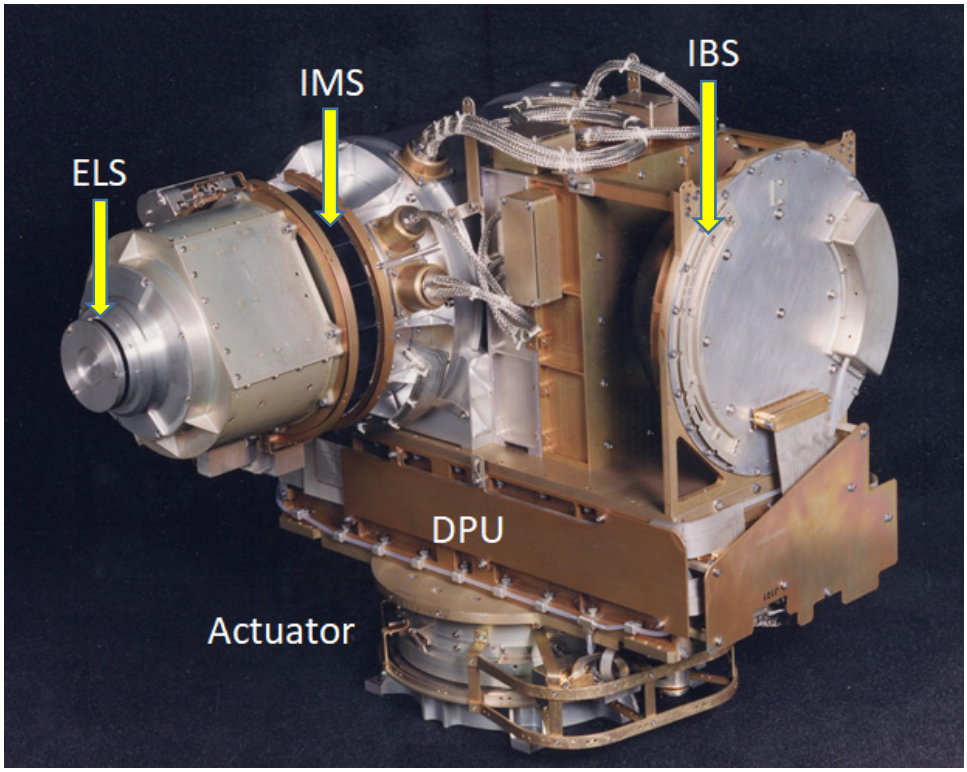

Figure CAPS-1. The CAPS flight unit prior to integration on the Cassini spacecraft late in 1997.

The ELS is an electrostatic energy-angle analyzer that measures electron velocity distributions with medium energy resolution ($\Delta E/E = 0.17$) and azimuthal resolution $\Delta\alpha = 5.2º$ (the angle α is in the plane of the drawing). ELS covers an elevation range of 160° in elevation with a resolution of $\Delta\beta = 20°$ corresponding to eight sectors on the microchannel plate detector. (These response characteristics were chosen to match those of the IMS.) As for all three CAPS sensors the azimuthal range of coverage when the instrument is scanned is ~160° corresponding to the actuator rotation range (the actuator axis of rotation is perpendicular to the plane of the paper). The energy range of 1 eV to 28 keV is sufficient to cover thermal energy electrons found near the icy satellites and rings and all but the most energetic trapped populations found in the outer magnetosphere. A scan over the energy range requires 2.0 s.

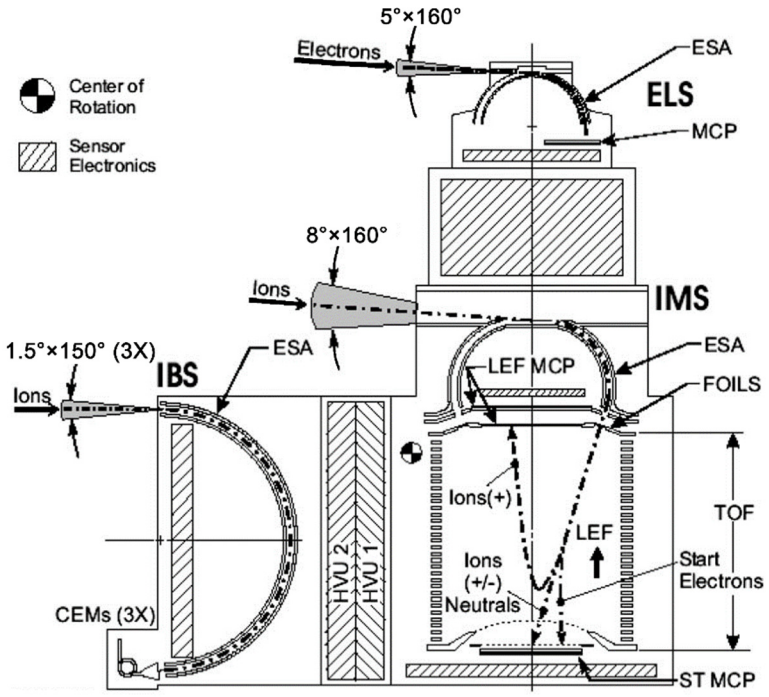

Figure CAPS-2. Cross-section of the three CAPS sensors showing schematic optical paths.

An important feature of the ELS that was not anticipated prior to arrival at Saturn was its ability to measure negative ions as well as electrons. Some scientists miss the point that an energy/charge analyzer is insensitive to the mass/charge of particles passing through its electric field and reaching the detector. It is easy to see why this is the case. The centrifugal force on a charged particle is $F = mv^2/qR_0$, where R_0 is the central radius of the analyzer and the velocity squared of the same particle is $v^2 = (2\ E/q)/(m/q)$, E/q is ion energy/charge, and m/q is its mass/charge. If we substitute the second equation into the first, then m/q cancels out and the force bending the particle through the analyzer is dependent only on energy per charge: $F = 2\ E/qR_0$. The ELS energy distribution can then be converted from E/q to $m/q = 2\ E/qV_{SC}^2$ where V_{SC} is the spacecraft ram velocity (this equation is conceptual—the actual conversion from ion energy to mass/charge must account for both the ELS passbands and the thermal velocity of the measured distribution).

ELS sensitivity, like those of the other two CAPS sensors, is proportional to its geometric factor G, which is defined such that:

$$C = J\ G\ \Delta t,$$

where C is the detector counting rate in counts/s, J is the differential particle energy flux in eV/cm^2 s sr eV, and Δt is the sampling interval in seconds. The geometric factor is made up of several elements and in its approximate (conceptual) form is given by:

$$G \sim A\ \varepsilon\ \tau\ \Delta\alpha\ \Delta\beta\ \Delta E/E,$$

where A is the effective analyzer sensitive area in cm^2, ε is the detector efficiency in counts/ion, τ is the transmission of any grids in the optical path (dimensionless), Δα and Δβ (radians) are the angle passbands introduced above, and ΔE/E is the energy passband (in units of eV/eV). The geometric factor of ELS is calibrated to be $G = 1.4 \times 10^{-2}$ cm^2 sr eV/eV.

The IBS is also an electrostatic energy-angle analyzer, but with the very high resolution required to resolve high Mach number ion flows (~10 or greater) found in the solar wind in the outer solar system, and during flybys through the cold ionospheres of Titan and Enceladus. An advantage of this design that turned out to be far more important than anticipated, is that the high spacecraft flyby velocities (~7 km/s at Titan) and low ion thermal speeds (<100 m/s) yielded very high Mach number flows in the spacecraft frame of reference that allowed IBS to effectively resolve ion velocity distributions into mass spectra.

IBS energy resolution is ΔE/E = 0.014 with an angle resolution in azimuth x elevation of Δα × Δβ = 1.4° × 1.5°. Although the range in azimuth is very limited by its high resolution, IBS has an unresolved elevation response of 160° for a single detector (out of three). IBS energy range is 1 eV to 50 keV which is covered in 2.0 s. The very high resolution makes the IBS sensitivity of 4.7×10^{-5} about two orders of magnitude smaller than that of the other two sensors.

The IMS is a time-of-flight (TOF) ion mass spectrometer that has certain advantages in terms of sensitivity, energy range and mass resolution in comparison to other types of mass spectrometers flown on space missions [Young et al. 2004]. Figure CAPS-2 shows a cross-section schematic of the IMS optics.

The IMS measures ion energy and angle distributions with a resolution similar to ELS (ΔE/E = 0.17 and Δα = 8.3°). Its elevation range, and resolution is the same as ELS: Δβ = 20° in eight sectors covering 160°. The IMS energy range is 1 to 50,000 eV which is covered in 4.0 seconds.

Ions enter the IMS via an electrostatic energy analyzer (ESA) operating on the same principle as the ELS and IBS sensors. After leaving the ESA ions are accelerated by 15 kV before striking one of eight ultra-thin carbon foils (~1 $\mu g/cm^2$) and entering the TOF analyzer. As ions leave the foils they emit secondary electrons that strike the Straight Through (ST) microchannel plate (MCP) detector, initiating timing electronics. When ions (which may be positive, negative, or neutral) strike either the ST or LEF detectors (Figure CAPS-2) the event stops the timing and the ion TOF is recorded together with ion energy and angle of arrival.

IMS makes two independent TOF measurements, medium and high resolution. Medium resolution measurements are made with ST optics (Figure CAPS-2) at M/ΔM ~8 with a range M/q 1 to ~400 amu/q. The sensitivity in this mode is typically ~5×10^{-3} cm^2 sr eV/eV depending on ion species and energy. High resolution measurements are made with time-focusing linear electric field (LEF) reflectron optics at resolutions M/ΔM ~60 depending on ion energy and species. The mass range in this mode is 1 to ~100 amu/q.

Ion mass/charge is given approximately by the simple equation $M/q \approx 2E/q\ (T/L)^2$ where E/q is ion energy/charge, T is the time-of-flight, and L is the effective distance the ion travels from carbon foil to detector about 18 cm. However, this equation is only approximate because energy lost in the foils and optics has to be considered and the flight distance depends on the angle at which the ion leaves the foil.

This abbreviated description of the IMS optics makes clear that there are several factors dependent on averages over random processes that affect TOF measurements. The width of the TOF peaks, and therefore mass resolution, are affected by ESA energy resolution, by scattering in the carbon foils and the effect that that has on trajectories. Sensitivity depends on ion species, transmission through the foils, and the secondary electron yield of the foils and the two detectors. In addition, "ghost" peaks caused by scattering may appear, further complicating TOF spectra. The complexity of IMS optics and electronics, and its dependence on random atomic processes that are essential to its functioning, were addressed by extensive pre-flight calibration as well as post-flight calibration of a high-precision ion optical model, and extensive numerical simulations. In the end these post-flight efforts allowed accurate determinations of even minor ion species. Prominent examples are measurements of very small amounts of nitrogen and nitrogen-bearing compounds in the outer magnetosphere [Smith et al. 2005, 2007, 2008].

> The complexity of IMS optics and the multiple random processes that contribute to CAPS measurements of mass spectra were addressed by extensive post-flight calibration of a high precision model of the optics, and literally years of numerical simulations.

CAPS collects data based on two measurement cycles. During the shorter A-Cycle (32 seconds) CAPS acquires ion and electron count rate distributions consisting of energy × eight elevation-angle "pixels" × TOF (in the case of IMS). The longer B-Cycle (256 seconds) consists of 8 A-Cycles and corresponds very roughly to the amount of time needed for the CAPS turntable, which moves approximately 1°/s, to rotate through an azimuth range of ~160°. Data are acquired and buffered for one B-Cycle in one side of a ping-pong memory while a second B-Cycle is acquired in the other side. The first side is then read out to telemetry and the next cycle of data acquired.

A critically important aspect of the CAPS instrument that greatly affected scientific aspects of the investigation was that because CAPS was mounted on the Particles and Fields Pallet, which is fixed to the spacecraft (Figure CAPS-3), it was not possible to view the full sky (4π sr) at any one time. Being able to scan the entire sky is critical to plasma observations because plasma distributions are seldom isotropic and are typically distorted in many ways (e.g., field-aligned, pancaked, rammed), all of which are key to understanding the phenomena causing the anisotropy in the first place.

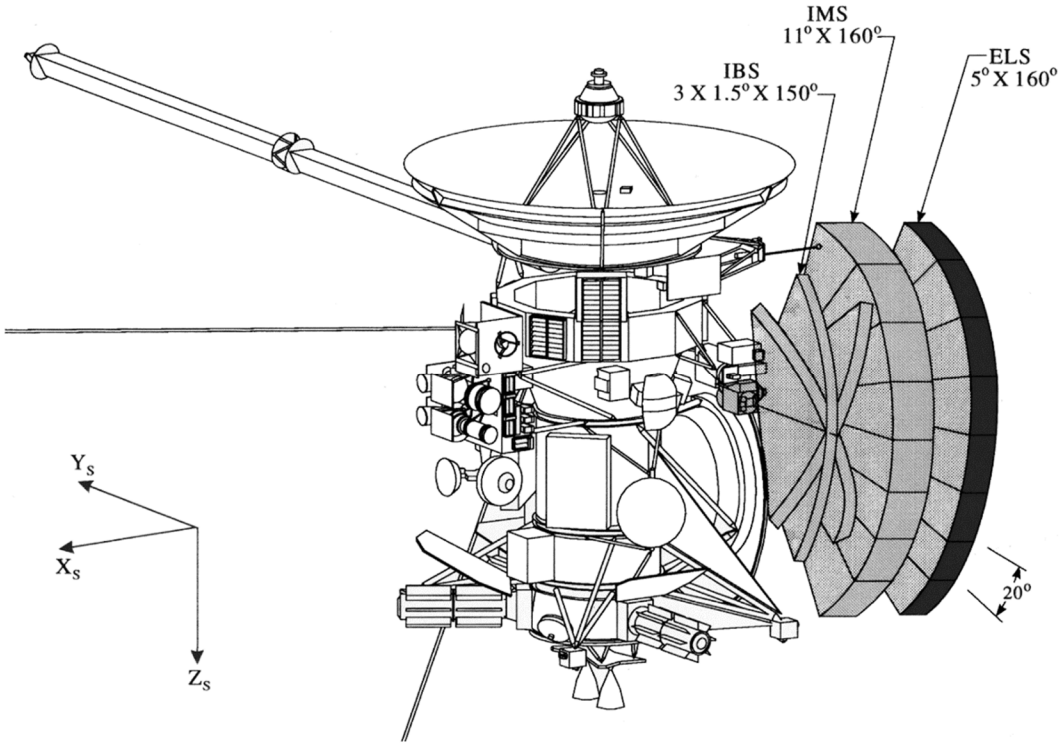

Figure CAPS-3. Location of CAPS on the Fields and Particles Platform showing the sense of CAPS rotation and location of the fields-of-view.

To address the problem of a limited field-of-view (FOV) the design team began by mounting the entire complement of CAPS sensors and the DPU on an actuator (ACT) capable of scanning the sensor FOVs around an axis parallel to the spacecraft Z-axis over a range of ±104° centered on the spacecraft −Y axis. After launch there was an indication that CAPS rotation caused it to snag on a piece of multi-layer insulation (MLI) thermal protection blanket. Out of caution that CAPS might get stuck in one position for the remainder of the mission the ACT scan was limited to +104° (the direction along the spacecraft +X axis) and −80°.

Limited to a scan range of 184° about the Z-axis, the ACT solved only part of the FOV access problem and only in the azimuthal direction. When combined with the elevation acceptance angle of 160° and protrusions of portions of the spacecraft into the FOV (i.e., the high gain antenna, Radioisotope Thermoelectric Generator (RTG) shielding, and other instruments on the pallet—see Young et al. [2004] and Figure CAPS-5) the solid angle commanded by CAPS was limited to approximately 5.8 sr or about 45% of the full sky.

The solution to these limitations was to rotate or otherwise re-orient the spacecraft to enable CAPS (as well as other MAPS particle instruments) to observe a region of the sky closer to 4π sr, albeit slowly. This made operations more difficult for CAPS, MAPS, remote sensing instruments, and indeed the entire spacecraft operations team (see Cassini Final Mission Report Volume 5: Mission Operations System Performance Assessment).

Calibration of ELS and IBS, which are conventional plasma energy-angle analyzers, was relatively straightforward. Calibration of IMS was an entirely different, and far more complex, matter. Figure CAPS-4 shows an example of IMS calibration data taken in an ion beam of m/q = 16 ions. The mass separation optics used to form the calibration ion beam did not have resolution sufficient to separate ion species with virtually the same m/q, it was possible to form beam containing O^+, NH_2^+ and CH_4^+ simultaneously and use it to probe the ability of IMS to separate these species using TOF.

Figure CAPS-4 shows a sample of IMS straight-through (ST) and LEF calibration data from a beam containing O^+, NH_2^+ and CH_4^+at 1024 eV, one of the standard IMS calibration energies. The LEF spectrum shows H^+ and C^+ from the breakup of CH_4^+ in the foils, H^+ and N^+ from the breakup of NH_2^+, and O^+ and O^{++} from oxygen ions in the beam. This spectrum demonstrates the ability of the IMS TOF system to separate three ion species with nearly identical mass/charge ratios that could not otherwise be separated by conventional magnetic or quadrupole spectrometers flown on space missions. The ST spectrum shows H^- ions from the breakup of NH_2^+ and CH_4^+ together with C^- from the latter and O^- from oxygen. All three species in the calibration beam produce neutral atoms that show up as a single peak. There are two ghost peaks centered at 250 and 270 channels caused by electrons leaving structures around the LEF detector and reaching the ST detector. These can be identified and calibrated out.

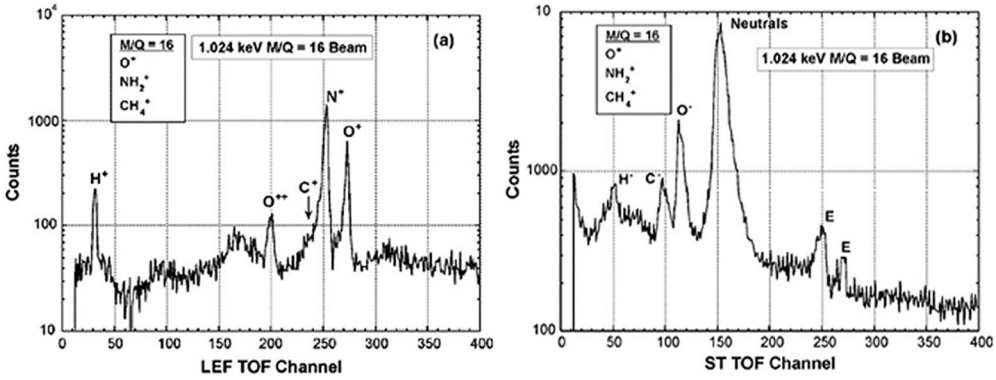

Figure CAPS-4. IMS TOF calibration data for an input beam of M/q = 16⁺ ions at 1024 eV.

Key Goals and Objectives of the CAPS Investigation

The overarching scientific objectives of the CAPS investigation spelled out in the AO were to perform the highest quality measurements that would allow the CAPS team to understand the physical, compositional, and temporal characteristics of Titan's ionosphere, the icy satellites, the rings, and Saturn and their interactions with Saturn's magnetosphere. A second goal was to achieve those measurements with a quality that was at least ten times better than that of Voyager since their measurements and analysis had been considered the gold standard for studies of Saturn's magnetosphere. In fact, it was data from the Voyager mission that were used to develop the CAPS science objectives, performance guidelines, and sensor requirements. In the following section we briefly summarize the specific objectives of the CAPS investigation.

Note: In the short discussion of AO and CSM objectives given below there are several sections in which we hybridized goals by combining objectives such as Titan-Magnetosphere Interactions, Rings-Magnetosphere Interactions, etc. In those sections we list and discuss objectives from both disciplines, e.g., Titan-Magnetosphere Interactions contains both Titan and Magnetosphere AO and CSM Objectives in order to capture the full breadth of the science objective.

Titan

Because of its mass-resolving capabilities, the CAPS investigation was expected to contribute to measurements of the overall composition and abundances of complex and trace ions in the upper atmosphere (**T_AO1, T_AO2, T_AO5, TN1c**), and explore their vertical and horizontal distributions (**T_AO2**) as well as seasonal dependence (**TC1a**) in order to help determine the evolution of Titan's atmosphere. CAPS contributed also to understanding the magnetosphere as a source of ionization at Titan, and the contribution made by Titan to the outer magnetosphere (**T_AO5**).

Titan AO objectives

- **Titan Atmospheric Formation and Evolution (T_AO1):** Determine abundances of atmospheric constituents (including any noble gases), establish isotope ratios for abundant elements, constrain scenarios of formation and evolution of Titan and its atmosphere.
- **Titan Atmospheric Composition and Distribution (T_AO2):** Observe vertical and horizontal distributions of trace gases, search for more complex organic molecules, investigate energy sources for atmospheric chemistry, model the photochemistry of the stratosphere, study formation and composition of aerosols.
- **Titan Upper Atmosphere (T_AO5):** Investigate the upper atmosphere, its ionization, and its role as a source of neutral and ionized material for the magnetosphere of Saturn.

Titan CSM objectives

- **Titan's Great Seas (TC1a):** Determine seasonal changes in the methane-hydrocarbon hydrological cycle of lakes, clouds, aerosols, and their seasonal transport.
- **Determine intrinsic and/or internal induced magnetic field (TN1b):** Characterize possible inducing magnetic fields by measuring the draping of the magnetic field. Study the decay of ionospheric magnetic fields.
- **Measure aerosol and heavy molecule layers and properties (TN1c).**

Titan-Magnetosphere Interactions

- With sensors that functioned as both energy and mass analyzers CAPS was uniquely positioned to study the interactions between Titan and the magnetosphere (**M_AO4**), and the reverse situation (**M_AO5**), including specifically contributions to the magnetodisk (**TC2a**) which, it turns out, was very little. Measurements of heavy ion layers (**TN1c**) were a continuation of the (**T_AO1**) objective to study atmosphere/ionosphere composition. Plasma flow past Titan drags magnetospheric magnetic field lines across Titan's ionosphere inducing magnetic fields that may affect the ability to observe intrinsic fields (**TN1b**).

Titan-magnetosphere AO objectives

- **Titan Atmospheric Formation and Evolution (T_AO1):** Determine abundances of atmospheric constituents (including any noble gases), establish isotope ratios for abundant elements, constrain scenarios of formation and evolution of Titan and its atmosphere.
- **Magnetosphere and Solar Wind Interactions with Titan (M_AO4):** Study the effect of Titan's interaction with the solar wind and magnetospheric plasma.
- **Plasma Interactions with Titan's Atmosphere and Ionosphere (M_AO5):** Investigate interactions of the surrounding magnetospheric plasma with Titan's atmosphere and exosphere.

Titan-magnetosphere CSM objectives

- **Titan-Magnetosphere Interaction (TC2a):** Observe Titan's plasma interaction as it goes from south to north of Saturn's solar-wind-warped magnetodisk from one solstice to the next.
- **Titan Atmospheric Composition (TN1c):** Measure aerosol and heavy molecule layers and properties.

Enceladus

CAPS was uniquely able to measure both negative and heavy positive ions from Enceladus plumes (**M_AO2**) together with charged nano-grains over a long period of time, thus contributing to our understanding of plume composition and variability (**MC1a**) as well as surface composition from material falling back to the surface (**I_AO3**). Enceladus water-based plasma turned out to completely dominate the composition of the magnetosphere and, through mass loading, much of its dynamics (**I_AO5**).

Icy satellites AO objectives

- **Icy Satellite Surface Composition (I_AO3):** Investigate the composition and distribution of surface materials, particularly dark, organic rich materials and low melting point condensed volatiles.
- **Icy Satellite Magnetosphere and Ring Interactions (I_AO5):** Investigate satellite interactions with the magnetosphere and ring systems and possible satellite gas injections into the magnetosphere.
- **Magnetosphere Charged Particles (M_AO2):** Determine current systems, composition, sources, and sinks of magnetospheric charged particles.

Icy satellites CSM objectives

- **Enceladus Plume Variability (MC1a):** Determine the temporal variability of Enceladus' plumes.

Icy Satellite Science

In addition to contributing in major ways to determining composition and sources and sinks of plasma (**M_AO2**), CAPS was able to identify and measure small amounts of plasma surrounding Dione, Rhea, and Tethys (**IN1c, IN2a, IN2b**), which went on to interact with the magnetosphere (**I_AO5**). Measurements of material returning from the magnetosphere to the satellite could be used to infer origins of surface coatings (**I_AO3**).

Icy satellites AO objectives

- **Icy Satellite Surface Composition (I_AO3):** Investigate the compositions and distributions of surface materials, particularly dark, organic rich materials and low melting point condensed volatiles.
- **Icy Satellite Magnetosphere and Ring Interactions (I_AO5):** Investigate interactions with the magnetosphere and ring systems and possible gas injections into the magnetosphere.
- **Magnetosphere Charged Particles (M_AO2):** Determine current systems, composition, sources, and sinks of magnetospheric charged particles.

Icy satellites CSM objectives

- **Dione (IN1c):** Determine whether Dione exhibits evidence for low-level activity, now or in recent geological time. Investigate Dione's current level of activity.

- **Rhea (IN2a):** Determine whether there is ring material orbiting Rhea, and if so, what its spatial and particle size distribution is. Investigate the interaction of Rhea material with Saturn's magnetosphere.
- **Tethys (IN2b):** Determine whether Tethys contributes to the E-ring and the magnetospheric ion and neutral populations.

Rings

Although CAPS could not participate in the final Cassini orbits over the rings, it did establish that there is an atmosphere and ionosphere formed by UV photolysis hovering over the main rings (**R_AO2**) with the resulting plasma moving along field lines connected to Saturn's ionosphere (**R_AO1, RAO_5**). An unexpected finding is that very clean O_2^+ and O^+ peaks in mass spectra indicate the dearth of contaminants in surface ices of ring particles (**RN1a**). The origin of locally formed negative ions is likely nano-grain particles ejected from the rings themselves (**R_AO4, RN1a**) which likely extend beyond the edge of the A-ring. Observed changes in the plasma composition outside the rings over time are caused by changes in solar UV illumination of the ring particles (**RC1a**).

Rings AO objectives

- **Ring Structure and Dynamics (R_AO1):** Study configuration of the rings and dynamical processes (gravitational, viscous, erosional, and electromagnetic) responsible for ring structure.
- **Ring Particle Composition and Size (R_AO2):** Map composition and size distribution of ring material.
- **Dust and Meteoroid Distribution (R_AO4):** Determine dust and meteoroid distributions both in the vicinity of the rings and in interplanetary space.
- **Ring Magnetosphere-Ionosphere Interactions (R_AO5):** Study interactions between the rings and Saturn's magnetosphere, ionosphere, and atmosphere.

Rings CSM objectives

- **Changing Rings (RC1a):** Determine the seasonal variation of key ring properties and the microscale properties of ring structure, by observing at the seasonally maximum opening angle of the rings near Solstice.
- **Ring Age and Origin (RN1a):** Constrain the origin and age of the rings by direct determination of the ring mass, and of the composition of ring ejecta trapped on field lines.

Rings-Magnetosphere Interactions

Material from the outer rings is found in the inner magnetosphere (**R_AO5**) while the rings are the major supplier of neutral H_2 ionized to form H_2^+ farther out in the magnetosphere and a highly seasonal supplier of neutral O_2 (**M_AO2**).

Rings-magnetosphere AO objectives

- **Ring Magnetosphere-Ionosphere Interactions (R_AO5):** Study interactions between the rings and Saturn's magnetosphere, ionosphere, and atmosphere.
- **Magnetosphere Charged Particles (M_AO2):** Determine current systems, composition, sources, and sinks of magnetospheric charged particles.

Magnetosphere Composition, Sources, Transport, and Losses

CAPS explored the structure of Saturn’s magnetosphere, which shares some features with Earth’s, whereas its composition is dominated by water-group ions produced by the plumes of Enceladus (**M_AO2, SC2a**). Many phenomena exhibit diurnal periodicities associated with the plasma sheet, but little in the way of seasonal variability except near the rings due to changes in UV illumination (**MC1b, SC2a**). Rather surprisingly, N^+ was shown to originate primarily at Enceladus and not Titan (**M_AO2, M_AO4, M_AO5**). Plasma outflows from Saturn’s ionosphere carry tens of kg/s of ions and field-aligned currents connecting Enceladus to its auroral footprint (**MN1b, SC2a**).

MAPS AO objectives

- **Magnetosphere Charged Particles (M_AO2):** Determine current systems, composition, sources, and sinks of magnetosphere charged particles.
- **Magnetosphere and Solar Interactions with Titan (M_AO4):** Study the effect of Titan's interaction with the solar wind and magnetospheric plasma.
- **Plasma Interactions with Titan’s Atmosphere and Ionosphere (M_AO5):** Investigate interactions of Titan's atmosphere and exosphere with the surrounding plasma.

MAPS CSM objectives

- **Seasonal and Solar Cycle Variations (MC1b):** Observe Saturn’s magnetosphere over a solar cycle, from one solar minimum to the next.
- **Saturn’s Ionosphere and Radiation Belts (MN1b):** Investigate the temporal dependence and effects of solar wind coupling on the aurora, ionosphere, and magnetosphere. Probe for UV satellite footprints on Saturn.

- **Aurorae, Chemistry, and Upper Atmosphere (SC2a):** Observe the magnetosphere, ionosphere, and aurora as they change on all time scales—minutes to years—and are affected by seasonal and solar cycle forcing.

Magnetosphere Dynamics

Plasma created in the Enceladus plume at a rate of 100 kg/s deep in Saturn's magnetosphere (**M_AO2**) is transported inward by scattering and outward by the centrifugal interchange instability (**M_AO3**) and eventually, primarily through plasmoid formation, is ejected down the magnetotail (**MN1a**). Dynamical processes (not yet understood) lead to periodicities in plasma characteristics near Saturn's rotation period that are associated with motion of the plasma sheet and possibly a plasma cam structure (**MN1a, MN1c**).

MAPS AO objectives

- **Magnetosphere Charged Particles (M_AO2):** Determine current systems, composition, sources, and sinks of magnetospheric charged particles.
- **Magnetosphere Wave-Particle Interactions (M_AO3):** Investigate wave-particle interactions and dynamics of the dayside magnetosphere and the magnetotail of Saturn and their interactions with the solar wind, the satellites, and the rings.

MAPS CSM objectives

- **Magnetotail (MN1a):** Determine the dynamics of Saturn's magnetotail.
- **Magnetosphere Periodicities (MN1c):** Investigate magnetospheric periodicities, their coupling to the ionosphere, and how the Saturn Kilometric Radiation (SKR) periods are imposed from close to the planet (3–5 R_S) out to the deep tail.

Shock, Magnetopause, Outer Magnetosphere

Cassini crossed Saturn's bow shock on numerous occasions as it and the magnetopause (average standoff 21 to 27 R_S) swept back and forth over the spacecraft (**M_AO3**). The magnetosheath flow carries both solar wind and W^+ ions, but there is little evidence for N^+ from Titan in part because its orbit lies just inside the average magnetopause distance from Saturn (**M_AO4**).

MAPS AO objectives

- **Magnetosphere Wave-Particle Interactions (M_AO3):** Investigate wave-particle interactions and dynamics of the dayside magnetosphere and the magnetotail of Saturn and their interactions with the solar wind, the satellites, and the rings.

- **Magnetosphere and Solar Interactions with Titan (M_AO4):** Study the effect of Titan's interaction with the solar wind and magnetospheric plasma.

Saturn

Both the aurora and SKR are dynamic phenomena controlled to varying degrees by both the solar wind and internal rotation of the magnetosphere. These dynamic phenomena have been observed to vary on all timescales from minutes up to the rotation period (~10 hours). They can be expected to vary on seasonal time scales because of the connection of the magnetosphere with the solar wind, which varies with solar activity (**SC2a**).

Saturn CSM objectives

- **Magnetosphere, Ionosphere and Aurora (SC2a):** Observe the magnetosphere and ionosphere as they change on all time scales—minutes to years—and are affected by seasonal and solar cycle forcing.

Solar Wind

Measurements of the solar wind were carried out at intervals during cruise primarily to study the evolution of solar wind transients propagating through the solar system (**C_AO2**). CAPS also served as an upstream solar wind monitor during studies of Jupiter's magnetosphere (**J_AO3**) and helped show that Saturn's aurora is controlled by solar wind dynamic pressure (**SC2a**).

Cruise AO objectives

- **Cruise Solar Wind Investigations (C_AO2):** Investigate the behavior of the solar wind during solar minimum for comparison with earlier Galileo and Ulysses measurements.
- **Jupiter Magnetospheric Studies (J_AO3):** Explore the dusk side of the magnetosphere and intermediate regions of the magnetotail unvisited by previous spacecraft.

Venus

CAPS was not operating during the two Venus encounters.

Earth's Magnetosphere

Earth's magnetosphere was a target-of-opportunity with no specific objectives. CAPS operated for 10 hours upstream of Earth in the solar wind and then spent nine hours as Cassini flew through

virtually every major plasma structure in the magnetosphere. This gave an unusual cross-section freeze-frame snapshot including two substorms that took place during the fly-through.

Jupiter's Magnetosphere

Cassini flew down the Jovian magnetosheath in early 2001. The shock and sheath passed over the spacecraft about 40 times allowing observations that were shown to be consistent with a slow mode shock (**J_AO3**).

Jupiter flyby AO objectives

- **Jupiter Magnetospheric Studies (J_AO3):** Explore the dusk side of the magnetosphere and intermediate regions of the magnetotail unvisited by previous spacecraft.

Heliosphere

During cruise phase between Jupiter and Saturn, CAPS made the first observations of interstellar hydrogen, helium and oxygen as pickup ions (**C_AO1**). Modeling of the data also showed that Cassini was in the interstellar hydrogen shadow.

Cruise AO objectives

- **Interstellar Ion Composition (C_AO1):** Extend the sensitivity of composition measurements of interstellar ions by approximately three orders of magnitude.

CAPS Science Assessment

Table CAPS-1 shows the CAPS, AO, and Traceability Matrix (TM)/CSM Science objectives and the CAPS assessment.

Table CAPS-1 CAPS Science Assessment.

CAPS Objectives	AO and TM/CSM Science Objectives	CAPS Assessment
TITAN		
Atmospheric and ionosphere composition	T_AO1, TC1a, TN1c	
Ionospheric structure	T_AO2	
Magnetosphere interactions	T_AO5, T_AO6, M_AO5, TC2a, TN1b	
Seasonal variations	MC2a, TC1a	
MAGNETOSPHERE-TITAN INTERACTIONS		
Interactions with magnetosphere, solar wind	M_AO4, TC2a	
Interactions with plasma	M_AO5, TN1b	

Table CAPS-1 CAPS Science Assessment.

CAPS Objectives	AO and TM/CSM Science Objectives	CAPS Assessment
ENCELADUS		
Plume variability	MC1a	
Plume gas composition	IC1a	
Plume dust and ice composition	IN1a	
ICY SATELLITES		
Dione activity and interactions	IN1c	
Rhea activity, ring, interactions	IN2a	
Tethys contributions to E-ring, magnetosphere	IN2b	
Hyperion plasma environment	IN2e	
MAGNETOSPHERE - ICY SATELLITE INTERACTIONS		
Magnetosphere	I_AO5	
RINGS		
Composition of ring material	R_AO2	
Ejecta composition	RN1a	
MAGNETOSPHERE-RING INTERACTIONS		
Magnetosphere-ring interactions	R_AO5, I_AO5	
Ring coupling	MN2a	
GENERAL MAGNETOSPHERE		
Magnetosphere solar cycle variation	MC1b, SC2a	
Radiation belt	MN1b	
MAGNETOSPHERE DYNAMICS		
Wave-particle interactions	M_AO3	
Magnetotail dynamics	MN1a	
Aurora and ionosphere	MN1b	CAPS was off at low altitudes
Periodicities and SKR	MN1c	
SHOCK AND MAGNETOPAUSE		
Dayside magnetosphere	M_AO3	
SATURN		
Aurora, magnetosphere, ionosphere	SC2a	
CRUISE		
Solar wind	C_AO2	
VENUS		CAPS did not operate at Venus
EARTH		
Dusk side magnetosphere	Same as J_AO3	
JUPITER		
Magnetosphere	J_AO3	

Table CAPS-1 CAPS Science Assessment.

CAPS Objectives	AO and TM/CSM Science Objectives	CAPS Assessment
HELIOSPHERE		
Interstellar composition	C_AO1	

Detailed Magnetospheric Science Results

Composition of Titan's Atmosphere and Ionosphere

Discovery of heavy positive and negative ions

Before proceeding with this section, it should be understood that ELS and IBS, which are electrostatic energy/charge analyzers, have no intrinsic capabilities as mass spectrometers. Rather the detection of negative ions and very heavy positive ions, discovered by CAPS and discussed in detail below, is made possible because the ram velocity of the spacecraft in the Titan rest frame is far higher (at 6 to 6.4 km/s) than ion thermal speeds of at most a few hundred meters/s. Using the relationship $m/q = 2E/qV_{ram}^2$, where E is the ion energy and V_{ram} is the spacecraft velocity, the energy spectra of ions entering ELS or IBS (or for that matter IMS) can be treated as mass spectra albeit with relatively low mass resolution. Since ELS is designed to detect electrons, its measurements can be interpreted as negative ion mass spectra.

Measurements made by CAPS sensors between altitudes of 950 to 1400 km were responsible, along with those of INMS, for one of the major surprises of the Cassini mission—the high level of chemical complexity observed in Titan's ionosphere. From the earliest close encounters ELS detected heavy negatively charged ions with mass/charge up to 13,800 amu/q (Figure CAPS-5 and Fgiure CAPS-6). In addition, heavy positive ions up to ~350 amu/q [Crary et al. 2009] and as high as 1000 amu/q [Coates et al. 2010a] were detected by IBS. An unexpected level of chemical complexity was seen in the neutrals as well [Waite et al. 2007]. Before Cassini, models of Titan's chemistry had shown some complexity in the interaction of the neutral atmosphere with positive ions [Wilson and Atreya 2004]. The observations from Cassini necessitated more sophisticated modelling of the positive ion composition [Cravens et al. 2006, 2009]. The negative ion observations by ELS were completely unexpected at the altitudes sampled by Cassini, opening a whole new field for modeling and understanding the complex chemistry of Titan's atmosphere.

With these discoveries, Titan's ionosphere is now known to be the most chemically complex in the solar system. This complexity extends to altitudes sampled by Cassini and, based on models, even deeper in the atmosphere. Much of this complexity relative to other terrestrial planets, including Earth, is due to the cold, dense nitrogen-methane atmosphere and Titan's relatively low gravity compared to the other planets. CAPS pioneering discovery of large negative ions has been followed up by further studies of the spatial distribution and density of these ions on altitude and solar zenith angle [Ali et al. 2013; Wellbrock et al. 2013; Desai et al. 2017].

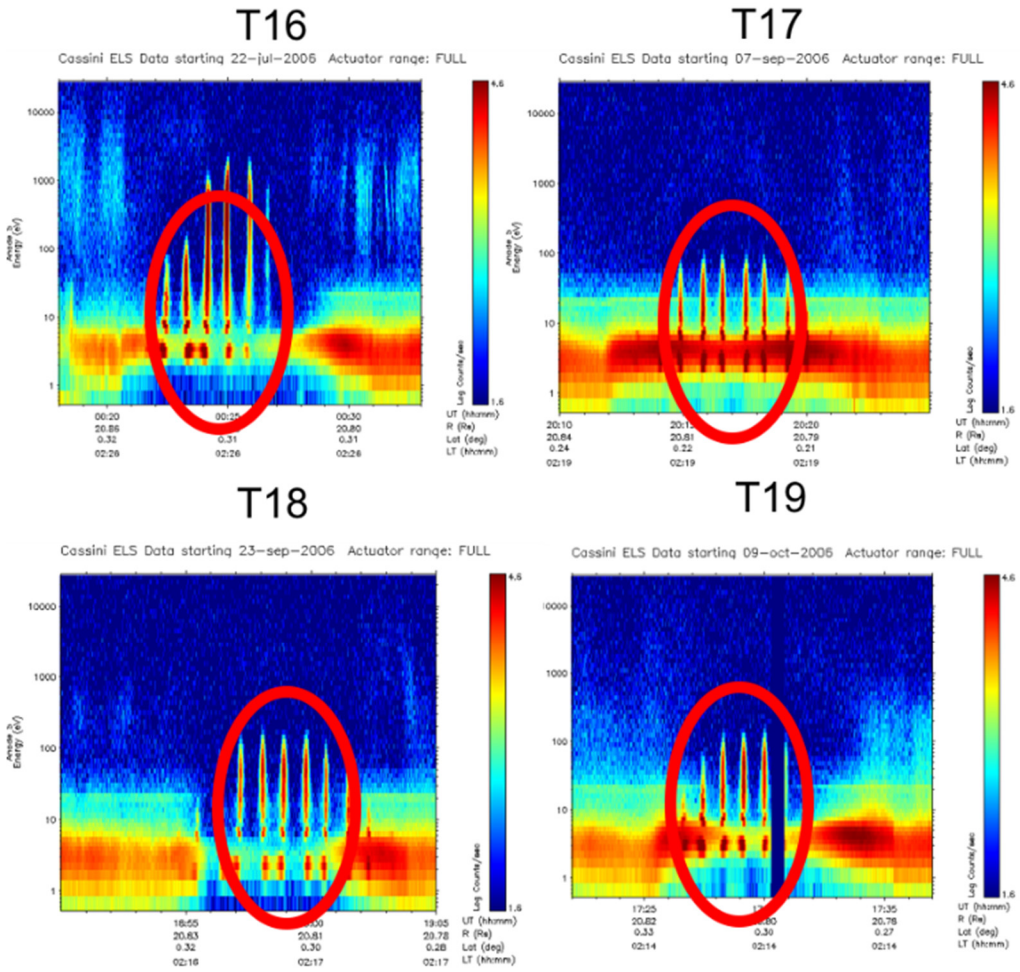

Figure CAPS-5. Energy-time spectrograms of negative ions taken over 15-minute intervals by CAPS ELS during successive Titan encounters T16, T17, T18, and T19. The sharp spikes encircled in red are compressed spectra measured each time the CAPS turntable swept the ELS field-of-view across the ram direction. Figure from Coates et al. [2007a].

Wellbrock et al. [2013] have shown that the highest densities of negative ions are found at lower altitudes. Moreover, the average altitudes where peak ion densities occur decrease with increasing ion mass. In addition, the maximum altitudes at which ions from a specific mass group are observed (the reference altitude) decrease with increasing mass group. This study provides the first step in investigating conditions which affect the densities of different negative ion mass groups.

The highest mass negative ions were observed during the T16 encounter (Figure CAPS-6). A recent analysis of this data shows that polar winter is where the heaviest negative ions are seen [Wellbrock et al. 2018]. This helps to constrain the chemical processes that produce these large ions.

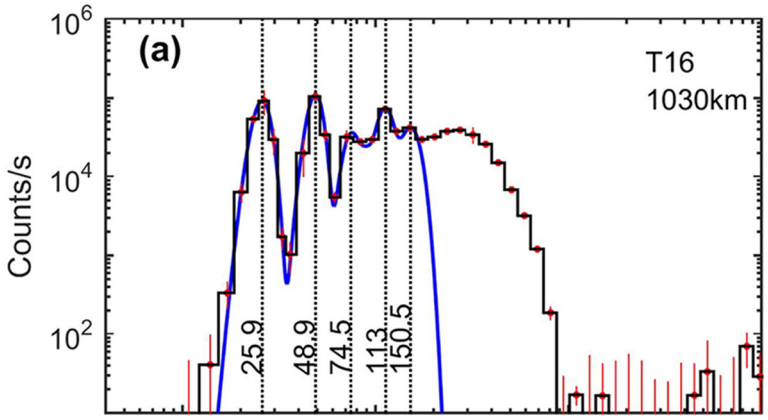

Figure CAPS-6. Fitting negative ion spectra using the instrument response function reveals that intermediate mass negative ions provide a steppingstone in producing the spectacularly heavy ions up to 13,800 amu/q [Desai et al. 2017]. The existence of negative ions was confirmed using RPWS Langmuir probe data, initially using observations at the lowest altitude encounter T70 [Ågren et al. 2012], where CAPS was not oriented in the ram direction for safety reasons, and subsequently at other encounters [Shebanits et al. 2016].

Chemical source of heavy ions

The relatively low-mass negative ions were identified as CN^-, C_3N^- and C_5N^- in the first chemical models used to describe the negative ions seen at these altitudes [Vuitton et al. 2009]. Considering several processes and estimating chemical reaction rates, they suggested that the most likely production process is dissociative electron attachment. They also suggested the most likely loss processes to be associative detachment supplemented by photo-detachment.

While some progress has been made on formation of higher mass ions, this topic is still under study. The geometric configuration of heavy ions is relatively unconstrained, and chains, rings or even fullerenes may be possible. Sittler et al. [2009a] have suggested that the latter may trap and transport oxygen [de Kok et al. 2007] to the surface although there are no observations that confirm this hypothesis. Agglomeration of large molecules caused by charging [Michael et al. 2011] or chemical processes [Lavvas et al. 2013] have been suggested as potential mechanisms to produce the large negative ions. However recent work by Desai et al. [2017] shows that chains of negative ions at intermediate masses may provide another pathway for heavy ion formation (Figure CAPS-7). Heavy negative and positive ions may also link up to form embryo aerosols of both negative and positive charge [Coates et al. 2007a; Crary et al. 2009].

Desai et al. [2017] use observations of negative ions by CAPS/ELS to show mass peaks where unsaturated carbon-chain negative ions such as CN^-/C_2H^-, C_3N^-/C_4H^-, C_5N^-/C_6H^-, etc., might exist (see also the comprehensive review by Millar et al. [2017]). Higher mass ions ~117 ±3 amu/q and 154 ±8 amu/q could be longer negatively charged carbon chains with 10 or 12 or more carbon atoms in saturated aromatic versions. Thus, negative ions exist at masses where INMS cannot measure positive ions. This makes the two instruments not only complementary in their measurements but also makes them highly dependent on each other if we are going to achieve

deeper insights into the composition of Titan's ionosphere. A second example of INMS/CAPS interdependence are IBS observations of heavy positive ions above 1000 amu/q [Crary et al. 2009] which complements INMS measurements that are limited to m/q ≤ 100 amu/q (Figure CAPS-7).

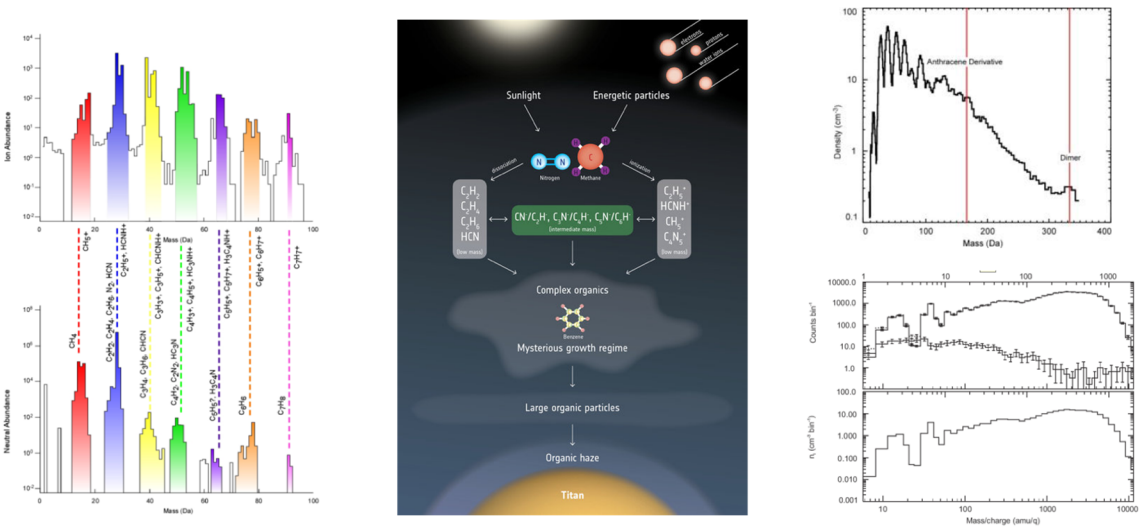

Figure CAPS-7. Observations of negative ions by CAPS/ELS show mass peaks where unsaturated carbon-chain negative ions might exist. The combination of the *Left panel:* INMS neutrals [Waite et al. 2007], *Middle panel:* IBS positive ions [Crary et al. 2009], and *Right panel:* ELS negative ions [Coates. et al. 2007] with a schematic illustrating the process of large ion formation. Figure from Desai et al. [2017].

Tholin formation

The maximum mass of negative ions increases with decreasing altitude [Coates et al. 2009]. Additionally, the number density of the higher mass group increases there [Wellbrock et al. 2013]. Furthermore, a depletion of the low mass (<150 amu/q) negative ions at a rate proportional to the increase of higher mass ions has been observed at the lowest altitudes (950 km) sampled by CAPS [Desai et al. 2017]. Additionally, non-mass-resolved negative ions were inferred from Langmuir probe data at 870 km [Ågren et al. 2012]. Taken together, the CAPS data provide evidence that the space plasma environment in the ionosphere produces these larger ions, while the RPWS data provide in situ evidence that they reach the lowest altitudes ever sampled by Cassini. The large ions then provide the source for aerosols and tholins that float down through Titan's atmosphere, forming the well-known haze layers. This idea is supported by UV occultation measurements—for example, Liang et al. [2007], which show that the density of tholins is measurable at 950 km and increases in density at lower altitudes, possibly all the way to the surface. Based on a combination of RPWS and CAPS data it is estimated that 10^5 to 10^6 metric tons per year of heavy organic aerosol compounds are added to the atmosphere from the ionosphere.

At the surface, the heaviest constituents of the haze could contribute hydrocarbons and nitriles to the dunes seen by the radar and could also provide material that would sink to the bottom of Titan's lakes. However, this process has not been observed directly in situ which leaves several

open questions for future Titan exploration [Tobie et al. 2014]. Several mission concepts have been proposed which could follow this process. These include the ESA-NASA TANDEM mission [Coustenis et al. 2009] and the NASA Dragonfly rotorcraft lander mission [Turtle et al. 2017].

Titan – Magnetosphere Interactions

The main themes of CAPS studies of the Titan-magnetosphere interaction are summarized in Figure CAPS-8. The particular goals were to: 1) measure the kinetic interaction between Titan's upper atmosphere and ionosphere with Saturn's magnetosphere where ion gyro-radii can be larger than Titan itself; 2) measure the composition of the plasma environment around Titan including its exosphere and ionosphere; 3) contribute to our understanding of the surface composition and its organic chemistry; and 4) contribute to our understanding of atmospheric loss and the required

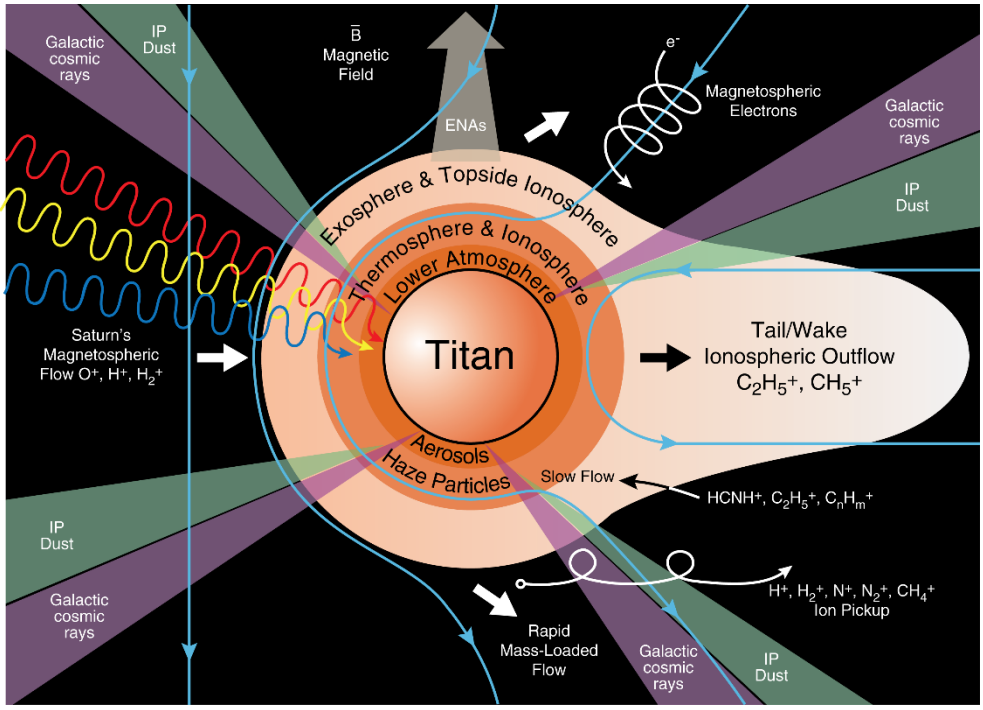

Figure CAPS-8. The main themes of CAPS studies of the Titan-magnetosphere interaction. Colorized figure of Titan includes: various atmospheric layers; surface and incoming photons, plasma, dust, energetic neutral atoms; and energetic charged particles, as well as other processes related to the interaction with the magnetosphere.

replacement timescales from the sub-surface of Titan for the content of methane within Titan's atmosphere, lakes, and surfaces. Lunine et al. [2009] have estimated the lifetime of methane due to photochemical reactions alone to be < 10 million years. Ultimately CAPS may contribute to the larger theme of understanding Titan's origins and the nebula from which the Saturn system was born—see Lunine [2009] and references within.

Kinetic interactions

CAPS discovered pickup ions in the form of beams of CH_4^+ and N_2^+ that can be explained theoretically as the result of kinetic interactions between Titan and the magnetosphere [Hartle and Killen 2006; Hartle and Sittler 2007; Hartle et al. 2011]. It is no surprise that beam composition is consistent with the composition of Titan's exosphere and atmosphere which are dominated by N_2 (98.4%) and CH_4 (1.4%)—cf. Waite et al. [2005].

Sittler et al. [2010] observed nearly field-aligned outflows from the topside ionosphere during the T9 flyby and estimated the loss of methane ions due to pick up from the exosphere at ~5×10^{22} molecules/s [Sittler et al. 2009b]. The outflows serve ultimately as a sink from Titan's atmosphere of roughly ~5×10^{24} molecules/s. Later, Coates et al. [2007b, 2012] observed similar amounts of ionospheric outflows during the T9, T63 and T75 flybys. The theoretical cause of these outflows was originally discussed in Hartle et al. [2008]. They are produced by a field-aligned polarization electric field $E_{pol} \sim -1/ne\nabla_{||}P_e$ so that above the ionospheric density peak the outward acceleration is > 10 times the force of gravity for m/q ~28 amu/q ions (note that the ionospheric electron temperature T_e ~1000° K is much greater than the ionospheric ion temperature T_{ION} < 180° K, which gives rise to charge separation and hence the dipolar electric field). Sittler et al. [2010] found that the resulting ion outflow speeds were ~7 km/s with T_{ION} ~50,000° K. Therefore, both significant acceleration and heating must have occurred at altitudes above 5000 km. Later, using electron observations, Coates et al. [2007b; 2015] measured the total potential drop of this electric field to be ~0.2 μV/m up to heights ~15,000 km, which is sufficient to accelerate methane ions to the observed speeds ~5–6 km/s. Future 3-D hybrid simulations similar to that done by Lipatov et al. [2011, 2012, 2014] will be required to understand the heating (e.g., due to wave-particle interactions) of ions to the observed high temperatures. In addition to the outflows, Sittler et al. [2010] also found evidence of Alfven waves during the T9 flyby with transverse velocity and magnetic field fluctuations that were anti-correlated with time and thus consistent with field-aligned propagation.

One other surprising observation that affects Titan atmospheric chemistry was CAPS discovery of kilovolt oxygen ions with inflows arriving from the magnetosphere at the exobase of Titan's atmosphere ranging up to ~10^{23} O^+/s [Hartle et al. 2006a, 2006b]. Its likely origins are Enceladus and the rings—see Johnson et al. [2005]; Cassidy and Johnson [2010]. Oxygen combined with the complex chemical makeup of the ionosphere is most likely the source of CO in the atmosphere [Hörst et al. 2008; Krasnopolsky 2012]. The influx of O^+ into the atmosphere, where it undoubtedly affects Titan's already complex chemistry, is one more unusual and interesting aspect of Saturn's magnetosphere in which it acts as a conduit for the chemistry of one moon (Enceladus plumes) to affect the chemistry of another.

Aerosol formation and surface composition

Heavy negative ions with m/q > 10,000 amu/q [Coates et al. 2007a; Wahlund et al. 2009], and positive ions with m/q > 1000 amu/q [Crary et al. 2009], can combine to form embryo aerosol particles which can then settle to lower altitudes [Waite et al. 2008]. As they drift down, they grow

to larger sizes to form tholins that make up the well-known smog haze layers extending down to ~400 km altitude. Eventually the particles settle to the surface [Lavvas et al. 2008; Sittler et al. 2009a, 2009b). In the Lavvas et al. [2008] model, more saturated versions of hydrocarbons and nitriles are assumed to form the aerosols, while Sittler et al. [2009a, 2009b] argue for the formation of large negatively charged carbon chains that eventually fold into fullerenes [Kroto et al. 1985; Kroto et al. 1991]. In an interesting connection to Titan chemistry, fullerenes are also thought to exist in interstellar molecular clouds and planetary nebula [Herbst 1981; McCarthy et al. 2006; Millar et al. 2007; Brünken et al. 2007; Remijan et al. 2007; Sakai et al. 2007, 2008; Thaddeus et al. 2008; Herbst and Osamura 2008].

Desai et al. [2017] present clear observational evidence that long-chain negative carbon ions can form and eventually grow into larger embryo aerosols. Vuitton et al. [2007, 2009], reporting on negative ion chemistry at Titan, also argue in favor of negative ion carbon chains, but with nitrogen appendages such as CN^-, C_3N^- and C_5N^-. Desai et al. [2017] also noted that stable multiply-charged heavier fullerenes might also be present within the ELS mass spectrum at m/q ~360 amu/q for C_{60}^{-2} or 420 amu/q for C_{70}^{-2} (see spectra in Figure CAPS-2 and Figure CAPS-3). When heavier negative ions above 150 amu/q are present at altitudes below the main ionospheric peak, broad mass peaks between 300 amu/q to 800 amu/q are present. This suggests that multiple charge state negatively charged fullerenes may exist in Titan's ionosphere—see Wang et al. [2009]; Shebanits et al. [2016]. Sittler et al. [2009a, 2009b] made the argument that the keV O^+ ions reported by Hartle et al. [2006a, 2006b] can penetrate to lower altitudes [Cravens et al. 2008], and become trapped inside the fullerenes—a condition known to occur with noble gasses such as ^{40}Ar, and nitrogen atoms [Pietzak et al. 1997]. Once trapped inside the fullerenes, the latter can condense into embryonic aerosols within the ionosphere. This process isolates the oxygen atom from reactions with Titan's reducing atmosphere. The oxygen ions will then ultimately end up on the surface of Titan where further chemical processing, driven by highly energetic galactic cosmic rays that penetrate to the surface, could lead to still more complex exobiological molecules [Sittler et al. 2009a, 2009b].

Atmospheric loss

Both CAPS and the INMS have provided crucial data for estimating processes that contribute to atmospheric loss. The review article by Johnson et al. [2009] highlights mechanisms and estimates of loss. They are primarily H_2 thermal (Jeans) escape, CH_4 destruction/precipitation, N_2/CH_4 sputtering, and ion pickup causing ionospheric outflows. Loss of CH_4 by hydrodynamic outflow [Yelle et al. 2008; Strobel 2008] thought to also contribute, was later shown not to be the case.

Waite et al. [2005] presented the first observations of H_2, CH_4 and N_2 altitude profiles extending above the exobase to ~1400 km. There is a break in the altitude profiles above the exobase that is consistent with atmospheric escape. Cui et al. [2008] and Bell et al. [2009] estimated H_2 escape to be ~10^{10} amu/q/cm^2/s locally, and ~1.6×10^{28} amu/q/s globally (integrated over the surface area of the atmosphere). Sittler et al. [2010] reported that during the T9 and T18 flybys H^+ and H_2^+ ions were present in the flow of plasma moving towards Titan. The ions also

happened to be moving perpendicular to the local magnetic field, leading Sittler et al. [2010] to conclude that they were seeing pickup ions from Titan's hydrogen corona which can extend to ~20 Titan radii (i.e., out to the Hill sphere).

Primary chemical losses occur when methane is dissociated and ionized by photochemical reactions initiated by solar UV and particle impact. Further reactions with neutrals and ions then make heavier hydrocarbons and nitriles, which can eventually grow into aerosols that precipitate to Titan's surface. Sittler et al. [2009a], using an analogy to molecular clouds and planetary nebulas, suggested that negative chains of carbon atoms form and eventually fold into fullerenes, implying that the same might be going on at Titan. They estimated precipitation to the surface to be ~2.7 × 10^{-14} kg/m^2/s at 950 km altitude and a global rate of ~4 × 10^{27} amu/q/s. This mass loss rate appears to dominate all other present-day atmospheric loss mechanisms—for example, Johnson et al. [2009]. Because the rate is large, in order to maintain a steady state methane concentration an upward diffusion of methane would be required, presumably from a source of methane on Titan's surface.

Sittler et al. [2009b] estimated the loss rate due to pick up ions to be between ~5 × 10^{22} ions/s and ~10^{24} amu/q/s, which is much smaller than the lower bound given by Johnson et al. [2009] of ~10^{26} amu/q/s, possibly due to the inclusion of scavenging down Titan's ion tail—see Sillanpaa et al. [2006]; Hartle et al. [2006b]. Woodson et al. [2015] showed the ion outflow detected between ~1 and 5 Titan radii consisted of H^+, H_2^+ and H_3^+ as well as two hydrocarbon groups with mass ranges between 12–19 amu and 24–32 amu. The net escape caused by ionospheric outflows is ~5 × 10^{24} mol/s or ~10^{26} amu/q/s [Sittler et al. 2010; Coates et al. 2012] which should be included in the Johnson et al. [2009] estimate. The escape fluxes caused by sputtering, hot atomic recoils and charge transfer by energetic neutral atoms also cause heating of the thermosphere and corona [De La Haye et al. 2007a, 2007b]. Adding all these terms Johnson et al. [2009] find a total escape rate of ~0.32 to ~3.8 x 10^{28} amu/q/s.

Recent work highlights the need to reanalyze INMS data … in order to understand the energy distribution of neutral molecules in the exosphere region.

Recent work highlights the need to reanalyze INMS data using detailed models of sputtering and energy deposition in the upper atmosphere in order to understand the energy distribution of neutral molecules in the exosphere region. Snowden and Yelle [2014] used Fourier's Law to extract energy deposition rates in the upper atmosphere from INMS data. They suggested that precipitation of magnetospheric ions observed by CAPS is likely too small to explain the observed temperature variations [Snowden et al. 2013] and escape rates. They also suggest that gravity waves produced in the lower atmosphere could cause the variability, but a source for the waves has not been identified, and it has recently been shown that the means of estimating the local temperature in an atmosphere with significant density structure might be problematic.

Tucker et al. [2016] showed that using the Louisville Theorem approach, with a non-thermal energy distribution at the exobase, can lead to incorrect estimations of the upper atmospheric thermal structure and, consequently, escape rates due to collisions in the transitional region. Furthermore, such corona fits obtain different exobase energy distributions for N_2 and CH_4 density distributions, which is suggestive of different heating mechanisms occurring between species. Therefore, ion/pickup fluxes and spectra extracted from CAPS data and model development of gas-kinetic models are needed for detailed simulations of the ion-neutral interaction. Such models can consider the ion-neutral interaction at the microscopic level and include the production of hot recoil molecules. This has led to a re-evaluation of an earlier Titan atmosphere model investigated by Johnson et al. [2016].

The final topic is hydrodynamic loss proposed by Yelle et al. [2008] and Strobel [2008]. By using CH_4 and N_2 ingress altitude profiles with methane diffusing through atmospheric N_2, and then using the ^{40}Ar density profiles, they were able to separate the molecular and eddy diffusivities, which then required an upward methane flux ~4–5 × 10^{10} amu/q/cm^2/s and globally ~4.5 × 10^{28} amu/q/s. This estimate is close to the chemical destruction/precipitation of methane to heavier molecules and aerosols. The model by Strobel [2008] called slow wind ague that solar UV penetrates below the ionosphere where it is deposited. This excess heat is then conducted upward to higher altitudes to drive the hydrodynamic slow wind. But, in order to meet the upward flux required by Yelle et al. [2008] this heat must be transported above the exobase where there are no collisions to conduct the heat, which is its major weakness. Direct Simulation Monte Carlo (DSMC) simulations by Tucker and Johnson [2009] did not show any enhancement of the methane escape rate significantly greater than the Jeans escape rate ~3 × 10^{22} amu/q/s. Therefore, it is highly unlikely that hydrodynamic escape of $CH_4$is currently occurring at Titan. Tucker et al. [2013] showed that H_2 escape cools the background gas resulting in non-isothermal density profiles without requiring a significant escape rate. Volkov et al. [2011] examined the hydrodynamic escape problem in detail using DSMC simulations. They found that above a Jeans parameter of 6 at the exobase the thermal escape rate is enhanced towards the analytical Jeans rate only by a factor of 1.4–1.7. This contrasts with Strobel [2008] who predicts a CH_4 escape rate orders of magnitude larger than the Jeans rates, possibly due to an overestimation of heat conduction in the transitional region.

Enceladus

In 2005, and far from Enceladus, IMS measured pick-up water group ions (O^+, OH^+, H_2O^+ and H_3O^+ or, collectively, W^+) throughout Saturn's inner magnetosphere [Young et al. 2005; Sittler et al. 2005; 2006; Tokar et al. 2008]. The source of these ions is charge-exchange collisions that scatter water group neutrals, replacing a fraction of the co-rotating core distribution with a new and slower-moving ion population without changing the total ion content. The newly created ions are moving near the local Keplerian speed, which is slower than the co-rotation speed, and hence are picked-up by Saturn's magnetic field. IMS detected these water-group ions within their source region, the Enceladus torus, thus providing the first measurements of W^+ ions throughout their toroidal source region and far from Enceladus. High ion count rates in IMS were observed at the

ion pick-up energies as shown in Figure CAPS-9 with largest signals near the Enceladus and Dione orbits. Another surprising measurement was the discovery of negative ions in the Enceladus plume, a result as surprising for Enceladus as it was for Titan [Coates et al. 2010a, 2010b].

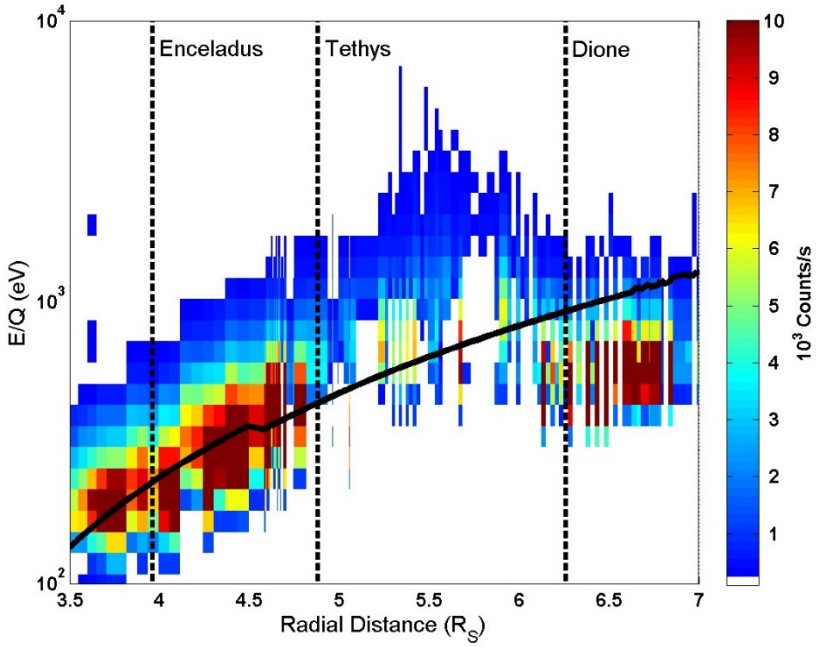

Figure CAPS-9. Energy charge of detected ions versus radial distance from Saturn in Saturn radii (1Rs = 6.03x10^5 km). Figure from Tokar et al. [2008].

Striking observations were also obtained with IMS during the close encounters of Cassini with Enceladus. Early in the Cassini mission, on July 14, 2005, the spacecraft flew within 175 km of Enceladus, passing through its surrounding cloud of neutrals and plasma. Although encounters with Enceladus later in the mission would be at much closer distances, CAPS was still able to detect indications of a strong interaction between Enceladus and magnetospheric plasma [Tokar et al. 2006]. Originally detected by the Hubble space telescope, Enceladus was known to sit in a cloud of neutral OH forming a torus around Saturn. The cloud detected by CAPS extends from about 3 to 8 R_S with maximum concentration of ~10^3 cm^{-3} inferred to exist near the orbit of Enceladus (3.95 R_S). The OH cloud is produced by dissociation of H_2O, and although the peak concentration suggested that the largest source of water molecules was in the region near the orbit of Enceladus, the nature of this source was unknown. IMS measurements during the 2005 encounter established a strong perturbation of the plasma flow caused by Enceladus, and perhaps most importantly, the presence of W^+ ions (Figure CAPS-10). This population had been detected earlier during Saturn orbit insertion [Young et al. 2005].

Later in the mission, during closer encounters with Enceladus, CAPS obtained in situ measurements of W^+ ions freshly produced in the dense Enceladus plume. The dominant species there are light ions (H^+, H_2^+), W^+ ions, and single water cluster ions, ($H_2O^*H_2O^+$). All were observed close to, and nearly due south, of Enceladus. The ions have kinetic energies in the IMS frame

roughly equal to ions that are at rest with respect to Enceladus and rammed into the CAPS sensors at the spacecraft speed. This is the signature of freshly produced ions in the plume due, e.g., to charge exchange interactions of incoming magnetospheric ions with neutral plume gas. Figure CAPS-11 shows an example of these ions detected by IMS during the E3 encounter only 52 km from Enceladus. The high counting rates close to the ion ram energies (denoted by vertical arrows) are clearly visible. Further details of these data are discussed in Tokar et al. [2009].

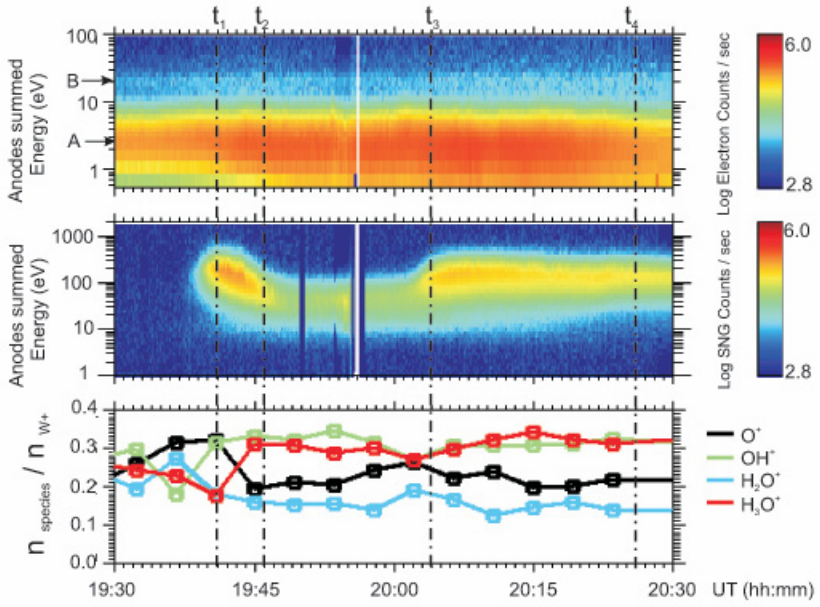

Figure CAPS-10. Data from CAPS on July 14, 2005. *Upper panel:* ELS electron counting rates summed over all direction anodes. Cold and hot electron components were detected with peak counts near A and B. *Middle panel:* Ion counting rates from IMS, with the slowing of the of the ion flow evident between t_1 and t_2. *Bottom panel:* Individual water group (W^+) ion densities divided by the total water group ion density, obtained from IMS time-of-flight measurements. Reduced χ^2 fits for mass spectra give high confidence for identification of the ions. Figure from Tokar et al. [2006].

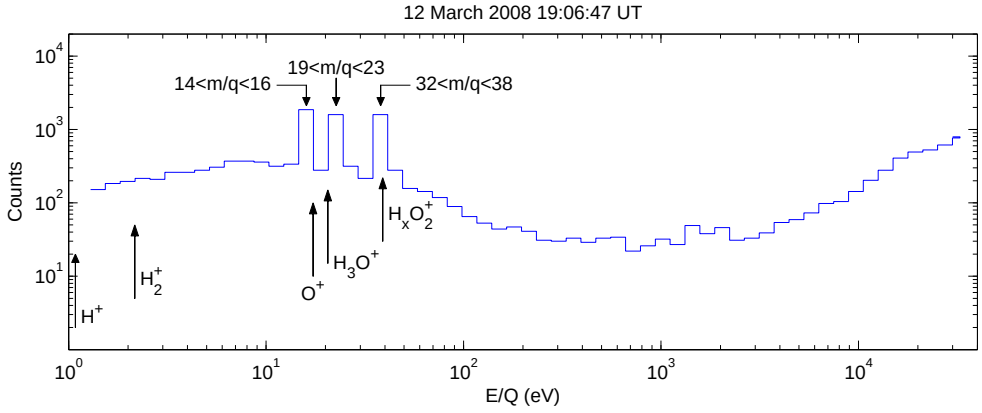

Figure CAPS-11. Individual ion counting rates versus energy per charge measured by IMS anode 5 within the plume during the March 12, 2008 (E3) flyby of Enceladus. Figure from Tokar et al. [2009].

The E7 encounter on November 2, 2009 provided additional observations of the plume stagnation region as Cassini passed directly through the Enceladus plume. The IMS detector sensitive to rammed ions observed stagnation and fresh ions at the ion ram energies (Figure CAPS-12). The strong interaction region within the plume is clearly visible in the CAPS IMS data as are the water group ions near 10 eV that are at rest in the Enceladus frame.

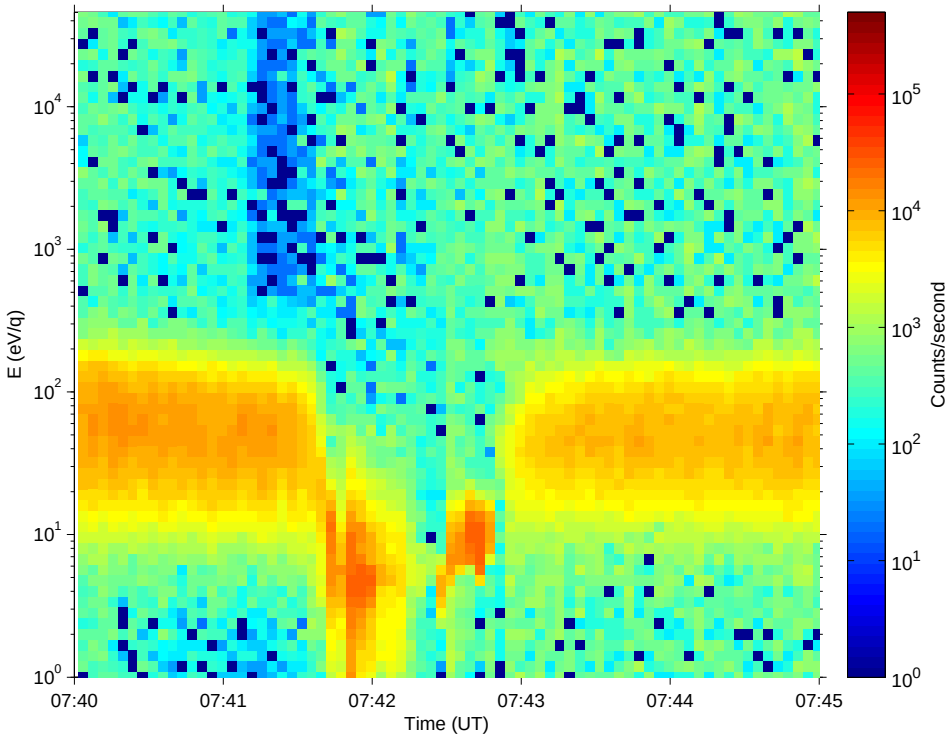

Figure CAPS-12. CAPS energy-time spectrogram from the E7 encounter. Figure from Smith et al. [2017].

Data from the E7 encounter also exhibited the close correspondence between IMS observations of ion slowing and the observed entry into the dense water vapor plume measured by INMS. This is depicted in Figure CAPS-13, which shows the IMS ion flow speed and the INMS mass 44 counts, a proxy for plume water vapor concentration. The E7 closest approach (C/A) is at ~07:41:58 universal time (UT) when IMS observed a rapid decrease in the ion flow speed ~20 sec before C/A. Similarly, INMS observed an increase from 29 to 399 counts at m/q = 44 from 17.5s to 11.3s before C/A. The data suggest that magnetospheric plasma enters the dense plume leading to charge exchange with plume water vapor followed by subsequent pick-up into the co-rotating flow. The signature of this process is very sharp on the Saturn-ward side of the plume as the new ions are picked-up and gyrate away from Saturn. The transition out of the plume opposite Saturn for E7 is more extended due to several factors, e.g., ion drift velocity and variable ion gyroradius for the various masses created. Note in the figure that the observed ion flow speed obtained from count distributions in the ram direction imply speeds as low as a few km/s in the Enceladus frame.

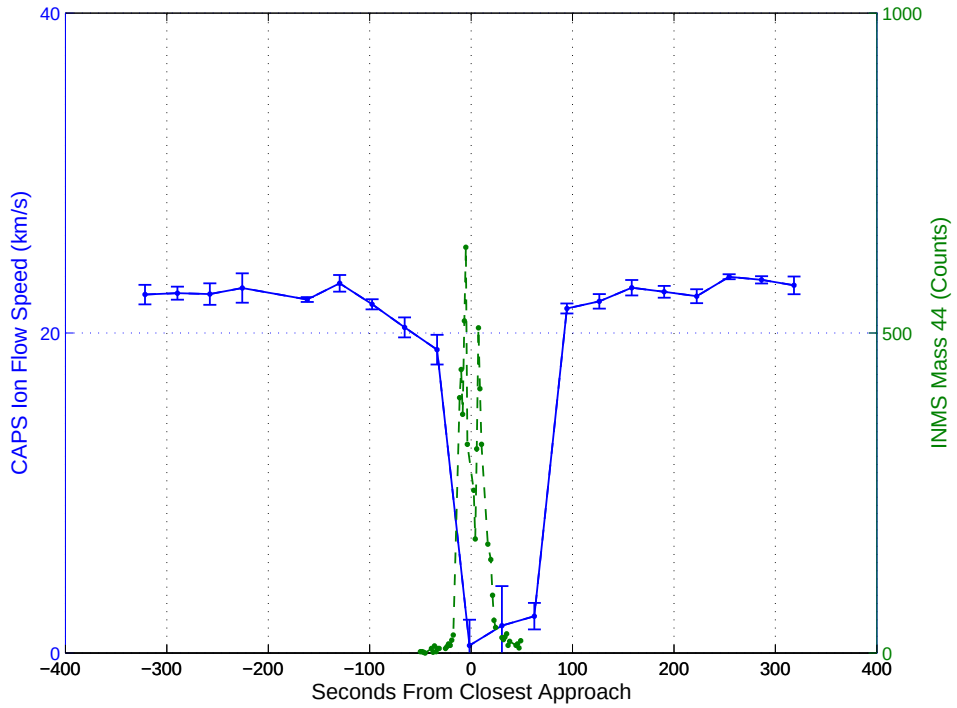

Figure CAPS-13. The CAPS IMS ion flow speed and the INMS mass 44 counts which serve as a proxy for plume water vapor concentration. The E7 closest approach was at ~07:41:58 UT on November 2, 2009.

In addition to the dense neutral water vapor measured by INMS and the resulting cold plasma measured by CAPS and RPWS Langmuir Probe, the south-polar plume of Enceladus was also found by CAPS to carry singly charged nanometer-size water-ice grains [Coates et al. 2009; Jones et al. 2009; Hill et al. 2012; Meier et al. 2014; Dong et al. 2015; Meier et al. 2015]. Such nano-grains had been inferred to exist in various cold, tenuous geophysical and astrophysical environments, but the close Enceladus plume encounters by Cassini offered the first opportunity to measure and characterize nano-grains in situ. Before the CAPS shutdown in June 2012 there were three close Enceladus encounters that provided the ram pointing required to measure these high mass-per-charge particles—E3 on 12 Mar 2008, E5 on 9 Oct 2008, and E7 on 2 Nov 2009. The detailed analysis was reported by Hill et al. [2012].

Hill's analysis confirms that the nano-grains are largely uncharged when they emerge from the surface vents and become increasingly (mostly negatively) charged as they approach Cassini a few tenths of Enceladus radii away. The charged nano-grain density versus distance from the surface source is shown in Figure CAPS-14, from Hill et al. [2012]. The dashed line shows the r^{-2} dependence that would be expected if the grains were already charged when they emerged from the source. The most plausible charging mechanism is electron attachment from the dense plume plasma. The non-neutrality of the nano-grains observed by CAPS, n(−) >> n(+), plausibly cancels the opposite non-neutrality of the plume plasma observed by RPWS-Langmuir Probe (LP). Most of the electrons missing from the plume plasma reside on the nano-grains.

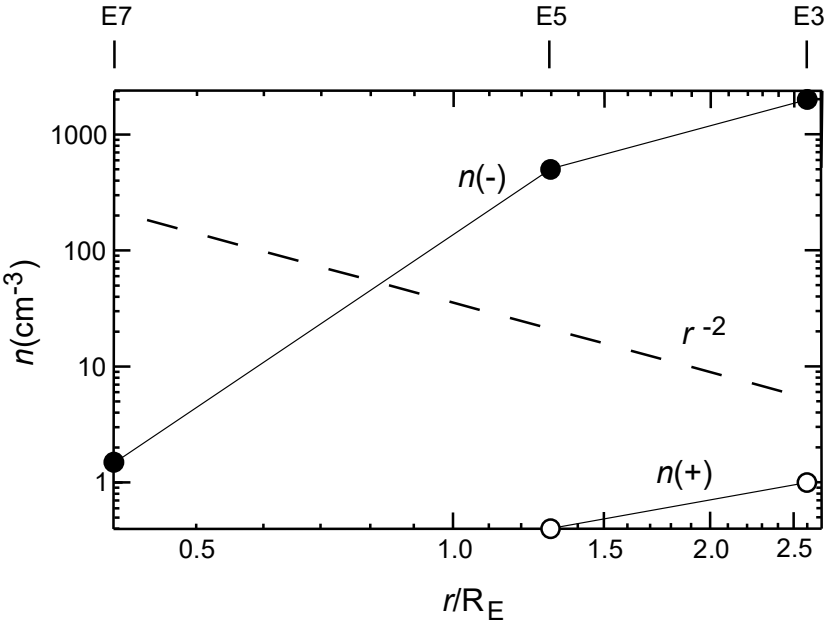

Figure CAPS-14. Total charged nano-grain number density within the CAPS E/q range versus distance from the south-pole source vent.

The link between Jupiter's aurora and its inner large moons was well known, which raised the question of whether a similar relationship might exist between Enceladus and Saturn's aurora. The necessary electrodynamic coupling was established by combining ELS data showing strong field-aligned electron beams, with magnetic field measurements indicating field-aligned currents. Pryor et al. [2011] then used the Cassini UVIS camera to take UV images of the region around Saturn's north pole about two weeks later. The Enceladus footprint was seen as predicted by field line tracing at 64.5° N latitude and the correct longitude.

Icy Satellites

In addition to Enceladus, IMS also detected signatures of magnetosphere-moon interactions at both Dione and Rhea. Dione is in an approximately circular orbit at a radial distance from Saturn of about 6.3 R_S, which is outside Enceladus (R = 3.9 R_S) and Tethys (R = 4.9 R_S) and inside Rhea (R = 8.7 R_S) orbits. Early in the mission IMS observations suggested the presence of an exosphere around Rhea—for example, Martens et al. [2008]—that was produced by radiolysis and sputtering of the surfaces by magnetospheric particles [Johnson et al. 2008]. Subsequent data from CAPS and INMS led to confirmation of very tenuous exospheres around both Dione and Rhea—for example, Tokar et al. [2012] and Teolis et al. [2010]—that have similar density and chemical composition consisting primarily of carbon dioxide and molecular oxygen. During Cassini's April 7, 2010, flyby of Dione (D2), at an altitude of about 500 km, IMS detected O_2^+ pick-up ions that likely originated from a neutral O_2 exosphere. The interaction is depicted in Figure CAPS-15.

Figure CAPS-16 shows IMS and ELS observations of pickup ions. The positive ions are from Rhea's exosphere (denoted by blue trajectories) and are identified as O_2^+ in the IMS data. The distribution of ion arrival directions in the vicinity of Rhea also indicate the presence of a tenuous dust ring or halo [Jones et al. 2008]. Note that negative ions are also visible in the ELS spectrogram.

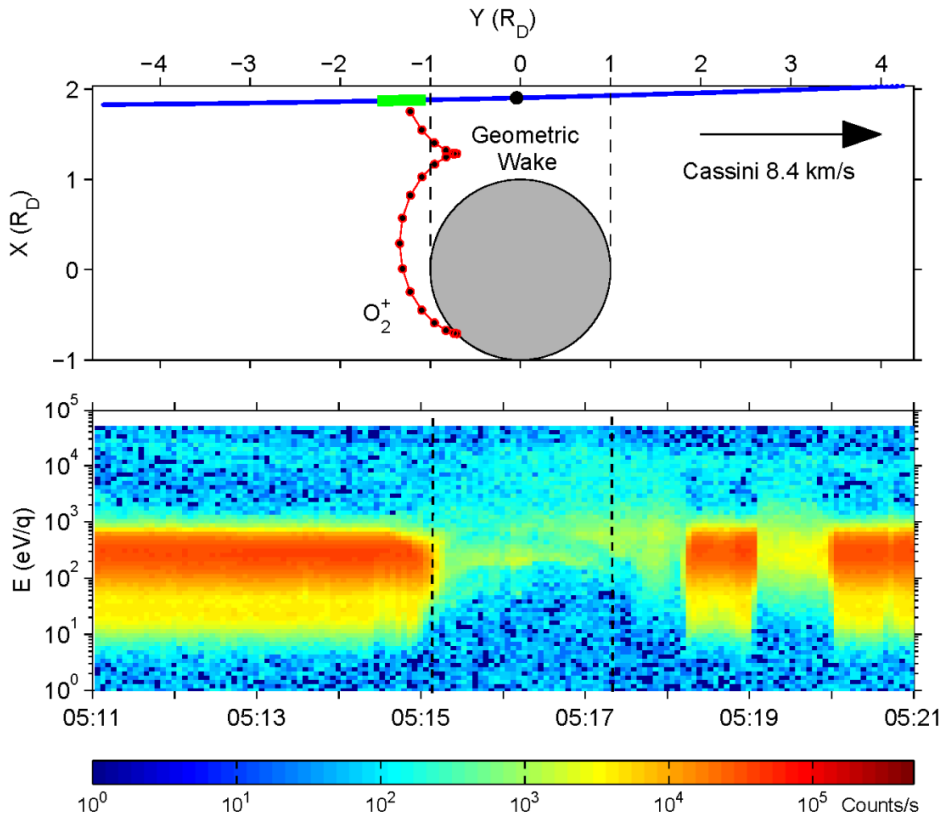

Figure CAPS-15. Depiction of the orbit of O_2^+ at Dione showing the mapping of O_2^+ ions from the observation point of CAPS (green line along trajectory) back to the moon. Figure from Tokar et al. [2012].

The observation of the so-called Pac-Man thermal feature on Mimas by the Independent Review (IR) Team came to be interpreted and modeled by the CAPS team. Schaible et al. [2017] developed a quantitative description of the effect of highly penetrating energetic electrons observed by CAPS causing sintering of the ice grains which increased the thermal inertia of the icy regolith causing the Pac-Man feature.

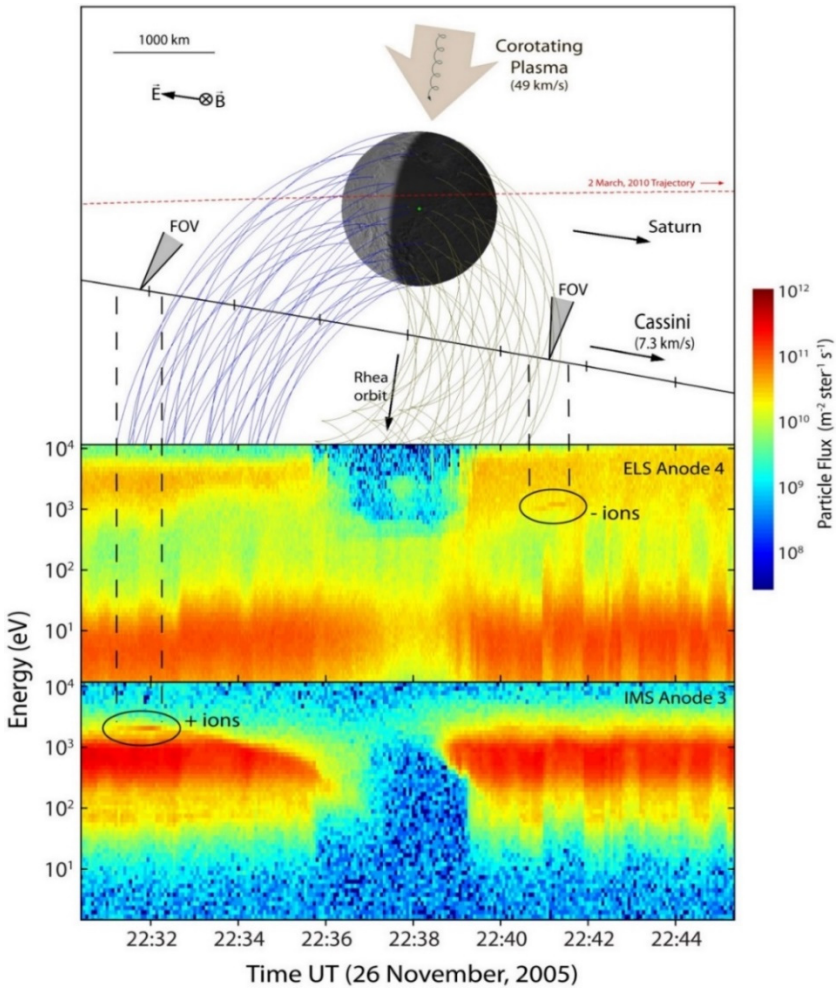

Figure CAPS-16. IMS and ELS observations of pickup ions. Energy spectrograms of ELS (top panel) and IMS (bottom panel) data for the March 10, 2010 shows the encounter with Rhea. Figure from Teolis et al. [2010].

Rings

IMS observed an enhanced ion flux (compared to background outside the rings) outside of the main rings and in the vicinity of the F-ring and G-ring as Cassini crossed the ring plane during orbit insertion on July 1, 2004. Near the edge of the main rings the ion flux as a function of energy per charge provided strong evidence for the presence of O_2^+. Analysis led to the conclusion that the enhanced ion flux between the F-ring and G-ring consisted of the water group ions O^+, OH^+, and H_2O^+ (the other water group ion H_3O^+ could not be identified) coming from Enceladus with an admixture of O_2^+, predominantly from the extended ring O_2 atmosphere. The O_2^+ component appeared to be dominant at Saturn Orbit Insertion (SOI) and was later found to vary with season [Elrod et al. 2012; 2014] due to the changing orientation of the ring plane relative to the solar UV flux (Figure CAPS-17).

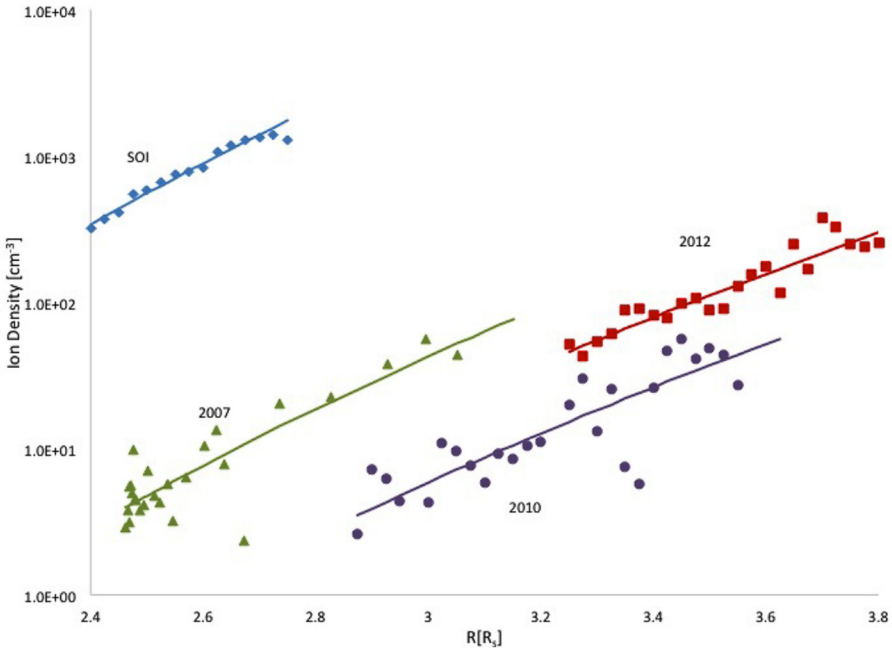

Figure CAPS-17. Ion densities extracted from IMS data at SOI in 2004, and inferred for subsequent years by modelling. The modeling indicates the seasonal dependence of ring plasma. This region contains ions formed from neutrals scattered out of the ring atmosphere as well as ions formed from neutrals in the Enceladus torus. SOI observations were dominated by O_2^+ and in the later years by water group ions. Figure from Elrod et al. [2014].

The seasonal dependence observed and modeled using CAPS data (Figure CAPS-16) confirmed that the O_2^+ ionization source was indeed solar UV acting on oxygen in the ring atmosphere as predicted by Tseng et al. [2010]. Seasonally varying oxygen was subsequently observed at much larger radii by the MIMI instrument, confirming that oxygen originating in the rings can be scattered throughout the inner magnetosphere and, consequently, also into Saturn's atmosphere. This likely accounts for oxygen observed in Saturn's thermosphere. Subsequent modeling [Tseng et al. 2013a] shows that model calculations based on the CAPS data were in reasonable agreement with that data.

Laboratory data showed that radiation decomposition of ice would lead to the production of roughly twice as much H_2 as O_2, thereby maintaining the near stoichiometry of irradiated ice grains —for example, Brown et al. [1982]. Indeed, CAPS measurements have shown that the Saturnian magnetosphere is permeated with H_2^+ and H^+ from a variety of sources (Titan, the Enceladus torus, and Saturn's atmosphere as discussed above), including the ring atmosphere [Tseng et al. 2011; 2013b]. Since H_2 is much lighter than O_2 it has a proportionately larger neutral scale height and can also be easily scattered throughout the magnetosphere by the heavier molecules. Ionization of the H_2 component of the extended ring atmosphere, and the pick-up of H_2^+ formed by this process, was shown by Tseng et al. [2011] to be an important component of magnetospheric H_2^+ detected by CAPS [Thomsen et al. 2010].

Possibly even more important, the very clean mass spectrum seen by CAPS over the rings (Figure CAPS-18) is indicative of the absence of significant levels of contaminants in the ring's ice particles [Cuzzi et al. 2009). In other words, irradiation of samples containing, for instance, carbon, would have produced CO molecules as well as other volatiles, all of which would subsequently have been scattered into the outer magnetosphere, forming pick-up ions that would be detected by CAPS. Although Cassini never flew over the main rings again, INMS data taken during the proximal orbits (when CAPS was off) did suggest that carbon species were indeed coming from the main rings.

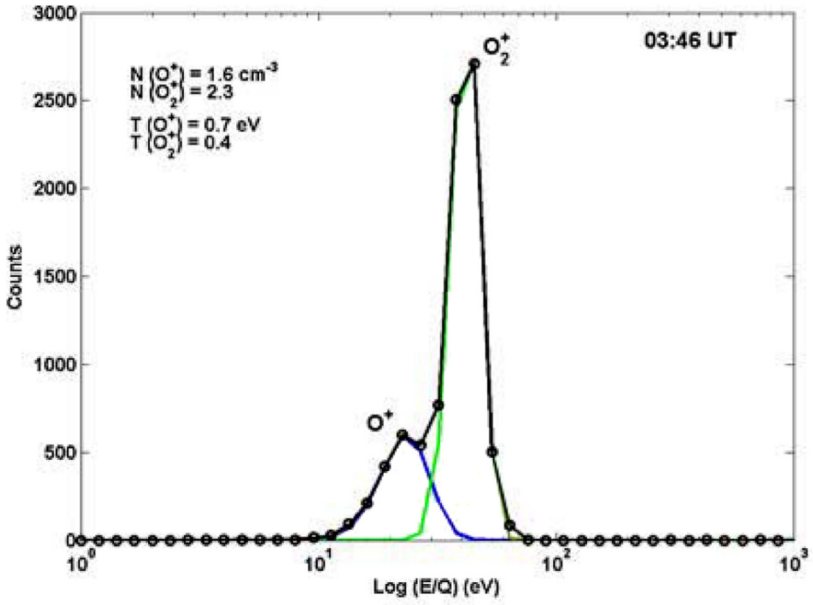

Figure CAPS-18. IMS mass spectrum over the rings taken during SOI at an altitude of ~0.2 R_S above the magnetic equator. Figure from Tokar et al. [2005].

It is worth noting that the INMS team is of the opinion that mass 28 signals seen during the Grand-Finale mission were mostly made by impact dissociation of CO_2 inside the INMS spectrometer ionization chamber. It is, therefore, unclear which molecule would be easier to produce from radiolysis of carbon-contaminated water ice. Both CO_2 and CO are possibilities. The INMS team detected only O_2 and CO_2 in Rhea and Dione exospheres.

Surprisingly, the ion densities observed by IMS between the outer edge of the main rings and Mimas (Figure CAPS-18) are derived from ionization of neutrals from the ring atmosphere and the Enceladus torus and exhibited an unexpected radial dependence [Elrod et al. 2012; 2014]. Not only did the plasma detected by CAPS in this region exhibit a seasonal dependence, with the O_2^+ component dominated by the water products from the Enceladus torus at Equinox, but the observed radial dependence suggested that an ion loss process other than electron-ion recombination, charge exchange or diffusion was acting [Elrod et al. 2014; Tseng et al. 2013a]. Since the CAPS ion densities and the RPWS electron densities differed, particularly at SOI, the observed radial dependence of the CAPS ion data was subsequently determined to be due to quenching of the

ions on nano-grains. These grains, a fraction of which were negatively charged, were presumed to be emitted from the edge of the main rings and present in the tenuous F-ring and G-ring, acted as ion sinks [Johnson et al. 2017]. That this process was occurring in this region of the magnetosphere was subsequently confirmed by the RPWS instrument during the F-ring orbits when, unfortunately, the CAPS instrument was turned off.

Rings-Magnetosphere Interactions

During SOI on July 1, 2004, the spacecraft passed over the B-ring, A-ring, and F-ring and the Cassini division before descending, inside the G-ring, through the ring plane. The trajectory provided the first in situ plasma measurements over Saturn's main rings, complementing data obtained by the Voyager 2 plasma science instrument outside the main rings. During SOI, IMS observed ion fluxes over the main rings consistent with the presence of atomic and molecular oxygen ions [Young et al. 2005]. IMS observations over the main rings detected both O^+ and O_2^+ at densities of a few per cm^3 using the IMS TOF sensor (Figure CAPS-19) [Tokar et al. 2005; Elrod et al. 2012]. Further analysis by Elrod et al. [2012] shows much higher densities of O^+ when CAPS was over the outer edge of the B-ring and again when CAPS was over the inner edge of the A-ring.

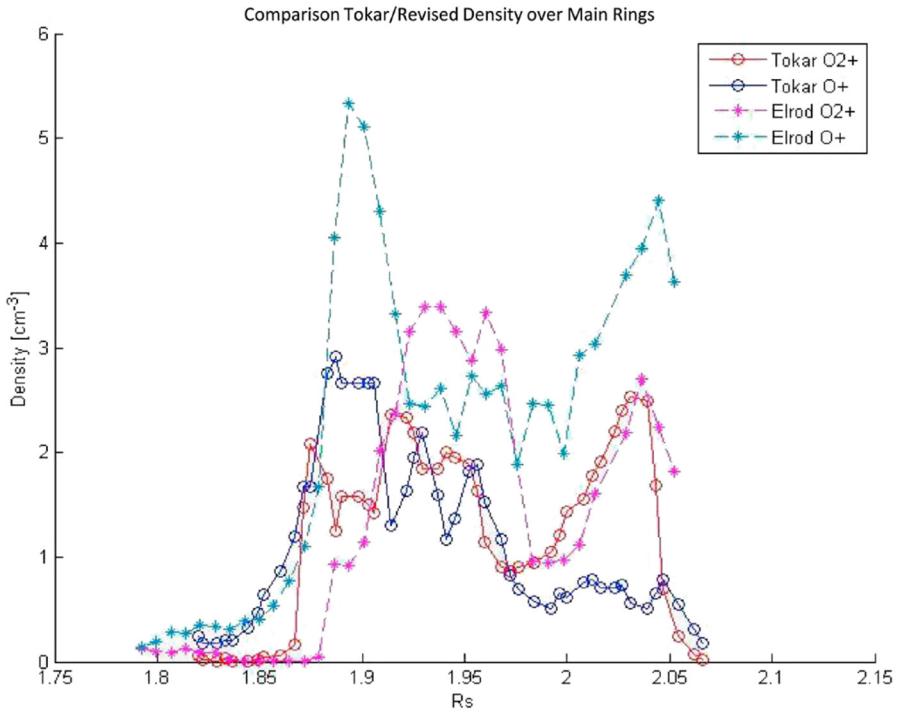

Figure CAPS-19. Densities of O^+ and O_2^+ obtained from IMS data over the main rings as a function of radial distance from Saturn in R_S. Data from Tokar et al. [2005] and re-analyzed by Elrod et al. [2012].

The IMS data suggested the presence of a ring atmosphere that was predominantly O_2 rather than H_2O and much more robust than predicted. Since the energetic ion density in this region is highly depleted due to absorption by ring particles—for example, Cooper et al. [2015], the CAPS

team proposed that the atmosphere was produced by UV-induced decomposition of ice on the ring particles [Johnson et al. 2006b]. Such a neutral atmosphere would have a scale height confining it close to the ring plane. Because ions were detected well above the ring plane, this also led to the prediction that ion-neutral scattering would produce both a ring ionosphere with a much larger scale height, and a neutral oxygen cloud that permeated Saturn's magnetosphere [Johnson et al. 2006b; Luhman et al. 2006; Bouhram et al. 2006]. Following ionization, pick-up and scattering of the neutrals from this atmosphere was shown to populate the magnetosphere with oxygen atoms and molecules which are eventually ionized far from the main rings [Johnson et al. 2006b]. Molecular oxygen ions were eventually discovered in the inner magnetosphere as well [Martens et al. 2008]. This has been subsequently confirmed by additional data and modeling as discussed in the section entitled Rings and Satellites.

Magnetosphere Composition, Sources, Transport, and Losses

The Cassini mission enabled an extensive exploration of Saturn's magnetosphere: its structure, plasma sources, transport, dynamics, loss mechanisms, and interaction with satellites, rings, and other neutral material. In this section we address CAPS findings regarding magnetosphere structure, plasma sources, transport, variability, and loss. More extensive discussions of the magnetospheric dynamics, the interaction with satellites and rings, and the interaction with the solar wind at the bow shock and magnetopause are presented in the separate section entitled Magnetosphere Dynamics. Thomsen [2013] has given a short but very useful overview of magnetosphere dynamics.

Structure

Global Structure. The orbital coverage of Cassini allowed a good determination of the global structure of Saturn's magnetosphere. Based on multiple-instrument observations, summary descriptions of the global structure have been published [Gombosi et al. 2009; Arridge et al. 2011b; Krupp et al. 2018]. As suspected from previous fly-by missions, Saturn's magnetosphere is similar in some respects to the Earth's: Its strong intrinsic magnetic field creates a bubble standing in the incident supersonic solar wind, separated from it by a magnetopause, magnetosheath, and bow shock. The magnetospheric bubble is bullet-shaped, compressed by solar wind dynamic pressure on the dayside and stretching out into a long magnetotail on the night side. The distinguishing factors that determine the structure and dynamics of Saturn's magnetosphere are its strong magnetic field, rapid rotation, and dominant source of magnetospheric plasma deep within the magnetosphere (i. e., neutral water molecules from Enceladus).

Radial Variation. The primary spatial dependence of magnetospheric properties is in the radial direction. From the first pass through the magnetosphere during SOI [Young et al. 2005], several distinct magnetospheric regions could be identified: an outer region (inside the magnetopause) with extremely low density, later understood as magnetospheric lobe; then a significantly denser region with variable density dominated by H^+, later understood as the higher-latitude manifestation of the plasma sheet/ring current; and finally, a much denser inner

plasmasphere dominated by W^+. Subsequent analyses of the SOI data [Rymer et al. 2005; Sittler et al. 2005, 2006a, 2008] provided quantitative estimates of the H^+, W^+, and electron plasma parameters in the inner magnetosphere and demonstrated that the plasma flow velocity is near co-rotation throughout the region (co-rotation is the azimuthal flow that results from essentially rigid rotation with the planet; it is enforced by currents flowing along the magnetic field lines between the upper atmosphere and the magnetospheric plasma). The proton and water-group temperatures were consistent with local ionization and pick-up into the co-rotating flow. The electrons in the inner magnetosphere consist of two populations: 1) a cool component whose temperature tracks the proton temperature; and 2) a hotter population that increases in energy with decreasing radial distance [Young et al. 2005; Sittler et al. 2006b; Schippers et al. 2008]. Later work [Rymer et al. 2007; Rymer 2010; Schippers et al. 2009] showed that the cold electron component was consistent with a local pick-up source and subsequent heating via Coulomb collisions with the protons. The hot component was consistent with adiabatic transport inwards from a source in the plasma sheet/ring current region.

Calculation of the ion plasma moments (density, temperature, flow velocity) from CAPS data is complicated by incomplete and variable viewing directions. Nonetheless, application of a numerical computational scheme to the full data set through March 2009 enabled a survey of the properties of H^+, W^+, and H_2^+ (the third most common ion species in the magnetosphere, as revealed by CAPS time-of-flight measurements) throughout the magnetosphere (Figure CAPS-20)

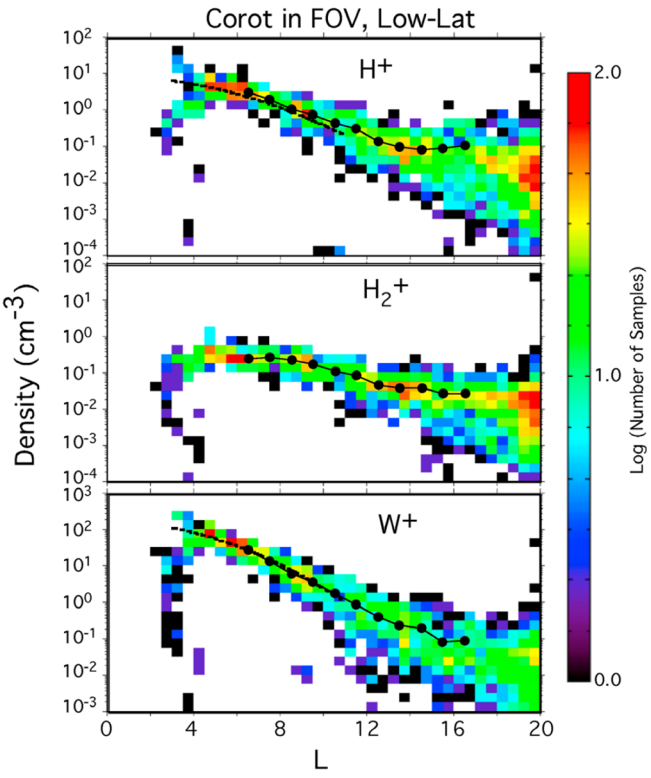

Figure CAPS-20. Radial dependence of low-latitude plasma density when co-rotation was in the CAPS field of view. Figure from Thomsen et al. [2010].

[Thomsen et al. 2010]. The survey confirmed that densities decrease, and temperatures increase, with radial distance inside ~20 R_S, and the W^+ density declines more rapidly than light ions. The flow velocity remains primarily in the co-rotational direction essentially all the way to the magnetopause, but the speed is lower than full co-rotation, as discussed below in the Transport section. Combined with the higher-energy measurements of MIMI, the CAPS data enabled a comprehensive survey of the total plasma pressure throughout the magnetosphere and thus an understanding of the currents that distort the dipole field within the plasma sheet and ring current region [Sergis et al. 2010, 2017]. A more recent survey of plasma moments calculated with a forward modeling approach that includes anisotropic temperatures explores both the radial and local time variations of the plasma (Figure CAPS-21) [Wilson et al. 2017].

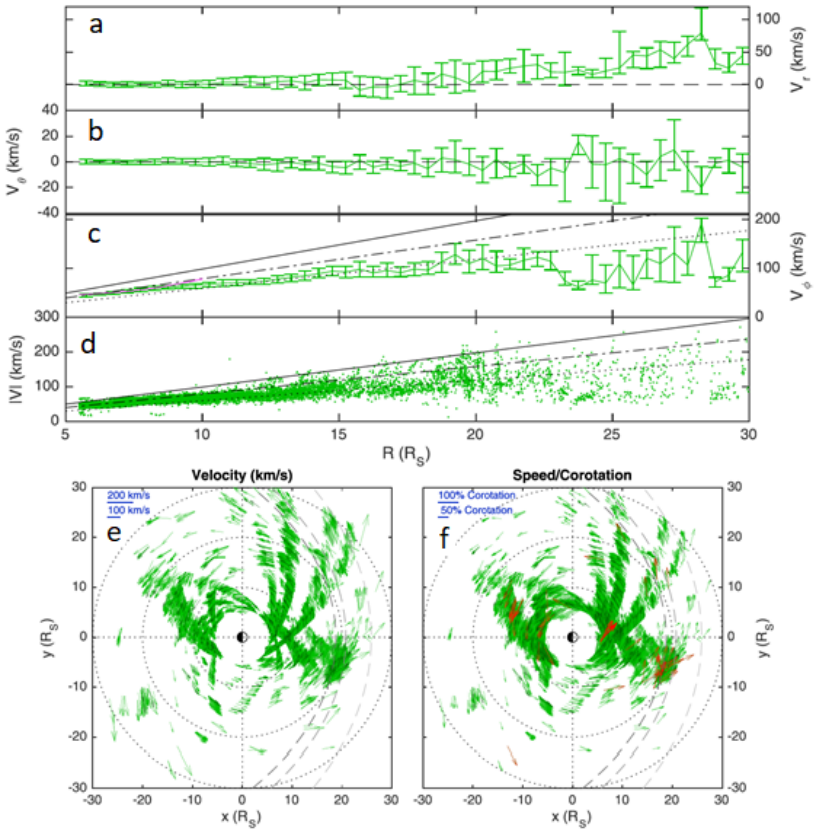

Figure CAPS-21. A low-latitude heavy ion layer displaying narrow substructures, and a higher-latitude, smooth, broad ion layer composed dominantly of light ions. *Panels a–c:* Radial profiles of plasma velocity components, in 0.5-R_S bins. *Panel d:* All measured flow speeds. *Panel e:* Equatorial plane projections of flow vectors with length proportional to flow speed. *Panel f:* Same as panel e, but with length proportional to the fraction of co-rotation. All data points are shown in green, while dark green shows every thirtieth data point. Figure from Wilson et al. [2017].

Disk structure, low-latitude confinement. Because of strong centrifugal forces on co-rotating plasma, Saturn's magnetosphere is flattened into a disk shape, especially on the night side and during times of relatively low solar wind dynamic pressure—for example, Arridge et al. [2007, 2008]. CAPS data allow determination of the latitudinal scale heights of H^+, W^+, and H_2^+ and show

that the heavy ions are more strongly confined to the equatorial plane—for example, Thomsen et al. [2010]. In the magnetotail, the magnetodisk structure is particularly prominent, with the current flowing in a relatively thin region of dense plasma separating the lobes of oppositely directed magnetic field. The magnetodisk consists of a structured plasma sheet: a low-latitude heavy ion layer displaying narrow substructures, and a higher-latitude, smooth, broad ion layer composed predominantly of light ions (Figure CAPS-22) [Szego et al. 2011]. The density and azimuthal flow speed decline with increasing latitude [Nemeth et al. 2015] as a direct consequence of the sub-corotation of the plasma in the outer magnetosphere—for example, McAndrews et al. [2009]; Thomsen et al. [2013, 2014b]; Wilson et al. [2017]. Highest speeds occur on field lines at lowest latitudes mapping to the rapidly rotating inner regions of the plasma sheet, and the speed falls as one moves to higher latitudes where the field lines are connected to strongly sub-co-rotating plasma at large radial distances.

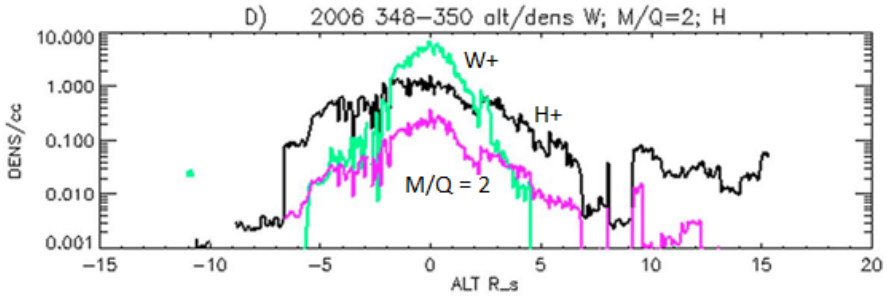

Figure CAPS-22. Density of three species: water W^+ (green), hydrogen H^+ (black), and mass/charge 2 (magenta); as a function of distance from the equatorial plane for a crossing of the magnetic equator at ~9 R_S. W^+ is more confined to the equator than light ions, so the relative composition varies with latitude. Figure from Szego et al. [2011].

Local time dependence. Although CAPS had relatively little low-latitude coverage with appropriate viewing near dawn, several observations were made of the local time dependence of plasma properties. For example, interchange injections (see the section entitled Magnetosphere Dynamics and Radial Transport) appear to be stronger and penetrate more deeply into the inner magnetosphere on the night side compared to the dayside [DeJong et al. 2011]. Also, in the inner magnetosphere, there is a day-night asymmetry in both ion and electron temperatures [Thomsen et al. 2012], which is further discussed in the section entitled Magnetosphere Dynamics and Radial Transport. The day-night asymmetry in the hot electron component extends to high latitudes, but there is no such asymmetry in the plasma sheet thickness, at least in the cold electron population [Carbary and Rymer 2014]. At larger radial distances, there is only modest variation with local time [Wilson et al. 2017].

Cusp and Polar Cap. As seen already during SOI [Young et al. 2005], at latitudes above the extended plasma-sheet/ring-current there is a region that is largely devoid of plasma, known as the magnetospheric lobe. The lobe is commonly seen in the magnetotail—for example, Thomsen et al. 2015b]—as the plasma sheet rocks and flaps up and down (see discussion in the section entitled Periodicities). Lobe field lines are thought to be connected by magnetopause reconnection into the solar wind and have thus lost their magnetospheric contents. At low altitudes, the lobe maps into

the polar cap. The polar cap boundary is identified based on a sharp drop in ELS electron fluxes and corresponding signatures in other data sets (Figure CAPS-23)—e.g., Jinks et al. [2014]. A survey of polar cap boundary crossings showed that the main upward field-aligned currents associated with the aurorae reside equatorward of the open-closed boundary [Jinks et al. 2014].

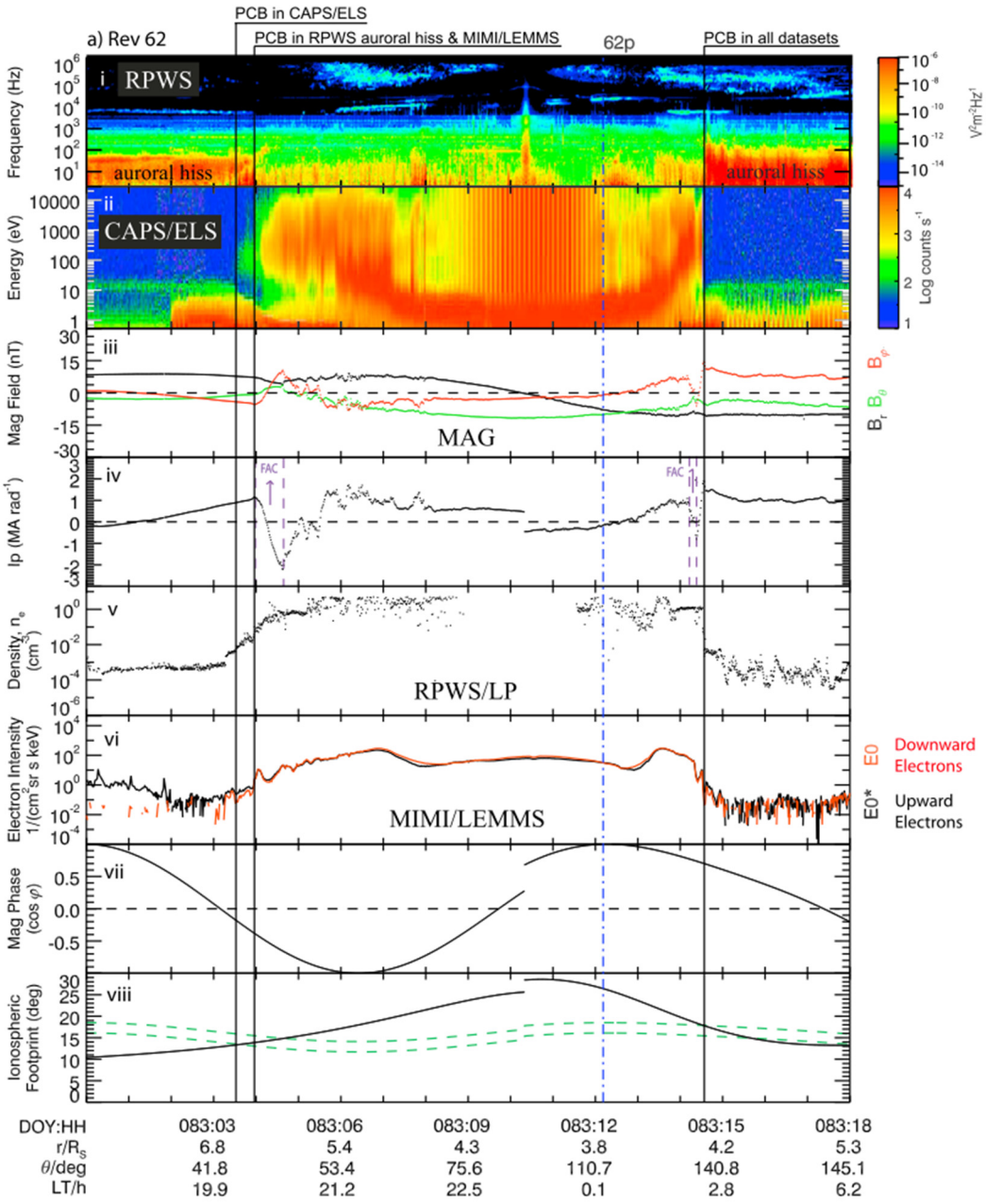

Figure CAPS-23. Polar cap boundary as seen in several different Cassini data sets. The sharp change in the ELS electron spectrum is the most definitive signature. The polar cap is largely devoid of electrons (counts below ~20 eV are due to spacecraft photoelectrons). Figure from Jinks et al. [2014].

Near noon, open magnetic field lines (which will ultimately become the lobe/polar cap) are filled with incoming magnetosheath plasma, which penetrates down to low altitudes. CAPS observations of this region, known as the cusp, demonstrate that the process of reconnection occurs at Saturn's magnetopause, with indications that the reconnection is pulsed [Jasinski et al. 2014]. The first cusp observation was associated with the arrival of a solar wind shock front, which compressed the magnetosphere and probably provided more favorable conditions for magnetopause reconnection [Jasinski et al. 2014]. Evidence for both bursty and more continuous reconnection is observed during different cusp events, and the locations of the reconnection site vary along the subsolar magnetopause. Magnetic reconnection and plasma injection into the cusp can occur for a variety of upstream conditions [Jasinski et al. 2016, 2017; Arridge et al. 2016].

Temporal variability

Seasonal and long-time scale. On the time scale of months to years, most of Saturn's magnetospheric plasma does not exhibit strong variability—less than a factor of three [Wilson et al. 2017]—in spite of the fact that the Enceladus plume source (see Figure CAPS-17) does appear to vary on the scale of several months [Smith et al. 2010; Elrod et al. 2014]. In the innermost magnetosphere, just outside the main rings, heavy ion densities (O_2^+ and W^+) show a seasonal dependence, as could be expected for a ring source that depends on the solar illumination angle [Elrod et al. 2012, 2014] (see the section entitled Rings in Plasma Sources).

Short time scale. On the scale of minutes to hours or days, there is significant variability in plasma properties (Figure CAPS-24)—for example, Young et al. [2005]; Gombosi et al. [2009], Figures 9.28 and 9.29; Thomsen et al. [2015a], Figure 1. Variability at this scale may be due to the

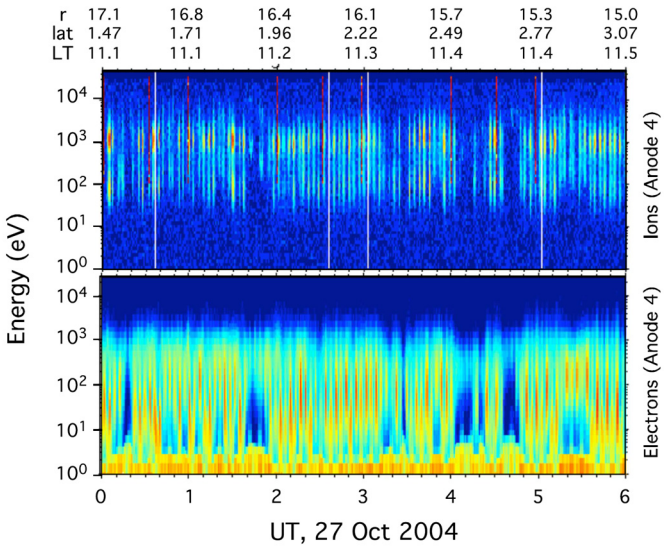

Figure CAPS-24. Temporal variability in plasma found in the middle magnetosphere ~16 R_S. Both panels show CAPS count rate as a function of energy and time for ions (*top panel*) and electrons (*bottom panel*). Regularly periodic variations are due to the CAPS actuator scanning the instrument into different look directions. Aperiodic variations show frequent changes in the spectral shape and intensity of magnetospheric plasma. Figure from Gombosi et al. [2009].

outward transport of interchanged flux tubes from the inner magnetosphere (see the section entitled Magnetosphere Dynamics). At the orbit of Titan, the ambient plasma environments are variable but can be organized into four types by the nature of the electron populations [Rymer et al. 2009a; Smith and Rymer 2014]. The plasma environment at Titan's orbit appears to be determined by the motion of the magnetodisk current sheet [Arridge et al. 2008; Szego et al. 2011].

Periodicity. Many properties of Saturn's magnetosphere exhibit periodicities at approximately the planetary rotation rate, a significant puzzle given the near-alignment of the magnetic and rotational axes. In the plasma data, the periodicities are clearest in the plasma sheet region. The density varies by more than an order of magnitude, depending on the SLS3 longitude [Arridge et al. 2008]. This variability is likely due to periodic up-and-down motion of the plasma sheet. The temporal and spatial variations in plasma and field parameters are well organized by the flapping of the plasma disk about a periodically varying position [Arridge et al. 2008; Szego et al. 2011, 2012, 2013; Nemeth et al. 2016]. Asymmetries in Cassini's periodic plasma sheet crossings [Thomsen et al. 2017] are consistent with predictions of plasma sheet rocking and thickness variation made both by the global magneto-hydrodynamic (MHD) models that incorporate the effects of hypothesized atmospheric vortices [Jia and Kivelson 2012] and by the closely-related dual rotating current systems inferred from magnetic field observations—for example, Cowley et al. [2017] and references therein.

In the inner to middle magnetosphere, evidence was found for a plasma cam in which the plasma density varies roughly sinusoidally with SLS3 (Figure CAPS-25) [Burch et al. 2008, 2009; Goldstein et al. 2016]. Theoretical arguments suggest that asymmetric ring-current pressure coupled to Saturn's ionosphere can initiate a rotating two-cell interchange potential that is long-lived and stable [Goldstein et al. 2014]. Outflow from the dense sector was suggested as the driver of recurrent tail reconnection and plasmoid production (see sections entitled Plasma Sources and Magnetosphere Dynamics) inferred from periodic magnetic field variations in the tail [Burch et al. 2009], but subsequent authors argued that the field variations were more consistent with simple wave-like motion or periodic rocking of the plasma sheet rather than plasmoid formation [Jackman et al. 2009]. In the more recent forward-modeling dataset of ion densities [Wilson et al. 2017], the cam is not seen, so there remain questions about its existence and its consequences.

Response to Solar Wind. Because of its strong magnetic field, rapid rotation, and internal plasma source, most magnetospheric dynamics appear to be internally driven (see the section entitled Magnetosphere Dynamics). Nonetheless, evidence has been found for significant dynamical effects attributable to solar wind variability. CAPS observations in the pre-dawn tail outbound from SOI, showed sudden energization of plasma associated with a field dipolarization, which was interpreted as evidence of a solar wind compression-related tail collapse via magnetic reconnection. Under conditions of high solar wind dynamic pressure, the magnetotail appears to enter a state of sustained lobe reconnection, resulting in a more Dungey-like configuration [Thomsen et al. 2015b]. In the inner magnetosphere, there is no apparent relation between the depth of electron penetration and solar wind properties [Thomsen et al. 2016a], although the energization of ions in a large-scale standing wave might be caused by a solar wind pressure impulse [Thomsen et al. 2017].

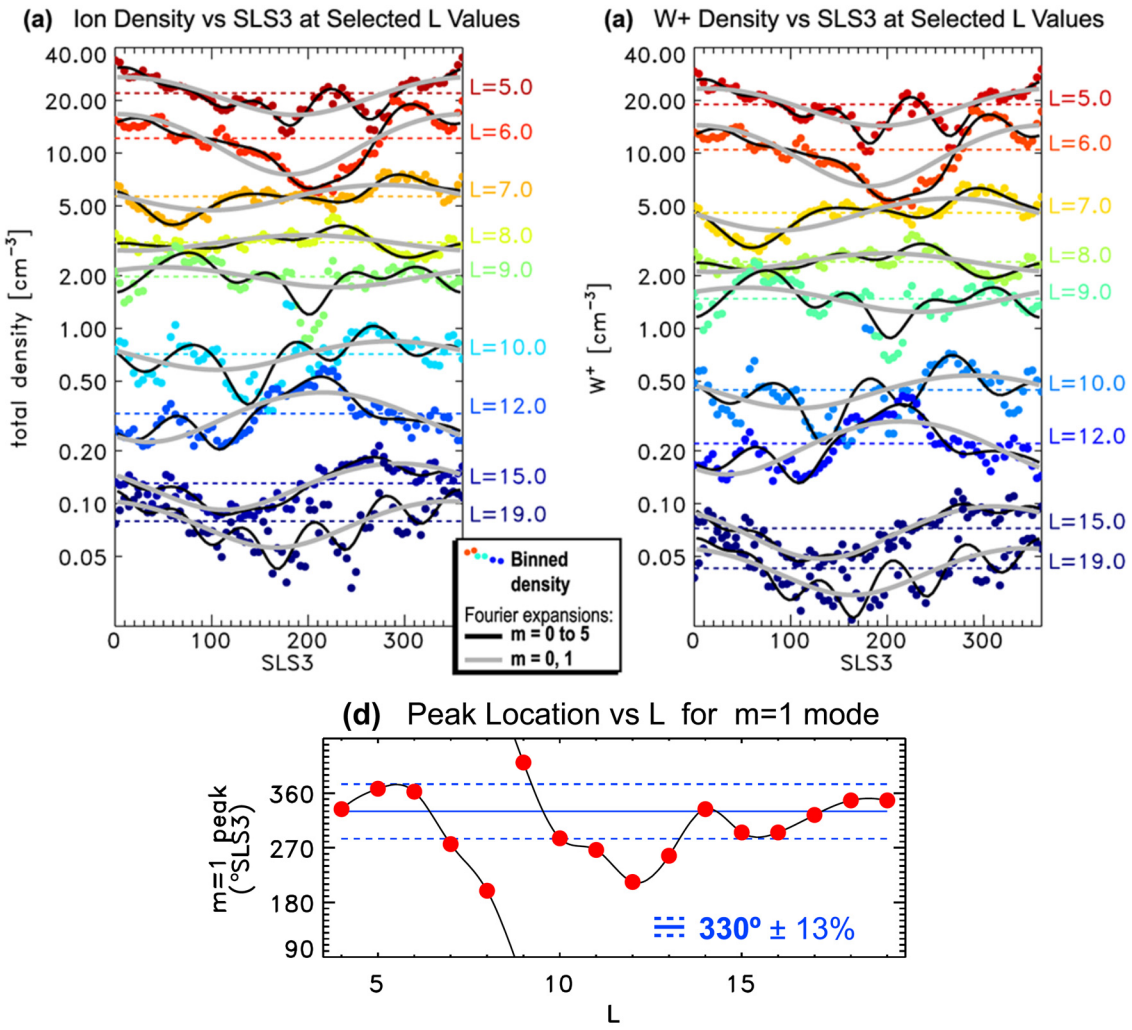

Figure CAPS-25. Evidence for the existence of a plasma cam, in which the density is generally highest in a particular SLS3 longitude sector. Figure from Goldstein et al. [2016].

Plasma sources

Clues from Composition. The composition of plasma ions is one of the best pointers to the source of the plasma. CAPS findings that the dominant magnetospheric ions are W^+, H^+, and H_2^+ [Young et al. 2005; Thomsen et al. 2010] were well explained by the later discovery of the prodigious output of water from the south-polar plumes of Enceladus. It was noted by Young et al. [2005] that the presence of H_3O^+ within the W^+ ion group indicated ion-molecule reactions occurring in a water-rich atmosphere, attributed to the E-ring and inner icy satellites, which ultimately was determined to be Enceladus. A careful separation of the individual components of the water-group species and determination of the radial distance dependence of their relative proportions [Tokar et al. 2008; Wilson et al. 2015] provided vital constraints on models of the physics and chemistry of Enceladus-originating material.

Another example of source determination through composition is N^+ [Smith et al. 2005, 2007, 2008]. Originally expected from Titan, the radial dependence of the N^+ phase space density and the energy of this population suggested instead an inner magnetosphere source [Sittler et al. 2006b], probably Enceladus, with both molecular nitrogen and ammonia emitted there (Figure CAPS-26). Surprisingly little N^+ has been found in the outer magnetosphere, indicating that nitrogen ions coming from Titan do not accumulate to significant densities [Smith and Rymer 2014].

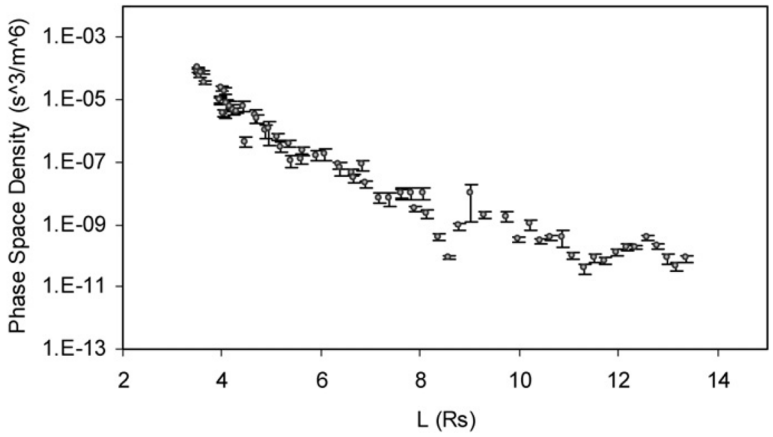

Figure CAPS-26. Nitrogen ion phase space density averaged over energy and angle, as a function of distance from Saturn. Clear decline with distance indicates a source in the inner region, inconsistent with a Titan source in the outer magnetosphere (L ~20). Figure from Smith et al. [2007].

Clues from Energy and Pitch-Angle Distributions. Examples of how the energy distribution illuminates plasma sources were noted above. For example, the way ion energies in the inner magnetosphere track the co-rotational energy was strong evidence for local pick-up from a distributed neutral gas source [Young et al. 2005; Thomsen et al. 2010]. Similarly, the different radial dependence of the two electron populations suggested a local pick-up source with subsequent collisional heating of the cold electrons, while the hot electrons are more likely adiabatically transported inward from the outer magnetosphere (Figure CAPS-27)—for example, Schippers et al. [2008]; Rymer et al. [2007]; Rymer [2010]. Butterfly angular distributions found in inner magnetosphere electrons adjacent to interchange injections (see the section entitled Hot Plasma Injections in Magnetosphere Dynamics) suggest an origin near Dione and Tethys [Burch et al. 2007] but might also be consistent with a hot electron circulation process associated with the injections, rather than an inner magnetospheric source [Rymer et al. 2008].

Enceladus. As can be seen from Figure CAPS-20 and Figure CAPS-22, the dominant ion species seen throughout the magnetosphere are well explained by ionization of material from the water plumes of Enceladus. CAPS observations of the plumes themselves are detailed in the section entitled Enceladus. CAPS data also showed Enceladus to be the probable source of most of the N^+ observed in Saturn's inner magnetosphere (Figure CAPS-26), and CAPS measurements further helped reveal the existence of temporal variability in the plume source [Smith et al. 2010].

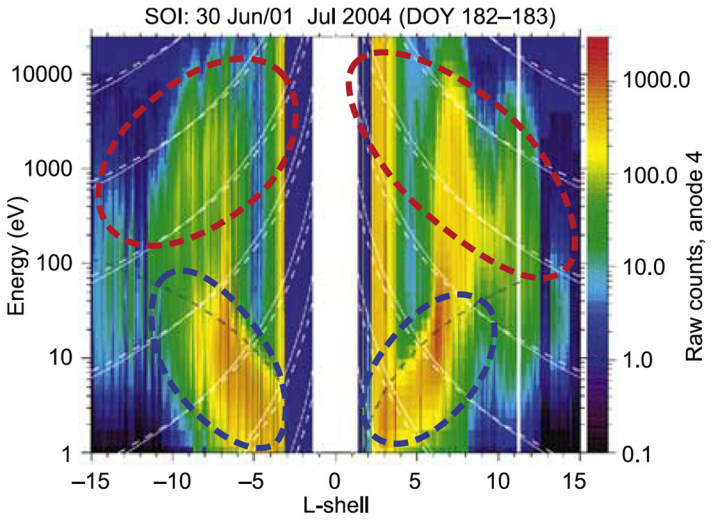

Figure CAPS-27. Two-component electron spectra from the part of the orbit insertion trajectory passing through the inner magnetosphere. White dotted curves show expected L dependence of the energy of particles conserving their first adiabatic invariant. Blue dotted lines show expected energy for local pickup of H^+. The cold electrons are most consistent with non-adiabatic collisional coupling to pick up H^+, whereas the hotter electrons are consistent with adiabatic transport from outside the inner region. Figure from Rymer et al. [2007].

Titan. A summary of CAPS observations during the many encounters with Titan are described elsewhere. The primary tracers of Titan's contributions to magnetospheric plasma, have been N^+ and H_2^+. The finding of very little N^+ in the outer magnetosphere [Smith et al. 2005] indicates that Titan's contribution to the heavy-ion plasma is limited, whereas the fact that H_2^+ becomes comparable to H^+ and W^+ in the outer magnetosphere [Thomsen et al. 2010] indicates that Titan is an important source of lighter ions in that region. From observations during passage through Titan's wake region, the total mass loss rate from Titan is estimated to be a few × 10^{25} amu/q/sec (~0.8 kg/s) [Coates et al. 2012], compared to estimates of ~60-100 kg/s from Enceladus [Fleshman et al. 2013].

Rings. CAPS was turned off before the F-Ring and Proximal Orbits, so the only direct exploration of ring-associated plasma occurred during SOI, where a layer of O^+ and O_2^+ was discovered over the A-ring and B-ring [Young et al. 2005]. Subsequent analysis of the SOI data [Tokar et al. 2005] produced densities and temperatures of these two species (Figure CAPS-28). The ring atmosphere and ionosphere are likely produced by UV photosputtering of the icy rings and subsequent photoionization of O_2^+. Significant O_2^+ was also detected outside the main rings, near the F-ring [Tokar et al. 2005], and analysis of the O_2^+ and W^+ profiles showed the seasonal dependence mentioned above, consistent with a ring source that depends on the solar illumination angle [Elrod et al. 2012, 2014; Tseng et al. 2010]. The result indicates that the rings are an important source of O_2^+ and O^+ ions inside the orbit of Mimas.

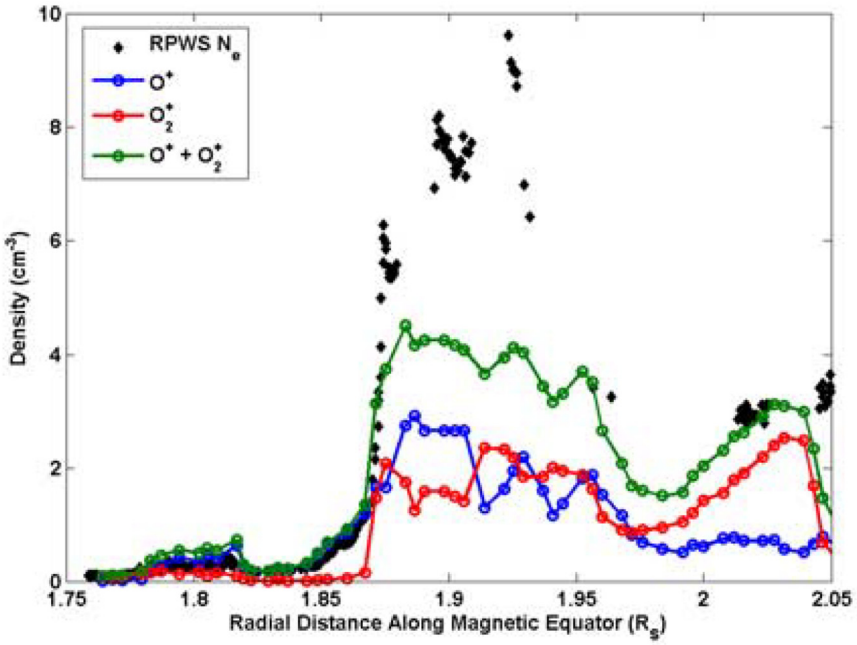

Figure CAPS-28. Radial dependence of O^+ and O_2^+ densities from CAPS observations over the main rings during SOI. Figure from Tokar et al. [2005].

Other satellites. CAPS has also detected O_2^+ in the vicinity of Dione [Tokar et al. 2012], and the observed radial dependence of the ratio O_2^+/W^+ suggested that there is a neutral O_2 source in the vicinity of Rhea [Martens et al. 2008]. Although the evidence for oxygen from Rhea is somewhat skimpy, CAPS has clearly detected non-gyrotropic outflowing CO_2^+ there, as well as another negatively charged species, previously thought to be O^- but now found to be closer to mass 23 [Desai et al. 2018]. The latter is perhaps a carbon-based ion deriving from implanted exogenic compounds. Examination of the plasma conditions on flybys of Rhea [Wilson et al. 2010] revealed that the plasma flowing near it had no radial component on the Saturn-side of the moon but had a radially outward component on the anti-Saturn-side. This is potentially due to an electric field enhancement near the moon, which is suggested in hybrid simulations.

Saturn ionosphere. Observation of probable plasma outflows from the ionosphere at the outer edge of the night side plasma sheet and extending into the lobes led to an estimate of some tens of kg/s lofted from the ionosphere (Figure CAPS-29) [Felici et al. 2016].

The observations occurred during a probable solar wind dynamic pressure enhancement, which may be important for producing significant outflow. It is not yet clear how often such outflow occurs, nor whether the outflow is captured into the closed region of the magnetosphere, rather than just escaping into the solar wind. Additionally, the field-aligned angular distributions of the suprathermal electrons within the plasma sheet/ring current region may indicate an ionospheric origin [Schippers et al. 2008], but no supporting evidence from the ion data has been reported.

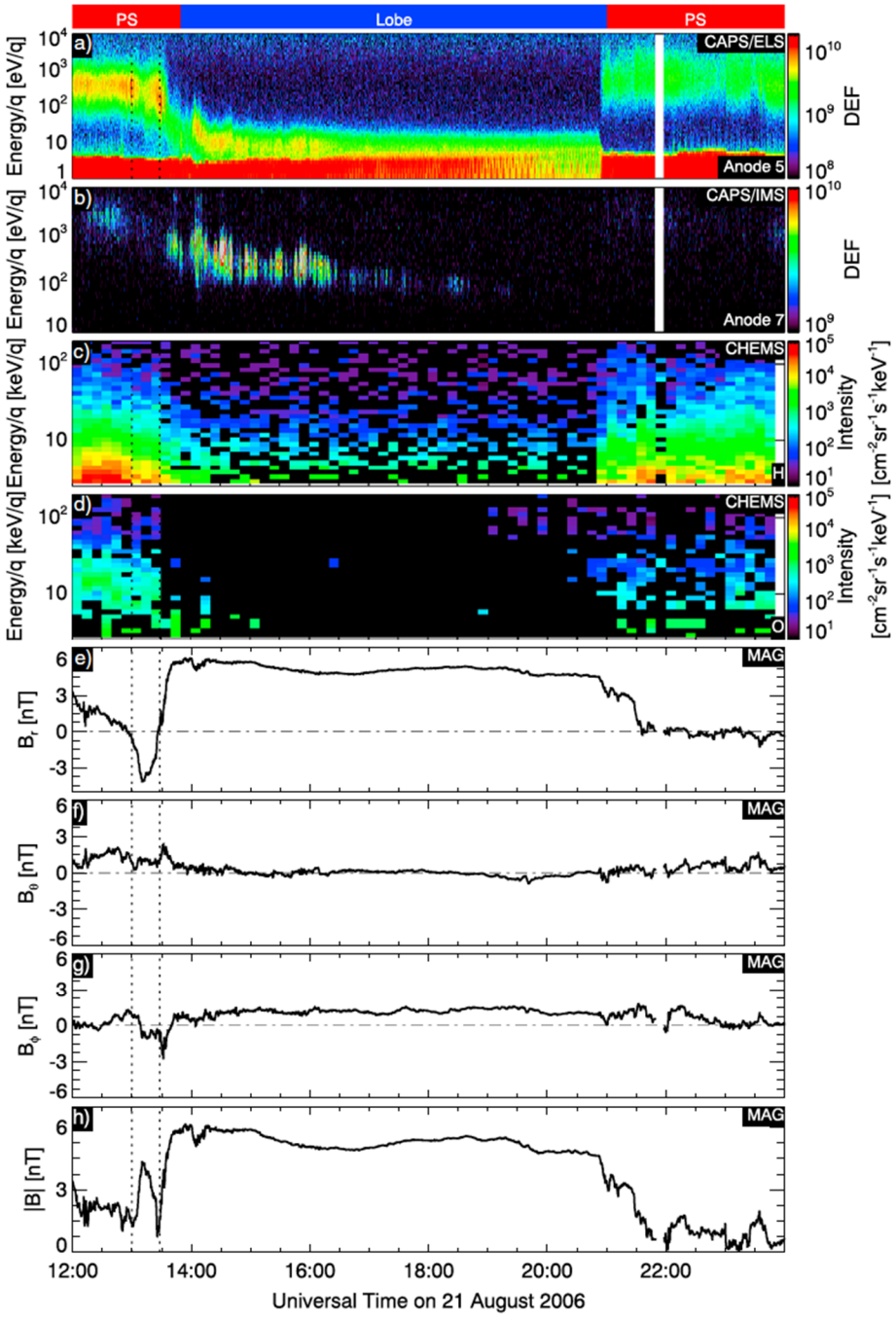

Figure CAPS-29. CAPS observations of an outflowing H^+ population from Saturn's ionosphere, seen in the lobe near the plasma sheet boundary at 36 R_J down tail. Figure from Felici et al. [2016].

Solar wind. Regarding dayside entry of solar wind plasma via reconnection or the Kelvin-Helmholtz instability, there is considerable evidence that both processes take place (see the section entitled Bow Shock, Magnetosheath, and Outer Magnetosphere). Magnetopause encounters frequently exhibit a low-latitude boundary layer (LLBL), in which magnetosheath

plasma can be found just inside the magnetopause. From a survey of 354 crossings of the LLBL [Masters et al. 2011a, 2011b], the estimated thickness is only of the order of one Saturn radius, with no clear dawn-dusk asymmetry. Thus, while solar wind plasma can and does enter the magnetosphere on the dayside, it does not get very far in. This is supported by the fact that the ratio of m/q = 2 to H^+ ions in the outer magnetosphere is almost always significantly greater than the values of 1 to 10% typically seen within the solar wind [Thomsen et al. 2010], indicating that plasma in the outer magnetosphere is predominantly of inner magnetospheric and/or Titan origin, with very little contribution from solar wind plasma.

On the night side, plasma with solar wind-like composition has been observed at 37 R_S near local midnight [Thomsen et al. 2015b]. In that event, it appeared that prolonged high solar wind dynamic pressure may have caused erosion of the tail plasma sheet through ongoing Vasyliunas-type reconnection that then involved open lobe field lines and created a more Earth-like, Dungey-style outer plasma sheet predominantly of solar wind origin. Other evidence for Dungey-style reconnection following a Vasyliunas-style reconnection event is the post-plasmoid plasma sheet— for example, Jackman et al. [2011]. One other event that showed the possibility of a Dungey region, in which field lines were probably closed but the densities were quite low and there was very little O^+, was seen in a rapid high-latitude pass near dawn with clear evidence of Vasyliunas-type reconnection at latitudes just equatorward of the Dungey region [Thomsen et al. 2015a].

One unanticipated discovery of the Cassini mission is the existence of an inner magnetospheric convection pattern superimposed on the dominant co-rotation pattern.

Transport

Inner Magnetosphere. As noted in the section entitled Magnetosphere Structure and in Figure CAPS-21, CAPS measurements consistently show that plasma flow in the inner magnetosphere is predominantly in the co-rotation direction, with a magnitude near full co-rotation at low radial distances but tending toward a fraction (~60%) of full co-rotation by 10 R_S—see Sittler et al. [2005]; Wilson et al. [2008, 2009, 2017]; Thomsen et al. [2010]; Livi et al. [2014]. Radial velocities are much smaller and difficult to measure [Wilson et al. 2008].

There is widespread agreement that the primary mechanism for radial transport within the inner magnetosphere, which is needed to remove the continuously-produced plasma from Enceladus, is the process of centrifugally-driven flux-tube interchange. This process is described in detail in the section entitled Magnetosphere Dynamics, but CAPS data have been instrumental in the discovery [Young et al. 2005; Hill et al. 2005; Burch et al. 2005] and diagnosis [Andre et al. 2007; Chen and Hill 2008; Menietti et al. 2008; Rymer et al. 2009b; Chen et al. 2010; DeJong et al. 2010; Thomsen et al. 2014b; Paranicas et al. 2016] of hot-plasma injection events that are the inward-moving half of the flux-tube interchange. There has been only one reported observation of outward-moving cold plasma fingers that should form the other half of the process [Thomsen et al.

2015a]. Estimates of the inflow speeds within the injection channels range from a few km/s to ~260 km/s [Burch et al. 2005; Rymer et al. 2009b; Chen et al. 2010; Paranicas et al. 2016]. Composition suggests that the plasma inside the injection channels comes from the outer magnetosphere [Thomsen et al. 2014b].

One unanticipated discovery of the Cassini mission is the existence of an inner magnetospheric convection pattern superimposed on the dominant co-rotation pattern [Andriopoulou et al. 2012, 2014; Thomsen et al. 2012; Wilson et al. 2013]. The pattern consists of a general dusk-to-dawn drift, such that particles drift inward while they co-rotate from noon to midnight and outward as they return from midnight to noon (Figure CAPS-30). The result is an inward displacement at midnight compared to noon. Several hypotheses regarding this convection have been advanced, but it remains an unsolved puzzle.

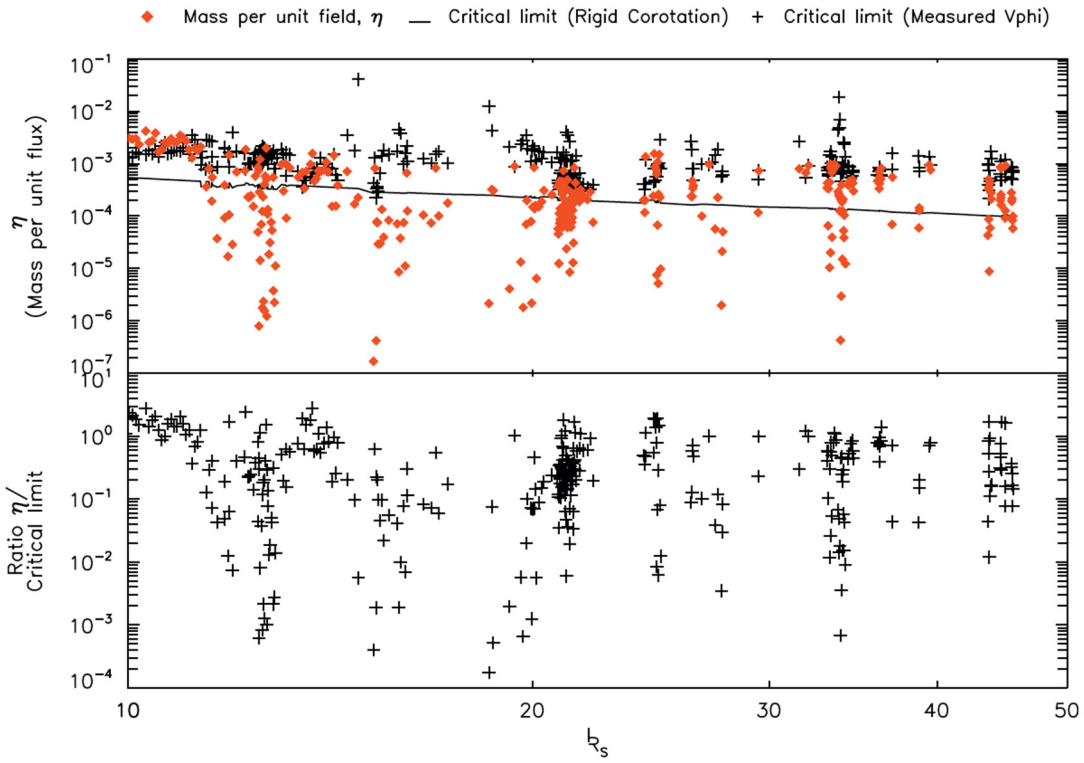

Figure CAPS-30. Comparison of night-side flux-tube content (red ♦), estimated from CAPS/IMS data, with the theoretical critical limit above which the flux tube will pinch off and release a plasmoid downtail (black +). The observed flux-tube content is roughly bounded by the critical limit, suggesting that night-side reconnection and plasmoid formation keep the tail near marginal stability. Figure from McAndrews et al. [2009].

Outer Magnetosphere. Beyond 10 R_S, CAPS measurements show consistently that the plasma flow overwhelmingly remains in the co-rotational direction at essentially all local times, indicating continued influence of connection to the co-rotating ionosphere, but the speed of the flow is well below full co-rotation—for example, McAndrews et al. [2009]; Thomsen et al. [2010, 2013, 2014a]; Wilson et al. [2017]. Beyond about 15–20 R_S, there is little evidence for inflowing plasma

on the night side, where, particularly near the flanks, flows tend to have more of an outward component. From the lack of inward flow in the pre-dawn sector, it appears that dense plasma is not often able to make the turn and return sunward to the dayside magnetosphere at distances beyond ~15 R_S (see Figure CAPS-21).

Plasma loss

Plasmoid formation. One of the principal ways in which plasma produced in the inner magnetosphere can be shed to the solar wind is through the process of magnetic reconnection in the tail. This is covered in greater detail later in the section entitled Magnetosphere Dynamics. Essentially, flux tubes loaded with inner magnetospheric plasma are transported via interchange to the outer magnetosphere. Strong centrifugal forces distend them radially, especially near the equatorial plane. On the dayside, the pressure of the solar wind helps confine the distended flux tubes, but when they rotate into the night side, that confinement goes away, and centrifugal force can overwhelm the magnetic tension. The result is that the flux tubes pinch off (or reconnect), shedding a plasmoid that is no longer connected to the planet and which carries away the load of plasma the flux tube bore before reconnection occurred (Figure CAPS-30). This is the so-called Vasyliunas cycle. CAPS data have been instrumental in identifying the resulting down-tail flows of the disconnected plasmoids [Hill et al. 2008; McAndrews et al. 2009; Jackman et al. 2014, 2015; Arridge et al. 2015; Smith et al. 2016, 2018]. There is ongoing debate as to whether plasmoids can carry away enough plasma to balance new production in the inner magnetosphere.

Magnetopause processes. Magnetic reconnection and nonlinear Kelvin-Helmholtz waves at the magnetopause could both potentially allow magnetospheric mass loss. Evidence for the operation of both processes has been seen—for example, McAndrews et al. [2008]; Masters et al. [2009, 2010, 2012]; Wilson et al. [2012]; Delamere et al. [2013]; Fuselier et al. [2014]; Jasinski et al. [2016]. However, to date the contribution of neither process to the overall mass balance problem has been quantitatively assessed. While energetic W^+ ions are commonly seen in the dayside magnetosheath, there is no evidence for thermal W^+ there [Sergis et al. 2013] or in the upstream region [Thomsen et al. 2007].

Planetary wind. As mentioned above, plasma flows along the night side flanks of the magnetosphere tend to have an outward component, suggesting the likelihood that plasma is lost as a planetary wind down the flanks. An estimate of total mass loss from the tail (excluding plasmoids) [Thomsen et al. 2014a] is within the range of previous estimates of the total mass-loading rate from ionization of water gas from Enceladus.

Magnetosphere Dynamics

Radial transport – centrifugal interchange instability

Magnetospheric plasma motion transverse to the magnetic field, usually called magnetospheric convection, is key to dynamics in any magnetosphere. As discussed in the section entitled

Magnetosphere Composition, Sources, Transport and Losses, such motion in Saturn's magnetosphere is dominated throughout the equatorial region by (partial) co-rotation with the planet. This was widely expected before the Cassini encounter, and although the expectation was not universally held, the basic result was no big surprise.

The surprises are in the details. It is now clear that the dominant source of plasma for Saturn's entire equatorial magnetosphere is the inner icy satellites, in particular, the south-polar geyser plumes of Enceladus orbiting Saturn at L = 3.95, where L is the planet-centered distance normalized to Saturn's equatorial radius, $R_S \approx 60{,}300$ km—see the section entitled Magnetosphere Composition, Sources, Transport and Losses; and Young et al. [2005]. If tiny Enceladus is to dominate the source of Saturnian plasma, and hence its dynamics, there must be a mechanism for transporting this plasma radially from its inner-magnetospheric source to a sink in the outer magnetosphere and ultimately to the downstream solar wind. This transport mechanism is now known to be the centrifugal interchange instability.

A schematic illustration of this process, projected on the equatorial plane, is shown in Figure CAPS-31 [Hill et al. 2005].

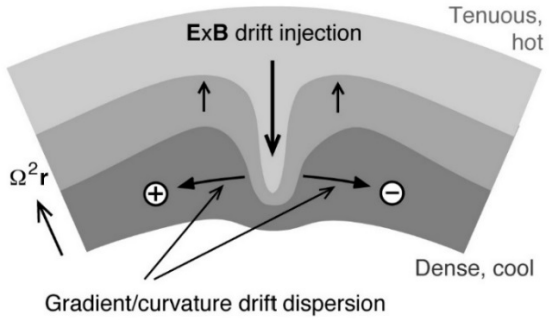

Figure CAPS-31. In the centrifugally driven interchange convection process, flux tubes containing hot but tenuous plasma (*light gray shading*) from an exterior source move inward, toward Saturn, and are replaced by outward moving flux tubes of cooler but denser plasma (*dark gray shading*) moving outward from an interior source.

The centrifugal acceleration Ω^2/r is outward and exceeds Saturn's inward gravitational acceleration beyond L ~2. Outward moving flux tubes release centrifugal potential energy from the system at a rate Ω^2/r per unit mass, and inward moving flux tubes add centrifugal potential energy to the system at the same rate per unit mass. Because of the inward density gradient of the combined plasma distribution (per unit magnetic flux), the combined flux-tube interchange process releases potential energy from the system and is therefore gravitationally unstable. The reverse would be true if the background density gradient (per unit magnetic flux) were reversed. In this sense the interchange motion is centrifugally driven. Flux-tube interchange motions, by definition, involve no net radial transport of magnetic flux.

Hot plasma injections

Figure CAPS-31 also illustrates the azimuthal gradient and curvature drifts of the hot tenuous plasma injected inward by the interchange process, relative to a co-rotating frame of reference. This drift is prograde (eastward) for positive ions and retrograde (westward) for negative ions and electrons. Its speed at a given distance is proportional to particle thermal energy. The injection process thus gives rise to an energy-longitude dispersion signature of the injected plasma, which has been called the smoking gun of interchange convection. This signature was repeatedly observed by CAPS on every Cassini pass through the inner magnetosphere, (L between ~5 and ~12), where the magnetic configuration is well described by an aligned dipole model [Burch et al. 2005; Hill et al. 2005; Young et al. 2005; Chen and Hill 2008; Chen et al. 2010; Rymer et al. 2008, 2009]. An early example of this injection-dispersion signature, appropriate to this off-equatorial orbit, is shown in Figure CAPS-32 from Hill et al. [2005]. In the inner magnetosphere the interchange convection scenario accounts for all key aspects of the morphology and composition results summarized in the section entitled Magnetosphere Composition, Sources, Transport and Losses.

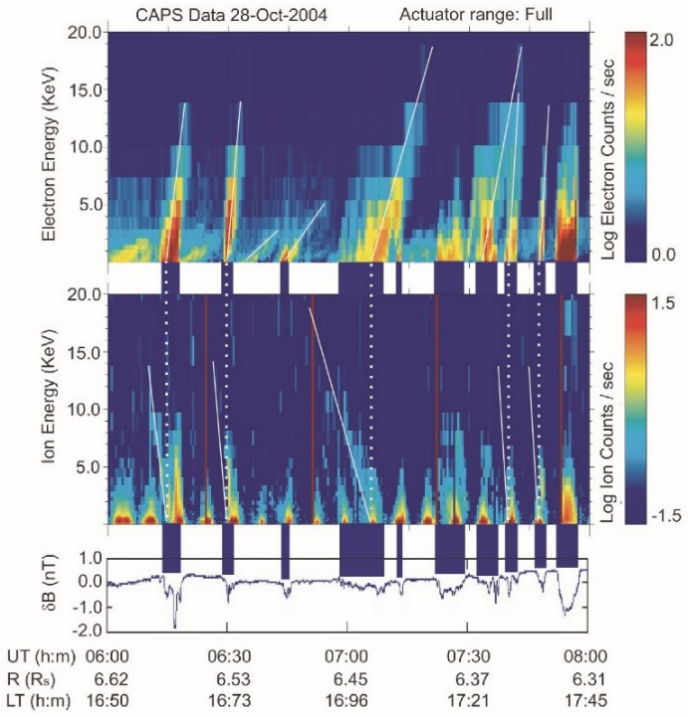

Figure CAPS-32. Energy-longitude dispersion signature of injected plasma. Linear energy-time spectrograms for electrons (*top panel*) and positive ions (*middle panel*) from the CAPS detectors during the second Cassini orbit of Saturn. The *bottom panel* shows simultaneous magnetic-field magnitude perturbations.

One unexpected feature of these observations is that Saturn's inflow channels (containing hot tenuous plasma) are always narrower in longitude than the neighboring outflow channels (containing cooler denser plasma), by a factor ~10 [Chen and Hill 2008; Chen et al. 2010]. All

previous theoretical models of interchange convection had inflow and outflow channels of equal width, because of assumptions made for analytical convenience. Recent numerical simulations using the more flexible Rice Convection Model (RCM), driven by CAPS observational inputs [Liu et al. 2010; Liu and Hill 2012; Hill 2016, 2017; Hill et al. 2018], have clarified the reason for this apparent discrepancy between observation and theory. At Saturn (unlike at Jupiter) the source region for newly injected plasma, both from new ionization and from charge-exchange reactions with ambient neutral molecules, is broadly distributed throughout the radial range in which the resultant interchange radial transport occurs (L between ~5 and ~12).

Co-rotation lag and plasma loading

There are useful and well-established relationships between the local rate of plasma mass or momentum loading (through new ionization, charge exchange, or outward mass transport), on one hand, and the radial variation of the rotational lag behind rigid co-rotation with the planet, on the other. Rates of ionization, charge exchange, and net outward mass transport are difficult if not impossible to measure directly. But the co-rotation lag is straightforward to measure directly if one has access to reliable in situ plasma measurements. If one side of the equation is measurable, it can provide proxy information about the other side of the equation that is not. This method of data analysis has been developed and employed successfully at Jupiter for several decades using Voyager, Galileo, and even Earth-based spectroscopic data, and has now been generalized and employed successfully by the CAPS team.

Tokar et al. [2006] reported surprisingly strong and asymmetric plasma flow perturbations during the distant and highly inclined July 2005 Cassini encounter with Enceladus. The flow measurements are depicted by arrows in Figure CAPS-33, projected onto the equatorial plane. The background flow contours are provided by an analytical model [Pontius and Hill 2006] that is based on earlier Jupiter-Io models, but generalized to account for, among other things, the fact that the Enceladus plasma source is centered, not at Enceladus, but at a position clearly southward of Enceladus, thus anticipating the more-or-less concurrent discovery of the south polar Enceladus plumes. This study also concluded that plasma mass is added to Saturn's magnetosphere at a rate > ~100 kg/s in the near vicinity of Enceladus, a conclusion that was controversial at the time but was subsequently verified by many independent analyses—for example, Chen et al. [2010].

Pontius and Hill [2009] applied a similar analysis, not to the localized plasma loading in the immediate vicinity of Enceladus, but to the much broader region ~3 < L < ~10 where significant co-rotation lag was reported by Wilson et al. [2008, 2009] from their analysis of CAPS data. This study utilized the modeled neutral gas distribution of Johnson et al. [2006b], also based on CAPS results. The red symbols in Figure CAPS-34 [Wilson et al. 2009, Figure 4] show the co-rotation lag as a fraction of the local rigid co-rotation speed. The data-model comparison of Pontius and Hill [2009] concludes that the plasma loading rate in this much larger volume is also > ~100 kg/s, comparable to that in the near vicinity of Enceladus.

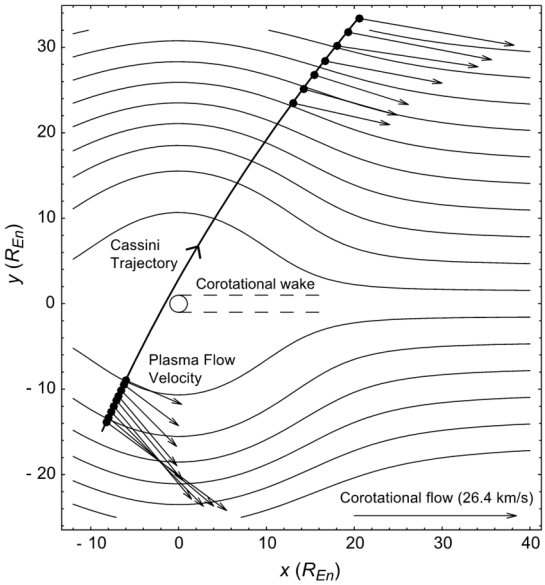

Figure CAPS-33. Strong and asymmetric plasma flow perturbation measurements. Observed plasma flow vectors (arrows), projected onto the equatorial plane, during the July 2005 Cassini encounter with Enceladus, at times (indicated by large dots) when the Cassini orientation was favorable for detection of such flows [Tokar et al. 2006]. The background flow contours are from the theoretical model of Pontius and Hill [2006] as described in the text.

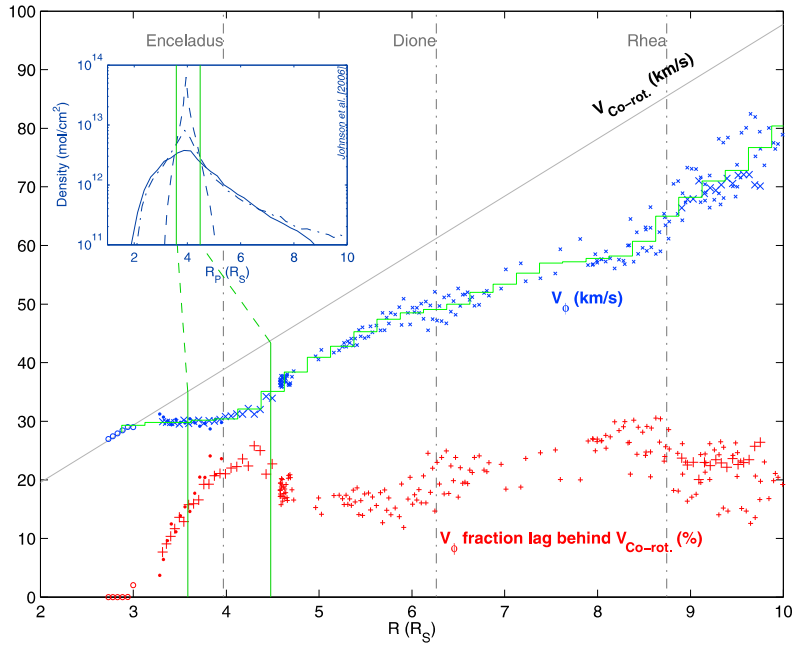

Figure CAPS-34. CAPS plasma flow measurements. Data for L > 5.5 are from forward modeling of thermalized ion velocity moments [Wilson et al. 2008]. Data for L < 5.5 are obtained from analysis of freshly picked-up charge-exchange products under the assumption of gyrotropy. Red symbols at the bottom show azimuthal speeds as a fraction of the local co-rotation speed. Figure from Wilson et al. [2009], Figure 4.

Magnetotail plasmoids and their consequences

Magnetic reconnection in the magnetotail current sheet can produce plasmoids, magnetic flux ropes (or closed magnetic loops) that are disconnected from the planet at one (or both) ends. These structures have been routinely observed in the magnetotails of Earth and Jupiter. Observations at Saturn were limited by orbital geometry because the deep magnetotail passes in 2006 occurred near Saturn's northern winter solstice, when the warped magnetotail current sheet was presumably displaced well northward of Cassini's orbital plane—see Figure CAPS-35. Despite this problem, three plasmoid-like magnetic signatures were identified in the Cassini magnetometer data [Jackman et al. 2007]. Two of these events crossed the current sheet, where ion fluxes were sufficient to permit composition and velocity-moment information to be extracted from CAPS data. These two events were analyzed in detail by Hill et al. [2008]. The most dramatic event occurred on March 4, 2006 at a planet-centered distance of 44 R_S and at 0300 local time (LT). Results are shown in Figure CAPS-36.

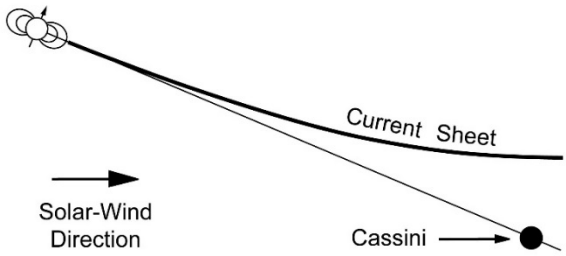

Figure CAPS-35. Orbital geometry during the deep-tail passes of Cassini. Figure from Hill et al. [2008], Figure 1.

Early in this event, before the sharp B_θ reversal near 2300 UT, water-group ions dominated plasma composition, indicating pinching off of a formerly closed flux tube containing plasma from the interior source, as in Vasyliunas-cycle reconnection. At about 23:10 UT the W^+ peak went off-scale above the energy-per-charge range of the CAPS IMS (50 keV), so W^+ velocity moments became unavailable though their flux remained high. The velocity moments (based on H^+ after 23:10) indicate sub-co-rotational azimuthal flow throughout the event and a dramatic tailward acceleration (with V_r increasing up to ~800 km/s) late in the event. Rigid co-rotation at this distance would be 430 km/s in the V_Φ direction.

A particularly interesting feature of this event is that Cassini was in a position to see not only the plasmoid properties observed in situ by CAPS and MAG, but also the plasmoid's earlier initiation closer to Saturn as observed by MIMI in energetic neutral atom (ENA) bursts. The viewing geometry is shown in Figure CAPS-37. The ENAs were hydrogen and oxygen atoms having speeds consistent with covering the distance from source to Cassini (~26.5 R_S) in the allotted time (~25 min). The plasmoid structure itself could also have covered the same distance in the same time interval [Hill et al. 2008].

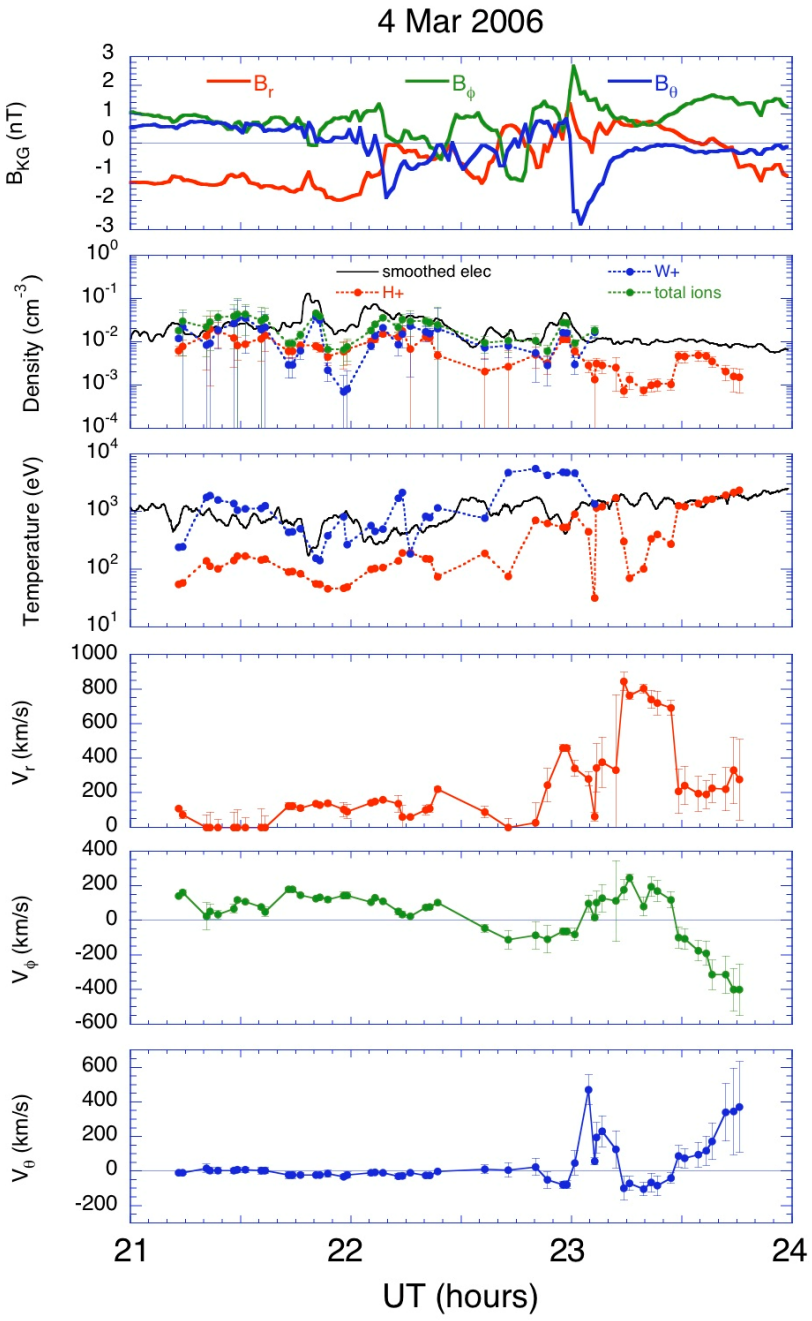

Figure CAPS-36. Magnetic field components and particle velocity moments for the plasmoid encountered by Cassini at 44 R_S near 0300 LT [Hill et al. 2008, Figure 3].

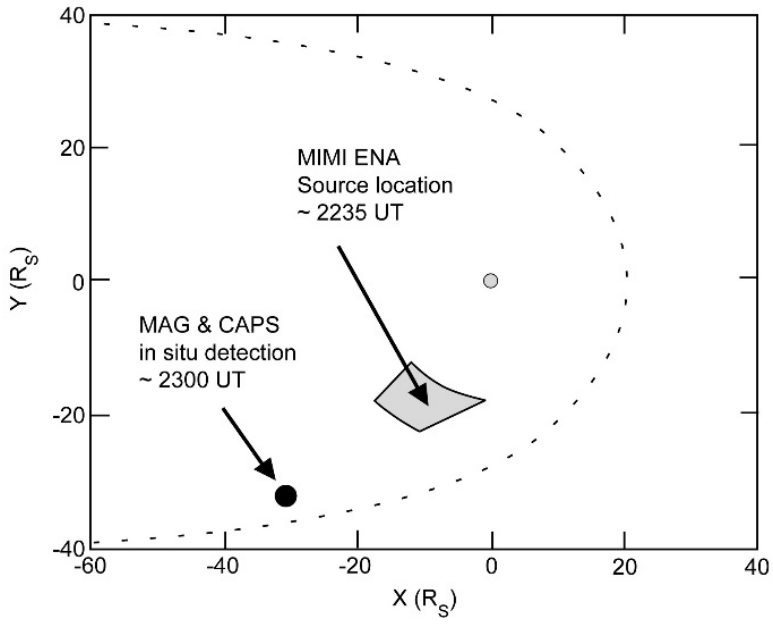

Figure CAPS-37. During the in situ CAPS and MAG plasmoid observations on March 4, 2006 (see Figure CAPS-36 above), Cassini was within the large dot indicated. The ENA bursts observed from the same location ~25 min earlier were deduced to have a source within the quasi-rectangular shaded box. The dashed contour is a cartoon depiction of the typical shape and location of Saturn's magnetopause.

Plasmoid formation provides an escape route for cool W^+ plasma that has accumulated from the interior source region. There remains some controversy as to whether this escape route is adequate to balance the interior source rate, estimated to be roughly 100 kg/s or more. It is plausible, but not yet demonstrated, that an unseen spectrum of smaller but more frequent plasmoids could contribute importantly to the escape rate.

Magnetotail reconnection also provides a fresh source of hot, tenuous plasma to the region planetward of the reconnection site, where it causes a dipolarization signature in the magnetic field. It can also provide seed particles both for the inflow channels of the interchange cells in the inner magnetosphere, as described earlier, and for the intermittent ENA bursts observed by MIMI from the middle and outer magnetosphere, and the associated SKR bursts observed by RPWS from the footprints of the same field lines.

Theoretically, there is a clear distinction between Vasyliunas-cycle reconnection involving the pinching off of formerly closed flux tubes containing cool dense plasma from the inner-magnetosphere source, and the more Earth-like Dungey-cycle reconnection involving the closure of formerly open flux tubes of the magnetotail lobes, containing hotter and more tenuous plasma of magnetosheath origin. The large plasmoid event described above (Figure CAPS-36) is readily explained by the Vasyliunas cycle alone. But two detailed multi-instrument event studies [Thomsen et al. 2015a, 2015b] have also found evidence of both Vasyliunas and Dungey cycles occurring either simultaneously or sequentially.

Thomsen et al. [2015a] examined a high-latitude dawn-side Cassini pass moving from the low-density lobe region into the higher-density closed field-line region. They inferred a stripping of plasma from the outer region of closed magnetic flux tubes as those tubes cross the night side magnetosphere from dusk to dawn, attributable to Vasyliunas-cycle reconnection, together with an interval (or region) of Dungey-cycle reconnection at the high-latitude boundary between open and closed field lines.

Thomsen et al. [2015b] also examined a deep-tail near-equatorial Cassini pass near 37 R_S near midnight LT. They found a prolonged period (~5 hr) of planet-ward plasma-sheet flow attributable to an even more prolonged period of magnetotail compression due to the passage of a recurrent solar-wind structure containing enhanced dynamic pressure. They concluded that Dungey-cycle reconnection takes precedence over Vasyliunas-cycle reconnection when the solar-wind pressure is high.

Bow Shock, Magnetosheath, and Outer Magnetosphere

The Cassini spacecraft crossed Saturn's bow shock for the first time at 09:45 UT on June 27, 2004, at a radial distance of 49.2 R_S from the planet. Clarke et al. [2010] investigated 35 orbits on which the spacecraft crossed Saturn's magnetopause and bow shock during 2004–2007 and concluded that the bow shock and magnetopause oscillate approximately in phase, within a phase uncertainty of about ±25°. The typical amplitude is 1–2 R_S and the period is organized by the phase of the interior magnetic field oscillations, with a period near that of planetary rotation. Saturn's (dayside) bow shocks are predominantly quasi-perpendicular by virtue of the shape of the Parker spiral at 10 AU. Sulaiman et al. [2016], analyzing data between 2004 and 2014, found that Saturn's bow shock, which is principally controlled by the upstream magnetic field strength, exhibits characteristics similar to both terrestrial and astrophysical regimes (Alfven Mach number of order 100). Went et al. [2011] used a semi-empirical model to show that the shock is axisymmetric about the solar wind flow direction.

The Cassini spacecraft crossed the bow shock of Saturn for the first time at 09:45 UT on June 27, 2004, at a radial distance of 49.2 R_S from Saturn.

How stable is the bow shock? Sulaiman et al. [2015] carried out a study of very high Mach number shocks in a parameter space that has been poorly explored previously. They identified re-formation of the shock at 10 AU using in situ magnetic field observations from the MAPS suite of instruments. They found evidence for cyclic re-formation of the shock (Figure CAPS-38) controlled by specular ion reflection occurring on a predicted time scale of ~0.3 τ_C, where τ_C is the ion gyro period. In addition, they showed that the magnetic structure of re-forming shocks at the same M_A, a re-forming shock exhibits stronger magnetic field amplification than a shock that is not re-forming.

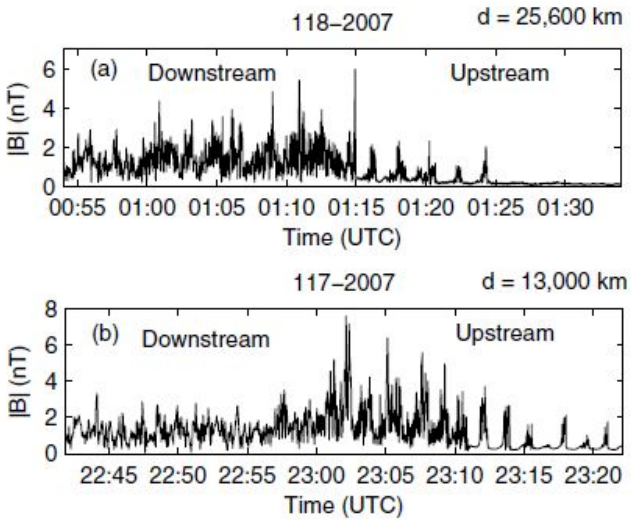

Figure CAPS-38. Magnetic field plots. The panels are two examples of magnetic field plots showing quasi-perpendicular bow shock crossings with re-formation cycles occurring upstream of the shock.

The long-term statistical behavior of the large-scale structure of Saturn's magnetosphere has been investigated by Achilleos et al. [2008]—see also the section entitled Magnetosphere Composition, Sources, Transport and Losses. Statistical techniques established for Jupiter have been applied to the kronian system, employing Cassini magnetometer data and a new empirical model of the shape of the magnetopause based on these data. The resulting distribution of the standoff distance R_{MP} for Saturn, covering a time interval of ~400 days, is well described by a bimodal model—the sum of two normal distributions with different means at ~22 and ~27 planetary radii. Achilleos et al. [2008] also produced a new mathematical model of magnetopause shape. It was noted that the shape of the magnetopause obstacle has an elliptical cross-section with a major (equatorial) axis ~25% larger than its minor (polar) axis. Saturn's bow shock can occasionally reach a high Mach number typical of astrophysical shocks. In this regime Cassini measurements have provided the first in situ evidence for suprathermal electron acceleration under quasi-parallel upstream magnetic conditions [Masters et al. 2016].

Using CAPS and other MAPS data, Sergis et al. [2013] investigated the properties of the magnetosheath. At energies of a few keV the magnetosheath is comprised of shocked solar wind plasma, while at energies above a few keV there is a strong presence of water group ions forming localized structures that are being convected downstream in the plasma flow. Under average magnetic field conditions in the magnetosheath, the kinetic properties of these hot water group ions can enable their escape upstream from the bow shock—see also the section entitled Magnetosphere Composition, Sources, Transport and Losses.

A new magnetosheath data set introduced by Thomsen et al. [2017] is based on a comprehensive survey of intervals in which the observed magnetosheath flow was encompassed within the CAPS plasma analyzers' fields-of-view, and for which the computed numerical moments are accurate. The data extend over eight years from 2004 day 299 to 2012 day 151 and comprise 19,155 measurements of 416 s each. In addition to the plasma ion moments (density, temperature,

and flow velocity), merged values of the plasma electron density and temperature, the energetic particle pressure, and the magnetic field vector are also included in the data set. The magnetosheath population is characterized by ion energies between ~100 eV and ~2 keV and electrons up to about 100 eV. The solar wind is best identified in the electrons, which have energies generally below 10 eV.

The proton-to-electron temperature ratio is very similar to typical values found in Earth's magnetosheath. Approximately 95% of the flows in Saturn's magnetosheath are found to be super-Alfvénic. The proton temperature tracks the predicted solar wind speed well. The clear correspondence between the magnetosheath proton temperature and the predicted solar wind speed suggests that temperature might provide a useful means of monitoring the upstream solar wind flow speed. Although the presence of the magnetosphere obstacle and its influence on the flow certainly affects the overall energy balance, one might nonetheless expect a rough equivalence between the upstream energy per particle and the downstream energy per particle. An analysis of the total magnetosheath energy (defined as magnetosheath bulk flow energy plus thermal energy plus magnetic energy per particle) using CAPS data, compared to the upstream bulk flow energy at several terrestrial bow shock crossings reported by Song et al. [1999], gives ratios ~0.4 to 0.6. This is similar to simulations of the total energy of plasma carried in Saturn's magnetosheath. On average, the solar wind bulk flow energy is ~1.860 ±0.797 times the combined magnetosheath bulk flow energy and proton temperature. Similarly, it is ~1.69 ±0.76 times the total magnetosheath energy.

The large set of magnetosheath electron temperature measurements made by ELS in this dataset, combined with the statistically-based estimates of the upstream flow speed based on IMS data, reveals how the magnetosheath temperature is related to the solar wind bulk flow energy, in a statistical sense. The median ratio of 3.8% is consistent with the findings of Masters et al. [2011a]. Accounting for other factors, the typical fraction of electron heating is probably closer to 4 than 3.5, which is significantly lower than the typical value for lower-Mach number shocks at Earth.

The rotation period of Saturn's magnetosphere was found to vary with time, and changing periodicities were identified in magnetic fields, radio emissions, and charged particles [Andrews et al. 2008, 2011, 2012; Provan et al. 2009, 2011, 2013, 2014]. The motion of the magnetodisk is very much affected by the oscillating magnetic field of Saturn, which is different in the two hemispheres. These planetary period oscillations strongly influence the magnetic and plasma properties of the outer magnetosphere [Andrews et al. 2010; Provan et al. 2012] as well as the density of thermal ions [Nemeth et al. 2011; Szego et al. 2011]. The thermal plasma sheet properties are different for the different ion species. The proton sheet is smoothly modulated by the flapping of the magnetodisk while heavy ions form a narrow sheet surrounding the magnetic equator—see also the section entitled Magnetosphere Composition, Sources, Transport and Losses. The periodicity of the observed heavy-ion rich events was found to be close to the SKR period of the southern hemisphere.

Szego et al. [2012] observed that the ion density moments derived by Thomsen et al. [2010] exhibit peaks around zero-crossings of the magnetic field. The proton peaks are broader while the

heavy ion peaks are sharper. They found that the positions of these peaks can be explained by the simple structural model of Arridge et al. [2011a]. Szego et al. [2013] modified this simple structural model to include the dual periodicity of the magnetic field and found an even better agreement for the positions of the ion peaks.

Using numerical ion moments, Nemeth et al. [2015] investigated the azimuthal flow velocities measured by CAPS along with their periodicities. They observed a significant positive correlation between the azimuthal plasma speed and the plasma density, while both are anti-correlated with the magnitude of the radial component of the magnetic field. They found that the dense plasma near the magnetic equator rotates around the planet at high speed, but the dilute plasma of higher latitudes is rotating significantly slower.

Nemeth et al. [2016] analyzed the quasi-periodic variation of several plasma parameters. The variation of the magnetic field was used to recover the position of the magnetodisk, and the position information was further used to model the variation of the density and azimuthal velocity moments of the thermal ions. This simple technique provides very good fits for all three parameters simultaneously.

Synergistic Science

Many plasma observations during the mission featured data collected simultaneously by most, if not all, of the particles and fields instruments (CAPS, INMS, MAG, MIMI, and RPWS), collectively referred to as MAPS. Prior to the Cassini mission it was understood from the experience of Voyager at Saturn and investigations of other magnetospheres, as well as space plasma physics in general, that many of Cassini's science objectives could only be met by synergistic measurements made by the MAPS instrument suite. Many details of synergistic science emerging from these measurements are discussed in the section entitled Detailed Magnetosphere Science Results and can easily be judged by the multitude of references cited in this volume. Below is a short list of the most important contributions made by CAPS to synergistic science.

- CAPS and INMS collaborations to elucidate the composition of neutral and charged particles at Titan and Enceladus. This is undoubtedly one of the most productive examples of synergistic science.
- CAPS, MAG and MIMI collaborations on the acceleration and transport of plasma throughout the magnetosphere.
- CAPS and MAG studies of periodic oscillations of the magnetodisk and plasma sheet, as well as investigations of the properties of shocks at Jupiter and Saturn.
- CAPS data inputs to the Rice Convection Model which was then used to simulate plasma convection throughout the magnetosphere.
- CAPS, RPWS, INMS, and CDA—Investigations of the makeup of charged ions, nano-grains and dust in the Enceladus plume.

Open Questions

Although CAPS operated for only the first eight years of the 13-year Cassini mission (2004 through 2012), as might be expected it left behind numerous open questions. Some of the most significant remaining questions concern the nature of the chemistry and formation of heavy negative ions in the atmosphere of Titan and the plumes of Enceladus. Other issues include the source, acceleration, transport and loss of cold, heavy water group ions, and finally, the role of the magnetodisk in controlling plasma sheet dynamics and generation of plasmoids.

Titan and Titan-magnetosphere interactions

Titan's atmosphere and its interaction with the magnetosphere are so complex that there remain many issues to address. Foremost among them are:

1. Search for methane ions in Saturn's outer magnetosphere which should be detectable if the high outward fluxes of methane estimated by Yelle et al. [2008] and Strobel [2008] are correct.

2. Continue IMS composition measurements of ionospheric outflows initiated by Sittler et al. [2010], and later by Woodson et al. [2015]. Look for evidence of minor species such as N^+, H_2O^+, NH_4^+ and more specific identifications of the mass 12–17 amu/q ions and mass 28–30 amu/q ions.

3. Perform more theoretical modeling of the ion composition of these outflows.

4. The Desai et al. [2017] analysis of negative ions measured by ELS showed that negative long carbon chains are forming in Titan's ionosphere, and that doubly-charged fullerenes could explain the main heavy negative ion peak at ~400 amu/q at lower altitudes. More work is required in this area including studies of the conversion of oxygenated fullerenes on Titan's surface, and on the bottom of its hydrocarbon lakes, into exobiological molecules such as amino acids by galactic cosmic rays.

5. Clearly studies of the kinetic interactions between Titan's upper atmosphere and upstream flow (light or heavy ion dominated) need to be continued, but such analysis will require the continued development of hybrid codes so the observed interaction details can be fully understood.

6. Detailed analysis of pickup ions and ionospheric outflows for Titan flybys at different heights still needs to be carried out, for example using ELS data as Coates et al. [2015] have done.

7. In order to characterize neutral energy distributions in the exosphere region, continued development of rarefied gas dynamics theory is needed in order to

understand the energy deposited by pickup ions and the population of hot recoil atoms and molecules that result.

8. Further calibration of the IMS prototype using molecular ions such as HCN^+, and NO^+ is needed in order to get C/N and N/O efficiency ratios. Calibration measurements of NH_4^+ would also be useful.

9. INMS data indicates that Titan's upper atmosphere is highly variable on timescales less than a Titan day [Cui et al. 2009]. However, the dynamics driving the variability are not well understood. Current ideas include gravity waves propagating from the lower atmosphere [Snowden and Yelle 2014], and/or magnetospheric energy inputs [Sillanpaa and Johnson 2015; Johnson et al. 2016; Jiang et al. 2017]. CAPS measurements of plasma energy spectra can provide constraints for numerical simulations of the effect that precipitation has on the thermal structure and escape of Titan's upper atmosphere. Understanding the physics of escape in Titan's current atmospheric environment will provide insight on how Titan and other bodies have evolved over their lifetimes.

Enceladus, rings, and the icy satellites

1. How are heavy negative ions formed in the plume at Enceladus, and what is their contribution to nano-grain formation?

2. How are ions such as O_2^+ which originate over and near the rings distributed throughout the magnetosphere?

3. What happens to the charged nano-grains? Do they contribute to a dusty plasma near Enceladus orbit, or are they eroded by local energetic plasmas?

4. What processes remove material from icy satellite surfaces to create their exospheres, and are they steady-state?

Magnetosphere structure and dynamics

The CAPS data set is exceedingly rich and has enabled great progress in identifying and understanding the structure and behavior of Saturn's magnetosphere. Further understanding will almost certainly be derived from the data in the future. Some of the findings described in this report have been clear and definitive; others need additional confirmation, either by inclusion of more data or by other means such as modeling. The interpretation of many of the findings need more rigorous examination or development. (Note: Some open questions identified in the sections entitled Magnetosphere Composition, Sources, Transport and Losses and Magnetosphere Dynamics dealing with magnetospheric structure and dynamics and seasonal variations of Saturn's magnetosphere appear in the book, Saturn in the 21st Century, Cambridge, 2019).

1. Are the growth of the Kelvin-Helmholtz instability and magnetic reconnection coupled?

2. What is the dominant mode of solar wind interaction with the magnetosphere, the viscous interaction or the large-scale reconnection interaction?

3. How is plasma transported outward, and magnetic flux returned, in the region between ~12 and ~20 to 25 R_S?

4. Where in the Saturnian system does Vasyliunas-type reconnection take place, and where does Dungey-type reconnection take place? Is there a region in Saturn's magnetosphere where one or the other dominates?

5. Where and how does the magnetosphere unload its cold, dense plasma?

6. How does the solar wind drive magnetospheric dynamics at Saturn? Is solar wind dynamic pressure the primary influence?

7. What causes the inner magnetospheric electric field that drives the noon-midnight asymmetry in plasma temperature, plasma density, energetic particle intensity, etc.?

8. What other solar cycle effects can be found in Saturn's magnetosphere?

9. How important is Titan as a source of magnetospheric H_2^+? What is the fraction of N^+ contributed by Titan?

10. What is the relationship between large-scale, tail-reconnection-driven injections and small-scale interchange injections?

11. What determines the scale size and inflow speed of interchange injections? What determines the apparently variable rate and depth of such injections?

12. What is the nature of the very low density layer often seen in lower energy electrons between the plasma sheet and the lobes? Is it related to ionospheric outflow reported by Felici et al. [2016]?

Cruise Science Results

CAPS took advantage of two gravity-assist flybys to gather data on the magnetospheres of Earth and Jupiter and, particularly at Earth, to perform calibration measurements and analysis. During those two flybys CAPS contributed measurements never made before—at Earth with a high-speed traverse that gave a freeze-frame picture of the magnetosphere in addition to real-time observations of the substorm cycle in progress [Khan et al. 2001]—and at Jupiter by establishing characteristics of its bow shock and magnetosheath.

Solar Wind and Heliosphere

During cruise, the CAPS investigation made its first major discovery with the in situ observation of interstellar pickup ions beyond the orbit of Jupiter …

On October 15, 1997, the Cassini-Huygens spacecraft was launched on an almost seven-year journey to Saturn. On its way, Cassini-Huygens performed gravity-assist maneuvers at Venus (on April 25, 1998 and June 24, 1999), Earth (August 17, 1999), and before arriving at Jupiter (technically) on December 29, 2000. The Jupiter flyby was followed by a ~3-month long exploration down the dusk flank of the magnetosphere. CAPS then operated at programmed intervals between 6.4 and 8.2 AU searching for interstellar pickup ions, before arriving at Saturn on July 1, 2004. During much of the cruise before Jupiter and for two years afterwards CAPS was in hibernation as were other MAPS instruments. The Cruise phase was partly devoted to commissioning the instrument, but also to making measurements in the solar wind that led to new science.

Interstellar pickup ions. During cruise, the CAPS investigation made its first major discovery with in situ observations of interstellar pickup ions beyond the orbit of Jupiter. [Gloeckler et al. [1998] had previously measured pickup ions inside Jupiter's orbit using the Solar Wind Ion Composition Spectrometer (SWICS) instrument onboard Ulysses. This was the first direct detection of mass-resolved interstellar pickup ions. It confirmed the existence of helium focusing at these distances caused by the solar gravitational field (Figure CAPS-39). CAPS also made the first direct, in situ, measurements of a large shadow in the interstellar atomic hydrogen population downstream from the Sun caused by its motion through the interstellar medium [McComas et al. 2004]. The shape of the distribution function of He^{+} as a function of energy was characteristic of a pickup distribution with a flat top and cut off at about four times of the solar wind energy.

Saturn's aurora. Geomagnetic storms and associated auroral activity at Earth are tied to the interaction of the disturbed solar wind with the magnetosphere. Saturn's magnetosphere is dominated by co-rotating plasma out to large distances from the planet, and it is unclear to what extent the solar wind plays a role in high latitude phenomena such as the aurora. Crary et al. [2005] combined Hubble Space Telescope (HST) images of Saturn's aurora taken over one month in 2004, with solar wind data from IBS taken while Cassini was ~3 × 10^7 km (~500 R_S) upstream from Saturn, to show that Saturn's aurora responds strongly to changes in solar wind conditions. Auroral power was best correlated with solar wind dynamic pressure (which is similar to that found at Earth) rather than the direction of the interplanetary field. This is a finding apparently unique to Saturn.

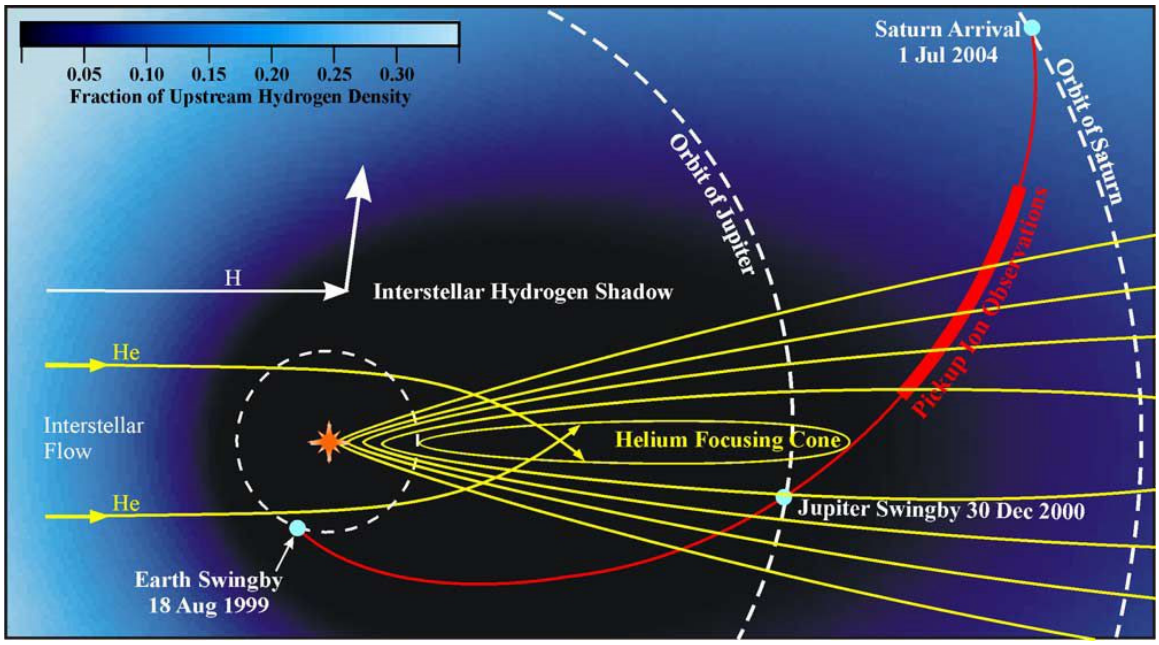

Figure CAPS-39. Schematic diagram of Cassini's trajectory between Earth swing-by and arrival at Saturn. Pickup ion measurements were made between 6.4 and 8.2 AU (heavy line) as Cassini emerged from the down-stream direction. Simulation results show: 1) the gravitational focusing of interstellar He in contours of 5/3, 2, 7/3, 8/3, and 3 times the upstream He density; and 2) the color-coded H density as a fraction of the interstellar value. The dark region downstream from the Sun represents the interstellar hydrogen shadow. Figure from McComas et al. [2004].

Venus

CAPS was not operating during the Venus encounters.

Earth

Earth's gravity-assist encounter on August 18, 1999, was the fastest traversal of Earth's magnetosphere to date. It was effectively a freeze-frame picture of the magnetosphere and an important chance to sample phenomena and boundaries that could later be compared with Saturn's. Inter-comparison of planetary magnetospheres, including that of Jupiter, was a critical, but usually overlooked, feature of the Cassini mission. Most of the following discussion is a condensed version of the definitive study by Rymer [2004] and Rymer [2001].

The spacecraft trajectory allowed CAPS, and particularly ELS, to make measurements of all large structures within the magnetosphere. Since Earth's magnetosphere is a well-known object, the flyby was also an excellent opportunity to calibrate CAPS sensors, particularly ELS, which is subject to spacecraft-plasma interactions that obscure part of its FOV. Figure CAPS-40 shows the Cassini trajectory through the magnetosphere.

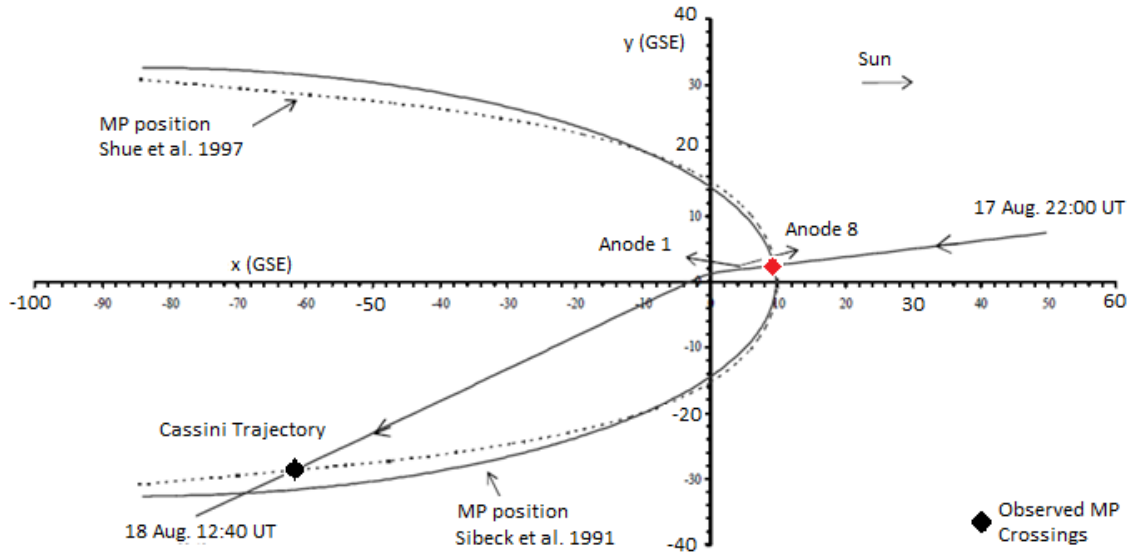

Figure CAPS-40. The Cassini trajectory through the magnetosphere in the x-y Geocentric Solar Ecliptic (GSE) co-ordinate plane showing a model for expected magnetopause shape and position based on Sibeck et al. [1991] and Shue et al. [1997] together with the positions of magnetopause crossings observed by ELS.

During the encounter ELS collected almost ten hours of solar wind data upstream of Earth, and almost nine hours inside the magnetosphere. During the pass ELS sampled electrons in the solar wind, bow shock, magnetosheath, magnetopause, radiation belts, an eclipse, the plasmasphere, plasma sheet, and lobes, and made several crossings of the tail magnetopause. Although this was a period of enhanced solar activity, results were mainly consistent with previous observations of various parts of the magnetosphere with a few exceptions. In addition, two substorms were taking place and there was evidence for low-energy field-aligned electron beams in the plasma sheet [Khan et al. 2001].

A spectacular energy-time spectrograph from ELS covering the entire pass and magnetosphere structures (Figure CAPS-41) can be used to briefly discuss magnetosphere features.

Data taken in the solar wind demonstrated ELS response to photoelectrons down to 0.5 eV, and solar wind electrons up to ~110 eV. Cassini then crossed the very sharp bow shock into the magnetosheath, jumping from solar wind conditions (energy ~10 eV) to the magnetosheath (~52 eV). The radial standoff distance of the bow shock was measured at 15.18 R_E while the magnetopause was at 9.88 R_E, a ratio of 1.55, in good agreement with theoretical predictions of 1.53 [Rymer 2004].

Inside the magnetosheath the core electron population was heated to between 20 eV and 110 eV. The photoelectron flux increased while the energy dropped, which is typical of spacecraft charge becoming more positive. The shift in spacecraft potential was typical of what would be seen

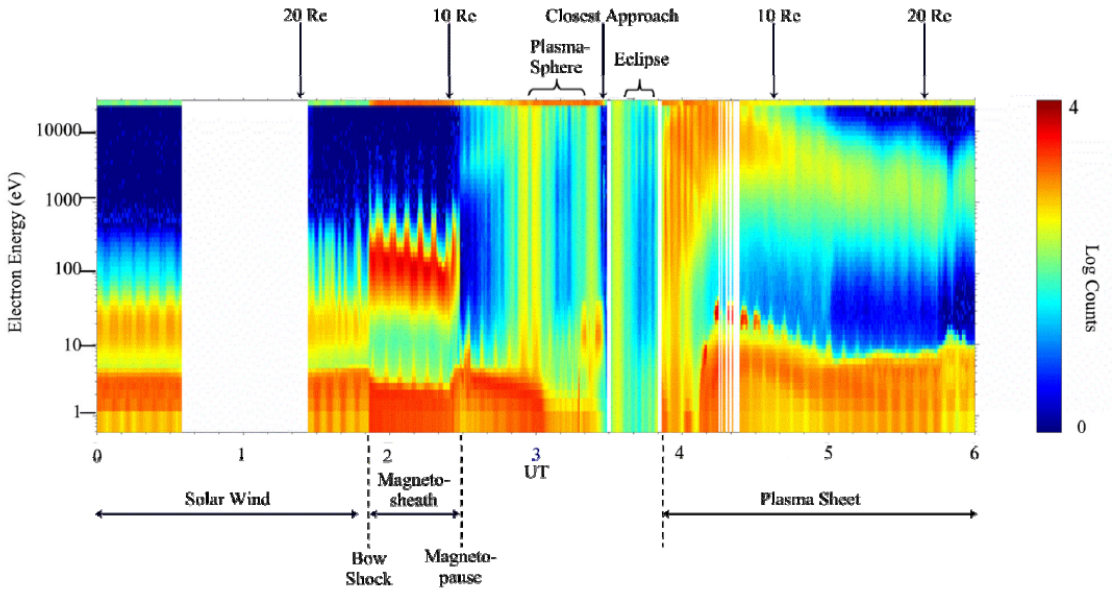

Figure CAPS-41. Six hour energy versus time spectrogram of ELS data from 0000–0600 UT August 18, 1999, for one central anode (out of eight). Counts per accumulation interval (23.4 ms) are indicated by the color scale. Modulation visible in the spectrogram is caused by actuator sweep cycles lasting four minutes.

later at Saturn. Thickness of the magnetopause boundary appears to be rather sharp (956 ±32 km) but its speed past the spacecraft position has an effect on the measurement and is unknown. The LLBL (an appendage of the magnetosheath electron population) is an important feature also seen at Saturn (see the section entitled Bow Shock, Magnetosheath, and Outer Magnetosphere). It carries a mix of both magnetosheath and magnetosphere plasmas and is an important loss process in both magnetospheres.

Once inside the magnetosphere at ~2:30 UT at a distance of 9.38 R_E, Cassini encountered the plasmapause, another feature also seen regularly at Saturn [Young et al. 2005]. The spectrum shows the plasma temperature dropping, which is characteristic of the response expected in the relatively cold plasma of the plasmasphere. Just prior to the encounter Cassini passed through the trapped radiation belts, confirming that shielding of ELS and the other CAPS sensors is effective.

Following the geometric encounter at 03:28 UT, Cassini entered an eclipse period, and then entered the plasma sheet just before local midnight. Electron energies within the plasmapause extended from ~100 eV (identified as accelerated photoelectrons), to above the ELS energy rage of 26 keV. The latter is identified as the plasma sheet distribution calculated to have a density of 0.2 cm^{-3} and a temperature of 2.4 keV about as expected and in agreement with values found with other measurements—for example, Lui et al. [1987].

Starting at 07:27 UT at 36.7 R_E Cassini crossed into and then out of (07:35 UT, 37.9 R_E) the magnetosphere lobe region [Abel et al. 2001]. Finally, at ~6000 R_E downstream from Earth and 12:00 to 22:00 UT, about where the extended magnetotail might be expected under the then current

solar wind conditions, data from several MAPS instruments suggested an encounter with the extended magnetotail. Unfortunately, the measurements were all at the extreme limits of detection and the issue was never resolved [Lagg et al. 2001].

Jupiter

Cassini carried out a gravity assist maneuver at Jupiter on December 30, 2000 at 10:05 UT. The closest approach brought Cassini to within about 9.7 million km of Jupiter's cloud tops. The science it made possible was an additional bonus, more so because Cassini had much superior instrumentation compared to that that of the previous two Voyagers, Ulysses and Galileo missions. The Galileo probe was still active during the flyby (Figure CAPS-42) and joint MAPS measurements provided a chance to study the dynamic effects of the solar wind perturbations on the global configuration of the Jovian magnetosphere [Joy et al. 2002]. The dual Cassini/Galileo spacecraft measurements by MAPS showed clearly that magnetospheric particles leak directly into the interplanetary medium from the closed magnetosphere and are the source for upstream particle events [Krupp 2002].

Cassini made at least five bow shock crossings, one at ~1929 LT and four more between 2100 and 2130 LT on DOY 21. During the flyby, shock activity was high and variable making a moving target for Cassini instruments. Cassini found that the shock is enormous, extending at least 700 R_J down the flank.

All three CAPS sensors were used to identify shock conditions and the times at which Cassini crossed into and out of it—see Szego et al. [2003] for a full description of shock studies based on all Cassini observations. By combining RPWS identification of Langmuir waves and IBS energy spectra, the upstream density could be measured at 0.5 to 1 cm^{-3} while at the same time ELS provided a measure of electron temperature at 2.6 eV. The data allowed the team to solve the Rankine-Hugoniot relations for transitions between the upstream and downstream conditions, deriving plasma density ratios of 2.74, and a downstream ion bulk energy of ~360 eV. The calculated downstream electron bulk temperature prediction was ~44 eV whereas ELS data gave ~11 eV and IMS ~24 eV, in decent agreement with the total energy jump predicted by theory.

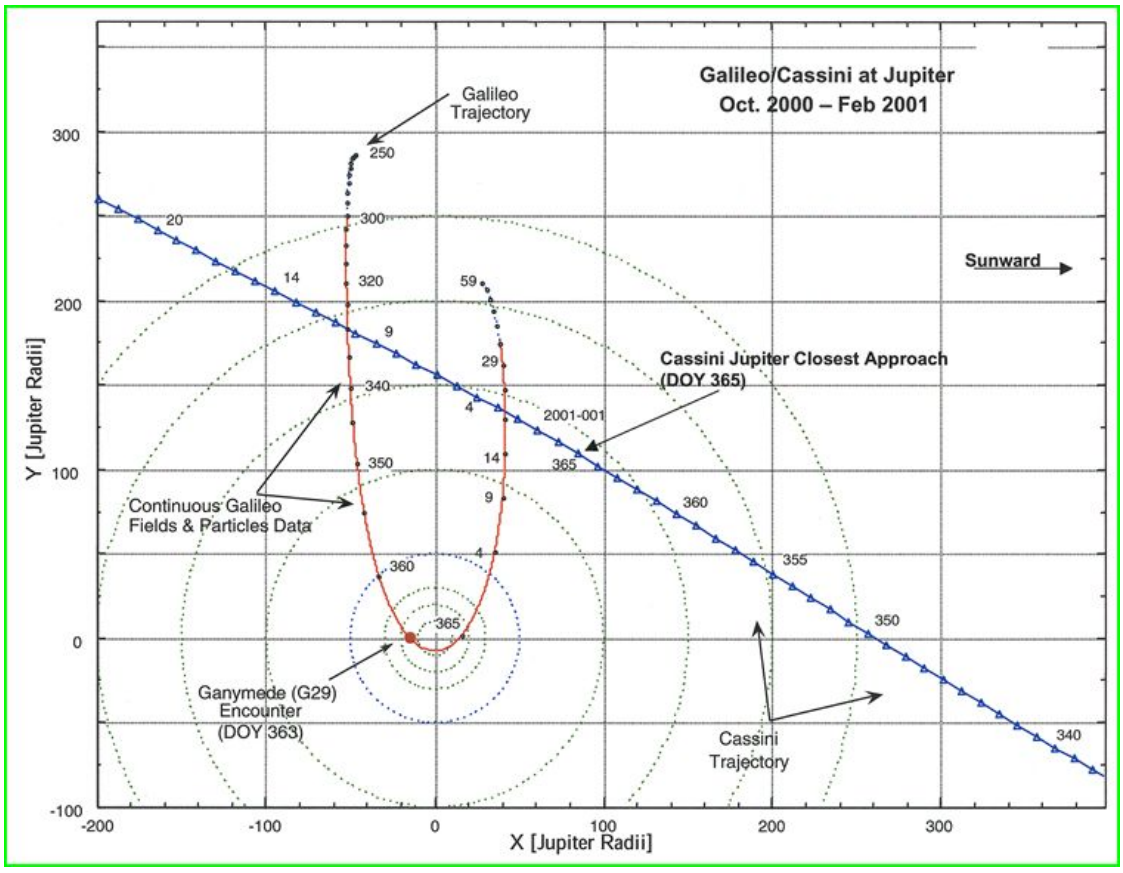

Figure CAPS-42. The orbits of Galileo and Cassini at Jupiter.

IBS energy-time spectrograms were used to easily identify shock crossings far down the flank of the magnetosphere. Figure CAPS-43 is one example of four that were observed at 576, 618, 744, and 770 R_J [Szego et al. 2003].

Using primarily IBS and ELS data in addition to MAG and RPWS, Bebesi et al. [2010] were able to investigate features of the downstream Jovian shock and magnetosheath out to ~700 R_J; a region not previously visited by any other spacecraft. As might be expected, the shock transition layer was broad and turbulent at that distance, but the transits were always easily observed using IBS data.

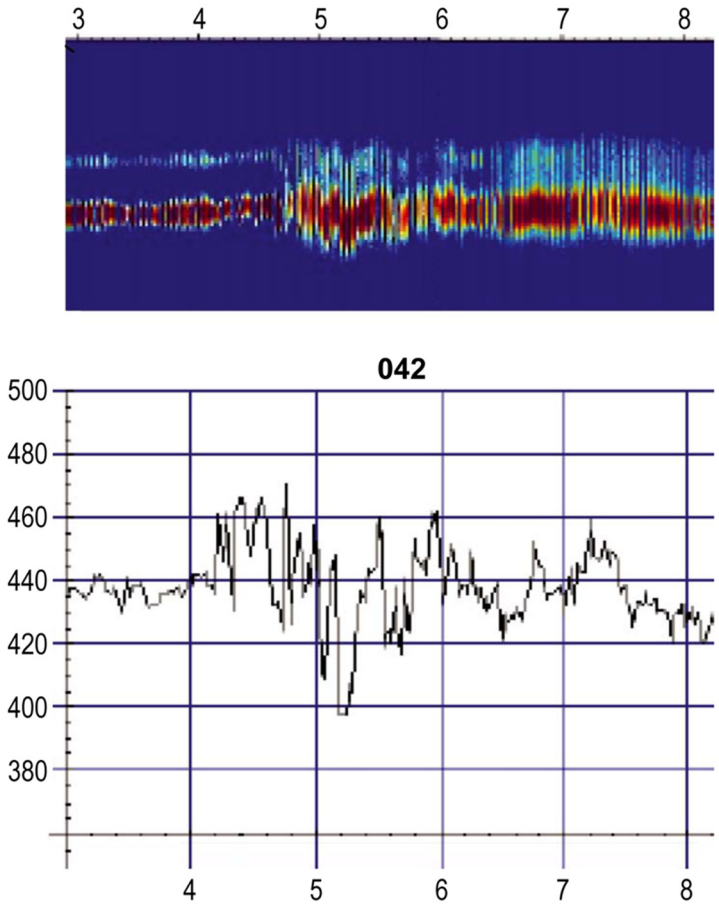

Figure CAPS-43. IBS data taken on DOY 042, 2000, 0300 to 0900 UT along the flanks of the Jovian magnetosphere. The velocity jump across the shock shows up as a jump in the velocity measured by IBS beginning at approximately 0420 UT. The most apparent feature is at ~4:40 UT when Cassini is inside the sheath and density and temperature both increase.

ACRONYMS

Note: For a complete list of Acronyms, refer to Cassini Acronyms – Attachment A.

ACT	actuator
amu	atomic mass unit
AO	Announcement of Opportunity
au	astronomical unit
C/A	closest approach
CAPS	Cassini Plasma Spectrometer
CSM	Cassini Solstice Mission
DPU	data processing unit
DSMC	Direct Simulation Monte Carlo
ELS	Electron Spectrometer
ENA	energetic neutral atom
ESA	electrostatic energy analyzer
eV	electron volt
FOV	field-of-view
GSE	Geocentric Solar Ecliptic
HST	Hubble Space Telescope
IBS	Ion Beam Spectrometer
IMS	Ion Mass Spectrometer
INMS	Ion and Neutral Mass Spectrometer
IR	Independent Review
keV	kiloelectron volt
kg	kilograms
km	kilometer
LEF	linear electric field
LLBL	low-latitude boundary layer
LP	Langmuir Probe
LT	local time
MAG	Magnetometer
MAPS	Magnetospheres and Plasma Science
MHD	magneto-hydrodynamic
MIMI	Magnetospheric Imaging Instrument
MLI	multi-layer insulation
NESC	NASA Engineering and Safety Center
NESC	National Electrical Safety Code
RCM	Rice Convection Model
RPWS	Radio and Plasma Wave Science
R_S	Saturn radii

s	seconds
SKR	Saturn Kilometric Radiation
SOI	Saturn Orbit Insertion
ST	straight through
SWICS	Solar Wind Ion Composition Spectrometer
TM	Traceability Matrix
TOF	time-of-flight
UT	universal time
UV	ultraviolet
UVIS	Ultraviolet Imaging Spectrograph

REFERENCES

Disclaimer: The partial list of references below correspond with in-text references indicated in this report. For all other Cassini references, refer to Attachment B – References & Bibliographies; Attachment C – Cassini Science Bibliographies; the sections entitled References contributed by individual Cassini instrument and discipline teams located in Volume 1 Sections 3.1 and 3.2 Science Results; and other resources outside of the Cassini Final Mission Report.

Abel, G. A., A. J. Coates, A. M. Rymer, D. R. Linder, M. F. Thomsen, D. T. Young, M. K. Dougherty, (2001), Cassini Plasma Spectrometer observations of bidirectional lobe electrons during the Earth flyby, August 18, 1999, Journal of Geophysical Research, 106(A12), 30199–30208, doi: 10.1029/2001JA900076.

Achilleos, N., C. S. Arridge, C. Bertucci, C. M. Jackman, M. K. Dougherty, K. K. Khurana, C. T. Russell, (2008), Large-scale dynamics of Saturn's magnetopause: Observations by Cassini, Journal of Geophysical Research, 113, A11209, doi: 10.1029/2008JA013265.

Ågren, K., N. J. T. Edberg, J.-E. Wahlund, (2012), Detection of negative ions in the deep ionosphere of Titan during the Cassini T70 flyby, Geophysical Research Letters, 39, L10201.

Ali, A., E. C. Sittler Jr., D. Chornay, B. R. Rowe, C. Puzzarini, (2013), Cyclopropenyl cation – the simplest Huckel's aromatic molecule – and its cyclic methyl derivatives in Titan's upper atmosphere, Planetary and Space Science, 109, 46.

André, N., A. M. Persoon, J. Goldstein, J. L. Burch, G. R. Lewis, A. M. Rymer, A. J. Coates, W. S. Kurth, E. C. Sittler Jr., M. F. Thomsen, M. K. Dougherty, D. A. Gurnett, D. T. Young, (2007), Magnetic signatures of plasma-depleted flux tubes in the Saturnian inner magnetosphere, Geophysical Research Letters, 2007GL030374R, doi: 10.1029/2007GL030374.

Andrews, D. J., S. W. H. Cowley, M. K. Dougherty, et al., (2012), Planetary period oscillations in Saturn's magnetosphere: Evolution of magnetic oscillation properties from southern summer to post-equinox, Journal of Geophysical Research, 117, p. A04224, doi: 10.1029/2011JA017444.

Andrews, D. J., B. Cecconi, S. W. H. Cowley, et al., (2011), Planetary period oscillations in Saturn's magnetosphere: Evidence in magnetic field phase data for rotational modulation of Saturn kilometric radiation emissions, Journal of Geophysical Research, 116, p. A09206, doi: 10.1029/2011JA016636.

Andrews, D. J., S. W. H. Cowley, M. K. Dougherty, G. Provan, (2010), Magnetic field oscillations near the planetary period in Saturn's equatorial magnetosphere: Variation of amplitude and phase with radial distance and local time, Journal of Geophysical Research, 115, A04212, doi: 10.1029/2009JA014729.

Andrews, D. J., E. J. Bunce, S. W. H. Cowley, et al., (2008), Planetary period oscillations in Saturn's magnetosphere: Phase relation of equatorial magnetic field oscillations and SKR modulation, Journal of Geophysical Research, 113, p. A09205, doi: 10.1029/2007JA012937.

Andriopoulou, M., E. Roussos, N. Krupp, C. Paranicas, M. Thomsen, S. Krimigis, M. K. Dougherty, K.-H. Glassmeier, (2014), Spatial and temporal dependence of the convective electric field in Saturn's inner magnetosphere, Icarus, 229, 57.

Andriopoulou, M., E. Roussos, N. Krupp, C. Paranicas, et al., (2012), A noon-to-midnight electric field and nightside dynamics in Saturn's inner magnetosphere, using microsignature observations, Icarus, 220, 503, doi: 10.1016/j.icarus.2012.05.010.

Arridge, C. S., J. M. Jasinski, N. Achilleos, Y. V. Bogdanova, et al., (2016), Cassini observations of Saturn's southern polar cusp, Journal of Geophysical Research, 121, 3006–3030, doi: 10.1002/2015JA021957.

Arridge, C. S., J. Eastwood, C. Jackman, G. K. Poh, J. Slavin, M. F. Thomsen, N. André, X. Jia, A. Kidder, L. Lamy, A. Radioti, N. Sergis, M. Volwerk, A. Walsh, P. Zarka, A. Coates, M. Dougherty, (2015), Cassini in situ observations of long duration magnetic reconnection in Saturn's magnetotail, Nature Physics, doi: 10.1038/nphys3565.

Arridge, C. S., N. Andrew, K. K. Khurana, C. T. Russell, S. W. H. Cowley, G. Provan, et al., (2011a), Periodic motion of Saturn's nightside plasma sheet, Journal of Geophysical Research, 116, 11205, doi: 10.1029/2011JA016827.

Arridge, C. S., N. André, H. J. McAndrews, E. J. Bunce, M. H. Burger, K. C. Hansen, H.-W. Hsu, R. E. Johnson, G. H. Jones, S. Kempf, K. K. Khurana, N. Krupp, W. S. Kurth, J. S. Leisner, C. Paranicas, E. Roussos, C. T. Russell, P. Schippers, E. C. Sittler, H. T. Smith, M. F. Thomsen, M. K . Dougherty, (2011b), Mapping magnetospheric equatorial regions at Saturn from Cassini prime mission observations, Space Science Review, 164, 1, doi: 10.1007/s11214-011-9850-4.

Arridge, C. S., C. T. Russell, K. K. Khurana, N. Achilleos, S. W. H. Cowley, M. K. Dougherty, E. J. Bunce, (2008), Saturn's magnetodisc current sheet, Journal of Geophysical Research, 113, A04214, doi: 10.1029/2007JA012540.

Arridge, C. S., C. T. Russell, K. K. Khurana, N. Achilleos, N. André, A. M. Rymer, M. K. Dougherty, A. J. Coates, (2007), Mass of Saturn's magnetodisc: Cassini observations, Geophysical Research Letters, vol 34, CiteID L09108, doi: 10.1029/2006GL028921.

Bebesi, Z., K. Szego, A. Balogh, G. Erdos, M. K. Dougherty, D. T. Young, (2010), Slow-mode shock candidates in the Jovian magnetosheath, Planetary and Space Science, 58, pp. 807–813.

Bell, J. M., J. H. Waite, B. A. Magee, K. E. Mandt, J. Westlake, (2009), Simulating the 3-D structure of Titan's upper atmosphere, American Geophysical Union (AGU), Spring Meeting 2009, abstract P11A-04.

Bouhram, M., R. E. Johnson, J.-J. Berthelier, J.-M. Illiano, R. L. Tokar, D. T. Young, F. J. Crary, (2006), A test-particle model of the atmosphere/ionosphere system of Saturn's main rings, Geophysical Research Letters, 33, L05106, doi: 10.1029/2005GL025011.

Brown, W.L., W. M. Augustyniak, E. Simmons, K. J. Marcantonio, L. J. Lanzerotti, R. E. Johnson, J. W. Boring, C. T. Reimann, G. Foti, V. Pirronello, (1982), Erosion and molecule formation in

condensed gas films by electronic energy loss of fast ions, Nuclear Instruments and Methods in Physics Research, vol. 198, issue 1 pp. 1–8, doi: 10.1016/0167-5087(82)90043-6.

Brünken, S., H. Gupta, C. A. Gottlieb, M. C. McCarthy, P. Thaddeus, (2007), Detection of the carbon chain negative ion C_8H^- in TMC-1, The Astrophysical Journal Letters, 664, L43−L46.

Burch, J. L., A. D. Dejong, J. Goldstein, D. T. Young, (2009), Periodicity in Saturn's magnetosphere: Plasma cam, Geophysical Research Letters, doi: 10.1029/2009GL039043.

Burch, J. L., J. Goldstein, P. Mokashi, W. S. Lewis, C. Paty, D. T. Young, A. J. Coates, M. K. Dougherty, N. André, (2008), On the cause of Saturn's plasma periodicity, Geophysical Research Letters, 35, L14105, doi: 10.1029/2008GL034951.

Burch, J. L., J. Goldstein, W. S. Lewis, D. T. Young, A. J. Coates, M. K. Dougherty, N. André, (2007), Tethys and Dione as sources of outward flowing plasma in Saturn's magnetosphere, Nature, Vol 447, doi: 10.1038/nature05906.

Burch, J. L., J. Goldstein, T. W. Hill, D. T. Young, F. J. Crary, A. J. Coates, N. André, W. S. Kurth, E. C. Sittler, (2005), Properties of local plasma injections in Saturn's magnetosphere, Geophysical Research Letters, 32, L14S02, doi: 10.1029/2005GL02261.

Carbary, J. F. and A. M. Rymer, (2014), Meridional maps of Saturn's thermal electrons, Journal of Geophysical Research, 119, 1721–1733, doi: 10.1002/2013JA019436.

Cassidy, T. A. and R. E. Johnson, (2010), Collisional spreading of Enceladus' neutral cloud, Icarus 209, 696–703.

Cassini Plasma Spectrometer (CAPS), (2019), Cassini Final Mission Report Voloume 1: Mission Overview, Science Objectives, and Science Results.

Cassini Plasma Spectrometer (CAPS), (2019), Cassini Final Mission Report Volume 3: Instrument Performance Assessment.

Cassini Plasma Spectrometer (CAPS), (2019), Cassini Final Mission Report Volume 5: Mission Operations System Performance Assessment.

Cassini Plasma Spectrometer (CAPS), (2019) Cassini Final Mission Report Volume 6: Lessons Learned.

Chen, Y., T. W. Hill, A. M. Rymer, R. J. Wilson, (2010), Rate of radial transport of plasma in Saturn's inner magnetosphere, Journal of Geophysical Research, 115, A10211, doi: 10.1029/2010JA015412.

Chen, Y. and T. W. Hill, (2008), Statistical analysis of injection/dispersion events in Saturn's inner magnetosphere, Journal of Geophysical Research, 113, A07215, doi: 10.1029/2008JA013166.

Clarke, K. E., D. J. Andrews, A. J. Coates, S. W. H. Cowley, A. Burch, (2010), Magnetospheric period oscillations of Saturn's bow shock, Journal of Geophysical Research, 115, A05202, doi: 10.1029/2009JA015164.

Coates, A. J., A. Wellbrock, J. H. Waite, G. H. Jones, (2015), A new upper limit to the field-aligned potential near Titan, Geophysical Research Letters, vol. 42, issue 12, pp. 4676–4684, doi: 10.1002/2015GL064474.

Coates, A. J., A. Wellbrock, G. R. Lewis, C. S. Arridge, F. J. Crary, D. T. Young, M. F. Thomsen, D. B. Reisenfeld, E. C. Sittler Jr., R. E. Johnson, K. Szego, Z. Bebesi, G. H. Jones, (2012), Cassini in Titan's tail: CAPS observations of plasma escape, Journal of Geophysical Research, vol. 117, issue A5, doi:10.1029/2012JA017595.

Coates, A. J., A. Wellbrock, G. R. Lewis, G. H.Jones, D. T. Young, F. J. Crary, J. H. Waite, R. E. Johnson, T. W. Hill, E. C. Sittler Jr., (2010a), Negative ions at Titan and Enceladus: recent results, Faraday Discussion, vol. 147(1), 293–305, doi: 10.1039/C004700G.

Coates, A.J., G. H. Jones, G. R. Lewis, A. Wellbrock, D. T. Young, F. J. Crary, R. E. Johnson, T. A. Cassidy, T. W. Hill, (2010b), Negative Ions in the Enceladus Plume, Icarus, 206, no. 2, pp. 618–622, doi: 10.1016/j.icarus.2009.07.013.

Coates, A. J., A. Wellbrock, G. R. Lewis, G. H. Jones, D. T. Young, F. J. Crary, J. H. Waite Jr., (2009), Heavy negative ions in Titan's ionosphere: altitude and latitude dependence, Planetary and Space Science, 57, Issues 14–15, 1866–1871, doi: 10.1016/j.pss.2009.05.009.

Coates, A.J ., F. J. Crary, G. R. Lewis, D. T. Young, J. H. Waite Jr., E. C. Sittler Jr., (2007a), Discovery of heavy negative ions in Titan's ionosphere, Geophysical Research Letters, 34, L22103, doi: 10.1029/2007GL030978.

Coates, A. J., F. J. Crary, D. T. Young, K. Szego, C. S. Arridge, Z. Bebesi, E. C. Sittler Jr., R. E. Hartle, T. W. Hill, (2007b), Ionospheric electrons in Titan's tail: plasma structure during the Cassini T9 encounter, Geophysical Research Letters, 34, L24S05, doi: 10.1029/2007GL030919.

Coates, A. J., H. J. McAndrews, A. M. Rymer, D. T. Young, F. J. Crary, S. Maurice, R. E. Johnson, R. A. Baragiola, R. L. Tokar, E. C. Sittler, G. R. Lewis, (2005), Plasma electrons above Saturn's main rings: CAPS observations, Geophysical Research Letters, 32, 14S09, doi: 10.1029/2005GL022694.

Cooper, J. F, E. C. Sittler, R. E. Johnson, P. Kollman, E. Roussos, Atmospheric, ionospheric, and energetic radiation environments of Saturn's rings, (2015), American Geophysical Union (AGU) Fall Meeting, abstract P51B-2064.

Coustenis, A., S. K. Atreya, T. Balint, R. H. Brown, et al., (2009), Titan and Enceladus Mission, Experimental Astronomy, vol. 23, issue, pp. 893–946, doi: 10.1007/s10686-008-9103-z.

Coustenis, A., A. Salama, E. Lellouch, T. Encrenaz, G. L. Bjoraker, R. E. Sameulson, T. de Graauw, H. Feuchtgruber, M. F. Kessler, (1998) Evidence for water vapor in Titan's atmosphere from ISO/SWS data, Astronomy & Astrophysics, 336, L85–L89.

Cowley, S. W. H., G. Provan, G. J. Hunt, C. M. Jackman, (2017), Planetary period modulations of Saturn's magnetotail current sheet: A simple illustrative mathematical model, Journal of Geophysical Research: Space Physics, 122, 258–279, doi:10.1002/2016JA023367.

Cowley, S. W. H., C. S. Arridge, E. J. Bunce, J. T. Clarke, A. J. Coates, M. K. Dougherty, J.-C. Gérard, D. Grodent, J. D. Nichols, D. L. Talboys, (2008), Auroral current systems in Saturn's magnetosphere: Comparison of theoretical models with Cassini and HST observations, Annales Geophysicae, 26, pp. 2613–2630.

Crary, F.J., B. A. Magee, K. Mandt, J. H. Waite Jr., J. Westlake, D. T. Young, (2009), Heavy ions, temperatures and winds in Titan's ionosphere: Combined Cassini CAPS and INMS observations, Planetary Space Science, 57, 1847–1856, doi: 10.1016/j.pss.2009.09.006.

Crary, F. J., J. T. Clarke, M. K. Dougherty, P. Hanlon, K. C. Hansen, J. T. Steinberg, B. L. Barraclough, A. J. Coates, J.-C. Gérard, D. Grodent, W. S. Kurth, D. G. Mitchell, A. M. Rymer, D. T. Young, (2005), Solar wind dynamic pressure and electric field as main factors controlling Saturn's aurorae, Nature, 433, 720–722.

Cravens, T. E., R. V. Yelle, J.-E. Wahlund, D. E. Shemansky, A. F. Nagy, (2009), Composition and structure of the ionosphere and thermosphere, In Titan from Cassini-Huygens, Chapter 11, (eds.) R. E. Brown, J.-P. Lebreton, J. H. Waite, Springer, Dordrecht, pp. 259–295, doi: 10.1007/978-1-4020-9215-2_11.

Cravens, T. E., I. P. Robertson, S. A. Ledvina, D. Mitchell, S. M. Krimigis, J. H. Waite Jr., et al., (2008), Energetic ion precipitation at Titan, Geophysical Research Letters, 35, no. 3, doi: 10.1029/2007GL032451.

Cravens, T. E., I. P. Robertson, J. H. Waite Jr., R. V. Yelle, W. T. Kasprzak, C. N. Keller, S. A. Ledvina, et al., (2006), The composition of Titan's ionosphere, Geophysical Research Letters, 33, L07105, doi: 10.1029/2005GL025575.

Cui, J., M. Galand, R. V. Yelle, V. Vuitton, J.-E. Wahlund, P. P. Lavvas, I. C. F. Muller-Wodarg, T. E. Cravens, W. T. Kasprzak, J. H. Waite Jr., (2009), Diurnal variations of Titan's ionosphere, Journal of Geophysical Research, vol. 114, issue A6, doi: 10.1029/2009JA014228.

Cui, J., R. V. Yelle, K. Volk, (2008), Distribution and escape of molecular hydrogen in Titan's thermosphere and exosphere,Journal of Geophysical Research: Planets 113, no. E10.

Cuzzi, J., R. Clark, G. Filacchione, R. French, R. Johnson, E. Marouf, L. Spilker, (2009), Ring particle composition and size distribution, Chapter 15, In Saturn from Cassini- Huygens (eds.) M. K. Dougherty, Springer, Dordrecht, pp. 459–509, doi: 10.1007/978-1-4020-9217-6_15.

de Kok, R., P. G. J. Irwin, N. A . Teanby, E. Lellouch, B. Bézard, S. Vinatier, C. A. Nixon, L. Fletcher, C. Howett, S. B. Calcutt, N. E. Bowles, F. M. Flasar, F. W. Taylor, (2007), Oxygen compounds in Titan's stratosphere as observed by Cassini CIRS, Icarus 186, 354–363.

De La Haye, V., J. H. Waite Jr., T. E. Cravens, A. F. Nagy, R. V. Yelle, R. E. Johnson, S. Lebonnois, I. P. Robertson, (2007a), Titan's corona: the contribution of exothermic chemistry, Icarus, 191, 236–250.

De La Haye, V., J. H. Waite Jr., R. E. Johnson, et al., (2007b), Cassini ion and neutral mass spectrometer data in Titan's upper atmosphere and exosphere: observations of a suprathermal corona, Journal of Geophysical Research, vol. 112, issue A7, doi: 10.1029/2006JA0122.

DeJong, A. D., J. L. Burch, J. Goldstein, A. J. Coates, F. Crary, (2011), Day-night asymmetries of low-energy electrons in Saturn's inner magnetosphere, Geophysical Research Letters, 38, L08106, doi:1 0.1029/2011GL047308.

DeJong, A. D., J. L. Burch, J. Goldstein, A. J. Coates, D. T. Young, (2010), Low-energy electrons in Saturn's inner magnetosphere and their role in interchange injections, Journal of Geophysical Research, vol. 115, issue A10, doi: 10.1029/2010JA015510.

Delamere, P. A., R. J. Wilson, S. Eriksson, F. Bagenal, (2013), Magnetic signatures of Kelvin-Helmholtz vortices on Saturn's magnetopause: Global survey, Journal of Geophysical Research: Space Physics, 118, 393–404, doi: 10.1029/2012JA018197.

Desai, R. T., S. A. Taylor, L. H. Regoli, A. J. Coates, T. A. Nordheim, M. A. Cordiner, B. D. Teolis, et al., (2018), Cassini CAPS identification of pickup ion compositions at Rhea, Geophysical Research Letters, vol. 45, issue 4, pp. 1704–1712, doi: 10.1002/2017GL076588.

Desai, R. T., A. J. Coates, A. Wellbrock, V. Vuitton, F. J. Crary, D. González-Caniulef, O. Shebanits, G. H. Jones, G. R. Lewis, J. H. Waite, M. Cordiner, S. A. Taylor, D. O. Kataria, J.-E. Wahlund, N. J. T. Edberg, E. C. Sittler, (2017), Carbon chain anions and the growth of complex organic molecules in Titan’s ionosphere, Astrophysical Journal Letters, 844, L18, doi: 10.3847/2041-8213/aa7851.

Dong, Y., T. W. Hill, S.-Y. Ye, (2015), Characteristics of ice grains in the Enceladus plume from Cassini observations, of Geophysical Research: Space Physics, vol. 120, issue 2, pp. 915–937, doi: 10.1002/2014JA020288.

Elrod, M. K., W.-L. Tseng, A. K. Woodson, R. E. Johnson, (2014), Seasonal and radial trends in Saturn's thermal plasma between the main rings and Enceladus, Icarus 242, 130–137.

Elrod, M. K., W.-L. Tseng, R. J. Wilson, R. E. Johnson, (2012), Seasonal variations Saturn's plasma between the main rings and Enceladus, Journal of Geophysical Research, vol. 117, issue A3, doi: 10.1029/2011JA017332.

Felici, M., C. S. Arridge, A. J. Coates, S. V. Badman, M. K. Dougherty, C. M. Jackman, W. S. Kurth, H. Melin, D. G. Mitchell, D. B. Reisenfeld, et al., (2016), Cassini observations of ionospheric plasma in Saturn's magnetotail lobes, Journal of Geophysical Research, 121, 338–357, doi: 10.1002/2015JA021648.

Fleshman, B. L., P. A. Delamere, F. Bagenal, T. Cassidy, (2013), A 1-D model of physical chemistry in Saturn's inner magnetosphere, Journal of Geophysical Research: Planets, 118, 1567–1581, doi: 10.1002/jgre.20106.

Fuselier, S. A., R. Frahm, W. S. Lewis, A. Masters, J. Mukherjee, S. M. Petrinec, I. J. Sillanpaa, (2014), The location of magnetic reconnection at Saturn's magnetopause: A comparison with Earth, Journal of Geophysical Research: Space Physics, 119, 2563–2578, doi: 10.1002/2013JA019684.

Galand, M., A. J. Coates, T. E. Cravens, J.-E. Wahlund, (2013), Titan's ionosphere, In Titan: Surface, atmosphere and magnetosphere, (eds.) I. Mueller-Wodarg, C. Griffith, E. Lellouch, T. Cravens, Cambridge Planetary Science Series, Cambridge University Press.

Garnier, P., M. K. G. Holmberg, J.-E. Wahlund, G. R. Lewis, S. Grimald, M. F. Thomsen, D. A. Gurnett, A. J. Coates, F. Crary, I. Dandouras, (2013), The influence of the secondary electrons induced by energetic electrons impacting the Cassini Langmuir probe at Saturn, Journal of Geophysical Research: Space Physics 118, no. 11, 7054–7073.

Gloeckler, G. and J. Geiss (1998), Interstellar and inner source pickup ions observed with SWICS on ULYSSES, Space Science Review 86, 127–159.

Goldstein, J., J. H. Waite, J. L. Burch, R. Livi, (2016), Evidence of m = 1 density mode (plasma cam) in Saturn's rotating magnetosphere, Journal of Geophysical Research: Space Physics, 121, 2335–2348, doi: 10.1002/2015JA022131.

Goldstein, J., T. W. Hill, J. H. Waite, J. L. Burch, (2014), Analytical model of rotating two-cell convection at Saturn, Journal of Geophysical Research, 119, doi: 10.1002/2013JA019615.

Gombosi, T. I., T. P. Armstrong, C. S. Arridge, K. K. Khurana, S. M. Krimigis, N. Krupp, A. M. Persoon, M. F. Thomsen, (2009), Saturn's magnetospheric configuration, In Saturn after Cassini-Huygens, (eds.) M. Dougherty, L. Esposito, S. M. Krimigis, Springer, Dordecht, pp. 203–255.

Hanel, R., B. Conrath, F. M. Flasar, V. Kunde, W. Maguire, J. C. Pearl, J. Pirraglia, R. Samuelson, L. Herath, M. Allison, et al., (1981), Infrared observations of the Saturnian system from Voyager 1, Science, 212, 192–200.

Hartle, R. E., M. Sarantos, E. C. Sittler Jr., (2011), Pickup ion distributions from three-dimensional neutral exospheres, Journal of Geophysical Research, vol. 116, issue A10, doi: 10.1029/2011JA016859.

Hartle, R. E., E. C. Sittler Jr., A. Lipatov, (2008), Ion Escape from the Ionosphere of Titan, European Geosciences Union Annual Meeting, Vienna Austria, 14–18 April 2008.

Hartle, R. E. and E. C. Sittler Jr., (2007), Pickup ion phase space distributions: Effects of atmospheric spatial gradients, Journal of Geophysical Research, vol. 112, issue A7, doi: 10.1029/2006JA012157.

Hartle, R. E., E. C. Sittler Jr., F. M. Neubauer, R. E. Johnson, H. T. Smith, F. Crary, D. J. McComas, D. T. Young, A. J. Coates, D. Simpson, S. Bolton, D. Reisenfeld, K. Szego, J. J. Berthelier, A. Rymer, J. Vilppola, J. T. Steinberg, N. Andre, (2006a), Preliminary interpretation of Titan plasma interaction as observed by the Cassini plasma spectrometer: Comparisons with Voyager 1, Geophysical Research Letters, 33, L08201, doi: 10.1029/2005GL024817.

Hartle, R. E., E. C. Sittler Jr., F. M. Neubauer, R. E. Johnson, H. T. Smith, F. Crary, D. J. McComas, D. T. Young, A. J. Coates, D. Simpson, S. Bolton, D. Reisenfeld, K. Szego, J. J. Berthelier, A. Rymer, J. Vilppola, J. T. Steinberg, N. Andre, (2006b), Initial interpretation of Titan plasma interaction as observed by the Cassini plasma spectrometer: Comparisons with Voyager 1, Planetary and Space Science, 54, 1211.

Hartle, R. E. and R. Killen, (2006), Measuring pickup ions to characterize the surfaces and exospheres of planetary bodies: applications to the moon, Geophysical Research Letters, 33(5), L05201.

Herbst, E. and Y. Osamura, (2008),Calculations on the formation rates and mechanisms for CnH anions in interstellar and circumstellar media, The Astrophysical Journal 679, no. 2, 1670.

Herbst, E., (1981), Can negative molecular ions be detected in dense interstellar clouds?, Nature 289, no. 5799, 656–657.

Hill, T. W., A. Jaggi, S. Sazykin, R. A. Wolf, (2018), Plasma circulation time scale of Saturn's magnetosphere, in preparation.

Hill, T. W., (2017), Magnetosphere-Ionosphere coupling at Jupiter and Saturn, In Magnetosphere-Ionosphere Coupling in the Solar System, Part VI: Chapter 24, (eds.) C. R. Chappell, R. W. Schunk, P. M. Banks, J. L. Burch, R. M. Thorne, pp. 307–318, doi: 10.1002/9781119066880.ch24.

Hill, T. W., (2016), Penetration of external plasma into a rotation-driven magnetosphere, Journal of Geophysical Research: Space Physics, 121, doi: 10.1002/ 2016JA023430.

Hill, T. W., M. F. Thomsen, R. L. Tokar, A. J. Coates, G. R. Lewis, D. T. Young, F. J. Crary, R. A. Baragiola, R. E. Johnson, Y. Dong, R. J. Wilson, G. H. Jones, J.-E. Wahlund, D. G. Mitchell, M. Hornyi, (2012), Charged nanograins in the Enceladus plume, Journal of Geophysical Research: Space Physics, 117, A05209, doi: 10.1029/2011JA017218.

Hill, T. W., M. F. Thomsen, M. G. Henderson, R. L. Tokar, A. J. Coates, H. J. McAndrews, G. R. Lewis, D. G. Mitchell, C. M. Jackman, C. T. Russell, M. K. Dougherty, F. J. Crary, D. T. Young, (2008), Plasmoids in Saturn's magnetotail, Journal of Geophysical Research, 113, A01214, doi: 10.1029/2007JA012626.

Hill, T. W., A. M. Rymer, J. L. Burch, F. J. Crary, D. T. Young, M. F. Thomsen, D. Delapp, N. André, A. J. Coates, G. R. Lewis, (2005), Evidence for rotationally-driven plasma transport in Saturn's magnetosphere, Geophysical Research Letters, 32, L14S10, doi: 10.1029/2005GL022620.

Hörst, S. M., V. Vuitton, R. V. Yelle, (2008), Origin of oxygen species in Titan's atmosphere, Journal of Geophysical Research, 113, E10006, doi: 10.1029/2008JE003135.

Jackman, C. M., M. F. Thomsen, D. G. Mitchell, N. Sergis, C. S. Arridge, M. Felici, S. V. Badman, C. Paranicas, X. Jia, G. B. Hospodarsky, M. Andriopoulou, K. K. Khurana, A. W. Smith, M. K. Dougherty, (2015), Field dipolarization in Saturn's magnetotail with planetward ion flows and energetic particle flow bursts: Evidence of quasi-steady reconnection, Journal of Geophysical Research, 120, doi: 10.1002/2015JA020995.

Jackman, C. M., J. A Slavin, M. G. Kivelson, D. J. Southwood, N. Achilleos, M. F. Thomsen, G. A. DiBraccio, J. P. Eastwood, M. P. Freeman, M. K. Dougherty, (2014), Saturn's dynamic magnetotail: A comprehensive magnetic field and plasma survey of plasmoids and traveling compression regions and their role in global magnetospheric dynamics, Journal of Geophysical Research, 119, 5465–5494, doi: 10.1002/ 2013JA019388.

Jackman, C. M., J. A. Slavin, S. W. H. Cowley, (2011), Cassini observations of plasmoid structure and dynamics: Implications for the role of magnetic reconnection in magnetospheric circulation at Saturn, Journal of Geophysical Research, 116, A10212, doi: 10.1029/2011JA016682.

Jackman, C. M., C. S. Arridge, H. J. McAndrews, M. G. Henderson, R. J. Wilson, (2009), Northward field excursions in Saturn's magnetotail and their relationship to magnetospheric periodicities, Geophysical Research Letters, 36, L16101, doi: 10.1029/2009GL039149.

Jackman, C. M., C. T. Russell, D. J. Southwood, C. S. Arridge, N. Achilleos, M. K. Dougherty, (2007), Strong rapid dipolarizations in Saturn's magnetotail: In situ evidence of reconnection, Geophysical Research Letters, 34, L11203, doi: 10.1029/2007GL029764.

Jasinski, J. M., C. S. Arridge, A. J. Coates, G. H. Jones, N. Sergis, M. F. Thomsen, N. Krupp, (2017), Diamagnetic depression observations at Saturn's magnetospheric cusp by the Cassini spacecraft, Journal of Geophysical Research, doi: 10.1002/2016JA023738.

Jasinski, J. M., C. S. Arridge, A. J. Coates, G. H. Jones, N. Sergis, M. F. Thomsen, D. B. Reisenfeld, N. Krupp, J. H. Waite Jr., (2016), Cassini plasma observations of Saturn's magnetospheric cusp, Journal of Geophysical Research: Space Physics, 121, 12,047–12,067, doi: 10.1002/2016JA023310.

Jasinski, J. M., C. S. Arridge, L. Lamy, J. S. Leisner, M. F. Thomsen, D. G. Mitchell, A. J. Coates, A. Radioti, G. H. Jones, E. Roussos, N.Krupp, D. Grodent, M. K. Dougherty, J. H. Waite, (2014), Cusp observation at Saturn's high latitude magnetosphere by the Cassini spacecraft, Geophysical Research Letters, 41, doi: 10.1002/2014GL0593.

Jia, X. and M. G. Kivelson, (2012), Driving Saturn's magnetospheric periodicities from the upper atmosphere/ionosphere: Magnetotail response to dual sources, Journal of Geophysical Research, 117, A11219, doi: 10.1029/2012JA018183.

Jiang, F., J. Cui, J. Xu, (2017), The structure of Titan's N_2 and CH_4 coronae, The Astronomical Journal, 154, 271.

Jinks, S. L., E. J. Bunce, S. W. H. Cowley, G. Provan, et al., (2014), Cassini multi-instrument assessment of Saturn's polar cap boundary, Journal of Geophysical Research: Space Physics, 119, 8161–8177, doi: 10.1002/2014JA020367.

Johnson, R. E., W.-L. Tseng, M. K. Elrod, A. M. Persoon, (2017), Nanograin density outside Saturn's A-ring, The Astrophysical Journal Letters 834, L6 (4 pp.) doi: 10.384/2041-8213/834/L6.

Johnson, R. E., O. J. Tucker, W. Waalkes, V. M. Tenishev, et al., (2016), Evolution of an early Titan atmosphere, Icarus, 271, 202–206, doi: 10.1016/j.icarus.2016.01.014.

Johnson, R. E., O. J. Tucker, M. Michael, E. C. Sittler, H. T. Smith, D. T. Young, J. H. Waite, (2009), Mass loss processes in Titan's upper atmosphere, In Titan from Cassini-Huygens, Chapter 15, (eds.) R. H. Brown, J. P. Lebreton, J. H. Waite, Springer, Dordrecht, pp. 373–391, doi: 10.1007/978-1-4020-9215-2_15.

Johnson, R. E., M. Fama, M. Liu, R. A. Baragiola, E. C. Sittler, H. T. Smith, (2008), Sputtering of ice grains and icy satellites in Saturn's inner magnetosphere, Planetary and Space Science, 56, pp. 1238–1243, doi: 10.1016/j.pss.2008.04.003.

Johnson, R. E., H. T. Smith, O. J. Tucker, M. Liu, M. H. Burger, E. C. Sittler, R. L. Tokar, (2006a), The Enceladus and OH tori at Saturn, The Astrophysical Journal Letters, 644, L137-L139, doi: 10.1086/505750.

Johnson, R. E., J. G.Luhmann, R. L. Tokar, M. Bouhram, J. J. Berthelier, E. C. Sittler, J. F. Cooper, T. W. Hill, H. T. Smith, M. Michael, M. Liu, F. J. Crary, D. T. Young, (2006b), Production, ionization and redistribution of O_2 Saturn's ring atmosphere, Icarus180, 393–402.

Johnson, R. E., M. Liu, E. C. Sittler Jr., (2005), Plasma-induced clearing and redistribution of material embedded in planetary magnetospheres, Geophysical Research Letters, 32, L24201, doi: 10.1029/2005GL024275.

Jones, G. H., C. S. Arridge, A. J. Coates, G. R. Lewis, S. Kanani, A. Wellbrock, D. T. Young, F. J. Crary, R. L. Tokar, R. J. Wilson, T. W. Hill, R. E. Johnson, D. G. Mitchell, J. Schmidt, S. Kempf, U. Beckmann, C. T. Russell, Y. D. Jia, M. K. Dougherty, J. H. Waite Jr., B. A. Magee, (2009), Fine jet structure of electrically charged grains in Enceladus' plume, Geophysical Research Letters, 36, L16204, doi: 10.1029/2009GL038284.

Jones, G. H., E. Roussos, N. Krupp, U. Beckmann, A. J. Coates, F. Crary, I. Dandouras, V. Dikarev, M. K. Dougherty, P. Garnier, C. J. Hansen, A. R. Hendrix, G. B. Hospodarsky, R. E. Johnson, S. Kempf, K. K. Khurana, S. M. Krimigis, H. Kröger, W. S. Kurth, A. Lagg, H. J. McAndrews, D. G. Mitchell, C. Paranicas, F. Postberg, C. T. Russell, J. Saur, M. Seiß, F. Spahn, R. Srama, D. F. Strobel, R. Tokar, J.-E. Wahlund, R. J. Wilson, J. Woch, D. Young, (2008), The dust halo of Saturn's largest icy moon, Rhea, Science, vol. 319, issue 5868, pp. 1380–1384, doi: 10.1126/science.1151524.

Joy, S. P., M. G. Kivelson, R. J. Walker, K. K. Khurana, C. T. Russell, T. Ogino, (2002), Probabilistic models of the Jovian magnetopause and bow shock locations, Journal of Geophysical Research, 107(A10), 1309, doi: 10.1029/2001JA009146.

Khan, H., S. W. H. Cowley, E. Kolesnikova, M. Lester, M. J. Brittnacher, T. J. Hughes, W. J. Hughes, et al., (2001), Observations of two complete substorm cycles during the Cassini Earth swing-by: Cassini magnetometer data in a global context, Journal of Geophysical Research, pp. 30141–30175.

Krasnopolsky, V. A., (2012), Titan's photochemical model: Further update, oxygen species, and comparison with Triton and Pluto, Planetary and Space Science, 73, 318–326.

Kroto, H. W., A. W. Allaf, S. P. Balm, (1991), C_{60}: Buckminsterfullerene, Chemical Reviews, 91, 6, pp. 1213–1235, doi: 10.1021/cr00006a005.

Kroto, H. W., J. R. Heath, S. C. O'Brien, R. F. Curl, R. E. Smalley, (1985), C_{60}: Buckminsterfullerene, Nature, 318, 162–163.

Krupp, N., P. Kollmann, M. F. Thomsen, D. G. Mitchell, X. Jia, A. Masters, P. Zarka, (2018), Global configuration an seasonal variations of Saturn's magnetosphere, In Saturn in the 21st Century, (eds.) K. H. Baines, F. M. Flasar, N. Krupp, and T. Stallard, Cambridge University Press, in press.

Krupp, N., J. Woch, A. Lagg, S. Livi, D. G. Mitchell, S. M. Krimigis, M. K. Dougherty, P. G. Hanlon, T. P. Armstrong, S. A. Espinosa, (2004), Energetic particle observations in the vicinity of Jupiter: Cassini MIMI/LEMMS results, Journal of Geophysical Research, vol. 109, issue A9, doi: 10.1029/2003JA010111.

Krupp, N., J. Woch, A. Lagg, S. A. Espinosa, et al., (2002), Leakage of energetic particles from Jupiter's dusk magnetosphere: dual spacecraft observations, Geophysical Research Letters, 29, doi: 10.1029/2001GL014290.

Lagg, A., N. Krupp, S. Livi, J. Woch, S. M. Krimigis, M. K. Dougherty, (2001), Energetic particle measurements during the Earth swing-by of the Cassini spacecraft in August 1999, Journal of Geophysical Research, 106(A12), 30209–30222, doi: 10.1029/2001JA900048.

Lavvas, P., R. V. Yelle, T. Koskinen, A. Bazin, V. Vuitton, E. Vigren, M. Galand, A. Wellbrock, A. J. Coates, J.-E. Wahlund, F. J. Crary, D. Snowden, (2013), Aerosol growth in Titan's ionosphere, PNAS early edition, February 4, 2013, 110, 2729–2734, doi: 10.1073/pnas.1217059110.

Lavvas, P. P., A. Coustenis, I. M. Vardavas, (2008), Coupling photochemistry with haze formation in titan's atmosphere, Part II: Results and validation with Cassini-Huygens data, Planetary and Space Science, 56(1), 67–99.

Liang, M.-C., Y. L. Yung, D. E. Shemansky, (2007), Photolytically generated aerosols in the mesosphere and thermosphere of Titan, The Astrophysical Journal Letters, 661, L199-L202, doi: 10.1086/518785.

Lipatov, A. S., E. C. Sittler Jr., R. E. Hartle, J. F. Cooper, D. G. Simpson, (2014), Titan's plasma environment: 3D hybrid kinetic modeling of the TA flyby and comparison with CAPS-ELS and RPWS LP observations, Planetary and Space Science, 93–94, 119–128.

Lipatov, A. S., E. C. Sittler, R. E. Hartle, J. F. Cooper, D. G. Simpson, (2012), Saturn's magnetosphere interaction with Titan for T9 encounter: 3D hybrid modeling and comparison with CAPS's observations, Planetary and Space Science, 61, 66–78.

Lipatov, E. C., E. C. Sittler Jr., R. E. Hartle, J. F. Cooper, D. G. Simpson, (2011), Background and pickup ion velocity distribution dynamics in Titan's plasma environment: 3D hybrid simulation and comparison with CAPS T9 observations, Advances in Space Research, 48, 1114–1125.

Liu, X. and T. W. Hill, (2012), Effects of finite plasma pressure on centrifugally driven convection in Saturn's inner magnetosphere, Journal of Geophysical Research, 117, A07216, doi: 10.1029/2012JA017827.

Liu, X., T. W. Hill, R. A. Wolf, S. Sazykin, R. W. Spiro, H. Wu, (2010), Numerical simulation of plasma transport in Saturn's inner magnetosphere using the Rice Convection Model, Journal of Geophysical Research, 115, A12254, doi: 10.1029/2010JA015859.

Livi, R. J., J. L. Burch, J. L. Burch, F. Crary, A. M. Rymer, D. G. Mitchell, A. M. Persoon, (2014), Multi-instrument analysis of plasma parameters in Saturn's equatorial, inner magnetosphere using corrections for spacecraft potential and penetrating background radiation, Journal of Geophysical Research: Space Physics, 119, 3683–3707, doi: 10.1002/2013JA019616.

Luhmann, J. G, R. E. Johnson, R. L. Tokar, T. Cravens, (2006), A model of the ionosphere of Saturn's rings and its implications, Icarus 181, 465–474.

Lui, A. T. Y, R. W. McEntire, S. M. Krimigis, (1987), Evolution of the ring current during two geomagnetic storms, Journal of Geophysical Research: Space Physics 92, no. A7, pp. 7459–7470, doi: 10.1029/JA092iA07p07459.

Lunine, J., M. Choukroun, D. Stevenson, G. Tobie, (2009), The origin and evolution of Titan, In Titan from Cassini-Huygens, Chapter 3, (eds.) R. H. Brown, J.-P. Lebreton, J. H. Waite, Springer, Dordrecht, pp. 35–60, doi: 10.1007/978-1-4020-9215-2_3.

Martens, H. R., D. B. Reisenfeld, J. D. Williams, R. E. Johnson, H. T. Smith, (2008), Observations of molecular oxygen ions in Saturn's inner magnetosphere, Geophysical Research Letters, 35, L20103, doi: 10.1028/2008GL035433, 2008.

Masters, A., A. H. Sulaiman, N. Sergis, L. Stawarz, M. Fujimoto, A. J. Coates, M. K. Dougherty, (2016), Suprathermal electrons at Saturn's bow shock, The Astrophysical Journal, vol. 826, np. 1, article 48, 7 pp., doi: 10.3847/0004-637X/826/1/48.

Masters, A., N. Achilleos, J. C. Cutler, A. J. Coates, M. K. Dougherty, G. H. Jones, (2012), Surface waves on Saturn's magnetopause, Planetary and Space Science, 65(1), doi: 10.1016/j.pss.2012.02.007.

Masters, A., D. G. Mitchell, A. J. Coates, M. K. Dougherty, (2011a), Saturn's low-latitude boundary layer: 1. Properties and variability, Journal of Geophysical Research, 116, A06210, doi: 10.1029/2010JA016421.

Masters, A., A. P. Walsh, A. N. Fazakerley, A. J. Coates, M. K. Dougherty, (2011b), Saturn's low-latitude boundary layer: 2. Electron structure, Journal of Geophysical Research, 116, A06211, doi: 10.1029/2010JA016422.

Masters, A., N. Achilleos, M. G. Kivelson, N. Sergis, M. K. Dougherty, M. F. Thomsen, C. S. Arridge, S. M. Krimigis, H. J. McAndrews, S. J. Kanani, N. Krupp, A. J. Coates, (2010), Cassini observations of a Kelvin-Helmholtz vortex in Saturn's outer magnetosphere, Journal of Geophysical Research, 115, A07225, doi: 10.1029/2010JA015351.

Masters, A., N. Achilleos, C. Bertucci, M. K. Dougherty, et al., (2009), Surface waves on Saturn's dawn flank magnetopause driven by the Kelvin–Helmholtz instability, Planetary Space Science, vol. 57, issues 14–15, pp. 1769–1778, doi: 10.1016/j.pss.2009.02.010.

McAndrews, H. J., M. F. Thomsen, C. S. Arridge, C. M. Jackman, et al. (2009), Plasma in Saturn's nightside magnetosphere and the implications for global circulation, Planetary and Space Science, vol. 57, issues 14–15, pp. 1714–1722, doi: 10.1016/j.pss.2009.03.003.

McAndrews, H. J., C. J. Owen, M. F. Thomsen, B. Lavraud, A. J. Coates, M. K. Dougherty, D. T. Young, (2008), Evidence for reconnection at Saturn's magnetopause, Journal of Geophysical Research, 113, A04210, doi: 10.1029/2007JA012581.

McCarthy, M. C., C. A. Gottlieb, H. Gupta, P. Thaddeus, (2006) Laboratory and astronomical identification of the negative molecular ion C_6H^-, The Astrophysical Journal Letters, 652, L141-L144.

McComas, D. J., N. A. Schwardron, F. J. Crary, H. A. Elliott, D. T. Young, J. T. Gosling, M. F. Thomsen, E. Sittler, J. J. Berthelier, K. Szegö, A. J. Coates, (2004), The interstellar hydrogen shadow: Observations of interstellar pickup ions beyond Jupiter, Journal of Geophysical Research: Space Physics, 109, A02104, doi: 10.1029/2003JA010217.

Meier, P., H. Kriegel, U. Motschmann, J. Schmidt, F. Spahn, T. W. Hill, Y. Dong, G. H. Jones, (2014), A model of the spatial and size distribution of Enceladus′ dust plume, Planetary and Space Science 104, 216–233.

Meier, P., U. Motschmann, J. Schmidt, F. Spahn, T. W. Hill, Y. Dong, G. H. Jones, H. Kriegel, (2015), Modeling the total dust production of Enceladus from stochastic charge equilibrium and simulations, Planetary and Space Science 119, 208–221.

Menietti, J. D., O. Santolik, A. M. Rymer, G. B. Hospodorsky, A. M. Persoon, D. A. Gurnett, A. J. Coates, D. T. Young, (2008), Analysis of plasma waves observed within local plasma injections seen in Saturn's magnetosphere, Journal of Geophysical Research, 113, A05213, doi: 10.1029/2007JA012856.

Michael, M., S. N. Tripathi, P. Arya, A. Coates, A. Wellbrock, D. T. Young, (2011), High-altitude charged particles in the atmosphere of Titan, Planetary and Space Science, 59, 880–885.

Millar, T. J., C. Walsh, T. A. Field, (2017), Negative ions in space, Chemical Reviews, 117, 1765−1795 doi: 10.1021/acs.chemrev.

Millar, T. J., C. Walsh, M. A. Cordiner, R. Ní Chuimín, E. Herbst, (2007) Hydrocarbon anions in interstellar clouds and circumstellar envelopes, The Astrophysical Journal Letters, vol. 662, issue 2, L87−L90.

NASA Engineering and Safety Center (NESC), (2014), Cassini Plasma Spepctrometer (CAPS) Short Circuit Anomaly Assessment, Technical Assessment Report NESC-RP-12-00803, August 15, 2014.

NASA Engineering and Safety Center (NESC), (2013), Cassini Plasma Spectrometer (CAPS) Short Circuit Anomaly Assessment, Technical Assessment Report NESC-2013, August 15, 2013.

Nemeth, Z., K. Szego, L. Foldy, S. W. H. Cowley, G. Provan, M. F. Thomsen, (2016), Periodic motion of the magnetodisk as a cause of quasi-periodic variations in the Kronian magnetosphere, Planetary and Space Science, 130, 54.

Nemeth, Z., K. Szego, L. Foldy, M. G. Kivelson, X. Jia, K. M. Ramer, S. W. H. Cowley, G. Provan, M. Thomsen, (2015), The latitudinal structure of the nightside outer magnetosphere of Saturn as revealed by velocity moments of thermal ions, Annales Geophysicae 33(9) pp. 1195–1202.

Nemeth, Z., K. Szego, Z. Bebesi, G. Erdos, L. Foldy, A. Rymer, E. C. Sittler, A. J. Coates, A. Wellbrock, (2011), Ion distributions of different Kronian plasma regions, Journal of Geophysical Research, vol. 116, issue A9, pp.8, doi: 10.1029/2011JA016585.

Paranicas, C., M. F. Thomsen, N. Achilleos, M. Andriopoulou, S. Badman, G. Hospodarsky, C. Jackman, X. Jia, T. Kennelly, K. Khurana, P. Kollmann, N. Krupp, P. Louarn, E. Roussos, N. Sergis, (2016), Effects of radial motion on interchange injections at Saturn, Icarus, 264, 342, doi: 10.1016/j.icarus.2015.10.002.

Pietzak, B., M. Waiblinger, T. A. Murphy, A. Weidinger, et al., (1997) Buckminsterfullerene C_{60}: a chemical Faraday cage for atomic nitrogen, Chemical Physics Letters, 21, 259–263.

Pontius Jr., D. H. and T. W. Hill, (2009), Plasma mass loading from the extended neutral gas torus of Enceladus as inferred from the observed plasma corotation lag, Geophysical Research Letters, 36, L23103, doi: 10.1029/2009GL041030.

Pontius Jr., D. H. and T. W. Hill, (2006) Enceladus: A significant plasma source for Saturn's magnetosphere, Journal of Geophysical Research, 111, A09214, doi: 10.1029/2006JA011674.

Provan, G., L. Lamy, S. W. H. Cowley, et al., (2014) Planetary period oscillations in Saturn's magnetosphere: Comparison of magnetic oscillations and SKR modulations in the post-equinox interval Journal of Geophysical Research, 119, pp. 7380–7401, doi: 10.1002/2014JA020011.

Provan, G., S. W. H. Cowley, J. Sandhu, et al., (2013) Planetary period magnetic field oscillations in Saturn's magnetosphere: Post-equinox abrupt non-monotonic transitions to northern system dominance Journal of Geophysical Research, 118, pp. 3243–3264, doi: 10.1002/jgra.50186.

Provan, G., Andrews D. J., Arridge C. S., et al., (2012), Dual periodicities in planetary period magnetic field oscillations in Saturn's tail, Journal of Geophysical Research, vol. 117, issue A1, doi: 10.1029/2011JA017104.

Provan, G., D. J. Andrews, B. Cecconi, et al., (2011), Magnetospheric period magnetic field oscillations at Saturn: Equatorial phase 'jitter' produced by superposition of southern- and northern-period oscillations Journal of Geophysical Research, vol. 116, issue A4, doi: 10.1029/2010JA016213.

Provan, G., D. J. Andrews, C. S. Arridge, et al., (2009), Polarization and phase of planetary period oscillations on high latitude field lines in Saturn's magnetosphere Journal of Geophysical Research, vol. 114, issue A2, doi: 10.1029/2008JA013782.

Pryor, W. R., A. M. Rymer, D. G. Mitchell, T. W. Hill, D. T. Young, J. Saur, G. H. Jones, S. Jacobsen, S. W. Cowley, B. H. Mauk, A. J. Coates, (2011), The auroral footprint of Enceladus on Saturn, Nature, 472, pp. 331–333.

Remijan, A. J., J. M. Hollis, F. J. Lovas, M. A. Cordiner, T. J. Millar, A. J. Markwick-Kemper, P. R. Jewell, (2007), Detection of C_8H^- and comparison with C_8H toward IRC+10 216, The Astrophysical Journal Letters, vol. 664, issue 1, L47-L50.

Rymer, A. M., D. G. Mitchell, T. W. Hill, E. A. Kronberg, N. Krupp, C. M. Jackman, (2013), Saturn's magnetospheric refresh rate, Geophysical Research Letters, 40, doi: 10.1002/grl.50530.

Rymer, A. M., (2010), Electron-Ion Thermal Equilibration At Saturn: Electron Signatures Of Ion Pick-Up?, In AIP Conference Proceedings, vol. 1302, no. 1, pp. 250–255.

Rymer, A. M., H. T. Smith, A. Wellbrock, A. J. Coates, D. T. Young, (2009a), Discrete classification and electron energy spectra of Titan's varied magnetospheric environment, Geophysical Research Letters, 36, L15109, doi: 10.1029/2009GL039427.

Rymer, A. M., B. H. Mauk, T. W. Hill, N. André, D. G. Mitchell, C. Paranicas, D. T. Young, H. T. Smith, A. M. Persoon, J. D. Menietti, G. B. Hospodarsky, A. J. Coates, M. K. Dougherty, (2009b), Cassini evidence for rapid interchange transport at Saturn, Planetary and Space Science, doi: 10.1016/j.pss.2009.04.010.

Rymer, A. M., B. H. Mauk, T. W. Hill, C. Paranicas, D. G. Mitchell, A. J. Coates, D. T. Young, (2008), Electron circulation in Saturn's magnetosphere, Journal of Geophysical Research, 113, A01201, doi: 10.1029/2007JA012589.

Rymer, A. M., B. H. Mauk, T. W. Hill, C. Paranicas, N. André, E. C. Sittler Jr., D. G. Mitchell, H. T. Smith, R. E. Johnson, A. J. Coates, D. T. Young, S. J. Bolton, M. F. Thomsen, M. K. Dougherty, (2007), Electron sources in Saturn's magnetosphere, Journal of Geophysical Research, 112, A02201, doi: 10.1029/2006JA012017.

Rymer A. M., F. Crary, D. J. McComas, D. T. Young, D. Reisenfeld, M. Dougherty, N. André, (2005), Preliminary results on Saturn's inner plasmasphere as observed by Cassini: Comparison with Voyager, Geophysical Research Letters, 32, L14S07, doi: 10.1029/2005GL022653.

Rymer, A. M., (2004), Analysis of Cassini plasma and magnetic field mea- surements from 1–7 AU, Ph.D. thesis, University College London, London, United Kingdom.

Rymer, A. M., A. J. Coates, G. A. Abel, D. R. Linder, K. Svenes, B. Narheim, M. Thomsen, D. T. Young, (2001), Cassini CAPS electron spectrometer measurements during the Earth swingby on 18 August 1999, Journal of Geophysical Research, 106, pp. 30177–30198.

Sakai, N., T. Sakai, S. Yamamoto, (2008), Tentative detection of C_4H^- toward the low-mass protostar IRAS 04368+2557 in L1527, The Astrophysical Journal Letters, vol. 673, issue 1, L71–L74.

Sakai, N., T. Sakai, S. Yamamoto, (2007), Detection of C_6H^- toward the low-mass protostar IRAS 04368+2557 in L1527, The Astrophysical Journal Letters, 667, L65–L68.

Schaible, M. J., R. E. Johnson, L. V. Zhigilei, S. Piqueux, (2017), High energy electron sintering of icy regoliths: formation of the PacMan anomalies on the icy Saturnian moons, Icarus 285, pp. 211–123.

Schippers, P, Schenk, P., D. P. Hamilton, R. E. Johnson, W. B. McKinnon, C. Paranicas, J. Schmidt, M. R., N. André, M. Blanc, I. Dandouras, A. J. Coates, S. M. Krimigis, D. T. Young,

(2009), Identification of photoelectron energy peaks in Saturn's inner neutral torus, Journal of Geophysical Research 114, A12212, doi: 10.1029/2009JA014368.

Schippers, P., M. Blanc, N. André, I. Dandouras, G. R. Lewis, L. K. Gilbert, A. M. Persoon, N. Krupp, D. A. Gurnett, A. J. Coates, S. M. Krimigis, D. T. Young, M. K. Dougherty, (2008), Multi-instrument analysis of electron populations in Saturn's magnetosphere, Journal of Geophysical Research, 113, A07208, doi: 10.1029/2008JA013098.

Sergis, N., C. M. Jackman, M. F. Thomsen, S. M. Krimigis, D. G. Mitchell, D. C. Hamilton, M. K. Dougherty, N. Krupp, R. J. Wilson, (2017), Radial and local time structure of the Saturnian ring current revealed by Cassini, Journal of Geophysical Research, 122, 1803.

Sergis, N., C. M. Jackman, A. Masters, S. M. Krimigis, M. F. Thomsen, D. C. Hamilton, D. G. Mitchell, M. K. Dougherty, A. J. Coates, (2013), Particle and magnetic field properties of the Saturnian magnetosheath: Presence and upstream escape of hot magnetospheric plasma, Journal of Geophysical Research: Space Physics, 118, 1620–1634, doi: 10.1002/jgra.50164.

Sergis, N., S. M. Krimigis, E. C. Roelof, C. S. Arridge, A. M. Rymer, D. G. Mitchell, D. C. Hamilton, N. Krupp, M. F. Thomsen, M. K. Dougherty, A. J. Coates, D. Y. Young, (2010), Particle pressure, inertial force, and ring current density profiles in the magnetosphere of Saturn, based on Cassini measurements, Geophysical Research Letters, 37, L02102, doi: 10.1029/2009GL041920.

Shebanits, O., J.-E. Wahlund, N. J. T. Edberg, F. J. Crary, A. Wellbrock, D. J. Andrews, E. Vigren, R. T. Desai, A. J. Coates, K. E. Mandt, J. H. Waite Jr., (2016), Ion & aerosol precursor densities in Titan's ionosphere: a multi-instrument case study, Journal of Geophysical Research, 121, 10,075–10,090, doi: 10.1002.2016JA022980.

Shue, J. H., J. K. Chao, H. C. Fu, C. T. Russell, P. Song, K. K. Khurana, H. J. Singer, (1997), A new functional form to study the solar wind control of the magnetopause size and shape, Journal of Geophysical Research, 102, 9497–9511.

Sibeck, D. G., R. E. Lopez, E. C. Roelof, (1991), Solar wind control of the magnetopause shape, location, and motion, Journal of Geophysical Research, 96(A4), 5489–5495, doi: 10.1029/90JA02464.

Sillanpää, I. J. and Johnson, R. E., (2015), The role of ion-neutral collisions in Titan's magnetospheric interaction, PSS 108, 73–88.

Sillanpää, I., E. Kallio, P. Janhunen, W. Schmidt, K. Mursula, J. Vilppola, P. Tanskanen, (2006), Hybrid simulation study of ion escape at Titan for different orbital positions, Advances in Space Research, 38, 799–805, doi: 10.1016/j.asr.2006.01.005.

Sittler Jr., E. C., R. E. Hartle, R. E. Johnson, J. F. Cooper, A. S. Lipatov, C. Bertucci, A. J. Coates, K. Szego, M. Shappirio, D. G. Simpson, J.-E. Wahlund, (2010), Saturn's magnetospheric interaction with Titan as defined by Cassini encounters T9 and T18: New results, Planetary and Space Science 58, 327–350.

Sittler Jr., E. C., A. Ali, J. F. Cooper, R. E. Hartle, R. E. Johnson, A. J. Coates, D. T. Young, (2009a), Heavy ion formation in Titan's ionosphere: Magnetospheric introduction of free

oxygen and a source of Titan's aerosols?, Planetary and Space Science, 57, 1547–1557, doi: 10.1016/j.pss.2009.07.017.

Sittler Jr., E. C., R. E. Hartle, C. Bertucci, A. Coates, T. Cravens, I. Dandouras, D. Shemansky, (2009b), Energy deposition processes in Titan's upper atmosphere and its induced magnetosphere, In Titan from Cassini-Huygens, Chaper 16, (eds.) R.H. Brown, J. P. Lebreton, J. H. Waite, Springer, Dordrecht, pp, 393-453, doi: 10.1007/978-1-4020-9215-2_16.

Sittler Jr., E. C., N. Andre, M. Blanc, M. Burger, R. E. Johnson, A. Coates, A. Rymer, et al. (2008), Ion and neutral sources and sinks within Saturn's inner magnetosphere: Cassini results, Planetary and Space Science, 56, 3, doi: 10.1016/j.pss.2007.06.006.

Sittler Jr., E. C., M. Thomsen, R. E. Johnson, R. E. Hartle, M. Burger, D. Chornay, M. D. Shappirio, D. Simpson, H. T. Smith, A. J. Coates, A. M. Rymer, D. J. McComas, D. T. Young, D. Reisenfeld, M. Dougherty, N. André, (2006a), Cassini observations of Saturn's inner plasmasphere: Saturn orbit insertion results, Planetary and Space Science, 54, 1197–1210, doi: 10.1016/j.pss.2006.05.038.

Sittler Jr., E. C., R. E. Johnson, H. T. Smith, J. D. Richardson, S. Jurac, M. Moore, J. F. Cooper, B. H. Mauk, M. Michael, C. Paranicas, T. P. Armstrong, B. Tsurutani, (2006), Energetic nitrogen ions within the inner magnetosphere of Saturn, Journal of Geophysical Research 111, A09223, doi: 10.1029/2004JA010509.

Sittler Jr., E. C., M. Thomsen, D. Chornay, M. D. Shappirio, D. Simpson, R. E. Johnson, H. T. Smith, A. J. Coates, A. M. Rymer, F. Crary, D. J. McComas, D. T. Young, D. Reisenfeld, M. Dougherty, N. André, (2005), Preliminary results on Saturn's inner plasmasphere as observed by Cassini: Comparison with Voyager, Geophysical Research Letters, 32, L14S07, doi: 10.1029/2005GL022653.

Smith, A. W., C. M. Jackman, M. F. Thomsen, L. Lamy, N. Sergis, (2018), Multi-instrument investigation of the location of Saturn's magnetotail X-line, Journal of Geophysical Research: Space Physics 123, no. 7, 5494–5505.

Smith, A. W., C. M. Jackman, M. F. Thomsen, (2016), Magnetic reconnection in Saturn's magnetotail: A comprehensive magnetic field survey, Journal of Geophysical Research, 121, 2984, doi: 10.1002/2015JA022005.

Smith, H. T. and A. M. Rymer, (2014), An empirical model for the plasma environment along Titan's orbit based on Cassini plasma observations, Journal of Geophysical Research: Space Physics, 119, 5674–5684, doi: 10.1002/2014JA019872.

Smith, H. T., R. E. Johnson, M. E. Perry, D. G. Mitchell, R. L. McNutt, D. T. Young, (2010), Enceladus plume variability and the neutral gas densities in Saturn's magnetosphere, Journal of Geophysical Research, 115, A10252, doi: 10.1029/2009JA015184.

Smith, H. T., M. Shappirio, R. E. Johnson, D. Reisenfeld, E. C. Sittler, F. J. Crary, D. J. McComas, D. T. Young, (2008), Enceladus: a potential source of ammonia products and molecular nitrogen for Saturn's magnetosphere, Journal of Geophysical Research 113, A11206, doi: 10.1029/2008JA013352.

Smith, H. T., R. E. Johnson, E. C. Sittler, M. Shappirio, D. Reisenfeld, O. J. Tucker, M. Burger, F. J. Crary, D. J. McComas, D. T. Young, (2007), Enceladus: The likely dominant nitrogen source in Saturn's magnetosphere, Icarus, 188, 356–366, doi: 10.1016/j.icarus.2006.12.007.

Smith, H. T., M. Shappirio, E. C. Sittler, D. Reisenfeld, R. E. Johnson, R. A. Baragiola, F. J. Crary, D. J. McComas, D. T. Young, (2005), Discovery of nitrogen in Saturn's inner magnetosphere, Geophysical Research Letters 32, L14S03, doi: 10.1029/2005GL022654.

Snowden, D. and R. V. Yelle, (2014), The thermal structure of Titan's upper atmosphere, II: Energetics Icarus, 228, pp. 64–77.

Snowden, D., R. V. Yelle, J. Cui, et al., (2013), The thermal structure of Titan's upper atmosphere, I: Temperature profiles from Cassini INMS observations, Icarus, 226, pp. 522–582.

Song, P., C. T. Russell, X. X. Zhang, S. S. Stahara, J. R. Spreiter, T. I. Gombosi, (1999), On the processes in the terrestrial magnetosheath 2. Case study. Journal of Geophysical Research, 104, 22357, doi: 10.1029/1999JA900246.

Strobel, D. F., (2008), Titan’s hydrodynamically escaping atmosphere, Icarus, 193, 588–594.

Sulaiman, A. H., A. Masters, M. K. Dougherty, (2016), Characterization of Saturn’s bow shock: Magnetic field observations of quasi-perpendicular shocks, Journal of Geophysical Research: Space Physics, 121, 4425–4434, doi: 10.1002/2016JA022449.

Sulaiman, A., H., A. Masters, M. K. Dougherty, D. Burgess, M. Fujimoto, G. B. Hospodarsky, (2015), Quasiperpendicular high mach number shocks, Physical Review Letters, 115, 125001, doi: 10.1103/PhysRevLett.115.125001.

Szegö, K., Z. Nemeth, L. Foldy, S. W. H. Cowley, G. Provan, (2013), Dual periodicities in the flapping of Saturn's magnetodisk, Journal of Geophysical Research 118:(6) pp. 2883–2887.

Szegö, K., Z. Nemeth, G. Erdos, L. Foldy, Z. Bebesi, M. Thomsen, D. Delapp, (2012), Location of the magnetodisk in the nightside outer magnetosphere of Saturn near equinox based on ion densities, Journal of Geophysical Research, 117, A09225, doi: 10.1029/2012JA017817.

Szegö, K., Z. Nemeth, G. Erdos, L. Földy, M. Thomsen, D. Delapp, (2011), The plasma environment of Titan: The magnetodisk of Saturn near the encounters as derived from ion densities measured by the Cassini/CAPS plasma spectrometer, Journal of Geophysical Research: Space Physics, 116, A10219, doi: 10.1029/2011JA016629.

Szegö, K., D. T. Young, B. Barraclough, J.-J. Berthelier, et al., (2003) Cassini plasma spectrometer measurements of Jovian bow shock structure, Journal of Geophysical Research, 108, 1287, doi: 10.1029/2002JA009517.

Teolis, B. D., G. H. Jones, P. F. Miles, R. L. Tokar, B. A. Magee, J. H. Waite, E. Roussos, D. T. Young, et al., (2010), Cassini finds an oxygen–carbon dioxide atmosphere at Saturn’s icy moon Rhea, Science, vol. 330, issue 6012, pp. 1813–1815, doi: 10.1126/science.1198366.

Thaddeus, P., C. A. Gottlieb, H. Gupta, S. Brünken, M. C. McCarthy, M. Agundez, M. Guélin, J. Cernicharo, (2008), Laboratory´ and astronomical detection of the negative molecular ion C_3N^-, The Astrophysical Journal, 677, pp. 1132−1139.

Thomsen, M. F., S. V. Badman, C. M. Jackman, X. Jia, M. G. Kivelson, W. S. Kurth, (2017), Energy-banded ions in Saturn's magnetosphere, Journal of Geophysical Research, 122, doi: 10.1002/2017JA024147.

Thomsen, M. F., A. J. Coates, E. Roussos, R. J. Wilson, K. C. Hansen, G. R. Lewis, (2016a), Suprathermal electron penetration into the inner magnetosphere of Saturn, Journal of Geophysical Research, 121, 5436, doi: 10.1002/2016JA022692.

Thomsen, M. F., C. M. Jackman, S. W. H. Cowley, X. Jia, M. G. Kivelson, G. Provan, (2016b), Evidence for periodic variations in the thickness of Saturn's nightside plasma sheet, Journal of Geophysical Research, 121, doi: 10.1002/2016JA023368.

Thomsen, M. F., D. G. Mitchell, X. Jia, C. M. Jackman, G. Hospodarsky, A. J. Coates, (2015a), Plasmapause formation at Saturn, Journal of Geophysical Research, 120, 2571, doi: 10.1002/2015JA021008.

Thomsen, M. F., C. M. Jackman, D. G. Mitchell, G. Hospodarsky, W. S. Kurth, K. C. Hansen, (2015b), Sustained lobe reconnection in Saturn's magnetotail, Journal of Geophysical Research, doi: 10.1002/2015JA021768.

Thomsen, M. F., C. M. Jackman, R. L. Tokar, R. J. Wilson, (2014a), Plasma flows in Saturn's nightside magnetosphere, Journal of Geophysical Research, 119, 4521–4535.

Thomsen, M. F., D. B. Reisenfeld, R. J. Wilson, M. Andriopoulouet, et al., (2014b), Ion composition in interchange injection events in Saturn's magnetosphere, Journal of Geophysical Research: Space Physics, 119, 9761–9772, doi: 10.1002/2014JA020489.

Thomsen, M. F., R. J. Wilson, R. L. Tokar, D. B. Reisenfeld, C. M. Jackman, (2013), Cassini/CAPS observations of duskside tail dynamics at Saturn, Journal of Geophysical Research, 118, 5767, doi: 10.1002/jgra.50552.

Thomsen, M. F., (2013), Saturn's magnetospheric dynamics, Geophysical Research Letters, vol. 40, issue 20, pp. 5337–5344, doi: 10.1002/2013GL057967.

Thomsen, M. F., E. Roussos, M. Andriopoulou, P. Kollmann, C. S. Arridge, C. P. Paranicas, D. A. Gurnett, R. L. Powell, R. L. Tokar, D. T. Young, (2012), Saturn's inner magnetospheric convection pattern: Further evidence, Journal of Geophysical Research, vol. 117, issue A9, doi: 10.1029/2011JA017482.

Thomsen, M. F., D. B. Reisenfeld, D. M. Delapp, R. L. Tokar, D. T. Young, F. J. Crary, E. C. Sittler, M. A. McGraw, J. D. Williams, (2010), Survey of ion plasma parameters in Saturn's magnetosphere, Journal of Geophysical Research, vol. 115, issue A10, doi: 10.1029/2010JA015267.

Thomsen, M. F., J. P. DiLorenzo, D. J. McComas, D. T. Young, F. J. Crary, D. Delapp, D. B. Reisenfeld, N. André, (2007), Assessment of the magnetospheric contribution to the

suprathermal ions in Saturn's foreshock region, Journal of Geophysical Research, vol. 112, issue A5, doi: 10.1029/2006JA012084.

Tobie, G., N. A. Teanby, A. Coustenis, R. Jaumann, F. Raulin, J. Schmidt, N. Carrasco, A. J. Coates, D. Cordier, R. De Kok, W. D. Geppert, J.-P. Lebreton, A. Lefevre, T. A. Livengood, K. E. Mandt, G. Mitri, F. Nimmo, C. A. Nixon, L. Norman, R. T. Pappalardo, F. Postberg, S. Rodriguez, D. Schulze-Makuch, J. M. Soderblom, A. Solomonidou, K. Stephan, E. R. Stofan, E. P. Turtle, R. J. Wagner, R. A. West, J. H. Westlake, (2014), Science goals and mission concept for the future exploration of Titan and Enceladus, Planetary and Space Science, 104, pp. 59–77.

Tokar, R. L., R. E. Johnson, M. F. Thomsen, E. C. Sittler, A. J . Coates, R. J. Wilson, F. J. Crary, D. T. Young, G. H. Jones, (2012), Detection of exospheric O_2^+ at Saturn's moon Dione, Geophysical Research Letters 39, L03105, doi: 10.1029/2011GL050452.

Tokar, R. L., R. E. Johnson, M. F. Thomsen, R. J. Wilson, D. T. Young, F. J. Crary, A. J. Coates, G. H. Jones, C. S. Paty, (2009), Cassini detection of Enceladus' cold water-group plume ionosphere, Geophysical Research Letters 36, L13203, doi: 10.1029/2009GL038923.

Tokar, R. L., R. J. Wilson, R. E. Johnson, M. G. Henderson, M. F. Thomas, M. M. Cowee, E. C. Sittler Jr., D. T. Young, H.J . McAndrews, H. T. Smith, (2008), Cassini detection of water-group pick-up ions in the Enceladus torus, Geophysical Research Letters 35, L14202, doi: 10.1029/2008GL034749.

Tokar, R. L, R. E. Johnson, T. W. Hill, D. H. Pontius, W. S. Kurth, F. J. Crary, D. T. Young, M. F. Thomsen, D. B. Reisenfeld, A. J. Coates, G. R. Lewis, E. C. Sitter, D. A. Gurnett, (2006), The interaction of the atmosphere of Enceladus with Saturn’s plasma, Science 311, 1409–1412.

Tokar, R. L., R. E. Johnson, M. F. Thomsen, D. M. Delapp, R. A. Baragiola, M. F. Francis, D. B. Reisenfeld, B. A. Fish, D. T. Young, F. J. Crary, A. J. Coates, D. A. Gurnett, W. S. Kurth, (2005), Cassini observations of the thermal plasma in the vicinity of Saturn's main rings and the F and G rings, Geophysical Research Letters, 32, L14S04, doi: 10.1029/2005GL022690.

Tseng, W.-L., R. E. Johnson, M. K. Elrod, (2013a), Modeling the seasonal variability of the plasma environment in Saturn's magnetosphere between main rings and Mimas, Planetary and Space Science 77, 126–135.

Tseng, W.-L., R. E. Johnson, W.-H. Ip, (2013b), The atomic hydrogen cloud in the Saturnian system, Planetary and Space Science 85, 164–174.

Tseng, W.-L., R. E. Johnson, M. F. Thomson, T. A. Cassidy, Meredith K. Elrod, (2011), Neutral H2 and H2+ ions in the Saturnian magnetosphere, Journal of Geophysical Research, vol. 116, issue A3, doi: 10.1029/2010JA016145.

Tseng, W.-L., W.-H. Ip, R. E. Johnson, T. A. Cassidy, M. K. Elrod, (2010), The Structure and time variability of the ring atmosphere and ionosphere, Icarus 206, 382–389.

Tucker, O. J., W. Waalkes, V. M. Tenishev, et al., (2016), Examining the exobase approximation: DSMC models of Titan's upper atmosphere, Icarus, 272, 290–300.

Tucker, O. J., R. E. Johnson, J. I. Deighan, et al., (2013), Diffusion and thermal escape of H2 from Titan's atmosphere: Monte Carlo simulations, Icarus 222, 149–158.

Turtle, E. P., J. W. Barnes, M. G. Trainer, R. D. Lorenz, S. M. MacKenzie, et al., (2017), Dragonfly: Exploring Titan's prebiotic organic chemistry and habitability, vol. 48, id. 1958, 48th Lunar and Planetary Science Conference, March 20–24, 2017, TX.

Volkov, A. N., O. J. Tucker, J. T. Erwin, et al., (2011), Kinetic simulations of thermal escape from a single component atmosphere, Physics of Fluids, vol. 23, issue 6, 1–16, doi: 10.1063/1.3592253.

Vuitton, V., P. Lavvas, R. V. Yelle, M. Galand, A. Wellbrock, G. R. Lewis, A. J. Coates, J.-E. Wahlund, (2009), Negative ion chemistry in Titan's upper atmosphere, Planetary and Space Science, 57, 1558−1572.

Vuitton, V., R. V. Yelle, M. J. McEwan, (2007), Ion chemistry and N-containing molecules in Titan's upper atmosphere, Icarus, 191, 722–742.

Wahlund, J.-E., M. Galand, I. Müller-Wodarg, J. Cui, R. V. Yelle, F. J. Crary, K. Mandt, B. Magee, J. H. Waite Jr, D. T. Young, A. J. Coates, P. Garnier, K. Ågren, M. André, A. I. Eriksson, T. E. Cravens, V. Vuitton, D. A. Gurnett, W. S. Kurth, (2009), On the amount of heavy molecular ions in Titan's ionosphere, Planetary and Space Science, 57, 1857–1865, doi: 10.1016/j.pss.2009.07.014.

Waite Jr., J. H., D. T. Young, A. J. Coates, F. J. Crary, B. Magee, K. Mandt, J. Westlake, (2008), The source of heavy organics and aerosols in Titan's atmosphere, Proceedings of the International Astronomical Union, vol. 4, issue S251, February 2008, pp. 321–326, doi: 10.1017/S1743921308021844.

Waite Jr., J. H., D. T. Young, T. E. Cravens, A. J. Coates, F. J. Crary, B. Magee, J. Westlake, (2007), The process of Tholin formation in Titan's upper atmosphere, Science 316, 870, doi: 10.1126/science.1139727.

Waite, J. H., H. Niemann, R. V. Yelle, W. Kasprzak, T. Cravens, et al., (2005), Ion Neutral Mass Spectrometer (INMS) results from the first flyby of Titan, Science, 308, 982–986.

Wang, X.-B. and Wang, L.-S., (2009), Photoelectron spectroscopy of multiply charged atoms, Annual Review of Physical Chemistry, vol. 60, pp. 105–126.

Wellbrock, A., A. J. Coates, G. H. Jones, V. Vuitton, P. Lavvas, J. H. Waite, (2018), Heavy negative ions in Titan's ionosphere: The effect of polar winter conditions, submitted.

Wellbrock, A., A. J. Coates, G. H. Jones, G. R. Lewis, J. H. Waite, (2013), Cassini CAPS-ELS observations of negative ions in Titan's ionosphere: Trends of density with altitude, Geophysical Research Letters, vol. 40, issue 17, pp. 4481–4485, doi: 10.1002/grl.50751.

Wellbrock A., A. J. Coates, I. Sillanpää, G. H. Jones, C. S. Arridge, G. R. Lewis, D. T. Young, F. J. Crary, A. D. Aylward, (2012), Cassini observations of ionospheric photoelectrons at large distances from Titan: Implications for Titan's exospheric environment and magnetic tail, Journal of Geophysical Research, vol. 117, issue A3, doi: 10.1029/2011JA017113.

Went, D. R., G. B. Hospodarsky, A. Masters, K. C. Hansen, M. K. Dougherty, (2011), A new semiempirical model of Saturn's bow shock based on propagated solar wind parameters. Journal of Geophysical Research: Space Physics 116, issue A7.

Wilson, R. J., F. Bagenal, A. M. Persoon, (2017), Survey of thermal plasma ions in Saturn's magnetosphere utilizing a forward model, Journal of Geophysical Research: Space Physics, 122, 7256–7278, doi: 10.1002/2017JA024117.

Wilson, R. J., F. Bagenal, T. Cassidy, B. L. Fleshman, F. Crary, (2015), The relative proportions of water group ions in Saturn's inner magnetosphere: A preliminary study, Journal of Geophysical Research: Space Physics, 120, 6624–6632, doi: 10.1002/2014JA020557.

Wilson, R. J., F. Bagenal, P. A. Delamere, M. Desroche, B. L. Fleshman, V. Dols, (2013), Evidence from radial velocity measurements of a global electric field in Saturn's inner magnetosphere, Journal of Geophysical Research: Space Physics, vol. 118, issue 5, 2122–2132, doi: 10.1002/jgra.50251.

Wilson, R. J., P. A. Delamere, F. Bagenal, A. Masters, (2012), Kelvin-Helmholtz instability at Saturn's magnetopause: Cassini ion data analysis, Journal of Geophysical Research: Space Physics, vol. 117, issue A3, doi: 10.1029/2011JA016723.

Wilson, R. J., R. L. Tokar, W. S. Kurth, A. M. Persoon, (2010), Properties of the thermal ion plasma near Rhea as measured by the Cassini plasma spectrometer, Journal of Geophysical Research, vol. 115, issue A5, doi: 10.1029/2009JA014679.

Wilson, R. J., R. L. Tokar, M. G. Henderson, (2009), Thermal ion flow in Saturn's inner magnetosphere measured by the Cassini plasma spectrometer: A signature of the Enceladus torus?, Geophysical Research Letters, 36, L23104, doi: 10.1029/2009GL040225.

Wilson, R. J., R. L. Tokar, M. G. Henderson, T. W. Hill, M. F. Thomsen, D. H. Pontius Jr., (2008), Cassini plasma spectrometer thermal ion measurements in Saturn's inner magnetosphere, Journal of Geophysical Research, vol. 113, issue A12, doi: 10.1029/2008JA013486.

Wilson, E. H. and Atreya, S. K., (2004), Current state of modeling the photochemistry of Titan's mutually dependent atmosphere and ionosphere, Journal of Geophysical Research, 109, E06002, doi: 10.1029/2003JE002181.

Woodson, A. K., H. T. Smith, F. J. Crary, R. E. Johnson, (2015), Ion composition in Titan’s exosphere via the Cassini plasma spectrometer I: T40 encounter, Journal of Geophysical Research: Space Physics, 120, 212–234, doi: 10.1002/2014JA020499.

Yelle, R. V., J. Cui, I. C. F. Muller-Wodarg, (2008), Methane escape from Titan’s atmosphere, Journal of Geophysical Research, 113, doi: 10.1029/2007JE003031.

Young, D. T., J-J. Berthelier, M. Blanc, J. L. Burch, S. Bolton, A. J. Coates, F. J. Crary, et al., (2005), Composition and dynamics of plasma in Saturn's magnetosphere, Science, vol. 307, issue 5713, pp. 1262–1266, doi: 10.1126/science.1106151.

Young, D. T., J. J. Berthelier, M. Blanc, J. L. Burch, A. J. Coates, R. Goldstein, M. Grande, et al., (2004), Cassini plasma spectrometer investigation, Space Science Reviews, vol. 114, issues 1–4, pp. 1–112, doi: 10.1007/s11214-004-1406-4.

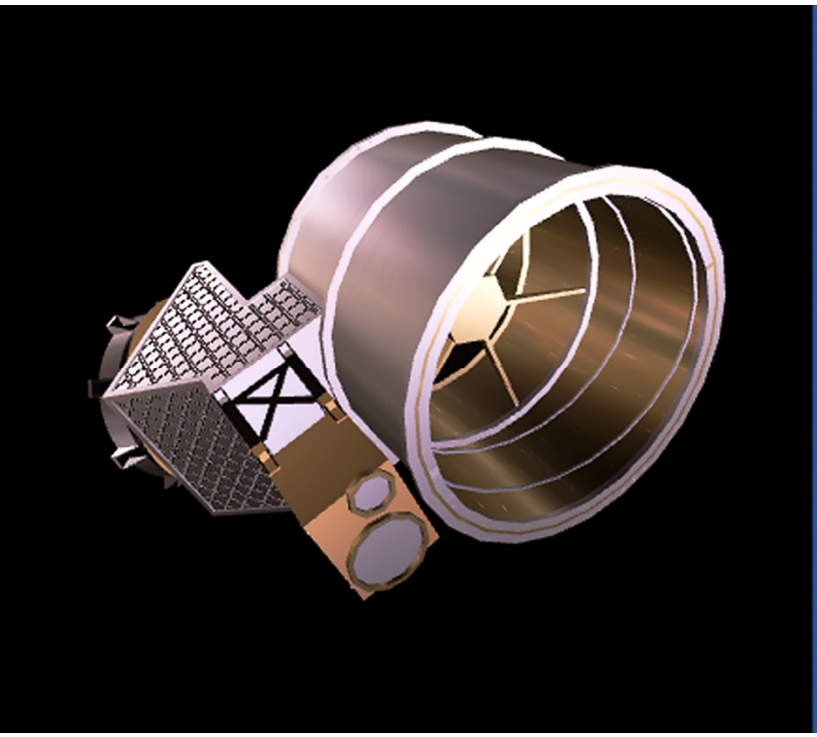

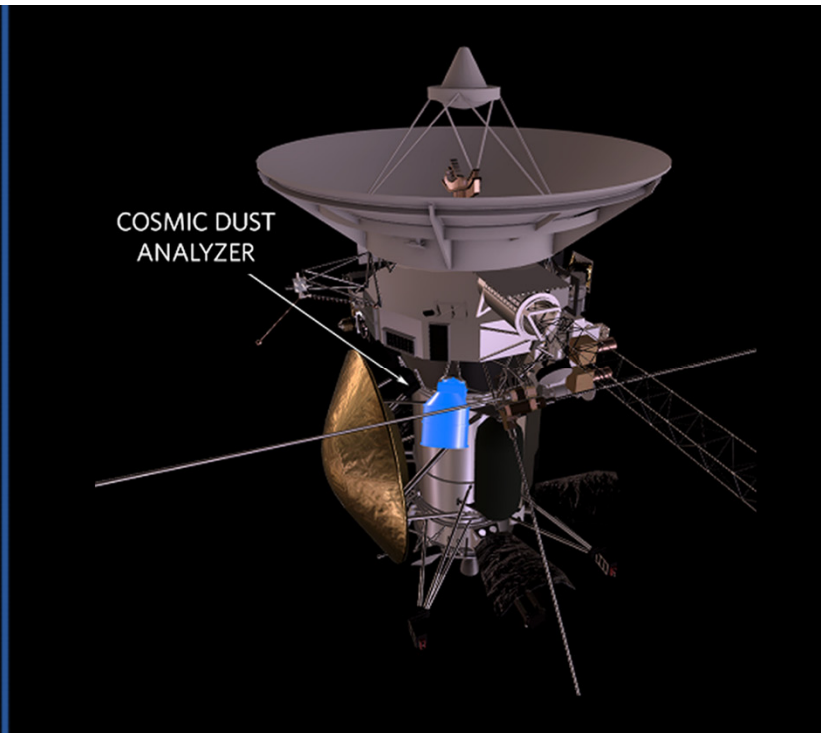

Cosmic Dust Analyzer

The Cosmic Dust Analyzer (CDA) directly sampled the composition, mass, impact direction, and speed of dust and ice particles in the Saturn system, as well as the Jupiter system and in interplanetary space. The **science objectives** of CDA included mapping the size distribution and chemical composition of ring material in the Saturn system, studying dynamical processes responsible for the diffuse E-ring structure, obtaining information on the chemical composition of satellites, and determining the role that dust plays as source and sink of charged particles in the magnetosphere.

CDA was composed of two sensors, the high-rate detectors (HRDs) designed to measure high impact rates in dust-rich environments such as ring plane crossings and the dust analyzer (DA) that measured the electric charge carried by dust particles, their impact directions, speeds, masses, and chemical composition. CDA was on an articulated mechanism that enabled the entire instrument to rotate and reposition to enable measurements of particle fluxes over a wide range of directions.

CONTENTS

Figures

Tables

EXECUTIVE SUMMARY

The science objectives of the Cassini-Huygens CDA were to carry out in situ characterization of the dust environments in order to infer properties of the dust-emitting sources as well as to study the underlying processes associated with dust. The capability to measure both the compositional and dynamical properties of incident dust grains makes the CDA measurements uniquely useful to explore the dust environment in the Saturnian system, as well as other dust populations from the Jovian system (i.e., the nanodust stream particles), and from interplanetary and interstellar space.

The CDA instrument performance over the entire time from 1999 until the last second of Cassini in September 2017 was outstanding.

At Saturn, CDA has successfully characterized the structure and the composition of Saturn's diffuse E-ring, its relation to the geologically active icy moon Enceladus, and how the E-ring interacts with the magnetosphere. CDA results contributed significantly to our understanding of Enceladus and its subsurface ocean, promoting the exploration of the habitability of the ocean worlds in the outer solar system. CDA also provided observational constraints for other diffuse rings (e.g., G-ring and Pallene ring) and the ejecta cloud around the major icy moons of Saturn. During the Grand Finale orbits, CDA detected material directly from Saturn's main rings and revealed ring-planet interactions through charged nanodust.

In addition, the dust populations arriving at the Saturnian system, i.e., interplanetary dust particles (IDPs) and interstellar dust (ISD), were also characterized thanks to the extended mission. Tiny grains expelled from both the Jovian and Saturnian systems by electromagnetic forces were also detected, providing additional information about their source moons and helping to understand the coupling between the interplanetary magnetic field (IMF) and the dynamics of these charged grains.

The CDA instrument performance over the entire time was outstanding. CDA switched on in 1999 and measured almost continuously until the last second of Cassini in September 2017. All five measurement channels (primary charge grid, targets, ion grid, and multiplier) worked the entire time. The multiplier of the spectrometer showed only a minor gain change. No issues with instrument high voltage were identified and the CDA thermal parameters were in the nominal range. The only instrument degradation that occurred was related to close Enceladus plume crossings where the gain of the two target channels decreased. This had no effect on charge or compositional measurements, instead the lower sensitivity was used to perform measurements in the dense E-ring with a higher mass threshold to avoid instrument saturation. A major concern was the Cassini pointing profile and although CDA used its articulation platform approximately once a day in order to track the dust RAM direction, many observations were not possible. Updates of the CDA flight software optimized the instrument performance during special events (Enceladus flybys). Very high impact rates required special instrument settings due to the long instrument dead time of one second. The noise behavior of CDA remained constant during the entire time and no significant interference with the spacecraft or other subsystems was observed. Only the Radio and Plasma

Wave Science (RPWS) active sounder operation led to interferences in the primary charge channel (QP) of CDA.

The major CDA findings are listed below for each science working group as well as during the cruise phase:

Rings

- The exogenous mass influx and the age of the main rings are determined.
- In situ measurement of E-ring particles shows the large extension of the ring all the way to Titan's orbit (~20 R_S).
- Charged grains are the result of dust-plasma interactions in Saturn's magnetosphere. The grain charge polarity switches from negative to positive at a radial distance of around 7 R_S as predicted by models.
- The E-ring is asymmetrical with respect to local time—it is denser and the peak locations are closer to Saturn near local noon and vice versa.

Icy satellites

- In situ characterization of the dusty plume of Enceladus.
- Discovery of the subsurface liquid water reservoir below the icy crust of Enceladus, inferred from the salt-rich E-ring ice grains.
- Ongoing hydrothermal activities within Enceladus' subsurface ocean, inferred from nano-phase silica particles.
- Discovery of complex organic molecules in ice grains from Enceladus.

Magnetosphere and plasma sciences

- Discovery of fast nanodust from Saturn.
- Fast nanograins are probes of the interplanetary magnetic field, as a result of their dynamical interactions with the interplanetary magnetic field.

Others

- Interstellar dust grains penetrate deep into the heliosphere and reach the Earth orbit. Its composition is found to be homogeneous and rich in silicates.
- Sodium chloride is the dominant constituent of the Jovian stream particles, implying they are early condensates from the volcanic plumes of Io.

- Interplanetary dust particles carry surface charges in agreement with the charging models in interplanetary space.
- In situ analysis of two metal-rich interplanetary dust particles by time-of-flight mass spectrometry (TOF MS) in the inner solar system.

CDA is the first dedicated dust instrument operated at Saturn. While its results have changed our view on the role of microscopic dust grains in the system and space exploration, several open questions remain to be resolved in the future:

- What expected ejecta clouds stemming from interplanetary micrometeorite impacts have not been detected around major icy moons (except Rhea) embedded in the E-ring?
- What is the production yield and the size distribution of impact-ejecta particles produced from Saturn's icy moons and the main rings?
- What is the original origin of silicates apparently coming from Saturn's main rings, as detected during the Grand Finale orbits?
- What, if any, are the effects on Saturn's upper atmosphere of nanograins from the main rings?
- What is the dusty plasma status in the plume of Enceladus and the core of the E-ring? What would be its impact on E-ring grain dynamics?

CDA was a highly reliable and versatile instrument with a mass sensitivity 10^6 times higher than those of the Pioneer 10 and 11 dust detectors that measured dust at Saturn prior to Cassini.

CDA Instrument Summary

The CDA was designed to provide direct observations of the impacting dust grains. CDA investigated the physical, chemical, and dynamical properties of impacting dust particles, and their interactions with satellites, rings, and Saturn's magnetosphere [Srama et al. 2004]. The chemical composition of interplanetary meteoroids was successfully compared with asteroidal and cometary dust, as well as with dust in orbit about Saturn and the ejected dust particles from rings and satellites at Saturn and during the flyby at Jupiter. The electrical charging of dust particles in the magnetosphere and the subsequent effects of the ambient plasma and magnetic fields on the trajectories of dust particles have been successfully observed by CDA.

CDA was a highly reliable and versatile instrument with a mass sensitivity 10^6 times higher than those of the Pioneer 10 and 11 dust detectors that measured dust at Saturn prior to Cassini. CDA had significant heritage from former space instrumentation developed for the Vega, Giotto, Galileo, and Ulysses missions.

CDA consisted of two independent subsystems, the High Rate Detector (HRD) and the Dust Analyzer (DA). HRD was designed to monitor high impact rates (up to 10^6 m^{-2} s^{-1}) in dust-rich environments such as during the Saturn ring plane crossings. HRD uses polyvinylidene difluoride (PVDF) foils to detect the impact energy of particles larger than approximately 1 micrometer.

The DA was sensitive to particles within a large mass range of 5×10^{-18} to 10^{-12} kg for impact speeds of ~20 km s^{-1} and covered an impact velocity range of 1 to 100 km s^{-1}, measuring the electrical charge, mass, impact velocity, and elemental composition of the impacting dust grains. This was accomplished by a suite of three DA detectors: 1) a charge sensing unit (QP) in front of the instrument; 2) a classical impact ionization detector (IID); and 3) a time-of-flight mass spectrometer (TOF MS), the chemical analyzer (CA) as a compositional mass analyzer with a mass resolution of up to 50. Both subsystems, HRD and DA, point in the same direction. The units are mounted at 45 degrees on an articulation platform with one rotation axis and an angular range of 270 degrees. The field of views of the subsystems are 180 degrees (HRD), 90 degrees (IID), and 56 degrees (CA), respectively. The instrument had a total mass of 17 kg, a data rate between 0.1 and 4 kbps, and consumed 12 W of electrical power.

Key Objectives for the CDA Instrument

The scientific goals of the Cassini dust instrument were defined as:

- **Cruise science**. Extended studies of interplanetary dust from the Earth to the orbit of Saturn. Sample the chemical composition and the charging state of dust in interplanetary space. Determine the flux of interstellar particles during solar maximum conditions. Search for dust streams originating from Saturn.
- **Jupiter flyby**. Investigate the dynamics of the Io dust streams discovered by Ulysses and Galileo. Characterize their direction, size-mass-distribution, and correlation with the Jovian and interplanetary magnetic field. Investigate the dust stream fluxes caused by the Jovian system with respect to Jupiter distance. Analyze dust stream particles at a different epoch from Galileo. Characterize the elemental composition of dust stream particles.
- **Rings**. Map size distribution of ring material, search for ring particles beyond the known E-ring. Determine the sources and sinks of E-ring dust grains. Analyze the chemical composition of ring particles. Study dynamical processes (erosional, plasma, and electromagnetic) responsible for the E-ring structure, study interactions between the E-ring and Saturn's magnetosphere, and search for electromagnetic resonances. Study ring interaction with Titan. Determine dust and meteoroid distribution both in the vicinity of the rings and in interplanetary space.
- **Icy satellites**. Define the role of meteoroid impacts as a mechanism for surface modification. Obtain information on the chemical composition of satellites from the analysis of gravitationally bound ejecta particles in the vicinity of the satellites (within Hill spheres). Investigate interactions with the ring system and determine the

importance of the various satellites as sources of ring particles. Search for particles from retrograde moons.

- **Magnetosphere of Saturn**. Determine the role that dust plays as source and sink for charged particles in the magnetosphere. Search for electromagnetically dominated dust (small particles) and for dust streams. Constrain the origin of dust streams.

CDA Science Assessment

Table CDA-1 contains an assessment of CDA science based on the objectives in the original Announcement of Opportunity (AO) and the Cassini Traceability Matrix (TM) developed for the Equinox and Solstice missions. The key AO and TM objectives addressed are:

- **Cruise Interplanetary Dust Studies (C_AO4)** – Extend studies of interplanetary dust to the orbit of Saturn.
- **Icy Satellite Geology and History (I_AO1)** – Determine the general characteristics and geological histories of the satellites.
- **Icy Satellite Surface and Crustal Modifications (I_AO2)** – Define the mechanisms of crustal and surface modifications, both external and internal.
- **Icy Satellite Surface Composition (I_AO3)** – Investigate the compositions and distributions of surface materials, particularly dark, organic-rich materials and low melting point condensed volatiles.
- **Icy Satellite Interior Properties (I_AO4)** – Constrain models of the satellites' bulk compositions and internal structures.
- **Icy Satellite Magnetosphere and Ring Interactions (I_AO5)** – Investigate interactions with the magnetosphere and ring systems and possible gas injections into the magnetosphere.
- **Enceladus Seasonal Changes (IC1a)** – Identify long-term secular and seasonal changes at Enceladus, through observations of the south polar region, jets, and plumes.
- **Enceladus Ocean (IN1a)** – Determine the presence of an ocean at Enceladus as inferred from induced magnetic field and plume composition, search for possible anomalies in the internal structure of Enceladus as associated with plume sources, and constrain the mechanisms driving the endogenic activity by in situ observations and remote sensing.
- **Magnetosphere Wave-Particle Interactions (M_AO3)** – Investigate wave-particle interactions and dynamics of the dayside magnetosphere and the magnetotail of Saturn and their interactions with the solar wind, the satellites, and the rings.

- **Enceladus Plume Variability (MC1a)** – Determine the temporal variability of Enceladus' plumes.
- **Ionosphere and Ring Coupling (MN2a)** – Determine the coupling between Saturn's rings and ionosphere.
- **Ring Structure and Dynamics (R_AO1)** – Study configuration of the rings and dynamical processes (gravitational, viscous, erosional, and electromagnetic) responsible for ring structure.
- **Ring Particle Composition and Size (R_AO2)** – Map composition and size distribution of ring material.
- **Ring-Satellite Interaction (R_AO3)** – Investigate interrelation of rings and satellites, including embedded satellites.
- **Dust and Meteoroid Distribution (R_AO4)** – Determine dust and meteoroid distribution both in the vicinity of the rings and in interplanetary space.
- **Ring Magnetosphere-Ionosphere Interactions (R_AO5)** – Study interactions between the rings and Saturn's magnetosphere, ionosphere, and atmosphere.
- **Changing Rings (RC1a)** – Determine the seasonal variation of key ring properties and the microscale properties of ring structure, by observing at the seasonally maximum opening angle of the rings near solstice.
- **F-ring (RC2a)** – Focus on F-ring structure, and distribution of associated moonlets or clumps, as sparse observations show clumps, arcs, and possibly transient objects appearing and disappearing.
- **Ring Age and Origin (RN1a)** – Constrain the origin and age of the rings by direct determination of the ring mass, and of the composition of ring ejecta trapped on field lines.
- **Ring Composition (RN1b)** – Determine the composition of the close-in "ringmoons" as targets of opportunity.
- **Ring Structure (RN1c)** – Determine structural and compositional variations at high resolution across selected ring features of greatest interest, using remote and in situ observations.
- **Titan Upper Atmosphere (T_AO5)** – Investigate the upper atmosphere, its ionization, and its role as a source of neutral and ionized material for the magnetosphere of Saturn.

Table CDA-1. CDA Science Assessment: AO and TM objectives are paired with CDA science objectives.

Fully/Mostly Accomplished: **Partially Accomplished:**

CDA Science Objective	AO and TM Science Objective	CDA Ring Science Assessment	Comments if yellow (partly fulfilled)
Ring Science			
Structure and dynamics of E-ring	R_AO1, R_AO2, R_AO3, R_AO4, T_AO5, RN1c, RC1a		
Seasonal variation of E-ring	RC1a		Analysis is not complete.
Composition of E-ring	R_AO2, RN1b, RN1c		
E-ring origin	R_AO1, I_AO1, I_AO2, I_AO3, I_AO5, IN1a		
G-ring	R_AO1, RC2a		HRD was damaged by a grain larger than 100 microns during a near G-ring crossing in 2005.
Other diffuse rings / ring arcs	R_AO1, R_AO2, R_AO3		
In situ composition measurements of main ring material	R_AO1, R_AO2, RN1a		
Ring rain mass flux and structure	R_AO1, R_AO2, R_AO4, R_AO5, RN1a, MN2a		
Icy Satellites			
Enceladus			
Plume ice grain structure and size distribution	R_AO2, R_AO3, I_AO2, I_AO3, I_AO4, I_AO5, IC1a, IN1a, MC1a		
Plume ice grain mass output	R_AO3, I_AO4, IN1a		
Plume ice grain composition	I_AO1, I_AO4, IN1a		
Plume dynamics			
Ejecta from hypervelocity impacts on icy moons	R_AO1, R_AO2, R_AO3, R_AO4, I_AO5		Ring/ring arcs associated with moons were detected and studied. Despite multiple attempts, the existence of ejecta clouds around other mid-sized icy moons remains ambiguous because of the higher than expected E-ring background.
Magnetosphere			
E-ring grain charge	R_AO4, R_AO5, M_AO3		
Dynamics of Saturnian stream Particles	R_AO2, R_AO3, R_AO4, R_AO5, M_AO3		
Composition of Saturnian stream particles	R_AO2, R_AO3, R_AO5, M_AO3, I_AO1, I_AO4, IN1a		
Other (including cruise, Jupiter flyby)			
IDP (cruise)	C_AO4		
Exogenous mass infall	C_AO4, R_AO4, RN1a		
Interstellar dust	R_AO4		
Jovian nanograins (Jupiter flyby)	J_AO1		

CDA Saturn System Science Results

Rings

E-ring

Saturn's E-ring was one of the prime targets of CDA from the beginning of the mission. After the discovery of the plume activity on Enceladus and its recognition as the major source of the E-ring grains—see section entitled Enceladus and Spahn et al. [2006a]—the E-ring measurements became more important. Sampling the E-ring provides insights into not only the dynamical evolution of micron-sized grains but also the structure and composition of Enceladus' interior [Postberg et al. 2009b; Postberg et al. 2011]. In situ CDA measurements have characterized the E-ring spatial distribution, the grain size distribution, the electrostatic charge state, and the grain composition [Srama et al. 2006; Kempf et al. 2006, 2008a, 2010; McBride et al. 2007; Hillier et al. 2007a; Postberg et al. 2008; Ye et al. 2014, Hsu et al. 2015]. Both DA and HRD data have been used to derive the E-ring spatial distribution and the grain size distribution. The grain charge is measured by the entrance grid signal (QP) and the grain composition by the CA.

A side projection of the global apparent dust density is shown in Figure CDA-1. One has to keep in mind that the mass threshold during the related measurements was not fixed. The mass

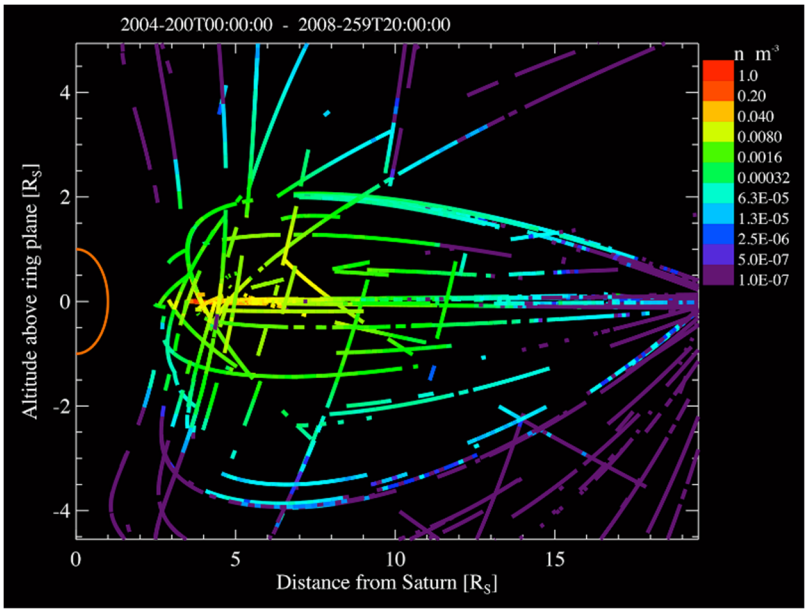

Figure CDA-1. Global apparent dust density measured by CDA in the Saturnian system. The densities are color coded along the Cassini trajectory in the time range of 2004-200 to 2008-259 (Cassini Prime Mission). High impact rates and densities are observed outside the optically measured E-ring, which was defined between 3 to 9 R_S. Enhanced dust densities are found as far as 250,000 km away from the ring plane and extend to radial distances of 20 R_S and beyond. From Srama et al. [2006].

threshold varied with relative impact speed and CDA becomes more sensitive for higher relative impact speeds. Assuming a typical relative impact speed of 8 km s^{-1}, the lower mass threshold would be 1.2×10^{-16} kg. This mass corresponds to compact water ice particles with a diameter of 0.6 µm.

Spatial Distribution

The densest part of the E-ring lies at ρ_c = 3.98 R_S (1 R_S is the radius of Saturn, 60,268 km), slightly outside the orbit of Enceladus (3.95 R_S) as known from pre-Cassini Earth-based observations [de Pater et al. 1996a]. The peak number density ranges from 16 to 21 × 10^{-2} m^{-3} for grains larger than 0.9 µm, and 2.1 to 7.6 × 10^{-2} m^{-3} for grains larger than 1.6 µm. The radial extension of the E-ring inferred from CDA measurements is much broader than that from the remote sensing observations. The E-ring encompasses all major icy moons of Saturn from 3 to 20 R_S [Srama et al. 2006, 2011], i.e., from the orbit of Mimas to that of Titan. The ring's vertical profiles are generally Gaussian, yet the vertical extension varies with the radial distance [Kempf et al. 2008b]. The narrowest part is located at ρ_c = 3.98 R_S with a full-width-half-maximum (FWHM) of 4,300 km. The vertical ring thickness increases both inwards and outwards from ρ_c. The density peak offsets towards the south with respect to the geometric ring plane at radial distances inside ρ_c. The offset is about 1,200 km at Mimas' orbit. No clear offset was found outside ρ_c in CDA data prior to 2008. An empirical, axisymmetric E-ring density model based on the CDA measurements is described in Kempf et al. [2008b].

The E-ring encompasses all major icy moons of Saturn from 3 to 20 R_S …, i.e., from the orbit of Mimas to that of Titan.

As reported by Hedman et al. [2012] based on imaging data, CDA measurements also indicate that the E-ring is asymmetric with respect to the local time [Kempf et al. 2012]. The data analysis and modeling efforts in understanding the day-night asymmetry of the E-ring are still ongoing.

Radial scans were performed by DA in the ring plane in order to determine the radial density profile of smaller grains (Figure CDA-2). As described earlier, the mass threshold was in the submicron range and variable. The density profile is compatible with a power law function of the type $n(r) = 20\ (r - 2.8)^{-4.6}$. This has to be considered a minimum density since particles below the detection threshold were not considered.

Grain Size Distribution

The grain size distribution of a diffuse ring sheds light on the grain production mechanism and the dynamical evolution of the ring. Under nominal encounter speeds in the E-ring, i.e., several km s^{-1}, DA was able to measure grains as small as 0.1 µm and HRD was sensitive to grain radii ranging from ~1 to 10 µm. The grain size distribution information is mostly derived from HRD because of the long dead time of the DA (~1 second)—see Kempf [2008b].

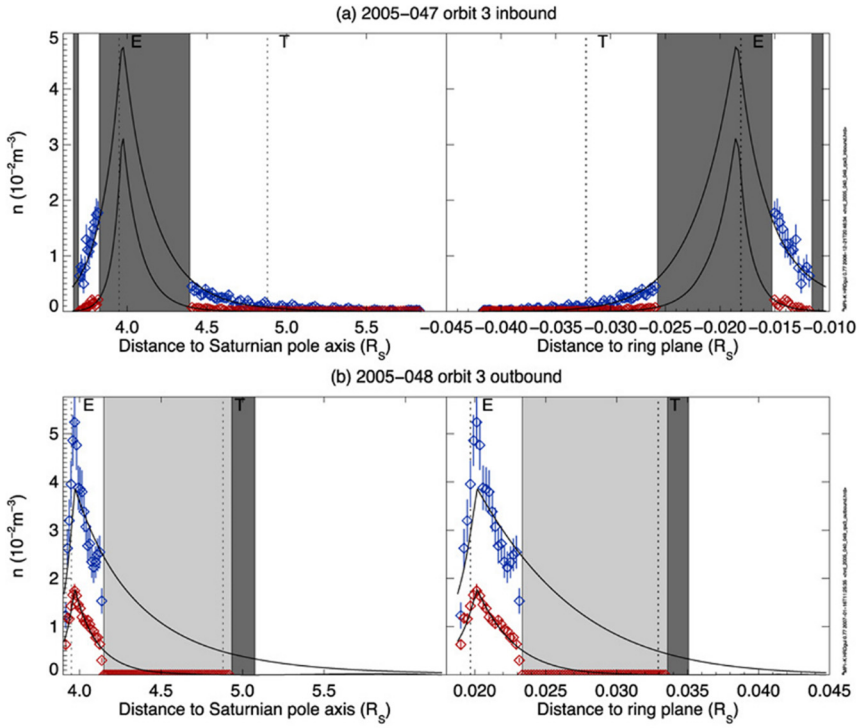

Figure CDA-2. E-ring number density profiles measured by CDA/HRD. Spatial distribution of E-ring particles 1.3 µm (red) and 2.4 µm inferred from HRD rate measurements inside 6 R_S in orbit 3. Solid curves are the empirical model given in Kempf et al. [2008b].

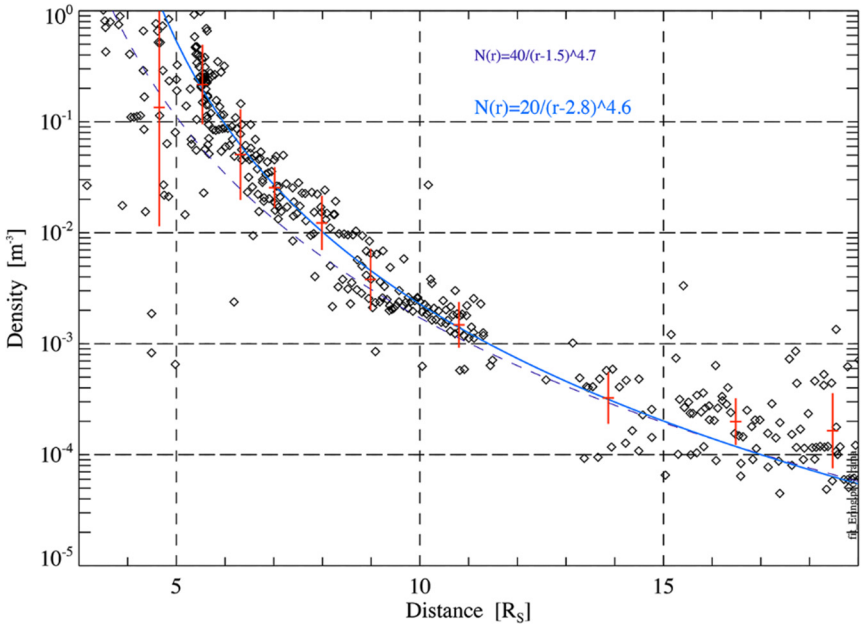

Figure CDA-3. Radial density profile of Saturn's E-ring measured in the ring plane. Data from the years between 2004 and 2008 were considered. Figure from [Srama et al. 2006].

The differential size distribution of E-ring grains is consistent with a power-law distribution, $n(s_d)\, ds_d \sim sd^{-q}\, ds_d$, with slope q = 4 to 5 for grains >0.9 μm [Kempf et al. 2008b]. s_d is the grain radius. The size slopes derived from the RPWS instrument are consistent within a range of q = 3 to 5 (Figure CDA-4) [Ye et al. 2014, 2016]. The steep size distribution slope is related to the E-ring's peculiar blue spectral color [Showalter et al. 1991; de Pater et al. 1996; Nicholson et al. 1996] and stems from the size-speed dependence of grains emitted from the plume of Enceladus (see section entitled Enceladus). In comparison, for diffuse rings supplied by ejecta from hypervelocity impacts on the source bodies, the size slopes are flatter (q ~ 2), resulting in a redder spectral color (e.g., G-ring, see section entitled Other Rings).

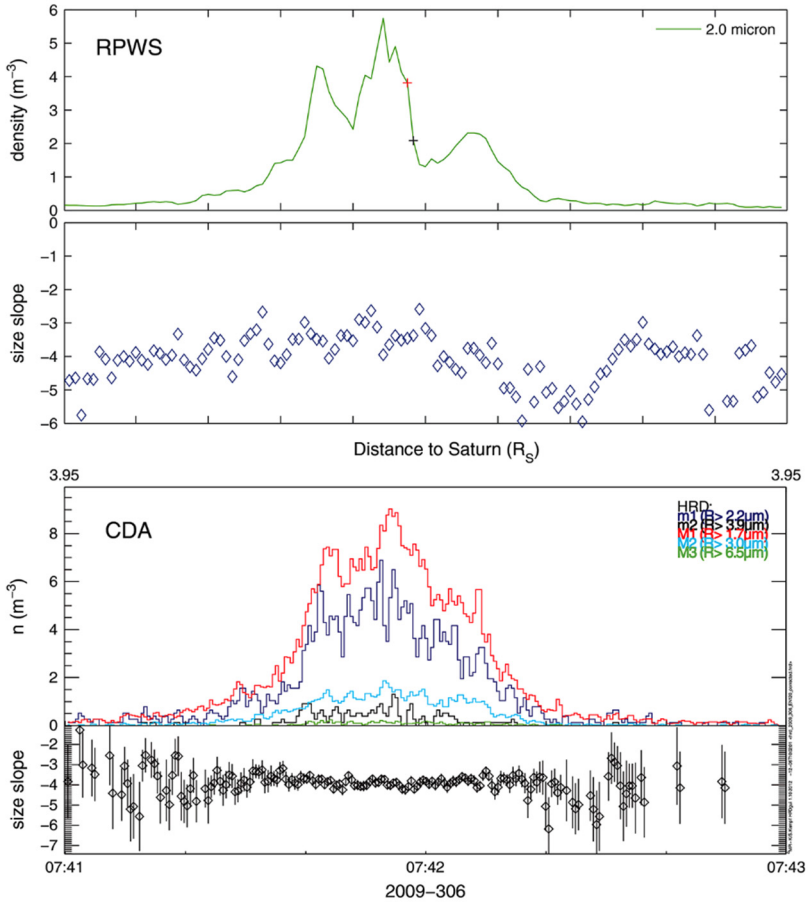

Figure CDA-4. Grain number density and the size distribution slope during E7 flyby by RPWS and CDA/HRD. Figure from Ye et al. [2014].

Grain Electrostatic Charge State

The Lorentz forces acting on a grain are determined by the number and the polarity of electric charges of a grain. The grain charge is determined by various charging processes, e.g., plasma electron and ion collections, photoemission and secondary electron emission, and thus is expected to vary with the magnetospheric plasma conditions [Horányi et al. 1992]. Figure CDA-5 shows the

CDA measurements of E-ring grain charges at various distances [Kempf et al. 2006]. Near Enceladus' orbit the grain potential is about −3 Volts, consistent with, but slightly lower than, the previous estimates based on Voyager plasma measurements [Horányi et al. 1992]. The grain potential becomes more positive with increasing distance and the polarity turns positive roughly outside the orbit of Rhea [Kempf et al. 2006] because of the decreasing plasma electron density and the increasing secondary electron emission resulting from the presence of more energetic electrons in the middle to outer magnetosphere [Arridge et al. 2011; Hsu et al. 2011b].

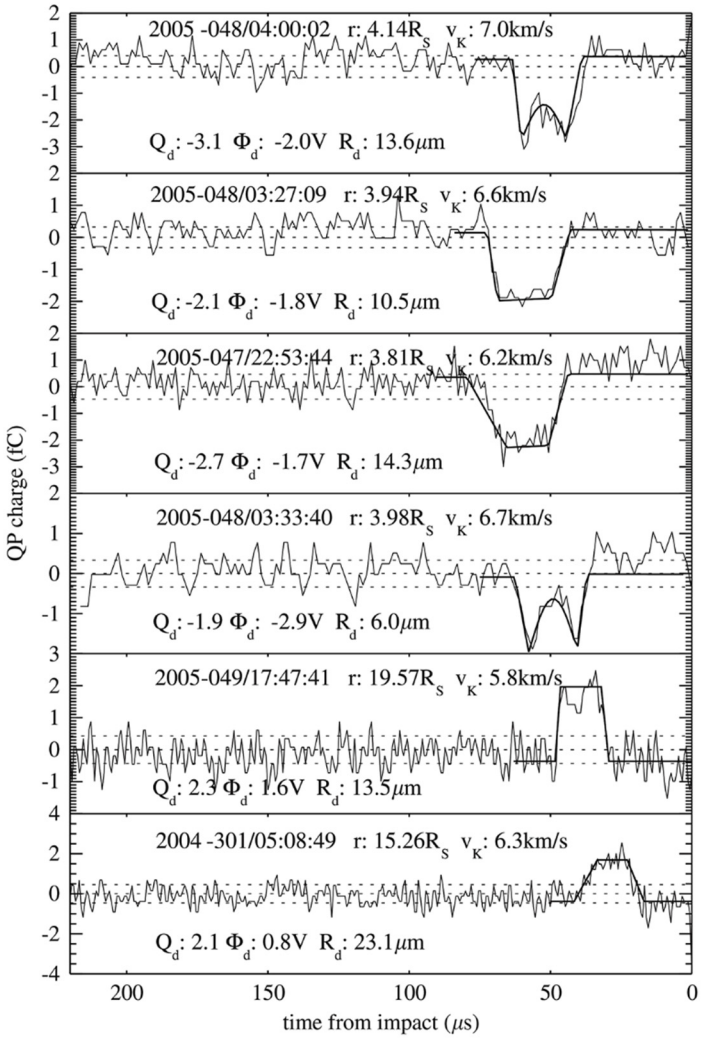

Figure CDA-5. Particle charge signals from the QP channel as measured by CDA in the E-ring at various radial distances from Saturn. The signal shape varies with particle speed (signal width), incident angle (signal asymmetry) and particle surface charge (signal amplitude). The signal sag is dependent upon the particle trajectory and its distance from the outer housing. From Kempf et al. [2006].

GRAIN COMPOSITION

E-ring grains are predominantly composed of water ice [McBride et al. 2007, Hillier et al. 2007a; Postberg et al. 2008]. The presence of minor grain constituents (up to a few percent levels), however, drastically changes mass spectral appearance because of the nature of impact ionization time-of-flight spectroscopy. Three major types of E-ring grain mass spectra have been identified (Figure CDA-6): Type I - pure water ice particles; Type II - water ice with organic compounds and/or silicate minerals impurities; and Type III - water ice rich in sodium salts [Postberg et al. 2008, 2009b, 2011]. The majority of the E-ring grains are either Type I or II, with only ~6% belonging to Type III.

The presence of Type III salty E-ring grains suggests the existence of subsurface liquid water underneath Enceladus' south polar terrain [Postberg et al. 2009b, 2011], in good agreement with the calculated thermodynamics result [Schmidt et al. 2008]. They are interpreted as frozen droplets lofted from liquid plume sources at the bottom of the fissures, representing direct samples of the subsurface waters within Enceladus [Postberg et al. 2009b, Postberg et al. 2011]. The salinity (0.5 to 2% by mass) and pH values (8 to 11) of the subsurface waters are also inferred [Postberg et al. 2009b]. Other findings about the icy moon Enceladus are addressed in the section entitled Enceladus.

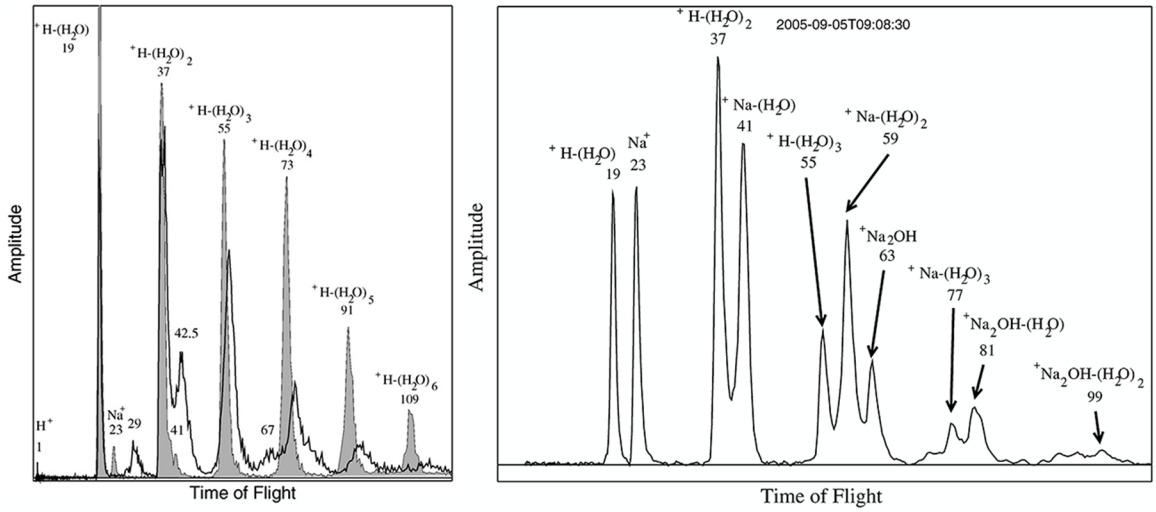

Figure CDA-6. Three major E-ring grain composition types. *Left*: Type I (pure water ice, gray) and Type II (water ice and organic compounds and/or silicate minerals, bright) E-ring grain mass spectra. The horizontal axis shows the cation time of flight. The vertical axis shows the peak amplitude. The Type I spectrum is characterized by the presence of water clusters, $H\text{-}(H_2O)^+_n$, where n = 1 to 6. Type II spectrum often show a wide feature at 42 to 43 u and 65 to 68 u. A shift of the water cluster peaks starts at n > 2 and increases towards longer times of flight. *Right*: Type III salt-rich E-ring grain mass spectrum. Water clusters ($H\text{-}(H_2O)^+_n$) seen in Type I spectrum are joined by sodium-water clusters, $Na\text{-}(H_2O)^+_n$ and $(Na_2OH)\text{-}(H_2O)^+_n$, because of the abundant Na^+. From Postberg et al. [2008].

GRAIN DYNAMICS MODELING

Joining pre-Cassini results, for example, Showalter et al. [1991]; de Pater et al. [1996]; Nicholson et al. [1996], the "ground truth" measurements provided by Cassini make Saturn's E-ring the most studied diffuse ring in the solar system. While the E-ring is particularly special because of its cryovolcanic origin, the same processes shaping the E-ring operate similarly elsewhere. Modeling efforts enable us to readily apply what has been learned from Saturn's E-ring to other environments.

> … Saturn's E-ring is the most studied diffuse ring in the solar system.

Regarding the E-ring dynamics, early modeling shows that the gravity from the oblate planet and the Lorentz forces from the electromagnetic fields lead to a size-dependent orbital precession rate ($\dot{\omega}$). For grains with radii around 1 μm, this leads to $\dot{\omega} \sim 0$ and allows a fast increase in the grains' orbital eccentricities by the solar radiation pressure force on timescales of a few years [Horányi et al. 1992; Hamilton 1993]. Additionally, the drag force asserted by the co-rotating magnetospheric plasma overtaking grains in semi-Keplerian orbits leads to an increase of the grains' orbital semi-major axes (i.e., grains gain orbital energy) [Dikarev 1999; Horányi et al. 2008]. Simultaneously, grain sizes are reduced by plasma sputtering erosion [Jurac et al. 2001; Juhasz and Horányi 2002; Horányi et al. 2008]. The combined effect of plasma drag and sputtering causes a reduction in grain sizes towards larger Saturn-centric distances without changing the size distribution [Horányi et al. 2008]. The radial extension of the E-ring up to Titan's orbit [Srama et al. 2006] also implies that Enceladus has been actively supplying the E-ring for at least hundreds of years.

Ejecta cloud and diffuse rings

In addition to the cryovolcanic E-ring, CDA also explored other diffuse rings, which are most likely supplied by impact ejecta produced from the embedded source bodies through continuous bombardment of micrometeoroids and the consequent fragmentation. Ejecta produced from airless bodies could appear in three forms, depending on the gravitational influences of the source body and its neighbors: a dust exosphere around the source body (e.g., around Galilean moons and Rhea), a complete ring (e.g., Saturn's G-ring), or a ring arc (a partial ring, e.g., the Anthe and Methone ring arcs). Modeling efforts provided theoretical support for characterizing the exogenous interplanetary mass infall [Han et al. 2011; Poppe and Horányi 2012] (see section entitled Interplanetary Dust) and the resulting ejecta cloud around major [Krivov et al. 2003; Sremčević et al. 2003; Dikarev et al. 2006; Spahn et al. 2006b] and minor [Sun et al. 2017] moons in the Saturnian system.

EJECTA CLOUD AROUND RHEA

In contrast to the clear detection of dust exospheres around Galilean moons [Krüger et al. 1999], the identification of such ejecta clouds around Saturn's major icy moons was ambiguous except at Rhea (8.75 R_S) [Jones et al. 2008], the major icy moon located furthest from the E-ring source

moon Enceladus (Figure CDA-7). Clearly, the background of the extensive E-ring renders a clear detection of a dust exosphere around the inner icy moons difficult.

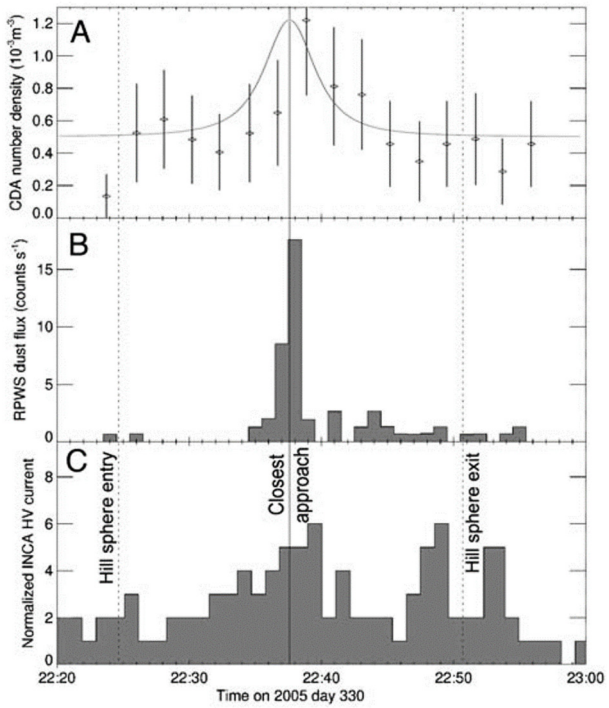

Figure CDA-7. In situ dust observations reveal the dust cloud around Rhea. Measurements from three in situ instruments during the Rhea flyby on November 26, 2005: (A) CDA (grains > 1 µm), (B) Radio and Plasma Wave Science instrument (grains ≥ 3 µm), and (C) Magnetosphere Imaging Instrument. From Jones et al. [2008].

Pallene ring

The dusty ring associated with a tiny moon, Pallene (mean radius ~2 km), at 3.52 R_S [Hedman et al. 2009b] has been detected by CDA/HRD in 2010 [Seiß et al. 2014]. The cross-section of the ring measured by HRD can be fitted with a double-Gaussian distribution, yielding a radial and vertical FWHM of 2,300 km and 270 km, respectively, and a maximum particle density of 2.7×10^{-3} m^{-3}. Additionally, the data clearly show an enhancement of larger particles in the Pallene ring compared to the background E-ring particles. In comparison, no in situ CDA detection of the ring arcs associated with Anthe (3.28 R_S) and Methone (3.23 R_S) has been reported so far.

G-ring

Collisions are expected to be the major dust production process that resupplies Saturn's G-ring, as indicated from its spectrally red color [de Pater et al. 1996; Nicholson et al. 1996]. However, no source was known prior to Cassini's arrival. The source of the G-ring was then identified, based on Cassini imaging data [Hedman et al. 2007], as a 60°-long arc. Collisional fragmentation of

centimeter- to meter-sized objects within this bright arc is believed to replenish the G-ring, which would otherwise disappear over relatively short timescales.

An impact of an exceptionally large dust grain (>100 μm) was registered and damaged HRD on September 5, 2005, when the spacecraft passed the ring plane at a radial distance of 2.93 R_S, less than 0.15 R_S from the core of the G-ring [Hedman et al. 2007]. The size of that grain is consistent with the impactor-ejecta production origin.

JANUS-EPIMETHEUS RING

During the ring grazing orbits, the spacecraft passed near the orbits of the co-orbital moons Janus and Epimetheus [Buratti et al. 2019]. A Gaussian distribution fit to the radial profile of grains larger than 1.6 μm registered by HRD show that the peak density is located very close to the orbits of Janus and Epimetheus at 151,500 km (2.51R_S) with a radial width of about 4,300 km.

Grand finale mission

The major science goals of CDA for the Grand Finale were: (1) perform in situ composition measurements of materials from the Main rings and (2) study the ring–planet interactions.

An analysis of CDA and RPWS measurements suggests that the region interior to Saturn's D-ring sampled during Cassini's Grand Finale Mission is predominantly populated by grains 10s of nm in radii, whose dynamics are consistent with high-speed impact ejecta from Saturn's main rings [Hsu et al. 2018]. Electromagnetic forces lead to the fast transport of tiny, charged ejecta grains (within hours, see Hsu et al. [2017]), which comprises a ring mass loss pathway (10^2 to 10^3 kg s^{-1}). About 20% of this ejecta falls into Saturn, mainly in the equatorial region and the southern hemisphere, leading to the observed H_3^+ ionospheric signature, i.e., the Ring Rain effect [O'Donoghue et al. 2013; Moore et al. 2015]. Two grain composition types were identified from ~25% of recorded mass spectra—water ice and silicates, with an ice fraction varying with the distance from the ring plane—decreasing from around 70–90% near the ring plane towards high latitudes. No indication of grains with pure organics, iron or iron-oxide compositions has been found in the dataset.

Icy Satellites

Enceladus

Ice grains emitted from Enceladus provide a unique window to probe the interior of Enceladus, as these tiny solid particles preserve information differently from that in gaseous and plasma phases. The micron-sized ice grains and the nanometer-sized silica stream particles probe the conditions of the subsurface water of Enceladus at different depths: the silica nanoparticles probe the pH, salinity and water temperature at the bottom of Enceladus' ocean, while the micrometer-sized ice

grains reveal composition and thermodynamical processes at near-surface liquid plume sources and in the vents.

Several sets of CDA measurements contribute to the study of Enceladus: (a) in the E-ring (described in the section entitled E-ring), (b) during the close Enceladus flybys, and (c) the Saturnian nanodust stream particles.

CLOSE ENCELADUS FLYBYS

Information provided by the CDA measurements during the plume crossings include the structure of the dusty plume (HRD) and the composition of freshly emitted grains (DA). The HRD data from the close encounter on July 14, 2005, showed that the grains in the vicinity of Enceladus are produced from a localized source near the south polar region [Spahn et al. 2006a], suggesting endogenic dust production at Enceladus as the major source of Saturn's diffuse E-ring. In addition, the structure of the plume provides constraints on the thermodynamics of the grains and vapor in the vents. The grain size distribution sampled by HRD is best explained by ice grain formation from condensation as water vapor reaches saturation when passing through the nozzles in the subsurface fissures (Figure CDA-8) [Schmidt et al. 2008]. A key characteristic successfully explained by this nozzle model is the size-dependent grain initial speeds, larger grains are emitted slower due to the longer time required to recover to the gas flow speed after a wall collision in the vent. This leads in a steepening of grain size distribution towards higher altitudes in the plume, consistent with measurements from the Visual and Infrared Imaging Spectrometer (VIMS) [Hedman et al. 2009a].

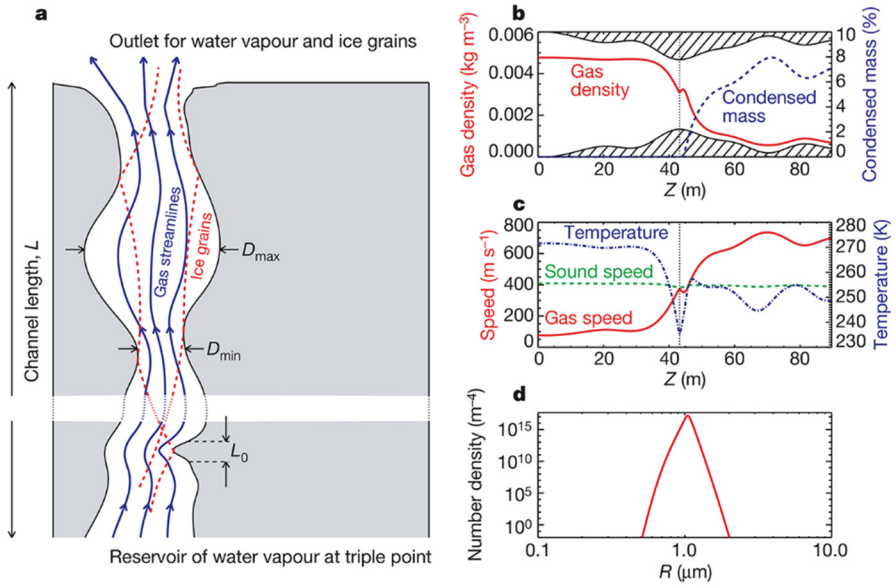

Figure CDA-8. The nozzle grain formation model. (a) Schematic sketch of the subsurface fissure profile describing the gas flow and ice grain condensation. (b, c) Thermodynamics conditions in the channel as a function of depth. (d) The resulting grain size distribution of one single channel. Figure from Schmidt et al. [2008].

Constrained by the HRD measurements, the mass production rate of micron-sized ice grains from the plume was estimated to be approximately 10 kg s^{-1} [Southworth et al. 2019], comparable with independent estimates from the imaging data [Ingersoll and Ewald 2011; Gao et al. 2016]. In addition, the deposition of plume ice grains onto Enceladus simulated with the same model shows a pattern resembling an infrared-ultraviolet brightness ratio map of Enceladus (Figure CDA-9) [Kempf et al. 2010; Schenk et al. 2011]. While this reinforces notions about the effects of the E-ring deposition and the surface albedo patterns of the major icy moons [Buratti et al. 1990; Verbiscer et al. 2007; Schenk et al. 2011], the detailed mechanisms remain unknown.

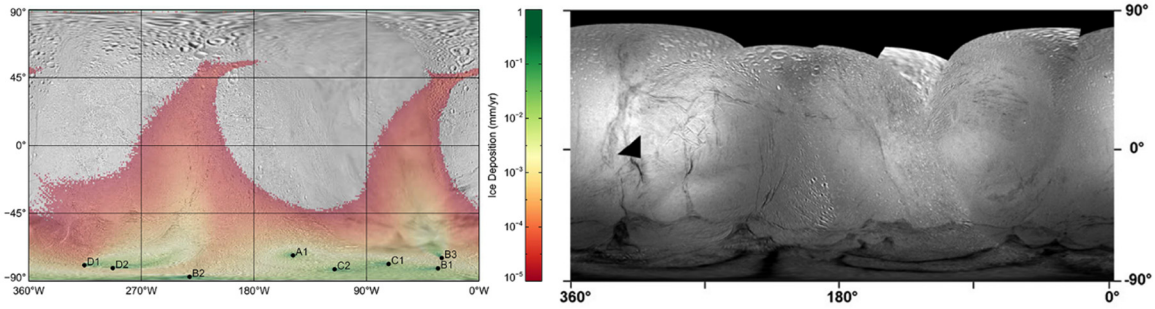

Figure CDA-9. Modeled plume deposition map (left) and the observed infrared/ultraviolet (IR/UV) ratio map of Enceladus (right). From Kempf et al. [2010] and Schenk et al. [2011].

Grain composition provides information about the subsurface waters of Enceladus. As mentioned, the presence of Type III (salt-rich) E-ring grains indicates salty, alkaline subsurface waters within Enceladus [Postberg et al. 2009b]. The grain composition profile recorded during the E5 close encounter in 2008 shows that the ratio of Type III grains increases from the E-ring background of around 6% to 40% at the closest approach (altitude of 25 km) [Postberg et al. 2011]. A clear decrease of the proportion of Type I grains in the dense plume region was confirmed by data of the E17 flyby in 2012 [Khawaja et al. 2017]. The dominance of the larger, salty ice grains at lower altitudes indicates a stratified plume [Hedman et al. 2009a; Postberg et al. 2011] and is consistent with the aforementioned modeling results [Schmidt et al. 2008]. In other words, the grain composition stratification reflects the grain formation processes in the fissures (Figure CDA-10) and thus strongly suggests that subsurface waters are the direct source of the plume [Postberg et al. 2011]. This result also agrees with the low abundance of salty ice grain (Type III) in the E-ring [Postberg et al. 2008]—most grains capable of escaping Enceladus to resupply the E-ring are smaller, and therefore faster, pure ice grains forming from condensation in the vents. Salty grains tend to be heavier/slower and mostly fall back onto the moon [Kempf et al. 2010; Postberg et al. 2011].

A subset of E-ring Type II spectra was found to contain a series of mass lines indicating the presence of complex organic molecules with a mass fraction of about 1% of the ice grain [Postberg et al. 2018]. As shown in Figure CDA-11, the species marked high mass organic cation (HMOC) show regular ~12.5 u separation and extend to beyond ~200 u mass range, indicating that they are fragments of larger parent molecules whose mass may be in the 1,000s u region. The observation suggests the existence of a thin film at the subsurface water liquid-vapor interface composed of complex organics likely originating from hydrothermal activities deep inside Enceladus.

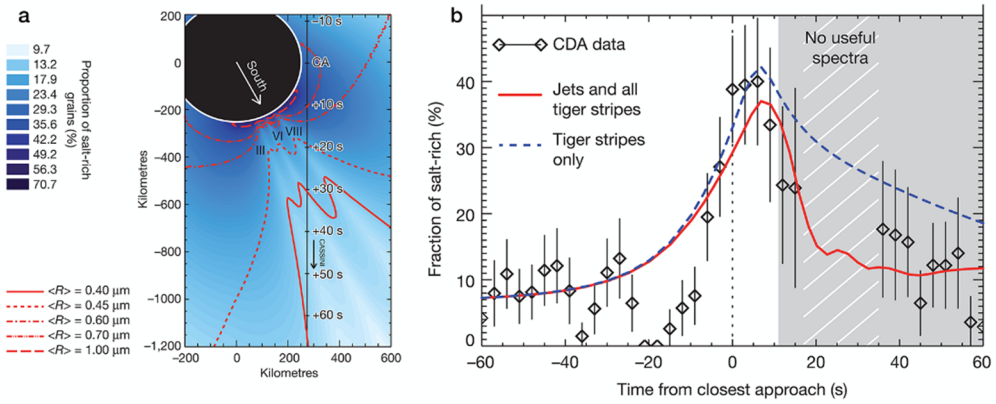

Figure CDA-10. Compositional and size profile of the ice plume of Enceladus. (a) The background color and the contour lines show the modeled fraction of salt-rich grains and the mean particle radius <*R*> of grains emitted from the plume of Enceladus. (b) Measured Type III spectrum fraction as a function of time during the E5 Enceladus flyby. Model and measurement results consistently show that the closer to the surface, the higher the fraction of Type III ice grains. Figure from Postberg et al. [2011].

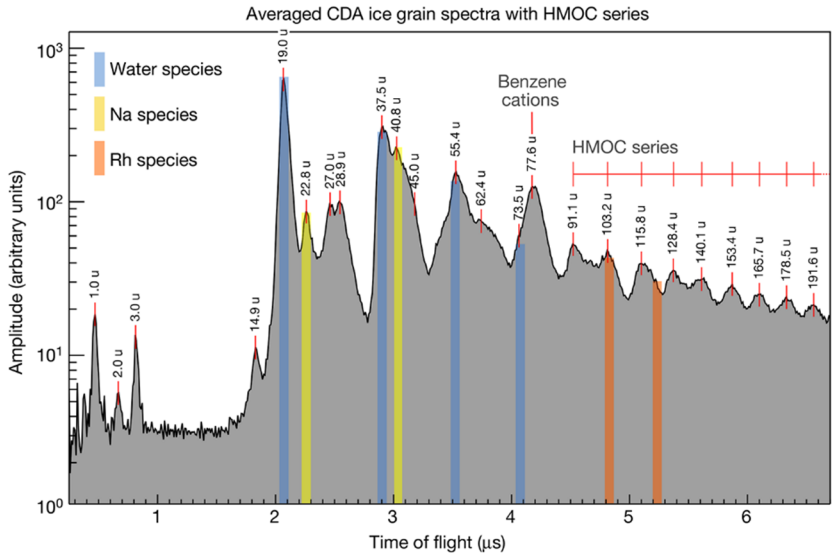

Figure CDA-11. CDA HMOC spectrum. This spectrum is co-added from 64 Type II E-ring spectra containing complex organic features. Benzene-like cations (77.6 u) and their fragments (C2 to C4 species) as well as the (HMOC, 91 u, and higher) appear distinctively from water (blue) and CDA target (Rh, orange) and target contamination (Na, yellow) mass lines. Figure from Postberg et al. [2018].

NANO-PHASE SILICA PARTICLES

The fast, nanometer-scale silicon-rich grains emitted into interplanetary space from the Saturnian system were the first CDA discovery [Kempf et al. 2005a, 2005b], despite the theoretical prediction [Horányi 2000] based on the knowledge of their Jovian counterparts [Grün et al. 1993]. These nanoparticles are in fact the silicon fingerprint of the ongoing hydrothermal activities within Enceladus [Hsu et al. 2015; Sekine et al. 2015].

Since the dynamical properties of the nanograins are beyond the CDA calibrated range, their sizes (2 to 8 nm) and ejection speeds (50 to 200 km s^{-1}) are derived based on the interactions with the IMF [Hsu et al. 2010a, 2010b, 2011a, 2011b, 2012b]. These grains are interpreted to be of Enceladus origin—they are erosion-resistant impurities embedded in micron-sized E-ring grains, which are released after the surrounding ice matrix is removed by the plasma sputtering erosion [Hsu et al. 2011b].

One surprising factor regarding their composition is their extremely low metal concentration. Detailed analysis, including the laboratory hydrothermal reaction experiments, show that these grains are nanometer-sized metal-free silicon-oxide, i.e., nano-phase silica (SiO_2, Figure CDA-12b), which is best explained as nm-sized colloidal silica stemming from hydrothermal interactions within Enceladus [Hsu et al. 2015; Sekine et al. 2015]. The instability of the nano-phase silica sets strong constraints on the internal conditions of Enceladus subsurface waters (see Figure CDA-13), including (a) a water-rock reaction temperature of >90°C; (b) a low salinity ocean region (<4%) and an alkaline pH value (8.5 to 10.5), in good agreement with [Postberg et al. 2009b]; (c) Enceladus' rocky core is likely undifferentiated and porous, with a primordial composition similar to carbonaceous chondrites;

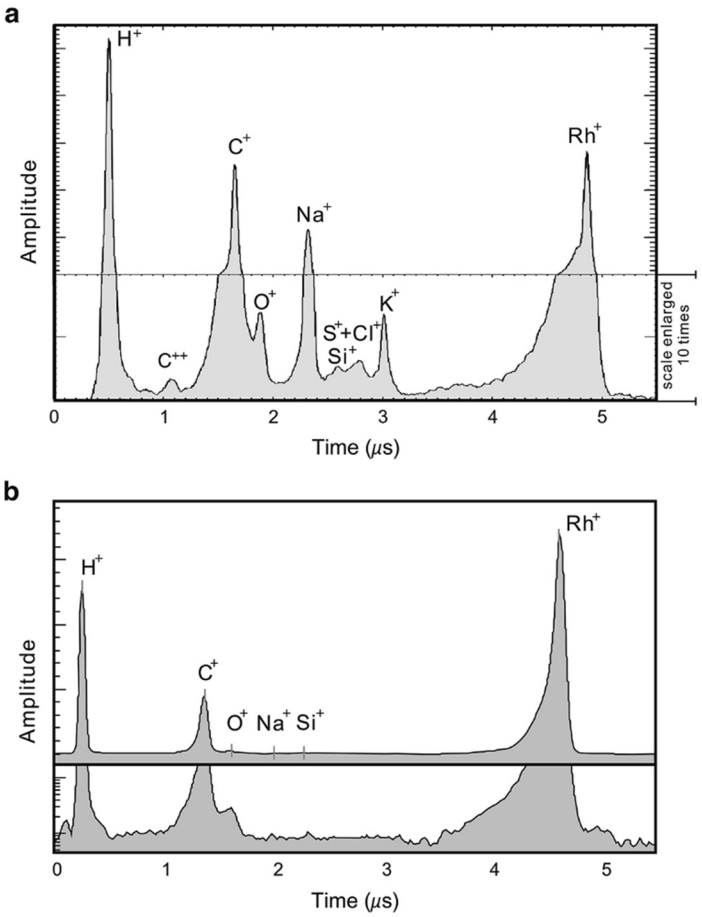

Figure CDA-12. CDA mass spectra of Jovian (*a*) and Saturnian (b) stream particles. Figure from Hsu et al. [2012b].

and (d) fast vertical transportation of the hydrothermal fluid from Enceladus' subsurface ocean to the plume within several years [Hsu et al. 2015; Sekine et al. 2015].

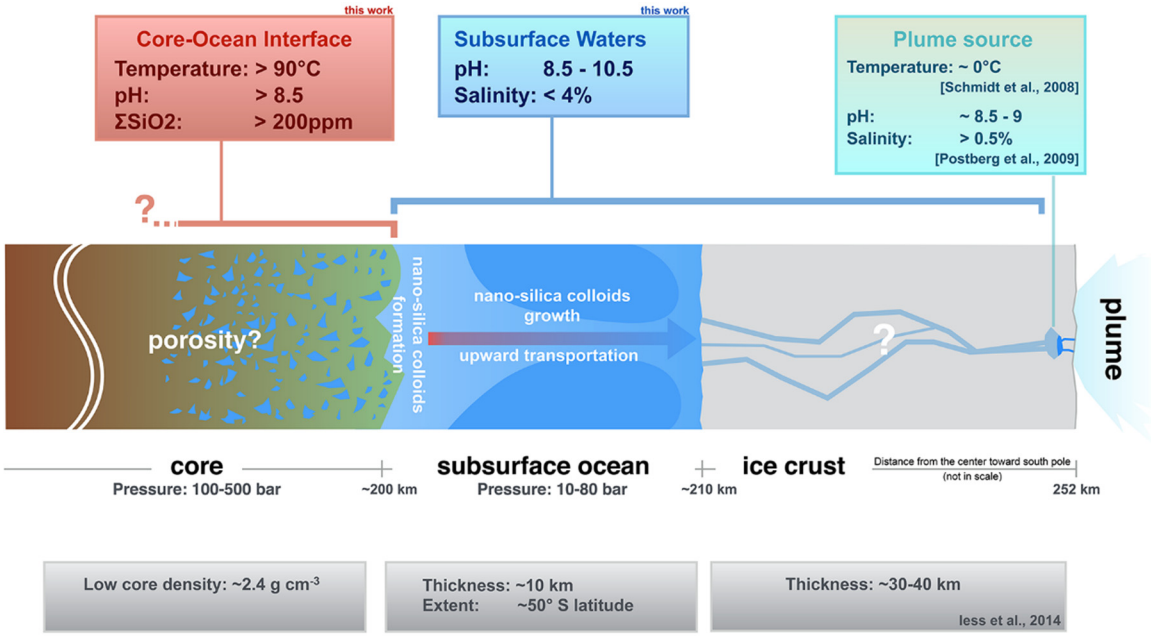

Figure CDA-13. A schematic of Enceladus' interior derived from the nano-phase silica results. Figure from Hsu et al. [2015].

Ejecta from Saturn's moons

As discussed in the section entitled Other Rings, the only major moon of Saturn around which an ejecta cloud was detected is Rhea [Jones et al. 2008]. The dusty rings associated with Pallene [Seiß et al. 2014], and Janus and Epimetheus [Buratti et al. 2019] were also explored in situ by CDA.

Magnetospheric and Plasma Science

Dust-magnetospheric plasma interactions

Grain charging, plasma sputtering, and plasma drag force

Magnetospheric plasma influences the charging, erosion, and dynamical processes of circumplanetary dust populations. In addition to the grain charge measurements in Saturn's E-ring [Kempf et al. 2006], as described in the section entitled E-ring, in situ E-ring characterization by CDA also provides constraints on the effects of the plasma sputtering erosion and the drag force. As illustrated in the modeling work by [Horányi et al. 2008], due to the plasma drag, grains from Enceladus can be transported from 4 to 20 R_S, and will arrive there with a few percentage of their

original radius due to sputtering losses, consistent with CDA measurements [Srama et al. 2006, 2011]. These calculations also indicate that the geysers on Enceladus have been supplying the E-ring material at an approximately constant rate for at least the last 300 years [Horányi et al. 2008].

Spacecraft charging

Strong interferences caused by dust impacts during the crossings of Enceladus' dusty plume have been reported from several instrument teams [Morooka et al. 2011; Ye et al. 2014; Krupp et al. 2018], likely caused by impact plasma produced from intense dust-spacecraft impacts. Because of the low plasma temperature of such an impact plasma cloud (~1 eV), this impact-generated plasma cloud may act as a buffer that reduces the spacecraft potential when traversing through a dust-rich region at high speed. The proposed effect has been examined by comparing the modeled spacecraft potential based on the CDA measurements to the Langmuir probe results during the plume and E-ring crossings [Hsu et al. 2012a, 2013a].

Nanodust dynamics in interplanetary space

CDA measurements also reveal the dynamical interactions of the Saturnian stream particles with the interplanetary magnetic field. After entering interplanetary space, the dynamics of the charged nanodust is governed by the IMF. CDA observed an identical detection pattern when the spacecraft crossed two similar solar wind compression regions associated with the Corotation Interaction Region (CIR), during the declining phase of solar activity in 2004 [Hsu et al. 2010b, 2011a]. These measurements illustrate that the nature of the dust stream phenomenon, first discovered by the Ulysses at Jupiter [Grün et al. 1993], is not in a form of collimated beams but a gust of electromagnetic acceleration of charged nanodust within a thick, warped dust sheet extending up to several astronomical units (AUs) from the source planets [Hsu et al. 2010a, 2010b].

Solar wind-magnetosphere interactions

The nanodust stream particle dataset is also relevant for studying the solar wind-magnetosphere interactions at Saturn. Serendipitous detections of a recurring pattern consisting of energetic stream particles coming from oblique directions are interpreted as the reentry of emitted stream particles back into their source magnetosphere due to the interaction with IMF [Hsu et al. 2013b]. Numerical simulation results show that this is simply due to the pick-up of the charged nanodust by the solar wind. The returning nanograins acquired kinetic energies higher than their initial kinetic energies gained from the magnetosphere, by being picked up in the compressed, high magnetic field strength solar wind regions. This means that this population can be easily identified and, more importantly, their directionality reflects the tangential component of the IMF. The latter provides additional information about the sector structure of the solar wind at Saturn's location. In other words, these measurements demonstrate an alternative method by which a single spacecraft can probe the solar wind conditions from within the magnetosphere [Hsu et al. 2013b; Hsu et al. 2016].

Instrument

In addition to the description of the CDA instrument [Srama et al. 2004], two publications provide information relevant for the CDA data analysis: (a) the DA dead time correction [Kempf 2008b] and (b) the contamination of the rhodium target of the integrated time-of-flight mass spectrometer [Postberg et al. 2009a].

Non-Saturn Science Results

Jovian Nanodust Stream Particles

"Ashes" from the volcanic plumes of Io, having acquired sufficient electric charges, may be accelerated by Jupiter's powerful magnetosphere and ejected with speeds comparable to the solar wind [Horányi et al. 1993; Graps et al. 2000]. These so-called stream particles were discovered during the first Ulysses flyby of Jupiter in 1992 by the onboard dust detector [Grün et al. 1993]. The detection patterns as registered by the Galileo Dust Detection System [Grün et al. 1992] suggest that they are modulated by the structure of the Io plasma torus (IPT) [Krüger et al. 2003b] as well as the temporal variation of Io's volcanic activities [Krüger et al. 2003a]. The stream could be detected by Galileo and Ulysses many 100 Mkm away from Jupiter.

Cassini CDA performed the first composition measurement of the Jovian stream particles before and after its Jupiter flyby in 2000/2001.

Cassini CDA performed the first composition measurement of the Jovian stream particles before and after its Jupiter flyby in 2000/2001 [Postberg et al. 2006]. Figure CDA-14 shows that these ash particles are mainly composed of sodium chloride (NaCl). In contrast to the sulfur-rich environment of Io, sulfur or sulfurous components and potassium-bearing components are only identified as minor constituents. Trace amounts of silicates or rocky minerals are often found. It is suggested that sodium chloride particles are formed inside Pele-type plumes prior to the condensation of the volatile SO_2. The less refractory sulfur compounds, in particular SO_2, either do not condense abundantly onto the grains, or are lost in bow shock regions at the top of the plumes, before the grains acquire sufficient electric charges to escape into Io's exosphere [Postberg et al. 2006]. The proposed scenario is in good agreement with the New Horizons observation of plume particle condensation in the eruption of Tvashtar [Spencer et al. 2007].

The CDA measurements of Jovian stream particles lasted about 10 months, roughly from day of year (DOY) 240 of 2000 to DOY 170 of 2001. A qualitative analysis of the CDA impact rate shows a correlation with the Galileo measurements [Hsu et al. 2010a, 2012b; Krüger et al. 2003b], reinforcing the idea of using Jovian stream particles as a monitor of Io's volcanic activities [Krüger et al. 2003a].

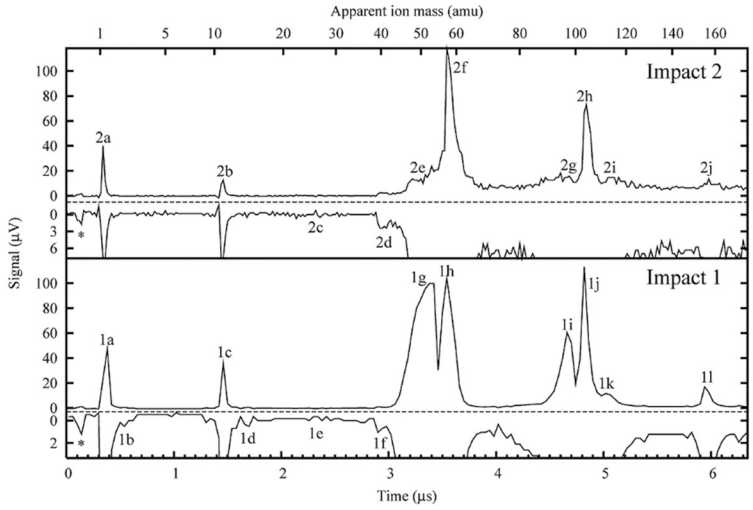

Ion abundances for both impacts

Species (key in Fig. 1)	Time (μs)	$\int Q_M$	Ions
Impact 1			
H^+ (1a), H_2^+ (1b)	0.28–0.64	2.71×10^{-12}	52,200
C^+ (1c)	1.36–1.58	2.22×10^{-12}	42,800
O^+ (1d)	1.6–1.72	3.16×10^{-14}	600
K^+ (1f)	2.84–2.96	1.09×10^{-13}	2100
'Fast Fe^+' (1g)	2.96–3.44	2.61×10^{-11}	503,300
'Slow Fe^+' (1h)	3.44–3.84	1.24×10^{-11}	239,300
'Fast Rh^+' (1i)	4.00–4.72	1.06×10^{-11}	204,200
'Slow Rh^+' (1j)	4.72–4.96	9.92×10^{-12}	191,400
RhC^+/Fe_2^+ (1k)	4.96–5.20	1.92×10^{-12}	37,000
$RhFe^+$ (1l)	5.80–6.12	1.77×10^{-12}	34,100
Total			1,307,000
Impact 2			
H^+ (2a)	0.3–0.42	1.25×10^{-12}	44,700
C^+ (2b)	1.42–1.58	5.41×10^{-13}	19,300
K^+ (2d)	2.88-3.02	2.99×10^{-13}	10,700
'Fast Fe^+' (2e)	3.02–3.46	5.25×10^{-12}	187,400
'Slow Fe^+' (2f)	3.46–3.88	1.56×10^{-11}	557,800
'Fast Rh^+' (2g)	4.16–4.74	6.67×10^{-12}	238,100
'Slow Rh^+' (2h)	4.74–4.98	7.72×10^{-12}	275,600
RhC^+/Fe_2^+ (2i)	4.98–5.22	2.96×10^{-12}	105,600
$RhFe^+$ (2j)	5.88–6.12	2.10×10^{-12}	74,900
Total			1,514,100

Figure CDA-14. CDA IDP TOF mass spectra detected during the cruise phase. *Left*: The time-of-flight mass spectra of two interplanetary dust particles detected in 1999. *Right*: The table shows the identified cation of each corresponding mass peak. From Hillier et al. [2007b].

Interplanetary Dust

Cruise phase

The interplanetary dust environment in between the orbits of Earth and Jupiter was explored during the cruise phase, during 1999 to early 2000 when the spacecraft was around 1 to 2.5 AUs away from the Sun [Kempf et al. 2004; Hillier et al. 2007b]. The detections of bound IDPs and unbound ISD in between the Jupiter flyby (2000-365) and the Saturn Orbit Insertion (SOI, 2004-183) are reported by Altobelli et al. [2007a, 2007b]. While the CDA dataset is limited by the spacecraft pointing, the CDA IDP measurements are in general consistent with the Pioneer results from the 70s. However, due to spacecraft activities no dust measurements were possible during the asteroid belt crossing.

Two mass spectra of IDPs were registered on 1999-147 and 1999-314, at heliospheric distances of 0.89 and 1.87 AU, respectively. These grains are roughly 2 μm in radii and both have an iron-rich composition [Hillier et al. 2007b]. Surprisingly, silicates and magnesium do not feature predominantly in the spectra. They are likely to have originated from near-Earth asteroid families (Aten and Apollo family, respectively), or Jupiter-family comets.

Kempf et al. [2004] reported in total 37 registered IDP impacts between November 1999 and January 2000. Among them, 6 impacts were obtained whose QP signals identified show a clear feature caused by charged grains, corresponding to Q_d between 1.3 and 5.4 fC [Auer et al. 2002; Kempf et al. 2004]. Assuming a potential of $\varphi_d \approx +5$ V and spheroidal grain morphologies, the corresponding grain masses are found to be in excess of 10^{-13} kg. The detection rate reasonably matches the IDP flux prediction [Staubach et al. 1997].

Between the Jupiter flyby and SOI, 7 of the total of 17 impact events were identified as IDPs based on their directionality [Altobelli et al. 2007a, 2007b]. These grains show a large spread in mass, ranging from 2×10^{-16} to 10^{-11} kg, corresponding to grain radii of 3 to 11 μm assuming a bulk grain density of 2 kg m^{-3}. These grains are most likely in orbits with low inclination and low eccentricity and likely originate from the short-period external Jupiter family comets and Edgeworth-Kuiper Belt objects [Altobelli et al. 2007b].

Exogenous mass infall at Saturn

Grains migrating inwards from the Edgeworth-Kuiper belt are expected to be an important exogenous dust population entering the Saturnian system [Han et al. 2011; Poppe and Horányi 2012]. Recent modeling results suggest grains approach Saturn's Hill sphere with speeds lower than expected (<3 km s^{-1}), meaning that the IDP flux enhancement by the gravitational focusing of Saturn is significant and the exogenous flux highly depends on the location of the moons/rings [Poppe and Horányi 2012].

Interstellar Dust

ISD is the major ingredient in planetary formation. The flow of these charged grains is mainly shaped by the solar radiation pressure force and the IMF configuration [Grün et al. 2000; Sterken et al. 2012]. The interplanetary cruise of Cassini during the first half of year 1999 provided an ideal window to monitor these interstellar messengers as the spacecraft traveled upstream with respect to the ISD flow [Altobelli et al. 2003]. The mean interstellar flux measured during this period of time, corresponding to heliospheric distances between 0.7 and 1.2 AU, is $2.5 \pm 0.5 \times 10^{-5}$ m^{-2} s^{-1}, in the grain mass range of $5 \times 10e^{-17}$ kg to 10^{-15} kg [Altobelli et al. 2003], in good agreement with the ISD flux measured by Ulysses at 3 AU during the same time period [Landgraf et al. 2003]. These simultaneous measurements demonstrate that relatively large interstellar grains (radii > 0.4 μm) can penetrate deeply into the inner solar system.

At 5 to 9 AU from the Sun, corresponding to the time in between the Jupiter flyby and SOI, 6 out of the 17 events registered are consistent with interstellar origin [Altobelli et al. 2007b]. The grain sizes are around 0.4 μm and the upper limit value of the flux is estimated to be 2×10^{-5} m^{-2} s^{-1}, consistent with the previous results.

ISD composition has been studied based on measurements at Saturn during 2004 to 2013 [Altobelli et al. 2016]. The mass distribution of 36 interstellar grains, their elemental composition, and a lower limit for the ISD flux at Saturn were determined [Altobelli et al. 2016]. Mass spectra and grain dynamics suggest the presence of magnesium-rich grains of silicate and oxide composition, partly with iron inclusions. Major rock-forming elements (magnesium, silicon, iron, and calcium) are present in cosmic abundances, with only small grain-to-grain variations, but sulfur and carbon are depleted. The ISD grains in the solar neighborhood appear to be homogenized, likely by repeated processing in the interstellar medium (Figure CDA-15).

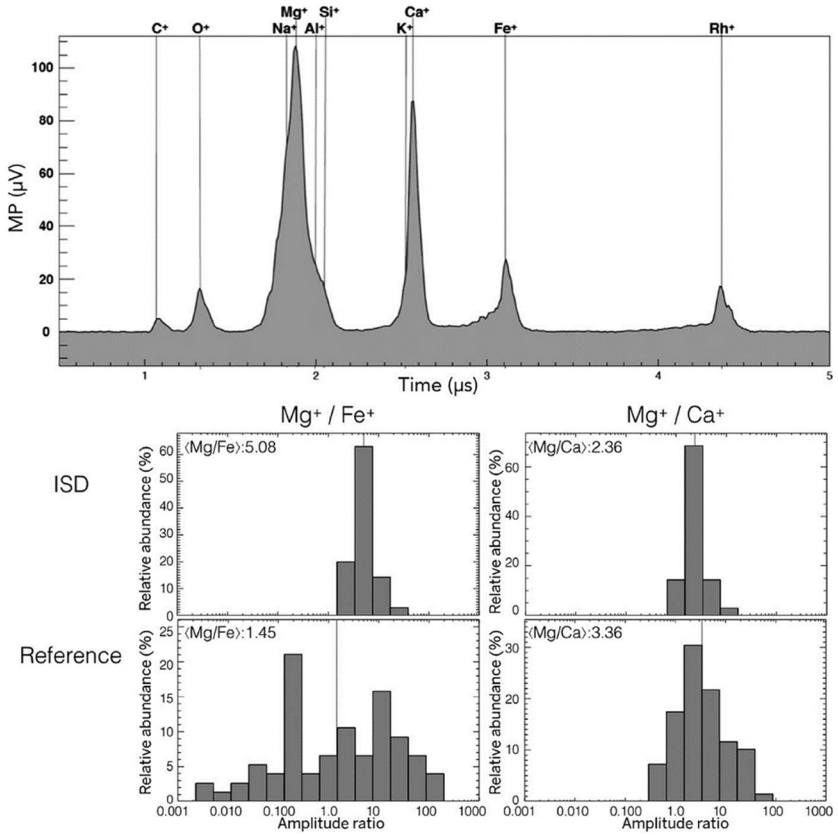

Figure CDA-15. Typical CDA ISD TOF mass spectrum and spectra comparison. *Top*: An example CDA time-of-flight mass spectrum of an ISD grain. *Bottom*: The comparison of cations from ISD spectra to that from the reference group spectra shows that ISD grains have a similar composition. From Altobelli et al. [2016].

ACRONYMS

Note: For a complete list of Acronyms, refer to Cassini Acronyms – Attachment A.

AO	Announcement of Opportunity
AU	astronomical unit
CA	chemical analyzer
CDA	cosmic dust analyzer
CIR	Corotation Interaction Region
DA	dust analyzer
DOY	day of year
FWHM	full-width-half-maximum
HMOC	high mass organic cation
HRD	high-rate detector
IDP	interplanetary dust particle
IID	impact ionization detector
IMF	interplanetary magnetic field
IPT	Io Plasma Torus
IR/UV	infrared/ultraviolet
ISD	interstellar dust
NaCl	sodium chloride
PVDF	polyvinylidene fluoride
RPWS	Radio and Plasma Wave Science
SOI	Saturn Orbit Insertion
TM	Traceability Matrix
TOF MS	time-of-flight mass spectrometry
VIMS	Visual and Infrared Imaging Spectrometer

REFERENCES

Disclaimer: The partial list of references below correspond with in-text references indicated in this report. For all other Cassini references, refer to Attachment B – References & Bibliographies; Attachment C – Cassini Science Bibliographies; the sections entitled References contributed by individual Cassini instrument and discipline teams located in Volume 1 Sections 3.1 and 3.2 Science Results; and other resources outside of the Cassini Final Mission Report.

Altobelli, N., F. Postberg, K. Fiege, M. Trieloff, H. Kimura, V. J. Sterken, H.-W. Hsu, J. Hillier, N. Khawaja, G. Moragas-Klostermeyer, J. Blum, M. Burton, R. Srama, S. Kempf, E. Grün, (2016), Flux and composition of interstellar dust at Saturn from Cassini's Cosmic Dust Analyzer, Science, 352, 312–318.

Altobelli, N., V. Dikarev, S. Kempf, R. Srama, S. Helfert, G. Moragas-Klostermeyer, M. Roy, E. Grün, (2007a), Cassini/Cosmic Dust Analyzer in situ dust measurements between Jupiter and Saturn, Journal of Geophysical Research, 112(A11), 7105.

Altobelli, N., S. Kempf, M. Roy, R. Srama, S. Helfert, G. Moragas-Klostermeyer, E. Grün, (2007b), Preliminary results on analysis of the Cosmic Dust Analyzer data between Jupiter and Saturn, Dust in Planetary Systems, 643, 65–68.

Altobelli, N., S. Kempf, M. Landgraf, R. Srama, V. Dikarev, H. Krüger, G. Moragas-Klostermeyer, G., E. Grün, (2003), Cassini between Venus and Earth, Detection of interstellar grains, Journal of Geophysical Research, 108(A10), 7–1.

Arridge, C. S., N. André, H. J. McAndrews, E. J. Bunce, M. H. Burger, K. C. Hansen, H.-W. Hsu, R. E. Johnson, G. H. Jones, S. Kempf, K. K. Khurana, N. Krupp, W. S. Kurth, J. S. Leisner, C. Paranicas, E. Roussos, C. T. Russell, P. Schippers, E. C. Sittler, H. T. Smith, M. F. Thomsen, M. K. Dougherty, (2011), Mapping magnetospheric equatorial regions at Saturn from Cassini Prime Mission observations, Space Science Reviews, 164, 1–83.

Auer, S., E. Grün, R. Srama, S. Kempf, R. Auer, (2002), The charge and velocity detector of the Cosmic Dust Analyzer on Cassini, Planetary and Space Science, 50, 773–779.

Buratti, B. J., P. C. Thomas, E. Roussos, C. Howett, M. Seiß, A. R. Hendrix, P. Helfenstein, R. H. Brown, R. N. Clark, T. Denk, G. Filacchione, H. Hoffmann, G. H. Jones, N. Khawaja, P. Kollmann, N. Krupp, J. Lunine, T. W. Momary, C. Paranicas, F. Postberg, M. Sachse, F. Spahn, J. Spencer, R. Srama, T. Albin, K. H. Baines, M. Ciarniello, T. Economou, H.-W. Hsu, S. Kempf, S. M. Krimigis, D. Mitchell, G. Moragas-Klostermeyer, P. D. Nicholson, C. C. Porco, H. Rosenberg, J. Simolka, L. A. Soderblom (2019), Close Cassini flybys of Saturn's ring moons Pan, Daphnis, Atlas, Pandora, and Epimetheus, Science, 364(6445), eaat2349, doi: 10.1126/science.aat2349.

Buratti, B. J., J. A. Mosher, J. A., T.V. Johnson, (1990), Albedo and color maps of the Saturnian satellites, Icarus, 87, 339–357.

de Pater, I., M. R. Showalter, J. J. Lissauer, J. R. Graham, (1996), Keck infrared observations of Saturn's E and G rings during Earth's 1995 ring plane crossings, Icarus, 121, 195–198.

Dikarev, V. V., A. V. Krivov, E. Grün, (2006), Two stages of dust delivery from satellites to planetary rings, Planetary and Space Science, 54, 1014–1023.

Dikarev, V., (1999), Dynamics of particles in Saturn's E ring, effects of charge variations and the plasma drag force, Astronomy and Astrophysics, 346, 1011–1019.

Gao, P., P. Kopparla, X. Zhang, A. P. Ingersoll, (2016), Aggregate particles in the plumes of Enceladus, Icarus, 264, 227–238.

Graps, A., E. Grün, H. Svedhem, H. Krüger, M. Horányi, A. Heck, S. Lammers, (2000), Io as a source of the Jovian dust streams, Nature, 405, 48–50.

Grün, E., M. Landgraf, M. Horányi, J. Kissel, H. Krüger, R. Srama, H. Svedhem, P. Withnell, (2000), Techniques for galactic dust measurements in the heliosphere, Journal of Geophysical Research, 105, 10403–10410.

Grün, E., H. Zook, M. Baguhl, A. Balogh, S. Bame, H. Fechtig, R. Forsyth, M. Hanner, M. Horányi, J. Kissel, B.-A. Lindblad, D. Linkert, G. Linkert, I. Mann, J. McDonnel, G. Morfill, J. Phillips, C. Polanskey, G. Schwehm, N. Siddique, P. Staubach, J. Svestka, A. Taylor, (1993), Discovery of Jovian dust streams and interstellar grains by the Ulysses spacecraft, Nature, 362, 428–430.

Grün, E., H. Fechtig, M. S. Hanner, J. Kissel, B.-A. Lindblad, D. Linkert, D. Maas, G. E. Morfill, H. A. Zook, (1992), The Galileo Dust Detector, Space Science Reviews, 60, 317–340.

Hamilton, D. P., (1993), Motion of dust in a planetary magnetosphere - orbit-averaged equations for oblateness, electromagnetic, and radiation forces with application to Saturn's E ring, Icarus, 101, 244–264.

Han, D., A. R. Poppe, M. Piquette, E. Grün, M. Horányi, (2011), Constraints on dust production in the Edgeworth-Kuiper Belt from Pioneer 10 and New Horizons measurements, Geophysical Research Letters, 38, L24102.

Hedman, M. M., J. A. Burns, D. P. Hamilton, M. R. Showalter, (2012), The three-dimensional structure of Saturn's E ring, Icarus, 217, 322–338.

Hedman, M. M., C. D. Murray, N. J. Cooper, M. S. Tiscareno, K. Beurle, M. W. Evans, J. A. Burns, (2009a), Three tenuous rings/arcs for three tiny moons, Icarus, 199, 378–386.

Hedman, M. M., P. D. Nicholson, M. R. Showalter, R. H. Brown, B. J. Buratti, R. N. Clark, (2009b), Spectral observations of the Enceladus plume with Cassini-VIMS, The Astrophysical Journal, 693, 1749–1762.

Hedman, M. M., J. A. Burns, M. S. Tiscareno, C. C. Porco, G. H. Jones, E. Roussos, N. Krupp, C. Paranicas, S. Kempf, (2007), The source of Saturn's G ring, Science, 317, 653–656.

Hillier, J. K., S. F. Green, N. McBride, N. Altobelli, F. Postberg, S. Kempf, J. Schwanethal, R. Srama, J. A. M. McDonnell, E. Grün, (2007a), Interplanetary dust detected by the Cassini CDA Chemical Analyzer, Icarus, 190, 643–654.

Hillier, J. K., S. F. Green, N. McBride, J. P. Schwanethal, F. Postberg, R. Srama, S. Kempf, G. Moragas-Klostermeyer, J. A. M. McDonnell, E. Grün, (2007b), The composition of Saturn's E ring, Monthly Notices of the Royal Astronomical Society, 377, 1588–1596.

Horányi, M., A. Juhasz, G. E. Morfill, (2008), Large-scale structure of Saturn's E-ring, Geophysical Research Letters, 35, L04203.

Horányi, M., (2000), Dust streams from Jupiter and Saturn, Physics of Plasmas, 7(10), 3847–3850.

Horányi, M., G. Morfill, E. Grün, (1993), Mechanism for the acceleration and ejection of dust grains from Jupiter's magnetosphere, Nature, 363, 144–146.

Horányi, M., J. Burns, D. Hamilton, (1992), The dynamics of Saturn's E ring particles, Icarus, 97, 248–259.

Hsu, H. W., J. Schmidt, S. Kempf, F. Postberg, G. Moragas-Klostermeyer, M. Seiß, H. Hoffmann, M. Burton, S.-Y. Ye, W. S. Kurth, M. Horányi, N. Khawaja, F. Spahn, D. Schirdewahn, J. O'Donoghue, L. Moore, J. Cuzzi, G. H. Jones, R. Srama, (2018), In situ collection of dust grains falling from Saturn's rings into its atmosphere, Science, 362(6410), eaat3185, doi: 10.1126/science.aat3185.

Hsu, H., M. Horányi, S. Kempf, (2017), On the time-dependent grain charging and its effects on ring-atmosphere interactions at Saturn, American Institute of Physics Conference Proceedings.

Hsu, H.-W., S. Kempf, S. V. Badman, W. S. Kurth, F. Postberg, R. Srama, (2016), Interplanetary magnetic field structure at Saturn inferred from nanodust measurements during the 2013 aurora campaign, Icarus, 263, 10–16.

Hsu, H.-W., F. Postberg, Y. Sekine, T. Shibuya, S. Kempf, M. Horányi, A. Juhasz, N. Altobelli, K. Suzuki, Y. Masaki, T. Kuwatani, S. Tachibana, S.-I. Sirono, G. Moragas-Klostermeyer, R. Srama, (2015), Ongoing hydrothermal activities within Enceladus, Nature, 519, 207–210.

Hsu, H.-W., K. C. Hansen, M. Horányi, S. Kempf, A. Mocker, G. Moragas-Klostermeyer, F. Postberg, R. Srama, B. Zieger, (2013a), Probing IMF using nanodust measurements from inside Saturn's magnetosphere, Geophysical Research Letters, 40, 2902–2906.

Hsu, H.-W., M. Horányi, S. Kempf, (2013b), Dust and spacecraft charging in Saturn's E ring, Earth, Planets, and Space, 65, 149–156.

Hsu, H.-W., M. Horányi, S. Kempf, E. Grün, (2012a), Spacecraft charging near Enceladus, Geophysical Research Letters, 39, 6108.

Hsu, H.-W., H. Krüger, F. Postberg, (2012b), Dynamics, composition, and origin of Jovian and Saturnian dust-stream particles, in Astrophysics and Space Science Library, (eds.) I. Mann, N. Meyer-Vernet, A. Czechowski, Volume 385, p. 77.

Hsu, H.-W., S. Kempf, F. Postberg, M. Trieloff, M. Burton, M. Roy, G. Moragas-Klostermeyer, R. Srama, (2011a), Cassini dust stream particle measurements during the first three orbits at Saturn, Journal of Geophysical Research, 116, A08213.

Hsu, H.-W., F. Postberg, S. Kempf, M. Trieloff, M. Burton, M. Roy, G. Moragas-Klostermeyer, R. Srama, (2011b), Stream particles as the probe of the dust-plasma-magnetosphere interaction at Saturn, Journal of Geophysical Research, 116, A09215.

Hsu, H., S. Kempf, C. M. Jackman, (2010a), Observation of Saturnian stream particles in the interplanetary space, Icarus, 206, 653–661.

Hsu, H., S. Kempf, F. Postberg, R. Srama, C. M. Jackman, G. Moragas-Klostermeyer, S. Helfert, E. Grün, (2010b), Interaction of the solar wind and stream particles, results from the Cassini dust detector, Twelfth International Solar Wind Conference, American Institute of Physics Conference Proceedings, 1216, 510–513.

Ingersoll, A. P. and S. P. Ewald, (2011), Total particulate mass in Enceladus plumes and mass of Saturn's E ring inferred from Cassini ISS images, Icarus, 216, 492–506.

Jones, G. H., E. Roussos, N. Krupp, U. Beckmann, A. J. Coates, F. Crary, I. Dandouras et al. (2008), The dust halo of Saturn's largest icy moon, Rhea, Science 319, 5868, 1380–1384.

Juhasz, A. and M. Horányi, (2002), Saturn's E ring, A dynamical approach, Journal of Geophysical Research, 107, 1–10.

Jurac, S., R. E. Johnson, J. D. Richardson, (2001), Saturn's E ring and production of the Neutral Torus, Icarus, 149, 384–396.

Kempf, S., R. Srama, G. Moragas-Klostermeyer, J. Schmidt, F. Spahn, M. Horányi, (2012), Saturn's egg-shaped E ring, in EGU General Assembly Conference Abstracts, (eds.) A. Abbasi and N. Giesen, 14, 11409.

Kempf, S., U. Beckmann, J. Schmidt, (2010), How the Enceladus dust plume feeds Saturn's E ring, Icarus, 206, 446–457.

Kempf, S., (2008a), Interpretation of high rate dust measurements with the Cassini dust detector CDA, Planetary and Space Science, 56, 378–385.

Kempf, S., U. Beckmann, G. Moragas-Klostermeyer, F. Postberg, R. Srama, T. Economou, J. Schmidt, F. Spahn, E. Grün, (2008b), The E ring in the vicinity of Enceladus I, Spatial distribution and properties of the ring particles, Icarus, 193, 420–437.

Kempf, S., U. Beckmann, R. Srama, M. Horányi, S. Auer, E. Grün, (2006), The electrostatic potential of E ring particles, Planetary and Space Science, 54, 999–1006.

Kempf, S., R. Srama, M. Horányi, M. Burton, S. Helfert, G. Moragas-Klostermeyer, M. Roy, E. Grün, (2005a), High-velocity streams of dust originating from Saturn, Nature, 433, 289–291.

Kempf, S., R. Srama, F. Postberg, M. Burton, S. F. Green, S. Helfert, J. K. Hillier, N. McBride, J. A. M. McDonnell, G. Moragas-Klostermeyer, M. Roy, E. Grün, (2005b), Composition of Saturnian stream particles, Science, 307, 1274–1276.

Kempf, S., R. Srama, N. Altobelli, S. Auer, V. Tschernjawski, J. Bradley, M. Burton, S. Helfert, T. Johnson, H. Krüger, G. Moragas-Klostermeyer, E. Grün, (2004), Cassini between Earth and asteroid belt, First in-situ charge measurements of interplanetary grains, Icarus, 171, 317–335.

Khawaja, N., F. Postberg, J. Schmidt, (2017), The compositional profile of the Enceladus ice plume from the latest Cassini flybys, Lunar and Planetary Science Conference, 2005.

Krivov, A. V., M. Sremcevic, F. Spahn, V. V. Dikarev, K. V. Kholshevnikov, (2003), Impact-generated dust clouds around planetary satellites, Spherically symmetric case, Planetary and Space Science, 51, 251–269.

Krüger, H., P. Geissler, M. Horányi, A. Graps, S. Kempf, R. Srama, G. Moragas-Klostermeyer, R. Moissl, T. Johnson, E. Grün, (2003a), Jovian dust streams, A monitor of Io's volcanic plume activity, Geophysical Research Letters, 30(21), 2101.

Krüger, H., M. Horányi, E. Grün, (2003b), Jovian dust streams, Probes of the Io plasma torus, Geophysical Research Letters, 30(2), 1058.

Krüger, H., A. Krivov, D. Hamilton, E. Grün, (1999), Detection of an impact-generated dust cloud around Ganymede, Nature, 399, 558–560.

Krupp, N., E. Roussos, C. Paranicas, D. G. Mitchell, P. Kollmann, S. Ye, W. S. Kurth, K. K. Khurana, R. Perryman, H. Waite, R. Srama, D. C. Hamilton, (2018), Energetic electron measurements near Enceladus by Cassini during 2005–2015, Icarus, 306, 256–274.

Landgraf, M., H. Krüger, N. Altobelli, E. Grün, (2003), Penetration of the heliosphere by the interstellar dust stream during solar maximum, Journal of Geophysical Research, 108, 5–1.

McBride, N., J. K. Hillier, S. F. Green, R. Srama, S. Kempf, F. Postberg, G. Moragas-Klostermeyer, J. A. M. McDonnell, E. Grün, (2007), Cassini Cosmic Dust Analyzer, Composition of dust at Saturn, Dust in Planetary Systems, 643, 107–110.

Moore, L., J. O'Donoghue, I. Müller-Wodarg, M. Galand, M. Mendillo, (2015), Saturn ring rain, Model estimates of water influx into Saturn's atmosphere, Icarus, 245, 355–366.

Morooka, M. W., J.-E. Wahlund, A. I. Eriksson, W. M. Farrell, D. A. Gurnett, W. S. Kurth, A. M. Persoon, M. Shafiq, M. André, M. K. G. Holmberg, (2011), Dusty plasma in the vicinity of Enceladus, Journal of Geophysical Research (Space Physics), 116, 12221.

Nicholson, P. D., M. R. Showalter, L. Dones, (1996), Observations of Saturn's ring-plane crossing in August and November, Science, 272, 509–516.

O'Donoghue, J., T. S. Stallard, H. Melin, G. H. Jones, S. W. H. Cowley, S. Miller, K. H. Baines, J. S. D. Blake, (2013), The domination of Saturn's low-latitude ionosphere by ring 'rain', Nature, 496, 193–195.

Poppe, A. R. and M. Horányi, (2012), On the Edgeworth-Kuiper Belt dust flux to Saturn, Geophysical Research Letters, 39, L15104.

Postberg, F., N. Khawaja, B. Abel, G. Choblet, C. Glein, M. Gudipati, B. L. Henderson, H. Hsu, S. Kempf, F. Klenner, G. Moragas-Klostermeyer, B. Magee, L. Nölle, M. Perry, R. Reviol,

J. Schmidt, R. Srama, F. Stolz, G. Tobie, M. Trieloff, J. H. Waite, (2018), Macromolecular organic compounds from the depths of Enceladus, Nature, 558(7711), 564.

Postberg, F., J. Schmidt, J. Hillier, S. Kempf, R. Srama, (2011), A salt-water reservoir as the source of a compositionally stratified plume on Enceladus, Nature, 474, 620–622.

Postberg, F., S. Kempf, D. Rost, T. Stephan, R. Srama, M. Trieloff, A. Mocker, M. Goerlich, (2009a), Discriminating contamination from particle components in spectra of Cassini's dust detector CDA, Planetary and Space Science, 57, 1359–1374.

Postberg, F., S. Kempf, J. Schmidt, N. Brilliantov, A. Beinsen, B. Abel, U. Buck, R. Srama, (2009b), Sodium salts in E-ring ice grains from an ocean below the surface of Enceladus, Nature, 459, 1098–1101.

Postberg, F., S. Kempf, J. K. Hillier, R. Srama, S. F. Green, N. McBride, E. Grün, (2008), The E-ring in the vicinity of Enceladus II, Signatures of Enceladus in the elemental composition of E-ring particles, Icarus, 193, 438–454.

Postberg, F., S. Kempf, R. Srama, S. F. Green, J. K. Hillier, N. McBride, E. Grün, (2006), Composition of Jovian dust stream particles, Icarus, 183, 122–134.

Schenk, P., D. P. Hamilton, R. E. Johnson, W. B. McKinnon, C. Paranicas, J. Schmidt, M. R. Showalter, (2011), Plasma, plumes and rings, Saturn system dynamics as recorded in global color patterns on its midsize icy satellites, Icarus, 211, 740–757.

Schmidt, J., N. Brilliantov, F. Spahn, S. Kempf, (2008), Slow dust in Enceladus' plume from condensation and wall collisions in tiger stripe fractures, Nature, 451, 685–688.

Seiß, M., R. Srama, K.-L. Sun, M. Seiler, G. Moragas-Klostermeyer, S. Kempf, F. Spahn, (2014), Pallene dust torus observations by the Cosmic Dust Analyzer, European Planetary Science Congress, 9, EPSC2014–375.

Sekine, Y., T. Shibuya, F. Postberg, H. Hsu, K. Suzuki, Y. Masaki, T. Kuwatani, M. Mori, P. K. Hong, M. Yoshizaki, S. Tachibana, S.-I Sirono, (2015), High-temperature water–rock interactions and hydrothermal environments in the chondrite-like high-temperature water-rock interactions and hydrothermal environments in the chondrite-like core of Enceladus, Nature Communications, 6(8604).

Showalter, M. R., J. N. Cuzzi, S. M. Larson, (1991), Structure and particle properties of Saturn's E ring, Icarus, 94, 451–473.

Southworth, B. S., S. Kempf, J. Spitale, (2019), Surface deposition of the Enceladus plume and the zenith angle of emissions, Icarus, 319, 33–42.

Spahn, F., N. Albers, M. Hörning, S. Kempf, A. V. Krivov, M. Makuch, J. Schmidt, M. Seiß, M. Sremcevic, (2006a), E ring dust sources, Implications from Cassini's dust measurements, Planetary and Space Science, 54, 1024–1032.

Spahn, F., J. Schmidt, N. Albers, M. Hörning, M. Makuch, M. Seiß, S. Kempf, R. Srama, V. Dikarev, S. Helfert, G. Moragas-Klostermeyer, A. V. Krivov, M. Sremcevic, A. J. Tuzzolino,

T. Economou, E. Grün, (2006b), Cassini dust measurements at Enceladus and implications for the origin of the E ring, Science, 311, 1416–1418.

Spencer, J. R., S. A. Stern, A. F. Cheng, H. A. Weaver, D. C. Reuter, K. Retherford, A. Lunsford, J. M. Moore, O. Abramov, R. M. C. Lopes, J. E. Perry, L. Kamp, M. Showalter, K. L. Jessup, F. Marchis, P. M. Schenk, C. Dumas, (2007), Io volcanism seen by New Horizons, A major eruption of the Tvashtar volcano, Science, 318, 240–.

Srama, R., S. Kempf, G. Moragas-Klostermeyer, N. Altobelli, S. Auer, U. Beckmann, S. Bugiel, M. Burton, T. Economomou, H. Fechtig, K. Fiege, S. F. Green, M. Grande, O. Havnes, J. K. Hillier, S. Helfert, M. Horányi, S. Hsu, E. Igenbergs, E. K. Jessberger, T. V. Johnson, E. Khalisi, H. Krüger, G. Matt, A. Mocker, P. Lamy, G. Linkert, F. Lura, D. Möhlmann, G. E. Morfill, K. Otto, F. Postberg, M. Roy, J. Schmidt, G. H. Schwehm, F. Spahn, V. Sterken, J. Svestka, V. Tschernjawski, E. Grün, H.-P. Röser, (2011), The Cosmic Dust Analyzer onboard Cassini, Ten years of discoveries, CEAS Space Journal, 2, 3–16.

Srama, R., S. Kempf, G. Moragas-Klostermeyer, S. Helfert, T. J. Ahrens, N. Altobelli, S. Auer, U. Beckmann, J. G. Bradley, M. Burton, V. V. Dikarev, T. Economou, H. Fechtig, S. F. Green, M. Grande, O. Havnes, J. K. Hillier, M. Horányi, E. Igenbergs, E. K. Jessberger, T. V. Johnson, H. Krüger, G. Matt, N. McBride, A. Mocker, P. Lamy, D. Linkert, G. Linkert, F. Lura, J. A. M. McDonnell, D. Mohlmann, G. E. Morfill, F. Postberg, M. Roy, G. H. Schwehm, F. Spahn, J. Svestka, V. Tschernjawski, A. J. Tuzzolino, R. Wäsch, E. Grün, (2006), In situ dust measurements in the inner Saturnian system, Planetary and Space Science, 54, 967–987.

Srama, R., M. Stübig, E. Grün, (2004), Laboratory detection of organic dust with the Cassini-CDA instrument, Advances in Space Research, 33, 1289–1293.

Sremcevic, M., A. V. Krivov, F. Spahn, (2003), Impact-generated dust clouds around planetary satellites, asymmetry effects, Planetary and Space Science, 51, 455–471.

Staubach, P., E. Grün, R. Jehn, (1997), The meteoroid environment near earth, Advances in Space Research, 19, 301–308.

Sterken, V. J., N. Altobelli, S. Kempf, G. Schwehm, R. Srama, E. Grün, (2012), The flow of interstellar dust into the solar system, Astronomy and Astrophysics, 538, A102.

Sun, K.-L., M. Seiß, M. M. Hedman, F. Spahn, (2017), Dust in the arcs of Methone and Anthe, Icarus, 284, 206–215.

Verbiscer, A., R. French, M. Showalter, P. Helfenstein, (2007), Enceladus, Cosmic graffiti artist caught in the act, Science, 315, 815.

Ye, S.-Y., D. A. Gurnett, W. S. Kurth, (2016), In-situ measurements of Saturn's dusty rings based on dust impact signals detected by Cassini RPWS, Icarus, 279, 51–61.

Ye, S.-Y., D. A. Gurnett, W. S. Kurth, T. F. Averkamp, S. Kempf, H.-W. Hsu, R. Srama, E. Grün, (2014), Properties of dust particles near Saturn inferred from voltage pulses induced by dust impacts on Cassini spacecraft, Journal of Geophysical Research, 119, 6294–6312.

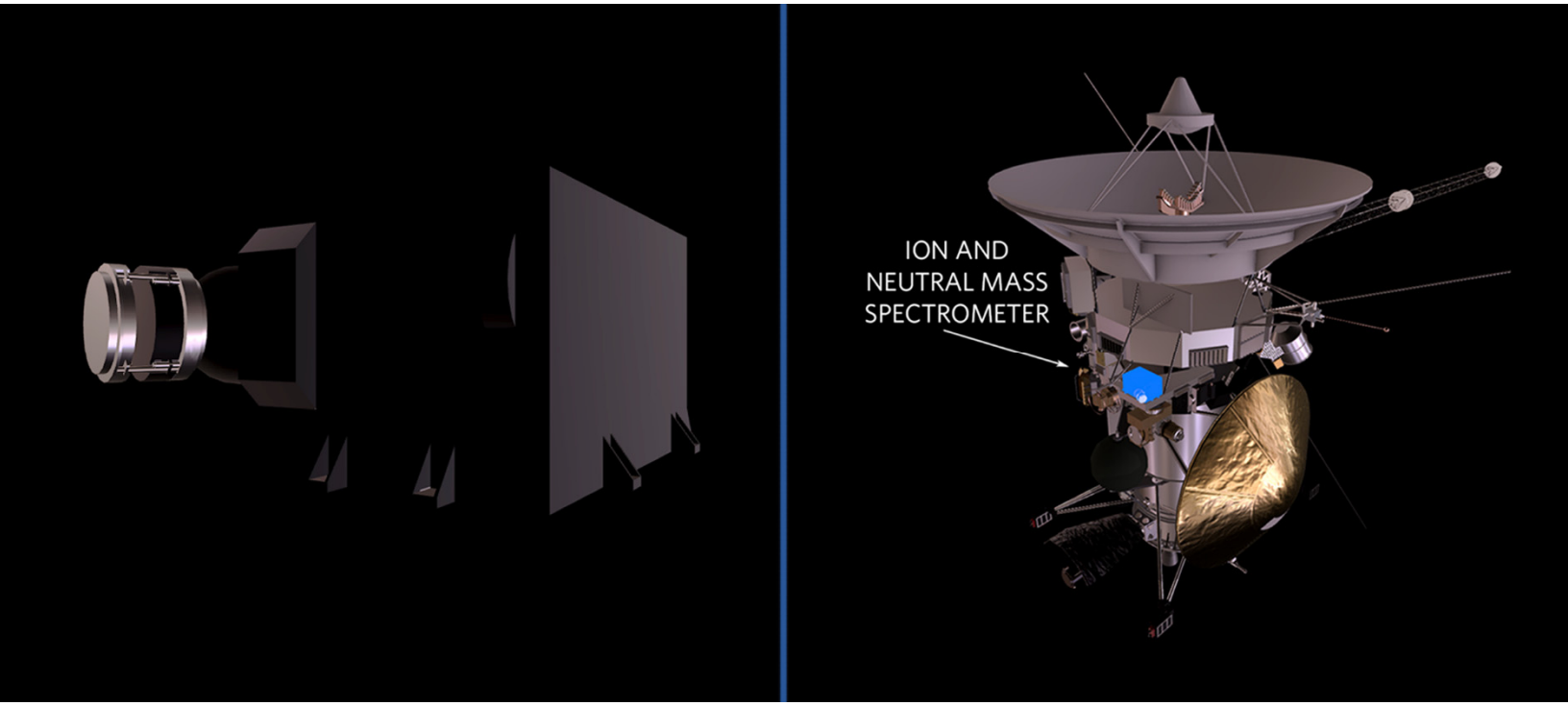

Ion and Neutral Mass Spectrometer

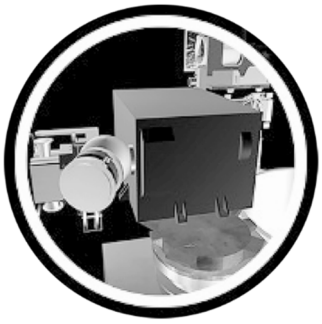

The Ion and Neutral Mass Spectrometer (INMS) was designed to determine the chemical, elemental and isotopic composition of the gaseous and volatile components of the neutral particles and the low energy ions in the Saturn system. The **science objectives** of INMS were to determine the composition and structure of Titan's ionosphere and upper atmosphere, to investigate the neutral and plasma environments of the rings and icy satellites and the interaction with the magnetosphere of Saturn. INMS directly sampled the gas in the Enceladus plume.

The instrument was a quadrupole mass spectrometer with two ion source inlets, a closed ion source for measurement of non-reactive neutral gas and an open ion source for the measurement of ions and reactive neutrals.

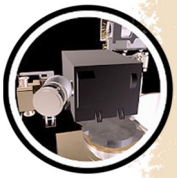

CONTENTS

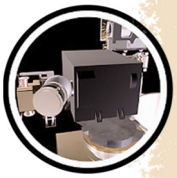

Figures

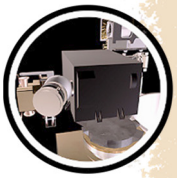

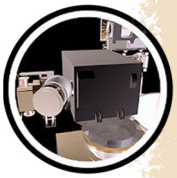

Tables

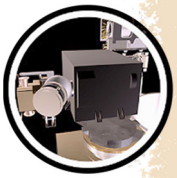

EXECUTIVE SUMMARY

The two primary scientific objectives of the Cassini Ion Neutral Mass Spectrometer (INMS) investigation were: 1) to characterize the composition, structure, and chemical behavior of Titan's upper atmosphere and its interaction with Saturn's magnetosphere; and 2) to investigate the neutral and plasma environments of the rings and icy satellites and their magnetospheric interactions [Waite et al. 2004]. Careful determination of the gas densities of the environment is necessary for the proper execution of these objectives. The ion density extraction process has been discussed in detail by Mandt et al. [2012b] for ram pointed flybys, and many other aspects of the INMS calibration and instrument response to ions and neutrals have been addressed in literature [Teolis et al. 2015; Cui et al. 2009a; Magee et al. 2009; Perry et al. 2010; Teolis et al. 2010b; Vuitton et al. 2008; Waite et al. 2004]. These include compositional extraction from mass spectra, wall adsorption of sticky gases such as H_2O and NH_3, thruster firing contamination, radiation background, high-pressure background effects, residual gas tails, high-sensitivity detector saturation, and on-going work to refine the instrument calibration with the ground-based refurbished engineering unit.

INMS produced results beyond expectation for all objects examined: Titan, Enceladus, Dione, Rhea, the inner magnetosphere, the rings, and the ring/atmosphere interaction in Saturn's equatorial atmosphere.

INMS produced results beyond expectation for all objects examined: Titan, Enceladus, Dione, Rhea, the inner magnetosphere, the rings, and the ring/atmosphere interaction in Saturn's equatorial atmosphere. The expectations at Titan were the measurement of the principal components of the atmosphere (nitrogen and methane) and their primary photochemical products (acetylene, ethane, hydrogen cyanide, and their ion counterparts). What emerged was the measurement of a plethora of organic compounds across the whole mass range of INMS that provided a window on a novel way to produce organics through ion neutral chemistry, perhaps an insight into the world of interstellar molecular clouds. There were no expectations for Enceladus, but in reality, this became the most compelling satellite in the system with INMS working in tandem with cosmic dust analyzer (CDA) to demonstrate the habitability of an internal ocean that no one even knew existed before the mission began. The crowning achievement was INMS measurements of molecular hydrogen in the plume that allowed the team to demonstrate that the interior ocean had the latent chemical energy to support methanogenic archea. Dione, Rhea, and the inner magnetosphere provided examples of sputtering of icy satellites, the first time this had been quantitatively investigated in the space environment. The Grand Finale proved *grand* indeed by providing the most complex spectra of the mission (Figure INMS-1) and uncovering a complex chemical interaction between the Saturn atmosphere and rings involving methane, water, carbon dioxide, and ammonia and a host of nanograin organic material—a truly amazing finish to an extraordinary mission.

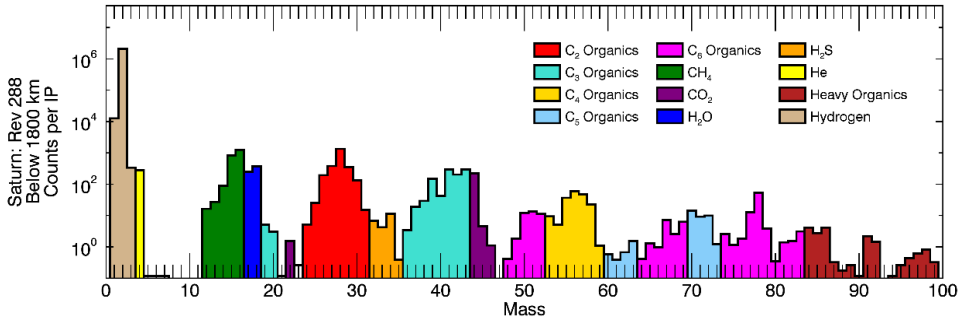

Figure INMS-1. INMS mass spectra of Saturn's upper atmosphere from the Grand Finale. Preliminary mass deconvolution of compounds measured by INMS on the last six orbits of the mission between 1700 and 1800 km at latitudes within 10° of the equator. The spectrum shown here is from the first of these orbits. The axis is in units of mass (u) and extends over the full mass range of INMS (1–99 u).

Instrument Summary

The INMS (Figure INMS-2) is a mass spectrometer described in detail by Waite et al. [2004]. The instrument is a quadrupole mass spectrometer (Figure INMS-3) with two source inlets: 1) a closed ion source (CS) for measurement of non-reactive neutral gas; and 2) an open ion source (OS) for the measurement of ions and reactive neutrals without wall collisions within the instrument interior (Figure INMS-4). The sources are housed in an Ion Source Enclosure (ISE). In flight, measurements alternate in a programmable fashion between the two sources. Gas enters the CS inlet through the entrance aperture as a well collimated molecular beam since the relative gas-spacecraft speed is typically much greater than the molecule thermal speeds. Molecule velocities are isotropized and slowed (thermally accommodated) by colliding (roughly 120 times) with the walls of the inlet's antechamber and antechamber-to-CS transfer tube [Teolis et al. 2015] before passing through the tube to the CS ionization region (Figure INMS-4, labeled with density n_s). The resulting density enhancement in the antechamber and CS is a function of the ram angle between the spacecraft velocity vector and the entrance aperture normal. A typical Titan flyby at 6 km/s produces a ram factor of ~71 for nitrogen relative to the density for a spacecraft at rest if one neglects the leakage paths out of the CS. Scaling the ram factor by $\sqrt{T_a/T_s}$ yields the CS to ambient density ratio at the CS and ambient gas temperatures T_s and T_a (see Teolis et al. [2015], Eq. A17). The side vent (Figure INMS-3 and Figure INMS-4) limits the accumulation of residual gas inside the instrument, and constitutes a major leakage pathway out of the instrument. Neutral gas is ionized in the CS using an electron beam (commandable to ~25 or 70 eV) generated by one of two redundant hot filaments. The OS inlet is located below the CS inlet, and consists of an entrance aperture and ion beam collimator. In-flight measurement of ambient ion densities is described by Mandt et al. [2012b]. In-flight measurement of ambient neutral densities is described by Teolis et al. [2015]. Positive ions from the CS or OS are extracted into the electrostatic quadrupole lens (Figure INMS-4), which is used as a deflector to switch ion trajectories between the two sources [Mahhafy and Lai 1990]. The quadrupole lens voltages are set to transfer the ions into the analyzer ion focus lenses and in turn into the quadrupole mass analyzer (QMA). The voltage setting on the ion focus lenses can increase or reduce the sensitivity by affecting how well the beam of ionized neutrals is focused into the mass analyzer.

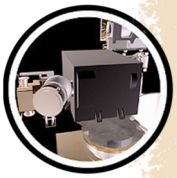

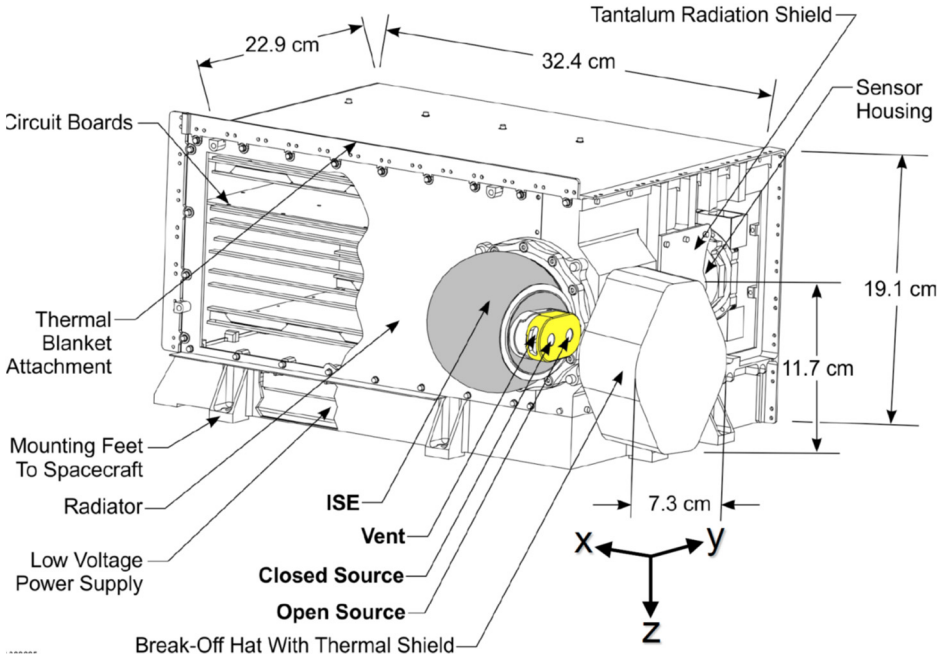

Figure INMS-2. Drawing of the INMS. Showing (*gray*) the ISE and CS and OS inlet apertures, and vent, in relation to (no color) the instrument and electronics housing. The Break-Off Hat was jettisoned after the launch of Cassini.

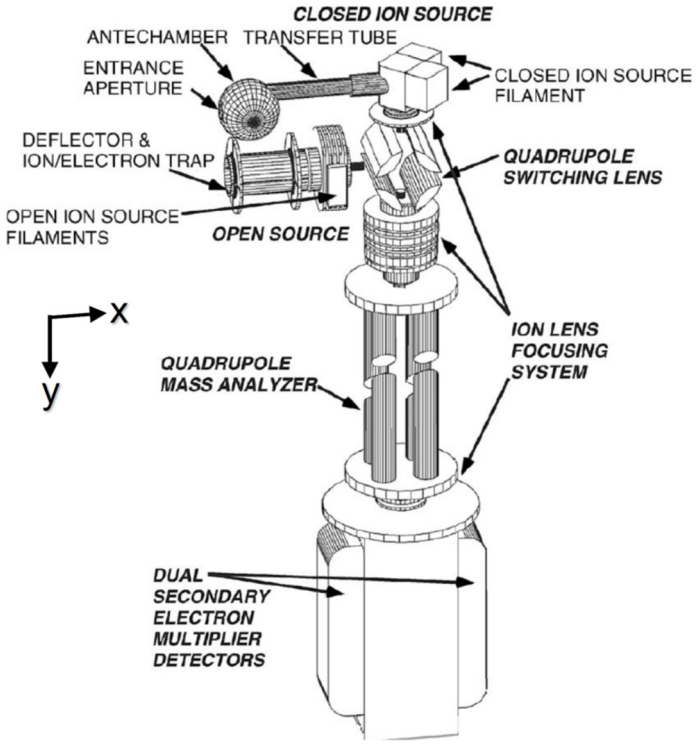

Figure INMS-3. Schematic showing the main components of the INMS. The ram factor model considers the sections above the quadrupole mass analyzer within the ISE (not shown).

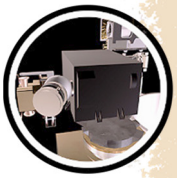

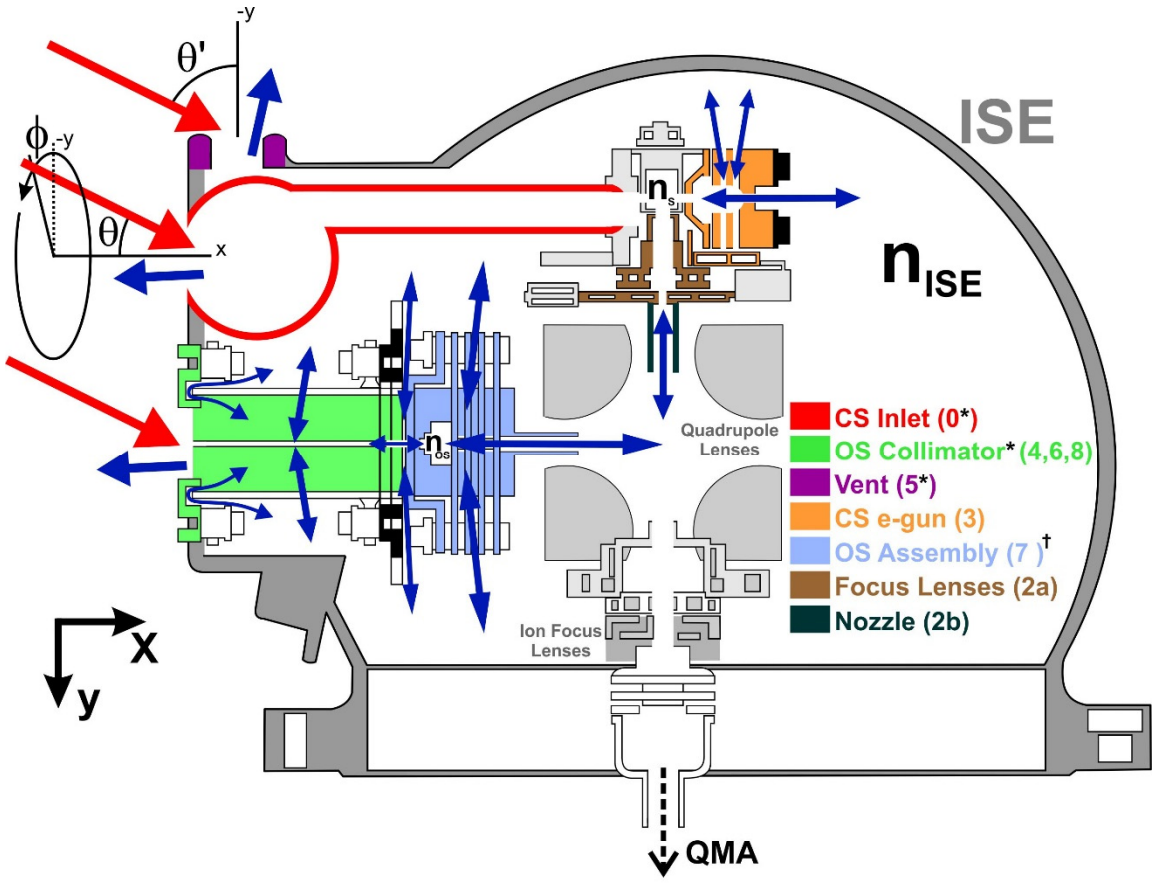

Figure INMS-4. Cross-section diagram (to scale) of the INMS ISE (shown in yellow in Figure INMS-2) with ion sources and gas inlet system shown, together with the azimuthal (ϕ), ram (θ) and vent ram (θ′) angles, spacecraft coordinates axes, gas flows (*Red arrows:* ram flux; *Blue arrows:* thermalized flows), and the approximate locations of densities n_s, n_{os}, and n_{ISE}. Conduction paths considered in the ram factor model are colored as indicated by the legend, with number-letter notation (detailed in Teolis et al. [2015], Appendix A) in parentheses. *Asterisks:* effective area estimated by Monte Carlo simulations. *Dagger:* effective area estimated by fit to Cassini T85 and T88 data. For remaining pathways, we estimated the effective areas analytically. For clarity, leakage through both CS electron guns is shown here as a single conduction pathway. See Teolis et al. [2015], Figure 4 for multiple pathways considered in the CS e-gun conductance calculation. *Grey components*: are neglected in the model, since these sections are treated as having either negligible (e.g., CS enclosure around n_s, ion focus lenses and QMA) or maximum (quadrupole lenses) conductance.

The QMA selects the mass-per-charge ratio (m/q) in the range of 0.5 to 8.5 and 11.5 to 99.5 u per charge, by way of a quadrupole radio frequency mass filter. The detector fore optics consists of three lenses: 1) the Einzel; 2) the Mask I; and 3) the Mask II, which together focus the ions into the detectors. The lens voltage settings can modify the INMS sensitivity depending on how well they focus the beam exiting the QMA into the detectors. Two secondary electron multipliers detect the resulting ion beam operating in a pulse counting mode. These detectors differ in effective sensitivity, with the lower sensitivity detector operating off of secondary electrons produced from the adjacent higher sensitivity detector [Waite et al. 2004]. INMS neutral species-dependent sensitivity factors s_f (for species f) are calibrated on the ground by seven factors: 1) the electron

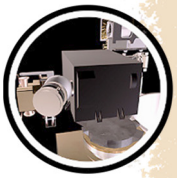

impact efficiency in the sources as determined by the ionization cross-sections of each neutral species; 2) the efficiency for extraction of ions from the CS or OS into the quadrupole lens; 3) the transmission band-pass of the quadrupole switching lens; 4) the degree of focusing in the ion focus lenses into the mass analyzer; 5) the QMA transmission; 6) the detector fore optics transmission; and 7) the detector efficiency.

The OS has three modes of operation: open source ion (OSI), open source neutral beam (OSNB), and open source neutral thermal (OSNT). In the OSI and OSNB modes the OS is used to analyze the ram flux (or molecular beam) of ambient ions and neutrals entering the OS at spacecraft speed, respectively. For more details on the OSNT, see Teolis et al. [2015]; for the OSI see, Mandt et al. [2012]; and for the OSNB, see Waite et al. [2004, 2017].

Over the course of the mission the INMS measurements of Titan's atmospheric neutral mass density were found to be systematically lower than that measured by the Cassini Attitude and Articulation Control System (AACS) and by Navigation (NAV), both of which use spacecraft drag data and aerodynamic models of the spacecraft to derive mass density, as reported by the Titan Atmospheric Working Group (TAMWG); Lee and Hanover [2005]. RPWS Langmuir probe (LP) electron densities can serve as a proxy for total ion densities, while ion densities can be retrieved from Cassini Plasma Spectrometer-Ion Beam Spectrometer (CAPS-IBS) data [Crary et al. 2009]. Comparisons of these sources of ion densities also show systematic differences with the ion densities measured by INMS. Teolis et al. [2015] traced the differences between INMS neutral density measurements and other spacecraft systems in part to gas escape from the CS through leakage pathways not accounted for in the original INMS calibration model. The escape competes with the ram dynamic pressure entering the INMS, yielding lower CS gas densities than indicated by the original calibration, and resulting in a lower INMS neutral gas sensitivity estimate. Therefore, the INMS original calibration model that assumed a sealed CS, used until 2015 to relate the CS density to the ambient density was replaced by a more accurate approach. Teolis et al. [2015] also re-analyzed the INMS detector gain, and found that the gain reduction that occurred during pre-launch characterization testing [Waite et al. 2004], had not been accounted for in the original calibration model. This gain reduction contributes to the reduced INMS sensitivity estimate in the model of Teolis et al. [2015]. The new calibration model brought Cassini INMS results into agreement within expected errors (30%) with the other Cassini systems on the Titan ion and neutral atmospheric densities, and enabled the extraction of Titan neutral density profiles from several previous flybys that yielded unusual and unreasonable densities using the original calibration model.

Key Objectives For INMS

The Announcement of Opportunity (AO) and Cassini Solstice Mission (CSM) objectives listed below have been drawn from the original documents and filtered for relevance to INMS. The objectives are given by key target or working group. Under each key target the AO objectives are first listed followed by the CSM objectives. The AO objectives are fairly general and, in most cases, apply to the overall mission. On the other hand, the CSM objectives largely pertain to new discoveries during the first half of the mission or to seasonal variation objectives during the CSM.

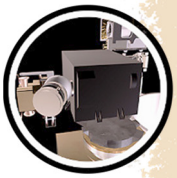

Saturn

The Grand Finale phase of the Cassini mission provided a unique opportunity to study the Saturn Ionosphere Magnetosphere interaction as anticipated. However, what was not expected was information on the equatorial composition and thermal structure (**S_AO1**), the variability of trace gases (**SN1c**), unique H/D and He/H_2 ratio measurements (**S_AO5**), and information on short time scale variations between the rings and the atmosphere (**SC2a**).

Saturn AO objectives

- **Saturn Temperature, Clouds, Composition (S_AO1)** - Determine temperature field, cloud properties, and composition of the atmosphere of Saturn.
- **Saturn Ionosphere-Magnetosphere Interaction (S_AO4)** - Study the diurnal variations and magnetic control of the ionosphere of Saturn.
- **Saturn Formation and Evolution (S_AO5)** - Provide observational constraints (gas composition, isotope ratios, heat flux …) on scenarios for the formation and the evolution of Saturn.

CSM objectives

- *Priority 1* **SN1c** - Measure the spatial and temporal variability of trace gases and isotopes.
- *Priority 2* **SC2a** - Observe the magnetosphere, ionosphere, and aurora as they change on all time scales—minutes to years—and are affected by seasonal and solar cycle forcing.

Rings

Once again, the Grand Finale phase of the mission allowed unique opportunities to address the rings composition (**R_AO2**) and the magnetosphere ring interaction (**R_AO5**) as anticipated, but also allowed unanticipated contributions in understanding ring structure and dynamics (**R_AO1, RN1a, RN1c,** and **RC1b**).

Rings AO objectives

- **Ring Structure and Dynamics (R_AO1)** - Study configuration of the rings and dynamical processes (gravitational, viscous, erosional, and electromagnetic) responsible for ring structure.
- **Ring Particle Composition and Size (R_AO2)** - Map composition and size distribution of ring material.

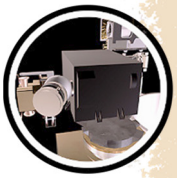

- **Ring Magnetosphere-Ionosphere Interactions (R_AO5)** - Study interactions between the rings and Saturn's magnetosphere, ionosphere, and atmosphere.

CSM objectives

- *Priority 1* **RN1a** - Constrain the origin and age of the rings by direct determination of the ring mass, and of the composition of ring ejecta trapped on field lines.
- *Priority 1* **RC1b** - Determine the temporal variability of ring structure on all timescales up to decadal for regions including Encke gap, D-ring, F-ring, and ring edges by substantially increasing the cadence and time baseline of observations.
- *Priority 1* **RN1c** - Determine structural and compositional variations at high resolution across selected ring features of greatest interest, using remote and in situ observations.

MAPS

INMS was generally expected to address the MAPS AO and CSM objectives listed below (**M_AO2, M_AO4, M_AO5, MC1a, MN1b, MC2a,** and **MN2a**) and did indeed contribute in a meaningful way to all of the listed objectives.

MAPS AO objectives

- **Magnetosphere Charged Particles (M_AO2)** - Determine current systems, composition, sources, and sinks of magnetosphere charged particles.
- **Magnetosphere and Solar Interactions with Titan (M_AO4)** - Study the effect of Titan's interaction with the solar wind and magnetospheric plasma.
- **Plasma Interactions with Titan’s Atmosphere and Ionosphere (M_AO5)** - Investigate interactions of Titan's atmosphere and exosphere with the surrounding plasma.

CSM objectives

- *Priority 1* **MC1a** - Determine the temporal variability of Enceladus’ plumes.
- *Priority 1* **MN1b** - Conduct in situ and remote sensing studies of Saturn’s ionosphere and inner radiation belt.
- *Priority 2* **MC2a** - Observe seasonal variation of Titan’s ionosphere, from one Solstice to the next.
- *Priority 2* **MN2a** - Determine the coupling between Saturn’s rings and ionosphere.

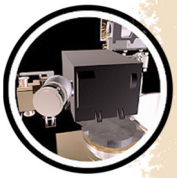

Icy Satellites

INMS was anticipated to contribute to AO objectives (**I_AO5** and **IN1c**). However, the plumes of Enceladus were not anticipated and thrust INMS into a fundamental role in addressing objectives (**I_AO1, I_AO3, I_AO4, IN1a,** and **IC1a**). INMS was unable to contribute to objectives (**IN2b** and **IN2e**) as a result of low satellite outgassing, proximity to the body, or a combination of both, which led to a very low signal to noise ratio in the measurements.

Icy Satellites AO objectives

- **Icy Satellite Geology and History (I_AO1)** - Determine the general characteristics and geological histories of the satellites.
- **Icy Satellite Surface Composition (I_AO3**) - Investigate the compositions and distributions of surface materials, particularly dark, organic rich materials and low melting point condensed volatiles.
- **Icy Satellite Interior Properties (I_AO4)** - Constrain models of the satellites' bulk compositions and internal structures.
- **Icy Satellite Magnetosphere and Ring Interactions (I_AO5)** - Investigate interactions with the magnetosphere and ring systems and possible gas injections into the magnetosphere.

CSM objectives

- *Priority 1* **IN1a** - Determine the presence of an ocean at Enceladus as inferred from induced magnetic field and plume composition, search for possible anomalies in the internal structure of Enceladus as associated with plume sources, and constrain the mechanisms driving the endogenic activity by in situ observations and remote sensing.
- *Priority 1* **IC1a** - Identify long-term secular and seasonal changes at Enceladus, through observations of the South Polar Region, jets, and plumes.
- *Priority 1* **IN1c** - Determine whether Dione exhibits evidence for low-level activity, now or in recent geological time.
- *Priority 2* **IN2b** - Determine whether Tethys contributes to the E-ring and the magnetospheric ion and neutral population.
- *Priority 2* **IN2e** - Understand the unusual appearance of Hyperion with remote sensing observations of the highest resolution possible.

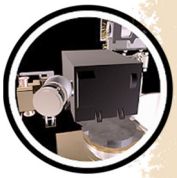

Titan

Titan was always a primary objective of interest for INMS (**T_AO1** and **T_AO5**). However, the importance of ion neutral chemistry in producing organic compounds that are connected to the aerosols and surface deposits (**T_AO2, TC1a, TC1b,** and **TN1c**) was an unanticipated objective. An unfortunate oversight of these processes in Phase B led to descoping the mass range of INMS during development, which in hindsight was a significant impediment in understanding the full extent of the ion neutral chemistry (**T_AO2** and **T_AO5**). Objective **TN2a** on resolving atmospheric density discrepancies between INMS, AACS, and NAV was discovered during the mission and was a direct result of descoping the calibration system for INMS during development.

Titan AO objectives

- **Titan Atmospheric Formation and Evolution (T_AO1)** - Determine abundances of atmospheric constituents (including any noble gases), establish isotope ratios for abundant elements, constrain scenarios of formation and evolution of Titan and its atmosphere.
- **Titan Atmospheric Composition and Distribution (T_AO2)** - Observe vertical and horizontal distributions of trace gases, search for more complex organic molecules, investigate energy sources for atmospheric chemistry, model the photochemistry of the stratosphere, study formation and composition of aerosols.
- **Titan Upper Atmosphere (T_AO5)** - Investigate the upper atmosphere, its ionization, and its role as a source of neutral and ionized material for the magnetosphere of Saturn.

CSM objectives

- *Priority 1* **TC1a** - Determine seasonal changes in the methane-hydrocarbon hydrological cycle: of lakes, clouds, aerosols, and their seasonal transport.
- *Priority 1* **TC1b** - Determine seasonal changes in the high-latitude atmosphere, specifically the temperature structure and formation and breakup of the winter polar vortex.
- *Priority 1* **TN1c** - Measure aerosol and heavy molecule layers and properties.
- *Priority 2* **TN2a** - Resolve current inconsistencies in atmospheric density measurements (critical to a future Flagship mission).

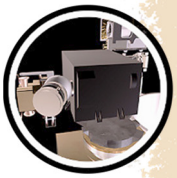

INMS Science Assessment

Rating of Relevant Cassini AO and Solstice Objectives

The Key Objectives for INMS detailed above provide some rationale for the color-coded ratings given in Table INMS-1 for summary purposes.

Table INMS-1. Science Assessment. Note: This table is an Assessment of Data collected to satisfy an objective. It is not an assessment of the status of data analysis/publications.

Fully/Mostly Accomplished: **Partially Accomplished:** **Not Accomplished:**

INMS Science Objectives	AO and TM Science Objectives	INMS Science Assessment	Comments if yellow (partially fulfilled)
Saturn			
Saturn Temperature, Clouds, Composition	S_AO1		Measured temperatures and composition in the exosphere of Saturn near the equator.
Saturn Ionosphere-Magnetosphere Interaction	S_AO4		
Saturn Formation and Evolution	S_AO5		
Measure the spatial and temporal variability of trace gases and isotopes. *(Priority 1)*	SN1c		
Observe the magnetosphere, ionosphere, and aurora as they change on all time scales - minutes to years - and are affected by seasonal and solar cycle forcing. *(Priority 2)*	SC2a		Observed inner magnetospheric composition throughout the mission. Unable to sample in the auroral region close enough to the planet to see any atmospheric or ionospheric effects associated with the aurora.
Rings			
Ring Structure and Dynamics	R_AO1		Positively contributed to understanding the exchange of material between the C-ring and D-ring during the proximal orbits.
Ring Particle Composition and Size	R_AO2		
Ring Magnetosphere-Ionosphere Interactions	R_AO5		
Determine the temporal variability of ring structure on all timescales up to decadal for regions including Encke gap, D-ring, F-ring, and ring edges by substantially increasing the cadence and time baseline of observations. *(Priority 1)*	RC1b		Positively contributed to understanding the exchange of material between the C-ring and D-ring during the proximal orbits.
Constrain the origin and age of the rings by direct determination of the ring mass, and of the composition of ring ejecta trapped on field lines. *(Priority 1)*	RN1a		Positively contributed to understanding the exchange of material between the C-ring and D-ring during the proximal orbits. Also observed material infalling from the D-ring into the atmosphere and determined it to be an important source of ring decay.
Determine structural and compositional variations at high resolution across selected ring features of greatest interest, using remote and in situ observations. *(Priority 1)*	RN1c		INMS contributions limited to comparisons of material infall to Imaging Science Subsystem (ISS) brightness measurements of D68 ringlet during the proximal orbits.

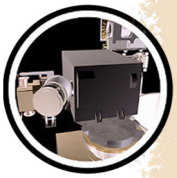

Table INMS-1. Science Assessment. Note: This table is an Assessment of Data collected to satisfy an objective. It is not an assessment of the status of data analysis/publications.

Fully/Mostly Accomplished: **Partially Accomplished:** **Not Accomplished:**

INMS Science Objectives	AO and TM Science Objectives	INMS Science Assessment	Comments if yellow (partially fulfilled)
MAPS			
Magnetosphere Charged Particles	M_AO2		The INMS contribution to the magnetospheres studies was very limited due to the energy range covered by the open source ions.
Magnetosphere and Solar Interactions with Titan	M_AO4		
Plasma Interactions with Titan's Atmosphere and Ionosphere	M_AO5		
Determine the temporal variability of Enceladus' plumes. *(Priority 1)*	MC1a		
Conduct in situ and remote sensing studies of Saturn's ionosphere and inner radiation belt. *(Priority 1)*	MN1b		
Observe seasonal variation of Titan's ionosphere, from one Solstice to the next. *(Priority 2)*	MC2a		
Determine the coupling between Saturn's rings and ionosphere. *(Priority 2)*	MN2a		
Icy Satellites			
Icy Satellite Geology and History	I_AO1		Measured evolutional implications for Enceladus.
Icy Satellite Surface Composition	I_AO3		
Icy Satellite Interior Properties	I_AO4		
Icy Satellite Magnetosphere and Ring Interactions	I_AO5		
Identify long-term secular and seasonal changes at Enceladus, through observations of the south polar region, jets, and plumes.	IC1a		Measured variability but were unable to distinguish secular versus seasonal changes.
Determine the presence of an ocean at Enceladus as inferred from induced magnetic field and plume composition, search for possible anomalies in the internal structure of Enceladus as associated with plume sources, and constrain the mechanisms driving the endogenic activity by in situ observations and remote sensing. *(Priority 1)*	IN1a		
Determine whether Dione exhibits evidence for low-level activity, now or in recent geological time. *(Priority 1)*	IN1c		
Determine whether Tethys contributes to the E-ring and the magnetospheric ion and neutral population. *(Priority 2)*	IN2b		INMS was unable to contribute as a result of low outgassing, proximity to the body, or a combination of both, which led to a very low signal to noise ratio in the measurements.

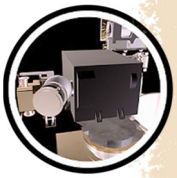

Table INMS-1. Science Assessment. Note: This table is an Assessment of Data collected to satisfy an objective. It is not an assessment of the status of data analysis/publications.

Fully/Mostly Accomplished: **Partially Accomplished:** **Not Accomplished:**

INMS Science Objectives	AO and TM Science Objectives	INMS Science Assessment	Comments if yellow (partially fulfilled)
Understand the unusual appearance of Hyperion with remote sensing observations of the highest resolution possible. *(Priority 2)*	IN2e		INMS was unable to contribute as a result of low outgassing, proximity to the body, or a combination of both, which led to a very low signal to noise ratio in the measurements.
Titan			
Titan Atmospheric Formation and Evolution	T_AO1		
Titan Atmospheric Composition and Distribution	T_AO2		
Titan Upper Atmosphere	T_AO5		
Determine seasonal changes in the methane-hydrocarbon hydrological cycle: of lakes, clouds, aerosols, and their seasonal transport. *(Priority 1)*	TC1a		
Determine seasonal changes in the high-latitude atmosphere, specifically the temperature structure and formation and breakup of the winter polar vortex. *(Priority 1)*	TC1b		Measurements at INMS in situ altitudes provided little information on processes in the stratosphere.
Measure aerosol and heavy molecule layers and properties. *(Priority 1)*	TN1c		
Resolve current inconsistencies in atmospheric density measurements (critical to a future Flagship mission). *(Priority 2)*	TN2a		

Alternative Science Performance Assessment – Mapping of Refereed Publications

An alternative way to assess INMS science performance is to take the science performance requirements compiled prelaunch and match them with the complete list of INMS refereed publications. A relationship between the science performance and functional requirements for INMS was spelled out in the Cassini Orbiter Functional Requirements Book Ion and Neutral Mass Spectrometer (INMS), Rev. A, CAS-4-2074, dated July 4, 1997 prepared just before launch. The performance is encapsulated in a series of science objectives spelled out in Section 3.3.1 of Functional Requirements Book and repeated below in summary assessment form with references of related published INMS papers.

Titan – atmospheric structure

1. What gases (and isotopes) are present besides the N_2, CH_4, and C_2H_2 detected by the Voyager UltraViolet Spectrometer (UVS)?

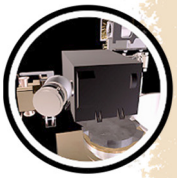

2. What is the extent of diffusive separation (or, where is the homopause)? This may require a comparison with Cassini Probe data.

RELEVANT PAPERS

There are 31 refereed papers listed below that discuss the bulk structure and composition of Titan's atmosphere. The methane homopause was located at ~1100 km above the surface. The papers range in topics from major species structure to isotope and minor species structure in altitude, longitude, and latitude. The quality and quantity of papers far exceeds performance expectations. Solar cycle variability was also examined.

Bell, J. M., J. H. Waite, J. H. Westlake, S. W. Bougher, A. J. Ridley, R. Perryman, K. Mandt, (2014), Developing a self-consistent description of Titan's upper atmosphere without hydrodynamic escape, Journal of Geophysical Research, 119, 4957–4972.

Bell, J. M., J. Westlake, J. H. Waite Jr., (2011a), Simulating the time-dependent response of Titan's upper atmosphere to periods of magnetospheric forcing, Geophysical Research Letters, 38, L06202.

Bell, J., S. W. Bougher, J. H. Waite Jr., A. J. Ridley, B. Magee, K. Mandt, J. Westlake, A. D. DeJong, A. Bar-Nun, R. Jacovi, G. Toth, V. de la Haye, (2011b), Simulating the one-dimensional structure of Titan's upper atmosphere, Part III: Mechanisms determining methane escape, Journal of Geophysical Research, 116, E11002.

Bell, J., S. W. Bougher, J. H. Waite Jr., A .J. Ridley, B. Magee, K. Mandt, J. Westlake, A. D. DeJong, A. Bar-Nun, R. Jacovi, G. Toth, V. de la Haye, (2010a), Simulating the one-dimensional structure of Titan's upper atmosphere, Part I: Formulation of the Titan global ionosphere-thermosphere model and benchmark simulations, Journal of Geophysical Research, 115, E12002.

Bell, J., S. W. Bougher, J. H. Waite Jr., A.J. Ridley, B. Magee, K. Mandt, J. Westlake, A. D. DeJong, V. de la Haye, D. Gell, G. Fletcher, A. Bar-Nun, R. Jacovi, G. Toth, (2010b), Simulating the one-dimensional structure of Titan's upper atmosphere, Part II: Alternative scenarios for methane escape, Journal of Geophysical Research, 115, E12018.

Cui, J., Y. Lian, I. C. F. Müller-Wodarg, (2013), Compositional effects in Titan's thermospheric gravity waves, Geophysical Research Letters, 40, 43–47, doi: 1 0.1029/2012GL054621.

Cui, J., R. V. Yelle, D. F. Strobel, I. C. F. Müller-Wodarg, D. S. Snowden, T. T. Koskinen, M. Galand, (2012), The CH4 structure in Titan's upper atmosphere revisited, Journal of Geophysical Research, 117, E11006, doi: 10.1029/2012JE004222.

Cui, J., R. V. Yelle, I. C. F. Müller-Wodarg, P. P. Lavvas, M. Galand, (2011), The implications of the H2 variability in Titan's exosphere, Journal of Geophysical Research, 116, A11324.

Cui, J., R. V. Yelle, V. Vuitton, J. H. Waite, W. T. Kasprzak, D. A. Gell, H. B. Niemann, I. C. F. Müller-Wodarg, N. Borggren, G. G. Fletcher, E. L. Patrick, E. Raaen, B. A. Magee, (2009a),

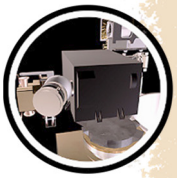

Analysis of Titan's neutral upper atmosphere from Cassini ion neutral mass spectrometer measurements, Icarus, 200, 581–615, doi: 10.1016/j.icarus.2008.12.005.

Cui, J., R. V. Yelle, K. Volk, (2008), Distribution and escape of molecular hydrogen in Titan's thermosphere and exosphere, Journal of Geophysical Research, 113, E10004, doi: 10.1029/2007JE003032.

De La Haye, V., J. H. Waite Jr., T. E. Cravens, I. P. Robertson, S. Lebonnois, (2008a), Coupled ion and neutral rotating model of Titan's upper atmosphere, Icarus, 197, 110–136, doi: 10.1016/j.icarus.2008.03.022.

De La Haye, V., J. H. Waite, R. E. Johnson, R. V. Yelle, et al., (2007a), Cassini Ion and Neutral Mass Spectometer data in Titan's upper atmosphere and exosphere: Observation of a suprathermal corona, Journal of Geophysical Research, 12, A07309.

Magee, B. A., J. H. Waite, K. E. Mandt, J. Bell, J. Westlake, D. A. Gell, V. De la Haye, (2009), INMS derived composition of Titan's upper atmosphere: Analysis methods and model comparison, Planetary and Space Science, 57, 1895–1916.

Mandt, K. E., J. H. Waite Jr., B. Teolis, B. A. Magee, J. Bell, J. Westlake, C. Nixon, O. Mousis, J. Lunine, (2012a), The 12C/13C ratio on Titan from Cassini INMS measurements and implications for the evolution of methane, Astrophysical Journal, 749, 160, doi: 10.1088/0004-637X/749/2/160.

Mandt, K. E., J. H. Waite Jr., W. Lewis, J. I. Lunine, O. Mousis, J. Bell, B. A. Magee, D. Cordier, (2009), Isotopic evolution of the major constituents of Titan's atmosphere based on Cassini data, Planetary and Space Science, 57, 1917–1930.

Mousis, O., J. I. Lunine, S. Picaud, D. Cordier, J. H. Waite, Jr., K. E. Mandt, (2011), Removal of Titan's atmospheric noble gases by their sequestration in surface clathrates, The Astrophysical Journal, 740, L9.

Mousis, O., J. I. Lunine, M. Pasek, D. Cordier, J. H. Waite Jr., K. E. Mandt, W. S. Lewis, M.-J. Nguyen, (2009b), A primordial origin for the atmospheric methane of Saturn's moon Titan, Icarus, 204, 749–751.

Müller-Wodarg, I. C. F., R. V. Yelle, J. Cui, J. H. Waite, (2008), Horizontal structures and dynamics of Titan's thermosphere, Journal of Geophysical Research, 113, E10003, doi: 10.1029/2007JE003031.

Müller-Wodarg, I. C. F., R. V. Yelle, N. Borggren, J. H. Waite, (2006a), Waves and horizontal structures in Titan's thermosphere, Journal of Geophysical Research, 111, A12315.

Müller-Wodarg, I. C. F., R. V. Yelle, M. J. Mendillo, A. D. Aylward, (2003), On the global distribution of neutral gases in Titan's upper atmosphere and its effect on the thermal structure, Journal of Geophysical Research: Space Physics, vol. 108, issue A12, doi: 10.1029/2003JA010054.

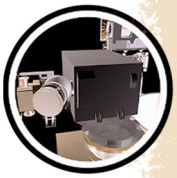

Müller-Wodarg, I. C. F. and R. V. Yelle, (2002a), The effect of dynamics on the composition of Titan's upper atmosphere, Geophysical Research Letters, vol. 29, issue 23, 54-1–54-4, doi: 10.1029/2002GL016100.

Müller-Wodarg, I. C. F., (2002b), The application of general circulation models to the atmospheres of terrestrial-type moons of the giant planets, In Atmoshperes in the Solar System: Comparative Aeronomy, Volume 120, Part IV: Models of Aeronomic Systems, (eds.) M. Mendillo, A. Nagy, J. H. Waite, American Geophysical Union, Geophysical Monograph Series, pp. 307–318, doi: 10.1029/GM130.

Müller-Wodarg, I. C. F., R. V. Yelle, M. Mendillo, L. A. Young, A. D. Aylward, (2000), The thermosphere of Titan simulated by a global three-dimensional time-dependent model, Journal of Geophysical Research, 105, pp. 20833–20856, doi: 10.1029/2000JA000053.

Shematovich, V. I., R. E. Johnson, M. Michael, J. G. Luhmann, (2003), Nitrogen loss from Titan, Journal of Geophysical Research, 108, E8, id. 5087, doi: 10.1029/2003JE002094.

Strobel, D. F., S. K. Atreya, B. Bézard, F. Ferri, F. M. Flasar, M. Fulchignoni, E. Lellouch, I. C. F. Müller-Wodarg, (2009), Atmospheric structure and composition, In Titan from Cassini-Huygens, (eds.) R. Brown, J.-P. Lebreton, J. H. Waite, Springer Dordrecht, pp. 235–257, doi: 10.1007/978-1-4020-9215-2_10.

Vuitton, V., R. V. Yelle, J. Cui, (2008), Formation and distribution of benzene on Titan, Journal of Geophysical Research, doi: 1 0.1029/2007JE002997.

Waite, J. H., J. Bell, R. Lorenz, R. Achterberg, F. M. Flasar, (2013), A model of variability in Titan's atmospheric structure, Planetary and Space Science, 86, 45–56, doi: 10.1016/j.pss.2013.05.018.

Waite, J. H., H. Niemann, R. V. Yelle, W. T. Kasprzak, T. E. Cravens, J. G. Luhmann, R. L. McNutt, W.-H. Ip, D. Gell, V. de la Haye, I. Müller-Wordag, B. McGee, N. Borggren, S. Ledvina, G. Fletcher, E. Walter, R. Miller, S. Scherer, R. Thorpe, J. Xu, B. Block, K. Arnett, (2005a), Ion Neutral Mass Spectrometer (INMS) results from the first flyby of Titan, Science, 308 (5724), 982–986.

Westlake, J. H., J. H. Waite, J. M. Bell, R. Perryman, (2014a), Observed decline in Titan's thermospheric methane due to solar cycle drivers, Journal of Geophysical Research, 119, 8586–8599, doi: 10.1002/2014JA020394.

Yelle, R.V., J. Cui, and I.C.F. Müller-Wodarg, (2008), Methane Escape from Titan's Atmosphere, Journal of Geophysical Research, 113, E10003, doi: 10.1029/2007JE003031.

Yelle, R. V., N. Borggren, V. De La Haye, W. T. Kasprzak, H. B. Niemann, I. Müller-Wodarg, J. H. Waite Jr., (2006), The vertical structure of Titan's upper atmosphere from Cassini ion neutral mass spectrometer measurements, Icarus, 182, 567–576.

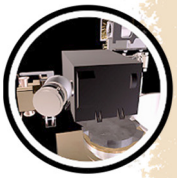

Titan – thermal structure and energetics

1. What is the exospheric temperature and how does it vary (diurnally, spatial, or long term)?

2. What energy sources and sinks determine the heat balance of the exosphere and lower thermosphere?

3. What role do radiatively active species play in the upper atmospheric heat balance and the coupling of the lower and upper atmosphere thermal processes?

RELEVANT PAPERS

There are 10 papers listed below that report the thermal structure of the atmosphere including solar heating, particle precipitation, and gravity wave forcing. Solar heating was found to be the primary energy source and hydrogen cyanide rovibrational emissions the major cooling process. The papers met expectations for the performance noted prior to the mission.

Cui, J., R. V. Yelle, T. Li, D. S. Snowden, I. C. F. Müller-Wodarg, (2014), Density waves in Titan's upper atmosphere, Journal of Geophysical Research, 119, 490–518, doi: 10.1001/2013JA019113.

Cravens T. E., I. P. Robertson, S. A. Ledvina, D. Mitchell, S. M. Krimigis, J. H. Waite Jr., (2008a), Energetic ion precipitation at Titan, Geophys. Res. Lett., 35, L03103, doi: 10.1029/2007GL032451.

De La Haye, V., J. H. Waite, Jr., T. E. Cravens, S. W. Bougher, I. P. Robertson, J. M. Bell, (2008b), Heating Titan's upper atmosphere, Journal of Geophysical Research, 113, A11314.

De La Haye, V., J. H. Waite Jr., T. E. Cravens, A. F. Nagy, R. E. Johnson, S. Lebonnois, I. P. Robertson, (2007b), Titan's Corona: The contribution of exothermic chemistry, Icarus, 191, 236–250.

Snowden, D. and R. V. Yelle, (2014a), The global precipitation of magnetospheric electrons into Titan's upper atmosphere, Icarus, 243, 1–15, doi: 10.1016/j.icarus.2014.08.027.

Snowden, D. and R. V. Yelle, (2014b), The thermal structure of Titan's upper atmosphere, II: Energetics, Icarus, vol. 228, pp. 64–77, doi: 10.1016/j.icarus.2013.08.027.

Snowden, D., R. Yelle, J. Cui, J.-E. Wahlund, N. J. T. Edberg, K. Ågren, (2013a), The thermal structure of Titan's upper atmosphere, I: Temperature profiles from Cassini INMS observations, Icarus, vol. 226, pp. 552–582, doi: 10.1016/j.icarus.2013.06.006.

Snowden, D., R. V. Yelle, M. Galand, A. J. Coates, A. Wellbrock, G. H. Jones, and P. Lavvas, (2013b), Auroral electron precipitation and flux tube erosion in Titan's upper atmosphere, Icarus, 226, 186-204, doi: 10.1016/j.icarus.2013.05.021.

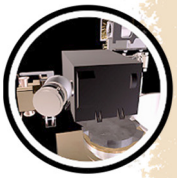

Vigren, E., M. Galand, R. V. Yelle, J. Cui, J.-E. Wahlund, K. Ågren, P. P. Lavvas, I. C. F. Müller-Wodarg, D. F. Strobel, V. Vuitton, A. Bazin, (2013), On the thermal electron balance in Titan's sunlit upper atmosphere, Icarus, vol. 223, pp. 234–251, doi: 10.1016/j.icarus.2012.12.010.

Westlake, J. H., J. Bell, J. H. Waite, Jr., R. E. Johnson, J. G. Luhmann, K. E. Mandt, B. A. Magee, A. M. Rymer, (2011), Titan's thermospheric response to various plasma and solar environments, Journal of Geophysical Research, 116, A03318.

Titan – ionospheric structure

1. What are the sources of ionization? What is the chemistry of positive ions? How important are vertical and horizontal transports of ions and electrons?

2. What are the energy sources and sinks for ions and electrons? What ions and neutrals are escaping from Titan? What is the environment in which the intense airglow (aurora?) is produced?

RELEVANT PAPERS

There are 51 papers listed below that deal with the ionosphere—its formation and chemistry, especially the complex ion neutral chemistry that forms the heavy organic compounds found on the Titan surface. This work far exceeds the pre-flight expectations.

Ågren, K., J. E. Wahlund. R. Modolo, D. Lummerzheim, M. Galand, I. Müller-Wodarg, P. Canu, W. S. Kurth, T. E. Cravens, R. V. Yelle, J. H. Waite Jr., A. J. Coates, G. R. Lewis, D. T. Young, C. Bertucci, M. K. Dougherty, (2007), On magnetospheric electron impact ionisation and dynamics in Titan's ram-side & polar ionosphere-a Cassini case study, Annales Geophysicae, 25.

Brecht, S. H., J. G. Luhmann, D. J. Larson, (2000), Simulation of the Saturnian magnetospheric interaction with Titan, Journal of Geophysical Research, vol. 105, issue A6, 13119–13130, doi: 10.1029/1999JA900490.

Coates, A. J., A. Wellbrock, G. R. Lewis, G. H. Jones, D. T. Young, F. J. Crary, J. H. Waite Jr., (2009), Heavy negative ions in Titan's ionosphere: Altitude and latitude dependence, Planetary and Space Science, 57, 1866–1871.

Crary, F. J., B. A. Magee, K. E. Mandt, J. H. Waite, J. Westlake, D. T. Young, (2009), Heavy ions, temperatures and winds in Titan's ionosphere: Combined Cassini CAPS and INMS observations, Planetary and Space Science, 57, 1847–1856.

Cravens, T. E., M. Richard, Y.-J. Ma, C. Bertucci, J. G. Luhmann, S. Ledvina, I. P. Robertson, J.-E. Wahlund, K. Ågren, J. Cui, I. Müller-Wodarg, J. H. Waite, M. Dougherty, J. Bell, D. Ulusen, (2010), Dynamical and Magnetic Field Time Constants for Titan's Ionosphere - Empirical Estimates, Journal of Geophysical Research, 115, A08319.

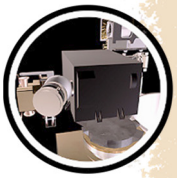

Cravens, T. E., R. V. Yelle, J.-E. Wahlund, D. E. Shemansky, A. F. Nagy, (2009a), Composition and structure of the ionosphere and thermosphere, In Titan from Cassini-Huygens, Chapter 11, (eds.) R. H. Brown, J. P. Lebreton, J. H. Waite, Springer, Dordrecht, pp. 259–295, doi: 10.1007/978-1-4020-9215-2_11.

Cravens, T. E., I. P. Robertson, J. H. Waite Jr., R. V. Yelle, V. Vuitton, A. J. Coates, J.-E. Wahlund, K. Ågren, M. S. Richard, V. De La Haye, A. Wellbrock, F. N. Neubauer, (2009b), Model-data comparisons for Titan's nightside ionosphere, Icarus, 199, 174–188, doi: 10.1016/j.icarus.2008.09.005.

Cravens, T. E., I. P. Robertson, J. H. Waite Jr., R. V. Yelle, V. Vuitton, A. J. Coates, J.-E. Wahlund, K. Ågren, M. S. Richard, V. De La Haye, A. Wellbrock, F. N. Neubauer, (2008b), Model-data comparisons for Titan’s nightside ionosphere, Icarus, doi: 10.1016/j.icarus.2008.09.005.

Cravens, T. E., I. P. Robertson, J. H. Waite Jr., R. V. Yelle, W. T. Kasprzak, C. N. Keller, S. A. Ledvina, H. B. Niemann, J. G. Luhmann, R. L. McNutt, W.-H. Ip, V. De La Haye, I. Müller-Wodarg, J.-E. Wahlund, V. G. Anicich, V. Vuitton, (2006), The composition of Titan's ionosphere, Geophysical Research Letters, 33, L07105.

Cravens, T. E., I. P. Robertson, J. Clark, J.-E. Wahlund, J. H. Waite Jr., S. A. Ledvina, H. B. Niemann, R. V. Yelle, W. T. Kasprzak, J. G. Luhmann, R. L. McNutt, W.-H. Ip, V. De La Haye, I. Müller-Wodarg, D. T. Young, A. J. Coates, (2005), Titan's ionosphere: Model comparisons with Cassini Ta data, Geophysical Research Letters, vol. 32, issue 12, doi: 10.1029/2005GL023249.

Cravens, T. E., J. Vann, J. Clark, J. Wu, C. N. Keller, C. Brull, (2004), The ionosphere of Titan: An updated theoretical model, Advances in Space Research, 33, 212.

Cravens, T. E., C. N. Keller, B. Ray, (1997), Photochemical sources of non-thermal neutrals for the exosphere of Titan, Planetary and Space Science, 45, 889.

Cui, J., M. Galand, R. V. Yelle, J.-E. Wahlund, K. Ågren, J. H. Waite Jr., M. K. Dougherty, (2010), Ion transport in Titan's upper atmosphere, Journal of Geophysical Research, 115, A06314.

Cui, J., M. Galand, R. V. Yelle, V. Vuitton, I. C. F. Müller-Wodarg, J. -E. Wahlund, P. P. Lavvas, T. E. Cravens, W. T. Kasprzak, J. H. Waite Jr., (2009b), Diurnal variations of Titan's ionosphere, Journal of Geophysical Research, 114, A06310.

Edberg, N. J. T., D. J. Andrews, O. Shebanits, K. Ågren, J.-E. Wahlund, H. J. Opgenoorth, T. E. Cravens, Z. Girazian, (2013a), Solar cycle modulation of Titan’s ionosphere, Journal of Geophysical Research, 118, 5255–5264, doi: 10.1002/jgra.50463.

Edberg, N. J. T., D. J. Andrews, O. Shebanits, K. Ögren, J.-E. Wahlund, H. J. Opgenoorth, E. Roussos, P. Garnier, T. E. Cravens, S. V. Badman, R. Modolo, C. Bertucci, M. K. Dougherty, (2013b), Extreme densities in Titan’s ionosphere during the T85 magnetosheath encounter, Geophysical Research Letters, 40, 2879–2883, doi: 10.1002/grl.50579.

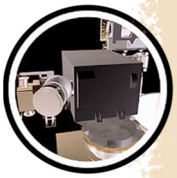

Galand, M., A. J. Coates, T. E. Cravens, J.-E. Wahlund, (2014), Titan's ionosphere, In Titan: Interior, Surface, Atmosphere, and Space Environment, Chapter 11, (eds.) I. Müller-Wodarg, C. A. Griffith, E. Lellouch, T. E. Cravens, Cambridge University Press, pp. 376–419.

Garnier, P., J.-E. Wahlund, L. Resnqvist, R. Modolo, K. Ågren, N. Sergis, P. Canu, M. Andre, D. A. Gurnett, W. S. Kurth, S. M. Krimgis, A. Coates, M. Dougherty, J. H. Waite Jr., (2009), Titan's ionosphere in the magnetosheath: Cassini RPWS results during the T32 flyby, Annales Geophysicae, 27, 4257–4272.

Keller, C. N., V. G. Anicich, T. E. Cravens, (1998), Model of Titan's ionosphere with detailed hydrocarbon ion chemistry, Planetary and Space Science, 46, 1157.

Ledvina, S. A. and S. H. Brecht, (2012a), Consequences of negative ions for Titan's plasma interaction, Geophysical Research Letters, 39, L20103, doi: 10.1029/2012GL053835.

Ledvina, S. A., S. H. Brecht, T. E. Cravens, (2012b), The orientation of Titan's dayside ionosphere and its effects on Titan's plasma interaction, Earth Planets Space, 64, 207–230.

Ledvina, S. A., Y. Ma, E. Kallio, (2008), Modeling and simulating flowing plasmas and related phenomena, Space Science Reviews, doi: 10.1007/s11214-008-9384-6.

Ledvina, S. A., T. E. Cravens, K. Kecskemety, (2005), Ion distributions in Saturn's magnetosphere near Titan, Journal of Geophysical Research, 110, A06211, doi: 10.1029/2004JA010771.

Ledvina, S. A., J. G. Luhmann, S. H. Brecht, T. E. Cravens, (2004a), Titan's induced magnetosphere, Advances in Space Research, 33, 2092.

Ledvina, S. A., J. G. Luhmann, T. E. Cravens, (2004b), Ambient ion distributions in Saturn's magnetosphere near Titan during a non-Voyager type interaction, Advances in Space Research, 33, 221.

Ledvina, S. A., S. H. Brecht, J. G. Luhmann, (2004c), Ion distributions of 14 amu pickup ions associated with Titan's plasma interaction, Geophysical Research Letters, 31, L17S10, doi: 10.1029/2004GL019861.

Luhmann, J. G., D. Ulusen, S. A. Ledvina, K. Mandt, B. Magee, J. H. Waite, J. Westlake, T. E. Cravens, I. Robertson, N. Edberg, K. Ågren, J.-E. Wahlund, Y.-J. Ma, H. Wei, C. T. Russell, M. K. Dougherty, (2012), Investigating magnetospheric interaction effects of Titan's ionosphere with the Cassini orbiter ion neutral mass spectrometer, Langmuir Probe and magnetometer observations during targeted flybys, Icarus, 219, 534–555, doi: 10.1016/j.icarus.2012.03.015.

Luhmann, J. G., S. A. Ledvina, C. T. Russell, (2004), Induced magnetospheres, Advances in Space Research, 33, 1905.

Luhmann, J. G., (1996), Titan's ion exosphere wake: A natural ion mass spectrometer? Journal of Geophysical Research, 101, E12, pp. 29387–29393, doi: 10.1029/96JE03307.

Ma, Y., K. Altwegg, T. Breus, M. R. Combi, et al., (2008), Plasma flow and related phenomena in planetary aeronomy, Space Science Reviews, 139, no. 1–4, 311–353, doi: 10.1007/s11214-008-9389-1.

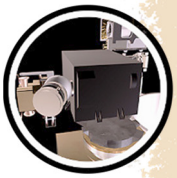

Ma, Y., A. F. Nagy, T. E. Cravens, I. V. Sokolov, K. C. Hansen, J.-E. Wahlund, F. J. Crary, A. J. Coates, M. K. Dougherty, (2006), Comparisons Between MHD Model Calculations and Observations of Cassini Flybys of Titan, Journal of Geophysical Research, 111, A05207, doi: 10.1029/2005JA011481.

Ma, Y.-J., A. F. Nagy, T. E. Cravens, I. G. Sokolov, J. Clark, K. C. Hansen, (2004), 3-D global MHD model prediction of the first close flyby of Titan by Cassini, Geophysical Research Letters, 31, doi: 10.1029/2004GL021215.

Madanian, H., T. E. Cravens, M. S. Richard, J. H. Waite, N. J. T. Edberg, J. H. Westlake, J.-E. Wahlund, (2016), Solar cycle variations in ion composition in the dayside ionosphere of Titan, Journal of Geophysical Research, 121, 8013–8037, doi: 10.1002/2015JA022274.

Mandt, K. E. , D. A. Gell, M. Perry, J. H. Waite Jr., F. A. Crary, D. Young, B. A. Magee, J. H. Westlake, T. Cravens, W. Kasprzak, G. Miller, J.-E. Wahlund, K. Ågren, N. J. T. Edberg, A. N. Heays, B. R. Lewis, S. T. Gibson, V. de la Haye, M.-C. Liang, (2012b), Ion densities and composition of Titan's upper atmosphere derived from the Cassini ion neutral mass spectrometer: Analysis methods and comparison of measured ion densities to photochemical model simulations, Journal of Geophysical Research, 117, E10006, doi: 10.1029/2012JE004139.

Michael, M., R. E. Johnson, F. Leblanc, M. Liu, J. G. Luhmann, V. I. Shematovich, (2005), Ejection of nitrogen from Titan's atmosphere by magnetospheric ions and pick-up ions, Icarus, vol. 175, Issue 1, pp. 263–267, doi: 10.1016/j.icarus.2004.11.004.

Nagy, A. F. and T. E. Cravens, (1998), Titan's ionosphere: A review, Planetary and Space Science, 46, 1149, doi: 10.1016/S0032-0633(98)00049-X.

Richard, M. S., T. E. Cravens, C. Wylie, D. Webb, Q. Chediak, R. Perryman, K. Mandt, J. Westlake, J. H. Waite, I. Robertson, B. A. Magee, N. J. T. Edberg, (2015a), An empirical approach to modeling ion production rates in Titan’s ionosphere I: Ion production rates on the dayside and globally, Journal of Geophysical Research, 120, 1264–1280, doi: 10.1002/2013JA019706.

Richard, M. S., T. E. Cravens, C. Wylie, D. Webb, Q. Chediak, K. Mandt, J. H. Waite, A. Rymer, C. Bertucci, A. Wellbrock, A. Windsor, A. J. Coates, (2015b), An empirical approach to modeling ion production rates in Titan’s ionosphere II: Ion production rates on the nightside, Journal of Geophysical Research, 120, 1281–1298, doi: 10.1002/2014JA020343.

Richard, M. S., T. E. Cravens, I. P. Robertson, J. H. Waite, J.-E. Wahlund, F. J. Crary, A. J. Coates, (2011), Energetics of Titan's ionosphere: model comparisons with Cassini data, Journal of Geophysical Research, 116, A09310.

Robertson, I. P., T. E. Cravens, J. H. Waite Jr., R. V. Yelle, V. Vuitton, A. J. Coates, J. E. Wahlund, K. Ågren, B. Magee, K. Mandt, M. S. Richard, (2009), Structure of Titan's ionosphere: model comparisons with Cassini data, Planetary and Space Science, 57, 1834–1846.

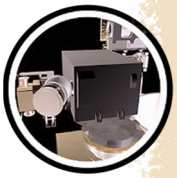

Rosenqvist, L., J.-E. Wahlund, K. Ågren, R. Modolo, H. J. Opgenoorth, D. Strobel, I. Müller-Wodarg, P. Garnier, C. Bertucci, (2009), Titan ionospheric conductivities from Cassini measurements, Planetary and Space Science, 57, 1828–1833, doi: 10.1016/j.pss.2009.01.007.

Sagnières, L. B. M., M. Galand, J. Cui, P. P. Lavvas, E. Vigren, V. Vuitton, R. V. Yelle, A. Wellbrock, A. J. Coates, (2015), Influence of local ionization on ionospheric densities in Titan's upper atmosphere, Journal of Geophysical Research, 120, 5899–5921, doi: 10.1002/2014JA020890.

Shebanits, O., J.-E. Wahlund, N. J. T. Edberg, F. J. Crary, A. Wellbrock, D. J. Andrews, E. Vigren, R. T. Desai, A. J. Coates, K. E. Mandt, J. H. Waite, (2016), Ion and aerosol precursor densities in Titan's ionosphere: A multi-instrument case study, Journal of Geophysical Research, 121, 10075–10090, doi: 10.1002/2016JA022980.

Ulusen, D., J. G. Luhmann, Y. J. Ma, K. Mandt, J. H. Waite, M. K. Dougherty, J.-E. Wahlund, C. T. Russell, T. A. Craven, N. Edberg, K. Agren, (2012), Comparisons of Cassini flybys of the Titan magnetospheric interaction with an MHD model: Evidence for organized behavior at high altitudes, Icarus, 217, 43–54, doi: 10.1016/j.icarus.2011.10.009.

Ulusen, D., J. Luhmann, Y. Ma, S. Ledvina, T. Cravens, K. Mandt, J. H. Waite Jr., J.-E. Wahlund, (2010), Investigation of the force balance in the Titan ionosphere: Cassini T5 flyby model/data comparisons, Icarus, 210, 867–880.

Vigren, E., M. Galand, R. V. Yelle, A. Wellbrock, A. J. Coates, D. Snowden, J. Cui, P. Lavvas, N. J. T. Edberg, O. Shebanits, J.-E. Wahlund, V. Vuitton, K. Mandt, (2015), Ionization balance in Titan's nightside ionosphere, Icarus, 248, 539–546, doi: 10.1016/j.icarus.2014.11.012.

Vuitton, V., P. Lavvas, R. V. Yelle, M. Galand, A. Wellbrock, G. R. Lewis, A. J. Coates, J.-E. Wahlund, (2009), Negative ion chemistry in Titan's upper atmosphere, Planetary and Space Science, 57, 1558–1572.

Wahlund, J.-E., M. Galand, I. Meuller-Wodarg, J. Cui, R. V. Yelle, F. J. Crary, K. Mandt, B. Magee, J. H. Waite, Jr., D. T. Young, A. J. Coates, P. Garnier, K. Ågren, M. Andre, A. I. Eriksson, T. E. Cravens, V. Vuitton, D. A. Gurnett, W. S. Kurth, (2009), On the amount of heavy molecular ions in Titan's ionosphere, Planetary and Space Science, 57, 1857–1865.

Westlake, J. H., J. H. Waite, N. Carrasco, M. Richard, T. Cravens, (2014b), The role of ion-molecule reactions in the growth of heavy ions in Titan's ionosphere, Journal of Geophysical Research, 119, 5951–5963, doi: 10.1002/2014JA0202008.

Westlake, J. H., C. P. Paranicas, T. E. Cravens, J. G. Luhmann, K. E. Mandt, H. T. Smith, D. G. Mitchell, A. M. Rymer, M. E. Perry, J. H. Waite Jr., J.-E. Wahlund, (2012a), The observed composition of ions outflowing from Titan, Geophysical Research Letters, 39, L19104, doi: 10.1029/2012GL053079.

Westlake, J. H., J. H. Waite Jr., K. E. Mandt, N. Carrasco, J. M. Bell, B. A. Magee, J.-E. Wahlund, (2012b), Titan's ionospheric composition and structure: Photochemical modeling of Cassini INMS data, Journal of Geophysical Research, 117, E01003, 21, doi: 10.1029/2011JE003883.

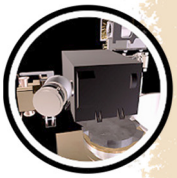

Titan – unanticipated findings

There are five papers listed below that detail unanticipated findings by INMS. The complex nature and complexity of the ion neutral chemistry was totally unanticipated, as was our overall characterization of the formation of the Saturn system through compositional measurements.

RELEVANT PAPERS

Carrasco, N., J. Westlake, P. Pernot, J. H. Waite Jr., (2013), Nitrogen in Titan's Atmospheric Aerosol Factory, The Early Evolution of the Atmospheres of Terrestrial Planets, 35, doi: 10.1007/978-1-4614-5191-4_11.

Glein, C. R., (2017), A whiff of nebular gas in Titan's atmosphere – Potential implications for the conditions and timing of Titan's formation, Icarus, 293, 231–242.

Vuitton, V., R. V. Yelle, M. J. McEwan, (2007), Ion Chemistry and N-containing Molecules in Titan's Upper Atmosphere, Icarus, doi: 10.1016/j.carus.2007.06.023.

Waite, J. H., D. T. Young, A. J. Coates, F. J. Crary, B. A. Magee, K. E. Mandt, J. H. Westlake, (2008), The source of heavy organics and aerosols in Titan's atmosphere, Proceedings of the International Astronomical Union, vol. 4, issue S251 (Organic Matter in Space), pp. 321-326, doi: 10.1017/S1743921308021844.

Waite Jr., J. H., D. T. Young, T. E. Cravens, A. J. Coates, F. J. Crary, B. Magee, J. Westlake, (2007), The process of tholin formation in Titan's upper atmosphere, Science, 316, 870–875.

Rings and icy satellites

There are 11 papers listed below that discuss Saturn's rings and icy satellites. INMS allowed a characterization of the E-ring and F-ring as expected. The sputtered atmospheres of Dione and Rhea were well characterized, including the unexpected seasonal variations associated with those atmospheres. The D-ring interaction with Saturn's atmosphere during the Grand Finale exceeded all expectations.

RELEVANT PAPERS

Ip W.-H., (2006), On a ring origin of the equatorial ridge of Iapetus, Geophysical Research Letters, 33, L16203.

Ip, W.-H., (2005), An update on the ring exosphere and plasma disc of Saturn, Geophysical Research Letters, doi: 10.1029/2004GL022217.

Johnson, R. E., J. G. Luhmann, R. L. Tokar, M. Bouhram, J. J. Berthelier, E. C. Sittler, J. F. Cooper, T. W. Hill, H. T. Smith, M. Michael, M. Liu, F. J. Crary, D. T. Young, (2006), Production, ionization and redistribution of O2 in Saturn's ring atmosphere, Icarus, 180, 393.

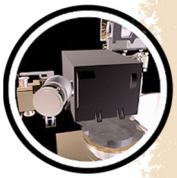

Luhmann, J. G., R. E. Johnson, R. L. Tokar, S. A. Ledvina, T. E. Cravens, (2006), A model of the ionosphere of Saturn's rings and its implications, Icarus, 181 (2), 465–474.

Perry, M. E., B. Teolis, H. T. Smith, R. L. McNutt, G. Fletcher, W. Kasprzak, B. Magee, D. G. Mitchell, J. H. Waite Jr., (2010), Cassini INMS observations of neutral molecules in Saturn's E-ring. Journal of Geophysical Research, 115, A10206.

Teolis, B. D. and J. H. Waite, (2016), Dione and Rhea seasonal exospheres, revealed by Cassini CAPS and INMS, Icarus, 272, 277–289, doi: 10.1016/j.icarus.2016.02.031.

Teolis, B. D., I. Sillanpää, J. H. Waite, K. K. Khurana, (2014), Surface current balance and thermoelectric whistler wings at airless astrophysical bodies: Cassini at Rhea, Journal of Geophysical Research, 119, 8881–8901, doi: 10.1002/2014JA020094.

Teolis, B., G. H. Jones, P. F. Miles, R. L. Takar, B. A. Magee, J. H. Waite, E. Roussos, D. T. Young, F. J. Crary, A. J. Coates, R. E. Johnson, W.-L. Tseng, R. A. Baragiola, (2010a), Cassini Finds an Oxygen-Carbon Dioxide Atmosphere at Saturn's Icy Moon Rhea, Science, 330, 24.

Waite Jr., J. H., R. Perryman, M. Perry, K. Miller, J. Bell, T. E. Cravens, C. R. Glein, J. Grimes, M. Hedman, J. Cuzzi, T. Brockwell, B. Teolis, L. Moore, D. Mitchell, A. Persoon, W. S. Kurth, J-E. Wahlund, M. Morooka, L. Z. Hadid, S. Chocron, J. Walker, A. Nagy, R. Yelle, S. Ledvina, R. Johnson, W. Tseng, O. J. Tucker, W.-H. Ip, (2018), Chemical Interactions between Saturn’s Atmosphere and its Rings, Science, doi: 10.1126/science.aat2382.

Waite Jr., J. H., M. Combi, W.-H. Ip, T. E. Cravens, R. L. McNutt, Jr., W. Kasprzak, R. Yelle, J. Luhmann, H. Niemann, D. Gell, B. Magee, G. Fletcher, J. Lunine, W.-L. Tseng, (2006), Cassini Ion and Neutral Mass Spectrometer: Enceladus plume composition and structure, Science, 311, 1419–1422.

Waite, J. H., T. E. Cravens, W.-H. Ip, W. T. Kasprzak, J. G. Luhmann, R. L. McNutt, H. B. Niemann, R. V. Yelle, I. Müller-Wodarg, S. A. Ledvina, S. Scherer, (2005b), Oxygen ions observed near Saturn’s A Ring, Science, 307 (5713), 1260–1262.

Magnetosphere

There is one paper listed below that discusses the magnetosphere. The INMS contribution to the magnetospheres studies was limited due to the energy range covered by the open source ions.

RELEVANT PAPERS

Blanc, M., S. Bolton, J. Bradley, M. Burton, T. E. Cravens, I. Dandouras, M. K. Dougherty, M. C. Festou, J. Feynman, R. E. Johnson, T. G. Gombosi, W. S. Kurth, P. C. Liewer, B. H. Mauk, S. Maurice, D. Mitchell, F. M. Neubauer, J. D. Richardson, D. E. Shemansky, E. C. Sittler, B. T. Tsurutani, P. Zarka, L. W. Esposito, E. Grün, D. A. Gurnett, A. J. Kliore, S. M. Krimigis, D. Southwood, J. H. Waite Jr., D. T. Young, (2002), Magnetospheric and plasma science with Cassini-Huygens, Space Science Reviews, 104, 1, 253–346.

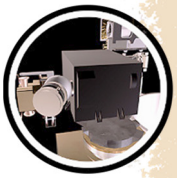

Enceladus

The most startling and unanticipated contribution from INMS was the characterization of the gas composition of the Enceladus plume. The 18 papers listed below discuss the composition, structure, and dynamics of the plume. Most noteworthy were the discovery that the water in the plumes has the same D/H ratio of some Oort cloud comets, and that the plume contained molecular hydrogen that showed a positive chemical affinity to the reaction for methanogenesis $[4\ H_2 + CO_2 \rightarrow CH_4 + 2\ H_2O]$. There is food for microbes in the global ocean.

RELEVANT PAPERS

Bouquet, A., C. R. Glein, D. Wyrick, J. H. Waite Jr., (2017), Alternative energy: Production of H_2 by radiolysis of water in the rocky cores of icy bodies, The Astrophysical Journal Letters, 840, L8, doi:10.3847/2041-8213/aa6d56.

Cravens, T. E., R. L. McNutt Jr., J. H. Waite Jr., I. P. Robertson, J. G. Luhmann, R. V. Yelle, W. Kasprzak, W.-H. Ip, (2009c), Plume ionosphere of Enceladus as seen by the Cassini Ion and Neutral Mass Spectrometer, Geophysical Research Letters, 36, L08106, doi: 10.1029/2009GL037811.

Dong, Y., T. W. Hill, B. D. Teolis, B. A. Magee, J. H. Waite Jr., (2011), The water vapor plumes of Enceladus, Journal of Geophysical Research, 116, A10204.

Farrell, W. M., W. S. Kurth, D. A. Gurnett, R. E. Johnson, M. L. Kaiser, J.-E. Wahlund, J. H. Waite Jr., (2009), Electron density dropout near Enceladus in the context of water-vapor and water-ice, Geophysical Research Letters, 36, L10203.

Glein, C. R., J. A. Baross, J. H. Waite Jr., (2015), The pH of Enceladus' ocean, Geochimica et Cosmochimica Acta, 162, 202–219, doi: 10.1016/j.gca.2015.04.017.

Hansen, C. J., D. E. Shemansky, L. W. Esposito, A. I. F. Stewart, B. R. Lewis, J. E. Colwell, A. R. Hendrix, R. A. West, J. H. Waite Jr., B. Teolis, B. A. Magee, (2011), The composition and structure of the Enceladus plume, Geophysical Research Letters, 38, L11202.

Hurley, D. M., M. E. Perry, H. J. Waite Jr., (2015), Modeling insights into the locations of density enhancements from the Enceladus water vapor jets, Journal of Geophysical Research, 120, 1763–1773, doi: 10.1002/21015JE004872.

Jones, G. H., C. S. Arridge, A. J. Coates, G. R. Lewis, S. Kanani, A. Wellbrock, D. T. Young, F. J. Crary, R. L. Tokar, R. J. Wilson, R. E. Johnson, D. G. Mitchell, J. Schmidt, S. Kempf, U. Beckmann, C. T. Russell, Y. D. Jia, M. K. Dougherty, J. H. Waite Jr., B. A. Magee, (2009), Fine jet structure of electrically charged grains in Enceladus' plume, Geophysical Research Letters, 36, L16204.

Magee, B. A. and J. H. Waite, (2017), Neutral gas composition of Enceladus' plume - Model parameter insights from Cassini-INMS, 48th Lunar and Planetary Science Conference, 20–24 March 2017, The Woodlands, TX, LPI Contribution No. 1964, id. 2974.

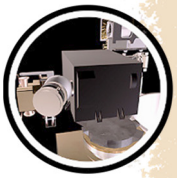

Mousis, O., J. I. Lunine, J. H. Waite Jr., B. Magee, W. S. Lewis, K. E. Mandt, D. Marquer, D. Cordier, (2009a), Formation conditions of Enceladus and origin of its methane reservoir, The Astrophysical Journal Letters, 701, L39-L42.

Ozak, N., T. E. Cravens, G. H. Jones, A. J. Coates, I. P. Robertson, (2012), Modeling of electron fluxes in the Enceladus plume, Journal of Geophysical Research, 117, A06220, doi: 10.1029/2011JA017497.

Perry, M. E., B. D. Teolis, D. M. Hurley, B. A. Magee, J. H. Waite, T. G. Brockwell, R. S. Perryman, R. L. McNutt, (2015), Cassini INMS measurements of Enceladus plume density, Icarus, 257, 139–162, doi: 10.1016/j.icarus.2015.04.037.

Sakai, S., T. E. Cravens, N. Omidi, M. E. Perry, J. H. Waite Jr.,(2016) Ion energy distributions and densities in the plume of Enceladus, Planetary and Space Science, 130, 60–79, doi: 10.1016/j.oss.2016.05.007.

Tenishev, V., D. C. S. Öztürk, M. R. Combi, M. Rubin, J. H. Waite Jr., M. Perry, (2014), Effect of the Tiger Stripes on the water vapor distribution in Enceladus' exosphere, Journal of Geophysical Research, 119, 2658–2667, doi: 10.1002/2014JE004700.

Tenishev, V., M. R. Combi, B. D. Teolis, J. H. Waite Jr., (2010). An approach to numerical simulation of the gas distribution in the atmosphere of Enceladus, Journal of Geophysical Research, 115, A09302.

Teolis, B., M. E. Perry, B. A. Magee, J. Westlake, J. H. Waite Jr., (2010b), Detection and measurements of ice grains and gas distribution in the Enceladus plume by Cassini's ion neutral mass spectrometer, Journal of Geophysical Research, 115, A09222.

Waite Jr., J. H., C. R. Glein, R. S. Perryman, B. D. Teolis, B. A. Magee, G. Miller, J. Grimes, M. E. Perry, K. E. Miller, A. Bouquet, J. L. Lunine, T. Brockwell, S. J. Bolton, (2017), Cassini finds molecular hydrogen in the Enceladus plume: Evidence for hydrothermal processes, Science, 356, 155–159.

Waite Jr., J. H., W. S. Lewis, B. A. Magee, J. I. Lunine, W. B. McKinnon, C. R. Glein, O. Mousis, D. T. Young, T. Brockwell, J. Westlake, M.-J. Nguyen, B. D. Teolis H. B. Niemann, R. L. McNutt, M. Perry, W.-H. Ip, (2009), Liquid water on Enceladus from observations of ammonia and 40Ar in the plume, Nature, 460, 487–490.

Instrument

The four papers listed below describe the INMS instrument, including instrument operations, calibrations, and lab activities.

Kasprzak, W. T., H. Niemann, D. Harpold, J. Richards, H. Manning, E. Patrick, P. Mahaffy, (1996), Cassini orbiter ion neutral mass spectrometer instrument, Proceedings SPIE, vol. 2803, Cassini-Huygens: A Mission to the Saturnian Systems, International Symposium on Optical Science, Engineering, and Instrumentation, Denver, CO, doi: 10.1117/12.253413.

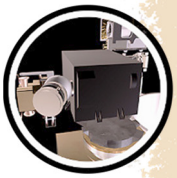

Patrick, E. L. , (2006), Silicon carbide nozzle for producing molecular beams, Review of Scientific Instruments, 77, 043301, doi:10.1063/1.2188907.

Teolis, B. D., H. B. Niemann, J. H. Waite, D. A. Gell, R. S. Perryman, W. T. Kasprzak, K. E. Mandt, R. V. Yelle, A. Y. Lee, F. J. Pelletier, G. P. Miller, D. T. Young, J. M. Bell, B. A. Magee, E. L. Patrick, J. Grimes, G. G. Fletcher, and V. Vuitton, (2015), A revised sensitivity model for Cassini INMS: Results at Titan, Space Science Reviews, doi: 10.1007/s11214-014-0133-8.

Waite Jr., J. H., W. S. Lewis, W. T. Kasprzak, V. G. Anicich, B. P. Block, T. C. Cravens, G. G. Fletcher, W.-H. Ip, J. G. Luhmann, R. L. McNutt, H. B. Niemann, J. K. Parejko, J. E. Richards, R. L. Thorpe, E. M. Walter, R. V. Yelle, (2004), The Cassini Ion and Neutral Mass Spectrometer (INMS) investigation, Space Science Reviews, 114, 113–231.

INMS Saturn System Science Results

Titan Science

Titan highlights

- **Complex Ion Neutral Chemistry:** Existence demonstrated of a complex ionospheric chemistry on Titan dominated by hydrocarbon and nitrogen-bearing species.
- **Solar Radiation as the Primary Ionospheric Source:** Demonstration that solar radiation dominates as the global source of Titan's ionosphere but that locally on the nightside particle precipitation from Saturn's magnetosphere is an important source.
- **Atmospheric Escape:** Early studies by Yelle et al. [2006, 2008] and Strobel [2008, 2010] demonstrated possible need for enhanced methane escape from Titan to explain the data. Later studies by Bell et al. [2014] and Tucker et al. [2013] that combined thermal balance, dynamical, and chemical calculations reproduced INMS without hydrodynamic escape of methane. The New Horizons mission also demonstrated that hydrodynamic escape is not likely at Pluto and by extension, Titan. However, the possibility remains that high escape rates could be possible due to other non-thermal mechanisms. Definite implications for evolution of Titan [Mandt et al. 2012a].
- **Thermosphere Temperatures:** Rapid changes in upper atmosphere temperatures could be due to a combined effect of upward propagating gravity waves (see Müller-Wodarg et al. [2006a, 2008]; Strobel [2006]; Snowden et al. [2013a, 2013b]) and downwelling plasma from Saturn's co-rotating magnetosphere [Westlake et al. 2011; Bell et al. 2011a]. Thus, this is a thermosphere driven from above and below in unique ways in the solar system.

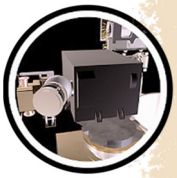

Summary of Titan science

Instruments on the Cassini Orbiter carried out extensive measurements of the upper atmosphere and ionosphere of Titan over a 12-year period of time, starting in 2005. The first INMS neutral measurements were made during the TA pass and the first ion composition were made on Titan's nightside during the T5 pass. The INMS measured densities of ion species up to a mass number of 99 throughout the main and topside ionosphere, on the dayside and nightside, the ramside and wakeside (with respect to the external flow of magnetospheric plasma), and when Titan was in different regions of Saturn's magnetosphere. The measured ion composition and densities provided insight into several aspects of Titan's ionosphere and its linkage between the neutral atmosphere and the external environment including the Sun (solar ionizing radiation), Saturn's magnetosphere, and the solar wind. In particular, ionospheric processes were shown to play a critical role in how external particles and radiation, combined with a nitrogen and methane neutral atmosphere, in driving photochemistry in the upper atmosphere that leads to complex organic composition and also to aerosol growth.

TITAN UPPER ATMOSPHERE/IONOSPHERE MAJOR FINDINGS (NEUTRAL)

- INMS made first in situ measurements of the major constituents of Titan's upper atmosphere and ionosphere, discovering an unexpectedly complex and rich ion and neutral chemistry occurring above 1000 km. **(T_AO2, T_AO1,** and **T_AO5)**.
- The INMS measurements of the $^{12}C/^{13}C$ and $^{14}N/^{15}N$ isotopic ratios have allowed for assessments of Titan's evolutionary history. **(T_AO1)**.
- INMS observations have revealed significant variations in thermal structures that suggest a combination of magnetospheric and wave/tide energy deposition. **(T_AO5)**.
- INMS observations over time have revealed that the atmospheric content of methane above 1000 km is sensitive to the solar cycle.
- INMS measurements over time demonstrated that solar ionizing radiation is the dominant source of the ionosphere and correlated with solar activity, although ionization by energetic particle precipitation from Saturn's magnetosphere is important on the nightside **(T_AO5)**.

Table INMS-2 shows the INMS Titan objective, the AO and TM/CSM science objective, and the color-coded rating assessment.

Figure INMS-5 shows the inferred neutral temperatures from INMS nitrogen density measurements.

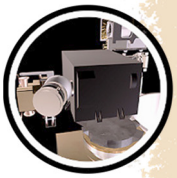

Table INMS-2. Final Report INMS – Titan Science.

Fully/Mostly Accomplished: Partially Accomplished: Not Accomplished:

INMS Objectives	AO and TM/CSM Science Objectives	Assessment
Titan Objectives		
Titan Atmospheric Formation and Evolution	T_AO1	
Titan Atmospheric Composition and Distribution	T_AO2	
Titan Upper Atmosphere	T_AO5	

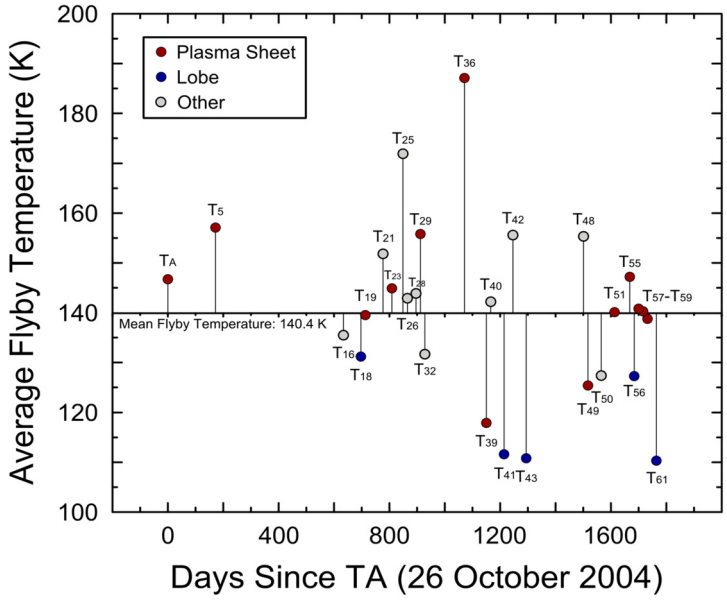

Figure INMS-5. Inferred neutral temperatures (vertical axis) from INMS nitrogen density measurements over time since the TA.

Titan's neutral atmosphere

Observations of neutral densities (mainly N_2), have allowed us to make inferences into the thermal structure of Titan's upper atmosphere [cf. Müller-Wodarg et al. 2006a, 2008; Cui et al. 2008, 2009a; Magee et al. 2009; Westlake et al. 2011; Snowden et al. 2013a]. The average thermospheric temperature derived from INMS data is around 150 K, which is in good agreement with pre-Cassini estimates [Müller-Wodarg et al. 2000, 2003; Müller-Wodarg and Velle 2002a]. However, the temperature of Titan's thermosphere exhibits a high degree of variability that was not predicted prior to Cassini—see, for example, Müller-Wodarg et al. [2000, 2003]; Müller-Wodarg and Velle [2002a]. Pre-Cassini models calculated day-night variations on the order of 10–15 K. Cassini has observed temperature variations much larger than this over the course of a single Titan day, even when observing the same region of atmosphere at a similar local time. The variations in

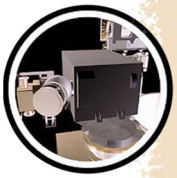

temperature are not correlated with solar input, indicating there are additional heating/cooling mechanisms with magnitudes that are similar to solar insulation. The short-timescales associated with the large variations in temperature has led some to postulate that the magnetosphere may provide sporadic and localized inputs [Westlake et al. 2011] or internal gravity waves may be depositing significant energy into the upper atmosphere [Müller-Wodarg et al. 2006a; Snowden et al. 2013a]. Atmospheric escape may also significantly alter the temperature of the upper thermosphere [Tucker et al. 2013] as can spatial and temporal variation of minor species that are strong sources of radiative cooling such as HCN and CH_4.

INMS data indicates that, similar to other atmospheres, waves are a persistent feature in Titan's thermosphere. Wave characteristics derived by fitting INMS data (Figure INMS-6) indicates vertical wavelengths are the order of several hundred kilometers, amplitudes are on the order of 10%, and wave periods are on the order of several hours [Müller-Wodarg et al. 2006a; Snowden et al. 2013a; Cui et al. 2013]. The persistence of waves in Titan's thermosphere indicates that the zonal wind speed must exceed 100 m/s [Snowden et al. 2013a]. Super rotating winds around 100 m/s have also been employed to explain day-night variation in short and long-lived ions observed by INMS in Titan's upper atmosphere [Cui et al. 2009b].

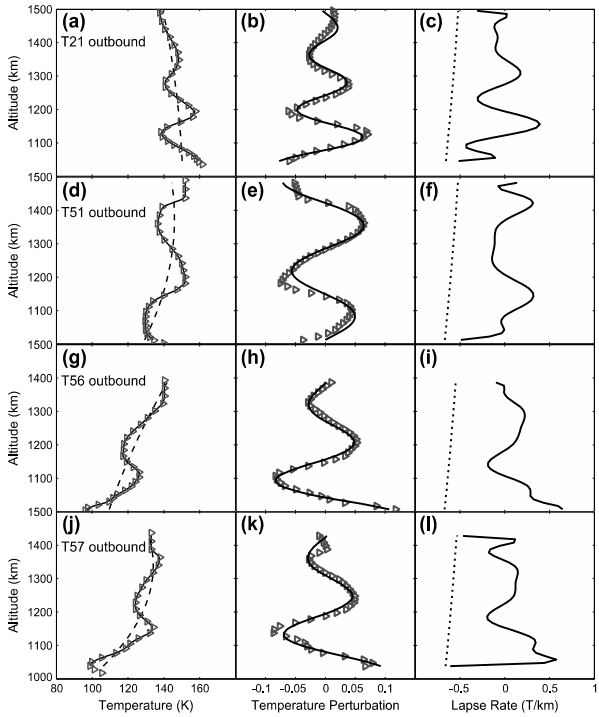

Figure INMS-6. The panels show how wave properties are determined by fitting the vertical temperature profiles derived from INMS data from four flybys. Panels on the right compare the vertical gradient in temperature to the adiabatic lapse rate to show that waves of this scale can be stable in Titan's thermosphere. [Snowden et al. 2013a].

Not only has INMS revealed the nature of Titan's upper atmospheric thermal structure, but it has also shown that the methane in the upper atmosphere can exhibit significant solar cycle

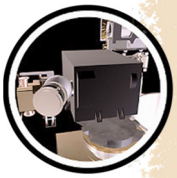

variations. As seen in Figure INMS-7, the methane densities (abundances) during the extended solar minimum remained relatively stable and consistent relative to the major background species N_2. However, as the solar activity levels increased (Figure INMS-7, panels 4 and 5), methane was significantly reduced relative to N_2. This occurred despite the fact that, as shown by the panel 3 in Figure INMS-7, Titan was moving farther away from the Sun, and all things being equal, should have experienced reduced solar insolation. These observations demonstrated that methane is a chemically active species, responding relatively quickly to increases in solar insolation, again highlighting the surprisingly dynamic nature of Titan's upper atmosphere.

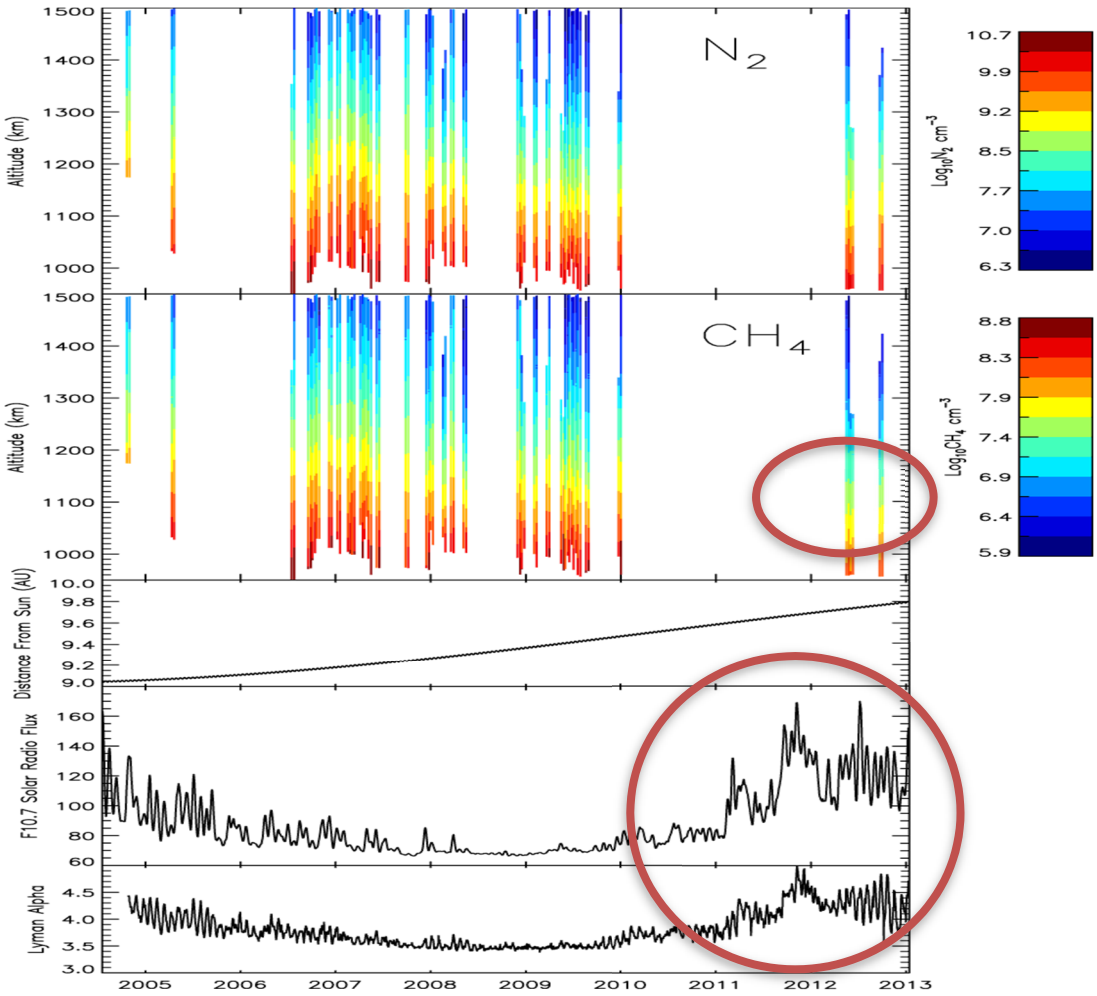

Figure INMS-7. Titan's upper atmospheric thermal structure shows that the methane in the upper atmosphere can exhibit significant solar cycle variations. Multipanel plot showing N_2 densities (*panel 1*), CH_4 densities (*panel 2*), Titan-Saturn orbital distance (*panel 3*), Solar $F_{10.7\text{-cm}}$ radio flux (*panel 4*), and Lyman-alpha fluxes at Titan's orbit (*panel 5*) as a function of time (horizontal axis). The circles point to the time periods of significantly reduced methane measured by INMS that correlates with high solar activity [Westlake et al. 2012a].

While no direct thermosphere wind measurements could be made with the INMS or any other Cassini or Earth based instrumentation, the horizontal density variations in the thermosphere as

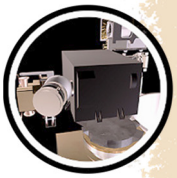

measured by the INMS were used in conjunction with balance of forces calculations as well as more sophisticated General Circulation Model (GCM) simulations to infer horizontal wind speeds reaching around 150 m/s [Müller-Wodarg et al. 2008]. These calculations also determined the important influence of thermospheric winds on the distribution of atmospheric gases such as CH_4. More recent calculations with the Titan thermosphere GMC [Müller-Wodarg et al. 2003] demonstrated that much of the significant variability in densities and temperatures observed by the INMS [Snowden et al. 2013a] could be explained by variability in the stratosphere which strongly affected the thermosphere.

Titan's ionosphere

Voyager measurements, both in situ of the magnetotail and radio occultation of the main ionosphere, showed the existence of an ionosphere at Titan [Neubauer et al. 1984; Bird et al. 1997]. Subsequent theoretical modeling suggested that the ionospheric composition could be quite complex, largely due to the presence of hydrocarbons associated with dissociation and ionization of methane [Nagy and Cravens 1998; Keller et al. 1992, 1998; Fox and Yelle 1997]. But the series of Cassini measurements by INMS, CAPS, and the Radio and Plasma Wave Science (RPWS) LP quantified the ionospheric densities and the extent of the ionosphere. The INMS science of Titan's ionosphere is organized into 3 sub-sections: 1) sources, 2) chemistry, and 3) dynamics.

Sources of Titan's ionosphere

The major ion species produced is N_2^+, since N_2 is the major neutral species. However, chemical considerations told us that the main ion species at mass 28 is not N_2^+ but $HCNH^+$, so another ion species, CH_3^+, was used to almost directly deduce ion production rates [Richard et al. 2015a, 2015b; Vigren et al. 2015; Sagnières et al. 2015]. The rapid chemical reaction of N_2^+ with CH_4 produces CH_3^+ (mass 15). The ionization rate of CH_4 can be deduced by the measured CH_4^+ ions at mass 16 [Richard et al. 2015a, 2015b].

It was found that solar ionizing radiation is the dominant source of the dayside ionosphere, not surprisingly, and the quantification of the source rate was largely as expected given the solar flux and the relevant photoionization cross-sections for N_2 and CH_4. Given that Cassini spanned a large part of a solar cycle, the INMS-deduced ion production rates were shown to increase with increasing solar activity [Madanian et al. 2016].

Sources of ionization deep on the nightside were also studied by Cassini and INMS. Globally, solar radiation accounts for 90% of total ionization, but precipitation of energetic electrons and ions leading to ionization is obviously locally important on the nightside [Ågren et al. 2007; Cravens et al. 2008a, 2008b; Cravens et al. 2009b; Vigren et al. 2015; Snowden and Yelle 2014a, 2014b; Edberg et al. 2013a, 2013b; Robertson et al. 2009; Galand et al. 2014]. As on Venus and Mars, the two possible sources of the nightside ionosphere are local/direct ionization from precipitation (i.e., a diffuse aurora) and transport of plasma from the dayside. Evidence for the precipitation source was provided by INMS by measurements of primary or almost primary ion species (CH_3^+,

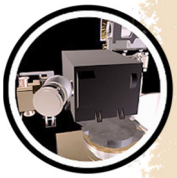

CH_4^+, CH_5^+…), which have short chemical lifetimes and could only be produced locally. On T5 a correlation between secondary auroral electron fluxes measured by CAPS ELS correlated with the CH_5^+ densities [Cravens et al. 2008a]. Longer-lived ion species (e.g., $HCNH^+$) can also be transported from day to night and both sources can operate [Cui et al. 2009a]. Modeling combined with INMS, CAPS, and RPWS data determined that the precipitation ionization source depend on magnetic topology and on the location of Titan in Saturn's magnetosphere. Incident magnetospheric electron fluxes, and the associated nightside ionosphere, were more robust when Titan was located in the plasmasheet region as opposed to the magnetic lobes of Saturn's magnetosphere [Richard et al. 2015a; Rymer et al. 2009].

Chemistry of the Upper Atmosphere and Ionosphere

The chemistry of Titan's upper atmosphere and ionosphere is complex due to the presence of a large number of organic species extending up to high mass numbers. The neutral and ion chemistry is linked together [Waite et al. 2007]. The INMS has played a key role in improving our understanding of this chemistry. Photodissociation and photoionization of N_2 and CH_4 form ion and neutral species that are very reactive and that initiate a series of reactions producing increasing larger species, up to aerosol-sized particles [Waite et al. 2007]. Primary N_2^+ ions react with CH_4 to produce CH_3^+, which again reacts with CH_4 to produce $C_2H_5^+$. $C_2H_5^+$ reacts with HCN to produce the very abundant species $HCNH^+$. Reactions of $C_2H_5^+$ and $HCNH^+$ with C_2H_2, C_2H_4, and C_4H_2 drive a chain of reactions leading to families of $C_nH_m^+$ species, including protonated benzene ($C_6H_7^+$), and up to masses exceeding 99 Da [Anicich and McEwan 1997; Cravens et al. 2006; Vuitton et al. 2006, 2007, 2009; Westlake et al. 2014b; Cui et al. 2009a; Mandt et al. 2012a] (Figure INMS-8 and Figure INMS-9). Figure INMS-10 shows INMS ion density profiles versus neutral density (i.e., altitude). CAPS measurements, albeit at low mass resolution, indicated the presence of species up to at least 1100 Da [Crary et al. 2009; Coates et al. 2010]. For example, CH_2NH_2, CH_3CN, and other nitrogen-bearing species react with lower mass ion species to produce protonated ion species [Vuitton et al. 2007].

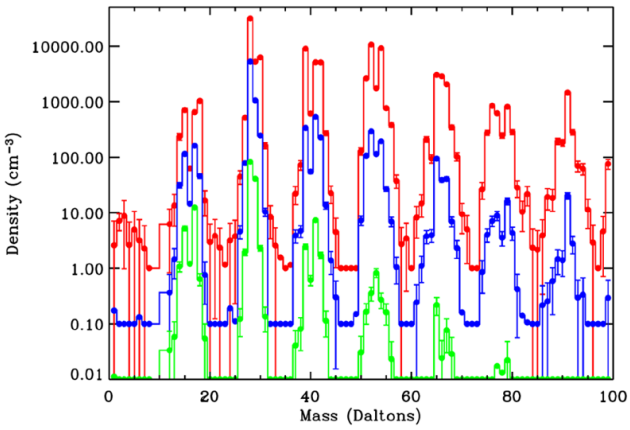

Figure INMS-8. Shown are the first INMS measurements of ion densities versus mass number at three different altitudes for the T5 nightside ionosphere [Cravens et al. 2006]. *Red:* 1027–1200 km. *Blue:* 1200–1400 km. *Green:* 1400–1600 km. Chemical complexity increases with decreasing altitude.

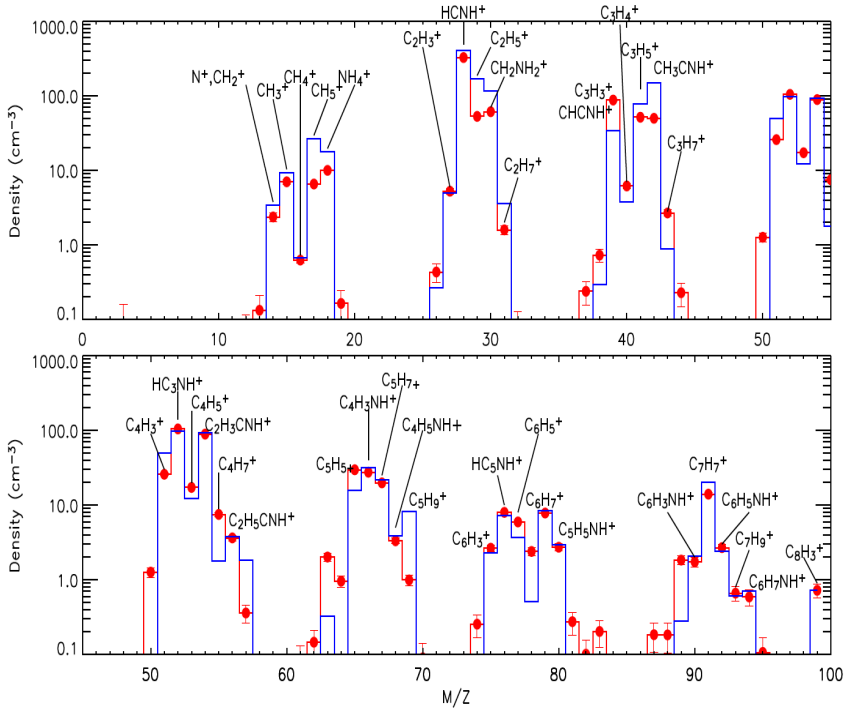

Figure INMS-9. INMS T5 data compared with a photochemical model which put forward the presence of protonated nitrogen ion species. The *blue line* is the modeled mass spectrum [Vuitton et al. 2007].

INMS data for 4 ion species. *Ion Density vs. neutral density*.

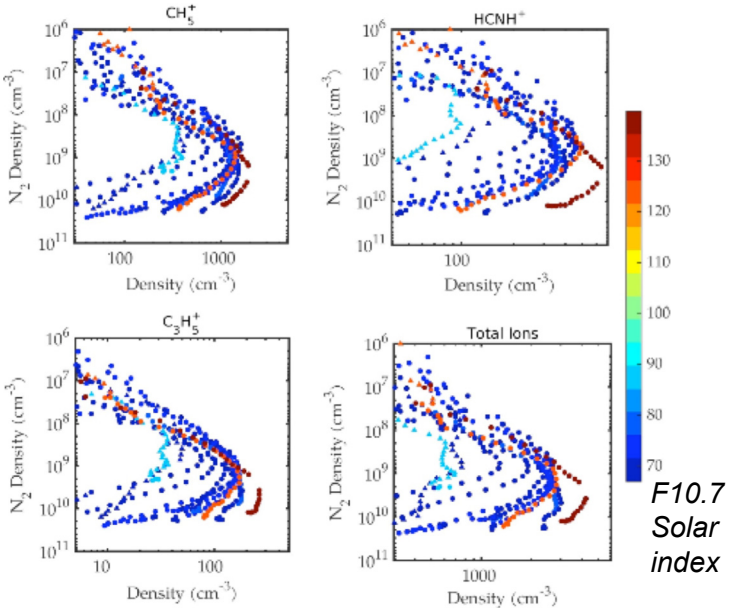

Figure INMS-10. INMS ion density profiles versus neutral density measured throughout the mission with different solar activity levels (as given by the solar extreme ultraviolet (EUV) proxy F10.7—*color bar*). Total ions denote the total INMS ion density. In general, higher solar activity correlates with higher density. [Madanian et al. 2016].

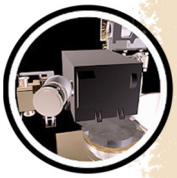

Titan's ionosphere consists of positive and negative ions, some of which have masses of up to and possibly beyond 1000s u [Waite et al. 2007; Coates et al. 2007]. The study of Vuitton et al. [2007] identified over 100 ions in the INMS spectrum including several N-bearing species such as protonated ammonia (NH_4^+), $CH_2NH_2^+$, and CH_3CNH^+. Titan's atmosphere is a reducing atmosphere (little or no oxygen species are present) and as such the ionization will flow from species whose parent neutral molecules have low proton affinities (PA) to those whose parent neutral molecules have greater PAs. The proton affinity of a molecule is a measure of the gas-phase basicity or its propensity to undergo a reaction in which a proton is gained. In general, molecules containing unsaturated carbon bonds (those which have double or triple covalent bonds between adjacent molecules) have larger proton affinities.

The hydrocarbon chemistry at Titan has been shown to lead to the production of benzene [Waite et al. 2007; De La Haye et al. 2008b; Vuitton et al. 2008]. There have been several attempts by the modeling community to reproduce the INMS observed benzene abundances including those based solely on radical neutral and termolecular processes [Lebonnois 2005], some ion-molecule reactions coupled with neutral processes [Wilson et al. 2003], and intricately coupled ion-molecule chemical schemes [De La Haye et al. 2008b; Vuitton et al. 2008]. The INMS measured molar fraction of benzene was found to be about 2×10^{-6} at 1050 km altitude [Magee et al. 2009]. The study of Vuitton et al. [2008] argues that most of the observed benzene is a product of reactions between phenyl radicals (C_6H_5) and hydrogen within the INMS instrument's antechamber yielding a benzene abundance that contributes one-third of the total observed peak level. This implies significant amounts of the phenyl radical are present in Titan's upper atmosphere. Further analysis of the INMS data revealed that it is difficult to disentangle heterogeneous surface chemistry of radicals from adsorption/desorption of the parent molecule [Cui et al. 2009b]. Regardless of interpretation, the Cassini INMS data shows that the mixing ratio of benzene or benzene and phenyl is a few times 10^{-6} indicating that the chemistry is efficient in producing not only unsaturated hydrocarbons but also aromatic hydrocarbons.

Although NH_3 and CH_2NH were not directly detected on Titan, we have shown that the mass spectra obtained by Cassini indicate the presence of NH_4^+ and $CH_2NH_2^+$. This implies quantities of NH_3 and CH_2NH close to 10 ppm in the upper atmosphere, because the NH_4^+/NH_3 and $CH_2NH_2^+/CH_2NH$ couples are connected to each other by proton exchange and electron recombination reactions. However, the presence of such an amount of NH_3 in the upper atmosphere of Titan was not predicted by photochemical models.

In order to tackle this problem, we have proposed a new way for the formation of NH_3, by reaction of the radical NH_2 with H_2CN, the latter being also the precursor of HCN. To confirm this hypothesis, we calculated the kinetic constant and showed that it is indeed fast (7.5×10^{-11} cm^3 s^{-1} at 150 K). The calculated NH_4^+ and $CH_2NH_2^+$ densities are then in agreement with the densities measured for the entire altitude range for which observations are available, which leads to the conclusion that the main mechanisms of production and loss of NH_3 and CH_2NH have been properly identified. More generally, we have shown that ammonia and methanimine are formed from a complex network of reactions involving both neutral and charged species, which, as for

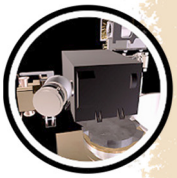

C_6H_6, shows the importance of ion chemistry for the composition of the neutral atmosphere [Yelle et al. 2010].

Below about 1200 km in Titan's atmosphere positive ions with masses greater than 100 u have been found [Waite et al. 2007; Crary et al. 2009]. A sample spectrum obtained by the CAPS-IBS instrument during the T26 flyby is shown in Figure INMS-11. The composition of the high mass ions has been suggested to primarily consist of polycyclic aromatic hydrocarbon (PAH) that are multi-ringed molecules built from benzene [Crary et al. 2009]. PAH ions are likely the precursors to the tholins observed in the haze layer at about 500 km [Waite et al. 2007; Lavvas et al. 2008a, 2008b]. Models have shown that the most efficient pathway for production of the haze layer is through PAHs [Wilson et al. 2003]. Several theoretical models have also been developed to describe the process of producing PAHs from benzene through neutral chemistry in the context of flame chemistry [Wang and Frenklach 1997; Richter and Howard 2000], and interstellar environments [Bohme 1992; Snow et al. 1998]. Computational models have been developed to describe the energy required to build PAHs through neutral chemistry [Bauschlicher and Ricca 2000], cation chemistry [Bauschlicher et al. 2002], as well as, the efficiency for incorporating nitrogen into PAHs [Ricca et al. 2001a, 2001b].

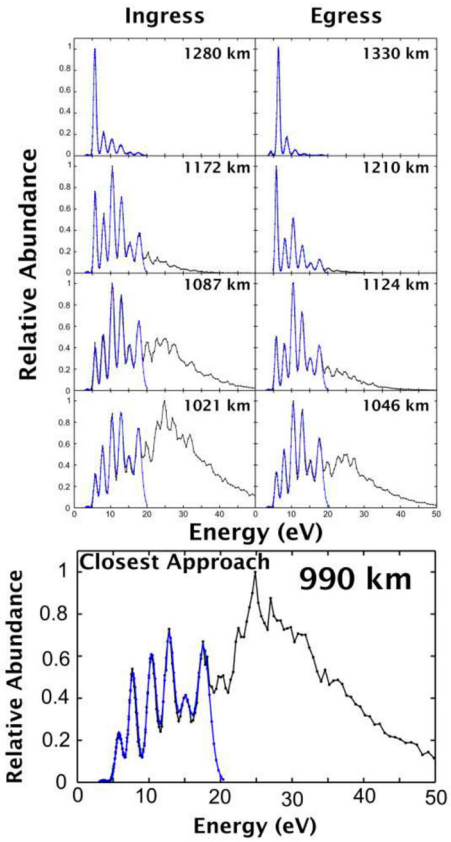

Figure INMS-11. Shown are nine ion mass spectra obtained by the CAPS-IBS instrument at various altitudes during the T26 flyby. The *blue lines* show the INMS data converted using the CAPS-IBS instrument response model.

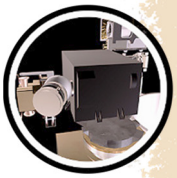

The Cassini INMS measures positive ions with masses up to 100 u. The CAPS-IBS can be used to measure positive ions with much larger masses at lower resolution. The CAPS-IBS measures the energy per charge of incident ions with an energy resolution of 1.4% [Young et al. 2004]. The energy per charge spectrum can be converted to a mass per charge spectrum by fitting the CAPS-IBS and INMS measurements using the spacecraft potential, ion temperature, and crosstrack winds as free parameters [Crary et al. 2009]. The high mass ion densities were found to increase exponentially with altitude down to the lowest observed Cassini altitudes [Crary et al. 2009]. An analysis of the chemical production mechanisms studied by Wilson et al. [2003] was compared to the peak spectrum, and it was found that the most likely compounds were aromatic in character. This further supports that aromatic chemistry is efficient in Titan's ionosphere, and that it is likely to proceed past benzene.

Westlake et al. [2014b] analyzed the T57 flyby in detail between the CAPS and INMS observations to determine the characteristics of the processes responsible for the production and loss of the large hydrocarbons observed at Titan. Altitude profiles (Figure INMS-12) of heavy ions

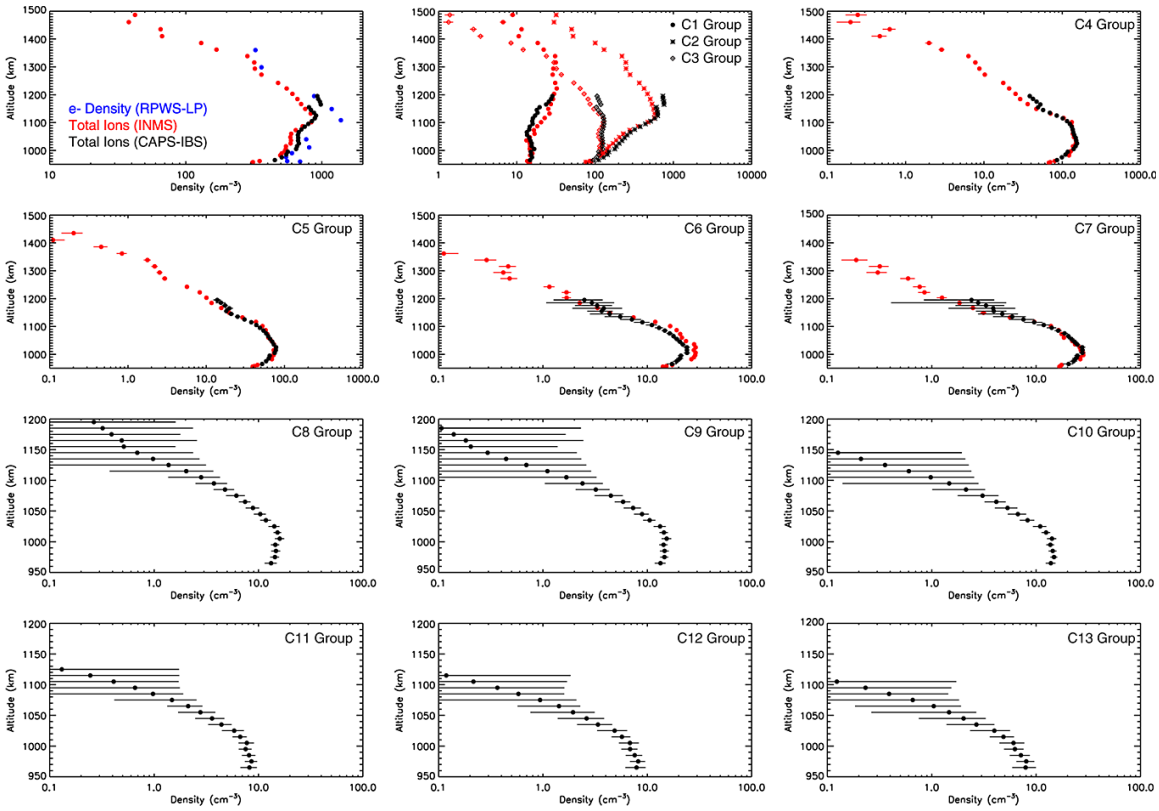

Figure INMS-12. Hydrocarbon group densities from the C1 to the C13 groups for the T57 flyby. A group density is simply the integrated density between the minima in the mass spectrum. The labeling using carbon number (C_i) indicates the number of heavy atoms (carbon, nitrogen, oxygen, etc.) expected within this mass grouping. The *black points* represent CAPS-IBS data, the *red points* give the INMS data, and the *blue points* give the RPWS-LP total electron density. The CAPS-IBS data are both summed within carbon groups and 10 km height bins. The *error bars* in the CAPS-IBS and INMS data represent the statistical counting errors.

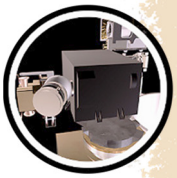

from the C6–C13 group (C_i indicates the number, i, of heavy atoms in the molecule) using a CAPS-IBS/INMS cross calibration reveal structure that indicates a region of initial formation and growth at altitudes below 1200 km followed by a stagnation and dropoff at the lowest altitudes (1050 km). Westlake et al. [2014b] suggested that an ion-molecule reaction pathway could be responsible for the production of the heavy ions, namely reactions that utilize abundant building blocks such as C_2H_2 and C_2H_4, which have been shown to be energetically favorable and that have already been identified as ion growth patterns for the lighter ions detected by the INMS. This growth scenario, in contrast with alternative growth scenarios, has implications for the densities of the source heavy neutrals in each scenario. Westlake et al. (2014b) showed that the high-mass ion density profiles are consistent with ion-molecule reactions as the primary mechanism for large ion growth and derived a production rate for benzene from electron recombination of $C_6H_7^+$ of 2.4×10^{-16} g cm^{-2} s^{-1} and a total production rate for large molecules of 7.1×10^{-16} g cm^{-2} s^{-1}.

Magnetosphere – Titan Interactions Science

The INMS and other Cassini instruments including RPWS, Magnetospheric Imaging Instrument (MIMI), CAPS, and Magnetometer (MAG) provided data, that with associated modeling (including global magneto-hydrodynamic (MHD) and hybrid models) has increased our understanding of Titan's plasma interaction with Saturn's magnetosphere and, rarely, with the solar wind plasma [Ledvina et al. 2012a, 2012b; Ulusen et al. 2010, 2012]. As alluded to earlier, the precipitation of energetic particles can lead to the ionization and heating of the neutral atmosphere. The pressure (thermal and magnetic) of the external plasma affects the dynamics [Cui et al. 2010; Cravens et al. 2010] and energetics [Richard et al. 2011; Vigren et al. 2013] of the ionosphere. Magnetic fields are induced in the ionosphere by this interaction, which then acts to help constrain and control the plasma motion. Put simply, plasma flows in response to magnetic forces and thermal pressure forces. INMS data contributed to our understanding of these processes. For example, INMS measurements show that chemically complex species (e.g., $HCNH^+$) flow out the wake (i.e., downstream of the external magnetospheric flow) of Titan eroding Titan's atmosphere [Westlake et al. 2012a, 2012b].

Data from the open source supra thermals mode from Titan showed ions escaping from Titan. In this mode, we tuned the quadrupole switching lens to look for ions with velocities above the spacecraft ram velocity. We fine-tuned these sweeps to look for ions of mass 2, 15, 16, 17, 28, 29, and 30 to characterize Titan's ion outflow and determine the actual velocity of these ions, looking for changes in their apparent temperature, understanding their spatial distribution, looking for acceleration mechanisms, and understanding the instrument response. We have included a Figure INMS-13 that shows these observations for several ions during the T100 flyby.

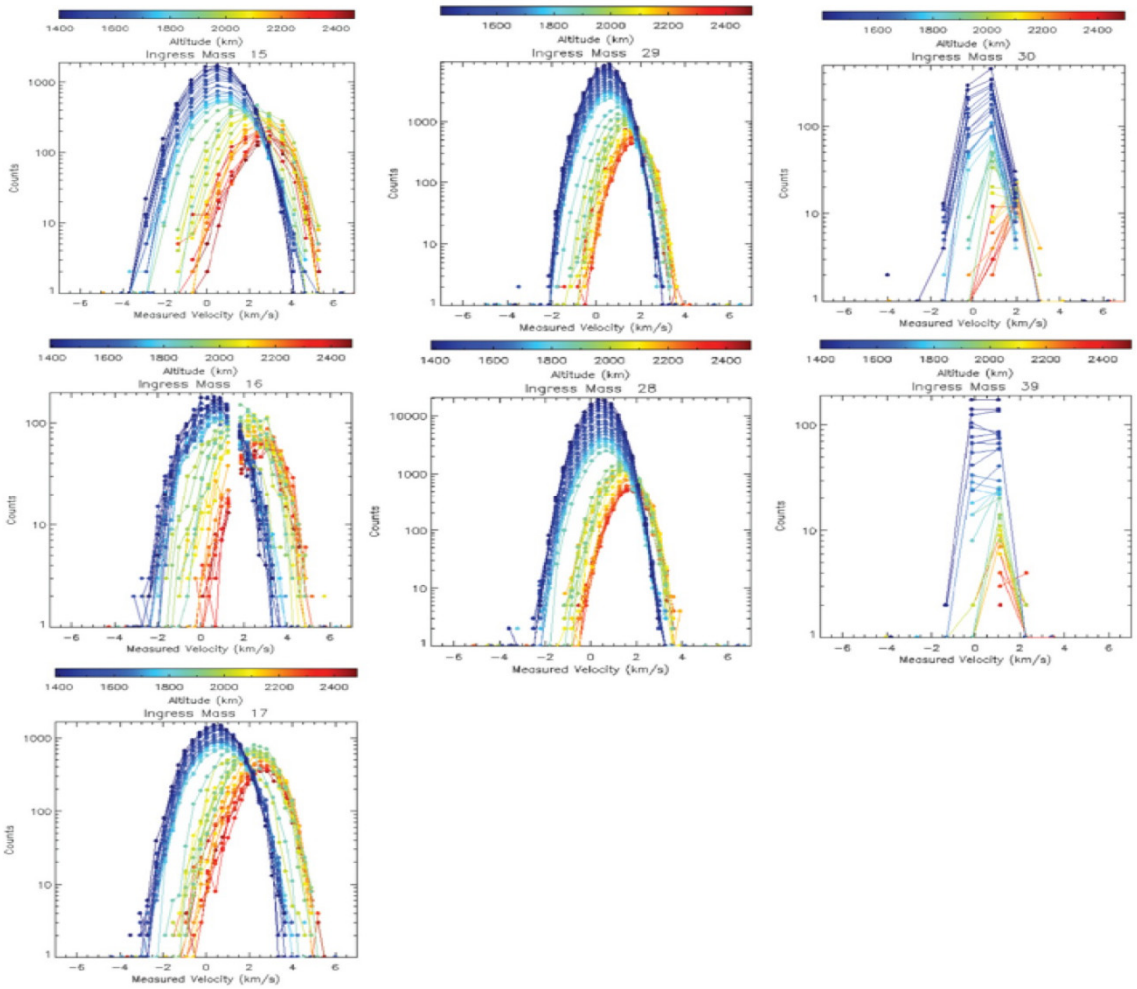

Figure INMS-13. INMS ion measurements from the T100 flyby.

Titan open questions

1. INMS discovered a new regime for organic chemistry in the solar system in Titan's upper atmosphere. Observations indicated the presence of large organic molecules with masses greater than 100 u. This could include biological precursors such as amino acids and nucleotide bases, but the mass range and resolution were insufficient for unique identifications. Thus, detailed knowledge of the organic composition, including the extent of nitrogen incorporation into the large organic molecules, and the associated chemistry remains an open question.

2. INMS found that the thermal structure of Titan's upper atmosphere was highly variable both in space and time. The mean temperature is ~150 K but pass-to-pass variability can be as large as 50 K and there may be long term trends. The variability has been poorly characterized and the cause of the variability has not been

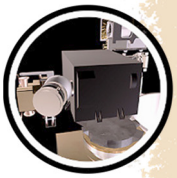

definitively identified. The high level of variability has stymied studies of the dynamics of Titan's upper atmosphere.

3. We have numerous examples of the effect of Titan's interaction with Saturn's magnetosphere on the structure of Titan's upper atmosphere, but insufficient data to thoroughly characterize the interaction.

    a. Why is there no Titan torus about Saturn?

    b. What is the energetic ion environment along Titan's orbit?

    c. How do the upstream plasma conditions affect Titan?

    d. What is the energy and momentum deposited into Titan's atmosphere as a result of the different bulk plasma conditions?

    e. What effect do the deposition of energetic ions have on Titan's atmosphere and its plasma interaction?

    f. How do the different upstream plasma conditions affect ion loss from Titan?

    g. How do the answers to these questions vary along Titan's orbit about Saturn?

    h. How does re-configurations of Saturn's magnetosphere effect Titan's plasma interaction?

    i. How does Titan respond to changes in the upstream conditions and how long does it take those changes to occur?

    j. What role do negative ions play in each of these situations?

4. INMS measured the structure of Titan's ionosphere but a factor of 2–3 disagreement between the observed and modeled electron densities has not yet been fully resolved. What explains the difference between the modeled ionospheric electron densities and the observed ionospheric electron densities? Is there a missing loss process? Are new recombination rates needed? Might ion transport be an answer?

5. There is evidence for both in situ ionization on the nightside of Titan and transport of ions from the dayside, but the relative contributions and characteristics of these two sources remain an open question.

6. How does the coupled neutral and ion dynamics in the ionosphere affect the magnetic structure that is observed? In fact, ionospheric dynamics at Titan was not well-described with Cassini data.

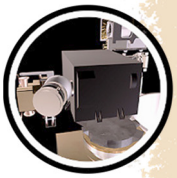

7. The variability of major gasses in the upper atmosphere as a response to solar input? Are there differing variations across species?

8. What are the large volatiles in Titan's upper atmosphere and how are they created?

    a. What is the extent of nitrogen in the larger organic compounds?

    b. What is the relative importance of day/night transport and in situ ion production on the nightside ionosphere?

    c. What is the role of day to night transfer in maintaining the ionosphere.

9. How does the system change with the solar cycle?

10. How does the system change throughout the Saturn year?

11. What are the boundary conditions at Titan? Is there a subsurface ocean and could it be detectable from the Cassini data?

12. What controls the magnetic field signatures below 1200 km? What role does the ionosphere and atmosphere play?

    a. How does the magnetic field topology around Titan and in its ionosphere effect ion and electron transport within Titan's ionosphere and linking them to Saturn's magnetosphere?

    b. What is the role of the Hall and Pederson conductivities in controlling Titan's ionospheric dynamo region? What role do the resulting ion and electron current have in heating Titan's ionosphere/atmosphere?

    c. What are the time constants of the remnant magnetic fields in Titan's ionosphere?

    d. How might atmospheric processes (such as gravity waves) effect Titan's ionosphere and its' resulting plasma interaction?

    e. What is the day to night ion transport rate in the ionosphere?

    f. How do the above processes affect the ion loss rate from Titan?

    g. What happens during morning energetic neutral atom (ENA) storms?

    h. Why is there no Titan torus about Saturn?

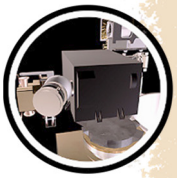

Enceladus Science

The initial INMS planning considered Enceladus as another small icy satellite albeit of some additional interest due to the fact that it was embedded in the E-ring. This perception soon changed. The Cassini MAG measurements on the first flyby of Enceladus redirected flyby E2 close to the satellite and thus began the important compositional exploration of Enceladus by INMS that culminated in a startling assessment that the internal global ocean was habitable; there was food for the microbes.

The first close flyby of Enceladus with a ram pointing orientation for INMS occurred on the July 14, 2005 when Cassini passed within 168.2 km of the flank of Enceladus. The presence of water vapor emanating from the south polar cap was noted over 4000 km before the encounter. Water, carbon dioxide, methane, and a mass 28 compound (carbon dioxide and molecular nitrogen were suggested) were observed during the flyby. Trace detections of ammonia, acetylene, and propane were noted. Figure INMS-14 shows a reproduction of the integrated mass spectra during the E2 flyby (~8 km/s relative velocity) taken from Waite et al. [2006], Figure 2.

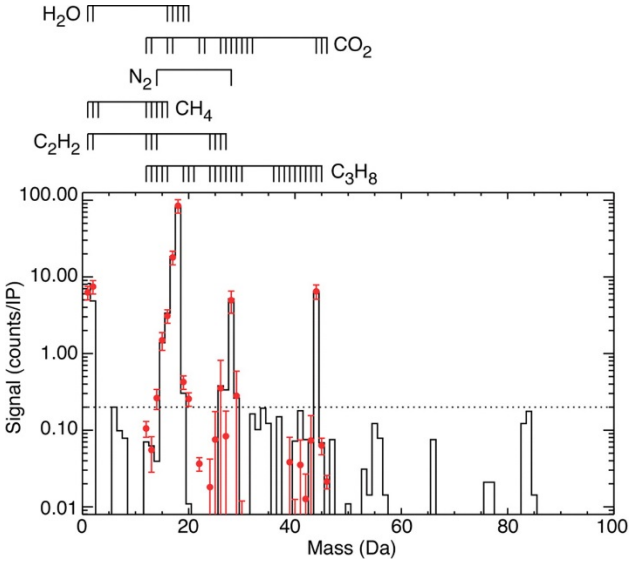

Figure INMS-14. Average mass spectrum for altitudes below 500 km. (Reproduced from Waite et al. [2006], Figure 2). The solid *black line* indicates the measured average spectrum and the *red symbols* represent the reconstructed spectrum. The *error bars* displayed are the larger of the 20% calibration uncertainty or the 1σ statistical uncertainty. The *dotted line* is indicative of the 1σ noise level. The dissociative ionization products produced by the electron ionization source for each constituent are also shown in the figure. Legend: Da = Daltons; IP = integration period.

Enceladus highlights

1. Determination of the major composition of the Enceladus plume gas.

2. Measurement of the deuterium/hydrogen ratio of water in the Enceladus plume.

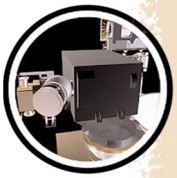

3. Discovery of organic molecules in the Enceladus plume. From fragmentation we know that there are large organic molecules.

4. Discovery of molecular hydrogen in the Enceladus plume.

5. Dynamics of the plume—speed of the gas measured with the open source and more evidence of it with the closed source. Also, angular structure told us about the dynamics. See very narrow jets that suggest that some jets have very high-Mach numbers.

6. Discovery of grains in an intermediate size range between CDA and CAPS.

7. The ion composition measured in Enceladus's plume by INMS confirms the strong interaction between the plume and the external Saturnian magnetosphere and was strongly dominated by H_3O^+.

Velocity-dependent mass spectra and impact fragments

The next major milestone occurred during the E5 flyby that occurred at a much higher relative velocity of ~18 km/s, approached from the Northern hemisphere and flyout along the south polar axis. This produced the highest signal to noise mass spectra of Enceladus of the entire mission due to the long outbound duration in the plume. The integrated mass spectra in Figure INMS-15 (reproduced from Waite et al. [2009], Figure 1) shows a much more complex spectrum extending out to the limits of the INMS mass range (99 u).

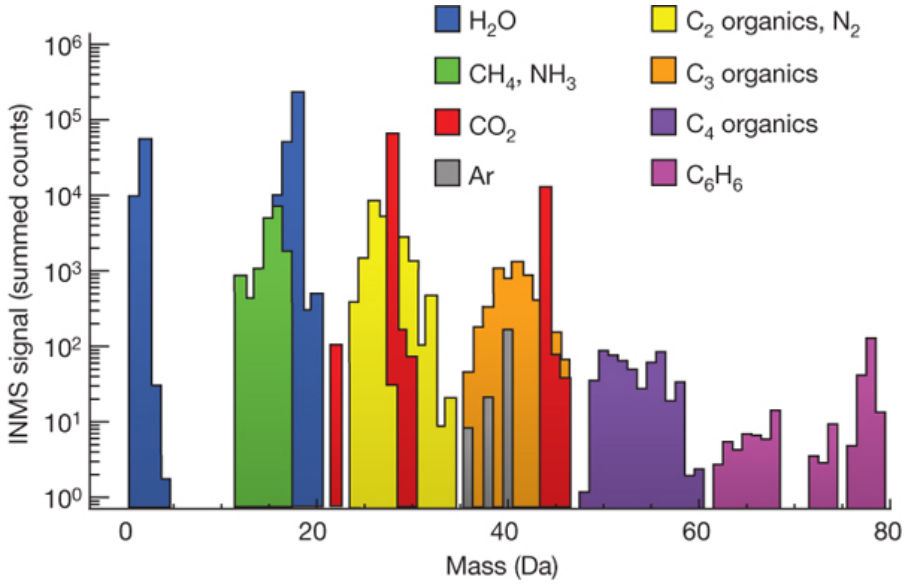

Figure INMS-15. A complex spectrum extending out to the limits of the INMS mass range (99 u). From Waite et al. [2009], Figure 1.

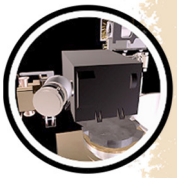

A mass deconvolution of the E5 integrated mass spectra is given in Table INMS-3 indicating a host of complex organic compounds, as well as, the compounds previously cited on flyby E2: water, carbon dioxide, methane, mass 28, ammonia, acetylene, and propane. Of particular note was that water seems to be converted into molecular hydrogen and some other compounds abundance altered due to the high flyby speed. This conversion was interpreted and later verified [Walker et al. 2015] as due to raw titanium vapor from ice grain impacts reacting with water to form TiO and TiO_2 and leaving behind the H_2. The serendipitous side effect of this reaction allowed the INMS team to determine the D/H ratio in water from Enceladus, which was found to be similar to comet Halley ($2.9\ (+1.5/-0.7) \times 10^{-4}$) suggesting that Enceladus had never come into chemical equilibrium with the protoplanetary nebula of Saturn otherwise the ratio would have been much closer to the protoplanetary value of 2×10^{-5}.

The first INMS measurements of the plume's composition were made in the plume's outer edge on July 15, 2005 (E2 encounter), and revealed that the plume consists predominantly of water vapor, with small amounts of carbon dioxide, methane, a species of mass 28, and trace quantities of acetylene and propane. During the October 9, 2008 (E5) encounter, favorable spacecraft pointing and the high spacecraft velocity relative to Enceladus significantly increased the neutral gas density in the closed source antechamber. This density enhancement, together with the proximity of the measurements to the center of the plume, enabled a considerably improved signal-to-noise ratio compared with that obtained during the earlier four encounters. (The y-axis shows counts summed over the period of plume influence.) With their higher signal-to-noise ratio, the E5 measurements provide the first clear evidence of the presence of higher-order (C_4^+) hydrocarbons in the plume, including benzene, and allow the tentative identification of individual species within each hydrocarbon group and of other organics, such as methanol and formaldehyde (Table INMS-3). As described in the Supplementary Information of Waite et al. [2009], interpretation of the INMS spectra requires careful deconvolution of a complex pattern of mass peaks representing both parent species and dissociative ionization products. Fractionation by energetic impact as well as interaction of the gas with the titanium antechamber walls must also be taken into account. Owing to the low mass resolution of INMS, overlapping mass peaks cannot in a number of cases be uniquely separated, resulting in some ambiguity in the interpretation of the data.

The mixing ratios shown for CO and H_2 (values in parenthesis) are included in the mixing ratios for H_2O and CO_2 (first two rows). Analysis of the data from all five encounters shows that the ratios of mass 44 (CO_2) to mass 28, and mass 18 (H_2O) to mass 2 (H_2) decrease with increasing spacecraft velocity, suggesting that H_2 and CO are produced by the dissociation of H_2O and CO_2 through hypervelocity impact on (and reaction with) the walls of the INMS antechamber, see supplementary information of Waite et al. [2009]. We estimate that 40–80% of the signal in mass channel 28 is due to CO produced in this way. A small contribution of CO from Enceladus is also possible, but cannot be distinguished from the dissociation product. The residual mass 28 signal is attributed to N_2, C_2H_4, or a combination of both, with either HCN or the ethene dissociation product C_2H_3 contributing to the signal in mass channel 27. The values given for these species are upper limits based on the two alternative scenarios (N_2 + HCN versus C_2H_4). Neither scenario can be given preference over the other on the basis of the present INMS data set.

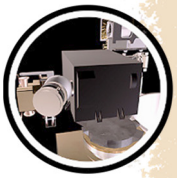

Table INMS-3. With higher signal-to-noise ratio, E5 measurements provide the first clear evidence of the presence of higher-order hydrocarbons in the plume, including benzene, and allow the tentative identification of individual species within each hydrocarbon group and of other organics. From Waite et al. [2009], Table 1.

Species	Volume Mixing Ratio
H_2O	0.90 ±0.01
CO_2	0.053 ±0.001
CO	(0.044)
H_2	(0.39)
H_2CO	$(3.1 \pm 1) \times 10^{-3}$
CH_3OH	$(1.5 \pm 0.6) \times 10^{-4}$
C_2H_4O	$< 7.0 \times 10^{-4}$
C_2H_6O	$< 3.0 \times 10^{-4}$
H_2S	$(2.1 \pm 1) \times 10^{-5}$
^{40}Ar	$(3.1 \pm 0.3) \times 10^{-4}$
NH_3	$(8.2 \pm 0.2) \times 10^{-3}$
N_2	< 0.011
HCN†	$< 7.4 \times 10^{-3}$
CH_4	$(9.1 \pm 0.5) \times 10^{-3}$
C_2H_2	$(3.3 \pm 2) \times 10^{-3}$
C_2H_4	< 0.012
C_2H_6	$< 1.7 \times 10^{-3}$
C_3H_4	$< 1.1 \times 10^{-4}$
C_3H_6	$(1.4 \pm 0.3) \times 10^{-3}$
C_3H_8	$< 1.4 \times 10^{-3}$
C_4H_2	$(3.7 \pm 0.8) \times 10^{-5}$
C_4H_4	$(1.5 \pm 0.6) \times 10^{-5}$
C_4H_6	$(5.7 \pm 3) \times 10^{-5}$
C_4H_8	$(2.3 \pm 0.3) \times 10^{-4}$
C_4H_{10}	$< 7.2 \times 10^{-4}$
C_5H_6	$< 2.7 \times 10^{-6}$
C_5H_{12}	$< 6.2 \times 10^{-5}$
C_6H_6	$(8.1 \pm 1) \times 10^{-5}$

Later, subsequent orbits at relative flyby velocities of < 8 km/s E14, E17, and E18 also helped establish that much of the organic content beyond the C_3 (> mass 40 u) were likely fragments of a heavier organic compound CDA identified in E-ring ice grains. This is the subject of a paper in Science [Postberg et al. 2018]. Figure INMS-16 shows the differences of the combined E14, E17, and E18 relative to the E5 spectra.

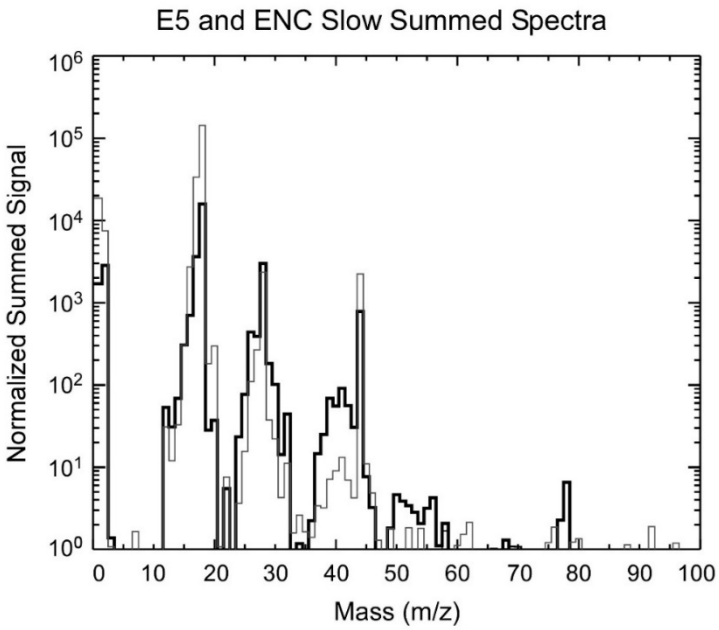

Figure INMS-16. The effects of impact fragmentation of organics within the ice grains and the effect of Titanium vapor on the water signal can be seen in this comparison mass spectra. The E5 spectra are the bold lines, and the summed E14, E17, and E18 spectra are the light lines. The normalization is performed by setting the spectra equal at mass 15 u.

The composition of plume vapor

The data obtained during the E14, E17, and E18 flybys all at relative flyby speeds of 7–8 km/s and all along or in parallel tracks near the Baghdad tiger stripe provide a consistent and repeatable depiction of the mass spectra at relative speeds low enough that fragmentation effects are minimized. These spectra are shown in Figure INMS-17. The spectra above 50 u (not shown) were near the noise level and further reinforce the point that the relative speeds above 8 km/s can lead to significant fragmentation of heavy organics buried in ice grains that complicate the interpretation of the mass spectra from E3 (~14 km/s) and E5 (~18 km/s). One can mass deconvolve the combined spectra from the slower flybys (E14, E17, and E18). The detailed analysis of this data set is the subject of Magee and Waite [2017]. A preliminary deconvolution is shown in Table INMS-4 taken from Magee and Waite [2017].

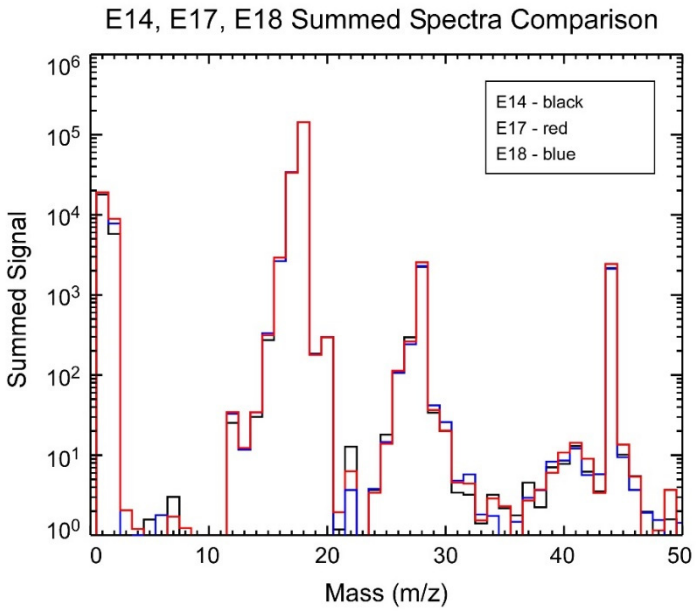

Figure INMS-17. Overlaid mass spectra for flybys E14, E17, and E18. Note the consistency of the spectra.

Table INMS-4. Preliminary mass deconvolution of mass spectra from E14, E17, and E18.

Minor Species I	Minor Species II				
Moderate Ambiguity	High Ambiguity				
< 0.2% and > 100 ppm	< 100 ppm				
	Hydrocarbons	**N-bearing**	**O-bearing**	**NO-bearing**	**Others**
C_2H_2 (26)	C_3H_4 (40)	CH_5N (31)	O_2 (32)	C_2H_7NO (61)	H_2S (34)
HCN (27)	C_3H_6 (42)	C_2H_3N (41)	CH_3OH (32)	$C_2H_5NO_2$ (75)	PH_3 (34)
C_2H_4 (28)	C_3H_8 (44)	C_2H_7N (45)	C_2H_2O (42)	$C_3H_7NO_2$ (89)	Ar (36, 38, 40)
CO (28)	C_4H_8 (56)	$C_2H_6N_2$ (58)	C_2H_4O (44)		C_3H_5Cl (76)
N_2 (28)	C_4H_{10} (58)	C_4H_9N (71)	C_2H_6O (46)		
C_2H_6 (30)	C_5H_{10} (70)	$C_4H_8N_2$ (84)	C_3H_6O (58)		
CH_2O (30)	C_5H_{12} (72)	$C_6H_{12}N_4$ (140)	C_3H_8O (60)		
NO (30)	C_8H_{18} (114)		$C_2H_4O_2$ (60)		
			$C_2H_6O_2$ (62)		
			$C_4H_{10}O$ (74)		
			$C_4H_6O_2$ (86)		

INMS measurement of ice-grain composition

Another serendipitous data product that INMS obtained from the Enceladus plume was a record of the ice grain composition. When an ice grain impacted the antechamber, a burst of material passed through the instrument creating a spike in the data [Perry et al. 2015; Teolis et al. 2010b]. Since

material flowed through the instrument in 2–3 milliseconds, these bursts occurred within one sampling period (i.e., one mass step), which had a dwell time of 31 milliseconds. Compiling the spikes from the E14, E17, and E18 data sets produces a mass spectrum of the portion of the ice grain material that does not chemically interact with the walls of the antechamber. This spectrum is shown in Figure INMS-18 (reproduced from Postberg et al. [2018], Figure 10).

The ice grain spectrum is related but distinct from the spectrum of the plume vapor. If present, C_2H_4 is limited to less than approximately 6% of the 28-u signal, and N_2 has an upper limit of approximately 10% due to the low signal at 14 u. This leaves a requirement for CO as the dominant species at 28 u, which matches well the signal at 12 u and 14 u (C^+ and CO^{++} dissociative peaks). Acetonitrile (C_2H_3N) also appears to be present. The signal pattern of 39–42 u suggests a species with its highest signal peak at 41 u and lower signal in the surrounding masses. C_2H_3N is the best candidate as it matches this stairstep pattern.

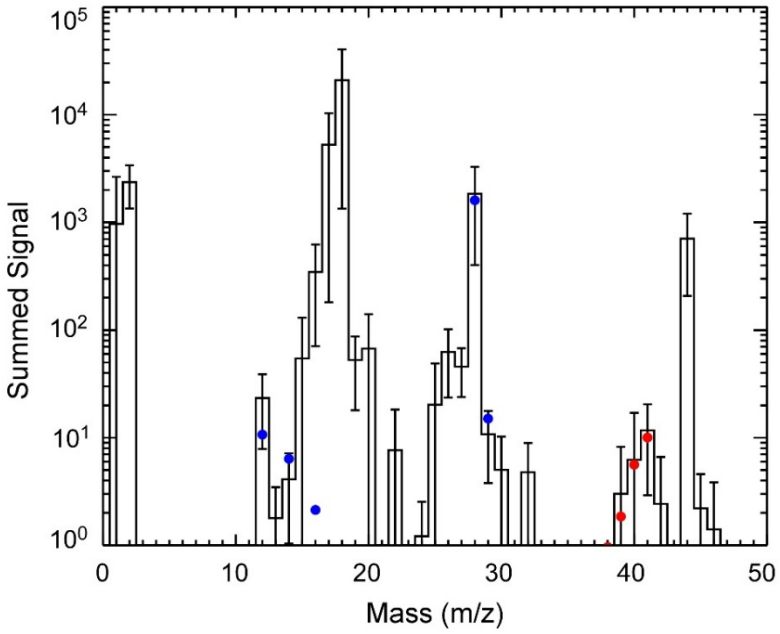

Figure INMS-18. Co-added INMS ice grain spike spectrum from three plume encounters. *Error bars* are derived from the dispersion of the count rate from the three encounters. The spectrum proves the presence of CO fragments (*blue circles*) as an oxygen bearing species: N_2 has very low abundance and contributes < ~10% of the 28 u signal. CO_2 and C_2H_4 collectively contribute < ~10% of the 28 u signal. CO (*blue circles*) is required to fit the rest of the 28 u signal and matches its other dissociative peaks well. The spectrum also indicates the presence of nitrogen bearing species: the stairstep pattern around 41 u matches best to the C_2H_3N spectrum (*red circles*). From Postberg et al. [2018], Figure 10.

Velocity of plume vapor

During four Enceladus encounters between November 2009 and October 2015, INMS operated in its seldom-used OSNB mode. In the OSNB mode, INMS makes direct measurement of the

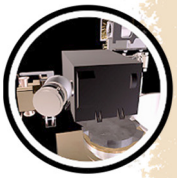

velocities of the neutrals. Although the velocity data from OSNB measurements are coarse, they provide strong constraints on the speed distribution of H_2O molecules within and surrounding the plumes.

In the OSNB mode, the velocity of the neutrals measured by INMS are determined by the angle of the INMS boresight, which sets the direction of the molecules, and the INMS compensation velocity parameter (V_{COMP}), which sets the speed of the molecules. The vector addition of this velocity with Cassini's velocity provides the neutrals' velocity relative to Enceladus. During E8, E11, and E16, V_{COMP} was fixed, but Cassini rotated so that INMS scanned the velocity of neutrals. (E21 operations were different: Cassini's attitude was fixed and V_{COMP} was scanned throughout the encounter to purposely sample the velocity distribution of the plume multiple times.) For each encounter, Cassini's rotation produced a single velocity scan, where the measured molecules had velocities that were radial from Enceladus with speeds increasing from 0 to 2 km/s. Figure INMS-19 shows the results of the velocity scan for E8. The fitted shape peaks at 1.25 km/s, but reduces to 1.1 ±0.2 after correction for INMS pointing calibration. The width of 300 m/s corresponds to a temperature of 65 K, which is similar to the low temperatures predicted by the models of Yeoh et al. [2015].

The ultimate velocity of adiabatic expansion for water at its triple point reflects the energy available per molecule of H_2O and is equivalent to 1.0 km/s, which is within the uncertainty of the measurement for the bulk velocity of E8. These results are reconciled with a previous higher-velocity estimate due to the modeling that shows the observed high-Mach jets have lower temperatures than previously assumed. INMS measured molecules leaving Enceladus at both high and low velocities.

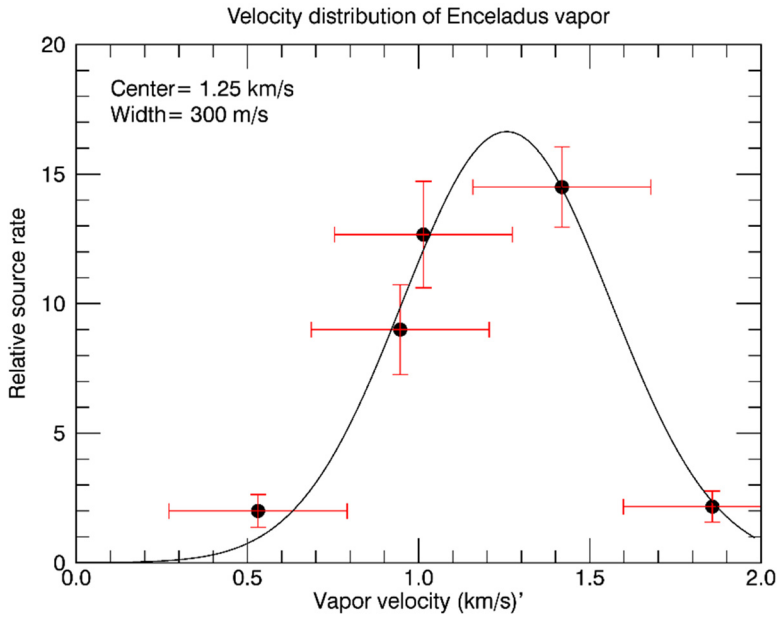

Figure INMS-19. Results of the E8 OSNB velocity scan. After adjustment for pointing calibration, the distribution peaks at ±0.2 km/s.

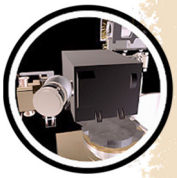

The measurements from the other OSNB encounters show a range of speeds that reflect the different environments surrounding Enceladus (Figure INMS-20).

- E8 had the highest velocities, and was sampling the strong jets.
- E11 velocities are slower and may represent the broader plume, outside of the dense, fast jets. E11 velocities are also consistent with early modeling of data from the higher-altitude encounters where the jets had merged with lower-velocity sources such as the tiger stripes, and the broad distribution of E11 may indicate a combination of multiple sources.
- E16 measured the neutral cloud that surrounds Enceladus and is fed by the plumes.

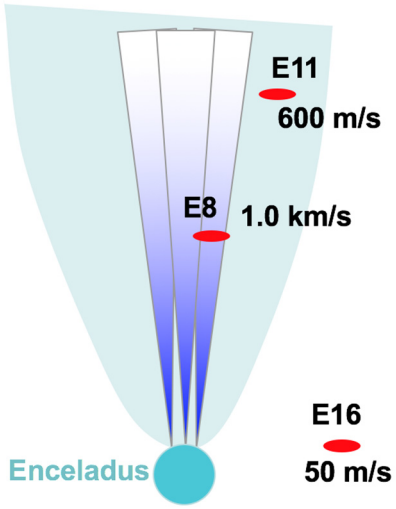

Figure INMS-20. The vertical speed of H_2O molecules measured during the E8, E11, and E16 encounters, showing several different velocity regimes.

The vapor-density structure of the Enceladus plumes

During six encounters between 2008 and 2013, the Cassini INMS made in situ measurements deep within the Enceladus plumes (Table INMS-5). Throughout each encounter, those measurements showed density variations that reflected the nature of the source, particularly of the high-velocity jets. Since the dominant constituent of the vapor, H_2O, interacted with the walls of the INMS inlet, changes in the external vapor density are tracked by using more-volatile species that responded promptly to those changes. To understand the plumes requires examination of each of the three components of Enceladus ejecta, fast and dense jets, slower diffuse gas, and ice grains.

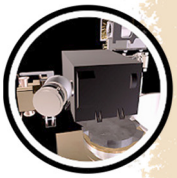

Table INMS-5. Information on the Enceladus encounters with the best INMS data. Perry et al. [2015] contains plume-structure data for the six un-shaded encounters. The last three encounters follow nearly identical trajectories but are offset several kilometers from each other.

Encounter	Features
E2	Relatively far from ejected vapor; minimal data useful for plume structure; first INMS identification of H_2O.
E3, E5	Steeply inclined, fast (14, 17 km/s) north-south trajectories, following the plume.
E7	Horizontal, slow pass (7 km/s) at 100 km min altitude, perpendicular to stripes, outbound from Saturn.
E8	Horizontal, slow pass south of Enceladus 1,200 km below the equatorial plane. Includes vapor velocity measurements from OSNB data. Minimal closed source neutral (CSN) data.
E14	Horizontal, slow pass at 100 km, high res, parallel to stripes, inbound to Saturn.
E17	Horizontal, slow pass at 75 km, high res, parallel to stripes, inbound to Saturn.
E18	Horizontal, slow pass at 75 km, high res, parallel to stripes, inbound to Saturn.

When INMS operated in the Closed Source Neutral (CSN) mode, Teolis et al. [2010b] described H_2O adsorption onto the walls of the INMS inlet system and the consequential delayed passage of H_2O through INMS. The delays can be tens of seconds to hours, depending on the amount of water already adsorbed onto the walls, and measurements of H_2O do not represent the conditions at the time and location of the measurement. Molecules with higher volatility respond to external flux in a tenth of an IP, 34 milliseconds, the temporal resolution of INMS [Waite et al. 2004], and these volatile gases (referred to as volatiles) are used to track changes in density.

The ice grains entering the INMS aperture add complexity and uncertainty to the physical interpretation of the data because the grains modified the INMS measurements. On entering the CSN aperture, an ice grain causes a high count or spike for a single measurement. The larger grains cause spikes that mask the gas density, confuse interpretation of INMS measurements, and add uncertainty. Since the resident time for volatiles in the INMS CSN inlet system is 2−3 milliseconds, the grain usually affects the measurement of only one IP.

The size of ice grains spans a range from molecular clusters to several microns in radius [Spahn et al. 2006; Jones et al. 2009; Coates et al. 2010]. Only grains that cause count rates much larger than the neighboring measurements can be clearly identified, and these were removed from the vapor-density data. Slightly smaller grains can cause two types of ambiguity in the INMS measurement: small spikes may be misinterpreted as local increases in vapor density, and rapid density variations may be misinterpreted as grain spikes. Grains that are still smaller cannot individually cause a noticeable change in count rate, but nanometer-scale grains are so plentiful that many enter the INMS aperture during a single IP, and these combine to create a background. Figure INMS-21 shows an example of INMS data with ice-grains spikes removed.

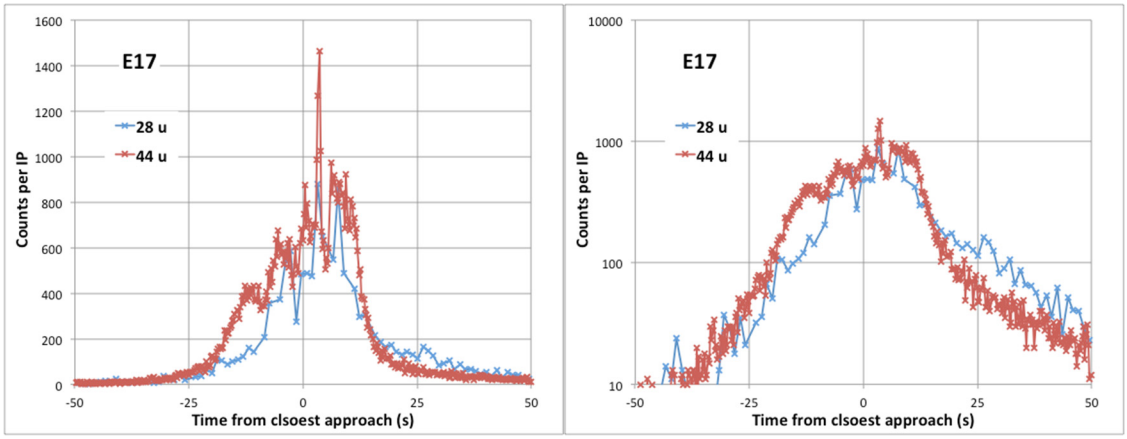

Figure INMS-21. Linear and log-plot profiles for the E17 Enceladus encounters. (Perry et al. [2015] has the profiles for all Enceladus encounters before 2016 with structure data.) The plots contain count rates for species with masses of 28 u and 44 u. Measurements that were clearly affected by ice grains have been removed.

For molecules emitted at the same supersonic velocity and in thermal equilibrium with each other at the time they are emitted, the cone angle or spreading of the molecules depends on mass (Figure INMS-22). This behavior causes differences in spatial composition that are measured by INMS and are independent of variations in source composition. Depending on the temperature, bulk velocity and mass, spreading angles vary from 10 to 45 degrees for Mach numbers from 1 to higher than 5, see Teolis et al. [2017].

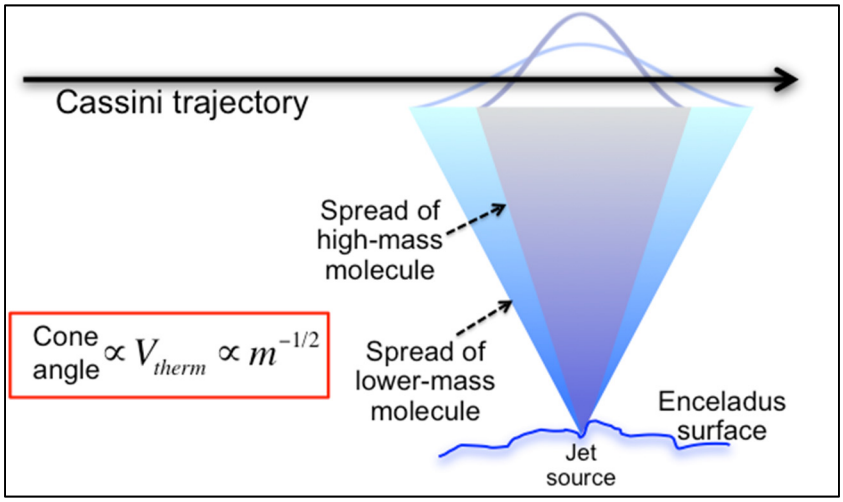

Figure INMS-22. Illustration of the mass-dependent behavior of high-velocity molecules emitted by the jets.

Based on ground [Waite et al. 2004] and flight calibration at Titan [Teolis et al. 2015], each INMS count during E7, E14, E17, and E18, corresponds to 2,100 molecules/cm^3 for the 28 u mass channel and 1,500 molecules/cm^3 for the 44 u channel (25% uncertainty). For E3 and E5, which had higher velocities, the calibration factors are 890 and 660 molecules/cm^3 for 28 u and 44 u

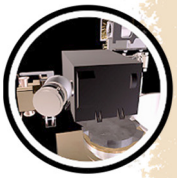

channels, respectively. Since high-velocity fragmentation products of molecules with masses greater than 100 u increase the counts of lower masses, E3 and E5 counts are higher than they would be without the added molecular fragments. Consequently, the actual 28 u and 44 u densities for E3 and E5 are a factor of two-to-five lower than the values based on the calibration factor provided for E7, E14, E17, and E18 [Teolis et al. 2015].

In lieu of modeling each individual molecule separately to account for mass-dependent behavior, the total-count ratios between the 18 u mass channel and the volatile masses provide an approximate density for H_2O. For the later, lower-velocity encounters, the total counts summed over the flyby for the 28 u and 44 u channels were each 0.5 % to 1% of the total 18 u counts after adjusting for the higher measurement frequency of the 44 u channel. At the high velocity of E3 and E5, larger molecules dissociate on impact with the INMS inlet, modifying the measurements for lower masses. This increased the counts for the measured volatiles and the ratio to water counts increased to 2–5% for each species [Teolis et al. 2015].

The vapor plumes show variability that was first reported by Hedman et al. [2013]. A comparison of data from the last three encounters, E14, E17, and E18, are consistent with the Visual and Infrared Imaging Spectrometer (VIMS) observation of variability in jet production and a slower, more diffuse gas flux from the four sulci or tiger stripes. Teolis et al. [2017] used data from all INMS and Ultraviolet Imaging Spectrograph (UVIS) encounters to constrain a time-dependent and high-resolution model of the plumes.

Two-component and multi-component models of INMS plumes

During the final low-altitude flybys of Enceladus, the most abundant, non-sticky species in the plume, CO_2 at 44 u, was sampled at a higher rate, to enable higher-resolution measurements of local density variations along Cassini's trajectory, achieving resolution of 0.25 s temporal and 1.9 km spatial. As shown in Figure INMS-24, CO_2 data from E17 clearly resolved density variations, indicative of gas jets, along Cassini's trajectory. Hurley et al. [2015] suggested on the basis of Monte Carlo models (Figure INMS-23) that the plume source may be continuously distributed, albeit variable, along the tiger stripes. These models included one lower-velocity component for the tiger stripes and a second, higher-velocity component for the jets. The complete plume three-dimensional structure is difficult to uniquely constrain solely on the basis of the few INMS flybys as multiple combinations of jet pointing directions and intensities can fit the data, and temporal variability further increases the potential solutions.

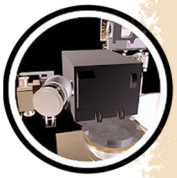

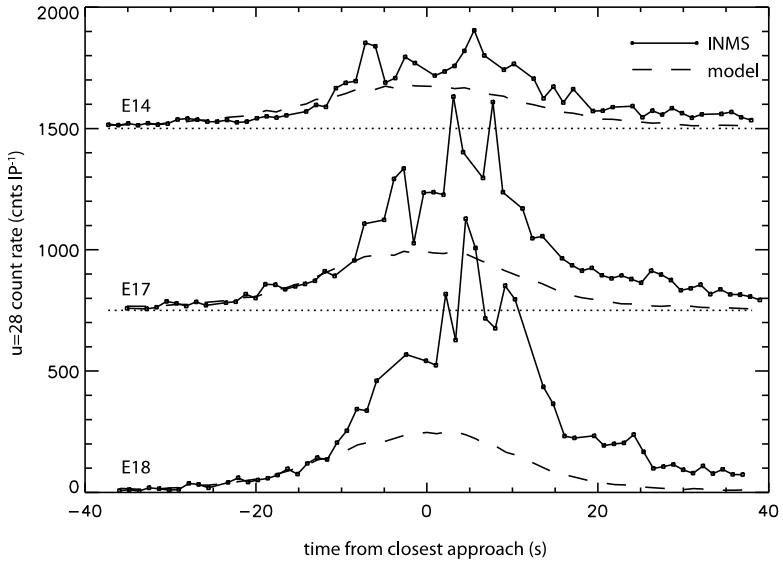

Figure INMS-23. Using the model described in Hurley et al. [2015], the *dashed lines* are simulated count rates with a continuous source along the tiger stripes as the only source of vapor. The temperature (270 K) and velocity (500 m/s) of the emitted tiger-stripe vapor were chosen to fit the rise and fall of the INMS data for mass 28 u. The best fit to the data is for E14, which occurred during a phase that corresponds to lower activity in the jets according to Hedman et al. [2013]. E17 and E18 occurred near Enceladus' apoapsis, when VIMS observed higher ice-grain emissions, and the higher, variable measurements in E17 and E18 may be due to more-active jets.

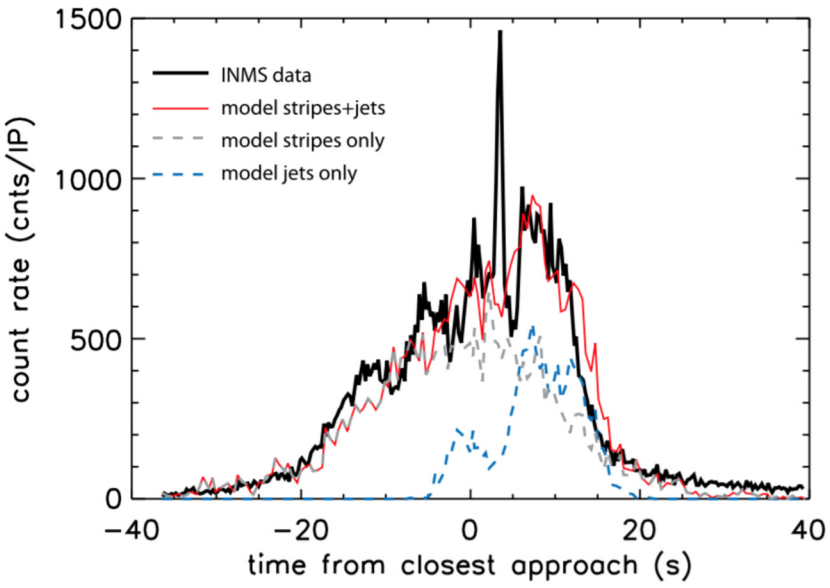

Figure INMS-24. INMS measurements of mass 44 u species during the E17 flyby are shown in *black*. Model [Hurley et al. 2015] predictions using constant emission along the tiger stripes at 500 m/s and 270 K (*gray dashed line*) are selected to match the rise and fall on the outskirts of the plume. The jet model using Mach 4 (1500 m/s and 270 K) are included (*blue dashed line*) to reproduce the overall enhancement near closest approach. The sum of the two models (*red line*) reproduces the overall structure of the plume, but misses some of the fine structure.

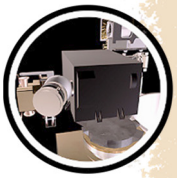

Alternate Enceladus plume structure

During Cassini's close (99, 74, 74 km) E14, E17 and E18 flybys through the Enceladus gas/dust plume on October 1, 2011, March 27, 2012, and April 14, 2012, the INMS measured in situ the detailed spatial structure of the neutral gas along the trajectories. These encounters were the first to fly close enough to the plume sources with the required pointing and sufficient data acquisition rate, to enable resolution of individual gas jets within the broad plume by INMS. During these flybys two INMS objectives were to: 1) constrain the locations, magnitudes and gas velocity from the plume surface sources, and 2) extrapolate the three-dimensional structure of the plume, including the diffuse plume and individual major jets. Since these flybys, the INMS team have carried out detailed plume modeling, combining the along-track densities measured at different times/dates by INMS, with and occultation, surface temperature, and imaging data from UVIS, Composite Infrared Spectrometer (CIRS) and ISS. The goals were to constrain the physics of the jet sources, i.e., the nozzle dimension and gas thermodynamic properties including temperature, density, flow and expansion rate, and provide necessary inputs for future modeling of the plume interaction with the Saturn system, i.e., the E-ring and magnetospheric sources and mass loading.

The results of our studies are now published in the papers by Perry et al. [2015] and Teolis et al. [2017]. Teolis et al. [2017] describes a detailed comparison of several plume source scenarios. The findings indicate that a time variable source, consisting of a source continuously (but non-uniformly) distributed along the tiger stripes, and sharp gas jets as inferred from ISS data [Porco et al. 2014], provide the best fit to the INMS and UVIS data. Figures INMS-26–INMS-30 compare the results of plume modeling for several different plume source models, considering both a curtain source with upward (normally) directed emission continuously distributed along the tiger stripes, and a source consisting of discrete gas jets with locations and pointing direction matching the grain jets identified by Porco et al. [2014] in ISS data.

In both the curtain and jet cases, the model suggests that a gas source with a Mach number distribution, containing a slow (with thermal velocity, Mach 0) isotropic emission, and a super-sonic (high velocity) component, was required to fit the broad distribution, and the fine structure, respectively, observed in the UVIS/INMS data. The fits use a 4-point Mach number distribution ranging from zero (gas at rest) to 16 (the fast component), as necessary to best fit the shapes of the features in the INMS and UVIS data. The curtain model considered three cases: 1) a uniform emission along the tiger stripes; 2) emission correlated to the tiger stripe temperature from CIRS data (Figure INMS-25); and 3) emission optimized to fit the INMS and UVIS data. For jets, the model considered two cases: 1) jets with equal intensities; and 2) jet intensity optimized to fit the data. The optimized models typically give multiple solutions, corresponding to reductions/enhancements in different combinations of jets, or different vapor source distributions along the tiger stripes. Figures INMS-26–INMS-30 show the averages over these solution families to compare and contrast the quality of the fits in the cases of continuous distributed emission and of discrete gas jets. It is clear on the basis of the plots, that neither the thermal plume cases, nor the cases of uniform curtains or jets, provide very good fits to the data. Both optimized curtains and jets yield rough agreement with the data but, as shown in the plots, some features of the data are better matched by the jets. The models could not fit all of the INMS and UVIS data simultaneously

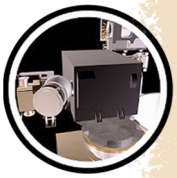

with a unique model solution. Therefore, given the curtain and [Porco et al. 2014], jets as a modeling constraint, an assumption of time variability of plume source distribution and/or individual jets between the Cassini flybys, is required to fit the data. The changes over time of the individual jets appears to be chaotic, exhibiting no obvious correlation to the Enceladus mean anomaly, as seen (for the plume as a whole) in VIMS data [Hedman et al. 2013].

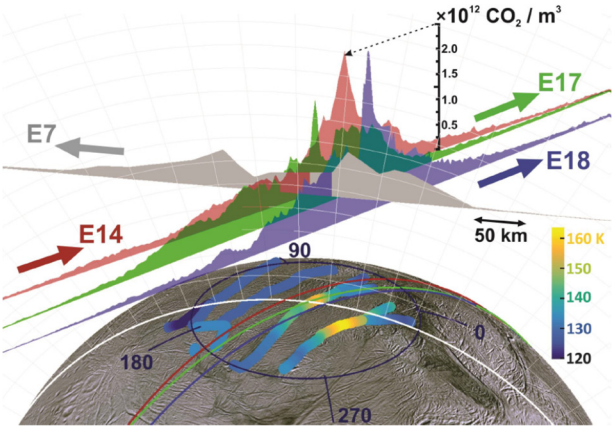

Figure INMS-25. Emission correlated to the tiger stripe temperature from CIRS data. To scale 3-D representation of the E14, E17, E18, and also (lower resolution) E7 INMS data with vertical areas representing (in linear scale) the density, and the flat base of the areas corresponding to the Cassini trajectories. Lines across the surface are the ground tracks. The Tiger stripes are colored according to the temperature estimated by CIRS. Figure from Teolis et al. [2017].

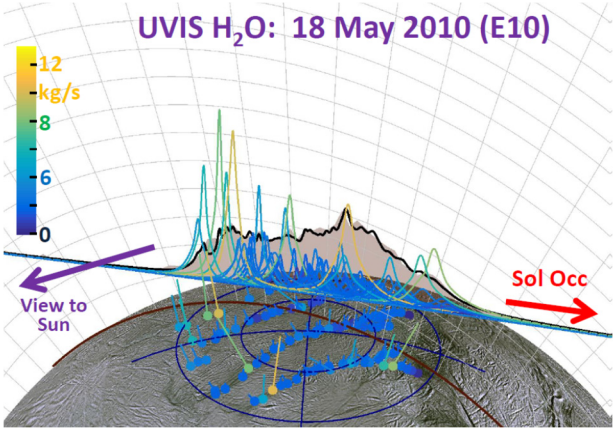

Figure INMS-26. Results of plume modeling. To scale 3-D representation of the 2010 Enceladus plume UVIS Solar Occultation with vertical areas representing (in linear scale) the occulted intensity fraction (corresponding to the water vapor column density), and the flat base of the area corresponding to the line of minimum ray height (*brown line* on surface is the ground track of this ray). For example, Cassini's viewpoint onto the plume is from the upper right of the figure, and UVIS is scanned from left to right as shown by the *arrow*. *Dots on surface:* [Porco et al. 2014] jet source locations, with *straight lines* showing jet directions. The colors and jet line lengths are given by the optimized jet strength; i.e., *orange* (*blue*), long (short) jets represent high (low) intensity jets. Colored curves: line height from min ray height line gives the estimated column density profile of each jet along the UVIS line of sight. *Black curve:* the best fit total column density of all jets across the UVIS line of sight: the colored curves sum to yield the *black curve*. Figure from Teolis et al. [2017].

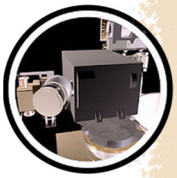

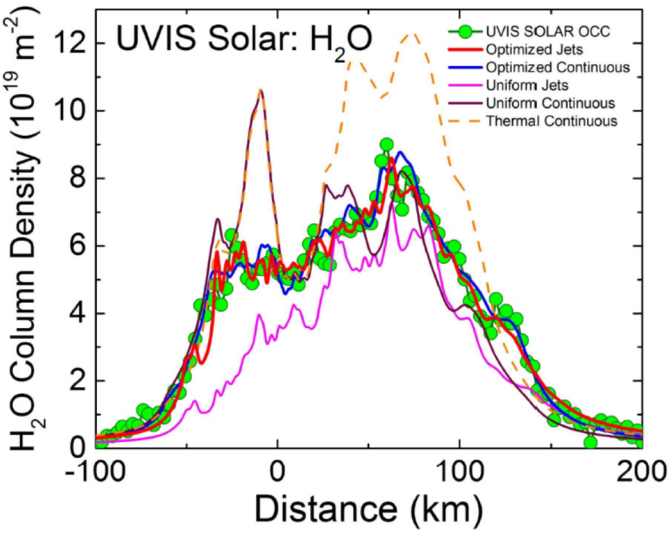

Figure INMS-27. Results of plume modeling. Enceladus plume water vapor column density measurement from the UVIS 2010 solar occultation (*Green circles*), plotted versus distance across the plume along the occultation line of sight minimum ray height. *Red line:* Average model solution for the optimized [Porco et al. 2014] jets. *Blue line:* Average solution for continuous emission along the tiger stripes. *Magenta line:* Jets with equal intensity. *Brown line:* Uniformly distributed continuous emission along the tiger stripes. *Orange dashed line:* Continuous emission with emission strength dependent on tiger stripe temperature (proportional in this example to Tn, with n = 7). Figure from Teolis et al. [2017].

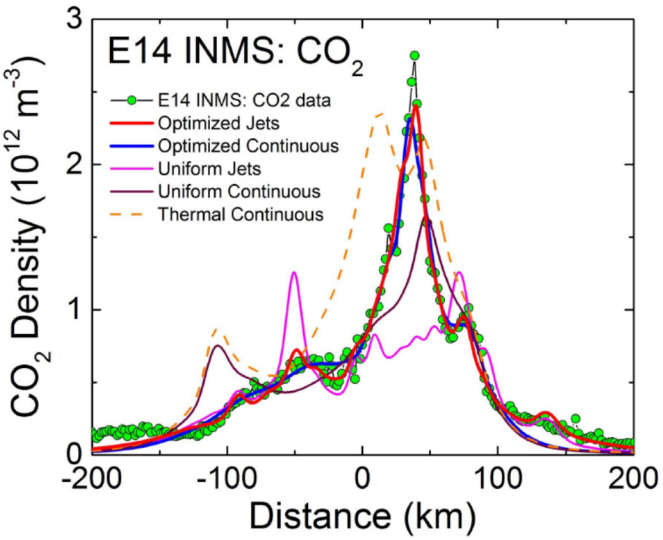

Figure INMS-28. Results of plume modeling. INMS CO_2 density measurement (*Green circles*) along the E14 flyby trajectory showing structure in the plume density along trajectory. *Red line:* Average model solution for the optimized (Porco et al., 2014) jets. *Blue line:* Average solution for continuous emission along the tiger stripes. *Magenta line:* Jets with equal intensity. *Brown line:* Uniformly distributed continuous emission along the tiger stripes. *Orange dashed ine:* Continuous emission with emission strength dependent on tiger stripe temperature. Figure from Teolis et al. (2017).

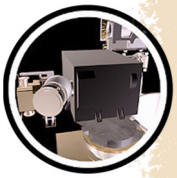

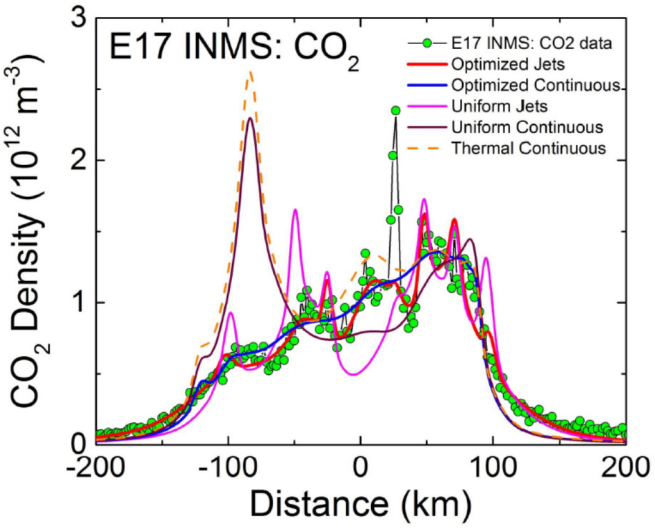

Figure INMS-29. Results of plume modeling. Same as Figure INMS-28 for the E17 flyby. Figure from Teolis et al. [2017].

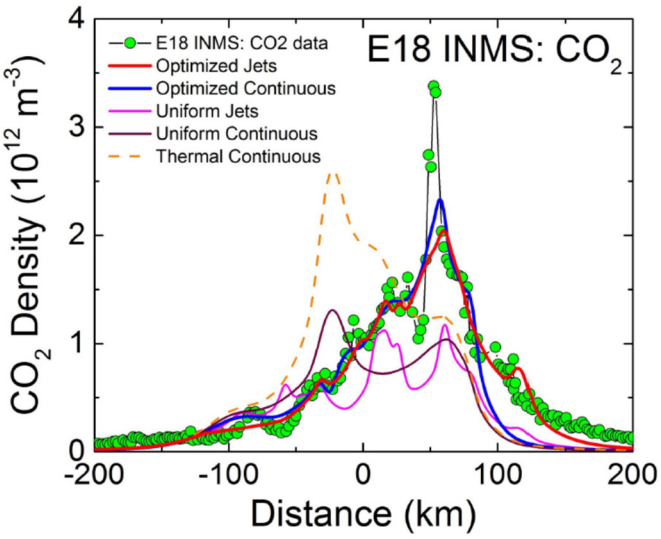

Figure INMS-30. Results of plume modeling. Same as Figures INMS-28 and INMS-29 for the E18 flyby. Figure from Teolis et al. [2017].

Confirmation of H_2 in the plume vapor and hydrothermal activity

Finally, one of the most important findings of the Cassini mission by INMS was the open source detection of molecular hydrogen within the plume. Previous observations by the closed source had indicated the presence of molecular hydrogen, but were fraught with ambiguity due to the unearthing of fresh titanium from the walls of the antechamber from ice grain impacts as noted in the E5 discussion in the section entitled Velocity-Dependent Mass Spectra and Impact Fragments. E21 used the open source to measure molecular hydrogen and then after a lengthy and careful

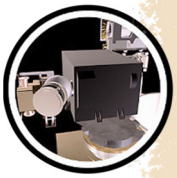

study of the instrumental background this result was verified and published in Science [Waite et al. 2017]. Figure INMS-31 data (reproduced from Waite et al. [2017], Figure 2) indicates a two sigma detection of molecular hydrogen in the plume and an indication of the other important minor constituents, see Table INMS-6 (reproduced from Waite et al. [2017] Table1). The important implications of this measurement are shown in Figure INMS-32 (reproduced from Waite et al. [2017], Figure 4), which illustrates that a positive chemical affinity for the reaction that represents methanogenesis in Earth's ocean can be shown to be present on Enceladus. This constitutes evidence that food for microbes is present Enceladus' ocean, the crowning achievement for demonstrating habitability at Enceladus.

Comparison of OSNB measurements of mass 2 (H_2) with the estimated total mass 2 instrumental background

The detected count rates and estimated background rates are plotted (Figure INMS-31) as a function of time from closest approach to Enceladus. The bottom panel of the plot is on a linear scale showing all the data points at or below ten counts. The top panel, plotted on the common log scale, shows the remaining data points that are above ten counts. Data points are color-coded according to the statistical uncertainties and background estimation: **open black circles** - no distinguishable separation from the background signal; **light blue circles** - at least one sigma separation; **dark blue diamonds** - at least two sigma separation; **purple triangles** - at least three sigma separation.

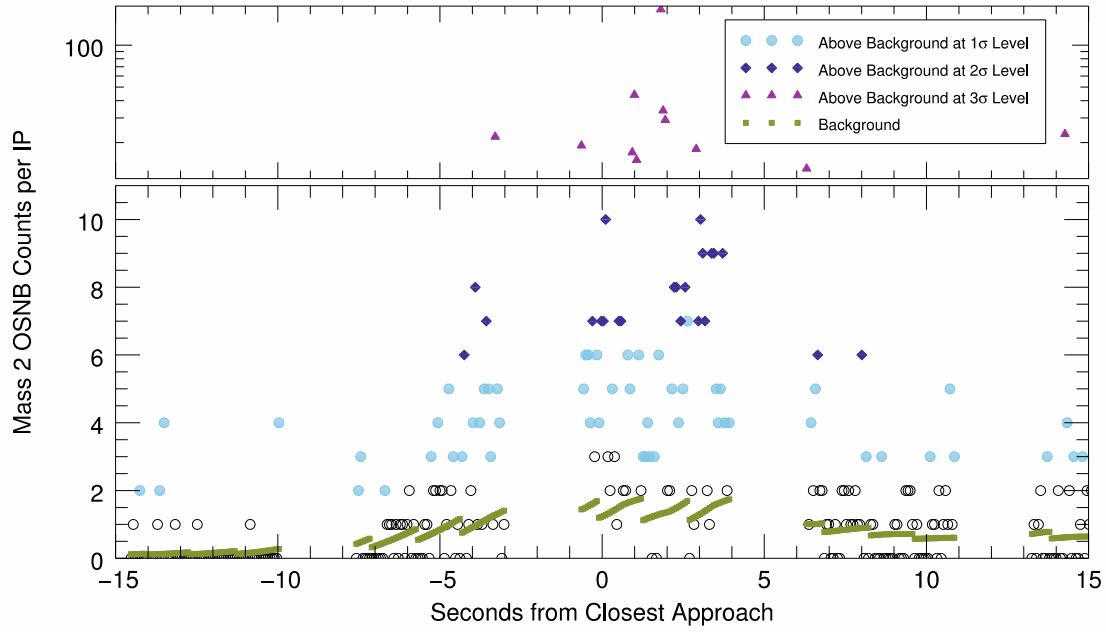

Figure INMS-31. Detection of molecular hydrogen in the plume. Figure from Waite et al. [2017].

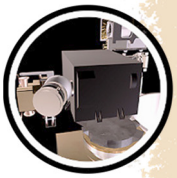

Table INMS-6. Other important minor constituents. Table from Waite et al. [2017]*.

Constituent	Mixing Ratio (%)
H_2O	96 to 99
CO_2	0.3 to 0.8
CH_4	0.1 to 0.3
NH_3	0.4 to 1.3
H_2	0.4 to 1.4

* Waite et al. [2017], Table 1. The major species composition of Enceladus' plume gas. Volume mixing ratios are derived from Cassini INMS measurements—supplementary materials [20], sections 2.4 and 3.2.

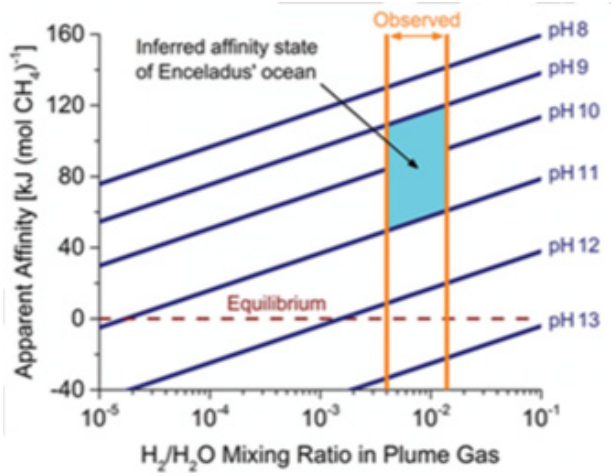

Figure INMS-32. A positive chemical affinity for the reaction that represents methanogenesis in Earth's ocean can be shown to be present on Enceladus. (Reproduced from Waite et al. [2017] Figure 4.) Apparent chemical affinity for hydrogenotrophic methanogenesis in Enceladus' ocean (273 K, 1 bar). The *orange lines* bracket the observed range in the mixing ratio of H_2 in the plume gas (Waite et al. [2017], Table 1). The *blue lines* are contours of constant ocean pH, a key model parameter. The *cyan region* indicates affinities for a pH range that may provide the greatest consistency between the results of (13, 15, 25). The *dashed red line* designates chemical equilibrium, where no energy would be available from methanogenesis. These nominal model results are based on CH_4/CO_2 = 0.4 (Waite et al. [2017], Table 1), a chlorinity of 0.1 molal, and 0.03 molal total dissolved carbonate (*25*). Reported ranges in these parameters propagate to give an uncertainty in the computed affinities of ~10 kJ (mol CH_4)$^{-1}$.

Detection of a plume ionosphere by INMS

As will be discussed later, the INMS (and CAPS) measured plasma in the Enceladus torus that mainly consisted of H_2O^+, OH^+, and O^+. In addition to closed source measurements of neutrals, INMS during the E3 flyby of Enceladus also made measurements in its open source ion mode [Cravens et al. 2009c]. The mass spectrum primarily showed a species with a mass of 19 u, and localized to the region of the neutral plume. Almost no signal at mass 18 was detected. Mass 19 corresponds to H_3O^+. We interpret the INMS measurements of cold H_3O^+ ions and the almost complete absence of cold H_2O^+ ions as being a consequence of ion-neutral chemistry taking place

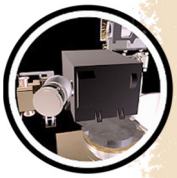

in a plume "ionosphere" where the H_3O^+ is produced by reaction of H_2O^+ ions (incident from outside or locally from phototionization of water) with H_2O [Sakai et al. 2016].

Enceladus Open Questions

1. Extremely narrow vapor jets with Mach numbers as high as ten were sampled by INMS along Cassini's E14, E17 and E18 trajectories. What is the temperature and speed of the gas in the jets?

2. Drastic stochastic time variability in the vapor jets detected by INMS between Cassini's plume traversals. How does the time variability relate to subsurface tidal stresses and fluid flow in the tiger stripes?

3. What chemistry produces a mass 28 species in the closed source of INMS?

4. What is the isotopic composition of non-water plume gases?

5. Are there noble gases in the plume?

6. Is the methane detected by INMS abiotic or biotic in origin?

7. What is the relationship between plume gas abundances and the concentrations of dissolved species in Enceladus's ocean?

8. What is the composition of those large organics that are outside the mass range of the instrument?

Icy Satellite Science

> INMS results provide essential clues regarding the origin of O_2 and CO_2 at Dione and Rhea, and invaluable insight into the physics of icy satellite exospheres generally.

A major original objective of the Cassini mission, and of the INMS in particular, was to measure the abundance and composition of atmospheric gases around Saturn's large icy moons. Unlike Enceladus, which has insufficient gravity to retain an appreciable bound exosphere, sputtered and/or cryovolcanic emissions from Saturn's other large airless moons may fall back to their surfaces, and more volatile molecules can accumulate in the exosphere, adsorbing and desorbing to and from the surface many times before escaping to space. The ability of INMS to capture and analyze exospheric ions (with the OS) and/or neutrals (with the CS) is a strong function of Cassini's distance from these moons, with close flybys most likely to encounter detectable exospheric densities. Of Saturn's five large airless moons Mimas, Tethys, Dione, Rhea, and Iapetus, Cassini only flew close enough to

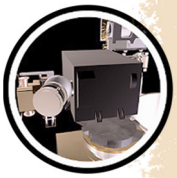

two, Dione and Rhea, to enable the detection of neutral O_2 and CO_2 exospheres by INMS at both moons (Figure INMS-33 and Figure INMS-34). INMS found evidence that the exospheres of Dione and Rhea exhibit complex structure, and observed drastic changes in the exosphere over time during the mission, as the Saturn system transitioned between equinox and solstice.

Owing to the diversity of multiple flyby dates and geometries (altitude, latitude, local time) the INMS was able to carry out exospheric density measurements over different geographic regions of Dione and Rhea, and at different flyby dates throughout the Saturnian year. The constraints provided by these INMS data, provide critical context and interpretation for the exospheric pickup ions detected by Cassini CAPS, and paint a highly detailed picture of the exospheric structure and time evolution. These data, together with high fidelity exospheric modeling, reveal highly seasonal exospheres at both Dione and Rhea, and inform interpretation of the exospheric measurements reported by Cassini's other instruments at these two moons [Simon et al. 2011; Tokar et al. 2012]. INMS results provide essential clues regarding the origin of O_2 and CO_2 at Dione and Rhea, and invaluable insight into the physics of icy satellite exospheres generally. For these reasons, INMS exploration of Saturn's large icy moons must be judged a spectacular success, meeting and in fact exceeding the original science objectives.

Icy satellites highlights

1. Discovery of oxygen and carbon dioxide exospheres at Dione and Rhea.
2. The exospheres change with time seasonally.
3. The exospheres have complex structure.
4. The measurements of the INMS place limits on the exospheric density that allowed aspects of the magnetometer data to be interpreted such that new types of current systems were discovered.

The Rhea and Dione flybys

Table INMS-7 summarizes Cassini's close flybys of Dione and Rhea, and the flybys for which INMS (and CAPS) had priority. At Rhea, Cassini carried out five major flybys ranging in speed from 6.8 to 9.3 km/s: the high altitude R1 and R1.5 flybys through the plasma wake, the low altitude R2 and R3 flybys approximately over the north and south poles, and the high altitude R4 flyby over the northern hemisphere. At Dione, five 6.5–9.0 km/s flybys were performed: the high altitude D1 flyby over the south, the high-altitude D2 flyby through the plasma wake, the low altitude D3 flyby near the dusk terminator, and the high altitude D4 and D5 flybys over the north. Cassini's traversal across the solar terminator, from night to day on all of the low altitude flybys (R2, R3, D3, see Figure INMS-33, Figure INMS-35, Figure INMS-36), was fortunate and essential, enabling INMS to detect the drastic differences of exospheric density between the night and day hemispheres. This constraint is key to the interpretation and understanding of the INMS data as discussed in the rest of this section.

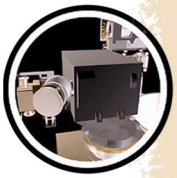

Table INMS-7. Dione and Rhea flyby observations.

Flyby	Body	Date	UTC	Speed	Alt	Detection	Species	References	Description
D1	Dione	11-Oct-05	17:52:00	9.12 km/s	500 km	MAG	-	Simon et al. 2011	Upstream southern flux tube, Saturn inbound.
R1	Rhea	26-Nov-05	22:37:38	7.28	500	CAPS	CO_2^+, O^-	Teolis et al. [2010a]; Teolis and Waite [2016]	Equatorial Wake, toward night side, Saturn inbound.
R1.5	Rhea	30-Aug-07	01:18:55	6.76	5725	CAPS	CO_2^+	Teolis and Waite [2016]	Northern Wake, toward night side, Saturn outbound.
R2	Rhea	2-Mar-10	17:40:36	8.58	100	INMS	O_2, CO_2	Teolis et al. [2010a]; Teolis and Waite [2016]	Low altitude, north polar, toward day side, Saturn inbound.
D2	Dione	7-Apr-10	05:16:11	8.34	500	CAPS	O_2^+	Tokar et al. [2012]	Equatorial Wake, toward day side, Saturn inbound.
R3	Rhea	11-Jan-11	04:53:25	8.05	72	INMS	O_2	Teolis and Waite [2016]	Low altitude, south polar, toward day side, Saturn outbound.
D3	Dione	12-Dec-11	09:39:23	8.73	99	INMS	O_2, CO_2	Teolis and Waite [2016]	Low altitude, equatorial wake, toward day side, Saturn outbound. CAPS offline.
R4	Rhea	9-Mar-13	18:17:26	9.29	996	-	None	Teolis and Waite [2016]	South-to-north, over anti-Saturn night side. CAPS offline. Altitude too high, and pointing poor, for INMS: Non-detection.
D4	Dione	16-Jun-15	20:11:52	7.32	516	INMS	O_2	Teolis and Waite [2016]	North polar, toward night side, Saturn outbound. CAPS offline.
D5	Dione	17-Aug-15	18:33:25	6.45	476	-	None	Teolis and Waite [2016]	North polar, toward night side, Saturn inbound. CAPS offline.

Detection of exospheric oxygen and carbon dioxide

Figure INMS-33 and Figure INMS-34 show the densities of exospheric O_2 and CO_2 at Rhea and Dione as they were measured by the INMS closed source along Cassini's flyby trajectories [Teolis et al. 2010a; Teolis and Waite 2016]. While O_2 is an expected product of sputtering, produced by radiolysis of highly abundant water ice on the surfaces of many icy satellites, the detection of exospheric CO_2 at a high relative abundance compared to O_2 was not expected.

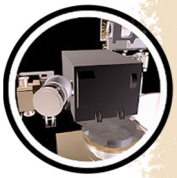

Before addressing the origin of CO_2, we first point to several other extraordinary aspects of these INMS data sets that are key to their interpretation:

- Exospheric densities, as measured during the R2, R3 and D3 flybys, were higher over the dayside than the night side (Figure INMS-33).
- The day-night asymmetry is in all cases far more pronounced for CO_2 than for O_2 (Figure INMS-33).
- Despite the lower altitude of the R3 flyby (minimum 72 km) relative to R2 (minimum 100 km), ten times less O_2, and no CO_2 was detected on R3 (Figure INMS-33).

The observation of higher exospheric densities over the daysides of Dione and Rhea is consistent with higher exospheric scale heights over that hemisphere, as exospheric gas interacts and thermally accommodates to the warmer dayside surface temperatures. However, the day-night exospheric asymmetry is far more pronounced for CO_2 than for O_2 at both Dione and Rhea (Figure INMS-33, Figure INMS-35, Figure INMS-36), suggesting that the less volatile CO_2 molecules may, unlike O_2, actually freeze out onto the night sides of both moons.

However, the detection of far less O_2, and non-detection of CO_2 at R3 was entirely unexpected at the time of the flyby, since the R3 trajectory was at a lower altitude than the previous R2 flyby. This raised the question of whether the drastically different O_2 and CO_2 densities between R2 and R3 were the result of exospheric spatial structure (a gas source in the north), or changes in the exospheric structure with time?

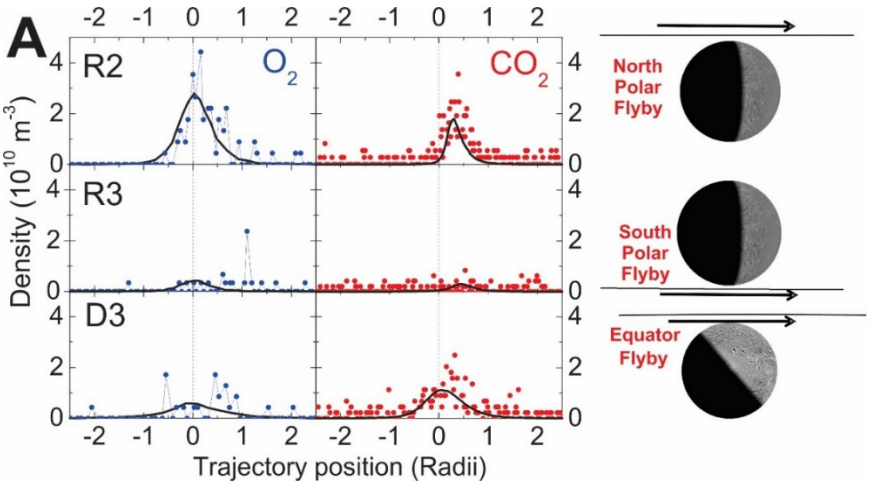

Figure INMS-33. Densities of exospheric O_2 and CO_2 at Rhea and Dione as they were measured by the INMS closed source along Cassini's flyby trajectories. The Dione and Rhea O_2 and CO_2 exospheric densities measured by Cassini INMS versus distance (in planetary radii) from closest approach (*dashed line*) along the night-to-day R2, R3 and D3 trajectories (*shown on right*). The data are un-binned, such that single counts are visible. Time increases left to right in the plots, with Cassini moving from the night to the dayside hemisphere on all flybys. As shown, the exospheric profiles are concentrated (especially for CO_2) over the dayside when equivalent inbound-outbound altitudes are compared. Lines: exosphere model results, see Figure INMS-35 and Figure INMS-36. Figure from Teolis and Waite [2016].

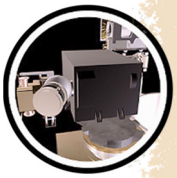

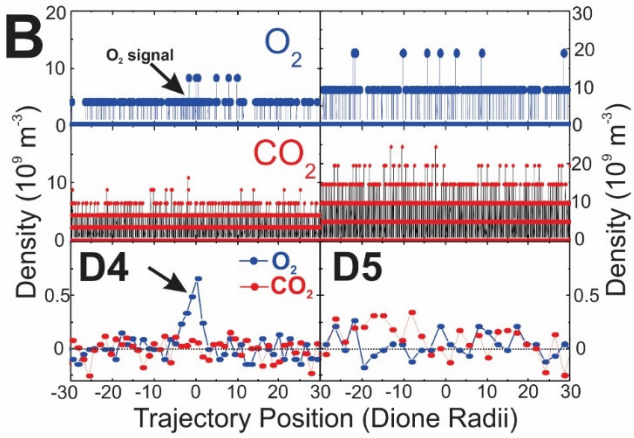

Figure INMS-34. Densities of exospheric O_2 and CO_2 at Rhea and Dione as they were measured by the INMS closed source along Cassini's flyby trajectories. Exospheric data (*top-center:* raw counts converted to density; *bottom:* binned/background subtracted) from the recent Dione northern high (516 km) altitude (day-to-night) D4 and D5 flybys, showing the detection of O_2 but not CO_2 at D4 and the non-detection of either species at D5. Time increases left to right with Cassini moving from the day to the night side hemisphere on both flybys. Figure from Teolis and Waite [2016].

Exospheric structure and seasons at Dione and Rhea

To address this puzzle Teolis et al. [2010a] and Teolis and Waite [2016] created a state-of-the-art icy satellite exospheric model code that specifically takes into account the effects of surface thermal accommodation and sticking observed by INMS. The model considers the rotation of Dione and Rhea, the variability of surface temperature between day and night, and the change in the solar declination with Saturn's seasons, which varies from between ±26.7 degrees over the 29.5 (Earth) year Saturn orbit. Molecules of O_2 and CO_2 are ejected into the simulated exosphere uniformly from all points on the surface to approximate a surface sputtered source, but can stick (transiently) to the night side and (for much longer periods) at the winter latitudes.

The exospheres of Dione and Rhea are, according to the models, highly seasonal with exospheric O_2 and CO_2 freezing onto the cold terrain in the winter latitudes, which remain in shadow drop as low as 20 Kelvin over the 14 year Saturn system winter [Howett et al. 2016]. However, with the approach of spring equinox the solar terminator advances across the polar terrain resulting in the rapid desorption of condensed gasses and a drastic ramp up of the exospheric gas density. In fact, the Rhea R2 flyby over the north occurred shortly after northern equinox and thus the exospheric O_2 and CO_2 were still desorbing from the northern terrain as previously shadowed areas were coming into sunlight. The main exospheric gas source was in the north at the time of the R2 and R3 flybys, due to desorption of condensed O_2 and CO_2 (built up over the prior winter) from that region. This can be seen in Figure INMS-35 and Figure INMS-36 where we plot the modeled exospheric CO_2 and O_2 densities at Rhea and compare predicted with measured densities along the R2 and R3 flyby trajectories. For CO_2 it can be seen (Figure INMS-35) that Rhea's exospheric gas density was higher over the north than the south according to the model, since CO_2 was

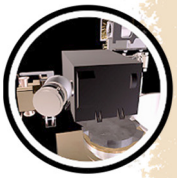

desorbing from the north at that time. This interpretation, shown in Figure INMS-35, successfully accounts for INMS non-detection of CO_2 on R3 in the south.

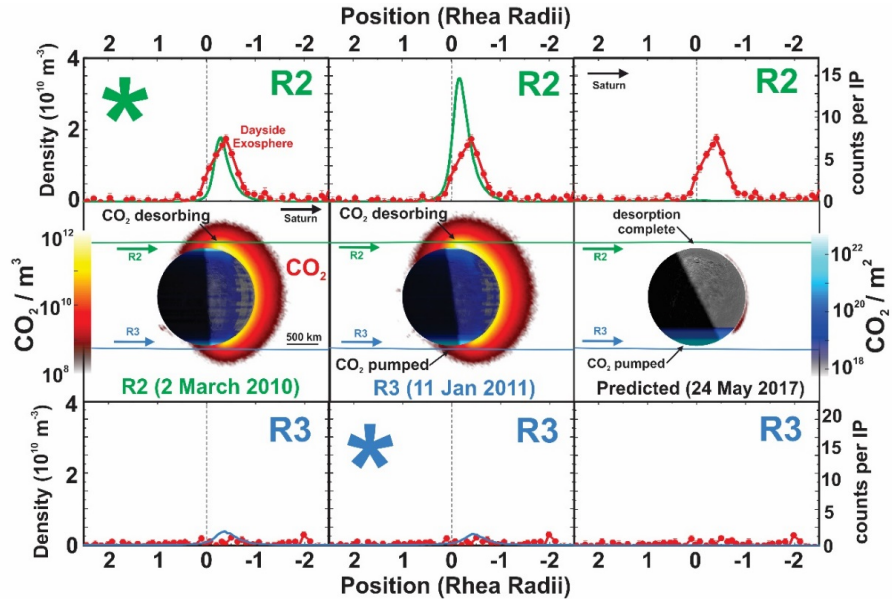

Figure INMS-35. Plot of the modeled exospheric CO_2 and O_2 densities at Rhea, and the comparison of predicted with measured densities along the R2 and R3 flyby trajectories. Rhea CO_2 exospheric model results, showing (*center row*) the surface solar illumination (dawn terminator as viewed over the equator), and predicted gas density cross-sections and surface frost column density at the R2 (*left*) and R3 (*center column*) flyby dates and times, and prediction (*right*) for the 2017 Saturn solstice. *Top*: comparison of the observed (*red points*, data binned) and predicted (*green line*) CO_2 densities versus position from closest approach along the R2 trajectory (x-axis, in Rhea radii, *dashed line:* closest approach). *Bottom*: same for the R3 flyby trajectory. *Asterisks* denote model-data comparisons with the same flyby date; all other plots show model projections to different dates. The model assumed a 3.7×10^{21} CO_2/s source rate as required to match the observed peak density on both flybys. The observation of CO_2 concentrated on the dayside is consistent with the modeled exospheric structure due to night side and polar cryopumping. CO_2 was desorbing from the north, and cryopumping onto the southern polar surface during the flybys. Accordingly, as anticipated by the model (*bottom center*), CO_2 was undetectable in the south on R3. As shown (*right*) exhaustion of the northern frost cap should result in the collapse of the CO_2 exosphere by the time of the 2017 solstice. Figure from Teolis and Waite [2016].

Surprisingly the O_2 data has a somewhat different interpretation than CO_2 according to the model, owing to the greater volatility of O_2 as compared to CO_2. The less volatile CO_2 (unlike O_2) is was beginning to freeze out onto the south polar terrain at the time of the R2 flyby according to the model, even before its desorption from the north had completed. For CO_2 (unlike O_2) the adsorption of exospheric gas onto one pole overlaps in time with its desorption from the opposite pole, meaning that CO_2 exhibited a more drastic difference of density between north and south at the time of the R2 and R3 flybys than O_2. Therefore, as can be seen in Figure INMS-36, the drop in O_2 between R2 and R3 is indicative of a rapid collapse of the entire exosphere in the ten months between R2 and R3. The exosphere's collapse occurs as all of the O_2 frozen onto the northern terrain is depleted, having fully desorbed off of the northern surface. The CO_2, being less volatile, takes longer to desorb from the north, and therefore CO_2 exosphere is predicted to have collapsed

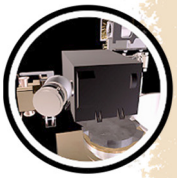

only after the R3 flyby took place. In this way exospheric O_2 and CO_2 desorb and re-freezing, moving from pole to pole every equinox, in a repeating seasonal cycle, leading to changing exospheric densities at Dione and Rhea that are minimal near Saturn's solstices and maximal near the its equinox's. The model of a seasonal exosphere not only accounts for the INMS data, but also the spatial distribution, composition, flux of pickup ions observed by CAPS discussed by Teolis and

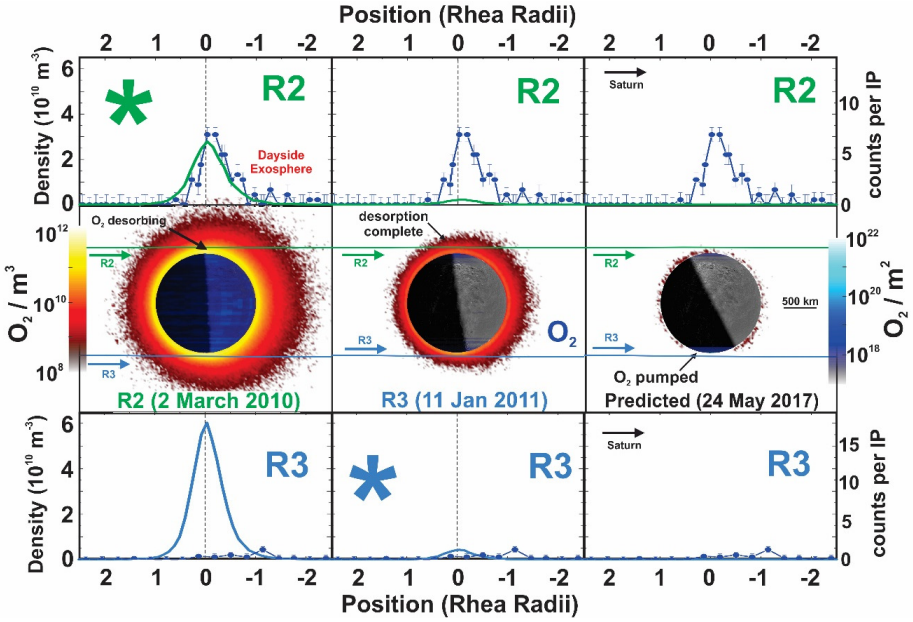

Figure INMS-36. Plot of the modeled exospheric CO_2 and O_2 densities at Rhea, and the comparison of predicted with measured densities along the R2 and R3 flyby trajectories. Rhea O_2 exospheric model results, showing (center row) the surface solar illumination (dawn terminator as viewed over the equator), and predicted gas density cross-sections and surface frost column density at the R2 (left) and R3 (center) flyby dates and times, and prediction (right) for the 2017 Saturn solstice. (Top) comparison of the observed (data binned) and predicted O_2 densities versus position from closest approach along the R2 trajectory (x-axis, in Rhea radii, dashed line: closest approach). (Bottom) same for the R3 flyby trajectory. Asterisks denote model-data comparisons with the same flyby date; all other plots show model projections to different dates. The model assumed a 7.2×10^{21} O_2/s source rate as required to match the observed peak density on both flybys. An O_2 tail is detected on the dayside, consistent with the anticipated greater dayside scale height. Unlike CO_2, the southern latitudes are not yet cold enough to cryopump O_2 from the southern exosphere on the R2 and R3 flybys dates. However, the modeled O_2 frost cap is exhausted between the R2 and R3 flybys, resulting in an anticipated collapse of the global exosphere, consistent with the reduced O_2 detection on R3. Figure from Teolis and Waite [2016].

Waite [2016]. CAPS observed 50% more CO_2^+ pickup ions during the distant 2007 R1.5 flyby than the 2005 R1 flyby, consistent with the expected ramp up of Rhea's exospheric CO_2 densities as the 2009 Saturn system equinox was approaching. See the publication by Teolis and Waite [2016] for a much more detailed description of these (and other) aspects of the analysis.

The source of O_2 and CO_2 at icy satellites

Another spectacular facet of these INMS data and models is that, together, they fully constrain the source rates O_2 and CO_2 to the exospheres of Dione and Rhea. Since both the exospheric density

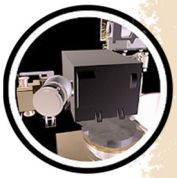

and ionization/escape rates are constrained by INMS and CAPS, the O_2 and CO_2 source rates can be directly estimated by fitting the exospheric model to obtain agreement with the INMS and CAPS data—as Teolis and Waite [2016] have done. These source rates can, in the case of O_2, be compared to known yields of sputtered radiolytic O_2 from water ice measured in the laboratory [Teolis et al. 2017a] to infer the composition and radiation chemistry of the surface material on Rhea and Dione subject to magnetospheric sputtering.

The results of this analysis are remarkable—the O_2 source rates at Dione and Rhea are lower, by approximately two orders of magnitude, than that expected from water ice subject to sputtering by Saturn's magnetospheric plasma [Thomsen et al. 2010]. Teolis and Waite [2016] concluded that, if pure water ice were present on their surfaces, Dione and Rhea ought to have two orders of magnitude more O_2 in their exospheres than observed.

A clue to this puzzle may be the high CO_2 abundance CO_2 (relative to O_2) in the exospheres of Dione and Rhea. Teolis and Waite [2016] proposed that preferential sputtering and removal of radiolytic volatile water products such as O_2 and H_2, and of H_2O itself, may enrich the topmost nanometers of surface material of these moons in carbonaceous sputter-resistant refractory material. As a result, the surfaces of surface regolith grains, composed in bulk of water ice and (likely) small amounts of carbon-bearing organic species, may be coated with a nanometer thick rind of radiolytically processed refractory material, for example, graphitic oxide, which is carbon-rich and yields small amounts of O_2 and CO_2 when sputtered. Recent composition analysis [Desai et al. 2018] of negative pickup ions detected by Cassini CAPS during the Rhea R1 flyby [Teolis et al. 2010] also supports the interpretation of a carbonaceous material on Rhea's surface ice. Thus, by constraining the source rates of O_2 and CO_2 to the exospheres of Dione and Rhea, the findings of Cassini INMS at these two Saturnian icy satellites have provided fundamental clues about the physics of surface sputtering and radiolysis, and of exospheric gas production, at icy bodies generally.

… the findings of Cassini INMS at these two Saturnian icy satellites have provided fundamental clues about the physics of surface sputtering and radiolysis, and of exospheric gas production, at icy bodies generally.

ICY SATELLITES OPEN QUESTIONS

1. O_2 and CO_2 exospheres at Rhea and Dione confirmed by INMS. Is CO_2, like O_2, a sputtered surface radiolysis product?

2. Exospheric seasonal variability, and complex spatial structure, in the exospheres of Dione and Rhea, suggests that diurnal and seasonal adsorption and desorption play a major role in exospheric structure and dynamics. What is the effect of regolith porosity on the exospheric gas adsorption, desorption and diffusion rates on the surfaces of Dione, Rhea, and other solar system icy satellites?

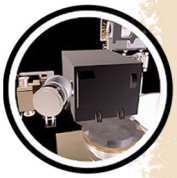

3. Lower than expected O_2 exospheric densities at Dione and Rhea O_2 suggest surface sputtering rates two orders of magnitude less than those measured from water ice in the laboratory. Do surface refractory impurities suppress sputtering from ice satellites, and do carbonaceous refractories contribute radiolytic CO_2 to their atmospheres?

4. Rhea's INMS-measured exospheric densities are insufficient to account for strong magnetic perturbations in Rhea's vicinity, leading to the conclusion that Cassini's Magnetometer measured two new electric current systems never before observed at a plasma absorbing planetary body. These are an Alfvenic current system generated by Rhea's plasma wake, and a thermo-electric flux-tube current system which maintains electric charge balance on Rhea's surface. How widespread are these newly discovered current systems at other plasma absorbing planetary bodies in the solar system?

Magnetosphere–icy satellite Interactions science

Saturn inner magnetosphere highlights

1. INMS measured the individual ions and determined the fractional abundance within the water group (O^+, H_2O^+, OH^+, H_3O^+) and derived those fractions relative to the various parameters (velocity phase space and distance from Saturn).

2. INMS measured neutral water and was able to derive an azimuthal distribution with respect to Enceladus via in situ measurements.

Current systems at Rhea

The constraints provided by INMS on the exospheric gas abundances at Dione and Rhea have been essential to the interpretation of the Magnetometer (MAG) readings from these two moons, resulting in the discovery of two previously unknown current systems at inert plasma absorbing planetary bodies. These discoveries a fantastic demonstration of the power of a diverse instrument payload; in this case Cassini’s INMS, CAPS and MAG; to reveal new and previously unknown fundamental physics operating in planetary systems.

MAG has been a powerful tool for the detection of exospheres in the Saturn system, having been in part responsible for the initial discovery of the Enceladus plume. Exospheric neutral gas disrupts the flow of Saturn’s co-rotating magnetosphere plasma by contributing new pickup ions to magnetosphere, generating electric currents and draped magnetic field perturbations, which can be measured by MAG to infer the presence of an exosphere. In addition to Enceladus, a major effort was made to detect the exospheres of Saturn’s other large icy satellites with the magnetometer, and to compare these data with the in situ measurements from CAPS and INMS. In fact, MAG did detect field-aligned currents at both Dione [Simon et al. 2011] and Rhea [Khurana

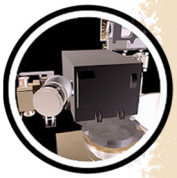

et al. 2017; Santolik et al. 2011; Simon et al. 2012] which appeared, initially, to be consistent with exospheres at these moons as found by INMS. Remarkably, after taking into consideration the rates of pickup ion generation and the electrical conductivity, it became clear that the exospheres measured by CAPS [Tokar et al. 2012] and INMS [Teolis et al. 2010] at Dione at Rhea (Chapter 1.4) were two orders of magnitude too tenuous to account for the Magnetometer data. At Rhea these limits on the exospheric abundances from INMS spurred a fundamental new re-interpretation of the MAG data which, together with new modeling approaches, resulted in the discovery of two new current systems. In the next few paragraphs we briefly summarize these current systems at Rhea, but we refer the reader to papers by [Khurana et al. 2017; Simon et al. 2012; Teolis et al. 2014] for a much more detailed analysis.

The first current system, detected by MAG in Rhea's plasma wake, results from the combination of ion kinetic effects in a hot plasma, and relative motion between the plasma and an inert plasma absorbing body like Rhea. As the wake is refilled with plasma in the downstream co-rotation flow [Roussos et al. 2008], the plasma pressure gradient directed back toward Rhea results in diamagnetic current closure across the wake and perpendicular to the co-rotation flow. The pressure gradient exerts a force directed towards Rhea and mimics a real exosphere by generating a field-aligned Alfvénic current system, which extracts momentum from the co-rotating plasma outside the wake and transfers it to the wake. The Alfvén wings from the wake [Khurana et al. 2017] produce flow-directed magnetic field perturbations north and south of Rhea's equatorial plane, detected by MAG at the locations of R2 and R3 and also during two distant (102 R_H and 54 R_H away from Rhea on June 3 and October 17, 2010 [Khurana et al. 2012] downstream flybys. However, MAG also found indications of a second field aligned current system in Rhea's flux tube which, remarkably, is not generated by Rhea's motion relative to the plasma. Evidence for this current system comes from sharp magnetic field perturbations detected during Cassini's R2 and R3 flybys through Rhea's northern and southern flux tubes [Teolis et al. 2014]. The perturbations point in opposite directions on opposite sides of the flux tube, indicating a field twisting about the flux tube, consistent with a wire of flux tube current flowing away, north and south, from Rhea [Santolik et al. 2011; Simon et al. 2012]. The small ~100 km thickness of these field perturbations, much less than the ~500 km ion inertial length, makes them too small to be Alfvénic.

This current system, investigated by [Teolis et al. 2014], results from the requirement to balance ion and electron currents at Rhea's non-conductive surface, and the difference of gyroradius between the positive (ion) and negative (electron) charge carriers. The ions which (owing to their larger gyroradius) discharge into the plasma absorber's surface from all directions are balanced by the electrons, which are constrained to flow along the magnetic field lines. More magnetic field lines connect to the planetary equator due to the oblique angle and, therefore, the electron current is most intense at the edge of the flux tube. The resulting magnetic field perturbation circles about the flux tube and is maximal at the edges, as observed by the Cassini spacecraft. A fundamental property of this flux tube current system is its proportionality only to the ion flux into Rhea, i.e., the plasma density times the ion thermal speed, and its independence of the motion of the moon's conductive atmosphere through the magnetosphere. This spectacular, albeit unexpected outcome of Cassini's magnetic field data at Rhea, would not have been possible

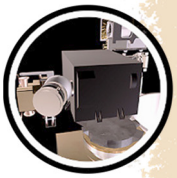

without the exospheric abundance limits provided by Cassini CAPS [Tokar et al. 2012] and INMS [Teolis and Waite 2016].

Inner magnetosphere science

INMS has extracted the water-group ion fractions from OSI measurements in Saturn's inner magnetosphere. These fractions are sensitive probes of the source, transport, and loss mechanisms that govern Saturn's magnetosphere. INMS samples only a small portion of velocity space at a time (Figure INMS-37), which enables investigation of the distributions within velocity space but also limits sensitivity and complicates the separation of various factors that affect the relative ion fractions. Densities and count rates can be low, sometimes requiring the sum of 10,000 IPs for a two-sigma result. Figure INMS-38 shows that ion fractions depend on distance from the orbit of Enceladus. Models show that the water-group fractions depend most strongly on the local fraction of neutrals. In contrast to CAPS results, INMS data show H_3O^+ fractions less than 0.1 except for measurements taken directly in the plumes. These fractions are now being used to calibration ion and neutral models of Saturn's magnetosphere.

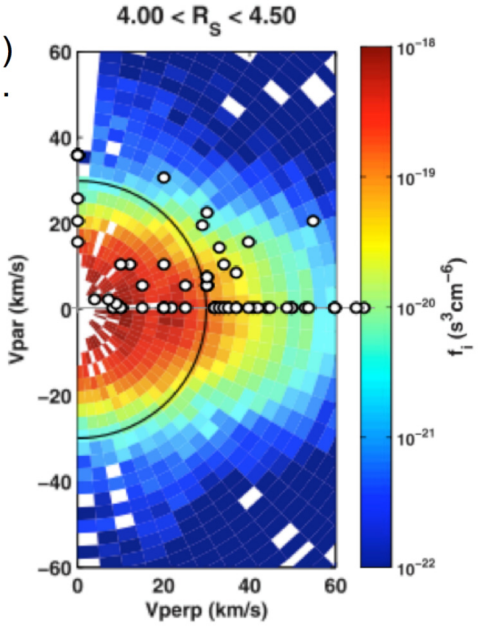

Figure INMS-37. INMS samples only a small portion of velocity space at a time. The *small white circles*, displayed on the CAPS distribution of ion density in velocity space [Tokar et al. 2008], show the location of the INMS measurements of water-group fractions. Although coverage is sparse, the INMS measurements take spot samples of a wide region of velocity space.

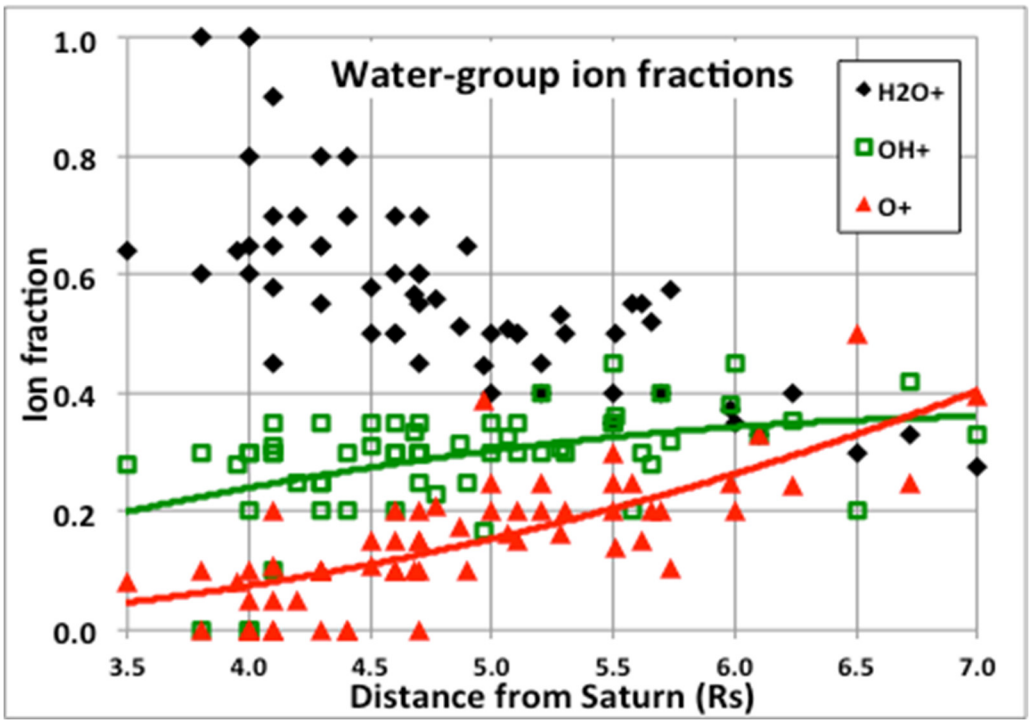

Figure INMS-38. The fraction of water-group ions plotted as a function of distance from Saturn. INMS finds that the highest fraction of H_3O^+ is near 4 R_S, as expected, as that is the orbit of Enceladus, the source of the neutral water that becomes the plasma.

Neutrals in Saturn's inner magnetosphere

In 2008, the Cassini INMS investigation made in situ measurements of neutral species near Saturn's equatorial plane within 0.5 Saturn radii (R_S) of the orbit of Enceladus. After removing the large background and modeling to interpret instrumental effects, the data provide constraints on the neutral distribution and composition. These data show an azimuthal asymmetry in the neutral densities (Figure INMS-39) and provide measurements used to compare simulations of neutral H_2O emitted from Enceladus (Figure INMS-40). Far from Enceladus, the neutral water densities, at a few times 10^3 molecules/cm^3, are near the detection limit of INMS. Near Enceladus, but outside of the plumes and north of the equatorial plane, the INMS detects particles within 5,000 km of Enceladus, with the density increasing to approximately 10^5 molecules/cm^3 at the equatorial plane.

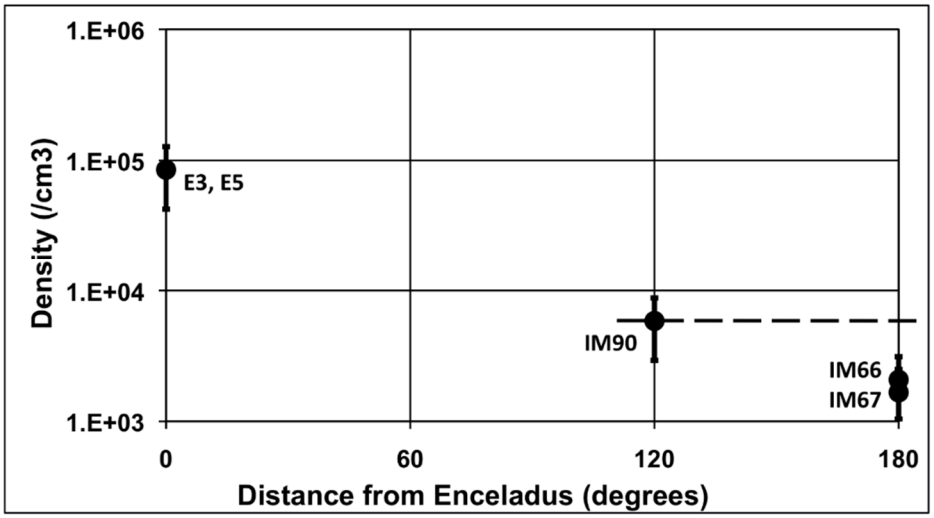

Figure INMS-39. Average densities near 4 R_S show the dependence on azimuth. The densities at 0 (near Enceladus) are north of Enceladus, outside the plumes. The difference between the measurements at 0° and 120° are much larger than the uncertainties. The measurements at 180° are at 4.5 R_S. The data at 180° are a factor of three below the data at 120°. The displayed *error bars* are ±50%.

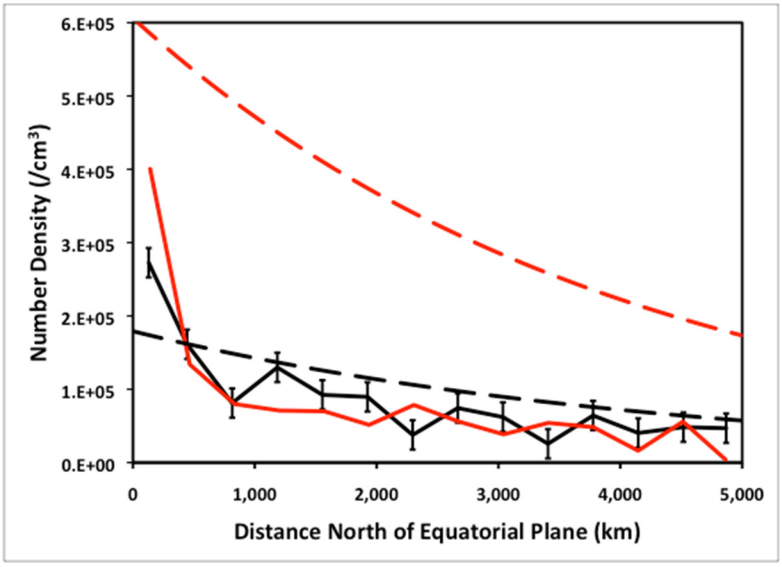

Figure INMS-40. Neutral cloud density north of Enceladus, before close approach and outside of proximal influence of the south-pole plumes. The solid lines are the INMS data. The *dashed lines* are simulations using the charge-exchange model of the neutral cloud [Smith et al. 2010]. The E5 simulation is based on the source rate derived from modeling the E5 plumes, and the E3 simulation is based on the source rate derived from modeling the E3 plumes. The E3 and E5 INMS densities are similar to each other and to the E3 simulation. E5 error bars (not shown to reduce clutter) are the same size as E3 error bars.

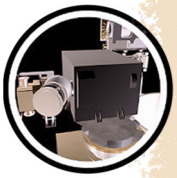

28 u neutrals in Saturn's inner magnetosphere

INMS observes inner-magnetosphere neutrals with a mass of 28 u that have unexpectedly high densities, no apparent source, and no clear molecular identification. With densities as high as 30% of the neutral-water density, the candidate molecules, N_2 and CO, should be abundant in the Enceladus emissions, but multiple observational approaches show that neither molecule comprises more than 3% of the H_2O density (Figure INMS-41).

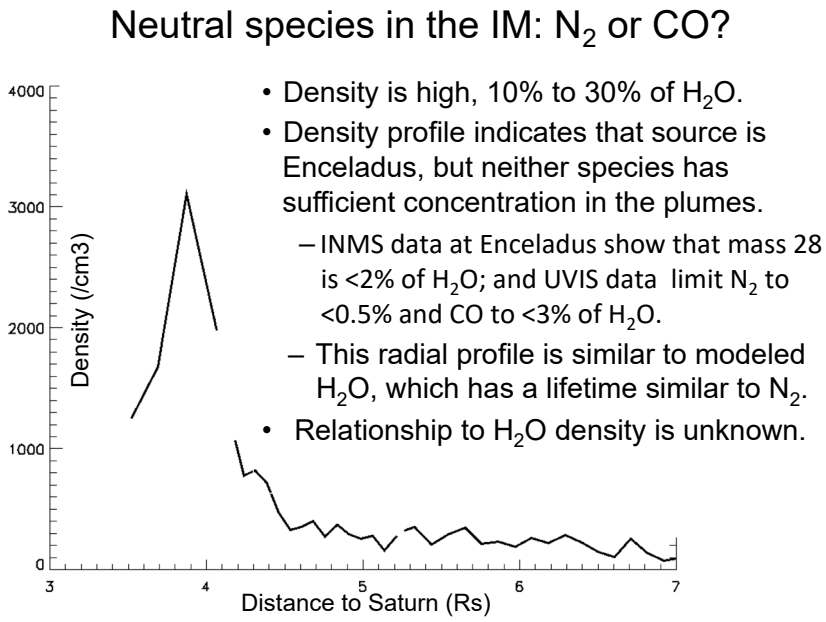

Figure INMS-41. Mass 28 u mystery compound in the inner magnetosphere.

SATURN INNER MAGNETOSPHERE OPEN QUESTIONS

1. What explains the mass 28 signal?

F-ring Science

F-ring observations: primary neutrals

INMS found two neutral species with remarkable consistency during the F-ring passes: H_2 and a species at 28 u (Figure INMS-42). The scale height, or the half-width-half-max of the INMS counts, for both of these species was approximately 3,000 km, or 0.05 Saturn radii (R_S). This parameter and the total counts were nearly identical in each pass.

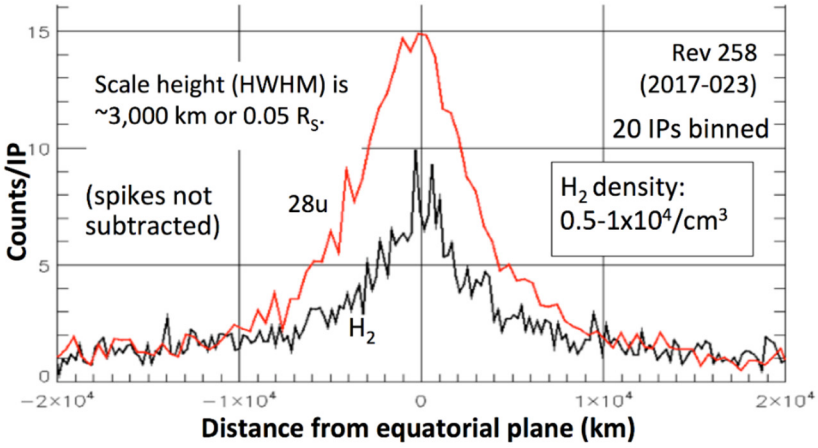

Figure INMS-42. The major neutrals measured by INMS in the F-ring. Twenty measurements (integration periods or IPs) were binned for this plot.

Although H_2 was expected in this area of the rings, models and Earth-based observations predicted a larger scale height for H_2 from Saturn's atmosphere, and the narrow distribution of the observed H_2 suggests that it is more liked to originate in the rings. The lack of variability indicates a stable ring atmosphere. Atomic hydrogen is not measured by INMS due to instrumental noise at 1 u.

A complication for INMS neutral observations is the high speed of Cassini relative to the ring particles. At 20 km/s, the molecules carry 2.1 eV per nucleon, which is sufficient energy to cause some dissociation in the INMS antechamber, particularly for larger molecules. If a molecule dissociates, only volatile products are measured. Without considering dissociation, the density of the H_2 is 0.5-1 × 10^4 cm^{-3}.

F-ring observations: other neutrals and 28 u

CH_4 (16 u) and CO_2 (44 u) are the only other measured species. They both have a count rate that is approximately 20% of the H_2 rate. CH_4 is confirmed by the presence of 15 u counts at the correct electron impact dissociative ionization ratio, the amount produced from CH_4 in the INMS ionization chamber. CO_2 is not a common dissociation product and may be a native species, it exists on the surface of several icy moons. Count rates for both CH_4 and CO_2 are depressed due to dissociation and they may be more abundant than indicated by the measurements. There are small amounts of 26 u and 27 u, which are expected products from ionization of C_2H_4, one possibility for the 28 u measurements. However, the count rates for these two cracking products are lower than expected if the entire 28 u signal was produced by C_2H_4. This deficiency implies that another species such as CO may contribute to the 28 u signal.

Several expected neutral species are missing, most notably H_2O and O_2. Since water is temporarily adsorbed onto the walls of the INMS inlet, H_2O counts are suppressed and delayed. Combined with the radiation background, which increases after passing through the equatorial plane, INMS would not detect low densities of H_2O particularly after some loss due to high-velocity

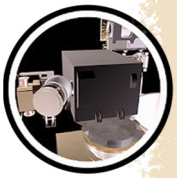

dissociation. Models show that O_2 could be abundant, but that densities decrease a factor of 1,000 approaching the location of Cassini's trajectory, moreover, much of the O_2 would be lost due to dissociation.

F-ring observations: ions

INMS observed only water-group ions in the F-ring. Unlike the neutrals, the ion densities were not symmetrical with respect to the equatorial plane, varying in both total density and the relative fractions within the water group (Figure INMS-43). The predominance of O^+ versus the other water-group ions indicates that there may be a source of O^+ other than as a byproduct of water. One possibility is that CH_4^+ contributes a fraction of the 16 u ions.

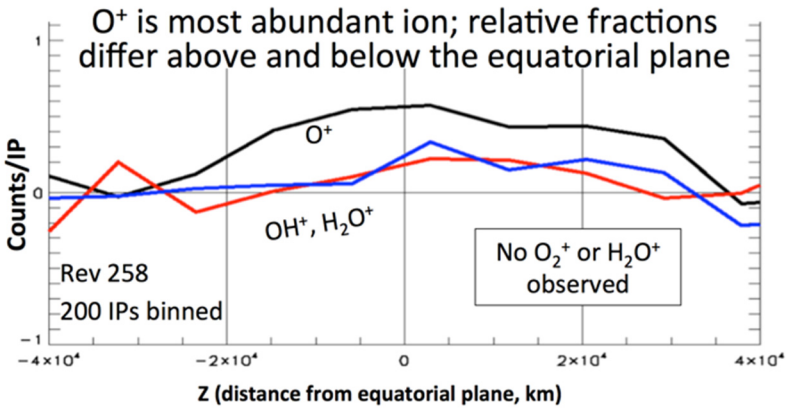

Figure INMS-43. Distribution of water-group ions south and north of the equatorial plane. O+ comprises a higher fraction of the ions in the south.

The velocity distribution of the ions (Figure INMS-44) shows that the ions are cold, with a mean velocity below the pickup velocity of 8 km/s, corresponding to a temperature of approximately 3 eV. These results are consistent with analyses and modeling of data from the CAPS.

The lack of O_2^+ in the F-ring, which INMS previously observed during Cassini's insertion into orbit about Saturn, is likely due to the INMS energy limit at the F-ring speeds—O_2^+ exceeds the INMS energy limit for ions. The lack of H_2^+ is surprising and not yet explained. As with neutrals, noise prevents INMS measurement of H^+ at 1 u.

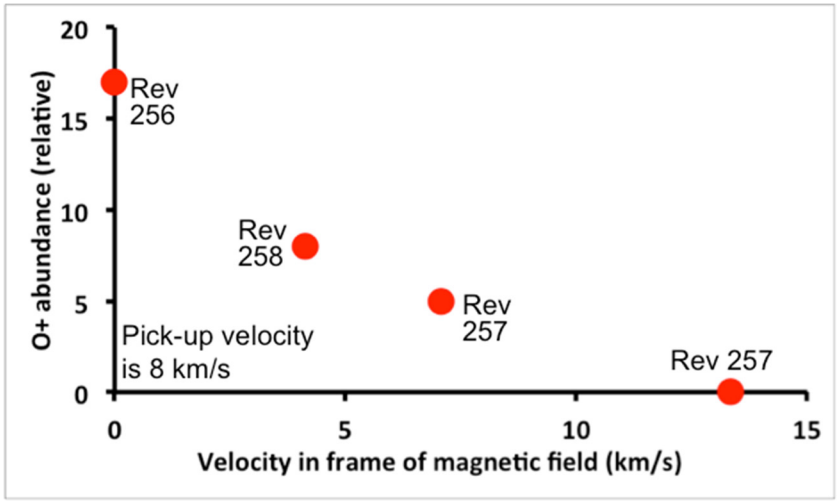

Figure INMS-44. The distribution of ions in the rest frame of the magnetic field. Ions are concentrated near the core, as expected for cold ions.

Saturn Ionosphere, Atmosphere, and Atmosphere-Ring Interaction Science

Saturn Upper Atmosphere Major Findings (Neutral Thermosphere):

- INMS made the first in situ measurements of Saturn's atmosphere, and made surprising discoveries of several species of high mass neutrals, e.g., CH_4, CO, CO_2.
- The INMS made the first in situ characterization of the thermal structure in the upper atmosphere of Saturn, indirectly through its measurements of the H_2 densities.
- Helium has been measured for the first time in Saturn's upper atmosphere, providing constraints on possible deep-atmosphere mixing ratios of Helium and whether or not Saturn has a solar-like composition or something else.

During the Cassini Grand Finale, the INMS made an unprecedented series of measurements of Saturn's upper atmosphere during the Proximal Orbit Phase, sampling from ~3500–1370 km altitude above the one bar pressure level. Prior to these orbits, it was anticipated that Saturn's upper atmosphere consisted primarily of H, H_2, with trace amounts of H_2O and He. However, the INMS measurements revealed an atmosphere with an unexpectedly rich composition, containing significant amounts of organics spanning the entire mass range sampled by INMS, shown in Figure INMS-45. These results were completely unanticipated and they have effectively turned our understanding of the high altitude thermosphere-ionosphere chemistry on its head [Waite et al. 2018; Perry et al. 2018; Yelle et al. 2018].

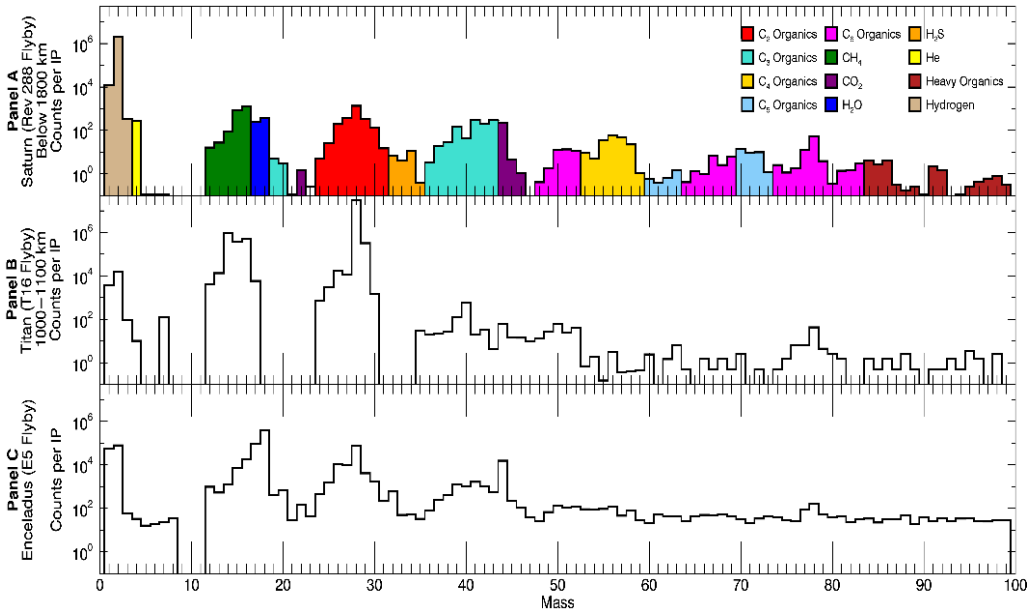

Figure INMS-45. INMS mass spectra from the Grand Finale orbits at Saturn (*Panel A*), compared with those of Titan (*Panel B*), and Enceladus (*Panel C*). Horizontal axis is in units of mass per charge. See Waite et al. [2018] for details.

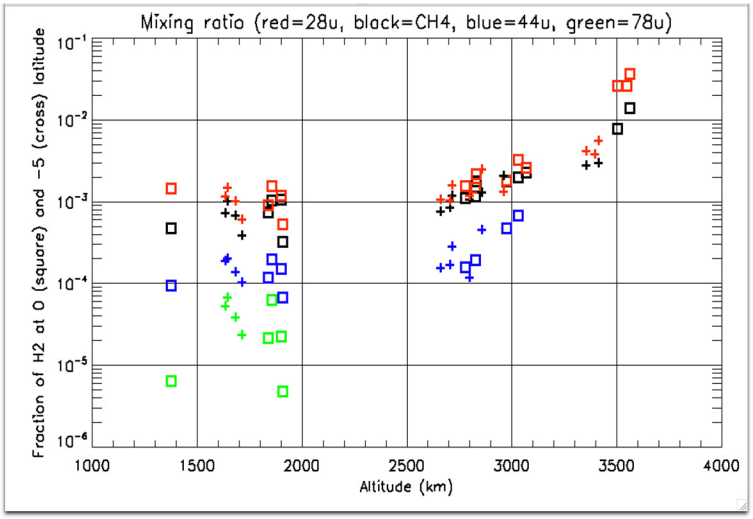

Figure INMS-46. Volume mixing ratios (*vertical axis*) of the heavy species identified by INMS in the Saturnian upper atmosphere as a function of altitude above the 1-bar pressure level (*horizontal axis*).

In particular, INMS has identified methane (CH_4) as a significant component of the upper atmosphere of Saturn above 1370 km. As shown in Figure INMS-46, INMS has found significant amounts of methane that reach up to ~10% of the composition near 3500 km altitude above the 1-bar pressure level. Additional heavy species (masses 28 u, 44 u, and 78 u) have also been

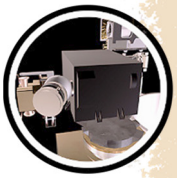

identified. All of these species can potentially play major photochemical roles in the atmosphere of Saturn [cf. Moses and Bass 2000; Kim et al. 2014].

Using a combination of National Institute of Standards and Technology (NIST) data and calibration data collected using the refurbished engineering unit, preliminary fits to spectra at altitudes between 1700 and 1800 km for three representative orbits were made to identify contributing species in the measured mass spectra (for example, Figure INMS-45). In general, the spectrum below ~70 u can be fit by a combination of species that is dominated by hydrocarbons. Ammonia (NH_3) is detected at 17 u. Other N-bearing species are neither excluded nor required by the spectra. The same is true for O-bearing organics. Inclusion of S species, especially H_2S, improves the fit of the spectrum. However, of the non-H_2, non-He material, less than 1 mol percent is contributed by S-bearing species. We estimate that between 30 and 50 mol percent of the non-H_2, non-He material measured by INMS is comprised of organics other than methane, which may constitute an additional 20 to 35 mol percent. C_4 species, including butane (C_4H_{10}) at 58 u, are particularly abundant compared to other hydrocarbons. Above 70 u, the spectra are consistent with contributions from heavier aromatic species, including species such as naphthalene ($C_{10}H_8$, 128 amu) with primary peaks that are beyond the range of INMS.

Other Cassini instruments, including the Charge-Energy-Mass Spectrometer (CHEMS) from the MIMI, reported detections of heavy (8,000 to 40,000 amu) particles during the Grand Finale orbits [Mitchell et al. 2018]. To understand the relationship of these particles to INMS data, we compared the total amount of material detected by INMS to the particle sizes observed by MIMI [Perry et al. 2018]. The results suggest that INMS may have mainly sampled smaller particles that were dominated by volatile and organic material with very little contribution from refractory mineral phases. The altitude-density profiles of these particles indicate very low densities, likely on the order of 0.1 g/cm^3 or less. These densities may be consistent with the densities of interplanetary dust particles from small bodies [Rietmeijer 1993]. Some masses, including 15 u (mainly from CH_4), 28 u (possibly N_2 or CO) and 17 u (mainly NH_3), have altitude-density profiles that are consistent with molecular radii. Other masses, including 58 u (possibly butane, C_4H_{10}) and 78 u (possibly benzene, C_6H_6), have profiles that suggest larger radii, on the order of nanometers or tens of nanometers.

In addition to the heavy species in the upper atmosphere of Saturn, INMS has also made the first in situ measurements of H_2, He, and H-D in the atmosphere of Saturn (shown in Figure INMS-47). Molecular hydrogen (H_2) is the dominant species in the thermosphere, and its density scale height reveals the expected background temperature of Saturn's upper atmosphere. Thus, measurements of H_2 reveal information about the thermal state of Saturn's upper atmosphere. Prior to the INMS measurements, only remote sensing observations were possible [cf. Koskinen et al. 2015; Vervack and Moses 2015], which provide temperatures through inversion techniques. The measurements in **SIA3**, however, provide the first-ever direct sampling of the Saturn atmosphere [Waite et al., 2018; Yelle et al. 2018], allowing us to infer thermal structure from these measurements using models of the atmosphere, such as Müller-Wodarg et al. [2006b, 2012].

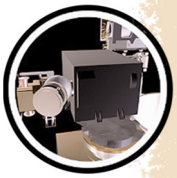

Finally, there has been considerable uncertainty about the amount of Helium in the Saturnian atmosphere [Ben-Jaffel and Abbes 2015]. He abundances are key to determining the most likely formation scenarios for Saturn's atmosphere. Currently, it has been suggested that Saturn would be depleted in Helium relative to Jupiter (~13.5% volume mixing ratio) or the protosolar value (~15.6%) due to Helium raining out in the lower atmosphere. The measurements provided by INMS, combined with diffusive modeling, can lead to constraints on the Helium content in the lower atmosphere providing a missing component in our understanding of planetary evolution.

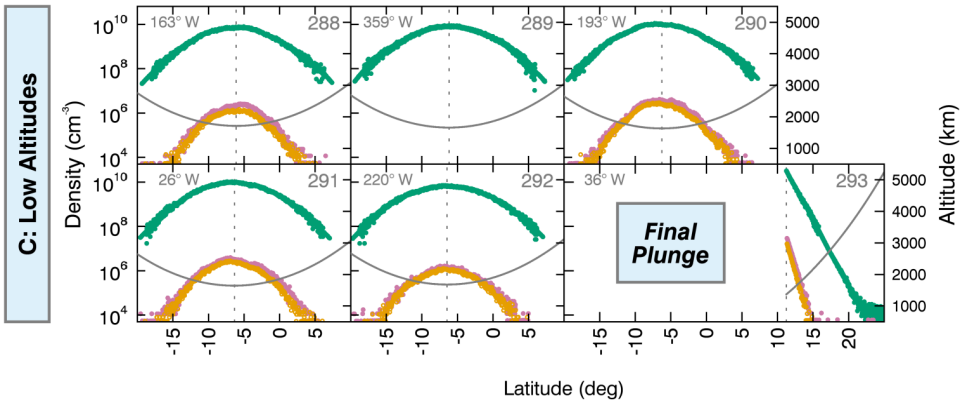

Figure INMS-47. INMS measurements of H_2 (green), He (red), and Mass 3 u (orange) as a function of altitude (*right-hand axis*) and latitude (*horizontal axis*).

Saturn Upper Atmosphere Major Findings (Charged Gases, i.e, the Ionosphere):

- The INMS made the first in situ measurements of the ion composition of the ionosphere of a gas giant planet (i.e., Saturn), allowing the first determination of ion mixing ratios and number densities as well as their temporal variabilities.
- INMS measurements of the minor ion (H_2^+) represent a strong constraint on local ion production rates providing a check on outer planet projections of solar irradiances, including evidence for ring shadowing of the ionosphere.
- Combined with RPWS and MIMI measurements, INMS in situ data paint a clear picture of Saturn's equatorial ionosphere being dominated by heavy molecular ions that result from ring-derived material.

Prior to the Cassini Grand Finale, observations of Saturn's ionosphere were limited to altitude profiles of electron density (the presumed sum of the ion densities) at dawn or dusk, periods of rapid change in an ionosphere. Trace emissions from an expected major ion (H_3^+) were also detected, but column-integrated densities could only be derived at auroral latitudes. Therefore, ion densities throughout the majority of Saturn's ionosphere were based solely on model comparisons with radio occultation measurements, for example, Moses and Bass [2000]; Moore et al. [2006, 2010]. In situ measurements by INMS provided key constraints on the expected major ion species, H^+ and H_3^+ [Waite et al. 2018; Cravens et al. 2018; Moore et al. 2018], finally providing closure on a decades-long debate regarding the dominant chemical losses of H^+, for example, Connerney and Waite [1984].

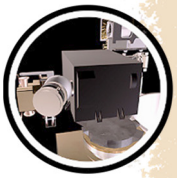

In addition, INMS was able to measure the expected minor ion species H_2^+ and He^+. The chemistry of these ions is relatively straightforward, and the extremely short chemical lifetime of H_2^+ makes it an ideal tracer of the in situ ion production rate. Therefore, H_2^+ densities from INMS measurements can be used to gauge the accuracy of commonly used projections of solar irradiances at Saturn. These projections rely on Earth-based data, and the assumption of a relatively stable solar irradiance over a period of days. Comparisons between measured H_2^+ with modeled H_2^+ based on projected solar irradiances find a ~50% discrepancy, implying that future outer planet modeling will require better estimates of the solar irradiance. A drop-off in the H_2^+ density (i.e., ionization rate) observed by INMS near 15° S latitude is consistent with shadowing by the B-ring [Waite et al. 2018; Cravens et al. 2018].

Finally, Cassini's high speed near periapsis during the Grand Finale (~32 km s^{-1}), meant that INMS could only sample ions with masses up to 7 u. The sums of the light ion densities measured by INMS were found to be an excellent match with the electron densities from RPWS, for example, Persoon et al. [2019], at high altitudes (> ~2200 km), implying that Saturn's high-altitude ionosphere was charge-neutral and dominated by H^+ with minor contributions from H_3^+, as expected (Figure INMS-48). However, at low altitudes the total ion densities from INMS differed significantly from the electron densities. This massive discrepancy was interpreted as a signature of an ionosphere dominated by heavy (> 7 u) ions, which would be entirely consistent with the expected ion chemistry to follow from the ring-derived influx of complex neutrals measured by INMS (Figure INMS-46). Detailed model-data comparisons indicated that in the main ionosphere, a complex, and heavy, neutral species was needed to react with H^+ and H_3^+, and thus reduce the model densities of these light species to measured values [Cravens et al. 2018; Moore et al. 2018]. The neutral mixing ratios required were consistent with the values measured by the closed source and described earlier. The ion species produced by these reactions were suggested to be those needed to fill the ion-electron density gap evident in Figure INMS-48.

The ionosphere was demonstrated to be chemically controlled at lower altitudes where the heavy ions are dominant [Cravens et al. 2018; Moore et al. 2018], but at higher altitudes, where H^+ dominates the measured ion composition, transport processes should become important. During the relatively high altitude proximal orbit 287, the INMS open source was operated in a special energy scan mode and some limited information on proton flow speeds was obtained [Cravens et al. 2018]. Proton speeds of a couple km/s were detected in the Northern Hemisphere at latitudes connecting to the B-ring shadow in the Southern Hemisphere.

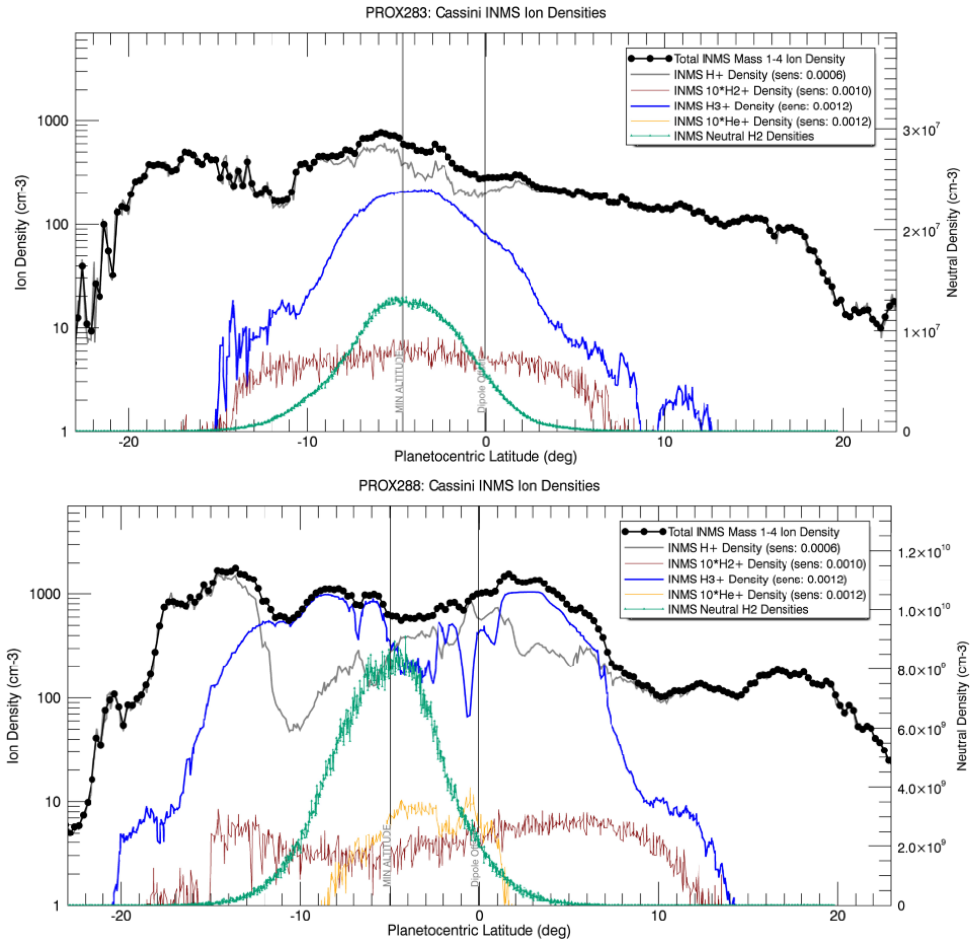

Figure INMS-48. INMS measurements of H_2 (*green*), H^+ (*gray*), H_2^+ (*red*, multiplied by 10), H_3^+ (*blue*), He^+ (*gold*, multiplied by 10), and total light ion density (1–4 u, *black*) as a function of planetocentric latitude (*horizontal axis*). Ion measurements were taken for four proximal orbits, 283, 287, 288, and 292, though only one representative high altitude (283, top) and low altitude (288, bottom) orbit is presented here.

Saturn proximals open questions

1. INMS made the first in situ measurements of He and HD in Saturn's atmosphere. What are the implications of the upper atmosphere He measurements for the abundance of He in the bulk atmosphere? How is the measured HD affected by ring inflow?

2. INMS measured the temperature structure of Saturn's upper atmosphere with significantly higher precision and altitude resolution than is possible with remote sensing techniques. The energy balance in Saturn's upper atmosphere remains an open question.

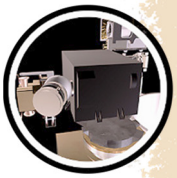

3. INMS measurements revealed significant influx of material from the rings to the atmosphere.

    a. What causes this inflow, how it relates to ring erosion processes and magnetospheric processes, as well as the implications for atmospheric chemistry remain open questions.

    b. Is the ring influx uniformly distributed about Saturn?

    c. Is the ring influx constant or is there a time dependence?

    d. Does the ring influx respond to magnetospheric processes or solar wind drivers?

    e. How long has the ring influx been taking place? Is the time the same for all species (methane, nanograins, etc.)?

    f. What are the dynamics in equatorial region and how are they affected by the Joule heating measured by MAG??

    g. Presence of negative ions in the equatorial region (and auroral regions too)?

    h. What is the balance between chemistry and transport operating in the low-latitude Saturnian ionosphere?

Open Questions for Saturn System Science

The open questions are found under each subtopic. The big open question for the Saturn system—Is there life in the ocean of Enceladus?

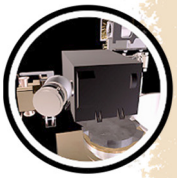

ACRONYMS

Note: For a complete list of Acronyms, refer to Cassini Acronyms – Attachment A.

AACS	Attitude and Articulation Control System
AO	Announcement of Opportunity
CAPS	Cassini Plasma Spectrometer
CDA	cosmic dust analyzer
CHEMS	Charge-Energy-Mass Spectrometer
CIRS	Composite Infrared Spectrometer
CS	closed source
CSM	Cassini Solstice Mission
CSN	Closed Source Neutral
Da	Daltons
ELS	Electron Spectrometer
ENA	energetic neutral atom
EUV	extreme ultraviolet
GCM	General Circulation Model
IBS	Ion Beam Spectrometer
IP	integration period
ISE	Ion Source Enclosure
ISS	Imaging Science Subsystem
LP	Langmuir probe
MAG	Magnetometer
MAPS	Magnetospheres and Plasma Science
MHD	magneto-hydrodynamic
MIMI	Magnetospheric Imaging Instrument
NAV	Navigation
NIST	National Institute of Standards and Technology
OS	open source
OSI	open source ion
OSNB	open source neutral beam
OSNT	open source neutral thermal
PA	proton affinities
PAH	polycyclic aromatic hydrocarbon
QMA	quadrupole mass analyzer
RPWS	Radio and Plasma Wave Science
TAMWG	Titan Atmospheric Working Group
UVIS	Ultraviolet Imaging Spectrograph
UVS	Ultraviolet Spectrometer
VIMS	Visual and Infrared Imaging Spectrometer

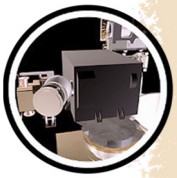

REFERENCES

Disclaimer: The partial list of references below correspond with in-text references indicated in this report. For all other Cassini references, refer to Attachment B – References & Bibliographies; Attachment C – Cassini Science Bibliographies; the sections entitled References contributed by individual Cassini instrument and discipline teams located in Volume 1 Sections 3.1 and 3.2 Science Results; and other resources outside of the Cassini Final Mission Report.

Ågren, K., J. E. Wahlund. R. Modolo, D. Lummerzheim, M. Galand, I. Müller-Wodarg, P. Canu, W. S. Kurth, T. E. Cravens, R. V. Yelle, J. H. Waite Jr., A. J. Coates, G. R. Lewis, D. T. Young, C. Bertucci, M. K. Dougherty, (2007), On magnetospheric electron impact ionisation and dynamics in Titan's ram-side & polar ionosphere-a Cassini case study, Annales Geophysicae, 25.

Anicich, V. G. and M. J. McEwan, (1997), Ion-molecular chemistry in Titan's ionosphere, Planetary Space Science, 45, 897–921, doi: 10.1016/S0032-00633(97)00053-6.

Bauschlicher, C. W., A. Ricca, M. Rosi, (2002), Mechanisms for the growth of polycyclic aromatic hydrocarbon (PAH) cations, Chemical Physics Letters, vol. 355, issues 1–2, pp. 159–163.

Bauschlicher Jr., C. and A. Ricca, (2000), Mechanisms for polycyclic aromatic hydrocarbon (PAH) growth, Chemical Physics Letters, vol. 326, Issues 3–4, 283–287.

Bell, J. M., J. H. Waite, J. H. Westlake, S. W. Bougher, A. J. Ridley, R. Perryman, K. Mandt, (2014), Developing a self-consistent description of Titan's upper atmosphere without hydrodynamic escape, Journal of Geophysical Research, 119, 4957–4972.

Bell, J. M., J. Westlake, J. H. Waite Jr., (2011a), Simulating the time-dependent response of Titan's upper atmosphere to periods of magnetospheric forcing, Geophysical Research Letters, 38, L06202.

Bell, J., S. W. Bougher, J. H. Waite Jr., A. J. Ridley, B. Magee, K. Mandt, J. Westlake, A. D. DeJong, A. Bar-Nun, R. Jacovi, G. Toth, V. de la Haye, (2011b), Simulating the one-dimensional structure of Titan's upper atmosphere, Part III: Mechanisms determining methane escape, Journal of Geophysical Research, 116, E11002.

Bell, J., S. W. Bougher, J. H. Waite Jr., A .J. Ridley, B. Magee, K. Mandt, J. Westlake, A. D. DeJong, A. Bar-Nun, R. Jacovi, G. Toth, V. de la Haye, (2010a), Simulating the one-dimensional structure of Titan's upper atmosphere, Part I: Formulation of the Titan global ionosphere-thermosphere model and benchmark simulations, Journal of Geophysical Research, 115, E12002.

Bell, J., S. W. Bougher, J. H. Waite Jr., A.J. Ridley, B. Magee, K. Mandt, J. Westlake, A. D. DeJong, V. de la Haye, D. Gell, G. Fletcher, A. Bar-Nun, R. Jacovi, G. Toth, (2010b), Simulating the one-dimensional structure of Titan's upper atmosphere, Part II: Alternative scenarios for methane escape, Journal of Geophysical Research, 115, E12018.

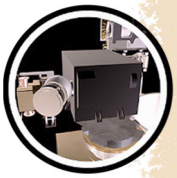

Ben-Jaffel, L. and I. Abbes, (2015), Helium abundance in giant planets and the local interstellar medium, Journal of Physics: Conference Series, 577, doi: 10.1088/1742-6596/577/1/012003.

Bird, M. K., R. Dutta-Roy, S. W. Asmar, T.A. Rebold, (1997), Detection of Titan's ionosphere from Voyager 1 radio occultation observations, Icarus, vol. 130, issue 2, pp. 426—436, doi: 10.1006/icar.1997.5831.

Blanc, M., S. Bolton, J. Bradley, M. Burton, T. E. Cravens, I. Dandouras, M. K. Dougherty, M. C. Festou, J. Feynman, R. E. Johnson, T. G. Gombosi, W. S. Kurth, P. C. Liewer, B. H. Mauk, S. Maurice, D. Mitchell, F. M. Neubauer, J. D. Richardson, D. E. Shemansky, E. C. Sittler, B. T. Tsurutani, P. Zarka, L. W. Esposito, E. Grün, D. A. Gurnett, A. J. Kliore, S. M. Krimigis, D. Southwood, J. H. Waite Jr., D. T. Young, (2002), Magnetospheric and plasma science with Cassini-Huygens, Space Science Reviews, 104, 1, 253–346.

Bohme, D. K., (1992), PAH [polycyclic aromatic hydrocarbons] and fullerene ions and ion/molecule reactions in interstellar and circumstellar chemistry, Chemical Reviews, 92 (7), 1487.

Bouquet, A., C. R. Glein, D. Wyrick, J. H. Waite Jr., (2017), Alternative energy: Production of H2 by radiolysis of water in the rocky cores of icy bodies, The Astrophysical Journal Letters, 840, L8, doi:10.3847/2041-8213/aa6d56.

Brecht, S. H., J. G. Luhmann, D. J. Larson, (2000), Simulation of the Saturnian magnetospheric interaction with Titan, Journal of Geophysical Research, vol. 105, issue A6, 13119–13130, doi: 10.1029/1999JA900490.

Carrasco, N., J. Westlake, P. Pernot, J. H. Waite Jr., (2013), Nitrogen in Titan's Atmospheric Aerosol Factory, The Early Evolution of the Atmospheres of Terrestrial Planets, 35, doi: 10.1007/978-1-4614-5191-4_11.

Coates, A. J., A. Wellbrock, G. R. Lewis, G. H. Jones, D. T. Young, F. J. Crary, J. H. Waite, R. E. Johnson, T. W. Hill, E. C. Sittler Jr., (2010), Negative ions at Titan and Enceladus: recent results, Faraday Discussions, 147(1), 293-305, doi: 10.1039/C004700G2010.

Coates, A. J., A. Wellbrock, G. R. Lewis, G. H. Jones, D. T. Young, F. J. Crary, J. H. Waite Jr., (2009), Heavy negative ions in Titan's ionosphere: Altitude and latitude dependence, Planetary and Space Science, 57, 1866–1871.

Coates, A. J., F. J. Crary, G. R. Lewis, D. T. Young, J. H. Waite, Jr., E. C. Sittler Jr., (2007), Discovery of heavy negative ions in Titan's ionosphere, Geophysical Research Letters, 34, L22103, doi: 10.1029/2007GL030978.

Connerney, J. and J. Waite, (1984), New model of Saturn's ionosphere with an influx of water from the rings, Nature, 312, 136–138.

Coustenis, A., J. I. Lunine, J.-P. Lebreton, D. Matson, C. Erd, K. Reh, P. Beauchamp, R. Lorenz, J. H. Waite Jr., C. Sotin, L. Gurvits, M. Hirtzig, (2009), Earth-based support for the Titan Saturn System Mission, Earth, Moon and Planets, 105, 135–142.

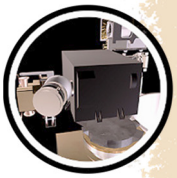

Coustenis, A., S. K. Atreya, T. Balint, R. H. Brown., et al., (2008), TandEM: Titan and Enceladus mission, Experimental Astronomy, 23, issue 3, pp. 893–946, doi: 10.1007/s10686-008-9103-z.

Crary, F. J., B. A. Magee, K. E. Mandt, J. H. Waite, J. Westlake, D. T. Young, (2009), Heavy ions, temperatures and winds in Titan's ionosphere: Combined Cassini CAPS and INMS observations, Planetary and Space Science, 57, 1847–1856.

Cravens, T. E., M. Morooka, A. Renzaglia, L. Moore, J. H. Waite Jr., R. Perryman, et al., (2019). Plasma transport in Saturn's low-latitude ionosphere: Cassini data, Journal of Geophysical Research: Space Physics, 124, 4881–4888, doi: 10.1029/2018JA026344.

Cravens, T. E., L. Moore, J. H. Waite Jr., R. Perryman, M. Perry, J.-E. Wahlund, A. Persoon, W. Kurth, (2018), The ion composition of Saturn's equatorial ionosphere as observed by Cassini. Geophysical Research Letters, doi: 10.1029/2018GL077868.

Cravens, T. E., M. Richard, Y.-J. Ma, C. Bertucci, J. G. Luhmann, S. Ledvina, I. P. Robertson, J.-E. Wahlund, K. Ågren, J. Cui, I. Müller-Wodarg, J. H. Waite, M. Dougherty, J. Bell, D. Ulusen, (2010), Dynamical and Magnetic Field Time Constants for Titan's Ionosphere - Empirical Estimates, Journal of Geophysical Research, 115, A08319.

Cravens, T. E., R. V. Yelle, J.-E. Wahlund, D. E. Shemansky, A. F. Nagy, (2009a), Composition and structure of the ionosphere and thermosphere, In Titan from Cassini-Huygens, Chapter 11, (eds.) R. H. Brown, J. P. Lebreton, J. H. Waite, Springer, Dordrecht, pp. 259–295, doi: 10.1007/978-1-4020-9215-2_11.

Cravens, T. E., I. P. Robertson, J. H. Waite Jr., R. V. Yelle, V. Vuitton, A. J. Coates, J.-E. Wahlund, K. Ågren, M. S. Richard, V. De La Haye, A. Wellbrock, F. N. Neubauer, (2009b), Model-data comparisons for Titan's nightside ionosphere, Icarus, 199, 174–188, doi: 10.1016/j.icarus.2008.09.005.

Cravens, T. E., R. L. McNutt Jr., J. H. Waite Jr., I. P. Robertson, J. G. Luhmann, R. V. Yelle, W. Kasprzak, W.-H. Ip, (2009c), Plume ionosphere of Enceladus as seen by the Cassini Ion and Neutral Mass Spectrometer, Geophysical Research Letters, 36, L08106, doi: 10.1029/2009GL037811.

Cravens, T. E., I. P. Robertson, S. A. Ledvina, D. Mitchell, S. M. Krimigis, J. H. Waite Jr., (2008a), Energetic ion precipitation at Titan, Geophys. Res. Lett., 35, L03103, doi: 10.1029/2007GL032451.

Cravens, T. E., I. P. Robertson, J. H. Waite Jr., R. V. Yelle, V. Vuitton, A. J. Coates, J.-E. Wahlund, K. Ågren, M. S. Richard, V. De La Haye, A. Wellbrock, F. N. Neubauer, (2008b), Model-data comparisons for Titan’s nightside ionosphere, Icarus, doi: 10.1016/j.icarus.2008.09.005.

Cravens, T. E., I. P. Robertson, J. H. Waite Jr., R. V. Yelle, W. T. Kasprzak, C. N. Keller, S. A. Ledvina, H. B. Niemann, J. G. Luhmann, R. L. McNutt, W.-H. Ip, V. De La Haye, I. Müller-Wodarg, J.-E. Wahlund, V. G. Anicich, V. Vuitton, (2006), The composition of Titan's ionosphere, Geophysical Research Letters, 33, L07105.

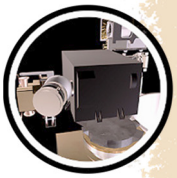

Cravens, T. E., I. P. Robertson, J. Clark, J.-E. Wahlund, J. H. Waite Jr., S. A. Ledvina, H. B. Niemann, R. V. Yelle, W. T. Kasprzak, J. G. Luhmann, R. L. McNutt, W.-H. Ip, V. De La Haye, I. Müller-Wodarg, D. T. Young, A. J. Coates, (2005), Titan's ionosphere: Model comparisons with Cassini Ta data, Geophysical Research Letters, vol. 32, issue 12, doi: 10.1029/2005GL023249.

Cravens, T. E., J. Vann, J. Clark, J. Wu, C. N. Keller, C. Brull, (2004), The ionosphere of Titan: An updated theoretical model, Advances in Space Research, 33, 212.

Cravens, T. E., C. N. Keller, B. Ray, (1997), Photochemical sources of non-thermal neutrals for the exosphere of Titan, Planetary and Space Science, 45, 889.

Cui, J., R. V. Yelle, T. Li, D. S. Snowden, I. C. F. Müller-Wodarg, (2014), Density waves in Titan's upper atmosphere, Journal of Geophysical Research, 119, 490–518, doi: 10.1001/2013JA019113.

Cui, J., Y. Lian, I. C. F. Müller-Wodarg, (2013), Compositional effects in Titan's thermospheric gravity waves, Geophysical Research Letters, 40, 43–47, doi: 10.1029/2012GL054621.

Cui, J., R. V. Yelle, D. F. Strobel, I. C. F. Müller-Wodarg, D. S. Snowden, T. T. Koskinen, M. Galand, (2012), The CH4 structure in Titan's upper atmosphere revisited, Journal of Geophysical Research, 117, E11006, doi: 10.1029/2012JE004222.

Cui, J., R. V. Yelle, I. C. F. Müller-Wodarg, P. P. Lavvas, M. Galand, (2011), The implications of the H2 variability in Titan's exosphere, Journal of Geophysical Research, 116, A11324.

Cui, J., M. Galand, R. V. Yelle, J.-E. Wahlund, K. Ågren, J. H. Waite Jr., M. K. Dougherty, (2010), Ion transport in Titan's upper atmosphere, Journal of Geophysical Research, 115, A06314.

Cui, J., R. V. Yelle, V. Vuitton, J. H. Waite, W. T. Kasprzak, D. A. Gell, H. B. Niemann, I. C. F. Müller-Wodarg, N. Borggren, G. G. Fletcher, E. L. Patrick, E. Raaen, B. A. Magee, (2009a), Analysis of Titan's neutral upper atmosphere from Cassini ion neutral mass spectrometer measurements, Icarus, 200, 581–615, doi: 10.1016/j.icarus.2008.12.005.

Cui, J., M. Galand, R. V. Yelle, V. Vuitton, I. C. F. Müller-Wodarg, J. -E. Wahlund, P. P. Lavvas, T. E. Cravens, W. T. Kasprzak, J. H. Waite Jr., (2009b), Diurnal variations of Titan's ionosphere, Journal of Geophysical Research, 114, A06310.

Cui, J., R. V. Yelle, K. Volk, (2008), Distribution and escape of molecular hydrogen in Titan's thermosphere and exosphere, Journal of Geophysical Research, 113, E10004, doi: 10.1029/2007JE003032.

De La Haye, V., J. H. Waite Jr., T. E. Cravens, I. P. Robertson, S. Lebonnois, (2008a), Coupled ion and neutral rotating model of Titan's upper atmosphere, Icarus, 197, 110–136, doi: 10.1016/j.icarus.2008.03.022.

De La Haye, V., J. H. Waite Jr., T. E. Cravens, S. W. Bougher, I. P. Robertson, J. M. Bell, (2008b), Heating Titan's upper atmosphere, Journal of Geophysical Research, 113, A11314.

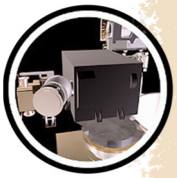

De La Haye, V., J. H. Waite, R. E. Johnson, R. V. Yelle, et al., (2007a), Cassini Ion and Neutral Mass Spectometer data in Titan's upper atmosphere and exosphere: Observation of a suprathermal corona, Journal of Geophysical Research, 12, A07309.

De La Haye, V., J. H. Waite Jr., T. E. Cravens, A. F. Nagy, R. E. Johnson, S. Lebonnois, I. P. Robertson, (2007b), Titan's Corona: The contribution of exothermic chemistry, Icarus, 191, 236–250.

Desai, R. T., S. A. Taylor, L. H. Regoli, A. J. Coates, et al. (2018), Cassini CAPS identification of pickup ion compositions at Rhea, Geophysical Research Letters, vol. 45, Issue 4, pp. 1704–1712, doi: 10.1002/2017GL076588.

Dong, Y., T. W. Hill, B. D. Teolis, B. A. Magee, J. H. Waite Jr., (2011), The water vapor plumes of Enceladus, Journal of Geophysical Research, 116, A10204.

Edberg, N. J. T., D. J. Andrews, O. Shebanits, K. Ågren, J.-E. Wahlund, H. J. Opgenoorth, T. E. Cravens, Z. Girazian, (2013a), Solar cycle modulation of Titan's ionosphere, Journal of Geophysical Research, 118, 5255–5264, doi: 10.1002/jgra.50463.

Edberg, N. J. T., D. J. Andrews, O. Shebanits, K. Ögren, J.-E. Wahlund, H. J. Opgenoorth, E. Roussos, P. Garnier, T. E. Cravens, S. V. Badman, R. Modolo, C. Bertucci, M. K. Dougherty, (2013b), Extreme densities in Titan's ionosphere during the T85 magnetosheath encounter, Geophysical Research Letters, 40, 2879–2883, doi: 10.1002/grl.50579.

Farrell, W. M., W. S. Kurth, D. A. Gurnett, R. E. Johnson, M. L. Kaiser, J.-E. Wahlund, J. H. Waite Jr., (2009), Electron density dropout near Enceladus in the context of water-vapor and water-ice, Geophysical Research Letters, 36, L10203.

Fox, J. L. and R. V. Yelle, (1997), Hydrocarbon ions in the ionosphere of Titan, Geophysical Research Letters, 24, Issue 17, pp. 2179–2182.

Galand, M., A. J. Coates, T. E. Cravens, J.-E. Wahlund, (2014), Titan's ionosphere, In Titan: Interior, Surface, Atmosphere, and Space Environment, Chapter 11, (eds.) I. Müller-Wodarg, C. A. Griffith, E. Lellouch, T. E. Cravens, Cambridge University Press, pp. 376–419.

Garnier, P., J.-E. Wahlund, L. Resnqvist, R. Modolo, K. Ågren, N. Sergis, P. Canu, M. Andre, D. A. Gurnett, W. S. Kurth, S. M. Krimgis, A. Coates, M. Dougherty, J. H. Waite Jr., (2009), Titan's ionosphere in the magnetosheath: Cassini RPWS results during the T32 flyby, Annales Geophysicae, 27, 4257–4272.

Glein, C. R., (2017), A whiff of nebular gas in Titan's atmosphere – Potential implications for the conditions and timing of Titan's formation, Icarus, 293, 231–242.

Glein, C. R., J. A. Baross, J. H. Waite Jr., (2015), The pH of Enceladus' ocean, Geochimica et Cosmochimica Acta, 162, 202–219, doi: 10.1016/j.gca.2015.04.017.

Hansen, C. J., D. E. Shemansky, L. W. Esposito, A. I. F. Stewart, B. R. Lewis, J. E. Colwell, A. R. Hendrix, R. A. West, J. H. Waite Jr., B. Teolis, B. A. Magee, (2011), The composition and structure of the Enceladus plume, Geophysical Research Letters, 38, L11202.

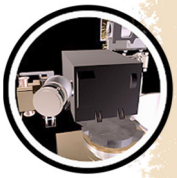

Hedman, M. M., C. M. Gosmeyer, P. D. Nicholson, C. Sotin, R. H. Brown, R. N. Clark, K. H. Baines, B. J. Buratti, M. R. Showalter, (2013), An observed correlation between plume activity and tidal stresses on Enceladus, Nature, 500, 182–184.

Howett, C. J. A., J. R. Spencer, T. Hurford, A. Verbiscer, M. Segura, (2016), Thermal properties of Rhea's poles: Evidence for a meter-deep unconsolidated subsurface layer, Icarus, 272, 140, doi: 10.1016/j.icarus.2016.02.033.

Hurley, D. M., M. E. Perry, H. J. Waite Jr., (2015), Modeling insights into the locations of density enhancements from the Enceladus water vapor jets, Journal of Geophysical Research, 120, 1763–1773, doi: 10.1002/21015JE004872.

Ip W.-H., (2006), On a ring origin of the equatorial ridge of Iapetus, Geophysical Research Letters, 33, L16203.

Ip, W.-H., (2005), An update on the ring exosphere and plasma disc of Saturn, Geophysical Research Letters, doi: 10.1029/2004GL022217.

Johnson, R. E., J. G. Luhmann, R. L. Tokar, M. Bouhram, J. J. Berthelier, E. C. Sittler, J. F. Cooper, T. W. Hill, H. T. Smith, M. Michael, M. Liu, F. J. Crary, D. T. Young, (2006), Production, ionization and redistribution of O2 in Saturn's ring atmosphere, Icarus, 180, 393.

Jones, G. H., C. S. Arridge, A. J. Coates, G. R. Lewis, S. Kanani, A. Wellbrock, D. T. Young, F. J. Crary, R. L. Tokar, R. J. Wilson, R. E. Johnson, D. G. Mitchell, J. Schmidt, S. Kempf, U. Beckmann, C. T. Russell, Y. D. Jia, M. K. Dougherty, J. H. Waite Jr., B. A. Magee, (2009), Fine jet structure of electrically charged grains in Enceladus' plume, Geophysical Research Letters, 36, L16204.

Kasprzak, W. T., H. Niemann, D. Harpold, J. Richards, H. Manning, E. Patrick, P. Mahaffy, (1996), Cassini orbiter ion neutral mass spectrometer instrument, Proceedings SPIE, vol. 2803, Cassini-Huygens: A Mission to the Saturnian Systems, International Symposium on Optical Science, Engineering, and Instrumentation, Denver, CO, doi: 10.1117/12.253413.

Keller, C. N., V. G. Anicich, T. E. Cravens, (1998), Model of Titan's ionosphere with detailed hydrocarbon ion chemistry, Planetary and Space Science, 46, 1157.

Keller, C. N., T. E. Cravens, L. Gan, (1992), A model of the ionosphere of Titan, Journal of Geophysical Research: Space Physics, vol. 97, Issue A8, pp. 12117–12135, doi: 10.1029/92JA00231.

Khurana, K. K., S. Fatemi, J. Kindkvist, E. Roussos, N. Krupp, M. Holmstrom, C. T. Russell, M. K. Dougherty, (2017), The role of plasma slowdown in the generation of Rhea’s Alfvén wings, Journal of Geophysical Research: Space Physics, 122, doi: 10.1002/2016JA023595.

Khurana, K. K., N. Krupp, M. G. Kivelson, E. Roussos, M. K. Dougherty, (2012), Cassini’s flyby through Rhea’s distant Alfven wing, in European Planetary Science Congress 2012, pp. EPSC2012-2309, Europlanet RI, Madrid.

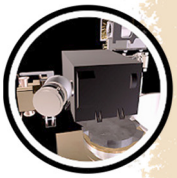

Kim, Y. H., J. L. Fox, J. H. Black, J. I. Moses, (2014), Hydrocarbon ions in the lower ionosphere of Saturn, Journal of Geophysical Research: Space Physics, 119, 1–12, doi: 10.1002/2013JA019022.

Koskinen, T. T., B. R. Sandel, R. V. Yelle, D. F. Strobel, I. C. F. Müller-Wodarg, J. T. Erwin, (2015), Saturn's variable thermosphere from Cassini/UVIS occultations, Icarus, 260, 174–189, doi: 10.1016/j.icarus.2015.07.008.

Lavvas, P., A. Coustenis, I. Vardavas, (2008a), Coupling photochemistry with haze formation in Titan's atmosphere, part I: Model description, Planetary and Space Science, 56(1), 27–66.

Lavvas, P., A. Coustenis, I. Vardavas, (2008b), Coupling photochemistry with haze formation in Titan's atmosphere, Part II: Results and validation with Cassini/Huygens data, Planetary and Space Science, 56(1), 67–99.

Lebonnois, S., (2005), Benzene and aerosol production in Titan and Jupiter's atmospheres: a sensitivity study, Planetary and Space Science, 53(5), 486–497.

Ledvina, S. A. and S. H. Brecht, (2012a), Consequences of negative ions for Titan's plasma interaction, Geophysical Research Letters, 39, L20103, doi: 10.1029/2012GL053835.

Ledvina, S. A., S. H. Brecht, T. E. Cravens, (2012b), The orientation of Titan's dayside ionosphere and its effects on Titan's plasma interaction, Earth Planets Space, 64, 207–230.

Ledvina, S. A., Y. Ma, E. Kallio, (2008), Modeling and simulating flowing plasmas and related phenomena, Space Science Reviews, doi: 10.1007/s11214-008-9384-6.

Ledvina, S. A., T. E. Cravens, K. Kecskemety, (2005), Ion distributions in Saturn's magnetosphere near Titan, Journal of Geophysical Research, 110, A06211, doi: 10.1029/2004JA010771.

Ledvina, S. A., J. G. Luhmann, S. H. Brecht, T. E. Cravens, (2004a), Titan's induced magnetosphere, Advances in Space Research, 33, 2092.

Ledvina, S. A., J. G. Luhmann, T. E. Cravens, (2004b), Ambient ion distributions in Saturn's magnetosphere near Titan during a non-Voyager type interaction, Advances in Space Research, 33, 221.

Ledvina, S. A., S. H. Brecht, J. G. Luhmann, (2004c), Ion distributions of 14 amu pickup ions associated with Titan's plasma interaction, Geophysical Research Letters, 31, L17S10, doi: 10.1029/2004GL019861.

Lee, A. Y. and G. Hanover, (2005), Cassini spacecraft attitude control system flight performance, in AIAA Guidance, Navigation, and Control Conference, American Institute of Aeronautics and Astronautics, San Francisco, CA, AIAA-2005-6269.

Luhmann, J. G., D. Ulusen, S. A. Ledvina, K. Mandt, B. Magee, J. H. Waite, J. Westlake, T. E. Cravens, I. Robertson, N. Edberg, K. Ågren, J.-E. Wahlund, Y.-J. Ma, H. Wei, C. T. Russell, M. K. Dougherty, (2012), Investigating magnetospheric interaction effects of Titan's ionosphere with the Cassini orbiter ion neutral mass spectrometer, Langmuir Probe and magnetometer observations during targeted flybys, Icarus, 219, 534–555, doi: 10.1016/j.icarus.2012.03.015.

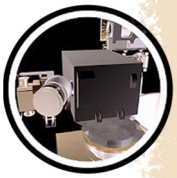

Luhmann, J. G., R. E. Johnson, R. L. Tokar, S. A. Ledvina, T. E. Cravens, (2006), A model of the ionosphere of Saturn's rings and its implications, Icarus, 181 (2), 465–474.

Luhmann, J. G., S. A. Ledvina, C. T. Russell, (2004), Induced magnetospheres, Advances in Space Research, 33, 1905.

Luhmann, J. G., (1996), Titan's ion exosphere wake: A natural ion mass spectrometer? Journal of Geophysical Research, 101, E12, pp. 29387–29393, doi: 10.1029/96JE03307.

Ma, Y., K. Altwegg, T. Breus, M. R. Combi, et al., (2008), Plasma flow and related phenomena in planetary aeronomy, Space Science Reviews, 139, no. 1–4, 311–353, doi: 10.1007/s11214-008-9389-1.

Ma, Y., A. F. Nagy, T. E. Cravens, I. V. Sokolov, K. C. Hansen, J.-E. Wahlund, F. J. Crary, A. J. Coates, M. K. Dougherty, (2006), Comparisons Between MHD Model Calculations and Observations of Cassini Flybys of Titan, Journal of Geophysical Research, 111, A05207, doi: 10.1029/2005JA011481.

Ma, Y.-J., A. F. Nagy, T. E. Cravens, I. G. Sokolov, J. Clark, K. C. Hansen, (2004), 3-D global MHD model prediction of the first close flyby of Titan by Cassini, Geophysical Research Letters, 31, doi: 10.1029/2004GL021215.

Madanian, H., T. E. Cravens, M. S. Richard, J. H. Waite, N. J. T. Edberg, J. H. Westlake, J.-E. Wahlund, (2016), Solar cycle variations in ion composition in the dayside ionosphere of Titan, Journal of Geophysical Research, 121, 8013–8037, doi: 10.1002/2015JA022274.

Magee, B. A. and J. H. Waite, (2017), Neutral gas composition of Enceladus' plume - Model parameter insights from Cassini-INMS, 48th Lunar and Planetary Science Conference, 20–24 March 2017, The Woodlands, TX, LPI Contribution No. 1964, id. 2974.

Magee, B. A., J. H. Waite, K. E. Mandt, J. Bell, J. Westlake, D. A. Gell, V. De la Haye, (2009), INMS derived composition of Titan's upper atmosphere: Analysis methods and model comparison, Planetary and Space Science, 57, 1895–1916.

Mahhafy, P. M. and K. Lai, (1990), An electrostatic quadrupole deflector for mass spectrometer applications, Journal of Vacuum Science A8, 3244.

Mandt, K. E., J. H. Waite Jr., B. Teolis, B. A. Magee, J. Bell, J. Westlake, C. Nixon, O. Mousis, J. Lunine, (2012a), The 12C/13C ratio on Titan from Cassini INMS measurements and implications for the evolution of methane, Astrophysical Journal, 749, 160, doi: 10.1088/0004-637X/749/2/160.

Mandt, K. E. , D. A. Gell, M. Perry, J. H. Waite Jr., F. A. Crary, D. Young, B. A. Magee, J. H. Westlake, T. Cravens, W. Kasprzak, G. Miller, J.-E. Wahlund, K. Ågren, N. J. T. Edberg, A. N. Heays, B. R. Lewis, S. T. Gibson, V. de la Haye, M.-C. Liang, (2012b), Ion densities and composition of Titan's upper atmosphere derived from the Cassini ion neutral mass spectrometer: Analysis methods and comparison of measured ion densities to photochemical model simulations, Journal of Geophysical Research, 117, E10006, doi: 10.1029/2012JE004139.

- - - - - - - - - - - - - -

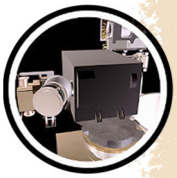

Mandt, K. E., J. H. Waite Jr., W. Lewis, J. I. Lunine, O. Mousis, J. Bell, B. A. Magee, D. Cordier, (2009), Isotopic evolution of the major constituents of Titan's atmosphere based on Cassini data, Planetary and Space Science, 57, 1917–1930.

Michael, M., R. E. Johnson, F. Leblanc, M. Liu, J. G. Luhmann, V. I. Shematovich, (2005), Ejection of nitrogen from Titan's atmosphere by magnetospheric ions and pick-up ions, Icarus, vol. 175, Issue 1, pp. 263–267, doi: 10.1016/j.icarus.2004.11.004.

Mitchell, D. G., M. E. Perry, D. C. Hamilton, J. H. Westlake, P. Kollmann, H. T. Smith, J. F. Carbary, J. H. Waite Jr., R. Perryman, H.-W. Hsu5, J.-E. Wahlund, M. W. Morooka, L. Z. Hadid, A. M. Persoon, W. S. Kurth, (2018), Dust grains fall from Saturn’s D-ring into its equatorial upper atmosphere, Science, 362, no. 6410, p. eaat2236.

Moore, L., T. E. Cravens, I. Müller-Wodarg, M. E. Perry, J. H. Waite Jr., R. Perryman, et al., (2018), Models of Saturn’s equatorial ionosphere based on in situ data from Cassini’s Grand Finale, Geophysical Research Letters, 45, 9398–9407, doi: 10.1029/2018GL078162.

Moore, L., I. Müller-Wodarg, M. Galand, A. Kliore, M. Mendillo, (2010), Latitudinal variations in Saturn’s ionosphere: Cassini measurements and model comparisons, Journal of Geophysical Research, 115(A11), A11317, doi: 10.1029/2010JA015692.

Moore, L., A. F. Nagy, A. J. Kliore, I. Müller-Wodarg, J. D. Richardson, M. Mendillo, (2006), Cassini radio occultations of Saturn’s ionosphere: Model comparisons using a constant water flux, Geophysical Research Letters, 33(22), L22202, doi: 10.1029/2006GL027375.

Moses, J. and S. Bass, (2000), The effects of external material on the chemistry and structure of Saturn’s ionosphere, Journal of Geophysical Research, 105(1999), 7013–7052.

Mousis, O., J. I. Lunine, S. Picaud, D. Cordier, J. H. Waite Jr., K. E. Mandt, (2011), Removal of Titan's atmospheric noble gases by their sequestration in surface clathrates, The Astrophysical Journal, 740, L9.

Mousis, O., J. I. Lunine, J. H. Waite Jr., B. Magee, W. S. Lewis, K. E. Mandt, D. Marquer, D. Cordier, (2009a), Formation conditions of Enceladus and origin of its methane reservoir, The Astrophysical Journal Letters, 701, L39-L42.

Mousis, O., J. I. Lunine, M. Pasek, D. Cordier, J. H. Waite Jr., K. E. Mandt, W. S. Lewis, M.-J. Nguyen, (2009b), A primordial origin for the atmospheric methane of Saturn's moon Titan, Icarus, 204, 749–751.

Müller-Wodarg, I. C. F., L. Moore, M. Galand, S. Miller, M. Mendillo, (2012), Magnetosphere–atmosphere coupling at Saturn: 1 – Response of thermosphere and ionosphere to steady state polar forcing, Icarus, 221(2), 481–494, doi: 10.1016/j.icarus.2012.08.034.

Müller-Wodarg, I. C. F., R. V. Yelle, J. Cui, J. H. Waite, (2008), Horizontal structures and dynamics of Titan’s thermosphere, Journal of Geophysical Research, 113, E10003, doi: 10.1029/2007JE003031.

Müller-Wodarg, I. C. F., R. V. Yelle, N. Borggren, J. H. Waite, (2006a), Waves and horizontal structures in Titan’s thermosphere, Journal of Geophysical Research, 111, A12315.

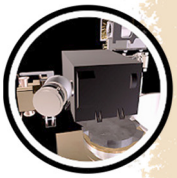

Müller-Wodarg, I. C. F., M. Mendillo, R. Yelle, A. Aylward, (2006b), A global circulation model of Saturn's thermosphere, Icarus, 180(1), 147–160, doi: 10.1016/j.icarus.2005.09.002.

Müller-Wodarg, I. C. F., R. V. Yelle, M. J. Mendillo, A. D. Aylward, (2003), On the global distribution of neutral gases in Titan's upper atmosphere and its effect on the thermal structure, Journal of Geophysical Research: Space Physics, vol. 108, issue A12, doi: 10.1029/2003JA010054.

Müller-Wodarg, I. C. F. and R. V. Yelle, (2002a), The effect of dynamics on the composition of Titan's upper atmosphere, Geophysical Research Letters, vol. 29, issue 23, 54-1–54-4, doi: 10.1029/2002GL016100.

Müller-Wodarg, I. C. F., (2002b), The application of general circulation models to the atmospheres of terrestrial-type moons of the giant planets, In Atmoshperes in the Solar System: Comparative Aeronomy, Volume 120, Part IV: Models of Aeronomic Systems, (eds.) M. Mendillo, A. Nagy, J. H. Waite, American Geophysical Union, Geophysical Monograph Series, pp. 307–318, doi: 10.1029/GM130.

Müller-Wodarg, I. C. F., R. V. Yelle, M. Mendillo, L. A. Young, A. D. Aylward, (2000), The thermosphere of Titan simulated by a global three-dimensional time-dependent model, Journal of Geophysical Research, 105, pp. 20833–20856, doi: 10.1029/2000JA000053.

Nagy, A. F. and T. E. Cravens, (1998), Titan's ionosphere: A review, Planetary and Space Science, 46, 1149, doi: 10.1016/S0032-0633(98)00049-X.

Neubauer, F. M., et al., (2006). Titan's near magnetotail from magnetic field and electron plasma observations and modeling: Cassini flybys, TA, TB and T3, Journal of Geophysical Research, 111, doi: 10.1029/2006011676.

Neubauer, F. M., D. A. Gurnett, J. D. Scudder, R. E. Hartle, (1984), Titan's magnetospheric interaction, Saturn, 1, 760–787.

Ozak, N., T. E. Cravens, G. H. Jones, A. J. Coates, I. P. Robertson, (2012), Modeling of electron fluxes in the Enceladus plume, Journal of Geophysical Research, 117, A06220, doi: 10.1029/2011JA017497.

Patrick, E. L., (2006), Silicon carbide nozzle for producing molecular beams, Review of Scientific Instruments, 77, 043301, doi:10.1063/1.2188907.

Perry, M. E., J. H. Waite Jr., D. G. Mitchell, K. E. Miller, T. E. Cravens, R. S. Perryman, et al., (2018), Material flux from the rings of Saturn into its atmosphere, Geophysical Research Letters, 45, 10,093–10,100, doi: 10.1029/2018GL078575.

Perry, M. E., B. D. Teolis, D. M. Hurley, B. A. Magee, J. H. Waite, T. G. Brockwell, R. S. Perryman, R. L. McNutt, (2015), Cassini INMS measurements of Enceladus plume density, Icarus, 257, 139–162, doi: 10.1016/j.icarus.2015.04.037.

Perry, M. E., B. Teolis, H. T. Smith, R. L. McNutt, G. Fletcher, W. Kasprzak, B. Magee, D. G. Mitchell, J. H. Waite Jr., (2010), Cassini INMS observations of neutral molecules in Saturn's E ring. Journal of Geophysical Research, 115, A10206.

- - - - - - - - - - - - - -

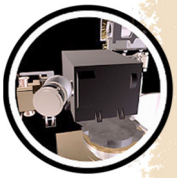

Persoon, A. M., W. S. Kurth, D. A. Gurnett, J. B. Groene, A. H. Sulaiman, J.-E. Wahlund, et al., (2019), Electron density distributions in Saturn's ionosphere, Geophysical Research Letters, 46, 3061–3068, doi: 10.1029/2018GL078020.

Porco, C., D. DiNino, F. Nimmo, (2014), How the geysers, tidal stresses, and thermal emission across the south polar terrain of Enceladus are related, The Astronomical Journal, 148, 45.

Postberg, F., N. Khawaja, B. Abel, G. Choblet, C. R. Glein, M. S. Gudipati, B. L. Henderson, H.-W. Hsu, S. Kempf, F. Klenner, G. Moragas-Klostermeyer, B. Magee, L. Nölle, M. Perry, R. Reviol, J. Schmidt, R. Srama, F. Stolz, G. Tobie, M. Trieloff, J. H. Waite, (2018), Macromolecular organic compounds from the depths of Enceladus, Nature, 558, 564–568, doi: 10.1038/s41586-018-0246-4.

Ricca, A., C. Bauschlicher Jr., E. L. O. Bakes, (2001a), A computational study of the mechanisms for the in- corporation of a nitrogen atom into polycyclic aromatic hydrocarbons in the Titan haze, Icarus, 154(2), 516–521.

Ricca, A., C. Bauschlicher Jr., M. Rosi. (2001b), Mechanisms for the incorporation of a nitrogen atom into polycyclic aromatic hydrocarbon cations, Chemical Physics Letters, 347(4-6), 473–480.

Richard, M. S., T. E. Cravens, C. Wylie, D. Webb, Q. Chediak, R. Perryman, K. Mandt, J. Westlake, J. H. Waite, I. Robertson, B. A. Magee, N. J. T. Edberg, (2015a), An empirical approach to modeling ion production rates in Titan's ionosphere I: Ion production rates on the dayside and globally, Journal of Geophysical Research, 120, 1264–1280, doi: 10.1002/2013JA019706.

Richard, M. S., T. E. Cravens, C. Wylie, D. Webb, Q. Chediak, K. Mandt, J. H. Waite, A. Rymer, C. Bertucci, A. Wellbrock, A. Windsor, A. J. Coates, (2015b), An empirical approach to modeling ion production rates in Titan's ionosphere II: Ion production rates on the nightside, Journal of Geophysical Research, 120, 1281–1298, doi: 10.1002/2014JA020343.

Richard, M. S., T. E. Cravens, I. P. Robertson, J. H. Waite, J.-E. Wahlund, F. J. Crary, A. J. Coates, (2011), Energetics of Titan's ionosphere: model comparisons with Cassini data, Journal of Geophysical Research, 116, A09310.

Richter, H. and J. B. Howard, (2000), Formation of polycyclic aromatic hydrocarbons and their growth to soot—a review of chemical reaction pathways, Progress in Energy and Combustion Science, 26, 565.

Rietmeijer, F. J., (1993) Size distributions in two porous chondritic micrometeorites, Earth and Planetary Science Letters, 117, 609–617.

Robertson, I. P., T. E. Cravens, J. H. Waite Jr., R. V. Yelle, V. Vuitton, A. J. Coates, J. E. Wahlund, K. Ågren, B. Magee, K. Mandt, M. S. Richard, (2009), Structure of Titan's ionosphere: model comparisons with Cassini data, Planetary and Space Science, 57, 1834–1846.

Rosenqvist, L., J.-E. Wahlund, K. Ågren, R. Modolo, H. J. Opgenoorth, D. Strobel, I. Müller-Wodarg, P. Garnier, C. Bertucci, (2009), Titan ionospheric conductivities from Cassini

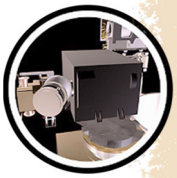

measurements, Planetary and Space Science, 57, 1828–1833, doi: 10.1016/j.pss.2009.01.007.

Roussos, E., J. Wuller, S. Simon, A. Boswetter, U. Motschmann, N. Krupp, M. Franz, J. Woch, K. K. Khurana, M. K. Dougherty, (2008), Plasma and fields in the wake of Rhea: 3-D hybrid simulation and comparison with Cassini data, Annales Geophysicae, 26, 619.

Rymer, A. M., H. T. Smith, A. Wellbrock, A. J. Coates, D. T. Young, (2009), Discrete classification and electron energy spectra of Titan's varied magnetospheric environment, Geophysical Research Letters, 36, L15109, doi: 10.1029/2009GL039427

Sagnières, L. B. M., M. Galand, J. Cui, P. P. Lavvas, E. Vigren, V. Vuitton, R. V. Yelle, A. Wellbrock, A. J. Coates, (2015), Influence of local ionization on ionospheric densities in Titan's upper atmosphere, Journal of Geophysical Research, 120, 5899–5921, doi: 10.1002/2014JA020890.

Sakai, S., T. E. Cravens, N. Omidi, M. E. Perry, J. H. Waite Jr.,(2016) Ion energy distributions and densities in the plume of Enceladus, Planetary and Space Science, 130, 60–79, doi: 10.1016/j.oss.2016.05.007.

Santolik, O., D. A. Gurnett, G. H. Jones, P. Schippers, F. J. Crary, J. S. Leisner, G. B. Hospodarsky, W. S. Kurth, C. T. Russell, M. K. Dougherty, (2011), Intense plasma wave emissions associated with Saturn's moon Rhea, Geophysical Research Letters, 38, L19204.

Shebanits, O., J.-E. Wahlund, N. J. T. Edberg, F. J. Crary, A. Wellbrock, D. J. Andrews, E. Vigren, R. T. Desai, A. J. Coates, K. E. Mandt, J. H. Waite, (2016), Ion and aerosol precursor densities in Titan's ionosphere: A multi-instrument case study, Journal of Geophysical Research, 121, 10075–10090, doi: 10.1002/2016JA022980.

Shematovich, V. I., R. E. Johnson, M. Michael, J. G. Luhmann, (2003), Nitrogen loss from Titan, Journal of Geophysical Research, 108, E8, id. 5087, doi: 10.1029/2003JE002094.

Simon, S., H. Kriegel, J. Saur, A. Wennmacher, F. M. Neubauer, E. Roussos, U. Motschmann, M. K. Dougherty, (2012), Analysis of Cassini magnetic field observations over the poles of Rhea, Journal of Geophysical Research, 117, A07211.

Simon, S., J. Saur, F. M. Neubauer, A. Wennmacher, M. K. Dougherty, (2011), Magnetic signatures of a tenuous atmosphere at Dione, Journal of Geophysical Research, 38, L15102.

Smith, H. T., R. E. Johnson, M. E. Perry, D. G. Mitchell, R. L. McNutt, D. T. Young, (2010), Enceladus plume variability and the neutral gas densities in Saturn's magnetosphere, Journal of Geophysical Research, 115, A10252, doi: 10.1029/2009JA015184.

Snow, T., V. Le Page, Y. Keheyan, V. Bierbaum, (1998), The interstellar chemistry of PAH cations, Nature, 391(6664), 259–260

Snowden, D. and R. V. Yelle, (2014a), The global precipitation of magnetospheric electrons into Titan's upper atmosphere, Icarus, 243, 1–15, doi: 10.1016/j.icarus.2014.08.027.

Snowden, D. and R. V. Yelle, (2014b), The thermal structure of Titan's upper atmosphere, II: Energetics, Icarus, vol. 228, pp. 64–77, doi: 10.1016/j.icarus.2013.08.027.

- - - - - - - - - - - - - -

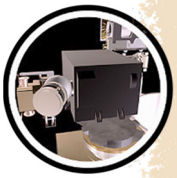

Snowden, D., R. Yelle, J. Cui, J.-E. Wahlund, N. J. T. Edberg, K. Ågren, (2013a), The thermal structure of Titan's upper atmosphere, I: Temperature profiles from Cassini INMS observations, Icarus, vol. 226, pp. 552–582, doi: 10.1016/j.icarus.2013.06.006.

Snowden, D., R. V. Yelle, M. Galand, A. J. Coates, A. Wellbrock, G. H. Jones, and P. Lavvas, (2013b), Auroral electron precipitation and flux tube erosion in Titan's upper atmosphere, Icarus, 226, 186-204, doi: 10.1016/j.icarus.2013.05.021.

Spahn, F., N. Albers, M. Hörning, S. Kempf, A. V. Krivov, M. Makuch, J. Schmidt, M. Seiß, M. Sremčević, (2006), E-ring dust sources: Implications from Cassini's dust measurements, Planetary and Space Science, vol. 54, Issues 9–10, pp. 1024–1032, doi: 10.1016/j.pss.2006.05.022.

Strobel, D. F., (2010), Molecular hydrogen in Titan's atmosphere: Implications of the measured tropospheric and thermospheric mole fractions, Icarus, vol. 208, no. 2, pp. 878–886.

Strobel, D. F., S. K. Atreya, B. Bézard, F. Ferri, F. M. Flasar, M. Fulchignoni, E. Lellouch, I. C. F. Müller-Wodarg, (2009), Atmospheric structure and composition, In Titan from Cassini-Huygens, (eds.) R. Brown, J.-P. Lebreton, J. H. Waite, Springer Dordrecht, pp. 235–257, doi: 10.1007/978-1-4020-9215-2_10.

Strobel, D. F., (2008), Titan's hydrodynamically escaping atmosphere, Icarus, vol. 193, no. 2, pp. 588–594.

Strobel, D. F., (2006), Gravitational tidal waves in Titan's upper atmosphere, Icarus, vol. 182, no. 1, pp. 251–258.

Tenishev, V., D. C. S. Öztürk, M. R. Combi, M. Rubin, J. H. Waite Jr., M. Perry, (2014), Effect of the Tiger Stripes on the water vapor distribution in Enceladus' exosphere, Journal of Geophysical Research, 119, 2658–2667, doi: 10.1002/2014JE004700.

Tenishev, V., M. R. Combi, B. D. Teolis, J. H. Waite Jr., (2010). An approach to numerical simulation of the gas distribution in the atmosphere of Enceladus, Journal of Geophysical Research, 115, A09302.

Teolis, B. D., C. Plainaki, T. A. Cassidy, U. Raut, (2017a), Water Ice Radiolytic O2, H2, and H2O2 Yields for Any Projectile Species, Energy, or Temperature: A Model for Icy Astrophysical Bodies, Journal of Geophysical Research: Planets, 122, doi: 10.1002/2017JE005285.

Teolis, B. D., M. E. Perry, C. J. Hansen, J. H. Waite, C. C. Porco, J. R. Spencer, C. J. A. Howett, (2017b), Enceladus Plume Structure and Temporal Variability: Comparison of Cassini Observations, Astrobiology (special issue), 17, no. 9, 926–940.

Teolis, B. D. and J. H. Waite, (2016), Dione and Rhea seasonal exospheres, revealed by Cassini CAPS and INMS, Icarus, 272, 277–289, doi: 10.1016/j.icarus.2016.02.031.

Teolis, B. D., H. B. Niemann, J. H. Waite, D. A. Gell, R. S. Perryman, W. T. Kasprzak, K. E. Mandt, R. V. Yelle, A. Y. Lee, F. J. Pelletier, G. P. Miller, D. T. Young, J. M. Bell, B. A. Magee, E. L. Patrick, J. Grimes, G. G. Fletcher, and V. Vuitton, (2015), A revised sensitivity model for Cassini INMS: Results at Titan, Space Science Reviews, doi: 10.1007/s11214-014-0133-8.

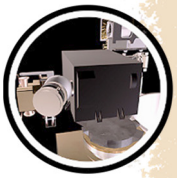

Teolis, B. D., I. Sillanpää, J. H. Waite, K. K. Khurana, (2014), Surface current balance and thermoelectric whistler wings at airless astrophysical bodies: Cassini at Rhea, Journal of Geophysical Research, 119, 8881–8901, doi: 10.1002/2014JA020094.

Teolis, B., G. H. Jones, P. F. Miles, R. L. Takar, B. A. Magee, J. H. Waite, E. Roussos, D. T. Young, F. J. Crary, A. J. Coates, R. E. Johnson, W.-L. Tseng, R. A. Baragiola, (2010a), Cassini Finds an Oxygen-Carbon Dioxide Atmosphere at Saturn's Icy Moon Rhea, Science, 330, 24.

Teolis, B., M. E. Perry, B. A. Magee, J. Westlake, J. H. Waite Jr., (2010b), Detection and measurements of ice grains and gas distribution in the Enceladus plume by Cassini's ion neutral mass spectrometer, Journal of Geophysical Research, 115, A09222.

Thomsen, M. F., D. B. Reisenfeld, D. Delapp, R. L. Tokar, D. T. Young, F. J. Crary, E. C. Sittler, M. A. McGraw, J. D. Williams, (2010), Survey of Ion Plasma Parameters in Saturn’s Magnetosphere, Journal of Geophysical Research, 115, A10220.

Tokar, R. L., R. E. Johnson, M. F. Thomsen, E. C. Sittler, A. J. Coates, R. J. Wilson, F. J. Crary, D. T. Young, G. H. Jones, (2012), Detection of Exospheric O2+ at Saturn’s Moon Dione, Journal of Geophysical Research, 39, L03105.

Tokar, R. L., R. J. Wilson, R. E. Johnson, M. G. Henderson, M. F. Thomas, M. M. Cowee, E. C. Sittler, Jr., D. T. Young, H. J. McAndrews, H. T. Smith, (2008), Cassini Detection of Water - group pick - up ions in Saturn's torus, Geophysical Research Letters 35, L14202, doi: 10.1029/2008GL034749.

Tucker, O. J., R. E. Johnson, J. I. Deighan, A. N. Volkov, (2013), Diffusion and thermal escape of H2 from Titan’s atmosphere: Monte Carlo simulations, Icarus, 222, 149–158, doi: 10.1016/j.icarus.2012.10.016.

Ulusen, D., J. G. Luhmann, Y. J. Ma, K. Mandt, J. H. Waite, M. K. Dougherty, J.-E. Wahlund, C. T. Russell, T. A. Craven, N. Edberg, K. Agren, (2012), Comparisons of Cassini flybys of the Titan magnetospheric interaction with an MHD model: Evidence for organized behavior at high altitudes, Icarus, 217, 43–54, doi: 10.1016/j.icarus.2011.10.009.

Ulusen, D., J. Luhmann, Y. Ma, S. Ledvina, T. Cravens, K. Mandt, J. H. Waite Jr., J.-E. Wahlund, (2010), Investigation of the force balance in the Titan ionosphere: Cassini T5 flyby model/data comparisons, Icarus, 210, 867–880.

Vervack, R. J. and J. I. Moses, (2015), Saturn’s upper atmosphere during the Voyager era: Reanalysis and modeling of the UVS occultations, Icarus, 258, 135–163, doi: 10.1016/j.icarus.2015.06.007

Vigren, E., M. Galand, R. V. Yelle, A. Wellbrock, A. J. Coates, D. Snowden, J. Cui, P. Lavvas, N. J. T. Edberg, O. Shebanits, J.-E. Wahlund, V. Vuitton, K. Mandt, (2015), Ionization balance in Titan’s nightside ionosphere, Icarus, 248, 539–546, doi: 10.1016/j.icarus.2014.11.012.

Vigren, E., M. Galand, R. V. Yelle, J. Cui, J.-E. Wahlund, K. Ågren, P. P. Lavvas, I. C. F. Müller-Wodarg, D. F. Strobel, V. Vuitton, A. Bazin, (2013), On the thermal electron balance in Titan’s sunlit upper atmosphere, Icarus, vol. 223, pp. 234–251, doi: 10.1016/j.icarus.2012.12.010.

- - - - - - - - - - - - - -

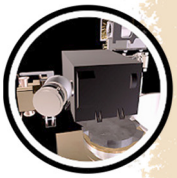

Vuitton, V., P. Lavvas, R. V. Yelle, M. Galand, A. Wellbrock, G. R. Lewis, A. J. Coates, J.-E. Wahlund, (2009), Negative ion chemistry in Titan's upper atmosphere, Planetary and Space Science, 57, 1558–1572.

Vuitton, V., R. V. Yelle, J. Cui, (2008), Formation and distribution of benzene on Titan, Journal of Geophysical Research, doi: 1 0.1029/2007JE002997.

Vuitton, V., R. V. Yelle, M. J. McEwan, (2007), Ion Chemistry and N-containing Molecules in Titan’s Upper Atmosphere, Icarus, doi: 10.1016/j.carus.2007.06.023.

Vuitton, V., R. V. Yelle, V. Anicich, (2006), The Nitrogen Chemistry of Titan’s Upper Atmosphere Revealed, The Astrophysical Journal Letters, vol. 647, no.2, L175-L178

Wahlund, J.-E., M. Galand, I. Meuller-Wodarg, J. Cui, R. V. Yelle, F. J. Crary, K. Mandt, B. Magee, J. H. Waite, Jr., D. T. Young, A. J. Coates, P. Garnier, K. Ågren, M. Andre, A. I. Eriksson, T. E. Cravens, V. Vuitton, D. A. Gurnett, W. S. Kurth, (2009), On the amount of heavy molecular ions in Titan's ionosphere, Planetary and Space Science, 57, 1857–1865.

Waite Jr., J. H., R. Perryman, M. Perry, K. Miller, J. Bell, T. E. Cravens, C. R. Glein, J. Grimes, M. Hedman, J. Cuzzi, T. Brockwell, B. Teolis, L. Moore, D. Mitchell, A. Persoon, W. S. Kurth, J-E. Wahlund, M. Morooka, L. Z. Hadid, S. Chocron, J. Walker, A. Nagy, R. Yelle, S. Ledvina, R. Johnson, W. Tseng, O. J. Tucker, W.-H. Ip, (2018), Chemical Interactions between Saturn’s Atmosphere and its Rings, Science, doi: 10.1126/science.aat2382.

Waite Jr., J. H., C. R. Glein, R. S. Perryman, B. D. Teolis, B. A. Magee, G. Miller, J. Grimes, M. E. Perry, K. E. Miller, A. Bouquet, J. L. Lunine, T. Brockwell, S. J. Bolton, (2017), Cassini finds molecular hydrogen in the Enceladus plume: Evidence for hydrothermal processes, Science, 356, 155–159.

Waite, J. H., J. Bell, R. Lorenz, R. Achterberg, F. M. Flasar, (2013), A model of variability in Titan’s atmospheric structure, Planetary and Space Science, 86, 45–56, doi: 10.1016/j.pss.2013.05.018.

Waite Jr., J. H., W. S. Lewis, B. A. Magee, J. I. Lunine, W. B. McKinnon, C. R. Glein, O. Mousis, D. T. Young, T. Brockwell, J. Westlake, M.-J. Nguyen, B. D. Teolis H. B. Niemann, R. L. McNutt, M. Perry, W.-H. Ip, (2009), Liquid water on Enceladus from observations of ammonia and 40Ar in the plume, Nature, 460, 487–490.

Waite, J. H., D. T. Young, A. J. Coates, F. J. Crary, B. A. Magee, K. E. Mandt, J. H. Westlake, (2008), The source of heavy organics and aerosols in Titan’s atmosphere, Proceedings of the International Astronomical Union, vol. 4, issue S251 (Organic Matter in Space), pp. 321-326, doi: 10.1017/S1743921308021844.

Waite Jr., J. H., D. T. Young, T. E. Cravens, A. J. Coates, F. J. Crary, B. Magee, J. Westlake, (2007), The process of tholin formation in Titan’s upper atmosphere, Science, 316, 870–875.

Waite Jr., J. H., M. Combi, W.-H. Ip, T. E. Cravens, R. L. McNutt, Jr., W. Kasprzak, R. Yelle, J. Luhmann, H. Niemann, D. Gell, B. Magee, G. Fletcher, J. Lunine, W.-L. Tseng, (2006), Cassini Ion and Neutral Mass Spectrometer: Enceladus plume composition and structure, Science, 311, 1419–1422.

- - - - - - - - - - - - - -

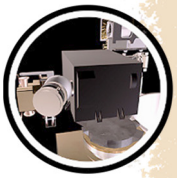

Waite, J. H., H. Niemann, R. V. Yelle, W. T. Kasprzak, T. E. Cravens, J. G. Luhmann, R. L. McNutt, W.-H. Ip, D. Gell, V. de la Haye, I. Müller-Wordag, B. McGee, N. Borggren, S. Ledvina, G. Fletcher, E. Walter, R. Miller, S. Scherer, R. Thorpe, J. Xu, B. Block, K. Arnett, (2005a), Ion Neutral Mass Spectrometer (INMS) results from the first flyby of Titan, Science, 308 (5724), 982–986.

Waite, J. H., T. E. Cravens, W.-H. Ip, W. T. Kasprzak, J. G. Luhmann, R. L. McNutt, H. B. Niemann, R. V. Yelle, I. Müller-Wodarg, S. A. Ledvina, S. Scherer, (2005b), Oxygen ions observed near Saturn's A Ring, Science, 307 (5713), 1260–1262.

Waite Jr., J. H., W. S. Lewis, W. T. Kasprzak, V. G. Anicich, B. P. Block, T. C. Cravens, G. G. Fletcher, W.-H. Ip, J. G. Luhmann, R. L. McNutt, H. B. Niemann, J. K. Parejko, J. E. Richards, R. L. Thorpe, E. M. Walter, R. V. Yelle, (2004), The Cassini Ion and Neutral Mass Spectrometer (INMS) investigation, Space Science Reviews, 114, 113–231.

Walker, J. D., S. Chocron, J. H. Waite, T. Brockwell, (2015), The vaporization threshold: Hypervelocity impacts of ice grains into a titanium Cassini spacecraft instrument chamber, Procedia Engineering, 103, 628–635, doi: 10.1016/j.proeng.2015.04.081.

Wang, H. and M. Frenklach, (1997), A detailed kinetic modeling study of aromatics formation in laminar premixed acetylene and ethylene flames, Combustion and Flame, vol. 110, issues 1–2, pp. 173–221.

Westlake, J. H., J. H. Waite, J. M. Bell, R. Perryman, (2014a), Observed decline in Titan's thermospheric methane due to solar cycle drivers, Journal of Geophysical Research, 119, 8586–8599, doi: 10.1002/2014JA020394.

Westlake, J. H., J. H. Waite, N. Carrasco, M. Richard, T. Cravens, (2014b), The role of ion-molecule reactions in the growth of heavy ions in Titan's ionosphere, Journal of Geophysical Research, 119, 5951–5963, doi: 10.1002/2014JA0202008.

Westlake, J. H., C. P. Paranicas, T. E. Cravens, J. G. Luhmann, K. E. Mandt, H. T. Smith, D. G. Mitchell, A. M. Rymer, M. E. Perry, J. H. Waite Jr., J.-E. Wahlund, (2012a), The observed composition of ions outflowing from Titan, Geophysical Research Letters, 39, L19104, doi: 10.1029/2012GL053079.

Westlake, J. H., J. H. Waite Jr., K. E. Mandt, N. Carrasco, J. M. Bell, B. A. Magee, J.-E. Wahlund, (2012b), Titan's ionospheric composition and structure: Photochemical modeling of Cassini INMS data, Journal of Geophysical Research, 117, E01003, 21, doi: 10.1029/2011JE003883.

Westlake, J. H., J. Bell, J. H. Waite, Jr., R. E. Johnson, J. G. Luhmann, K. E. Mandt, B. A. Magee, A. M. Rymer, (2011), Titan's thermospheric response to various plasma and solar environments, Journal of Geophysical Research, 116, A03318.

Wilson, E. H., S. K. Atreya, A. Coustenis, (2003), Mechanisms for the formation of benzene in the atmosphere of Titan, Journal of Geophysical Research: Planets, vol. 108, Issue E2, doi: 10.1029/2002JE001896.

Yelle, R. V., J. Serigano, T. T. Koskinen, S. M. Hörst, M. E. Perry, R. S. Perryman, J. H. Waite Jr., (2018), Thermal Structure and Composition of Saturn's Upper Atmosphere From

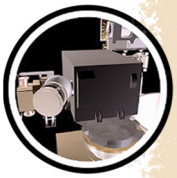

Cassini/Ion Neutral Mass Spectrometer Measurements, Geophysical Research Letters 45, no. 20, pp. 10951–10958, doi: 10.1029/2018GL078454.

Yelle, R. V., V. Vuitton, P. Lavvas, S. J. Klippenstein, M. A. Smith, S. M. Hörst, J. Cui, (2010), Formation of NH 3 and CH 2 NH in Titan's upper atmosphere, Faraday Discussions 147, pp. 31–49. doi: 10.1039/C004787M.

Yelle, R.V., J. Cui, I.C.F. Müller-Wodarg, (2008), Methane Escape from Titan's Atmosphere, Journal of Geophysical Research, vol. 113, Issue E10, doi: 10.1029/2007JE003031.

Yelle, R. V., N. Borggren, V. De La Haye, W. T. Kasprzak, H. B. Niemann, I. Müller-Wodarg, J. H. Waite Jr., (2006), The vertical structure of Titan's upper atmosphere from Cassini ion neutral mass spectrometer measurements, Icarus, 182, 567–576.

Yeoh, S. K., T. A. Chapman, D. B. Goldstein, P. L. Varghese, L. M. Trafton, (2015), On understanding the physics of the Enceladus south polar plume via numerical simulation, Icarus, 253, 205–222

Young, D. T., J. J. Berthelier, M. Blanc, J. L. Burch, A. J. Coates, R. Goldstein, M. Grande, T. W. Hill, R. E. Johnson, V. Kelha, D. J. McComas, , E. C. Sittler, K. R. Svenes, K. Szegö, P. Tanskanen, K. Ahola, D. Anderson, S. Bakshi, R. A. Baragiola, B. L. Barraclough , R. K. Black, S. Bolton, T. Booker, Bowman, P. Casey, G. Dirks, N. Eaker, J. T. Gosling, H. Hannula, C. Holmlund, H. Huomo, J. M. Illiano, P. Jensen, M. A. Johnson, D. Linder, T. Luntama, S. Mayrice, K. McCabe, B. T. Narheim, J. E. Nordholt, A. Preece , J. Rudzki, A. Ruitberg, K. Smith, S. Szalai, M. F. Thomsen, K. Viherkanto, T. Vollmer, T. E. Wahl, M. Wuest, T. Ylikorpi, C. Zinsmeyer, (2004), Cassini Plasma Spectrometer Investigation, Space Science Review, vol. 114, pp. 1– 112, doi: 10.1007/s11214-004-1406-4.

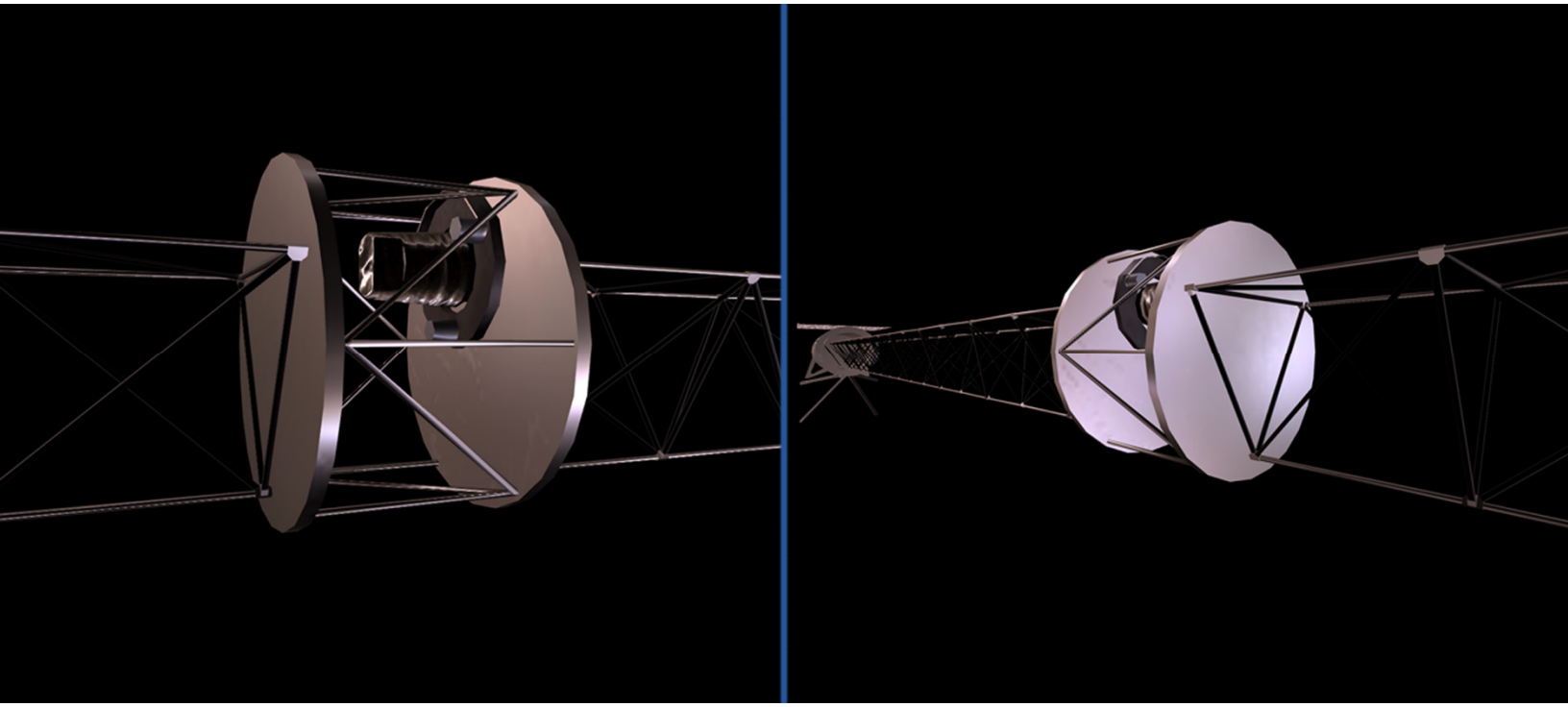

MAGNETOMETER

The Magnetometer (MAG) experiment/instrument onboard the Cassini spacecraft consisted of two magnetometers that measured the magnetic field in and near Saturn's magnetosphere. The **science objectives** of MAG were to determine Saturn's internal magnetic field, map the magnetospheric magnetic field, and characterize the magnetospheric interaction with Titan and the icy satellites. MAG was the first instrument to detect an unusual signature from Enceladus that foreshadowed the Enceladus plume.

MAG consisted of a three-axis Flux-Gate Magnetometer (FGM) and a Vector/Scalar Helium Magnetometer (V/SHM) designed to record the direction and strength of magnetic fields in the Saturn system. On the Cassini spacecraft, the FGM was located midway out on the 11-meter (36-foot) magnetometer boom, and the V/SHM was located at the end of the boom.

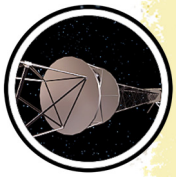

CONTENTS

Tables

Executive Summary

The key science results from the Cassini MAG team include, but are not restricted to:

- Discovery of the atmosphere of Enceladus via its magnetospheric interaction.
- Confirmation of the extreme axisymmetry of Saturn's magnetic field (this work, as well as an attempt to pin down the internal rotation rate, continues with analysis of the Grand Finale data set).
- Discovery of low-latitude, intra-D-ring field-aligned current system at Saturn.
- Mission-long magnetic field measurements of Saturn's planetary period oscillations (PPOs) demonstrate strong, but not simple, seasonal control.
- Saturn's atmosphere-ionosphere-magnetosphere coupling current system consists of two interlinked components.
- Much better understanding of Saturn magnetospheric dynamics.
- MAG-led discovery of Titan's magnetic memory.
- MAG-led discovery of Saturn's two-state magnetosphere.
- MAG/ Magnetospheric Imaging Instrument (MIMI) discovery of the internal inflation for Saturn's magnetosphere.

The key outstanding questions from Cassini MAG data and science output include:

- What are the implications of the extremely axisymmetric planetary magnetic field for the internal structure and dynamics of Saturn?
- What is the dynamo process generating this unique planetary field?
- How are the PPOs driven in the atmosphere/ionosphere of Saturn?
- Understand the variety of currents observed during the periapse periods of the Grand Finale orbits and their implications for coupling between the atmosphere-ionosphere-magnetosphere-rings.

MAG Instrument Summary

The Cassini dual technique MAG consisted of a FGM and a V/SHM capable of operating in scalar mode. The instrument was intended to measure small changes in fields spanning four orders of magnitude with extremely high sensitivity. This was achieved in part by mounting the sensors on an 11-meter spacecraft boom, the V/SHM at the end of the boom, the FGM halfway along it. The FGM was based on three single-axis ring core fluxgate sensors mounted orthogonally on a machinable glass ceramic block. In each sensor, a drive coil was wound around a high permeability ring core, which was completely enclosed in a sense winding. The drive coil was driven by a square wave that was used to generate a magnetic field driving the core into saturation twice per cycle.

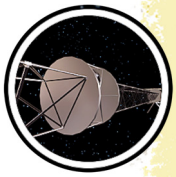

The presence of an ambient magnetic field component parallel to the axis of the sense coil caused the saturation of the core to become asymmetrical. This induced a second harmonic of the drive frequency in the sense coil, which was proportional to the magnitude of the magnetic field component along that axis. The V/SHM was based on field-dependent light absorption (the Zeeman Effect) and optical pumping to sense the magnetic field. Helium in an absorption cell was excited by a radio frequency discharge to maintain a population of metastable long-lived atoms. Infrared radiation at 1,083 nm from a helium lamp passed through a circular polarizer and the cell to an infrared detector. The absorption of the helium in the cell was dependent on the ambient magnetic field direction. The normal data rate for the instrument was 32 vectors/second with the ability to take data in a burst mode at 64 vectors/second. Magnetic field information was needed by other investigations on the spacecraft and to this end, magnetic field data were made available to Magnetospheres and Plasma Science (MAPS) [Blanc et al. 2002] onboard users every second.

Calibration plans had to be changed a year after arrival at Saturn when the V/SHM stopped operating with regular calibration rolls around two separate axes required for the rest of the mission lifetime to enable calibration of the single FGM and hence resolution of the science objectives of the MAG team. MAG is described in detail in Dougherty et al. [2004]; Kellock et al. [1996]; Smith et al. [2001].

KEY OBJECTIVES FOR MAG

The key science objectives for MAG, as described in the Dougherty et al. [2004] paper, are listed below and divided into two main areas, focusing on the planet and its magnetosphere and on Titan. The third area examining the icy satellites of Saturn gained much more importance of course after the initial observations during the first four years of the mission and the water vapor plume discovery [Dougherty et al. 2006] at Enceladus.

All of the MAG objectives have been achieved, with only the 3-D global field model remaining until all of the end-of-mission data has been completely analyzed and modelled.

Saturn

- Resolve the internal planetary magnetic field to at least fourth order.
- Establish relative contributions to electromagnetic and mechanical stress balance.
- Identify the energy sources for dynamical processes.
- Understand the coupling that occurs between the magnetosphere and ionosphere.
- Characterize the phenomena of the distant dayside/flank planetary environment.
- Survey satellite/dust/ring/torus electromagnetic interactions.
- Determine the tail structure and dynamic processes.

- Provide a three-dimensional (3-D) global model of the magnetospheric magnetic field.

Titan

- Determine the magnetic state of the body and conditions of the atmosphere.
- Characterize and model the Titan electromagnetic environment.
- Interpret and model all Titan-plasma flow interactions and the variation of the Titan-magnetosphere interaction with respect to the Titan orbital phase.
- Determine the nature of the low-frequency waves in the near-Titan plasma environment.

Saturnian satellites other than Titan

- Probe the magnetic state and plasma environment of the Saturnian satellites to the extent possible within the limitation of the chosen trajectory.

All of the above objectives have been achieved, with the exception of the 3-D global field model, which still requires work and will be achieved once all of the end-of-mission data has been completely analyzed and modelled.

Key Objectives for MAG from Announcement of Opportunity (AO) and Cassini Solstice Mission (CSM)

- R_AO5—Ring Magnetosphere-Ionosphere Interactions. Study interactions between the rings and Saturn's magnetosphere, ionosphere, and atmosphere.
- M_AO1—Determine the configuration of the nearly axially symmetric magnetic field and its relation to the modulation of Saturn kilometric radiation (SKR).
- M_AO2—Magnetosphere Charged Particles. Determine current systems, composition, sources, and sinks of magnetosphere charged particles.
- M_AO03—Investigate wave-particle interactions and dynamics of the dayside magnetosphere and the magnetotail of Saturn and their interactions with the solar wind, the satellites, and the rings.
- M_AO4—Magnetosphere and Solar Interactions with Titan. Study the effect of Titan’s interaction with the solar wind and magnetospheric plasma.
- M_AO5—Plasma Interactions with Titan’s Atmosphere and Ionosphere. Investigate interactions of Titan’s atmosphere and exosphere with the surrounding plasma.
- I_AO5—Icy Satellite Magnetosphere and Ring Interactions. Investigate interactions with the magnetosphere and ring systems and possible gas injections into the magnetosphere.

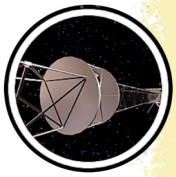

- J_AO3—Explore the dusk side of the magnetosphere and intermediate regions of the magnetotail unvisited by previous spacecraft.
- C_AO2—Investigate the behavior of the solar wind during solar minimum, for comparison with earlier Galileo and Ulysses measurements.
- S_AO3—Saturn Interior Structure and Rotation. Infer the internal structure and rotation of the deep atmosphere.
- S_AO4—Saturn Ionosphere-Magnetosphere Interaction. Study the diurnal variations and magnetic control of the ionosphere of Saturn.
- T_AO4—Determine the physical state, topography, and composition of the surface; infer the internal structure of the satellite.
- IN1a—Determine the presence of an ocean at Enceladus as inferred from induced magnetic field and plume composition, search for possible anomalies in the internal structure of Enceladus as associated with plume sources, and constrain the mechanisms driving the endogenic activity by in situ observations and remote sensing.
- IN1c—Determine whether Dione exhibits evidence for low-level activity, now or in recent geological time.
- IN2b—Determine whether Tethys contributes to the E-ring and the magnetospheric ion and neutral population.
- SC2a—Observe the magnetosphere, ionosphere, and aurora as they change on all time scales—minutes to years—and are affected by seasonal and solar cycle forcing.
- SN1a—Determine Saturn's rotation rate and internal structure despite the planetary magnetic field's unexpected high degree of axisymmetry.
- MC1a—Determine the temporal variability of Enceladus' plumes.
- MC1b—Observe Saturn's magnetosphere over a solar cycle, from one solar minimum to the next.
- MC2a—Observe seasonal variation of Titan's ionosphere from one solstice to the next.
- MN1a—Determine the dynamics of Saturn's magnetotail.
- MN1b—Conduct in situ and remote sensing studies of Saturn's ionosphere and inner radiation belt.
- MN1c—Investigate magnetospheric periodicities, their coupling to the ionosphere, and how the SKR periods are imposed from close to the planet (3–5 R_S) out to the deep tail.
- MN2a—Determine the coupling between Saturn's rings and ionosphere.

- TC2a—Observe Titan's plasma interaction as it goes from south to north of Saturn's solar-wind-warped magnetodisk from one solstice to the next.
- TN1b—Determine internal and crustal structure: liquid mantle, crustal mass distribution, rotational state of the surface with time, intrinsic and/or internal induced magnetic field.

MAG Science Assessment

Table MAG-1. AO and TM objectives are paired with MAG science objectives.

Fully/Mostly Accomplished: **Partially Accomplished:** **Not Accomplished:**

MAG Science Objectives Characterize the following:	AO and TM Science Objectives	MAG Science Assessment	Comments, if yellow (partially fulfilled)
Planetary magnetic field	S_AO3, M_AO1, SN1a		
Magnetospheric structure and dynamics			
Magnetospheric periodicities	MN1c, SC2a		
Saturn magnetosphere-ionosphere coupling	R_AO5, S_AO4, MN1b, MN1c, MN2a		
Magnetospheric current systems	M_AO2		
Magnetosphere—dayside, middle magnetosphere, magnetotail, solar wind interaction	M_AO3, MN1a		
Seasonal and solar wind variation	SC2a, MC1b		
Ring-magnetosphere interactions	R_AO5, MN2a		
Titan			
Titan and magnetospheric interaction	M_AO4, M_AO5, T_AO4, MC2a, TC2a, TN1b		
Icy satellites			
Enceladus internal structure and activity	MC1a, IN1a		
Moon-magnetosphere interaction	I_AO5		
Icy satellite activity, Dione, Tethys	IN1c, IN2b		
Non-Saturn science			
Jovian magnetosphere	J_AO3		
Properties of the solar wind	C_AO2		

MAG Saturn System Science Results

Saturn's Bow Shock

The distant apoapsis orbits by the Cassini spacecraft around Saturn over many years enabled hundreds of bow shock crossings. This allowed for thorough analyses from modelling the (3-D) shape and predicting the location of the boundary to investigating the microphysics of high Mach

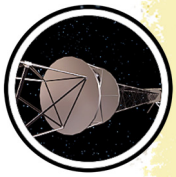

number shocks. The magnetometer instrument proved indispensable in advancing our understanding of Saturn's bow shock. Below are the highlights:

Detailed characterization of Saturn's bow shock

Masters et al. [2008a] and Went et al. [2011a] developed the most comprehensive semi-empirical model of Saturn's dayside bow shock. The average 3-D shape of the boundary was constructed and equations relating the response of the subsolar point to variations in solar wind dynamic pressure were derived. The identification of bow shock crossings was most reliably and straightforwardly achieved using MAG. The classic signature for an inbound crossing, i.e., from the solar wind to the magnetosheath, was an abrupt rise from a low and steady to a large (~4x) and turbulent magnetic field strength. The reverse was the case for an outbound crossing.

The magnetometer instrument proved indispensable in advancing our understanding of Saturn's bow shock.

Achilleos et al. [2006] presented magnetic field signatures of some of the earliest crossings in the mission. Their results showed clearly defined overshoot and foot signatures that are typical of quasi-perpendicular shocks. This is one of two configurations of shocks in magnetized plasmas (the other being quasi-parallel) where the local normal to the shock surface makes an angle of >45° to the interplanetary magnetic field. This is by virtue of the Parker spiral structure of the interplanetary magnetic field (IMF) at 10 AU, where the magnetic fields met the bow shock with very large azimuthal components. Sulaiman et al. [2016] characterized Saturn's bow shock using the largest sample of crossings to date. With the utility of the aforementioned models, they showed Saturn's dayside bow shock was in the quasi-perpendicular configuration for a large majority of the time. Further, they estimated the Alfvén Mach numbers (a measure of the shock's strength) for all crossings to show that Saturn's bow shock spans over a very wide range of parameter space. The bow shock was found to exhibit characteristics akin to both terrestrial and astrophysical regimes. This laid the foundation for further detailed studies specific to astrophysical shocks (e.g., surrounding young supernova remnants), providing an in situ insight into such regimes, which were otherwise studied using remote observations and/or simulations. Masters et al. [2008b, 2009a] presented a survey of hot flow anomalies at Saturn's bow shock, all of which were associated with energization of solar wind electrons. Having been a well-established phenomenon at the Earth's bow shock, these works underlined hot flow anomalies as a solar system-wide phenomenon.

Dissipation at high Mach number shocks

In the presence of an obstacle, shock waves in a neutral gas efficiently dissipate the supersonic flow to subsonic through the action of collisions. In space plasmas, however, shocks cannot rely on collisions to adequately dissipate the flow since the collisional mean free path is many orders of magnitude larger than the shock's width. Here, electromagnetic forces play important roles to compensate for the additional dissipation required. Their roles are well understood for modest Mach

numbers (e.g., 2–10). However, the dissipation becomes more complicated at larger Mach numbers since additional kinetic processes, namely ion reflection and reformation, come into play to complete the process. Fortunately, such high Mach number phenomena were explored using the Cassini magnetometer dataset. Sulaiman et al. [2015] showed evidence for the timescales of ions reflection at a shock undergoing reformation to be 0.3 times the upstream gyroperiod. This was in excellent agreement with what had been theorized.

Masters et al. [2011a] investigated the Mach number dependence of electron heating across a bow shock. Their work presented a positive correlation between the electron temperature increase across the shock and kinetic energy of an incident proton, where electron heating accounts for ~3%–7% of the incident ram energy. Further, they confirmed that the trend of the decreasing percentage with increasing Alfvén Mach number continues into the poorly explored high Mach number regime, up to ~150. Masters et al. [2013a] compared observations of overshoots between Mercury's and Saturn's bow shocks, both of which represent drastically different Mach numbers in parameter space. They showed, on average, the overshoots at Saturn's bow shock were much higher than those observed at Mercury's. This supported the larger role of particle dynamics at higher Mach numbers. The low Mach number class of shocks were also explored. Sulaiman et al. [2017a] examined the dispersive properties of Saturn's bow shock through the identification of electromagnetic precursors consistent with whistler waves. These waves were believed to play a limited role in the dissipation process and were found to be right-handed circularly polarized with a frequency of 0.2–0.4 Hz in the spacecraft frame.

Electron acceleration at high Mach number shocks

Collisionless shock waves are also known to be efficient particle accelerators. It is widely believed that a large proportion of cosmic rays originate from energetic charged particles accelerated at collisionless shocks associated with supernova explosions in our galaxy. Masters et al. [2013b] confirmed, for the first time, electron acceleration up to relativistic energies at an unusually strong Saturn bow shock under a quasi-perpendicular configuration. This contradicted previous knowledge purporting a magnetic dependence on this phenomenon. Further works by Masters et al. [2016] and Masters et al. [2017] provided the full picture of suprathermal electrons at Saturn's bow shock. They showed results that are consistent with the theory in which the injection of thermal electrons into an acceleration process is possible for all magnetic field configurations at high Mach numbers.

Additionally, MAG provided important observations to study the properties of Saturn's foreshock, the portion of the upstream solar wind magnetically connected to Saturn's bow shock. An in-depth characterization of the waves originating from solar wind-charged particles backstreaming from the shock [Bertucci et al. 2007a] was followed by the identification of the spatial extent of the region where these waves are observed [Andres et al. 2013] with a technique that was also successfully applied to the Earth's foreshock [Andres et al. 2015].

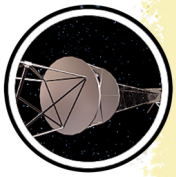

Saturn's Magnetosheath

Long-term sampling of Saturn's magnetosheath by Cassini afforded the most complete coverage of this intermediary region between the unshocked solar wind and Saturn's magnetosphere. A relatively high Alfvén Mach number solar wind and a polar-flattened magnetosphere make Saturn's magnetosheath both physically and geometrically distinct from the Earth's. Fast rotating gas giants, such as Saturn, are bulged along the equator and flattened along the poles owing to their embedded plasma disks and for this reason, Sulaiman et al. [2014] showed that the magnetic structure of Saturn's magnetosheath significantly deviated from axisymmetry. Their results showed large northward/southward components in the magnetic field despite the prevailing Parker spiral configuration being largely in the equatorial plane.

Sulaiman et al. [2017b] addressed the impact of nonaxisymmetry with the aid of magneto-hydrodynamic (MHD) simulations. They showed that Saturn's polar-flattened magnetosphere channels ~20% more flow over the poles than around the flanks at the terminator. They further showed the pressure gradient force is the primary driver accelerating the magnetosheath plasma. This is by virtue of the high-β plasma and, in turn, the high Mach number bow shock. This translated into larger pressure gradients over shorter paths (over poles) compared to longer paths (around flanks), which explained the net torque on magnetic field lines to produce the large northward/southward components. These results are anticipated to provide a more accurate insight into the global conditions upstream of Saturn and the outer planets.

Saturn's Magnetopause

Data taken by MAG at the magnetopause boundary of Saturn's giant magnetosphere have allowed us to examine the ways in which energy can be transferred into and out of near-Saturn space. Understanding this is crucial for revealing the dynamics of the coupled planetary system of magnetosphere, moons, rings, and atmosphere.

A good understanding of the geometry of the magnetopause, and how its position changes with the pressure of the solar wind, is important for characterizing the distant dayside magnetosphere and in developing a 3-D global model of the magnetospheric magnetic field. Arridge et al. [2006] used early measurements of the magnetopause from Cassini/MAG, combined with measurements from Voyager 1 and 2, and Pioneer 11, to develop a new model of Saturn's magnetopause. This study employed a new mathematical formulation, borrowed from studies of the terrestrial magnetosphere, and a new modelling methodology. This revealed that Saturn's magnetosphere was more compressible than previously thought: more compressible than Earth's magnetosphere, but less than that of Jupiter. This was confirmed and enhanced in further studies using larger datasets from Cassini/MAG [Kanani et al. 2010; Pilkington et al. 2015a]. In a study by Achilleos et al. [2008], the MAG team analyzed some of the early orbits and the points along those orbits where the spacecraft crossed the magnetopause. By analyzing the distribution of the magnetopause crossings, we concluded that the size of the magnetosphere was certainly being controlled by the dynamic pressure of the solar wind upstream of the planet, but that there was also

evidence for an additional influence, probably due to a process internal to the magnetosphere. The system preferentially spent most of the time in one of two states, characterized by subsolar magnetopause distances near ~22 and ~27 Saturn radii.

A study some years later [Pilkington et al. 2015b] built upon this work by constructing an up-to-date empirical model of Saturn's magnetopause, based on an extensive set of magnetopause crossings observed by the spacecraft. We found that we could not satisfactorily fit these crossings in their entirety by assuming a system whose size responded only to solar wind pressure. By separating the crossings into subsets based on additional plasma data from the MIMI instrument, we were able to demonstrate that Saturn's magnetosphere plausibly made transitions between states that were plasma-light and plasma-loaded, this form of internal control exerting additional influence on the magnetopause size. The work of Pilkington et al. [2015b] represented a natural progression from an earlier version of the Saturn magnetopause model developed by Arridge et al. [2006], based on a necessarily more limited dataset from several years earlier in the mission.

The structure of the magnetopause boundary itself provides information about the processes at work in this region of Saturn's space environment. MAG data have shown that the magnetopause current layer itself is typically in motion at speeds of order 100 km s^{-1} [Masters et al. 2011b]. This very high speed is considerably faster than that of the spacecraft during magnetopause encounters (a few km s^{-1}). The data also provide the first clear evidence for the existence of a boundary layer of mixed plasma immediately inside the magnetopause [Masters 2011a]. This low-latitude boundary layer is particularly important because it is the direct result of the mass and energy transport that we wish to understand. Magnetic field measurements have played a crucial role in determining that the typical thickness of the layer is approximately 1 Saturn radius (~60,000 km).

The observed variability in low-latitude boundary layer properties between spacecraft crossings of the near-magnetopause region led to a number of surprises. Firstly, the basic thermal electron structure of the layer is significantly variable—a phenomenon not reported in the context of Earth's magnetosphere, and yet to be explained [Masters et al. 2011c]. Secondly, the thickness of the layer itself shows no clear response to the direction of the Sun's interplanetary magnetic field in the vicinity of Saturn, in stark contrast with the behavior of the equivalent region of Earth's magnetosphere [Masters et al. 2011b]. The latter of these two unexpected results can help us to reveal the nature of a particular boundary process.

Magnetic reconnection is a fundamental process that can operate at a current sheet. It results in the release of energy stored in the local magnetic field, leading to acceleration of charged particles and allowing the direct transfer of mass and energy across an otherwise closed boundary. While evidence for the known operation of reconnection at Saturn's magnetopause has been sparse, MAG observations have formed the basis of important assessments that have broad implications. The first such assessment demonstrated that conditions at the magnetopause boundary of Saturn's magnetosphere are dramatically unlike those at Earth's magnetopause. As a result, reconnection at Saturn's magnetopause should be more restricted to regions where magnetic field lines adjacent to the boundary are locally anti-parallel to each other [Masters 2012a].

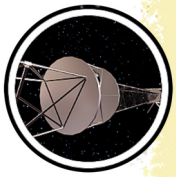

This Cassini result led to a shift in how we think about the solar wind-magnetosphere interaction at Saturn, with implications for other magnetized planets.

> Understanding the ways in which energy can be transferred into and out of near-Saturn space is crucial for revealing the dynamics of the coupled planetary system of magnetosphere, moons, rings, and atmosphere.

MAG data has also shown that when reconnection operates at Saturn's magnetopause it likely does so at a speed that is far slower than that associated with reconnection in environments closer to the Sun—for example, the solar corona, the solar wind, Earth's magnetopause, Earth's magnetotail [Masters et al. 2014a]. The reason for this is the way that solar wind properties change as the plasma moves away from the Sun. The Alfvén speed, which dictates the speed of reconnection, drops with heliocentric distance, producing a relatively slow reconnection process at Saturn's magnetopause and consistent with the lack of evidence for rapid boundary later response discussed above. This result directly contributed to further work that showed that driving of Saturn's magnetosphere by global magnetopause reconnection is rarely strong enough to compete with the internal driving of the system that results from the combination of fast planetary rotation and plasma production due to the plumes of Enceladus [Masters 2015].

A search for reconnection signatures at the Saturnian magnetopause from 10:00 to 14:00 Saturn local time (SLT) was carried out. We found brief intervals during which the normal component of the magnetic field across the magnetopause becomes significantly enhanced for typically 1 to 10 minutes. Through these magnetic bridges, the magnetosphere is connected to the magnetosheath. To determine if the magnetic reconnection leads to a measurable transfer of magnetic flux from the dayside, we checked the location of the magnetopause standoff distance for both northward and southward magnetosheath field. We found no obvious dependence of the distance on the direction of the magnetosheath field, indicating that dayside reconnection does not play a significant role in Saturnian magnetospheric dynamics [Lai et al. 2012].

The other important mechanism by which solar wind energy can enter a planetary magnetosphere is via a viscous-like interaction. This is underpinned by another fundamental process: Growth of the Kelvin-Helmholtz (K-H) instability. Where there are large plasma flow shears across a magnetopause this instability can lead to the evolution of small boundary perturbations in to gentle waves and eventually in to large, rolled-up vortices. The first evidence for magnetopause surface waves from Cassini came in the form of normals to the boundary determined from magnetic field observations that exhibited an oscillation in a preferred direction from one magnetopause crossing to the next [Masters et al. 2009b]. The direction of wave propagation (direction of boundary normal oscillation) was controlled by the local direction of the magnetic field inside the boundary, consistent with K-H-driven waves.

Extension of this initial study to consider hundreds of magnetopause crossings over a period of years subsequently revealed the bigger picture [Masters et al. 2012a]. Such waves are

ubiquitous, present at approximately half of all magnetopause encounters made by Cassini. Further evidence of the influence of adjacent magnetic fields on the wave propagation direction and a dawn-dusk difference in typical wave period demonstrated that growth of the K-H instability is one of the major drivers of these waves and, potentially, the dominant driver.

Perhaps the most compelling evidence for K-H instability at Saturn's magnetopause is the reported evidence that the spacecraft flew through a K-H–driven plasma vortex on the magnetopause in December 2004 [Masters et al. 2010]. Surprisingly, this vortex encounter coincided with detection of electrons with energies exceeding ~20 keV. This unexpected feature led Cassini scientists to speculate that there may be electrodynamic coupling between boundary vortices and Saturn's upper atmosphere, potentially producing some of the spot-like features regularly observed in the sources of planetary auroral emissions.

Similar to many topics, Cassini has revolutionized our understanding of how the solar wind influences Saturn's giant magnetosphere, where magnetic field observations are an essential element. Many questions have been answered, with a number of unexpected results. Cassini has made us redefine major open questions, to be addressed by future missions. An important open question relevant for this topic in the post-Cassini era is: Does the solar wind primarily interact with Saturn's magnetosphere through K-H instability?

Saturn's Magnetosphere

Saturn's cusp

At Earth, the solar wind is the primary energy source that can drive dynamical processes in the magnetosphere, and it is also a primary source of plasma. Before Cassini's arrival, it was not clear what role the solar wind played in driving the Saturnian magnetosphere, and so understanding the coupling between the solar wind and the magnetosphere, characterizing the phenomena of the distant dayside/flank planetary environment was an important goal. This included studying viscous and magnetic reconnection processes at the magnetopause. Flux transfer events are a signature of dayside magnetic reconnection at Earth, Mercury, and Jupiter, and consist of a rope of magnetic flux and plasma peeling away from the magnetopause. Jasinski et al. [2016] presented an example of a flux transfer event at Saturn (the only one) and showed that this single event made a fairly small contribution (<10%) to the magnetic flux transport budget, although it was not clear how typical this event was, and if they are more prevalent at locations on the magnetopause not sampled by Cassini.

At higher latitudes, a region known as the cusp maps to a very wide region of the magnetopause and so is ideal for remote monitoring of the magnetopause for reconnection signatures, revealing coupling between the solar wind and the magnetosphere. Cassini's inclined orbits during 2007/2008 and 2013/2014 were ideal to study this coupling process in plasma—Cassini Plasma Spectrometer (CAPS)—and the magnetic field—MAG. Some of the early inclined orbits in early 2007 showed evidence of solar wind plasma gaining entry into the magnetosphere

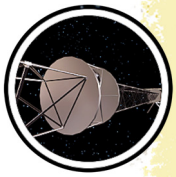

[Arridge et al. 2016a]. This work showed evidence for movement of the cusp region in phase with magnetospheric (so-called planetary-period) oscillations, indicating the presence of current systems in the magnetosphere. It was also found that magnetopause reconnection was possible under both compressed and expanded magnetospheric conditions [Jasinski et al. 2016; Arridge et al. 2016a], and that the reconnection process could proceed in an unsteady fashion and at various locations on the magnetopause [Jasinski et al. 2014, 2016; Arridge et al. 2016a]. Cavities, where the plasma reduced the local magnetic field strength, were also detected, similar to Earth and Mercury, but at Saturn, the plasma was less capable of reducing the magnetic field strength, and there were important morphological differences due to the presence of internal plasma in the magnetosphere [Jasinski et al. 2017]. Saturn's cusp is the most thoroughly surveyed amongst the giant planets, and sets important context for the Juno mission at Jupiter.

Disk-like magnetosphere

Saturn's magnetosphere is an example of a rapidly rotating system dominated over much of its extent by a large magnetodisk of rotating plasma, this material falling further behind corotation with the planet as we go to larger distances from the planet. Because the system is so large, centrifugal force becomes very effective at keeping the cold plasma confined as this near-equatorial disk. In order to develop a first-principles model of Saturn's magnetodisk region, Achilleos et al. [2010a] adapted a model of field and plasma developed for the Jovian system by Caudal [1986], using plasma data available at that time to constrain the model's boundary conditions. This model was successfully used to explain the observed response of the planet's magnetospheric field to changes in system size. We were also able to compare the model contributions to the total magnetodisk current associated with the various forces on the plasma—centrifugal force and pressure gradient force—for both the Kronian and Jovian magnetodisk systems. A follow-up study by Achilleos et al. [2010b] explored particularly the influence of global changes in the energetic particle population on Saturn's magnetodisk structure. This model was also used in a study by Sorba et al. [2017], who developed theoretical compressibility curves showing how the magnetodisk size responds to changes in solar wind pressure and internal plasma content (energetic particles). These theoretical results were in good agreement with the observational analysis of Pilkington et al. [2015b] and we were also able to use the model to explain why one would expect the compressibility of the system to vary with system size. We have also had some success in using this magnetodisc model, combined with the current sheet elevation model of Arridge et al. [2011a], in order to model global, near-planetary-period oscillations in the magnetic field and plasma properties [Achilleos et al. 2014].

It has been shown that periodic variations of the plasma density peak at different rotation phases depending on radial distance in the magnetosphere. We showed that this variation arises as a consequence of the interaction between simple rotation and the expansion and contraction of the magnetosphere associated with propagating compressional disturbances [Ramer et al. 2017]. Propagating compressional disturbances also cause the magnetopause to move in and out non-sinusoidally and somewhat asymmetrically [Kivelson and Jia 2014]. The simulation also explains

the dawn–dusk asymmetry of field configuration and plasma flows in Saturn's magnetosphere [Jia and Kivelson 2016].

Drivers of magnetospheric dynamics

Saturn is often placed in between Earth (solar wind driven) and Jupiter (internally driven) in terms of its magnetospheric dynamics, but this is an oversimplified picture. Much work has been done to characterize the structure of the solar wind upstream of the planet. Jackman et al. [2004] analyzed several solar rotations worth of upstream IMF data while Cassini was approaching Saturn, and Jackman et al. [2005a] followed up with an analysis of the solar wind excursion on Cassini's long first capture orbit. Overall, it was found that during the declining phase of the solar cycle, the IMF is structured into a very clear pattern of two compressions per solar rotation separated by rarefactions. This structuring is very useful because it helps to predict the phasing of intermittent driving of the magnetosphere by the solar wind. Jackman et al. [2004] developed an empirical formula to calculate how much open flux is generated through dayside reconnection, dependent on the IMF direction, the solar wind velocity, and assuming a certain length of a predicted reconnection x-line at the dayside magnetopause. This formula has since been widely used by many other authors, in particular to compare to auroral images that seem to indicate addition and removal of flux—for example, Badman et al. [2005, 2012]. The solar wind conditions at Saturn (and Jupiter) spanning all stages of the solar cycle were summarized in Jackman and Arridge [2011a]. Reconnection voltages were predicted to be slightly lower at solar minimum than solar maximum, while increased photoionization of the Enceladus torus at solar maximum can lead to a more plasma dominated system at this stage of the solar cycle.

In a review article [Khurana et al. 2018], we showed that both azimuthal and radial currents in Saturn's magnetosphere exhibit local time asymmetries as has been reported in Jupiter's magnetosphere. Further, in these magnetospheres, the corotation enforcement currents (CEC), which flow in the radial direction in the current sheet, rival the strengths of their azimuthal ring currents. We also reviewed our knowledge of the field-aligned currents (FACs) in these magnetospheres.

> Before Cassini's arrival, it was not clear what the role the solar wind played in driving the magnetosphere, and so understanding the coupling between the solar wind and the magnetosphere … was an important goal.

Magnetic flux and plasma circulation

In Lai et al. [2016], we investigated the returning flux tubes in the inner Saturnian magnetosphere. By studying the location distribution of the flux tubes, we confirmed that their magnetic signatures are different depending on the background plasma environments. Inside the plasma disk, the returning magnetic field is enhanced in strength, while outside the plasma disk, the magnetic field is depressed in strength. We also suggested that the flux tubes break into smaller ones as they convect in. By statistically comparing the entrance and exit normal vectors of the flux tubes, we

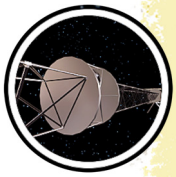

determined the shape of their cross-section. We found that it is closer to circular than fingerlike as produced in the simulations based on the interchange mechanism. In addition, no sudden changes in any flux tube properties can be found at the boundary, which has been claimed to separate the reconnection and interchange-dominant regions. By matching the magnetic flux transporting rate with the tail reconnection rate, a reasonable cold plasma loss rate (~150 kg/s) is derived. Meanwhile, the estimated outflow velocity agrees with earlier observations [Wilson et al. 2008].

Magnetotail structure

Cassini MAG measurements (often in concert with plasma measurements) have been used to characterize the tail in terms of distinguishing the lobe and plasma sheet regions and exploring how they change with distance from the planet. The current sheet is found to be warped out of the equatorial plane [Arridge et al. 2008a], with a characteristic hinging distance of ~25 R_S. This warping made a significant impact in Saturn's southern hemisphere summer in 2006 when Cassini executed its deepest tail orbits, first in the equatorial plane (below the hinged current sheet) and later at higher latitudes (close to the hinged current sheet). The current sheet has also been found to flap, or oscillate vertically with a period close to the ~10 hours linked to the mysterious planetary periodicities. Jackman and Arridge [2011b] performed a statistical study of Saturn's lobes and plasma sheet during 2006, developing numerical definitions for these regions, and deriving the falloff of the field strength in the lobes with radial distance. They found that the near magnetotail of Saturn is similar to that of Jupiter and Earth (when scaled to a common distance). Unlike at Earth, we do not have spacecraft coverage of the asymptotic tail region, but rather have likely only covered the part of the tail where the magnetopause boundary is still flaring outward and where the lobe field strength is falling off before reaching a steady asymptotic level. We do not know the exact length of Saturn's tail, but can consider arguments first made by Dungey [1965] for the Earth where length was estimated by time for open field lines to be dragged over the poles before ultimately sinking in toward the center of the tail before reconnection (giving ~1,000 R_E). Milan et al. [2005] examined the case at Saturn where the polar cap refresh time (i.e., the time for magnetic flux to be cycled through dayside to nightside reconnection) is expected to be many days—for example, Jackman et al. [2004] compared to a much shorter (~10–11 hours) planetary rotation period. This may be expected to twist the lobes of the tail and Milan argued each turn of a twisted lobe could be ~900 R_S long. They theorized that Saturn is a last-in–first-out system in which recently opened field lines are the first to be closed by reconnection in the tail, due to this twist. This implies that Saturn's tail lobes contain a core of old open field lines that can be stretched to incredible lengths (>15,000 R_S).

It has been described how periodic compressional waves can account for periodic variation in the thickness of Saturn's nightside plasma sheet and proposed resonances as an explanation for the appearance of banded structure in ion dynamic spectra [Thomsen et al. 2017].

In situ observations of reconnection

Saturn's magnetosphere is observed to undergo dramatic, explosive energy release events. The first indication of such behavior was on the outbound pass of Saturn Orbit Insertion (SOI) where Bunce et al. [2005] reported an episode of solar wind compression-induced tail reconnection, with dipolarizing field and injection of hot plasma. The products of reconnection tailward of the x-line (plasmoids and travelling compression regions [TCRs]), were first observed with the Cassini magnetometer by Jackman et al. [2007]. They are identified primarily by a bipolar deflection in the north-south component of the field, with northward turnings implying reconnection products tailward of the x-line and southward turnings implying dipolarizations planetward of the x-line. Multi-instrument views of reconnection events reveal changes in the flow pattern from azimuthal to tailward and local heating of the plasma—for example, Jackman et al. [2008a]. It is sometimes observed that northward turnings are not purely bipolar but instead have an extended interval where the field remains northward. This has been interpreted as the Kronian equivalent of the post-plasmoid plasma sheet [Jackman et al. 2011], which represents an interval where previously open flux is being closed by reconnection.

Over the years, catalogs of reconnection events were built up from by-eye surveys and basic automation involving simple background thresholding of the magnetic field and searching for significant deflections above or below these thresholds. Surveys covering the deepest tail orbits of 2006 revealed a significant imbalance between the rate of mass loss inferred from plasmoid release and the rate of mass loading from the moon Enceladus, which has been termed the mass budget problem [Jackman et al. 2014]. More sophisticated automated event searches have returned surveys of >2,000 events from tail orbits during 2006, 2009, and 2010, and Smith et al. [2016] revealed that the rate of observed reconnection events peaked post-midnight, with a highly variable radial location of the reconnection x-line, with an average ranging from 20–30 R_S from the planet. To date only one study has identified the x-line region itself [Arridge et al. 2016b], while more recently Smith et al. [2018a] presented a series of very short duration reconnection-related inward and outward flows in quick succession on the dusk flank. Their interpretation was that over a 7-hour interval investigated, reconnection sites had formed both tailward and planetward of the spacecraft, showing that reconnection can operate on small spatial/temporal scales. A second case study showed an event during which the reconnection site was inferred to retreat tailward, resulting in progressively hotter, dipolarizing material reaching Cassini.

The properties of dipolarizations planetward of the x-line give us another view of the impact of reconnection on the magnetosphere. Jackman et al. [2013] published a case study that showed rapid acceleration of newly-reconnected field lines back toward the planet. The transition from a radially stretched to dipolar field configuration can cause a current which usually flows across the tail to divert into the ionosphere, potentially leading to bright, distinct spots of auroral emission. Jackman et al. [2015] further showed that dipolarization of the field can be accompanied by ion flows at speeds of up to 1,500 km/s toward the planet following tail reconnection, representing a significant departure from the slower, subcorotational flow typically seen in the tail. A reconnection event that starts at a small x-line can have a big impact on the magnetosphere as a whole.

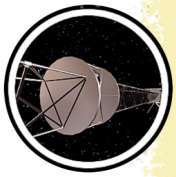

Dipolarizations themselves have also been shown to have a dramatic effect on the local plasma: Smith et al. [2018b] investigated dipolarizations as identified from southward deflections of the magnetic field and found they were clustered preferentially post-midnight. The analysis of the accompanying CAPS data showed that the dipolarizing material was systematically hotter and less dense than the ambient plasma sheet. This density depletion and heating was found to be much more variable post-midnight, suggesting a more variable reconnection site.

Remote observations of global impact of reconnection

It is also important to consider how reconnection fits into the bigger picture of global magnetospheric dynamics. Jackman et al. [2016] reported that, like so many other phenomena, tail reconnection at Saturn is organized by northern and southern magnetic phase. Events are specifically linked to current sheet thinning and outward displacement of field and plasma. Little evidence was found for visibility effects associated with the north-south motion of the plasma sheet.

The question of whether reconnection is linked to internal or external drivers is an important one, and one approach to exploring this is to examine the radio data that accompany the magnetometer observations. Jackman et al. [2005b] explored concurrent IMF and SKR data from Cassini during Saturn Orbit Insertion. They showed that the SKR intensified and extended to lower frequencies coincident with the arrival of a solar wind compression, while many other studies have also explored this strong link between the radio power (and frequency) and the nature of the solar wind.

Jackman et al. [2009a] explored the SKR in more detail, focusing on several case studies where reconnection had been observed in Saturn's magnetotail. In general, they found a good correlation between the timing of reconnection events and enhancements in the SKR emissions. A physical mechanism was put forward whereby reconnection increases the precipitation of energetic particles into the auroral zones, leads to the formation of a potential drop, and thus stimulates the motion of the SKR source region to higher altitudes along the field line (and, hence, lower frequencies of radio emission). These low frequency extensions (LFEs) of the SKR were seen as strong proxies for dynamic solar wind compression and/or tail reconnection events.

Reed et al. [2018] attempted to automate the search for these LFEs in the SKR data and correlated 282 LFEs found during 2006 with a larger catalogue of reconnection events. LFEs were grouped into two categories, with short events of duration <20 hours separated by a median waiting time of ~10 hours, and strongly correlated with the northern and southern SKR phases. 60% of short LFEs have a reconnection event within the preceding 6 hours. The second category, long events, had duration >20 hours, often lasting multiple planetary rotations and associated with increases in solar wind dynamic pressure.

Saturn's magnetodisk current

Amongst the central goals of the Cassini magnetic field investigation is the characterization of the large-scale current systems that flow in Saturn's magnetosphere, their typical properties together

with their variability and dynamical behavior. The largest of these is Saturn's ring/magnetodisk current. This current flows in the equatorial magnetosphere eastward around the planet, extending the field lines radially outward and carried by the differential drift of ions and electrons in the plasma trapped on Saturn's magnetic field lines, which grades into the cross-tail plasma sheet current separating the lobes of the magnetic tail on the nightside. Although the existence of the ring current was first established from magnetic data acquired during the Pioneer-11 and Voyager flybys, little was known of the variability of the current, and its physical nature remained a matter of controversy, whether due to centrifugal action of the plasma mass or to the effect of plasma pressure. Data from the initial sequence of near-equatorial Cassini orbits was first used to determine the strength and radial extent of the current, showing that these vary strongly with the size of the magnetosphere dependent on the dynamic pressure of the impinging solar wind [Bunce et al. 2007]. While the inner edge of the current lies nearly unvaryingly at an equatorial radial distance of ~7 R_S, the radius of the outer edge varies between ~15 R_S when the magnetosphere is strongly compressed to ~22 R_S when it is significantly expanded, these distances typically lying only few R_S inside the dayside magnetopause. Correspondingly, the total eastward current varies from ~9 to ~15 MA, with a magnetic dipole moment that varies between ~0.2 and ~0.6 that of the internal field of the planet. A consequence is that while the dayside and comparably near nightside field is quasi-dipolar in form when the system is compressed, the field lines extend into an equatorial magnetodisk when it is expanded [Bunce et al. 2008a]. Later, when data from the first highly inclined Cassini orbits became available, the first direct measurements of the north-south thickness of the current sheet were also made, with values being typically ~3 R_S on the dayside, while varying between ~1 and ~5 R_S on the nightside [Kellett et al. 2009].

Cassini/MAG data revealed the magnetodisc [Arridge et al. 2008b; Bunce et al. 2008a] was particularly sensitive to the solar wind pressure, essentially disappearing on the dayside when the magnetosphere was compressed by the solar wind and explaining why it was not detected by Pioneer 11 or Voyager 1 and Voyager 2 [Arridge et al. 2008b].

The current sheet was also found to be warped out of the equatorial plane, as expected by analogy with Earth and Jupiter, but it was also found to be deformed at noon. Effectively the current sheet had the geometry of a shallow bowl, or upturned umbrella [Arridge et al. 2008a]. Subsequently, a detailed study of data from Earth's magnetosphere, inspired by Cassini/MAG measurements at Saturn, has revealed a similar effect at Earth [Tsyganenko and Andreeva 2014]. Superimposed upon this global warping was a flapping motion that occurred in phased with other periodicities in Saturn's magnetosphere [Arridge et al. 2008c, 2011b] and which had a lag or delay that propagated into the outer magnetosphere. However, latitudinal effects were also shown to play an important role, connected with differing periods in the northern and southern hemispheres [Provan et al. 2012].

Small ripples were also found superimposed on this bowl-shape [Arridge et al. 2007] that are largely propagating away from Saturn, indicating a source closer to the planet, possibly produced by plasma transport in the inner/middle magnetosphere [Martin and Arridge 2017].

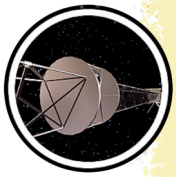

The presence of the current sheet, and its deformation into a bowl shape, has important consequences for Titan's magnetic and plasma environment, and so the structure of its induced magnetosphere [Backes et al. 2005; Arridge et al. 2011b; Simon et al. 2013], as not only is the magnetic field (oriented in a different location to that found by Voyager 1) but also the bowl-shaped current sheet means that the Titan is not continuously immersed in Saturn's magnetospheric plasma.

Detailed collaborative work with the CAPS, MIMI, and Radio and Plasma Wave Science (RPWS) teams also examined the physical nature of the current [Kellett et al. 2010, 2011; Sergis et al. 2018]. It was shown that inside ~10–12 R_S the current is carried principally by the relatively unvarying population of warm (~100 eV) water plasma picked up from the Enceladus torus, comprising principally of inertia and pressure anisotropy currents. Beyond these distances it is carried mainly by the more variable hot tenuous plasma (~10 keV and above) periodically injected from the tail, forming a pressure gradient current (see section entitled Saturn Storms). While, by analogy with Earth, the term ring current particles is often taken to be synonymous with hot injected plasma, this usage has thus proven to be inappropriate at Saturn, since the outwardly-transported warm water plasma is at least as significant in carrying the current.

In a publication dealing with periodic current sheet tilt [Khurana et al. 2009], we provided evidence that Saturn's inner/middle magnetosphere contains semi-permanent azimuthal anomalies in the magnetodisk current region in the fluxes of energetic charged particles, plasma density, magnetic field, and electrical current with a longitudinal wave number m = 1. We demonstrated that in the presence of these anomalies and a finite solar elevation angle, the solar wind lifts Saturn's magnetosphere asymmetrically in longitude, generating a tilt in the current sheet of Saturn.

Current sheet dynamics

Current sheets are also locations where dynamical behavior can be detected and studied. Magnetic reconnection is one important dynamical process that has been studied in detail with Cassini/MAG. Most studies only remotely or indirectly inferred that reconnection was happening—they were detecting the smoke from a distant fire. The location of the fire, the ion diffusion region, remained undetected until MAG played a critical role in the detection and analysis of an ion diffusion region in Saturn's magnetotail [Arridge et al. 2016a]—the only diffusion region to be detected and studied at a giant planet. This revealed the presence of fast magnetic reconnection and highlighted the possible effects of a multicomponent plasma, as studied in the terrestrial magnetosphere. The observations were used to examine the poorly understood mass and magnetic flux transport process, previously referred to as the mass crisis, where the observations of mass loss and magnetic flux transport were insufficient to balance transport and sources in other parts of the system. The observations showed that mass and flux could be conserved, and that undersampling may play a role in generating an apparent crisis. Using MAG, we were able to show that the geometry of the current sheet was important in the correct detection and interpretation of reconnection signatures [Jackman et al. 2009a]. Study of the current sheet has also revealed dynamical behavior connected with the ionosphere. Felici et al. [2016] presented evidence for

plasma flowing out of the ionosphere into the magnetotail where magnetic reconnection was also occurring. This revealed evidence for strong magnetosphere-ionosphere coupling associated with magnetic reconnection that drove outflow from the ionosphere into the magnetosphere.

Planetary period oscillations

Although the singular phenomenon of Saturn's PPOs was first observed by the Voyagers in modulated SKR emissions observed remotely from the planet, and later noted in both Voyager and Pioneer-11 magnetospheric magnetic data, Cassini observations have demonstrated the near ubiquity of oscillations near the planetary rotation period in essentially all magnetospheric plasma, field, and wave data despite the close axisymmetry of the internal planetary magnetic field. Initial work on the magnetic PPOs established their basic properties, first confirming the rotational nature of the oscillations via the Doppler effect of the azimuthal spacecraft motion [Cowley et al. 2006], and second showing that while the perturbation fields in the equatorial region are quasi-uniform in nature [Andrews et al. 2010a], rotating in the equatorial plane as indicated by the earlier flyby studies, the fields at high latitudes are instead quasi-dipolar in form [Provan et al. 2009a], associated with a rotating transverse dipole. The dipole moment is not internally generated by the planet, however, but by an external current system coupling the ionosphere and magnetosphere (see section entitled Field-Aligned Currents). The PPOs are thus associated with a second large-scale current system, and, due to their ubiquitous nature, have proved to be a major aspect of the Cassini Magnetic Field Investigation throughout the mission. In addition, their imprint is seen more widely in the entire Cassini magnetosphere data set. It was shown that the radial distance of the dayside magnetopause and bow shock are also significantly modulated by this phenomenon [Clarke et al. 2006, 2010a, 2010b].

With the further realization, initially from SKR data, that two such oscillations are generally present at the same time with slightly different periods, one associated with the northern polar region and the other with the southern, it was shown that the phase jitter in the equatorial magnetic oscillations previously observed is due to the vector superposition of the two systems [Provan et al. 2011], while the polar oscillations were found to be pure northern and southern on the central polar field lines in the two hemispheres [Andrews et al. 2012]. Cassini data from the deeper tail passes in 2006 correspondingly showed that while the two tail lobes are modulated at their separate polar periods, mixed signals are again present within the plasma sheet that are associated with both north-south oscillations of the current layer together with significant modulations in its thickness [Provan et al. 2012; Szego et al. 2013; Nemeth et al. 2015, 2016]. A model of these PPO-related variations has been derived, which provides a simple explanation of the sawtooth plasma sheet field variations observed during equinoctial conditions of near-equal northern and southern PPO amplitudes [Cowley et al. 2017; Thomsen et al. 2017]. The model has further been

> The final proximal orbits have provided access to previously unexplored field lines crossing and inside Saturn's ring system.

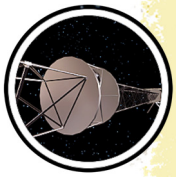

successfully applied to the more northern-dominated conditions prevailing during northern spring [Cowley and Provan 2017].

With the additional realization that the two PPO periods slowly change with Saturn's seasons by ~±1% about ~10.7 h (i.e., ~±6 min), a long-term program of precise (~±10 s) measurement of the magnetic oscillation rotation period and phase has been carried out over the whole Cassini mission [Andrews et al. 2008, 2010b, 2012; Provan et al. 2013, 2014, 2016, 2018]. The results have subsequently been employed by many Cassini and Hubble Space Telescope (HST) teams as a framework to organize their data. The two PPO periods were found to be well-separated in late southern summer conditions at the beginning of the Cassini mission, ~10.6 h for the northern system and ~10.8 h for the dominant southern system, but then slowly converged with near-equal amplitudes to a near-common value ~10.7 h over a ~2 (Earth) year interval centered near vernal equinox (August 2009) [Andrews et al. 2012]. There followed a ~3-year interval in early northern spring when the relative amplitudes changed abruptly at ~100–200-day intervals between southern and northern dominance and near-equal amplitudes [Provan et al. 2013], the southern period ~10.69 h remaining slightly longer than the northern ~10.65 h, before the periods of the two systems coalesced at ~10.70 h in antiphase during the first half of 2014 [Provan et al. 2016]. In mid-2014, the period of the then-dominant northern system began to increase towards ~10.8 h, similar to the southern system in southern summer, while the southern period remained near-fixed at ~10.7 h, thus leading to the first enduring reversal in PPO periods, northern longer than southern, during the Cassini era. The periods remained close to these values across northern summer solstice in May 2017 to the end of mission [Provan et al. 2018]. Possible physical origins of the post-equinox interval of abrupt changes have been discussed in terms of both atmospheric effects [Cowley and Provan 2013] and solar wind influences during the rising phase of the solar cycle [Provan et al. 2015], though clear causality remains to be demonstrated. An additional important theme of these studies has been the comparison of the magnetic field phases and periods with those derived independently by others from analysis of SKR modulations. Although some areas of contention have been debated [Yates et al. 2015a, 2015b; Cowley and Provan 2015, 2016], the overall picture is one of good agreement [Andrews et al. 2008, 2010b, 2011, 2012; Provan et al. 2014, 2016].

The final proximal orbits have provided access to previously unexplored field lines crossing and inside Saturn's ring system. The behavior of the PPO oscillations on these field lines is presently under intense investigation.

Theoretical work [Southwood and Kivelson 2007] describes how a system of rotating field-aligned currents (cam currents) located on a magnetic shell in the range L = 12–15 would account for the periodicity observed in the magnetic field perturbations near the equator. Later, it was shown that the interaction of the rotating cam currents would interact with the global magnetic structure of the magnetosphere to produce periodic variations of current intensity and account for the modulation of the power of SKR [Southwood and Kivelson 2009].

A series of papers elucidated how appropriately placed vortical flows in a rotating ionosphere drive field-aligned currents consistent with the cam current previously proposed. These rotating

currents were shown to provide a quantitatively consistent description of all of the periodic dynamics reported in the system [Jia, X. et al. 2012a; Jia and Kivelson 2016; Kivelson and Jia 2014]. Theoretical work continues to best understand the origin of the two rotations rates [Southwood 2011, 2014, 2015; Southwood and Cowley 2014; Southwood and Chane 2016].

Field-aligned currents

A further major area of study for the Cassini Magnetic Field Investigation relates to large-scale field-aligned current systems, which couple the magnetosphere to the planet's upper atmosphere, ultimately producing the auroral displays seen in images, for example, at ultraviolet (UV) wavelengths. As in other magnetized environments, field-aligned currents in Saturn's magnetosphere play a fundamental role in the transfer of momentum along field lines between the ionosphere, the magnetosphere, and (potentially) the solar wind. At their ends, such currents close cross-field in association with $j \times B$ forces on the corresponding plasmas. Field-aligned currents further relate to the generation of bright discrete auroral forms at ionospheric heights, if current densities directed away from the planet exceed that which can be carried by the ambient precipitating magnetospheric electrons, at which point the latter are accelerated downward into the ionosphere by field-aligned voltages where they deposit their charge and energy. Initial theoretical expectations for Saturn related to meridional magnetosphere-ionosphere currents associated with the transfer of angular momentum from the planet's ionosphere to the net radially-outward transported equatorial plasma principally of Enceladus origin, i.e., the subcorotation currents [Cowley et al. 2004], together with dawn-dusk asymmetries associated with the solar wind interaction [Jackman and Cowley 2006].

Observationally, field-aligned currents are detected and quantified via variations in the azimuthal magnetic field on high-latitude and relatively low-altitude passes across the planet's polar regions. The first such data were acquired by Cassini/MAG in 2006/2007, with simultaneous HST UV imagery on one pass confirming that Saturn's auroral oval indeed maps into a region of upward current requiring downward acceleration of the observed magnetospheric electrons [Bunce et al. 2008b; Cowley et al. 2008]. An overall survey of these data showed that while their basic properties are consistent with theoretical expectations for subcorotation currents, with ~6 MA flowing down into the central polar ionosphere and the same return current flowing upward at lower latitudes in the auroral region, the currents are also modulated by the PPOs [Talboys et al. 2009a]. A much larger data set was then acquired in 2008 that allowed statistical studies to be undertaken [Talboys et al. 2009b, 2011]. It further allowed detailed exploration of the PPO dependence by comparing currents observed under conditions of differing PPO phase [Hunt et al. 2014, 2015, 2018a].

The principal PPO currents are found to be directed upward in a given hemisphere and downward on the opposite hemisphere of the planet's polar ionosphere, and rotate around the pole at the PPO period of the corresponding hemisphere. They are also approximately colocated with the upward current region of the subcorotation system, and of comparable strength, such that where the PPO current flows down, the total field-aligned current is reduced near to zero, while where it flows up the current is doubled, thus suggesting a dynamical connection. It is also found

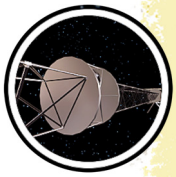

that the auroral region oscillates in latitude with amplitude ~1° in concert with these rotating modulations [Nichols et al. 2008; Provan et al. 2009b; Hunt et al. 2014; Bunce et al. 2014]. A complementary multi-instrument study also established the typical locations of the boundary of open field lines in the two hemispheres at ~13° colatitude in the north and ~16° in the south [Jinks et al. 2014], showing that the main PPO field-aligned currents flow just equatorward of this boundary on closed field lines. Correspondingly, interhemispheric coupling along closed magnetospheric field lines also occurs between the two PPO systems [Hunt et al. 2015; Provan et al. 2018]. Overall, the form of the PPO currents is consistent with driving by rotating twin-vortex flows in the two polar thermospheres/ionospheres [Hunt et al. 2014; Southwood and Cowley 2014].

Comparison between the 2008 data, obtained in the midnight sector, with the dawn-dayside data from 2006/2007 showed little difference, confounding expectations of observing long-term current asymmetries associated with the solar wind interaction [Hunt et al. 2016]. Highly unusual current distributions are observed in a small subset of passes, however, some of which have been associated with Saturn auroral storm solar wind compression events (see section entitled Saturn Storms) [Bunce et al. 2010]. Significant solar wind-related currents thus do flow in Saturn's magnetosphere at least intermittently. Indirect evidence of less dramatic solar wind effects have been obtained from HST studies of the dayside auroras (though not directly in field data), using Cassini as an upstream monitor of the IMF. Morphological auroral differences are found depending on the sense of the north-south component of the IMF, suggestive of dayside reconnection and related driving of flows and currents when the IMF points north [Meredith et al. 2014]. More generally, collaboration with colleagues at Moscow State University has resulted in the development of Saturn magnetospheric field models validated with Cassini data, which incorporate ring/tail and magnetopause currents, and are also parameterized by the strength and direction of the IMF [Alexeev et al. 2006; Belenkaya et al. 2006, 2007, 2010, 2011, 2014, 2016]. These models have been used during intervals when Cassini was located in the solar wind measuring the impinging IMF to map auroral features observed by the HST along field lines into their magnetospheric source regions, namely the middle and outer ring current region typically at dawn, and to the vicinity of the open-closed field boundary for high-latitude emissions near noon.

While the 2006/2007 and 2008 high-latitude data sets both correspond to Saturn's late southern summer, a third interval of high-latitude data was obtained in 2012/2013 during northern spring [Bradley et al. 2018]. The PPO currents were found to be of similar form but somewhat weaker than in 2008, while the subcorotation currents exhibited strong opposite seasonal asymmetries in the north and south polar regions, indicative of weak polar ionospheric conductivity in the winter polar cap. Investigation of the current signatures observed on the F-ring and proximal orbits spanning northern summer solstice at the end of the Cassini mission are currently ongoing [Hunt et al. 2018b].

Saturn auroral storms

Although Voyager radio data had previously demonstrated that SKR emissions are strongly positively correlated with solar wind dynamic pressure, the nature of the related magnetospheric

dynamics remained unknown. This was partially revealed in early 2004 during the Cassini approach to Saturn when an intensive HST campaign imaging Saturn's UV auroras was undertaken, with Cassini acting as upstream solar wind/IMF monitor. As expected during the declining phase of the solar cycle, the recurrent solar wind structure consisted of two corotating interaction regions (CIRs) per ~25-day solar rotation, exhibiting two few-day compression events of enhanced dynamic pressure, one major and one minor [Jackman et al. 2004]. The HST caught the impingement of the major compression region on Saturn's magnetosphere towards the end of the campaign, and observed a major increase in UV and SKR emissions with bright auroral forms extending throughout the dawn sector up to the planetary pole itself [Clarke et al. 2005; Bunce et al. 2006]. It was suggested that such auroral storms are caused by major bursts of compression-induced reconnection in Saturn's nightside tail, that inject hot plasma towards Saturn, which subsequently flows around the planet via dawn under the action of magnetosphere-ionosphere coupling [Cowley et al. 2005]. Estimates of the reconnection rate yielded associated voltages of at least several hundred kV [Badman et al. 2005]. Monitoring of the interplanetary field prior to SOI showed that the same compression region would likely impinge on the system during the SOI fly-through of the magnetosphere [Jackman et al. 2005a, 2005b], and indeed did, with a corresponding magnetic dipolarization event, plasma energization, and enhanced SKR emissions being observed in the nightside magnetosphere on the outbound pass [Bunce et al. 2005]. Analysis of a larger number of compression events observed by Cassini acting as upstream IMF monitor during the approach phase, as well as outbound after SOI in late 2004, also showed characteristic enhancements in SKR, but with the regular pulsing at the PPO period generally being undisturbed in phase [Badman et al. 2008].

Studies led elsewhere subsequently detected numerous reconnection-related events during the main Cassini tail exploration interval in 2006, namely planetward-travelling dipolarizations and tailward-travelling plasmoid structures, which were found to be related in timing to both the pulsing of the SKR emissions and the magnetic PPO phase [Jackman et al. 2009a, 2016]. Specifically, the events were found to be preferentially initiated during intervals when the PPO perturbations stretch the field lines radially outward from the planet and thin the plasma sheet leading to instability (see section entitled Planetary Period Oscillations), especially when the two PPO systems act in this manner in concert, i.e., when they are near antiphase. Ongoing work is presently investigating dipolarization events and auroral storms during the sequence of proximal orbits observed just prior to end of mission.

A further important related topic concerns the mass loss associated with plasmoid release down-tail as part of the Vasyliunas cycle, compared with the ~100 kg s^{-1} Enceladus water plasma source rate. Although simple estimates based on the duration of observed plasmoid field perturbations yield mass loss values at least an order of magnitude smaller than this, given the typically several-hour interval between plasmoid releases, it has been suggested that the overall plasma structure released by such events may be at least an order of magnitude longer than the few tens of R_S lengths inferred from the magnetic data directly [Cowley et al. 2015].

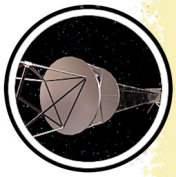

Wave analysis

Preparatory studies concentrated on ultra-low frequency (ULF) waves in the Kronian magnetosphere and the resonant mode coupling process—for example, Cramm et al. [1998]. Later studies on plasma waves were conducted using observations made during the Cassini Earth flyby and after orbit insertion—for example, Bogdanov et al. [2003]; Kleindienst et al. [2009]. A more recent study of ULF waves has been carried out [Yates et al. 2016].

Saturn's Internal Magnetic Field and Implications for Interior Structure

Numerous planetary magnetic field models have been developed over the time of the Cassini orbital mission at Saturn beginning with Saturn Orbit Insertion [Dougherty et al. 2005]. Burton [2009] derived a model of Saturn's internal planetary magnetic field based on data obtained from the first three years of the mission, from July 1, 2004–July 1, 2007. Due to the uncertainty in the rotation rate, the model was constrained to be axisymmetric. In that analysis, one-minute averages of the vector magnetic field data obtained by the fluxgate magnetometer from all orbits within 10 R_S (1 R_S = 60268 km). Data from 45 orbits were used in that study. The contribution of the eastward flowing ring current is known to be significant close to the planet. Its contribution was modeled using the analytical expression derived by Giampieri and Dougherty [2004a] based on the simple axisymmetric equatorial current sheet centered on the planet's equator, first described by Connerney et al. [1981]. The ring current magnetic field was modeled separately for the inbound and outbound legs of each orbit because the current sheet structure and characteristics are known to vary with local time [Arridge et al. 2008b] and temporal variations in the solar wind and magnetosphere are likely to occur over time scales corresponding to that of a periapsis pass (several days). The ring current field was modeled and removed from the data and standard generalized inversion techniques were used to model the magnetic field presumed to originate in Saturn's interior.

The internal field model derived in that study was found to be quite consistent with previous models. An axisymmetric octupolar (degree 3) model was found to fit the data adequately based on an examination of the root-mean-square misfit or residual for each orbit. The spherical harmonic coefficients derived were g_{10} = 21,162, g_{20} = 1514, g_{30} = 2283. Units are nanoteslas (nT) and are based on a planetary radius of 60,268 km. Saturn's magnetic was found to be offset northward by 0.036 Saturn radii, consistent with earlier Pioneer-11 and Voyager models. Reanalysis and comparison with data obtained by Pioneer 11 and Voyager 1 and 2 showed little evidence for secular variation in the field in the almost 30 years since those data were obtained.

A subsequent study [Burton 2010] used data from the entire Cassini Prime Mission (through July 2008) and a methodology that differed in significant ways from the earlier modeling approach [Burton 2009]. Only data obtained at radial distances closer than the L-shell of Enceladus (dipole L-value of 3.8) were used to derive the model. Measurements obtained by all Cassini fields and particles instruments had demonstrated that the structure and dynamics of Saturn's inner magnetosphere are governed by plasma created at Enceladus [Kivelson 2006]. The observed field

at radial distances outside the orbit of Enceladus is modified by processes in the inner magnetosphere and does not necessarily reflect the magnetic field generated in Saturn's interior.

The approach to modeling the external ring current field also differed from the earlier modeling approach. As time went on, our understanding of Saturn's magnetodisc had evolved and a simple symmetric ring current centered on the equator was no longer thought to be an accurate representation. Instead, the current sheet was found to be displaced from Saturn's rotational equator and to assume the shape of a bowl or basin, referred to as a magnetodisc [Arridge et al. 2008b]. Instead of modeling the external field as an oversimplified axisymmetric ring current as in Burton [2009], the internal plus external field was modeled using the standard spherical harmonic formulation and a single set of spherical harmonic coefficients was obtained that describes the internal and external field in a least squares sense. Accordingly, the axisymmetric model coefficients differ somewhat from the previous model.

In Burton [2010], an attempt was made to determine the planetary rotation rate by deriving a number of non-axisymmetric magnetic field models for a plausible range of planetary rotation periods and assessing the power in the non-axisymmetric components of the field and the root-mean-square misfit between the model and the data. The methodology is as follows. A presumed planetary rotation period was varied in one-second increments from 10 hours 28 minutes to 10 hours 40 minutes and a pseudo-longitude calculated for each measured data point. A degree 3, non-axisymmetric magnetic field model was derived and the power in the non-axial magnetic field and the misfit were calculated. The underlying premise is that the planetary rotation period could be determined based on a peak in the non-axial power and minimum in the misfit. Although no such peak was identified unambiguously, the analysis did provide an upper limit on the extent of the dipole tilt. Based on the distribution of the non-axial spherical harmonic model coefficients for the range of rotation rates, a mean value for the dipole tilt was determined to be 0.03 degree. The upper limit of all tilt angles was found to be 0.1 degree.

We have further developed the state-of-the-art internal magnetic field model for Saturn using Cassini magnetometer measurements prior to the Grand Finale, which placed the most stringent constraint to date on the tilt and secular variation of Saturn's intrinsic magnetic field [Cao et al. 2011]. The tilt of Saturn's dipole must be smaller than 0.06 degree from the spin-axis of Saturn, and the time variation of Saturn's intrinsic magnetic field must be an order of magnitude slower than that of the Earth's [Cao et al. 2011]. These results are very challenging for dynamo theory, as Cowling's theorem excludes the possibility of a purely axisymmetric magnetic field being maintained by dynamo action.

We have also derived degree 4 and degree 5 internal magnetic moments for Saturn, albeit with relatively large uncertainties, from reanalyzing the Cassini SOI MAG measurements [Cao et al. 2012]. Based on these observational findings, we worked out the implications on helium rain inside Saturn [Cao et al. 2011, 2012]. These also provided the framework for our current analysis of the magnetometer measurements from the Cassini Grand Finale.

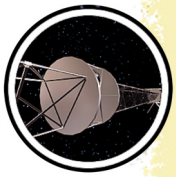

The latest Cassini Grand Finale gravity measurements indicate that the ~100 m/s zonal flows observed at the cloud deck of Saturn extend almost 10,000 kilometers into the planetary interior. Given that the electrical conductivity at such depth are high enough for significant MHD effects, zonal flow magnetic field interaction in the semi-conducting region of Saturn is now a central issue in understanding the interior dynamics. On the theoretical side, we have developed a mean-field model for zonal flow magnetic field interaction in the semi-conducting region of Saturn [Cao and Stevenson 2017]. In this work, we proposed that the interaction between zonal flow and a magnetic field in the semi-conduction region of Saturn would generate small-scale axisymmetric magnetic fields that are spatially correlated with zonal flows [Cao and Stevenson 2017]. The amplitude of the wind-induced magnetic perturbations would depend on the amplitude of the deep differential rotation as well as the amplitude of the small-scale deep convective flow. Thus, measuring/constraining wind-induced magnetic perturbations along the Cassini Grand Finale orbits would place important constraints on the properties (profile and amplitude) of deep differential rotation and convective flow in the semi-conducting region of Saturn.

With magnetic field measurements at unprecedented proximity to Saturn by the Cassini Grand Finale [Dougherty et al. 2018], we are working on deriving: 1) non-axisymmetric internal magnetic moments of Saturn from the Cassini Grand Finale magnetometer measurements, which can tell us about the deep interior rotation rate of Saturn and/or helium rainout and stable stratification inside Saturn; 2) small-scale axisymmetric magnetic features—for example, high-degree axisymmetric internal magnetic moments—which can be used to constrain deep differential rotation inside Saturn; and 3) time variations in the internal magnetic fields, which would reveal characteristic time scale in Saturn's internal magnetic field and deep interior dynamics. These expected results would constitute the observational facts about the internal magnetic fields of Saturn for many years to come, which would further serve as tests for theories about giant planet interiors and have profound implications about giant planets outside the solar system.

Titan Science

The MAG team has significantly contributed to the understanding of the interaction between Saturn's major moon, Titan, and its plasma environment. The virtual absence of an intrinsic field at Titan makes this interaction mainly atmospheric as fields and charged particles from Saturn or the Sun impinge on the moon's chemically complex atmosphere, exosphere, and ionosphere. Atmospheric interactions are common elsewhere in the solar system with Mars and Venus as their most typical examples. In these cases, as well as in Titan's, charged particles from its atmosphere (originating from photoionization, charge exchange, and electron impact) become electro-magnetically coupled to those carried by the plasma winds that flow past it [Bertucci et al. 2011].

The exchange of momentum and energy between the atmospheric charged particles and those being part of the external wind lead to a steady perturbation in the ambient external magnetic field known as induced magnetosphere and characterized by the draping of the external magnetic field lines around the unmagnetized, atmospheric body. Cassini MAG observations were crucial in

providing constraints to the structure of Titan's magnetotail [Bertucci et al. 2007b] and characterizing Saturn's magnetic field at Titan's location [Bertucci et al. 2009].

However, one of the most remarkable features revealed by MAG was that Titan's induced magnetosphere is formed by layers of different polarity of the external magnetic field that allows for reconstruction of the history of the moon's magnetic environment. Indeed, in the same way as older sediments lay beneath more recent deposits in geology, the magnetic fields fossilized in the deep layers of Titan's induced magnetosphere provide information about the orientation of the external field Titan was exposed up to three hours before the encounter with Cassini [Bertucci et al. 2008]. This magnetic memory of Titan is significantly longer than those at Venus and Mars and is a result of the capacity of Titan plasma to remove momentum from the external plasma. Cassini MAG data were also essential to characterize Titan's unique example of interaction with the supersonic solar wind [Bertucci et al. 2015] as structures found at Mars and Venus (an induced magnetospheric boundary and a collisional bow shock) were successfully captured by the instrument.

The Cassini Titan mission consisted of the encounters TA, TB, TC, T3, T4 … T126 in project nomenclature, all with useful magnetic field data. The magnetic field conditions upstream of these flybys were strongly variable and different from the single encounter during the Voyager 1 mission—for example, Neubauer et al. [1984]. For example, the simple model derived from Voyager 1 with the flow along the direction of orbital motion and the magnetic field perpendicular to Titan's orbital plane was at most approximately fulfilled in rare cases.

Titan's orbit is typically located inside Saturn's magnetosphere, but could occasionally move outside it into the magnetosheath or even into the solar wind.

The first part of the exploration strategy was to analyze individual encounters with particularly noteworthy characteristics. The first encounter TA on October 26, 2004, was carefully investigated and compared with the results of a newly developed numerical model. The comparison showed best agreement with a MHD-model, which separately described ionospheric (cold) electrons and magnetospheric (hot) electrons [Backes et al. 2005]. In joint studies of the TA flyby a comparison between MAG and RPWS-data was done by Wahlund et al. [2005] and a comparison between Cassini and Voyager data using both plasma spectrometer (PLS) and magnetic field data by Hartle et al. [2006]. The next more detailed study was using magnetic field and PLS electron data and included TA, TB, and T3 [Neubauer et al. 2006]. The data showed a draping boundary as the outer boundary of strong magnetic field draping. Further, the induced magnetospheric tail near Titan was investigated. The shape of the tail was found to be similar to a delta wing in aerodynamics. It was shown that the long travel time of frozen-in magnetic field lines into the lower ionosphere of Titan led to the observation of old or fossil field lines compared with their times of arrival in front of Titan. This concept was later called memory effect by Bertucci et al. [2008] in a paper discussing Titan encounter T32 which occurred for the first time in the Saturnian magnetosheath, but also contained old Saturnian magnetospheric field as a memory effect—see also Ma et al. [2009].

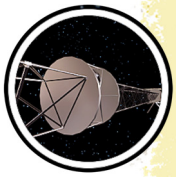

The first opportunity to study the induced tail at medium distances occurred at T9, which led to a data analysis paper by Bertucci et al. [2007b]. It also led to a number of modelling papers that helped to disentangle the detailed plasma and magnetic field characteristics [Kallio et al. 2007; Wei et al. 2007; Ma et al. 2007] of the complex magnetotail.

These early Cassini/MAG data at Titan also led to the conclusion that an internal magnetic field of Titan was at most very small. Using the magnetic field observations on flyby orbits very close to Titan. Wei et al. [2010a] found an upper limit on the dipole moment of 0.78 nT × R_T^3 improving the Voyager 1 upper limit by a factor of five.

Considering further the ionosphere of Titan with its embedded magnetic field, a study of Titan's nightside ionosphere was published by Cravens et al. [2009]. Data collected along T96, the first encounter presumably occurring in the supersonic solar wind, was also compared to modeling results from a hybrid kinetic code [Feyerabend et al. 2016].

An important kinetic process in the interaction between a streaming magnetized plasma and Titan's atmosphere is the pick-up process, which has been observed to lead to the generation of often strong ion cyclotron waves in the cases of atmospheric interactions (Venus, Mars, Galilean satellites of Jupiter, Saturnian satellites, comets). In the case of Titan, only two flybys T63 and T98 were associated with ion cyclotron waves of relatively high amplitude, as a study of the MAG team shows [Russell et al. 2016].

In parallel to the studies of single flybys, we have also undertaken a systematic study of all Titan flybys by looking at the characteristics of the magnetic field variations upstream and also downstream of the interaction region proper close to Titan with duration ±1 h. Most of the regions of ±8 h around the interaction region can be characterized as a sequence of intervals with magnetic fields of the northern/southern magnetospheric lobe type and the magnetospheric current sheet [Arridge et al. 2008c], which can be found near the magnetic equator. Mixtures of these regions do also occur. In rare cases, encounters occurred in the magnetosheath of Saturn (T32, T42, and T85) and in the solar wind (T96).

The individual results have been collected in Simon et al. [2010a, b] for TA–T62, Simon et al. [2013] for TA–T85 and Kabanovic et al. [2017] for the remainder. The latter paper also indicates appreciable variations of the occurrence of the types of magnetic field regions as a function of Saturnian season. Results are given for 2004–2008, 2009–2010, 2011–2017 for about half a Saturn year.

A special study of the magnetotails of Titan has investigated the tails by wake flybys with closest approach (CA) distances >2.5 R_T in the whole set of flybys TA–T84 [Simon et al. 2014a]. The resulting eight flybys confirmed the delta wing structure found in Neubauer et al. [2006] leading to a thickness of the wing of ±3 R_T. Magnetotail studies in the set T85–T126 have not been done yet.

Titan's orbit is typically located inside Saturn's magnetosphere, but could occasionally move outside it into the magnetosheath or even into the solar wind. To better understand the magnetic and plasma environment of Titan, the plasma environment at Titan's orbit is compared with Titan present and absent from 06/2004 to 12/2008. Cassini observations reveal that the presence of Titan appears to affect the magnetopause location. Near noon, the Saturn magnetopause is more frequently inside of Titan's orbit with the moon absent than with it present. Titan's presence near noon appears to locally enhance the total pressure and reduce the magnetosphere compressibility, possibly by mass-loading. Near local midnight, the stretching and sweepback angles for cases with Titan present and absent suggest that the moon enhances the tail reconnection rate, in agreement with previous studies of the moon's influence on the Saturnian magnetosphere [Wei et al. 2009].

Due to Titan's thick atmosphere, ion cyclotron waves are expected to be created when the atmospheric particles are ionized and picked up by Saturn's magnetospheric plasma. However, ion cyclotron waves are rarely observed near Titan, due to the long growth times of waves associated with the major ion species from Titan's ionosphere, such as CH_4^+ and N_2^+ [Cowee et al. 2010]. In the more than 100 Titan flybys obtained by Cassini, there are only two wave events, for just a few minutes during T63 flyby and for tens of minutes during T98 flyby. These waves occur near the gyrofrequencies of proton and singly ionized molecular hydrogen. From hybrid simulations for T63, we find the pickup protons with densities ranging from 0.01/cc to 0.02/cc and singly ionized molecular hydrogens with densities ranging from 0.015/cc to 0.25/cc can drive ion cyclotron waves with amplitudes of ~0.02 nT and of ~0.04 nT within appropriate growth times at Titan, respectively [Russell et al. 2016].

During the interaction between Titan's ionosphere and its ambient plasma, Cassini observations find that the lower ionosphere of Titan is often magnetized, with large-scale magnetic fields and some structures resemble magnetic flux ropes. These flux ropes are either starting to form or maturely formed, with their axial orientations in agreement with the theoretical formation mechanism [Wei et al. 2010b]. A special example of ionospheric flux rope is observed during Titan flyby T42. The observed magnetic field attained a maximum value of 37 nT between an altitude of 1,200 and 1,600 km, much larger than other similar passes. Cassini observations from the plasma and magnetic instruments indicate that Titan's ionosphere was strongly magnetized during an enhanced solar wind dynamic pressure interval right before this flyby, and it caused this large fossil field that later got further twisted while sinking into lower ionosphere [Wei et al. 2011].

The interaction between Titan and the corotating Saturnian plasma forms an induced magnetosphere with an elongated Alfven-wing-style magnetotail. During the first mid-tail flyby T9, Cassini plasma and magnetic field instruments detected in one tail lobe a magnetic flux tube connected with ionosphere and filled with cold ionospheric plasma. This magnetic structure indicates that Titan's ionosphere appears to be escaping along field lines down the tail, leading to particle loss from the atmosphere [Wei et al. 2007].

To understand the internal magnetic moments of Titan, the radial component of Cassini magnetometer observations near Titan surface (from 950 km to 1,100 km) was used to calculate the permanent dipole moment. The upper limit to Titan's permanent dipole moment is

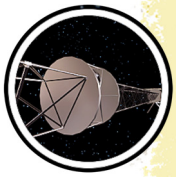

0.78 nT × R_{Ti}^3, using the observations during the southern summer season of Saturn (April 2005 to March 2009). This weak internal field indicates the interior of Titan may not contain a liquid core sufficiently electrically conductive for a magnetic dynamo to be generated inside Titan or even for the simple amplification of the external magnetic field [Wei et al. 2010a]. For the signs of the calculated internal field components, the g11 and h11 component, corresponding with the Titan-to-Saturn direction and the corotation direction, respectively, are in agreement with the signs of the averaged ambient field around Titan during the observation period. This indicates that these estimated internal moments may be due to the penetration of the ambient field into the interior of Titan, generating induced fields. After Saturn's equinox, August 2009, the ambient field of Titan changes sign in the Titan-to-Saturn direction and the corotation direction, as Titan moved from below Saturn's current sheet to above it. Thus, we compared the calculated internal moments using the observations before and after Saturn's equinox, and found that the g11 and h11 moment changed sign in agreement with the sign of Titan's ambient field.

A multispecies MHD model has been employed to study plasma interaction with Titan, model results have been compared with several Cassini Titan flybys to better understand the plasma environment of Titan.

1. Ta and Tb flyby [Ma et al. 2006]: The Cassini spacecraft passed by Titan on October 26, 2004 (Ta flyby), and December 13, 2004 (Tb flyby). In both cases, the Cassini spacecraft entered Titan's ionosphere and flew through Titan's dynamic wake region. We simulated both flybys using our three-dimensional multispecies MHD model. The calculations used the best available upstream plasma and magnetic field parameters obtained by Cassini. Model results were compared with relevant plasma measurements and showed close agreement between the two, demonstrating that the general interaction features can be pretty well reproduced by the MHD model.

2. T9 flyby [Ma et al. 2007]: The wake region of Titan is an important component of Titan's interaction with its surrounding plasma. The Cassini spacecraft passed through the distant downstream region of Titan on December 26, 2005 (T9 flyby). In this study, we compared the observational data with numerical results using a three-species Hall MHD Titan model. There is a good agreement between the observed and modeled parameters, given the uncertainties in plasma measurements and the approximations inherent in the Hall MHD model. Our simulation results also show that Hall MHD model results fit the observations better than the non-Hall MHD model for the flyby, consistent with the importance of kinetic effects in the Titan interaction. Based on the model results, we also identified the controlling physical processes in different plasma regions based on ion gyroradius.

3. T32 flyby [Ma et al. 2009]: When the Cassini spacecraft flew by Titan on June 13, 2007, at 13.6 hr Saturn local time, Titan was directly observed to be outside Saturn's magnetopause. Cassini observations showed dramatic changes of magnetic field orientation as well as other plasma flow parameters during the inbound and outbound segments. We studied Titan's ionospheric responses to such a sudden change in the

upstream plasma conditions using our multispecies global MHD model. Simulation results are compared against Cassini MAG, Langmuir Probe, and CAPS observations. The main interaction features, as observed by the Cassini spacecraft, are well reproduced by the time-dependent simulation cases. The simulation results provide clear evidence for the existence of a fossil field that was induced in the ionosphere due to a different convection time around Titan. These simulations also reveal how the fossil field was trapped during the interaction and shows the coexistence of two pileup regions with opposite magnetic orientation, as well as the formation of a pair of new Alfvén wings and tail disconnection during the magnetopause crossing process.

4. T34 flyby [Ma et al. 2011]: We improved the previously used multispecies MHD model by solving both the electron and ion pressure equations instead of a single plasma pressure equation. This improvement enabled a more accurate evaluation of ion and electron temperatures inside Titan's ionosphere. The model is first applied to an idealized case, and the results are compared in detail with those of the single-pressure MHD model to illustrate the effects of the model improvement. These simulation results show that the dayside ionosphere thermal pressure is larger than the upstream pressure during normal conditions, when Titan is located in the dusk region; thus Saturn's magnetic field is shielded by the highly conducting ionosphere, similar to the interaction of Venus during solar maximum conditions. This model is also applied to a special flyby of Titan, the T34 flyby, which occurred near the dusk region. It is shown that better agreement with the MAG data can be achieved using the improved MHD model with the inclusion of the effects of super thermal electron heating. This clearly demonstrates the importance of super thermal-electron heating in Titan's ionosphere.

Enceladus Science

The most significant highlight of the MAG investigation during the Cassini mission was the discovery of an atmospheric plume at Enceladus by the MAG team [Dougherty et al. 2006] on February 17, 2005, and confirmed and strengthened by subsequent measurements on later flybys and other instruments. The discovery of a thin neutral atmosphere by the magnetic signature of an electrodynamic interaction proved to point to one of the unique capabilities of the MAG experiment. In another MAG publication on Enceladus [Khurana et al. 2007], we showed that the effective diameter of the obstacle (the plume) is at least 6 R_E, and the obstacle is displaced by >2 R_E south of Enceladus and downstream by at least 1 R_E. The total current produced in the interaction is $<10^5$ Amps (40–60% of the Neubauer limit). We estimated that the mass picked up by the plasma within 5 R_E of Enceladus is <3 kg/s.

This dynamic atmospheric plume was later shown by the Imaging team to be due to geyser activity on the southern hemisphere of Enceladus. The electrodynamic interaction involves southern and northern Alfvén wings such that the atmospheric influence not only shows up in the

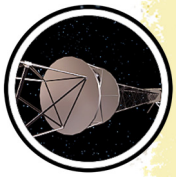

southern but also the northern wing—hemispheric coupling [Saur et al. 2007]. Using these concepts and magnetic field observations of flybys E0, E1, E2 and neutral density measurements at E2 the time variability of the plumes was investigated [Saur et al. 2008]. Subsequent modelling based on analytical theory clearly showed that the MAG results required the presence of negatively charged dust particles [Simon et al. 2011a]. The paper also proves the presence of the hemispheric coupling currents required by Saur et al. [2007]. The interaction was later modelled numerically in detail using a hybrid (fluid electron) kinetic code including charged dust particles [Kriegel et al. 2011]. As a unique feature at Enceladus, dust–plasma interactions play an important role to explain the observations.

Since Saturn has a rotation dominant magnetosphere powered by the plasma sources in its inner magnetosphere, quantifying the gas and plasma torus is crucial to understand the magnetospheric dynamics of Saturn. The primary source of the Saturnian torus is ejections from Enceladus. This newly released gas, dust, and plasma interacts with Saturn's magnetosphere, and strong disburbations in the magnetic field are generated. We studied the magnetic signals observed by Cassini/MAG at Enceladus, to determine the gas and dust production rate at Enceladus and how do they vary with time.

The neutrals sent to space from Enceladus are partly ionized via photoionization, electron or proton impact ionization, and charge exchange processes. These new ions are loaded into the magnetosphere, which is, in turn, slowed down into an 80% subcorotation.

We employed a 3-D MHD model to simulate the plasma interaction at Enceladus. The model is applied to the Block Adaptive Tree Solar-wind Roe Upwind Scheme (BATS-R-US) code in an 80 x 80 x 160 Enceladus radii computational domain. The neutrals are treated as a background condition, with a density described by analytical functions: the torus component and a moon component that falls off by a factor of r^{-2} with distance. The upstream boundary is an inflow boundary, with density, velocity, temperature and field conditions obtained from the Cassini flyby data. The inner boundary at the Enceladus surface is absorbing the moon condition, which absorbs the inflow plasma, and fixes the outflow density as a floor value. The field has no gradient at the inner boundary. This code has been applied to a spherical obstacle in a plasma flow to show the effect of the moon and local pickup separately [Jia, Y. -D. et al. 2010a]. With this model, we have refined the plume geometry with E2 data [Jia, Y. -D. et al. 2010b] and constrained the outgassing rate of the Enceladus plume with data from the nine early flybys [Jia, Y. -D. et al. 2010c, 2010d].

Plume brightness is found to be varying by a factor of a few around the apocenter of Enceladus orbit, using visual images. In contrast, outgassing rate deduced from our data-modeling comparison suggested 50% variation in gas production rate during the first nine passes E0-E8 [Jia, Y. -D. et al. 2010c, 2010d]. The magnetometer could not confirm this postulation with local interaction data. Then, the field perturbation perpendicular to both the direction of magnetospheric flow, and to the magnetic field has been studied with our multi-fluid code, to illustrate the effect of charged dust in creating such a field perturbation [Jia, Y. et al. 2011].

Other Icy Satellite Science

In addition to the large number of flybys at Titan and Enceladus, there was also a small number of targeted flybys of some of the other icy satellites. The magnetic signatures observed were used to investigate in detail the magneto-plasma interaction with these satellites with the help of 3-D hybrid kinetic models introduced before. On September 24, 2005, the only Tethys encounter took place close enough to the satellite to be diagnostically useful. No evidence for an atmosphere/ionosphere system was found. Instead, the magnetic field signatures were explained by the plasma absorption by the satellite [Simon et al. 2009a]. The Dione encounters on October 11, 2005 and April 7, 2010, led to the observation of Alfvén wing signatures. The analysis yielded an atmospheric column density of 10^{17} m^{-2} [Simon et al. 2011b]. The two flybys at Rhea on March 2, 2010, and January 11, 2011, were not associated with magnetic signatures due to the atmosphere, which was identified by other means. The magnetic signature was also dominated by plasma absorption features [Simon et al. 2012].

We characterized the submagnetosonic plasma interaction of Rhea in Khurana et al. [2008]. Main conclusions were: 1) Rhea is also an inert moon and devoid of any internal magnetic field; 2) no induction field was observed from any subsurface conductor; 3) no appreciable mass-loading occurs near Rhea; and 4) the region of plasma depletion is greatly elongated along the field direction. The submagnetosonic interaction of Rhea with the Saturnian plasma was further explored in Khurana et al. [2017] where we showed that the wake refilling process generates Alfvén wings in the wake region from a plasma density gradient force directed in the direction of corotating plasma. The plasma pressure gradient force slows down the plasma streaming into the wake along field lines. As on the same field lines, outside of the wake, the plasma continues to move close to its full speed; this differential motion of plasma bends the magnetic flux tubes, generating Alfvén wings in the wake. The current system excited by the Alfvén wings transfers momentum from plasma outside the wake to the wake plasma. Our work demonstrates that Alfvén wings can be excited even when a moon does not possess a conducting exosphere. In another work on Rhea's interaction with the Saturnian plasma [Teolis et al. 2014], we showed that sharp magnetic perturbations are present at the edge of the Rhea flux tube, which are consistent with field-aligned flux tube currents. We showed that the current system results from the difference of ion and electron gyroradii and the requirement to balance currents on the sharp Rhea surface.

On September 26, 2005, Cassini conducted its only close targeted flyby of Saturn's small, irregularly shaped moon Hyperion. Approximately 6 minutes before the closest approach, the electron spectrometer (ELS), part of the CAPS instrument detected a field-aligned electron population originating from the direction of the moon's surface. We showed that this constituted a remote detection of a strongly negative (~200 V) surface potential on Hyperion, consistent with the predicted surface potential in regions near the solar terminator [Nordheim et al. 2014].

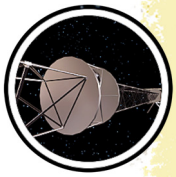

MAG Non-Saturn Science Results

Early science used the measurements along the flyby of Earth and Jupiter. The Earth flyby produced fairly original observations at high resolution of what appeared to be interchange motions on the nightside outbound pass. Inbound, high-resolution measurements of the whistler waves in the electron foreshock were reported. In addition, the down-tail passage allowed observation of two geomagnetic sequential substorm cycles [Southwood et al. 2001; Smith et al. 2001; Khan et al. 2001; Tsurutani et al. 2001]. Passage by Jupiter allowed coordination with Galileo during its 28th and 29th orbits. The most important conclusion was good evidence of changed magnetospheric shape in response to local solar wind magnetic field changes in the north-south component. There is increased flaring when the field is northward, opposite of what happens at Earth. As the Jovian dipole is oppositely oriented, this is consistent with reconnection being important to magnetospheric configuration at Jupiter despite the rapid planetary rotation [Kivelson and Southwood 2003, 2005].

ACRONYMS

Note: For a complete list of Acronyms, refer to Cassini Acronyms – Attachment A.

AO	Announcement of Opportunity
AU	astronomical unit
BATS-R-US	Block Adaptive Tree Solar-wind Roe Upwind Scheme
CA	closest approach
CAPS	Cassini Plasma Spectrometer
CEC	corotation enforcement currents
CIR	corotating interaction region
CSM	Cassini Solstice Mission
ELS	electron spectrometer
FAC	field-aligned current
FGM	Flux Gate Magnetometer
HST	Hubble Space Telescope
IMF	interplanetary magnetic field
LFE	low frequency extension
MAG	Magnetometer
MAPS	Magnetospheres and Plasma Science
MHD	magneto-hydrodynamic
MIMI	Magnetospheric Imaging Instrument
PLS	plasma spectrometer
PPO	planetary period oscillation
RPWS	Radio and Plasma Wave Science
SKR	Saturn kilometric radiation
SLT	Saturn local time
SOI	Saturn orbit insertion
TCR	travelling compression region
ULF	ultra-low frequency
UV	ultraviolet
V/SHM	Vector/Scalar Helium Magnetometer

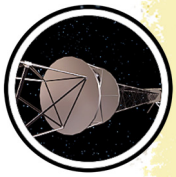

REFERENCES

Disclaimer: The partial list of references below correspond with in-text references indicated in this report. For all other Cassini references, refer to Attachment B – References & Bibliographies; Attachment C – Cassini Science Bibliographies; the sections entitled References contributed by individual Cassini instrument and discipline teams located in Volume 1 Sections 3.1 and 3.2 Science Results; and other resources outside of the Cassini Final Mission Report.

Abel, G. A., A. J. Coates, A. M. Rymer, D. R. Linder, M. F. Thomsen, D. T. Young, M. K. Dougherty, (2001), Cassini Plasma Spectrometer observations of bidirectional lobe electrons during the Earth flyby, August 18, 1999, Journal of Geophysical Research: Space Physics, 106(A12):30199–30208, doi: 10.1029/2001JA900076.

Achilleos, N., C. S. Arridge, C. Bertucci, P. Guio, N. Romanelli, N. Sergis, (2014), A combined model of pressure variations in Titan's plasma environment, Geophysical Research Letters, 41(24):8730–8735, doi: 10.1002/2014GL061747.

Achilleos, N., P. Guio, C. S. Arridge, (2010a), A model of force balance in Saturn's magnetodisc, Monthly Notices of the Royal Astronomical Society, 401(4):2349–2371, doi: 10.1111/j.1365-2966.2009.15865.x.

Achilleos, N., P. Guio, C. S. Arridge, N. Sergis, R. J. Wilson, M. F. Thomsen, A. J. Coates, (2010b), Influence of hot plasma pressure on the global structure of Saturn's magnetodisk, Geophysical Research Letters, 37, L20201, doi: 10.1029/2010GL045159.

Achilleos, N., C. S. Arridge, C. Bertucci, C. Jackman, M. K. Dougherty, K. K. Khurana, C. T. Russell, (2008), Large-scale dynamics of Saturn's magnetopause: Observations by Cassini, Journal of Geophysical Research: Space Physics, 113(A11):14 pp., doi: 10.1029/2008JA013265.

Achilleos, N., C. Bertucci, C. T. Russell, G. B. Hospodarsky, A. M. Rymer, C. S. Arridge, M. E. Burton, M. K. Dougherty, S. Hendricks, E. J. Smith, B. T. Tsurutani, (2006), Orientation, location, and velocity of Saturn's bow shock: Initial results from the Cassini spacecraft, Journal of Geophysical Research, 111(A03201), doi: 10.1029/2005JA011297.

Achilleos, N., M. K. Dougherty, D. T. Young, F. Crary, (2004), Magnetic signatures of Jupiter's bow shock during the Cassini flyby. Journal of Geophysical Research: Space Physics, 109(A9):14 pp., doi: 10.1029/2003JA010258.

Agren, K., D. J. Andrews, S. C. Buchert, A. J. Coates, S. W. H. Cowley, M. K. Dougherty, A. Wellbrock, (2011), Detection of currents and associated electric fields in Titan's ionosphere from Cassini data, Journal of Geophysical Research: Space Physics, 116:13 pp., doi: 10.1029/2010JA016100.

Agren, K., J. -E. Wahlund, R. Modolo, D. Lummerzheim, M. Galand, I. Mueller-Wodarg, M. K. Dougherty, (2007), On magnetospheric electron impact ionisation and dynamics in Titan's ram-

side and polar ionosphere - a Cassini case study, Annales Geophysicae, 25(11):2359–2369, doi: 10.5194/angeo-25-2359-2007.

Alexeev, I. I., V. V. Kalegaev, E. S. Belenkaya, S. Y. Bobrovnikov, E. J. Bunce, S. W. H. Cowley, J. D. Nichols, (2006), A global magnetic model of Saturn's magnetosphere, and a comparison with Cassini SOI data, Geophysical Research Letters, 33, L08101, doi: 10.1029/2006GL025896.

André, N., M. Blanc, S. Maurice, P. Schippers, E. Pallier, T. I. Gombosi, J. T. Clarke, (2008), Identification of Saturn's magnetospheric regions and associated plasma processes: Synopsis of Cassini observations during orbit insertion, Reviews of Geophysics, 46(4):22 pp., doi: 10.1029/2007RG000238.

André, N., A. M. Persoon, J. Goldstein, J. L. Burch, P. Louarn, G. R. Lewis, D. T. Young, (2007), Magnetic signatures of plasma-depleted flux tubes in the Saturnian inner magnetosphere, Geophysical Research Letters, 34(14):7 pp., doi: 10.1029/2007GL030374.

André, N., M. K. Dougherty, C. T. Russell, J. S. Leisner, K. K. Khurana, (2005), Dynamics of the Saturnian inner magnetosphere: First inferences from the Cassini magnetometers about small-scale plasma transport in the magnetosphere, Geophysical Research Letters, 32(14):5 pp., doi: 10.1029/2005GL022643.

André, N., G. Erdos, M. Dougherty, (2002), Overview of mirror mode fluctuations in the Jovian dusk magnetosheath: Cassini magnetometer observations, Geophysical Research Letters, 29(20):4 pp., doi: 10.1029/2002GL015187.

Andrés, N., K. Meziane, C. Mazelle, C. Bertucci, D. Gómez, (2015), The ULF wave foreshock boundary: Cluster observations, Journal of Geophysical Research: Space Physics, 120(6):4181–4193, doi: 10.1002/2014JA020783.

Andrés, N., D. O. Gomez, C. Bertucci, C. Mazelle, M. K. Dougherty, (2013), Saturn's ULF wave foreshock boundary: Cassini observations, Planetary and Space Science, 79–80:64–75, doi: 10.1016/j.pss.2013.01.014.

Andrews, D. J., S. W. H. Cowley, M. K. Dougherty, L. Lamy, G. Provan, D. J. Southwood, (2012), Planetary period oscillations in Saturn's magnetosphere: Evolution of magnetic oscillation properties from southern summer to post-equinox, Journal of Geophysical Research: Space Physics, 117:31 pp., doi: 10.1029/2011JA017444.

Andrews, D. J., B. Cecconi, S. W. H. Cowley, M. K. Dougherty, L. Lamy, G. Provan, P. Zarka, (2011), Planetary period oscillations in Saturn's magnetosphere: Evidence in magnetic field phase data for rotational modulation of Saturn kilometric radiation emissions, Journal of Geophysical Research: Space Physics, 116:24 pp., doi: 10.1029/2011JA016636.

Andrews, D. J., A. J. Coates, S. W. H. Cowley, M. K. Dougherty, L. Lamy, G. Provan, P. Zarka, (2010a), Magnetospheric period oscillations at Saturn: Comparison of equatorial and high-latitude magnetic field periods with north and south Saturn kilometric radiation periods, Journal of Geophysical Research: Space Physics, 115:21 pp., doi: 10.1029/2010JA015666.

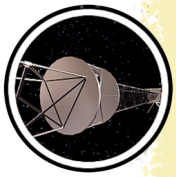

Andrews, D. J., S. W. H. Cowley, M. K. Dougherty, G. Provan, (2010b), Magnetic field oscillations near the planetary period in Saturn's equatorial magnetosphere: Variation of amplitude and phase with radial distance and local time, Journal of Geophysical Research: Space Physics, 115:28 pp., doi: 10.1029/2009JA014729.

Andrews, D. J., E. J. Bunce, S. W. H. Cowley, M. K. Dougherty, G. Provan, D. J. Southwood, (2008), Planetary period oscillations in Saturn's magnetosphere: Phase relation of equatorial magnetic field oscillations and Saturn kilometric radiation modulation, Journal of Geophysical Research: Space Physics, 113(A9):19 pp., doi: 10.1029/2007JA012937.

Andriopoulou, M., E. Roussos, N. Krupp, C. Paranicas, M. Thomsen, S. Krimigis, K. -H. Glassmeier, (2014), Spatial and temporal dependence of the convective electric field in Saturn's inner magnetosphere, Icarus, 229:57–70, doi: 10.1016/j.Icarus.2013.10.028.

Andriopoulou, M., E. Roussos, N. Krupp, C. Paranicas, M. Thomsen, S. Krimigis, K. -H. Glassmeier, (2012), A noon-to-midnight electric field and nightside dynamics in Saturn’s inner magnetosphere, using microsignature observations, Icarus, 220(2):503–513, doi: 10.1016/j.Icarus.2012.05.010.

Arridge, C. S., J. M. Jasinski, N. Achilleos, Y. V. Bogdanova, E. J. Bunce, S. W. H. Cowley, N. Krupp, (2016b), Cassini observations of Saturn’s southern polar cusp, Journal of Geophysical Research: Space Physics, 121(4):3006–3030, doi: 10.1002/2015JA021957.

Arridge, C. S., J. P. Eastwood, C. M. Jackman, G. -K. Poh, J. A. Slavin, M. F. Thomsen, M. K. Dougherty, (2016b), Cassini in situ observations of long-duration magnetic reconnection in Saturn's magnetotail, Nature Physics, 12(3):268–271, doi: 10.1038/NPHYS3565.

Arridge, C. S., N. Achilleos, J. Agarwal, C. B. Agnor, R. Ambrosi, N. Andre, S. V. Badman, K. Baines, D. Banfield, M. Barthelemy, M. M. Bisi, J. Blum, T. Bocanegra-Bahamon, B. Bonfond, C. Bracken, P. Brandt, C. Briand, C. Briois, S. Brooks, J. Castillo-Rogez, T. Cavalie, B. Christophe, A. J. Coates, G. Collinson, J. F. Cooper, M. Costa-Sitja, R. Courtin, I. A. Daglis, I. De Pater, M. Desai, D. Dirkx, M. K. Dougherty, R. W. Ebert, G. Filacchione, L. N. Fletcher, J. Fortney, I. Gerth, D. Grassi, D. Grodent, E. Grun, J. Gustin, M. Hedman, R. Helled, P. Henri, S. Hess, J. K. Hillier, M. H. Hofstadter, R. Holme, M. Horanyi, G. Hospodarsky, S. Hsu, P. Irwin, C. M. Jackman, O. Karatekin, S. Kempf, E. Khalisi, K. Konstantinidis, H. Kruger, W. S. Kurth, C. Labrianidis, V. Lainey, L. L. Lamy, M. Laneuville, D. Lucchesi, A. Luntzer, J. MacArthur, A. Maier, A. Masters, S. McKenna-Lawlor, H. Melin, A. Milillo, G. Moragas-Klostermeyer, A. Morschhauser, J. I. Moses, O. Mousis, N. Nettelmann, F. M. Neubauer, T. Nordheim, B. Noyelles, G. S. Orton, M. Owens, R. Peron, C. Plainaki, F. Postberg, N. Rambaux, K. Retherford, S. Reynaud, E. Roussos, C. T. Russell, Am. Rymer, R. Sallantin, A. Sanchez-Lavega, O. Santolik, J. Saur, Km. Sayanagi, P. Schenk, J. Schubert, N. Sergis, E. C. Sittler, A. Smith, F. Spahn, R. Srama, T. Stallard, V. Sterken, Z. Sternovsky, M. Tiscareno, G. Tobie, F. Tosi, M. Trieloff, D. Turrini, E. P. Turtle, S. Vinatier, R. Wilson, P. Zarkat, (2014), The science case for an orbital mission to Uranus: Exploring the origins and evolution of ice giant planets, Planetary and Space Science, 104:122–140, doi: 10.1016/j.pss.2014.08.009.

Arridge, C. S., N. Andre, K. K. Khurana, C. T. Russell, S. W. H. Cowley, G. Provan, D. T. Young, (2011a), Periodic motion of Saturn's nightside plasma sheet, Journal of Geophysical Research: Space Physics, 116:22 pp., doi: 10.1029/2011JA016827.

Arridge, C. S., N. Achilleos, P. Guio, (2011b), Electric field variability and classifications of Titan's magnetoplasma environment, AnGeo Communicates, 29:1253–1258, doi: 10.5194/angeo-29-1253-2011.

Arridge, C. S., H. J. McAndrews, C. M. Jackman, C. Forsyth, A. P. Walsh, E. C. Sittler, D. T. Young, (2009), Plasma electrons in Saturn's magnetotail: Structure, distribution and energization, Planetary and Space Science, 57(14–15):2032–2047, doi: 10.1016/j.pss.2009.09.007.

Arridge, C. S., K. K. Khurana, C. T. Russell, D. J. Southwood, N. Achilleos, M. K. Dougherty, H. K. Leinweber, (2008a), Warping of Saturn's magnetospheric and magnetotail current sheets, Journal of Geophysical Research: Space Physics, 113(A8):13 pp., doi: 10.1029/2007JA012963.

Arridge, C. S., C. T. Russell, K. K. Khurana, N. Achilleos, S. W. H. Cowley, M. K. Dougherty, E. J. Bunce, (2008b), Saturn's magnetodisc current sheet, Journal of Geophysical Research: Space Physics, 113(A4):9 pp., doi: 10.1029/2007JA012540.

Arridge, C. S., N. Andre, N. Achilleos, K. K. Khurana, C. L. Bertucci, L. K. Gilbert, M. K. Dougherty, (2008c), Thermal electron periodicities at 20R(S) in Saturn's magnetosphere, Geophysical Research Letters, 35(15):5 pp., doi: 10.1029/2008GL034132.

Arridge, C. S., C. T. Russell, K. K. Khurana, N. Achilleos, N. Andre, A. M. Rymer, A. J. Coates, (2007), Mass of Saturn's magnetodisc: Cassini observations, Geophysical Research Letters, 34(9):5 pp., doi: 10.1029/2006GL028921.

Arridge, C. S., N. Achilleos, M. K. Dougherty, K. K., Khurana, C. T. Russell, (2006), Modeling the size and shape of Saturn's magnetopause with variable dynamic pressure, Journal of Geophysical Research: Space Physics, 111(A11):13 pp., doi: 10.1029/2005JA011574.

Backes, H., F. M. Neubauer, M. K. Dougherty, N. Achilleos, N. Andre, C. S. Arridge, A. Wennmacher, (2005), Titan's magnetic field signature during the first Cassini encounter, Science, 308(5724):992–995, doi: 10.1126/science.1109763.

Badman, S. V., G. Provan, E. J. Bunce, D. G. Mitchell, H. Melin, S. W. H. Cowley, M. K. Dougherty, (2016), Saturn's auroral morphology and field-aligned currents during a solar wind compression, Icarus, 263:83–93, doi: 10.1016/j.Icarus.2014.11.014.

Badman, S. V., C. M. Jackman, J. D. Nichols, J. T. Clarke, J.- C. Gérard, (2014), Open flux in Saturn's magnetosphere, Icarus, 231:137–145, doi: org/10.1016/j.Icarus.2013.12.004.

Badman, S. V., A. Masters, H. Hasegawa, M. Fujimoto, A. Radioti, D. Grodent, A. J. Coates, (2013), Bursty magnetic reconnection at Saturn's magnetopause, Geophysical Research Letters, 40(6):1027–1031, doi: 10.1002/grl.50199.

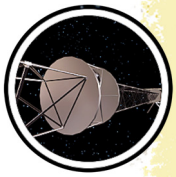

Badman, S. V., N. Achilleos, C. S. Arridge, K. H. Baines, R. H. Brown, E. J. Bunce, C. Tao, (2012), Cassini observations of ion and electron beams at Saturn and their relationship to infrared auroral arcs, Journal of Geophysical Research: Space Physics, 117, doi: 10.1029/2011JA017222.

Badman, S. V., N. Achilleos, K. H. Baines, R. H. Brown, E. J. Bunce, M. K. Dougherty, T. Stallard, (2011), Location of Saturn's northern infrared aurora determined from Cassini VIMS images, Geophysical Research Letters, 38:6 pp., doi: 10.1029/2010GL046193.

Badman, S. V., S. W. H. Cowley, B. Cecconi, L. Lamy, P. Zarka, (2008), Relationship between solar wind corotating interaction regions and the phasing and intensity of Saturn kilometric radiation bursts, Annales Geophysicae, 26:3641–3651.

Badman, S. V. et al., (2005), Open flux estimates in Saturn’s magnetosphere during the January 2004 Cassini-HST campaign, and implications for reconnection rates, Journal of Geophysical Research, 110(A11216), doi: 10.1029/2005JA011240.

Barnes, J. W., A. A. Simon-Miller, E, P. Turtle, M. K. Dougherty, R. H. Brown, (2009), Special issue: Titan, Saturn, and Saturn's Magnetosphere Preface, Planetary and Space Science, 57(14–15):1649, doi: 10.1016/j.pss.2009.09.015.

Bebesi, Z., N. Krupp, K. Szego, M. Fraenz, Z. Nemeth, S. M. Krimigis, M. K. Dougherty, (2012), Analysis of energetic electron drop-outs in the upper atmosphere of Titan during flybys in the dayside magnetosphere of Saturn, Icarus, 218(2):1020–1027, doi: 10.1016/j.Icarus.2012.01.009.

Bebesi, Z., K. Szego, A. Balogh, N. Krupp, G. Erdos, A. M. Rymer, M. K. Dougherty, (2011), Response to Comment on Slow-mode shock candidate in the Jovian magnetosheath by Bebesi et al., Planetary and Space Science, 59(5–6):445–446, doi: 10.1016/j.pss.2010.10.007.

Bebesi, Z., K. Szego, A. Balogh, N. Krupp, G. Erdos, A. M. Rymer, M. K. Dougherty, (2010), Slow-mode shock candidate in the Jovian magnetosheath, Planetary and Space Science, 58(5):807–813, doi: 10.1016/j.pss.2009.12.008.

Belenkaya, E. S., V. V. Kalegaev, S. W. H. Cowley, G. Provan, M. S. Blokhina, O. G. Barinov, A. A. Kirillov, M. S. Grigoryan, (2016), Optimization of Saturn paraboloid magnetospheric field model parameters using Cassini equatorial magnetic field data, Annales Geophysicae, 34:641–656, doi: 10.5914/angeo-34-641-2016.

Belenkaya, E. S., S. W. H. Cowley, C. J. Meredith, J. D. Nichols, V. V. Kalegaev, I. I. Alexeev, O. G. Barinov, W. O. Barinova, M. S. Blokhina, (2014), Magnetospheric magnetic field modelling for the 2011 and 2012 HST Saturn aurora campaigns – implications for auroral source regions, Annales Geophysicae, 32:689–704, doi: 10.5914/angeo-32-689-2014.

Belenkaya, E. S., S. W. H. Cowley, J. D. Nichols, M.S. Blokhina, V.V. Kalegaev, (2011), Magnetospheric mapping of the dayside UV auroral oval at Saturn using simultaneous HST images, Cassini IMF data, and a global magnetic field model, Annales Geophysicae, 29:1233–1246.

Belenkaya, E. S., I. I. Alexeev, M. S. Blokhina, E. J. Bunce, S. W. H. Cowley, J. D. Nichols, V. V. Kalegaev, V. G. Petrov, G. Provan, (2010), IMF dependence of Saturn's auroras: Modelling study of HST and Cassini data from 12–15 February 2008, Annales Geophysicae, 28:1559–1570.

Belenkaya, E. S., I. I. Alexeev, M. S. Blokhina, S. W. H. Cowley, S. V. Badman, V. V. Kalegaev, M. S. Grigoryan, (2007), IMF dependence of the open-closed field line boundary in Saturn's ionosphere and its relation to the UV auroral oval observed by the Hubble Space Telescope, Annales Geophysicae, 25:1215–1226.

Belenkaya, E. S., S. W. H. Cowley, I. I. Alexeev, (2006), Saturn's aurora in the January 2004 events, Annales Geophysicae, 24:1649–1663.

Bertucci, C., D. C. Hamilton, W. S. Kurth, G. Hospodarsky, D. Mitchell, N. Sergis, M. K. Dougherty, (2015), Titan's interaction with the supersonic solar wind, Geophysical Research Letters, 42(2):193-200, doi: 10.1002/2014GL062106.

Bertucci, C., F. Duru, N. Edberg, M. Fraenz, C. Martinecz, K. Szego, O. Vaisberg, (2011), The Induced Magnetospheres of Mars, Venus, and Titan, Space Science Reviews, 162(1–4):113–171, doi: 10.1007/s11214-011-9845-1.

Bertucci, C., B. Sinclair, N. Achilleos, P. Hunt, M. K. Dougherty, C. S. Arridge, (2009), The variability of Titan's magnetic environment, Planetary and Space Science, 57(14–15), 1813–1820, doi: 10.1016/j.pss.2009.02.009.

Bertucci, C., N. Achilleos, M. K. Dougherty, R. Modolo, A. J. Coates, K. Szego, A. Masters, Y. Ma, F. M. Neubauer, P. Garnier, J. E. Wahlund, D. T. Young, (2008), The magnetic memory of Titan's ionized atmosphere, Science, 321(5895):1475–1478, doi: 10.1126/science.1159780.

Bertucci, C., N. Achilleos, C. Mazelle, G. B. Hospodarsky, M. Thomsen, M. K. Dougherty, W. Kurth, (2007a), Low-frequency waves in the foreshock of Saturn: First results from Cassini, Journal of Geophysical Research: Space Physics, 112(A9):13 pp., doi: 10.1029/2006JA012098.

Bertucci, C., F. M. Neubauer, K. Szego, J. -E. Wahlund, A. J. Coates, M. K. Dougherty, D. T. Young, W. S. Kurth, (2007b), Structure of Titan's mid-range magnetic tail: Cassini magnetometer observations during the T9 flyby, Geophysical Research Letters, 34(24):4 pp., doi: 10.1029/2007GL030865.

Bertucci, C., N. Achilleos, C. T. Russell, M. K. Dougherty, E. J. Smith, M. Burton, B. T. Tsurutani, C. Mazelle, (2005), Bow shock and upstream waves at Jupiter and Saturn: Cassini magnetometer observations, in Physics Of Collisionless Shocks, (eds.) G. Li, G. P. Zank, C. T. Russell, Volume 781, American Institute of Physics, Palm Springs, CA, pp. 109–115.

Blanc, M., S. Bolton, J. Bradley, M. Burton, T. E. Cravens, I. Dandouras, M. K. Dougherty, M. C. Festou, J. Feynman, R. E. Johnson, T. G. Gombosi, W. S. Kurth, P. C. Liewer, B. H. Mauk, S. Maurice, D. Mitchell, F. M. Neubauer, J. D. Richardson, D. E. Shemansky, E. C. Sittler, B. T. Tsurutani, P. H. Zarka, L. W. Esposito, E. Grun, D. A. Gurnett, A. J. Kliore, S. M. Krimigis, D. Southwood, J. H. Waite, D. T. Young, (2002), Magnetospheric and plasma science with

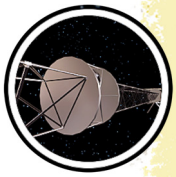

Cassini-Huygens, Space Science Reviews, 104(1–2):253–346, doi: 10.1023/A:1023605110711.

Bogdanov, A. T., K. H. Glassmeier, G. Musmann, M. K. Dougherty, S. Kellock, P. Slootweg, B. Tsurutani, (2003), Ion cyclotron waves in the Earth's magnetotail during Cassini's Earth swing-by, Annales Geophysicae, 21(10):2043–2057, doi: 10.5194/angeo-21-2043-2003.

Bradley, T. J., S. W. H. Cowley, G. Provan, G. J. Hunt, E. J. Bunce, S. J. Wharton, I. I. Alexeev, E. S. Belenkaya, V. V. Kalegaev, M. K. Dougherty, (2018), Field-aligned currents in Saturn's nightside magnetosphere: Subcorotation and planetary period oscillation components during northern spring, Journal of Geophysical Research: Space Physics, 123(5):3602–3636, doi: 10.1029/2017JA024885.

Brandt, P. C., K. K. Khurana, D. G. Mitchell, N. Sergis, K. Dialynas, J. F. Carbary, E. C. Roelof, C. P. Paranicas, S. M. Krimigis, B. H. Mauk, (2010), Saturn's periodic magnetic field perturbations caused by a rotating partial ring current, Geophysical Research Letters, 37(L22103):5 pp., doi: 10.1029/2010GL045285.

Branduardi-Raymont, G., P. G. Ford, K. C. Hansen, L. Lamy, A. Masters, B. Cecconi, A. J. Coates, M. K. Dougherty, G. R. Gladstone, P. Zarka, (2013), Search for Saturn's X-ray aurorae at the arrival of a solar wind shock, Journal of Geophysical Research: Space Physics, 118(5):2145–2156, doi: 10.1002/jgra.50112.

Bunce, E. J., D. C. Grodent, S. L. Jinks, D. J. Andrews, S. V. Badman, A. J. Coates, G. Provan, (2014), Cassini nightside observations of the oscillatory motion of Saturn's northern auroral oval, Journal of Geophysical Research: Space Physics, 119(5):3528–3543, doi: 10.1002/2013JA019527.

Bunce, E. J., S. W. H. Cowley, D. L. Talboys, M. K. Dougherty, L. Lamy, W. S. Kurth, A. J. Coates, (2010), Extraordinary field-aligned current signatures in Saturn's high-latitude magnetosphere: Analysis of Cassini data during Revolution 89, Journal of Geophysical Research: Space Physics, 115:9 pp., doi: 10.1029/2010JA015612.

Bunce, E. J., C. S. Arridge, S. W. H. Cowley, M. K. Dougherty, (2008a), Magnetic field structure of Saturn's dayside magnetosphere and its mapping to the ionosphere: Results from ring current modeling, Journal of Geophysical Research: Space Physics, 113(A2):8 pp., doi: 10.1029/2007JA012538.

Bunce, E. J., C. S. Arridge, J. T. Clarke, A. J. Coates, S. W. H. Cowley, M. K. Dougherty, D. L. Talboys, (2008b), Origin of Saturn's aurora: Simultaneous observations by Cassini and the Hubble Space Telescope, Journal of Geophysical Research: Space Physics, 113(A9):11 pp., doi: 10.1029/2008JA013257.

Bunce, E. J., S. W. H. Cowley, I. I. Alexeev, C. S. Arridge, M. K. Dougherty, J. D. Nichols, C. T. Russell, (2007), Cassini observations of the variation of Saturn's ring current parameters with system size, Journal of Geophysical Research: Space Physics, 112(A10):21 pp., doi: 10.1029/2007JA012275.

Bunce, E. J., S. W. H. Cowley, C. M. Jackman, J. T. Clarke, F. J. Crary, M. K. Dougherty, (2006), Cassini observations of the Interplanetary Medium Upstream of Saturn and their relation to the Hubble Space Telescope aurora data, Advances in Space Research, mercury, mars and saturn, 38(4):806–814, doi: 10.1016/j.asr.2005.08.005.

Bunce, E. J., S. W. H. Cowley, D. M. Wright, A. J. Coates, M. K. Dougherty, N. Krupp, A. M. Rymer, (2005), In situ observations of a solar wind compression-induced hot plasma injection in Saturn's tail, Geophysical Research Letters, 32(20):4 pp., doi: 10.1029/2005GL022888.

Burch, J. L., J. Goldstein, P. Mokashi, W. S. Lewis, C. Paty, D. T. Young, N. Andre, (2008), On the cause of Saturn's plasma periodicity, Geophysical Research Letters, 35(14):4 pp., doi: 10.1029/2008GL034951.

Burch, J. L., J. Goldstein, W. S. Lewis, D. T. Young, A. J. Coates, M. K. Dougherty, N. Andre, (2007), Tethys and Dione as sources of outward-flowing plasma in Saturn's magnetosphere, Nature, 447(7146):833–835, doi: 10.1038/nature05906.

Burton, M. E., M. K. Dougherty, C. T. Russell, (2010), Saturn's internal planetary magnetic field, Geophysical Research Letters, 37:5 pp., doi: 10.1029/2010GL045148.

Burton, M. E., M. K. Dougherty, C. T. Russell, (2009), Model of Saturn's internal planetary magnetic field based on Cassini observations, Planetary and Space Science, 57(14–15):1706–1713, doi: 10.1016/j.pss.2009.04.008.

Cao, H., D.J. Stevenson, (2017) Zonal flow magnetic field interaction in the semi-conducting region of giant planets, Icarus, 296:59–72.

Cao, H., C. T. Russell, J. Wicht, U. R. Christensen, M. K. Dougherty, (2012), Saturn's high degree magnetic moments: Evidence for a unique planetary dynamo, Icarus, 221(1):388–394, doi: 10.1016/j.Icarus.2012.08.007.

Cao, H., C. T. Russell, U. R. Christensen, M. K. Dougherty, M. E. Burton, (2011), Saturn's very axisymmetric magnetic field: No detectable secular variation or tilt, Earth and Planetary Science Letters, 304(1–2):22–28, doi: 10.1016/j.epsl.2011.02.035.

Carbary, J. F., N. Achilleos, C. S. Arridge, K. K. Khurana, M. K. Dougherty, (2010), Global configuration of Saturn's magnetic field derived from observations, Geophysical Research Letters, 37:6 pp., doi: 10.1029/2010GL044622.

Caudal, G., (1986), A self-consistent model of Jupiter’s magnetodisc including the effects of centrifugal force and pressure, Journal of Geophysical Research, 91(A4):4201–4221.

Clarke, K. E., D. J. Andrews, C. S. Arridge, A. J. Coates, S. W. H. Cowley, (2010a), Magnetopause oscillations near the planetary period at Saturn: Occurrence, phase, and amplitude, Journal of Geophysical Research, 115(A08209), doi: 10.1029/2009JA014745.

Clarke, K. E., D. J. Andrews, A. J. Coates, S. W. H. Cowley, A. Masters, (2010b), Magnetospheric period oscillations of Saturn’s bow shock, Journal of Geophysical Research, 115(A05202), doi: 10.1029/2009JA015164.

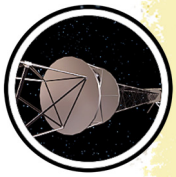

Clarke, K. E., N. Andre, D. J. Andrews, A. J. Coates, S. W. H. Cowley, M. K. Dougherty, D. M. Wright, (2006), Cassini observations of planetary-period oscillations of Saturn's magnetopause, Geophysical Research Letters, 33(23):6 pp., doi: 10.1029/2006GL027821.

Clarke, J. T., J. C. Gerard, D. Grodent, S. Wannawichian, J. Gustin, J. Connerney, J. Kim, (2005), Morphological differences between Saturn's ultraviolet aurorae and those of Earth and Jupiter, Nature, 433:717–719.

Coates, A. J., M. K. Dougherty, (2001), Cassini-Huygens by Jove, Frontiers, 10(4).

Connerney, J. E. P., (1981), The magnetic field of Jupiter: A generalized inverse approach, Journal of Geophysical Research: Space Physics, 86(A9):7679–7693, doi: 10.1029/JA086iA09p07679.

Coustenis, A., S. K. Atreya, T. Balint, R. H. Brown, M. K. Dougherty, F. Ferri, E. F. Young, (2009), TandEM: Titan and Enceladus mission, Experimental Astronomy, 23(3):893–946, doi: 10.1007/s10686-008-9103-z.

Cowee, M. M., S. P. Gary, H. Y. Wei, R. L. Tokar, C. T. Russell, (2010), An explanation for the lack of ion cyclotron wave generation by pickup ions at Titan: 1-D hybrid simulation results, Journal of Geophysical Research: Space Physics, 115(A10), doi: 10.1029/2010JA015769.

Cowley, S. W. H., G. Provan, (2017), Planetary period modulations of Saturn’s magnetotail current sheet during northern spring: Observations and modeling, Journal of Geophysical Research, 122:6049–6077, doi: 10.1002/2017JA023993.

Cowley, S. W. H., G. Provan, G. J. Hunt, C. M. Jackman, (2017), Planetary period modulations of Saturn’s magnetotail current sheet: A simple illustrative mathematical model, Journal of Geophysical Research, 122:258–279, doi: 10.1002/2016JA023367.

Cowley, S. W. H., G. Provan, (2016), Planetary period oscillations in Saturn’s magnetosphere: Further comments on the relationship between post-equinox properties deduced from magnetic field and Saturn kilometric radiation measurements, Icarus, 272:258–276, doi: 10.1016/j.Icarus.2016.02.051.

Cowley, S. W. H., J. D. Nichols, C. M. Jackman, (2015), Down-tail mass loss by plasmoids in Jupiter’s and Saturn’s magnetospheres, Journal of Geophysical Research, 120:6347–6356, doi: 10.1002/2015JA021500.

Cowley, S. W. H., G. Provan, (2015), Planetary period oscillations in Saturn’s magnetosphere: Comments on the relation between post-equinox periods determined from magnetic field and SKR emission data, Annales Geophysicae, 33:901–912.

Cowley, S. W. H., G. Provan, (2013), Saturn’s magnetospheric planetary period oscillations, neutral atmosphere circulation, and thunderstorm activity: Implications, or otherwise, for physical links, Journal of Geophysical Research, 118:7246–7261, doi: 10.1002/2013JA019200.

Cowley, S. W. H., C. S. Arridge, E. J. Bunce, J. T. Clarke, A. J. Coates, M. K. Dougherty, D. L. Talboys, D. L., (2008), Auroral current systems in Saturn's magnetosphere: comparison of

theoretical models with Cassini and HST observations, Annales Geophysicae, 26(9):2613–2630, doi: 10.5194/angeo-26-2613-2008.

Cowley, S. W. H., D. M. Wright, E. J. Bunce, A. C. Carter, M. K. Dougherty, G. Giampieri, T. R. Robinson, (2006), Cassini observations of planetary-period magnetic field oscillations in Saturn's magnetosphere: Doppler shifts and phase motion, Geophysical Research Letters, 33(7):4 pp., doi: 10.1029/2005GL025522.

Cowley, S. W. H., S. V. Badman, E. J. Bunce, J. T. Clarke, J. C. Gérard, D. Grodent, C. M. Jackman, S. E. Milan, T. K. Yeoman, (2005), Reconnection in a rotation-dominated magnetosphere and its relation to Saturn’s auroral dynamics, Journal of Geophysical Research, 110(A02201), doi: 10.1029/2004JA010796.

Cowley, S. W. H., E. J. Bunce, J. M. O’Rourke, (2004), A simple quantitative model of plasma flows and currents in Saturn’s polar ionosphere, Journal of Geophysical Research, 109(A05212), doi: 10.1029/2003JA010375.

Cramm, R. et al., (1998), Evidence for resonant mode coupling in Saturn’s magnetosphere, Journal of Geophysical Research, 103:11951–11960.

Crary, F. J., J. T. Clarke, M. K. Dougherty, P. G. Hanlon, K. C. Hansen, J. T. Steinberg, D. T. Young, (2005), Solar wind dynamic pressure and electric field as the main factors controlling Saturn's aurorae, Nature, 433(7027):720–722, doi: 10.1038/nature03333.

Cravens, T. E., M. Richard, Y. -J. Ma, et al., (2010), Dynamical and magnetic field time constants for Titan's ionosphere: Empirical estimates and comparisons with Venus, Journal of Geophysical Research, 115(A08319), doi: 10.1029/2009JA015050.

Cravens, T. E., I. P. Robertson, J. H. Waite, R. V. Yelle, V. Vuitton, A. J. Coates, J. -E. Wahlund, K. Agren, M. S. Richard, V. De La Haye, A. Wellbrock, F. M. Neubauer, (2009), Model-data comparisons for Titan's nightside ionosphere, Icarus, 199:174–188, doi: 10.1016/j.Icarus.2008.09.005.

Cui, J., M. Galand, R. V. Yelle, J. -E. Wahlund, K. Agren, J. H. Waite, M. K. Dougherty, (2010), Ion transport in Titan's upper atmosphere, Journal of Geophysical Research: Space Physics, 115:12 pp., doi: 10.1029/2009JA014563.

Cutler, J. C., M. K. Dougherty, E. Lucek, A. Masters, (2011), Evidence of surface wave on the dusk flank of Saturn's magnetopause possibly caused by the Kelvin-Helmholtz instability, Journal of Geophysical Research: Space Physics, 116:9 pp., doi: 10.1029/2011JA016643.

Davies, E. H., A. Masters, M. K. Dougherty, K. C. Hansen, A. J. Coates, G. J. Hunt, (2017), Swept forward magnetic field variability in high-latitude regions of Saturn's magnetosphere, Journal of Geophysical Research: Space Physics, 122(12):12328–12337, doi: 10.1002/2017JA024419.

Dougherty, M. K., H. Cao, K. K. Khurana, G. J. Hunt, G. Provan, S. Kellock, M. E. Burton, T. A. Burk, E. J. Bunce, S. W. H. Cowley, M. G. Kivelson, C. T. Russell, D. J. Southwood, (2018), Saturn’s magnetic field revealed by the Cassini Grand Finale, Science, 362, aat5434, doi:10.1126/science.aat5434.

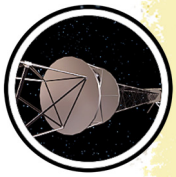

Dougherty, M. K., (2017), Cassini-Huygens Saturn in the infrared, Nature Astronomy, 1(9):579, doi: 10.1038/s41550-017-0245-7.

Dougherty, M. K., A. Coustenis, R. D. Lorenz, (2009), Titan beyond cassini-huygens, in Titan from Cassini-Huygens, doi: 10.1007/978-1-4020-9215-2_18, pp. 479–488.

Dougherty, M. K., K. K. Khurana, F. M. Neubauer, C. T. Russell, J. Saur, J. S. Leisner, M. E. Burton, (2006), Identification of a dynamic atmosphere at Enceladus with the Cassini magnetometer, Science, 311(5766):1406–1409, doi: 10.1126/science.1120985.

Dougherty, M. K., N. Achilleos, N. Andre, C. S. Arridge, A. Balogh, C. Bertucci, B. T. Tsurutani, (2005), Cassini magnetometer observations during Saturn orbit insertion, Science, 307(5713):1266–1270, doi: 10.1126/science.1106098.

Dougherty, M. K., S. Kellock, D. J. Southwood, A. Balogh, E. J. Smith, B. T. Tsurutani, S. W. H. Cowley, (2004), The Cassini magnetic field investigation, Space Science Reviews, 114(1–4):331–383, doi: 10.1007/s11214-004-1432-2.

Dougherty, M. K., (2001), Saturn: magnetosphere, in Encyclopedia of Astronomy and Astrophysics, (ed.) P. Murdin, Institute of Physics Publishing, Nature Publishing Group, London, pp. 2361–2367.

Dungey, J. W., (1965), The length of the magnetospheric tail, Journal of Geophysical Research, 70:1753.

Dunlop, M. W., M. K. Dougherty, S. Kellock, D. J. Southwood, (1999), Operation of the dual magnetometer on Cassini: science performance, in Planetary and Space Science, Vol. 47, Pergamon-Elsevier Science Ltd, Nantes, France, doi: 10.1016/S0032-0633(99)00060-4, pp. 1389–1405.

Edberg, N. J. T., D. J. Andrews, O. Shebanits, K. Agren, J. -E. Wahlund, H. J. Opgenoorth, M. K. Dougherty, (2013), Extreme densities in Titan's ionosphere during the T85 magnetosheath encounter, Geophysical Research Letters, 40(12):2879–2883, doi: 10.1002/grl.50579.

Edberg, N. J. T., K. Agren, J. -E. Wahlund, M. W. Morooka, D. J. Andrews, S. W. H. Cowley, M. K. Dougherty, (2011), Structured ionospheric outflow during the Cassini T55-T59 Titan flybys, Planetary and Space Science, 59(8):788–797, doi: 10.1016/j.pss.2011.03.007.

Edberg, N. J. T., J. -E. Wahlund, K. Agren, M. W. Morooka, R. Modolo, C. Bertucci, M. K. Dougherty, (2010), Electron density and temperature measurements in the cold plasma environment of Titan: Implications for atmospheric escape, Geophysical Research Letters, 37:5 pp., doi: 10.1029/2010GL044544.

Engelhardt, I. A. D., J. -E. Wahlund, D. J. Andrews, A. I. Eriksson, S. Ye, W. S. Kurth, M. K. Dougherty, (2015), Plasma regions, charged dust and field-aligned currents near Enceladus, Planetary and Space Science, 117:453–469, doi: 10.1016/j.pss.2015.09.010.

Espinosa, S. A., D. J. Southwood, M. K. Dougherty, (2003a), How can Saturn impose its rotation period in a noncorotating magnetosphere?, Journal of Geophysical Research: Space Physics, 108(A2):8 pp., doi: 10.1029/2001JA005084.

- - - - - - - - - - - - - -

Espinosa, S. A., D. J. Southwood, M. K. Dougherty, (2003b), Reanalysis of Saturn's magnetospheric field data view of spin-periodic perturbations, Journal of Geophysical Research: Space Physics, 108(A2):8 pp., doi: 10.1029/2001JA005083.

Espinosa, S. A., M. K. Dougherty, (2001), Unexpected periodic perturbations in Saturn's magnetic field data from Pioneer 11 and Voyager 2, in Planetary Magnetospheres, (eds.) M. Dougherty, J. D. Menietti, Vol. 28.Elsevier Science BV, Warsaw, Poland, doi: 10.1016/S0273-1177(01)00518-X, pp. 919–924.

Espinosa, S. A., M. K. Dougherty, (2000), Periodic perturbations in Saturn's magnetic field, Geophysical Research Letters, 27(17):2785-2788, doi: 10.1029/2000GL000048.

Felici, M., C. S. Arridge, A. J. Coates, S. V. Badman, M. K. Dougherty, C. M. Jackman, N. Sergis, (2016), Cassini observations of ionospheric plasma in Saturn's magnetotail lobes, Journal of Geophysical Research: Space Physics, 121(1):338–357.

Feyerabend, M., S. Simon, F. M. Neubauer, U. Motschmann, C. Bertucci, N. J. T. Edberg, G. B. Hospodarsky, W. S. Kurth, (2016), Hybrid simulation of Titan's interaction with the supersonic solar wind during Cassini's T96 flyby, Geophysical Research Letters, 43:35–42, doi: 10.1002/2015GL066848.

Gerard, J. -C., D. Grodent, S. W. H. Cowley, D. G. Mitchell, W. S. Kurth, J. T. Clarke, A. J. Coates, (2006), Saturn's auroral morphology and activity during quiet magnetospheric conditions, Journal of Geophysical Research: Space Physics, 111(A12):10 pp., doi: 10.1029/2006JA011965.

Giampieri, G., M. K. Dougherty, E. J. Smith, C. T. Russell, (2006), A regular period for Saturn's magnetic field that may track its internal rotation, Nature, 441(7089):62–64, doi: 10.1038/nature04750.

Giampieri, G., M. K. Dougherty, C. T. Russell, E. J. Smith, (2005), Reply to comment by M. L. Kaiser et al., on Rotation rate of Saturn's interior from magnetic field observations, Geophysical Research Letters, 32(2):2 pp., doi: 10.1029/2004GL021684.

Giampieri, G., M. K. Dougherty, (2004a), Modelling of the ring current in Saturn's magnetosphere, Annales Geophysicae, 22(2):653–659, doi: 10.5194/angeo-22-653-2004.

Giampieri, G., M. K. Dougherty, (2004b), Rotation rate of Saturn's interior from magnetic field observations, Geophysical Research Letters, 31(16):4 pp., doi: 10.1029/2004GL020194.

Gladstone, G. R., J. H. Waite, D. Grodent, W. S. Lewis, F. J. Crary, R. F. Elsner, T. E. Cravens, (2002), A pulsating auroral X-ray hot spot on Jupiter, Nature, 415(6875):1000–1003, doi: 10.1038/4151000a.

Gurnett, D. A., T. F. Averkamp, P. Schippers, A. M. Persoon, G. B. Hospodarsky, J. S. Leisner, M. K. Dougherty, (2011), Auroral hiss, electron beams and standing Alfven wave currents near Saturn's moon Enceladus, Geophysical Research Letters, 38:4 pp., doi: 10.1029/2011GL046854.

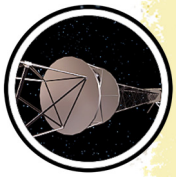

Gurnett, D. A., A. M. Persoon, A. J. Kopf, W. S. Kurth, M. W. Morooka, J. -E.Wahlund, N. Krupp, (2010), A plasmapause-like density boundary at high latitudes in Saturn's magnetosphere, Geophysical Research Letters, 37:5 pp., doi: 10.1029/2010GL044466.

Gurnett, D. A., A. M. Persoon, W. S. Kurth, J. B. Groene, T. F. Averkamp, M. K. Dougherty, D. J. Southwood, (2007), The variable rotation period of the inner region of Saturn's plasma disk, Science, 316(5823):442–445, doi: 10.1126/science.1138562.

Gurnett, D. A., W. S. Kurth, G. B. Hospodarsky, A. M. Persoon, P. Zarka, A. Lecacheux, M. K. Dougherty, (2002), Control of Jupiter's radio emission and aurorae by the solar wind, Nature, 415(6875):985–987, doi: 10.1038/415985a.

Hadid, L. Z., F. Sahraoui, K. H. Kiyani, A. Retino, R. Modolo, P. Canu, M. K. Dougherty, (2015), Nature of the MHD and kinetic scale turbulence in the magnetosheath of Saturn: Cassini observations, Astrophysical Journal Letters, 813(2):6 pp., doi: 10.1088/2041-8205/813/2/L29.

Hanlon, P. G., M. K. Dougherty, N. Krupp, K. C. Hansen, F. J. Crary, D. T. Young, G. Toth, (2004a), Dual spacecraft observations of a compression event within the Jovian magnetosphere: Signatures of externally triggered supercorotation?, Journal of Geophysical Research: Space Physics, 109(A9):8 pp., doi: 10.1029/2003JA010116.

Hanlon, P. G., M. K. Dougherty, R. J. Forsyth, M. J. Owens, K. C. Hansen, G. Toth, D. T. Young, (2004b), On the evolution of the solar wind between 1 and 5 AU at the time of the Cassini Jupiter flyby: Multispacecraft observations of interplanetary coronal mass ejections including the formation of a merged interaction region, Journal of Geophysical Research: Space Physics, 109(A9):10 pp., doi: 10.1029/2003JA010112.

Hansen, K. C., A. J. Ridley, G. B. Hospodarsky, N. Achilleos, M. K. Dougherty, T. I. Gombosi, G. Toth, (2005), Global MHD simulations of Saturn's magnetosphere at the time of Cassini approach, Geophysical Research Letters, 32(20):5 pp., doi: 10.1029/2005GL022835.

Hartle, R. E., E. C. Sittler, F. M. Neubauer, R. E. Johnson, H. T. Smith, F. Crary, D. J. McComas, D. T. Young, A. J. Coates, D. Simpson, S. Bolton, D. Reisenfeld, K. Szego, J. J. Berthelier, A. Rymer, J. Vilppola, J. T. Steinberg, N. Andre, (2006), Initial interpretation of Titan plasma interaction as observed by the Cassini plasma spectrometer: Comparisons with Voyager 1, Planet, Planetary and Space Science, 54(12):1211–1224, doi: 10.1016/j.pss.2006.05.029.

Hendricks, S., F. M. Neubauer, M. K. Dougherty, N. Achilleos, C. T. Russell, (2005), Variability in Saturn's bow shock and magnetopause from Pioneer and Voyager: Probabilistic predictions and initial observations by Cassini, Geophysical Research Letters, 32(20):4 pp., doi: 10.1029/2005GL022569.

Hill, T. W., M. F. Thomsen, M. G. Henderson, R. L. Tokar, A. J. Coates, H. J., McAndrews, D. T. Young, (2008), Plasmoids in Saturn's magnetotail, Journal of Geophysical Research: Space Physics, 113(A1):9 pp., doi: 10.1029/2007JA012626.

Hospodarsky, G. B., T. F. Averkamp, W. S. Kurth, D. A. Gurnett, J. D. Menietti, O. Santolik, M. K. Dougherty, (2008), Observations of chorus at Saturn using the Cassini Radio and Plasma

Wave Science instrument, Journal of Geophysical Research: Space Physics, 113(A12):13 pp., doi: 10.1029/2008JA013237.

Hospodarsky, G. B., T. F. Averkamp, W. S. Kurth, D. A. Gurnett, M. Dougherty, U. Inan, T. Wood, (2001), Wave normal and Poynting vector calculations using the Cassini radio and plasma wave instrument, Journal of Geophysical Research: Space Physics, 106(A12):30253–30269, doi: 10.1029/2001JA900114.

Hunt, G. J., S. W. H. Cowley, J. D. Nichols, (2018a), Ionospheric currents due to ionosphere-magnetosphere coupling at Jupiter and Saturn, in Electric Currents in Geospace and Beyond, (eds.) A. Keiling, O. Marghitu, and M. Wheatland, John Wiley & Sons, Inc., p. 459.

Hunt, G. J., G. Provan, E. J. Bunce, S. W. H. Cowley, M. K. Dougherty, D. J. Southwood, (2018b), Field-aligned currents in Saturn's magnetosphere: Observations from the F-ring orbits, Journal of Geophysical Research, 123(5):3806–3821, doi: 10.1029/2017JA025067.

Hunt, G. J., Cowley, S. W. H., Provan, G., Bunce, E. J., Alexeev, I. I., Belenkaya, E. S., Coates, A. J., (2016), Field-aligned currents in Saturn's magnetosphere: Local time dependence of southern summer currents in the dawn sector between midnight and noon, Journal of Geophysical Research: Space Physics, 121(8):7785–7804, doi: 10.1002/2016JA022712.

Hunt, G. J., Cowley, S. W. H., Provan, G., Bunce, E. J., Alexeev, I. I., Belenkaya, E. S., Coates, A. J., (2015), Field-aligned currents in Saturn's northern nightside magnetosphere: Evidence for interhemispheric current flow associated with planetary period oscillations, Journal of Geophysical Research: Space Physics, 120(9):7552–7584, doi: 10.1002/2015JA021454.

Hunt, G. J., Cowley, S. W. H., Provan, G., Bunce, E. J., Alexeev, I. I., Belenkaya, E. S., Coates, A. J., (2014), Field-aligned currents in Saturn's southern nightside magnetosphere: Subcorotation and planetary period oscillation components, Journal of Geophysical Research: Space Physics, 119(12):53 pp., doi: 10.1002/2014JA020506.

Jackman, C.M., C. M., G. Provan, S. W. H. Cowley, (2016), Reconnection events in Saturn's magnetotail: Dependence of plasmoid occurrence on planetary period oscillation phase, Journal of Geophysical Research Space Physics, 121, doi: 10.1002/2015JA021985.

Jackman, C. M., M. F. Thomsen, D. G. Mitchell, N. Sergis, C. S. Arridge, M. Felici, M. K. Dougherty, (2015), Field dipolarization in Saturn's magnetotail with planetward ion flows and energetic particle flow bursts: Evidence of quasi-steady reconnection, Journal of Geophysical Research: Space Physics, 120(5):3603–3617, doi: 10.1002/2015JA020995.

Jackman, C. M., J. A. Slavin, M. G. Kivelson, D. J. Southwood, N. Achilleos, M. F. Thomsen, M. F. Vogt, (2014), Saturn's dynamic magnetotail: A comprehensive magnetic field and plasma survey of plasmoids and traveling compression regions and their role in global magnetospheric dynamics, Journal of Geophysical Research: Space Physics, 119(7):5465–5494, doi: 10.1002/2013JA019388.

Jackman, C. M., N. Achilleos, S. W. H. Cowley, E. J. Bunce, A. Radioti, D. Grodent, W. Pryor, (2013), Auroral counterpart of magnetic field dipolarizations in Saturn's tail, Planetary and Space Science, 82–83:34-42, doi: 10.1016/j.pss.2013.03.01.

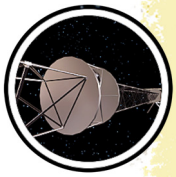

Jackman, C. M., J. A. Slavin, S. W. H. Cowley, (2011), Cassini observations of plasmoid structure and dynamics: Implications for the role of magnetic reconnection in magnetospheric circulation at Saturn, Journal of Geophysical Research, 116(A10212), doi: 10.1029/2011JA016682.

Jackman, C. M., C. S. Arridge, (2011a), Solar cycle effects on the dynamics of Jupiter's and Saturn's magnetospheres, Solar Physics, 274:481–502, doi 10.1007/s11207-011-9748-z.

Jackman, C. M., C. S. Arridge, (2011b), Statistical properties of the magnetic field in the Kronian magnetotail lobes and current sheet, Journal of Geophysical Research, 116(A05224), doi: 10.1029/2010JA015973.

Jackman, C. M., C. S. Arridge, J. A. Slavin, S. E. Milan, L. Lamy, M.K. Dougherty, A. J. Coates, (2010), In situ observations of the effect of a solar wind compression on Saturn's magnetotail, Journal of Geophysical Research: Space Physics, 115:12 pp., doi: 10.1029/2010JA015312.

Jackman, C. M., C. S. Arridge, H. J. McAndrews, M. G. Henderson, R. J. Wilson, (2009a), Northward field excursions in Saturn's magnetotail and their relationship to magnetospheric periodicities, Geophysical Research Letters, 36(L16101), doi: 10.1029/2009GL039149.

Jackman, C. M., L. Lamy, M. P. Freeman, P. Zarka, B. Cecconi, W. S. Kurth, M. K. Dougherty, (2009b), On the character and distribution of lower-frequency radio emissions at Saturn and their relationship to substorm-like events, Journal of Geophysical Research: Space Physics, 114:13 pp., doi: 10.1029/2008JA013997.

Jackman, C. M., C. S. Arridge, N. Krupp, E. J. Bunce, D. G. Mitchell, H. J. McAndrews, A. J. Coates, (2008a), A multi-instrument view of tail reconnection at Saturn, Journal of Geophysical Research: Space Physics, 113(A11):9 pp., doi: 10.1029/2008JA013592.

Jackman, C. M., R. J. Forsyth, M. K. Dougherty, (2008b), The overall configuration of the interplanetary magnetic field upstream of Saturn as revealed by Cassini observations, Journal of Geophysical Research: Space Physics, 113(A8):10 pp., doi: 10.1029/2008JA013083.

Jackman, C. M., C. T. Russell, D. J. Southwood, C. S. Arridge, N. Achilleos, M. K. Dougherty, (2007), Strong rapid dipolarizations in Saturn's magnetotail: In situ evidence of reconnection, Geophysical Research Letters, 34(11):5 pp., doi: 10.1029/2007GL029764.

Jackman, C. M., S. W. H. Cowley, (2006), A model of the plasma flow and current in Saturn's polar ionosphere under conditions of strong Dungey-cycle driving, Annales Geophysicae, 24:1029–1055.

Jackman, C. M., N. Achilleos, E. J. Bunce, S. W. H. Cowley, S. E. Milan, (2005a), Structure of the interplanetary magnetic field during the interval spanning the first Cassini fly-through of Saturn's magnetosphere and its implications for Saturn's magnetospheric dynamics, Advances in Space Research, 36:2120–2126, doi: 10.1016/j.asr.2004.12.023.

Jackman, C. M., N. Achilleos, E. J. Bunce, B. Cecconi, J. T. Clarke, S. W. H. Cowley, W. S. Kurth, P. Zarka, (2005b), Interplanetary conditions and magnetospheric dynamics during the Cassini orbit insertion fly-through of Saturn's magnetosphere, Journal of Geophysical Research, 110(A10212), doi: 10.1029/2005JA011054.

Jackman, C. M., N. Achilleos, E. J. Bunce, S. W. H. Cowley, M. K. Dougherty, G. H. Jones, E. J. Smith, (2004), Interplanetary magnetic field at similar to 9 AU during the declining phase of the solar cycle and its implications for Saturn's magnetospheric dynamics, Journal of Geophysical Research: Space Physics, 109(A11):19 pp., doi: 10.1029/2004JA010614.

Jasinski, J. M., C. S. Arridge, A. J. Coates, G. H. Jones, N. Sergis, M. F. Thomsen, N. Krupp, (2017), Diamagnetic depression observations at Saturn's magnetospheric cusp by the Cassini spacecraft, Journal of Geophysical Research Space Physics, 122:6283–6303, doi: 10.1002/2016JA023738.

Jasinski, J. M., J. A. Slavin, C. S. Arridge, G. Poh, X. Jia, N. Sergis, A. J. Coates, G. H. Jones, J. H. Waite, (2016), Flux transfer event observation at Saturn's dayside magnetopause by the Cassini spacecraft, Geophysical Research Letters, 43:6713–6723, doi: 10.1002/2016GL069260.

Jasinski, J. M., C. S. Arridge, L. Lamy, J. S. Leisner, M. F. Thomsen, D. G. Mitchell, J. H. Waite, (2014), Cusp observation at Saturn's high-latitude magnetosphere by the Cassini spacecraft, Geophysical Research Letters, 41(5):1382–1388, doi: 10.1002/2014GL059319.

Jia, X., M. G. Kivelson, (2016), Dawn-dusk asymmetries in rotating magnetospheres: Lessons from modeling Saturn, Journal of Geophysical Research, 121:1413–24, doi: 10.1002/2015JA021950.

Jia, X., M. G. Kivelson, (2012), Driving Saturn's magnetospheric periodicities from the upper atmosphere/ionosphere: Magnetotail response to dual sources, Journal of Geophysical Research, 117(A11219), doi: 10.1029/2012JA018183, described in Research Spotlight, Eos, 94(6), 5 February 2013, p. 68.

Jia, X., M. G. Kivelson, T. I. Gombosi, (2012a), Driving Saturn's magnetospheric periodicities from the upper atmosphere/ionosphere, Journal of Geophysical Research, 117(A04215), doi: 10.1029/2011JA017367.

Jia, X., K. C. Hansen, T. I. Gombosi, M. G. Kivelson, G. Tóth, D. L. DeZeeuw, A. J. Ridley, (2012b), Magnetospheric configuration and dynamics of Saturn's magnetosphere: A global MHD simulation, Journal of Geophysical Research, 117(A05225), doi: 10.1029/2012JA017575.

Jia, X., M.G. Kivelson, K.K. Khurana, R.J. Walker, (2010), Magnetic fields of the satellites of Jupiter and Saturn, Space Science Reviews (proceedings of an ISSI workshop on Planetary Magnetism), 152:271–305, doi: 10.1007/s11214-009-9507-8.

Jia, Y. -D., H. Wei, C. T. Russell, (2016), Characterizing the Enceladus torus by its contribution to Saturn's magnetosphere, in Magnetosphere-Ionosphere Coupling in the Solar System, Geophysical Monograph 222, Chapter 27, doi: 10.1002/9781119066880.ch27, pp. 345–354.

Jia, Y. -D., Y. J. Ma, C. T. Russell, H. R. Lai, G. Toth, T. I. Gombosi, (2012), Perpendicular flow deviation in a magnetized counter-streaming plasma, Icarus, 218:895–905, doi: 10/1016/j.Icarus.2012.01.017, 2012.

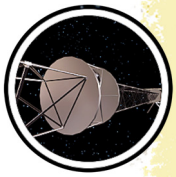

Jia, Y. -D., C. T. Russell, K. K. Khurana, H. Y. Wei, Y. J. Ma, J. S. Leisner, M. K. Dougherty, (2011), Cassini magnetometer observations over the Enceladus poles, Geophysical Research Letters, 38:5 pp., doi: 10.1029/2011GL049013.

Jia, Y. -D., C. T. Russell, K. K. Khurana, J. S. Leisner, T. I. Gombosi, (2010a), The interaction of Saturn's magnetosphere and its moons 1: Interaction between co-rotating plasma and standard obstacles, Journal of Geophysical Research, 115(A04214), doi: 10.1029/2009JA014630.

Jia, Y. -D., C. T. Russell, K. K. Khurana, Y. J. Ma, D. Najib, and T. I. Gombosi, (2010b), The interaction of Saturn's magnetosphere and its moons 2: Shape of the Enceladus plume, Journal of Geophysical Research, 115(A04215), doi: 10.1029/2009JA014873.

Jia, Y. -D., C. T. Russell, K. K. Khurana, J. S. Leisner, Y. J. Ma, M. K. Dougherty, (2010c), Time-varying magnetospheric environment near Enceladus as seen by the Cassini magnetometer, Geophysical Research Letters, 37:5 pp., doi: 10.1029/2010GL042948.

Jia, Y. -D., C. T. Russell, Y. J. Ma, K. K. Khurana, W. Kurth, T. I. Gombosi, (2010d), The interaction of Saturn's magnetosphere and its moons 3: Time Variation of the Enceladus Plume, Journal of Geophysical Research, 115(12):A12243, doi: 10.1029/2010JA015534.

Jinks, S. L., E. J. Bunce, S. W. H. Cowley, G. Provan, T. K. Yeoman, C. S. Arridge, J. -E. Wahlund, (2014), Cassini multi-instrument assessment of Saturn's polar cap boundary, Journal of Geophysical Research: Space Physics, 119(10):8161–8177, doi: 10.1002/2014JA020367.

Jones, G. H., C. S. Arridge, A. J. Coates, G. R. Lewis, S. Kanani, A. Wellbrock, B. A., Magee, (2009), Fine jet structure of electrically charged grains in Enceladus' plume, Geophysical Research Letters, 36:6 pp., doi: 10.1029/2009GL038284.

Jones, G. H., E. Roussos, N. Krupp, U. Beckmann, A. J. Coates, F. Crary, D. Young, (2008), The dust halo of Saturn's largest icy moon, Rhea, Science, 319(5868):1380–1384, doi: 10.1126/science.1151524.

Jones, G. H., E. Roussos, N. Krupp, C. Paranicas, J. Woch, A. Lagg, M. K. Dougherty, (2006a), Enceladus' varying imprint on the magnetosphere of Saturn, Science, 311(5766):1412–1415, doi: 10.1126/science.1121011.

Jones, G. H., N. Krupp, H. Krueger, E. Roussos, W. -H. Ip, D. G. Mitchell, H. J. McAndrews, (2006b), Formation of Saturn's ring spokes by lightning-induced electron beams, Geophysical Research Letters, 33(21):6 pp., doi: 10.1029/2006GL028146.

Kabanovic, S., S. Simon, F. M. Neubauer, Z. Meeks, (2017), An empirical model of Titan's magnetic environment during the Cassini era: Evidence for seasonal variability, Journal Geophysical Research, 122:11,076–11,085, doi: 10.1002/2017JA024402.

Kallio, E., I. Sillanpää, R. Jarvinen, P. Janhunen, M. Dougherty, C. Bertucci, F. Neubauer, (2007), Morphology of the magnetic field near Titan: Hybrid model study of the Cassini T9 flyby, Geophysical Research Letters, 34(24), doi: 10.1029/2007GL030827=.

- - - - - - - - - - - - - -

Kanani, S. J., C. S. Arridge, G. H. Jones, A. N. Fazakerley, H. J. McAndrews, N. Sergis, N. Krupp, (2010), A new form of Saturn's magnetopause using a dynamic pressure balance model, based on in situ, multi-instrument Cassini measurements, Journal of Geophysical Research: Space Physics, 115:11 pp., doi: 10.1029/2009JA014262.

Kellett, S., C. S. Arridge, E. J. Bunce, A. J. Coates, S. W. H. Cowley, M. K. Dougherty, R. J. Wilson, (2011), Saturn's ring current: Local time dependence and temporal variability. Journal of Geophysical Research: Space Physics, 116:25 pp., doi: 10.1029/2010JA016216.

Kellett, S., C. S. Arridge, E. J. Bunce, A. J. Coates, S. W. H. Cowley, M. K. Dougherty, R. J. Wilson, (2010), Nature of the ring current in Saturn's dayside magnetosphere, Journal of Geophysical Research: Space Physics, 115:10 pp., doi: 10.1029/2009JA015146.

Kellett, S., E. J. Bunce, A. J. Coates, S. W. H. Cowley, (2009), Thickness of Saturn’s ring current determined from north-south Cassini passes through the current layer, Journal of Geophysical Research, 114(A04209), doi: 10.1029/2008JA013942.

Kellock, S., P. Austin, A. Balogh, B. Gerlach, R. Marquedant, G. Musmann, E. Smith, D. Southwood, S. Szalai, (1996), Cassini dual technique magnetometer instrument (MAG), in Cassini/Huygens: A Mission to the Saturnian Systems, 2803:141–152, doi: 10.1117/12.253414.

Kellogg, P. J., M. K. Dougherty, R. J. Forsyth, D. A. Gurnett, G. B. Hospodarsky, W. S. Kurth, (2003a), Electric fluctuations and ion isotropy, in 10th international solar wind conference, (eds.) M. Velli, R. Bruno, F. Malara, Pisa, Italy, 17–21 June 2002, American Institute of Physics, Melville, pp. 383–388.

Kellogg, P. J., D. A. Gurnett, G. B. Hospodarsky, W. S. Kurth, M. K. Dougherty, R. J. Forsyth, (2003b), Ion isotropy and ion resonant waves in the solar wind: corrected Cassini observations, Journal of Geophysical Research: Space Physics, 108(1045).

Khan, H., S. W. H. Cowley, E. Kolesnikova, M. Lester, M. J. Brittnacher, T. J. Hughes, W. J. Hughes, W. S. Kurth, D. J. McComas, L. Newitt, C. J. Owen, (2001), Observations of two complete substorm cycles during the Cassini Earth swing-by: Cassini magnetometer data in a global context, Journal of Geophysical Research: Space Physics, 106(A12):30141–30175, doi: 10.1029/2001JA900049.

Khurana, K.K., J. Liu, (2018), Current systems in planetary magnetospheres: A comparative overview, in Electric Currents in Geospace and Beyond, Geophysical Monograph 235, (eds.) A. Keiling, O. Marghitu, M. Wheatland, Chapter 2, 2018 American Geophysical Union, John Wiley & Sons, Inc.

Khurana, K. K., S. Fatemi, J. Lindkvist, E. Roussos, N. Krupp, M. Holmstroem, M. K. Dougherty, (2017), The role of plasma slowdown in the generation of Rhea's Alfven wings, Journal of Geophysical Research: Space Physics, 122(2):1778-1788, doi: 10.1002/2016JA023595.

Khurana, K. K., D. G. Mitchell, C. S. Arridge, M. K. Dougherty, C. T. Russell, C. Paranicas, A. J. Coates, (2009), Sources of rotational signals in Saturn's magnetosphere, Journal of Geophysical Research: Space Physics, 114:11 pp., doi: 10.1029/2008JA013312.

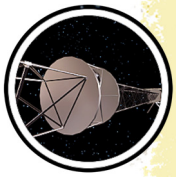

Khurana, K. K., C. T. Russell, M. K. Dougherty, (2008), Magnetic portraits of Tethys and Rhea, Icarus, 193(2):465–474, doi: 10.1016/j.Icarus.2007.08.005.

Khurana, K. K., M. K. Dougherty, C. T. Russell, J. S. Leisner, (2007), Mass loading of Saturn's magnetosphere near Enceladus, Journal of Geophysical Research: Space Physics, 112(A8):12 pp., doi: 10.1029/2006JA012110.

Kinrade, J., S. V. Badman, E. J. Bunce, C. Tao, G. Provan, S. W. H. Cowley, T. Kimura, (2017), An isolated, bright cusp aurora at Saturn, Journal of Geophysical Research: Space Physics, 122(6):6121–6138, doi: 10.1002/2016JA023792.

Kivelson, M. G., (2015), Planetary magnetodiscs: Some unanswered questions, Space Science Reviews, 187:5–21, doi: 10.1007/s11214-014-0046-6.

Kivelson, M. G., X. Jia, (2014), Control of periodic variations in Saturn’s magnetosphere by compressional waves, Journal of Geophysical Research: Space Physics, 119:8030–8045, doi: 10.1002/2014JA020258.

Kivelson, M. G., (2007), Planetary Science: A twist on periodicity at Saturn, Nature, 450:178–179, doi: 10.1038/450178a.

Kivelson, M. G., (2006), Does Enceladus govern magnetospheric dynamics at Saturn?, Science, 311:1391, doi: 10.1126/science.1124494.

Kivelson, M. G., (2005a), The current systems of the Jovian magnetosphere and ionosphere and predictions for Saturn, Space Science Reviews, 116, 299–318, also in The Outer Planets and Their Moons, (eds.) T. Encrenaz, R. Kallenbach, T. C. Owen, C. Sotin, Springer, Dordrecht, The Netherlands (IGPP Pub. No. 6209), SSR11629905, doi: 10.1007/s11214-005-1959-x.

Kivelson, M. G., (2005b), Transport and acceleration of plasma in the magnetospheres of Earth and Jupiter and expectations for Saturn, Advances in Space Research, 36:2077.

Kivelson, M. G., D. J. Southwood, (2005), Dynamical consequences of two modes of centrifugal instability in Jupiter's outer magnetosphere, Journal of Geophysical Research, 110(A12209), doi: 10.1029/2005JA011176.

Kivelson, M. G., D. J. Southwood, (2003), First evidence of IMF control of Jovian magnetospheric boundary locations: Cassini and Galileo magnetic field measurements compared, Planetary and Space Science, 51:891.

Kleindienst, G., K. -H. Glassmeier, S. Simon, M. K. Dougherty, N. Krupp, (2009), Quasiperiodic ULF-pulsations in Saturn's magnetosphere, Annales Geophysicae, 27(2):885–894, doi: 10.5194/angeo-27-885-2009.

Kopf, A. J., D. A. Gurnett, J. D. Menietti, P. Schippers, C. S. Arridge, G. B. Hospodarsky, M. K. Dougherty, (2010), Electron beams as the source of whistler-mode auroral hiss at Saturn, Geophysical Research Letters, 37:5 pp., doi: 10.1029/2010GL042980.

Kriegel, H., S. Simon, P. Meier, U. Motschmann, J. Saur, A. Wennmacher, M. K. Dougherty, (2014), Ion densities and magnetic signatures of dust pickup at Enceladus, Journal of Geophysical Research: Space Physics, 119(4):2740–2774, doi: 10.1002/2013JA019440.

Kriegel, H., S. Simon, U. Motschmann, J. Saur, F. M. Neubauer, A. M. Persoon, D. A. Gurnett, (2011), Influence of negatively charged plume grains on the structure of Enceladus' Alfven wings: Hybrid simulations versus Cassini Magnetometer data, Journal of Geophysical Research: Space Physics, 116:19 pp., doi: 10.1029/2011JA016842.

Kriegel, H., S. Simon, J. Mueller, U. Motschmann, J. Saur, K. -H. Glassmeier, M. K. Dougherty, (2009), The plasma interaction of Enceladus: 3D hybrid simulations and comparison with Cassini MAG data, Planetary and Space Science, 57(14–15):2113–2122, doi: 10.1016/j.pss.2009.09.025.

Kronberg, E. A., K. H. Glassmeier, J. Woch, N. Krupp, A. Lagg, M. K. Dougherty, (2007), A possible intrinsic mechanism for the quasi-periodic dynamics of the Jovian magnetosphere, Journal of Geophysical Research: Space Physics, 112(A5):12 pp., doi: 10.1029/2006JA011994.

Krupp, N., E. Roussos, H. Kriegel, P. Kollmann, M. G. Kivelson, A. Kotova, Paranicas, D. G. Mitchell, S. M. Krimigis, K. K. Khurana, (2013), Energetic particle measurements in the vicinity of Dione during the three Cassini encounters 2005–2011, Icarus, 226(1):617–628, doi: 10.1016/j.Icarus.2013.06.007, 2013.

Krupp, N., E. Roussos, A. Lagg, J. Woch, A. L. Mueller, S. M. Krimigis, N. Sergis, (2009), Energetic particles in Saturn's magnetosphere during the Cassini nominal mission (July 2004–July 2008), Planetary and Space Science, 57(14–15):1754–1768, doi: 10.1016/j.pss.2009.06.010.

Krupp, N., A. Lagg, J. Woch, S. M. Krimigis, S. Livi, D. G. Mitchell, M. K. Dougherty, (2005), The Saturnian plasma sheet as revealed by energetic particle measurements, Geophysical Research Letters, 32(20):5 pp., doi: 10.1029/2005GL022829.

Krupp, N., J. Woch, A. Lagg, S. Livi, D. G. Mitchell, S. M. Krimigis, S. A. Espinosa, (2004), Energetic particle observations in the vicinity of Jupiter: Cassini MIMI/LEMMS results, Journal of Geophysical Research: Space Physics, 109(A9):10 pp., doi: 10.1029/2003JA010111.

Kurth, W. S., G. B. Hospodarsky, D. A. Gurnett, L. Lamy, M. K. Dougherty, J. Nichols, F. J. Crary, (2016), Saturn kilometric radiation intensities during the Saturn auroral campaign of 2013, Icarus, 263:2–9, doi: 10.1016/j.Icarus.2015.01.003.

Kurth, W. S., D. A. Gurnett, J. T. Clarke, P. Zarka, M. D. Desch, M. L. Kaiser, F. J. Crary, (2005), An Earth-like correspondence between Saturn's auroral features and radio emission, Nature, 433(7027):722–725, doi: 10.1038/nature03334.

Kurth, W. S., D. A. Gurnett, G. B. Hospodarsky, W. M. Farrell, A. Roux, M. K. Dougherty, C. J. Alexander, (2002), The dusk flank of Jupiter's magnetosphere, Nature, 415(6875):991–994, doi: 10.1038/415991a.

Lagg, A., N. Krupp, S. Livi, J. Woch, S. M. Krimigis, M. K. Dougherty, (2001), Energetic particle measurements during the Earth swing-by of the Cassini spacecraft in August 1999, Journal of Geophysical Research: Space Physics, 106(A12):30209–30222, doi: 10.1029/2001JA900048.

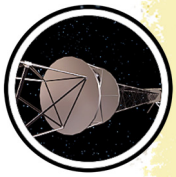

Lai, H. R., C. T. Russell, Y. D. Jia, H. Y. Wei, M. K. Dougherty, (2016), Transport of magnetic flux and mass in Saturn's inner magnetosphere, Journal of Geophysical Research: Space Physics, 121(4):3050–3057, doi: 10.1002/2016JA022436.

Lai, H. R., H. Y. Wei, C. T. Russell, C. S. Arridge, M. K. Dougherty, (2012), Reconnection at the magnetopause of Saturn: Perspective from FTE occurrence and magnetosphere size, Journal of Geophysical Research: Space Physics, 117:9 pp., doi: 10.1029/2011JA017263.

Lamy, L., P. Schippers, P. Zarka, B. Cecconi, C. S. Arridge, M. K. Dougherty, A. J. Coates, (2010), Properties of Saturn kilometric radiation measured within its source region, Geophysical Research Letters, 37:6 pp., doi: 10.1029/2010GL043415.

Lario, D., S. Livi, E. C. Roelof, R. B. Decker, S. M. Krimigis, M. K. Dougherty, (2004), Heliospheric energetic particle observations by the Cassini spacecraft: Correlation with 1 AU observations, Journal of Geophysical Research: Space Physics, 109(A9):23 pp., doi: 10.1029/2003JA010107.

Leisner, J. S., C. T. Russell, H. Y. Wei, M. K. Dougherty, (2011), Probing Saturn's ion cyclotron waves on high-inclination orbits: Lessons for wave generation, Journal of Geophysical Research: Space Physics, 116:5 pp., doi: 10.1029/2011JA016555.

Leisner, J. S., C. T. Russell, K. K. Khurana, M. K. Dougherty, (2007), Measuring the stress state of the Saturnian magnetosphere, Geophysical Research Letters, 34(12):4 pp., doi: 10.1029/2007GL029315.

Leisner, J. S., C. T. Russell, M. K. Dougherty, X. Blanco-Cano, R. J. Strangeway, C. Bertucci, (2006), Ion cyclotron waves in Saturn's E ring: Initial Cassini observations, Geophysical Research Letters, 33(11):5 pp., doi: 10.1029/2005GL024875.

Leisner, J. S., C. T. Russell, K. K. Khurana, M. K. Dougherty, N. Andre, (2005), Warm flux tubes in the E-ring plasma torus: Initial Cassini magnetometer observations, Geophysical Research Letters, 32(14):4 pp., doi: 10.1029/2005GL022652.

Luhmann, J. G., D. Ulusen, S. A. Ledvina, K. Mandt, B. Magee, J. H. Waite, M. K. Dougherty, (2012), Investigating magnetospheric interaction effects on Titan's ionosphere with the Cassini orbiter Ion Neutral Mass Spectrometer, Langmuir Probe and magnetometer observations during targeted flybys, Icarus, 219(2):534–555, doi: 10.1016/j.Icarus.2012.03.015.

Ma, Y. J., C. T. Russell, A. F. Nagy, G. Toth, M. K. Dougherty, A. Wellbrock, F. J. Crary, (2011), The importance of thermal electron heating in Titan's ionosphere: Comparison with Cassini T34 flyby, Journal of Geophysical Research: Space Physics, 116:10 pp., doi: 10.1029/2011JA016657.

Ma, Y. J., C. T. Russell, A. F Nagy, G. Toth, C. Bertucci, M. K. Dougherty, F. J. Crary, (2009), Time-dependent global MHD simulations of Cassini T32 flyby: From magnetosphere to magnetosheath, Journal of Geophysical Research: Space Physics, 114:13 pp., doi: 10.1029/2008JA013676.

Ma, Y. -J., A. F. Nagy, G. Toth, T. E. Cravens, C. T. Russell, T. I. Gombosi, J. -E. Wahlund, F. J. Crary, A. J. Coates, C. L. Bertucci, F. M. Neubauer, (2007), 3D global multi-species Hall-MHD

simulation of the Cassini T9 flyby, Geophysical Research Letters, 34, doi: 10.1029/2007GL031627.

Ma, Y., A. F. Nagy, T. E. Cravens, I. V. Sokolov, K. C. Hansen, J. -E. Wahlund, M. K. Dougherty, (2006), Comparisons between MHD model calculations and observations of Cassini flybys of Titan, Journal of Geophysical Research: Space Physics, 111(A5):14 pp., doi: 10.1029/2005JA011481].

Martin, C. J., C. S. Arridge, (2017), Cassini observations of aperiodic waves on Saturn's magnetodisc, Journal of Geophysical Research Space Physics, 122:8063–8077, doi: 10.1002/2017JA024293.

Masters, A., A. H. Sulaiman, L. Stawarz, B. Reville, N. Sergis, M. Fujimoto, M. K. Dougherty, (2017), An in situ comparison of electron acceleration at collisionless shocks under differing upstream magnetic field orientations, Astrophysical Journal, 843(2):9 pp., doi: 10.3847/1538-4357/aa76ea.

Masters, A., A. H. Sulaiman, N. Sergis, L. Stawarz, M. Fujimoto, A. J. Coates, M. K. Dougherty, (2016), Suprathermal electrons at Saturn's bow shock, Astrophysical Journal, 826(1):7 pp., doi: 10.3847/0004-637X/826/1/48.

Masters, A., (2015), The dayside reconnection voltage applied to Saturn's magnetosphere, Geophysical Research Letters, 42, doi: 10.1002/2015GL063361.

Masters, A., M. Fujimoto, H. Hasegawa, C. T. Russell, A. J. Coates, M. K. Dougherty, (2014a), Can magnetopause reconnection drive Saturn's magnetosphere?, Geophysical Research Letters, 41(6):1862–1868, doi: 10.1002/2014GL059288.

Masters, A., T. D. Phan, S. V. Badman, H. Hasegawa, M. Fujimoto, C. T. Russell, M. K. Dougherty, (2014b), The plasma depletion layer in Saturn's magnetosheath, Journal of Geophysical Research: Space Physics, 119(1):121–130, doi: 10.1002/2013JA019516.

Masters, A., J. A. Slavin, G. A. DiBraccio, T. Sundberg, R. M. Winslow, C. L. Johnson, B. J. Anderson, H. Korth, (2013a), A comparison of magnetic overshoots at the bow shocks of Mercury and Saturn, Journal of Geophysical Research Space Physics, 118:4381–4390, doi: 10.1002/jgra.50428.

Masters, A., L. Stawarz, M. Fujimoto, S. J. Schwartz, N. Sergis, M. F. Thomsen, M. K. Dougherty, (2013b), Electron acceleration to relativistic energies at a strong quasi-parallel shock wave, Nature Physics, 9(3):164–167, doi: 10.1038/nphys2541.

Masters, A., L. Stawarz, M. Fujimoto, S. J. Schwartz, N. Sergis, M. F. Thomsen, M. K. Dougherty, (2013c), In situ observations of high-Mach number collisionless shocks in space plasmas, Plasma Physics and Controlled Fusion, 55(12):6 pp., doi: 10.1088/0741-3335/55/12/124035.

Masters, A., N. Achilleos, J. C. Cutler, A. J. Coates, M. K. Dougherty, G. H. Jones, (2012a), Surface waves on Saturn's magnetopause, Planetary and Space Science, 65(1):109–121, doi: 10.1016/j.pss.2012.02.007.

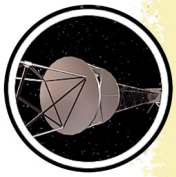

Masters, A., J. P. Eastwood, M. Swisdak, M. F. Thomsen, C. T. Russell, N. Sergis, S. M. Krimigis, (2012b), The importance of plasma beta conditions for magnetic reconnection at Saturn's magnetopause, Geophysical Research Letters, 39:6 pp., doi: 10.1029/2012GL051372.

Masters, A., S. J. Schwartz, E. M. Henley, M. F. Thomsen, B. Zieger, A. J. Coates, N. Achilleos, J. Mitchell, K. C. Hansen, M. K. Dougherty, (2011a), Electron heating at Saturn's bow shock, Journal of Geophysical Research: Space Physics, 116(A10107), doi: 10.1029/2011JA016941.

Masters, A., D. G. Mitchell, A. J. Coates, M. K. Dougherty, (2011b), Saturn's low-latitude boundary layer: 1. Properties and variability, Journal of Geophysical Research: Space Physics, 116:13 pp., doi: 10.1029/2010JA016421.

Masters, A., A. P. Walsh, A. N. Fazakerley, A. J. Coates, M. K. Dougherty, (2011c), Saturn's low-latitude boundary layer: 2. Electron structure, Journal of Geophysical Research: Space Physics, 116:7 pp., doi: 10.1029/2010JA016422.

Masters, A., M. F. Thomsen, S. V. Badman, C. S. Arridge, D. T. Young, A. J. Coates, M. K. Dougherty, (2011d), Supercorotating return flow from reconnection in Saturn's magnetotail, Geophysical Research Letters, 38:5 pp., doi: 10.1029/2010GL046149.

Masters, A., N. Achilleos, M. G. Kivelson, N. Sergis, M. K. Dougherty, M. F. Thomsen, A. J. Coates, (2010), Cassini observations of a Kelvin-Helmholtz vortex in Saturn's outer magnetosphere, Journal of Geophysical Research: Space Physics, 115:13 pp., doi: 10.1029/2010JA015351.

Masters, A., H. J. McAndrews, J. T. Steinberg, M. F. Thomsen, C. S. Arridge, M. K. Dougherty, A. J. Coates, (2009a), Hot flow anomalies at Saturn's bow shock, Journal of Geophysical Research: Space Physics, 114:10 pp., doi: 10.1029/2009JA014112.

Masters, A., N. Achilleos, C. Bertucci, M. K. Dougherty, S. J. Kanani, C. S. Arridge, A. J. Coates, (2009b), Surface waves on Saturn's dawn flank magnetopause driven by the Kelvin-Helmholtz instability, Planetary and Space Science, 57(14–15):1769–1778, doi: 10.1016/j.pss.2009.02.010.

Masters, A., N. Achilleos, M. K. Dougherty, J. A. Slavin, G. B. Hospodarsky, C. S. Arridge, A. J. Coates, (2008a), An empirical model of Saturn's bow shock: Cassini observations of shock location and shape, Journal of Geophysical Research: Space Physics, 113(A10):18 pp., doi: 10.1029/2008JA013276.

Masters, A., C. S. Arridge, M. K. Dougherty, C. Bertucci, L. Billingham, S. J. Schwartz, M. F. Thomsen, (2008b), Cassini encounters with hot flow anomaly-like phenomena at Saturn's bow shock, Geophysical Research Letters, 35(2):6 pp., doi: 10.1029/2007GL032371.

McAndrews, H. J., M. F. Thomsen, C. S. Arridge, C. M. Jackman, R. J. Wilson, M. G. Henderson, M. K. Dougherty, (2009), Plasma in Saturn's nightside magnetosphere and the implications for global circulation, Planetary and Space Science, 57(14–15):1714–1722, doi: 10.1016/j.pss.2009.03.003.

McAndrews, H. J., C. J. Owen, M. F. Thomsen, B. Lavraud, A. J. Coates, M. K. Dougherty, D. T. Young, (2008), Evidence for reconnection at Saturn's magnetopause, Journal of Geophysical Research: Space Physics, 113(A4):12 pp., doi: 10.1029/2007JA012581.

Meredith, C. J., I. I. Alexeev, S. V. Badman, E. S. Belenkaya, S. W. H. Cowley, M. K. Dougherty, J. D. Nichols, (2014), Saturn's dayside ultraviolet auroras: Evidence for morphological dependence on the direction of the upstream interplanetary magnetic field, Journal of Geophysical Research: Space Physics, 119(3):1994–2008, doi: 10.1002/2013JA019598.

Milan, S. E., E. J. Bunce, S. W. H. Cowley, C. M. Jackman, (2005), Implications of rapid planetary rotation for the Dungey magnetotail of Saturn, Journal of Geophysical Research, 110(A02201), doi: 10.1029/2004JA010716.

Mistry, R., M. K. Dougherty, A. Masters, A. H. Sulaiman, E. J. Allen, (2014), Separating drivers of Saturnian magnetopause motion, Journal of Geophysical Research: Space Physics, 119(3):1514–1522, doi: 10.1002/2013JA019489.

Mitchell, D. G., W. S. Kurth, G. B. Hospodarsky, N. Krupp, J. Saur, B. H. Mauk, D. C. Hamilton, (2009a), Ion conics and electron beams associated with auroral processes on Saturn, Journal of Geophysical Research: Space Physics, 114:10 pp., doi: 10.1029/2008JA013621.

Mitchell, D. G., S. M. Krimigis, C. Paranicas, P. C. Brandt, J. F. Carbary, E. C. Roelof, W. R. Pryor, (2009b), Recurrent energization of plasma in the midnight-to-dawn quadrant of Saturn's magnetosphere, and its relationship to auroral UV and radio emissions, Planetary and Space Science, 57(14–15):1732–1742, doi: 10.1016/j.pss.2009.04.002.

Mitchell, D. G., P. C. Brandt, E. C. Roelof, J. Dandouras, S. M. Krimigis, B. H. Mauk, D. E. Shemansky, (2005), Energetic ion acceleration in Saturn's magnetotail: Substorms at Saturn?, Geophysical Research Letters, 32(20):4 pp., doi: 10.1029/2005GL022647.

Nemeth, Z., K. Szego, L. Foldy, S. W. H. Cowley, G. Provan, M. Thomsen, (2016), Periodic motion of the magnetodisk as a cause of quasi-periodic variations in the kronian magnetosphere, Planetary and Space Science, 130:54–59.

Nemeth, Z., K. Szego, L. Foldy, M. G. Kivelson, X. Jia, K. M. Ramer, S. W. H. Cowley, G. Provan, M. Thomsen, (2015), The latitudinal structure of the nightside outer magnetosphere of Saturn as revealed by the velocity moments of thermal ions, Annales Geophysicae, 33:1195–1202.

Neubauer, F. M., H. Backes, M. K. Dougherty, A. Wennmacher, C. T. Russell, A. Coates, J. Saur, (2006), Titan's near magnetotail from magnetic field and electron plasma observations and modeling: Cassini flybys TA, TB, and T3, Journal of Geophysical Research: Space Physics, 111(A10):15 pp., doi: 10.1029/2006JA011676.

Neubauer, F. M., D. A. Gurnett, J. D. Scudder, R. E. Hartle, (1984), Titan’s magnetospheric interaction, in Saturn, (eds.) Gehrels, T., Matthews, M.S., University of Arizona Press, Tucson, Arizona, pp. 760–787.

Nichols, J. D., S. V. Badman, K. H. Baines, R. H. Brown, E. J. Bunce, J. T. Clarke, T. S. Stallard, (2014), Dynamic auroral storms on Saturn as observed by the Hubble Space Telescope, Geophysical Research Letters, 41(10):3323–3330, doi: 10.1002/2014GL060186.

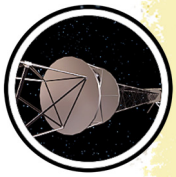

Nichols, J. D., S. V. Badman, E. J. Bunce, J. T. Clarke, S. W. H. Cowley, F. J. Crary, S. Wannawichian, (2009), Saturn's equinoctial auroras, Geophysical Research Letters, 36:5 pp., doi: 10.1029/2009GL041491.

Nichols, J.D., J. T. Clarke, S. W. H. Cowley, J. Duval, A. J. Farmer, J. C. Gérard, D. Grodent, S. Wannawichian, (2008), Oscillation of Saturn's southern auroral oval, Journal of Geophysical Research, 113(A11205), doi: 10.1029/2008JA013444.

Nordheim, T. A., G. H. Jones, E. Roussos, J. S. Leisner, A. J. Coates, W. S. Kurth, J. H. Waite, (2014), Detection of a strongly negative surface potential at Saturn's moon Hyperion, Geophysical Research Letters, 41(20):7011–7018, doi: 10.1002/2014GL061127.

Omidi, N., A. H. Sulaiman, W. Kurth, H. Madanian, T. Cravens, N. Sergis, N. J. T. Edberg, (2017), A single deformed bow shock for Titan-Saturn system, Journal of Geophysical Research: Space Physics, 122(11):11058–11075, doi: 10.1002/2017JA024672.

Paranicas, C., D. G. Mitchell, S. M. Krimigis, J. F. Carbary, P. C. Brandt, F. S. Turner, E. Roussos, N. Krupp, M. G. Kivelson, K. K. Khurana, (2010), Asymmetries in Saturn's radiation belts, Journal of Geophysical Research, 115(A07216), doi: 10.1029/2009JA014971.

Persoon, A. M., D. A. Gurnett, W. S. Kurth, G. B. Hospodarsky, J. B. Groene, P. Canu, M. K. Dougherty, (2005), Equatorial electron density measurements in Saturn's inner magnetosphere, Geophysical Research Letters, 32(23):4 pp., doi: 10.1029/2005GL024294.

Pilkington, N. M., N. Achilleos, C. S. Arridge, P. Guio, A. Masters, L. C. Ray, M. K. Dougherty, (2015a), Asymmetries observed in Saturn's magnetopause geometry. Geophysical Research Letters, 42(17):6890–6898, doi: 10.1002/2015GL065477.

Pilkington, N. M., N. Achilleos, C. S. Arridge, P. Guio, A. Masters, L. C. Ray, M. K. Dougherty, (2015b), Internally driven large-scale changes in the size of Saturn's magnetosphere, Journal of Geophysical Research: Space Physics, 120(9):7289–7306, doi: 10.1002/2015JA021290.

Pilkington, N. M., N. Achilleos, C. S. Arridge, A. Masters, N. Sergis, A. J. Coates, M. K. Dougherty, (2014), Polar confinement of Saturn's magnetosphere revealed by in situ Cassini observations, Journal of Geophysical Research: Space Physics, 119(4):2858–2875, doi: 10.1002/2014JA019774.

Porco, C. C., P. Helfenstein, P. C. Thomas, A. P. Ingersoll, J. Wisdom, R. West, G. Neukum, T. Denk, R. Wagner, T. Roatsch, S. Kieffer, E. Turtle, A. McEwen, T. V. Johnson, J. Rathbun, J. Veverka, D. Wilson, J. Perry, J. Spitale, A. Brahic, J. A. Burns, A. D. Del Genio, L. Dones, C. D. Murray, S. Squyres, (2006), Cassini observes the active south pole of Enceladus, Science, 311:1393–1401, doi: 10.1126/science.1123013.

Provan, G., S. W. H. Cowley, T. J. Bradley, E. J. Bunce, G. J. Hunt, M. K. Dougherty, (2018), Planetary period oscillations in Saturn's magnetosphere: Cassini magnetic field observations over the northern summer solstice interval, Journal of Geophysical Research: Space Physics, 123:3859–3899, doi: 10.1029/2018JA025237.

Provan, G., S. W. H. Cowley, L. Lamy, E. J. Bunce, G. J. Hunt, P. Zarka, M. K. Dougherty, (2016), Planetary period oscillations in Saturn's magnetosphere: Coalescence and reversal of

northern and southern periods in late northern spring, Journal of Geophysical Research: Space Physics, 121(10):9829–9862, doi: 10.1002/2016JA023056.

Provan, G., C. Tao, S. W. H. Cowley, M. K. Dougherty, A. J. Coates, (2015), Planetary period oscillations in Saturn's magnetosphere: Examining the relationship between abrupt changes in behavior and solar wind-induced magnetospheric compressions and expansions, Journal of Geophysical Research: Space Physics, 120(11):9524–9544, doi: 10.1002/2015JA021642.

Provan, G., L. Lamy, S. W. H. Cowley, M. K. Dougherty, (2014), Planetary period oscillations in Saturn's magnetosphere: Comparison of magnetic oscillations and SKR modulations in the postequinox interval, Journal of Geophysical Research: Space Physics, 119(9):22 pp., doi: 10.1002/2014JA020011.

Provan, G., S. W. H. Cowley, J. Sandhu, D. J., Andrews, M. K. Dougherty, (2013), Planetary period magnetic field oscillations in Saturn's magnetosphere: Postequinox abrupt nonmonotonic transitions to northern system dominance, Journal of Geophysical Research: Space Physics, 118(6):3243–3264, doi: 10.1002/jgra.50186.

Provan, G., D. J. Andrews, C. S. Arridge, A. J. Coates, S. W. H. Cowley, G. Cox, C. M. Jackman, (2012), Dual periodicities in planetary-period magnetic field oscillations in Saturn's tail, Journal of Geophysical Research: Space Physics, 117:20 pp., doi: 10.1029/2011JA017104.

Provan, G., D. J. Andrews, B. Cecconi, S. W. H. Cowley, M. K. Dougherty, L. Lamy, P. M. Zarka, (2011), Magnetospheric period magnetic field oscillations at Saturn: Equatorial phase "jitter" produced by superposition of southern and northern period oscillations, Journal of Geophysical Research: Space Physics, 116:22 pp., doi: 10.1029/2010JA016213.

Provan, G., D. J. Andrews, C. S. Arridge, A. J. Coates, S. W. H. Cowley, S. E. Milan, D. M. Wright, (2009a), Polarization and phase of planetary-period magnetic field oscillations on high-latitude field lines in Saturn's magnetosphere, Journal of Geophysical Research: Space Physics, 114:36 pp., doi: 10.1029/2008JA013782.

Provan, G., S. W. H. Cowley, J. D. Nichols, (2009b), Phase relation of oscillations near the planetary period of Saturn’s auroral oval and the equatorial magnetospheric magnetic field, Journal of Geophysical Research, 114(A04205), doi: 10.1029/2008JA013988.

Pryor, W. R., A. M. Rymer, D. G. Mitchell, T. W. Hill, D. T. Young, J. Saur, X. Zhou, (2011), The auroral footprint of Enceladus on Saturn, Nature, 472(7343):331–333, doi: 10.1038/nature09928.

Radioti, A., D. Grodent, J. -C. Gérard, D. J. Southwood, E. Chané, B. Bonfond, W. Pryor, (2017), Stagnation of Saturn’s auroral emission at noon, Journal of Geophysical Research: Space Physics, 122:6078–6087, doi: 10.1002/2016JA023820.

Radioti, A., J. Woch, E. A. Kronberg, N. Krupp, A. Lagg, K. -H. Glassmeier, M. K. Dougherty, (2007), Energetic ion composition during reconfiguration events in the Jovian magnetotail, Journal of Geophysical Research: Space Physics, 112(A6):9 pp., doi: 10.1029/2006JA012047.

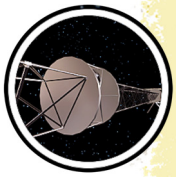

Ramer, K. M., M. G. Kivelson, N. Sergis, K. K. Khurana, X. Jia, (2017), Spinning, breathing, and flapping: Periodicities in Saturn's middle magnetosphere, Journal of Geophysical Research 122:393–416, doi: 10.1002/2016JA023126.

Reed, J. J., C. M. Jackman, L. Lamy, W. S. Kurth, D. K. Whiter, (2018), Low-frequency extensions of the Saturn Kilometric Radiation as a proxy for magnetosphericdynamics, Journal of Geophysical Research, 123:443–463, doi: 10.1002/2017JA024499.

Regoli, L. H., E. Roussos, M. Feyerabend, G. H. Jones, N. Krupp, A. J. Coates, M. K. Dougherty, (2016), Access of energetic particles to Titan's exobase: A study of Cassini's T9 flyby, Planetary and Space Science, 130:40–53, doi: 10.1016/j.pss.2015.11.013.

Rodriguez-Martinez, M., X. Blanco-Cano, C. T. Russell, J. S. Leisner, R. J. Wilson, M. K. Dougherty, H. R. Perez-Enriquez, (2011), Waves and instabilities in the magnetospheric plasma of Saturn, in XIII Latin American Regional IAU Meeting Vol. 40, (eds.) W. J. Henney, S. Torres Peimbert, Universidad Nacional Autonoma Mexico Instituto Astronomia, Morelia, Mexico, pp. 295.

Rodriguez-Martinez, M., X. Blanco-Cano, C. T. Russell, J. S. Leisner, R. J. Wilson, M. K. Dougherty, (2010), Harmonic growth of ion-cyclotron waves in Saturn's magnetosphere, Journal of Geophysical Research: Space Physics, 115:13 pp., doi: 10.1029/2009JA015000.

Roussos, E., N. Krupp, D. G. Mitchell, C. Paranicas, S. M. Krimigis, M. Andriopoulou, M. K. Dougherty, (2016), Quasi-periodic injections of relativistic electrons in Saturn's outer magnetosphere, Icarus, 263:101–116, doi: 10.1016/j.Icarus.2015.04.017.

Roussos, E., N. Krupp, C. P. Paranicas, P. Kollmann, D. G. Mitchell, S. M. Krimigis, G. H. Jones, (2011), Long- and short-term variability of Saturn's ionic radiation belts. Journal of Geophysical Research: Space Physics, 116:21 pp., doi: 10.1029/2010JA015954.

Roussos, E., J. Mueller, S. Simon, A. Boesswetter, U. Motschmann, N. Krupp, M. K. Dougherty, (2008), Plasma and fields in the wake of Rhea: 3-D hybrid simulation and comparison with Cassini data, Annales Geophysicae, 26(3):619–637, doi: 10.5194/angeo-26-619-2008.

Roussos, E., G. H. Jones, N. Krupp, C. Paranicas, D. G. Mitchell, A. Lagg, M. K. Dougherty, (2007), Electron microdiffusion in the Saturnian radiation belts: Cassini MIMI/LEMMS observations of energetic electron absorption by the icy moons, Journal of Geophysical Research: Space Physics, 112(A6):22 pp., doi: 10.1029/2006JA012027.

Roussos, E., N. Krupp, J. Woch, A. Lagg, G. H. Jones, C. Paranicas, U. Motschmann, (2005), Low energy electron microsignatures at the orbit of Tethys: Cassini MIMI/LEMMS observations, Geophysical Research Letters, 32(24):4 pp., doi: 10.1029/2005GL024084.

Rucker, H. O., M. Panchenko, K. C. Hansen, U. Taubenschuss, M. Y. Boudjada, W. S. Kurth, C. H. Barrow, (2008), Saturn kilometric radiation as a monitor for the solar wind?, Advances in Space Research, 42(1):40–47, doi: 10.1016/j.asr.2008.02.008.

Russell, C. T., H. Y. Wei, M. M. Cowee, F. M. Neubauer, M. K. Dougherty, (2016), Ion cyclotron waves at Titan, Journal of Geophysical Research: Space Physics, 121(3):2095–2103, doi: 10.1002/2015JA022293.

Russell, C. T., M. K. Dougherty, (2010), Magnetic fields of the outer planets, Space Science Reviews, 152(1–4):251–269, doi: 10.1007/s11214-009-9621-7.

Russell, C. T., K. K. Khurana, C. S. Arridge, M. K. Dougherty, (2008a), The magnetospheres of Jupiter and Saturn and their lessons for the Earth, Advances in Space Research, 41(8):1310–1318, doi: 10.1016/j.asr.2007.07.037.

Russell, C. T., C. M. Jackman, H. Y. Wei, C. Bertucci, M. K. Dougherty, (2008b), Titan's influence on Saturnian substorm occurrence, Geophysical Research Letters, 35(12):5 pp., doi: 10.1029/2008GL034080.

Russell, C. T., J. S. Leisner, C. S. Arridge, M. K. Dougherty, X. Blanco-Cano, (2006), Nature of magnetic fluctuations in Saturn's middle magnetosphere, Journal of Geophysical Research: Space Physics, 111(A12):13 pp., doi: 10.1029/2006JA011921.

Russell, C. T., J. S. Leisner, K. K. Khurana, M. K. Dougherty, X. Blanco-Cano, J. L. Fox, (2005), Ion cyclotron waves in the Saturnian magnetosphere associated with Cassini's engine exhaust, Geophysical Research Letters, 32(14):3 pp., doi: 10.1029/2005GL022672.

Rymer, A. M., B. H. Mauk, T. W. Hill, N. Andre, D. G. Mitchell, C. Paranicas, M. K. Dougherty, (2009), Cassini evidence for rapid interchange transport at Saturn, Planetary and Space Science, 57(14–15):1779–1784, doi: 10.1016/j.pss.2009.04.010.

Rymer, A. M., B. H. Mauk, T. W. Hill, C. Paranicas, N. Andre, E. C. Sittler, M. K. Dougherty, (2007), Electron sources in Saturn's magnetosphere, Journal of Geophysical Research: Space Physics, 112(A2):11 pp., doi: 10.1029/2006JA012017.

Santolik, O., D. A. Gurnett, G. H. Jones, P. Schippers, F. J. Crary, J. S. Leisner, M. K. Dougherty, (2011), Intense plasma wave emissions associated with Saturn's moon Rhea, Geophysical Research Letters, 38:7 pp., doi: 10.1029/2011GL049219.

Saur, J., N. Schilling, F. M. Neubauer, D. F. Strobel, S. Simon, M. K. Dougherty, R. T. Pappalardo, (2008), Evidence for temporal variability of Enceladus' gas jets: Modeling of Cassini observations, Geophysical Research Letters, 35(20):5 pp.

Saur, J., F. M. Neubauer, N. Schilling, (2007), Hemisphere coupling in Enceladus' asymmetric plasma interaction, Journal of Geophysical Research, 112(A11209), doi: 10.1029/2007JA012479.

Saur, J., B. H. Mauk, D. G. Mitchell, N. Krupp, K. K. Khurana, S. Livi, M. K. Dougherty, (2006), Anti-planetward auroral electron beams at Saturn, Nature, 439(7077):699–702, doi: 10.1038/nature04401.

Schippers, P., C. S. Arridge, J. D. Menietti, D. A. Gurnett, L. Lamy, B. Cecconi, D. T. Young, (2011), Auroral electron distributions within and close to the Saturn kilometric radiation source region, Journal of Geophysical Research: Space Physics, 116:19 pp., doi: 10.1029/2011JA016461.

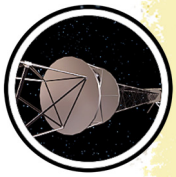

Schippers, P., M. Blanc, N. Andre, I. Dandouras, G. R. Lewis, L. K. Gilbert, M. K. Dougherty, (2008), Multi-instrument analysis of electron populations in Saturn's magnetosphere, Journal of Geophysical Research: Space Physics, 113(A7):10 pp., doi: 10.1029/2008JA013098.

Schneider, N. M., M. H. Burger, E. L. Schaller, M. E. Brown, R. E. Johnson, J. S. Kargel, N. A. Achilleos, (2009), No sodium in the vapour plumes of Enceladus, Nature, 459(7250):1102–1104, doi: 10.1038/nature08070.

Sergis, N., E. J. Bunce, J. F. Carbary, S. W. H. Cowley, X. Jia, S. M. Krimigis, D. G. Mitchell, M. K. Dougherty, D. C. Hamilton, (2018), The ring current of Saturn, in Electric Currents in Geospace and Beyond, (eds.) A. Keiling, O. Marghitu, M. Wheatland, John Wiley & Sons, Inc., pp. 139–154.

Sergis, N., C. M. Jackman, M. F. Thomsen, S. M. Krimigis, D. G. Mitchell, D. C. Hamilton, R. J. Wilson, (2017), Radial and local time structure of the Saturnian ring current, revealed by Cassini, Journal of Geophysical Research: Space Physics, 122(2):1803–1815, doi: 10.1002/2016JA023742.

Sergis, N., C. M. Jackman, A. Masters, S. M. Krimigis, M. F. Thomsen, D. C. Hamilton, A. J. Coates, (2013), Particle and magnetic field properties of the Saturnian magnetosheath: Presence and upstream escape of hot magnetospheric plasma, Journal of Geophysical Research: Space Physics, 118(4):1620–1634, doi: 10.1002/jgra.50164.

Sergis, N., C. S. Arridge, S. M. Krimigis, D. G. Mitchell, A. M. Rymer, D. C. Hamilton, A. J. Coates, (2011), Dynamics and seasonal variations in Saturn's magnetospheric plasma sheet, as measured by Cassini, Journal of Geophysical Research: Space Physics, 116:11 pp., doi: 10.1029/2010JA016180.

Sergis, N., S. M. Krimigis, E. C. Roelof, C. S. Arridge, A. M. Rymer, D. G. Mitchell, D. T. Young, (2010), Particle pressure, inertial force, and ring current density profiles in the magnetosphere of Saturn, based on Cassini measurements, Geophysical Research Letters, 37:5 pp., doi: 10.1029/2009GL041920.

Sergis, N., S. M. Krimigis, D. G. Mitchell, D. C. Hamilton, N. Krupp, B. H. Mauk, M. K. Dougherty, (2009), Energetic particle pressure in Saturn's magnetosphere measured with the Magnetospheric Imaging Instrument on Cassini, Journal of Geophysical Research: Space Physics, 114:17 pp., doi: 10.1029/2008JA013774.

Simon, S., F. M. Neubauer, A. Wennmacher, M. K. Dougherty, (2014a), Variability of Titan's induced magnetotail: Cassini magnetometer observations, Journal of Geophysical Research: Space Physics, 119(3):2024–2037, doi: 10.1002/2013JA019608.

Simon, S., J. Saur, S. C. van Treeck, H. Kriegel, M. K. Dougherty, (2014b), Discontinuities in the magnetic field near Enceladus, Geophysical Research Letters, 41(10):3359–3366, doi: 10.1002/2014GL060081.

Simon, S., S. C. van Treeck, A. Wennmacher, J. Saur, F. M. Neubauer, C. L. Bertucci, M. K. Dougherty, (2013), Structure of Titan's induced magnetosphere under varying background

magnetic field conditions: Survey of Cassini magnetometer data from flybys TA-T85, Journal of Geophysical Research: Space Physics, 118(4):1679–1699, doi: 10.1002/jgra.50096.

Simon, S., H. Kriegel, J. Saur, A. Wennmacher, F. M. Neubauer, E. Roussos, M. K. Dougherty, (2012), Analysis of Cassini magnetic field observations over the poles of Rhea, Journal of Geophysical Research: Space Physics, 117:18 pp., doi: 10.1029/2012JA017747.

Simon, S., J. Saur, H. Kriegel, F. M. Neubauer, U. Motschmann, M. K. Dougherty, (2011a), Influence of negatively charged plume grains and hemisphere coupling currents on the structure of Enceladus' Alfven wings: Analytical modeling of Cassini magnetometer observations, Journal of Geophysical Research: Space Physics, 116:33 pp., doi: 10.1029/2010JA016338.

Simon, S., J. Saur, F. M. Neubauer, A. Wennmacher, M. K. Dougherty, (2011b), Magnetic signatures of a tenuous atmosphere at Dione, Geophysical Research Letters, 38:5 pp., doi: 10.1029/2011GL048454.

Simon, S., A. Wennmacher, F. M. Neubauer, C. L. Bertucci, H. Kriegel, J. Saur, M. K. Dougherty, (2010a), Titan's highly dynamic magnetic environment: A systematic survey of Cassini magnetometer observations from flybys TA-T62, Planetary and Space Science, 58(10):1230–1251, doi: 10.1016/j.pss.2010.04.021.

Simon, S., A. Wennmacher, F. M. Neubauer, C. L. Bertucci, H. Kriegel, C. T. Russell, M. K. Dougherty, (2010b), Dynamics of Saturn's magnetodisk near Titan's orbit: Comparison of Cassini magnetometer observations from real and virtual Titan flybys, Planetary and Space Science, 58(12):1625–1635, doi: 10.1016/j.pss.2010.08.006.

Simon, S., J. Saur, F. M. Neubauer, U. Motschmann, M. K. Dougherty, (2009a), Plasma wake of Tethys: Hybrid simulations versus Cassini MAG data, Geophysical Research Letters, 36:5 pp., doi: 10.1029/2008GL036943.

Simon, S., U. Motschmann, G. Kleindienst, J. Saur, C. L. Bertucci, M. K. Dougherty, A. J. Coates, (2009b), Titan's plasma environment during a magnetosheath excursion: Real-time scenarios for Cassini's T32 flyby from a hybrid simulation, Annales Geophysicae, 27(2):669–685, doi: 10.5194/angeo-27-669-2009.

Simon, S., U. Motschmann, G. Kleindienst, K. -H. Glassmeier, C. Bertucci, M. K. Dougherty, (2008), Titan's magnetic field signature during the Cassini T34 flyby: Comparison between hybrid simulations and MAG data, Geophysical Research Letters, 35(4):4 pp., doi: 10.1029/2007GL033056.

Simon, S., G. Kleindienst, A. Boesswetter, T. Bagdonat, U. Motschmann, K. -H. Glassmeier, M. K. Dougherty, (2007), Hybrid simulation of Titan's magnetic field signature during the Cassini T9 flyby, Geophysical Research Letters, 34(20):5 pp., doi: 10.1029/2007GL029967.

Sittler, E. C., M. Thomsen, D. Chornay, M. D. Shappirio, D. Simpson, R. E. Johnson, N. Andre, (2005), Preliminary results on Saturn's inner plasmasphere as observed by Cassini: Comparison with Voyager, Geophysical Research Letters, 32(14):5 pp., doi: 10.1029/2005GL022653.

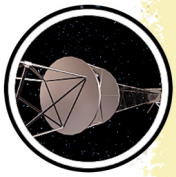

Smith, A. W., C. M. Jackman, M. F. Thomsen, L. Lamy, N. Sergis, (2018a), Multi-instrument investigation of the location of Saturn's magnetotail X-line, Geophysical Research Letters: Space Physics, 123:5494–5505, doi: 10.1029/2018JA025532.

Smith, A. W., C. M. Jackman, M. F. Thomsen, N. Sergis, D. G. Mitchell, E. Roussos, (2018b), Dipolarization fronts with associated energized electrons in Saturn’s magnetotail, Journal of Geophysical Research: Space Physics, 123(4):2714–2735.

Smith, A. W., C. M. Jackman, M. F. Thomsen, (2016), Magnetic reconnection in Saturn's magnetotail: A comprehensive magnetic field survey, Journal of Geophysical Research: Space Physics, 121:2984–3005, doi: 10.1002/2015JA022005.

Smith, E. J., M. K. Dougherty, C. T. Russell, D. J. Southwood, (2001), Scalar helium magnetometer observations at Cassini Earth swing-by, Journal of Geophysical Research: Space Physics, 106(A12):30129–30139, doi: 10.1029/2001JA900115.

Snowden, D., R. Winglee, C. Bertucci, M. Dougherty, (2007), Three-dimensional multifluid simulation of the plasma interaction at Titan, Journal of Geophysical Research: Space Physics, 112(A12), doi: 10.1029/2007JA012393.

Sorba, A. M., N. A. Achilleos, P. Guio, C. S. Arridge, N. M. Pilkington, A. Masters, M. K. Dougherty, (2017), Modeling the compressibility of Saturn's magnetosphere in response to internal and external influences, Journal of Geophysical Research: Space Physics, 122(2):1572–1589, doi: 10.1002/2016JA023544.

Southwood, D. J., E. Chané, (2016), High-latitude circulation in giant planet magnetospheres, Journal of Geophysical Research Space Physics, 121:5394–5403, doi: 10.1002/2015JA022310.

Southwood, D. J., (2015), Formation of magnetotails: Fast and slow rotators compared, in Magnetotails in the Solar System, (eds.) A. Keiling, C. M. Jackman, P. A. Delamere, John Wiley & Sons, Inc., doi: 10.1002/9781118842324.ch12.

Southwood, D. J., (2014), Saturn's mysterious magnetism, Astronomy & Geophysics, 55(1):1–13, doi: 10.1093/astrogeo/atu034.

Southwood, D. J., S. W. H. Cowley, (2014), The origin of Saturn magnetic periodicities: Northern and southern current systems, Journal of Geophysical Research, 119:1563–1571, doi: 10.1002/2013JA019632.

Southwood, D. J., (2011), Direct evidence of differences in magnetic rotation rate between Saturn's northern and southern polar regions, Journal of Geophysical Research, 116(A01201), doi: 10.1029/2010JA016070, 2011.

Southwood, D.J., M.G. Kivelson, (2009), The source of Saturn’s periodic radio emission, Journal of Geophysical Research, 114(A09201), doi: 10.1029/2008JA013800.

Southwood, D. J., M. G. Kivelson, (2007), Saturnian magnetospheric dynamics: Elucidation of a camshaft model, Journal of Geophysical Research, 112(A12222), doi: 10.1029/2007JA012254.

Southwood, D. J., M. K. Dougherty, A. Balogh, S. W. H. Cowley, E. J. Smith, B. T. Tsurutani, F. M. Neubauer, (2001), Magnetometer measurements from the Cassini Earth swing-by, Journal of Geophysical Research: Space Physics, 106(A12):30109–30128, doi: 10.1029/2001JA900110.

Stallard, T. S., A. Masters, S. Miller, H. Melin, E. J. Bunce, C. S. Arridge, S. W. H. Cowley, (2012), Saturn's auroral/polar H-3(+) infrared emission: The effect of solar wind compression, Journal of Geophysical Research: Space Physics, 117:12 pp., doi: 10.1029/2012JA018201.

Stallard, T., S. Miller, M. Lystrup, N. Achilleos, E. J. Bunce, C. S. Arridge, P. Drossart, (2008), Complex structure within Saturn's infrared aurora, Nature, 456(7219):214–217, doi: 10.1038/nature07440.

Sulaiman, A. H., D. A. Gurnett, J. S. Halekas, J. N. Yates, W. S. Kurth, M. K. Dougherty, (2017a), Whistler mode waves upstream of Saturn, Journal of Geophysical Research: Space Physics, 122(1):227–234, doi: 10.1002/2016JA023501.

Sulaiman, A. H., X. Jia, N. Achilleos, N. Sergis, D. A. Gurnett, W. S. Kurth, (2017b), Large-scale solar wind flow around Saturn’s nonaxisymmetric magnetosphere, Journal of Geophysical Research, 122:9198–9206, doi: 10.1002/2017JA024595.

Sulaiman, A. H., A. Masters, M. K. Dougherty, (2016), Characterization of Saturn's bow shock: Magnetic field observations of quasi-perpendicular shocks, Journal of Geophysical Research: Space Physics, 121(5):4425–4434, doi: 10.1002/2016JA022449.

Sulaiman, A. H., A. Masters, M. K. Dougherty, D. Burgess, M. Fujimoto, G. B. Hospodarsky, (2015), Quasiperpendicular high mach number shocks, Physical Review Letters, 115(12):5 pp., doi: 10.1103/PhysRevLett.115.125001.

Sulaiman, A. H., A. Masters, M. K. Dougherty, X. Jia, (2014), The magnetic structure of Saturn's magnetosheath, Journal of Geophysical Research: Space Physics, 119(7):5651–5661, doi: 10.1002/2014JA020019.

Szego, K., Z. Nemeth, L. Foldy, S.W.H. Cowley, G. Provan, (2013), Dual periodicities in the flapping of Saturn’s magnetodisk, Journal of Geophysical Research, 118:2883–2887, doi: 10.1002/jgra.50316.

Szego, K., D. T. Young, T. Bagdonat, B. Barraclough, J. J. Berthelier, A. J. Coates, M. F. Thomsen, (2006), A pre-shock event at Jupiter on 30 January 2001, Planetary and Space Science, 54(2):200–211, doi: 10.1016/j.pss.2005.10.011.

Szego, K., D. T. Young, B. Barraclough, J. -J. Berthelier, A. J. Coates, D. J. McComas, M. F. Thomsen, (2003), Cassini plasma spectrometer measurements of Jovian bow shock structure, Journal of Geophysical Research: Space Physics, 108(A7):14 pp., doi: 10.1029/2002JA009517.

Talboys, D. L., E. J. Bunce, S. W. H. Cowley, C. S. Arridge, A. J. Coates, M. K. Dougherty, (2011), Statistical characteristics of field-aligned currents in Saturn's nightside magnetosphere, Journal of Geophysical Research: Space Physics, 116:24 pp., doi: 10.1029/2010JA016102.

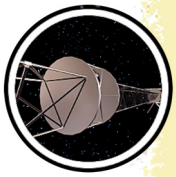

Talboys, D. L., C. S. Arridge, E. J. Bunce, A. J. Coates, S. W. H. Cowley, M. K. Dougherty, K. K. Khurana, (2009a), Signatures of field-aligned currents in Saturn's nightside magnetosphere, Geophysical Research Letters, 36:6 pp., doi: 10.1029/2009GL039867.

Talboys, D. L., C. S. Arridge, E. J. Bunce, A. J. Coates, S. W. H. Cowley, M. K. Dougherty, (2009b), Characterization of auroral current systems in Saturn's magnetosphere: High-latitude Cassini observations, Journal of Geophysical Research: Space Physics, 114:24 pp., doi: 10.1029/2008JA013846.

Taubenschuss, U., H. O. Rucker, W. S. Kurth, B. Cecconi, P. Zarka, M. K. Dougherty, J. T. Steinberg, (2006), Linear prediction studies for the solar wind and Saturn kilometric radiation, Annales Geophysicae, 24(11):3139–3150, doi: 10.5194/angeo-24-3139-2006.

Teolis, B. D., I. Sillanpää, J. H. Waite, K. K. Khurana, (2014), Surface current balance and thermoelectric whistler wings at airless astrophysical bodies: Cassini at Rhea, Journal of Geophysical Research Space Physics, 119:8881–8901, doi: 10.1002/2014JA020094.

Thomsen, M. F., C. M. Jackman, S. W. H. Cowley, X. Jia, M. G. Kivelson, G. Provan, (2017), Evidence for periodic variations in the thickness of Saturn’s nightside plasma sheet, Journal of Geophysical Research, 122:280–292, doi: 10.1002/2016JA023368.

Tomas, A., J. Woch, N. Krupp, A. Lagg, K. H. Glassmeier, M. K. Dougherty, P. G. Hanlon, (2004), Changes of the energetic particles characteristics in the inner part of the Jovian magnetosphere: a topological study, in Planetary and Space Science Vol. 52, Pergamon-Elsevier Science LTD, Lisbon, Portugal, doi: 10.1016/j.pss.2003.06.011, pp. 491–498.

Tsurutani, B. T., E. J. Smith, M. E. Burton, J. K. Arballo, C. Galvan, X. Y. Zhou, J. K. Chao, (2001), Oblique "1-Hz" whistler mode waves in an electron foreshock: The Cassini near-Earth encounter, Journal of Geophysical Research: Space Physics, 106(A12):30223–30238, doi: 10.1029/2001JA900108.

Tsyganenko, N. A., V. A. Andreeva, (2014), On the bowl-shaped deformation of planetary equatorial current sheets, Geophysical Research Letters, 41:1079–1084, doi: 10.1002/2014GL059295.

Ulusen, D., J. G. Luhmann, Y. J. Ma, K. E. Mandt, J. H. Waite, M. K. Dougherty, K. Agren, (2012), Comparisons of Cassini flybys of the Titan magnetospheric interaction with an MHD model: Evidence for organized behavior at high altitudes, Icarus, 217(1):43–54, doi: 10.1016/j.Icarus.2011.10.009.

Ulusen, D., J. G Luhmann, Y. J. Ma, S. Ledvina, T. E Cravens, K. Mandt, J. H. Waite, J. -E. Wahlund, (2010), Investigation of the force balance in the Titan ionosphere: Cassini T5 flyby model/data comparisons, Icarus, 210(2):867–880, https://doi.org/10.1016/j.icarus.2010.07.004.

Wahlund, J. E., R. Bostrom, G. Gustafsson, D. A. Gurnett, W. S. Kurth, A. Pedersen, I. Muller-Wodarg, (2005), Cassini measurements of cold plasma in the ionosphere of Titan, Science, 308(5724):986–989, doi: 10.1126/science.1109807.

Wei, H. Y., C. T. Russell, M. K. Dougherty, Y. J. Ma, K. C. Hansen, H. J. McAndrews, D. T. Young, (2011), Unusually strong magnetic fields in Titan's ionosphere: T42 case study, Advances in Space Research, 48(2):314–322, doi: 10.1016/j.asr.2011.02.009.

Wei, H. Y., C. T. Russell, M. K. Dougherty, F. M. Neubauer, Y. J. Ma, (2010a), Upper limits on Titan's magnetic moment and implications for its interior, Journal of Geophysical Research-Planets, 115:14 pp., doi: 10.1029/2009JE003538.

Wei, H. Y., C. T. Russell, T. L. Zhang, M. K. Dougherty, (2010b), Comparison study of magnetic flux ropes in the ionospheres of Venus, Mars and Titan, Icarus, 206(1):174–181, doi: 10.1016/j.Icarus.2009.03.014.

Wei, H. Y., C. T. Russell, A. Wellbrock, M. K. Dougherty, A. J. Coates, (2009), Plasma environment at Titan's orbit with Titan present and absent, Geophysical Research Letters, 36:5 pp., doi: 10.1029/2009GL041048.

Wei, H. Y., C. T. Russell, J. -E. Wahlund, M. K. Dougherty, C. Bertucci, R. Modolo, F. M. Neubauer, (2007), Cold ionospheric plasma in Titan's magnetotail, Geophysical Research Letters, 34(24):5 pp., doi: 10.1029/2007GL030701.

Wellbrock, A., A. J. Coates, M. F. Thomsen, D. T. Young, (2008), Unusually strong magnetic fields in Titan’s ionosphere: T42 analysis, Advances in Space Research, doi: 10.1016/j.asr.2011.02.009.

Went, D. R., G. B. Hospodarsky, A. Masters, K. C. Hansen, M. K. Dougherty, (2011a), A new semiempirical model of Saturn's bow shock based on propagated solar wind parameters, Journal of Geophysical Research: Space Physics, 116:9 pp., doi: 10.1029/2010JA016349.

Went, D. R., M. G. Kivelson, N. Achilleos, C. S. Arridge, M. K. Dougherty, (2011b), Outer magnetospheric structure: Jupiter and Saturn compared, Journal of Geophysical Research: Space Physics, 116:14 pp., doi: 10.1029/2010JA016045.

Williams, J. D., L. J. Chen, W. S. Kurth, D. A. Gurnett, M. K. Dougherty, (2006), Electrostatic solitary structures observed at Saturn, Geophysical Research Letters, 33(6):4 pp., doi: 10.1029/2005GL024532.

Williams, J. D., L. J. Chen, W. S. Kurth, D. A. Gurnett, M. K. Dougherty, A. M. Rymer, (2005), Electrostatic solitary structures associated with the November 10, 2003, interplanetary shock at 8.7 AU, Geophysical Research Letters, 32(17):4 pp., doi: 10.1029/2005GL023079.

Wilson, R. J., R. L. Tokar, M. G. Henderson, T. W. Hill, M. F. Thomsen, D. H. Pontius, Jr., (2008), Cassini plasma spectrometer thermal ion measurements in Saturn’s inner magnetosphere, Journal of Geophysical Research, 113(A12218), doi:10.1029/2008JA013486.

Witasse, O., B. Sanchez-Cano, M. L. Mays, P. Kajdic, H. Opgenoorth, H. A. Elliott, R. F. Wimmer-Schweingruber, (2017), Interplanetary coronal mass ejection observed at STEREO-A, Mars, comet 67P/Churyumov-Gerasimenko, Saturn, and New Horizons en route to Pluto: Comparison of its Forbush decreases at 1.4, 3.1, and 9.9 AU, Journal of Geophysical Research: Space Physics, 122(8):7865–7890, doi: 10.1002/2017JA023884.

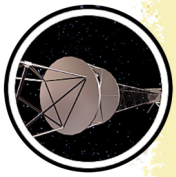

Yao, Z. H., A. J. Coates, L. C. Ray, I. J. Rae, D. Grodent, G. H. Jones, W. R. Dunn, (2017a), Corotating magnetic reconnection site in Saturn's magnetosphere, Astrophysical Journal Letters, 846(2):7 pp., doi: 10.3847/2041-8213/aa88af.

Yao, Z. H., A. Radioti, I. J. Rae, J. Liu, D. Grodent, L. C. Ray, J. H. Waite, (2017b), Mechanisms of Saturn's near-noon transient aurora: In situ evidence from Cassini measurements, Geophysical Research Letters, 44(22):11217–11228, doi: 10.1002/2017GL075108.

Yates, J. N., D. J. Southwood, M. K. Dougherty, A. H. Sulaiman, A. Masters, S. W. H. Cowley, A. J. Coates, (2016), Saturn's quasiperiodic magnetohydrodynamic waves. Geophysical Research Letters, 43(21):11102–11111, doi: 10.1002/2016GL071069.

Yates, J. N., D. J. Southwood, M. K. Dougherty, (2015a), Magnetic phase structure of Saturn's 10.7h oscillations, Journal of Geophysical Research: Space Physics, 120(4):2631–2648, doi: 10.1002/2014JA020629.

Yates, J. N., D. J. Southwood, M. K. Dougherty, (2015b), Reply to the comment by Cowley et al., on Magnetic phase structure of Saturn's 10.7h oscillations, Journal of Geophysical Research: Space Physics, 120(7):5691–5693, doi: 10.1002/2015JA021559.

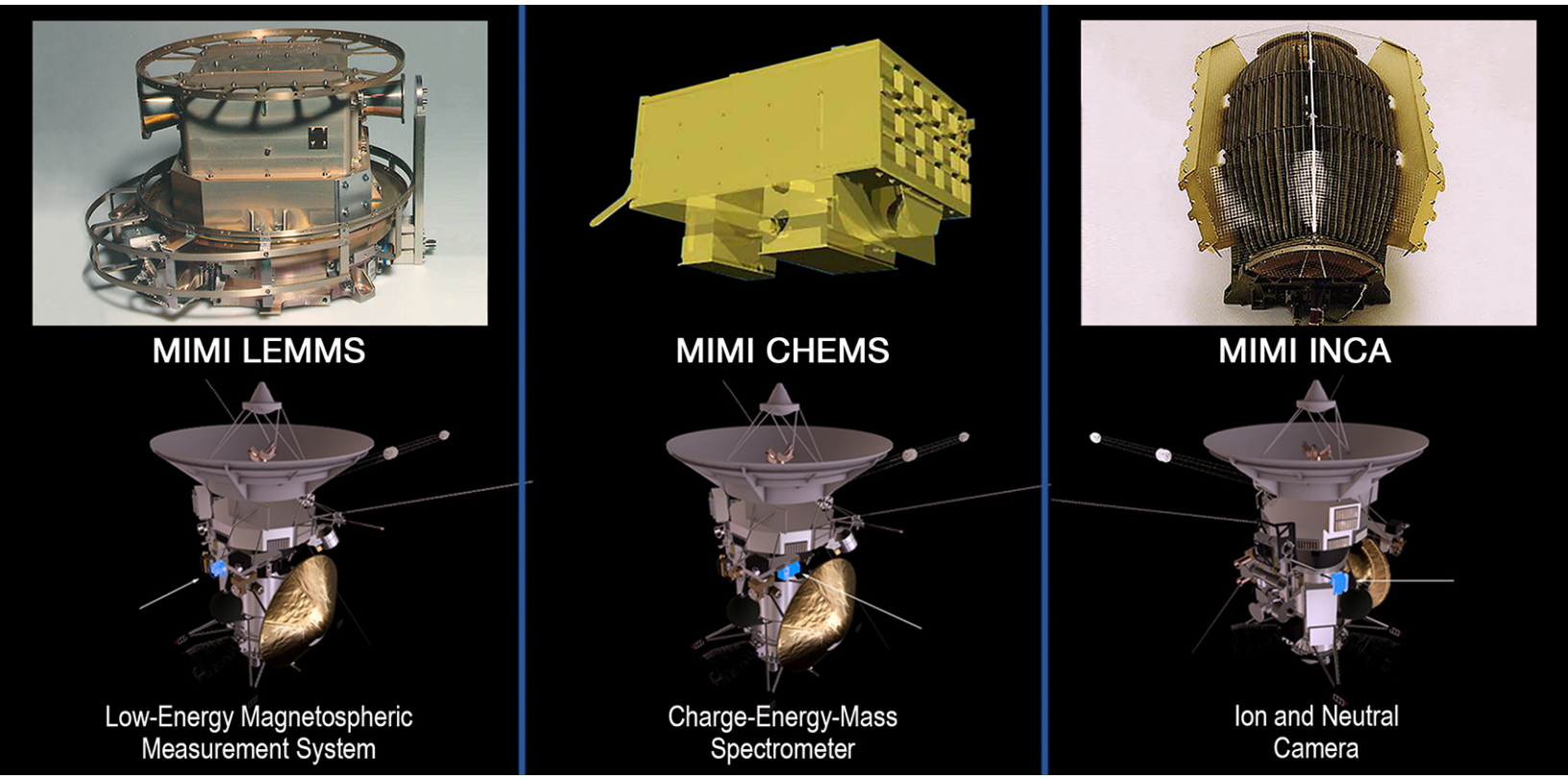

Magnetosphere Imaging Instrument

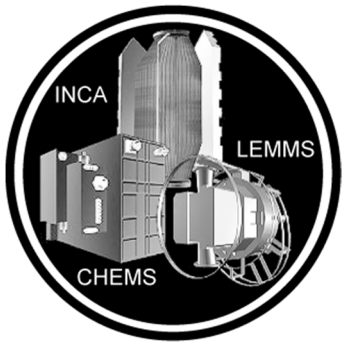

The Magnetosphere Imaging Instrument (MIMI) was comprised of three sensors designed to measure energetic electrons, ions, and neutrals in the Saturn system: the Low Energy Magnetospheric Measurement System (LEMMS), the Charge-Energy-Mass Spectrometer (CHEMS), and the Ion and Neutral Camera (INCA). Each sensor made in situ particle measurements and INCA had the additional capability of creating images out of energetic neutral atoms (ENAs) that can reach the spacecraft from large distances. The **science objectives** of MIMI were to map the charged particle populations of Saturn's magnetosphere, study the global configuration and dynamics of Saturn's magnetosphere and its interaction with the solar wind, Saturn's atmosphere, Titan, and the icy satellites. In concert, MIMI's three sensors extensively characterized the planetary radiation belts of Saturn, discovered a transient radiation belt, and characterized magnetospheric dynamics with global ENA images of Saturn's magnetosphere.

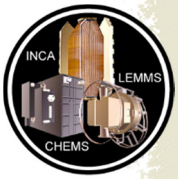

CONTENTS

Figures

Tables

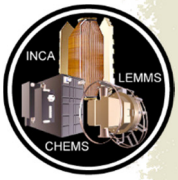

Executive Summary

MIMI measured energetic electrons, ions, and neutrals using three separate sensors: 1) LEMMS, 2) CHEMS, and 3) INCA. Each of these sensors detected particles in the local environment of the spacecraft and INCA had the additional capability of creating images out of ENAs that can reach the spacecraft from large distances. The sensors were able to carry out some separation by species and CHEMS could also separate ions by charge state. MIMI made measurements in cruise and around the planetary flybys and, at Saturn, was operated essentially continuously from orbit insertion in 2004 to the end of mission in 2017. MIMI data characterized Saturn's ion and electron radiation belts; the space environments of the rings, inner satellites, and Titan; and the magnetosphere, high latitude regions, and boundaries, and made advances in our understanding of the dynamics of Saturn's magnetosphere. Through ENA imaging, MIMI also expanded our understanding of the heliosphere.

MIMI extensively characterized the planetary radiation belts of Saturn, including the segmentation of the belts due to the rings and moons and discovered a transient belt.

Highlights from MIMI science. MIMI extensively characterized the planetary radiation belts of Saturn, including the segmentation of the belts due to the rings and moons and discovered a transient belt. INCA obtained global ENA images of Saturn's magnetosphere showing detailed dynamics such as injections, planetary rotational periodicities in ring current intensity, images of the heliosphere and its structure, images of ion acceleration in the auroral region, global ENA emissions of Jupiter, and images of Titan's interaction with the magnetosphere. Satellite and ring absorption signatures predicted a global electric field with no known source. CHEMS and LEMMS data were used to infer regions dominated by the neutral gas torus. MIMI LEMMS measured the inner radiation belts between the middle of the D-ring and the planetary atmosphere. MIMI INCA and CHEMS data led to the discovery of ring dust precipitating into the equatorial atmosphere. MIMI data found periodic features in the magnetosphere.

Key open questions. Some of the open questions relevant to this science are (this follows and expands on the ones in the individual sections below):

- What is the relationship between small and large-scale injections at Saturn and what is the role of injections in the flow of mass and energy through the system?
- What are the mechanisms that create the injections, both in the outer magnetosphere (Titan's orbit and beyond) and between ~18 R_S and Enceladus?
- How do periodicities in charged particle fluxes come about?
- How is the radiation belt inward of the C-ring formed and sustained?

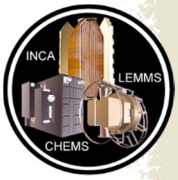

- How can we explain the fluxes of the MeV particles, both inward and outward of the rings and how does the radiation belt co-existing with the F-ring form? What is the source rate of cosmic ray albedo neutron decay (CRAND) neutrons?
- To what extent are the accessible satellite surfaces and atmospheres (including Titan) modified by charged particles?
- What influence does the solar wind have on the magnetosphere?
- Is the mass loss rate from the rings to the atmosphere episodic, or continuous?
- What would Saturn's magnetosphere look like without Enceladus?

Instrument Summary

MIMI comprised three separate sensors and is described in complete detail in Krimigis et al. [2004]. MIMI/LEMMS was a two-ended telescope with oppositely directed fields of view (low and high energy). Detected electrons and ions that entered the apertures were collimated and then reached a solid-state detector (SSD) stack. The stack used a series of coincidence and anti-coincidence requirements related to the energy deposited in the detectors within a timing window to separate species and energies. Electrons entering the low-energy end were magnetically deflected onto detectors for which direct ion pathways are much less probable. Up until about March 2005, a stepping motor changed the telescope fields of view so that good local pitch-angle sampling could be achieved. MIMI/INCA was like a pin-hole camera used to detect ions and ENAs. Collimator blades in front of the detection system could be used to significantly reduce the local charged environment that enters the aperture so that ENAs can be detected more cleanly. When the collimator blade voltages were off, INCA detected the local environment of energetic ions, which typically dominates the neutral intensities. Both ions and neutrals were then measured in a time-of-flight (TOF) system. Secondary electrons triggered start and stop pulses whose positions also identify the particle trajectory. The system was capable of a crude light/heavy ion separation. MIMI/CHEMS measured ions in three directions using an electrostatic analyzer (ESA) followed by a TOF and SSD system. CHEMS stepped through E/q ESA values from about 3 keV/q to 220 keV/q, and selected ions then passed through the TOF system and into one of three SSDs. This allowed for good species and charge state separation (the only sensor on MIMI that can measure charge state). Because of the duty cycle inherent in stepping through 32 E/q steps, CHEMS required more time integration to get good signal statistics.

Key Objectives for MIMI (Announcement of Opportunity (AO) first, then Cassini Solstice Mission (CSM))

- R_AO5 – Ring Magnetosphere-Ionosphere Interactions. Study interactions between the rings and Saturn's magnetosphere, ionosphere, and atmosphere.
- M_AO2 – Magnetosphere Charged Particles. Determine current systems, composition, sources, and sinks of magnetosphere charged particles.

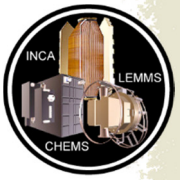

- M_AO4 – Magnetosphere and Solar Interactions with Titan. Study the effect of Titan's interaction with the solar wind and magnetospheric plasma.
- M_AO5 – Plasma Interactions with Titan's Atmosphere and Ionosphere. Investigate interactions of Titan's atmosphere and exosphere with the surrounding plasma.
- I_AO2 – Icy Satellite Surface and Crustal Modifications. Define the mechanisms of crustal and surface modifications, both external and internal.
- I_AO5 – Icy Satellite Magnetosphere and Ring Interactions. Investigate interactions with the magnetosphere and ring systems and possible gas injections into the magnetosphere.
- J_AO3 – Explore the dusk side of the magnetosphere and intermediate regions of the magnetotail unvisited by previous spacecraft.
- C_AO2 – Investigate the behavior of the solar wind during solar minimum, for comparison with earlier Galileo and Ulysses measurements.
- SC2a – Observe the magnetosphere, ionosphere, and aurora as they change on all time scales—minutes to years—and are affected by seasonal and solar cycle forcing.
- MC1a – Determine the temporal variability of Enceladus' plumes.
- MC1b – Observe Saturn's magnetosphere over a solar cycle, from one solar minimum to the next.
- MC2a – Observe seasonal variation of Titan's ionosphere, from one solstice to the next.
- MN1a – Determine the dynamics of Saturn's magnetotail.
- MN1b – Conduct in situ and remote sensing studies of Saturn's ionosphere and inner radiation belt.
- MN1c – Investigate magnetospheric periodicities, their coupling to the ionosphere, and how the Saturn kilometric radiation (SKR) periods are imposed from close to the planet (3–5 R_S) out to the deep tail.
- MN2a – Determine the coupling between Saturn's rings and ionosphere.
- TC2a – Observe Titan's plasma interaction as it goes from south to north of Saturn's solar-wind-warped magnetodisk from one solstice to the next.

MIMI Science Assessment

Table MIMI-1 shows the MIMI science objectives and assessment.

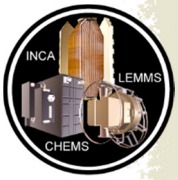

Table MIMI-1. MIMI Science Assessment. AO and Traceability Matrix (TM) objectives are paired with MIMI science objectives.

Fully/mostly accomplished: **Partially accomplished:** **Not accomplished:**

MIMI Science Objectives Characterize the following:	AO and TM Science Objectives	MIMI Science Assessment	Comments if yellow (partially fulfilled)
Magnetospheric structure			
Radiation belts and time variations	MN1b		
Composition, sources, and sinks	M_AO2		
Infer neutral properties	MC1a		
Proximal orbits, D-ring gap	M_AO2		
Middle magnetosphere and tail	MN1a		
High latitude magnetosphere, aurorae	SC2a		
Magnetospheric dynamics			
Dynamic phenomena	SC2a		
Periodicities, solar cycle, seasonal effects			
Periodic phenomena	SC2a, MN1c		
Response to season and solar wind	SC2a, MC1b		
Ring and moon interactions			
Moon-magnetosphere interactions	I_AO2, I_AO5		
Ring-magnetosphere interactions	R_AO5, MN2a		
Titan			
Titan-magnetosphere interactions	M_AO4, M_AO5, MC2a, TC2a		
Non-Saturn results			
Properties of the heliosphere			
Jovian magnetosphere	J_AO3		
Properties of the solar wind	C_AO2		

MIMI Saturn Results

Magnetospheric Structure (Roussos)

The structure of Saturn's magnetosphere is complex, due to its colocation with numerous moons, dense and dusty rings, and active plasma sources. Despite that, it is useful to identify several major regions based on which we can organize the MIMI findings. The regions can be naively divided on the basis of the L-shell (which is the field line distance along the magnetic equator in a dipole representation of the magnetic field):

- Inner magnetosphere, containing the radiation belts (L < 9)
- Middle magnetosphere and plasma/sheet (9 < L < 15)
- Outer magnetosphere and magnetotail (L > 15 out to the magnetopause)
- Upstream of the magnetopause

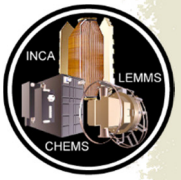

All locations have been extensively sampled by MIMI with different cadence at different mission periods. Below we summarize some of the key results for each region.

Inner magnetosphere and radiation belts: MIMI measurements achieved the most comprehensive description of the radiation belts of a planet besides Earth. More than 200 orbits crossed into the radiation belts, allowing us to understand and quantify their average structure, but also to monitor time variations, despite the single point measurements. The most detailed description of the radiation belts is given by Kollmann et al. [2011] where the L-shell, local time, and pitch angle (latitudinal) structure of the belts is given for electrons and protons of different energies. Heavier ions and their charge states are studied by DiFabio et al. [2011], Dialynas et al. [2009], Carbary et al. [2010a], and Christon et al. [2013, 2014, 2015]. The latter three studies provide the most detailed characterization of trace energetic ions and their charge states at an outer planet, showing how their origin may be connected to the planet's rings, the activity of Enceladus, and seasonal or solar cycle effects.

Allen et al. [2018] conducted a mission-long overview of internal to external sources of energetic plasma at Saturn. They found that solar wind-originating He^{++} ions are able to penetrate into the inner magnetosphere, although the fractional abundance in the inner magnetosphere is only about 0.001%.

Detailed investigations of the proton radiation belts in the MeV range have been published by Roussos et al. [2011, 2016a, 2018a], Kollmann et al. [2013, 2015, 2017], Armstrong et al. [2009], Paranicas et al. [2008, 2010a], and Buratti et al. [2019]. All studies establish how the proton belts are segmented by the icy moons of Saturn (Pandora, Prometheus, Janus, Epimetheus, Mimas, Enceladus, and Tethys) and the planet's main rings. They highlight interaction features with minor rings or ring arcs, such as those from Methone, Pallene, the G-ring, and the ringlets of the D-ring, most of which were unknown prior to Cassini. All studies established that the proton radiation belts inward of Tethys are disconnected from the short-term and large-scale changes that occur in the rest of the magnetosphere, and develop only over long time scales due to the combined influence from variable particle transport effects and the solar cycle, with the former being much more important. The origin of those belts is attributed to CRAND, rather than to extreme solar wind transients, a possibility that was considered before Cassini. Transient extensions of these belts, outside Tethys, have been linked with certainty to the occurrence of interplanetary coronal mass ejections (CMEs) in the vicinity of Saturn [Roussos et al. 2008a, 2018b], one of the first direct demonstrations of space weather at an outer planet with in situ data.

The electron radiation belts in the MeV range have been studied in a series of papers by Roussos et al. [2006, 2014, 2016b, 2019a], Paranicas et al. [2010b, 2012, 2014], Mauk et al. [2010], and Buratti [2019]. They are much more variable and longitudinally asymmetric than the corresponding proton belts, but on average they tend to increase monotonically in intensity inward towards the main rings at which point electrons get instantly absorbed. They evolve in time scales of weeks (as opposed to years for the protons) and are controlled by numerous factors, including the solar wind and internal magnetospheric dynamics. Interaction features of MeV electrons with material—for example, scattering and energy loss in collisions with material—and moons have

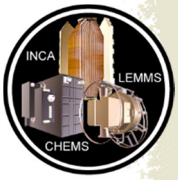

helped to constrain radial transport rates in the magnetosphere and discover previously unknown ring arcs. The source population of the MeV electron belts is now believed to reside in the ring current (middle magnetosphere).

Between energies of tens of keV and few hundred keV, both electrons and ions are on average diminished significantly inward of the orbit of Tethys, due to interactions of these particles with the neutral cloud of Enceladus, the dust of the E-ring or due to absorption by the moons [Paranicas et al. 2007; Kollmann et al. 2011; Carbary et al. 2009a]. The region between 5 and 9 R_S has been found to be dominated by a transient population of interchange injection events, which have been analyzed in single case studies as well as statistically [Paranicas et al. 2007, 2008, 2010b; Mueller et al. 2010; Mauk et al. 2005; and Rymer et al. 2007, 2008, 2009a]. The results have been used to constrain the plasma corotation speed in the inner magnetosphere and the inward radial transport velocities of plasma, and assess the importance of interchange for energetic particle transport and acceleration with respect to other processes like diffusion. The inner magnetosphere is also dominated by energetic electron microsignatures (gaps in the electron fluxes caused by electron absorption by Saturn's moons), which have been used to define the convective flows in the inner magnetosphere (a noon-to-midnight electric field) and radial diffusion rates [Paranicas et al. 2005a; Roussos et al. 2007, 2008a, 2013, 2019a; Andriopoulou et al. 2012, 2014; and Thomsen et al. 2012]. Statistically significant results on the angular distributions and energy spectra of electrons have been described for the first time in Carbary et al. [2011a, 2011b] and Clark et al. [2014].

Middle magnetosphere/ring current: The middle magnetosphere is the region where the so-called ring current of Saturn resides. This current likely has important components below the energy range of MIMI. But it has been found to contain energetic ions and electrons below 1 MeV, with relatively high fluxes. It is populated by large-scale injections in the nightside magnetosphere of Saturn, which sustain the ring current with a series of rotating, energetic ion and electron bundles, sometimes called blobs due to their appearance as such in remote sensing images by MIMI/INCA. The energy density of the energetic ion population is high enough to increase the plasma beta (the ratio of total particle pressure divided by magnetic pressure) above one, therefore causing a significant stretching of the magnetic field lines. Depending on the abundance of oxygen in the energetic ion distributions, the dynamics of the current sheet may be dominated by the presence of energetic particles. All these results are summarized in a series of studies by Sergis et al. [2007, 2009, 2010, 2011, 2013, 2017], Krimigis et al. [2007], Dialynas et al. [2009, 2013a], Carbary et al. [2008a, 2010b, 2012a, 2014a], and Kollmann et al. [2011]. All these measurements provided a most comprehensive, average description of Saturn's ring current, which can inform numerous empirical and physical models of Saturn's magnetosphere—for example, Achilleos et al. [2010]. The time variations in the ring current have been linked to changes in the radiation belts [Roussos et al. 2014, 2018a; Kollmann et al. 2017] and injections [Mitchell et al. 2009a, 2015, 2016], revealing the coupling of the system with different

All these measurements provided a most comprehensive, average description of Saturn's ring current, which can inform numerous empirical and physical models of Saturn's magnetosphere …

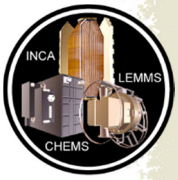

regions of the magnetosphere and the interplanetary space and the aurora—for example, Mitchell et al. [2009b]. The average properties of the ring current, as monitored by ENAs, have been inverted in order to probe the characteristics of Saturn's neutral gas cloud [Dialynas et al. 2013b]. Meanwhile, the average distribution of the middle magnetosphere energetic particles has been studied using observations from CHEMS [Allen et al. 2018].

Many of the studies focusing of the inner magnetosphere extended into the region of the ring current, meaning that energy spectra, angular and L-shell distributions, composition, as well as asymmetries are equally well quantified for $9 < L < 15$.

Outer magnetosphere: Since the outer magnetosphere is very dynamic, it is very challenging to describe its average properties. Still, the continuous in situ measurements by CHEMS and LEMMS and the remote monitoring by INCA have provided unique insights into that region. The most detailed study of the outer magnetosphere's average structure is given by Krimigis et al. [2007] and Sergis et al. [2009], which highlight the distinct day-night asymmetry in the vertical extent of the ring current (or plasma sheet). INCA images have been used to determine the most active sites for dipolarization (or large-scale injection events) in the outer magnetosphere being in the post-midnight sector of the magnetosphere [Mitchell et al. 2005a, 2009b; Carbary et al. 2008b]. They have revealed the wavy structure of the magnetodisk [Carbary 2013; Carbary et al. 2008a, 2015, 2016] and links to auroral emissions. LEMMS measurements have been used to identify an unexpected source of high energy electrons, seen as quasi-periodic pulsations with a period of about 65 minutes. These events are seen globally, they can accelerate electrons to the MeV range instantly and have been linked to reconnection, auroral transients, and similar periodic observations in magnetic field and plasma wave data [Roussos et al. 2016b; Palmaerts et al. 2016a, 2016b; Carbary et al. 2016]. The magnetospheric topology (e.g., open vs. closed field lines or the cusp) has been discussed in the context of MIMI observations—for example, Gurnett et al. [2010] and Arridge et al. [2016a]—while MIMI data have been central in the study and interpretation of reconnection/dipolarization events, in combination with other datasets—for example, Badman et al. [2013, 2016], Jackman et al. [2008, 2015], and Masters et al. [2010]. CHEMS observations also revealed outer magnetosphere asymmetries in the fractional abundance of solar wind-originating ions penetrating into the magnetosphere of Saturn [Allen et al. 2018]. These asymmetries indicate that solar wind He^{++} particles may be entering the magnetosphere due to a combination of Dungey-type reconnection as well as Kelvin-Helmholtz instabilities [Allen et al. 2018].

Upstream of the magnetopause: MIMI measurements have been used to characterize the environment also upstream of the magnetopause. In particular, Sergis et al. [2013] described the conditions of the planet's magnetosheath (the region of shocked solar wind outside the magnetopause), showing how it is strongly modified in the absence or presence of escaping, heavy energetic ions. Kanani et al. [2010] has factored in MIMI measurements to improve empirical models of the shape of Saturn's magnetopause. Measurements of Cassini in the solar wind extend the findings of Sergis et al. [2013], showing the escape of magnetospheric species into interplanetary space [Krimigis et al. 2009a]. Masters et al. [2013] have used MIMI measurements of energetic electrons to demonstrate how the bow shock at very high Mach numbers can be an efficient accelerator of electrons into relativistic energies.

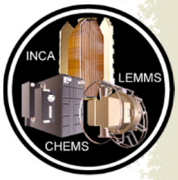

Open questions: What processes form and sustain the newly discovered radiation belt inward of the C-ring? How are energetic particles accelerated at Saturn and how are two-component spectra formed?

Magnetospheric Dynamics (Paranicas)

In addition to the magnetospheric structure presented above, a key aspect of Saturn's magnetosphere is its dynamics. This includes changes on long time scales (months to years) such as the formation and subsequent decay of transient radiation belts [Roussos et al. 2008a] or the gradual evolution of the main radiation belts [Kollmann et al. 2017]. On much shorter time scales, there are both global and more spatially limited injections of hotter plasma or energetic charged particles into the magnetosphere; see Thomsen et al. [2013] for a complete review of the subject. Other dynamics, like pulsations [Palmaerts et al. 2016b] and [Mitchell et al. 2016], are considered in the section entitled Periodicities, Solar Cycle, and Seasonal Effects.

Injections at Saturn have been coarsely characterized as small and large scale. The latter would likely be accompanied by reconfigurations of the planetary magnetic field. Small-scale injections are probably narrow in planetary longitude and physically can be flux tube bundles, flow channels, or more elaborate structures. This group of injections also perturbs the magnetic field locally—for example, Andre et al. [2005, 2007]—but probably at the level of a few percent of the planetary field. Andre et al. [2007] and Rymer et al. [2009a] present multi-instrument displays of interchange events in the magnetosphere of Saturn. This group of injections have been characterized as particle distributions with phase space densities that are very different from the surrounding medium in which they are observed [Mauk et al. 1999; Paranicas et al. 2016]. Mitchell et al. [2015] summarized the observational differences between small-scale and large-scale injections at Saturn. They found that small-scale injections tended to be found inward of about 12–15 R_S, although they also found large-scale injections that could be inward of that distance. It is probably the case that small-scale injections (which are found very frequently in the data) extend in energy up to the tens of keV or so. Rymer et al. [2007] used phase space density profiles derived from Cassini Plasma Spectrometer (CAPS) data to approximate a starting radial distance of interchange injections that are observed by Cassini. Paranicas et al. [2016] approximated the inward flow speed of injections and found values comparable to the theoretical computations of Hill et al. [2016] for $5 < L < 10$. It is believed that the radial speed of injections decreases as they approach Saturn.

Large-scale injections at Saturn have received much less attention in the literature than small-scale ones. Thomsen et al. [2013] have provided a good summary of the situation. Large-scale injections have been characterized by the MIMI data set. Mitchell et al. [2009b] linked some of these injections to ultraviolet (UV) data from Hubble Space Telescope (HST) and Cassini. Paranicas et al. [2007, 2010b] looked at the radial range of injection remnants. Because these extend into the hundreds of keV, it is likely Paranicas was studying large-scale injections. The effects of tail collapse, plasmoid production, and related processes have been documented with the help of magnetometer data—for example, Jackman [2011, 2015].

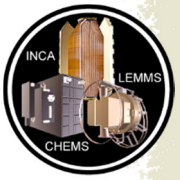

Because of their ubiquity, injections at Saturn have been used to characterize other features of the magnetosphere. Mauk et al. [2005] and Mueller et al. [2010] created azimuthal plasma flow speeds as a function of Saturn distance using MIMI injection data. Plasma flow speeds were later found using the plasma data—for example, Thomsen et al. [2010].

Open questions: What is the connection between large-scale and small-scale injections at Saturn? How much material do injections transport relative to radial diffusion? What creates the injections? How is radial diffusion driven?

Saturn's magnetosphere displays a wealth of periodicities at a wide range of frequency scales.

Periodicities, Solar Cycle, and Seasonal Effects (Carbary)

Saturn's magnetosphere displays a wealth of periodicities at a wide range of frequency scales. The best known of these periodicities is the putative planetary period at ~10.7 hours. This periodicity was discovered in charged particles by the Voyager Low Energy Charged Particle (LECP) instrument in the early 1980s [Carbary and Krimigis 1982]. LEMMS and CHEMS instruments monitored this planetary periodicity throughout the 13-year Cassini mission, and, along with the Radio and Plasma Wave Science (RPWS) and Magnetometer (MAG) instruments, discovered that this periodicity slowly varied by ~1% over several years and that it split into dual periods, one associated with the northern hemisphere and the other with the southern [Carbary et al. 2009b, 2011a]. This dual periodicity is not always detected, however, which may be a consequence of the observer location and/or its actual disappearance [Carbary et al. 2014a, 2016]. Single and dual periodicities were also observed in ENA fluxes detected by INCA [Carbary et al. 2008b, 2014a; Carbary and Mitchell 2017]. INCA's global view of these periodicities revealed a local time dependence, namely, that one period might be detected at one local time but absent at another [Carbary et al. 2014a]. Finally, the energetic electrons apparently have the same period (~10.8 h) during the summer season when either the North or the South Pole tilts with respect to the direction to the Sun [Carbary et al. 2017a]. This discovery, made possible by Cassini's solstice-to-solstice extension, has strong implications for the solar driving of these planetary periodicities. A complete review of Saturn's magnetospheric periodicities, as of 2013, appeared in Reviews of Geophysics [Carbary and Mitchell 2013], and should be consulted for the overall context within which particle periodicities can be placed.

MIMI also discovered that energetic particles display oscillations at the much longer solar wind period (~26 d). This solar wind periodicity was discerned during solar minimum (i.e., 2008–2010) when the solar wind structure was not disrupted by solar activity. The solar wind periodicity was first recognized in the energetic electrons [Carbary et al. 2009c], but was perhaps even stronger in the energetic ions [Carbary et al. 2013a]. Because solar activity varied with the ~22-year solar cycle, the appearance of this 26-day periodicity itself should vary with the solar cycle.

The solar cycle is also evident in LEMMS measurements of Saturn's radiation belts. The very energetic protons (E > 1 MeV) that form Saturn's ionic radiation belts were found to be modulated

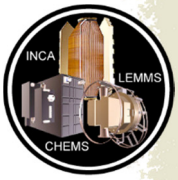

with the solar cycle, which provided clues that they might derive from CRAND from Saturn's atmosphere [Roussos et al. 2011]. As at Earth, the cosmic rays causing CRAND at Saturn are themselves modulated by the solar cycle, and LEMMS detected this for the first time using observations over many years. The ring current boundary, deduced from LEMMS observations, also appears to fluctuate in response to solar energetic particle (SEP) events, which are themselves conditioned according to the solar cycle [Roussos et al. 2014].

The LEMMS instrument also discovered another, completely unexpected periodicity at the relatively short time scale of ~1 hour [Roussos et al. 2016b]. These quasi-periodic (QP) oscillations have periods near ~60 minutes, tend to occur on the dusk side, and suggest acceleration at high latitude [Palmaerts et al. 2016a]. Similar QP-60 oscillations were detected in the polar cusp regions and are probably related to similar periodicities observed in the magnetic field and radio emissions [Palmaerts et al. 2016b]. The ~60-minute periodicities may be related to pulsed dayside reconnection, which generates Alfvén waves having these periods.

Open questions: What is the underlying cause of Saturn's periodicities? How are the observed periodicities related to the actual rotation of Saturn, and does it matter?

Particle Interactions with Moons and Ring Arcs (Krupp)

MIMI studied the environment during 23 Enceladus flybys, 5 Dione flybys, 4(5) Rhea flybys, 1 Tethys flyby, a distant Hyperion flyby, and a distant Mimas flyby.

Simon et al. [2015] summarized the moon magnetosphere interaction and compared Cassini data with hybrid code simulations.

Mimas: Hendrix et al. [2012] analyzed the Mimas UV albedo where the space weather effects caused by the energetic particles in the LEMMS energy range play a major role.

Enceladus: Krupp et al. [2012], Krupp et al. [2018a], and Jones et al. [2006a] studied the particle distributions and absorptions features near Enceladus with ramp-like, spike-like, and dust-related features.

Tethys: Roussos et al. [2005] reported low energy electron microsignature observations by LEMMS in the vicinity of Tethys' L-shell, during the first seven orbits of the Cassini mission. Double microsignatures seen for the first time suggest low radial diffusion coefficients and point to dynamic events in the magnetosphere.

Dione: Kotova et al. [2015] studied the particle distributions using particle tracing in hybrid code simulations and Krupp et al. [2013] summarized the LEMMS measurements near Dione.

Rhea: Jones et al. [2008] reported about particle observations possibly due to orbiting dust near Rhea. In Roussos et al. [2008b], three-dimensional hybrid simulations were performed in the vicinity of Rhea, and Roussos et al. [2012] reviewed the energetic electron environment of Rhea's

magnetospheric interaction. Khurana et al. [2017] identified the distant Alfven wing signature of Rhea several hundred moon radii away.

Hyperion: Nordheim et al. [2014] detected a dropout in energetic electrons observed by LEMMS, indicating that the moon and the spacecraft were magnetically connected when the field-aligned electron population was observed. It was shown that this constitutes a remote detection of a strongly negative (about -200 V) surface potential on Hyperion, consistent with the predicted surface potential in regions near the solar terminator.

Roussos et al. [2005] used LEMMS-displaced microsignature measurements near Tethys to study magnetospheric parameters, including a convective electric field.

Paranicas et al. [2005a] showed some of the earliest evidence of two microsignatures from Enceladus and Tethys in the LEMMS data.

Microsignature analysis from Roussos et al. [2007] revealed a high n dependence in D_{LL} ~L^n and an increase of its value toward equatorial pitch angles. This supports the idea that electron micro-diffusion refills microsignatures and partly accounts for transporting electrons at low L. It is driven by magnetic field pulsations.

Roussos et al. [2008c] looked at several energetic charged particle microsignatures of two Lagrange moons, Telesto and Helene, measured by the LEMMS instrument and inferred the possibility that the 3 km satellite Methone is responsible for two electron microsignatures detected by Cassini close to this moon's orbit; a previously undetected arc of material exists at Methone's orbit (R/2006 S5) (Figure MIMI-1).

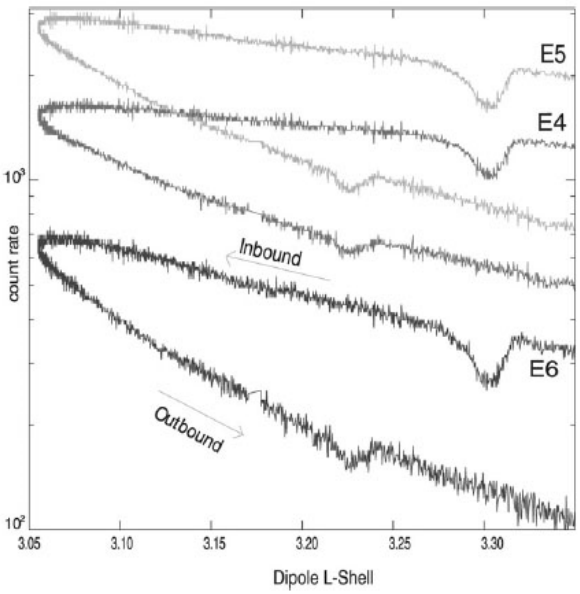

Figure MIMI-1. Flux depletions around Methone's orbit in the LEMMS E4–E6 channels as a function of dipole L shell. [Roussos et al. 2008c]

Roussos et al. [2010a] analyzed energetic electron microsignatures as tracers of radial flows and dynamics in Saturn's innermost magnetosphere including numerical simulation of energetic electron microsignature drifts [Roussos et al. 2013].

Andriopoulou et al. [2012, 2014] discovered a formerly unknown global noon-midnight electric field in Saturn's inner magnetosphere inferred from moon microsignature displacements, by carrying out an analysis of a large amount of LEMMS data (Figure MIMI-2 and Figure MIMI-3).

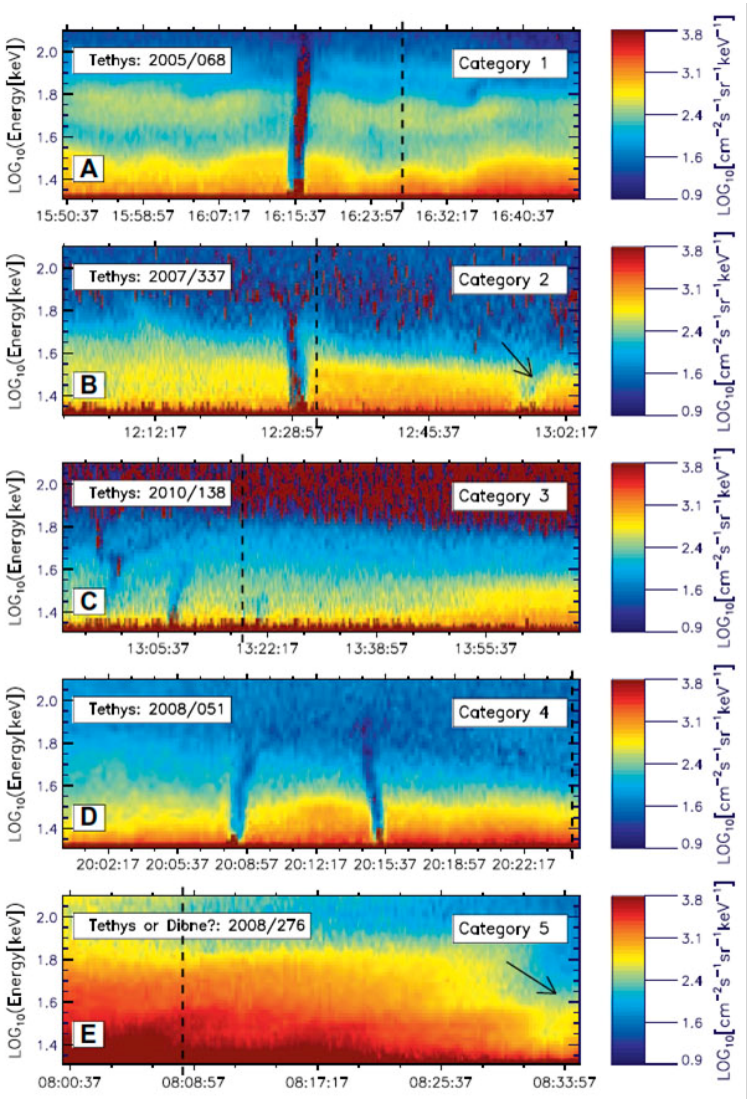

Figure MIMI-2. Microsignatures in the LEMMS data. [Andriopoulou et al. 2012]

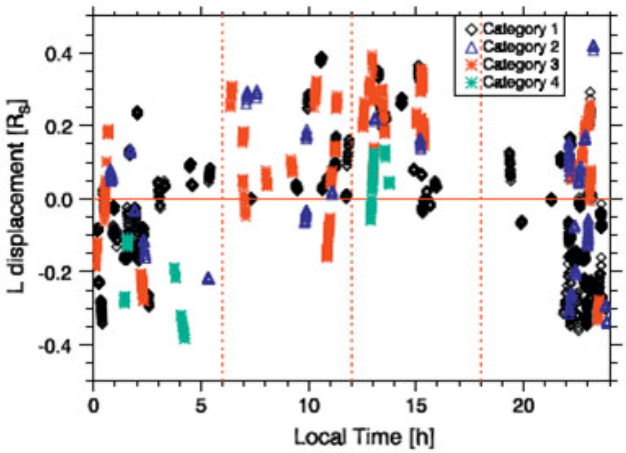

Figure MIMI-3. Microsignature displacements that led to the discovery of a global noon-to-midnight electric field at Saturn. [Andriopoulou et al. 2012]

Some other highlights included a study by Hedman et al. [2007] on the source of Saturn's G-ring and a study by Jones et al. [2006] that found evidence of lightning-induced electron beams in the formation of ring spokes at Saturn.

Open question: What would Saturn's magnetosphere look like without Enceladus?

Space Weathering, Surface Interactions, and Charging (Krupp and Paranicas)

Several optical studies related bombardment patterns by MIMI-range electrons to surface features. Schenk et al. [2011], using a color ratio from Cassini data, found a dark lens shape on the leading hemispheres of Mimas and Tethys that they related to energetic electron bombardment patterns. Howett et al. [2011], using Cassini data from the thermal infrared (IR), predicted that the bombardment of the same energetic electrons could cause regions of thermally anomalous surface ice, meaning the ice would not change temperature in sunlight in a predictable manner. Schiable et al. [2017] expanded on the possible nature of energetic electron bombardment of ice, its effects on spacing in the regolith grains and thermal conductivity.

Paranicas et al. [2014] presented the magnetospheric underpinnings of the lens feature that is observed by Schenk and Howett, following their earlier bombardment model [Paranicas et al. 2001]. Nordheim et al. [2017] expanded on Paranicas's model to include predictions for the bombardment of the leading and trailing hemispheres of Mimas and considered other species in their work.

Paranicas et al. [2018] discussed the energetic proton fluxes at the orbits of the inner moons and argued that the relatively low proton fluxes at the Saturnian moons (compared with the Jovian ones) might be the reason there is little to no amorphous ice in the Saturnian system [Clark et al. 2012]. Buratti et al. [2017] also discussed weathering issues.

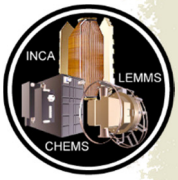

Roussos et al. [2010b] considered the question of the surface charging of Saturn's inner moons.

Open question: Is all the ice in the Saturnian system in the crystalline state and if so why does radiation play no role in causing a transformation to the amorphous state?

Titan (Regoli)

The spacecraft performed 127 flybys of Titan over the course of the whole Cassini mission. The flybys, varying in trajectory and closest approach altitude, served as gravity assists to change Cassini's trajectory, but also to bring our understanding of the moon's environment to an unprecedented level. MIMI's three separate sensors provided a large dataset of the environment surrounding Titan that has already produced important scientific results and that will certainly continue to be analyzed in the decades to come.

The INCA instrument had the capability of remotely measuring the exosphere of Titan, an ambient neutral population too tenuous to be measured by in situ mass spectrometers.

The INCA instrument had the capability of remotely measuring the exosphere of Titan, an ambient neutral population too tenuous to be measured by in situ mass spectrometers. Prior to the arrival of Cassini at Saturn, modeling of the production of ENAs began as a preparation for the first observations. Amsif et al. [1997] developed a model including the inner and outer exosphere, including the five major species contained in Titan's atmosphere, namely, H, H_2, N, N_2, and CH_4. The ENA production was modeled using a proton spectrum from the Voyager flyby. Taking into account the production from both the inner and outer exosphere (estimated using a Chamberlain model), they predicted that Cassini would be able to image the exosphere out to at least 5 Titan radii. Dandouras and Amsif [1999] analyzed the production of synthetic ENA images considering the same exospheric model from Amsif et al. [1997] but including the geometry of the interaction region and the expected ENA trajectories. They concluded that the INCA instrument would be able to provide information regarding the ion fluxes and spectra, as well as the magnetic field environment in the vicinity of Titan, based on a shadowing effect produced by the presence of the moon itself.

Using data from the INCA instrument collected during the first two close flybys of Titan by Cassini, namely TA and TB, Mitchell et al. [2005a] reported a variable halo of ENA emissions that is asymmetric around the moon, confirming the predictions made by the Dandouras and Amsif [1999] model. The overall shape of the ENA images showed a complex interaction region dominated by the variable magnetospheric environment present at the outer magnetosphere and the large gyroradii of the energetic parent ions.

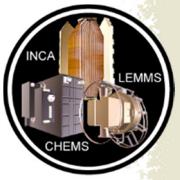

Analyzing the images returned by INCA during the TA flyby, Garnier et al. [2007] found a discrepancy between the maximum flux altitude estimated by the models and the one derived by the data. In order to account for this, they proposed an updated exospheric model, adapted to fit the data provided by the Ion Neutral and Mass Spectrometer (INMS). Using the updated model and energetic ion data obtained by LEMMS, they obtained improved ENA flux profiles that were more consistent with the INCA data.

In a follow-up paper, Garnier et al. [2008] improved the shadowing by the moon by including the corotation velocity of the parent ions. They also found that, to properly interpret INCA data, multiple ionization and neutralization processes for a single parent ion need to be considered. Apart from changing the trajectories, this leads to a thermalization of the energetic ion population.

Combining data from the INCA and the INMS instruments, Dandouras et al. [2009] calculated profiles of the main exospheric species that revealed the non-thermal nature of their distributions. They also found that the ENA emissions from the interaction region get absorbed below an altitude of about 1000 km, where energetic ions deposit their energy. In terms of the extension of the atmosphere, they were able to measure it up to an altitude of 40,000 km.

Using data from Saturn Orbit Insertion (SOI) to 2007, Brandt et al. [2012] studied the exospheric composition of Titan. For this, 36 min accumulation time hydrogen data from the INCA detector when observing Titan without the magnetosphere behind it were analyzed. Combining these observations with a model for the production of ENAs, they found that the molecular hydrogen exosphere of Titan extends to a distance of about 50,000 km—almost 20 Titan radii, confirming the lower-limit of 5 Titan radii obtained by Amsif et al. [1997]. Taking into account the profiles obtained and the fact that ENAs have direct access to Titan's atmosphere, they estimated a precipitating energy flux from ENAs of 5×10^6 keV/(cm^2s), a number comparable to previous estimates of precipitating energetic ions [Sittler et al. 2009] and solar extreme ultraviolet (EUV) [Tobiska 2004].

Apart from remote-sensing studies of the exospheric structure and the interaction region using INCA, CHEMS, and LEMMS also provided in situ data to understand the upstream conditions at Titan's orbit as well as the energy deposition by energetic ions in the atmosphere. Cravens et al. [2008] studied the energy deposition by energetic H^+ and O^+ ions using two different LEMMS spectra: one for the T5 flyby that presented especially high fluxes, and one for a more typical condition. Using a combination of INMS measurements and an engineering model by Yelle et al. [1997] of Titan's atmosphere, they calculated the ionization rates for the precipitating ions concluding that these are important for the formation of the ionospheric layers below the main ionospheric peak as well as for the creation of negative ions observed by the CAPS instrument [Coates et al. 2007].

Smith et al. [2009] focused on the T18 flyby to study the energetic proton penetration in the atmosphere. They used LEMMS to obtain the incoming flux of energetic particles and INCA to analyze the proton penetration at lower altitudes than the Cassini closest approach distance. With these data, they derived an updated atmospheric model that they successfully used to reproduce the INCA observations.

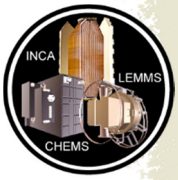

Using a combination of a test particle code and hybrid simulations, Regoli et al. [2016a] analyzed the effect that the magnetic field configuration has on the access and subsequent energy deposition of energetic ions from the Saturnian magnetosphere. Using upstream fluxes detected by CHEMS during the T9 flyby, they found that the ionization rates can vary by up to 80% from one location to another, due to finite gyroradius effects.

From the beginning of the Cassini mission, it became clear that the conditions assumed using the data collected by Voyager in the vicinity of Titan were not representative of the highly variable magnetospheric environment surrounding the moon. The fact that the moon is located at the outskirts of the magnetosphere and that the Saturnian current sheet is constantly moving up and down [Arridge et al. 2008] means that Titan can be located at completely different environments in rapid succession.

Rymer et al. [2009b] used a combination of the electron measurements taken by the Electron Spectrometer (ELS; part of CAPS) and LEMMS instruments to classify the plasma environment at Titan in four different categories, namely plasma sheet, lobe-like, magnetosheath, and bimodal, each with a distinct electron spectrum. They found that the bimodal distribution seems to arise from enhanced local pickup, introducing a cold electron population not present in the other environments. They also found that current sheet encounters were the more common ones, with magnetosheath ones being fairly rare, even though over half of the analyzed encounters occurred within two hours of noon, in terms of Saturn local time.

Using the same technique and instrumentation, Smith and Rymer [2014] extended the study up to the final data sampled by CAPS, before the instrument was switched off in 2012. For that study, they included the remaining dedicated flybys as well as all the orbit crossings when Titan was not there. With this extended dataset (77 encounters and 111 orbit crossings), they derived an empirical model for the electron distribution and also for the rate of occurrence of each environment with respect to Saturn local time.

A similar statistical analysis, but only looking at the energetic ions was made by Garnier et al. [2010] using LEMMS data for ions with energies from 27 to 255 keV and H ENA images corresponding to energies between 24 and 55 keV. They found that the ion population seems to be quasi-isotropic and a dawn-dusk asymmetry in the flux of energetic ions, with higher fluxes in the dawn sector of the magnetosphere. They also concluded that the variability observed in the ENA images from INCA are due to the variability in the magnetospheric fluxes, with the exosphere being roughly stable.

Bebesi et al. [2012] analyzed the locations of the mass-loading boundary (defined as the region where corotating plasma starts to slow down) and the electron drop-out region (where energetic electrons strongly interact with the moon’s atmosphere). They found that the location of these regions presents a scattering that they attributed to the highly variable magnetospheric environment.

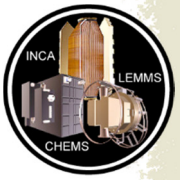

Roussos et al. [2018c] took advantage of the ability of SEPs to penetrate the magnetospheric boundaries to use LEMMS as an upstream monitor to detect solar events even when Cassini is located inside the Saturnian magnetosphere. By performing a statistical study, they identified times with enhanced energetic protons, some of them occurring during dedicated Titan flybys, opening up the possibility of studying the effect that these events have on the energy deposition of energetic particles in the moon's atmosphere.

Using LEMMS and CHEMS data, Regoli et al. [2018] analyzed the energetic environment at the orbit of Titan from a statistical perspective, also finding a highly variable environment, but with a relatively clear distinction for the times when Titan is located inside and outside the Saturnian current sheet. In addition, using Kappa distribution functions, they derived an empirical model of the energetic protons that the moon encounters while orbiting Saturn.

Open questions: How do changes in the energetic environment affect the ionization of Titan's atmosphere? How does the induced magnetosphere of Titan react to changes in the solar wind when Titan is located beyond the Saturnian bow shock?

The Final Year (Kollmann)

The last year of the Cassini mission facilitated a variety of unique measurement opportunities that were not possible throughout the entire previous mission. This began in November 2016 with the so-called F-ring or ring-grazing orbits. Cassini not only came close to the edge of the main rings, it also kept revisiting this region every week. This allowed studying the time dependence of energetic charged particles in this region. Roussos et al. [2018d] reported on a strong enhancement of >1 MeV electrons inward of 6 R_S, possibly due to acceleration in the magnetotail. The fast sequence of orbits allowed observing the time evolution of the enhancement. It is consistent with radial diffusion driven by fluctuations of the noon-to-midnight electric field. Electrons that are quasi stationary in local time (because magnetic and corotation drifts cancel out) are affected the most. Their transport and subsequent loss is much faster than for the stably trapped protons in the same region.

In April 2017, the proximal orbits began, also called the mission Grand Finale. This enabled a comprehensive study of the proton radiation belt trapped approximately between the F-ring and A-ring. MIMI also found a previously unknown partial, electron belt within the F-ring (called "microbelt")—partial because it is only observed outbound at local noon. This microbelt is variable in intensity, although permanently present and stable in local time and L-shell. These results are compiled in Buratti et al. [2019] and Roussos et al. [2019a]. As part of the latter study, it was also shown that a small flux of particles observed on field lines above Saturn's main rings, are actually secondary MeV electrons that were produced by galactic cosmic ray (GCR) impacts on ring material, less than 1 sec before their observation. A clear radial profile of the rings, including the signature of the Cassini division, was visible on the MeV electron rates from LEMMS. This signal has been observed in the past by Pioneer 11 measurements, but it was unclear if those secondary electrons were from GCR impacts on the atmosphere or the rings.

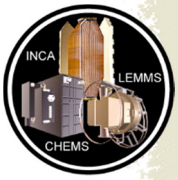

The LEMMS instrument discovered a previously unknown radiation belt collocated with the D-ring and extending up to the dense atmosphere of Saturn. This belt was predicted earlier [Kollmann et al. 2015] but its properties were unknown. It was found that the belt is dominated by protons up to the GeV range, which is the first time that such high energies were directly observed at any of the giant planets. The suggested source is CRAND because protons are unable to diffuse past Saturn's dense A–C rings. There is no evidence for the presence of energetic electrons or ions heavier than protons. These results are compiled in Roussos et al. [2018d]. A follow-up study by Kollmann et al. [2018a] studied the pitch angle distribution and explained its steepness with a strong interaction with Saturn's atmosphere and D-ring. Particle fluxes inward of the main rings can therefore be diagnostic of properties of the D-ring and high-altitude exosphere that are difficult to constrain by other Cassini instruments or remote observations. During SOI, Cassini remotely detected protons at tens of kiloelectron volt (keV) from low (atmospheric) altitudes [Krimigis et al. 2005]. The proximal orbits revealed that this was a huge coincidence since similar observations were only found once during the proximal orbits [Krupp et al. 2018b], suggesting this ion population is transient. Since the ions derive from ENAs produced in the magnetosphere, their intensity likely depends on the conditions in the magnetosphere. Because these ions were not observed in situ, they must be located at altitudes below 3,800 km.

The most surprising measurement during the proximal orbits was likely that the MIMI/INCA and CHEMS instruments, which were designed to measure energetic particles, were detecting signatures of D-ring dust falling into Saturn's equatorial atmosphere. These particles are of 1–3 nm size, much smaller than what is detected by the Cosmic Dust Analyzer (CDA) instrument designed to measure dust. The dust is reaching the atmosphere within 4 h and provides a continuous influx of about 5 kg/s from the rings into the atmosphere. These results are compiled in Mitchell et al. [2018].

Open questions: How can we explain the fluxes of the MeV particles, both inward and outward of the rings and how does the radiation belt co-existing with the F-ring form? What is the source rate of CRAND neutrons?

Grand Finale Orbits (Paranicas, Kollmann)

Other research articles that significantly included MIMI data from the Grand Finale orbits are described next. Mitchell et al. [2018] participated in a series of articles about D-ring dust falling into the planet. They looked at signatures of this process in two of the MIMI sensors and found evidence for grain sizes that cannot be measured by the dedicated dust instrument CDA on Cassini. The spiraling dust may be an explanation for Saturn's hydrogen plume [Shemansky et al. 2009]. Roussos et al. [2018b] described heliospheric conditions inferred from MIMI data obtained at Saturn. Buratti et al. [2019] showed the relationship between trapped charged particles and the locations of small bodies close to the planet.

MIMI Non-Saturn Results

Cruise Observations (Carbary)

Ion conics were observed in proximity to a shock structure in the solar wind between the orbits of Jupiter and Saturn. These conics appear in energetic protons (~30–350 keV) detected by INCA during its approach to Saturn on October 8, 2003 (d 281) and again on October 20, 2003 (d 293).

Both conics have a distinct ring structure centered approximately on the magnetic field, but the first one was peaked along the field at ~35° pitch angles while the second peaked near ~145° anti-parallel to the field. Figure MIMI-4 shows these rings at several energies. The conics lasted for about an hour and display a time and energy dependence. Such events are seen rarely during the Cassini transit between Jupiter and Saturn, even when the spacecraft pointing was favorable near a shock. The conic structures can be explained as a consequence of back-scattering from a nearby shock in the solar wind [Decker et al. 1988]. These results were described by Hill et al. [2006].

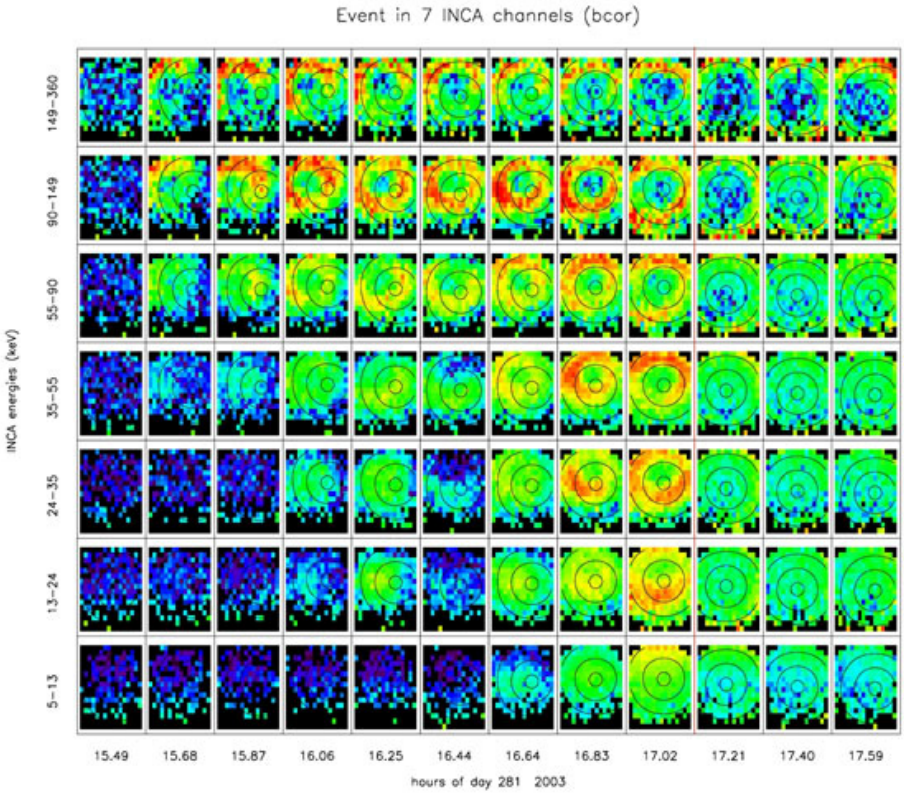

Figure MIMI-4. Sequence of INCA ion images at the highest time resolution available for the ion conic event. With pitch angles contours shown at increments of 10°, 30°, 50°, the images are arranged with time on the horizontal axis and INCA energy on the vertical. Images have been corrected for background and the solar wind flow. The vertical red line between 17.02 h and 17.21 h marks the time of the forward shock. The intensity scales in all cases are logarithmic, although they have different low- and high-energy limits.

Planetary Flybys (Carbary)

The Cassini spacecraft obtained gravity-assists at Earth (August 1999) and Jupiter (December 2000–January 2001). During the Earth flyby, MIMI operated for the first time in a planetary magnetosphere. INCA observed Earth's ring current from long range, CHEMS detected H^+ and O^+ from the outer ring current, and LEMMS reported complete energy spectra of ions and electrons during the pass, including bow shock and magnetopause crossings [Krimigis et al. 2004; Lagg et al. 2001; Ogasawara et al. 2011]. During the Jupiter flyby, INCA observed large fluxes of energetic neutral atoms, primarily H and O, from the planet [Mitchell et al. 2004]. INCA discovered an ENA torus associated with and located just outside the orbit of Europa [Mauk et al. 2003]. The neutral densities in this torus were comparable to those found in the Io-associated cloud, and suggested that Europa is a strong source of neutrals. Figure MIMI-5 shows the discovery ENA image of the Europa torus.

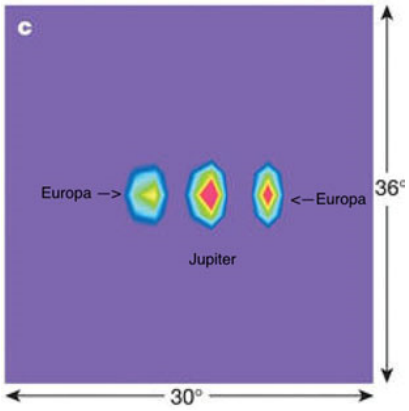

Figure MIMI-5. ENA image of the Europa torus. Seen from the side during the Cassini flyby of Jupiter in early 2001, the Europa torus appears on either side of Jupiter. The image was deconvolved for point sources and corrected for background. The intensity scale is linear.

Jupiter Cassini-Galileo Comparisons (Krupp)

During the Jupiter flyby of Cassini at the end of 2000/beginning of 2001, the Galileo spacecraft was still orbiting the gas giant. The LEMMS sensor was flown on both missions with nearly the same capabilities and identical energy channel configurations. This offered the opportunity to study the duskside Jovian magnetosphere from two different locations simultaneously. The comparison of both energetic particle measurements is summarized in Krupp et al. [2002, 2004].

Figure MIMI-6 shows the differential fluxes and the pitch angle distributions of ions and electrons measured with LEMMS onboard Galileo and Cassini in the vicinity of the Jovian magnetopause. The main results are:

- Passage of closed to open planetary field lines with distributions from bidirectional to monodirectional, with respect to the magnetic field near the magnetopause;
- Periodic variations of electron fluxes on both spacecraft with 40 min periods near Cassini and about 60 min at Galileo's location;

- Leakage of magnetospheric particles into the interplanetary space; and
- Sporadic electron beams outside the magnetosphere (Cassini at 300–900 R_J and Galileo at 130 R_J).

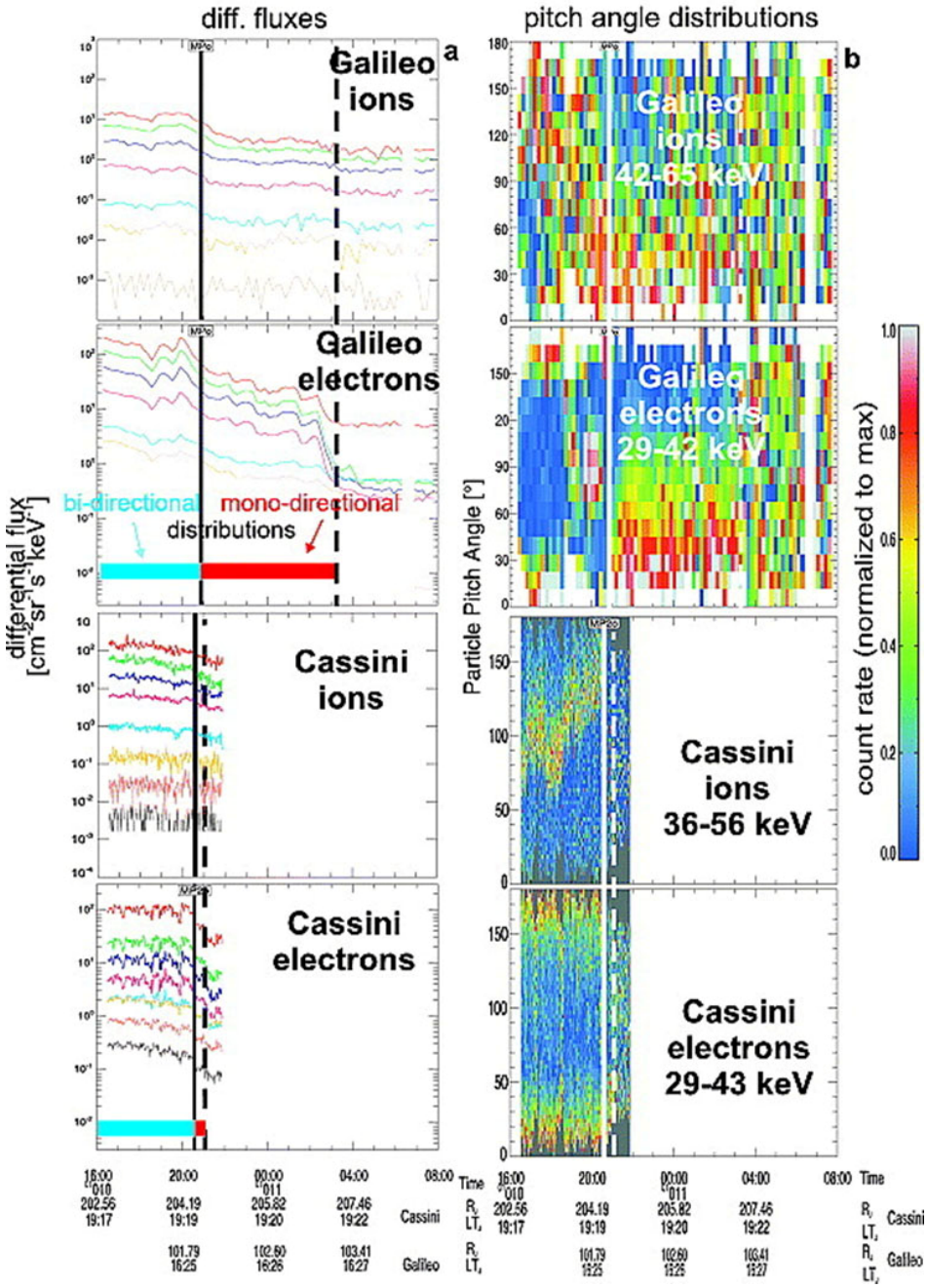

Figure MIMI-6. Differential fluxes and pitch angle distributions of ions and electrons. These ions and electrons are measured with the LEMMS sensors onboard Galileo and Cassini [Krupp et al. 2002] in the vicinity of the magnetopause of Jupiter.

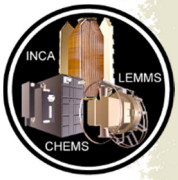

Hanlon et al. [2004] also studied dual spacecraft observations near Jupiter. Cassini data were used as upstream monitors while Galileo was deep inside the Jovian magnetosphere.

Interplanetary Suprathermal and Energetic Particles (Hill)

During the cruise to Saturn, the MIMI suite was able to make unique measurements of heliospheric suprathermal particles in the 2–60 keV/nuc range. There has never been an investigation with species separation of this important class of particles, which ties the solar wind plasma to the energetic particles, beyond Jupiter. Hill et al. [2009] made CHEMS measurements that revealed that the radial intensity profiles of He^{+} and He^{++} are very different from both analytical and numerical theory, with the observations showing an increasing intensity with distance from the Sun, while the theory predicts the intensity should fall. This observation remains unexplained.

CHEMS measurements of pickup ions were used to determine solar wind speeds, which enabled a study [Hill and Hamilton 2010] of the spectral index of suprathermal particles. The slopes of the spectra were reported and widely put into and used to create context by the community, but Hill and Hamilton [2010] showed that the expected velocity v dependence was approximately v-5 as reported by Fisk and Gloeckler [2008]. This study was followed up by Kollmann et al. [2019]. They compared Cassini and New Horizons measurements of interplanetary suprathermal ions. This revealed that there is no obvious dependence of the average spectral shape with distance to the Sun but that that the variability at Cassini's location was much larger. They also suggested a mechanism through which the suprathermal ions are accelerated. The data are consistent with acceleration happening largely in corotating interaction regions. Particles leaving these regions and flowing along magnetic field lines are cooled, so that their spectral shape is changing with distance to the emission region.

The solar wind speeds that were derived with CHEMS data are of inherent value for investigating the heliosphere and, near Saturn, as an input to magnetospheric studies. Data from 2001 to 2004, inclusive, at a 12-hour cadence, were published on the Cassini project's MAPSview website in 2014 (mapskp.cesr.fr/index.php).

The energetic particle population was studied by Lario et al. [2004] using LEMMS observations. They found that intensity enhancements up to ~1 MeV were due to the passage of interplanetary shocks while at the highest energy (>25 MeV), the prompt component of solar energetic particle events was responsible. For all but the largest SEP events, the presence of magnetic field structures between the Sun and the spacecraft significantly modulates the intensity enhancements.

Furthermore, the extension of LEMMS's capabilities to monitor galactic cosmic rays, was used to disprove a theory and Earth-based observations that Jupiter contributes up to 5% of the 80 MeV-2.5 GeV proton flux in the heliosphere [Roussos et al. 2019b].

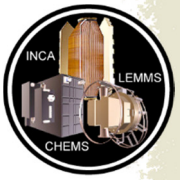

The Heliosphere Imaged with INCA (Dialynas)

The Sun's atmosphere is not static, but expands in the form of a magnetized fluid called the solar wind [Parker 1958], reaching to distances of potentially hundreds of astronomical units (1 AU = 1.5 × 108 km), shaping our local bubble, called the heliosphere, through its interaction with the Local Interstellar Medium (LISM). Voyager 1 and Voyager 2 (hereafter, V1 and V2) crossed the termination shock, where the supersonic solar wind presumably terminates at the shock front, at respective distances of ~94 and ~84 AU in 2004 and 2007 at +35° and −26° ecliptic latitudes [Decker et al. 2005, 2008], pinpointing both the—previously unanticipated—size of the local heliosphere and the scale of the heliospheric asymmetry.

After the discovery of the reservoir of ions and electrons that constitute the heliosheath (a region past the termination shock), V1 passed through an unexpected depletion region, where a decrease in ions of solar origin (by a factor of ~103) and a simultaneous increase of high-energy cosmic rays (~9.3%) occurred, that forms part of the interface between the solar plasma and the galaxy, namely the heliopause [Krimigis et al. 2013], at a distance of ~122 AU. Since August 2012, V1 has continued its journey to the galaxy, measuring the distant and unexplored LISM (V1 is currently located at a distance of ~19 AU past the heliopause), while V2 is still surveying the heliosheath (expected to cross the heliopause in the next few years). Due to the powerful synergy between in situ ions from V1/Low Energy Charged Particle (LECP) instrument and ENAs from INCA (in overlapping energy bands), MIMI, beginning in about 2009, has made key discoveries that altered our past notions on the formation and interactions of the heliosphere, leading to a number of surprises concerning the physics that governs this enormous system, and providing insights on the plasma processes at ~100 AU that were substantially at variance with previous theories and models.

In 2009, the MIMI team published one of the most historic papers, of worldwide appeal, in the field of Heliosphere Physics in Science [Krimigis et al. 2009b]. They showed, for the first time, images of the global heliosphere using >5.2 keV ENA measurements obtained with INCA over the 2003–2009 time period, and identified two striking, previously unexpected, heliospheric signatures: (a) the Belt, a broad band of emission in the sky, identified as a high intensity, relatively wide ENA region that wraps around the celestial sphere in ecliptic coordinates, passing through the nose the anti-nose (tail) and the North and South Heliosphere poles; and (b) the Basins, identified as two extended heliosphere lobes where the ENA minima occur. Interestingly, the ENA measurements are moderately well organized in galactic coordinates, with the Belt presenting a prominent tilt of ~30° with respect to the galactic equator, whereas the Basins were found to roughly coincide with the galactic North and South Poles, although their boundaries were also tilted ~30° to the galactic equator. The same *Science* issue hosted yet another significant publication (with contribution from the then-MIMI PI, S. M. Krimigis), from the Interstellar Boundary Explorer team [McComas et al. 2009], showing, for the first time, images of the heliosphere in <6 keV ENAs. A narrow bright ENA stripe known as the ribbon forms an incomplete circle around the heliospheric nose, most prominent at ~1.1 keV, surrounded by a broad ENA emission that became known as Globally Distributed Flux (GDF).

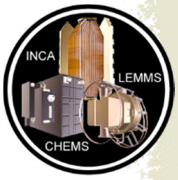

In a later publication, Dialynas et al. [2013a] found that the deviation of the ENA emissions from the equator is effectively minimized in a rotated frame—interpreted as interstellar magnetic field frame (ISMF)—where its North Pole points toward 190° ecliptic longitude and 15° ecliptic latitude. The ENA spectra showed a power-law form in energy, presenting higher spectral slopes in the belt region and lower outside ($3.4 < \gamma < 4.4$), which are almost indistinguishable between the tail and the nose regions, i.e., no noticeable asymmetry was observed. Notably, the morphology of the belt (peak, width, and structure) is nearly energy independent of energy from 5.2 keV to 30 keV. The authors speculated that Interstellar Boundary Explorer (IBEX)-GDF evolves with increasing ENA energy to form the belt at high GDF energies, explaining that the GDF and the ribbon are distinct features that originate from different source plasma populations (heliosheath and outside the heliopause, respectively). This was recently confirmed by the IBEX team [McComas et al. 2017].

Taking into account the local partial pressure over the $\sim 5 < E < 4000$ keV energy range from V1, V2, and INCA (~0.1 pPa), an assumed thickness of the heliosheath (~50 AU) and the simulated PUI (pick-up ion) distribution [Giacalone and Decker 2010] that was used to estimate the $E < 6$ keV contribution (~0.12 pPa), Krimigis et al. [2010] concluded that there is a need for a substantially stronger magnetic field upstream of the heliopause than assumed before, in order to balance the non-thermal PUI pressure against the stagnation pressure of the interstellar plasma and the local ISMF at the heliospheric nose. The interstellar magnetic field was estimated to be ~0.5 nT and have an upper bound of ~0.64 nT. This calculation was confirmed a few years later after V1 crossed the heliopause and measured a strong interstellar magnetic field of ~0.5 nT [Burlaga et al. 2013] that exhibited a jump right outside the heliopause of ~0.6 nT. V1 is currently located at ~19 AU past the heliopause and still measures a magnetic field of ~0.5 nT [Burlaga and Ness 2016], and a relatively dense plasma of $>0.09/cm^3$ that reached densities of $\sim 0.12/cm^3$ [Gurnett et al. 2013, 2015].

A different study, Dialynas et al. [2015] analyzed separately INCA images of the heliosphere and found that the very low (basin) and high (tail) ENA emissions in the heliosheath are separated with a relatively smooth boundary (called transition region), with a spatial width of ~30° in ecliptic longitude, which no theory had predicted to date. The ENA intensity gradient in this transition region was found to be almost invariant as a function of both ecliptic latitude and energy, with an average value of ~2.4% per degree and translates to a corresponding partial pressure gradient that occurs in the transition region, enabling a discussion on the Parker field towards the tail. Bearing in mind that the plasma-β inside the heliosheath showed large fluctuations about an average of ~5–10, i.e., much larger than unity [Decker et al. 2015], this pressure gradient is possibly not consistent with a tail magnetic field configuration that is similar to the measured magnetic fields by the Voyagers in the nose hemisphere. Notably, the pick-up ion populations in the keV range play a dominant role in maintaining the pressure balance in the heliosheath.

In the pre-INCA imaging era, the size of the heliosphere had been estimated using several different models, where the heliosheath varied between 70 and 160 AU. By combining Voyager in situ ion measurements and remotely sensed INCA ENAs in overlapping energy bands, Krimigis et al. [2009b, 2010], calculated that the heliosheath thickness should be ~54 (+30, −15) AU. A more

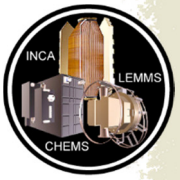

detailed analysis performed by the MIMI team also included the possible contributions from the Compton-Getting effect due to the radial velocity of the heliosheath plasma and concluded that the heliosheath appears to be twice as thick along the V2 line of sight (LOS) as it is along the LOS to V1: L_{V1} = 31 (+31, −18) AU and L_{V2} = 71 (+30, −15) AU [Roelof et al. 2012]. A breakthrough occurred in 2011 when the MIMI and Voyager teams published a brief report [Krimigis et al. 2011] showing that the radial component of the bulk plasma velocity had been decreasing almost linearly for three years, from 70 km/s to 0 km/s, and then stabilized around this value for ~8 months. This study concluded that the ENA and ion spectra could be brought into agreement at V2 with a heliosheath thickness of L_{V2} ~54 (+30, −15) AU, whereas the same normalization procedure applied to Voyager 1 results in L_{V1} ~27 (+26, −11) AU. Surprisingly, the V1 crossing from the heliopause occurred ~1 month later than anticipated by Krimigis et al. [2011] in August 2012 [Krimigis et al. 2013], showing that the heliosheath thickness towards the nose (at V1 direction) is ~29 AU, i.e., much smaller and more compressed than expected in past models.

Admittedly, one of the milestones in the heliosphere research concerns the shape of this enormous system, because it strongly relates to the interpretation of several phenomena that were either theorized in the literature and/or resulted from measurements performed by modern detectors. For more than five decades, the shape and interactions of the heliosphere with the local interstellar medium have been discussed in the context of either a magnetosphere-like heliotail or a more symmetric bubble shape, posited in 1961 [Parker 1961]. Although past models broadly assumed the magnetosphere-like concept, the accurate heliospheric configuration remained largely undetermined due to lack of measurements.

Building upon previous analyses made by Krimigis et al. [2009b] and Dialynas et al. [2013a], and employing both Voyager in situ and INCA remote measurements, a recent MIMI publication, Dialynas et al. [2017a] used >5.2 keV ENA measurements obtained with MIMI/INCA over the 2003–2014 time period and provided a new paradigm on the heliosphere interaction with the LISM: the belt corresponds to a reservoir of particles that exist within the heliosheath, constantly replenished by new particles from the solar wind, while the ENAs that INCA detects are most likely associated with a region of enhanced particle pressure that is formed inside the heliopause and contributes to balancing the pressure of the ISMF. The authors showed that the heliosheath ions are the source of >5.2 keV ENA and that the heliosphere responds promptly, within ~2–3 years, to outward propagating solar wind changes (controlled by solar sunspot numbers and solar wind energy input) in both the upstream (nose) and downstream (tail) directions. These observations, taken together with the V1 measurement of a ~0.5 nT interstellar magnetic field, plasma density of >0.09/cm^3 and the enhanced ratio between particle pressure and magnetic pressure in the heliosheath, strongly suggest a diamagnetic bubble-like heliosphere with few substantial tail-like features. A follow-up MIMI publication [Dialynas et al. 2017b] discussed the details of these results, and by calculating the recovery times of ENAs in the heliosphere, they found that the rough width of the heliosheath can be ~80–120 AU (or more) towards the tail, due to the ~2–3 year delay after solar minimum (Figure MIMI-7).

Dialynas et al. [2017a] also included two important implications concerning the heliosphere interaction with the LISM: 1) A perfectly symmetric and stable heliosphere in time would not be

possible and/or physically correct, i.e., as the heliosphere cannot be a closed system, the heliosphere bubble can (and must) inflate with time in either the anti-nose direction (tail models) or along the direction of the interstellar magnetic field (note that the polar jets [Opher et al. 2015; Drake et al. 2015], provide one of the possible mechanisms through which the solar wind input is evacuated from the system); and 2) due to the strong interstellar magnetic field, the Mach number of the local interstellar medium can be significantly decreased and the flow can become submagnetosonic, leading to the inability of forming a bow shock, as previously explained by Fahr et al. [1986] and simulated from Kivelson and Jia [2013] using the mini magnetosphere of Ganymede as a rough analogy to the heliosphere.

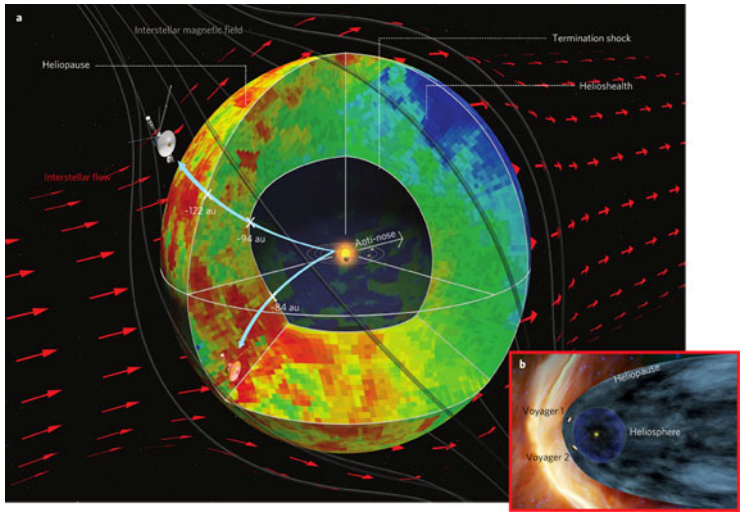

Figure MIMI-7. A conceptual model of the global heliosphere. Adapted from Dialynas et al. [2017b] showing: (a) The gross shape and basic properties of the global heliosphere in three dimensions, summarizing our current understanding, based on both remote ENA and in situ ion measurements from Cassini/INCA and LECP/V1&V2, respectively. It shows a belt of varying ENA intensities surrounding the termination shock and extending to the outer boundary of the heliosphere, called the heliopause, as identified by V1; it is anticipated that the heliopause south of the ecliptic will be crossed by V2 within the next few years. The red arrows represent the interstellar plasma flow deflected around the heliosphere bubble. The termination shock and heliopause are marked at the distances (in AU) observed by the Voyagers from 2004 through 2012 in their traversal of the heliosheath. The cutout illustrates the possible distribution of hot ion plasma in the heliosheath discerned by line-of-sight (LOS) ENA images (E > 5.2 keV); relative scale ranging from 1 (blue) to 12 (red). As the ENA emissions detected by INCA are LOS integrated, the third dimension in this composite, conceptual representation of the global heliosheath (presenting the possible ENA distribution confined between the termination shock and the heliopause) is based on the knowledge of the variation of ion intensities measured at the Voyagers towards the nose hemisphere. These ion intensities are representative of the average ENA intensities along any LOS inside the heliosheath. Note that this concept of the heliosphere does not imply a closed system that cannot change its shape towards the tail to release the solar wind energy input. Inside the termination shock the ion intensities are lower by at least ×100. The orbits of the outer planets are drawn to scale around the Sun. Concept (a) is compared with (b), a magnetosphere-like configuration (http://voyager.jpl.nasa.gov/mission/) widely adopted as one of two possibilities put forward by Parker [1961]. The termination shock is ~10 AU further out in the V1 direction, but the heliosheath (HS) is possibly ~30–50% thicker towards the V2 direction (as detailed in the text), inconsistent with a compressed heliosheath in the Southern Hemisphere. That will be determined when V2 crosses the heliopause (HP), expected in the next few years.

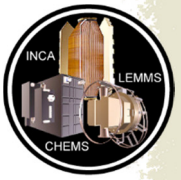

ACRONYMS

Note: For a complete list of Acronyms, refer to Cassini Acronyms – Attachment A.

AU	astronomical unit
CAPS	Cassini Plasma Spectrometer
CDA	cosmic dust analyzer
CHEMS	Charge-Energy-Mass Spectrometer
CRAND	cosmic ray albedo neutron decay
CSM	Cassini Solstice Mission
ELS	Electron Spectrometer
ENA	energetic neutral atom
ESA	electrostatic analyzer
EUV	extreme ultraviolet
e/Q	energy per charge
GCR	galactic cosmic ray
GDF	Globally Distributed Flux
gEV	giga electron volt
HP	heliopause
HS	heliosheath
HST	Hubble Space Telescope
IBEX	Interstellar Boundary Explorer
INCA	Ion and Neutral Camera
INMS	Ion Neutral and Mass Spectrometer
IR	infrared
ISMF	interstellar magnetic field frame
keV	kiloelectron volt
LECP	Low Energy Charged Particle
LEMMS	Low-Energy Magnetospheric Measurement System
LISM	Local Interstellar Medium
LOS	line of sight
MAG	Magnetometer
meV	megaelectron volt
MIMI	Magnetosphere Imaging Instrument
PI	Principal Investigator
PUI	pick-up ion
QP	quasi-periodic
R_J	Jupiter radius
R_S	Saturn radius
RPWS	Radio and Plasma Wave Science
SEP	solar energetic particle

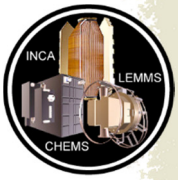

SKR	Saturn Kilometric Radiation
SOI	Saturn Orbit Insertion
SSD	solid-state detector
TM	Traceability Matrix
TOF	time of flight
UV	ultraviolet

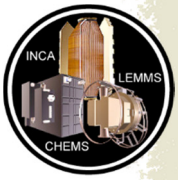

REFERENCES

Disclaimer: The list of references below correspond with in-text references indicated in this report and other articles that rely heavily on MIMI data. For all other Cassini references, refer to Attachment B – References & Bibliographies; Attachment C – Cassini Science Bibliographies; the sections entitled References contributed by individual Cassini instrument and discipline teams located in Volume 1 Sections 3.1 and 3.2 Science Results; and other resources outside of the Cassini Final Mission Report.

Achilleos N., C. S. Arridge, C. Bertucci, P. Guio, N. Romanelli, N. Sergis, (2014), A combined model of pressure variations in Titan's plasma environment, Geophysical Research Letters, 41(24):8730–8735.

Achilleos, N., P. Guio, C. S. Arridge, N. Sergis, R. J. Wilson, M. F. Thomsen, A. J. Coates, (2010), Influence of hot plasma pressure on the global structure of Saturn's magnetodisk, Geophysical Research Letters, 37(L20201).

Allen, R. C., et al. (2018), Internal versus external sources of plasma at Saturn: Overview from MIMI/CHEMS data, Journal of Geophysical Research: Space Physics, 123:4712–4727, doi: 10.1029/2018JA025262.

Amsif, A., J. Dandouras, E. C. Roelof, (1997), Modeling the production and imaging of energetic neutral atoms from Titan's exosphere, Journal of Geophysical Research, 102(22):169–22,181.

André, N., et al., (2008), Identification of Saturn's magnetospheric regions and associated plasma processes: Synopsis of Cassini observations during orbit insertion, Reviews of Geophysics, 46, doi: 10.1029/2007RG000238.

André, N., et al., (2007), Magnetic signatures of plasma-depleted flux tubes in the Saturnian inner magnetosphere, Geophysical Research Letters, 34(L14108).

André, N., et al., (2005), Dynamics of the Saturnian inner magnetosphere: First inferences in the Cassini magnetometers about small-scale plasma transport in the magnetosphere, Geophysical Research Letters, 32(L14SO6).

Andriopoulou, M., E. Roussos, N. Krupp, C. Paranicas, M. Thomsen, S. Krimigis, M. K. Dougherty, K. H. Glassmeier, (2014), Spatial and temporal dependence of the convective electric field in Saturn's inner magnetosphere, Icarus, 229:57–70.

Andriopoulou, M., E. Roussos, N. Krupp, C. Paranicas, M. Thomsen, S. Krimigis, M. K. Dougherty, K. H. Glassmeier, (2012), A noon-to-midnight electric field and nightside dynamics in Saturn's inner magnetosphere, using microsignature observations, Icarus, 220:503–513.

Armstrong, T. P., et al., (2009), Energetic ions trapped in Saturn's inner magnetosphere, Planetary and Space Science, 57(14–15):1723–1731, doi: 10.1016/j.pss.2009.03.008.

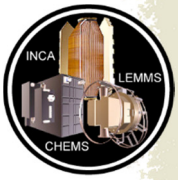

Arridge, C. S., et al., (2016a), Cassini observations of Saturn's southern polar cusp, Journal of Geophysical Research: Space Physics, 121:3006.

Arridge, C. S., et al., (2016b), Cassini in situ observations of long-duration magnetic reconnection in Saturn's magnetotail, Nature Physics, 12:268–271.

Arridge, C. S., M. Kane, N. Sergis, K. K. Khurana, C. M. Jackman, (2015), Sources of local time asymmetries in magnetodiscs, Space Science Reviews, 187:301.

Arridge, C. S., et al., (2011a), Mapping magnetospheric equatorial regions at Saturn from Cassini prime mission observations, Space Science Reviews, 164:1–83.

Arridge, C. S., et al., (2011b), Upstream of Saturn and Titan, Space Science Reviews, 162:25–83.

Arridge, C. S. et al., (2008), Warping of Saturn's magnetospheric and magnetotail current sheets, Journal of Geophysical Research, 113(A8).

Badman, S. V., et al., (2016), Saturn's auroral morphology and field-aligned currents during a solar wind compression, Icarus, 263:83–93.

Badman, S. V., G. Branduardi-Raymont, M. Galand, S. L. G. Hess, N. Krupp, L. Lamy, H. Melin, C. Tao, (2015), Auroral processes at the giant planets: Energy deposition, emission mechanisms, morphology, and spectra, Space Science Reviews, 187(1–4):99–179, doi: 10.1007/s11214-014-0042-x.

Badman, S. V., et al., (2013), Bursty magnetic reconnection at Saturn's magnetopause, Geophysical Research Letters, 40:1027.

Badman, S. V., et al., (2012), Cassini observations of ion and electron beams at Saturn and their relationship to infrared auroral arcs, Journal of Geophysical Research, 117(A01211).

Bebesi, Z., et al., (2012), Analysis of energetic electron drop-outs in the upper atmosphere of Titan during flybys in the dayside magnetosphere of Saturn, Icarus, 218:1020–1027.

Bebesi, Z., et al., (2010), Slow mode shock candidate in the Jovian magnetosheath, Planetary and Space Science, 58:807–813.

Bell, J. M., J. Hunter Waite Jr., J. H. Westlake, S. W. Bougher, A. J. Ridley, R. Perryman, K. Mandt, (2014), Developing a self-consistent description of Titan's upper atmosphere without hydrodynamic escape, Journal of Geophysical Research Space Physics, 119:4957.

Bertucci, C., D. C. Hamilton, W. S. Kurth, G. Hospodarsky, D. G. Mitchell, M. K. Dougherty, (2015), Titan's interaction with the supersonic solar wind, Geophysical Research Letters, 42:193–200.

Beth, A., P. Garnier, D. Toublanc, C. Mazelle, A. Kotova, (2014), Modeling the satellite particle populations in planetary exospheres: Application to Earth, Titan, and Mars, Icarus, 227:21–36.

Blanc, M., D. J. Andrews, A. J. Coates, D. C. Hamilton, C. M. Jackman, X. Jia, A. Kotova, M. Morooka, H. T. Smith, J. H. Westlake, (2015), Saturn plasma sources and associated

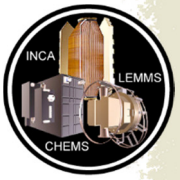

transport processes, Space Science Reviews, 192(1–4):237–283, doi: 10.1007/s11214-015-01792-9.

Blanc, M., et al., (2002), Magnetospheric and plasma science with Cassini-Huygens, Space Science Reviews, 104(1).

Brandt, P. C., K. Dialynas, I. Dandouras, D. G. Mitchell, P. Garnier, S. M. Krimigis, (2012), The distribution of Titan's high altitude (out to ~50,000 km) exosphere from energetic neutral atom (ENA) measurements by Cassini/INCA, Planetary and Space Science, 60:107–114.

Brandt, P. C., et al., (2010), Saturn's periodic magnetic field perturbations caused by a rotating partial ring current, Geophysical Research Letters, 37(L22103), doi: 10.1029/2010GL045285.

Brandt, P. C., C. P. Paranicas, J. F. Carbary, D. G. Mitchell, B. H. Mauk, S. M. Krimigis, (2008), Understanding the global evolution of Saturn's ring current, Geophysical Research Letters, 35(L17101), doi: 10.1029/2008GL034969.

Bunce, E. J., S. W. H. Cowley, D. M. Wright, A. J. Coates, M. K. Dougherty, N. Krupp, W. S. Kurth, A. M. Rymer, (2005), In situ observations of a solar wind compression-induced hot plasma injection in Saturn's tail, Geophysical Research Letters, 32(L20S04), doi: 10.1029/2005GL022888.

Buratti, B. J., et al., (2019), Close Cassini flybys of Saturn's ring moons Pan, Daphnis, Atlas, Pandora, and Epimetheus, Science, 364(6445):eaat2349, doi: 10.1126/science.aat2349.

Buratti, B. J., R. N. Clark, F. Crary, C. J. Hansen, A. R. Hendrix, C. J. A. Howett, J. Lunine, C. Paranicas, (2017), Cold cases: What we don't know about Saturn's moons, Planetary and Space Science, 155:41–49, doi: 10.1016/j.pss.2017.11.017.

Burlaga, L. F., N. F. Ness, (2016), Observations of the interstellar magnetic field in the outer heliosheath: Voyager 1, The Astrophysical Journal, 829:134.

Burlaga, L. F., N. F. Ness, E. C. Stone, (2013), Magnetic field observations as Voyager 1 entered the heliosheath depletion region, Science, 341:147–150.

Carbary, J. F., (2019a), Magnetodisk coordinates for Saturn, Journal of Geophysical Research: Space Physics, 124:451–458.

Carbary, J. F., (2019b), Three dimensional currents in Saturn's magnetosphere, Journal of Geophysical Research: Space Physics, 124:971–981.

Carbary, J. F., D. C. Hamilton, D. G. Mitchell, (2019), Global maps of energetic ions in Saturn's magnetosphere, Journal of Geophysical Research: Space Physics, 123:8557–8571.

Carbary, J. F., (2018), The meridional magnetic field lines of Saturn, Journal of Geophysical Research: Space Physics, 123:6264–6276.

Carbary, J. F., et al., (2018), Energetic electron pitch angle distributions during the Cassini final orbits, Geophysical Research Letters, 45:2911–2917.

Carbary, J. F., (2017), Update on Saturn's energetic electron periodicities, Journal of Geophysical Research: Space Physics, 122:156–165, doi: 10.1002/2016JA023405.

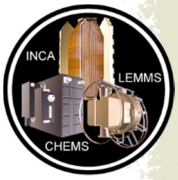

Carbary, J. F., D. G. Mitchell, P. Kollmann, N. Krupp, E. Roussos, (2017a), Energetic electron periodicities during the Cassini grand finale, Journal of Geophysical Research: Space Physics, 122, doi: 10.1002/2017JA024836.

Carbary, J. F., D. G. Mitchell, A. M. Rymer, N. Krupp, D. Hamilton, S. M. Krimigis, S. V. Badman, (2017b), Local time asymmetries in Saturn's magnetosphere, in Dawn-Dusk Asymmetries in Planetary Plasma Environments, (eds.) S. Haaland, A. Runov, C. Forsythm, Geophysical Monograph 230, pp. 323–336.

Carbary, J. F., G. Provan, (2017), Saturn's magnetic field periodicities at high latitudes and the effects of spacecraft motion and position, Journal of Geophysical Research: Space Physics, 122, doi: 10.1002/2016JA023611.

Carbary, J. F., D. G. Mitchell, (2017), Midnight flash model of ENA periodicities at Saturn, Journal of Geophysical Research: Space Physics, 122(7), doi: 10.1002/2017JA024296.

Carbary, J. F., A. M. Rymer, (2017), Solar wind periodicities in thermal electrons at Saturn, Journal of Geophysical Research: Space Physics, 122, doi: 10.1002/2016JA023531.

Carbary, J. F., W. S. Kurth, D. G. Mitchell, (2016), Short periodicities in low-frequency plasma waves at Saturn, Journal of Geophysical Research: Space Physics, 121:6562–6572.

Carbary, J. F., D. G. Mitchell, (2016), Seasonal variations in Saturn's plasma sheet warping, Geophysical Research Letters, 43:11,957–11,962, doi: 10.1002/2016GL071790.

Carbary, J. F., (2016), A new spiral model of Saturn's magnetosphere, Geophysical Research Letters, 43:501–507.

Carbary, J. F., (2015a), A new approach to Saturn's periodicities, Journal of Geophysical Research: Space Physics, 120:6436–6442.

Carbary, J. F., (2015b), Doppler effects on periodicities in Saturn's magnetosphere, Journal of Geophysical Research: Space Physics, 120:9457–9470.

Carbary, J. F., N. Sergis, D. G. Mitchell, N. Krupp, (2015), Saturn's hinge parameter from Cassini magnetotail passes in 2013–2014, Journal of Geophysical Research: Space Physics, 120:4438.

Carbary, J. F., M. Kane, B. H. Mauk, S. M. Krimigis, (2014a), Using the kappa function to investigate hot plasmas in the magnetospheres of the giant planets, Journal of Geophysical Research, 119, doi: 10.1002/2014JA020324.

Carbary, J. F., D. G. Mitchell, P. C. Brandt, (2014b), Local time dependences of oxygen ENA periodicities at Saturn, Journal of Geophysical Research, 119, 2014JA020214.

Carbary, J. F., D. G. Mitchell, (2014), Keogram analysis of ENA images at Saturn, Journal of Geophysical Research, 119, doi: 10.1002/2014JA019784.

Carbary, J. F., A. M. Rymer, (2014), Meridional maps of Saturn's thermal electrons, Journal of Geophysical Research: Space Physics, 119, doi: 10.1002/2013JA019436.

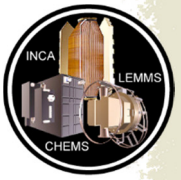

Carbary, J. F., (2013), Wavy magnetodisk in Saturn's outer magnetosphere, Geophysical Research Letters, 40:5024.

Carbary, J. F., D. G. Mitchell, (2013), Periodicities in Saturn's magnetosphere, Reviews of Geophysics, 51:1–30.

Carbary, J. F., E. C. Roelof, D. G. Mitchell, D. C. Hamilton, (2013a), Solar periodicity in energetic ions at Saturn, Journal of Geophysical Research, 118, doi: 10.1002/jgra.50282.

Carbary, J. F., et al., (2013b), Longitude dependences of Saturn's ultraviolet aurora, Geophysical Research Letters, 40, doi: 10.1002/grl.50430.

Carbary, J. F., (2012), The morphology of Saturn's ultraviolet aurora, Journal of Geophysical Research, 117(A06210).

Carbary, J. F., N. Achilleos, C. S. Arridge, (2012a), Statistical ring current of Saturn, Journal of Geophysical Research, 117(A06223).

Carbary, J. F., D. G. Mitchell, S. M. Krimigis, N. Krupp, (2012b), Unusually short period in electrons at Saturn, Geophysical Research Letters, 39(L22103).

Carbary, J. F., D. G. Mitchell, S. M. Krimigis, N. Krupp, (2011a), Post-equinox periodicities in Saturn's energetic electrons, Geophysical Research Letters, 28(L24104), 2011GL050259.

Carbary, J. F., et al., (2011b), Energetic electron spectra in Saturn's plasma sheet, Journal of Geophysical Research, 116(A07210).

Carbary, J. F., D. G. Mitchell, P. C. Brandt, S. M. Krimigis, D. A. Gurnett, (2011c), ENA periodicities and their phase relations to SKR emissions at Saturn, Geophysical Research Letters, 38(L16106).

Carbary, J. F., D. G. Mitchell, C. P. Paranicas, E. C. Roelof, S. M. Krimigis, N. Krupp, K. Khurana, M. Dougherty, (2011d), Pitch angle distributions of energetic electrons at Saturn, Journal of Geophysical Research, 116(A01216), doi: 10.1029/2010JA015987.

Carbary, J. F., D. C. Hamilton, S. P. Christon, D. G. Mitchell, S. M. Krimigis, (2010a), Longitude dependencies of energetic H+ and O+ at Saturn, Journal of Geophysical Research, 115(A07226), doi: 10.1029/2009JA015133.

Carbary, J. F., N. Achilleos, C. S. Arridge, K. K. Khurana, M. K. Dougherty, (2010b), Global configuration of Saturn's magnetic field derived from observations, Geophysical Research Letters, 37(L21806), doi: 10.1029/2010GL044622.

Carbary, J. F., D. G. Mitchell, S. M. Krimigis, D. A. Gurnett, W. S. Kurth, (2010c), Phase relations between energetic neutral atom intensities and kilometric radio emissions at Saturn, Journal of Geophysical Research, 115(A01203).

Carbary, J. F., D. G. Mitchell, N. Krupp, S. M. Krimigis, (2009a), L shell distribution of energetic electrons at Saturn, Journal of Geophysical Research, 114(A09210), doi: 10.1029/2009JA014341.

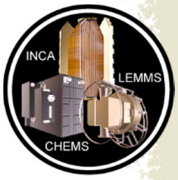

Carbary, J. F., D. G. Mitchell, S. M. Krimigis, N. Krupp, (2009b), Dual periodicities in energetic electrons at Saturn, Geophysical Research Letters, 36(L20103), doi: 10.1029/2009GL040517.

Carbary, J. F., E. C. Roelof, D. G. Mitchell, S. M. Krimigis, N. Krupp, (2009c), Solar wind periodicity in energetic electrons at Saturn, Geophysical Research Letters, 36(L22104), doi: 10.1029/2009GL041086.

Carbary, J. F., S. M. Krimigis, D. G. Mitchell, C. Paranicas, P. Brandt, (2009d), Energetic neutral atom (ENA) and charged particle periodicities in Saturn's magnetosphere, Advances in Space Research, 44:483–493, doi: 10.1016/j.asr.2009.04.019.

Carbary, J. F., D. G. Mitchell, C. Paranicas, E. C. Roelof, S. M. Krimigis, (2008a), Direct observation of warping in the plasma sheet of Saturn, Geophysical Research Letters, 35(L24201), doi: 10.1029/2008GL035970.

Carbary, J. F., D. G. Mitchell, P. Brandt, E. C. Reolof, S. M. Krimigis, (2008b), Track analysis of energetic neutral atom blobs at Saturn, Journal of Geophysical Research, 113(A01209), doi: 10.1029/2007JA012708.

Carbary, J. F., D. G. Mitchell, P. Brandt, C. Paranicas, S. M. Krimigis, (2008c), ENA periodicities at Saturn, Geophysical Research Letters, 35(L07102), doi: 10.1029/2008GL033230.

Carbary, J. F., D. G. Mitchell, P. Brandt, E. C. Roelof, S. M. Krimigis, (2008d), Periodic tilting of Saturn's plasma sheet, Geophysical Research Letters, 35(L24101), doi: 10.1029/2008GL036339.

Carbary, J. F., D. G. Mitchell, P. Brandt, E. C. Reolof, S. M. Krimigis, (2008e), Statistical morphology of ENA emissions at Saturn, Journal of Geophysical Research, 113(A05210), doi: 10.1029/2007JA012873.

Carbary, J. F., D. G. Mitchell, S. M. Krimigis, D. C. Hamilton, N. Krupp, (2007a), Charged particle periodicities in Saturn's outer magnetosphere, Journal of Geophysical Research, 112, 2007JA012351.

Carbary, J. F., D. G. Mitchell, S. M. Krimigis, D. C. Hamilton, N. Krupp, (2007b), Spin-period effects in magnetospheres with no axial tilt, Geophysical Research Letters, 34(L18107), doi: 10.1029/2007GL030483.

Carbary, J. F., D. G. Mitchell, S. M. Krimigis, N. Krupp, (2007c), Evidence for spiral pattern in Saturn's magnetosphere using the new SKR longitudes, Geophysical Research Letters, 34(L13105), doi: 10.1029/2007GL030167.

Carbary, J. F., D. G. Mitchell, S. M. Krimigis, N. Krupp, (2007d), Electron periodicities in Saturn's outer magnetosphere, Journal of Geophysical Research, 112, doi: 10.1029/2006JA012077.

Carbary, J. F., S. M. Krimigis, (1982), Charged particle periodicity in the Saturnian magnetosphere, Geophysical Research Letters, 9:1073–1076.

Carrasco N., J. H. Westlake, P. Pernot, J. H. Waite, Jr., (2013), Nitrogen in Titan's atmospheric aerosol factory, in The Early Evolution of the Atmospheres of Terrestrial Planets, Springer.

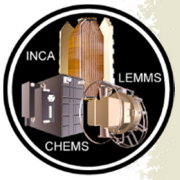

Chen, Y., T. W. Hill, A. M. Rymer, R. J. Wilson, (2010), Rate of radial transport of plasma in Saturn's inner magnetosphere, Journal of Geophysical Research, 115(A10211), doi: 10.1029/2010JA015412.

Christon S. P., D. C. Hamilton, J. M. C. Plane, D. G. Mitchell, J. M. Grebowsky, W. N. Spjeldvik, S. R. Nylund, (2017), Discovery of suprathermal ionospheric origin Fe+ in and near Earth's magnetosphere, Journal of Geophysical Research: Space Physics, 122, doi: 10.1002/2017JA024414.

Christon, S. P., D. C. Hamilton, D. G. Mitchell, R. B. DiFabio, S. M. Krimigis, J. M. C. Plane, (2015), Discovery of suprathermal Fe+ in Saturn's magnetosphere, Journal of Geophysical Research, 120:2720.

Christon, S. P., D. C. Hamilton, D. G. Mitchell, R. B. DiFabio, S. M. Krimigis, (2014), Suprathermal magnetospheric minor ions heavier than water at Saturn: Discovery of 28M+ seasonal variations, Journal of Geophysical Research, 119, 2014JA020010.

Christon, S. P., D. C. Hamilton, R. D. DiFabio, D. G. Mitchell, S. M. Krimigis, D. S. Jontof-Hutter, (2013), Saturn suprathermal O2+ and mass-28+ molecular ions: Long-term seasonal and solar variation, Journal of Geophysical Research, 118, doi: 10.1002/jgra.50383.

Christensen, U., N. Krupp (2009), Die Geschwister der Erde, Physik Journal, 8(5):31–36.

Clark, G., C. Paranicas, D. Santos-Costa, S. Livi, N. Krupp, D. G. Mitchell, E. Roussos, W. L. Tseng, (2014), Evolution of electron pitch angle distributions across Saturn's middle magnetospheric region from MIMI/LEMMS, Planetary and Space Science, 104:18–28, doi: 10.1016/pss.2014.07.004.

Clark, R. N., et al., (2012), The surface composition of Iapetus: Mapping results from Cassini VIMS, Icarus, 218:831–860.

Coates, A. J., et al. (2007), Discovery of heavy negative ions in Titan's ionosphere, Geophysical Research Letters, 34(L22103).

Cooper, J. F., P. D. Cooper, E. C. Sittler, S. J. Sturner, A. M. Rymer, (2009), Old faithful model for radiolytic gas-driven cryovolcanism at Enceladus, Planetary and Space Science, 57:1607–1620.

Crary, F., et al., (2005), Solar wind dynamic pressure and electric field as the main factors controlling Saturn's aurorae, Nature, 433:720–722.

Cravens, T. E., N. Ozak, M. S. Richard, M. E. Campbell, I. P. Robertson, M. Perry, A. M. Rymer, (2011), Electron energetics in the Enceladus torus, Journal of Geophysical Research, 116(A09205).

Cravens, T. E., et al., (2008), Energetic ion precipitation at Titan, Geophysical Research Letters, 35(L03103), doi: 10.1029/2007GL032451.

Dandouras, I., P. Garnier, D. G. Mitchell, E. C. Roelof, P. C. Brandt, N. Krupp, S. M. Krimigis, (2009), Titan's exosphere and its interaction with Saturn's magnetosphere, Philosophical Transactions of the Royal Society, 367, doi: 10.1098/rsta.2008.0249.

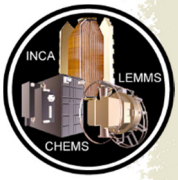

Dandouras, J., A. Amsif, (1999), Production and imaging of energetic neutral atoms from Titan's exosphere: A 3-D model, Planetary and Space Science, 47:1355–1369.

Decker, R. B., S. M. Krimigis, E. C. Roelof, M. E. Hill, (2015), Recent particle measurements from Voyagers 1 and 2, Journal of Physics: Conference Series, 577.

Decker, R. B., S. M. Krimigis, E. C. Roelof, M. E. Hill, T. P. Armstrong, G. Gloeckler, D. C. Hamilton, L. J. Lanzerotti, (2008), Mediation of the solar wind termination shock by non-thermal ions, Nature, 454:67–70.

Decker, R. B., S. M. Krimigis, E. C. Roelof, M. E. Hill, T. P. Armstrong, G. Gloeckler, D. C. Hamilton, L. J. Lanzerotti, (2005), Voyager 1 in the foreshock, termination shock, and heliosheath, Science, 309:2020–2024.

Decker, R. B., (1988), Computer modeling of test particle acceleration at oblique shocks, Space Science Reviews, 48:195–262.

Delamere, P. A., et al., (2015), Solar wind and internally driven dynamics: Influences on magnetodiscs and auroral responses, Space Science Reviews, 187(1–4):51–97, doi: 10.1007/s11213-013-0075-1.

Dessler, A. J., (1985), Differential rotation of the magnetic fields of gaseous planets, Geophysical Research Letters, 12:299–302.

Dialynas, K., et al., (2018), Energetic ion moments and polytropic index in Saturn's magnetosphere using Cassini/MIMI measurements: A simple model based on k-distribution functions, Journal of Geophysical Research: Space Physics, 123, doi: 10.1029/2018JA025820.

Dialynas, K., et al., (2017a), The bubble-like shape of the heliosphere observed by Voyager and Cassini, Nature Astronomy, 1:115.

Dialynas, K., S. M. Krimigis, D. G. Mitchell, R. B. Decker, E. C. Roelof, (2017b), Response times of Cassini/INCA > 5.2 keV ENAs and Voyager ions in the heliosheath over the solar cycle, Journal of Physics: Conference Series, 900(1).

Dialynas, K., C. P. Paranicas, J. F. Carbary, M. Kane, S. M. Krimigis, B. H. Mauk, (2017c), The kappa-shaped particle spectra in planetary magnetospheres, in, Kappa Distributions, Theory and Applications in Plasmas, (ed.) G. Livadiotis, Elsevier, pp. 481–522.

Dialynas, K., S. M. Krimigis, D. G. Mitchell, E. C. Roelof, (2015), Energetic neutral atom (ENA) intensity gradients in the heliotail during year 2003, using Cassini/INCA measurements, Journal of Physics: Conference Series, 577, doi: 10.1088/1742-6596/577/1/012007.

Dialynas, K., S. M. Krimigis, D. G. Mitchell, E. C. Roelof, R. B. Decker, (2013a), A three-coordinate system (Ecliptic, Galactic, ISMF) spectral analysis of heliospheric ENA emissions using Cassini/INCA measurements, The Astrophysics Journal, 778:40.

Dialynas, K., et al., (2013b), The extended Saturnian neutral cloud as revealed by global ENA simulations using Cassini/MIMI measurements, Journal of Geophysical Research, 118:1–15, doi: 10.1002/jgra.50295.

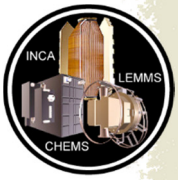

Dialynas, K. S., S. M. Krimigis, D. G. Mitchell, D. C. Hamilton, N. Krupp, P. C. Brandt, (2009), Energetic ion spectral characteristics in the Saturnian magnetosphere using Cassini/MIMI measurements, Journal of Geophysical Research, 114(A01212), doi: 10.1029/2008JA013761.

DiFabio, R. D., D. C. Hamilton, S. M. Krimigis, D. G. Mitchell, (2011), Long term time variations of the suprathermal ions in Saturn's magnetosphere, Geophysical Research Letters, 38(L18103).

Dougherty, M. K., L. W. Esposito, S. M. Krimigis, (2009), Overview, in Saturn from Cassini-Huygens, (eds.) M. K. Dougherty, L. W. Esposito, S. M. Krimigis, Springer, Dordrecht, pp. 1–8.

Drake, J. F., M. Swisdak, M. Opher, (2015), A model of the heliosphere with jets, The Astrophysical Journal Letters, 808, doi: 10.1088/2041-8205/808/2/L44.

Edberg, N. J. T., et al., (2013), Extreme densities in Titan's ionosphere during the T85 magnetosheath encounter, Geophysical Research Letters, 40:1–5, doi: 10.1002/grl.50579.

Fahr, H. J., (1986), Is the heliospheric interface submagnetosonic? Consequences for the LISM presence in the heliosphere, Advances in Space Research, 6:13–25.

Felici, M., et al., (2016), Cassini observations of ionospheric plasma in Saturn's magnetotail lobes, Journal of Geophysical Research: Space Physics, 121:338.

Fisk, L. A., G. Gloeckler, (2008), Acceleration of suprathermal tails in the solar wind, The Astrophysical Journal, 686:1466.

Frisch, P. C., et al., (2010), First global observations of the interstellar interaction from the Interstellar Boundary Explorer (IBEX), Bulletin of the American Astronomical Society, 42:263.

Futaana, Y., J. Chaufray, H. T. Smith, P. Garnier, H. Lichtenegger, M. Delva, H. Groeller, A. Mura, (2011), Exospheres and energetic neutral atoms of Mars, Venus, and Titan, Space Science Reviews, 162:213–266.

Garnier, P., et al., (2012), The detection of energetic electrons with the Cassini Langmuir probe at Saturn, Journal of Geophysical Research, 117(A10202).

Garnier, P., et al., (2010), Statistical analysis of the energetic ion and ENA data for the Titan environment, Planetary and Space Science, 58:1811–1822.

Garnier, P., et al., (2009), Titan's ionosphere in the magnetosheath: Cassini RPWS results during the T32 flyby, Annales Geophysicae, 27:4257–4272.

Garnier, P., et al., (2008), The lower exosphere of Titan: Energetic neutral atom absorption and imaging, Journal of Geophysical Research, 113(A10216), doi: 10.1029/2008JA013029.

Garnier, P., et al., (2007), The exosphere of Titan and its interaction with the kronian magnetosphere: MIMI observations and modeling, Planetary and Space Science, 55:165–173.

Gérard, J. -C., et al., (2006), Saturn's auroral morphology and activity during quiet magnetospheric conditions, Journal of Geophysical Research, 111(A12210), doi: 10.1029/2006JA011965.

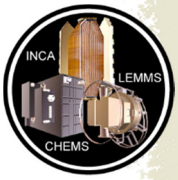

Giacalone, J., R. B. Decker, (2010), The origin of low-energy anomalous cosmic rays at the solar-wind termination shock, The Astrophysical Journal, 710:91–96.

Gombosi, T. I., T. P. Armstrong, C. S. Arridge, K. K. Khurana, S. M. Krimigis, N. Krupp, A. M. Persoon, M. F. Thomsen, (2009), Saturn's magnetospheric configuration, in Saturn from Cassini-Huygens, (eds.) M. K. Dougherty, L. W. Esposito, S. M. Krimigis, Springer, Dordrecht, pp. 203–255.

Gurnett, D. A., W. S. Kurth, E. C. Stone, A. C. Cummings, S. M. Krimigis, R. B. Decker, N. F. Ness, L. F. Burlaga, (2015), Precursors to interstellar shocks of solar origin, The Astrophysical Journal, 809:121.

Gurnett, D. A., W. S. Kurth, L. F. Burlaga, N. F. Ness, (2013), In situ observations of interstellar plasma with Voyager 1, Science, 341:1489–1492.

Gurnett, D. A., et al., (2010), A plasmapause-like density boundary at high latitudes in Saturn's magnetosphere, Geophysical Research Letters, 37(L16806), doi: 10.1029/2010GL044466.

Gurnett, D. A., A. Lecacheux, W. S. Kurth, A. M. Persoon, J. B. Groene, L., Lamy, P. Zarka, J. F. Carbary, (2009), Discovery of a north-south asymmetry in Saturn's radio rotation period, Geophysical Research Letters, 36(L16102), doi: 10.1029/2009GL039621.

Hanlon, P. G., (2004), Dual spacecraft observations of a compression event within the Jovian magnetosphere: Signatures of externally triggered supercorotation, Journal of Geophysical Research, 109(A09S09).

Hedman, M. M., et al., (2007), The source for Saturn's G ring, Science, 317:653–656.

Helled, R., E. Galanti, Y. Kaspi, (2015), Saturn's fast spin determined from its gravitational field and oblateness, Nature, 520:202–204, doi: 10.1038/nature14278.

Hendrix, A. R., G. Filacchione, C. Paranicas, P. Schenk, F. Scipioni, (2018), Icy Saturnian satellites: Disk-integrated UV-IR characteristics and links to exogenic processes, Icarus, 300:103–114.

Hendrix, A. R., et al., (2012), Mimas' far-UV albedo: Spatial variations, Icarus, 220:922–931.

Hill, M. E., D. C. Hamilton, (2010), Interim report on the power law index of interplanetary suprathermal ion spectra, American Institute of Physics Conference Proceedings, 1302:58–63.

Hill, M. E., N. A. Schwadron, D. C. Hamilton, R. D. DiFabio, R. K. Squier, (2009), Interplanetary suprathermal He+ and He++ observations during periods from 1 to 9 AU and implications for particle acceleration, The Astrophysical Journal, 699:L26–L30.

Hill, M. E., C. P. Paranicas, R. B. Decker, D. G. Mitchell, (2006), "Smoke ring" pitch angle distributions of energetic particles associated with shock passage in the middle heliosphere, American Geophysical Union Spring Meeting, Baltimore, MD, May 25, 2006, abstract SH44A-04.

Hill, T., (2016), Penetration of external plasma into a rotation-driven magnetosphere, Journal of Geophysical Research Space Physics, 121:10,032–10,036.

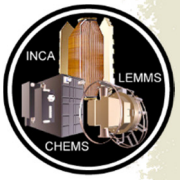

Hill, T. W., et al., (2011), Charged nanograins in the Enceladus plume, Journal of Geophysical Research, 117(A05209).

Hill, T. W., et al., (2008), Plasmoids in Saturn's magnetotail, Journal of Geophysical Research, 113(A01214), doi: 10.1029/2007JA12626.

Howett, C. J. A., A. R. Hendrix, T. A. Nordheim, C. Paranicas, J. R. Spencer, A. J. Verbiscer, (2018), Ring and magnetosphere interactions with satellite surfaces, Enceladus and the icy moons of Saturn, 2(4):343.

Howett, C. J. A., J. R. Spencer, P. Schenk, R. E. Johnson, C. Paranicas, T. A. Hurford, A. Verbiscer, M. Segura, (2011), A high-amplitude thermal inertia anomaly of probable magnetospheric origin on Saturn's moon Mimas, Icarus, 216:221–226.

Jackman, C. M., et al., (2015), Field dipolarization in Saturn's magnetotail with planetward ion flows and energetic particle flow bursts: Evidence of quasi-steady reconnections, Journal of Geophysical Research: Space Physics, 120:3603–3617.

Jackman, C. M., J. A. Slavin, S. W. H. Cowley, (2011), Cassini observations of plasmoid structure and dynamics: Implications for the role of magnetic reconnection in magnetospheric circulation at Saturn, Journal of Geophysical Research, 116(A10212).

Jackman, C. M., et al., (2008), A multi-instrument view of tail reconnection at Saturn, Journal of Geophysical Research, 113(A11), 2008JA013592.

Jasinski, J. M., C. S. Arridge, A. J. Coates, G. H. Jones, N. Sergis, M. F. Thomsen, N. Krupp, (2017), Diamagnetic depression observations at Saturn's magnetospheric cusp by the Cassini spacecraft, Journal of Geophysical Research: Space Physics, 122:6283–6303.

Jasinski, J. M., et al., (2016a), Flux transfer event observation at Saturn's dayside magnetopause by the Cassini spacecraft, Geophysical Research Letters, 43:6713.

Jasinski, J. M., et al., (2016b), Cassini plasma observations of Saturn's magnetospheric cusp, Journal of Geophysical Research: Space Physics, 121.

Jasinski, J. M., et al., (2014), Cusp observation at Saturn's high-latitude magnetosphere by the Cassini spacecraft, Geophysical Research Letters, 41:1382–1388.

Jinks, S. L., et al., (2014), Cassini multi-instrument assessment of Saturn's polar cap boundary, Journal of Geophysical Research, 119:8161–8177.

Johnson, R. E., et al., (2009), Mass loss processes in Titan's upper atmosphere, in Titan from Cassini-Huygens, (eds.) R. H. Brown, J. -P. Lebreton, J. H. White, Springer, Dordrecht, pp. 373–391.

Johnson, R. E., et al., (2008), Sputtering of ice grains and icy satellites in Saturn's inner magnetosphere, Planetary and Space Science, 56, doi: 10.1016/j.pss.2008.04.003.

Jones, G. H., et al., (2008), The dust halo of Saturn's largest icy moon, Rhea, Science, 319:1380–1384.

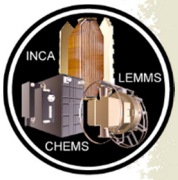

Jones, G. H., et al., (2006a), Enceladus's varying imprint on the magnetosphere of Saturn, Science, 311:1412–1415.

Jones, G. H., et al., (2006b), Formation of Saturn's ring spokes by lightning-induced electron beams, Geophysical Research Letters, 33(L21202), doi: 10.1029/2006GL028146.

Kanani, S. J., et al., (2010), A new form of Saturn's magnetopause using a dynamic pressure balance model, based on in-situ, multi-instrument Cassini measurements, Journal of Geophysical Research, 115(A06207), doi: 10.1029/2009JA014262.

Kane, M., D. G. Mitchell, J. F. Carbary, S. M. Krimigis (2014), Plasma convection in the nightside magnetosphere of Saturn determined from energetic ion anisotropies, Planetary and Space Science, 91(1).

Kane, M., D. G. Mitchell, J. F. Carbary, S. M. Krimigis, F. J. Crary, (2008), Plasma convection in Saturn's outer magnetosphere determined from ions detected by the Cassini INCA experiment, Geophysical Research Letters, 35(L04102), doi: 10.1029/2007GL032342.

Kellett, S., et al., (2011), Saturn's ring current: Local time dependence and temporal variability, Journal of Geophysical Research, 116(A05220).

Kellett, S., et al., (2010), Nature of the ring current in Saturn's dayside magnetosphere, Journal of Geophysical Research, 115(A08201), doi: 10.1029/2009JA015146.

Khurana, K. K., S. Fatemi, J. Lindkvist, E. Roussos, N. Krupp, M. Holmström, C. T. Russell, M. K. Dougherty, (2017), The role of plasma slowdown in the generation of Rhea's Alfvén wings, Journal of Geophysical Research: Space Physics, 122, doi: 10.1002/2016JA023595.

Khurana, K. K., et al., (2009), Sources of rotational signals in Saturn's magnetosphere, Journal of Geophysical Research, 114(A02211), doi: 10.1029/2008JA013312.

Kivelson, M. G., X. J. Jia, (2013), An MHD model of Ganymede's mini-magnetosphere suggests that the heliosphere forms in a sub-Alfvénic flow, Journal of Geophysical Research: Space Physics, 118(11):6839–6846.

Kliore, A. J., A. F. Nagy, T. E. Cravens, M. S. Richard, A. M. Rymer, (2011), Unusual electron density profiles observed by Cassini radio occultations in Titan's ionosphere: Effects of enhanced magnetospheric electron precipitation, Journal of Geophysical Research, 116(A11318).

Kollmann, P., et al., (2019), Suprathermal ions in the outer heliosphere, The Astrophysical Journal, 876:46(10pp), doi: 10.3847/1538-4357/ab125f.

Kollmann, P., et al., (2018a), Saturn's innermost radiation belt throughout and inward of the D ring, Geophysical Research Letters, 45:10,912–10,920, doi: 10.1029/2018GL077954.

Kollmann, P., et al., (2018b), Electron acceleration to MeV energies at Jupiter and Saturn, Journal of Geophysical Research: Space Physics, 123:9110–9129, doi: 10.1029/2018JA025665.

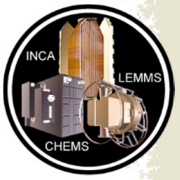

Kollmann, P., E. Roussos, A. Kotova, C. Paranicas, N. Krupp, (2017), The evolution of Saturn's radiation belts modulated by changes in radial diffusion, Nature Astronomy, doi: 10.1038/s41550-017-0287-x.

Kollmann, P., E. Roussos, A. Kotova, J. F. Cooper, D. G. Mitchell, N. Krupp, C. Paranicas, (2015), MeV protons flux predictions near Saturn's D ring, Journal of Geophysical Research Space Physics, 120:8586–8602.

Kollmann, P., E. Roussos, C. Paranicas, N. Krupp, D. K. Haggerty, (2013), Processes forming and sustaining Saturn's proton radiation belts, Icarus, 222:323–341.

Kollmann, P., E. Roussos, C. Paranicas, N. Krupp, C. M. Jackman, E. Kirsch, K. -H. Glassmeier, (2011), Energetic particle phase space densities at Saturn: Cassini observations and interpretations, Journal of Geophysical Research, 116(A05222), doi: 10.1029/2010JA016221.

Kotova, A., E. Roussos, N. Krupp, I. Dandouras, (2015), Modeling of the energetic ion observations in the vicinity of Rhea and Dione, Icarus, 258:402.

Krimigis, S. M., R. B. Decker, E. C. Roelof, M. E. Hill, T. P. Armstrong, G. Gloeckler, D. C. Hamilton, L. J. Lanzerotti, (2013), Search for the exit: Voyager 1 at heliosphere's border with the galaxy, Science, 341(6142):144–147.

Krimigis, S. M., (2011), Saturn's magnetosphere: An example of dynamic planetary systems, American Institute of Physics Conference Proceedings, 1320:213–220, doi: 10.1063/1.3544327.

Krimigis, S. M., E. C. Roelof, R. B. Decker, M. E. Hill, (2011), Zero outward flow velocity for plasma in a heliosheath transition layer, Nature, 474:359–361.

Krimigis, S. M., D. G. Mitchell, E. C. Roelof, R. B. Decker (2010), ENA (E > 5 keV) images from Cassini and Voyager "ground truth": Suprathermal pressure in the heliosheath, American Institute of Physics Conference Proceedings, 1302:79–85, doi: 10.1063/1.3529994.

Krimigis, S. M., et al., (2009a), Analysis of a sequence of energetic ion and magnetic field events upstream from the Saturnian magnetosphere, Planetary and Space Science, 57(14–15):1785–1794, doi: 10.1016/j.pss.2009.02.013.

Krimigis, S. M., D. G. Mitchell, E. C. Roelof, K. C. Hsieh, D. J. McComas, (2009b), Imaging the interaction of the heliosphere with the interstellar medium from Saturn with Cassini, Science, 326:971–973.

Krimigis, S. M., N. Sergis, D. G. Mitchell, N. Krupp, (2007), A dynamic, rotating ring current around Saturn, Nature, 450:1050–1053.

Krimigis, S. M., et al., (2005), Dynamics of Saturn's magnetosphere from MIMI during Cassini's orbital insertion, Science, 307:1270–1273.

Krimigis, S. M., et al., (2004), Magnetosphere imaging instrument (MIMI) on the Cassini mission to Saturn/Titan, Space Science Reviews, 114:233–329.

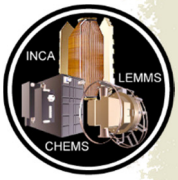

Krimigis, S. M., et al., (2002), A nebula of gases from Io surrounding Jupiter, Nature, 415:994–996.

Krupp, N., et al., (2018a), Energetic electron measurements near Enceladus by Cassini during 2005-2015, Icarus, 306:256–274.

Krupp, N., et al., (2018b), Energetic neutral and charged particle measurements in the inner Saturnian magnetosphere during the Grand Finale orbits of Cassini 2016/2017, Geophysical Research Letters, 45:10,847–10,854, doi: 10.1029/2018GL078096.

Krupp, N., (2016), 12-Energetic-particle environments in the solar system, in Heliophysics: Active stars, their astrospheres, and impacts on planetary environments, (eds.) C. J. Schrijver, F. Bagenal, J. J. Sojka, Cambridge University Press.

Krupp, N., P. Kollmann, M. F. Thomsen, D. G. Mitchell, X. Jia, A. Masters, P. Zarka, (2016a), Global configuration and seasonal variations of Saturn's magnetosphere, in Saturn in the 21st Century, (eds.) K. H. Baines, F. M. Flasar, N. Krupp, Cambridge University Press.

Krupp, N., E. Roussos, C. Paranicas, A. Sicard, G. Hospodarsky, Y. Shprits, (2016b), Energetic particles and waves in the outer planet radiation belts, in Waves, Particles, and Storms in Geospace: A complex Interplay, pp. 373–410.

Krupp, N., (2015), Comparison of plasma sources in solar system magnetospheres, Space Science Reviews, 192:285–295.

Krupp, N., E. Kronberg, A. Radioti, (2015), Jupiter's magnetotail, in Magnetotails in the Solar System, (eds.) A. Keiling, C. M. Jackman, P. A. Delamere, Geophysical Monograph Series, 207, American Geophysical Union, John Wiley & Sons, pp. 85–98.

Krupp, N., (2014), Giant magnetospheres in our solar system: Jupiter and Saturn compared, The Astronomy and Astrophysics Review, 22:75, s00159-014-0075-x.

Krupp, N., et al., (2013), Energetic particle measurements in the vicinity of Dione during the three Cassini encounters 2005-2011, Icarus, 226:617.

Krupp, N., et al., (2012), The Cassini Enceladus encounters 2005-2010 in the view of energetic electron measurements, Icarus, 18:433–447.

Krupp, N., et al., (2010), Environments in the outer solar system, Space Science Reviews, 153:11–59.

Krupp, N., et al., (2009), Energetic particles in Saturn's magnetosphere during the Cassini nominal mission (July 2004 -- July 2008), Planetary and Space Science, 57(14–15):1754–1768, doi10.1016/j.pss.2009.06.010.

Krupp, N., et al., (2005), The Saturnian plasma sheet as revealed by energetic particle measurements, Geophysical Research Letters, 32, 2005GL022829.

Krupp, N., (2005), Energetic particles in the magnetosphere of Saturn and a comparison with Jupiter, Space Science Reviews, 116:345–369.

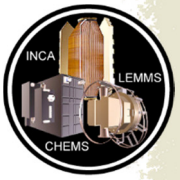

Krupp, N., et al., (2004), Energetic particle observations in the vicinity of Jupiter: Cassini MIMI/LEMMS results, Journal of Geophysical Research, 109, doi: 10.1029/2003JA010111.

Krupp, N., et al., (2002), Leakage of energetic particles from Jupiter's dusk magnetosphere: Dual spacecraft observations, Geophysical Research Letters, 29, doi: 10.1029/2001GL014290.

Kurth, W. S., et al., (2009), Auroral processes, in Saturn from Cassini-Huygens, (eds.) M. K. Dougherty, L. W. Esposito, S. M. Krimigis, Springer, Dordrecht, pp. 333–374.

Lagg, A., N. Krupp, S. Livi, J. Woch, S. Krimigis, M. Dougherty, (2001), Energetic particle measurements during the Earth swing-by of the Cassini spacecraft in August, 1999, Journal of Geophysical Research, 106:30,209–30,222.

Lamy, L., et al., (2013), Multispectral simultaneous diagnosis of Saturn's aurorae throughout a planetary rotation, Journal of Geophysical Research: Space Physics, 118:4817.

Lario, D., S. Livi, E. C. Roelof, R. B. Decker, S. M. Krimigis, M. K. Dougherty, (2004), Heliospheric energetic particle observations by the Cassini spacecraft: Correlation with 1 AU observations, Journal of Geophysical Research, 109(A09S02).

Lebreton, J. P., et al., (2004), High ambitions for an outstanding planetary mission: Cassini-Huygens, European Space Agency Bulletin, 120.

Lewis, G. R., et al., (2010), The calibration of the Cassini-Huygens electron spectometer, Planetary and Space Science, 58:427–436.

Martens, H. R., D. B. Reisenfeld, J. D. Williams, R. E. Johnson, H. T. Smith, (2008), Observations of molecular oxygen ions in Saturn's inner magnetosphere, Geophysical Research Letters, 35(L20103).

Masters, A., et al., (2017), An in-situ comparison of electron acceleration at collionless shocks under differing upstream magnetic field orientations, The Astrophysical Journal, 843:147.

Masters, A., A. H. Sulaiman, N. Sergis, L. Stawarz, A. J. Coates, M. K. Dougherty (2016), Suprathermal electrons at Saturn's bow shock, The Astrophysical Journal, 826:48.

Masters, A., et al., (2013), Electron acceleration to relativistic energies at a strong quasi-parallel shock wave, Nature Physics, 9:164–167.

Masters, A., et al., (2012), The importance of plasma beta conditions for magnetic reconnection at Saturn's magnetopause, Geophysical Research Letters, 39(L08103).

Masters, A., D. G. Mitchell, A. J. Coates, M. K. Dougherty, (2011), Saturn's low-latitude boundary layer 1: Properties and variability, Journal of Geophysical Research, 116(A06210).

Masters, A., et al., (2010), Cassini observations of a Kelvin-Helmholtz vortex in Saturn's outer magnetosphere, Journal of Geophysical Research, 115(A07225), doi: 10.1029/2010JA015351.

Mauk, B. H., (2014), Comparative investigation of the energetic ion spectra comprising the magnetospheric ring currents of the solar system, Journal of Geophysical Research, 119:9729–9746.

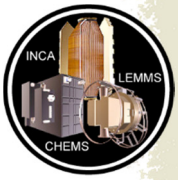

Mauk, B. H., (2012), Radiation belts of the solar system and universe, in Dynamics of the Earth's radiation belts and inner magnetosphere, Geophysical Monograph Series, 199, (eds.) D. Summers, I. R. Mann, D. Baker, M. Schulz, American Geophysical Union, Washington, DC, pp. 405–414.

Mauk, B., F. Bagenal, (2012), Comparative auroral physics: Earth and other planets, in Auroral Phenomenology and Magnetospheric Process, Geophysical Monograph Series, 197, (eds.) A. Keiling et al., American Geophysical Union, Washington, DC, pp. 3–26.

Mauk, B. H., N. J. Fox, (2010), Electron radiation belts of the solar system, Journal of Geophysical Research, 115, A12, doi: 10.1029/2010JA015660

Mauk, B. H., et al. (2009), Fundamental plasma processes in Saturn's magnetosphere, in Saturn from Cassini-Huygens, (eds.) M. K. Dougherty, L. W. Esposito, S. M. Krimigis, Springer, Dordrecht, pp. 281–331.

Mauk, B. H., et al., (2005), Energetic particle injections in Saturn's magnetosphere, Geophysical Research Letters, 32, 2005GL022485.

Mauk, B. H., et al., (2004), Energetic ion characteristics and neutral gas interactions in Jupiter's magnetosphere, Journal of Geophysical Research, 109(A09S12), doi: 10.1029/2003JA010270.

Mauk, B. H., D. G. Mitchell, S. M. Krimigis, E. C. Roelof, C. P. Paranicas, (2003), Energetic neutral atoms from a trans-Europa gas torus at Jupiter, Nature, 421:920–922.

Mauk, B. H., et al., (1999), Storm-like dynamics of Jupiter's inner and middle magnetosphere, Journal of Geophysical Research, 104:22,759-22,778.

Mauk, B. H., S. M. Krimigis, D. G. Mitchell, E. C. Roelof, (1998a), Energetic neutral atom imaging of Jupiter's magnetosphere using the Cassini MIMI instrument, Advances in Space Research, 21:1483–1486.

Mauk, B. H., S. M. Krimigis, D. G. Mitchell, E. C. Roelof, J. Dandouras (1998b), Imaging Saturn's dust rings using energetic neutral atoms, Planetary and Space Science, 46:1349–1362.

McComas, D. J., et al., (2017), Seven years of imaging the global heliosphere with IBEX, Astrophysical Journal Supplement, 229.

McComas, D. J., et al., (2009), Global observations of the interstellar interaction from the Interstellar Boundary Explorer (IBEX), Science, 326, 959.

Menietti, J. D., P. H. Yoon, S. Y. Ye, B. Cecconi, A. M. Rymer, (2010), Source mechanism of Saturn narrowband emission, Annales Geophysicae, 28:1013–1021.

Menietti, J. D., S. -Y. Ye, P. H. Yoon, O. Santolik, A. M. Rymer, D. A. Gurnett, A. J. Coates, (2009), Analysis of narrowband emission observed in the Saturn magnetosphere, Journal of Geophysical Research, 114(A06206).

Menietti, J. D., O. Santolik, A. M. Rymer, G. B. Hospodarsky, A. M. Persoon, D. A. Gurnett, A. J. Coates, D. T. Young, (2008), Analysis of plasma waves observed within local plasma

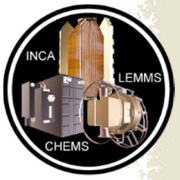

injections seen in Saturn's magnetosphere, Journal of Geophysical Research, 113(A05213), doi: 10.1029/2007JA012856.

Mitchell, D. G., M. E. Perry, D. C. Hamilton, J. H. Westlake, P. Kollmann, H. T. Smith, J. F. Carbary, J. H. Waite Jr., R. Perryman, H. -W. Hsu, J. -E. Wahlund, M. W. Morooka, L. Z. Hadid, A. M. Persoon, W. S. Kurth, (2018), Dust grains fall from Saturn's D-ring into its equatorial upper atmosphere, Science, 362(6410), doi: 10.1126/science.aat2236

Mitchell, D. G., et al., (2016), Recurrent pulsations in Saturn's high latitude magnetosphere, Icarus, 263:94–100.

Mitchell, D. G., et al., (2015), Injection, interchange, and reconnection: Energetic particle observations in Saturn's magnetosphere, in Magnetotails in the Solar System, (eds.) A. Keiling, C. M. Jackman, P. A. Delamere, Geophysical Monograph Series, 207, American Geophysical Union, John Wiley & Sons, pp. 327–344.

Mitchell, D. G., J. F. Carbary, S. W. H. Cowley, T. W. Hill, P. Zarka, (2009a), The dynamics of Saturn's magnetosphere, in Saturn from Cassini-Huygens, (eds.) M. K. Dougherty, L. W. Esposito, S. M. Krimigis, Springer, Dordrecht, pp. 257–279.

Mitchell, D. G., et al., (2009b), Recurrent energization of plasma in the midnight-to-dawn quadrant of Saturn's magnetosphere, and its relationship to auroral UV and radio emissions, Planetary and Space Science, 57(14–15):1732–1742, doi: 10.1016/j.pss.2009.04.002.

Mitchell, D. G., et al., (2009c), Ion conics and electron beams associated with auroral processes at Saturn, Journal of Geophysical Research, 114(A02212), doi: 10.1029/2008JA013621.

Mitchell, D. G., et al., (2005a), Energetic neutral atom emissions from Titan interactions with Saturn's magnetosphere, Science, 308:989–992.

Mitchell, D. G., et al., (2005b), Energetic ion acceleration in Saturn's magnetotail: Substorms on Saturn, Geophysical Research Letters, 32, 2005GL022647.

Mitchell, D. G., C. Paranicas, B. H. Mauk, E. C. Roelof, S. M. Krimigis, (2004), Energetic neutral atoms from Jupiter measured with the Cassini Magnetospheric Imaging Instrument: Time dependence and composition, Journal of Geophysical Research, 109, 2003JA010120.

Mueller, A. L., J. Saur, N. Krupp, E. Roussos, B. H. Mauk, A. M. Rymer, D. G. Mitchell, S. M. Krimigis, (2010), Azimuthal plasma flows in the Kronian magnetosphere, Journal of Geophysical Research, 115(A08203), doi: 10.1029/2009JA015122.

Nordheim, T. A., K. P. Hand, C. Paranicas, C. J. A. Howett, A. R. Hendrix, G. H. Jones, A. J. Coates, (2017), The near surface electron radiation environment of Saturn's moon Mimas, Icarus, 286:56–68.

Nordheim, T. A., et al., (2014), Detection of a strongly negative surface potential at Saturn's moon Hyperion, Geophysical Research Letters, 41:7011–7018.

Ogasawara, K., S. A. Livi, D. G. Mitchell, T. P. Armstrong, N. Krupp, (2011), Properties of energetic particle bursts at dawnside magnetosheath: Cassini observations during the 1999 swing-by, Journal of Geophysical Research, 116(A12207).

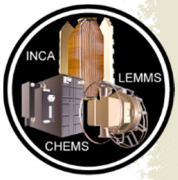

Opher, M., J. F. Drake, B. Zieger, T. I. Gombosi, (2015), Magnetized jets driven by the Sun: The structure of the heliosphere revisited, The Astrophysical Journal of Letters, 800(7).

Orton, G. S., et al., (2009), Review of knowledge prior to the Cassini-Huygens missions and concurrent research, in Saturn from Cassini-Huygens, (eds.) M. K. Dougherty, L. W. Esposito, S. M. Krimigis, pp. 9–54, Springer, Dordrecht.

Palmaerts, B., E. Roussos, N. Krupp, W. S. Kurth, D. G. Mitchell, J. N. Yates, (2016a), Statistical analysis and multi-instrument overview of the quasi-periodic 1-hour pulsations in Saturn's magnetosphere, Icarus, 271:1–18.

Palmaerts, B., A. Radioti, E. Roussos, D. Grodent, J.-C. Gérard, N. Krupp, D. G. Mitchell, (2016b), Pulsations of the polar cusp aurora at Saturn, Journal of Geophysical Research, Space Physics, 121:11,952–11,963, doi: 10.1002/2016JA023497.

Paranicas, C., et al., (2018), Magnetospheric considerations for solar system ice state, Icarus, 302:560–564.

Paranicas, C., et al., (2016), Effects of radial motion on interchange injections at Saturn, Icarus, 264:342–351.

Paranicas, C., et al., (2014), The lens feature on the inner Saturnian satellites, Icarus, 234:155.

Paranicas, C., et al., (2012), Energetic charged particle weathering of Saturn's inner satellites, Planetary and Space Science, 61:60–65.

Paranicas, C., et al., (2010a), Asymmetries in Saturn's radiation belts, Journal of Geophysical Research, 115(A07216), doi: 10.1029/2009JA014971.

Paranicas, C., et al., (2010b), Transport of energetic electrons into Saturn's inner magnetosphere, Journal of Geophysical Research, 115(A09214), doi: 10.1029/2010JA015853.

Paranicas, C., et al., (2008), Sources and losses of energetic protons in Saturn's magnetosphere, Icarus, 197:519–525.

Paranicas, C., et al., (2007), Energetic electrons injected into Saturn's neutral gas cloud, Geophysical Research Letters, 34, 2006GL028676.

Paranicas, C., et al., (2005a), Evidence of Enceladus and Tethys microsignatures, Geophysical Research Letters, 32, 2005GL024072.

Paranicas, C., et al., (2005b), Periodic intensity variations in global ENA images of Saturn, Geophysical Research Letters, 32, 2005GL023656.

Paranicas, C., R. W. Carlson, R. E. Johnson, (2001), Electron bombardment of Europa, Geophysical Research Letters, 28:673.

Parker, E. N., (1961), The stellar-wind regions, The Astrophysical Journal, 134.

Parker, E. N., (1958), Dynamics of the interplanetary gas and magnetic fields, The Astrophysical Journal, 128.

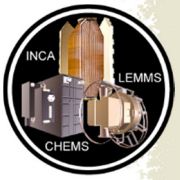

Perry, M. E., et al., (2010), Cassini INMS observations of neutral molecules in Saturn's E-ring, Journal of Geophysical Research, 115(A10206).

Pilkington, N. M., et al., (2015a), Asymmetries observed in Saturn's magnetopause geometry, Geophysical Research Letters, 42:6890–6898.

Pilkington, N. M., et al., (2015b), Internally driven large-scale changes in the size of Saturn's magnetosphere, Journal of Geophysical Research: Space Physics, 120:7289–7306.

Pilkington, N. M., N. Achilleos, C. S. Arridge, A. Masters, N. Sergis, A. J. Coates, M. K. Dougherty, (2014), Polar confinement of Saturn's magnetosphere revealed by in situ Cassini observations, Journal of Geophysical Research: Space Physics, 119:2858–2875.

Pisa, D., G. B. Hospodarsky, W. S. Kurth, O. Santolik, J. Soucek, D. A. Gurnett, A. Masters, M. E. Hill, (2015), Statistics of Langmuir wave amplitudes observed inside Saturn's foreshock by the Cassini spacecraft, Journal of Geophysical Research, 120:2531–2542.

Pryor, W. R., A. Rymer, et al., (2011), The auroral footprint of Enceladus on Saturn, Nature, 472(7343):331–333.

Radioti, A., et al., (2016), A multi-scale magnetotail reconnection event at Saturn and associated flows: Cassini/UVIS observations, Icarus, 263:75–82.

Radioti, A., et al., (2013), Signatures of magnetospheric injections in Saturn's aurora, Journal of Geophysical Research, 118:1922.

Radioti, A., et al., (2009), Transient auroral features at Saturn: Signatures of energetic particle injections in the magnetosphere, Journal of Geophysical Research, 114(A03210), doi: 10.1029/2008JA013632.

Ramer, K. M., M. G. Kivelson, N. Sergis, K. K. Khurana, X. Jia, (2016), Spinning, breathing, and flapping: Periodicities in Saturn's middle magnetosphere, Journal of Geophysical Research: Space Physics, 122:393–416, doi: 10.1002/2016JA023126.

Regoli, L. H., et al., (2018), Statistical study of the energetic proton environment at Titan's orbit from the Cassini spacecraft, Journal of Geophysical Research: Space Physics 123(6):4820–4834.

Regoli, L. H., E. Roussos, M. Feyerabend, G. H. Jones, N. Krupp, A. J. Coates, S. Simon, U. Motschmann, M. K. Dougherty, (2016a), Access of energetic particles to Titan's exobase: A study of Cassini's T9 flyby, Planetary and Space Science, 130:40–53.

Regoli, L. H., A. J. Coates, M. F. Thomsen, G. H. Jones, E. Roussos, J. H. Waite, N. Krupp, G. Cox, (2016b), Survey of pickup ion signatures in the vicinity of Titan using CAPS/IMS, Journal of Geophysical Research: Space Physics, 121, doi: 10.1002/2016JA022617.

Roelof, E. C., (2015), The group abundance fraction: A statistically robust measure of particle composition and of spatial structure in images, Journal of Physics: Conference Series, 577(1):012026.

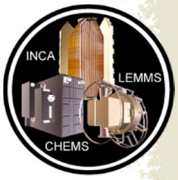

Roelof, E. C., S. M. Krimigis, D. G. Mitchell, R. B. Decker, K. Dialynas, (2012), Cassini ENA images of the heliosheath and Voyager “ground truth”: Thickness of the heliosheath, 10th Anniversary International Astrophysics Conference, American Institute of Physics Conference Proceedings, 1436:265–272.

Roelof, E. C., et al., (2010), Implications of generalized Rankine-Hugoniot conditions for the PUI population at the Voyager 2 termination shock, American Institute of Physics Conference Proceedings, 1302:133–141, doi: 10.1063/1.3529960.

Roussos, E., et al., (2019a), Sources, sinks and transport of energetic electrons near Saturn's main rings, Geophysical Research Letters, 46, doi: 10.1029/2018GL078097.

Roussos, E., et al., (2019b), Jovian cosmic-ray protons in the heliosphere: Constraints by Cassini observations, The Astrophysical Journal, 871:223.

Roussos, E., et al., (2018a), A radiation belt of energetic protons located between Saturn and its rings, Science, 362(6410), doi: 10.1126/science.aat1962.

Roussos, E., et al., (2018b), Heliospheric conditions at Saturn during Cassini's ring-grazing and proximal orbits, Geophysical Research Letters, 45:10,812–10,818, doi: 10.1029/2018GL078093.

Roussos, E., et al., (2018c), Solar energetic particles (SEP) and galactic cosmic rays (GCR) as tracers of solar wind conditions near Saturn: Event lists and applications, Icarus, 300:47–71.

Roussos, E., et al., (2018d), Drift-resonant, relativistic electron acceleration at the outer planets: Insights from the response of Saturn’s radiation belts to magnetospheric storms, Icarus, 305:160–173.

Roussos, E., et al., (2016a), Evidence for dust-driven, radial plasma transport in Saturn’s inner radiation belts, Icarus, 274:272–283.

Roussos, E., et al., (2016b), Quasi-periodic injections of relativistic electrons in Saturn’s outer magnetosphere, Icarus, 263:101–116.

Roussos, E., N. Krupp, C. Paranicas, J. F. Carbary, P. Kollmann, S. M. Krimigis, D. G. Mitchell, (2014), The variable extension of Saturn’s electron radiation belts, Planetary and Space Science, 104(3).

Roussos, E., M. Andriopoulou, N. Krupp, A. Kotova, C. Paranicas, S. M. Krimigis, D. G. Mitchell, (2013), Numerical simulation of energetic electron microsignature drifts at Saturn: Methods and applications, Icarus, 226:1595.

Roussos, E., et al., (2012), Energetic electron observations of Rhea’s magnetospheric interaction, Icarus, 221:116–134.

Roussos, E., et al., (2011), Long- and short-term variability of Saturn’s ionic radiation belts, Journal of Geophysical Research, 116(A02217), doi: 10.1029/2010JA015954.

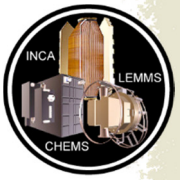

Roussos, E., et al., (2010a), Energetic electron microsignatures as tracers of radial flows and dynamics in Saturn's innermost magnetosphere, Journal of Geophysical Research, 115(A03202), doi: 10.1029/2009JA014808.

Roussos, E., N. Krupp, H. Kruger, G. H. Jones, (2010b), Surface charging of Saturn's plasma absorbing moons, Journal of Geophysical Research, 115(A08225), doi: 10.1029/2010JA015525.

Roussos, E., et al., (2008a), Discovery of a transient radiation belt at Saturn, Geophysical Research Letters, 35, doi: 10.1029/2008GL035767.

Roussos, E., et al., (2008b), Plasma and fields in the wake of Rhea: 3-D hybrid simulation and comparison with Cassini data, Annales Geophysicae, 26:619–637.

Roussos, E., et al., (2008c), Energetic electron signatures of Saturn's smaller moons: Evidence of an arc of material at Methone, Icarus, 193:455–464.

Roussos, E., et al., (2007), Electron microdiffusion in the Saturnian radiation belts: Cassini MIMI/LEMMS observations of energetic electron absorption by the icy moons, Journal of Geophysical Research, 112(A06214), doi: 10.1029/2006JA012027.

Roussos, E., G. H. Jones, N. Krupp, S. M. Krimigis, D. Mitchell, C. Paranicas, (2006), R/2006 S 5, International Astronomical Union Circular, 8773(3).

Roussos, E., et al., (2005), Low energy electron microsignatures at the orbit of Tethys: Cassini MIMI/LEMMS observations, Geophysical Research Letters, 32, 2005GL024084.

Rymer, A. M., D. G. Mitchell, T. W. Hill, E. A. Kronberg, N. Krupp, C. M. Jackman, (2013), Saturn's magnetospheric refresh rate, Geophysical Research Letters, 40:1–5, doi: 10.1002/grl.50530.

Rymer, A. M., (2010), Electron-ion thermal equilibration at Saturn: Electron signatures of ion pick-up, American Institute of Physics Conference Proceedings, 1302:250–255.

Rymer, A., et al., (2009a), Cassini evidence for rapid interchange transport at Saturn, Planetary and Space Science, 57(14–15):1779–1784, doi: 10.1016/j.pss.2009.04.010.

Rymer, A. M., H. T. Smith, A. Wellbrock, A. J. Coates, D. T. Young, (2009b), Discrete classification and electron energy spectra of Titan's varied magnetospheric environment, Geophysical Research Letters, 36(L15109), doi: 10.1029/2009GL039427.

Rymer, A. M., B. H. Mauk, T. W. Hill, C. Paranicas, D. G. Mitchell, A. J. Coates, D. T. Young, (2008), Electron circulation in Saturn's magnetosphere, Journal of Geophysical Research, 113(A01201), doi: 10.1029/2007JA012589.

Rymer, A., et al., (2007), Electron sources in Saturn's magnetosphere, Journal of Geophysical Research, 112(A02201), doi: 10.1029/2006JA012017.

Saur, J., et al., (2006), Anti-planetward auroral electron beams at Saturn, Nature, 439:699–702.

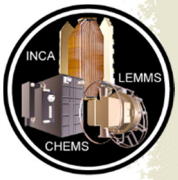

Schenk, P., D. P. Hamilton, R. E. Johnson, W. B. McKinnon, C. Paranicas, J. Schmidt, M. R. Showalter, (2011), Plasma, plumes and rings: Saturn system dynamics as recorded in global color patterns on its midsize satellites, Icarus, 211:740–757.

Schiable, M. J., et al., (2017), High energy electron sintering of icy regoliths: Formation of the PacMan thermal anomalies on the icy Saturnian moons, Icarus, 285:211.

Schippers, P., et al., (2011), Auroral electron distributions within and close to Saturn Kilometric Radiation source region, Journal of Geophysical Research, 116(A05203).

Schippers, P., N. André, R. E. Johnson, M. Blanc, I. Dandouras, A. J. Coates, S. M. Krimigis, D. T. Young, (2009), Identification of photoelectron energy peaks in Saturn’s inner neutral torus, Journal of Geophysical Research, 114(A12212), doi: 10.1029/2009JA014368.

Schippers, P., et al., (2008), Multi-instrument analysis of electron populations in Saturn’s magnetosphere, Journal of Geophysical Research, 113(A07208), 2008JA013098.

Sergis, N., et al., (2018), Mapping Saturn's night side plasma sheet using Cassini's proximal orbit, Geophysical Research Letters, 45:6798–6804, doi: 10.1029/2018GL078141.

Sergis, N., et al., (2017), Radial and local time structure of the Saturnian ring current, revealed by Cassini, Journal of Geophysical Research: Space Physics, 122, doi: 10.1002/2016JA023742.

Sergis, N., et al., (2013), Particle and magnetic field properties of the Saturnian magnetosheath: Presence and upstream escape of hot magnetospheric plasma, Journal of Geophysical Research, 118:1620-1634.

Sergis, N., et al., (2011), Dynamics and seasonal variations in Saturn’s magnetospheric plasma sheet, as measured by Cassini, Journal of Geophysical Research, 116(A04203), doi: 10.1029/2010JA016180.

Sergis, N., et al., (2010), Particle pressure, inertial force, and ring current density profiles in the magnetosphere of Saturn based on Cassini measurements, Geophysical Research Letters, 37, doi: 10.1029/2009GL041920.

Sergis, N., et al., (2009), Energetic particle pressure in Saturn’s magnetosphere measured with the Magnetospheric Imaging Instrument on Cassini, Journal of Geophysical Research, 114(A02214), doi: 10.1029/2008JA013774.

Sergis, N., et al., (2007), Ring current at Saturn: Energetic particle pressure in Saturn’s equatorial magnetosphere measured with Cassini/MIMI, Geophysical Research Letters, 34(L09102), 10.1029/2006GL029223.

Shemansky, D. F., et al., (2009), The Saturn hydrogen plume, Planetary and Space Science, 57:1659–1670.

Simon, S., E. Roussos, C. S. Paty, (2015), The interaction between Saturn’s moons and their plasma environments, Physics Reports, 602:1–65.

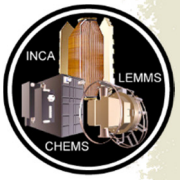

Simon, S., H. Kriegel, J. Saur, A. Wennmacher, F. M. Neubauer, E. Roussos, U. Motschmann, M. K. Dougherty, (2012), Analysis of Cassini magnetic field observations over the poles of Rhea, Journal of Geophysical Research, 117(A07211).

Sittler, E. C., et al., (2009), Energy Deposition Processes in Titan's Upper Atmosphere and Its Induced Magnetosphere, in Titan from Cassini-Huygens, (eds.) R. H. Brown, J. -P. Lebreton, J. H. White, Springer, Dordrecht.

Sittler, E. C., Jr., et al., (2008), Ion and neutral sources and sinks within Saturn's inner magnetosphere: Cassini results, Planetary and Space Science, 56, doi: 10.1016/j.pss.2007.06.006.

Sittler, E. C., et al., (2006), Energetic nitrogen ions within the inner magnetosphere of Saturn, Journal of Geophysical Research, 111(A09223), doi: 10.1029/2004JA010509.

Smith, C. G. A., (2018), Interaction of Saturn’s dual rotation periods, Icarus, 302:330–342, doi: 10.1016/j.icarus.2017.11.016.

Smith, H. T., A. M. Rymer, (2014), An empirical model for the plasma environment along Titan's orbit based on Cassini plasma observations, Journal of Geophysical Research, 119, 2014JA019872.

Smith, H. T., (2010), Neutral clouds and their influence on pick-up ions in Saturn’s magnetosphere, American Institute of Physics Conference Proceedings, 1302:256–262.

Smith, H. T., R. E. Johnson, M. E. Perry, D. G. Mitchell, R. L. McNutt, D. T. Young, (2010), Enceladus plume variability and the neutral gas densities in Saturn’s magnetosphere, Journal of Geophysical Research, 115(A10252), doi: 10.1029/2009JA015184.

Smith, H. T., et al., (2009), Investigation of energetic proton penetration in Titan’s atmosphere using the Cassini INCA instrument, Planetary and Space Science, 57(13):1538–1546, doi: 10.1016/j.pss.2009.03.013.

Smith, H. T., M. Shappirio, R. E. Johnson, D. Reisenfeld, E. C. Sittler, F. J. Crary, D. J. McComas, D. T. Young, (2008), Enceladus: A potential source of ammonia products and molecular nitrogen for Saturn's magnetosphere, Journal of Geophysical Research, 113(A11206), doi: 10.1029/2008JA013352.

Sorba, A.M., N. A. Achilleos, P. Guio, C. S. Arridge, N. M. Pilkington, A. Masters, N. Sergis, A. J. Coates, M. K. Dougherty, (2017), Modeling the compressibility of Saturn's magnetosphere in response to internal and external influences, Journal of Geophysical Research: Space Physics, 122(2):1572–1589.

Stephan, K., et al., (2016), Cassini's geological and compositional view of Tethys, Icarus, 274:1–22, doi: 10.1016/j.icarus.2016.03.002.

Stevens, M. H., J. S. Evans, J. Lumpe, J. H. Westlake, J. M. Ajello, E. T. Bradley, L. W. Esposito, (2015), Molecular nitrogen and methane density retrievals from Cassini UVIS dayglow observations of Titan’s upper atmosphere, Icarus, 247:301.

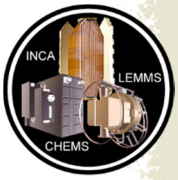

Teolis, B. D., et al., (2010), Cassini finds an oxygen-carbon-dioxide atmosphere at Saturn's icy moon Rhea, Science, 330:1813–1815.

Thomsen, M. F., D. G. Mitchell, X. Jia, C. Jackman, G. Hospodarsky, A. Coates, (2015), Plasmapause formation at Saturn, Journal of Geophysical Research: Space Physics, 120, 2015JA021008.

Thomsen, M. F., et al., (2014), Ion composition in interchange injection events in Saturn's magnetosphere, Journal of Geophysical Research, 119:9761–9772.

Thomsen, M., et al., (2013), Saturn's magnetospheric dynamics, Geophysical Research Letters, 40:5337–5344.

Thomsen, M. F., et al., (2012), Saturn's inner magnetospheric convection pattern: Further evidence, Journal of Geophysical Research, 117(A09208).

Thomsen, M. F., D. B. Reisenfeld, D. M. Delapp, R. L. Tokar, D. T. Young, F. J. Crary, E. C. Sittler, M. A. McGraw, J. D. Williams, (2010), Survey of ion plasma parameters in Saturn's magnetosphere, Journal of Geophysical Research: Space Physics 115:A10.

Tobie, G., et al., (2014), Science goals and mission concept for the future exploration of Titan and Enceladus, Planetary and Space Science, 104:59.

Tobiska, W. K., (2004), SOLAR2000 irradiances for climate change research, aeronomy and space system engineering, Advances in Space Research, 34:1736–1746.

Tokar, R. L., et al., (2008), Cassini detection of water-group pick-up ions in the Enceladus torus, Geophysical Research Letters, 35, doi: 10.1029/2008GL034749.

Westlake, J. H., J. H. Waite, J. M. Bell, R. Perryman, (2014), Observed decline in Titan's thermospheric methane due to solar cycle drivers, Journal of Geophysical Research: Space Physics, 119:8586–8599, doi: 10.1002/2014JA020394.

Westlake, J. H., J. H. Waite, Jr., N. Carrasco, M. Richard, T. Cravens, (2014), The role of ion-molecule reactions in the growth of heavy ions in Titan's ionosphere, Journal of Geophysical Research, 119:5951–5963.

Westlake, J. H., et al., (2012), The observed composition of ions outflowing from Titan, Geophysical Research Letters, 39(L19104).

Westlake, J. H., J. M. Bell, J. H. Waite, Jr., R. E. Johnson, J. G. Luhmann, K. E. Mandt, B. A. Magee, A. M. Rymer, (2011), Titan's thermospheric response to various plasma environments, Journal of Geophysical Research, 116(A03318).

Wulms, V., J. Saur, D. F. Strobel, S. Simon, D. G. Mitchell, (2010), Energetic neutral atoms from Titan: Particle simulations in draped magnetic and electric fields, Journal of Geophysical Research, 115(A06310), doi: 10.1029/2009JA014893.

Yelle, R.V., D. F. Strobel, E. Lellouch, D. Gautier, (1997), Engineering models for Titan's atmosphere, in Huygens: Science, Payload and Mission, pp. 243–256.

- - - - - - - - - - - - - -

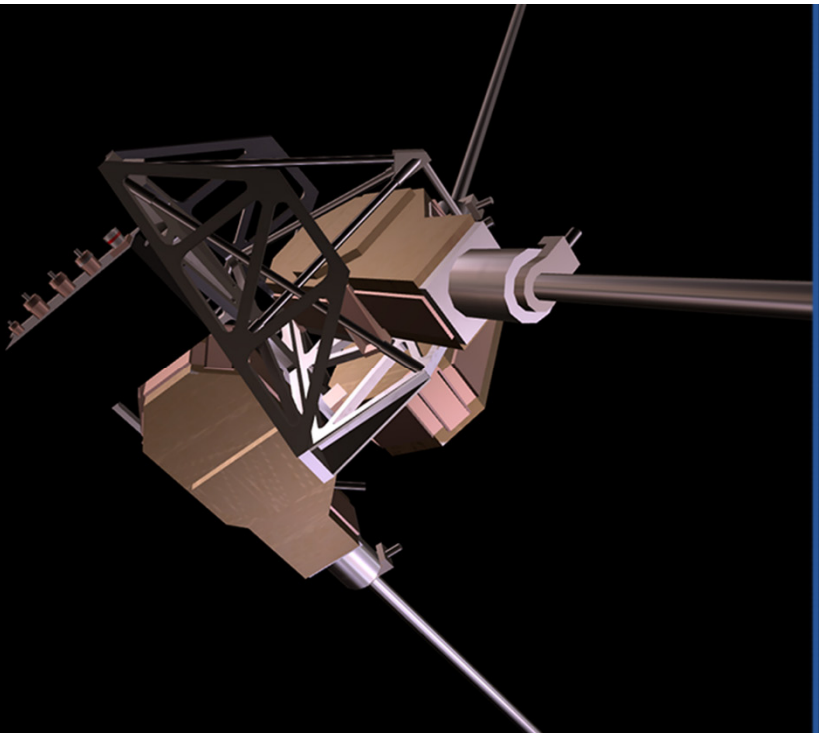

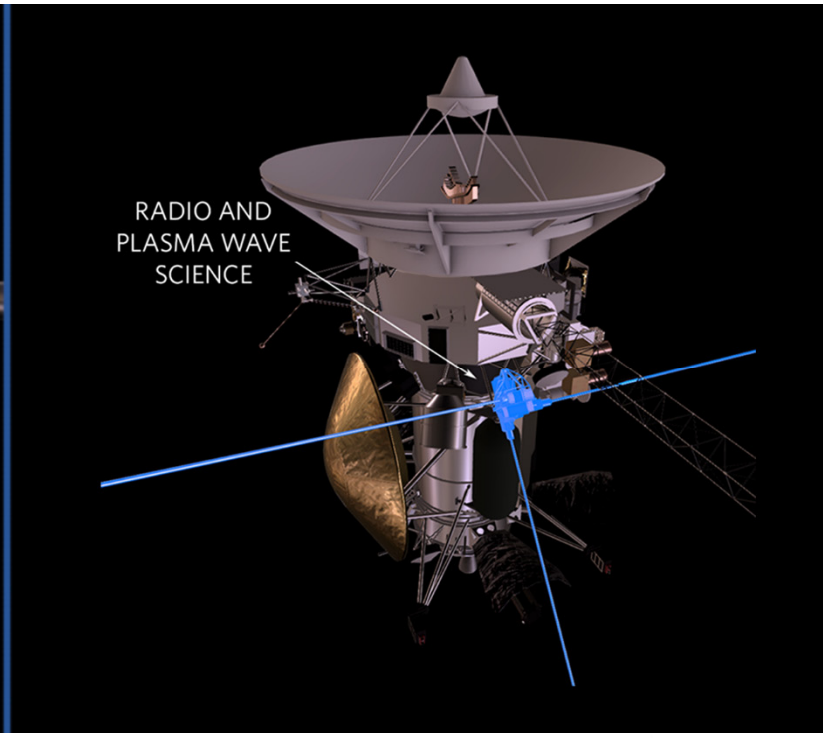

Radio and Plasma Wave Science

The Radio and Plasma Wave Science (RPWS) investigation was designed to study radio emissions, plasma waves, thermal plasma, and dust in the vicinity of Saturn. The **science objectives** included improving our knowledge of the rotational modulation of Saturn's intense radio emission (SKR) and hence Saturn's rotation rate, characterizing plasma waves associated with Saturn's icy satellites and characterizing plasma density in the inner magnetosphere. RPWS was able to detect the dust hitting Cassini throughout the Saturn system and characterize lightning in Saturn's atmosphere.

RPWS was composed of an electric field sensor, a magnetic search coil assembly and a Langmuir probe. The electric field sensor consisted of three deployable antennas. The Langmuir probe, which measured electron density and temperature, was a metallic sphere that measured currents and voltages induced in the probe.

ACKNOWLEDGEMENTS

The following investigators contributed to the Final Mission Report Volume 1: Mission Overview, Science Objectives and Results; Section 3.2: Instruments Science Results – Fields, Particles, and Waves Sensing Instruments – Radio and Plasma Wave Science (RPWS).

RPWS Principal Investigator (PI) and Deputy Principal Investigator (DPI):

Donald A. Gurnett, PI (through October 2015)	*University of Iowa, U.S.*
William S. Kurth, PI (after October 2015); DPI (through October 2015)	

RPWS Investigators:

George B. Hospodarsky, J. Douglas Menietti, Ann M. Persoon	*University of Iowa, U.S.*
Paul Kellogg, Keith Goetz	*University of Minnesota, U.S.*
William M. Farrell, Robert J. MacDowall, Michael D. Desch, Michael L. Kaiser	*Goddard Space Flight Center, U.S.*
Philippe Zarka, Alain Lecacheu, Baptiste Cecconi, Laurent Lamy	*Observatoire de Paris, France*
Philippe Louarn, Christopher C. Harvey	*CESR-CNRS, France*
Patrick Canu, Nicole Cornilleau-Wehrlin, Alain Roux	*CNET/LPP, France*
Patrick Galopeau, Ronan Modolo	*LATMOS/IPSL/UVSQ, France*
Les Woolliscroft, Hugo St. C. Alleyne	*University of Sheffield, United Kingdom*
Helmut O. Rucker, Peter Ladreiter, Georg Fischer	*Austrian Academy of Science, Space Research Institute, Austria*
Rolf Boström, Georg Gustafsson, Jan-Erik Wahlund, Michiko W. Morooka	*Swedish Institute of Space Physics (IRF-U), Sweden*
Arne Pedersen	*University of Oslo, Norway*

RPWS Publication Contributors:

W. S. Kurth, W. M. Farrell, G. Fischer, D. A. Gurnett, G. B. Hospodarsky, L. Lamy, A. M. Persoon, A. H. Sulaiman, J.-E. Wahlund, S.-Y. Ye, P. Zarka

CONTENTS

Figures

Tables

Executive Summary

The Cassini Radio and Plasma Wave Science (RPWS) investigation was successfully carried out over a seven-year cruise and more than thirteen years in orbit at Saturn. As described elsewhere, the instrument performed almost flawlessly; even some occasional processor hangs were understood to the point that we could anticipate modes that might cause them and sequence commands to allow the instrument to recover without ground intervention. While questions were certainly left to answer with future missions (see section entitled Open Questions for Saturn System Science), all of the RPWS science objectives were addressed and advances were made in areas not anticipated at launch, at least partially due to the long mission extensions and agile orbital mechanics involved in the mission and extended mission design.

Top Scientific Findings

The RPWS team debated the top scientific findings of the investigation at length and it is safe to say that while the following is a representative list, it is by no means a consensus in terms of either completeness or order of priority. It does, however, convey the breadth of the investigation, touching on all of Cassini's disciplines including the magnetosphere, satellites, Titan, rings, and Saturn, itself.

- Confirmation of a variable radio period and the discovery of hemispherically differing radio periods.
- First in situ measurements of Saturn's topside ionosphere and evidence of significant interactions with the ring system.
- Comprehensive study of the occurrence of lightning in Saturn's atmosphere and the evolution of a once-per-Saturn-year Great White Spot storm.
- In situ measurements of the Enceladus plumes and their interaction with Saturn's magnetosphere; in situ studies of a dusty plasma.
- Plasma wave phenomena associated with icy satellites, notably Enceladus and Rhea, revealing their electromagnetic connection to Saturn via its magnetic field.
- First in situ characterization of a non-terrestrial cyclotron maser instability-driven radio source (Saturn kilometric radiation).
- In situ measurements of Titan's extensive ionosphere, including the electron density and temperature, evidence for negative ions, and solar cycle dependencies.
- The development of a plasma density model for Saturn's inner magnetosphere.
- Interdisciplinary studies of Saturn's auroras including Saturn kilometric radiation, ultraviolet (UV) and infrared (IR) observations, energetic particles, and the influence of magnetospheric dynamics and solar wind compression events.

- Imaging of SKR source regions and the confirmation that they align with the UV auroras.
- The discovery of Z-mode waves as the source of ~5 kHz narrowband radio emissions first observed by Voyager.
- Anomalously low plasma densities over the unlit side of the B-ring.
- A new low-frequency radio emission phenomenon consisting of drifting tones.
- Finding Titan ahead of Saturn's bow shock and the realization that a complex shock forms ahead of the Titan-Saturn system as opposed to separate shocks.
- The discovery of a seasonally-dependent source of plasma between the A-ring and Enceladus.
- New insights on high Mach number shocks and upstream phenomena through studies of Saturn's bow shock and foreshock region.

The above list demonstrates that RPWS met and exceeded all of its objectives and made significant progress in areas not anticipated prior to arrival at Saturn.

Open Questions for Saturn System Science

Any mission, however extended, always raises questions based on the new knowledge gained. Here we give a brief list of open questions for radio and plasma wave science at Saturn, after Cassini.

- What is the rotation period of Saturn? How do the multiple, variable magnetospheric periods observed in radio, magnetic fields, energetic particles, plasma, aurora, and other phenomena tie to the internally-generated magnetic field at Saturn?
- Given the extraordinarily axi-symmetric magnetic field, why are there such prominent rotational modulations in Saturn's magnetosphere?
- What drives the episodic lightning on Saturn; why is there ~one Great White Spot storm per Saturnian year?
- How does the dust in the Saturnian system interact with Saturn and its atmosphere? How are the rings coupled to the planet other than through gravity?
- What is the predominant form of the electron distribution function at the source of SKR?
- How does the abundant neutral population in Saturn's magnetosphere make it different from fully or mostly ionized magnetospheres?
- What are the various populations of charged dust and molecules that balance charges in dusty media such as in the plumes of Enceladus and in Saturn's topside equatorial ionosphere?

> … all of the RPWS science objectives were addressed and advances were made in areas not anticipated at launch … .

The key open questions are listed above and in the section entitled Open Questions for Saturn System Science. One of the objectives of Cassini was to understand the rotational modulation of Saturn kilometric radiation in the presence of an axi-symmetric magnetic field. Rather than understanding this, the question became more complex. The rotational modulation of SKR was confirmed to be variable and there are often different periods associated with the northern and southern hemispheres. Furthermore, such multiple, variable periods are seen in many aspects of the magnetosphere including the magnetic field, energetic particles, and even the auroral oval. While models exist that reproduce many of these observations, the fundamental origin of this asymmetric behavior in a symmetric system is not understood.

Another aspect of the Saturnian system which is ripe with follow-on questions is the complex processes involving the magnetized plasma in Saturn's magnetosphere in the presence of a large neutral population and pervaded with charged dust grains with sizes ranging from microns to nanometers.

The Cassini mission provided the first opportunities to observe a cyclotron maser instability (CMI) source (of Saturn kilometric radiation) in situ at a location other than at Earth. While these opportunities allowed for the confirmation of a CMI mechanism, only two such source crossings occurred when the Cassini Plasma Science (CAPS) instrument was functioning. Hence, the multiple additional source crossings in the Ring Grazing and Grand Finale orbits did not have the advantage of the CAPS measurements, meaning we do not have more than a couple samples of the electron distribution function responsible for driving the CMI at Saturn. The theory for CMI allows one to infer the resonant energy of electrons and even something about the form of free energy in the source, but having the plasma measurements for additional sources would be beneficial.

RPWS Instrument Summary

The RPWS instrument is a radio and plasma wave spectrometer with the capability of determining the density and temperature of plasmas. The instrument utilizes seven sensors including three monopole electric field antennas with the ability to use two of them as a dipole antenna, a triaxial search coil magnetometer, and a Langmuir probe. Electric fields in the frequency range of 2 Hz to 16 MHz and magnetic fields in the range of 2 Hz to 12 kHz can be measured by the RPWS. The Langmuir probe can determine plasma densities and temperatures in the range of 10 to 10^5 cm^{-3} and below 8 eV through the analysis of voltage-current sweeps. By using the spacecraft potential as a proxy for the electron density, much lower densities, down to 10^{-5} cm^{-3} can be inferred. The instrument is fully described by Gurnett et al. [2004].

The RPWS utilizes a number of receivers to analyze signals from the various sensors. These include a high frequency receiver (HFR) covering electric fields from 3.5 kHz to 16 MHz with the capability of making full polarization and direction-finding measurements in certain modes. The HFR also includes a sounder which can actively stimulate characteristic frequencies of the plasma that enable an alternate approach to determining the plasma density. The medium frequency receiver (MFR) provides electric and magnetic spectral information in the range of 24 Hz to 12 kHz. The low frequency receiver (LFR) provides spectral information for both electric and magnetic fields in the frequency range of ~1 Hz to 26 Hz. The five-channel waveform receiver (WFR) simultaneously captures waveforms from up to five sensors selected from two electric antennas, three magnetic antennas, and the Langmuir probe. Finally, the wideband receiver (WBR) can collect waveform measurements from a selected sensor in a bandwidth of 60 Hz to 10.5 kHz or 0.8 to 75 kHz. The WBR can also provide a 25-kHz band downconverted from selected frequency bands in the HFR.

A typical temporal resolution for survey measurements (covering the full instrument spectrum) is one spectrum per 8 to 16 seconds. The spectral resolution for survey data are Δf/f of 7 to 13%. The HFR has selectable spectral resolutions of 5 to 20% below 318 kHz and n × 25 kHz at higher frequencies. The typical operation of the Langmuir probe provides a full voltage sweep every 24 seconds and can collect currents at fixed bias at rates as high as 20 Hz. Because of the possibility of interference with other instruments, the sounder is only operated briefly every 10 minutes, or so. The WFR and WBR provide the highest resolution observations because actual waveforms are telemetered to the ground for processing optimized to the wave feature under study. However, because of the tremendous data rate generated by these receivers, only relatively short waveform acquisitions can be afforded. These are typically targeted near satellite flybys or regions of interest in the magnetosphere.

Key Objectives for RPWS Instrument

The key RPWS science objectives listed below are taken from Gurnett et al. [2004] and are discussed in the section entitled Science Results. While they were written with the prime mission in mind, the same objectives flow easily into the mission extensions.

Radio emissions

- Improve our knowledge of the rotational modulation of Saturn's radio sources, and hence of Saturn's rotation rate.
- Determine the location of the SKR source as a function of frequency, and investigate the mechanisms involved in generating the radiation.
- Obtain a quantitative evaluation of the anomalies in Saturn's magnetic field by performing direction-finding measurements of the SKR source.

- Establish if gaseous ejections from the moons Rhea, Dione, and Tethys are responsible for the low frequency narrow-band radio emissions.
- Determine if SKR is controlled by Dione's orbital position.
- Establish the nature of the solar wind-magnetosphere interaction by using SKR as a remote indicator of magnetospheric processes.
- Investigate the relationship between SKR and the occurrence of spokes and other time-dependent phenomena in the rings.
- Study the fine structure in the SKR spectrum, and compare with the fine structure of terrestrial and Jovian radio emissions in order to understand the origin of this fine structure.

Plasma waves

- Establish the spectrum and types of plasma waves associated with gaseous emissions from Titan, the rings, and the icy satellites.
- Determine the role of plasma waves in the interaction of Saturn's magnetospheric plasma (and the solar wind) with the ionosphere of Titan.
- Establish the spectrum and types of plasma waves that exist in the radiation belt of Saturn.
- Determine the wave-particle interactions responsible for the loss of radiation belt particles.
- Establish the spectrum and types of waves that exist in the magnetotail and polar regions of Saturn's magnetosphere.
- Determine if waves driven by field-aligned currents along the auroral field lines play a significant role in the auroral charged particle acceleration.
- Determine the electron density in the magnetosphere of Saturn, near the icy moons, and in the ionosphere of Titan.

Lightning

- Establish the long-term morphology and temporal variability of lightning in the atmosphere of Saturn.
- Determine the spatial and temporal variation of the electron density in Saturn's ionosphere from the low frequency cutoff and absorption of lightning signals.
- Carry out a definitive search for lightning in Titan's atmosphere during the numerous close flybys of Titan.
- Perform high-resolution studies of the waveform and spectrum of lightning in the atmosphere of Saturn, and compare with terrestrial lightning.

Thermal plasma

- Determine the spatial and temporal distribution of the electron density and temperature in Titan's ionosphere.
- Characterize the escape of thermal plasma from Titan's ionosphere in the downstream wake region.
- Constrain and, when possible, measure the electron density and temperature in other regions of Saturn's magnetosphere.

Dust

- Determine the spatial distribution of micron-sized dust particles throughout the Saturnian system.
- Measure the mass distribution of the impacting particles from pulse height analyses of the impact waveforms.
- Determine the possible role of charged dust particles as a source of field-aligned Currents.

RPWS Science Assessment

Tables RPWS-1–RPWS-5 contain assessments of RPWS science based on the objectives in the original Announcement of Opportunity (AO) and the Cassini Traceability Matrix (TM) developed for the Equinox and Solstice missions. Each RPWS science objective is paired with an AO and TM science objective. RPWS objectives span all disciplines addressed by the Cassini mission, to some extent. These include Titan, Icy Satellites, Rings, Saturn, and the Magnetosphere.

Table RPWS-1. RPWS Saturn Science Assessment: AO and TM Objectives are paired with RPWS Science objectives. Objectives are accomplished in terms of acquiring relevant data to address.

Fully/Mostly Accomplished: **Partially Accomplished:**

RPWS Saturn Science Objectives	AO and TM Science Objectives	RPWS Saturn Science Assessment	Comments, if yellow (partially fulfilled)
Saturn Interior Structure and Rotation			
--- Rotation of the Deep Atmosphere	SP3, SN1a		Still unknown
Saturn Ionosphere-Magnetosphere Interaction			
--- Saturn I-M interaction, Auroras	SP4, SC2a		
Saturn Lightning Sources and Morphology			
--- Saturn Lightning	SP6, SN2a, SC1b		
--- Great Storm	SN1b		
Aurorae, Chemistry, and Upper Atmosphere	SC2a		Analysis ongoing

Table RPWS-2. RPWS Rings Science Assessment: AO and TM Objectives are paired with RPWS Science objectives. Objectives are accomplished in terms of acquiring relevant data to address.

Fully/Mostly Accomplished: **Partially Accomplished:**

RPWS Rings Science Objectives	AO and TM Science Objectives	RPWS Rings Science Assessment	Comments, if yellow (partially fulfilled)
Ring Structure and Dynamics			
--- Structure of the dusty rings	RP1, RN1c		
--- Dust in vicinity of F-ring	RC1b, RC2a		
Ring Particle Composition and Size			
--- Size distribution of dust	RP2, RC1a		
Ring-Satellite Interaction			
--- Interaction of Enceladus and E-ring	RP3		
Dust and Meteoroid Distribution			
--- Micron-sized dust within and inside D-ring	RP4		Analysis ongoing
Ring Magnetosphere-Ionosphere Interactions	RP5		Analysis ongoing

Table RPWS-3. RPWS MAPS Science Assessment: AO and TM Objectives are paired with RPWS Science objectives. Objectives are accomplished in terms of acquiring relevant data to address.

Fully/Mostly Accomplished: **Partially Accomplished:**

RPWS MAPS Science Objectives	AO and TM Science Objectives	RPWS MAPS Science Assessment	Comments, if yellow (partially fulfilled)
Saturn Magnetic Field Configuration and SKR			
--- Modulation of SKR	MP1, MN1c		Still do not understand variations
--- Seasonal and Solar Cycle Variations	MC1b		
Magnetosphere Charge Particles	MP2		
--- Enceladus as a source of plasma			
--- Rings as a source of plasma			
Magnetosphere Wave-Particle Interactions	MP3		
--- Upstream waves and waves at shock and magnetopause			
--- Wave-particle interactions in middle magnetosphere			
--- Correlations of SKR and tail reconnection			
Magnetosphere and Solar Interactions with Titan	MP4		
Plasma Interactions with Titan's Atmosphere and Ionosphere	MP5		
Enceladus Plume Variability	MC1a		
Titan's Ionosphere	MC2a		
Magnetotail	MN1a		
Saturn's Ionosphere and Radiation Belts	MN1b		
Ionosphere and Ring Coupling	MN2a		

Table RPWS-4. RPWS Icy Satellite Science Assessment: AO and TM Objectives are paired with RPWS Science objectives. Objectives are accomplished in terms of acquiring relevant data to address.

Fully/Mostly Accomplished: Partially Accomplished:

RPWS Icy Satellite Science Objectives	AO and TM Science Objectives	RPWS Icy Satellite Science Assessment	Comments, if yellow (partially fulfilled)
Icy Satellite Magnetosphere and Ring Interactions			
--- Enceladus plume-magnetosphere interaction	IP5, IC1a, IN1a		
--- Evidence for Dione activity	IN1c		
--- Rhea ring material	IN2a		
--- Tethys contribution to E-ring, magnetosphere	IN2b		
--- Appearance of Hyperion	IN2e		

Table RPWS-5. RPWS Titan Science Assessment: AO and TM Objectives are paired with RPWS Science objectives. Objectives are accomplished in terms of acquiring relevant data to address.

Fully/Mostly Accomplished: Partially Accomplished:

RPWS Titan Science Objectives	AO and TM Science Objectives	RPWS Titan Science Assessment	Comments, if yellow (partially fulfilled)
Titan Meteorology			
--- Search for lightning	TP3		
Titan Upper Atmosphere	TP5		
--- Seasonal variations of Titan's ionosphere	TC1a, TC1b		
Titan-Magnetosphere Interaction	TC2a		
--- Induced magnetic field/magnetosphere interaction	TN1b		

RPWS Saturn System Science Results

Titan Science

The RPWS contributions to Titan science are foremost to map the structure, dynamics and long-term variability of its ionosphere and its induced magnetosphere, both interacting continuously with Saturn's magnetosphere and the solar extreme ultraviolet (EUV) radiation, and occasionally also directly with the enhanced solar wind during more active solar conditions when the magnetopause is pushed back toward Saturn past the orbit of Titan. The RPWS contributions, mostly from the Langmuir probe sensor, were recently reviewed in the Cambridge University Press book Titan, primarily in Chapters 12 and 13 [Galand et al. 2013; Wahlund et al. 2013]. Many more RPWS science results have been produced since then. A total of more than 70 publications with RPWS participation in peer-reviewed journals have resulted regarding Titan science up to 2018. Here we dwell only on the main key results.

The first in situ measurements of Titan's ionosphere and space environment were made by Cassini/RPWS during the Titan A flyby in October 26, 2004 [Wahlund et al. 2005a], and the Langmuir probe sensor has been successfully monitoring the cold plasma, charged aerosol and electron temperature during every Titan flyby since then—a total of 127 flybys. A slight degradation of the Langmuir probe sensitivity was induced by the Saturn radiation belt passes in late 2008, but had no effect on the subsequent science output. The RPWS/Langmuir probe therefore provided good science data from Titan for the full period October 2004 to September 2017 (almost 13 years of data).

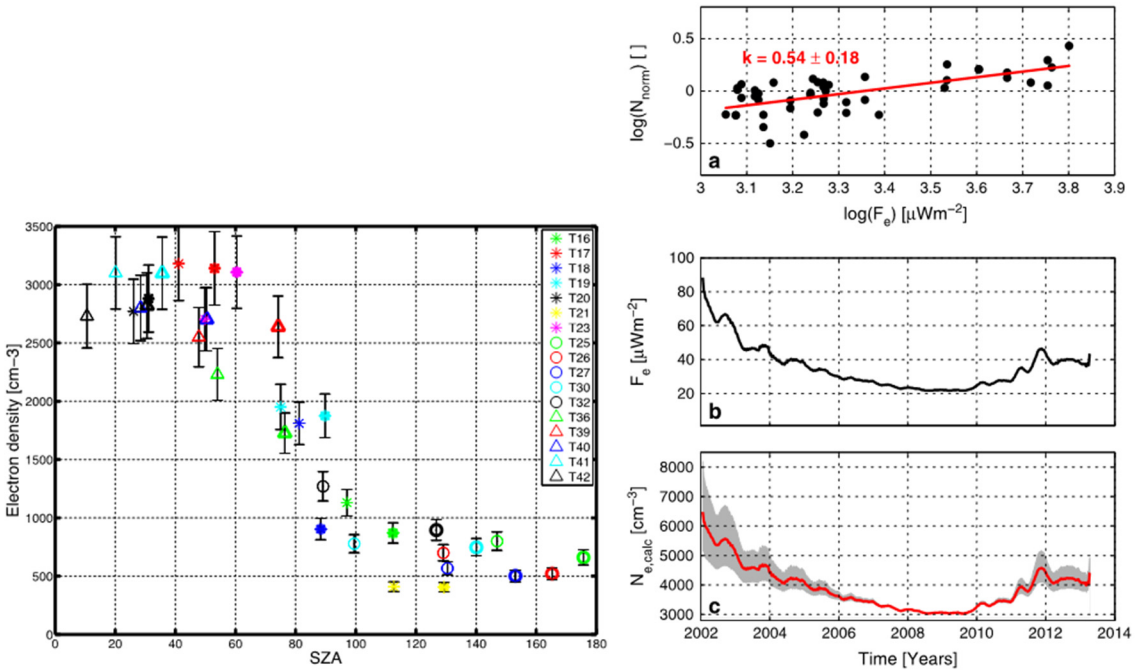

Figure RPWS-1. ***Left*****: Ionospheric peak electron number density versus solar zenith angle [Ågren et al. 2009].** ***Right*****: The variation of the peak electron number density solar EUV flux [Edberg et al. 2013b].**

The main structure of Titan's ionosphere emerged after a few flybys [Ågren et al. 2007, 2009; Robertson et al. 2009] and it became clear that solar EUV radiation dominated the ionization of Titan's upper atmosphere, and varied with the long-term EUV output from the Sun [Edberg et al. 2013b; Shebanits et al. 2017]. Energetic particle precipitation from the magnetosphere is important on the nightside of Titan, but only occasionally makes a significant difference on the dayside [Edberg et al. 2013a]. A most surprising find was the importance of the ionosphere for the production of complex organic chemistry and aerosol particles (dust) below about 1100 km altitude [Coates et al. 2007, 2011; Wahlund et al. 2009b; Vuitton et al. 2009; Ågren et al. 2012; Lavvas et al. 2013; Shebanits et al. 2013, 2016], where the Langmuir probe provided a measure of the detailed amounts of organic ions and charged aerosol particles. The mechanism starts with EUV producing an N_2^+ ion that then reacts primarily with methane, with subsequently more complex C-H-N chemistry and aerosol formation [Lavvas et al. 2013].

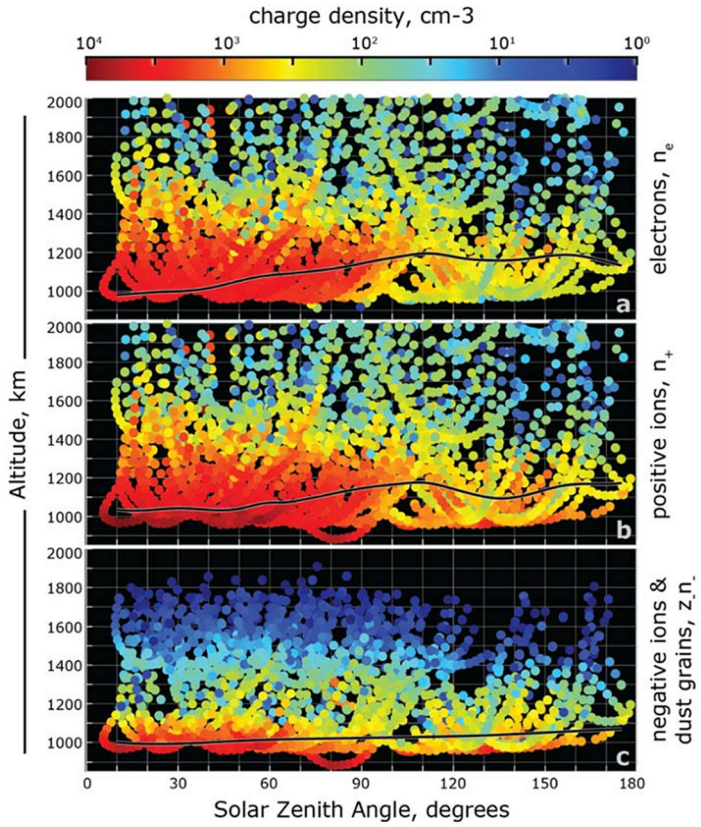

Figure RPWS-2. The ionosphere of Titan. The number densities of electrons (T*op panel*), positively charged ions (*Middle panel*), and negatively charged ions and aerosol particles (*Bottom panel*). Adapted from Shebanits et al. [2013].

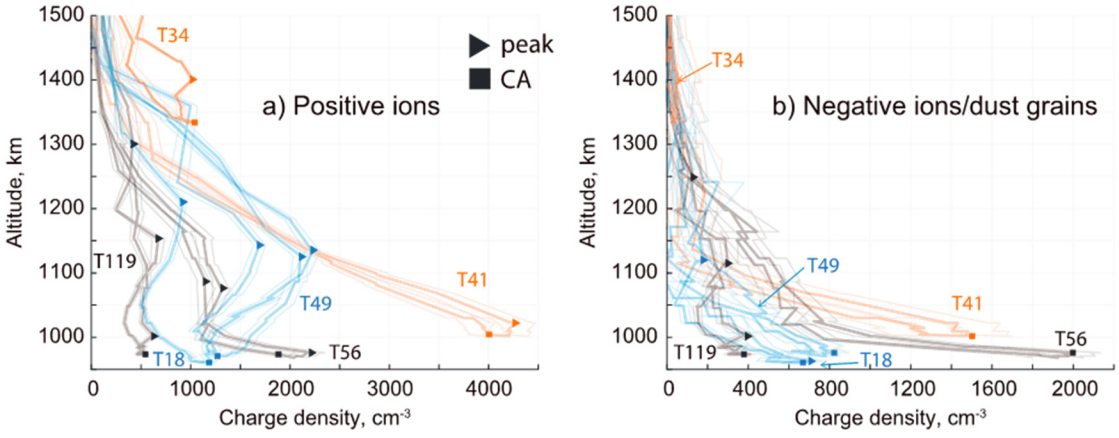

Figure RPWS-3. Examples from six flybys of Titan of altitude profiles of the positive ion and negative ion/aerosol number densities as derived from the RPWS Langmuir probe measurements [Shebanits et al. 2017]. Note the dominance of charged aerosol particles below 1100 km. Dayside flybys are colored in orange, terminator in blue, and nightside in black; the triangles mark the peaks and the squares mark the closest approach (CA) maxima.

Titan's interaction with the magnetosphere of Saturn results in the formation of an induced magnetosphere around Titan. The RPWS sensors have mapped the interaction region [Modolo et al. 2007a, 2007b], proved the existence of cold ionospheric flows from Titan—for example, Edberg et al. [2010, 2011], as well as more energetic ion pickup [Modolo et al. 2007b], and studied how these processes change when Titan enters the magnetosheath [Bertucci et al. 2008; Garnier et al. 2009]. Titan's ionosphere also acts as a conductive medium where electric currents generated in the induced magnetosphere close [Rosenqvist et al. 2009; Ågren et al. 2011]. The escape rate through the cold plasma was determined to be a few kg/s (10^{25} ions/s), which is considered small compared to the exosphere escape rates.

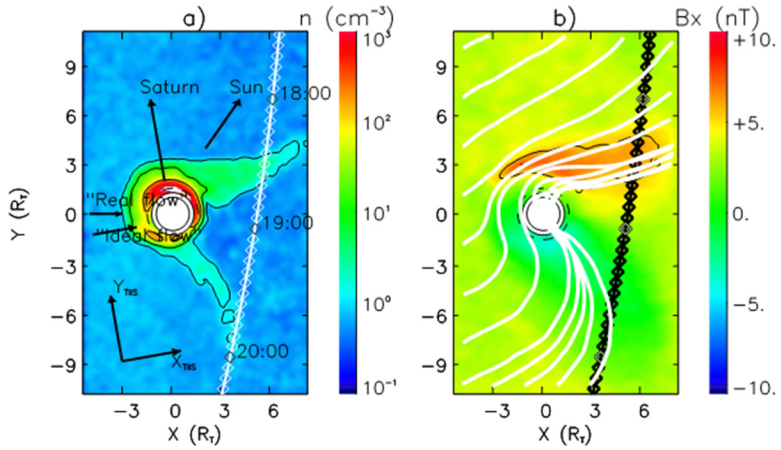

Figure RPWS-4. The induced magnetosphere of Titan as measured and modelled during the T9 flyby through the tail [Modolo et al. 2007b].

Icy Satellite Science

RPWS at Enceladus

PLASMA WAVES

Cassini made 22 close flybys of the icy moon Enceladus which enabled the RPWS to study plasma waves in the moon's near-environment, auroral processes associated with these waves, and the interaction between the magnetospheric plasma and the dust originating in Enceladus' plume. Gurnett et al. [2011a] reported observations of whistler mode auroral hiss emissions produced by magnetic field-aligned electron beams. A ray path analysis of the funnel emission shows the hiss source region within a few moon radii of the Enceladus surface. Figure RPWS-5 is adapted from Figure 2 in Gurnett et al. [2011a] and shows the auroral hiss funnel from the E8 flyby in the top panel and the nearly field-aligned electron beams from the CAPS electron spectrometer (ELS) instrument in the second panel. The magnetometer observations of the field-aligned currents which accelerate the electron beams are shown in the bottom panel. The ramp-like signature of the southward current is associated with a shear-mode Alfven wave excited by the moon-plasma

interaction. Parallel electric fields often associated with the Alfven wave are believed to be accelerated by these waves along magnetic field lines that map to the Enceladus footprint in Saturn's aurora [Gurnett and Pryor 2012].

Leisner et al. [2013] observed northward and southward auroral hiss funnels on both flanks of Enceladus. They found that these funnels are consistently observed on all low-inclination flybys through the Enceladus flux tube, suggesting that the electron beams associated with these auroral hiss funnels are a steady state feature of the Enceladus interaction with the plasma. Sulaiman et al. [2018a] observed an auroral hiss funnel on the ionospheric end of the flux tube connecting the planet to Enceladus.

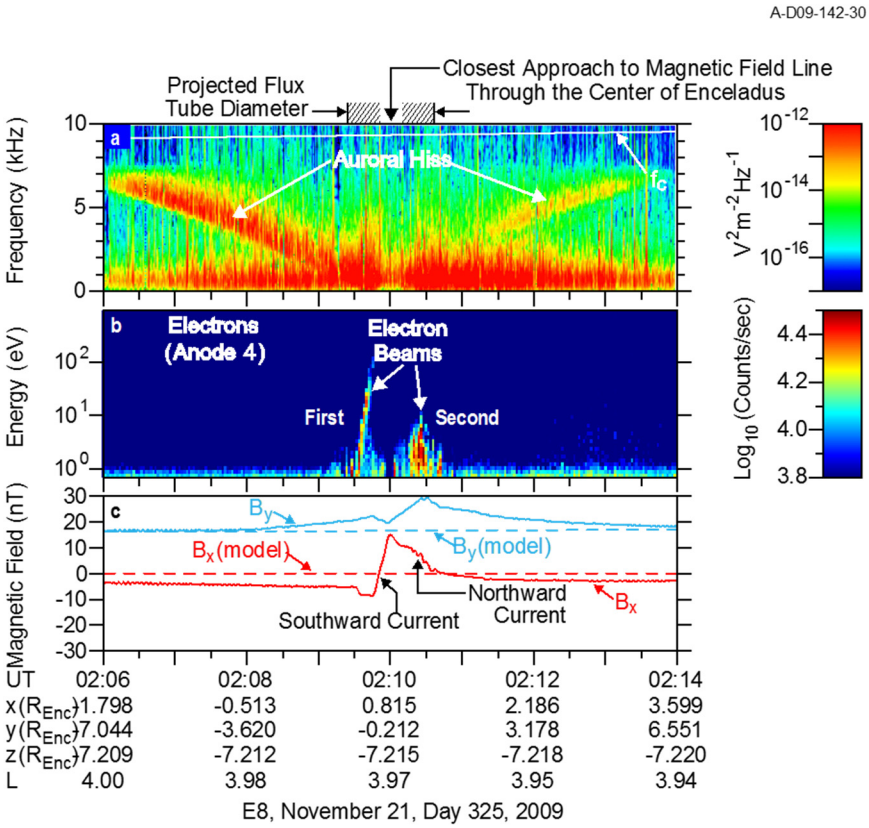

Figure RPWS-5. Evidence of an electrodymanic interaction between Enceladus and Saturn's magnetosphere in the form of auroral hiss generated by electron beams.

PLASMA-DUST INTERACTIONS

The measurement of dust grains in the vicinity of Enceladus and the interaction of these grains with the ambient plasma became a focus of RPWS research. Farrell et al. [2009] presented high-time resolution spectral evidence from the E3 flyby of small water-ice grain impacts on the electric antennas in the vicinity of Enceladus and a sudden, large drop in the electron density in the same region, a density depletion that they attribute to the absorption of electrons by submillimeter-sized

icy particles. Morooka et al. [2011] presented Langmuir probe observations to provide evidence for the presence of dusty plasma in the Enceladus plume region. The data show large increases in the ion and electron densities just south of the equatorial plane in the plume region for four Enceladus flybys in 2008, but there is a two order of magnitude difference in these plasma densities with $n_e/n_i < 0.01$. This plasma signature is attributed to electron absorption by dust grains in the plume, which subsequently become negatively charged. The ion and electron density increases in the plume region just south of the equatorial plane are shown in the top panel of Figure RPWS-6, which is adapted from Figure 5 in Morooka et al. [2011]. No plasma wake signature is observed in this data. The middle panel of Figure RPWS-6 shows the strong drop in the n_e/n_i density ratio in this same region where the presence of dust grains had been previously determined [Farrell et al. 2009]. The bottom panel in Figure RPWS-6 shows almost Keplerian ion speeds measured by the Langmuir probe which are well below the plasma corotation speed, reaching a minimum below Keplerian speeds in the plume region. The interaction between the cold plasma and the negatively charged small dust grains is believed to cause this slowing of the plasma that moves with Enceladus, explaining the lack of a plasma wake behind the moon.

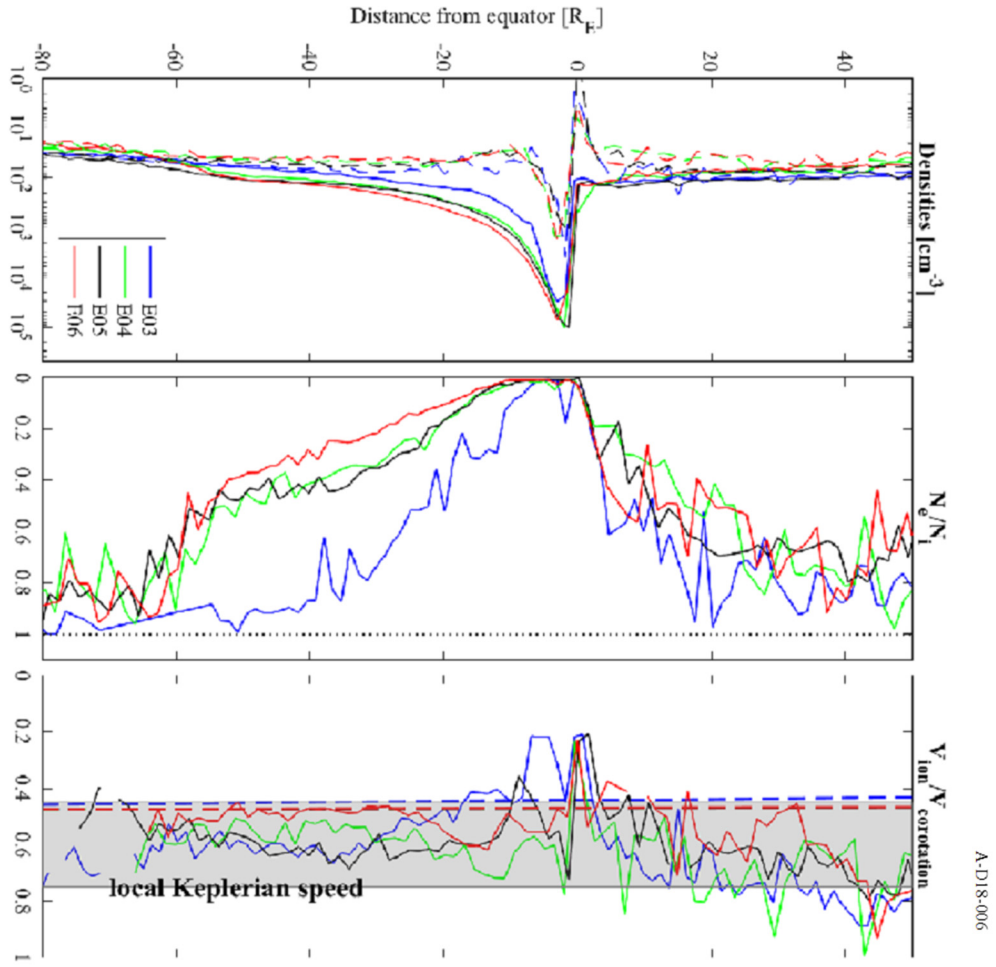

Figure RSWS-6. The variation of electron densities (*Top*), ratio of electron to ion densities (*Middle*) and the ratio of the ion velocity relative to corotation in the vicitnity of Enceladus.

The presence of dust grains inferred by the ion-electron density difference led to a number of research results. Ye et al. [2014a] discovered that, after a dust grain impacted the RPWS electric antennas, a dust ringing effect was observed by the RPWS Wideband Receiver, characterized as periodic plasma oscillations. The frequency of these oscillations was shown to be consistent with the local electron plasma frequency, providing a measurement of the electron density. Densities derived from this method in the Enceladus plume region were found to be consistent with electron densities derived by the Langmuir probe for four consecutive Enceladus flybys in 2008. Shafiq et al. [2011] presented Langmuir probe observations of the E3 flyby to derive estimates of the dusty plasma parameters and found that the dust density would vary depending on the grain size. The submicron-sized dust grains dominate in the plume region with densities of 10^2 cm^{-3}. The micrometer-sized and larger sized grains are estimated to have densities of only 6.3×10^{-5} cm^{-3}.

OTHER RESEARCH

Omidi et al. [2012] used an electromagnetic hybrid simulation to explore the impact of charge exchange between the plasma and the neutral gas and the electron absorption by dust particles on the deceleration of the corotating plasma near Enceladus. They found that the charge exchange between the corotating ions and the neutral gas in the plume played a dominant role in the deceleration of the plasma.

Farrell et al. [2012] found that, in Enceladus' northern hemisphere within ~5 R_E, there is a quasi-time stationary plasma feature, a clear electron density dropout in the RPWS data coincident with a sharp deceleration in the plasma flow. They infer the presence of dust in the northern hemisphere by this plasma feature. They further suggest that the submicron dust population in the northern hemisphere is secondary ejecta, small fast dust grains resulting from surface impacts by larger micron-sized dust grains which originated in, among other possible sources, the moon's plume.

Engelhardt et al. [2015] presented evidence for the existence of a dust trail downstream of Enceladus and extending north of the moon up to 4 R_E. The trail region is characterized by a strong electron density depletion coincident with a nearly constant ion density profile, suggesting that some fraction of the electrons have been absorbed by the dust grains that have been observed in this region.

Farrell et al. [2017a] used a particle-in-cell electrostatic simulation to examine the cold, low-energy ions produced in the Enceladus plume and the development of plasma sheaths about the negatively-charged, submicron dust grains that can act to trap these newly created ions which subsequently exit the plume region at the subcorotational speed of the dust grains. The authors further suggest that only about 3% of the ion population, with energies exceeding the sheath trapping potential, contribute to the ion pickup current and the associated magnetic field perturbations. The Langmuir probe measures both of these ion populations.

Rhea interaction

The moon Rhea orbits at a distance of 8.74 R_S (1 R_S = 60,268 km) from Saturn and is its largest icy satellite, with a radius of 764 km. Since Rhea has essentially no internal geological activity [Pitman et al. 2008] and only a very tenuous exosphere consisting of oxygen and carbon dioxide [Teolis et al. 2010] the moon was expected to be essentially a passive absorber, with little interaction with Saturn's corotating magnetosphere which streams by at a nominal corotational velocity of 85.4 km/s. Nonetheless, Cassini plasma measurements [Wilson et al. 2010] show that the plasma ions in the vicinity of the moon are slowed down by about 30% relative to rigid corotation due to their interaction with the moon. Measurements of the fluxes of energetic (several hundred keV) electrons [Roussos et al. 2012] shows that these electron fluxes have a broad depletion extending out to as much as 5 to 7 times the radius of Rhea. This extended depletion region has been interpreted by Roussos et al. [2012] as possibly being caused by dust or ring particles orbiting Rhea within the Hill sphere which is estimated to have a radius of about 7.7 times the radius of the moon. At lower energies, below about 100 keV, the electron fluxes show sharper depletion boundaries consistent with the geometric wake generated by absorption at the surface of the moon. Curiously, electron density measurements of the cold plasma by the Langmuir probe and by RPWS measurements of the upper hybrid resonance frequency show only a small decrease in the plasma density in the wake region, suggesting that the moon might be a significant source of cold plasma. Measurements of the electric and magnetic fields of plasma waves by the RPWS [Santolik et al. 2011] show that intense plasma waves are generated in the magnetic flux tube connected to the surface of the moon. Three types of plasma waves were observed: (i) bursty electrostatic waves near the electron plasma frequency, (ii) intense whistler-mode waves below one half the electron cyclotron frequency, and (iii) broadband electrostatic waves at frequencies well below the ion plasma frequency. The waves near the electron plasma frequency are believed to be driven by low energy (35 eV) electron beams accelerated in the vicinity of Rhea, and the whistler mode emissions are thought to be generated by the loss-cone anisotropy introduced in the low energy (230 eV) electron distribution by absorption at the surface of the moon. Pitch angle scattering by these waves may be able to explain some of the structure in the flux of energetic electrons reported in the vicinity of the moon.

Dust and Dusty Ring Science

One of RPWS's scientific goals is to detect the micron-sized dust particles that concentrate near the ring plane of Saturn [Gurnett et al. 2004]. In addition to gravity, these particles are also subject to solar radiation pressure and electromagnetic forces, making their orbit dynamics drastically different from the meter-sized main ring particles [Horányi 1996]. The dynamic orbit evolution and plasma sputtering make the lifetime of these particles less than a few thousand years [Burns et al. 2001], which requires these diffuse rings to be replenished continuously. During the Cassini mission, cryovolcanic activity near the south pole of Enceladus was discovered to be the source of E-ring material [Spahn et al. 2006b; Porco et al. 2006]. Other diffuse rings are formed mainly through collisions (meteoroid-moonlet impacts or collisions among the small bodies) and diffusion of collisional debris by non-gravitational forces [Hedman et al. 2007; Williams and Murray 2011].

The longevity of the Cassini mission and good coverage of space by the orbits allowed ample opportunities to explore the dusty rings of Saturn and the plume of Enceladus, providing important in situ measurements of dust density profiles and size distributions in these regions.

During Cassini's Saturn orbit insertion (SOI), RPWS WBR detected micron-sized dust particles at ~500 to 2000 impacts per second around the ring plane crossings [Gurnett et al. 2005]. Due to the high gain antenna (HGA) to ram pointing (protecting the spacecraft from dust hazards), the designated dust instrument Cosmic Dust Analyzer (CDA) [Srama et al. 2004] was not operating during SOI, so RPWS provided the only in situ measurement of dust particles then in this crucial region [Wang et al. 2006]. Based on the power spectrum measured by the monopole antenna, Wang et al. [2006] estimated the root mean square size of the particles detected to be around 2.6 micron. The particles detected near the ring plane were shown to have a power law distribution with power index −2.

In the first few years of the mission, Cassini made a number of inclined and equatorial crossings of the E-ring, particularly near the orbit of Enceladus.

In the first few years of the mission, Cassini made a number of inclined and equatorial crossings of the E-ring, particularly near the orbit of Enceladus. The ice particles detected by RPWS in this region were estimated to be a few microns [Kurth et al. 2006b]. The peak impact rates measured around the orbit of Enceladus were around 50 per second, corresponding to densities of order of 5×10^{-4} m^{-3}. The vertical dust flux profiles could be described by Gaussian function with a scale height of about 2800 km. It was also noted that density peaks could have a vertical offset of a few hundred km. Radial density profiles derived from the equatorial orbit measurements showed a peak near the Enceladus orbit and power law decreases inside and outside the Enceladus orbit, consistent with the previous optical measurements of the ring profile.

Ye et al. [2016a] analyzed the ring plane crossing data (within 6 R_S) collected by RPWS between SOI and equinox (85 crossings). Since the WBR can record the voltage waveform of each individual impact, they were able to derive the dust size distribution based on the sizes of the voltage jumps. It was found that the E-ring particle size distribution can be characterized by a power law function with a power law index around −4. Figure RPWS-7 shows the trajectories of Cassini during 53 high inclination ring plane crossings before equinox. The color code indicates dust density estimated for particles with radius larger than 1 micron. The density profiles derived based on the impact rates showed that dusty ring near the G-ring has a narrow profile (~240 km FWHM). In contrast, E-ring is much thicker. The thickness of E-ring has a minimum ~4000 km FWHM at Enceladus' orbit, and increases with the distance away from Enceladus' orbit. Ye et al. [2016a] constructed an E-ring density model based on fitting the vertical density profiles with Lorentzian functions and radial profiles with power law functions. Near Enceladus' orbit, the vertical dust density profiles showed slight dips around the ring plane, likely due to the gravitational scattering of the particles by the moon. The E-ring peak location was shown to be shifted to the north outside Enceladus' orbit and to the south inside Enceladus' orbit, consistent with optical measurements [Hedman et al. 2012]. The E-ring warp is due to the locking of the pericenters and apocenters of

the dust orbits out of the ring plane by the vertical component of the solar radiation pressure [Hamilton 1993]. So, it was predicted that the E-ring warp would change with time due to the seasonal change of solar radiation pressure normal direction relative to the ring plane.

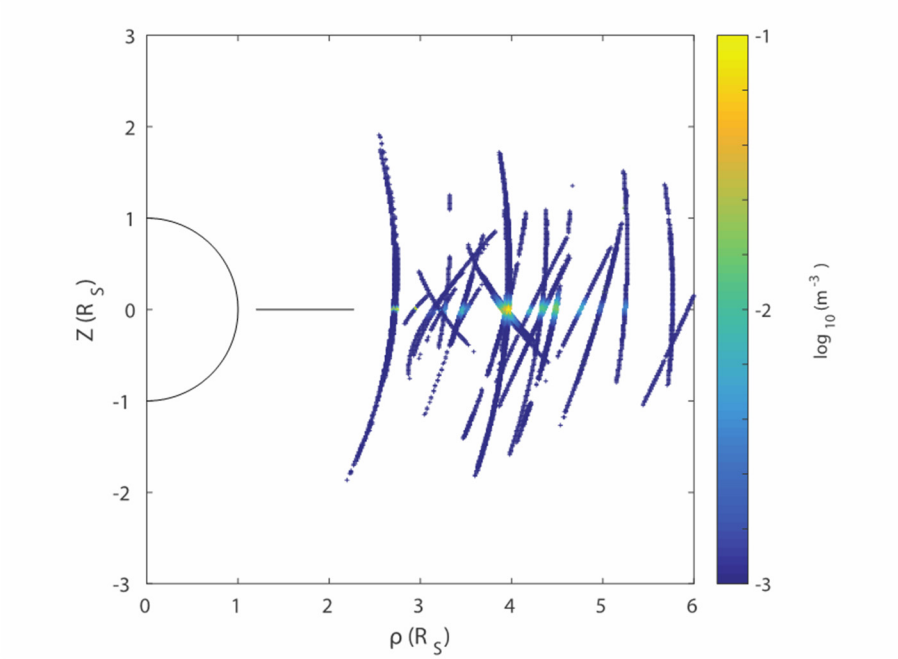

Figure RPWS-7. Trajectories of Cassini during 53 high inclination crossings between SOI and equinox in polar coordinates. The color code shows base ten logarithm of estimated dust density (>1 micron), so that yellow represents 0.1/m^3 and blue represents 0.001/m^3.

Cassini shifted to high inclination orbits and crossed the E-ring multiple times in 2016, providing opportunities to compare the vertical dust density profiles to those measured before equinox. The density profiles showed that the E-ring warp indeed reversed after equinox, with the dust density peak shifting to the south of the ring plane outside Enceladus' orbit and to the north inside Enceladus' orbit. These results confirm the seasonal control of the E-ring warp and role of solar radiation pressure in the dynamics of micron-sized dust particles in the E-ring.

Another asymmetry in the E-ring is the day-night asymmetry, as revealed by both remote sensing [Hedman et al. 2012] and in situ measurements (CDA and RPWS). The E-ring appears to be more compressed and bright on the noon side and more stretched out and faint on the night side. This local time asymmetry is likely related to two factors. One is the dependence of the orbital precession rate on the particles properties like size and charge-to-mass ratio and the other one is the recently discovered noon-to-midnight electric field which is of particular importance in driving the E-ring dynamic evolution.

The plume of water vapor and icy particles ejected from the south pole of Enceladus is perhaps the most exciting discovery of the Cassini mission [Dougherty et al. 2006; Porco et al. 2006]. The ejected material constitutes the major contents of the E-ring and Enceladus torus and

after ionization they become a major source of plasma in the magnetosphere of Saturn. Several instruments onboard Cassini are sensitive to the ice particles in the plume. On the small end of the size spectrum, nanoparticles are directly detected by the CAPS, where nanograins appear as energetic charged particles in the ELS and ion mass spectrometer (IMS) [Jones et al. 2009; Hill et al. 2012; Dong et al. 2015]. In a dusty plasma, electrons are attached to these nanograins, leading to a large difference between the electron and ion densities measured by the RPWS Langmuir probe in and around the plume [Wahlund et al. 2009a; Yaroshenko et al. 2009; Shafiq et al. 2011; Morooka et al. 2011; Engelhardt et al. 2015]. On the large end of the size spectrum, both CDA and RPWS are sensitive to micron-sized dusts [Srama et al. 2006; Kempf et al. 2008; Farrell et al. 2009, 2010; Omidi et al. 2012]. During the plume crossing when both CDA and RPWS were operating, the dust density profiles measured by the two instruments are consistent within the estimated uncertainty range for RPWS [Ye et al. 2014b]. Recently, it has been found that the Magnetospheric Imaging Instrument (MIMI) / Low-Energy Magnetospheric Measurement System (LEMMS) instrument is also sensitive to dust impacts in the plume of Enceladus, and the dust peak matches well with the dust density profile measured by RPWS [Krupp et al. 2017].

The plasma charge balance in the vicinity of Enceladus has been shown by the Langmuir probe measurements to be modified by the presence of dust particles. During the crossings of the Enceladus plume, Cassini RPWS observed sharp frequency decreases of the upper hybrid resonance in the vicinity of the moon, indicating electron density dropouts most likely due to absorption by the dust particles [Farrell et al. 2009]. Inside the plume, however, the dust impact signals are so intense that the upper hybrid resonance is hard to identify. Ye et al. [2014a] presented an independent method of determining the electron density inside the dusty plume of Enceladus, using the plasma oscillations induced by dust impacts and detected by the WBR. The frequencies of these oscillations were shown to be consistent with the local plasma frequency, thus providing a measurement of the electron density. It was proposed that the electrons from the impact plasma constitute a fast beam relative to the background plasma, which will excite Langmuir waves through the bump-on-tail instability.

During the Ring Grazing orbits between December 2016 and April 2017, Cassini crossed through the Janus/Epimetheus ring 20 times. The WBR was scheduled to collect waveform data during the ring plane crossings, from which dust density profiles and size distributions have been derived [Ye et al. 2018a]. Figure RPWS-8 shows the statistics of dust impacts observed during the ring plane crossing on day of year (DOY) 361, 2016. *Panel a* shows the impact counts as a function of voltage and time. *Panel b* shows the gain of the receiver, which is set based on waveform amplitudes to maximize the use of the analog-to-digital converter (A/D) dynamic range while minimizing clipping (exceeding the range of the A/D converter) [Gurnett et al. 2004]. *Panel c* shows the dust density (1 micron size threshold) calculated from the impact rates, assuming an effective impact area of 1 m^2. The red line in *panel c* represents a horizontal cut of *Panel a* situated at 0.034 Volts, the voltage that corresponds to 1 micron dust size. The count rate profile for 1 micron particles has a width (~600 km) similar to the CDA high-rate detector (HRD) density profile. *Panel d* shows the size distribution slope estimated within a 10-second moving window (blue diamonds). The scatter of the blue diamonds indicates the uncertainty of the estimated size distribution slope, increased when the number of impacts detected within the moving window decreases.

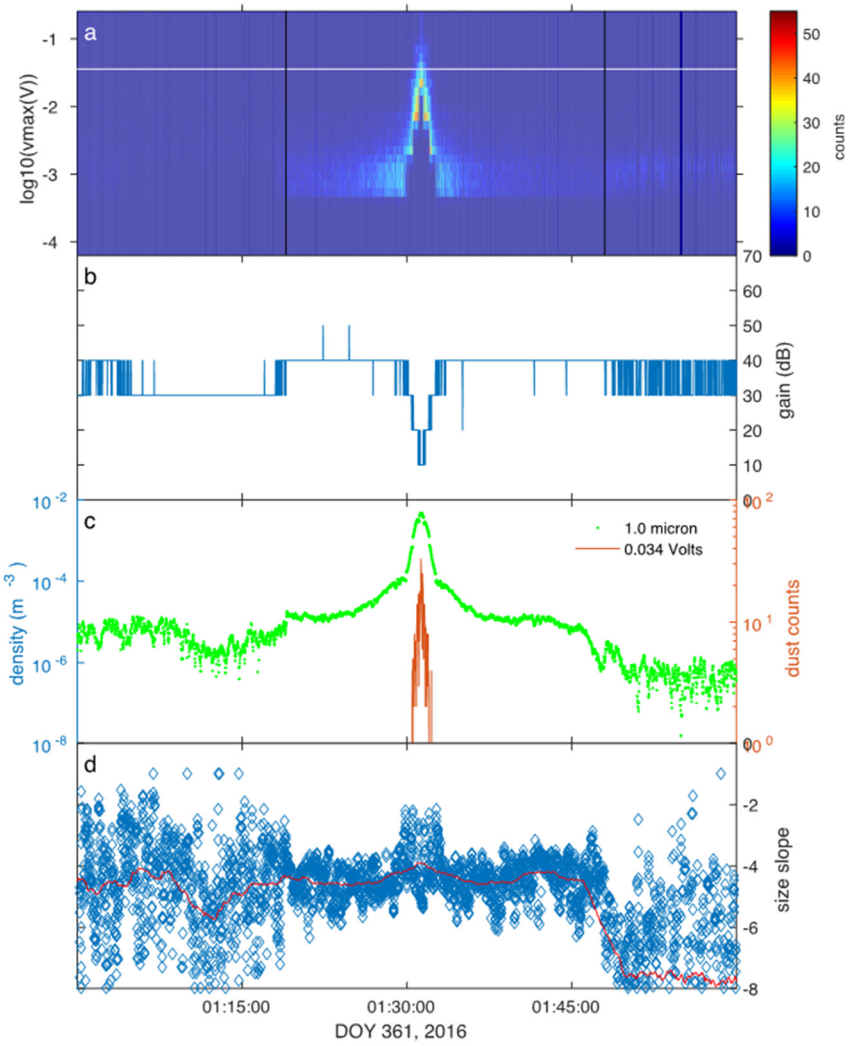

Figure RPWS-8. Dust analysis for the ring plane crossing on DOY 361, 2016. *Panel a*: Impact counts as a function of voltage and time. Black vertical lines mark the times of mode changes, between which the monopole antenna was used. *Panel b*: Gain of the receiver. *Panel c*: Dust density (1 micron size threshold) calculated from the impact rates. The red line shows the horizontal cut of *Panel a* situated at 0.046 Volts (marked with white horizontal line in *Panel a*). *Panel d*: Differential size (radius) distribution slope estimated within a 10-second moving window (blue diamonds, red line shows smoothed value with a 120-second moving window).

For example, when the antenna mode was switched to dipole, fewer impacts were detected, causing higher uncertainty level of the size slope. The red line indicates smoothed values of the individual size slopes (blue diamonds) using a 120-second moving window. This smoothed size slope is also used to scale the density values to the fixed size threshold shown in *Panel c*.

The RPWS dust density profiles were fitted with Lorentzian functions and compared to that measured by the CDA HRD (Figure RPWS-9). There is one order of magnitude difference between the two results, which is within the uncertainty limit estimated for the RPWS measurement.

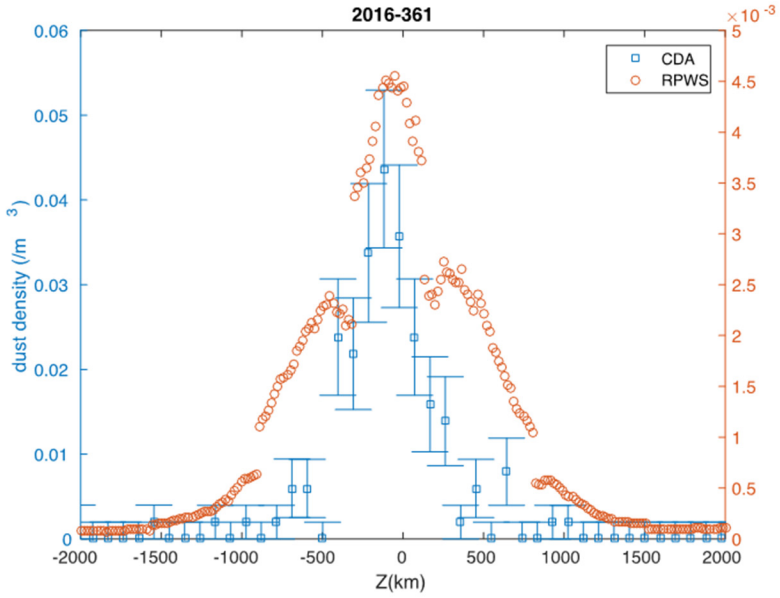

Figure RPWS-9. Comparison of vertical dust density profiles measured by RPWS and CDA HRD during the ring plane crossing on DOY 361, 2016.

The HRD profile also has a slightly narrower peak width. The dust densities inferred from the Langmuir probe sweep data (assuming a differential size distribution slope −4.5) agree with the WBR results [Morooka et al. 2018]. The peak locations of the RPWS dust density profiles shift north and south but are within 100 km of the ring plane (CDA HRD density profiles show a systematic southward shift of 130 km). These peak offsets are within the maximum offsets of the moons Janus and Epimetheus due to their slight orbit inclinations.

On April 26, 2017, Cassini dived into the gap between Saturn's main ring system and its atmosphere starting the 22 Grand Finale orbits. RPWS observed few micron dust impacts during the first five and last ten proximal orbits, not enough for characterizing the size distribution [Ye et al. 2018b]. The lack of micron dust in this region is probably due to the plasma drag in the ionosphere, where the cold density plasma corotate with the planet at a speed lower than the Keplerian speed of the dust particles. So, the micron dusts would lose speed and fall into the planet. During the higher altitude D-ring crossings (rev 276–282), RPWS detected more dust impacts with the density estimated to be about two orders of magnitude lower than F-ring orbits. The monopole antenna measurements near the D-ring indicated that spacecraft was charged positively (the impact signals were mostly positive, whereas at larger radial distances the impacts detected by monopole were mostly negative). The Langmuir probe also measured positive spacecraft potentials and electron bite-outs around the ring plane. The positive potential might be due to kinetic ion impacts, similar to what Langmuir probe (LP) observed in the deep ionosphere. Close inspection of the waveforms indicates a possible dependence of the impact signal decay time on ionosphere plasma density, which showed large variations from orbit to orbit.

RPWS was also able to detect nanoparticles originated from the inner solar system (0.2 AU) [Schippers et al. 2014, 2015] and Jupiter's moons [Meyer-Vernet et al. 2009], based on the bursty noise spectrum measured on the monopole antenna of RPWS. During the cruise phase of Cassini, the RPWS instrument was turned on with setup suitable for dust detection at three different heliocentric distances: 1, 1.6, and 2.9 AU. Signature of nanoparticle impacts were detected during all three operating periods, suggesting ubiquitous presence of these particles in the solar wind. The observed flux distribution is consistent with nanodust produced in the inner heliosphere, picked up by the solar wind, and carried to the outer heliosphere [Mann et al. 2007; Mann and Czechowski 2012]. Meyer-Vernet et al. [2009] analyzed RPWS observations during the Jovian flyby and estimated the flux of streaming nanoparticles ejected by the Jovian moon Io based on the bursty wave spectrum, which is consistent with the flux measured by the onboard dust analyzer CDA and Galileo dust instrument.

Magnetosphere-Ring Interaction Science

The Cassini mission brought about a profound new view the interaction of the amazing Saturnian main ring system with the magnetospheric space environment. During the Voyager era, it was presumed that meteors continually bombarded the rings. The spokes were thought to represent a stunning visual manifestation of these intense impacts. The associated impact-ionized vapor plume then delivered ring water and oxygen ions along connecting magnetic field lines to the ionosphere. These water ions were thought to chemically disrupt the ionosphere hydrogen cycle and deplete the ionosphere locally of electrons. It was also thought that these ring-generated ions possibly modify the color of the cloud tops. In this view, the rings were considered a source of quasi-energetic plasma delivering heavy ions to the exobase above the cloud-tops. Figure RPWS-10

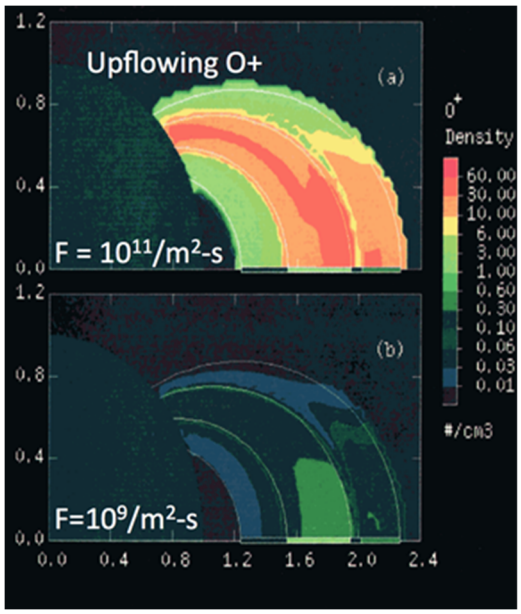

Figure RPWS-10. Impact-driven Ring Plasma Model [Wilson and Waite 1989].

shows the predicted impact-generated plasma flux from the rings, with peak densities over the dense portion of the central B-ring [Wilson and Waite 1989]. Voyager, unfortunately, did not actually fly over the rings and thus confirmation of this impact-driven ring plasma source could only be inferred.

At both the very beginning (SOI) and very end of the Cassini mission, the spacecraft flew directly across magnetic field lines that connect back down to the main rings, and thus obtained unique direct measurements of the plasma environment across the main A-ring, B-ring, and C-ring.

Saturn orbit insertion

Gurnett et al. [2005] presented a new view of the plasma environment over the main rings from the SOI overflight of the shadowed face of the rings. Figure RPWS-11 shows the corresponding plasma density as derived from the narrow-banded upper hybrid waves, electron plasma oscillations, and high frequency edge of the auroral hiss. All of these plasma wave features allow a high resolution direct derivation of the local electron density (see Gurnett et al. [2005] for a more detailed description of that derivation). In the profile, the various plasma wave sources are identified.

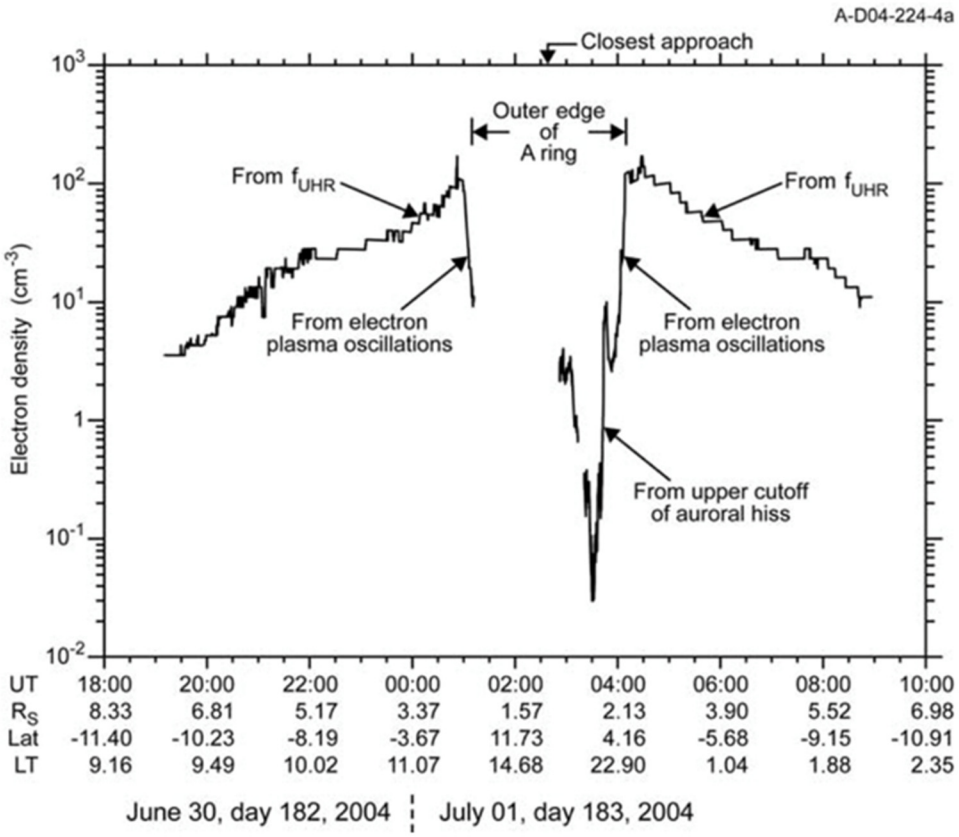

Figure RPWS-11. The electron density over the main rings as derived by the plasma waves detected by RPWS (see Gurnett et al. [2005] for more details).

There are two stunning features to this profile:

1. That immediately adjacent to the dense A-ring, there is an electron density maximum at over 100 electrons/cm^3, with the high density region (>10/cm^3) extending out to beyond L = 5. It would later be found [Persoon et al. 2009, 2015] that this high density region is a plasma torus created by ionization and pickup of new ions born in the Enceladus plume and a seasonal contribution from photo-ionized neutrals originating from the rings themselves. Thus, at equinox, the maximum in plasma density in this torus shifts radially outward to 4 R_S, but at solstice, the Sun-facing rings become a neutral and plasma source shifting the torus plasma maximum closer to the A-ring (see Figure 6 and 7 of Persoon et al. [2015]). The peak density in the torus is about 10% of the Io torus at Jupiter and represents a dominant controlling element in the inner magnetosphere of Saturn [Gurnett et al. 2007].

2. That the region over the main rings is devoid of plasma, with an electron density drop of near 10000 from the outer edge of the A-ring to values of 0.04 electrons/cm^3 at 1.76 R_S over the central portion of the B-ring [Xin et al. 2006; Farrell et al. 2017b]. This void region has been identified as a ring plasma cavity (RPC) with its lowest density near the synchronous location. The profile of electron density over the main rings varied inversely with ring optical depth, with the lowest plasma densities observed over the central dense B-ring and a local maxima sense when passing over field lines connected to the Cassini Division. (In Figure RPWS-11, this Cassini Division plasma maxima is seen near 03:45 spacecraft event time (SCET) with the local peak near 10/cm^3.)

This electron density profile was unexpected and almost diametrically opposite to what would have been predicted from an impact-driven ring plasma system, where the maximum in plasma density is expected in the central B-ring (like in Figure RPWS-10).

Evidence for photolytic-driven rings

RPWS SOI observations confirm the model of Tseng et al. [2013] that the ring-ionosphere-magnetosphere interaction is driven by photolytic processes, not impact processes [Farrell et al. 2017b]. Specifically, the sun-facing side of the main rings are a source of photo-dissociated neutrals that then get ionized to form a relatively low energy exo-ionosphere. This exo-ionosphere cannot directly access the shadowed/unlit side of the rings: the ring particles represent obstacles to their transport. Thus, the plasma density on the unlit side is modulated by ring density, being lowest where the ring obstruction is the highest—in the central B-ring. Local maxima are expected where the local ring particle density is low, like across the Cassini Division. There is little evidence of impact-generated plasma like that predicted during the Voyager era.

New main ring-magnetosphere current system

Xin et al. [2006] reported a strong auroral hiss signal detected at the deepest depletion of the electrons within the RPC near 1.76 R_S. The whistler-mode auroral hiss emission is a classic signature of the presence of energetic-field-aligned electron beams, in this case flowing outward from the rings along field lines connecting to the ionosphere. They reported that the RPC environment had a stunning similarity to plasma cavities found in polar auroral regions, usually associated with field-aligned currents that drive the aurora. The observation suggested that there is a current system driven by the rings-magnetosphere interaction, with the electron beams and currents near the synchronous point at 1.76 R_S possibly being part of the current closure system.

Figure RPWS-12 illustrates the concept of this new ring current system presented in Xin et al. [2006]. While the plasma on field lines over the rings would be corotating, the particles and associated photo-dissociated gas of the rings would be moving in Keplerian motion, creating drag on the plasma. This drag creates an associated change in plasma speed, ΔV. Beyond the synchronous point, the plasma is slowed by the Keplerian-moving particles and gas, creating an outward radially-directed E-field in order to maintain the new subcorotation speed $E' = \Delta V \times B$. This new E-field drives an outward current, J, which acts to then form a magnetohydrodynamic $J \times B$ force to balance the plasma-ring drag force. Inward of the synchronous point, the corotating plasma is accelerated by the ring drag force, creating an inward radial E-field and current that forms a $J \times B$ force to offset the acceleration. At the edges of the rings, these cross-ring currents become field-aligned parallel current that close down to the ionosphere along connecting magnetic field lines at the outer edge of the A-ring near L = 2.25 and inner edge of the D-ring near L ~ 1.11. The rings thus behave as an electrical generator in the plasma, driving currents from the ring surfaces along magnetic field lines down to the ionosphere.

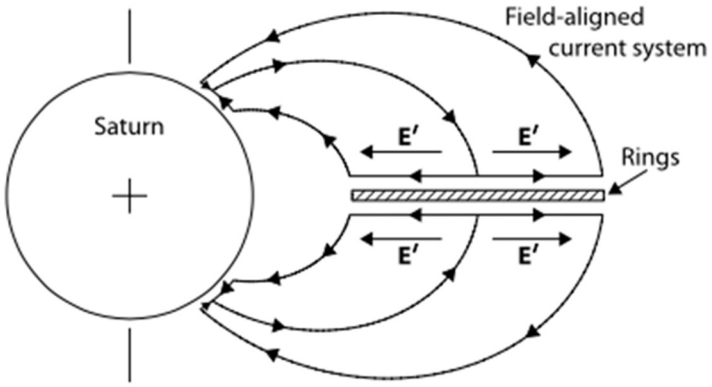

Figure RPWS-12. The proposed large-scale current system that would be induced in Saturn's magnetosphere by the interaction of the rings (including any associated gas) with the corotating magnetospheric plasma. Figure from Xin et al. [2006].

Subsequent RPWS observations confirm the presence of the various elements of this current system:

1. After SOI, Gurnett reported that bursts of auroral hiss emission were observed during SOI at the outer edge of the A-ring by RPWS. These events were initially reported to possibly be from impacts on the rings. However, the burst localization limited to only the very outer edge of the A-ring suggests the non-unique possibility that these auroral hiss emissions are associated with bursty field-aligned electron beams that make up the outer edge of the Xin et al. current system at L ~ 2.2.

2. Farrell et al. [2005b, 2008] reported on z-mode radiation emitted from active plasma hot spots along the outer edge of the A-ring where the rings and corotating magnetospheric plasma disk interact. Newly-born corotating ions created by photo-ionization of neutrals from the Enceladus torus or sunlit side of the rings would be the source of this ring-plasma interaction. Farrell et al. [2005b] and Menietti et al. [2016b] proposed wave generation mechanisms to explain the z-mode emitted from active regions.

3. Kopf et al. [2011] reported on the fine structure of Saturnian Kilometric Radiation from active auroral regions. They found there was a population of events having fine structure emission frequency vs time emission drifts consistent with emission at low latitudes from the L = 2.2 field line. The observation suggests the L = 2.2 field line at the outer edge of the A-ring is active, with parallel currents creating SKR at the field line footprint above the cloud-tops.

4. As discussed in this section, auroral hiss indicative of electron beams and inward flowing currents were detected near the synchronous point at 1.76 R_S [Xin et al. 2006]. This observation was the inspiration for the model of the main ring-magnetosphere current system.

Some added key evidence for this current system is still being derived from the ongoing analysis of the proximal orbit sequence that occurred in 2017.

Proximal orbit analysis and added evidence for the main ring-magnetosphere current system

While detailed analysis of the proximal orbits is still ongoing, Wahlund et al. [2018] reported on a very strong Saturnian ionosphere-D-ring electrical connection, which would represent the current closure of the Xin et al. [2006] model at the inner radial edge of the main rings. Using the RPWS Langmuir probe, they found that Cassini passed through a cold, dense electron region during proximal perigee, which has been interpreted to be entry into the Saturnian ionosphere. Figure RPWS-13 shows an example proximal electron density profile from orbit 271. The peak densities are in excess of $10^3/cm^3$, consistent with passing through the ionosphere. However, as evident in this and other passes, the ionospheric densities had relative maxima and/or unusual fluctuations

on field lines connected to the D-ring (near ±10° latitude). This effect was reported by Wahlund et al. [2018] to be associated with the Keplerian D-ring charged particles driving currents on field lines connected to the corotating ionosphere plasma.

At higher altitude proximal perigee passes, like orbit 277, Cassini passed through the inner edge of the D-ring (also immersed in the outer edge of the ionosphere). In these cases, the electron density had a distinct bite-out or decrease near the equator which is believed to be due to the presence of D-ring particulates that have absorbed the local ionospheric plasma. The RPWS instrument also detected micron-sized dust grain impacts revealing the presence of these D-ring particulates. The complex dusty plasma interactions remain a subject of considerable study even after the end of the mission.

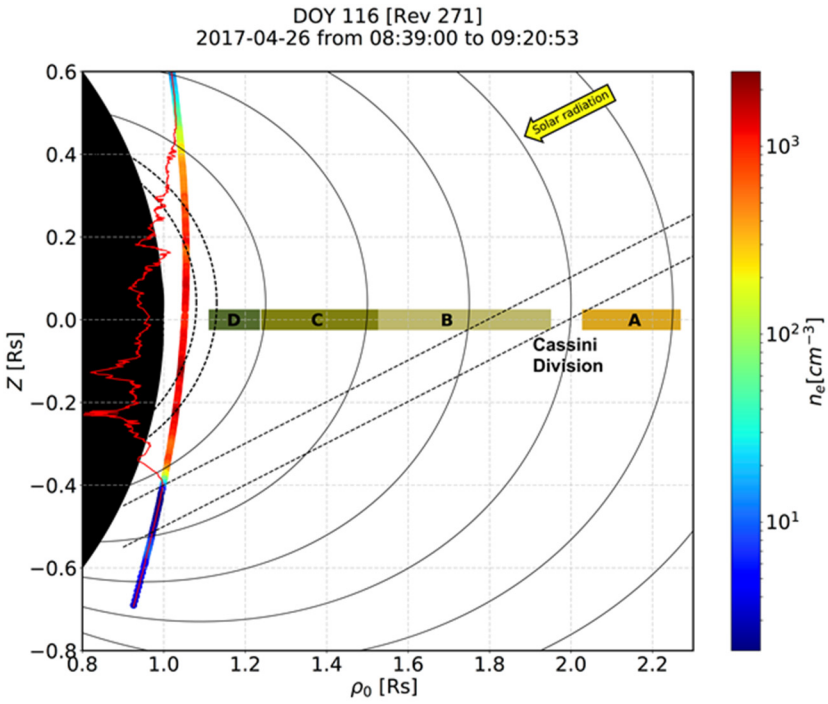

Figure RPWS-13. The Cassini spacecraft trajectory during April 26, 2017, crossed through the gap between the planet Saturn (solid black) and its rings (denoted D, C, B, Cassini Division, A) from north to south. The color code signifies the electron number density as measured by RPWS, which is also shown as a red line (in linear scale, density increases toward the left) where detailed structures can be detected. Four dominant electron density enhancements are connected via Saturn's magnetic field to, or inside, the inner edge of the D-ring (dashed lines). The solar elevation angle was 26.7° during the event, and the shadows of the B- and A-rings result in decreased ionization in the south. From Wahlund et al. [2018].

With repeated sampling of magnetic field lines connected to the main rings during the proximal orbit, Sulaiman et al. [2018b] reported the first observations of VLF saucers originating from Saturn's ionosphere, similar to what was observed at the Earth by the Fast experiment [Ergun et al. 2003]. Furthermore, Sulaiman et al. [2019] found evidence to strongly support the single observation that Xin et al. [2006] reported, hinting a ring-ionosphere current system. This concluded

the existence of a persistent, large-scale, and ordered electrodynamic connection between Saturn and its main rings.

The spokes in the context of the ring-plasma cavity and ring current environmental systems

The enigmatic spokes found near the center of the B-ring (near the synchronous location) were the source of numerous observation and theoretical works during the Voyager era. Their amazing observation captured the imagination since they represented a dynamic, impulsive, modern process occurring on the ring surfaces. Unfortunately, Voyager did not pass over the rings so the space environment associated with the spokes remained unknown until Cassini.

The review by Goertz [1989] described the spokes as being a result of a meteoric impact onto the rings that releases high volumes of charged dust, neutrals, ions, and electrons from the ring surface. Immediately after impact, the plume charged species undergo pickup, with electrons getting picked up immediately, then ions and then the more massive dust. This spatial spread in charged species created by local pickup thus was hypothesized to form an azimuthally-directed transient E-field. The various species then were predicted undergo an ExB drift to migrate radially forming spokes from the central B-ring.

However, during SOI and the proximal orbits, Cassini transited field lines that connect to the spoke locations (although spoke activity was not reported during these times). Farrell et al. [2006] reported that the Voyager spoke occurrences are spatially co-aligned with the ring-plasma cavity observed during SOI. Figure RPWS-14 overlays the SOI observations of the RPC with the Voyager-detected spoke occurrences [Grün et al. 1992]. The stunning spatial coincidence suggests that the spokes might then be some visual manifestation of the larger electrical current system containing the electron beam, auroral hiss, and plasma cavity detected during the Cassini SOI passage.

Any new dusty-plasma plume forming in the central B-ring is thus injected into the low density RPC environment with a radially-directed E-field (see Figure RPWS-12) along the ring surface [Xin et al. 2006]. The radial E-field may then provide the acceleration the spoke's charged dust in the radial direction. This new acceleration process would replace the more complex requirement of having to form a transient azimuthal E-field to create the subsequent radial transport.

HST observations [McGhee et al. 2005] indicated that the spokes on the sun-lit faces of the rings—those visible to Hubble Space Telescope (HST)—tended to disappear when the ring tilt angles exceeded ~15°, under increasing solar UV radiation conditions. Farrell et al. [2006] noted that at these angles the local photo-electron emission from the ring surfaces would exceed the electron densities in the plasma cavity—thus destroying the RPC environment and changing the local surface potential polarity from negative to positive. They suggested this photo-electron effect from solar exposure might explain the reported loss of the spokes at relatively large tilt angles observed by HST.

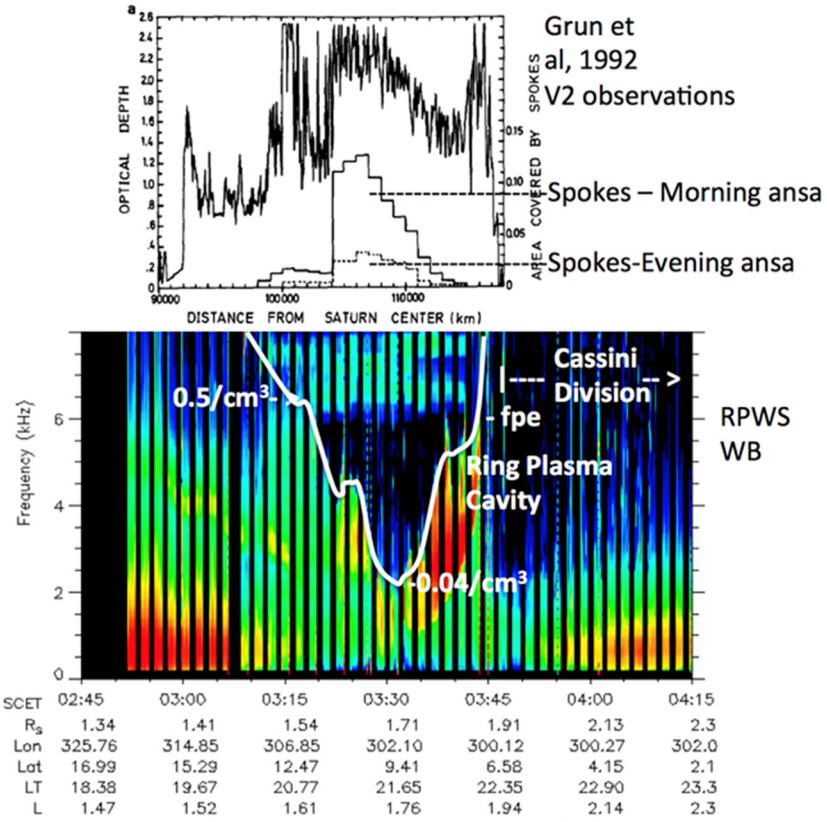

Figure RPWS-14. The ring plasma cavity detected during SOI as evident by the deep minimum in electron plasma frequency (indicated with the white line) in the RPWS wideband spectrogram. *Top panel*: location of the Voyager-observed spokes occurrence from Grun et al. [1992] with the two plots co-aligned by L-shell value. Presented by W. M. Farrell, M. D. Desch, M. L. Kaiser, W. S. Kurth, and D. A. Gurnett at the Joint Juno-Cassini workshop 2015.

Radio Emissions and Periodicities

Saturn's radio emissions started to be observed by Cassini/RPWS over the 10–1000 kHz range (see section entitled Kilometric Radiation) from distances of a few astronomical units. From late 2002 to early 2003, they were embedded in Jovian radio emissions and solar radio bursts. Their signal-to-noise ratio increasing with decreasing distance to Saturn, they became the dominant emission for the mid-2003 to mid-2004 year preceding Saturn's orbit insertion. These emissions divided into three main components, which have been analyzed separately or comparatively, as described below, to address most of the scientific objectives described in previous sections. Figure RPWS-15 shows examples of Saturn Kilometric Radiation (SKR), 5- and 20-kHz narrowband (NB) emissions and Saturn Drifting Bursts (SDBs) along with Saturn Electrostatic Discharges (SEDs) at the higher frequencies.

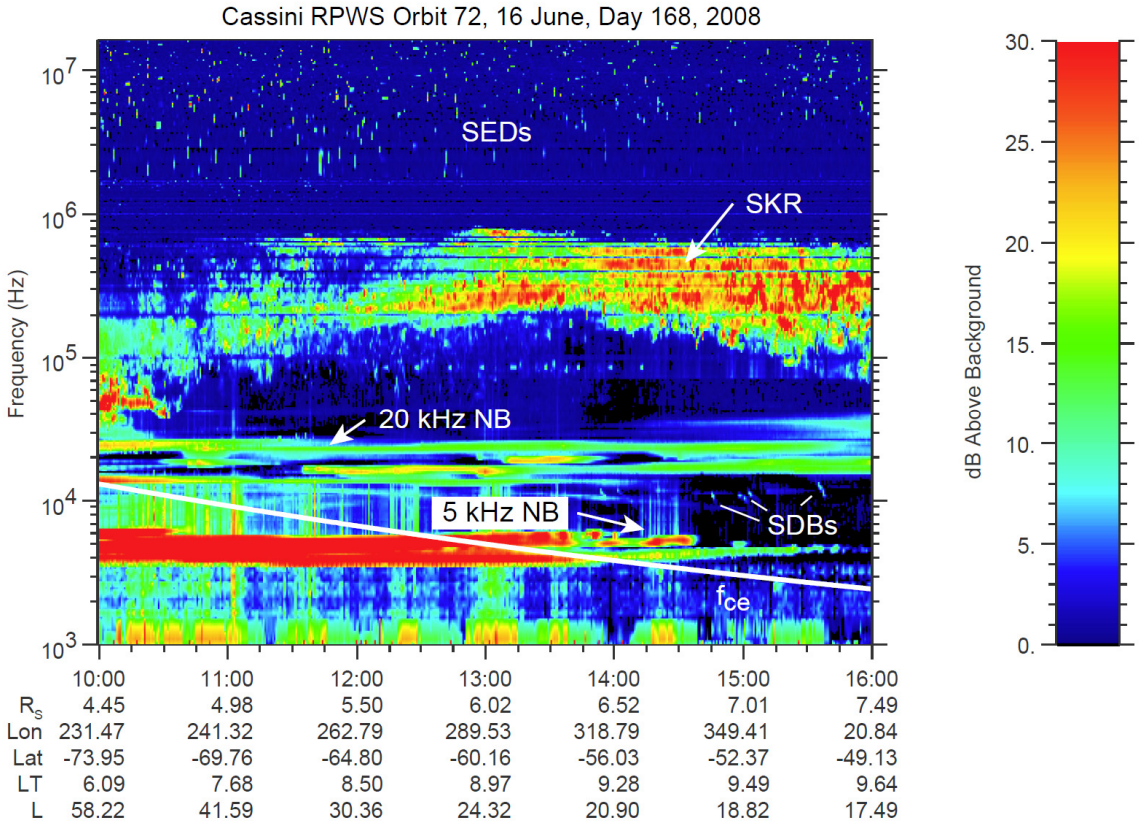

Figure RPWS-15. An illustration of the the major Saturnian radio emissions. From highest frequencies: SEDs, Saturn electrostatic discharges from lightning; SKR, Saturn Kilometric Radiation, 20- and 5-kHz NB, emissions, and SDBs, Saturn drifting bursts.

Kilometric radiation

Saturn's Kilometric Radiation is the most intense radio emission component, produced in the auroral regions. Several reviews of SKR properties have accompanied the Cassini mission [Kurth et al. 2009; Badman et al. 2014], the most recent one summarizing our current knowledge before Cassini Grand Finale [Lamy 2017] (see in particular Figure 1 of Lamy [2017] which plots all RPWS observations of SKR over the course of the Cassini mission).

REMOTE PROPERTIES

- The SKR spectrum was studied statistically with RPWS observations from a wide variety of Cassini's positions. It extends from a few kHz to 1 MHz and appears to be most intense when observed from the dawn-side at mid-latitude [Lamy et al. 2008a; Kimura et al. 2013]. Southern SKR was predominant up to 2010 to mid-2011 (slightly after the equinox of 2009), while the northern SKR was predominant after,

consistent with a seasonal control of field-aligned currents driving auroral emissions by solar illumination of Saturn's ionosphere.

- The SKR sources were routinely located by RPWS/HFR direction-finding (goniopolarimetric analysis, which additionally provided the apparent wave beaming angle. The radio sources were observed to be hosted by magnetic field lines at all longitudes whose footprints map to the circumpolar auroral oval [Farrell et al. 2005a; Cecconi et al. 2006; Lamy et al. 2009]. The emission is strongly anisotropic, with a beaming angle decreasing with frequency, which produces arc-shaped emissions in the t-f plane [Lamy et al. 2008b; Cecconi et al. 2009; Lamy et al. 2013].
- SKR is a right-handed (RH) fully elliptically polarized emission. It is seen predominantly in the R-X (and marginally in the L-O) mode, with RH/LH (LH/RH) polarization witnessing emissions coming from the northern/southern (southern/northern) hemispheres, respectively. SKR was remotely found to display quasi-purely circular polarization at latitudes below 30° and strongly linearly polarized above [Cecconi and Zarka 2005a; Masters et al. 2009].
- SKR displays several types of dynamics. At timescales of a few minutes, SKR displays fine structures drifting in frequency and reminiscent of auroral kilometric radiation (AKR) fine structures observed at Earth. Multiple origins accounting for the slow drifts of a few kHz/min are debated [Kurth et al. 2005b]. At timescales of hours, active flux tubes hosting anisotropic radio sources produce isolated arcs in the time-frequency plane, whose characteristics relate to the wave beaming angle and the position/motion of the source with respect to the observer. At timescales of 11 h, the emission is strongly rotationally modulated (see section entitled Radio Periodicities). At longer timescales, SKR strongly brightens episodically, indicating auroral storms driven or not by the solar wind and thus probing large-scale magnetospheric dynamics [Kurth et al. 2005a, 2016; Clarke et al. 2005; Crary et al. 2005; Jackman et al. 2005, 2009, 2010; Badman et al. 2008a, 2016; Nichols et al. 2009; Lamy et al. 2013; Reed et al. 2018].

In situ characteristics:

SKR sources were crossed twice at 10–20 kHz before the Cassini Grand finale. Their detailed study revealed that SKR is fully consistent with the Cyclotron Maser Instability (CMI) developed for AKR at Earth. It is radiated perpendicular to the magnetic field-lines from shell-like electron distribution functions of 6–9 keV [Lamy et al. 2010a; Mutel et al. 2010; Bunce et al. 2010; Schippers et al. 2011; Kurth et al. 2011; Menietti et al. 2011a, 2011b]. SKR polarization turned to be strongly linearly polarized at the source, as expected for perpendicular emission, and was found to be circularized along its propagation through the surrounding environment in agreement with expectations from the magneto-ionic theory in a cold, weakly inhomogeneous, plasma [Lamy et al. 2011a]. A statistical survey of the ring-grazing orbits revealed three additional passes of the spacecraft within low frequency dawnside northern SKR sources. The amplified waves were again

found to be strongly linearly polarized, radiated quasi-perpendicularly from the field lines through the CMI from 6-12 keV unstable electrons. Additionally, the SKR source region was interestingly seen to be only partially colocated with the UV auroral oval as the local plasma density was surprisingly variable and sometimes high enough to quench the CMI [Lamy et al. 2018a]. Cassini proximal orbits will provide further insights to the statistical characterization of SKR high frequency sources.

Narrowbanded emissions

At the lower edge of SKR spectrum, narrowbanded (NB) emissions have been observed between 3 and 70 kHz, and divide in two main components around 5 kHz and 20–40 kHz. Their observation by RPWS has been reviewed by [Ye et al. 2011].

The 5 kHz emissions, early labelled n-SMR for NB myriametric emissions in analogy with narrowband kilometer (nKOM) at Jupiter, were observed to rise in association with sudden SKR intensifications and related to ejection events from the plasma disk [Louarn et al. 2007]. The 5 kHz component was found to be intense and weakly circular polarized while the 20–40 kHz component, proposed to be referred to as n-SKR, appeared to be weaker and highly circularly polarization, both being better observed from high latitudes [Lamy et al. 2008a].

The source locus, dynamics, and wave growth of NB emissions were investigated in depth through a series of statistical and case studies [Menietti et al. 2009, 2010b, 2016b; Ye et al. 2009, 2010a; Wang et al. 2010; Gu et al. 2013]. Both components were found to propagate in the L-O ordinary mode. The 20–40 kHz component was proposed to be generated by mode conversion of electrostatic upper hybrid waves on the boundary of the plasma torus. The 5 kHz component is produced on the Z-mode from the lower density region near the inner edge of the Enceladus torus and possibly from the auroral regions as well by a generation mechanism not unambiguously identified yet.

Saturn Drifting Bursts

Another type of low frequency radio emissions called Saturn Drifting Bursts (SDBs) was detected with RPWS below 50 kHz [Taubenschuss et al. 2011]. These bursty emissions are highly circularly polarized, propagating in R-X and L-O modes and display emission at the fundamental and first harmonic frequencies. They last for a few minutes and occur intermittently as slowly drifting events in the time-frequency spectrogram. Possible generation mechanism include CMI and linear or nonlinear mode conversion.

Radio periodicities

RPWS brought crucial observations to the study of the rotational modulation of Saturn's magnetosphere through measurements of periods of SKR and NB emissions (see reviews in Gurnett [2011]; Lamy et al. [2011a]; Lamy [2017]; Carbary and Mitchell [2013]; Szego et al. [2015]).

The first SKR periodicity measured by RPWS witnessed a value differing by 1% to the SKR period identified from Voyager/Planetary Radio Astronomy (PRA) observations 25 years earlier [Gurnett et al. 2005]. Such a large variation implies that the SKR period does not probe the internal rotation rate. The measured SKR period was then found to display weak variations associated with those of solar wind speed [Cecconi and Zarka 2005b; Zarka et al. 2007].

The major discovery brought by RPWS was then the identification of two SKR periods [Kurth et al. 2008] corresponding to the two kronian hemispheres, differing by ~1%. These periods were found to both vary with time in anti-correlation over yearly timescales and crossed closely after equinox, a trend which was interpreted as a seasonal driving of solar illumination [Gurnett et al. 2009a, 2010b, 2011b; Lamy 2011]. These dual periods were later noticed in NB emissions and auroral hiss as well [Gurnett et al. 2010a; Ye et al. 2010b; Ye et al. 2017] and more generally observed in numerous magnetospheric observables including magnetic oscillations, energetic neutral atom (ENA) emissions, aurorae [Mitchell et al. 2009c; Carbary et al. 2010, 2011; Nichols et al. 2010; Andrews et al. 2010, 2011; Provan et al. 2011; Badman et al. 2012a, 2012b]. It is now accepted that these dual rotational modulations all originate from two rotating hemispheric systems of field-aligned currents, whose origin may be atmospheric vortices [Jia et al. 2012].

The post-equinox period displayed a confused situation with poorly determined radio and magnetospheric periods. Over 2010–2012, they remained close to each other at locked phases, suggesting retro-interaction between both currents systems [Garnier et al. 2014], while sudden jumps of periods were tentatively attributed to Saturn's great whit spot activity [Fischer et al. 2014b] or to variable solar wind conditions [Provan et al. 2015]. Both periods eventually merged between mid-2013 and mid-2014 before crossing and diverging from each other after mid-2014 up to September 2017 [Provan et al. 2016; Ye et al. 2016b, 2017; Lamy 2017]. Figure RPWS-16 summarizes the variation of northern and southern SKR periods found by Ye et al. [2018c].

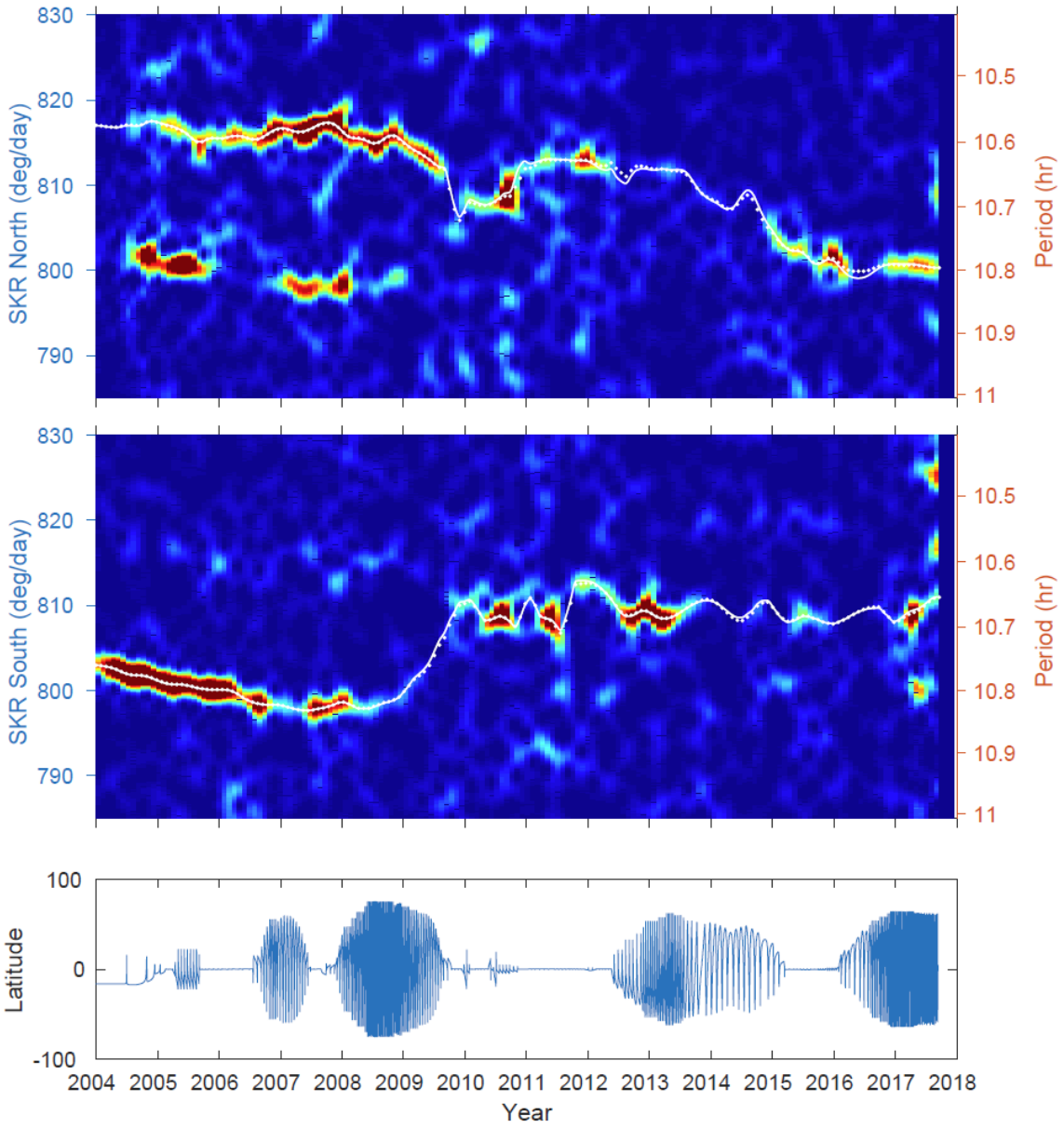

Figure RPWS-16. Rotational modulation spectrograms for SKR. *Top panel*: northern, *Middle panel*: southern hemispheres. The spectrograms show normalized modulation power (calculated using the least-squares spectral analysis) as a function of rotation rate and time. The white dotted lines show the automatically traced rotation rates (zeroth order) of north/south SKR. The white solid lines are corrected SKR rotational modulation rates (based on the zeroth-order rates and corrected by the phase drifts traced in Figure 1 of Ye et al. [2018c]). *Bottom panel*: is the latitude of Cassini.

Magnetosphere and Solar Wind Interactions Science

The Cassini RPWS instrument has helped investigate many different effects due to the interaction of the solar wind and the Saturnian magnetosphere, … .

The Cassini RPWS instrument has helped investigate many different effects due to the interaction of the solar wind and the Saturnian magnetosphere, how shock to the variations in the SKR intensity and frequency range, the presence of upstream Langmuir waves in the solar wind, and the detection of lion-roar like emissions in the magnetosheath. The following sections briefly discuss these observations and the various studies that RPWS has contributed to.

Solar wind influence on the Saturnian magnetosphere and aurora

The exact nature and importance of the solar wind influence on the Saturnian magnetosphere has long been debated. At Earth, the solar wind is the primary source of plasma in the magnetosphere and solar wind dynamics drive changes in the magnetosphere, including magnetic storms that lead to magnetic reconnection, plasma transport, and aurora. At Jupiter, the rapid rotation, large spatial scales, and internal source of plasma from the moon of Io, cause the magnetospheric dynamics to be primarily driven by centrifugal stresses rather than solar wind dynamics. The solar wind influence on the Saturnian magnetosphere has generally been considered to have both internal and solar-wind-driven processes. For example, the Voyager results suggested that the SKR pulsed at a period close to the planetary rotation period, but also that the emitted intensity was correlated with the solar wind dynamic pressure. This possible solar wind influence on the magnetospheric dynamics was an active area of research throughout the Cassini mission.

The approach to Saturn and the many orbits in which Cassini was located in the solar wind during apogee allowed in situ measurements of the solar wind while remote sensing measurements of the Saturn system were obtained. The remote sensing included Saturnian auroral imaging from the Hubble telescope and Cassini, plus observations by RPWS of the auroral radio emissions. During the approach to Saturn in early 2004, the Hubble Space Telescope took a number of ultraviolet images of the Saturn aurora and the comparison of these images to the Cassini observations were reported in a series of papers [Clarke et al. 2005; Crary et al. 2005; Kurth et al. 2005a]. During these observations, Saturn's auroras respond strongly to solar wind conditions, with the main controlling factor being solar wind dynamic pressure and electric field, with the orientation of the interplanetary magnetic field playing a much more limited role [Crary et al. 2005]. Clarke et al. [2005] reported that Saturn's auroral emissions varied slowly, with some features appearing to be related to corotation, and others are fixed to the solar wind direction. The auroral oval shifts quickly in latitude and is often not centered on the magnetic pole. In response to a large increase in solar wind dynamic pressure Saturn's aurora brightened dramatically, the brightest auroral emissions moved to higher latitudes, and the dawn side polar regions were filled with more intense emissions. The SKR emissions were also found to increase in intensity and drop in frequency

during the dynamic pressure increase and this intensity was correlated with the intensity of the aurora as shown in Figure RPWS-17 [Kurth et al. 2005a].

The relationship between solar wind dynamics, SKR, other magnetospheric properties, and the variation in the aurora continued in a number of different studies. During the SOI period, Jackman et al. [2005] suggested a major compression of Saturn's magnetosphere took place. Bunce et al. [2005] examined the in situ affects measured by Cassini that the corotating interaction region (CIR)-related compression had on Saturn's magnetospheric dynamics. For example, at ~02:00 UT on day 184, a burst of SKR emission is observed which disrupts the existing pattern of planetary modulated emission seen both upstream of the magnetosphere and during the inbound pass [Jackman et al. 2005; Kurth et al. 2005a]. Simultaneously, inside the magnetosphere, Cassini experienced a region of depressed and variable magnetic field. In addition, ion and electron observations show that this occurs as the spacecraft is engulfed by a hot, tenuous plasma population. They proposed that this behavior is indicative of a major episode of tail reconnection, triggered by the impact of the compression region on Saturn's magnetosphere.

The MIMI Ion and Neutral Camera (INCA) on the Cassini spacecraft also detected abrupt increases in energetic neutral atom flux coming from the general direction of Saturn's magnetotail that are well correlated with the enhancements in the Saturn kilometric radiation. Given the similarities between these events and substorm activity on Earth, including their dependence on interplanetary conditions, Mitchell et al. [2005] concluded that Earth-like substorms occur within Saturn's magnetosphere.

Taubenschuss et al. [2006b] examined the external control of SKR by the solar wind in the frame of the Linear Prediction Theory (LPT). Four basic solar wind quantities (solar wind bulk velocity, the solar wind ram pressure, the magnetic field strength of the interplanetary magnetic field (IMF) and the y-component of the IMF) were found to exert a clear influence on the SKR intensity profile. All four inputs exhibit nearly the same level of efficiency for the linear prediction indicating that all four inputs are possible drivers for triggering SKR, but all showed different lag times, ranging from ~13 hours for the ram pressure to ~52 h for the bulk velocity.

In contrasts to these earlier observations of direct correlations between solar wind magnetospheric dynamics, Gérard et al. [2006] reported results from a coordinated Hubble Space Telescope-Cassini campaign that took place between October 26 and November 2, 2005. During this period, Saturn's magnetosphere was in an expanded state and the solar wind was quiet, as indicated by the location of the magnetopause, in situ particle measurements, weak auroral SKR emission, and the generally low brightness of the aurora. The aurora exhibited considerable longitudinal structure and time variations over intervals of a few hours, in spite of the absence of observable external triggers and generally low intensity. In particular, enhancements of the dawn-morning oval were seen while no apparent indication of solar wind activity was observed. These features rotated at a speed corresponding to about 65% of the planet's angular velocity. Also, an ENA acceleration event occurred in the magnetotail on October 26 without any measured signature of solar wind activation. These observations suggest an intrinsically dynamical magnetosphere where injection of hot plasma occasionally takes place in the night or dawn sector during quiet

magnetospheric conditions, possibly connected with either the Dungey or the Vasyliunas convection cycle.

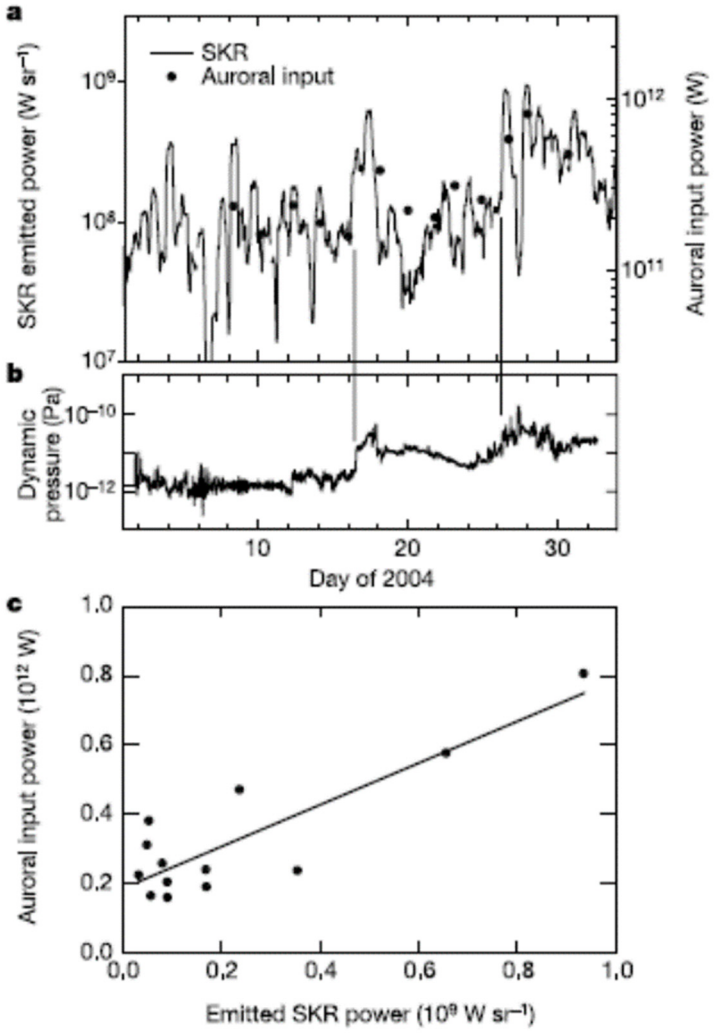

Figure RPWS-17. Correlations between auroral input power and emitted SKR power. *Panel a*: shows the time-averaged power emitted as SKR over plotted with the estimated auroral input power based on the ultraviolet aurora integrated intensity. *Panel b*: shows the solar wind dynamic pressure determined from Cassini measurements of the solar wind density and speed, and propagated to Saturn with a simple radial magnetohydrodynamic model. *Panel c*: compares the auroral input power and emitted radio power. Based on Figure 1 of Kurth et al. [2005a].

Louarn et al. [2007] reported on radio signatures observed at Saturn which are strikingly similar to the Jovian energetic events observed by Galileo. These radio signals consist of a sudden intensification of the SKR followed by the detection of a periodic narrowband radiation at about 5 kHz which most likely originates with plasma evacuation from Saturn's plasma disk. These radio signatures suggest that although Saturn's auroral activity is largely triggered by the solar wind,

energetic processes developing in the plasma disk are also involved, possibly associated with plasma transports and consequent releases of rotational energy.

In a study with a slightly different emphasis, Zarka et al. [2007] examined the possible role of the solar wind on the SKR radio period. As discussed in detail in the section entitled Radio Periodicities, as Cassini approached Saturn, the SKR period was measured to vary on the order of ~1% [Gurnett et al. 2005], and measurements over the first few years of the mission found that it actually exhibits two different periods [Kurth et al. 2008], and that each auroral polar region has its own dominate period that also varied with time [Gurnett et al. 2009a]. Zarka et al. [2007] found that the SKR period varied systematically by about ±1% with a characteristic timescale of 20–30 days, and that these fluctuations were correlated with solar wind speed at Saturn, suggesting that SKR is controlled in part, by conditions external to the planet's magnetosphere. No correlation was found with the solar wind density, dynamic pressure or magnetic field; suggesting that the solar wind speed therefore has a special role in this variation.

Rucker et al. [2008] reexamined the relationship between the SKR intensity and solar wind dynamics (both measured by Cassini and measured by Ulysses at ~5 AU and propagated to Saturn) for the year 2004. This study also found that the SKR intensity is positively correlated with solar wind pressure, and suggested that it may be possible to use the measured SKR properties as a monitor for the solar wind conditions.

Badman et al. [2008a] looked for variation of the SKR power observed by Cassini following arrival of thirteen solar wind compression event and investigated the phasing of the intensified or reduced emission peaks during the compression event, and the relative phasing and intensity of the emission peaks before and after the compression compared to the predictions of the drifting SKR period [Kurth et al. 2007]. They found that even though the behavior of the SKR following the compressions was somewhat variable, they confirmed that there was an overall positive correlation between the change in solar wind dynamic pressure and the change in emitted SKR power, and that the timings of the initial SKR intensifications following the compressions could be independent of the long-term phasing of the SKR bursts, but during the disturbed interval the SKR continues to pulse close to the expected times. Distinct extra bursts of SKR emission were also detected both before and during the compressions. The intensity of the detected emissions during the disturbed intervals was variable, sometimes remaining intense for several days, sometimes reducing, and in rare cases it disappeared. This variability showed that the SKR emissions cannot be simply used as a diagnostic of the prevalent solar wind conditions (e.g., when Cassini is inside Saturn's magnetosphere), without careful consideration of other influencing factors.

Clarke et al. [2009] built on the Cassini approach observations by using more aurora imaging data from a large campaign of observations in 2007 and 2008 of Saturn using the Hubble Space Telescope, in association with measurements from Cassini and determining solar wind conditions both by propagating measurements from 1 AU and by using Cassini observations when it was in the solar wind. The data found a one to one correspondence between the arrival of solar wind shocks at Saturn and increases in Saturn's auroral power and SKR emission, plus a decrease in the auroral oval radius. At the times of two reverse shocks, the SKR emission appeared to increase,

and possibly also the UV emission although the statistics were poor. These data are consistent with a causal relationship between solar wind disturbances and auroral and SKR emission increases as suggested in the earlier studies.

Mitchell et al. [2009c] adds to the above Clarke et al. [2009] results by examining the MIMI ENA results in conjunction with the auroral images and SKR observations. In the ENA observations, recurrent ring current oxygen intensity enhancements are usually detected that begin near midnight and increase in intensity and area as they rotate through the dawn meridian toward noon, and there is a close temporal association between recurrent ring current enhancements and recurrent SKR enhancements. For the single example of this recurring phenomenon for which continuous UV auroral imaging was available, bright corotating auroral emissions distributed in latitude from about 70 to 80 degrees tracked the ring current ion enhancement as it moved in local time from post-midnight to late morning. It was suggested that these recurrent events are caused by recurrent reconfiguration of the thin night-side current sheet in the 15–20 R_S region, probably associated with Vasyliunas-cycle reconnection and plasmoid release in the tail initiated relatively close to Saturn. The energy in such events presumably derives from Saturn's rotation, in combination with the mass loading of the cold plasma produced from Enceladus' extended gas cloud. However, a strong correlation was also found to exist between a solar wind pressure pulse resulting in magnetospheric compression and a ring current event, a sudden SKR power increase, and dawn-side auroral brightening. This correlation suggest a link between the asymmetric ring current enhancements and a rotating field aligned current system that drives both SKR enhancements and auroral displays. Such a relationship is implied for both the recurrent events with the Saturn rotation period and the solar wind pressure induced events.

The exploration of the nightside magnetosphere is reported in a series of papers by Jackman and coauthors. Jackman et al. [2009] revealed evidence of plasmoid-like magnetic structures and other phenomena indicative of the Saturnian equivalent of terrestrial substorms. In general, there was a good correlation between the timing of reconnection events and enhancements in the auroral SKR emission. Eight of nine reconnection events studied occur at SKR phases where the SKR power would be expected to be rising with time. Thus, while the recurrence rate of substorm-like events at Saturn is likely much longer than the planetary rotation timescale, the events are favored to occur at a particular phase of the rotation. Three examples were found in which the SKR spectrum extended to lower frequencies than usual. These low frequency extension SKR events were labeled low frequency extension (LFE) and were interpreted as an expansion of the auroral particle acceleration region to higher altitudes (lower radio frequency) along magnetic field lines as a direct consequence of an increase in the magnetosphere-ionosphere current density driven by substorm-like events. Saturnian substorms are likely a much more prevalent phenomenon than this small number of observations suggests, but the statistics in this study were hampered by viewing geometries, primary the small amount of time that Cassini spent in the deep magnetotail near the nominal current sheet location. Many examples of LFEs are observed by

In general, there was a good correlation between the timing of reconnection events and enhancements in the auroral SKR emission.

Cassini from a wide set of vantage points, but the spacecraft is only in the right position to observe the corresponding magnetic signature (if any) a fraction of the time.

Jackman et al. [2010] explored the dynamic response of Saturn's magnetotail to an episode of solar wind compression that took place while Cassini was sampling Saturn's nightside equatorial magnetosphere in 2006. Following an initial increase in solar wind dynamic pressure, the magnetosphere was compressed and became more streamlined, with an elevated lobe field strength as external pressure compressed the tail. Then, assuming a favorable IMF direction (for at least part of the interval, as seems entirely plausible), dayside reconnection may have been ongoing, leading to an increase in the amount of open flux inside the magnetosphere, flaring of the magnetotail, and continued elevated lobe field strength. Because of the longer time scales involved at Saturn for loading of the tail with open flux, it can take several days for the tail to be inflated to a point where reconnection is likely to occur, and this study suggested that the time scale observed in this case was of order ~6–7 days. No strong evidence for magnetotail reconnection events during this loading phase were detected, however, toward the end of this period a sharp decrease in lobe field strength and what appears to be significant current sheet deflection toward the equator from its previously hinged position was observed. Several days later the current sheet was displaced southward from its previously hinged position, and magnetic signatures consistent with the passage of a plasmoid were observed. These field signatures are closely correlated with intense radio emission, evidenced by LFEs of radio emission, corresponding to radio sources detected at higher altitudes. All of the above features are believed to be a common consequence of the impact of a solar wind compression on Saturn's magnetosphere.

Jackman et al. [2015] presented a rare observation of strong planetward flow following a reconnection episode in Saturn's tail from August 2006, when the Cassini spacecraft was sampling the region near 32 R_S and 22 h LT. Cassini observed a strong northward-to-southward turning of the magnetic field, which is interpreted as the signature of dipolarization of the field as seen by the spacecraft planetward of the reconnection X line. This event was accompanied by very rapid (up to ~1500 km s^{-1}) thermal plasma flow toward the planet. At energies above 28 keV, energetic hydrogen and oxygen ion flow bursts were observed to stream planetward from a reconnection site downtail of the spacecraft. Meanwhile, a strong field-aligned beam of energetic hydrogen was also observed to stream tailward, likely from an ionospheric source. SKR radio emissions enhancements similar to ones previously associated with plasmoid formation and release were detected slightly more than an hour after the observation of the dipolarization. The reconnection episode as inferred from the planetward directional flow duration lasts on the order of ~1.5 h, a significant fraction of a planetary rotation. The continuing presence of energetic O+ ions throughout the event demonstrates that this must be a case of long-lasting Vasyliunas-type reconnection occurring beyond 32 R_S in the premidnight region, perhaps indicating quasi-steady reconnection of the type. Because of the persistent presence of O+, we find little evidence for lobe involvement in the reconnection.

Kimura et al. [2013] investigated the very long-term (six years of measurements) variations of northern and southern SKR spectra, separated by polarization. This study confirms the prominent

role of solar wind pressure over one solar cycle, and additionally identified a seasonal dependence of the SKR activity, with a maximum in summer.

Kurth et al. [2016] reports on the SKR measurements obtained during a Saturn auroral campaign carried out in the spring of 2013 which used multiple Earth-based observations, remote-sensing observations from Cassini, and in situ-observations from Cassini. Saturn kilometric radiation was remotely monitored nearly continuously providing a measure of the auroral activity and a means of understanding the temporal relationships between the sometimes widely spaced remote sensing observations of the auroral activity. While beaming characteristics of the radio emissions are known to prevent single spacecraft observations of this emission from being a perfect auroral activity indicator, a good correlation between the radio emission intensity and the level of UV auroral activity was observed, when both measurements are available, similar to what the previous studies had shown. Given the known influence of solar wind dynamics on both SKR intensity and auroral activity as discussed above, the SKR integrated power is also a proxy for solar wind activity. This study found that there is a good correlation between the 10-h averages of SKR power flux and the power estimated input to the aurora on the basis of the UV brightness, justifying the SKR as a simple proxy for auroral activity through the campaign. The SKR emissions also give evidence for a recurrent pattern of solar wind interaction with Saturn's magnetosphere, suggesting a two-sector structure and associated corotating interaction regions influencing the level of auroral activity on Saturn. However, there are other SKR intensifications that may be due to internal processes.

Bunce et al. [2014] presented an unusual case in January 2009, where Ultraviolet Imaging Spectrograph (UVIS) observes the entire northern UV auroral oval during a 2 h interval while Cassini traverses the magnetic flux tubes connecting to the auroral regions near 21 LT, sampling the related magnetic field, particle, and radio and plasma wave signatures. The motion of the auroral oval evident from the UVIS images was found to be consistent with the appropriate phase of the magnetosphere oscillations in the northern hemisphere, whereas previous interpretations have assumed a static current system. Concurrent observations of the auroral hiss (typically generated in regions of downward directed field-aligned current) support this revised interpretation of an oscillating current system.

Thomsen et al. [2015b] presented observations that suggest that under some conditions the solar wind governs the character of the plasma sheet in the outer magnetosphere. Observations from September 2006, near local midnight at a radial distance of 37 R_S, showed a planetward flowing ion population for ~5 hours, which was accompanied by enhanced SKR emissions. This ion beam was interpreted as the outflow from a long-lasting episode of Dungey-type reconnection, i.e., reconnection of previously open flux containing magnetosheath material. The beam occurred in the middle of a several-day interval of enhanced SKR activity and lobe magnetic field strength, likely caused by the arrival of a solar wind compression region with significantly higher than average dynamic pressure (magneto-hydrodynamic (MHD) propagation models of the solar wind from 1 AU observations to Saturn during this period suggest the presence of higher density solar wind). There was also a change in the composition of the plasma-sheet plasma, from water-group-dominated material clearly of inner-magnetosphere origin to material dominated by light-ion composition,

consistent with captured magnetosheath plasma. This event suggests that under the influence of prolonged high solar wind dynamic pressure, the tail plasma sheet, which normally consists of inner-magnetospheric plasma, is eroded away by ongoing reconnection that then involves open lobe field lines. This process removes open magnetic flux from the lobes and creates a more Earth-like, Dungey-style outer plasma sheet dominantly of solar wind origin. This behavior is potentially a recurrent phenomenon driven by repeating high-pressure streams (corotating interaction regions) in the solar wind.

During a coordinated auroral observing campaign on April 21–22, 2013, instruments onboard Cassini and the Hubble Space Telescope observed Saturn's northern and southern aurora while Cassini traversed Saturn's high latitude auroral field lines [Badman et al. 2016]. Signatures of upward and downward field-aligned currents were detected in the nightside magnetosphere, with the location of the upward current corresponded to the bright ultraviolet auroral arc seen in the auroral images, and the downward current region located poleward of the upward current in an aurorally dark region. In the area poleward of the auroral oval, magnetic field and plasma fluctuations were identified with periods of ~20 and ~60 min. During April 21, 2013 the northern and southern auroral ovals were observed to rock in latitude in phase with the respective northern and southern planetary period oscillations. A solar wind compression impacted Saturn's magnetosphere at the start of April 22, 2013, identified by the intensification and extension to lower frequencies of the SKR. At this time, a bulge appeared along the pre-dawn auroral oval, which appeared to have moved sunward when this region was next observed. The midnight sector aurora remained a narrow arc at this time. Subsequently, the post-midnight aurora broadened in latitude and contracted towards the pole. The motion in this sector was in the opposite direction to that expected from the planetary period oscillation. There was also an intensification of the auroral field-aligned currents. These observations are interpreted as the response to tail reconnection events instigated by solar wind compression, initially involving Vasyliunas-type reconnection of closed mass-loaded magnetotail field lines, and then proceeding onto open lobe field lines, causing the contraction of the polar cap region on the post-midnight sector.

Felici et al. [2016] presented a case study of data from Saturn's magnetotail, when Cassini was located at ~22-hour Local Time at 36 R_S from Saturn that suggests for the first time that a low-energy ionospheric outflow event has been detected at planets other than Earth. During several entries into the magnetotail lobe, tailward flowing cold electrons and a cold ion beam were observed directly adjacent to the plasma sheet and extending deeper into the lobe. The electrons and ions appear to be dispersed, dropping to lower energies with time. The composition of both the plasma sheet and lobe ions show very low fluxes (sometimes zero within measurement error) of water group ions. The magnetic field has a swept-forward configuration which is atypical for this region, and the total magnetic field strength is larger than expected at this distance from the planet. Ultraviolet auroral observations show a dawn brightening, SKR is enhanced and extends down to lower frequencies, and upstream heliospheric models suggest that the magnetosphere is being compressed by a region of high solar wind ram pressure. This event is interpreted as the observation of ionospheric outflow in Saturn's magnetotail, with the active atmospheric regions most likely the main auroral oval.

The majority of the previously discussed studies involved periods where Saturn's magnetosphere encountered a high density solar wind. The study by Kinrade et al. [2017] discusses observations during a period that Saturn's magnetosphere was in a rarified solar wind region. During this period on June 14, 2014 (day 165), the Hubble Space Telescope observed an unusual auroral morphology, where for 2 h, the Saturn's far ultraviolet (FUV) aurora faded almost entirely, with the exception of a distinct emission spot at high latitude. The spot remained fixed in local time between 10 and 15 LT and moved poleward to a minimum colatitude of ~4°. Interestingly, the spot constituted the entirety of the northern auroral emission, with no emissions present at any other local time—including Saturn's characteristic dawn arc, the complete absence of which is rarely observed. Solar wind parameters from propagation models, together with a Cassini magnetopause bow shock crossing, indicate that Saturn's magnetosphere was in an expanded magnetosphere configuration during the interval, suggesting it was likely embedded in a rarefaction region. The spot was possibly sustained by reconnection either poleward of the cusp or at low latitudes under a strong component of interplanetary magnetic field transverse to the solar wind flow. The subsequent poleward motion could then arise from either reconfiguration of successive open field lines across the polar cap or convection of newly opened field lines. The spot's fixed LT position may be attributed to the negative IMF BY conditions incident at the time, combined with increased subcorotation of open flux toward higher latitudes. The emission intensity was also possibly enhanced by a sector of upward planetary period oscillation (PPO) current rotating through the region. These observations show conclusively that the mechanisms producing noon auroral spots and the main oval auroras (i.e., the dawn arc) are distinct, since in this case the cusp spot occurred without the arc. These observations also suggest that reconnection can occur in an expanded magnetosphere, in agreement with the cusp observations of Arridge et al. [2016a, 2016b], who found evidence of reconnection under a range of upstream solar wind conditions.

Solar wind parameters from propagation models, …, indicate that Saturn's magnetosphere was in an expanded magnetosphere configuration during the interval, suggesting it was likely embedded in a rarefaction region.

A recent study by Roussos et al. [2018] uses a novel technique to overcome the lack of an upstream solar wind monitor at Saturn. Cassini MIMI/LEMMS observations of solar energetic particle (SEP) and galactic cosmic ray (GCR) transients, that are both linked to energetic processes in the heliosphere such us interplanetary coronal mass ejections (ICMEs) and CIRs, are used to trace enhanced solar wind conditions at Saturn's distance. A survey of the MIMI/LEMMS dataset between 2004 and 2016 resulted in the identification of 46 SEP events. Most events last more than two weeks and have their lowest occurrence rate around the extended solar minimum between 2008 and 2010, suggesting that they are associated to ICMEs rather than CIRs, which are the main source of activity during the declining phase and the minimum of the solar cycle. Also, 17 time periods (> 50 days each) are identified where GCRs show a clear solar periodicity (~13 or 26 days). The 13-day period that derives from two CIRs per solar rotation dominates over the 26-day period in only one of the 17 cases catalogued. This interval belongs to the second half of 2008 when

expansions of Saturn's electron radiation belts were previously reported to show a similar periodicity. That observation not only links the variability of Saturn's electron belts to solar wind processes, but also indicates that the source of the observed periodicity in GCRs may be local. In this case GCR measurements can be used to provide the phase of CIRs at Saturn. The survey results also suggest that magnetospheric convection induced by solar wind disturbances associated with SEPs is a necessary driver for the formation of transient radiation belts that were observed throughout Saturn's magnetosphere on several occasions during 2005 and on day 105 of 2012. Also, an enhanced solar wind perturbation period that is connected to an SEP on day 332 of 2013 was the definite source of a strong magnetospheric compression (enhanced SKR and LFEs were also detected at this time) which led to open flux loading in the magnetotail. This event lists can a guide to better constrain or identify the arrival times of interplanetary shocks or solar wind compressions for single case studies or statistical investigations on how Saturn and its moons (particularly Titan) respond to extreme solar wind conditions or on the transport of SEPs and GCRs in the heliosphere.

OTHER AURORAL OBSERVATIONS

X-ray aurorae are detected at Jupiter, but no detection has been made at Saturn. Saturnian X-ray aurorae may be expected to be powered by charge exchange between energetic ions and the planet's atmospheric neutrals. If the ions are of solar origin, the emission should be brightest during episodes of enhanced solar wind activity. Using propagating SW parameters measured near the Earth to Saturn to estimate the timing of solar wind enhancements to reach Saturn, a number of Chandra observations were obtained in April–May 2011. Cassini in situ measurements confirm that two of the observations were carried out at the time when a significant SW disturbance reached Saturn. Variability was observed between the two Chandra datasets, but no evidence for X-ray brightening in the auroral regions were detected during this period, suggesting that the strength of any charge exchange auroral X-ray emission on Saturn was below Chandra's detectability threshold [Branduardi-Raymont et al. 2013].

Upstream Langmuir waves

Langmuir waves are often detected by Cassini in the foreshock region upstream of the Saturnian bow shock [Hospodarsky et al. 2006]. In planetary foreshocks, electrostatic Langmuir waves at frequencies close to the local plasma frequency (f_{pe}) are generated by electrons reflected from the bow shock via the beam-plasma instability. The fact that the Langmuir waves are generated near f_{pe} allows an estimate of the solar wind electron plasma density (n_e) to be determined from the frequency of the waves when they are present. This ability to estimate the density was used in a study by Bertucci et al. [2007a] to compared low frequency (<<1 Hz) waves detected by the Magnetometer instrument to similar variations observed in ne as determined from the Langmuir wave frequency. Langmuir wave derived solar wind density measurements have also been used in a number of studies investigating the bow shock shape and stand-off distance. These studies are discussed in the section entitled Bow Shock Shape and Location.

Using the RPWS Wideband Receiver measurements, Píša et al. [2015, 2016] examined the characteristics of the Langmuir waves detected upstream of Saturn. Typical Langmuir wave amplitudes observed by the RPWS at Saturn are in a range of 0.01 to 1 mV/m, with the largest amplitudes detected ~10 mV/m. The estimated energy density for the largest measured amplitudes at Saturn does not exceed the threshold for strong turbulence processes, suggesting that weak turbulence saturation processes are more important in the Langmuir wave saturation inside Saturn's foreshock. The maximum wave intensity is observed around the upstream foreshock boundary with a slight shift behind the tangent magnetic field line toward the downstream position and with a decrease in intensity along the solar wind direction deeper in the foreshock. The wave amplitude also decreases with distance along the tangent field line, but decreases more slowly compared to the dependence on the depth. This dependence shows an amplitude decrease of almost one order of magnitude over the distance of 100 R_S.

The typical Langmuir wave spectrum at Saturn exhibits a single intense peak (62% of all selected waveforms). However, spectra with a superposition of two (25%) or more (13%) intense peaks are also observed [Píša et al. 2016]. Using magnetic field observations and a model of the bow shock, plasma wave activity across Saturn's foreshock has been mapped. The single peak spectra are observed across the entire foreshock, while more complicated spectra are more likely measured deeper inside the foreshock and closer to the bow shock. A gap in wave occurrence and intensity at the tangent point delimits two foreshock regions similar to those observed at Venus and Earth. In the case of Saturn's foreshock, this gap is caused by the larger radius of curvature of the shock.

Lion Roar emissions

Electromagnetic waves with similar properties known as “lion roars” have been reported by numerous missions in the terrestrial magnetosheath.

Píša et al. [2018] presented an observation of intense electromagnetic emissions in Saturn's magnetosheath as detected by the Cassini spacecraft in the dawn sector (magnetic local time ~06:45) over a time period of 11 hours. The waves were narrow-banded in frequency with a peak frequency of about 0.16 f_{ce}, where f_{ce} is the local electron gyrofrequency. Using plane wave propagation analysis, the waves were found to be right hand circularly polarized in the spacecraft frame and propagate at small wave normal angles (<10°) with respect to the ambient magnetic field. Electromagnetic waves with similar properties known as “lion roars” have been reported by numerous missions in the terrestrial magnetosheath. These Cassini observations are the first evidence of such emission outside the terrestrial environment.

Bow shock shape and location

Studying the global shape, location, and dynamics of the bow shock offers important insights into the physics governing its formation and the magnetospheres response to solar wind dynamics. A

number of authors [Achilleos et al. 2006; Masters et al. 2008; Went et al. 2011] have used the Cassini data to develop models of the average shape of Saturn's bow shock as well as the response of this surface to changes in the dynamic pressure of the upstream solar wind. RPWS data has contributed to these studies by detecting the occurrence of bow shock crossings and by providing upstream solar wind densities from the frequency of the Langmuir waves near these crossings. The solar wind density has been used both as an in situ verification of solar wind propagation models [Hansen et al. 2005; Zieger and Hansen 2008] and to estimate the solar wind dynamic pressure.

A number of studies have investigated the properties of the bow shocks themselves at Saturn [Masters et al. 2013a, 2013b, 2017; Sulaiman et al. 2015; Sundberg et al. 2017], and the particles and regions associated with the bow shock, including hot flow anomalies [Masters et al. 2009], superthermal electrons [Masters et al. 2016], and upstream whistler mode waves [Sulaiman et al. 2017a]. The T96 Titan encounter (see the section entitled Titan Science for more details) occurred during a period of high solar wind pressure that caused Saturn's bow shock to be pushed inside Titan's orbit, exposing the moon and its ionosphere to the solar wind. Omidi et al. [2017] using electromagnetic hybrid (kinetic ions and fluid electrons) simulations and Cassini observations, showed a formation of a single deformed bow shock for the Titan-Saturn system.

Saturn Science—Lightning

The first indication of lightning in Saturn's atmosphere was obtained in November 1980 by the radio instrument on-board Voyager 1. Strong impulsive signals in the frequency range of a few MHz were detected and termed Saturn electrostatic discharges (SEDs) [Warwick et al. 1981]. The Voyager SEDs were thought to stem from an atmospheric source in the equatorial region of Saturn, and a source in Saturn's B-ring was excluded by Kaiser et al. [1983] with an argument of visibility. However, no storm clouds in the equatorial region could be identified in the Voyager images. The Cassini mission has greatly enhanced our knowledge about Saturn lightning, and combined radio and imaging observations have clearly established the atmospheric origin of the SEDs. This is discussed in the first subsection below, and the subsequent subsections will describe the occurrence of SED storms in the Cassini era, the fascinating great white spot (GWS) event of 2010/2011, the physical parameters of the SEDs, the usage of the SEDs as a tool to investigate Saturn's ionosphere, and the scarcity of lightning whistler observations. Finally, we will mention that the new discoveries by Cassini will enable limited future ground-based observations of Saturn's thunderstorm and lightning even without a spacecraft in Saturn's orbit.

New discoveries by Cassini will enable limited future ground-based observations of Saturn's thunderstorm and lightning even without a spacecraft in Saturn's orbit.

Radio and imaging observations of Saturn lightning storms

The first link between SEDs and cloud features in Saturn's atmosphere was found in 2004: Cassini Imaging Science Subsystem (ISS) imaged the so-called dragon storm, and the RPWS instrument detected SEDs at the same time [Porco et al. 2005; Fischer et al. 2006a]. These combined observations revealed consistent longitudes and longitudinal drift rates of the cloud feature and the SED source. Later, the white storm clouds were also found to be brighter when the SED rates were high [Dyudina et al. 2007; Fischer et al. 2007a]. Finally, Saturn lightning flashes were first detected optically on the nightside of Saturn around equinox, when the reflected light from the rings towards the planet (ring-shine) was minimized. The Cassini cameras spotted flash-illuminated cloud tops with a diameter of about 200 km, suggesting that the lightning comes from 125–250 km below [Dyudina et al. 2010], and most likely from the water-cloud layer. At Earth, the charging of water cloud particles in thunderstorms is most effective in a temperature range of −10° C to −25° C. At Saturn this temperature range is located at a level of 8–10 bars, about 200 km below the cloud tops, i.e., consistent with the altitude range found by Dyudina et al. [2010]. Another indication that the Saturn lightning source is in the water cloud layer comes from Cassini Visual and Infrared Mapping Spectrometer (VIMS) near-infrared spectra of the Great White Spot. They revealed spectroscopic evidence for ammonia and water ices [Sromovsky et al. 2013] brought up to higher altitudes by strong vertical convection. So it is thought that the same particle charging mechanisms are at work on Saturn and Earth. As most of the sunlight is absorbed above 2 bars, Saturn's weather and thunderstorms at deep pressure levels should be powered by the planet's internal energy [Desch et al. 2006]. It drives the vertical convection which brings up the water cloud to the visible atmospheric level where it is observed as a bright eruption by Cassini ISS and VIMS. Dyudina et al. [2010] also measured the optical flash energy to be about 10^9 J, which suggests that Saturn lightning is superbolt-like with total energies of about 10^{12} J [Fischer et al. 2011a], and not a fast and weak discharge as hypothesized by Farrell et al. [2007].

The left side of Figure RPWS-18 shows an image made by Cassini ISS of a Saturn lightning storm with two outbreaks, separated by about 25° in longitude [Fischer et al. 2018]. They are both located at the same planetocentric latitude of 35°South, a region nicknamed storm alley since many SED storms occurred there. They can be easily seen as the bright white features with a size of about 2000 km. Saturn's thunderstorms could also be imaged with the backyard telescopes of amateur astronomers as the right side of Figure RPWS-18 shows. The observations of amateur astronomers turned out to be very useful: they provided information on the location and the morphological evolution of the thunderstorms when the Cassini cameras were not looking [Fischer et al. 2011d; Mousis et al. 2014]. On the other hand, the Cassini optical instruments were able to study Saturn's thunderstorms in a very high spatial resolution [e.g., Dyudina et al. 2007; Sayanagi et al. 2013] revealing their exact sizes and dynamics. In the Cassini images, one can also see dark ovals that spew out of the stormy regions over the course of weeks [Dyudina et al. 2007] (see also Figure RPWS-18). These dark ovals show no SED activity since they are still visible for several weeks after the end of an SED storm. Baines et al. [2009] believe that their dark color originates from carbon soot particles that could have been produced by the dissociation of methane in the high-temperature lightning channels.

Figure RPWS-18. Two outbreaks of a Saturn lightning storm during the year 2008. The left image was obtained by Cassini ISS on June 18, 2008; and the right image was made by the amateur astronomer Christopher Go on May 1, 2008 (cloud features marked with white arrows).

Occurrence of SED storms

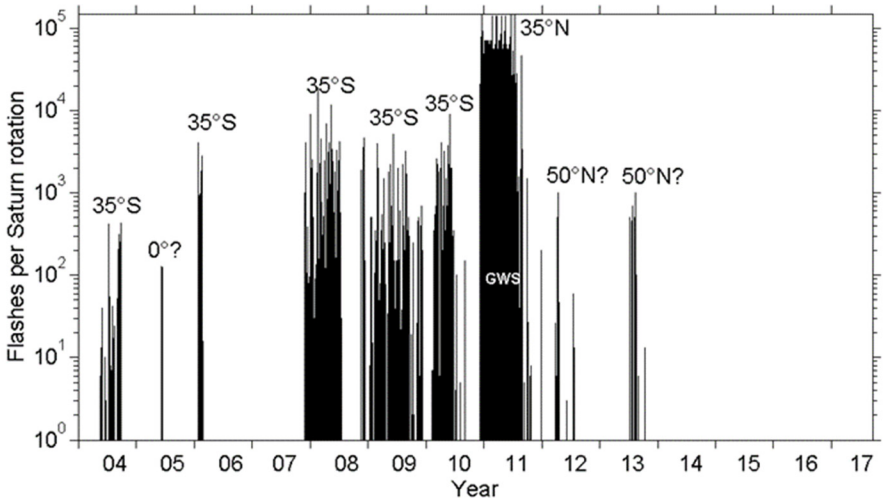

Figure RPWS-19. Number of flashes/SEDs per Saturn rotation detected by Cassini RPWS as a function of time (years from 2004 until 2017). The text in the figure denotes the planetocentric latitudes of the thunderstorms, and GWS marks the SEDs from the Great White Spot.

Figure RPWS-19 shows the number of SEDs per Saturn rotation as a function of time (year from 2004 until 2017) throughout Cassini's orbital tour around Saturn. Some bursty SED-like emissions recorded in July 2003 at a distance of 1.08 AU from Saturn [Gurnett et al. 2005] turned out to be Jovian decametric arcs [Fischer et al. 2006c]. The first SEDs were detected by Cassini RPWS in May 2004, and the last SEDs were seen in October 2013.

Figure RPWS-19 shows that Saturn lightning storms can last from a few days up to several months, and there was one storm that almost lasted throughout the year 2009. There are also long

time intervals with no SED activity, especially from February 2006 until November 2007 and during the last four years of the mission. The absence of SEDs after October 2013 could be explained by a kind of convective inhibition state of the atmosphere after the GWS of 2010/2011 [Li and Ingersoll 2015]. The flash rate during the GWS was about 1–2 orders of magnitude higher than during the other regular 2000 km-sized SED storms. For the GWS the flash rate was about 10 SEDs per second [Fischer et al. 2011c], whereas the regular storms typically have flash rates of a few SEDs per minute [Fischer et al. 2008]. Saturn's thunderstorms only raged at specific latitudes, preferentially at the so-called storm alleys around 35° South (regular storms) and 35° North (GWS). At those latitudes there are broad minima in wind speed with small westward velocities with respect to the Voyager Space Launch System (SLS). Only a few smaller storms were potentially located at different latitudes (equator or 50° N). Since Cassini RPWS could not exactly determine the locations of the thunderstorms on Saturn, a good collaboration with the Cassini imaging team and ground-based amateur astronomers was essential as pointed out in the previous subsection. Most SEDs occurred ±2 years around equinox (August 2009), and the SED storms switched from the southern hemisphere to the northern hemisphere one year after equinox, suggesting a seasonal influence [Fischer et al. 2011c].

The Great White Spot

There are two different classes of thunderstorms on Saturn [Aplin and Fischer 2017], (i) regular 2000 km-sized storms, and (ii) the rare and giant GWS that usually occur only once per Saturn year (29.5 Earth years). The previous GWS on Saturn broke out in 1990 and was located in the northern equatorial region [Sanchez-Lavega et al. 1991].

The 2010/2011 GWS was located around a planetocentric latitude of 35° N, and it reached a latitudinal extension of about 10,000 km about three weeks after it started in early December 2010 (first SEDs detected on December 5). The storm developed an elongated eastward tail with additional storm cells that wrapped around the whole planet (a distance of 300,000 km) by February 2011 [Fischer et al. 2011c]. In Figure RPWS-20, one can see an image of the GWS from March 2011. The main lightning activity took place in the so-called head of the storm (westernmost bright white clouds on the left side in the top panel of Figure RPWS-20), which drifted westward with a velocity of −27 m/s (westward motion w.r.t. Voyager SLS). The head spawned the largest anticyclonic vortex ever seen on Saturn that drifted with −8 m/s [Sayanagi et al. 2013]. The different drift velocities led to a collision between the head and the anticyclonic vortex in mid-June 2011, which caused a significant drop in SED activity. After the collision, the SED activity became intermittent and SEDs finally disappeared at the end of August 2011.

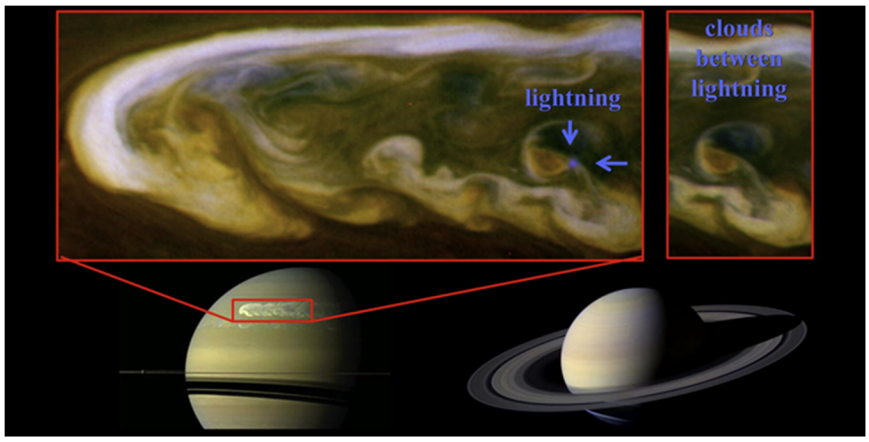

Figure RPWS-20. The upper part of this figure shows two Cassini images taken on March 6, 2011. The *left panel* shows a blue spot attributed to a lightning flash which is absent in the *right panel* image taken half an hour later. The lower part of this figure displays two Saturn images to show the large extent of the Great White Spot. Figure from Dyudina et al. [2013].

Dyudina et al. [2013] could also identify visible flashes in blue wavelengths on Saturn's dayside, which is also shown in Figure RPWS-20. The optical flashes appeared in the cyclonic gaps between anticyclonic vortices where the atmosphere looked clear down to the level of deep clouds. Dyudina et al. [2013] also estimated the optical power of the flashes to be about 10^{10} W, and the total convective power of the GWS to be of the order of 10^{17} W. Since this power is similar to Saturn's global power radiated to space, storms like the GWS should be important factors in the thermal balance of Saturn's atmosphere. Fischer et al. [2014b] suggested that the powerful storm was an intense source of gravity waves that may have caused a global change in Saturn's thermospheric winds via energy and momentum deposition. These changes might have also influenced the periodicity of SKR, which should be driven by the upper atmosphere. The GWS also caused a large stratospheric vortex with temperatures of 80 K above the normal level and an enhanced abundance of stratospheric acetylene [Fletcher et al. 2012].

Physical parameters of SEDs in comparison to Earth lightning

The radio emissions of Saturn lightning are stronger by a factor of 10^4 than the radio emissions from terrestrial lightning in the frequency range of a few MHz. Zarka et al. [2006] and Fischer et al. [2006b] found spectral radio powers of the order of 10 to 100 W/Hz, confirming previous Voyager measurements by Zarka and Pedersen [1983]. RPWS detected the first SEDs from beyond 300 Saturn radii [Fischer et al. 2006a] in May 2004. This corresponds to a staggering distance of about 3000 Earth radii compared to only 14 Earth radii, within which RPWS detected terrestrial lightning during its Earth flyby [Gurnett et al. 2001]. Similarly, the total energy of one superbolt SED is about 10^{12} J, a factor of 10^4 larger than the typical total energy of a terrestrial flash with 10^8 J. The large SED energy could be related to the fact that the breakdown voltage increases with pressure, and the SED source should be located at a pressure level of 8–10 bars. Higher breakdown fields would allow more charges to accumulate before it comes to a powerful breakdown [Fischer et al. 2008].

Similar to terrestrial intracloud lightning, an SED consists of many subpulses, and the total duration of one SED can be as long as a few hundred milliseconds. Most SEDs are somewhat shorter, and the average SED duration is around 60–70 ms [Zarka et al. 2006]. The SED duration can be well described by a distribution with an exponential decrease in SED numbers with increasing burst duration. Such distributions are characterized by a so-called e-folding time, and for SEDs this e-folding time is in the range from 35–50 ms [Fischer et al. 2007a]. The RPWS instrument had a millisecond mode with which the signal amplitude could be measured at a fixed frequency with a high temporal resolution of 1 ms. However, it turned out that this time is still too long to resolve the substructures of an SED. High temporal resolution observations were provided by ground-based SED observations (see the section entitled Ground-based Saturn lightning observations for the future), and Mylostna et al. [2013] found substructures with a duration of the order of 100 microseconds. The temporal structure of a burst should be related to its frequency spectrum. The frequency spectrum of terrestrial lightning shows a roll-off with $1/f^2$ or even steeper above 1 MHz. Zarka et al. [2006] and Fischer et al. [2006b] found a distinctly different spectrum for SEDs which is almost flat or with a slight roll-off of $1/f^{0.5}$ from 4–16 MHz. The reason for such a flat spectral behavior of SEDs is unknown.

Lightning as a tool to investigate Saturn's ionosphere

SEDs usually occur in episodes of a few hours when the thunderstorm is on the side of Saturn facing Cassini, whereas the SEDs are absent when the storm is on the backside of the planet. However, some SEDs can propagate from beyond the visible horizon due to ducted ionospheric propagation, and we call this the over-the-horizon effect [Zarka et al. 2006].

Figure RPWS-21 shows an SED episode that lasts for about six hours. The SEDs are the short vertical bursts, which appear as narrow-banded signals due to the frequency sweeping receiver, although they are intrinsically broadband. Assuming straightline SED propagation, the peak electron plasma frequency of Saturn's ionosphere can be easily determined from the low frequency cutoff denoted by the white line [Fischer et al. 2011b]. Therefore, it is necessary to know the exact location of the storm cloud, and it is indicated in Figure RPWS-21 when the storm cloud was appearing at the horizon, passing the central meridian (CM), and disappearing again. Fischer et al. [2011b] found peak electron densities of 10^4 cm^{-3} at midnight and 10^5 cm^{-3} at noon for the storms at the kronocentric latitude of 35° S. This diurnal variation of about 1 order of magnitude is still too large to be explained by ionospheric models [Moore et al. 2012]. The SED measurements are still the only technique to obtain the electron densities of Saturn's ionosphere at all local times, since radio occultation only works for local times at dawn and dusk. Figure RPWS-19 shows the different SED behavior when the storm cloud is close to the horizon: SEDs get weaker when the cloud comes near the day-side horizon due to the oblique angle of propagation leading to absorption in Saturn's ionosphere. On the other hand, SEDs were detected about one hour before the cloud reached the visible night-side horizon, and the over-the-horizon SEDs are denoted in the figure. This effect not only exists when Cassini is on the morning side, but also with Cassini on the evening side with an SED storm that disappears towards the night-side [Fischer et al. 2018]. The typical over-the-horizon effect extends 30° to 45° beyond the night-side horizon and has been modelled by ray tracing [Gautier et al. 2011].

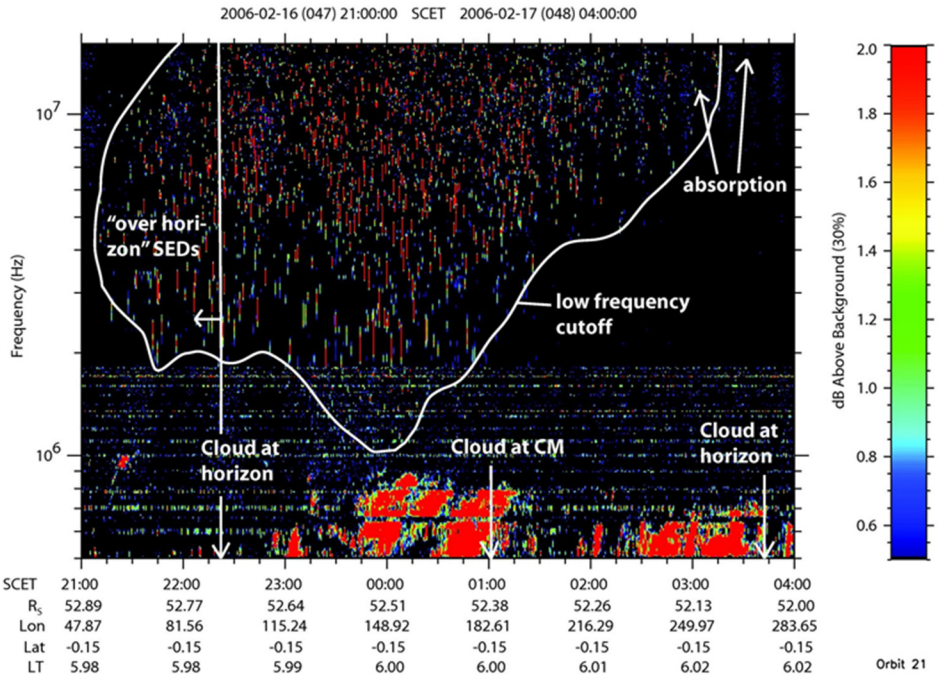

Figure RPWS-21. Dynamic spectrum (color-coded radio wave intensity as function of time and frequency) of an SED episode as measured by RPWS on February 16–17, 2006. The white line denotes the low frequency cutoff and other features are described in the text. The bottom numbers show the Spacecraft Event Time (SCET), the distance of Cassini to Saturn's center in Saturn radii, and the longitude, latitude, and local time of Cassini. Figure from Fischer et al. [2008].

The wave polarization of SEDs has been measured below 2 MHz (in the so-called quasi-static frequency range), and it is thought that it is fixed in Saturn's ionosphere. Fischer et al. [2007c] found SEDs to be highly polarized (80%) with just one sense of rotation, which was right-handed with respect to the wave propagation direction for SEDs originating from the southern hemisphere. They explained this by the dominance of the ordinary mode and the absorption of the extraordinary mode in the ionosphere. Consequently, SEDs from the northern hemisphere were found to be left-hand circularly polarized [Fischer et al. 2011c], since the magnetic field and the wave propagation vector point to the same direction in the northern hemisphere, whereas they are opposite to each other in the southern hemisphere.

Saturn lightning whistlers

Lightning is known to emit whistler waves at very low frequencies which propagate along magnetic field lines from the source to the observer. For Saturn the detection of only one lightning whistler has been reported in the literature. Akalin et al. [2006] detected one whistler signal in the frequency range of 200–400 Hz that lasted for 2 seconds. It was detected by the RPWS wideband receiver on October 28, 2004, on a magnetic field line with an L-shell value of 6.5. They concluded that the whistler originated from the northern hemisphere from a latitude of 67°, but no corresponding SED activity was seen. The scarcity of whistler observations by Cassini can be explained by Cassini's trajectory, since the stormy regions at latitudes around 35° N and S are connected to low magnetic

L-shells which were traversed by Cassini only during orbit insertion and the proximal orbits of 2017. However, an intense search for lightning whistlers led to the detection of only three tentative events during the proximal orbits. This is probably due to the absence of lightning storms in 2017 as shown in Figure RPWS-17.

Ground-based Saturn lightning observations for the future

We already mentioned that SEDs are typically 10,000 times stronger than terrestrial lightning in the frequency range of a few MHz. This has led to their first detection with an Earth-based radio telescope, which was achieved by the giant UTR-2 facility (effective area of 150,000 m²) in the Ukraine [Zakharenko et al. 2012; Konovalenko et al. 2013]. At Earth, the SEDs have a radio flux of a few hundred Jansky (1 Jy = 10^{-26} W/m²/Hz), and the sensitivity of UTR-2 is a few Jansky. The new discoveries about Saturn's thunderstorm by Cassini will enable some limited future observations of Saturn's lightning and thunderstorms even without a spacecraft in Saturn's orbit. During the times of Saturn apparition we should be able to identify thunderstorms in Saturn's atmosphere with a high confidence from the images of the ground-based amateurs, since we now know what they should look like. Saturn can be well-observed from Earth for roughly 6–9 months per year, and a confirmation of a storm's SED activity is now possible with large Earth-based radio telescopes. It is interesting to know when the next SED storm will take place after the long inactivity of more than four years at the end of the Cassini mission.

Search for Titan lightning

The existence of lightning on Saturn's enigmatic moon Titan has been suggested soon after the Voyager 1 flyby in 1980, although no corresponding radio emissions were detected by Voyager [Desch and Kaiser 1990]. The potential effects of lightning on Titan's atmospheric chemistry have been widely investigated up to the production of organic compounds that could be essential precursors for the evolution of life [Plankensteiner et al. 2007]. Furthermore, the Cassini cameras observed convective cloud activity in Titan's atmosphere. However, no radio bursts that would clearly indicate the existence of Titan lightning were found by RPWS during the numerous flybys [Fischer et al. 2007b; Fischer and Gurnett 2011]. Hence, Titan lightning is a very rare event if it exists at all.

Saturn Science—Ionosphere

The ionosphere of Saturn is still a work in progress, and the first in situ measurements by RPWS of the cold ionosphere properties have just been reported [Wahlund et al. 2018]. Several other manuscripts have been submitted, and they all show a very strong interaction between the D-ring and the ionosphere of Saturn, causing the ionosphere to become extremely variable with more than two orders of magnitude and trigger a dust-ionosphere layer near the equator.

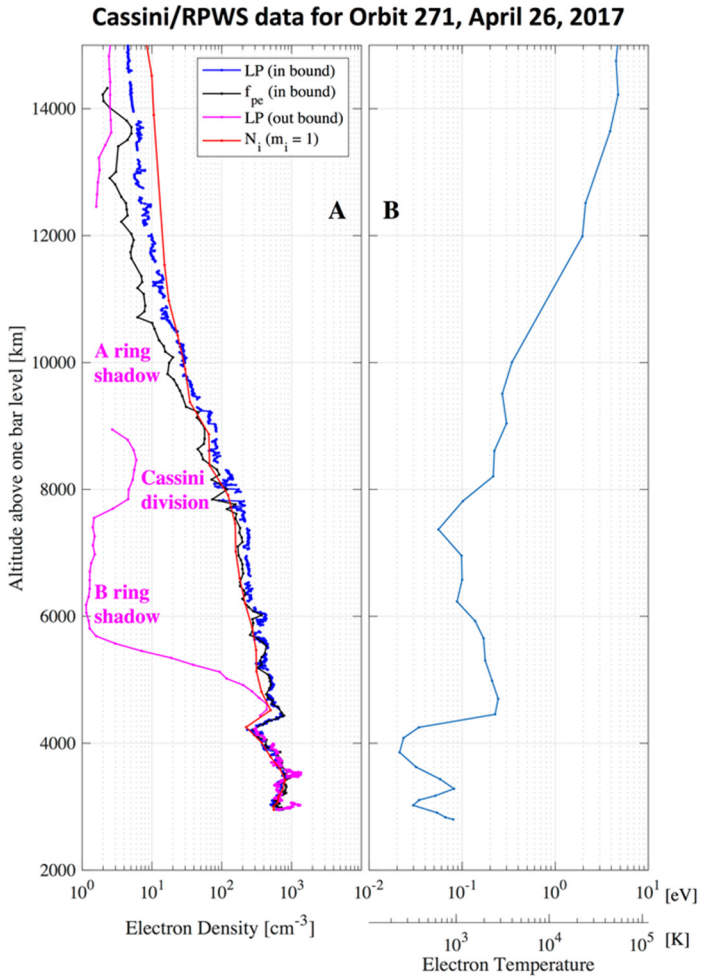

Figure RPWS-20. Cassini/RPWS altitude profiles of the ionosphere number density (*Panel A*) and inbound electron temperature (*Panel B*) during the crossing on April 26, 2017. Two independent methods for estimating the inbound electron density (blue and black) gave almost identical results, confirming their validity. The Langmuir probe ion density (N_i, assuming H^+) also produces values in agreement with the estimated electron densities, confirming that hydrogen ions dominated during this first flyby. The lower LP electron densities over the outbound sector (magenta) indicate that much of the A- and B-rings are opaque to ionizing extreme ultraviolet radiation.

Sulaiman et al. [2017c] reported the first observations of lower hybrid resonance waves in Saturn's ionosphere. They are believed to be generated through the interaction of whistler-mode waves and density gradients present in the ionosphere.

Plasma Waves

The almost 300 orbits by Cassini have allowed the RPWS to study a variety of plasma and radio waves in the magnetosphere of Saturn. See Gurnett et al. [2005]; Mauk et al. [2009]; Kurth et al. [2009]; Hospodarsky et al. [2012, 2016] for overviews of the Saturn magnetosphere and some of the wave observations.

In the inner magnetosphere (<10 R_S), whistler mode chorus [Hospodarsky et al. 2008; Menietti et al. 2013a, 2013b, 2014a, 2014b], quasi-periodic (QP) whistler mode emissions [Hospodarsky et al. 2012], electron cyclotron harmonic (ECH) emissions [Menietti et al. 2008a, 2008b, 2012; Tao et al. 2010], and upper hybrid resonance (UHR) emissions [Persoon et al. 2005, 2006a, 2006b, 2009, 2013, 2015] are observed. At higher magnetic latitudes (> ~25°), auroral hiss is detected [Mitchell et al. 2009a; Gurnett et al. 2009b; Kopf et al. 2010]. RPWS observations of ion cyclotron waves have also been made in the Saturn downward auroral current region. Menietti et al. [2011c] showed that these waves can be generated by the observed upward electron beams and modeling suggested that they can produce significant ion heating as has been observed in the terrestrial auroral region.

Evidence of lightning in Saturn's atmosphere is shown from observations of lightning whistlers [Akalin et al. 2006] and from observations of Saturn Electrostatic Discharges (SEDs) (see the section entitled Saturn Science—Lightning for detailed discussion of the lightning observations). A number of radio emissions are also observed, including Z- and O-mode narrowband emissions [Louarn et al. 2007; Ye et al. 2009, 2010a, 2011; Menietti et al. 2009, 2010b, 2012; Wang et al. 2010], and SKR [Kurth et al. 2005a, 2005b, 2011; Cecconi et al. 2006; Lamy et al. 2008a, 2010a; Fischer et al. 2009; Mutel et al. 2010; Menietti et al. 2011b]. Plasma waves have also been detected in association with many of the Saturnian moons, including Enceladus [Tokar et al. 2006; Gurnett et al. 2011a; Leisner et al. 2013; Pickett et al. 2015] and Rhea [Santolik et al. 2011]. The RPWS instrument also detects dust impacts on the Cassini spacecraft, providing information on the properties of dust [Kurth et al. 2006b; Wang et al. 2006; Ye et al. 2014a] and sometimes information on the electron density [Ye et al. 2014b] (see the section entitled Dust and Dusty Ring Science for a more detailed discussion of the RPWS dust results].

Whistler mode chorus emissions

Whistler mode emissions are often observed in Saturn's inner magnetosphere with many characteristics similar to chorus detected at Earth and Jupiter. Due to these similar characteristics, the majority of the literature on these emissions has called the whistler mode emission chorus even though some of the emissions lack discrete elements or fine structure [Hospodarsky et al. 2008; Menietti et al. 2013b, 2014a]. Hospodarsky et al. [2008] performed an initial survey of these emissions and characterized them into two types based on their spectral characteristics and where they were observed. The most common type was defined as magnetospheric chorus that was observed within ~30 degrees of the magnetic equator between L shells of about 4.5 to 10. This emission usually has a bandwidth of a few hundred Hz and is detected below 1/2 f_{ce} as Cassini crosses through the inner magnetosphere. A variety of fine structure is associated with the chorus, from a structureless, hiss-like emission to narrowband frequency tones rising in frequency. The rising tone structure is similar to structures associated with chorus detected at Earth and Jupiter, but the timescales of the structure detected at Saturn are usually longer than those observed at Earth or Jupiter [Hospodarsky et al. 2008].

There is a subset of the magnetospheric chorus that have rising tones with periods on the order of many minutes. These emissions have been referred to as rising whistler mode emission, QP whistler emission, or sometimes as worms. They are observed about 5% of the time when Cassini is near the magnetic equator within 5.5 R_S of Saturn, and appear to be related to electrons with energies of a few keV. The cause of the many-minute periodicity is not well understood [Hospodarsky et al. 2016]. Although Hospodarsky et al. [2008] included these many-minute period rising tone whistler mode emissions with the magnetospheric chorus emissions, their spectral characteristics are more similar to the QP whistler mode emissions detected at Earth. However, it is currently unclear if the same type of source generation can explain the Earth and Saturn QP emissions.

The second type of whistler mode chorus emission reported by Hospodarsky et al. [2008] is detected in association with local plasma injections and were defined as injection event chorus. Local plasma injection events are injections of hot, less dense plasma produced by the interchange instability in rapidly rotating magnetospheres such as Saturn. These injections flow towards the planet while the colder and denser plasma from the inner magnetosphere flows outward [Mauk et al. 2009; Rymer et al. 2009; Mitchell et al. 2009b; Paranicas et al. 2016]. Young injection events are usually easy to detect with RPWS due to the changes in the spectral properties of the plasma waves associated with the injection compared to the waves detected outside of the events [Menietti et al. 2008a, 2008b; Hospodarsky et al. 2008; Kennelly et al. 2013]. Specifically, the frequency of the UHR usually decreases due to the lower electron plasma density inside of the injection and the ECH and chorus emissions are enhanced. Injection event chorus is often observed in two bands located above and below 1/2 f_{ce}, with a gap in the emission intensity at 1/2 f_{ce}, very similar to chorus detected at the Earth. The injection event chorus often contains fine structure (primarily rising tones) at a much smaller timescale (less than a second to a few seconds) than the magnetospheric chorus, again more similar to chorus at Earth and Jupiter [Hospodarsky et al. 2008]. Menietti et al. [2008a] showed that the chorus emissions observed inside the injection region can be at least partially generated by the measured temperature anisotropies in the electron population.

The occurrence, intensity, local time, and latitude variations of both types of chorus emission at Saturn have been examined by Hospodarsky et al. [2008, 2012] and in a series of papers by Menietti et al. [2012, 2013b, 2014a, 2014b]. These studies found that the peak in chorus intensity is detected at about ±5 degrees in magnetic latitude, with the intensity decreasing at the magnetic equator. The emissions are observed at all LT, but display maximum intensity on the nightside between L of 4.5 to 7. The small scale fine structure is more likely to be observed at higher frequencies and at latitudes greater than ~5°. The injection event chorus was typically found to be more intense than the chorus outside of the injection events [Menietti et al. 2014a], and the amplitude and structure of the rising tones was found to reasonably match predictions from non-linear theories of chorus generation [Menietti et al. 2013a]. Calculations of the wave normal and Poynting vector using the WFR data show that the chorus emissions propagate away from the magnetic equator at Saturn—see Figure 7 of Hospodarsky et al. [2008]—similar to results obtained for chorus at Earth.

Intense whistler mode waves were also detected in the magnetic flux tube connected to the surface of the Saturnian moon Rhea during a close flyby on March 2, 2010 [Santolik et al. 2011]. The whistler mode emission was observed below 1/2 f_{ce}, had peak amplitudes >0.5 nT, and was found to be propagating toward Rhea. Santolik et al. [2011] showed that these waves could be generated by the loss-cone anisotropy caused by absorption of electrons by the surface of the moon. Strong, bursty electrostatic waves near the electron plasma frequency and broadband electrostatic waves at frequencies well below the ion plasma frequency were also detected during this flyby. The waves near the electron plasma frequency have many of the characteristics of Langmuir waves observed in the solar wind and are believed to be produced by a low energy (~35 eV) electron beam propagating away from Rhea. The low-frequency waves may be related to the higher frequency waves through a nonlinear three-wave interaction.

Whistler mode auroral hiss emission

Auroral hiss is produced by electron beams and, when plotted on a time-frequency spectrogram, usually exhibits a funnel shaped spectrum.

Cassini also observes at magnetic latitudes greater than about 25° at Saturn a whistler mode emission that has many of the characteristics of auroral hiss [Mitchell et al. 2009a; Gurnett et al. 2009b; Kopf et al. 2010]. Auroral hiss is produced by electron beams and, when plotted on a time-frequency spectrogram, usually exhibits a funnel shaped spectrum. Auroral hiss has only been detected by Cassini propagating away from the auroral zone of Saturn and the emission is often observed out to distances of many tens of Saturn radii (R_S). Before 2008, the emission often exhibited a modulation in its intensity with a period of about 10.6 hours in the northern hemisphere and about 10.8 hours in the southern hemisphere, very similar to the periods of the SKR emission [Gurnett et al. 2009a, 2009b]. Shorter scale periodicity on the order of one hour is also often detected, and these short scale structures are often correlated with ion conics [Mitchell et al. 2009a, 2016; Palmaerts et al. 2016]. Kopf et al. [2010] analyzed electron beams detected by the CAPS during a Cassini high latitude pass and found that the detected beams coincided with observations of auroral hiss emissions. Examination of the predicted emission growth rate demonstrated that each of the measured beams possessed large whistler-mode growth rates, sufficient to produce the observed emission intensities.

Similar auroral hiss-like emissions have also been detected near Saturn's B-ring during the SOI period [Xin et al. 2006], and near the Saturnian moon Enceladus [Gurnett et al. 2011a]. Using ray tracing and the observed spectral funnel characteristics of the emission observed on seven different Enceladus flybys, Leisner et al. [2013] found two possible source regions near the moon, the quadrant upstream of the Saturnward flow terminator and the quadrant downstream of the anti-Saturnward flow terminator. The result of similar source regions for multiple flybys separated by over five years suggests that the electron beam acceleration near the moon is a quasi-time-stationary feature of the plasma interaction.

Electrostatic ECH and UHR emissions

Electrostatic emissions detected in Saturn's inner magnetosphere include ECH and UHR emissions. ECH emissions usually occur in frequency bands at $(n + 1/2)f_{ce}$, where n is an integer. Just like the chorus emissions discussed earlier, the ECH emissions are observed on most orbits when Cassini crosses the inner magnetosphere [Menietti et al. 2017]. The ECH waves also exhibit very different spectral characteristics inside and outside of injection events. ECH emissions observed outside of injection events are primarily found in the first harmonic band centered at ~1.5 f_{ce}, with higher harmonic bands being weaker and more sporadic. Inside of injection events the ECH emissions usually increase in both intensity and the number of harmonic bands present. A number of studies have attempted to explain the characteristics of the ECH waves using the electron plasma distributions measured by CAPS [Rymer et al. 2009] both outside [Menietti et al. 2008b] and inside [Menietti et al. 2008a; Tao et al. 2010] of an injection event. Menietti et al. [2008a, 2008b] found that phase space distributions with an assumed narrow, empty loss cone of the lower energy (< 100 eV) electron populations both inside and outside the injection event could generate the observed ECH emissions. However, Tao et al. [2010] found that inside the injection events, assuming a non-empty loss cone for electrons with energy near a few hundred eV and a few keV (higher than those predicted by Menietti et al. [2008b] could produce ECH waves with the observed harmonic structure. The precise ECH wave gain in the Tao et al. [2010] and Menietti et al. [2008b] models is very sensitive to the electron distribution used, which for this event is not measured at the smallest pitch angles. These uncertainties in modeling the actual cold electron components may explain the differences in these studies.

The UHR emissions are detected on most orbits in the inner magnetosphere [Moncuquet et al. 2005; Schippers et al. 2013] and during close flybys of Saturn's moons—for example, Farrell et al. [2009], especially Titan [e.g., Modolo et al. 2007a]. Because the frequency of the UHR emissions (fuhr) is related to the electron plasma frequency (f_{pe}) by $f_{uhr}^2 = f_{pe}^2 + f_{ce}^2$, determining f_{uhr} and obtaining f_{ce} from the magnetic field strength provides the electron plasma density (n_e) from $f_{pe} = 8980\ n_e^{1/2}$. By measuring f_{uhr} for each pass through the inner magnetosphere, Persoon et al. [2009, 2013] have developed an empirical plasma density model for the Saturnian system.

Open Questions for Saturn System Science

Any mission, however extended, always raises questions based on the new knowledge gained. Here we give a brief list of open questions for radio and plasma wave science at Saturn, after Cassini.

- What is the rotation period of Saturn? How do the multiple, variable magnetospheric periods observed in radio, magnetic fields, energetic particles, plasma, aurora, and other phenomena tie to the internally-generated magnetic field at Saturn?
- Given the extraordinarily axi-symmetric magnetic field, why are there such prominent rotational modulations in Saturn's magnetosphere?

- What drives the episodic lightning on Saturn; why is there ~one Great White Spot storm per Saturnian year?
- How does the dust in the Saturnian system interact with Saturn and its atmosphere? How are the rings coupled to the planet other than through gravity?
- What is the predominant form of the electron distribution function at the source of SKR?
- How does the abundant neutral population in Saturn's magnetosphere make it different from fully or mostly ionized magnetospheres?
- What are the various populations of charged dust and molecules that balance charges in dusty media such as in the plumes of Enceladus and in Saturn's topside equatorial ionosphere?

RPWS Non-Saturn Science Results

Cruise Science

The bulk of science carried out in the cruise phase by the RPWS was at planetary targets as detailed in the following sections, although there were considerable efforts employed during cruise to check out the instrument and exercise and improve various observing modes planned for use at Saturn. However, Schippers et al. [2014, 2015] reported nanograins in the solar wind detected by the RPWS and Meyer-Vernet et al. [2009], reported nanograins originating from Jupiter's moons.

Venus

During two Cassini very close gravity-assist flybys of Venus, the first on April 26, 1998, and the second on June 24, 1999, the RPWS instrument conducted a search for high-frequency (0.125 to 16 MHz) radio impulses from Venus lightning. Despite the excellent sensitivity of the high-frequency RPWS receiver (down to the cosmic background), no impulses were detected [Gurnett et al. 2001]. During a subsequent close gravity-assist flyby of Earth on August 18, 1999, radio signals from lightning were observed essentially continuously at all radial distances inside of about 14 Earth radii, with maximum occurrence rates up to about 30 pulses per minute. If Venus lightning exists then it must be much weaker and at much lower frequencies than terrestrial lightning.

Earth

Cassini executed a flyby of Earth on August 18, 1999, in order to gain sufficient energy to get to Saturn. However, the flyby also offered an opportunity to understand how some of the instruments, including RPWS, perform in a planetary magnetosphere nearly five years prior to arrival at Saturn [Kurth et al. 2001b]. The Earth flyby provided the opportunity to test a number of observation modes and capabilities to determine their efficacy in time to make adjustments prior to the prime mission.

In addition, the flyby provided a swift flyby of Earth that allowed a unique set of observations of terrestrial magnetospheric radio and plasma wave phenomena.

Figure RPWS-21 shows an overview of the RPWS observations during the Earth flyby. The trajectory brings Cassini into the magnetosphere just past noon local time and carries it down the magnetotail in the post-midnight sector. Closest approach to Earth was just under 1200 km. As one would expect, the RPWS observed broadband electrostatic waves at the bow shock, electron cyclotron harmonics and whistler mode chorus in the outer radiation belts and emissions between the plasma frequency and upper hybrid frequency in the ionosphere. Evidence for electron phase space holes was found in the near-Earth plasma sheet. At higher frequencies auroral kilometric radiation was observed on the night side indicating a series of auroral substorms and fixed frequency narrowband lines from man-made terrestrial radio stations were observed. Even Jovian hectometric radiation was observed from a position far downstream from Earth.

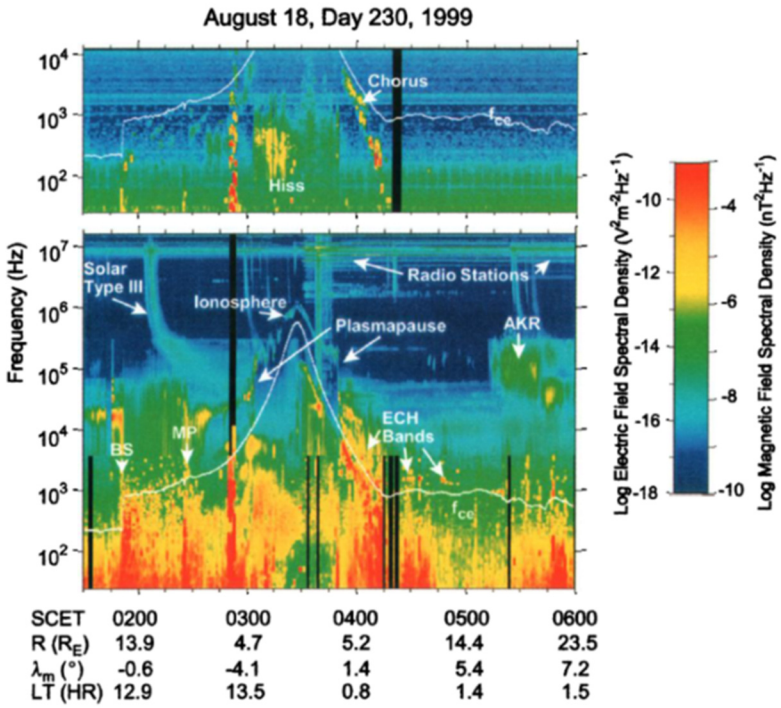

Figure RPWS-21. An overview of RPWS observations of the Earth flyby with magnetic fields shown in the *Top panel* and electric fields below. The white trace is the electron cyclotron frequency fce derived from |*B*|. *BS* refers to the bow shock, *MP* refers to the magnetopause, *ECH* refers to electron cyclotron harmonics, and *AKR* refers to auroral kilometric radiation.

Using a number of techniques, the plasma density was measured. The electron plasma frequency and upper hybrid resonance frequency are characteristic frequencies of the plasma dependent on the electron density. RPWS also includes a Langmuir probe that can determine the electron density and temperature. Finally, a relaxation sounder was used to stimulate the plasma frequency.

Wideband waveform measurements were used in various regions of the magnetosphere to acquire examples of chorus and ECH bands. These are also necessary to identify solitary-like structures associated with electron phase space holes.

Another feature of the RPWS instrument that was tested during the Earth flyby was the capability of determining the wave normal angle of whistler mode waves using 5-channel WFR measurements of three magnetic and two electric sensors. Hospodarsky et al. [2001b] used the WFR measurements to examine the propagation characteristics of a lightning whistler, chorus, and electromagnetic emissions in the magnetosheath, presumably lion roars.

Hospodarsky et al. [2001b] determined that the whistler analyzed was also detected at Palmer Station in Antarctica. The chorus waves were observed near the magnetic equator and appeared to reverse their direction of propagation at the equator, consistently propagating away from the equator where it is assumed the chorus source is located. The lion roars were found to consistently propagate nearly along the magnetic field but varied from burst to burst with some propagating near parallel and others near antiparallel to the field, suggesting multiple sources.

As mentioned above, Cassini detected intense, fixed frequency emissions at close range to Earth in the frequency range above about 1 MHz that are attributed to man-made radio transmissions. Fischer and Rucker [2006] studied the occurrence of these in detail and demonstrated that most of the emissions could be identified with shortwave radio bands. A few brief detections of scientific transmitters including the High-frequency Active Auroral Research Program (HAARP) and the Russian SURA station—see also Tokarev et al. [2006]. Fischer and Rucker point out an interesting quiet period when Cassini was near closest approach over the Pacific Ocean where a combination of the rarity of transmitters in this location and ionospheric propagation characteristics effectively shielded Cassini from the radio transmission for a period of about 20 minutes.

Jupiter

Cassini flew by Jupiter on December 30, 2000, on its way to Saturn. Arriving from the pre-noon sector, closest approach occurred in the afternoon sector at 138 Jovian radii ($\sim 10^7$ km) from the planet, and was followed by an exploration of the dusk flank of the Jovian magnetosphere. In spite of the large distance of the flyby, several Cassini- Magnetospheres and Plasma Science (MAPS) instruments including RPWS recorded high-quality data for about 6 months around closest approach. These observations benefited from the simultaneous presence of Galileo in orbit around Jupiter, enabling two-point measurements, and were complemented by remote observations by HST, Chandra, and ground-based radio observations (e.g., with the Nançay decameter array, France). This resulted in a very rich data set that was the basis of many publications and will be further exploited in the coming years.

The distant observations were well adapted to the study of the complex zoo of Jupiter's magnetospheric radio emissions, nicely covered by the Kronos receiver of RPWS, an example of which is given in Figure RPWS-22. An early overview is given in [Lecacheux 2001]. The intensity

spectrum of all Jovian radio components was accurately measured [Zarka et al. 2004a] through calibration on the Galactic background and Nançay observations, demonstrating in particular the absence of peak at 10 MHz in the decameter spectrum. The beaming of the decametric (DAM) and hectometric (HOM) components (a widely opened hollow cone of a few degrees thickness) were measured via two point Cassini-Wind measurements [Kaiser et al. 2000] as well as frequency-longitude statistics and modelling [Imai et al. 2008, 2011a, 2011b]. The HOM low-frequency cutoff measured by Ulysses and Cassini provided constraints of its source location, in the outer regions of the Io plasma torus [Zarka et al. 2001a].

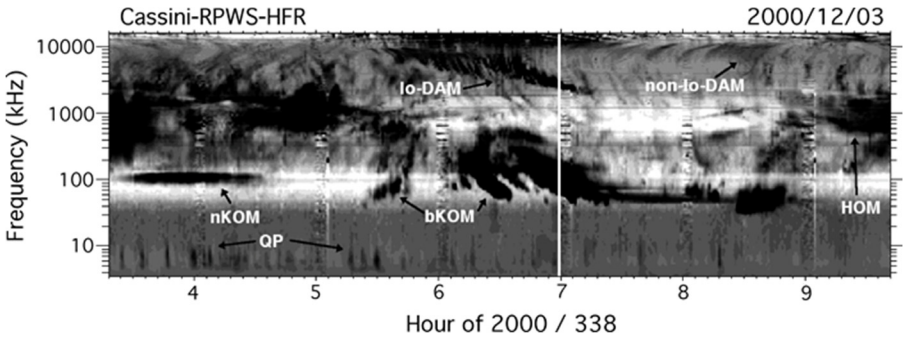

Figure RPWS-22. Jovian low-frequency radio emissions detected on December 3, 2000, by the RPWS experiment onboard Cassini approaching Jupiter. Frequency range is 3.5 kHz to 16.1 MHz. The Io-induced decameter emission (Io-DAM) appears here down to about 2 MHz, while weaker Io-independent (non-Io-DAM) arcs merge with the HOM component detected down to ~400 kHz. The auroral broadband kilometer (bKOM) component is detected down to ~40 kHz. The narrowband emission (nKOM) about 100 kHz is generated at or near the plasma frequency f_{pe} in Io's torus. The QP bursts, spaced by 5 to > 15 min, are detected in the ~5 to 20 kHz range. Distance to Jupiter was 383 R_J (2.7×10^7 km) at the time of this observation.

The six month series of continuous homogeneous measurements provided unique measurements of time variations of the radio emission. Burst of auroral (non-Io) DAM emission were found to reoccur at a period slightly longer than the system III rotation period [Panchenko et al. 2010, 2013; Panchenko and Rucker 2011]. Gurnett et al. [2002] found from Cassini and Galileo observations that Jupiter's auroral radio and UV emissions were triggered by interplanetary shocks inducing magnetospheric compressions, in disagreement with theoretical predictions [Southwood and Kivelson 2001]. Hess et al. [2014] reconciled these views by a finer analysis of dawn and dusk radio emissions seen by Cassini, Galileo and Nançay, only dusk emissions being driven by both compressions and dilatations of the magnetosphere. They also used radio observations to deduce the subcorotation velocity of the magnetospheric plasma. Clarke et al. [2009] compared the effect of solar wind compressions on radio and UV aurora at Jupiter and Saturn, and found a weaker effect at Jupiter. Radio (non-Io-DAM, HOM, and bKOM) and UV comparisons are used quite systematically in the study of Jupiter's aurora [Clarke et al. 2004, 2005; Pryor et al. 2005]. Comparison of Galileo/Jupiter and Cassini/Saturn observations also revealed similar energetic events where auroral radio intensifications are related to centrifugal plasma ejections, from the Io torus at Jupiter and from the equatorial plasma sheet at Saturn [Louarn et al. 2007].

Cassini, Galileo, and Voyager radio observations were used to try to demonstrate the influence of satellites other than Io on DAM emissions. Marginal results were obtained statistically [Hospodarsky et al. 2001a], whereas clear evidence was obtained for Europa and Ganymede by comparison of observations with modelled dynamic spectra [Louis et al. 2017a]. The ExPRES simulation tool developed in Meudon [Hess et al. 2008] and the experienced gained with Cassini on Jupiter's radio emissions were used to build simulations preparing the re-exploration of the Jovian magnetosphere by the electrostatic energy analyzer (ESA) Juice mission [Cecconi et al. 2012].

Fast recording modes of RPWS (spectral and waveform) allowed us to characterize the fine structure of Jovian radio emissions in the kilometer (bKOM) to decameter range [Kurth et al. 2001a; Lecacheux et al. 2001], including zebra-like patterns in the bKOM emission. Those were tentatively interpreted by bubble-like plasma inhomogeneities [Farrell et al. 2004] or the double plasma resonance mechanism involving ion cyclotron waves [Zlotnik et al. 2016]. Similar patterns have been observed at decameter wavelengths [Panchenko et al. 2016, 2018].

At the very low-frequency end of the radio spectrum (below a few 10s of kHz), Cassini together with Ulysses and Galileo characterized the Jovian Quasi-Periodic bursts [Kaiser et al. 2001, 2004], stereoscopic observations demonstrated their strobe-like behavior and wide beaming [Hospodarsky et al. 2004], and direction-finding techniques localized their sources at high latitude regions of the magnetopause, implying complex propagation [Hospodarsky et al. 2004; Kimura et al. 2012]. QP bursts were tentatively related to the so-called Jovian anomalous continuum radiation [Ye et al. 2012]. Propagation of radio waves near the edges of the Io plasma torus were shown to generate the HOM attenuation lane, an intensity gap oscillating between ~1 and ~3 MHz, described by Boudjada et al. [2011] and modelled by Menietti et al. [2003] and Imai et al. [2015]. Occultations of Jovian radio emissions were used to probe the Io plasma torus [Boudjada et al. 2014a].

Analysis of local low-frequency plasma waves recorded by RPWS was used to study the Jovian dust flank magnetopause and bow shock [Kurth et al. 2002; Szego et al. 2003], magnetosheath [Bebesi et al. 2010, 2011] and pre-shock [Szego et al. 2006]. The magnetopause was found to be in the process of being compressed by a solar wind pressure increase at the time of the Cassini flyby [Kurth et al. 2002]. Langmuir waves were detected upstream of the bow shock, and their level compared with that at other planets: the ratio of the energy density of the waves electric field to the plasma was found to increase with distance from the Sun [Hospodarsky et al. 2006].

Z-mode radiation and electron cyclotron harmonics (at low latitudes) and whistler-mode chorus (at higher latitudes) were measured [Menietti et al. 2012, 2016a] and their effect on electron acceleration was evaluated [de Soria-Santacruz et al. 2017]. RPWS spectral and waveform measurements also permitted to detect nanodust particles in the interplanetary medium, of likely Jovian origin [Meyer-Vernet et al. 2009; Schippers et al. 2014, 2015].

Observations of Jupiter radio emissions were used to calibrate the Direction-Finding (actually Gonio-Polarimetric) capability of RPWS/Kronos [Vogl et al. 2001, 2004], which proved extremely successful at Saturn. Early use of this directional capability permitted to check the origin of lightning-like signals observed in Cassini's inbound leg to Saturn, which proved to be Jovian radio bursts [Fischer et al. 2006c].

Overall, the Cassini RPWS experiment was very successful at Jupiter. The obtained results were reported in several review papers about comparisons of radio waves [Zarka 2000, 2004; Zarka and Kurth 2005; de Pater and Kurth 2007; Rucker et al. 2014] and plasma waves [Hospodarsky et al. 2012] at the magnetized planets, as well as in reviews about auroras [Badman et al. 2014], magnetospheric processes [Blanc et al. 2002; Seki et al. 2015], or dust detection [Meyer-Vernet et al. 2017]. They greatly helped to prepare the magnetospheric measurements of the Juno mission in Jovian polar orbit [Bagenal et al. 2017]. Two PhD theses were largely based on Cassini RPWS measurements at Jupiter [Cecconi 2004; Imai 2016].

ACRONYMS

Note: For a complete list of Acronyms, refer to Cassini Acronyms – Attachment A.

A/D	analog-to-digital converter
AKR	auroral kilometric radiation
AO	Announcement of Opportunity
AU	astronomical unit
bKOM	broadband kilometer
CA	closest approach
CAPS	Cassini Plasma Science
CDA	Cosmic Dust Analyzer
CIR	corotating interaction region
CM	central meridian
CMI	cyclotron maser instability
DAM	decametric
DOY	day of year
ECH	electron cyclotron harmonic
ELS	electron spectrometer
ENA	energetic neutral atom
ESA	electrostatic energy analyzer
EUV	extreme ultraviolet
FUV	far ultraviolet
FWHM	full width at half-maximum
GCR	galactic cosmic ray
GWS	great white spot
HAARP	High-frequency Active Auroral Research Program
HFR	high frequency receiver
HGA	high gain antenna
HOM	hectometric
HRD	high-rate detector
HST	Hubble Space Telescope
ICME	interplanetary coronal mass ejection
IMF	interplanetary magnetic field
IMS	ion mass spectrometer
INCA	Ion and Neutral Camera
IR	infrared
ISS	Imaging Science Subsystem
LEMMS	Low-Energy Magnetospheric Measurement System
LFR	low frequency receiver
LP	Langmuir probe

LPT	Linear Prediction Theory
LT	local time
MAPS	Magnetospheres and Plasma Science
MFR	medium frequency receiver
MHD	magneto-hydrodynamic
MIMI	Magnetospheric Imaging Instrument
NB	narrowbanded
nKOM	narrowband kilometer
PPO	planetary period oscillation
PRA	Planetary Radio Astronomy
QP	quasi-periodic
RH	right-handed
RPC	ring plasma cavity
RPWS	Radio and Plasma Wave Science
RS	Saturn radii
SCET	spacecraft event time
SED	Saturn electrostatic discharges
SEP	solar energetic particle
SKR	Saturn kilometric radiation
SLS	Space Launch System
SOI	Saturn orbit insertion
TM	Traceability Matrix
UHR	upper hybrid resonance
UT	universal time
UV	ultraviolet
UVIS	Ultraviolet Imaging Spectrograph
VIMS	Visual and Infrared Mapping Spectrometer
WBR	wideband receiver
WFR	waveform receiver

REFERENCES

Disclaimer: The partial list of references below correspond with in-text references indicated in this report. For all other Cassini references, refer to Attachment B – References & Bibliographies; Attachment C – Cassini Science Bibliographies; the sections entitled References contributed by individual Cassini instrument and discipline teams located in Volume 1 Sections 3.1 and 3.2 Science Results; and other resources outside of the Cassini Final Mission Report.

Achilleos, N., C. Bertucci, C. T. Russell, G. B. Hospodarsky, A. M. Rymer, C. S. Arridge, M. E. Burton, M. K. Dougherty, S. Hendricks, E. J. Smith, B. T. Tsurutani, (2006), Orientation, location, and velocity of Saturn's bow shock: Initial results from the Cassini spacecraft, Journal of Geophysical Research, 111, A03201, doi: 10.1029/2005JA011297.

Ågren, K., (2012), On the formation and structure of the ionosphere of Titan, Ph.D. Thesis, Uppsala University, Uppsala, Sweden.

Ågren, K., N. J. T. Edberg, J.-E. Wahlund, (2012), Detection of negative ions in the deep ionosphere of Titan during the Cassini T70 flyby, Geophysical Research Letters, 39, L10201, doi: 10.1029/2012GL051714.

Ågren, K., D. J. Andrews, S. C. Buchert, A. J. Coates, S. W. H. Cowley, M. K. Dougherty, N. J. T. Edberg, P. Garnier, G. R. Lewis, R. Modolo, H. Opgenoorth, G. Provan, L. Rosenqvist, D. L. Talboys, J.-E. Wahlund, A. Wellbrock, (2011), Detection of currents and associated electric fields in Titan's ionosphere from Cassini data, Journal of Geophysical Research, 116, A04313, doi: 10.1029/2010JA016100.

Ågren, K., J.-E. Wahlund, P. Garnier, R. Modolo, J. Cui, M. Galand, I. Muller-Wodarg, (2009), On the ionospheric structure of Titan, Planetary and Space Science, 57, 1821–1827, doi: 10.1016/j.pss.2009.04.012.

Ågren, K., J.-E. Wahlund, R. Modolo, D. Lummerzheim, M. Galand, I. Muller-Wodarg, P. Canu, W. S. Kurth, T. E. Cravens, R. V. Yelle, J. H. Waite, Jr., A. J. Coates, G. R. Lewis, D. T. Young, C. Bertucci, M. Dougherty, (2007), On magnetospheric electron impact ionisation and dynamics in Titan's ram-side and polar ionosphere - A Cassini Case Study, Annales Geophysicae, 25, 2359–2369, doi: 10.5194/angeo-25-2359-2007.

Akalin, F., D. A. Gurnett, T. F. Averkamp, A. M. Persoon, O. Santolik, W. S. Kurth, G. B. Hospodarsky, (2006), First whistler observed in the magnetosphere of Saturn, Geophysical Research Letters, 33, L20107, doi: 10.1029/2006GL027019.

Akalin, F., (2005), Observation of a whistler in the magnetosphere of Saturn, M.S. Thesis, University of Iowa, Iowa City, Iowa.

Amatucci, W. E., P. W. Schuck, D. N. Walker, P. M. Kintner, S. Powell, B. Holback, D. Leonhardt, (2001), Contamination-free sounding rocket Langmuir probe, Review of Scientific Instruments, 72, 2052–2057.

Andre, N., M. Blanc, S. Maurice, P. Schippers, E. Pallier, T. I. Gombosi, K. C. Hansen, D. T. Young, F. J. Crary, S. Bolton, E. C. Sittler, H. T. Smith, R. E. Johnson, R. A. Baragiola, A. J. Coates, A. M. Rymer, M. K. Dougherty, N. Achilleos, C. S. Arridge, S. M. Krimigis, D. G. Mitchell, N. Krupp, D. C. Hamilton, I. Dandouras, D. A. Gurnett, W. S. Kurth, P. Louarn, R. Srama, S. Kempf, J. H. Waite, L. W. Esposito, J. T. Clarke, (2008), Identification of Saturn's magnetospheric regions and associated plasma processes: Synopsis of Cassini observations during orbit insertion, Reviews of Geophysics, 46, RG4008, doi: 10.1029/2007RG000238.

Andre, N., A. M. Persoon, J. Goldstein, J. L. Burch, P. Louarn, G. R. Lewis, A. M. Rymer, A. J. Coates, W. S. Kurth, E. C. Sittler, Jr., M. F. Thomsen, F. J. Crary, M. K. Dougherty, D. A. Gurnett, D. T. Young, (2007), Magnetic signatures of plasma-depleted flux tubes in the Saturnian inner magnetosphere, Geophysical Research Letters, 34, L14108, doi: 10.1029/2007GL030374.

Andrews, D. J., S. W. H. Cowley, M. K. Dougherty, L. Lamy, G. Provan, and D. J. Southwood, (2012), Planetary period oscillations in Saturn's magnetosphere: Evolution of magnetic oscillation properties from southern summer to post-equinox, Journal of Geophysical Research, 117, A04224, doi: 10.1029/2011JA017444.

Andrews, D. J., B. Cecconi, S. W. H. Cowley, M. K. Dougherty, L. Lamy, G. Provan, P. Zarka, (2011), Planetary period oscillations in Saturn's magnetosphere: Evidence in magnetic field phase data for rotational modulation of Saturn kilometric radiation emissions, Journal of Geophysical Research, 116, A09206, doi: 10.1029/2011JA016636.

Andrews, D. J., A. J. Coates, S. W. H. Cowley, M. K. Dougherty, L. Lamy, G. Provan, P. Zarka, (2010), Magnetospheric period oscillations at Saturn: Comparison of equatorial and high-latitude magnetic field periods with north and south SKR periods, Journal of Geophysical Research, 115, A12252, doi: 10.1029/2010JA015666.

Aplin, K. and G. Fischer, (2019), Atmospheric electricity in the solar system, Oxford Research Encyclopedia, Planetary Science, Oxford University Press, doi: 10.1093/acrefore/9780190647926.013.112.

Aplin, K. L. and G. Fischer, (2017), Lightning detection in planetary atmospheres, Weather, 72, 2, 46–50, doi: 10.1002/wea.2817.

Arridge, C. S., J. P. Eastwood, C. M. Jackman, G.-K. Poh, J. A. Slavin, M. F. Thomsen, N. Andre, X. Jia, A. Kidder, L. Lamy, A. Radioti, D. B. Reisenfeld, N. Sergis, M. Volwerk, A. P. Walsh, P. Zarka, A. J. Coates, M. K. Dougherty, (2016a), Cassini in situ observations of long duration magnetic reconnection in Saturn's magnetotail, Nature Physics, 12, 268–271, doi: 10.1038/nphys3565.

Arridge, C. S., J. M. Jasinski, N. Achilleos, Y. V. Bogdanova, E. J. Bunce, S. W. H. Cowley, A. N. Fazakerley, K. K. Khurana, L. Lamy, J. S. Leisner, E. Roussos, C. T. Russell, P. Zarka, A. J. Coates, M. K. Dougherty, G. H. Jones, S. M. Krimigis, N. Krupp, (2016b), Cassini observations of Saturn's southern polar cusp, Journal of Geophysical Research, 121, 3006–3030, doi: 10.1002/2015JA021957.

Arridge, C. S., N. André, H. J. McAndrews, E. J. Bunce, M. H. Burger, K. C. Hansen, H.-W. Hsu, R. E. Johnson, G. H. Jones, S. Kempf, K. K. Khurana, N. Krupp, W. S. Kurth, J. S. Leisner, C. Paranicas, E. Roussos, C. T. Russell, P. Schippers, E. C. Sittler, H. T. Smith, M. F. Thomsen, M. K. Dougherty, (2011), Mapping magnetospheric equatorial regions at Saturn from Cassini Prime Mission Observations, Space Science Reviews, 164, Nos. 1–4, 1–83, doi: 10.1007/s11214-011-9850-4.

Azari, A. R., X. Jia, M. W. Liemohn, G. B. Hospodarsky, G. Provan, S.-Y. Ye, S. W. H. Cowley, C. Paranicas, N. Sergis, A. M. Rymer, M. F. Thomsen, D. G. Mitchell, (2019), Are Saturn's interchange injections organized by rotational longitude? Journal of Geophysical Research, 124, 1806–1822, doi: 10.1029/2018Ja026196.

Azari, A. R., M. W. Liemohn, X. Jia, M. F. Thomsen, D. G. Mitchell, N. Sergis, A. M. Rymer, G. B. Hospodarsky, C. Paranicas, J. Vandegriff, (2018), Interchange injections at Saturn: Statistical survey of energetic H^+ sudden flux intensifications, Journal of Geophysical Research, 123, 4692–4711, doi: 10.1029/2018JA025391.

Bader, A., S. V. Badman, Z. H. Yao, J. Kinrade, W. R. Pryor, (2019), Observations of continuous quasiperiodic auroral pulsations on Saturn in high time-resolution UV auroral imagery, Journal of Geophysical Research, 124, 2451–2465, doi: 10.1029/2018JA026320.

Badman, S. V., G. Provan, E. J. Bunce, D. G. Mitchell, H. Melin, S. W. H. Cowley, A. Radioti, W. S. Kurth, W. R. Pryor, J. D. Nichols, S.L. Jinks, T. S. Stallard, R. H. Brown, K. H. Baines, M. K. Dougherty, (2016), Saturn's auroral morphology and field-aligned currents during a solar wind compression, Icarus, 263, 83–93, doi: 10.1016/j.icarus.2014.11.014.

Badman, S. V., G. Branduardi-Raymont, M. Galand, S. L. G. Hess, N. Krupp, L. Lamy, H. Melin, C. Tao, (2014), Auroral processes at the giant planets: Energy deposition, emission mechanisms, morphology and spectra, Space Science Reviews, 187, Issue 1–4, doi: 10.1007/s11214-014-0042-x.

Badman, S. V., N. Achilleos, C. S. Arridge, K. H. Baines, R. H. Brown, E. J. Bunce, A. J. Coates, S. W. H. Cowley, M. K. Dougherty, M. Fujimoto, G. Hospodarsky, S. Kasahara, T. Kimura, H. Melin, D. G. Mitchell, T. Stallard, C. Tao, (2012a), Cassini observations of ion and electron beams at Saturn and their relationship to infrared auroral arcs, Journal of Geophysical Research, 117, A01211, doi: 10.1029/2011JA017222.

Badman, S. V., N. Achilleos, C. S. Arridge, K. H. Baines, R. H. Brown, E. J. Bunce, A. J. Coates, S. W. H. Cowley, M. K. Dougherty, M. Fujimoto, G. Hospodarsky, S. Kasahara, T. Kimura, H. Melin, D. G. Mitchell, T. Stallard, C. Tao, (2012b), Correction to Cassini observations of ion and electron beams at saturn and their relationship to infrared auroral arcs, Journal of Geophysical Research, 117, A04220, doi: 10.1029/2012JA017617.

Badman, S. V., D. J. Andrews, S. W. H. Cowley, L. Lamy, G. Provan, C. Tao, S. Kasahara, T. Kimura, M. Fujimoto, H. Melin, T. Stallard, R. H. Brown, K. H. Baines, (2012c), Rotational Modulation and Local Time Dependence of Saturn's Infrared H_3^+ Auroral Intensity, Journal of Geophysical Research, 117, A09228, doi: 10.1029/2012JA017990.

Badman, S. V., S. W. H. Cowley, L. Lamy, B. Cecconi, P. Zarka, (2008a), Relationship between solar wind corotating interaction region compressions and the phasing and intensity of Saturn kilometric radiation bursts, Annales Geophysicae, 26, 3641–3651, doi: 10.5194/angeo-26-3641-2008.

Badman, S. V., S. W. H. Cowley, L. Lamy, B. Cecconi, P. Zarka, (2008b), Saturn's radio clock, Astronomy & Geophysics, No. 4, pp. 4.13–4.15, Blackwell Publishing, doi: 10.1111/j.1468-4004.2008.49413.x.

Bagenal, F., A. Adriani, F. Allegrini, S. J. Bolton, B. Bonfond, E. J. Bunce, J. E. P. Connerney, S. W. H. Cowley, R. W. Ebert, G. R. Gladstone, C. J. Hansen, W. S. Kurth, S. M. Levin, B. H. Mauk, D. J. McComas, C. P. Paranicas, D. Santos-Costas, R. M. Thorne, P. Valek, J. H. Waite, P. Zarka, (2017), Magnetospheric science objectives of the Juno Mission, Space Science Reviews, 213, 219–287, doi: 10.1007/s11214-014-0036-8.

Baines, K. H., M. L. Delitsky, T. W. Momary, R. H. Brown, B. J. Buratti, R. N. Clark, P. D. Nicholson, (2009), Storm clouds on Saturn: Lightning-induced chemistry and associated materials consistent with Cassini/VIMS spectra, Planetary and Space Science, 57, 1650–1658.

Bebesi, Z., K. Szego, A. Balogh, N. Krupp, G. Erdos, A. M. Rymer, G. R. Lewis, W. S. Kurth, D. T. Young, M. K. Dougherty, (2011), Response to– Comment on– Slow-mode shock candidate in the Jovian magnetosheath by Bebesi et al. 2010, Planetary and Space Science, 59, Issues 5–6, 445–446, doi: 10.1016/j.pss.2010.10.007.

Bebesi, Z., K. Szego, A. Balogh, N. Krupp, G. Erdos, A. M. Rymer, G. R. Lewis, W. S. Kurth, D. T. Young, M. K. Dougherty, (2010), Slow-mode shock candidate in the Jovian magnetosheath, Planetary and Space Science, 58, Issue 5, 807–813, doi: 10.1016/j.pss.2009.12.008.

Beghin, C., P. Canu, E. Karkoschka, C. Sotin, C. Bertucci, W. S. Kurth, J. J. Berthelier, R. Grard, M. Hamelin, K. Schwingenschuh, F. Simoes, (2009), New insights on Titan's plasma-driven Schumann resonance inferred from Huygens and Cassini data, Planetary and Space Science, 57, 1872–1888, doi: 10.1016/j.pss.2009.04.006.

Bertucci, C., D. C. Hamilton, W. S. Kurth, G. B. Hospodarsky, D. Mitchell, N. Sergis, N. J. T. Edberg, M. K. Dougherty, (2015), Titan's interaction with the supersonic solar wind, Geophysical Research Letters, 42, 193–200, doi: 10.1002/2014GL062106.

Bertucci, C., F. Duru, N. Edberg, M. Fraenz, C. Martinecz, K. Szego, O. Vaisberg, (2011), The induced magnetospheres of Mars, Venus, and Titan, Space Science Reviews, 162, 113–171, doi: 10.1007/s11214-011-9845-1.

Bertucci, C., N. Achilleos, M. K. Dougherty, R. Modolo, A. J. Coates, K. Szego, A. Masters, Y. Ma, F. M. Neubauer, P. Garnier, J.-E. Wahlund, D. T. Young, (2008), The magnetic memory of Titan's ionized atmosphere, Science, 321, 1475–1478, doi: 10.1126/science.1159780.

Bertucci, C., N. Achilleos, C. Mazelle, G. B. Hospodarsky, M. Thomsen, M. K. Dougherty, W. Kurth, (2007a), Low-frequency waves in the foreshock of Saturn: First results from Cassini, Journal of Geophysical Research, 112, A09219, doi: 10.1029/2006JA012098.

Bertucci, C., F. M. Neubauer, K. Szego, J.-E. Wahlund, A. J. Coates, M. K. Dougherty, D. T. Young, W. S. Kurth, (2007b), Structure of Titan's mid-range magnetic tail: Cassini Magnetometer observations during the T9 flyby, Geophysical Research Letters, 34, L24S02, doi: 10.1029/2007GL030865.

Blanc, M., S. Bolton, J. Bradley, M. Burton, T. E. Cravens, I. Dandouras, M. K. Dougherty, M. C. Festou, J. Feynman, R. E. Johnson, T. G. Gombosi, W. S. Kurth, P. C. Liewer, B. H. Mauk, S. Maurice, D. Mitchell, F. M. Neubauer, J. D. Richardson, D. E. Shemansky, E. C. Sittler, B. T. Tsurutani, Ph. Zarka, L. W. Esposito, E. Gruen, D. A. Gurnett, A. J. Kliore, S. M. Krimigis, D. Southwood, J. H. Waite, D. T. Young, (2002), Magnetospheric and plasma science with Cassini-Huygens, Space Science Reviews, 104, 253–346, doi: 10.1023/A:1023605110711.

Boudjada, M. Y., P. H. M. Galopeau, S. Sawas, H. Lammer, (2014a), Remote sensing of the Io torus plasma ribbon using natural radio occultation of the Jovian radio emission, Annales Geophysicae, 32, 1119–1128, doi: 10.5194/angeo-32-1119-2014.

Boudjada, M. Y., P. H. M. Galopeau, M. Maksimovic, H. O. Rucker, (2014b), Visibility of Type III burst source location as inferred from stereoscopic space observations, Advances in Radio Science, 12, 167–170, doi: 10.5194/ars-12-167-2014.

Boudjada, M. Y., P. H. M. Galopeau, H. O. Rucker, A. Lecacheux, N. Mebarki, W. Macher, W. Voller, (2011), Morphological aspects of the attenuation bands associated with Jovian hectometric radiation, Journal of Geophysical Research, 116, A11208, doi: 10.1029/2010Ja016354.

Branduardi-Raymont, G., P. G. Ford, K. C. Hansen, L. Lamy, A. Masters, B. Cecconi, A. J. Coates, M. K. Dougherty, G. R. Gladstone, P. Zarka, (2013), Search for Saturn's x-ray aurorae at the arrival of a solar wind shock, Journal of Geophysical Research, 118, 2145–2156, doi: 10.1002/jgra.50112.

Bunce, E. J., D. C. Grodent, S. L. Jinks, D. J. Andrews, S. V. Badman, A. J. Coates, S. W. H. Cowley, M. K. Dougherty, W. S. Kurth, D. G. Mitchell, G. Provan, (2014), Cassini nightside observations of the oscillatory motion of Saturn's northern auroral oval, Journal of Geophysical Research, 119, 3528–3543, doi: 10.1002/2013JA019527.

Bunce, E. J., S. W. H. Cowley, D. L. Talboys, M. K. Dougherty, L. Lamy, W. S. Kurth, P. Schippers, B. Cecconi, P. Zarka, C. S. Arridge, A. J. Coates, (2010), Extraordinary field-aligned current signatures in Saturn's high-latitude magnetosphere: Analysis of Cassini data during Revolution 89, Journal of Geophysical Research, 115, A10238, doi: 10.1029/2010JA015612.

Bunce, E. J., S. W. H. Cowley, D. M. Wright, A. J. Coates, M. K. Dougherty, N. Krupp, W. S. Kurth, A. M. Rymer, (2005), In situ observations of a solar wind compression-induced hot plasma injection in Saturn's tail, Geophysical Research Letters, 32, L20S04, doi: 10.1029/2005GL022888.

Burch, J. L., J. Goldstein, T. W. Hill, D. T. Young, F. J. Crary, A. J. Coates, N. Andre, W. S. Kurth, E. C. Sittler, Jr., (2005), Properties of local plasma injections in Saturn's magnetosphere, Geophysical Research Letters, 32, L14S02, doi: 10.1029/2005GL022611.

Burns, J. A., D. P. Hamilton, M. R. Showalter, (2001), Dusty rings and circumplanetary dust: Observations and simple physics, In Interplanetary Dust, (eds.) E. Grün, B. A. S. Gustafson, S. Dermott, H. Fechtig, Springer, Berlin.

Carbary, J. F., W. S. Kurth, D. G. Mitchell, (2016), Short periodicities in low-frequency plasma waves at Saturn, Journal of Geophysical Research, 121, 6562–6572, doi: 10.1002/2016JA022732.

Carbary, J. F. and D. G. Mitchell, (2013), Periodicities in Saturn’s magnetosphere, Reviews of Geophysics, 51, 1–30, doi: 10.1002/rog.20006.

Carbary, J. F., D. G. Mitchell, P. C. Brandt, S. M. Krimigis, D. A. Gurnett, (2011), ENA periodicities and their phase relations to SKR emissions at Saturn, Geophysical Research Letters, 38, L16106, doi: 10.1029/2011GL048418.

Carbary, J. F., D. G. Mitchell, S. M. Krimigis, D. A. Gurnett, W. S. Kurth, (2010), Phase relations between energetic neutral atom intensities and kilometric radio emissions at Saturn, Journal of Geophysical Research, 115, A01203, doi: 10.1029/2009JA014519.

Cecconi, B., S. Hess, A. Herique, M. R. Santovito, D. Santos-Costa, P. Zarka, G. Alberti, D. Blankenship, J.-L. Bougeret, L. Bruzzone, W. Kofman, (2012), Natural radio emission of Jupiter as interferences for radar investigations of Icy Satellites of Jupiter, Planetary and Space Science, 61, 32–45, doi: 10.1016/j.pss.2011.06.012.

Cecconi, B., L. Lamy, P. Zarka, R. Prange, W. S. Kurth, P. Louarn, (2009), Goniopolarimetric study of the revolution 29 perikrone using the Cassini Radio and Plasma Wave Science instrument high-frequency radio receiver, Journal of Geophysical Research, 114, A03215, doi: 10.1029/2008JA013830.

Cecconi, B., (2009), Comment on– Spectral features of SKR observed by Cassini/RPWS: Frequency bandwidth, flux density and polarization by Patrick Galopeau et al. 2007, Journal of Geophysical Research, 114, A07206, doi: 10.1029/2007JA012970.

Cecconi, B., (2007), Influence of an extended source on goniopolarimetry (or direction finding) with Cassini and solar terrestrial relations observatory radio receivers, Radio Science, 42, RS2003, doi: 10.1029/2006RS003458.

Cecconi, B., P. Zarka, W. S. Kurth, (2006), SKR polarization and source localization with the Cassini/RPWS/HFR instrument: First results, In Planetary Radio Emissions VI, (eds.) H. O. Rucker, W. S. Kurth, G. Mann, Austrian Academy of Sciences Press, Vienna, Austria, pp. 37–49.

Cecconi, B. and P. Zarka, (2005a), Direction finding and antenna calibration through analytical inversion of radio measurements performed using a system of two or three electric dipole wire antennas on a three-axis stabilized spacecraft, Radio Science, 40, RS3003, doi: 10.1029/2004RS003070.

Cecconi, B. and P. Zarka, (2005b), Model of a variable radio period for Saturn, Journal of Geophysical Research, 110, A12203, doi: 10.1029/2005JA011085.

Cecconi, B., (2004), Étude goniopolarimétrique des émissions radio de Jupiter et Saturne à l'aide du récepteur radio de la sonde Cassini, Ph.D. Thesis, University of Paris, Meudon, France.

Clarke, J. T., J. Nichols, J.-C. Gerard, D. Grodent, K. C. Hansen, W. Kurth, G. R. Gladstone, J. Duval, S. Wannawichian, E. Bunce, S. W. H. Cowley, F. Crary, M. Dougherty, L. Lamy, D. Mitchell, W. Pryor, K. Retherford, T. Stallard, B. Zieger, P. Zarka, B. Cecconi, (2009), The response of Jupiter's and Saturn's auroral activity to the solar wind, Journal of Geophysical Research, 114, A05210, doi: 10.1029/2008JA013694.

Clarke, J. T., J.-C. Gerard, D. Grodent, S. Wannawichian, J. Gustin, J. Connerney, F. Crary, M. Dougherty, W. Kurth, S. W. H. Cowley, E. J. Bunce, T. Hill, J. Kim, (2005), Morphological differences between Saturn's ultraviolet aurorae and those of Earth and Jupiter, Nature, 433, 717–719, doi: 10.1038/nature03331.

Clarke, J. T., D. Grodent, S. W. H. Cowley, E. J. Bunce, P. Zarka, J. E. P. Connerney, T. Satoh, (2004), Jupiter's aurora, In Jupiter: the Planet, Satellites, and Magnetosphere, (eds.) F. Bagenal, W. McKinnon, T. Dowling, Cambridge University Press, Cambridge.

Coates, A. J., A. Wellbrock, G. H. Jones, J. H. Waite, P. Schippers, M. F. Thomsen, C. S. Arridge, R. L. Tokar, (2013), Photoelectrons in the Enceladus plume, Journal of Geophysical Research, 118, 5099–5108, doi: 10.1002/jgra.50495.

Coates, A. J., J.-E. Wahlund, K. Ågren, N. J. T. Edberg, J. Cui, A. Wellbrock, K. Szego, (2011), Recent results from Titan’s ionosphere, Space Science Review, 162, 85–211, doi: 10.1007/s11214-011-9826-4.

Coates, A. J., F. J. Crary, G. R. Lewis, D. T. Young, J. H. Waite, E. C. Sittler Jr., (2007), Discovery of heavy negative ions in Titan's ionosphere, Geophysical Research Letters, 34, L22103, doi: 10.1029/2007GL030978.

Crary, F. J., J. T. Clarke, M. K. Dougherty, P. G. Hanlon, K. C. Hansen, J. T. Steinberg, B. L. Barraclough, A. J. Coates, J.-C. Gerard, D. Grodent, W. S. Kurth, D. G. Mitchell, A. M. Rymer, D. T. Young, (2005), Solar wind dynamic pressure and electric field as the main factors controlling Saturn's aurorae, Nature, 433, 720–722, doi: 10.1038/nature03333.

Cravens, T., L. Moore, H. J. Waite, R. Perryman, M. Perry, J.-E. Wahlund, A. M. Persoon, W. S. Kurth, (2018), The ion composition of Saturn's equatorial ionosphere as observed by Cassini, Geophysical Research Letters 46, no. 12, 6315-6321.

Cravens, T. E., M. Richard, Y. J. Ma, C. Bertucci, J. G. Luhmann, S. Ledvina, I. P. Robertson, J.-E. Wahlund, K. Ågren, J. Cui, I. Müller-Wodarg, J. H. Waite, M. Dougherty, J. Bell, D. Ulusen, (2010), Dynamical and magnetic field time constants for Titan’s ionosphere: Empirical estimates and comparisons with Venus, Journal of Geophysical Research, 115, A08319, doi: 10.1029/2009JA015050.

Cravens, T. E., I. P. Robertson, J. H. Waite, R. V. Yelle, V. Vuitton, A. J. Coates, J.-E. Wahlund, K. Ågren, M. S. Richard, V. de La Haye, A. Wellbrock, F. M. Neubauer, (2009a), Model-data

comparisons for Titan's nightside ionosphere, Icarus, 199, 174–188, doi: 10.1016/j.icarus.2008.09.005.

Cravens, T. E., R. V. Yelle, J.-E. Wahlund, D. E. Shemansky, A. F. Nagy, (2009a), Composition and structure of the ionosphere and thermosphere, In Titan from Cassini-Huygens, (eds.) R. H. Brown, J.-P. Lebreton, J. H. Waite, Springer, Dordrecht, doi: 10.1007/978-1-420-9215-2_11, pp. 259-295.

Cravens, T. E., I. P. Robertson, J. H. Waite, R. V. Yelle, W. T. Kasprzak, C. N. Keller, S. A. Ledvina, H. B. Niemann, J. G. Luhmann, R. L. McNutt, W.-H. Ip, V. De La Haye, I. Mueller-Wodarg, J.-E. Wahlund, V. G. Anicich, V. Vuitton, (2006), Composition of Titan's ionosphere, Geophysical Research Letters, 33, L07105, doi: 10.1029/2005GL025575.

Cravens, T. E., I. P. Robertson, J. Clark, J.-E. Wahlund, J. H. Waite, Jr., S. A. Ledvina, H. B. Niemann, R. V. Yelle, W. T. Kasprzak, J. G. Luhmann, R. L. McNutt, W.-H. Ip, V. De La Haye, I. Muller-Wodarg, D. T. Young, A. J. Coates, (2005), Titan's ionosphere: Model comparisons with Cassini Ta data, Geophysical Research Letters, 32, L12108, doi: 10.1029/2005GL023249.

Cui, J., M. Galand, R. V. Yelle, J.-E. Wahlund, K. Ågren, J. H. Waite, Jr., M. K. Dougherty, (2010), Ion transport in Titan's upper atmosphere, Journal of Geophysical Research, 115, A06314, doi: 10.1029/2009JA014563.

Cui, J., M. Galand, R. V. Yelle, V. Vuitton, J.-E. Wahlund, P. P. Lavvas, I. C. F. Muller-Wodarg, T. E. Cravens, W. T. Kasprzak, J. H. Waite, Jr., (2009), Diurnal variations of Titan's ionosphere, Journal of Geophysical Research, 114, A06310, doi: 10.1029/2009JA014228.

de Pater, I. and W. S. Kurth, (2007), The solar system at radio wavelengths, In Encyclopedia of the Solar System, 2nd Edition, (eds.) L.-A. McFadden, P. Weissman, T. Johnson, Academic Press/Elsevier, San Diego, pp. 695–718.

de Soria-Santacruz, M., Y. Y. Shprits, A. Drozdov, J. D. Menietti, H. B. Garrett, H. Zhu, A. C. Kellerman, R. B. Horne, (2017), Interactions between energetic electrons and realistic whistler mode waves in the Jovian magnetosphere, Journal of Geophysical Research, 122, 5355–5364, doi: 10.1002/2017JA023975.

Desai, R. T., A. J. Coates, A. Wellbrock, V. Vuitton, F. J. Crary, D. Gonzalez-Caniulef, O. Shebanits, G. H. Jones, G. R. Lewis, J. H. Waite, S. A. Taylor, D. O. Kataria, J.-E. Wahlund, N. J. T. Edberg, E. C. Sittler, (2017), Carbon chain anions and the growth of complex organic molecules in Titan's ionosphere, Astrophysical Journal Letters, 844, doi: 10.3847/2041-8212/aa/7851.

Desch, M. D., G. Fischer, M. L. Kaiser, W. M. Farrell, W. S. Kurth, D. A. Gurnett, P. Zarka, A. Lecacheux, C. C. Porco, A. P. Ingersoll, U. Dyudina, (2006), Cassini RPWS and imaging observations of Saturn lightning, In Planetary Radio Emissions VI, (eds.) H. O. Rucker, W. S. Kurth, G. Mann, Austrian Academy of Sciences Press, Vienna, Austria, pp. 103–110.

Desch, M. D. and M. L. Kaiser, (1990), Upper limit set for level of lightning activity on Titan, Nature, 343, 442–444.

Dong, Y., T. W. Hill, S.-Y. Ye, (2015), Characteristics of Ice grains in the Enceladus plume from Cassini observations, Journal of Geophysical Research, 120, 915–937, doi: 10.1002/2014JA020288.

Dougherty, M. K., K. K. Khurana, F. M. Neubauer, C. T. Russell, J. Saur, J. S. Leisner, M. E. Burton, (2006), Identification of a dynamic atmosphere at Enceladus with the Cassini magnetometer, Science, 311, 1406–1409, doi: 10.1126/science.1120985.

Dyudina, U. A., A. P. Ingersoll, S. P. Ewald, C. C. Porco, G. Fischer, Y. Yair, (2013), Saturn's visible lightning, its radio emissions, and the structure of the 2009–2011 lightning storms, Icarus, 225, 1029–1037, doi: 10.1016/j.icarus.2013.07.013.

Dyudina, U. A., A. P. Ingersoll, S. P. Ewald, C. C. Porco, G. Fischer, W. S. Kurth, R. A. West, (2010), Detection of visible lightning on Saturn, Geophysical Research Letters, 37, L09205, doi: 10.1029/2010GL043188.

Dyudina, U. A., A. P. Ingersoll, S. P. Ewald, C. C. Porco, G. Fischer, W. S. Kurth, M. D. Desch, A. Del Genio, J. Barbara, J. Ferrier, (2007), Lightning storms on Saturn observed by Cassini ISS and RPWS during 2004–2006, Icarus, 190, 545–555, doi: 10.1016/j.icarus.2007.03.035.

Edberg, N. J. T., E. Vigren, D. Snowden, L. H. Regoli, O. Shebanits, J.-E. Wahlund, D. J. Andrews, C. Bertucci, J. Cui, (2019), Titan's variable ionosphere during the T118-T119 Cassini flybys, Geophysical Research Letters, 45, 8721–8728, doi: 10.1029/2018GL078436.

Edberg, N. J. T., D. J. Andrews, C. Bertucci, D. A. Gurnett, M. Holmberg, C. M. Jackman, W. S. Kurth, J. D. Menietti, H. Opgenoorth, O. Shebanits, E. Vigren, and J.-E. Wahlund, (2015), Effects of Saturn's magnetospheric dynamics on Titan's ionosphere, Journal of Geophysical Research, 120, 8884–8898, doi: 10.1002/2015JA021373.

Edberg, N. J. T., D. J. Andrews, O. Shebanits, K. Ågren, J.-E. Wahlund, H. J. Opgenoorth, E. Roussos, P. Garnier, T. E. Cravens, S. V. Badman, R. Modolo, C. Bertucci, M. K. Dougherty, (2013a), Extreme densities in Titan's ionosphere during the T85 magnetosheath encounter, Geophysical Research Letters, 40, 1–5, doi: 10.1002/grl.50579.

Edberg, N. J. T., D. J. Andrews, O. Shebanits, K. Ågren, J.-E. Wahlund, H. J. Opgenoorth, T. E. Cravens, Z. Girazian, (2013b), Solar cycle modulation of Titan's ionosphere, Journal of Geophysical Research, 118, 5255–5264, doi: 10.1002/jgra.50463.

Edberg, N. J. T., K. Ågren, J.-E. Wahlund, M. W. Morooka, D. J. Andrews, S. W. H. Cowley, A. Wellbrock, A. J. Coates, C. Bertucci, M. K. Dougherty, (2011), Structured ionospheric outflow during the Cassini T55–T59 Titan flybys, Planetary and Space Science, 59, 788–797, doi: 10.1016/j.pss.2011.03.007.

Edberg, N. J. T., J.-E. Wahlund, K. Ågren, M. W. Morooka, R. Modolo, C. Bertucci, M. K. Dougherty, (2010), Electron density and temperature measurements in the cold plasma environment of Titan: Implications for atmospheric escape, Geophysical Research Letters, 37, L20105, doi: 10.1029/2010GL044544.

Encrenaz, T., J.-P. Bibring, M. Blanc, A. Barucci, F. Roques, P. Zarka, (2004), The solar system, 3rd edition, Astronomy and Astrophysics Library, Springer, Germany.

Engelhardt, I. A. D., J.-E. Wahlund, D. J. Andrews, A. I. Erikkson, S. Ye, W. S. Kurth, D. A. Gurnett, M. W. Morooka, W. M. Farrell, M. K. Dougherty, (2015), Plasma regions, charged dust, and field-aligned currents near Enceladus, Planetary and Space Science, 117, 453–469, doi: 10.1016/j.pss.2015.09.010.

Ergun, R. E., C. W. Carlson, J. P. McFadden, R. J. Strangeway, M. V. Goldman, D. L. Newman, (2003), Fast auroral snapshot satellite observations of very low frequency saucers, 10, 454, doi: 10.1063/1.1530160.

Eriksson, A. I., T. Nilsson, J.-E. Wahlund, (2012), Interpretation of Langmuir probe data obtained close to a spacecraft, In Proceedings of the 39th EPS Conference/16th International Congress on Plasma Physics, (eds.) S. Ratynskaya, L. Blomberg, A. Fasoli, European Physical Society, Stockholm, Sweden, ISBN 2-914771-79-7, vol. 36F, P4.185.

Farrell, W. M., L. Z. Hadid, M. W. Morooka, W. S. Kurth, J.-E. Wahlund, R. J. MacDowall, A. H. Sulaiman, A. M. Persoon, D. A. Gurnett, (2018), Saturn's plasma density depletions along magnetic field lines connected to the main rings, Geophys. Res. Lett., 45, 8104–8110, doi: 10.1029/2018GL078137.

Farrell, W. M., J.-E. Wahlund, M. Morooka, W. S. Kurth, D. A. Gurnett, R. J. MacDowall, (2017a), Ion trapping to dust grains: Simulation applications to the Enceladus plume, Journal of Geophysical Research: Planets, 122, Issue 4, 729–743, doi: 10.1002/2016JE005235.

Farrell, W. M., W. S. Kurth, D. A. Gurnett, A. M. Persoon, R. J. MacDowall, (2017b), Saturn's rings and associated ring plasma cavity: Evidence for slow ring erosion, Icarus, 292, 48–52, doi: 10.1016/j.icarus.2017.03.022.

Farrell, W. M., J.-E. Wahlund, M. Morooka, D. A. Gurnett, W. S. Kurth, R. J. MacDowall, (2014), An estimate of dust pickup current at Enceladus, Icarus, 239, 217–221, doi: 10.1016/j.icarus.2014.05.034.

Farrell, W. M., J.-E. Wahlund, M. Morooka, D. A. Gurnett, W. S. Kurth, R. J. MacDowall, (2012), The electromagnetic pickup of submicron-sized dust above Enceladus' northern hemisphere, Icarus, 219, 498–501, doi: 10.1016/j.icarus.2012.02.033.

Farrell, W. M., W. S. Kurth, R. L. Tokar, J.-E. Wahlund, D. A. Gurnett, Z. Wang, R. J. MacDowall, M. W. Morooka, R. E. Johnson, J. H. Waite, Jr., (2010), Modification of the plasma in the near-vicinity of Enceladus by the enveloping dust, Geophysical Research Letters, 37, L20202, doi: 10.1029/2010GL044768.

Farrell, W. M., W. S. Kurth, D. A. Gurnett, R. E. Johnson, M. L. Kaiser, J.-E. Wahlund, J. H. Waite, Jr., (2009), Electron density dropout near Enceladus in the context of water-vapor and water-ice, Geophysical Research Letters, 36, L10203, doi: 10.1029/2008GL037108.

Farrell, W. M., M. L. Kaiser, D. A. Gurnett, W. S. Kurth, A. M. Persoon, J.-E. Wahlund, P. Canu, (2008), Mass unloading along the inner edge of the Enceladus Plasma torus, Geophysical Research Letters, 35, L02203, doi: 10.1029/2007GL032306.

Farrell, W. M., M. L. Kaiser, G. Fischer, P. Zarka, W. S. Kurth, D. A. Gurnett, (2007), Are Saturn electrostatic discharges really superbolts? A temporal dilemma, Geophysical Research Letters, 34, L06202, doi: 10.1029/2006GL028841.

Farrell, W. M., M. D. Desch, M. L. Kaiser, W. S. Kurth, D. A. Gurnett, (2006), Changing Electrical nature of Saturn's rings: Implications for spoke formation, Geophysical Research Letters, 33, L07203, doi: 10.1029/2005GL024922.

Farrell, W. M., M. D. Desch, M. L. Kaiser, A. Lecacheux, W. S. Kurth, D. A. Gurnett, B. Cecconi, P. Zarka, (2005a), A nightside source of Saturn's kilometric radiation: Evidence for an inner magnetosphere energy driver, Geophysical Research Letters, 32, L18107, doi: 10.1029/2005GL023449.

Farrell, W. M., W. S. Kurth, M. L. Kaiser, M. D. Desch, D. A. Gurnett, P. Canu, (2005b), Narrowband Z-mode emissions interior to Saturn's plasma torus, Journal of Geophysical Research, 110, A10204, doi: 10.1029/2005JA011102.

Farrell, W. M., M. L. Kaiser, W. S. Kurth, M. D. Desch, D. A. Gurnett, G. B. Hospodarsky, R. J. MacDowall, (2004), Remote sensing of possible plasma density bubbles in the inner Jovian dayside magnetosphere, Journal of Geophysical Research, 109, A09S14, doi: 10.1029/2003JA010130.

Farrell, W. M., D. A. Gurnett, D. L. Kirchner, W. S. Kurth, L. J. C. Woolliscroft, (1993), Data compression for the Cassini Radio and Plasma Wave experiment, 1993 Space and Earth Science Data Compression Workshop, NASA Conference Publication 3183, p. 111, Snowbird, UT.

Felici, M., C. S. Arridge, A. J. Coates, S. V. Badman, M. K. Dougherty, C. M. Jackman, W. S. Kurth, H. Melin, D. G. Mitchell, D. B. Reisenfeld, N. Sergis, (2016), Cassini observations of ionospheric plasma in Saturn's magnetotail lobes, Journal of Geophysical Research, 121, 338–357, doi: 10.1002/2001JA021648.

Feyerabend, M., S. Simon, F. M. Neubauer, U. Motschmann, C. Bertucci, N. J. T. Edberg, G. B. Hospodarsky, W. S. Kurth, (2016), Hybrid simulation of Titan's interaction with the supersonic solar wind during Cassini's T96 flyby, Geophysical Research Letters, 43, 35–42, doi: 10.1002/2015GL066848.

Fischer, G. J. P. Pagaran, P. Zarka, M. Delcroix, U. A. Dyudina, W. S. Kurth, D. A. Gurnett, (2018), Analysis of a long-lived, two-cell lightning storm on Saturn, Astronomy & Astrophysics, 621, A113, doi:10.1051/0004-6361/201833014.

Fischer, G., D. A. Gurnett, W. S. Kurth, S.-Y. Ye, J. B. Groene, (2015), Saturn kilometric radiation periodicity after equinox, Icarus, 254, 72–91, doi: 10.1016/icarus.2015.03.014.

Fischer, G., (2015), Im Kontext: Blitze am Saturn, In Physik fuer Wissenschaftler und Ingenieure (7. Auflage), (eds.) P. A. Tipler, G. Mosca, J. Wagner, Springer-Verlag, Berlin-Heidelberg, pp. 752–753.

Fischer, G., W. Macher, M. Panchenko, (2014a), Space-based radio observations of Saturn at IWF, In Planetary Radio Emissions 7.5, Planetary Retirement Edition, (eds.) N. I. Kömle, G. Fischer, W. Macher, Living Edition Publishers, Pöllauberg, pp. 55–70.

Fischer, G., S.-Y. Ye, J. B. Groene, A. P. Ingersoll, K. Sayanagi, J. D. Menietti, W. S. Kurth, D. A. Gurnett, (2014b), A possible influence of the Great White Spot on Saturn kilometric radiation periodicity, Annales Geophysicae, 32, 1463–1476, doi: 10.5194/angeo-32-1463-2014.

Fischer, G., D. A. Gurnett, Y. Yair, (2011a), Extraterrestrial lightning and its past and future investigation, lightning; properties, formation and types, (eds.) M. D. Wood, NOVA Science Publishers, Inc., New York.

Fischer, G., D. A. Gurnett, P. Zarka, L. Moore, U. Dyudina, (2011b), Peak electron densities in Saturn's ionosphere derived from the low-frequency cutoff of Saturn lightning, Journal of Geophysical Research, 116, A04315, doi: 10.1029/2010JA016187.

Fischer, G., W. S. Kurth, D. A. Gurnett, P. Zarka, U. A. Dyudina, A. P. Ingersoll, S. P. Ewald, C. C. Porco, A. Wesley, C. Go, M. Delcroix, (2011c), A giant thunderstorm on Saturn, Nature, 475, 75–77, doi: 10.1038/nature10205.

Fischer, G., U. A. Dyudina, W. S. Kurth, D. A. Gurnett, P. Zarka, T. Barry, M. Delcroix, C. Go, D. Peach, R. Vandebergh, A. Wesley, (2011d), Overview of Saturn lightning observations, In Planetary Radio Emissions VII, (eds.) H. O. Rucker, W. S. Kurth, P. Louarn, G. Fischer, Austrian Academy of Sciences, Vienna, Austria, pp. 135–144.

Fischer, G. and D. A. Gurnett, (2011), The search for Titan lightning radio emissions, Geophysical Research Letters, 38, L08206, doi: 10.1029/2011GL047316.

Fischer, G., B. Cecconi, L. Lamy, S. Ye, U. Taubenschuss, W. Macher, P. Zarka, W. S. Kurth, D. A. Gurnett, (2009), Elliptical polarization of Saturn Kilometric radiation observed from high latitudes, Journal of Geophysical Research, 114, A08216, doi: 10.1029/2009JA014176.

Fischer, G., D. A. Gurnett, W. S. Kurth, F. Akalin, P. Zarka, U. A. Dyudina, W. M. Farrell, M. L. Kaiser, (2008), Atmospheric electricity at Saturn, Space Science Reviews, 137, 271–285, doi: 10.1007/s11214-008-9370-z.

Fischer, G., W. S. Kurth, U. A. Dyudina, M. L. Kaiser, P. Zarka, A. Lecacheux, A. P. Ingersoll, D. A. Gurnett, (2007a), Analysis of a giant lightning storm on Saturn, Icarus, 190, 528–544, doi: 10.1016/j.icarus.2007.04.002.

Fischer, G., D. A. Gurnett, W. S. Kurth, W. M Farrell, M. L. Kaiser, P. Zarka, (2007b), Nondetection of Titan lightning radio emissions with Cassini/RPWS after 35 close Titan flybys, Geophysical Research Letters, 34, L22104, doi: 10.1029/2007GL031668.

Fischer, G., D. A. Gurnett, A. Lecacheux, W. Macher, and W. S. Kurth, (2007c), Polarization measurements of Saturn electrostatic discharges with Cassini/RPWS below a frequency of 2 MHz, Journal of Geophysical Research, 112, A12308, doi: 10.1029/2007JA012592.

Fischer, G., M. D. Desch, P. Zarka, M. L. Kaiser, D. A. Gurnett, W. S. Kurth, W. Macher, H. O. Rucker, A. Lecacheux, W. M. Farrell, B. Cecconi, (2006a), Saturn lightning recorded by Cassini/RPWS in 2004, Icarus, 183, 1, 135–152, doi: 10.1016/j.icarus.2006.02.010.

Fischer, G., W. Macher, M. D. Desch, M. L. Kaiser, P. Zarka, W. S. Kurth, W. M. Farrell, A. Lecacheux, B. Cecconi, D. A. Gurnett, (2006b), On the intensity of Saturn lightning, In Planetary Radio Emissions VI, (eds.) H. O. Rucker, W. S. Kurth, G. Mann, Austrian Academy of Sciences Press, Vienna, Austria, pp. 123–132.

Fischer, G., W. Macher, D. A. Gurnett, M. D. Desch, A. Lecacheux, P. Zarka, W. S. Kurth, M L. Kaiser, (2006c), The discrimination between Jovian radio emissions and Saturn electrostatic discharges, Geophysical Research Letters, 33, L21201, doi: 10.1029/2006GL026766.

Fischer, G. and H. O. Rucker, (2006), Man-made radio emissions recorded by Cassini/RPWS during Earth flyby, In Planetary Radio Emissions VI, (eds.) H. O. Rucker, W. S. Kurth, G. Mann, Austrian Academy of Sciences Press, Vienna, Austria, pp. 299–306.

Fischer, G., (2004), Energy dissipation and HF radiation of lightning on Titan and Earth, Ph.D. Thesis, Karl-Franzens Universitat, Graz, Austria.

Fischer, G., T. Tokano, W. Macher, H. Lammer, H. O. Rucker, (2004), Energy dissipation of possible Titan lightning strokes, Planetary and Space Science, 52, 447–458.

Fischer, G., W. Macher, H. O. Rucker, H. P. Ladreiter, D. F. Vogl, Cassini RPWS Team, (2001), Wire-grid modeling of Cassini spacecraft of the determination of effective antenna length vectors of the RPWS antennas, In Planetary Radio Emissions V, (eds.) H. O. Rucker, M. L. Kaiser, Y. Leblanc, Austrian Academy of Sciences Press, Vienna, Austria, pp. 347–356.

Fletcher, L. N., B. E. Hesman, R. K. Achterberg, P. G. J. Irwin, G. Bjoraker, N. Gorius, J. Hurley, J. Sinclair, G. S. Orton, J. Legarreta, E. Garcia-Melendo, A. Sanchez-Lavega, P. L. Read, A. A. Simon-Miller, F. M. Flasar, (2012), The origin and evolution of Saturn’s 2011–2012 Stratospheric Vortex, Icarus, 221, 560–586.

Galand, M., A. J. Coates, T. E. Cravens, J.-E. Wahlund, (2013), Titan's ionosphere, In Titan – Interior, surface, atmosphere and space environment, (eds.) I. C. F. Müller-Wodarg, C. A. Griffith, E. Lellouch, T. E. Cravens, Cambridge University Press, Cambridge.

Galand, M., R. Yelle, J. Cui, J.-E. Wahlund, V. Vuitton, A. Wellbrock, A. Coates, (2010), Ionization sources in Titan's deep ionosphere, Journal of Geophysical Research, 115, A07312, doi: 10.1029/2009JA015100.

Galand, M., R. V. Yelle, A. J. Coates, H. Backes, J.-E. Wahlund, (2006), Electron temperature of Titan's sunlit ionosphere, Geophysical Research Letters, 33, L21101, doi: 10.1029/2006GL027488.

Galopeau, P. H. M., M. Y. Boudjada, A. Lecacheux, (2009), Reply to– Comment by B. Cecconi on– Spectral features of SKR observed by Cassini/RPWS: Frequency bandwidth, flux density and polarization, Journal of Geophysical Research, 114, A07207, doi: 10.1029/2008JA013177.

Galopeau, P. H. M., M. Y. Boudjada, A. Lecacheux, (2007), Spectral features of SKR observed by Cassini/RPWS: Frequency bandwidth, flux density and polarization, Journal of Geophysical Research, 112, A11213, doi: 10.1029/2007JA012573.

Garnier, P., M. K. G. Holmberg, J.-E. Wahlund, G. R. Lewis, P. Schippers, A. Coates, D. A. Gurnett, J. H. Waite, I. Dandouras, (2014), Deriving the characteristics of warm electrons (100 - 500 eV) in the magnetosphere of Saturn with the Cassini Langmuir probe, Planetary and Space Science, 104, 173–184, doi: 10.1016/j.pss.2014.09.008.

Garnier, P., M. Holmberg, J.-E. Wahlund, G. Lewis, S. R. Grimald, M. Thomsen, D. A. Gurnett, A. J. Coates, F. Crary, I. Dandouras, (2013), The influence of the secondary electrons induced by energetic electrons impacting the Cassini Langmuir probe at Saturn, Journal of Geophysical Research, 118, 7054–7073, doi: 10.1002/2013JA019114.

Garnier, P., J.-E. Wahlund, M. K. G. Holmberg, M. Morooka, S. Grimald, A. Eriksson, P. Schippers, D. A. Gurnett, S. M. Krimigis, N. Krupp, A. J. Coates, F. Crary, G. Gustafsson, (2012), The detection of energetic electrons with the Cassini Langmuir probe at Saturn, Journal of Geophysical Research, 117, A10292, doi: 10.1029/2011JA017298.

Garnier, P., I. Dandouras, D. Toublanc, E. C. Roelof, P. C. Brandt, D. G. Mitchell, S. M. Krimigis, N. Krupp, D. C. Hamilton, J.-E. Wahlund, (2010), Statistical analysis of the energetic ion and ENA data for the Titan environment, Planetary and Space Science, 58, 1811–1822, doi: 10.1016/j.pss.2010.08.009.

Garnier, P., J.-E. Wahlund, L. Rosenqvist, R. Modolo, K. Ågren, N. Sergis, P. Canu, M. Andre, D. A. Gurnett, W. S. Kurth, S. M. Krimigis, A. J. Coates, M. K. Dougherty, J. H. Waite, (2009), Titan's ionosphere in the magnetosheath: Cassini RPWS results during the T32 flyby, Annales Geophysicae, 27, 4257–4272, doi: 10.5194/angeo-27-4257-2009.

Garnier, P., I. Dandouras, D. Toublanc, E. C. Roelof, P. C. Brandt, D. G. Mitchell, S. M. Krimigis, N. Krupp, D. C. Hamilton, O. Dutuit, J.-E. Wahlund, (2008), The lower exosphere of Titan: Energetic neutral atoms absorption and imaging, Journal of Geophysical Research, 113, A10216, doi: 10.1029/2008JA013029.

Gautier, A. L., B. Cecconi, P. Zarka, G. Fischer, (2011), Propagation of Saturn's radio lightning studied by three-dimensional ray tracing, In EPSC-DPS Joint Meeting, p. 917.

Gérard, J.-C., D. Grodent, S. W. H. Cowley, D. G. Mitchell, W. S. Kurth, J. T. Clarke, E. J. Bunce, J. D. Nichols, M. K. Dougherty, F. J. Crary, A. J. Coates, (2006), Saturn's auroral morphology and activity during quiet magnetospheric conditions, Journal of Geophysical Research, 111, A12210, doi: 10.1029/2006JA011965.

Goertz, C. K., (1989), Dusty plasmas in the solar system, Reviews of Geophysics, 27, 271–292.

Gombosi, T. I., T. P. Armstrong, C. S. Arridge, K. K. Khurana, S. M. Krimigis, N. Krupp, A. M. Persoon, M. F. Thomsen, (2009), Saturn's magnetospheric configuration, In Saturn from Cassini-Huygens, (eds.) M. K. Dougherty, L. W. Esposito, S. M. Krimigis, Springer, Dordrecht, pp. 203–255, doi: 10.1007/978-1-4020-9217-6_9.

Grün, E., C. K. Goertz, G. E. Morfill, O. Havnes, (1992), Statistics of Saturn's spokes, Icarus, 99, 191–201.

Gu, X., R. M. Thorne, B. Ni, S.-Y. Ye, (2013), Resonant diffusion of energetic electrons by narrowband Z mode waves in Saturn's inner magnetosphere, Geophysical Research Letters, 40, 255–261, doi: 10.1029/2012GL054330.

Gurnett, D. A. and A. Bhattacharjee, (2017), Introduction to plasma physics with space, laboratory, and astrophysical applications, 2nd Edition, Cambridge University Press, Cambridge, UK.

Gurnett, D. A. and W. R. Pryor, (2012), Auroral processes associated with Saturn's moon Enceladus, In Auroral phenomenology and magnetospheric processes: Earth and other planets, (eds.) A. Keiling, E. Donovan, F. Bagenal, T. Karlsson, American Geophysical Union Geophysical Monograph Series, Washington DC, vol. 197, pp. 305–313, doi: 10.1029/2011BK001174.

Gurnett, D. A., T. F. Averkamp, P. Schippers, A. M. Persoon, G. B. Hospodarsky, J. S. Leisner, W. S. Kurth, G. H. Jones, A. J. Coates, F. J. Crary, M. K. Dougherty, (2011a), Auroral hiss, electron beams and standing Alfven wave currents near Saturn's moon Enceladus, Geophysical Research Letters, 38, L06102, doi: 10.1029/2011GL046854.

Gurnett, D. A., J. B. Groene, T. F. Averkamp, W. S. Kurth, S.-Y. Ye, G. Fischer, (2011b), A SLS4 longitude system based on a tracking filter analysis of the rotational modulation of Saturn kilometric radiation, In Planetary Radio Emissions VII, (eds.) H. O. Rucker, W. S. Kurth, P. Louarn, G. Fischer, Austrian Academy of Sciences, Vienna, Austria, pp. 51–63.

Gurnett, D. A., A. M. Persoon, J. B. Groene, W. S. Kurth, M. Morooka, J.-E. Wahlund, J. D. Nichols, (2011c), The rotation of the plasmapause-like boundary at high latitudes in Saturn's magnetosphere and its relation to the eccentric rotation of the northern and southern auroral ovals, Geophysical Research Letters, 38, L21203, doi: 10.1029/2011GL049547.

Gurnett, D. A., (2011), An overview of the time-dependent rotational modulation of Saturnian radio emissions, abstract, In Planetary Radio Emissions VII, (eds.) H. O. Rucker, W. S. Kurth, P. Louarn, G. Fischer, Austrian Academy of Sciences, Vienna, Austria, p. 37.

Gurnett, D. A., A. M. Persoon, A. J. Kopf, W. S. Kurth, M. W. Morooka, J.-E. Wahlund, K. K. Khurana, M. K. Dougherty, D. G. Mitchell, S. M. Krimigis, N. Krupp, (2010a), A plasmapause-like density boundary at high latitudes in Saturn's magnetosphere, Geophysical Research Letters, 37, L16806, doi: 10.1029/2010GL044466.

Gurnett, D. A., J. B. Groene, A. M. Persoon, J. D. Menietti, S.-Y. Ye, W. S. Kurth, R. J. MacDowall, A. Lecacheux, (2010b), The reversal of the rotational modulation rates of the north and south components of Saturn kilometric radiation near equinox, Geophysical Research Letters, 37, L24101, doi: 10.1029/2010GL045796.

Gurnett, D. A., A. Lecacheux, W. S. Kurth, A. M. Persoon, J. B. Groene, L. Lamy, P. Zarka, J. F. Carbary, (2009a), Discovery of a north-south asymmetry in Saturn's radio rotation period, Geophysical Research Letters, 36, L16102, doi: 10.1029/2009GL039621.

Gurnett, D. A., A. M. Persoon, J. B. Groene, A. J. Kopf, G. B. Hospodarsky, W. S. Kurth, (2009b), A north-south difference in the rotation rate of auroral hiss at Saturn: Comparison to Saturn's kilometric radio emission, Geophysical Research Letters, 36, L21108, doi: 10.1029/2009GL040774.

Gurnett, D. A., (2009), The search for life in the solar system, Transactions of the American Clinical and Climatological Association, 120, 299–325, doi: PMCID:PMC2744519.

Gurnett, D. A., A. M. Persoon, W. S. Kurth, J. B. Groene, T. F. Averkamp, M. K. Dougherty, D. J. Southwood (2007), The variable rotation period of the inner region of Saturn's plasma disk, Science, 316, No. 5823, 442–445, doi: 10.1016/science.1138562.

Gurnett, D. A., W. S. Kurth, G. B. Hospodarsky, A. M. Persoon, T. F. Averkamp, B. Cecconi, A. Lecacheux, P. Zarka, P. Canu, N. Cornilleau-Wehrlin, P. Galopeau, A. Roux, C. Harvey, P. Louarn, R. Bostrom, G. Gustafsson, J.-E. Wahlund, M. D. Desch, W. M. Farrell, M. L. Kaiser, K. Goetz, P. J. Kellogg, G. Fischer, H.-P. Ladreiter, H. Rucker, H. Alleyne, A. Pedersen, (2005), Radio and plasma wave observations at Saturn from Cassini's approach and first orbit, Science, 307, 1255–1259, doi: 10.1126/science.1105356.

Gurnett, D. A., W. S. Kurth, D. L. Kirchner, G. B. Hospodarsky, T. F. Averkamp, P. Zarka, A. Lecacheux, R. Manning, A. Roux, P. Canu, N. Cornilleau-Wehrlin, P. Galopeau, A. Meyer, R. Bostrom, G. Gustafsson, J.-E. Wahlund, L. Aahlen, H. O. Rucker, H. P. Ladreiter, W. Macher, L. J. C. Woolliscroft, H. Alleyne, M. L. Kaiser, M. D. Desch, W. M. Farrell, C. C. Harvey, P. Louarn, P. J. Kellogg, K. Goetz, A. Pedersen, (2004), The Cassini radio and plasma wave science investigation, Space Science Reviews, 114, 395–463, doi: 10.1007/s11214-004-1434-0.

Gurnett, D. A., W. S. Kurth, G. B. Hospodarsky, A. M. Persoon, P. Zarka, A. Lecacheux, S. J. Bolton, M. D. Desch, W. M. Farrell, M. L. Kaiser, H.-P. Ladreiter, H. O. Rucker, P. Galopeau, P. Louarn, D. T. Young, W. R. Pryor, M. K. Dougherty, (2002), Control of Jupiter's radio emission and aurorae by the solar wind, Nature, 415, 985–987, doi: 10.1038/415985a.

Gurnett, D. A., P. Zarka, R. Manning, W. S. Kurth, G. B. Hospodarsky, T. F. Averkamp, M. L. Kaiser, W. M. Farrell, (2001), Non-detection at Venus of high-frequency radio signals characteristic of terrestrial lightning, Nature, 409, 313–315, doi: doi: 10.1038/35053009.

Gustafsson, G. and J.-E. Wahlund, (2010), Electron temperatures in Saturn's plasma disc, Planetary and Space Science, 58, 1018–1025, doi: 10.1016/j.psss.2010.03.007.

Gustin, J., J.-C. Gerard, D. Grodent, G. R. Gladstone, J. T. Clarke, W. R. Pryor, V. Dols, B. Bonfond, A. Radioti, L. Lamy, J. M. Ajello, (2013), effects of methane on giant planet's UV emissions and implications for the auroral characteristics, Journal of Molecular Spectroscopy, 291, 108–117, doi: 10.1016/j.jms.2013.03.010.

Guzman, M., R. Lorenz, D. Hurley, W. Farrell, J. Spencer, C. Hansen, T. Hurford, J. Ibea, P. Carlson, C. P. McKay, (2018), Collecting amino acids in the Enceladus plume, International Journal of Astrobiology, 18, 47–59, doi: 10.1017/S1473550417000544.

Hadid, L. Z., M. W. Morooka, J.-E. Wahlund, A. M. Persoon, D. Andrews, O. Shebanits, W. S. Kurth, E. Vigren, N. J. T. Edberg, A. F. Nagy, A. I. Ericksson, (2018), Saturn's Ionosphere: Electron Density Altitude Profiles and D-ring Interaction from the Cassini Grand Finale, Geophysical Research Letters, vol. 46, Issue 15, pp. 9362–9369, doi: 10.1029/2018GL078004.

Hadid, L. Z., M. W. Morooka, J.-E. Wahlund, L. Moore, T. E. Cravens, M. M. Hedman, N. J. T. Edberg, E. Vigren, J. H. Waite, R. Perryman, W. S. Kurth, W. M. Farrell, A. I. Eriksson, (2018), Ring shadowing effects on Saturn's ionosphere: Implications for ring opacity and plasma transport, Geophysical Research Letters, 45, 10084–10184, doi: 10.1029/2018GL079150.

Hadid, L., (2017), In-situ observations of compressible turbulence in planetary magnetosheaths and solar wind, Ph.D. Thesis, University of Paris-Saclay, France.

Hamilton, D. P., (1993), Motion of dust in a planetary magnetosphere - orbit-averaged equations for oblateness, electromagnetic, and radiation forces with application to Saturn's E ring, Icarus, 101, 244–264.

Hansen, K. C., A. J. Ridley, G. B. Hospodarsky, M. K. Dougherty, T. I. Gombosi, G. Toth, (2005), Global MHD simulations of Saturn's magnetosphere at the time of Cassini approach, Geophysical Research Letters, 32, L20S06, doi: 10.1029/2005GL022835.

Hedman, M. M., J. A. Burns, D. P. Hamilton, M. R. Showalter, (2012), The Three-dimensional structure of Saturn's E ring, Icarus, 217, 322–338, doi: 10.1016/j.icarus.2011.11.006.

Hedman, M. M., J. A. Burns, M. S. Tiscareno, C. C. Porco, G. Jones, E. Roussos, N. Krupp, C. Paranicas, S. Kempf, (2007), The source of Saturn’s G ring, Science, 317, 653, doi: 10.1126/science.1143964.

Hess, S., E. Echer, P. Zarka, L. Lamy, P. Delamere, (2014), Multi-instrument study of the Jovian radio emissions triggered by solar wind shocks and inferred magnetospheric subcorotation rates, Planetary and Space Science, 99, 136–148, doi: 10.1016/j.pss.2014.05.015.

Hess, S., B. Cecconi, P. Zarka, (2008), Modeling of Io-Jupiter decameter arcs, emission beaming and energy source, Geophysical Research Letters, 35, 13, doi: 10.1029/2008GL033656.

Hill, T. W., M. F. Thomsen, R. L. Tokar, A. J. Coates, G. R. Lewis, D. T. Young, F. J. Crary, et al., 92012), Charged nanograins in the Enceladus plume, Journal of Geophysical Research: Space Physics, 117, no. A5 (2012).

Hill, T. W., M. F. Thomsen, R. L. Tokar, A. J. Coates, G. R. Lewis, D. T. Young, F. J. Crary, R. A. Baragiola, R. E. Johnson, Y. Dong, R. J. Wilson, G. H. Jones, J.-E. Wahlund, D. G. Mitchell, M. Horányi, (2011), Charged nanograins in the Enceladus plume, Journal of Geophysical Research, vol. 117, Issue A5, doi: 10.1029/2011JA017218.

Holmberg, M. K. G., O. Shebanits, J.-E. Wahlund, M. W. Morooka, E. Vigren, N. André, P. Garnier, A. M. Persoon, V. Génot, L. K. Gilbert, (2017), Density structures, dynamics, and seasonal and solar cycle modulations of Saturn's inner plasma disk, Journal of Geophysical Research, 122, 12258–12273, doi: 10.1002/2017JA024311.

Holmberg, M. K. G., J.-E. Wahlund, E. Vigren, T. A. Cassidy, D. J. Andrews, (2016), Transport and chemical loss rates in Saturn's inner plasma disk, Journal of Geophysical Research, 121, 2321–2334, doi: 10.1002/2015JA021784.

Holmberg, M. K. G., J.-E. Wahlund, M. W. Morooka, (2014), Dayside/nightside asymmetry of ion densities and velocities in Saturn's inner magnetosphere, Geophysical Research Letters, 41, 3717–3723, doi: 10.1002/2014GL060229.

Holmberg, M. K. G., J.-E. Wahlund, M. W. Morooka, A. M. Persoon, (2012), Ion densities and velocities in the inner plasma torus of Saturn, Planetary and Space Science, 73, 151–160, doi: 10.1016/j.pss.2012.09.016.

Holmberg, M. K. G., (2013), On the structure and dynamics of Saturn's inner plasma disk, Licentiate Thesis (Ph.D.), Uppsala University, Uppsala, Sweden.

Holmberg, M. K. G., (2010), Determination of solar EUV intensity and ion flux from Langmuir probe current characteristics, M.S. Thesis, Uppsala University, Uppsala, Sweden.

Horányi, M., (1996), Charged dust dynamics in the solar system, Annual Review of Astronomy and Astrophysics, 34, 383–418, doi: 10.1146/annurev.astro.34.1.383.

Hospodarsky, G. B., J. D. Menietti, D. Píša, W. S. Kurth, D. A. Gurnett, A. M. Persoon, J. Leisner, T. F. Averkamp, (2016), Plasma wave observations with Cassini at Saturn, Chapter 22, In Magnetosphere-Ionosphere Coupling in the Solar System, (eds.) C. R. Chappell, R. W. Schunk, P. M. Banks, J. L. Burch, R. M. Thorne, Wiley & Sons, Inc., pp. 277–289, doi: 10.1002/9781119066880.

Hospodarsky, G. B., J. S. Leisner, K. Sigsbee, J. D. Menietti, W. S. Kurth, D. A. Gurnett, C. A. Kletzing, O. Santolik, (2012), Plasma wave observations at Earth, Jupiter, and Saturn, In Dynamics of Earth's Radiation Belts and Inner Magnetosphere, (eds.) D. Summers, I. R. Mann, D. N. Baker, M. Schulz, American Geophysical Union Geophysical Monograph Series, Washington DC, vol. 199, pp. 415–430, doi: 10.1029/2012GM001342.

Hospodarsky, G. B., T. F. Averkamp, W. S. Kurth, D. A. Gurnett, M. K. Dougherty, O. Santolik, (2011), Observations of chorus at Saturn by Cassini (abstract), In Planetary Radio Emissions VII, (eds.) H. O. Rucker, W. S. Kurth, P. Louarn, G. Fischer, Austrian Academy of Sciences, Vienna, Austria, pp. 127.

Hospodarsky, G. B., T. F. Averkamp, W. S. Kurth, D. A. Gurnett, J. D. Menietti, O. Santolik, M. K. Dougherty, (2008), Observations of chorus at Saturn using the Cassini Radio and Plasma Wave Science Instrument, Journal of Geophysical Research, 113, A12206, doi: 10.1029/2008JA013237.

Hospodarsky, G. B., W. S. Kurth, D. A. Gurnett, P. Zarka, P. Canu, M. Dougherty, G. H. Jones, A. Coates, A. Rymer, (2006), Observations of Langmuir waves detected by the Cassini spacecraft, In Planetary Radio Emissions VI, (eds.) H. O. Rucker, W. S. Kurth, G. Mann, Austrian Academy of Sciences Press, Vienna, Austria, pp. 67–79.

Hospodarsky, G. B., W. S. Kurth, B. Cecconi, D. A. Gurnett, M. L. Kaiser, M. D. Desch, P. Zarka, (2004), Simultaneous observations of Jovian quasi-periodic radio emissions by the Galileo and

Cassini spacecraft, Journal of Geophysical Research, 109, A09S07, doi: 10.1029/2003JA010263.

Hospodarsky, G. B., I. W. Christopher, J. D. Menietti, W. S. Kurth, D. A. Gurnett, T. F. Averkamp, J. B. Groene, P. Zarka, (2001a), Control of Jovian radio emissions by the Galilean moons as observed by Cassini and Galileo, In Planetary Radio Emissions V, (eds.) H. O. Rucker, M. L. Kaiser, Y. Leblanc, Austrian Academy of Sciences Press, Vienna, Austria, pp. 155–164.

Hospodarsky, G. B., T. F. Averkamp, W. S. Kurth, D. A. Gurnett, M. Dougherty, U. Inan, T. Wood, (2001b), Wave normal and poynting vector calculations using the Cassini Radio and Plasma Wave instrument, Journal of Geophysical Research, 106, 30253–30269, doi: 10.1029/10.1029/2001JA900114.

Hsu, H.-W., J. Schmidt, S. Kempf, F. Postberg, G. Moragas-Klostermeyer, M. Seiss, H. Hoffmann, M. Burton, S.-Y. Ye, W. S. Kurth, M. Horanyi, N. Khawaja, F. Spahn, D. Schirdewahn, J. O'Donoghue, L. Moore, J. Cuzzi, G. H. Jones, R. Srama, (2018), In situ collection of dust grains falling from Saturn's rings into its atmosphere, Science, 362, Issue 6410, eaat3185, doi: 10/1126/science.aat3195.

Hsu, H.-W., S. Kempf, S. V. Badman, W. S. Kurth, F. Postberg, R. Srama, (2016), Interplanetary magnetic field structure at Saturn inferred from nanodust measurements during the 2013 auroral campaign, Icarus, 263, 10–16, doi: 10.1016/j.icarus.2015.02.022.

Imai, M., (2016), Characteristics of Jovian low-frequency radio emissions during the Cassini and Voyager flyby of Jupiter, Ph.D. Thesis, Kyoto University, Kyoto, Japan.

Imai, M., A. Lecacheux, M. Moncuquet, F. Bagenal, C. A. Higgins, K. Imai, J. R. Thieman, (2015), Modeling Jovian hectometric attenuation lanes during the Cassini flyby of Jupiter, Journal of Geophysical Research, 120, 1888–1907, doi: 10.1002/2014JA020815.

Imai, M., A. Lecacheux, K. Imai, C. A. Higgins, J. R. Thieman, (2011a), Jupiter's decametric and hectomectric radio emissions observed by Voyager PRA and Cassini RPWS, In Planetary Radio Emissions VII, (eds.) H. O. Rucker, W. S. Kurth, P. Louarn, G. Fischer, Austrian Academy of Sciences, Vienna, Austria, pp. 167–176.

Imai, M., K. Imai, C. A. Higgins, J. R. Thieman, (2011b), Comparison between Cassini and Voyager observations of Jupiter’s decametric and hectometric radio emissions, Journal of Geophysical Research, 116, A12233, doi: 10.1029/2011JA016456.

Imai, M., K. Imai, C. A. Higgins, J. R. Thieman, (2008), Angular beaming model of Jupiter's decametric radio emissions based on Cassini RPWS data analysis, Geophysical Research Letters, 35, L17103, doi: 10.1029/2008GL034987.

Jackman, C. M., M. F. Thomsen, D. G. Mitchell, N. Sergis, C. S. Arridge, M. Felici, S. V. Badman, C. Paranicas, X. Jia, G. B. Hospodarsky, M. Andriopoulou, K. K. Khurana, A. W. Smith, M. K. Dougherty, (2015), Field depolarization in Saturn’s magnetotail with planetward ion flows and energetic particle flow bursts: Evidence of quasi-steady connection, Journal of Geophysical Research, 120, 3603–3617, doi: 10.1002/2015JA020995.

Jackman, C. M., C. S. Arridge, J. A. Slavin, S. E. Milan, L. Lamy, M. K. Dougherty, A. J. Coates, (2010), In situ observations of the effect of a solar wind compression on Saturn's magnetotail, Journal of Geophysical Research, 115, A10240, doi: 10.1029/2010JA015312.

Jackman, C. M., L. Lamy, M. P. Freeman, P. Zarka, B. Cecconi, W. S. Kurth, S. W. H. Cowley, M. K. Dougherty, (2009), On the character and distribution of lower-frequency radio emissions at Saturn, and their relationship to substorm-like events, Journal of Geophysical Research, 114, A08211, doi: 10.1029/2008JA013997.

Jackman, C. M., N. Achilleos, E. J. Bunce, B. Cecconi, J. T. Clarke, S. W. H. Cowley, W. S. Kurth, P. Zarka, (2005), Interplanetary conditions and magnetospheric dynamics during the cassini orbit insertion fly-through of Saturn's magnetosphere, Journal of Geophysical Research, 110, A10212, doi: 10.1029/2005JA011054.

Jacobsen, K. S., J.-E. Wahlund, A. Pedersen, (2009), Cassini Langmuir probe measurements in the inner magnetosphere of Saturn, Planetary and Space Science, 57, 48–52, doi: 10.1016/j.pss.2008.10.012.

Jasinski, J. M., C. S. Arridge, L. Lamy, J. S. Leisner, M. F. Thomsen, D. G. Mitchell, A. J. Coates, A. Radioti, G. H. Jones, E. Roussos, N. Krupp, D. Grodent, M. K. Dougherty, J. H. Waite, (2014), Cusp observation at Saturn's high latitude magnetosphere by the Cassini spacecraft, Geophysical Research Letters, 41, 1382–1388, doi: 10.1002/2014GL059319.

Jia, X., M. G. Kivelson, T. I. Gombosi, (2012), Driving Saturn’s magnetospheric periodicities from the upper atmosphere/ionosphere, Journal of Geophysical Research, 117, A04215, doi: 10.1029/2011JA017367.

Jia, Y.-D., C. T. Russell, K. Khurana, H. Y. Wei, Y. J. Ma, J. S. Leisner, A. M. Persoon, M. K. Dougherty, (2011), Cassini magnetometer observations over the Enceladus poles, Geophysical Research Letters, 38, L19109, doi: 10.1029/2011GL049013.

Jia, Y.-D., C. T. Russell, K. K. Khurana, G. Toth, J. S. Leisner, T. I. Gombosi, (2010a), The interaction of Saturn's magnetosphere and its moons 1: Interaction between corotating plasma and standard obstacles, Journal of Geophysical Research, 115, A04214, doi: 10.1029/2009JA014630.

Jia, Y.-D., C. T. Russell, K. K. Khurana, Y. J. Ma, W. Kurth, T. I. Gombosi, (2010b), Interaction of Saturn's magnetosphere and its moons: 3. Time variation of the Enceladus plume, Journal of Geophysical Research, 115, A12243, doi: 10.1029/2010JA015534.

Jinks, S., E. Bunce, S. Cowley, G. Provan, T. Yeoman, C. Arridge, M. Dougherty, D. Gurnett, N. Krupp, W. Kurth, D. Mitchell, M. Morooka, J.-E. Wahlund, (2014), Cassini multi-instrument assessment of Saturn's polar cap boundary, Journal of Geophysical Research, 119, 8161–8177, doi: 10.1002/2014JA020367.

Jones, G. H., C. S. Arridge, A. J. Coates, G. R. Lewis, S. Kanani, A. Wellbrock, D. T. Young, F. J. Crary, R. L. Tokar, R. J. Wilson, T. W. Hill, R. E. Johnson, D. G. Mitchell, J. Schmidt, S. Kempf, U. Beckmann, C. T. Russell, Y. D. Jia, M. K. Dougherty, J. H. Waite, B. A. Magee,

(2009), Fine jet structure of electrically charged grains in Enceladus' plume, Geophysical Research Letters, 36, L16204, doi: 10.1029/2009GL038284.

Jones, G. H., E. Roussos, N. Krupp, U. Beckmann, A. J. Coates, F. Crary, I. Dandouras, V. Dikarev, M. K. Dougherty, P. Garnier, C. J. Hansen, A. R. Hendrix, G. B. Hospodarsky, R. E. Johnson, S. Kempf, K. Khurana, S. M. Krimigis, H. Krüger, W. S. Kurth, A. Lagg, H. J. McAndrews, D. G. Mitchell, C. Paranicas, F. Postberg, C. T. Russell, J. Saur, M. Seis, F. Spahn, R. Srama, D. F. Strobel, R. Tokar, J.-E. Wahlund, R. J. Wilson, J. Woch, D. Young, (2008), The dust halo of Saturn's largest icy moon: Evidence of rings at Rhea?, Science, 319, 1380–1384, doi: 10.1126/science.1151524.

Kaiser, M. L., W. M. Farrell, W. S. Kurth, G. B. Hospodarsky, D. A. Gurnett, (2004), New observations from Cassini and Ulysses of Jovian VLF radio emissions, Journal of Geophysical Research, 109, A09S08, doi: 10.1029/2003JA010233.

Kaiser, M. L., W. M. Farrell, M. D. Desch, G. B. Hospodarsky, W. S. Kurth, D. A. Gurnett, (2001), Ulysses and Cassini at Jupiter: Comparison of the quasi-periodic radio bursts, In Planetary Radio Emissions V, (eds.) H. O. Rucker, M. L. Kaiser, Y. Leblanc, Austrian Academy of Sciences Press, Vienna, Austria, pp. 41–48.

Kaiser, M. L., P. Zarka, W. S. Kurth, G. B. Hospodarsky, D. A. Gurnett, (2000), Cassini and wind stereoscopic observations of Jovian nonthermal radio emissions: Measurement of beam widths, Journal of Geophysical Research, 105, 16053–16062, doi: 10.1029/1999JA000414.

Kaiser, M. L., J. E. P. Connerney, M. D. Desch, (1983), Atmospheric storm explanation of Saturnian electrostatic discharges, Nature, 303, 50–53.

Karlsson, R., W. Macher, U. Taubenschuss, H. O. Rucker, Cassini/RPWS Team, (2007), In flight calibration of the Cassini Radio and Plasma Wave Science (RPWS) antennas after the Huygens probe release, In Proceedings of the Nordic Shortwave Conference HF07 (in Faro, Gotland), pp. 3.4.1–3.4.9.

Kasaba, Y., T. Kimura, D. Maruno, A. Morioka, B. Cecconi, L. Lamy, C. M. Jackman, C. Tao, H. Kita, H. Misawa, T. Tsuchiya, A. Kumamoto, (2017), A flux comparison of northern and southern Saturn kilometric radio bursts during southern summer, In Planetary Radio Emissions VIII, (eds.) G. Fischer, G. Mann, M. Panchenko, P. Zarka, Austrian Academy of Sciences Press, Vienna, Austria, pp. 205–215.

Kellett, S., C. Arridge, E. Bunce, A. Coates, S. Cowley, M. Dougherty, A. Persoon, N. Sergis, R. Wilson, (2011), Saturn's ring current: Local time dependence and temporal variability, Journal of Geophysical Research, 116, A05220, doi: 10.1029/2010JA016216.

Kellett, S., C. Arridge, E. Bunce, A. Coates, S. Cowley, M. Dougherty, A. Persoon, N. Sergis, R. Wilson, (2010), Nature of the ring current in Saturn's dayside magnetosphere, Journal of Geophysical Research, 115, A08201, doi: 10.1029/2009JA015146.

Kelley, M. C., S. Pancoast, S. Close, Z. Z. Wang, (2012), Analysis of electromagnetic and electrostatic effects of particle impacts on spacecraft, Advances in Space Research, 49, Issue 6, doi: 10.1016/j.asr.2011.12.023, 1029-1033.

Kellogg, P., D. A. Gurnett, G. B. Hospodarsky, W. S. Kurth, M. Dougherty, R. Forsyth, (2003a), Ion isotropy and ion resonant waves in the solar wind: Corrected Cassini observations, Journal of Geophysical Research, 108(A1), 1045, doi: 10.1029/2002JA009312.

Kellogg, P., D. A. Gurnett, G. B. Hospodarsky, W. S. Kurth, M. Dougherty, R. Forsyth, (2003b), Electric fluctuations and ion isotropy, AIP Conference Proceedings, American Institute of Physics, vol. 679, Issue 1, pp. 383–388, doi: 10.1063/1.1618618.

Kellogg, P. J., D. A. Gurnett, G. B. Hospodarsky, W. S. Kurth, (2001a), Ion isotropy and ion resonant waves in the solar wind: Cassini observations, Geophysical Research Letters, 28, 87–90, doi: 10.1029/10.1029/2000GL012100.

Kellogg, P. J., D. A. Gurnett, G. B. Hospodarsky, W. S. Kurth, (2001b), Comment on– Ion isotropy and ion resonant waves in the solar wind: Cassini observations, Geophysical Research Letters, 28, 4061–4061.

Kempf, S., U. Beckmann, G. Moragas-Klostermeyer, R. Srama, T. Economou, J. Schmidt, F. Spahn, E. Grün, (2008), The E ring in the vicinity of Enceladus I: Spatial distribution and properties of the ring particles, Icarus, 193, 420–437, doi: 10.1016/j.icarus.2007.06.027.

Kennelly, T., J. S. Leisner, G. B. Hospodarsky, D. A. Gurnett, (2013), Ordering of injection events within Saturnian SLS longitude and local time, Journal of Geophysical Research, 118, 832–838, doi: 10.1002/jgra.50152.

Khan, H., S. W. H. Cowley, E. Kolesnikova, M. Lester, M. J. Brittnacher, T. J. Hughes, W. J. Hughes, W. S. Kurth, D. J. McComas, L. Newitt, C. J. Owen, G. D. Reeves, H. J. Singer, C. W. Smith, D. J. Southwood, J. F. Watermann, (2001), Observations of two complete substorm cycles during the Cassini Earth swing-by: Cassini magnetometer data in a global context, Journal of Geophysical Research, 106, 30,141–30,175, doi: 10.1029/2001JA900049.

Kimura, T., L. Lamy, C. Tao, S. Badman, S. Kasahara, B. Cecconi, P. Zarka, A. Morioka, Y. Miyoshi, D. Maruno, Y. Kasaba, M. Fujimoto, (2013), Long-term modulations of Saturn's auroral radio emissions by the solar wind and seasonal variations controlled by the solar ultraviolet flux, Journal of Geophysical Research, 118, 7019–7035, doi: 10.1002/2013JA018833.

Kimura, T., B. Cecconi, P. Zarka, Y. Kasaba, F. Tsuchiva, H. Misawa, A. Morioka, (2012), Polarization and direction of arrival of Jovian quasiperiodic bursts observed by Cassini, Journal of Geophysical Research, 117, A11209, doi: 10.1029/2012JA017506.

Kinrade, J., S. V. Badman, E. J. Bunce, C. Tao, G. Provan, S. W. H. Cowley, A. Grocott, R. L. Gray, D. Grodent, T. Kimura, J. D. Nichols, C. S. Arridge, A. Radioti, J. T. Clarke, F. J. Crary, W. R. Pryor, H. Melin, K. H. Baines, M. K. Dougherty, (2017), An Isolated, bright cusp aurora at Saturn, Journal of Geophysical Research, 122, 6121–6138, doi: 10/1002/2016JA023792.

Kivelson, M. G. and X. Jia, (2018), Coupled SKR emissions in Saturn's northern and southern ionospheres, Geophysical Research Letters, 45, 2893–2900, doi: 10.1002/2017GL075425.

Konovalenko, A. A., N. N. Kalinichenko, H. O. Rucker, A. Lecacheux, G. Fischer, P. Zarka, V. V. Zakharenko, K. Y. Mylostna, J.-M. Griessmeier, E. P. Abranin, I. S. Falkovich, K. M. Sidorchuk,

W. S. Kurth, M. L. Kaiser, D. A. Gurnett, (2013), Earliest recorded ground-based decameter wavelength observations of Saturn's lightning during the giant E-storm detected by Cassini spacecraft in early 2006, Icarus, 224, 14–23, doi: 10.1016/j.icarus.2012.07.024.

Kopf, A. J., D. A. Gurnett, J. D. Menietti, R. L. Mutel, W. M. Farrell, (2011), A statistical study of kilometric radiation fine structure striations observed at Jupiter and Saturn, Magnetospheres of the Outer Planets Conference, July 11–15, 2011, Hosted by John Clarke, sponsored by Boston University, Session 5 Aurora, #53, Kopf_AJ_MOP-1.ppt.

Kopf, A. J., (2010), A multi-instrument study of auroral hiss at Saturn, Ph.D. Thesis, University of Iowa, Iowa City, Iowa.

Kopf, A. J., D. A. Gurnett, J. D. Menietti, P. Schippers, C. S. Arridge, G. B. Hospodarsky, W. S. Kurth, S. Grimald, N. Andre, A. J. Coates, M. K. Dougherty, (2010), Electron beams as the source of whistler-mode auroral hiss at Saturn, Geophysical Research Letters, 37, L09102, doi: 10.1029/2010GL042980.

Kriegel, H., S. Simon, U. Motschmann, J. Saur, F. M. Neubauer, A. M. Persoon, M. K. Dougherty, D. A. Gurnett, (2011), Influence of negatively charged plume grains on the structure of Enceladus' Alfven wings: Hybrid simulations versus Cassini Magnetometer data, Journal of Geophysical Research, 116, A102233, doi: 10.1029/2011JA016842.

Krupp, N., E. Roussos, C. Paranicas, D. G. Mitchell, P. Kollmann, S. Ye, W. S. Kurth, K. R. Khurana, R. Perryman, H. Waite, R. Srama, D. C. Hamilton, (2017), Energetic electron measurements near Enceladus by Cassini during 2005–2015, Icarus, 306, 256–274, doi: 10.1016/j.icarus.2017.10.022.

Kurth, W. S., G. B. Hospodarsky, D. A. Gurnett, L. Lamy, M. K. Dougherty, J. Nichols, E. J. Bunce, W. Pryor, K. H. Baines, U. Dyudina, T. Stallard, H. Melin, F. J. Crary, (2016), Saturn kilometric radiation intensities during the Saturn auroral campaign of 2013, Icarus, 263, 2–9, doi: 10.1016/j.icarus.2015.01.003.

Kurth, W. S., D. A. Gurnett, J. D. Menietti, R. L. Mutel, M. G. Kivelson, E. J. Bunce, S. W. H. Cowley, D. L. Talboys, M. K. Dougherty, C. Arridge, A. Coates, S. Grimald, L. Lamy, P. Zarka, B. Cecconi, P. Schippers, N. Andre, P. Louarn, D. Mitchell, J. S. Leisner, M. Morooka, (2011), A close encounter with a Saturn kilometric radiation source region, In Planetary Radio Emissions VII, (eds.) H. O. Rucker, W. S. Kurth, P. Louarn, G. Fischer, Austrian Academy of Sciences, Vienna, Austria, pp. 75–86.

Kurth, W. S., E. J. Bunce, J. T. Clarke, F. J. Crary, D. C. Grodent, A. P. Ingersoll, U. A. Dyudina, L. Lamy, D. G. Mitchell, A. M. Persoon, W. R. Pryor, J. Saur, T. Stallard, (2009), Auroral processes, Chapter 12, In Saturn from Cassini-Huygens, (eds.) M. K. Dougherty, L. W. Esposito, S. M. Krimigis, Springer, Dordrecht, pp. 333–374, doi: 10.1007/978-1-4020-9217-6_12.

Kurth, W. S.,T. F. Averkamp, D. A. Gurnett, J. B. Groene, A. Lecacheux, (2008), An update to a Saturn longitude system based on kilometric radio emissions, Journal of Geophysical Research, 113, A05222, doi: 10.1029/2007JA012861.

Kurth, W. S., A. Lecacheux, T. F. Averkamp, J. B. Groene, D. A. Gurnett, (2007), A Saturnian longitude system based on a variable kilometric radiation period, Geophysical Research Letters, 34, L02201, doi: 10.1029/2006GL028336.

Kurth, W. S., B. Cecconi, D. A. Gurnett, M. L. Kaiser, P. Zarka, A. Lecacheux, (2006a), Is Titan a radio source?, In Planetary Radio Emissions VI, (eds.) H. O. Rucker, W. S. Kurth, G. Mann, Austrian Academy of Sciences Press, Vienna, Austria, pp. 133–142.

Kurth, W. S., T. F. Averkamp, D. A. Gurnett, Z. Wang, (2006b), Cassini RPWS Observations of dust in Saturn's E ring, Planetary and Space Science, 54, 988–998, doi: 10.1016/j.pss.2006.05011.

Kurth, W. S., D. A. Gurnett, J. T. Clarke, P. Zarka, M. D. Desch, M. L. Kaiser, B. Cecconi, A. Lecacheux, W. M. Farrell, P. Galopeau, J.-C. Gerard, D. Grodent, R. Prange, M. K. Dougherty, F. J. Crary, (2005a), An Earth-like correspondence between Saturn's auroral features and radio emission, Nature, 433, 722–725, doi: 10.1038/nature03334.

Kurth, W. S., G. B. Hospodarsky, D. A. Gurnett, B. Cecconi, P. Louarn, A. Lecacheux, P. Zarka, H. O. Rucker, M. Boudjada, M. L. Kaiser, (2005b), High spectral and temporal resolution observations of Saturn kilometric radiation, Geophysical Research Letters, 32, L20S07, doi: 10.1029/2005GL022648.

Kurth, W. S., (2003), Cassini, The World Book Encyclopedia, 3, 276–277.

Kurth, W. S., D. A. Gurnett, G. B. Hospodarsky, W. M. Farrell, A. Roux, M. K. Dougherty, S. P. Joy, M. G. Kivelson, R. J. Walker, F. J. Crary, C. J. Alexander, (2002), The dusk flank of Jupiter's Magnetosphere, Nature, 415, 991–994, doi: 10.1038/415991a.

Kurth, W. S., G. B. Hospodarsky, D. A. Gurnett, A. Lecacheux, P. Zarka, M. D. Desch, M. L. Kaiser, W. M. Farrell, (2001a), High-resolution observations of low-frequency Jovian radio emissions by Cassini, In Planetary Radio Emissions V, (eds.) H. O. Rucker, M. L. Kaiser, Y. Leblanc, Austrian Academy of Sciences Press, Vienna, Austria, pp. 15–28.

Kurth, W. S., G. B. Hospodarsky, D. A. Gurnett, M. L. Kaiser, J.-E. Wahlund, A. Roux, P. Canu, P. Zarka, Y. Tokarev, (2001b), An overview of observations by the Cassini radio and plasma wave investigation at Earth, Journal of Geophysical Research, 106, 30,239-30,252, doi: 10.1029/2001JA900033.

Kurth, W. S. and P. Zarka, (2001), Saturn radio waves, In Planetary Radio Emissions V, (eds.) H. O. Rucker, M. L. Kaiser, Y. Leblanc, Austrian Academy of Sciences Press, Vienna, Austria, pp. 247–259.

Ladreiter, H. P., P. Zarka, A. Lecacheux, W. Macher, H. O. Rucker, R. Manning, D. A. Gurnett, W. S. Kurth, (1995), Analysis of electromagnetic wave direction finding performed by spaceborne antennas using singular value decomposition techniques, Radio Science, 30, 1699–1712, doi: 10.1029/95RS02479.

Lammer, H., J. H. Bredehöft, A. Coustenis, M. L. Khodachenko, L. Kaltenegger, O. Grasset, D. Prieur, F. Raulin, P. Ehrenfreund, M. Yamauchi, J.-E. Wahlund, J.-M. Grießmeier, G. Stangl,

C. S. Cockell, Yu. N. Kulikov, J. L. Grenfell, H. Rauer, (2009), What makes a planet habitable? Astronomy and Astrophysics Review, 17, 181–249, doi: 10.1007/s00159-009-0019-z.

Lammer, H., T. Tokano, G. Fischer, W. Stumptner, G. J. Molina-Cuberos, K. Schwingenschuh, H. O. Rucker, (2001a), Lightning activity on Titan: Can Cassini detect it?, Planetary and Space Science, 49, 561–574, doi: 10.1016/S0032-0633(00)00171-9.

Lammer, H., T. Tokano, G. Fischer, G. J. Molina-Cuberos, W. Stumptner, K. Schwingenschuh, H. O. Rucker, (2001b), Detection capability of Cassini for thundercloud generated lightning discharges on Titan, In Planetary Radio Emissions V, (eds.) H. O. Rucker, M. L. Kaiser, Y. Leblanc, Austrian Academy of Sciences Press, Vienna, Austria, pp. 261–270.

Lamy, L., P. Zarka, B. Cecconi, R. Prange, W. S. Kurth, G. B. Hospodarsky, A. M. Persoon, M. Morooka, J.-E. Wahlund, G. J. Hunt, (2018a), The low frequency source of Saturn's kilometric radiation, Science, 362, Issue 6410, eaat2027, doi: 10.1126/science.aat2027.

Lamy, L., R. Prange, C. Tao, T. Kim, S. V. Badman, P. Zarka, B. Cecconi, W. S. Kurth, W. Pryor, E. J. Bunce, A. Radioti, (2018b), Saturn's northern aurorae at solstice from HST observations coordinated with Cassini's Grand Finale, Geophysical Research Letters, 45, 9353–9362, doi: 10.1029/2018GL078211.

Lamy, L., (2017), The Saturnian kilometric radiation before the Cassini Grand Finale, In Planetary Radio Emissions VIII, G. Fischer, G. Mann, M. Panchenko, P. Zarka, (eds.) Austrian Academy of Sciences Press, Vienna, Austria, pp. 171–190.

Lamy, L., R. Prange, W. Pryor, J. Gustin, S. V. Badman, H. Melin, T. Stallard, D. G. Mitchell, P. C. Brandt, (2013), Multispectral simultaneous diagnosis of Saturn's aurorae throughout a planetary rotation, Journal of Geophysical Research, 118, 4817–4843, doi: 10.1002/jgra.50404.

Lamy, L., B. Cecconi, P. Zarka, P. Canu, P. Schippers, W. S. Kurth, R. L. Mutel, D. A. Gurnett, D. Menietti, P. Louarn, (2011a), Emission and propagation of Saturn kilometric radiation: Magnetoionic modes, beaming pattern, and polarization state, Journal of Geophysical Research, 116, A04212, doi: 10.1029/2010JA016195.

Lamy, L., (2011), Variability of southern and northern periodicities of Saturn Kilometric Radiation, In Planetary Radio Emissions VII, (eds.) H. O. Rucker, W. S. Kurth, P. Louarn, G. Fischer, Austrian Academy of Sciences, Vienna, Austria, pp. 38–50.

Lamy, L., P. Schippers, P. Zarka, B. Cecconi, C. Arridge, M. K. Dougherty, P. Louarn, N. Andre, W. S. Kurth, R. L. Mutel, D. A. Gurnett, A. J. Coates, (2010a), Properties of Saturn kilometric radiation measured within its source region, Geophysical Research Letters, 37, L12104, doi: 10.1029/2010GL043415.

Lamy, L., P. Zarka, B. Cecconi, R. Prange, (2010b), Auroral kilometric radiation diurnal, semi-diurnal, and shorter-term modulations disentangled by Cassini/RPWS, Journal of Geophysical Research, 115, A09221, doi: 10.1029/2010JA015434.

Lamy, L., P. Schippers, P. Zarka, B. Cecconi, C. S. Arridge, M. K. Dougherty, P. Louarn, N. Andre, W. S. Kurth, R. L. Mutel, D. A. Gurnett, A. J. Coates, (2010c), Properties of Saturn

kilometric radiation measured within its source region (abstract), In Planetary Radio Emissions VII, (eds.) H. O. Rucker, W. S. Kurth, P. Louarn, G. Fischer, Austrian Academy of Sciences, Vienna, Austria, p. 97.

Lamy, L., B. Cecconi, R. Prange, P. Zarka, J. D. Nichols, J. T. Clarke, (2009), An auroral oval at the footprint of Saturn's kilometric radio sources, colocated with the UV aurorae, Journal of Geophysical Research, 114, A10212, doi: 10.1029/2009JA014401.

Lamy, L., P. Zarka, B. Cecconi, R. Prange, W. S. Kurth, D. A. Gurnett, (2008a), Saturn kilometric radiation: Average and statistical properties, Journal of Geophysical Research, 113, A07201, doi: 10.1029/2007JA012900.

Lamy, L., P. Zarka, B. Cecconi, S. Hess, R. Prange, (2008b), Modeling of Saturn kilometric radiation arcs and equatorial shadow zone, Journal of Geophysical Research, 113, A10213, doi: 10.1029/2008JA013464.

Lamy, L., (2008), Etudes des emissions radio aurorales de Saturne, modelisation et aurores UV, Ph.D. Thesis, l'Universite Pierre et Marie Curie, Meudon, France.

Lavvas, P. P., R. V. Yella, T. Koskinen, A. Bazin, V. Vuitton, E. Vigren, M. Galand, A. Wellbrock, A. J. Coates, J.-E. Wahlund, F. Crary, D. Snowden, (2013), Aerosol growth in Titan’s ionosphere, In Proceedings of the National Academy of Sciences, doi: 10.1073/pnas.1217059110.

Lecacheux, A., W. S. Kurth, R. Manning, (2001), Sub-second time scales in Jovian radio emissions as measured by Cassini/RPWS: Comparison with ground-based observations, In Planetary Radio Emissions V, (eds.) H. O. Rucker, M. L. Kaiser, Y. Leblanc, Austrian Academy of Sciences Press, Vienna, Austria, pp. 29–39.

Lecacheux, A., (2001), Radio observations during the Cassini flyby of Jupiter, In Planetary Radio Emissions (eds.) V, H. O. Rucker, M. L. Kaiser, Y. Leblanc, Austrian Academy of Sciences Press, Vienna, Austria, pp. 1–13.

Leisner, J. S., G. B. Hospodarsky, D. A. Gurnett, (2013), Enceladus auroral hiss observations: Implications for electron beam locations, Journal of Geophysical Research, 118, 160–166, doi: 10.1029/2012JA018213.

Lewis, G. R., C. S. Arridge, D. R. Linder, L. K. Gilbert, D. O. Kataria, A. J. Coates, A. Persoon, G. A. Collinson, N. Andre, P. Schippers, J.-E. Wahlund, M. Morooka, G. H. Jones, A. M. Rymer, D. T. Young, D. G. Mitchell, A. Lagg, S. A. Livi, (2010), The calibration of the Cassini-Huygens CAPS electron spectrometer, Planetary and Space Science, 58, 427–436, doi: 10.1016/j.pss.2009.11.008.

Li, C. and A.P. Ingersoll, (2015), Moist convection in hydrogen atmospheres and the frequency of Saturn’s giant storms, Nature Geoscience, 8, 398–403.

Livi, R., J. Goldstein, J. L. Burch, F. Crary, A. M. Rymer, D. G. Mitchell, A. M. Persoon, (2014), Multi-instrument analysis of plasma parameters in Saturn's equatorial, inner magnetosphere using corrections for corrections for spacecraft potential and penetrating background radiation, Journal of Geophysical Research, 119, 3683–3707, doi: 10.1002/2013JA019616.

- - - - - - - - - - - - - -

Louarn, P., W. S. Kurth, D. A. Gurnett, G. B. Hospodarsky, A. M. Persoon, B. Cecconi, A. Lecacheux, P. Zarka, P. Canu, A. Roux, H. O. Rucker, W. M. Farrell, M. L. Kaiser, N. Andre, C. Harvey, M. Blanc, (2007), Observation of similar radio signatures at Saturn and Jupiter: Implications for the magnetospheric dynamics, Geophysical Research Letters, 34, L20113, doi: 10.1029/2007GL030368.

Louis, C. K., L. Lamy, P. Zarka, B. Cecconi, S. L. G. Hess, (2017a), Detection of Jupiter decametric emissions controlled by Europa and Ganymede with Voyager/PRA and Cassini/RPWS, Journal of Geophysical Research, 122, 9228–9247, doi: 10.1002/2016JA023779.

Louis, C., L. Lamy, P. Zarka, B. Cecconi, M. Imai, W. Kurth, G. Hospodarsky, S. Hess, X. Bonnin, S. Bolton, J. Connerney, S. Levin, (2017b), Io-Jupiter decametric arcs observed by Juno/Waves compared to ExPRES simulations, Geophysical Research Letters, vol. 44, Issue 18, pp 9225–9232, doi: 10.1002/2017GL073036.

Luhmann, J. G., D. Ulusen, S. A. Ledvina, K. Mandt, B. Magee, J. H. Waite, J. Westlake, T. E. Cravens, I. Robertson, N. J. T. Edberg, K. Ågren, J.-E. Wahlund, Y.-J. Ma, H. Y. Wei, C. T. Russell, M. K. Dougherty, (2012), Investigating magnetospheric interaction effects on Titan's ionosphere with the Cassini orbiter Ion Neutral Mass Spectrometer, Langmuir probe, and magnetometer observations during targeted flybys, Icarus, 2192, Issue 2, 534–555, doi: 10.1016/j.icarus.2012.03.015.

Ma, Y.-J., C. T. Russell, A. F. Nagy, G. Toth, M. K. Dougherty, A. Wellbrock, A. J. Coates, P. Garnier, J.-E. Wahlund, T. E. Cravens, M. S. Richard, F. J. Crary, (2011), The importance of thermal electron heating in Titan’s ionosphere: Comparison with Cassini T34 flyby, Journal of Geophysical Research, 116, A10213, doi: 10.1029/2011JA016657.

Ma, Y.-J., C. T. Russell, A. F. Nagy, G. Toth, C. Bertucci, M. K. Dougherty, F. M. Neubauer, A. Wellbrock, A. J. Coates, P. Garnier, J.-E. Wahlund, T. E. Cravens, F. J. Crary, (2009), Time-dependent global MHD simulations of Cassini T32 flyby: From magnetosphere to magnetosheath, Journal of Geophysical Research, 114, A03204, doi: 10.1029/2008JA013676.

Ma, Y.-J., A. F. Nagy, G. Toth, T. E. Cravens, C. T. Russell, T. I. Gombosi, J.-E. Wahlund, F. J. Crary, A. J. Coates, C. L. Bertucci, F. M. Neubauer, (2007), 3D global multi-species Hall-MHD simulation of the Cassini T9 flyby, Geophysical Research Letters, 34, L24S10, doi: 10.1029/2007GL031627.

Ma, Y.-J., A. F. Nagy, T. E. Cravens, I. V. Sokolov, K. C. Hansen, J.-E. Wahlund, F. J. Crary, A. J. Coates, M. K. Dougherty, (2006), Comparisons between MHD model calculations and observations of Cassini flybys of Titan, Journal of Geophysical Research, 111, A05207, doi: 10.1029/2005JA011481.

Madanian, H., T. E. Cravens, M. S. Richard, J. H. Waite Jr., N. J. T. Edberg, J. H. Westlake, J.-E. Wahlund, (2016), Solar cycle variations in ion composition in the dayside ionosphere of Titan, Journal of Geophysical Research, 121, 8013–8037, doi: 10.1002/2015JA022274.

Mandt, K. E., D. A. Gell, M. Perry, J. H. Waite, F. Crary, D. Young, B. A. Magee, J. H. Westlake, T. Cravens, W. Kasprzak, G. Miller, J.-E. Wahlund, K. Ågren, N. J. T. Edberg, A. N. Heays, B. R. Lewis, S. T. Gibson, V. de la Haye, M-C. Liang, (2012), Ion densities and composition of Titan's upper atmosphere derived from the Cassini Ion Neutral Mass Spectrometer: Analysis methods and comparison of measured ion densities to photochemical model simulations, Journal of Geophysical Research, 117, E10006, doi: 10.1029/2012JE004139.

Mann, I. and A. Czechowski, (2012), Causes and consequences of the existence of nanodust in interplanetary space, In Nanodust in the solar system: Discoveries and interpretations, Astrophysics and Space Science Library, Springer-Verlag, Berlin, p. 385, doi: 10.1007/978-3-642-27543-2_10.

Mann, I., E. Murad, A. Czechowski, (2007), Nanoparticles in the inner solar system, Planetary and Space Science, 55, 1000–1009, doi: 10.1016/j.pss.2006.11.015.

Marty, B., T. Guillot, Athena Coustenis, N. Achilleos, Y. Alibert, S. Asmar, D. Atkinson, S. Atreya, G. Babasides, K. Baines, T. Balint, D. Banfield, S. Barber, B. Bézard, G. L. Bjoraker, M. Blanc, S. Bolton, N, Chanover, S. Charnoz, E. Chassefière, J. E. Colwell, E. Deangelis, M. K. Dougherty, P. Drossart, F. M. Flasar, T. Fouchet, R. Frampton, I. Franchi, D. Gautier, L. Gurvits, R. Hueso, B. Kazeminejad, S. M. Krimigis, A. Jambon, G. Jones, Y. Langevin, M. Leese, E. Lellouch, J. Lunine, A. Milillo, P. Mahaffy, B. Mauk, A. Morse, M. Moreira, X. Moussas, C. Murray, I. Mueller-Wodarg, T. C. Owen, S. Pogrebenko, R. Prangé, P. Read, A. Sánchez-Lavega, P. Sarda, D. Stam, G. Tinetti, P. Zarka, J. Zarnecki, (2008), Kronos: Exploring the Depths of Saturn With Probes and Remote Sensing Through an International Mission, Experimental Astronomy, doi: 10.1007/s10686-008-9094-9, pp. 8–37.

Masters, A., A. H. Sulaiman, L. Stawarz, B. Reville, N. Sergis, M. Fujimoto, D. Burgess, A. J. Coates, M. K. Dougherty, (2017), An In Situ comparison of electron acceleration at collisionless shocks under differing upstream magnetic field orientations, Astrophysical Journal, 843, doi: 10.3847/1538-4357/aa76ea.

Masters, A., A. H. Sulaiman, N. Sergis, L. Stawarz, M. Fujimoto, A. J. Coates, M. K. Dougherty, (2016), Suprathermal electrons at Saturn's bow shock, Astrophysical Journal, 826, doi: 10.3847/0004-637X/826/1/48.

Masters, A., L. Stawarz, M. Fujimoto, S. J. Schwartz, N. Sergis, M. F. Thomsen, A. Retino, H. Hasegawa, B. Zieger, G. R. Lewis, A. J. Coates, P. Canu, M. K. Dougherty, (2013a), Electron acceleration to relativistic energies at a strong quasi-parallel shock wave, Nature Physics, 9, 164–167, doi: 10.1038/nphys2541.

Masters, A., L. Stawarz, M. Fujimoto, S. J. Schwartz, N. Sergis, M. F. Thomsen, A. Retino, H. Hasegawa, B. Zieger, G. R. Lewis, A. J. Coates, P. Canu, M.K. Dougherty, (2013b), In situ observations of high-mach number collisionless shocks in space plasmas, Plasma Physics and Controlled Fusion, 55, 124035, doi: 10.1088/0741-3335/55/12/124035.

Masters, A., H. J. McAndrews, J. T. Steinberg, M. F. Thomsen, C. S. Arridge, M. K. Dougherty, L. Billingham, S. J. Schwartz, N. Sergis, G. B. Hospodarsky, A. J. Coates, (2009), Hot flow

anomalies at Saturn's bow shock, Journal of Geophysical Research, 114, A08217, doi: 10.1029/2009JA014112.

Masters, A., N. Achilleos, M. K. Dougherty, J. A. Slavin, G. B. Hospodarsky, C. S. Arridge, A. J. Coates, (2008), An empirical model of Saturn's bow shock: Cassini observations of shock location and shape, Journal of Geophysical Research, 113, A10210, doi: 10.1029/2008JA013276.

Mauk, B. H., D. C. Hamilton, T. W. Hill, G. B. Hospodarsky, R. E. Johnson, C. Paranicas, E. Roussos, C. T. Russell, D. E. Shemansky, E. C. Sittler, Jr., R. M. Thorne, (2009), Fundamental Plasma Processes in Saturn's Magnetosphere, in Saturn from Cassini-Huygens, (eds.), M. K. Dougherty, L. W. Esposito, and S. M. Krimigis, pp. 281–331, Springer, Dordrecht, doi: 10.1007/978-1-4020-9217-6_11.

McGhee, C. A., R. G. French, L. Dones, J. N. Cuzzi, H. J. Salo, R. Danos, (2005), HST Observations of the Spokes in Saturn’s B Ring, Icarus, 173, 508–521.

Mendillo, M., L. Moore, J. Clarke, I. Mueller-Wodarg, W. S. Kurth, M. L. Kaiser, (2005), Effects of ring shadowing on the detection of electrostatic discharges at Saturn, Geophysical Research Letters, 32, L05107, doi: 10.1029/2004GL021934.

Menietti, J. D., T. F. Averkamp, S.-Y. Ye, A. M. Persoon, M. W. Morooka, J. B. Groene, W. S. Kurth, (2018a), Extended survey of Saturn Z-mode wave intensity through Cassini's Final Orbits, Geophysical Research Letters, 45, 7330–7336, doi: 10.1029/2018GL079287.

Menietti, J. D., T. V. Averkamp, S.-Y. Ye, A. Sulaiman, M. Morooka, A. M. Persoon, G. B. Hospodarsky, W. S. Kurth, D. A. Gurnett, J.-E. Wahlund, (2018b), Analysis of intense Z-mode emission observed during the Cassini proximal orbits, Geophysical Research Letters, 45, 6766–6772, doi: 10.1002/2018GL077354.

Menietti, J. D., T. F. Averkamp, W. S. Kurth, S.-Y. Ye, D. A. Gurnett, B. Cecconi, (2017), Survey of Saturn electrostatic cyclotron harmonic wave intensity, Journal of Geophysical Research, 122, 8214–8227, doi: 10.1002/2017JA023929.

Menietti, J. D., J. B. Groene, T. F. Averkamp, R. B. Horne, E. E. Woodfield, Y. Y. Shprits, M. de Soria-Santacruz Pich, D. A. Gurnett, (2016a), Survey of whistler mode chorus intensity at Jupiter, Journal of Geophysical Research, 121, 10, 9758–9770, doi: 10.1002/2016JA022969.

Menietti, J. D., P. H. Yoon, D. Píša, S.-Y. Ye, O. Santolik, C. S. Arridge, D. A. Gurnett, A. J. Coates, (2016b), Source region and growth analysis of narrowband Z-mode emission at Saturn, Journal of Geophysical Research, 121, 12, 11929–11942, doi: 10.1002/2016JA022913.

Menietti, J. D., T. F. Averkamp, S.-Y. Ye, R. B. Horne, E. E. Woodfield, Y. Y. Shprits, D. A. Gurnett, J.-E. Wahlund, (2015), Survey of Saturn Z-mode emission, Journal of Geophysical Research, 120, 6176–6187, doi: 10.1002/2015JA021426.

Menietti, J. D., G. B. Hospodarsky, Y. Shprits, D. A. Gurnett, (2014a), Saturn chorus latitudinal variations, Journal of Geophysical Research, 119, Issue 6, 4656–4667, doi: 10.1002/2014JA019914.

Menietti, J. D., T. F. Averkamp, J. B. Groene, R. Horne, Y. Shprits, E. Woodfield, G. B. Hospodarsky, D. A. Gurnett, (2014b), Survey analysis of chorus intensity at Saturn, Journal of Geophysical Research, 119, 8415–8425, doi: 10.1002/2014JA020523.

Menietti, J. D., Y. Katoh, G. B. Hospodarsky, D. A. Gurnett, (2013a), Frequency drift of Saturn chorus emission compared to nonlinear theory, Journal of Geophysical Research, 118, 982–990, doi: 10.1002/jgra.50165.

Menietti, J. D., P. Schippers, Y. Katoh, J. S. Leisner, G. B. Hospodarsky, D. A. Gurnett, O. Santolik, (2013b), Saturn chorus intensity variations, Journal of Geophysical Research, 118, 1–11, doi: 10.1002/jgra.50529.

Menietti, J. D., Y. Shprits, R. Horne, E. Woodfield, G. B. Hospodarsky, D. A. Gurnett, (2012), Chorus, ECH, and Z-mode emissions observed at Jupiter and Saturn and possible electron acceleration, Journal of Geophysical Research, 117, A12214, doi: 10.1029/2012JA018187.

Menietti, J. D., R. L. Mutel, P. Schippers, S.-Y. Ye, O. Santolik, W. S. Kurth, D. A. Gurnett, B. Cecconi, (2011a), Saturn kilometric radiation near a source center on day 73, 2008, In Planetary Radio Emissions VII, (eds.) H. O. Rucker, W. S. Kurth, P. Louarn, G. Fischer, Austrian Academy of Sciences, Vienna, Austria, pp. 87–96.

Menietti, J. D., R. L. Mutel, P. Schippers, S.-Y. Ye, D. A. Gurnett, L. Lamy, (2011b), Analysis of Saturn kilometric radiation near a source center, Journal of Geophysical Research, 116, A12222, doi: 10.1029/2011JA017056.

Menietti, J. D., P. Schippers, O. Santolik, D. A. Gurnett, F. Crary, A. J. Coates, (2011c), Ion cyclotron harmonics in the Saturn downward current auroral region, Journal of Geophysical Research, 116, A12234, doi: 10.1029/2011JA017102.

Menietti, J. D., S.-Y. Ye, C. W. Piker, B. Cecconi, (2010a), The influence of Titan on Saturn kilometric radiation, Annales Geophysicae, 28, 395–406, doi: 10.5194/angeo-28-395-2010.

Menietti, J. D., P. H. Yoon, S.-Y. Ye, B. Cecconi, A. M. Rymer, (2010b), Source mechanism of Saturn narrowband emission, Annales Geophysicae, 28, 1013–1021, doi: 10.5194/angeo-28-1013-2010.

Menietti, J. D., S.-Y. Ye, P. H. Yoon, O. Santolik, A. M. Rymer, D. A. Gurnett, A. J. Coates, (2009), Analysis of narrowband emission observed in the Saturn magnetosphere, Journal of Geophysical Research, 114, A06206, doi: 10.1029/2008JA013982.

Menietti, J. D., O. Santolik, A. M. Rymer, G. B. Hospodarsky, A. M. Persoon, D. A. Gurnett, A. J. Coates, D. T. Young, (2008a), Analysis of plasma waves observed within local plasma injections seen in Saturn's magnetosphere, Journal of Geophysical Research, 113, A05213, doi: 10.1029/2007JA012856.

Menietti, J. D., O. Santolik, A. M. Rymer, G. B. Hospodarsky, D. A. Gurnett, A. J. Coates, (2008b), Analysis of plasma waves observed in the inner Saturn magnetosphere, Annales Geophysicae, 26, 2631–2644, doi: 10.5194/angeo-26-2631-2008.

Menietti, J. D., P. H. Yoon, D. A. Gurnett, (2007a), Possible eigenmode trapping in density enhancements in Saturn's inner magnetosphere, Geophysical Research Letters, 34, L04103, doi: 10.1029/2006GL028647.

Menietti, J. D., J. B. Groene, T. F. Averkamp, G. B. Hospodarsky, W. S. Kurth, D. A. Gurnett, P. Zarka, (2007b), Influence of Saturnian moons on Saturn kilometric radiation, Journal of Geophysical Research, 112, A08211, doi: 10.1029/2007JA012331.

Menietti, J. D. and W. S. Kurth, (2006), Ordered fine structure in radio emission observed by Cassini, Cluster, and Polar, In Planetary Radio Emissions VI, (eds.) H. O. Rucker, W. S. Kurth, and G. Mann, Austrian Academy of Sciences Press, Vienna, Austria, pp. 265–272.

Menietti, J. D., D. A. Gurnett, G. B. Hospodarsky, C. A. Higgins, W. S. Kurth, P. Zarka, (2003), Modeling radio emission attenuation lanes observed by the Galileo and Cassini spacecraft, Planetary and Space Science, 51, 533–540, doi: 10.1016/S0032-0633(03)00078-3.

Meyer-Vernet, N., M. Moncuquet, K. Issautier, P. Schippers, (2017), Frequency range of dust detection in space with radio and plasma wave receivers: Theory and application to interplanetary nanodust impacts on Cassini, Journal of Geophysical Research, 122, 8–22, doi: 10.1002/2016JA023081.

Meyer-Vernet, N., Z. Czechowski, I. Mann, M. Maksimovic, A. Lecacheux, K. Goetz, M. L. Kaiser, O. C. St. Cyr, S. D. Bale, G. Le Chat, (2010), Detection of fast nanoparticles in the solar wind, 12th International Solar Wind Conference, AIP Conference Proceedings, American Institute of Physics Publishing, vol. 1216, pp. 502–505,doi: 10.1063/1.3395912.

Meyer-Vernet, N., A. Lecacheux, M. L. Kaiser, D. A. Gurnett, (2009), Detecting nanoparticles at radio frequencies: Jovian dust stream impacts on Cassini/RPWS, Geophysical Research Letters, 36, L03103, doi: 10.1029/2008GL036752.

Mitchell, D. G., M. E. Perry, D. C. Hamilton, J. H. Westlake, P. Kollmann, H. T. Smith, J. F. Carbary, J. H. Waite, R. Perryman, H.-W. Hsu, J.-E. Wahlund, M. W. Morooka, L. Z. Hadid, A. M. Persoon, W. S. Kurth, (2018), Dust grains fall from Saturn's D-ring into its equatorial upper atmosphere, Science, 362, Issue 6410, eaat2236, doi:10.1126/science.aat2236.

Mitchell, D. G., J. F. Carbary, E. J. Bunce, A. Radioti, S. V. Badman, W. R. Pryor, G. B. Hospodarsky, W. S. Kurth, (2016), Recurrent pulsations in Saturn's high latitude magnetosphere, Icarus, 263, 94–100, doi: 10.1016/j.icarus.2014.10.028.

Mitchell, D. G., P. C. Brandt, J. F. Carbary, W. S. Kurth, S. M. Krimigis, C. Paranicas, N. Krupp, D. C. Hamilton, B. H. Mauk, G. B. Hospodarsky, M. K. Dougherty, W. R. Pryor, (2015), Injection, interchange, and reconnection: Energetic particle observations in Saturn's magnetosphere, Chapter 19, In Magnetotails in the solar system, Geophysical Monograph 207, (eds.) A. Keiling, C. M. Jackman P. A. Delamere, American Geophysical Union and John Wiley & Sons, Inc., pp. 327-343.

Mitchell, D. G., W. S. Kurth, G. B. Hospodarsky, N. Krupp, J. Saur, B. H. Mauk, J. F. Carbary, S. M. Krimigis, M. K. Dougherty, D. C. Hamilton, (2009a), Ion conics and electron beams

associated with auroral processes on Saturn, Journal of Geophysical Research, 114, A02212, doi: 10.1029/2008JA013621.

Mitchell, D. G., J. F. Carbary, S. W. H. Cowley, T. W. Hill, P. Zarka, (2009b), The dynamics of Saturn's magnetosphere, In Saturn from Cassini-Huygens, (eds.) M. K. Dougherty, L. W. Esposito, S. M. Krimigis, Springer, Dordrecht, pp. 257–279, doi: 10.1007/978-1-4020-9217-6_10.

Mitchell, D. G., S. M. Krimigis, C. Paranicas, P. C. Brandt, J. F. Carbary, E. C. Roelof, W. S. Kurth, D. A. Gurnett, J. T. Clarke, J. D. Nichols, J.-C. Gerard, D. C. Grodent, M. K. Dougherty, W. R. Pryor, (2009c), Recurrent energization of plasma in the midnight-to-dawn quadrant of Saturn's magnetosphere, and its relationship to auroral UV and radio emissions, Planetary and Space Science, 57, 1732–1742, doi: 10.1016/j.pss.2009.04.002.

Mitchell, D. G., P. C. Brandt, E. C. Roelof, J. Dandouras, S. M. Krimigis, B. H. Mauk, C. P. Paranicas, N. Krupp, D. C. Hamilton, W. S. Kurth, P. Zarka, M. K. Dougherty, E. J. Bunce, D. E. Shemansky, (2005), Energetic ion acceleration in Saturn's magnetotail: Substorms at Saturn?, Geophysical Research Letters, 32, L20S01, doi: 10.1029/2005GL022647.

Modolo, R. and G. M. Chanteur, (2008), A global hybrid model for Titan's interaction with the Kronian plasma: Application to the Cassini Ta flyby, Journal of Geophysical Research, 113, A01317, doi: 10.1029/2007JA012453.

Modolo, R., G. Chanteur, J.-E. Wahlund, P. Canu, W. S. Kurth, D. A. Gurnett, A. P. Matthews, C. Bertucci, (2007a), Plasma environment in the wake of Titan from hybrid simulation: A case study, Geophysical Research Letters, 34, L24S07, doi: 10.1029/2007GL030489.

Modolo, R., J.-E. Wahlund, R. Bostrom, P. Canu, W. S. Kurth, D. A. Gurnett, G. R. Lewis, A. J. Coates, (2007b), Far plasma wake of Titan from the RPWS observations: A case study, Geophysical Research Letters, 34, L24S04, doi: 10.1029/2007GL030482.

Molina-Cuberos, G. J., H. Lammer, W. Stumptner, K. Schwingenschuh, H. O. Rucker, J. J. Lopez-Moreno, R. Rodrigo, T. Tokano, (2001), Ionospheric layer induced by meteoric ionization in Titan's atmosphere, Planetary and Space Science, 49, 143–153, doi: 10.1016/S0032-0633(00)00133-1.

Moncuquet, M., N. Meyer-Vernet, A. Lecacheux, B. Cecconi, W. S. Kurth, (2006), Quasi Thermal Noise in Bernstein waves at Saturn, In Planetary Radio Emissions VI, (eds.) H. O. Rucker, W. S. Kurth, G. Mann, Austrian Academy of Sciences Press, Vienna, Austria, pp. 93–100.

Moncuquet, M., A. Lecacheux, N. Meyer-Vernet, B. Cecconi, W. S. Kurth, (2005), Quasi thermal noise spectroscopy in the inner magnetosphere of Saturn with Cassini/RPWS: Electron temperatures and density, Geophysical Research Letters, 32, L20S02, doi: 10.1029/2005GL022508.

Moore, L., T. E. Cravens, I. Mueller-Wodarg, M. Perry, J. H. Waite, R. Perryman, A. Nagy, D. Mitchell, A. Persoon, J.-E. Wahlund, M. W. Morooka, (2018), Models of Saturn's equatorial ionosphere based on in situ data from Cassini's Grand Finale, Geophysical Research Letters, 45, 9398–9407, doi: 10.1029/2018GL078162.

Moore, L., G. Fischer, I. Mueller-Wodarg, M. Galand, M. Mendillo, (2012), Diurnal variation of electron density in the Saturn ionosphere: Model comparisons with Saturn Electrostatic Discharge (SED) observations, Icarus, 221, 508–516, doi: 10.1016/j.icarus.2012.08.010.

Morooka, M. W., J.-E. Wahlund, L. Hadid, A. I. Ericksson, N. J. T. Edberg, E. Vigren, D. J. Andrews, A. M. Persoon, W. S. Kurth, D. A. Gurnett, W. M. Farrell, J. H. Waite, R. S. Perryman, M. Perry, (2019), Saturn's dusty ionosphere, Journal of Geophysical Research, 124, 1679–1697, doi: 10.1029/2018JA026154.

Morooka, M. W., J.-E. Wahlund, D. Andrews, A. M. Persoon, S.-Y. Ye, W. S. Kurth, D. A. Gurnett, W. M. Farrell, (2018), The dusty plasma disk around the Janus/Epimetheus ring, Journal of Geophysical Research, 123, 4668–4678, doi: 10.1002/2017JA024917.

Morooka, M. W., J.-E. Wahlund, D. Andrews, A. M. Persoon, S.-Y. Ye, W. S. Kurth, D. A. Gurnett, W. M. Farrell, (2018), Cassini RPWS dust observation near Janus and Epimetheus orbits, Journal of Geophysical Research: Space Physics, 123, no. 6, 4952–4960, doi: 10.1029/2017JA025112.

Morooka, M. W., J.-E. Wahlund, M. Shafiq, W. M. Farrell, D. A. Gurnett, W. S. Kurth, A. M. Persoon, M. Andre, A. I. Ericksson, M. Holmberg, (2011), Dusty plasma in the vicinity of Enceladus, Journal of Geophysical Research, 116, A12221, doi: 10.1029/2011JA017038.

Morooka, M. W., R. Modolo, J.-E. Wahlund, M. Andre, A. I. Eriksson, A. M. Persoon, D. A. Gurnett, W. S. Kurth, A. J. Coates, G. R. Lewis, K. K. Khurana, M. Dougherty, (2009), The electron density of Saturn's magnetosphere, Annales Geophysicae, 27, 2971–2991, doi: angeo-27-2971-2009.

Mousis, O., R. Hueso, J.-P. Beaulieu, S. Bouley, B. Carry, F. Colas, A. Klotz, C. Pellier, J.-M. Petit, P. Rousselot, M. Ali-Dib, W. Beisker, M. Birlan, C. Buil, A. Delsanti, E. Frappa, H. B. Hammel, A. C. Levasseur-Regourd, G. S. Orton, A. Sanchez-Lavega, A. Santerne, P. Tanga, J. Vaubailoon, B. Zanda, D. Baratoux, T. Böhm, V. Boudon, A. Bouquet, L. Buzzi, J.-L. Dauvergne, A. Decock, M. Delcroix, P. Drossart, N. Esseiva, G. Fischer, L. N. Fletcher, S. Foglia, J. M. Gomez-Forrellad, J. Guarro-Flo, D. Herald, E. Jehin, F. Kugel, J.-P. Lebreton, J. Lecacheux, A. Leroy, L. Maquet, G. Masi, A. Maury, F. Meyer, S. Perez-Hoyos, A. S. Rajpurohit, C. Rinner, J. H. Rogers, F. Roques, R. W. Schmude, B. Sicardy, B. Tregon, M. Vanhuysse, A. Wesley, T. Widemann, (2014), Instrumental methods for professional and amateur collaborations in planetary astronomy, Experimental Astronomy, vol. 38, Issue 1–2, pp. 91–191, doi: 10.1007/s10686-014-9379-0.

Mutel, R. L., J. D. Menietti, D. A. Gurnett, W. Kurth, P. Schippers, C. Lynch, L. Lamy, C. Arridge, B. Cecconi, (2010), CMI growth rates for Saturnian kilometric radiation, Geophysical Research Letters, 37, L19105, doi: 10.1029/2010GL044940.

Mylostna, K., V. Zakharenko, A. Konovalenko, V. Kolyadin, P. Zarka, J.-M. Griessmeier, G. Litvinenko, M. Sidorchuk, H. O. Rucker, G. Fischer, B. Cecconi, A. Coffre, L. Denis, V. Nikolaenko, V. Shevchenko, (2013), Study of Saturn electrostatic discharges in a wide range of time scales, Odessa Astronomical Publication, 26, p. 251.

Nichols, J. D., S. V. Badman, K. H. Baines, R. H. Brown, E. J. Bunce, J. T. Clarke, S. W. H. Cowley, F. J. Crary, M. K. Dougherty, J.-C. Gerard, A. Grocott, D. Grodent, W. S. Kurth, H. Melin, D. G. Mitchell, W. R. Pryor, T. S. Stallard, (2014), Dynamic auroral storms on Saturn as observed by the Hubble Space Telescope, Geophysical Research Letters, 41, 3323–3330, doi: 10.1002/2014GL060186.

Nichols, J. D., B. Cecconi, J. T. Clarke, S. W. H. Cowley, J.-C. Gerard, A. Grocott, D. Grodent, L. Lamy, P. Zarka, (2010), Variation of Saturn's UV aurora with SKR phase, Geophysical Research Letters, 37, L15102, doi: 10.1029/2010GL044057.

Nichols, J. D., S. V. Badman, E. J. Bunce, J. T. Clarke, S. W. H. Cowley, F. J. Crary, M. K. Dougherty, G.-C. Gerard, D. Grodent, K. C. Hansen, W. S. Kurth, D. G. Mitchell, W. R. Pryor, T. S. Stallard, D. L. Talboys, S. Wannawichian, (2009), Saturn's equinoctial auroras, Geophysical Research Letters, 36, L24102, doi: 10.1029/2009GL041491.

Nilsson, T., (2009), Modeling of Cassini Langmuir probe measurements, M.S. Thesis, Uppsala University, Uppsala, Sweden.

Nordheim, T. A., G. H. Jones, E. Roussos, J. S. Leisner, A. J. Coates, W. S. Kurth, K. K. Khurana, N. Krupp, M. K. Dougherty, J. H. Waite, (2014), Detection of a strongly negative surface potential at Saturn's moon Hyperion, Geophysical Research Letters, 41, 7011–7018, doi: 10.1002/2014GL061127.

Olson, J., N. Brenning, J.-E. Wahlund, H. Gunell, (2010), On the interpretation of Langmuir probe data inside a spacecraft sheath, Review of Scientific Instruments, 81, 105–106, doi: 10.1063/1.3482155.

Omidi, N., A. H. Sulaiman, W. Kurth, H. Madanian, T. Cravens, N. Sergis, M. K. Dougherty, N. J. Edberg, (2017), A single deformed bow shock for Titan-Saturn system, Journal of Geophysical Research, 122, 11058–11075, doi: 10.1002/2017JA024672.

Omidi, N., R. Tokar, T. Averkamp, D. Gurnett, W. Kurth, Z. Wang, (2012), Flow stagnation at Enceladus: The effects of neutral gas and charged dust, Journal of Geophysical Research, 117, A06230, doi: 10.1029/2011JA017488.

Omidi, N., C. T. Russell, R. L. Tokar, W. M. Farrell, W. S. Kurth, D. A. Gurnett, Y. D. Jia, L. S. Leisner, (2010), Hybrid simulations of plasma-neutral-dust interactions at Enceladus, In Pickup Ions Throughout the Heliosphere and Beyond, (eds.) J. A. le Roux, V. Florinski, G. Zank, AIP Conference Proceedings, American Institute of Physics Publishing, pp. 237–242.

Palmaerts, B., A. Radioti, D. Grodent, Z. H. Yao, T. J. Bradley, E. Roussos, L. Lamy, E. J. Bunce, S.W.H. Cowley, N. Krupp, W. S. Kurth, J.-C. Gerard, W. R. Pryor, (2018), Auroral storm and polar arcs at Saturn: Final Cassini/UVIS auroral observations, Geophysical Research Letters, 45, 6832–6842, doi: 10.1029/2018GL078094.

Palmaerts, B., E. Roussos, N. Krupp, W. S. Kurth, D. G. Mitchell, J. N. Yates, (2016), Statistical analysis and multi-instrument overview of the quasi-periodic 1-hour pulsations in Saturn's outer magnetosphere, Icarus, 271, 1–18, doi: 10.1016/j.icarus.2016.01.025.

Panchenko, M., S. Rošker, H. O. Rucker, A. Brazhenko, P. Zarka, G. Litvinenko, V. E. Shaposhnikov, A. A. Konovalenko, V. Melnik, A. V. Franzuzenko, J. Schiemel, (2018), Zebra pattern in decametric radio emission of Jupiter, Astronomy and Astrophysics, 610, A69.

Panchenko, M., S. Rošker, H. O. Rucker, A. Brazhenko, A. A. Konovalenko, G. Litvinenko, P. Zarka, V. Melnik, V. E. Shaposhnikov, A. V. Franzuzenko, (2016), Zebra-like fine spectral structures in Jovian decametric radio emission, In Planetary Radio Emissions VIII, (eds.) G. Fischer, G. Mann, M. Panchenko, P. Zarka, Austrian Academy Science Press, Vienna, Austria, pp. 103–114.

Panchenko, M., G. Fischer, W. Macher, (2014), Space-based observations of Jupiter's radio emission at IWF, In Planetary Radio Emissions 7.5, Planetary Retirement Edition, (eds.) N. I. Kömle, G. Fischer, W. Macher, Living Edition Publishers, Pöllauberg, 71–78.

Panchenko, M., H. O. Rucker, W. M. Farrell, (2013), Periodic bursts of Jovian non-Io decametric radio emission, Planetary and Space Science, 77, 100, 3–11, doi: 10.1016/j.pss.2012.08.015.

Panchenko, M. and H. O. Rucker, (2011), New type of periodic bursts of non-Io Jovian decametric radio emission, In Planetary Radio Emissions VII, (eds.) H. O. Rucker, W. S. Kurth, P. Louarn, G. Fischer, Austrian Academy of Sciences, Vienna, Austria, pp. 157–166.

Panchenko, M., H. O. Rucker, M. L. Kaiser, O. C. St. Cyr, J.-L. Bougeret, K. Goetz, S. D. Bale, (2010), New periodicity in Jovian decametric radio emission, Geophysical Research Letters, 37, L05106, doi: 10.1029/2010GL042488.

Paranicas, C., M. F. Thomsen, N. Achilleos, M. Andriopoulou, S. V. Badman, G. Hospodarsky, C. M. Jackman, X. Jia, T. Kennelly, K. Khurana, P. Kollman, N. Krupp, P. Louarn, E. Roussos, N. Sergis, (2016), Effects of radial motion on interchange injections at Saturn, Icarus, 264, 342–351, doi: 10.1016/j.icarus.2015.10.002.

Persoon, A. M., W. S. Kurth, D. A. Gurnett, J. B. Groene, A. Sulaiman, J.-E. Wahlund, M. W. Morooka, L. Z. Hadid, A. F. Nagy, J. H. Waite, T. E. Cravens, (2019), Electron density distributions in Saturn's ionosphere, Geophysical Research Letters, 46, 3061–3068, doi: 10.1029/2018GL078020.

Persoon, A. M., D. A. Gurnett, W. S. Kurth, J. B. Groene, (2015), Evidence for a seasonally dependent ring plasma in the region between Saturn's A-ring and Enceladus' orbit, Journal of Geophysical Research, 120, 6276–6285, doi: 10.1002/2015JA021180.

Persoon, A. M., D. A. Gurnett, J. S. Leisner, W. S. Kurth. J. B. Groene, J. B. Faden, (2013), The plasma density distribution in the inner region of Saturn's magnetosphere, Journal of Geophysical Research, 118, 1–5, doi: 10.1002/jgra.50182.

Persoon, A. M., D. A. Gurnett, J. S. Leisner, M. Morooka, J.-E. Wahlund, J. B. Groene, W. S. Kurth, G. B. Hospodarsky, (2011), The location of the high-density boundary in Saturn's inner magnetosphere (extended abstract), In Planetary Radio Emissions VII, (eds.) H. O. Rucker, W. S. Kurth, P. Louarn, G. Fischer, Austrian Academy of Sciences, Vienna, Austria, pp. 129–132.

Persoon, A. M., D. A. Gurnett, O. Santolik, W. S. Kurth, J. B. Faden, J. B. Groene, G. R. Lewis, A. J. Coates, R. J. Wilson, R. L. Tokar, J.-E. Wahlund, M. Moncuquet, (2009), A diffusive

equilibrium model for the plasma density in Saturn's magnetosphere, Journal of Geophysical Research, 114, A04211, doi: 10.1029/2008JA013192.

Persoon, A. M., D. A. Gurnett, W. S. Kurth, J. B. Groene, (2006a), A simple scale height model of the electron density in Saturn's plasma disk, Geophysical Research Letters, 33, L18106, doi: 10.1029/2006GL027090.

Persoon, A. M., D. A. Gurnett, W. S. Kurth, G. B. Hospodarsky, J. B. Groene, P. Canu, M. K. Dougherty, (2006b), An electron density model for Saturn's inner magnetosphere, In Planetary Radio Emissions VI, (eds.) H. O. Rucker, W. S. Kurth, G. Mann, Austrian Academy of Sciences Press, Vienna, Austria, pp. 81–91.

Persoon, A. M., D. A. Gurnett, W. S. Kurth, G. B. Hospodarsky, J. B. Groene, P. Canu, M. K. Dougherty, (2005), Equatorial electron density measurements in Saturn's inner magnetosphere, Geophysical Research Letters, 32, L23105, doi: 10.1029/2005GL024294.

Pickett, J. S., W. S. Kurth, D. A. Gurnett, R. L. Huff, J. B. Faden, T. F. Averkamp, D. Píša, G. H. Jones (2015), Electrostatic solitary waves observed at Saturn by Cassini inside 10 R_S near Enceladus, Journal of Geophysical Research, 120, 6569–6580, doi: 10.1002/2015JA021305.

Píša, D., A. H. Sulaiman, O. Santolik, G. B. Hospodarsky, W. S. Kurth, D. A. Gurnett, (2018), First observations of lion roar emission in Saturn’s magnetosheath, Geophysical Research Letters, 45, 486–492, doi: 10.1002/2017GL075919.

Píša, D., O. Santolik, G. B. Hospodarsky, W. S. Kurth, D. A. Gurnett, J. Soucek, (2016), Spatial distribution of Langmuir waves observed upstream of Saturn's bow shock by Cassini, Journal of Geophysical Research, 121, 7771–7784, doi: 10.1002/2016JA022912.

Píša, D., G. B. Hospodarsky, W. S. Kurth, O. Santolik, J. Soucek, D. A. Gurnett, A. Masters, M. E. Hill, (2015), Statistics of Langmuir wave amplitudes observed inside Saturn's foreshock by the Cassini spacecraft, Journal of Geophysical Research, 120, 2531–2542, doi: 10.1002/2014JA020560.

Pitman, K. M., B. J. Buratti, J. A. Mosher, J. M. Bauer, T. W. Momary, R. H. Brown, P. D. Nicholson, M. M. Hedman, (2008), First high solar phase angle observations of Rhea using Cassini VIMS: Upper limits on water vapor and geologic activity, The Astrophysical Journal Letters, 680, L65, doi: 10.1086/589745.

Plankensteiner, K., H. Reiner, B. M. Rode, T. Mikoviny, A. Wisthaler, A. Hansel, T. D. Mark, G. Fischer, H. Lammer, H. O. Rucker, (2007), Discharge experiments chemical evolution on the surface of Titan – Simulation experiments, Icarus, 187, 616–619, doi: 10.1016/j.icarus.2006.12.018.

Porco, C. C., P. Helfenstein, P. C. Thomas, A. P. Ingersoll, J. Wisdom, R. West, G. Neukum, et al., (2006), Cassini observes the active south pole of Enceladus, Science, 311, 1393–1401, doi: 10.1126/science.1123013.

Porco, C. C., E. Baker, J. Barbara, K. Beurle, A. Brahic, J. A. Burns, S. Charnoz, N. Cooper, D. D. Dawson, A. D. Del Genio, T. Denk, L. Dones, U. Dyudina, M. W. Evans, B. Giese, K. Grazier, P. Helfenstein, A. P. Ingersoll, R. A. Jacobson, T. V. Johnson, A. McEwen, C. D.

Murray, G. Neukum, W. M. Owen, J. Perry, T. Roatsch, J. Spitale, S. Squyres, P. Thomas, M. Tiscareno, E. Turtle, A. R. Vasavada, J. Veverka, R. Wagner, R. West, (2005), Cassini imaging science: Initial results on Saturn's atmosphere, Science, 307, 1243–1247.

Provan, G., L. Lamy, S. W. H. Cowley, E. J. Bunce, (2019), Planetary period oscillations in Saturn's magnetosphere: Comparison of magnetic and SKR modulation periods and phases during northern summer to the end of the Cassini Mission, Journal of Geophysical Research, 124, 1157–1172, doi: 10.1029/2018JA026079.

Provan, G., S. W. H. Cowley, L. Lamy, E. J. Bunce, G. J. Hunt, P. Zarka, M. K. Dougherty, (2016), Planetary period oscillations in Saturn's magnetosphere: Coalescence and reversal of northern and southern periods in late northern spring, Journal of Geophysical Research, 121, 10, 9829–9862, doi: 10.1002/2016JA023056.

Provan, G., C. Tao, S. W. H. Cowley, M. K. Dougherty, A. J. Coates, (2015), Planetary period oscillations in Saturn's magnetosphere: Examining the relationship between abrupt changes in behavior and solar wind-induced magnetospheric compressions and expansions, Journal of Geophysical Research, 120, 9524–9544, doi: 10.1002/ 2015JA021642.

Provan, G., L. Lamy, S. W. H. Cowley, M. K. Dougherty, (2014), Planetary period oscillations in Saturn's magnetosphere: Comparison of magnetic oscillations and SKR modulations in the post-equinox interval, Journal of Geophysical Research, 119, 7380–7401, doi: 10.1002/2014JA020011.

Provan, G., D. J. Andrews, B. Cecconi, S. W. H Cowley, M. K. Dougherty, L. Lamy, P. M. Zarka, (2011), Magnetospheric period magnetic field oscillations at Saturn: Equatorial phase "jitter" produced by superposition of southern and northern period oscillations, Journal of Geophysical Research, 116, A04225, doi: 10.1029/2010JA016213.

Pryor, W., A. M. Rymer, D. G. Mitchell, T. W. Hill, D. T. Young, J. Saur, G. H. Jones, S. Jacobsen, S. W. H. Cowley, B. H. Mauk, A. J. Coates, J. Gustin, D. Grodent, J.-C. Gerard, L. Lamy, J. D. Nichols, S. M. Krimigis, L. W. Esposito, M. K. Dougherty, A. J. Jouchoux, A. F. Stewart, W. E. McClintock, G. M. Holsclaw, J. M. Ajello, J. E. Colwell, A. R. Hendrix, F. J. Crary, J. T. Clarke, X. Zhou, (2011), The auroral footprint of Enceladus on Saturn, Nature, 472, 331–333, doi: 10.1038/nature09928.

Pryor, W. R., A. I. F. Stewart, L. W. Esposito, W. E. McClintock, J. E. Colwell, A. J. Jouchoux, A. J. Steffl, D. E. Shemansky, J. M. Ajello, R. A. West, C. J. Hansen, B. T. Tsurutani, W. S. Kurth, G. Hospodarsky, D. A. Gurnett, J. T. Clarke, D. Grodent, M. K. Dougherty, (2005), Cassini UVIS observations of Jupiter's auroral variability, Icarus, 178, 312–326, doi: 10.1016/j.icarus.2005.05.021.

Reed, J. J., C. M. Jackman, L. Lamy, D. Whiter, W. Kurth, (2018), Low frequency extensions of the Saturn kilometric radiation as a proxy for magnetospheric dynamics, Journal of Geophysical Research, 123, 443–463, doi: 10.1002/2017JA024499.

Richard, M. S., T. E. Cravens, C. Wylie, D. Webb, Q. Chediak, R. Perryman, K. Mandt, J. Westlake, J. H. Waite Jr., I. Robertson, B. A. Magee, N. J. T. Edberg, (2015), An empirical

approach to modeling ion production rates in Titan's ionosphere I: Ion production rates on the dayside and globally, Journal of Geophysical Research, 120, 1264–1280, doi: 10.1002/2013JA019706.

Richard, M. S., T. E. Cravens, I. P. Robertson, J. H. Waite, J.-E. Wahlund, F. J. Crary, A. J. Coates, (2011), Energetics of Titan’s ionosphere: Model comparisons with Cassini data, Journal of Geophysical Research, 116, A09310, doi: 10.1029/2011JA016603.

Rief, G., (2013), Numerical calibration of the Cassini RPWS antenna system, M.S. Thesis, Karl-Franzens-Universitat, Graz, Austria.

Robertson, I. P., T. E. Cravens, J. H. Waite Jr., R. V. Yelle, V. Vuitton, A. J. Coates, J.-E. Wahlund, K. Ågren, B. Magee, K. Mandt, M. S. Richard, (2009), Structure of Titan's ionosphere: Model comparisons with Cassini data, Planetary and Space Science, 57, 1834–1846, doi: 10.1016/j.pss.2009.07.011.

Rodriguez-Martinez, M., X. Blanco-Cano, C. T. Russell, J. S. Leisner, R. J. Wilson, M. K. Dougherty, (2010), Harmonic growth of ion-cyclotron waves in Saturn's magnetosphere, Journal of Geophysical Research, 115, A09207, doi: 10.1029/2009JA015000.

Romanelli, N., R. Modolo, E. Dubinin, J.-J. Berthelier, C. Bertucci, J.-E. Wahlund, F. Leblanc, P. Canu, N. J. T. Edberg, H. Waite, W. Kurth, D. Gurnett, A. Coates, M. Dougherty, (2014), Outflow and plasma acceleration in Titan's induced magnetotail: Evidence of magnetic tension forces, Journal of Geophysical Research, 119, 9992–10005 doi: 10.1002/2014JA020391.

Rosenqvist, L., J.-E. Wahlund, K. Ågren, R. Modolo, H. J. Opgenoorth, D. Strobel, I. Muller-Wodarg, P. Garnier, C. Bertucci, (2009), Titan Ionospheric conductivities from Cassini measurements, Planetary and Space Science, 57, 1828–1833, doi: 10.1016/j.pss.2009.01.007.

Roussos, E., C. M. Jackman, M. F. Thomsen, W. S. Kurth, S. V. Badman, C. Paranicas, P. Kollmann, N. Krupp, R. Bucik, D. G. Mitchell, S. M. Krimigis, D. C. Hamilton, A. Radioti, (2018), Solar Energetic Particles (SEP) and Galactic Cosmic Rays (GCR) as tracers of solar wind conditions near Saturn: Event lists and applications, Icarus, 300, 47–71, doi: 10.1016/j.icarus.2017.08.040.

Roussos, E., N. Krupp, D. G. Mitchell, C. Paranicas, S. M. Krimigis, M. Andriopoulou, W. S. Kurth, S. V. Badman, A. Masters, M. K. Dougherty, (2016), Quasi-periodic injections of relativistic electrons in Saturn's outer magnetosphere, Icarus, 263, 101–116, doi: 10.1016/j.icarus.2015.04.017.

Roussos, E., P. Kollmann, N. Krupp, C. Paranicus, S. M. Krimigis, D. G. Mitchell, A. M. Persoon, D. A. Gurnett, W. S. Kurth, H. Kriegel, S. Simon, K. K. Khurana, G. H. Jones, J.-E. Wahlund, M. K. G. Holmberg, (2012), Energetic electron observations of Rhea's magnetospheric interaction, Icarus, 221, Issue 1, 116–134, doi: 10.1016/j.icarus.2012.07.006.

Royer, E. M., E. L. W. Esposito, F. Crary, J.-E. Wahlund, (2018), Enhanced airglow signature observed at Titan in response to its fluctuating magnetospheric environment, Geophysical Research Letters, 45, 8864–8870, doi: 10.1029/2018GL078870.

Rucker, H. O., M. Panchenko, C. Weber, (2014), Planetary radio astronomy: Earth, giant planets, and beyond, advances in radio science, 12, 211–220, doi: 10.5194/ars-12-211-2014.

Rucker, H. O., M. Panchenko, K. C. Hansen, U. Taubenschuss, M. Y. Boudjada, W. S. Kurth, M. K. Dougherty, J. T. Steinberg, P. Zarka, P. H. M. Galopeau, D. J. McComas, C. H. Barrow, (2008), Saturn kilometric radiation as a monitor for the solar wind?, Advances in Space Research, 42, 40–47, doi: 10.1016/j.asr.2008.02.008.

Rucker, H. O., W. Macher, S. Albrecht, (1997), Experimental and theoretical investigations on the Cassini RPWS antennas, In Planetary Radio Emissions IV, (eds.) H. O. Rucker, S. J. Bauer, A. Lecacheux, Osterreichischen Akademie Der Wissenschaften, Wien, Austria, pp. 327–337.

Rucker, H. O., W. Macher, R. Manning, H. P. Ladreiter, (1996), Cassini model rheometry, Radio Science, 31, 1299–1311, doi: 10.1029/10.1029/96RS01972.

Rymer, A. M., B. H. Mauk, T. W. Hill, N. Andre, D. G. Mitchell, C. Paranicas, D. T. Young, H. T. Smith, A. M. Persoon, J. D. Menietti, G. B. Hospodarsky, A. J. Coates, M. K. Dougherty, (2009), Cassini evidence for rapid interchange transport at Saturn, Planetary and Space Science, 57, 1779–1784, doi: 10.1016/j.pss.2009.04.010.

Sakai, S., T. E. Cravens, N. Omidi, M. E. Perry, J. H. Waite Jr., (2016), Ion energy distributions and densities in the plume of Enceladus, Planetary and Space Science, 130, 60–79, doi: 10.1016/j.pss.2016.05.007.

Sakai, S.-T., S. Watanabe, M. W. Morooka, M. K. G. Holmberg, J.-E. Wahlund, D. A. Gurnett, W. S. Kurth, (2013), Dust-plasma interaction through magnetosphere-ionosphere coupling in Saturn's plasma disk, Planetary and Space Science, 75, 11–16, doi: 10.1016/j.pss.2012.11.003.

Sanchez-Lavega, A., G. Fischer, L. N. Fletcher, E. Garcia-Melendo, B. Hesman, S. Perez-Hoyos, K. M. Sayanagi, L. A. Sromovsky, (2018), The great Saturn storm of 2010–2011, Chapter 13, In Saturn in the 21st Century, (eds.) K. Baines, M. Flasar, N. Krupp, T. Stallard, Cambridge University Press, Cambridge, pp. 377–416, doi: 10.1017/9781316227220.

Sanchez-Lavega, A., F. Colas, J. Lecacheux, P. Laques, D. Parker, I. Miyazaki, (1991), The great white spot and disturbances in Saturn’s equatorial atmosphere during 1990, Nature, 353, 397–401.

Santolik, O., D. A. Gurnett, G. H. Jones, P. Schippers, F. J. Crary, J. S. Leisner, G. B. Hospodarsky, W. S. Kurth, C. T. Russell, M. K. Dougherty, (2011), Intense plasma wave emissions associated with Saturn's moon Rhea, Geophysical Research Letters, 38, L19204, doi: 10.1029/GL049219.

Saur, J., F. M. Neubauer, J. E. P. Connerney, M. G. Kivelson, P. Zarka, (2004), Plasma interaction of Io with its plasma torus, Chapter 22, In Jupiter: The Planet, Satellites and Magnetosphere 1, (eds.) F. Bagenal, W. McKinnon, T. Dowling, Cambridge University Press, Cambridge, pp. 537–560.

Sayanagi, K. M., U. A. Dyudina, S. P. Ewald, G. Fischer, A. P. Ingersoll, W. S. Kurth, G. D. Muro, C. C. Porco, R. A. West, (2013), Dynamics of Saturn's great storm of 2010–2011 from Cassini ISS and RPWS, Icarus, 223, Issue 1, 460–478, doi: 10.1016/j.icarus.2012.12.013.

Schippers, P., N. Meyer-Vernet, A. Lecacheux, S. Belheouane, M. Moncuquet, W. S. Kurth, I. Mann, D. G. Mitchell, N. Andre, (2015), Nanodust detection between 1 and 5 AU using Cassini wave measurements, The Astrophysical Journal, 806, 77, doi: 10.1088/0004-637X/806/1/77.

Schippers, P., N. Meyer-Vernet, A. Lecacheux, W. S. Kurth, D. G. Mitchell, N. Andre, (2014), Nanodust detection near 1 AU from spectral analysis of Cassini/RPWS radio data, Geophysical Research Letters, 41, 5382-5388, doi: 10.1002/2014GL060566.

Schippers, P., M. Moncuquet, N. Meyer-Vernet, A. Lecacheux, (2013), Core electron temperature and density in the innermost Saturn magnetosphere from HF power spectra analysis on Cassini, Journal of Geophysical Research, 118, 7170–7180, doi: 10.1002/2013JA019199.

Schippers, P., N. Andre, D. A. Gurnett, G. R. Lewis, A. M. Persoon, A. J. Coates, (2012), Identification of electron Field-aligned current systems in Saturn's magnetosphere, Journal of Geophysical Research, 117, A05204, doi: 10.1029/2011JA017352.

Schippers, P., C. Arridge, J. D. Menietti, D. Gurnett, L. Lamy, B. Cecconi, D. Mitchell, N. Andre, W. Kurth, S. Grimald, M. Dougherty, A. Coates, D. Young, (2011), Auroral electron distributions within and close to the Saturn kilometric radiation source region, Journal of Geophysical Research, 116, A05203, doi: 10.1029/2011JA016461.

Schippers, P., M. Blanc, N. Andre, I. Dandouras, G. R. Lewis, L. K. Gilbert, A. M. Persoon, N. Krupp, D. A Gurnett, A. Coates, S. M. Krimigis, D. Young, M. K. Dougherty, (2008), Multi-instrument analysis of electron populations in Saturn's magnetosphere, Journal of Geophysical Research, 113, A07208, doi: 10.1029/2008JA013098.

Seki, K., A. Nagy, C. Jackman, F. Crary, D. Fontaine, P. Zarka, P. Wurz, A. Milillo, J. A. Slavin, D. C. Delcourt, M. Wiltberger, R. Ilie, X. Jia, S. A. Ledvina, M. W. Liemohn, R. W. Schunk, (2015), A review of general processes related to plasma sources and losses for solar system magnetospheres, Space Sciences Reviews, 192, 27–89.

Shafiq, M., J.-E. Wahlund, M. W. Morooka, W. S. Kurth, W. M. Farrell, (2011), Characteristics of the dust-plasma interaction near Enceladus' south pole, Planetary and Space Science, 59, Issue 1, 17–25, doi: 10.1016/j.pss.2010.10.006.

Shebanits, O., E. Vigren, J.-E. Wahlund, M. K. G. Holmberg, M. Morooka, N. J. T. Edberg, K. E. Mandt, J. H. Waite Jr., (2017), Titan's ionosphere: A survey of solar EUV influences, Journal of Geophysical Research, 122, 7491–7503, doi: 10.1002/2017JA023987.

Shebanits, O., J.-E. Wahlund, N. J. T. Edberg, F. J. Crary, A. Wellbrock, D. J. Andrews, E. Vigren, R. T. Desai, A. J. Coates, K. E. Mandt, J. H. Waite Jr., (2016), Ion and aerosol precursor densities in Titan's ionosphere: A multi-instrument case study, Journal of Geophysical Research, 121, 10, 10075–10090, doi: 10.1002/2016JA022980.

Shebanits, O., J.-E. Wahlund, K. Mandt, K. Ågren, N. J. T. Edberg, J. H. Waite, (2013), Negative ion densities in the ionosphere of Titan-Cassini RPWS/LP results, Planetary and Space Science, 84, 154–162, doi: 10.1016/j.pss.2013.05.021.

Shprits, Y. Y., J. D. Menietti, X. Gu, K. C. Kim, R. B. Horne, (2012), Gyroresonant interactions between the radiation belt electrons and whistler mode chorus waves in the radiation environments of Earth, Jupiter, and Saturn: A comparative study, Journal of Geophysical Research, 117, A11216, doi: 10.1029/2012JA018031.

Sillanpaa, I., D. T. Young, F. Crary, M. Thomsen, D. Reisenfeld, J.-E. Wahlund, C. Bertucci, E. Kallio, R. Jarvinen, P. Janhunen, (2011), Cassini plasma spectrometer and hybrid model study on Titan's interaction: Effect of oxygen ions, Journal of Geophysical Research, 116, A07223, doi: 10.1029/2011JA016443.

Sittler Jr., E. C., R. E. Hartle, R. E. Johnson, J. F. Cooper, A. S. Lipatov, C. Bertucci, A. J. Coates, K. Szego, M. Shappiro, D. G. Simpson, J.-E. Wahlund, (2010), Saturn's magnetospheric interaction with Titan as defined by Cassini encounters T9 and T18: New results, Planetary and Space Science, 58, 327–350, doi: 10.1016/j.pss.2009.09.017.

Sittler Jr., E. C., N. Andre, M. Blanc, M. Burger, R. E. Johnson, A. Coates, A. Rymer, D. Reisenfeld, M. F. Thomsen, A. Persoon, M. Dougherty, H. T. Smith, R. A. Baragiola, R. E. Hartle, D. Chornay, M. D. Shappirio, D. J. McComas, D. T. Young, (2008), Ion and Neutral Sources and Sinks within Saturn's Inner Magnetosphere: Cassini Results, Planetary and Space Science, 56, 3–18, doi: 10.1016/j.pss.2007.06.006.

Smith, A. W., C. M. Jackman, M. F. Thomsen, L. Lamy, N. Sergis, (2018), Multi-instrument investigation of the location of Saturn's magnetotail x-Line, Journal of Geophysical Research, 123, 5494–5505, doi: 10.1029/2018025532.

Snowden, D., R. V. Yelle, J. Cui, J.-E. Wahlund, K. Ågren, N. J. T. Edberg, (2013), The thermal structure of Titan's upper atmosphere, I: Temperature profiles from Cassini INMS observations, Icarus, 226, Issue 1, 552–582, doi: 10.1016/j.icarus.2013.06.006.

Southwood, D. J. and M. G. Kivelson, (2001), A new perspective concerning the influence of the solar wind on the Jovian magnetosphere, Journal of Geophysical Research, 106, 6123–6130.

Spahn, F., J. Schmidt, N. Albers, M. Hörning, M. Makuch, M. Seiß, S. Kempf, et al., (2006a), Cassini dust measurements at Enceladus and implications for the origin of the E ring, Science, 311, 1416–1418, doi: 10.1126/science.1121375.

Srama, R., S. Kempf, G. Moragas-Klostermeyer, S. Helfert, T. J. Ahrens, N. Altobelli, S. Auer, et al., (2006), In situ dust measurements in the inner Saturnian system, Planetary and Space Science, 54, 967–987, doi: 10.1016/j.pss.2006.05.021.

Srama, R., T. J. Ahrens, N. Altobelli, et al., (2004), The Cassini Cosmic Dust Analyzer, Space Science Reviews, 114, 465–518, doi: 10.1007/s11214-004-1435-z.

Sromovsky, L. A., K. H. Baines, P. M. Fry, (2013), Saturn's great storm of 2010–2011: Evidence for ammonia and water ices from analysis of VIMS spectra, Icarus, 226, 402–418.

Sulaiman, A. H., W. M. Farrell, S.-Y. Ye, W. S. Kurth, D. A. Gurnett, G. B. Hospodarsky, J. D. Menietti, D. Píša, G. J. Hunt, O. Agiwal, M. K. Dougherty, (2019), A persistent, large-scale, and ordered electrodynamic connection between Saturn and its main rings, Geophysical Research Letters, In press, June 16, 2019, doi:10.1029/2019GL083541.

Sulaiman, A. H., W. S. Kurth, G. B. Hospodarsky, T. F. Averkamp, S.-Y. Ye, J. D. Menietti, W. M. Farrell, D. A. Gurnett, M. K. Dougherty, G. J. Hunt, (2018a), Enceladus auroral hiss emissions during Cassini's Grand Finale, Geophysical Research Letters, 45, 7347–7353, doi: 10.1029/2018GL078130.

Sulaiman, A. H., W. S. Kurth, G. B. Hospodarsky, T. F. Averkamp, A. M. Persoon, J. D. Menietti, S.-Y. Ye, D. A. Gurnett, D. Píša, W. M. Farrell, M. K. Dougherty, (2018b), Auroral hiss emissions during Cassini's Grand Finale: Diverse electrodynamic interactions between Saturn and its rings, Geophysical Research Letters, 45, 6782–6789, doi:10.1029/2018GL077875.

Sulaiman, A. H., D. A. Gurnett, J. S. Halekas, J. N. Yates, W. S. Kurth, M. K. Dougherty, (2017a), Whistler-mode waves upstream of Saturn, Journal of Geophysical Research, 122, 227–234, doi: 10.1002/2016GL070405.

Sulaiman, A., X. Jia, N. Achilleos, N. Sergis, D. A. Gurnett, W. S. Kurth, (2017b), Large-scale solar wind flow around Saturn's nonaxisymmetric magnetosphere, Journal of Geophysical Research, 122, 9198–9206, doi: 10.1002/2017JA024595.

Sulaiman, A. H., W. S. Kurth, A. M. Persoon, J. D. Menietti, W. M. Farrell, S.-Y. Ye, G. B. Hospodarsky, D. A. Gurnett, L. Z. Hadid, (2017c), Intense harmonic emissions observed in Saturn's ionosphere, Geophysical Research Letters, 44, 12049–12056, doi: 10.1002/2017GL076184.

Sulaiman, A. H., A. Masters, M. K. Dougherty, D. Burgess, M. Fujimoto, G. B. Hospodarsky, (2015), Quasiperpendicular high mach number shocks, Physical Review Letters, 115, 125001, doi: 10.1103/PhysRevLett.115.125001.

Sundberg, T., D. Burgess, M. Scholer, A. Masters, A. H. Sulaiman, (2017), The dynamics of very high Alfvén Mach number shocks in space plasmas, Astrophysical Journal Letters, 836, 1, L4, doi: 10.3847/2041-8213/836/1/L4.

Szego, K., Achilleos, N., Arridge, C., Badman, S. V., Delamere, P., Grodent, D., Kivelson, M. G., Louarn, P., (2015), Giant planet magnetodiscs and aurorae – An introduction, Space Science Reviews, 187, 1, 1–3, doi: 10.1007/s11214-014-0131-x.

Szego, K., D. T. Young, T. Bagdonat, B. Barraclough, J.-J. Berthelier, A. J. Coates, F. J. Crary, M. K. Dougherty, G. Erdos, D. A. Gurnett, W. S. Kurth, A. Opitz, A. Rymer, M. F. Thomsen, (2006), A pre-shock event at Jupiter on 30 January 2001, Planetary and Space Science, 54, 200–211, doi: 10.1016/j.pss.2005.10.011.

Szego, K., D. T. Young, B. Barraclough, J.-J. Berthelier, A. J. Coates, D. J. McComas, F. J. Crary, M. K. Dougherty, G. Erdos, D. A. Gurnett, W. S. Kurth, M. F. Thomsen, (2003), Cassini plasma spectrometer measurements of Jovian bow shock structure, Journal of Geophysical Research, 108, No. A7, 1287, doi: 10.1029/2002JA009517.

Tao, C., L. Lamy, and R. Prange, (2014), The brightness ratio of H Lyman-α/H_2 bands in FUV auroral emissions: A diagnosis for the energy of precipitating electrons and associated magnetospheric acceleration processes applied to Saturn, Geophysical Research Letters, 41, 6644–6651, doi: 10.1002/2014GL061329.

Tao, X., R. Thorne, R. B. Horne, S. Grimald, C. S. Arridge, G. B. Hospodarsky, D. A. Gurnett, A. J. Coates, F. J. Crary, (2010), Excitation of electron cyclotron harmonic waves in the inner Saturn magnetosphere within local plasma injections, Journal of Geophysical Research, 115, A12204, doi: 10.1029/2010JA015598.

Taubenschuss, U., J. S. Leisner, G. Fischer, D. A. Gurnett, F. Nemec, (2011), Saturnian low frequency drifting radio bursts: Statistical properties and polarization, In Planetary Radio Emissions VII, (eds.) H. O. Rucker, W. S. Kurth, P. Louarn, G. Fischer, Austrian Academy of Sciences, Vienna, Austria, pp. 115–124.

Taubenschuss, U., H. O. Rucker, W. S. Kurth, B. Cecconi, M. D. Desch, P. Zarka, M. K. Dougherty, J. T. Steinberg, (2006a), External control of Saturn kilometric radiation, In Planetary Radio Emissions VI, (eds.) H. O. Rucker, W. S. Kurth, G. Mann, Austrian Academy of Sciences Press, Vienna, Austria, pp. 51–60.

Taubenschuss, U., H. O. Rucker, W. S. Kurth, B. Cecconi, P. Zarka, M. K. Dougherty, J. T. Steinberg, (2006b), Linear prediction studies for the solar wind and Saturn kilometric radiation, Annales Geophysicae, 24, 3139–3150, doi: 10.5194/angeo-24-3139-2006.

Taubenschuss, U., (2005), The linear prediction theory applied to Cassini Data, M.S. Thesis, Karl Franzens University of Graz, Graz, Austria.

Taylor, S. A., A. J. Coates, G. H. Jones, A. Wellbrock, A. N. Fazakerley, R. T. Desai, R. Caro-Carretero, M. W. Morooka, P. Schippers, J. H. Waite, (2018), Modeling, analysis, and interpretation of photoelectron energy spectra at Enceladus observed by Cassini, Journal of Geophysical Research, 123, 287–296, doi: 10.1002/2017JA024536.

Teolis, B. D., G. H. Jones, P. F. Miles, R. L. Tokar, B. A. Magee, J. H. Waite, E. Roussos, et al., (2010), Cassini finds an oxygen-carbon dioxide atmosphere at Saturn’s icy moon Rhea, Science, 330, 1813, doi: 10.1126/science.1198366.

Thomsen, M. F., S. V. Badman, C. M. Jackman, X. Jia, M. G. Kivelson, W. S. Kurth, (2017), Energy-banded ions in Saturn's magnetosphere, Journal of Geophysical Research, 122, 5181–5202, doi: 10.1002/2017JA024147.

Thomsen, M. F., D. G. Mitchell, X. Jia, C. M. Jackman, G. B. Hospodarsky, A. J. Coates, (2015a), Plasmapause formation at Saturn, Journal of Geophysical Research, 120, 2571–2583, doi: 10.1002/2015JA021008.

Thomsen, M. F., C. M. Jackman, D. G. Mitchell, G. Hospodarsky, W. S. Kurth, K. C. Hansen, (2015b), Sustained lobe reconnection in Saturn's magnetotail, Journal of Geophysical Research, 120, 10257–10274, doi: 10.1002/2015JA021768.

Thomsen, M. F., D. B. Reisenfeld, R. J. Wilson, M. Andriopoulou, F. J. Crary, G. B. Hospodarsky, C. M. Jackman, X. Jia, K. K. Khurana, C. Paranicas, E. Roussos, N. Sergis, R. L. Tokar,

(2014), Ion composition in interchange injection events in Saturn's magnetosphere, Journal of Geophysical Research, 119, 9761–9772, doi: 10.1002/2014JA020489.

Thomsen, M. F., E. Roussos, M. Andriopoulou, P. Kollmann, C. S. Arridge, C. P. Paranicas, D. A. Gurnett, R. L. Powell, R. L. Tokar, D. T. Young, (2012), Saturn's inner magnetospheric convection pattern: Further evidence, Journal of Geophysical Research, 117, A09208, doi: 10.1029/2011JA017482.

Tokar, R. L., R. E. Johnson, T. W. Hill, D. H. Pontius, W. S. Kurth, F. J. Crary, D. T. Young, M. F. Thomsen, D. B. Reisenfeld, A. J. Coates, G. R. Lewis, E. C. Sittler, D. A. Gurnett, (2006), The interaction of the atmosphere of Enceladus with Saturn's plasma: Cassini observations, Science, 311, 1409–1412, doi: 10.1126/science.1121061.

Tokar, R. L., R. E. Johnson, M. F. Thomsen, D. M. Delapp, R. A. Baragiola, M. Francis, D. B. Reisenfeld, B. Fish, D. T. Young, F. J. Crary, A. J. Coates, D. A. Gurnett, W. S. Kurth, (2005), Cassini observations of the thermal plasma in the vicinity of Saturn's main rings and the F and G rings, Geophysical Research Letters, 32, L14S04, doi: 10.1029/2005GL022690.

Tokarev, Y., J.-L. Bougeret, B. Cecconi, A. Lecacheux, M. Kaiser, W. Kurth, (2006), SURA-WAVES experiments: Calibration of the Cassini/RPWS/HFR instrumentation, In Planetary Radio Emissions VI, (eds.) H. O. Rucker, W. S. Kurth, an G. Mann, Austrian Academy of Sciences Press, Vienna, Austria, pp. 531–541.

Tokarev, Yu. V., D. A. Gurnett, W. S. Kurth, M. L. Kaiser, R. Manning, G. N. Boiko, S. P. Terent'ev, (2001), Observations of low-frequency cosmic background at various distances from the Sun, All-proceedings of the Russian Astronomical Conference: 2001, August 6–12, 2001, St. Petersburg, Russia, p. 175.

Tseng, W.-L., R. E. Johnson, M. K. Elrond, (2013), Modeling the seasonal variability of the plasma environment in Saturn’s magnetosphere between main rings and Mimas, Planetary and Space Science, 77, 126–135.

Ulusen, D., J. G. Luhmann, Y. J. Ma, K. E. Mandt, J. H. Waite, M. K. Dougherty, J.-E. Wahlund, C. T. Russell, T. E. Cravens, N. J. T. Edberg, K. Ågren, (2012), Comparisons of Cassini flybys of the Titan magnetospheric interaction with an MHD Model: Evidence for organized behavior at high altitudes, Icarus, 217, Issue 1, 43–54, doi: 10.1016/j.icarus.2011.10.009.

Ulusen, D., J. G. Luhmann, Y. J. Ma, S. Ledvina, T. E. Cravens, K. Mandt, J. H. Waite, J.-E. Wahlund, (2010), Investigation of the force balance in the Titan ionosphere: Cassini T5 flyby model/data comparisons, Icarus, 210, 867–880, doi: 10.1016/j.icarus.2010.07.004.

Vigren, E., M. Galand, R. V. Yelle, A. Wellbrock, A. J. Coates, D. Snowden, J. Cui, P. Lavvas, N. J. T. Edberg, O. Shebanits, J.-E. Wahlund, V. Viutton, K. Mandt, (2015), Ionization balance in Titan's nightside ionosphere, Icarus, 248, 539–546, doi: 10.1016/j.icarus.2014.11.012.

Vigren, E., M. Galand, O. Shebanits, J.-E. Wahlund, W. D. Geppert, P. Lawas, V. Vuitton, R. V. Yelle, (2014), Increasing positive ion number densities below the peak of ion-electron pair production in Titan's ionosphere, The Astrophysical Journal, 786, 69–73, doi: 10.1088/0004-637X/786/1/69.

Vigren, E., M. Galand, R. V. Yelle, J. Cui, J.-E. Wahlund, K. Ågren, P. P. Lavvas, I. C. F. Mueller-Wodarg, D. F. Strobel, V. Vuitton, A. Bazin, (2013), On the thermal electron balance in Titan's sunlit upper atmosphere, Icarus, 223, Issue 1, 234–251, doi: 10.1016/j.icarus.2012.12.010.

Vogl, D. F., B. Cecconi, W. Macher, P. Zarka, H.-P. Ladreiter, P. Fedou, A. Lecacheux, T. Averkamp, G. Fischer, H. O. Rucker, D. A. Gurnett, W. S. Kurth, G. B. Hospodarsky, (2004), In-flight calibration of the Cassini-Radio and Plasma Wave Science (RPWS) antenna system for direction-finding and polarization measurements, Journal of Geophysical Research, 109, A09S17, doi: 10.1029/2003JA010261.

Vogl, D. F., H. P. Ladreiter, P. Zarka, H. O. Rucker, W. Macher, W. S. Kurth, D. A. Gurnett, G. Fischer, (2001), First results on the calibration of the Cassini RPWS antenna system, In Planetary Radio Emissions V, (eds.) H. O. Rucker, M. L. Kaiser, Y. Leblanc, Austrian Academy of Sciences Press, Vienna, Austria, pp. 357–365.

Vuitton, V., P. Lavvas, R. V. Yelle, M. Galand, A. Wellbrock, G. R. Lewis, A. J. Coates, J.-E. Wahlund, (2009), Negative ion chemistry in Titan's upper atmosphere, Planetary and Space Science, 57, 1558–1572, doi: 10.1016/j.pss.2009.04.004.

Wahlund, J.-E., M. W. Morooka, L. Z. Hadid, A. M. Persoon, W. M. Farrell, D. A. Gurnett, G. B. Hospodarsky, W. S. Kurth, S.-Y. Ye, D. J. Andrews, N. J. T. Edberg, A. I. Eriksson, E. Vigren, (2018), In situ measurements of Saturn's ionosphere show it is dynamic and interacts with the rings, Science, 359, Issue 6371, 66–68, doi: 10.1126/science.aao4134.

Wahlund, J.-E., R. Modolo, C. Bertucci, A. J. Coates, (2013), Titan's magnetospheric and plasma environment (Chapter 12), In Titan – Interior, Surface, Atmosphere and Space Environment, (eds.) I. C. F. Müller-Wodarg, C. A. Griffith, E. Lellouch, T. E. Cravens, Cambridge University Press, Cambridge.

Wahlund, J.-E., M. Andre, A. I. E. Eriksson, M. Lundberg, M. W. Morooka, M. Shafiq, T. F. Averkamp, D. A. Gurnett, G. B. Hospodarsky, W. S. Kurth, K. S. Jacobsen, A. Pedersen, W. Farrell, S. Ratynskaia, N. Piskunov, (2009a), Detection of dusty plasma near the E-ring of Saturn, Planetary and Space Science, 57, 1795–1806, doi: 10.1016/j.pss.2009.03.011.

Wahlund, J.-E., M. Galand, I. Mueller-Wodarg, J. Cui, R. V. Yelle, F. J. Crary, K. Mandt, B. Magee, J. H. Waite, Jr., D. T. Young, A. J. Coates, P. Garnier, K. Ågren, M. Andre, A. I. Ericksson, T. E. Cravens, V. Vuitton, D. A. Gurnett, W. S. Kurth, (2009b), On the amount of heavy molecular ions in Titan's ionosphere, Planetary and Space Science, 57, 1857–1865, doi: 10.1016/j.psss.2009.07.014.

Wahlund, J.-E., R. Bostrom, G. Gustafsson, D. A. Gurnett, W. S. Kurth, A. Pedersen, T. F. Averkamp, G. B. Hospodarsky, A. M. Persoon, P. Canu, F. M. Neubauer, M. K. Dougherty, A. I. Eriksson, M. W. Morooka, R. Gill, M. Andre, L. Eliasson, I. Muller-Wodarg, (2005a), Cassini measurements of cold plasma in the ionosphere of Titan, Science, 308, 986–989, doi: 10.1126/science.1109807.

Wahlund, J.-E., R. Bostrom, G. Gustafsson, D. A. Gurnett, W. S. Kurth, T. Averkamp, G. B. Hospodarsky, A. M. Persoon, P. Canu, A. Pedersen, M. D. Desch, A. I. Eriksson, R. Gill, M. W.

Morooka, M. Andre, (2005b), The inner magnetosphere of Saturn: Cassini RPWS cold plasma results from the first encounter, Geophysical Research Letters, 32, L20S09, doi: 10.1029/2005GL022699.

Waite, J. H., R. Perryman, M. Perry, K. Miller, J. Bell, T. E. Cravens, C. Glein, J. Grimes, H. Hedman, T. Brockwell, B. Teolis, L. Moore, D. Mitchell, A. Persoon, W. S. Kurth, J.-E. Wahlund, M. Morooka, L. Hadid, S. Chocron, A. Nagy, R. Yelle, S. Ledvina, R. Johnson, (2018), Chemical interactions between Saturn's atmosphere and rings, Science, 362, Issue 6410, eaat2382, doi:10/1126/science.aat2382.

Wang, Z., D. A. Gurnett, G. Fischer, S-Y. Ye, W. S. Kurth, D. G. Mitchell, J. S. Leisner, C. T. Russell, (2010), Cassini observations of narrowband radio emissions in Saturn's magnetosphere, Journal of Geophysical Research: Space Physics, vol. 115, Issue A6, doi: 10.1029/2009JA014847.

Wang, Z., D. A. Gurnett, T. F. Averkamp, A. M. Persoon, W. S. Kurth, (2006), Characteristics of dust particles detected near Saturn's ring plane with the Cassini Radio and Plasma Wave instrument, Planetary and Space Science, 54, 957-966, doi: 10.1016/j.pss.2006.05015.

Wang, Z., (2006), The characteristics of dust particles detected by Cassini near Saturn's ring plane, Ph.D. Thesis, University of Iowa, Iowa City, Iowa.

Wang, Z., D. A. Gurnett, G. Fischer, S.-Y. Ye, W. S. Kurth, D. G. Mitchell, J. S. Leisner, C. T. Russell, (2010), Cassini observations of narrowband radio emissions in Saturn's magnetosphere, Journal of Geophysical Research, 115, A06213, doi: 10.1029/2009JA014847.

Warwick, J. W., J. B. Pearce, D. R. Evans, T. D. Carr, J. J. Schauble, J. K. Alexander, M. L. Kaiser, M. D. Desch, M. Pedersen, A. Lecacheux, G. Daigne, A. Boischot, C. H. Barrow, (1981), Planetary radio astronomy observations from Voyager 1 near Saturn, Science, 212, 239–243.

Wei, H. Y., C. T. Russell, J.-E. Wahlund, M. K. Dougherty, C. Bertucci, R. Modolo, Y. J. Ma, F. M. Neubauer, (2007), Cold ionospheric plasma in Titan's magnetotail, Geophysical Research Letters, 34, L24S06, doi: 10.1029/2007GL030701.

Went, D. R., G. B. Hospodarsky, A. Masters, K. C. Hansen, M. K. Dougherty, (2011), A new semiempirical model of Saturn's bow shock based on propagated solar wind parameters, Journal of Geophysical Research, 116, A07202, doi: 10.1029/2010JA016349.

Westlake, J. H., J. H. Waite Jr., K. E. Mandt, N. Carrasco, J. M. Bell, B. A. Magee, J.-E. Wahlund, (2012a), Titan’s ionospheric composition and structure: Photochemical modelling of Cassini INMS data, Journal of Geophysical Research, 117, E01003, doi: 10.1029/2011JE003883.

Westlake, J. H., C. P. Paranicas, T. E. Cravens, J. G. Luhmann, K. E. Mandt, H. T. Smith, D. G. Mitchell, A. M. Rymer, M. E. Perry, J. H. Waite, J.-E. Wahlund, (2012b), The observed composition of ions outflowing from Titan, Geophysical Research Letters, 39, L19104, doi: 10.1029/2012GL053079.

Williams, G. A. and C. D. Murray, (2011), Stability of co-orbital ring material with applications to the Janus-Epimetheus system, Icarus, 212, 275–293, doi: 10.1016/j.icarus.2010.11.038.

Williams, J. D., L.-J. Chen, W. S. Kurth, D. A. Gurnett, M. K. Dougherty, (2006), Electrostatic solitary structures observed at Saturn, Geophysical Research Letters, 33, L06103, doi: 10.1029/2005GL024532.

Williams, J. D., L.-J. Chen, W. S. Kurth, D. A. Gurnett, M. K. Dougherty, A. M. Rymer, (2005), Electrostatic solitary structures associated with the November 10, 2003 interplanetary shock at 8.7 AU, Geophysical Research Letters, 32, L17103, doi: 10.1029/2005GL023079.

Willis, I. C., L. J. Woolliscroft, T. F. Averkamp, D. A. Gurnett, R. A. Johnson, D. L. Kirchner, W. S. Kurth, W. Robison, (1995), The implementation of data compression in the Cassini RPWS dedicated data compression processor, In Proceedings, Data Compression Conference (DCC), Space and Earth Science Data Compression Workshop, Snowbird, UT, March 28–30, 1995, doi: 10.1109/DCC.1995.515601.

Wilson, R., F. Bagenal, A. Persoon, (2017), Survey of thermal plasma ions in Saturn's magnetosphere utilizing a forward model, Journal of Geophysical Research, 122, 7256–7278, doi: 10.1002/2017JA024117.

Wilson, R. J., R. L. Tokar, W. S. Kurth, A. M. Persoon, (2010), Properties of the thermal ion plasma near Rhea as measured by the Cassini Plasma Spectrometer, Journal of Geophysical Research, A05201, doi: 10.1029/2009JA014679.

Wilson, G. R. and J. H. Waite Jr., (1989), Kinetic modeling of the Saturn ring-ionosphere plasma environment, Journal of Geophysical Research, 94, 17287–17298.

Woodfield, E. E., R. B. Horne, S. A. Glauert, J. D. Menietti, Y. Y. Shprits, W. S. Kurth, (2018), Formation of electron radiation belts at Saturn by Z-mode wave acceleration, Nature Communications, 9, article 5062, doi: 10.1038/s41467-018-07549-4.

Woolliscroft, L. J. C., W. M. Farrell, H. St. C. Alleyne, D. A. Gurnett, D. L. Kirchner, W. S. Kurth, J. A. Thompson, (1993), Cassini radio and plasma wave investigation: Data compression and scientific application, Journal of the British Interplanetary Society, 46, 115.

Xin, L., D. A. Gurnett, O. Santolik, W. S. Kurth G. B. Hospodarsky, (2006), Whistler-mode auroral hiss emissions observed near Saturn's B ring, Journal of Geophysical Research, 111, A06214, doi: 10.1029/2005JA011432.

Xin, L., (2005), A study of whistler-mode resonance-cone emissions, Ph.D. Thesis, University of Iowa, Iowa City, Iowa.

Yair, Y., G. Fischer, F. Simoes, N. Renno, P. Zarka, (2008), Updated review of planetary atmospheric electricity, Space Science Reviews, 137, 29–49, doi: 10.1007/s11214-008-9349-9.

Yamauchi, M. and J.-E. Wahlund, (2007), Role of the ionosphere for the atmospheric evolution of planets, Astrobiology, 7, 783–800, doi: 10.1089/ast.2007.0140.

Yao, Z. H., A. Radioti, D. Grodent, L. C. Ray, B. Palmaerts, N. Sergis, K. Dialynas, A. C. Coates, C. S. Arridge, R. Roussos, S. V. Badman, S.-Y. Ye, J.-C. Gerard, P. A. Delamere, R. L. Guo, Z. Y. Pu, J. H. Waite, N. Krupp, D. G. Mitchell, M. K. Dougherty, (2018), Recurrent magnetic

dipolarization at Saturn: Revealed by Cassini, Journal of Geophysical Research, 123, 8502–8517, doi: 10.1029/2018JA025837.

Yaroshenko, V. V., S. Ratynskaia, J. Olson, N. Brenning, J.-E. Wahlund, M. Morooka, W. S. Kurth, D. A. Gurnett, G. E. Morfill, (2009), Characteristics of charged dust inferred from the Cassini RPWS measurements in the vicinity of Enceladus, Planetary and Space Science, 57, 1807–1812, doi: 10.1016/j.pss.2009.03.002.

Yates, J. N., D. J. Southwood, M. K. Dougherty, A. H. Sulaiman, A. Masters, S. W. H. Cowley, M. G. Kivelson, C. H. K. Chen, G. Provan, D. G. Mitchell, G. B. Hospodarsky, N. Achilleos, A. M. Sorba, A. J. Coates, (2016), Saturn's quasi-periodic magnetohydrodynamic waves, Geophysical Research Letters, 43, 11102–11111, doi: 10.1002/2016GL071069.

Ye, S.-Y., W. S. Kurth, G. B. Hospodarsky, A. M. Persoon, D. A. Gurnett, M. Morooka, J.-E. Wahlund, H.-W. Hsu, M. Seiss, R. Srama, (2018a), Cassini RPWS dust observation near Janus and Epimetheus orbits, Journal of Geophysical Research, doi: 10.1002/2017JA025112.

Ye, S.-Y., W. S. Kurth, G. B. Hospodarsky, A. M. Persoon, A. H. Sulaiman, D. A. Gurnett, M. Morooka, J.-E. Wahlund, H.-W. Hsu, Z. Sternovsky, X. Wang, M. Horanyi, M. Seiss, S. Srama, (2018b), Dust observations by the Radio and Plasma Wave Science Instrument during Cassini's Grand Finale, Geophysical Research Letters, 45, 10101–10109, doi: 10.1029/2018GL078059.

Ye, S.-Y., G. Fischer, W. S. Kurth, J. D. Menietti, D. A. Gurnett, (2018c), An SLS5 longitude system based on the rotational modulation of Saturn radio emissions, Geophysical Research Letters, 45, 7297–7305, doi: 10.1029/2018GL077976.

Ye, S.-Y., G. Fischer, W. S. Kurth, J. D. Menietti, D. A. Gurnett, (2017), Rotational modulation of Saturn kilometric radiation, narrowband emission, and auroral hiss, In Planetary Radio Emissions VIII, (eds.) G. Fischer, G. Mann, M. Panchenko, P. Zarka, Austrian Academy of Sciences Press, Vienna, Austria, pp. 191–204.

Ye, S.-Y., D. A. Gurnett, W. S. Kurth, (2016a), In-situ measurements of Saturn's dusty rings based on dust impact signals captured by Cassini RPWS, Icarus, 279, 51–61, doi: 10.1016/j.icarus.2016.05.006.

Ye, S.-Y., G. Fischer, W. S. Kurth, J. D. Menietti, D. A. Gurnett, (2016b), Rotational modulation of Saturn's radio emissions after equinox, Journal of Geophysical Research, 121(12), 11714–11728, doi: 10.1002/2016JA023281.

Ye, S.-Y., D. A. Gurnett, W. S. Kurth, T. F. Averkamp, M. Morooka, S. Sakai, J.-E. Wahlund, (2014a), Electron density inside Enceladus plume inferred from plasma oscillations excited by dust impacts, Journal of Geophysical Research, 119, Issue 5, 3373–3380, doi: 10.1002/2014JA019861.

Ye, S.-Y., D. A. Gurnett, W. S. Kurth, T. F. Averkamp, S. Kempf, H.-W. Hsu, R. Srama, E. Gruen, (2014b), Properties of dust particles near Saturn inferred from voltage pulses induced by dust impacts on Cassini spacecraft, Journal of Geophysical Research, 119, 6294–6312, doi: 10.1002/2014JA020024.

Ye, S.-Y., D. A. Gurnett, J. D. Menietti, W. S. Kurth, G. Fischer, (2012), Cassini observation of Jovian anomalous continuum radiation, Journal of Geophysical Research, 117, A04211, doi: 10.1029/2011JA017135.

Ye, S.-Y., G. Fischer, J. D. Menietti, Z. Wang, D. A. Gurnett, W. S. Kurth, (2011), An overview of Saturn narrowband radio emissions observed by Cassini RPWS (invited), In Planetary Radio Emissions VII, (eds.) H. O. Rucker, W. S. Kurth, P. Louarn, G. Fischer, Austrian Academy of Sciences, Vienna, Austria, pp. 99–114.

Ye, S.-Y., J. D. Menietti, G. Fischer, Z. Wang, B. Cecconi, D. A. Gurnett, W. S. Kurth, (2010a), Z-mode waves as the source of Saturn narrowband radio emissions, Journal of Geophysical Research, 115, A08228, doi: 10.1029/2009JA015167.

Ye, S.-Y., D. A. Gurnett, J. B. Groene, Z. Wang, W. S. Kurth, (2010b), Dual periodicities in the rotational modulation of Saturn narrowband emissions, Journal of Geophysical Research, 115, A12258, doi: 10.1029/2010JA015780.

Ye, S.-Y., D. A. Gurnett, G. Fischer, B. Cecconi, J. D. Menietti, W. S. Kurth, Z. Wang, G. B. Hospodarsky, P. Zarka, A. Lecacheux, (2009), Source locations of narrowband radio emissions detected at Saturn, Journal of Geophysical Research, 114, A06219, doi: 10.1029/2008JA013855.

Zaitsev, V. V., V. E. Shaposhnikov, M. L. Khodachenko, H. O. Rucker, M. Panchenko, (2010), Acceleration of electrons in Titan's ionosphere, Journal of Geophysical Research, 115, A03212, doi: 10.1029/2008JA013958.

Zakharenko, V., C. Mylostna, A. Konovalenko, P. Zarka, G. Fischer, J.-M. Griessmeier, G. Litvinenko, H. Rucker, M. Sidorchuk, B. Ryabov, D. Vavriv, V. Ryabov, B. Cecconi, A. Coffre, L. Denis, C. Fabrice, L. Pallier, J. Schneider, R. Kozhyn, V. Vinogradov, D. Mukha, R. Weber, V. Shevchenko, V. Nikolaenko, (2012), Ground-based and spacecraft observations of lightning activity on Saturn, Planetary and Space Science, 61, Issue 1, 53-59, doi: 10.1016/j.pss.2011.07.021.

Zarka, P., W. M. Farrell, G. Fischer, A. A. Konovalenko, (2008), Ground-based and space-based radio observations of planetary lightning, Space Science Reviews, 137, 257–269, doi: 10.1007/s11214-008-9366-8.

Zarka, P., L. Lamy, B. Cecconi, R. Prange, H. Rucker, (2007), Modulation of Saturn's radio clock by solar wind speed, Nature, 450, 265–267, doi: 10.1038/nature06237.

Zarka, P., B. Cecconi, L. Denis, W. M. Farrell, G. Fischer, G. B. Hospodarsky, M. L. Kaiser, W. S. Kurth, (2006), Physical properties and detection of Saturn's lightning radio bursts, In Planetary Radio Emissions VI, (eds.) H. O. Rucker, W. S. Kurth, G. Mann, Austrian Academy of Sciences Press, Vienna, Austria, pp. 111–122.

Zarka, P. and W. S. Kurth, (2005), Radio wave emission from the outer planets before Cassini, Space Science Reviews, 116, 371–397, doi: 10.1007/s11214-005-1962-2.

Zarka, P., B. Cecconi, W. S. Kurth, (2004a), Jupiter's low-frequency radio spectrum from Cassini/Radio and Plasma Wave (RPWS) absolute flux density measurements, Journal of Geophysical Research, 109, A09S15, doi: 10.1029/2003JA010260.

Zarka, P., W. M. Farrell, M. L. Kaiser, E. Blanc, W. S. Kurth, (2004b), Study of solar system planetary lightning with LOFAR, Planetary and Space Science, 52, 1435–1447, doi: 10.1016/j.pss.2004.09.011.

Zarka, P., (2004), Radio and plasma waves at the outer planets, Advances in Space Research, 33, 2045–2060, doi: 10.1016/j.asr.2003.07.055.

Zarka, P., J. Queinnec, F. J. Crary, (2001a), Low-frequency limit of Jovian radio emissions and implications on source locations and Io plasma wake, Planetary and Space Science, 49, 1137–1149, doi: 10.1016/S0032-0633(01)00021-6.

Zarka, P., R. A. Treumann, B. P. Ryabov, V. B. Ryabov, (2001b), Magnetically-driven planetary radio emissions and applications to extrasolar planets, Astrophysics and Space Science, 277, 293–300, doi: 10.1023/A:1012221527425.

Zarka, P., (2000), Radio emissions from the planets and their moons, In Radio Astronomy at Long Wavelengths, (eds.) R. G. Stone, K. W. Weiler, M. L. Goldstein, J.-L. Bougeret, American Geophysical Union Geophysical Monograph Series, vol. 119, pp. 167–178, doi: 10.1029/GM119p0167.

Zarka, P. and B. M. Pedersen, (1983), Statistical study of Saturn electrostatic discharges, Journal of Geophysical Research, 88, 9007–9018.

Zieger, B. and K. C. Hansen, (2008), Statistical validation of a solar wind propagation model from 1 to 10 AU, Journal of Geophysical Research, 113, A8, doi: 10.1029/2008JA013046.

Zlotnik, E. Ya., V. E. Shaposhnikov, V. V. Zaitsev, (2016), Interpretation of the zebra pattern in the Jovian kilometric radiation, Journal of Geophysical Research, 121, 5307–5318, doi: 10.1002/2016JA022655.

Microwave Remote Sensing Instruments

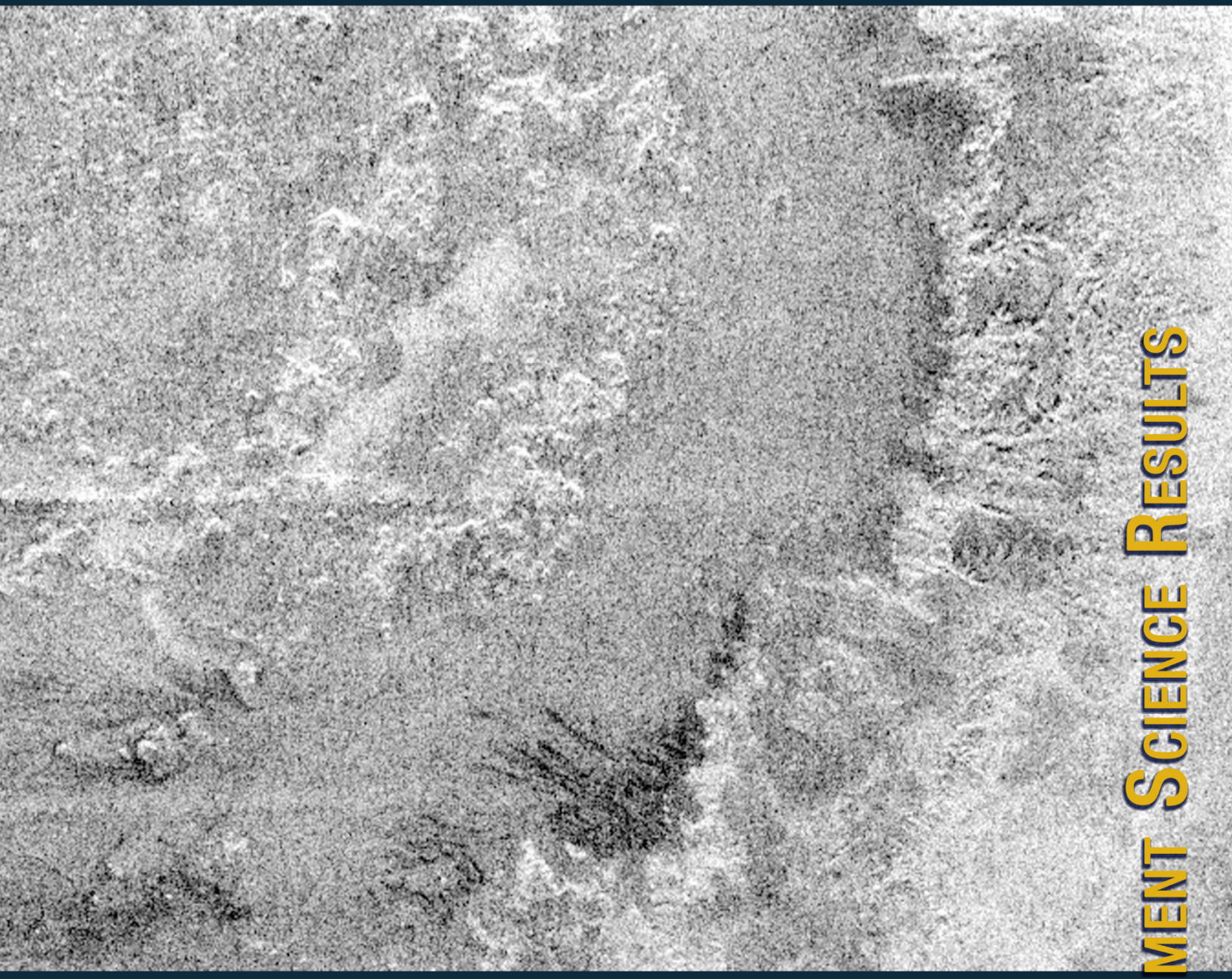

– Titan Radar Mapper (RADAR)

– Radio Science Subsystem (RSS)

INSTRUMENT SCIENCE RESULTS

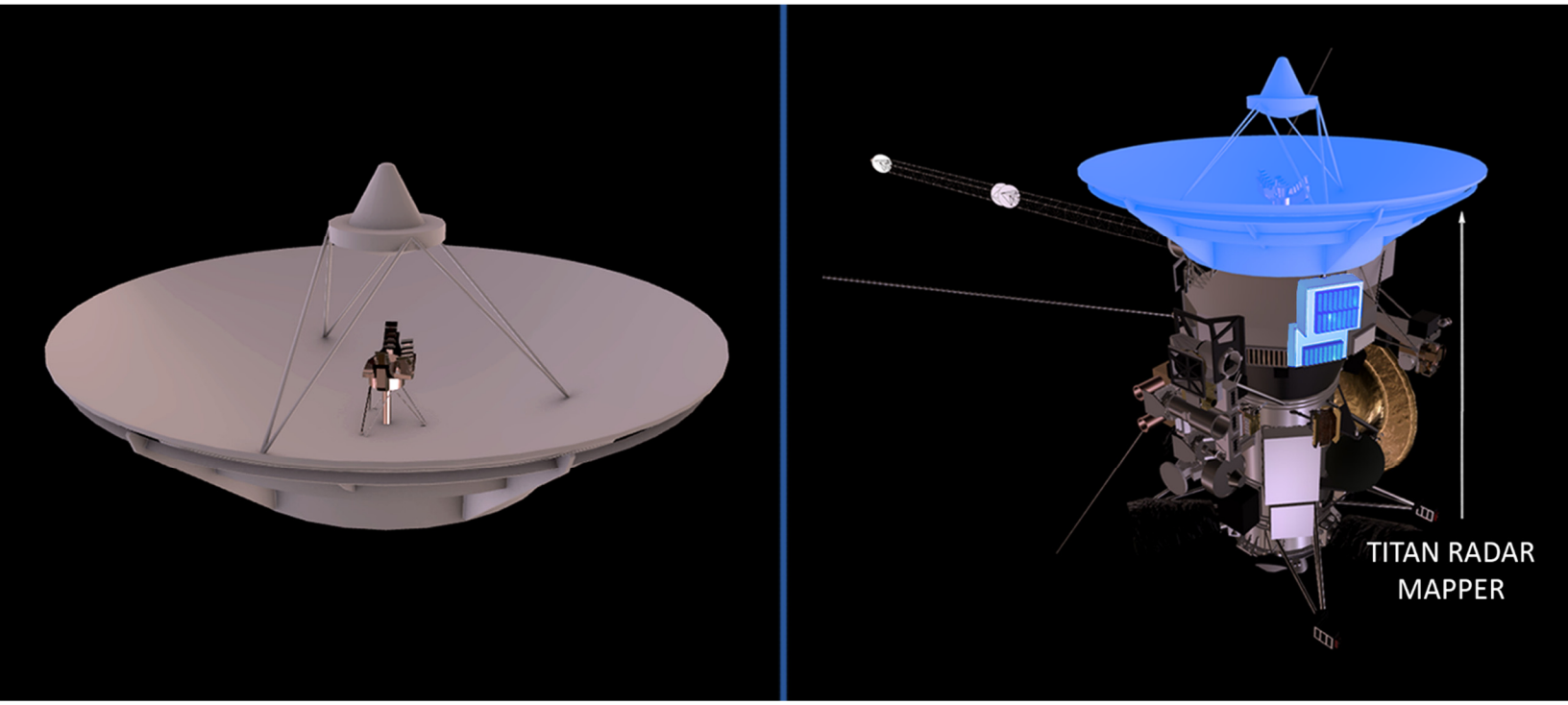

TITAN RADAR MAPPER

The Titan Radar Mapper (RADAR) Instrument investigated Saturn, its rings and moons, but it was primarily built to study Saturn's moon Titan, which has a thick atmosphere that hides its surface. The **science objectives** of RADAR were to perform Synthetic Aperture Radar (SAR) imaging, altimetry, scatterometry, and radiometry of Titan's surface to determine the distribution of lakes and seas, investigate the geologic features and topography of the solid surface of Titan, and acquire data on non-Titan targets (Saturn, rings, icy satellites). RADAR bounced radio waves at microwave frequencies off Titan's surface, and created images of the surface by recording slight differences in the reflected signal's arrival time and wavelength back at the spacecraft. RADAR detected how smooth or rough surfaces are, making it useful for studying Titan's methane seas.

The RADAR used the spacecraft's high-gain antenna (HGA) and its associated five-beam Ku-band feed assembly to send radar transmissions (at a wavelength of 2.2 cm, equivalent to a frequency of 13.8 GHz) toward targets and capture reflected radar signals and blackbody radiation. In its altimetry mode, the RADAR could also measure the height profile of terrain beneath the spacecraft.

CONTENTS

Figures

Tables

EXECUTIVE SUMMARY

Throughout the Cassini mission, Titan Radar Mapper (RADAR) obtained Synthetic Aperture Radar (SAR) images, altimetry, scatterometry, and (passive) radiometry of Titan, Saturn, some of the icy satellites, and Saturn's rings. Over the course of the mission, the Radar Science Team planned, commanded, processed, and archived these datasets. Taken together with other Titan-observing Cassini instruments' data, their analysis has produced many scores of discoveries: we have revolutionized our understanding of Titan, which despite its low temperatures has shown its surface to be unexpectedly Earth-like, both in terms of observed features and the geologic processes that formed them. These include mountains, sand dunes, oceans and lakes, rivers, and a complex hydrologic system where the working fluid is primarily methane. Analysis of repeat SAR coverage was a major contributor to the conclusion that there is a subsurface ocean within Titan. Radar observations of Saturn have improved microwave observations by nearly an order of magnitude and revealed deeper structure than was previously thought possible. Icy satellite data have been used to explore hemispheric dichotomies or regional anomalies and, where higher spatial resolution was possible, to examine specific areas of interest—in particular of Enceladus. Microwave scans of Saturn's rings suggest that particles in the A-ring, B-ring, and C-ring may be highly porous, and that the rings may be very young—perhaps less than 150 million years. Both passive and active radar data from Cassini's last orbits of Saturn, still under analysis, promise to provide new information about particle size distribution and its variation across the rings.

Radar observations of Saturn have improved microwave observations by nearly an order of magnitude and revealed deeper structure than was previously thought possible.

To rank the team's discoveries is difficult, both because of their wide variety and because discoveries often involve analyses of more than one instrument's data. After some debate we have developed these top ten major new facts resulting at least in part from radar data. The body of this report explains these in detail.

1. Titan's surface is dynamic and Earthlike, with an active hydrological cycle that includes several large seas, hundreds of lakes, and numerous rivers and channels.

2. Titan's surface is relatively young, perhaps hundreds of millions of years, with few impact craters identified.

3. A band of linear sand dunes, likely made of organic material, stretches across most of Titan's equator.

4. Titan's seas have depths of 100s of meters; the liquid in them is remarkably pure methane-ethane-nitrogen.

5. A large, previously identified feature known as Xanadu is not elevated relative to surrounding terrain as previously suspected. It seems to be younger and rougher than the rest of Titan and it likely has a high content of highly fractured water ice bedrock.

6. Titan is internally differentiated, and has an outer ice shell, a subsurface ocean, a high pressure layer at the base of the ocean, and a deep rocky interior.

7. Liquid is transported from one Titan hemisphere to the other, resulting in more lakes that are currently dry in the south.

8. Cryovolcanism exists or has recently existed on Titan. Several surface features have been identified as likely cryovolcanic vents.

9. By probing its ammonia at depth, radiometric data have revealed deeper structure in Saturn than was previously thought possible.

10. The south pole of Enceladus has the brightest radar backscatter of any planetary surface in the solar system, suggesting a retroreflective near surface, for reasons that remain puzzling but appear to be linked in some way to the presence of the E-ring.

RADAR Instrument Summary

The Titan Radar Mapper (henceforth RADAR[1] [Elachi et al. 2004]) was one of twelve instruments aboard the Cassini spacecraft. It was developed by NASA's Jet Propulsion Laboratory (JPL), the Italian Space Agency (ASI), and the Cassini Radar Science Team, primarily to reveal the surface of Titan but also to explore Saturn, its rings and the icy satellites. Nearly opaque at most visible and near-infrared wavelengths, Titan's atmosphere is transparent at RADAR operating wavelength of 2.17 cm (Ku-band). RADAR had four operating modes: SAR imaging, altimetry, scatterometry, and radiometry. In its SAR mode, used at altitudes under ~4,000 km, RADAR imaged surfaces of Titan and Saturn's icy satellites and rings in various modes, including SAR at incidence angles from 15 to 35 degrees and spatial resolutions varying as low as 350 m, sufficient to identify major structures and to make geologic maps. SAR images characterize the surface roughness at scales near the radar wavelength, to surface slopes at the scale of the radar resolution, and to dielectric properties of the constituent materials. In addition, microwaves can penetrate many wavelengths into some materials on Titan. But for the most part, SAR images are observationally similar to optical images and allow us to identify major structures and geomorphologic units. Altimetry results when the antenna is pointed within a fraction of a beam width (0.35 deg) of nadir resulting in a range resolution of approximately 30 m and spatial resolution depending on altitude. The altimetry data have two broad applications. First, the aggregate of all data define an absolute geoid for Titan and constrain any rotational or tidal bulge. Second, relative topographic profiles from each RADAR

[1] In this report, we distinguish radar, a microwave sensing technique, and RADAR, an instrument aboard the Cassini spacecraft.

pass characterize landforms (e.g., impact craters, mountains), yielding important constraints on geophysical models. Altimetry was obtained over 2% of Titan's surface, in some cases measuring the depth and absorption of liquids.

An amplitude monopulse comparison technique called SARTopo [Stiles et al. 2009] added an additional 5% topographic coverage using SAR data [Corlies et al. 2017]. The SARTopo technique depends on the precise manner in which the location and magnitude of each SAR pixel are affected by variation in surface height between each of the five antenna beams (feeds) [Elachi et al. 2004]. The technique estimates surface heights from observed differences between beams. Cassini's antenna had multiple beams, so that some points on the ground were observed from two different beams. For different beams, the mislocation error due to surface height is the same, but the miscalibration error is different and of opposite sign. Nonzero surface heights, therefore, result in apparent differences in pixel positions between overlapping single beam SAR images. In addition, altimetry was able to obtain depths of several lakes and seas [Mastrogiuseppe et al. 2014]. Scatterometry is obtained by pointing the transmitter off-nadir, but processing the echoes using the real aperture rather than the synthetic aperture. The data indicate the backscatter efficiency at various incidence angles at relatively low resolution (real aperture resolution depends on range to

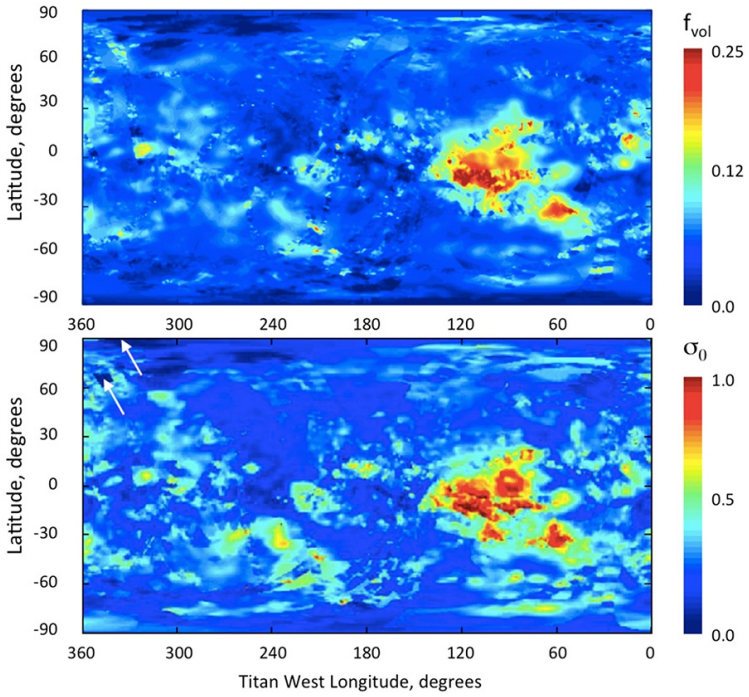

Figure RADAR-1. Predicted and observed maps of scattering from Titan's surface. The upper panel is a map of the volume scattering parameter f_{vol} for a simple surface model composed of a smooth dielectric interface separating free space from an inhomogeneous and isotropically scattering subsurface. The f_{vol} is the probability that a photon entering the surface (as determined by the effective dielectric constant) scatters and escapes from the subsurface before it is absorbed. The map of f_{vol} reconciles the maps of effective dielectric constant and emissivity and predicts the overall magnitude of the scattering. The lower panel is a global mosaic of Titan's normalized radar cross-section from all real aperture data through T71 [Wye 2011], showing the actually observed scattering. The white arrows in the upper left-hand corner indicate two small regions that were not mapped.

surface). Scatterometry coverage is near-global (Figure RADAR-1); it can be used as a basemap for SAR and as a broad characterization of global terrains. As an independent constraint on surface roughness, scatterometry data are an important complement to radiometry data in order to constrain surface composition. Used as a passive microwave radiometer, RADAR collected near-global measurements (Figure RADAR-2) of Ku-band brightness temperature with an accuracy of 1 K [Janssen et al. 2016]. Radiometry data produce polarized brightness temperatures of the observed scene, obtained from the antenna temperature measurements. The microwave brightness temperature of a solid surface depends on many properties besides physical temperature; e.g., emission angle, polarization, dielectric constant, porosity, surface, and subsurface roughness, etc.

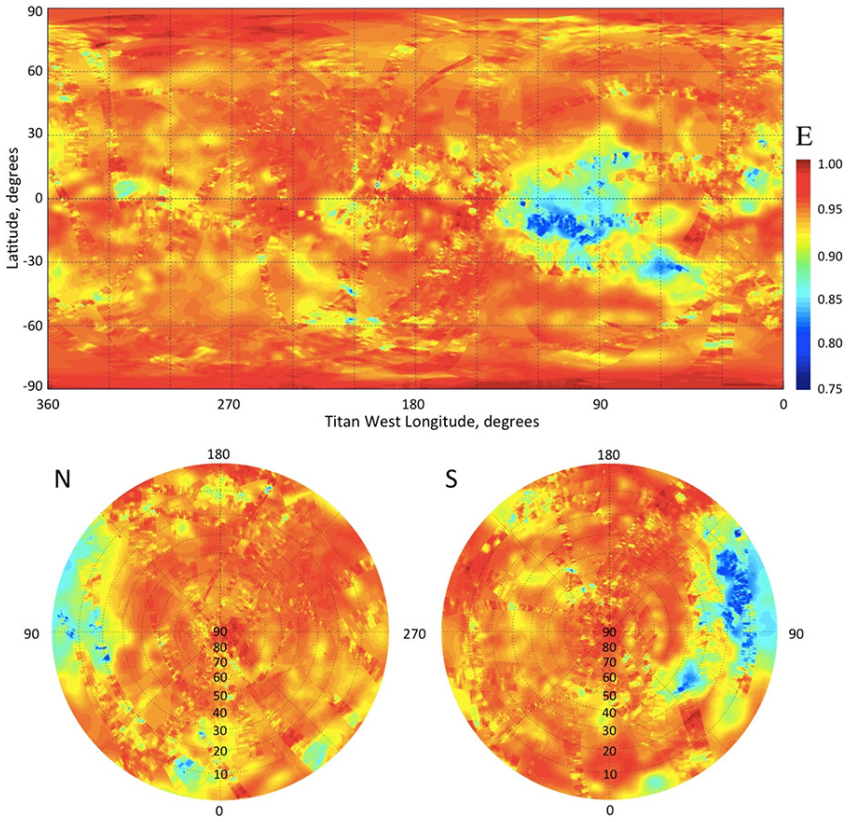

Figure RADAR-2. Global mosaic of emissivity of Titan at the 2 cm wavelength of the Cassini RADAR. This is the final result of the brightness temperature mapping of Titan incorporating all radiometric data obtained from Titan passes, a nearly 10-year span. The brightness temperature was measured as a function of position, polarization and time over a wide range of geometries and ranges, and calibrated to about 1% absolute accuracy using Huygens probe and Composite Infrared Spectrometer (CIRS) temperature measurements as described in Janssen et al. [2016]. The polarization data were used to construct a global mosaic of effective dielectric constant, enabling the conversion of all measured brightness temperatures to their equivalent values at normal incidence. The data were then folded into a massive least-squares solution for the seasonally varying brightness temperature distribution of Titan over the time scale of the observations. Comparison with surface temperature measurements obtained in the infrared (IR) using Kirchhoff's law then enabled the construction of the emissivity map shown. Note that Xanadu, the equatorial region centered on 100 W longitude, is extremely cold and non-emissive, characteristic of a high content of highly fractured water ice bedrock.

KEY OBJECTIVES FOR RADAR INSTRUMENT

The key RADAR science objectives are listed below, and discussed in further detail in the section entitled RADAR Science Results.

Titan Science

Surface units

TN1a: Determine the types, composition, distribution, and ages of surface units and materials, most notably lakes (i.e., filled vs. dry & depth; liquid versus solid & composition; polar versus other latitudes and lake basin origin).

CSM: T_AO4: Titan surface characteristics and internal structure—determine the physical state, topography, and composition of the surface; infer the internal structure of the satellite.

TC1a: Determine seasonal changes in the methane-hydrocarbon hydrological cycle—of lakes, clouds, aerosols, and their seasonal transport.

Internal structure

TN1b: Determine internal and crustal structure—liquid mantle, crustal mass distribution, rotational state of the surface with time, intrinsic and/or internal induced magnetic field.

TN2b: Determine icy shell topography and viscosity.

TN2c: Determine the surface temperature distribution, cloud distribution, and tropospheric winds.

Saturn Science

SN1b: Observe the aftermath of the 2010–2011 storm. Study the life cycles of Saturn's newly discovered atmospheric waves, south polar hurricane, and rediscovered north polar hexagon.

Ring Science

RN1c (R_AO2): Determine structural and compositional variations at high resolution across selected ring features of greatest interest, using remote and in situ observations.

Icy Satellite Science

IN1a: Determine the presence of an ocean at Enceladus as inferred from induced magnetic field and plume composition, search for possible anomalies in the internal structure of Enceladus as

associated with plume sources, and constrain the mechanisms driving the endogenic activity by in situ observations and remote sensing.

IN1c: Determine whether Dione exhibits evidence for low-level activity, now or in recent geological time.

I_AO1: Icy satellite geology and history—determine the general characteristics and geological histories of the satellites.

RADAR Science Assessment

Table RADAR-1 contains an assessment of RADAR science based on the objectives in the original Announcement of Opportunity (AO) and the Cassini Traceability Matrix (TM) developed for the Equinox and Solstice missions.

Table RADAR-1. Matrix of RADAR science objectives. Green color indicates that RADAR data with sufficient quality were obtained during the Cassini mission to contribute to a given science objective.

RADAR Science Objectives	AO and TM Science Objectives	RADAR Science Assessment	Comments
Titan Science			
Surface units	TN1a, CSM:T_AO4, TC1a		
Internal structure	TN1b, TN2b, TN2c		
Saturn Science	SN1b		
Icy Satellite Science			
Enceladus plumes	IN1a		
Dione	IN1c		Data acquired, not yet analyzed
Satellite geology and history	I_AO1		
Ring Science	RN1c (R_AO2)		

RADAR Science Results

Titan Science

In its 13-year presence at Saturn, Cassini made a total of 127 passes by Titan, some as close as 950 km. Forty-eight of these were used by RADAR, with one lost in downlink—for a detailed description of results from individual flybys, see Lorenz et al. [2018]. SAR coverage was limited by both Cassini's orbital path, which used Titan for gravity assists, and by intense competition among instruments for observation time—resulting in a seemingly random set of strips 100–200 km wide (Figure RADAR-3). However, the swaths were well distributed in latitude and longitude, allowing for an emerging global picture of the surface. Aerial SAR coverage at the end of the mission was

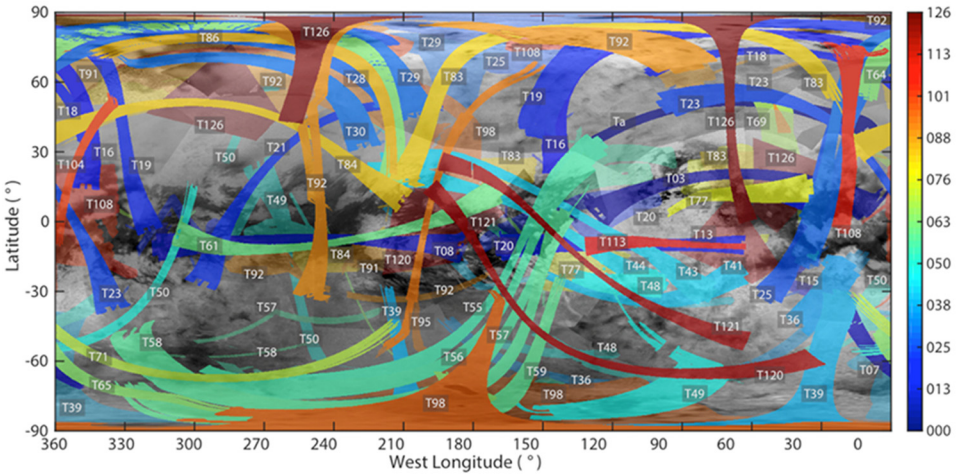

Figure RADAR-3. Combined Titan SAR coverage from the entire Cassini mission. Swaths are shown over an ISS basemap.

46% using nominal SAR mode and 74% including coarser-resolution (>1.5 km) HiSAR. Repeat images were obtained over 14% of the surface, and 1.5% was covered four or more times [Lorenz et al. 2018]. Real-aperture scatterometry and passive radiometry data exist over the entire surface, at varying resolutions.

Together with near-infrared and mid-infrared images taken by other Cassini instruments—Visual and Infrared Mapping Spectrometer (VIMS) [Brown et al. 2004] and the Imaging Science Subsystem (ISS) [Porco et al. 2004]—RADAR has given us an opportunity to discover a new world that is both Earth-like and unearthly. We find familiar geomorphology in its mountains, dunes, rivers, and seas, but note that these features are composed of unfamiliar materials. In this section, we review RADAR's contributions to geology, hydrology, and surface-atmospheric interaction in an attempt to summarize our knowledge of Titan at the end of the Cassini mission.

Interior

Static and time-varying gravity field measurements [Iess et al. 2010, 2012], rotational dynamics measurements [Stiles et al. 2008, 2010; Lorenz et al. 2008a; Meriggiola et al. 2016], and shape models [Zebker et al. 2009a; Mitri et al. 2014; Corlies et al. 2017] have been used to infer the interior structure of Titan. Magnetic field measurements have shown that an intrinsic magnetic field is not present on Titan [Wei et al. 2010]. The determination of the rotational dynamics from Cassini RADAR SAR images has been key to constraining the interior structure of Titan. As described in the previous section, Cassini RADAR SAR coverage of Titan is dependent on orbit dynamics and competition for observation time. As a result, SAR swaths appear somewhat randomly distributed with coincidental overlaps (with only a few exceptions). Where overlap occurs, and assuming that the same surface features appear in both images, it is possible to determine how quickly Titan has rotated between observations and thus estimate Titan's pole location and spin rate [Stiles et al. 2008, 2010], analogous to previous work using Magellan SAR imagery to estimate the spin model of Venus [Davies et al. 1992]. First, a set of recognizable landmarks observed in two different SAR

images are obtained at different times located in a Titan centered inertial, non-rotating (J2000) reference frame. Pixels chosen in each SAR image corresponding as closely as possible to the same point on the landmark are aligned, using several techniques to minimize landmark mismatches. The spin state parameters are estimated by minimizing the misregistration error—that is, the apparent movement in Titan body-fixed coordinates of the landmarks between observation times. Feature mapping is much more robust for radar than for passive optimal imagery, because radar geolocation is independent of spacecraft pointing knowledge except that the general direction (within 10 degrees or so) must be known to exclude mirror ambiguities. Accurate radar pixel locations in inertial space depend only on the accuracy of the measurement of delay, Doppler shift, spacecraft velocity and position, and presumed target body topography. Nearby SARTopo [Stiles et al. 2009] measurements of topography help determine more precisely variations in feature locations in inertial space. Using similar methodology and a more extensive set of observations, Meriggiola et al. [2016] also provided a rotational model of Titan estimating the spin pole location, the spin rate, the precession, and the nutation. Further, these authors show that the pole location is compatible with the Cassini State 1 (a dynamical equilibrium wherein the spin axis, the orbit norma,l and the normal to the invariable plane are coplanar).

Stiles et al. [2008] and Meriggiola et al. [2016] have provided an estimate of Titan's obliquity (0.31°). The obliquity together with the quadrupole moment of the gravity field (J2 and C22) measurements [Iess et al. 2010, 2012] constrain the moment of inertia of Titan. These results were used by Bills and Nimmo [2011] to estimate the radial mass distribution of Titan and, when combined with the low-degree gravity field derived from Cassini spacecraft Doppler tracking data [Iess et al. 2010], suggest that Titan's outer shell is mechanically decoupled from the deeper interior. Bills and Nimmo [2011] and Meriggiola et al. [2016] find that the estimated obliquity is compatible with a deep interior decoupled from the outer ice shell by a global subsurface ocean. Note that Lorenz et al. [2008a] interpreted the initial indication in Stiles et al. [2008] of nonsynchronous rotation as indicating a subsurface ocean, drawing on predictions of atmospheric angular momentum exchange with a decoupled shell by Tokano and Neubauer [2005]. However, the spin state determination has significant degeneracy between nonsynchronous rotation and precession of the spin pole, and subsequent observations seem to favor synchronous rotation. Thus, the conclusion of Lorenz et al. [2008a] of an internal global ocean indicated by RADAR spin measurements remains correct, but for perhaps the wrong reasons. The presence of a subsurface ocean inferred from the rotational dynamics of Titan is consistent with the large tidal response of Titan (tidal Love number $k_2 = 0.589 \pm 0.150$) [Iess et al. 2012; Mitri et al. 2014]. In agreement with this scenario, the Permittivity, Wave and Altimetry (PWA) instrument on board Huygens' probe measured a Schumann-like resonance, also suggesting the presence of a subsurface ocean [Bèghin et al. 2012]. In summary, the gravity, topography and rotational dynamics measurements in combination with thermal-evolution models indicate that Titan is internally differentiated (Figure RADAR-4), and has an outer ice shell, a subsurface ocean, a high pressure layer at the base of the ocean, and a deep rocky or rock-ice mix interior [Hemingway et al. 2013; Mitri et al. 2014; Tobie et al. 2014].

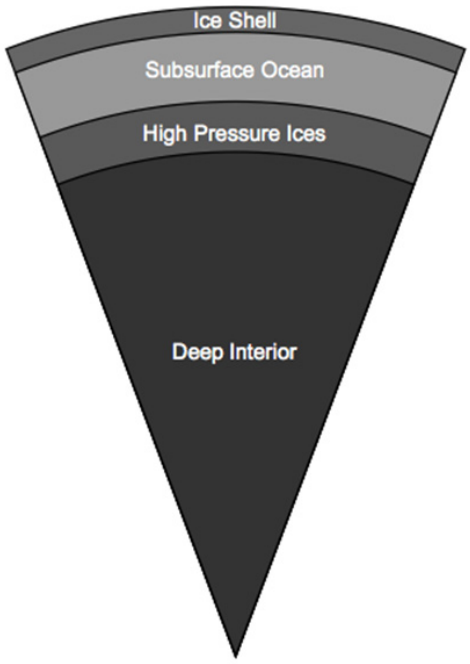

Figure RADAR-4. Possible present-day structure of Titan's interior showing that Titan is internally differentiated with a deep rocky or rock-ice mix core.

Global shape

RADAR observations using both the altimetry and SARTopo modes reveal Titan's global shape and yield insights to its interior structure. The roughly 60 satellite-derived elevation surface traces—Figure RADAR-5 [Zebker et al. 2009a]—show that Titan's polar radius is less than, and the equatorial radii are greater than, predicted by its gravity field. Best-fitting solutions are shown in Table RADAR-2.

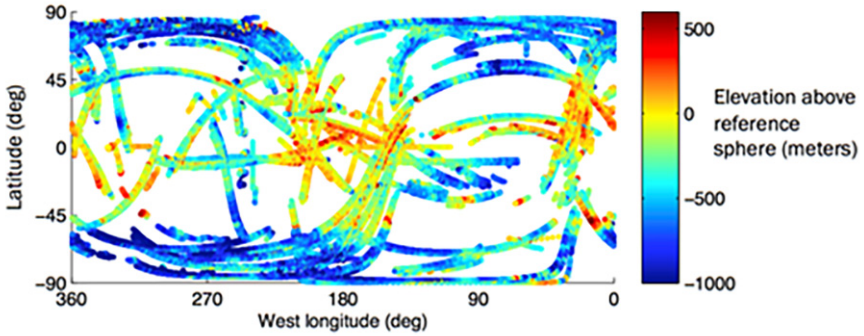

Figure RADAR-5. Cassini measurements of Titan surface height above a reference sphere of 2575 km radius. As expected, the shape is dominantly triaxial ellipsoidal, with topographic lows near the poles and topographic highs at the prime-meridians and anti-meridians. However, the polar flattening is greater than expected for a hydrostatic body, meaning the equatorial topography stands higher than expected and the polar depressions are lower than expected, suggesting that the depth to the subsurface ocean is smaller at the poles than at the equator.

Table RADAR-2. Titan gravity and shape triaxial ellipsoids (m).

	Gravity	Elevations	Difference
a axis	2574875 ± 7.3	2575124 ± 26	−249
b axis	2574716 ± 7.4	2574746 ± 45	−30
c axis	2574660 ± 4.5	2574414 ± 28	246
a translation	0.8 ± 5.6	69.8 ± 6.2	
b translation	0.1 ± 5.6	68.3 ± 8.0	
c translation	1.7 ± 3.9	45.8 ± 6.4	
Mean eq. rad.	2574795	2574761	−34
Hydrostatic ratio (a-c)/(b-c)	3.83	2.14	

The hydrostatic ratio (a-c)/(b-c), which is exactly 4 for a spin-locked satellite in hydrostatic equilibrium, for Titan's figure is observed to be only 2.14 [Zebker et al. 2009a; Corlies et al. 2017]. The hydrostatic ratio obtained from the third-degree gravity observations is 3.83—that is, the gravity field reflects approximate hydrostatic equilibrium. While the gravity field is consistent with a hydrostatically relaxed body, Titan's figure is not. If both of these data constraints pertain, Titan's interior does not conform to a set of spherically symmetric shells, as these data imply that the average satellite density at the equator is less than at the poles. If Titan has a vast interior ocean of liquid water, then some ice layers (less dense than liquid water) are thinner at the poles than the equator. A simple model satisfying both sets of data and assuming isostatic compensation (Figure RADAR-6) could be the result of uneven heat dissipation in Titan's interior, such as may result from tidal interaction with Saturn or its other moons.

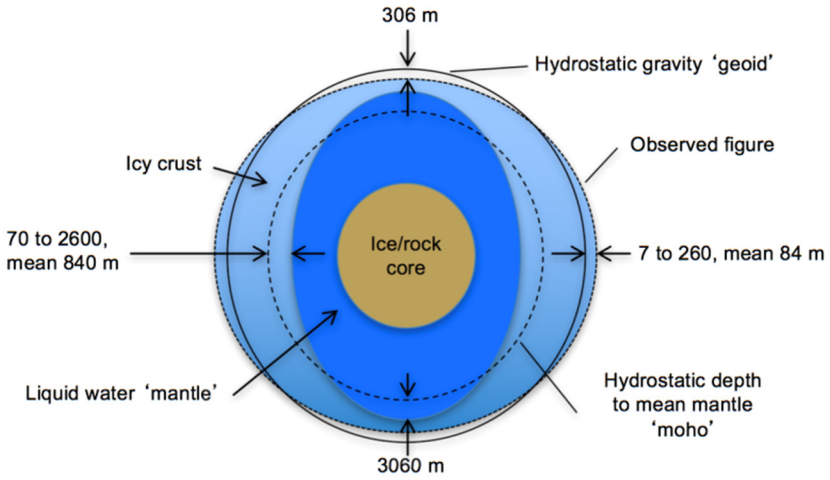

Figure RADAR-6. Model consistent with Cassini gravity and figure measurements, assuming isostatic compensation. The thinner ice shell (exaggerated for visibility in the figure) at the poles could result from uneven heat dissipation within Titan from tidal interactions, and the relatively shallower geoid at the poles is one explanation for the preponderance of lakes at the most northern and southern latitudes. The shallower geoid allows mobile liquids to lie closer to the surface.

Another simple model explaining the overly oblate topographic figure assumes that there is greater precipitation of hydrocarbon snow or loosely packed hydrocarbon particulates at the equator than at the poles, perhaps with a net equatorward transport from the poles, which would also be consistent with the data. This could account for increased distance from the surface to the planet center at the equator if sufficient material were so transported. We note that this is consistent with the observation of 100 m tall dune structures near Titan's equator (see the section entitled Dunes), so that poorly consolidated material may indeed collect there to a greater extent. Several hundred meters of deposition at the equator would match the mean equatorial radii of both models, but precipitation would have to preferentially occur in the sub- and anti-Saturnian directions, which seems unlikely.

Further comparisons of the gravity and shape observations constrain the depth of any outer ice shell enclosing a global subsurface ocean [Zebker and Wong 2016]. While the exact value varies depending on how the spherical expansion is constrained, the observed gravity to topography ratio is 0.070 for the third order terms and 0.042 for fourth order [Zebker and Wong 2016]. These imply ice shell thicknesses of 327 and 187 km, respectively, a factor of ≥2 more than the 100 km expected from thermal models [Sohl et al. 2003; Nimmo and Bills 2010]. The Zebker and Wong solution yields a tidal Love number h_{2t} of about 0.5, and a basal heat flow of 2.5 mW/m^2. This would suggest that heat from Titan's core is lower than often assumed, hence the amount of radiogenic material in the core is likely less as well. These data also constrain the depth of Titan's mantle and density of its core, placing added restrictions on its composition and evolution. Supposing that Titan has an undifferentiated ice/rock core beneath the ocean, and that the moment of inertia is most likely in the range 0.33–0.34 [Iess et al. 2010], then a 200 km crust estimate from above and Titan's well-known mean density of 1.88 g cm^{-3} implies an ocean depth and core density ranging from 308 km and 2.74 g cm^{-3} (MOI = 0.33), to 226 km and 2.55 g cm^{-3} (MOI = 0.34).

The Cassini-Huygens mission has revealed the surface of Titan in unprecedented detail, enabling us to discern different geomorphological units on the surface … .

Composition and surface and subsurface properties

The Cassini-Huygens mission has revealed the surface of Titan in unprecedented detail, enabling us to discern different geomorphological units on the surface (see the section entitled RADAR Science Results), constrain the relative times of emplacement of these units, and place constraints on composition. Titan has an ice shell (Figure RADAR-4), but water ice signatures are not easily detected due to atmospheric scattering and absorption that hamper the observations and the presence of complex organic molecules on the surface. The extended, dense, and hazy N_2-CH_4 dominated atmosphere shields the surface from direct optical observations, except at certain wavelengths where the methane absorption is weak. These methane atmospheric windows [McCord et al. 2006] are exploited by the Cassini VIMS to obtain compositional information of the top few microns of the surface, as discussed in the section entitled Surface. Composition from

VIMS and RADAR, while RADAR can probe the surface and subsurface scattering properties, and hence place additional constraints on composition.

SURFACE AND SUBSURFACE SCATTERING PROPERTIES

Compared to the surface of the Moon or Earth, the off-nadir radar response from most of Titan's surface is quite strong at Ku-band. This indicates that more complex processes than simple surface scattering, such as a significant volume scattering component, have to be considered [Elachi et al. 2005; Wye et al. 2007; Paganelli et al. 2007; Janssen et al. 2016]. Indeed, given the low Titan surface temperatures and the low loss tangent of analogs of materials relevant to Titan's surface, signals from Cassini RADARs Ku-band instrument should penetrate the surface down to a depth ranging from a few decimeters for an organic and compacted near-surface, to several meters for a pure water ice near-surface [Paillou et al. 2008a], and thus have multiple opportunities to be scattered. The RADAR observations of Titan are consistent with subsurface volume scattering processes, in addition to pure surface scattering. Analysis of Cassini scatterometer and radiometer measurements obtained simultaneously (see Figure RADAR-7) are best fit using models where volume scattering, enabled by the low material losses, is enhanced by coherent backscatter processes [Zebker et al. 2008; Janssen et al. 2011].

Janssen et al. [2016] further advance that a regionally enhanced degree of volume scattering is indicative of a higher abundance of water ice in the near-surface. This is because water ice is more transparent to microwaves than common organic materials, allowing for more opportunities for scattering. This would be consistent with about 10% of Titan's near-surface being water ice-rich while the composition of the remaining terrains is dominated by more absorbing organic materials, likely byproducts of the intense atmospheric photochemistry [Lorenz et al. 2008b; Hörst 2017]. The regions that contain a high degree of volume scattering include mountainous terrains, impact craters, fluvial and fan-like features, all of which possibly correspond to highly fractured or unconsolidated sedimentary materials derived from erosion. Many of these materials could also have originated from cryovolcanism, in which the radar signature could be explained by a strong volume scattering effect in a thick water-ammonia ice layer using a two-layer scattering model [Paillou et al. 2006]. Radar-bright sinuous channels in the southwest of Xanadu (see section entitled Xanadu), showing very large radar cross-sections, are also consistent with the presence of icy, low-loss, rounded scatterers, acting as efficient natural retro-reflectors [Le Gall et al. 2010].

Weaker radar reflectors such as Titan's dunes are most likely organic in nature (as also supported by VIMS—for example, Barnes et al. [2008], Soderblom et al. [2009], and Clark et al. [2010]). However, we note that these features exhibit somewhat high backscatter at large incidence angles compared to Earth analogs, which suggests even aeolian sediments may contain centimeter-scale gravels producing a significant volume scattering component [Paillou et al. 2014]. Features interpreted as mega-yardangs were observed on Titan, and they also exhibit a much brighter radar signature than their terrestrial analogs, indicating that additional scattering processes, such as volume scattering, occur in those materials as well [Paillou et al. 2016].

Lastly, and of particular interest, is the case of Titan's methane-dominated lakes, where radar waves can penetrate down to several thousand wavelengths (at least 150 m) and be subsequently backscattered by the bottoms of a lake or seabed [Mastrogiuseppe et al. 2014]. These results are consistent with recent laboratory investigations of the electrical properties of liquid hydrocarbons [Mitchell et al. 2015].

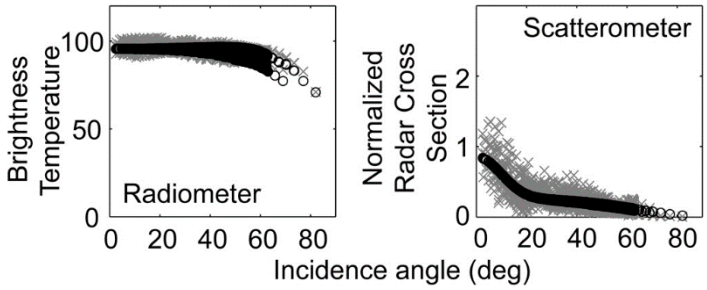

Figure RADAR-7. Angular dependence of radiometer (left) and scatterometer (right) measurements of a portion of Titan's surface. Grey X's are observations, while black circles are modeled values assuming both surface and volume scattering terms. Both sets of curves fall off slowly with incidence angle, indicative of significant volume scattering.

Surface composition from VIMS and RADAR

A combination of RADAR and near-infrared multispectral imaging data—VIMS—is a powerful way to distinguish and categorize geomorphological features into units with distinct chemical compositions (that remain to be identified). Spectroscopic observations of Titan's surface are severely hindered by the presence of an optically thick, scattering and absorbing atmosphere, allowing direct investigation of the surface within only a few spectral windows in the near-infrared. Based on the 1.29/1.08 μm, 2.03/1.27μm, and 1.59/1.27 μm band ratios measured by VIMS at low to moderate latitudes, three main spectral units were initially distinguished on the surface of Titan: 1) bright material mainly distributed in the topographically high and mid-latitude areas; 2) blue material adjacent to the bright-to-dark boundaries; and 3) brown material that correlates with radar-dark dune fields [Barnes et al. 2007; Soderblom et al. 2007; Jaumann et al. 2008].

Even though these spectral units are distinct, their actual compositions remain elusive. A number of chemical species was proposed to exist on the surface of Titan, but only a few absorptions were unambiguously detected from remote-sensing observations carried out by VIMS during Cassini flybys. A methane-ethane dominated composition seems to be present in the polar lakes and seas of Titan—for example, Brown et al. [2008], and Lunine and Lorenz [2009]. IR spectroscopy, microwave radiometry and scatterometry are sensitive to the physical structure of the surface to a different extent and at different scales. IR spectroscopy measurements are used to determine surface composition, but they are also affected, down to depths of micrometers, by the physical properties of the surface material like roughness, photometric geometry, and porosity.

Correlations between near-infrared and microwave data of Titan's surface are useful to gather a broader understanding of surface properties. These were quantified at coarse spatial resolution

by Tosi et al. [2010a], who applied a multivariate statistical analysis to an aggregated dataset made up of infrared spectra acquired by VIMS at spatial resolution of tens of km together with scatterometry and radiometry data measured by RADAR. This technique allowed for the identification of regional surface units at equatorial to mid-latitudes. Some of these units matched both the major dark and bright features seen in the ISS mosaic of Titan [Porco et al. 2005; Turtle et al. 2009], whereas other units showed boundaries not apparent from the visible and near-infrared remote-sensing data set. In particular, while dark equatorial basins are very similar to each other in terms of infrared and microwave reflectance at this spatial scale, the major bright features do not share the same characteristics.

A comprehensive investigation of Titan's surface features using the VIMS and RADAR-SAR datasets at the best available spatial resolution is still the best approach to characterize geomorphologic units using both spectral and morphologic characteristics. For example, the correlation between the 5 μm bright materials and RADAR empty lakes suggests the presence of sedimentary or organic-rich evaporitic deposits in dry polar lakebeds [Barnes et al. 2011a; MacKenzie et al. 2014]. Langhans et al. [2012] extensively studied the morphology, distribution, and spectral properties of Titan’s fluvial valleys showing that these are mostly associated with the bright surface unit.

In recent years, several investigators have applied radiative transfer models in addition to comparison between datasets—for example, Hirtzig et al. [2013]; Solomonidou et al. [2014]; Lopes et al. [2016]. These studies allow definition of both the surface and the atmospheric contributions from VIMS spectral imaging data after performing the appropriate pixel selection of areas of interest with the help of SAR data.

The application of radiative transfer analyses to the VIMS Titan data yields extracted weighted surface albedos in the seven methane windows, which have been tested against a variety of Titan candidate ice and organic constituents to provide constraints on the possible material present in various geomorphological units [Solomonidou et al. 2018]. An updated material library is used based on Bernard et al. [2006], Brassé et al. [2015], and the Grenoble Astrophysics and Planetology Solid Spectroscopy and Thermodynamics (GhoSST) database (https://ghosst.osug.fr). This library includes several materials at different grain sizes, such as ices of acetylene (C_2H_2), ethylene (C_2H_4), ethane (C_2H_6), propane (C_3H_8), cyanoacetylene (HC_3N), water (H_2O), ammonia (NH_3), methane (CH_4), and carbon dioxide (CO_2), in addition to spectra of laboratory tholins [Bernard et al. 2006; Brassé et al. 2015], and spectra of dark materials such as asphalite, kerite, different types of anthraxolite and amorphous carbon, which have been proposed to lower the total surface albedo of Titan’s surface—[Lellouch et al. 2006; GhoSST database].

Considering the different grain sizes, the library consists of 148 different constituent possibilities that can also be mixed. By using this constituent library, spectral simulations are made and an iterative process is used to obtain the best fit to the observations, bearing in mind that there is no unique solution for the whole mixtures. With these and other caveats, Solomonidou et al. [2018] have derived constraints on the possible major constituent for each geological unit and reported a latitudinal dependence of Titan’s surface composition with water ice being the major

constituent at latitudes poleward of 30° N and 30° S, while Titan's equatorial region appears to be dominated by a very dark organic material, possibly aromatic in character [Clark et al. 2010]. The surface albedo differences and similarities among the various geomorphological units also have implications for the geological processes that govern Titan's surface and interior (e.g., aeolian, cryovolcanic, tectonic).

Surface geology

MAJOR GEOLOGIC UNITS AND MAPPING

SAR data have been used since the early days of the mission to interpret different types of terrains (Figure RADAR-8) [Stofan et al. 2006; Paganelli et al. 2007, 2008; Lopes et al. 2010]. More recent work used not only SAR data but added correlations with data from other RADAR modes (altimetry, SARTopo, scatterometry, and radiometry), and also from VIMS and ISS to provide sufficient information on Titan's surface to distinguish the major types of terrain units [Malaska et al. 2016a; Lopes et al. 2016]. Also see Lopes et al. [2019] for the recently produced global geologic map. These data were also used to establish the major geomorphologic unit classes on Titan and their ages using contacts between units. In order of total surface area, the classes of units are: plains, dunes, mountainous/hummocky terrains, labyrinth terrains, lakes, and impact craters. The oldest units are the mountainous/hummocky and the labyrinth terrains; it is not possible with currently available data to differentiate the relative ages of these two oldest types of terrain. The mountainous/hummocky terrains consist of mountain chains and isolated radar-bright terrains. The labyrinth terrains consist of highly incised and dissected plateaus with medium radar backscatter. The plains are younger than both mountainous/hummocky and labyrinthic unit classes. Dunes and lakes of liquid hydrocarbons are the youngest unit classes on Titan. Additionally, we have identified individual features such as crater rims, channels, and candidate cryovolcanic features. Crater rims and candidate cryovolcanic features are locations more likely to expose materials from the icy crust, while the hummocky/mountainous materials are thought to be exposed remnants of the icy crust.

Characterization and comparison of the properties of the unit classes and individual features with data from radar radiometry, ISS, and VIMS provide information on their composition and possible provenance and shed light on the interconnection between the interior, the surface, and the atmosphere. Both microwave emissivity and VIMS are helpful in characterizing the units, although both have different penetration depths with microwave emissivity penetrating 10s of cm into the surface, while infrared-based responses such as VIMS and ISS, penetrate only the top surface coating, on the order of microns. Microwave emissivity data infer that the hummocky/mountainous terrains and impact crater rim features have relatively low emissivity (and greater radar scattering) in radiometric data, consistent with more water ice near the surface (Figure RADAR-2). The undifferentiated plains, dunes, labyrinth terrains, and lakes all have high emissivity (lower radar scattering) in radiometric data, which is consistent with low-dielectric organic materials.

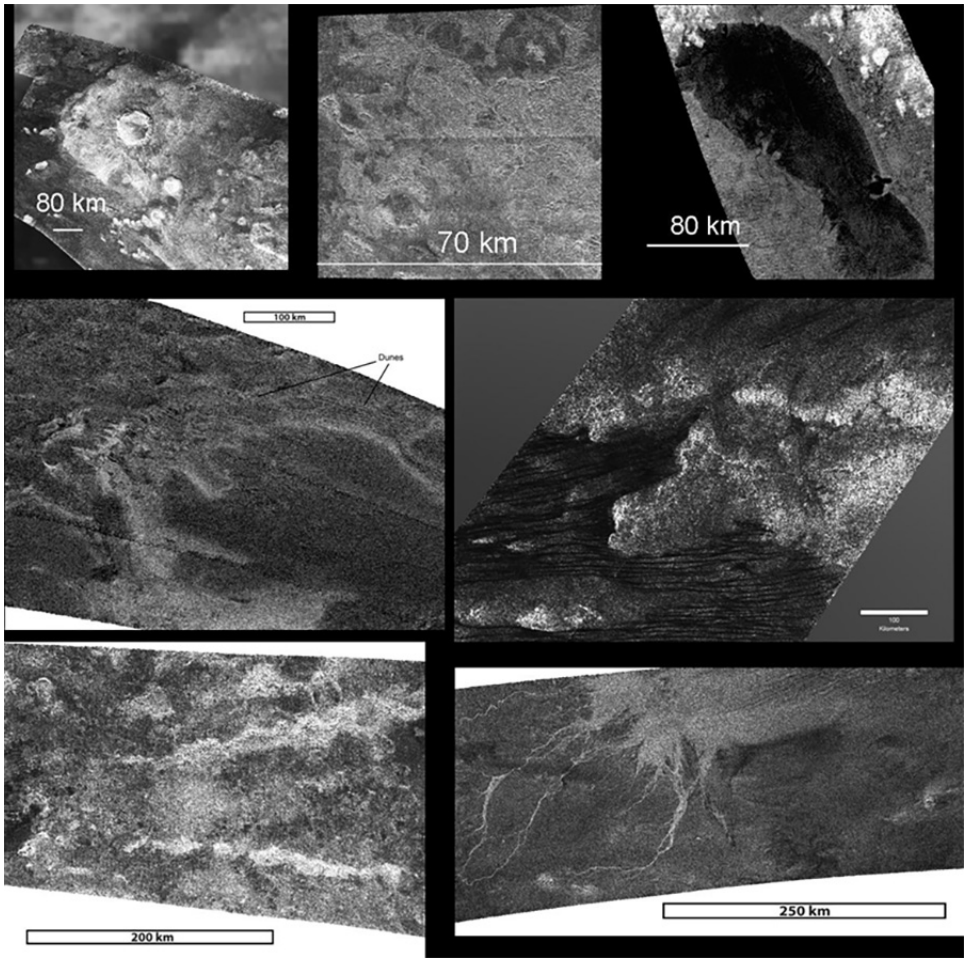

Figure RADAR-8. Examples of geologic features on Titan. Top row from left: Sinlap crater with its well defined ejecta blanket. Middle: Crateriform structure (suspected impact crater) on Xanadu. Right: Ontario Lacus near Titan's South Pole. Middle row, left: Bright (high radar backscatter) deposit Winia Fluctus abutting darker undifferentiated plains, the dunes indicated by arrows overlie part of deposit. Middle row, right: Dunes abutting against hummocky and mountainous terrain. Bottom left: Mountains (radar bright) in the equatorial region. Right: Elivagar Flumina, interpreted as a large fluvial deposit, showing braided radar-bright channels that overlie radar-dark undifferentiated plains.

Spectral coatings of the terrain units were described in Solomonidou et al. [2018] and discussed in the section entitled Surface Composition from VIMS and RADAR. From this analysis, three groups of compositional mixtures are reported, which include the major geomorphological units mentioned there: water ice, tholin, and a dark component. The units with spectral responses most similar to water ice are the labyrinth terrains and a number of different types of plains such as the streak-like, the scalloped, and the undifferentiated plains that are concentrated at the higher parts of the mid-latitudes. The impact crater ejecta and the alluvial fans are part of a different compositional group in which a tholin-like material is dominant. The units covered with an unknown dark constituent are the hummocky/mountainous terrains, the variable plains, the dunes, and the undifferentiated plains that are close to the equator and possibly contaminated by dune material

[Lopes et al. 2016; Solomonidou et al. 2018]. Since microwave radiometry and VIMS are global datasets (at lesser spatial resolution than SAR), we can also use these correlations to infer global distributions of regions not covered by SAR. This is particularly important as SAR data did not provide complete coverage of Titan at the end of the Cassini mission.

PLAINS

Plains are the most widespread type of terrain on Titan [Lopes et al. 2016]. Although there are several different types of plains, by far the most extensive are the Undifferentiated Plains, first mapped by Lopes et al. [2010]. These are vast expanses of radar-dark terrains that appear fairly uniform in SAR images, with no major topographic units, and are for this reason often referred to as blandlands. Lopes et al. [2016] mapped the distribution of the Undifferentiated Plains using SAR swaths up to flyby T92 (July 2013) and found that these terrains are located mainly at mid-latitudes. Their gradational boundaries and paucity of recognizable features in SAR data make geologic interpretation challenging, so Lopes et al. [2016] used all the RADAR datasets available, plus VIMS and ISS, to examine and evaluate different formation mechanisms including: (i) cryovolcanic origin, consisting of overlapping flows of low relief; or (ii) sedimentary origins, resulting from fluvial/lacustrine or aeolian deposition, or accumulation of photolysis products created in the atmosphere. Their analysis showed that exposure of Undifferentiated Plains in the lower mid-latitudes are consistent with a composition predominantly containing organic rather than icy materials and formed by depositional and/or sedimentary processes, unlike the undifferentiated plains in the higher mid-latitudes, which are consistent with water ice [Solomonidou et al. 2018]. The study concluded that aeolian processes played a major part in the formation of the Undifferentiated Plains, though other processes (fluvial, deposition of photolysis products) are likely to have contributed, possibly in differing proportions depending on location. However, the distribution of Undifferentiated Plains, both at local and global scales, is consistent with aeolian deposition being the major process contributing to their formation.

Spectral differences between the Plains and Dunes seen in VIMS data imply that the materials, at least on the top layers of the surface, are not exactly the same. Spectral differences in terms of surface albedo values between locations of Undifferentiated Plains [Lopes et al. 2016; Solomonidou et al. 2018] show that Plains at lower latitudes (closer to the dune seas) are more spectrally similar to dune materials, suggesting that they are related and supporting the idea that dune materials are transported by wind to mid-latitudes [Malaska et al. 2016a]. The Undifferentiated Plains located at lower mid-latitudes (and therefore closer to the equatorial dunes) appear to be composed predominantly of organic materials, which may have been cemented by an organic substance and/or wetted by methane, causing them to become spectrally different from dune materials, at least at a surficial level. Work by Malaska et al. [2016a] and Lopes et al. [2016] suggests that the plains deposits may be derived from modified dune materials—thus tying two of the major geomorphologic units together. If the Undifferentiated Plains materials are mainly the result of aeolian deposition but contain liquids due to methane rain or fluids transported by channels, this could explain why they show relatively high emissivity (lower global dielectric constant, less efficient volume scattering) as well as why they are free of observable dunes (reduced sediment mobility). It would also be consistent with the high level of degradation of craters

found at mid-latitudes, potentially due to efficient erosion by fluvial, pluvial, or subsurface flow activity [Neish et al. 2016].

DUNES

One of the youngest and most areally extensive geomorphologic units on Titan consists of sand dunes [Lorenz et al. 2006]. These appear as long, narrow, and SAR-dark features against a SAR-brighter substrate or interdune (Figure RADAR-9), presumably because dune sands are smooth to RADAR at the 2.17 cm Cassini SAR wavelength. The dunes are generally 1–2 km wide, spaced by 1–4 km and can be over 100 km long [Lorenz et al. 2006; Radebaugh et al. 2008]. Limited measurements of heights from radarclinometry suggest they are 80–130 m [Neish et al. 2010]. They are grouped together in large dune fields, or sand seas, equatorward of ± 30° latitude. The Titan's dunes interact with topographic obstacles, seen as SAR-bright and generally isolated mountains, in a way that indicates general W-E transport of sand; they pile up on the west side of obstacles, divert in their azimuth around the obstacles, and are sparser on the east side [Radebaugh et al. 2010]. Their size, general morphology and relationship with underlying terrain and obstacles, and their style of collection are nearly identical to large, linear dunes in Earth's sand seas of the Sahara, Arabia and Namibia [Lorenz et al. 2006; Radebaugh et al. 2008; Le Gall et al. 2011; Le Gall et al. 2012]. Such dunes on Earth typically form under bimodal winds [Fryberger and Dean 1979; Tsoar 1983]. A more recent model calls on a dominant, slightly off-axis wind and a secondary wind causing sand flux down the dune long axis [Courrech du Pont et al. 2014; Lucas et al. 2014].

Figure RADAR-9. Sand dunes on Titan appear as long, narrow, and SAR-dark features against a SAR-brighter substrate or interdune. Dunes on Titan as seen by the Cassini SAR, wavelength 2.17 cm, with spatial resolution of 350 m in the Belet Sand Sea, from the T61 (August 2009) swath on the equatorial leading hemisphere, at 11° S, 255° W. Dune surfaces are generally smooth and absorbing to SAR and thus typically, as here, appear as SAR-dark lines against a rougher and/or fractured, and thus radar- bright substrate, unless the RADAR is pointed directly at a dune face, in which case it appears as a thin, SAR-bright line. Occasionally the radar incidence is such as to give bright glints from dune slopes. The open arrows indicate the direction of SAR illumination and incidence angle. Figure from Radebaugh et al. [2013].

Regardless of whether the classical (bimodal) or fingering-mode dune growth mechanisms applies, a fundamental challenge raised by the RADAR observations of the dunes is the eastward direction of growth and sand transport [Lorenz et al. 2006; Radebaugh et al. 2010]. This contrasts with expectations that low-latitude near-surface winds should generally blow to the west. The solution appears to be that the dunes reflect strong but infrequent eastward winds, either associated with vertical mixing in the atmosphere at equinox leading to strong westerly gusts [Tokano 2010] or methane rainstorms having a similar effect [Charnay et al. 2015]. Additionally, convergence of the meridional transport predicted in models—for example, Lucas et al. [2014] can further explain why Titan's dunes are confined within ±30° latitudes, where sediment fluxes converge—see also Malaska et al. [2016a].

Titan's dune sands are not only dark to SAR but they are also some of the darkest materials seen by ISS [Porco et al. 2005; Karkoschka et al. 2017] and have a low albedo and "red" slope as seen by VIMS, thus comprising the VIMS dark brown spectral unit [Soderblom et al. 2007; Barnes et al. 2008; Clark et al. 2010; Rodriguez et al. 2014]. Volume scattering within the dunes is very low, consistent with smooth, homogeneous surfaces in general, and lacking large voids or clasts [Janssen et al. 2009; Le Gall et al. 2011], although modeling by Paillou et al. [2014] suggests shallow surface ripples and some volume scattering. The observations indicate the dunes cannot be composed of water ice, but rather must be made of organics, ultimately derived from photolytic processing of methane in the upper atmosphere, and precipitation to the surface [Lorenz et al. 2006, 2008a; Soderblom et al. 2007]. Sand sources could include river channels, as on Earth [Radebaugh 2013], low-latitude evaporite deposits, which can show similar VIMS properties [Barnes et al. 2011a]; or the mid-latitude blandlands, though it is more likely that sands are being transported there from the equatorial regions [Lopes et al. 2016; Malaska et al. 2016a]. The extent of the dunes indicates that sand has been generated on Titan in great volumes and transported by wind, and that processes have acted on the surface long enough to produce extensive and morphologically consistent landforms [Radebaugh 2013].

Gathering all exploitable SAR and HiSAR images since the start of the Cassini mission, Rodriguez et al. [2014] built a global map of the dune coverage available at that time, accounting for observations from TA to T92 flybys (from October 2004 to July 2013) and more than 30 individual RADAR SAR and HiSAR swaths. They evaluated that dunes cover 13 ± 2% of the 58.1% of Titan's surface observed with SAR and HiSAR, considering only those images having sufficient spatial resolution to identify individual dunes—that is, excluding HiSAR swaths with a resolution coarser than 2 km/pixel. In terms of latitudinal distribution, 99.6% of the imaged dunes are found within the equatorial belt (within ±30° latitudes—61.3% of which has been imaged after flyby T92. The overlapping of a VIMS global mosaic and the global distribution of dunes as seen by the RADAR highlights the strong correlation between the dunes and a specific infrared unit spectrally compatible with complex solid organics (the dark brown unit). This allowed an extrapolation of the dune geographic distribution to the entire spatial extent of the VIMS dark brown unit, even in locations where dunes are not seen because of lack of RADAR coverage, and extending the previously estimated total surface area of Titan covered by dunes up to ≈17% (≈14×10^6 km^2, 1.5 times the surface area of the Sahara desert on Earth), the same as early estimates from Lopes et al. [2010]. A simple calculation of the volume—for example, Lorenz et al.

[2008b]—indicates that dunes are a major surface reservoir of organics, probably originating from the atmosphere.

In addition to dunes, there are other aeolian features and landforms on Titan's surface. These are wind streaks and yardangs, or wind-carved ridges. The wind streaks are visible in ISS images as bright features that extend in the downwind direction from obstacles—for example, Porco et al. [2005]; Lorenz et al. [2006]; Malaska et al. [2016a]. They can be several tens of kilometers wide and long, can have flow-like, teardrop shapes, and appear as though wind has shaped the bright landscapes and deposited dark materials, likely sand, in the low regions downwind of the obstacles. These features help indicate the direction of the winds, which also broadly parallels the linear dunes seen in Cassini SAR images [Malaska et al, 2016a].

Deposits that are SAR-bright, circular in planform and likely elevated into small mounds or domes are found in some regions in the northern mid-latitudes [Lopes et al. 2016]. These domes are easily eroded as revealed by deep, badlands-like river channels that flow outwards from their centers. Cutting across the channels and the domes are a series of parallel, long lineation ~1 km wide, spaced by a few km, and tens of kilometers long [Paillou et al. 2016; Northrup et al. 2018]. They are similar in appearance and SAR brightness, radiometry and scatterometry to yardangs, or wind-carved ridges [Paillou et al. 2015]. These appear to have formed in easily eroded materials, similar to yardangs on Earth and Mars, and further indicate the action of wind at moderate to high latitudes now or in the past [Northrup et al. 2018].

IMPACT CRATERS

Before Cassini arrived at Saturn, the impact cratering history on Titan was unknown from direct observations. Estimates of the cratering rate were made by extrapolating the crater distributions observed on other Saturnian satellites, or by predicting impact rates by comet populations. Such estimates suggested that at least several hundred craters larger than 20 km in diameter should be present on Titan [Zahnle et al. 2003]. Impactors that would create craters smaller than 20 km in diameter are expected to be disrupted by Titan's atmosphere [Artemieva and Lunine 2005; Korycansky and Zahnle 2005]. Cassini RADAR observations show an extreme paucity of craters. Only 23 certain or nearly certain craters and ~10 probable craters >20 km in diameter have been observed on Titan, with a handful of smaller crater candidates [Wood et al. 2010; Neish and Lorenz 2012; Buratti et al. 2012; Neish et al. 2016]. This suggests that Titan has a crater retention age of several hundred million years [Wood et al. 2010; Neish and Lorenz 2012], with the oldest surfaces located near the equator and the youngest surfaces located near the poles [Neish et al. 2016].

The craters that are observed on Titan all show evidence for extensive modification by erosional processes (Figure RADAR-10). Channels are observed to cut through the ejecta blankets and floors of several impact craters [Wood et al. 2010; Soderblom et al. 2010; Neish et al. 2015]. Many of Titan's impact craters are located in its equatorial sand seas, and also show evidence for extensive infilling by sand [Wood et al. 2010; Le Mouelic et al. 2008; Neish et al. 2013]. In addition to the morphologic evidence for erosion and burial, Titan's craters are consistently shallower than similarly sized fresh craters on Ganymede (often by many hundreds of meters), suggestive of infill

[Neish et al. 2013]. Given the distribution of depths, aeolian infilling appears to be the dominant modification process on Titan [Neish et al. 2013], but fluvial erosion seems to play an important secondary role [Neish et al. 2016]. Modification by viscous relaxation is expected to be minimal given the cold lithospheric temperatures on Titan, although insulation by sand could enable some relaxation in Titan's larger craters [Schurmeier and Dombard 2018].

In addition to being highly modified, Titan's impact craters are not uniformly distributed across the moon. There is an almost complete absence of impact craters near Titan's poles, with the majority of the craters found in the topographically high, equatorial sand seas [Neish and Lorenz 2014]. There have been several hypotheses advanced to explain this observation. Neish and Lorenz [2014] proposed the lack of craters near Titan's poles might be indicative of marine impacts into a former ocean in this region. Moore et al. [2014] suggested that extreme climate change occurred in Titan's recent past, causing global methane rainfall that produced sediment that settled in Titan's topographically low polar regions, burying any craters there. Finally, Neish et al. [2016] suggested that an increased rate of fluvial erosion near the poles could degrade Titan's craters to the point where they would be unrecognizable from orbit. In any case, Titan's cratering record demonstrates that it is an extremely dynamic world, and studying its impact structures can reveal much about the processes that have shaped it.

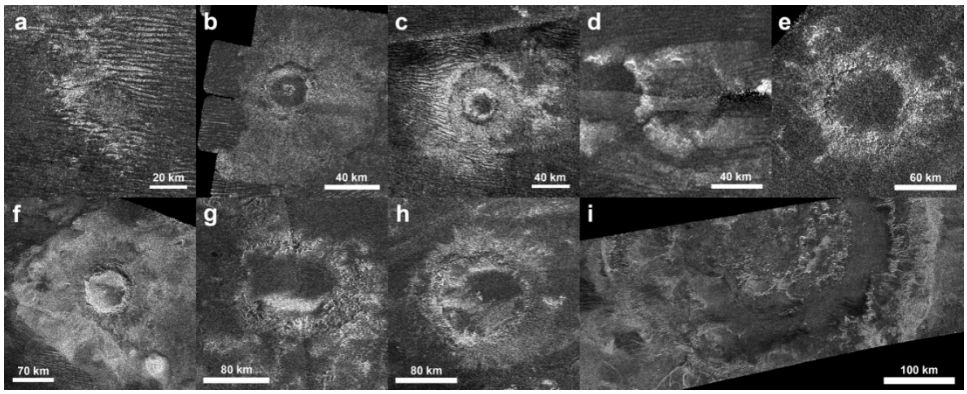

Figure RADAR-10. Nine probable impact craters observed on Titan by Cassini RADAR. From smallest (a) to largest (i) the impact craters on Titan show modification by exogenic processes such as fluvial erosion and infilling by sand [Neish et al. 2013].

MOUNTAINS AND TECTONICS

Features of relatively high topography, termed mountains, have been observed across Titan (Figure RADAR-11). Topography on icy satellites is rare, taking the form of, for example, impact crater rims, grooved terrain on Ganymede, or the towering scarps of Miranda. This is in part because water ice generally loses strength with increasing depth, making high topographies difficult to support. However, the exceptional amount of erosion on Titan may also be responsible for terrain height reduction. Overall, topography on Titan is rather subdued, having a range of just a few kilometers [Lorenz et al. 2013; Corlies et al. 2017]; nevertheless, there are features on the surface aside from impact crater rims that are elevated. These take the form of isolated blocks, chains, ridges, and elevated plateaus [Radebaugh et al. 2007]. Mountains of all types are SAR-bright due

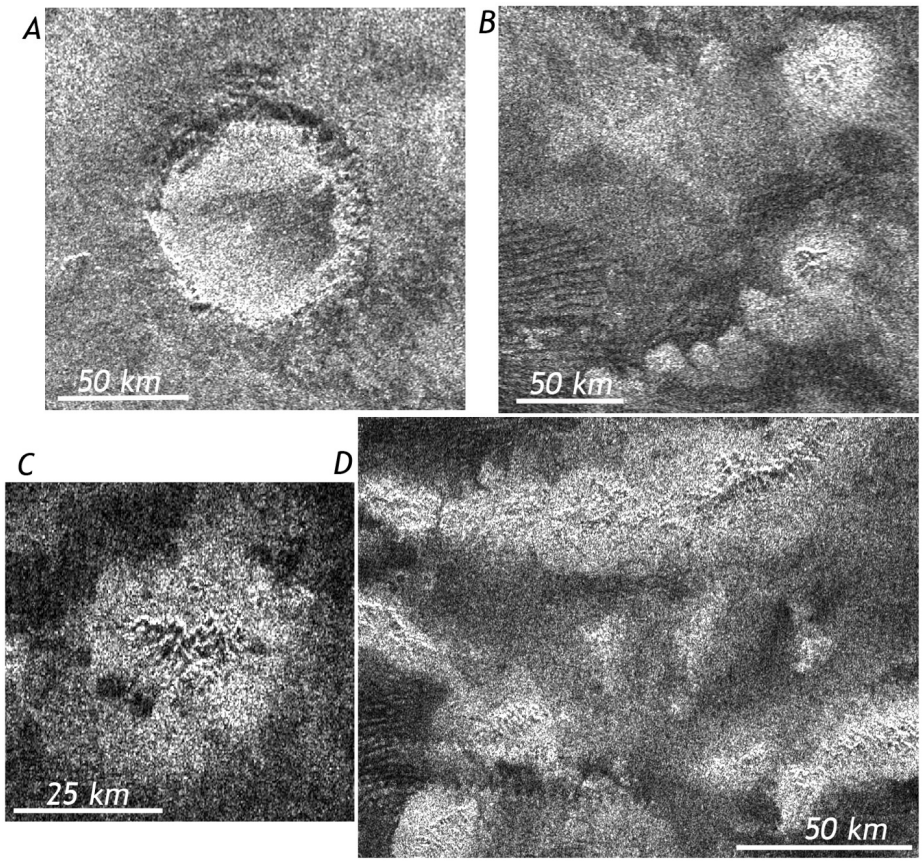

Figure RADAR-11. Some examples of mountains on Titan. Radar illumination is from the top in all cases, and north is up. Bright, possibly erosional, blankets surround the central, high elevation features visible as bright/dark pairs. A) Sinlap crater, shown to demonstrate the effects of radar illumination on a rimmed depression; B) Individual mountain blocks in the T3 swath south of Sinlap crater; C) Rugged mountain from the T3 swath; D) A portion of mountain ranges west of the Huygens landing site from the T8 swath. Figure from Radebaugh et al. [2007].

to the roughness and fractured nature of the materials, as well as the slope geometry with respect to the SAR antenna look direction and incidence angle. Mountains also exhibit high scattering and have a high emissivity as seen by RADAR [Janssen et al. 2009, 2016], and are part of the VIMS bright blue unit [Barnes et al. 2007], indicating a higher water-ice component, which is dominant in Titan's lithosphere.

Isolated mountain blocks are found only in a few select regions and tend to be several km across and a few hundred meters high as calculated from radarclinometry [Radebaugh et al. 2007]. More frequently, mountains are found in small belts near the middle and high latitudes. They are only few to tens of kilometers in length and a few hundred meters high. Mountain chains are the most areally extensive rugged features (aside from Xanadu) and are the most dramatic on the surface, being found dominantly at the equatorial regions and generally aligned E-W. They are up to several hundred kilometers in length, are arcuate in planform, and can be up to several kilometers high [Radebaugh et al. 2007; Radebaugh et al. 2016]. In Xanadu, there are extensive, mountainous and rugged terrains. These appear crenulated to SAR and exhibit multiple

overlapping peaks concentrated in regions over tens to hundreds of square kilometers. They are interspersed with lineations that indicate a regional tectonic fabric, likely extensional, given the straight nature of the lineations [Radebaugh et al. 2011]. All mountains on Titan are highly rugged and exhibit signs of extensive erosion from methane rainfall and possibly mass wasting. All mountain ridges and chains exhibit a preferential orientation [Cook-Hallett et al. 2015; Liu et al. 2016a] indicating internal tectonic forces operating on their formation. The equatorial mountain chains differ in morphology from long, narrow tectonic features on other icy satellites: they sit on elevated topography [Radebaugh et al. 2016], they are arcuate in morphology, and they have low slopes [Liu et al. 2016b]. This indicates they are more likely to have been created by contractional tectonism, by N-S directed forces in the interior and at the equator. Such thrust faulting could have been enabled by liquid methane within the crust, which could act to lubricate fault zones, much as occurs on Earth with water [Liu et al. 2016b]. A similar conclusion is reached for the mountain ridges north of Xanadu, which contain the highest peak on Titan at just over 3,300 m [Radebaugh et al. 2016]: that they were formed by contractional tectonism [Mitri et al. 2010]. Some very large-scale tectonic rises, several hundred kilometers across, may be topographic rises related to laccolithic activity [Schurmeier et al. 2017].

CRYOVOLCANISM

The possibility of finding cryovolcanic features on Titan had been discussed prior to Cassini by Lorenz [1993, 1996]. The case for cryovolcanism was strengthened by results from the Gas Chromatograph Mass Spectrometer (GCMS) instrument on board the Huygens probe, which detected the radiogenic isotope of argon in Titan's atmosphere [Niemann et al. 2005] in concentrations suggesting that the atmosphere was in communication with a reservoir of the parent atom. Prior to the first Titan flyby using RADAR, VIMS imaged a bright feature (later named Tortola Facula) that Sotin et al. [2005] proposed to be cryovolcanic in origin. However, SAR images obtained later in the mission showed Tortola Facula to be a local topographic high similar to others elsewhere on Titan [Lopes et al. 2013] and not a candidate for a cryovolcanic feature. Sotin et al. [2005] further suggested that the upwelling of large cryovolcanic plumes might be releasing sufficient methane into the atmosphere to account for the known atmospheric composition.

Cassini RADAR and VIMS revealed several features interpreted as formed by cryovolcanism [Barnes et al. 2006; Sotin et al. 2005; Lopes et al. 2007; Soderblom et al. 2009; Wall et al. 2009; Lopes et al. 2013; Solomonidou et al. 2016]. However, the interpretation has been the subject of some debate—for example, Moore and Pappalardo [2011]—and has not been entirely resolved by Cassini data [Nixon et al. 2018], primarily due to limitations in spatial resolution and coverage. The cryovolcanic interpretations by RADAR (using several data sets including SAR, stereogrammetry [Kirk et. al. 2010], SARTopo, and radiometry) and VIMS (surface albedo retrievals, surface composition constraints, and temporal variations) are based on morphology, differences in surface albedo between the cryovolcanic areas, their surrounding terrains and several other geomorphological features, and temporal variations detected by VIMS [Barnes et al. 2005; Solomonidou et al. 2014, 2016, 2018]. However, the Cassini mission did not reveal any hot spots, i.e., thermal enhancements, that would have provided conclusive proof. The detection of thermal activity at Titan’s surface using radiometry data (which is sensitive to variations of ~1K) or VIMS,

would require Cassini's instruments to be observing the right locations at the right times and in multiple occasions, an unlikely scenario given the consensus that cryovolcanic candidate features are not ubiquitous on Titan [Lopes et al. 2010].

Landforms considered as possibly cryovolcanic include flow-like terrains seen on the western margin of Xanadu [Wall et al. 2010], spectrally different regions in Tui Regio [Barnes et al. 2005] and tangled flow regions in Hotei Regio [Soderblom et al. 2009; Wall et al. 2010]. These flow-like morphologies even exhibit elevated, lobate margins typical of flows. Other possible cryovolcanic features are the steep-sided, small lakes at the north polar region (see section entitled Lakes). These landforms have slightly elevated rims, steep sides, flat floors, and deposits diffuse to SAR surrounding them. All of these characteristics are typical of maar craters on Earth [Wood et al. 2007] though they are also generally consistent with dissolution and sublimation-related features [Hayes et al. 2017].

The strongest evidence for cryovolcanic features on Titan was put forward by Lopes et al. [2013] who combined SAR imaging (including stereogrammetry, Figure RADAR-12) and VIMS data (Figure RADAR-13) for a region that includes two mountains, Doom Mons (40.4° W, 14.7° S) and Erebor Mons (36.2° W, 5.0° S), as well as a depression, Sotra Patera (40.0° W, 14.5° S), and a region consisting of flow-like features, Mohini Fluctus (centered at 38.5° W, 11.8° S). Doom and Erebor Montes are tall mountains (Doom being ~70 km in diameter and 1.5 ± 0.2 km high,), Sotra Patera is

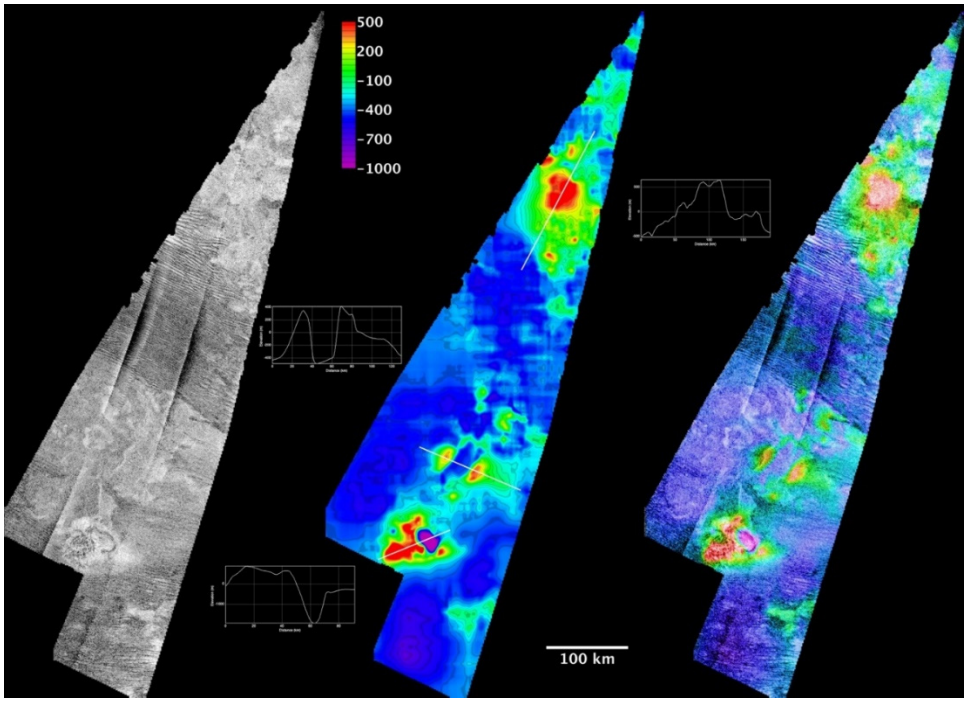

Figure RADAR-12. Topography of Doom Mons, Sotra Patera and (at the top) Erebor Mons region from SAR stereo. The image on the left is SAR over the region. The central image shows a color-coded DTM (scale shown), with the tops of Doom and Erebor Montes being the highest points, the white lines show the locations of the three profiles shown. The SAR and DTM are merged at the right. Figure from Lopes et al. [2013].

the deepest depression found on Titan (1.7 ± 0.2 km deep, relative to surrounding terrain). It is non-circular and interpreted as a collapse feature adjacent to Doom Mons (Figure RADAR-13). Mohini Fluctus appears to emerge from Doom Mons. Other non-circular, collapsed depressions are located between the two Montes, and flow-like features also surround Erebor Mons.

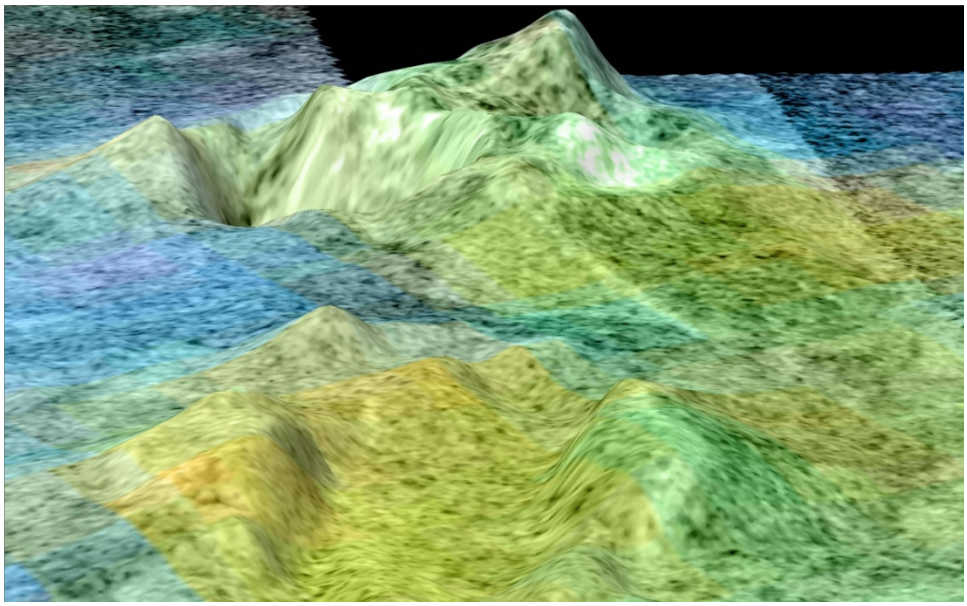

Figure RADAR-13. Perspective view of Doom Mons and Sotra Patera. This 3-D image was obtained by combining a digital topographic model (produced from two SAR swaths) and VIMS data showing compositional differences in representative color, which shows that the dune fields (in blue) are of a different composition from the candidate cryovolcanic materials in shades of green and yellow. The image shows one of the tallest peaks on Titan, Doom Mons, which is ~70 km in diameter and 1.5 ± 0.2 km high. Doom Mons is adjacent to the deepest depression so far found on Titan, Sotra Patera, an elongated pit ~30 km in diameter and 1.7 ± 0.2 km deep. The DTM data have a vertical exaggeration of 10:1. A movie showing the whole region can be seen at http://photojournal.jpl.nasa.gov/catalog/PIA13695.

A criticism by Moore and Pappalardo [2011] of initial interpretations by RADAR of cryovolcanic candidates reported by Lopes et al. [2007] is that flow-like features could have been produced by fluvial activity, since channels are seen in areas such as Hotei Regio and Ganesa Macula (which topography later obtained by RADAR showed it was not a shield or dome as initially interpreted). However, the Doom Mons-Sotra Patera-Erebor Mons region is totally devoid of visible fluvial channels, making a fluvial origin for Mohini Fluctus and other flows unlikely. A vast dune field is located between Doom and Erebor Montes, indicating a dry region. The depressions seen in the region, including Sotra Patera, are not circular, are very deep, and are therefore unlikely to have had an impact origin [Lopes et al. 2013]. VIMS data analysis has contributed to the cryovolcanic interpretation via two different types of investigation. First, analysis of VIMS data using a radiative transfer model [Solomonidou et al. 2014] showed that the surface albedo of the candidate cryovolcanic features is different from that of plains or dunes, indicating differences in composition [Solomonidou et al. 2014]. Following this and again using a radiative transfer model on a large selection of VIMS data, Solomonidou et al. [2016] revealed temporal changes for the Sotra Patera

and Mohini Fluctus areas, which became brighter up to a factor of two in terms of pure surface albedo and brightness during one year (2005–2006), while surrounding areas and the undifferentiated plains and dunes did not present any significant change for the same period of time. The surface albedo variations, together with the presence of volcanic-like morphological features consistent with volcanism, suggest that the regions might be active and possibly connected to the deep interior via cryovolcanic processes. Additional support for cryovolcanic origin of these features comes from interior structure models of Titan and corresponding calculations of the spatial pattern of maximum tidal stresses [Sohl et al. 2014], which indicate that the Doom Mons-Sotra Patera-Erebor Mons area is a likely region for cryovolcanic activity.

LABYRINTH

The enigmatic labyrinthic terrains of Titan are defined as elevated highly-dissected plateaus with intersecting valleys or remnant ridges of low to medium backscatter with a generally >5,000 km^2 extent [Malaska et al. 2010; Moore et al. 2014; Malaska et al. 2016b; Malaska et al. 2017a]. The Katain Labyrinth (Figure RADAR-14) is a typical example. SARTopo suggests that labyrinth terrains are among the locally highest units on Titan [Stiles et al. 2009]. Often the valley floors contain radar-dark floors or fill. The valley and upland widths are variable: in areas where the valleys are narrow and the intervening uplands (or valley spacing) are wide, the terrain appears in the form of a dissected plateau; when the widths of the valleys and the widths of the intervening plateaus are about equal, the terrain appears as a series of valleys and intervening plateaus; and when the valleys are wide and the widths of the intervening plateaus are small, the terrain can appear as a series of remnant ridges. Closed valleys may also be present, although this may be a misinterpretation due to the coarse resolution of the Cassini RADAR.

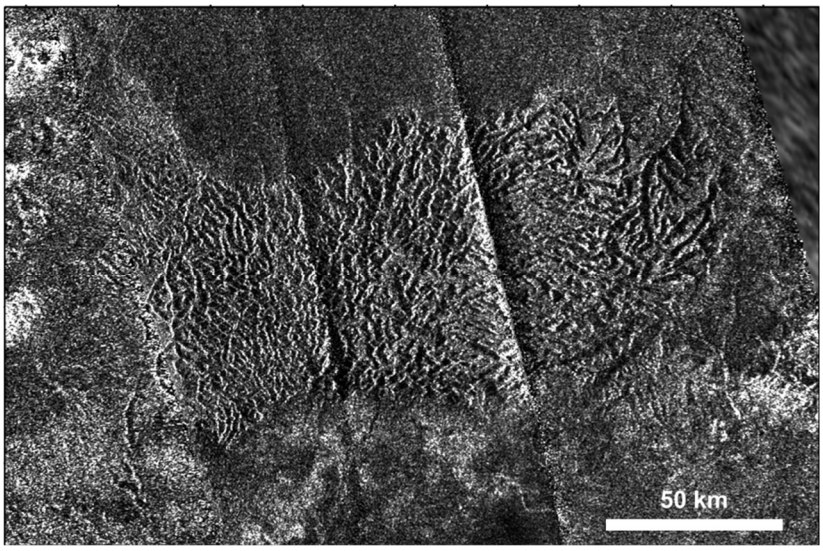

Figure RADAR-14. SAR image of Katain Labyrinth. The highly dissected feature at center is Katain Labyrinth. SAR illumination is from right (large straight lines through center are SAR artifacts due to beam overlap). Sinusoidal projection centered at 349 W. North is at top.

Wide valleys may appear suddenly in the plateaus, suggestive of amphitheater-headed valleys. The overall planforms of the labyrinth terrain units are circular, ovoid, or tabular. The valley density at a scale of 300 m/pixel is above 0.02, significantly higher than the density of valley networks described elsewhere on Titan such as the network in western Xanadu [Burr et al. 2009]. The valley networks inside the labyrinth units are rectangular to dendritic, suggesting varying amounts of structural and topographic control. Some of the more circular planform labyrinths have valley or ridge networks that are radial, extending away from the center of the region, suggesting that doming occurred prior to erosion, possibly as a result of a liquid water laccolith injection at depth [Shurmeier et al. 2017, 2018]. At the terminus of the valley networks and in contact with the labyrinths, undifferentiated plains units are found, suggesting a close connection between the two types of units, at least at the local scale.

The labyrinth terrains are composed almost wholly of a possibly uplifted thick plateau of organic materials, with very little water ice materials present.

The labyrinth terrains are composed almost wholly of a possibly uplifted thick plateau of organic materials, with very little water ice materials present. The emissivity data shows that labyrinth terrains have significantly higher emissivity than mountain and hummocky terrains and have similar emissivities to dunes or undifferentiated plains. The microwave data are consistent with the labyrinths being composed of low dielectric organic materials and are not consistent with materials containing significant amounts of water ice.

The labyrinths were likely formed from the uplifted plateaus through a combination of dissolution coupled with mechanical erosion, or other phase changes that could allow the development of closed valleys with transport of the remaining materials to the outlying plains. Karstic dissolution is a likely scenario, and many of the labyrinth terrains have morphologic analogs with terrestrial karst terrains [Malaska et al. 2010]. Theoretical predictions and laboratory work have shown that organic materials on Titan may dissolve when exposed to Titan hydrocarbon rainfall or liquids [Raulin 1987; Lorenz and Lunine 1996; Cordier et al. 2009; Malaska et al. 2011a; Glein and Shock 2013; Malaska and Hodyss 2014; Cornet et al. 2015; Cornet et al. 2017]. Dissolution geology on Titan may create a landscape that is similar to terrestrial karst terrain present in water-soluble materials such as limestone and gypsum on Earth [Malaska et al. 2011a; Malaska and Hodyss 2014; Cornet et al. 2015]. Preliminary modelling by Cornet et al. [2017] suggests that blocks of Titan soluble materials could dissolve under Titan conditions to form the features observed by SAR that are similar to polygonal karst. The evolution sequence begins with incised valleys in a plateau, then widening to form the end-stage wide-floored remnant ridges. Type examples of each stage are found in close proximity near Sikun Labyrinth in Titan's south polar terrain and are shown in Figure RADAR-15. However, other formation scenarios are possible, including differential hardening and deflation, aeolian deflation, or other phase change and removal processes such as sublimation. From superposition relations, the organic labyrinths represent an ancient terrain [Malaska et al. 2016b]. Thus, the labyrinth terrains unit represents a significant deposit of organic materials on Titan, and suggests that significant organic deposition, lithification, and uplift/exposure occurred early in Titan's history.

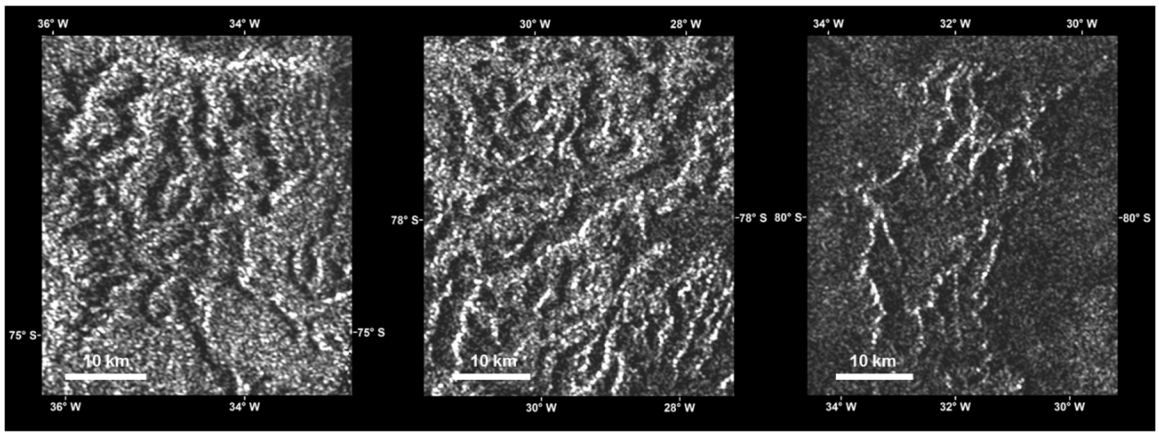

Figure RADAR-15. SAR images of different types of labyrinth terrains found in close proximity in Titan's south polar terrain. Left: Naraj Labyrinth, represents thin valleys incised in a plateau, Center: Sikun Labyrinth, represents valleys and plateaus of near equal width, Right: Tupile Labyrinth, a type example of remnant ridge. Sinusoidal projection. North is at top.

Xanadu

Much of Titan's geology has a regional organization; dunes and mountain belts are found near the equator, lakes and seas are found near the poles, and relatively bland regions are located in the mid-latitudes [Lopes et al. 2010]. Xanadu (Figure RADAR-16), however, is a continent-sized region that breaks with all predictions. It is 4,000 × 2,500 km wide, is located on Titan's leading hemisphere, and interrupts the equator-encircling sand seas. The feature was observed before Cassini arrived [Lemmon et al. 1993; Smith et al. 1996], and efforts were made to observe and understand Xanadu by Cassini SAR and other instruments. Xanadu is generally SAR-bright, which indicates it is composed of rough and fractured terrains [Radebaugh et al. 2011]. It has a high backscatter but low brightness temperature as indicated by scatterometry and radiometry measurements, which is consistent with a water-ice composition in the bedrock [Wye et al. 2007; Zebker et al. 2008; Janssen et al. 2009, 2016]. Furthermore, some portions of Xanadu are correlated with the VIMS dark blue unit, indicating there is a higher than average percentage of water-ice exposed at the surface [Barnes et al. 2007].

Xanadu is unique in several respects to other regions on Titan. While geologically diverse, many regions in Xanadu have extremely rugged terrains, manifest as many adjacent, deeply eroded, and incised mountain ranges [Radebaugh et al. 2011]. There are broad scale linear features characteristic of NE-SW and NW-SE extensional tectonism, and broadly arcuate mountain ranges indicative of N-S directed contractional tectonism [Radebaugh et al. 2011]. These features all indicate a long and complicated tectonic history for Xanadu. Extensive, dendritic networks of varying morphologies [Burr et al. 2009], large channels that distribute fans and cobbles to the south [Le Gall et al. 2010], and the extensive erosion of the mountains also reveal a long erosional history. Over twice as many impact craters or possible impact craters can be found in Xanadu as on the rest of Titan [Wood et al. 2010; Radebaugh et al. 2011], which is further evidence of the generally old nature of Xanadu compared with the rest of the surface of Titan [Radebaugh et al. 2011; Wood

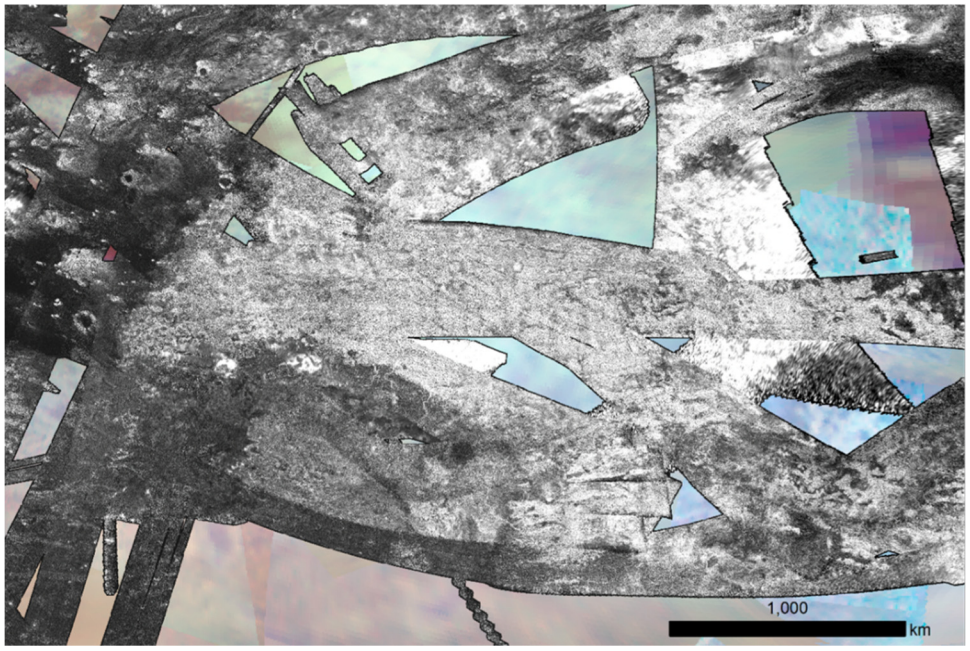

Figure RADAR-16. Xanadu region. All Cassini SAR and HiSAR image swaths covering the Xanadu region, overlain on a VIMS basemap. Xanadu is generally SAR-bright because of rough terrain and fractured ice, which is interspersed with valleys filled with SAR-darker sediment. Some regions of Xanadu are VIMS dark blue, consistent with the presence of exposed water ice. The southwest margin of Xanadu has large river channels emptying to the south.

et al. 2010]. A region of mottled terrain is found on the western margin, with arcuate depositional morphologies and lack of integrated drainage, postulated to be a possible cryovolcanic deposit [Wall et al. 2009]. These morphologies are consistent with other possible cryovolcanic zones in Hotei Regio, bordering Xanadu's southern margin [Soderblom et al. 2009]. These landforms may instead be related to swamp-like deposits entirely fluvial in origin, but they are unique and not widespread.

Xanadu's most puzzling characteristic is that despite the abundance of mountains and high local topographic differences, the region as a whole appears to be regionally lower in elevation than anywhere else near the equator [Zebker et al. 2009a; Stiles et al. 2009]. This is evidenced by radar altimetry measurements as well as SARTopo observations [Stiles et al. 2009]. It is possible that after a time period of mountain-building and contraction, there was gravitational collapse of the water ice crust [Mitri et al. 2010], resulting in broad extensional tectonism and down-dropping of Xanadu [Radebaugh et al. 2011]. This scenario might have led to Xanadu-bounding fault zones, along which the possible cryolavas of western Xanadu and Hotei in the south could have ascended [Radebaugh et al. 2011].

What could have driven this N-S directed contractional tectonism is unknown but might have resulted from global contraction related to interior cooling, tidal spin-up or spin-down, or internal convection [Radebaugh et al. 2011]. Another scenario hypothesized for the formation of Xanadu

involves a large impact event early in Titan's history, leaving behind a disrupted terrain [Brown et al. 2011].

Several outstanding questions about Xanadu remain, in addition to its origin: Why is it regionally depressed? Why do the dunes of the equatorial sand seas not cover and fill Xanadu? Why is water ice more exposed here than in most other places on Titan? Much remains to be learned about this unusual region.

Lakes

While ISS revealed ~50 dark features poleward of 70° S during one of Cassini's first observations of Titan, these features were not initially referred to as lakes as they could not be distinguished from dark equatorial dune fields at optical wavelengths [Porco et al. 2004]. The first high-resolution and definitive observations of Titan's hydrocarbon lakes were acquired by the RADAR in July 2016 (T16), when ~75 features with exceptionally low backscatter, high emissivity, and distinctly lacustrine morphology were identified in SAR images [Stofan et al. 2007]. Subsequent observations have revealed more than 650 such features, both dry and filled, scattered throughout Titan's polar terrain [Hayes et al. 2008; Birch et al. 2017]. These features have diameters that follow a log-normal distribution with a median of 77 ± 20 km [Hayes et al. 2016]. The morphology of both dry and filled lakes and seas on Titan provide a record of past and current climatic conditions and surface evolution processes. For example, while Titan's large seas have complex shorelines that are consistent with drowning of pre-existing topography, most of the smaller lakes are steep-sided depressions that are more consistent with dissolution-based erosion driven by karstic processes [Hayes et al. 2017; Cartwright et al. 2011; Langhans et al. 2012]. For a recent and more detailed review of Cassini's exploration of Titan's lakes and seas, see Hayes et al. [2016].

Lakes and seas encompass 1% of Titan's total surface area [Hayes et al. 2016]. The majority of surface liquids (97% by area) reside in the north polar region, with 80% of all liquid-filled surface area contained in three large seas; Kraken Mare, Ligeia Mare, and Punga Mare (Figure RADAR-17; note that the coloration in this figure is artificial). The largest modern liquid body in the south polar region is Ontario Lacus, although several large empty basins that encompass an area similar to the northern maria (7.6×10^5 km^2) have been identified and interpreted as paleoseas [Hayes et al. 2010, 2011; Birch et al. 2018b]. The observed dichotomy in lake distribution has been attributed to a net transport of ~5×10^{14} kg of methane per Titan year from the South Pole to the north, driven by a seasonal asymmetry in solar insolation that is the result of Saturn's eccentric orbit around the sun [Aharonson et al. 2009; Lora and Mitchell 2015]. Summer solstice in Titan's southern hemisphere occurs near perihelion while northern summer solstice occurs at aphelion, resulting in 25% higher peak insolation during southern summer as compared to northern summer. Long timescale (~100,000 year) orbital cycles can switch the direction and magnitude of the seasonal asymmetry driving this transport, moving liquid deposits between the poles similar to the way Croll-Milankovitch cycles drive ice ages and other long-term climate effects on Earth [Aharonson et al. 2009]. The presence of drowned river valleys at the terminus of channels flowing into the northern seas [Stofan et al. 2006], as well as the presence of exposed and abandoned river deltas adjacent

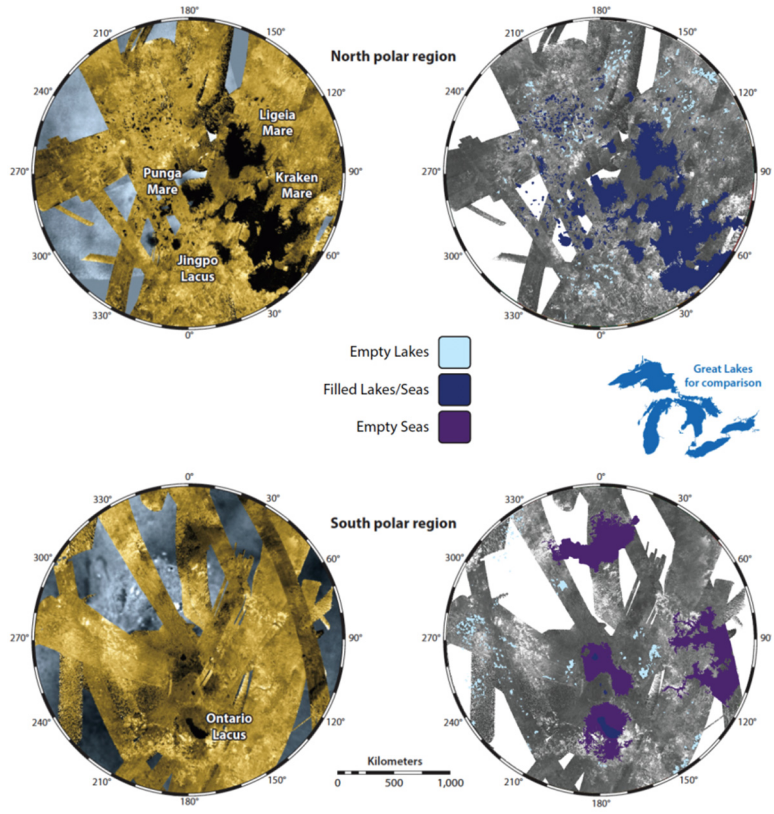

Figure RADAR-17. Map of lakes and seas on the northern (top) and southern (bottom) polar regions of Titan.

to the shores of southern Ontario Lacus [Wall et al. 2009], support the theory of rising and falling liquid levels as the magnitude and direction of net pole-to-pole methane transport varies with Titan's orbital cycles [Lora et al. 2014].

While a few small lakes have been observed to disappear or brighten in both the north and south over the 13 years of Cassini observations, no large-scale changes in the sea shorelines have been observed over the course of the mission. Given the resolution of the RADAR, however, this is not surprising. Although confirmed and stable liquid deposits are currently restricted to polar terrain, the equatorial features Hotei and Tui Regiones have been interpreted as possible low-latitude paleoseas [Moore and Howard 2010]. Both regions are surrounded by fluvial networks that appear to converge on a field of radar-bright, lobate, depressions that are morphologically similar to high-latitude lakes [Moore and Howard 2010]. Dark flow-like features identified adjacent to the radar-bright depressions have been interpreted as cryovolcanic deposits [Barnes et al. 2006; Wall et al. 2009], suggesting that both paleo-lakes and cryovolcanic flows may be present at Tui Regio and Hotei Regio [Lopes et al. 2013]. The existence of modern equatorial lakes has been proposed based on the longevity of low albedo localities observed by Cassini VIMS [Griffith et al. 2012; Vixie et al. 2015], although none of these features have been observed in higher-resolution SAR or altimetry datasets of the regions. Ample evidence exists (e.g., at the Huygens landing site) for at least transient liquids at low latitudes, and very flat areas exist that may be lake beds. Indeed, strong specular reflections

were observed at low latitude by the Arecibo radar on Earth (the longest-range radar astronomy experiment conducted to date) before Cassini's arrival, and the favored interpretation at the time was as extant bodies of smooth liquid hydrocarbons [Campbell et al. 2003]. A recent reinterpretation of the Arecibo returns is in progress at the time of this writing [Hofgartner et al. 2014b].

In May 2014, the RADAR acquired nadir-pointed altimetry over Ligeia Mare. The resulting altimetry echoes revealed waveforms that displayed two distinct returns, one from the surface of Ligeia Mare and one from its seabed [Mastrogiuseppe et al. 2014]. The difference in the received timing between these returns was a direct measure of Ligeia's depth (Figure RADAR-18), while the relative intensity difference between the surface and subsurface return was a measurement of the liquid's loss tangent (i.e., absorbance). While several studies—for example, Brown et al. [2008]; Lorenz et al. [2008a]; Lunine and Lorenz [2009]; Cordier et al. [2012]; Cornet et al. [2012]; Ventura et al. [2012]—have used indirect measurements to constrain the depth of Titan's lakes and seas, the altimetry observations over Ligeia represent the first direct measurement of extraterrestrial bathymetry profiles. Following the identification of Ligeia Mare's seabed, several passes of Titan were modified to repeat the experiment over Punga Mare and Kraken Mare [Mastrogiuseppe et al. 2016]. A reprocessing of altimetry data acquired over Ontario Lacus in December 2008 allowed the technique to be applied to Ontario Lacus as well [Mastrogiuseppe et al. 2018]. Ligeia Mare was determined to have a depth of 170 m at the deepest point along the observed track [Mastrogiuseppe et al. 2014] and, in combination with SAR images, the total volume of the basins was found to be around 14,000 km^3 of liquid [Hayes et al. 2016]. The estimated Ku-band loss tangent was $4.4 \pm 1 \times 10^{-5}$ [Mastrogiuseppe et al. 2016]. Assuming a methane-ethane-nitrogen composition and using the laboratory measurements of Mitchell et al. [2015] with the Lorentz-Lorenz formulation, the best-fit loss tangent is consistent with a methane-dominated composition of 71% CH_4: 12% C_2H_6: 17% N_2. As large quantities of liquid ethane should have been produced by photolysis of methane in the upper atmosphere, and as at least trace amounts of ethane have been detected in Ontario Lacus [Brown et al. 2008], the lack of significant ethane—and other higher order hydrocarbons such as propane—in Titan's lakes and seas requires that the ethane be sequestered in reservoirs (e.g., subsurface liquid deposits or sequestration in crustal clathrate hydrate).

To within error, the loss tangents of Punga Mare and the shallower parts of Kraken Mare (Figure RADAR-18) suggested a similar composition to Ligeia [Mastrogiuseppe et al. 2018]. Along most of Kraken Mare the seafloor was not detected, indication that the seas are either too deep or too absorptive in these areas. Within Punga Mare, a clear detection of the subsurface was observed up to 120 m along-track [Mastrogiuseppe et al. 2018]. At Ontario Lacus, however, the loss tangent was observed to be greater ($7 \pm 3 \times 10^{-5}$), consistent with a composition of ~47% CH_4, ~40% C_2H_6, and ~13% N_2,and suggesting an increased abundance of high-order hydrocarbons as compared to the northern seas. This higher loss tangent could be related to an increased abundance of more involatile hydrocarbons and/or nitriles or suspended particulates that represent a lag deposit generated as methane is transported from the south to the north over multiple seasonal cycles. The final RADAR observation of the bathymetry campaign was the T126 (April 22, 2017) final flyby of Titan, which observed several small-to-medium size (10–50 km) hydrocarbons lakes present at the northern polar terrain, revealing that such lakes can exceed one hundred meters of depth and have similar loss tangents, and therefore composition, to the northern seas. When the bathymetry

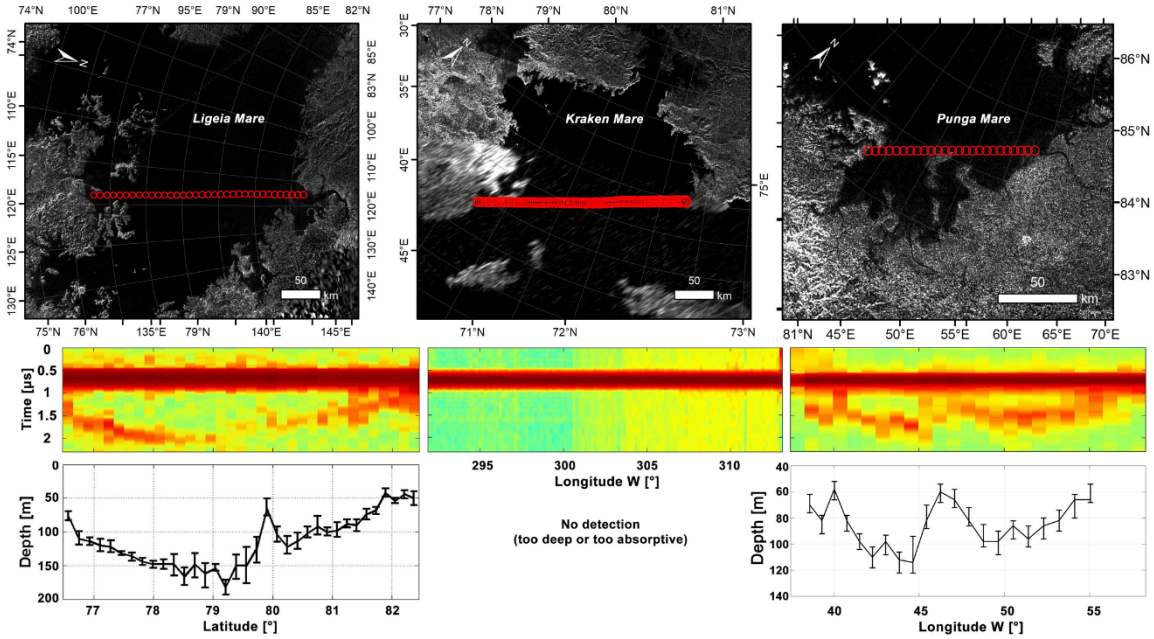

Figure RADAR-18. SAR mosaics, radargrams, and relative bathymetries (respectively in the upper, middle, and bottom panels) relative to the flyby T91 over Ligeia Mare (left), the flyby T104 over Kraken Mare (center), and the flyby T108 over Punga Mare (right) altimetry observations. Note that seafloor echoes have been detected for Ligeia and Punga Maria, while only surface returns are present over the open sea of Kraken Mare.

measurements are used to anchor models of sea and lake depth from SAR images, the estimated volume of all Titan's observed lakes and seas is ~70,000 km^3 [Hayes et al. 2016]. It is interesting to note that this represents only 1/7 the amount of methane that currently resides in Titan's atmosphere, suggesting that the lakes and seas do not drive global-scale heat transport or meteorology. It is also worthwhile mentioning that measuring the bathymetry and microwave absorptivity of Titan's seas was not planned initially and represents an exciting discovery made during the Cassini spacecraft lifetime.

T126 data (together with previous passes) revealed that some of the northern lakes have raised rims. Recent analysis of these features have produced different hypotheses for their origins [Birch et al. 2018a; Mitri et al. 2019].

RIVERS/CHANNELS

When water falls to the surface of the Earth, the most visible conduits on its journey downslope are networks of fluvial channels that slowly transport it toward the oceans. These networks take on many different forms that are the result of the mechanical and chemical properties of the surface [Burr et al. 2006], the climate and weather that generate fluid flow, and the mechanisms that produce topographic relief [Black et al. 2017]. The observation of channels on Titan by Cassini and Huygens [Collins 2005; Lorenz et al. 2008c; Lunine et al. 2008; Burr et al. 2009; Black et al. 2012; Burr et al. 2013] has thus provided similar constraints on the nature of Titan's surface and the

climatic conditions that proved favorable for the formation of these features, albeit in a far more limited fashion.

Cassini's RADAR imaged large portions of the moon and showed that valley networks are distributed at all latitudes [Lorenz et al. 2008c; Burr et al. 2009; Lopes et al. 2010] and have a wide variety of surface morphologies (Figure RADAR-19). Cassini has observed canyon networks at the poles with a diversity of valley networks analogous to Earth [Poggiali et al. 2016], including both dendritic and rectilinear networks globally [Burr et al. 2013], and even a meandering like feature in

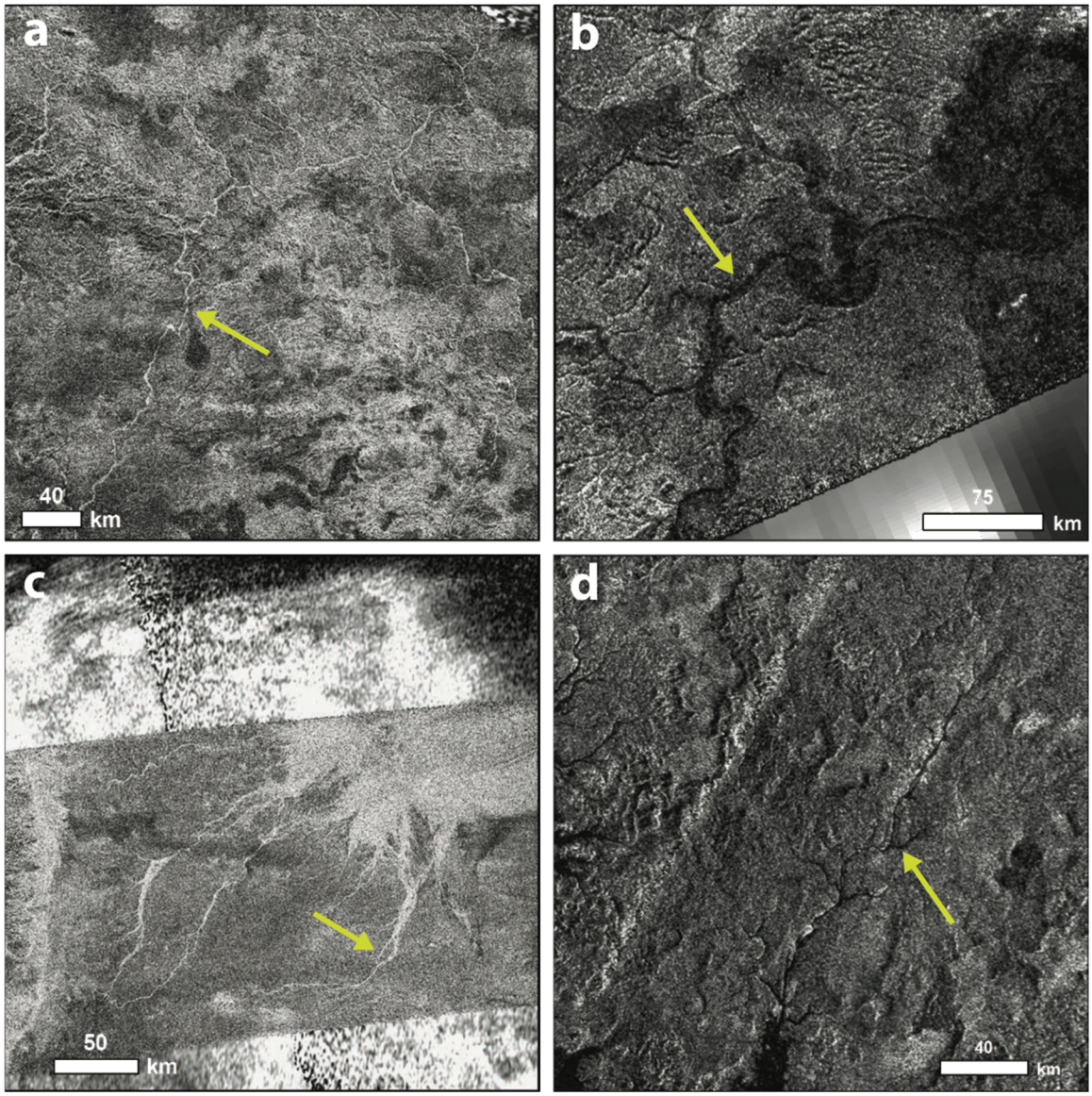

Figure RADAR-19. Erosions on Titan. (a) Rectilinear networks in eastern Xanadu; (b) Celadon Flumina, a meandering network near the South Pole; (c) Elvigar Flumina, a braided network that deposits into an alluvial fan; (d) Vid Flumina, a dendritic canyon network up to 500 m deep that drains into Ligeia Mare.

the south polar region [Malaska et al. 2011b; Birch et al. 2018b]. The presence of canyons implies a vertically weak bedrock, which may be influenced by fractures in the crust and/or a relatively highly erodible material. Similarly, rectilinear channels imply a fractured bedrock, where channels are forced to follow tectonically controlled paths of weakness. Meandering networks, meanwhile, imply the presence of a cohesive substrate [Howard et al. 2009]. A critical unknown following the Cassini mission, however, is whether there are any systematic variations in morphologic type that may be indicative of crustal heterogeneities [Burr et al. 2013] and/or variations in transport efficiencies/climate change [Moore et al. 2014].

Due to the coarse resolution of the Cassini RADAR, we have been limited to studying only the largest valley networks on Titan. We therefore have a limited idea about the extent to which Titan's landscapes are dissected by fluvial networks. The one exception to this was the region where the Huygens lander descended, where descent images, with an order-of-magnitude higher resolution [Tomasko et al. 2005], showed a highly dissected network of dendritic valleys [Perron et al. 2006]. It is likely that Titan is dissected everywhere at the scale observed by Huygens, however, a definitive answer to this question requires image data and topography with a resolution finer than the scale of fluvial dissection (10s of meters).

While it is not surprising that Titan has a global network of fluvial valleys, the mere presence of channelized flow conduits implies that the surface material can be eroded either physically or chemically, and that flows of sufficient magnitude, either from precipitation or groundwater, are able to erode Titan's surface. However, using estimates for the initial topography and erodibility of the substrate, channels may be very inefficient agents of erosion on Titan [Black et al. 2012] or there may be a gravel lag deposit that inhibits erosion under Titan's current climate [Howard et al. 2016]. Better estimates for the physical and chemical properties of both the bedrock and the fluid(s) [Burr et al. 2006; Cordier et al. 2017; Malaska et al. 2017a; Richardson et al. 2018] are needed to provide better understanding about the role that fluvial channels have played in sculpting Titan's surface.

In some locations, fluvial channels terminate in alluvial or fluvial fans—distributary landforms that indicate a transition from a high to a low elevation [Radebaugh et al. 2017; Birch et al. 2017]. These are fairly low in slope, and in some cases can run out to large distances, indicating the carrying power by methane fluid of organic sedimentary rock [Radebaugh et al. 2017]. These landforms are widely distributed across the surface, but they are not abundant [Birch et al. 2017]. This may indicate there is not frequent rainfall that can generate surface erosion, or that topographic gradients are gentle on a global scale such that these landforms are not readily generated.

Temporal change

Temporal changes were detected on Titan during the course of the Cassini mission, due to seasonal or other effects. Data from more than one instrument are key for determining the possible causes of change. For example, as mentioned in the section entitled Cryovolcanism, the radiative transfer code analysis of VIMS data from Tui Regio (2005–2009) and Sotra Patera (2005–2006) showed temporal surface albedo changes in two areas identified by SAR as cryovolcanic

candidates: Tui Regio darkened by 50% and Sotra Patera brightened by a factor of 2 [Solomonidou et al. 2016]. These changes could be due to endogenic and/or exogenic processes, possibly cryovolcanism or atmospheric deposition.

Magic Islands

For the majority of the Cassini mission, Titan's lakes and seas were observed to be quiescent, with no temporal changes and maximum vertical surface roughness on the order of millimeters [Barnes et al. 2011b; Stephan et al. 2010; Wye et al. 2009; Zebker et al. 2014; Grima et al. 2017]. This lack of observable surface roughness has been attributed to a seasonal effect in which polar winds were too weak to create waves or other dynamic features [Hayes et al. 2013]. As the northern hemisphere transitioned from spring equinox to summer solstice, temporal changes were observed in all three of Titan's seas. Specular reflections offset from the geometric specular point were observed by VIMS in Punga Mare [Barnes et al. 2014], transient bright features were observed by RADAR in Ligeia Mare [Hofgartner et al. 2014a, 2016], and both offset specular reflections and transient radar-bright features were observed in Kraken Mare [Hayes et al. 2016].

The transient bright features were nicknamed "Magic Islands" due to their appearing/disappearing act and similarity in appearance to islands in SAR images.

The transient radar-bright features were nicknamed "Magic Islands" due to their appearing/disappearing act and similarity in appearance to islands in SAR images. The features are not islands, however, and are most consistent with waves, or floating and/or suspended solids and bubbles. Based on the frequency of these phenomena in analogous terrestrial settings, wind-driven waves (intended to mean roughness of the liquid surface regardless of the process causing the roughness) are the most probable hypothesis. Tides, changes of sea level, and changes of the seafloor are unlikely to be the primary cause of the temporal changes. Magic Islands were observed in three regions; two in Ligeia Mare [Hofgartner et al. 2014a, 2016] and one in Kraken Mare [Hayes et al. 2016].

Figure RADAR-20 shows the time evolution of the first and most observed Magic Island region. This region was observed to have Magic Islands on two occasions; the transient bright features were in the same location on both occasions but differed in areal extent and morphology. HiSAR and VIMS observations acquired between the two SAR detections did not detect Magic Islands, however, the possibility that the Magic Islands were present but not detected in these observations could not be ruled out. Magic Islands were definitely not present in SAR observations before the first appearance and after the second appearance (Figure RADAR-20 includes a subset of the images of the region).

The Kraken Magic Island was also observed as a 5-micron sunglint by VIMS within two hours after the radar detection. The co-detection of the Kraken Magic Island by both RADAR and VIMS

suggests that it is likely caused by surface waves, as the reflecting facets must be smooth at both microwave and micron length scales [Hayes et al. 2016].

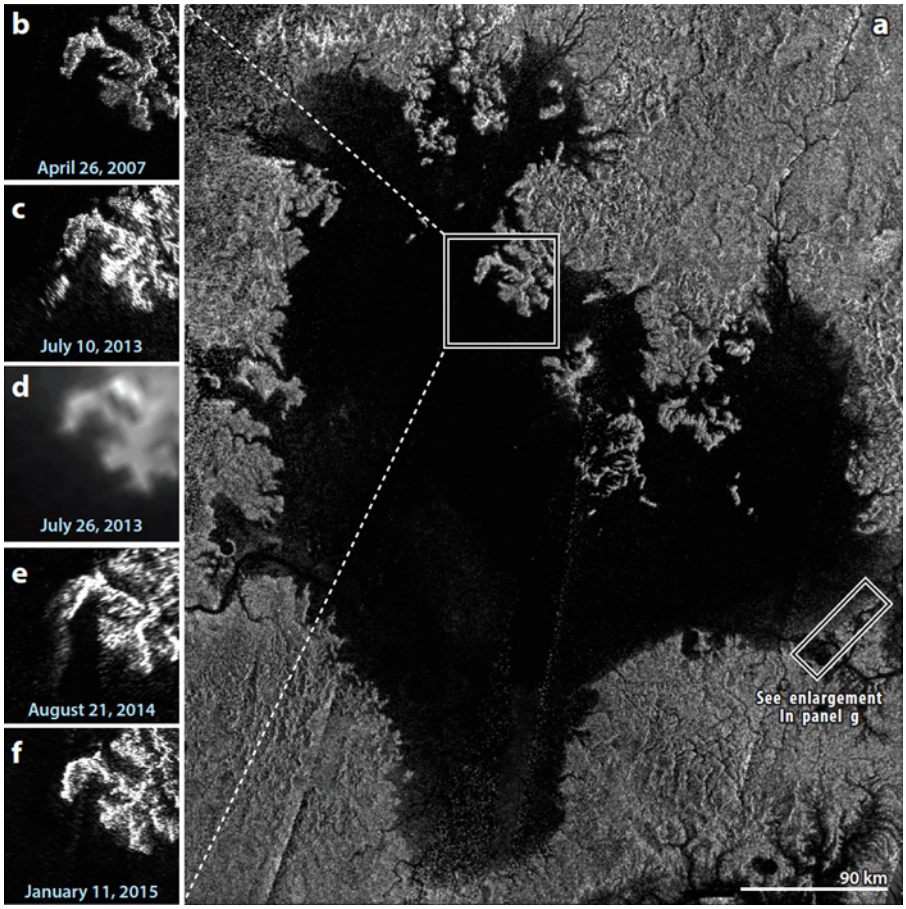

Figure RADAR-20. Time evolution of the first and most observed Magic Island region. The large panel on the right is a SAR mosaic of Titan's hydrocarbon sea, Ligeia Mare. The panels on the left show the temporal variation of a region observed to have Magic Islands. Transient bright features (Magic Islands) are observed in the images from July 10, 2013 and August 21, 2014 that are not present in any other images of this region [Hayes 2016]. The VIMS observation on July 26, 2013 (panel d) did not detect Magic Islands, however, the possibility that they were present but not detected in these observations could not be ruled out. Magic Islands were definitely not present in SAR observations before the first appearance and after the second appearance. The figure shows only a subset of Cassini observations of the region, see Hofgartner et al. [2016] for all observations with a resolution sufficient to observe the Magic Islands.

ARRAKIS PLANITIA PRECIPITATION AND OTHER TRANSIENT EVENTS

The first Cassini observations of surface change on Titan were obtained over Arrakis Planitia, near the South Pole, where ISS observed the appearance of dark splotches (interpreted as ponded hydrocarbon liquid) in June 2005 that were not present in the previous observation acquired in July 2004 [Turtle et al. 2009]. In October 2004, between those two observations, a large cloud outburst was observed near Titan's South Pole from Earth-based telescopes [Schaller et al. 2006].

SAR images and SARTopo later found that the ISS dark splotches occurred in topographic depressions that are morphologically similar to steep-sided depressions interpreted as empty lakes in the north [Soderblom et al. 2016]. VIMS observations of this area acquired between 2007 and 2009 show that the dark splotches had become brighter than the surrounding terrain [Soderblom et al. 2016]. SAR images of the area obtained in October 2007 and December 2008 showed the absence of dark splotches in the same topographic depressions, this time in the microwave, that were interpreted as either the evaporation or infiltration of ponded liquid [Hayes et al. 2011].

In addition to Arrakis Planitia, temporal changes have also been observed at other locations in the South Pole as well as within the northern lakes and seas and at equatorial latitudes. The largest observed surface change occurred in 2010 when an equatorial area of over 500,000 km in size was observed to darken, presumably by methane precipitation, after a chevron-shaped cloud passed over the region [Turtle et al. 2011]. SAR images of the area suggest that the darkened region represented local topographic lows. The area was later observed to return to its original albedo [Barnes et al. 2013]. Whereas there have been no definitive changes observed in the shorelines of the northern lakes and seas through April 2017 (flyby T126), there have been several surface changes reported for lacustrine features in the south polar region. Turtle et al. [2011] argued for shoreline recession at Ontario Lacus between ISS images acquired June 2005 and March 2009, although the poor resolution of T51 makes quantitative measures difficult. Hayes et al. [2011] found that, while inter-instrument comparisons can be dangerous, SAR images acquired in 2009 (T57/T58) and 2010 (T65) were consistent with a receded shoreline when compared to the June 2005 images obtained by ISS. However, Cornet et al. [2012b] argued that, to within measurement error, the data are consistent with no changes at all. Hayes et al. [2011] also discussed repeat RADAR passes of the south acquired in 2007 and 2008/2009 that contain lacustrine features that seem to disappear between subsequent SAR observations. The observed ten-fold increase in SAR backscatter cannot easily be explained by geometric effects and suggests that, between the observations, liquid either infiltrated into the ground, evaporated, or did both [Hayes et al. 2011]. Other temporal changes, including roughening events interpreted as wave or fluvial activity as well as Titan's mysterious magic islands have been observed within the northern seas. These changes are discussed in the section entitled Magic Islands.

Although the Cassini mission's exploration of Titan's methane cycles has ended, ground-based observations can continue to monitor Titan's weather until future missions can map fluvial features at a higher resolution and characterize the composition of surface material (including the lakes and seas) through in situ exploration.

Observation of a Summer Lag in the North Pole (by Radiometry)

One of the main scientific objectives of the Cassini Extended Mission (2008–2017) was to monitor the changing seasons on Titan. If any change were to occur, it should be primarily in Titan's arctic regions where the most important temperature variations are expected (though limited to 2-4 K over the course of a year).

Onboard Cassini, both the Composite Infrared Spectrometer (CIRS) and the microwave radiometer had the ability to measure the variations of surface/near-surface temperature with time [Jennings et al. 2009; Cottini et al. 2012; Janssen et al. 2016] and both instruments observed a lag in the summer warming of the northern polar terrains [Jennings et al. 2016; Le Gall et al. 2016]. They reported a much slower rise of temperature in late spring (2014–2015) than predicted by a global circulation model (GCM), even assuming a very high thermal inertia for lakes and seas [Tokano 2005]. Further, there seems to be no significant temperature difference between the land and the seas, which suggests that the solid surface surrounding the lakes and seas of Titan are saturated with liquid and behave thermally like the liquids. They may as well experience evaporative cooling which would explain the low measured temperatures in the north polar region and have important implication for the hydrocarbon cycle on Titan.

Surface and atmosphere interaction

Winds and temperature

In contrast to the contemporary instantaneous winds revealed by sea surface roughness (see section entitled Major Geologic Units and Mapping), the widespread observations of dunes on Titan attest to winds that have acted over significant periods in the past, and indeed the possibility that aeolian landforms might shed light on Titan's climate history was recognized before Cassini's launch—for example, Lorenz et al. [1995]. Since so few trackable cloud features have been observed on Titan, the aeolian features in Titan's landscape have emerged as one of the principal constraints on Titan's meteorology. Specifically, it has been estimated that the saltation threshold for the movement of dry sediment on Titan requires surface winds of the order of 1 m/s—for example, Greeley and Iversen [1987], Lorenz et al. [1995], and Lorenz [2014]. This estimate is based on an assumption of interparticle cohesion not too different from terrestrial sands: some laboratory measurements suggest they could be slightly larger [Burr et al. 2015] and it is possible or even likely that (methane/ethane) moisture [Yu et al. 2017] and/or electrostatic charging [Lorenz 2014; Mendez-Harper et al. 2017] could be responsible for stronger cohesion. In any case, the presence of dunes requires winds sometimes exceeding this threshold in the past.

The construction or reorientation time for dunes of the size (~100 m tall) observed by Cassini is substantial, of the order of 50,000 years [Ewing et al. 2015; Lorenz et al. 1995; Lorenz 2014]. Thus, not only does the presence of dunes require that the winds have been above the saltation threshold for a substantial integrated period, but also that the dune pattern observed today retains some memory of winds extending into the past by a substantial part or multiple of an astronomical (Croll-Milankovich) climate cycle—see, for example, Aharonson et al. [2009]; Lora et al. [2014]. In particular, Ewing et al. [2015] noted that some of Titan's dunes are somewhat crescentic, implying a recent dominance of a northward meridional component to the winds—see McDonald et al. [2016].

The generally-eastwards direction of sand transport implied by the dune morphology was noted early [Lorenz et al. 2006; Radebaugh et al. 2008; Lorenz and Radebaugh 2009] and was a

challenge to meteorological expectations, since low-latitude near-surface winds should have on average an easterly (westwards) flow, much like the trade winds on Earth. Tokano [2008] made some of the first systematic experiments with a GCM to attempt to reproduce the observed pattern by positing the influence of Xanadu as a highland or bright region. The vexing paradox—see for example Lorenz and Zimbelman [2014]—was resolved by invoking occasional westward gusts [Tokano 2010; Charnay et al. 2015] such that even though the average wind direction is eastwards, these typical winds are below the threshold speed and so are not reflected in the sand transport. Thus, the landscape is shaped only by the stronger (westward) gusts—with the saltation threshold acting like a diode in an electrical analogy of alternating winds. Tokano [2010] found that a threshold of order 1 m/s was consistent with obtaining a dune pattern similar to that observed, and suggested that stronger vertical mixing in the low-latitude troposphere during the equinox period might cause the required westward flows. This idea has been developed somewhat further by Charnay et al. [2015], who suggested that methane rainstorms in particular may be responsible. Significant developments in the mapping of dune morphology and orientation to wind diversity and sand supply/mobility have taken place in the last decade and a half, stimulated in no small part by the Cassini discovery of large linear dunes as well as other wind-borne features [Lorenz and Radebaugh 2009; Malaska et al. 2016a]. Detailed observations suggest that there is a divergence of material transport in the equatorial regions, and a convergence in the mid-latitude regions around latitude 35°. This suggests that a relationship exists between two major land units on Titan: the longitudinal dunes and the undifferentiated plains, as discussed in the section entitled Plains. It has been suggested [Rubin and Hesp 2009] that sticky sand may yield longitudinal features, and laboratory results with organic material have shown that electrostatic charging may be significant for Titan organics under cryogenic, dry conditions [Mendez-Harper et al. 2017]. Nonetheless, the interaction of multiple modes of dune growth may be important in decoding Titan's winds from dunes—for example, Lucas et al. [2014].

In contrast to the complex wind story, the overall distribution of dunes on Titan is somewhat straightforward from the standpoint of wetness. Early Titan GCM studies—for example, Rannou et al. [2006]; Mitchell [2008]—indicated that Titan's low latitudes should be dried out by the general circulation, as a result of the meridional (Hadley) cells on this slowly rotating world. Thus, the dunes form a broad equatorial belt on Titan, whereas they form belts at about 20 degrees north or south on the faster-rotating Earth. The size and spacing of dunes, assuming that they have been allowed to grow to their full extent without being limited by growth time or sand supply, has been determined—for example, Andreotti et al. [2009]—to correlate to the thickness of the atmospheric boundary layer. Essentially, the layer caps the dune growth once the spacing is roughly equal to the layer thickness. Lorenz et al. [2010] showed that the Huygens descent data were consistent with a boundary layer thickness of the order of 3 km, matching the typical dune spacing on Titan. Extensive dune spacing measurements—for example, Le Gall et al. [2011], and Savage et al. [2014]—show only small minimal variations with latitude. Charnay et al. [2012] found that a GCM with an improved boundary layer scheme reproduced the 3 km thickness, interpreting this as a seasonal boundary layer.

The full meteorological interpretation of the dune pattern revealed by Cassini's RADAR will require a finer scale of modeling than has been performed so far, including regional topography

and albedo effects. It may be that the dune fields, by virtue of having a low thermal inertia and albedo, cause their own sea breeze effect, modifying the local winds. The role of evolving ground moisture remains to be elucidated, although some hints of moisture effects on ground thermal inertia have been suggested in the RADAR radiometry data [Janssen et al. 2016].

Although the radiometer in principle is an indicator of surface temperature and could be used to independently constrain gradients with latitude etc. [Lorenz et al. [2003], in practice, the surface temperature estimates from the Cassini CIRS and the Huygens probe have been adopted as ground truth and the interpretation of the microwave radiometry has been principally in terms of the surface dielectric properties. However, future studies might profitably examine small-scale radiometer variations and their correlation with surface elevation—in principle, the ~1 K/km lapse rate may have a signature in surface brightness temperature.

METHANALOGIC CYCLE

Titan is the only place in the solar system, other than Earth, that is known to have an active hydrologic cycle.

Titan is the only place in the solar system, other than Earth, that is known to have an active hydrologic cycle. Titan's methane-based hydrologic cycle is an extreme analog to Earth's water cycle. Exchange processes between atmospheric, surface, and subsurface reservoirs produce methane and ethane cloud systems, as well as erosional and depositional landscapes that have strikingly similar forms to their terrestrial counterparts. Over its 13-year exploration of the Saturn system, Cassini has revealed that Titan's hydrocarbon-based hydrology is driven by nested methane cycles that operate over a range of timescales including geologic, orbital, seasonal, and that of a single convective storm. A fast physical (phase change) cycle drives active weather and fluvial processes over seasonal to orbital timescales. A medium-paced chemical cycle siphons off methane for photochemical synthesis in the upper atmosphere, depositing the products on the surface over timescales of millions of years. A long-term geologic cycle may sporadically inject methane into the system from Titan's interior over the age of the solar system. For a recent review of Titan's hydrologic cycle, see Hayes et al. [2018].

Titan as a system

Titan is the only moon in the solar system with an atmosphere so massive that it dominates the total volatile inventory in the surface-atmosphere system and provides strong radiative forcing and an active meteorology [Lorenz et al. 2005]. It also obscures the surface from view in both the optical and infrared, which is why the Cassini RADAR has been such a crucial tool. However, by the irreversible deposition of heavy hydrocarbons, nitriles, and other photochemical products from methane and nitrogen, the atmosphere also obscures the underlying surface geology to some extent. Were the current inventory of methane to condense onto the surface, it would form a layer 5 m thick [Mitchell and Lora 2016], but a variety of evidence suggests that many times that number is present in various solid and liquid deposits of organics on and within the crust [Hayes et al. 2018].

Therefore, Titan's geologic history is poorly constrained and in particular there is a significant uncertainty as to what fraction of the body's 4.5 billion years of existence is recorded on the surface. Observations relevant to its history include:

1. The low observed numbers of impact craters [Porco et al. 2005] yield an age of hundreds of millions of years, not billions [Lorenz et al. 2007; Wood et al. 2010; Neish and Lorenz 2012].

2. The rate of photodissociation of methane in Titan's atmosphere implies that the current gaseous inventory will be depleted in some tens of millions of years [Yung et al. 1984].

3. Titan's interior has at least partially differentiated, resulting in a rock-metal core, a high-pressure ice mantle of uncertain thickness, a liquid water ocean [Iess et al. 2010] perhaps with salts and ammonia [Mitri et al. 2014], and an ice crust 50 to 150 km thick. The core is either significantly hydrated [Castillo-Rogez and Lunine 2010], or there is a mixed rock-ice layer somewhere in the interior [Tobie et al. 2014].

4. A range of chemical and physical data from the atmosphere to the interior suggest that a significant event, or change in the way Titan evolves, occurred sometime between a few hundred million and a billion years ago [Horst 2017].

The relatively youthful age of the surface, which may be the result of geologic activity, older impacts occurring on surfaces covered by liquids [Neish and Lorenz 2014], extensive erosion, or substantial burial in organic matter, means that there is little if any geologic evidence of the first 3/4 of Titan's history. Two unanswered questions are: 1) what was the process/processes that eroded or covered older impact craters and other landforms; and 2) did the obscuration of features older than a few hundred million years occur continuously over time, or in some singular event?

There is no evidence of the answer to the second question, but a theoretical model of the evolution of Titan's interior by Tobie et al. [2006] provides an intriguing scenario that implies Titan had a significant change in the working of its interior, crust, and atmosphere about 500 million years ago [Wood 2018]. In the Tobie et al. [2006] model, Titan had a thin and rigid clathrate crust—with methane as the dominant guest species—up until 500 million to one billion years ago. During that earlier epoch, several major heating events resulted in the release of large (compared to the present atmospheric inventory) amounts of methane from the clathrate hydrate into the surface-atmosphere system. Within the last 500–1000 million years the interior has cooled sufficiently to allow an ice I crust to form underneath the buoyant clathrate hydrate crust, with diapirism in the thickening ice I crust providing one or several episodes of further release of methane into the surface-atmosphere system.

Wood [2018] called the onset of the ice I subcrust the Great Crustal Thickening Event and noted that the mode of geologic processes would change dramatically as Titan transitioned from a

body with a thin rigid conductive crust over the ocean to one with a thicker and rheologically heterogeneous crust.

Models of Titan's interior look broadly similar but with substantial disagreements on the thickness of the high pressure ice layer and the extent of silicate core hydration [Tobie et al. 2014]. How much this affects the surface evolution is unclear. While the idea is commonly held that the source of the methane to resupply the atmosphere is in crustal clathrate hydrate—such as that predicted in pre-Voyager days [Lewis 1971]—how the resupply works is unclear. Simple forcing out of the methane from the clathrate by the photochemically produced ethane eventually fails because of the stoichiometry (two methane molecules making one ethane), although this replacement could eventually weigh down the crust and cause an overturn because clathrate with predominantly ethane is heavier than ice I [Choukroun and Sotin 2012]. This could cause interesting geologic consequences in the present era when the clathrate is nominally underlain by warm ice I. Whether the methane hydrological cycle that we see today shaping so many aspects of Titan's surface is ancient or recent, episodic [Lunine et al. 1998] or continuous, remains a mystery that may be directly coupled to the poorly understood interior evolution. Or it may reflect a series of external events whose record in the Saturn system has yet to be properly read.

Birch et al. [2017] have pointed to geologic evidence (notably the presence of large sedimentary deposits) suggesting that the present epoch of lakes and seas of methane, ethane, and nitrogen might have been preceded by one with a widespread ocean of methane and other hydrocarbons. The longevity of such an ocean, in particular its decline, may be constrained by the limits on tidal dissipation of the orbital eccentricity during ocean shrinkage [Sagan and Dermott 1982; Sears 1992], since we now have measured global Titan topography. Finally, it is possible that Titan has run out of atmospheric and surface methane multiple times in its history, leading to dramatic atmospheric changes [Lorenz et al. 1997] and possibly epochs in the which the surface is worked by liquid nitrogen seas and rivers [Charnay et al. 2014].

If Titan's geologic and atmospheric nature have changed in a secular way over its history, it would join the other terrestrial planets—Venus, Earth, and Mars, in this regard. In each case, interior and surface-atmosphere changes over time have led to present-day characteristics that are likely to have been dramatically different from those in the past.

Open questions

Now that we have a global view of Titan contributed by several Cassini instruments, the questions that remain become more detailed and in general require more than one data type to address. Some also require a different type of sensing platform as well. NASA plans to send a rotorcraft to Titan called Dragonfly, scheduled to launch in 2026 and land in 2034 [Lorenz et al, 2018; http://dragonfly.jhuapl.edu/]. Dragonfly's primary objective is to look for prebiotic chemical processes, and it will also address open questions atmospheric, surface and subsurface properties. Other open questions are addressed in Lunine's Interdisciplinary Scientist (IDS) report on Titan elsewhere in this report.

Below we list a subset of those questions that might be addressed by future spaceborne radar instruments, keeping in mind that they have proven to be a challenge from several standpoints. In fact, because of Cassini's success, the minimum orbiter science payload considered worthwhile for such purposes is now fairly large [Reh 2007].

Direct benefit from higher resolution (<100m) SAR

- To what extent is the surface fluvial dissected?
- How do the organic compounds produced in the atmosphere evolve on the surface?
- Does cryovolcanism occur on Titan?
- What is the composition of the dune particles and how are they produced?
- What is the nature of the asymmetry in seasonal effects?

Indirect benefit from higher resolution SAR/HiSAR/scatterometry/ altimeter

- How did the lakes and sea basins form?
- What is the organic and inorganic composition of the surface?
- What is the circulation in the lakes and seas and how is it affected by the atmosphere?
- What is the salinity and composition of the deep ocean and is it in contact with rock beneath?

Direct benefit from a radar sounder

- What is the nature and extent of the exchange between the surface/atmosphere and deep subsurface and ocean?
- What is the depth and thickness of the subsurface ocean?

Saturn Science

Introduction

The thermal emission from the gas-giant planets was first observed by single-antenna telescopes in the 1950s [Mayer 1958], and quantitatively related to fundamental atmospheric properties in the following decade [Thornton and Welch 1963; Gulkis et al. 1969; Wrixon and Welch 1970]. Subsequent observations through the 1980s filled in the disk-temperature spectra of Jupiter and Saturn through the millimeter- and centimeter-wavelength range. This combined with advances in understanding the high-pressure microwave absorption of ammonia, which possesses a strong inversion band just longward of 1 cm wavelength, led to a consistent story of deeply convective

atmospheres with ammonia as the dominant absorber [Gulkis and Poynter 1972; Berge and Gulkis 1976; Klein and Gulkis 1978]. The advent around the same time of radio interferometers capable of using aperture synthesis to image the planets led to the first microwave image of Saturn, reported by Schloerb et al. [1979] using the interferometric Owens Valley Radio Observatory at 3.7 cm wavelength. The completion of the National Radio Astronomical Observatory's Very Large Array (VLA) in New Mexico was followed by a series of images of Saturn and its rings made with this instrument reported by a number of authors at wavelengths ranging from 2–21 cm wavelength (de Pater and Dickel [1982, 1991]; Grossman et al. [1989]; Grossman [1990]). These studies have resulted in a better understanding of Saturn's rings and atmospheric microwave spectrum, and have provided evidence of large-scale structure in Saturn's ammonia distribution including variable broad bands in the mid-latitudes. However, they have been limited by the capabilities of the VLA in spatial resolution and dynamic range for imaging extended objects; in addition, the process of Earth-rotational aperture synthesis used for imaging averages out longitudinal structure.

The microwave radiometer contained in the Cassini RADAR provides a unique opportunity to image Saturn with the advantage of close range and without the limitations of a ground-based approach other than the restriction to a single wavelength. This has resulted in nearly an order-of-magnitude improvement in both spatial resolution and sensitivity over Saturn microwave observations published up to the Cassini era, although improvements made to the VLA since then promise to close this gap. In this report we summarize the mapping campaign of Saturn carried out by the RADAR radiometer during the Cassini mission and its main results, leaving the details to papers already in the literature.

Observations

The thermal emission from Saturn's atmosphere was mapped globally on six occasions by the RADAR radiometer at its single wavelength (2.2 cm) and half-power beamwidth of 0.36°. Imaging was achieved by controlling the spacecraft orientation to scan the source using the spacecraft momentum wheels to scan back and forth from pole to pole. We obtained six global maps of the 2 cm thermal emission from Saturn distributed over a period from 2005–2015, each obtained using a period of approximately 14 hours centered on an equatorial periapsis pass. The motion of the spacecraft and Saturn's rotation combined to provide nearly complete global maps of Saturn in each pass. Janssen et al. [2013] presented the first five of these maps and described in detail the techniques used, calibrations, and general interpretations. A companion paper by Laraia et al. [2013] focused on the interpretation in terms of the ammonia vapor distribution in the ammonia cloud and sub-cloud region. A sixth map was obtained in May 2015 and a paper presenting its results is in preparation at the time of this report.

The five published maps are shown in Figure RADAR-21 as cylindrical maps of brightness temperature relative to a model Saturn atmosphere with nominal composition and fully saturated ammonia—for example, 0 K in the map indicates an absolute brightness as given by the fully

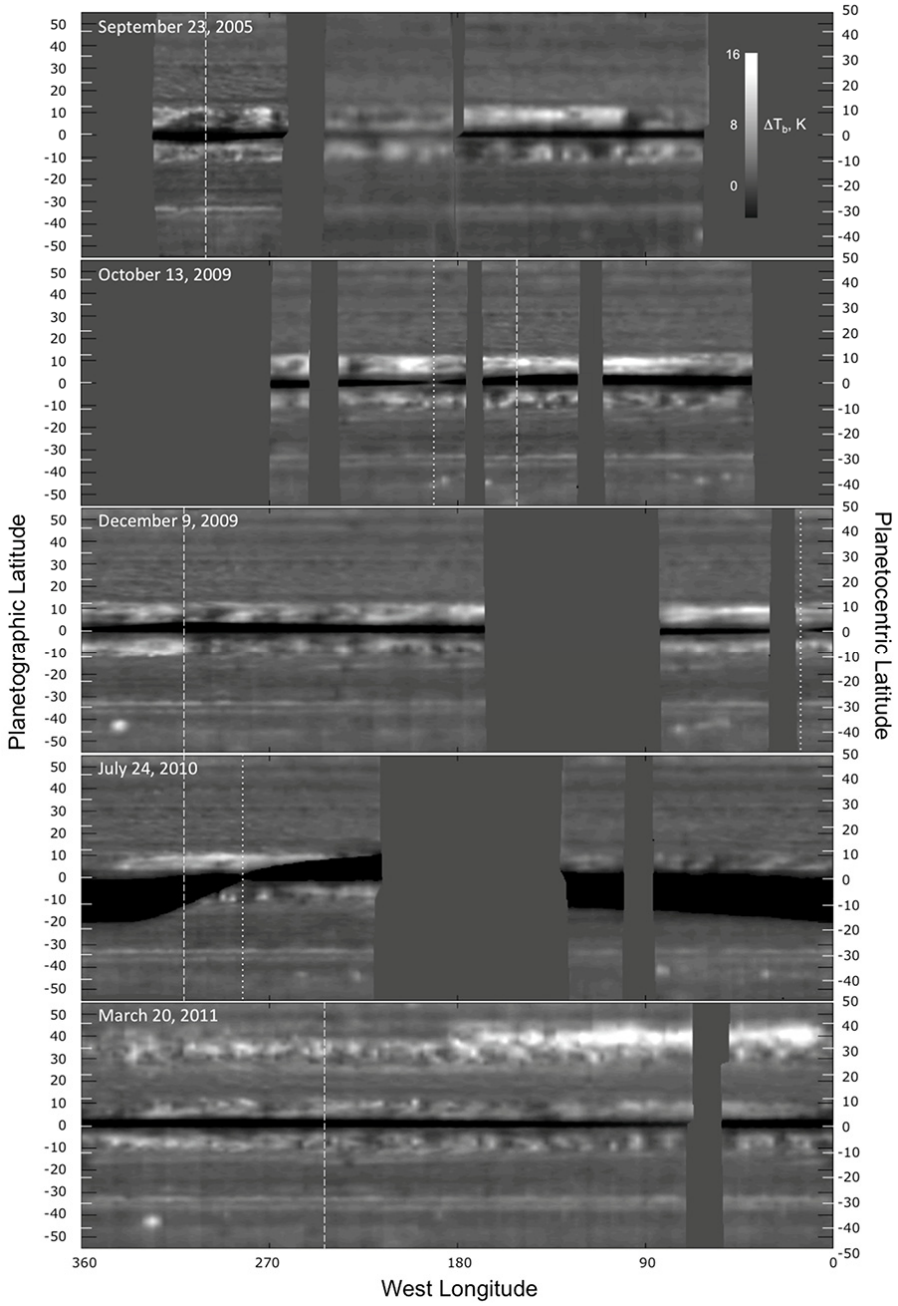

Figure RADAR-21. Global cylindrical maps of Saturn's thermal emission obtained at 2.2 cm wavelength during the Cassini prime and equinox missions. This was obtained by accumulating north-south scans from pole to pole during an approximately 14-hour period surrounding Saturn periapsis.

saturated model (see section entitled Key Objectives for RADAR Instrument). The Saturn brightness measurements themselves were calibrated to an absolute accuracy approaching 1% by transferring absolute calibrations obtained from Titan observations [Janssen et al. 2009, 2016] to Saturn. All observations were made during periods in the mission when the spacecraft was in Saturn's equatorial

plane. The inclination of the rings as seen by the spacecraft was less than 1° for all observations except for that of July 24, 2010 where it approached 4°. The dark band with variable width seen in the equatorial region is due to blockage by the rings. Gaps indicated by the uniform grey shading (corresponding to 0 K relative brightness) are lapses in data-taking where time had to be taken to unload the spacecraft momentum wheels. The dashed and dotted lines indicate periapsis and ring plane crossings respectively (there were no observations made exactly at ring plane crossing for the 2005 and 2011 maps). Planetographic latitudes are indicated by black ticks on the vertical scales, planetocentric by white. Mapping of the regions outside approximately ±50° latitude is of lower quality because of high emission angle and the results obtained there are not shown. The resolution in latitude is as good as 0.86° at the equator, and the sensitivity of each observation is ~0.1 K. The longitude resolution is limited by the scan rate of the spacecraft but averages about 2° at the equator.

Interpretation

The maps are interpreted in terms of a reference model for Saturn's atmospheric structure and composition based on Atreya [2010] and shown in Figure RADAR-22, using current values for the known constituents of the atmosphere [Hanley et al. 2009; Deveraj 2011]. The weighting function in

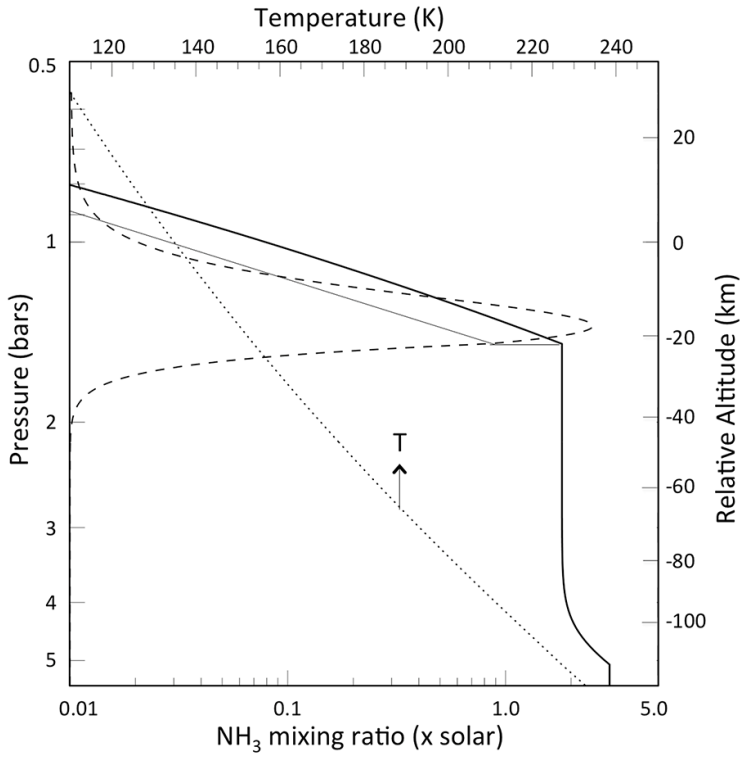

Figure RADAR-22. Atmospheric model used to compute reference brightness temperatures. The temperature (dotted line) and NH_3 mixing ratio in units of solar abundance (thick solid line) are shown as a function of pressure and altitude in the vicinity of the ammonia cloud region in the atmosphere. The reference model assumes 100% relative humidity for ammonia above its saturation level, while the light solid line shows a case for 50% relative humidity. The decrease in NH_3 mixing ratio above the 5-bar level is due to reaction with H_2S to form NH_4SH ice. The dashed line shows the 2.2 cm wavelength weighting function in arbitrary linear units at normal incidence for the reference model.

Figure RADAR-22 shows the region responsible for the thermal emission assuming that the ammonia is fully saturated in the cloud region. In this model, the microwave absorption, and hence thermal emission, is seen to be due almost entirely to gaseous ammonia and is located primarily within the ammonia cloud region. Any depletion of ammonia relative to the fully saturated model leads to excess brightness. The maps indicate that the ammonia cloud region is everywhere unsaturated (at least away from the equator where the atmosphere is blocked by the rings), and variations in the ammonia can be expected to trace atmospheric circulations in and below the clouds.

The maps in Figure RADAR-21 reveal features either never before seen or known features viewed from a perspective never before available. The region of the atmosphere responsible for the microwave brightness variations, roughly 0.5 to 2 bars, has been extensively observed with high-resolution instruments at infrared wavelengths. Nevertheless, the unique value of observations at 2.2 cm wavelength is the simple origin of the observed structure—it is just ammonia vapor and variations in its distribution. Low residual brightness indicate the presence of gas phase ammonia in the cloud region at concentrations approaching but not exceeding its saturation level, whereas higher brightness indicates a relative depletion. The variability of the brightness distribution across Saturn suggests the existence of circulations that cause the depletion or enhancement of the ammonia by means of gas flow into and out of the ammonia condensation region, while the morphologies of these variations give clues as to the nature of the dynamical forcing causing these flows. Obvious features include the bright bands that are symmetric about the equator from approximately 3° to 10° latitude north and south respectively, where regions of high brightness alternate with low brightness regions resulting in longitudinal variability not seen at higher latitudes (until the Great Northern Storm in the 2011 map). These regions are similar to Jupiter's equatorial belts as seen recently by the Juno microwave instrument on the Juno spacecraft [Bolton et al. 2017]. The regions of high brightness in these bands are dry in the sense of low ammonia abundance, and therefore resemble the dry sub-tropics of Earth.

In between the north and south equatorial bands, at the equator, is a central band of relative calm with the lowest brightness seen on Saturn, similar to that seen by Juno in Jupiter's equatorial zone. The low brightness seen here indicates ammonia concentration to be near saturation, consistent with the greatly enhanced NH_3 abundances found by VIMS in this region [Fletcher et al. 2011]. Although difficult to discern because of the ring blockage, this band is apparent at or near the ring crossings, most notably in the central segment of the 2005 map. Although at relatively low resolution, the ring inclination in this segment is near 0.01° as seen from the spacecraft, with the blockage causing less than a 1 K influence on the brightness. Laraia et al. [2013] present a more thorough examination of the ring blockage, using a ring model to retrieve the equatorial brightness at the ring plane crossings for all maps to confirm the presence of generally uniform near-saturated ammonia in the equatorial belt.

We investigated the significance of these maps more quantitatively by assuming a simple model for the ammonia distribution. In particular, we allowed the ammonia concentration to vary only in the cloud region only, assuming that it could be described there by a constant relative humidity (RH) in the range 0% < RH < 100%. Figure RADAR-23 shows an analysis using this model carried out by Laraia et al. [2013] of the March 2011 map, which fortuitously captured the Great

Northern Storm of 2010–2011 in progress. The map in panel (a) shows the relative humidity derived from the relative brightness and illustrates that, in general, most of the variation in brightness can be interpreted as variation of ammonia within the cloud region. Significantly, some regions cannot be described this way since the brightness temperature exceeds the model brightness with all cloud ammonia removed. Hence, in these regions, some of the sub-cloud ammonia must be removed as well. The Great Northern Storm (seen in panel (b) around the same time by the Imaging Subsystem) had progressed about halfway around the globe at the time of this map, and shows a dramatic decrease in ammonia extending well beneath the clouds. This supports a model describing the cause and consequences of this storm that predicts such an ammonia depletion [Li and Ingersoll 2015]. The north and south equatorial belts, and isolated storms in a region near 40°S latitude, show evidence of such strong depletion in this map, and all others as well.

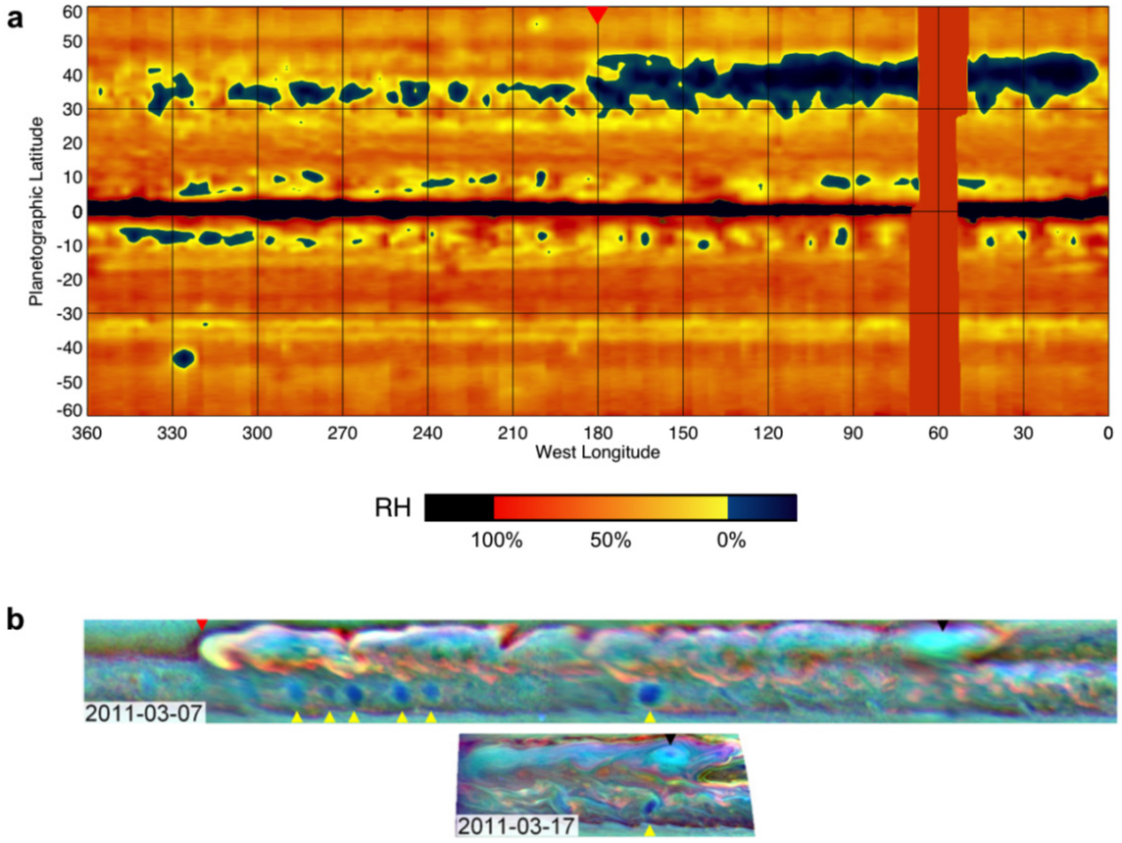

Figure RADAR-23. A simple model used for the ammonia distribution. (a) Map of ammonia cloud humidity from March 20, 2011. Black regions would indicate super saturation of ammonia in the cloud layer (we do not see any). Here, the black regions are due to the cold rings blocking the emission from the atmosphere. Blue regions are regions that require ammonia depletion below the ammonia cloud layer (i.e., RH < 0 in the cloud layer). The northern storm is blue, indicating low ammonia concentrations in the storm that extend to layers beneath the clouds. There are many local regions in the subtropical bands, as well as a storm in the southern hemisphere near 325°W, −43°, that require ammonia depletion below the clouds. (b) Two Cassini ISS images of the northern storm from Sayanagi et al. [2013] Figure 4. These are the closest dates we have to the 2.2 cm map date. Cloud heights are distinguished by the three color filters—red (CB2−750 nm), green (MT2–727 nm), and blue (MT3–889 nm).

A final global map was obtained in 2015, more than four years after the onset of the storm. This map is shown in Figure RADAR-24 in context with maps from 2010 and 2011, all together showing Saturn's atmosphere prior to, in the midst of, and after the storm onset. Figure RADAR-25 shows the relative humidity as described in Figure RADAR-23. This map shows the long-lived ammonia depletion in the latitudes affected by the storm as it has evolved, and contains valuable information on the nature of convection, meridional and zonal circulations in Saturn's sub-cloud atmosphere. A paper discussing the implications for the dynamics of Saturn's atmosphere is in preparation as of this writing.

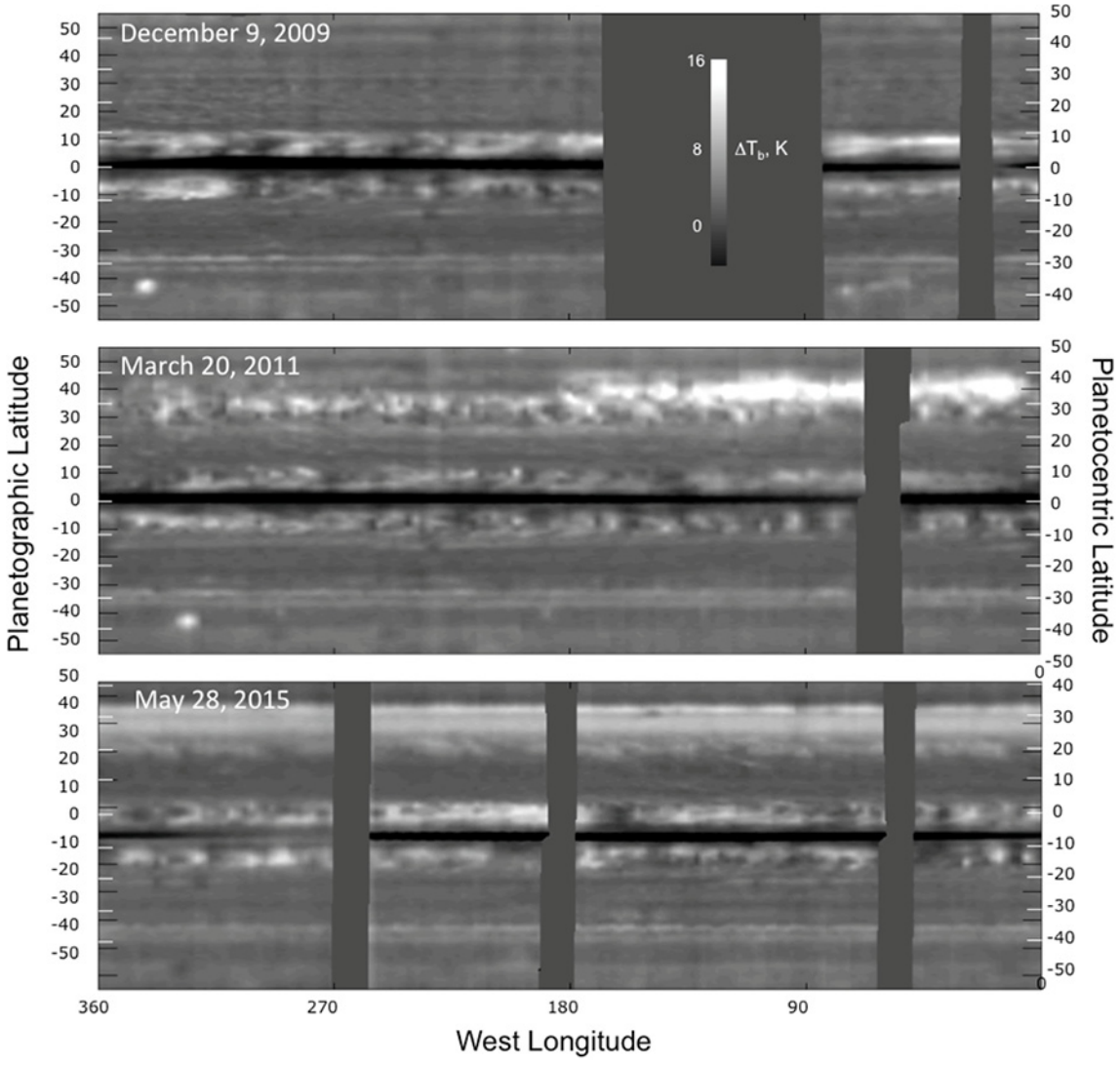

Figure RADAR-24. The global map of 2015 shown in context with earlier maps to show the development of the Great Northern Storm of 2010–2011. The relative brightness for each is shown as in Figure RADAR-21.

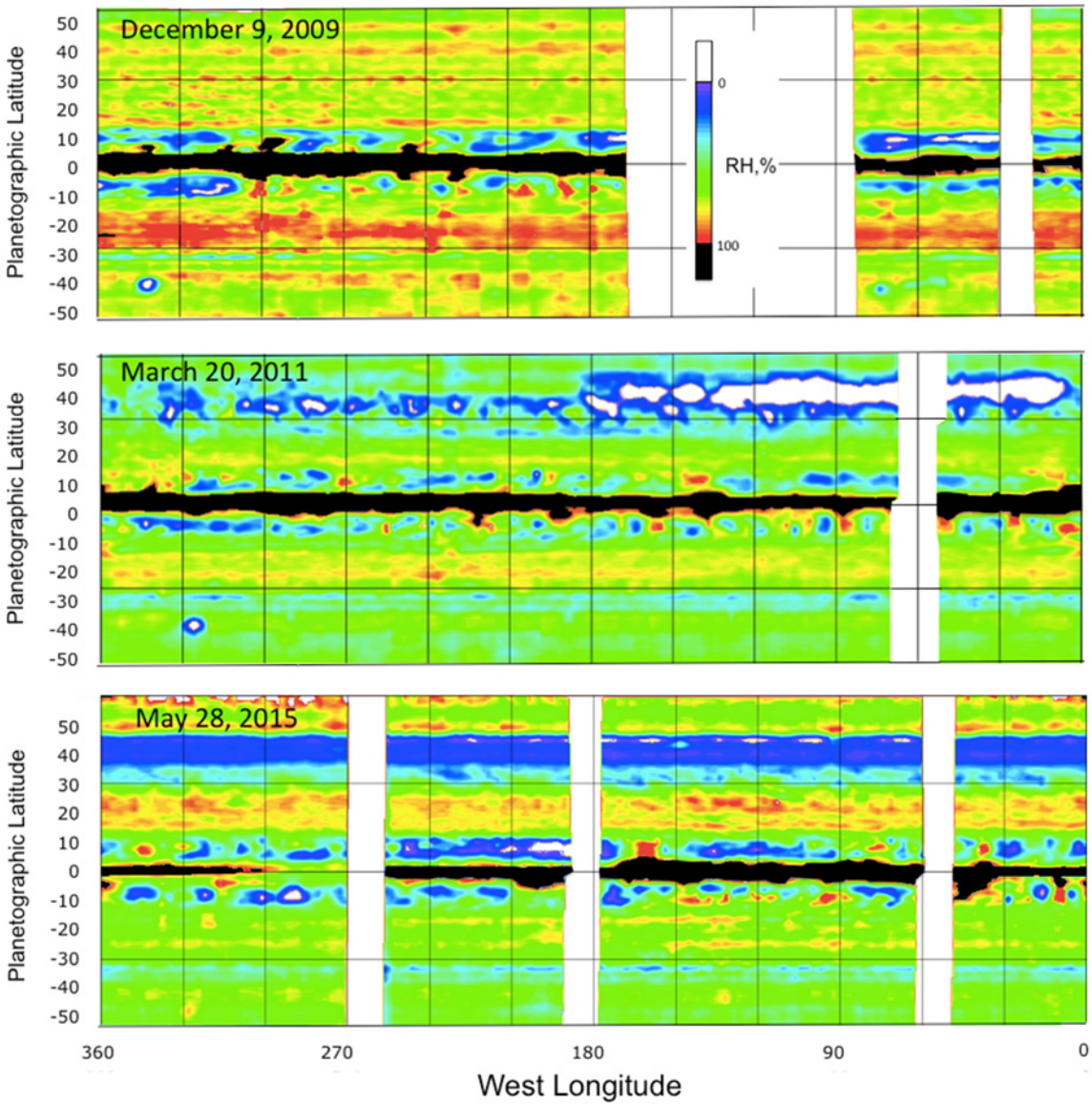

Figure RADAR-25. Ammonia cloud relative humidity for the brightness maps in Figure RADAR-24. Here regions of black are due to ring blockage, while white indicates regions where ammonia additional depletion below the cloud base is required to fit the observations.

Open Questions

The Cassini RADAR radiometer has provided unprecedented images of Saturn's equatorial and mid-latitude atmosphere at 2 cm wavelength. It has uniquely measured the cloud and sub-cloud humidity through the period of the Great Northern Storm of 2010–2011. This provides a basis for ground-based observations of Saturn over multiple frequencies using the VLA and Atacama Large Millimeter/Submillimeter Array (ALMA) radio interferometers to extend the atmospheric depths sounded and follow the slow decay of the 2010–2011 storm, which remains a puzzle. A follow-on

radiometric experiment based on the Juno orbiter's Microwave Radiometer [Janssen et al. 2017; Bolton 2017] would be an excellent complement to an atmospheric sounder assuming that difficulties in obtaining a close orbit and achieving deep sounding in Saturn's more absorbing atmosphere can be overcome. This would enable a comparative examination of the deep atmospheres of both gas giants, which appear to have strikingly different dynamical properties based on present results from Cassini and Juno.

Saturn Ring Science

Introduction

Saturn's rings are the most massive, extensive and diverse ring system in the solar system, …, their origin and age continue to be a subject of debate.

Saturn's rings are the most massive, extensive and diverse ring system in the solar system, yet despite decades of ground and spacecraft-based observations [Dougherty et al. 2009; Grossman 1990; de Pater and Dickel 1991; van der Tak et al. 1999; Dunn et al. 2002, 2005; Poulet et al. 2003; Nicholson et al. 2008], their origin and age continue to be a subject of debate. Although water ice has long been accepted as the most prominent component of ring composition [Cuzzi et al. 1984; Esposito et al. 1984], it is the small fraction of non-icy material that is crucial in understanding their origin and age through source composition and exposure time to extrinsic micrometeoroid bombardment [Cuzzi and Estrada 1998]. However, the abundance and character of this non-icy material remained poorly understood until the extensive observations of Saturn's rings by RADAR, in both its active and passive modes.

Microwave observations at mm- to cm- wavelengths provide an ideal window through which to study the non-icy material fraction in Saturn's main rings, as these are wavelengths where the absorptivity of water ice is negligible compared to that of most non-icy material, and thus the intrinsic thermal radiation from the ring layer is dominated by the non-icy components. Moreover, whereas visible and near-IR spectra are only sensitive to the top millimeter or less of ring particle surfaces, microwave observations are able to sample the bulk of the ring mass. Furthermore, microwave measurements at mm- to cm- wavelengths are most sensitive to mm- and cm- scale particles, which are known to be the most dominant sizes of the ring particles.

Passive radiometry observations at 2.2 cm

During the Cassini Prime Mission, the radiometer scanned Saturn and its rings at 2.2 cm wavelength on 12 occasions between December 2004 and October 2008. There are two categories of radiometric observations of Saturn's rings: low-resolution map scans from a distance of ~20 RS (where RS = 60,330 km is Saturn's radius) and high-resolution spoke scans (not related to the

fuzzy features seen in the B-ring) from a distance of ~5–8 RS. The map scan footprints cover all of the main rings at all azimuthal angles. The projection of the line connecting Saturn's center and the spacecraft onto the ring plane lies at zero degree azimuth, and the azimuthal angle increases anti-clockwise in the ring plane. At small azimuthal angles, the observed ring regions occult Saturn. These observations are comparable to stellar and radio occultations except that the light source is due to the planet's radiation. On the other hand, high-resolution spoke scan footprints only cover the main rings at five distinct intermediate azimuthal angles where the rings are not occulting Saturn. While map scans reveal the complete angular scattering profile, spoke scans show finer radial structures. RADAR has a main beam size of 0.36° in angular diameter (full width at half maximum (FWHM) power), which results in radial resolution of ~2,000 km in high resolution scans and ~6,000 km in low resolution maps.

While this dataset presents several advantages, it is also very challenging to process. Each measurement of antenna temperature is the convolution of the radiometer's broad gain pattern and the brightness temperature of all targets in the field of view [Janssen et al. 2009]. In order to remove the contribution to the signal from the sidelobes and obtain values of the brightness temperature, we developed an iterative adaptation of the successful calibration and sidelobe removal algorithms [Zhang et al. 2017a] developed for Titan and Saturn [Janssen et al. 2009, 2013, 2016]. Figure RADAR-26 shows the output of our calibration and processing applied to a low-resolution map scan of Saturn's rings. Figure RADAR-27 shows the brightness temperature T_b profile versus distance from Saturn center after one high-resolution spoke-scan; all such scans were collected when the rings were not occulting Saturn, at azimuthal angles larger than 20 degrees. Going from the C-ring to B-ring and then to A-ring, the distance from Saturn increases, and hence the planet's angular size decreases as seen from Cassini's vantage point. The dashed curves in Figure RADAR-27 illustrate the decreasing trend of incoming radiation from Saturn as the observation point moves further away from Saturn center. While T_b follows the trend of incoming Saturn radiation in most parts of the rings, the distinct bump (with a peak at ~83,000 km) in the C-ring's brightness is too large to be attributed simply to optical depth variation, which suggests some unusual properties. We will show that this effect may result from a radially variable increase in non-icy material fraction that produces an extra amount of intrinsic thermal emission.

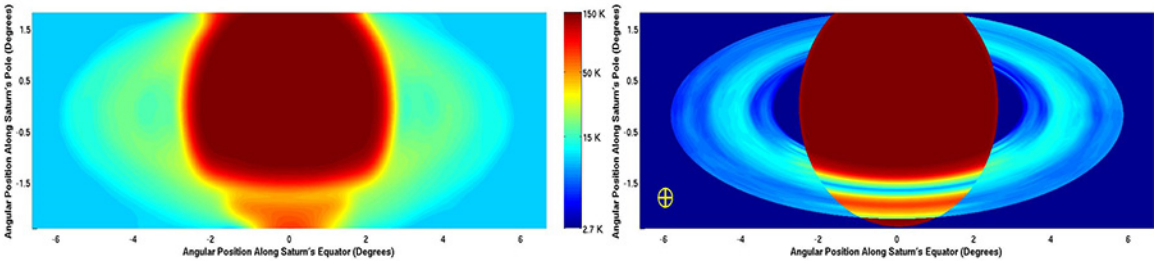

Figure RADAR-26. Calibration of low-resolution Cassini RADAR map scans as projected onto the sky in degrees. Left panel: The collected antenna temperature map. Due to the wide antenna pattern and extensive sidelobe contribution from Saturn, the antenna temperature shows very little clear structure of the main rings. Right panel: The output brightness temperature map obtained through our calibration. The yellow circle in the lower left corner shows the main beam size.

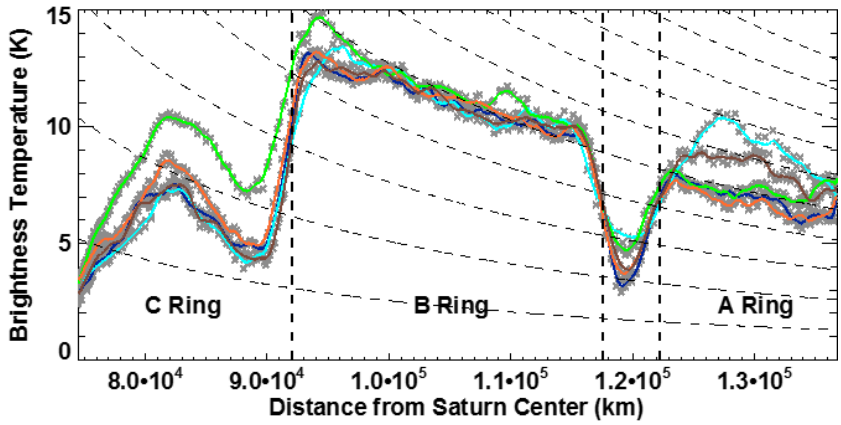

Figure RADAR-27. Brightness temperature T_b versus ring radius obtained from one high-resolution spoke scan. Solid lines of different color indicate spoke scans at different azimuthal angles. The black dashed lines show the trend of incident Saturn radiation, which decreases as one moves further away from Saturn's center.

Brightness temperature model

The observed brightness temperature has four components: 1) directly transmitted Saturn radiation (which exists in occultation data only); 2) scattered Saturn radiation; 3) intrinsic thermal emission; and 4) cosmic microwave background (CMB) contributions. To simulate the observed brightness we use the Monte-Carlo-based photon counting code SimRings [Dunn et al. 2002]. SimRings is able to deal with multiple scattering within the ring layer (where the light source is from extended Saturn emission) and derive the amount of directly transmitted Saturn radiation, scattered Saturn radiation and the intrinsic thermal emission from the ring particles that arrives at the observer. The rings' intrinsic thermal emission mainly depends on the non-icy material fraction since the emissivity of water ice at 2.2 cm is negligible. SimRings requires knowledge of the ring particles' composition and size distribution, which determines the scattering phase function, absorption rate, and the local optical depth.

The ring particle composition is used to determine the material's effective dielectric constant based on the Maxwell-Garnett mixing rule of Effective Medium Theory (EMT)—see Bohren and Huffman [1983]. We assume that the ring particles are made of porous water ice with non-icy material embedded in the form of small inclusions. We primarily use silicates as the candidate for the intermixed non-icy material which has dielectric constant $\varepsilon_{silicate} = 5.38 - i \cdot 0.134$ [Cuzzi et al. 1980].

The ring particles sizes are assumed to have a power law distribution, $n(a) = n_0 a^{-q}$, with minimum size a_{min}, maximum size a_{max}, power law index q and a constant n_0, which depends on the particle areal number density in the rings. Table RADAR-3 summarizes the nominal size distribution parameters we employed for each ring region. The size distribution parameters are determined from previous stellar and solar occultation observations [Zebker et al. 1985; Harbison et al. 2013; Cuzzi et al. 2009; Marouf et al. 2008; French and Nicholson 2000; Dones et al. 1993].

An important result derived from density wave measurements that relate the particle sizes and their mean densities is the opacity, which can be approximated as:

$$\kappa \sim \frac{3(4-q)}{4(3-q)} \cdot \frac{a_{max}^{3-q} - a_{min}^{3-q}}{a_{max}^{4-q} - a_{min}^{4-q}} \cdot \frac{1}{\bar{\rho}}.$$

Table RADAR-3. Particle size distribution parameters in the main rings.

Ring Radius (km)	a_{min}(cm)	a_{max}(m)	q
C-ring: 74,510–92,000	0.4	4.5	3.15
B-ring: 92,000–117,580	30.0	6.3	2.75
Cassini Division: 117,580–122,170	0.1	7.5	2.79
A-ring			
– A0: 122,170–127,900	30.0	5.4	2.75
– A1: 127,900–130,860	30.0	6.3	2.75
– A2: 130,860–133,423	30.0	11.2	2.75

In Saturn's C-ring and Cassini Division, millimeter-centimeter scale particles are dominant in the scattering process and a Mie phase function is a good approximation in these regions. However, in Saturn's B-ring and A-ring, particles are much larger than the wavelength and the particle non-sphericity effect becomes important. The phase function deviates from being simply Mie scattering and become more isotropic. In addition, due to the larger number density found in the middle B-ring and A-ring wakes, close packing of ring particles can also cause the phase function to be more isotropic. To that end, where Mie scattering alone is inadequate, we introduce a phase function that is a linear combination of Mie and isotropic scattering phase functions [Dunn et al. 2002].

$$p(\theta) = (1 - f_{iso}) \cdot p_{mie}(\theta) + f_{iso} \cdot \frac{1}{4\pi}$$

Here f_{iso} is the fraction of isotropic scattering, which is determined by matching the observed data.

The C-ring

Non-Icy Material Fraction Determined by Cassini Radiometry

In the low-resolution maps, the C-ring regions at near-zero azimuthal angles that occult Saturn reveal the forward scattering profile for the C-ring particles. We found that the modeled brightness temperature is much smaller than observed when assuming non-porous ring particles (see Figure RADAR-28). However, we are able to match the observation by either making the whole particle uniformly 75% porous or by assuming a core-mantle ring particle structure with a solid core and porous mantle, both of which result in a more forward-directed scattering phase [Zhang et al. 2017a]. Due to the complication of the core-mantle ring particle structure in our simulation, we defer treatment of the core-mantle particles to the section entitled Ring opacity favors large rocky chunks.

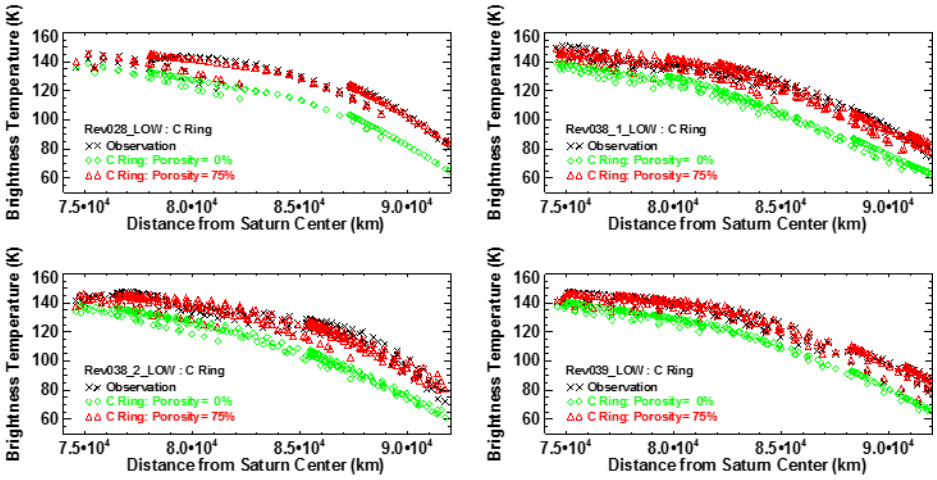

Figure RADAR-28. Brightness temperature model as compared to actual observations for C-ring particles with 75% porosity. Plotted is the brightness temperature versus ring radius for occultation observations of the C-ring low resolution maps during Rev028_LOW (upper left), Rev038_1_LOW (upper right), Rev038_2_LOW (lower left), and Rev039_LOW (lower right). Black crosses: Observed brightness temperature. Green diamonds: Simulated brightness temperature assuming zero porosity. Red triangles: Simulated brightness when assuming C-ring particles are 75% porous.

By adding 75% porosity, the bending angle of intrinsic refraction tends to be smaller and more light gets scattered into the forward direction.

Given that some of the smaller satellites in the Saturn system have bulk porosities in excess of 60% [Thomas et al. 2007; Johnson et al. 2005], and the recent works by the Rosetta team that reported a bulk porosity of 70–80% for comet 67P/Churyumov-Gerasimenko [Sierks et al. 2015; Kofman et al. 2015], it may not be surprising that individual ring particles can be so porous. One possible explanation might be that impact gardening due to micrometeoroid bombardment, which creates a regolith of increasing depth over time—Elliott and Esposito [2011]—may play a role in increasing particle porosity. Collisions among ring particles occur frequently within the C-ring, but at relatively low (mm/s) velocities, when compared to impacts by extrinsic micron-sized meteoroids (~10 times more frequent for the nominal choice of flux, see the section entitled Exposure time due to micrometeoroid bombardment). However, secondary impacts that arise as a result of the ejected material from the primary micrometeoroid impact should occur much more frequently than inter-particle collisions and at velocities of up to tens of meters per second—ballistic transport process as discussed in Cuzzi and Estrada [1998]. These secondary impacts might kick up loosely bound regolith particles such that a considerable exchange of material may happen locally between neighboring ring particles, keeping their regoliths fluffy. Thus, even though inter-particle collisions may have a tendency to compact a ring particle surface, it might be possible that the ring particles can achieve a quasi-equilibrium porous regolith that results from a balance of these combined impact and collisional processes.

While occultation observations mainly reveal the strength of the forward directed part of the scattering phase function, non-occultation observations in high-resolution spoke scans depend more on the scattering phase function at intermediate scattering angles. Figure RADAR-29 shows

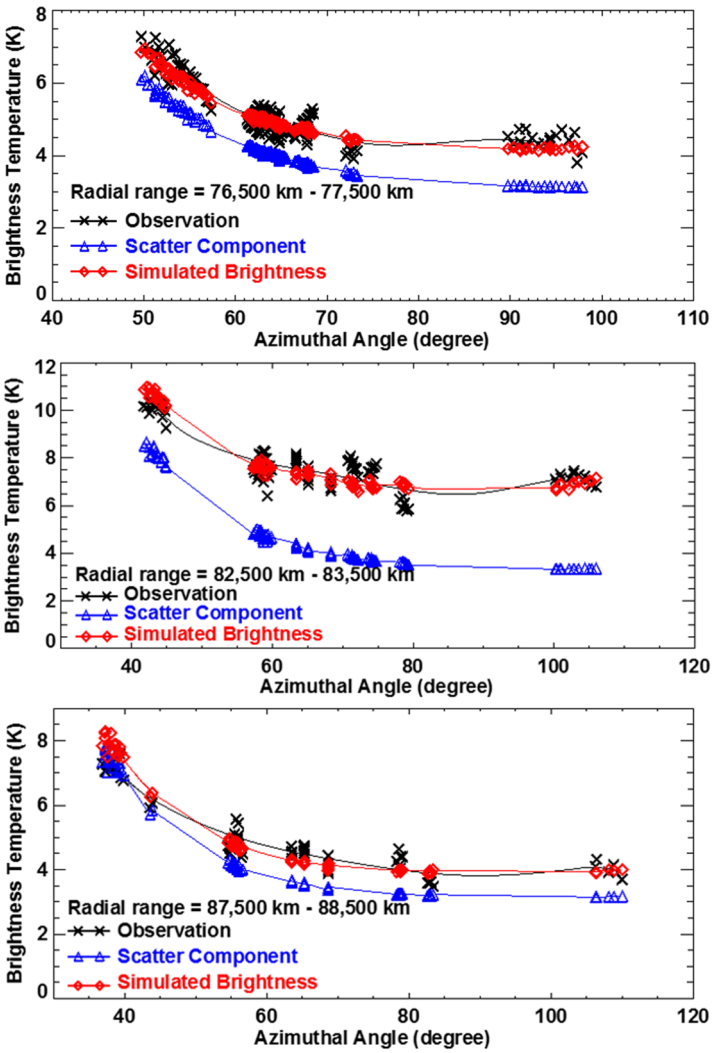

Figure RADAR-29. High-resolution spokes observations and simulations for three ring annuli. Brightness temperature versus azimuthal angle curves at three different ring radii for the: inner (76,500 km–77,500 km); middle (82,500 km–83,500 km); and outer C-ring (87,500 km–88,500 km). All observation data come from high-resolution scan Rev028_HIGH. We plot the observed brightness temperature (black crosses), scattering component with CMB contribution (blue triangles), and simulated brightness temperature (red diamonds—addition of scatter component, CMB contribution and intrinsic thermal emission). We have added ~2%, ~6% and ~1.5% non-icy material in the ring annulus for panels 1, 2 and 3, respectively. The simulated brightness temperature matches the observations well.

high resolution spokes observations and simulations for three ring annuli in the inner, middle and outer C-ring at intermediate azimuthal angles. The simulated scattering profile (brightness temperature versus azimuthal angle) matches the data fairly well with a radially varying non-icy material fraction as shown in Figure RADAR-30. The results of this analysis justify the necessity for including intrinsic thermal emission in order to match the observed brightness temperature, especially around ~83,000 km in the middle C-ring, where the brightness is observed to increase significantly beyond what can be attributed to scattered radiation from Saturn [Zhang et al. 2017a].

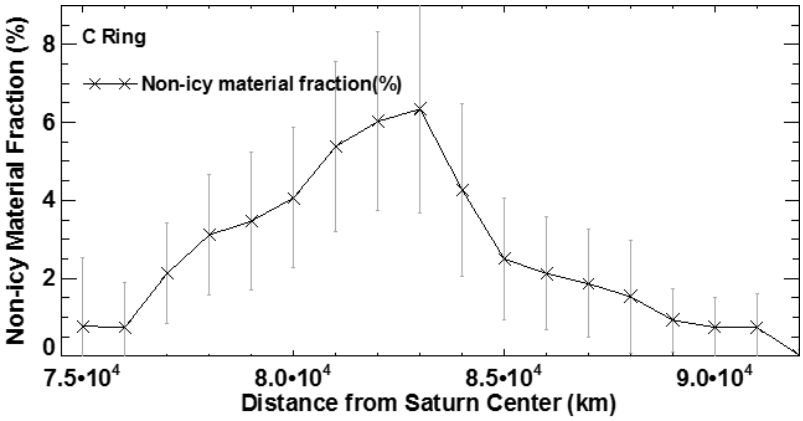

Figure RADAR-30. Simulated scattering profile. The derived radial variation of non-icy fraction reaches its maximum of ~6.3% silicate by volume in the middle of the C-ring and gradually decreases inward, and more sharply outward. The grey vertical lines show the range of one standard deviation.

In the previous paragraphs, we have treated C-ring particles as water ice with a fraction of voids and non-icy material as inclusions. The Maxwell-Garnett mixing rule of the EMT calculates the ring particle's averaged (effective) dielectric constant taking water ice as the host medium. This mixing rule treats one material as the matrix (host material) in which other materials (guest materials) are embedded in the form of small inclusions. However, this model is not symmetric as the host and guest materials do not contribute on an equal basis to the effective dielectric constant. Therefore, it makes a difference what one chooses as the host material. An alternative is to use vacuum as the host medium, which will result in 70% porous C-ring particles and 50% more non-icy material fraction in the C-ring (see Figure RADAR-31). These two cases, using either water ice or vacuum as the host medium, set the upper and lower limit of the non-icy material fraction in the ring particles. The non-icy material fraction will lie in between these two limits depending on which mixing rule is used.

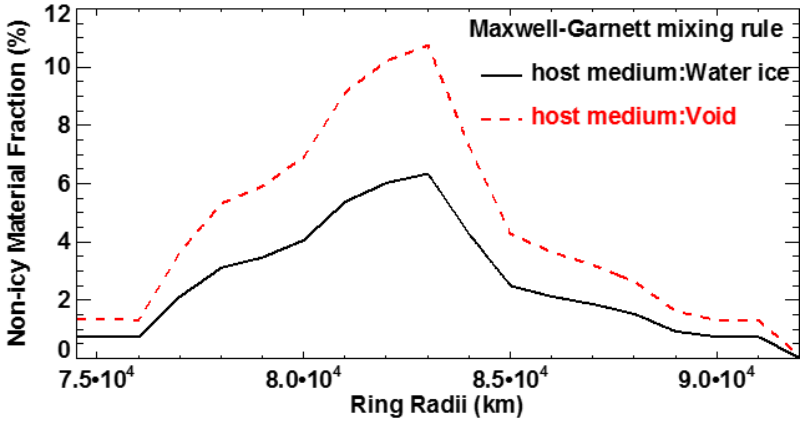

Figure RADAR-31. Using vacuum as an alternative model host medium. Black curve: Maxwell-Garnett mixing rule with water ice as the host material, and 75% porous C-ring particles. Red curve: Maxwell-Garnett mixing rule with vacuum as the host medium, and 70% porous C-ring particles.

EXPOSURE TIME DUE TO MICROMETEOROID BOMBARDMENT

After their formation, the rings have been continuously bombarded by extrinsic meteoroid impacts that have the effect of polluting them with non-icy material over time. The required exposure time to accumulate the observed fraction of non-icy material implies a lower limit on the rings' age. The exposure time scale due to micrometeoroid bombardment is inversely proportional to the local impact flux onto the ring plane.

The radial variability of the derived non-icy material fraction is surprising and warrants discussion. Considering that the local impacting flux depends approximately linearly on the local geometric optical depth in most regions of the C-ring, the final non-icy material fraction should be proportional to opacity, which equals geometric optical depth divided by surface density ($\kappa = \tau_{geometry}/\sigma$). The larger the opacity, the higher the non-icy material fraction should become, if meteoroid bombardment is the only pollution source. Though a complete opacity radial profile for the C-ring is still unknown, the current values at a few radial locations from density wave measurements suggest a higher opacity in the inner (and outer) C-ring of ~0.15 $cm^2\ g^{-1}$, and a significantly lower opacity in the middle C-ring of ~0.022 $cm^2\ g^{-1}$ [Baillie et al. 2011; Hedman and Nicholson 2013], which is the opposite trend to the shape of the non-icy material fraction we have found. In Figure RADAR-32, we demonstrate how the non-icy material fraction would evolve over 15 and 45 million years (upper panel) and 30 and 90 million years (lower panel) after the C-ring first formed assuming that the rings were initially pure water ice, that meteoroid bombardment is the only pollution source and that the C-ring optical depth and surface density have not changed significantly during that time. The opposite trend between the observed (black curve) and simulated (red dashed curve) non-icy material fraction profiles in Figure RADAR-32 implies that if the rings started as mainly pure ice ~15–90 million years ago, there must be some non-icy material source other than the nearly radially constant micrometeoroid flux in order to explain the enhanced non-icy fraction in the middle C-ring [Zhang et al. 2017a].

On the other hand, in order to accumulate the observed peak non-icy material fraction merely from meteoroid bombardment in the middle C-ring, it would require ~900 million years, which sets an upper bound on the age. However, if this is the case, it would imply that the non-icy material fraction in the inner and outer C-ring would be much higher than the observed values and a process that preferentially removes non-icy material from the inner and outer C-ring regions would be required in order to account for the observed distribution. Another alternative is that the C-ring did not start out as nearly pure ice. In such a case, if the non-icy material was intramixed within the initial ring composition, any radial variability that may have existed most likely would have already been smoothed out as a result of ballistic transport [Cuzzi and Estrada 1998; Estrada et al. 2015]. That is, ballistic transport, which behaves much like both a diffusive and advective process [Cuzzi and Estrada 1998] (see next section), generally works to smooth out any compositional differences that may have existed or that might arise in the rings. Indeed, how material is diffused/advected through ballistic transport in the rings is an effective means by which the age of ring features or the rings themselves can be determined. Therefore, the exceptionally high non-icy material fraction in the middle C-ring requires either the recent introduction of a high concentration of non-icy material, or a process that preferentially removes non-icy material from the inner and outer C-ring regions

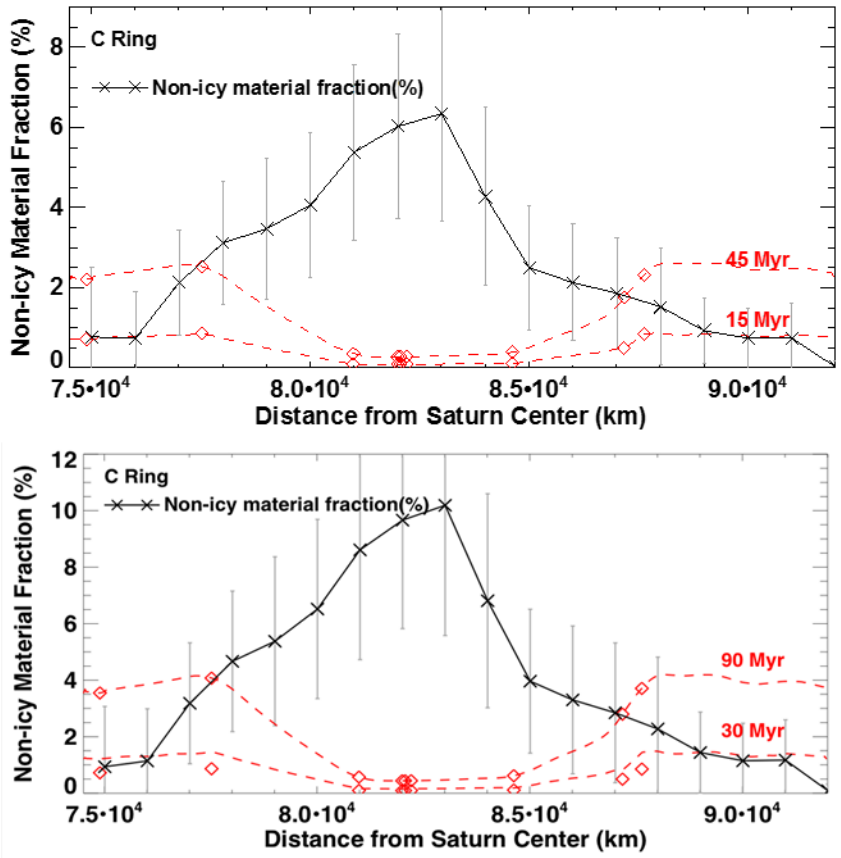

Figure RADAR-32. How the non-icy material fraction would evolve over millions of years. Black curve: Derived non-icy material fraction from the observations. Both cases using Maxwell-Garnett mixing rule with water ice (upper panel) and vacuum (lower panel) as the host material are shown. Red dashed curve: The non-icy material fraction evolution over 15 and 45 million years (upper panel) and 30 and 90 million years (lower panel), if meteoroid bombardment is the only source of contamination. Red diamonds demonstrate the positions where opacity measurements [Baillie et al. 2011; Hedman and Nicholson 2013] have been made through density waves.

[Zhang et al. 2017a]. We argue that the persistence of a non-uniform distribution of silicates within the middle C-ring strongly favors the former scenario. In the next sections, we describe the former scenario in more detail that attempt to address this observation.

A BAND OF NON-ICY MATERIAL FROM AN IMPACTING CENTAUR AT C-RING CENTER

In the first scenario, we assume that meteoroid bombardment has continuously contaminated the whole of the C-ring since it first formed, and that a higher concentration of non-icy material was injected into the middle C-ring at a more recent time. Barring any process that might dilute the non-icy fraction—for example, a by-product of ballistic transport is that icier material spills over from the B-ring to C-ring [Durisen et al. 1992; Estrada et al. 2015]—the implied age of the C-ring from this evolution is between 15 and 90 million years based only on the pollution of the inner and outer

C-ring for the nominal micrometeoroid flux (see Figure RADAR-32). Note that this estimate is inversely proportional to the time-averaged micrometeoroid flux.

Any additional contribution to the effective dielectric constant of material must be attributed to an alternative, more localized source. In order to further examine this source, we investigated a scenario in which the middle C-ring was contaminated by a debris cloud derived from a Centaur disrupted by previous encounters with Saturn [Hedman et al. 2011]. Centaurs captured into orbit around Saturn might break apart into debris through tidal disruption as they pass close to the planet, or even through direct collision with the rings. This debris will follow the same bound trajectory and crash into the rings potentially across a range of radii at later periapses [Hedman et al. 2011]. Assuming the non-icy material is all silicates, and that this material is now finely ground and intramixed within the ring particles, we find that the observed non-icy material distribution may be produced during the break-up of a Centaur with radius R ~7–20 km. The capture of the Centaur would likely involve it passing through the ring plane several times leaving little material behind initially, becoming weaker and rubblized until tides break up the object into smaller fragments which could then be captured and integrated into the rings [Hyodo and Ohtsuki 2014]. In such a scenario, it is not clear that the material would initially be concentrated into a narrow annulus of material. However, in the case that a narrow annulus is the initial condition, the spreading timescale of the high concentration of non-icy material through ballistic transport [Cuzzi and Estrada 1998] could help constrain the earliest possible time the initial contamination occurred. A conservative estimate of the time it would take for the intramixed pollutant that initially occupies an annulus at ~83,000 km to spread into the observed distribution is about 9.3 million years. Therefore the non-uniform radial peak in our intramixed, non-icy material fraction profile would be a relatively new structure, with an age on the order of ~10 million years, though the absolute time scale depends on the meteoroid flux rate at infinity and how gravitationally focused the micrometeoroids are by Saturn. Such Centaur crossing events are fairly likely to occur over this time period. On average, about 5 to 52 Centaurs larger than 7 km in radius may have hit the Saturn system within the last ~10 million years. Once the Centaur is disrupted into debris by Saturn's gravity, the debris is likely to be absorbed by the rings after several orbits. The observational evidence would suggest, however, that successful disruption and capture events of such large Centaurs have not happened so frequently otherwise we might expect to see relatively large peaks in non-icy material concentration in other C-ring regions rather than the single, well-defined peak we observe in the middle C-ring.

RING OPACITY FAVORS LARGE ROCKY CHUNKS

In the previous section, we have discussed the case where non-icy material brought in by the incoming Centaur is intramixed within the ring particles as envisioned in the EMT model. However, it seems unlikely that an incoming Centaur, basically a rocky object that may have substantial internal strength, torn apart gently by tides and ultimately broken into pieces that reside in the C-ring, could be ground to powder this way, especially if it were done fairly recently. It seems more likely that there would still be many chunks of solid silicates in the centimeter-decimeter-meter size range left, which have now been coated by the icy ring material. This would require more total non-icy material in the middle C-ring since non-icy material affects emission most efficiently when

finely divided as in the EMT intramixed assumption versus a salt and pepper, or intramixing type model—Cuzzi and Estrada [1998]; Poulet and Cuzzi [2002]; Cuzzi et al. [2014].

Moreover, 75% porous ring particles containing less than 11% intramixed non-icy material implies a ring layer opacity of ~0.07–0.08 $cm^2\ g^{-1}$ using our nominal particle size distribution, which is inconsistent with the opacity measured through density wave. Recall that the derived radial opacity profile from density wave measurements is notably non-uniform. In order to have a radially varying opacity profile, the C-ring particles must have a radially-varying particle size distribution or a radially varying mean particle density $\bar{\rho}$. At the inner and outer C-ring, the measured opacity is higher than our calculated value, possibly suggesting fewer large particles in those regions. We are able to match the measured opacity by decreasing the maximum particle size from 4.5 m to 1.5 m −2.2 m in the inner C-ring and 1.3 m in the outer C-ring. However, by merely increasing the maximum particle size it is not possible to lower the opacity in the middle C-ring to the measured value ~0.022 $cm^2\ g^{-1}$. Therefore, the exceptionally low opacity in the middle C-ring suggests a potentially considerable amount of extra mass hidden in the ring particles, just where the finely distributed non-icy material also is. A particle in the middle C-ring is likely to contain large chunks of silicates, which originated from the disrupted Centaur.

We proposed a silicate-core and porous-dirty-icy-mantle model in which the mass of the Centaur is initially contained in a narrow annulus located at the peak of the current non-icy material fraction bump in the C-ring center (83,000 km) [Zhang et al. 2017a]. This annulus can viscously spread to the feature's current width (78,000 km–87,000 km) and surface density in as little as ~20–30 million years. It is possible that a combination of viscous spreading and ballistic transport acting together could shorten this time further. We find this variant more compelling because it successfully fulfills the requirements for a strong forward-directed scattering phase function, while explaining both our derived radially-variable thermal emission and the low opacity in the middle C-ring, without requiring the Centaur to be ground to powder.

Other main rings

Though the ring particles in the Cassini Division are very similar to the C-ring particles, and thus a pure Mie scattering phase function matches the observation well, B-ring and A-ring are much optically thicker and comprise particles much larger as compared to the wavelength. We found that a hybrid phase function that varies between Mie half-isotropic to purely isotropic fits the observations best in A-ring and B-ring. By fitting the shape of the scattering profile in the Cassini Division, we found that Cassini Division particles are likely to have 90% porosity, which is consistent with the high opacity ~0.064–0.111 $cm^2\ g^{-1}$ derived from density waves [Colwell et al. 2009]. Though we are not able to determine the porosity values for B-ring and A-ring particles only based on our data, the high opacities measured through density waves [Hedman and Nicholson 2016] suggest that B-ring particles have porosities in excess of 85% while A-ring particles are likely to have porosity value in between 55% and 90%. The radial profile of the derived non-icy material fraction and the corresponding required exposure time to meteoroid flux is rather flat in the B-ring, Cassini Division and A-ring as compared to that in the C-ring, which indicates that the non-icy material observed in these regions has been

accumulated from meteoroid bombardment. In Table RADAR-4, we summarize the derived results (i.e., particle porosity, scattering phase function, silicate fraction, and exposure time) for all the main rings [Zhang et al. 2017b].

Table RADAR-4. Summary of the main finds in C-ring, B-ring, Cassini Division, and A-ring from Cassini passive radiometry observations.

Rings	Radial Range (km)	Porosity	Phase Function	Silicate Fraction	Exposure Time (million years)
C-ring	74,510–92,000	70%–75%	Mie	Baseline: 1–2% Maximum: 6–11%	15–90
B-ring	92,000–117,580	85%–90%	From 50% Mie / 50% Isotropic to Isotropic	Inner/Outer:0.3–0.5% Middle: 0.1–0.2%	30–100
Cassini Division	117,580–122,170	≳90%	Mie	1–2%	60–100
A-ring	122,170–133,423	55%	Isotropic	0.2–0.3%	80–150
Inside Encke Gap		90%	30% Mie / 70% Isotropic		

Conclusion

We conclude that ring particles in the C-ring, B-ring, Cassini Division, and A-ring are likely to be highly porous [Zhang et al. 2017b]. The result that ring particles are very porous across all the main rings may come as some surprise, especially in dense, high particle packing fraction regions like the A-ring and B-ring wakes, since it might be expected that collisions between particles would lead to compaction. Yet relative velocities, and thus impact velocities between ring particles even in these dense regions are small, and is especially true if they are very dissipative—for example, Porco et al. [2008]—making collisions more gentle, and perhaps causing particles to spend more time being stuck in larger clumps—see, for example, Robbins et al. [2010]. Collisions at such low velocities might lead to sticking of ring particles, or only bouncing with some compaction of the particle's surface layers—for example, Güttler et al. [2010]. Meanwhile, micrometeoroid bombardment is continuously acting to garden those same ring particle surfaces, perhaps producing fluffy regoliths, not just from direct bombardment, but even more so from the secondary impacts due to the ballistic transport of the large amounts of impact ejecta. It may be that these competing effects might account for and/or maintain particle porosity.

The C-ring non-icy material fraction shows the most significant and interesting radial variation, reaching a maximum of 6%–11% by volume in the center of the C-ring near 83,000 km, and decreasing gradually to 1%–2% inward and rapidly outward from this radial location [Zhang et al. 2017a]. A possible scenario that nicely explains this trend has a passing Centaur providing the necessary material for post-formation enhancement of the C-ring non-icy material in addition to the micrometeoroid in-fall component. That is to say, the non-icy material fraction in the inner and outer C-ring, which is about 1%–2%, is due to meteoroid bombardment and indicates an exposure time of 15–90 million years. On the contrary, the non-icy material fraction radial profile in the B-ring, A-ring and Cassini Division are relatively flat and can be explained by merely meteoroid bombardment pollution.

Our derived results for the radial distribution of the mass fraction of non-icy material due to direct micrometeoroid bombardment in general support the idea that Saturn's rings are geologically young, formed ≲150 million years ago. The high contamination rate in the middle C-ring, which we have explained as being due to the breakup and deposition of a Centaur, occurs within this time frame [Zhang et al. 2017a]. It further suggests a formation scenario in which the rings are derived from the relatively recent breakup of an icy moon, perhaps of Mimas' mass consistent with the post Voyager ring mass estimate [Esposito 1984], though recently Hedman and Nicholson [2016] suggest that the total mass of the rings may be as little as 0.4 times Mimas' mass. However, no model for the origin of the rings in which they form within the indicated timescale has thus far been proposed. It might be argued that such a ring progenitor may have had a rocky core that could still in one form or another remain hidden within the rings [Charnoz et al. 2009b] which might then account for the anomalous fraction in the C-ring. However, how that rocky material ends up solely in the C-ring but apparently not elsewhere, combined with the fact that the radial distribution of non-icy material and observed opacity in the middle C-ring can be simulated through viscous diffusion of an initially high density annulus of rocky chunks embedded within icy mantles (core-mantle model) suggests that the Centaur capture scenario can readily account for the observations.

Active radar observation during Cassini's Grand Finale

During the Grand Finale, RADAR scanned along the line connecting the ring plane crossing point with Saturn's center in the active mode. These observations looked at the rings' backscattering as a function of radial distance. Although similar observations have been done at optical wavelengths, RADAR saw a different population of ring particles because our measurements will be dominated by cm-scale and larger particles, while the optical observations are seeing a wider spectrum of particle sizes. Figure RADAR-33 shows calibrated normalized backscattering cross-section in F-ring orbit Rev 260 and Proximal orbit Rev 282. These data have not gone through the range compression process and the resolution is therefore equal to the aperture resolution with angular diameter of 0.36°, which is about hundreds of kilometer as projected onto the ring plane. After the

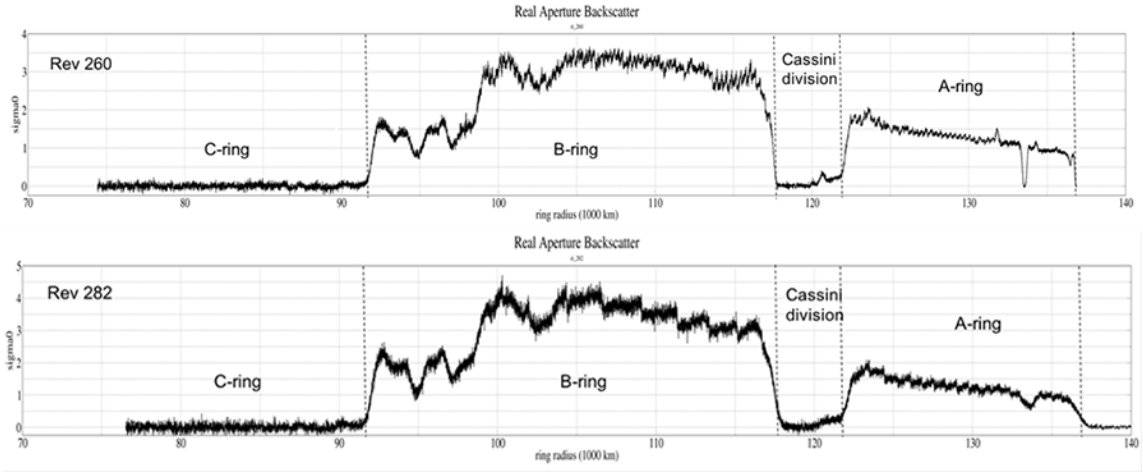

Figure RADAR-33. Normalized back scattering cross-section obtained in Rev 260 and Rev 282.

range compression we would expect the radial resolution to be as high as several kilometers. The Rev 260 observation was shortly after the ring plane crossing and thus has a shorter observation range and thus higher resolution.

In order to compare the observation with the known ring structure, we plot the rings optical depth with the red curve over the Rev 260 data (see Figure RADAR-34). We notice that the backscattering signal in the C-ring and inner Cassini Division is below the noise level, which is consistent with the previous Arecibo observation, which is due to the low optical depth, smaller particle size, and relatively larger absorption loss there. However, we do see backscattering from the outer Cassini Division, suggesting that the ring particles at the outer Cassini Division are more similar to those in the inner A-ring. These particles might have been spilled from the inner A-ring through ballistic transportation. We also notice that the backscattering in the A-ring interior Encke Gap (located at 133,590 km) is much higher than that exterior Encke Gap, suggesting that particles in the exterior Encke Gap tend to be smaller than those in the interior Encke Gap. The observed backscattering in B-ring and A-ring

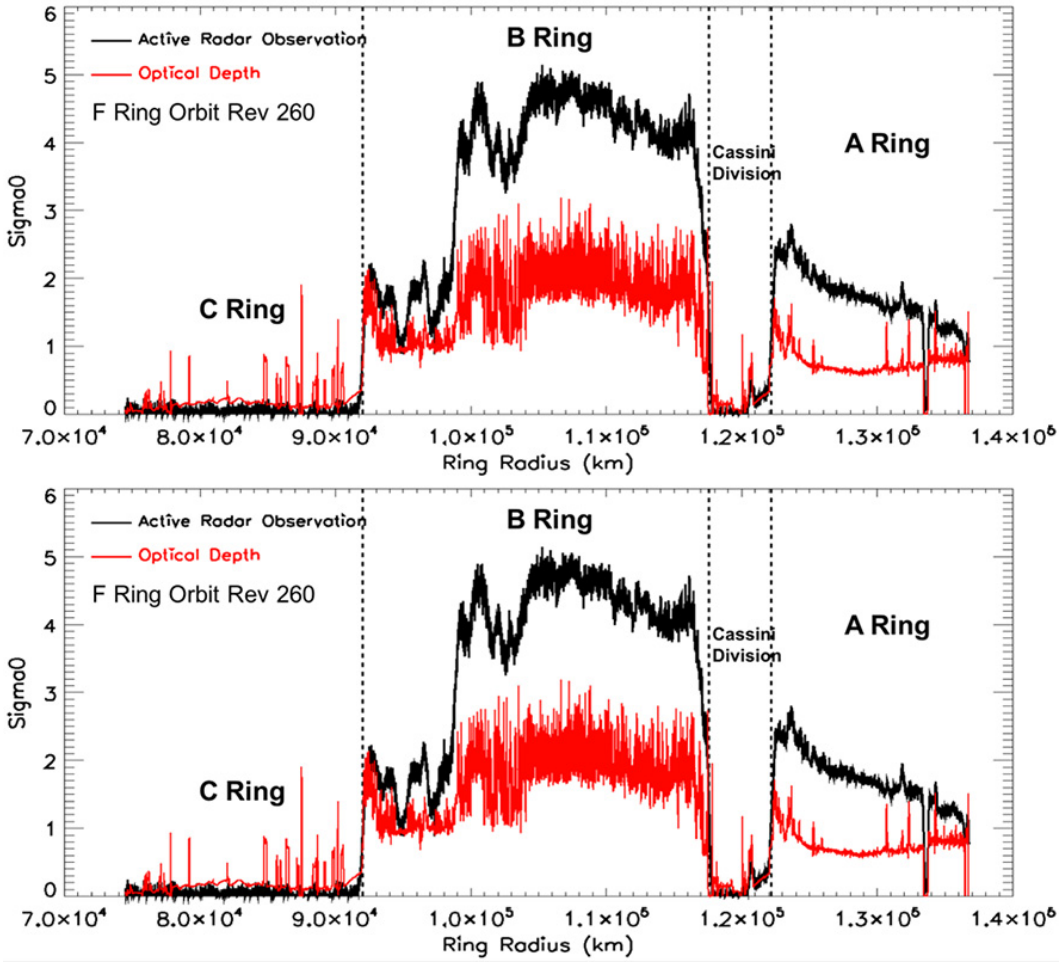

Figure RADAR-34. Comparison between the Rev 260 normalized backscattering cross-section (black curve) and rings optical depth (red curve). In the lower panel, we further zoom in and focus on the A-ring. For better comparison, we have rescaled the optical depth in the lower panel.

is lower than as predicted by a pure Mie scattering phase function. An accurate backscattering phase function is required in order to match the simulation with the observation, which will then help determining the non-spherical shape of the A-ring and B-ring particles. In the lower panel, we further zoom in and focus on the A-ring and Cassini Division. Despite the difficulty in calibrating these observations, we have successfully had the observation line up with the known fine structures. We are able to resolve the Encke Gap, which is about 300 km wide. Furthermore, we have captured all the density and bending waves structures, which are the dynamical structures we are interested in. There is still a great deal to be done, but we must acknowledge that these results of the Cassini era will stand firmly as the benchmark until that point in a possibly uncertain future that we may return to observe Saturn and its majestic rings up close once again.

Icy Satellite Science

Introduction

While it was initially designed to examine the surface of Titan through the veil of its optically opaque atmosphere, RADAR was occasionally used to observe Saturn's airless icy moons from long ranges (>50,000 km) and, less frequently, during targeted flybys. In this section, we give an overview of the Cassini radar/radiometry observations of Mimas, Enceladus, Tethys, Dione, Rhea, Hyperion, Iapetus, and Phoebe, many of which have not been published as of this writing. These observations have taught us much about the about the near-surface of the middle-sized satellites of Saturn, but many questions remain about their composition, structure and what it tells us about their geological history and interaction with Saturn and its rings.

Science objectives

Investigating the microwave properties … provides insights into the various physical and geological processes … and thus into what is common and what is specific to the history of each satellite.

After Titan, the six largest Saturnian satellites are, in order of distance from Saturn: Mimas, Enceladus, Tethys, Dione, Rhea, and Iapetus (Figure RADAR-35). Phoebe and Hyperion are smaller and exhibit irregular shapes. The collective formation of these moons and subsequent evolution remains an outstanding problem. All of them are composed largely of water ice [Clark et al. 1986]. However, their respective evolution history and near environment have led to different regolith composition and structure. In particular, they show evidence of varying degrees of geologic activity in the past and, in the case of Enceladus, the present [Porco et al. 2006]. Investigating the microwave properties of Saturn's airless satellites' near-surface provides insights into the various physical and geological processes that have affected them and thus into what is common and what is specific to the history of each satellite.

Figure RADAR-35. Saturnian icy airless satellites observed by the Cassini RADAR (with the exception of Hyperion). They are here presented at scale (in size, not in distance) and by order of distance from Saturn.

Microwave observations of Saturnian satellites are rare and recent. Until the 2004 through 2007 oppositions of the Saturn system, Earth-based radar measurements in the outer system were limited to Galilean satellites and Titan [Muhleman et al. 1990; Campbell et al. 2003; Roe et al. 2004]. Black et al. [2004, 2007] observed both hemispheres of Iapetus and the middle-sized Saturnian satellites Rhea, Dione, Tethys, and Enceladus with the Arecibo Observatory's 13 cm wavelength (2.38 GHz) radar system. The other Earth-based planetary radar system, Goldstone—equipped with a 3.5 cm transmitter (X-band)—has not been used to observe these objects or other Saturnian airless satellites yet. In addition, passive microwave observations of Saturnian moons from Earth are difficult to make due to confusion with emissions from the planet, the faintness of some targets and their small apparent size. That is the reason why, with the exception of Titan and Iapetus, they have never been conducted. In that regard, the Cassini RADAR and radiometry observations of Saturn's icy moons are pioneer.

RADAR operates at a wavelength (2.2 cm, f = 13.78 GHz), which is a factor of 6 times smaller than the 12.6 cm wavelength used by Arecibo, and 22 times longer than the millimeter wavelengths at the limit of Cassini's CIRS instrument. It has thus expanded the observation of the icy satellites of Saturn to a new and revealing length scale. The Cassini RADAR likely probes icy subsurfaces down to depths of several meters against few millimeters for CIRS. Its main scientific objective was to provide constraints on the thermal, physical and compositional properties of the first few meters below the surface of the investigated objects and, doing so, insights into the degree of purity and maturity of their water-ice regolith. The goal was also to further explore existing hemispheric dichotomies or regional anomalies such as the dramatic two-tone coloration of Iapetus. In addition, operations at closer ranges (i.e., spatially resolved) offered a unique opportunity to examine or detect features of interest at the surface and identify potential hot spots in the near-surface, in particular of Enceladus. Overall, RADAR observations of Saturn's icy moons were to enhance our understanding of the diversity of icy regoliths in the solar system by comparison with radio observations of other objects such as the Galilean satellites (e.g., de Pater et al. [1984], Muhleman and Berge [1991], and Black et al. [2001]), trans-Neptunian objects (e.g., Lellouch et al. 2017], or comets (e.g., Gulkis et al. [2015]).

Data acquisition, calibration, and reduction

Most of the Cassini icy satellite observations are distinguished by the relatively long range to the target. Notable exceptions are one close flyby of Iapetus that is partially analyzed in Le Gall et al.

[2014], two close flybys of Enceladus where one is partially analyzed in Ries and Janssen [2015] and Le Gall et al. [2017], one close flyby of Dione (not yet analyzed), and one close flyby of Rhea that is partially analyzed in Wye [2011] during which spatially resolved data were acquired in both the active (scatterometry) and passive (radiometry) modes of the instrument.

Background

RADAR data come in two flavors: active and passive. In its active mode, the instrument measures the radar albedo which describes the reflectivity of a target. The radar cross-section (RCS) of a target is the projected area of a perfectly reflective, isotropic target that would return an identical echo power to what is measured, if it was observed at the same distance from the radar and with the same transmitted and received polarizations. The radar albedo is derived by normalizing the radar cross-section by the projected geometric area of the target or equivalently by the RCS of a perfectly reflective target such as a smooth metallic sphere. It is thus a dimensionless quantity which is a measure of how reflective the target is in the backscatter direction. RADAR receives echoes in the same linear polarization as it transmits, so it provides same-linear radar albedos at 2.2 cm. For more details, see Ostro et al. [2006] and Wye [2011].

In its passive mode, RADAR records the microwave thermal emission from the near-surface through the measurements of its brightness temperature essentially at the same wavelength (2.2 cm) and with the same aperture as in active mode. By virtue of the Rayleigh-Jeans approximation, the 2.2 cm emissivity of the surface can be estimated from the measured brightness temperature dividing it by the effective physical temperature of the near-surface.

In best cases, active and passive distant observations follow each other so that the same (or almost the same) disk is observed in both modes and thus the derived disk-integrated radar albedo and brightness temperature can be compared, which is key for understanding the near-surface properties. When active and passive measurements are too separated in time, the sub-spacecraft point has changed between observations (both due to the motion of the spacecraft and the rotation of the satellite) and it is not relevant to compare active and passive measurements, especially for satellites that exhibit a hemispheric dichotomy.

Lastly, we note that there were two Hyperion observations, HY15 and HY39. However, these data are not included in this report because their reduction, which requires a shape model is still a work in progress.

Distant observations

Typical distant RADAR observations of Saturn's moons occur at ranges between 50,000 km and 500,000 km where the antenna beamwidth is comparable to or greater than the apparent angular extent of the target's disk. These experiments were designed largely for disk-integrated albedo and average temperature calculation. The derivation of these quantities is described in the next paragraph. Ostro et al. [2006, 2010] report on the distant observations of Saturn's major airless

satellites measured at the beginning of the mission. Since then, the observational database has significantly increased.

DISTANT ACTIVE STARES

During distant active observations, often referred to as stares, RADAR transmits 46 W through the 4 meter dish antenna with a half-power beamwidth of 0.37°. The receiver operates with a relatively high noise temperature around 900 K, and the received echo power is well below the noise floor. To overcome the low signal strength, the radar stares at the target body while accumulating echo measurements (see Figure RADAR-36 left). Spacecraft power constraints limit RADAR to a 7% transmit duty cycle, so the actual integration time is less than the total staring time, which usually runs 5 to 10 minutes for a single observation. In order to maximize the signal to noise ratio (SNR), the echo data is Fourier-transformed and then summed in the frequency domain. The transmit events consist of bursts of single frequency pulses at 13.78 GHz. The received echo power is spread out in the frequency domain by Doppler variation, which arises from the relative motion of the spacecraft and the rotation of the target body (see Figure RADAR-36 right). For the icy satellites, the Doppler variation ranges from a few hundred Hz up to about 4 kHz. The pulsed nature of the transmit events introduces grating lobes spaced at the pulse repetition frequency (PRF). The PRF is set to a frequency higher than the Doppler spread of the target, so the central spectral peak is separated from the grating lobes and shows the natural variation of the echo power over the target body.

The sum of the echo power in the power spectrum is then scaled by the radar equation to give a radar albedo for the target body. More especially, the radar equation is applied assuming azimuthal homogeneity and a diffuse surface scattering function given by $\sigma^0 = Acos^n\theta$ where θ is the incidence angle. The values of A and n are obtained from a least-squares fit to the observed power spectrum with a model consisting of the surface scattering function and the antenna gain pattern integrated over the illuminated area (see Figure RADAR-36). The resulting disk-integrated radar albedo is the uniform normalized backscattering value, which reproduces the observed integrated power assuming that the fit model is correct. Therefore, it is derived from the best-fit values of A and n as follows:

$$A_{\mathrm{SL}-2}^{\mathrm{disk}} = \frac{2\pi R_t^2 \int_0^{\frac{\pi}{2}} \sigma^0(\theta) \sin\theta d\theta}{\pi R_t^2} = 2\int_0^{\frac{\pi}{2}} Acos^n\theta \sin\theta \, d\theta. \qquad \text{Eq. 1}$$

It results:

$$A_{\mathrm{SL}-2}^{\mathrm{disk}} = \frac{2A}{n+1}. \qquad \text{Eq. 2}$$

For more details, see Ostro et al. [2006] and Wye [2011].

Table RADAR-5 presents the results of 79 active stares. These results are discussed in the next section (see also Figure RADAR-41). Note that it corrects a factor of 2 error in the originally published values in Ostro et al. [2006, 2010]. The original calculation was normalized by the total surface area of the visible hemisphere (i.e., $2\pi R_t^2$); but to be consistent with Earth-based

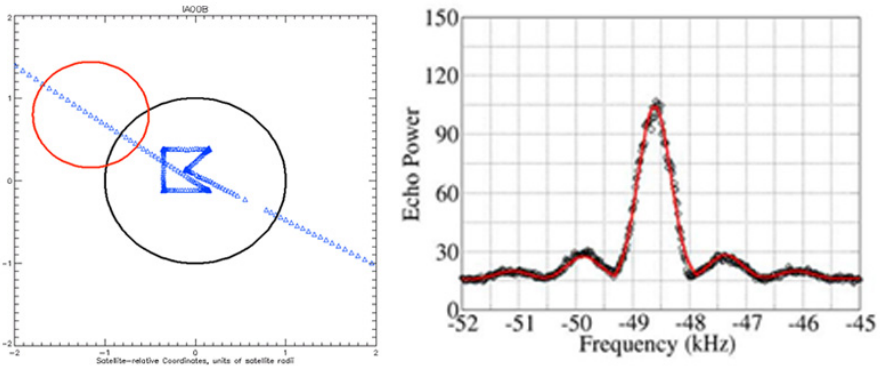

Figure RADAR-36. Distant active RADAR observations. Left: Boresight pointing directions (blue triangles) during the IA-B active stare observation. Iapetus' disk is in black. The beam size at the beginning of the observation is indicated in red. Right: Cassini 2.2-cm radar echo power spectrum (black circle symbols) acquired during the IA-B stare observation and model fit (red line). Figures extracted from Ostro et al. [2006].

observations and the usual convention for the definition of radar albedo, the correct normalization is the disk cross-sectional area (i.e., πR_t^2). This gives an albedo of 1 for a conducting sphere.

The last column of Table RADAR-5 shows the relative errors on the derived disk-integrated albedos. These describe the statistical uncertainties and were derived from the goodness of the fit. The absolute error is about 1.5 dB (1.4 in linear scale). It was estimated adding all known uncertainties on the transmitter power, receiver path losses, receiver gain, and beam solid angle.

We highlight that the choice of a surface scattering function as just a diffuse cosine law is supported by the shape of the measured spectra. As stated in Ostro et al. [2006], none of them, and none of the ground-based echo spectra from any of our targets or the icy Galilean satellites, show any hint of the specular (narrowband) scattering expected if the echoes were dominated by single backreflections from surface elements that are large and smooth at scales near the wavelength. Rather, the spectral shapes are broad, indicating diffuse scattering from structural complexity at some scale(s) comparable to the wavelength or larger.

We further note that radiometry data were also acquired during active stares. However, because the transmitter has just been turned ON at the beginning of the observation and/or because it is turned OFF and ON at least once during these observations, the receiver temperature is not stabilized and the calibration of the radiometry data is not straightforward.

Table RADAR-5. Cassini active-stare observations of Mimas (MI), Tethys (TE), Enceladus (EN), Dione (DI), Rhea (RH), Iapetus (IA), and Phoebe (PH).

Obs ID[a]	Latitude (°)	W Longitude (°)	Beam size (diameter)	Range (km)	n	A_{SL-2}^{disk}	Error
MI47	−2.2	59.3	3.56	219,539	1.9	**2.45**	0.022
MI53	16.2	136.4	2.89	177,750	1.9	**2.69**	0.005
MI64	−48.3	150.7	1.78	109,554	1.9	**2.37**	0.005
MI126	−5.0	271.8	0.68	42,047	1.3	**2.69**	0.005

Table RADAR-5. Cassini active-stare observations of Mimas (MI), Tethys (TE), Enceladus (EN), Dione (DI), Rhea (RH), Iapetus (IA), and Phoebe (PH).

Obs ID[a]	Latitude (°)	W Longitude (°)	Beam size (diameter)	Range (km)	n	A_{SL-2}^{disk}	Error
EN3	0.0	232.0	2.14	165,480	2.0	**2.16**	0.004
EN4	−12.8	70.1	1.08	83,059	1.8	**2.82**	0.002
EN28	60.7	186.5	2.11	162,678	1.2	**3.01**	0.005
EN32	−29.2	243.0	1.18	90,772	1.7	**3.15**	0.002
EN50	16.7	120.0	1.54	119,321	1.9	**3.21**	0.004
EN61In	68.9	108.6	1.88	145,225	1.7	**3.49**	0.004
EN120	−0.5	313.5	0.97	75,735	1.8	**2.63**	0.005
EN61Out	−70.3	331.9	1.09	83,845	1.7	**3.04**	0.005
TE15	−0.2	207.3	0.74	120,908	1.8	**2.76**	0.002
TE21	3.2	254.6	1.47	240,696	1.7	**2.66**	0.004
TE48	1.9	107.7	0.58	95,421	2.1	**3.10**	0.003
DI16	−1.3	14.9	0.64	111,107	1.5	**1.64**	0.005
DI16C1	19.2	18.0	0.66	115,330	1.9	**1.70**	0.005
DI16C2	−3.5	36.2	0.69	119,692	2.9	**1.40**	0.005
DI16C3	0.9	358.4	0.72	124,780	1.3	**2.18**	0.005
DI16C4	−19.1	14.9	0.75	129,270	1.4	**1.56**	0.004
DI27	−33.6	266.8	0.98	169,413	1.9	**1.94**	0.003
DI33**	17.1	355.7	0.44	76,199	2.4	**1.31**	0.004
DI33C1	43.1	27.4	0.45	77,546	1.8	**1.93**	0.005
DI33C2	8.3	26.2	0.45	78,600	2.1	**1.35**	0.005
DI33C3	−10.5	353.3	0.46	79,847	4.8	**1.25**	0.005
DI33C4	15.0	321.3	0.47	81,148	1.1	**1.36**	0.005
DI50	−12.6	227.0	0.46	79,275	2.3	**1.58**	0.003
DI50C1	−11.3	242.9	0.57	98,379	2.8	**1.46**	0.005
DI50C2	−42.7	215.9	0.54	93,688	1.4	**1.88**	0.004
DI50C3	−10.8	187.4	0.51	89,125	1.8	**1.85**	0.004
DI50C4	19.7	222.7	0.49	84,676	1.9	**1.66**	0.004
RH11	−74.4	61.7	0.82	193,603	1.7	**1.84**	0.003
RH18*	0.4	17.5	0.51	120,829	1.9	**1.83**	0.005
RH18C1	27.6	17.6	0.53	125,575	1.9	**1.81**	0.003
RH18C2	0.3	44.0	0.57	135,169	2.7	**1.32**	0.004
RH18C3	−23.5	20.1	0.61	144,896	1.4	**1.89**	0.004
RH18C4	−0.0	0.2	0.65	154,761	1.3	**2.36**	0.004
RH22	0.9	109.1	0.40	93,867	5.2	**1.09**	0.002
RH22C1	−35.2	102.7	0.40	95,353	1.0	**2.39**	0.003
RH22C2*	−2.9	76.0	0.41	96,415	1.1	**2.18**	0.003

Table RADAR-5. Cassini active-stare observations of Mimas (MI), Tethys (TE), Enceladus (EN), Dione (DI), Rhea (RH), Iapetus (IA), and Phoebe (PH).

Obs ID[a]	Latitude (°)	W Longitude (°)	Beam size (diameter)	Range (km)	n	A_{SL-2}^{disk}	Error
RH22C3	35.8	100.0	0.41	97,476	1.5	**1.60**	0.003
RH22C4	23.2	145.4	0.42	98,647	3.0	**1.22**	0.004
RH22C5	−16.1	149.9	0.42	99,771	3.1	**1.36**	0.004
RH27	26.7	320.2	0.77	181,621	1.6	**2.18**	0.003
RH45	−45.0	63.2	0.83	195,637	1.5	**2.12**	0.003
RH47	−2.7	234.2	0.64	152,183	1.2	**2.62**	0.002
RH49	−0.4	346.8	0.45	105,925	2.1	**1.86**	0.005
RH49C1	−35.1	347.4	0.44	103,287	1.0	**2.34**	0.006
RH49C2	−1.8	315.8	0.43	100,710	1.8	**1.97**	0.007
RH49C3	27.9	322.4	0.41	98,206	1.6	**1.89**	0.006
RH49C4	28.6	9.2	0.40	95,652	1.3	**2.04**	0.006
RH127	0.8	163.5	0.27	63,927	2.7	**1.43**	0.007
RH49C5	−9.0	24.8	0.39	93,559	1.0	**2.38**	0.006
IAIn	38.8	66.5	0.68	150,823	1.1	**0.54**	0.009
IAInC1	52.0	41.6	0.68	150,229	2.3	**0.54**	0.008
IAInC2	52.0	91.6	0.67	149,611	1.9	**0.42**	0.009
IAInC3	23.1	82.2	0.67	148,993	1.2	**0.41**	0.011
IAInC4	23.8	49.2	0.67	148,375	0.7	**0.56**	0.011
IAOut	45.6	296.0	0.91	202,360	1.3	**1.02**	0.006
IA17	37.1	358.3	1.88	419,001	3.1	**0.71**	0.020
IA49Obs1	10.9	61.2	1.10	244,226	1.5	**0.34**	0.019
IA49Obs2	10.4	65.5	0.45	100,193	1.9	**0.28**	0.011
IA49Obs2C1	−15.4	72.6	0.49	109,270	1.4	**0.34**	0.017
IA49Obs2C2	3.0	39.8	0.48	107,855	0.4	**0.43**	0.016
IA49Obs2C3	35.6	57.2	0.48	106,450	1.1	**0.39**	0.016
IA49Obs2C4	16.7	91.3	0.47	105,049	1.3	**0.36**	0.016
IA49Obs4	−10.3	247.3	0.50	110,290	2.2	**0.66**	0.018
IA49Obs4C1	−16.6	274.9	0.50	111,345	1.5	**0.92**	0.018
IA49Obs4C2	−36.6	238.3	0.50	112,121	1.8	**0.66**	0.019
IA49Obs4C3	−1.6	220.5	0.51	112,763	2.1	**0.48**	0.019
IA49Obs4C4*	16.3	255.0	0.51	113,460	1.8	**0.82**	0.019
PHIn	−21.9	245.5	2.72	92,525	1.1	**0.29**	0.044
PHOut	26.7	327.8	1.71	58,238	1.3	**0.31**	0.007

[a] Observations for which there is a discrepancy in the best-fit n and derived radar albedo compared to what was published in Ostro et al. [2010] are marked by a * when the discrepancy is small and by ** when the discrepancy is significant.

DISTANT PASSIVE RASTER SCANS

Distant radiometry observations use the spacecraft reaction wheels to raster-scan a rectangular area centered on the target and extending off the disk for baseline calibration (see Figure RADAR-37). The rasters are approximately 2° in length with spacing less than half of the 0.37° beamwidth. First, the measured antenna temperatures are calibrated using the best current calibration of the instrument. This calibration is based on Titan and Saturn observations and described in Janssen et al. [2016], where it is argued that the resulting absolute uncertainty on non-Titan objects is better than 2%. The cold sky reference level (i.e., the Cosmic Microwave Background brightness temperature at 2.7 K) is determined by averaging the off-disk observations. Second, a limb-darkening brightness temperature model (see Figure RADAR-37 bottom) is used to derive the total emission from the moon, expressed as its disk-averaged brightness temperature $T_{\mathrm{b}}^{\mathrm{disk}}$. This model is convolved with the well-determined beam pattern of the radiometer along the raster-scan path in order to produce synthetic data with the same viewing geometry as the time-ordered measured data (see Figure RADAR-37). The model parameters, namely the pointing error,

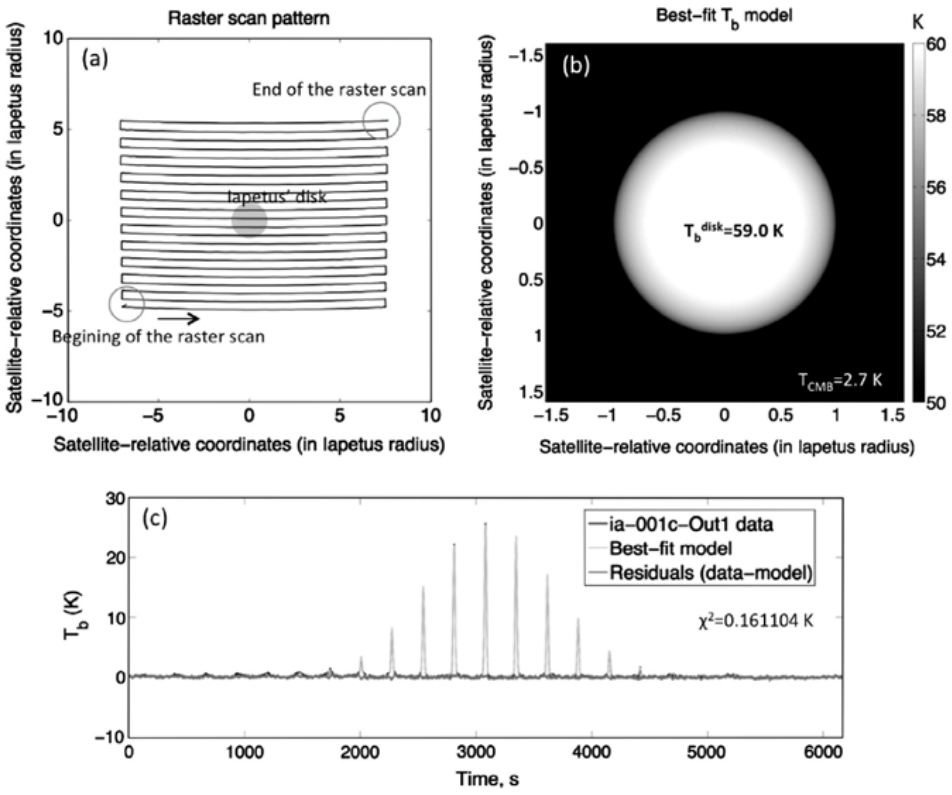

Figure RADAR-37. IA01c-1-Out1 distant radiometry observation of Iapetus. Top Left: Raster-scan pattern performed to collect radiometry data. The beam sizes at the beginning and the end of the raster scan are indicated; they are about the size of Iapetus' diameter (see also Table RADAR-6). Top Right: Measured calibrated antenna temperature compared to the best-fit model as a function of time. Radiometry distant raster-scan typically last one or two hours. Bottom: Best-fit model and corresponding disk-averaged temperature. The model assumes a circularly symmetric bright disk (730 km in diameter) with a $\cos^n\theta$ brightness taper to account for limb darkening (where θ is the emission angle and n = 0.04). Figure is extracted from Le Gall et al. [2014].

the timing offset and the brightness scale factor, are adjusted until the chi-squared sum of the residuals is minimized. T_b^{disk} is derived from the best-fit brightness temperature model as follows:

$$T_{\mathrm{b}}^{\mathrm{disk}} = \frac{1}{\Omega^{\mathrm{disk}}} \int T_{\mathrm{b}}^{m} d\Omega, \qquad \text{Eq. 3}$$

where Ω^{disk} is the disk solid angle and T_b^m the best-fit modeled brightness temperature of each element of solid angle dΩ. The errors on T_b^{disk} are estimated from the least-squares fit. The results are almost insensitive to the choice of a priori model parameters. More details can be found in Janssen et al. [2009].

Table RADAR-6 summarizes all 40 distant radiometry observations of Mimas, Tethys, Enceladus, Dione, Rhea, Iapetus, and Phoebe during the Cassini mission. Note that some radiometer footprints are as small as about 0.4–0.5 satellite diameter. These observations are able to resolve large-scale features at the surface. However, in this report we have chosen to classify them as distant because no scatterometry data were acquired concurrently with the radiometry.

Table RADAR-6. Cassini radiometry distant observations of Mimas, Tethys, Enceladus, Dione, Rhea, Iapetus, and Phoebe.

Target Distant Observation ID[g]	Date Start time End time M, D, Y h:m:s	Sub-spacecraft Point[a] (°E, °N)	Sub-solar Point[b] (°E, °N)	Beam size[c] (Diameter)	$T_b^{disk[d]}$ (K)	Emissivity[e]	Radar albedo[f]
MIMAS MI47	2007 Jun 28 03:38:47 04:01:17	(−50.5, −2.0)	(−40.3, −10.4)	3.89	43.1±1.5	0.56	2.45
MIMAS MI53	2007 Dec 03 00:25:31 03 00:59	(−92.9, 14.8)	(141.0, −10.3)	4.59	41.0±1.8	0.53	N/A
MIMAS MI64	2008 Apr 11 10:21:18 10:54:08	(−166.6, −67.9)	(6.1, −7.5)	2.06	42.7±1.3	0.55	N/A
MIMAS MI126	2010 Feb 13 14:51:31 15:15:11	(97.3, −3.3)	(−76.9, 2.0)	0.77	43.0±0.9	0.56	2.69
ENCELADUS EN03	2005 Feb 17 10:33:29 11:26:59	(128.2, 0.7)	(−65.4, −22.8)	3.29	39.3±1.4	0.66	2.16
ENCELADUS EN04	2005 Mar 09 13:04:24 13:52:58	(−74.1, 0.3)	(51.6, −22.5)	1.29	32.9±0.8	0.54	N/A
ENCELADUS EN32	2006 Nov 09 02:20:41 02:31:06	(114.0, −14.3)	(130.8, −15.2)	1.23	38.8±0.9	0.64	N/A
ENCELADUS EN50	2007 Sep 30 15:21:43 16:00:46	(−131.5, 16.0)	(−71.1, −10.6)	1.59	31.0±0.8	0.51	3.21

Table RADAR-6. Cassini radiometry distant observations of Mimas, Tethys, Enceladus, Dione, Rhea, Iapetus, and Phoebe.

Target Distant Observation ID[g]	Date Start time End time M, D, Y h:m:s	Sub-spacecraft Point[a] (°E, °N)	Sub-solar Point[b] (°E, °N)	Beam size[c] (Diameter)	T_b^{disk}[d] (K)	Emissivity[e]	Radar albedo[f]
ENCELADUS EN61-1	2008 Mar 12 15:01:01 15:49:46	(−108.0, 68.6)	(46.6, −8.0)	2.33	35.0±1.0	0.58	3.49
ENCELADUS EN88-1	2008 Oct 09 12:06:44 12:57:04	(−40.6, 64.4)	(89.7, −4.8)	4.42	36.8±1.6	0.61	N/A
ENCELADUS EN120-1	2009 Nov 02 01:46:02 02:27:42	(60.5, -0.6)	(-107.7, 1.3)	2.02	39.7±1.1	0.66	2.63
ENCELADUS EN120-2	2009 Nov 02 02:44:22 03:21:02	(54.5, −0.7)	(−118.2, 1.3)	1.73	40.6±1.0	0.67	2.63
ENCELADUS EN16-1#	2011 Nov 06 03:02:26 03:14:09	(172.0, 0.0)	(18.0, 11.7)	0.65	Data contamined with Saturn	N/A	N/A
ENCELADUS EN16-2#	2011 Nov 06 03:22:53 03:37:36	(167.8, −0.1)	(14.1, 11.7)	0.51	Data contamined with Saturn	N/A	N/A
ENCELADUS EN16-9#	2011 Nov 06 06:32:49 06:46:30	(−43.3, −0.8)	(−19.1, 11.7)	0.58	37.9±0.9	0.63	N/A
ENCELADUS EN16-10#	2011 Nov 06 06:58:09 07:12:51	(−47.3, −0.7)	(−23.8, 11.7)	0.74	37.5±0.9	0.62	N/A
TETHYS TE15	2005 Sep 24 06:49:46 07:21:41	(152.6, −0.3)	(−42.2, −19.3)	0.94	32.9±0.7	0.47	2.76
DIONE DI16	2005 Oct 11 22:52:51 23:30:41	(−23.6, 0.2)	(140.4, −20.1)	1.12	54.2±1.2	0.76	1.64
DIONE DI50	2007 Sep 30 00:19:29 01:12:39	(152.7, −13.1)	(34.3, −10.4)	0.64	52.8±1.1	0.74	1.58
DIONE DI177-1	2012 Dec 23 05:08:11 05:22:41	(−95.1, 45.7)	(−14.4, 16.9)	1.35	47.6±1.0	0.67	N/A
DIONE DI177-2	2012 Dec 23 05:34:21 05:47:41	(−93.9, 49.0)	(−16.7, 16.9)	1.37	47.3±1.0	0.66	N/A
RHEA RH11	005 Jul 14 09:05:44 09:41:44	(−48.3, −74.7)	(174.8, −20.6)	0.79	46.6±1.0	0.64	1.84

Table RADAR-6. Cassini radiometry distant observations of Mimas, Tethys, Enceladus, Dione, Rhea, Iapetus, and Phoebe.

Target Distant Observation ID[g]	Date Start time End time M, D, Y h:m:s	Sub-spacecraft Point[a] (°E, °N)	Sub-solar Point[b] (°E, °N)	Beam size[c] (Diameter)	T_b^{disk}[d] (K)	Emissivity[e]	Radar albedo[f]
RHEA RH18	2005 Nov 27 04:35:35 05:21:55	(−21.8, 0.2)	(156.8, −19.1)	0.74	50.1±1.1	0.69	1.83
RHEA RH22-1	006 Mar 21 11:03:26 12:57:06	(−135.5, 0.9)	(52.4, −17.8)	0.51	46.5±1.0	0.64	N/A
RHEA RH22-2	2006 Mar 21 13:03:16 14:57:06	(−153.0, 0.7)	(45.8, −17.8)	0.64	47.4±1.0	0.65	1.43
RHEA RH45	2007 May 27 11:21:28 11:49:44	(−57.7, −44.0)	(−157.2, −11.9)	0.84	47.3±1.0	0.65	2.12
RHEA RH49	2007 Aug 29 20:05:06 20:47:36	(15.2, −0.3)	(−114.3, −10.6)	0.51	49.2±1.1	0.68	1.86
RHEA RH127-1	2010 Mar 02 13:42:57 14:30:12	(−159.5, 0.3)	(19.3, 3.1)	0.47	47.2±1.0	0.65	1.43
RHEA RH127-2	2010 Mar 02 14:31:57 15:23:02	(−162.1, 0.4)	(16.6, 3.1)	0.35	47.5±1.1	0.65	1.43
RHEA RH177-1#	2012 Dec 22 20:06:52 20:28:42	(−102.2, −76.0)	(−11.7, 16.6)	0.40	43.7±1.0	0.60	N/A
RHEA RH177-2#	2012 Dec 22 20:38:32 20:57:16	(−91.6, −77.0)	(13.4, 16.6)	0.33	43.5±1.1	0.60	N/A
IAPETUS IA01b-1-In	2004 Dec 31 05:13:48 06:27:51	(−72.1, 37.1) L	(−111.5, −7.5) ☼	0.68	69.6±1.5	0.81	0.54
IAPETUS IA01c-1-Out1	2005 Jan 01 19:04:23 20:45:33	(60.9, 41.0) T	(−118.7, −7.5) ☾	0.97	56.0±1.2	0.65	N/A
IAPETUS IA01c-1-Out2	2005 Jan 01 20:44:23 22:27:13	(61.7, 39.6) T	(119.0, −7.5) ☾	1.02	55.8±1.2	0.65	N/A
IAPETUS IA17-1	2005 Nov 12-13 23:18:50 00:04:40	(1.3, 36.9) T/L	(−97.5, −4.7) ☾/☼	1.84	62.2±1.4	0.72	0.71

Table RADAR-6. Cassini radiometry distant observations of Mimas, Tethys, Enceladus, Dione, Rhea, Iapetus, and Phoebe.

Target Distant Observation ID[g]	Date Start time End time M, D, Y h:m:s	Sub-spacecraft Point[a] (°E, °N)	Sub-solar Point[b] (°E, °N)	Beam size[c] (Diameter)	T_b^{disk}[d] (K)	Emissivity[e]	Radar albedo[f]
IAPETUS IA49-1	2007 Sep 09 07:41:52 08:23:32	(−65.4, 10.8) L	(146.4, 1.5) ☾	1.12	73.4±1.5	0.85	0.34 0.28
IAPETUS IA49-2	2007 Sep 10 00:13:00 01:07:10	(−69.2, 10.7) L	(143.3, 1.5) ☾	0.50	74.1±1.7	0.86	0.34 0.28
IAPETUS IA49-4	2007 Sep 11 03:51:15 04:51:45	(106.8, −10.8) T	(138.1, 1.5) ☼	0.52	59.3±1.3	0.69	0.66
PHEOBE PH3-1	2004 Jun 11 14:31:11 15:22:52	(136.5, −21.7)	(−137.7, −12.8)	3.10	78.7±3.6	0.88	0.29
PHEOBE PH3-2	2004 Jun 12 00:01:19 00:23:48	(−45.5, 22.2)	(−137.2, −12.8)	3.13	69.0±1.9	0.77	N/A
PHEOBE PH3-3	2004 Jun 12 00:25:17 00:47:56	(−61.4, 22.7)	(−152.3, −12.5)	3.42	71.5±2.1	0.80	N/A

a The planetographic coordinate of the apparent sub-spacecraft point is given at the center of the scan. It may change a few degrees along the scan. L and T flag observations of the leading or trailing sides.

b The sub-solar point is given at the center of the raster scan. ☾ and ☼ flag observations of the day or night sides.

c The beam size at the center of the raster scan is expressed in satellite diameter. It is related to the encounter distance by the following relationship: beam size = distance*tan(0.37/2)/radius, where 0.37° is the antenna beamwidth and radius is the mean of the two equatorial radii of the satellite.

d 2.2-cm absolute brightness temperature over the satellite disk. The derived values include statistical and calibration uncertainties.

e Estimate of the disk-integrated emissivity. As in Ostro et al. [2006], we use the isothermal equilibrium temperature T_{eq} as a proxy for the effective physical temperature at 2.2 cm with $T_{eq} = 91.4\ (1-A_{Bond})^{1/4}$, where 91.4 K is the equilibrium temperature for a grey body at Saturn's distance from the Sun and A_{Bond} is the bolometric Bond albedo of the satellite. For this parameter, we use the up-to-date values published in Howett et al. [2010] based on CIRS observations. Note that these Bond albedo values are different from those used in Ostro et al. [2006] and should be more accurate. Indeed, prior to Cassini measurements, only much less accurate and complete Voyager and ground-based data were available, and the leading and trailing values had been measured solely for a few icy satellites. The emissivity is estimated by $T_{\mathrm{b}}^{\mathrm{disk}}/T_{eq}$.

f Radar albedo value for comparison. Only the values acquired during the same flyby and over (almost) the same disk are shown.

g Observations marked with a # are observations that are preceded or followed in an observation of the same disk in the orthogonal polarization.

SCATTEROMETRY-RADIOMETRY RESOLVED OBSERVATIONS

Over the course of the Cassini mission, RADAR had few opportunities to collect spatially resolved scatterometry and radiometry data during close-targeted encounters of icy satellites. For instance, during Cassini's 49th orbit around Saturn (Sept. 9–10, 2007), RADAR was assigned a time slot while the spacecraft was at a range of ~20,000 km from Iapetus. The SAR image obtained during this close encounter is described in Ostro et al. [2010] while the scatterometry data were processed

and analyzed by Wye [2011] and the radiometry data by Le Gall et al. [2014] (see Figure RADAR-38).

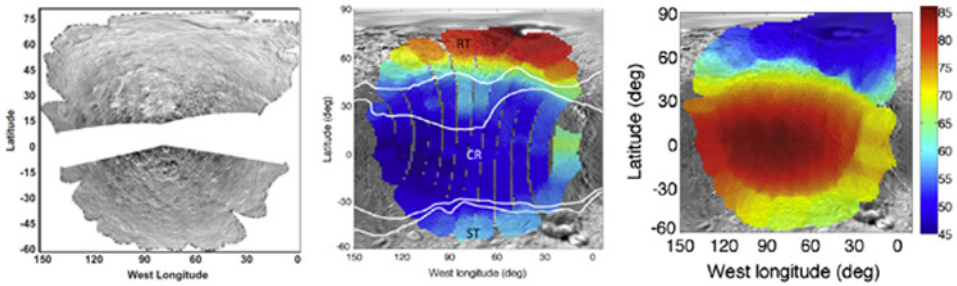

Figure RADAR-38. SAR-scatterometry-radiometry IA49-3 observation. (See Table RADAR-6). Left: SAR image of the leading side of Iapetus acquired during flyby IA49 (September 2007). For this SAR image, a cosine scattering law with exponent 1.5 was subtracted from the original image. Extracted from Ostro et al. [2010]. Middle: Scatterometry data collected during the IA49-3 experiment overlaid on an ISS base map (PIA08406). The normalized backscattering cross-sections are in linear scale and corrected to an incidence angle of 32° using the backscatter analysis conducted by Wye [2011]. Extracted from Le Gall et al. [2014]. Right: Calibrated antenna temperatures recorded during the radiometry IA49-3 experiment overlaid on an ISS base map of Iapetus (PIA08406). Extracted from Le Gall et al. [2014].

Table RADAR-7 lists all resolved scatterometry-radiometry observations of icy satellites during the Cassini mission and, when they exist, the published papers describing these observations.

Table RADAR-7. Cassini radar/radiometry spatially-resolved observations of Enceladus, Dione, Rhea, and Iapetus.

Target Distant Observation ID[g]	Date Start time End time M, D, Y h:m:s	Sub-spacecraft Point[a] (°E, °N)	Sub-solar Point[b] (°E, °N)	Beam size[c] Start End (Diameter)	$T_b^{disk^d}$ (K)	Comments and References
ENCELADUS EN120-3	2009 Nov 02 04:51:52 06:36:52	(34.3, −1.2)	(−179.9, 26.2)	0.50 0.39	N/A	SAR image and scatterometry analysis: Wye [2011]. The radiometry data cannot be calibrated.
ENCELADUS E16 In 1[#]	2011 Nov 06 03:38:37 03:48:15	(165.2, −0.2)	(11.8, 11.6)	0.47 0.33	N/A	The low-resolution SAR images acquired during E16 In 1, 2 and 3 are shown in the SI of Le Gall et al. [2017]. The concurrent radiometry data are contaminated by Saturn's emission.
ENCELADUS E16 In 2[#]	2011 Nov 06 03:59:49 04:20:23	(159.7, −0.5)	(7.1, 11.6)	0.23 0.22	N/A	
ENCELADUS E16 In 3	2011 Nov 06 04:24:29 04:51:26	(152.4, −1.8)	(2.2, 11.6)	0.19 0.04	N/A	
ENCELADUS E16 closest approach	2011 Nov 06 04:58:15 05:00:00	(60, 30)	(-1.5, 11.8)	0.019 0.023	N/A	Active (including high-res SAR) and passive data are shown and discussed in Le Gall et al. [2017].

Table RADAR-7. Cassini radar/radiometry spatially-resolved observations of Enceladus, Dione, Rhea, and Iapetus.

Target Distant Observation ID[g]	Date Start time End time M, D, Y h:m:s	Sub-spacecraft Point[a] (°E, °N)	Sub-solar Point[b] (°E, °N)	Beam size[c] Start End (Diameter)	$T_b^{disk^d}$ (K)	Comments and References
ENCELADUS E16 Out 1	2011 Nov 06 05:07:27 05:52:10	(−29.9, −1.9)	(−6.6, 11.6)	0.05 0.33	43.5±4.9	E16 Out 1 radiometry data are analyzed in Ries and Janssen [2015].
ENCELADUS E16 Out 2#	2011 Nov 06 05:57:10 06:10:22	(−37.3, −1.1)	(−12.8, 11.7)	0.33 0.41	42.5±2.3	E16 Out 2 and 3 radiometry data are shown in Ries and Janssen [2015].
E16 Out 3#	2011 Nov 06 06:22:30 06:31:42	(−41.3, −0.9)	(−16.9, 11.7)	0.48 0.53	40.5±1.5	
DIONE DI163-1	2012 Mar 28 02:01:07 03:36:07	(−16.2, −0.9)	(−135.3, 13.7)	0.56 0.49	57.3±1.7	None
DIONE DI163-2	2012 Mar 28 03:39:07 03:49:07	(−36.4, −1.0)	(−140.4, 13.7)	0.34 0.32	56.1±1.3	None
RHEA RH127-3	2010 Mar 02 15:50:04 16:50:30	(−166.9, 1.1)	(11.7, 3.1)	0.24 0.11	N/A	The SAR image and scatterometry observation are shown and analyzed in Wye [2011].
IAPETUS IA49-3	2007 Sep 10 11:19:42 12:17:47	(−76.9, 10.4)	(141.2, 1.5)	0.11 0.07	76.8±6.5	SAR image: Ostro et al. [2010]. Scatterometry analysis: Wye [2011]. Radiometry analysis : Le Gall et al. [2014].

a The planetographic coordinate of the apparent sub-spacecraft point is given at the center of the scan. L and T flag observations of the leading or trailing sides.

b The sub-solar point is given at the center of the raster scan. ☾ and ☼ flag observations of the day or night sides.

c The beam size at the center of the raster scan is expressed in satellite diameter.

d 2.2-cm absolute brightness temperature over the satellite disk. When possible, the values are derived as described in the section entitled Distant passive raster-scans.

e Observations marked with a # are observations that are preceded or followed in an observation of the same disk in the orthogonal polarization.

Note that flyby E16 was the only Enceladus' encounter dedicated to RADAR. The SAR image was acquired within 2 min centered around closest approach, while the spacecraft passed the moon at distance of about 500 km, has the highest spatial resolution (~50 m in the cross-track direction, ~200 m in the along-track direction) ever achieved for SAR imagery on any icy satellite. These high-resolution datasets and the concurrent radiometry were analyzed in Le Gall et al. [2017]. Medium-resolution radar/radiometry data were also acquired before and after the E16 closest approach—see the inbound and outbound low-resolution SAR images in Figure RADAR-39 and West et al. [2012]. Unfortunately, half of the concurrent radiometry data were contaminated by

emission from Saturn (and its rings), which was behind Enceladus' disk during the inbound leg of the observation [Ries and Janssen 2015].

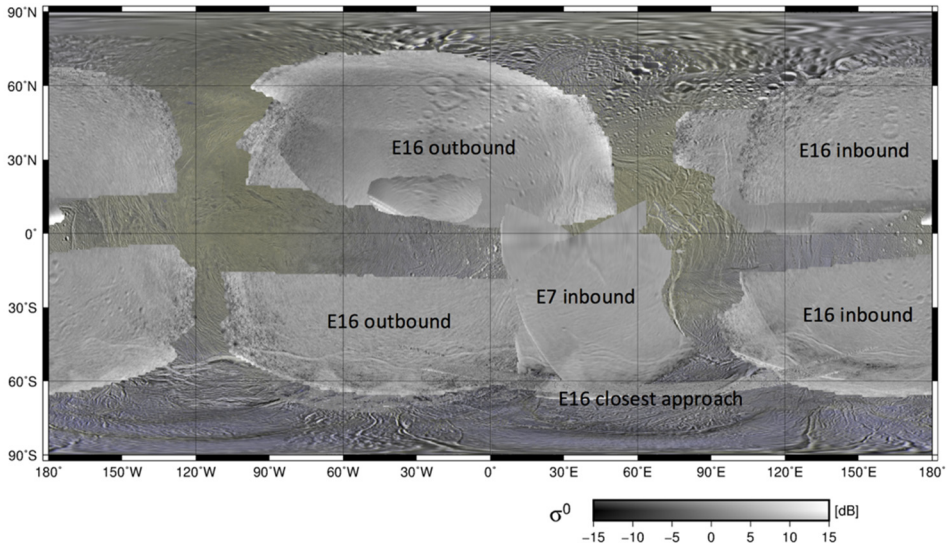

Figure RADAR-39. Mosaic of the EN120 (also called E7) and E16 SAR images of Enceladus overlaid on a color mosaic of Enceladus produced by the Cassini ISS (PIA18435). The measured normalized backscatter cross-sections are in dB and have been corrected for incidence-angle effects and biases due to thermal and quantization noises. Figure is extracted from the Supplementary Material of Le Gall et al. [2017].

Lastly, the first resolved observation of Enceladus was acquired during the inbound leg of the 7th targeted encounter of the moon (often referred to as E7 or EN120) that occurred on November 2, 2009. Following a distant observation, the spacecraft turned to offset the central beam to a suitable imaging area and RADAR collected high-altitude scatterometry imaging and radiometry data down to an altitude of about 30,000 km [Wye 2011]. The resulting low-resolution SAR image has some overlap with the E16 high-resolution SAR observation (see E7 inbound in Figure RADAR-39). However, the concurrent radiometry data cannot be properly calibrated because the receiver temperature was not stabilized during this observation.

Science results and open questions

In this section, we summarize the major science results obtained thanks to RADAR observations of Saturn's icy satellites. When possible, these observations are analyzed in light of observations at other wavelengths or by comparison with radio observations of other icy objects.

Measure of the degree of scattering in the subsurface

Among all the radar-detected planetary bodies in the solar system, the ice-rich satellites of both the Saturn and Jovian systems have the most unusual radar properties. Their reflectivities are very high and they exhibit peculiar polarization properties [Black et al. 2001]. The general understanding

gained so far about the radar properties of the Saturnian satellites icy surfaces, including Titan, at the Cassini 2.2 cm wavelength is that they are dominated by subsurface volume scattering [Ostro et al. 2006; Wye et al. 2007; Zebker et al. 2009a; Janssen et al. 2009].

More accurately, if refraction scattering from dielectric inclusions [Hagfors et al. 1985; Hagfors et al. 1997] or interface cracks [Goldstein and Green 1980] can play a role, the generally accepted explanation is that most icy satellites' radar behavior is related to an effect called the coherent backscatter effect [Hapke 1990; Ostro 1993; Black et al. 2001]. This effect is due to volume scattering from within the satellites' regolith, which, on icy satellites, can be regarded as an extremely low-loss and disordered random medium.

The high radar transparency of ice at temperatures as low as 100 K [Thompson and Squyres 1990; Matzler 1998; Lorenz 1998] compared with that of silicates indeed permits deeper radar sounding (10–100 wavelengths), longer photon path lengths, and thus higher order scattering from regolith heterogeneities (voids, rocks) producing large backscatter and reducing the emissivity (Figure RADAR-40). The purer and the more structurally complex the subsurface, the higher the radar albedo and the lower the emissivity. Both in its active and passive modes, the Cassini RADAR therefore measures quantities that are closely related to the degree of purity of the regolith and to its structural heterogeneity/complexity.

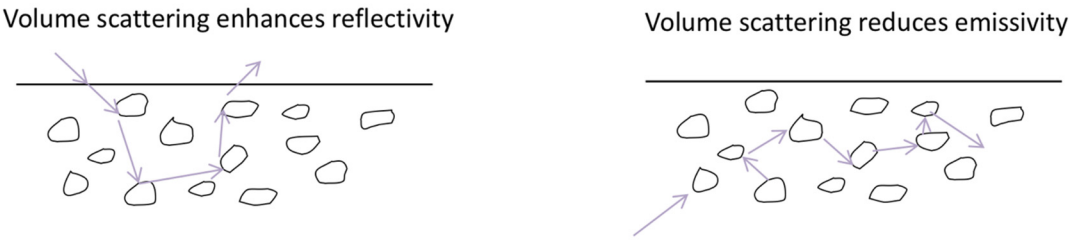

Figure RADAR-40. Effect of volume scattering on the measured reflectivity and emissivity. A low-loss and structurally complex regolith provides enhanced opportunity for scattering, which increases the reflectivity and reduces the emissivity (because it prevents the emitted waves from escaping the subsurface).

INTER-SATELLITE RADAR ALBEDO AND EMISSIVITY VARIATIONS

Figures RADAR-41, RADAR-42, and RADAR-43 show that active and passive signatures differ from one satellite to another—see also Black et al. [2007]; Ostro et al. [2006]—thus indicating various degrees of volume scattering in their subsurface, i.e., various degree of purity and/or complexity of their regolith and thus differences in their composition and/or the various processes that have modified their structure.

For Ostro et al. [2006], variations in terms of composition, rather than structure, is the main source of satellite-to-satellite variabilities. More specifically, they invoke an increase in surface contaminants of Saturnian satellites to explain the observed proportional decrease in radar albedo and the concurrent increase in emissivity in the order Enceladus/Tethys, Mimas, Rhea, Dione,

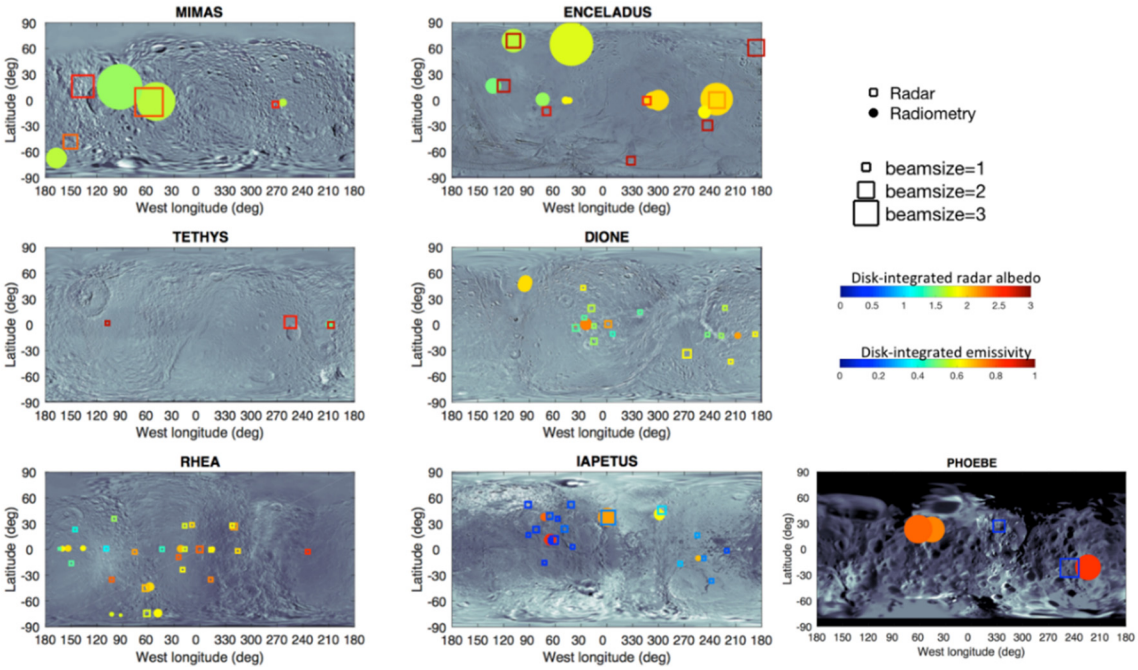

Figure RADAR-41. Sub-radar locations of distant active-radar and radiometry observations of Mimas, Tethys, Enceladus, Dione, Rhea, Iapetus, and Phoebe acquired during the Cassini mission, overlaid on the near-IR ISS mosaics of each satellite. The square symbols correspond to active stare observations while the circle symbols correspond to distant radiometry measurements. The color codes indicate the value of the derived disk-integrated radar albedo for the squares and that of the derived disk-integrated emissivity for the circles, respectively. The size of the symbols indicates the ratio between the beamwidth of the observation and the target angular diameter. The sub-Saturn longitude occurs at zero and the leading side is centered on 90° W longitude.

Iapetus, and Phoebe (see Figures. RADAR-42 and RADAR-43). An argument in favor of this hypothesis is the strong correlation between the radar and optical albedos of the satellites—see Figure 4 in Ostro et al. [2006]. This suggests that an increasing concentration of optically dark contaminant(s) in the near-surface leads to the attenuation of the high-order multiple scattering in the subsurface (water ice being transparent to radio wavelengths) and thus to smaller albedos and larger emissivities. Note that Phoebe, the dimmest of the targets, is nevertheless twice as radar bright as the Moon [Ostro et al. 2006]. The nature of the contaminant(s) remains unknown but Ostro et al. [2006] propose possible candidates including silicates, metallic oxides, and polar organics such as nitriles or complex tholins.

Taking a step further, the active radar and radiometry sequences shown in Figures RADAR-42 and RADAR-43 as well as the hemispheric dichotomies observed at 2.2 cm can be, at first order, explained by variations in term of surface contamination as the result of the competition between several effects including:

- The coating effect of the E-ring
- The coating effect of the vast debris ring from Phoebe

- The geological and thermal history of the icy satellite
- The efficiency of space weathering at the position of the icy satellite within Saturn's magnetosphere

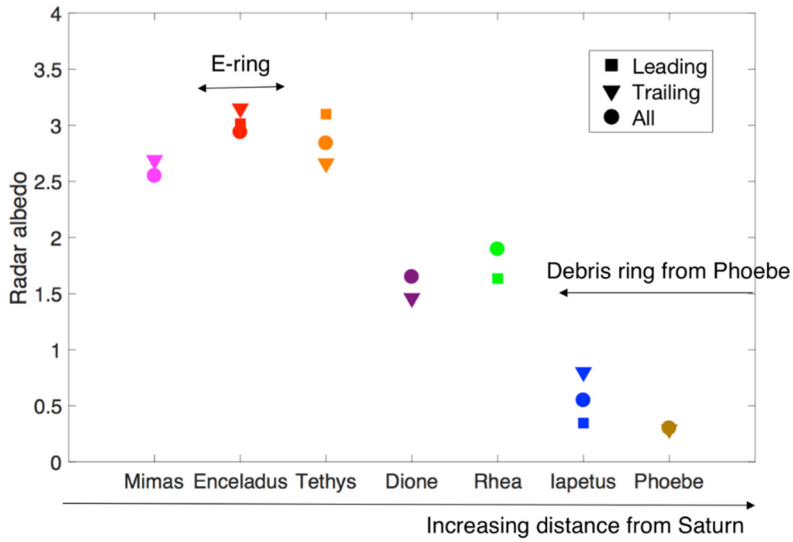

Figure RADAR-42. Radar albedos derived from Cassini active stare observations of Mimas, Enceladus, Tethys, Dione, Rhea Iapetus, and Phoebe. For each satellite, when available, values are shown separately for the leading and trailing sites (in the latitudinal band (−30°, 30°)) in order to reveal possible hemispheric dichotomy. The locations of the E-ring and the vast debris ring from Phoebe are indicated.

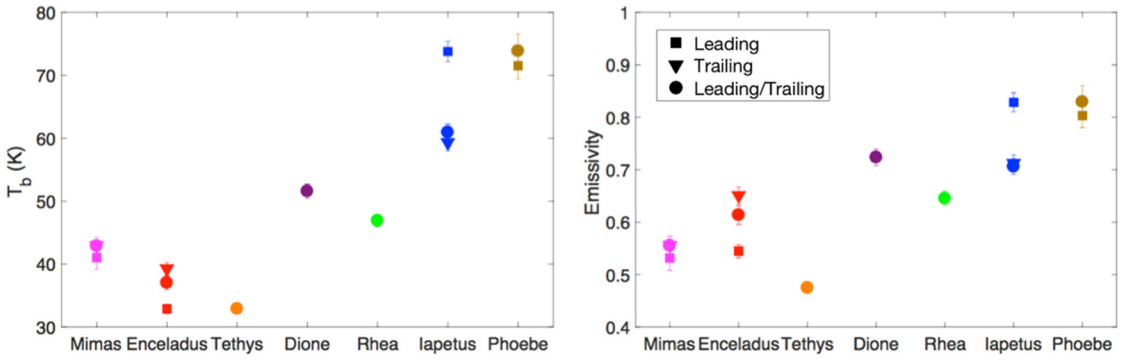

Figure RADAR-43. Disk-integrated brightness temperatures (left) and estimated emissivities (right) derived from Cassini passive distant observations of Mimas, Enceladus, Tethys, Dione, Rhea, Iapetus, and Phoebe. For each satellite, when available, values are shown separately for the leading and trailing sites (in the latitudinal band (−30°, 30°)) in order to reveal possible hemispheric dichotomy. Note that the error bars on the emissivity results only take into account the measurement errors, not the error related to the fact that the isothermal equilibrium temperature was taken as a proxy for the effective physical temperature of the near-surface. A more accurate method to constrain emissivity is described in Le Gall et al. [2014].

Around Enceladus, the E-ring guarantees the deposition at the surface of extremely clean water ice that may also be structurally complex and thus very favorable to volume scattering. The decrease in radar brightness from Enceladus outward would then be due to the outward decrease in E-ring flux [Verbiscer et al. 2007] and hence the endowment of the satellite surface with ultra-clean ice. At the other extreme (moving inward from Phoebe), on the contrary, the diffuse debris ring from Phoebe progressively coats surfaces with material of low reflectivity. Geological activity brings fresh water ice at the surface and, if not too ancient, should therefore be associated with especially high albedos. Lastly, the efficiency of space weathering decreases with the distance to Saturn, which may have various implications on the microwave signatures of the icy satellites. For instance, close to Saturn, the magnetospheric ion bombardment should favor ammonia depletion in the near-surface and thus a higher degree of a purity of the water-ice regolith [Lanzerotti et al. 1984; Ostro et al. 2006]. On the other hand, gravitational focusing enhances the meteoroid flux close to Saturn—for example, Morfill et al. [1983]—which should lead to a higher contamination by non-ice compounds.

The differences between Saturn's icy satellites at 2.2 cm wavelength are further discussed in the section entitled Intra-satellite variations: Hemispheric dichotomies.

VARIATIONS WITH WAVELENGTH/DEPTH

Hints on the vertical variations of the regolith can be inferred from comparison of radio observations at different wavelengths. The 13 cm wavelength radar albedos measured from the Arecibo radar system [Black et al. 2004, 2007], once converted into same-sense albedos—from total power albedos as described in Ostro et al. [2010]—are all lower than the albedos obtained with the Cassini radar instrument at 2.2 cm (see Figure RADAR-44).

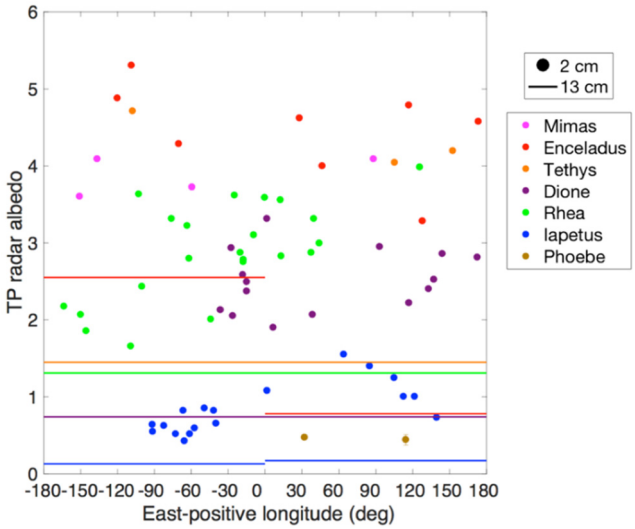

Figure RADAR-44. Total-power (TP) radar albedos of Saturn's icy satellites at the 2.2 cm (dots) and the 13 cm wavelengths (lines). The TP albedos at 2.2 cm were derived from the same-sense radar albedos measured by the Cassini radar as described in Ostro et al. [2010]. The TP albedos at 13 cm are Arecibo measurements averaged over the indicated longitude spans. See the caption of Figure 4 in Ostro et al. [2010] for more details.

The strong drop in radar albedo from 2.2 to 13 cm suggests that either the composition and/or structure is a function of depth everywhere (with e.g., electrical loss much greater at depths or a decrease with depth in the number density of efficient scatterers), or the regolith material is dispersive (with higher losses at higher wavelength). Ostro et al. [2010] favor the hypothesis of a decreasing ice cleanness with depth. Black and al. [2004] and Ostro et al. [2010] both invoke ammonia as the most likely contaminant: a lower abundance of ammonia within the upper one or two decimeters of the ice-rich regolith than at greater depths would account for the observations.

The specific cases of Enceladus and Iapetus for which Arecibo data show, respectively, a hemispheric dichotomy and no hemispheric dichotomy are discussed in the following subsections.

INTRA-SATELLITE VARIATIONS: HEMISPHERIC DICHOTOMIES

Almost all Saturnian icy satellites exhibit longitudinal variations in their microwave signatures, especially between their leading and trailing sides (see Figures RADAR-41, RADAR-42, and RADAR-43). These hemispheric dichotomies provide essential clues on the mechanisms that have primarily affected their near-surface.

IAPETUS' TWO-FACE

The most dramatic hemispheric dichotomy in the Saturnian system occurs at Iapetus, whose trailing side and poles are about an order of magnitude optically brighter than most of its leading hemisphere. The origin of this two-tone coloration has long been controversial, but there seems to now be a consensus toward an exogenic deposition of low-albedo materials probably originated in the region of Phoebe, or the vast debris ring from Phoebe, that crosses Iapetus' orbit—for example, Cruikshank et al. [1983], Buratti et al. [2002], Verbiscer et al. [2009], and Tosi et al. [2010b]. It has also been proposed that the darkening of the leading hemisphere is enhanced by the thermal segregation of water ice leaving behind a darker remnant material in the relatively warm equatorial region [Dalle Ore et al. 2012].

At 2.2 cm, the satellite's radar albedo and emissivity mimic the optical dichotomy, which implies that the leading side's optically dark contaminant must be present to depths of at least one to several decimeters [Ostro et al. 2006, 2010; Le Gall et al. 2014] (see Figures RADAR-41, RADAR-42, RADAR-43, and RADAR-44). On the other hand, at 13 cm, values of the radar albedo from the Arecibo radar system show no significant longitudinal pattern [Black et al. 2004] (see Figure RADAR-44). This strongly suggests that the thickness of the dark layer is no more than a few meters, which is also consistent with the discovery of small bright-ray and bright-floor craters within the dark terrain.

As a further argument, the thermal inertia of Iapetus' dark terrains inferred from Cassini IA49-3 resolved radiometry observations (see Table RADAR-6 and Figure RADAR-38) is much higher than that inferred from CIRS measurements [Howett et al. 2010], which sense only the uppermost layers of the surface [Le Gall et al. 2014]. This suggests a gradient in density with depth or, more

likely, that the radiometer has probed the icy substrate underlying the dark layer. Radiometry measurements also indicate a progressive thinning of the dark layer away from the equator.

In addition, Le Gall et al. [2014] show that the measured thermal emission during IA49-3 arises from several meters of the subsurface, which points to tholins, rather than iron oxide compounds, as the primary contaminants of the dark material. They also find that the dark terrains of Iapetus exhibit a 2.2 cm emissivity close to the emissivity of Phoebe (see Figure RADAR-43), which brings a further argument in favor of a common origin of their darkening agent.

ENCELADUS' YOUNG LEADING HEMISPHERE

Enceladus' 2.2 cm active observations show no dramatic leading/trailing asymmetry (see Figures RADAR-39 and RADAR-42), but passive observations, both unresolved (see Figure RADAR-43) and resolved (see Figure RADAR-45) do. Radiometry observations indeed show that the leading side of Enceladus is about 30% less emissive than its trailing side [Ries and Janssen 2015]. Such a dichotomy is also observed in Arecibo 13 cm measurements, which reveal a much brighter leading side [Black et al. 2007] (see Figure RADAR-44.)

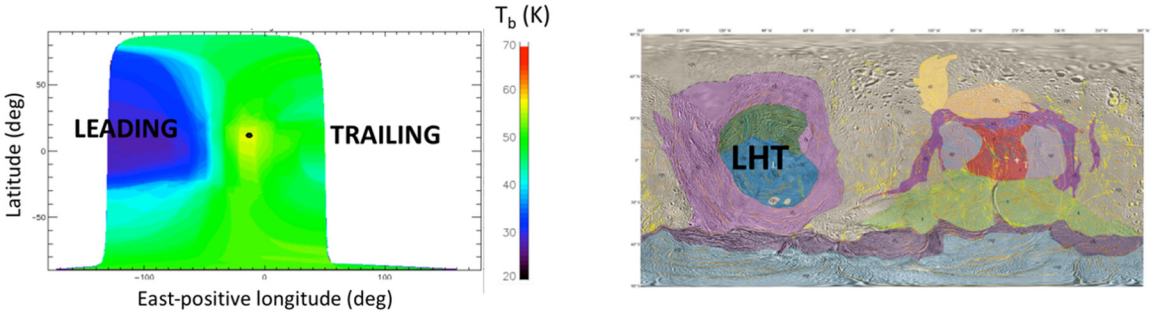

Figure RADAR-45. Resolved passive observations. Left: Deconvolved brightness temperatures measured during E16-Out1 (see Table RADAR-6). Credits: L. Bonnefoy. Right: Structural units of Enceladus as mapped by Crow-Willard and Pappalardo [2015].

Ries and Janssen [2015] propose that the leading side anomaly is an anomaly of scattering, associated with a seemingly young tectonized terrain called the Leading Hemisphere Terrain (LHT)—see Figure RADAR-44 and Crow-Willard and Pappalardo [2015]. In this picture, the LHT would be young enough (75–200 million years) to have been reprocessed (e.g., by micrometeoritic bombardment) only down to a depth shallower than the electrical skin depth at 2.2 cm (a few meters at most) contrary to the trailing side. This would be the reason why the leading/trailing dichotomy is not visible in 2.2 cm active data, which probe the subsurface down to a smaller depth than concurrent passive measurements and observations at 13 cm.

Alternatively, we note in Figure RADAR-42 that the trailing side of Enceladus is actually slightly brighter at 2.2 cm than its leading side. This suggests that, at the depth sensed by RADAR in active mode, the coating effect of the E-ring (which should be more widespread on the trailing side of Enceladus [Kempf et al. 2010]) prevails over the effect of space weathering and/or over the detection of the underneath leading-side young terrain. This would imply that the deposition rate of plume

particles at the surface of Enceladus is larger than estimated by Kemp et al. [2010] and, more specifically, larger than the reprocessing rate by micrometeoritic gardening [Cooper et al. 2001].

AROUND THE E-RING

The coating effect of the E-ring may also be responsible for the clear leading/trailing radar albedo dichotomy observed on Tethys and the hint of similar asymmetry observed on Mimas (see Figure RADAR-42).

We recall that for Rhea, Dione, and Tethys, which lie outside the densest part of Saturn's E-ring, the deposition of icy particles from Enceladus' plumes should be preferentially on the leading side. But Mimas and Enceladus, which are inside the E-ring, should be bombarded on their trailing side [Hamilton and Burns 1994; Buratti et al. 1998]. This is consistent with Figure RADAR-42, which shows a brighter leading hemisphere for Tethys while it is Mimas' trailing side that is brighter.

Cassini active observations also support the idea that the Pac-Man anomalies detected by the CIRS instrument are shallow. We recall that the CIRS instrument has detected, first on the leading side of Mimas and then of that of Tethys, a thermally anomalous extensive region shaped like the 1980s video game icon Pac-Man [Howett et al. 2011, 2012]. Both on Mimas and Tethys, the anomalous region coincides, in shape and location, with a region of preferential bombardment by high-energy electrons from Saturn's magnetosphere. The anomaly occurs because the MeV electrons penetrate into the subsurface gluing the water grains along their path and thus enhancing the thermal inertia. Evidence for a similar surface alteration by high-energy electrons was also detected on the leading side of Dione [Howett et al. 2014] but with a more tenuous expression as expected since the efficiency of the alteration must decrease with increasing distance to Saturn.

Given the small penetration depths of the MeV electrons into the subsurface (a few cm), the Pac-Man effect should not be detectable at 2.2 cm wavelength and the fact that we observe opposite albedo dichotomies on Mimas and Tethys (Figure RADAR-42) is a further argument for the dominant effect of coating by plume particles around Enceladus.

However, the Pac-Man effect may explain why slightly higher disk-integrated brightness temperatures were measured on the trailing side of Mimas (Figure RADAR-43). This can be confirmed or refuted by comparison of the radiometry data with a thermal model that accounts for the season and local hour of passive observations. In addition, the E-ring coating scenario implies the presence of at least a few meters of fresh water-ice material at the surface, which must be validated by model predictions of the deposition rate of particles from the plumes at the surface of Enceladus' neighbors.

DIONE'S PAST GEOLOGICAL ACTIVITY

The leading side of Dione is much brighter than its trailing side (see Figures RADAR-42 and RADAR-46). As for Enceladus, this is most likely the result of past geologic activity and the resultant resurfacing by fresh water ice. Most of Dione's leading side is indeed covered by smooth terrains [Schenk and Moore 2009] and must have a long resurfacing history [Kirchoff and Schenk 2015].

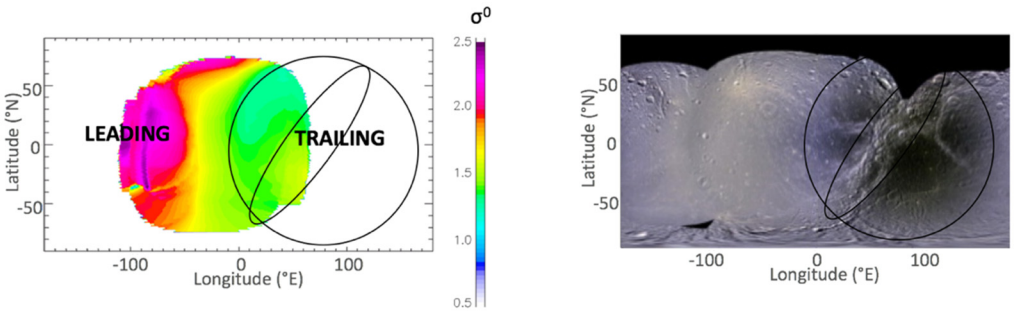

Figure RADAR-46. Trailing side of Dione. Left: Normalized backscattering cross-sections measured during DI 163-1. Credits: L. Bonnefoy. Right: Global mosaic of Dione composed of Cassini Imaging Science Subsystem images [Schenk et al. 2011].

RHEA'S PUZZLING HEMISPHERIC DICHOTOMY AND ENHANCED BRIGHTNESS

Figure RADAR-42, as well as the spatially resolved observations acquired during RH 127-3 (see Table RADAR-6), suggest that Rhea's leading side is radar-darker than its trailing side. Interestingly, Rhea has an optically brighter leading side—so, contrary to Tethys and Dione, there is an opposite correlation between the radar and the optical albedos. In addition, Rhea is surprisingly brighter (and concurrently less emissive) than Dione (see Figures RADAR-42 and RADAR-43). Rhea is also brighter than Dione at 13 cm (see Figure RADAR-44). The cause of this enhanced brightness is not well understood but it could be related to the weaker efficiency of space weathering at the location of Rhea's orbit as suggested by Scipioni et al. [2014] to explain VIMS observations.

Figure RADAR-47 summarizes the likely origins of the inter- and intra-satellites' radar albedo and emissivity variations.

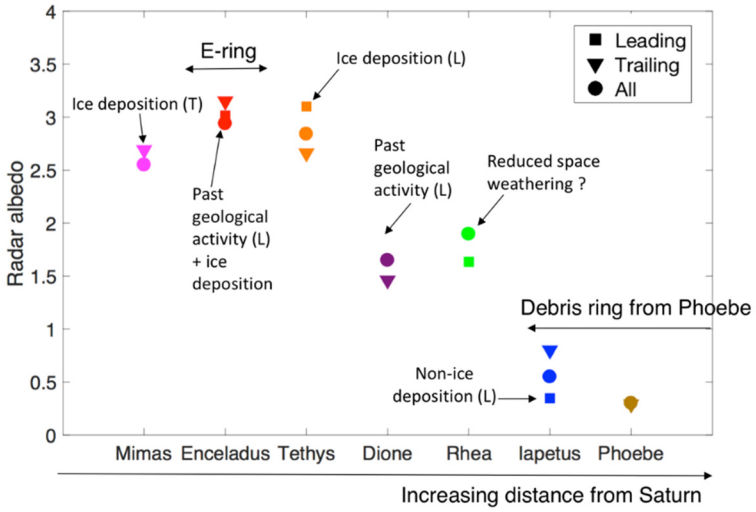

Figure RADAR-47. Radar albedos derived from Cassini active stare observations of Mimas, Enceladus, Tethys, Dione, Rhea, Iapetus, and Phoebe. (See section Distant Active Stares). For each satellite, when available, values are shown separately for the leading and trailing sites (in the latitudinal band (−30°, 30°)) in order to reveal possible hemispheric dichotomy. The possible mechanisms at the origin of the observed inter- and intra-satellite radar albedo and emissivity variations are indicated.

ENCELADUS' SOUTH POLE THERMAL ANOMALY

In 2005, the Cassini spacecraft witnessed for the first time water-rich jets venting from four anomalously warm fractures (also called sulci) near its South Pole [Porco et al. 2006; Spencer et al. 2009]. Since then, several observations have provided evidence that the source of the materials ejected from Enceladus is a large-scale underground ocean whose depth is still debated [Iess et al. 2014; Thomas et al. 2016].

In November 2011, during the closest approach of the 16th Enceladus encounter (flyby E16), RADAR had its first and only opportunity to closely observe Enceladus' south polar terrain (SPT), a few tens of km north of the active sulci (see Figure RADAR-48). At a distance of ~500 km from the surface, the instrument acquired a SAR image (see Figure RADAR-39) and recorded the 2.2 cm wavelength thermal emission of a ~500 km long, ~25 km wide, arc-shaped region centered at 63° S and 295° W and located 30–50 km north of the thermally active sulci identified as the sources of Enceladus' jets.

Le Gall et al. [2017] demonstrate that the brightness temperatures measured during E16 are too high for a purely exogenic explanation, with implications for endogenic processes and heat transport in the Enceladus' SPT. More specifically, they report the detection of prominent thermal anomalies that had not been identified before in the South Pole of Saturn's moon Enceladus (Figure RADAR-48). These anomalies coincide with large fractures, similar or structurally related to the four faults from which Enceladus jets are venting. Their presence implies a broadly distributed heat production and transport system below the south polar terrain of the icy moon with plate-like features. It also suggests that a liquid reservoir could exist at a depth of only a few kilometers under the ice shell at the South Pole—as also supported by interpretation of the libration, topography,

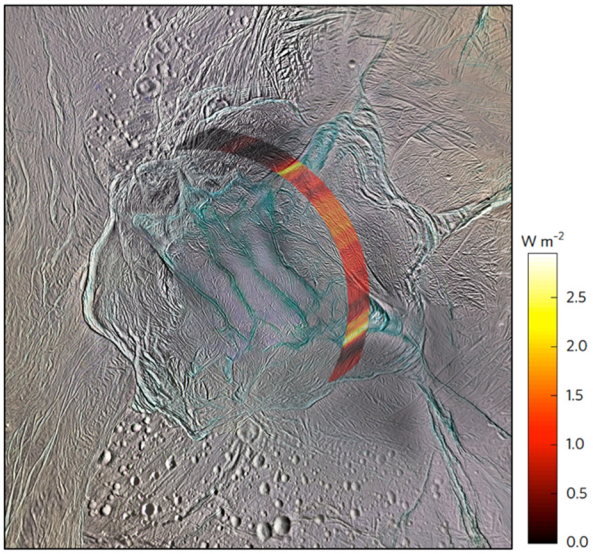

Figure RADAR-48. Minimum flux in excess in the region of Enceladus' SPT observed by the Cassini radar during the closest approach of E16. These values were derived from the E16 resolved radiometry observations by comparison with a thermal + radiative transfer model.

and gravity data [Čadek et al. 2016]—which has important implications for the search of habitable worlds in the solar system.

WHY ARE THEY SO BRIGHT?

Despite our good first-order understanding of the origins of the observed satellite-to-satellite variations and hemispheric dichotomies, an open question persists: why are these icy objects so bright at centimetric wavelengths? In the following subsection, we show that the radar albedos measured over most of Saturn's moons are enhanced beyond what can be explained by random scattering models commonly invoked for icy solar system surfaces. We then propose some explanations.

BACKGROUND: RELATIONSHIP BETWEEN RADAR ALBEDO AND EMISSIVITY FOR SATELLITES WITH IDEAL UNIFORM SURFACES

Radar reflectivity and thermal radiometry for any surface are related through Kirchhoff's law of thermal radiation, and the comparison of these quantities offers an approach to understanding the nature of planetary surfaces that is complementary to that using either radar or radiometry alone.

The emissivity of a surface at a given wavelength and its reflectivity at the same wavelength are related through the Kirchhoff's law of thermal radiation combined with the principle of conservation of energy, as follows:

$$e_p(\theta,\varphi) = 1 - A_p(\theta,\varphi). \quad \text{Eq. 4}$$

A_p is the reflectivity of the surface, i.e., the hemispheric albedo obtained by integrating the reflectivity of a wave incident from the direction (θ,φ) and for the polarization p over the hemisphere.

With radar applications specifically in mind, Peake [1959]—see also Ulaby et al. [1981, 1982]—derived an expression that relates the reflectivity of the surface to its bistatic radar cross-sections:

$$A_p(\theta,\varphi) = \frac{1}{4\pi}\iint_{upper\ hemisphere}\left(\frac{\sigma^0_{pp}(\theta,\varphi;\theta_s,\varphi_s)+\sigma^0_{pq}(\theta,\varphi;\theta_s,\varphi_s)}{\cos\theta}\right)\sin\theta_s d\theta_s d\varphi_s, \quad \text{Eq. 5}$$

where σ^0_{pp} and σ^0_{pq} are the bistatic cross-sections for the scattering of the incident wave into the direction (θ_s,φ_s) in respective orthogonal polarizations p and q.

The Cassini RADAR, like most radars, only measures the cross-section in the backscattering direction (i.e., for $\theta=\theta_s$ and $\varphi=\varphi_s+\pi$) in same-sense polarization (i.e., σ^0_{pp}). However, Janssen et al. [2011] show that for an idealized diffuse scattering surface following a cosine power law (i.e., $\sigma^0_{pp}(\theta,\varphi;\theta,\varphi)=Acos^n\theta$), the emissivity viewed in the (θ,φ) direction can be obtained from:

$$e_p(\theta,\varphi) = 1-\left(\frac{1+\mu_L(\theta,\varphi)}{2n}\right)A, \quad \text{Eq. 5}$$

where $\mu_L$is the linear polarization ratio : $\mu_L(\theta,\varphi) = \sigma^0_{pp}(\theta,\varphi;\theta,\varphi)/\sigma^0_{pq}(\theta,\varphi;\theta,\varphi)$. By definition, $\mu_L$is between 0 (no depolarization) and 1 (full depolarization).

Further, if the coherent backscattering effect [Hapke 1990] is considered:

$$e_p(\theta,\varphi) = 1 - \left(\frac{1+\mu_L(\theta,\varphi)}{2f_{cbe}n}\right)A, \quad \text{Eq. 6}$$

where f_{cbe} is between 1 (no coherent backscattering effect) and 2 (maximum coherent backscattering effect).

The disk-integrated radar albedo $A^{\text{disk}}_{\text{SL}-2}$ was derived from distant active stares based on the same assumption of a purely diffuse scattering surface (see the section entitled Distant Active Stares) and according to Eq. 2:

$$A = \frac{(n+1)}{2}A^{\text{disk}}_{\text{SL}-2}. \quad \text{Eq. 7}$$

The disk-integrated emissivity is thus related to the disk-integrated radar albedo as follows:

$$e^{disk} = 1 - \left(\frac{1+\mu_L(\theta,\varphi)}{2f_{cbe}n}\right)\frac{(n+1)}{2}A^{\text{disk}}_{\text{SL}-2}. \quad \text{Eq. 8}$$

It follows that if the surface is isotropic ($n = 1$) and fully depolarizing ($\mu_L(\theta,\varphi) = 1$):

$$1 - A^{\text{disk}}_{\text{SL}-2} \leq e^{disk} \leq 1 - \frac{A^{\text{disk}}_{\text{SL}-2}}{2}. \quad \text{Eq. 9}$$

If the surface is Lambertian ($n = 2$) and fully depolarizing ($\mu_L(\theta,\varphi) = 1$):

$$1 - \frac{3}{4}A^{\text{disk}}_{\text{SL}-2} \leq e^{disk} \leq\leq 1 - \frac{3}{8}A^{\text{disk}}_{\text{SL}-2}. \quad \text{Eq. 10}$$

Distant active and passive data acquired over icy satellites are discussed in the following subsection in light of this purely random-scattering model.

RADAR VERSUS RADIOMETRY, MODEL VERSUS OBSERVATIONS

Even if there is some variability that is primarily indicative of various degrees of cleanness of the water-ice regolith. Figure RADAR-49 shows that all Saturnian icy satellites, except maybe for Phoebe and Iapetus, are anomalously radar-bright.

Indeed, generic scattering models that depend on purely random scattering processes alone cannot explain the combined radiometric and radar distant observations of Mimas, Enceladus, Tethys, Dione, and Rhea. The distribution of the observed emissivities show an approximately linear relationship with the radar albedo as predicted by the modeling, but with a slope a factor of two larger than the most extreme model considered. The factor of two discrepancy between model expectation and observation already allows for maximum coherent scattering, and is well beyond the range that could be accommodated by any conceivable imbalance in the distribution of bistatic

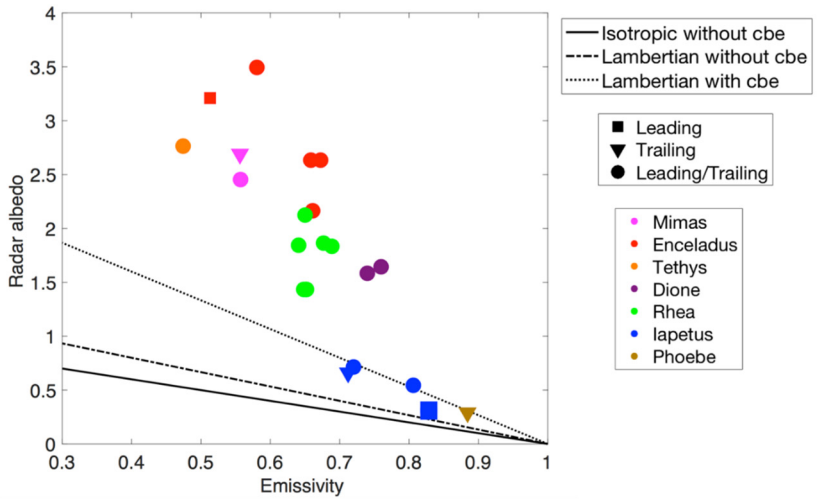

Figure RADAR-49. Disk-integrated same-sense radar albedos versus disk-integrated emissivities derived from the Cassini distant observations of Mimas, Enceladus, Tethys, Dione, Rhea, Iapetus, and Phoebe. When available, the values are shown separately for the leading and trailing sites (in the latitudinal band (−30°, 30°)). The black lines are predictions from the purely random-scattering model described earlier. The measured radar albedos are much larger than expected.

polarization, which is assumed to be the equal in the model. Further, the absolute uncertainties in both emissivity (0.02) and radar albedo (1.4) would have to be seriously underestimated to accommodate the difference as well.

A similar discrepancy has been observed on Titan, on a radar-bright region called Xanadu. Janssen et al. [2011] argue that on Xanadu the mechanism responsible for the enhanced backscatter is related to the presence of ordered structures on or within the surface. There are many theoretical possibilities for such an enhancement, for example a layer of corner cube reflectors, while the challenge is to select those that are geologically plausible for all Saturnian icy satellites. For example, Le Gall et al. [2010] have explained the high radar brightness of some river channels on Titan as due to layers of rounded ice river rocks created by fluvial processes. Maybe more relevant to the surface of Saturn's atmosphereless icy satellites, the unusual radar cross-sections seen in the percolation zone of the Greenland ice sheet were modeled as due to ice cylinders/pipes [Rignot et al. 1993; Rignot 1995]. The presence of cracks or fissures with a preferred orientation in the icy crusts of the Saturnian airless moons is another possibility to be examined.

More recently, Mitchell et al. [2018] have advanced other explanations to accommodate the extreme brightness of Enceladus including the presence of ferroelectric Ice XI, which has unknown backscattering properties, and the sintering of fine particles, which creates larger subsurface particles and/or layering effects that could enhance volumetric radar backscatter. More modeling and laboratory work are required to place more detailed constraints on these hypotheses.

Open questions

RADAR has provided unique insights into the thermal, structural, and compositional properties of the near-surface of Saturn's airless satellites, namely Mimas, Enceladus, Tethys, Dione, Rhea, Hyperion, Iapetus, and Phoebe. It has revealed a number of regional anomalies and satellite-to-satellite variabilities. However, many questions remain about the origin and evolution of Saturn's moons and, in particular, about their respective geological history and interaction with Saturn and its rings. Until the Cassini mission, microwave observations of Saturnian satellites were rare. RADAR observations have set the stage for future researches using ground-based measurements at multiple frequencies in the radio domain—with, for example, the VLA and ALMA radio interferometers or the Institut de Radio Astronomie Millimétrique (IRAM) radio telescope. These measurements will nicely complement Cassini's observations by exploring the thermophysical and compositional properties of the regolith of Saturn's moons at different depths and epochs. Furthermore, future missions to Saturn could include an instrument sounder similar to Mars Advanced Radar for Subsurface and Ionosphere Sounding (MARSIS) /Mars Express, Shallow Radar (SHARAD) / Mars Reconnaissance Orbiter (MRO), or Radar for Europa Assessment and Sounding: Ocean to Near-surface (REASON) / Europa Clipper. Such a radar could, in particular, determine the vertical extent and structure of the dark cover of Iapetus's leading side and confirm the recently advanced hypothesis that the liquid ocean of Enceladus is only a few kilometers under the ice shell at the South Pole of the moon.

ACRONYMS

Note: For a complete list of Acronyms, refer to Cassini Acronyms – Attachment A.

ALMA	Atacama Large Millimeter/submillimeter Array
AO	Announcement of Opportunity
ASI	Italian Space Agency
CIRS	Composite Infrared Spectrometer
GCM	global circulation model
GCMS	Gas Chromatograph Mass Spectrometer
GhoSST	Grenoble Astrophysics and Planetology Solid Spectroscopy and Thermodynamics
HGA	high-gain antenna
IDS	Interdisciplinary Scientist
IR	infrared
IRAM	Institut de Radio Astronomie Millimétrique
ISS	Imaging Science Subsystem
JPL	Jet Propulsion Laboratory
MARSIS	Mars Advanced Radar for Subsurface and Ionosphere Sounding
MRO	Mars Reconnaissance Orbiter
PWA	Permittivity, Wave and Altimetry
RADAR	Titan Radar Mapper
REASON	Radar for Europa Assessment and Sounding: Ocean to Near-surface
RH	relative humidity
SAR	Synthetic Aperture Radar
SHARAD	Shallow Radar
TM	Traceability Matrix
VIMS	Visual and Infrared Mapping Spectrometer
VLA	very large array

REFERENCES

Disclaimer: The partial list of references below corresponds with in-text references indicated in this report. For all other Cassini references, refer to Attachment B – References & Bibliographies; Attachment C – Cassini Science Bibliographies; the sections entitled References contributed by individual Cassini instrument and discipline teams located in Volume 1 Sections 3.1 and 3.2 Science Results; and other resources outside of the Cassini Final Mission Report.

Aharonson, O., A. G. Hayes, J. I. Lunine, R. D. Lorenz, M. D. Allison, C. Elachi, (2009), An asymmetric distribution of lakes on Titan as a possible consequence of orbital forcing, Nature Geoscience, 2(12):851.

Andreotti, B., A. Fourriere, F. Ould-Kaddour, B. Murray, P. Claudin, (2009), Giant aeolian dune size determined by the average depth of the atmospheric boundary layer, Nature, 457(7233):1120.

Artemieva, N., J. I. Lunine, (2005), Numerical calculations of the longevity of impact oases on Titan, Icarus, 173:243–253.

Artemieva, N., J. Lunine, (2003), Cratering on Titan: Impact melt, ejecta, and the fate of surface organics, Icarus, 164:471–480.

Atreya, S. K., (2010), Atmospheric moons Galileo would have loved, in Galileo's Medicean Moons - Their Impact on 400 Years of Discovery, Chapter 16, Cambridge University Press, pp. 130–140.

Baillié, K., J. E. Colwell, J. J. Lissauer, L. W. Esposito, M. Sremčević, (2011), Waves in Cassini UVIS stellar occultations: 2. The C ring, Icarus, 216(1):292–308.

Barnes, J. W., C. Sotin, J. M. Soderblom, et al., (2014), Cassini/VIMS observes rough surfaces on Titan's Punga mare in specular reflection, Planetary Science, 3(17), doi: 10.1186/ s13535-014- 0 0 03-4.

Barnes, J. W., B. J. Buratti, E. P. Turtle, J. Bow, P. A. Dalba, J. Perry, R. H. Brown, S. Rodriguez, S. Le Mouélic, K. H. Baines, C. Sotin, R. D. Lorenz, M. J. Malaska, T. B. McCord, R. N. Clark, R. Jaumann, P. O. Hayne, P. D. Nicholson, J. M. Soderblom, L. A. Soderblom, (2013), Precipitation-induced surface brightenings seen on Titan by Cassini VIMS and ISS, Planetary Science, 2(1), doi: 10.1186/2191-2521-2-1.

Barnes, J. W., J. Bow, J. Schwartz, R. H. Brown, J. M. Soderblom, A. G. Hayes, G. Vixie, S. Le Mouelic, S. Rodriguez, C. Sotin, R. Jaumann, K. Stephan, L. A. Soderblom, R. N. Clark, B. J. Buratti, K. H. Baines, P. D. Nicholson, (2011a), Organic sedimentary deposits in Titan's dry lakebeds: Probable evaporate, Icarus, 216:136–140.

Barnes, J. W., J. M. Soderblom, R. H. Brown, (2011b), Wave constraints for Titan's Jingpo Lacus and Kraken Mare from VIMS specular reflection lightcurves, Icarus, 211:722–731, doi: 10.1016/j.icarus.2010.09.022.

Barnes, J. W., R. H. Brown, L. Soderblom, C. Sotin, S. Le Mouelic, S. Rodriguez, R. Jaumann, R. A. Beyer, R. Clark, P. Nicholson, (2008), Spectroscopy, morphometry, and photoclinometry of Titan's dunefields from Cassini/VIMS, Icarus, 195:400–414.

Barnes, J., J. Radebaugh, R. H. Brown, S. Wall, L. Soderblom, J. Lunine, D. Burr, C. Sotin, S. Le Mouelic, S. Rodriguez, B. J. Buratti, R. Clark, K. H. Baines, R. Jaumann, P. D. Nicholson, R. L. Kirk, R. Lopes, R. Lorenz, K. Mitchell, and C. A. Wood, (2007), Near-infrared spectral mapping of Titan's mountains and channels, Journal of Geophysical Research, 112(E11006), doi: 10.1029/2007JE002932.

Barnes, J. W., R. H. Brown, J. Radebaugh, B. J. Buratti, C. Sotin, S. Le Mouelic, S. Rodriguez, E. P. Turtle, J. Perry, R. Clark, K. H. Baines, P. D. Nicholson, (2006), Cassini observations of flow-like features in western Tui Regio, Titan, Geophysical Research Letters, 33(L16204), doi: 10.1029/2006GL026843.

Barnes, J. W., R. H. Brown, E. P. Turtle, A. S. McEwen, R. D. Lorenz, M. Janssen, E. L. Schaller, M. E. Brown, B. J. Buratti, C. Sotin, C. Griffith, R. Clark, J. Perry, S. Fussner, J. Barbara, R. West, C. Elachi, A. H. Bouchez, H. G. Roe, K. H. Baines, G. Bellucci, J. -P. Bibring, F. Capaccioni, P. Cerroni, M. Combes, A. Coradini, D. P. Cruikshank, P. Drossart, V. Formisano, R. Jaumann, Y. Langevin, D. L. Matson, T. B. McCord, P. D. Nicholson, B. Sicardy, (2005), A 5-micron-bright spot on Titan: evidence for surface diversity, Science, 310:92–95, doi: 10.1126/science.1117075.

Béghin, C., O. Randriamboarison, M. Hamelin, E. Karkoschka, C. Sotin, R. C. Whitten, J. -J. Berthelier, R. Grard, F. Simoes, (2012), Analytic theory of Titan's Schumann resonance: Constraints on ionospheric conductivity and buried water ocean, Icarus, 218:1028–1042.

Berge, G. L., S. Gulkis, (1976), Earth-based radio observations of Jupiter: millimeter to meter wave-lengths, in Jupiter, (ed.) T. Gehrels, University of Arizona Press, Tucson, pp. 621–692.

Bernard, J. -M., E. Quirico, O. Brissaud, G. Montagnac, B. Reynard, B. P. McMillan, P. Coll, M. -J. Nguyen, F. Raulin, B. Schmitt, (2006), Reflectance spectra and chemical structure of Titan's tholins: Application to the analysis of Cassini Huygens observations, Icarus, 185:301–307.

Bills, B.G., F. Nimmo, (2011), Rotational dynamics and internal structure of Titan, Icarus, 214(1):351–355.

Birch, S. P. D., A. G. Hayes, J. D. Hofgartner, (2018a), The raised rims of Titan's small lakes, 49th Lunar and Planetary Science Conference, March 19–23, 2018, The Woodlands, Texas, LPI Contribution No. 2083, id.2076.

Birch, S. P. D., A. G. Hayes, P. Corlies, E. R. Stofan, J. D. Hofgartner, R. M. C. Lopes, R. D. Lorenz, J. I. Lunine, S. M. MacKenzie, M. J. Malaska, C. A. Wood, (2018b), Morphological evidence that Titan's southern hemisphere basins are paleoseas, Icarus, 310:140–148.

Birch, S. P. D., A. G. Hayes, W. E. Dietrich, A. D. Howard, C. S. Bristow, M. J. Malaska, J. M. Moore, M. Mastrogiuseppe, J. D. Hofgartner, D. A. Williams, O. L. White, (2017), Geomorphologic mapping of Titan's polar terrains: Constraining surface processes and landscape evolution, Icarus, 282:214–236.

- - - - - - - - - - - - - -

Black, B. A., J. T. Perron, D. Hemingway, E. Bailey, F. Nimmo, H. Zebker, (2017), Global drainage patterns and the origins of topographic relief on Earth, Mars, and Titan, Science, 356:727–731.

Black, B. A., J. T. Perron, D. M. Burr, S. A. Drummond, (2012), Estimating erosional exhumation on Titan from drainage network morphology, Journal of Geophysical Research: Planets, 117(E08006).

Black, G. J., D. B. Campbell, L. M. Carter, (2007), Arecibo radar observations of Rhea, Dione, Tethys, and Enceladus, Icarus, 191:702–711.

Black, G. J., D. B. Campbell, L. M. Carter, S. J. Ostro, (2004), Radar detection of Iapetus, Science, 304:553.

Black, G. J., D. B. Campbell, P. D. Nicholson, (2001), Icy Galilean satellites: Modeling radar reflectivities as a coherent backscattering effect, Icarus, 151:167–180.

Bohren, C., D. R. Huffman, (1983), Absorption and scattering of light by small particles, John Wiley & Sons.

Bolton, S. J., A. Adriani, V. Adumitroaie, M. Allison, J. Anderson, S. Atreya, J. Bloxham, S. Brown, J. E. P. Connerney, E. DeJong, W. Folkner, (2017), Jupiter's interior and deep atmosphere: The initial pole-to-pole passes with the Juno spacecraft, Science, 356(6340):821–825.

Brassé, C., O. Munoz, P. Coll, F. Raulin, (2015), Optical constants of Titan aerosols and their tholins analogs: Experimental results and modeling/observational data, Planetary and Space Science, 109–110(159–174).

Brown, R. H., J. W. Barnes, H. J. Melosh, (2011), On Titan's Xanadu region, Icarus, 214:556–560.

Brown, R. H., L. A. Soderblom, J. M. Soderblom, R. N. Clark, R. Jaumann, J. W. Barnes, C. Sotin, B. Buratti, K. H. Baines, P. D. Nicholson, (2008), The identification of liquid ethane in Titan's Ontario Lacus, Nature, 454:607–610, doi: 10.1038/nature 07100.

Brown, R. H., K. H. Baines, G. Bellucci, J. -P. Bibring, B. J. Buratti, F. Capaccioni, et al., (2004), The Cassini Visual And Infrared Mapping Spectrometer (VIMS) investigation, Space Science Reviews, 115:111–168, doi: 10.1007/s11214-004-1453-x.

Buratti, B. J., C. Sotin, K. Lawrence, R. H. Brown, S. Le Mouélic, J. M. Soderblom, et al., (2012), A newly discovered impact crater in Titan's Senkyo Cassini VIMS observations and comparison with other impact features, Planetary and Space Science, 60:18–25.

Buratti, B. J., M. D. Hicks, K. A. Tryka, M. S. Sittig, R. L. Newburn, (2002), High-resolution 0.33–0.92 μm spectra of Iapetus, Hyperion, Phoebe, Rhea, Dione, and D-type asteroids: how are they related?, Icarus, 155:375–381.

Buratti, B. J., J. A. Mosher, P. D. Nicholson, C. A. McGhee, R. G. French, (1998), Near-infrared photometry of the Saturnian satellites during ring plane crossing, Icarus, 136:223–231.

Burr, D. M., N. T. Bridges, J. R. Marshall, J. K. Smith, B. R. White, J. P. Emery, (2015), Higher-than-predicted saltation threshold wind speeds on Titan, Nature, 517(7532):60.

Burr, D. M., S. A. Drummond, R. Cartwright, B. A. Black, J. T. Perron, (2013), Morphology of fluvial networks on Titan: Evidence for structural control, Icarus, 226:742–759.

Burr, D. M., R. E. Jacobsen, D. L. Roth, C. B. Phillips, K. L. Mitchell, D. Viola, (2009), Fluvial network analysis on Titan: Evidence for subsurface structures and west-to-east wind flow, southwestern Xanadu, Geophysical Research Letters, 36(L22203).

Burr, D. M., J. P. Emery, R. D. Lorenz, G. C. Collins, P. A. Carling, (2006), Sediment transport by liquid surficial flow: Application to Titan, Icarus, 181:235–242.

Čadek, O., G. Tobie, T. Van Hoolst, M. Massé, G. Choblet, A. Lefèvre, G. Mitri, R. -M. Baland, M. Behounková, O. Bourgeois, A. Trinh, (2016), Enceladus's internal ocean and ice shell constrained from Cassini gravity, shape, and libration data, Geophysical Research Letters, 43, 5653–5660.

Campbell, D. B., G. J. Black, L. M. Carter, and S. J. Ostro, (2003), Radar evidence for liquid surfaces on Titan, Science, 302:431–434.

Cartwright, R., J. A. Clayton, R. L. Kirk, (2011), Channel morphometry, sediment transport, and implications for tectonic activity and surficial ages of Titan basins, Icarus, 214(2):561–570.

Castillo-Rogez, J. C., J. I. Lunine, (2010), Evolution of Titan's rocky core constrained by Cassini observations, Geophysical Research Letters, 37(L20205), doi: 10.1029/2010GL044398.

Charnay, B., E. Barth, S. Rafkin, C. Narteau, S. Lebonnois, S. Rodriguez, S. C. Du Pont, A. Lucas, (2015), Methane storms as a driver of Titan's dune orientation, Nature Geoscience, 8(5):362.

Charnay, B., F. Forget, G. Tobie, C. Sotin, R. Wordsworth, (2014), Titan's past and future: 3D modeling of a pure nitrogen atmosphere and geological implications, Icarus, 241:269–279.

Charnay, B., S. Lebonnois, (2012), Two boundary layers in Titan's lower troposphere inferred from a climate model, Nature Geoscience, 5(2):106–109.

Charnoz, S. et al., (2009), Origin and evolution of Saturn's ring system, in Saturn after Cassini-Huygens, (eds.) M. K. Dougherty, L. W. Esposito, S. M. Krimigis, Springer-Verlag Press, pp. 537–576.

Choukroun, M., S. Sotin, (2012), Is Titan's shape caused by its meteorology and carbon cycle?, Geophysical Research Letters, 39(L04201), doi: 10.1029/2011GL050747.

Clark, R. N., J. M. Curchin, J. W. Barnes, R. Jaumann, L. Soderblom, D. P. Cruikshank, R. H. Brown, S. Rodriguez, J. Lunine, K. Stephan, T. M. Hoefen, (2010), Detection and mapping of hydrocarbon deposits on Titan, Journal of Geophysical Research: Planets, 115(E10), doi: 10.1029/2009JE003369.

Clark, R. N., et al., (1986), Surface composition of natural satellites, in Satellites, (eds.) J. Burns, M.S. Mathews, University of Arizona Press, Tucson, pp. 437–491.

- - - - - - - - - - - - - -

Collins, G. C., (2005), Relative rates of flucial bedrock incision on Titan and Earth, Geophysical Research Letters, 32(22), CiteID L22202.

Colwell, J. E., et al., (2009), The structure of Saturn's rings, in Saturn From Cassini-Huygens, (eds.) M. K. Dougherty, L. W. Esposito, S. M. Krimigis, Springer-Verlag Press, pp. 375–412.

Cook-Hallett, C., J. W. Barnes, S. A. Kattenhorn, T. Hurford, J. Radebaugh, B. Stiles, M. Beuthe, (2015), Global contraction/expansion and polar lithospheric thinning on Titan from patterns of tectonism, Journal of Geophysical Research: Planets, 120(6):1220–1236.

Cooper, J. F., R. E. Johnson, B. H. Mauk, H. B. Garrett, N. Gehrels, (2001), Energetic ion and electron irradiation of the icy Galilean satellites, Icarus, 149(1):133–159.

Cordier, D., F. García-Sánchez, D. N. Justo-García, G. Liger-Belair, (2017), Bubble streams in Titan's seas a product of liquid N_2 +CH_4 + C_2H_6 cryogenic mixture, Nature Astronomy, 1:1–4, doi: 10.1038/s415550017-0102.

Cordier, D., O. Mousis, J. I. Lunine, S. Lebonnois, P. Rannou, P. Lavvas, L. Q. Lobo, A. G. M. Ferreira, (2012), Titan's lakes chemical composition: Sources of uncertainties and variability, Planetary and Space Science, 61(1):99–107.

Cordier, D., O. Mousis, J. I. Lunine, P. Lavvas, V. Vuitton, (2009), An estimate of the chemical composition of Titan's lakes, The Astrophysical Journal, 707(L128–L131), doi: 10.1088/0004-637X/707/2/L128.

Corlies, P., A. G. Hayes, S. P. D. Birch, R. D. Lorenz, B. Stiles, R. L. Kirk, V. Poggiali, H. Zebker, L. Iess, (2017), Titan's topography and shape at the end of the Cassini mission, Geophysical Research Letters, 44:11754–1176.

Cornet, T., C. Fleurant, B. Signovert, D. Cordier, O. Bourgois, S. Le Mouélic, S. Rodriguez, A. Lucas, (2017), Landscape formation through dissolution on Titan: A 3D landscape evolution model, Lunar and Planetary Science 2017, abstract 1835.

Cornet, T., D. Cordier, T. Le Bahers, O. Bourgeois, C. Fleurant, S. Le Mouélic, N. Altobelli, (2015), Dissolution on Titan and on Earth: Toward the age of Titan's karstic landscapes, Journal of Geophysical Research: Planets, 120:1044–1074, doi: 10.1002/2014JE004738.

Cornet, T., O. Bourgeois, S. Le Mouélic, S. Rodriguez, T. Lopez Gonzalez, C. Sotin, G. Tobie, C. Fleurant, J. W. Barnes, R. H. Brown, (2012), Geomorphological significance of Ontario Lacus on Titan: Integrated interpretation of Cassini VIMS, ISS and RADAR data and comparison with the Etosha Pan (Namibia), Icarus, 218(2):788–806.

Cottini, V., C. A. Nixon, D. E. Jennings, R. de Kok, N. A. Teanby, P. G. J. Irwin, F. M. Flasar, (2012), Spatial and temporal variations in Titan's surface temperatures from Cassini CIRS observations, Planetary Space Science, 60(1):62–71, doi: 10.1016/j.pss.2011.03.015.

Courrech du Pont, S., C. Narteau, X. Gao, (2014), Two modes for dune orientation, Geology, doi: 10.1130/G35657.1.

Crow-Willard, E. N., R. T. Pappalardo, (2015), Structural mapping of Enceladus and implications for formation of tectonized regions, Journal of Geophysical Research: Planets, 120:928–950.

- - - - - - - - - - - - - -

Cruikshank, D. P., J. F. Bell, M. J. Gaffey, R. H. Brown, R. Howell, C. Beerman, M. Rognstad, (1983), The dark side of Iapetus, Icarus, 53:90–104.

Cuzzi, J. N., et al., (2014), Utilitarian opacity model for aggregate particles in protoplanetary nebulae and exoplanet atmospheres, The Astrophysical Journal Supplement, 210(2), article id. 21.

Cuzzi, J. N., et al., (2009), Ring particle composition and size distribution, in Saturn From Cassini-Huygens, (eds.) M. K. Dougherty, L. W. Esposito, S. M. Krimigis, Springer-Verlag Press, pp. 459.

Cuzzi, J. N., P. R. Estrada, (1998), Compositional evolution of Saturn's rings due to meteoroid bombardment, Icarus, 132:1–35.

Cuzzi, J. N., et al., (1984), Saturn’s rings: Properties and processes; in Planetary Rings, (eds.) R. Greenberg, A. Brahic, University of Arizona Press, Tucson.

Cuzzi, J. N., J. B. Pollack, A. L. Summers, (1980), Saturn's rings - Particle composition and size distribution as constrained by observations at microwave wavelengths, II - Radio interferometric observations, Icarus, 44:683–705.

Dalle, O., et al., (2012), Infrared spectroscopic characterization of the low-albedo materials on Iapetus, Icarus, 221(2):735–743.

Davies, M. E., T. R. Colvin, P. G. Rogers, P. W. Chodas, W. L. Sjogren, E. L. Akim, V. A. Stepaniants, Z. P. Vlasova, A. I. Zakharov, (1992), The rotation period, direction of the North Pole, and geodetic control network of Venus, Journal of Geophysical Research, 97(E8):13,141–13,151.

Davies, M. E., et al., (1989), Report of the IAU/IAG/COSPAR working group on cartographic coordinates and rotational elements of the planets and satellites, Celestial Mechanics and Dynamical Astronomy, 46:187–204.

de Pater, I., J. R. Dickel, (1991), Multifrequency radio observations of Saturn at ring inclination angles between 5 and 26 degrees, Icarus, 94:474.

de Pater, I., (1990), Radio images of the planets, Annual Review of Astronomy and Astrophysics, 28:347–399.

de Pater, I., R. A. Brown, J. R. Dickel, (1984), VLA observations of the Galilean satellites, Icarus, 57:93–101.

de Pater, I., J. R. Dickel, (1982), VLA observations of Saturn at 1.3, 2, and 6 cm, Icarus, 50(1):88–102.

Deveraj, K., (2011), The centimeter- and millimeter-wavelength ammonia absorption spectra under Jovian conditions, Ph.D. thesis, Georgia Institute of Technology, Atlanta.

Dones, L., et al., (1993), Voyager photometry of Saturn’s A-ring, Icarus, 105:184–215.

Dougherty, M. K., et al., (2009), Saturn from Cassini-Huygens, Springer-Verlag Press.

- - - - - - - - - - - - - -

Dunn, D. E., et al., (2005), High-Quality BIMA-OVRO images of Saturn and its rings at 1.3 and 3 millimeters, The Astronomical Journal, 129:1109.

Dunn, D. E., et al., (2002), More microwave observations of Saturn: Modeling the ring with a Monte Carlo radiative transfer code, Icarus, 160:132.

Durisen R. H., P. W. Bode, J. N. Cuzzi, S. E. Cederbloom, B. W. Murphy, (1992), Ballistic transport in planetary ring systems due to particle erosion mechanisms. II - Theoretical models for Saturn's A- and B-ring inner edges, Icarus, 100(2):364–393, doi.org/10.1016/0019-1035(92)90106-H.

Elachi, C., M. D. Allison, L. Borganelli, P. Encrenaz, E. Im, M. A. Janssen, W. T. K. Johnson, R. L. Kirk, R. D. Lorenz, J. I. Lunine, D. O. Muhleman, S. J. Ostro, G. Picardi, F. Posa, C. G. Rapley, L. E. Roth, S. Seu, L. A. Soderblom, S. Vetrella, S. D. Wall, C. A. Wood, H. A. Zebker, (2004), RADAR: The Cassini Titan radar mapper, Space Science Reviews, 115(1–4):71–110.

Elachi, C., et al., (2005), Cassini Radar Views the Surface of Titan, Science, 308:970–974.

Elliot J. P., L. W. Esposito, (2011), Regolith depth growth on an icy body orbiting Saturn and evolution of bidirectional reflectance due to surface composition changes, Icarus, 212.

Esposito, L. W., et al., (1984), Saturn’s rings: Structure, dynamics, and particle properties, in Saturn, (eds.) T. Gehrels, M. Matthews, University of Arizona Press, Tucson.

Estrada, P. R., et al., (2015), Combined structural and compositional evolution of planetary rings due to micrometeoroid impacts and ballistic transport, Icarus, 252:415–439.

Ewing, R. C., A. G. Hayes, A. Lucas, (2015), Sand dune patterns on Titan controlled by long-term climate cycles, Nature Geoscience, 8(1):15–19.

Fletcher, L. N., K. H. Baines, T. W. Momary, A. P. Showman, P. G. J. Irwin, G. S. Orton, M. Roos-Serote, C. Merlet, (2011), Saturn’s tropospheric composition and clouds from Cassini/VIMS 4.6–5.1 μm nightside spectroscopy, Icarus, 214:510–533.

French, R. G., P. D. Nicholson, (2000), Saturn's rings II. Particle sizes inferred from stellar occultation data, Icarus, 145:502–523.

Fryberger, S. G., G. Dean, (1979), Dune forms and wind regime, in A study of global sand seas, (ed.) E. D. McKee, U.S. Geological Survey Professional Paper, 1052:137–169.

Glein, C. R., E. L. Shock, (2013), A geochemical model of non-ideal solutions in the methane-ethane-propane-nitrogen-actylene system on Titan, Geochemica et Cosmochimica Acta, 115:217–240, doi: 10.1016/j.gca.2013.03.030.

Goldstein, R. M., R. R. Green, (1980), Ganymede: Radar surface characteristics, Science, 207:179–180.

Greeley, R., J. D. Iversen, (1987), Wind as a geological process: on Earth, Mars, Venus and Titan, Vol. 4, Cambridge University Press.

Griffith, C. A., L. Doose, M. G. Tomasko, P. F. Penteado, C. See, (2012), Radiative transfer analyses of Titan's tropical atmosphere, Icarus, 218(2):975–988.

- - - - - - - - - - - - - -

Grima, C., M. Mastrogiuseppe, A. G. Hayes, S. D. Wall, R. D. Lorenz, J. D. Hofgartner, B. C. Stiles, C. Elachi, the Cassini RADAR Team, (2017), Surface roughness of Titan's hydrocarbon seas, Earth and Planetary Science Letters, 474:20–24.

Grossman, A. W., (1990), Microwave imaging of Saturn's deep atmosphere and rings, Ph.D. thesis, California Institute of Technology, Pasadena.

Grossman, A. W., D. O. Muhleman, G. L. Berge, (1989), High resolution microwave observations of Saturn, Science, 245:1211–1215.

Gulkis, S., et al., (2015), Subsurface properties and early activity of comet 67P/Churyumov-Gerasimenko, Science, 347(6220), doi: 10.1126/science.aaa0709.

Gulkis, S., et al., (2007), MIRO: Microwave instrument for Rosetta Orbiter, Space Science Reviews, 128-1:561–597.

Gulkis, S., R. Poynter, (1972), Thermal radio emission from Jupiter and Saturn, Physics of the Earth and Planetary Interiors, 6:36–43.

Gulkis, S., T. R. McDonough, H. Craft, (1969), The microwave spectrum of Saturn, Icarus, 10:421.

Güttler, C., et al., (2010), The outcome of protoplanetary dust growth: pebbles, boulders or planetesimals? I. Mapping the zoo of laboratory collision experiments, Astronomy & Astrophysics, 513, id.A56.

Hagfors, T., I Dahlstrom, T. Gold, S. -E. Hamran, R. Hansen, (1997), Refraction scattering in the anomalous reflections from icy surfaces, Icarus, 130:313–322.

Hagfors, T., T. Gold, H. M. Ierkic, (1985), Refraction scattering as origin of the anomalous radar returns of Jupiter's satellites, Nature, 315:637–640.

Hamilton, D. P., J. A. Burns, (1994), Origin of Saturn's E ring: Self-sustained, naturally, Science, 264(5158):550–553.

Hanley, T. R., P. G. Steffes, B. M. Karpowicz, (2009), A new model of the hydrogen and helium broadened microwave opacity of ammonia based on extensive laboratory measurements, Icarus, 202:316–335.

Hapke, B., (1990), Coherent backscatter and the radar characteristics of outer planet satellites, Icarus, 88:407–417.

Harbison, R. A., et al., (2013), The smallest particles in Saturn's A and C rings, Icarus, 226(2).

Harper, J. M., G. D. McDonald, J. Dufek, M. J. Malaska, D. M. Burr, A. G. Hayes, J. McAdams, J. J. Wray, (2017), Electrification of sand on Titan and its influence on sediment transport, Nature Geoscience, 10(4):260.

Hayes, A. G., R. D. Lorenz, J. I. Lunine, (2018), A post-Cassini view of Titan's methane-based hydrologic cycle, Nature Geoscience, 11(5):306.

- - - - - - - - - - - - - -

Hayes, A. G., S. P. D. Birch, W. E. Dietrich, A. D. Howard, R. L. Kirk, V. Poggiali, M. Mastrogiuseppe, R. J. Michaelides, P. M. Corlies, J. M. Moore, et al., (2017), Topographic constraints on the evolution and connectivity of Titan's lacustrine basins, Geophysical Research Letters, 44(23):11,745–11,753.

Hayes, A. G., (2016), The lakes and seas of Titan, Annual Review of Earth and Planetary Sciences, 44:57–83.

Hayes, A. G., R. D. Lorenz, M. A. Donelan, et al., (2013), Wind driven capillary-gravity waves on Titan’s lakes: Hard to detect or non-existent?, Icarus, 225:403–412, doi: 10.1016/j.icarus.2013.04.004 .

Hayes, A. G., O. Aharonson, J. I. Lunine, R. L. Kirk, H. A. Zebker, L. C. Wye, R. D. Lorenz, E. P. Turtle, P. Paillou, G. Mitri, et al., (2011), Transient surface liquid in Titan's polar regions from Cassini, Icarus, 211(1):655–671.

Hayes, A. G., A. S. Wolf, O. Aharonson, H. Zebker, R. Lorenz, R. L. Kirk, P. Paillou, J. Lunine, L. Wye, P. Callahan, et al., (2010), Bathymetry and absorptivity of Titan's Ontario Lacus, Journal of Geophysical Research, 115(E9), citeID E09009.

Hayes, A., O. Aharonson, P. Callahan, C. Elachi, Y. Gim, R. Kirk, K. Lewis, R. Lopes, R. Lorenz, J. Lunine, et al., (2008), Hydrocarbon lakes on Titan: Distribution and interaction with a porous regolith, Geophysical Research Letters, 35(9), citeID L09204.

Hedman, M. M., P. D. Nicholson, (2016), The B-ring’s surface mass density from hidden density waves: Less than meets the eye?, Icarus, 279:109–124.

Hedman M. M., P. D. Nicholson, (2013), Kronoseismology: Using density waves in Saturn’s C ring to probe the planet’s interior, The Astronomical Journal, 146.

Hedman, M. M., et al., (2011), Saturn’s curiously corrugated C ring, Science, 332(6030).

Hemingway, D., F. Nimmo, H. Zebker, L. Iess, (2013), A rigid and weathered ice shell on Titan, Nature, 500:550–552.

Hirtzig, M., B. Bézard, E. Lellouch, A. Coustenis, C. de Bergh, P. Drossart, A. Campargue, V. Boudon, V. Tyuterev, P. Rannou, T. Cours, S. Kassi, A. Nikitin, D. Mondelain, S. Rodriguez, S. Le Mouélic, (2013), Titan’s surface and atmosphere from Cassini/VIMS data with updated methane opacity, Icarus, 226:470–486.

Hoffman, J. P., P. G. Steffes, D. R. DeBoer, (2001), Laboratory measurements of the microwave opacity of phosphine: Opacity formalism and application to the atmospheres of the outer planets, Icarus, 152:172–184.

Hofgartner, J. D., A. G. Hayes, J. I. Lunine, et al., (2016), Titan’s “Magic Islands”: Transient features in a hydrocarbon sea, Icarus, 271:338–349.

Hofgartner, J. D., A. G. Hayes, J. I. Lunine, et al., (2014a), Transient features in a Titan sea, Nature Geoscience, 7(7):493–496, doi: 10.1038/ngeo2190.

Hofgartner, J. D., D. B. Campbell, A. Hayes, J. I. Lunine, (2014b), Specular reflections from Titan's equatorial region: Solving the decade old mystery, American Geophysical Union Fall Meeting 2014, abstract P42B-06.

Hörst, S. M., (2017), Titan's atmosphere and climate, Journal of Geophysical Research: Planets, 122(3):432–482.

Howard, M., S. Bastea, L. E. Fried, B. Khare, C. P. McKay, (2009), Titans' interior chemical composition: A thermo-chemical assessment, American Astronomical Society DPS meeting #41, id.7.03.

Howett, C. J. A., J. R. Spencer, T. Hurford, A. Verbiscer, M. Segura, (2014), Thermophysical property variations across Dione and Rhea, Icarus, 241:239–247.

Howett, C. J. A., J. R. Spencer, T. A. Hurford, A. Verbiscer, M. Segura, (2012), PacMan returns: an electron-generated thermal anomaly on Tethys, Icarus, 221(2):1084–1088.

Howett, C. J. A., J. R. Spencer, P. Schenk, R. E. Johnson, C. Paranicas, T. A. Hurford, A. Verbiscer, M. Segura, (2011), A high-amplitude thermal inertia anomaly of probable magnetospheric origin on Saturn's moon Mimas, Icarus, 216:221–226.

Howett, C. J. A., J. R. Spencer, J. Pearl, M. Segura, (2010), Thermal inertia and bolometric bond albedo values for Mimas, Enceladus, Tethys, Dione, Rhea and Iapetus as derived from Cassini/CIRS measurements, Icarus, 206:573–593.

Hyodo, R., K. Ohtsuki, (2014), Collisional disruption of gravitational aggregates in the tidal environment, The Astrophysical Journal, 787:56.

Iess, L., et al., (2014), The gravity field and interior structure of Enceladus, Science, 344:78–80.

Iess, L., et al., (2012), The tides of Titan, Science, 337:457, doi: 10.1126/ Science.1219631.

Iess, L., et al., (2010), Gravity field, shape, and moment of inertia of Titan, Science, 327:1367, doi:10.1126/science.1182583.

Janssen, M. A., J. E. Oswald, S. T. Brown, S. Gulkis, S. M. Levin, S. J. Bolton, M. D. Allison, S. K. Atreya, D. Gautier, A. P. Ingersoll, J. I. Lunine, (2017), MWR: Microwave radiometer for the Juno mission to Jupiter, Space Science Reviews, 213(1–4):139–185.

Janssen, M. A., A. Le Gall, M. J. Malaska, R. M. Lopes, A. Solomonidou, R. D. Lorenz, C. D. Neish, K. L. Mitchell, J. Radebaugh, P. J. Encrenaz, M. Mastrogiuseppe, (2016), Titan's surface at 2.2-cm wavelength imaged by the Cassini RADAR radiometer: Results and interpretations through the first ten years of observation, Icarus, 270:443–459.

Janssen, M. A., A. Ingersoll, M. D. Allison, S. Gulkis, A. Laraia, K. Baines, S. Edgington, Y. Anderson, K. Kelleher, (2013), Saturn's thermal emission at 2.2-cm wavelength as imaged by the Cassini radar radiometer, Icarus, 226:522–535.

Janssen, M. A., A. Le Gall, L. C. Wye, (2011), Anomalous radar backscatter from Titan's surface?, Icarus, 212:321–328.

- - - - - - - - - - - - - -

Janssen, M. A., R. D. Lorenz, R. West, F. Paganelli, R. M. Lopes, R. L. Kirk, C. Elachi, S. D. Wall, W. T. K. Johnson, Y. Anderson, R. A. Boehmer, P. Callahan, Y. Gim, G. A. Hamilton, K. D. Kelleher, L. Roth, B. Stiles, A. Le Gall, the Cassini Radar Team, (2009), Titan's Surface at 2.2-cm wavelength imaged by the Cassini RADAR Radiometer: Calibration and first results, Icarus, 200:222–239.

Jaumann, R., R. H. Brown, K. Stephan, J. W. Barnes, L. A. Soderblom, C. Sotin, S. Le Mouélic, R. N. Clark, J. Soderblom, B. J. Buratti, et al., (2008), Fluvial erosion and post-erosional processes on Titan, Icarus, 197(2):526–538.

Jennings, D. E., et al., (2016), Surface temperatures on Titan during northern winter and spring, The Astrophysical Journal Letters, 816(L17).

Jennings, D. E., F. M. Flasar, V. G. Kunde, R. E. Samuelson, J. C. Pearl, C. A. Nixon, R. C. Carlson, A. A. Mamoutkine, J. C. Brasunas, E. Guandique, R. K. Achterberg, (2009), Titan's surface brightness temperatures, The Astrophysical Journal Letters, 691(2):L103.

Johnson, T. V., J. I. Lunine, (2005), Saturn's moon Phoebe as a captured body from the outer solar system, Nature, 435(7038).

Karkoschka, E., A. McEwen, J. Perry, (2017), Creating the best global mosaic of Titan's surface albedo using cassini Images, American Astronomical Society Division for Planetary Sciences Meeting, abstract #49, 301.06.

Kempf, S., U. Beckmann, J. Schmidt, (2010), How the Enceladus dust plume feeds Saturn's E ring, Icarus, 206(2):446–457.

Kirchoff, M., P. Schenk, (2015), Dione's resurfacing history as determined from a global impact crater database, Icarus, 256:78–89.

Kirk, R. L., E. Howington-Kraus, A. G. Hayes, R. M. C. Lopes, R. D. Lorenz, J. I. Lunine, K. L. Mitchell, E. R. Stofan, S. D. Wall, (2010), La Sotra y los otros: Topographic evidence for (and against) cryovolcanism on Titan, Eos: Transactions American Geophysical Union, 91(52), abstract P22A-03.

Klein, M. J., S. Gulkis, (1978), Jupiter's atmosphere: Observations and interpretation of the microwave spectrum near 1.25-cm wavelength, Icarus, 35:44–60.

Kofman, W., A. Herique, Y. Barbin, J. P. Barriot, V. Ciarletti, S. Clifford, P. Edenhofer, C. Elachi, C. Eyraud, J. P. Goutail, E. Heggy, (2015), Properties of the 67P/Churyumov-Gerasimenko interior revealed by CONSERT radar, Science, 349(6247), aab0639.

Korycansky, D. G., K. J. Zahnle, (2005), Modeling crater populations on Venus and Titan, Planetary and Space Science, 53:695–710.

Langhans, M. H., R. Jaumann, K. Stephan, R. H. Brown, B. J. Buratti, R. N. Clark, K. H. Baines, P. D. Nicholson, R. D. Lorenz, L. A. Soderblom, et al., (2012), Titan's fluvial valleys: Morphology, distribution, and spectral properties, Planetary and Space Science, 60(1):34–51.

Lanzerotti, L. J., W. L. Brown, K. J. Marcantonio, R. E. Johnson, (1984), Production of ammonia-depleted surface layers on the Saturnian satellites by ion sputtering, Nature, 312:139–140.

Laraia, A. L., A. P. Ingersoll, M. A. Janssen, S. Gulkis, F. A. Oyafuso, M. D Allison, (2013), Analysis of Saturn's thermal emission at 2.2-cm wavelength: Spatial distribution of ammonia vapor, Icarus, 226:641–654.

Le Gall, A., C. Leyrat, M. A. Janssen, G. Choblet, G. Tobie, O. Bourgeois, A. Lucas, C. Sotin, C. Howett, R. Kirk, R. D. Lorenz, (2017), Thermally anomalous features in the subsurface of Enceladus's south polar terrain, Nature Astronomy, 1(4):0063.

Le Gall, A., M. J. Malaska, R. D. Lorenz, M. A. Janssen, T. Tokano, A. G. Hayes, M. Mastrogiuseppe, J. I. Lunine, G. Veyssière, P. Encrenaz, O. Karatekin, (2016), Composition, seasonal change and bathymetry of Ligeia Mare, Titan, derived from its microwave thermal emission, Journal of Geophysical Research: Planets, 121:233–251.

Le Gall, A., C. Leyrat, M. A. Janssen, S. Keihm, L. C. Wye, R. West, R. D. Lorenz, F. Tosi, (2014), Iapetus' near surface thermal emission modeled and constrained using Cassini RADAR radiometer microwave observations, Icarus, 241:221–238.

Le Gall, A., A. G. Hayes, R. Ewing, M. A. Janssen, J. Radebaugh, C. Savage, P. Encrenaz, the Cassini RADAR Team, (2012), Latitudinal and altitudinal controls on Titan's dune field morphometry, Icarus, 217:231–242.

Le Gall, A., M. A. Janssen, L. C. Wye, A. G. Hayes, J. Radebaugh, C. Savage, H. Zebker, R. D. Lorenz, J. I. Lunine, R. L. Kirk, R. M. C. Lopes, S. Wall, P. Callahan, E. R. Stofan, T. Farr, the Cassini Radar Team, (2011), Cassini SAR, radiometry, scatterometry and altimetry observations of Titan's dune fields, Icarus, 213:608–624.

Le Gall, A., M. A. Janssen, P. Paillou, R. D. Lorenz, S. D. Wall, the Cassini RADAR Team, (2010), Radar-bright channels on Titan, Icarus, 207:948–958.

Le Mouelic, S., P. Paillou, M. A. Janssen, J. W. Barnes, S. Rodriguez, C. Sotin, R. H. Brown, K. H., Baines, B. J. Buratti, R. N. Clark, M. Crapeau, P. J. Encrenaz, R. Jaumann, D. Geudtner, F. Paganelli, L. Soderblom, G. Tobie, S. Wall, (2008), Mapping and interpretation of Sinlap crater on Titan using Cassini VIMS and RADAR data, Journal of Geophysical Research, 113(E04003), doi: 10.1029/2007JE002965.

Lellouch, E., R. Moreno, T. Müller, S. Fornasier, P. Santos-Sanz, A. Moullet, M. Gurwell, J. Stansberry, R. Leiva, B. Sicardy, B. Butler, (2017), The thermal emission of Centaurs and trans-Neptunian objects at millimeter wavelengths from ALMA observations, Astronomy & Astrophysics, 608:A45.

Lellouch, E., (2006), Titan's zoo of clouds, Science, 311:186–187.

Lemmon, M. T., E. Karkoschka, M. Tomasko, (1993), Titan's rotation – Surface feature observed, Icarus, 103(2):329–332.

Lewis, J. S., (1971), Satellites of the outer planets: Their physical and chemical nature, Icarus, 15:174–185.

Li, C., A. P. Ingersoll, (2015), Moist convection in hydrogen atmospheres and the frequency of Saturn's giant storms, Nature Geoscience, 8:398–403, doi: 10.1038/ngeo2405.

- - - - - - - - - - - - - -

Liu, Z. Y. -C., J. Radebaugh, R. A. Harris, E. H. Christiansen, C. D. Neish, R. L. Kirk, R. D. Lorenz, the Cassini RADAR Team, (2016a), The tectonics of Titan: Global structural mapping from Cassini RADAR, Icarus, 270:14–29.

Liu, Z. Y. -C., J. Radebaugh, R. A. Harris, E. H. Christiansen, S. Rupper, (2016b), Role of fluids in the tectonic evolution of Titan, Icarus, 270:2–13.

Lopes, R. M.C., S. D. Wall, C. Elachi, et al., (2019), Titan as revealed by the Cassini Radar, Space Science Review, 215(33), doi: 10.1007/s11214-019-0598-6.

Lopes, R. M. C., M. J. Malaska, A. Solomonidou, A. LeGall, M. A. Janssen, C. Neish, E. P. Turtle, S. P. D. Birch, A. G. Hayes, J. Radebaugh, A. Coustenis, A. Schoenfeld, B. W. Stiles, R. L. Kirk, K. L. Mitchell, E. R. Stofan, K. J. Lawrence, the Cassini RADAR Team, (2016), Nature, distribution, and origin of Titan's undifferentiated plains ("blandlands"), Icarus, 270:162–182.

Lopes, R. M. C., R. L. Kirk, K. L. Mitchell, A. LeGall, J. W. Barnes, A. Hayes, J. Kargel, L. Wye, J. Radebaugh, E. R. Stofan, M. Janssen, C. Neish, S. Wall, C. A. Wood, J. I. Lunine, M. Malaska, (2013), Cryovolcanism on Titan: New results from Cassini RADAR and VIMS, Journal of Geophysical Research: Planets, 118:1–20, doi: 10.1002/jgre.20062.

Lopes, R. M. C., E. R. Stofan, R. Peckyno, J. Radebaugh, K. L. Mitchell, G. Mitri, C. A. Wood, R. L. Kirk, S. D. Wall, J. I. Lunine , A. Hayes , R. Lorenz, T. Farr, L. Wye, J. Craig, R. J. Ollerenshaw, M. Janssen, A. LeGall, F. Paganelli, R. West, B. Stiles, P. Callahan, Y. Anderson, P. Valora, L. Soderblom, the Cassini RADAR Team, (2010), Distribution and Interplay of geologic processes on Titan from Cassini RADAR data, Icarus, 205:540–588, doi: 10.1016/j.icarus.2009.08.010.

Lopes, R. M. C., K. L. Mitchell, E. R. Stofan, J. I. Lunine, R. Lorenz, F. Paganelli, R. L. Kirk, C. A. Wood, S. D. Wall, L. E. Robshaw, A. D. Fortes, C. D. Neish, J. Radebaugh, E. Reffet, S. J. Ostro, C. Elachi, M. D. Allison, Y. Anderson, R. Boehmer, G. Boubin, P. Callahan, P. Encrenaz, E. Flamini, G. Francescetti, Y. Gim, G. Hamilton, S. Hensley, M. A. Janssen, W. T. K. Johnson, K. Kelleher, D. O. Muhleman, G. Ori, R. Orosei, G. Picardi, F. Posa, L. E. Roth, R. Seu, S. Shaffer, L. A. Soderblom, B. Stiles, S. Vetrella, R. D. West, L. Wye, H. A. Zebker, (2007), Cryovolcanic features on Titan's surface as revealed by the Cassini Titan radar mapper, Icarus, 186:395–412.

Lora, J. M., J. I. Mitchell, (2015), Titan's asymmetric lake distribution mediated by methane transport due to atmospheric eddies, Geophysical Research Letters, 42(15):6213–6220.

Lora, J. M., J. I. Lunine, J. L. Russell, A. G. Hayes, (2014), Simulations of Titan's paleoclimate, Icarus, 243:264–273.

Lorenz, R. D., E. P. Turtle, J. W. Barnes, M. G. Trainer, D. S. Adams, K. E. Hibbard, C. Z. Sheldon, K. Zacny, P. N. Peplowski, D. J. Lawrence, M. A. Ravine, (2018), Dragonfly: a Rotorcraft Lander Concept for scientific exploration at Titan, Johns Hopkins APL Technical Digest.

Lorenz, R. D., (2014), Physics of saltation and sand transport on Titan: A brief review, Icarus, 230:162–167.

Lorenz, R. D., J. R. Zimbelman, (2014), Dune worlds: How windblown sand shapes planetary landscapes, Springer Science & Business Media.

Lorenz, R.D., B. W. Stiles, O. Aharonson, A. Lucas, A. G. Hayes, R. L. Kirk, H. A. Zebker, E. P. Turtle, C. D. Neish, E. R. Stofan, J. W. Barnes, (2013), A global topographic map of Titan, Icarus, 225(1):367–377.

Lorenz, R. D., P. Claudin, B. Andreotti, J. Radebaugh, T. Tokano, (2010), A 3 km atmospheric boundary layer on Titan indicated by dune spacing and Huygens data, Icarus, 205(2):719–721.

Lorenz, R. D., J. Radebaugh, (2009), Global pattern of Titan's dunes: Radar survey from the Cassini prime mission, Geophysical Research Letters, 36(3).

Lorenz, R. D., B. Stiles, R. L. Kirk, M. Allison, P. Persi del Marmo, L. Iess, J. I. Lunine, S. J. Ostro S. Hensley, (2008a), Titan's rotation reveals an internal ocean and changing zonal winds, Science, 319:1649–1651.

Lorenz, R. D., K. L. Mitchell, R. L. Kirk, A. G. Hayes, H. A. Zebker, P. Paillou, J. Radebaugh, J. I. Lunine, M. A. Janssen, S. D. Wall, R. M. Lopes, B. Stiles, S. Ostro, G. Mitri, E. R. Stofan, the Cassini RADAR Team, (2008b), Titan’s Inventory of Organic Surface Materials, Geophysical Research Letters, 35(L02206), doi: 10.1029/2007GL032118.

Lorenz, R. D., R. M. Lopes, F. Paganelli, J. I. Lunine, R. L. Kirk, K. L. Mitchell, L. A. Soderblom, E. R. Stofan, G. Ori, M. Myers, H. Miyamoto, J. Radebaugh, B. Stiles, S. D. Wall, C. A. Wood, the Cassini RADAR Team, (2008c), Fluvial channels on Titan: Initial Cassini RADAR observations, Planetary and Space Science, 56:1132–1144.

Lorenz, R. D., C. A. Wood, J. I. Lunine, S. D. Wall, R. M. Lopes, K. L. Mitchell, F. Paganelli, Y. Z. Anderson, L. Wye, C. Tsai, H. Zebker, E. R. Stofan, (2007), Titan's young surface: Initial impact crater survey by Cassini RADAR and model comparison, Geophysical Research Letters, 34(L07204).

Lorenz, R. D., S. Wall, J. Radebaugh, G. Boubin, E. Reffet, M. Janssen, E. Stofan, R. Lopes, R. Kirk, C. Elachi, J. Lunine, (2006), The sand seas of Titan: Cassini RADAR observations of longitudinal dunes, Science, 312(5774):724–727.

Lorenz, R. D., C. A. Griffith, J. I. Lunine, C. P. McKay, N. O. Rennò, (2005), Convective plumes and the scarcity of Titan's clouds, Geophysical Research Letters, 32(1).

Lorenz, R. D., G. Biolluz, P. Encrenaz, M. A. Janssen, R. D. West, D. O. Muhleman, (2003), Cassini RADAR: prospects for Titan surface investigations using the microwave radiometer, Planetary and Space Science, 51(4–5):353–364.

Lorenz, R. D., (2000), Post-Cassini exploration of Titan: Science rationale and mission concepts, Journal-British Interplanetary Society, 53(7/8):218–234.

Lorenz, R. D., (1998), Preliminary measurements of the cryogenic dielectric properties of water–ammonia ices: Application to radar observations of icy satellites, Icarus, 136:344–348.

Lorenz, R. D., C. P. McKay, J. I. Lunine, (1997), Photochemically driven collapse of Titan’s atmosphere, Science, 275:642–644.

- - - - - - - - - - - - - -

Lorenz, R. D., (1996), Pillow lava on Titan: expectations and constraints on cryovolcanic processes, Planetary and Space Science, 44(9):1021–1028.

Lorenz, R. D., J. I. Lunine, (1996), Erosion on Titan: Past and present, Icarus, 196:79–91.

Lorenz, R. D., J. I. Lunine, J. A. Grier, M. A. Fisher, (1995), Prediction of aeolian features on planets: Application to Titan paleoclimatology, Journal of Geophysical Research: Planets, 100(E12):26377–26386.

Lorenz, R. D., (1993), The surface of Titan in the context of ESA's Huygens probe, ESA Journal, 17:275–292.

Lucas, A., S. Rodriguez, C. Narteau, B. Charnay, S. C. Pont, T. Tokano, A. Garcia, M. Thiriet, A. G. Hayes, R. D. Lorenz, O. Aharonson, (2014), Growth mechanisms and dune orientation on Titan, Geophysical Research Letters, 41(17):6093–6100, doi: 10.1002/2014GL060971.

Lunine, J. I., R. D. Lorenz, (2009), Rivers, lakes, dunes, and rain: Crustal processes in Titan's methane cycle, Annual Review of Earth and Planetary Sciences, 37(1):299–320.

Lunine, J. I., C. Elachi, S. D. Wall, M. A. Janssen, M. D. Allison, Y. Anderson, et al., (2008), Titan's diverse landscapes as evidenced by Cassini RADAR's third and fourth looks, Icarus, 195:415–433.

Lunine, J. I., R. D. Lorenz, W. K. Hartmann, (1998), Some speculations on Titans past, present and future, Planetary and Space Science, 46(9–10):1099–1107.

MacKenzie, S. M., J. W. Barnes, C. Sotin, J. M. Soderblom, S. Le Mouélic, S. Rodriguez, K. H. Baines, B. J. Buratti, R. N. Clark, P. D. Nicholson, T. B. McCord, (2014), Evidence of Titan's climate history from evaporite distribution, Icarus, 243:191–207.

Malaska, M. J., R. M. C. Lopes, K. L. Mitchell, J. Radebaugh, T. Verlander, A. Schoenfeld, (2017a), Classification of labyrinth terrains on Titan, Lunar and Planetary Science Conference, abstract 2406.

Malaska, M. J., R. Hodyss, J. I. Lunine, A. G. Hayes, J. D. Hofgartner, G. Hollyday, R. D. Lorenz, (2017b), Laboratory measurements of nitrogen dissolution in Titan lake fluids, Icarus, 289:94–105, doi: 10.1016/j.icarus.2017.01.033.

Malaska, M. J., R. M. Lopes, A. G. Hayes, J. Radebaugh, R. D. Lorenz, E. P. Turtle, (2016a), Material transport map of Titan: The fate of dunes, Icarus, 270:183–196, doi: 10.1016/j.icarus.2015.09.029.

Malaska, M. J., R. M. C. Lopes, D. A. Williams, C. D. Neish, A. Solominidou, J. M. Soderblom, A. M. Schoenfeld, S. P. D. Birch, A. G. Hayes, A. Le Gall, M. A., Janssen, T. G. Farr, R. D. Lorenz, J. Radebaugh, E. P. Turtle, (2016b), Geomorphological map of the Afekan Crater region, Titan: Terrain relationships in the equatorial and mid-latitude regions, Icarus, 270:130–161, doi: 10.1016/j.icarus.2016.02.021.

Malaska, M. J., R. Hodyss, (2014), Dissolution of benzene, naphthalene, and biphenyl in a simulated Titan lake, Icarus, 242:74–81, doi: 10.1016/j.icarus.2014.07.022.

Malaska, M., J. Radebaugh, K. Mitchell, R. Lopes, S. Wall, R. Lorenz, (2011a), Surface dissolution model for Titan karst, First International Planetary Cave Research Workshop, October 2011, abstract 8018.

Malaska, M., J. Radebaugh, A. Le Gall, K. Mitchell, R. Lopes, S. Wall, (2011b), High-volume meandering channels in Titan's south polar region, Lunar and Planetary Science Conference, abstract 1562.

Malaska, M., J. Radebaugh, R. Lorenz, K. Mitchell, T. Farr, E. Stofan, (2010), Identification of Karst-like terrain on Titan from valley analysis, Lunar and Planetary Science Conference, 41, abstract 1544.

Marouf, E., R. French, N. Rappaport, C. McGhee, K. Wong, F. Thomson, A. Anabtawi, (2008), Structure and physical properties of Saturn's rings from Cassini radio occultations, in Abstracts for ''Saturn after Cassini–Huygens'' Symposium, 28:113, Imperial College London, UK.

Mastrogiuseppe, M., A. G. Hayes, V. Poggiali, J. I. Lunine, R. D. Lorenz, R. Seu, A. Le Gall, C. Notarnicola, K. L. Mitchell, M. Malaska, S. P. D. Birch, (2018), Bathymetry and composition of Titan's Ontario Lacus derived from Monte Carlo-based waveform inversion of Cassini RADAR altimetry data, Icarus, 300:203–209.

Mastrogiuseppe, M., A. Hayes, V. Poggiali, R. Seu, J. I. Lunine, J. D. Hofgartner, (2016), Radar sounding using the Cassini altimeter: Waveform modeling and Monte Carlo approach for data inversion of observations of Titan's seas, IEEE Transactions on Geoscience and Remote Sensing, 54(10):5646–5656.

Mastrogiuseppe M., V. Poggiali, A. Hayes, R. Lorenz, J. Lunine, G. Picardi, R. Seu, E. Flamini, G. Mitri, C. Notarnicola, P. Paillou, H. Zebker, (2014), The bathymetry of a Titan sea, Geophysical Research Letters, 41(5):1432–1437.

Matzler C., (1998), Microwave properties of ice and snow, in Solar System Ices, (eds.) B. Schmitt, C. De Bergh, M. Festou, Astrophysics and Space Science Library, Vol. 227, Springer, Dordrecht, doi.org/10.1007/978-94-011-5252-5_10.

Mayer, C. H., T. P. McCullough, R. M. Sloanaker, (1958), Observations of Mars and Jupiter at a wave length of 3.15 cm, The Astrophysical Journal, 127:11.

McCord, T. B., G. B. Hansen, B. J. Buratti, R. N. Clark, D. P. Cruikshank, E. D'Aversa, C. A. Griffith, E. K. H. Baines, R. H. Brow, C. M. Dalle Ore, G. Filacchione, V. Formisano, C. A. Hibbitts, R. Jaumann, J. I. Lunine, R. M. Nelson, C. Sotin, the Cassini VIMS Team, (2006), Composition of Titan's surface from Cassini VIMS, Planetary and Space Science, 54(15):1524–1539, doi:10.1016/j.pss.2006.06.007.

McDonald, G. D., A. G. Hayes, R. C. Ewing, J. M. Lora, C. E. Newman, T. Tokano, A. Lucas, A. Soto, G. Chen, (2016), Variations in Titan's dune orientations as a result of orbital forcing, Icarus, 270:197–210.

Méndez-Harper, J., G. D. McDonald, J. Dufek, M. J. Malaska, D. M. Burr, A. G. Hayes, J. McAdams, J. J. Wray, (2017), The electrified sands of Titan, Nature Geoscience, 10:260–265, doi: 10.1038/ngeo2921.

- - - - - - - - - - - - - -

Meriggiola, R., L. Iess, B. W. Stiles, J. I. Lunine, G. Mitri, (2016), The rotational dynamics of Titan from Cassini RADAR images, Icarus, 275:183–192.

Mitchell, K. L., R. Hodyss, M. Choukroun, J. Molaro, A. Le Gall, (2018), Enceladus' brilliant surface 2: Rationalizing Cassini RADAR and optical remote sensing, in Lunar and Planetary Science Conference, 49.

Mitchell, J. L., J. M. Lora, (2016), The climate of Titan, Annual Review of Earth and Planetary Sciences, 44.

Mitchell, K. L., M. B. Barmatz, C. S. Jamieson, R. D. Lorenz, J. I. Lunine, (2015), Laboratory measurements of cryogenic liquid alkane microwave absorptivity and implications for the composition of Ligeia Mare, Titan, Geophysical Research Letters, 42.

Mitchell, J. L., (2008), The drying of Titan's dunes: Titan's methane hydrology and its impact on atmospheric circulation, Journal of Geophysical Research, 113(E8), citeID E08015.

Mitri, G., J. I. Lunine, M. Mastrogiuseppe, V. Poggiali, (2019), Possible explosion crater origin of small lake basins with raised rims on Titan, Nature Geoscience, 1–6.

Mitri, G., et al., (2014), Shape, topography, gravity anomalies and tidal deformation of Titan, Icarus, 236:169–177.

Mitri, G., M. T. Bland, A. P. Showman, J. Radebaugh, B. Stiles, R. M. C. Lopes, M. C. Rosaly, J. I. Lunine, R. T. Pappalardo, (2010), Mountains on Titan: Modeling and observations, Journal of Geophysical Research, 115(E10), citeID E10002.

Mohammed, P., (2004), Laboratory measurements of the W band (3.2 mm) properties of phosphine (PH_3) and ammonia (NH_3) under simulated conditions of the outer planets, Journal of Geophysical Research, 109:1–9.

Moore, J. M., A. D. Howard, A. M. Morgan, (2014), The landscape of Titan as witness to its climate evolution, Journal of Geophysical Research: Planets, 119, doi: 10.1002/2014JE004608.

Moore, J. M., R. T. Pappalardo, (2011), Titan: An exogenic world?, Icarus, 212:790–806.

Moore, J. M., A. D. Howard, (2010), Are the basins of Titan's Hotei Regio and Tui Regio sites of former low latitude seas?, Geophysical Research Letters, 37(22).

Morfill, G. E., H. Fechtig, E. Grun, C. K. Goertz, (1983), Some consequences of meteoroid impacts on Saturn’s rings, Icarus, 55:439–447.

Muhleman, D. O., G. L. Berge, (1991), Observations of Mars, Uranus, Neptune, Io, Europa, Ganymede, and Callisto at a wavelength of 2.66 mm, Icarus, 92:263–71.

Muhleman, D., A. Grossman, B. Butler, M. Slade, (1990), Radar reflectivity of Titan, Science, 248:975−980.

Neish, C. D., J. L. Molaro, J. M. Lora, A. D. Howard, R. L. Kirk, P. Schenk, et al., (2016), Fluvial erosion as a mechanism for crater modification on Titan, Icarus, 270:114–129.

- - - - - - - - - - - - - -

Neish, C. D., J. W. Barnes, C. Sotin, S. MacKenzie, J. M. Soderblom, S. Le Mouélic, et al., (2015), Spectral properties of Titan's impact craters imply chemical weathering of its surface, Geophysical Research Letters, 42:3746–3754.

Neish, C. D., R. D. Lorenz, (2014), Elevation distribution of Titan's craters suggests extensive wetlands, Icarus, 228:27–34.

Neish, C. D., R. L. Kirk, R. D. Lorenz, V. J. Bray, P. Schenk, B. W. Stiles, et al., (2013), Crater topography on Titan: Implications for landscape evolution, Icarus, 223:82–90.

Neish, C. D., R. D. Lorenz, (2012), Titan's global crater population: A new assessment, Planetary and Space Science, 60(1):26–33.

Neish, C. D., R. D. Lorenz, R. L. Kirk, L. C. Wye (2010), Radarclinometry of the sand seas of Africa's Namibia and Saturn's moon Titan, Icarus, 208:385–394.

Nicholson P. D., et al., (2008), A close look at Saturn's rings with Cassini VIMS, Icarus, 193(1).

Niemann, H. B., S. K. Atreya, J. Demick, D. Gautier, J. Haverman, D. Harpold, W. Kasprzak, J. Lunine, T. Owen, F. Raulin, (2010), Composition of Titan's lower atmosphere and simple surface volatiles as measured by the Cassini-Huygens probe gas chromatograph mass spectrometer experiment, Journal of Geophysical Research, 115(E12006).

Niemann, H. B., S. K. Atreya, S. J. Bauer, G. R. Carignan, J. E. Demick, R. L. Frost, D. Gautier, J. A. Haberman, D. N. Harpold, D. M. Hunten, G. Israel, J. I. Lunine, W. T. Kasprzak, T. C. Owen, M. Paulkovich, F. Raulin, E. Raaen, S. H. Way, (2005), Huygens Probe Gas Chromatograph Mass Spectrometer: The atmosphere and surface of Titan, Nature, doi: 10.1038/nature04122.

Nimmo, F., B. G. Bills, (2010), Shell thickness variations and the long-wavelength topography of Titan, Icarus, 208:896–904.

Nixon, C. A., R. D. Lorenz, R. K. Achterberg, A. Buch, P. Coll, R. N. Clark, R. Courtin, A. Hayes, L. Iess, R. E. Johnson, R. M. C. Lopes, (2018), Titan's cold case files-Outstanding questions after Cassini-Huygens, Planetary and Space Science, 155:50–72.

Northrup, D., J. Radebaugh, E. H. Christiansen, S. Tass, L. Kerber, (2018), Yardang and dune classification on Titan through length, width, and sinuosity, Lunar and Planetary Science Conference, 49.

Ostro, S. J., R. D. West, L. C. Wye, H. A. Zebker, M. A. Janssen, B. Stiles, K. Kelleher, Y. Z. Anderson, R. A. Boehmer, P. Callahan, Y. Gim, G. A. Hamilton, W. T. K. Johnson, C. Veeramachaneni, R. D. Lorenz, the Cassini Radar Team, (2010), New Cassini RADAR results for Saturn's icy satellites, Icarus, 206:498–506.

Ostro, S. J., R. D. West, M. A. Janssen, R. D. Lorenz, H. A. Zebker, G. J. Black, J. I. Lunine, L. C. Wye, R. M. Lopes, S. D. Wall, C. Elachi, L. Roth, S. Hensley, K. Kelleher, G. A. Hamilton, Y. Gim, Y. Z. Anderson, R. A. Boehmer, W. T. K. Johnson, (2006), Cassini RADAR observations of Enceladus, Tethys, Dione, Rhea, Iapetus, Hyperion, and Phoebe, Icarus, 183(2):479-490.

- - - - - - - - - - - - - -

Ostro, S. J., 1993, Planetary radar astronomy, Reviews of Modern Physics, 65:1235–1279.

Paganelli, F., M. A. Janssen, R. M. Lopes, E. Stofan, S. D. Wall, R. D. Lorenz, J. I. Lunine, R. L. Kirk, L. Roth, C. Elachi, the Cassini Radar Team, (2008), Titan's surface from the Cassini RADAR radiometry data during SAR mode, Planetary and Space Science 56:100–108.

Paganelli, F., M. A. Janssen, B. Stiles, R. West, R. D. Lorenz, J. I. Lunine, S. D. Wall, P. Callahan, R. M. Lopes, E. Stofan, R. L. Kirk, W. T. K Johnson, L. Roth, C. Elachi, the Cassini RADAR Team, (2007), Titan's surface from the Cassini Radar SAR and high resolution radiometry data of the first five flybys, Icarus, 191:211–222.

Paillou, P., B. Seignovert, J. Radebaugh, S. Wall, (2016), Radar scattering of linear dunes and mega-yardangs: Application to Titan, Icarus, 270:211–221.

Paillou, P., D. Bernard, J. Radebaugh, R. Lorenz, A. Le Gall, T. Farr, (2014), Modeling the SAR backscatter of linear dunes on Earth and Titan, Icarus, 230:208–214.

Paillou, P., J. I. Lunine, G. Ruffié, P. Encrenaz, S. D. Wall, R. D. Lorenz, M. A. Janssen, (2008a), Microwave dielectric constant of Titan-relevant materials, Geophysical Research Letters, 35(L18202).

Paillou, P., K. L. Mitchell, S. D. Wall, G. Ruffié, C. A. Wood, R. D. Lorenz, E. R. Stofan, J. I. Lunine, R. M. Lopes, P. Encrenaz, (2008b), Microwave dielectric constant of liquid hydrocarbons: Application to the depth estimation of Titan's lakes, Geophysical Research Letters, 35(L05202).

Paillou, P., M. Crapeau, C. Elachi, S. Wall, P. Encrenaz, (2006), Models of SAR backscattering for bright flows and dark spots on Titan, Journal of Geophysical Research, 111(E11011), doi: 10.1029/2006JE002724.

Peake, W. H., (1959), Interaction of electromagnetic waves with some natural surfaces, IRE Transactions on Antennas and Propagation, 7:324–329.

Perron, J. T., M. P. Lamb, C. D. Koven, I. Y. Fung, E. Yager, M. Adamkovics, (2006), Valley formation and methane precipitation rates on Titan, Journal of Geophysical Research, 111(E11001).

Poggiali, V., M. Mastrogiuseppe, A. G. Hayes, R. Seu, S. P. D. Birch, R. Lorenz, C. Grima, J. D. Hofgartner, (2016), Liquid-filled canyons on Titan, Geophysical Research Letters, 43:7887–7894.

Porco, C. C., J. W. Weiss, D. C. Richardson, L. Dones, T. Quinn, H. Throop, (2008), Simulations of the dynamical and light-scattering behavior of Saturn's rings and the derivation of ring particle and disk properties, The Astronomical Journal, 136(5):2172.

Porco, C. C., et al., (2006), Cassini observes the active south pole of Enceladus, Science, 311:1393–1401.

Porco, C. C., E. Baker, J. Barbara, K. Beurle, A. Brahic, J. A. Burns, S. Charnoz, N. Cooper, D. D. Dawson, A. D. Del Genio, T. Denk, L. Dones, U. Dyudina, M. W. Evans, S. Fussner, B. Giese, K. Grazier, P. Helfenstein, A. P. Ingersoll, R. A. Jacobson, T. V. Johnson,

A. McEwen, C. D. Murray, G. Neukum, W. M. Owen, J. Perry, T. Roatsch, J. Spitale, S. Squyres, P. Thomas, M. Tiscareno, E. P. Turtle, A. R. Vasavada, J. Veverka, R. Wagner. R. West, (2005), Imaging of Titan from the Cassini spacecraft, Nature, 434:159–168, doi: 10.1038/nature03436.

Porco, C. C., R. A. West, S. Squyres, A. McEwen, P. Thomas, C. D. Murray, A. Del Genio, A. P. Ingersoll, T. V. Johnson, G. Neukum, et al., (2004), Cassini Imaging Science: Instrument characteristics and anticipated scientific investigations at Saturn, Space Science Reviews, 115(1–4):363–497, doi: 10.1007/s11214-004-1456-7.

Poulet, F., et al., (2003), Compositions of Saturn's rings A, B, and C from high resolution near-infrared spectroscopic observations, Astronomy and Astrophysics, 412:305–316.

Poulet, F., J. N. Cuzzi, (2002), The composition of Saturn's rings, Icarus, 160:350–358.

Radebaugh, J., R. C. Lewis, B. Bishop, E. H. Christiansen, L. Kerber, S. Rodriguez, C. Narteau, A. A. Le Gall, A. Lucas, M. Malaska, (2017), Aeolian landscapes of Titan from Cassini RADAR reveal winds, elevation constraints and sediment characteristics, American Geophysical Union Fall Meeting Abstracts.

Radebaugh, J., D. Ventra, R. D. Lorenz, T. Farr, R. Kirk, A. Hayes, M. J. Malaska, S. Birch, Z. Y. -C. Liu, J. Lunine, J. Barnes, A. Le Gall, R. Lopes, E. Stofan, S. Wall, P. Paillou, (2016), Alluvial and fluvial fans on Saturn's moon Titan reveal processes, materials and regional geology, in Geology and Geomorphology of Alluvial and Fluvial Fans: Terrestrial and Planetary Perspectives, (eds.) D. Ventra, L. E. Clarke, Geological Society, London, Special Publications, 440, doi: 10.1144/SP440.6.

Radebaugh, J., (2013), Dunes on Saturn's moon Titan at the end of the Cassini Equinox Mission, Aeolian Research, 11:23–41.

Radebaugh, J., R. D. Lorenz, S. D. Wall, R. L. Kirk, C. A. Wood, J. I. Lunine, E. R. Stofan, R. M. C. Lopes, P. Valora, T. G. Farr, A. G. Hayes, B. Stiles, G. Mitri, H. Zebker, M. Janssen, L. Wye, A. Le Gall, K. L. Mitchell, F. Paganelli, R. D. West, E. L. Schaller, the Cassini RADAR Team, (2011), Regional geomorphology and history of Titan's Xanadu province, Icarus, 211:672–685.

Radebaugh, J., R. Lorenz, T. Farr, P. Paillou, C. Savage, C. Spencer, (2010), Linear dunes on Titan and Earth: Initial remote sensing comparisons, Geomorphology 121:122–132, doi: 10.1016/j.geomorph.2009.02.022.

Radebaugh, J., R. Lorenz, J. Lunine, S. Wall, G. Boubin, E. Reffet, R. Kirk, R. Lopes, E. Stofan, L. Soderblom, M. Allison, M. Janssen, P. Paillou, P. Callahan, the Cassini RADAR Team, (2008), Dunes on Titan observed by Cassini RADAR, Icarus, 194:690–703, doi: 10.1016/j.icarus.2007.10.015.

Radebaugh, J., R. Lorenz, R. Kirk. J. Lunine, E. Stofan, R. Lopes, S. Wall, the Cassini RADAR Team, (2007), Mountains on Titan observed by Cassini Radar, Icarus, 192:77–91, doi: 10.1016/j.icarus.2007.06.020.

Rannou, P., F. Montmessin, F. Hourdin, S. Lebonnois, (2006), The latitudinal distribution of clouds on Titan, Science, 311(5758):201–205.

Raulin, F., (1987), Organic chemistry in the oceans of Titan, Advances in Space Research, 7(5):71–81.

Reffet, E., S. Courrech du Pont, P. Hersen, S. Douady, (2010), Formation and stability of transverse and longitudinal sand dunes, Geology, 38:491–494.

Reh, K., (2007), Titan and Enceladus $1B mission feasibility study report, JPL D-37401 B.

Richardson, L. A., J. W. Hartwig, J. W. Leachman, (2018), Fluid phase equilibria, 462:38–43, doi: 10.1016/j.fluid.2018.01.023.

Ries, P. A., M. A. Janssen, (2015), A large-scale anomaly in Enceladus microwave emission, Icarus, 257:88–102.

Rignot, E., (1995), Backscatter model for the unusual radar properties of the Greenland ice sheet, Journal of Geophysical Research, 100(E5):9389–9400.

Rignot, E., S. J. Ostro, J. J. Van Zyl, K. C. Jezek, (1993), Unusual radar echoes from the Greenland ice sheet, Science, 261:1710–1713.

Robbins, S. J., et al., (2010), Estimating the masses of Saturn's A and B rings from high-optical depth N-body simulations and stellar occultations, Icarus, 206:431–445.

Rodriguez, S., A. Garcia, A. Lucas, T. Appéré, A. Le Gall, E. Reffet, L. Le Corre, S. Le Mouélic, T. Cornet, S. Courrech du Pont, C. Narteau, O. Bourgeois, J. Radebaugh, K. Arnold, J. W. Barnes, K. Stephan, R. Jaumann, C. Sotin, R. H. Brown, R. D. Lorenz, E. P. Turtle, (2014), Global mapping and characterization of Titan's dune fields with Cassini: Correlation between RADAR and VIMS observations, Icarus, 230:168–179.

Roe, H. G., I. de Pater, S. G. Gibbard, B. A Macintosh, C. E. Max, E. F. Young, M. E. Brown, A. H. Bouchez, (2004), A new 1.6 micron map of Titan's surface, Geophysical Research Letters, 31(L17S03).

Rubin, D. M., P. A. Hesp, (2009), Multiple origins of linear dunes on Earth and Titan, Nature Geoscience, 2(9):653.

Sagan, C., S. F. Dermott, (1982), The tide in the seas of Titan, Nature, 300:731–733.

Savage, C. J., J. Radebaugh, E. H. Christiansen, R. D. Lorenz, (2014), Implications of dune pattern analysis for Titan's surface history, Icarus, 230:180–190.

Sayanagi, K., U. A. Dyudina, S. P. Ewald, G. Fischer, A. P. Ingersoll, W. S. Kurth, G. D. Muro, C. C. Porco, R. A. West, (2013), Dynamics of Saturn's great storm of 2010–2011 from Cassini ISS and RPWS, Icarus, 223:460–478.

Schaller, E. L., M. E. Brown, H. G. Roe, A. H. Bouchez, (2006), A large cloud outburst at Titan's south pole, Icarus,182(1):224–229.

Schenk, P., D. P. Hamilton, R. E. Johnson, W. B. McKinnon, C. Paranicas, J. Schmidt, M. R. Showalter, (2011), Plasma, plumes and rings: Saturn system dynamics as recorded in global color patterns on its midsize icy satellites, Icarus, 211(1):740-–57.

Schenk, P. M., J. M. Moore, (2009), Eruptive volcanism on saturn's icy moon Dione, Lunar and Planetary Science Conference, 40.

Schloerb, F. P., D. O. Muhleman, G. L. Berge, (1979), Interferometric observations of Saturn and its rings at a wavelength of 3 3.71 cm, Icarus, 39(2):214–231.

Schurmeier, L. R., A. J. Dombard, (2018), Crater relaxation on Titan aided by low thermal conductivity sand infill, Icarus, 305:314–323.

Schurmeier, L., A. J. Dombard, J. Radebaugh, M. Malaska, (2018), Intrusive and extrusive cryovolcanism and the composition of Titan’s icy crust, Lunar and Planetary Science Conference, 49, abstract 2934.

Schurmeier, L., A. J. Dombard, M. Malaska, J. Radebaugh, (2017), Are Titan’s radial labyrinth terrains surface expressions of large laccoliths?, American Geophysical Union Fall Meeting, New Orleans.

Scipioni, F., F. Tosi, K. Stephan, G. Filacchione, M. Ciarniello, F. Capaccioni, P. Cerroni, the VIMS Team, (2014), Spectroscopic classification of icy satellites of Saturn II: Identification of terrain units on Rhea, Icarus, 234:1–16.

Scipioni, F., F. Tosi, K. Stephan, G. Filacchione, M. Ciarniello, F. Capaccioni, P. Cerroni, the VIMS Team, (2013), Spectroscopic classification of icy satellites of Saturn I: Identification of terrain units on Dione, Icarus, 226(2):1331–1349.

Sears, W. D., (1995), Tidal dissipation in oceans on Titan, Icarus, 113:39–56.

Sears, W. D., (1992), Tidal dissipation and the giant impact origin for the Moon, Lunar and Planetary Science Conference, 23.

Sierks, H., et al., (2015), On the nucleus structure and activity of comet 67P/Churyumov-Gerasimenko, Science, 347(6220).

Smith, P. H., M. T. Lemmon, R. D. Lorenz, L. A. Sromovsky, J. J. Caldwell, M. D. Allison, (1996), Titan's surface, revealed by HST imaging, Icarus, 119(2):336–349.

Soderblom, J. M., J. W. Barnes, R. H. Brown, V. Chevrier, K. Farnsworth, L. A. Soderblom, (2016), Evidence for frozen hydrocarbons on Titan, American Astronomical Society, DPS meeting #48, id.502.04.

Soderblom, J. M., R. H. Brown, L. A. Soderblom, J. W. Barnes, R. Jaumann, S. Le Mouélic, C. Sotin, K. Stephan, K. H. Baines, B. J. Buratti, R. N. Clark, (2010), Geology of the Selk crater region on Titan from Cassini VIMS observations, Icarus, 208(2):905–912.

Soderblom, L. A., R. H. Brown, J. M. Soderblom, J. W. Barnes, R. L. Kirk, C. Sotin, R. Jaumann, D. J. Mackinnon, D. W. Mackowski, K. H. Baines, B. J. Buratti, (2009), The geology of Hotei Regio, Titan: correlation of Cassini VIMS and RADAR, Icarus, 204(2):610–618.

- - - - - - - - - - - - - -

Soderblom, L., J. Anderson, K. Baines, J. Barnes, J. Barrett, R. Brown, B. Buratti, R. Clark, D. Cruikshank, C. Elachi, M. Janssen, R. Jaumann, R. Kirk, E. Karkoschka, S. Lemouelic, R. Lopes, R. Lorenz, J. Lunine, T. McCord, P. Nicholson, J. Radebaugh, B. Rizk, C. Sotin, E. Stofan, T. Sucharski, M. Tomasko, S. Wall, (2007), Correlations between Cassini VIMS spectra and RADAR SAR images: Implications for Titan's surface composition and the character of the Huygens Probe landing site, Planetary and Space Science, 55:2025–2036.

Sohl, F., A. Solomonidou, F. W. Wagner, A. Coustenis, H. Hussmann, D. Schulze-Makuch, (2014), Tidal stresses on Titan and implications for its geology and habitability, Journal of Geophysical Research, 119:1013–1036.

Sohl, F., H. Hussmann, B. Schwentker, T. Spohn, R. D. Lorenz, (2003), Interior structure models and tidal Love numbers of Titan, Journal of Geophysical Research, 108(E12):5130, doi: 10.1029/2003JE002044.

Solomonidou, A., A. Coustenis, R. M. Lopes, M. J. Malaska, S. Rodriguez, P. Drossart, C. Elachi, B. Schmitt, S. Philippe, M. Janssen, M. Hirtzig, (2018), The spectral nature of Titan's major geomorphological units: constraints on surface composition, Journal of Geophysical Research: Planets, 123(2):489–507.

Solomonidou, A., A. Coustenis, M. Hirtzig, S. Rodriguez, K. Stephan, R. M. C. Lopes, P. Drossart, C. Sotin, S. Le Mouélic, K. Lawrence, E. Bratsolis, R. Jaumann, R. H. Brown, (2016), Temporal variations of Titan's surface with Cassini/VIMS, Icarus, 270:85–99.

Solomonidou, A., et al., (2014), Surface albedo spectral properties of geologically interesting areas on Titan, Journal of Geophysical Research, 119:1729–1747.

Sotin, C., R. Jaunmann, B. J. Buratti, R. H. Brown, R. N. Clark, L. A. Soderblom, K. H. Baines, G. Bellucci, J. -P. Bribing, F. Capaccioni, P. Cerroni, A. Coradini, D. P. Cruikshank, P. Drossart, V. Formisano, Y. Langevin, D. L. Matson, T. B. McCord, R. M. Nelson, P. D. Nicholson, B. Sicardy, S. LeMouelic, S. Rodriguez, K. Stephan, C. K. Scholz, (2005), Release of volatiles from a possible cryovolcano from near-infrared imaging of Titan, Nature, 435:786–789.

Spencer, J. R., A. C. Barr, L. W. Esposito, P. Helfenstein, A. P. Ingersoll, R. Jaumann, C. P. McKay, F. Nimmo, J. H. Waite, (2009), Enceladus: An active cryovolcanic satellite, in Saturn from Cassini-Huygens,, Springer, Dordrecht, pp. 683–724.

Spencer, J. R., J. C. Pearl, M. Segura, F. M. Flasar, A. Mamoutkine, P. Romani, B. J. Buratti, A. R. Hendrix, L. J. Spilker, R. M. C. Lopes, (2006), Cassini encounters Enceladus: Background and the discovery of a south polar hot spot, Science, 311(5766):1401–1405.

Stephan, K., et al., (2010), Specular reflection on Titan: Liquids in Kraken Mare, Geophysical Research Letters, 37(L07104), doi: 10.1029/2009GL042312.

Stiles, B., R. Kirk, R. Lorenz, S. Hensley, E. Lee, S. Ostro, M. Allison, P. Callahan, Y. Gim, L. Iess, P. Perci del Marmo, G. Hamilton, W. Johnson, R. West, the Cassini RADAR Team, (2010), Determining Titan's spin State from Cassini radar images, The Astronomical Journal, 139(1):311.

Stiles, B. W., S. Hensley, Y. Gim, D. M. Bates, R. L. Kirk, A. Hayes, J. Radebaugh, R. D. Lorenz, K. L. Mitchell, P. S. Callahan, H. Zebker, W. T. K. Johnson, S. D. Wall, J. I. Lunine, C. A. Wood, M. Janssen, F. Pelletier, R. D. West, C. Veeramacheneni, (2009), Determining Titan surface topography from Cassini SAR data, Icarus, 102:584–598, doi: 10.1016/j.icarus.2009.03.032.

Stiles, B. W., R. L. Kirk, R. D. Lorenz, S. Hensley, E. Lee, S. J. Ostro, M. D. Allison, P. S. Callahan, Y. Gim, L. Iess, (2008), Determining Titan's spin state from Cassini radar images, The Astronomical Journal, 135(5).

Stofan, E. R., C. Elachi, J. I. Lunine, R. D. Lorenz, B. Stiles, K. L. Mitchell, S. Ostro, L. Soderblom, C. Wood, H. Zebker, S. Wall, M. Janssen, R. Kirk, R. Lopes, F. Paganelli, J. Radebaugh, L. Wye, Y. Anderson, M. Allison, R. Boehmer, P. Callahan, P. Encrenaz, E. Flamini, G. Francescetti, Y. Gim, G. Hamilton, S. Hensley, W. T. K. Johnson, K. Kelleher, D. Muhleman, P. Paillou, G. Picardi, F. Posa, L. Roth, R. Seu, S. Shaffer, S. Vetrella, R. West, (2007), The lakes of Titan, Nature, 445:61–64, doi: 10.1038/nature05438.

Stofan, E. R., J. I. Lunine, R. Lopes, F. Paganelli, R. D. Lorenz, C. A. Wood, R. Kirk, S. Wall, C. Elachi, L. A. Soderblom, S. Ostro, M. Janssen, J. Radebaugh, L. Wye, H. Zebker, Y. Anderson, M. Allison, R. Boehmer, P. Callahan, P. Encrenaz, E. Flamini, G. Francescetti, Y. Gim, G. Hamilton, S. Hensley, W. T. K. Johnson, K. Kelleher, D. Muhleman, G. Picardi, F. Posa, L. Roth, R. Seu, S. Shaffer, B. Stiles, S. Vetrella, R. West, (2006), Mapping of Titan: Results from the first Titan radar passes, Icarus, 185:443–456.

Thomas, P. C., R. Tajeddine, M. S. Tiscareno, J. A. Burns, J. Josepth, T. J. Loredo, P. Helfenstein, C. C. Porco, (2016), Enceladus’s measured physical libration requires a global subsurface ocean, Icarus, 264:37–47.

Thomas, P.C., et al., (2007), Hyperion's sponge-like appearance, Nature, 448:50–56.

Thompson, W. D., S. W. Squyres, (1990), Titan and other icy satellites: Dielectric properties of constituent materials and implications for radar sounding, Icarus, 86:336–354.

Thornton, D. D., W. J. Welch, (1963), 8.35 mm radio emission from Jupiter, Icarus, 2:228–232.

Tobie, G., J. I. Lunine, J. Monteux, O. Mousis, F. Nimmo, (2014), The origin and evolution of Titan, in Titan Interior, Surface, Atmosphere, and Space Environment, (eds.) I. Müller-Wodarg, C. A. Griffith, E. Lellouch, T. E. Cravens, Cambridge University Press, doi.org/10.1017/CBO9780511667398, pp. 29–62.

Tobie, G., J. I. Lunine, C. Sotin, (2006), Episodic outgassing as the origin of atmospheric methane on Titan, Nature, 440:61–64.

Tokano, T., (2010), Relevance of fast westerlies at equinox for the eastward elongation of Titan’s dunes, Aeolian Research, 2(2–3):113–127.

Tokano, T., (2008), Dune-forming winds on Titan and the influence of topography, Icarus, 194(1):243–262.

- - - - - - - - - - - - - -

Tokano T., (2005), Meteorological assessment of the surface temperatures on Titan: constraints on the surface type, Icarus, 173:222–42.

Tokano, T., F. M. Neubauer, (2005), Wind-induced seasonal angular momentum exchange at Titan's surface and its influence on Titan's length-of-day, Geophysical Research Letters, 32(24), doi: 10.1029/2005GL024456.

Tomasko, M., B. Archinal, T. Becker, B. Bézard, M. Bushroe, M. Combes, D. Cook, A. Coustenis, C. de Bergh, L. Dafoe, L. Doose, S. Douté, A. Eibl, S. Engel, F. Gliem, B. Grieger, K. Holso, E. Howington-Kraus, E. Karkoschka, H. Keller, R. Kirk, R. Kramm, M. Küppers, P. Lanagan, E. Lellouch, M. Lemmon, J. Lunine, E. McFarlane, J. Moores, M. Prout, B. Rizk, M. Rosiek, P. Rueffer, S. Schröder, B. Schmitt, C. See, P. Smith, L. Soderblom, N. Thomas, R. West, (2005), Rain, winds, and haze during the Huygens probe descent to Titan’s surface, Nature, 438:765–778.

Tosi, F., R. Orosei, R. Seu, A. Coradini, J. I. Lunine, G. Filacchione, A. I. Gavrishin, F. Capaccioni, P. Cerroni, A. Adriani, et al., (2010a), Correlations between VIMS and RADAR data over the surface of Titan: Implications for Titan’s surface properties, Icarus, 208(1):366–384.

Tosi, F., D. Turrini, A. Coradini, G. Filacchione, (2010b), Probing the origin of the dark material on Iapetus, Monthly Notices of the Royal Astronomical Society, 403:1113–1130.

Tsoar, H., (1983), Dynamic processes acting on a longitudinal (seif) dune, Sedimentology, 30:567–578.

Turtle, E. P., J. E. Perry, A. G. Hayes, R. D. Lorenz, J. W. Barnes, A. S. McEwen, R. A. West, A. D. Del Genio, J. M. Barbara, E. L. Schaller, T. L. Ray, J. I. Lunine, R. M. C. Lopes, E. R. Stofan, (2011), Rapid and extensive surface changes near Titan’s equator: evidence of April showers, Science, 331(1414), doi: 10.1126/science.1201063.

Turtle, E. P., J. E. Perry, A. S. McEwen, A. D. Del Genio, J. Barbara, R. A. West, D. D. Dawson, C. C. Porco, (2009), Cassini imaging of Titan's high-latitude lakes, clouds, and south-polar surface changes, Geophysical Research Letters, 36(2), citeID L02204.

Ulaby, F. T., R. K. Moore, A. K. Fung, (1982), Microwave remote sensing, active and passive, Vol. II: Radar remote sensing and surface scattering and emission theory, Addison-Wesley Publishing Company Advanced Book Program/World Science Division.

Ulaby, F. T., R. K. Moore, A. K. Fung, (1981), Microwave remote sensing active and passive-Volume I: Microwave remote sensing fundamentals and radiometry, Addison-Wesley Publishing Company Advanced Book Program/World Science Division.

van der Tak, F., et al., (1999), Time variability in the radio brightness distribution of Saturn, Icarus, 142:125.

Ventura, B., C. Notarnicola, D. Casarano, F. Posa, A. G. Hayes, L. Wye, (2012), Electromagnetic models and inversion techniques for Titan’s Ontario Lacus depth estimation from Cassini RADAR data, Icarus, 221:960–969.

Verbiscer, A. J., M. F. Skrutskie, D. P. Hamilton, (2009), Saturn’s largest ring, Nature, 461:1098.

Verbiscer, A., R. French, M. Showalter, P. Helfenstein, (2007), Enceladus: Cosmic graffiti artist caught in the act, Science, 315:815.

Vixie, G., J. W. Barnes, B. Jackson, S. Rodriguez, S. Le Mouélic, C. Sotin, S. MacKenzie, P. Wilson, (2015), Possible temperate lakes on Titan, Icarus, 257:313–323.

Wall, S., A. Hayes, C. Bristow, R. Lorenz, E. Stofan, J. Lunine, A. Le Gall, M. Janssen, R. Lopes, L. Wye, L. Soderblom, P. Paillou, O. Aharonson, H. Zebker, T. Farr, G. Mitri, R. Kirk, K. Mitchell, C. Notarnicola, D. Casarano, B. Ventura, (2010), Active shoreline of Ontario Lacus, Titan: A morphological study of the lake and its surroundings, Geophysical Research Letters, 37(L05202), doi: 10.1029/2009GL041821.

Wall, S. D., R. M. Lopes, E. R. Stofan, C. A. Wood, J. L. Radebaugh, B. W. Stiles, R. M. Nelson, L. W. Kamp, M. A. Janssen, R. L. Lorenz, J. I. Lunine, T. G. Farr, G. Mitri, P. Paillou, F. Paganelli, K. L. Mitchell, (2009), Cassini RADAR images at Hotei Arcus and Western Xanadu, Titan: Evidence for recent cryovolcanic activity, Geophysical Research Letters, 36(L04203), doi: 1029/2008GL036415.

Wei, H. Y., C. T. Russell, M. K. Dougherty, F. M. Neubauer, Y. J. Ma, (2010), Upper limits on Titan's magnetic moment and implications for its interior, Journal of Geophysical Research, 115(E10007).

West, R., K. Mitchell, B. Stiles, Y. Anderson, A. Le Gall, A. Hayes, M. Janssen, R. Kirk, R. Lopes, R. Lorenz, S. Wall, (2012), Observation design and early results from Cassini Radar SAR imaging of Enceladus, Lunar and Planetary Science Conference, 43.

Wood, C. A., (2018), Titan’s great crustal thickening event and recent geologic history, Lunar and Planetary Science Conference, 49:1343.

Wood, C. A., R. Lorenz, R. Kirk, R. Lopes, K. Mitchell, E. Stofan, (2010), Impact craters on Titan, Icarus, 206:334–344.

Wood, C. A., K. L. Mitchell, R. M. C. Lopes, J. Radebaugh, E. Stoffan, J. Lunine, the Cassini RADAR Team, (2007), Volcanic calderas in the north polar region of Titan, Lunar and Planetary Science Conference, abstract 1454.

Wrixon, G. T., W. J. Welch, (1970), The millimeter wave spectrum of Saturn, Icarus, 13(2):163–172.

Wye, L., (2011), Radar scattering from Titan and Saturn's icy satellites using the Cassini spacecraft, Ph.D. Thesis, Stanford University, Faculty of Engineering, 316.

Wye, L. C., H. A. Zebker, the Cassini RADAR Team, (2011), Backscatter analysis of Saturn's icy moons with Cassini RADAR, American Geophysical Union Fall Meeting 2011, abstract id.P11E-1624.

Wye, L. C., H. A. Zebker, R. D. Lorenz, (2009), Smoothness of Titan’s Ontario Lacus: Constraints from Cassini RADAR specular reflection data, Geophysical Research Letters, 36:16201, doi: 10.1029/2009GL039588.

Wye, L. C., H. A. Zebker, S. J. Ostro, R. D. West, Y. Gim, R. D. Lorenz, the Cassini RADAR Team, (2007), Electrical properties of Titan's surface from Cassini RADAR scatterometer measurements, Icarus, 188:367–385.

Yu, X., S. M. Hörst, C. He, N. T. Bridges, D. M. Burr, J. A. Sebree, J. K. Smith, (2017), The effect of adsorbed liquid and material density on saltation threshold: Insight from laboratory and wind tunnel experiments, Icarus, 297:97–109.

Yung, Y. L., M. Allen, J. P. Pinto, (1984), Photochemistry of the atmosphere of Titan: comparison between model and observations, The Astrophysical Journal Supplement, 55:465–506.

Zahnle, K., P. Schenk, H. Levison, L. Dones, (2003), Cratering rates in the outer solar system, Icarus, 163:263–289.

Zebker, K., Y. -Q. Wong, (2016), Shape of Titan from Cassini radar elevation measurements and implications for interior structure and composition, American Geophysical Union Fall Meeting, Dec. 12–16, San Francisco, CA, paper no. P33F-01.

Zebker, H., A. Hayes, M. Janssen, A. Le Gall, R. Lorenz, L. Wye, (2014), Surface of Ligeia Mare, Titan, from Cassini altimeter and radiometer analysis, Geophysical Research Letters, 41:308–313, doi: 10.1002/2013GL058877.

Zebker, H. A., B. Stiles, S. Hensley, R. Lorenz, R. L. Kirk, J. I. Lunine, (2009a), Size and shape of Saturn’s moon Titan, Science, 324:921–923.

Zebker, H. A., Y. Gim, P. Callahan, S. Hensley, R. D. Lorenz, the Cassini RADAR Team, (2009b), Analysis and interpretation of Cassini Titan radar altimeter echoes, Icarus, 200:240–255.

Zebker, H., L. Wye, M. Janssen, the Cassini RADAR Team, (2008), Titan's surface from reconciled Cassini microwave reflectivity and emissivity observations, Icarus, 194(2):704–710.

Zebker, H. A., E. A. Marouf, G. L. Tyler, (1985), Saturn's rings: Particle size distributions for thin layer models, Icarus, 64(3):531–548.

Zhang, Z., et al., (2017a), Cassini microwave observations provide clues to the origin of Saturn's C ring, Icarus, 281:297–321.

Zhang, Z., A. G. Hayes, M. A. Janssen, P. D. Nicholson, J. N. Cuzzi, I. de Pater, D. E. Dunn, (2017b), Exposure age of Saturn's A and B rings, and the Cassini Division as suggested by their non-icy material content, Icarus, 294:14–42.

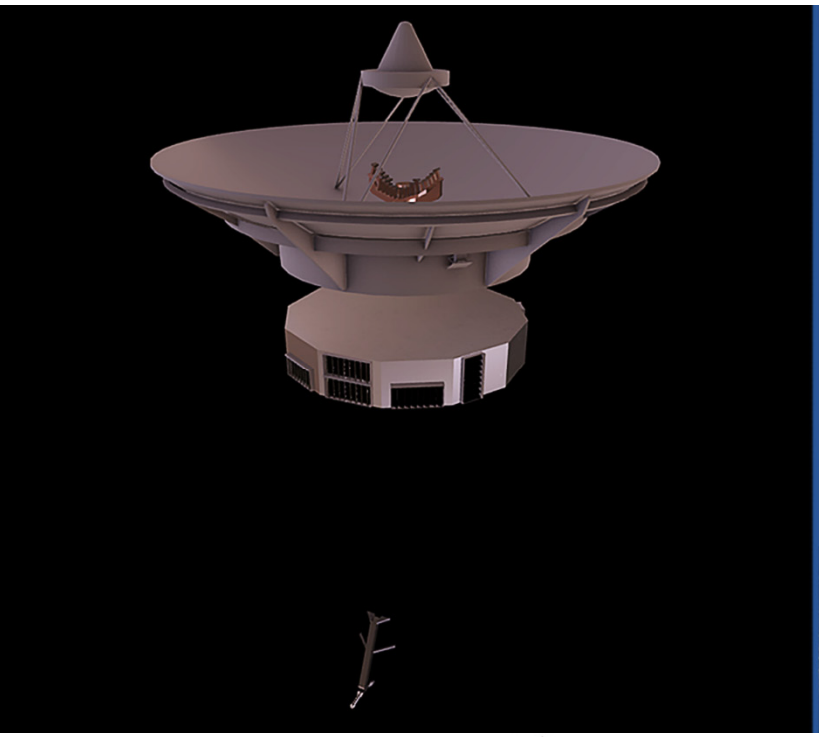

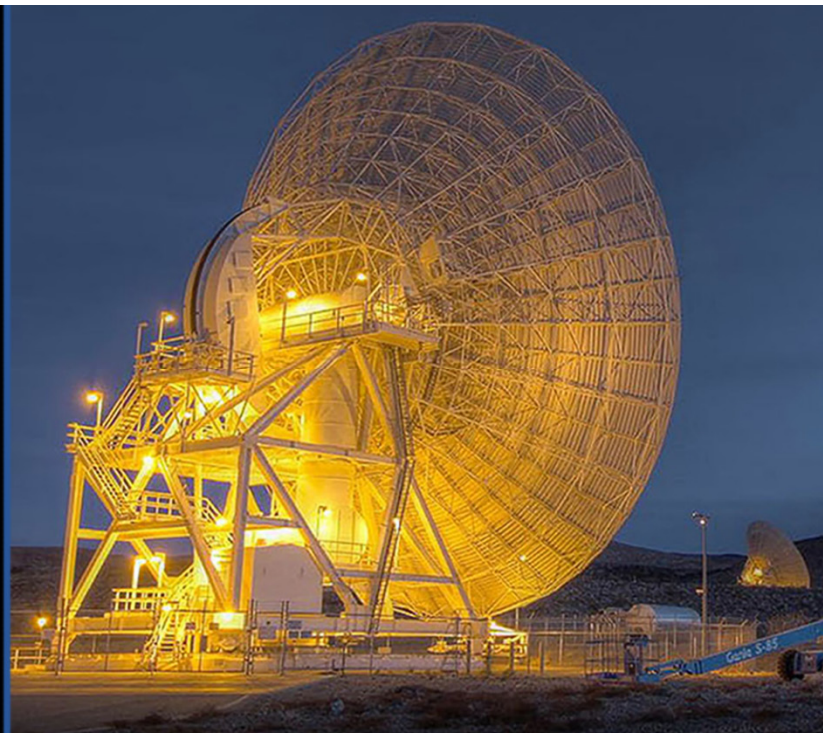

Radio Science Subsystem

The Radio Science Subsystem (RSS) used the spacecraft X-band communication link, an S-band downlink and a Ka-band uplink and downlink to study structure, composition, pressure, and temperature of atmospheres and ionospheres, ring structure, surface properties and particle sizes, body and system masses, gravity fields and gravitational waves. The **science objectives** of RSS were to study the atmospheres and ionospheres of Saturn and Titan, properties of rings, and gravity fields of Saturn and its satellites. During Cassini's cruise phase, RSS was also used to search for gravitational waves coming from beyond our solar system. Some of these experiments measured Doppler shifts (frequency shifts) and other changes to radio signals that occurred when the spacecraft passed behind Saturn, moons, as viewed from Earth to derive information about the structure and composition of the occulting bodies, atmospheres, and the rings.

RSS consists of a Ka-band traveling wave tube amplifier, a translator, an exciter; an S-band transmitter; and various microwave components. RSS used the spacecraft's Radio Frequency Subsystem (RFS) and one or more of the three Deep Space Network (DSN) antenna complexes to obtain the required scientific data. The RFS sent radio signals from Cassini spacecraft to Earth (DSN) using the spacecraft's high-gain antenna (HGA). In route, the radio signal interacted with Saturn's moons, rings or Saturn's atmosphere.

CONTENTS

Figures

Tables

Executive Summary

The Cassini RSS team conducted a wide-ranging series of experiments spanning the entire mission. En route to Saturn, the RSS team observed Cassini at solar conjunction, providing what is still today the most rigorous test of Einstein's theory of general relativity, and the single most frequently cited publication of the entire Cassini mission [Bertotti et al. 2003]. A second cruise experiment set new limits on the strength of low-frequency gravitational waves. Upon arrival at Saturn, a series of diametric ring occultations at three wavelengths revealed stunning detail in the rings at sub-km resolution, periodic structure in Saturn's C-ring (possible evidence of a pair of cometary collisions hundreds of years ago), incomplete clumps in the core of Saturn's F-ring, evidence of wake-driven periodic microstructure in rings A and B, and estimates of particle sizes through the main ring system. Companion Saturn atmosphere occultations over the course of the mission provided regional and seasonal information about the atmospheric thermal structure, including evidence of an equatorial oscillation, zonal winds, and complex wave structure. A suite of ionospheric observations revealed highly variable electron density profiles with evidence of ring/ionosphere interactions. Multiple Titan occultations provided accurate thermal profiles from the surface to the stratosphere over a broad range of latitudes and over the course of Saturn's seasons, and ionospheric profiles as well. Bistatic scattering experiments probed the reflectivity of Titan's surface and provided estimates of the dielectric constant of the liquid norther seas. An exquisite series of gravity field measurements during flybys revealed the presence of subsurface oceans on Titan and Enceladus, established firm measurements for the shape and degree of hydrostatic equilibrium for other icy satellites, and during the Grand Finale, determined the gravitational field of Saturn to extraordinary accuracy and determined the mass of Saturn's ring system to be lower than expected, providing strong evidence that the rings are younger than the planet itself.

En route to Saturn, the RSS team observed Cassini at solar conjunction, providing what is still today the most rigorous test of Einstein's theory of general relativity, … .

Top 20 RSS Science Highlights

Titan Science

1. **Measurement of Titan's hydrostatic gravity quadrupole and moment of inertia**, implying a partially differentiated body very different from its Jovian cousin Ganymede, with a low-density core made up by hydrated silicates.

2. **Seasonal variations in Titan's atmospheric thermal structure** from the surface to the stratosphere, with muted variations in the troposphere but larger in the middle atmosphere above 100 km, and a global minimum in the vertical profile of the zonal wind.

3. **Spatial and temporal variations of Titan's electron density structure**, with large low altitude secondary peak, possibly related to energetic ion precipitation.

4. **Bistatic observations of Titan's surface and Northern seas.**

Saturn Science

5. **Discovery of a strong differential rotation in Saturn's atmosphere**, extending down to 9000 km below the cloud level.

6. **Seasonal variations in Saturn's atmospheric thermal structure** from the cloud deck to the stratosphere, with evidence of an equatorial oscillation forced by vertically propagating waves.

7. **Spatial and temporal variations of Saturn's ionosphere**, likely affected by latitudinal variation of neutral molecules.

Enceladus Science

8. Discovery of Enceladus' subsurface ocean and interior structure.

9. Electron density observations at Enceladus.

Icy Satellite Science

10. Measurement of Rhea's quadrupole gravity field.

11. Measurement of Dione's quadrupole gravity field.

Ring Science

12. Measurement of a low mass of Saturn's rings.

13. Particle size determination of Saturn's rings.

14. Orbital properties of Saturn's rings.

15. Periodic microstructure in rings A and B.

16. Evidence for ancient impacts on Saturn's rings.

Cruise Science

17. Precision test of General Relativity.

18. Low-frequency gravitational waves.

19. Plasma turbulence in the inner heliosphere.

20. Precision navigation at solar conjunction.

RSS Instrument Summary

Radio Science experiments are typically divided into two categories: gravitation and propagation. For gravitation, the Cassini spacecraft serves as a point-mass probe within the gravity field of Saturn and its satellites; precision measurements of the Earth-Cassini distance and relative velocity can be used to infer the target body mass and higher order field components. Propagation experiments are radio occultation experiments where the occulting objects under study are planetary and satellite ionospheres and neutral atmospheres, rings, and solar plasma.

Figure RSS-1 shows typical radio science (RS) observational configuration for planetary occultations. The spacecraft transmits a signal that is refracted by the target atmosphere before being received on Earth at a ground station of NASA DSN. The direction of the arrow on the dashed ray path indicates that this is a one-way downlink observation. As the spacecraft moves, the ray probes more deeply into the atmosphere until it is absorbed or occulted by the planet itself. Stability of the signal during the observation depends on the quality of the reference oscillator onboard the spacecraft. Cassini was equipped with an ultra-stable oscillator (USO) to improve stability of its transmitted one-way signal. In two-way mode, a signal is transmitted from Earth and received at the spacecraft; this uplink signal can then be used to control the frequency of the downlink transmission. In general, the two-way mode provides better overall frequency stability than the one-way mode because of the superior quality of the atomic clocks at the ground stations. However, passage of the uplink signal through an atmosphere, ring, or plasma cloud, or reflection from a surface distorts the uplink signal making a USO-referenced one-way mode preferable. In three-

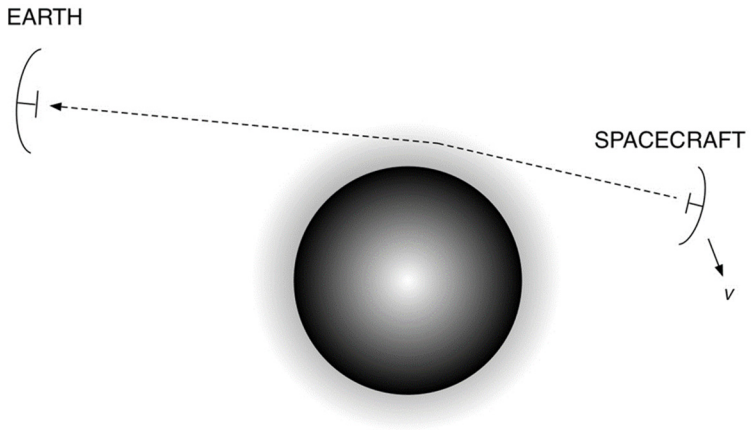

Figure RSS-1. Configuration for radio science observations at a generic planet. Spacecraft moving at velocity *v* gets occulted by the atmosphere then the planet itself.

way mode, one ground station transmits to the spacecraft and a different ground station receives; this is used when an observation spans the handover from one ground station to another. In the Cassini case, three-way was necessary because of the long one-way light time between Saturn and Earth, ranging from 68 to 84 minutes.

During occultations by Saturn, its rings, or its satellites, one-way operation yield observables which are inverted to give temperature-pressure and absorption profiles of neutral atmospheres, electron density profiles of ionospheres, and optical depth and particle size distribution profiles of rings. Most measurements are wavelength dependent and some may include polarization effects, so a wide range of transmitting and receiving equipment is desirable.

During close encounters, the spacecraft antenna is deflected from the Earth direction to point at satellite surfaces or Saturn's ring plane. Such one-way bistatic radar (BSR) experiments require the highest sampling rates of the receivers at the ground stations and contain the most interesting polarization information. Inversions can yield dielectric constant of target surfaces and size distributions for ring particles.

Cruise Phase Science

During the long Cassini phase, RS observations included gravitational wave experiments (GWEs) near solar oppositions and solar conjunction experiments (SCEs). In a GWE, subtle changes in the apparent Earth-spacecraft distance and/or relative velocity, which cannot be attributed to other causes, would indicate passage of gravitational wavefronts through space between Earth and Cassini. GWE observations were conducted in two-way mode for highest clock stability. When the spacecraft's radio signal is occulted by the Sun, then an SCE investigates the solar corona. Operationally, two-way data are collected at large solar radii; but one-way operation with open-loop reception is the practical choice for small solar radii and high solar activity. The shortest radio wavelengths are least affected by the solar plasma; multiple wavelength measurements yield total electron content along the radio path directly.

Radio Frequency Subsystem

The RFS, in conjunction with the Antenna Subsystem, provides communications between the spacecraft and ground stations of the DSN. It also provides a signal source for RS measurements. In earlier documentation—for example, Kliore et al. [2004]—a distinction was made between multi-use radio components (RFS) and RS-only components called the Radio Frequency Instrument Subsystem (RFIS) but that distinction is not maintained here and all radio components fall within the RFS. The RFS includes a pair of redundant X-band transponders for reception and transmission, an S-band transmitter, and a Ka-band transmitter. The USO provided an onboard highly stable time and frequency reference, but it failed in 2011. A Ka-band translator (KaT), which received at 34 GHz and transmitted coherently at 32 GHz, supported general relativity observations during Cruise; it failed before Saturn orbit insertion.

The RFS produces an X-band carrier modulated with data received from the Command & Data Subsystem (CDS), amplifies the modulated carrier, and delivers the signal stream to the Antenna Subsystem for transmission to Earth. It also receives and demodulates X-band commands from the ground via the Antenna Subsystem. At Saturn, where the one-way distance to Earth is 8.2–10.2 astronomical units (AU) and the one-way travel time is 68–84 minutes, commands and instructions from Earth have been received at 1000 bits per second (bps) by the HGA; and data have been transmitted to Earth at selectable rates ranging from 14,220 to 165,900 bps. Data can be recorded on the solid- state recorders for about 15 hours, while the HGA is not pointed at Earth; then they are played back for nine hours. About one gigabit of data can be returned each day via a 34-m DSN antenna; nearly four times that can be returned via a 70-m ground antenna. The two redundant recorders can record and read out nearly 2 gigabits of data simultaneously. The CDS handles combined data rates in excess of 430,000 bps from the instruments while carrying on its functions of command and control. Since RS observables are generated at the DSN, only a very small fraction of telemetry, such as equipment status and spacecraft attitude measurements, are of interest to RS.

The Antenna Subsystem includes the 4-meter diameter HGA reflector (which was also used for Sun shading in the early cruise phase); a frequency-selective subreflector; HGA feeds for S-band, X-band, Ka-band, and Ku-band; and two low-gain antennas (LGA). All antennas operate at X-band; only the HGA operates at S-band, X-band, Ka-band, and Ku-band. The X-band components are for communications and navigation as well as RS; the S-band and Ka-band components are only for RS and the Ku-band components are for the Cassini Titan Radar Mapper (RADAR). Table RSS-1 lists the RS bands.

Table RSS-1. Cassini Radio Science Bands and Wavelengths.

Band	Wavelength (cm)	Frequency (MHz) Uplink	Frequency (MHz) Uplink
S	13	N/A	2298
X	3.6	7175	8425
Ka	0.9	34316	32028

Notes: Separate S-band channels existed to receive the Huygens probe relay in two polarizations at 2040 and 2098 MHz. The X-band uplink polarization is left circular (LCP) when Transponder A is selected and right circular (RCP) when Transponder B is selected. The X-band downlink polarization is LCP when traveling wave tube amplifier A (TWTA-A) is selected and RCP when TWTA-B is selected.

Ultra-stable oscillator

Key to RS instrumentation onboard the Cassini spacecraft, the USO provided the highly stable reference generated on-board the spacecraft until it failed in 2011. The Cassini oscillator is in the class of highest performance thermally-controlled quartz crystal oscillators flown on planetary missions. It was manufactured by Johns Hopkins University, Applied Physics Laboratory. Figure RSS-2 shows the X-band output frequency of the USO over several years showing long-term aging behavior (without accounting for time dilation effects).

Figure RSS-3 shows the excellent Allan Deviation performance of the USO stability as a function of integration time from one representative test in 2011. These data in reality characterize

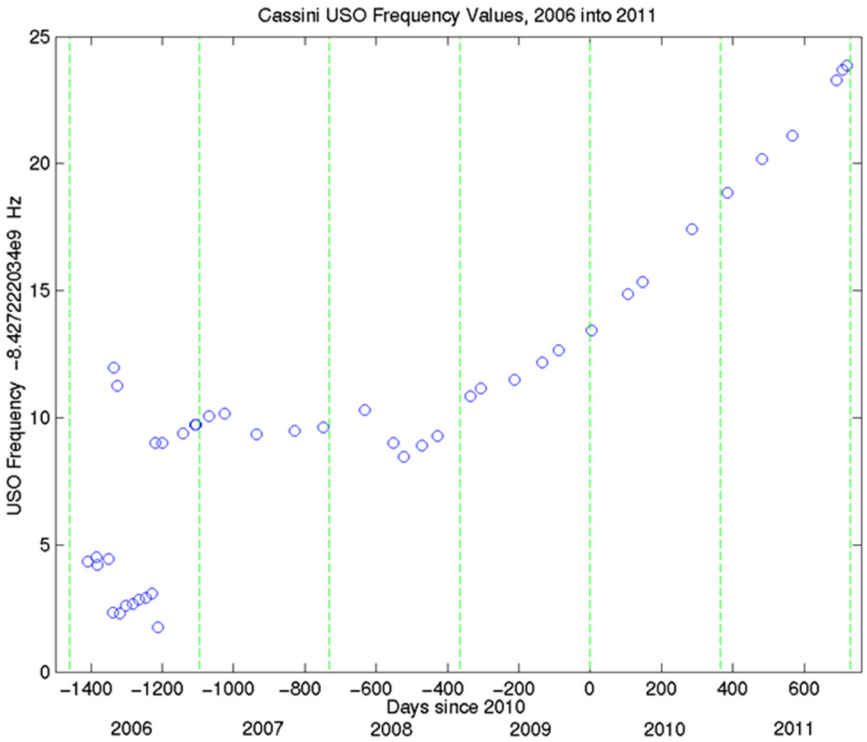

Figure RSS-2. The USO output frequency scaled to X-band by the Cassini transponder over several years, showing long-term aging process as expected.

the end-to-end performance of the radio systems on both the spacecraft and ground station, although independent calibration of the DSN stations have shown that these results are dominated primarily by the limit of the USO performance.

Attitude and Articulation Control Subsystem

The Attitude and Articulation Control Subsystem (AACS) maintains the spacecraft's orientation and consists of redundant Sun sensors mounted on the HGA, redundant stellar reference units mounted on the remote-sensing platform, three mutually perpendicular reaction wheels mounted in the lower equipment module (LEM), plus a fourth backup reaction wheel mounted in the upper equipment module (UEM). Redundant inertial reference units, along with an accelerometer to measure changes in the spacecraft's velocity, are located in the UEM.

The AACS points the selected communication antenna toward Earth and points the remote sensing pallet toward selected targets. It also points one of the two redundant main propulsion engines in the desired direction during engine burns and performs small trajectory correction maneuvers using the onboard thrusters. The AACS uses a pointing system known as inertial vector propagation that keeps track of spacecraft orientation, the direction of the Sun and distance to the Sun, Earth, Saturn, and other possible remote- sensing targets, and the spacecraft-relative pointing

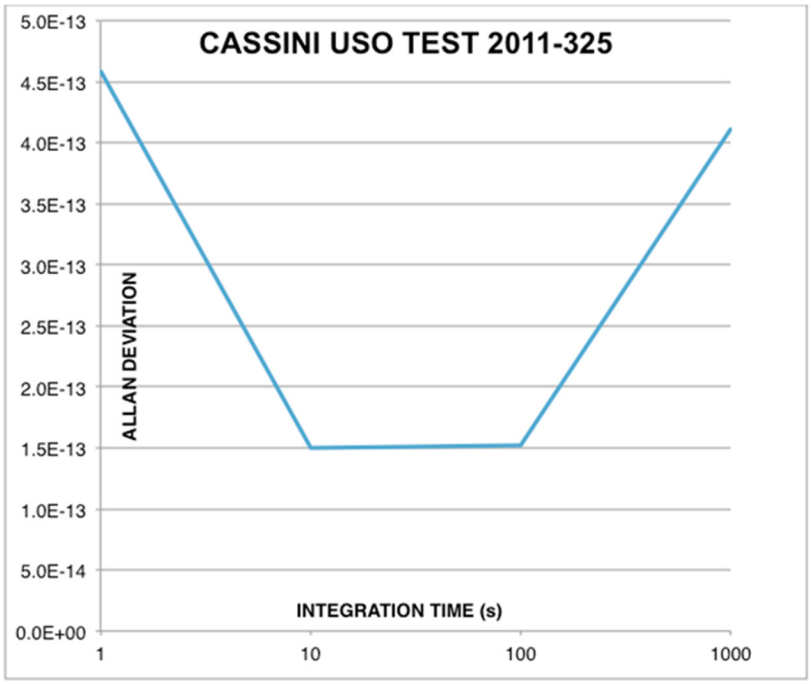

Figure RSS-3. Allan Deviation of the Cassini USO as a function of integration time from a representative test. Four points are plotted at 1, 10, 100, and 1000 seconds.

directions of all science instruments. This subsystem provides sufficient engineering data to support science data interpretation and mission operations.

Other Subsystems

The Propulsion Module Subsystem (PMS) is the largest and most massive subsystem. It consists of a bipropellant element for trajectory changes and a hydrazine element for attitude control, small maneuvers, and reaction wheel desaturation. The Power and Pyrotechnics Subsystem (PPS) converts the radioisotope thermoelectric generator (RTG) power output to provide a regulated 30-V direct-current power bus and provides the capability to turn various users on or off when commanded. Power conditioning equipment can detect over-current conditions and switch the affected user off. The pyrotechnic switching unit also provides redundant power conditioning and energy storage, and it controls the firing of pyrotechnic devices.

The Temperature Control Subsystem (TCS) maintains the temperatures of all critical spacecraft components within their specified limits via electrical temperature sensors. Even at 9 AU from the Sun, spacecraft orientations that expose radiator plates to the Sun can severely degrade the data collected by some of the science instruments. The TCS can turn electric heaters on or off, open or shut thermal louvers in the UEM, use small radioisotope heaters to raise the temperature of selected regions, and utilize thermal blankets and shields. Several instruments have radiator plates for cooling.

Ground Systems

RS data are acquired by the ground instrumentation at DSN stations at Goldstone, California; Canberra, Australia; and Madrid, Spain. During the Grand Finale orbits, additional electrostatic energy analyzer (ESA) ground stations at New Norcia, Australia and Malargue, Argentina, contributed to Cassini RSS experiments. The microwave signals are captured using 34 m or 70 m diameter antennas and are mixed to lower frequencies where they are sampled, averaged, and recorded for later analysis. Two-way and three-way uplink transmissions can be modulated with ranging codes, which allow determination of round-trip times after correlation with the modulation on the downlink signal. Status and performance of the uplink, downlink, and ground antenna systems is recorded in files of monitor data. RS data are acquired via two types of receivers: closed-loop and open-loop.

During the Grand Finale orbits, additional ESA ground stations at New Norcia and Malargue contributed to Cassini RSS experiments.

The ground stations are pointed via the following techniques. Conical scan is dynamical ground antenna pointing during which the boresight is offset from the predicted pointing by a small amount; the observed degradation in signal level is used to determine a new best pointing direction. This is repeated in such a way that the pointing follows a conical path around the best direction; it is not used when the signal is expected to undergo significant amplitude changes. The monopulse technique uses relative amplitude and phase between TE_{11} and TE_{21} circular waveguide mode signals generated in a special Ka-band feed. Aberration correction is a pointing adjustment to account for real motion of the signal source against the sky background during the one-way light travel time. During uplink, the antenna is pointed to the location where the spacecraft will be at the time the signal arrives rather than toward its geometric location at the time of transmission.

Closed-loop tracking receiver

In order to track a spacecraft signal carrier, the closed-loop receiver utilizes a phase-locked loop (PLL) that precisely measures and record the carrier's phase. The Doppler shift is estimated from the phase and converted to relative velocity. Separately, ranging code modulation is extracted and correlated with the uplink code to determine absolute range. The closed-loop tracking receiver provides a Doppler estimate every 0.1 seconds; ranging samples are generated at a rate that depends on the code repetition period and user-selected averaging interval. The tracking receiver also provides a signal to the antenna pointing process.

Open-loop radio science receiver

In open-loop reception, an independent broadband receiver is used without the PLL tracking mechanism described above. The radio science receiver (RSR) down-converts the spacecraft signal via a local oscillator heterodyne process guided by a prediction of the expected frequency.

Additional description of the RSR structure and data format and content is available in the DSN document 820-013, module 0159-Science; a functional description in Asmar et al. [2013]. It captures and records the predetection radio signal at a user-selected sampling rate via an analog-to-digital converter. The digital samples of the propagating electromagnetic wave are stored to disk. Because the received downlink signal can be precisely reconstructed, this mode of data acquisition provides great flexibility in signal processing. The RSR provides superior phase stability, captures the signal during high amplitude or frequency dynamics (where the closed-loop receiver would lose lock), is resilient to multipath effects, and preserves all the information contained in the signal. On the other hand, this method requires additional operational procedures, resources, and generation of predictions sometimes containing complex planetary atmospheric or other models. It also involves handling large file sizes and requires expertise in digital signal processing.

Each DSN complex has at least three RSRs, each capable of independently capturing the output from a different antenna feed, i.e., a different band polarization combination. Similar receivers are also available for very-long-baseline interferometry (VLBI) work; their output can be easily converted to the RSR format, and they can be used when Cassini RS observations require more support than the RSRs alone can provide. The Radio Science Systems Group (RSSG) remotely operates the RSR and VLBI Science Receiver (VSR) from Jet Propulsion Laboratory (JPL).

Key Objectives for RSS Instrument

The key RSS ring science objectives are listed below and discussed in further detail in the section entitled Science Results.

Titan Science

Gravity

Gravity provides unique and crucial information about the interior structure of Titan. When combined with other measurements, such as altimetry and rotation, gravity measurements enable a full tomography of the body. The high-level science questions addressed by the gravity science investigation include:

1. Is Titan in hydrostatic equilibrium?
2. How differentiated is the interior? Is Titan as differentiated as its Jovian cousin Ganymede?
3. What is the density of the core? What is its chemical composition?
4. Is Titan hosting an ocean at depth? If a subsurface ocean exists, what is its density (therefore, its enrichment with salts)?

5. What is the gravitational shape of the moon, and how does it compare with the physical shape?

6. If a higher degree gravity field is measurable, can gravity-topography correlations constrain the thickness of the outer ice shell?

Prior to Cassini, only the density of the moon was sufficiently well determined from Pioneer 11 and Voyager 1 and 2 radiometric measurements [Null et al. 1981; Campbell and Anderson 1989]. Although uncertainties and ambiguities are unavoidable, RSS has been able to answer directly or in combination with other instruments to all these questions, providing a comprehensive picture of the interior structure of the moon.

Atmosphere

The key objectives for Titan atmospheric science were to determine the surface-to-stratospheric thermal structure over a range of latitudes and seasons on Titan, from multiple radio occultation experiments; to measure the wavelength-dependent atmospheric extinction; to investigate atmospheric wave activity; to infer zonal wind characteristics; to characterize diurnal, regional, and seasonal variations in atmospheric structure.

Ionosphere

The key objectives for Titan atmospheric science were to determine the surface-to-stratospheric thermal structure over a range of latitudes and seasons on Titan, from multiple radio occultation experiments; to measure the wavelength-dependent atmospheric extinction; to investigate atmospheric wave activity; to infer zonal wind characteristics; to characterize diurnal, regional, and seasonal variations in atmospheric structure.

Surface—bistatic experiments

The Cassini RSS team carried out a number of bistatic experiments near the Brewster angle at Titan to determine reflectivity and dielectric constant estimates at its three radio wavelengths. A particular focus was to determine the dielectric constant of the liquids in the northern seas.

Saturn Science

Gravity

The key objective for Saturn gravity science was to determine measure gravitational mass (GM), the lower order gravitational moments, and the low-order tidal Love numbers to infer Titan's internal mass distribution from multiple gravitational flybys. During the nominal Cassini tour, the pericenters of the petal orbits were too far from the planet to measure the fine structure of the gravity and magnetic field, the only available tools to probe Saturn's interior. The Grand Finale Orbits (GFO)

brilliantly completed the investigation of the Saturnian system by peeking through the upper cloud deck down to the inner recesses of Saturn's core. In addition, the unique geometry of the GFO orbits, with the pericenters between the planet and the ring system, allowed the determination of the mass of the B-ring, a quantity of utmost importance to reveal the age, hence the nature, of the ring system.

Extensive numerical simulations were carried out in the years preceding the GFO to set the science goals for the RSS gravity investigation at Saturn. The team benefitted from the experience gained with the Juno mission, whose main goal was to probe the deep interior of Jupiter using the same observational tools (Doppler and magnetic measurements), although with dedicated and more accurate instrumentation. The science questions addressed by RSS-Gravity were:

1. To what depth is Saturn differentially rotating? How deep are the flows detected by optical imaging of the clouds?

2. What is the allowed range of core masses? What is the abundance of heavy elements in the interior of Saturn?

3. What is the mass of the B-ring? Are Saturn's rings young or did they form together with the planet?

For a review of the pre-Cassini understanding of the interior of Saturn and the expected improvements from gravity measurements, see Fortney et al. [2016], with earlier references therein. For the relation between the mass and the age of the rings, see Cuzzi and Estrada [1998]. The gravity harmonics of Saturn before the GFO were determined by Jacobson et al. [2006] from the orbital perturbations on the orbits of Saturn's moons.

Atmosphere

The key objectives for Saturn atmospheric science were to determine the surface-to-stratospheric thermal structure over a range of latitudes and seasons on Saturn, from multiple radio occultation experiments; to measure the wavelength-dependent atmospheric extinction; to investigate atmospheric wave activity; to infer zonal wind characteristics; to characterize diurnal, regional, and seasonal variations in atmospheric structure; to help constrain the H/He ratio in Saturn's atmosphere.

Ionosphere

The key objectives for Saturn ionospheric science were to determine the surface-to-stratospheric thermal structure over a range of latitudes and seasons on Saturn, from multiple radio occultation experiments; to measure the wavelength-dependent atmospheric extinction; to investigate atmospheric wave activity; to infer zonal wind characteristics; to characterize diurnal, regional, and seasonal variations in atmospheric structure; to help constrain the H/He ratio in Saturn's atmosphere.

Enceladus Science

Gravity

Enceladus was a special focus of interdisciplinary science in the Cassini mission. Indeed, two major objectives of the Cassini Satellite Surface Working Group were to acquire optical remote sensing observations of Enceladus and to measure its gravity field. This interest is explained by the intriguing characteristics of Enceladus, among which figure the remarkably high and uniform albedo and the presence of old and recent terrains. In the pre-Cassini era, the mean geometric albedo was known to be close to unity, and the total range of albedo over the surface is 20%. This was even more intriguing considering that Enceladus topography contains both old cratered terrains dating from the period of heavy bombardment and smooth terrains recently resurfaced, indicating endogenic activity. Buratti [1998] investigated the photometric properties of Enceladus and concluded that the satellite is completely covered by a young, bright surface layer. Buratti argues that the E-ring, whose thickness peaks at the orbit of Enceladus, is the most likely source for this layer, and that the E-ring itself is probably the result of active surface processes on Enceladus. Alternatively, the bright surface of Enceladus may result from dissipation associated with tidal interactions, perhaps with Dione.

This interest is explained by the intriguing characteristics of Enceladus, among which figure the remarkably high and uniform albedo and the presence of old and recent terrains.

Enceladus' mean radius was known to be ~250 km. How could such a small satellite have undergone substantial evolution? This may be due to the fact that ammonia ice, which plays an important role in lowering the melting point, may have been incorporated into Enceladus. Evidently, the surface properties alone are insufficient to provide information on the interior composition. To understand the nature and history of Enceladus and the other Saturn's satellites, modeling of the interiors and of the thermal evolutions was in order.

As far as Enceladus is concerned, even the most basic parameter, i.e., the mass density, was very poorly known (with about 50% accuracy). A determination of the mass of Enceladus and of its harmonic coefficients of at least degree 2 from data acquired during targeted flybys was deemed a crucial goal to determine its moment of inertia, and hence to constrain models of internal structure.

Atmosphere/ionosphere

The tenuous atmosphere/ionosphere of Enceladus was probed during a serendipitous RSS occultation.

Icy Satellite Science

The objective was to determine the masses (and, where possible, the gravity field) of the icy satellites (especially Dione, Hyperion, Iapetus, Phoebe, and Rhea) in order to determine their mean density to high accuracy, and hence constrain their bulk composition. For Dione and Rhea, which had multiple flybys with radio tracking during the closest approach, the goal was to find out whether these bodies are differentiated and to compare their internal structure to that of Titan and Enceladus.

The mass determination is essential for an improved understanding of their dynamical behavior and evolution. Tyler et al. [1981] determined the masses of Titan and Rhea from Voyager 1 Radio Science measurements at Saturn, and Voyager 2 permitted Tyler et al. [1982] to determine the masses of Tethys and Iapetus. Using the mass of Tethys in combination with the theory of the Tethys-Mimas resonance, they derived the mass of Mimas. Campbell and Anderson [1989] used the combined data set of Pioneer and Voyager data to redetermine the masses of Tethys, Rhea, Titan and Iapetus, but recommended the earlier ground-based determination [Kozai 1957] for Tethys. No mission, before Cassini, yielded a direct determination of the masses of Mimas, Enceladus, Dione, Hyperion, and Phoebe. Phoebe, on an inclined, retrograde orbit, may be a captured object. Determining its density is important to find out whether or not Phoebe is asteroidal in nature.

Ring Science

The primary objective of Cassini Radio Science Subsystem ring experiments was to take advantage of the capability of simultaneous observations at three wavelengths (0.94, 3.6, and 13 cm, or Ka-band, X-band, and S-band, respectively) over multiple occultation opportunities at large, intermediate, and small ring opening angle *B*, to investigate ring structure and physical properties, including:

- High-resolution profiling of radial ring structure and characterization of its variability with wavelength, longitude, ring opening angle, and time. Profiling of the relative abundance of millimeter to decimeter radius particles and characterizing of their variability across resolved ring features.
- Determination of the full particle size distribution over the approximate size range 1 mm to 20 m of broad ring features that can be resolved in the spectra of the near-forward scattered signal. Determination of the vertical ring structure, of the physical ring thickness, and of the particle packing fraction within such features.
- Determination of ring surface mass density, ring viscosity, and bulk density of particle material. Characterization of the variability of these parameters among global ring features (A, B, C …) and within local broad features.

Goals of studies of ring kinematics and dynamics included:

- Determination of the geometry of the Saturn ring system, including determination of Saturn's pole direction and precession rate and a highly accurate (few hundred meter) absolute radius scale of the rings.
- Investigations of ring morphology: A major goal of ring dynamics studies is to explain the presence of non-axisymmetric features such as eccentric ringlets and density waves, and nonequatorial features such as inclined ringlets and bending waves.
- Exploration of ring evolution by characterizing and modeling viscous stresses, and the transport of angular momentum and energy within the rings and their transfer between rings and satellites.

Cruise Science

During the long Cassini phase, RS observations included GWEs near solar oppositions and SCEs. In a GWE, subtle changes in the apparent Earth-spacecraft distance and/or relative velocity, which cannot be attributed to other causes, would indicate passage of gravitational wavefronts through space between Earth and Cassini. GWE observations were conducted in two-way mode for highest clock stability. When the spacecraft's radio signal is occulted by the Sun, then an SCE investigates the solar corona. Operationally, two-way data are collected at large solar radii; but one-way operation with open-loop reception is the practical choice for small solar radii and high solar activity. The shortest radio wavelengths are least affected by the solar plasma; multiple wavelength measurements yield total electron content along the radio path directly.

RSS Science Assessment

Table RSS-2 contains an assessment of RSS ring science based on the objectives in the original Announcement of Opportunity (AO) and the Cassini Traceability Matrix (TM) developed for the Equinox and Solstice missions. Each RSS ring science objective is paired with an AO and TM science objective, with the exception of the Solar Conjunction Experiment (a test of general relativity).

Table RSS-2. Matrix of RSS Science Objectives. Green indicates that RSS data with sufficient quality were obtained during the Cassini mission to contribute to a given science objective.

RSS Science Objectives	AO and TM Science Objectives	RSS Science Assessment	Comments if yellow (partially fulfilled)
Titan Science			
Titan Meteorology	T_AO3, TN2a, TN2c		
Titan Surface and Internal Structure	T_AO4		
Titan Upper Atmosphere	T_AO5		
Titan's Great Seas	TC1a		

Table RSS-2. Matrix of RSS Science Objectives. Green indicates that RSS data with sufficient quality were obtained during the Cassini mission to contribute to a given science objective.

RSS Science Objectives	AO and TM Science Objectives	RSS Science Assessment	Comments if yellow (partially fulfilled)
Titan's Global Seasons	TC1b		
Titan's Interior Ocean	TN1b		
Titan's Internal Structure	TN2b		
Titan's Ionosphere	MC2a		
Saturn Science			
Saturn Temperature	S_AO1		
Saturn Winds and Weather	S_AO2		
Saturn interior structure and rotation	S_AO3, SN1a		
Saturn ionosphere/magnetosphere interaction	S_AO4		
Seasonal variations	SC1a		
Saturn's winds	SC1b		
Ionosphere and ring coupling	MN2a		
Enceladus Science			
Enceladus ocean	IN1a		
Enceladus plume variability	MC1a		
Icy Satellite Science			
Icy satellite interior properties	I_AO4,IN2c		
Ring Science			
Ring structure and dynamics	R_AO1, RC1a, RC1b		
Ring particle size	R_AO2		
Ring-Satellite interaction	R_AO3		
Ring/Ionosphere interactions	R_AO5, MN2a		
F-ring	RC2a		
Ring age and Origin	RN1a		
Ring structure at high resolution	RN1c		
Ring microstructure	RN2a		
Cruise Science			
Gravitational wave experiment	C_AO3		
Solar conjunction experiment			
Solar wind experiment	C_AO2		

RSS Saturn System Science Results

Titan Science

Gravity

Titan played a special role in Cassini: it was at the same time one of the main science targets of the mission, and at the same time its true engine. Titan gravity was used to change the orbital elements of the spacecraft, enabling its complex and extraordinary tour of the Saturnian system. But Titan's gravity, in its fine details, revealed the interior structure of the moon by answering the Key Objectives for RSS Instrument-Titan Science-Gravity. Indeed, lacking an internal dynamo and in the absence of a detectable induction magnetic field, gravity and rotation are the only available tools to peek through the surface and reach the deep interior.

Cassini's observations have unveiled a variety of features and phenomena not found on any other solar system satellite, such as hydrocarbon lakes, river channels, and dune fields, making it a unique object.

Cassini's observations have unveiled a variety of features and phenomena not found on any other solar system satellite, such as hydrocarbon lakes, river channels, and dune fields, making it a unique object. While exogenic processes driven by the dense, hydrocarbon-rich atmosphere, play a crucial role in shaping the complex topography determined by Cassini's radar, contributions from endogenic processes are far less clear. Assessing the presence of active endogenic processes and understanding the origin of the complex topography revealed by Cassini's radar requires the knowledge of Titan's interior structure, which can be indirectly inferred from gravity and rotation data.

Prior to Cassini measurements, models of Titan's interior generally envisaged a core made up of silicates, surrounded by a layer of high-pressure ice, possibly a liquid water or water-ammonia ocean, and an ice-I outer shell, with variations associated with the dehydration state of the core or the presence of mixed rock-ice layers. It was generally expected that Titan could be significantly differentiated [Sohl et al. 2003], although models with higher moment of inertia factor (MOIF) and partial differentiation were also proposed [Fortes et al. 2007]. The determination of Titan's MOIF became therefore a crucial goal for RSS gravity investigations. The MOIF can be inferred from the quadrupole field under the assumption of hydrostatic equilibrium, a hypothesis that Cassini could easily test from the measurement of the J2/C22 ratio (equal to 10/3 for a relaxed body).

Models of Titan's interior envisaging small amounts of ammonia indicated that a subsurface ocean made up of liquid water could exist to the present day—for example, Tobie et al. [2005]. Such a liquid layer has profound implications for the geologic history of Titan and the source of methane. However, one can construct a fully frozen Titan by including only water and rock/metal as bulk

materials, excluding ammonia, and assuming that the crust contains little methane clathrate which acts to lower the thermal conductivity and plasticity of Titan's upper thermal lid [Tobie et al. 2006].

The first hint for a conductive layer came from the analysis of the electric signal acquired during the descent of the Huygens probe in January 2005 [Béghin et al. 2012]. The Huygens Atmospheric Structure Instrument and Permittivity, Wave, and Altimetry (HASI–PWA) observed an electromagnetic (EM) signal at around 36 Hz interpreted as the second harmonic of a Schumann resonance. This physical characteristics of the resonating cavity required a conductive layer at a depth of 65-km (±15-km) that was interpreted as the upper layer of a salty ocean. The measurement of a large obliquity from SAR processing of crossovers was also interpreted as an indication of an outer icy shell decoupled from the interior [Lorenz et al. 2008; Bills and Nimmo 2008].

A conclusive test for the presence of an interior ocean requires the measurement of Titan's time-variable gravity. Therefore, direct testing for the presence of an ocean within Titan's interior became a key goal of the Cassini-Huygens mission. The large eccentricity (e = 0.03) of Titan's orbit causes significant variations in the tidal field from Saturn and induces periodic stresses in the satellite body at the orbital period (about 16 days). Peak-to-peak variations of the tidal field (from pericenter to apocenter) are about 18%. If Titan hosts a liquid layer, the gravity field would exhibit significant periodic variations, controlled by the tidal Love numbers, defined for each spherical harmonic as the ratio between the perturbed and perturbing potential. For Titan the largest effect is by far on the quadrupole field, and the corresponding Love number is indicated by k_2 (assumed to be identical for all degree 2 harmonics).

Analysis of Titan's tidal response [Rappaport et al. 2008] shows that k_2 depends crucially on the presence or absence of an internal ocean. k_2 was found to vary from about 0.03 for a purely rocky interior to 0.48 for a rigid rocky core surrounded by an ocean and a thin (20 km) ice shell. Larger values of k_2, such as 0.7–0.8, are possible if the density of the ocean and the external shell is large (1.1–1.2 g/cm^3). A large k_2 entails changes in the satellite's quadrupole coefficients by a few percent, enough to be detected by accurate range rate measurements of the Cassini spacecraft.

CASSINI FLYBYS OF TITAN

Due to competition with other science goals, the opportunities for gravitational measurements were limited. Titan's main deviations from spherical symmetry are caused by centrifugal and tidal forces, associated respectively with the rotation about its spin axis and the gradient of Saturn's gravity. During the Cassini mission, 10 Titan flybys were committed to gravitational measurements. Table RSS-3 tabulates characteristics of the flybys. The flyby identification is shown in the first column. The color codes identifying each flyby in the table are used also in Figure RSS-4 and Figure RSS-5. The second column indicates the epoch of closest approach (C/A). The gravity signal is stronger for lower pericenter altitudes (third column) while Doppler noise due to interplanetary plasma turbulence decrease for larger Sun-Earth-Probe (SEP) angles (fourth column). T110 was carried out using Cassini's LGA, as the attitude was set by the needs of other instruments. The first four flybys provided the static gravity field and the moment of inertia factor of

Table RSS-3. Main characteristics of Titan's gravity flybys.

Flyby	Closest Approach (C/A) Date	Altitude	SEP
T011	27-FEB-2006 08:25:18 ET	1812 km	150°
T022	28-DEC-2006 10:05:21 ET	1297 km	131°
T033	29-JUN-2007 17:00:51 ET	1933 km	46°
T045	31-JUL-2008 02:14:16 ET	1614 km	30°
T068	20-MAY-2010 03:25:26 ET	1397 km	120°
T074	18-FEB-2011 16:05:17 ET	3651 km	131°
T089	17-FEB-2013 01:57:42 ET	1978 km	106°
T099	06-MAR-2014 16:27:53 ET	1500 km	111°
T110	16-MAR-2015 14:30:55 ET	2274 km	109°
T122	10-AUG-2016 08:32:00 ET	1698 km	113°

the body [Iess et al. 2010]. Two additional flybys (T68 and T74) were needed to ensure a robust determination of k_2 [Iess et al. 2012].

During gravity flybys the spacecraft was tracked from the antennas of NASA's DSN using microwave links at X-band and Ka-band frequencies (8.4 and 32.5 GHz), referred to a common uplink. The state-of-the-art instrumentation enables range rate measurements accurate to 20–50 micron/s at integration times of 60 s.

In order to obtain the optimal gravity measurements, the goal would be to obtain even global sampling of Titan's gravity; however, orbital limitations and competition with other Cassini goals prevented this. Figure RSS-4 shows ground tracks achieved within the limited observational opportunities and emphasizes the scarcity of high latitudinal sampling.

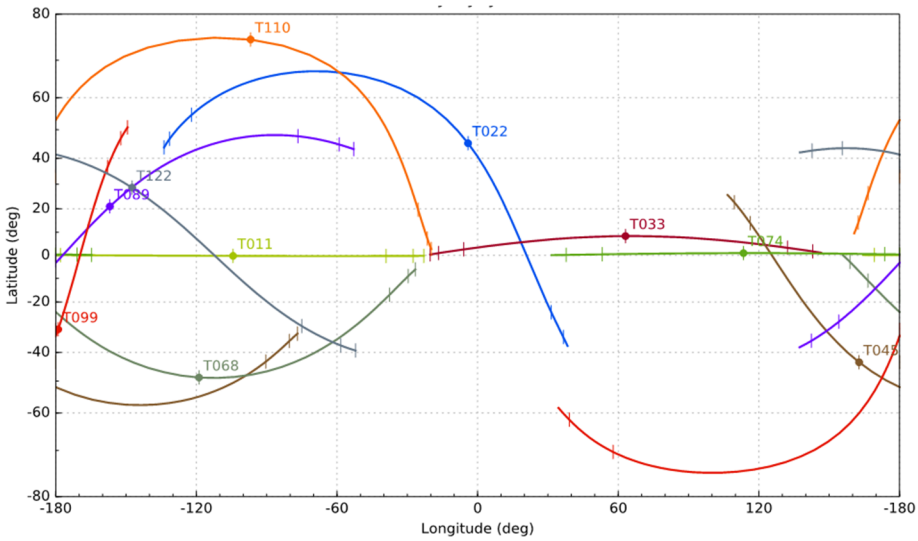

Figure RSS-4. Ground tracks of the 10 Titan gravity flybys showing uneven sampling of the moon's gravity. Each track corresponds to a time window of 3-hours centered at C/A, with tick marks for 30-minute intervals. Lack of coverage on high latitude regions produce larger uncertainties in the reconstructed geoid on those regions.

Figure RSS-5 shows the distribution of the mean anomalies among the 10 flybys. With Titan's orbital eccentricity being about one-half that of our moon at 0.0288, this leads to the ratio of the tidal field at apocenter relative to that at pericenter being about 84%, allowing for considerable response.

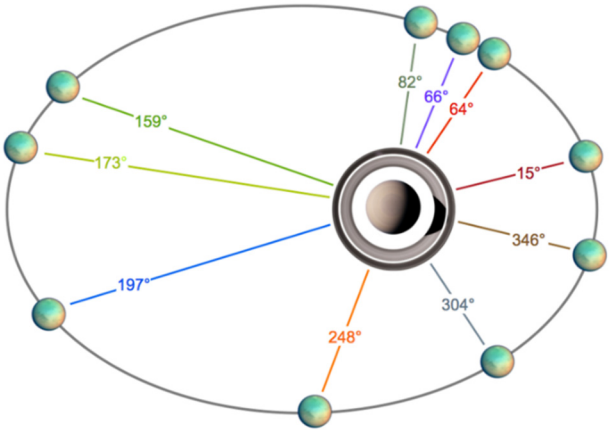

Figure RSS-5. Distribution of Titan mean anomalies of the 10 gravity flybys at the time of closest approach. Measuring Titan's gravity field at different mean anomalies allows a better determination of eccentricity tides (Love number k_2). If the tidal bulge has no phase lag, the tidal variation of the quadrupole gravity coefficients J2 and C22 peaks at pericenter (M = 0°) and apocenter (M = 180°).

Titan Gravity Results

The first four gravity flybys (T11, T22, T33, and T45) provided a determination of Titan's mass and gravity harmonics to degree 3. The quadrupole field was found to be consistent with a hydrostatically relaxed body shaped by tidal and rotational effects. The MOIF inferred from the Radau-Darwin equation is about 0.34, implying incomplete differentiation, either in the sense of imperfect separation of rock from ice or a core in which a large amount of water remains chemically bound in silicates. As has been suggested for Callisto, the proposed incomplete differentiation of Titan may have arisen because of a long accretion time (of order a million years), perhaps because both bodies are at large distance from the parent planet, measured in units of planet radii. The unexpectedly large MOIF has been interpreted in many ways, all ending up in a generally low core density consistent with hydrated silicates.

The equilibrium figure is a triaxial ellipsoid whose semi-axes a, b, and c differ by 410 meters (a–c) and 103 meters (b–c). The nonhydrostatic geoid height variations (up to 19 meters) are small compared to the observed topographic anomalies of hundreds of meters, suggesting a high degree of compensation appropriate to a body that has warm ice at depth. The construction of the geoid and gravity disturbances requires defining a reference ellipsoid. We define the reference ellipsoid as the equipotential surface around the sphere of radius equal to the mean radius of Titan, whose potential is composed of the sum of: (i) the gravitational potential produced by the monopole potential, $J_2^H = (10/3)C_{22}$, and C_{22} ; (ii) the tidal potential due to Saturn; and (iii) the rotational

potential. The equations and the values for the semi-axes of the reference ellipsoid (derived from SOL1 in Iess et al. [2010] are:

$$a = R_t\left[1 + \frac{14}{3}C_{22} + \frac{7}{6}q_r\right] = 2575.239 \text{ km},$$
$$b = R_t\left[1 - \frac{4}{3}C_{22} - \frac{1}{3}q_r\right] = 2574.932 \text{ km},$$
$$c = R_t\left[1 - \frac{10}{3}C_{22} - \frac{5}{6}q_r\right] = 2574.829 \text{ km},$$

for a reference radius R_t = 2575 km. The formal errors are less than 1 m. These values change by about the same amount if SOL2 [Iess et al. 2010] is adopted. A non-hydrostatic reference ellipsoid, constructed from the measured values of J_2 and C_{22}, would differ from the hydrostatic one by at most −9 m for SOL1 and only +0.2 m for SOL2. In both solutions $(a - c)/(b - c) \approx 4$, as expected for a synchronously rotating satellite in hydrostatic equilibrium subjected to the rotational and tidal deformation.

The axes of the reference ellipsoid are larger than the radii found from radar altimetry [Zebker et al. 2009] (a = 2575.15 ±0.02 km, b = 2574.78 ±0.06 km, c = 2574.47 ±0.06 km). The mean planetary radius (2574.73 ±0.09 km) determined by the Cassini radar is slightly smaller than the value of 2575 km adopted in gravity determinations. If this smaller value is used, the axes of the reference ellipsoid become 2574.969 km, 2574.662 km, and 2574.559 km. These values differ respectively by −181 m, −118 m, and +89 m from those determined from radar altimetry, a statistically significant difference especially for the long axis. This interesting discrepancy may stem from several mechanisms. Latitudinal changes of the ice shell thickness resulting from spatial variations of tidal heating [Tobie et al. 2012] and by the subsidence associated with the substitution of methane with ethane-rich liquids percolating into the crust which be composed of methane clathrate hydrates [Choukroun and Sotin 2012].

By combining radio tracking data acquired at different mean anomalies of Titan (see Figure RSS-5) Cassini RSS measurements detected the signature of the periodic stresses [Iess et al. 2012] induced by eccentricity tides. Precise measurements of the acceleration of the Cassini spacecraft during six close flybys between 2006 and 2011 (T11, T22, T33, T45, T68, T74) revealed that Titan responds to the variable tidal field exerted by Saturn with periodic changes of its quadrupole gravity, at about 4% of the static value. Two independent determinations of the corresponding degree 2 Love number yield k_2 = 0.589 ±0.150 and k_2 = 0.637 ±0.224 (2σ). Such a large response to the tidal field requires that Titan's interior is deformable over time scales of the orbital period, in a way that is only consistent with a global ocean at depth. The large value of k_2 points also to an ocean heavily enriched by salts, although the uncertainties are large. The large value of k_2 was confirmed by the yet unpublished analysis of the remaining gravity flybys (T89, T99, T110, T122).

Table RSS-4—from Iess et al. [2012] Table 1 and Table S3 (uncertainties are 2-σ.)—reports the estimated spherical harmonics coefficients for the unnormalized Titan gravity field (degree and

order 4). Eccentricity tides are also included in the model and described by the degree 2 Love number k_2 (last row).

The weak and not so well resolved higher degree gravity (3 × 3 and 4 × 4) was also used to attempt an estimate of the outer shell thickness [Hemingway et al. 2013]. The marked anticorrelation of the 3 × 3 gravity and topography was interpreted as an indication that Titan's ice shell is rigid (elastic thickness >50 km) and that several hundred meters of erosion/deposition have taken place over length scales of ~1000 km, suggesting aeolian transport. However, the gravity topography anti-correlation is much less evident in the latest results. Gravity-topography correlations (Figure RSS-6) were addressed by Mitri et al. [2014], who concluded that a 100 km thick outer ice I shell is underlain by a dense subsurface water ocean containing a high concentration of dissolved salts. The large correlation between the surface topography and the Bouguer anomalies are also consistent the presence of subsurface topographic features under the ice shell. Bouguer anomalies are produced by variations of the ice shell thickness where the surface topography is isostatically compensated. These authors concluded that the ice shell is typically thinner at the poles and thicker in the equatorial and middle latitude regions.

Durante et al. [2019] performed a subsequent analysis of Titan's gravity field and interior structure after Cassini. The results from less et al. [2012] indicated that Titan is subject to large eccentricity tides in response to the time varying perturbing potential exerted by Saturn. The magnitude of the response quadrupole field, expressed in the tidal Love number k_2, was used to infer the existence of an internal ocean. The new gravity field determination provides an improved estimate of k_2 of about 0.62, accurate to a level of a few percent. The value is higher than the simplest models of Titan suggest and the interpretation is unclear; possibilities include a high-density ocean (as high as 1300 kg/m^3), a partially viscous response of the deeper region, or a dynamic contribution to the tidal response. The new solution includes higher degree and order harmonic coefficients (up to 5) and offers an improved map of gravity anomalies. The geoid is poorly correlated with the topography, implying strong compensation. In addition, the updated geoid and its associated uncertainty could be used to refine the gravity-altimetry correlation analysis and for improved interpretation of radar altimetric data.

Table RSS-4. Estimated spherical harmonics coefficients.

	SOL1b Value ±1σ (× 10^6)
J_2	34.227 ±0.477
C_{21}	0.125 ±0.111
S_{21}	0.816 ±0.351
C_{22}	10.263 ±0.069
S_{22}	0.111 ±0.055
J_3	−1.635 ±0.838
C_{31}	0.681 ±0.207
S_{31}	−0.073 ±0.475
C_{32}	0.150 ±0.125
S_{32}	0.104 ±0.114

Table RSS-4. Estimated spherical harmonics coefficients.

	SOL1b Value ±1σ (× 10^6)
C_{33}	−0.221 ±0.016
S_{33}	−0.232 ±0.016
J_4	2.043 ±0.759
C_{41}	0.175 ±0.203
S_{41}	0.033 ±0.250
C_{42}	0.059 ±0.080
S_{42}	0.093 ±0.058
C_{43}	0.026 ±0.015
S_{43}	0.008 ±0.020
C_{44}	−0.007 ±0.002
S_{44}	−0.014 ±0.002
k_2	0.670 ±0.090

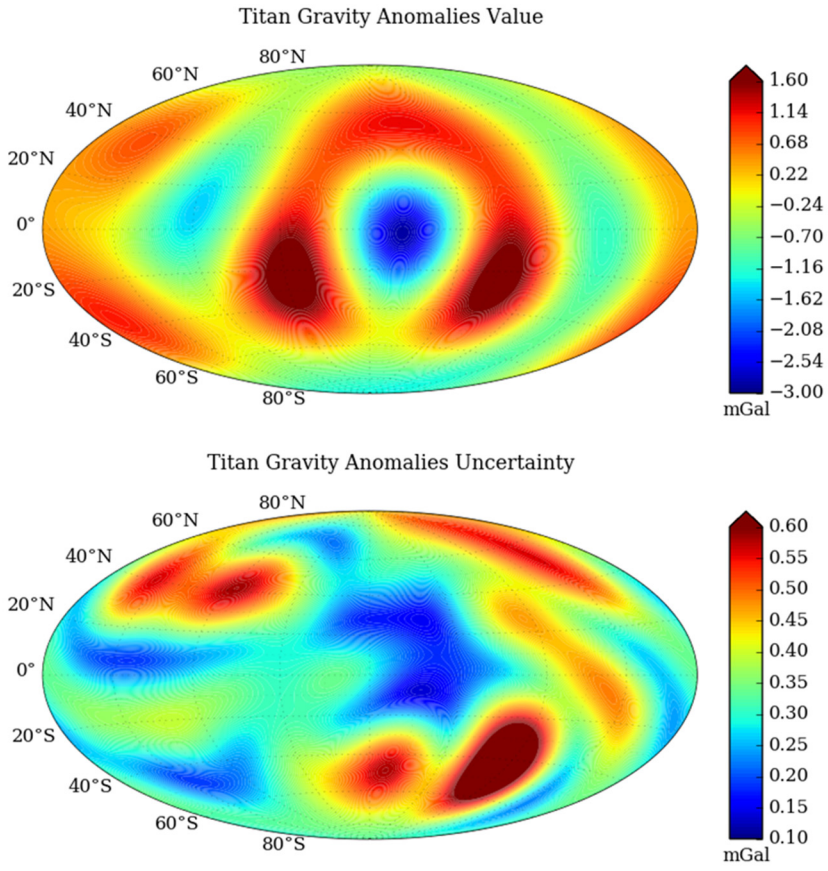

Figure RSS-6. Estimated gravity anomalies (*upper panel*) and related formal uncertainties (*lower panel*) from the analysis of the first six Titan gravity flybys (T11–T74 (4 × 4). The anomalies are computed in mGal over the reference gravity of the ellipsoid defined by the estimated monopole and quadrupole coefficients (GM, J_2, and C_{22}), the tidal field and the rotational state of Titan. Based on the solution SOL1.b from Iess et al. [2012].

Atmosphere

Titan is an interesting object to study, because it is a hybrid combining characteristics of Earth and Venus. Like Earth, its atmosphere is composed mainly of N_2 and it has a hygrological cycle, with methane assuming a role analogous to that of water on Earth. It has seasons, which are determined by the obliquity of Saturn, which is comparable to Earth's. On the other hand, Titan is a slow rotator, and its circulation is cyclostrophic—the winds aloft are globally much larger than the equatorial rotation of its surface, like Venus, but not at all like Earth, where the winds are much smaller than the equatorial surface rotation. Much of what we know about Titan's atmosphere initially came from the Voyager spacecraft flybys in 1980–1981. Although the Voyager soundings were limited, both spatially and in time (early northern spring), the small hemispheric thermal contrasts in Titan's tropospheres suggested that the seasonal response was muted there. In contrast, the large contrasts seen in the upper stratosphere suggested that there were large seasonal swings at those altitudes. A simple calculation of the radiative damping times at different atmospheric levels were consistent with these inferences, the response times being large in the lower atmosphere, and much smaller than the seasonal timescale in the middle atmosphere (stratosphere and mesosphere). The larger meridional temperature contrasts in the stratosphere implied strong zonal winds at these altitudes, especially in the colder northern hemisphere coming out of winter. The implied large seasonal variation expected in the upper stratosphere implied that there would be a large cross-equatorial transport of angular momentum from the northern hemisphere to the southern, as that hemisphere moved into its winter. Thus, there were many meteorological drivers to return to Titan (as Cassini did): first to observe the details of its hygrological cycle near the surface, but also to define better the global spatial structure of the atmosphere and also its seasonal behavior. The last offered a new probe to elucidate the maintenance of cyclostrophic wind systems, which are poorly understood. Titan brings the seasonality card to the analyst's table, which Venus lacks.

The review chapters by Flasar et al. [2014] and Lebonnois et al. [2014] summarize our current understanding of Titan's atmospheric temperature and wind structure, and its seasonal behavior, based in large part on Cassini observations.

There were 20 Cassini radio-occultation soundings of Titan's atmosphere (counting ingress and egress separately). These had relatively high vertical resolution, typically ~1 km through most of the atmosphere, decreasing in the lower troposphere, where differential refraction becomes important, to 10^2 m near the surface. With the failure of the Ultra Stable Oscillator in December 2010, the later occultations were executed in two-way mode. Here, the ground station transmitted a monochromatic signal at X-band to the spacecraft. Upon reception, the electronics onboard multiplied the received X-band signal by 880/749, generated S-band and Ka-band signals from this X-band signal by multiplying by 3/11 and 3.8, respectively, and coherently retransmitted the signal in S-band, X-band, and Ka-band back to Earth. Schinder et al. [2015] describe in detail how the experiment was set up and the received signal record analyzed.

The approach in analyzing radio occultations is to compare the frequency received at the Earth tracking station to what would be expected in the absence of the atmosphere of the target body through which the radio ray passes and is refracted. The difference is the residual frequency.

Knowing the geometry of the occultation, one can derive the bending angle of the ray, i.e., the angle between the incoming ray and that which exits the atmosphere. This can be inverted to retrieve a vertical profile of refractivity—for example, Kliore et al. [2004] and Schinder et al. [2011b]. For Titan, one can assume spherical symmetry in the inversion and use an Abel transform to invert the bending angle profile to retrieve refractivity. Saturn is oblate and the inversions requires ray tracing.

GLOBAL SPATIAL STRUCTURE OF ATMOSPHERIC TEMPERATURES AND ZONAL WINDS

VERTICAL AND MERIDIONAL STRUCTURE

Although the number of soundings were limited, the latitude coverage included high latitudes in both hemispheres, as well as a sampling of low and mid latitudes. Over half the soundings were obtained in northern late winter and early spring. Away from the surface, the troposphere showed little variation with latitude, consistent with the large radiative damping time. In the lowest few kilometers above the surface, variations on the order of a few kelvin appeared. In the northern winter and equinox seasons, variations were small in the summer hemisphere, and the largest variations were seen at high northern latitudes. Near the surface (at the base of the retrieved profiles), the temperature at 80° N was approximately 4 K cooler than at low southern latitudes. The tropopause region, near 40–50 km altitude, exhibited larger variations: high northern latitudes were 4 K cooler than temperatures at 30° S, for example, and even at high southern latitudes in late summer, tropopause temperatures were 2 K cooler [Schinder et al. 2012; Flasar et al. 2014].

Larger meridional contrasts were observed at higher altitudes, consistent with the decrease in radiative damping time. Again, during the northern winter-early spring season the largest contrasts were observed between low latitudes and high northern latitudes, up to 70 K between 100 km and 130 km altitude.

TRANSITION BETWEEN TROPOSPHERE AND STRATOSPHERE

The largest meridional thermal contrasts were observed in the winter/early spring hemisphere at high latitudes, where stratospheric temperatures were much colder than at other latitudes. However, the vertical structure of the transition between the tropopause region and the middle stratosphere—the transition between radiative damping times large compared to seasonal time scales and small damping times—was dramatic [Schinder et al. 2012]. At most latitudes, away from the winter polar region, temperatures above the tropopause region exhibited a rapid increase with altitude from 60 to 130 km, with the vertical gradient gradually becoming smaller at high altitudes. At the high northern latitudes in winter, the usual increase of stratospheric temperatures with altitude, abruptly changed at 80 km, with temperatures decreasing between 80 km and 100 km (by 10 K in the profile at 80° N). The effect decreases at lower latitudes in the winter hemisphere: near 50° N, the decrease has fallen to 1 K. At higher altitudes temperatures resume their increase with altitude, but offset from what one might have expected from the behavior of the temperate profile below 80 km in comparison with profiles observed at lower latitudes. In a manner of speaking, the temperature profiles have abruptly offset from lower

altitudes where there is little meridional (and seasonal) variation to higher altitudes, where these variations become larger. The temperature lapse rate in the transition is statically stable (subadiabatic). What causes it remains speculative, but a radiative origin might be a good guess. Composite Infrared Spectrometer (CIRS) spectra have suggested that organic condensates can form in the lower stratosphere at high latitudes in winter. They also indicate that these latitudes are rich in trace organic compounds that can act as effective radiative coolants. Possibly the increase in infrared opacity at these altitudes can affect the observed destabilization.

One of the most interesting results of the Huygens Doppler Wind Experiment was the minimum at 80 km in the vertical profile of the zonal wind at 10° S, which dipped to just a few meters per second. An analysis of the radio-occultation soundings, composited from 2006 to 2009 and based on the assumption of balanced flow, which relates the zonal winds to meridional gradients in geopotential heights along isobars, indicated that this minimum is global, i.e., it occurs over all latitudes. This is the same altitude, just described, for the abrupt destabilization in the temperature profiles, but only at high latitudes in the winter season. Whether this is coincidental remains to be determined. Possible sources could be damping by interaction of the mean flow with internal gravity waves, but a quantitative analysis remains to be done.

SURFACE TEMPERATURES AND PLANETARY BOUNDARY LAYER

LATITUDE DISTRIBUTION OF SURFACE TEMPERATURES

Because of the weak solar heating and the thickness of Titan's atmosphere (surface pressure ≈ 1.4 bar) the difference between surface temperature and that a few meters higher is expected to be small, so the contrasts discussed above likely hold for the surface itself.

Radio occultations have provided the only means from the Cassini orbiter to map temperatures in the lowest 1½ scale heights of Titan's atmosphere … .

VERTICAL STRUCTURE NEAR THE SURFACE

Radio occultations have provided the only means from the Cassini orbiter to map temperatures in the lowest 1½ scale heights of Titan's atmosphere [Kliore et al. 2004; Schinder et al. 2011b, 2012]. In the earlier part of the mission, when northern hemisphere was in winter and early spring, the occultation profiles had lapse rates in the lowest few kilometers that were close to adiabatic at in the southern hemisphere and at low latitudes in the northern hemisphere. Near 30° S the temperatures lay right on dry adiabats in the lowest 2 km, suggesting efficient vertical mixing from thermal convection. However, the dawn terminator profiles exhibit a more stable structure below the adiabatic layer within 200 m of the surface. This is reminiscent of the nocturnal inversions on Earth, where the surface cools more quickly than the overlying atmosphere during the night, and the atmosphere radiatively cools to the surface and forms a stable layer. However, radiative cooling on Titan is too inefficient to form such a layer over diurnal time scales (16 days), but a turbulent transport with a modest eddy diffusivity ~0.1 m^2/s would suffice.

At high latitudes in the winter hemisphere, temperature profiles become noticeably more stable at the lowest 5 km, being nearly isothermal in the lowest kilometer [Schinder et al. 2012]. Again, this probably reflects cooling to the surface, but over seasonal time scales. In this case, radiative cooling could affect the stable inversion, although turbulent diffusion could also play a role.

Seasonal behavior of temperatures and winds

Radio-occultation soundings near 65° N and S in 2014 and later, as the northern hemisphere moved toward the summer solstice and the southern toward winter, validated the inference of seasonal variation based on the observed meridional structure earlier in the mission. At 65° S the stratosphere above 80 km was rapidly cooling, at a greater rate at higher altitudes [Schinder et al. 2019]. The abrupt transition between 80 and 100 km that was observed at high northern latitudes was not yet evident. At 62° and 66° in the north, the sharp transition seen earlier at high latitudes was decaying, although a remnant persisted. Higher up, the temperatures had not yet attained the larger values seen in the southern hemisphere in late northern winter. Unfortunately, the Cassini tour did not extend a full half year, so a direct comparison that might provide evidence of hemispheric asymmetry is not possible.

Waves

As implied above, absorption of upwardly propagating waves (internal gravity and other types) could effect a drag on the zonal winds in the lower stratosphere, producing the observed minimum in the zonal winds. However, only preliminary analyses of the phase fluctuations (i.e., the small-scale fluctuations in the retrieved temperature profiles) has been done.

Ionosphere

Until the arrival of Cassini, the only direct information concerning the ionosphere of Titan came from the Voyager 1 radio occultation observation. After the careful reanalysis of the original data an electron density peak of about 2.7×10^3 cm^{-3} at an altitude near 1190 km for a solar zenith angle of 90° was found [Bird et al. 1997]. Now we have quite an extended collection of data about Titan's ionosphere from radio occultation, the Langmuir probe, and the ion-neutral mass spectrometer.

The first set of radio occultation observations by Cassini were published in 2009 [Kliore et al. 2008]. This paper presented eight electron density profiles. Figure RSS-7 shows the average of these profiles, along with the Voyager 1 and early Cassini Langmuir probe observations along with a 3-D magneto-hydrodynamic (MHD) model results. A fairly general agreement was found in that there was a density peak in the range of about $2–4 \times 10^3$ cm^{-3} at an altitude near 1200 km. There is a shoulder in the observed densities around a 100 km, which is very likely due to photoionization by soft X-rays. Both the entry and exit T31 results indicated a statistically significant secondary electron density peak near 500 km. Theoretical modeling by Cravens et al. [2008] indicate that ion

precipitation is quite possibly the source of this, somewhat intermittent, secondary peak. Further occultation results were presented in a subsequent paper [Kliore et al. 2011]. This paper presented data from 13 observations obtained by that time (overall only five more profiles were obtained during the lifetime of Cassini and these results were also submitted to the PDF and were similar to previous and published results). The peak electron densities of three of the observed electron density profiles were found to be significantly greater than the average of the others. Using the measured Cassini Plasma Spectrometer (CAPS) Electron Spectrometer (ELS) energetic electron spectra it was shown that these higher peak densities are very likely the result of electron impact ionization.

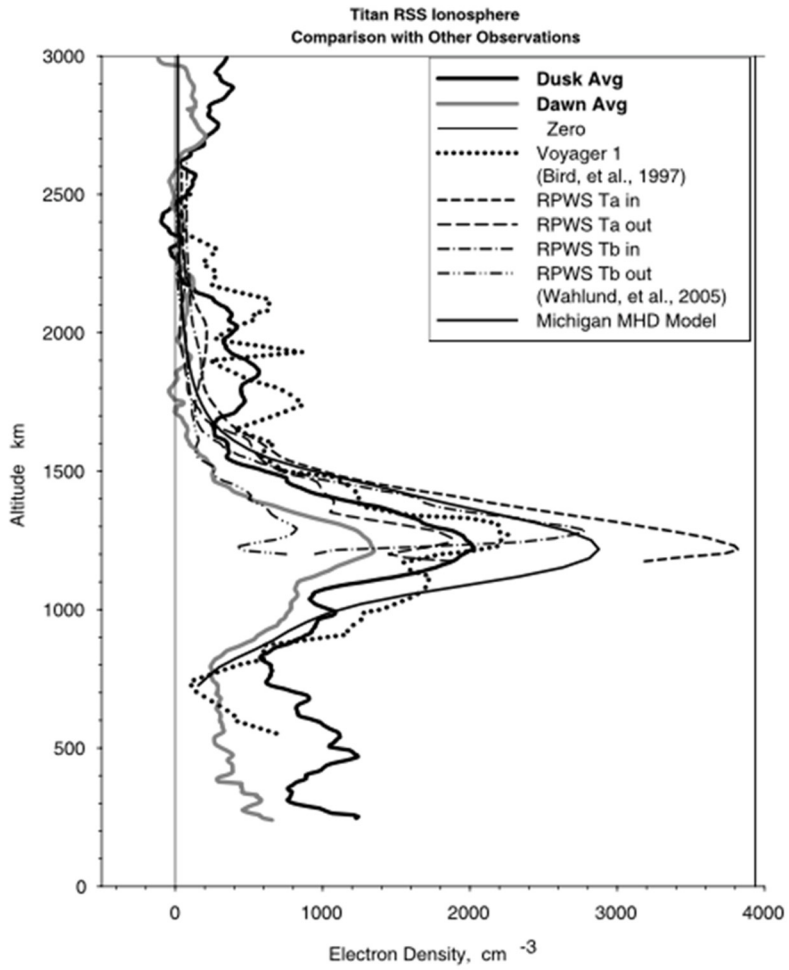

Figure RSS-7. Vertical profiles of electron density from Titan RSS occultations, compared with other observations.

Titan surface scattering results

BSR is the active probing of planetary surfaces by oblique reflection and scattering of microwave signals. Such observations provide statistical information on root-mean-square (rms) surface

slopes and on dielectric constant and density at scales comparable to the radio wavelength (centimeters to meters). An unmodulated radio signal, transmitted from the spacecraft, is scattered by the surface, and the echo is received at a ground station on Earth. A direct signal (from the spacecraft) is often received at the same time, providing a frequency reference for the echo. Fjeldbo [1964] utilized physical optics theory to explain the specular component of the echo as an aggregation of mirror-like reflections from properly oriented elements of the undulating surface. For typical spacecraft transmitters of 1–100 watts, surface echoes as small as 1 zeptowatt (10^{-21} W) can be detected. BSR experiments have been carried out on the Moon, Venus, Mars, and Titan using Soviet, U.S., and European spacecraft [Simpson 2007].

Differential Doppler effects between the direct and reflected paths separates the received echo from the carrier. Dispersion of the echo itself, caused by differential Doppler within the reflecting region, provides a measure of the rms slope of the undulations. Where echo dispersion is not large, the Doppler difference between the two primary paths can be used to infer large-scale topography of the surface. An incident signal with known polarization will generate a reflected signal with both the original and orthogonal components; application of Fresnel reflection theory to absolutely calibrated echoes in one polarization or to relatively calibrated echoes in orthogonal pairs can be used to recover the dielectric constant of the surface material. A simple model relating dielectric constant to porosity then allows estimation of material density.

The first Cassini detectable X-band RS bistatic echoes from Titan's surface were observed on flyby T14 on May 20, 2006 (DOY 140) (Table RSS-5), making Titan the most distant solar system object for which bistatic echoes were successfully detected. The echoes were weak but clearly detectable. Right circularly polarized sinusoidal signal was transmitted by Cassini and both the right and left circularly polarized (RCP and LCP) surface reflected components were observed at the 70 m station of the DSN at Madrid, Spain, Deep Space Station (DSS)-63).

Table RSS-5. Cassini Bistatic Radar Experiments

Start Date	Data Set	Target
2006-03-18	CO-SSA-RSS-1-TBOC1-v1.0	Titan
2006-05-20	CO-SSA-RSS-1-TBOC2-v1.0	Titan
2007-03-25	CO-SSA-RSS-1-TBOC3-v1.0	Titan
2007-07-18	CO-SSA-RSS-1-TBIS1-v1.0	Titan
2008-11-03	CO-SSA-RSS-1-TBOC4-v1.0	Titan
2009-03-27	CO-SSA-RSS-1-TBIS2-v1.0	Titan
2009-04-04	CO-SSA-RSS-1-TBOC5-v1.0	Titan

Cassini was maneuvered continuously to track the region of Titan's surface where mirror- like (quasi-specular) reflected signals may be observed. The ground receivers were tuned to compensate for the large Doppler shift due to relative spacecraft-Titan-Earth motion, allowing detection of the echoes near the center of the recording bandwidth (Figure RSS-8 and Figure RSS-9).

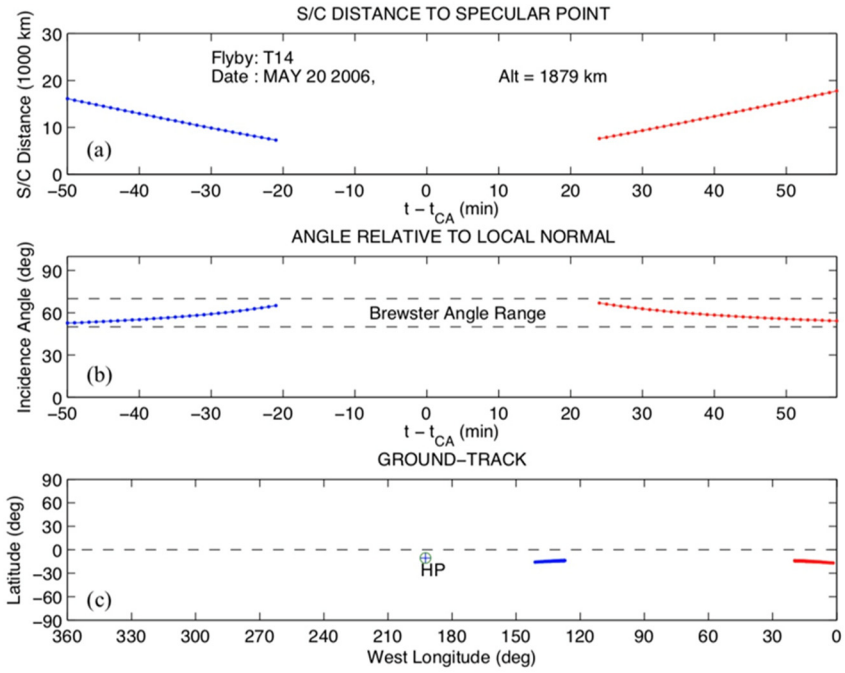

Figure RSS-8. *Panel (a)* and *Panel (b)* depict selected geometry parameters of the Cassini T14 observations and *Panel (c)* depicts the corresponding ground tracks. The Huygens Probe landing site is shown for reference purposes.

The experiment was designed to probe incidence angles θ close to the Brewster, or polarization, angle of likely surface compositions. Careful measurements of the system noise temperature allowed determination of the absolute power in each polarized echo component and, hence, their ratio. The polarization ratio, the known observation geometry, and Fresnel reflectivity were then used to determine the dielectric constant ε.

The T14 surface echoes were detectable on both the inbound and outbound sides, but were intermittent along the ground tracks, suggesting mostly rough terrain occasionally interrupted by patches of relatively flat areas. Polarization ratio measurements were obtained for two localized surface regions of similar latitude ~15° S, well separated longitudes ~14 and ~140° W, and incidence angle θ ~56° and ~64°, respectively. For both regions, the measurements implied surface dielectric constant ε ~1.6, suggesting liquid hydrocarbons, although alternative interpretations are possible [Marouf et al. 2006, 2008].

In Figure RSS-8 panel (a) and panel (b) depict selected geometry parameters of the Cassini T14 bistatic scattering observations. The parameters are plotted versus time relative to closest approach. Inbound (blue) and outbound (red) bistatic observations were implemented before and after the T14 ionospheric/atmospheric occultation (the empty gap in both panels). Panel (c) depicts the corresponding ground tracks. The Huygens Probe landing site is shown for reference purposes. The polarization ratio measurements were obtained for two localized surface regions of similar latitude ~15° S, well separated longitudes ~14 and ~140° W, and incidence angle θ ~56° and ~64°, respectively.

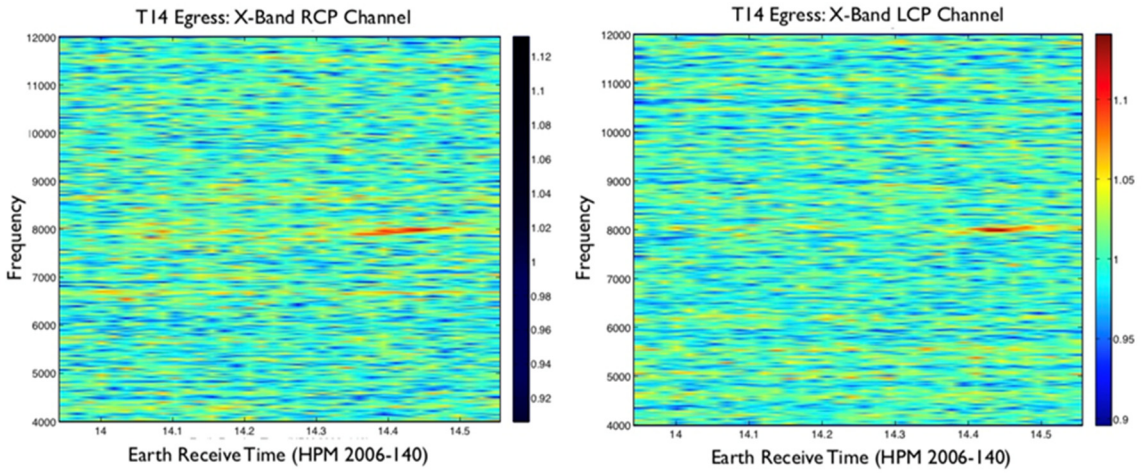

Figure RSS-9. Uncalibrated spectrograms of the first positive detection of bistatic echoes from Titan surface observed on the T14 flyby on May 20, 2006 (DOY 140). The weak echoes were simultaneously detectable in both the RCP and LCP 16 kHz bandwidth X-band channels of the 70 m ground station of the Madrid, Spain DSN complex (DSS-63).

Open questions

Ionosphere

It would be desirable to have more measurements at Titan to enable further examination of the lower ionosphere, which direct measurements cannot probe.

Gravity

The Cassini-Huygens mission provided answers to many key questions on Titan's interior structure. Titan is now a full-fledged member of the Ocean Worlds family, with a low-density core possibly in direct contact with silicates [Castillo and Lunine 2010]. However, major unsolved mysteries remain to understand its interior structure and the exchange processes between the interior, the surface and the atmosphere [Nixon et al. 2018].

The physical mechanism underlying the discrepancy between the gravity equipotential and the global shape is still an open question. The depth of the ocean and the thickness of the outer icy shell remain vaguely determined. Another unsolved mystery is whether the silicate core is in contact with the deep-water ocean, providing an interface similar to the terrestrial seafloor, one of the places where life may have emerged on Earth. Ruling out the existence of a high-pressure ice layer between the core and the ocean would have important consequences for the life-hosting potential of the moon.

Exchange mechanisms between the deep interior and the surface/atmosphere are certainly at play, but Cassini-Huygens has not provided clues on the nature, the extent and timing of these

processes. Whether or not ice convection is taking place in the icy shell is still an unresolved question. No active volcanism has been detected. The presence of methane into Titan's atmosphere requires geologically recent exchange between the interior and the atmosphere, as methane is irreversibly transformed in the atmosphere and its presence requires a supply mechanism. Similar arguments hold for ^{40}Ar, which is found in the atmosphere although its origin is in the decay of ^{40}K contained in the silicates.

Saturn Science

Atmosphere

INTRODUCTION

Saturn's oblateness, a result of its self-gravitation and rapid rotation, is sufficiently large that the usual Abel transform used to analyze spherical atmospheres, cannot be used to retrieve vertical profiles of refractivity from the bending angle ray as it traverses the atmosphere (leading to density, pressure, and temperature). This is particularly true in the troposphere, where refraction of the radio signal as it passes through the atmosphere becomes large. The difficulty emerges because the ray bends toward the local gradient in refractivity (or density in an atmosphere with uniform composition), and not toward the center of the planet, as would be the case with spherical symmetry. This means that the inversions must use ray tracing to retrieve refractivity profiles from the residual Doppler frequency.

Inverting the occultation data requires some assumption of symmetry. The assumption of at least local spherical symmetry is generally used for most atmospheres, but that doesn't work for rapid rotating oblate atmospheres. Here, the assumption used was that the atmosphere was axisymmetric and barotropic, i.e., the mean zonal winds were assumed to only vary with cylindrical radius. In this case, the resulting surfaces of constant density, pressure, temperature, and geopotential height coincide, and the inversion becomes tractable [Schinder et al. 2011a]. Of course, observations from remote-sensing instruments, like CIRS indicate that Saturn's atmosphere is baroclinic, particularly at low latitudes. One can use the occultations to check for consistency and obtain some measure of the error that the assumption of a barotropic atmosphere in the ray tracing introduces.

As with Titan occultations, those of Saturn after December 2010 needed to be done in the two-way mode, described earlier.

There were over 50 occultation soundings from Cassini, spanning low and high latitudes in both hemispheres.

THERMAL AND ZONAL-WIND STRUCTURE

Most of the analysis so far has concentrated on the equatorial region, where there are a large number of soundings within 10 degrees of the equator. The zonal winds can be derived assuming balanced flow, in which the meridional gradient of equipotential height is proportional to the mean zonal wind. A priori, there is no reason why the balanced flow relation does not hold down to the equator, but because the winds are proportional to 1/sin (latitude) in the geostrophic approximation, errors in the geopotential height magnify as one approaches zero latitude. The advantage of radio occultation soundings stems from the ability to refer the retrieved profiles to altitude (or planetary radius). This is possible since a reference body is tracked, namely the virtual image of Earth on the limb. Other remote-sensing instruments, like CIRS, cannot do this, unless they are in an occultation mode, for example tracking a star. In general, they can only obtain a temperature-pressure profile, and must impose a boundary condition, usually at a lower boundary. This becomes complicated in the thermal wind relation, because vertical gradients in the zonal wind must be along cylinders concentric with the rotation axis, rather than truly vertical, as is the case at higher latitudes.

The advantage of radio occultation soundings stems from the ability to refer the retrieved profiles to altitude (or planetary radius).

Retrieving zonal winds from the gradient wind balance first required applying a low-pass filter to the vertical profiles, to avoid small-scale fluctuations, perhaps from waves, from confusing meridional gradients. Then, to allow for the fact that the occultation soundings are not that densely distributed, the meridional distribution was smoothed. The results were encouraging: a vertical oscillation in the zonal winds was observed with a separation of ~2 pressure scale heights between maxima and minima, with peak-to-peak values of ~200 m/s, which is substantial.

SATURN'S SHAPE

Vertical profiles of pressure versus radius were retrieved from all radio occultation soundings, assuming a barotropic atmosphere and winds derived from cloud tracking, as described above. The shape of an isobar depends both on the gravitational potential and the centrifugal potential associated with the atmospheric rotation. The former is calculated using the measured J_n coefficients obtained from two-way radio Doppler tracking. Note that the partitioning between atmospheric winds and any assumed uniform interior rotation is not important, because what the cloud tracking measures are transit times across the visible disk, in other words the total angular rotation of the atmosphere, which determines the centrifugal potential in the atmospheric shell probed by the occultation soundings. With the retrieved profiles at latitudes spanning much of Saturn, the radius of the 1 bar and 1 mbar surfaces were determined as functions of latitude. Were the actual atmosphere barotropic corresponding to the wind model used, then the retrieved pressure surfaces would correspond to that used in the ray tracing. Instead, the retrieved pressures deviated from the model—which used the Voyager winds given by Sanchez-Lavega et al. [2000]—

by ±15 km, which is small compared to Saturn's pressure scale height at these altitudes, ~50 km. Currently the calculation is being redone using the Cassini winds reported by Garcia-Melendo et al. [2011].

Equatorial Oscillation

One of the interesting results from Cassini and ground-based observations is that Jupiter and Saturn exhibit quasi-periodic oscillations in the equatorial stratosphere similar to those observed on Earth. The ground-based observations provided a lengthy time record of several decades, but with limited vertical resolution. Cassini observations provided much more detailed vertical resolution, showing that the equatorial stratosphere consisted of alternating layers of warmer and colder regions. On Saturn, these were two pressure scale heights apart (~100 km). Because of thermal wind balance, these warm and cold anomalies are associated with peak to peak variations in the zonal winds with altitude of ~200 m/s. This structure appears to be zonally symmetric. Cassini observations enabled one to study the temporal evolution of this structure. The equatorial radio occultation soundings, separated by 4–5 years, showed that the pattern descended, but not in a rigid pattern [Schinder et al. 2011a]. This is reminiscent of the situation on Earth, where the oscillation is driven by the absorption of vertically propagating waves with eastward and westward zonal phase velocities.

Waves

Little quantitative analysis of the small-scale structure in the vertical profiles of temperature and pressure has been completed, but it is clearly of interest for studying phenomena like the equatorial oscillation.

NH_3

The extinguishing of the radio occultation signal around 1–2 bar results from a combination of refractive defocusing and absorption by species with large microwave opacities: NH_3, PH_3, etc. This area has yet not received much analysis.

Helium

The tropospheric helium abundance can be determined by using CIRS infrared spectra in the far infrared, using the collision-induced absorption in the translation continuum, and S(0) and S(1) lines of H_2. Helium does not absorb but affects the induced dipole moment of H_2. This analysis can be performed using CIRS spectra alone, but it is consistent with a wide range of helium mole fractions. A more sensitive approach is to combine radio occultations with thermal infrared spectra. For atmospheres with uniform composition, temperatures are proportional to the molecular mass. One can compute synthetic infrared spectra using retrieved occultation temperature profiles for various

assumed masses. The difficulty here is that this approach is that the inferred He mole fraction is smaller than interior modelers predict, which is not easily explained. No obvious systematic errors have been identified in the radio-infrared technique. This work is currently being prepared for publication.

Ionosphere

Until Cassini began to orbit Saturn the only information we had available concerning Saturn's ionosphere came from a handful of decades old radio occultation measurements of electron density profiles by Pioneer 11 and Voyager 1 and 2. Over the lifetime of the Cassini mission over 60 radio occultation observations were carried covering a latitude region from near the equator to 72°.

The results of the early radio occultation observations (12 profiles) were published in 2006 [Nagy et al. 2006]. The resulting electron density profiles all correspond to low latitudes (< 10°) and as all such observations at Saturn were within a few degrees of the terminator as a result of orbital geometry. There were significant orbit to orbit variations observed, an in order to see if noticeable differences existed between dusk and dawn observations averages were obtained as shown in Figure RSS-10. The mean peak densities for the dusk and dawn conditions are about 5.4×10^3

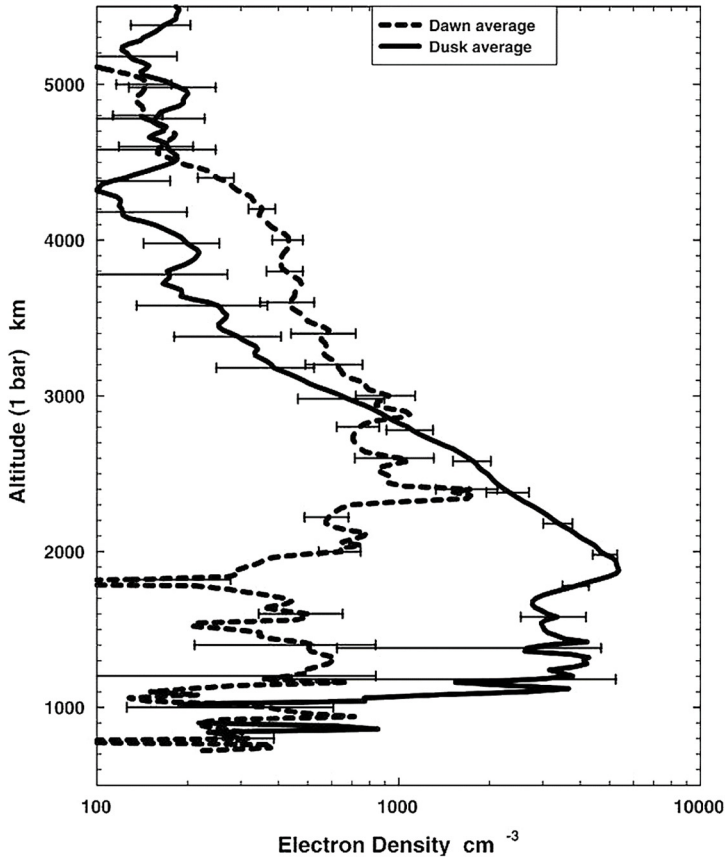

Figure RSS-10. Weighted averages of dusk and dawn electron density profiles.

and 1.7 × 10^3 cm^{-3} and the altitudes of the peaks are at about 1880 and 2360 km, respectively. The measured solar zenith angle for the dusk cases is 95.1 while it is 86 degrees for the observations. The model calculations have indicated that the main ion below and near the peak is H_3^+ and the lifetime of these molecular ions is short, less than a few hundred seconds and thus significant decay is plausible during the five hours of Saturn's nighttime. The decrease in the peak density and the increase in the height of the peak are consistent with such a decay. As the ionosphere decreases at night, it is the bottomside which decreases more rapidly, where the loss rates are higher. This can explain the decrease in the peak density and the rise of the peak height.

The mean observed topside scale heights for the dusk and dawn occultations are about 500 and 1230 km, respectively. It is very dangerous to assume that the topside is in diffusive equilibrium and that temperature gradients are negligible, however at that time there was no information on the plasma temperature and ion composition, thus the scale heights were used to make some estimates on the temperature. Assuming that H^+ is the major topside ion at dawn, the dawn scale height indicates a plasma temperature of about 625°. This value is not inconsistent with the Langmuir probe electron temperature measured during the proximate orbits [Wahlund et al. 2017]. If one assumes that the dusk temperature is at least as large as the dawn one, one arrives at a mean ion mass of about 2.46, which in turn implies the presence of about 72% H_3^+ or 7.7% H_3O^+ or other possible molecular ions; this is also not inconsistent with the Ion and Neutral Mass Spectrometer (INMS) results from the proximal orbits [Waite 2017].

The results of all (except for four, which will be analyzed in the future by Paul Withers, PhD, Boston University) ionospheric radio occultations were published in 2014 [Kliore et al. 2014]. Table RSS-6 shows important aspects of these results, along with numerous relevant parameters. Early indications that the electron densities increase with increasing latitudes was reconfirmed with these more complete results. The original idea to explain this trend was that particle impact ionization increases with latitude and plays a more important role in the total ionization rate [Kliore et al. 2009].

Table RSS-6. Summary of Cassini Radio Science Results on the Saturn Ionosphere.

Orbit ID	Year and Day	Peak Altitude (km)	Peak Electron Density (cm^{-3})	SZA (deg)	Latitude (deg)	L Shell (RS)	EPS Angle (deg)	Ionopause Height (km)	TEC (cm^{-2})	Ring Connection
7N	2005 123	1326.3	6693.5	84.4	−4.9	1.0074	75	6512	8.356E+11	—
7X	2005 123	2472	2215.7	95.9	−9.0	1.0251	75	4808	2.751E+11	—
8N	2005 141	1312	9469.1	85.2	−3.1	1.0029	58	6320	1.013E+12	—
8X	2005 141	1792	1339.4	95.1	−8.3	1.0213	58	5344	2.526E+11	—
9X	2005 159	1168	1688.6	93.8	−7.5	1.0173	41	4728	1.092E+11	—
10N	2005 177	1913.4	7736.1	87.7	1.6	1.0008	25	3640	6.785E+11	—
10X	2005 177	2409.6	1481.3	92.4	−6.1	1.0114	25	5232	3.628E+11	—
11X	2005 196	2528	4287.6	90.8	−4.5	1.0062	8	4096	1.121E+12	—
12N	2005 214	1379.4	10783.9	90.9	7.5	1.0173	9	3144	8.649E+11	—

Table RSS-6. Summary of Cassini Radio Science Results on the Saturn Ionosphere.

Orbit ID	Year and Day	Peak Altitude (km)	Peak Electron Density (cm^{-3})	SZA (deg)	Latitude (deg)	L Shell (RS)	EPS Angle (deg)	Ionopause Height (km)	TEC (cm^{-2})	Ring Connection
12X	2005 214	1326	546.1	89.1	−2.6	1.0021	9	2160	2.993E+11	—
13X	2005 232	2921.9	925.5	87.6	−0.5	1.0001	26	5072	2.131E+11	—
14N	2005 248	1712	12606.9	93.3	−8.4	1.0218	41	3280	7.428E+11	—
28N	2006 260	1360	7965.9	93	−4.3	1.0049	36	3408	1.013E+12	—
44N	2007 130	3032	19028.2	80.4	72.0	10.4721	96	7888	2.806E+12	—
44X	2007 130	1664	757.4	95.5	3.5	1.0037	96	3400	8.343E+10	—
46N	2007 162	2274	11671.2	85.2	−4.1	1.0051	65	7888	4.823E+11	—
47X	2007 179	2637.2	12217.5	94.4	−35.4	1.5050	51	9840	1.964E+12	C
51N	2007 297	2264	2719.8	92.4	−28.4	1.2924	60	6728	9.953E+11	C
51X	2007 297	2916	9466.7	85	−37.9	1.6060	60	9136	1.428E+12	B
54N	2007 353	1456	9615.3	94.3	−14.5	1.0669	114	3160	8.662E+11	—
54X	2007 353	2382	21567.7	85.5	−65.6	5.8598	114	9952	5.073E+12	E
56X	2008 15	2178.4	18436.9	89.6	−68.9	7.7162	141	9920	2.868E+12	E
58X	2008 39	1656	20864.5	89.9	−70.6	9.0636	165	9808	3.573E+12	—
68N	2008 138	1960	8071.5	83.8	23.3	1.1855	101	6552	1.837E+12	D
68X	2008 138	2376	11098.3	90.1	−60.8	4.2016	101	11960	3.037E+12	E
70N	2008 153	2376	2733.5	83.9	37.0	1.5678	86	5144	8.707E+11	B
70X	2008 153	2346.1	10769.6	90.4	−65.1	5.6411	86	10600	1.645E+12	E
72N	2008 168	1672	4803.6	84.2	35.3	1.5013	74	7616	9.005E+11	C
72X	2008 168	2400	14289.4	90.1	−62.9	4.8188	74	9760	2.444E+12	E
73X	2008 175	2472	26192.9	89.9	−61.5	4.3921	67	7328	3.215E+12	E
75N	2008 189	1128	11635.6	85.3	30.0	1.3333	54	9392	1.275E+12	C
75X	2008 189	2184	13083.4	89.5	−57.7	3.5022	54	11336	1.797E+12	E
120N	2009 305	2328	7510.8	93.8	28.5	1.2948	43	5368	1.227E+12	C
120X	2009 305	3216	5140.5	87.6	20.8	1.1443	43	9560	1.391E+12	D
121X	2009 324	2796.1	7090.8	87.1	25.2	1.2214	86	6056	5.138E+11	D
122N	2009 343	2460	5145.2	95.6	41.4	1.7773	80	6648	6.857E+11	B
122X	2009 343	1810.6	16447.2	86.9	29.7	1.3253	80	5488	2.175E+12	C
123X	2009 360	2076.8	4984.6	84.8	1.5	1.0007	96	5256	4.491E+11	—
125N	2010 26	1477.6	5994.6	94.5	−1.4	1.0006	127	8024	2.178E+12	—
125X	2010 26	1888	1540.4	85.5	2.1	1.0013	127	5432	9.119E+11	—
130N	2010 117	1594	10034.2	86.3	17.2	1.0958	145	9920	1.128E+12	—
130X	2010 117	1498.7	24059.9	92.7	12.7	1.0508	145	8344	7.776E+11	—
133N	2020 170	1835.4	6772.3	84.6	−0.4	1.0000	97	4640	5.960E+11	—
133X	2020 170	1309.3	752.3	95.4	0.3	1.0000	96	1464	2.074E+11	—

Table RSS-6. Summary of Cassini Radio Science Results on the Saturn Ionosphere.

Orbit ID	Year and Day	Peak Altitude (km)	Peak Electron Density (cm^{-3})	SZA (deg)	Latitude (deg)	L Shell (RS)	EPS Angle (deg)	Ionopause Height (km)	TEC (cm^{-2})	Ring Connection
135N	2010 205	1685.9	14783.4	86	−13.5	1.0576	64	4856	6.295E+11	—
137N	2010 245	1640	6069.6	87.6	3.8	1.0044	27	4112	6.920E+11	—
151N	2011 213	1624	5571.8	86.5	48.3	2.2597	69	8024	9.328E+11	A
151X	2011 213	2288	6003.3	93.5	40.3	1.7192	69	6176	8.879E+11	B
167N	2012 157	1492.7	7161.7	85.6	4.7	1.0068	133	3888	9.214E+11	—
170N	2012 225	2248	6594.0	89.7	−60.4	4.0987	70	4648	1.803E+12	E
170X	2012 225	1384.9	330.4	95	−1.0	1.0003	70	1896	1.833E+10	—
171N	2012 246	2048	6061.0	88.4	−44.6	1.9725	50	6446	1.546E+12	C. Div.
178X	2013 5	2368	4876.5	89.2	56.1	3.2146	70	6360	2.265E+12	E
180X	2013 31	2344	21488.9	90.4	66.1	6.0924	96	6456	3.774E+12	E
182X	2013 56	2256.8	24509.0	89.5	61.0	4.2546	121	6480	4.526E+12	E
189N	2013 130	2328	10294.0	90.8	−71.9	10.3606	168	6056	2.262E+12	—
190N	2013 140	2584	6246.8	91.3	−70.5	8.9745	159	8552	6.058E+12	—
191N	2013 151	2512	4940.6	93	−44.6	1.9725	149	3640	1.015E+12	C. Div.
191X	2013 151	1314.8	561.1	93.2	−10.2	1.0317	149	1968	2.960E+10	—

An alternate and/or supplemental suggestion was also raised in the 2014 paper [Kliore et al. 2014]. Connerny and Waite [1984] suggested that water inflow from the rings can rapidly convert H^+ into a molecular ion recombines dissociatively and, thus, lead to lower electron densities. The inflow of any other molecule, for example methane, will have the same effect. They called this the ring-rain effect. At that time, there was very little information on the presence of water, but the very little data on the presence and variation of stratospheric water abundances [Bjoraker 2013] was consistent with this suggestion. O'Donoghue et al. [2013] used the W. M. Keck Telescope to observe two bright H_3^+ rotational-vibrational infrared emission lines at Saturn. They reported that their observations was consistent with the so-called ring-rain suggestions of Connerney and Waite [1984]. They detected increased H_3^+ densities where the ionosphere is magnetically connected to the gaps between the rings. An attempt was made to see if this phenomena was noticeable with our ionospheric occultation results. There were only two observations corresponding to the Cassini Division and no noticeable effect was seen. It was somewhat surprising not to see such an effect if it is present, but it is important to note that the two possible opportunities do not provide a statistically meaningful answer.

Gravity

INTRODUCTION

The interior of Saturn is schematically separated into three layers: (i) a helium-depleted, molecular hydrogen envelope, where pressures reach the value of 2 Mbar; (ii) a metallic hydrogen layer, with pressures in the range 2–10 Mbar; and (iii) a heavy element core, with a mass in the range 5–20 Earth masses [Fortney et al. 2016]. Gravity, being determined by the internal distribution of masses, is the primary source of information in the construction of interior models of the planet. Saturn's magnetic field was also expected to provide important additional information, especially on the location of the envelope-metallic hydrogen boundary. If the H-He envelope is fully convective and well mixed, the atmospheric composition may give further constraints, distinct and complementary from those of gravity.

Saturn is a fluid and rapidly rotating planet whose internal mass distribution is largely driven by gravity and centrifugal forces.

Saturn is a fluid and rapidly rotating planet whose internal mass distribution is largely driven by gravity and centrifugal forces. The gravity field is therefore dominated by an axially and hemispherically symmetric component described by even zonal coefficients $J_{2n} \approx q^n$, where q is the ratio of the centrifugal and gravity acceleration at the equator. Deviations from this law are related to two effects: the radial density distribution, and differential rotation associated to flows in the envelope.

Determining the density distribution inside Saturn requires some assumptions on the equation of state (EOS). Due to the lower mass, the dependence of interior models on the assumed EOS is however less critical than for Jupiter. However, models suffer to some extent the uncertainty in rotation rate of the uniformly rotating deep interior.

Dynamical phenomena associated to zonal flows and differential rotation seen in optical images may generate peculiar perturbations in the gravity field. If the differential rotation associated to surface velocity is deep-seated, then internal dynamics affects the gravity field in two ways. Firstly, it perturbs the equipotential surfaces symmetrically, giving rise to a redistribution of mass that appears as a correction to the even zonal coefficients [Hubbard 1999] and a high degree field that does not follow the law $J_{2n} \sim q^n$. Secondly, any north-south asymmetry in the velocity field would necessarily lead to nonzero values for the odd zonal harmonics [Kaspi 2013]. Gravity results from the Juno mission at Jupiter verified these theoretical expectations and were interpreted as an indication of a diffuse core [Wahl et al. 2017] and a wind depth of 2000–3000 km [Iess et al. 2018; Kaspi et al. 2018]. Cassini has repeated these measurements at Saturn, revealing large differences between the two planets.

Another important result of Cassini gravity measurements during the GFO is the determination of the mass of the rings. This quantity, when combined with the percentage of silicate in the ice grains and with the dust flow (both measured by Cassini) can be related to the age of the ring system [Cuzzi and Estrada 1998]. While the masses of the A-ring and C-ring were determined with good accuracy from stellar occultations, the mass of the opaque B-ring remained matter of speculation. Prior to the GFO, Cassini's pericenter was always outside the A-ring, so that the gravitational effects of the rings on the spacecraft motion could not be separated from those of the oblateness of the planet. In the final phase of the mission, Cassini flew between the planet and the rings thus allowing to single out the gravitational pull from the B-ring.

Gravity observations during Cassini's Grand Finale orbits

The range rate of Cassini was the primary observable quantity for gravity determination. Range-rate measurements were obtained from the Doppler shift of a carrier sent from the ground at 7.2 GHz (X-band) and retransmitted back by the onboard transponder at 8.4 GHz. An auxiliary downlink at Ka-band (32.5 GHz) was also available. The nearly edge-on view of the GFO from Earth generated a particularly strong Doppler signature due to Saturn's gravity.

Of the 22 GFO (sequentially labeled as Rev271 through Rev293) six were selected for gravity measurements: Rev273, Rev274, Rev275, Rev278, Rev280, and Rev284. These orbits were chosen to minimize neutral particle drag and tropospheric noise (large spacecraft elevation at closest approach). Unfortunately, data near pericenter for Rev275 could not be used due to a configuration error at the ground station.

Cassini was continuously tracked through pericenter for 24–36 hours from the antennas of the DSN and from the ESA's ESTRACK antennas located in the southern hemisphere (Malargue, Argentina, and New Norcia, Australia). The gravity GFO represented a major coordination effort for the Radio Science group at JPL.

Two-way Doppler measurements at X-band make up 98% of the data. Noise from solar plasma was low due to the large solar elongation angle (> 142° on all six gravity orbits). The data quality was statistically equivalent in X-band and Ka-band data, with an RMS Doppler noise between 0.020 and 0.088 mm/s at 30 s integration time. The main characteristics of the gravity GFO are shown in Table RSS-7 and Figure RSS-11.

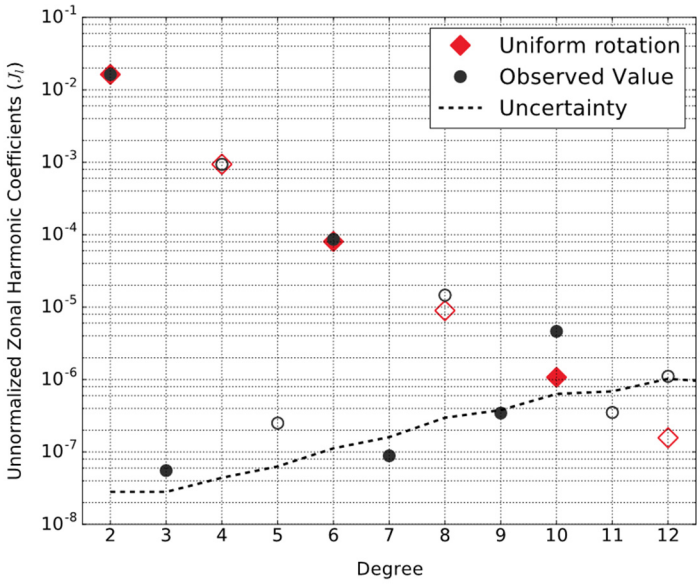

Figure RSS-11. Zonal gravity harmonic coefficients J_2–J_{12}. The dashed line shows the uncertainty from Table RSS-8. Positive values are marked as solid circles, negative values as empty circles. The red diamonds are the theoretical predictions for uniform rotation.

Table RSS-7. Parameters of the osculating orbit at C/A from the RSS reconstructed trajectory. Orbit inclination and C/A latitude are relative to the ring plane. The C/A altitude is relative to the Saturn 1 bar surface (equatorial radius of 60268 km, flattening of 0.09796). The reported noise level refers to the C/A pass only, for Doppler observables at 30 s integration time.

Parameter	Units	Rev273	Rev274	Rev278	Rev280	Rev284
Day (2017)		9 May	15 May	10 June	23 June	19 July
Eccentricity		0.92	0.92	0.92	0.92	0.92
Inclination	(deg)	63	63	62	62	62
EBO	(deg)	96	96	98	99	101
C/A altitude	(km)	2720	2668	3427	3409	2817
C/A latitude	(deg)	−5	−5	−6	−6	−7
SEP	(deg)	142	148	175	172	146
Noise RMS	(μm/s)	29	23	20	88	44

The X-band data were favored for our analysis because of the higher measurements signal to noise ratio (SNR) during ring occultation periods. As predicted, the radio link was lost when the line of sight passed through the densest region of the B-ring, causing a blockage of about 10 minutes. Diffraction and near-forward scattering resulted in a larger Doppler noise at Ka-band than X-band when the beam passed through the rings.

GRAVITY RESULTS

The gravity measurements carried out by Cassini during the Grand Finale orbits reveal a planet with many surprising features. Range rate measurements were successfully used to estimate the zonal field of the planet till degree 10 and the mass of the B-ring, as shown in Table RSS-8. Note: these are preliminary results; for authoritative results, refer to Iess et al. [2019].

Surprisingly, and differently from what was found on Jupiter by Juno, Saturn's gravity shows residual, unexplained, accelerations (at the level of 4×10^{-7} m/s^2) that affected the motion of Cassini and were detected by the Doppler tracking system. These accelerations were absorbed using three different models: stochastic accelerations, acoustic normal modes (zonal component only), and a static tesseral field. As the nature of the unexplained accelerations is unknown at the time of this writing, the stochastic model is preferred. A tesseral field must originate from deep-seated density anomalies in the region of uniform rotation in order to be seen as a static field over the two months of the gravity measurements. This cannot be excluded, although the magnitude of the accelerations and the large degree of the required field (from 8 × 8 to 12 × 12, depending on the assumed rotation period) militates against this hypothesis. In spite of these unexpected features, the solution for the zonal field and the ring mass, relevant for the interpretation, is stable and all parameters are sufficiently well determined.

Table RSS-8. Saturn's gravity harmonic coefficients (unnormalized; reference radius 60330 km) and B-ring mass (in units of Mimas' mass), obtained from the analysis of Cassini's Grand Finale gravity orbits. The uncertainties are 3-sigma for the zonal harmonics and 1-sigma for the B-ring mass.

	Value	Uncertainty
J_2 (× 10^6)	16290.573	0.064
J_3 (× 10^6)	0.059	0.023
J_4 (× 10^6)	−935.314	0.037
J_5 (× 10^6)	−0.224	0.054
J_6 (× 10^6)	86.340	0.087
J_7 (× 10^6)	0.108	0.122
J_8 (× 10^6)	−14.624	0.205
J_9 (× 10^6)	0.369	0.260
J_{10} (× 10^6)	4.672	0.420
J_{11} (× 10^6)	−0.317	0.458
J_{12} (× 10^6)	−0.997	0.672
B ring mass (M_m)	0.23	0.19

The main outcomes of gravity measurements [Iess et al. 2019] can be summarized as follows:

1. The even zonal harmonic coefficients J_6, J_8, J_{10} are so large that only a deep and intense differential rotation can explain their value. The analysis using two different methods (differential rotation on cylinders with the concentric Maclaurin spheroids and differential rotation with finite depth flows from the thermal wind equation) indicate that the flows extend to a depth of ~9000km and must involve a large

fraction of the mass of the planet. This differs from Jupier, where winds are shallower (~3000 km).

2. The favored EOS leads to a core mass in the range 15–18 Earth masses.

3. The mass of the B-ring is not very different from the Voyager-era expectations, pointing to a ring age in the range 10–100 million years. The estimate of the mass under different models for the unexplained accelerations is shown in Table RSS-9. The low value of the ring mass suggests a scenario where the present rings of Saturn are young, probably just 10 million to 100 million years old, to be consistent with their pristine icy composition. Nevertheless, the rings may have evolved substantially since their formation and were perhaps once more massive than they are today. Models for a young ring system invoke the chance capture and tidal disruption of a comet or an icy outer solar system body, suggesting that catastrophic events continued to occur in the solar system long after its formation 4.6 billion years ago.

Table RSS-9. Estimates of the ring masses for the three dynamical models (stochastic, tesseral field, normal modes), in units of Mimas mass (GM_M = 2.5026 km^3/s^2). The uncertainties are 1σ. The solution with the tesseral field shows larger uncertainties due to the large number of free parameters to be estimated. The reference solution (random accelerations) and the solution using normal modes are in good agreement. Although the masses of the three rings are highly correlated, their sum is well determined and consistent at the 1σ level.

	A-ring (M_M)	B-ring (M_M)	C-ring (M_M)	A+B+C-rings (M_M)
A priori	0.11	10.00	0.024	10.00
Random accelerations	0.15 ±0.11	0.23 ±0.20	0.024 ±0.024	0.41 ±0.13
8 × 8 field (10h 32min 45s)	0.14 ±0.11	0.16 ±0.31	0.025 ±0.024	0.32 ±0.27
12 × 12 field (10h 39min 22s)	0.17 ±0.11	0.10 ±0.46	0.024 ±0.024	0.29 ±0.43
10 × 10 field (10h 45min 45s)	0.16 ±0.11	0.43 ±0.37	0.025 ±0.024	0.62 ±0.34
10 × 10 field (10h 47min 06s)	0.17 ±0.11	0.16 ±0.38	0.024 ±0.024	0.35 ±0.35
f-modes	0.10 ±0.11	0.37 ±0.15	0.023 ±0.024	0.49 ±0.07
f- and p- modes	0.13 ±0.11	0.29 ±0.18	0.023 ±0.024	0.45 ±0.12
g- and f- modes	0.10 ±0.11	0.36 ±0.18	0.023 ±0.024	0.48 ±0.13

Open questions

We never got really high latitude occultations of Saturn. Non-radio science efforts includes quite a bit of modeling of Saturn's ionosphere given the proximal orbit observations. The loss of CAPS means that we have no direct information of the ion temperature in Saturn's ionosphere.

What accounts for the tesseral components of Saturn's gravity field?

What accounts for the differences between the overall structure of Saturn's and Jupiter's interior, as revealed by their gravity fields?

Enceladus Science

Gravity

After Titan, Enceladus has been the most observed satellite by the Cassini spacecraft during its exploration of the Saturnian system. Flybys of this small moon revealed a large plume ejected from the south-polar region, with the source being long fractures from which vapor and ice emerge as discrete jets [Spitale and Porco 2007]. Concurrent observations of sodium and potassium salts in the plume [Postberg et al. 2011], and the measured temperatures within the fractures [Spencer et al. 2006], strongly argue for the presence of liquid water in the subsurface source region. The plume exhibits a time variability well correlated to the predicted tidal stresses of the body [Hedman et al. 2013].

The endogenic (non-solar) power emitted from the south-polar region, derived from Cassini CIRS data, is 15.8 gigawatt (GW), with a 20% formal uncertainty [Howett et al. 2011]. This is equivalent to an average surface heat flux of about 20 mW/m^2 and is an order of magnitude larger than conventional estimates of tidal heating if Enceladus' current orbital eccentricity represents a so-called equilibrium resonant state with other satellites [Meyer and Wisdom 2007]. It indicates time-variability in its internal properties [Ojakangas and Stevenson 1986], in a resonant state with other nearby moons [Zhang and Nimmo 2009], or in the rate of heat transport. In any or all of these cases, a plausible internal structure is that of a liquid water ocean overlain by a (thermally conductive) crust [Howett et al. 2011].

Cassini Gravity Flybys and Data Analysis

The design of the Cassini spacecraft did not allow radio tracking from Earth during remote sensing observations. Therefore, only three of the 23 flybys of Enceladus have been used for gravity measurements. In these close encounters the spacecraft was continuously tracked from ground antennas while flying within 100 km of the moon's surface, twice above the southern hemisphere (in the flybys labeled E9 and E19) and once over the northern hemisphere (E12). Enceladus' quadrupole gravity field and degree-3 zonal harmonic coefficient J_3 were determined [Iess et al. 2014] from measurements of spacecraft range-rate. With a radius about 10 times smaller than that of Titan, and about the same density, the gravitational signature of Enceladus in Doppler measurements is much weaker than that of Saturn's largest moon. However, the small perturbation due to J_3 (about 0.2–0.3 mm/s) was still clearly detectable by the Cassini tracking system, whose accuracy was 0.02–0.09 mm/s on a time scale of $\tau \approx 60$ s.

Microwave links between the onboard transponder and ground stations of NASA's DSN enabled precise measurements of the spacecraft range-rate. In addition to gravitational forces, the RSS analysis accounted for the main non-gravitational accelerations, most notably neutral particle drag exerted by the substantial gas plume formed by the jets of the south-polar region. Flying by the moon at latitudes below −70°, the spacecraft interacted with the plume at distances up to 500 km from Enceladus' surface, although most of the effect is localized within 20 seconds from

closest approach. Given the uncertainties in the gas density along the spacecraft flight path, and the short time scale of the interaction, the effect of the drag could be modeled as an unknown, impulsive, vectorial acceleration at closest approach at E9 and E19. The orbital solutions yielded a velocity variation almost parallel to the spacecraft velocity, as expected for a drag force, of magnitude 0.25 mm/s for E9 and 0.26 mm/s for E19, comparable to the J_3 signature. The inclusion of the neutral particle drag in the south-polar flybys is therefore essential for obtaining Doppler residuals free of any signatures, essential for a faithful gravity solution.

As in other Cassini gravity analyses [Iess et al. 2010, 2012; Tortora et al. 2016] the solution for Enceladus' gravity field was obtained from a multi-arc analysis where all data from the three flybys were fitted using separate initial conditions for the spacecraft state vector at each arc (local parameters). The Enceladus state vector, the five degree-2 harmonic coefficients and J_3, were considered global parameters common to all arcs. To avoid biased estimates, the a priori uncertainties on the gravity coefficients were at least 30 times larger than the formal uncertainties obtained from the orbital solution. The non-gravitational accelerations due to anisotropic thermal emission from the three radioisotope thermoelectric generators and solar radiation pressure were modeled using values determined by the spacecraft navigation team from the past eight years of the Saturn tour. By processing the data into a multi-arc least squares filter, all local and global parameters were estimated (Table RSS-10). Furthermore, the solution was proven to be stable with respect to perturbations of the dynamical model, such as the estimation of a full degree-3 field.

The ratio J_2/C_{22} differs from the value required for hydrostatic equilibrium (J_2/C_{22} = 10/3), suggesting that the satellite is not in a fully relaxed shape. The equipotential surface of the tidal, rotational and gravitational potential (the latter limited to 2,0 and 2,2 harmonics) has semiaxis differences of $a–c$ = 6.00 km and $b–c$ = 2.07 km. The tesseral coefficients C_{21}, S_{21}, and S_{22} are null within 3σ, indicating that the adopted rotational model is correct and that the orientation of the principal axes is that expected for a tidally locked body with a fully damped pole. The estimated value of J_3 implies a 2.5 mGal, negative gravity anomaly at the south pole (Figure RSS-12).

Table RSS-10. Solution for the gravity field of Enceladus. Estimated gravity harmonic coefficients from the multi-arc fit of E9, E12, and E19 Doppler data.

Coefficient	Central Value ± 1σ
J_2 (× 10^6)	5435.2 ±34.9
C_{21} (× 10^6)	9.2 ±11.6
S_{21} (× 10^6)	39.8 ±22.4
C_{22} (× 10^6)	1549.8 ±15.6
S_{22} (× 10^6)	22.6 ±7.4
J_3 (× 10^6)	−115.3 ±22.9
J_2/C_{22}	3.51 ±0.05

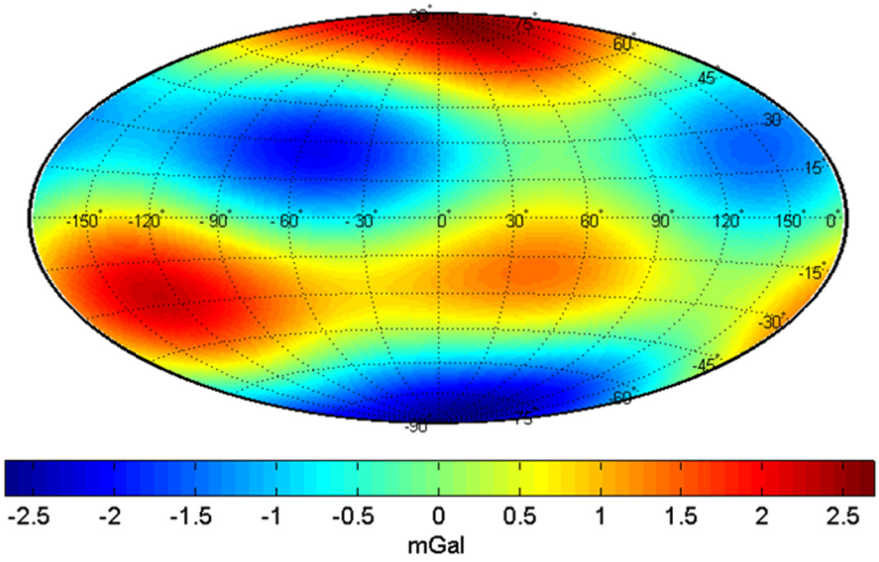

Figure RSS-12. The gravity field due to C_{21}, S_{21}, S_{22}, and J_3 as in Table RSS-10 is mapped onto the reference ellipsoid. The negative anomaly at the south pole, representing the asymmetry between the two hemispheres, is ~2.5 mGal.

INTERIOR MODELS

The interpretation of Enceladus gravity presented a greater difficulty and uncertainty than usual, given the strikingly different appearances of the northern and southern hemisphere, and the apparent confinement of endogenic activity to the high southern latitudes. Still, the deviation of J_2/C_{22} from 10/3 (the value for a laterally homogeneous body) is modest (of order 6%) and the non-degree 2 gravity is small (of order 2% relative to J_2), suggesting that there is some prospect of useful inferences.

The topography of Enceladus [Nimmo et al. 2011] is not that of a relaxed hydrostatic body under the action of tides and rotation in a synchronous orbit. Based on the global shape data which show a topographic depression at the south pole [Thomas et al. 2007], it has long been proposed that the liquid reservoir may be located only in the southern hemisphere [Collins and Goodman 2007], thus explaining why the activity is concentrated around the south pole [Tobie et al. 2008]. First interpretation of the topography and gravity data [Iess et al. 2014; McKinnon 2015] suggests that the ice shell is about 30–40 km thick at the south pole, and its thickness increases to about 60 km in the equatorial region. However, from these data alone, it is not possible to definitively conclude whether the ocean is global or only located in the southern hemisphere. More recently, the detection of a significant physical libration [Thomas et al. 2016] has indicated that the ice shell is mechanically decoupled from the rocky core, thus providing the first direct evidence for a global subsurface ocean. Thomas et al. [2016] have shown that the observed libration is consistent with an average ice shell thickness of 21–26 km, which is significantly less than the value predicted from gravity and topography. Čadek et al. [2016] show that the Cassini observations can be reconciled by considering isostatic compensation including the effect of a few hundred meter thick elastic

lithosphere. Their model predicts that the core radius is 180–185 km, the ocean density is at least 1030 kg/m^3, and the ice shell is 18–22 km thick on average. The ice thicknesses are reduced at poles decreasing to less than 5 km in the south polar region.

Interior modeling of Enceladus remains an active area of research and is important because its internal structure tells us about the thermal state, evolution, and energy budget of this ocean world.

Ionosphere

An unplanned opportunity to observe the Enceladus plume was discovered in a routine search, which indicated that the radio path will pass within a few hundred kilometers from Enceladus' south pole shortly before a scheduled Saturn occultation during orbit 125. The Cassini science engineers were able to adjust the orbit to obtain a plume occultation with the radio path passing about 45 km below the south pole. At the time of the passage of the Cassini radio line-of–sight (LOS) through the center of the plume, its velocity relative to Enceladus was about 13 km s^{-1}, and the distance of Cassini from Enceladus was about 577,400 km. The occultation was observed by two DSN stations near Canberra, Australia: (i) DSS-43 with a 70-m diameter antenna receiving S-band (~13 cm) and X-band (~3.5 cm) signals; and (ii) DSS-34 with a 34-m antenna receiving X-band and Ka-band (~1 cm) signals. The two frequencies from both stations were coherently differenced to obtain frequency data that is sensitive only to the electron plasma.

The differenced frequency residuals were inverted using an Abel integral inversion, cf. Kliore et al. [2004], for the case of circular cylindrical symmetry (with the axis of the cylinder being the north-south polar axis of Enceladus), to obtain the refractivity as a function of distance from the south pole axis, which then can be used to obtain the profiles of electron density shown in Figure RSS-13. This clearly indicates an electron density enhancement with a maximum density of

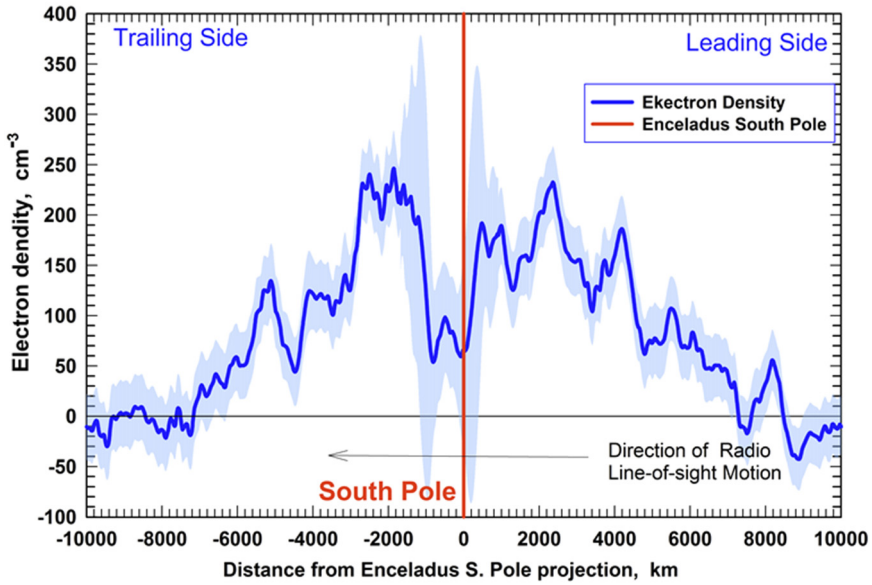

Figure RSS-13. RSS observations of Rev125 Enceladus occultation.

about 225 cm^{-3} on the entry (leading) side, at a distance of about 2000 km from the plume center, and approximately 245 cm^{-3} maximum density on the exit (trailing) side, also at a distance of about 2,000 km from the plume center, extending to about 7,000 km (~28 R_E), in both directions from the plume axis. A significant asymmetric drop in the electron density to about 50 cm^{-3} in the neighborhood of the Enceladus plume, beginning near the plume centerline on the leading side, and continuing for about 1,000 km on the trailing side, can also be seen clearly in the figure. A few smaller dips on both sides are also observable.

The Radio and Plasma Wave Spectrometer (RPWS) in situ observations [Morooka et al. 2011] based on both the Langmuir Probe and the upper hybrid emissions were taken along the E3, E4, E5, and E6 Cassini flybys, which were also close to Enceladus, but basically at right angles to the RSS results. Therefore, no direct comparisons between these data sets can be made, nevertheless, a few comparative statements are possible. The combined data sets indicate significant electron density plumes extending to about 28 R_E in both directions close to the equatorial plane. Both the RPWS and RSS electron density observations indicate a large drop of the density in the immediate vicinity of the Enceladus neutral density plume and smaller fluctuations further out in the wings. These observations are consistent with the direct RPWS measurements in terms of densities, but are in a direction about 72° away, which implies that the extended plasma plume extends in both directions in the equatorial plane. The large electron density bite-out is very likely caused by electron attachment to grains with sizes ranging from nanometers to micron-sized. We also showed by simple calculations that the peak electron densities observed outside this depletion region are consistent with photoionization of neutral gas plus removal by plasma transport.

These results were presented at numerous national and international meetings—for example, Kliore et al. [2006, 2010].

Open questions

What are the long-term spatial and temporal variations in the ionosphere of Enceladus, associated with its plumes originating from the southern hemisphere?

Icy Satellite Science

The determination of the gravity fields of the Saturnian satellites was one of the main scientific goals and responsibilities of the Cassini Radio Science team [Kliore et al. 2004]. Radiometric tracking data were acquired during the flybys of Phoebe, Iapetus, Hyperion, Dione, and Rhea, allowing an accurate determination of the masses of these satellites as well as the gravity quadrupole field of Dione and Rhea [Rappaport et al. 2005; Iess et al. 2005, 2007; Thomas et al. 2007; Mackenzie et al. 2008; Zannoni et al. 2015; Tortora et al. 2016]. These experiments consisted in using X-band and Ka-band coherent, two-way Doppler data and fit them in JPL's Orbit Determination Program in short data arcs. Doppler data were fitted using a spacecraft dynamical model that included the gravitational accelerations from all Saturn system bodies, as well as non-

gravitational accelerations from the spacecraft Radioisotope Thermoelectric Generators and from solar radiation pressure. The noise introduced by the Earth troposphere was calibrated at Goldstone (California) and Madrid (Spain) complexes of the DSN using an Advanced Media Calibration (AMC) system [Resch et al. 2002] at Canberra (Australia) the standard Tracking System Analytical Calibrations (TSAC) is used instead [Bar-Sever et al. 2007], being an AMC not available. AMC devices were specifically developed in support of the cruise Cassini radio science experiments (see the section entitled RSS Non-Saturn Science Results – Cruise Science) and consisted of water vapor radiometers, digital pressure sensors and microwave temperature profilers assembled in a single unit installed a short distance from the DSS-25 and 55 at Goldstone and Madrid, respectively. Since the loss of the Cassini onboard Ka-band transponder in 2003, which in the past allowed a full calibration of the solar and interplanetary plasma [Tortora et al. 2003, 2004], the Sun-Earth-Probe angle also became an important factor in determining the radio link frequency stability [Asmar et al. 2005] and, in turn, the achievable accuracy in the orbit determination and parameter estimation process. Thus, to mitigate the effect of the charged particles in the solar corona, interplanetary space, and the Earth ionosphere X-band uplink, Ka-band downlink (X/Ka) Doppler data were preferred to X/X data, if acquired simultaneously (Ka-band data are more immune to plasma noise); similarly, in order to maximize the phase stability, 2-way data were preferred to 3-way data, if acquired simultaneously.

A close encounter with Phoebe, was performed by Cassini just prior to the Saturn Orbit Insertion (SOI) maneuver, on June 11, 2004.

Phoebe

A close encounter with Phoebe, was performed by Cassini just prior to the Saturn Orbit Insertion (SOI) maneuver, on June 11, 2004. This was the only opportunity during the whole Cassini mission because, after SOI, its maximum distance from Saturn was designed to be smaller than Phoebe's orbital radius. Phoebe's C/A took place at an altitude of about 2000 km and a relative velocity of about 6.4 km/s.

For the determination of Phoebe's GM [Rappaport et al. 2005], X-band Doppler data and optical images of the Saturnian satellites were used. The optical navigation images were used to constrain Phoebe's ephemerides and determine its position relative to the spacecraft, so that the intrinsic correlation (in terms of satellite mass and spacecraft impact parameter) of a hyperbolic flyby could be removed.

Iapetus

Iapetus moves around Saturn on a large orbit of radius ~59 Saturn radii. For the first Cassini encounter (October 17, 2004), the distance at closest approach of Cassini to the satellite was 1.11×10^6 km, so large that the encounter barely deserves the name of flyby. However, Iapetus is a big body with a radius of 733 km, so even a distant encounter allowed to determine its mass. The

large distance at closest approach had a positive effect, in that the determination has only a weak dependence on the impact parameter, and more generally, on the relative orbit of Cassini with respect to Iapetus. Indeed, we expected the correlations between the mass of Iapetus and the orbital elements of both Cassini and Iapetus to be small. The relative velocity between Cassini and Iapetus at closest approach of the first flyby was 3.7 km/s. This relatively small velocity was an advantage since it resulted in a relatively large velocity change of Cassini, due to Iapetus, of about 3.2 cm/s, greater by more than three orders of magnitude than the sensitivity of the radio signal to velocity changes. The SEP angle at C/A was 87°. This implied a solar plasma noise of about 9.2×10^{-14} at 300 s integration time, i.e., larger than the noise introduced by the Earth troposphere [Asmar et al. 2005]. For this reason, the Cassini Radio Science Team requested Ka-band passes to reduce the detrimental effect of plasma noise on Doppler data. For the first Iapetus flyby, the data used for our determination [Iess et al. 2005] consisted of closed-loop tracking data acquired in the period from October 10–25, 2004. The set of data includes Doppler X/X and X/Ka data as well as ranging data at X-band. The Doppler data before and after C/A were compressed at 300 seconds, while those acquired on October 17 and 18 were compressed to 60 seconds.

The second Cassini encounter of Iapetus occurred on December 31, 2004. The distance at C/A of Cassini to the satellite was 123,363 km, the relative velocity was 2.0 km/s and the SEP angle was 165°. As explained in the section entitled Key Objectives for RSS Instrument, this short distance at C/A implied that the uncertainty in the distance at C/A was predominant on the uncertainty in the velocity change so that the estimation (and an update) of the satellite ephemerides was mandatory. The data used for our determination [Iess et al. 2005] consisted of closed-loop tracking data acquired in the period from December 28, 2004 to January 2, 2005. The set of data includes only X-band Doppler coherent with X-band uplink. The Doppler data were compressed at 300 seconds.

Hyperion

The Cassini flyby of Hyperion occurred on September 25–26, 2005. The C/A took place on September 26, 2005, 02:24:47 UTC at a distance of 618 km from the center of mass of the satellite and with a relative velocity between the spacecraft and the moon of about 5.6 km/s. The data used for our determination [Thomas et al. 2007] consisted of closed-loop tracking data acquired in the period from 07:54:07 UTC of September 25 to 21:29:11 UTC of September 26, 2005. The data set was originally designed to comprise four segments of observation: two of them just before and after C/A, acquired over the Goldstone and Madrid complexes, respectively, and two additional passes—the so-called gravity science enhancement (GSE)—to be acquired far from C/A (in the wings of the hyperbolic flyby) about 12 hours before (Madrid) and after (Goldstone) C/A. However, due to a complex-wide failure, all data to be acquired over the Madrid complex on the egress part of the flyby just after C/A were lost, leading to a significant degradation in the GM estimation error. Thus, the exploitable data set consists only of three segments of observation (two before and one after C/A) where the Doppler data are a combination of two-way and three-way, X/X and X/Ka data, predominantly sampled at 60 s.

Dione

During its time in the Saturn system, Cassini has performed five close flybys of Dione, three of which included radio tracking during closest approach: one in December 2011, and two in summer of 2015. As in previous works, the gravity field of Dione was estimated by reconstructing the spacecraft trajectory during these encounters, making use of precise measurements of the Doppler shift of a highly stable microwave radio link between Cassini and the ground station antennas of NASA's DSN.

The available data were analyzed [Zannoni et al. 2015] in a multi-arc fit estimating a fully unconstrained quadrupole gravity field for Dione, the Dione and the spacecraft initial state vectors for each flyby, and modeling parameters for the non-gravitational accelerations. The stability of the solution was tested by perturbing the dynamical model in various ways, including estimating a full 3 × 3 gravity field and changing the a priori uncertainties. The Saturn system dynamics were modeled on the basis of the most recent satellite ephemerides.

Rhea

Before Cassini's arrival in the Saturn system, only the gravitational parameter GM was known from the analysis of Pioneer and Voyager data [Campbell and Anderson 1989]. Using this and the estimated volume (from camera images), a bulk density of about 1200 kg/m^3 was derived, relatively small and compatible with a mixture of about 75% by mass water ice (density 1000 kg/m^3) and 25% rock-metal (density 3000 kg/m^3).

During its mission in the Saturn system, Cassini performed four close encounters of Rhea, of which only two were devoted to gravity investigations. The first gravity flyby, referred to as R1, according to the numbering scheme used by the Cassini project, was performed on November 26, 2005, during the main mission, and the second and last gravity flyby, referred to as R4, was performed on March 9, 2013, during the Solstice mission.

Radiometric data acquired during the first encounter (R1) were used to estimate the gravity field of Rhea. A first estimate [Anderson and Schubert 2007] was obtained under the assumption of hydrostatic equilibrium, i.e., constraining the unnormalized gravity coefficients J_2 and C_{22} to a ratio of 10/3. From this estimation, by applying the Radau-Darwin relation the authors obtained a normalized moment of inertia of about 0.3911 ±0.0045 (a value of 0.4 would imply a constant density interior). The authors concluded that the satellite's interior is a homogeneous, undifferentiated mixture of ice and rock, with possibly some compression of the ice and transition from ice I to ice II at depth.

In parallel, the radiometric data acquired during R1 were independently analyzed by the Cassini Navigation team [MacKenzie et al. 2007] and by the Cassini Radio Science team [Iess et al. 2007]. Both analyses estimated the moon's GM and quadrupole gravity coefficients J_2 and C_{22}, obtaining different solutions, but consistent at the 2σ level, as a result of different analysis approaches. The two approaches were then combined to obtain a joint best unconstrained

estimation of the quadrupole field [MacKenzie et al. 2008]. The solution obtained is not statistically compatible with hydrostatic equilibrium, hence, no useful constraint on Rhea's interior structure could be imposed. Hydrostatic equilibrium was also ruled out by applying this constraint to the estimated quadrupole field coefficients, and this led to a significant degradation of the orbital fit at closest approach. To explain the non-hydrostatic ratio J_2/C_{22}, the authors theorized that a large collision occurred after the completion of the thermal evolution of the satellite, causing a redistribution of mass and a reorientation of the tidal bulge.

Successively, Anderson and Schubert [2010] stated that the differences in the previously published gravity fields are probably caused by a mismodeling of the non-gravitational acceleration acting on Cassini caused by anisotropic thermal emission. To avoid this issue, Anderson and Schubert [2010] restricted the analysis to a subset of data around the closest approach (± 2000 s), where the information from Rhea's quadrupole gravitational field is confined. They obtained a new solution in agreement with Anderson and Schubert [2007] using the hypothesis of hydrostatic equilibrium. Moreover, they concluded that non-hydrostaticity is not supported by the data.

To resolve these discrepancies, a second and final gravity flyby was planned in Cassini's Solstice.

To resolve these discrepancies, a second and final gravity flyby was planned in Cassini's Solstice. R1 was characterized by a very low inclination, about 17° at the closest approach (C/A), in order to decorrelate the estimation of J_2 and C_{22}, while R4 was designed to be nearly polar, with a high inclination at C/A, about 106°. However, the C/A of R4 was about 999 km, twice as high as R1 (about 502 km), thus significantly reducing the information content about Rhea's quadrupole gravity field in this second flyby. The SEP angle was larger than 110° during both encounters, thus range-rate measurements were only slightly affected by the harmful effect of solar plasma.

During the encounters, Doppler data at X-band (8.4 GHz) and Ka-band (32.5 GHz) were acquired by the antennas of NASA's DSN at the three complexes of Goldstone, Madrid, and Canberra. In addition to data obtained around the closest approach, the analysis also used data obtained up to two days before and after the closest approach, during standard navigation tracking passes. The additional data allow an improvement of the orbit determination, in particular, the estimation of Rhea's ephemerides and Rhea's GM, because of the stronger constraints that are imposed on the relative trajectories between Cassini, Rhea, and Saturn.

It is important to note that the closest approach of R1 was tracked only in three-way mode, meaning that the receiving and transmitting stations were different. This represents a suboptimal condition, due to the possible delay between the reference oscillators of the two different uplink and downlink stations. During R4, the closest approach was tracked in two-way mode.

Dual frequency X-band uplink and Ka-band downlink (X/Ka) Doppler data were preferred to the standard X/X data when available, to reduce the effects of the dispersive noise sources, mainly the solar corona and the Earth ionosphere. Two-way Doppler data were preferred to three-way

data in the same band when both were available, to remove the errors due to the clock synchronization between the uplink and downlink ground stations.

When only two-way X/X data and three-way X/Ka data were available, the selection was made on a case-by-case basis.

When available, the wet path delay due to Earth's troposphere was calibrated using measurements from advanced water vapor radiometers [Resch et al. 2002]. When not available, the Earth's troposphere was calibrated using a combination of weather data and dual frequency GPS measurements [Bar-Sever et al. 2007].

The mass estimation results obtained by the Cassini Radio Science team for Phoebe, Iapetus, and Hyperion are summarized in Table RSS-11, along with the rank of each solution (the number of estimated variables) and the tropospheric calibrations used.

The gravity field results obtained by the Cassini Radio Science team are summarized in Table RSS-12 for Rhea.

Table RSS-11. Mass estimation results for the Saturn icy satellites encountered by Cassini.

Saturn Icy Satellite	Estimated GM (km^3/s^s)	Solution Rank	Estimation of Cassini SV	Estimation of Satellite SV	Use of Optical Navigation Images	Tropospheric Calibrations[1]
Phoebe	0.5517 ±0.0007	13	Yes	Yes	Yes[2]	TSAC
Iapetus	120.2064 ±0.0631	7	Yes	No[3]	No	TSAC
Hyperion	0.375 ±0.003	13	Yes	Yes	No	TSAC

[1] AMC = Advanced Media Calibration, TSAC = Tracking System Analytical Calibrations.

[2] The use of optical navigation data for Phoebe's flyby helped constraining the relative distance between the spacecraft and the satellite.

[3] The ODP version used for Iapetus data analysis did not possess the capability to estimate and update the planetary satellite ephemerides as part of the orbit determination procedure.

Table RSS-12. Estimated values and 1-σ formal uncertainties of Rhea's quadrupole gravity unnormalized coefficients for the Cassini Radio Science Team solution [Tortora et al. 2016], compared to the results published in MacKenzie et al. [2008] and Anderson and Schubert [2010]. MacKenzie et al. [2008] did not provide the correlation between J_2 and C_{22}, a zero value was assumed. Anderson and Schubert [2010] solution was obtained by constraining the J_2/C_{22} ratio to the hydrostatic value 10/3. A priori values and uncertainties used by RSS are also shown in the first column.

	Unit	(a priori)	RSS Team	(MacKenzie et al. 2008)	(Anderson and Schubert 2010)
J_2	(× 10^6)	930 ±600	946.0 ±13.9	931.0 ±12.0	892.0 ±1.6
C_{21}	(× 10^6)	0 ±300	−19.9 ±11.0	0 ±0.0	0 ±0.0
S_{21}	(× 10^6)	0 ±300	23.5 ±21.3	0 ±0.0	0 ±0.0
C_{22}	(× 10^6)	240 ±250	242.1 ±4.0	237.2 ±4.5	267.6 ±4.9
S_{22}	(× 10^6)	0 ±250	−15.3 ±5.0	3.8 ±3.8	0 ±0.0
J_2/C_{22}		3.9 ±4.8	3.91 ±0.10	3.92 ±0.9	3.33 ±0.0
corr J_2-C_{22}		0.0	−0.34	0.0 (N/A)	1.00

The results obtained by the Cassini Radio Science team, summarized in Tables RSS-11 and RSS-12, represent a major improvement in the knowledge of the Saturn icy satellite gravitational parameters, with respect to the pre-Cassini published results [Campbell and Anderson 1989; Jacobson 2004]. These more accurate results, along with the satellite geometrical information coming from the Cassini Imaging team, were used by the Cassini Radio Science team to build interior models and allow their geophysical interpretation for some of the encountered icy satellites.

Open questions

- How close to hydrostatic equilibrium are the icy satellites? What does this say about their internal structure and geophysical history?

Ring Science

During a ring occultation observation, Cassini transmits three coherent sinusoidal signals simultaneously through the rings. They are generated from the common onboard USO, allowing measurement of their amplitude, frequency, and phase, as well as their relative phases.

As a transmitted signal passes through the rings, the ring material perturbs it. Two signal components can be identified in the measured spectrum of the perturbed signal. The first is the direct signal, a narrow spectral line that is the remnant of the coherent incident sinusoid after being attenuated and phase shifted by ring material. The time histories of estimated average power and phase change of the direct signal provide a measured extinction and phase shift profile. The extinction is characterized in terms of an optical depth and, with the help of a reconstructed spacecraft trajectory, is used to compute an optical depth versus radius profile of the ring system as a function of wavelength. The initial profile is diffraction-limited. Accurate measurement of the signal phase allows reconstruction of the profile to remove diffraction effects [Marouf et al. 1986].

The second component is the near-forward scattered signal, a frequency-broadened signal that originates from incoherent superposition of the signals scattered by ring particles located within the intersection of the main-lobe of the Cassini high-gain antenna and the rings plane (antenna footprint). The Doppler shift caused by the relative motion of the spacecraft, ring particles, and ground station broadens the spectrum of this signal component. The time history of the scattered signal spectra can be used to determine the size distribution of large (> 1 meter) particles as well as other physical properties [Marouf et al. 1983; Zebker et al. 1985].

RSS ring occultations during the Cassini Prime Mission

Twenty-four one-sided radio occultations of Saturn's rings were observed during the Cassini Prime Mission (Table RSS-13), with additional occultations observed through the Grand Finale orbits. The spacecraft trajectory was chosen so that the path of the radio signals transmitted from Cassini to an observing ground receiving station would be interrupted by the ring system.

The Prime Mission occultation observations sampled a broad range of ring-opening angles, *B*. In particular, a set from Revs 7 to 14 of mostly diametric occultations captured relatively large angles, 19.5–23.5°, allowing detailed profiling of the optically thick ring B for the first time. Another set from Revs 53–67 of mostly chord occultations sampled small ring opening angles ~6-10°. The limited intermediate range of angles, 14–15°, was sampled by occultations from Revs 28, 44, and 46. These 24 occultation cuts also sampled a broad range of ring longitudes both inertial and Earth-relative.

Table RSS-13. RSS Ring Occultations Completed During Cassini Prime Mission.

Occ #	YYYY-DOY[1]	Cassini Rev #	Ingress/Egress/Chord	B (deg)[2]
1	2005-123	7	I	−23.57
2	2005-123	7	E	−23.57
3	2005-141	8	I	−23.17
4	2005-141	8	E	−23.17
5	2005-159	9	E	−22.64
6	2005-177	10	I	−22.01
7	2005-177	10	E	−22.01
8	2005-196	11	E	−21.29
9	2005-214	12	I	−20.54
9	2005-214	12	E	−20.54
11	2005-232	13	E	−19.76
12	2005-248	14	I	−19.12
13a[3]	2006-258	28	I	−14.35
13b[3]	2006-259	28	I	−14.35
14	2007-130	44	E	−15.23
15	2007-162	46	I	−14.37
16	2007-337	53	I	−6.68
17	2007-353	54	C	−6.63
18	2008-015	56	C	−7.04
19	2008-027	57	C	−7.38
20	2008-039	58	C	−7.80
21	2008-062	60	C	−8.65
22	2008-092	63	C	−9.60
23	2008-102	64	C	−9.79
24	2008-130	67	C	−9.91

[1]Observation Year and Day-of-Year.

[2]Ring opening angle.

[3]Ingress occultation was interrupted over Ring B by a high-phase orbiter remote sensing observation.

A gallery of the Earth view of selected RSS occultations is shown in Figure RSS-14, with the spacecraft path shown in blue.

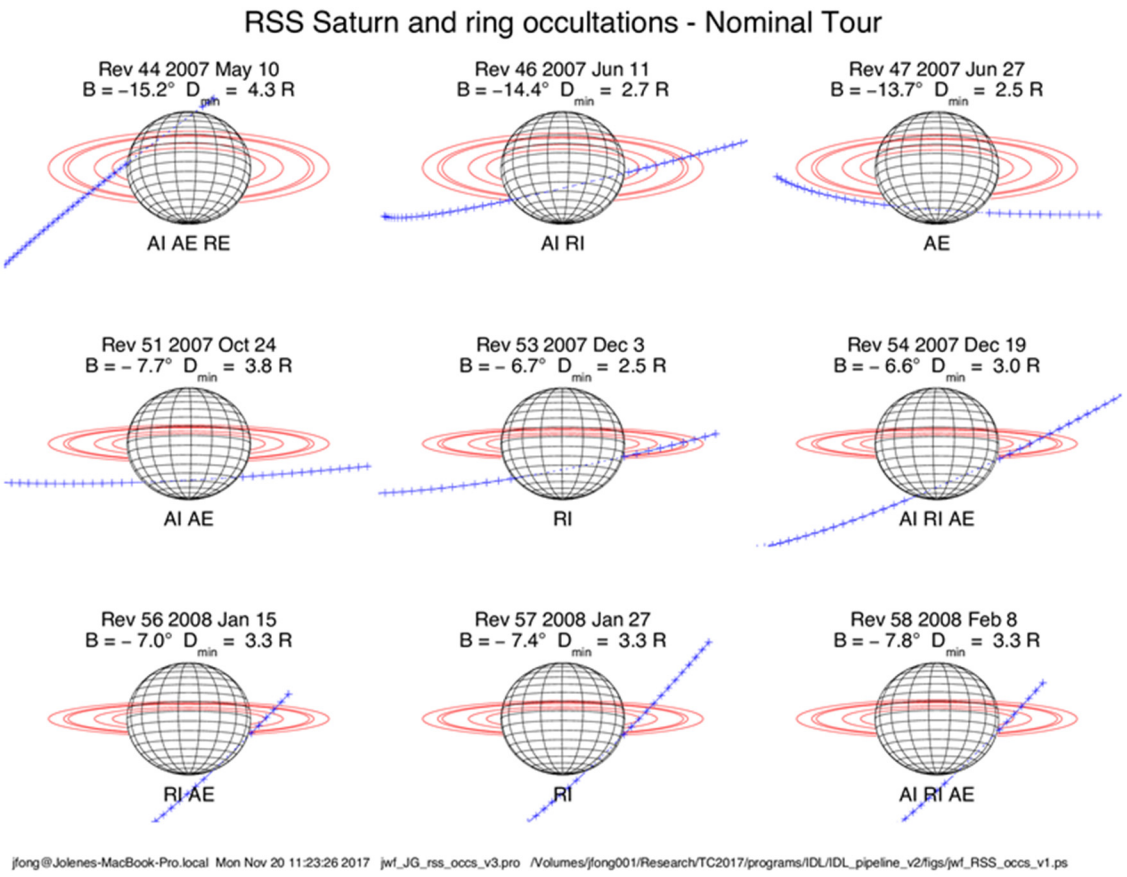

Figure RSS-14. Gallery of Earth-based views of selected RSS ring and atmosphere occultations in 2007 and 2008.

Radial structure in the rings

A major objective of the RSS ring occultation experiments was to determine highly accurate orbits of the rings and to investigate the dynamics and kinematics of ring and gap edges. This work was carried out in collaboration with the Visual and Infrared Imaging Spectrometer (VIMS) and Ultraviolet Imaging Spectrograph (UVIS) teams, in order to combine the full set of occultation data obtained from Cassini instruments. A series of four major papers summarized the results of this joint effort: the edge of Saturn's B-ring [Nicholson et al. 2014a], the C-ring [Nicholson et al. 2014b], the Cassini Division [French et al. 2016], and a determination of the absolute radius scale and pole direction of Saturn [French et al. 2017]. Representative examples of the results from these papers are shown in Figure RSS-15 and Figure RSS-16.

Figure RSS-15 shows the broad influence of Titan's 1:0 inner Lindblad resonance (ILR) over the inner C-ring—from Nicholson et al. [2014b]. Figure RSS-16 shows the structure of the inner C-ring—from Nicholson et al. [2015b]—from the RSS Rev 007 occultation.

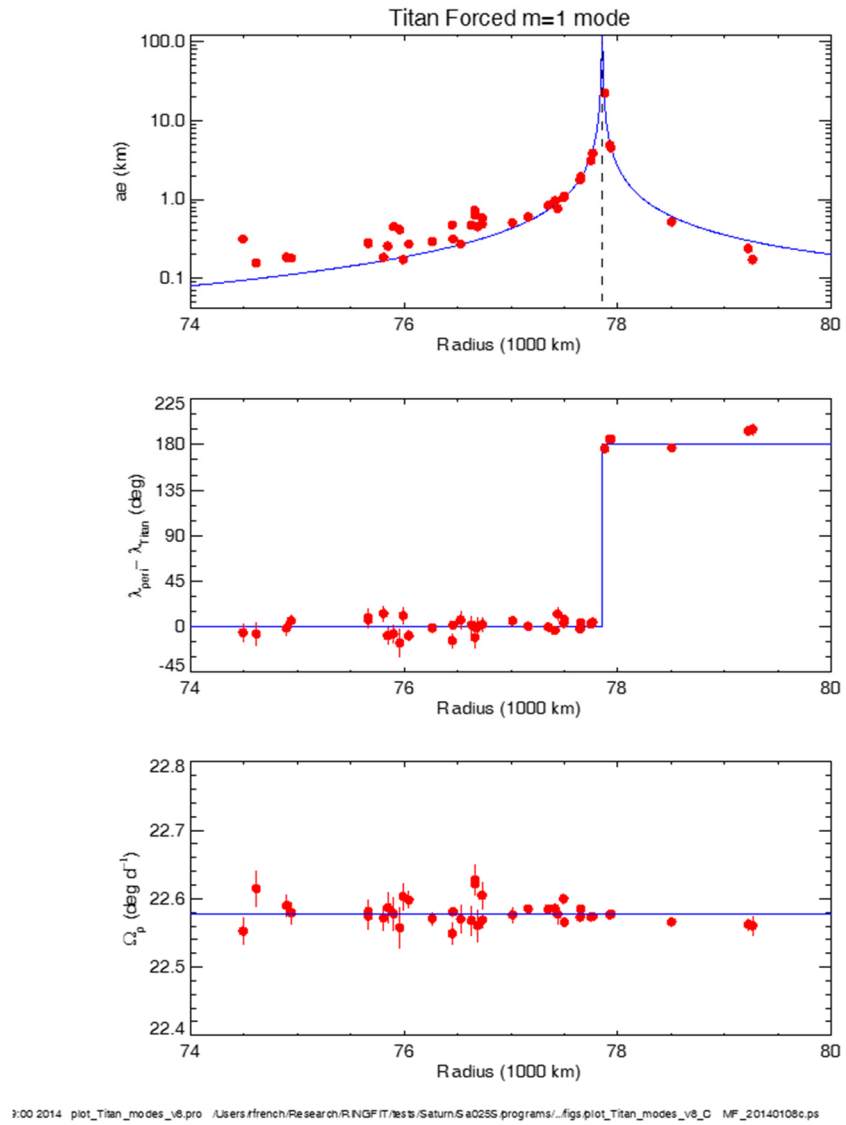

Figure RSS-15. Fitted amplitudes, phases, and pattern speeds versus radius for perturbations induced at a distance by the strong Titan 1:0 ILR. *Upper panel*: curve shows the predicted amplitude, based on a simple test-particle model. *Middle panel*: shows the phase of the perturbation relative to Titan. Note: the orientation changes by 180 from inside to outside the resonant radius, in accord with the same model. *Lower panel*: shows the best-fitting pattern speed compared to Titan's mean motion of 22:577 deg/day. Figure from Nicholson et al. [2014b].

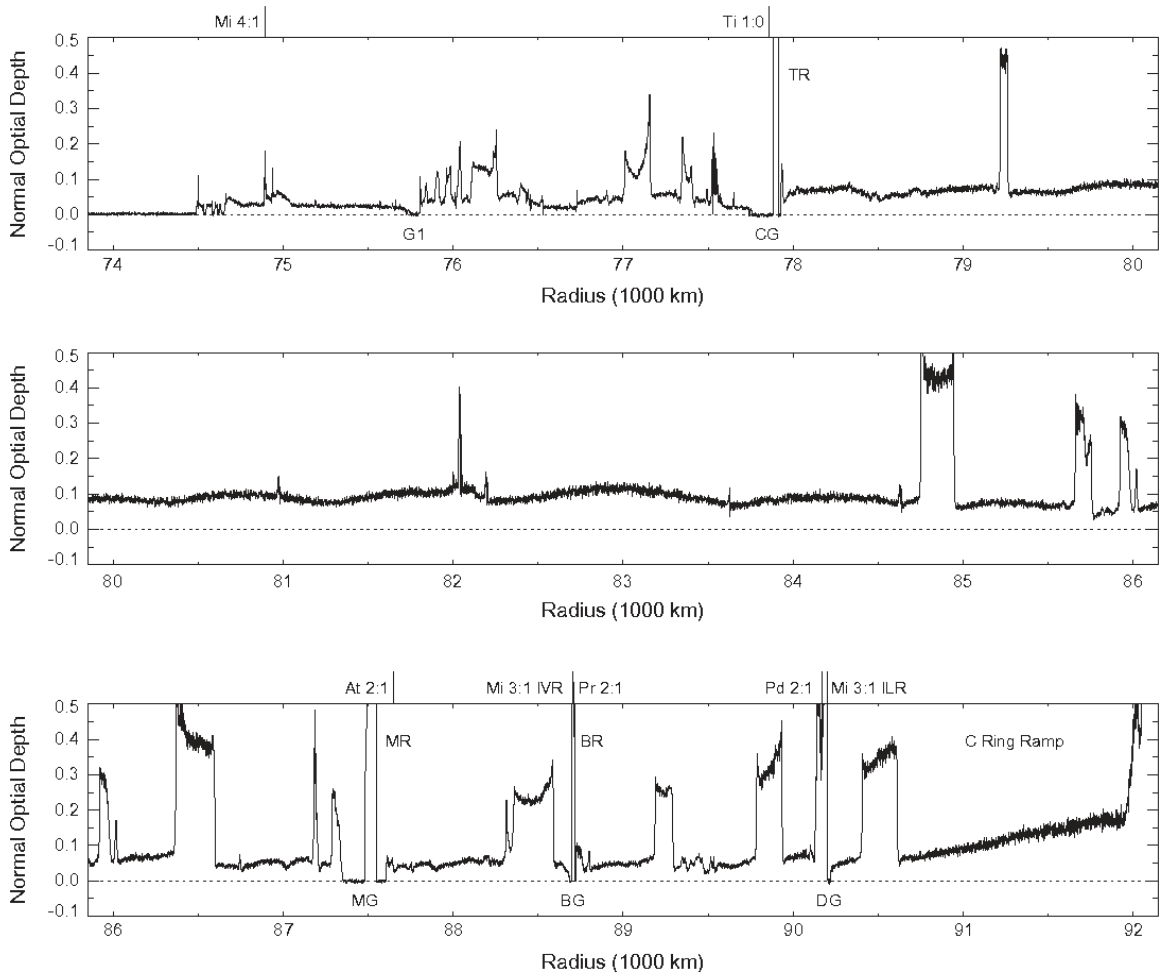

Figure RSS-16. An optical depth profile of the C-ring, derived from the Cassini radio occultation on Rev 7. Abbreviations refer to the Titan ringlet (TR) and Colombo gap (CG), the Maxwell gap and ringlet (MG, MR), the Bond gap and ringlet (BG, BR), and Dawes gap (DG). Tick marks across the top of the plot indicate the locations of significant satellite resonances with Ti = Titan, Mi = Mimas, At = Atlas, Pr = Prometheus, and Pd = Pandora.

From nearly edge-on occultation observations of the C-ring later in the mission, RSS measurements revealed a conspicuous periodic beating pattern between two km-scale waves (Figure RSS-17). From spectral measurements of the power spectrum of the waves and direct model fits, the observations can be interpreted as 10-meter scale vertical corrugations in the C-ring with horizontal wavelengths of order 1 km, increasingly tightly wound as one approaches Saturn (Figure RSS-18). This hints at the possibility that two ancient impacts in the 1300s tilted Saturn's rings—detailed analysis remains to be completed for this provocative possibility.

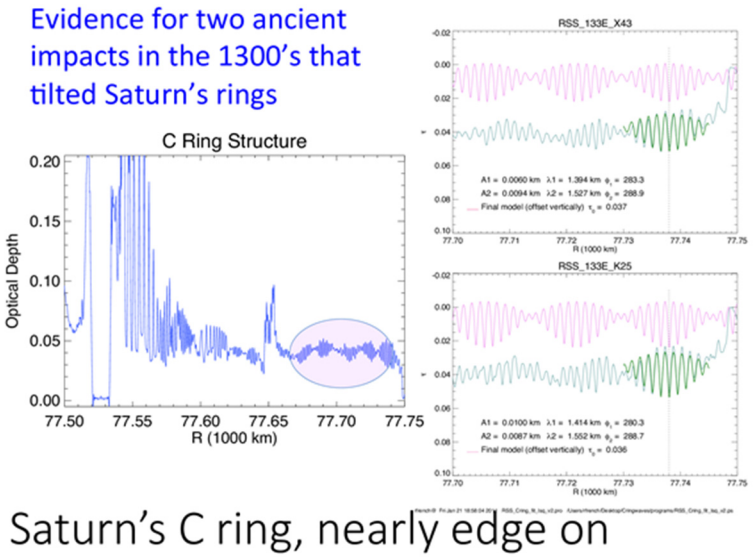

Figure RSS-17. Optical depth profile of the inner C-ring from a nearly edge-on RSS ring occultation.

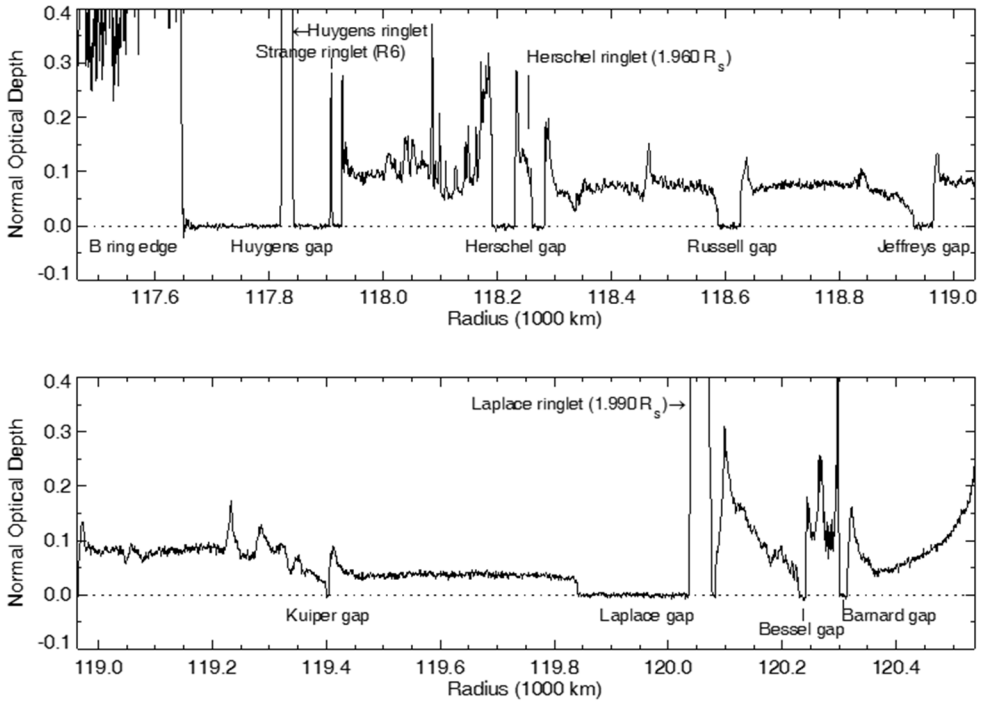

Figure RSS-18. Prominent ringlets and gaps in the Cassini Division shown in an optical depth profile from the Cassini RSS egress occultation on Rev 7. Figure from French et al. [2016].

Among the interesting results found from the analysis of the Cassini Division occultation data is evidence of anomalous precession rates for noncircular features, as shown in Figure RSS-19 from French et al. [2016].

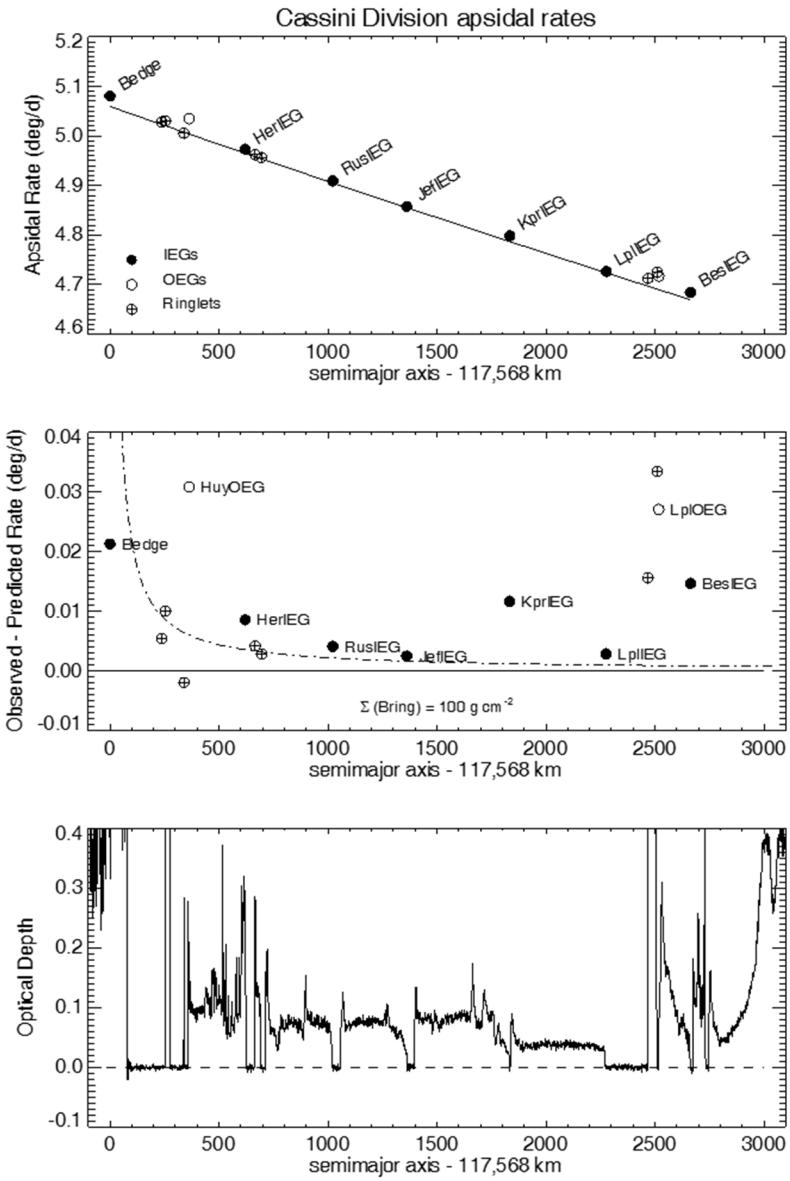

Figure RSS-19. Results found from the analysis of the Cassini Division occultation data *Upper panel*: fitted apsidal precession rates versus mean radius for eccentric features. Note: the quasi-regular sequence in the precession rates for the gap inner edges. The solid line shows the predicted precession rates, calculated from Saturn's zonal gravity coefficients. *Middle panel*: The differences between the fitted and calculated precession rates in the upper panel, using the same symbols. The dot-dashed curve shows the contribution to the apsidal precession rates from the nearby B-ring, assuming a uniform surface mass density of 100 g cm^{-2}. *Lower panel*: Optical depth profile, for context. Figure from French et al. [2016a].

Additional targeted studies of individual ring features were also conducted by the RSS team, including the identification of an m = 2 Saturn-driven density wave in the Maxwell Ringlet [French et al. 2016b]. Figure RSS-20 shows the results of a simulation of the strongly nonlinear density wave embedded in a highly eccentric ringlet.

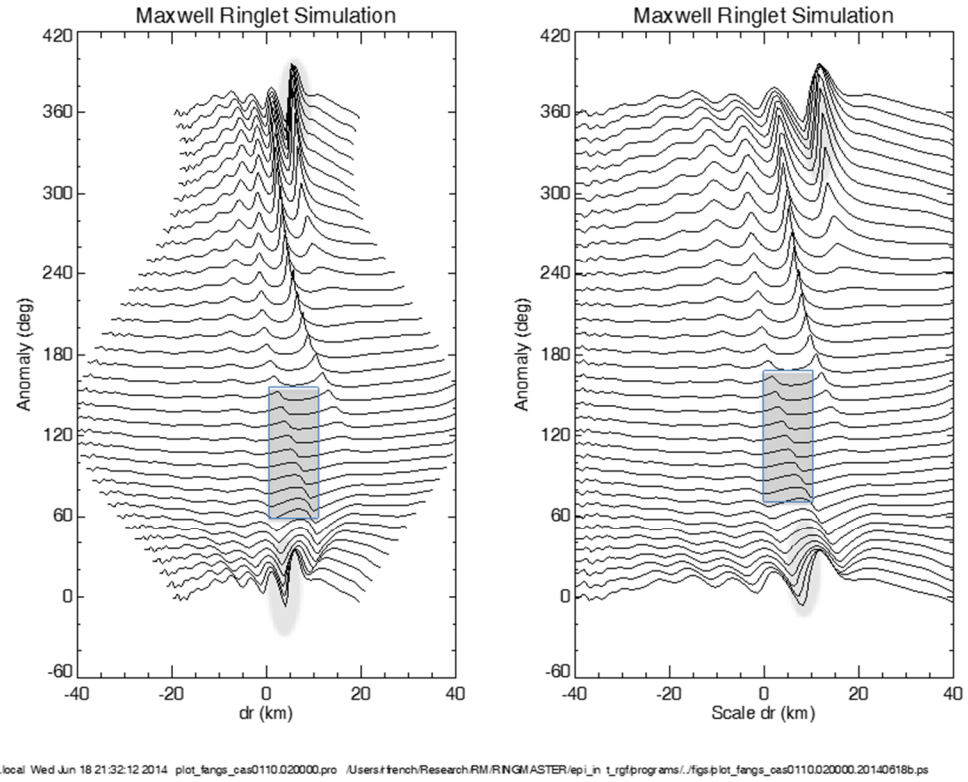

Figure RSS-20. Simulation of non-linear density wave embedded in the eccentric Maxwell Ringlet.

In a recent study of Saturn's F-ring [Cuzzi et al. 2018], RSS F-ring observations, such as those shown in Figure RSS-21, were used to provide evidence for an incomplete core of the F-ring, with arcs of material confined by an unusual resonance with Prometheus.

Density waves in Saturn's rings

Saturn's rings are replete with density waves, and the RSS ring occultations are a rich resource for investigating their properties. Rappaport et al. [2009] developed a novel procedure to analyze nonlinear density waves using multiple occultations, with the goal of determining the underlying unperturbed optical depth of the material in the wave region, and other properties of dynamical interest (Figure RSS-22).

A comparison of density wave profiles observed from RSS, VIMS, and UVIS (Figure RSS-23) shows the exquisite quality of all three occultation techniques.

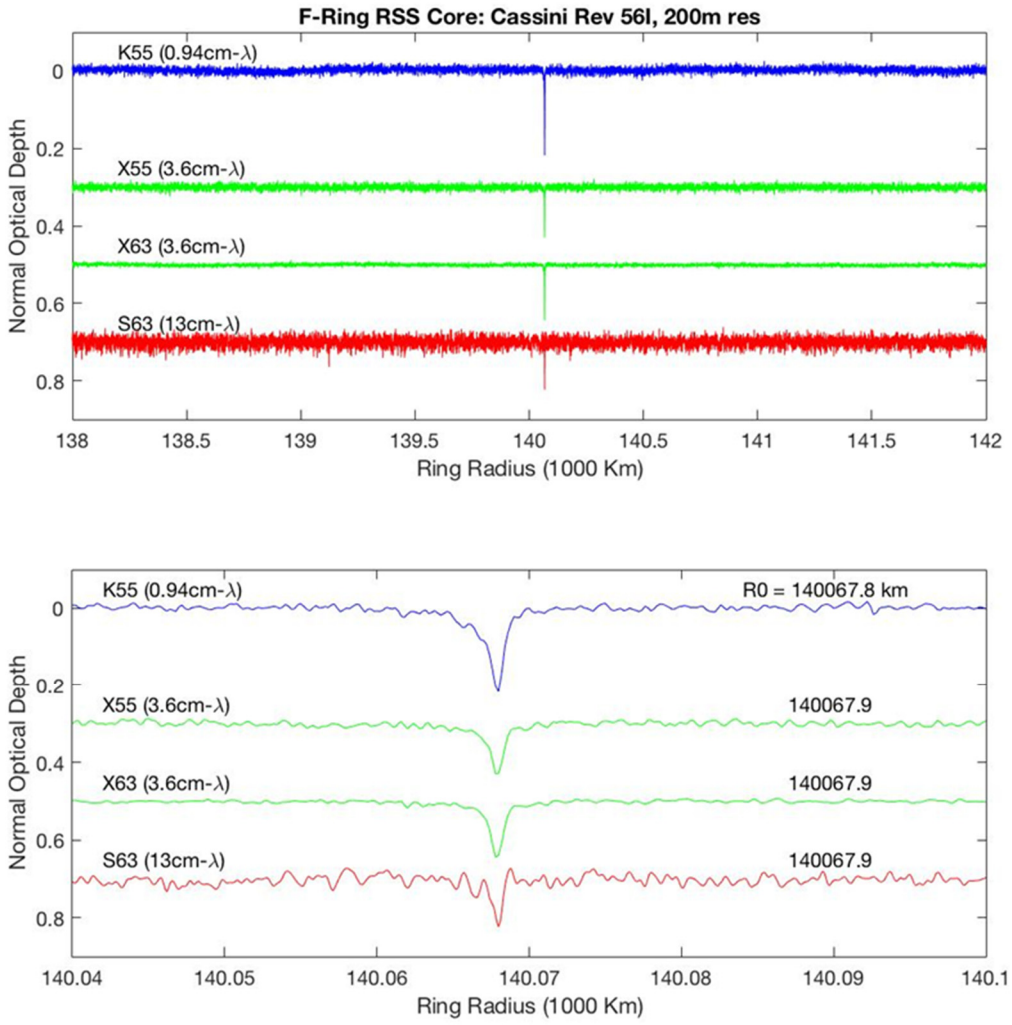

Figure RSS-21. Example Cassini RSS F-ring core detection (ingress occultation on Rev 54, December 19, 2007). The core was detectable in the 0.94, 3.6, and 13 cm-wavelength measurements (Ka-band, X-band, and S-band, respectively; blue, green, and red lines). The measurements were acquired by two of the NASA DSN stations at the Madrid, Spain, complex. DSS-63, a 70-m station, acquired X-band and S-band; DSS-55, a 34-m station, acquired X-band and Ka-band, hence, the four profiles in each panel. The measurements were reconstructed to remove diffraction effects, yielding 200 m radial resolution optical depth profiles. The upper panel shows the profiles over a broad 4000 km wide region outside the outer edge of the A-ring, primarily to provide a free-space baseline for the experiment. A single feature of optical depth large compared with the baseline noise fluctuations is evident in all three bands at ring radius of about 140,100 km. The stretched radius scale of the lower panel (60 km wide) reveals a single feature about 900 m wide of wavelength-dependent peak normal optical depth < 0.2. The narrow RSS F-ring core was detectable in 23 out of 66 ingress or egress Cassini RSS ring occultations completed between May 2005 and August 2013 (~35%). The S-band core was not detectable in all 23.

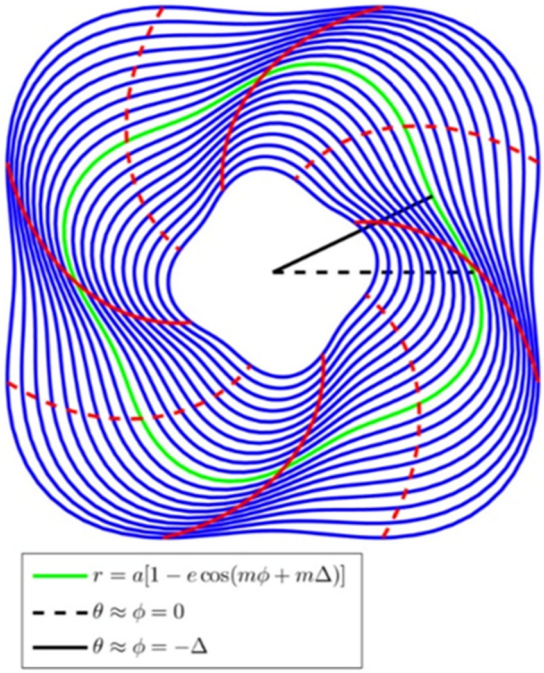

Fig. 1. Streamlines of a 4-lobe ($m = 4$) density wave, such as Mimas 5:3. The lag angle Δ provides the relative shift in angle of one streamline to the next. The loci of constant profile phase ψ corresponding to the density maxima ($\psi = 2\pi n$ with $n = 1$ to 5, solid line) and minima ($\psi = \pi$ modulo 2π, dashed line) are also shown to illustrate the geometrical meaning of ψ. A streamline has been singled out, to show the phase angle Δ.

Figure RSS-22. Density wave model used to analyze RSS observations of Mimas 5:3 density wave. Figure from Rappaport et al. [2009].

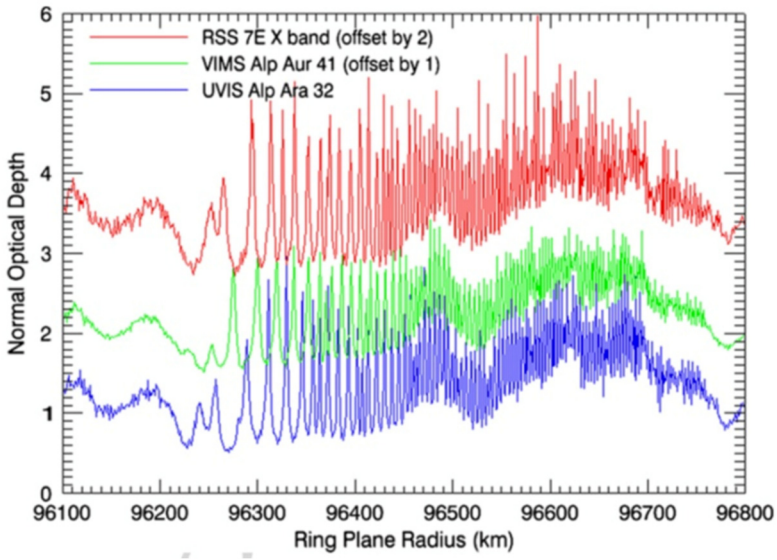

Figure RSS-23. Occultation profiles of the Janus/Epimetheus 2:1 density wave in the B1 region. The resonance locations for Janus and Epimetheus shift when the satellites perform their horseshoe orbit swap every four years and are between 96,210 and 96,250 km. Figure from Colwell et al. [2009].

Particle size distribution

The three-wavelength capability of the RSS observations provides the opportunity to measure the wavelength dependence of the ring optical depth, which can be related to the ring particle size distribution using scattering theory. Figure RSS-24 shows an example of the differential extinction over eight different ring features [Cuzzi et al. 2009]. Figure RSS-25 shows the optical depth contrasts at multiple wavelengths, and the inferred minimum and maximum particle sizes, based on an analysis of RSS occultation data [Cuzzi et al. 2009].

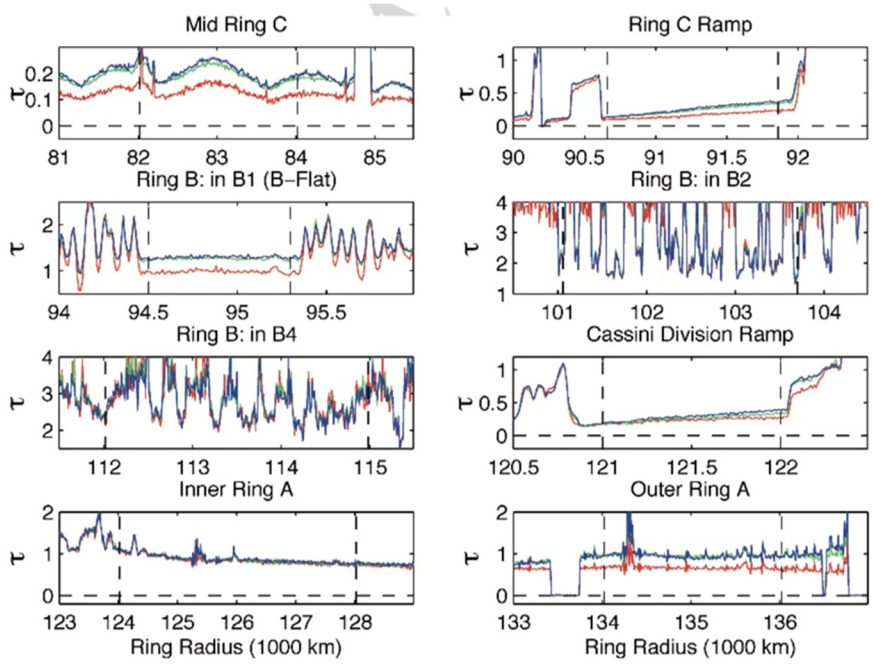

Figure RSS-24. Three-wavelength RSS optical depth profiles of eight ring features identified for examination of the constraints imposed by observed interesting differential extinction, or lack thereof, on parameters of a power-law size distribution model. Figure from Cuzzi et al. [2009].

Periodic microstructure in Saturn's rings A and B

Radio occultation of Saturn's rings by the Cassini spacecraft on May 3, 2005, revealed several remarkable phenomena in rings A and B. In limited regions of the rings, the observations indicate the presence of fine-scale structure characterized by periodic variations in optical depth of period 100–250 meters, which we refer to as periodic microstructure (PM). Our discovery of these structures [Thomson et al. 2006] is based on observation of diffraction effects in 0.94 cm and 3.6 cm wavelength coherent sinusoidal signals transmitted from Cassini through the rings, and received at the ground stations of the DSN. Figure RSS-26 shows the geometry of the ring occultation experiment used to determine the ring microstructure, seen in the spectra illustrated in Figure RSS-27.

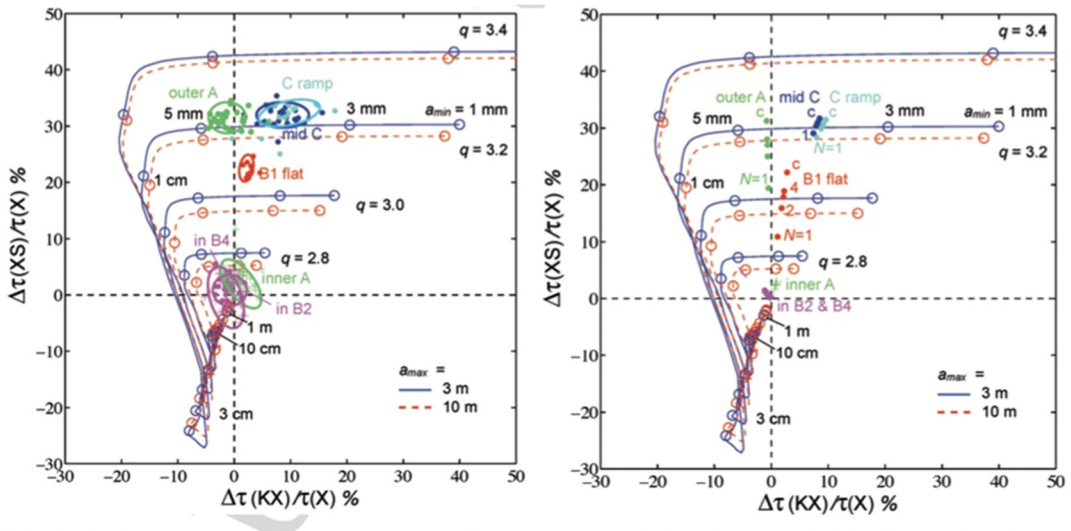

Fig. 15.3 (*Left*) Comparison of the measured X-S (*vertical axis*) and Ka-X (*horizontal axis*) differential optical depth with predictions of a power-law size distribution model of the indicated parameters. For a given power-law index q, the predicted differentials are plotted using the minimum radius a_{min} as a parameter. Points $a_{min} = 0.1, 0.3, 0.5, 1, 3, 10$, and 100 cm are as identified. For each case, dependence on a_{max} is illustrated for the two cases $a_{axn} = 3$ (*solid blue*) and 10 m (*dashed red*). The seven clusters are the values measured for seven of the ring features identified in Figure 3, as labeled. Individual points within each cluster are 80 km resolution samples. The comparison is based on the assumption of a classical (many-particle-thick) ring model. (*right*) Same figure, except that the measured values are scaled based on the thin layers ring model. The five points for each feature correspond to number of layers fours N = 1 to 4 and the classical model result 'c', as labeled. Each point is an average over the radial width of the corresponding ring feature (Marouf et al. 2009)

Figure RSS-25. Optical depth contrasts at multiple wavelengths and the inferred minimum and maximum particle sizes. Figure from Cuzzi et al. [2009].

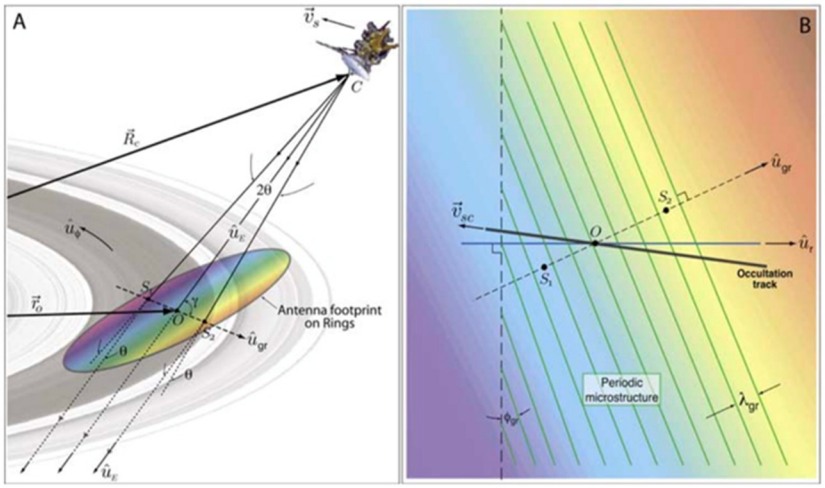

Figure 1. Geometry of the ring occultation experiment. (a) Line-of-sight ray linking Cassini and Earth is directed along $\hat{u}_E$ and pierces the ring plane at point **O**; $\hat{u}_{gr}$ is in the plane of the rings, and defines the orientation of the periodic structure. Points S_1 and S_2 correspond to locations in the ring plane where first-order diffraction grating lobes of the structure originate and propagate along $\hat{u}_E$ to the Earth-based receiver. The grating lobes are directed at angle $\pm\theta$ relative to $\hat{u}_E$. All angles shown are in the plane defined by $\hat{u}_E$ and $\hat{u}_{gr}$. Color within the antenna footprint represents variations in Doppler shift of signals scattered to Earth by the rings; footprint size is exaggerated for clarity. (b) View is of the ring plane. Signals diffracted to Earth from S_1 and S_2 are Doppler-shifted by f_{D1} and f_{D2} relative to the signal along the line-of-sight, represented by the colors at S_1 and S_2. $\hat{u}_r$ is a radial unit vector pointing from the center of Saturn to **O**, and $\vec{v}_{sc}$ is the projection in the ring plane of Cassini velocity $\vec{v}_c$.

Figure RSS-26. The geometry of the ring occultation experiment used to determine the ring microstructure. Figure from Thomson et al. [2006].

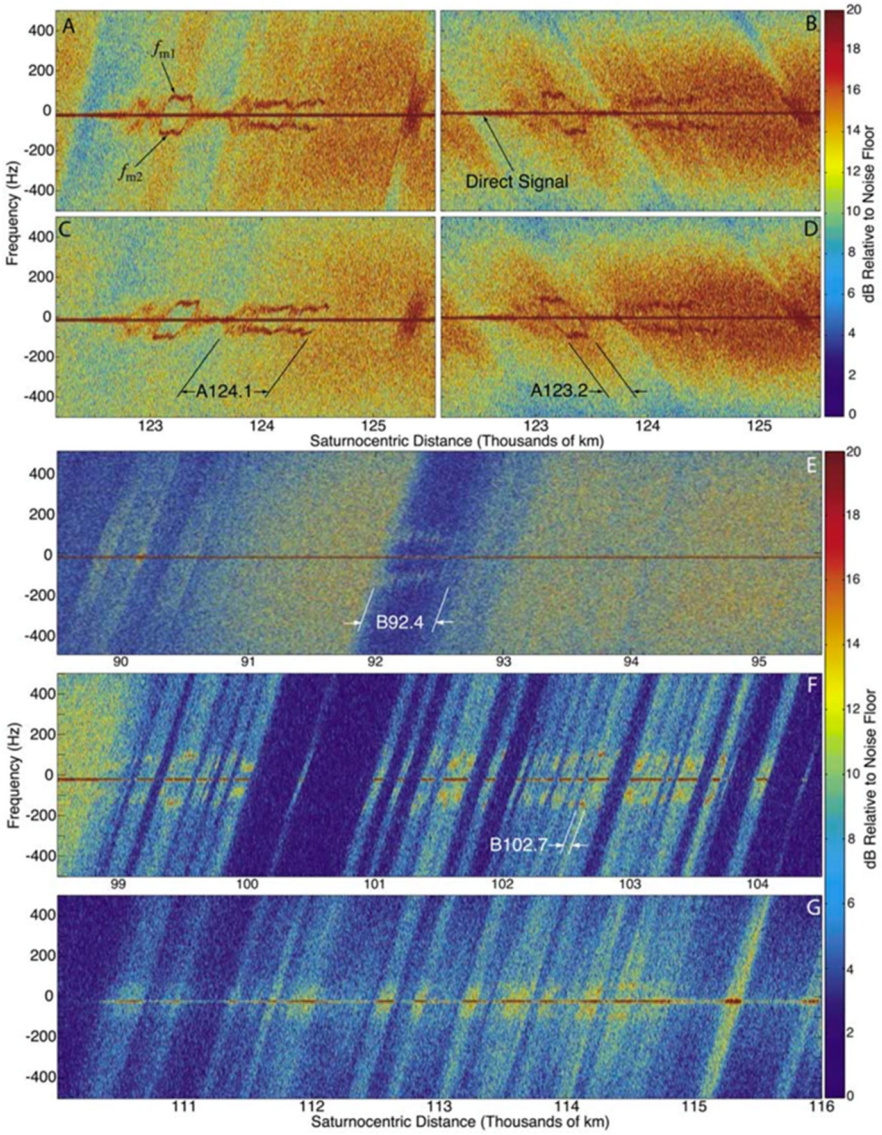

Figure 2. Spectrograms of 3.6 cm-λ signal observed during May 3, 2005, ring occultation (a, e, f, g) ingress and (b) egress; and on August 2, 2005, occultation (c) ingress and (d) egress. The direct signal is the horizontal brown line near the center of each panel. The diffraction signature of periodic microstructure appears as roughly parallel horizontal lines displaced ±70–100 Hz from the direct signal in Ring A (Figures 2a–2d) and ±50–120 Hz Ring B (Figures 2e–2g). The signature is clearly evident for the two indicated features in inner Ring A, over the roughly 500 km inner part of region B1 (Figure 2e) and over most of the detectable subregions of the ≈5000 km-wide region B2 (Figure 2f). It is more muted over most of region B4 (Figure 2g). Other evident broadband features correspond to energy forward scattered by the background wake structure in the rings.

Figure RSS-27. The geometry of the ring occultation experiment seen in the spectra. Figure from Thomson et al. [2006].

Open questions

After more than a decade of ring observations at Saturn, fundamental questions remain about the origin of ring structure and confinement mechanisms for sharp-edged ring features.

- What confines the Titan and Maxwell ringlets?
- Is it a coincidence that the Maxwell ringlet harbors a density wave?
- Did the driving resonance behind the density wave contribute in some fashion to the formation of the ringlet?
- Did the Titan ringlet form in response to its near-resonance with Titan itself?
- Where did the C-ring plateaus originate?
- What drives the host of normal modes detected in sharp ring and edge gaps?
- Is there detectable radial evolution of ring features on the time scale of decades and centuries?

RSS Non-Saturn Science Results

Cruise Science

Gravitational wave experiment

Introduction[1]

One of the cruise-phase Cassini science investigations was to use Cassini's precision Doppler tracking capability to search for GWs. The idea [Estabrook and Wahlquist 1975] is that Earth and Cassini act as electromagnetically-tracked free test masses. The Earth-spacecraft relative velocity is continuously measured via Doppler shifts of microwave links referenced to a ground-based precision frequency standard. Such as system can be used to search for low-frequency (~10^{-6} to 10^{-1} Hz) GWs.[2]

Signal response

Figure RSS-28 shows the effect of a burst GW incident on the Earth-Cassini system. The Doppler responds to a projection of the time-dependent wave metric, in general producing a three-pulse

---

[1] *Much of this report, including the figures, comes from Armstrong, et al. [2003], and Armstrong [2006].*

[2] *Gravitational wave bands conventionally divide based on detector technology [Thorne 1987]: extremely-low-frequency (~10^{-18} to ~10^{-15} Hz) search programs are based on mapping the intensity and polarization of the cosmic microwave background; very-low frequency observations (~10^{-9} to ~10^{-6} Hz) use pulsar timing observations; low-frequency (~10^{-6} to ~10^{-1} Hz) observations currently use Doppler tracking of spacecraft (in the 2030s, a laser interferometer in space); high-frequency (~10 to ~10^{3} Hz) observations involve ground-based laser interferometers. The ground-based LIGO detectors made the first detection of GWs in 2015, for which the 2017 Nobel Prize in physics was awarded.*

response to a pulse of incident gravitational radiation: one event due to buffeting of the Earth by the GW, one event due to buffeting of the spacecraft by the GW, and a third event in which the original Earth buffeting is transponded a two-way light time later. The amplitudes and locations of the pulses depend on the arrival direction of the GW with respect to the Earth-spacecraft line, the two-way light time, and the wave's polarization state [Estabrook and Wahlquist 1975]. Technical details of the detector, including polarization response, are in references in Armstrong [2006].

The Cassini experiment is distinguished by its 5-link radio system. This system (X-up, X-down coherent with X-up, Ka-down coherent with X-up, Ka-up, Ka-down coherent with Ka-up) allowed essentially perfect rejection of plasma scintillation noise, a dominant noise source for earlier-generation spacecraft observations—for example, Tortora et al. [2004]; Asmar et al. [2005]; Mariotti and Tortora [2013]. Cassini observations also benefitted from an Advanced Media Calibration unit—water vapor radiometer and microwave temperature profiler—which allowed measurement and removal of a substantial fraction of propagation noise from the neutral atmosphere [Keihm et al. 2004]. Discussion of the noise budget is in Bertotti et al. [2003]; Asmar et al. [2005]; and Armstrong [2006].

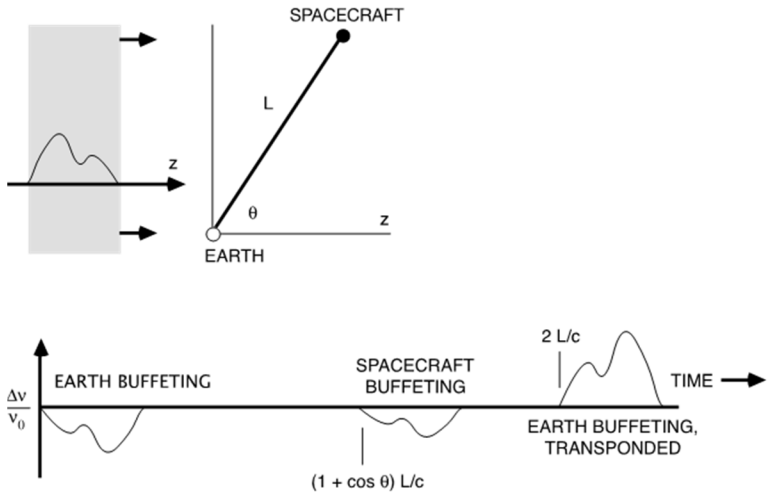

Figure RSS-28. Schematic response of two-way Doppler tracking to a GW [Estabrook and Wahlquist 1975]. The Doppler exhibits three pulses having amplitudes and relative locations which depend on the GW arrival direction, the two-way light time, and the wave's strain amplitude and polarization state. The sum of the three pulses is zero, so the pulses overlap and partially cancel when the characteristic time of the GW pulse is comparable to or larger than the light time between the Earth and spacecraft.

Three GW observing campaigns were done during Cassini cruise: (i) November 25, 2001 to January 4, 2002; (ii) December 5, 2002 to January 14, 2003; and (iii) November 10, 2003 to November 28, 2003—the last being done with X-up and X-down only due to the failure of the Cassini Ka-band translator.

The spectrum of the propagation-corrected data from the first observing campaign is shown in Figure RSS-29. The associated 1000-second Allan deviation (fractional frequency variation), for

the full 40 days of the observation, is 6×10^{-15}. The velocity noise is thus about 1 μm/sec in a 1000-second integration. These are the most sensitive deep space Doppler measurements ever made.

Sensitivity is conventionally stated as the sky- and polarization-averaged sinusoidal signal strength required to achieve a given signal to noise ratio in a specified integration time, as a function of Fourier frequency. This is shown in Figure RSS-30 for a signal-to-noise ratio of unity in a 40-day integration. This ~10^{-16} value (in the ~decade Fourier range of best sensitivity) is also the SNR = 1 sensitivity limit for sinusoidal GWs or linear chirps.

For GW signals having more complicated Fourier composition the sensitivity is lower and in general depends on waveform shape and angle-of-arrival of the GW relative to the Earth-Cassini line. Figure RSS-31 shows the characteristic strain sensitivity for generic burst waves (bandwidth = center frequency) averaged over the sky and polarization states.

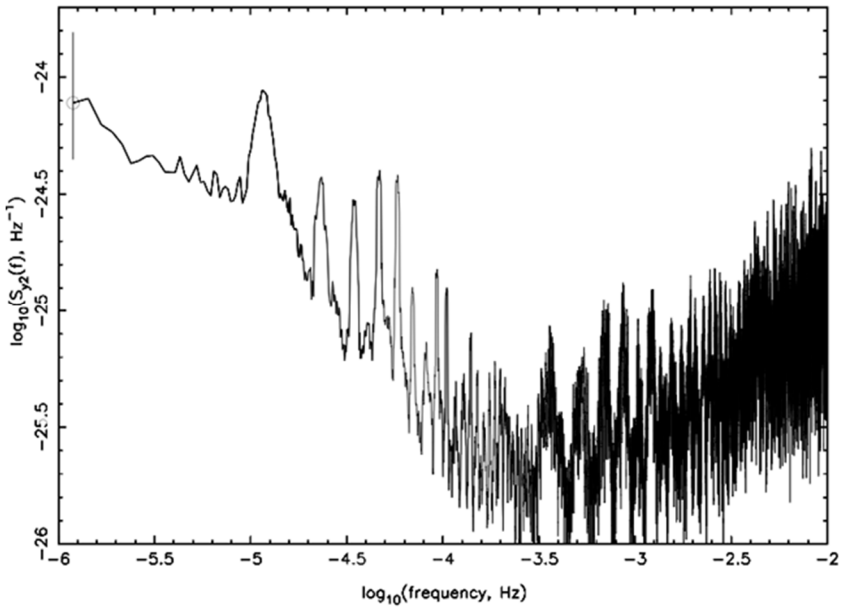

Figure RSS-29. Spectrum of two-way Doppler for the 2001–2002 Cassini observations. The associated 1000s Allan deviation is 6×10^{-15}, corresponding to 1 μm/sec velocity noise on a 1000s integration time [Armstrong et al. 2003].

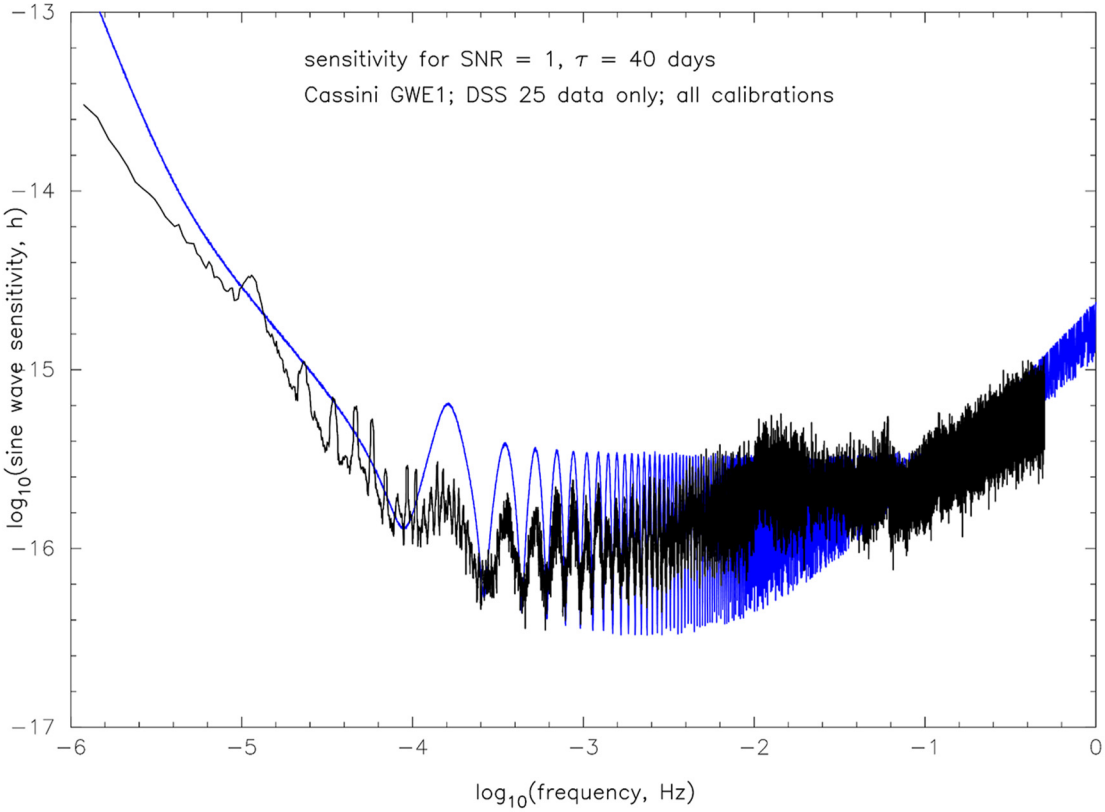

Figure RSS-30. Sensitivity of the Cassini 2001–2002 gravitational wave observations, expressed as the equivalent sinusoidal strain sensitivity required to produce SNR = 1 for a randomly polarized isotropic background, as a function of Fourier frequency. This reflects both the levels, spectral shapes, and transfer functions of the instrumental noises and the GW signal transfer function. Black curve: sensitivity computed using smoothed version of observed Doppler spectrum. Blue curve: sensitivity computed from pre-observation predicted noise spectrum. Figure from Armstrong [2006].

The Cassini data can also be used to bound the level of a stochastic background of GWs [Armstrong et al. 2003]. This is shown in Figure RSS-32 relative to the density required to gravitationally close the universe. These limits are about three orders of magnitude more stringent than any others from Doppler tracking.

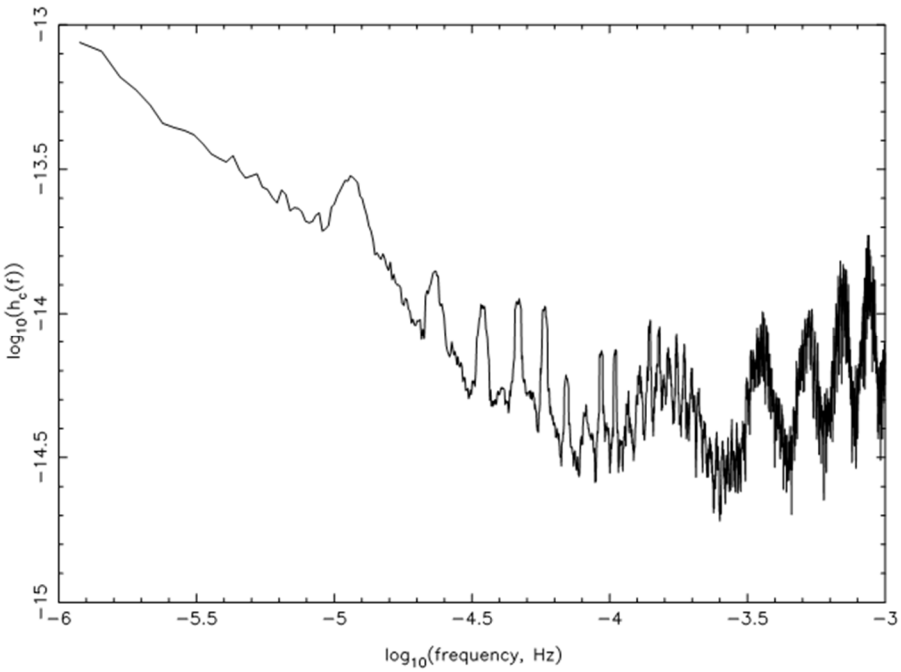

Figure RSS-31. Sensitivity of the Cassini 2001–2002 burst gravitational wave observations, expressed as characteristic strain sensitivity (GW bandwidth = center frequency) averaged over the sky and polarization state. Figure from Armstrong [2006].

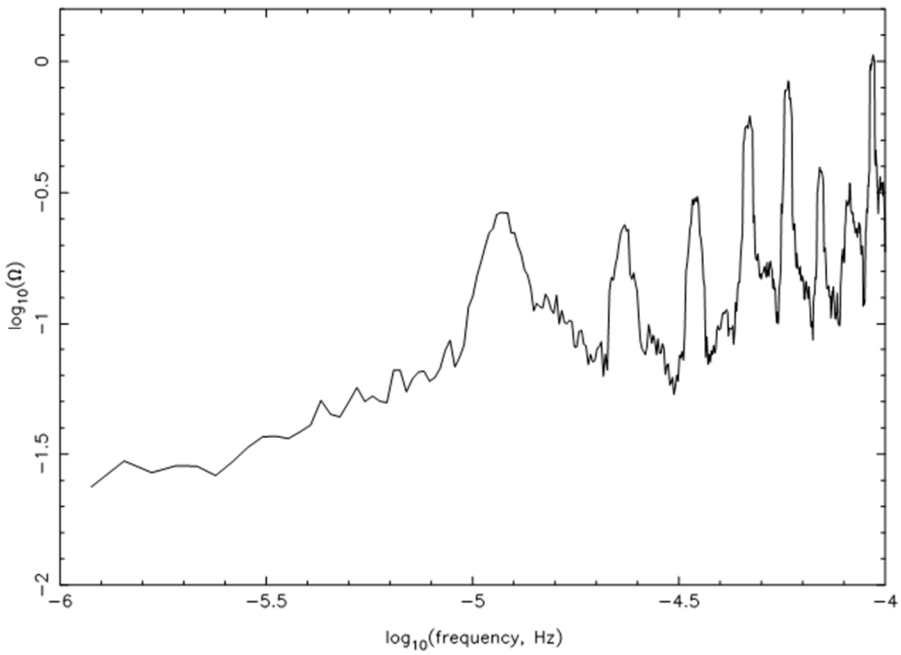

Figure RSS-32. Upper limits to GW energy density (bandwidth = center frequency) divided by the critical density required to close the universe of an isotropic GW background. Figure from Armstrong et al. [2003].

Solar conjunction experiment

INTRODUCTION[3]

In addition to the gravitational wave experiment, another cruise-phase Cassini science investigation was to use Cassini's radiometric data to measure the space components of the Sun's metric tensor. In the parameterized post-Newtonian formalism, this quantity is controlled by a parameter (γ) which is unity in General Relativity but may assume slightly different values in other metric theories of gravity. The measurement of γ with Cassini is based upon a new observable quantity: the frequency shift induced on a radio wave when the spacecraft is near solar conjunction. The calibration of the large frequency fluctuations induced by the solar corona, necessary in order to guarantee the required signal stability, was performed using the novel Cassini radio frequency system, based on a multi-frequency link.

PREVIOUS TESTS AND CASSINI'S EXPERIMENTAL CONFIGURATION

During a SCE, radio-metric data are used to measure the space curvature produced by the Sun. The parametrized post-Newtonian (PPN) parameter γ was estimated by other space-based experiments which allowed to bound the value of γ-1 to less than 0.001 using range measurements to the Viking landers [Reasenberg et al. 1979], an experiment carried out more than 20 years before Cassini's one, and more recently, using Very Long Baseline Interferometry techniques [Eubanks et al. 1997].

The measurement of γ with Cassini is based upon a new observable quantity: the frequency shift induced on a radio wave when the spacecraft is near solar conjunction. For this experiment, the geometry is particularly favorable and the relativistic relative frequency shift is on the order of 10^{-9}. On the other hand, this large Doppler signal is obtained only at small impact parameters, when the radio beam, well inside the solar corona, exhibits large frequency fluctuations. The solar plasma calibration, made possible by the multi-frequency link [Bertotti et al. 1993; Tortora et al. 2003, 2004; Mariotti and Tortora 2013], plays a crucial role in the experiment. In this method, the sky-frequencies in the three bands (X/X, X/Ka, Ka/Ka) are coherently combined to remove the effects of the solar plasma, the major noise source in the Doppler observable. Furthermore, the use of water vapor radiometers and microwave temperature profilers [Resch at al. 2002; Keihm et al. 2004], developed for the Cassini RSE, provides a precise calibration of the frequency shift due to the troposphere. The predicted stability of the radio link, once all media calibrations were applied, was in the order of 10^{-14} at integration times of 1000 s, showing that the Cassini experiment may have provided a measurement of γ to a level between 10^{-5} and 10^{-4}, one or two orders of magnitude better than previous experimental tests.

---

[3] *Much of this report, including the figures, comes from Iess et al [2003], and Bertotti et al [2003].*

CASSINI EXPERIMENT

The increase Δt produced by the gravitational field of the Sun (with mass M_S and radius R_S) in the roundtrip light-time between the ground antenna and the spacecraft, respectively, at the distances r_1 and r_2 from the Sun, is [Will 1993]:

$$\Delta t = 2(1+\gamma)\frac{GM_S}{c^3}\ln\left(\frac{4r_1r_2}{b^2}\right), \quad \text{(Eq. 1)}$$

where G is the gravitational constant and b (<< r_1, r_2) the impact parameter. The motion of the spacecraft and Earth produces a change in b and Δt, equivalent to a change in distance, hence to a relative radial velocity. The corresponding fractional frequency $y_{gr} = \Delta v/v$ shift for a two-way radio signal is [Iess et al. 1999]:

$$y_{gr} = \frac{d\Delta t}{dt} = -2(1+\gamma)\frac{GM_S}{c^3 b}\frac{db}{dt} = -(1\times 10^{-5}\ \text{sec})(1+\gamma)\frac{1}{b}\frac{\mathrm{d}b}{\mathrm{d}t}. \quad \text{(Eq. 2)}$$

For a spacecraft much farther away from the Sun than Earth, db/dt is not very different from the Earth's velocity v_E = 30 km/sec. In the Cassini solar conjunction the peak value of y_{gr} is 6×10^{10}. The Cassini experiment, exploiting this new observable [Iess et al. 1999; Bertotti and Giampieri 1992], has been carried out from June 6, 2002 to July 7, 2002, when the spacecraft was on its way to Saturn, around the time of a solar conjunction (Figure RSS-33).

The gravitational signal and the tracking passes which provided useful data [Iess et al. 2003] are shown in Figure RSS-34.

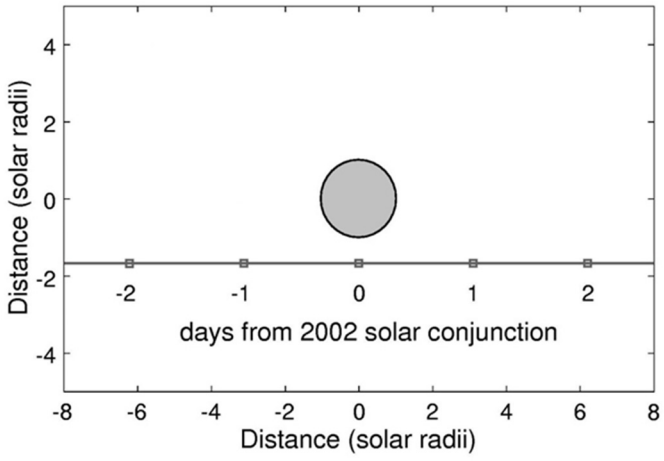

Figure RSS-33. Geometry of the 2002 Cassini solar conjunction. Cassini's motion in the sky relative to the Sun, as a function of days from the 2002 solar conjunction; coordinates are in solar radii. The conjunction, at which the spacecraft (at a geocentric distance of 8.43 AU) Sun and Earth were almost aligned (in this order), occurred on 21 June 2002 with a minimum impact parameter b_{min} = 1.6 R_S, and no occultation.

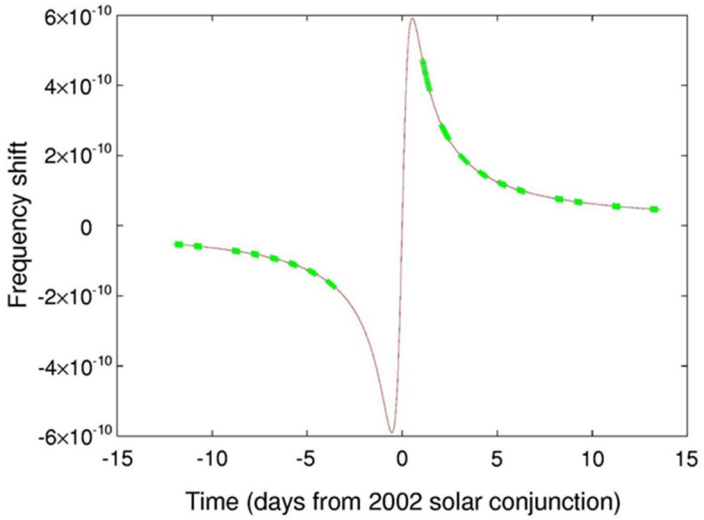

Figure RSS-34. The gravitational signal. The two-way relativistic frequency shift y_{gr} due to the sun and the available 18 passages, each lasting about 8 hours. Unfortunately, no data could be acquired for three days just before conjunction, due to a failure of the ground transmitter; moreover, the tracking data acquired near closest approach were particularly noisy. A much larger plasma noise was detected in some passes after conjunction and was fully removed by the multilink technique. Remarkably, in these days Solar and Heliospheric Observatory (SOHO) observations have shown large coronal mass ejections (CME) traversing the radio beam.

The main reason why the Doppler method has not been applied before is the overwhelming noise contribution due to the solar corona. The Cassini mission has overcome this hindrance with: a) high-frequency carriers in Ka-band, in addition to the X-band for standard operation; and b) a multi-frequency link in which three different phases are measured at the ground station. The resulting measurement errors are four orders of magnitude smaller than the relativistic signal (Eq. 2).

The dynamical model used in the orbital fit of Doppler data is particularly simple, thanks to the large distance from the Sun, the location of the spacecraft in interplanetary space and the lack of unknown gravitational perturbations by solar system bodies. JPL's Orbit Determination Program has been used in the integration of the equations of motion and the orbital solution, based upon planetary ephemerides and ancillary data, such as station location and Earth orientation parameters.

We have used up to 12 free solve-for parameters: a) the six components of the state vector at the start of the experiment; b) the three components of the non-gravitational acceleration due to the RTG in the spacecraft frame; c) the specular and diffuse reflectivity of the high gain antenna, which determine the magnitude (and the direction) of the non-gravitational acceleration due to solar radiation pressure; and d) the relativistic parameter γ. Consider-parameters (quantities not solved-for, but whose uncertainty is taken into account in the solution) include the dry troposphere, the station location, polar motion, and the Earth Love numbers (which intervene in the solid tide model).

Among the five parameters which control the nongravitational acceleration, three (the nonradial components of the thermal thrust from the RTG and one of the two optical coefficients of the high gain antenna) are poorly determined. It is, therefore, appropriate to investigate a solution including

only the other two, namely the radial acceleration due to the RTG and the diffuse reflectivity of the antenna; by so doing, most nongravitational perturbations are accounted for at a level consistent with the accuracy of the tracking data. The value of the other three parameters, the specular reflectivity and the nonradial components of the RTG acceleration, together with their uncertainties, have been taken from a separate fit carried out on the data from the Cassini solar opposition experiment, as mentioned earlier. This is our main orbital fit (see Figure RSS-35), with only nine parameters to be determined. The a priori uncertainty of the parameters which are not estimated, but affect the solution (such as the station geocentric coordinates and those derived from the gravitational wave experiment) has been included in the computation of the covariance matrix.

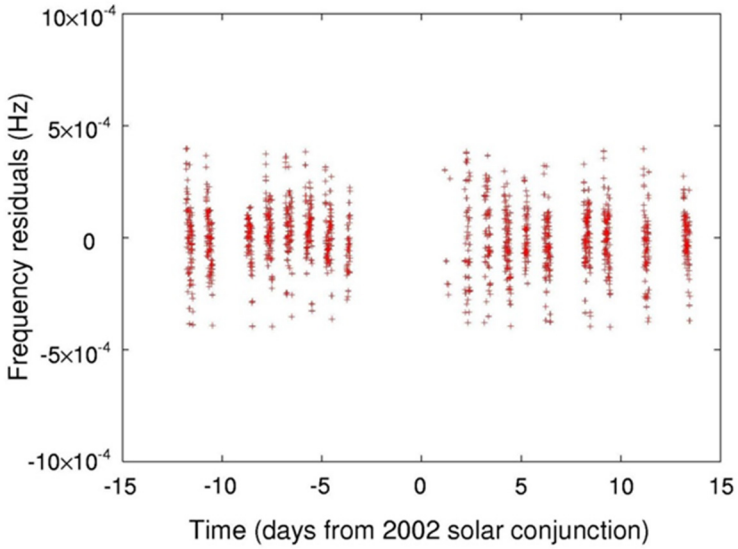

Figure RSS-35. The Doppler residuals. Two-way frequency residuals, relative to an 8.4 GHz carrier, as a function of time (in days from solar conjunction), obtained from the final 9-parameter fit on the calibrated data. The rms value of the 1094 data points (compressed at a 300 s integration time) is 1.2×10^{-4}, Hz corresponding to a one-way range rate of 2.2×10^{-6} m/s; this is an unprecedented accuracy for tracking data at solar conjunction.

Our result [Bertotti et al. 2003] $\gamma = 1 + (2.1 \pm 2.3) \times 10^{-5}$ agrees with Einstein's, with an accuracy ≈ 50 times better than published measurements. While a fundamental force such as gravity must always be investigated as accurately as possible, our result approaches a sensitivity at which, theoretically, deviations from General Relativity are expected.

Conclusions

The question, at what level violations of General Relativity can be expected, does not have a satisfactory answer yet. A long-range scalar field is currently assumed to play a fundamental role in primordial cosmology; although it decays with the expansion of the Universe, its present remnant would entail not only violations of the two main tests of General Relativity, but also a lack of universality of the constants of microphysics, as assumed in the Equivalence Principle [Damour et al. 1994, 2002].

A claim, based upon quasar absorption lines, that the fine structure constant α was weaker in the distant past has been recently made, thereby violating the Equivalence Principle [Murphy 2001a, 2001b, 2001c, 2001d]; if confirmed, and reconciled with other constraints on the variation of fundamental constants [Damour 2003], such finding would be the first serious challenge to Einstein's paradigm. No detailed theory is available about the expected amounts of these violations, but $\gamma - 1$ should be negative and, possibly, in the range 10^{-5}–10^{-7}. Therefore, our result, with an accuracy not far from this range, places an important constraint on this cosmological scenario.

Solar wind

INTRODUCTION

Before the failure of the Ka-band translator, Cassini's five-link radio system (X-up, X-down coherent with X-up; Ka-down coherent with X-up; Ka-up; Ka-down coherent with Ka-up) allowed a decomposition of the Doppler time series into three components: a non-dispersive component, the uplink-path plasma component, and the downlink-path plasma component [Iess et al. 2003; Bertotti et al. 2003; Tortora et al. 2003, 2004]. Having the up- and downlink plasma time series separately allowed the first localization along the line-of-sight and time of plasma turbulence between the ground station and the Cassini spacecraft.

Before the failure of the Ka-band translator, Cassini's five-link radio system … allowed a decomposition of the Doppler time series into three components: a non-dispersive component, the uplink-path plasma component, and the downlink-path plasma component … .

The idea has its origin in noise budget analysis of precision Doppler tracking experiments [Estabrook and Wahlquist 1975; Estabrook 1978; Vessot and Levine 1978] and is illustrated in Figure RSS-36. The upper plot is a space-time diagram, showing the ground station continuously transmitting a signal to Cassini and continuously receiving a signal from the spacecraft. In the two-way mode, the Doppler time series $y_2(t)$ has its phase perturbed by a localized plasma blob at distance x along the line-of-sight as illustrated, giving rise to two events in the two-way tracking time series separated by a time lag depending on the Earth-blob distance: $T_2 - 2\ x/c$, where T_2 is the two-way light time.

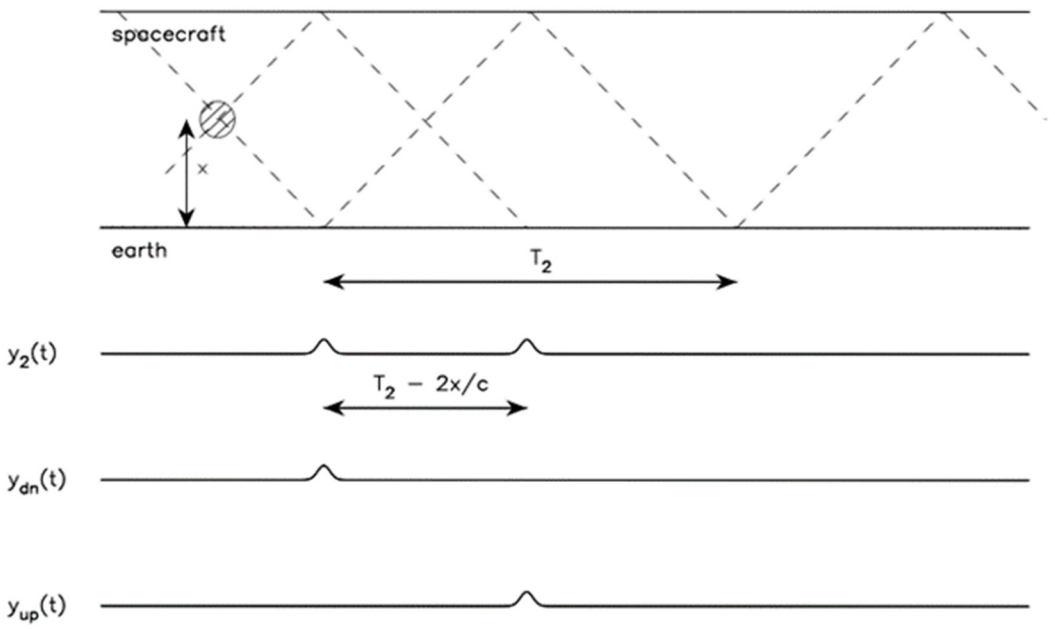

Figure RSS-36. Transfer function of plasma fluctuations to one-way and two-way phase/Doppler scintillation allows localization of plasma blobs along the line-of-sight. Upper plot is a space-time diagram (space vertically, time horizontally). The ground station and the spacecraft are continuously exchanging microwave signals, some of which are shown as dashed lines. If the signals pass through a well-localized plasma blob (indicated by the crosshatched circular area) the phase is perturbed. This perturbation is observed on both the uplink and downlink signals and on the two-way Doppler. The two-way, $y_2(t)$, and the one-way plasma-contribution Doppler time series, $y_{up}(t)$ and $y_{dn}(t)$, are shown in the *lower plot*. The phase perturbation is seen initially on the downlink, and (in the two-way Doppler) latter when the perturbation on the uplink is phase-coherently retransmitted back to the ground. The effect in $y_2(t)$ is two positively-correlated features in the time series, separated in time by $T_2 - 2x/c$, where T_2 is the two-way light time and x is the distance of the blob from the Earth. The one-way up and down Doppler time series detect the blob once each, but also separated by $T_2 - 2x/c$. Cross-correlation or windowed matched filtering between y_{up} and y_{dn} allows an estimate of the time delay thus the location of the blob.

Demonstration with Cassini Data on 2001 DOY 149

As described more completely in Richie-Halford et al. [2009] (from which the discussion and figures here are taken), the proof of concept observations were made with Cassini and DSS25 on 2001 DOY 149 (= 2001 May 29; Sun-Earth-spacecraft angle ≈ 6.6 degrees; $T_2 \approx 6825$ seconds, varying by ≈ 2 seconds over the pass). The full five-link system was used and Figure RSS-37 shows the inferred uplink and downlink plasma scintillation as a function of time. It is usually thought that plasma scintillation arises from distributed scattering along a large fraction of the line of sight. In this case, however, large, similarly-shaped events in the two time series are obvious. The time-offset is indicative of highly localized plasma turbulence in the solar wind on this day. Figure RSS-38 shows the location of this dominant screen in the solar wind as a function of time on DOY 149.

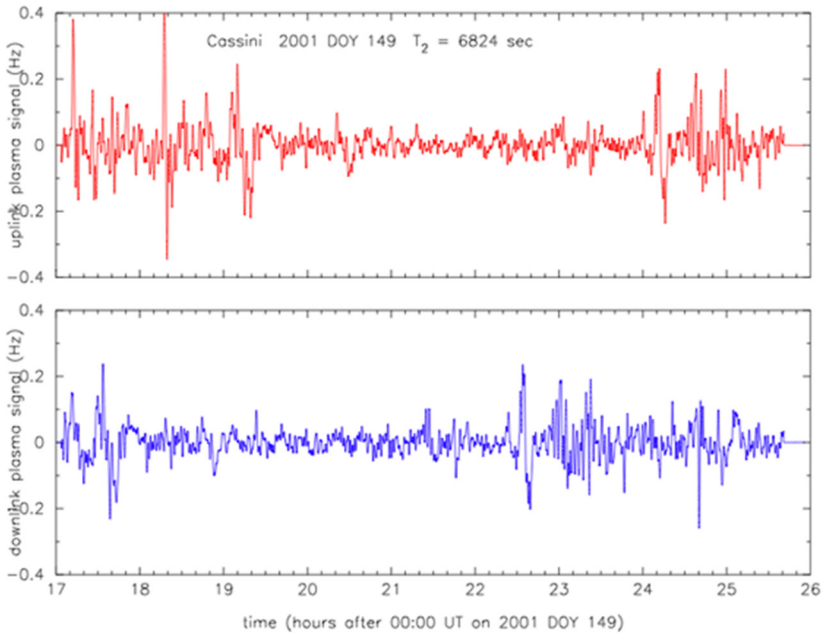

Figure RSS-37. Time series of the plasma contribution to the X-band up- and down links, $y_{up}(t)$ and $y_{dn}(t)$, for DSS25 Cassini track on 2001 DOY 149 = 2001 May 29. The two-way light time T_2 was ≈ 6824 seconds. Several large amplitude features in the downlink time series, for example at about 1730 UT, 2230 UT, 2300 UT, have clear echoes in the uplink time series with time difference ~T_2 − 2∗1.028 AU/c.

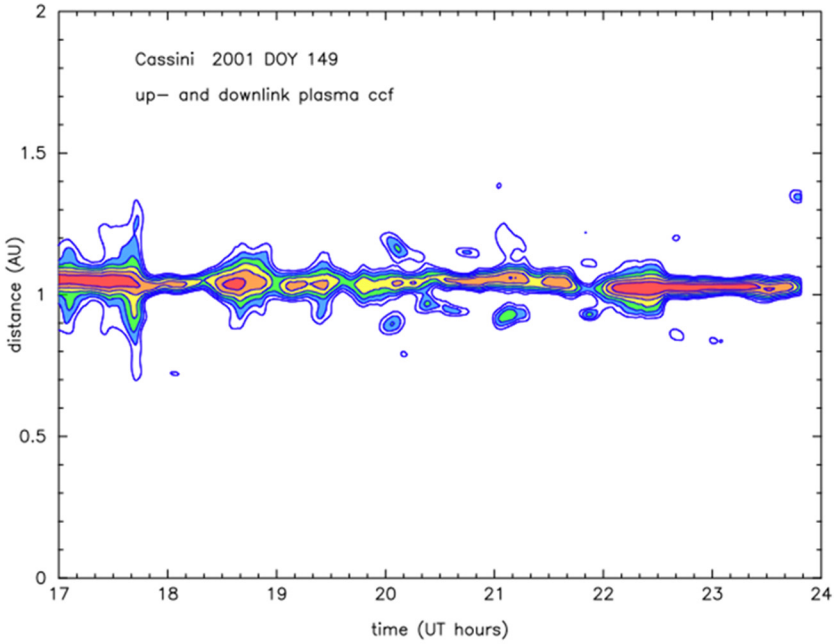

Figure RSS-38. Space-time cross-correlation function of the 2001 DOY 149 plasma up- and downlink time series plotted in Figure RSS-37. Y-axis is the distance from the Earth; x-axis is downlink received time. Contours of cross correlation value are plotted between 0.9 and 0.4, in 0.1 increments. Correlations > 0.9 are shaded red, those between 0.8 and 0.9 in orange, etc.

CONTEXT FROM NEAR-SUN CORONAL DENSITY OBSERVATIONS

Richie-Halford et al. [2009] looked at coronal data to see if there was an obvious plane-of-sky counterpart for the localized plasma on 2001 DOY 149. Figure RSS-39 shows a map of the coronal density structure at a height of four solar radii for Carrington Rotation 1976. Red is high density, black is low. The x-axis is Carrington rotation longitude, the y-axis is solar latitude. The point along the Earth-Cassini line of sight closest to the Sun is shown as a diamond on the map. The three dotted and dashed lines are the position of the heliospheric current sheet, calculated using various models. The positional agreement suggests the highly-localized plasma seen by Cassini is associated with the heliospheric current sheet on DOY 149.

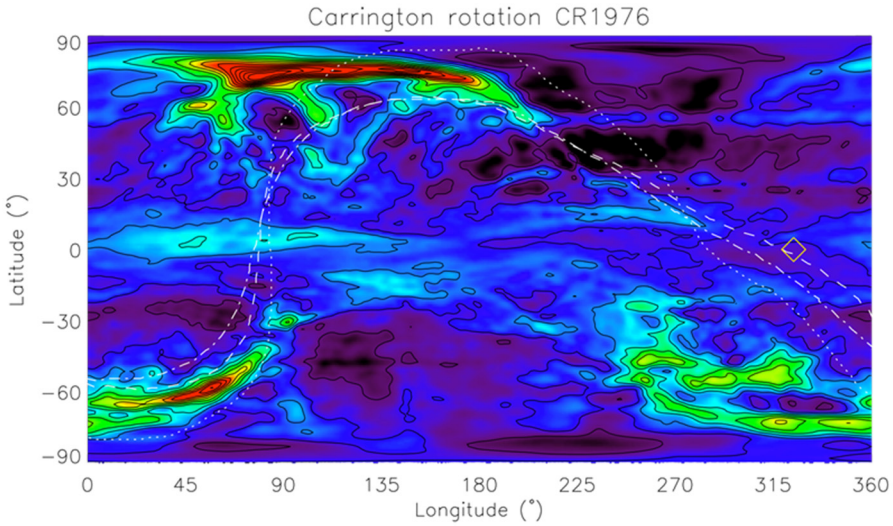

Figure RSS-39. Map of coronal density structure at a height of 4 solar radii for Carrington Rotation 1976, calculated using a solar rotational tomography technique from ~2 weeks of LASCO/SOHO C2 coronagraph observations. Red is high density, black is low. The x-axis refers to Carrington longitude, the y-axis to solar latitude. The point along the Earth-Cassini line of sight closest to the Sun is shown as a diamond. The three dotted and dashed lines are the position of the heliospheric current sheet, calculated using different models. The positional agreement suggests the highly-localized plasma seen by Cassini is associated with the heliospheric current sheet on this day.

LOCALIZATION ON OTHER DAYS

The localization of the dominant plasma turbulence on 2001 DOY 149 is remarkable but perhaps not typical. Figure RSS-40 shows analysis for 2002 DOY 160 = 2002 June 9 (Sun-Earth-spacecraft angle ≈ 9.5 degrees; two-way light time ≈ 8365 seconds). Correlation levels are in general lower than those in Figure RSS-38 for 2001 DOY 149. At the start of the track a scattering region nearer to the Earth than the ray path closest approach point (≈ 1AU∗cos(9.5 degrees) = 0.986 AU) is indicated. In mid-track, the correlation is particularly low, indicative of extended, rather than localized, scattering for much of this day.

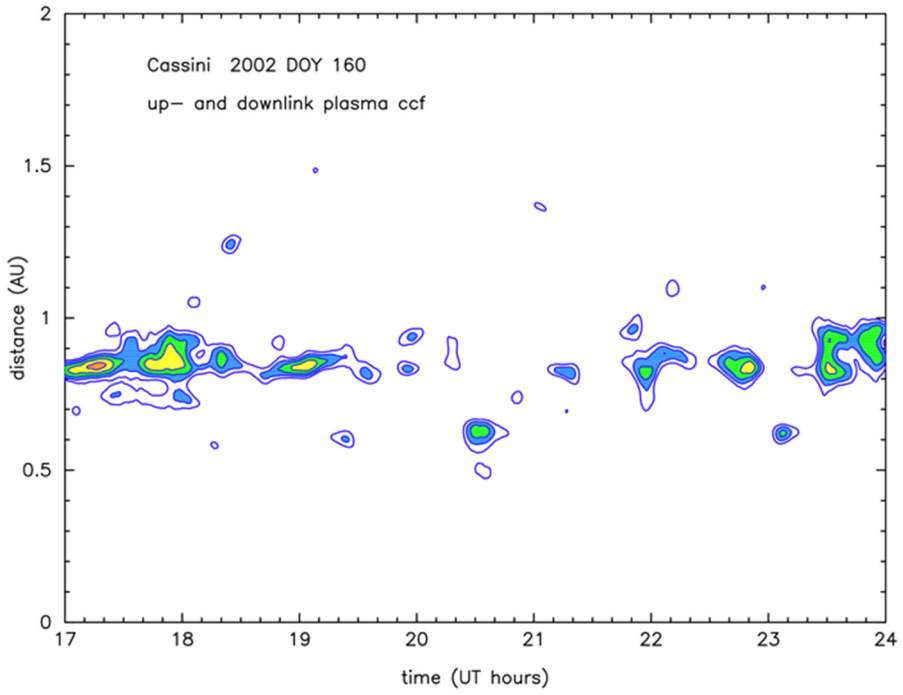

Figure RSS-40. As Figure RSS-38, but for 2002 DOY 160 = 2002 June 9. The Sun-Earth-spacecraft angle was about 9.5 degrees and the two-way light time was about 8365 seconds. Correlation levels in general lower than those in Figure RSS-38. At the start of the track a scattering region nearer to Earth than the ray path closest approach point (≈ 1AU cos (9.5 degrees) = 0.986 AU) is indicated. In mid-track the correlation is particularly low, indicative of extended, rather than localized, scattering.

OTHER SOLAR CONJUNCTION OBSERVATIONS

In addition to the 2001–2002 observations analyzed by Richie-Halford et al. [2009], subsequent solar conjunction data were collected. Full information (including Doppler modes, link information, spacecraft operational modes, exact start/stop times, etc.) are included in Project documentation [Anabtawi 2018]. Table RSS-14, for reference, is an overview of times when data were taken.

Table RSS-14. Overview of data times.

Year	Day-of-Year	Comment	Year	Day-of-Year	Comment
2005	196, 198, 208		2011	270–300	SCE8
2006	203–233	SCE3	2012	279–319	SCE9
2007	219–247	SCE4	2013	297–324	SCE10
2008	233–259	SCE5	2014	308–335	SCE11
2009	245–275	SCE6	2015	322–348	SCE12
2010	261–285	SCE7	2016	330–360	SCE13

SCE = solar conjunction experiment

Open questions

Cassini's principal non-Saturn science investigations were the gravitational wave experiment, solar conjunction relativity experiment, and solar wind plasma localization experiment. In all cases, Doppler tracking between Cassini and the DSN was used as the raw observation. The scientific objectives of future spacecraft cruise experiments would be to improve on current results.

The search for low frequency gravitational waves in space is the goal of the ongoing LISA mission, to be launched in the early 2030. This major undertaking of ESA and NASA confirms the motivations of the Cassini GWE, an attempt to search for gravitational wave sources in the mHz band at distances reaching the Virgo cluster.

The Cassini SCE increased our confidence in the validity of general relativity (GR), pushing possible violations of the metric in the solar system to the fifth decimal place. However, in spite of its apparent success, the Cassini test is just one more step in the quest for the breakdown of GR. Unfortunately, the theoretical framework does not give any clue on the level at which GR could be violated. Every test capable of improving the Cassini results is therefore significant. The BepiColombo Mission, which has a multilink radio system similar to Cassini's, with the additional feature of a pseudo-noise, high accuracy, ranging system, is expected to improve the SCE result by a factor 5–10 [Iess and Asmar 2007; Imperi and Iess 2017]. Remarkably, astrometric measurements of the gravitational deflection with the mission GAIA will reach a similar accuracy.

Here we comment on limiting noises in Cassini's precision Doppler observations and how these might be mitigated in future spacecraft cruise experiments. This section draws heavily on Bertotti et al. [2003]; Armstrong et al. [2003]; Asmar et al. [2005]; Armstrong [2006]; and Richie-Halford et al. [2009].

Precision Doppler tracking: noise in two-way observations

The Earth and the Cassini spacecraft act as separated test masses, electromagnetically tracked using microwaves. The ground stations for the Doppler system are the antennas of the NASA/JPL DSN. In particular, DSS25 was instrumented with Ka-band uplink and an advanced tropospheric calibrations system. The Cassini spacecraft was gravitationally very quiet when its attitude was controlled by reaction wheels and it had a sophisticated radio system. A precision frequency standard provided the frequency reference to both the transmitter and receiver chains. On the transmitter side, the exciter produced a near-monochromatic signal, referenced to the Fourier Transform Spectrometer (FTS) signal but at the desired transmit frequency. This was amplified by the transmitter—with closed-loop feedback around the power amplifier to ensure frequency stability was not degraded—and routed via waveguide to the transmitter feed horn in the basement of DSS25. To correct for aberration the Ka-band transmit feed horn was on a table which articulated in the horizontal plane. This allowed the Ka-band transmitted beam to be pointed correctly relative to the received beam. In a DSN beam waveguide antenna, the transmitted beam is reflected off six mirrors within the antenna up to the subreflector (near the prime focus), then back to the main dish

and out to the spacecraft (passing first through the troposphere, ionosphere, and solar wind). When the signal is received at the spacecraft, it is amplified and phase-coherently retransmitted to Earth. The received beam bounces off the main reflector to the subreflector and then, via mirrors and dichroic plates, to the receiver feed horn. The received signal is downconverted to an intermediate frequency where it is digitized. The digital samples are processed to tune out the (predictable) gross Doppler shift, and reduce the bandwidth of the samples.

For cruise operations, the bandwidth of the predetection data was typically reduced to 1 kHz and those data were recorded to disk along with the tuning information. The phase of the signal was detected in software and, using the tuning information, the received sky frequency could be reconstructed. This and the known frequency of the transmitted signal was used to compute the Doppler time series. Removal of the orbital signature and correction for charged particle and tropospheric scintillation gave Doppler residuals, which were used in subsequent processing steps for cruise experiments.

The main noises, along with the transfer functions of the noises to the two-way Doppler observable, are listed in Table RSS-15—see also Bertotti et al. [2003]; Asmar et al. [2005]; Armstrong [2006]. Cassini's multilink radio system, plus tropospheric corrections using the Advanced Media Calibration system, allowed: a) precise measurement of the PPN parameter γ [Bertotti et al. 2003]; b) improved limits to gravitational wave signal strength in the 10^{-6} to 10^{-1} Hz band [Armstrong et al. 2003]; and c) the first space-time localization of plasma turbulence in the inner heliosphere [Richie-Halford et al. 2009].

Table RSS-15. Cassini Cruise-phase Doppler noises and their transfer functions to two-way observations.

Noise source	Noise level (approx. Allan deviation at 1000s integration) during Cassini cruise phase	Transfer function of raw noise to Doppler observation (T_2 = two-way light time)
Frequency standard	8×10^{-16}	$\delta(t) - \delta(t - T_2)$
Antenna mechanical	2×10^{-15}	$\delta(t) + \delta(t - T_2)$
Ground electronics	2×10^{-16}	$\delta(t)$
Plasma scintillation	$< 10^{-15}$ at Ka-band for Sun-Earth-spacecraft angle > 150 degrees	variable, depending on effective phase screen location
Stochastic spacecraft motion	2×10^{-16}	$\delta(t - T_2/2)$
Receiver thermal	few $\times 10^{-16}$	$\delta(t)$
Spacecraft transponder	10^{-16}	$\delta(t - T_2/2)$
Tropospheric scintillation	$< 3 \times 10^{-15}$ to 30×10^{-15} (raw) $< 1.5 \times 10^{-15}$ to 3×10^{-15} (corrected)	$\delta(t) + \delta(t - T_2)$

Noise Mitigation in Future Precision Two-Way Doppler Observations

This section briefly outlines how future spacecraft Doppler observations might be made with 10x lower noise level, to a few times 10^{-16} Allan deviation at 1000s. In addition to possible innovation in Doppler extraction in the presence of moderate-to-strong interplanetary scintillation (relevant for

near-Sun relativity tracking and the decomposition of Doppler into dispersive uplink and downlink components for turbulence localization close to the Sun), Table RSS-16 shows the required improvements to the various subsystems or other noise contributors for typical tracking conditions—adapted from Armstrong [2006].

Table RSS-16. Required Noise improvement factors to reach ~10^{-16} Doppler noise.

Noise source	Comment/Allan deviation	Approximate improvement required
Frequency standard	currently ~8 × 10^{-16}	~8×
Antenna mechanical	currently ~2 × 10^{-15} under favorable conditions	~20×
Ground electronics	currently ~2 × 10^{-16}	~2×
Plasma scintillation	Cassini-class radio system probably adequate for ~10^{-16} with multilink calibration	~1×
Stochastic spacecraft motion	currently ~2 × 10^{-16}	~2×
Receiver thermal	few × 10^{-16}	~few ×
Spacecraft transponder	10^{-16}	~1×
Tropospheric scintillation	currently ~few × 10^{-15}, under favorable conditions and with calibration	~20×

Improving frequency standards and frequency distribution over what was possible in the Cassini cruise era by 8× is thought to be straightforward. Ground electronics can probably be improved by 2× by even more careful design. Similarly, spacecraft buffeting can probably be improved by 2× by careful design. Thermal noise can be improved by increasing the downlink SNR.

The big problems are antennal mechanical noise and tropospheric scintillation. These enter with the same transfer function: $\delta(t) + \delta\ (t - T_2)$. A possible way to mitigate this noise is to simultaneously track with an additional 3-way link (i.e., with a separate, listen only, ground antenna). As suggested by Estabrook [1978] and Hellings [private communication] in the context of tropospheric mitigation, a linear combination of the 2-way and 3-way Doppler data streams can be used to remove both the antenna mechanical and tropospheric noise of the 2-way station and replace it with those of the 3-way station [Armstrong et al. 2008]. If the 3-way station is located in a favorable tropospheric site and if it is mechanically stiff, this can in principle significantly improve the quality of the observation. Experiments demonstrating proof of concept have been done [Armstrong et al. 2008] and the practical limits of this approached are being investigated [Notaro et al. 2018]. These techniques may be useful in future precision radio science observations, for example BepiColombo, where substantial improvement in selected PPN parameters is possible, as well as future highly-accurate spacecraft navigation determinations [Tortora et al. 2004].

ACRONYMS

Note: For a complete list of Acronyms, refer to Cassini Acronyms – Attachment A.

AACS	Attitude and Articulation Control Subsystem
AMC	Advanced Media Calibration
AO	Announcement of Opportunity
AU	astronomical units
AU	astronomical unit
bps	bits per second
BSR	bistatic radar
C/A	closest approach
CAPS	Cassini Plasma Spectrometer
CDS	Command & Data Subsystem
CIRS	Composite Infrared Spectrometer
CME	coronal mass ejections
DOY	day of year
DSN	Deep Space Network
DSS	Deep Space Station
ELS	Electron Spectrometer
EM	electromagnetic
EOS	equation of state
ESA	electrostatic energy analyzer
FTS	Fourier Transform Spectrometer
GFO	Grand Finale Orbits
GM	gravitational mass
GR	general relativity
GSE	gravity science enhancement
GW	gigawatt
GWE	gravitational wave experiment
HASI–PWA	Huygens Atmospheric Structure and Permittivity, Wave, and Altimetry
HGA	high-gain antenna
ILR	inner Lindblad resonance
INMS	Ion and Neutral Mass Spectrometer
JPL	Jet Propulsion Laboratory
KaT	Ka-band translator
LCP	left circularly polarized
LEM	lower equipment module
LGA	low-gain antennas
LOS	line-of–sight
MHD	magneto-hydrodynamic

MOIF	moment of inertia factor
PLL	phase-locked loop
PM	periodic microstructure
PMS	Propulsion Module Subsystem
PPN	parametrized post-Newtonian
PPS	Power and Pyrotechnics Subsystem
RADAR	Titan Radar Mapper
RCP	right circularly polarized
RFIS	Radio Frequency Instrument Subsystem
RFS	Radio Frequency Subsystem
rms	root-mean-square
RPWS	Radio and Plasma Wave Spectrometer
RS	radio science
RSR	radio science receiver
RSS	Radio Science Subsystem
RSSG	Radio Science Systems Group
RTG	radioisotope thermoelectric generator
SCE	solar conjunction experiment
SEP	Sun-Earth-Probe
SNR	signal to noise ratio
SOHO	Solar and Heliospheric Observatory
SOI	Saturn Orbit Insertion
TCS	Temperature Control Subsystem
TM	Traceability Matrix
TSAC	Tracking System Analytical Calibrations
UEM	upper equipment module
USO	ultra-stable oscillator
UTC	Coordinated Universal Time
UVIS	Ultraviolet Imaging Spectrograph
VIMS	Visual and Infrared Imaging Spectrometer
VLBI	very-long-baseline interferometry
VSR	VLBI Science Receiver

REFERENCES

Disclaimer: The partial list of references below correspond with in-text references indicated in this report. For all other Cassini references, refer to Attachment B – References & Bibliographies; Attachment C – Cassini Science Bibliographies; the sections entitled References contributed by individual Cassini instrument and discipline teams located in Volume 1 Sections 3.1 and 3.2 Science Results; and other resources outside of the Cassini Final Mission Report.

Anabtawi, A., (2018), RSS Datasheet, PDS: The Planetary Atmosheres Node https://atmos.nmsu.edu/data_and_services/atmospheres_data/Cassini/logs/PDS_RSSArchivedDataProducts_Final_sorted.htm.

Anderson, J. D. and G. Schubert, (2010), Rhea's gravitational field and interior structure inferred from archival data files of the 2005 Cassini flyby, Physics of the Earth and Planetary Interiors 178, 176–182.

Anderson, J. D. and G. Schubert, (2007), Saturn's satellite Rhea is a homogeneous mix of rock and ice, Geophysical Research Letters, 34, 4–7.

Armstrong, J. W., F. B. Estabrook, S. W. Asmar, L. Iess, P. Tortora, (2008), Reducing antenna mechanical noise in precision spacecraft tracking. Radio Sci. 43, RS3010.

Armstrong, J. W., (2006), Low-frequency gravitational wave searches using spacecraft Doppler tracking, Living Reviews in Relativity, 9, 1, updated 11 January 2016.

Armstrong, J. W., L. Iess, P. Tortora, B. Bertotti, (2003), Stochastic gravitational wave background: Upper limits in the 10^{-6}–10^{-3} Hz band, The Astrophysical Journal, 599, 806–813.

Asmar,S. W., A. S. Konopliv, M. M. Watkins, J. G. Williams, R. S. Park, G. Kruizinga, M. Paik, D.-N. Yuan, E. Fahnestock, D. Strekalov, N. Harvey, W. Lu, D. Kahan, K. Oudrhiri, D. E.Smith, M. T.Zuber, (2013), The scientific measurement system of the Gravity Recovery and Interior Laboratory (GRAIL) Mission, Space Science Reviews, 178, 25–55, doi: 10.1007/s11214-013-9962-0.

Asmar, S. W, J. W. Armstrong, L. Iess, P. Tortora, (2005), Spacecraft Doppler tracking: Noise budget and accuracy achievable in precision radio science observations, Radio Science, 40, 1.

Bar-Sever Y. E., C. S. Jacobs, S. Keihm, G. E. Lanyi, C. J. Naudet, H. W. Rosenberger, T. F. Runge, A. B. Tanner, Y. Vigue-Rodi, (2007), Atmospheric media calibration for the deep space network, Proceedings of the IEEE, 95, 2180–2192.

Béghin, C., O. Randriamboarison, M. Hamelin, E. Karkoschka, C. Sotin, R. C. Whitten, J.-J. Berthelier, R. Grard, F. Simões, (2012), Analytic theory of Titan's Schumann resonance: Constraints on ionospheric conductivity and buried water ocean, Icarus, 218, 1028–1042.

Bertotti, B., L. Iess, P. Tortora, (2003), A test of general relativity using radio links with the Cassini spacecraft, Nature, 425, 374–376.

Bertotti, B., G. Comoretto, L. Iess, (1993), Doppler tracking of spacecraft with multifrequency links, Astronomy & Astrophysics, 269, 608–616.

Bertotti B. and G. Giampieri, (1992), Relativistic effects for Doppler measurements near solar conjunction, Classical and Quantum Gravity, 9, 777–793.

Bills, B. G. and F. Nimmo, (2011), Rotational dynamics and internal structure of Titan, Icarus 214, 351–355.

Bills, B. G. and F. Nimmo, (2008), Forced obliquity and moments of inertia of Titan, Icarus, 196, pp. 293–296.

Bird, M. K., R. Dutta-Roy, S. W. Asmar, T. A. Rebold, (1997), Detection of Titan’s ionosphere from Voyager 1 radio occultation observations, Icarus 130, 426–436.

Bjoraker, G., (2013), Oxygen compounds in Saturn’s atmosphere during the 2010 northern storm, American Geophysical Union (AGU) Fall Meeting, abstracts.

Buratti, B. J., (1988), Enceladus: Implications of its unusual photometric properties, Icarus 75, 113–126.

Čadek, O., G. Tobie, T. Van Hoolst, M. Massé, G. Choblet, A. Lefèvre, G. Mitri, et al., (2016), Enceladus's internal ocean and ice shell constrained from Cassini gravity, shape, and libration data, Geophysical Research Letters, 43, 5653–5660.

Campbell, J. K. and J. D. Anderson, (1989), Gravity field of the Saturnian system from Pioneer and Voyager tracking data, The Astronomical Journal, 97, 1485–1495

Castillo-Rogez, J. C. and J. I. Lunine, (2010), Evolution of Titan's rocky core constrained by Cassini observations, Geophysical Research Letters, 37, 20.

Choukroun, M. and C. Sotin, (2012), Is Titan's shape caused by its meteorology and carbon cycle? Geophysical Research Letters, 39, 4.

Collins, G. C. and J. C. Goodman, (2007), Enceladus' south polar sea, Icarus, 189, 72–82, doi: 10.1016/j.icarus.2007.01.010.

Colwell, J. E., P. D. Nicholson, M. S. Tiscareno, C. D. Murray, R. G. French, E. A. Marouf, (2009), The structure of Saturn's rings, Chapter 13, In Saturn from Cassini-Huygens, (eds.) M. K. Dougherty, L. W. Esposito, S. M. Krimigis, Springer, Dordrecht, pp. 375–412.

Connerney, J. A. P. and J. H. Waite, (1984), New model of Saturn’s ionosphere with an influx of water from the rings, Nature, 312, 136–138.

Cravens, T. E., I. P. Robertson, S. A. Ledvina, D. Mitchell, S. M. Krimigis, J. H. Waite Jr, (2008), Energetic ion precipitation at Titan, Geophysical Research Letters, 35, 3 CiteID L03103.

Cuzzi, J. N., E. A. Marouf, R. G. French, R.A. Jacobson, C. D. Murray, N. J. Cooper, (2018), Saturn’s F Ring is shepherded by Prometheus, Science Advances, in review.

Cuzzi, J., R. Clark, G. Filacchione, R. French, R. Johnson, E. Marouf, L. Spilker, (2009), Ring particle composition and size distribution, Chapter 15, In Saturn from Cassini-Huygens, (eds.) M. K. Dougherty, L. W. Esposito, S. M. Krimigis, Springer, Dordrecht, pp. 459–509.

Cuzzi, J. N. and P. R. Estrada, (1998), Compositional evolution of Saturn's rings due to meteoroid bombardment, Icarus, 132, 1–35.

Damour, T., (2003), String theory, cosmology and varying constants, Astrophysics and Space Science, 283, 445–456.

Damour T., F. Piazza, G. Veneziano, (2002), Violations of the equivalence principle in a dilaton-runaway scenario, Physical Review, D 66, no. 4, 046007, doi: 10.1103/PhysRevD.66.046007.

Damour, T. and A. M. Polyakov, (1994), The string dilaton and a least coupling principle, Nuclear Physics B, vol. 423, Issues 2–3, pp. 532–558, doi: 10.1016/0550-3213(94)90143-0.

Durante, D., D. J. Hemingway, P. Rachioopa, L. Iess, D. J. Stevenson, (2019), Titan's gravity field and interior structure after Cassini, Icarus, 326, 123–132.

Estabrook, F. B., (1978), Gravitational wave detection with the Solar Probe. II. The Doppler tracking method, In A Close-Up of the Sun (JPL Publication 78-70), September 1, 1978, pp. 441–449.

Estabrook, F. B. and H. D. Wahlquist, (1975), Response of Doppler spacecraft tracking to gravitational radiation, General Relativity and Gravitation, 6, 439–447.

Eubanks, T. M., D. N. Matsakis, J. O. Martin, B. A. Archinal, A. L. Fey, F. J. Josties, D. D. McCarty, S. A. Klioner, E. Formalont, A. J. Beasley, I. I. Shapiro, (1997), Advances in solar system tests of gravity, Joint American Physical Society (APS)/American Association of Physics Teachers (AAPT) Meeting, Washington D.C., 1997 April 18–21, paper K11.05, http://flux.aps.org/meetings/YR97/BAPSAPR97/abs/S1280005.html.

Fjeldbo, G., (1964), Bistatic radar methods for studying planetary ionospheres and surfaces, Science Report, no. 2, Stanford Electronics Laboratories, Stanford, CA, NsG-377, SU-SEL-64-025.

Flasar, F. M., R. K. Achterberg, P. J. Schinder, (2014), Thermal structure of Titan's troposphere and middle atmosphere, Chapter 3, Titan: Interior, Surface, Atmosphere, and Space Environment, (eds.) I. Müller-Wodarg, C. A. Griffith, E. Lellouch, T, E. Cravens, Cambridge University Press.

Fortes, A. D., P. M. Grindrod, S. K. Trickett, L. Vočadlo, (2007), Ammonium sulfate on Titan: Possible origin and role in cryovolcanism, Icarus, 188, 139–153.

Fortney, J. J., R. Helled, N. Nettelmann, D. J. Stevenson, M. S. Marley, W. B. Hubbard, L. Iess, (2016), The Interior of Saturn, Astrophysics: Earth and Planetary Astrophysics Cornell University, http://www.ucolick.org/~jfortney/Saturn21st.pdf.

French, R. G., C. A. McGhee-French, K. Lonergan, T. Sepersky, R. A. Jacobson, P. D. Nicholson, M. M. Hedman, E. A. Marouf, J. E. Colwell, (2017), Noncircular features in Saturn's rings IV: Absolute radius scale and Saturn's pole direction, Icarus, 290, 14–45.

French, R. G., P. D. Nicholson, C. A. McGhee-French, K. Lonergan, T. Sepersky, M. M. Hedman, E. A. Marouf, J. E. Colwell, (2016), Noncircular features in Saturn's rings III: The Cassini Division, Icarus 274, 131–162.

French, R. G., P. D. Nicholson, M. M. Hedman, J. M. Hahn, C. A. McGhee-French, J. E. Colwell, E. A. Marouf, N. J. Rappaport, (2016), Deciphering the embedded wave in Saturn's Maxwell ringlet, Icarus, 279, 62–77.

García-Melendo, E., S. Pérez-Hoyos, A. Sánchez-Lavega, R. Hueso, Saturn's zonal wind profile in 2004–2009 from Cassini ISS images and its long-term variability, Icarus, 215, no. 1, 62–74.

Hedman, M. M., C. M. Gosmeyer, P. D. Nicholson, C. Sotin, Robert H. Brown, R. N. Clark, K. H. Baines, B. J. Buratti, M. R. Showalter, (2013), An observed correlation between plume activity and tidal stresses on Enceladus, Nature, 500, 182–184, doi: 10.1038/nature12371.

Hellings, R., (private communication).

Hemingway, D., F. Nimmo, H. Zebker, L. Iess, (2013), A rigid and weathered ice shell on Titan, Nature, 500, 550–552, doi: 10.1038/nature12400.

Howett, C. J. A., J. R. Spencer, J. Pearl, M. Segura, (2011), High heat flow from Enceladus' south polar region measured using 10-600 cm^{-1} Cassini/CIRS data, Journal of Geophysical Research, vol. 116, Issue E3, doi: 10.1029/2010JE003718.

Hubbard, W. B., (1999), Gravitational signature of Jupiter's deep zonal flows, Icarus, vol. 137, Issue 2, pp. 357–359, doi: 10.1006/icar.1998.6064.

Iess, L., B. Militzer, Y. Kaspi, P. Nicholson, D. Durante, P. Racioppa, A. Anabtawi, et al., (2019), Measurement and implications of Saturn's gravity and ring mass, Science, vol. 364, Issue 6445, eaat2965, doi: 10.1126/science.aat2965.

Iess, L., W. M. Folkner, D. Durante, M. Parisi, Y. Kaspi, E. Galanti, and D. R. Buccino, (2018), Measurement of Jupiter's asymmetric gravity field, Nature, 555, 220–222, doi: 10.1038/nature25776.

Iess, L., D. J. Stevenson, M. Parisi, D. Hemingway, R. A. Jacobson, J. I. Lunine, F. Nimmo, et al., (2014), The gravity field and interior structure of Enceladus, Science, 344, 78–80, doi: 10.1126/science.1250551.

Iess, L., P. Racioppa, N. J. Rappaport P. Tortora, (2012), The tides of Titan, Science, 337, 457–459, doi: 10.1126/science.1219631.

Iess, L., N. J. Rappaport, R. A. Jacobson, P. Racioppa, D. J. Stevenson, P. Tortora, J. W. Armstrong, S. W. Asmar, (2010), Gravity field, shape, and moment of inertia of Titan, Science, 327, 1367, doi: 10.1126/science.1182583.

Iess, L., N. J. Rappaport, P. Tortora, J. Lunine, J. W. Armstrong, S. W. Asmar, L. Somenzi, F. Zingoni, (2007), Gravity field and interior of Rhea from Cassini data analysis, Icarus, 190, 585–593.

Iess, L. and S. Asmar, (2007), Probing space-time in the solar system: from Cassini to BepiColombo, International Journal of Modern Physics D, vol. 16, no. 12a, pp. 2117–2126, doi: 10.1142/S0218271807011449.

Iess, L., N. Rappaport, P. Tortora, G. Rapino, L. Somenzi, (2005), The determination of Iapetus mass from Doppler tracking of the Cassini spacecraft, In Geophysical Research Abstracts, European Geosciences Union General Assembly, Vienna, Austria, 24–29 April 2005, vol. 7, Union Symposia, US9 Titan-Huygens-Cassini: First Results, US9/PS1.5-1MO4O-002, EGU05-A-11176, https://www.cosis.net/abstracts/EGU05/11176/EGU05-J-11176-1.pdf.

Iess, L., R. A. Jacobson, M. Ducci, D. J. Stevenson, J. I. Lunine, J. W. Armstrong, S. W. Asmar, S. J. Keihm, A. Tanner, H. Rosenberger, (2004), Measurements and calibration of tropospheric delay at Goldstone from the Cassini Media Calibration System, IPN Progress Report, 42–158.

Iess L., P. Tortora, J. D. Anderson, S. W. Asmar, E. Barbinis, B. Bertotti, D. U. Fleischman, M. S. Gatti, et al., (2003), The Cassini solar conjunction experiment: a new test for general relativity, IEEE Aerospace Conference, Big Sky, MT, 8–15 March 2003, IEEE Aerospace Conference Proceedings (Cat. No.03TH8652), https://ieeexplore.ieee.org/stamp/stamp.jsp?tp=&arnumber=1235053.

Iess, L., G. Giampieri, J. D. Anderson, B. Bertotti, (1999), Doppler measurement of the solar gravitational deflection, Classical and Quantum Gravity, 16, 5, 1487–1502.

Imperi, L. and L. Iess, (2017), The determination of the post-Newtonian parameter γ during the cruise phase of BepiColombo, Classical and Quantum Gravity, vol. 34, no. 7, 075002, doi: 10.1088/1361-6382/aa606d.

Jacobson, R. A., P. G. Antreasian, J. J. Bordi, K. E. Criddle, R. Ionasescu, J. B. Jones, R. A. Mackenzie, et al., (2006), The gravity field of the Saturnian system from satellite observations and spacecraft tracking data, The Astronomical Journal, vol. 132, no. 6, pp. 2520–2526.

Jacobson, R. A., (2004), The orbits of the major Saturnian satellites and the gravity field of Saturn from spacecraft and Earth-based observations, The Astronomical Journal, vol. 128, no. 1, pp. 492–501.

Kaspi, Y., E. Galanti, W. B. Hubbard, D. J. Stevenson, S. J. Bolton, L. Iess, and D. Durante, (2018), Jupiter’s atmospheric jet streams extend thousands of kilometres deep, Nature, 555, 223–226, doi: 10.1038/nature25793.

Kaspi, Y., (2013), Inferring the depth of the zonal jets on Jupiter and Saturn from odd gravity harmonics, Geophysical Research Letters, 40, 676–680.

Kliore, A. J., A. Nagy, S. Asmar, A. Anabtawi, E. Barbinis, D. Fleischman, D. Kahan, J. Klose, (2014), The ionosphere of Saturn as observed by the Cassini radio science system, Geophysical Research Letters, 41, no. 16, 5778–5782.

Kliore, A. J., A. F. Nagy, T. E. Cravens, M. S. Richard, A. M. Rymer, (2011), Unusual electron density profiles observed by Cassini radio occultation in Titan’s ionosphere: Effects of enhanced magnetospheric electron precipitation, Journal of Geophysical Research, 116, A11, CiteID A11318.

- - - - - - - - - - - - - -

Kliore, A. J., A. Nagy, E. Marouf, (2010), The plasma cloud of Enceladus, In European Planetary Science Congress, Angelicum Centre – Pontifical University of Saint Thomas Aquinas, 19–24 September 2010, Rome, Italy, EPSC abstracts, vol. 5, EPSC2010-113.

Kliore, A. J., A. F. Nagy, E. A. Marouf, A. Anabtawi, E. Barbinis, D. U. Fleischman, D. S. Kahan, (2009), Mid-latitude and high latitude electron density profiles in the ionosphere of Saturn obtained by radio occultations, Journal of Geophysical Research: Space Physics, 114, A4, CiteID A04315.

Kliore, A. J., A. F. Nagy, E. A. Marouf, R. G. French, F. M. Flasar, N. J. Rappaport, A. Anabttawi et al., (2008), First results from the Cassini radio occultations of the Titan ionosphere, Journal of Geophysical Research: Space Physics, 113, A9, CiteID A09317.

Kliore, A. J., J. Armstrong, F. Flasar, R. French, E. Marouf, A. Nagy, N. Rappaport, et al., (2006), Cassini radio occultation by Enceladus plume, American Geophysical Union (AGU) Fall Meeting, abstract.

Kliore, A. J., J. D. Anderson, J. W. Armstrong, S. W. Asmar, C. L. Hamilton, N. J. Rappaport, H. D. Wahlquist, R. Ambrosini, F. M. Flasar, R. G. French, L. Iess, E. A. Marouf, A. F. Nagy, (2004), Cassini Radio Science, Space Science Reviews, 115, Issue 1–4, 1–70.

Kozai, Y., (1957), Observations of the satellites of Saturn, Annals of the Tokyo Astronomical Observatory, Series 25, 73.

Lebonnois, S., F. M. Flasar, T. Tokano, C. Newman, (2014), The general circulation of Titan's lower and middle atmosphere, Chapter 4, In Titan: Interior, Surface, Atmosphere, and Space Environment, (eds.) I. Müller-Wodarg, C. A. Griffith, E. Lellouch, T. E. Cravens, Cambridge University Press, pp. 122–157, doi: 10.1017/CBO9780511667398.007.

Lorenz, R. D., B. W. Stiles, R. L. Kirk, M. D. Allison, P. Persi del Marmo, L. Iess, J. I. Lunine, S. J. Ostro, S. Hensley, (2008), Titan's rotation reveals an internal ocean and changing zonal winds, Science, 319, 5870, 1649–1651.

Mackenzie, R. A., L. Iess, P. Tortora, N. J. Rappaport, (2008), A non-hydrostatic Rhea, Geophysical Research Letters, 35, L05204, doi: 10.1029/2007GL032898, pp. 1–5.

Mackenzie, R. A., P. G. Antreasian, J. J. Bordi, K. E. Criddle, R. Ionasescu, R. A. Jacobson, J. B. Jones, D. W. Parcher, F. J. Pelletier, D. C. Roth, J. R. Stauch, (2007), A determination of Rhea’s gravity field from Cassini navigation analysis. Proceedings of the American Astronomical Society (AAS)/American Institute of Aeronautics and Astronautics (AIAA) 17th Space Flight Mechanics Meetings, 28 January–1 February 2007, Sedona, AZ.

Mariotti, G. and P. Tortora, (2013), Experimental validation of a dual uplink multifrequency dispersive noise calibration scheme for Deep Space tracking, Radio Science, vol. 48, Issue 2, pp. 111–117, doi: 10.1002/rds.20024.

Marouf, N. Rappaport, R. French, R. Simpson, A. Kliore, C. McGhee, P. Schinder, A. Anabtawi, (2008), Dialectric constant of Titan’s south polar region from Cassini Radio Science bistatic scattering observations, American Geophysical Union (AGU) Fall Meeting, abstract P21A-1319.

Marouf, E., M. Flasar, R. French, A. Kliore, A. Nagy, N. Rappaport, C. McGhee et al., (2006), Evidence for likely liquid hydrocarbons on Titan's surface from Cassini Radio Science bistatic scattering observations, American Geophysical Union (AGU) Fall Meeting, abstract P11A-07.

Marouf, E. A., G. L. Tyler, P. A. Rosen, (1986), Profiling Saturn's rings by radio occultation, Icarus vol. 68, Issue 1, pp. 120–166, doi: 10.1016/0019-1035(86)90078-3.

Marouf, E. A., G. L. Tyler, H. A. Zebker, R. A. Simpson, V. R. Eshleman, (1983), Particle-size distributions in Saturn's rings from Voyager 1 radio occultation, Icarus, 54, pp. 189–211.

McKinnon, W. B., (2015), Effect of Enceladus's rapid synchronous spin on interpretation of Cassini gravity, Geophysical Research Letters, 42, 2137–2143, doi: 10.1002/2015GL063384.

Meyer, J. and J. Wisdom, (2007), Tidal heating in Enceladus, Icarus, 188, 535–539.

Mitri, G., R. Meriggiola, A. Hayes, A. Lefevre, G. Tobie, A. Genova, J. I. Lunine, H. Zebker, (2014), Shape, topography, gravity anomalies and tidal deformation of Titan, Icarus, 236, 169–177.

Morooka, M. W., J.-E. Wahlund, A. I. Eriksson, W. M. Farrell, D. A. Gurnett, W. S. Kurth, A. M. Persoon, M. Shafiq, M. Andre, M. K. G. Holmberg, (2011), Dusty plasma in the vicinity of Enceladus, Journal of Geophysical Research, 116, A12221, doi: 10.1029/2011JA017038.

Murphy, M. T., J. K. Webb, V. V. Flambaum, V. A. Dzuba, C. W. Churchill, J. X. Prochaska, J. D. Barrow, A. M. Wolfe, (2001a), Possible evidence for a variable fine-structure constant from QSO absorption lines: Motivations, analysis and results, Monthly Notices of the Royal Astronomical Society (MNRAS), 327, 1208–1222.

Murphy, M. T., J. K. Webb, V. V. Flambaum, C. W. Churchill, J. X. Prochaska, (2001b), Possible evidence for a variable fine-structure constant from QSO absorption lines: systematic errors. Monthly Notices of the Royal Astronomical Society (MNRAS), 327, 1223–1236.

Murphy, M. T., J. K. Webb, V. V. Flambaum, J. X. Prochaska, A. M. Wolfe, (2001c), Further constraints on variation of the fine-structure constant from alkali-doublet QSO absorption lines. Monthly Notices of the Royal Astronomical Society (MNRAS), 327, 1237–1243.

Murphy, M. T., J. K. Webb, V. V. Flambaum, M. J. Drinkwater, F. Combes, T. Wiklind, (2001d), Improved constraints on possible variations of physical constants from H I 21-cm and molecular QSO absorption lines, Monthly Notices of the Royal Astronomical Society (MNRAS), 327, 1244–1248.

Nagy, A. F., A. J. Kliore, E. Marouf, R. French, M. Flasar, N. J. Rappaport, A. Anabtawi, et al., (2006), First results from the ionospheric radio occultations of Saturn by the Cassini spacecraft, Journal of Geophysical Research, 111, A6, CiteID A06310.

Nicholson, P. D., R. G. French, M. M. Hedman, E. A. Marouf, J. E. Colwell, (2014a), Noncircular features in Saturn’s rings I: The edge of the B ring, Icarus, 227, 152–175.

Nicholson, P.D., R. G. French, C. A. McGhee-French, M. M. Hedman, E. A. Marouf, J. E. Colwell, K. Lonergan, T. Sepersky, (2014b), Noncircular features in Saturn’s rings II: The C ring, Icarus 241, 373–396.

Nimmo, F., B. G. Bills, P. C. Thomas, (2011), Geophysical implications of the long-wavelength topography of the Saturnian satellites, Journal of Geophysical Research, 116, E11001.

Nixon, C. A., R. D. Lorenz, R. K. Achterberg, A. Buch, P. Coll, R. N. Clark, R. Courtin, et al., (2018), Titan's cold case files - Outstanding questions after Cassini-Huygens, Planetary and Space Science, 155, 50–72.

Notaro, V., M. J. Mariani, A. Di Duscio, L. Iess, J. W. Armstrong, S. W. Asmar, (2018), Feasibility of an innovative technique for noise reduction in spacecraft doppler tracking, IEEE Aerospace Conference, 3–10 March 2018, Big Sky, MT, paper 2187 3.

Null, G. W., E. L. Lau, E. D. Biller, J. D. Anderson, (1981), Saturn gravity results obtained from Pioneer 11 tracking data and Earth-based Saturn satellite data, The Astronomical Journal, 86, 456–468.

O'Donoghue, J., T. S. Stallard, H. Melin, G. H. Jones, S. W. H. Cowley, S. Miller, K. H. Baines, J. S. D. Blake, (2013), The domination of Saturn's low-latitude ionosphere by ring 'rain', Nature, 496, 193–195.

Ojakangas, G. W. and D. J. Stevenson, (1986), Episodic volcanism of tidally heated satellites with application to Io, Icarus, 66, 341.

Postberg, F., J. Schmidt, J. Hillier, S. Kempf, R. Srama, (2011), A salt-water reservoir as the source of a compositionally stratified plume on Enceladus, Nature, 474, 620.

Rappaport, N. J., P.-Y. Longaretti, R. G. French, E. A. Marouf, C. A. McGhee, (2009), A procedure to analyze nonlinear density waves in Saturn's rings using several occultation profiles, Icarus, vol. 199, Issue 1, pp. 154–173, doi: 10.1016/j.icarus.2008.08.014.

Rappaport, N. J., L. Iess, J. Wahr, J. I. Lunine, J. W. Armstrong, S. W. Asmar, P. Tortora, M. Di Benedetto, P. Racioppa, (2008), Can Cassini detect a subsurface ocean in Titan from gravity measurements?, Icarus, 194, 711–720.

Rappaport, N. J., L. Iess, P. Tortora, S. W. Asmar, L. Somenzi, A. Anabtawi, E. Barbinis, D. U. Fleischman, G. L. Goltz, (2005), Gravity science in the Saturnian system: the masses of Phoebe, Iapetus, Dione and Enceladus, 37th Annual Meeting of the Division for Planetary Sciences of the American Astronomical Society, Cambridge, UK, 4–9 September 2005, presentation 39.02.

Reasenberg, R. D., I. I. Shapiro, P. E. MacNeil, R. B. Goldstein, J. C. Breidenthal, J. P. Brenkle, D. L. Cain, T. M. Kaufman, T. A. Komarek, A. I. Zygielbaum, (1979), Viking Relativity Experiment: Verification of signal retardation by solar gravity, The Astrophysical Journal, 234, 219–221.

Resch, G. M., S. J. Keihm, G. E. Lanyi, R. P. Linfield, C. J. Naudet, A. L. Riley, H. W. Rosenberger, A. B. Tanner, (2002), The media calibration system for Cassini Radio Science: Part III, IPN Progress Report, 42–148.

Richie-Halford, A. C., L. Iess, P. Tortora, J. W. Armstrong, S. W. Asmar, R. Woo, S. R. Hab-bal, H. Morgan, (2009), Space-time localization of heliospheric plasma turbulence using multiple spacecraft links, Space Weather 7, S12003, doi: 10.1029/2009SW000499.

Sanchez-Lavega, A., J. F. Rojas, P. V. Sada, (2000), Saturn's zonal winds at cloud level, Icarus, vol. 147, Issue 2, pp. 405–420, doi: 10.1006/icar.2000.6449.

Schinder, P. J., F. M. Flasar, E. A. Marouf, R. G. French, E. Barbinis, D. Fleischman, A. Anabtawi, R. K. Achterberg, (2019), The structure of Titan's atmosphere from Cassini radio occultations: One- and two- way occultations, Icarus, submitted 26 July 2019.

Schinder, P. J., F. M. Flasar, E. A. Marouf, R. G. French, A. Anabtawi, E. Barbinis, A. J. Kliore, (2015), A numerical technique for two-way radio occultations by oblate axisymmetric atmospheres with zonal winds, Radio Science, 50, 712–727.

Schinder, P. J., F. M. Flasar, E. A. Marouf, R. G. French, C. A. McGhee, A. J. Kliore, N. J. Rappaport, E. Barbinis, D. Fleischman, A. Anabtawi, (2012), The structure of Titan's atmosphere from Cassini radio occultations: Occultations from the Prime and Equinox missions, Icarus, 221, 1020–1031.

Schinder, P. J., F. M. Flasar, E. A. Marouf, R. G. French, C. A. McGhee, A. J. Kliore, N. J. Rappaport, E. Barbinis, D. Fleischman, A. Anabtawi, (2011a), Saturn's equatorial oscillation: Evidence of descending thermal structure from Cassini radio occultations, Geophysical Research Letters, 38, L08205.

Schinder, P. J., F. M. Flasar, E. A. Marouf, R. G. French, C. A. McGhee, A. J. Kliore, N. J. Rappaport, E. Barbinis, D. Fleischman, A. Anabtawi, (2011b), The structure of Titan's atmosphere from Cassini radio occultations, Icarus 215, 460–474.

Simpson, R. A., (2007), Planetary Exploration, Chapter 5, In Advances in Bistatic Radar, (eds.) N. J. Willis, H. D. Griffiths, SciTech Publishing Inc., pp. 56–77.

Sohl, F., H. Hussmann, B. Schwentker, T. Spohn, R. D. Lorenz, (2003), Interior structure models and tidal Love numbers of Titan, Journal of Geophysical Research: Planets, vol. 108, Issue E12, doi: 10.1029/2003JE002044.

Spencer, J. R., J. C. Pearl, M. Segura, F. M. Flasar, A. Mamoutkine, P. Romani, B. J. Buratti, A. R. Hendrix, L. J. Spilker, R. M. C. Lopes, (2006), Cassini encounters Enceladus: Background and the discovery of a south polar hot spot, Science, 311, 1401–1405.

Spitale, J. N. and C. C. Porco, (2007), Association of the jets of Enceladus with the warmest regions on its south-polar fractures, Nature, 449, 695.

Thomas, P. C., R. Tajeddine, M. S. Tiscareno, J. A. Burns, J. Joseph, T. J. Loredo, P. Helfenstein, C. Porco, (2016), Enceladus's measured physical libration requires a a global subsurface ocean, Icarus, 264, 37–47.

Thomas, P. C., J. A. Burns, P. Helfenstein, S. Squyres, J. Veverka, C. Porco, E. P. Turtle, et al., (2007), Shapes of the Saturnian icy satellites and their significance, Icarus, 190, 573–584, doi: 10.1016/j.icarus.2007.03.012.

Thomas, P. C., J. W. Armstrong, S. W. Asmar, J. A. Burns, T. Denk, B. Giese, P. Helfenstein, L. Iess, T. V. Johnson, A. McEwen, L. Nicolaisen, C. Porco, N. Rappaport, J. Richardson, L., Somenzi, P. Tortora, E. P. Turtle, J. Veverka, (2007), Hyperion sponge-like appearance, Nature, 448, 50–53.

Thomson, F. S., E. A. Marouf, G. L. Tyler, R. G. French, N. J. Rappaport, (2007), Periodic microstructure in Saturn's rings A and B, Geophysical Research Letters, 34, L24203.

Thorne, K. S., (1987) Gravitational radiation, In Three Hundred Years of Gravitation, (eds.) S. W. Hawking, W. Israel, Cambridge University Press, pp. 330–458.

Tobie, G., D. Gautier, F. Hersant, (2012), Titan's bulk composition constrained by Cassini-Huygens: implication for internal outgassing, The Astrophysical Journal, 752, no. 2, 125.

Tobie, G., O. Čadek, C. Sotin, (2008), Solid tidal friction above a liquid water reservoir as the origin of the south pole hotspot on Enceladus, Icarus, 196, 642–652, doi: 10.1016/j.icarus.2008.03.008.

Tobie, G., J. I. Lunine, C. Sotin, (2006), Episodic outgassing as the origin of atmospheric methane on Titan, Nature, 440, 7080, 6.

Tobie, G., A. Mocquet, C. Sotin, (2005), Tidal dissipation within large icy satellites: Applications to Europa and Titan, Icarus 177, 534–549.

Tortora, P., M. Zannoni, D. Hemingway, F. Nimmo, R. A. Jacobson, L. Iess, M. Parisi, (2016), Rhea gravity field and interior modeling from Cassini data analysis, Icarus, 264, 264–273, doi: 10.1016/j.icarus.2015.09.022.

Tortora, P., M. Zannoni, D. Hemingway, F. Nimmo, R.A. Jacobson, L. Iess, M. Parisi, (2015), Rhea gravity field and interior modeling from Cassini data analysis, Icarus, 264, 264–273, doi: 10.1016/j.icarus.2015.09.022.

Tortora, P., J. W. Armstrong, S. W. Asmar, L. Iess, N. J. Rappaport, A. Ardito, L. Somenzi, (2009), Cassini's determination of the gravity fields of the Saturnian satellites, 58th International Astronautical Congress, 24–28 September 2009, Hyderabad, India, paper IAC-07- A3.I.A.29, pp. 1263–1271.

Tortora, P., L. Iess, J. J. Bordi, J. E. Ekelund, D. C. Roth, (2004), Precise Cassini navigation during solar conjunctions through multifrequency plasma calibrations, Journal of Guidance, Control and Dynamics, 27, 251–257.

Tortora, P., L. Iess, R. G. Herrera, (2003), The Cassini multifrequency link performance during 2002 solar conjunction, IEEE Aerospace Conference, 8–15 March 2003, Big Sky, MT, vol. 3, 1465–1473.

Tortora, P., L. Iess, J. E. Ekelund, (2002), Accurate navigation of deep space probes using multifrequency links: The Cassini breakthrough during solar conjunction experiments, The World Space Congress, 10–19 October 2002, Houston, TX.

Tyler, G. L., V. R. Eshleman, J. D. Anderson, G. S. Levy, G. F. Lindal, G. E. Wood, T. A. Croft, (1982), Radio science with Voyager 2 at Saturn: Atmosphere and ionosphere and the masses of Mimas, Tethys, and Iapetus, Science, 215, 553–558.

Tyler, G. L., V. R. Eshleman, J. D. Anderson, G. S. Levy, G. F. Lindal, G. E. Wood, T. A. Croft, (1981), Radio science investigations of the Saturn system with Voyager 1: Preliminary results, Science, 212, 201–206.

Vessot, R. F. C. and B. W. Levine, (1978), A timed-correlated four-link Doppler tracking system, In a close-up of the Sun, JPL Publication 78-70, pp. 457–497.

Wahl, S. M., W. B. Hubbard, B. Militzer, T. Guillot, Y. Miguel, N. Movshovitz, Y. Kaspi, et al., (2017), Comparing Jupiter interior structure models to Juno gravity measurements and the role of a dilute core, Geophysical Research Letters, vol. 44, Issue 10, 4649–4659, doi: 10.1002/2017GL073160.

Wahlund, J. E., M. W. Morooka, L. Hadid, D. J. Andrews, W. S. Kurth, G. Hospodarsky, A. M. Persoon, (2017), First in-situ determination of the ionospheric structure of Saturn by Cassini/RPWS, In European Planetary Science Congress, vol. 11.

Waite, J. H., C. R. Glein, R. S. Perryman, B. D. Teolis, B. A. Magee, G. Miller, J. Grimes, et al., (2017), Cassini finds molecular hydrogen in the Enceladus plume: evidence for hydrothermal processes, Science, 356, no. 6334, 155–159.

Waite Jr., J. H., (2017), Cassini INMS Measurements of Saturn's Atmosphere and Ionosphere, In American Geophysical Union (AGU) Fall Meeting, abstract.

Will, C. M., (1993), Theory and experiment in gravitational physics, Cambridge University Press.

Zannoni, M., P. Tortora, L. Iess, R. A. Jacobson, J. W. Armstrong, S. W. Asmar, (2015), The determination of Dione’s gravity field after four Cassini flybys, European Geoscience Union (EGU) General Assembly, 12–17 April 2015, Vienna, Austria, Id.13211.

Zebker, H. A., B. Stiles, S. Hensley, R. Lorenz, R. L. Kirk, J. Lunine, (2009), Size and shape of Saturn's moon Titan, Science, vol. 324, Issue 5929, pp. 921–923, doi: 10.1126/science.1168905.

Zebker, H. A., E. A. Marouf, G. Leonard Tyler, (1985), Saturn's rings: Particle size distributions for thin layer models, Icarus, 64, no. 3, 531–548.

Zhang, K. and F. Nimmo, (2009), Recent orbital evolution and the internal structures of Enceladus and Dione, Icarus, 204, 597.

- - - - - - - - - - - - - -

4 PROJECT PUBLIC ENGAGEMENT PROGRAM

Social media did not exist when Cassini launched to Saturn. The interactivity and accessibility enabled by the internet was only just beginning to emerge. Streaming video was limited to pixelated, postage stamp-sized windows that often required great patience to view. But over the years, as the world—and the World Wide Web—changed, Cassini's public engagement activities evolved to embrace an ever-larger audience.

In 1998, JPL communications manager Alice Wessen was asked to lead the reformulation of the Cassini Mission's Education and Public Outreach (EPO) Plan. Then head of NASA's Office of Space Science, Jeff Rosendahl, funded each science mission individually, and each mission was required to have its own communications plan, which included EPO. The charge was to update Cassini outreach for the 21st century—make it more relevant and more impactful nationally. Wessen worked with the project to create a new vision for Cassini public engagement for NASA review. Early versions of the plan included ideas for a public-friendly mission website, a Saturn observing campaign, printed outreach products, and a planetary data access function (which did not survive the development process due to the projected level of effort needed to support it).

From that original 1998 plan, Cassini's public engagement program evolved to embrace the ever-expanding role of digital media.

From that original 1998 plan, Cassini's public engagement program evolved to embrace the ever-expanding role of digital media. Over the mission's final decade, from 2008 to 2018, the project transitioned from primarily dealing in printed outreach products (such as posters, lithographs, trading cards, and educational binders for teachers) to almost exclusively digital outreach. By the mission's end, there were millions of visits to the Cassini mission website per year, and Cassini could boast of 1.6 million followers on Twitter and close to half a million followers on Facebook. (In fact, the mission was an early adopter of social media, in 2008, leading the agency as one of the most followed NASA accounts on Twitter throughout its lifetime.)

The most visible element of the mission (and perhaps most memorable for the public) has always been its dazzling images. Cassini set a new standard at NASA for openness and public access to scientific data by making all of the spacecraft's raw imaging science observations available on the mission website almost as soon as the data hit the ground. This level of access was game changing in public engagement, and allowed a whole community to spring up and evolve over the years as people perused the images, processed them, discussed them, and shared them. This was the most trafficked area of the mission website for its entire history, but it should also be noted that the overall website won two judges' Webby awards ("the Internet's highest honor") for best science website, in 2009 and 2017.

The hallmark of Cassini public engagement was to serve up Saturn's awe-inspiring vistas and to seize on emerging trends in the digital landscape. The mission consistently did this in ways that drew in people from diverse backgrounds and many walks of life, bestowing on them a sense of

personal ownership of the mission as they imagined dancing with the spacecraft among the icy moons of Saturn.

4.1 Formal Education

4.1.1 READING, WRITING & RINGS (RW&R)

"Reading, Writing & Rings" is a comprehensive language arts education program for young learners. The program was developed in partnership by the Cassini-Huygens EPO program; the Jet Propulsion Laboratory education office; the Bay Area Writing Project (an affiliate of the California Writing Project); Project FIRST at the University of California, Berkeley; the Caltech Precollege Science Initiative; and selected classroom educators.

4.1.2 CASSINI "SCIENTIST FOR A DAY" (SFAD)

The Cassini Scientist for a Day essay program challenges students to become NASA scientists studying Saturn. Participants write a short essay about which of three possible Cassini observations they think will yield the best science. SFAD meets U.S. National English and Science Education Standards. Since its 2004 inception, SFAD reached over 10,000 students in over 500 U.S. classrooms; the international version reached tens of thousands worldwide on five continents and 65 countries. See https://solarsystem.nasa.gov/scientist-for-a-day/home/.

4.2 Informal Education

"Ring World" Planetarium Show Content transitioned from original planetarium show (slides, music, and storyboard) for 200 mid-sized planetariums in 2004, to digital slides in 2005, to three updated versions of a DVD video "Ring World." All copies were distributed before end of mission. The Grand Finale video replaced the previous programs, is widely available, and remains on the Cassini Website, which transitioned to the NASA Solar System website in fall 2018.

Ring World won a 2004 Telly award, and has been shown nationally and internationally in hundreds of planetariums in multiple languages. Versions for schools in English, Spanish, Letterbox (for hearing impaired), and Podcast (or "vodcast") are available for download. The third and final Ring World HD video was completed in 2012, and a print run of 50,000 was completed and sent to NASA networks with a Spanish translation and closed-captioning for the hearing impaired.

The "Saturn Observing Campaign" shared the excitement of the Cassini mission with amateur astronomers and public groups around the world. Since 2004, Saturn Observation Events reached more than 750,000 members of the public. The Juno Observing program (JunoCam) gleaned lessons learned from the Saturn Observation Campaign, as did other citizen science programs throughout NASA. The Saturn Observing Campaign was created from U.S. members of the Solar System Ambassador program, and opened to international volunteers to honor the International Cassini-

Huygens mission. At its peak in 2013, the program had over 500 worldwide members in 100 countries, and all 50 states of the U.S.

Now known as "Eyes on the Solar System" (http://eyes.nasa.gov), the application provides 3-D simulations of all of NASAs planetary missions using authentic NASA SPICE navigation data.

The "What's Up?" podcast featured a 2-minute video highlight of a current NASA mission and what is viewable in the night sky. Originally developed by Cassini EPO and featured Cassini and Saturn in many of the monthly episodes, it is now supported by the NASA Planetary Science directorate. In November 2017, NASA Communications selected "What's Up?" as one of four NASA video series to debut on Facebook Watch. As of April 2018, 165,000 users subscribed to the What's Up show, and each episode reached between 800,000 and 3 million views each month. In its 12th year (began by Cassini in April 2007), What's Up's 130 monthly episodes now reach over 10 million views each month on NASA websites, YouTube, Facebook, Instagram, Tumblr, Twitter, and other social platforms, and are imbedded in TV Weather websites, science websites, and used in museums, planetariums, and shown in amateur astronomy club meetings.

4.3 Reaching Underserved Schools

DonorsChoose.org (http://www.youtube.com/watch?v=PUSdjfh2YjM&feature=player_embedded) is a nonprofit organization matching donors with public school educators. Seventy-five percent are high poverty and all were unaware that NASA provides high-quality materials for free.

Through DonorsChoose.org:

- Cassini reached ~3,000 K–12 teachers and ~300,000 students in all 50 states;
- Cassini EPO invited all students to participate in Cassini Scientist for a Day and other NASA networks. This program has been transferred to the Solar System Public Engagement team for continuation.

4.4 Public Outreach: NASA Data Shared with the Public

"Eyes on the Solar System": In 2004, Cassini EPO started a unique visualization program called "CASSIE" (Cassini Internet Explorer), which allowed the public to experience the Cassini spacecraft going into Saturn Orbit Insertion. Now known as "Eyes on the Solar System" (http://eyes.nasa.gov), the application provides 3-D simulations of all of NASA's planetary missions using authentic NASA SPICE navigation data. It has been downloaded millions of times by members of the public. The

family of applications known as NASA's Eyes on the Earth, Eyes on Exoplanets, and DSN now owe their start to Cassini's CASSIE.

Cassini Huygens Analysis and Results of the Mission (CHARM): Teleconferences presented since 2004 by Cassini Mission experts to NASA's outreach networks (NASA Museum Alliance members, Cassini Saturn Observation Campaign volunteers, Solar System Ambassadors, Night Sky Network astronomy clubs, solar system educators. Now hosted on NASA's Museum Alliance website.

4.5 Website

The Cassini website (https://solarsystem.nasa.gov/missions/cassini) was one of the most-visited NASA websites, garnering Webby awards for Best Science Website in 2009 and 2017 for outstanding work highlighting science. In 2009, the site received approximately half a million unique users monthly and is over 100,000 pages deep. The raw images, which were made available to the public eight hours after being downlinked from the spacecraft, continued to receive the most traffic throughout the mission's lifetime.

During 2015–2017, content was created to highlight the Cassini Grand Finale (https://solarsystem.nasa.gov/missions/cassini/mission/grand-finale/overview/) with resources, orbit guides, photo galleries, 3-D interactives, and features such as "Why Cassini Matters," End of Mission timeline, Quick facts and What's Next, and Cassini People, while older content was rewritten or retired. Since October 2017, the website was further streamlined, and in October 2018, the Cassini Legacy Website was transferred to the NASA Solar System website for historic preservation.

Cassini Archive Updates:

- https://saturn.jpl.nasa.gov has been redirected to https://solarsystem.nasa.gov/missions/cassini
- https://solarsystem.nasa.gov/missions/cassini has been expanded
- Cassini pages have been migrated into the new architecture and redirects provided for key content
- The archive site has fewer sections, but content offered in a deeper dive
- News, features, images, videos, graphics, etc., archived in SSE news section, but filterable by mission
- Raw images and search remain intact

The Journey: https://saturn/solarsystem.nasa.gov/missions/cassini/the-journey/

- Spacecraft model: https://solarsystem.nasa.gov/missions/cassini/the-journey/the-spacecraft/

- Timeline: https://solarsystem.nasa.gov/missions/cassini/the-journey/timeline/#launch-from-cape-canaveral
- Grand Finale Interactive: https://solarsystem.nasa.gov/missions/cassini/the-journey/the-grand-finale/
- Behind the Scenes (images from this section archived in galleries): https://solarsystem.nasa.gov/missions/cassini/galleries/images

Science: https://solarsystem.nasa.gov/missions/cassini/science/overview/

Mission: https://solarsystem.nasa.gov/missions/cassini/mission/about-the-mission/

- About the Mission: https://solarsystem.nasa.gov/missions/cassini/mission/about-the-mission/
- The Grand Finale: https://solarsystem.nasa.gov/missions/cassini/mission/grand-finale/overview/
- Saturn Tour Flybys, Highlights, and All Dates: https://solarsystem.nasa.gov/missions/cassini/mission/tour/flybys/
- Ten Ways Cassini Mattered: https://solarsystem.nasa.gov/missions/cassini/overview/#10_ways_cassini_mattered_otp
- Spacecraft Section: https://solarsystem.nasa.gov/missions/cassini/mission/spacecraft/cassini-orbiter/
- The Team: https://solarsystem.nasa.gov/missions/cassini/mission/team/
- Cassini Inspires (images from this section archived in galleries): https://solarsystem.nasa.gov/missions/cassini/galleries/images

Galleries: https://solarsystem.nasa.gov/missions/cassini/galleries/images

- Raw image search: https://solarsystem.nasa.gov/missions/cassini/galleries/featured-raw-images/

News & Features: https://solarsystem.nasa.gov/news/

Resources: https://solarsystem.nasa.gov/resources/all/

4.6 Social Media

Cassini had a significant presence on social media. Cassini Twitter (@CassiniSaturn) had 1.6 million followers and NASA Cassini Facebook had 450,000+ followers as of April 2018. The accounts are now managed by the Solar System Exploration Social/Web team.

4.7 Other Notable Programs

Wave at Saturn: The EPO team partnered with NASA Media Relations to produce the viral "Wave at Saturn" event on July 19, 2013, which captured a mosaic of the Saturn and Earth/Moon systems. The event was the first time Earthlings were told in advance that their picture was being taken from interplanetary distances. A photomosaic, or collage version of the image features about 1,600 pictures submitted by members of the public, in which they captured themselves waving at Cassini (and Saturn) during the event. Other NASA missions and programs have since used the Wave At Saturn model for their own public engagement campaigns (#EarthRightNow photos and mosaic #HiJuno (in Morse code) and others).

Cassini hosts a regular whimsical gallery of holiday graphics which have their own cult following. No other mission has matched Cassini in this endeavor, and the collection, along with all photo galleries, will remain on the legacy website.

4.8 And the Emmy goes to … NASA/JPL!

The Cassini team pulled out all the stops for their coverage of the spacecraft's Grand Finale. Mixing traditional media coverage with interactive components, they developed a multi-faceted, multi-platform campaign that allowed them to share the mission's last weeks and hours. Their efforts in showcasing the mission earned NASA/JPL an Emmy for Outstanding Original Interactive Program in 2018, the first such award the agency has ever received.

4.9 Summary

As Cassini winds down, the mission's decades-long public engagement effort continues to pay dividends—its products and programs now influencing the next generation of space missions.

The Saturn Observation Campaign has fed into the ongoing efforts of the NASA-sponsored Night Sky Network and helped inform the Juno mission's JunoCam amateur observation program. Cassini's long-running Scientist for a Day program is planned to continue indefinitely as NASA Solar System Scientist for a Day.

NASA's Eyes on the Solar System application (eyes.nasa.gov), which began life as the Cassini Interactive Explorer, continues to be developed and diversified. The application shows all of NASA's space missions over the period of 1950 to 2050, and (of course) includes a detailed dive into Cassini's Grand Finale. It has branched out into two additional interactives, called Eyes on the Earth and Eyes on Exoplanets. This innovative and groundbreaking visualization tool owes credit for much of its early development to Cassini.

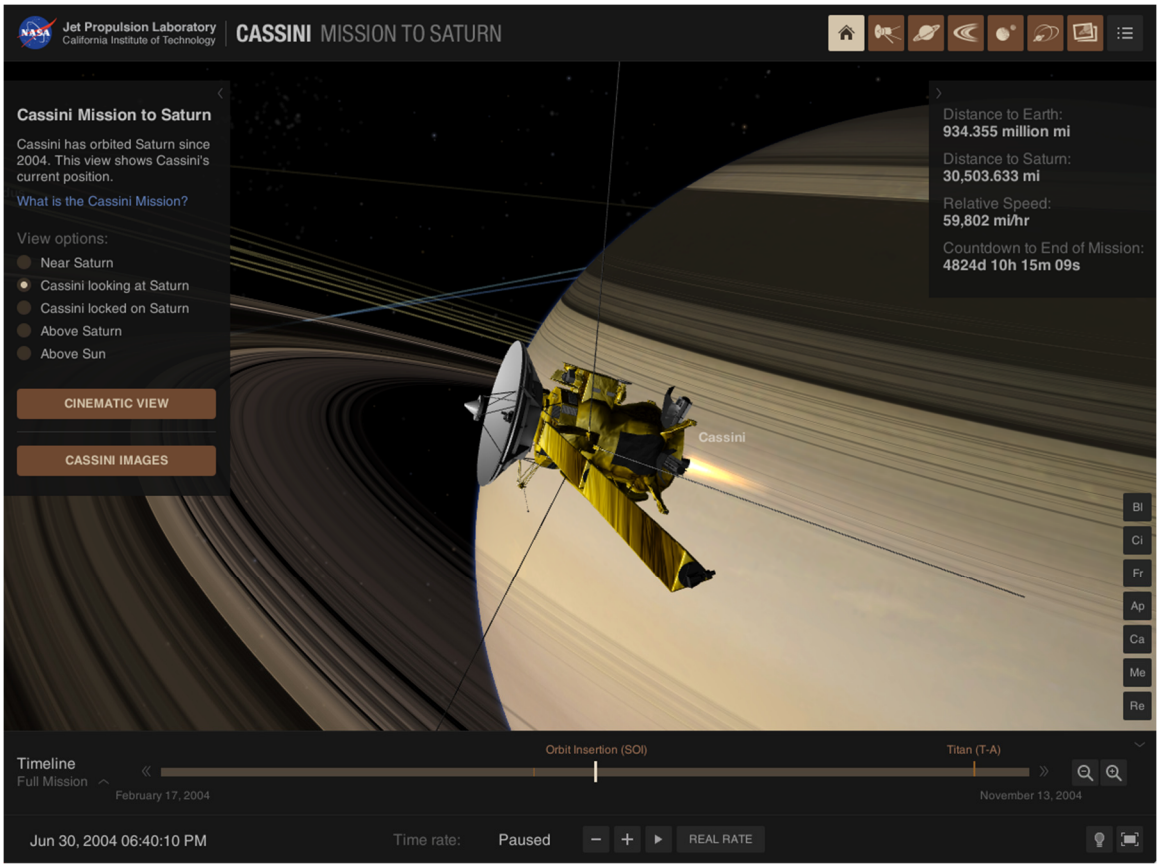

Screenshot from NASA's Eyes on the Solar System interactive application, which began life as a Cassini simulator in 2004.

The Cassini Twitter account, with its >1.6 million followers, was rechristened as the NASA Solar System Exploration account in September 2018. (The account serves the Planetary Science Division's Solar System Exploration website, solarsystem.nasa.gov.) This decision reflects the enormous influence Cassini has had on pivoting planetary exploration toward ocean worlds, and also helps NASA hold onto the huge space-science hungry audience the mission has painstakingly built over a decade.

The mission website is permanently archived as part of the Solar System Exploration website (https://solarsystem.nasa.gov/missions/cassini/overview/), similar to the model employed for Deep Impact and Galileo. A major difference is that the post-mission archiving of the Cassini site was planned for and budgeted well in advance, and the site's final redesign (including the content itself)

was produced with this end-state in mind. Digital storytelling tools and image gallery filtering tools developed for Cassini are also being deployed on the solar system site at large. The website for NASA's next flagship outer planets mission, Europa Clipper, is being directly modeled on key elements of the Cassini site. Examples include: science instrument profiles, which provide accessible, high-level "How It Works and How We Use It" summaries before delving into details; visually rich interactives like Cassini's timelines and short-form digital stories (as seen in "The Journey" section of the website); and the mission's planned raw image gallery, which will follow the same basic design as Cassini.

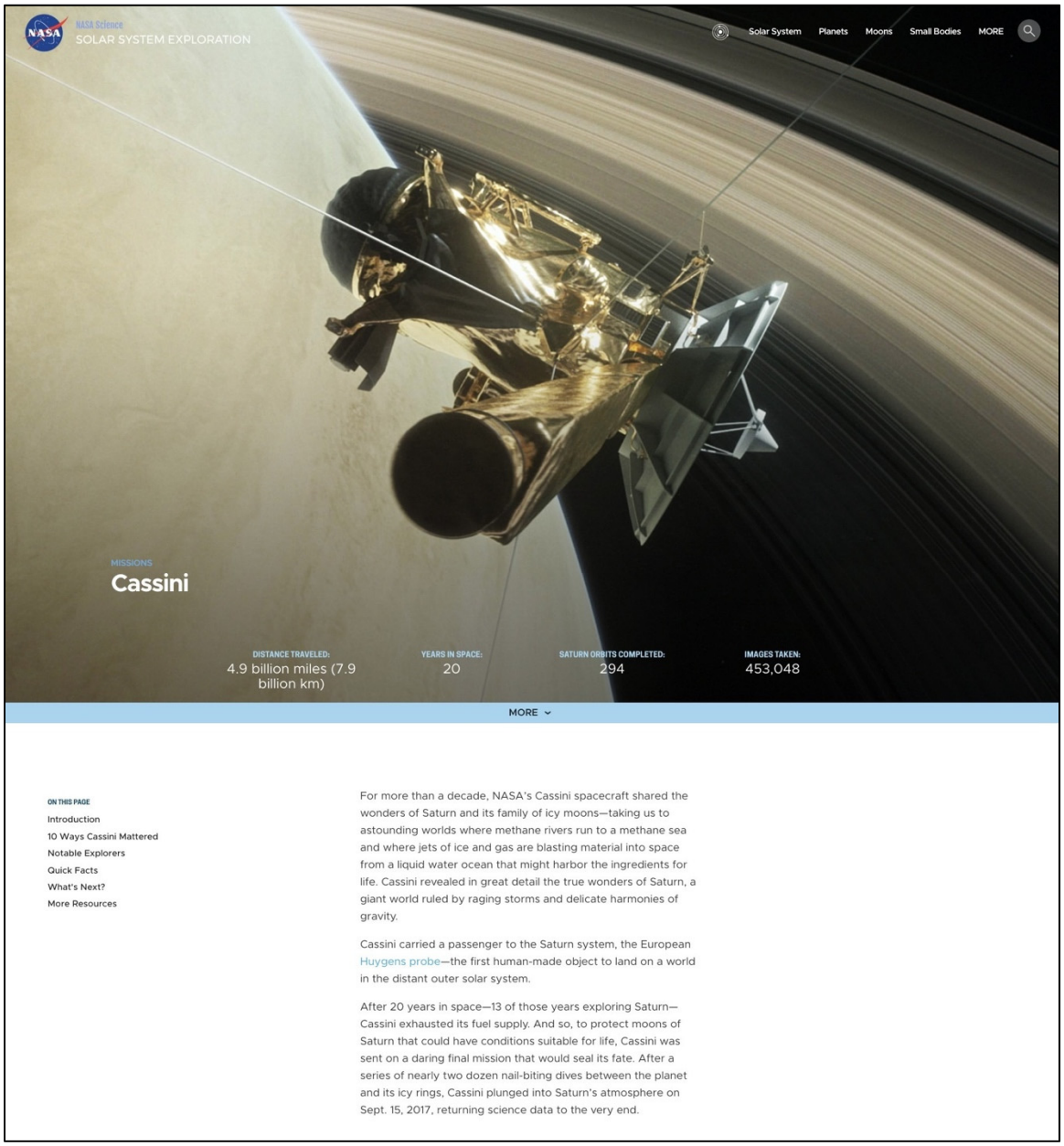

Screenshot from the Cassini website, now archived on NASA's Solar System Exploration site.

5 PROJECT ARCHIVES

Due to the complexity and amount of information (engineering and scientific) that the Cassini Project acquired and processed, the archive of this information has been divided into the following main systems: the PDS, JPL DocuShare, JPL Records Storage, JPL Line Management Archives, Amazon Web Services (AWS), and the JPL Solar System Exploration Web Presence.

5.1 The Planetary Data System

The PDS is the primary organization within NASA responsible for the archive of planetary science data obtained from NASA sponsored missions and, thus, provides a long-term archive system for Cassini science data. It consists of an Engineering Node located at JPL and several Discipline Nodes located around the country. For Cassini, the Lead Node is the Atmospheres (ATMOS) Node at New Mexico State University in Las Cruces, New Mexico. The full list of Nodes supporting the Cassini Mission, and the corresponding instrument team delivering to them, is shown in the table below.

Table 5.1-1. PDS discipline nodes for Cassini/Huygens data.

Data from:	Delivered to PDS Node:
CAPS, INMS, MAG, MIMI, RPWS	Planetary Plasma Interactions Node (PPI), University of California, Los Angeles, CA https://pds-ppi.igpp.ucla.edu/
CDA	Small Bodies Node (SBN) – Dust Sub-node, University of Arizona, Tucson, AZ https://pds-smallbodies.astro.umd.edu/
CIRS, RSS, UVIS	*Atmospheres Node (ATMOS), New Mexico State University, Las Cruces, NM https://pds-atmospheres.nmsu.edu/
ISS, VIMS	Cartography and Imaging Sciences Node, JPL, Pasadena, CA https://pds-imaging.jpl.nasa.gov/portal/
RADAR	Cartography and Imaging Sciences Node, JPL, Pasadena, CA https://pds-imaging.jpl.nasa.gov/portal/
SPICE (Kernels: SPK, PCK, IK, CK, EK, FK, SCLK and LSK)	Navigation and Ancillary Information Facility (NAIF), JPL, Pasadena, CA https://naif.jpl.nasa.gov/
Huygens probe: ACP, DISR, DWE, GCMS, HASI, SSP	1. Planetary Science Archive, ESA http://open.esa.int/esa-planetary-science-archive/ 2. ATMOS, New Mexico State University, Las Cruces, NM https://pds-atmospheres.nmsu.edu/

* Lead node for Cassini

The Cassini and Huygens probe data sets are archived separately. The Huygens data are housed online at the PDS Atmospheres Node in the U.S. as well as in Europe at the European Space Agency's Planetary Science Archive.

The first scheduled archive delivery took place on July 1, 2005. Data coverage was from launch on October 15, 1997 through September 30, 2004.

After the first data delivery on July 1, 2005, data deliveries were made quarterly and lagged the acquisition of data in operations by 9 months. The final data delivery took place October 2018.

In addition to the data from the Cassini science instruments, the project created the Cassini Science Research Support System (SRSS). The Cassini SRSS is a cohesive set of PDS web pages with links to science research support data and science data. The SRSS is located on the PDS Atmospheres node: https://pds-atmospheres.nmsu.edu/data_and_services/atmospheres_data/Cassini/Cassini.html.

5.2 JPL Archives

Cassini has created two institutionally supported libraries: the Cassini Program Archival Library and the Cassini Software Repository.

The Cassini Program Archival Library consists of the following collections:

- Project Document Archive – contains official project documents, interoffice memorandums, requirements, plans, reviews, and science proposals
- Project Records and Products – contains operational products, such as sequence products, log files, and process documents, and records, such as test reports, and records, such as instrument heating predicts. Files are organized by team.
- Project Discreet Documents and Records – contains project- and business-discreet documents, such as management reviews, program status reports, and program plan
- Science Research Support Products
- Records Storage Requests – contains inventories of storage requests
- Cassini Electronic File Cabinet (EFC) – contains over 18,000 memos, presentations, and documents

The Cassini Software Repository library contains copies of the latest versions of flight and ground software delivered to the Cassini Program Software Library (PSL). It is organized into two collections: Flight Software and Ground Software.

The Project Document Archive collection contains official project documents, such as plans, requirements, test plans, reports, and reviews.

5.3 JPL Records Storage

Hardcopy records and documents are archived with JPL Records Storage. The JPL internal online Paper Records Inventory (PRI) System is used to create a Records Storage Request or to perform a search and request the return of boxes sent to storage.

5.4 JPL Line Management Archives

Teams with domain-specific information and data have arranged to archive this data with their JPL Line Management. For example, navigation software, documentation, and data are archived on the Section 392 System for Archival of Navigation Data (SAND).

5.5 Amazon Web Services

Files used and shared in operations that were stored in the Cassini file catalog system, known as the DOM and the project web server, were copied into the AWS cloud storage as a deep archive, or backup, to other archives. A web portal provides a limited, file-name–based search capability to the archive.

5.6 JPL Solar System Exploration Web Presence

The mission's public website (saturn.jpl.nasa.gov)—including the entire searchable raw image gallery—was permanently archived as part of the NASA Solar System Exploration website (solarsystem.nasa.gov) in September 2018 (as solarsystem.nasa.gov/cassini). New Cassini science results are shared by the Solar System Exploration Twitter account (@NASASolarSystem) and are retweeted and amplified by the Cassini Twitter account (@CassiniSaturn).

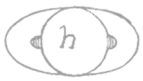

6 ADDITIONAL INFORMATION

6.1 Quick Facts about the Cassini Mission

6.1.1 MILESTONES

- Launch: October 15, 1997, from Cape Canaveral Air Force Station, Florida
- Launch vehicle: Titan IVB/Centaur
- Venus flybys: April 26, 1998, at 176 miles (234 km); June 24, 1999, at 370 miles (600 km)
- Earth flyby: August 18, 1999, at 727 miles (1,171 km)
- Jupiter flyby: December 30, 2000, at 6 million miles (10 million kilometers); closest approach at 5:12 a.m. EST Saturn arrival: July 1, 2004, UTC (June 30, 2004 PDT)
- Huygens probe: Titan release December 24, 2004; Titan descent January 14, 2005

6.1.2 CASSINI ORBITER

- Dimensions: 22 feet (6.7 meters) high; 13.1 feet (4 meters) wide
- Weight at launch: 12,593 pounds (5,712 kilograms) with fuel, Huygens probe, adapter, etc.
- Weight at end of mission: 4,685 pounds (2,125 kilograms)
- Propellant used: 6,504 pounds out of 6,565 pounds (2,950 kilograms out of 2,978 kilograms)
- Power: 885 watts (633 watts at end of mission) from radioisotope thermoelectric generators
- Orbiter science instruments (12 total): CIRS, ISS, UVIS, VIMS, RADAR, RSS, CAPS, CDA, INMS, MAG, MIMI, RPWS. Details about all of Cassini's science instruments: https://solarsystem.nasa.gov/missions/cassini/mission/spacecraft/cassini-orbiter/.

6.1.3 MISSION

- Commands executed: 2.5 million
- GB of science data collected: 635 GB
- Saturn orbits completed: 294
- Targeted moon flybys: 162
- Targeted Titan flybys: 127
- Targeted Enceladus flybys: 23
- Images taken: 453,048
- Main engine burns: 183
- Oceans discovered: 2 (Titan, Enceladus)
- Titan seas and lakes discovered: 3 seas, hundreds of small lakes
- Named moons discovered: 6
- Science papers published: 3,948
- Prime Mission: 4 years
- Two Extended Missions: Equinox (2008–2010) and Solstice (2010–2017)

- Total distance traveled: At Cassini's end of mission, the spacecraft had traveled about 4.9 billion miles (7.8 billion kilometers) with respect to the Sun. This distance includes its 2.1 billion-mile (3.4-billion kilometer) interplanetary trajectory from Earth to Saturn. With respect to Saturn, Cassini traveled a total of 1.2 billion miles (1.9 million kilometers) from arrival to end of mission.
- Saturn's average distance from Earth: 890 million miles (1.43 billion kilometers)
- One-way speed-of-light time from Saturn to Earth during orbital tour: Varied between 67 and 85 minutes
- One-way speed-of-light time from Saturn to Earth at end of mission: 83 minutes
- Spacecraft speed at loss of signal (relative to Saturn): 69,368 mph (111,637 kph)

6.1.4 PROGRAM

- Partners: NASA, ESA, ASI
- Number of people who worked on some portion of Cassini-Huygens: More than 5,000
- Cost of mission: $3.9 billion*. This figure includes $2.5 billion* in pre-launch costs (including launch vehicle and contributions from ESA and the Italian Space Agency) and $1.4 billion* in post-launch costs (including operations and tracking for 20 years in flight).

**The cost information contained in this document is of a budgetary and planning nature and is intended for informational purposes only. It does not constitute a commitment on the part of JPL and/or Caltech.*

ACRONYMS

Note: For a complete list of Acronyms, refer to Cassini Acronyms – Attachment A.

AACS	Attitude and Articulation Control Subsystem
ACP	Aerosol Collector and Pyrolyzer
AFC	AACS Flight Computer
AMMOS	Advanced Multi-Mission Operations System
ASI	Italian Space Agency (Agenzia Spaziale Italiana)
ASIC	Application-Specific Integrated Circuit
ATMOS	Atmospheres
AWS	Amazon Web Services
BAIL	Backup Assisted Load Format Injection Loader
BIU	Bus Interface Unit
bps	Bits Per Second
C/CAM	collision and contamination avoidance maneuver
Caltech	California Institute of Technology
CAPS	Cassini Plasma Spectrometer
Cassini Internet Explorer	CASSIE
CCL	Channel Conversion Language
CDA	Cosmic Dust Analyzer
CDS	Command and Data Subsystem
CEM	Cassini Equinox Mission
CHARM	Cassini Huygens Analysis and Results of the Mission
CHEMS	Change-Energy-Mass Spectrometer
CIRS	Composite Infrared Spectrometer
CM	Configuration Management
CPT	Channel Parameter Table
CRAF	Comet Rendezvous/Asteroid Flyby
CSM	Cassini Solstice Mission
DGDS	Downlink Ground Data System
DISR	Descent Imager/Spectral Radiometer
DMD	Data Monitor and Display
DOM	Distributed Object Manager
DSN	Deep Space Network
DSOT	Data Services Operations Team
DSS	Digital Subsystem
DWE	Doppler Wind Experiment
EFC	Engineering Flight Computer
EFC	Electronic File Cabinet
EGA	Engine Gimbal Assembly

EPO	Education and Public Outreach
ESA	European Space Agency
ESB	Earth Swing-By
ESS	Energy Storage Subsystem
ESTEC	European Space Technology and Research Center
FIR	Far-Infrared
FOP	Flight Operations Plan
FPW	Fields, Particles and Waves
GCMS	Gas Chromatograph Mass Spectrometer
GCMS	Gas Chromatograph and Mass Spectrometer
GVSC	Generic VHSIC Spaceborne Computer
HASI	Huygens Atmospheric Structure Instrument
HPOC	Huygens Probe Operations Centre
ICD	Interface Control Document
IEB	Instrument Expanded Block
INCA	Ion and Neutral Camera
INMS	Ion and Neutral Mass Spectrometer
IRU	Inertial Reference Unit
ISS	Imaging Science Subsystem
IT	Information Technology
ITSDB	Information Technology Security Database
JunoCam	Juno Observing Program
kbps	Kilobits Per Second
LEMMS	Low Energy Magnetospheric Measurement Subsystem
LV	Latch Valve
MAG	Magnetometer
MAG	Magnetometer
MDAS	Mission Control, Data Management & Accountability, and Spacecraft Analysis Subsystem
MGSS	Multi-Mission Ground Data System and Services
MIM	Mission Interface Manager
MIMI	Magnetospheric Imaging Instrument
MMH	Monomethylhydrazine
MOA	Mission Operations Assurance
MOAM	Mission Operations Assurance Manager
MOS	Mission Operations System
MSC	Magnetic Search Coils
MSS	Mission Sequencing System
NAC	Narrow-Angle Camera
NAIF	Navigation and Ancillary Information Facility
NGSS	National Next Generation Science Standards

NPD	NASA Policy Directive
NTO	nitrogen tetroxide
ODM	Orbiter Deflection Maneuver
OIA	Operational Interface Agreement
OIT	Operational Interface Test
ORS	Optical Remote Sensing Instruments
OTM	Orbit Trim Maneuver
PAR	Perimeter Access Request
PAT	PSG Automation Tool
PB	Playback
PCO	Probe Checkout
PDS	Planetary Data System
PDT	Pointing Design Tool
PI	Principal Investigator
PM	Prime Mission
PPI	Planetary Plasma Interactions
PR	Pressure Regulator
PRI	Paper Records Inventory
PSA	Probe Support Avionics
PSL	Program Software Library
PSLA	Program Service Level Agreement
PV	Pyro Valve
RADAR	Titan Radar Mapper
RCS	Reaction Control Subsystem
RF	Radio Frequency
RFES	Radio Frequency Electronics Subsystem
RFIS	Radio Frequency Instrument Subsystem
RPWS	Radio and Plasma Wave Science
RSP	Remote Sensing Pallet
RSS	Radio Science Subsystem
RTE	Real-Time Engineering
RTG	Radioisotope Thermoelectric Generator
RTO	Real-Time Operations
RW&R	Reading, Writing, & Rings
RWA	Reaction Wheel Assembly
SAND	System for Archival of navigation Data
SAUL	Science and Uplink
SBN	Small Bodies Node
SCAS	Science Calibration Subsystem
SCCM	Standard Cubic Centimeters Per Minute

SCET	Spacecraft Event Time
SCIOP	Science Operations
SCLK	Spacecraft Clock Time
SED	Spin/Eject Device
SEQ_GEN	Sequence Generator
SEQTRAN	Sequence Translator
SFAD	Scientist for a Day
SIS	Software Interface Specification
SOPC	Science Operations and Planning Computer
SPE	Sun-Spacecraft-Earth
SRAM	Static Random-Access Memory
SRU	Stellar Reference Unit
SSI	Space Science Institute
SSP	Surface Science Package
SSPS	Solid-State Power Switch
SwRI	Southwest Research Institute
TCM	Trajectory Correction Maneuver
TDS	Telemetry Delivery System
TT&C	Telemetry, Tracking and Command
UEM	Upper Equipment Module
UVIS	Ultraviolet Imaging Spectrograph
V&V	Verification and Validation
VHSIC	Very High-Speed Integrated Circuit
VIMS	Visible and Infrared Mapping Spectrometer
WAC	Wide-Angle Camera